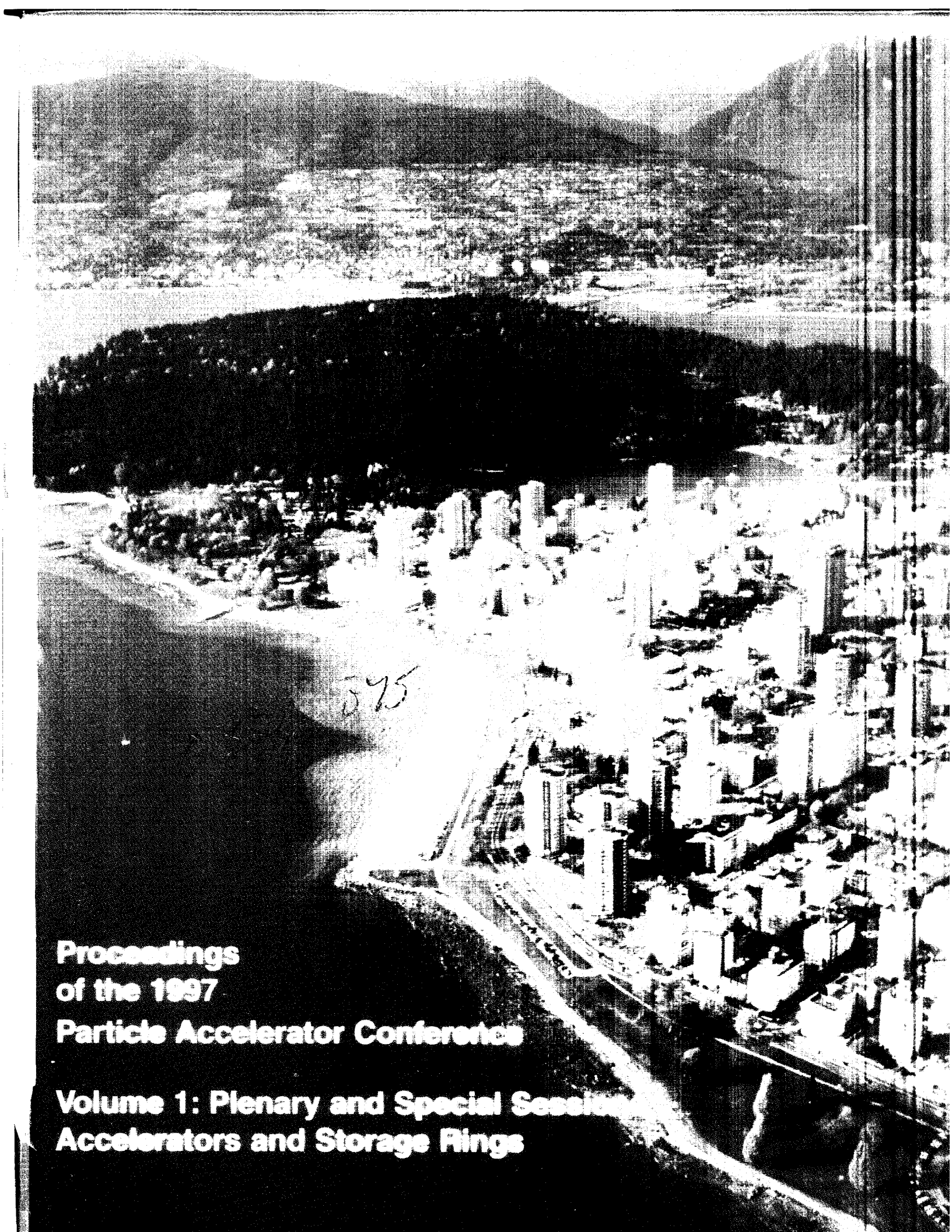


Proceedings of the 1997 Particle Accelerator Conference

Volume 1: Plenary and Special Sessions, Accelerators and Storage Rings



Proceedings of the 1997 Particle Accelerator Conference

DISTRIBUTION STATEMENT A
Approved for Public Release
Distribution Unlimited

Vancouver, B.C., Canada
12–16 May 1997

Editors
M. Comyn, M.K. Craddock, M. Reiser, J. Thomson

Volume 1 of 3
Plenary and Special Sessions; Accelerators and Storage Rings

19990326 075

Organized by
TRIUMF
University of Maryland

Held under the joint auspices of
Institute of Electrical and Electronics Engineers
(Nuclear and Plasma Sciences Society)
American Physical Society
(Division of Physics of Beams)

IEEE

Sponsored by
US Department of Energy
National Science Foundation
Office of Naval Research

The American Physical Society

DTIC QUALITY INSPECTED 4

PROCEEDINGS OF THE 1997 PARTICLE ACCELERATOR CONFERENCE

Copyright and Reprint Permission: Abstracting is permitted with credit to the source. Libraries are permitted to photocopy beyond the limits of U.S. copyright law for private use of patrons those articles in this volume that carry a code at the bottom of the first page, provided the per-copy fee indicated in the code is paid through the Copyright Clearance Center, 222 Rosewood Drive, Danvers, MA 01923. For other copying, reprint, or republication permission, write to the IEEE Copyrights Manager, IEEE Operations Center, 445 Hoes Lane, Piscataway, NJ 08855-1331. All rights reserved.
Copyright © 1998 by The Institute of Electrical and Electronics Engineers, Inc.

IEEE Catalog Number:	97CH36167 (softbound) 97CB36167 (casebound)
Library of Congress Number:	88-647453
ISBN Softbound:	0-7803-4376-X
ISBN Casebound:	0-7803-4377-8
ISBN Microfiche:	0-7803-4378-6
ISBN CD-ROM:	0-7803-4379-4

Additional copies of this publication are available from

IEEE Operations Center
P. O. Box 1331
445 Hoes Lane
Piscataway, NJ 08855-1331
USA

Phone:	1-800-678-IEEE (1-800 678-4333) 1-732-981-0060 1-732-981-1393
FAX:	1-732-981-9667 (FAX)
Telex:	833-233
E-mail:	customer.service@ieee.org

REPORT DOCUMENTATION PAGE

Form Approved
OMB No. 0704-0188

Public reporting burden for this collection of information is estimated to average 1 hour per response, including the time for reviewing instructions, searching existing data sources, gathering and maintaining the data needed, and completing and reviewing the collection of information. Send comments regarding this burden estimate or any other aspect of this collection of information, including suggestions for reducing this burden, to Washington Headquarters Services, Directorate for Information Operations and Reports, 1215 Jefferson Davis Highway, Suite 1204, Arlington, VA 22202-4302, and to the Office of Management and Budget, Paperwork Reduction Project (0704-0188), Washington, DC 20503.

1. AGENCY USE ONLY *(Leave Blank)*	2. REPORT DATE	3. REPORT TYPE AND DATES COVERED
	1998	Final

4. TITLE AND SUBTITLE
1997 Particle Accelerator Conference , Proceedings of the
Vol. 1: Plenary and Special Sessions; Accelerators & Storage Rings
Vol. 2: Beam Dynamics, Instrumentation and Control
Vol. 3: Subsystems, Technology and Applications

5. FUNDING NUMBERS
G

6. AUTHORS
M. Comyn, M.K. Craddock, M. Reiser, J. Thomson (Editors)

7. PERFORMING ORGANIZATION NAME(S) AND ADDRESS(ES)
Institute of Electrical and Electronics Engineers, Inc.
445 Hoes Lane, P.O. Box 1331
Piscataway, NJ 08855-1331

8. PERFORMING ORGANIZATION REPORT NUMBER
GG231

9. SPONSORING / MONITORING AGENCY NAME(S) AND ADDRESS(ES)
Office of Naval Research
800 North Quincy Street
Arlington, VA 22217-5660

10. SPONSORING / MONITORING AGENCY REPORT NUMBER
N00014-97-1-0399

11. SUPPLEMENTARY NOTES

12a. DISTRIBUTION / AVAILABILITY STATEMENT

12b. DISTRIBUTION CODE

13. ABSTRACT *(Maximum 200 words)*

The Proceedings contains 1261 papers presented at PAC'97, held in Vancouver in May, 1997. With one third of the 1221 delegates coming from 23 countries outside North America, these papers present a comprehensive picture of accelerator science, technology and applications worldwide. Highlights include the initial operation of the SPring-8 light source, the PEP-II B-factory high-energy ring, the CERN LEP2 collider, and one sextant of RHIC. Construction reports range from the CERN Large Hadron Collider and the Fermilab Main Injector and Recycler, to the BESSY-II light source and the TRIUMF-ISAC radioactive beam facility. Upcoming projects described include the US Spallation Neutron Source, the Japanese Hadron Facility and the RIKEN Beam Factory. Important progress is reported on advanced accelerators - linear colliders, muon colliders and laser accelerators - and on pulsed-power and high-intensity beams. There are also details of interesting advances on superconducting rf and magnets, ion sources and electron guns, controls, instrumentation, and other technology. Free-electron lasers now offer novel photon beams for users, while the standard industrial and medical applications have been joined by new schemes for contraband detection and high-energy proton radiography.

14. SUBJECT TERMS
Particle Accelerators

15. NUMBER OF PAGES
3874

16. PRICE CODE

17. SECURITY CLASSIFICATION OF REPORT	18. SECURITY CLASSIFICATION OF THIS PAGE	19. SECURITY CLASSIFICATION OF ABSTRACT	20. LIMITATION OF ABSTRACT
Unclassified	**Unclassified**	**Unclassified**	**UL**

FOREWORD

The 17th Particle Accelerator Conference was held at the Hotel Vancouver, Vancouver, British Columbia, from May 12–16, 1997, under the joint auspices of the Nuclear and Plasma Sciences Society of the IEEE, and the Division of Physics of Beams of the APS. This was the second time the meeting has been held in Canada and once again TRIUMF was honoured to have been chosen as host; the Institute for Plasma Research at the University of Maryland was responsible for organizing the program. Though the attendance (1221) was not an all-time record, it was up 20% from the 1985 Vancouver meeting and up 15% from PAC'95, indicating the continuing vitality of the discipline even in these fiscally stringent times. The international component is also growing, with 33% of the delegates coming from 23 countries outside North America.

PAC'97 might well be said to mark the centenary of accelerator technology, since Thomson's measurement of the mass of the electron and his identification of it as sub-atomic were published 100 years ago to the month, and his was the first important experiment to rely on the accurate formation and measurement of a particle beam in well-defined electric and magnetic fields. As the first speaker noted, the masses of the electron and its sister particles remain of central interest in physics today!

Scientific Program: The opening plenary session covered four highlights of the conference: recent important advances for both normal and superconducting linear colliders (B. Richter), and for several varieties of laser accelerators (C. Joshi); and the initial operation of two major accelerator projects – the CERN LEP2 collider, which has reached 93 GeV, comfortably exceeding the W-production threshold (S. Myers), and the highest energy third-generation light source SPring-8 (H. Kamitsubo). Several more machines reported initial beam commissioning, including the PEP-II B-factory high-energy ring, RHIC (one sextant) and the IUCF Cooler Injection Synchrotron. Many reports described projects under construction, ranging from the Large Hadron Collider at CERN and the Main Injector at Fermilab (now joined by a permanent-magnet Recycler) to the BESSY-II light source and various radioactive ion-beam accelerators, including the development of a cw RFQ at TRIUMF. A number of major proposals are also close to approval: the 1 GeV 1 MW National Spallation Neutron Source at Oak Ridge, the compact 2.9 GeV Canadian Light Source at Saskatoon, the 50 GeV 0.01 mA Japanese Hadron Facility at KEK, and the RI-Beam Factory at RIKEN, which includes a 400 MeV/A superconducting ring cyclotron and the MUSES storage rings. Somewhat further off are the challenging prospects of the APT linac for producing tritium and the muon collider.

Interesting advances were reported in all areas of accelerator technology, especially superconducting rf and magnets. In the related areas of high-current multi-particle beam dynamics and pulsed-power and high-intensity beams, noteworthy progress was reported through the Z-pinch and the induction-linac flash X-radiography approaches. In beam instrumentation, novel measurements were reported on ultrashort bunches: emittance measurements with picosecond resolution at BNL, and bunch-length measurements down to 100 femtoseconds using coherent radiation at Jefferson Lab. Controls highlights were the growing acceptance of the EPICS system and a growing trend to use more programmable devices in safety systems.

Accelerators continue to serve a multitude of applications: cancer therapy, neutron radiography, sterilization, and production of isotopes, spallation neutrons and synchrotron light, are now joined by interesting schemes for contraband detection and high-energy proton radiography. Notable developments were reported at free-electron laser facilities: provision of photon beams from sub-eV to multi-MeV energies at the Duke FEL user facility, first operation of the Jefferson Lab's cw FEL, and the use of self-amplified spontaneous emission (SASE) for the TESLA FEL at DESY.

The final plenary session offered a look to the future. J. Peoples and K. Gelbke surveyed future directions for high-energy physics and nuclear physics respectively, H. Winick described the bright prospects for fourth-generation light sources, and finally W. Weng (who will be chairing the next PAC, to be held in New York, March 29 - April 2, 1999) reviewed a new class of machines with a variety

of applications - ultra-high-intensity proton accelerators.

In all, 1564 abstracts were submitted, for 76 invited and 120 contributed talks, and 1368 posters. In addition, a very successful 3-day industrial exhibition was held, limited by space to 30 participants, and over 40 satellite topical and committee meetings were scheduled.

Social Program and Awards: The social program began on Monday evening with a Pacific Coast salmon barbecue for 1000 at TRIUMF, followed by a tour of the laboratory. The conference banquet was held in the Hotel Vancouver on Wednesday evening and attended by a record 980 – attracted perhaps by the subsequent Awards Ceremony and some memorable entertainment by the Physics Chanteuse, Lynda Williams. The conference is indebted to Advanced Ferrite Technology, MDS Nordion and TRIUMF for their generous contributions as co-sponsors of these events.

The IEEE/PAC Technology Awards went to K. Leung (LBNL) for ion source development and to D. Sutter (DOE) for developing federal R&D programs for advanced accelerator technologies. The US Particle Accelerator School Prizes were given to D. Boussard (CERN) for contributions to superconducting rf, beam dynamics and feedback, and to C. Joshi (UCLA) for pioneering plasma beatwave accelerators. The APS Award for Outstanding Doctoral Thesis Research went to L. Spentzouris for her application of plasma physics to measurements of non-linear coherent phenomena, and finally the APS R.R. Wilson Prize was presented to A.M. Sessler for a broad range of advances in beam dynamics, including the negative-mass and resistive-wall instabilities, free-electron lasers and the two-beam accelerator concept.

The number of companions registered was 211, and many of these enjoyed a Welcome Breakfast and orientation talk and walk, various tours of Vancouver, and excursions to Victoria and Whistler – all assisted by a week of good weather.

Proceedings: As at PAC'95, electronic publication was the norm, but with the innovation of direct submission of abstracts to the APS. This relieved the organizers of a huge task and resulted in the early posting of the complete program of abstracts on the Web version of the APS Bulletin. The proceedings are being published by IEEE in both book and CD-ROM form, and are also available on a combined PAC/EPAC/APAC Web site. The sessions do not follow the same order as in the conference program: instead, oral and poster sessions on the same topic have been grouped together under the title of the oral session, and these amalgamated sessions have been grouped with ones on similar topics:

Volume 1: Plenary and Special Sessions; Accelerators and Storage Rings.

Volume 2: Beam Dynamics, Instrumentation and Controls.

Volume 3: Subsystems, Technology and Applications.

Altogether, 1261 papers are included, just 1.5% below the all-time record, and the highest number per registrant (1.04) so far. Publication has been supported by generous grants from the US Department of Energy, National Science Foundation and Office of Naval Research.

Acknowledgements: Space is unfortunately too short to thank individually all those people whose dedicated efforts, often over a period of many months, were responsible for the success of the conference – especially the members of the Organizing Committee, Program Committee, Local Arrangements Committee, and members of IEEE, APS and TRIUMF staff. Exceptions must be made however for Elly Driessen, the Conference Coordinator, who showed an amazing facility for dealing with all manner of inquiries from all quarters of the globe; Martin Comyn, the database manager, responsible for organizing the vast amount of information relating to the abstracts and registration, and for the technical editing of the proceedings; and to Raso Samarasekera and Carol Bellamy, who not only acted as our respective secretaries, but took on other major responsibilities connected with registration and the program respectively.

M.K. Craddock — Conference Chairman

M. Reiser — Program Chairman

CONFERENCE ORGANIZATION

Organizing Committee

M.K. Craddock, *UBC & TRIUMF, Chairman*
M. Allen, *SLAC*
W. Barletta, *LBNL*
J. Bisognano, *TJNAF*
Y. Cho, *ANL*
L. Costrell, *NIST*
W.K. Dawson, *TRIUMF & IEEE*
D. Finley, *FNAL*
D. Friesel, *IUCF*
D. Hartill, *Cornell U.*
Y. Kimura, *KEK*
S. Krinsky, *BNL*
C. Leemann, *TJNAF*
M. Olivier, *CEA & EPAC*
M. Reiser, *U. Maryland*
B. Ripin, *APS*
C. Roberson, *ONR*
S. Schriber, *LANL*
R. Siemann, *SLAC*
D. Sutter, *DOE*
S. Tazzari, *U. Roma & INFN-LNF*
W-T. Weng, *BNL*
G. Westenskow, *LLNL*
R. York, *NSCL*

Program Committee

M. Reiser, *U. Maryland, Chairman*
C. Bellamy, *Secretary*
G. Alton, *ORNL*
I. Ben-Zvi, *BNL*
M. Berz, *MSU*
J. Bisognano, *TJNAF*
E. Blackmore, *TRIUMF*
J.M. Brennan, *BNL*
D. Burke, *SLAC*
K. Cahill, *FNAL*
D. Chan, *LANL*
S. Chattopadhyay, *LBNL*
Y. Cho, *ANL*
P. Colestock, *FNAL*
J.N. Corlett, *LBNL*
M.K. Craddock, *UBC & TRIUMF*
P. Debenham, *DOE*
D. Douglas, *TJNAF*
G. Dutto, *TRIUMF*
D. Finley, *FNAL*
J. Flanz, *MGH*
J. Fox, *SLAC*
A. Friedman, *LLNL*
D. Friesel, *IUCF*
J. Galayda, *ANL*
E. Gluskin, *ANL*
R. Humphrey, *SLAC*
A. Jackson, *LBNL*
T. Katsouleas, *USC*
D. Kovar, *DOE*
S. Krinsky, *BNL*
W. Lawson, *U. Maryland*
S-Y. Lee, *IUCF*
A. Lennox, *FNAL*
K-N. Leung, *LBNL*
W. MacKay, *BNL*
M. McAshan, *FNAL*
W. McDowell, *ANL*
D. McGinnis, *FNAL*
N. Mistry, *Cornell U.*
S. Myers, *CERN*
J. Nolen, *ANL*
C. Olson, *Sandia NL*
P. O'Shea, *Duke U.*
H. Padamsee, *Cornell U.*
S. Peggs, *BNL*
R.E. Pollock, *IUCF*
T. Raubenheimer, *SLAC*
D. Rees, *LANL*
L. Reginato, *LBNL*
D. Rice, *Cornell U.*
J. Rifkin, *SLAC*
J. Rosenzweig, *UCLA*
D. Rubin, *Cornell U.*
R. Ryne, *LANL*
O. Sander, *LANL*
R.D. Schlueter, *LBNL*
R. Servranckx, *U. Saskatchewan*
R. Siemann, *SLAC*
J. Simpson, *ANL*
C. Sinclair, *TJNAF*
W. Stoeffl, *LLNL*
J. Strait, *FNAL*
D. Sutter, *DOE*
M. Syphers, *BNL*
A. Ting, *NRL*
A. Todd, *Northrop Grumman*
J. Watson, *LANL*
M. White, *ANL*
F. Willeke, *DESY*
M. Wilson, *DOE*
Y. Yamazaki, *KEK*
R. York, *MSU*
A. Zolfaghari, *MIT & Bates*

Local Arrangements

M.K. Craddock, *Chairman*
M. Barnes, *Equipment*
E. Blackmore, *Tour*
M. Comyn, *Database*
E. Driessen, *Co-ordinator*
M. D'yachkov, *WWW pages*
S. Koscielniak, *Proceedings*
M. La Brooy, *Printing*
S. Reeve, *Treasurer*
K. Reiniger, *Posters*
J. Richards, *Database*
R. Samarasekera, *Registration*
J. Thomson, *Proceedings*
G. Wait, *Exhibits*

INDUSTRIAL EXHIBITORS

Advanced Ferrite Technology, Inc.
Alpha Scientific Electronics
Bergoz
Ceramic Magnetics, Inc.
CERN Accelerator School
CPI
Copley Controls Corp.
Danfysik A/S
Ebco Technologies
EEV, Inc.
Engineered Magnetics, Inc.
Everson Electric Co.
Glassman Europe Ltd.
GMW Associates
Inverpower Controls Ltd.
Ion Beam Applications s.a.
JP Accelerator Works, Inc.
LINAC Systems
Mega Industries
Metaceram
NTG Neue Technologien GmbH & Co. KG
Oxford Instruments, Inc.
Pearson Electronics, Inc.
Philips
SICN
SIGMAPHI
Svetlana Electron Devices, Inc.
Thomson Components & Tubes Corp.
Titan Beta
Vista Control Systems, Inc.

OUTLINE OF CONTENTS

VOLUME 1
PLENARY AND SPECIAL SESSIONS; ACCELERATORS AND STORAGE RINGS

OPENING PLENARY SESSION 1
SPECIAL SESSION 16
FINAL PLENARY SESSION 29
HIGH-ENERGY HADRON ACCELERATORS AND COLLIDERS 47
High-Energy Hadron Accelerators and Colliders 89
Beam Injection, Extraction, Transport and Targetry W 156
Beam Injection, Extraction, Transport and Targetry X 207
LEPTON ACCELERATORS AND COLLIDERS 281
Electron Storage Rings and Accelerators 324
Circular Electron Colliders 363
Muon Colliders 393
LINEAR COLLIDERS 425
Linear Collider Beam Dynamics 467
Linear Collider Structure 518
Linear Colliders (Other) 557
ADVANCED CONCEPTS 611
New Acceleration Techniques 633
LIGHT SOURCES AND FREE ELECTRON LASERS 698
Synchrotron Radiation Facilities 742
Free Electron Lasers 871
LOW- AND MEDIUM-ENERGY ACCELERATORS AND RINGS 915
Proton Synchrotrons and Storage Rings 959
Low- and Medium-Energy Circular Accelerators 1027
RFQ Linacs 1078
Proton and Ion Linacs 1111
Electron Linacs 1197
Electrostatic and Other Accelerators 1224
PULSED-POWER AND HIGH-INTENSITY BEAMS 1230
Pulsed Power Accelerators 1254
Pulsed Power Technology 1269

VOLUME 2
BEAM DYNAMICS, INSTRUMENTATION AND CONTROLS

SINGLE-PARTICLE BEAM DYNAMICS AND OPTICS 1331
Lattice Design and Optics 1371
Maps, Tracking and Dynamic Aperture 1418
Error Effects, Experiments, Spin Dynamics 1460
Other Single-Particle Beam Dynamics 1493
MULTIPARTICLE BEAM DYNAMICS I 1532
Instabilities and Cures (High Energy) 1575
Wake Field 1658
Impedance 1700

Beam-Beam Interaction 1759
Beam Cooling 1792
Other Multiparticle Beam Dynamics 1810
MULTIPARTICLE BEAM DYNAMICS II 1837
High-Current Dynamics 1858
Space Charge 1882
BEAM INSTRUMENTATION 1971
Short-Bunch Instrumentation 1996
Instrumentation Electronics 2023
Tune Measurement 2052
Beam Position Monitors 2069
Emittance and Profile Instrumentation 2149
Other Beam Instrumentation 2207
INSTABILITIES AND FEEDBACK 2276
Feedback Systems (including Beam) 2290
CONTROLS AND COMPUTING 2395
Control Systems W 2437
Control Systems X 2487
Computer Codes W 2538
Computer Codes X 2606

VOLUME 3
SUBSYSTEMS, TECHNOLOGY AND APPLICATIONS

SOURCES AND INJECTORS 2657
Particle Sources (including Polarized Sources) 2696
RF Guns and Linac Injectors 2787
RADIOFREQUENCY SYSTEMS 2879
Room-Temperature RF 2920
Superconducting RF 3072
RF Sources/Systems 3111
Related Hardware 3174
MAGNETS 3201
Room-Temperature Magnets 3227
Superconducting Magnets 3338
Power Supplies 3449
Insertion Devices 3491
VACUUM, ALIGNMENT, RADIATION MONITORING AND OTHER TECHNOLOGY 3542
Vacuum Technology 3580
Alignment and Survey 3645
Radiation Monitoring and Safety 3669
Other Subsystems Technology and Components 3687
APPLICATIONS OF ACCELERATORS 3770
Medical Therapy 3813
Medical Isotope Production 3834
High-Power Accelerator Applications 3848
Electron Beam Processing 3854
Non-Destructive Evaluation and Other Applications 3866

CONTENTS OF VOLUME 1

OPENING PLENARY SESSION

Chair: M. Reiser, *University of Maryland*

LEP2: Present and Future Performance and Limitations *(Invited)* — *S. Myers* 1
Linear Collider Research & Development: World Status *(Invited)* — *B. Richter* ..... no manuscript submitted
First Commissioning of SPring-8 *(Invited)* — *H. Kamitsubo* 6
Laser Accelerators: Experiments, Computations and Prospects *(Invited)* — *C. Joshi* 11

SPECIAL SESSION

Chair: C. Pellegrini, *University of California at Los Angeles*

The Development of Colliders *(Invited)* — *Andrew Sessler* ..... no manuscript submitted
Coherent Nonlinear Longitudinal Phenomena in Unbunched Synchrotron Beams *(Invited)* — *L. Spentzouris, P.L. Colestock* 16
The National Spallation Neutron Source (NSNS) Project *(Invited)* — *Bill R. Appleton* 20
The Duke Free Electron Laser Light Source Facility *(Invited)* — *J.M.J. Madey, and the Faculty and Staff* 24

FINAL PLENARY SESSION

Chair: M. Craddock, *University of British Columbia and TRIUMF*

Future Directions of High Energy Physics *(Invited)* — *J. Peoples Jr.* 29
Future Directions for Nuclear Physics *(Invited)* — *C.K. Gelbke* 34
Fourth Generation Light Sources *(Invited)* — *Herman Winick* 37
Ultra-High Intensity Proton Accelerators and Their Applications *(Invited)* — *W.T. Weng* 42

HIGH-ENERGY HADRON ACCELERATORS AND COLLIDERS

Chair: A. Astbury, *TRIUMF*

Status of the Fermilab Main Injector and Recycler *(Invited)* — *Stephen D. Holmes* 47
HERA Status and Upgrade Plans *(Invited)* — *F. Willeke* 51
RHIC Status *(Invited)* — *S. Peggs* 56
LHC Status and Plans *(Invited)* — *L.R. Evans* 61
Dynamic Effects and their Control at the LHC — *R. Bailey, F. Bordry, L. Bottura, P. Burla, P. Collier, K. Henrichsen, J.P. Koutchouk, R. Lauckner, R. Parker, J. Pett, P. Proudlock, H. Schmickler, R. Schmidt, L. Walckiers, R. Wolf* 66
RHIC Sextant Test - Physics and Performance — *J. Wei, W. Fischer, L. Ahrens, J.M. Brennan, K. Brown, R. Connolly, G.F. Dell, M. Harrison, J. Kewisch, W.W. MacKay, V. Mane, S. Peggs, F. Pilat, T. Satogata, M. Tanaka, S. Tepikian, P. Thompson, C.G. Trahern, D. Trbojevic, N. Tsoupas* 69
Measurement of Tevatron Extraction Parameters and Comparison of Model to Measurements — *M.A. Martens, J. Marriner, J. Holt* 72
Surface Resistance Measurements for the LHC Beam Screen — *F. Caspers, M. Morvillo, F. Ruggiero* 75
820 GeV/c Polarized Protons in HERA — *V.A. Anferov* 78
Record Deflection Efficiencies Measured for High Energy Protons in a Bent Germanium Crystal — *C. Biino, M. Clément, N. Doble, K. Elsener, L. Gatignon, P. Grafström, U. Mikkelsen, K. Kirsebom, S.P. Møller, E. Uggerhøj, T. Worm, A. Freund* 80
Overview of the APT High-Energy Beam Transport and Beam Expanders — *R.E. Shafer, B. Blind, E.R. Gray, J.D. Gilpatrick, D. Barlow, G.P. Lawrence* 83
The National Spallation Neutron Source Target Station: A General Overview — *Tony A. Gabriel, John N. Barnes, Lowell A. Charlton, James DiStefano, Ken Farrell, John Haines, Jeffrey O. Johnson, Louis K. Mansur, Steve J. Pawel, Moshe Siman-Tov, Rusi Taleyarkhan, Thomas J. McManamy, Mark J. Rennich* 86

High-Energy Hadron Accelerators and Colliders

High Intensity Proton Acceleration at the Brookhaven AGS - An Update — *L. Ahrens, J. Alessi, M. Blaskiewicz, E. Bleser, J.M. Brennan, K. Brown, C. Gardner, J.W. Glenn, H. Huang, K. Reece, T. Roser, W. van Asselt, K. Zeno, S.Y. Zhang* 89

Spin Tracking in RHIC — *A.U. Luccio, T. Katayama, H. Wu* 92

Flat Beams in a 50 TeV Hadron Collider — *S. Peggs, F. Pilat, M. Syphers* 95

RHIC Sextant Test: Accelerator Systems and Performance — *F. Pilat, D. Trbojevic, L. Ahrens, K. Brown, R. Connolly, G.F. Dell, W. Fischer, J. Kewisch, W. MacKay, V. Mane, S. Peggs, T. Satogata, S. Tepikian, P. Thompson, N. Tsoupas, J. Wei* 98

Preparing Accelerator Systems for the RHIC Sextant Commissioning — *D. Trbojevic, F. Pilat, L. Ahrens, D. Barton, T. Clifford, R. Connolly, W. Fischer, M. Harrison, W. MacKay, B. Olsen, S. Peggs, T. Satogata, S. Tepikian, P. Thompson, C. Trahern, R. Witkover* 101

Synchrotron Radiation Dominated Hadron Colliders — *E. Keil* 104

Summary of the Single-Beam Collective Effects in the LHC — *F. Ruggiero, J.S. Berg, O. Brüning, F. Caspers, M. Morvillo, M. D'Yachkov* 107

Proposal for an Aluminum Beam Screen in the LHC — *W. Chou, H. Ishimaru* 110

Dynamic Aperture Studies During Collisions in the LHC — *W. Chou, D. Ritson* 113

Optimization of the LHC Beam Cleaning System with Respect to Beam Loss in the High Luminosity Insertions — *A.I. Drozhdin, N.V. Mokhov* 116

Local Chromaticity Correction of the LHC — *C.J. Johnstone* 119

Perturbation of the Periodic Dispersion Under Beam Crossing Optics in LHC — *F. Méot* 121

Towards the Optimal LHC Interaction Region: Beam-Induced Energy Deposition — *N.V. Mokhov, J.B. Strait* 124

Measurement and Analysis of Longitudinal Bunched Beam Echoes in the Fermilab Tevatron — *S. Assadi, P.L. Colestock* 127

Accelerator Physics Issues of a Very Large Hadron Collider — *W. Chou* 130

Beam Loss Handling at Tevatron: Simulations and Implementations — *A.I. Drozhdin, N.V. Mokhov* 133

Using Luminosity Distributions to Determine Luminosity in a Collider with a Coupled Lattice — *M.A. Martens* 136

Excitation Characteristics of Fermilab Main Injector Dipoles and Magnetic Assignment to Reduce Closed Orbit Errors — *P.S. Martin, C.S. Mishra* 139

Status of the Fermilab Fixed Target Program — *C.D. Moore* 141

Slip Stacking for the Fermilab Luminosity Upgrade — *S. Shukla, C. Ankenbrandt, D. Capista, I. Kourbanis, J. Marriner, D. McGinnis, J. Steimel, R. Tomlin* 144

Experiments with Separated Beams in Run I at the Tevatron Collider — *M.A. Tartaglia* 147

Capture from Pair Production as a Beam Loss Mechanism for Heavy Ions at RHIC — *B. Feinberg, A. Belkacem, N. Claytor, T. Dinneen, H. Gould* 150

Numerical Optimization of Collimator Jaw Orientations and Locations in the LHC — *D. Kaltchev, M.K. Craddock, R.V. Servranckx, J.B. Jeanneret* 153

Beam Injection, Extraction, Transport and Targetry W

The IPNS Accelerator 50 MeV and 500 MeV Transport Lines — *J.C. Dooling, F.R. Brumwell, G.E. McMichael* 156

H^- Charge Exchange Injection for the NSNS Accumulator — *L.N. Blumberg, Y.Y. Lee* 159

The NSNS High Energy Beam Transport Line — *D. Raparia, J. Alessi, Y.Y. Lee, W.T. Weng* 162

First Observation of the Deflection of a 33 TeV Pb Ion Beam in a Bent Silicon Crystal — *C. Biino, M. Clément, N. Doble, K. Elsener, L. Gatignon, P. Grafström, U. Mikkelsen, A. Taratin, S.P. Møller, E. Uggerhøj, P. Keppler, J. Major* 165

Energy Dependence of Crystal Assisted Extraction at the CERN SPS — *G. Arduini, K. Elsener, G. Fidecaro, M. Gyr, W. Herr, J. Klem, U. Mikkelsen, E. Weisse* 168

Extraction of 22 TeV/c Lead Ions from the CERN SPS Using a Bent Silicon Crystal — *G. Arduini, K. Cornelis, K. Elsener, G. Ferioli, G. Fidecaro, M. Gyr, W. Herr, J. Klem, E. Weisse* 171

Gabor-Plasma Lens Focusing for LEBT Systems — *J. Pozimski, R. Dölling, A. Jakob, P. Groß, H. Klein* 174

An Idea for Selection of Short-Lived Particles by a Focusing Crystal — *V. Biryukov* 177

An Idea for Studying a Multipass Crystal Extraction by the Energy Loss Detector — *V. Biryukov* 179

Expected Characteristics of the Nuclotron Beams for Experimental Setups — *I. Issinsky, O. Kozlov, V. Mikhailov, P. Rukoyatkin, B. Vasilishin* 181

Beam Injection into the Nuclotron — *V.N. Buldakovsky, V.I. Chernikov, I.B. Issinsky, A.D. Kovalenko, V.A. Mikhailov, V.A. Monchinsky, S.A. Novikov, M.A. Voevodin, V.I. Volkov* 184
Carbon Stripper Foils Used in the Los Alamos PSR — *M.J. Borden, M.A. Plum, I. Sugai* 187
LANSCE Short-Pulse Spallation Source Target Upgrade — *J.B. Donahue, G.D. Baker, N.K. Bultman, T.O. Brun, P.D. Ferguson, R.J. Macek, M.M. Njegomir, M.A. Plum, J.E. Roberts, G.J. Russell, W.F. Sommer* 190
Overview of the Bump-Magnet System at the LANSCE Proton Storage Ring — *C.R. Rose, D.B. Barlow, B. Blind, F. Neri, J.F. Power, P.L. Walstrom* 193
Design and Simulation Studies of a One-Tenth Scale Final Focus System for Heavy Ion Fusion — *X. Wu, R.C. York, A. Faltens, D. Judd, E. Lee* 195
Tracking Studies and Performance Simulations of the NSCL A1900 Fragment Separator — *X. Wu, D.J. Morrissey, B.M. Sherrill, R.C. York, A.F. Zeller* 198
Measurements on Injection Property in HIMAC Synchrotron — *K. Noda, M. Kanazawa, E. Takada, A. Itano, S. Sato, S. Yamada, T. Nomura, T. Kohno, N. Araki* 201
Predicted Foil Temperatures in the Brookhaven Accumulator Ring for the NSNS — *Jonathan Duke* 204

Beam Injection, Extraction, Transport and Targetry X

Transfer of a Polarized Proton Beam From AGS to RHIC — *N. Tsoupas, T. Roser, M. Syphers, A. Luccio, D. Underwood* 207
Beam Injection into RHIC — *W. Fischer, H. Hahn, W.W. MacKay, T. Satogata, N. Tsoupas, W. Zhang* 210
The RHIC Injection Kicker — *H. Hahn, N. Tsoupas, J.E. Tuozzolo* 213
Equivalent Circuit Analysis of the RHIC Injection Kicker — *H. Hahn, A. Ratti* 216
A Study of Betatron and Momentum Collimators in RHIC — *D. Trbojevic, A.J. Stevens, M.A. Harrison, F. Dell, S. Peggs* 219
Focusing and Matching Properties of the ATR Transfer Line — *N. Tsoupas, W. Fischer, J. Kewisch, W.W. MacKay, S. Peggs, F. Pilat, S. Tepikian, J. Wei* 222
Design Aspects Related to the Reliability of the LHC Beam Dump Kicker Systems — *J.H. Dieperink, J.-L. Bretin, E. Carlier, L. Ducimetière, G.H. Schröder, E. Vossenberg* 225
The CERN PS East Area in the LHC Era — *L. Durieu, O. Ferrando, J.-Y. Hemery, J.-P. Riunaud, B. Williams* .. 228
PETRA Bunch Rotation — *Wilhelm Kriens* 231
Development of a Beam Sweeping System for the Fermilab Antiproton Source Target — *F.M. Bieniosek, O. Kurnaev, A. Cherepakhin, John Dinkel* 234
Test of Very Fast Kicker for TESLA Damping Ring — *B.I. Grishanov, F.V. Podgorny, J. Rümmler, V.D. Shiltsev* . 237
Optics and Field Error Compensation in the FNAL Permanent Magnet 8.9 GeV/c Proton Transfer Line — *John A. Johnstone* 240
A High Intensity Beam Absorber Corebox for the Fermilab Main Injector Abort System — *M. Reichanadter, C.M. Bhat, C. Crawford, P.S. Martin* 243
Diagnostic of the Compensation Process of Ion Beams with a Time-Resolving Ion Energy Spectrometer — *A. Jakob, K. Reidelbach, J. Pozimski, R. Dölling, H. Klein* 246
Development of Crystal Extraction Studies at the IHEP Accelerator — *V.M. Biryukov, V.N. Chepegin, Yu. Chesnokov, V.I. Kotov, E.A. Lyudmirskiy, V.A. Maisheev, E.F. Troyanov, N.K. Vishnevskiy, V.G. Zarucheiskiy* . 249
Efficiency of the UNK Scraper System — *I.I. Degtyarev, A.E. Lokhovitskii, I.A. Yazynin* 252
Substance Choice of the Scraper System Elements — *I.I. Degtyarev, Yu.S. Fedotov, A.E. Lokhovitskii, I.A. Yazynin* 255
RTS&T Monte-Carlo Code (Facilities and Computation Methods) — *A.I. Blokhin, I.I. Degtyarev, A.E. Lokhovitskii, M.A. Maslov, I.A. Yazynin* 258
Perturbation of Relevant Resonance for Slow Extraction Efficiency Increase — *N.N. Alexeev, S.L. Bereznitsky, A.E. Bolshakov* 261
Beam Extraction System for the Cooler Injector Synchrotron at IUCF — *X. Kang, G.P.A. Berg, D. Friesel, S.Y. Lee, T. Sloan* 264
Intensity Asymmetric Multiple Slow Extraction at the KEK-PS — *M.J. Shirakata, K. Marutsuka, H. Sato, Y. Shoji* 267
PSR Injection-Line Upgrade — *Barbara Blind, Andrew J. Jason* 270
Multi-Pulse Extraction from Los Alamos Proton Storage Ring for Radiographic Applications — *H.A. Thiessen, F. Neri, K.R. Rust, D.B. Redd* 273
Bremsstrahlung from a New Type of Target: Increased Intensity and Average Energy, and Reduced Divergence — *B. Bogdanovich, V. Kudinov, A. Nesterovich, Yu. Pomasan, E. Tsygankov, V. Janenko* 276
Thermo Mechanical Calculations of a Cyclotron Deflector — *J. DeKamp, F. Marti* 278

LEPTON ACCELERATORS AND COLLIDERS

Chair: S. Tazzari, *University of Roma/INFN-LNF*

Operation of CEBAF with Heavy Beamloading *(Invited)* — *A. Hutton* 281
Progress on $\mu^+\mu^-$ Colliders *(Invited)* — *Robert B. Palmer* 286
Performance of the CESR High Luminosity Interaction Region *(Invited)* — *S. Henderson* 291
B-Factory Interaction Region Design *(Invited)* — *M. Sullivan* 296
High Beam Current Experiments for the KEKB Conducted at the TRISTAN Accumulation Ring *(Invited)* — *Y. Funakoshi* 301
Experimental Study of the Ion Trapping Phenomenon in TRISTAN-AR — *S. Matsumoto, H. Fukuma, M. Tobiyama, E. Kikutani, M. Suetake, K. Satoh, Y. Funakoshi* 306
Experience with Bunch Trains in LEP — *W. Herr, B. Goddard, E. Keil, M. Lamont, M. Meddahi, E. Peschardt* .. 309
Low Emittances Lattices for LEP — *Y. Alexahin, P. Beloshitsky, D. Brandt, W. Herr, J.M. Jowett, M. Meddahi, G. Roy, A. Verdier* 312
Status and Early Commissioning Results for the PEP-II High Energy Ring — *U. Wienands, E. Reuter, P. Bellomo, A. Fisher, J. Gracia, R. Gray, M. Pietryka, T. Taylor, V. Bharadwaj, R. Iverson, A. Kulikov, J.T. Seeman, J. Turner, C. Besler, M. Zisman, S. Zholents* 315
Dual Aperture High Luminosity Collider at Cornell — *D. Rubin, G. Dugan, A. Mikhailichenko, J. Rogers* 318
Beijing Tau-Charm Factory Design Study — *Y.Z. Wu* 321

Electron Storage Rings and Accelerators

Automated Tuning of the Advanced Photon Source Booster Synchrotron — *S.G. Biedron, S.V. Milton* 324
Concepts for a Slow-Positron Target at the Advanced Photon Source — *E. Lessner, M. White* 327
ELFE@DESY: Slow Extraction from HERA — *M. Gentner, D. Husmann, P. Nghiem, J. Payet, A. Tkatchenko* .. 330
Beam Lifetime at the SRS — *H. Owen* 333
Design of a Damping Ring for the SB-Linear-Collider Project at DESY — *R. Brinkmann, D. Einfeld, M. Plesko, J. Schaper* 336
KSR as a Pulse Stretcher — *A. Noda, H. Fujita, M. Inoue, Y. Iwashita, H. Okamoto, T. Shirai, T. Sugimura, H. Tonguu, K. Mashiko* 339
Accelerator Modeling at SPEAR — *G. LeBlanc, W.J. Corbett* 342
Status of the MAX-II Storage Ring — *G. LeBlanc, Å. Andersson, M. Eriksson, L-J. Lindgren, P. Röjsel, S. Werin* 345
High Duty Factor Beams Extracted from the MIT-Bates South Hall Ring — *K. Jacobs, R. Averill, S. Bradley, G. Dodson, K. Dow, M. Farkhondeh, S. Kowalski, B. McAllister, D. Tieger, C. Tschalaer, E. Tsentalovich, W. Turchinetz, F. Wang, A. Zolfaghari, T. Zwart* 348
Transverse Kick in Misaligned Traveling Wave Structures Driven at the Fundamental Mode — *D.H. Whittum, H. Henke* 351
Low-Level RF System Design for the Accelerator Test Facility (ATF) Damping Ring — *M.G. Minty, K. Kubo, F. Hinode, S. Sakanaka, J. Urakawa* 354
Low-Level RF System Design for the Next Linear Collider Damping Ring — *M.G. Minty* 357
Centroid and Emittance of a Kicked Beam in Rings — *Chun-xi Wang, John Irwin* 360

Circular Electron Colliders

An e^+e^- Top Factory in a 50+50 TeV Hadron Collider Tunnel — *J. Norem, J. Jagger, S. Sharma, E. Keil, G.W. Foster, E. Malamud, E. Chojnacki, D. Winn* 363
Transverse Polarization Beyond the Z Energy at LEP — *A. Blondel, M. Böge, E. Bravin, B. Dehning, M. Placidi, F. Tecker, J. Wenninger* 366
Trapped Modes in CESR Sliding Joints — *E.B. Anderson, J. Rogers* 369
CESR Status — *D.L. Rubin, for the CESR Operations Group* 372
Beam-Beam Simulation Using the Unified Accelerator Libraries — *T. Koyama, N. Malitsky, R. Talman* 375
Interaction Region Design for Beijing τ-Charm Factory — *Y.Z. Wu, Q.L. Peng* 378
Status of the KEKB Project — *Shin-ichi Kurokawa* 381
Simulation of Tail Distributions Due to Random Processes and Beam-Beam Interaction in KEKB — *Eun-San Kim, Kohji Hirata* 384
HOM Heating at the PEP-II IR Beryllium Vacuum Pipe — *X. Lin, C.-K. Ng, K. Ko* 387
The PEP-II Injection Kicker System — *G.C. Pappas, A.R. Donaldson, D. Williams* 390

Muon Colliders

Target Options and Yields for a Muon Collider Source — *D. Ehst, N.V. Mokhov, R.J. Noble, A. Van Ginneken* .. 393
Bunch Shortening Experiments in the Fermilab Booster and the AGS — *J. Norem, C. Ankenbrandt, J. Griffin, C. Johnstone, S.Y. Lee, K.Y. Ng, M. Popovic, M. Brennan, T. Roser, J. Wei, D. Trbojevic* 396
The Proton Driver for the $\mu\mu$ Collider — *J. Norem, C. Ankenbrandt, J. Griffin, C. Johnstone, S.Y. Lee, M. Popovic, K.Y. Ng, M. Brennan, T. Roser, D. Trbojevic, J. Wei* 399
Optimization of the Target for Muon Colliders — *H. Takahashi, Y. An, X. Chen, M. Nomura* 402
A Lattice for the Muon Collider Demonstration Ring in the RHIC Tunnel — *D. Trbojevic, R.B. Palmer, E.D. Courant, J. Gallardo, S. Peggs, S. Tepikian, K.Y. Ng* 405
A Normal Conducting Accelerator for a Muon Collider Demonstration Machine — *Y. Zhao, R. Palmer, R. Fernow, J. Gallardo, H. Kirk* 408
A Ring Lattice for a 2-TeV Muon Collider — *C.J. Johnstone, A. Garren* 411
Shielding the Muon Collider Interaction Region — *C. Johnstone, N. Mokhov* 414
Simulation Studies of Ionization Cooling — *D. Neuffer, A. Van Ginneken* 417
An Asymmetric Muon-Proton Collider: Luminosity Consideration — *V.D. Shiltsev* 420
Control of Longitudinal Collective Behavior in the Muon Collider Rings — *Wen-Hao Cheng, Andrew M. Sessler, William C. Turner, Jonathan S. Wurtele* 422

LINEAR COLLIDERS

Chair: V. Balakin, *Branch of Budker Institute of Nuclear Physics, Protvino*

Results from the DESY TESLA Test Facility *(Invited)* — *B. Aune, for the TESLA collaboration* 425
The SLAC Damped Detuned Structure: Concept and Design *(Invited)* — *Norman M. Kroll* 429
Studies of Beam Induced Dipole-Mode Signals in Accelerating Structures at the SLC *(Invited)* — *Mike Seidel* 434
Results from the SLAC NLC Test Accelerator *(Invited)* — *R.D. Ruth, C. Adolphsen, S. Allison, R. Atkinson, W. Baumgartner, P. Bong, V. Brown, M. Browne, G. Caryotakis, R. Cassel, G. Cisneros, S.L. Clark, T. Constant, C. Corvin, T. Dean, J. Eichner, R. Fowkes, R. Fuller, S. Gold, J. Grippe, S. Hanna, H. Hoag, P. Holik, S. Holmes, R. Humphrey, L. Johnson, R. Jones, E. Jongewaard, K. Ko, R. Koontz, N. Kroll, T. Lavine, G.A. Loew, R. Loewen, R.H. Miller, J. Minister, V. Nesterov, C. Nantista, J.M. Patterson, C. Pearson, R. Phillips, M. Pietryka, R. Pope, T. Porter, J. Rifkin, W. Roster, M. Seidel, H. Smith, S. Smith, J. Spencer, N. Spencer, D. Sprehn, S. Tantawi, P. Tenenbaum, A. Tillghman, A. Vlieks, V. Vylet, J.W. Wang, P.B. Wilson, Z. Wilson, E. Wright, D. Yeremian, J. Zelinski, C. Ziomek* 439
KEK/ATF Damping Ring *(Invited)* — *Junji Urakawa* 444
Super-ASSET: A Technique for Measuring and Correcting Accelerator Structure Misalignments at the SLC — *F.-J. Decker, R. Assmann, M.G. Minty, P. Raimondi, G. Stupakov* 449
Limitations of Interaction-Point Spot-Size Tuning at the SLC — *P. Emma, L.J. Hendrickson, P. Raimondi, F. Zimmermann* 452
Development of C-Band RF Pulse Compression System for e^+e^- Linear Collider — *T. Shintake, N. Akasaka, H. Matsumoto* 455
Beam Characteristics versus Cavity Models in CLIC — *G. Guignard, J. Hagel* 458
LIGA-Fabrication of mm-Wave Accelerating Cavity Structures at the Advanced Photon Source (APS) — *J.J. Song, S. Bajikar, Y.W. Kang, R.L. Kustom, D. Mancini, A. Nassiri, B. Lai, A.D. Feinerman, V. White* 461
Design and Fabrication of a Traveling-Wave Muffin-Tin Accelerating Structure at 90 GHz — *P.J. Chou, G.B. Bowden, M.R. Copeland, H. Henke, A. Menegat, R.H. Siemann* 464

Linear Collider Beam Dynamics

Wakefield Dynamics in Quasi Periodical Structures — *A. Novokhatski, A. Mosnier* 467
A Statistical Approach to Analyse Effect of Misalignments and Correction Algorithms in High-Energy Linacs — *S. Fartoukh* 470
Emittance Dilution in 1 and 5 TeV 3 GHz Linear Colliders — *G. Guignard, T.O. Raubenheimer* 473
A Low Emittance Lattice for the CLIC Damping Ring — *J.P. Potier* 476
Nulling Emittance Measurement Technique for CLIC Test Facility — *P. Tenenbaum, H.H. Braun, F. Chautard* 479
A 30 GHz 5-TeV Linear Collider — *J.P. Delahaye, G. Guignard, J. Irwin, T.O. Raubenheimer, R.D. Ruth, I. Wilson, P.B. Wilson* 482
Simulation of Ground Motion Induced Beam Jitter in the SBLC Main Linac — *C. Montag* 485

Theoretical Study of Power Relativistic Amplifiers for Electron Beam Bunching — *E.A. Perelstein, L.V. Bobyleva, A.V. Elzhov, V.I. Kazacha* 488
Emittance Dilution and Magnet Design for the TTF FEL Second Bunch Compressor — *I.N. Ivanov, S.I. Kukarnikov, A.Yu. Molodozhentsev, V.A. Petrov, V.Ph. Shevtsov, T. Limberg, M. Marx* 491
Possibility of Precise Wakefield Measurement at ATF Extraction Line — *S. Kashiwagi, H. Hayano, T. Higo, K. Kubo, K. Oide, K. Takata, S. Takeda, N. Terunuma, J. Urakawa* 494
Beam-Based Monitoring of the SLC Linac Optics with a Diagnostic Pulse — *R.W. Assmann, F.J. Decker, L.J. Hendrickson, N. Phinney, R. Siemann, K.K. Underwood, M. Woodley* 497
Observation of Dark-Current Signals from the S-Band Structures of the SLAC Linac — *R.W. Assmann, F.J. Decker, M. Seidel, R.H. Siemann, D. Whittum* 500
Observation and Analysis of Static Deflections from Transverse Long-Range Wakefields in the SLC — *R.W. Assmann, F.J. Decker, P. Raimondi, T.O. Raubenheimer* 503
Beam-Based Analysis of Day-Night Performance Variations at the SLC Linac — *F.-J. Decker, R. Akre, R.W. Assmann, K.L.F. Bane, M.G. Minty, N. Phinney, W.L. Spence* 506
Longitudinal Phase Space Setup for the SLC Beams — *F.-J. Decker, K.L.F. Bane, M.G. Minty, P. Raimondi, R.L. Holtzapple* 509
Dynamic Focusing Schemes for Linear Colliders — *J. Irwin* 512
The Short-Range Wakefields in the SBLC Linac — *K.L.F. Bane, M. Timm, T. Weiland* 515

Linear Collider Structure

Design of a 30 GHz Damped Detuned Accelerating Structure — *M. Dehler, R.M. Jones, N.M. Kroll, R.H. Miller, I. Wilson, W. Wuensch* 518
Analysis of HOM Interaction Between Cavities by Multimodal S-Parameter Measurements — *H.-W. Glock, F. Marhauser, P. Hülsmann, M. Kurz, H. Klein* 521
The 36-Cell Structure - Calculations and Experiments — *P. Hülsmann, W.F.O. Müller, H. Klein, U. van Rienen, T. Weiland* 524
Search for Trapped Modes in TESLA Cavities — *F. Marhauser, H.-W. Glock, P. Hülsmann, M. Kurz, H. Klein* .. 527
Development of C-Band (5712 MHz) High Power Waveguide Components — *H. Matsumoto, T. Shintake, N. Akasaka, H. Baba, A. Miura* 530
Development of C-Band 50 MW Pulse Klystron for e^+e^- Linear Collider — *T. Shintake, N. Akasaka, H. Matsumoto, Y. Ohkubo, H. Yonezawa* 533
Input Coupler Design for C-Band Accelerating Structure — *C. Suzuki, N. Akasaka, T. Shintake* 536
Development of Characterization Techniques for X-Band Accelerator Structures — *S.M. Hanna, R.J. Loewen, H.A. Hoag, R.H. Miller, R.D. Ruth, J.W. Wang* 539
High-Gradient Cavity Beat-Wave Accelerator at W-Band — *D.H. Whittum, H. Henke, P.J. Chou* 542
Minimizing RF System Costs in a Linear Collider by an Optimized Choice of Beam and Structure Parameters — *R.M. Jones, P.B. Wilson* 545
Advanced Damped Detuned Structure Development at SLAC — *R.M. Jones, N.M. Kroll, R.H. Miller, R.D. Ruth, J.W. Wang* 548
Spectral Function Calculation of Angle Wakes, Wake Moments, and Misalignment Wakes for the SLAC Damped Detuned Structures (DDS) — *R.M. Jones, N.M. Kroll, R.H. Miller* 551
Analysis and Application of Microwave Radiation from the Damping Manifolds of the SLAC Damped Detuned Structures (DDS) — *R.M. Jones, M. Seidel, N.M. Kroll, R.H. Miller, C. Adolphsen, K.L.F. Bane, R.D. Ruth, J.W. Wang* 554

Linear Colliders (Other)

Spotsize Stabilization Studies for the TESLA Beam Delivery System — *Andrey Sery* 557
Pre-Alignment of CLIC Using the Double-Wire Method — *W. Coosemans, H. Mainaud* 560
A Multi-Drive Beam Scheme for Two-Beam Acceleration in a TeV Linear Collider — *R. Corsini, J.P. Delahaye, C. Johnson, A. Millich, A. Riche* 563
Analysis of a Symmetric Triplet and its Application to Ring Insertions — *T. d'Amico, G. Guignard* 566
The S-Band Linear Collider Test Facility at DESY — *S. Schmitz* 569
An Asymmetric Linac-Ring Collider for Baryon Timelike Form Factor Measurements with Existing High Energy Storage Rings — *P. Patteri, C. Bini* 572
MOPA FEL Scheme as a Source of Primary Photons for Gamma-Gamma Collider at TESLA and SBLC — *E.L. Saldin, E.A. Schneidmiller, M.V. Yurkov* 575

A Conventional Read-Out Electronics of Button-Type BPM in the ATF Damping Ring — *F. Hinode, J. Urakawa, Y. Yoribayashi* 578
Design Study of Cooling Water System for a Large Scale Linear Collider — *H. Matsumoto, Shigeru Takeda, Yasunori Takeuchi, M. Yoshioka, N. Holtkamp, J.S. Oh* 581
SR Monitor for ATF Damping Ring — *T. Naito, H. Hayano, N. Terunuma, J. Urakawa, Y. Hashimoto, M. Muto, T. Okugi* 584
Status of 1.54 GeV ATF Linac — *Seishi Takeda, H. Hayano, M. Akemoto, T. Naito, H. Matsumoto, J. Urakawa, K. Oide, N. Terunuma, K. Kubo, F. Hinode, T. Korhonen, Y. Funahashi, S. Araki, S. Kashiwagi, T. Okugi, S. Kagaya, T. Sakamoto, M. Takano* 587
Design of a 1-MV Induction Injector for the Relativisitic Two-Beam Accelerator — *D.E. Anderson, S. Eylon, S. Lidia, L. Reginato, D. Vanecek, S. Yu, T. Houck, G.A. Westenskow, E. Henestroza* 590
Efficiency Issue in C-Band Klystron-Modulator System for Linear Collider — *J.S. Oh, M.H. Cho, W. Namkung, T. Shintake, H. Matsumoto, K. Watanabe, H. Baba* 593
SLAC Accelerator Operations Report: 1995-1997 — *R. Erickson, C.W. Allen, S. Anderson, W. Linebarger, M. Stanek* 596
A Combined $\Delta T + \Delta F$ Beam Loading Compensation Scheme for Power Saving — *Zenghai Li, Roger Miller, David Farkas, Tor Raubenheimer, Huan Tang, Dian Yeremian* 599
Neutral Beam Collisions at 5 TeV — *David H. Whittum, Robert H. Siemann* 602
RF System for a 30 GHz, 5 TeV Linear Collider Based on Conventional Technology — *P.B. Wilson, T. Raubenheimer, R.D. Ruth* 605
Performance Issues, Downtime Recovery and Tuning in the Next Linear Collider (NLC) — *F. Zimmermann, C. Adolphsen, R. Assmann, K. Bane, D. Burke, F.J. Decker, P. Emma, R. Helm, L. Hendrickson, S. Hertzbach, J. Irwin, H. Jarvis, P. Krejcik, M.G. Minty, N. Phinney, P. Raimondi, M. Ross, J. Spencer, H. Tang, P. Tenenbaum, K. Thompson, D. Walz, A.D. Yeremian* 608

ADVANCED CONCEPTS

Chair: D. Sutter, *US Department of Energy*

Channeling and Time Evolution of Laser Wakes and Electron Acceleration in a Self-Modulated Laser Wakefield Accelerator Experiment *(Invited)* — *A. Ting, C.I. Moore, K. Krushelnick, H.R. Burris, C. Manka, R. Fischer, M. Baine, E. Esarey, R.F. Hubbard, P. Sprangle* 611
Inverse Free Electron Laser Accelerator Development *(Invited)* — *A. van Steenbergen, Juan C. Gallardo* 616
Experimental Observation of IFEL Micro-Bunching Using Coherent Transition Radiation — *Y. Liu, D.B. Cline, X.J. Wang, M. Babzien, J.M. Fang, J. Gallardo, K.P. Kusche, I. Pogorelsky, J. Skaritka, A. van Steenbergen* 621
Acceleration for the $\mu^+ - \mu^-$ Collider — *D. Summers, D. Neuffer, Q.-S. Shu, E. Willen* 624
Results of Blowout Regime Propagation Experiments of an Electron Beam in a Plasma — *N. Barov, M. Conde, W. Gai, J.B. Rosenzweig* 627
Femtosecond Electron Bunches from Colliding Laser Pulses in Plasmas — *E. Esarey, R.F. Hubbard, W.P. Leemans, A. Ting, P. Sprangle* 630

New Acceleration Techniques

The Argonne Wakefield Accelerator: Upgrade Scenarios and Future Experiments — *W. Gai, M. Conde, R. Konecny, X. Li, J. Power, P. Schoessow, J. Simpson* 633
Externally Powered Dielectric Loaded Waveguides as Accelerating Structures — *Wei Gai, R. Konecny, J. Simpson* 636
High Gradient Dielectric Wakefield Device Measurements at the Argonne Wakefield Accelerator — *P. Schoessow, M. Conde, W. Gai, R. Konecny, J. Power, J. Simpson* 639
Enhanced IFEL Performance Using a Novel Wiggler — *Z. Parsa, T. Marshall* 642
Emerging Terawatt Picosecond CO_2 Laser Technology and Possible Applications in Accelerator Physics — *I.V. Pogorelsky, I. Ben-Zvi* 645
High Energy-Gain Laser Wakefield Acceleration — *K. Nakajima, M. Kando, H. Ahn, H. Dewa, H. Kotaki, F. Sakai, S. Kondoh, H. Nakanishi, T. Ueda, M. Uesaka, T. Watanabe, A. Ogata* 648
Focusing of Relativistic Electron Bunches at the Wake-Field Excitation in Plasma — *Ya.B. Fainberg, N.I. Ayzatsky, V.A. Balakirev, A.K. Berezin, A.N. Dovbnya, V.I. Karas', V.A. Kiselev, V.A. Kushnir, A.F. Linnik, V.V. Mitrochenko, V.D. Stepin, I.N. Onishchenko, A.P. Tolstoluzhsky, V.V. Uskov* 651

Experimental Observation of Electron Beam Focusing Through Plasma Lenses — *R. Govil, S.J. Wheeler, W.P. Leemans* 654
Driving Laser Pulse Evolution in a Laser Wakefield Accelerator — *P. Volfbeyn, P.B. Lee, J.S. Wurtele, W.P. Leemans, G. Shvets* 657
Laser Acceleration in Vacuum with an Open Iris-Loaded Waveguide — *Ming Xie* 660
Ion Cyclotron Resonance Accelerator — *T.L. Grimm, C.T. Ramsell, R.C. York* 663
Stimulated Dielectric Wakefield Accelerator — *T.B. Zhang, J.L. Hirshfield, T.C. Marshall, B. Hafizi* 666
Beam Slicing with Lasers and Plasmas for a High-Transformer-Ratio Plasma Wakefield Accelerator — *G. Shvets, P. Stoltz* 669
RF Measurements of a Traveling-Wave Muffin-Tin Accelerating Structure at 90 GHz — *P.J. Chou, G.B. Bowden, M.R. Copeland, H. Henke, A. Menegat, D.P. Pritzkau, R.H. Siemann* 672
Design and Model Simulations of Inverse Cerenkov Acceleration Using Inverse Free Electron Laser Prebunching — *W.D. Kimura, M. Babzien, I. Ben-Zvi, D.B. Cline, R.B. Fiorito, J.R. Fontana, J.C. Gallardo, S.C. Gottschalk, P. He, K.P. Kusche, Y. Liu, R.H. Pantell, I.V. Pogorelsky, D.C. Quimby, K.E. Robinson, D.W. Rule, J. Sandweiss, J. Skaritka, A. van Steenbergen, V. Yakimenko* 675
The NEPTUNE Facility for 2nd Generation Advanced Accelerator Experiments — *C.E. Clayton, C. Joshi, K.A. Marsh, C. Pellegrini, J. Rosenzweig* 678
Optical Bunching of Relativistic Electrons for Injection into a GeV Plasma Beatwave Accelerator — *D. Gordon, C.E. Clayton, W.B. Mori, C. Joshi, T. Katsouleas* 681
Laser Acceleration in Vacuum — *J.L. Hus, T. Katsouleas, W.B. Mori, C.B. Schroeder, J.S. Wurtele* 684
A Proposal for a 1 GeV Plasma-Wakefield Acceleration Experiment at SLAC — *T. Katsouleas, S. Lee, S. Chattopadhyay, W. Leemans, R. Assmann, P. Chen, F.J. Decker, R. Iverson, T. Kotseroglou, P. Raimondi, T. Raubenheimer, S. Rokni, R.H. Siemann, D. Walz, D. Whittum, C. Clayton, C. Joshi, K. Marsh, W. Mori, G. Wang* 687
Approximate Analytical Description of the Underdense Plasma Lens — *A.Ts. Amatuni* 690
Self-Acceleration of Electrons in One-Dimensional Bunches, Moving in Cold Plasma — *A.Ts. Amatuni* 693
Generator-Invertor-Damper System of Electron (Positron) Bunches Moving in Cold Plasma — *A.Ts. Amatuni, S.G. Arutunian, M.R. Mailian* 695

LIGHT SOURCES AND FREE ELECTRON LASERS

Chair: M. Poole, *Daresbury Laboratory, CLRC*

Performance of the Advanced Photon Source *(Invited)* — *Glenn Decker* 698
Improving and Extending Performance at Synchrotron Radiation Facilities *(Invited)* — *A. Jackson* 703
Beam-Based Modeling and Control of Storage Rings *(Invited)* — *P.W. Lisowski* 708
Status of the High Brilliance Synchrotron Light Source BESSY-II — *E. Jaeschke* 713
Canadian Light Source Proposal — *L.O. Dallin, D.M. Skopik* 716
The TESLA Free Electron Laser *(Invited)* — *J. Rossbach* 719
Recent Results of the Commissioning of the DELTA Facility — *J. Friedl, DELTA Group* 724
Insertion Device Development in the X13 Straight of the NSLS X-Ray Ring — *P.M. Stefan, S. Krinsky, C.C. Kao, G. Rakowsky, O. Singh, L. Solomon* 727
Operation of FIR- and UV-FEL Facilities and FEL Beam Sharing to User's Rooms at the FELI — *T. Tomimasu, S. Okuma, K. Wakita, T. Takii, E. Oshita, K. Wakisaka, E. Tongu* 730
Stimulated Transition Radiation in the Far-Infrared — *Chitrlada Settakorn, Michael Hernandez, Helmut Wiedemann* 733
Measurements of High Gain and Noise Fluctuations in a SASE Free Electron Laser — *M. Hogan, S. Anderson, K. Bishofberger, P. Frigola, A. Murokh, N. Osmanov, C. Pellegrini, S. Reiche, J. Rosenzweig, G. Travish, A. Tremaine, A. Varfolomeev* 736
Use of Jefferson Lab's High Average Power FEL as a Thomson Backscatter X-Ray Source — *G.A. Krafft* 739

Synchrotron Radiation Facilities

Advances in Orbit Drift Correction in the Advanced Photon Source Storage Ring — *L. Emery, M. Borland* ... 742
Investigation of Open-Loop Beam Motion in Low Frequencies at the APS — *S.H. Kim, G. Decker, C. Doose, D. Mangra, R. Merl* 745
Experimental Calibration of VUV Ring Optics — *J. Safranek, S.L. Kramer* 748
Status Report on the ESRF — *J-M. Filhol, L. Hardy* 751
Lattice Related Brilliance Increase at the ESRF — *A. Ropert* 754

VUV and Soft X-Ray Light Source "new SUBARU" — *A. Ando, S. Amano, S. Hashimoto, H. Kinosita, S. Miyamoto, T. Mochizuki, M. Niibe, Y. Shoji, M. Terasawa, T. Watanabe* 757
A Short Pulse X-Ray Generation via Thomson Scattering of Ultrashort Laser Pulses by Relativistic Electron Beams — *K. Nakajima, H. Nakanishi, A. Ogata, H. Kotaki, H. Ahn, H. Dewa, M. Kando, S. Kondoh, F. Sakai, T. Watanabe, T. Ueda, M. Uesaka* 760
ANKA - Status of the 2.5 GeV Synchrotron Light Source at Forschungszentrum Karlsruhe — *D. Einfeld, A. Hagestedt, E. Huttel, A. Krüssel, H.O. Moser, F. Perez, M. Plesko, R. Rossmanith, J. Schaper, R. Simon, R. Steininger, D. Tommasini, S. Voigt* 763
Spatial Coherency of the Synchrotron Radiation at the Visible Light Region and its Application for the Electron Beam Profile Measurement — *T. Mitsuhashi* 766
Longitudinal Beam Transfer Function Diagnostics in the ALS — *John Byrd* 769
Controlling the Vertical Mode Coupling Instability with Feedback in the Advanced Light Source — *J.M. Byrd, W. Barry* 772
Commissioning of the Advanced Light Source Dual-Axis Streak Camera — *J. Hinkson, R. Keller, J. Byrd, A. Lumpkin* 775
ALS-N - A Candidate for a Next-Generation Synchrotron Light-Source — *A. Jackson, J. Byrd, W. Decking, M. Howells, R. Keller, C.H. Kim, D. Massoletti, H. Nishimura, D. Robin, H. Zyngier* 778
Transfer Functions for the ALS Lattice Magnets — *R. Keller* 781
Orbit Stability of the ALS Storage Ring — *R. Keller, H. Nishimura, the Stability Task Force Advanced Light Source Center* 784
Tune-Split Effects at the ALS Storage Ring — *R. Keller* 787
A Code for Calculating the Time Evolution of Beam Parameters in High Intensity Circular Accelerators — *C.H. Kim* 790
Measurement of Storage Ring Motion at the Advanced Light Source — *Gary F. Krebs* 793
Measurement of the Radiation Incident on ALS NdFeB Permanent Magnet Insertion Device Structures and a Determination of their Lifetime — *Gary F. Krebs, Michael Holmes* 796
Global Beta-Beating Compensation of the ALS W16 Wiggler — *D. Robin, J. Safranek, W. Decking, H. Nishimura* 799
Crossed Elliptical Polarization Undulator — *Shigemi Sasaki, Ross Schlueter, Steve Marks* 802
Accelerator Control Software Construction Based on Software Object Components — *C. Timossi, H. Nishimura* 805
Modification of the ALS Booster Synchrotron for an Experiment on Optical Stochastic Cooling — *A. Zholents, M. Fahmie, J. Johnson, C. Kim, K. Luchini, D. Massoletti, J. de Vries* 808
Commissioning and Operations of the Brazilian Synchrotron Light Source — *A.R.D. Rodrigues, R.H.A. Farias, M.J. Ferreira, G.S. Franco, L.C. Jahnel, Liu Lin, A.C. Lira, R.T. Neuenschwander, C. Pardine, F. Rafael, A. Rosa, C. Scorzato, C.E.T. Gonçalves da Silva, A. Romeu da Silva, P.F. Tavares, D. Wisnivesky, A. Craievich* . 811
Current Status of the LSB Project — *M. Muñoz* 814
Status of the SOLEIL Project — *J.-L. Laclare, M.-P. Level, P. Bosland, P. Brunelle, R. Chaput, S. Chel, M. Corlier, G. Flynn, M. Juillard, X. Hanus, C. Herbeaux, A. Loulergue, J.-L. Marlats, A. Mosnier, A. Nadji, J. Neel, P. Nghiem, S. Palanque, J. Payet, P. Peaupardin, J.-P. Pénicaud, M. Sommer, A. Tkatchenko, M. Tkatchenko, M.-A. Tordeux* 817
A Plan of Synchrotron Light Source for Medical Applications at NIRS — *M. Torikoshi, M. Endo, M. Kumada, K. Noda, S. Yamada, K. Kawachi* 820
Operational Status of Pohang Light Source — *J. Choi, T. Lee, M. Kwon, J.Y. Huang, S.H. Nam, M. Yoon, M.H. Cho, I.S. Ko, W. Namkung* 823
ELETTRA Performance and Upgrades — *C.J. Bocchetta, D. Bulfone, F. Daclon, G. D'Auria, A. Fabris, R. Fabris, M. Ferianis, A. Galimberti, F. Iazzourene, E. Karantzoulis, M. Lonza, C. Pasotti, C. Rossi, C. Scafuri, M. Svandrlik, L. Tosi, R. Visintini, R.P. Walker, F. Wei, A. Wrulich, D. Zangrando* 826
Beam Density Manipulations in the ELETTRA Storage Ring — *C.J. Bocchetta, A. Fabris, F. Iazzourene, E. Karantzoulis, M. Svandrlik, L. Tosi, R.P. Walker, A. Wrulich* 829
Ideas for Fast Accelerator Model Calibration — *J. Corbett, G. LeBlanc* 832
The SPEAR RF Cavity Characterization at Stanford Synchrotron Radiation Laboratory — *Sanghyun Park, James J. Sebek* 835
SPEAR-III: A Brighter Source at SSRL — *R. Hettel, R. Boyce, S. Brennan, J. Corbett, M. Cornacchia, W. Davies-White, A. Garren, A. Hofmann, C. Limborg, Y. Nosochkov, H.-D. Nuhn, T. Rabedeau, J. Safranek, H. Wiedemann* 838
Experimental Calibration of SRRC Lattice Optics — *C.C. Kuo, J. Safranek, H.P. Chang, K.T. Hsu* 841

Preliminary Study of the Wavelength Shifter Effect in SRRC Storage Ring — *J.C. Lee* 844
Operation Experience at SRRC — *Y.C. Liu, J.R. Chen, K.T. Hsu, C.C. Kuo, W.K. Lau, G.H. Luo, R.C. Sah, T.S. Ueng* 847
Analyzing the Relationship Between the Beam Life Time and Average Gas Pressure — *Gwo-Huei Luo, Glory Lin, C.C. Kuo, John Chiang, Y.J. Hsu, D.H. Lee, R.C. Sah, Ian C. Hsu* 850
The 1.5 GeV Operation Parameters and Performance at SRRC — *Gwo-Huei Luo, Peace Chang, K.T. Hsu, Jenny Chen, C.C. Kuo, Y.K. Lin, R.C. Sah, Y.C. Liu* 853
A Lattice for the Future Project of VUV and Soft X-Ray High-Brilliant Light Source — *Hiroyuki Takaki, Tadashi Koseki, Norio Nakamura, Yukihide Kamiya, Yukinori Kobayashi, Toshiya Nagatsuka* 856
Wavefront Distortion Measurement of a SR Extraction Mirror for the Beam Profile Monitor Using Shack-Hartmann Method — *N. Takeuchi, T. Mitsuhashi, M. Itoh, T. Yatagai* 859
Instability Analysis of an Active Higher-Harmonic Cavity — *R.A. Bosch* 862
Aladdin, Present and Future — *Walter Trzeciak, and SRC Staff* 865
An Alternative Lattice Design for a Compact Light Source Ring — *A.A. Garren, M.A. Green* 868

Free Electron Lasers

Planned Optical Diagnostics for the APS Low-Energy Undulator Test Line — *A.H. Lumpkin, W.J. Berg, B.X. Yang* 871
Initial Application of a Dual-Sweep Streak Camera to the Duke Storage Ring OK-4 Source — *A.H. Lumpkin, B.X. Yang, V. Litvinenko, S. Park, P. Wang, Y. Wu* 874
The Advanced Photon Source Low-Energy Undulator Test Line — *S.V. Milton, J.N. Galayda, E. Gluskin* 877
Gamma-Ray Production Using Multi-Photon Compton Scattering — *H. Takahashi, Y. An, M. Nomura* 880
Unique Features of the OK-4/Duke Storage Ring XUV FEL and Monochromatic γ-Ray Source — *V.N. Litvinenko, Y. Wu, B. Burnham, S.H. Park, M. Emamian, J. Faircloth, S. Goetz, N. Hower, J.M.J. Madey, J. Meyer, P. Morcombe, O. Oakeley, J. Patterson, R. Sachtschale, G. Swift, P. Wang, I.V. Pinayev, M.G. Fedotov, N.G. Gavrilov, V.M. Popik, V.N. Repkov, L.G. Isaeva, G.N. Kulipanov, G.Ya. Kurkin, S.F. Mikhailov, A.N. Skrinsky, N.A. Vinokurov, P.D. Vobly, E.I. Zinin, A. Lumpkin, B. Yang* 883
A Laser Pulse Trapper for Compton Backscattering Applications — *D. Yu, B. Stuart* 886
High Current FEL Oscillator on Base of MSU Electron Accelerators — *V.K. Grishin, B.S. Ishkhanov, T.A. Novicova* 889
Possibility of X-Ray Free Electron Laser with Single Crystal Optical Resonator for Bragg Reflection — *Y. Miyahara* 891
On the Analytic Representation of Periodic Magnetostatic Fields — *A.V. Smirnov* 894
A High-Power Compact Regenerative Amplifier FEL — *D.C. Nguyen, R.L. Sheffield, C.M. Fortgang, J.M. Kinross-Wright, N.A. Ebrahim, J.C. Goldstein* 897
W-Band Free Electron Laser for High Gradient Structure Research — *S.M. Lidia, D.H. Whittum, J.T. Donohue* 900
Linac Design for the LCLS Project at SLAC — *V.K. Bharadwaj, K. Bane, J. Clendenin, P. Emma, J.C. Sheppard, M.D. Woodley* 903
First Lasing of the Israeli Tandem Electrostatic Accelerator Free Electron Laser — *J.S. Sokolowski, A. Abramovich, A. Arensburg, D. Chairman, M. Draznin, A. Eichenbaum, A. Gover, H. Kleinman, Y. Pinchasi, I.M. Yakover, A. Rosenberg, J. Shiloh, M. Cohen, L.A. Levin, O. Shahal* 906
Recirculating Accelerator Driver for a High-Power Free-Electron Laser: A Design Overview — *Courtlandt L. Bohn* 909
Electron-Beam Diagnostics for Jefferson Lab's High Power Free Electron Laser — *G.A. Krafft, K. Jordan, D. Kehne, S. Benson, J. Denard, E. Feldl, P. Piot, J. Song, R. Ursic* 912

LOW- AND MEDIUM-ENERGY ACCELERATORS AND RINGS

Chair: S. Schriber, *Los Alamos National Laboratory*

New High Power Linacs and Beam Physics Issues *(Invited)* — *Thomas P. Wangler, E.R. Gray, S. Nath, K.R. Crandall, K. Hasegawa* 915
The Japanese Hadron Facility *(Invited)* — *Y. Mori* 920
Review of Radioactive Beam Accelerators *(Invited)* — *Pierre G. Bricault* 925
RIKEN RI-Beam Factory Project *(Invited)* — *Y. Yano, A. Goto, T. Katayama* 930
Status of the IUCF Cooler Injector Synchrotron — *D.L. Friesel, S.Y. Lee* 935

Acceleration Test of Radioactive Nuclear Beam at INS — *M. Tomizawa, S. Arai, Y. Arakaki, Y. Hashimoto, A. Imanishi, S.C. Jeong, I. Katayama, T. Katayama, H. Kawakami, S. Kubono, T. Miyachi, H. Miyatake, K. Niki, T. Nomura, M. Okada, M. Oyaizu, Y. Shirakabe, P. Strasser, Y. Takeda, J. Tanaka, M.H. Tanaka, E. Tojyo, M. Wada* 938
Acceleration Test of the Folded-Coaxial RFQ Linac for the RILAC — *O. Kamigaito, A. Goto, Y. Miyazawa, T. Chiba, M. Hemmi, M. Kase, S. Kohara, T. Nakagawa, Y. Batygin, Y. Yano* 941
Recent Lead Ion Storage Tests on LEAR — *J. Bosser, J. Broere, C. Carli, M. Chanel, C. Hill, R. Ley, A. Lombardi, R. Maccaferri, S. Maury, D. Möhl, G. Molinari, H. Mulder, E. Tanke, G. Tranquille, M. Vretenar* . 944
The REX-ISOLDE Project — *R. von Hahn, M. Grieser, H. Podlech, R. Repnow, D. Schwalm, D. Habs, O. Kester, T. Sieber, A. Schempp, G. Bollen, F. Ames, U. Ratzinger, L. Liljeby, K.G. Rensfelt, P. Van Duppen* 947
Development of HILBILAC for Initial Part of ADTT Accelerator — *G.I. Batskikh, V.M. Pirozhenko, A.J. Favale, T.J. Myers* 950
A 1- to 5-MW, RCS-Based, Short-Pulse Spallation Neutron Source — *Y. Cho, Y.-C. Chae, E. Crosbie, K. Harkay, D. Horan, R. Kustom, E. Lessner, W. McDowell, D. McGhee, H. Moe, R. Nielsen, G. Norek, K. Peterson, K. Thompson, J. Wang, M. White* 953
Status of the TRIUMF ISAC-Facility for Accelerating Radioactive Beams — *P.W. Schmor, R. Baartman, P. Bricault, M. Dombsky, G. Dutto, S. Koscielniak, R.E. Laxdal, F. Mammarella, G.H. Mackenzie, R. Poirier, L. Root, G. Stanford, G. Stinson, I. Thorson, J. Welz* 956

Proton Synchrotrons and Storage Rings

Anomalous, Intensity Dependent Losses in Au(32+) Beams — *M. Blaskiewicz, L. Ahrens, H. Calvani* 959
Accumulator Ring Lattice for the National Spallation Neutron Source — *C.J. Gardner, Y.Y. Lee, A.U. Luccio* .. 962
Mini-Bunching the AGS Slow External Beam — *J.W. Glenn, L. Ahrens, T. Hayes, R. Lee* 965
Micro-Bunching the AGS Slow External Beam — *J.W. Glenn, M. Brennan, L. Littenberg, J. Rose, C. Woody, A. Zaltsman, P. Bergbusch, Dick Majka* 967
Accumulator Ring Design for the NSNS Project — *W.T. Weng, J. Alessi, J. Beebe-Wang, M. Blaskiewicz, L. Blumberg, J.M. Brennan, C. Gardner, Y.Y. Lee, A. Luccio, H. Ludewig, D. Maletic, D. Raparia, A. Ruggiero, S.Y. Zhang* 970
Conversion of the PS Complex as LHC Proton Pre-Injector — *F. Blas, R. Cappi, V. Chohan, D. Cornuet, G. Daems, D. Dekkers, R. Garoby, D. Grier, J. Gruber, E. Jensen, H. Koziol, A. Krusche, K.D. Metzmacher, F. Pedersen, J. Pedersen, U. Raich, J.P. Riunaud, J.P. Royer, M. Sassowsky, K. Schindl, H. Schönauer, M. Thivent, H. Ullrich, F. Völker* 973
Combined Longitudinal and Transverse Multiturn Injection in a Heavy Ion Accumulator — *Ch. Carli, S. Maury, D. Möhl* 976
The Antiproton Decelerator: AD — *S. Baird, D. Berlin, J. Boillot, J. Bosser, M. Brouet, J. Buttkus, F. Caspers, V. Chohan, D. Dekkers, T. Eriksson, R. Garoby, R. Giannini, O. Gröbner, J. Gruber, J.Y. Hemery, H. Koziol, R. Maccaferri, S. Maury, C. Metzger, K. Metzmacher, D. Möhl, H. Mulder, M. Paoluzzi, F. Pedersen, J.P. Riunaud, C. Serre, D.J. Simon, G. Tranquille, J. Tuyn, A. Van der Schueren* 979
Overview of the Recent Operation of the AAC and LEAR for the Low-Energy Antiproton Physics Programme — *S. Baird, J. Boillot, F. Caspers, M. Chanel, V. Chohan, T. Eriksson, R. Ley, S. Maury, C. Metzger, D. Möhl, H. Mulder, F. Pedersen, G. Tranquille* 982
The Proton Synchrotron DESY III — *J.R. Maidment, W. Ebeling* 985
Status of the European Spallation Source Design Study — *I.S.K. Gardner, H. Lengeler, K. Bongardt, H. Klein, G.H. Rees, C.M. Warsop, on behalf of the ESS Study Group* 988
Intensity Limitations in the FNAL Main Injector — *W. Chou* 991
The Design of a γ_t-Jump System for the FNAL Main Injector — *W. Chou, B.C. Brown, S. Fang, J. Leibfritz, K.-Y. Ng, H. Pfeffer, I. Terechkine* 994
Design and Simulation of the Antiproton Recycler Lattice — *D.E. Johnson, C.S. Mishra, S.D. Holmes, N. Gelfand, J.A. Holt, L. Michelotti* 997
An Imaginary-γ_t Lattice with Dispersion-Free Straights for the 50 GeV High-Intensity Proton Synchrotron — *K.Y. Ng* 1000
Multiple Injections with Barrier Buckets — *K.Y. Ng* 1003
The Fermilab Accumulator Ring Lattice Upgrade — *S. O'Day, M. Church* 1006
Intensity Upgrade Studies at the KEK-PS — *Hikaru Sato, Crew of the Intensity Upgrade Study* 1009
Overview and Status of the Los Alamos PSR Injection Upgrade Project — *D.H. Fitzgerald, H. Ahn, B. Blind, M.J. Borden, R.J. Macek, F. Neri, M.A. Plum, C.R. Rose, H.A. Thiessen, C.A. Wilkinson, M.V. Zumbro* 1012

Comparison of Beam Transport Simulations to Measurements at the Los Alamos Proton Storage Ring — *C. Wilkinson, F. Neri, D.H. Fitzgerald, B. Blind, R. Macek, M. Plum, O. Sander, H.A. Thiessen* 1015
Accumulator Ring H^- Injection Optimization Studies — *J.D. Galambos, J.A. Holmes, D.K. Olsen* 1018
A Possible Upgrade for ISIS — *M.R. Harold, R.G. Bendall, T.A. Broome, I.S.K. Gardner, M.G. Glover, C.R. Prior, C.W. Planner, G.H. Rees* 1021
Design of Booster Synchrotron for MUSES — *T. Ohkawa, T. Katayama* 1024

Low- and Medium-Energy Circular Accelerators

ELISA - An Electrostatic Storage Ring for Atomic Physics — *Søren Pape Møller* 1027
A Proton Driver for the Muon Collider Source with a Tunable Momentum Compaction Lattice — *D. Trbojevic, J.M. Brennan, E.D. Courant, T. Roser, S. Peggs, K.Y. Ng, C. Johnstone, M. Popovic, J. Norem* 1030
Correction of Depolarizing Resonances in ELSA — *C. Steier, D. Husmann* 1033
Continuous Electron-Energy Variation of the Eindhoven Racetrack Microtron — *W.H.C. Theuws, J.I.M. Botman, H.L. Hagedoorn* 1036
The ANKA Injector — *D. Einfeld, F. Perez, R. Rossmanith, R. Walther* 1039
The IASA RaceTrack Microtron Facility, a Progress Report — *E. Stiliaris, H. Avramopoulos, D. Baltadoros, M. Barbarosou, S. Cohen, D. Economou, T.A. Filippas, E.N. Gazis, A. Karabarbounis, M. Malagari, D. Maroulis, N.H. Papadakis, C.N. Papanicolas, N. Patavalis, P. Phinou, H. Rahmani, N. Sparveris, N. Uzunoglou, N. Vodinas, H. Herminghaus* 1042
Extracted Beams from IBA's C235 — *D. Vandeplassche, W. Beeckman, S. Zaremba, Y. Jongen, T. Tachikawa* 1045
The Cooler Synchrotron COSY Facility — *H. Stockhorst, U. Bechstedt, J. Dietrich, R. Maier, S. Martin, D. Prasuhn, A. Schnase, H. Schneider, R. Toelle* 1048
Beams for Gammasphere at the LBNL 88-Inch Cyclotron — *D.J. Clark, D. Collins, R. Dwinell, A. Guy, S. Lundgren, C.M. Lyneis, M.A. McMahan, D. Syversrud, Z. Xie* 1051
A Compact Superconducting Cyclotron for the Production of High Intensity Protons — *H. Blosser, D. Johnson, D. Lawton, F. Marti, R. Ronnigen, J. Vincent* 1054
A Separated Sector Cyclotron for the Production of High Intensity Protons — *F. Marti, H. Blosser, D. Johnson, D. Lawton, J. Vincent* 1057
Conceptual Design of a High Field Ultra-Compact Cyclotron for Nuclear Physics Research — *J. Schubert, H. Blosser* 1060
Polarized Electrons in the AmPS Storage Ring — *G. Luijckx, P.W. van Amersfoort, H. Boer-Rookhuizen, J.F.J. van den Brand, F.B. Kroes, C.W. de Jager, L.H. Kuijer, J.B. van der Laan, R. Maas, J.G. Noomen, I. Passchier, M.J.J. van den Putte, I. Koop, B. Militsyn, A.S. Terekhov* 1063
Numerical Analyses of the Injection and Extraction Trajectories for the RIKEN Superconducting Ring Cyclotron — *S. Fujishima, H. Okuno, T. Tominaka, T. Mitsumoto, T. Kubo, T. Kawaguchi, J.-W. Kim, K. Ikegami, N. Sakamoto, S. Yokouchi, T. Morikawa, Y. Tanaka, A. Goto, Y. Yano* 1066
Orbit Analysis for the RIKEN Superconducting Ring Cyclotron — *T. Mitsumoto, A. Goto, T. Kawaguchi, J.-W. Kim, Y. Tanaka, T. Kubo, H. Okuno, T. Tominaka, S. Fujishima, K. Ikegami, N. Sakamoto, T. Morikawa, S. Yokouchi, Y. Yano* 1069
Design Study of Accumulator Cooler Ring for MUSES — *K. Ohtomo, T. Katayama* 1072
Design Study of the Injection and Extraction Systems for the RIKEN Superconducting Ring Cyclotron — *H. Okuno, T. Tominaka, S. Fujishima, T. Mitsumoto, T. Kubo, T. Kawaguchi, J.-W. Kim, K. Ikegami, N. Sakamoto, S. Yokouchi, T. Morikawa, Y. Tanaka, A. Goto, Y. Yano* 1075

RFQ Linacs

Status of the HMI-RFQ-Injector — *O. Engels, A. Schempp, H. Homeyer, W. Pelzer* 1078
A Two-Beam RFQ for Ion Beam Funneling — *A. Firjahn-Andersch, J. Madlung, A. Schempp, H. Zimmermann* . 1081
Design of a High Current H^- RFQ Injector — *A. Schempp, H. Vormann* 1084
Prototype of a Superconducting RFQ for a Heavy Ion Injector Linac — *G. Bisoffi, V. Andreev, E. Bissiato, F. Chiurlotto, M. Comunian, E. Corradini, H. Dewa, A. Lombardi, A. Pisent, A.M. Porcellato, T. Shirai, E. Tovo, T. Tovo* 1087
Development of the ITEP 27 MHz Heavy Ion RFQ — *V.A. Andreev, A.A. Kolomiets, V.I. Pershin, V.N. Sidorenko, R.M. Vengrov, S.G. Yaramyshev, O.V. Ershov, G. Parisi* 1090
A 6.7 MeV CW RFQ Linac — *D. Schrage, L. Young, W. Clark, T. Davis, F. Martinez, A. Naranjo, P. Roybal* 1093
NSNS RFQ Mechanical Design — *Matthew D. Hoff, Craig Fong, Martin Fong, John W. Staples* 1096
Status of the RFD Linac Prototype — *D.A. Swenson, F.W. Guy, J.W. Lenz, K.R. Crandall, J.M. Potter* 1099

Beam Dynamics Studies on the ISAC RFQ at TRIUMF — *S. Koscielniak, R.E. Laxdal, R. Lee, L. Root* 1102
Construction Criteria and Prototyping for the ISAC RFQ Accelerator at TRIUMF — *R.L. Poirier, P. Bricault, G. Dutto, K. Fong, K. Jensen, R. Laxdal, A.K. Mitra, G. Stanford* 1105
A High-Power Radiofrequency Focusing Continuous Wave Electron Linac — *N.P. Sobenin, D.V. Kostin, V.I. Shvedunov, W.P. Trower* 1108

Proton and Ion Linacs

The Beam Loading Effect in the Multicavity Linear Accelerator and the Requirements for the RF Control System — *Yu. Senichev* 1111
A Superconducting Linac for the Energy Amplifier — *Alessandro G. Ruggiero* 1114
Low-Beta Structures for CW Operation — *H. Leboutet, S. Joly, C. Perraudin* 1117
IPHI, the Saclay High-Intensity Proton Injector Project — *J-M. Lagniel, S. Joly, J-L. Lemaire, A.C. Mueller* ... 1120
Status on Linacs Developed at Institute of Atomic Physics - Bucharest, Romania — *D. Martin, C. Oproiu, A. Radu, S. Marghitu, I. Indreias, R. Cramariuc, A. Margaritescu, G. Cojocaru* 1123
A High-Current Superconducting Proton Linac for an Accelerator-Driven Transmutation System — *C. Pagani, G. Bellomo, P. Pierini, G. Travish, D. Barni, A. Bosotti, R. Parodi* 1126
The New Positive Ion Injector PIAVE at LNL — *A. Lombardi, G. Bassato, A. Battistella, M. Bellato, G. Bezzon, L. Bertazzo, G. Bisoffi, E. Bissiato, S. Canella, M. Cavenago, F. Cervellera, F. Chiurlotto, M. Comunian, A. Facco, P. Favaron, G. Fortuna, S. Gambalonga, M. Lollo, M.F. Moisio, V. Palmieri, R. Pengo, A. Pisent, M. Poggi, A.M. Porcellato, F. Scarpa, L. Ziomi, I. Kulik, A. Kolomiets, S. Yaramishev, H. Dewa* 1129
Complete Simulation of the Heavy Ion Linac PIAVE — *A. Pisent, M. Comunian* 1132
A Triple Gap Resonator Design for the Separated Function DTL at TRIUMF — *Y. Bylinsky, V. Kukhtiev, P. Ostroumov, V. Paramonov, R.E. Laxdal* 1135
BBU Gain Measurements on the ITS 6-MeV, 4-kA Linac — *Paul Allison, David C. Moir* 1138
Quadrupole Image-Current Effects in the ITS 6-MeV, 4-kA Linac — *Paul Allison, David C. Moir* 1141
Observation of Self-Steering Effects on the ITS 6-MeV Linac — *Paul Allison, David C. Moir, Gary Sullivan, Thomas P. Hughes* 1144
An Overview of the Low Energy Demonstration Accelerator (LEDA) Project RF Systems — *J. Bradley III, K. Cummings, M. Lynch, D. Rees, W. Roybal, P. Tallerico, L. Toole* 1147
Commissioning Plan for a High-Current Proton Linac — *K.C.D. Chan, R.L. Barber, R.W. Garnett, J.D. Gilpatrick, K.F. Johnson, G.P. Lawrence, S. Nath, A. Regan, L. Rybarcyk, R.E. Shafer, H.V. Smith, T.P. Wangler, L.M. Young, W. Funk, K. Crandall* 1150
Simulated Performance of the Superconducting Section of the APT Linac Under Various Fault and Error Conditions — *E.R. Gray, S. Nath, T.P. Wangler* 1153
Integrated Normal-Conducting/Superconducting High Power Proton Linac for APT Project — *G.P. Lawrence, T.P. Wangler* 1156
Overview of Progress on the Improvement Projects for the LANSCE Accelerator and Target Facilities — *R.J. Macek, J.C. Browne, T. Brun, J.B. Donahue, D.H. Fitzgerald, R. Pynn, S.O. Schriber, D. Weinacht* 1159
Beam Dynamics Aspects for the APT Integrated Linac — *S. Nath, K.R. Crandall, E.R. Gray, T.P. Wangler, L.M. Young* 1162
Availability Results for the LANSCE Accelerator Complex — *N.T. Callaway, R.W. Garnett, K.W. Jones, M.A. Oothoudt, B.D. Ray* 1165
Progress Update on the Low-Energy Demonstration Accelerator (LEDA) — *J.D. Schneider, K.C.D. Chan* 1168
Physics Design of the National Spallation Neutron Source Linac — *H. Takeda, J.H. Billen, S. Nath* 1171
The NSNS Front End Accelerator System — *John W. Staples* 1174
A Proposed Superconducting Booster Linac for the HRIBF — *J.D. Bailey, D.K. Olsen* 1177
A 100 MeV MultiTank Drift Tube Linac for Proton Acceleration — *G. D'Auria, C. Rossi* 1180
RF Low Level and Power Distribution of the 100 MeV Proton Multi-Tank Drift Tube Linear Accelerator — *G. D'Auria, C. Rossi* 1182
Linear Beam Dynamics in the Superconducting Linear Accelerator of the Energy Amplifier — *F. Iazzourene, C. Pasotti, A. Wrulich* 1185
Optimization of the Accelerating Structures for the Superconducting Linear Accelerator of the Energy Amplifier — *A. Wrulich* 1188
A DTL with Short Tanks and External Focusing for High Power CW Linacs — *C. Bourat, C. Perraudin* 1191
A Separated Function Drift-Tube Linac for the ISAC Project at TRIUMF — *R.E. Laxdal, P.G. Bricault, T. Ries, D.V. Gorelov* 1194

Electron Linacs

Design of the Source Development Lab Bunch Compressor — *W.S. Graves, I. Ben-Zvi, E.D. Johnson, S. Krinsky, J. Skaritka, M.H. Woodle, L.-H. Yu, T.O. Raubenheimer* 1197
Electron Beam Dynamics for a Low-Energy Electron Linac — *A.F.J. Hammen, J.I.M. Botman, R.W. de Leeuw, H.L. Hagedoorn, W.H.C. Theuws* 1200
Fabrication of Biperiodic DAW Cavity — *Y. Iwashita, H. Ao, A. Noda, H. Okamoto, T. Shirai, M. Inoue, T. Kawakita, M. Matsuoka, K. Koyama* 1203
Present Status of the Electron Linac as the Injector for KSR — *T. Sugimura, T. Shirai, H. Tonguu, Y. Iwashita, A. Noda, M. Inoue* 1206
Upgrading of the LNLS Injection System — *D. Wisnivesky, F.S. Rafael, O.R. Bagnato, R.A. Picoli, A.C. Lira, A.R. Silva, C. Pardine* 1209
Operation and Status of the ELETTRA Injector Linac — *G. D'Auria, D. Daclon, P. Del Giusto, M. Milloch, A. Milocco, A. Pozzer, V. Rizzi, C. Rossi, A. Tomicich* 1212
Backward Traveling Wave Electron Linac — *Huaibi Chen, Yuanzhong Huang, Yuzheng Lin, Dechun Tong, Xiaodong Ding* 1215
A 14 MeV Single-Section SW Guide for Medical Accelerators — *Qingxiu Jin, Yuzheng Lin, Dechun Tong, Quanfeng Li, Yue Yang, Jingqing Sun, Shaoguang Hu, Bingyi Chen, Yuezeng Li, Baoyu Sun, Yang Zou, Wensheng Hu* 1218
A Portable X-Band On-Axis Standing Wave Linac Structure — *Xiang Sun, Dechun Tong, Qingxiu Jin, Yuzheng Lin, Jingqing Sun, Shaoguang Hu, Taibin Du, Xiuming Duan, Bingyi Chen, Yuezeng Li, Yang Zou, Wensheng Hu* 1221

Electrostatic and Other Accelerators

Beijing Radioactive Nuclear Beam Facility (BRNBF) — *Guan Xia Ling, and the BRNBF Project Group* 1224
Development of the Holifield Radioactive Ion Beam Facility — *B.A. Tatum, and the HRIBF Operations Staff* ... 1227

PULSED-POWER AND HIGH-INTENSITY BEAMS

Chair: C. Olson, *Sandia National Laboratory*

Experiments in Heavy-Ion Fusion Beam Physics at LBNL, LLNL, and the University of Maryland *(Invited)* — *J.W. Kwan* 1230
PBFA Z: A 55 TW/4.5 MJ Electrical Generator *(Invited)* — *R.B. Spielman, W.A. Stygar, K.W. Struve, J.F. Seamen* 1235
3D Particle Simulations of Space-Charge-Dominated Beams in HIF Accelerator Experiments *(Invited)* — *D.P. Grote, A. Friedman, S.M. Lund, I. Haber* 1240
Experiments Investigating the Generation and Transport of 10-12 MeV, 30-kA, mm-Size Electron Beams with Linear Inductive Voltage Adders — *M.G. Mazarakis, J.W. Poukey, J.E. Maenchen, D.C. Rovang, P.R. Menge, J.S. Lash, D.L. Smith, J.A. Halbleib, S.R. Cordova, K. Mikkelson, J. Gustwiller, W.A. Stygar, D.R. Welch, I. Smith, P. Corcoran* 1245
Linear Induction Accelerator Approach for Advanced Radiography — *George J. Caporaso* 1248
Performance of the Spiral Line Induction Accelerator — *J.R. Smith, V.L. Bailey, H. Lackner, S.D. Putnam* 1251

Pulsed Power Accelerators

AIRIX Prototype Technological Results at CESTA — *P. Anthouard, J. Bardy, C. Bonnafond, P. Delsart, A. Devin, P. Eyharts, P. Eyl, D. Guilhem, J. Labrouche, J. Launspach, J. de Mascureau, A. Roques, M. Thevenot, D. Villate, L. Voisin, E. Merle, J.C. Picon* 1254
Beam Transport and Characterization on AIRIX Prototype at CESTA — *P. Eyharts, P. Anthouard, J. Bardy, C. Bonnafond, P. Delsart, A. Devin, P. Eyl, D. Guilhem, J. Labrouche, J. Launspach, J. de Mascureau, A. Roques, D. Villate, L. Voisin, E. Merle, J.C. Picon* 1257
ETA-II Experiments for Determining Advanced Radiographic Capabilities of Induction Linacs — *J.T. Weir, G.J. Caporaso, J.C. Clark, H.C. Kirbie, Y.-J. Chen, S.M. Lund, G.A. Westenskow, A.C. Paul* 1260
800-keV Electron Induction Injector with High Average Power — *G. Mamaev, A. Ctcherbakov, A. Glazov, V.. Krasnopolsky, T. Latypov, S. Mamaev, S. Pouchkov, I. Tenyakov, Y. Teryoshkin, S.I. Vlasenko* 1263
Output Beam Characteristics of 150 MeV Microtron — *T. Hori, H. Tsutsui, D. Amano, M. Washio, J. Yang, K. Tani* 1266

Pulsed Power Technology

Constant-Current Charging Supplies for the Advanced Photon Source (APS) Linear Accelerator Modulators — *R. Fuja, A.E. Grelick, D. Meyer, G. Pile, M. White* 1269
New Results on Electron Emission from PZT Ferroelectric Cathodes — *D. Flechtner, Cz. Golkowski, J.D. Ivers, G.S. Kerslick, J.A. Nation, L. Schächter* 1272
A Ferroelectric Cathode Electron Gun for High Power Microwave Research — *J.D. Ivers, D. Flechtner, Cz. Golkowski, G.S. Kerslick, J.A. Nation* 1275
Thirty Mega-Watt Klystron Modulator Development at the Duke University Free-Electron Laser Laboratory — *Richard J. Sachtschale, P.G. O'Shea, G. Swift* 1278
A Thyratron Trigger with Low Jitter — *C. Jensen, D. Qunell* 1281
A 40 kV, 3.1 Ω PFN for the Main Injector Abort Kicker — *C.C. Jensen* 1284
Kicker System for 8 GeV Proton Injection — *D. Qunell, C. Jensen, D. Tinsley* 1287
High Power Modulator for Linear Induction Accelerator SILUND-21 — *G.V. Dolbilov, A.A. Fateev* 1290
A 200-A, 500-Hz, Triangle Current-Wave Modulator and Magnet Used for Particle Beam Rastering — *C.R. Rose, R.E. Shafer* 1293
Arbitrary Waveform Generator for Electrostatic Dipoles in a Heavy Ion Recirculator — *D.P. Berners, L.L. Reginato* 1296
Dynamics of Magnetic Insulation Violation in Smooth-Bore Magnetrons — *A.V. Agafonov, V.M. Fedorov, V.P. Tarakanov* 1299
Brillouin Flow in a Magnetron Diode as the Kinetic Model Limit — *A.V. Agafonov, V.S. Voronin* 1302
A Novel Design for a High Power Superconducting Delay Line — *Yu Ju (Judy) Chen, George J. Caporaso* 1305
High-Performance Insulator Structures for Accelerator Applications — *S.E. Sampayan, G.J. Caporaso, D.M. Sanders, R.D. Stoddard, D.O. Trimble, J. Elizondo, M.L. Krogh, T.F. Wieskamp* 1308
150 kV Magnetic Pulse Compressor — *G. Mamaev, T. Latypov, S. Mamaev, S. Puchkov, A. Shcherbakov, I. Tenyakov* 1311
Technology for Production of Amorphous Alloy Large Scale Cores — *G. Mamaev, I. Bolotin, A. Ctcherbakov, S. Mamaev, S. Puchkov, I. Tenyakov* 1313
The PEP-II Abort Kicker System — *J. de Lamare, A. Donaldson, A. Kulikov, J. Lipari* 1316
NLC Klystron Pulse Modulator R&D at SLAC — *R. Koontz, M. Akemoto, S. Gold, A. Krasnykh, Z. Wilson* 1319
Development of the Pulse Transformer for NLC Klystrom Pulse Modulator — *M. Akemoto, S. Gold, A. Krasnykh, R. Koontz* 1322
A Fast 60 kV Resonant Charging Power Supply for the LHC Inflectors — *M.J. Barnes, G.D. Wait, E. Carlier, L. Ducimetière, U. Jansson, G.H. Schröder, E.B. Vossenberg* 1325
The Application of Saturating Inductors for Improving the Performance of the CERN PS Kicker Systems — *G.D. Wait, M.J. Barnes, K.D. Metzmacher, L. Sermeus* 1328

LEP2: PRESENT AND FUTURE PERFORMANCE AND LIMITATIONS

S. Myers (for the LEP2 team), CERN, Geneva, Switzerland

Abstract

The LEP collider was operated during 1996 for the first time at beam energies beyond the W pair threshold. In the first period, lasting about six weeks, operation was possible at 80.5GeV per beam by powering all of the 144 superconducting cavities (sc) as well as the original 120 room temperature cavities. After the summer shutdown, when an additional 32 sc cavities were installed, operation for physics was performed at 86GeV per beam for about four weeks. The integrated luminosity at high energy, delivered to the detectors, was 25pb^{-1} in the two fairly short running periods. The maximum integrated luminosity over a 24 hour period exceeded 1.1pb^{-1}. The present performance and limitations of the machine are reviewed as well as some of the crucial technical systems.

1 INTRODUCTION

The CERN Large Electron Positron (LEP) collider is a 26.6km circumference e^+e^- storage ring which has, until the end of 1995, operated with 4 and 8 bunches per beam in an energy range of 20 to 50GeV (see previous conference reports, [1],[2])

The energy upgrade (LEP2), foreseen to allow study of W pairs at energies around 90GeV per beam, involves a total of 272 new sc cavities with gradients of 6MV/m. In addition to the sc cavities the following technical modifications were necessary for the upgrade.

- Civil engineering for klystron galleries. Two new klystron galleries were excavated near points 4 and 8.
- 4 new 12 kW (at 4.5K) cryogenics plants were installed in the four regions which house sc cavities.
- The RF straight-sections were rearranged in all four interaction regions to allow the installation of the sc cavities which had different lengths to the existing copper cavities.
- The sc low β insertion quadrupoles were upgraded for the higher energy, as were nearly all of the power converters

2 PERFORMANCE AND HIGHLIGHTS OF 1996

Due to the long shutdown periods imposed by the installation of the sc cavities, the available time for physics in 1996 was limited to about 10 weeks. The initial physics operation was foreseen with an optics configuration with 108^0 phase advance per cell in the horizontal plane, designed to produce higher specific luminosity due to the inherent smaller horizontal emittance. It was soon discovered that the usable dynamic aperture was significantly lower than

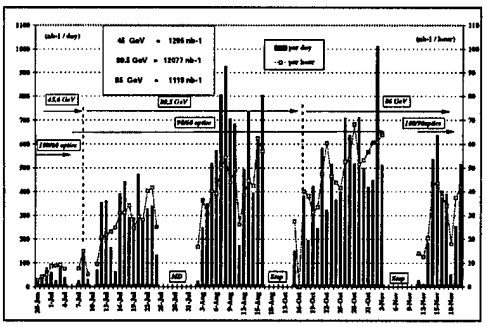


Figure 1: Measured Daily and Hourly Luminosity for 1996

computer simulations had predicted. For this reason, after nearly three weeks of attempted running the sextupoles were recabled and the older, well tried 90^0(H) and 60^0(V) optics was reinstalled in the machine and re-commissioned. Physics conditions were soon re-established and the collider was operated initially at 80.5GeV per beam and, after an additional installation of 32 sc cavities in the summer, at 86GeV. The performance for 1996 is shown in Fig.1.

Although the maximum operational beam energy for physics production was 86GeV, a record single beam energy of 88GeV was reached by operating the RF at the all-out limit. In this mode of operation, the average gradient of the 176 sc cavities was the design value of 6MV/m and a spurious trip of a single module would inevitably cause total beam loss. In "operational mode" the total voltage available is such that, in the event of simultaneous tripping of 2 klystron (feeding 16 cavities) there remains sufficient RF voltage for a longitudinal quantum lifetime of around 15 hours.

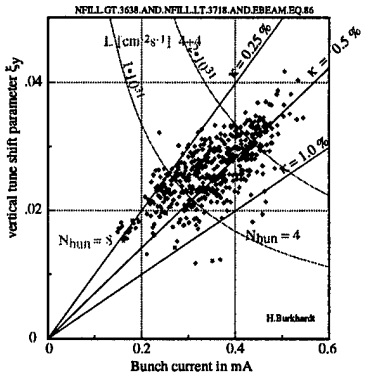


Figure 2: Measured ξ_y as a Function of Bunch Current

After initial conditioning and commissioning, the RF system behaved very reliably at its design gradient and with a total beam current of 4 mA. The current was limited by

0-7803-4376-X/98/$10.00 © 1998 IEEE

the "electro-acoustic" instability [3] in the cavities, and for normal operation the cavity conditions were optimized for this intensity value. Although the total current was limited, a record peak luminosity of 3.4×10^{31} $cm^{-2}s^{-1}$ was reached due to the very small emittance ratio of 0.25% achieved (refer to Fig.2). The maximum integrated daily luminosity reached $1.1pb^{-1}$ (see Fig.1) which bodes well for 1997. For 1997 a new feedback system (which was tested on a limited number of cavities in 1996) will be commissioned to combat the cavity instability [3]. During machine studies, single bunch currents of more than $600\mu A$ were successfully accumulated and ramped to high energy.

The 4×12kW cryogenic plants were operated without serious problems and with high reliability throughout the year [4].

On the beam dynamics front the vertical beam-beam tune shift (ξ_y), as measured from the average of the luminosities in the four detectors, reached values $\geq .04$ (see Fig.2) without any signs of saturation.

In LEP the precision measurement of the beam energy is of crucial importance for the precision of the physics. For LEP1 the beam energy was measured around the Z^0 equivalent energy by transverse resonant depolarization. For LEP2 it is likely that the polarization level at high energies will be too small to be measured. Hence the beam energy at W$\pm$ must be estimated by extrapolation from resonant depolarization at lower energies [5]. The extrapolation will be performed by the use of NMR monitors and the LEP "flux loop". The accuracy of the extrapolation depends on the energy range over which the calibrations can be performed. Precision measurements have been systematically performed at 43 and 45GeV for the Z^0 data. In addition, in 1996, a successful calibration was performed for the first time at 50GeV. An attempt was also made to extend the calibration to 55GeV where, although polarization levels of 2% were measures no accurate calibration could be performed.

3 PERFORMANCE LIMITATIONS

The two most important parameters for consideration of the performance of LEP2 are:

- the maximum beam energy, and
- the integrated luminosity

3.1 Maximum Energy

The over-riding limitation to the beam energy comes from the available RF voltage. The available RF is simply the product of the active length of the cavities and the average gradient per meter. The former limit is set by funding and the latter by technological constraints.

The energy spread of the RF bucket is approximately given by

$$\left(\frac{\Delta E}{E}\right)_{bk} \simeq Q_h\sqrt{\frac{eV_{RF}}{hE_b}f(\phi_s)} \qquad (1)$$

Hence, given the RF installation, an optics with stronger focussing provides relatively larger energy spreads and therefore allow a larger fraction of the RF voltage to be used to compensate synchrotron radiation, thereby permitting higher energies. In LEP2 the difference between the 90^0 and the 108^0 horizontal phase advance per cell is approximately 0.8GeV at 90GeV beam energy.

In the transverse plane there is an additional advantage to stronger focusing optics coming from the horizontal emittance.

$$\epsilon_x \propto \frac{\gamma^2}{Q_h^3 J_x} \qquad (2)$$

Clearly, for a dynamic or physical aperture which is independent of energy, then with the horizontal emittance growing with γ^2, at a high enough energy the aperture will be insufficient. This situation can be alleviated by operating with the "high tune optics". The alternative is to reduce the horizontal emittance by increasing the damping partition numbers (J_x) which unfortunately increases the energy spread of the bunches and thereby reduces slightly the maximum energy.

In general substantial gains in beam energy require either more RF cavities or higher gradients. The constraints on the LEP optics is treated in detail elsewhere in this conference [6].

3.1.1 Dynamic Aperture

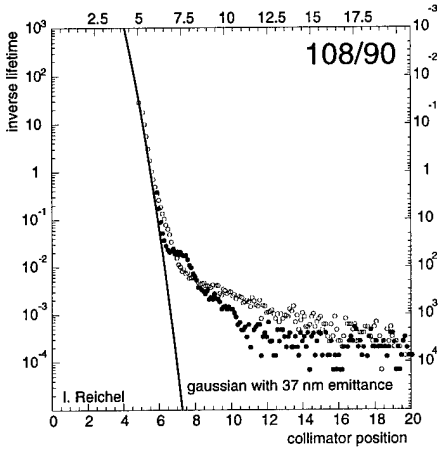


Figure 3: Measurement of Tail Distribution with $108^0/90^0$ Optics

As stated previously, the usable dynamic apertures with the $108^0/60^0$ and later in the year with the $108^0/90^0$ optics were measured to be less than predicted by simulations. The dynamic aperture is measured in LEP in two independent ways, firstly by the "emittance inflation" technique where the damping partition numbers are varied so as to increase the horizontal emittance by a large factor. When the emittance becomes large enough to reduce the lifetime this defines the dynamic or physical aperture. The inflated emittance is measured by a carefully calibrated synchrotron light monitor and verified by measuring the tails of the distribution using loss monitors [7]. Figure 3 shows the

results of tails scans on the $108^0/90^0$ optics. It is clear that non-Gaussian tails exist at large amplitudes. Similar measurements with the $90^0/60^0$ optics showed that the development of tails ocurred at larger amplitudes. In practice these non-Gaussian tails can produce serious problems with background in the detectors before there is a serious reduction in the lifetime.

The second technique, the "kicker technique", involves deflecting the beam horizontally by an ever increasing amount until a sizeable fraction of the beam is lost thereby indicating that the aperture limitation had been reached. In general, both methods gave similar results, however the results of the kick method can be easier to interpret and with suitable diagnostics has indicated the presence of non-linear resonances at large amplitudes. This behaviour will be studied during 1997 (see [8] for a fuller description of these measurements and analyses).

3.2 *Integrated Luminosity*

The yearly integrated luminosity may be conveniently approximated by

$$\int Ldt = \eta L_{peak} t_{year} \tag{3}$$

where η is the "overall efficiency factor" and L_{peak} is the all-out maximum luminosity recorded in physics during the year.

The luminosity (L) is directly related to the vertical beam-beam tune shift (ξ_y) i.e.

$$L = \frac{\gamma}{2r_e e} \frac{k_b i_b \xi_y}{\beta_y^*} \tag{4}$$

where γ is the relative energy, k_b the number of bunches per beam, and i_b the bunch current.

3.2.1 The Overall Efficiency (η)

The overall efficiency parameter (η) is derived by using historical data and equation (3). Consequently this parameter includes factors such as:

- The loss in integrated luminosity since all runs do not necessarily reach the record luminosity (L_{peak}).
- The fall in luminosity during the course of the run due to the **intensity lifetime**
- The technical efficiency (down-time) of all components including the chain of injectors, defined as the ratio of actual time spent in physics data taking to the time scheduled.

The Intensity Lifetime In LEP, the intensity lifetime (τ) is predominated by the particle losses resulting from the collisions of the electrons and positrons in the 4 collision points.

$$\frac{1}{\tau} = \frac{dI_b}{I_b dt} = \frac{\sigma_b L n_{collisions}}{I_b} \propto \frac{\sigma_b \xi_y \gamma n_{collisions}}{\beta_y^*} \tag{5}$$

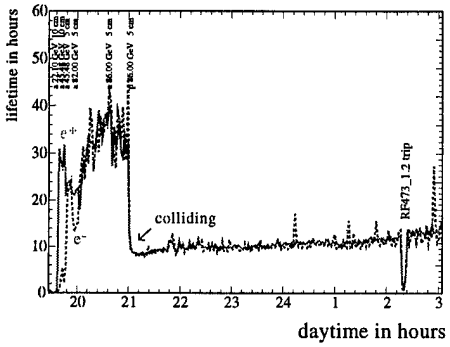


Figure 4: Lifetime Measurements during an 86 GeV Fill

where I_b is the total beam current, and σ_b is the cross-section. With the typical LEP parameters ($n_{collisions}$= 4, σ_b = .23barns (measured), β_y^* = 5cm) the intensity lifetime is approximately

$$\tau(hours) \approx \frac{1}{\xi_y} \frac{45}{E_{GeV}} \tag{6}$$

Figure 4 shows measurements [9] of the intensity lifetime during a typical physics run, involving accumulation at 22GeV, acceleration to 86GeV and colliding. The lifetime clearly drops by nearly a factor of 4 at the moment of going into collision and gradually increases during the duration of the physics run due to the reduction in ξ_y.

From equations (5) and (6) the intensity lifetime will decrease proportionately with energy. Consequently the durations of the runs at W± energies are shortened so as to optimize the integrated luminosity.

3.2.2 Beam-beam Contribution

From equation (4), it is clear that, when ξ_y remains constant during the physics run (i.e. at the beam-beam limit) then the luminosity lifetime is equal to the intensity lifetime. Alternatively when the ξ_y is linearly dependent on the bunch current (not beam-beam limited) then the luminosity lifetime is equal to the lifetime of i_b^2. Thus in order to maximize the integrated luminosity it is essential to remain beam-beam limited to the **end** of the physics run when the intensity has significantly dropped. In LEP1, this was accomplished [9] without difficulty due to the smaller beam sizes associated with the lower energies (see equation 2). The vertical beam-beam tune shift may be written

$$\xi_y = \xi_x \sqrt{\frac{\beta_y^*}{\beta_x^* k}} \propto \frac{i_b Q_h^3 J_x}{\gamma^3} \sqrt{\frac{\beta_y^*}{\beta_x^* k}} \tag{7}$$

where k is the emittance ratio ϵ_y/ϵ_x. For LEP2 where the energy is more than doubled, it will be necessary to gain about a factor of 8 in the combination of the free parameters in equation (7) if a similar beam-beam situation similar to Z^0 is to be achieved.

3.2.3 Beam Intensity

In LEP2, there are effects which limit the total beam current and others which limit the current per bunch and the

number of bunches. For LEP2 the limitations to the **total** beam current are given below starting with the highest limits and progressing to the lowest, most urgent limitations.

1. The power which can be transmitted through the main couplers. The couplers have been tested to 300kW per cavity which would correspond to 2.4MW equivalent from the klystrons, to be compared with their maximum power of 1.3 MW. This is no longer a limitation to beam intensity.
2. The total available klystron power which is available to compensate for the synchrotron power. (e.g. 30 klystrons giving 30MW would allow a total beam current of 16mA at 90GeV).
3. The electro-acoustic instability.
4. The current (and Energy) dependent cryogenic losses (see below)

Beam Current Provoked Cryogenic Power Losses Towards the end of 1996 measurements of the cryogenic losses with varying beam conditions indicated unexpected losses which were apparently dependent on the total bunch intensity and the beam energy [10].

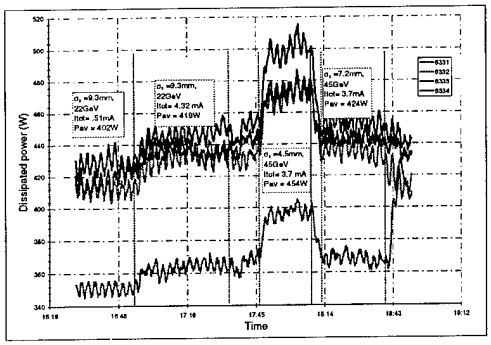


Figure 5: Measured Changes in Cryogenic Loads with Changing Beam Conditions

Fig. (5) shows the relative power changes during beam accumulation at 22GeV, followed by ramping to 45GeV where the bunch length was changed by excitation of wiggler magnets. The variation of the cryogenic power was also measured during the course of a physics run at 86GeV and is plotted as a function of beam current squared in Fig.(6). Superimposed on this plot are the measured points from Fig (5). There is a clear increase in the slope of about a factor of 4 between 22 and 86GeV. Similar results were obtained from measurements of the temperature rise of warm bellows between the sc modules. These results are however not irrefutable since the measurements were taken on different modules at different locations. However if the measurements made on the modules at 86GeV in Fig. (6) can be applied to all modules installed in a given region in LEP, then the total beam intensity may be limited to around 8mA with the presently installed and finely tuned cryogenics plant. A complete measurement campaign of this effect is planned as soon as LEP becomes operational in 1997.

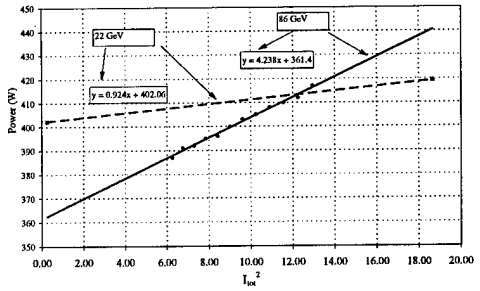


Figure 6: Crgryogenic Power Measurements as Function of I_b^2 for 22 and 86GeV.

Transverse Mode Coupling Instability This instability limits the current per bunch which can be accumulated at injection energy.

The approximate threshold for the instability is given by

$$i_{th} = \frac{2\pi Q_s E f_{rev}}{e \sum \beta_i k_{\perp i}(\sigma_s)} \tag{8}$$

where Q_s is the synchrotron tune, E the beam energy, and β_i the betatron amplitude function at the location of the transverse loss factor $k_{\perp i}$ which decreases with increasing bunch length (σ_s). In order to maximize the current per bunch for LEP2 operation, several schemes have been tested and reported in previous conferences [1],[11]

Number of Bunches LEP has been operated in 1995 and throughout 1996 with the new bunch train scheme allowing a maximum of 4 trains of 4 bunches per train in each beam. A detailed report on this scheme is to be presented elsewhere in this conference ([12]). It is foreseen to operate LEP during 1997 with 4 trains of 2 bunches per beam.

4 PERFORMANCE ESTIMATES (1997–1999)

Table 1: Performance Estimates

Parameter	45 GeV	92 GeV	96 GeV	96 GeV
	1994	1997	1998	1999
No. of sc cavities		240	272	272
'Operational' RF Voltage(MV)		2475	2722	2722
Overall Efficiency	0.220	0.165	0.165	0.165
i_b (bunch mA)	0.32	0.5	0.65	0.75
Beam-beam tune shift	0.038	0.0417	0.045	0.05
L peak (l0e31)	2	6.86	10	13.3
Days of Physics	148	108	120	120
Yearly Luminosity (pb-1)	65.0	122.2	198.0	263.3
Luminosity per day (pb-1)	0.439	1.132	1.650	2.195

The performance estimates for operation over the next three years (see Tab.1) are based on equation (3) with extrapolation from the year 1994 (the last full year of uninterrupted operation) and the following assumptions.

- the overall efficiency parameter η will be only 75% of the value attained (22%) at lower energy in 1994. This reduction is to take account of the possible increase in down time due to the large number of sc cavities and the reduction in integrated luminosity coming from

the increased difficulty in maintaining the beam-beam limit right to the end of the run as was done systematically at 45GeV .

- The peak luminosity is estimated from 8 bunches per beam with a bunch current of .5mA. Both these parameters have bee attained in the past however it remains to be seen if the inherent total beam current of 8mA will exceed the limit imposed by the cryogenics system.
- The total numbers of days operation is already scheduled definitively for 1997 and tentatively for 1998.

From this table it can be seen that the peak luminosity is estimated to reach beyond 10^{32} cm^{-2} s^{-1} and the total integrated luminosity over the three year period to exceed 500pb^{-1}.

5 MAXIMUM ENERGY WITH PRESENT RF INSTALLATION

Studies have begun recently to examine the possibility of extending the present beam energy range of LEP2 to around 100GeV with the presently installed RF system. This increase in beam energy would necessitate an average gradient in the 272 sc cavities of 7MV/m. The problems already encountered and the solutions being pursued are given below.

- **Cryogenics Power.** From the 12kW cryogenics power installed at each interaction point there remains about 6.8 kW for the RF dynamic load. At the higher gradients of 7MV/m and with the resulting reduction in Q value, the calculated required power is at least 10kW. Consequently the cryoplants must be upgraded before any significant increase in gradient is possible. The proposed solution is to plan an early installation of the required LHC cryogenics system which could be used by LEP2 from Spring 1999.
- **Electron emission in the cavities.** The present gradient of 6MV/m is for the most part limited by electron emission in the cavities with resulting high radiation. The proposal is to increase the threshold by Helium processing. This technique has been successfully tested on a number of occasions to reduce the electron emission at values below 6MV/m in "sick" cavities. However the procedure is inherently dangerous for the main couplers due to the significant reduction in vacuum pressure needed for the processing. Experimental tests are under way to try to develop a safe He processing technique.
- **Spread in cavity gradients.** When an RF module (8 cavities fed by one klystron) is operating at an average gradient per cavity of 6MV/m, the spread in the gradients is typically more than $\pm$1MV/m. Consequently some of the cavities in a module are already being operated at 7MV/m. It is clear that an average of 7MV/m will be more easily obtained if the spread of gradients in the modules is significantly reduced. This technical problem has been studied and one possible solution is to install waveguide transformers to allow individual control of the cavity gradients.

6 CONCLUSIONS

LEP2 has been sucessfully operated for a reduced running period during 1996. Physics data taking was performed at 80.5GeV/beam in the early part of the year and 86GeV later in the year. A total integrated luminosity of 25pb^{-1} was delivered to each of the four experiments and many technical problems were resolved with the newly installed very large RF system. The down-time of this system decreased dramatically during the course of the year as the steep learning curve was climbed.

Operation is planned for around 120 days in 1997 at 92GeV/beam allowed by the 240 sc cavities installed over the past few years. There is every hope for an integrated luminosity of nearly 100pb^{-1} in the search for new physics and for the precision study of the properties of the W$\pm$ particles.

The possibility of further extension of the LEP2 energy range is under active investigation.

7 REFERENCES

[1] S. Myers; "LEP Status and Plans", Proc. of the US particle Accelerator Conference and the 16th Int. Conf. on High Energy Accelerators, Dallas USA. (1995).

[2] A. Hofmann; "Performance Limitations in LEP", Proc. of the Fourth European Particle Accelerator Conference, held in London from 27 June until 1 July, 1994. (pp 73– 77), (1994)

[3] D. Boussard; "Performance of the LEP2 SRF System", invited contribution to this conference.

[4] P. Lebrun; "Cryogenics for Particle Accelerators; Present State of the Art and Future Trends", invited contribution to this conference.

[5] M. Böge et al., "Transverse Polarization beyond the Z Energy in LEP", contribution to this conference.

[6] D. Brandt et al., "Low Emittance lattices for LEP", contribution to this conference.

[7] I. Reichel et al.; "Observation and Simulation of Beam Tails in LEP", contribution to this conference

[8] J.M. Jowett; "Non-Linear resonances: Predictions, Effects and Measurements", Proc. 7th LEP Performance Workshop, January 1997, CERN-SL/97-06 (DI).

[9] H. Burkhardt, "Energy dependence of Beam-Beam Interactions at LEP", contribution to this conference.

[10] G. Cavallari et al. "Beam Related Thermal Losses in the LEP SC RF System", CERN LEP2 note 97-40 (21/4/97)

[11] S. Myers; "Synchro-Betatron Resonance Excitation in LEP", Proc. of the IEEE Particle Accelerator Conference held in Washington D.C., March 16–19, 1987, p. 1325.

[12] W. Herr, "Experience with Bunch Trains in LEP", contribution to this conference.

FIRST COMMISSIONING OF SPring-8

H. Kamitsubo
JAERI-RIKEN SPring-8 Project Team, Kamigori, Ako-gun, Hyogo 678-12,Japan

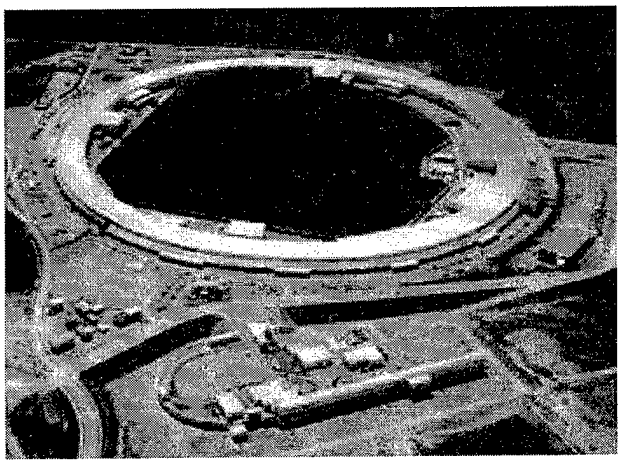
Abstract

SPring-8 is the third generation synchrotron radiation source in soft and hard X-ray region and consists of an injector linac of 1GeV, a booster synchrotron of 8GeV and a storage ring with a natural emittance of 5.5nmrad. The storage ring can accommodate 61 beamlines in total and 26 of them are under construction. Construction started in 1991 and inauguration is scheduled in October, 1997. We started commissioning of the injector linac on August 1, 1996, and succeeded to get 1GeV electron beam a week later. The synchrotron was commissioned in December and 8GeV electron beam was successfully extracted on January 27, 1997. By the end of February 1997, installation and precise alignment of the storage ring was completed and four insertion devices (in-vacuum undulators) were installed in the storage ring. On March 14 we started commissioning of the storage ring and immediately after we observed the first turn in the ring. After fine adjustment of the parameters we succeeded to store a 0.05mA beam in the storage ring on March 25. Next day the first synchrotron radiations from a bending magnet was clearly observed at the front end of the beamline. On April 17 we succeeded to increase the stored current to 20mA, which is a target value of the stored current in the first phase of commissioning. The first radiations from an undulator was observed on April 23.

1 INTRODUCTION

The SPring-8 (**S**uper **P**hoton **ring-8**GeV, sometimes abbreviated as SP8) facility[1] is one of the world's most brilliant synchrotron radiation sources in an energy range from 0.3 keV to several hundreds keV. It is composed of a 1 GeV electron/positron linac, an 8 GeV booster synchrotron and a low-emittance storage ring with a circumference of 1,436m. The storage ring has a Chasman-Green lattice structure and consists of 44 normal cells and 4 straight cells. In future each straight cell will be converted into a long straight section to accommodate a long insertion device. The storage ring can accommodate 38 beamlines from insertion devices (ID), including 4 long IDs. In addition to these ID beamlines, 23 beamlines from the bending magnet (BM) can be installed in the storage ring.

The estimated natural emittance of the storage ring is 5.5×10^{-9} mrad, allowing SPring-8 to realize a brilliance of 4×10^{19} (photons/s/mm^2/mrad^2/0.1%b.w.) with a 4.5m undulator and a stored current of 100 mA. SPring-8's 8GeV energy will allow us to obtain high-brilliance X-rays in the energy range from 5keV (fundamental) to 75keV (fifth harmonics) from a newly developed in-vacuum undulator with a period length of 32 mm simply by changing its gap.



Figuire 1: Aerial view of the SPring-8 facility. The storage ring is built surrounding a small mountain. The injectors are below the storage ring in the figure.

The storage ring is installed in the machine tunnel together with the front end parts of the beamlines. Optical system for synchrotron radiations (SR) and experimental devices are installed in hutches built in the experimental hall. The maximum length of beamlines in the experimental hall is 80 m from the exit of ID or BM. However we can extend 9 beamlines to 300m and 3 to 1,000m. The RI experimental hall is built neighboring the experimental hall to accommodate 3 beamlines for radioactive samples.

The facility is being constructed jointly by Japan Atomic Energy Research Institute (JAERI) and the Institute of Physical and Chemical Research (RIKEN) at the Harima Science Garden City in Hyogo Prefecture, which is 100 km west of Osaka. Construction was started in 1991 and is going one year ahead of the initial schedule. By now the linac, the synchrotron, and the storage ring was successfully commissioned.

Due to the geographical features of the SPring-8 campus, the storage ring is built surrounding a small mountain. The injector linac and the booster synchrotron are built separately from the storage ring. Figure 1 shows an aerial view of the SPring-8 facility. The injector linac will be used to inject electron beam to another accelerator, that is, a 1.5GeV SR source being constructed by Hyogo Prefecture for Himeji Institute of Technology.

0-7803-4376-X/98/$10.00 © 1998 IEEE

The facility has a legal status of a national user facility and will be open to researchers not only from Japan but also from abroad. The Japan Synchrotron Radiation Research Institute (JASRI) will have responsibility for SPring-8's operation, maintenance, and improvement, after the inauguration in October, 1997.

2 SPRING-8 ACCELERATORS

Table 1 lists the main performance specifications of SPring-8 accelerators. All the figures are design values.

2.1 The Injector Linac

The linac consists of a 250MeV high current linac and an electron/positron converter, and a 900MeV main linac with frequency of 2856 MHz [2]. Electron beam can be accelerated up to 1.15GeV by removing a tungsten target of the electron/positron converter. The linac has 26 accelerator columns which are of $2\pi/3$ traveling-wave and constant-gradient type. Average accelerating field is designed to be higher than 16 MV/m. One high-power klystron of 80MW (Toshiba E3712) supplies microwaves to two accelerator columns.

Modulators for the klystrons provide a maximum output power of 190MW with a pulse width of 4μsec and at the repetition rate of 60Hz.

The beam commissioning was started on August 1. We accelerated the electron beam up till the 7th accelerator column and analyzed the energy by bending magnets on August 7. Next day, August 8, we succeeded to accelerate the beam to the final energy of 1GeV. The final energy of the beam was measured when the beam was sent to the synchrotron in December.

2.2 The Booster Synchrotron

The synchrotron[3] has 64 bending magnets, 80 quadrupole and 60 sextupole magnets and 80 steerers. Integrated field strength was measured for all bending magnets and rms distribution is 8×10^{-4}. All the magnets were aligned within an accuracy of 0.2 mm. Power supplies for these magnets are operated in a ramping pattern of 1Hz and required to have high tracking accuracy and high reliability. The tracking accuracy of the bending magnet and the quadrupole magnet power supplies is less than 1×10^{-4}. Typical time structure of the output current of the magnet power supply is as follows; 0.15sec flat-bottom (for beam injection), 0.40sec ramping, 0.15sec flat-top (for beam extraction), and 0.30sec falling. Delay time of the output current was measured to be 0.33msec.

The RF system of the synchrotron consists of eight five-cells cavities, waveguides, two 508.58MHz klystron (Toshiba E3786) and their power supplies. The required maximum RF power is 1.69MW at 8GeV. The effective RF voltage changes from 8MV to 18.7MV during the electron acceleration from 1GeV to 8GeV. The five-cells cavity is made of OFHC copper and has an effective shunt impedance of 21MΩ.

Table 1: Major Parameters of the SPring-8 Accelerators

Injector Linac		
Energy	Electron	1.15 GeV
	Positron	0.9 GeV
Repetition Rate		60 Hz
RF		2856 MHz
Total Length		140 m
Electron Gun	Cathode	Y796
	Voltage	200 kV
Accelerator Columns	Number	26
Klystrons	Number	13
	Max. power	80 MW
Booster Synchrotron		
Injection Energy		1 GeV
Maximum Energy		8 GeV
Circumference		396.12 m
Repetition Rate		1 Hz
Number of Cells	FODO lattice	40
Super Period		2
RF		508.58MHz
No.of Klystrons	1MW output	2
No. of Cavities	5-cell type	8
Harmonic Number		672
Storage Ring		
Energy		8 GeV
Lattice Type	Chasman-Green	
No. of Cells	Normal Cell	44
	Straight Cell	4
Super Period		4
Circumference		1435.95 m
Stored Beam Current	Single Bunch	5 mA
	Multi-bunch	100 mA
Harmonic Number		2436
RF		508.58MHz
No.of Cavities		8 × 4
Revolution Period		4.79 μ sec
Natural Emittance		5.9×10^{-9} mrad
Coupling Constant		10%
Source Point Data		
No. of Straight	High β Sections	19
Sections	Low β Sections	15
	Long Sections	4
No.of BM Sources		23
Electron Beam Size	High β Sections	0.35 × 0.078
($\sigma_x \times \sigma y$, mm)	Low β Sections	0.069× 0.052
Beam Divergence	High β Sections	0.015× 0.007
($\sigma'_x \times \sigma' y$, mrad)	Low β Sections	0.073× 0.01

The beam position monitors (BPM) are located at up-stream positions of 80 quadrupole magnets. Four signal processing systems are used for 80 BPMs and it takes less than 30 msec to obtain all position data.

Installation of the synchrotron was completed in October and commissioning was started on December 10,

1996. We succeeded to accelerate the beam up to 8GeV on December 16. After the winter vacation the operation was restarted and the 8GeV beam was extraceted to the beam dump on January 27, 1997.

2.3 The Storage Ring

The storage ring is a four-fold symmetric ring with a circumference of 1,436 m. The magnet lattice is composed of two types of unit cells, that is, the normal cell and the straight cell. The former consists of 2 bending magnets, 10 quadrupole magnets, and 7 sextupole magnets and has a magnet-free space of 4.5m long with no dispersion. On the other hand, the latter has no bending magnet but has the same focusing magnet arrangement as that of the normal cell, thereby ensuring that both have approximately the same beam-dynamical property. In the first phase of operation, the storage ring will have a lattice structure of 4 × (11 normal cells + 1 straight cell) and be approximately 48-fold symmetric. In the second phase we will operate the storage ring under the condition that all the quadrupole and sextupole magnets in the straight cell are switched off. Then we will change the magnet arrangement of the straight cell to create a long straight section.

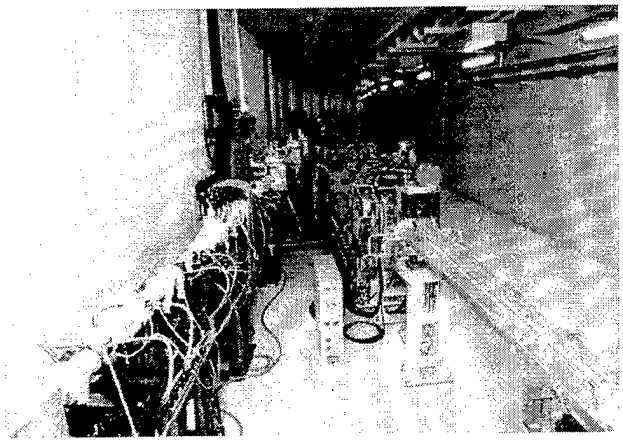


Figure 2: Picture of the storage ring. On the left side is a front end part of the ID beamline and on the right side is a dummy chamber for future ID.

2.3.1 Magnets

The storage ring has 88 bending magnets, 480 quadrupole magnets, and 336 sextupole magnets. In addition, four bump magnets and one pulsed and three DC septum magnets and 569 steering magnets with very low remnant field are installed in the storage ring. Performance of the low emittance ring depends strongly on the quality of these magnets and their precise alignment. Measured rms distributions of integrated field strength and gradient for all bending, quadrupole, and sextupole magnets are less than 5×10^{-4}. The bump magnets and the septum magnets are used for injection.

There are three groups of focusing magnets in one cell and each group is installed on one common girder. Magnetic centers of quadrupole and sextupole magnets on the common girder are aligned within an accuracy of 0.025 mm. On the other hand bending magnets and common girders are aligned within 0.1 mm along the whole ring. Final alignment was done in January 1997 and standard deviation of the alignment errors was 0.04 mm. This accuracy was confirmed at the commissioning of the storage ring. We observed the first turn of the electron beam without any correction by steering magnets.

Effective emittance of the beam increases if magnetic centers of quadrupole magnets vibrate. To reduce seismic vibrations as low as possible, the storage ring building is built on the firm bedrock. In addition, cooling system was carefully designed to reduce induced vibration on the storage ring. We observed the maximum vibration amplitude in horizontal and vertical planes was an order of 0.01μm when the cooling water system is in operation.

Control system of magnets power supplies consists of UNIX workstations, an optical fibre network and VME modules. Softwares of the control system has been developed by the magnet group in collaboration with the control group.

2.3.2 RF System

Although there are four straight sections reserved for RF stations in the storage ring, three RF stations were already installed. Each station is composed of eight single cell cavities of bell-shape type, one 1MW cw klystron, its high voltage power supply, and wave guide system. Shunt impedance of a cavity is 5.5MΩ. Frequency of higher order mode (HOM) for each cavity can be controlled by using two movable tuners and a plunger, keeping the fundamental frequency of 508.58MHz constant. Then dangerous HOM frequencies to cause coupled-bunch instability can be well separated from cavity to cavity, so that the threshold current for coupled-bunch instability becomes higher than 200mA. After high power test at the test stand all the cavities were installed in the storage ring.

As the injectors are built about 500m apart from the storage ring, timing system for them was made carefully. For example, temperature dependence of transit time of the reference signal and time jitter should be made as low as possible. We could realize precise timing by using optical fibre with low temperature dependence and newly developed E/O (electrical to optical) and O/E modules and achieved time jitter less than 10 psec.

2.3.3 Vacuum System

Main parts of the vacuum system of one unit cell consists of two bending magnet chamber (BMC), three straight section chamber (SSC) for the focusing magnets on one girder, two crotch chamber, one dummy chamber for an

insertion device to be built in future, and other components. The pumping system is based on non-evaporable getter (NEG) strips which are used in SSC and BMC, lumped NEG pumps for SR-induced gas load at crotches and absorbers, and sputter ion pumps. A distributed ion pump (DIP) is also used in the BMC.

The BMC and SSC are extrusions, made of aluminum alloy, A6063-T5. The BMC has a beam chamber with a slot-isolated antechambers for NEG strips and a rectangular pump chamber for DIP. On the other hand, SSC has a beam chamber and an antechamber for NEG strips. The injection section chamber consists of two parts, a stainless steel chamber and an aluminum alloy chamber. The former is equipped with a beryllium window for the injection of the electron beam from the synchrotron.

Each of 48 unit cells has six beam position monitors (BPM), giving a total of 288 BPMs. Because the BPM electrodes are welded directly to the SSC, SSCs should be supported on the common girder to make displacement and deformation of the chamber less than 50μm and 30μm, respectively, at BPM positions. Their sensitivity and difference between mechanical center and electrical center were calibrated for all BPMs. After final alignment of magnets, BPM centers were calibrated to fiducial points of neighboring sextupoles.

Baking and evacuation finished in September 1996 and vacuum pressure reaches below 10nPa.

2.3.4 Beam Diagnostics

Besides BPMs beam current monitors and a tune monitor are installed in a straight section together with absorbers to avoid unnecessary irradiation of SR. Two types of current monitors are developed; one is a DCCT of parametric current transformer type and used to measure the DC component of the stored current with a resolution of 5μA. The other is a pulse transformer with a signal processor to measure the charge of one bunch.

The tune monitor consists of a beam shaker, signal source for it, an amplifier, pick-up electrodes, signal processing circuits, and a spectrum analyzer. All these monitors were verified to work very well on the storage ring commissioning.

3 SPRING-8 BEAMLINES

3.1 Beamlines

SPring-8 can accommodate 61 beamlines(BL). They are divided into four groups according by the source types and source points. They may also classified by users. Table 2 lists the beamlines at SPring-8.

Now 26 beamlines are being constructed. They are 10 public BLs, 6 JAERI/RIKEN BLs, 3 for R&D, 2 for machine study, and five contract BLs. The public BLs are constructed by SPring-8 and will be open to general users. On the other hand, contract BLs are constructed by the specific organizations at their own expenses. In this case about 70% of beam time can be used by them. JAERI / RIKEN BLs are constructed by JAERI / RIKEN for their own use.

Table 2. SPring-8 Beamlines

Total Number of Beamlines	61
Classification by Source Type	
Standard Insertion Device Beamlines(BL)	38
BL from normal Straight Section (highβ)	(19)
BL from normal Straight Section (lowβ)	(15)
BL from long Straight Section (30m long)	4
Bending Magnet Beamlines	23
Classification by Users	
Public Beamlines	30
Contract Beamlines	10~20
JAERI / RIKEN Beamlines	6~10
R&D and Machine Study Beamlines	5

Seven of the public beamlines are ID BLs, four from in-vacuum undulators(U), one from twin-helical U, one from figure-8 U, and one from elliptical multipole wiggler (EMPW). The remaining three are beamlines from BM. On the other hand, JAERI and RIKEN are building three beamlines each, two of them are BLs from IDs. One of IDs being developed by JAERI is a variably-polarizing undulator which can produce circularly-polarized or linearly-polarized X-rays by changing relative phase of horizontal and vertical fields. One ID beamline and another BM beamline will be used for machine study.

3.2 Insertion Devices

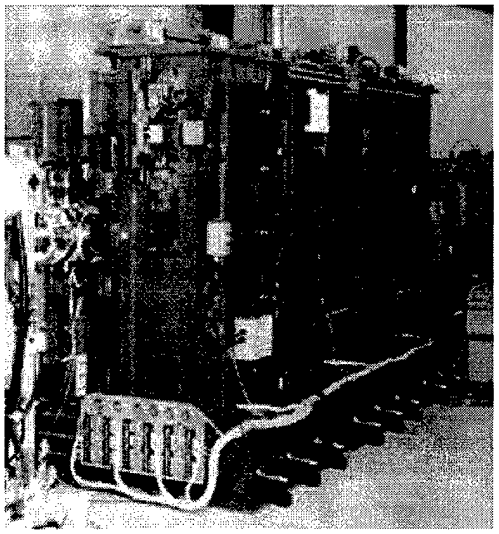


Figure 3: An in-vacuum undulator installed in the storage ring

Insertion device is a key technology for the third generation SR sources, especially for SPring-8. Most of excellent features of synchrotron radiations such as high brilliance, tunability over a wide range of wave length,

circular or linear polarization, coherency, microbeam, and time structure of the beam are realized by insertion devices, especially by an undulator. New types of insertion devices have been developed at SPring-8 as listed in Table 3 [4]. Development of in-vacuum undulators allow us to standardize the undulator for SPring-8. For example, an in-vacuum undulator (Figure 3) with a period length λ_u =32mm, one of the standard undulator, can provide X-rays in an energy range from 5.2 to 18.5keV (1st), 15.5 to 51keV (3rd) and 26 to 75 keV (5th) with the brilliance higher than 10^{19} (photons/sec/mm^2 /mrad^2 in 0.1% b.w.). Photon flux in a cone of 50 x 50μrad^2 is 10^{15} (photons/sec in 0.1% b.w.).

An in-vacuum vertical undulator has a horizontal field and provides X-rays linearly-polarized in vertical plane. A figure-8 undulator is composed of horizontal and vertical undulators with a period length of λ_u and $2\lambda_u$, respectively.

Table 3 Insertion devices under construction

Device	λ_u (mm)	N_0.	E(1st,keV)	No.
In-Vac. U	32	140	5.1~18	5
In-Vac Hybrid U	24	188	8.3~24	1
In-Vac. vertical U	37	37x2	4.5~16	1
Twin-Helical U	120	12x2	0.3~ 3	1
Figure-8 U	100	44	0.5~5	1
Variable-Pol. U	120	16	0.5~1.5 0.3~1.5	1
EMPW	120	37	Ec = 42.6	1

Energy range for the variably-polarizing undulator in Table 3 has two values, they are in the cases of circular polarization and linear polarization, respectively.

4 FIRST RESULTS OF COMMISSIONING

Commissioning of the storage ring was started on March 14, 1997. Test operation of the whole accelerator system had been carried on for a week before the commissioning. The strategy of the first phase commissioning is following; we will operate the storage ring and two beamlines, one from an in-vacuum undulator and the other from a bending magnet. A target current of the stored beam is 20mA. After we will succeed to store a current of 20 mA, we will extract SR to the beamlines. On March 14 we injected the beam from the synchrotron to the storage ring. Soon after we could observe the first turn of the beam in the ring. Then we spent five days for fine adjustment of the beam transport line from the synchrotron and the injection section of the ring. On March 21, we started again on-axis injection and after beam energy correction and tune survey, the sextupole magnets were excited. We observed 24 turns of the beam. On March 25, we started operation of RF system. After fine adjustment of phase and frequency we succeeded to store the beam of 0.05mA. The life time of the beam was 7 hours. Next day, March 26, we succeeded to observe the first synchrotron radiations at the front end of the bending magnet beamline (Figure 4). Then we made efforts to correct the COD and to increase the stored current. The target current of 20mA was cleared on April 17. The life time at 20mA was 3 hours but increased to 14 hours at 3.6mA .

Test operation of the in-vacuum undulator was started

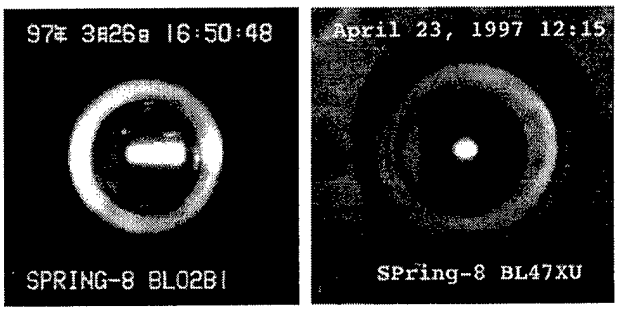


Figure 4: Pictures of the SR spots on the screen monitors in the BM (left) and ID (right) beamlines.

on April 23 and succeeded to observe the first radiations at the front end of the undulator beamline. The spot size of the photon beam on a screen monitor was around 1mm and the position of the spot did not move when the gap was changed from 50 mm to 20mm (Figure4).

4 CONCLUSION

So far the commissioning of SPring-8 has been carried out very smoothly and we found that the performance of the accelerators and the insertion devices is excellent. We will continue to extract photon beams from the bending magnet and the in-vacuum undulator to the mirrors and monochromaters in the optical hutches.

Inauguration of the SPring-8 facility is scheduled in October. The public beamlines will be open for domestic users from October.

REFERENCES

[1] SPring-8 Project Team: 'SPring-8 Project Part 1, Facility Design 1991 [Reviced]' , August 1991. H.Kamitsubo: 'SPring-8 Project' Rev. Sci. Instrum. **63**, 1586 (1992).

[2] H.Yokomizo et al: 'Linac and Synchrotron for SPring-8 Injector' Proc. EPAC'96, 688 (1996).

[3] H.Yonehara et al: 'Synchrotron of SPring-8' Proc. PAC'93, 2093 (1993).

[4] Beamline Handbook; to be published in June 1997 JASRI.

LASER ACCELERATORS: EXPERIMENTS, COMPUTATIONS AND PROSPECTS

C. JOSHI
Electrical Engineering Department
University of California, Los Angeles, CA 90095-1594

Abstract

Ever since the research on laser-based particle acceleration concepts began in earnest about a dozen years ago, there has been very significant progress in the field of Advanced Accelerator Research. Proof-of-principle experiments that demonstrate the physical principle of the various schemes have now been carried out. These experiments are guided by state-of-the-art computer simulations made possible by the recent revolution in computing power and techniques. The research is poised to move on to the next level where it will address both physics and technology issues that are at the very forefront of beam science.

1 INTRODUCTION

I will start off by giving a general motivation for advanced accelerator research. In most of the advanced accelerator schemes the accelerating structures are far smaller than the present structures driven by r.f. in the s or x band range. The wavelength of the structure is typically in the 1 mm to 10 μm range which means that these structures are powered by either optical frequency sources or short bunches of electrons. The beams produced by such structures are similarly expected to be ultrashort: in the subpicosecond to a few femtosecond range. The production, manipulation (preservation) and diagnostics of such ultrashort bunches represent the forefront of research in beam physics. Once such bunches become available, their interaction with matter or radiation will open new opportunities in the physical sciences. On the technology front the holy grail of advanced accelerator R & D is to produce a practical, table-top, 1 GeV electron accelerator that can deliver a peak current in the 10-100 Amp range. Finally, one hopes that in the long run, advanced accelerator R & D will yield a new technology for a future high energy collider.

The key physics milestones for any advanced accelerator scheme are as follows:

1. Demonstration of the physical principle for acceleration.
2. Demonstration of energy gain for externally injected electrons.
3. Demonstration of high gradients (say > 1 GeV/m).
4. Acceleration at this high gradient over a significant length (say 1 meter) or alternately an energy gain of 1 GeV.
5. Demonstration of a reasonably small energy spread and emittance.
6. Demonstration of staging.

It is gratifying to note that all the three laser acceleration schemes that I shall be discussing have demonstrated 1) and 2) above and laser-plasma schemes have in addition demonstrated 3). The second generation laser accelerator research then is moving on to topics 4), 5) and 6). It should be noted that technology and economy issues are at present not being addressed with the same degree of seriousness as the physics milestones.

I shall concentrate now on 3 laser-based particle acceleration schemes. The first is the laser driven plasma wave accelerators.[1] The second is known as the inverse free-electron laser accelerator (IFEL)[2] while the third is the inverse Cherenkov accelerator (ICA).[3] In all accelerators the accelerating particles obey the equation of motion[4]

$$\frac{d\gamma}{dz} = \frac{e\,(v \bullet E)}{mc^3}$$

which means that there are basically two ways a particle moving in the z direction can gain energy. First, if the electric field has a component E_z in the direction of motion of the particle and second if the particle is given a small but finite velocity component in the transverse direction so that it can interact with a transverse component $E_\perp$ of the electric field. Most acceleration schemes including the various laser-plasma schemes and the inverse Cherenkov scheme rely on the first method (i.e., $v_z E_z$) whereas the IFEL relies on the second (i.e., $v_\perp E_\perp$).

2 PHYSICAL PRINCIPLES

In the laser-plasma acceleration schemes the transverse electric field of a laser is transformed into a longitudinal electric field of a space charge wave using a plasma.[1] Physically this is accomplished as follows. In the so-called Laser Wake Field Accelerator (LWFA)[5] a short laser pulse roughly $\pi c/\omega_p$ long excites a wake in a plasma. This happens because the gradient of the intensity associated with the shape of the pulse exerts a force called the ponderomotive force on the plasma electrons which are pushed away from the regions of high intensity to the regions of lower intensity. After the pulse passes the electrons snap back because of the space charge force of the ions and set up an oscillation.

0-7803-4376-X/98/$10.00 © 1998 IEEE

In the Plasma Beat Wave Accelerator (PBWA),[6] two co-propagating laser pulses (ω_o,k_o) and (ω_1,k_1) of much lower intensity than required for LWFA are injected into a plasma which satisfy the resonance condition $\omega_o - \omega_1 = \omega_p$. This once again excites a plasma wave via the ponderomotive force.

In the self-modulated laser wake field accelerator[7] (SMLWFA), an intense but much longer single frequency laser pulse is used to excite the plasma wave. The excitation mechanism is the Raman Forward Scattering Instability (RFS)[8] which generates a whole band of Stokes and anti-Stokes e.m. waves by scattering from noise fluctuations in the plasma at ω_p. These in turn beat with the original wave to provide the ponderomotive buckets that reinforce the plasma wave. In all three schemes, the plasma oscillation in the 1D limit is purely electrostatic with the longitudinal electric field given by $\varepsilon(n_e)^{1/2}$ V/cm where ε is the level of density modulation and n_e is the plasma electron density in cm^{-3}. Thus for a plasma density in the range $10^{16} < n_e < 10^{18}$ cm^{-3} and ε = 0.1 one can expect $10^9 < E(v/m) < 10^{10}$.

In the inverse Cherenkov accelerator the laser beam is first slowed down in a gaseous dielectric and then made to interact with the particle at the Cherenkov angle θ_c such at $\beta \cos\theta_c = 1/n$ where n is the refractive index of the gas. In the zero order approximation if β and $\cos\theta_c$ do not change, the field seen by the particle remains constant in time. The particle sees an electric field E sin $\theta_c \cos\varphi$ which either accelerates or decelerates the particle depending on the sign of the phase angle φ. Unfortunately, there is a limit to the maximum accelerating field that can be expected in the ICA scheme. This is given by the breakdown threshold of the gas used to slow the laser down. If extremely short pulses are used, then the gas breakdown will occur because of tunnel ionization mechanism which becomes significant when the laser field produces a potential drop roughly corresponding to the ionization potential across the Bohr radius. This limits the laser intensity to less than 10^{14} W/cm^2 for a CO_2 laser in hydrogen which in turn means that the maximum accelerating field will be limited to less than 500 MeV/m.

Finally, in the IFEL the particle propagates along the axis of a static magnetic wiggler. The $\underline{v} \times \underline{B}$ force gives rise to a perpendicular component of the velocity of the particle which now can interact with the transverse field a co-propagating laser. A different way of looking at how this energy exchange can happen is as follows: The combined action of the laser (ω_o,k_o) and a static wiggler field (ω_o,k_w) on the electrons results in a ponderomotive wave. The ponderomotive wave has a phase velocity slightly less than c since $v_{ph} = \omega_o/(k_o + k_w) = c/(1+k_w/k_o)$. This ponderomotive well can trap and continuously accelerate electrons. However, for this to happen, the resonance condition which relates the electron energy to the wiggler and laser parameters must be maintained. This is given by $\gamma_R = (1+a_w)^{1/2}\ (\lambda_w/2\lambda_o)^{1/2}$ where a_w is the normalized vector potential.

3 CURRENT STATUS OF PLASMA ACCELERATORS

Laser Wake Field Accelerator

Experiments are being carried out at several laboratories around the world on LWFA.[9] The most ambitious current effort is the JAERI/KEK/U. Tokyo collaboration in Japan.[10] This collaboration has put together an impressive laboratory facility which combines a high repetition rate 2 TW, Ti-Saphire, T^3 laser and a 17 MeV linac. Their experimental arrangement is shown in Fig. 1.

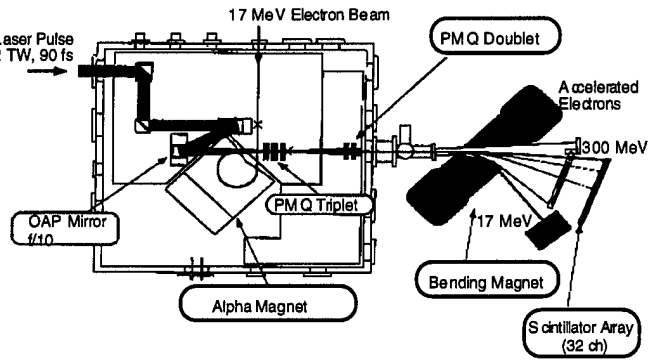


Figure 1. Experimental Set-up for Laser Wakefield Acceleration: KEK-JAERI-U. Tokyo

They have used the technique of frequency domain interferometry to measure the plasma density oscillation in a helium plasma that was produced by the laser. From this they clearly observe a relativistic plasma wave of the correct periodicity and infer a density fluctuation of ε = 0.15 or a longitudinal field of 4 GeV/m. They have also measured the electron spectra exiting the plasma and have found that when 17 MeV electrons are injected externally into the plasma, electrons up to 100 MeV at 2 Torr and 200+ MeV at 20 Torr are observed. To explain the observed maximum energies at the inferred gradients (from spectral interferometry) a coherent plasma wave must exist over many centimeters. Side on images of the plasma taken by the same group do show a plasma that is emitting light over this distance but its not clear if the laser beam is truly self guided or whether there is an alternative explanation for these images. The maximum laser power of 1.8 TW in these experiments is below the critical power for relativistic self-focusing.

Plasma Beat Wave Accelerator

The most definative experiments have been done by the UCLA group.[11] Using a 2 frequency, CO_2 laser they

have succeeded in accelerating a 2 MeV beam of electrons up to 30 MeV in about 1 cm giving an average gradient of 2.8 GeV/m. Similar results are reported by a group at AECL in Canada.[12] Furthermore, using a 1 μm laser operating on two lines, a group at Ecole Polytechnique[13] has also demonstrated acceleration of externally injected electrons using this technique. A group at Osaka University[14] in Japan also used a two frequency CO_2 laser. They observed the acceleration of plasma electrons without any external injection. It is clear that the beat wave acceleration is ready to move on to the next phase of research. The goal of the second generation experiments on the PBWA will be the demonstration of acceleration of a high quality, high current electron beam at the high accelerating gradients that have already been demonstrated.[15] The UCLA group has an ambitious program that proposes to accelerate electrons to 100 MeV while maintaining a small energy spread and emittance. The parameters for their experiment are shown in Table 1. They propose to use a synchronized photoinjector as a source of high current and low emittance injection beam. In order to bunch this beam on a sub 100 micron scale they are considering several bunching schemes.

Maximum Energy	100 MeV
Total number of particles accelerated	10^8
Number of bunches per macrobunch	1-4
Energy spread	< 5%
Emittance (normalized)	< 10 π.mm.mrad
Accelerated peak current	10-100 A
Acceleration gradient	3 GeV/m

Table 1. The parameters for UCLA 100 MeV PBWA experiment.

Figure 2 shows the results of computer simulations when a 15 MeV electron beam is injected into the plasma beat wave without and with prebunching. Without prebunching electrons are injected at all phases of the plasma wave whereas in the prebunched case a 60 fs bunch is injected into a 1 ps (300 μm wavelength) plasma wave. The plasma wave has a Lorentzian axial profile with a peak amplitude of 30% and a diameter of 500 μm. The initial emittance of the injected beam is 3π mm mrad. One can see that when a prebunched beam is injected more particles are accelerated to high energy as expected and the energy spread is much smaller. This is more clearly shown in Fig. 3. There is a clear peak at approximately 110 MeV with the phase space of particles above 75 MeV showing an emittance of 10 π mm mrad.

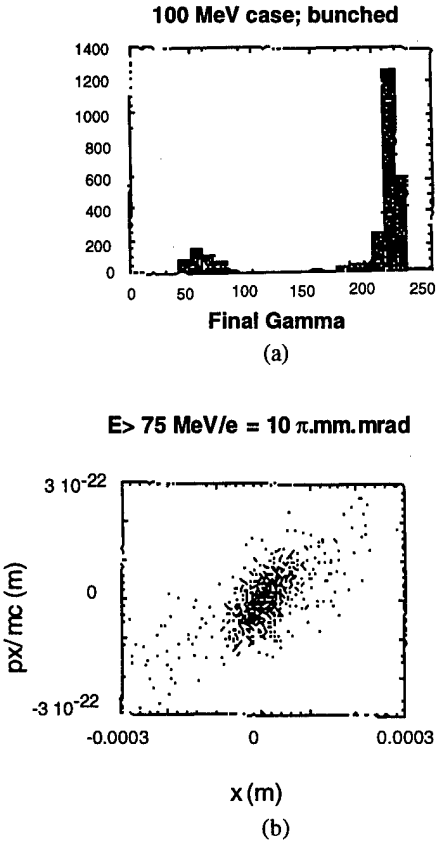


Figure 2.

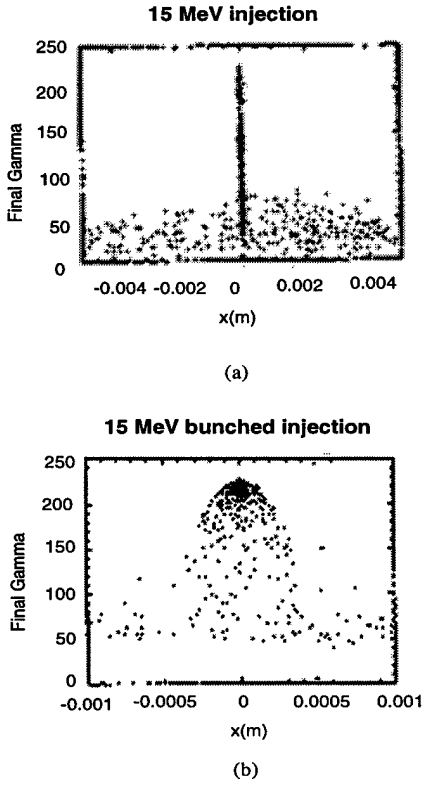


Figure 3.

Self-Modulated Laser Wake Field Accelerator

This scheme has received a lot of attention in the last three years. This is because chirped pulse amplification lasers have become commonplace. Many laboratories around the world have a terawatt class, subpicosecond laser suitable for the studies of SMLWFA. For instance experiments are underway at the Rutherford Laboratory (RAL)[16], NRL[17], Michigan[18] and JAERI[19] on this scheme. The most dramatic results come from the Imperial College/UCLA/Ecole Polytechnique collaboration at the RAL in England. Using a 20 TW, 1 ps, 1 μm laser this group observed acceleration of self-trapped electrons up to 100 MeV in a 1.5×10^{19} cm^{-3} density helium plasma.[20] The plasma wave length was simultaneously measured to be about 600 μm. An energy gain of 100 MeV in 600 μm implies an average acceleration gradient of 166 GeV/m, 3 orders of magnitude greater than what is obtained in current r.f. linacs. An interesting aspect of this experiment is that the maximum electron energies observed were larger than expected from the 2D, dephasing limit for externally injected electrons in a plasma wave. Furthermore, the distance over which the electrons were accelerated was greater than the dephasing distance. The explanation to this apparent contradiction is that what was being observed was the energy gain of self-trapped electrons and not externally injected electrons. In the wavebreaking process, the plasma wave amplitude is large enough to trap the main body of the distribution function of the electrons. This causes severe beam loading of the buckets. As the electrons are accelerated, the effective phase velocity of the later bucket speeds up since these buckets are formed as a consequence of the superposition of the original wave field and the wake-field induced by the accelerating electrons. Consequently some trapped particles in the later bucket continue to be accelerated by an accelerating field even though they have gone beyond the normal dephasing length.

What is the future for the SMLWFA scheme? In the near term, availability of 50-100 TW, 0.5 μm lasers would imply that we will quite likely see this scheme yielding the first 1 GeV energy gain of any advanced acceleration scheme. This is indeed a very exciting prospect. The eventual practicality of this scheme depends on whether one can phase-lock and inject extremely short bunches to the plasma wave. The plasma waves are sub 10 micron in wavelength so micron size bunches will be required as in the IFEL and ICA schemes.

Recently an all optical injector[21] that is particularly suitable for plasma accelerators has been proposed. In this scheme one intense laser excites the plasma wave while a second even shorter pulse laser ($\tau << \tau_{plasma}$) causes local "breaking" of the wave providing the electrons at the correct phase to be accelerated.

The SMLWFA experiments have also shown trantilizing evidence for self-guiding of these very powerful laser pulses.[22] Self-guiding increases the interaction length of the laser with the plasma. However, it remains to be seen if it is a practical way to extend the interaction length of a plasma accelerator since both the plasma density and the laser intensity can vary greatly inside the self-guided channel.

Inverse Free Electron Laser (IFEL)

There has been a successful IFEL acceleration experiment[23] at the Brookhaven National Laboratory's Accelerator Test Facility.[24] The CO_2 laser, the wiggler and the electron beam parameters are given in Table 2.

e^- beam			
	Injection Energy	40.0	MeV
	Exit Energy	42.3	MeV
	N(bunch)	10^9	e^-
	$\Delta E/E$ (one σ)	$\pm 3.10^{-3}$	
	Emittance (one σ)	7.10^{-8}	m.rad
Wiggler			
	Wiggler Length	0.47	m
	Period Length, λ_w	2.89-3.14	cm
	Wiggler Gap	4.0	mm
	Field max. (at 6kA)	10	kG
	Exc. Pulse, 1/2 sin.	200	μsec
CO_2 Laser			
	Power	10^9	Watts
	Pulse (FWHM)	300	psec
	Max. Field, E_0	$0.78\ 10^{-3}$	MV/m
	Guide Loss, α	0.05	m^{-1}
	R_0, Guide Radius	1.4	mm

Table 2. IFEL Accelerator Experiment, Phase I
(Accelerator Test Facility, Brookhaven National Lab.)

The CO_2 laser beam is guided in a saphire waveguide of 2.8 mm diameter to keep it interacting with the electron beam over the entire wiggler length. The wiggler design is very novel. An easily stakable, variable period, fast excitation driven wiggler is made by using geometrically alternating substacks of Venadium Permandur ferromagnetic laminations, interspaced with conductive nonmagnetic laminations. Although the wiggler period varied, the magnetic field strength is kept constant. They clearly observed the IFEL interaction. In the best case electron energy gain $\Delta P/P$ of 2% was observed for a laser power of less than 0.5 GW. This group intends to carry out a parametric study of the IFEL interaction with electron energy, laser intensity, magnetic field strength and laser spot size as variable parameters. In the future this group would like to attempt staging two IFEL modules.[25]

An interesting byproduct of the IFEL acceleration experiment is the bunching the accelerating electrons experience on the optical wavelength scale. Efforts are underway at BNL to measure the microbunching in the IFEL experiment.[26]

Inverse Cherenkov Accelerator (ICA)

A proof-of-principle ICA experiment[27] has been carried out at BNL's ATF using once again their CO_2 laser and the synchronized electron beam. A double-interferometer optical system is used to convert the CO_2 beam into a radially polarized beam which is sent in a gas cell containing 2 atmospheres of hydrogen gas using an axicon. The axicon converges the light so that it interacts with the e-beam at the correct phase matching angle. The experimental parameters are given in Table 3.

Electron Beam	
Source:	BNL ATF
Beam energy:	55 MeV
Instinsic Energy Spread(s):	$\approx \pm$ 0.1 MeV
Normalized emittance:	~3σ mm-mrad
Electron bunch length:	$\approx$ 10 ps (FWHM)
Pulse format:	Single pulse
Laser Beam	
Laser:	CO_2
Wavelength:	10.6 μm
Pulse Length:	220 ps
Peak power delivered to interaction region:	< 1 GW
Pulse repetition rate:	Single shot

Table 3. Typical ICA Experiment System Parameters

The electron beam energy is measured downstream of the gas cell using a dipole spectrometer. The electrons fall on a phosphor screen and are viewed using an image intensifier and CCD camera. Since the electrons are uniformly distributed over the laser phase both acceleration and energy loss are observed. They have observed an approximately 3.7 MeV energy gain over a 12 cm interaction length for 0.5 GW laser power, which gives a gradient of 31 MeV/m.

The next phase of the ICA experiment[28] involves using the IFEL as a prebuncher to inject microbunches into the ICA for more efficient acceleration. The length of the gas cell will be increased to 27 cm for an energy gain of 100 MeV. At the same time the IFEL and ICA experiments are being integrated, the laser is being upgraded to one terawatt level. Using 250 GW of CO_2 will lead to an accelerating gradient of 370 MeV/m in the next phase of ICA experiments.

4 CONCLUSIONS

As can be seen from the above discussions, there has been a tremendous progress in the laser-acceleration field. The future of this field looks very exciting with plasma schemes on the threshold of achieving 1 GeV energy gain, IFEL demonstrating microbunching and a combined IFEL/ICA experiment likely to demonstrate staging and phase-locking of charged particles at optical frequencies.

5 ACKNOWLEDGMENTS

I wish to thank Drs. Nakajima, A. Dangor, Kimura and van Steenbergen for their input to this paper. This work was supported by DOE grant number DE-AS03-92ER40727.

REFERENCES

1. J. M. Dawson, Scientific American 45, 267 (1979).
2. C. Pellegrini in Laser Acceleration of Particles, (AIP Conf. Proc. No. 91, ed., P. Channell, 1982).
3. J. R. Fontana, R. Pantell, J. Appl Phys. 54, 4285 (1962).
4. J. D. Jackson, Classical Electrodynamics, Ed. J. Wiley (1962).
5. T. Tajima and J. M. Dawson Phys. Rev. Lett. 43, 267 (1979).
6. C. Joshi et al., Nature 311, 525 (1984).
7. P. Sprangle et al., Phys. Rev. Lett. 69, 2200 (1992).
8. C. Joshi et al., Phys. Rev. Lett. 47, 1285 (1981).
9. J. R. Marqués et al., Phys. Rev. Lett. 76, 3566 (1996).
   C. Sider et al., Phys. Rev. Lett 76, 3570 (1996).
10. K. Nakajima, private communication.
11. C. Clayton et al., Phys. Rev. Lett. 70, 37 (1993).
    M. Everett et al., Nature 74, 1355 (1995).
12. N. Ebrahim, J. Appl. Phys. 76, 7645 (1994).
13. F. Amiranoff et al., Phys. Rev. Lett. 74, 5220 (1995).
14. Y. Kitagawa et al., Phys. Rev. Lett. 68, 48 (1992).
15. C. Joshi, Proceedings of the 3rd IAPS meeting, Vol. 5, Japan (1996).
16. A. Modena et al., Nature 377, 608 (1995).
17. A. Ting et al., Phys. Rev. Lett (1996).
18. D. Umstadter et al., Science 76, 2073 (1996).
19. Nakajima et al., 74, 4426 (1995).
20. D. Gordon et al., submitted to Phys. Rev. Lett.
21. D. Umstadter et al., Phys. Rev. Lett. 76, 2073 (1996).
22. C. Clayton et al., Phys. Rev. Lett. to be submitted.
23. A. van Steenbergen et al., Phys. Rev. Lett. 77, 2690 (1996).
24. I. Ben-Zvi, private communication.
25. A. van Steenbergen, private communication.
26. I. Ben-Zvi, private communication.
27. W. Kimura et al., (AIP Conf. Proc., Nov. 325, 1994) p. 131.
28. W. Kimura and A. van Steenbergen, private communication.

COHERENT NONLINEAR LONGITUDINAL PHENOMENA IN UNBUNCHED SYNCHROTRON BEAMS

L. K. Spentzouris and P. L. Colestock *,
Fermilab, P.O. Box 500, Batavia, IL 60510, USA

Abstract

Coherent nonlinear longitudinal dynamics have been investigated in unbunched hadron beams[1]. These phenomena may be described using a theoretical framework originally developed to describe interactions in plasmas[2]. Processes exhibiting the weakest degree of nonlinearity are known as wave-wave interactions. Manifestations of these interactions may be used to help characterize a beam. Echoes have been used to measure the collisional damping rate of weak diffusive processes which degrade a stored beam. Further information is contained in the echo shape, which depends on the form of the particle energy distribution. The echo shape may also be modified by the presence of wakefields, or nonlinearities in the machine lattice which affect the longitudinal motion of the particles.

1 ECHO MEASUREMENT AND DYNAMICS

Beam echoes may be generated transversely [3, 4], or else longitudinally in either a bunched beam [5] or an unbunched beam [1, 6, 7]. Although the underlying phenomena are the same in all cases, the discussion here pertains specifically to longitudinal echoes in an unbunched beam.

An echo is a coherent current oscillation which grows out of a quiet beam, with some delay after a sequence of two independent pulse excitations. In the absence of wakefields, the beam response to a longitudinal kick naturally decoheres, with a decoherence time that is inversely proportional to the energy spread of the beam. Even though the coherent motion of the beam damps away, the phases of the particles will remain correlated. Due to this correlation, the phase evolution of the decoherence is reversible. An echo is a partial reconstruction of the particle phase relation present during the coherent motion from the initial kicks. This reconstruction normally occurs some time after the beam response to the kicks has damped away.

Longitudinal echoes in an unbunched beam have been clearly observed in the Fermilab Accumulator. Figure 1 shows the time development of the peak beam current during echo production, as seen on a broadband longitudinal resistive-wall beam detector. The two large amplitude spikes within the first 100 ms correspond to the longitudinal kicks that were applied to the beam at harmonics $h = 9$ and $h = 10$, respectively. The frequency of the coherent response of the echo occurs at the difference frequency of the kicks, $f_{echo} = f_{kick2} - f_{kick1}$, which in this case is $h = 1$.

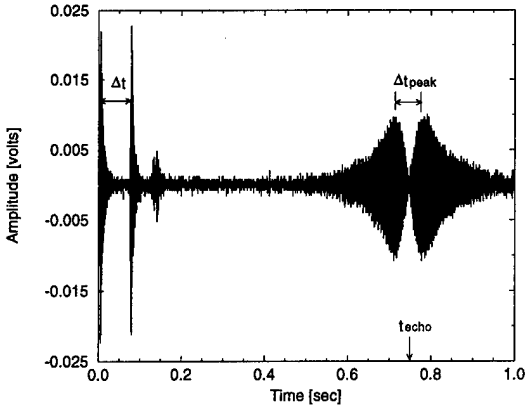


Figure 1: Beam response to a pair of impulse excitations separated in time by $\Delta t = .075$ seconds. The echo is centered at 0.75 seconds after the first kick. The beam parameters were: beam current $I_0 = 147$ mA, $\eta = .023$, total beam energy $E_0 = 8696$ MeV, beam energy spread $\sigma_\varepsilon = 3.2$ MeV, transverse normalized emittances $\epsilon_H = 1.75\pi$ mm-mrad, $\epsilon_V = .56\pi$ mm-mrad, and peak separation of the echo $\Delta t_{peak} = .07$ sec. Note the presence of a higher-order echo immediately following the second excitation pulse.

The timing of an echo is theoretically predicted to be $t_{echo} = [f_{kick2}/(f_{kick2} - f_{kick1})]\Delta t$, where Δt is the time separation between the two kicks. Verification of the scaling of t_{echo} with the kick frequencies is shown in figure 2.

2 DIFFUSION RATE MEASUREMENTS

Echoes are a useful tool for measuring the diffusion rate in a beam. Current methods of measuring thermal effects in a beam take on the order of hours. Echoes effectively amplify the effects of scattering, allowing the measurement of small collision frequencies in a much shorter time.

The presence of a diffusion mechanism destroys the reversibility of the decoherence of particle bunching. In the absence of diffusion, the phase evolution of the spreading particles depends strictly on their relative energies. The phase development of the particles due to their energy change from the second kick combines with their phase development from the first kick in such a way as to rebunch the particles. Partial decorrelation will reduce the echo amplitude, and full decorrelation will completely inhibit the echo. A collisional process, for example intrabeam scat-

* Operated by the Universities Research Association for the U.S. Dept. of Energy

0-7803-4376-X/98/$10.00 © 1998 IEEE

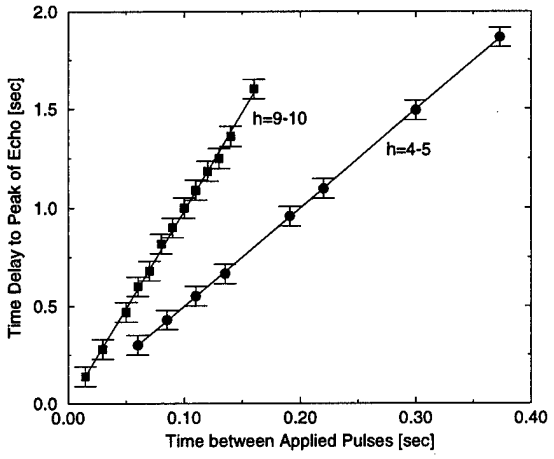


Figure 2: Measured echo delay time as a function of separation of the drive pulses. Upper curve: 1^{st} pulse at $h = 9$, 2^{nd} pulse at $h = 10$, giving expected time dependence $t_{echo} = [10/(10-9)]\Delta t = 10\Delta t$. Lower curve: 1^{st} pulse at $h = 4$, 2^{nd} pulse at $h = 5$, giving $t_{echo} = [5/(5-4)]\Delta t = 5\Delta t$.

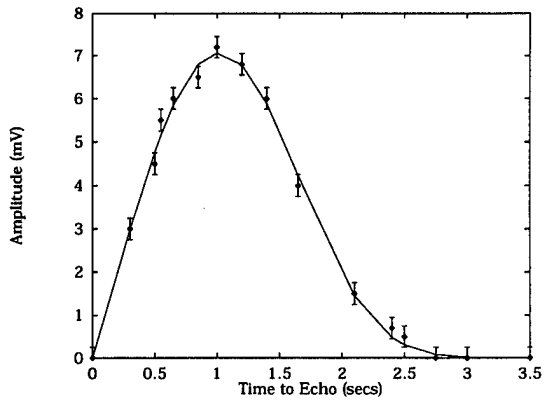


Figure 3: Peak echo response as a function of the time to echo following the initial pulse. The solid line represents a theoretical fit corresponding to a collision rate $\nu = (3.0 \pm 0.8) \times 10^{-4}$ Hz.

tering, will break down the correlation between energy and phase by knocking individual particles off their original trajectories. A diffusion process is thus expected to change the dependence of echo amplitude on the time at which the echo occurs, decreasing the amplitude until there is no echo at all.

In the presence of diffusion, the beam current at the echo harmonic goes as

$$I_{echo} = AJ_1(k_1\delta\Delta t)\exp\left(-k_2\nu t_{echo}^3\right) \qquad (1)$$

where A is a constant, δ is proportional to the kick strength of the excitation, k_1 is a constant equal to one of the kick harmonics, Δt is the time between kicks, k_2 is a constant which depends on the kick harmonics and the echo harmonic, ν is the collision rate, and t_{echo} is the time from the first kick to the center of the echo. Decorrelation due to collisions results in a decay as t^3, which modifies the otherwise Bessel function form of the echo amplitude response. Thus, by fitting a measurement of echo amplitude versus the time of the echo, the diffusion rate in the beam may be determined. Such a fit is shown in figure 3.

The diffusion rate is large enough in the Fermilab Accumulator that only a portion of the first lobe of the Bessel function is visible in the beam response. This was further verified by performing an echo amplitude scan at two different sets of kick harmonics, as shown in figure 4. A comparison of the time when the echo amplitude vanishes in the two scans indicates whether or not this zero is a node in the Bessel function dependence, because $k_1 \neq k_2$ in equation 1. The ratio of the vanishing time in the two scans of figure 4 is consistent with the ratio of the decay time constant in equation 1, and is not consistent with the ratio of

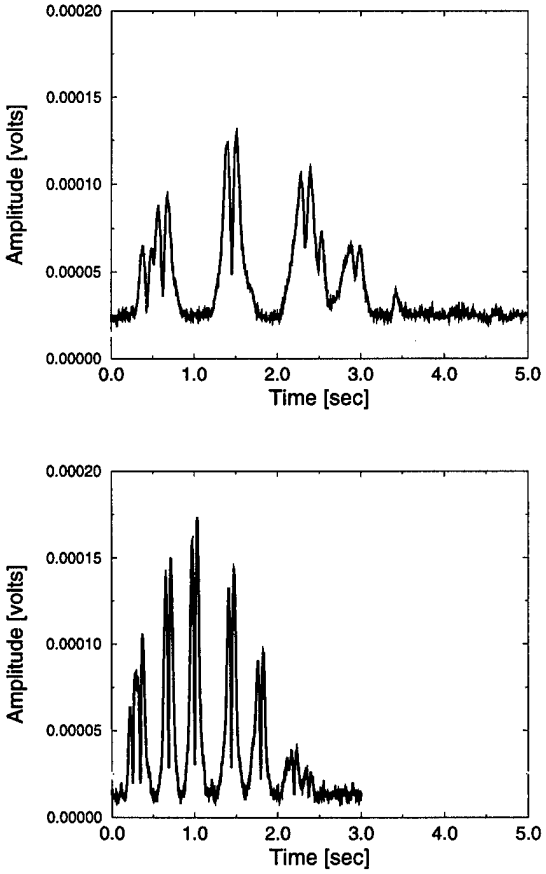


Figure 4: Echo amplitude vs. echo time t_{echo}. The top scan was done with kick harmonics $h_{kick1} = 9$ and $h_{kick2} = 10$, giving $h_{echo} = 1$. The bottom scan was done with $h_{kick1} = 8$ and $h_{kick2} = 10$, giving $h_{echo} = 2$. All other parameters were the same.

the argument of the Bessel function.

3 ECHO SHAPE

There is other information about the beam besides the diffusion rate residing in an echo. Knowledge of the beam energy sigma and the shape of the energy distribution of the particles may be extracted. It is perhaps even possible to learn about nonlinearities in the machine η function which governs the transit times of particles around the machine.

One of the major features of the observed echoes has been a deep notch in the center of the response. In the absence of wakefields, the echo current is dependent on the derivative of the unperturbed particle energy distribution. For a Gaussian beam, the slope of the distribution is zero at the center, hence the echo current goes to zero in the middle of the echo. The separation of the peaks on either side of this zero has a predicted dependence on the energy width of the beam. This goes as,

$$\Delta t_{peak} = \frac{\beta^2}{h_{echo}\pi f_{rev}|\eta|\frac{\sigma_E}{E_0}} \qquad (2)$$

where β is the relativistic β of the beam, h_{echo} is the harmonic of the echo frequency, f_{rev} is the revolution frequency of the machine, η is the slip factor governing the particle transit time, and $\frac{\sigma_E}{E_0}$ is the energy sigma over the central energy of the Gaussian beam. In figure 5, experimental results are shown to agree with equation 1 to within 20%.

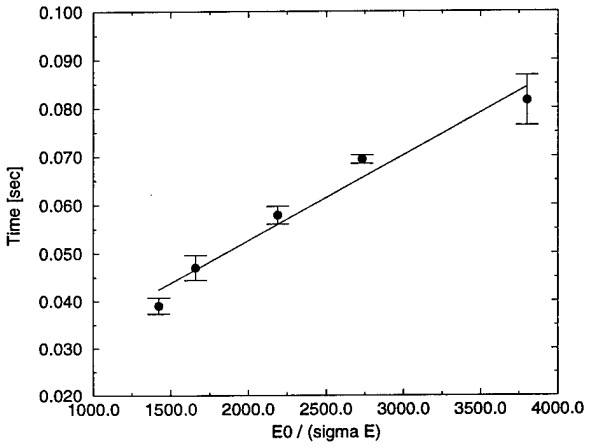


Figure 5: Peak separation of double-peaked echoes, Δt_{peak}, versus the inverse of $\frac{\sigma_\epsilon}{E_0}$, the energy spread of the beam. The value of the slope from the linear fit is 1.76E-5. The beam parameters were $I_0 = 147$ mA, $\eta = .023$, $\beta^2 = .988$, $h_{echo} = 1$, and $f_{rev} = 629$ kHz.

Departures of the particle energy distribution from a Gaussian will be reflected in the shape of the echo. For example, during one study period an instability developed which knocked particles out of the center of the distribution. This left a beam energy profile with a depression in the center and shoulders on either side. The corresponding shape of the beam echoes is shown in figure 6. The

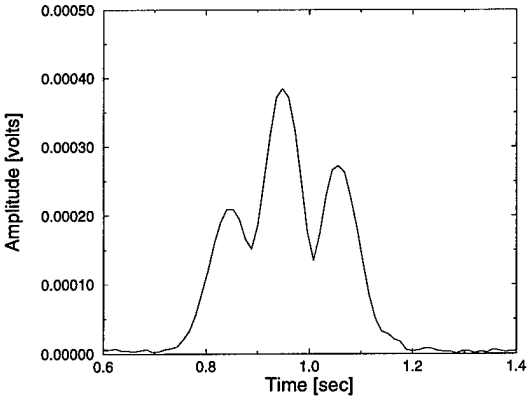


Figure 6: Beam echo from a non-Gaussian beam.

shape of the resulting beam profile can be constructed with a superposition of two offset Gaussians. By superposing the two corresponding normally notched echoes, a three-peaked echo such as that shown in figure 6 results. Since the echo shape is dependent on the slope of the beam distribution, perhaps a more careful and systematic algorithm for extraction of the beam profile can be developed.

While doing echo amplitude scans at various beam energy spreads, it was found that for large enough σ_ϵ the notch in the echo disappeared. Leaving all other parameters the same, scans were done for σ_ϵ in the range of 2.3 to 8 MeVc. As the beam energy spread increased, the echo amplitude decreased, and the central notch in the echo filled in, eventually vanishing completely. Figure 7 shows echoes from three of these scans. The echoes occur at approximately the same time relative to the driving pulses, but their shape is quite distinctive. Although only three echoes are shown in the figure, the trend is assiduously followed in all seven scans which were done. One possible explanation is that nonlinearities in the η function are mixing the particle distribution in such a way as to destroy the notch. The relation between the spread in particle revolution frequencies and the spread in particle energies is given by,

$$\frac{\Delta f}{f_0} = -\frac{\eta}{\beta^2}\frac{\Delta E}{E_0}$$
$$= -\frac{1}{\beta^2}\frac{\Delta E}{E_0}\left[\eta_0 + \eta_1\frac{1}{\beta^2}\frac{\Delta E}{E_0} + \cdots\right]$$

As the energy spread of the beam gets larger, the nonlinear terms will make a greater contribution to the motion, and destroy the linear correlation between the energy and phase of the particles.

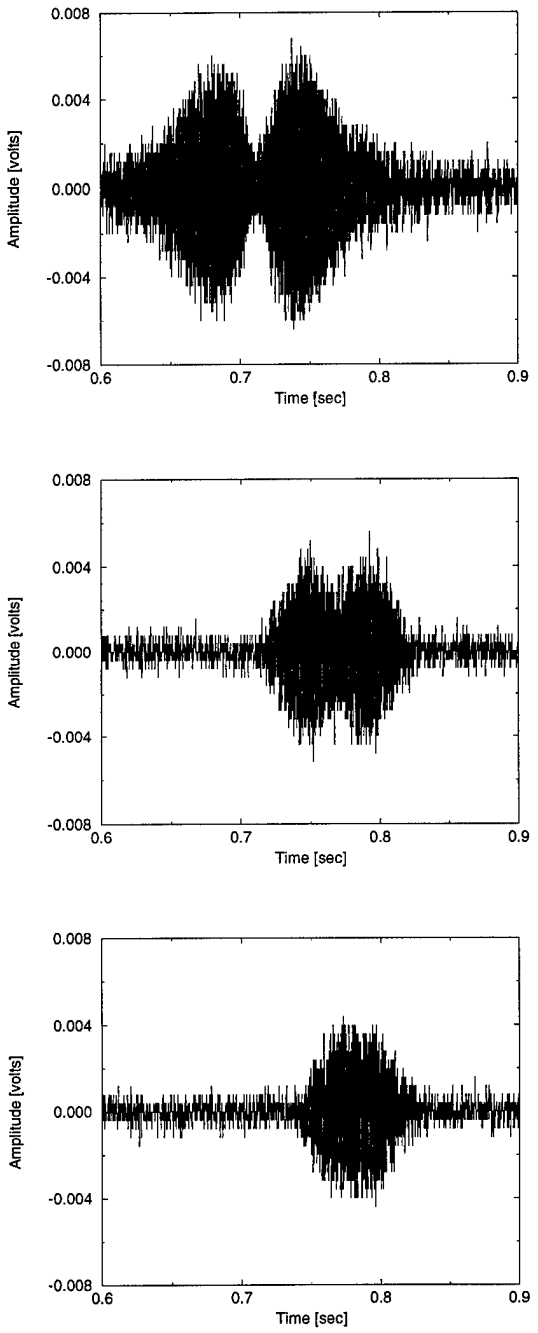


Figure 7: Three longitudinal beam echoes occurring in beams with different energy widths. The beam energy sigmas (σ_ε) were from top to bottom, 4.0, 6.1, and 8.0 MeVc. The energy spread was controlled with longitudinal stochastic cooling systems, all other beam conditions were the same. The beam intensity was 147 mA. Echoes which occurred at nearly the same time relative to the driving pulses were chosen for comparison.

4 CONCLUSIONS

High energy hadron beams are rich in nonlinear effects which are as of yet in the early stages of exploration. Echoes, which are a manifestation of weakly nonlinear wave-wave interactions, have been studied using an unbunched beam in a storage ring. Echoes can be used to explore the nature of the beam. The peak separation of the echoes generated in a Gaussian beam is proportional to the beam energy spread. In general, in the absence of wakefields, the shape of the echo depends on the slope of the energy distribution of the particles.

Echoes are sensitive to anything in a machine which disrupts the linear relation between particle energy and particle phase. As a result, it has been possible to make a fast measurement of the diffusion rate in a beam using longitudinal echoes. In the Fermilab Accumulator storage ring it has been observed that the notch normally present in the center of the echo fills in at large beam energy spreads. It may be that nonlinearities in the η function are responsible for this.

The investigation of beam echoes has demonstrated that studying nonlinear effects can be a useful tool in beam physics, allowing a deeper understanding of the behavior of particle storage rings.

5 ACKNOWLEDGEMENTS

This work was greatly facilitated through the support of Dr. David Finley and the Pbar group at Fermilab.

6 REFERENCES

[1] L.K. Spentzouris, *Ph.D. Thesis*, Northwestern University (1996).

[2] R.C. Davidson, *Methods in nonlinear plasma theory*, Academic Press, 1972.

[3] G.V. Stupakov, Superconducting supercollider laboratory report No. SSCL-579, 1992.

[4] G.V. Stupakov and K. Kauffmann, Superconducting supercollider laboratory report No. SSCL-587, 1992.

[5] P.L. Colestock and S. Assadi, Measurement and analysis of longitudinal bunched beam echoes in the Fermilab Tevatron, this proceedings

[6] O. Bruening, On the possibility of measuring longitudinal echoes in the SPS, CERN report SL/95-83, Sept 1995

[7] L.K. Spentzouris, J.F. Ostiguy, and P.L. Colestock, Direct measurement of diffusion rates in high energy synchrotons using longitudinal beam echoes, *Physical Review Letters*, 766, 620 (1996)

THE NATIONAL SPALLATION NEUTRON SOURCE (NSNS) PROJECT

Bill R. Appleton for the NSNS Collaboration
Oak Ridge National Laboratory*, P. O. Box 2008, Oak Ridge, Tennessee 37831, USA

Abstract

The need and justification for new sources and instrumentation in neutron science have been firmly established by numerous assessments since the early 1970s by the scientific community and the U.S. Department of Energy (DOE). In their 1996 budget, the DOE Office of Energy Research asked ORNL to lead the R&D and conceptual design effort for a next-generation spallation neutron source to be used for neutron scattering. To accomplish this, the NSNS collaboration involving five national laboratories (ANL, BNL, LANL, LBNL, and ORNL) has been formed. The NSNS reference design is for a 1-GeV linac and accumulator ring which delivers 1-MW proton beams in microsecond pulses to a mercury target; neutrons are produced by the spallation reaction, moderated, and guided into an experimental hall for neutron scattering. The design includes the necessary flexibility to upgrade the source in stages to significantly higher powers in the future and to expand the experimental capabilities. This paper describes the origins of NSNS, the current funding status, progress on the technical design, user community input and intended uses, and future prospects.

1.0 INTRODUCTION

The National Spallation Neutron Source (NSNS) is an accelerator-based facility that produces pulsed beams of neutrons by bombarding a mercury target with intense beams of 1-GeV protons. It is being designed to meet the needs of the neutron-scattering community in the United States well into the next century. The need and scientific justification for a more intense source of neutrons to keep pace with the burgeoning use of neutrons in science and technology have been well established in numerous assessments by the National Research Council and the U.S. Department of Energy (DOE) since the 1970s.[1]

Many advances in our society are driven by new technologies, and most of these new technologies depend on the development of new materials such as high-strength ceramics and composites, magnetic and electro-optic materials, or new high-transition- temperature superconductors. The approach to developing many of these materials requires understanding their interactions at the atomic level and relating these interactions to macroscopic properties. This usually requires the use of large facilities such as synchrotron radiation sources and neutron sources. Neutrons have several unique advantages for determining the structure and dynamics of a wide range of materials. This is why the demand for neutrons has increased so rapidly and has spread to so many fields of science in the last twenty years, and why there is a need for the NSNS.

2.0 ORGANIZING FOR THE CONCEPTUAL DESIGN

DOE provided $8 million in FY 1996 and FY 1997 to Oak Ridge National Laboratory (ORNL) to initiate the conceptual design and R&D for a next-generation spallation neutron source, the NSNS. Organizing to perform the conceptual design was a challenge. A design was needed in a short period of time and with limited funds. To accomplish this, ORNL formed a collaboration involving five DOE National Laboratories, Argonne National Laboratory (ANL), Brookhaven National Laboratory (BNL), Ernest Orlando Lawrence Berkeley National Laboratory (LBNL), Los Alamos National Laboratory (LANL), and ORNL. This approach assembles the best available expertise and latest technologies, utilizes the experience gained from all the laboratories in designing facilities and operating user facilities, leverages DOE resources, and allows ORNL to tailor the final staff at NSNS to user operations.

3.0 FUNCTIONAL REQUIREMENTS FOR NSNS

The functional requirements for the NSNS have been set by the scientific community and DOE through distillation of the many assessments and events dating from the 1970s that have firmly established the need and justification for a new neutron source.[1] From these studies and a recent NSNS User's Workshop on Performance Metrics and Instrumentation Needs held in Oak Ridge, October 31–November 1, 1996, the requirements the

*Managed by Lockheed Martin Energy Research Corporation for the U.S. Department of Energy under Contract No. E-AC05-96OR22464.

0-7803-4376-X/98/$10.00 © 1998 IEEE

community would like designed into the NSNS are basically the following:

- Short pulse (~1 microsecond) operation
- Initial operation at ~1 megawatt beam power
- A flexible initial design capable of being upgraded "to significantly higher power" in the future
- One target station initially at 30–60 Hz repetition rate, and provisions for a second at 10–20 Hz
- Rapid completion, high reliability, and high availability to the users
- A flexible design that preserves a long pulse (1 millisecond) mode of operation

4.0 ACCELERATOR REFERENCE DESIGN

To address the needs expressed by the neutron community, the NSNS team examined the relative merits of several technology options, including a full-energy linac plus accumulator ring vs a lower-energy linac and a rapid cycling synchrotron.

The NSNS team concluded that a full-energy linac injecting into an accumulator ring was the best combination of technologies for the accelerator system. The relatively modest cost for upgrading the 1-MW accumulator-ring scenario to 2 MW, and the flexibility of this option for additional upgrades to significantly higher powers and long-pulse operation in the future were the primary reasons. A liquid-mercury target rather than a solid target was chosen initially because this appeared the best option to accommodate higher power upgrades in the future, but as design activities have progressed, we now conclude this is the superior choice even at 1-MW power levels. A 60-Hz target was selected for the initial experiment system to accommodate the majority of recommendations from the User's Workshop, although there was a clear need expressed for both high- and low-frequency targets in the near future.

A schematic representation of the accelerator system layout and experiment building for the first 1-MW phase of NSNS is shown in Fig. 1.

4.1 Accelerator Reference Design

The performance parameters for the NSNS accelerator system reference design are listed in abbreviated form in Table 1. The first column of parameters are for the initial stage of the NSNS that would operate at a power of 1 MW.

The second column shows those parameters that would be changed for the NSNS to operate at the upgraded power of 2 MW. As mentioned in Table 1, the NSNS is designed so that the upgrade to 2 MW mainly requires increasing the ion source current to 70 milliamps and boosting the rf power to the existing linac structure to accelerate the additional beam, and this can all be accomplished quite economically.

ORNL 97-5011A/vlb

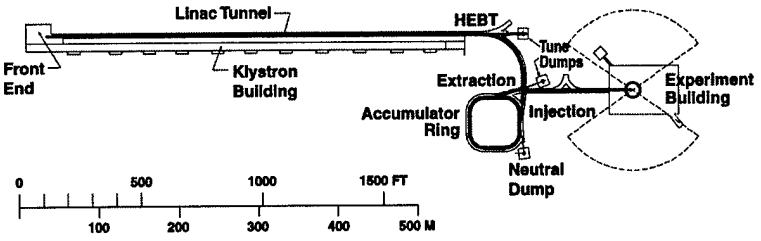


Fig. 1. Schematic representation of the accelerator system layout and experiment building for the first 1-MW phase of NSNS.

Table 1. National Spallation Neutron Source Performance Parameters

	Initial 1.0 MW	Upgrade to 2.0 MW
Pulse repetition rate	60 Hz	
Peak ion source H^- current	35 mA	70 mA
RFQ capture-bunching factor	>80%	
Linac length	493 m	
Linac capture-acceleration efficiency	100%	
Linac duty factor	6.2%	
Linac final beam energy	1.0 GeV	
Accumlator ring circumference	220.7 m	
Ring controlled injection loss	<10%	
Ring orbit rotation time	841 ns	
Pulse length at ring injection	546 ns	
Kicker gap at ring injection	295 ns	
Ring filling fraction	65%	
Number of injected turns	1225	
Ring filling time	1.03 ms	
Protons per pulse on target	1.04×10^{14}	2.08×10^{14}
Protons per second on target	6.3×10^{15}	1.25×10^{16}
Time average beam current on target	1.0 mA	2.0 mA
Beam power on target	1.0 MW	2.0 MW

LBNL has responsibility to design, develop, construct, and integrate the front-end system as a fully operational part of the NSNS accelerator system. The primary function of the front-end system is to produce a beam of H^- ions to be injected into the linac at 2.5 MeV. The ion source technology selected by LBNL to accomplish this is an rf-driven, rather than filament-operated, multi-cusp volume source, chosen primarily because of its stable, low-noise, and high-efficiency operation. This technology has been developed over many years and requires no major breakthroughs to achieve the performance goals.

LANL is responsible for the linac. The linac consists of a drift-tube linac (DTL) that accelerates beam from 2.5 to 20 MeV, a cavity-coupled drift-tube linac (CCDTL) that further accelerates beam to 95 MeV, and a cavity-coupled linac (CCL) that accelerates beam to 1.0 GeV. The DTL operates at an rf frequency of 402.5 MHz while the CCDTL and CCL operate at 805 MHz. Careful beam matching, large aperture-to-beam size ratios, and equipartitioning will greatly reduce the problem of beam halo. The linac and front end provide chopped beams suitable for injection into the accumulator ring.

The particular parameters chosen for the linac are the result of substantial experience with design, construction, and operation of the Los Alamos Neutron Science Center (LANSCE) linac, the Ground-Test Accelerator (GTA), and studies for the APT-linac design. The studies done for the European Spallation Source (ESS) accelerator systems have also been considered.

BNL is responsible for the high-energy beam transport (HEBT) from the linac to the ring, the accumulator ring, and the ring-to-target-beam-transport (RTBT) system. The HEBT system provides the beam transport between the linac and the accumulator ring. The accumulator ring is a simple FODO lattice with four-fold symmetry responsible for accumulating beam pulses from the linac, and bunching them into intense short pulses which are delivered to the target. Pulses of H^- ions from the linac are stripped in a carbon foil and injected into the accumulator ring as protons. The ring accumulates about 1200, 1.0-GeV pulses of about 1-msec length from the linac, overlaps these into a single pulse about 0.5 μsec in length, and ejects them onto the mercury target as intense proton pulses where neutrons are produced by the spallation reaction, and transports it to the neutron target.

4.2 Target Systems

ORNL has primary responsibility for the target systems. The NSNS target systems include two major elements: the neutron source system, which provides neutrons for the scattering instruments, and a set of three beam dumps for the accelerator systems.

The function of the neutron source system is to convert a 60-Hz short pulse (<1 μs), high-energy (17 kJ/pulse), high-average-power (1 MW), 1.0 GeV proton beam into intense, short (~tens of μs) neutron pulses optimized for use by 18 neutron beam lines. Pulse rates of less than 60 Hz are acceptable as long as the nominal 17 kJ/pulse is not exceeded. In addition to the proton beam target itself, the target systems include neutron moderators, reflectors, shielding, utilities, and maintenance systems.

A cross-sectional view of this neutron source system is shown in Fig. 2. The proton beam target will be liquid mercury flowing inside an austenitic stainless steel container. Two ambient temperature water moderators will be located under the target, and two cryogenic hydrogen moderators above the target. Each one of the 18 beam tubes view one of these four moderators. The moderators will be surrounded by a beryllium reflector cooled with heavy water.

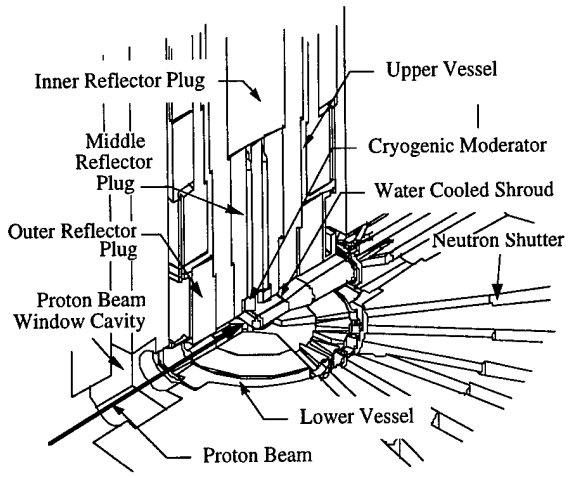


Fig. 2. Cross-sectional view of target station.

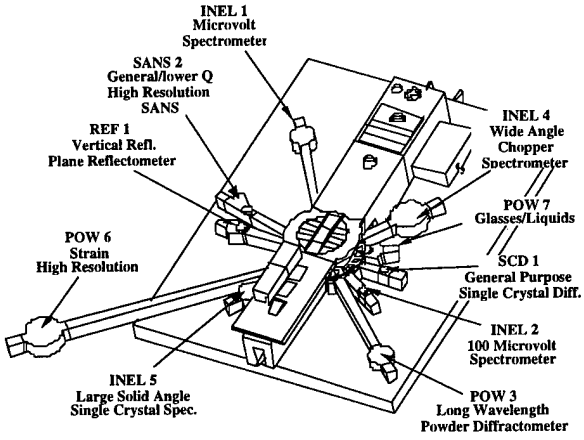


Fig. 3. Layout of experimental hall showing neutron beam lines and initial instrument set.

5.0 FACILITIES FOR SCIENTIFIC EXPERIMENTS

The purpose of the NSNS is to provide neutron beams for DOE and the scientific community. ANL and ORNL are jointly responsible for the instrumentation and experiment facilities.

The plan for staged upgrades of NSNS provides for an initial suite of state-of-the-art instruments and facilities that will grow as user needs evolve. The 1-MW first stage of operations will begin with construction of the target operating at 60 Hz with a reference design set of about 10 neutron-scattering instruments. The broad user community has been involved in the selection of these instruments. Based on recommendations from the NSNS User's Workshop, a layout of this reference set of instruments on NSNS neutron beams was developed and is shown schematically in Fig. 3. This layout was used in determining the size, shape, and other characteristics of the experiment hall shown on the facility footprint in Fig. 1.

6.0 FUTURE UPGRADES

Because of the reference design of NSNS, it is anticipated that the facility will be capable of operating at 2 MW in a short period and at modest cost. This would offer additional flexibility for the design and development of new instrumentation and a second low- frequency (10–20 Hz) target and experiment building. The suggested second stage of power upgrade would require building a second ion source, RFQ, MEBT, and DTL, and "funneling" of beam from two front-end systems operating at 70 mA into the linac. The initial accumulator ring is designed for maximum of 2 x 10^{14} particles per pulse, corresponding to 2 MW of beam power. A second ring would be built to accommodate the increased beam storage. While present plans have been carried only to the 4-MW level, the flexible nature of the baseline configuration and the potential of the planned site allow one to consider a variety of additional and alternate upgrade scenarios.

REFERENCES

1. DOE Basic Energy Sciences Advisory Committee (BESAC) Panel on Neutron Sources, Walter Kohn, Chairman, Michael Rowe, Vice-Chairman, *Neutron Sources for America's Future*, U.S. DOE Office of Energy Research, January 1993 and references therein.

THE DUKE FEL LIGHT SOURCE FACILITY

J. M. J. Madey, Director, and the Faculty and Staff of the FEL Laboratory
PO Box 90319, Duke University, Durham, NC 27708

Abstract

FEL research has proceeded during the last twenty five years from marginal proof of principle experiments to the construction and operation of devices optimized to provide the unique properties (peak power, tunability, and odd-wavelength capabilities) of most interest to the user community. The commissioning of the major facilities of the Duke FEL Laboratory constitutes another milestone along this path: the development of an integrated, FEL-based, research facility offering the opportunity to explore the capabilities and applications of high power, synchronized, multi-wavelength IR, UV and Gamma-ray FEL light sources. The size, cost and capabilities of such facilities appear uniquely well suited to the resources and interests of multi-disciplinary research universities.

1 INTRODUCTION

Since Ken Robinson's first musings more than thirty years ago that coherent radiation might be obtained from an appropriately designed undulator and accelerator-driver, free electron lasers have drawn attention as possible successors to incoherent e-beam based bend magnet and undulator light sources. That the technology has yet to reach the stage of widespread application is indicative of the barriers to understanding and implementation which have had to be surmounted.

Within this context, work on free electron lasers can be divided into three distinct, if overlapping, phases. The first phase, beginning with Robinson's work and continuing for perhaps 10 years past the first operation of an "optical" FEL at Stanford in 1976, focussed on the analysis of FEL operation. Though analysis and simulation continue through as vital and productive enterprises, it is also clear that the basic issues associated with FEL operation have been resolved. In this sense, the "theoretical" phase of FEL research can characterized as nearly complete.

The "hardware" phase of "optical" FELs (infrared and shorter wavelengths) began with the first experiments at Stanford, and continues through current date, with dramatic, continuing progress in the development of high performance linac and storage ring accelerator-drivers, precision undulators, and advanced optical systems. Indeed, it has largely been the progress in e-beam and undulator hardware which has transformed FEL technology from its humble and struggling beginnings to the very respectable levels of performance now routinely attainable in the infrared, and to the recent demonstrations of UV lasing, x-ray and gamma ray production via Compton backscattering. Continued progress in these supporting technologies make it reasonably certain that capabilities of FEL technology will also continue to advance, at least through the UV, XUV and soft x-ray regions.

The third phase of this effort might be called the "implementation" or "economic" phase, in which the objective has been to match the available technology with the applications best suited to exploit the capabilities of the technology, and most capable of supporting the costs to develop and operate the required hardware. The first efforts along these lines were begun in the mid 1980's as sponsors were found to support the exploration of the applications of the then-available prototype hardware in medicine and materials science in the United States, Europe, Japan and China.

While the results obtained to date in this third phase of the effort are encouraging, this third phase - perhaps the most critical with respect to the future of the technology - remains at an early stage of development. The developments described below reflect the efforts we have made at Duke to promote the advancement of FEL technology as part of this third phase of the effort to develop the free electron laser.

1.1 Comments on Siting Issues

The criteria by which success of an operating FEL light source facility will be measured are easy to identify: the facility should offer state-of-the-art performance, be inexpensive to build and operate, and be highly productive when evaluated in terms of the number of research projects accommodated or the utility or impact of the research performed. Note that these criteria involve both technical and siting issues: construction and operating costs will clearly depend both on the choice of technology and the skills and cost of labor, while productivity will depend both on the intrinsic capabilities of the technology and the skills and access of the investigators committed to exploring the technology.

A key issue for such FEL research centers is the number of users to be served. The challenge here is that FELs are, by their nature, devices which can serve only a limited number of users (typically one!) at a time. Though this restriction can be eased somewhat the implementation of one or more strategies to multiplex the electron beams and/or optical beams used or produced in such facilities, this restriction remains more or less intrinsic to the technology: like table-top lasers, FELs are limited in the number of users they can serve at any given time. As a consequence, FELs can not hope to justify their existence through the number of users they serve, but rather through the quality or impact of the of the research they support.

These three criteria: capabilities, cost, and productivity appear at this point in time to favor the deployment of small and medium-scale FEL technology, optimized to achieve one or more state-of-the-art capabilities, in university laboratories in which cost can

0-7803-4376-X/98/$10.00 © 1998 IEEE

be shared with these institutions' educational and training programs, and in which expedited access can be provided to a modest number of active research groups capable of pursuing the opportunities made possible by the technology. In general, this situation is reminiscent of the time 50 years ago in which the accelerator technology available to support nuclear and high energy physics was in its infancy, and the bulk of research was performed in small- and medium-scale university research facilities.

As described in further detail below, these considerations have led to the development at Duke University of a complementary series of FELs, FEL- and e-beam based light sources, and accelerator-drivers designed to facilitate the exploration of the capabilities and applications of FEL technology in basic and applied research. The site of the facility, on the Duke campus in the Research Triangle of North Carolina adjacent to North Carolina State University, the University of North Carolina at Chapel Hill, and Research Triangle Park promotes easy access to the facility by research groups affiliated with these centers.

2 THE DUKE FACILITY

The FEL light sources and accelerator-drivers available for use within the Duke FEL Laboratory are housed in a dedicated 50,000 sq. ft. facility sited on the Duke campus next to the Triangle Univesities Nuclear Laboratory. These devices include a 1 GeV electron storage ring located in the Laboratory's main bay, an ultraviolet FEL system (the OK-4 FEL) installed on the south straight section of this ring, the 280 MeV linac injector for the ring located in an underground tunnel extending 450' to the east of the Laboratory, and an independently operable infrared FEL (the MkIII FEL) located in a shielded cave adjacent to the Laboratory.

The choice of accelerator technology implemented in these devices reflects both the demanding technical requirements for FEL operation and the need to minimize acquisition and operating costs. The peak power output and tuning range of FELs are determined, primarily, by the peak current , emittance, and energy of the electron beam used as the lasing medium. Other characteristics of interest—optical pulse length, format, and average power output—follow from the time structure of the e-beam. Several means are now available to generate the e-beams required for state-of-the-art operation at infrared, ultraviolet, and extreme ultraviolet wavelengths, exploiting, respectively, the characteristics and capabilities of high gradient microwave gun injector technology and low emittance, medium energy storage ring technology.

For research facilities such as the FEL Lab at Duke, simple pulsed linac technology is attractive for operation at the lower electron energies required for infrared operation. As most of the infrared applications efforts to be pursued required either high pulse energies or high (Ghz) repetition rates, a single klystron S-band linac using a microwave thermionic gun and modified for long pulse operation to provide electron energies up to 45 MeV. With a peak current of 40 amps, this accelerator-driver permits operation of the MkIII infrared FEL system at wavelengths as short as 1.5 microns as described in further detail below.

For the e-beam energies and currents required for ultraviolet and extreme ultraviolet FEL operation, the economy and simplicity of storage ring accelerator-drivers make that technology an attractive choice for the exploratory short-wavelength research projects to be pursued in the Duke Laboratory. Storage ring technology also provides the means to generate high peak power optical pulses in the q-switched mode of FEL operation, and also the capability to support the operation of a range of conventional undulator and bend-magnet synchrotron radiation light sources as adjuncts to FEL operation. The recently commissioned OK-4 FEL system described below, based on the Laboratories 1 GeV storage ring driver, has generated coherent light at wavelengths as short as 345 nanometers in the ultraviolet, and also been used to demonstrate the generation via intracavity Compton backscattering of near-monoenergetic polarized gamma rays at energies up to 16 MeV.

The emittance, current, and energy of the e-beams produced by the injectors and accelerator-drivers for these FELs make them useful instruments in their own right for advanced research on high brightness and high current electron beam physics and technology, including the development of new e-beam based light sources.

2.1 The MkIII FEL

The MkIII FEL was designed to satisfy the requirements projected for research on the applications of tunable, short pulse infrared laser technology in laser surgery. Projected specifications for this application included a tuning range covering from 1 to 10 microns, megawatt instantaneous peak power, (micro)pulse widths of the order of a picosecond, (macro)pulse widths of the order of 10 microseconds, and (macro)pulse energies of the order of 10-100 millijoulses. Similar specifications apply for research in multiphoton photochemistry, the other major field of use for this device.

Analysis of these specifications in 1982 indicated that these requirements could be fulfilled using a single-section SLAC S-band linac driven by a long-pulse 30 megawatt klystron to achieve operation over the required energy range (28-45 MeV). A novel electron gun technology developed for this system, employing a thermionic lanthanum hexaboride button cathode mounted within a single-cell S-band accelerating cavity followed by an alpha-magnet momentum analyzer and buncher, provided the high current, low emittance e-beam required for operation [1].

The MkIII FEL system was first operated at Stanford University in 1985 [2]. Following the transfer of the FEL Laboratory to Duke in 1988, the MkIII was installed and recommissioned in the Laboratory's new facilities in 1991. The current operating specifications for this system are summarized in Table 1. Harmonic generation in phase-matched lithium niobate can be used to efficiently double the IR output of the MkIII for coverage of the spectral region at wavelengths shorter than 2 microns.

In addition to the uses contemplated for this system in surgery and multi-photon IR photochemistry, the high (2.856 GHz) rep rate train of optical pulses generated by the MkIII can be phase locked to enhance the spectral brightness by a factor of 39, thereby achieving unprecedented levels of spectrally pure, tunable, single mode optical radiation for applications requiring high spectral resolution and stability [3].

With the exception of the time lost due to the transfer of the Laboratory in 1988 and to a series of klystron-related problems in 1995 and 1996, the MkIII has reliably delivered more than 1000 hours a year of infrared radiation to its users in every year since it was first operated at Stanford.

Table: 1 Operating Parameters of the MKIII FEL System

Wavelength range	1.4 - 9.1 μm
Macropulse repetition rate	Single shot - 15 Hz
Macropulse duration	0.5 - 4 μs
Macropulse energy	1 - 100 mJ
Optical pulse repetition rate	2.86 GHz
Optical pulse width (uncompressed)	0.5 - 3 ps
Optical pulse energy	6 μJ
Peak power (uncompressed)	0.5 - 3 MW
Spectral width (transform limited	0.3% - 2%
Strehl ratio (diffraction limited)	> 0.8

2.2 The OK-4 FEL

The OK-4 FEL system was developed in collaboration with the Budker Institute of Nuclear Physics in Novosibirsk, Russia. The system utilizes Duke's 1.1 GeV electron storage ring, and the OK-4 undulator and optical system originally developed and commissioned at Budker for use on the VEPP-3 storage ring.

Table: 2 Recent Duke Storage Ring Electron Beam Parameters [10]

Operational Energy (GeV)	0.25 - 1.1
Circumference (m)	107.46
Impedance of the ring, Z/n (Ω)	2.75 ± 0.25
Stored current (mA)	
multibunch	155
single bunch	20 / 9
Bunch length, σs (ps)	
natural (low current)	15
with 5 mA in single bunch	60
Relative Energy spread σE/E	
natural (low current)	$2.9 \cdot 10^{-4}$
at 5 mA in single bunch	$1.1 \cdot 10^{-3}$
Peak Current (A)	
with 5 mA in single bunch	12
with 20 mA in single bunch	31
Horizontal Emittance (nm * rad)	
5 mA / bunch @ 700 MeV	< 10
3 mA / bunch @ 500 MeV	< 9

The Duke ring was designed with a 34 meter straight section to accommodate a long conventional undulators for FEL operation at extreme ultraviolet wavelengths, and to support circulating e-beams with the peak current and emittance required for operation at thesewavelengths. The design of the ring is particularly noteworthy for its dynamic aperture: the lattice will contain without loss a circulating electron beam with an energy spread as large as +/- 5%, permitting, in principle, the production of optical pulses with peak powers in excess of a gigawatt in the giant pulse mode [4].

The OK-4 undulator is configured as an optical klystron, comprised of two 10 cm period, 3.3 meter long electromagnetic wigglers separated by a buncher. The OK-4 optical resonator is symmetric, employing two spherical mirrors by one half the circumference of the ring with radii selected to achieve a 3.3 meter Rayleigh range equal to the length of the individual undulators [5].

The Duke storage ring was commissioned in the fall of 1994 prior to the installation of the OK-4 FEL system. The undulator and its vacuum system was installed in 1995. The e-beam parameters obtained following installation of the undulator are summarized in Table 2. Based on these e-beam parameters, the optical gain predicted for the OK-4 optical klystron and the optical losses estimated for the OK-4 resonator, the system has in its present configuration the capability to lase at wavelengths as short as 150 nanometers [6].

Table: 3 Measured Parameters of the OK-4 FEL [11]

Tuning Range (3.5 mA / bunch)	345 - 413 nm
Gain per pass (3.5 mA / bunch, 345 nm)	> 9%
Extracted Power (8 mA, single bunch, 380 nm)	0.15 W
Induced e-bunch length, σs (ps)	
low current	~35
with 3.5 mA in single bunch	~200
Induced energy spread (3.5 mA / bunch), σE/E	0.35%
FEL pulse length (ps)	
low current	~2.5
with 3.5 mA in single bunch	~20
Linewidth σλ/λ	$4 \cdot 10^{-4}$
Lasing life-time	2 - 4 hours

Lasing was demonstrated using the OK-4 system in the wavelength region between 345 and 413 nanometers in November 1996. The performance attained in this series of runs is summarized in Table 3. The parameters summarized in Table 3 correspond closely to those predicted by simulations of the system [7].

One of the most impressive results obtained during the November, 1996 run was the demonstration of the production of polarized, near monoenergetic gamma rays via intracavity Compton backscattering. In these experiments, a second bunch was injected into the ring separated from the first bunch by half the circumference of the ring. In this configuration, the laser radiation stored in the optical cavity collided head-on with the second stored bunch, yielding back-scattered Compton photons with energies up to 16 MeV. Measurements of the spectrum of

the backscattered photons showed that the energy spread could be reduced to 1.2% by collimation, in full accordance with theory [8]. The properties of the backscattered photons, allowing for the anticipated improvements in stored optical power and electron current, are of significant interest for applications ranging from precision nuclear spectroscopy to radiotherapy.

Instabilities in the power supply for the OK-4's buncher magnet in the November, 1996 run interfered with attempts to achieve lasing at shorter wavelength. However, the performance obtained at 375 nanometers, and the close correlation between simulations of the system and the observed laser parameters, give confidence that lasing can be extended to 193 nanometers and below in the system's present configuration. Improved performance should be possible following completion of the crotch chambers and absorbers required for high current operation.

2.3 Two-Color Operation

Considerable care was taken in the design of the Duke storage ring to insure that the circumference of the ring was an integral multiple of the RF wavelength (10.5 cm) at which the MkIII FEL operates. Given this integral relationship, the RF oscillators driving the high power RF systems for the ring and the MkIII can be phase-locked to permit the synchronized generation of infrared, ultraviolet, x-ray and gamma-ray pulses from these systems for use in two-color pulse-probe or two-color excitation experiments.

A proof of principle two-color IR/UV induced florescence experiment was conducted in 1995 to demonstrate this capability using the infrared light produced by the MkIII and the incoherent undulator radiation produced by the OK-4 FEL system [9].

3 ORGANIZATION AND FUNDING

The operating costs of the FEL light sources available in the Duke FEL Laboratory are financed by the Office of Naval Research's Medical FEL (MFEL) program through the Duke MFEL Center which provides beam time, specialized instrumentation, and other services to the researchers working in the fields of research supported by that program. These efforts currently include research on IR and UV laser surgery, imaging, and the detection and analysis of pathogens.

The development and commissioning of the MkIII and OK-4 systems, their injectors and accelerator drivers has been a joint effort of the Air Force Office of Scientific Research, the Army Strategic Defense Command and Army Research Office, the Office of Naval Research, and private donors. Special thanks are due the Office of Naval Research and the Medical FEL Program for the funds required to construct the beamlines and many other improvements required to serve the applications-oriented research efforts supported by that program.

4 FUTURE PROSPECTS

In the broadest terms, the mission of the Duke FEL Laboratory is to establish and nourish the partnership between researchers, technologists and engineers necessary to explore and evaluate the utility of FEL technology in basic and applied research. Only through such a partnership can the ingredients necessary to design, develop and apply this new technology be assembled in useful form.

It can reasonably be asserted that, with the commissioning of the major facilities of the Duke FEL Laboratory, a number of the key ingredients necessary to establish this partnership have been set in place: the operation of this facility demonstrates with reasonable clarity that the scientific and engineering community can provide the physical assets required to establish this partnership in a site as favorable as might be imagined with respect to the exploration of the technology. The commitment of operating funds by the Medical FEL program and the involvement of the researchers supported by that program is also reassuring.

What remains to be demonstrated is the broad intellectual contact and understanding which is a precondition both to the effective utilization of the technology and to the determination the lines of future development most critical to the interests of the research community. The attainment of this contact will require a continuing commitment not only to user support but to bilateral communications and understanding, a challenge equal to any of those with which we have had to deal in the prior phases of FEL development. The implementation of a collaborative, multidisciplinary approach to the applications research programs, encouraging the continued involvement and contributions of the FEL and accelerator technologists responsible for the facility, appears essential to bringing the technology to the point of successful application.

At Duke, we look forward in addition to the expansion of the physical facilities available to support the applications oriented research programs of the Laboratory and the MFEL Center, particularly the construction of the Keck Life Sciences Research Laboratory supported by a grant from the Keck Foundation, and the furnishing of this facility through an equipment grant funded by the Office of Naval Research. Construction of this facility will expand the space available for applications-oriented research by nearly an order of magnitude, to 5000 sq. ft.

We also look forward to the initiation of collaborative research programs in those additional areas of research which have the prospect of securing some benefit through the exploitation of FEL technology including those opportunities in spectroscopy, materials and nuclear research which have evoked the most active expressions of interest from our colleagues.

5 REFERENCES

[1] G.A. Westenkow and J.M.J. Madey, *Laser and Particle Beams* **2** (1985) 55.

[2] S.V. Benson, J.M.J. Madey, J. Schultz, M. Marc, W. Wadensweiler, and G.A. Westenskow *Nucl. Inst. and Meth.* **A250** (1986) 39.

[3] E.B. Szarmes, A.D. Madden, and J.M.J. Madey, *J. Opt. Soc. Am* **B13** (1986) 1588.

[4] V.N. Litvinenkow, B. Burnham, J.M.J. Madey, S.H. Park, and Y. Wu, *Nucl. Inst. and Meth.* **A375** (1996) 46.

[5] V.N. Litvinenko, *et al*, to be published in the proceeding of the conference **Free Electron Laser Challenges** (SPIE Photonics West, San Jose CA; February 1997).

[6] V.N. Litvinenko, B. Burnham, J.M.J. Madey, S.H. Park and Y. Wu, *op. cit.*

[7] V.N. Litvinenko, *et al; op. cit.*

[8] V.N. Litvinenko, *et al*; to be published in Physical Review Letters.

[9] G. Denbeaux, K.D. Straub, J.M.J. Madey, P.G. O'Shea, V. Litvinenko, E. Szarmes and G. Barnett, *Nucl Inst. and Meth.* **A375** (1996) 644.

[10] V.N. Litvinenko, *et al; op. cit.*

[11] V.N. Litvinenko, *et al; op. cit.*

FUTURE DIRECTIONS OF HIGH ENERGY PHYSICS

John Peoples, Jr., Fermi National Accelerator Laboratory
Batavia, Illinois 60510-0500 USA

Predicting the future is a risky enterprise, as the much-loved comic strip character Pogo once pointed out. Nearly 30 years ago, he confided to one of his friends that he stuck to predicting the past, because it was a lot safer than predicting the future. Pogo's observation was in my mind as I began a few months ago to think about what I would say to you on the subject of the future directions of high-energy physics.

I had thought that I would talk about global collaboration as the path to future high-energy colliders. Since the termination of the SSC in 1993, I and other directors of high-energy physics laboratories have told anyone who would listen that we must convince our government of the necessity of this collaborative approach to building future accelerators. However, just as I had grown comfortable with the idea of speaking to you on this subject, Representative Sensenbrenner, Chairman of the House Science Committee, began to question the terms of United States participation in the Large Hadron Collider at CERN, the highest-profile global collaboration in accelerator physics today. Congressman Sensenbrenner expressed serious concerns about the nature of the US agreement with CERN, and suddenly the prospects for global collaboration began to seem rather dim. It was then that I remembered Pogo's advice. Happily, the CERN Director General and the Secretary of Energy have since clarified the terms of the US involvement in the LHC to the satisfaction of Chairman Sensenbrenner and others, and he has expressed his support for US participation in the new accelerator.

To US physicists, it is very good news that global participation in the LHC is still on track. It is clear that there will be many more bumps in the road, but if we are cooperative and vigilant, we can succeed. While global participation may be the only path to the high-energy accelerators of the future, even Pogo could predict with confidence that it will not be easy.

One measure of the health of a field of science is the depth and significance of its unresolved questions. By this measure, the field of high-energy physics is in excellent health. Further, the nature of the important questions we confront can give us some guidance on the future directions of high-energy physics. I have chosen four questions to talk about, because the accelerators that we will need to answer them have been presented at this meeting.

I doubt that the current generation of accelerators, or even the next generation, will fully answer these questions. But I do believe that they will bring new knowledge and deeper insight into the questions. My four questions are these:

- What is the source of electroweak symmetry breaking?
- Why is there a preponderance of matter in our part of the universe, when the laws of physics that seem to govern the subatomic universe put matter and antimatter on the same footing?
- What is the cause of the unexpected and unexplained deficit of electron neutrinos emerging from the sun, and the cause of the unexplained ratio of electron neutrinos to muon neutrinos produced when cosmic rays slam into the upper atmosphere?
- What is the universe made of?

Before I speak more about the four important questions and their implications for future directions, I want to remind you of the current state of elementary particle physics. All of the familiar forms of matter, such as protons and electrons, and some not-so familiar forms of matter, such as B mesons and top quarks, can be reduced to a set of spin-1/2 particles named quarks and leptons. The quarks, of course, are what make up dull, uninteresting particles such as the proton. The quarks and leptons interact with one another through the exchange of three distinct types of spin-1 particles called gauge bosons. These three types of gauge bosons define the three forces familiar to all those of us who build accelerators. The photon, the boson of electricity and magnetism, is the most familiar to us, because it is what we manipulate to make all of our wonderful accelerators, storage rings, and power sources to create and control beams of charged particles in accelerators. Electricity and magnetism, which Maxwell unified, is the simplest of the forces: the photon is coupled to the charge of a particle, and it is just a simple number. It was the first field for which we understood the elegant properties of gauge interaction.

Of the other two forces, the weak interaction is next in importance, to accelerator builders. When the beams that we so carefully accelerate deviate from the desired path, they typically hit a piece of copper, iron, niobium, or some other piece of a vacuum chamber, RF cavity, or magnet. Sometimes the result is catastrophic, and we get a hole in a vacuum chamber; but most of the time we simply experience a loss of beam. Whenever our beams go astray, however, the objects they touch become radioactive. Thanks to the weak interaction, that radioactivity persists after the beams go away. The weak interactions show up as beta decay, carried by three gauge bosons: the W bosons, which come in positive and negative varieties, and the Z boson, which is neutral. The bosons are nearly a hundred times as massive as the proton, and because they are so massive, the range of the weak force is very small, roughly 2×10^{-16} cm or two thousandths of a fermi. Recall that a proton has a diameter of about one fermi, or 10^{-13} cm. The only way to explore this weak force is in very high energy collisions.

The model I have described is a great picture. It explains almost everything that we have been able to do with accelerators. But there are a few flaws. First of all,

0-7803-4376-X/98/$10.00 © 1998 IEEE

the Standard Model has a glaring mathematical weakness. It would be just fine mathematically if all of the particles in the theory, including the gauge bosons, were massless. However, this is not the case— all the quarks and the charged leptons do have masses, and so do the bosons, except for the photon. The W and Z are as massive as a silver atom.

If the particles were massless, then electricity, magnetism and the weak interaction would constitute a beautiful, unified, elegant theory. But the existence of massive particles leads to another question: Why are the W and Z different? The Standard Model gives mathematically inconsistent results for energies

$$E_{cm} > \sqrt{\frac{1}{2G_F}}$$

Peter Higgs proposed a way around the problem by introducing a spin-0, scalar "particle" that could give the W and Z a mass, retain the electroweak unification, and give the quarks and leptons masses. This particle, the Higgs, is named for him.

There is an aspect of the theory that is contrived. It explains the nine very different masses of the six quarks and three charged leptons by nine different coupling constants—not much of an explanation. Only one of these couplings, the coupling of the top quark to the Higgs, appears reasonable, because the mass of the top is 175 GeV, a value that may be an accident or may have deep significance.

The model that adds one spin-0 Higgs particle to what we already know is the minimum Standard Model. It has been highly successful for many years. LEP I, and now LEP II, have mounted challenge after challenge to the Standard Model, through incredibly precise experiments, and the theory has stood firm.

However, the Minimum Standard Model is not the only way to provide a consistent description of matter. There are at least two other ways: supersymmetry and dynamical symmetry breaking, both very interesting theories. Supersymmetry requires that for every spin-1/2 fermion, there must be a super partner with spin 0. The spin 1 gauge bosons should also have super partners with spin 1/2. Supersymmetry would automatically double the number of elementary particles and gauge bosons. In order for this theory to represent nature, the superparticles would have to be very massive, of order 246 GeV, although the lightest could be as light as 70 GeV. If it does turn out to be that light, experimenters will find it at LEP II in the not-too-distant future.

An alternative theory is that the quarks and leptons are made up of still smaller but more massive fermions—let me call them technifermions. The technifermions have very strong interactions, just as the quarks do. Again, this model would give us many new particles. If this were the correct theory, we would not expect technicolor to produce observable effects until collision energies exceed 1 TeV.

It really doesn't matter to accelerator builders whether nature chooses to break electroweak symmetry by supersymmetry or technicolor, because, either way, to find out one has to build much higher-energy accelerators than we have today.

The Tevatron and LEP II may get glimpses of the Higgs and perhaps even of the lightest supersymmetric particles. The LHC offers the best hope to explain the nature of electroweak symmetry breaking, but even that cannot be the end of the story. The pursuit of ever-higher energies will surely be one of the future directions of elementary particle physics. The course it takes will depend on whether we can continue to contain the cost of the great colliders. The SSC was touted as the most expensive scientific instrument ever to be started. In the end, it was too expensive for an era of deficit reduction.

As we pursue ever higher collision energies, lepton colliders offer different possibilities from hadron colliders. Leptons are fundamental particles with no internal structure, unlike hadrons, with their complex internal structure of quarks and gluons—"colliding garbage pails," in the late Luis Alvarez's well-known metaphor. When hadrons collide, among the banana peels and coffee grounds, every now and then they produce a pearl. The possibility of finding a pearl among the coffee grounds gives hadron colliders the name "discovery machines." Because of the complex hadron structure, it rarely happens that one gets as much mass in new particles from hadron collisions as goes in through the energy of particle acceleration, although occasionally one comes close.

In contrast, lepton collisions are clean; they don't produce the "garbage" of hadron collisions. All of the collision energy is available for new particles, at specified levels of energy. Thus a lepton collider can "sit on" the energy of a postulated "pearl" and go and look for it, rather than sending experimenters poking thought the coffee grounds and banana peels of hadron collisions. Electron accelerators take advantage of this property to create clean, high-energy collisions. However, at high energy, electrons lose energy to bremsstrahlung and synchrotron radiation; and the higher the energy the more of it they lose, effectively limiting the achievable energy of electron colliders. Muons, however, offer an interesting possibility for lepton colliders, because, with a mass 207 times the mass of the electron, accelerated muons do not suffer such large energy losses.

In fact, muons would appear to be the perfect particles for a collider—they give clean lepton collisions and they don't radiate energy—were it not for one flaw: they don't live very long. Muons are only muons for two microseconds before they decay into electrons and neutrinos. However, accelerating them to high energies can extend their lifetimes to 40 milliseconds, long enough to take 1,000 turns around a collider ring, and perhaps long enough to make themselves useful. The trick in building a successful muon collider is to find a way to take advantage of the muon's useful qualities within its short lifetime, and to deal with the products of its decay.

It's quite a trick, but here are the basics for creating muon collisions: Send an intense beam of protons to a target, producing pions. Capture the pions in a magnetic field, where they decay into positive and negative muons. Cool the muons into intense, coherent beams and quickly accelerate them to collision energy. Collide. Repeat as necessary.

Muon colliders are one avenue of exploration for future colliders at the energy frontier beyond the LHC. Another is the VLHC, or Very Large Hadron Collider, which would be a successor to the LHC, at higher energy and—of necessity—lower cost per TeV. It will take a great R&D effort to bring this cost down. To be successful, a new accelerator will need to probe physics at a scale at least on order of magnitude beyond the LHC, for an energy of 100-200 TeV in the center of mass. The VLHC could be built with either high-field or low-field magnets; the higher the field, the smaller the size of the collider.

About 150 physicists interested in a future VLHC held a conference at Fermilab in March. The conference poster showed Fermi's famous "Accelerator In Space" transparency, which Fermi used during his retiring presidential address to the American Physical Society at Columbia University on January 29, 1954. The title of his talk was "What can we learn with high energy accelerators?"

At the time, many more elementary particles were turning up than anyone had suspected. Physicists were barely making out the outlines of elementary particle physics. Fermi asked then: What should we do? and answered that question: Accumulate more data with higher and higher energy accelerators.

Fermi made a plot of energy and cost of accelerators as a function of time. He used that plot to extrapolate 40 years to 1994: he got a \$5 \10^{15} eV, for a 5 PeV accelerator, at a cost of \$170B (probably in 1954 dollars). Its energy was comparable to the highest-energy cosmic-ray proton known at the time. The design on the workshop poster is a fanciful "preliminary" design of such a gargantuan machine: around the earth with a radius of 8000 km and a magnetic field of 20,000 Gauss—above the orbit occupied by the space shuttle. The accelerator he was talking about was a fixed target one. If one converts the 5 PeV to a collider energy one obtains 3 TeV. So the energy in the center of mass of Fermi's "accelerator in space" is comparable to the Tevatron's energy today.

This is very interesting. Clearly, at the time of the talk, this extrapolation must have seemed completely impossible to reach, both technologically and financially. Yet Fermi's dream of reaching a center of mass energy of the order of the TeV has been achieved, not only for a much smaller price but also long before 1994. His extrapolation in energy by three orders of magnitude to the end of the century is actually amazingly accurate when compared to the SPS, Tevatron, and LHC. The TeV center of mass energy that accelerator physicists have now achieved should be compared to the few GeV the Bevatron would provide later in 1954. Fermi's machine did not take account of technical innovations, and no one in 1954 could have predicted all the milestones that would enable us to achieve that energy. To cite a few: discovery of the antiproton, of superconductivity that can achieve high fields and enormous savings in electric bills, the invention of stochastic cooling, advances in cryogenics and controls.

We can hope that other brilliant discoveries and ideas will allow us to reach the 100 TeV frontier in the lifetime of at least some of us.

Of course, the question of electroweak symmetry breaking is not the only question in particle physics, just as ever-higher energy colliders are not the only answer. There are other important questions, and other ways of answering them.

Color change does not appear to change the mass of the quarks, so irrespective of color, all quarks have the same mass. Up and down quarks have different masses because the weak force appears to distinguish between the weak isospin 1/2 quarks and the weak isospin -1/2 quarks. So we have six different masses for the quarks, and perhaps six different masses for the leptons. Although the theoretical structure is perfectly consistent with zero-mass neutrinos, as I will note later, certain astrophysical observations may not be.

Matter dominates our corner of the universe, the galaxy. Other than the paltry amount of antimatter created when high-energy cosmic rays collide with particles in our atmosphere, there is no evidence for antimatter in our galaxy. On the other hand, the interactions of our friendly quarks and leptons produce matter and antimatter in equal amounts. With one exception, there is no way to tell matter from antimatter. The exception comes in the decay of the long-lived neutral K meson, K_L^o . The K_L^o meson is made of nearly equal amounts of an anti-K^0 and a K^0. There is a small difference of two parts in 10^{-3}, and that is all that we know. The decay of K_L^o is said to violate the symmetry obtained by changing all particles into their antiparticles and changing their intrinsic parity. The electromagnetic and strong interactions are invariant separately under charge conjugation and parity, and the weak interaction. There is little room to incorporate the CP violation into the Standard Model.

The search for an understanding of the difference between matter and antimatter is for the moment focused on searching for a deeper understanding of CP violation in the decays of K_L^o and searching for CP violation in the decays of neutral and charged B mesons. There is an immense amount of activity in this area. The KEK synchrotron, the Brookhaven AGS, the CERN SPS, and the Fermilab Tevatron all support fixed-target experiments designed to look for further evidence of CP violation in K decays. The holy grail is direct CP violation. What we have found so far is CP violation that occurs as a consequence of the fact that the state vector that is a K_L^o has slightly unequal amounts of K^0 and anti-K^0. This is CP violation through mixing. By comparing very precise measurements of the relative rates of the K_L^o into two charged pions and two neutral pions with equally precise measurements of the relative rates of K_S^o decaying into two charged pions and two neutral pions, it may be possible to detect direct CP violation in K decays.

But nature could be unkind. This comparison of measurements could give a null result even though direct CP violation does exist. At a specific value of the top quark mass close to or equal to 175 GeV, the experiment could give a null result. Alternatively, the search for very rare decays of K mesons has been underway for more than a decade. The branching ratios of the K_L^o into two neutrinos and a neutral pion is only 10^{-11}, and yet it is a primary constituent. At this moment, the only way to observe such small branching ratios is with intense neutral kaon beams, and these can only be produced by proton collisions. In spite of the fact that these decays have gone undetected, two medium-energy proton synchrotrons—one, the Fermilab Main Injector, under construction and one, the KEK Japanese Hadron Collider, just proposed—could be used to produce kaon beams with enough intensity to reach these limits.

Because one expects a similar mixing to occur in neutral B decays, there is a strong expectation to observe CP violation in neutral B decays. There are three e^+e^- B factories nearing the end of construction, all designed to produce the Υ (4S), which decays into a $B\bar{B}$. The PEP II B factory and the KEK B factory use beams of unequal energies. Both should be in operation with complete detectors in 1999. Both B factories expect to reach and then exceed luminosity of $3x10^{33}$ $cm^{-2}sec^{-1}$. The luminosity record for colliders of any sort is held by CESR at Cornell. At these meeting, they have reported that CESR has reached a luminosity of $4x10^{32}$, well on their way to reaching their luminosity goal of $6x10^{32}$.

Certainly the exploitation of these factories by increasing the luminosity will be one of the future directions of high-energy physics. But this is a very hard way to make a living. There may be a quicker path to the goal of measuring everything that can be measured about B decays. B's are made of quarks, and quarks, even b quarks, can be more readily pair-produced in hadron collisions. Already, more B's decaying into the preferred decay mode of $B\rightarrow J/\psi K_S^o$ have been reconstructed by the CDF collaboration than anywhere else. At the Tevatron, the cross section for all $B\bar{B}$ is $3x10^4$ times larger than the cross section for e^+e^- production of $B\bar{B}$ pairs. The CDF detector is not particularly efficient at detecting B decays. When CDF and DZero begin running again in the year 2000, they will certainly contribute to the understanding of B decays, particularly B_S decays, which are not easily detected at e^+e^- B factories. When LHC-B begins operation sometime after the year 2005, it will bring an even more powerful detector to bear on the search for CP violation in the B system. Given all of that activity, CP violation will surely define one of the future directions of our field.

However, it is unlikely that K decays and B decays will reveal the whole story. In fact, they won't. There must be another set of interactions that transform quarks into leptons. These interactions will be characterized by a mass scale somewhere between the electroweak scale and the Planck scale. These interactions should lead to proton decay, and they must distinguish between matter and antimatter. The current view in particle physics is that they favor the production of quarks over antiquarks, and leptons over antileptons. The reaction rates must ultimately lead to the microwave background photon-to-baryon ratio of 10^9.

As in the case of electroweak symmetry breaking, we may learn a lot about CP violation from low-energy experiments, but a full explanation will require higher energy colliders, probably with energies that are beyond our dreams.

Let me now discuss a third future direction. As in the case of matter-antimatter asymmetry, there are also astrophysical results involving neutrinos that cannot be explained by the minimum Standard Model. The flux of electron neutrinos from the sun is a factor of 2 to 2.5 smaller than predicted by a well-developed model of the sun. Four experiments have measured the solar electron neutrino flux, and all give a consistently low result.

A second astrophysical neutrino experiment has also yielded unexpected and unexplained results. Neutrinos are produced in the upper atmosphere when cosmic rays slam into it and produce pions and kaons, some of which decay before they have a chance to interact again. The pion decays produce a muon neutrino and a muon. The kaon decays yield a muon and a muon neutrino most of the time, and some of the time and electron neutrino and an electron. Typically, the muons decay before they reach the ground to yield a muon neutrino, electron antineutrino, and an electron. If one builds a massive neutrino detector deep underground, where the only particles that can penetrate the earth and reach the detector are neutrinos, one expects to detect roughly twice as many muon neutrinos as electron neutrinos. But, in fact, the fraction of electron neutrinos is larger than expected. Five years ago, when experimenters first announced this puzzling result, the statistical accuracy and systematic errors were too large to allow a definitive statement. Five years make a very big difference, however, and now the errors are smaller and understood. Within the minimum Standard Model there is no explanation for this result. The precision of astrophysical measurements can and will be improved.

There is a plausible explanation for both the solar and atmospheric neutrino observations. If neutrinos have a small mass, less than a few electron volts, and if the mass eigenstates are just a little different from production eigenstates, then mixing can occur; and one kind of neutrino can change into another. For example, if an electron neutrino emerged from the sun and changed into a muon neutrino for part of the time as it traveled 150 million kilometers to the earth, this could account for the solar neutrino deficit. If the muon neutrinos produced as a consequence of collisions of cosmic rays with particles in the upper atmosphere changed into tau neutrinos, one could explain the relative paucity of atmospheric muon neutrinos. These proposals are plausible, but unproved. The only way to truly understand what is going on will be to build very intense neutrino beams with well-defined composition and momentum spectra. This will require

intense proton beams. Several laboratories with proton beams are currently considering proposals for long-baseline neutrino experiments

Although the Standard Model tells us that the fourth force, the strong force, transmitted by the gauge bosons known as gluons, gives rise to most of the mass of the matter that we can see, the stuff that makes up most of the universe remains a complete mystery. Neither particle physicists nor astrophysicists know the nature of 80 to 90 percent of the matter in the universe. For decades, since Zwicky's observations of galactic rotation curves in the 1930s, physicists have recognized that there must be more matter in the universe than meets the eye. During the past 60 years, still stronger evidence for unseen mass has come from observing the motions of clusters of galaxies and from examining the large-scale structure of the universe.

What is this unseen mass, this dark matter? Conjectures range from ordinary matter that takes the form of huge Jupiter-like objects that give off too little light to be observed, to small black holes, to fundamental particles such as neutrinos, or more speculative wisps of the fundamental fabric. Among the candidates is the class of weakly interacting massive particles, or WIMPSs, also known as cold dark matter. Such particles would have been created in the energetic early universe and have "frozen out" or stopped annihilating one another as the universe cooled and their energy decreased. According to this scheme, a large number of WIMPS could be left in the present universe. If so, the weak force provides the only means of detecting them. Experimenters have designed underground crystal detectors that they hope will be sensitive enough to detect the few WIMP scattering events expected to occur as the earth and sun move in their galactic orbit though the hypothesized sea of cold dark matter. Experiments such as these, together with neutrino experiments and other future high-energy physics experiments, and advances in astrophysics will all help to answer the last of our four questions, What is the universe made of?

The future of high-energy physics lies in the questions that are being posed in particle physics and astrophysics. For the last 50 years, particle physics and high-energy physics have been almost synonymous. We have made progress in understanding the structure of matter and energy by building accelerators with ever higher energy. Our future progress along this path toward answering the great questions that confront us will depend on our ability to collaborate with our colleagues in the global community that constitutes high energy physics.

FUTURE DIRECTIONS FOR NUCLEAR PHYSICS

C.K. Gelbke, National Superconducting Cyclotron Laboratory and Department of Physics and Astronomy, Michigan State University, East Lansing, MI 48824-1312

Abstract

I will summarize opportunities for nuclear science, particularly those given as priority recommendations by the DOE/NSF Nuclear Science Advisory Committee in the 1996 document "Nuclear Science: A Long Range Plan", and mention selected new initiatives abroad.

1 INTRODUCTION

The United States DOE/NSF Nuclear Science Advisory Committee (NSAC) provides advice to the agencies on nuclear science priorities. At approximately six-year intervals, NSAC is charged by the agencies to conduct a new study of scientific opportunities and priorities in U.S. nuclear physics research and to recommend a long rage plan which then becomes the guiding framework for a coordinated advancement of the nation's basic nuclear physics research program.

In October 1994, NSAC was charged to conduct a new study and formulate a new long range plan (LRP) for nuclear science with realistically achievable goals within budgetary guidelines provided by DOE and NSF. Summarized below are important elements of the planning process, key science opportunities, and NSAC's main recommendations.

2 THE PLANNING PROCESS

The NSAC long range planning process is done in close cooperation with Division of Nuclear Physics (DNP) of the American Physical Society, both in setting up the LRP Working Group and in seeking broad community input via a series of topical town meetings.

These town meetings were organized around six main topics:

- Nuclear Structure, Low Energy Nuclear Reactions, and Radioactive Beams;
- Electromagnetic Physics; Intermediate and High Energy Heavy-Ion Reactions;
- Theory;
- Electroweak Interactions, Astrophysics and Non-Accelerator Experiments;
- Intermediate-Energy and High-Energy Hadron Beams.

Each town meeting was planned by a steering group of widely recognized leaders in the field, who were also responsible for documenting the main findings and recommendations of the town meeting in a white paper.

Subsequent to obtaining this broad community input, in March 1995, the entire LRP Working Group (consisting of 64 scientists) convened for a week of presentations and deliberations at Caltech. The main recommendations for the new LRP were formulated at this meeting. In April 1995, these recommendations, together with an outline of the LRP document, were presented to the nuclear science community at the DNP spring meeting of the American Physical Society, and an interim report containing the main LRP recommendations was transmitted to the agencies.

The final LRP document, "Nuclear Science: A Long Range Plan", was published in February 1996 and widely distributed to the DNP membership, the U.S. Congress and other interested parties. Apart from discussing major research opportunities for nuclear science and the facilities and resources needed to do this research, the LRP document also addresses important issues concerning education, international collaboration, and interdisciplinary and societal applications.

3 NUCLEAR SCIENCE THRUSTS

Nuclear Science is a multi-faceted field of research primarily aimed at understanding how the elementary building blocks of matter interact to form complex mesoscopic systems, nuclei, or macroscopic systems, (neutron) stars, which form the underpinning of the material world as we know it. While much has been learned about nuclei close to the valley of stability and their properties at modest excitation energies, little is known about nuclei very far from the valley of stability or about nuclear matter at sub and supra-normal densities and high temperatures where phase transitions from liquid to gas to quark-gluon-plasma are predicted to take place. Understanding the origin of the elements, i.e. the detailed paths of nucleosynthesis in the cosmos, requires knowledge of the properties of many isotopes with unusual neutron and proton numbers. Detailed investigation of these "exotic" nuclei is becoming possible with newly emerging radioactive beam facilities and innovative experimental techniques. Also little is known about how the quark-structure of nucleons influences the detailed properties of nuclei. These broad (as well as many detailed) questions present major challenges to the field of nuclear science.

Modern nuclear science can be cast into four scientific thrust areas which are described in Chapters I - IV of the LRP document. These four chapters, together with some of the identified research topics, are:

0-7803-4376-X/98/$10.00 © 1998 IEEE

1. *Nuclear Structure and Dynamics: Exploring the Limits*

- Properties of nuclei far from stability:
  Limits of nuclear stability.
  Extended distributions of nearly pure neutron matter.
  Disappearance of shell structure.
  Neutron-proton pairing: new form of p-n superfluidity for N=Z nuclei.
  Proton emitters: tractable examples of three-dimensional quantum tunneling.

- New Aspects of Nuclear Rotation and Vibration:
  New regions of superdeformation; hyperdeformation?
  Identical bands in neighboring nuclei.
  Multi-phonon excitations.
  New symmetries.
  Transition from order to chaos.

2. *To the Quark Structure of Matter*

- Quark-Gluon Structure of Hadrons.
  Origin of the nucleon spin.
  The role of sea-quarks.
  Structure of the excited states of the nucleon.
  Glueballs.

- Hadronic Interactions.
  Breakdown of meson exchange picture.
  Λ–N, Δ–Δ interaction, hypernuclei.
  Meson-meson interaction ($\pi^+ - \pi^-$ "atoms").
  In-medium modifications.
  Quark-gluon content of nuclei.
  Vector meson production, color transparency.

3. *The Phases of Nuclear Matter*

- Liquid-Gas Phase Transition.
  Multi-fragment disintegration of hot and expanded nuclei.
  Equation of state and its isospin dependence.
- Quark-Gluon Plasma.
  Chiral symmetry restoration.
  Flavor equilibrium and strangeness production.
  Color deconfinement and J/Ψ suppression.

4. *Fundamental Symmetries and Nuclear Astrophysics*

- Nuclear Astrophysics with Beams of Rare Isotopes.
  Experimental benchmark tests for theories of nucleosynthesis.
  Supernovae physics: spin strength of unstable nuclei.
  Primordial nucleosynthesis of light elements in Big Bang.
- Solar neutrino puzzle, neutrino oscillations.
- Tests of symmetries in weak interactions.

4 MAIN LRP RECOMMENDATIONS

In view of these major scientific thrusts, the 1996 LRP made the following priority recommendations:

1. The highest priority for U.S. nuclear science is vigorous pursuit of the scientific opportunities provided by the nation's recent investments in forefront instrumentation and facilities. Scientific, technological and educational returns commensurate with these investments will require resources consistent with those in the charge requesting this Long Range Plan.

2. RHIC remains our highest construction priority. Its timely completion and operation are of utmost importance for discovery of the quark-gluon plasma and for study of this new form of matter.

Recommendations for new initiatives are:

3. The scientific opportunities made available by world-class radioactive beams are extremely compelling and merit very high priority. The U.S. is well-positioned for a leadership role in this important area; accordingly

- *We strongly recommend the immediate upgrade of the MSU facility to provide intense beams of radioactive nuclei via fragmentation.*

- *We strongly recommend development of a cost-effective plan for a next generation ISOL-type facility and its construction when RHIC construction is substantially complete.*

4. Multi-GeV proton beams are an essential tool for forefront studies aimed at elucidating the quark structure of nucleons and nuclei.

- *We strongly recommend funding for the Light-Ion Spin Synchrotron (LISS) as a major NSF research equipment initiative. This facility will build on Indiana University's leadership in stored, cooled, polarized proton beam technology to enable innovative experiments addressing the short-range behavior of nuclear forces.*

- *The RHIC/AGS complex, in addition to its core heavy-ion program, will offer significant capabilities with hadron beams. In particular, the collisions of polarized proton beams in RHIC will enable unique studies of quark and gluon distributions inside the nucleon. These studies are important for understanding hadron structure and should be pursued.*

Other recommendations address the pressing need for new equipment and support for theory, international collaboration, education and outreach, and interdisciplinary research.

5 INTERNATIONAL CONTEXT

The unique opportunities offered by intense beams of rare isotopes ("radioactive beams") are recognized world-wide, and a number of projects are underway or in the advanced stages of planning to provide significant radioactive beam capabilities.

In addition to small-scale ISOL facilities at Louvain-La-Neuve and (more recently) Oak Ridge National Laboratory, a number of new ISOL facilities are under construction, including the SPIRAL project at GANIL (E_{max}/A = 25 MeV, expected completion date: 1998), REX ISOLDE at CERN (E_{max}/A = 2.2 MeV, expected completion date: 1999), and ISAC at TRIUMF (E_{max}/A = 1.5 MeV, expected completion date: 2000).

A major new projectile fragmentation facility has been proposed by RIKEN and approval has been obtained for the first phase, consisting of a superconducting separate-sector cyclotron and a fragment separator. More recently, GSI has been discussing plans for a high-intensity heavy-ion facility for nuclear physics with radioactive beams which would also allow plasma-physics studies pertinent to the problem of inertial-confinement fusion driven by intense beams of heavy-ions.

ISOL-type radioactive beam capabilities are also being considered for the proposed Japanese Hadron Facility (JHF), using the 3 GeV, 200 μA beam from the booster synchrotron. The final beam energy and intensity of the JHF will be 50 GeV and 10 μA, respectively. If funded, the JHF would become the world's premier high-intensity, high-energy hadron facility; funding may be granted as early as 1998.

Well beyond the year 2000, new opportunities for research with ultra-relativistic heavy ion beams will become available at the Large Hadron Collider (LHC). In addition, there is interest in a new high-energy (E > 15 GeV) electron facility for nuclear physics research (possibly at DESY or at CEBAF), but no definitive proposals have been put forward.

6 PRESENT U.S. SITUATION

In the past year, the Department of Energy and the National Science Foundation have taken vigorous steps to implement the priority recommendations of the LRP. Positive developments for accelerator-based facilities include:

- Jefferson Lab now operates at the design energy of 4 GeV with experimental programs in all three experimental halls and plans to run experiments at 6 GeV in 1998.
- RHIC construction is proceeding well, and commissioning is expected in 1999.
- With significant funding contributions from Japan, the spin physics program at RHIC will be implemented and incorporated into the base program.
- The NSCL Coupled Cyclotron upgrade has been approved by the National Science Board in 1996, and construction funds have been provided by the NSF in FY97.
- Planning for a full-powered ISOL-type facility is moving ahead vigorously with workshops laying the foundation for a Conceptual Design Report scheduled for the second half of 1997.

In spite of these very positive developments, there is reason for concern. Congress's attempt of balancing the budget by reducing discretionary spending while protecting entitlements has lead to significant reductions in basic research funding. Adjusted for inflation, funding for basic nuclear physics research has decreased 31% for NSF and 5.3% for DOE between 1989 and 1997. Already in 1997, budgets for nuclear physics fall short of the minimum financial resources needed to properly implement the LRP. Nuclear Physics Funding by DOE is $315.9M for FY97, i.e. $9.1M short of the minimum estimate of the LRP. Funding by NSF is $39.81M for FY97, i.e. $5.2M below the minimum estimate of the LRP.

Careful long-term planning and consistent major investments in the past have provided forefront facilities such as the Jefferson Lab and RHIC, as well as a few unique smaller scale research facilities and programs at major universities. Together, these investments form the basis of the U.S. nuclear physics program. Even though the importance of nuclear science and its contributions to the country's technological infrastructure are widely recognized by Congress and the Executive Branch, our scientific and technological leadership in this critical field is now seriously threatened by decreases in funding. Fortunately, the science community is becoming increasingly effective in articulating the importance of basic research to Congress and positive statements by congressional leaders on the importance of science for the nation's well-being are becoming more frequent.

FOURTH GENERATION LIGHT SOURCES*

Herman Winick, Stanford Linear Accelerator Center
Stanford, CA 94309, USA

1 INTRODUCTION

Since the first indirect observation of synchrotron radiation (SR) in 1945[1] there has been a rapid growth in its scientific use. Starting in the 1950's cyclic electron synchrotrons were used, yielding to the superior properties of electron storage rings starting in 1968. Storage ring sources have evolved through three generations. First generation rings are those built for high energy physics research. The second generation are those built from the start as light sources. Third generation rings coming on-line since 1992 have many straight sections for insertion devices and lower electron beam emittance. Undulators on third generation rings provide ~10^4 higher brightness than bend magnet sources of earlier rings. There are now about 40 operational rings of all generations used as SR sources in 14 countries, 10 of which are third generation sources.

As remarkable as this performance improvement has been, even higher brightness and laser-like coherence appear achievable and are needed scientifically, particularly at soft and hard X-ray wavelengths. Reaching higher performance levels is the goal of fourth generation sources which we may define as sources which exceed the performance of previous sources by one or more orders of magnitude in an important parameter such as brightness, coherence, or shortness of pulse duration. The most promising directions for fourth generation sources in the wavelength range from the VUV to hard X-rays are storage rings with even lower emittance than third generation rings, and short wavelength free-electron lasers (FELs) which offer sub-picosecond pulses with full transverse coherence.

The extraordinary properties of SR stem largely from the fact that the copius emission by relativistic electrons curving in magnetic fields is concentrated into an instantaneous forward cone with opening angle given by $\gamma^{-1} = mc^2/E$, the electron's rest mass energy divided by its total energy. For example, this angle is only 0.1 mrad at 5 GeV. This small natural emission angle is key to understanding the properties of SR and the characteristics of the different source generations and types of insertion devices.

2 EARLY SOURCES

From the early 1950's to the early 1970's cycling electron synchrotrons, developed for high energy physics research, were used as SR sources. These are the ***zeroth generation***. Although their SR is intense, cycle-to-cycle fluctuations and spectral, intensity, and source position changes within a cycle pose limitations. With the development of high energy physics storage rings, SR became available with constant spectrum and source position, and long stored-beam lifetime. These are the ***first generation*** SR sources. The superior radiation from these rings led to a rapid growth in SR programs, and their evolution from a parasitic effort to partly dedicated, and often fully dedicated, use of the ring.

Radiation from the bend magnets of first generation rings provided about 10^5 times more tunable, continuum radiation than conventional sources, including rotating-anode X-ray tubes. The immediate successful use of this radiation, even in parasitic operation, resulted in an explosion of scientific interest[2]. The demand for SR in the mid-1970's led Europe, Japan and the US to construct ***second generation*** SR sources; rings fully dedicated to SR research. When designs of the first round of these were finalized there was no experience using SR from wiggler and undulator insertion devices. Thus these rings were designed for many bend magnet beam lines, and a few locations in which insertion devices could be added later.

3 WIGGLERS AND UNDULATORS

Starting in 1978 wiggler and undulator insertion devices (periodic magnets placed between the bending magnets of a ring) were tested in first generation rings[3], offering higher flux, brightness, and spectral range than bend magnet sources. Although wigglers and undulators are both periodic magnetic structures, they produce different spectra due to the different angular deflection in each pole. For a wiggler this deflection is larger than the natural emission angle of synchrotron radiation ($\gamma^{-1} = mc^2/E$). For an undulator it is typically $\leq\gamma^{-1}$, so undulators provide more concentrated radiation than wigglers or bend magnets. Furthermore, the small deflection in each undulator pole means that poles can be short, so that more can be accommodated in a given length. Permanent magnet technology has had a major impact on insertion device design, since the absence of coils allows for even more poles.

As an electron traverses an undulator, interference in the radiation at each of the collinear source points enhances intensity at certain wavelengths, resulting in a quasi-monochromatic spectrum rather than the broad continuum of bend magnet and wiggler sources. Peaks occur at wavelengths given by $\lambda=\lambda_u[1 + K^2/2 + \gamma^2\theta^2]/(2\gamma^2)$ and

* Work supported by the US Dept. of Energy, Office of Basic Energy Sciences, Contract DE-AC03-76SF00515

0-7803-4376-X/98/$10.00 © 1998 IEEE

its harmonics. λ_u is the undulator period, θ is the observation angle, and $K=0.934B[T]\lambda_u[cm]$ is the angular deflection in each pole in units of γ^{-1}. Peaks are tuned by varying the electron energy or the undulator field.

4 BRIGHTNESS, EMITTANCE, AND THIRD GENERATION SOURCES

The concentration of the radiation is called the brightness, measured in photons/(s,mm^2,mrad^2,0.1%bandwidth). The brightness produced by a beam of electrons depends on the electron beam transverse size and divergence, the product of which is called the emittance. Horizontal emittance ($\varepsilon_x=\sigma_x\sigma_{x'}$) is determined by the electron energy and the ring design. The vertical ($\varepsilon_y=\sigma_y\sigma_{y'}$) depends primarily on coupling to the horizontal and can be as small as ~0.5% of the horizontal emittance. Second generation sources were originally designed with horizontal emittances of one hundred to several hundred nm-rad, resulting in undulator beam brightness of up to ~10^{16}.

Since further reduction of electron beam emittance would result in even higher brightness, in the mid-1980's efforts began to design and construct a new round of storage rings, the ***third generation*** sources. These have many straight sections for insertion devices and electron beam emittance of about 5-20 nm-rad. These rings began operation in the early 1990's, reaching undulator brightness as high as 10^{20}, opening new opportunities for research. A brightness of 10^{20} is about 10^{13} times higher than that provided by rotating-anode X-ray tubes. Although spectacular, this brightness is far from fundamental limits. Further reduction of electron beam emittance would result in increased photon beam brightness, particularly at X-ray wavelengths. Achieving this is one of the most important objectives of fourth generation sources.

5 DIFFRACTION LIMITS

Diffraction sets an ultimate limit, on the geometric properties of photon beams. Because of diffraction the lower limit on the photon beam emittance is given approximately by the wavelength, λ. Using standard deviation values for Gaussian distributions, this diffraction-limited photon beam emittance is given by $\lambda/4\pi$. For light produced by electron beams, photon beam brightness increases as electron beam emittance decreases until the electron beam emittance reaches a value of ~$\lambda/4\pi$. Thus third generation rings with an emittance of 5 nm-rad can produce diffraction-limited light at wavelengths longer than ~60 nm, (photon energies below ~20 eV). An emittance three orders of magnitude lower, 5 pm-rad, would be needed to reach the diffraction limit at 0.06 nm (20 KeV).

6 FOURTH GENERATION SOURCES

As mentioned earlier, we consider a light source to be fourth generation if it exceeds the performance of previous sources by an order of magnitude or more in an important parameter such as brightness, coherence, or pulse duration. The main directions that have emerged for fourth generation light sources in the wavelength range from the VUV to hard X-rays are lower emittance rings and short wavelength FELs using both rings and linacs as drivers. Linac-based FELs offer sub-picosecond pulses compared to 10-50 ps for present storage rings. However, it may be possible to operate existing rings or design new rings with low momentum compaction factor[4] to produce a pulse duration of ~1 ps, albeit with relatively low current.

6.1 Lower Emittance Storage Rings

The relative ease with which third generation light sources have reached, and indeed exceeded, design goals indicates that fourth generation storage rings can reach even lower electron beam emittance, producing higher photon beam brightness and diffraction-limited light at shorter wavelengths. The challenges that must be met to accomplish this have been considered at workshops on fourth generation light sources[5,6]. Of concern are the various aspects of stability of the electron beam; position stability, reproducibility, single and multi-bunch instabilities, etc. A variety of countermeasures (such as feedback systems, Landau cavities, high-harmonic cavities) have been successfully developed to deal with these problems in presently operating rings. These will need to be pushed to higher performance levels to meet the stability demands of fourth generation rings. A major obstacle is the reduced lifetime and increased emittance due to intrabeam scattering (the Touschek effect) as bunch density increases.

6.1.1 Lattice design and dynamic aperture

A formidable challenge in the design of fourth generation storage ring sources is to develop a very low emittance magnet lattice with sufficient dynamic aperture to accommodate stable orbits with large amplitude oscillations resulting from, for example, Coulomb scattering of electrons on the residual gas and off-axis injection. The former results in the continuous population of a halo much larger than the core. As the large amplitude betatron oscillations of particles in this halo are damped, they coalesce with the core. If the aperture (dynamic or physical) is too small, particles in the halo are lost before being damped, reducing lifetime. It is difficult to maintain a large dynamic aperture in a low-emittance lattice because of the chromatic effects of the strong quadrupoles. This chromaticity, the energy dependence of the betatron tune, is corrected by sextupole magnets, whose non-linear fields reduce the dynamic aperture.

A possible countermeasure is the "modified sextupole"[7], which provides a magnetic field with a quadratic dependence over the core of the beam, but which then levels off or rises much less rapidly with distance from the axis, thereby lowering the non-linear fields experienced by particles with large amplitude oscillations. Dynamic aperture might also be enlarged by alternately rotating the lattice cells by +/- 45°, so that sextupoles can be placed at

locations of maximum dispersion in each plane for efficient chromaticity correction[8].

The large dynamic aperture needed for injection in present rings is due to the fact that stored beam is accumulated with off-axis injection of many low intensity "shots", each of which executes large amplitude betatron oscillations until they coalesce with the already stored beam due to radiation damping. The aperture requirement can be reduced with single-shot, on-axis injection from another ring, in which a high intensity beam has been accumulated with multi-shot, off-axis injection. Injection into synchrotron phase space is another possibility.

The horizontal emittance in an electron storage ring scales as the square of the electron energy and the third power of the bend magnet length. Thus, lower emittance fourth generation rings would have many bend magnets separated by quadrupoles, and many straight sections for insertion devices, leading to larger circumference at a given energy than third generation rings. For example, the lattice working group at the Grenoble Workshop[6] presented a "straw-man" design for a 2-3 GeV fourth generation ring with ~0.3 nm-rad emittance and a circumference the same as the 6 GeV ESRF machine, ~850 m. LBNL is studying a 2 GeV ring[9] also with ~0.5 nm-rad emittance and a circumference of about 350 m. Such rings might achieve a brightness at soft X-ray wavelengths of about $5x10^{23}$, more than 3 orders of magnitude greater than third generation VUV sources. Note that 0.3 nm-rad is the diffraction limit for light at 3.6 nm, or 0.34 keV.

Fourth generation rings for hard X-rays (below ~2 Å) would require higher electron energy and larger circumference. They would cost much more than the lower energy rings discussed above, even to reach an emittance of about 0.3 nm-rad, which is much larger than the diffraction limit for hard X-rays. Limited use has been made of undulators on the large circumference PEP[10] and TRISTAN[11] rings as third generation sources. However both are now being converted to B-Factories. Although the PETRA ring is part of the HERA injection system, an undulator has been installed in PETRA for use between HERA injections. Operating at 12 GeV, this undulator provides third generation brightness extending to very high photon energy. In the future fourth generation, hard X-ray rings may be installed in these tunnels.

6.1.2 Beam lifetime - Touschek effect

Very low emittance fourth generation rings will have very high bunch charge density, leading to short lifetime due to the collisions of electrons within a bunch; the Touschek effect. This is particularly severe at low energy and is already a problem in third generation 1-2 GeV rings. To achieve lifetime of the order of 10 hours, the bunch density must be reduced in several third generation rings. This is usually done by increasing the vertical emittance above its minimum value, trading brightness for lifetime. Multiple Touschek scattering also enlarges emittance. If all beam dimensions and the charge per bunch are kept constant, Touschek lifetime increases quadratically with electron energy and with the cube of the energy acceptance of the rf system. Thus lower emittance VUV/soft X-ray rings are designed with higher electron energy [the Swiss Light Source (2.1 GeV), Soleil in France(2.15 GeV) and the Shanghai Synchrotron Radiation Facility (2.2-2.5 GeV)] and with large rf overvoltage to increase the energy acceptance. The Swiss Light Source plans to use a high-Q superconducting passive rf cavity, tuned several bandwidths away from the main rf system, to increase the rf overvoltage and energy acceptance[12].

Short lifetime can also be compensated with frequent, or "top-up", injection. The nearly constant stored current also keeps a constant heat load on beam line optical elements and compensates for lifetime reduction if small gap, short period undulators, which extend the spectral range, are used. "Top-up" injection is planned for the 7 GeV APS facility at Argonne National Laboratory[13].

6.1.3 Other considerations

Reducing the energy at which a given ring is operated can be used to reduce the emittance, taking advantage of the quadratic dependence of emittance on electron energy, as has been done at PEP[10] and TRISTAN[11]. However damping time constants increase and instability threshold currents decrease as energy is reduced, limiting the effectiveness of this approach. To some extent this can be compensated by making more radiation with damping wigglers, which also reduce the emittance[14].

Improving unculator field quality by shimming[15] extends their spectral range beyond the 5th harmonic, previously the highest that could be used in practice. It also opens the possibility of designing future rings to produce hard X-ray brightness comparable to that of third generation hard X-ray sources with lower electron energy than 6-8 GeV. For example, high harmonics of undulators in a 3.5-4 GeV ring with a circumference of about 300-400 m and an emittance of ~10 nm-rad could produce a brightness of $\sim 10^{18}$ or greater at photon energies up to ~15 keV. Brightness of high harmonics is determined by emittance, undulator errors, and electron energy spread. A comprehensive code taking all these into account has been developed at APS[16]. As emittance is reduced and undulators are made more perfect, the energy spread ultimately determines high harmonic brightness.

6.2 FELs Based on Storage Rings

FELs produce extremely high brightness, transversely coherent radiation by inducing a bunch-density modulation of the electron beam at the optical wavelength. This is achieved by the interaction of a bright electron beam with an intense optical field in the spatially periodic magnetic field of an undulator. When electrons are bunched within an optical wavelength, the power radiated varies as the number of electrons squared, rather than linearly as for an unbunched beam. FELs have operated at wavelengths

from the IR to the UV for many years, using storage rings such as ACO, TERAS, UVSOR, VEPP-3, Super ACO, and others. Several storage rings have been designed with long straight sections to accommodate long FEL undulators. These include NIJI-IV in Japan and the new rings at Duke and Dortmund Universities. Long straight sections are also included in several proposed rings such as the Swiss Light Source, the Shanghai Synchrotron Radiation Facility, Soleil (France), and Diamond (U.K.).

Storage ring-based FELs provide light with very high brightness and coherence and may already be considered to be fourth generation sources in the wavelength range in which they now operate. Reviews of operating storage ring-based FELs and the prospects for future development, particularly the prospects for extending their operation to shorter wavelength, have been given[17]. Present storage ring FELs operate in the oscillator mode, using optical cavities to build up the radiation from many passes of the electron beam until the optical field is strong enough to induce a density modulation of the electron bunch at the optical wavelength, resulting in coherent, stimulated emission of radiation at that wavelength. It is difficult to make optical cavities at wavelengths below ~200 nm due to the lack of good reflectors. To overcome this, grazing incidence reflection, with higher reflectivity at shorter wavelength, can be used in a multiple-mirror, ring cavity configuration. Also, harmonics have been used to reach shorter wavelength. Using these approaches some groups are aiming for the 20-50 nm range.

An alternative approach is to eliminate the cavity and to achieve lasing in a single pass of a very bright electron beam through a long undulator, either by amplifying an input signal or with no input, in a process called self-amplified spontaneous emission (SASE)[18]. A design for such a single-pass, high-gain FEL amplifier operating down to 40 nanometers in a bypass of a 750 MeV storage ring was proposed at LBNL[19] and was considered for PEP[20].

6.3 FELs Based on LINACs

FELs using low energy linacs have operated for several years, providing coherent infra-red radiation at several user facilities. These use optical cavities in oscillator configurations, as do the storage ring-based FELs. Recent developments open the possibility to construct much shorter wavelength FELs, using bright electron beams from high energy linacs to achieve lasing in a single pass through a long undulator. With no optical cavity the lack of good short wavelength reflectors is no longer a limitation. However, the demands on the electron beam and undulator quality are severe, particularly to reach Ångstrom wavelengths. The developments opening the path to single-pass FELs operating at such short wavelengths are:

1. Photocathode rf electron guns[21], which provide short (5-10 ps), 1 nC pulses with normalized emittance (geometric emittance times γ) approaching 1 mm-mrad.
2. Control over emittance degradation during acceleration and compression, as demonstrated in the SLAC SLC project. Based on this and subsequent studies[22] it appears possible to accelerate and compress the beam from the gun to produce multi-GeV, kiloampere beams with emittance approaching the diffraction limit at wavelengths down to a few Ångstroms. Note that geometric emittance varies as γ^{-1} in a linac, as opposed to γ^2 in a storage ring.
3. Precision undulators as have been built at many SR sources. These must be extended to 50-100 m lengths, while including distributed focusing and maintaining tight tolerances on magnetic properties and alignment.

Designs are being developed for single-pass FELs operating from the VUV to the Ångstrom range, using photocathode rf guns and bunch length compressors to achieve high peak current in sub-picosecond pulses. BNL will use an existing 230 MeV linac to reach ~75 nm in a deep UV FEL by harmonic generation and single-pass amplification[23]. At DESY the TESLA Test Facility (TTF) superconducting linac will be used to drive a single-pass FEL[24] for SASE tests at ~250 Å. The linac will then be extended to ~1 GeV for an FEL user facility operating down to ~60 Å. The DESY group also proposes[25] to include several SASE-based FELs, operating down to about 1 Å, as an integral part of a proposed 250 GeV-per-beam linear collider. Energies up to about 30 GeV will be used for the FEL. Two approaches are being considered; a 1.3 GHz superconducting linac operating for the FEL at 5 Hz with 11,300 microbunches in each macropulse and a 3 GHz linac operating at 50 Hz with 125 microbunches per macropulse. The goal is average brightness of 10^{24}-10^{26} and peak brightness of 10^{33}-10^{34}.

The SLAC group[26] proposes to use the last third of the 3 km linac (the first 2 km will be used for injection to the B-Factory now in construction) to generate a 5-15 GeV beam for a 1.5-15 Å SASE FEL with an average brightness up to ~10^{23} and a peak brightness up to ~10^{34}. A design report for the project, called the Linac Coherent Light Source (LCLS), is in preparation. With an available 15 GeV linac, SLAC provides an opportunity to study the SASE process at very short wavelengths and to start using the remarkable brightness, coherence and short pulse duration of an X-ray FEL.

The calculated LCLS beam properties at 1.5 Å are: bandwidth = 0.1%, pulse duration (FWHM) = 280 fs, peak coherent power = 10 GW, coherent ph/pulse = 2 x 10^{12}, coherent ph/s = 2 x 10^{14} (120Hz), average coherent power = 0.3 W, transverse beam size (FWHM) = 70 microns, divergence (FWHM) = 10^{-6} radians. In addition, use will also be made of the broad spectrum of spontaneous undulator radiation with the same pulse duration, several times higher peak power and a larger opening angle.

Many laboratories (ANL, BNL, DESY, LANL, SLAC, TJNAF, UCLA) are pursuing single-pass FEL r&d including: SASE studies at micron wavelengths of startup from spontaneous radiation, exponential gain[27], and saturation; studies of the effects of space charge and coherent SR in bunch-length compressors; undulator design and alignment; photocathode rf gun design and characterization; electron and photon diagnostics; and X-ray optics.

The projected characteristics of linac-based short wavelength FELs, particularly their short pulse duration, peak brightness, and coherence, are extraordinary. The peak brightness of the X-ray FELs proposed at SLAC and DESY is ~10^{10} times higher than that of third generation storage ring sources, with ~100 times shorter pulses. These properties are likely to open entirely new opportunities in imaging, non-linear physics, and pump-probe experiments. There is increasing confidence in the accelerator community that linac-based, short wavelength FELs can be built. There is also increasing realization that their properties will open new science in the 21st century.

ACKNOWLEDGMENTS

It is a pleasure to acknowledge discussions with and comments on the manuscript by J. Barger, A. Bienenstock, R. Carr, J. Corbett, M. Cornacchia, J. Galayda, R. Gould, K. Halbach, A. Hofmann, A. Jackson, E. Johnson, C. Limborg, B. McSwain, H.-D. Nuhn, C. Pellegrini, J. Schmerge, R. Tatchyn, H. Wiedemann.

REFERENCES

[1] J. P. Blewett, Phys. Rev. 69 (1946) 87.

[2] H. Winick, S. Doniach, Synchrotron Radiation Research, Plenum Press, 1980.

[3] G. Brown, K. Halbach, J. Harris, H. Winick, Nucl. Instr. & Meth. 208 (1983) 65-77.

[4] D. Robin, A. Amiri, E. Forest, C. Pellegrini, Phys. Rev. E 48, 2149 (1993).

[5] M. Cornacchia, H. Winick, (eds.), Wkshp on Fourth Gen. Light Sources; Feb. 24-27, 1992, SSRL 92/02.

[6] J.-L. Laclare (ed) Workshop on Fourth Generation Light Sources; ESRF, Grenoble, Jan. 22-25, 1996.

[7] M. Cornacchia, K. Halbach, Nucl. Instr. & Meth. A290 (1990), 19-33.

[8] A. Hofmann, personal communication.

[9] A. Jackson, J. Byrd, W. Decking, R. Keller, C. Kim, D. Massoletti, H. Nishimura, D. Robin, H. Zyngier, Proc. of this conf.

[10] A. Bienenstock, G. Brown, H. Wiedemann, H. Winick, Rev. Sci. Instr. 60 (7), (1989), 1393-8.

[11] N. Yagi, K. Wakabayashi, H. Iwamoto, K. Horiuti, I. Kojima, T. Irving, Y. Takezawa, Y. Sugimoto, S. Iwamoto, T. Majima, Y. Amemiya, M. Ando, Jour. Synchr. Rad. 3 (1996) 305-312.

[12] SLS Design Handbk, 11/96. Also, P. Marchand, L. Rivkin, Proc. 1991 IEEE Part. Accel. Conf., page 78-82.

[13] G. Decker, Proc. of this conf.

[14] H. Wiedemann, Nucl. Instr. Meth. A266, 24 (1988).

[15] D.Quimby, S.Gottschalk, F.James, K.Robinson, J.Slater, A.Valla, Nucl. Instr. Meth. A285 (1989) 281; J. Chavanne,P.Elleaume,Rev. Sci. Instr. 66(2) (1995) 1868.

[16] R. Dejus, personal comm.; R. Dejus, M. Sanchez del Rio, Rev. Sci. Instrum. 67(9), (1996), CD-ROM

[17] M. E. Couprie, proc. FEL96, Rome, Nucl. Instr. & Meth. to be published; M. Poole summary in ref. 6.

[18] R. Bonifacio, C. Pellegrini, L. Narducci, Opt. Commun. 50 (6) (1985); J. Murphy, C. Pellegrini, Jour. Opt. Soc. of Amer. B2, 259 (1985); K.-J.Kim, Phys. Rev. Let. 57, 1871 (1986); C. Pellegrini, Nucl. Instr. & Meth. A272, 364 (1988).

[19] K.-J. Kim, J. Bisognano, S. Chattopadhyay, M. Cornacchia, A. Garren, K. Halbach, A. Jackson, H. Lancaster, J. Peterson, M. Zisman, C. Pellegrini, G. Vignola, Proc. 1985 IEEE Part. Accel. Conf. P. 3377-9.

[20] H-D.Nuhn, R.Tatchyn, H.Winick, A. Fisher, J. Gallardo, C.Pellegrini, Nucl. Instr. Meth., A319,89-96, 1992

[21] R. Sheffield, in Phys. of Part. Acc., AIP Vol. 184, 1500-31, M. Month, M. Dienes,eds. (1992); D. Palmer, R. Miller, H. Winick, X.-J.Wang, K.Batchelor, M. Woodle, I.Ben-Zvi; Proc.1995 IEEE Part. Acc. Conf. 982-4.

[22] T.Raubenheimer, Nucl. Instr. Meth.A358, 40 (1995).

[23] DUV FEL Concept. Des. Rep., BNL rep. 48713, Jan. 1994; I. Ben-Zvi, E. Blum, W. Graves, R. Heese, E. Johnson, S. Krinsky, J. Murphy, L.-H. Yu, Proc. FEL96

[24] DESY Report TESLA-FEL 95-03, June, 1995; J. Rossbach, proc. of this conf.

[25] R. Brinkman, G. Materlik, J. Rossbach, J.Schneider, B.-H. Wiik, Proc. FEL96, Nucl. Instr. Meth. to be pub.

[26] M. Cornacchia, Proc. SPIE Photonics West Conf, San Jose, CA, Feb. 8-14, 1997; R. Tatchyn et al. Nucl. Instr. & Meth. A375 (1996) 274-83; H. Winick, J. Electron Spectrosc. & Related Phenom. 75 (1995) 1-8.

[27] D. Bocek, P. Kung, H.-C. Lihn, C. Settakorn, H. Wiedemann, Nucl. Instr. & Meth. A375, (1996), 13-16; M. Hogan, C. Pellegrini, S. Reiche, J. Rosenzweig, G. Travish, A. Tremaine, S. Anderson, K. Bishofberger, P. Frigola, A. Murokh, A. Varfolomeev, Proc. of this conf.

ULTRA-HIGH INTENSITY PROTON ACCELERATORS AND THEIR APPLICATIONS *

W.T. Weng, AGS Department, Brookhaven National Laboratory, Upton, NY 11973

Abstract

The science and technology of proton accelerators have progressed considerably in the past three decades. Three to four orders of magnitude increase in both peak intensity and average flux have made it possible to construct high intensity proton accelerators for modern applications, such as: spallation neutron sources, kaon factory, accelerator production of tritium, energy amplifier and muon collider drivers. The accelerator design focus switched over from intensity for synchrotrons, to brightness for colliders to halos for spallation sources. An overview of this tremendous progress in both accelerator science and technology is presented, with special emphasis on the new challenges of accelerator physics issues such as: H^- injection, halo formation and reduction of losses.

1 INTRODUCTION

The road to ultra-high intensity proton accelerators has many origins. First is the availability of high current, low emittance, high duty factor H^+ and H^- ion sources. Second is the introduction of Radio Frequency Quadrapole (RFQ) to replace Cockcroft-Waton as effective pre-accelerator. Third is the advancement in the understanding of beam dynamics in the proton linac and the introduction of CCDTL as effective matching structure between low β DTL and high β CCL. The fourth is the development of synchrotrons to reach several tens of amperes in average current. For example, the evolution of synchrotron intensity from 1960 to the present is summarized in Fig. 1, where the numbers shown in the parenthesis refer to the rep-rate of operation.

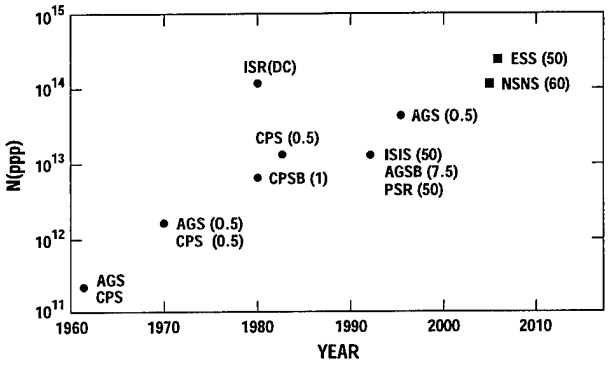


Figure 1: Evolution of synchrotron intensity.

Combined those four components together, a totally new picture emerges. All of a sudden, many mega watts of beam power, either in CW or pulsed form, becomes available. Many new ideas of how to utilize and exploit such a beam power surface.

The key developments in the accelerator science and technologies in the past thirty years will be reviewed in Sec. 2. Major new applications with high probability of been realized in the near future will be reviewed in Sec. 3.

2 KEY ACCELERATOR DEVELOPMENTS

The key developments in accelerator science and technologies are summarized in Table 1. Principles and merits of each development can be found in the references given. One recent review on traditional accelerator physics issues of how to achieve high intensity on proton synchrotrons can be found in ref. [12]. More recent concerns on issues pertaining to ultra-high intensity operation are explained in the following.

Table 1: Important accelerator scientific and technological developments (1960-1997).

DEVELOPMENTS	ADVANTAGES
H^- ion sources [1]	high current, low emittance, high duty factor
RFQ [2]	compact, bunching, low emittance
Linac [3]	CCDTL, S. C. linac, numerical simulations
H^- injection [4]	H^o population, many turns injection and painting
Resonance correction [5]	allow higher space charge tune shift
RF feedback [6]	beam loading compensation
Coherent instabilities [7]	impedance budget, damping
$e-p$ threshold [8]	$\eta < 10^{-3}$, electron loss control, beam clearing
Halo Formation [9]	lattice effect, dynamic aperture, collimation
Beam loss control [10]	design, injection, collimation
Accelerator operation [11]	beam-based modeling, orbit control

2.1 H^- Injection

In modern day application, for the injection of proton beam from a linac into a synchrotron, a H^- beam is prefered.

* Work performed under the auspices of U.S. Department of Energy.

0-7803-4376-X/98/$10.00 © 1998 IEEE

This is due to the foil-stripping process allows the repetitive stacking of incoming beam into the same phase space area which is impossible with a H^+ beam. Typical foil used is carbon or graphite foil of about 200 to 400 $\mu g/cm^2$. The stripping efficiency ranges from 98% to 99.5%. The critical issues faced in this process is the foil temperature, the collection of H^-, H^o and electrons. In the event that beam losses in the order of few 10^{-4} have to be realized, careful identification of H^o population in various excited states is necessary [4]. Another important design concern is the emittance blow up due to multiple traverse of foil which has to be minimized.

2.2 *e-p Instability [8]*

There are many ways electrons can be generated in a synchrotron. For example, they can be generated at stripping foil, by residual gas ionization, or by secondary electron emission from the wall. Experiences showed that if the population of electrons reaches certain level, characterized by the neutralization coefficient, η_e defined to be the ratio of electron to proton, the proton beam can become unstable due to coherent motion excited by the presence of electrons.

Ways to eliminate $e-p$ instability include better vacuum, collect electrons at stripping foil location, TiN coating of vacuum chamber, and clearing electrodes. In the event that the instability does occur, an active damping system can be provided to suppress the instability.

2.3 *Halo Formation*

It has been found that the large amplitude particle can interact with the core particles to move either closer to the center or away from the center [9, 13, 14, 15]. This process can be understood by an envelop oscillation created by the mismatch between the beam shape and the lattice of the focusing channels. A particle in the halo region tends to be driven away in such a mismatched focusing channel. Although the smaller amplitude particles stay close to the stable fixed point in the center, the larger amplitude particles can drift away following the multiple islands as show in Fig. 2 [14]. The crucial questions now, are first how far the islands can extend away from the center, what are the dynamical nature of the islands, and when the chaotic motion will set in. Those are all important questions to be answered by any new high power accelerators. It can happen both in the linac and in the circular rings.

A thorough understanding of the halo dynamics as function of mismatch, power supply ripple, space charge tune shift, and the lattice structure, etc., is necessary to be able to estimate the degree of beam losses with confidence.

Assuming Gaussian distribution, the development of proton synchrotron and main attention of accelerator physics in the past 40 years can be roughly classified into three period. Period 1 located roughly between 1960 to 1975 when the total intensity for fixed target research was a major concern. The figure of merit in this period is the

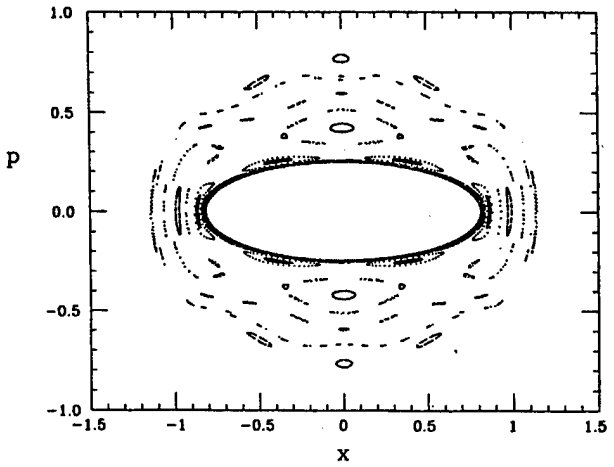


Figure 2: The Poincare surface of section in particle phase space from particle-core interaction [14].

total intensity,

$$N = \int_{-2.5\sigma}^{2.5\sigma} f(z)dz.$$

Period 2 located roughly between 1970 to 1990 when the brightness for colliding beam research was a major concern. The corresponding figure of merit is the brightness [16], $B = N/\sigma$. Period 3 started from 1990 and could well extend to 2010 when the loss of the halo particles is a major concern. The corresponding figure of merit will be the population and dynamics of the halo particles,

$$H = 2\int_{4\sigma}^{\infty} f(z)dy.$$

2.4 *Beam Loss Control*

Typical beam losses of existing low power proton synchrotron is in the order of a few percent. Let us use the AGS and the proposed NSNS ring as example. The relevant beam parameters are summarized in Table 2.

It can be clearly seen that 1% loss of the NSNS ring is equivalent to the entire flux of the AGS beam. Such a situation is totally unacceptable. That is why the design criterion for next generation spallation neutron sources is kept in the order of a few 10^{-4} to allow for hands-on maintenance after a long operation period.

To contain those particles inadvertently migrating toward the wall, after all careful considerations and provisions, a collimator system has to be designed to catch the bulk of them before hitting the wall. For example, for the

Table 2: AGS and NSNS parameters.

	AGS [12]	NSNS [17]
Proton Intensity	6×10^{13} ppp	10^{14} ppp
Rep-Rate	0.5	60
Flux	3×10^{13} pps	6×10^{15} pps
Loss 0f 1%	3×10^{11} pps	6×10^{13} pps

NSNS four collimators, 3.2m each, enclosing a 4π solid angle around the source point and stuffed with segmented material to capture all secondary particles generated by the incident protons will be provided to reduce the radiation effects by a factor of 100. This way, most of uncontrolled losses will occur at the collimator, leaving ring components relatively intact for reliable operation [18].

2.5 Accelerator Operation [11]

For high reliability and low loss operation of any high power accelerators, the performance standard of typical 3rd generation synchrotron radiation source should be achieved. Those accelerators routinely achieve orbit stability in the order of tens of microns and the measurement of betatron function to better than a few percent. To achieve such a performance, a well-thought out plan of diagnostic devices and realistic computer model-based operation have to be implemented.

3 EXAMPLE OF APPLICATIONS

By the early 1990's, there were a realization that the high intensity proton accelerator technology had come of age and a wide range of new demands from scientific, industrial, and governmental concerns can be met by the availability of this new technology. Listed in Table 3 are five interesting and promising applications of such ultra-high intensity proton accelerators.

3.1 Accelerator Production of Tritium (APT) [19]

The strategic reserve of Tritium could diminish due to natural decay of such material. Traditionally Tritium was produced by the reactors which are now perceived to be potentially unsafe and pollution-prone. The alternative is to use high power CW proton linac to produce sufficient number of neutrons for the production of Tritium.

The proposal under conceptual design at LANL uses a super-conducting proton linac of 1.7GeV with 100mA beam delivering 170MW power to the target. The technical challenges of this project is clearly in the attainment of high current, minimization of particle losses, and the design of target system. To safely and reliably operate a linac at such high current requires every care and ingenuity from the accelerator designers. The Las Alamos team payed special attentions to the design of RFQ to bunch and pre-accelerate the beam with very good emittance preservation, introduced CCDTL section to improve in matching between DTL and CCL, allowed for high "rms aperture ratios" the radio of transverse aperture to rms beam size and longitudinal bucket width to rms beam length. Typically, in the transverse dimension the rms aperture ratios of at least 10 are provided. Furthermore, the design is simulated in a fully nonlinear, 3-D particle-in-cell simulation code, using a large number of particles, and including various errors given by engineering tolerances. These runs have to show a well-matched beam, adequate aperture factors, and no particle losses before they can considered to be acceptable. The whole design procedure is a combination of beam dynamics, engineering configuration, numerical simulation, and finally cost optimization. Halo dynamics and associated beam losses have been thoroughly studied and measured in some occasions [3, 9] to ensure that beam losses of less than 1nA/m is achieved for "hands-on" maintenance and component reliability.

Super-conducting technology has been applied to accelerator through the CEBAF project for electron linac. The successful implementation of super-conducting technology to the APT will be a major breakthrough and will result in substantial cost saving for future operations. The U.S. Department of Energy will make final technological choice of APT in the fall of 1998.

Table 3: Examples of possible applications of ultra-high intensity proton accelerators.

Applications	Beam Energy (GeV)	Beam Current (mA)	Rep-Rate (Hz)	Average Beam Power (MW)
APT [19]	1.3-1.8	100	CW	130-180
Nuclear Transmutation [20, 21]	1.5	16	CW	25
Energy Amplifier [22]	1.0	12.5	CW	12.5
SNS [17, 23]	1.0-1.5	0.5-3.0	~50	1-3
μ-collider Driver [24]	30	0.25	15	7.0

3.2 Nuclear Transmutation [20, 21]

The nuclear power plants have been used to provide power for the past 50 years. One of the byproducts of the processes is the tremendous amount of long-lived nuclear waste. For environmental concern, those nuclear waste should be safely disposed. For the long term future of nuclear power, until the waste problem is solved, public opposition will undoubtedly continue. The required solution must reduce both the volume of existing waste and its radioactivity, so the waste becomes benign by the end of period over which a society might be able to retain control, say a few hundred years.

The ideas of breaking down long-lived radio-active product from nuclear power plants has been surfaced a while ago [20]. However, the need of fast neutron flux in the order of 10^{15}-10^{16}neutron/cm^2/sec was not readily available then. It took twenty years intensively R&D efforts to bring the accelerator technology closer to the requirements of viable and efficient application in this area. One of the original example suggested and tested is to convert Tc^{99} of half life 2.1×10^5 years by neutron capture to Tc^{100} which can quickly through β-decay (half life 15.8sec) become Ru^{100} which is stable. Another example are minor actinides , such as, Np^{237} or Am^{241} which have half life of ~1000 years by α-emission. Those can be fissioned by fast neutron to

become fission products of half life around a few years.

The soon-to-be-approved project of nuclear transmutation is the OMEGA project at JAERI [21]. As shown in Table 3, OMEGA requires a super-conducting linac of 1.5GeV, 16mA delivering average power of ~25MW. The major concerns of how to provide a reliable, high power proton source is the same as that required by APT, although the end use is some what different.

3.3 Energy Amplifier (EA)

The need of an industrialized society to have reliable supply of inexpensive power source can never be over-emphasized. However, the continuous application of nuclear power is hampered by both the safety and waste treatment problems. The two challenging problems can be substantially resolved by the proposal of the Energy Amplifier by C. Rubbia [22].

There are two important key concepts to modify nuclear reactors for new applications. First is to replace the UO_2 with ThO_2 as the core fuel whose production of neutron will stay sub-critical for sustained chain reaction. Secondly, the required additional fast neutrons will be provided by spallation neutron generated by high intensity proton accelerator. In the CERN proposal, the final stage of proton accelerator is a cyclotron of 1.0GeV with expected beam power of about 12.5MW. Through this arrangement, the fuel is used much more efficiently. For example, the power obtained from 780kg of Thorium is roughly the same as the one from 200 tons of native Uranium. Furthermore, the probability of a critical accident is suppressed since the device operates at all times far away from it. Spontaneous convective cooling by the surrounding air makes a "melt-down" leak impossible. In case of any incident, the accelerator can be shut down in a matter of a few micro-seconds, a much responsive operation than traditional Pressurized Water Reactor (PWR).

One more addition advantage is the life time of typical spent fuel from the EA facility is about 700 years which is many orders of magnitude lower than those products from PWR. The waste treatment becomes easier and more reliable.

3.4 Spallation Neutron Sources (SNS)

The potential of using neutron to probe material structure was immediately recognized when copious amount of neutrons became available in the 1930's. In the advent of high-intensity proton accelerators, the accelerator-driven spallation neutron sources became available in the 1980's. Notable examples are the ISIS at Rutherford, PSR at LANL, IPNS at ANL, and KENS at KEK.

By the 1990's, it became evident that the need of neutron sources is increasing and the availability of traditional neutron sources from nuclear reactors is decreasing. Many advances in industrial society are driven by new technologies, and most of these new technologies depend on the development of new materials such as high-strength ceramics and composited, magnetic and electro-optic materials, or new high transition temperature super-conductors. The approach to developing many of these materials requires understanding their interactions at atomic level and relating these interactions to macroscopic properties. This usually requires the use of large facilities such as synchrotron radiation sources and neutron sources. Neutrons have several unique advantages for determining the structure and dynamics of a wide range of materials. This is why the demand of neutrons has increased so rapidly and spread to so many fields of science in the last 20 years, and why there is a need for new spallation neutron sources.

Shown in Fig. 3 is the evolution of average neutron fluxes over the years from both the reactor sources and the SNS's. The advances of the accelerator technologies played a major role in making the high flux SNS possible. To meet the increasing demand of high flux neutron sources, there is a surge of new proposals for pulsed spallation neutron source in the few MW range all over the world. In Table 4, we list the parameters of three most powerful SNS in operation and four proposals for new SNS. At this moment, the probability of any of the proposal been approved in the next few years ranges from 80 to 20%. It would be very interesting to see which one actually get built and when.

All the four new proposals for SNS provide pulsed proton beam of ~1μsec long and spaced by ~20-50msec. Pulsed neutron beam is essential for studies of dynamical properties of materials and cell samples by time of flight technique. The signal to background / noise ratio is much enhanced due to the peak intensity of shout pulse.

For such a short pulse facility, an accumulator ring or rapid cycling synchrotron is needed to compress the ~1msec linac beam into less than 1μsec by H^- charge exchange injection mechanism over ~1000 turns. The modern choice is to use a liquid mercury target for the ease of design of cooling and long life time. Typical spallation process can generate more than 50 neutrons per incident proton. Complete description of various SNS can be found in references [17, 23, 29]. The accumulator ring design of the NSNS project is given in reference [30]. Currently NSNS is planned to start construction in 1999 and be completed

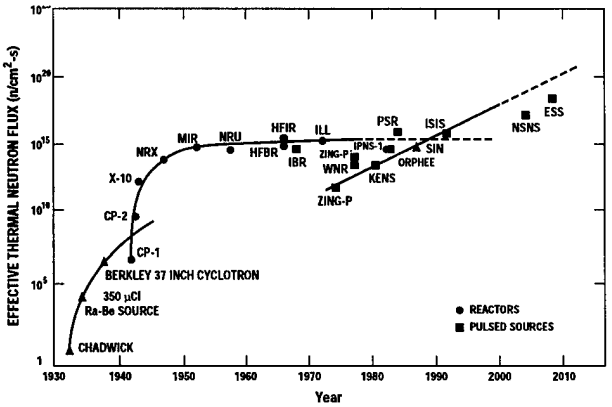


Figure 3: The evolution of average neutron fluxes.

Table 4: Design parameters of spallation neutron sources.

Name	Proton Energy (GeV)	Proton Intensity (ppp)	Rep-Rate (Hz)	Average Beam Power (MW)
Existing Facilities				
LANSCE [25]	0.8	2.3×10^{13}	20	0.07
ISIS[26]	0.8	2.5×10^{13}	50	0.2
SINQ[27]	0.59	1.5 mA	CW	1.0
Proposed Facilities				
JAERI[28]	1.5	2.8×10^{14}	50	2.7
JHF[29]	3.0	5.0×10^{13}	25	0.6
NSNS[17]	1.0	1.0×10^{14}	60	1.0
ESS[23]	1.334	2.3×10^{14}	50	2.5

in 2005. Upgrades to 2MW and eventually to 4MW can be implemented when fund is available [17].

From the above brief description, it is evident that all those new applications require new performance levels from both the accelerators and the target systems. it is such a ground breaking challenges and their potential pay-offs in the acquisition of new knowledge and contributions to societal needs, makes our field so interesting and rewarding.

4 ACKNOWLEDGMENTS

The author would like to thank for the information and presentation materials received from the following individuals: B. Appleton, G. Bauer, J. Browne, I. Gardner, J. M. Lagniel, S. Y. Lee, Y. Mori, T. Mukaiyama, G. Rees, J. Staples and N. Watanabe.

5 REFERENCES

[1] Eds L. Schroeder, K. Leung and J. Alonso, Proceedings of the Workshop on Ion Source Issues Relevant to a Pulsed Spallation Neutron Source, LBL-36347, October, 1994.

[2] M. Weiss, 'Radio-Frequency Quadrupole', CERN Accelerator School Proc., CERN 95-06, p.959, November, 1995.

[3] T.P. Wangler, 'New High-Power Linacs and Beam Physics Issues', these proceedings.

[4] M.S. Galley *et al.*, 'Mesurement of H^-, H^o, and H^+ yields produced by foil stripping of 800MeV H^- ions', Phys. Rev. A, Vol.53, p.3201, May,1996.

[5] C. Gardner *et al.*, 'Observation of Correction of Resonance Stopbands in the AGS Booster', Proc. of PAC'93, p.3633.

[6] J.M. Brennan, 'The Upgraded RF System for the AGS and High Intensity Proton Beams', Proc. of PAC'95, p.1489, May, 1995.

[7] J. Gareyte, 'Beam Observation and the Nature of Instabilities', AIP Conf. Proc. No.184, p.343-429, New York, 1989.

[8] D. Neuffer *et al.*, 'Observation of a Fast Transverse Instability in the PSR', Nucl. Inst. & Methods, A321, p.1-12, 1992.
M. Plum *et al.*, 'Experimental Evidence for the Las Alamos Proton Storage Ring Beam Instability', these proceedings.

[9] R.A. Jameson, 'Self-Consistent Beam Halo Studies and Halo Diagnostic Development', *Frontiers of Accelerator Technology*, World Scientific, p.530, November, 1994.

[10] P.E. Gear, 'Beam Induced Radiation Problems and cures', Proc. of EPAC'96, p.225, Sitges, Spain, June, 1996.

[11] J. Corbett and C. Wermelskirchen, 'Accelerator Controls and Modeling', *Synchrotron Radiation Sources*, ed. H. Winick, World Scientific, p.215, November, 1994.

[12] W.T. Weng, 'Performance and Measurements of the AGS and Booster Beams', AIP Conf. Proc. No.377, p.145, Bloomington, IN, Oct. 10-13, 1995.

[13] J-M. Lagniel, 'Halos and Chaos on Space-Charge Dominated Beams', Proc. of EPAC'96, p.163, Sitges, Spain, 1996.

[14] S.Y. Lee and A. Riabko, 'Envelop Hamiltonian of an Intense Charged-Particle Beam in Periodic Solenoidal Fields', Phys. Rev. E, Vol.51, Feb., 1995.

[15] G. Haonat, 'Experimental Results on Beam Halo', these proceedings.

[16] S. Machida, 'Space-Charge Effects in Low-Energy Proton Synchrotrons', Nucl. Inst. & Methods, A309, p.43-59, 1991.

[17] B.R. Appleton, 'The National Spallation Neutron Source (NSNS) Project', these proceedings.

[18] H. Ludewig, S. Mughabghab and M. Todosow, 'NSNS ring system design study, collimation and shielding', BNL/NSNS Tech. Note #5, November, 1996.

[19] W. Lisowski, 'The Accelerator production of Tritium (APT) Project', these proceedings.

[20] H. Takahashi, N. Mizov and M. Steinberg, 'Use of Linear Accelerator for Incinerating the Fission Produce of CS^{137} and Sr^{90}', Int. Conf. on Nucl. Waste Transmutation, Austin, USA, July 22-24, 1980.

[21] S. Saito, 'Research and Development program on Accelerator-driven Transmutation at JAERI', Proc. of 2nd Int. Conf. on Accelerator-driven Transmutation Technology and Applications, p.52, Kalmar, Sweden, 1996.

[22] C. Rubbia *et al.*, 'Conceptual Design of a Fast Neutron Operated High Power Energy Amplifier', CERN/AT/95-44, 1995.

[23] I. Gargner *et al.*, 'Status of the European Spallation Source Design Study', these proceedings.

[24] B. Palmer, 'Progress on $\mu^+\mu^-$ Colliders', these proceedings.

[25] R.J. Macek *et al.*, 'Overview of Progress on the LANSCE Accelerator and Target Facilities Improvement Program', these proceedings.

[26] M.R. Harold *et al.*, 'A Possible Upgrade for ISIS', these proceedings.

[27] G.S. Bauer *et al.*, 'Commissioning of the 1MW spallation Neutron Source', these proceedings.

[28] T. Mukaiyama, 'Neutron Science Project at JAERI', NSNS User's Workshop, Oct. 1996.

[29] Y. Mori, 'The Japanese Hadron Facility', these proceedings.

[30] W.T. Weng *et al.*, 'Accumulator Ring Design for the NSNS Project', these proceedings.

STATUS OF THE FERMILAB MAIN INJECTOR AND RECYCLER

Stephen D. Holmes, Fermi National Accelerator Laboratory*, P.O. Box 500 Batavia, IL 60510

Abstract

The Fermilab Main Injector is a new 150 GeV synchrotron under construction at the Fermi National Accelerator Laboratory. The FMI has been designed to support a factor of five increase in luminosity available from the Tevatron proton-antiproton collider while simultaneously providing a 2 mA resonantly extracted 120 GeV proton beam. Recently a new antiproton storage ring, the Recycler, has been incorporated within the scope of the project with an expected luminosity gain of a factor of two. Project status, schedule for completion, and expected performance characteristics of the Main Injector and Recycler will be presented.

1 INTRODUCTION

The Fermilab Tevatron is the highest energy collider operating in the world today. As such it is uniquely positioned as the world's forefront High Energy Physics "discovery facility"--a position it will retain until the advent of the LHC approximately eight years from now. Fermilab is committed to exploiting the Tevatron facility to the fullest extent possible over the period between now and 2005, and to that end has undertaken the construction of the Main Injector accelerator and the Recycler antiproton storage ring to provide improved Tevatron luminosity performance starting in 1999.

The Tevatron proton-antiproton collider currently operates at a center-of-mass energy of 1.8 TeV, accompanied by a luminosity greater than $1.5\times10^{31}\text{cm}^{-2}\text{sec}^{-1}$. The luminosity in the Tevatron collider is given by,

$$L=\frac{3\gamma f N_p(BN_{\bar{p}})}{\beta^*(\varepsilon_p+\varepsilon_{\bar{p}})}F(\sigma_z/\beta^*)$$

where γ is the relativistic factor, f is the revolution frequency, B is the number of bunches in each beam, N_p ($N_{\bar{p}}$) is the number of protons (antiprotons) in a bunch, ε_p ($\varepsilon_{\bar{p}}$) is the 95% normalized transverse beam emittance, σ_z is the rms bunch length, β^* is the beta function at the interaction point, and F is a form factor dependent on the ratio of the bunch length to β^*.

Under current operating conditions, the most important factor influencing luminosity performance is the total number of antiprotons in the ring, $BN_{\bar{p}}$. The second most important factor is the proton phase space density, N_p/ε_p. A large increase in N_p/ε_p is precluded by the beam-beam interaction. Hence, increasing antiproton availability remains, and will remain for the indeterminate future, the key to improving Tevatron collider performance.

2 RUN II PERFORMANCE GOALS

Run II is the name applied to the first operating period of the Tevatron collider following commissioning of the Main Injector. Goals established for this run include achievement of a luminosity of $5\times10^{31}\text{cm}^{-2}\text{sec}^{-1}$ early in the run, ultimately growing to $2\times10^{32}\text{cm}^{-2}\text{sec}^{-1}$ once the full capabilities of the Recycler ring are realized, accompanied by a capability of resonantly extracting 3×10^{13} protons per pulse at 120 GeV in support of a variety of fixed target experiments.

In order to achieve the collider goal the Fermilab complex will be required to support:

- More protons in collision
- Many more antiprotons in collision
- A significant increase in the antiproton stacking rate
- A capability for recovering antiprotons at the end of stores

The Main Injector, accompanied by a variety of improvements to the Antiproton Source facility, is designed to support a three-fold increase in the antiproton production rate, accompanied by good antiproton transmission efficiency from the Recycler to Tevatron and a modest increase in coalesced proton bunch intensity.

The Recycler is designed to capitalize on the existence of the Main Injector to extend further the performance potential of the Tevatron complex. The Recycler does this by relieving the Antiproton Source of responsibility for maintaining high stacking rate at high stacks, by doubling the effective stacking rate via antiproton recovery, and by providing a platform for further performance enhancements within the Tevatron complex.

Design parameters for the next Tevatron collider run (Run II) are listed in Table 1. For comparison typically achieved parameters and performance in the most recent collider run (Run IB) are listed in the first column. As can be seen from the table the factor of ten increase in luminosity is supported primarily through a factor of eight increase in the number of antiprotons in the collider. It should also be noted that the increased luminosity will require operations with 36 bunches per beam, rather than 6, in order to maintain the number of interactions per crossing as seen in the detectors at a reasonable level.

* Operated by Universities Research Association under contract to the United States Department of Energy

0-7803-4376-X/98/$10.00 © 1998 IEEE

Table 1: Collider operational achievement in Run IB and goals for Run II. Run II is the first run supported by the Main Injector and Recycler rings.

RUN	IB(1993-95)	II(1999-)	
Protons/bunch	2.32×10^{11}	2.70×10^{11}	
Pbars/bunch	5.50×10^{10}	7.00×10^{10}	
Total Pbars	3.30×10^{11}	2.5×10^{12}	
Pbar Production Rate	6.00×10^{10}	2.00×10^{11}	pbar/hour
Proton emittance	23π	20π	mm-mr
Pbar emittance	13π	15π	mm-mr
β^*	0.35	0.35	m
Energy	900	1000	GeV
Bunches	6	36	
Bunch length (rms)	0.60	0.38	m
Form Factor	0.59	0.70	
Typical Luminosity	1.6×10^{31}	2.0×10^{32}	$cm^{-2}sec^{-1}$
Bunch Spacing	~3500	396	nsec
Interactions/crossing (@ 50 mb)	2.7	5.8	

3 MAIN INJECTOR AND RECYCLER PERFORMANCE GOALS

The Main Injector is a 3319 meter circumference, 150 GeV, conventional-magnet-based accelerator. It is designed to perform all duties currently assigned to the Main Ring, the original 400 GeV accelerator at Fermilab, but with significantly improved performance. In addition the Main Injector creates a new capability at Fermilab for modest energy (120 GeV), high average intensity extracted beams.

Improved performance relative to Main Ring is largely attributable to a larger design aperture. The Main Injector is designed to provide an admittance of 40π mm-mr (normalized at 8.9 GeV) as compared to approximately 12π in the Main Ring. This improvement is the result of implementation of a lattice with beta functions reduced by a factor of two (55 meters vs. 110 meters) and dispersion reduced by a factor of three (2 meters vs. 6 meters), and by elimination of vertical dispersion. In addition better field quality is being achieved at injection through the use of lower coercivity steel (<1 Oe) and a higher injection field (0.1 Tesla vs. 0.04 Tesla).

As a result of these improvements the Main Injector is anticipated to have a capability of delivering more protons per cycle (5×10^{12} vs. 3×10^{12}) at a faster cycle rate (1.47 sec. vs. 2.4 sec.) than currently achieved in the Main Ring. A new capability of slow extracting 3×10^{13} protons per pulse at 120 GeV is also provided. Fast or slow resonant extraction cycles are planned with a 1.93 and 2.93 second cycle time respectively. A parametric description of the Main Injector is given in Table 2. It is expected that after some years of operation the delivered intensities may rise by a factor of two to three beyond the formal project goals.

Table 2: Main Injector parameter list

Circumference	3319.4	m
Injection Momentum	8.9	GeV/c
Peak Momentum	150	GeV/c
Cycle Time (@ 120 GeV)	1.5	s
Cycle Time (@150 GeV)	2.4	s
Protons/Bunch	6×10^{10}	
Number of Bunches	498	
Number of Protons	3×10^{13}	
Average Current	433	mA
Maximum Beta Function	57	m
Maximum Dispersion Function	1.9	m
Nominal Horizontal Tune	26.425	
Nominal Vertical Tune	25.415	
Transverse Emittance (Normalized @ 8.9 GeV/c)	20π	mm-mr
Transverse Admittance	$>40\pi$	mm-mr
Harmonic Number (@53 MHz)	588	
RF Frequency (Injection)	52.8	MHz
RF Frequency (Extraction)	53.1	MHz
RF Voltage	4	MV
Transition Gamma	21.8	
Longitudianl Emittance (95%, per bunch)	0.2	eV-s
Longitudinal Admittance	>0.5	eV-s
Number of Dipoles	216/128	
Dipole Lengths	6.1/4.1	m
Dipole Field (@150 GeV)	17.2	kG
Number of Quadrupoles	128/32/48	
Quadrupole Lengths	2.1/2.5/2.9	m
Quad. Gradient (@150 GeV)	200	kG/m

The Recycler is a 3319 meter, 8.0 GeV (kinetic energy), permanent-magnet-based storage ring situated within the Main Injector enclosure [1,2]. The choice of permanent combined function (or "gradient") magnet technology for this ring was based on considerations of construction and operational cost and reliability. The purpose of the Recycler is to improve the stacking

capability of the existing Antiproton Accumulator by relieving this facility of the responsibility of maintaining a high (>2×10^{11} antiprotons/hour) stacking rate at high stacks (>5×10^{11} antiprotons). Perhaps more importantly the Recycler will create the capability to recover unspent antiprotons at the end of collider stores. Since typically >70% of all antiprotons initially stored in the Tevatron remain at the end of a collider store, a significant increase in available antiprotons will be made possible through recycling. This operation will require deceleration of antiprotons from 1000 GeV to 8 GeV followed by transfer to and cooling in the Recycler.

Specific design goals for the Recycler include a stacking capability of 2×10^{11} antiprotons/hour up to a total stack size of 3×10^{12} antiprotons. The initial implementation is based on stochastic cooling. An R&D program aimed at developing electron cooling at 8 GeV is currently underway. Electron cooling will be required to support stack sizes in the range 3-10×10^{12} antiprotons at stacking rates up to 10^{12} antiprotons/hour for future applications.

Table 3: Recycler parameter list

Circumference	3319.4	m
Operating Momentum	8.9	GeV/c
Total Antiprotons	3×10^{12}	
Number of Bunches	498	
Average Current	43	mA
Maximum Beta Function	55	m
Maximum Dispersion Function	2.0	m
Nominal Horizontal Tune	24.425	
Nominal Vertical Tune	24.415	
Transverse Admittance (Normalized @ 8.9 GeV)	>40π	mm-mr
Momentum Acceptance (full)	0.6	%
Number of Gradient Magnets	216/128	
Dipole Lengths	4.5/3.1	m
Number of Quadrupoles	72	
Quadrupole Length	0.5	m

A detailed description of the lattice is contributed to these proceedings [3].

4 PROJECT STATUS

The Fermilab Main Injector Project is currently in its sixth year of funding. Funding over the period FY1992-97 amounts to $198.65M, with $30.95M scheduled for the final year of funding, FY1998. Currently (March 31, 1997) the project is 66% complete by cost and project completion is scheduled for March 1999.

4.1 Construction and Installation Status

Civil construction on the Main Injector is well advanced following completion of the underground ring enclosure and above ground service buildings in 1996. Currently under construction are the cooling ponds, a new substation, and the transmission line required to deliver 345 KV power to the substation. The major outstanding civil construction job involves the final connection of the Main Injector beam lines into the Tevatron at the interface between the two machines. This work is scheduled to start in the fall of 1997.

Magnet production is now nearing completion [4, 5]. Of the 344 dipole magnets required, 307 have been built and 280 are now installed in the ring. In addition all 80 new quadrupole magnets have been completed. These will be augmented by 128 quadrupoles recovered from the Main Ring following the shutdown of that machine in the fall. Dipole power supply installation is nearly complete and testing should be initiated in June. Prototype power amplifiers and modulators required to drive the 53 MHz cavities have been constructed and placed in service in the Main Ring where they have accumulated 24,000 and 14,000 hours respectively of failure free operations [6]. The actual accelerating cavities used in the Main Injector will be recovered from the Main Ring.

In September of 1995 it was decided to construct the 8 GeV transfer line connecting the Fermilab Booster to the Main Injector utilizing permanent magnets [7]. This choice was made in order to gain experience with the technology under consideration for the Recycler ring. The permanent magnets (about 120 in total) required for the 8 GeV line have now been constructed and installed, and procurements for Recycler permanent magnets have commenced.

4.2 Recycler Status

A proposal to incorporate the Recycler into the Main Injector project, without modification to the project budget or schedule, was presented to the Department of Energy in November 1996. As part of the proposal four prototype gradient magnets were built with field uniformity sufficient for use in a storage ring. These magnets culminated a nearly eighteen month period of R&D on permanent magnets for this application. The proposal was approved in February 1997 and work on Recycler construction commenced in April.

The Recycler itself is estimated to cost $12.6M. The low cost results from the utilization of permanent magnets and the already existing Main Injector enclosure and service buildings. The goal is to complete installation of the Recycler in the spring of 1998 and to commission over the remainder of the year.

4.3 Commissioning activities

The 8 GeV line is now completely installed over ~80% of its length. Commissioning with beam commenced on February 20, 1997 and beam was observed at the entrance to a temporary dump situated at the ~60% point after two

hours of tuning. Currently beam transmission is measured at 95±5% with most losses coming in the upstream, electromagnet, matching section where the most restrictive apertures are located. A measurement of the average bending in the line indicates that the dipole field in the permanent magnets is 0.4±0.2% less than that required for "8 GeV" beam delivered from the Booster. This offset is well within the acceptance of the line and will be corrected in the future by either realigning the gradient magnets or by reducing the Booster energy.

Commissioning of the 8 GeV line has occurred nearly a year ahead of schedule--the original plan called for utilizing magnets recovered from the Main Ring during the upcoming shutdown. Commissioning activities in the ring itself are expected to start in late winter/early spring 1998

5 SCHEDULE TO COMPLETE

The current working schedule to completion of the project is given below.

April 1997	Start Recycler construction
May 1997	Award F0 construction contract
September 1997	Start shutdown (Main Ring off)
October 1997	Start F0 construction (demolition)
March 1998	Start half turn commissioning of the Main Injector
June 1998	Main Injector under vacuum, start full turn commissioning
Summer 1998	Recycler under vacuum, start commissioning
July 1998	F0 partial occupancy. Start F0/beamline reinstallation
September 1998	Start Tevatron cooldown
November 1998	Complete F-0 construction. Start delivery of beam to the Tevatron. Parasitic commissioning of remaining beamlines.
January 1999	Complete Recycler installation & commissioning
March 1999	Project complete

We are planning to shut down the Main Ring for the final time on September 15, 1997. At this time equipment removal from the Main Ring and Tevatron will start, followed by demolition and reconstruction of the Tevatron enclosure with its connections to the Main Injector. During the same period Main Ring components destined for reuse in the Main Injector, primarily quadrupole magnets and rf cavities, will be removed, refurbished, and reinstalled.

It is anticipated that 50% of the Main Injector will be intact by February 1998, allowing half turn beam delivered to the permanent dump starting in March. The entire ring should be installed and under vacuum by May 1998. In parallel, but somewhat behind the Recycler magnet and vacuum systems will be installed, allowing commissioning with beam to commence in the summer of 1998. Final installation of beamlines and Recycler rf and stochastic cooling will not happen until the fall of 1998, to be followed by commissioning. Current planning calls for startup in fall 1998 with the Tevatron in a fixed target configuration. Parasitic collider commissioning activities will continue until the late spring of 1999 followed by a changeover to collider configuration.

6 SUMMARY

A plan for enhanced utilization of the Fermilab complex in the upcoming decade(s) is now well underway. By the end of the century the Fermilab community can expect to see:

- A luminosity in the range of $5\text{-}20\times10^{31}$ $cm^{-2}sec^{-1}$ in the Tevatron Collider.
- A new capability for study of neutrino oscillations and rare K decays based on 120 GeV resonantly extracted beams
- 120 GeV test beams to the experimental areas coincident with collider operations.
- A complex capable of being upgraded to $\sim1\times10^{33}$ $cm^{-2}sec^{-1}$ with further improvements to antiproton targeting and cooling.

Following the recent enhancement represented by the addition of the Recycler ring, the Main Injector project is proceeding rapidly to conclusion, with installation now well underway and completion scheduled for spring 1999.

7 ACKNOWLEDGMENTS

This work is reported by the author on behalf of a large number of members of the Beams, Technical, and Particle Physics Divisions, and the Business Services, Facilities Engineering Services, and ES&H Sections at Fermilab who are actively involved in the Main Injector Project.

REFERENCES

[1] Jackson, editor, "The Fermilab Recycler Ring Technical Design Report", Fermilab-TM-1991

[2] William Foster, "The Fermilab Permanent Magnet Antiproton Recycler Ring", Invited talk in these proceedings

[3] Gelfand, et al, "Design and Simulation of the Antiproton Recycler Lattice", Contributed paper to these proceedings.

[4] Harding, et al, "The making of the Main Injector Dipoles", Contributed paper to these proceedings.

[5] Harding et al, "Magnetic Field Strength and Shape Measurements of the Fermilab Main Injector Quadrupoles", Contributed paper to these proceedings.

[6] Reid, et al, "A 200 KW power Amplifier and Solid State Driver for the Fermilab Main Injector", Proceedings of the 1995 particle Accelerator Conference and International Conference on High Energy Accelerators, Dallas, TX, Page 1544 (1995)

[7] Glass, et al, "Permanent Gradient Magnets for the 8 GeV Transfer Line at FNAL", Contributed paper to these proceedings.

HERA STATUS AND UPGRADE PLANS

F. Willeke, Deutsches Elektronen-Synchrotron, Notkestr.85, 22603 Hamburg, Germany

Abstract

The HERA electron-proton collider at Hamburg Germany, designed for collisions of 820 GeV protons with 30 GeV electrons is now in its 6th year of operation. It delivers luminosity for the colliding beam detectors H1 and ZEUS and longitudinally polarized positrons for the internal target experiment HERMES. HERA is operated close to the design luminosity with peak values of $1.2 \times 10^{31} cm^{-2} sec{-}1$. While the beam currents still fall short of expectations, the luminosity was increased by focusing the beams very tightly at the interaction points at the expense of using up most of the margins on aperture, chromaticity and beam-beam tuneshift. In 1996, an integrated luminosity of $\int \mathcal{L} dt = 17.2 pb^{-1}$ has been delivered. Despite the strong beam-beam interactions, the degree of longitudinal polarization of the positron beam is, with (50-60)%, larger than expected.

Despite the good results of HERA, more luminosity is needed for the physics program in the next decade. Preparations are underway to increase the luminosity by rebuilding the low-β insertions. With unconventional new types of magnets, it seems to be possible to increase the luminosity substantially. The expected value is $\mathcal{L}_{peak} = 7.5 \times 10^{31} cm^{-2} sec^{-1}$ which is five times larger than the design value.

1 INTRODUCTION

The HERA collider[1] for 820 GeV protons (p-beam) and 30 GeV electrons or positrons (e-beam) in Hamburg is the only high-energy accelerator in which two completely different species of particles are brought into collision. The double ring collider has a length of 6.3 km. The proton ring has a superconducting magnet structure with 4.6 T magnets. The electron ring has conventional magnets but needs, besides 84 room temperature rf cavities, a superconducting cavity system to reach at the current top-energy of 27.5 GeV. HERA has two interaction regions for the colliding beam experiments H1 and ZEUS. In addition it hosts two fixed target experiments, the gas target experiment HERMES which needs a longitudinally polarized electron or positron beam and the new HERA-B experiment which is going to analyze the interactions of halo protons with a wire target.

The collider has been providing luminosity for more than five years now. It is operated close to the design values for luminosity and spin polarization. The recent incorporation of the HERA-B target operation in HERA operations was a success. At this point four different experiments with very different demands on the accelerator performance are running simultaneously without much detrimental interference.

The results from the HERA experiments open up a rich future physics programme. It is therefore highly desirable to produce luminosity in excess of what the present design can deliver. Therefore, plans are underway to rebuild the collider interaction regions (IR) to allow stronger focusing of both beams.

2 HERA LUMINOSITY OPERATION

HERA luminosity operation has made steady progress. The machine is now operated close to design conditions. Since 1994 HERA has been operated with 27.5 GeV positrons which collide with 820 GeV protons. At this point the peak luminosity is $1.2 \times 10^{31} cm^{-2} sec^{-1}$, the number of protons per bunch is up to 6×10^{10}, the total beam current of the positrons reaches values of up to 44 mA. The normalized emittance of the p-beam is in the order of 4 μm in collisions. The beam-beam tune shift of the positrons of $\Delta\nu_{ye} \simeq 0.03$ exceeds already the design value by a factor of 1.5. While the beam currents quoted above are still below expectations, the matched beam cross section at the interaction point is reduced by more than a factor compared to the design value. Thus high luminosity in HERA is achieved by cutting into the margins of aperture, chromaticity of the protons and of beam-beam tune-shift of the leptons.

Great progress has been made in the last two years on overall reliability. In 1997, HERA is delivering luminosity to the experiments for nearly 50% of the scheduled time. The minimum time needed to re-inject, to accelerate and to tune the two beams amounts to about 20% of the scheduled time. The remaining 30% are still needed at this point for optimizations or recovery from failures. The recent progress is the result of preventive maintenance on the more than thousand magnet power supplies[3] and regular reconditioning of the superconducting rf cavities. Furthermore a large effort is underway to store accelerator data in circular buffers to ease trouble shooting on the numerous components[2].

In 1996, HERA delivered an integrated luminosity of 17.2 pb^{-1} to the colliding beam experiments H1 and ZEUS. At present, luminosity is produced at a monthly rate of 4.5 pb^{-1}. The continuous improvement of HERA operations is reflected in Fig. 1 which shows the integrated luminosity versus the running time for the years 1992-1997.

Since 1995, the HERMES experiment investigates the reactions of high energy longitudinally spin-polarized positrons with a polarized gas target. HERA has a pair of spin rotator magnets installed around the experiment, which rotate the vertically oriented spin into the longitudinal direction and back into the vertical direction. The polarization is usually between 50% and 60% in routine

0-7803-4376-X/98/$10.00 © 1998 IEEE

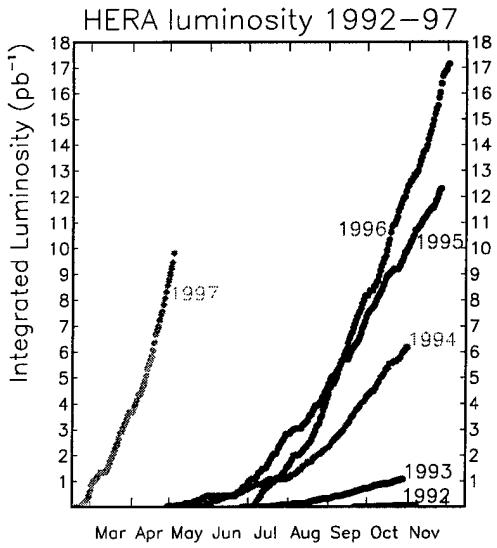


Figure 1: Accumulation of HERA Luminosities 1992-1997

operation. Peak values of up to 70% have been observed. The polarization is remarkably stable. Major tuning with harmonic orbit bumps[7] is performed only once or twice per year. High polarization can then be maintained by occasional orbit corrections. There is some indication, that high polarization is more difficult to obtain with strong beam-beam interactions. In 1996, there was some correlation was observed between beam-beam tune-shift of the positron beam and spin polarization. The tuneshift reached values of $\Delta\nu = 0.035$ and sometimes the polarization approached a level of 50% only after many hours of slow growth (The polarization time in HERA at 27.5 GeV is less than 37 minutes). More careful control of the tunes inside a very narrow window reduced this problem. Recently the vertical β function of the positron beam has been reduced at the interaction point (IP). Since then no correlation between proton beam intensity and positron spin polarization has been observed.

3 HERA ELECTRON OPERATION

A very unpleasant surprise was that the lifetime of intense electron beams in HERA is not determined by bremsstrahlung at desorbed gas molecules as expected but by effects which have been explained by dust trapped inside the beam. The present understanding is that dust particles are emitted from the chamber of the integrated ion getter pumps by an unknown mechanism. This effect makes the operation with electrons virtually impossible. Since 1994 HERA has been operated with positrons and there are no anomalies in the beam lifetime. The dust or micro-particles hypothesis has been supported by many experiments[5, 4, 6]. All efforts to overcome this problem have failed so far. It has been attempted to lower the voltage of the integrated pumps. This was not successful. Turning off the pumps completely seems to suppress the effect. This leads however to unsatisfactory lifetime due to increased pressure of desorbed gas. It has been attempted to drive out trapped particles by kicking the beam. This provides relief only for a period of several minutes. Then the lifetime breaks down again. BPM monitors have been used as clearing electrodes. But this did not solve the problem. The last attempt to resolve the problem, without major changes in the pumping system, was to equip all integrated pumps with pre-resistors of 5 $M\Omega$. This did not improve the situation.

In the winter shutdown period 1995-1996, an $\simeq$ 120 m long section of HERA has been equipped with passive non-evaporating getter pumps (NEG[8]). These pumps have been operated without any problems in the 1996 and 1997 luminosity operation. Pumping speed and required generation are within expectations. Experiments with electron beams indicate, that in this vacuum section, the local beam losses due to bremsstrahlung events have been drastically reduced after the NEG pumps have been installed. Electron beam experiments with all getter pumps turned off have been performed in December 1996. They seem also to indicate that the lifetime degradation is removed if there are no getter pumps present and electrons behave the same as positrons. Therefore, the pumping system in the HERA e-ring is planned to be replaced by NEG pumps in the winter shut-down 1997/1998.

4 HERA LUMINOSITY LIMITATIONS

The Luminosity of HERA is best written as

$$\mathcal{L} = \frac{N_p I_e}{4\pi e \sigma_x \sigma_y} \qquad (1)$$

(N_p is the number of protons per bunch, I_e is the total beam current of the lepton beam, e is the elementary charge, $\sigma_{x,y}$ are the rms beam sizes of the p-beam or e-beam with $\sigma^p_{x,y} = \sigma^e_{xy}$).

With a bunch spacing of 96 ns HERA luminosity is limited by the total lepton beam current and the beam current is limited by the available rf power. At present, the rf power is sufficient to store 45 mA reliably at 27.5 GeV, the lowest possible energy which allows longitudinal spin polarization. An eighth rf station is under construction to raise this limit above 50 mA. The total available rf power will be 12 MW which will allow the design beam current of 58 mA to be stored at 27.5 GeV.

The bunch intensity of the protons is limited by space charge effects at injection into the booster. The incoherent space charge tuneshift at 50 MeV injection into the synchrotron DESYIII is $\Delta Q_{incoh} = 0.4$ (see also[10]), which corresponds to about 1.2×10^{11} protons per bunch at extraction into the PETRA injector ring. Tight aperture in the beam lines and dynamic aperture limitations in the whole proton acceleration chain up to 70 GeV lead to beam losses so that only 6×10^{10} protons per bunch can be reached at present in HERA luminosity operation.

The beam cross sections of positrons and protons need to be matched to keep nonlinear effects of the beam-beam

interaction to a minimum. The beam width and height of the protons are given by the product of emittance and β-functions.

The limit on p-beam emittance, ε, is closely related to the p-beam intensity by the maximum brightness N_p/ε_N achieved in DESYIII. With the present intensity the normalized transverse emittance in HERA is $\varepsilon_N = (4 - 5)\ \mu m$. Electron-proton collisions require short proton bunch lengths. This means that the longitudinal emittance budget is also tight and the bunch intensity cannot be further increased by rf manipulations.

For the e-beam, the low-β quadrupoles are placed much closer to the IP than the p-beam quadrupoles. Despite the small proton emittance of 5 nm at 820 GeV the cross section is limited by the β-function of the protons. There are in the present lattice no limits on focusing of the e-beam.

There are many constraints on the choice of the e/p working point of the HERA collider. Nonlinear resonances for protons, synchro-betatron resonances, spin-orbit resonances for leptons and proton-lepton coupling-resonances need to be carefully avoided to prevent loss of spin polarization and damage to the proton beam, which causes increased backgrounds and loss of luminosity. Therefore the tunes are limited to a narrow window of

$$Q^e_{hor} = 47.147 \pm 0.002;\ Q^e_{vert} = 47.215 \pm 0.005 \quad (2)$$

$$Q^p_{hor} = 31.294 \pm 0.002;\ Q^p_{vert} = 32.297 \pm 0.002 \quad (3)$$

With the tunes inside this window and for present intensities, the lifetime, the emittance growth and the general stability of the proton are excellent in collision. The specific luminosity stays nearly constant over many hours and background conditions are tolerable. The proton beam-beam tuneshift parameters are

$$\Delta\nu^p_x = 0.0014; \Delta\nu^p_y = 0.0007 \quad (4)$$

which are apparently still below the beam-beam limit. At present, the e-beam experiences beam-beam tuneshifts of $\Delta\nu^e_x = 0.0026; \Delta\nu^e_x = 0.0032$. From the 1996 experience (with a larger β^2_y value at the IP), the tuneshift limit is expected to occur at values above 0.04. This means that no substantial increase in luminosity can be achieved by providing a smaller proton emittance.

Increasing the e-beam intensity could provide further increase of luminosity until the yet unexplored limit of the proton beam-beam tune shift is reached. However because of the high costs of rf power installation and consumption, this would be a very ineffective way to increase luminosity. Increasing the proton beam brightness is also quite expensive because is requires an upgrade of the linear accelerator or another small booster synchrotron or exotic beam cooling techniques. Taking into account that the e-beam beam-beam tuneshift does not have a large margin, this way to increase luminosity is not attractive either. The most effective way to increase HERA luminosity by a large factor compared to the design value is therefore to remove the limit on the proton beam β-functions by a new IR geometry. This will be discussed in the next section.

5 HERA LUMINOSITY UPGRADE

HERA beams collide head-on to avoid synchro-betatron resonances and loss of luminosity due to the long proton bunches. The beams need to be separated before the proton beam can be focused by strong low-β quadrupoles. In the present lattice this is accomplished by a dipole field generated by displaced e-beam low-β quadrupoles and by making use of the different magnetic rigidity of the two beams. A number of constraints limit the β in the present lattice. The hard synchrotron radiation generated upstream of the experiment by the separator field is a potential problem for the detector which limits the strength of separating fields. The separator field is a part of the spin rotator. Spin transparency of the beam optics is required. Dispersion generated in the separator gives rise to the excitation of synchro-betatron resonances in the adjacent rf sections. The result is that the first quadrupole magnet which focuses the protons can only be placed 27 m away from the interaction point and the design values for the β function at the IP are rather large with $\beta^*_x = 10$ m and $\beta^*_y = 1$ m. Meanwhile these values have been reduced to values of 7 m and 0.5 m respectively by using up all the aperture margin in the low β-quadrupoles.

A new interaction region has been laid out to overcome these limitations. It is based on two concepts: putting separator magnets much closer to the interaction point and making use of new types of septum quadrupoles. Both concepts help to achieve smaller β-functions at the IP.

The early separation fields will be generated by air-coil magnets inside the colliding beam detector. They are more than twice as strong as the present separators. The intense, hard synchrotron radiation (with a radiation power of $P_{rad} = 25$ kW, and a critical energy of $E_{crit} = 120$ keV) does not hit any components inside the detector and gets absorbed further downstream. The low-β magnets of the e-beam which are aligned on the e-beam axis need a gap between the coils to make way for the synchrotron radiation fan. At about 11 m from the IP, a factor of more than two closer than in the present lattice, the two beams are sufficiently separated by 56 mm. This is enough for a new type of quadrupole septum[11] which focuses only the proton beam. It is described below. The new lattice concept is illustrated in Fig. 2 which shows a top view of the magnets around the IP together with the synchrotron radiation fan.

The new scheme allows the β-functions of the protons to be reduced by a large factor. In order to fully exploit this advantage, the lepton beam must be focussed more tightly as well. Since large chromatic effects must be avoided, it is essential that the separator magnets have a gradient and provide some focusing to the e-beam. The outer diameter of these magnets is limited to 190 mm and the magnets have to be very compact. In addition sufficient aperture must be provided to avoid obstruction of the synchrotron radiation fan at the downstream end. This requires a non-conventional coil design. The conceptual design of this magnet promises a gradient of 7.6T/m and an average

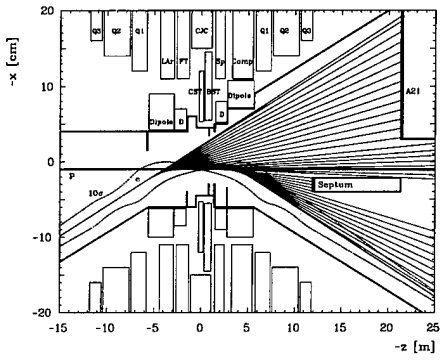


Figure 2: Top View of the New HERA IR: The beams are separated by a relatively strong dipole field generated by air-coil combined function magnets in the colliding beam detector. The intense synchrotron radiation fan passes through gaps between the coils of two iron quadrupoles which form, together with the air-coil magnets, a low-β triplet, for the e-beam. At about 11 m the two beams are sufficiently separated so that the first septum quadrupole to focus the proton beam can be placed there. The thin septum is protected by a small water-cooled absorber. Most of the synchrotron radiation passes along midplane gaps through the septum quadrupole and gets absorbed at 25 m by a power absorber.

dipole field of 0.22 T. About 100 kW of electrical power are dissipated in each of the eight separator magnets. These magnets present a challenge for the technical design. Figure 3 shows a cross-section of the separator magnet.

The new type of septum quadrupole has been developed from the half-quadrupole concept used in the present HERA lattice[11]. Since the field at the mirror plate in the magnet midplane is zero, the mirror plate can be reduced to zero thickness at this point. In this way a triangular cut out has been designed which separates the region of zero magnetic field and a strong gradient by a septum of quasi zero thickness. Figure 4 shows a cross-section of the septum quadrupole.

The second part of the first focusing lens of the protons is a current septum quadrupole which resembles the one of the PEPII design [12]. A layout is shown in Fig. 5.

As a result, the β-functions of the protons at the IP can be reduced from the design values $\beta_{xp} = 10$ m, $\beta_{yp} = 1$ m to $\beta_{xp} = 2.45$ m, $\beta_{yp} = 0.18$ m. The same aperture of $12.5\sigma_{x,y}$ is provided, which leaves sufficient margin. The vertical β is, with 0.18 m, touching on the bunch length limit ($\sigma_s \simeq (12 - 19)$ cm) and cannot be further reduced whereas in the horizontal plane there is still some room for improvement by giving up safety margins (present beam optics for protons in luminosity opertion provides only $10\sigma_{x,y}$ of aperture).

Using the focusing provided by the separator magnets, the β-functions of the e-beam must be reduced by a large factor as well. In addition, stronger focusing is required in the arc to produce an emittance as small as $\varepsilon_{ex} = 22$ nm.

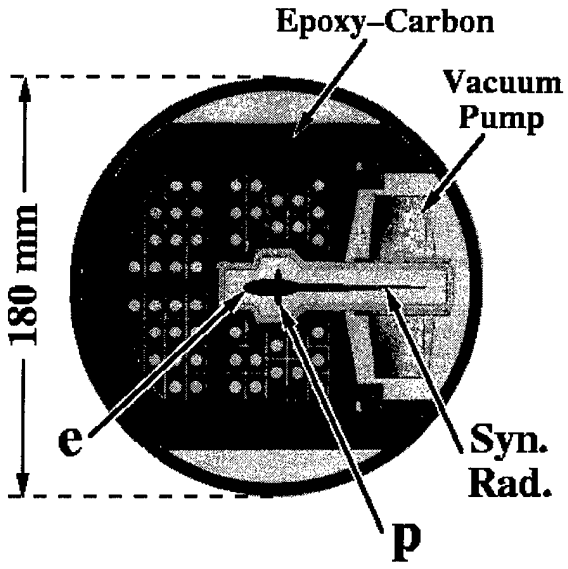


Figure 3: Section of an Air-coil Separator Combined Function Magnet which is placed inside the colliding beam detectors. The magnet fits into a circle of only 180 mm diameter. It has a length of 2 m. Its average field is about 0.22 T, its gradient is 7.6 T/m.

This is accomplished with a beam optics with 90 degree β-tron phase advance in the horizontal plane and 60 degree phase advance in the vertical plane. With this arrangement second order chromatic effects can be kept under control and sufficient dynamic aperture be provided. Table 1 gives the main parameters for the upgraded HERA lattice.

Lepton Beam Energy	30 GeV
Proton Beam Energy	820 GeV
Colliding Bunches	174
Leptons per Bunch	$4.18 \cdot 10^{10}$
Protons per Bunch	$10 \cdot 10^{10}$
Lepton Beam Current	58 mA
Lepton Emittance	22 nm
Proton Emittance	5 nm
Lepton Emittance ratio	0.18
Proton $\beta^*_{x,y}$ at IP	2.45 m/0.18 m
Lepton $\beta^*_{x,y}$ at IP	0.63 m/0.27 m
$\sigma^*_x \times \sigma^*_y$	118 μm$\times$32 μm
b-b tuneshift e $\Delta\nu^e_{x,y}$	0.027, 0.041
b-b tuneshift p $\Delta\nu^p_{x,y}$	0.0017, 0.00046
Specific Luminosity	$1.64 \cdot 10^{30}\ cm^{-2}s^{-1}\ mA^{-2}$
Luminosity	$7.36 \cdot 10^{31}\ cm^{-2}s^{-1}$
Improvement factor	4.9

Table 1: Parameters for Upgraded HERA IR Lattice

There are a number of difficulties which associated with this layout. There are many technical subtleties of mutual forces between the detector field and machine fields, with supports inside the detector, with cooling supply inside the detector with high power synchrotron radiation absorbers, with on-line alignment system, with technical layout of the

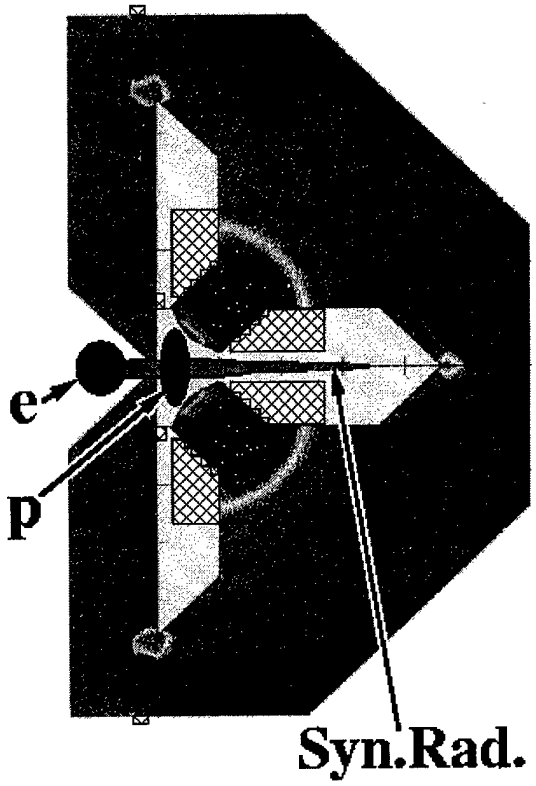


Figure 4: Cross Section of the septum quadrupole, the first focusing element for the protons next to the IP. Note the triangular cut-out which provides the field free space for the e-beam.

septum magnet which are described in a conceptual design report[14, 13]. Many difficulties with emittance and chromaticity control and dynamic aperture have been resolved. The spin dynamics in the new IR with uncompensated solenoid fields and tilted beam orbits is quite delicate but the problems appear to be solvable.

6 CONCLUSIONS

HERA has made good progress in recent years and is about to reach the limit of its design performance. Major technical improvement programmes are underway to overcome the limitations on beam current, overall reliability and the problem with breakdown of the electron beam lifetime.

Further progress in luminosity yield beyond the design values must come from an aggressive new design of the interaction region. A conceptual design of the HERA luminosity upgrade has been made and the feasibility of a luminosity increase by a factor of five compared to the design value has been demonstrated. The project is about to enter a detailed engineering layout. The expectations are to install the new interaction region components in the winter shut-down 1999/2000 providing high lepton-proton luminosity for the next decade.

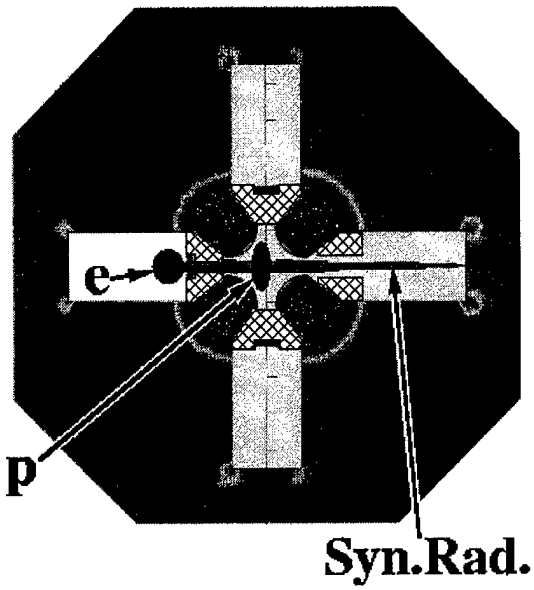


Figure 5: Cross Section of the quadrupole with a septum-coil.

7 REFERENCES

[1] "HERA, A Proposal for a Large Electron Proton Colliding Beam Facility at DESY", DESY HERA81-10 1981

[2] R. Bacher, these proceedings

[3] J. Eckolt, these proceedings

[4] W. Bialowons, "Status of HERA" Proceedings of the EPAC96, Sitges (1996) p.3

[5] D. Kelly *et al.*, Proceedings of the PAC95, Dallas (1995) D.Kelly, W. Bialowons, K.Wittenburg, Proceedings of the EPAC96, Sitges (1996)

[6] D. Kelly, these proceedings

[7] D.P. Barber, "The HERA Polarimeter and the First Observation of Electron Spin Polarisation at HERA", Nuclear Instruments and Methods A329(1993) pp. 79-111; D. Barber *et al.*, Phys.Letters B343 (1995) pp. 436-443

[8] C. Benvenuti, VACUUM 37 (1980) p. 699

[9] O. Bruening, W.Fischer, F. Schmidt and F. Willeke, DESY HERA 95-05 (1995)

[10] W. Ebeling, J. Maidment, these proceedings

[11] M. Marx, B. Parker and H. Wuempelmann , Proceedings of the EPAC96, Sitges (1996) 2170

[12] PEPII, An Asymmetric B-Factory at SLAC, SLAC 418, LBL-PUB 5379 (1993)

[13] G. Ingelmann, A. De Roeck, R. Klanner, ed's., Procedings of the Workshop on Future Physics of HERA, DESY 1995-1996 (1996)

[14] U. Schneekloth ed., "Conceptual Design of the HERA Luminosity Upgrade", DESY-HERA, in preparation

RHIC STATUS

S. Peggs,
Brookhaven National Laboratory, *
Upton, NY 11973, USA

Abstract

The design and construction status of the Relativistic Heavy Ion Collider, RHIC, which is in the seventh year of a nine year construction cycle, is discussed. Those novel performance features of a heavy ion collider that are distinct from hadron colliders in general are noted. These features are derived from the experimental requirements of operation with a variety of ion species over a wide energy range, including collisions between protons and ions, and between ions of unequal energies. Section 1 gives a brief introduction to the major parameters and overall layout of RHIC. A review of the superconducting magnet program is given in Section 2. Activities during the recent Sextant Test are briefly reviewed in Section 3. Finally, Section 4 presents the plans for RHIC commissioning in 1999.

1 INTRODUCTION

The primary motivation for colliding heavy ions at ultra-relativistic energies is the belief that it is possible to create macroscopic volumes of nuclear matter at such extreme conditions of temperature and energy density that a phase transition will occur from hadronic matter to a confined plasma of quarks and gluons. RHIC will provide head-on collisions at energies up to 100 GeV/u per beam for very heavy ions, nominally gold ($^{197}Au^{79+}$). The experimental program also calls for lighter ions all the way down to protons, including polarized protons. Luminosity requirements for the heaviest ions are in the 10^{26} - 10^{27} $cm^{-2}s^{-1}$ range. Although these luminosities are several orders of magnitude lower than p-p colliders, the higher Au-Au total cross-section results in comparable interaction rates.

The most influential experimental requirement is the need for collisions of different ion species (most notably p-Au) at identical Lorentz γ's. This necessitates accommodating mass-to-charge ratios (A/Z) in the range from 1 (p) to 2.5 (Au). Stabilizing the collision point location involves equalizing the rotation frequencies of the two beams, which requires the two rings to operate at different magnetic fields. The need for such beams to pass through common magnets in the interaction region (IR) dictates a lattice design different from conventional hadron colliders. Beams with large transverse and longitudinal sizes are a natural consequence of collider operations at relatively low energies, with enhanced intra beam scattering (IBS), which scales as Z^4/A^2. This in turn has ramifications for the lattice (strong focusing short cells of 29.6 m length) and for the magnet aperture (80 mm in the arcs). The RF system requirements are also determined by these considerations, and by the desire for a short interaction diamond length (< 0.2 m rms), for optimum detector design. Colliders, unlike fixed target machines, are designed to operate for extended periods at high energies. The economics of power consumption argue strongly for superconducting magnets. RHIC is such a superconducting machine.

Kinetic energy range, Au	10.8-100	GeV/u
Kinetic energy range, p	28.3-250	GeV
Number of bunches per ring	60	
Circumference	3833.845	m
Number of crossing points	6	
β^*, injection, H/V	10	m
β^*, low-β insertion, H/V	2	m
Betatron tunes, H/V	28.19/29.18	
Transition energy, γ_T	22.89	
Magnetic rigidity, injection	97.5	Tm
Magnetic rigidity, top energy	839.5	Tm
Bending radius, arc dipole	242.781	m
Maximum arc dipole field	3.45	T
Maximum arc quad gradient	71.2	T/m
Arc magnet coil ID	80	mm
Triplet magnet coil ID	130	mm

Table 1: Major Parameters for the Collider.

The RHIC machine parameters outlined in Table 1 are derived from these general requirements. The complete RHIC facility, including its existing injector complex, is shown schematically in Fig. 1. The internal collider layout is shown schematically in Fig. 2.

1.1 Layout

RHIC consists of two identical, quasi-circular rings separated horizontally by 0.90 m, and oriented to intersect one another at six locations. Each ring consists of three inner and three outer arcs, separated by six insertion regions. Each arc consists of 11 FODO cells, with each half cell consisting of a single dipole and a CQS assembly containing a quadrupole, sextupole, and concentric correction elements. Beam collisions occur at a crossing point in each IR. These IRs contain the optics necessary for producing small collision betatron functions β^* and a zero dispersion at the crossing point, in addition to bending the beams into head-on collisions. The focusing is relaxed at injection with $\beta^* = 10$ m, but during collisions at top energy it is

* Operated by Associated Universities Incorporated, under contract with the U.S. Department of Energy.

0-7803-4376-X/98/$10.00 © 1998 IEEE

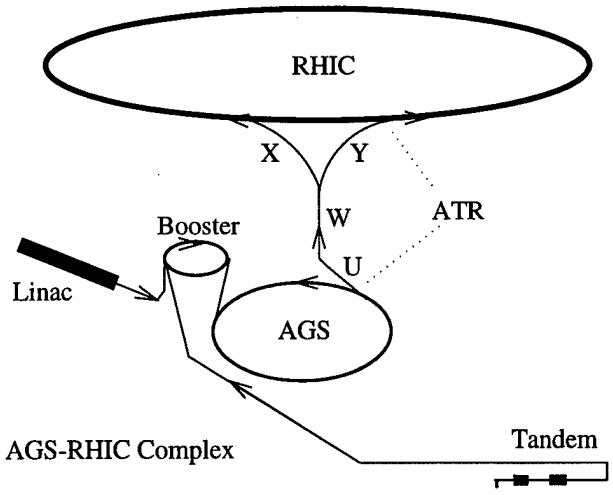


Figure 1: Schematic layout of the AGS-RHIC complex.

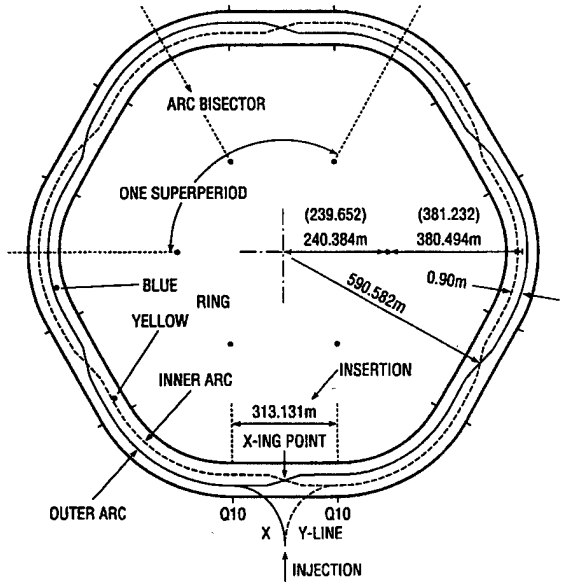


Figure 2: Layout of the collider and the tunnel.

squeezed down to a value of 2 m, resulting in a maximum β of about 700 m in the triplet quadrupoles. The warm parts of each IR contain machine utilities such as injection, beam abort, RF stations, collimators, and specialized instrumentation.

2 MAGNETS

RHIC magnets are conceptually similar to the HERA dipoles, with a "cold-iron" design and cryogenic transfer lines located in the cryostat. The arc dipoles and quadrupoles have a coil inner diameter (i.d.) of 80 mm, and a nominal maximum field and gradient of 3.45 T and 72 T/m, respectively. Interaction region triplet quads have a coil i.d. of 130 mm, with a maximum focusing strength of about 48 T/m. Beam splitting dipoles D0 and DX have apertures of 100 mm and 180 mm, respectively. The industrial production of 80 mm arc magnets was completed in a two year period from 1994 to 1996, and the BNL assembly of CQS cryogenic modules has just been completed. Arc dipoles were produced by the Northrop-Grumman Corporation in a build-to-print contract, as complete cryogenic elements ready for immediate installation.

Field quality and quench threshold are both crucial aspects of superconducting magnet performance. The limited cold testing of only 20% of the magnets is justified by a healthy 30% quench current operating margin. Arc dipole statistics on minimum and plateau quench currents for a set of 60 magnets are shown in Fig. 3. None of the magnets tested to date have had an initial quench current less than the nominal operating level. Limited cold testing is also justified by the good correlation between warm and cold magnetic field quality measurements, confirmed by a careful analysis of the complete data set. All of the smaller number of IR magnets (which have a smaller quench margin) will be cold tested in a vertical dewar.

The distribution of field harmonics for the full set of dipole magnets, shown in Fig. 4, demonstrates excellent

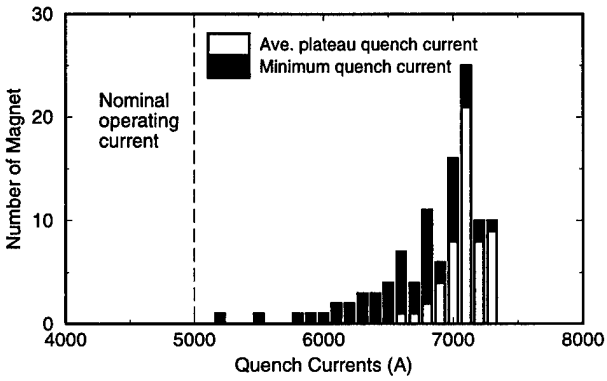


Figure 3: Arc dipole quench current distribution.

field quality with very small random multipole field components, by virtue of tight mechanical tolerances on the cable dimensions. The systematic component of the field harmonics is optimized for low-field performance at injection with yoke saturation apparent in the allowed harmonics at high field.

The dynamic aperture is determined by the triplet quadrupoles during collisions. For example, a maximum β of 1400 m would occur in the triplet under an upgrade scenario with $\beta^* = 1$ m. Under these conditions, the 5σ beam size is expected to increase from 35% to about 70% of the triplet magnet coil radius, due to strong IBS growth. Multiple sophisticated compensation techniques are used to optimize the field quality in triplet quadrupoles, including individual error correction with tuning shims, body-end harmonic compensation, magnet sorting, and lumped triplet multi-layer corrector packages. Especially tight alignment accuracies are required on these magnets [28]. Tuning shims are inserted into the eight empty slots of the IR

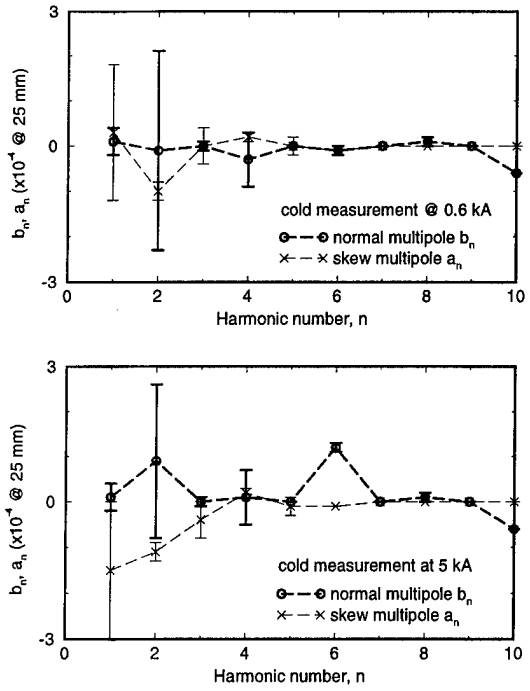


Figure 4: Arc dipole magnetic field multipole harmonics at injection (0.6 kA) and storage (5 kA) currents.

quadrupole body, as shown in Fig. 5, after the magnet is constructed and individually warm measured, in order to correct eight leading field harmonics. Recent experiments indicate that these multipole errors can be reduced to about 10% rms of their uncorrected values. The expected values for the mean and its uncertainty often become zero, while the final standard deviation is associated with a roll up of measurement errors, thermal cycling fluctuations, and quench fluctuations.

Continued production and assembly of IR magnets - correctors, triplet quadrupoles, and DX beam splitting dipoles - are the major items remaining on the RHIC magnet front. The first of the technically challenging DX beam splitting dipoles, with a field of 4.26 Tesla, is expected to finish construction in about October 1997. Prototype helical dipoles are being built at BNL and in industry, for use in Siberian snakes and spin rotators during polarized proton operations [2, 3, 4, 5, 6].

3 SEXTANT TEST

The Sextant Test was a full systems and beam test which occured from December 1996 through February 1997. Gold beam from the AGS was successfully passed through a single sextant in its final configuration, including injection kickers, RF cavities, et cetera. The only items missing were the DX beam splitting dipoles.

The BEAM test goals were to:

- transport beam through one cryogenic sextant to a dump

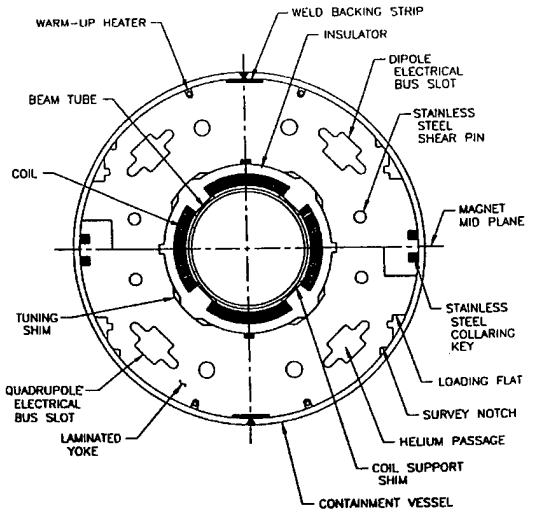


Figure 5: Triplet quadrupole cross-section showing empty slots for tuning shims.

- measure optical and dispersion functions
- study injection and establish nominal conditions
- commission beam diagnostic systems
- commission the low level RF controls
- perform radiation fault studies

The major SYSTEM test goals were to:

- verify cryogenic system performance
- verify the quench protection system
- test power supply ramping and storage
- observe mechanical motion during thermal cycles
- test the vacuum system performance

Beam operating conditions from the 1995 AtR Test were rapidly restored in late January, as beam was delivered 400 meters to the end of the straight part of the normal conducting AGS-to-RHIC (AtR) transfer line. Next, beam was maneuvered around a 90 degree bend, about 150 meters long, before encountering the Lambertson magnet. After the beam was steered through the Lambertson magnet and the injection kicker, gold ions immediately went through 400 meters of superconducting magnets, to a beam dump at the end of the sextant [7, 8, 9, 10].

Accelerator system tests continued after the end of the AGS gold run [11, 12, 13, 14]. During this time the sextant magnets were repeatedly ramped to 5,500 Amps, 10% beyond their nominal storage current, at a ramp rate 10% higher than nominal. This was the first time that many of the magnets had seen full current, since only approximately 20% of the industrially built magnets were cold tested. Tests and measurements of the vacuum, cryogenic, and quench protection systems were also performed. Finally, the magnets were taken through an additional complete thermal cycle.

With only minor caveats in some areas, the Sextant Test

was a great success. Since there are several other papers in these proceedings discussing RHIC Sextant Test performance results, only a brief summary is presented here.

3.1 Test results

The Integral Transfer Function (ITF) of the arc dipoles, measured with beam, differed from the test stand measurements by only about 0.2%. Multiple measurements of the phase advance per FODO cell were made with different QF and QD current settings, with the results shown in Fig. 6. The beam-based arc quadrupole ITF, derived from these data, agrees with magnet test bench measurements within the 0.6% accuracy of the beam measurements. The optimum excitation level of the injection kicker was measured as 32.3 kV, very close to its design value [15, 16, 17].

Various RHIC instrumentation systems have been fully commissioned, from hardware through to high level application codes, in single pass injection line mode [18, 19, 20, 21]. These include beam position monitors, beam loss monitors, current transformers, and flag profile monitors. The prototype of an innovative ionization profile monitor, which collects electrons instead of positive ions, was also successfully tested [22]. Electron collection is made practical by applying parallel electric and magnetic fields.

Tomographical algorithms were used to reconstruct the distribution of beam in an RF bucket, starting from a set of wall current monitor profiles recorded over half a synchrotron period. This application software, currently used to observe beam coalescence in the AGS, will be deployed in RHIC in due course [23].

High power testing of some of the 200 Mhz (storage) cavities was performed, under vacuum [24]. Although one complete 28 MHz (acceleration) cavity has been assembled, it has not yet been high power tested. The digital low level RF system that controls the transfer of single bunches from the AGS into arbitrarily defined bunches in RHIC was also successfully commissioned.

4 COMMISSIONING AND THE YEAR ONE RUN

Full beam commissioning is scheduled to begin in January 1999 in a "Test" run that will begin as soon as full cool down has been completed, and the final beam pipe has been installed. First circulating beam is expected in this run. A spring shutdown for final collider installation of collimators [28] et cetera, and for detector roll-in will, be followed by a "Commissioning" run. First collisions and RHIC project completion are nominally expected to occur about half way through this run. Production running for the experiments, with gold ions, is scheduled to begin in fall 1999, and will last 37 weeks. Spin physics with polarized protons may start in 2000 [25, 26, 27].

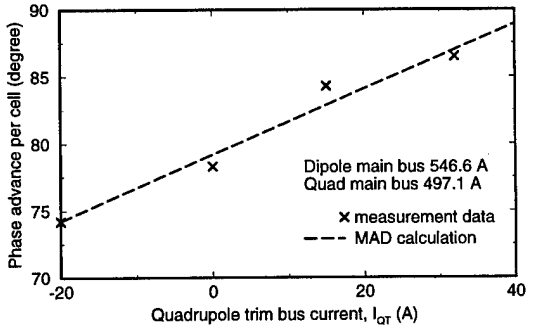


Figure 6: The horizontal phase advance per cell.

Goals for the end of the "Year One" production run include 50% uptime, a store set up time of less than 2 hours, and a luminosity of 10% of the design. This will require aggressive development of the luminosity parameters listed in Table 2, in particular the number of bunches and β^*, even with the more than satisfactory values of emittance and single bunch intensity that were measured in 1997. Based on Sextant Test experience, there is good reason to believe that it will be relatively easy to achieve design gold bunch intensities.

Approximately 40% of the bunch intensity is lost during the nominal gold storage time of 10 hours, mostly through IBS, but also with a significant contribution from Coulomb interactions. The cross sections for gold on gold at 100 GeV/u include:

$\sigma = 117$ barns for electron pair production and capture

$\sigma = 95$ barns for Coulomb nuclear dissociation

For example, if 2 experiments experience an instantaneous luminosity of $L = 8 \times 10^{26}$ cm^{-2}s^{-1}, the partial current lifetime due to nuclear interactions is approximately 49 hours. Figure 7 shows the expected "shot profile" performance for the beam parameters quoted in Table 2, using a beam dynamics model which, in addition to the above effects, includes emittance blow up due to IBS and beam losses to the dynamic aperture [29]. Emittance growth and beam loss lead to a factor of 8 loss in instantaneous luminosity during a nominal 10 hour store of gold ions.

	Gold 1997	Gold start	Gold end	Proton
No. of bunches		60	60	60
Bunch int., 10^9	.4	1.0	$\sim .6$	100.0
Lorentz gamma	12.1	108.4	108.4	268.2
Emittance, $\pi\mu$m	9.9	15.0	40.0	20.0
β^*, m		2.0	2.0	2.0
Lum., cm^{-2}s^{-1}		$8\ 10^{26}$	$1\ 10^{26}$	$1.5\ 10^{31}$

Table 2: Luminosity parameters in the Sextant Test, at the start and end of a 10 hour gold store, and in a proton store.

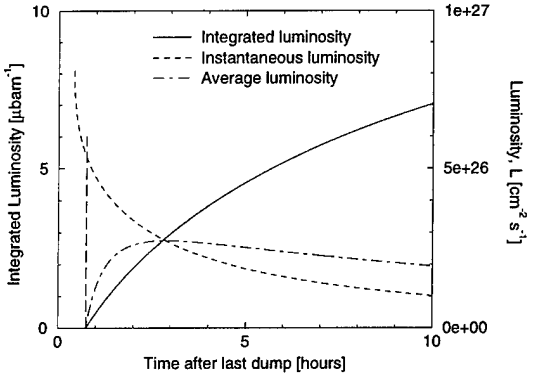


Figure 7: Integrated, instantaneous, and average luminosities during a nominal store of gold ions.

5 CONCLUSIONS

RHIC has two years of its nine year construction cycle to go before heavy ion operations begin in 1999. Industrial production of superconducting magnets has been completed, while in house production of specialized magnets continues. The major milestone of the Sextant Test was recently passed, successfully commissioning many of the beam and non-beam systems. Intra Beam Scattering is expected to be a dominant physical phenomenon limiting the ultimate performance of RHIC, with heavy ions. Polarized proton operations are scheduled to begin in 2000.

6 REFERENCES

[1] D. Trbojevic, "Alignment of the High Beta Magnets in the RHIC Interaction Regions", these proc.

[2] W. Fischer, M. Okamura, "Parameterization and Measurements of Helical Magnetic Fields", these proc.

[3] M. Okamura et al, "Three Dimensional Field Analysis of Helical Magnet for RHIC Siberian Snake", these proc.

[4] M. Syphers et al, "Helical Dipole Magnets for Polarized Protons in RHIC", these proc.

[5] T. Tominaka et al, "Analytical Field Calculation of Helical Dipole Magnets for RHIC Snake", these proc.

[6] E. Willen et al, "A Helical Magnet Design for RHIC", these proc.

[7] W. Fischer et al, "Beam Injection into RHIC", these proc.

[8] W.W. MacKay, "An Interactive Beam Line Simulator Module for RHIC", these proc.

[9] N. Tsoupas et al, "Focusing and Matching Properties of the AtR Transfer Line", these proc.

[10] J. Wei, W. Fischer, et al, "RHIC Sextant Test - Physics and Performance", these proc.

[11] D. Bruno et al, "Overview of the ATR Power Supplies", these proc.

[12] R.F. Lambiase et al, "Power Systems for the RHIC First Sextant Test", these proc.

[13] F. Pilat et al, "RHIC Sextant Test - Accelerator Systems and Performance", these proc.

[14] D. Trbojevic et al, "Preparing Accelerator Systems for the RHIC Sextant Commissioning", these proc.

[15] H. Hahn et al, "The RHIC Injection Kicker", these proc.

[16] H, Hahn, A. Ratti, "The Coupling Impedance of the RHIC Injection Kicker System", these proc.

[17] H. Hahn, A. Ratti, "Equivalent Circuit Analysis of the RHIC Injection Kicker", these proc.

[18] T.J. Shea et al, "Performance of the RHIC Injection Line Instrumentation Systems", these proc.

[19] Charles R. Conkling Jr., "RHIC Beam Permit and Quench Detection Communications System", these proc.

[20] H. Hartmann, "RHIC Real Time Data Link System", these proc.

[21] Lawrence T. Hoff, "Object oriented APIs for accelerator control systems", these proc.

[22] R. Connolly et al, "A Prototype Ionization Profile Monitor for RHIC", these proc.

[23] V. Mane et al, "Beam Tomography in Longitudinal Phase Space", these proc.

[24] R. Connolly et al., "Modifying CERN SPS Cavities and Amplifiers for use in RHIC", these proc.

[25] Peter Cameron et al, "Large Signal Enhancement in the RF Resonance Polarimeter", these proc.

[26] A.U. Luccio, T. Katayama, "Spin Tracking in RHIC", these proc.

[27] N. Tsoupas et al, "Transfer of a Polarized Proton Beam From AGS to RHIC", these proc.

[28] D. Trbojevic et al, "A Study of Betatron and Momentum Collimators in RHIC", these proc.

[29] F. Pilat et al, "Modeling RHIC Using the Standard Machine Format Accelerator Description", these proc.

LHC STATUS AND PLANS

L.R. Evans, CERN, CH - 1211 Geneva 23, Switzerland

Abstract

The Lagre Hadron Collider project (LHC) was approved by the CERN Council in December 1994 as a two-stage project, the first stage at two thirds of the final centre-of-mass energy of 14 TeV to become operational in 2004 and the final stage to be completed in 2008. The CERN management was also requested to solicit contributions to the machine construction from Non-member States involved in the experimental programme in order to allow construction of the machine in a single stage. Taking into consideration the strong support for the project from a number of countries outside the Member States, the CERN Council decided in December 1996 that the machine should be constructed in a single stage with first physics in 2005. Although global participation in detector construction has been well established for many years, this is the first large CERN project in which Non-member States have been involved in the construc-tion of a machine. A brief status report is given and future plans are discussed.

1 INTRODUCTION

The Large Hadron Collider, originally approved for construction as a two-stage machine in December 1994, has now been fully approved for construction in a single stage to be completed with a first physics run in 2005. The project has moved from a conceptual to an implementation phase with many large contracts in preparation, to be let by the end of 1997.

The basic parameters have not changed since the last report to this conference [1] and are reproduced for convenience in Table 1. The machine will provide proton-proton collisions with a centre-of-mass energy of 14 TeV and a nominal luminosity of 10^{34} cm^{-2} s^{-1} and heavy (Pb) ion collisions with a nominal luminosity of 10^{27} cm^{-2} s^{-1}.

The only parameters modified in Table 1, compared to the previous table, are the separation between the beams which has been increased from 180 to 194 mm and a slight decrease in field due to better optimisation of the interconnects.

Three experiments are now approved, the two high luminosity detectors ATLAS and CMS at intersection Points 1 and 5 respectively (Fig. 1), and the heavy ion experiment ALICE to be installed in the existing cavern at Point 2. A fourth detector optimised for B-physics (LHCB) is at the stage of preparation of a technical proposal.

The allocation of the eight straight sections for experiments and machine utilities remains unchanged with one major exception. The RF system has been moved from Point 8, where it was common for the two beams and cohabited with the LHCB detector and the counter-clockwise injection system, to Point 4. In addition, the common RF system has been replaced by separate systems for the two beams, which presents numerous advantages. However, in order to fit in the cavities, the beam separation has to be increased from its value of 194 mm in the arcs to 420 mm through the straight section at Point 4.

Table 1: *Machine parameters*

Energy	(TeV)	7.0
Dipole field	(T)	8.3
Coil aperture	(mm)	56
Distance between apertures	(mm)	194
Luminosity	(cm^{-2} s^{-1})	10^{34}
Beam-beam parameter		0.0032
Injection energy	(GeV)	450
Circulating current/beam	(A)	0.530
Bunch spacing	(ns)	25
Particles per bunch		1×10^{11}
Stored beam energy	(MJ)	332
Normalized transverse emittance	(μm)	3.75
R.m.s. bunch length	(m)	0.075
Beta values at I.P.	(m)	0.5
Full crossing angle	(μrad)	200
Beam lifetime	(h)	22
Luminosity lifetime	(h)	10
Energy loss per turn	(keV)	6.9
Critical photon energy	(eV)	45.6
Total radiated power per beam	(kW)	3.7

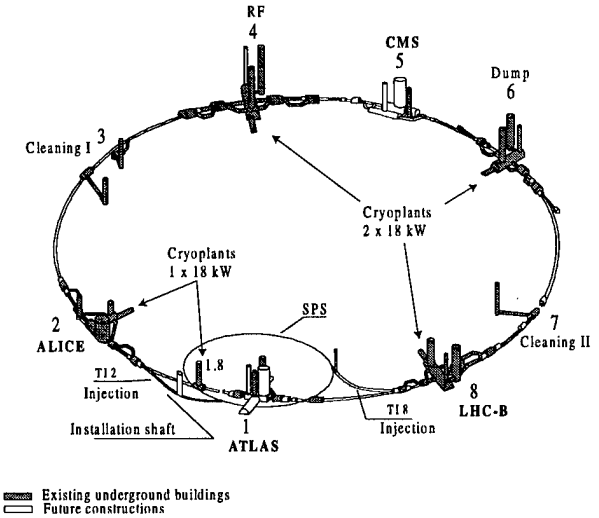


Figure 1: Overall layout

0-7803-4376-X/98/$10.00 © 1998 IEEE

2 OPTICS

A detailed status report on the optics is given elsewhere in these Proceedings [2]. The most visible change compared to previous versions is the addition of a fourth quadrupole in the outer triplet of the insertions in order to improve the flexibility of the machine and to reduce the maximum value of the beta function in the detuned low-beta insertions. However, many other improvements have been made at the level of the dispersion suppressors and at the beginning of the regular arcs in order to increase the tuning range of the machine .

3 INJECTOR CHAIN

In order to provide the beams with the required 25 ns bunch spacing and phase space density (10^{11} particles per bunch, <4 μm.rad, < 1 eV.s.), a considerable amount of work on the injector chain is required [3].The PS Booster and transfer lines are being upgraded from 1 to 1.4 GeV in order to alleviate space charge problems in the PS. The Booster also requires new h=1, 7 kV cavities. In the PS, a combination of 40 and 80 MHz cavities are needed in order to provide the required bunch spacing and bunch length.

In the SPS, considerable progress has been made in identifying the dominant impedances responsible for provoking the microwave instability and consequently diluting the longitudinal phase space density. A programme of work has started to shield the offending elements, mainly vacuum ports and septa. Among the other modifications in the SPS are a major upgrade of the 200 MHz accelerating system and the installation of a new extraction system in order to supply the counter-clockwise rotating beam to the LHC. Beams with nominal LHC parameters will be available in 1999.

4 MAGNETS

4.1 Dipoles and arc quadrupoles

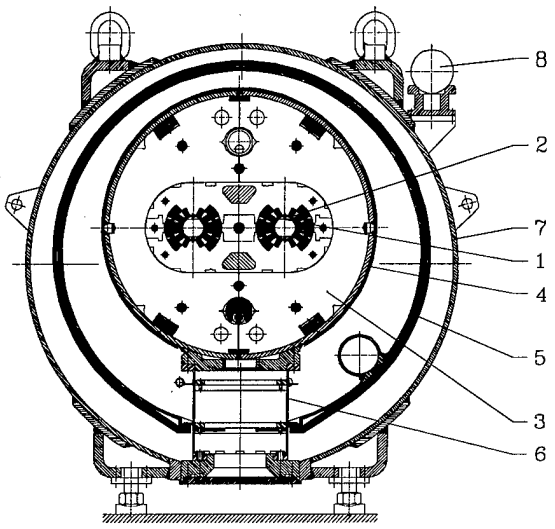
More than 8000 superconducting magnets are required, including 1232 two-in-one dipoles. Each dipole contains small sextupole and decapole correctors integrated into the space at the ends of the magnet in order to correct for persistent current multipoles at the injection field of 0.53 T. In order to achieve the high field (8.3 T) for 7 TeV operation, the magnets must operate in superfluid helium at 1.9 K.

A considerable amount of development work has already been done. More than a dozen short models have been constructed and tested. All of these models have exceeded 9 T with the best reaching 10.5 T. Seven 10 meter long first generation (50 mm aperture) industrially made prototypes have been tested. All have exceeded 9 T with some training. Since then, it has been decided to increase the coil inner diameter from 50 to 56 mm in order to improve the dynamic aperture at injection.

The new dipole design (Figs. 2 and 3) is identical to that presented in the last PAC except that the space between beam channels has been increased from 180 to 194 mm. This was done in order to reduce the prestress required during the collaring operation and to alleviate the design of the quadrupole. In addition, the cryogenic simplification (see below) has allowed much of the ancilliary piping to be removed from the magnet cryostat

Details of the dipole design and performance are given elsewhere in these Proceedings [4].

The arc quadrupoles are separately powered from the dipoles. Their design, undertaken by CEA/Saclay in collaboration with CERN, is based on the outer dipole cable The operational gradient is 223 T/m for 3.1 m length. Two first-generation prototypes have been built and tested successfully at their design gradient. Construction of final prototypes is now under way at Saclay.



1. Beam screen, 2. Cold bore, 3. Cold mass at 1.9 K,
4. Radiative insulation, 5. Thermal shield (55 to 75 K),
6. Support post, 7. Vacuum vessel, 8. Alignment target

Figure 2: Cross section of the dipole magnet and cryostat

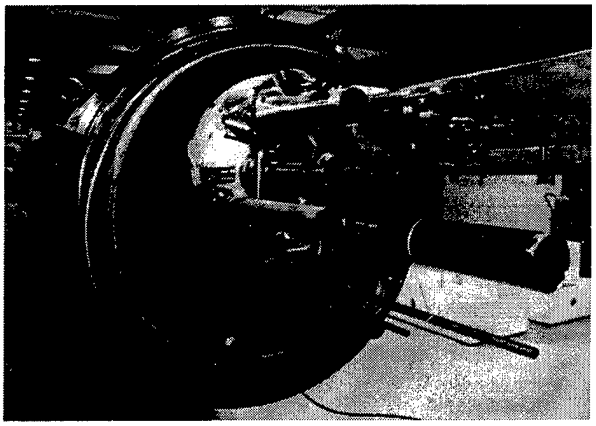


Figure 3: Prototype dipole

4.2 Cable

A lot of effort has gone into cable development. For the first generation of dipoles, more than 14 tons of 17 mm wide cable has been produced. For the final design, the cable width has been reduced to 15.1 mm in order to decrease cost and facilitate winding. Measurements of minimum quench energy, made in collaboration with BNL and LBL, have shown the importance of the degree of compaction of the strands in the cable, a lower compaction allowing more helium penetration and cooling of the strands. This has lead to a small change in cable dimensions and keystone angle. The main cable parameters are given in Table 2.

Table 2: *Dipole strand and cable characteristics*

	Inner layer	*Outer layer*
Strand:		
Diameter (mm)	1.065	0.825
Cu/Sc ratio	1.6	1.9
Filament size (μm)	7	6
Twist pitch (mm)	15	18
Critical current (A)		
at 10 T, 1.9 K	≥ 515	
at 9 T, 1.9 K		≥ 380
Cable:		
Number of strands	28	36
Cable dimensions		
width (mm)	15.1	15.1
keystone angle	1.25°	0.9°
mid thickness (mm)	1.9	1.48
Transposition pitch (mm)	115	105
Critical current (A)		
at 10 T, 1.9 K	≥ 13750	
at 9 T, 1.9 K		≥ 12960

The cable insulation has received a great deal of attention. In superfluid helium, it is particularly important that the helium penetrates the insulation in order to provide additional enthalpy and to profit from its very high thermal conductivity. Various insulation methods have been investigated in collaboration with CEA/Saclay. The classical b-stage epoxy has been abandoned in favour of an all polyimide insulation consisting of a 50 μm thick half-overlapping polyimide tape and a second wrap of adhesive coated tape wound with 3 mm spacing between turns, leaving open channels for helium penetration.

Another very important aspect of the cable development has been the search for a process that guarantees a consistent inter-strand resistance of between 10 and 30 μΩ in order to avoid current sharing between strands during ramping. Best results have been achieved with SnAg ("Stabrite") coated cables.

4.3 Insertion and corrector magnets

Recently a short model of a large aperture (70 mm) insertion quadrupole has been successfully tested in industry. More details are given in these Proceedings [5]. CERN is collaborating with FNAL and KEK to finalise the design of these magnets with a view to fabricating the full series. The RF insertion layout is based on RHIC coils and is being designed in collabo-ration with BNL.

Many prototype corrector and auxiliary magnets have been tested, including a combined dipole and sextupole for orbit and chromaticity correction, an octupole and the small sextupole and decapole correctors to be incorporated into the ends of the main dipoles.

5 CRYOGENICS

The design of the cryogenics system has undergone a number of detailed changes, although the basic design principles remain the same.

The four LEP cryoplants will be upgraded from 12 to 18 kW and supplemented by four new plants each of 18 kW capacity. These new plants will not be of the LEP type with split upper and lower cold boxes but will have a single cold box on the surface. The original layout grouped the plants in pairs at the four even points of the machine. This symmetry has now been broken by locating the new plant originally foreseen for Point 2 at point 1.8, where the large shaft that was used for the installation of LEP can be re-used to accommodate much of the cryogenic infrastructure feeding the octant from Point 1 to Point 2 (Fig. 1). This is also in close proximity to the hall used for magnetic measurements. A large cryoplant at this location is of considerable interest for component testing, particularly the cold compressor boxes. It also avoids major civil engineering at Point 2, where the surface and underground structures are quite different from the other three even points, and allows more efficient cooling at the 1.9 K level, since the tunnel slopes downwards between Points 2 and 1, facilitating the operation of the cold compressors located at Point 1.8.

Other substantial modifications made since last reported at this conference include the move of much of the cryogenic pipe work into a separate line and the extension of the cell cooling loop to a full period of 107 m (Fig. 4). Static superfluid helium pressurised at 1 bar permeating the magnet laminations is cooled by heat exchange with saturated superfluid helium flowing through a tube running over the whole length of a cell. The superfluid is produced by expanding sub-cooled helium to saturation through a Joule-Thomson valve (TCV1). Before expansion, helium at 4.3 K is pre-cooled in a small heat exchanger (HX), using the cold helium vapour at 1.8K, pumped to saturation pressure (15 mbar) through the line B. This allows one line carrying sub-cooled helium at 2.2 K line A in the previous design) to be suppressed. The connection between the cryogenic

line and the magnet cell is made by a jumper at the level of the short straight section. A major consequence of the move to a separate cryoline with connection to the magnet chain only once per period is that the quench discharge can be made only at each end of the cell through quench valves SRV and not at each individual magnet as originally foreseen. Tests on the string have shown that this can be tolerated.

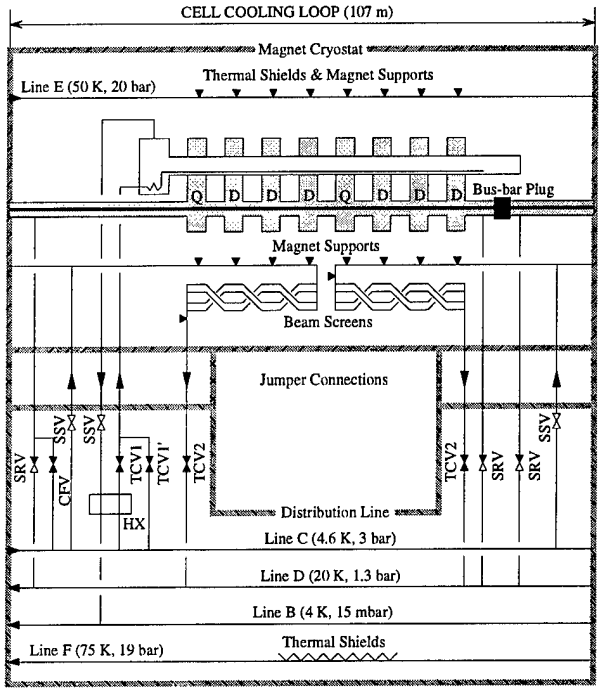


Figure 4: Cell cooling loop

6 THE STRING TEST FACILITY

The string test facility [6] consists of a simulation half-cell of the machine, containing a short straight section and three dipoles. The short straight section contains a prototype three meter long quadrupole and the cryogenic service module needed for cooling the string to 1.9 K. The dipoles are all "first-generation" prototypes, 10 meters in length with an internal coil diameter of 50 mm.

Since its commissioning in December 1994, the string has totalled more than 1500 hours of operation below 1.9 K and has undergone more than 30 forced quenches from its nominal current or above. It has validated the cooling scheme design and has given a great deal of valuable information which has been used to refine and optimise the machine design. For example, data on quench behaviour with all quench relief valves closed except the one at the end of the string has been invaluable in the decision to implement the separate cryogenic line with jumper connections separated by a full cell length.

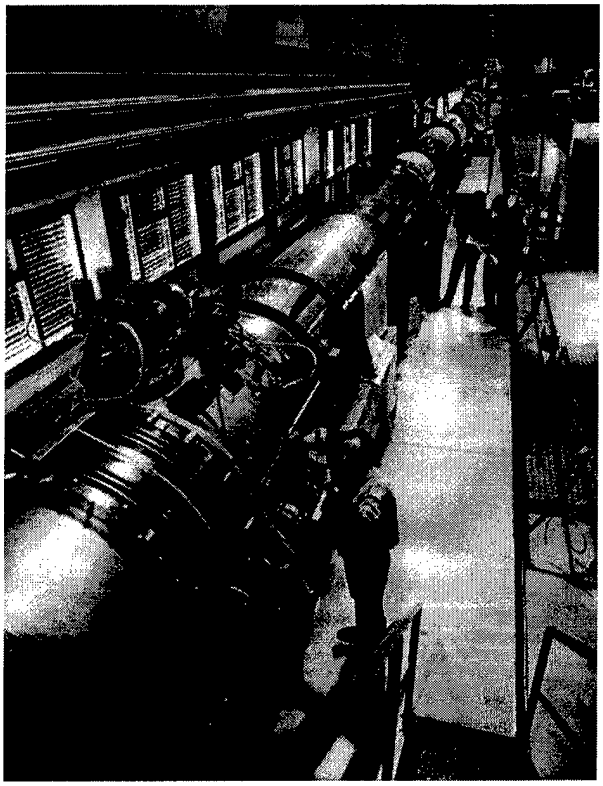


Figure 5: String test facility

Recently, the string has undergone a forced lifetime test, where it has been repetitively cycled more than 2100 times up to its nominal current of 12.5 kA at the nominal LHC ramp rate of 10 A/s, simulating more than 10 years of LHC operation. The current is kept stable for 150 s then ramped down to its nominal injection level of 800 A. This cycle is repeated 24 hours per day. The string dipoles have now been equipped with a prototype beam screen and additional instrumentation for detailed studies of quench propagation.

7 VACUUM

The LHC beam vacuum [7] poses particular problems. Due to the synchrotron radiation emitted by the protons (about 4 kW per ring at 7 TeV) and the heating due to image currents in the wall of the vacuum chamber, the magnet cold bore at 1.9 K must be shielded from the beam, otherwise the required cryogenic power would become excessive. An inner liner cooled to around 20 K through tubes carrying high pressure gas will therefore be installed in the cold bore. Synchrotron radiation impinging on this liner will cause gas to be desorbed from the bulk material which will in turn be cryopumped onto the surface of the liner. Once a substantial fraction of the surface is covered with gas molecules, particularly hydrogen, a catastrophic pressure rise would build up unless remedial action is taken. Slots, filling about 2% of the surface, are therefore cut in the liner so that hydrogen can be cryopumped by the much colder surface of the magnet cold bore. The inner surface must be of high

conductivity material but the liner must also be sufficiently strong to withstand the forces induced by eddy currents in case of magnet quench. It is therefore constructed from steel with a very low permeability (high-manganese) with a thin strip of copper on its inner surface. Tests have shown that co-lamination of copper and steel sheets at high pressure give much better results than electroplating. Once the composite strips are formed they are shaped into two half-shells and laser-welded along their edges. Great care is taken in order to adjust the weld parameters to avoid the formation of ferrite in the weld seams.

8 CIVIL CONSTRUCTION

The LHC makes use of the existing infrastructure of LEP, including the four existing experimental halls to house experimental detectors or machine utilities. Nevertheless, a considerable amount of extra investment in civil construction, amounting to about half of that already invested in LEP, is needed to house the two large detectors, for the long transfer tunnels between the SPS and the LHC, and for the surface infrastructure for assembly halls and cryogenic equipment.

At Point 1, the ATLAS detector requires an underground cavern of more than 50000 m^3 and an associated service cavern of nearly 20000 m^3 together with considerable surface hall space.

At Point 5, the CMS detector requires an experimental cavern of about 30000 m^3 and a service cavern of 17000 m^3 as well as considerable surface infrastructure for assembly and testing of the 14000 ton solenoid. The sinking of the shafts at Point 5 poses a particular challenge since they have to pass through water-bearing moraine.

At Points 2 and 8, ALICE and LHCB will use existing experimental halls with very little modification.

Two transfer tunnels, each more than 2.5 km in length, are needed to transport the beams from the SPS. The clockwise injection tunnel, TI2, will also be used for machine installation through a shaft located on the CERN site, needed for the excavation of the tunnel. Finally, two beam dump tunnels, each of some 700 m in length will house the transfer lines to the beam abort caverns. It is foreseen that all civil construction contracts will be let in November 1997, allowing site preparation to start at the beginning of 1998.

9 PLANNING

As mentioned in the introduction, the LHC project has now been approved for construction in a single stage with the first physics run in the second half of 2005. It is planned to run LEP until the end of 1999, although the LHC planning has been adapted in order to allow a further year of LEP running if the physics case justifies it and if appropriate funding can be found. The following major milestones can be identified:

– Start civil engineering	January 1998
– Dismount LEP	October 2000
– Deliver Point 1(ATLAS)	July 2002
– Deliver Point 5 (CMS)	July 2003
– Sector test	October 2003
– Circulating beams	July 2005

A sector test is foreseen in 2003. A beam will be injected in the counter-clockwise direction at Point 8 and transported through one octant to Point 7. It can be observed that the experimental area for CMS is available one year later than for ATLAS. This is due to the fact that geological conditions at Point 5 are less favourable than at Point 1 and is acceptable due to the fact that a complete assembly and test of the CMS magnet will be made on the surface before installation, whereas the ATLAS detector must be completely assembled under-ground.

10 CONCLUSIONS

The Large Hadron Collider project has now moved from a conceptual to an implementation phase, with machine construction to be completed in a single stage with a first physics run in 2005.

The main technical choices are now frozen and much effort is being devoted to the detailed technical specification of major hardware systems. By the end of the year, it is expected that several large contracts will be placed, including those for civil engineering.

The LHC is the first large CERN project in which there is a participaton of external institutes in the machine design and construction.

ACKNOWLEDGEMENTS

On behalf of the CERN LHC team, I would like to acknowledge the enthusiastic collaboration of colleagues from laboratories in Canada, India, Japan, Russia and the USA, as well as from a number of institutes in the CERN Member States, in the realisation of this project.

REFERENCES

[1] L.R. Evans, "The Large Hadron Collider", Proc. 1995 Part. Accel. Conf., Dallas (1995).
[2] A. Fauss-Golfe et al, , ".A More Robust and Flexible Lattice for LHC", these proceedings.
[3] K. Schindl, "Conversion of the PS Complex as LHC Proton Pre-Injector, these proceedings.
[4] R. Perin, "State of the LHC Main Magnets", these proceedings.
[5] R. Ostojic, "Quench Performance and Field Quality Measurements of the First LHC Low-beta Quadrupole Model", these proceedings.
[6] R. Saban, "Experiments and Cycling at the LHC Prototype Half-Cell", these proceedings.
[7] O. Gröbner, "The LHC Vacuum System", these proceedings.

DYNAMIC EFFECTS AND THEIR CONTROL AT THE LHC

R. Bailey, F. Bordry, L. Bottura, P. Burla, P. Collier, K. Henrichsen, J.P. Koutchouk, R. Lauckner, R. Parker, J. Pett, P. Proudlock, H. Schmickler, R. Schmidt, L. Walckiers, R. Wolf
CERN, Geneva, Switzerland

Abstract

Tune, chromaticity and orbit of the LHC beams have to be precisely controlled by synchronising the magnetic field of quadrupole, sextupole and corrector magnets. This is a challenging task for an accelerator using superconducting magnets, whose field and field errors will have large dynamic effects. The accelerator physics requirements are tight due to the limited dynamic aperture and the large energy stored in the beams. The power converters need to be programmed in order to generate the magnetic functions with defined tolerances. During the injection process and the energy ramp the magnetic performance cannot be predicted with sufficient accuracy, and therefore real-time feedback systems based on magnetic measurements and beam observations are proposed. Beam measurements are used to determine a correction factor for some of the power converters. From magnetic measurements the excitation of small magnets to compensate the sextupolar (b_3) and decapolar (b_5) field components in the dipole magnets will be derived. To meet these requirements a deterministic control system is envisaged.

1 INTRODUCTION

This paper summarises some of the findings of the LHC Dynamic Effects Working Group. It also reflects the discussions and conclusions of a three day workshop held at CERN in February 1997 [1] [2].

The injection and acceleration of the LHC proton beams without particle losses and emittance growth requires an accurate control of the beam parameters. The value of the betatron tune is about 63 units and needs to be controlled to a level of 0.003 (for ultimate performance) [3]. Orbit excursions should be limited to less than 0.5 mm (rms value of the closed orbit). The chromaticity should be limited to some units (the chromaticity is defined as the change of tune with energy). Therefore the magnetic fields of the dipole, quadrupole, sextupole and corrector magnets need to be precisely synchronised during the energy ramp. This must be done in the presence of varying response times and transfer functions of the power converters and magnets. For an accelerator with superconducting magnets, such as the LHC, the synchronisation is a particular challenge due to large variations in the field and field errors caused by coupling currents and persistent currents within the superconducting cable. Dynamic effects include changes of the magnetic field and its multipoles even at constant excitation current, and changes of the field depending on the speed of the ramp as well as on the powering history.

2 DYNAMIC EFFECTS IN SUPERCONDUCTING MAGNETS

Persistent current effects in superconducting magnets produce large allowed multipole components in the magnetic field. The phenomenon is strongest at low field and is highly non-linear in magnet excitation and temperature.

It was first observed at the TEVATRON that multipole fields exhibit slow time drifts even if the current is kept constant[4]. When the energy ramp is resumed, a rapid change of the multipole fields is observed ("snap-back"). Although it has been over 10 years since this phenomenon was first observed, the understanding of the time dependence of persistent currents is not complete. For the LHC prototype dipole magnets the results from detailed measurements of persistent current decay and snap-back are documented in [5] [6]. The decay at stable current and snap-back (Fig. 1) of the fundamental and multipole components depend on the previous powering history of the magnet and are not, at present, easy to predict. Theories have been put forward for this phenomena (interaction of the internal field with the cable magnetisation) suggesting that there is hope for a better predictability of these errors in the future[5][7]. From a practical point of view consistent behaviour can be best achieved by a precise and well defined cycle of the main magnets, as in the operational procedures for the TEVATRON, where the magnets are cycled six times before injection. Because of the time involved (about one hour for a complete cycle) multiple-cycling before injection can not be envisaged for the LHC. In the TEVATRON and at HERA the beam is only sensitive to the chromaticity due to sextupolar field components created by the persistent currents in the dipole magnets. For the LHC, decapolar as well as sextupolar field components in the dipole magnets require correction.

Dynamic effects during the ramp, due to coupling currents between the strands inside the cable, are now well understood[8]. By controlling the inter-strand contact resistance in the superconducting cable and limiting its spread it is expected to achieve a good reproducibility of the coupling currents for the series of LHC dipole magnets.

3 MAGNETS AND POWERING OF LHC

The large size and certain constraints imposed by the use of the existing infrastructure (for example the LEP tunnel and the existing underground structures) have resulted in an electrical segmentation of the machine into eight sectors requiring tracking amongst sectors as well as families of magnets. Each of the eight LHC sectors has one family of main dipole magnets and separately powered main

0-7803-4376-X/98/$10.00 © 1998 IEEE

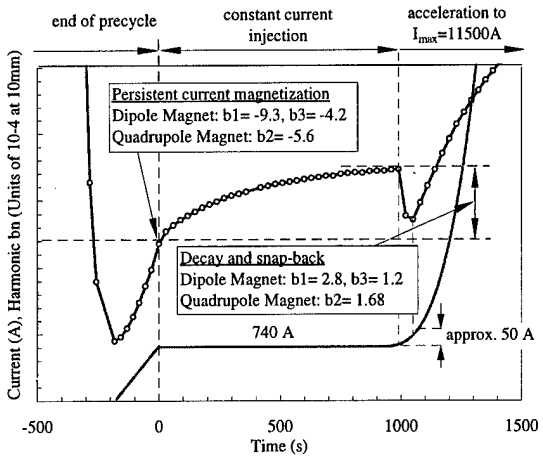


Figure 1: Schematic view of current and magnetic field versus time. The field decays during the injection plateau, and is re-established suddenly at the start of the ramp

quadrupoles (QD and QF). A dipole orbit corrector is associated with each quadrupole aperture. For the correction of the betatron tunes trim quadrupole magnets are foreseen, since a fast correction of the tune with the lattice quadrupoles is difficult to perform, due to the large inductance and therefore long time constant of the magnet chain. Families of tuning quadrupoles and dispersion suppressors are installed at both ends of each sector. Families of chromaticity sextupoles, octupoles and skew-quadrupoles are installed close to the quadrupole magnets in the arcs. Small sextupole and decapole corrector magnets will be installed at the end of each dipole magnet for local compensation of the multipoles in order to maximise the dynamic aperture.

In order to achieve the slow ramp rates as well as for fine adjustments, the main power converters will need a monotonic resolution of 1 ppm[9]. Because of the large hysteresis in the dc magnetisation curves it is important that the overshoot (and undershoot) is zero or at least kept below 5 ppm. Although absolute accuracy is not an issue, a short-term stability and dynamics of ± 3 ppm as well as a reproducibility and tracking between sectors of ± 5 ppm is required. The requirements, expressed in terms of maximum current, come from the needs at injection. These are 15 times less severe when expressed with respect to the actual current at injection. To meet these requirements, and because of the large electrical time-constants of the main circuits (23000s for the dipole), digital predictive regulation techniques will be used with a 20-bit Sigma-Delta ADC.

4 ORBIT AND BETATRON TUNE

The central momentum of the particles is determined by the integral dipole field. The frequency of the RF-system is nearly constant and determines the mean radial orbit. Differences of the integral field of the dipole magnets in the octants need to be smaller than 10^{-4} which requires an excellent tracking of the power converters. If this value is exceeded, the orbit is adjusted with correction dipole magnets. During the time to inject beam into the LHC (this will take at least eight minutes) the main dipole field increases slightly due to the decay of the persistent currents. To maintain the energy matching between LHC and SPS (as injector) the average strength of the orbit corrector magnets will be reduced to keep the integral dipole field and therefore the energy constant. At some critical locations, for example close to the collimators, a local orbit feedback is proposed.

To control the betatron tunes to a level of 0.003 the reproducibility of the quadrupole gradient with respect to the particle momentum needs to be better than 40 ppm. Since the power converter is always rated with respect to maximum current, a reproducibility of better than 2 ppm would be required. Not only the lattice quadrupoles need to be precisely synchronised to the particle momentum, but also the quadrupoles in the insertions. Due to magnet dynamic effects and power converter tolerances the energy cannot be ramped without correcting the tunes. Therefore on-line tune measurements and corrections are required at an early stage of the LHC operation using the tuning quadrupoles. The main dipole and quadrupole magnets will follow a predefined current ramp.

5 CHROMATICITY AND HIGHER ORDER MULTIPOLES

The chromaticity is generated by the optics and by the sextupolar field component (b_3) in the dipole magnets. The sextupole component of the persistent currents in the dipole magnets generates a chromaticity of about 550 units. The natural chromaticity is about 100 units. During the time to inject beam into the LHC the chromaticity changes slowly due to the decay of the persistent currents. A correction is performed with the sextupole correctors at the end of the dipoles, by either using a measurement of b_3 or a model for the persistent current decay. Since b_3 needs to be corrected to the 1% level or better, the required accuracy might not be achieved. Chromaticity measurements on the injection plateau will complement the magnetic measurements.

At the start of the energy ramp the snap-back leads to a chromaticity change of about 150 units, the time for this change depends on the initial speed of the ramp. It has been estimated, that after a field increase of about 35 mT the snap back is finished. This corresponds to a current increase of about 50 A. It is proposed to start the ramp very slowly so as to minimise the rate of change in the field and field errors. The sextupole corrector magnets will be ramped according to the results of magnetic measurements in the reference magnets. Again, chromaticity measurements can be performed for fine adjustments. Another option is to increase the current in small steps of, say, 0.5 A, and to measure and adjust the chromaticity for each step.

The control of the decapole corrector magnets relies on measurements of the b_5 component in reference magnets. At injection, the current will be adjusted to compensate the

b_5 component in the dipole magnets. During the snap-back, the corrector magnets have to be ramped, again based on magnetic measurements.

Schemes of injection on a very slow ramp to avoid the snap-back have also been considered but have no priority for the moment.

6 REFERENCE MAGNETS

The present layout of the LHC foresees a set of reference magnets connected in series with each of the main power converters of the eight separately powered sectors of the machine (8 dipole and 8 quadrupole magnets). The reference magnets were to provide the main observables within the machine for its control. However, it became apparent that they would not be able to achieve completely this role. Further reliance needed to be placed on good power converter performance where effects are reproducible and beam observation where this is not the case. Considering:

- the expected performance of the power converters;
- the availability of comprehensive beam observation (eventually on-line);
- the operating principle of correcting all dynamic effects with correcting magnets;

it is proposed to install the reference magnets remotely in a surface building in which the magnetic measurements will be made. There should be one reference magnet per type of dipole and one per type of quadrupole (total of about 6). To allow additional verification within the machine, these remote reference magnets should be complemented by flux-loops measuring the fundamental fields of the dipoles and quadrupoles of the machine magnets of each sector [10]. This results in a much simplified reference magnet system. It is accessible, can be developed from the magnet test benches, is flexible and can be used on-line to assist with machine operation or off-line for new developments. The disadvantages are associated with recovery from a failure of the powering or cryogenics systems and the fact that the remote infrastructure becomes important to machine operation until such time as it is not needed on-line.

7 BEAM INSTRUMENTATION AND CONTROLS

For the control of the LHC in presence of dynamic effects the measurement of orbit, tune, coupling and chromaticity is of prime importance. Fast orbit acquisition and good orbit correction software will be needed already at the commissioning stage. New techniques to observe coupling, tune and chromaticity need to be investigated with a view to use these signals for on-line corrections should they prove suitable. Although it is not clear today which parameters require on-line control, it is recommended that the machine is prepared to accept slow feedback as far as the control system, power converters and RF systems are concerned. Best estimates suggest a rate up to a few Hz, but this will depend, for instance, on the exact magnet ramping speed. The speed of the ramp will depend on the time required to measure and correct tunes, orbit and chromaticity. Therefore field and beam instrumentation should be suitable for inclusion in such a feedback system. Pilot projects are proposed for the SPS, which will concern mainly studies on tune and chromaticity control.

8 CONCLUSION

The Working Group on Dynamic Effects has been a very useful forum for discussions among specialist in different domains (magnet technology, beam dynamics, beam instrumentation, power converter, controls and operation). During these discussions, the accelerator physics requirements and specifications for various hardware have been established along with possible scenarios for operation. Considering the present understanding of the behaviour of superconducting magnets it is believed that the dynamic effects of LHC can be controlled using main power converters of reasonable precision (1 ppm resolution, ± 3 ppm short-term stability), benefiting from on-line magnetic measurements from a limited number of reference magnets. This will require a deterministic control system. For ultimate performance, however, the development of beam instrumentation suitable for feedback loops needs to be undertaken.

9 ACKNOWLEDGEMENTS

We would like to thank all participants to the 'LHC Workshop on Dynamic Effects and Their Control', in particular the representatives from DESY (HERA), FERMILAB (TEVATRON) and BNL (RHIC).

10 REFERENCES

[1] R. Schmidt, Progress Report from the Dynamic Effects Working Group, LHC Project Note 67, October 1996

[2] P. Proudlock, Summary of the LHC Workshop on Dynamic Effects, LHC Project Report 99, March 1997

[3] J.P. Koutchouk *et al.*, A Robust and Flexible Lattice for LHC, these proceedings

[4] D. Finley, PAC 87, Washington DC, USA, 16-19 March, 1987

[5] L. Bottura *et al.*, Field Errors Decay and "Snap-Back" in the LHC Model Dipoles, ASC'96, Pittsburgh, PA, USA, 25-30 August, 1996

[6] L. Walckiers *et al.*, Towards Series Measurements of the LHC Superconducting Magnets, these proceedings

[7] H.Mess *et al.*, Superconducting Accelerator Magnets, World Scientific, 1996

[8] A.P. Verweij, R. Wolf, Field Errors due to Inter-Strand Coupling Currents.., Internal Note CERN-AT-MA/AV 94-97, March 1994

[9] I. Barnett *et al.*, A strategy for controlling the LHC magnet currents, EPAC, Barcelona, Spain, June 10-14, 1996

[10] K. Henrichsen *et al.*, Proposal for in-situ measurements of dynamic effects in the LHC lattice magnets, LHC Project Report 89, January 1997

RHIC SEXTANT TEST – PHYSICS AND PERFORMANCE *

J. Wei, W. Fischer, L. Ahrens, J.M. Brennan, K. Brown, R. Connolly, G. F. Dell, M. Harrison, J. Kewisch, W. W. MacKay, V. Mane, S. Peggs, F. Pilat, T. Satogata, M. Tanaka, S. Tepikian, P. Thompson, C. G. Trahern, D. Trbojevic, N. Tsoupas
Brookhaven National Laboratory, Upton, New York 11973, USA

Abstract

This paper presents beam physics and machine performance results of the Relativistic Heavy Ion Collider (RHIC) Sextant and AGS-to-RHIC (AtR) transfer line during the Sextant Test in early 1997. Techniques used to measure both machine properties (difference orbits, dispersion, and beamline optics) and beam parameters (energy, intensity, transverse and longitudinal emittances) are described. Good agreement was achieved between measured and design lattice optics. The gold ion beam quality was shown to approach RHIC design requirements.

1 INTRODUCTION

The Sextant Test, a major test of the full accelerator systems and operational machine properties of a single completed sextant[1, 2] of RHIC, was performed with beams of fully stripped gold ions from December 1996 through February 1997. After being extracted from the AGS, the beam was first delivered to the AtR[3, 4] transfer line, where beam operating conditions from the 1995 AtR Test were rapidly restored. In late January, the superconducting magnets were cooled down to their operating temperature of 4.2 K in about 2 days and were subsequently powered to the injection current. On January 26, the first gold beam was steered through the Lambertson magnet, the injection kicker, and the 400 meters of superconducting magnets to a beam dump at the end of the Sextant. In total, 81 8-hour control-room shifts were devoted to the study of beam quality, machine properties, and accelerator system performance. This paper summarizes the physics results of these Sextant Test shifts.

2 BEAM QUALITY MEASUREMENTS

The main purpose of beam quality measurements was to demonstrate the design beam intensity and emittances. Various instrumentation systems[5, 6] in the AGS, AtR, and Sextant were employed, including beam position monitors (BPM), current transformers, wall current monitors, ionization profile monitors (IPM), and fluorescent screen profile monitors (flags).

2.1 Longitudinal Phase-Space Tomography

Particle motion in longitudinal phase space was reconstructed in the AGS using tomographical algorithms (RADON)[7] from a set of wall current monitor profiles recorded over half a synchrotron period. For the reconstruction, the rf voltage was calibrated by observing the synchronous phase difference as transition was crossed at a known ramp rate. Signal width broadening caused by finite cable bandwidth[8] was taken into account. Fig. 1 shows the phase space diagram at an early stage of the test when bunch coalescing was being tuned up to increase the beam intensity. The coalescing process was quickly improved to achieve an intensity of 4×10^8 ions per bunch with a 95% area of 0.5 ± 0.1 eV·s/u (Table 1).

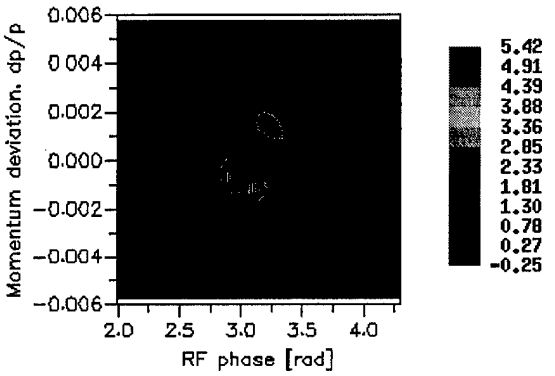


Figure 1: Longitudinal phase space diagram of a Au^{77+} beam in the AGS reconstructed with RADON showing imperfect bunch coalescing at an early stage of the test.

2.2 Transverse Emittances

Transverse beam emittances were measured (Table 1) in the AGS with ionization profile monitors located at places of measured β-functions ($\beta_{x,y} = 22$ m) and dispersion ($D_x = 2.2$ m). The normalized 95% emittances of 10 ± 1 mm·mr in both horizontal and vertical planes were confirmed by several independent self-consistent measurements[4] in the AtR with flag monitors at multiple locations. Choosing the thick flag uf2 at the minimum $\beta_{x,y}$ in the AtR for the final electron stripping minimized the emittance growth to about 0.7 mm·mrad (7%). A novel prototype IPM[9] was also successfully tested in the AtR, showing good agreement with the flag measurements (Fig. 2) of the transverse beam profile.

Table 1: Comparison of design and achieved Au^{79+} beam quality during the Sextant Test.

Quantity	Unit	Design	Achieved
Momentum	GeV/c/u	11.7	11.31±0.1
Intensity, N	10^9	1	0.4
Bunch area, S	eV·s/u	0.2	0.5±0.1
Emittance, $\epsilon_{Nx,y}$	mm·mrad	10	10±1

* Work supported by the U.S. Department of Energy.

0-7803-4376-X/98/$10.00 © 1998 IEEE

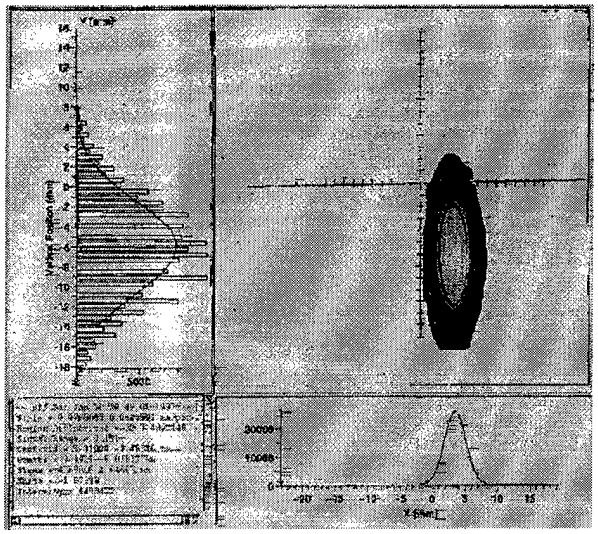


Figure 2: Transverse beam profile in the AtR recorded on flag wf3 (2D image and projections) and IPM (histogram).

2.3 *Other Beam Parameters*

The beam energy was obtained in the AGS by measuring the magnetic field in the main dipoles with the Gauss clock and a Hall probe. The measured energy with corresponding $\gamma = 12.15 \pm 0.1$ at AGS extraction was confirmed in the AtR by dipole deflection measurements with preset strengths. The beam intensity was consistently measured by several current transformers in the AGS, AtR, and Sextant. Multi-bunch transfer from the AGS to Sextant was also successfully tested and recorded by BPMs and flags.

3 MACHINE LATTICE STUDIES

The primary goals of machine lattice studies were to verify the design optical properties in the AtR and Sextant, and to establish nominal conditions for injection and operations.

3.1 *Orbit Correction and Aperture Scan*

Due to problems[6, 10] with the BPM system, reference orbits were established in most cases with flags and beam loss monitors, attempting to center the beam on the quadrupoles with three- and four-bump orbit correction schemes. Based on such a partially corrected orbit, Table 2 shows the minimum momentum aperture at critical places of the AGS, AtR, and Sextant. Variation of beam momentum in the AGS (via rf radial loop control) indicated that the momentum acceptance of the AGS extraction septum, the limiting aperture of the entire line, is about $\pm 0.5\%$. The momentum apertures in the AtR and Sextant were deduced from the range of variation in appropriate beamline magnet strengths that did not scrape the beam.

Table 2: Minimum momentum aperture.

Line	Bend	$\Delta p/p$	Comments & Methods
AGS	septum	$\pm 0.5\%$	bumps on, radial loop scan
U	4°, 8°	$\pm 1.5\%$	all ATR magnet scan
W	20°	$\pm 0.6\%$	all ATR magnet PS scan
Y	SWM	$\pm 1.7\%$	switching magnet PS scan
	90°	$\pm 1.0\%$	90° dipole PS scan
	Lamb.	$\pm 1.7\%$	Lambertson PS scan
Sextant	arc	$\pm 0.9\%$	main dipole PS scan

Table 3: Comparison of design and measured lattice optics.

Quantity	Units	Design	Measured
Phase adv./cell		79.2°	$78.3° \pm 1°$
Average β_{max}	m	49.4	49.4 ± 0.1
Average β_{min}	m	10.9	11.2 ± 0.3
Average $D_{x,max}$	m	1.8	2.5 ± 0.4*
Average $D_{y,max}$	m	0	0 ± 0.2*
ξ_x		-4.6	-7*

*) Possible systematic error in momentum calibration.

3.2 *Transfer Matrices and Difference Orbits*

Transfer matrix elements were measured by changing the strength of individual dipole correctors and observing the difference in the downstream orbits. Typical difference orbit excursions in these measurements were ± 5 mm. In both horizontal and vertical planes in the AtR, measured orbit differences agreed with those predicted from our lattice model within 1 mm. Due to BPM problems, no reliable difference orbit measurements were made in the Sextant.

3.3 *Dispersion*

The dispersions in the AtR and Sextant was measured by varying the beam momentum in the AGS while recording the beam displacements with BPMs and flags. The measured dispersions ($D_{x,y}$) at locations of maximum horizontal dispersion (D_x) in the Sextant is shown in Table 3. Compared with the design value, the relatively large measured dispersion is possibly caused by a systematic error in the calibration of beam momentum at AGS extraction.

3.4 *Lattice Optics*

The phase advance per cell of the Sextant was measured by varying the strength of a sequence of arc dipole correctors by a fixed amount (1 A) while observing the beam centroid shows the results of measurements made with

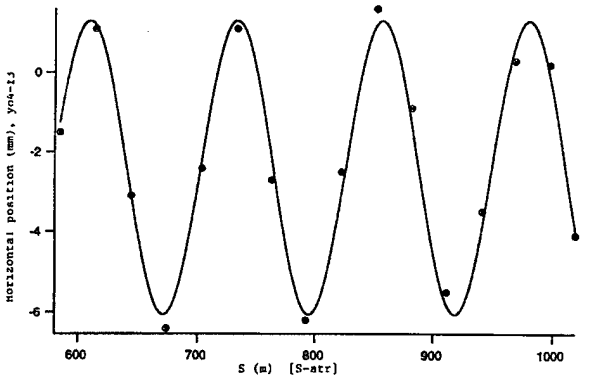


Figure 3: Beam position on the last flag versus perturbation location for Sextant phase advance measurement. The solid line is a sine-wave fit to the data.

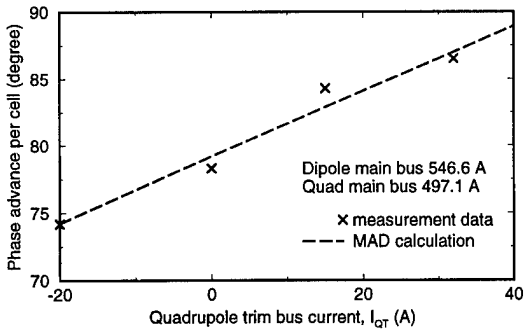


Figure 4: Comparison between the measurement and MAD lattice modeling on horizontal phase advance per cell as a function of arc focusing quadrupole strength.

different[11] focusing quadrupole settings. These agree very well with lattice modeling using test stand measurements of the quadrupole Integral Transfer Function (ITF). The β-functions deduced from the phase advance measurements also agreed well with the modeling (Table 3). Horizontal chromaticity ξ_x contributed by the Sextant was measured by evaluating the change in phase advance upon the change in beam momentum at AGS extraction.

4 SYSTEM PERFORMANCE

The primary interest in beam-based system performance analysis was to study stability and repeatability of both accelerator (power supply, kicker, magnet, etc.) and beam instrumentation systems.

4.1 Magnet Hysteresis

Hysteresis effects were measured for the sextant superconducting dipoles (see Fig. 5) and quadrupoles. Due to initial quench protection precautions, the main bus current was only ramped up to slightly above the injection current (about 560 A). After going through a hysteresis scan, differences of 1.1 A in the dipole current and 2.3 A in the quadrupole current were found to restore the original beam position and transmission efficiency. These results qualitatively agreed with test bench measurements, where magnets were ramped up to full current of 5.5 kA, and differences of 1.8 A and 2.3 A were found for dipoles and quadrupoles, respectively.

At the nominal dipole (547 A) and quadrupole (501 A) current settings derived from test bench ITF measurements, a 100% transmission efficiency was observed (Fig. 5). The range of transmission further indicated that the ITF of the arc dipoles (Fig. 5), measured with beam, agreed with the test stand measurements within an accuracy of 0.2%.

4.2 Injection and System Stability

The AGS extraction stability was measured in various ways. The intensity variation was typically $1.9 \pm 0.3 \times 10^8$. On the stripping flag uf2 near the entrance of the AtR, the beam position variations were typically 0.3 mm in the horizontal and 0.05 mm in the vertical plane. Variation in transverse beam size was typically 10%. Relative momentum variations were below the measurable level of 10^{-3}.

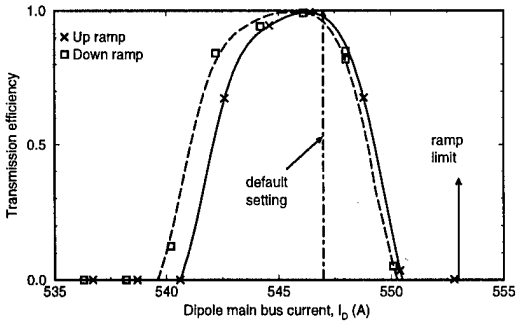


Figure 5: Sextant dipole and quadrupole hysteresis measurement by transmission efficiency scan.

Beam centroid positions recorded on nearby BPMs and flags were compared to determine the shot-to-shot repeatability of these systems. The flags showed a repeatability of less than 0.1 mm, and BPMs showed a repeatability of less than 1 mm. Effects produced by power supply noise in the AtR and Sextant were below measurable levels.

5 CONCLUSIONS

The Spring 1997 Sextant Test successfully fulfilled its goal of commissioning the full RHIC accelerator systems with beam. Very good agreement was achieved between measured and design phase advances, and other lattice optics parameters. The quality of the gold beam injected into the RHIC was satisfactory, with transverse emittances close to the design, and intensity only a factor of 2.5 below the design requirement. RHIC is on track towards its completion and operation in 1999.

6 ACKNOWLEDGMENTS

We are thankful to the AGS Main Control Room crews and the Controls Group for their support during the test.

7 REFERENCES

[1] J. Wei and M. Harrison, "The RHIC Project – Design, Status, Challenges, and Perspectives", Proc. XVI RCNP Osaka Intern. Sym. Multi-GeV High-Performance Accel., 1997.

[2] S. Peggs, "RHIC Status", these proceedings.

[3] W.W. MacKay, et al., Proc. 5th EPAC, Sitges, 2376 (1996).

[4] T. Satogata, et al., Proc. 5th EPAC, Sitges, 2379 (1996).

[5] D. Trbojevic, et al., "Preparing Accelerator Systems for the RHIC Sextant Commissioning", these proceedings.

[6] F. Pilat, et al., "RHIC Sextant Test – Accelerator Systems and Performance", these proceedings.

[7] V. Mane, et al., "Beam Tomography in Longitudinal Phase Space", these proceedings.

[8] J. Wei, J.M. Brennan, et al., Proc. 1995 Part. Accel. Conf. and Intern. Conf. on High-Energy Accel., Dallas, 3334 (1995).

[9] R. Connolly et al., "A Prototype Ionization Profile Monitor for RHIC", these proceedings.

[10] T. Shea et al., "Performance of the RHIC Injection Line Instrumentation Systems", these proceedings.

[11] N. Tsoupas et al., "Focusing and Matching Properties of the AtR Transfer Line", these proceedings.

MEASUREMENT OF TEVATRON EXTRACTION PARAMETERS AND COMPARISON OF MODEL TO MEASUREMENTS

M.A. Martens, J. Marriner, J. Holt
Fermi National Accelerator Laboratory *, P.O. Box 500, Batavia, IL 60510

Abstract

An accurate model of the half integer resonance extraction process in the Tevatron requires a knowledge of the extraction parameters such as the strengths of the 39th harmonic quadrupole and 0th harmonic octupole. This paper describes a series of experiments that determine the extraction parameters. Results of target wire scans, which measure the profile of the extracted beam, are then compared to the Tevatron model.

1 INTRODUCTION

During the 1996/1997 Fixed Target Run at Fermilab the Tevatron goal was to resonantly extract 2.5×10^{13} protons per pulse using fast spill pulses lasting several milliseconds and a slow spill period lasting 20 seconds. Extracting this beam intensity without quenching the superconducting magnets requires a precise knowledge of the extraction process to minimize particle losses. This paper describes measurements made to improve the accuracy of a model of Tevatron resonant extraction and shows comparisons of these measurements to the model calculation. The accurate extraction model led to a reduction of beam losses and an increased extracted intensity.

2 EXTRACTION PARAMETERS

Half integer resonant extraction in the Tevatron is implemented using two 39th harmonic quadrupole circuits (sine and cosine components) and a 0th harmonic octupole circuit [1]. Ignoring the effects of momentum spread and vertical motion, the horizontal phase space topology during the half integer extraction process is determined by the tune defect, $\delta_x = 0.5 - \nu_x$, the sine and cosine components of the 39th harmonic quadrupole,

$$Q_{39s} = \frac{1}{2B\rho} \oint ds \beta_x B'_y \sin(2\psi_x) ds \qquad (1)$$

$$Q_{39c} = \frac{1}{2B\rho} \oint ds \beta_x B'_y \cos(2\psi_x) ds \qquad (2)$$

and the zeroth harmonic octupole,

$$O_0 = \frac{3}{8B\rho} \oint ds \beta_x^2 \frac{B'''_y}{6} ds. \qquad (3)$$

The tune (ν_x), beta function (β_x), and phase advance (ψ_x) refer to the linear lattice values with the extraction devices deactivated ($Q_{39s} = Q_{39c} = O_0 = 0$). The integrals in Equations 1–3 are determined by the excitation level (B'_y and B'''_y) of the extraction circuits: the 39th harmonic quadrupoles and the 0th harmonic octupoles.

When $Q_{39s} = Q_{39c} = O_0 = 0$, the particle trajectories in the normalized phase space are circles centered on the origin. The excitation of the extraction circuits disturbs the phase space into that shown in Fig. 1 with the two circular separatrices given by

$$(x \mp \sqrt{\frac{Q_{39}}{O_o}} \sin\frac{\xi_0}{2})^2 + (y \pm \sqrt{\frac{Q_{39}}{O_o}} \cos\frac{\xi_0}{2})^2 = \frac{2\pi\delta}{O_0} \qquad (4)$$

where $y = \alpha x + \beta x'$, $Q_{39} = \sqrt{Q_{39s}^2 + Q_{39c}^2}$, and $\tan\xi_0 = Q_{39s}/Q_{39c}$. The region of overlap of the two circles is the stable region and the resonantly extracted particles stream out along the circles. Once the particles stream sufficiently far they are kicked transversely by passing through the field region of an electrostatic septum resulting in their separation from the circulating beam. One half turn later the separated particles are extracted with a Lambertson magnet and delivered to experiments.

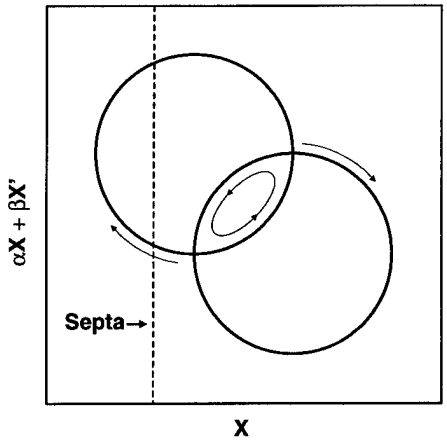


Figure 1: Sketch of separatrices in normalized horizontal phase space during resonant extraction. The arrows show the direction of motion in phase space.

3 TEVATRON MODEL

In developing a model of the extraction process we started with a design lattice of the Tevatron with the correction circuits set to reproduce the measured tunes and chromaticities. We then included effects we believed important for an accurate model: the tunes, the 39th harmonic quadrupole, the 0th harmonic octupole, the extraction septa position, the chromaticity, and the beam momentum spread. There

* Operated by University Research Association for the United States Department of Energy

0-7803-4376-X/98/$10.00 © 1998 IEEE

are several parameters which were not considered in this model but are not believed to have a large effect. These include vertical motion, transverse coupling, the 39th and 78th harmonic octupole component, and higher order magnetic multipoles in the dipole magnets. No attempt was made to understand the effects of coupling however the coupling resonance in the Tevatron was compensated with two families of skew quadrupoles.

Because of their importance to resonant extraction our model also included the effects of lattice errors (such as the octupole component in the main dipoles) which contribute to the integrals in Equations 1–3. The model included the lattice errors by adding an offset to each of the three extraction circuits: the sine and cosine 39th harmonic quadrupole and the 0th harmonic octupole. The idea is to set the values of Q_{39s}, Q_{39c}, and O_0 in the model equal the those in the Tevatron when lattices errors are present. The offsets were determined from beam measurements described in the next sections.

3.1 Tune and 39th Harmonic Quadrupole

To determine the amount of residual 39th harmonic in the Tevatron the horizontal tune was measured as a function of the strength of 39th harmonic sine and cosine quadrupole circuits denoted T:Q39S and T:Q39C. Figure 2 shows the measured tunes when T:Q39S is varied. The data were fit to the analytically expected form

$$\nu_x = 0.5 - \sqrt{\delta_o^2 - Q'(I_{39s} - I_{39s0})^2} \qquad (5)$$

where I_{39s0}, Q', and δ_o are determined from the data. I_{39s0} is the T:Q39S current that produces a 39th harmonic quadrupole component canceling that produced by the error fields. We find $I_{39s0} = 1.3$ Amps. A similar measurement was done with T:Q39C and with a fit we find $I_{39c0} = -1.35$ Amps. In the model these fit values, I_{39s0} and I_{39c0}, are subtracted from to the amounts intentionally added by the 39th harmonic quadrupole circuits. With these offsets included the tune versus strength of T:Q39S was calculated using the model and the results are shown in Fig. 2.

3.2 0th Harmonic Octupole

The bunched beam tune spectrum consists of a central tune line and several synchrotron sidebands. The width of the central line depends on the 0th harmonic octupoles and higher order multipoles. The width of the central tune line was measured [2] as a function of the 0th harmonic octupole circuit denoted T:OZF and the data is shown in Fig. 3. These data were fitted to the form

$$\Delta\nu = \sqrt{k^2(I - I_{\rm off})^2 + (\Delta f)^2} \qquad (6)$$

where k, $I_{\rm off}$, and Δf are determined from the data. The slope of the fitted curve, k, in the region with large current agrees well with the slope expected with a 20π mm-mrad horizontal emittance beam and the octupole circuit

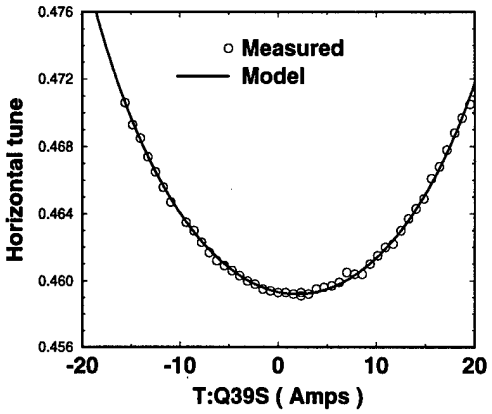


Figure 2: Measurement of horizontal tune versus setting of 39th harmonic quadrupole circuit T:Q39S. The circles are the measured tunes the solid line is the model calculation with an extra -1.3 Amps added to the T:Q39S circuit.

used. The value of $I_{\rm off}$ could be affected by the presence of higher order multipoles. However these higher order multipoles probably have similar effects on the extraction process as they do on the tune spread so we believe that Equation 6 should be an accurate description for the extraction model.

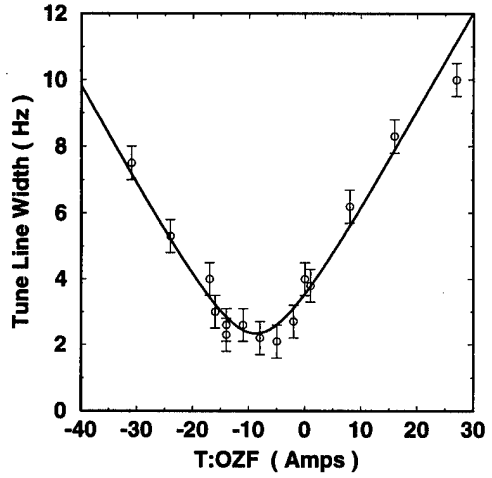


Figure 3: Measurement of horizontal tune width versus setting of the 0th harmonic octupole circuit T:OZF. The circles are the measured values and the solid line is a phenomenological fit described in the text.

3.3 Extraction Septa Position

An important parameter in accurately calculating the step size is the position of the electrostatic septa with respect to the center of the beam. To determine the septa position accurately we used survey information and verified the position using beam measurements. From survey data the upstream end of the electrostatic septa was determined to be 14.7 mm to the radial inside and aligned at an angle of 160 μrad with respect to the closed orbit. In an experiment

where the beam position was measured while a low intensity beam was slowly moved into the electrostatic septa until the beam was extinguished it was determined that the electrostatic septa was 0.4 mm closer to the beam than indicated by the survey data. The survey information and beam measurements are consistent when the uncertainty of the measurement and the accuracy of the beam position monitors are considered. We chose to use the survey data in our model.

3.4 Model Calculations

With the above measurement of the relevant extraction parameters the phase space of the beam during resonant extraction can be calculated at any location in the Tevatron. Figure 4 shows the calculated horizontal phase space (from particle tracking) just after the electrostatic septa. The particles were launched in horizontal phase space at points near the separatrix and with a momentum spread of $\sigma_p/p = 0.00017$ corresponding to a measured bunch length of $\sigma_\tau = 2$ ns. The disconnected segment in the upper left corner of the plot is the beam that has been kicked 62 μrad by passing through the septum. The width of the extracted beam is the step size (about 8 mm) and angle at which the beam is incident on the septa wires is 160 μrad.

While resonantly extracting in the Tevatron the electrostatic septa are aligned remotely to reduce the losses downstream of the septa. The loss minimum occurs when the particles hitting the septa are incident parallel to the septa wires. Thus the 160 μrad angle of incidence calculated by the model is consistent with the surveyed 160 μrad angle of the aligned septa.

To further test the accuracy of the Tevatron model a set of target scans was made near the extraction septa and extraction Lambertsons. By moving a wire horizontally into the extracted portion of the beam and measuring the losses on a downstream loss monitor as a function of target wire position we get a profile of the beam intensity as a function of position. Figure 5 is a comparison of one of these measurements with model calculations at a target location just downstream of the septa and shows good agreement between the model and measurements. The beam on the left is the extracted beam which is separated from the circulating beam by about 1.5 mm at the location of the wire target.

The knowledge gained from the modeling process described in this paper contributed to increasing the intensity of extracted beam. For instance the step size was increased from several millimeters in the early part of the fixed target run to the 8 mm shown in Fig. 4. The increased step size resulted in lower losses from the septa wires since a smaller percentage of beam hits and interacts with the septa wires. The calculated phase space at the entrance to the extraction Lambertsons resulted in a realignment of the Lambertsons which reduced the losses downstream of the Lambertson and again resulted in higher intensity extracted beam.

In conclusion, a model of the Tevatron extraction process was developed starting with basic theory and using a

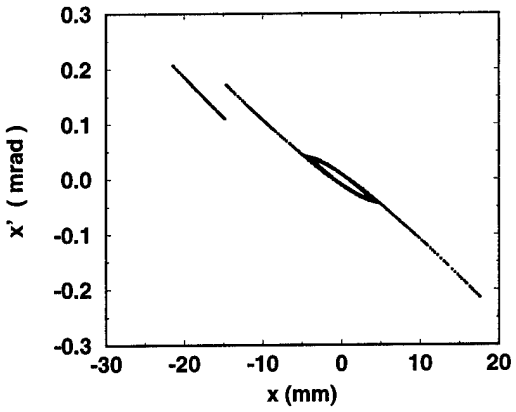


Figure 4: Horizontal phase space at the extraction septa as determined from tracking particles near the separatrices.

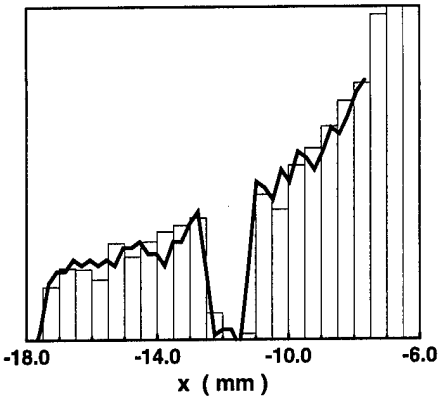


Figure 5: Measured (solid line) and modeled (histogram) profile of extracted beam and tail of circulating beam at the wire target scanner downstream of the electrostatic septa. The vertical scale is loss rate for the measurement and number of particles in the model.

set of measurements to refine the accuracy of the model. Comparisons of the model agreed well with the other independent measurements such as target wire scans. The understanding gained from this process led to improvements in the operation of the Tevatron during fixed target operations.

4 ACKNOWLEDGMENTS

We would like to thank Bruce Hanna for getting the wire target scanners working, Leo Michelotti for helping us understand the theory of resonant extraction.

5 REFERENCES

[1] M. Harrison, "Resonant Extraction at the Tevatron", *AIP Conference Proceedings* 184, pp. 2009–2032, (1989).

[2] J. Marriner, M. Martens, "Measurement of the Tune Spread in the Tevatron vs Octupole Strength", EXP-199, Fermilab Internal Publication. (1996).

SURFACE RESISTANCE MEASUREMENTS FOR THE LHC BEAM SCREEN

F. Caspers, M. Morvillo and F. Ruggiero, European Laboratory for Particle Physics (CERN)

Abstract

A critical review of resistive losses in the LHC beam screen, taking into account anomalous skin effect and surface roughness, has triggered a programme of surface resistance measurements at different temperatures, frequencies and magnetic field intensities. The aim is to establish a realistic heating budget for the LHC cryogenic system and to optimize the fabrication process for the copper coating of the beam screen. Preliminary results at cryogenic temperatures (without magnetic field) indicate a surface resistance about a factor two larger than previously estimated: an absolute measurement precision of a few per cent is reached by comparing the quality factors of even and odd TEM modes in a cylindrical structure with two inner conductors.

1 INTRODUCTION

The LHC beam screen is a stainless steel pipe (for mechanical strength during quench) with a 50 μm copper layer coated on its inner surface. It is cooled at a temperature ranging from 5 to 20 K. The purpose of the copper coating is to reduce the surface resistance R_S, i.e., the ratio between longitudinal component of the electric field at the wall surface and beam-induced wall current. This is important to minimize at the same time transverse resistive wall instability (a relatively low frequency phenomenon) and beam-induced wall heating. At top energy and for nominal beam parameters, the classically computed resistive wall heating of the LHC beam screen is 75 mW/m. Owing to the anomalous skin effect, this value should increase by 11%, but according to surface resistance measurements performed on samples of the SSC beam tube, the increase could be significantly larger [1].

For a circular screen of radius b, the parasitic heating power per unit length is given by

$$\frac{P}{L} = \frac{I_{\mathrm{av}}^2}{M f_0} \cdot \frac{c^2}{\pi} \int_0^\infty \left|\tilde{\lambda}(\omega)\right|^2 \frac{R_S(\omega)}{2\pi b}\, d\omega, \qquad (1)$$

where I_{av} is the average beam current, M the number of bunches, f_0 the revolution frequency, c the velocity of light and $\tilde{\lambda}(\omega)$ the bunch spectrum, which for the relatively short LHC bunches at 7 TeV (7.5 cm, r.m.s.) will cover a wide high frequency region (637 MHz, r.m.s.).

Since the parasitic heating scales with the square of I_{av}, for the ultimate beam intensity of 850 mA, it may become comparable to the synchrotron radiation power loss of 326 mW/m. Reliable data for the surface resistance up to a few GHz is therefore needed to establish a realistic heating budget for the cryogenic system and to optimize the fabrication process for the copper coating of the beam screen. The situation is complicated by the fact that the anomalous skin effect is accompanied by a strong magnetic field and by phenomena associated with the surface roughness. There is no valid theory for estimating the surface resistance in this complex environment and this has triggered a programme of surface resistance measurements on several samples of the LHC beam screen.

2 EXPERIMENTAL SETUP

To measure the surface resistance at several temperatures and with an 8.4 T magnetic field, we decided to avoid using supercondutors. With the experimental setup shown in Fig. 1, we measure the quality factors Q^{++} and Q^{+-} of even and odd modes excited in a 1 m long cylindrical TEM mode cavity with two inner conductors. Relying on the only assumption that R_S be the same for the two inner conductors, we then obtain the surface resistance of both inner conductors and outer tube in steps of about 150 MHz.

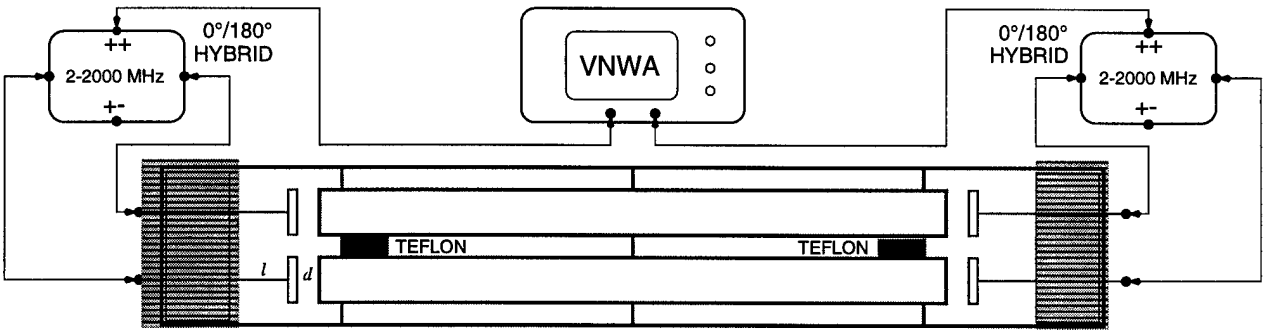


Figure 1: Experimental setup: a vector network analyser (VNWA) is used in conjunction with two hybrids, yielding either even (++) or odd (+-) mode excitation for a 1 m long cylindrical cavity with two inner conductors, held by 3 teflon supports. The near degeneracy of even and odd modes is removed by two teflon splitters placed between the inner conductors.

0-7803-4376-X/98/$10.00 © 1998 IEEE

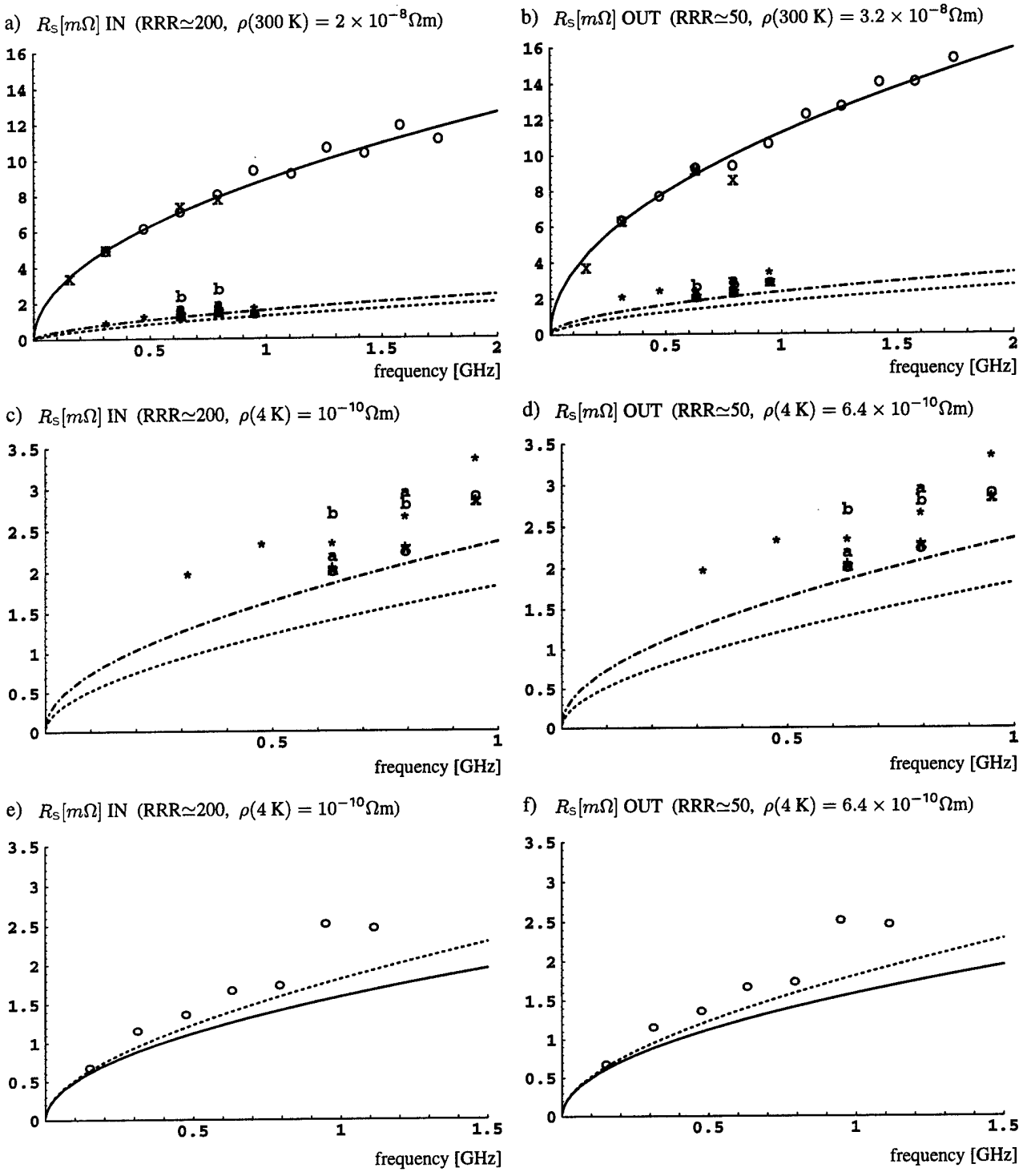


Figure 2: Surface resistance measured for the thermally treated inner conductors (a, c, e) having a dc RRR≃200, and for the outer tube (b, d, f) with *no* thermal treatment and a dc RRR≃50, compared to the predictions in the classic (solid line) and anomalous regime (dot-dashed lines: 40 K, dashed lines: 4 K). Figures (a) and (b) show data measured at room temperature, either before ("X") or after cryogenic measurements using shorter coupling networks ("O"), at 40 K, either before ("b") or after ("a") injection of He gas during cool down (leading to a sudden thermalisation of the inner conductors, otherwise thermally insulated) or with external heating ("*"), at 20 K ("+"), at 10 K ("x") and at 4 K ("o"). Some measurements at 40 K have a large temperature spread from top to bottom of the outer tube. The data at room temperature is best fitted assuming a resistivity $\rho(300\,K) = 2 \times 10^{-8}\Omega m$ for the inner conductors and $\rho(300\,K) = 3.2 \times 10^{-8}\Omega m$ for the outer tube. Figures (c) and (d) are a magnification of (a) and (b), respectively, showing only measurements at cryogenic temperatures. The data in (e) and (f) has been obtained at 4 K with shorter coupling networks, to allow measurements in a wider frequency range: data above 1.2 GHz, however, has been discarded due to strong or badly corrected coupling.

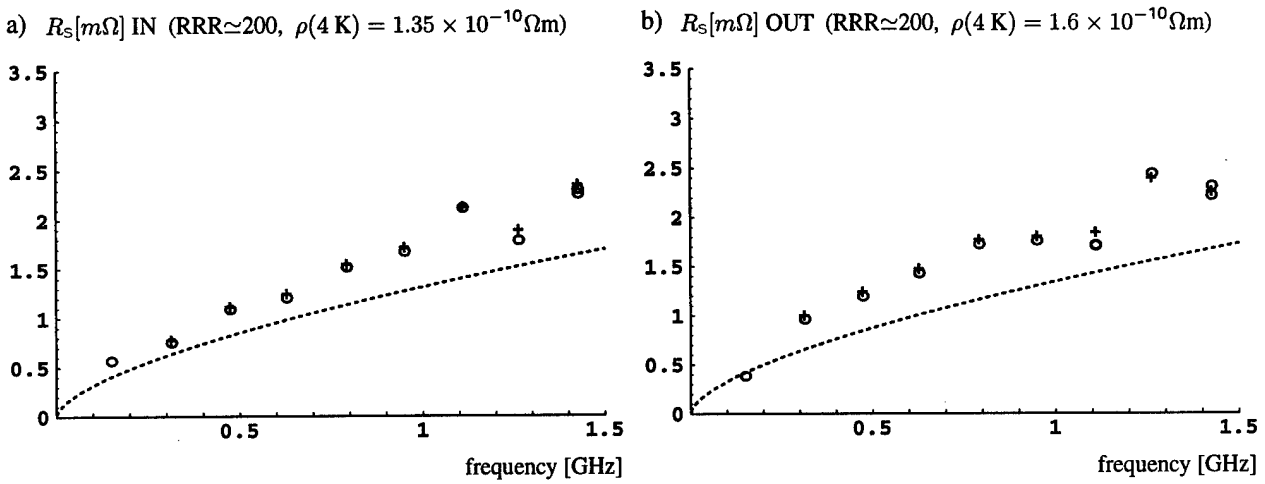


Figure 3: Surface resistance measured with shorter coupling networks at 4 K ("o") and at 20 K ("+") for the inner conductors (a) and the outer tube (b), *both* thermally treated at 350° C and having a measured dc RRR≃200, compared to the predictions in the anomalous regime (dashed lines). The corresponding data at room temperature (not shown in the figure) is best fitted assuming a resistivity $\rho(300\ K) = 2.7 \times 10^{-8}\Omega m$ for the inner conductors and $\rho(300\ K) = 3.2 \times 10^{-8}\Omega m$ for the outer tube. The slightly higher resistivity attributed to the inner conductors may be due to small scratches in their copper coating, caused by the sliding teflon supports repeatedly mounted during previous measurements.

Indeed the unloaded quality factor of each mode, given by $1/Q = \Gamma_{IN}/R_S^{IN} + \Gamma_{OUT}/R_S^{OUT}$, is related through calculable geometric coefficients [2] Γ_{IN} and Γ_{OUT} to the surface resistances R_S^{IN} and R_S^{OUT} of the inner conductors and of the outer tube. Measuring Q^{++} and Q^{+-}, therefore, we can solve a system of *two* equations in the *two* unknowns R_S^{IN} and R_S^{OUT}.

The two inner cylindrical conductors (of radius 8 mm) and the outer tube (of radius 19.6 mm) are all made out of stainless steel with a 50 μm electrodeposited copper layer, having a surface roughness of a few μm. Future measurements are planned also with a colaminated copper layer. The distance between the axes of the two inner conductors is 19.5 mm. The distance d between each coupling network and the inner conductors (a few cm) is adjusted to have sufficiently weak coupling coefficients $\beta_1(\omega)$ and $\beta_2(\omega)$ over the frequency range of interest. We calculate coupling by measuring reflection coefficients at each coupling port, while the loaded quality factor $Q_{load}(\omega)$ for each mode is obtained by a transmission coefficient measurement. The corresponding unloaded quality factor is then given by $Q(\omega) = [1 + \beta_1(\omega) + \beta_2(\omega)]\, Q_{load}(\omega)$. The length l of the coupling networks has been varied from 12 down to 4 cm, to allow measurements in a wider frequency range (up to about 1.5 GHz). Indeed coupling grows with frequency, but suddenly drops over a large frequency gap whose location depends critically on l. This phenomenon seems related to internal resonances of the coupling networks.

3 PRELIMINARY EXPERIMENTAL RESULTS

In Figs. 2 and 3 we present some preliminary surface resistance measurements without magnetic field, from room temperature down to 4.2 K, compared to the predictions in the classic and anomalous regime. The inner conductors have been thermally treated at 350° C and have a measured dc RRR around 200. Fig. 2 refers to an outer tube with no thermal treatment and a dc RRR≃50, while Fig. 3 refers to a thermally treated outer tube. The low temperature resistivity of the outer tube in the case of Fig. 2 is comparable to that of the LHC beam screen in a magnetic field of 8.4 T, but the measured surface resistance around 1 GHz is almost a factor two larger than previously estimated.

Both figures show a slight modulation of the surface resistance as a function of frequency; this modulation is anticorrelated for the IN versus OUT data and grows from a few per cent at low frequencies to about 10% beyond 1 GHz. We are currently investigating this effect, which might be due to the teflon supports, to the teflon splitters, to geometric imperfections or to the coupling networks.

4 ACKNOWLEDGEMENTS

We would like to thank several CERN colleagues who gave significant contributions to these measurements and, in particular, A. Poncet and C. Benvenuti for useful discussions of the experimental setup, A. Mathewson and N. Kos (beam screen prototypes), S. Sgobba (surface metrology and welding), C. Reymermier and L. Nikitina (designs), J. Rieubland, G. Ferlin and A. Jacquemot for their constant help in the cryolab, L. Walckiers and A. Arn (measurements in progress with magnetic field).

5 REFERENCES

[1] W. Chou and F. Ruggiero, LHC Project Note 2 (1995).

[2] G.S. Smith and J.D. Nordgård, IEEE Trans. Microwave Theory Tech., vol. MTT-28, pp. 887–893, Aug. 1980.

820 GeV/c POLARIZED PROTONS IN HERA

V. A. Anferov, Physics Department, University of Michigan, Ann Arbor, Michigan 48109-1120

Abstract

The SPIN Collaboration and DESY Polarization Team have studied the possible acceleration of a polarized proton beam to 820 GeV/c in the HERA accelerator complex at DESY [1]. This paper summarizes suggested changes at various stages of acceleration that would allow to maintain the beam polarization to the top energy.

1 INTRODUCTION

The interest in spin phenomena has significantly increased in recent years. It is now clear that spin effects in high energy interactions provide essential information about properties of the elementary particles and their fundamental interactions. The polarized proton beam capability at HERA would provide a powerful tool for high energy physics; it would allow unique spin studies in a polarized *e–p* collider.

While high energy electron and positron beams have selfpolarization mechanism due to the synchrotron radiation, an intense high energy polarized proton beam could only be obtained by acceleration from the source to the ring's maximum energy. Wide range of spin instabilities that become stronger at higher energies make the polarized protons acceleration a challenging problem. However, recently developed methods and techniques of overcoming the spin depolarizing resonances allow one to consider polarized proton beam acceleration in the high energy proton machines such as RHIC (250 GeV), HERA (820 GeV) and Tevatron (900 GeV).

2 POLARIZED ION SOURCE

A state-of-the-art polarized H^- ion source should be acquired and installed at DESY. This might be either an atomic beam source (ABS), or an optically pumped polarized ion source (OPPIS). Both types of sources have made tremendous progress in the recent years; the best ABS at INR (Moscow) has now achieved a current of 1 mA in pulsed operation [2], while the best OPPIS at TRIUMF has recently obtained a DC current of 1.6 mA with an emittance of 2π mm·mrad [3]. The source performance together with accumulation efficiency will be crucial issues for attaining a high intensity polarized proton beam at 820 GeV/c. Recent improvements tests at TRIUMF indicate that a 20 mA polarized H^- current might be possible to obtain with the OPPIS technology. Such source would make the polarized beam intensity in HERA equal to the intensity of unpolarized beam.

3 POLARIZED BEAM ACCELERATION

Polarized protons encounter many depolarizing resonances during acceleration in high energy proton synchrotrons. An unperturbed proton's spin would normally precess around the ring's vertical magnetic field that forms particle closed orbit. The frequency of the spin precession is energy dependent; the spin tune, which is the number of spin rotations during one particle revolution around the ring, is proportional to the Lorentz factor γ:

$$\nu_s = G\gamma\,, \tag{1}$$

where $G = 1.792847$ is the proton's anomalous magnetic moment. This vertical spin precession becomes unstable when the spin precession frequency is synchronized with a frequency of a small horizontal perturbation field. Such resonant perturbations can rapidly depolarize the beam in a circular accelerator and are called spin depolarizing resonances. During acceleration a large number of depolarizing resonances are crossed, whenever $G\gamma$ passes through a resonance frequency.

Various methods will be used in HERA in order to preserve the beam polarization during the acceleration. The required changes for each stage of polarized beam acceleration are shown in Fig. 1.

No depolarization occur in the new 750 keV RFQ, which should match the polarized ion source, and in the 50 MeV LINAC. Polarimeter installed after the LINAC would monitor the source output polarization.

The 50 MeV polarized beam would then be injected into the 7.5 GeV/c DESYIII synchrotron, where five strong depolarizing resonances occur during acceleration. The one strong and about 13 weak imperfection resonances, that are caused by magnets missalignment, could be overcome using a solenoidal partial Siberian snake of about 5%. The snake would rotate the spin by 9^0 and would cause a spin-flip every time $G\gamma$ crosses the integer value. The partial Siberian snake can not overcome four strong intrinsic resonances in DESYIII, which are caused by vertical betatron oscillations in the quadrupole fields. These resonances occur at integer harmonics of the vertical betatron tune, $G\gamma = n \pm k\nu_y$, and would require either pulsed quadrupoles, to use tune jump method of overcoming an intrinsic resonance, or vertical beam kicker magnets, to induce the spin-flip through each resonance by making them stronger. The novice betatron kick method, which was recently tested at IUCF [4], could be significantly cheaper and easier to use than the pulsed-quadrupoles method. To avoid emittance blow up after the beam kick one could use an RF-dipole for exciting and damping coherent betatron oscillations. This RF-dipole method will soon be tested for polarized beam acceleration at AGS.

Two full Siberian snakes would be needed in PETRA to overcome its many strong depolarizing resonances. The calculated maximum strength for the intrinsic and imperfection resonances in PETRA are $\varepsilon_{int} = 0.06$ and

0-7803-4376-X/98/$10.00 © 1998 IEEE

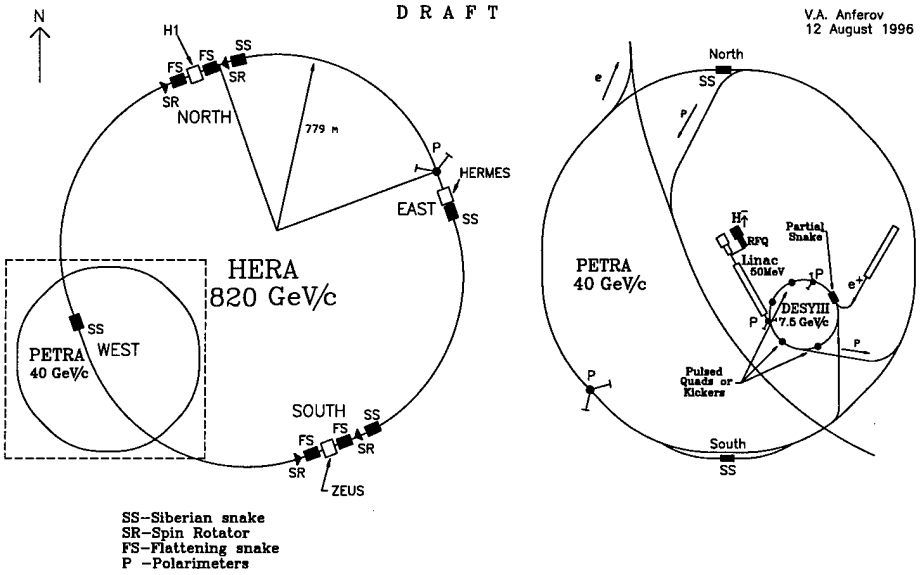


Figure 1: The proposed modifications for an 820 GeV/c polarized proton beam at DESY.

$\varepsilon_{imp} = 0.04$ assuming 25π mm mrad normalized beam emittance and 2.2 mm RMS vertical closed orbit distortion. Two snakes installed in the opposite straight sections would overcome all depolarizing resonances in PETRA and would provide vertical stable spin direction for easier polarization monitoring and spin matching during injection and extraction of the polarized beam. Each Siberian snake should rotate spin by 180^0 around a horizontal axis, while keeping the particle orbit unperturbed outside the snake. The spin rotation axes in PETRA snakes should be orthogonal to set the spin tune away from spin perturbations. The snake design is somewhat difficult in PETRA because, at its 7.5 GeV/c injection energy, full Siberian snakes would cause large orbit excursions. As a solution to this problem, a special helical Siberian snakes are proposed, which use helical dipoles to minimize the orbit excursions and normal dipole at the center to reduce the aperture of the helical dipoles.

Accelerating polarized protons to 820 GeV/c in HERA is difficult not only because of the very strong depolarizing resonances that occur during the acceleration, but also because of the requirement of a several hours polarization life time at the top energy in order to be useful for the experiments. Four Siberian snakes could be installed in each of the existing long straight sections. However, earlier studies by the DESY Polarization team have shown that the vertical orbit bumps around the interaction regions in HERA would interfere with any standard Siberian snake configuration. A solution to this problem was found, which would require four additional snakes to make the HERA ring "flat" for the spin motion. We called these snakes "flattening snakes" to emphasize their purpose of making the vertically bending beam lines near the interaction regions spin transparent.

Even after "flattening" the HERA lattice the spin perturbation remains very strong and four snakes in HERA would not provide adequate spin stability during the polarized beam acceleration. To reduce the strength of the spin perturbations one might consider various correction techniques that could reduce the rms orbit error to perhaps 0.2 mm and the emittance of the polarized beam to perhaps 5π mm mrad. One could also consider installing additional four snakes near the centers of each bending arcs. Both options are now under under careful analysis using various spin tracking techniques developed by the SPIN Collaboration and DESY Polarization team.

4 CONCLUSION

Polarized proton acceleration to 820 GeV/c at HERA would be an appropriate response to the growing interest in spin in high energy physics. It would extend the physics scope of the HERA collider and would enable unique studies of the spin and its role in the fundamental interactions at high energies. While most of the polarized beam problems appear to have straightforward solutions using existing techniques, two main problems will need further study:

- increasing the accumulated polarized beam intensity,
- providing adequate spin stability for polarized beam acceleration and storage in HERA.

This work was supported by the research grants from DESY and the U.S. Department of Energy.

5 REFERENCES

[1] SPIN Collaboration, *"Acceleration of Polarized Protons to 820 GeV/c at HERA"*,University of Michigan Report UM-HE 96-20, November 8 (1996).

[2] A.S. Belov *et al.*, Proc. 6th Int. Conf. on Ion Sources (Whistler); Rev. Sci. Instrum. **67**, 1293 (1996).

[3] A.N. Zelenski *et al.*, Proc. 6th Int. Conf. on Ion Sources (Whistler); Rev. Sci. Instrum. **67**, 1359 (1996).

[4] D.A. Crandell *et al.*, Phys. Rev. Lett. **77**, 1763 (1996).

RECORD DEFLECTION EFFICIENCIES MEASURED FOR HIGH ENERGY PROTONS IN A BENT GERMANIUM CRYSTAL

C. Biino, M. Clément, N. Doble, K. Elsener, L. Gatignon, P. Grafström,
U. Mikkelsen (CERN, Geneva, Switzerland), A. Freund (ESRF, Grenoble, France)
K. Kirsebom, S.P. Møller, E. Uggerhøj, T. Worm (ISA, Aarhus University, Denmark)

Abstract

New experimental results on the deflection of high energy protons in a bent germanium crystal are presented. At 450 GeV/c, the 50 mm long crystal gave record deflection efficiencies up to 60% for small angles (1 mrad), while at angles as large as 12 mrad, the efficiency is about 25 times larger than for a silicon crystal of the same size. The experimental results are in good agreement with a model for channeling and deflection developed by Ellison and give - together with a similar comparison for a 200 GeV/c beam - confidence in extrapolations to higher energies (e.g., to LHC), other crystal materials or different deflection angles.

1 INTRODUCTION

Proton deflection experiments using bent crystals have been performed at CERN and elsewhere since many years (reviewed in [1], [2]), and silicon crystals are being applied routinely as beam splitters [3] and for proton beam extraction [4]. Up to 50% of a parallel proton beam has been deflected by 1.5 mrad in a bent silicon crystal [5]. The experimental results are generally in good agreement with the deflection efficiencies expected from classical models [6]. A crucial test for these models, however, is to change to a different crystalline material. Besides silicon, germanium is the only crystal with a sufficiently good crystalline quality for a very high energy channeling experiment, available at a reasonable cost.

The deflection efficiency for a given incident beam / crystal configuration is influenced by four important factors: (1) the beam divergence; (2) the critical angle for channeling [7], which scales with $\sqrt{(Z_2)}$; (3) the dechanneling losses due to multiple scattering; and (4) the bending dechanneling. The 'acceptance' of the crystal, the so-called surface transmission, is determined by (1) and (2), as well as by the planar distance in the crystal and the lattice vibration amplitude. The higher charge of the atoms in a Ge crystal (Z_2=32 compared to Z_2=14 for Si) should lead to higher deflection efficiencies than obtained with Si, (a) due to the fact that the surface transmission is larger, (b) because the channeling potential 'trap' is deeper and thus the bending dechanneling less severe at the larger deflection angles. In order to test these hypotheses, we have conducted proton deflection experiments with a bent germanium crystal, over a large range of deflection angles, and compared the results with calculations.

2 EXPERIMENT

The present experiment continues the series of proton deflection experiments performed with bent crystals at the CERN-SPS. Information on the earlier experiments can be found in [1], [5] and [8], and further details on the recent tests with a germanium crystal (using 450 and 200 GeV/c beams) are described in [9]. In the following, a description of the H8 'micro-beam' option is given, together with a brief discussion of the experimental arrangement used for the 450 GeV/c proton experiment on a bent germanium crystal.

2.1 *The H8 micro-beam*

The micro-beam (H8 beam line) in the North Hall at the CERN-SPS has been designed in 1983 to serve the NA34 experiment. The requirement on this 450 GeV/c proton beam was to achieve an extremely small spot size (about 10μm rms.) at the target. The conceptual design of this beam is schematically shown in Fig. 1.

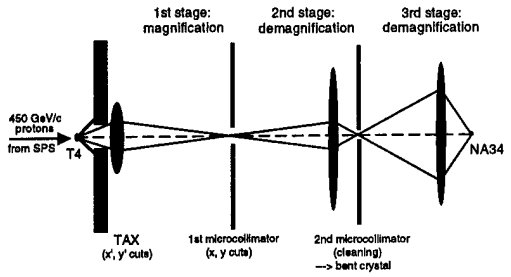


Figure 1: Conceptual layout of the H8 micro-beam (horizontal projection). For the present experiment, the cleaning collimator was removed, the bent crystal installed at its place and the beam tuned to be parallel at the crystal. For details, see text.

The beam has a large intermediate magnification in both planes (×2 horiz.(x), ×4 vert.(y)) as a first stage, followed by two stages with strong demagnification (overall ×0.2 horiz., ×0.1 vert.). The 450 GeV/c protons from the SPS are attenuated and scattered in the T4 target (30 cm beryllium) and in an additional 80 cm beryllium attenuator, in order to reach acceptable beam intensities at the experiment. The angular space is first cut to about 100 μrad by a 2 mm diameter tungsten lined aperture in a 160 cm long beam-dump collimator (TAX). The (x,y) space is then cut by precision 'micro-collimators', usually closed to $\pm$100μm,

0-7803-4376-X/98/$10.00 © 1998 IEEE

in the place of largest magnification. In order to correct for possible alignment errors in the installation or in beam steering, these collimators can be aligned with the beam for maximum transmission in angular steps of 0.05°. A second set of such micro-collimators is installed at an intermediate focus and serves beam-cleaning purposes. Note that this scheme reduces the beam intensity drastically, from some 10^{12} protons per spill on target T4 to a few 10^6 at the experiment. In order to minimize the contribution of momentum dispersion terms to the spot sizes, focii (or waists) were placed in all bending magnets. (Note that the 450 GeV/c beam from the SPS has an intrinsic 0.1% momentum bite as defined by the accelerator.)

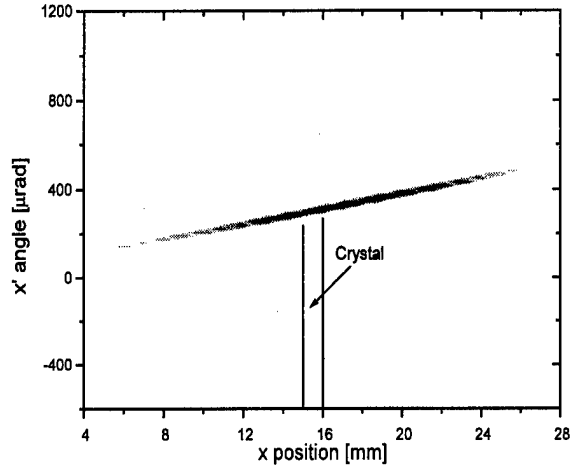


Figure 2: Horizontal phase space of the 450 GeV/c protons incident on the germanium crystal. This measurement stems from two drift chambers located 36.9 and 0.5 m upstream of the crystal (see Fig. 4). The horizontal width of the bent crystal is indicated to illustrate the relevant phase space for this experiment.

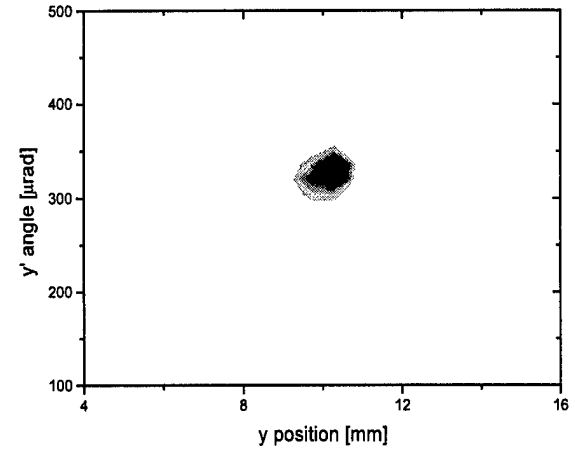


Figure 3: As Fig. 2, but for the vertical phase space (y,y'). (Note that the scale is different from the one in Fig. 2).

For the application of the bent crystal experiments in H8, the second set of micro-collimators was removed and the goniometer with the crystal installed in its place. For channeling experiments, it is important to achieve as parallel a beam as possible – in the case of planar channeling and bending, discussed here, the beam was therefore set-up to be parallel in the horizontal (channeling and deflection) plane, and focussed onto the crystal in the vertical plane. Finally, the last quadrupole upstream of the crystal was used to further increase the horizontal beam-size at the crystal position (i.e., to rotate the phase space ellipse), thus reducing the angular spread of protons inside the 1 mm wide 'slice' hitting the crystal, even if the overall divergence of the beam is increased. The resulting beam phase space as measured in the experiment is shown in Figs. 2 and 3. Note that due to the limited angular resolution in the experiment, the horizontal angular spread appears to be 6μrad (rms.). Angular scans with the goniometer (see below) indicate, however, that it is indeed much smaller, i.e., 2 to 3 μrad and thus inside the critical angle for channeling, which amounts to $\pm 7\mu$rad in this case.

2.2 *Crystal and Detectors*

The experimental arrangement is shown schematically in Fig. 4. The germanium crystal, 1 × 10 × 50 mm^3, was mounted in a 'classical' three-point bending device (see [9]) and was bent over 30 mm of its length. The curvature was thus normal to the (110) plane which lay along the 50 × 10 mm^2 face. The newly designed bending device was optimised for stability with respect to temperature variations (titanium block). The push-pin for the crystal bending includes a micrometre read-out. The device was placed on a goniometer with 1.7μrad step-size.

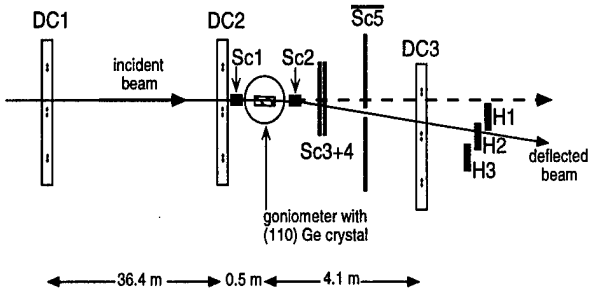


Figure 4: Schematic view of the experimental arrangement. Protons are deflected horizontally by the bent germanium crystal. Scintillators Sc1-4 are trigger counters for incident beam particles, H1, H2 and H3 for deflected particles. SC5 is a veto counter used during crystal alignment. Driftchambers DC1, DC2 and DC3 define the incoming and exiting beams, respectively.

To align the crystal, an array of scintillators, H1, H2, H3, (each 10 × 10 × 5 mm^3 in size), was used to detect the deflected beam and the goniometer was rotated until a maximum rate of deflected particles was observed. At large bending angles (above 15 mrad) for the 450 GeV/c beam, the low deflection efficiency resulted in a small signal to noise ratio in the five-fold hodoscope coincidence used for

alignment, H2·Sc1·Sc3·Sc4·$\overline{Sc5}$. However, the micrometre read-out on the bending device enabled a fairly accurate prediction of the new bend-angle after each change and thus a relatively fast re-alignment of the crystal was possible.

Driftchambers (DC) are used to track the incident and exiting protons in the beamline with a position resolution of about 100 μm (rms). The incident angles can be measured with DC1 and DC2, with an accuracy of about 6 μrad, which is larger than the horizontal beam divergence of the 450 GeV/c proton micro-beam, but was useful to cut the tails of the angular distribution in the 200 GeV/c experiment [9]. The experimentally determined deflection efficiency is defined as the ratio of the number of fully deflected particles (detected in DC3) originating from a specific area on the 1 x 10 mm^2 entrance-face of the crystal and the number of particles incident on this area. For each deflection angle, off-line cuts using the driftchambers were applied to determine the area with the highest deflection efficiency, thus avoiding edge and surface effects.

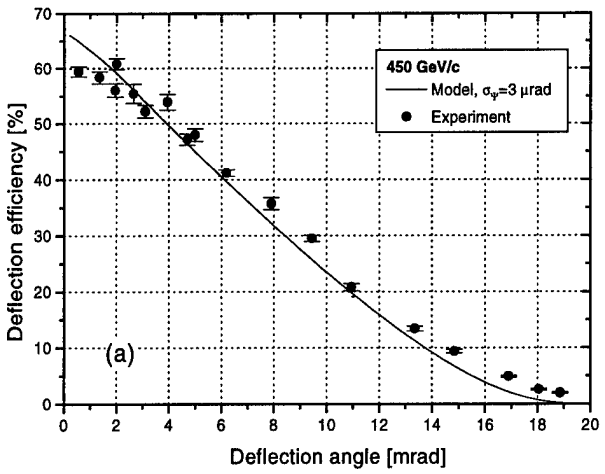


Figure 5: Deflection efficiencies measured for 450 GeV/c protons incident on a bent germanium crystal (dots) compared to calculations following the model of [6]. For details, see text.

3 RESULTS

Deflection efficiencies for 450 GeV/c protons were measured between 0.5 and 19 mrad deflection angle. The results are shown in Fig. 5. Statistical errors are shown in the figure. The systematic errors, which can stem from mechanical instabilities of the goniometer or bending device as well as from beam instabilities, can be estimated from the fluctuation of the data points. A new record deflection efficiency, 60%, for bent crystal proton deflection was found for the small deflection angles. The beam being very parallel, this can be attributed to the larger 'acceptance' – the so-called surface transmission - of the (110) Ge crystal when compared to the (111) Si used in earlier experiments [5].

The experimental results are compared in Fig. 5 to a model calculation along the lines described by Ellison [6]. In this model, the surface transmission, straight crystal dechanneling and bending dechanneling are parametrised (for more details, see [9]). The agreement with the data is found to be very good.

4 CONCLUSION

New experimental results on proton deflection with a bent germanium crystal have been obtained, and a record deflection efficiency of 60% has been obtained for the 450 GeV/c proton beam. The H8 microbeam of 450 GeV/c protons, originally designed to give a small spot size for an experiment, is here being used to provide as parallel a beam as possible at the crystal. Together with the good crystal quality, this makes record deflection efficiencies possible. The results shown here, together with the 200 GeV/c data reported elsewhere [9], provide a crucial test for models which had previously only been compared to data obtained with silicon crystals. The agreement between data and model for germanium is now found to be excellent, too. Therefore, one can conclude that reliable predictions are indeed possible, both for a different crystal material as well as for a large energy range, and that extrapolations to much higher energies, as will be available e.g., at the LHC, are trustworthy. For silicon, the radiation resistance of the crystals to large proton fluxes has been shown in a recent experiment [10]. In summary, bent crystals are thus a very useful tool to split, deflect or extract very high energy proton beams.

5 REFERENCES

[1] S.P. Møller, Nucl. Instr. Meth **A361**, 403 (1994)

[2] V. Biryukov *et al.*, Phys. Uspekhi **37**, 937 (1994)

[3] N. Doble, P. Grafström and L. Gatignon, Nucl Instr. Meth. **B119**, 181 (1996)

[4] A. Asseev and M.Yu. Gorin, Nucl. Instr. Meth **B119**, 210 (1996)

[5] S.P. Møller *et al.*, Nucl. Instr. Meth **B84**, 434 (1994)

[6] J. Ellison, Nucl. Phys. **B206**, 205 (1982)

[7] J. Lindhard, Mat. Fys. Medd. Dan. Vid. Selsk. **34**, 1 (1965)

[8] A. Baurichter *et al.*, Nucl. Instr. Meth **B119**, 172 (1996)

[9] C. Biino *et al.*, CERN-SL/97-05(EA), and Phys. Lett. B (in print), and U. Mikkelsen, PhD thesis, Aarhus (1997) (to be published as CERN-SL report).

[10] C. Biino *et al.*, contr. to 5th EPAC, eds. S. Myers, A. Pacheco, R. Pascual, Ch. Petit-Jean-Genaz and J. Poole, Vol. 3 (1996), 2385

OVERVIEW OF THE APT HIGH-ENERGY BEAM TRANSPORT AND BEAM EXPANDERS

R. E. Shafer, B. Blind, E. R. Gray, J. D. Gilpatrick, D. Barlow, and G. P. Lawrence.

Abstract

The APT high energy beam transport (HEBT) and beam expanders convey the 1700-MeV, 100-mA cw proton beam from the linac to the tritium target/blanket assembly, or a tuning beam stop. The HEBT includes extensive beam diagnostics, collimators, and beam jitter correction, to monitor and control the 170-MW beam prior to expansion. A zero-degree beamline conveys the beam to the beam stop, and an achromatic beand conveys the beam to the tritium production target. Nonlinear beam expanders make use of higher-order multipole magnets and dithering dipoles to expand the beam to a uniform-density, 16-cm wide by 160-cm high rectangular profile on the tritium-production target. The overall optics design will be reviewed, and beam simulations will be presented.

1 INTRODUCTION

The Accelerator for Production of Tritium (APT) is a 1700-MeV, 100-mA cw proton accelerator designed for the production of tritium in a target/blanket assembly via the reaction ^{3}He(n,p)T [1]. The beam from the 700-MHz superconducting (SC) rf linac [2] is transported to either a 4-MW low-duty-factor beam stop, or the tritium-production target by means of the high energy beam transport (HEBT), the switchyard and bend, and beam expanders.

The overall beamline layout is shown in Fig. 1. The approximate beamline length is 250 m from the linac to the beam stop, and 280 m from the linac to the tritium production target.

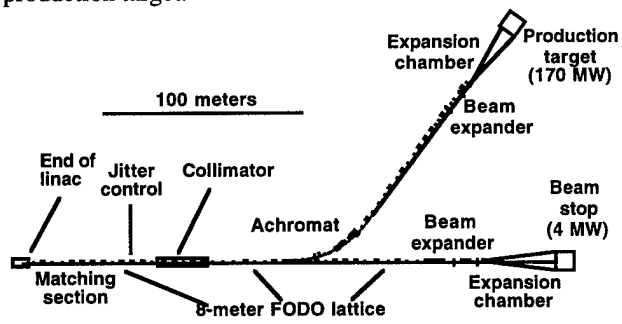


Fig. 1. The overall layout of the APT beam delivery system.

The purpose of the beam delivery system is to transport the beam to either of the end stations and expand it, to reduce the beam power density to acceptable levels. The HEBT includes beam diagnostics to characterize and monitor the beam, a system to correct beam position and angle jitter, and a collimator to intercept beam halo. The switchyard, which includes a 53.13°, 5-FODO-period achromat, directs the beam to either the beam stop or the tritium-production target. Finally, the beam expanders transform the beam to a 16-cm-wide by 160-cm-high uniform density distribution at the target windows. Each of these systems is described in more detail below.

2 HEBT AND EXPANDER LAYOUT

2.1 High Energy Beam Transport

The HEBT consists of an 8-meter-period FODO lattice, with a 72° zero-current phase advance per period. This 8-meter periodicity is maintained throughout the HEBT and switchyard to both end stations. The initial HEBT aperture is 16-cm diameter, to match the aperture in the superconducting (SC) linac [2]. The first 29 m is an adiabatic match from the SC linac focusing lattice. This FODO lattice also includes beam diagnostics to characterize and monitor beam energy, beam current, beam profiles, and a beam jitter control system to remove any residual transverse beam jitter and steering errors not corrected by the beam steering control system in the linac. The beam diagnostics for characterizing the linac is described elsewhere [3].

This HEBT section is followed by a 20-m-long adjustable-aperture collimator system to remove any excessive beam halo that might result from mismatches, beam turn-on transients, or component failure in the linac. The collimator is specifically designed to absorb up to about 1 kW of beam continuously, or individual pulses of 5 kJ, corresponding to about 30 μsec of full-power beam. This unit is heavily shielded, and is specifically designed to allow remote maintenance.

The remainder of the HEBT is a continuation of the same FODO lattice, but with the aperture reduced to 8-cm-diameter.

The nominal rms beam radius in the HEBT is about 1 mm, corresponding to a normalized rms emittance of 0.2 π-mm-mrad. The nominal aperture to beam-size ratio is 70:1 in the 16-cm dia. section, and 35:1 in the 8-cm dia. section.

2.2 Switchyard and Bend

The switchyard includes a 40-m section of the 8-m FODO lattice, a FODO cell with a dipole insertion for directing the beam to either the target or the beam stop, and a 5-FODO period, 360°-zero current phase advance, 53.13° achromat. The dipoles are placed immediately downstream of D-quads to minimize the dispersion in the achromat to about 2.6 cm per % Δp/p. Each dipole is about 1.3-m long, with a field of 1.2 T, and has a bend angle of 10.63°. Each quadrupole has a GL product of about 2.5 T. The beam aperture of the dipoles is 11 cm horizontally, and 7.3 cm vertically, while the beam aperture of the achromat quadrupoles is 9 cm. The energy acceptance of the achromat is ± 20 MeV.

The high-dispersion areas of the achromat will be used for both momentum collimation and for measurement of beam energy and energy spread. Beam

0-7803-4376-X/98/$10.00 © 1998 IEEE

energy is also measured in the HEBT using time of flight diagnostics. Momentum collimators will have adjustable apertures to intercept off-momentum beam halo, and off-momentum beams that may result from linac klystron trips. At the high dispersion points, the 2-MeV expected energy spread contributes about 2-mm to the horizontal beam size, compared to the 2-mm width in zero-dispersion areas. Thus both energy spread and energy changes can be observed in these high dispersion regions.

If needed, a second achromat can be inserted in the FODO lattice 40-m upstream of the first one.

2.3 Beam expander

The purpose of the beam expander is to expand the beam from its nominal 2-mm width to a uniform-density, 16-cm wide by 160-cm high image on the target. The nonlinear beam expander optics includes about 50-m of magnetic optics that sequentially folds the vertical and horizontal tails of the nearly Gaussian beam profile back onto the core, in order to achieve a nearly rectangular expanded-beam having a unifirm profile with a 10:1 aspect ratio [4]. The beam expander optics, shown in Fig. 2, include a 4-quadrupole matching section, a nonlinear magnet to fold the beam in the y-y′ phase space, a two-quadrupole intermediate lens, a second nonlinear magnet to fold the beam in the x-x′ phase space, two dithering dipoles to shake the expanded beam ± 1 cm horizontally and ± 2 cm vertically, and a final quadrupole-doublet objective lens to focus the beam through two neutron backshine shields in the beam expansion chamber.

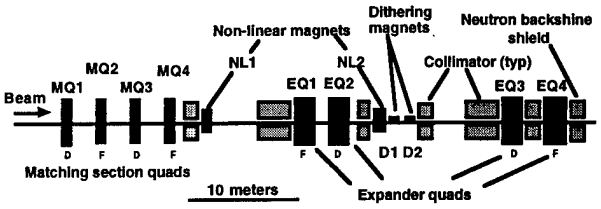


Fig. 2. Beam expander optics.

The beam folding in each plane is carried out in two stages, as illustrated in Fig. 3. First, the nonlinear magnetic fields, including octupole and higher-order terms, fold the beam phase-ellipse in y′ (or x′) space. Then, when the beam drifts in a long field-free region, the beam ellipse shears in y (or x) space, causing the tails in the transverse profile to fold back onto the core of the beam. This folding is done sequentially in the y-y′ and the x-x′ phase spaces.

Two nonlinear (multipole) magnets suitable for beam folding at 800 MeV have been built, and are now being tested at LANSCE in a prototype nonlinear beam expander [5].

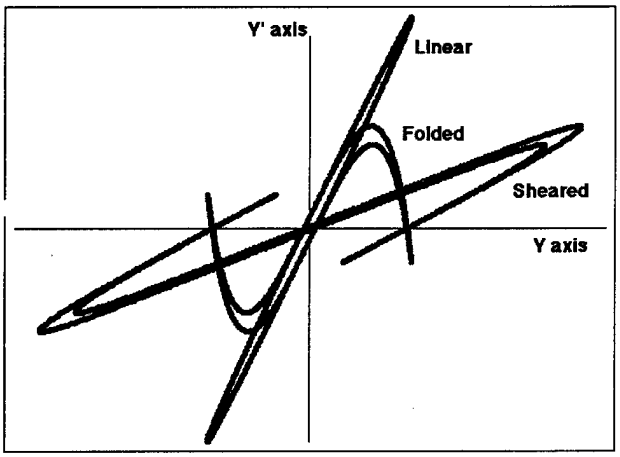


Fig. 3. The folding process for the nonlinear magnets.

Because of the concern about beam losses in the small apertures of the nonlinear expander, an alternate expansion scheme using rastering is being studied. This system is based on a high frequency triangle current-waveform modulator using IGBTs (insulated gate bipolar transistors) with ferrite dipole deflector magnets [6]. This triangular current waveform produces a uniform beam power density on the target. Four independently-powered deflectors, each about 40-cm long, are used in each plane to raster the beam at about 500 Hz vertically and 575 Hz horizontally. This beam-expansion concept has a much larger beam aperture than the nonlinear folding concept, and potentially improved control of the beam distribuion on the target (independent of the input beam), but has the additional risk of thermal fatigue in the target, and the possibility of target damage in the case of raster system failure. These issues are being addressed in the study.

2.4 Beam expansion chamber

Fig. 4 shows the 30-m long beam expansion chamber. In order to limit the backstreaming neutron flux from the target, the expansion chamber includes two neutron backshine shields. These shields are placed at the vertical waist in the expanding beam, about 0.5 m downstream of the last quadrupole, and at the horizontal waist, about 11-m downstream of the last quadrupole. These neutron shields are about 1.5-m-thick iron shields, with a 2-cm high by 15-cm wide contoured slit at the vertical waist, and a 3-cm wide by 80-cm high contoured slit at the horizontal waist. Their upstream side will be covered with a boron-loaded material to absorb low-energy neutrons. The expected backstreaming neutron flux inside the beam expander optics is about 3×10^9 n/cm^2/s, and the annual neutron fluence is of the order of 1×10^{17} neutrons/cm^2, because the neutron shields together limit the view of the target from the beam expander to about 2% of the target frontal surface area.

The beam expansion chamber includes extensive multiwire beam diagnostics (secondary emission and resistance wires) to determine and monitor the expanded beam profile. These beam diagnostics systems, described elsewhere [3], are inserted through either of two beam diagnostics towers, shown in Fig. 4.

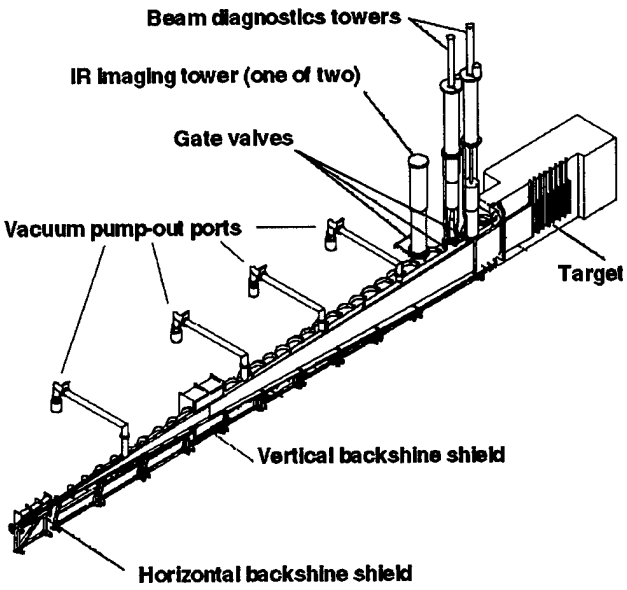


Fig. 4. 30-m long beam expansion chamber.

3 BEAM SIMULATIONS

Beam simulations using space-charge codes (PARMILA and TRACE-3D) show that the SC linac beam is easily matched into the 8-m period FODO lattice from the SC linac wihout any indication of space-charge effects in the transverse planes. The aperture to rms beam size ratio is about 70:1 in the 16 cm diameter HEBT, and 35:1 in the 8-cm diameter section. The longitudinal bunch length of the individual microbunches grows slightly in the HEBT as expected, but this is inconsequential. In addition, the beam simulations through the achromat show no space-charge effects. The maximum dispersion in the achromat is about 2.6 cm per % $\Delta p/p$. With a total energy spread of 2 MeV, the beam width increases by about 2 mm in the achromat. The residual dispersion after the achromat is near zero, and the beam shows no residual effects of the 53.13° bend.

In the beam expander, the 4-quadrupole matching section focuses the beam into the first nonlinear magnet with a horizontal beam waist, and into the second with a vertical waist. The folded beam then expands in both planes to the final quadrupole doublet.

End-to-end particle-tracking simulations, from the RFQ to the tritium-production target, are being used to evaluate the beam-expander design. These simulations include up to 100,000 particles, and include effects such as rf phase and amplitude errors, loss of one klystron, quadrupole field and alignment errors, etc. The simulations indicate that roughly 1 particle in 100,000 either may hit collimators shielding the nonlinear-magnet coils, or may be deflected by a nonlinear magnet into downstream collimators. This is equivalent to 1000 to 2000 watts of beam loss, and may lead to radiation damage and premature beamline-component failure (magnets and beam diagnostics), and indicates the need for remote maintenance capability. The beam expander physics model used in the simulations is being improved to better ascertain the expected beam loss, and design work is going on to increase the physical aperture of the nonlinear magnets [7].

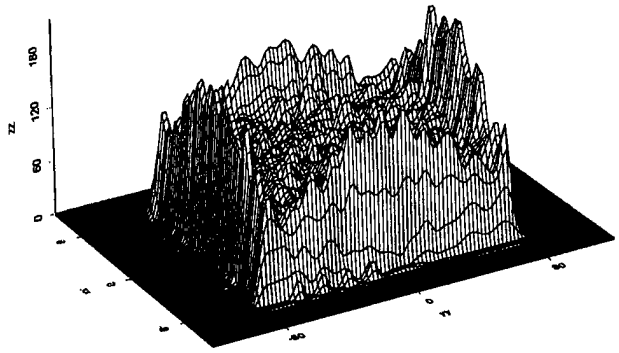


Fig. 5. Isometric plot of simulated particle distribution on target. The horizontal width is 16 cm, and the vertical height is 160 cm.

4 CONCLUSION

The conceptual design of the high energy beam transport to the beam expanders is nearly complete, and meets all the necessary requirements for the APT project. Design of the nonlinear beam expanders is still in progress, with the major effort being to improving the models used in the beam simulations, simulating a wide variety of off-normal linac operating conditions, and increasing the expander magnet apertures. A parallel effort is examining the alternate expansion scheme based on beam rastering.

5 REFERENCES

[1] P. W. Lisowski, "The Accelerator Production of Tritium (APT) Project", these proceedings.

[2] G. P. Lawrence and T. Wangler, "Integrated Normal/Superconducting Linac Design for APT", these proceedings.

[3] J. D. Gilpatrick et al., "LEDA and APT Beam Diagnostics Instrumentation," these proceedings.

[4] B. Blind, "Production of Uniform and Well-Confined Beams by Nonlinear Optics," Nucl. Inst. and Meth., Vol B56/57, pages 1099-1102 (1991).

[5] D. Barlow et al., "Magnetic Design and Measurement of Nonlinear Multipole Magnets for the APT Beam Expander System," these proceedings.

[6] C. R. Rose and R. E. Shafer, "A 200-A, 500-Hz Triangle Current-Wave Modulator and Magnet for Particle Beam Rastering," these proceedings.

[7] A. J. Jason, B. Blind, and K. Halbach, "Beam Expansion with Specified Final Distribution," these proceedings.

THE NATIONAL SPALLATION NEUTRON SOURCE TARGET STATION: A GENERAL OVERVIEW

Tony A. Gabriel, John N. Barnes, Lowell A. Charlton, James DiStefano, Ken Farrell, John Haines, Jeffrey O. Johnson, Louis K. Mansur, Steve J. Pawel, Moshe Siman-Tov, Rusi Taleyarkhan

Oak Ridge National Laboratory, P. O. Box 2008, Oak Ridge, Tennessee 37831, USA

Thomas J. McManamy and Mark J. Rennich

Engineering, Lockheed Martin Energy Systems, Inc., P. O. Box 2009, Oak Ridge, Tennessee 37830, USA

Abstract

The technologies that are being utilized to design and build a state-of-the-art neutron spallation source, the National Spallation Neutron Source (NSNS), are discussed. Emphasis is given to the technology issues that present the greatest scientific challenges. The present facility configuration, ongoing analysis and the planned hardware research and development program are also described.

1.0 INTRODUCTION

In many areas of physics, materials and nuclear engineering, it is extremely valuable to have a very intense source of neutrons so that the structure and function of materials can be studied. One facility proposed for this purpose is the National Spallation Neutron Source (NSNS). This facility will consist of two parts: 1) A high-energy (1 GeV) and high powered (1 MW) proton accelerator (60 Hertz, <1 μs/pulse), and 2) A target station which converts the protons through nuclear interactions to low-energy ($\lesssim$2 eV) neutrons and delivers them to the neutron scattering instruments.

This paper deals with the second part, i.e., the design and development of the NSNS target station and the scientifically challenging issues. Many scientific and technical disciplines are required to produce a successful target station. These include engineering, remote handling, neutronics, materials, thermal hydraulics, and instrumentation. Some of these areas will be discussed below.

2.0 TARGET STATION CONFIGURATION AND MAINTENANCE

The target for the NSNS is located in a single building. As shown in Fig. 1, the target is positioned within an iron and concrete shielding monolith approximately 12 m in diameter. The proton beam enters horizontally in the mercury target and produced neutrons, which (after moderation) are used by the scattering instruments, exit through 18 neutron beam tubes projecting from the sides. The majority of the 62 m x 83 m building is reserved for the scattering instruments located on the neutron beam lines, however, remote handling hot cells projecting from the back of the shielding are provided for handling the activated target, moderator and reflector components. This region also contains utilities used for the target. Another cell for utility systems is located beneath the main floor level.

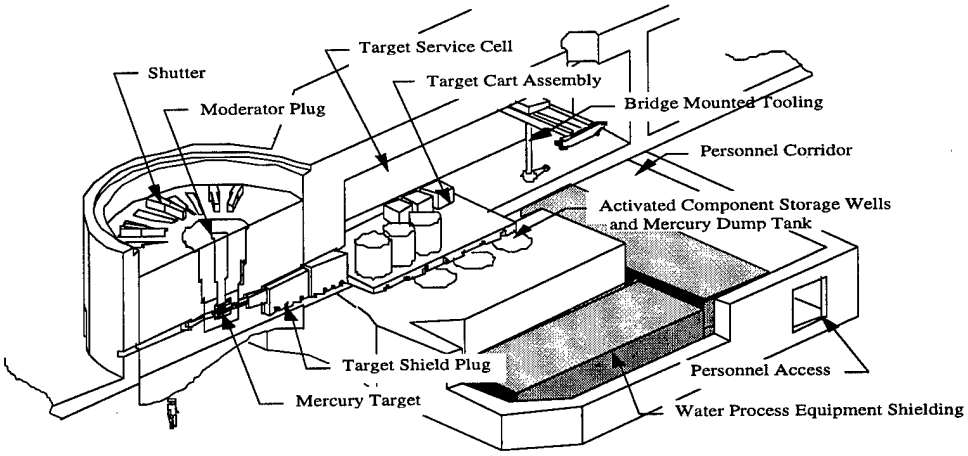
The reference design for the NSNS incorporates mercury as its target material. A heavy liquid metal target was selected over a water-cooled solid target because (1) increased power handling capability is possible with a liquid target, (2) the liquid target material lasts the entire lifetime of the facility, and (3) the radiation damage lifetime of a liquid target system, including its solid material container, should be considerably longer.

Mercury was also selected as the reference liquid target material because it: (1) is a liquid at room temperature, (2) has good heat transport properties, and (3) has high atomic number and mass density resulting in high neutron yield and source brightness. One significant result from recent neutronic analysis studies has been that the neutron flux from a short-pulse (~1 μs) neutron source is substantially greater for a mercury target than for either water-cooled tungsten or tantalum targets especially at power levels greater than 1 MW.

The mercury target design configuration, shown in Fig. 2, has a width of 400 mm, a height of 100 mm, and a length of 650 mm. The mercury is contained within a structure made from 316-type stainless steel. Mercury enters from the back side (side outermost from the proton beam window) of the target, flows along the two side walls to the front surface (proton beam window), and returns through a 224 mm x 80 mm rectangular passage in the middle of the target. The target window, i.e., portion of the target structure in the direct path of the proton beam is cooled by mercury which flows through the passage formed between two walls of a duplex structure. In this way, the window cooling and transport

0-7803-4376-X/98/$10.00 © 1998 IEEE

Fig. 1: Target System Configuration



of heat deposited in the bulk mercury are achieved with separate flow streams.

A shroud (safety container) is provided around the mercury target to guide the mercury to a dump tank in the event of a failure of the target container structure. The shroud is a water-cooled duplex structure made from austenitic, 316-type, stainless steel.

Detailed thermal hydraulic and stress calculations have been carried out for the mercury target system and a large fraction of our R&D program deals with thermal shock and hydraulic tests and analysis, radiation damage, and erosion/corrosion test and analysis.

The mercury target and the water cooled shroud, which are subject to intense interactions with the proton beam, must be replaced on a regular basis. For this reason, all major liquid target system components, except the dump tank, are located on a mobile cart, which is retracted into the target maintenance cell for maintenance activities. The mercury contained in the target system is drained to the dump tank prior to retracting the target assembly.

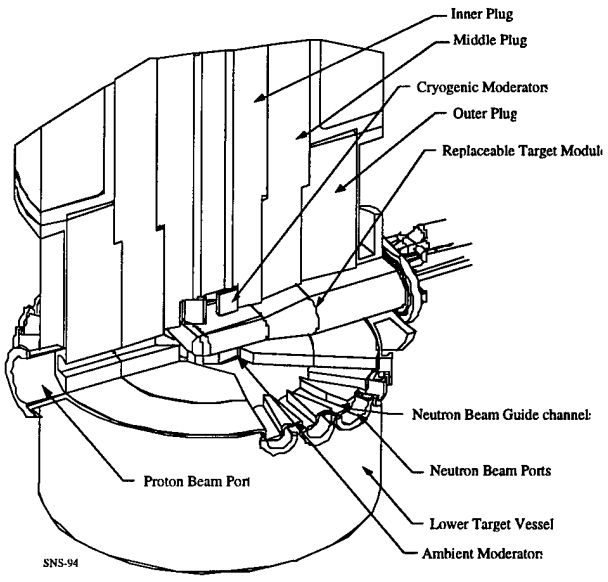
The heat deposited in the mercury target is transported away in the flowing mercury loop to a primary heat exchanger that is located on the target cart assembly, outside the target region shielding. In addition to this primary heat exchanger, the mercury flow loop also includes piping, valves, fittings, pumps, expansion tanks, and mercury processing equipment. The secondary (water) loop transports the heat to a secondary heat exchanger located in the floor below the target hot cell. The tertiary flow stream utilizes process water.

The mercury dump tank is located below all other components in the mercury system thus ensuring that most of the mercury can be drained to the dump tank even in a passive situation (failure of the electric power system). The capacity of the dump tank is greater than 1 m^3, which is slightly larger than the mercury inventory in the remainder of the system. The tank is passively cooled by natural convection to remove the nuclear afterheat in the mercury.

Figure 2 shows the two light-water moderators planned for the NSNS. They are located in wing geometry below the mercury target and water-cooled shroud. The upstream moderator has a thickness of 50 mm, relative to the proton beam, and is decoupled and poisoned to give high temporal resolution of the neutron flux. The second moderator is 100 mm thick and is coupled to produce higher neutron intensity but with less temporal resolution. Both moderators are approximately 120 mm wide and 150 mm high. Two cryogenic moderators, cooled with supercritical hydrogen, are located above the target as shown in Fig. 2. This configuration improves the cooling and warming characteristics of the moderators. Mechanically circulated supercritical hydrogen gas at a pressure of 1.5 MPa was chosen for the moderators because it improves the cooling operation, eliminates boiling and adds flexibility in operation. The hydrogen is maintained at supercritical pressures in all parts of the loop during normal operation. The calculated neutron current energy distribution per proton from the front cryogenic moderator is shown in Fig. 3.

The neutron beam tube systems provide the paths for moderated neutrons to travel through the bulk shielding to the scattering instruments. The configuration assumed at present consists of 18 beam lines looking at the four moderators as shown in Figs. 1 and 2. Each moderator face which is viewed illuminates three beam lines, one normal to the face and two at plus or minus 13.75 degrees. The upper and lower forward moderators have two faces viewed and the two rear moderators each have one face viewed for a total of 6 viewed faces. This arrangement allows a 70° degree arc for the proton beam entrance region and a similar 70° degree arc for the remote maintenance systems at the rear of the target.

Fig. 2: NSNS Mercury Target

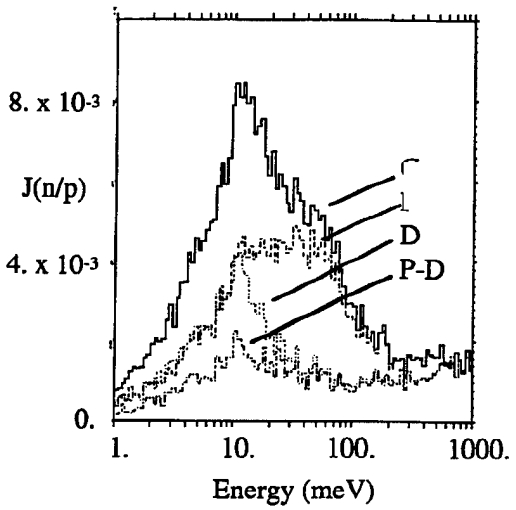


A neutron beam shutter concept similar to the ISIS vertical shutter design is planned. The shutters are in the form of stepped rectangular slabs. In the open position a hole in the shutter aligns with the neutron beam flight path and cross section. The shutter is lowered approximately 500 mm to close. This puts approximately 2 m of shielding in the neutron flight path. The drive for the shutters will be from the top. Each shutter will be made from several sections to reduce the height above the top of the bulk shielding required for removal and the size of the shielded flask required for transport. All shutters will be the same, except for the difference in beam elevation required between beam lines viewing the upper or lower moderators. The weight of one shutter assembly is approximately 25 tonnes.

Optimization of both the operating availability and predictability, while protecting personnel, is the primary goal of the maintenance systems for NSNS. Several techniques proven in successful facilities throughout the world are applied to assist the operators in meeting the operating goals. These include designing equipment from the earliest stages to reduce the need for remote handling. Operating equipment are packaged in modular assemblies designed to be replaced with on-site spares. This enables operations to continue while time-consuming repairs are performed in off-line facilities.

The As Low As Reasonably Achievable (ALARA) principle is used as guidance for all personnel and contamination control operations in NSNS. Thus, activated and contaminated equipment are shielded for transport around the facility and to the permanent storage site. Areas of potential contamination are isolated by seals and valves. Repair and replacement of active components are accomplished in the hot cell adjoining the target shielding stack as identified in Fig. 1.

Fig. 3: Neutron energy distribution from the face of the front cryogenic moderator, C=coupled, P=poisoned, D=decoupled, P-D=poisoned and decoupled.



A general maintenance cell is located behind the target maintenance cell primarily to maintain the moderator/reflector plug, proton beam window, neutron guide tubes and shutters. Generally all operations will be remote; however, personnel may enter the cell following extensive cleanup.

The enclosed, unshielded high-bay above the target system and maintenance cells will provide the primary means of handling components in the target system.

3.0 CONCLUSIONS

Preliminary design and analysis indicate that a very attractive short-pulse neutron source operating at 1 MW of proton beam power can be constructed for the NSNS using liquid mercury as the target material. Research and development activities have been identified to validate design concepts and to allow future upgrades to higher power levels. Reasonable design configurations have been proposed for major component assemblies and remote handling concepts have been developed. A detailed descriptions of the NSNS project can be found in Ref. 1.

REFERENCES

1. "The National Spallation Neutron Source Conceptual Design Report," ORNL, in press, June, 1997.

HIGH INTENSITY PROTON ACCELERATION AT THE BROOKHAVEN AGS - AN UPDATE

L.Ahrens*, J.Alessi, M.Blaskiewicz, E.Bleser, J.M.Brennan, K.Brown, C.Gardner,
J.W.Glenn,H.Huang, K.Reece, T.Roser, W.vanAsselt, K.Zeno,and S.Y.Zhang
AGS Department, Brookhaven National Laboratory, Upton, N.Y. 11973

Abstract

The AGS accelerator complex is into its third year of 60+ $x10^{12}$ (teraproton = Tp) per cycle operation. The hardware making up the complex as configured in 1997 is briefly mentioned. The present level of accelerator performance is discussed. This includes beam transfer efficiencies at each step in the acceleration process, i.e. losses; which are a serious issue at this intensity level. Progress made in understanding beam behavior at the Linac-to-Booster (LtB) injection, at the Booster-to-AGS (BtA) transfer as well as across the 450 ms AGS accumulation porch is presented. The state of transition crossing, with the gamma-tr jump is described. Coherent effects including those driven by space charge are important at all of these steps.

1 INTRODUCTION

The Brookhaven National Laboratory's Alternating Gradient Synchrotron (AGS) complex delivers slowly extracted protons at 24 GeV simultaneous into four beam lines with a spill length of 2 seconds in a total cycle time of 3.6 seconds. Over the last several years the available intensity in this mode has increased, from 25 Tp in '93, to 40 Tp in '94, then to just over the design goal of 60 Tp in '95 [1],[2]. During 1996 the total number of protons delivered per hour of running continued to increase, though the peak intensity achieved was unchanged.

Experience from each yearly running period suggests modifications both to the accelerator hardware and to acceleration strategies. Available resources including the time between runs, together with the flexibility of the complex and its control system allow some of these modifications to be implemented. This report summarizes the changes of this sort made prior to the 1997 high intensity proton run and operational experience during this ongoing run as these changes have been implemented.

2 THE RECENT PAST - THE 1996 RUN

Losses during acceleration and at extraction have grown as the intensity has increased but not so fast as to be a constraint on operations until the '96 run. Probably as a result of successful efforts to reduce losses experienced just at AGS extraction in '95, losses further down the extraction lines naturally increased somewhat. This creates a more serious problem to the operation of the machine simply because these losses occur closer to areas where ongoing work must be carried out. As a result efforts to reduce the chronic radiation levels associated with the extracted beam were the primary focus of activity during the 1996 run. These transport losses are dependent on beam handling throughout the acceleration cycle, and in particular with the setup of the four transfer accumulation on the AGS front porch, the passage through transition, and the machine quadrupole and sextupole settings between transition and extraction, as well as on the slow extraction dance itself.

For losses occurring earlier during the acceleration cycle, the sensitive spots are 1) transition crossing, at about 9 GeV, 2) AGS injection, including both losses in the transfer process, and losses incurred as the four Booster batches are accumulated on a magnetic porch and 3) injection from the Linac into the Booster at .2 GeV.

The transition losses, which are potentially serious radiation sources because of the beam energy, usually remained below 4%. Keeping them at this level required continual attention since the transition jump scheme with its inherent distortion of the machine dispersion function sets the machine momentum aperture.

The losses at AGS injection amounted to about 20 Tp, 25% of the beam available in the Booster, and so merited attention because of the associated activation and simply as a potential beam source for increasing the AGS output. The '96 AGS injection beam losses were categorized, from current transformers and the loss monitor arrays which cover all the regions (a new loss monitor system was commissioned in the AGS during the '96 run). A quarter of these loss, perhaps less, occurred in the Booster and in the BtA transfer line. A quarter occurred slowly, while the beam is stored on the porch and well away from the transfers. Progress on reducing this "drool" loss had been made the previous year ('95) by

* Work performed under the auspices of the U.S. Department of Energy

0-7803-4376-X/98/$10.00 © 1998 IEEE

powering some "prototype" octupoles in the AGS A modest extension to that system in '96 did not further reduce the drool. Sharp "coherence" losses can occur during these storage intervals, and are controlled by vertical betatron tune adjustments in conjunction with the AGS vertical damper. A third quarter of the losses could be seen on the AGS current transformer on a millisecond time scale at each of the four transfers. The remaining quarter was not explicitly accounted for either in the loss monitor or wall monitor analysis. It was most likely occurring in the AGS on a time scale of tens of turns around the machine, too fast for the usual transformer, to subtle each turn for the wall monitor, and ending in ring locations having low sensitivity in the loss monitors. These losses could be space charge driven[3].

The highest loss point, in terms of protons, was at Booster injection. The Linac delivers 35 mA beam current and is capable of maintaining this for pulse widths of 500 usec and so can totally saturate the Booster capacity. In fact the Booster is routinely delivering 22 Tp/ cycle x 4 cycles/ AGS cycle, operating 50% above its "design" intensity of 15 Tp. Space charge driven losses early in the cycle are expected, but pouring more Linac beam in is the obvious source (beside chipping away at losses later in the cycle) for higher AGS output. Losses at Booster injection vary significantly but are typically 30%.

3 CHANGES FOR THE 1997 RUN

Efforts to improve the transport efficiency of the extracted beam came first. By the end of the '96 run measurements of the emittance of the extracted beam had generated Twiss parameters credible enough to encourage a substantial rework of the optics at extraction and down the many transfer lines. The implementation of this optics under the highest intensity operation was the priority activity at the '97 startup and into the run. Instrumentation upgrades to further refine the emittance measurement and to allow quantitative measurements of the tails of the extracted beam were implemented (flags, and scanning targets) [4].

The transition situation, though satisfactory at this intensity was given additional tuning flexibility in that three of the twelve horizontal high field sextupoles in the AGS, the three most effective during the dispersion distortions of the transition jump, were equipped with additional power supplies - allowing them to function beyond their roles as chromaticity sextupoles. The objective is to reduce the expected nonlinear growth of the momentum compaction spread within the beam caused by the basic jump scheme itself [5]. The sextupole set has been powered without ill effects on the beam, and awaits higher intensity and study time.

The orbit correction system in the AGS was redone for the '97 proton run. Though this replacement was required by maintenance issues both for the hardware and controls, the replacement system addressed the fact that the injection momentum has increased four fold from the days of direct Linac injection. Each replacement dipole has 25 times the strength of a dipoles in the old system, the number of magnets is halved. This system allows significant 'local' aperture scanning on the AGS injection porch, yielding clean identification (plane and side) for observed losses. By combining several magnets there is sufficient strength to bump the orbit at transition, where millimeter motion at the jump quadrupoles significantly affects the jump induced orbit distortion. The system has been commissioned in these modes and has taking over the basic harmonic orbit correction from the old system.

The attack on the AGS injection porch drool loss continued with the addition of four powerful (4 inch radius, 2 KG pole tip field) octupoles to the AGS lattice. With these, and the four previously existing octupoles, the betatron tune space on the AGS injection porch has been revisited. Using a pencil beam probe, losses intentionally created by slowly sweeping the beam across the normal octupole lines passing through the point where both betatron tunes equal 8.75 were removed. The octupole currents yielding optimal survival in the study are not the currents demanded by the highest intensity machine. The addition of a large 'zero theta" octupole component is tolerated by the high intensity machine with no immediate effect either beneficial or destructive.

In another response to losses in the AGS at injection, a simplification was introduced into the injection situation. The orbit bump which deforms the equilibrium orbit against the injection septum had always been pulsed (2 ms width) for each of the four transfers. This bump is now held on throughout the injection porch, and then ramped down before acceleration. Having the new static situation allows the residuals from this 3/2 lambda bump to be corrected in a straight forward way (using in part the controls made available by the new orbit correction system), and provides a single orbit across the porch, a single sampling of the fields of the machine for stop band correction.

In the BtA a high loss region and residually hot spot could be associated with a slightly low beam pipe, which was repositioned. The '96 loss at this position was sensitive to vertical steering, which was impossible to adjust without affecting AGS survival. By redistributing the available trim dipoles in the BtA transfer line, steering at the tight point and steering into the AGS ring were decoupled. (The original positions of these magnets allowed creating a dog-leg between the Booster and AGS. The shift was never needed due to an early resurvey and local repositioning of the adjacent region of the AGS ring.)

The most interesting change at transfer between Booster and AGS implemented for the '97 run was an increase of the transfer kinetic energy, from 1.54 GeV to 1.91 GeV, an 18% increase in momentum. In conjunction

with this change several other variables for the acceleration strategy were also modified, and despite the pedagogical difficulties introduced, all the changes were applied simultaneously, during one four hour study period after a two hour prep session.

Each Booster acceleration cycle was lengthened by one clock tick of the super cycle, 1/60 sec. This allowed time for the Booster to rise to higher fields without forcing the Booster injection process to be fundamentally reworked. (To fit a cycle rising by 18% into the old 7.5Hz constraint, the derivative of the field at injection would have had to be higher or injection moved right to the beginning of the cycle - both interesting but risky choices given the available time). In fact the time increase is sufficient to also give systems such as the ring rf a bit more time to come to a stable starting value each cycle before beam is injected. The highest Booster extraction field occurs as the magnet is about to roll over - namely at a point of zero Bdot. Over the Booster history the extraction Bdot has been decreased from 8T/sec -(full ramp rate at the time) to 2 T/sec for the last two years, and now to zero. Along with allowing the highest momentum transfer, this also allows several other explorations in particular the reduction of the Booster rf gap volts. The Booster and AGS could be longitudinal matched were that desirable.

Of course the injection fields in the AGS had to be scaled up to accommodate the momentum increase. The actual frequency for the rf's and the "synchro" dance providing the clean bunch-to-bucket transfers required the appropriate parameter adjustments, as did the frequency sent to the dilution cavity which is active across the injection porch. The rest of the AGS cycle was unchanged as much as possible, with the exception that the cycle time lost due to the lengthening of the Booster cycles was recovered by a just slightly more enthusiastic acceleration in AGS.

Factors benefitting from the momentum increase include the 8% transverse beam size reduction simply due to the adiabatic shrinkage. The space charge tune shift in the AGS becomes lower due to the higher momentum and also to the extent that the longitudinal match strategy yields lower peak currents in the AGS bunches just after transfers before the dilution cavity can do its work[3]. Possible detrimental results include the obvious need to push the magnetic elements, and in particular the kickers at both ends of the transfer line, 18% harder. In addition, since the transverse phase space occupied by the beam in AGS tends to fill the AGS acceptance, - perhaps by the intentional space charge reducing mismatch during injection, the beam with which AGS extraction will have to cope may be larger.

The latest results from this step in the acceleration is that indeed the loss reported by the loss monitors within the BtA line is gone, and Booster extraction is relatively quiet. The overall beam lost in the transfer process is half that seen last year though the Booster late intensity is also a bit down.

In the Booster, improvements were made to the rf systems. The h = 4 second harmonic cavity system has been improved to allow the system to be active throughout the Booster cycle. A beam "feed forward" system has been introduced, again active throughout the cycle. The "orbit display" which has suffered from the high intensity runs, was brought back to life to allow orbits for the turn on.

4 STATUS AND CONCLUSIONS

The '97 high energy physics run started just six weeks ago but will end just six weeks hence. It is a physics production run; not a setup period. In addition, the sending of the AGS beam by eight fast extractions to the 'g-2' experiment (down the beam line that leads to RHIC) has occurred on a pulse stealing basis for the past three weeks. Study/setup activities typically use twelve hours each week. The changes described here, especially the many facets of the BtA momentum shift, have been applied quickly; and only by using the full capability of the accelerator control system which can keep several different machine setups available with 'pulse-to-pulse modulation'. There has not yet been much 'tuning' time for Operations to exploit the changes, which is ultimately how intensity increases come about. Nevertheless, the performance of the past has been equaled, and the protons/hour delivered this year is the highest yet. Next running period the plan is to commission a barrier bucket system in the AGS which will allow transfer of additional Booster batches into AGS [1], pushing the envelope.

5 ACKNOWLEDGMENTS

AGS progress results from the dedicated efforts of the entire accelerator staff, an effort we greatly appreciate.

6 REFERENCES

[1 J.M.Brennan and T.Roser: 'High Intensity Performance of the Brookhaven AGS', EPAC 96 Proceedings of the Fifth European Particle Acc. Conf., Vol 1, p 530.

[2] M. Blaskiewicz et al., 'High Intensity Proton Operations at Brookhaven', Proc. of the 1995 IEEE Particle Accelerator. Conference, Dallas, TX, May 1995, p 383.

[3] S.Y.Zhang, 'Space Charge Effects and the AGS Injection Loss',AGS Accelerator Div. Tech. Note #451, 29Oct96.

[4] K.A.Brown et al., 'A Scanning Target Profile Monitor for the Slow Extracted Beam at the AGS', these proceedings

[5] J. Wei et al., "Effects of Enhanced Chromatic Nonlinearity during the AGS Gamma-tr Jump', Proc. of the 1995 IEEE Particle Accelerator Conference, Dallas, TX, May 1995, p 3334.

SPIN TRACKING IN RHIC

A.U. Luccio *, Brookhaven National Laboratory, Upton, NY 11973
T. Katayama, INS, University of Tokyo
and H. Wu, Riken Institute, Tokyo

Abstract

In the acceleration of polarized protons in RHIC [1] many spin depolarizing resonances are encountered. Helical Siberian snakes [2] [3] will be used to overcome depolarizing effects. The behaviour of polarization can be studied by numerical tracking in a model accelerator, That allows one to check the strength of the resonances, to study the effect of snakes, to find safe lattice tune regions, and finally to study the operation of special devices like spin flippers. In this paper we describe numerical spin tracking. Results show that, for the design corrected distorted orbit and the design beam emittance, the polarization of the beam will be preserved in the whole range of proton energies in RHIC.

1 SPIN RESONANCES

Spin resonances that may lead to the loss of polarization [4] [5] [6] are of two main species: *intrinsic* resonances that depend on the lattice structure of the ring and arise from the coupling of betatron oscillations with horizontal magnetic fields, and *imperfection* resonances caused by orbit distorsions. In both cases, for vertical polarization (as in RHIC), the vertical motion of the beam is the main responsible for depolarization. If P is the superperiods of an accelerator, and ν_y the vertical betatron tune, along the acceleration cycle intrinsic resonances are located at $G\gamma = nP \pm \nu_y$ and imperfection resonances at $G\gamma = k$, with $G = 1.7928$ the proton gyromagnetic ratio, and n and k integers. Resonance strenght is proportional to the amplitude of the vertical motion of the beam, produced either by betatron oscillations or closed orbit distortion, then, ultimately, to the emittance of the beam. The strength is proportional to the energy of the beam γ for imperfections and to the square root of the energy for intrinsic.

Effects on depolarization are also due to the betatron horizontal and synchrotron longitudinal oscillations and to other causes, like the beam-beam interactions that take place in colliders. Resonances may also be enhanced in the vicinity of special fractional value of the betatron tune.

2 SPIN TRACKING

For spin tracking, we used an ad-hoc written computer code *Spink* [7], that follows an ensemble of particles through an accurate representation of the actual lattice of RHIC. Among special lattice modules are the helices of the Siberian snakes and spin rotators needed to bring the vertical polarization to a longitudinal orientation at the colliding points in RHIC. The most elegant representation of spin is in the 2-dimensional space throgh spinors and Pauli matrices. However, in the code we found it more convenient to represent the spin as a real vector in the ordinary space.

Tracking, hundreds particles for a number of revolutions of the order of 100,000 through a thousand matrices takes a computer time of the order of a few hours for a typical fast workstation. Some of the tracking with many particles has been performed on a supercomputer.

2.1 Orbit Matrices

Spink tracks a number of protons randomly generated in phase space, through the machine lattice. A proton is characterized by four transverse coordinates, *x, x', y, y'* and by two longitudinal coordinates dp/p, $d\phi$. Matrices used to transform orbit coordinates are built from the output of the code *Mad* [8]. We only retain the relevant ("active") modules for orbit tracking; everything else in the lattice is lumped in drift modules. Typically, for RHIC the number of *Spink* matrices is 981, each active element being surrounded by two drifts.

Acceleration by rf cavities is represented by a matrix in which the longitudinal momentum of a proton is changed at the expense of the transverse momentum [9]. In a cavity, the emittance of the beam changes as $\epsilon = \epsilon_N/\beta\gamma$, with ϵ_N the normalized emittance.

2.2 Spin Matrices

In the spin space, a proton has three coordinates S_x, S_y, S_z (where $S_x^2+S_y^2+S_z^2 = 1$). Spin is transformed by rotation, using matrices. In a bend, the rotation is around a vertical y-axis, in a quad, around a radial axis, in a snake, around an axis of orientation given as input, and in a spin flipper around a horizontal rotating or oscillating axis.

In general, a matrix representing a rotation in the ordinary space can be written as [10].

$$R = I\cos\varphi + W(1-\cos\varphi) + A\sin\varphi$$

where I is the unitary matrix, W a symmetric matrix, A an anti symmetric matrix, and φ the rotation angle. In the case of spin, if one writes the components of the rotation axis as follows

$$b_1 = \cos\theta\sin\phi$$
$$b_2 = \sin\theta$$
$$b_3 = \cos\theta\cos\phi$$

with θ the latitude and ϕ the azimuth, explicit expressions for the matrices are

$$W = \begin{pmatrix} b_1^2 & b_1b_2 & b_1b_3 \\ b_2b_1 & b_2^2 & b_2b_3 \\ b_3b_1 & b_3b_2 & b_3^2 \end{pmatrix} \quad A = \begin{pmatrix} 0 & b_3 & -b_2 \\ -b_3 & 0 & b_1 \\ b_2 & -b_1 & 0 \end{pmatrix}$$

* Work performed under the auspices of the U.S. Department of Energy

0-7803-4376-X/98/$10.00 © 1998 IEEE

2.3 *Synthetic Modules and Field Maps.*

Matrices for machine modules can be built directly with mathematical expressions ("synthetic" modules, e.g. a snake that rotates the spin exactly by 180^0 around an axis at 45^0) or can be calculated from field maps. In the latter case the technique is to integrate the differential equations of motion and the spin BMT equation [11] through the map for an ensemble of particles and averaging the results. For synthetic modules the orbit matrices are automatically symplectic and the spin matrices unitary, for field maps, some manipulation is needed, to make them so. This is important, since spin tracking is sometimetimes carried on for 10^5 to 10^6 turns, and systematic errors may lead to wrong results.

The orbit matrix M is symplectic if it satisfies the condition (equivalent to six independent conditions among the matrix elements)

$$M^T S M = S$$

where M^T is the transpose of M and S is the base anti symmetric matrix. The symplecticity condition in particular insures that the 4-dimensional emittance of the beam in transverse space is conserved.

If a syntehtic module, building spin matrices is immediate. In a field map, in terms of the elements of the spin matrices W and A, the angles of the rotation axis $\hat{b}$ and the spin precession angle μ are given by

$$\tan 2\phi = \frac{2W_{13}}{W_{33}-W_{11}}$$
$$\tan 2\theta = -\frac{A_{12}A_{13}\sin\phi}{A_{12}A_{23}-A_{13}^2\sin\phi\cos\phi}$$
$$\cos\phi = \frac{A_{12}A_{23}}{W_{13}-1}$$
$$\cos\mu = (R\vec{S_0})\cdot\vec{S_0}$$

with $\vec{S_0}$ the spin vector before the rotation.

Note that the elements of spin matrices for snakes (unless synthetic) are a function of beam energy. The magnetic field in the helices should be varied during the acceleration cycle to optimize spin rotation angle and axis angles. However, since it is convenient to keep the snake field constant, and since the strongest resonances take place at high energy, we tune the fields in the snakes at their optimum value for high energy and maintain these values. It is expected to operate this way with the real magnets.

3 EXAMPLES

Reference values of the main parameters for spin tracking are given in Table 1 [12]

Examples of spin tracking follow, both for the acceleration mode and for storage mode at constant energy.

3.1 *Acceleration Mode*

Figure 1 shows an example of spin tracking of one proton during the entire acceleration cycle in RHIC, for proton energy from 25 GeV to 250 GeV and snakes on. Initial transverse coordinates were taken at random on the contour of progressively larger emittances. In addition to the unavoidable intrinsic resonances, also imperfection resonances were present, induced by closed orbit distortions of different rms values. At a constant acceleration rate the full process took several million turns.

Table 1: RHIC parameters for spin tracking

Acceleration mode		
Acceleration rate	$d\gamma/dt$	3.9 /s
Betatron tunes	ν_y, ν_x	29.18, 29.19
Harmonic number	h	360
RF voltage	V_{RF}	300 kV
Beta-star (all interactions)	β^*	10 m
Normalized emittance	ϵ_N	$20\pi 10^{-6}$ m-rad
Momentum spread	dp/p	± 0.00056
Storage mode		
Beam energy	E	250 GeV
Harmonic number	h	2520
RF voltage	V_{RF}	6,000 kV
Beta-star (6, 8 o'clock)	β^*	1 m
Momentum spread	dp/p	± 0.00019

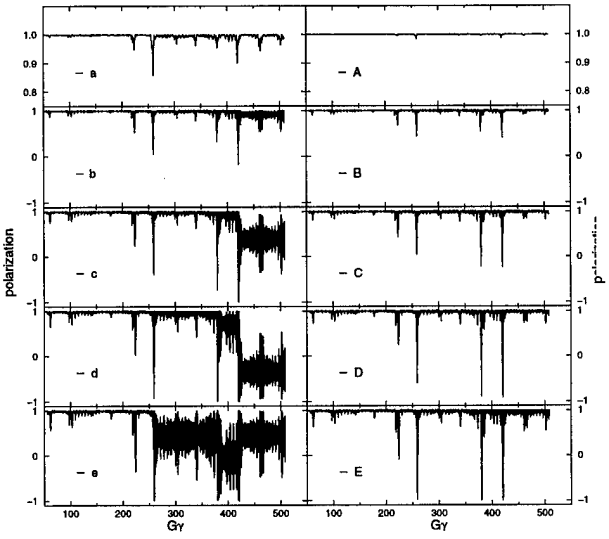


Figure 1: Spin tracking in acceleration mode. Plots on the left for vertical closed orbit deviation of 0.7 mm rms, on the right for 0.2 mm rms. From top to bottom, beam emittance of 0, 5, 10, 15 and 20 π mm-mrad.

The example showed that with a distorted orbit of 0.7 mm rms, the polarization is substantially reduced at high energies, while at 0.2 mm (the design value in RHIC, after corrections) the polarization will be preserved even at large values of the emittance. However it should be noted that a good orbit correction scheme for spin is not necessarily the best scheme for unpolarized beam, since the correcting dipoles may create additional spin resonances.

3.2 *Storage Mode*

Beam-beam collisions in RHIC for experiments will be performed at fixed energy and mostly with longitudinal polar-

ization. Spin rotators across the two collision regions will be used to rotate the spin from the vertical to the longitudinal and back to the vertical after the interaction. We studied by spin tracking the survival of beam polarization at fixed energy. In Figure 2 the longitudinal spin at an interaction point is plotted vs. number of turns (up to 10^6), for one particle extracted at random on a $20\pi 10^{-6}$ m-rad emittance on an uncorrected distorted closed orbit and snakes on. The polarization is shown to oscillate, but survive.

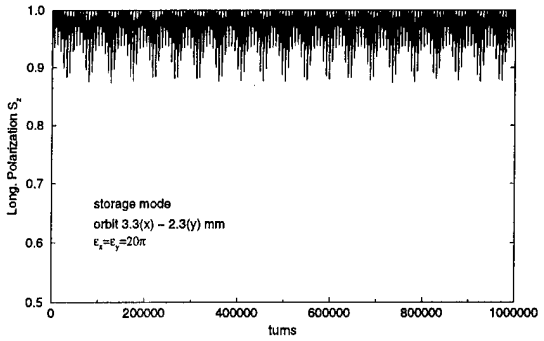


Figure 2: Spin Tracking at $\gamma = 250$. Longitudinal polarization at the 8 o'clock interaction point in RHIC. Snakes and spin rotators on.

3.3 Scanning Tune Space

The two previous examples were run at the nominal RHIC betatron tune. When the fractional value of the tune combines with the supersymmetry of RHIC lattice, one finds resonance strength enhanced. A typical value is the fraction 1/6 (or 5/6). Tune space has been previously explored [6]. We repeated the scanning of the tune line 1/6 by tracking a certain number of particles through a strong resonance $G\gamma = 411 - \nu_y$. The results, for fractional tunes close to the offending one, are shown in Figure 3. Systematic scan allowed us to determine the strength and the profile of the tune resonance.

To move the tune, it would be very cumbersome to run *Mad* and read its output for every tune in the range. To accomplish this, in *Spink* each quadrupole in the lattice is padded with two thin lenses of variable strength δq.

4 WORK IN PROGRESS

Many tracking runs have been executed, some on a large number of particles on a supercomputer at the Riken Institute, and the results averaged. Results in general agree with the conclusions drawn above from the tracking of one particle, but their discussion is beyond the limits of the present report.

5 ACKNOWLEDGEMENTS

We acnowledge frequent discussions with members of the Spin collaboration, at the AGS/Brookhaven and at Riken,

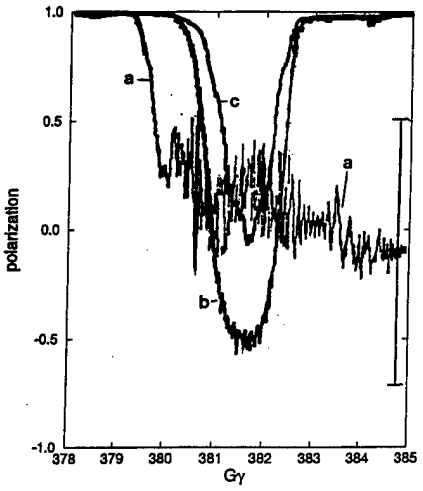


Figure 3: Crossing the $G\gamma = 381.82$ resonance with snakes on and varying the vertical fractional betatron tune in proximity of 1/16. (a) Spin tracking at $\Delta\nu = 0.16691$. (b) $= 0.16608$. (c) $= 0.16758$.

where the computing is done. In particular we acknowledge valuable comments and criticism of Drs. Ernest Courant, Thomas Roser and Michael Syphers.

6 REFERENCES

[1] Rhic-Spin Collaboration (T. Roser, Spokesperson, M. Syphers, Project Manager). Design Report BNL, Upton, NY, updated January 28, 1997

[2] Ya.S. Derbenev and A.M. Kondratenko, Sov. Phys. Doklady, 20 (1976) p.562.

[3] V.I. Ptitsin and Yu.M. Shatunov. in "Proc. Third Workshop on Siberian Snakes and Spin Rotators" (A. Luccio and T.Roser, Eds.) Brookhaven Report BNL-52453, p.15. Upton, NY, Sept. 12-13,1994

[4] E.D. Courant and R.D. Ruth. Brookhaven Report BNL 51270/UC-28, Upton, NY, September 12, 1980

[5] B.W. Montague. Phys. Reports 113, No.1 (1984) p.1-96

[6] S.Y. Lee. Lecture note presented at RCNP-Kikuchi School on Physics at Intermediate Energy, Osaka, Japan, Nov 15-19, 1992

[7] A.U. Luccio. Proc. Int. Adriatico Conf. (N.Paver, A. Penzo, M. Conte, Eds.) Trieste, Dec. 1995

[8] F.Ch. Iselin and J. Niederer. "Mad User's Manual". CERN/LEP-TH88, Geneva, July 13, 1988 (and later additions)

[9] J. Buon. Program *Snake*. Umpublished.

[10] A. Luccio, AGS/RHIC/Spin Note No. 039, Brookhaven, October 8, 1996

[11] A.W. Jackson. "Classical Electrodynamics". 2.nd ed. Wiley, NY 1962, p.558

[12] T. Roser. Private Communication.

FLAT BEAMS IN A 50 TeV HADRON COLLIDER

S. Peggs, M. Harrison, F. Pilat, M. Syphers,
Brookhaven National Laboratory, *
Upton, NY 11973, USA

1 INTRODUCTION

The basic beam dynamics of a next generation 50 x 50 TeV hadron collider based on a high field magnet approach have been outlined over the past several years [1, 2, 3]. Radiation damping not only produces small emittances, but also flat beams, just as in electron machines. Based on "Snowmass 96" parameters, we investigate the issues associated with flat beams in very high energy hadron colliders.

2 FLAT BEAMS

The energy loss per particle per turn is

$$U_s = \frac{C_g E_s^4}{2\pi} C < G^2 > \quad (1)$$

where E_s is the nominal storage energy, C is the total circumference, and $G = 1/\rho$ is the dipole bending strength. Angle brackets $<>$ denote an average over the entire design trajectory circumference. The constant C_g is

$$C_g = 8.846 \times 10^{-5}\ \mathrm{m\,GeV^{-3}}\ \text{(electron)} \quad (2)$$
$$= 7.783 \times 10^{-18}\ \mathrm{m\,GeV^{-3}}\ \text{(proton)} \quad (3)$$

The exponential damping times for the amplitudes of horizontal, vertical, and longitudinal oscillations are given by

$$\tau_{x,y,s} = \tau_0 / J_{x,y,s} \quad (4)$$

where the characteristic time $\tau_0 = 2T(E_s/U_s)$ is simply related to the revolution period, T. Natural partition number values $(J_x, J_y, J_s) = (1, 1, 2)$ are assumed. Note that $U_s \sim B\gamma^3$ and $\tau_0 \sim 1/(B^2\gamma)$, where B is the dipole field and γ is the Lorentz factor, independent of the lattice optics structure. The equilibrium rms momentum width is

$$\left(\frac{\sigma_p}{p}\right)^2 = \frac{C_q \gamma^2}{J_s} \frac{< G^3 >}{< G^2 >} \quad (5)$$

while the natural *normalized* rms horizontal emittance is

$$\epsilon_x \equiv \gamma \frac{\sigma^2}{\beta} = \frac{C_q \gamma^3}{J_x} \frac{< G^3 H >}{< G^2 >} \quad (6)$$

In these equations the constant C_q is

$$C_q = 3.832 \times 10^{-13}\ \mathrm{m}\ \text{(electron)} \quad (7)$$
$$= 2.087 \times 10^{-16}\ \mathrm{m}\ \text{(proton)} \quad (8)$$

while H is a property of the FODO cell optics

$$H = \gamma\eta^2 + 2\alpha\eta\eta' + \beta\eta'^2 \quad (9)$$

*Operated by Associated Universities Incorporated, under contract with the U.S. Department of Energy.

Energy, E_s	50.0	TeV
Peak luminosity, L	10^{34}	$\mathrm{cm^{-2}s^{-1}}$
Circumference, C	89.0	km
Dipole field, B	12.5	T
Number of bunches, M	20,000	
Initial bunch intensity, N	12.5×10^9	
Half cell length, L	260	m
Number of collision points	2	
Collision betas, β_x^*, β_y^*	5.0, 0.5	m
Natural emittance ratio, κ	0.1	
Full crossing angle, $\alpha/\sigma_y'^*$	10.0	
Separation distance, L_{sep}	50.0	
Bunch spacing	4.45	m
Stored energy	2.00	GJ
Synchrotron radiation power	492	kW
Dipole heat load	5.87	W/m
Damping time, τ_0	2.26	hr
Norm. rms H emittance, ϵ_x	0.59	μm
Natural mmtm. spread, σ_p/p	5×10^{-6}	

Table 1: Independent and dependent collider parameters.

(where α, β, γ, and η are Twiss functions). The momentum width is also independent of the lattice structure, and scales like $\sigma_p/p \sim \sqrt{B\gamma}$. By contrast, the natural horizontal emittance depends strongly on the lattice, scaling like $\epsilon_x \sim B^3 L^3$, where L is the half length of a FODO cell. The *normalized* emittance is independent of energy!

Figure 1 shows how the natural horizontal emittance may be tuned, for the primary parameters of Table 1, by adjusting the half cell length around its nominal value. The beam needs to be heated longitudinally to about $\sigma_p/p \simeq 10^{-4}$, to avoid significant intra beam scattering (IBS) consequences. If the linear coupling and the vertical dispersion in the arcs are both well controlled, the equilibrium vertical emittance will be much smaller the horizontal emittance, $\kappa \equiv (\epsilon_y/\epsilon_x) << 1$. There is no reason why hadron storage rings should not be able to achieve $\kappa \approx 0.1$ or less, in common with conventional electron storage rings.

3 BEAM-BEAM INTERACTIONS

The head on tune shift parameters are given by

$$\xi_{x,y} = \frac{r}{2\pi\gamma} \frac{N\beta_{x,y}^*}{\sigma_{x,y}^* \left(\sigma_x^* + \sigma_y^*\right)} \quad (10)$$

0-7803-4376-X/98/$10.00 © 1998 IEEE

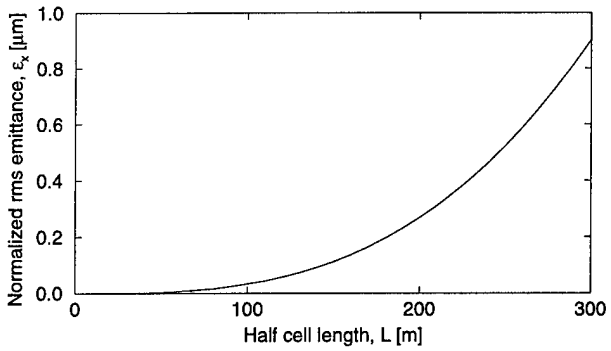


Figure 1: Equilibrium emittance versus half cell length

where N is the single bunch intensity, $r = 1.535 \times 10^{-18}$m is the classical radius of the proton, and values at the interaction point (IP) are denoted by a superscript asterisk*. The two tune shift parameters are made equal for flat beams by asserting that the β^* ratio is the same as the emittance ratio, so that

$$\kappa \equiv \frac{\epsilon_y}{\epsilon_x} = \frac{\beta_y^*}{\beta_x^*} = \frac{\sigma_y^*}{\sigma_x^*} << 1 \qquad (11)$$

The vertical tune shift due to n_{LR} long range beam-beam interactions near a single IP is approximately

$$\Delta Q_y \simeq \frac{n_{LR}}{\kappa} \frac{\xi_y}{(\alpha/\sigma_y'^*)^2} \qquad (12)$$

where α is the full vertical crossing angle, and $\sigma_y'^*$ is the vertical angular size at the IP. This expression is valid if the phase of the collisions is approximately ± 90 degrees, whether or not they occur in or beyond the first quadrupole.

When valid, this last expression is equivalent to the more general (but less convenient) expression

$$\Delta Q_{x,y} = \mp \frac{r}{2\pi\gamma} \left\langle \frac{\beta_{x,y}}{\Delta^2} \right\rangle MN \frac{4L_{sep}}{C} \qquad (13)$$

where M is the total number of bunches, Δ is the full vertical beam separation, and angle brackets <> indicate an average over the parasitic collision region, within $\pm L_{sep}$ of the IP. The horizontal tune shift is negative. This shows that, for fixed values of (MN), C, and Δ, the only two ways to ameliorate the long range tune shift are to reduce L_{sep}, and to reduce β values at the parasitic collisions.

If most of the parasitic collisions occur in the IP drift, the total horizontal tune shift is much smaller than the vertical,

$$\Delta Q_x \simeq -\kappa \, \Delta Q_y \qquad (14)$$

since $\beta_x/\beta_y \simeq \beta_y^*/\beta_x^* = \kappa$ in the drift. Even when there are many collisions in and beyond the first quadrupole, it is still reasonable to expect the horizontal long range tune shift to be less of a problem than the vertical.

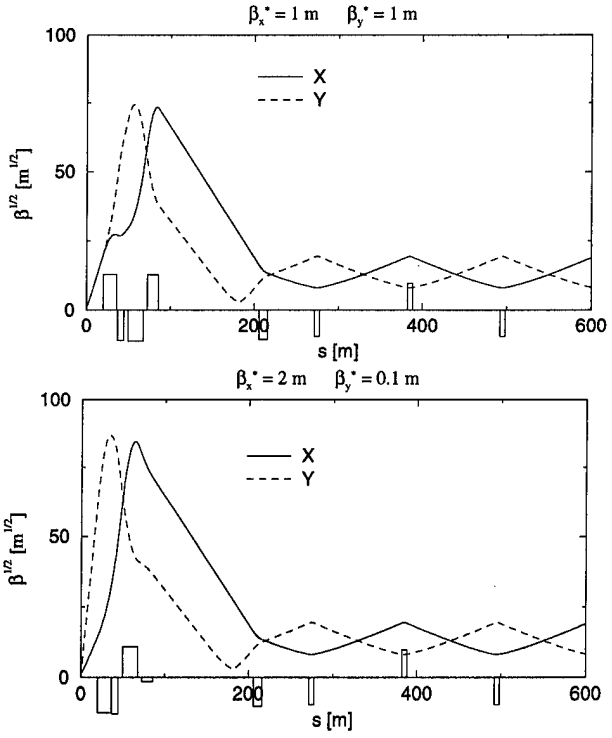


Figure 2: Round and flat ($\kappa = 0.05$) IR optics, with a common magnet layout.

4 INTERACTION REGION OPTICS

Flat beams allow the use of quadrupole doublets in the interaction region (IR), with many advantages over conventional triplet layouts. Figure 2 shows the same IR quadruplet layout accommodating both round and flat ($\kappa = .05$) optics. The height of each quadrupole rectangle is proportional to its strength, up to a maximum of about 500 T/m. While the round optics solution emulates a triplet, the flat optics solution emulates a shorter weaker doublet, with the fourth quad almost turned off. Because the "center of gravity" of the doublet is closer to the IP, maximum beta values $\widehat{\beta}$ with round and flat optics are comparable, even though the flat β_y^* value is reduced by a factor of 10. This is conveniently parameterized by an effective length, $L_{eff}^2 \equiv \beta^* \widehat{\beta}$, since L_{eff} is almost independent of β^* (at fixed κ). The horizontal and vertical effective lengths are approximately 74 m for the round optics, but are only 119 m and 27.4 m, respectively, in the flat optics. A true IR doublet layout would abandon the conservative round optics option, but would allow a beam splitting dipole between the two quadrupoles, justifying the nominal value $L_{sep} \approx 50$m.

The instantaneous luminosity may be written

$$L = \frac{M}{4\pi T} \frac{N^2\gamma}{\kappa \epsilon_x \beta_x^*} \qquad (15)$$

where T is the revolution period, showing that β_x^* may be increased as κ is decreased, with other parameters (including β_y^*) held constant. This explains why the collision betas in Table 1, $(\beta_x^*, \beta_y^*) = (5.0, 0.5)$m, are unusually large,

and is probably the most significant optical advantage of flat beams. Both the long range tune shifts and also $\widehat{\beta}$, and all the associated nonlinear problems, may be reduced by an order of magnitude.

5 STORE PERFORMANCE

A distinguishing characteristic of the strong emittance damping regime is the independence of integrated luminosity on the initial beam emittances. This allows the production of very dense beams and high luminosities with relatively weak bunch intensities. Particle burn-off then limits integrated luminosities and results in short store lengths. The Table 1 parameter set manipulates both the number and intensity of the bunches to produce $\sim$ 20 hr store lengths. The instantaneous luminosity shown in Fig. 3 increases rapidly at the beginning of the store as the emittances damp, rising to a peak of $10^{34}\mathrm{cm}^{-2}\mathrm{s}^{-1}$ when the beams have achieved equilibrium after 6 hr. The luminosity then falls to $4 \times 10^{33}\mathrm{cm}^{-2}\mathrm{s}^{-1}$ after 14 more hours, as the average bunch intensity falls.

Fig. 4 shows that the horizontal emittance achieves an equilibrium value determined by the cell length in 5 hr. The equilibrium vertical emittance, due to linear coupling and vertical dispersion, is assumed to result in a 10:1 emittance ratio. The bunch intensity shown in Fig. 5 falls by a factor of $\sim$ 2 during the 20 hr store, while the beam-beam tune shift parameters, determined by the bunch density and shape, peak at a relatively benign 0.003. Of more concern is the long range tune shift. With the IR outlined above, there are $\sim$ 40 parasitic crossings before the beams are fully separated. Fig. 6 shows the (vertical) crossing angle needed to restrict the vertical tune shift to 0.03 or less. Physical beam separations of only several mm are needed in the nearest quadrupoles. Enhancing the optimum store length by adding more particles increases the synchrotron power which must be absorbed by the cryogenic system, nominally 6 W/m emitted into the dipoles.

6 CONCLUSIONS

Flat beams produce denser bunches, allowing larger β^* values and leaving room for further performance enhancement. Luminosities in the range of $10^{35}\mathrm{cm}^{-2}\mathrm{s}^{-1}$ may be considered by reducing β^* values.

Flat beams also permit doublet IR optics, with more modest magnetic strength demands, lower maximum betas, easier beam separation, and reduced long range tune shifts.

7 REFERENCES

[1] "Proceedings of the Workshop on Future Hadron Facilities in the US", Fermilab-TM-1907, 1994.

[2] M. Syphers et al, Dallas, PAC Proc., 1995, p.431

[3] S. Peggs et al, Barcelona, EPAC Proc., 1996, p.377

Figure 3: Luminosity evolution during a 20 hour store.

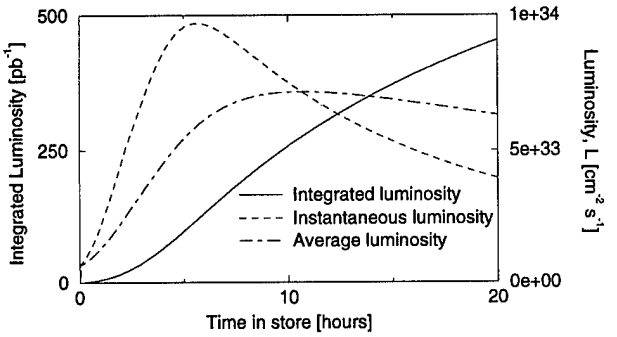


Figure 4: Emittance evolution, with radiation and IBS.

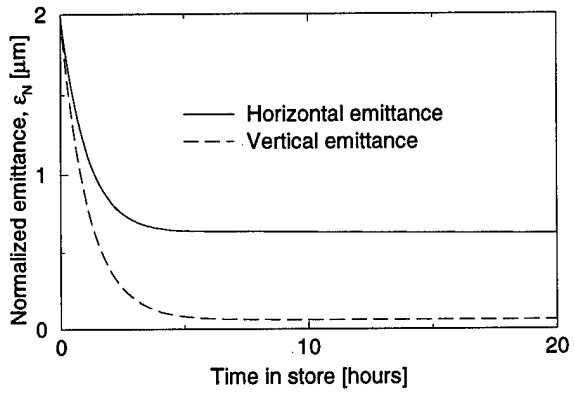


Figure 5: Beam-beam tune shift parameter evolution.

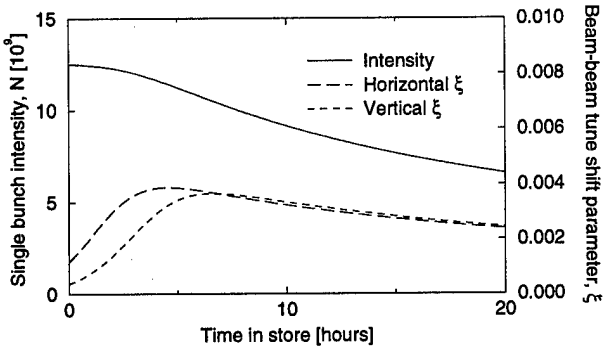
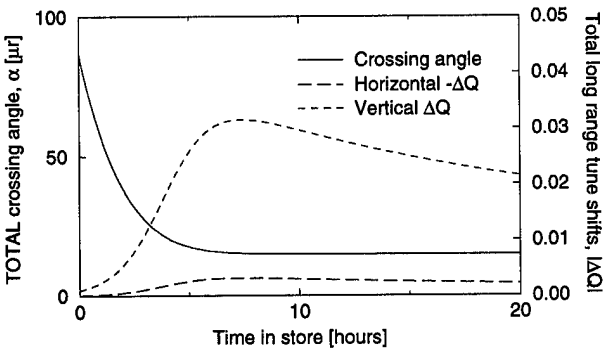


Figure 6: Long range tune shift evolution, per IR.



RHIC SEXTANT TEST: ACCELERATOR SYSTEMS AND PERFORMANCE*

F. Pilat, D. Trbojevic, L. Ahrens, K. Brown, R. Connolly, G.F. Dell, W. Fischer, J. Kewisch, W. MacKay, V. Mane, S. Peggs, T. Satogata, S. Tepikian, P. Thompson, N. Tsoupas, J. Wei
Brookhaven National Laboratory, Upton, NY 11973, USA

Abstract

One sextant of the RHIC Collider was commissioned in early 1997 with beam. We describe here the performance of the accelerator systems during the test, such as the mag-net and power supply systems, instrumentation subsystems and application software. We also describe a ramping test without beam that took place after the commissioning with beam. Finally, we analyze the implications of accelerator systems performance and their impact on the planning for RHIC installation and commissioning.

1 INTRODUCTION

A gold ion beam was transported through one sextant of RHIC on January 26, marking the successful beginning of the Sextant Test, the effective commissioning of one sixth of the RHIC accelerator. The commissioning milestones and the main physics results are discussed elsewhere in these proceedings [1][2]. The focus of this presentation is the performance of the various accelerator systems during the beam tests, from the point of view of the system commissioner. A description of the design of the systems and the planning for system integration can, again, be found elsewhere [3]. We will discuss the highlights of the beam systems one by one but will necessarily refer to individual papers for the details. We will also discuss some of the power supply tests that took place after the beam shutdown, in the areas that are closer to the physicist's concern such as ramping and stability. Finally we will analyze the experience gained from the sextant test in terms of system performance and its extrapolation to the full RHIC commissioning, and concern ourselves especially with system integration and application software.

2 SYSTEM PERFORMANCE WITH BEAM

We will now review the individual beam systems performance during the test. The AtR (AGS to RHIC transfer line [4]) or, more specifically the U and W line, was first commissioned in fall 1995 and the analysis of that test resulted in guidelines for modification and improvement of the application software. It was decided that each application for a system should consist of: a Manager, running on a Console level Computer (CLC), a Graphical User Interface, also running on a CLC and Accelerator Device Objects (ADOs) running on a Front End Computer (FEC)[5]. Managers provide global functionality, such as data handling, global commands, high level functionality such as physics algorithms and administration of resources. Managers are implemented as "virtual front end computers" and code is written in ADO style. The GUI is separated from the Manager so that the application can be operated as a building block in a sequencer program. ADO's are C++ class instances that provide interface to the hardware, device specific basic operations, and real time functionality.

2.1 Magnets and Power Supplies (PS)

All magnets performed flawlessly during the beam test. Once injected into RHIC, the beam hit the dump at the end of the sextant without need for corrections, validating the dipole integral transfer function measurements and magnet polarities. Phase advance measurements confirmed the quadrupole transfer functions and polarities. The sextant test power supply systems consisted of the PS for the main dipole bus (main quadrupole PS for RHIC), a 1000 A PS for the main quadrupole bus, a H/V quadrupole trim PS and 33 10 A PS for the independently powered dipole correctors.[3][6][7]. The power supplies delivered the required current of 550 A in the dipole and quadrupole buses. The power supplies worked very reliably in operations. Problem areas were a lack of precise current calibration between the DCCT, WFG and MADC readbacks, and occasional false power supply cutoffs and quench detection trips. These were caused by a sudden spurious increase in the set point on the current regulator, not requested by the WFG. The new ADO style manager for power supply control worked well, but improvements will be necessary in the low level communication software, as will be discussed later.

2.2 Instrumentation

2.2.1 Beam Loss Monitors (BLM)

The BLM system [3][8] was commissioned as a beamline system in single pass mode and the electronics for the Ring operation mode was also tested. During the beam test the hardware worked together with the low level software without problems. A new ADO style BLM Manager was developed for the test as well as a new BLM user interface. The BLM Manager and interface, a prototype of the way controls and user interface will be developed for RHIC commissioning, worked reliably during the run.

2.2.2 Beam Position Monitors (BPM)

The BPM system [3][8] worked satisfactorily in the U and W subsections of the AtR line. Orbit and difference orbit data were taken, and the orbit was flattened by the

* Work performed under the auspices of the U.S. Department of Energy

0-7803-4376-X/98/$10.00 © 1998 IEEE

orbit correction application. However, BPMs in the Sextant did not work reliably and that reduced the physics output of the test since precise and fast optics measurements require BPM data. During beam operations the BPM system was troubled by low level hardware and software problems, which manifested themselves as unreliable and inconsistent gain settings, orbit readings, etc. The ADO style BPM manager, after some initial configuration problems, worked but most of its functionality were rarely exercised because of the system problems.

2.2.3 Beam Current Monitors (BCM)

The current transformers were the same design and used the same application software as during the 1995 AtR test. Two additional transformers installed in the Y line and the Sextant performed reliably.

2.2.4 Beam Profile Monitors (Flags)

The flag hardware system, described in [3][9], was also already validated during the AtR test and the additional units installed in the sextant were essential to the successful outcome of the test. The high level software was completely rewritten, although not in ADO style, and provided 2 and 3 dimensional imaging (see Figure 1 for an picture of the beam on the last flag) as well as very useful online image fitting capabilities.

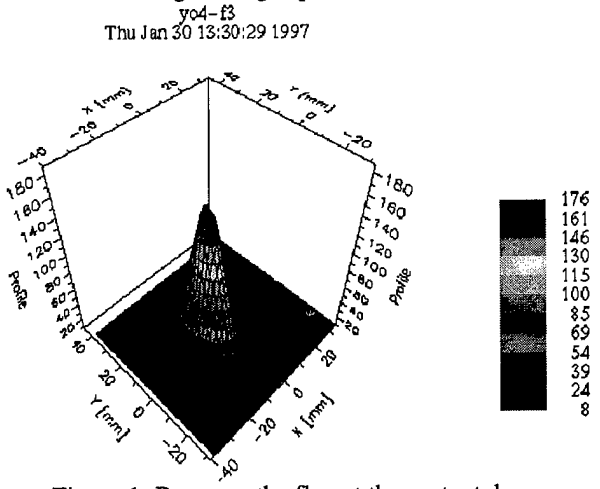


Figure 1: Beam on the flag at the sextant dump

2.2.5 Ionization Profile Monitor (IPM)

An IPM was commissioned that collects the electrons resulting from residual gas ionization during bunch passage. The prototype IPM measured vertical profiles of single bunches of Au nuclei containing 0.6 to 1 × 10^8 particles. These profiles were compared to those measured on a closeby flag and found to be in excellent agreement.[10]

2.3 Beam Permit

The goal of the beam permit link, which is described in more detail in [3], is to protect the cryogenic devices from the beam by preventing injection in RHIC and aborting the beam from storage. Only the first capability was commissioned during the sextant test. The system, which was tested before beam operations by simulating false inputs at the modules, performed well with beam. Three times the permit link disabled beam injection into the sextant because of closed vacuum valves.

2.4 Injection

The injection system into RHIC consists of a Lambertson septum magnet and 4 kicker modules, as described in [11]. At the beginning of the test a vertical corrector magnet, powered at 30 A, replaced the kickers by providing the requisite 1.86 mrad vertical deflection. Once good injection conditions were established, the kickers were brought on line. The kicker commissioning was very successful and all established goal were met: determining kicker timing and strength, measuring rise time and shot-to-shot stability for multi-bunch extraction. All requirements for RHIC injection were met [12]. A high-level application program to guide the beam into the sextant was only partially tested, because of lack of availability of BPM data.

2.5 RF

The RF contributions to the Sextant Test consisted of the preparation of 'RHIC like' bunches in the AGS and the high power operation of the 197 MHz storage RF system in the RHIC tunnel at the 4 o'clock area [13]. The final bunch coalescing of 8 to 4 bunches was implemented in the AGS. To perform this the AGS had to run 3 harmonic numbers in one cycle, with eight cavities running on harmonic 8 and two cavities running on harmonic 16 at injection, switching to harmonic 4 for the last coalescing. An intensity of 0.4 × 10^9 ions per bunch was attained. The RHIC low level RF Direct Digital Synthesizer (DDS) board successfully synchronized the AGS bunches to the RHIC 28 MHz bucket and provided the kicker triggers for beam extraction for the four successive bunches. The 28 MHz digital reference was sent back to RHIC via fiber optic link and, after bandpass filtering, used to drive the Step Recovery Diode (SRD) harmonic generator to derive the 197 MHz reference. This board also generated the bunch fiducial for triggering the BPM system. A single 197 MHz storage system cavity was successfully run at 1.1 MV gap volts after approximately 2 hours of RF conditioning, fully demonstrating the driver amplifier, power amplifier and cavity chain.

2.6 Cryogenics

The RHIC cryogenic system [14], which consists of the modified Isabelle refrigerator and new cryogenic components, was completed for the test from the refrigerator through 1 sextant up to the 4 o'clock valve box. The system performed very well during beam test: with a cold refrigerator, a helium delivery to load of about 4.5 K and mass flow of 50 g/s, cooldown was achieved in 48 h and cryogenics condition were stable throughout operations. After the beam test, a warmup time of only 24 h was achieved with the magnet warm-up heaters. During tests with beam and without beam several measurements were successfully done such as heat load measurements, warm pressure drop measurements, and the effect of an induced magnet quench on the system. Performance of cryogenics subsystems were found to be as per

manufacturers specifications. Functional tests of existing and new equipment proved very valuable to improve future performance of the system.

2.7 Vacuum

Large helium leaks were observed in the insulating vacuum volumes when the cold mass and helium lines were first pressurized. These leaks were located using helium profiling and repaired. A few smaller helium leaks were found and temporarily handled with additional turbopump stations. After cooldown the pressures in the insulating vacuum ranged from 10^{-7} to 10^{-3} Torr (at the leaks), adequate to maintain a low heat load to the cold surfaces. The warm bore beam vacuum sections were pumped down and maintained at 10^{-9} Torr with the ion sputter pumps. Neither an *in situ* bake nor titanium sublimation pumps were deployed for the first sextant. After cooldown the pressure readings at the cold cathode gauges of the cold bore beam vacuum sections ranged from 10^{-10} to 10^{-9} Torr, mostly due to the local outgassing of the gauge trees. The real pressure inside the cold bore was less than 10^{-11} Tor[15].

2.8 Controls and Database

The RHIC Control System [5] is the system that naturally integrates all others and as such benefited greatly from the beam test to validate its design. Design improvements from the analysis of the 1995 AtR run were included and overall the system performed well during beam operations. From the commissioner's point of view, the ADO programming environment proved to be a good framework for software development and high level applications worked reliably. Identified areas for future improvement include the low level asynchronous communication software, and the reliability of the FECs. A problem that will require attention is the scaling of the control system performance to the whole RHIC. A configuration database was developed for the Sextant Test to handle low and high level data requirements. High level applications relied directly on this database while at the low level configuration data for the FECs were handled via a networked file system. The latter functionality will be moved to the configuration database in the next phase of the project.

3 TESTS WITHOUT BEAM

After the test with beam was completed, the sextant was kept cold for 3 additional weeks in order to allow system tests without beam. The cryogenic system ran one additional full thermal cycle, the power supplies went through an extensive series of tests and some aspects of the high level software, such as the ramping manager and the sequencer, were exercised. During beam tests the main dipole bus was powered only by the flat-top power module, and the current was limited to less than 800 A. The goals of the power supply testing without beam [5][6] were to ramp the magnets to 5500 A with both the ramp and flat-top modules, to perform ramping cycles at the nominal ramp rate of 80 A/sec, to power the interaction region quadrupole shunts, to power all correction systems that were not used during beam tests (such as sextupoles and gamma-T quadrupoles) and to test thoroughly the quench protection system. All goals were accomplished. Dipole and quadrupole magnets were powered in series to 5500 A, 10% above nominal storage energy, and kept at full current for 12 hours, the time scale of a RHIC store. Over 200 ramp cycles were performed with ramp and flat-top modules run together from 500 to 5500 A at a rate of 80A/sec, also 10% above nominal. This allowed the high level ramping application software to be exercised together with the prototype sequencer for RHIC operations. All superconducting shunt buses in interaction regions 4 and 5 and the trim quadrupole circuits were powered to their maximum currents. The quench detection system was balanced for ramps to a threshold level of 0.025 volts, and was able to detect a dipole bus quench caused by a spot heater during ramping. Four magnet quenches were induced by warm-up heaters and the quench protection system performed as required by bringing the current down before any other magnet quenched. Problem areas identified included the poor performance of SCR switches, excessive noise on the current RTDL signal, and instability of the current set-point interface on the current regulator.

4 ANALYSIS AND CONCLUSIONS

Overall the Sextant test was a great success. From the systems point of view all fundamental design concepts of RHIC were validated: components, mechanical aspects, electrical systems, cryogenics, beam systems. Problem areas were discovered but nothing of the magnitude to impact the overall scope and plans for RHIC.

5 REFERENCES

[1] S.Peggs, "RHIC Status", These Proceedings
[2] J.Wei, et.al. "RHIC Sextant test -- Physics and Performance", These Proceedings
[3] D.Trbojevic, et.al., "Preparing Accelerator Systems for the RHIC Sextant Commissioning", These Proceedings
[4] N.Tsoupas, et al., "Focusing and matching properties of the AtR Transfer line", These Proceedings
[5] L.T. Hoff, "Object oriented APIs for accelerator control systems", These Proceedings
[6] R.Lambiase et.al."Power Systems for the RHIC First Sextant Test" These Proceedings
[7] G.Ganetis, "Electrical Systems", RHIC Accelerator Advisory Committee Meeting, March 1997
[8] T.J. Shea et.al., "Performance of the RHIC Injection Line Instrumentation Systems", These Proceedings
[9] R.L.Witkover, "Design of the Beam Profile Monitor System for the RHIC Injector Line", Proceedings of PAC 1995, Dallas, TX
[10] R.Connolly et.al.,"A Prototype Ionization Profile Monitor for RHIC", These Proceedings
[11] W.Fischer, et.al. "Beam Injection into RHIC", These Proceedings
[12] H.Hahn, et.al., "The RHIC Injection Kicker", These Proceedings
[13] J.Rose, et.al., "The RHIC 28 Mhz RF System", These Proceedings
[14] M.Iarocci, et.al., "RHIC 25 kW refrigerator and distribution system, construction, testing and initial operating experience",These Proceedings
[15] H.C. Hseuh, Private Communication

PREPARING ACCELERATOR SYSTEMS FOR THE RHIC SEXTANT COMMISSIONING *

D. Trbojevic, F. Pilat, L.Ahrens, D.Barton, T. Clifford, R.Connoly, W. Fischer, M. Harrison, W. MacKay, R. Olsen, S. Peggs, T. Satogata, S. Tepikian, P. Thompson, C.G. Trahern, and R. Witkover
Brookhaven National Laboratory, Upton, NY, 11973, USA

Abstract

The Relativistic Heavy Ion Collider (RHIC) construction is progressing steadily towards completion in 1999 when beams will circulate in both collider rings. One of the major tests of the RHIC project was the commissioning of the first sextant with gold ion beams in early 1997. This is a report on preparation of the RHIC accelerator systems for the first sextant test. It includes beam position monitors, timing, injection correction through the magnetic septum and kickers, current transformers, "flags" and the ionization beam profile monitors, beam loss monitors, beam and quench permit link system, power supply controls, and the configuration database system. The software and hardware development and coordination of the different systems before commissioning were regularly checked during bi-weekly, and (later) weekly, progress report meetings.

1 INTRODUCTION

The Relativistic Heavy Ion Collider (RHIC) construction has reached its final stage. The *sextant test* represents a crucial *proof of principle* for the whole RHIC machine. This report describes preparations of the accelerator systems for the test. It includes: Beam profile monitors (flags), Loss monitors (BLM), Beam current transformers (BCM), Beam and quench permit links, Power supply configurations, Ionization profile monitor (IPM), Injection kickers, Timeline events, Beam position monitors (BPM), and Database configuration. A goal of the RHIC *sextant test* was to verify the machine design and system performance by transporting a heavy-ion gold beam from the Alternating Gradient Synchrotron (AGS) through the already commissioned *U and W lines - ATR* , through the new *Y-arc line*, the magnetic septum-*Lambertson magnet*, through the sextant arc of the *yellow ring*, pass through the operating RF 200 MHz cavity, and through the high focusing triplet and *D0 dipole* magnets to reach a temporary beam dump. The sextant test required the same operating conditions as at RHIC injection (every magnet is at 4K temperature). During the test only the *yellow ring* was connected to the power supplies. The accelerator systems had to be prepared to steer the gold beam, to be able to measure the phase advance per cell, beam profiles, vertical and horizontal transverse emittances, transmission, losses etc. Preparations of the other systems in the *sextant test* are not mentioned in detail in this report. The test would not have been successful if magnets were not correctly installed, positioned, and electrically connected in the tunnel. This applies also to the cryogenic, vacuum, control system, power supply systems, etc. Very complicated installation procedures of cryogenic lines, valve boxes, vacuum beam pipes and other insulating vacuum connections were all part of the preparation for the *test*. Separate reports are available describing surveying and alignment procedures in RHIC [1]. Details of the cryogenic system [2], magnet installation, vacuum system, and other systems are also reported elsewhere [3].

* Work performed under the auspices of the U.S. Department of Energy

2 SYSTEM PREPARATION

Beam system commissioners were assigned before the *sextant test* and insured each system was progressing according to a coordinated plan. During preparation for the *sextant test*, sixteen commissioning meetings were held. This allowed integration between different systems and low and high level controls. At each meeting, first biweekly and later weekly, commissioners provided an update on their system with a separate report on a specific system.

- Beam Profile Monitors.

The beam profile monitors used in the *test* were the same type as during the AGS to RHIC beam line commissioning during the end of the 1995 (as previously reported [4]). Two additional profile monitors were installed at the end

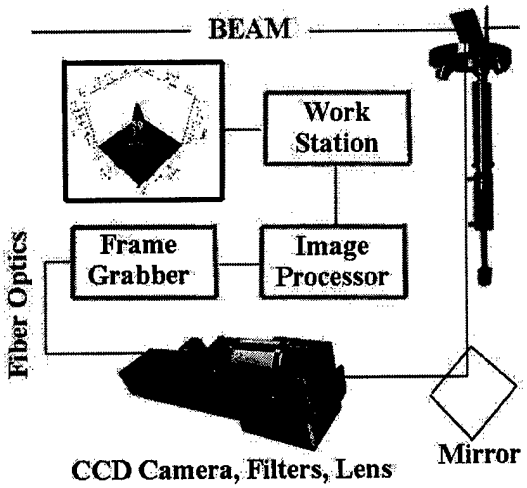


Figure 1: Beam Profile Monitor System

of the *y-arc* before the magnetic septum and at a temporary one at the end of the sextant. Preparation for the beam profile monitor system included new high level application software development which provided either two dimensional or even three dimensional beam profiles with inten-

0-7803-4376-X/98/$10.00 © 1998 IEEE

sity of the beam presented in the vertical axis. An automatic procedure fitted beam profiles to a Gaussian distribution, adjusting the σ_x and σ_y of the beams, the rotational angles of the beam ellipses in both *x-x'* and *y-y'* phase spaces, and the center of the beam position.(see the report at these proceedings [3]). The beam profile monitor system consists of a movable phosphor screen with mirror, CCD camera with filters, frame-grabber, image processor, and work station as shown in Figure 1. The beam loss monitor system (BLM) preparation for the sextant test included loss monitor bench calibration, installation in the RHIC tunnel, and signal checking. The sextant test operation of the system was in a single pass mode with many msec between the beam pulses, while for RHIC operations [5] different modes are being developed. The loss monitors were installed at each RHIC quadrupole. Every monitor was positioned between the two quadrupoles of parallel *blue* and *yellow* rings to record losses from both rings in the future.

- Loss monitors

Around the magnetic septum *the Lambertson magnet* and the injection kickers, more monitors were added. Signals from the loss monitors in the sextant test (more details are available in reference [5]) were brought to three service buildings where the integrator channels, high voltage power supplies, and MADC's (Multiplex Analog to Digital Converters) are located. Before the sextant test each monitor was tested in two ways from the control room. After the electrical connection was confirmed by a large resistor and applied voltage the signals from the MADC's were plotted by applying high voltage for a short time. The whole preparation procedure contributed to reliable system operation in the sextant test run [3].

- Beam current transformers

The beam current transformers used in the sextant test were of Integrating Current Transformer (ICT) type developed by Unser [7] for LEP. This design incorporates two toroidal transformer cores and is particularly suited to measuring the charge in short beam bunches. By passively stretching the initial pulse, the signal is converted downward in frequency prior to applying it to the transformer. This overcomes core losses at high frequencies, while preserving the relative charge and, in addition, allows the electronics to be located further from the detector. The charge transformers allowed precision measurements (to 1%) over a wide range of beam intensities. During the *sextant test* preparation two additional current transformers were installed: one upstream of the magnet septum at the end of the *y-arc*, and the second at the end of the sextant in front of the high focusing triplet quadrupoles.

- Beam and quench protection permit links

A new *beam and quench permit link* system has been designed for RHIC and partially commissioned during the *sextant test*. Full RHIC beam and quench protection permit links will be established when both rings are completed. A performance report of the system is presented elsewhere [3]. The system is also described in detail in reference [8]. The beam and quench permit links allowed beam entry into the RHIC sextant when RHIC accelerator support systems statuses were present. RHIC accelerator support systems include beam position and loss monitors, vacuum, power supply system status, and personnel safety. These systems report their status to the permit system. If any permit input or permit system connection fails, the beam permit system master module generates *blue* and *yellow* ring beam dump commands and triggers an abort event transmission. The 1 MHz carrier is created in a *master module* and the link is established throughout all other modules and back to the *master* unit (see Figure 2). There are three separate *links*: two quench protection links and one beam permit link. When one of the quench protection links is broken the whole beam permit link goes down. In the *sextant test* the three links were established around the RHIC sextant arc with a master and eight slave permit modules installed in the service buildings. An application program was developed during the preparation which displays the status of the link, location of a failure if occured, and the time stamp when the failure occured. A failure detected by the permit link in the sextant induces the shut-down of power to the *switching magnet* at the end of the previously commissioned *w-line*. This stops beam injection to RHIC.

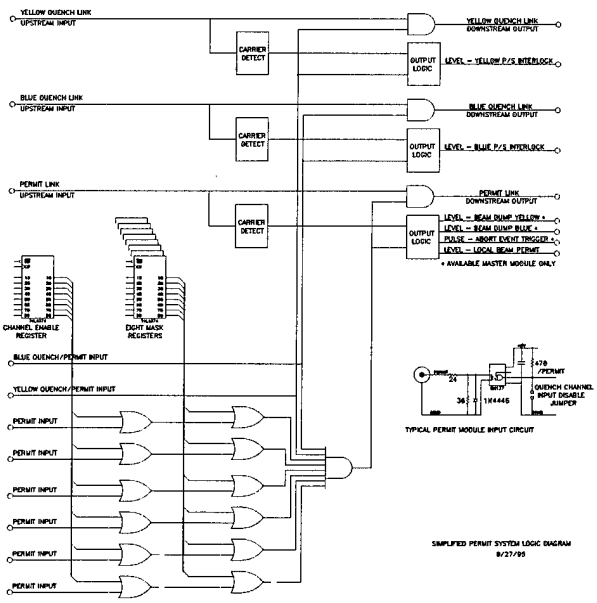


Figure 2: Beam and quench protection permit links logic diagram.

- Power Supply configurations

The ATR power supplies were provided to the: *switching magnet*, combined function magnets in the *y-arc*, the *Lambertson magnet*. Two separate quad buses, a dipole bus,

and every horizontal and vertical correction magnet were provided for the sextant. There was an additional trim quad magnet close to the end of the sextant connected to a power supply. More details about the lay-out and performance of the power supplies are reported elsewhere [3].

- Ionization profile monitor

A separate report [6] provides more details about this unique profile monitor developed during the preparation for the *sextant test*. The ionization profile monitor prototype was built to provide beam profiles from the electron signals which occur from the gold ion beam ionization of the residual gas in the beam vacuum pipe. A dipole magnet was used to prevent electron dispersal.

- Injection kickers

The injection kickers were not necessary for the *sextant test* because there was not circulating beam present and the beam could be steered by the correction magnets. But the whole injection kicker system was prepared on time to be completely commissioned during the *test*. A high level application code was developed during the preparation period to allow automatic tuning through the magnetic septum and the kickers as well as matching of the beam line to the RHIC.

- Timeline events

New RHIC beam events for the *sextant test* were established in addition to two existing AGS extraction events. These are three events for the wave form generators, and four events for the beam permit system: beam abort event, permit reset event, quench link reset event, and time stamp event to record the failure of the permit system.

- Beam position monitors-(BPM)

The BPM system will be operating in multi-turn mode when the RHIC accelerators are completed. The *sextant test* used them already in [9] one pass mode during commissioning of the ATR. Every corrector-quadrupole-sextupoles (CQS) assembly has a BPM's installed and optically and electrically checked [1]. The surveying data of the BPM's were used by a high level application code to correct for a small misalignment with respect to the quads (of the order of $\sigma = 0.6$mm). During the sextant preparation period a completely new high level application code was developed. During the sextant test not every BPM was connected to the control system.

- Database configuration

Beginning with the AtR test in 1995, configuration databases were developed to provide data for both controls applications and general information with use of the SYBASE relational database management system. For the 1996 sextant test these AtR data structures were both replicated and developed further as the sextant test configuration database. During the preparation for the *sextant test* all systems (BPM, BLM, Power Supply, flags, etc.) were developed with appropriate connections to the database.

3 CONCLUSIONS

A well organized system integration and preparation for the *sextant test* was essential for successful operation. Although there were few delays in development of some systems with respect to the coordinated plan, the total *sextant test* preparation has been very successful. This was shown by the superb performance [3] of almost every system during the test operation.

4 ACKNOWLEDGEMENTS

We would like to especially thank: the people from the magnet group for making superb quality magnets, measuring them with a highest possible precision, and defining their electrical and magnetical properties without a single error; the vacuum and installation group who made this test possible by an extreme effort; the surveying group which aligned the element to a high precision, where the beam went through the sextant without the use of any corrector magnet; and the cryogenic group for highly professional performance.

5 REFERENCES

[1] D. Trbojevic, A. Jain, S. Tepikian, R. Grandinetti, G. Ganetis, J. Wei, and F. Karl, "Alignment of the High Beta Magnets in the RHIC Interaction Region", these proceedings.

[2] M. Iarocci, et.al., "RHIC 24 kW refrigerator and distribution system, construction, testing, and initial operating experience", these proceedings.

[3] F. Pilat, "RHIC Sextant Test - Accelerator Systems and Performance", 7P.05,these proceedings.

[4] R.L. Witkover, "Design of the Beam Profile Monitor System for the RHIC injection line",Proceeding of the 1995 Particle Accelerator Conference and International Conference on High- Energy Accelerators, held May 1-5, 1995, Dallas, Texas, pp. 2589-2591.

[5] R.L. Witkover, "RHIC Loss monitors", these proceedings.

[6] R. Connolly, " A Prototype Ionization Profile Monitor for RHIC.", 5P.47, these proceedings.

[7] K. B. Unser, "Measuring Bunch Intensity, Beam Loss and Bunch Lifetime in LEP", Proc. IEEE Particle Accelerator, Conference EPAC 90, Nice, France, June 1991, pp.786-788.

[8] R. Conkling, "V120 RHIC Beam Permit System Module", RHIC-Internal Report, (available on world wide web as: www.rhichome.bnl.gov:80/Hardware/permit/permit.htm).

[9] P.R. Cameron, M.C. Grau, M. Morvillo, T.J. Shea, R.E. Sikora, "RHIC Beam Position Monitor Characterization", Proceedings of the 1995 PAC and International Conference on High Energy Accelerators, held May 1-5, 1995, Dallas, Texas, pp. 2458-2501.

SYNCHROTRON RADIATION DOMINATED HADRON COLLIDERS

E. Keil, CERN, Geneva, Switzerland

Abstract

The synchrotron radiation damping time becomes small compared to the beam lifetime when the beam energy in a circular hadron collider reaches about 100 TeV and the dipole field about 10 T. This paper discusses an approach to the design of these colliders such that the desired performance parameters, e.g. beam-beam tune shift and luminosity are achieved at the equilibrium values of the beam emittance and momentum spread. The design procedure is described, involving the design of the interaction regions, the arcs, and the RF system. The thresholds and/or growth rates of several collective effects, and the growth times for intra-beam scattering are estimated. The consequences of the synchrotron radiation are discussed in the conclusions.

1 INTRODUCTION

As noticed in the high-field option of really large hadron colliders (RLHC) [1], the damping time τ_z of the oscillations in the three degrees of freedom due to the emission of synchrotron radiation becomes about an hour at a beam energy $E \approx 100$ TeV and a dipole field $B \approx 12$ T:

$$\tau_z(h)J_z = \frac{16644}{E(\mathrm{TeV})B(\mathrm{T})^2}\left(\frac{C}{2\pi\rho}\right) \qquad (1)$$

Here, z labels the plane (x for horizontal, y for vertical betatron oscillations, s for synchrotron oscillations), J_z is the damping partition number, C is the circumference and ρ the bending radius in the arcs of the collider; $C/2\pi > R$ includes the long straight insertions for the experiments. Scaling their length like $\sqrt{E}$ from the SSC [2], and assuming four interaction regions, one gets $C/2\pi = R + 1708$ m.

Since the beam lifetime and the duration of a colliding beam run are usually many hours, the beams have the equilibrium beam parameters, given by the equilibrium of quantum excitation and synchrotron radiation damping, during most of their lifetime. Designing an RLHC such that the beam-beam limit and the desired luminosity are achieved at the equilibrium beam parameters has the advantage that the emittances of the injected and circulating beams are decoupled, and that the collider is insensitive to slow phenomena with growth times longer than the damping time.

2 DESIGN PROCEDURE

The design procedure for e^+e^- colliders [3] in the DESIGN program [4] adjusts the arc and RF system parameters to achieve a specified luminosity. Adapting it to p-p colliders implies setting the mass m_p, classical radius r_p, and Compton wavelength λ_p to their proton values.

2.1 Interaction Region Design

For round beams with equal normalised horizontal and vertical emittances $\epsilon_z = \gamma\sigma_z^2/\beta_z$, equal β-functions and vanishing dispersion at the interaction point IP, and ignoring crossing angle and "hourglass" effect, luminosity L and beam-beam tune shift ξ are with bunch population N and collision frequency f:

$$L = \frac{N^2 f}{4\pi\sigma_x\sigma_y} \qquad \xi = \frac{Nr_p}{4\pi\epsilon_n} \qquad (2)$$

The beams cross at an angle in order to separate them at the parasitic collision points at multiples of half the bunch spacing near the interaction point. Solving (2) for Nf yields with the usual relativistic factor γ:

$$Nf = L\beta_x r_p/(\gamma\xi) \qquad (3)$$

The choices of $\beta_x = \beta_y$ at the IP and of the crossing angle are related [5]. Tab. 1 shows the assumed and resulting IP parameters. The bunch spacing s fixes f by $s = c\beta/f$; c is the speed of light. For given $\beta_x = \beta_y$ and L, N follows from (3), and ϵ from (2). The beam-beam lifetime $\tau_{bb} = (r_p/c\sigma_{\mathrm{tot}})(\beta_x C/\gamma\xi)$ is calculated for one interaction region, independent of L, proportional to C and $1/E$, and small for good performance parameters (small β_x and large ξ); $\sigma_{\mathrm{tot}} = 120$ mb is the total cross section.The small RMS radii $\sigma_x = \sigma_y$, compared to LHC [6] or SSC [2], are largely due to the higher energy and adiabatic damping.The normalised emittance ϵ_n has about 1/3 of the SSC value.

Table 1: Interaction region parameters for a 100 TeV p-p collider with $\xi_x = \xi_y = 0.003$ [6], $\beta_x = \beta_y = 0.5$ m, $s = 3.75$ m, total inelastic cross section $\sigma_{\mathrm{inel}} = 60$ mb.

Bunch population $N/10^9$	9.03
Normalised emittance ϵ_n/nm	367.4
RMS beam radius $\sigma_x = \sigma_y/\mu$m	1.313
RMS divergence $\sigma'_x = \sigma'_y/\mu$r	2.626
Luminosity L/(nbs)$^{-1}$	30.1
Events/collision $n_c = L\sigma_{\mathrm{inel}}/f$	22.6
Beam-beam lifetime τ_{bb}/h	42.4

2.2 Arc Design

The arcs should provide just enough quantum excitation to achieve the emittance listed in Tab. 1. The average arc radius $R > \rho$ includes space for the quadrupoles, sextupoles, etc., and short straight sections in the arc cells. In separated function FODO cells with $\mu_x = \mu_y$, normalised horizontal emittance ϵ_n, arc tune Q and cell length L_p are related by:

$$\epsilon_n = \frac{1}{2}\frac{55\lambda_p}{32\sqrt{3}}\frac{RF(\mu)}{J_x\rho}\left(\frac{\gamma}{Q}\right)^3 \qquad L_p = \frac{\mu_x R}{Q} \qquad (4)$$

0-7803-4376-X/98/$10.00 © 1998 IEEE

The correction factor for finite phase advances $F(\mu)$ [7] tends towards unity for $\mu_x = \mu_y \to 0$. The insertions do not contribute to quantum excitation and momentum compaction $\alpha = (2\pi R/C)Q^{-2}$. I assume that round beams with $\epsilon_y \approx \epsilon_x$ are achieved by coupling horizontal and vertical betatron oscillations, and apply a factor 1/2 to the traditional form of (4). Tab. 2 shows the parameters of the arcs. The dipole field shown [8] is needed in order to obtain colliders in the parameter range I wish to study.

Table 2: Parameters of the arcs of a 100 TeV p-p collider with $B = 12$ T, $\rho = 27.78$ km and $R/\rho = 1.25$ [6]

Arc tune Q	80.62
Phase advance $\mu_x/2\pi = \mu_y/2\pi$	0.25
Cell length L_p/m	677
Maximum amplitude function β_x/m	1156
Maximum dispersion D_x/m	8.93

The cold vacuum chamber acts as a cryopump. The perforated beam screen absorbs the synchrotron radiation. Its temperature should be much higher than that of the vacuum chamber for good Carnot efficiency. Collective effects, in particular the resistive wall instability (cf. Section 3.1), and the forces during a magnet quench must also be considered.

2.3 Synchrotron Radiation

Tab. 3 shows several parameters related to the synchrotron radiation. The total synchrotron radiation power P per beam is three orders of magnitude higher than the 3.6 kW in the LHC. The normalised power $p = P/2\pi R$ is almost two orders of magnitude higher than the 0.2 W in the LHC. The photon flux Φ, the number of photons per metre of arc and per second, is about half the value in LEP2, operating at 96 GeV and a total current of 14 mA [9].

Table 3: Synchrotron radiation parameters of a 100 TeV p-p collider with synchrotron radiation loss $U_s = 28$ MeV and horizontal damping time $\tau_x = 1.5$ h.

Beam current I/mA	116
Synchrotron radiation power P/MW	3.24
Normalised radiation power p/Wm^{-1}	14.8
Critical energy E_c/keV	12.9
Photon flux $\Phi/10^{15}$(sm)$^{-1}$	23.3

2.4 RF System Design

The values of U_s in Tab. 3, σ_e and τ_q in Tab. 4, and the parameters of the super-conducting RF cavities, i.e. frequency $f_{\rm RF} = 400$ MHz, unloaded shunt impedance $Z = 60.3$ GΩ/m and filling time $T_f = 2.4$ s, similar to the LHC values, suffice for the design of the RF system. The DESIGN program finds the RF system parameters listed in Tab. 4; σ_e and σ_s are small. However, the bunch area $4\pi E\sigma_e\sigma_s/c$, is comparable to those of LHC and SSC.

Table 4: Parameters of the RF system of a 100 TeV p-p collider with circumference $C = 228.9$ km, harmonic number $h_{\rm RF} = 305415$, and quantum lifetime $\tau_q = 24$ h.

Voltage $V_{\rm RF}$/MV	35.9
Relative RMS energy spread $\sigma_e/10^{-6}$	6.53
Bucket height/10^{-6}	22.5
Synchrotron tune $Q_s/10^{-3}$	1.27
Bunch length σ_s/mm	27.5
Bunch area $4\pi E\sigma_e\sigma_s/c$/eVs	0.754

The time needed for a particle to radiate all its energy, and thus also the time needed for acceleration to the operating energy (when synchrotron radiation is neglected) is one half of τ_x. If the acceleration time T is to be shorter than $\tau_x/2$, the peak RF voltage must be higher than that listed in Tab. 4 in the ratio $\tau_x/(2T)$.

3 COLLECTIVE EFFECTS

The resistive wall instability, coherent synchrotron tune shift, longitudinal microwave instability, and transverse mode coupling instability TMCI are important [10] for the RLHC [11]. I only study the dominant contribution, and assume injection at 5 TeV, and a bunch area $4\pi E\sigma_e\sigma_s/c = 1$ eVs there. Below, I is the total beam current, and I_b is the bunch current. The effective impedances $Z_{\rm eff}$ are the weighted sums of $Z(\omega)$ and the bunch power spectrum [12]. Tab. 5 lists thresholds and growth rates at the energies where they are most critical.The longitudinal microwave and the transverse mode coupling instabilities are below threshold by good factors [13], and not discussed.

3.1 Transverse Resistive Wall Instability

The growth rate of the resistive wall instability τ_w^{-1} is [12]:

$$\tau_w^{-1} = \frac{r_p\bar{\beta}IF_w}{eZ_0\gamma b^3}\sqrt{\frac{\mu_0\rho_w Cc}{\pi(n-Q)}} \qquad (5)$$

Here, $(n - Q) = 0.25$ is the tune of the n-th mode, Z_0 is the impedance of free space, b is the radius of the beam screen, and $\bar{\beta} \approx R/Q$ is the average β-function. The wall penetration factor $F_w = 7.17$ describes the effects of a beam screen similar to that in the LHC [6], consisting of a thin inner Cu layer and a thicker layer of stainless steel. In the LHC, about half the wall resistivity is caused by the 10 % of the circumference with a Cu vacuum chamber at room temperature. I ignore this factor in the calculation of the growth rates. The growth rate τ_w^{-1} in Tab. 5 corresponds to 147 turns, which can be handled by feedback systems. Resistivity and thickness of the inner Cu layer are

critical issues in the design of the beam screen in the LHC [14]. If they are both increased by the same factor, the growth rates and the forces on the screen due to a magnet quench remain constant. This might open the possibility of reducing the cryogenic load of the beam screen by operating at a higher temperature. The resistive power losses due to the image current are much smaller than the synchrotron radiation power.

Table 5: Growth rates and threshold impedances at 100 TeV except where stated otherwise. The beam screen has a radius $b = 0.03$ m and consists of two layers. The inner layer is 50 μm of Cu at 5 to 20 K with a resistivity $\rho_w = 1.8 \cdot 10^{-10}$ Ωm, the outer layer is stainless steel.

Resistive wall growth rate at 5 TeV $\tau_w^{-1}/\mathrm{s}^{-1}$	8.88
Coh. synchrotron tune shift $\Im(Z_\mathrm{L}/n)_\mathrm{eff}/\mathrm{m}\Omega$	25.8
Long. μ-wave instability $\lvert(Z_\mathrm{L}/n)_\mathrm{eff}\rvert/\Omega$	0.968
TMCI threshold $\Im(Z_\mathrm{T})_\mathrm{eff}/\mathrm{G}\Omega\mathrm{m}^{-1}$ at 5 TeV	0.575

3.2 *Coherent Synchrotron Tune Shift*

To preserve longitudinal Landau damping, the synchrotron tune shift must remain smaller than the synchrotron tune spread. This leads to an upper limit for the imaginary part of the effective longitudinal impedance [10]:

$$\Im\left(\frac{Z_\mathrm{L}}{n}\right)_\mathrm{eff} \leq \frac{6}{\pi^3}\frac{h_\mathrm{RF}^3 V_\mathrm{RF}}{I_b}\left(\frac{2\pi\sigma_s}{C}\right)^5 \qquad (6)$$

The coherent synchrotron tune shift is driven by the longitudinal broad band impedance that is dominated by the shielded bellows [12] in the LHC. Assuming that the beam screen radius and the number of bellows per unit length are similar to those in the LHC, the effective longitudinal impedance $\Im(Z_\mathrm{L}/n)_\mathrm{eff} \approx 0.1\ \Omega$ is independent of the machine circumference, and about an order of magnitude higher than the threshold listed in Tab. 5. Increasing the harmonic number h_RF and raising the RF voltage V_RF do not help in overcoming this potential problem. The only promising way of increasing the threshold is increasing σ_s by a factor $10^{1/5} \approx 1.6$, by exciting the synchrotron oscillations with RF noise, by reducing the damping partition number J_s, or by reducing the slope of the RF wave form with a second RF system at a higher frequency [15]. Since the cut-off due to the bunch length is well above the resonant frequency of the bellows, the shorter bunches than in the LHC should not have much effect on the effective longitudinal impedance.

3.3 *Intra-Beam Scattering*

Intra-beam scattering IBS causes growth of the oscillation amplitudes. The amplitude growth times for synchrotron oscillations $\tau_s = 1.5$ h and for horizontal betatron oscillations $\tau_x = 3.2$ h, obtained with the actual β-functions and dispersion in the arc cells, are only about twice the corresponding synchrotron damping times. The vertical intra-beam scattering time is negative, implying damping, and orders of magnitude larger than the other two. In more tightly focused bunches, IBS may become a limitation [13].

4 CONCLUSIONS

An inevitable consequence of designing RLHCs to synchrotron radiation damping times of the order of hours is the synchrotron radiation power P. When (1) is used to eliminate B, P scales as follows:

$$P \propto E^{3/2} L \beta_x \xi^{-1} \tau_x^{-1/2} \qquad (7)$$

In the same variables, the stored energy G in one beam is:

$$G = EIC/ce = P\tau_x/2 \propto E^{3/2} L \beta_x \tau_x^{1/2}/\xi \qquad (8)$$

Eqs. (7) and (8) demonstrate how P and G are related by τ_x: For a given performance in terms of E, L, β_x and ξ, and large τ_x, P is small and G is large, while for small τ_x, P is large and G is small. Numerically, the stored energy in one beam is $G = 8.83$ GJ. This figure should be compared to 0.33 GJ for the LHC [6], and 0.4 GJ for the SSC [2].

Designing RLHCs such that the synchrotron radiation damping time is of the order of an hour and that the desired beam-beam tune shift parameter $\xi = 0.003$ and luminosity $L = 30\ (\mathrm{nbs})^{-1}$ are reached at the equilibrium beam parameters leads to interaction region, arc and RF system parameters not too far from extrapolated LHC and SSC parameters. The coherent synchrotron tune shift, driven by the longitudinal broad band impedance of the shielded bellows is above threshold by about an order of magnitude, unless one or the other of the measures listed in Section 3.2 are taken. The IBS growth times are only a factor of two larger than the synchrotron radiation damping times.

5 REFERENCES

[1] M.J. Syphers *et al.*, Part. Accel. Conf. (Dallas 1995) 431.

[2] SSC Central Design Group, SSC-SR-2020 (1986).

[3] J. Rees and B. Richter, SLAC Report SPEAR-167 (1973).

[4] DESIGN program written by P.M. Gygi-Hanney.

[5] E. Keil *et al.*, LHC Project Report 88 (CERN, 1997).

[6] The LHC Study Group, CERN/AC/95-05 (LHC) (1995).

[7] H. Wiedemann, PEP Note-303 (1979).

[8] L. Rossi, Proc. 34-th Eloisatron Workshop (Erice, 1996).

[9] The LEP2 Team, CERN-AC/96-01 (LEP2) (1996).

[10] J.T. Rogers, Cornell University CBN 96-14 (1996).

[11] G. Dugan *et al.*, Cornell University CBN 96-18 (1996).

[12] F. Ruggiero, Particle Accelerators **50** (1995) 83.

[13] E. Keil, CERN/SL/97-13 (AP) (1997).

[14] M.M. Karliner *et al.*, Particle Accelerators **50** (1995) 153.

[15] T. Linnecar, private communication (1996).

SUMMARY OF THE SINGLE-BEAM COLLECTIVE EFFECTS IN THE LHC

F. Ruggiero, J.S. Berg, O. Brüning, F. Caspers, M. Morvillo, CERN, Geneva, Switzerland
and M. D'Yachkov, TRIUMF, 4004 Wesbrook Mall, Vancouver, B.C., Canada V6T 2A3

Abstract

Single beam collective effects can limit the performance of the LHC and, together with parasitic losses, impose constraints on the design of the components of the LHC vacuum system. Because of the large number of bunches in the LHC, coherent losses and multibunch instability rise times generated by the impedance items can be rather large. For example, the vacuum chambers of the main experiments can lead to large parasitic losses and a continuous feedback from the impedance calculations during their design process is desirable. We first summarise the current status of the impedance model for the LHC and estimate rise times and threshold currents for different instabilities. In a second step, we discuss possibilities of controlling these instabilities, using feedback systems and Landau damping.

1 INTRODUCTION

The performance of the LHC will depend on the beam intensity, which may be limited by collective effects unless the impedance of the different vacuum chamber discontinuities is kept below certain limits. At the design stage of the machine, a fast and continuous feedback from impedance calculations or measurements to hardware builders is thus necessary. An impedance database program (ZBASE [1]) has therefore been setup and already successfully applied to estimate the LEP impedance budget: it helps keeping track of all the known impedance sources, of the corresponding betatron functions and of the input files used by different programs, such as ABCI or MAFIA, to compute high order modes and loss factors for several bunch lengths. In the near future, a further interface is foreseen to existing beam dynamics codes for detailed calculations of multibunch transverse mode-coupling and microwave instability thresholds both in the LHC and SPS.

In Sec. 2 and 3, we review parasitic losses and impedance estimates recently obtained for several LHC components, mentioning also some work in progress. We then present in Sec. 4 the results of the program VLASOV [2] for calculations of coherent mode frequencies including multibunch mode coupling. Finally we discuss possibilities of controlling potentially unstable modes using feedback systems and Landau damping [3]. The ongoing activity concerning collective effects in the LHC, including recent results on space charge, Laslett coefficients and the electron cloud instability, is documented on the world wide web at the address `http://wwwslap.cern.ch/collective/`.

2 PARASITIC LOSSES

2.1 *Beam screen*

The LHC beam screen is cooled at a temperature ranging from 5° to 20° K. It is a stainless steel pipe with a 50 μ copper coating that reduces its surface resistance, thus minimising at the same time transverse resistive wall instability and beam-induced wall heating. At top energy and for nominal beam parameters, the classically computed resistive wall heating of the LHC beam screen is 75 mW/m. Owing to anomalous skin effect and surface roughness, however, this value could be significantly underestimated. Since the parasitic heating scales with the square of the beam current, for the ultimate beam intensity of 850 mA, it may become comparable to the synchrotron radiation power loss of 326 mW/m. A programme of surface resistance measurements at different temperatures, frequencies, and magnetic field intensities has therefore been launched to provide a realistic heating budget for the LHC cryogenic system and to optimise the fabrication process of the beam screen. The measurements are based on the comparison of the quality factors for even and odd TEM modes excited in a cylindrical structure with two inner conductors [4]. Preliminary results at cryogenic temperatures (without magnetic field) indicate a surface resistance about a factor two larger than previously estimated.

Resistive losses in the longitudinal welds of the beam screen, with its new racetrack geometry, are 20 mW/m for nominal and 50 mW/m for ultimate beam intensity. Other losses, associated with TEM coaxial modes excited by the pumping slots and travelling synchronously with the beam are presently estimated to be less then 10 mW/m for nominal and 25 mW/m for ultimate beam intensity. About half of this power will be deposited on the cold bore at 1.9° K.

2.2 *Experimental vacuum chambers*

Another source of parasitic losses are the experimental beam pipes with their cavity like structures which give rise to a large number of narrow band HOM's. For a narrow band impedance, the wake fields of different bunches can overlap, leading to a coherent power loss proportional to the square of the total number of bunches N_b. If $\omega_0 = 2\pi \cdot f_{rev}$ is the angular revolution frequency, Q_b the charge per bunch, τ_n the position of the n^{th} bunch , σ_z the bunch length and $Z_{||}$ the longitudinal impedance, we have

$$P_{coh.} = -f_{rev}^2 \cdot Q_b^2 \cdot \sum_{p=-\infty}^{+\infty} \left| \sum_{n=1}^{N_b} \exp\left(-ip\omega_0 \cdot \tau_n\right) \right|^2 \times \exp\left(-[p \cdot \omega\sigma_z]^2/c^2\right) \cdot Z_{||}(p\omega_0). \quad (1)$$

0-7803-4376-X/98/$10.00 © 1998 IEEE

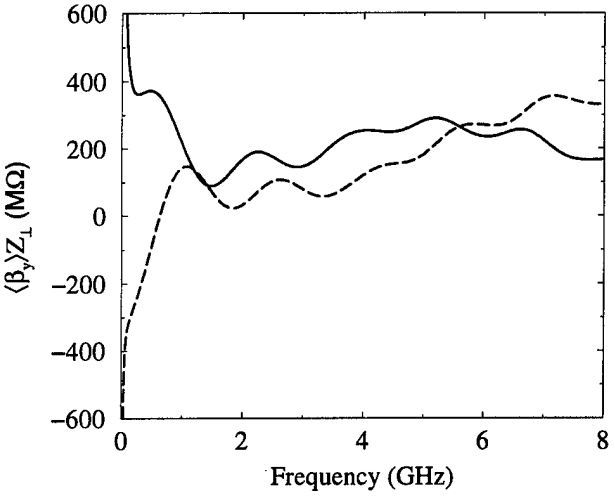


Figure 1: Vertical broad band impedance times average β function for the LHC: real (solid line) and imaginary part (dashed line).

The LHC has 2835 bunches with a bunch length of 13 cm at injection and 7.5 cm at top energy. At the moment there are four experiments foreseen in the LHC: the two main experiments CMS and ATLAS, plus LHC-B and ALICE. For example, the current design of the CMS vacuum chamber has about 30 HOM's with Q-values larger than 30000 and with mode frequencies within the bunch spectrum for a 13 cm long bunch. When lying on a line of the bunch spectrum, each of these HOM's can lead to a coherent power loss of more than 1 kW.

3 IMPEDANCE MODEL

A detailed description of the impedance model used for the LHC can be found in Refs. [5] and [6]. Here we discuss only recent updates in some of our impedance estimates. A plot of the broad band impedance used in the calculations is shown in Fig. 1. The narrow band impedance is the same as in [6], but we assume that the most prominent transverse mode in the longitudinal feedback cavities (the one at 516.7 MHz) is damped down to a Q-value of 1000.

3.1 Bellows and BPM's

Owing to the 3D geometry of the bellows, the code MAFIA was used for wake field and impedance calculations. The results presented in a companion paper [7] indicate that the latest bellows design, with smooth 10 mm transitions from racetrack to round geometry and shielding provided by sprung fingers which can slide along the beam screen, has impedances smaller than those previously estimated according to a rather conservative scaling of SSC calculations and LEP measurements. For a double 1 mm step and 3000 bellows, the low-frequency longitudinal impedance is $Z/n = 18.3$ mΩ and the vertical impedance is 753 kΩ/m. The transverse impedances of the bellows in the vertical and horizontal planes are not only different, but have also different signs (i.e., focusing in one plane and defocusing in the other). The effect of the gaps between fingers is found to be negligible.

A final design for the 500 beam position monitors is not yet available. Here we assume that each of them consists of four strip-lines, 10 cm long and 18 mm wide, located at a distance of 18 mm from the beam axis. A substantial reduction in length, compared to previous designs, is made possible by the proximity of the associated electronics, now located in the LHC tunnel.

3.2 Kickers

Impedance estimates are in progress for the LHC kickers, whose final design may depend on the outcome of possible impedance measurements foreseen in the near future.

The LHC abort kicker magnets have a total length $L = 14 \times 1.26$ m and are located in a region where the vertical β-function is about 600 m. They are equipped with a rectangular ceramic vacuum chamber of thickness $\Delta = 4.5$ mm and vertical aperture $b = 14$ mm. The inside of the chamber has a titanium coating of thickness $d = 1$ μm, with resistivity $\rho_{\rm Ti} = 7 \times 10^{-7}$ Ωm, to reduce the high-frequency impedance seen by the beam and to conduct away the static charge. The vertical impedance at frequencies well below 1 GHz can be written

$$Z_\perp(\omega) = \frac{-iR}{1 - i\omega/\omega_C}, \qquad (2)$$

where $R = \dfrac{Z_0 L}{2\pi b^2 \zeta} \simeq 8.5$ MΩ/m and $\omega_C = \dfrac{2\zeta\rho_{\rm Ti}}{bd\mu_0} \simeq 2\pi \times 8$ MHz. Here $\zeta = (b+\Delta)^2/[(b+\Delta)^2 + b^2] \simeq 0.636$. Note that (contrary to Refs. [5] and [6]) we have now assumed perfect magnetic boundary conditions, better suited for the (H-shaped) kicker ferrite.

The LHC injection magnet system must produce a kick of 1.36 Tm with a duration of 6.5 μs and consists of 4 units with a length of 2.17 m each. The kicker field rise time is 900 ns with a maximum ripple of 2 per mil. Ohmic losses in the (H-shaped) ferrite are substantially reduced by a round ceramic tube (with 18 mm inner radius and 4.5 mm thickness) painted in the inside with several 5 μm thick copper stripes, that should carry most of the high-frequency beam-induced image currents. To avoid loop currents in the stripes due to $\dot{B}$, they are not directly connected to the external beam pipe. Instead, a capacitive contact (about 800 pF) is established thanks to the high dielectric constant $\epsilon \simeq 10$ of the ceramic tube [8]. The field pattern of possible resonant modes associated with the stripes (behaving like a strip-line with unmatched load) shall be investigated to assess their penetration into the ferrite, with consequent strong damping.

According to BINP calculations [9] using the code ILANS, the effect of the injection kickers on the transverse resistive wall instability at 8.5 kHz is negligible: assuming an average vertical β-function of 70 m, the real part of the transverse impedance times β is 6 MΩ, to be compared to about 3 GΩ from the resistive wall. However, the calcula-

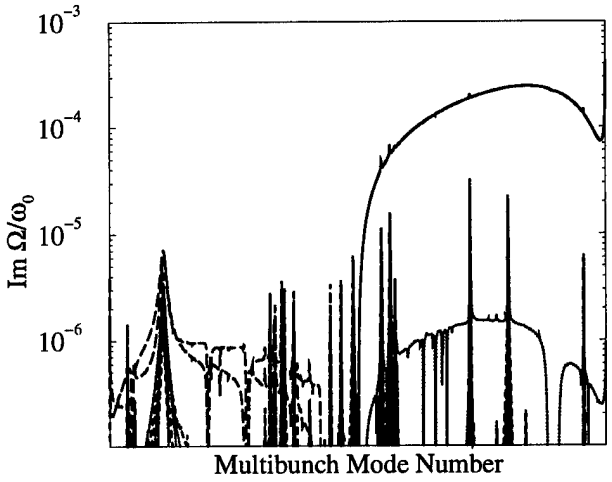


Figure 2: Vertical growth rates at injection versus multibunch mode number, for dipole (solid) and higher order modes.

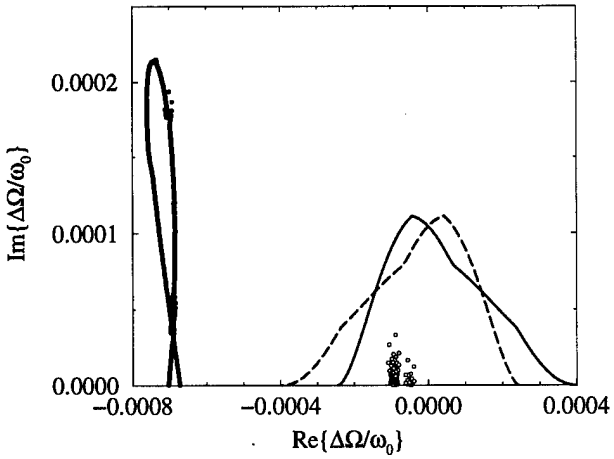


Figure 3: Vertical coherent tune shifts with 1 MHz half-bandwidth feedback, of $m = 0$ modes (filled circles, on the left) and $m = 1$ modes (open circles), compared to Landau damping stability curves.

tion is in quasi-static approximation and does not include the capacitive coupling of the stripes to the beam pipe.

As a temporary rough model for the injection kicker, we assume that the uncoated part of the ceramic chamber (about 36%) contributes a purely inductive impedance [10]

$$-0.4i\frac{Z_0 L}{2\pi b^2}\left(\frac{\alpha\epsilon-1}{\alpha\epsilon+1}+\frac{b^2}{(b+\Delta)^2}\right) \simeq -i\,1.63\ \mathrm{M\Omega/m},$$

where $\alpha = [(b+\Delta)^2 - b^2]/[(b+\Delta)^2 + b^2] \simeq 0.22$, while the region covered by copper stripes (64%) contributes a transverse impedance given by Eq. (2), with $\zeta \simeq 0.61$, $R \simeq 1.7\ \mathrm{M\Omega/m}$ and $\omega_C \simeq 2\pi \times 25.7$ kHz.

4 COHERENT INSTABILITIES

Using the impedance model of the previous section, the vertical multibunch growth rates computed at injection for nominal beam parameters by VLASOV are shown in Fig. 2.

The plot consists of several lines, one for each type of internal-bunch motion. Each line contains one point for each multibunch mode. The computation is done for N_b symmetrically placed bunches, with a total beam current of 674 mA. The peak on the left side of the figure is primarily caused by two of the septum cavity higher order modes: the one at 1117.9 MHz and the one at 516.7 MHz. The peak all the way to the right is primarily caused by the resistive-wall impedance, while the broad hump on the right is associated with the impedance of the abort kickers. Multibunch TMC occurs at about twice the nominal current.

The effect of a transverse feedback system with 1 MHz half-bandwidth and a gain corresponding to a damping time of 10 ms is shown in Fig. 3, where we compare the corresponding coherent tune shifts of rigid dipole and $m = 1$ head-tail modes to Landau damping stability curves for a transverse parabolic-like distributio collimated at anywhere from 3σ to 6σ. The dashed curve is for a shift in the vertical tune with vertical amplitude of 10^{-4} at 1 σ, whereas the solid curve is for -10^{-4}. The shift in the vertical tune with horizontal amplitude has opposite sign and is $\pm 7.2 \times 10^{-5}$. We see from the figure that, although Landau damping from octupoles (and space charge) stabilises all the $m = 1$ modes, some of the $m = 0$ modes are unstable (essentially those driven by the impedance of the abort kickers). This is a consequence of the insufficient feedback bandwidth, which we assumed to be the same as the bandwidth of the power amplifier required to damp injection oscillations. By suitable modifications of the feedback electronics, however, it should be possible to obtain a low-power half-bandwidth of about 20 MHz [11], thus stabilising all dipole modes at injection. Octupoles will be required at top energy to stabilise rigid dipole and higher order head-tail modes [12].

5 REFERENCES

[1] O. Brüning, these Proceedings.

[2] J.S. Berg, SLAC-TN-96-1 (1996).

[3] J.S. Berg and F. Ruggiero, these Proceedings, see also J.S. Berg, CERN LHC Project Report 100 (1997).

[4] F. Caspers, M. Morvillo and F. Ruggiero, these Proceedings.

[5] F. Ruggiero, Part. Accel. **50**, 83-104 (1995).

[6] J.S. Berg, CERN LHC Project Report 16 (1996).

[7] M. D'yachkov and F. Ruggiero, these Proceedings.

[8] G. Schröder, private communication (January 1997).

[9] M.M. Karliner, N.V. Mityanina, D.G. Myakishev and V.P. Yakovlev, private communication (May 1996), see also Proc. EPAC Conference, Sitges, 1996 (IPP, Bristol, 1996), pp. 1247-1249.

[10] S.S. Kurennoy, in Proc. of the IEEE 1993 Part. Acc. Conf., Washington, D.C., p. 3420 (1993).

[11] W. Höfle, private communication (May 1997).

[12] J. Gareyte, J.P. Koutchouk and F. Ruggiero, CERN LHC Project Report 91/rev (1997).

PROPOSAL FOR AN ALUMINUM BEAM SCREEN IN THE LHC

W. Chou, Fermilab,* P.O. Box 500, Batavia, IL 60510, USA
H. Ishimaru, KEK, Tsukuba, Japan

Abstract

This paper proposes a cold beam screen made of high strength, high electrical resistivity aluminum alloy (such as A7N01) as an alternative to the present LHC design that is based on a copper co-laminated high Mn content stainless steel. The main advantages of an aluminum screen are: simple manufacturing processes, low cost, elimination of millions of small slots and of TEM waves, no adhesion problem, no helium leak problem (vacuum tight), non-magnetic, and others. The available aperture is equivalent to the present design when a non-uniform wall thickness is adopted. A prototype was built to demonstrate the design and the end connections. Concerns about the multipactoring, electron cloud instability, surface resistance and cryopumping using anodized aluminum will be addressed.

1 INTRODUCTION

The present design of the beam screen in the LHC uses a copper co-laminated high Mn content stainless steel. Ref. [1] proposes an alternative candidate, namely, the high strength, high resistivity aluminum alloy, such as A7N01 or 7039-T61. (Note: The *high* resistivity is relative to pure aluminum and other aluminum alloys.) This paper revisits this proposal and gives some details in engineering design.

Table 1 is a comparison of the electrical resistivity and the yield tensile strength of copper (Cu), aluminum alloy (A7N01) and stainless steel (SS) at 4 K. It is seen that A7N01 has lower resistivity than SS and higher strength than Cu. It has been shown in [1] that a 1.5-mm thick A7N01 tube is mechanically stable during quench and its effect on beam instability can be under control.

Table 1: Electrical Resistivity and Yield Tensile Strength at 4 K.

Material	Electrical Resistivity (Ωm)	Yield Tensile Strength (MPa)
Cu	5×10^{-10}	44
A7N01	1.8×10^{-8}	520
SS	5×10^{-7}	1500

A preliminary sketch of the cross section of an aluminum beam screen is shown in Figure 1. It consists of a 1.5-mm thick aluminum pipe that contains two 3.7-mm diameter cooling holes, four 2-mm wide long slots and four mini-antechambers, which house the cryopump (such as anodized aluminum foils).

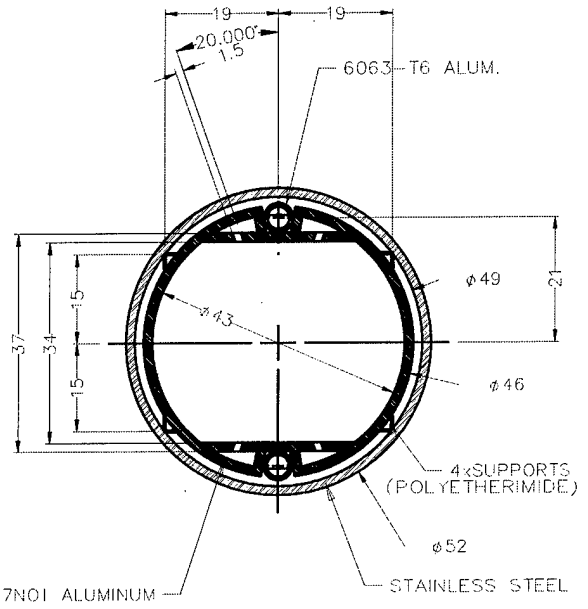


Figure 1: The cross section of an aluminum beam screen.

2 ADVANTAGES OF AN ALUMINUM SCREEN

2.1 *Good extrusion characteristics*

One may thus design a complex cross section as shown in Fig. 1. This would simplify the manufacturing process and provide higher reliability and easier quality control.

2.2 *Low cost*

A detailed break-down of the cost estimate has been carried out by the industry. The total (including overhead and contingency) is about 25 MCHF, which is lower than the projected cost of the copper-stainless steel design.

2.3 *Elimination of beam-induced rf fields outside the screen*

The beam-induced rf fields in Fig. 1 would be confined inside the beam screen. Therefore, there will be no TEM waves between the screen and cold bore.

* Operated by Universities Research Association Inc. under Contract No. DE-AC02-76CH03000 with the U.S. Department of Energy.

0-7803-4376-X/98/$10.00 © 1998 IEEE

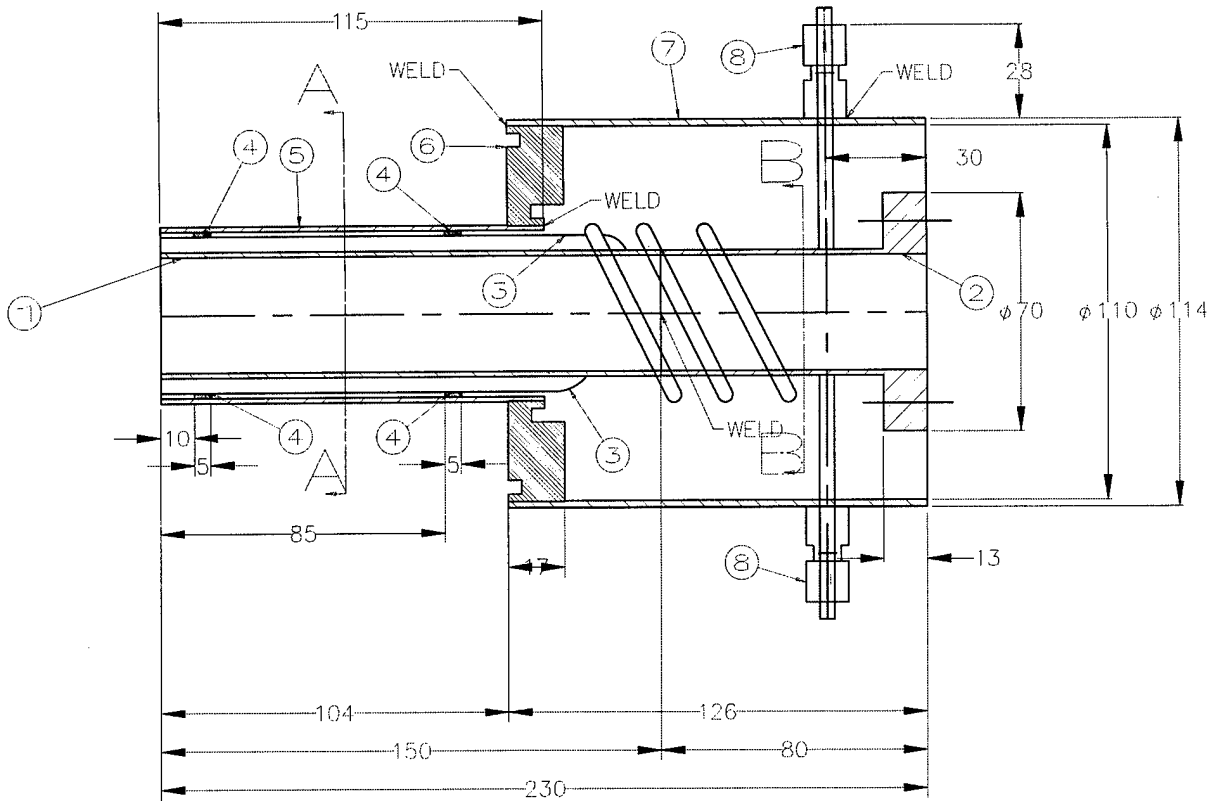


Figure 2: The inter-connection part of an aluminum beam screen.

2.4 *Replacing millions of pumping slots by a few long ones*

This would considerably reduce the machine impedance and simplify the manufacturing process.

2.5 *No adhesion problem*

There is no prior experience with the adherence of the copper to the stainless steel in a 30-year lifetime. This would no longer be a worry when a single-layer aluminum tube is used.

2.6 *Non-magnetic*

In order to minimize the magnetic susceptibility in a welded stainless steel pipe, special material (such as the high N_2 - high Mn steel) is needed. The aluminum alloy does not have this problem.

2.7 *Vacuum tight*

The aluminum beam screen system could be made vacuum tight provided that the bellows connections between the screens are vacuum tight. Any helium leak from the cooling tubes would not get into the beam vacuum.

3 INTER-CONNECTION DESIGN

Figure 2 shows an engineering drawing of the interconnection part. In order to absorb the differential thermal contraction between aluminum and stainless steel, the cooling tubes make several spirals before leaving the beam screen. The number of welding points is minimized. The installation procedure is simple. A prototype has been made for demonstration purpose.

4 CONCERNS ABOUT AN ALUMINUM SCREEN

4.1 *Aperture*

During quench, $B\dot{B} = 300\ \mathrm{T^2/s}$. The required thickness of aluminum screen is 1.5 mm. Compared with the present LHC beam screen which uses a 1 mm thick stainless steel tube, there could be an aperture loss of about 1 mm. However, it is known from beam collimation studies that the most critical part of the aperture limit is along the diagonal line.[2] Fortunately, the stress in the wall in this direction is small. Therefore, one may adopt a non-uniform wall thickness to reduce it from 1.5 mm to 1 mm near the diagonal region as shown in Figure 3. Thus, the usable physical aperture of an aluminum screen is equivalent to a stainless steel one.

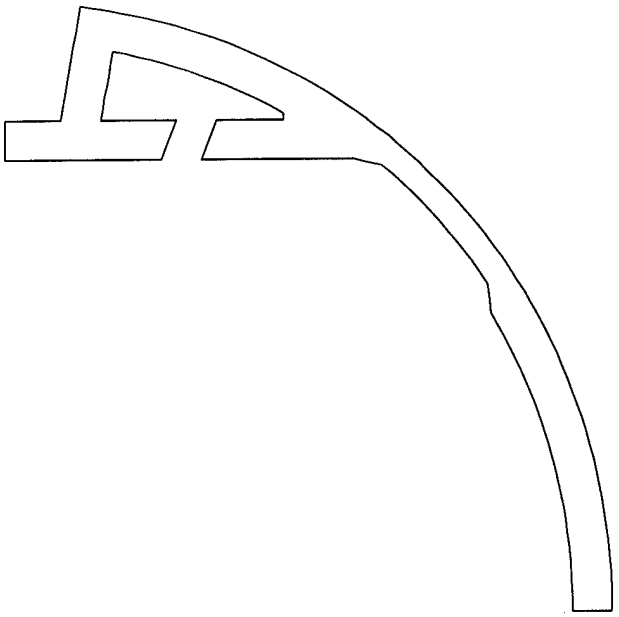


Figure 3: A quadrant of a beam screen with non-uniform wall thickness.

4.2 Surface resistance

At low frequencies, the concern is about the resistive wall instability. A 1.5-mm thick aluminum beam screen would give a growth time of about 11 ms. But this can easily be damped by a transverse feedback system.

At high frequencies, the concern is about the beam heating. Because of the anomalous skin effect[3], it is not clear if A7N01 is any worse than copper. A measurement program has been established at CERN and data will be made available soon.[4]

4.3 Photoelectrons

Photoelectrons may cause two types of problems: multipactoring and electron cloud instability. Because aluminum has higher secondary electron yield than stainless steel or copper, this is a genuine concern. A solution is to apply a thin (tens of nm) titanium-nitride (TiN) coating on the aluminum surface, which LBL is working on for the LER beam pipe of the SLAC B-Factory.

4.4 Cryopumping at 20 K

M.G. Rao at CEBAF has demonstrated that anodized aluminum is a good cryopump for hydrogen and helium at 4.3 K. [5] However, it is not clear if its pumping speed and adsorption capacity for hydrogen at 20 K could meet the LHC requirement. Three anodized aluminum pipes will be shipped to CERN for this measurement.

5 ACKNOWLEDGEMENTS

The authors are thankful to O. Gröbner, R. Calder, A. Mathewson, A. Poncet, F. Caspers, F. Ruggiero, J. Gareyte, B. Zotter, J.B. Jeanneret, M.G. Rao (CEBAF) and many others for stimulating discussions and critical comments. Thanks also to F.S. Mitchell for mechanical drawings and Z. Tang for ANSYS simulations.

6 REFERENCES

[1] W. Chou, LHC Project Note 3, CERN (October, 1995).

[2] Y. Baconnier, J.-B. Jeanneret and A. Poncet, CERN MT-ESH-Note 95-11, LHC-Note 326 (June 1995).

[3] W. Chou and F. Ruggiero, CERN LHC Project Note 2 (1995).

[4] F. Ruggiero, private communication.

[5] M. G. Rao, P. Kneisel and J. Susta, *Cryogenics,* V. 34, p. 377 (1994).

DYNAMIC APERTURE STUDIES DURING COLLISIONS IN THE LHC

W. Chou and D. Ritson, Fermilab,* P.O. Box 500, Batavia, IL 60510, USA

Abstract

The dynamic aperture during collisions in the LHC is mainly determined by the beam-beam interactions and by multipole errors of the high gradient quadrupoles in the interaction regions. The computer code JJIP has been modified to accommodate the LHC lattice configuration and parameters and is employed in this study. Simulations over a range of machine parameters are carried out, and results of preliminary investigation are presented.

1 INTRODUCTION

There has been an extensive study of the dynamic aperture of the LHC at injection, in which field errors of the arc magnets are dominant. However, things are quite different during collisions when field errors of the high gradient quadrupoles (the triplet) in interaction regions (IRs) and the beam-beam interactions play predominating roles. This is because the β-functions in the triplets are large and beam separations in the IRs are small. As a matter of fact, error multipoles in the arcs are small during collisions so that the tracking can be lumped into a few blocks. Thus large numbers of turns can be simulated with relative ease. This is particularly important for the LHC because beams, during experimental luminosity running, should circulate for 10 hours or longer.

The LHC has four interaction points (IPs): IP1 and 5 are high luminosity points, IP2 and 8 low luminosity points. The triplet magnets are identical in the four IRs. So is the head-on beam-beam interactions. However, the long-range beam-beam is important only in the high luminosity IRs, which has small β^* (0.5 m) and large $\beta_{\max}$ (4400 m). In order to minimize the beam-beam effects, there is a crossing angle at the IPs. A large crossing angle would certainly benefit as far as long-range beam-beam is concerned. But it would also reduce the luminosity, jeopardize the triplet field quality and enhance the synchro-betatron resonances. Moreover, larger crossing would require more aperture in the triplets. Therefore, a careful choice of an appropriate range of the crossing angle is a critical issue in the LHC IR design. This paper intends to provide some insights to help with making such a choice by means of a tracking code JJIP.

2 BRIEF DESCRIPTION OF THE CODE

The code JJIP was originally written for the IR studies of the former SSC project. It has been modified for accommodating the LHC lattice configuration and machine parameters. It consists of three basic tracking blocks — Tracking in the arcs is a simplified map with lumped errors; the triplet part is considered as thin-lense, in which each magnet is sliced; the head-on beam-beam is a simple kick and the multiple parasitic crossings are treated equally in the free space as well as in the triplet.[1]

The input data card provides a number of variables in the parameter space: launching positions, beam emittance, β^*, crossing angles, crossing planes, error tables of arc magnets and triplets, coupling strength, position errors in the 6-D phase space at IPs, tune modulations and noises, *etc.* On a single processor SUN Sparc-20 workstation, it takes about 15 minutes to track a million turns, equivalent to the 1.5 minutes required for a particle to travel 10^6 turns in the LHC in real time.

3 RESULTS OF PRELIMINARY INVESTIGATION

3.1 Bench test:

As a test case, the triplet error tables in Ref. [2] were adopted in the preliminary tracking study. Under similar conditions, the dynamic aperture obtained from JJIP is 10σ, while Ref. [2] gives 9.9σ. This justifies the use of the short cut in the arcs.

3.2 Scaling of dynamic aperture vs. β^**:*

Figure 1 shows the scaling of the dynamic aperture *vs.* β^* in the absence of beam-beam interactions. The beam separation n when expressed in terms of the beam size σ is:

$$\begin{aligned} n &= S(L)/\sigma(L) = L\theta_0/\sqrt{\epsilon\beta(L)} \approx \theta_0/\sqrt{\epsilon/\beta^*} \\ &= \theta_0/\sigma' \end{aligned} \quad (1)$$

in which S is the beam separation in meters, L the distance from the IP, θ_0 the full crossing angle, ϵ the beam emittance and σ' the *rms* beam angular spread. The separation n is kept constant in this scaling, which is 9.5σ that corresponds to θ_0 = 300 μrad and β^* = 0.5 m. When β^* increases, σ' will decrease and so does θ_0. Therefore, one would expect a larger dynamic aperture for a larger β^*. It is seen from Fig. 1 that the scaling is approximately linear. (Similar study for the SSC gave a scaling of $\beta^{*1.5}$, see [3].)

3.3 Relative weight of various sources limiting dynamic aperture:

Figure 2 decomposes the different sources that could limit the dynamic aperture (DA) and gives a quantitative comparison of each contribution. The tracking conditions are

* Operated by Universities Research Association Inc. under Contract No. DE-AC02-76CH03000 with the U.S. Department of Energy.

0-7803-4376-X/98/$10.00 © 1998 IEEE

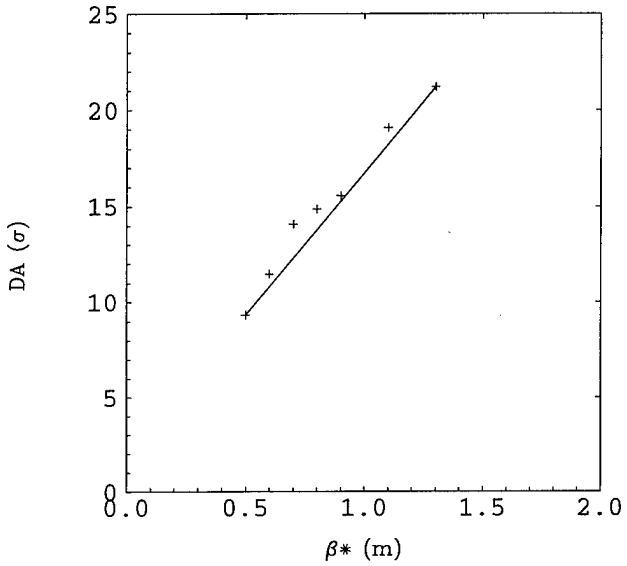


Figure 1: The scaling of dynamic aperture *vs.* β^* when the beam separation is kept constant at 9.5σ. It is approximately linear.

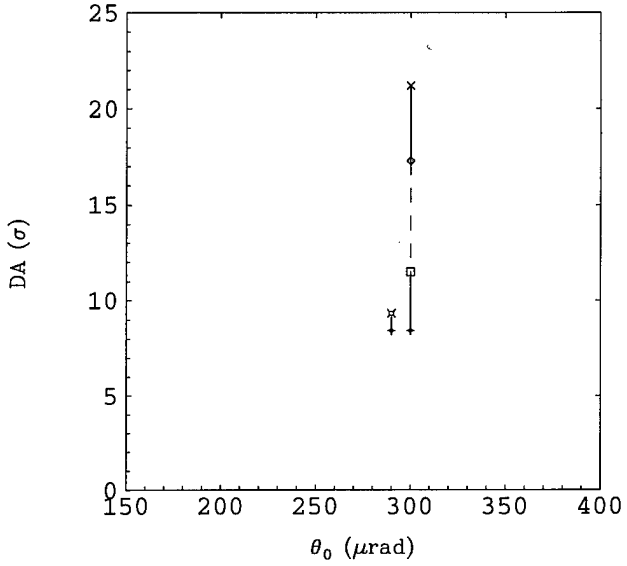


Figure 2: Contribution of various sources limiting the dynamic aperture. Right line from top down: (*a*) Arc errors only: DA $\geq 21\sigma$; (*b*) Arc errors + triplet errors (b_{10} off): DA = 17.3σ; (*c*) Arc errors + triplet errors (b_{10} on): DA = 11.5σ; (*d*) Arc errors + triplet errors (b_{10} on) + beam-beam: DA = 8.43σ. Left line from bottom up: (*d*) See above; (*e*) Same as (*d*), but the crossing plane is tilted by 45°: DA = 9.33σ.

as follows: collision optics, 10^5 turns, 5 seeds, field error tables from Ref. [2], and $\theta_0 = 300$ μrad. The results show that: (*a*) Arc errors only: DA $\geq 21\sigma$; (*b*) Arc errors + triplet errors (b_{10} off): DA = 17.3σ; (*c*) Arc errors + triplet errors (b_{10} on): DA = 11.5σ; (*d*) Arc errors + triplet errors (b_{10} on) + beam-beam: DA = 8.43σ; (*e*) Same as (*d*), but the crossing plane is tilted by 45°: DA = 9.33σ. From these results, the following observations are made:

- The arc magnets only minimally constrain the dynamic aperture during collisions.
- The systematic 20-pole b_{10} plays a major role in limiting the dynamic aperture, which is in agreement with Ref. [2]. However, the value of b_{10} (-0.005×10^{-4}) assumed here seems to be greatly exaggerated. In the present triplet design for the LHC at Fermilab, it has been reduced by more than a factor of five (0.0009×10^{-4}).[4]
- The beam-beam interactions limit the dynamic aperture even when the crossing angle is as big as 300 μrad.
- A 45°-tilted crossing plane improves the dynamic aperture if the particle oscillates horizontally. This is because for the same crossing angle, the beam distance becomes larger than that with horizontal crossings. However, this improvement disappears if the particle oscillates diagonally (not shown in the figure).

3.4 *Dynamic aperture* vs. *crossing angle:*

On the one hand, larger crossing means the beams are further away from the magnet axis, which leads to poor field qualities. Thus, the dynamic aperture limited by the triplet would become smaller. On the other hand, however, the dynamic aperture limited by beam-beam would become larger due to less beam-beam interactions. Therefore, one would expect that, when the crossing angle increases, the dynamic aperture would at first increase (which is the beam-beam dominated region); after reaching a maximum value, it would decrease (which is the triplet errors dominated region). Figure 3 is an illustration of this process at three crossing angles: 200, 300 and 350 μrad. The solid curve is the case when there are magnet errors but no beam-beam. The dashed one is when both magnet errors and beam-beam interactions are present. It is seen that, below 300 μrad, the beam-beam is dominating, while above that, the triplet errors seem to take over. The maximum dynamic aperture is achieved at about 300 μrad using the above error table.

3.5 *Space budget of the triplet aperture:*

One primary goal of these studies is to determine the required aperture of the triplets, which is 35 mm (radius) in the present design. Figure 4 demonstrates a proposed space budget for the aperture of the quadrupoles Q2 and Q3 (both are in the high-β region) at the high luminosity points IP1 and 5. (*a*) The radiation shielding takes 6 mm.[5] Another 2 mm is reserved for the helium flow. Thus, the available physical aperture is 27 mm. (*b*) The mechanical tolerance is 1.6 mm (0.6 mm for cold bore and 1 mm for misalignment).[6] (*c*) The peak closed orbit error is 4 mm.[7] (*d*) The β-beat is 10%. (*e*) The allowed beam oscillation around the equilibrium orbit is 9σ (which

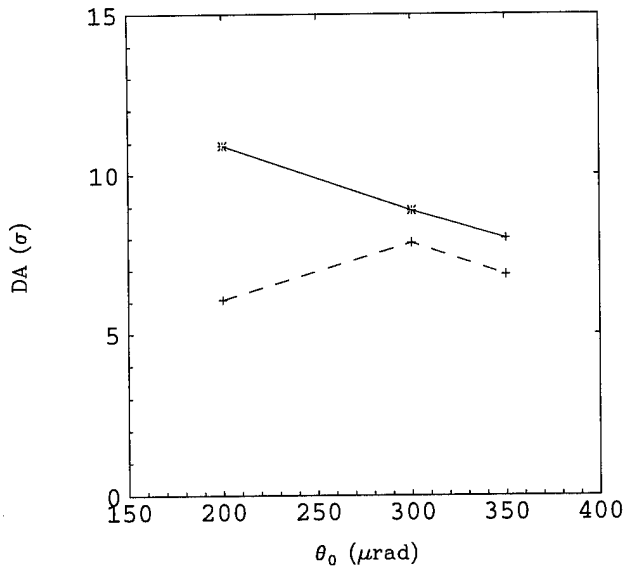


Figure 3: Dynamic aperture *vs.* crossing angle: The solid curve is the case when there are magnet errors but no beam-beam. The dashed one is when both magnet errors and beam-beam interactions are present. Below 300 μrad, the beam-beam is dominating, while above that, the triplet errors seem to take over.

corresponds to 7σ of the primary collimator and 9σ of the secondary halo).[8] Within the 9σ, the dynamic aperture needs to be $\geq 7\ \sigma$. (f) The crossing separation is $n\sigma/2$, where n is defined in Eq. (1). These numbers are still preliminary. The task of the tracking study is to find out how big the crossing angle needs to be (the value of n) in order to achieve a dynamic aperture of 7σ.

4 PLAN OF FUTURE STUDIES

A new iteration of tracking studies will include the following:

1. Use of the updated triplet error tables provided by the magnet builders Fermilab and KEK, respectively;

2. Study of the effects such as tune modulation, noises, x-y coupling, synchro-betatron resonances, particle offset in the 6-D phase space at the IP, closed orbit errors and Pacman, *etc.*

Based on these and other related studies to be made in collaboration with CERN, one should be able to:

- Determine the required triplet aperture;
- Make necessary trade-offs in the space budget;
- Identify the most damaging multipoles of the triplet for correction;
- work out a sorting strategy.

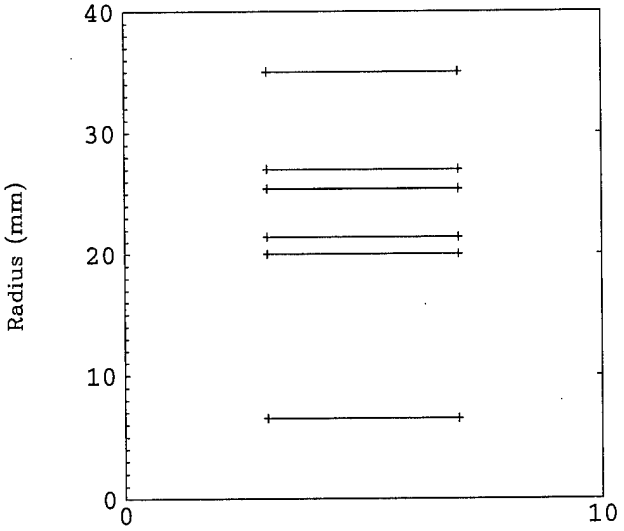


Figure 4: Space budget of the aperture of Q2 and Q3 at IP1 and 5. The quad radius is 35 mm. From that line down: (a) The radiation shielding takes 6 mm. Another 2 mm is reserved for the helium flow. (b) The mechanical tolerance is 1.6 mm (0.6 mm for cold bore and 1 mm for misalignment). (c) The peak closed orbit error is 4 mm. (d) The β-beat is 10%. (e) The allowed beam oscillation around the equilibrium orbit is 9σ (which corresponds to 7σ of the primary collimator and 9σ of the secondary halo). Within the 9σ, the dynamic aperture needs to be $\geq 7\ \sigma$. (f) The crossing separation is $n\sigma/2$, where n is defined in Eq. (1).

5 ACKNOWLEDGEMENTS

The authors are pleased to acknowledge that this study is in close collaboration with CERN colleagues (especially the LHC Division and SL/AP Group).

6 REFERENCES

[1] J. Irwin, SSC-233, SSC Laboratory (September 1989).

[2] A. Faus-Golfe and A. Verdier, 'Dynamic Aperture Limitations of the LHC in Physics Conditions due to Low-Beta Insertions,' Proc. European Particle Accelerator Conference, June 10-14 1996, Sitges, Spain.

[3] D. Ritson, SLAC-TN-91-2, also SSCL-N-752 (March 1991).

[4] G. Sabbi *et al.*, 'Magnetic Design of a High Gradient Quadrupole for the LHC Low-β Insertions,' this conference.

[5] N.V. Mokhov and J.B. Strait, 'Towards the Optimal LHC Interaction Region: Beam-Induced Energy Deposition,' this conference.

[6] R. Ostojic, private communication.

[7] J-P. Koutchouk, private communication.

[8] J.B. Jeanneret and T. Risselada, LHC Project Note 66, CERN (September 1996).

OPTIMIZATION OF THE LHC BEAM CLEANING SYSTEM WITH RESPECT TO BEAM LOSS IN THE HIGH LUMINOSITY INSERTIONS

A.I. Drozhdin and N.V. Mokhov*, Fermilab, P.O. Box 500, Batavia, IL 60510 USA

Abstract

The LHC design performance is achievable only with a dedicated beam cleaning system embedded in the lattice. The effect of the system on the beam loss distribution in the entire machine is studied with emphasis on the two high luminosity insertions. Realistic Monte-Carlo simulations are described, which include a model for beam halo interactions with collimators and other components, multi-turn particle tracking in the lattice, hadronic and electromagnetic shower simulations, and thermal and stress analyses. Methods to mitigate beam-induced effects in the interaction regions at operational and accidental beam loss are proposed, both for injection and collision conditions.

1 INTRODUCTION

The overall accelerator and detector performance at the Large Hadron Collider (LHC) [1] is strongly dependent on the beam loss and background particle rates in machine and detector components [2]. It was shown that the design performance of a high-luminosity collider is achievable only with a dedicated beam cleaning system embedded in the lattice [3, 4, 5, 6, 7]. Selected results on beam loss in the LHC lattice are presented below for various scenarios and beam cleaning system parameters.

2 BEAM LOSS SIMULATIONS

The calculations are based on the assumption of two high-luminosity experiments, ATLAS and CMS, operating simultaneously in the IP1 and IP5 interaction regions, respectively, at the nominal luminosity of $10^{34}\text{cm}^{-2}\text{s}^{-1}$ each. An inelastic *pp* cross section of 80 mb is used, including single diffraction. The calculations are performed for the clockwise 450 GeV proton beam at injection and 7 TeV beam at collisions.

Operational beam loss are simulated taking into account beam-gas scattering using the '97 version of the MARS code [8], *pp* collisions at IP1 and IP5 using the DPMJET code [9], and interactions of beam halo with primary collimators using the '97 version of the STRUCT code [10]. Consequent multi-turn particle tracking in the full LHC lattice, scoring particles lost at secondary collimators and at all other limiting apertures are performed with the STRUCT code. It is assumed that the beam loss rate in the beam cleaning system is evenly distributed among the two primary collimators (horizontal and vertical) in IP3 and horizontal collimator (momentum cleaning) in IP7, i. e. 10^9 p/s at each of them for each beam. Accidental beam loss are described in detail in the next section.

Starting with the calculated beam loss distributions in the lattice, shower simulations in the components of the beam cleaning system, IRs and arcs are performed with the MARS code taking into account all the lattice details, three-dimensional geometry, material and magnetic field descriptions. At this stage, energy deposition distributions in the machine components and particle fluxes in the CMS and ATLAS detectors are calculated.

3 ACCIDENTAL BEAM LOSS

Prefire of a single module of the abort kicker will result in high-amplitude coherent betatron oscillations of the beam. The disturbed beam can then cause the overheating of an limiting aperture component, a collimator jaw first of all. In the worst case, when abort kicker module prefires just after the longitudinal abort gap, one needs to wait the whole turn to extract the beam. In such a case, collimator overheating can be mitigated via [11]: early abort without synchronization with an abort gap (asynchronous firing of the beam abort kicker) or compensation of the prefired module with a special module with the opposite magnetic field (antikicker). In the second case, the beam abort can be safely delayed until the gap comes, thus eliminating beam loss during the kicker rise time. Beam loss depends on the time between the prefire and the antikicker start.

The collider injection kicker misfire and prefire will result in a coherent betatron oscillation of the injected portion of the beam with pretty large amplitude causing the deleterious effects in lattice components [11].

An asynchronous firing of the beam abort and beam injection kickers will spray the beam across the accelerator aperture. Number of protons sprayed by the abort kicker is equal to $\Delta t/T \times I \approx 10^{13}$, where $\Delta t = 3\mu s$ is a kicker rise time, $T = 89\mu s$ is a revolution time, and $I = 2.8\times10^{14}$ is the beam intensity. About half of this will be sprayed across the abort beam line, and another half will hit a primary collimator. A thin (fraction of radiation length X_0) scattering target, a spoiler of a few X_0 thick, or a thick shadow can be used to protect collimators from overheating. The material of targets, spoilers and shadows must withstand about 5×10^{12} protons at 7 TeV. The instantaneous temperature rise in a $0.42X_0$ thick beryllium, graphite, and even copper and tungsten primary collimator is below the melting point at the nominal size of the circulating beam. Actually, beam size is several times larger because of the beam sweeping across the primary collimator by the kicker. Therefore, the collimators can withstand even higher intensity, i.e., from a thermal standpoint, any of considered materials can be used

* Work supported by the U. S. Department of Energy under contract No. DE-AC02-76CH03000

0-7803-4376-X/98/$10.00 © 1998 IEEE

for targets and primary collimators. From the other hand, no material can withstand the total beam intensity.Further studies of thick spoilers and shadows are needed for specific conditions at injection and beam abort failures.

4 BETATRON CLEANING

A betatron cleaning system is located in IP3. In the collision mode at the nominal luminosity, the rate of protons per beam leaving the stable central core is estimated to be 2.4×10^9 p/s [1]. Slightly more conservative rate of 3×10^9 p/s is assumed in calculations. Proton impact parameter on the primary collimator is of the order of 1μm. Angular distributions of the beam after the primary collimators have angular spread with rms$\sim2\mu$rad, being wider for heavier materials.

Particles pass several times through the primary collimator before being absorbed by it or lost at secondary collimators or other accelerator apertures. At every interaction with a beryllium primary collimator, 25.2% of particles deposit more than 30% of their energy and they are lost in the nearest region downstream of the primary collimator and in the secondary collimators. Corresponding fraction of particles for graphite is 12.6% and for tungsten is 2.3%. Therefore, average number of particle passes through the primary collimator is three times larger for tungsten collimator compared to the beryllium one: 3.25 (Be), 4.55 (C) and 12 (W) passes, respectively.

Although primary and secondary collimators are placed at 6σ and 7σ from the beam axis, correspondingly [1], the tails of halo are extended up to 8σ at injection and up to 7.2σ at the top energy. Large amplitude particles, which escape from the cleaning system, are able to circulate without hitting the aperture in the cold part of the machine, before being captured by the collimators on the later turns. This defines the circulating beam size for the physical aperture calculations.

Calculated beam loss distribution in the LHC IP3 is shown in Fig. 1 for beryllium collimator. Distributions are similar for other collimators, but the rates are higher for heavier materials: maximum beam loss rate in a 14.2 m long superconducting magnet is 4.7×10^5 p/s for beryllium, 7.8×10^5 p/s for graphite and 2.7×10^6 p/s for tungsten. These rates are below the limit for the LHC magnets of $14.2\times7\times10^6$ p/s [1].

For the same thickness in units of radiation length ($0.42X_0$), higher rate of inelastic nuclear interactions in beryllium and graphite primary collimators results in increased irradiation of components in the collimation region and at the beginning of the arc downstream of IP3. With tungsten, this irradiation is lower, and significant fraction of outscattered protons is intercepted by the secondary collimators.

5 MOMENTUM CLEANING

A momentum cleaning system is located in IP7. The system consists of one horizontal primary and three secondary

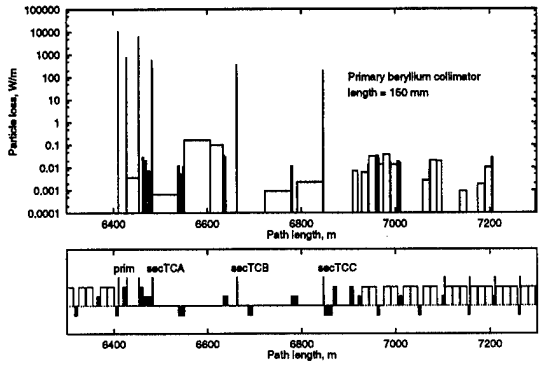


Figure 1: Beam loss distribution in the IP3 beam collimation region at collisions for 150 mm beryllium primary collimator.

collimators positioned similar to the betatron cleaning system. Beam loss distribution at collimation of 10^9 p/s in IP7 with a graphite horizontal primary collimator is shown in Fig. 2 for the entire LHC lattice. The distributions are not very different for other materials of the primary collimators in IP7.

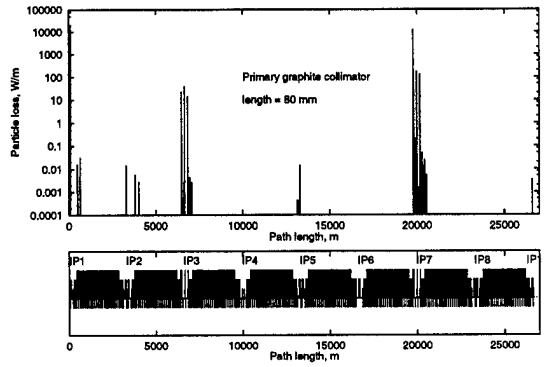


Figure 2: Beam loss distribution in the LHC lattice at momentum cleaning for a 80 mm graphite primary cillimator in IP7.

Figure 3 shows beam loss distributions in IP1 and IP5 for the simultaneous amplitude and momentum cleaning with graphite primary collimators. Total beam loss in IP1 ($26500\leq S\leq26650$ m) is 1.58×10^5 p/s with beryllium, 2.43×10^5 p/s with graphite and 6.17×10^6 p/s with tungsten primary collimators. These are mostly produced by the momentum cleaning system. Total beam loss in IP5 ($13129\leq S\leq13366$ m) is 8.47×10^5 p/s with beryllium, 1.52×10^6 p/s with graphite and 4.21×10^6 p/s with tungsten primary collimators. These are mostly produced by the amplitude cleaning system.

6 BEAM CLEANING AT INJECTION

Even in good operational conditions, about 5% of the beam (1.4×10^{13} particles) can be lost at the beginning of the acceleration ramp during 0.2–1 s. The quench level in the superconducting magnets at injection is estimated to be of the order of 10^{10} p/m [1]. If localized, the above loss can cause additionally a serious problem for cryogenics and for

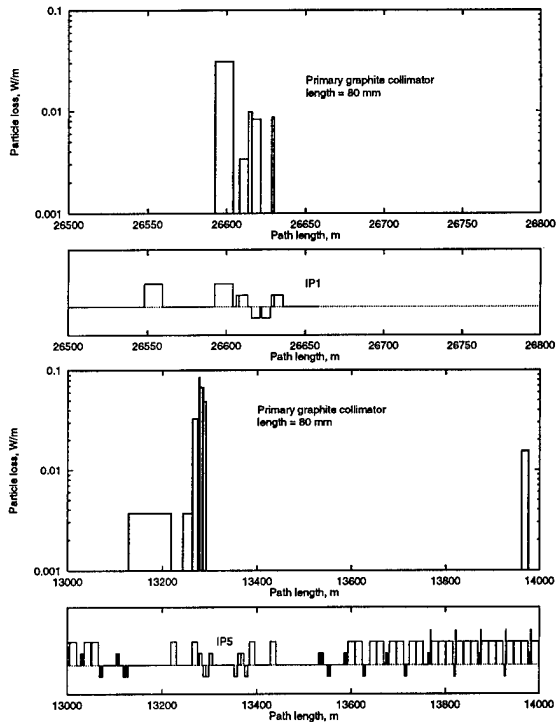


Figure 3: Beam loss distribution in IP1 (top) and IP5 (bottom) at collisions with simultaneous amplitude and momentum cleaning with a 80 mm graphite primary collimators.

the accelerator component lifetime. Experience says that detector components are also experience increased irradiation at injection. Therefore, the interaction regions must be well protected.

Beam loss distribution in the LHC lattice at injection is shown in Figure 4. The interception of 7.0×10^{12} protons during one second by each of the horizontal and vertical primary collimators in IP3 is assumed. The maximum beam loss rate in superconducting magnets is found to be 1.35×10^{9} p/(m·s) with beryllium, 1.86×10^{9} p/(m·s) with graphite and 2.56×10^{9} p/(m·s) with tungsten primary collimators, respectively. These rates are only a few times below the quench level. This can cause a problem if the beam loss rates at injection exceed at some moment the average expected rate. Fortunately, the injection lattice has no high-β region in the vicinity of the interaction regions. Therefore, the beam loss rates at injection are rather low in IP1 and IP5.

7 CONCLUSIONS

Effect of the LHC beam cleaning system operation on the beam induced radiation effects in the entire machine has been studied. Comparison of different materials for primary collimators has shown an advantage of beryllium and graphite compared to tungsten, with almost 10 times lower loss rates in the superconducting magnets. The beam loss with pyrolytic graphite is about 60% larger compared to beryllium, but taking into consideration allignement and

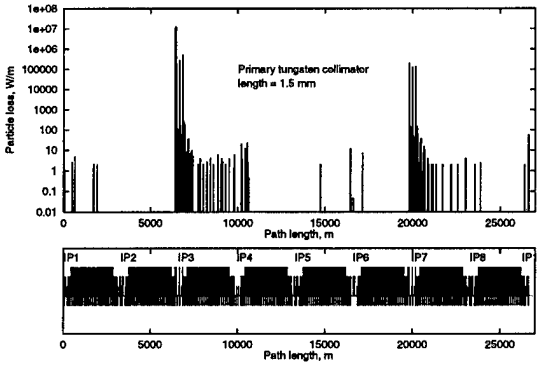


Figure 4: Beam loss distribution in the LHC lattice at injection with a 1.5 mm tungsten primary collimator.

safety issues, pyrolytic graphite seems to be the best material for the LHC primary collimators. The maximum beam loss rate in any single superconducting magnet is below the limit even with tungsten primary collimator. In the IP1 and IP5 high-luminosity insertions, beam loss rates produced by the beam cleaning system contribute about 10% to the total heat load in the inner triplet components, which is dominated by *pp* collisions. The maximum beam loss at injection, $(1.35\text{-}2.56)\times10^{9}$ p/(m·s), is 4 to 7 times below the limit defined in [1].

8 REFERENCES

[1] 'The Large Hadron Collider Conceptual Design', CERN/AC/95-05(LHC), 1995, P. Lefèvre and T. Pettersson, editors.

[2] A.I. Drozhdin, M. Huhtinen and N.V. Mokhov, Nucl. Instr. and Methods, A381, 531, 1996.

[3] L. Burnod and J. B. Jeanneret, 'Beam Losses and Collimation in the LHC: A Quantative Approach', CERN SL/91–39 (EA), LHC Note 167, 1991.

[4] P.J. Bryant, E. Klein, 'The Design of Betatron and Momentum Collimation Systems', CERN SL/92-40 (AP), 1992.

[5] T. Trenkler and J.B. Jeanneret, 'The Principles of Two Stage Betatron and Momentum Collimation in Circular Accelerators', CERN SL/95-03 (AP), LHC Note 312, 1995.

[6] M. Maslov, N. Mokhov and I. Yazynin, 'The SSC Beam Scraper System', SSCL-484, 1991.

[7] A. Drozhdin, N. Mokhov, R. Soundranayagam and J. Tompkins, 'Toward Design of the Collider Beam Collimation System', SSCL-Preprint-555, 1994.

[8] N. V. Mokhov, 'The MARS Code System User Guide, Version 13(95)', Fermilab–FN–628, 1995.

[9] J. Ranft, Phys. Rev., D51, 64, 1995.

[10] I. Baishev, A. Drozhdin and N. Mokhov, 'STRUCT Program User's Reference Manual', SSCL–MAN–0034, 1994.

[11] A. Drozhdin, N. Mokhov and B. Parker, 'Accidental Beam Loss in Superconducting Accelerators: Simulations, Consequences of Accidents and Protective Measures', SSCL-Preprint-556, 1994.

LOCAL CHROMATICITY CORRECTION OF THE LHC

C.J. Johnstone *, Fermilab, P.O. Box 500, Batavia, IL 60510 USA

Abstract

Local chromaticity correction of a low-beta region can under certain conditions enhance the momentum acceptance of a circular accelerator [1]. For this paper a local chromaticity scheme was explored for the LHC employing chromatic correction sextupoles in the arc cells nearest the final-focus triplet. Initially, existing optics and current sextupole locations [2] were used to correct the natural chromaticity of the LHC Interaction Region (IR) and preliminary tracking indicated an increase in dynamic aperture. However, calculated sextupole strengths were unrealistic. Therefore, work on a specialized chromatic correction region with increased beta functions at specific sextupole locations has begun. The higher beta functions allow the strengths required for the sextupoles to be reduced and, also, more optimal sextupole phase advances for chromatic correction. Progress towards an optical model for local chromatic correction for the LHC IR is the subject of this paper.

1 INTRODUCTION

The long-term stability and overall momentum acceptance of the LHC has been investigated using sextupole families to correct higher orders of chromaticity and also schemes which include multipoles [3]. Another approach which has been used in the design of the NLC and, recently, in the muon collider interaction regions [1] is a locally-applied correction for chromaticity. A local approach to chromatic correction of the LHC IR is the subject of this paper.

2 MINIMIZING AND LOCALLY CORRECTING CHROMATICITY

Since minimization of chromatic effects favors a symmetric reflection of the final-focus telescope, a symmetric layout of the LHC IR was considered. However, the existing antisymmetric implementation does not lend itself readily to a symmetric version, and, not surprisingly, rematching to the arcs proved difficult and disruptive.

Maximum momentum acceptance is achieved when the sextupole nearest the IP corrects the plane with the corresponding largest chromaticity. The largest chromaticity on a particular side is determined by the sign of the quadrupole nearest the IP. The plane which is defocussed nearest the IP will always have the largest chromaticity. In keeping with the antisymmetric nature of the IR, the Chromatic Correction Section (CCS) should also display antisymmetry about the IP–on the designated left side of the LHC IR, a vertical sextupole should be closest to the triplet and on the right side a horizontal one.

For calculation purposes, the LHC IR along with the twelve arc cells were extracted from the ring. Because of the 90 degree phase advance across the arc cells flanking the LHC IR, sextupoles could be conveniently placed in conventional π pairs for chromatic correction. For a noninterleaved layout (which is optimal for standard LHC arc cells), the correction sextupoles must be paired with an empty cell in between. Therefore, 6 normal arc cells on either side of the IR are required for both vertical and horizontal chromaticity correction; or 12 arc cells total.

The natural chromaticity of the LHC was calculated independently and found to be -34. Using only the 4 sextupole pairs, linear chromaticities arising from the LHC IR were cancelled. The 'locally-corrected' LHC IR was then embedded back into the ring, and rough tracking studies were performed. Tracking results indicated about a 20% increase in the dynamic aperture and improved momentum acceptance. However, the sextupole strengths required to cancel natural chromaticity of the LHC IR were a factor of 4 or 5 over and above present design currents. Since such sextupole strengths are not realistic, work began on a more feasible local correction scheme–one which modified existing optics in order to bring down the required sextupole strengths and one which would also incorporate more optimal phase advances.

To bring down sextupole strengths, a much larger β function value is required at the sextupole locations. Since the FODO separation is about 40-50 m, this scales the maximum and minimum beta to 1.2 km and 1.5 to 2.8 m, respectively. (Lower maximum/minimum beta functions cause the Chromatic Correction Section (CCS) to compete optically with the LHC IR in terms of chromaticity). The increase in β_{max} from 200 m to 1.1 km alone is sufficient to bring down the sextupole strengths to operational values. The changed FODO structure starts at Q5 and, beginning at sextupole locations, continues for two cells if the sextupoles are interleaved and four cells if they are not. Two additional arc units were perturbed to rematch from the CCS into the standard arc cell.

The large ratio in β functions, here, averaging 1200 to 2, generally allows sextupoles to be successfully interleaved with little cross-plane correlations. It is anticipated that the interleaved sextupole scheme will show the best acceptance due to a reduction in the overall length of the CCS.

In the standard LHC optics, the phase advance from the peak β in the final-focus quadrupoles to the correction sextupoles is not a multiple of π, and, correspondingly, it is

* Operated by Universities Research Association, Inc. under contract No. DE-AC02-76CH03000 with the U. S. Department of Energy

0-7803-4376-X/98/$10.00 © 1998 IEEE

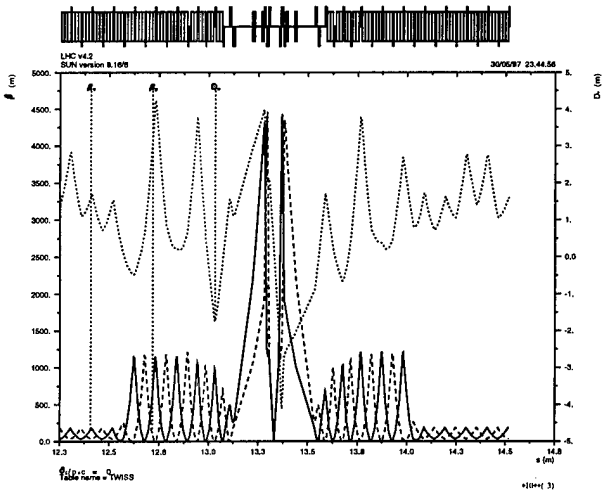


Figure 1: Horizontal (solid line) and vertical (dashed line) β-functions in the $\beta^* = 3$ mm IR lattice. Dot-dashed line shows the dispersion.

also not an odd multiple of $\pi/2$ from the IP. Therefore, the sextupole contributions to higher-order chromaticities and geometric aberrations are not minimized. In order to meet the optimal phase-advance criteria, the large $\sim$ 1km/2m ratios in maximum/minimum β functions were found to be critical. A full π phase advance is characteristic of the deeper minima and the phase advances to the high-beta locations and between sextupole pairs can be maintained in correct multiples of π. Geometric cancellation to second order is approximately achieved in the proposed configuration. The LHC low-β insertion with the CCS which was developed is given in Fig. 1. A smooth transition is achieved from the CCS into the arc in the lattice functions. The values of dispersion in the CCS and its present matching still need more work.

3 RESULTS

As has been already stated, apertures improved at the 20% level using a noninterleaved sextupole scheme in conventional arc cells. A CCS was subsequently designed which increased the β functions at the sextupole locations by a factor of 5–with the intended result of bringing down the required sextupole strengths. The larger values of betas combined with the large 40 to 50 m separations between quadrupoles conspired to raise quadrupole strengths in the pirated arc cells by as much as 30%. Although not technically insurmountable, the CCS will need to be refit to support operational values. In general, the new CCS showed a momentum aperture equivalent to the standard optics set even though machine tunes were displaced by $\pm.15$ from their optional fraction tune of .25. This is suggestive of increased momentum acceptance when tunes are readjusted near the quarter integer.

4 SUMMARY

In summary, a local chromatic correction has been applied to the LHC IR in the standard optics set and through a local modification about the final focus. Sextupole strengths in the former were not realistic, but appear to have acceptable values in the latter. Phase advances in the modified version are also close to optimal for sextupole chromatic correction. Work still remains to incorporate the dispersion and its matching in a more realizeable way. Also, the working tune needs to be restored to the optimum working point near the quarter integer (this does not appear to present any problems). Finally, tracking studies at the new working point need be performed to demonstrate and compare aperture and momentum acceptance.

5 REFERENCES

[1] 'Zeroth-Order Design Report for the Next Linear Collider', The NLC Design Group, LBNL-5424; SLAC-474; UCRL-ID-124161; UC-414, May, 1996. C. Johnstone and A. Garren, 'An Interaction Region and Chromatic Correction Design for a 2-TeV Muon Collider', to appear in the Proceedings of the Snowmass Workshop, June-July, 1996.

[2] J-P. Koutchouk, A. Faus-Golfe, H. Grote, T. Risselada, A Verdier, S. Weisz 'A Robust and Flexible Lattice for the LHC', to be published in the Proceedings of the PAC'97 Conference, Vancouver, Canada, May 12-16, 1997.

[3] A. Faus-Golfe, 'Multipole Compensation in the LHC Low-β Insertions', and F. Schmidt, M. Boge, 'Estimates for Long-term Stability for the LHC', to be published in the Proceedings of the PAC'97 Conference, Vancouver, Canada, May 12-16, 1997.

PERTURBATION OF THE PERIODIC DISPERSION UNDER BEAM CROSSING OPTICS IN LHC

F. Méot*, FNAL, Batavia, IL 60510-500, USA

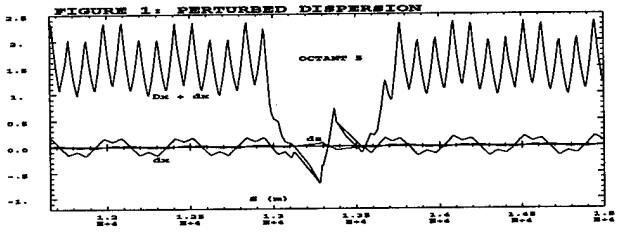
Abstract

Beam crossing and separation schemes in the LHC interaction regions impose non-zero closed orbit in the low-β triplets. The related perturbative dispersion is derived; propagation, multi-crossing interference, perturbative effects around the ring are investigated and quantified. Horizontal and vertical compensation schemes are presented.

1 INTRODUCTION

Crossing angle and orbit off-centering schemes at the interaction points (IP) in the LHC ring are foreseen [1][2], for the purpose of early separation of the beams so as to reduce harmful effects related to beam-beam interactions in that region where they share a common vacuum pipe. Such closed orbit (c.o.) geometry imposes horizontal and vertical off-centering in the low-β triplets, which has sensible effect on dispersion in collision optics when betatron functions reach very large values. This report provides an understanding and study of the building-up and effects of the anomalous dispersion in the LHC ring (Version 4.2), and investigates compensation schemes.

2 ANOMALOUS DISPERSION



2.1 *Equation of the anomalous dispersion*

The perturbative dispersion $d_y(s)$ due to $y_{co}(s)$ c.o. in the low-β triplets is the closed solution of [3]

$$d^2d_y/ds^2 + K(s)d_y = -\Delta B(s)/B\rho + K(s)y_{co} \quad (1)$$

with $y \equiv x$ *or* z, $B\rho$ = particle rigidity, K(s) = quadrupole strength, and the field term $\Delta B(s)/B\rho$ is introduced by the c.o. dipoles. Eq. (1) can be solved in the elementary kick approximation $K(s)y_{co}(s) = \int K(s)y_{co}(s)\delta(s - s_q)ds_q$ which yields the periodic solution (Fig. 1)

$$d_y(s) + y_{co}(s) = \frac{\sqrt{\beta(s)}}{2\sin\pi\nu}\sum(KL)_q y_{co}(s_q)\cdot \sqrt{\beta(s_q)}\cos\nu[\pi - |\phi(s) - \phi(s_q)|] \quad (2)$$

where $\phi(s) = 1/\nu\int ds/\beta$ = normalized betatron phase, $\phi(s_q)$ = phase at the kick, β = betatron function, ν = machine tune. The closed orbit $y_{co}(s_q)$ at the kick can be expressed in terms of its transport from the IP (optical functions β^*, ϕ^* while $\alpha^* \equiv 0$ is assumed). This yields

$$d_y(s) = -y_{co}(s) + \{\frac{\sqrt{\beta(s)/\beta^*}}{2\sin\pi\nu} \quad (3)$$
$$+y^*\sum(KL)_q\beta(s_q)\cos\nu[\phi(s_q)-\phi^*]\cos\nu[\pi-|\phi(s)-\phi(s_q)|]$$
$$+y'^*\beta^*\sum(KL)_q\beta(s_q)\sin\nu[\phi(s_q)-\phi^*]\cos\nu[\pi-|\phi(s)-\phi(s_q)|]\ \}$$

2.2 *Upper limits of the perturbation*

Beyond the low-β triplets associated with the non-zero c.o. Eq. (2) can be written under the form $d_y(s)/\sqrt{\beta(s)} = -y_{co}(s)/\sqrt{\beta(s)} + \bar{D}_y\cos\nu[\phi(s) + \Omega]$, with

$$\bar{D}_y = \{[\sum(KL)_q y_{co}(s_q)\sqrt{\beta(s_q)}\cos\nu(\pi + \epsilon\phi(s_q))]^2 \quad (4)$$
$$+[\sum(KL)_q y_{co}(s_q)\sqrt{\beta(s_q)}\sin\nu(\pi + \epsilon\phi(s_q))]^2\ \}^{1/2}/(2\sin\pi\nu)$$

($\epsilon = \pm 1$ for $\phi(s) \gtrless \phi(s_q)$, $\forall q$). Numerical calculation of the sums from first order optics yields [3]-[6]

$$\frac{\bar{D}_x|_{x^*=0}}{x'^*} \approx \frac{\bar{D}_z|_{z^*=0}}{z'^*} \approx 170,\ \frac{\bar{D}_x|_{x'^*=0}}{x^*} \approx \frac{\bar{D}_z|_{z'^*=0}}{z^*} \approx 2 \quad (5)$$

Since β_x and β_z have similar shapes Eq. (5) tells that the perturbation due to $10^{-4}rad$ c.o. angle ("d_x" plot in Fig. 1) is about ten times that due to $10^{-3}m$ c.o. off-centering ("d_z" plot in Fig. 1) . Extrema of $d_y(s) = \bar{D}_y\sqrt{\beta(s)}$ can be derived, this is studied in more details in Section 3.

2.3 *Comparison with the effects of D1/D2 dipoles*

Dispersive effects due to crossing can be compared to those due to the separator/recombiner dipoles $D1/D2$, in particular in view of simultaneous compensation by an optical assembly such as proposed in [7]. A single dipole (D1 or D2) with bend Θ_D excites a dispersion of closed form

$$\frac{^{D}d_x(s)}{\sqrt{\beta(s)}} = \frac{\Theta_D}{2\sin\pi\nu} < \sqrt{\beta(s_D)} > \cos\nu[\pi - |\phi(s) - \phi(s_D)|] \quad (6)$$

with $< \sqrt{\beta(s_D)} >$ = mean value of $\sqrt{\beta(s_D)}$ and assuming $\phi(s_D) \approx C^{ste}$, over a dipole. The overall perturbation is obtained by superposing the effects of the two pairs $D1/D2$, which, with $\phi(s_{D1}) \approx \phi(s_{D2})$, leads to

$$\frac{^{D1/D2}d_x(s)}{\sqrt{\beta(s)}} = {}^{D1/D2}\bar{D}_x\cos\nu[\phi(s) + \tau] \quad (7)$$
$$\approx \frac{\Theta_D}{2\sin\pi\nu}[< \sqrt{\beta(s_{D1})} > - < \sqrt{\beta(s_{D2})} >]$$

Given $< \sqrt{\beta(s_{D1})} > \approx \sqrt{<\beta(s_{D1})>}$ and $\Theta_D = 2.17\,10^{-3}rad$, it comes out ${}^{D1/D2}\bar{D}_x \approx 460\,10^{-4}$, which yields about $\pm 0.6\,m$ modulation at $\beta(s) = 180\,m$. This can be readily compared to the analogous coefficients due to $x'^* = 10^{-4}rad$ c.o. angle (Eq. 5), namely

$$^{Crossing}\bar{D}_x\ /\ {}^{D1/D2}\bar{D}_x \approx 170/460 \approx 35\% \quad (8)$$

* On leave from CEA/DSM-Saclay, France.

0-7803-4376-X/98/$10.00 © 1998 IEEE

In other words, the modulation in the arcs due to x'^* is $\pm 0.35 \times 0.6 \approx \pm 0.2\,m$ (Fig. 1). It also means that a correction scheme intended to compensate the dispersion due to $D1/D2$ can take care in addition of $10^{-4} rad$ c.o. angle by changing its strength (increase or decrease depending on the crossing sign) by about 35%.

3 TYPICAL EFFECTS OF CROSSING ANGLE GEOMETRY

We consider the sole crossing scheme ($y^* = 0, y'^* \neq 0$), which has the major perturbative effect as shown above (Eq. 5). Beyond the crossing region Eq. (3) leads to [3]

$$d_y(s < s_{qLeft}, s > s_{qRight}) = -y_{co}(s) \quad (9)$$

$$\pm y'^* \sqrt{\beta(s)\beta^*}/(2\sin\pi\nu)\sin\nu[\pi - |\phi(s) - \phi^*|]\sum(KL)_q\beta(s_q)$$

(± 1 for resp. $\phi(s) \gtrless \phi(s_q), \forall q$)

Extrema in the arcs

These are attained when $\sin\nu[\pi - |\phi(s) - \phi^*|] \approx 1$. Considering that $\beta_{max}(s) \approx 180\,m$ while $\sum(KL)_q\beta(s_q) \approx 370$ in odd-type IR's [3], it comes for x'^* *or* $z'^* = 10^{-4} rad$ c.o. angle, $d_{x,extr} < 0.228\,m$ ($\nu_x = 63.28$), i.e., about 10% of the first order dispersion ; or $d_{z,extr} < 0.212\,m$ ($\nu_z = 63.31$).

Extrema in low-β triplets

The phase in triplets is $\phi(s) \approx \phi(IP) \pm \pi/2\nu$ while $\beta_{max} \approx 4430\,m$ at *IP*1/5, $\approx 4020\,m$ at *IP*2/8. Given the c.o. angle $x'^* = 10^{-4} rad$ at *IP*5 and betatron phases $\phi(IP1) = 0, \phi(IP2) = 2\pi 8.985/\nu_x, \phi(IP5) = \phi^* = \pi, \phi(IP8) = 2\pi 55.745/\nu_x$, $\nu \equiv \nu_x = 63.28$ and $\beta^* = 0.5\,m$, Eq.(9) yields

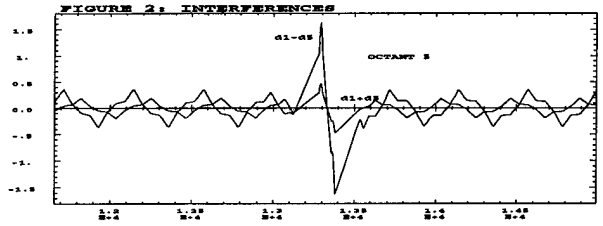
$$d_{x,extr}\ at\ IR1,2,5,8 = 1.13\,m,\ 1.07\,m,\ -0.71\,m,\ -1.05\,m \quad (10)$$

Dispersion at IP's

Eq. (9) with $\phi(s) = \phi(IP)$ and phase values above yield

$$d_x(IP1,2,5,8) = 0, 1.08\,10^{-3}m, 1.38\,10^{-3}m, -2.58\,10^{-3}m \quad (11)$$

which gives negligible beam size increase for $\delta p/p = 10^{-4}$.



Interferences

By virtue of the superposition principle interferences occur under crossings at several IP's. Two-IP interference for instance, in the case of a pair of inclined crossing geometries, or in the case of four alternating crossings [8]. Consider $z'^* = \pm 10^{-4} rad$ vertical c.o. angle at *IP*1 and *IP*5. Given $\phi(IP1) = 0$, $\phi(IP5) = \pi, \nu \equiv \nu_z = 63.31$, the resulting extremum in *IP*5 low-β triplets is (Eq. 9)

$$d_{z,extr} = \pm z'^* \frac{\sqrt{\beta_{max}\beta^*}}{2\sin\pi\nu}(1 + \epsilon\cos\pi\nu)\sum(KL)_q\beta(s_q)\ (\epsilon = \pm 1) \quad (12)$$

yielding, $d_{z,extr} \approx 0.46\,m$ for identical sign crossings ($\epsilon = 1$), $d_{z,extr} \approx 1.64\,m$ for opposite signs ($\epsilon = -1$) (Fig. 2).

Strong effects may arise from four-IP interference (non-alternating crossing configuration [8]). Consider c.o. angles $x'^* = \epsilon_{IP}\,10^{-4} rad$ with signs either identical, $\epsilon_1 = \epsilon_2 = \epsilon_5 = \epsilon_8 = 1$ or alternate, $\epsilon_1 = \epsilon_2 = 1$ and $\epsilon_5 = \epsilon_8 = -1$. The perturbation at *IP*5 low-β triplet reaches

$$d_{x,extr} = \pm x'^* \sqrt{\beta_{max}\beta^*}/(2\sin\pi\nu) \quad (13)$$

$$\sum_{IP=1-8}\epsilon_{IP}\cos\nu[\pi - |\phi(IP) - \phi(IP5)|]\sum(KL)_q\beta(s_q)$$

yielding, $d_{x,extr} \approx 0.42\,m$ if all crossings have identical signs, $d_{x,extr} \approx 4.1\,m$ in the second case.

4 CORRECTION SCHEMES

4.1 *Self-absorption within regular IR tuning procedures*

The simplest way to compensate the anomalous dispersion is by re-tuning the IR. As expected from $d_x(s) \approx 10\% D_x(s)$ under $\pm 10^{-4} rad$ c.o. angle (after Eq. 5), doing so leads to very limited changes in the Q1-Q10 IR quadrupole strengths. As to the optical functions, there is no meaningful difference with the unperturbed ones [3].

4.2 *Quadrupole correction of the horizontal dispersion*

Corrector strength

Quadrupole correctors excite a perturbative dispersion which superposes with that due to c.o. in the low-β triplets. This translates to additional term $\int K_Q(s)d_x(s)\delta(s - s_Q)ds_Q$ in Eq. (1) (index Q stands for the correctors). Besides, minimizing the corrector strength imposes on the one hand $\phi(s_Q) = \phi(s_q) + \pi/\nu[modulo\,\pi/\nu]$, on the other hand maximizing $D_x(s_Q)\sqrt{\beta_x(s_Q)}$ (which also minimizes effects on the orthogonal plane). Considering that $\phi(s_q)$ and $D_x(s_Q)\sqrt{\beta_x(s_Q)} \approx C^{ste}$ the correction strength writes

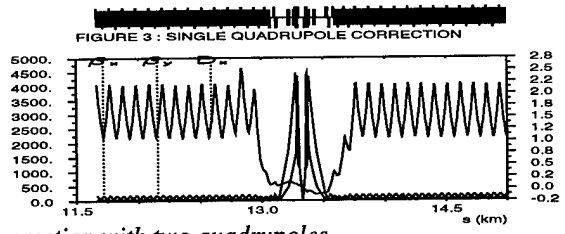
$$\sum_Q (KL)_Q = \pm \sum_q (KL)_q x_{co}(s_q)\sqrt{\beta_x(s_q)}\ /\ D_x(s_Q)\sqrt{\beta_x(s_Q)} \quad (14)$$

Numerical calculations for odd IR give $\sum(KL)_q\, x_{co}(s_q)\,\sqrt{\beta_x(s_q)}|_{Left/Right} = -1.12\,10^{-2} / 1.50\,10^{-2}$ for respectively the left and right low-β triplets. Hence the integrated strengths that independently close the left and right dispersion bumps : $|(KL)_Q|_{Left/Right}| \approx 3.9\,10^{-4} / 5.2\,10^{-4} m^{-1}$.

Correction with a single quadrupole

A single quadrupole with strength $9\,10^{-4} m^{-1}$ (after Eq. above) is sufficient to cure the anomalous dispersion, since the two π/ν apart low-β triplets sources of the defect excite independent perturbations that add in phase. It may be placed close to MSCBH multipole and would excite a defect in phase opposition thus canceling the anomalous dispersion beyond the local chromatic bump so determined. Fig. (3) shows the resulting second order dispersion at Octant 5, prior to any re-tuning of the IR, to be compared to the uncorrected situation (curve "$(D_x + d_x)$" in Fig. 1). Yet a single quadrupole has sensible effect on the tune and β mismatch, namely, $\Delta\nu_x = \beta_x(s_Q)(KL)_Q/4\pi \approx 1.3\,10^{-2}$ ($\beta_x(s_Q) = 178\,m$), $\Delta\nu_z = 0.23\,10^{-2}$ ($\beta_z(s_Q) = 32\,m$),

and $\Delta\beta_x/\beta_x < \beta_x(s_Q)|(KL)_Q|/2\sin(2\pi\nu_x) \approx \pm 8.5\%$, $\Delta\beta_z/\beta_z \approx \pm 1.5\%$ (with ν_x, $\nu_z \approx 63.3$).

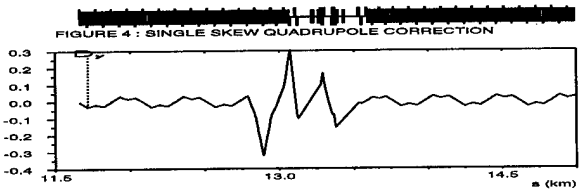


Correction with two quadrupoles

These effects can be taken care of to good level ($<$ 1% dispersion beating, $<$ 3% β-beat and at worst .0018 tune shift, prior to any re-tuning of the IR) by using two quadrupoles ; this could constitute a minimal correction scheme, yet there are several possibilities more or less beneficial w.r.t. residual dispersion, tune shift and β-beat : the two quadrupoles can be placed one at each end of the IR, or both at the same end, with each one half the strength $|(KL)_Q/2| \approx 4.5\,10^{-4}m^{-1}$; this has the effect of avoiding tune-shift and β-beats. They can be placed one at each end of the IR, with strengths $3.9\,10^{-4}/5.2\,10^{-4}m^{-1}$ to balance the opposite low-β triplet ; this brings quasi-zero dispersion and derivative at the IP.

Correction with four interlaced quadrupole pairs

Following a correction scheme proposed for SSC [9], the method above has been extended to four pairs of quadrupoles. Such correction scheme is also assimilable within the modular LHC IR tuning scheme [7] and other Q-shift system [10]. As expected from the discussions above, the correction is very efficient in terms of tune-shift, β-beat and dispersion. More details can be found in [3].



4.3 *Correction of the vertical dispersion*

The vertical anomalous dispersion can be compensated by skew quadrupoles (as proposed at SSC [9]) located at arc ends close to MSCBV correctors and maxima of $D_x\sqrt{\beta_z}$ and low β_x. Their role is to couple the horizontal dispersion into the vertical plane.

Corrector strength

The vertical dispersion verifies $d^2d_z/ds^2 + K(s)d_z = R(s)D_z$. The closed solution is (after Eq. 2)

$$d_z(s) = \frac{\sqrt{\beta_z(s)}}{2\sin\pi\nu_z} \cdot$$

$$\sum (RL)_{SQ} D_x(s_{SQ})\sqrt{\beta_z(s_{SQ})}\cos\nu[\pi - |\phi(s) - \phi(s_{SQ})|] \quad (15)$$

where index SQ denotes the correctors, R = skew quad strength. Taking $\phi(s_{SQ}) = \phi(s_q) + \pi/\nu[\pi/\nu]$ while $\phi(s_q)$ and $D_x(s_{SQ})\sqrt{\beta_z(s_{SQ})} \approx C^{ste}$ gives the correction strength

$$\sum (RL)_{SQ} = \sum (KL)_q z_{co}(s_q)\sqrt{\beta_z(s_q)}/D_x(s_{SQ})\sqrt{\beta_z(s_{SQ})}$$

$(RL)_{SQ}|_{Left/Right} \approx 10.6\,10^{-4}/7.9\,10^{-4}m^{-1}$ is necessary for balancing the effects of the left and right low-β triplets under $z'^* = 10^{-4}rad$ c.o. angle at IP [3]-[6].

Correction with a single skew quadrupole

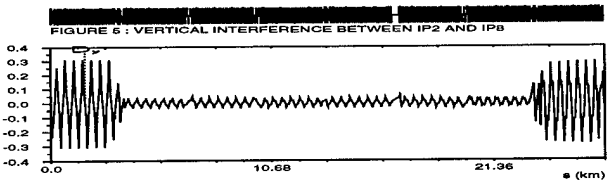
The corrector is placed at an arc end next to a MSCBV multipoles with the strength $18.2\,10^{-4}m^{-1}$ (Eq. above). Dispersion does not exceed 0.32 m in the crossing octant (Fig. 4), it is less than 0.05 m everywhere else in the ring (see the uncorrected situation, curve "d_x" in Fig. (1)).

Interlaced correction scheme

Residual effects on the first order focusing are weak ; however they can be improved by using quadrupole pairs ; doing so damps the dispersion to 0.2 m in the crossing low-β triplet. The philosophy is the same as above, for the horizontal plane ; more details can be found in [3].

Interferences

If no correction of the vertical dispersion is foreseen, yet some benefit may be drawn from interference, as long as adequate phase relation is fulfilled between IP's of concern. Fig. 5 shows such self-cancellation in the range IR2/IR8 when setting $z'^* = 10^{-4}rad$ c.o. angle at IP2 and IP8 simultaneously. This plot can be readily compared to the situation due to a single crossing (curve "dx" in Fig. 1, and extrema at all IP's, Eq. (10)).



5 REFERENCES

[1] The Large Hadron Collider, Conceptual Design, CERN/AC/95-05 (LHC), CERN, 20 Oct. 1995.

[2] W. Herr, Is there an alternative to alternating crossing scheme in LHC?, CERN/SL/93-45 (AP) LHC Note 258, CERN, Nov. 1993.

[3] F. Méot, Crossing Angle Induced Dispersion In LHC, Report FERMILAB-TM-2001, FNAL, BD/Physics (1997).

[4] H. Grote, F. C. Iselin, The MAD Program, CERN/SL/90-13 (AP), 19 Jan. 1995.

[5] T. Risselada, CERN/SL/AP, provided the MAD files : lhc42.K-collision, lhc42.K-injection, lhc42.sequence.

[6] J. Jowett, RDTWISS computer code, private communication, CERN, 1994.

[7] A. Faus-Golfe, J. P. Koutchouk, A. Verdier, Analysis and improvement of the dispersion matching in LHC, LHC Project Note 32, CERN, Feb. 26, 1996

[8] W. Herr, Luminosity limitations in the LHC [...], CERN SL/Note 92-51 (AP), CERN, 21 Sept. 1992.

[9] Y. Nosochkov, D. M. Ritson, The provision of IP crossing angles for the SSC, IEEE Trans. 1993.

[10] A. Verdier, Operational Q-shifts and b2 compensation in LHC, LHC Project Note 26, CERN, 8 Jan. 1996.

TOWARDS THE OPTIMAL LHC INTERACTION REGION: BEAM-INDUCED ENERGY DEPOSITION*

N.V. Mokhov and J.B. Strait, Fermilab, P.O. Box 500, Batavia, IL 60510 USA

Abstract

The overall machine and detector performances at the LHC are strongly dependent on the interaction region (IR) scheme and details. Beam-induced energy deposition in the components of the complex due to both p-p collisions and beam loss in the IR vicinity is a significant challenge for the design of the high luminosity insertions. It was shown in our previous studies that a set of collimators in the machine and absorbers within the low-beta quadrupoles would reduce both the peak power density and total heat load to tolerable levels with a reasonable safety margin. New optical configurations for the IRs developed in the past year may require changes in the absorber dimensions. In this paper we present studies of the radial and azimuthal distributions of the deposited power density and the dependence of peak power density on absorber thickness. These can be used to guide further studies of the optics and absorber systems.

1 INTRODUCTION

The Large Hadron Collider (LHC) [1] is designed to produce p-p collisions at $\sqrt{s}$=14 TeV and $L = 10^{34}$ cm^{-2}s^{-1}. The interaction rate of 8×10^8 s^{-1} represents a power of almost 900 W per beam, the large majority of which is directed towards the low-β insertions. Previous studies [1, 2, 3] have identified this as a potentially serious problem. The quadrupole fields sweep the secondary particles into the coils preferentially along the vertical and horizontal planes, giving rise to local peak power density P_{max} as much as an order of magnitude larger than the average. Tests of porous cable insulation systems [4] and calculations concerning the insulation system to be used in the Fermilab-built LHC IR quadrupoles [5] have shown that up to about 1 mW/g of heat can be removed while keeping the coil below the magnet quench temperature. Since our previous studies [3], which presented an optimized set of absorbers to protect the magnets, the optics design of the IRs has changed and not all parameters of the new design are firmly established yet. We present here studies of the distribution of the the power density in radius and azimuth within the magnet coils and the dependence of P_{max} on the thickness of internal absorbers placed inside the magnet bore, which can be used to guide future studies of the optics and absorber systems.

2 INNER TRIPLET CONFIGURATION

The studies described in this paper are based mainly on the IRs in version 4.2 of the LHC optics [1]. In that design the triplet consists of four 5.5 m long, 70 mm coil aperture quadrupoles – Q1, Q2a, Q2b and Q3 – which are powered in series and operate at 225 T/m at the high luminosity IRs (points 1 and 5). Two 1.8 m long, 85 mm aperture trim quadrupoles adjacent to Q1 and Q3 (Q01 and Q03 respectively) operate at a maximum gradient of 120 T/m; they provide tunability and the additional strength required of the outer two elements of the triplet. Superconducting beam separation-recombination dipoles D1 and D2 are 11.5 m long, have an 88 mm coil aperture and operate at 4.3 T. Under injection (collision) optics β^* = 6 (0.5) m, and a half crossing angle of 100 μrad is specified.

Recently a new version 5 of the LHC optics [6] has been introduced, which eliminates the trim quadrupoles and lengthens Q1 and Q3 to 6.3 m. The separation between D1 and D2 is increased allowing the use of lower field or shorter dipoles. At the high luminosity IRs D1 is replaced by a room temperature magnet. The half- crossing angle is now proposed to be 200 μrad at injection and 175 μrad under collision optics in the high luminosity IRs, and a $\pm$2 mm transverse separation at injection has been introduced. Under injection optics β^* = 12 m, but might be increased further. The optimization of these parameters is the subject of on-going studies (for example [7, 8]). The new conditions require changes of the absorber dimensions, typically increasing their apertures due to the larger crossing angle.

To understand the impact of these changes on the energy deposition and to guide future work, we have studied the dependence of P_{max} on internal absorber thickness. These studies have been carried out using both version 4.2 and version 5 configurations. Since the distance of the triplet from the interation point is the same and the overall length of the triplet is only slightly greater in version 5 than version 4.2 (30.6 m versus 29.6 m), the relation between power density and absorber thickness is the same for the two configurations within calculational uncertainties.

Figure 1 shows the version 4.2 inner triplet configuration and indicates the minimum mechanical half aperture, accounting for all the various errors considered in [1]. The positions and apertures of each magnet are shown as well as internal absorbers that come to the limiting aperture [3].

3 ENERGY DEPOSITION

The p-p collisions and showers in the IR components are simulated with the DPMJET event generator [9] and the MARS code [10], version 13(96), respectively. Charged particles are tracked through the lattice and the fields within each magnetic element. The cut-off energies are 1 MeV (charged particles), 0.2 MeV (photons) and 0.5 eV (neu-

* Work supported by the U. S. Department of Energy under contract No. DE-AC02-76CH03000

0-7803-4376-X/98/$10.00 © 1998 IEEE

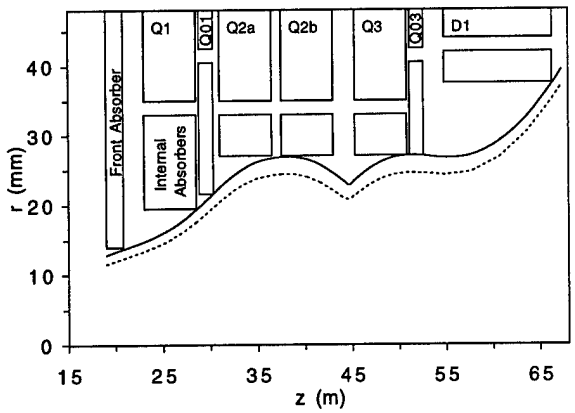


Figure 1: The LHC low-β insertions (version 4.2) including absorbers. The solid (dashed) curve is the approximate 10σ beam envelope for injection (collision) optics, including closed orbit and mechanical tolerances.

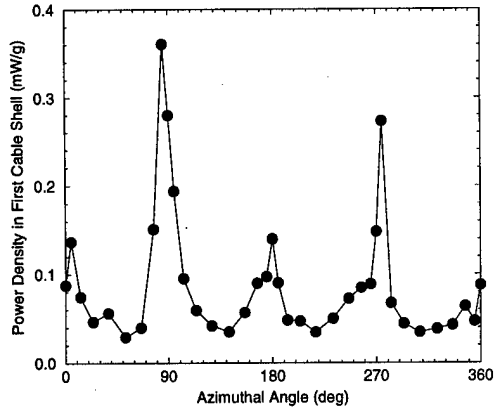


Figure 2: Azimuthal distribution of power density in the first cable shell at the downstream end of Q1. (0° is up.)

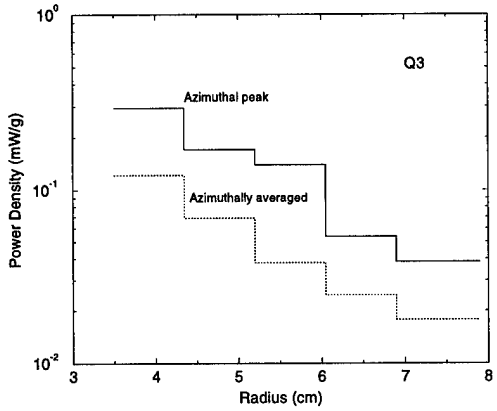


Figure 3: Radial distribution of P_{max} and azimuthally averaged power density at the upstream end of Q3.

trons). Magnet coils are modeled with 4 radial bins of 8.5 mm depth, azimuthal bins varying from 5° at the horizontal and vertical planes to 15° between, and axial bins range between 1.1 m (Q1) and 3.8 m (D1) long. The magnet coils, which are a mixture of NbTi, copper, insulation and helium, are simulated as a homogeneous material with A=50, Z=23 and ρ=7 g/cm^3. Details such as cooling channels in the yoke and coil ends are not included. Statistical errors on the Monte Carlo calculation are estimated to be $\pm$15% for P_{max}, based on comparison of results from different runs with independent random seeds.

The longitudinal distribution of P_{max} has been studied in detail in [3] for several triplet and absorber configurations. With the front collimator in place, P_{max} is always peaked at the downstream end of Q1, upstream end of Q2a, upstream end of Q3 and downstream end of D1. With no internal absorber P_{max} = 1.2$\pm$0.2 mW/g in Q2, at or above the allowable limit. With individually sized 10σ absorbers as shown in Fig. 1, P_{max} is substantially reduced, giving a factor of 3-4 safety margin. Cases in which the absorbers have larger or smaller inner radius have been studied to determine the dependence of P_{max} on absorber thickness.

Typical azimuthal structure of power density in the coils is shown in Fig. 2 for the 10σ absorber, showing the strong peaking at the horizontal and vertical planes. Left-right and vertical-horizontal asymmetries are apparent due to the excess of positive high energy particles in the forward direction and the horizontal crossing plane assumed in this study. Both P_{max} and azimuthally averaged power densities drop rapidly with radius (Fig. 3), so outer coil layers are in a much better situation than the innermost.

4 DEPENDENCE ON ABSORBER THICKNESS

A 1.8 m long copper absorber is placed in front of the triplet and stainless steel absorbers (thick beam pipes) are placed within the magnet bores to minimize the energy deposition in the coils. The LHC design requires [1] that the physical aperture, including effects of dispersion, closed orbit errors, construction and alignment tolerances, and the crossing angle in the IRs be everywhere at least 10σ (except at the beam cleaning collimators), where σ is the *rms* beam size. (A new method of computing the geometric aperture has been recently introduced [11], which will be incorporated in future studies.) Fig. 1 shows the 10σ limit for injection and collision conditions and absorbers with inner radii at this limit. The outer radius of the absorbers is 2 mm less than $r_{\rm coil}$.

Results on P_{max} for different triplet and absorber configurations, studied over 1995-1997, are collected in Fig. 4 through Fig. 6. The power density within a particular part of the triplet depends not only on the thickness of the absorber at that point but also on the apertures of the upstream absorbers. In Fig. 4 the aperture of the front absorber is r = 14 mm for the first three data points, and r = 12 mm for the last point. In Fig. 5 the pairs of data points at 8 mm and 9.5 mm thickness correspond to different absorber apertures in Q1 (Q1 aperture set to be the same as in Q2-Q3 or to the smallest allowed at its own location). Again, the right-most points correspond to a smaller front absorber aperture than the others. Here it is apparent that the effect of varying upstream apertures is comparatively

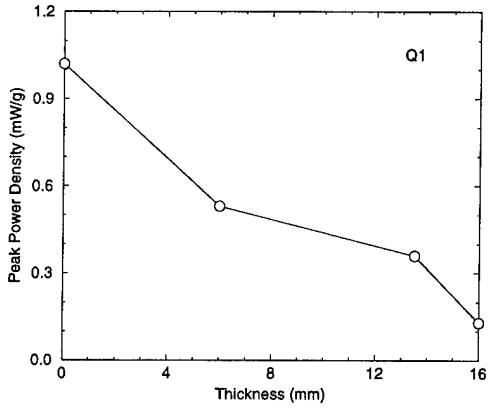


Figure 4: P_{max} in Q1 as a function of thickness d.

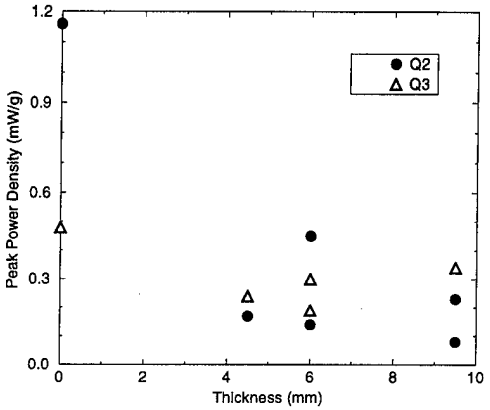


Figure 5: P_{max} in Q2 and Q3 as a function of thickness d.

local: P_{max} is less sensitive to front absorber aperture in Q2-Q3 than in Q1, especially for the case of a smaller Q1 absorber aperture. Similar trends are observed in Fig. 6 for D1.

To provide a reasonable margin with respect to expected quench level, the minimum absorber thickness should be 10-13 mm in Q1, 4.5-6 mm in Q2-Q3, and about 6 mm in D1. With this, the total power deposited in the inner triplet quadrupole cold mass is 82 Watts while the absorbers take about 60 Watts. One may consider cooling the internal absorbers at a higher temperature, as is done with the beam screen in the arcs. However, the insulating space required between a separate absorber and vacuum pipe would reduce the absorber thickness, making this option impractical.

5 CONCLUSIONS

Energy deposited in the superconducting magnets is an important issue in the overall design of the LHC IRs. Reducing P_{max} to an acceptable level requires the use of internal absorbers with the total thickness of 10-13 mm in Q1, 4.5-6 mm in Q2-Q3, and 6 mm in D1 (if this dipole is superconducting). Increasing the front absorber aperture above r = 14 mm will reduce the safety margin. Detailed analysis

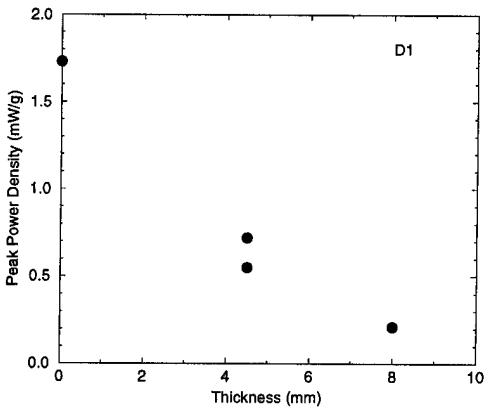


Figure 6: P_{max} in D1 as a function of thickness d.

of beam losses in the LHC high-luminosity interaction regions showed [12] that these contribute a few percent in the beam related energy deposition in Q2-Q3 quadrupoles and D1 and D2 dipoles, with pp-collisions as the main player.

6 REFERENCES

[1] 'The Large Hadron Collider Conceptual Design', CERN/AC/95-05(LHC), 1995, P. Lefèvre and T. Pettersson, editors.

[2] A. Morsch, R. Ostojic, T.M. Taylor, 'Progress in the Systems Design of the Inner Triplet of 70 mm Aperture Quadrupoles for the LHC Low-beta Insertions', Proc. 4th European Part. Accel. Conf., London, England, 1994.

[3] N.V. Mokhov and J.B. Strait, 'Optimization of the LHC Interaction Region with Respect to Beam-Induced Energy Deposition', EPAC96 and Fermilab–Conf–96/136, 1996.

[4] L. Burnod, et al., 'Thermal Modelling of the LHC Dipoles Funcitioning in Superfluid Helium,' Proc. 4th European Part. Accel. Conf., London, England, 1994.

[5] R. Bossert, et al., 'Development of a High Gradient Quadrupole for the LHC Interaction Regions,' IEEE Trans. Appl. Superconductivity **7**, 1997.

[6] A. Faus-Golfe, et al., 'A More Robust and Flexible Lattice for LHC,' submitted to the 1997 IEEE Part. Accel. Conf.

[7] M. Böge, et al., 'Overview of the LHC Dynamic Aperture Studies,' submitted to the 1997 IEEE Part. Accel. Conf.

[8] D. Ritson and W. Chou, 'Study of the Dynamic Aperture During Collisions in the LHC,' submitted to the 1997 IEEE Part. Accel. Conf.

[9] J. Ranft, Phys. Rev., D51, 64, 1995. Comput. Phys. Commun., **83**, p. 107, 1994.

[10] N.V. Mokhov, 'The MARS Code System User Guide, Version 13(95)', Fermilab–FN–628, 1995.

[11] J.B. Jeanneret and T. Risselada, 'Geometrical Aperture in LHC at Injection,' LHC Project Note 66, 23 Sept. 1996.

[12] A.I. Drozhdin, M. Huhtinen and N.V. Mokhov, Nucl. Instr. and Methods, A381, 531, 1996.

MEASUREMENT AND ANALYSIS OF LONGITUDINAL BUNCHED BEAM ECHOES IN THE FERMILAB TEVATRON

S. Assadi and P. L. Colestock
Fermi National Accelerator Laboratory*, P.O. Box 500, Batavia, IL 60510, USA

Abstract

Bunched beam echoes have been generated in the Fermilab Tevatron using a simple impulse kick technique involving the rf system. The echoes occur as a result of the nonlinear mixing of quadrupole and dipole components of successive impulse kicks, and may be readily observed using a bunch phase measurement system. The echo contains information on the synchrotron tune spread, as well as on various nonlinear phenomena, including the nonlinear tune spread and the effects of noise on the incoherent synchrotron motion. By measuring the detailed form of the echo response as well as its overall envelope as a function of the echo delay time, it is possible, in principle, to extract some of this information. In this paper we present experimental results along with a perturbation model which includes the effects of a nonlinear tune spread. In particular, we wish to explain the observed rapid decay of the echo envelope in terms of relevant beam parameters.

1 INTRODUCTION

Echoes have been studied in a variety of media for many years as a means of experimentally determining aspects of the dynamics of constituent particles (refs. [1] [2] [3]). In recent years, echoes have also been studied in high energy synchrotrons, and have been used to measure diffusion rates, although only in coasting beams [4] [5].

In this work we report the observation of bunched beam echoes in a high energy synchrotron and present a model which describes aspects of the experimental observations. At issue is whether such echoes can be used as diagnostic tools for determining experimentally various beam parameters.

Echoes are formally a nonlinear wave phenomenon whereby two harmonically related waves mix to provide a disturbance separated in time or space from the original excitation. Since echoes can occur at times much longer than a decoherence time, they may contain information about the long-term incoherent particle dynamics of a given system. Although echoes have often been viewed as a consequence of wave mixing, they can also occur in systems with negligible self-fields as a superposition of the motion of free-streaming particles, which is the view taken in this paper. We are interested in determining which aspects of the beam parameters can be determined from the properties of the echo response.

* Operated by the Universities Research Association,Inc, under contract with the U.S. Department of Energy.

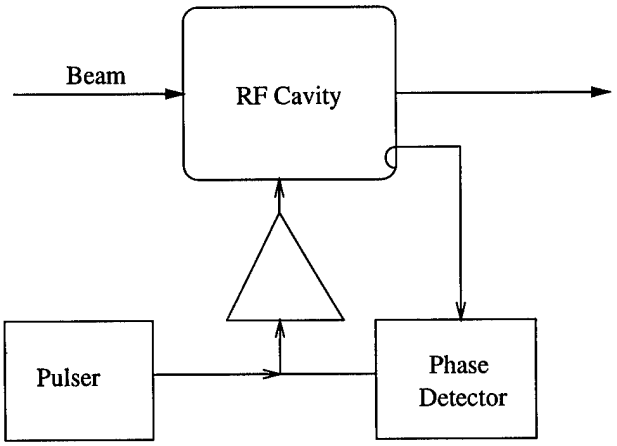


Figure 1: Sketch of the experimental setup. Successive impulses are applied with a pulser to the low-level phase feedback loop of the rf system. The resulting loop response applies a kick to the bunch energy.

2 EXPERIMENTAL RESULTS

Bunched beam echoes can be readily generated by two successive kicks in either energy or phase to a single stored bunch. The impulse must be much shorter than a synchrotron period, and sufficiently small so that the energy gain during a single kick is small compared to the bunch height. In the Tevatron, such a kick may be easily applied by introducing an impulse into the low-level rf phase loop, as shown in Fig. 1.

Two such kicks are applied separated by a variable delay, resulting in a response as shown in Fig. 2. Depicted is the bunch arrival phase relative to the synchronous phase established by the rf frequency. It is noted that the initial kicks decay in a time determined by the inverse frequency spread of the beam. The echo occurs as a temporally localized response at the synchrotron frequency at a time approximately equal to the delay between the two excitation impulses.

As the delay between the two excitation impulses is varied, the envelope of the echo maps out a characteristic curve, as shown in Fig. 3. Based on the experience with echoes in unbunched beams, it may be conjectured that the decay of the envelope may be due to stochastic processes affecting the beam dynamics, but it also may be due to the nonlinearity of the tune spread [6]. However, the observed echo decay is much faster than that seen in unbunched beams. It is our goal in the remainder of this paper to develop a model which would help determine the relative importance of these two effects.

0-7803-4376-X/98/$10.00 © 1998 IEEE

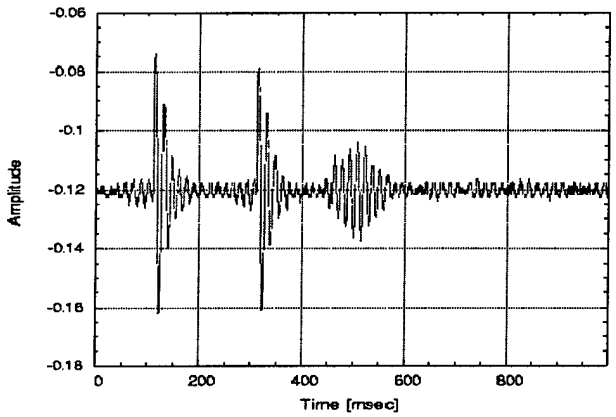


Figure 2: Bunched-beam echo generation in the Tevatron following two impulse kicks applied to a bunch through the rf system. A phase detector is used to detect the synchrotron oscillations associated with the impulse kicks. In this case the quadrupole portion of the second kick combines with the dipole portion of the first kick to produce a dipolar echo response. The phase amplitude is shown in arbitrary units.

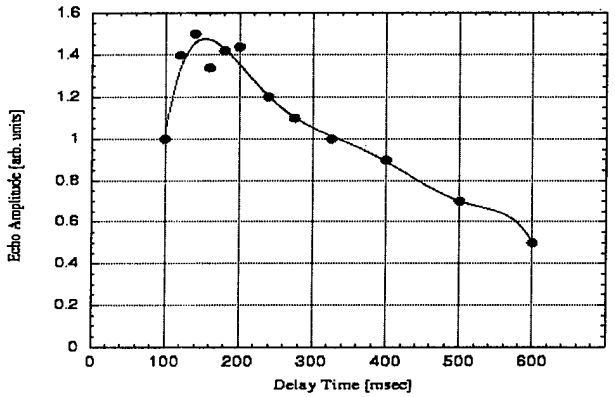


Figure 3: Decay of the echo envelope as a function of the delay time between impulse kicks. The decay rate indicates the combined influence of noise and nonlinear decoherence on the beam response.

3 PERTURBATION MODEL

A simplified expression for the dipole echo can be derived, assuming the absence of wakefields and external noise, using the same expansion of the Vlasov equation to second order used to describe three-wave coupling [6]. The analysis is carried out, however, in action-angle coordinates since the characteristics of the motion form level curves in this space. The transformation is given by

$$J = \tau^2 + (\frac{\dot{\tau}}{\omega_s})^2$$

$$\tau = \sqrt{J}cos\,\phi$$

$$\frac{\dot{\tau}}{\omega_s} = \sqrt{J}sin\,\phi$$

where τ is the arrival time of a particle relative to the synchronous time, and ω_s is the synchrotron frequency. We assume a Gaussian distribution of particles, which in normalized form is given as

$$\psi_o = \frac{1}{2\pi J_o} e^{\frac{-J}{J_o}}$$

After a kick of magnitude Δ_1 at t = 0, the perturbed particle distribution can be written

$$\psi_1 = \psi_o + \frac{\partial \psi_o}{\partial \frac{\dot{\tau}}{\omega_s}}\Delta_1 + \frac{1}{2}\frac{\partial^2 \psi_o}{\partial \frac{\dot{\tau}}{\omega_s}^2}\Delta_1^2 + \cdots$$

which, in action-angle coordinates is given by

$$\psi_1 = \psi_o + 2\sqrt{J}sin(\phi + \omega_s t)\frac{\partial \psi_o}{\partial J}\Delta_1$$
$$+\Delta_1{}^2(2\sqrt{J}sin[\phi+\omega_s t]\frac{\partial}{\partial J}[2\sqrt{J}sin\{\phi+\omega_s t\}\frac{\partial \psi_o}{\partial J}]$$
$$+\frac{cos[\phi+\omega_s t]}{\sqrt{J}}\frac{\partial}{\partial \phi}[2\sqrt{J}sin\{\phi+\omega_s t\}\frac{\partial \psi_o}{\partial J}])$$

We are only concerned with the dipolar part of the response, which is given by

$$<\tau> = \frac{1}{2}\int_0^\infty dJJ\int_0^{2\pi} d\phi\, cos\,\phi\,\psi_1(\phi, J, t)$$

Evaluation of this expression for a Gaussian distribution leads to the familiar result that the perturbation decoheres in a Landau damping time, given approximately by the inverse tune spread over the bunch radius, J_o. If now a second kick is made at $t = t_1$, the new particle distribution can be written as

$$\psi_2 = \psi_1 + 2\sqrt{J}sin(\phi + \omega_s[t-t_1])\frac{\partial \psi_1}{\partial J}\Delta_2$$
$$+\frac{cos(\phi+\omega_s[t-t_1])}{\sqrt{J}}\frac{\partial \psi_1}{\partial \phi}\Delta_2$$
$$+\frac{\Delta_2{}^2}{2}(2\sqrt{J}sin[\phi+\omega_s\{t-t_1\}]$$
$$\frac{\partial}{\partial J}[2\sqrt{J}sin\{\phi+\omega_s t\}\frac{\partial \psi_1}{\partial J} + \frac{cos[\phi+\omega_s t]}{\sqrt{J}}\frac{\partial \psi_1}{\partial \phi}]$$
$$+\frac{cos[\phi+\omega_s t]}{\sqrt{J}}\frac{\partial}{\partial \phi}[2\sqrt{J}sin\{\phi+\omega_s t\}\frac{\partial \psi_1}{\partial J}$$
$$+\frac{cos(\phi+\omega_s t)}{\sqrt{J}}\frac{\partial \psi_1}{\partial \phi}])$$

We may neglect the Δ_1 and Δ_2 terms, as they only describe the decoherence associated with the original kicks, as noted above. Similarly, the $\Delta_1{}^2$ and $\Delta_2{}^2$ terms do not produce echoes. Examination of the $\Delta_1\Delta_2$ terms shows they do not produce a dipole moment. Hence only the $\Delta_1\Delta_2{}^2$ and $\Delta_1{}^2\Delta_2$, which are the mixing of dipole and quadrupole excitations, are associated with the echo response. After considerable algebra, carrying out the ϕ integration, we arrive at the following expression for the dipole echo, which arises from the beating of the dipole and quadrupole oscillations of the successive impulses.

$$< \tau >_{echo} = \frac{\pi}{8} \int_0^\infty dJ \{ (JC)' \cos(\omega_s[t-t_1]) + (J[B-A])' \sin(\omega_s[t-t_1]) + 2J(A'+B') \sin(\omega_s[t-t_1]) \}$$

where primes correspond to $\frac{\partial}{\partial J}$ and

$$A(J) = 2\cos(\omega_s t_1)\frac{\partial \psi_o}{\partial J} + 4J\frac{\partial^2 \psi_o}{\partial J^2}\cos(\omega_s t)\cos(\omega_s[t-t_1]) - 4Jt\frac{\partial \omega_s}{\partial J}\frac{\partial \psi_o}{\partial J}\sin(\omega_s t)\cos(\omega_s[t-t_1])$$

$$B(J) = 2\cos(\omega_s t_1)\frac{\partial \psi_o}{\partial J} + 4J\frac{\partial^2 \psi_o}{\partial J^2}\sin(\omega_s t)\sin(\omega_s[t-t_1]) + 4Jt\frac{\partial \omega_s}{\partial J}\frac{\partial \psi_o}{\partial J}\cos(\omega_s t)\sin(\omega_s[t-t_1])$$

$$C(J) = 4Jt\frac{\partial \omega_s}{\partial J}\frac{\partial \psi_o}{\partial J}\cos(\omega_s[2t-t_1]) + 4J\frac{\partial^2 \psi_o}{\partial J^2}\sin(\omega_s[2t-t_1])$$

Finally, dropping further terms which do not lead to a delayed response, we obtain an expression for the echo response, including nonlinear synchrotron tune spread contributions, to second order.

$$< \tau >_{echo} = \frac{\pi}{2}\int_0^\infty dJ \{ (J^2\psi_o''' + 2J\psi_o'' - J^2{\omega_s'}^2 t t_1 \psi_o') \times \sin(\omega_s[t-2t_1]) - (2J\psi_o'\omega_s' t + 2J^2\omega_s' t\psi_o'' + J^2\omega_s'' t\psi_o') \times \cos(\omega_s[t-2t_1]) \}$$

where

$$\omega_s = \omega_{so} + \omega_{so}' J + \frac{1}{2}\omega_{so}'' J^2$$

4 DISCUSSION AND CONCLUSIONS

While this expression can be evaluated further analytically, we are running out of space, so we will simply show the results in Fig.4. It is seen that the model reproduces the measured echo form, which differs from the unbunched beam case through the influence of the nonlinearity of the synchrotron frequency; namely it is responsible for the Gaussian echo shape. However, the experimental results indicate a rapid characteristic decay of the echo envelope with t_1 and we find that the model cannot reproduce this effect at any reasonable value of synchrotron tune nonlinearity.

Therefore, we find that the tune nonlinearity must not be responsible for the echo envelope decay, at least not as included it in this model (to second order). One possibility is the fact that our pertubation approach breaks down at sufficiently long times, as evidenced by the continuously growing amplitude in Fig. 4. However, the observed decay occurs at very short times where our expansion should still be valid. The implication is that other mechanisms, such as noise, must be playing a role. This leaves open the possibility that the echoes may be used to directly measure this noise. The analysis of this possibility will be left for a future work.

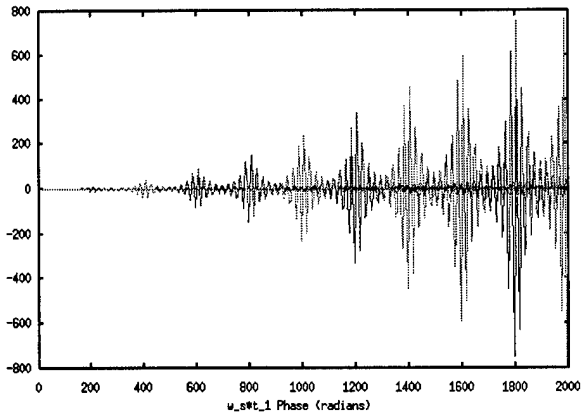


Figure 4: Theoretical echo response as a function of the delay time between excitation impulses. Multiple echoes are shown corresponding to equal increments of the impulse delay time, t_1. The echo amplitude increases nonlinearly with the delay time and the echo decoherence is determined by the inverse tune spread of the bunch.

5 REFERENCES

[1] R.W. Gould, *et al.*, *Phys. Rev. Lett.* **19**, 5 (1967).

[2] T. M. O'Neil, *Phys. Fluids*, Vol. 11, 1, 1968.

[3] G. V. Stupakov and K. Kauffmann, SSCL-587, 1992.

[4] O.S. Bruning, *CERN SL/95-83 (AP)*, Geneva (1995).

[5] L. K. Spentzouris, *et al.*, *Phys. Rev. Lett.* **76**, 4 (1996).

[6] L. K. Spentzouris, Ph.D. Thesis, Northwestern University, 1996.

ACCELERATOR PHYSICS ISSUES OF A VERY LARGE HADRON COLLIDER

W. Chou, Fermilab,* P.O. Box 500, Batavia, IL 60510, USA

Abstract

A Very Large Hadron Collider (VLHC) was proposed for the post-LHC future.[1] This paper gives a quick survey of a number of accelerator physics issues based on the information obtained from a parameter spreadsheet SSP.[2] The main technical challenges to build such a machine appear to be: the large number of events per crossing (in hundreds), enormous beam stored energy (equivalent to tens tons of TNT), ground motion (which is particularly harmful when the synchrotron frequency is in the sub-Hertz range), small dynamic aperture (due to long filling time), fast growth of the resistive wall instability (in a fraction of one turn), low threshold of the single bunch transverse instability (due to big machine size), strong synchrotron radiation (at a level close to the LEP) and short radiation damage lifetime, *etc.* Possible solutions to some of these problems will also be discussed.

1 INTRODUCTION

The VLHC is really very large in the low field approach. Although a coherent parameter list is yet to be developed, this paper will base its discussions on the following assumed "Level 0" specifications:

$$\begin{aligned} \text{Energy per beam } E &= 100 \text{ TeV} \\ \text{Luminosity } \mathcal{L} &= 1 \times 10^{35} \text{ cm}^{-2}\text{s}^{-1} \\ \text{Collision} &= p\text{–}p \\ \text{No. Detector} &= 1 \\ \text{Circumference} &= 10^6 \text{ meters} \end{aligned}$$

Because the interaction cross section is approximately proportional to $1/M^2$, where M is the equivalent parton beam energy, the luminosity should go as E^2. Anything below 10^{35} may be difficult to justify for a 100 TeV machine.

The physics of p-p and $\bar{p}$-p is similar at multi-TeV region. But p-p is easier to reach high luminosity. Besides, $\bar{p}$ may be just too expensive to fill up a megameter ring.

Starting from these top level parameters, one can generate their derivatives by running a spreadsheet. One such program is the SSP. It was originally written for the former project SSC, but can easily be modified to serve the VLHC. The next section will discuss a number of accelerator physics issues based on the output of this program.

* Operated by Universities Research Association Inc. under Contract No. DE-AC02-76CH03000 with the U.S. Department of Energy.

2 SELECTED ISSUES

2.1 *Events per crossing*

The number of events per crossing has a Poisson distribution. The average number n is:

$$n = \mathcal{L}\sigma_{\text{inel}}S_b \qquad (1)$$

in which σ_{inel} is the inelastic pp cross section, and S_b the bunch spacing. The value of σ_{inel} at 200 TeV center-of-mass energy is unknown. If the scaling law in the lower energy regions is employed, it could be estimated at about 150 mb. Thus, The only knob to reduce n is by reducing S_b, *i.e.,* increasing the number of bunches. But even at a 16 ns bunch spacing, the number of events per crossing could still reach about 300! This must be a serious challenge to the detector design.

2.2 *Beam stored energy*

This is one of the primary concerns. For $\mathcal{L} = 10^{35}$, $S_b = 16$ ns, $\beta^* = 0.3$ m, and $\epsilon_{\text{N}}(95\%) = 24\pi$, the current is about 0.6 A per beam. The stored energy of the two beams would be about 400 GJ, which is equivalent to 90 tons of TNT! Any accidental beam loss could be a catastrophe.

2.3 *Ground motion*

This is another primary concern for a machine of this size. It has two effects:

1. Relative movement of the magnets:
   This may be caused by tides, seismic effects, ground water level changes, *etc.,* which could lead to misalignment and mis-steering and result in an aperture problem.

2. Resonance with the synchrotron frequency:
   The small slip factor (3×10^{-6}) and low revolution frequency (300 Hz) lead to a very low synchrotron frequency (fraction of 1 Hz). This would make it vulnerable to external perturbations, such as the ground motion, which has large components in this low frequency range.

2.4 *Filling time and dynamic aperture*

Assuming two rings in the Tevatron tunnel as the injector, each capable to deliver 2.5 TeV protons (using 10 Tesla dipoles), cycle time 200 seconds. Then the filling time would be over 9 hours!

Such a long filling time would pose a threat to the dynamic aperture at injection. The big dynamic range of the

0-7803-4376-X/98/$10.00 © 1998 IEEE

beam energy (from 2.5 to 100 TeV, a factor of 40) would imply that the field quality at injection could not be very good. Assume the error field be similar to that of the SSC magnets. Then, scaled from the SSC simulation results, the dynamic aperture would shrink to less than 1 σ!

2.5 Beam instability scaling

This has been discussed in detail in Ref. [3]. We will apply those results to the VLHC.

2.5.1 Transverse mode coupling instability

The bunch current threshold of this instability decreases as the machine size increases:

$$I_{th} \propto R^{-3/2} \tag{2}$$

in which R is the machine radius. In terms of maximum number of particles per bunch, the scaling is:

$$N_b \propto R^{-1/2} \tag{3}$$

Therefore, for large machines this instability could become an intrinsic bottleneck. This is basically because the transverse impedance $Z_\perp$ is proportional to the machine radius R and to the 3rd power of the beam pipe radius b^3. Scaled from the SSC (a presumably low impedance machine) impedance budget, the transverse impedance of the VLHC (big R and small b) could reach several hundreds MΩ/m and the beam could become intrinsically unstable. In particular in the vertical plane, where b is the smallest. Ref. [3] suggested to apply local negative transverse impedance for compensating the total machine impedance so that $Z_\perp$ would not scale with the machine size in a linear way.

2.5.2 Resistive wall instability

The growth rate (in s^{-1}) of this instability is more or less independent of the machine size. However, when expressing the growth time in terms of turn number n_w, one has:

$$n_w \propto R^{-1} \tag{4}$$

In other words, in large machines the instability could grow quickly. For the VLHC, assuming the magnet aperture is 2 cm (corresponding to 1.57 Tesla at 50 kA) and the beam pipe 2 mm thick, then the growth time at 2.5 TeV would be 0.2 turn. One needs powerful feedback systems to keep it under control, such as the so-called criss-crossing feedback and one-turn correction scheme.

2.5.3 Longitudinal microwave instability

The threshold of this one is almost an invariant when machine size increases. Therefore, it should not be a major concern.

2.6 Synchrotron radiation

2.6.1 Comparison with the LEP

100 TeV = 2000×50 GeV. This means that, apart from the machine size factor, the synchrotron radiation of a 100 TeV proton beam is in many ways similar to that of a 50 GeV LEP, as listed in Table 1. The following remarks are made:

Table 1. Comparison of 100 TeV VLHC and 50 GeV LEP

	VLHC	LEP
Synch rad (W/m)	5	55
Photons emitted ($s^{-1}m^{-1}$)	4.6×10^{16}	1.3×10^{16}
Critical energy (keV)	2.24	89.5

1. The main heat load (and the cooling requirement) would actually come from the activation of the NEG (350 W/m) instead of the synchrotron radiation. Both machines would be the same in this regard.

2. Assuming the photo-desorption coefficient has a weak energy dependence (as generally believed), the gas load of the proton machine could be close to or even worse than the LEP.

3. The radiation is hard x-ray in the VLHC (critical wavelength 5.5 Å). It could be a concern when x-ray constantly hits the superconducting cable.

4. The damping time of the transverse amplitude of the protons is about 38 hours, which may be too long to be useful.

2.6.2 The NEG

The NEG (ST707) used at the APS/ANL is about $124/m for the material. The engineering cost is several times more. (The activation temperature is 450°C. Slots are needed for accommodating the thermal expansion.) This would mean several hundreds millions dollars for the NEG.

Moreover, the NEG alone cannot produce the required vacuum. Lumped pumps (e.g., TMP) are needed to pump down to 10^{-8} torr (APS data) before activating the NEG.

2.6.3 Beam lifetime problem

In the HERA electron ring (26 GeV), poor beam lifetime was observed at 3 mA when synchrotron radiation stroke the vicinity of several sections of the antechamber that houses distributed ion pumps. When these sections were removed, the problem disappeared.

In the present sketch of the low field option, the radiation from one of the two beams would land on the wall of the antechamber housing the NEG. This makes one to worry about if the HERA problem could also happen to this machine.

2.7 *Radiation damage lifetime*

The SSC maximum allowable dose on the kapton was 5000 Mrad. Scaled from the SSC calculation, the radiation damage lifetime of the kapton in this machine would only be a fraction of a year.

2.8 *Beam pipe*

The complex cross section may exclude the use of stainless steel. The concerns about an aluminum pipe are:

1. The eddy current:
   The ramp time from 0.05 to 2 Tesla doesn't seem too bad. But the rectangular shape of the pipe could generate sizable eddy current induced sextupole field that would have to be compensated.

2. The high secondary electron yield of aluminum:
   It could cause two types of problems. One is multipactoring induced by a bunched proton beam as observed in the ISR at CERN many years ago. Another is the recently found electron cloud instability. A solution is to apply a thin Ti-N coating on the surface of aluminum, which has been adopted by LBL for the Low Energy Ring of the SLAC B-Factory. But this would mean additional cost.

2.9 *Other issues*

These include beam-beam, space charge, intrabeam scattering, beam heating and luminosity lifetime *etc.* They do not seem to present any major problem. The coupled bunch instability still needs some study. The issue of reliability will not be addressed in this paper.

3 CONCLUSIONS

The VLHC is an interesting yet very difficult machine to build. The primary concerns seem to be the number of events per crossing, beam stored energy, ground motion, dynamic aperture during injection and transverse instabilities *etc.* However, the key issue regarding the building of such a machine is technology, in particular the magnet and tunnelling. All other issues can only take a second seat.

4 ACKNOWLEDGEMENTS

The author would like to thank P. Limon for introducing him to the study of this interesting subject.

5 REFERENCES

[1] G. W. Foster and E. Malamud, Fermilab-TM-1976 (June, 1996).

[2] R. Schwitters *et al.*, Proc. 1993 Particle Accelerator Conference, Washington, D.C., May 17-21, 1993, p. 3781.

[3] W. Chou and J. Griffin, 'Impedance Scaling and Impedance Control,' this conference.

BEAM LOSS HANDLING AT TEVATRON: SIMULATIONS AND IMPLEMENTATIONS

A.I. Drozhdin and N.V. Mokhov*, Fermilab, P.O. Box 500, Batavia, IL 60510 USA

Abstract

Summary of studies is presented towards minimization of beam loss in the critical locations at the Fermilab Tevatron to reduce background rates in the collider detectors and to protect machine components. Based on detailed Monte-Carlo simulations, measures have been proposed and incorporated in the machine to reduce accelerator-related instantaneous and residual background levels in the DØ and CDF detectors. Recent measurements are in good agreement with the predictions. A re-alignment of the electrostatic deflector and the Lambertson magnet and the addition of shielding in the AØ straight section has resulted in reduction of beam induced energy deposition in the superconducting magnets, which allowed an increase in the extracted beam intensity. Using the same simulation technique, it has been calculated that the total beam of 10^{13} protons can be removed from the Tevatron at the end of the store, leaving the antiproton beam in the machine for recycling. Using the EØ collimator with attached scattering targets, this process will require about 100 seconds to keep the power deposition in the superconducting magnets below the quench level.

1 INTRODUCTION

Tevatron is the world's first superconducting and most powerful hadron collider. Enormous efforts at Fermilab, reliably provided 900×900 GeV $p\bar{p}$ collisions with the peak luminosity up to $2.5 \times 10^{31}\,\mathrm{cm}^{-2}\,\mathrm{s}^{-1}$, recently resulted in the discovery of the top quark, among many other important achievements. The current fixed target run, begun in May 1996, exhibits the impressive performance of both the machine and experiments. At the same time, work progresses to upgrade the accelerator and detectors into even more powerful research tools [1]. The high performance of Tevatron both in the fixed target and collider modes is achievable only with a dedicated beam cleaning system embedded in the lattice [2, 3, 4].

2 BEAM LOSS HANDLING

In the Tevatron, as in any other accelerator, the creation of a beam halo is unavoidable: proton (antiproton) scattering in the IPs, in beam-gas interactions and on the limiting apertures, the diffusion of particles due to various nonlinear phenomena out of the beam-core, as well as various hardware and software errors – all result in emittance growth and eventually in beam loss in the lattice [2, 5, 6]. This causes irradiation of conventional and superconducting (SC) components of the machine, an increase of background rates in the detectors, possible radiation damage, quench, overheating of equipment and even a total destruction of some units. A very reliable multi-component beam collimation system is the main way to handle beam loss and is mandatory at any SC accelerator, providing [4, 5, 6]:

- reduction of beam loss in the vicinity of IPs to sustain favorable experimental conditions;
- minimization of radiation impact on personnel and environment by localizing beam loss in the predetermined regions and using appropriate shielding in these regions;
- protection of accelerator components against irradiation caused by operational beam loss and enhancement of reliability of the machine;
- prevention of quenching of SC magnets and protection of other machine components from unpredictable abort and injection kicker prefires/misfires and unsynchronized abort.

At the early Tevatron days the first collimation system was designed [2] on the basis of the MARS/STRUCT [7, 8] full-scale simulations of beam loss formation in the machine. The optimized system, consisted of primary and secondary collimators about 1 m long each, was installed in the Tevatron which immediately made it possible to raise by a factor of 5 the efficiency of fast resonant extraction system and intensity of the extracted 800 GeV proton beam. The data on beam loss rates and on their dependence on the collimator jaw positions were in an excellent agreement with the calculational predictions.

Later, we have refined the idea of a primary-secondary collimator set and shown that this is the only way to use such a system in the TeV region with a length of a primary collimator going down to a fraction of the radiation length. The whole system should consist then of a primary 'thin scattering target', followed immediately by 'a scraper' with a few 'secondary collimators' in the appropriate locations in the lattice [5, 6]. The purpose of a thin target is to increase amplitude of the betatron oscillations of the halo particles and thus to increase their impact parameter on the scraper face on the next turns. This results in a significant decrease of the outscattered proton yield and total beam loss in the accelerator, scraper jaws overheating and mitigating requirements to scraper alignment. Besides that, the scraper efficiency becomes independent of accelerator tuning, there is only one drastic restriction of accelerator aperture and only the scraper region needs heavy shielding and probably a dogleg structure. The method would give

*Work supported by the U. S. Department of Energy under contract No. DE-AC02-76CH03000

0-7803-4376-X/98/$10.00 © 1998 IEEE

an order of magnitude in beam loss reduction at multi-TeV machines, but even at the Tevatron we have got a noticeable effect. Recently the existing scraper at AØ was replaced with a new one with two 2.5 mm thick L-shaped tungsten targets with 0.3 mm offset relative to the beam surface on the either end of the scraper (to eliminate the misalignment problem), resulting in reduction of beam loss rate upstream of both collider detectors [3]. A few other recent studies are described in the following sections.

3 FORWARD PROTON DETECTOR

The detector [9] consists of four Roman Pot units placed in the DØ straight section upstream and downstream of the separators, and of three units at the C48 location. Each unit consists of two square 2×2 cm^2 detectors placed from both sides of the closed orbit.

Particle background in the Roman pot detectors is originated in proton and antiproton interactions with the primary and secondary collimators. The primary collimators are positioned at 5σ while secondary ones at 8σ. The Roman pot detectors are at $8\sigma_x$ for proton beam and $9.4\sigma_x$ for antiprotons. Moreover, antiproton intensity intercepted by the collimation system is 3.6 times lower compared to the proton intensity. Therefore, antiproton background in the Roman pots amounts only 2% of the total background, and backgrounds in the DØ detector due to Roman pots on the proton side about two orders of magnitude higher compared to the antiproton side.

Total background hit rates in Roman pots are (2.3-3.3)$\times10^6$ p/s for detectors at $8\sigma_x$ and (0.87-1.09)$\times10^6$ p/s for detectors at $9\sigma_x$, i. e. the rates are three times lower for the detectors at larger distance from the closed orbit. Beam loss distributions in Tevatron with the Roman pot detectors at $8\sigma_x$ are presented in Fig. 1.

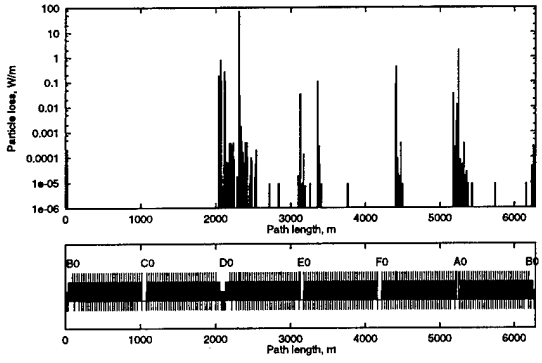


Figure 1: Beam loss distributions in Tevatron for D17 collimation with Roman pots at $8\sigma_x$.

4 FAST RESONANT EXTRACTION

Our recent simulations have shown that with the appropriate collimation, additional shielding in AØ and electrostatic deflector and Lambertson magnet realignment, one could reduce beam loss rates in Tevatron and increase the extracted intensity without quenches. It was found that in a narrow region of resonance phases used for extraction, the angle of the Lambertson magnet alignment depends mostly on the septa position, not on the resonance phase. This angle is equal to x'=-0.330 mrad for the septa at 20 mm from the beam orbit. Any misalignment can drastically increase the effective septum thickness and thus beam loss.

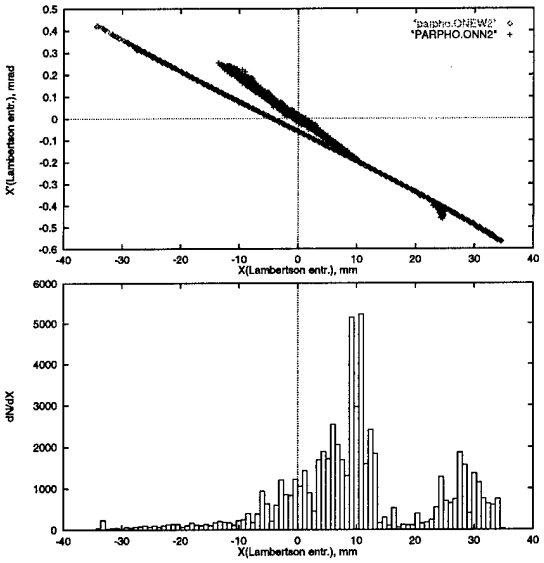


Figure 2: Fast extraction phase space at the AØ Lambertson magnet entrance. Top – extracted beam (black crosses) and protons outscattered from the DØ deflector (grey squares). Bottom – transverse distribution of outscattered protons.

Proton distributions at AØ are shown in Fig. 2 with proton beam kicked by the DØ electrostatic septum. Protons outscattered from the septum wires are intersepted by the Tevatron collimators. The EØ straight section is a very convenient place for the absorption of scattered protons, but unfortunately, there is no collimator in this location. It was found that the antiproton injection Lambertson magnet can be used as a collimator with particles catched by the normal conducting magnet yoke. Fast resonant extraction related beam losses (in SC magnets only) with and without collimation are presented in Fig. 3. Collimation system reduces beam losses in the superconducting magnets downstream of D17 by one order of magnitude. The DØ collimator right after the septum, catching the low-energy debries from the wires, unfortunately doesn't protect the DØ - D17 region.

Calculations show that a 1 m long collimator (r_{in}=15 mm) upstream of the extraction line superconducting skew dipoles will protect them from the secondaries produced in the Lambertson magnet. Similar collimator with a round aperture of r_{in}=20 mm upstream of the first and second quadrupoles will protect them and other ring superconducting magnets.

5 PROTON BEAM REMOVAL

The upgrade plan requires to remove proton beam from Tevatron before the deceleration leaving antiproton beam for recycling. There are two main concerns with the intense

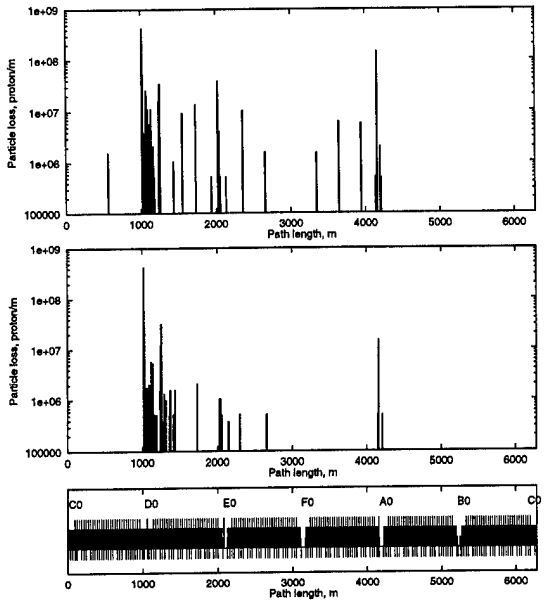


Figure 3: Fast resonant extraction losses without collimation (top), and with DØ , D17, F17, F49, AØ collimators and Lambertson magnet at EØ (bottom).

beam fast removal: superconducting magnet quenches caused by secondaries from a collimator and a target-collimator assembly overheating. A quench level of the Tevatron magnets at 1 TeV is about 3×10^8 p/m/s. This corresponds to about 50 W/m. A good practice is to keep a heat load to cryogenics below $\sim$ 1.5 W/m, or 1×10^7 p/m/s.

With the Main Injector, the EØ straight section becomes free of the magnets used for the beam injection into the Tevatron. With the first 15 m of EØ straight section reserved for RF, the rest 35 m can be successfully arranged for the proton beam removal (Fig. 4). Four DØ conventional bump-magnets are supposed to be used for the EØ dog-leg to protect the Tevatron magnets against neutral and low-energy charged particles out of a primary collimator. Two 1.5 m long L-shaped secondary collimators placed at 10σ downstream of the dog-leg at the entrance to the cold region intercept most secondaries. With such a system, the maximum beam loss in the Tevatron SC magnets is estimated to be 1.4 W/m. Moreover, the calculations show that it allows to get rid of other secondary collimators in the machine and, what is remarkable, reduce the beam loss level in the DØ - D17 region by about a factor of four.

The EØ target heating is a serious problem for short spills. An instantaneous target temperature rise is 10000°C. The target-collimator assembly cooling tremendously decreases this temperature. With this, for a 10 msec spill a stainless steel collimator edge is heated up to 1600°C, but already for a 1 sec spill, ΔT_{max} = 40°C, only. So, the target-scraper assembly overheating seams is not a restriction for the proton beam removal from Tevatron.

Calculations show that total beam intensity of 10^{13} can be removed from Tevatron during 100 s using EØ collimator. During the January 1997 experimental studies, proton

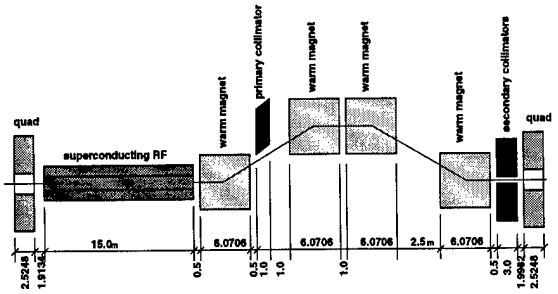


Figure 4: Dog-leg scheme for proton beam removal at EØ straight section.

beam was removed from Tevatron without problem until a SC magnet quench happened at the rate of 0.36×10^{11} p/s. This is three times below of that was expected, what is easily explained by absence of a scattering target in the collimator and possible closed orbit displacement. Moreover, analysis of the spill at beam removal has shown peaks of losses at frequency of 1, 4.6, 13.9, 21, 37, 73 and 90 Hz, which are understood from the Main Ring and Central Helium Liquefier performance and the beam position oscillations with synchrotron frequency. The experiment has shown that a feed-back system from the Beam Loss Monitors to the dipole correctors used for the beam displacement is necessary. This system would provide rectangular spill shape and eliminate low-frequency peaks (1-37 Hz).

6 REFERENCES

[1] D.A. Finley, J. Marriner and N.V. Mokhov, 'Tevatron Status and Future Plans', Fermilab–Conf–96/408, 1996.

[2] A.I. Drozhdin, M. Harrison and N.V. Mokhov, 'Study of Beam Losses During Fast Extraction of 800 GeV Protons from the Tevatron', Fermilab FN-418, 1985.

[3] J. Butler, D. Denisov, T. Diehl, A. Drozhdin, N. Mokhov and D. Wood, 'Reduction of Tevatron and Main Ring Induced Backgrounds in the DØ Detector', Fermilab–FN–629, 1995.

[4] N.V. Mokhov, 'Optimization of the Radiation Environment at the Tevatron', in Proc. of the Second Workshop on Simulating Accelerator Radiation Environments, CERN, October 1995, CERN/TIS-RP/97-05, 1997.

[5] M. Maslov, N. Mokhov and I. Yazynin, 'The SSC Beam Scraper System', SSCL-484, 1991.

[6] A. Drozhdin, N. Mokhov, R. Soundranayagam and J. Tompkins, 'Toward Design of the Collider Beam Collimation System', SSCL-Preprint-555, 1994.

[7] N. V. Mokhov, 'The MARS Code System User's Guide, Version 13(95)', Fermilab–FN–628, 1995.

[8] I. Baishev, A. Drozhdin and N. Mokhov, 'STRUCT Program User's Reference Manual', SSCL–MAN–0034, 1994.

[9] A. Brandt, A. Drozhdin, N. Mokhov et al., 'Proposal for Forward Proton Detector at DØ', Fermilab, October 1996.

USING LUMINOSITY DISTRIBUTIONS TO DETERMINE LUMINOSITY IN A COLLIDER WITH A COUPLED LATTICE

M.A. Martens, Fermi National Accelerator Laboratory *, P.O. Box 500, Batavia, IL 60510

Abstract

The traditional method for calculating luminosity in the Fermilab Tevatron during collider operations assumes a knowledge of the machine lattice at the locations of the flying wires and the luminous regions. In this paper we investigate an alternative method of determining the luminosity which does not require a knowledge of the lattice functions and can be applied even in the case of a transversely coupled lattice. By measuring a set of longitudinal luminosity distributions each with a different intentionally added separation between the proton and antiproton closed orbits the transverse widths of the luminous region can be determined and used to calculate the luminosity. As an example we apply this method to a set of Monte Carlo generated luminosity distributions using a Tevatron lattice that is transversely coupled due to a roll in one of the low beta quadrupole magnets.

1 INTRODUCTION

During Collider Run Ib operations in the Fermilab Tevatron there was disagreement by about 20% between the luminosity calculated from measured beam emittances and the luminosity as measured by CDF and D0. Traditionally the luminosity is calculated by measuring the proton and antiproton beam parameters such as emittance and bunch length and using these parameters, along with a set of lattice functions, to perform the overlap integral for the luminosity [1]. With this method errors in the lattice functions translate into errors in the calculated luminosity. Measurements of the lattice functions have been attempted in the Tevatron by making one-bump orbit distortions but these measurements give errors of at least 10% and furthermore has not led to a quantitative understanding of the coupling present in the Tevatron.

As an attempt to better understand the lattice in the interaction regions we investigate a method for measuring the transverse widths of the luminous region and use these results to calculate the luminosity. The method takes advantage of the fact that the longitudinal distribution of luminosity in the interaction region changes if the proton and antiproton orbits are separated using the electrostatic separators. As an example the dashed line in Figure 1 shows the expected luminosity distribution as a function of longitudinal position when the proton and antiproton beam closed orbits are separated horizontally by $180\mu m$ in the interaction region by using the electrostatic separators. The luminosity distributions generated in this example used a Tevatron lattice which was coupled due to a rolled low beta quadrupole.

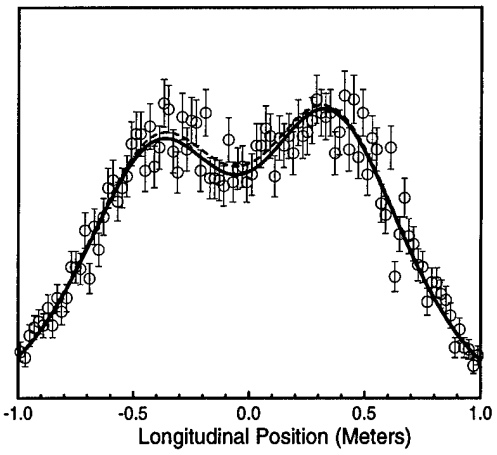


Figure 1: Luminosity distribution with added orbit separation of $\Delta X = +180$um. Circles with error bars are a Monte Carlo generated distribution. The solid line is the result of a fit to the data. The dashed line is the distribution used to generate the Monte Carlo data.

Two features are immediately evident in Figure 1. First, the luminosity distributions dips near the center of the interaction region due to the hourglass shape of the beams. The magnitude of the dip gives an indication of the transverse proton and antiproton beam widths. The second notable feature is that the luminosity distribution is not symmetric as would be expected from the ideal design lattice. In this example the asymmetry is caused by the coupling introduced by the rolled low beta quadrupole.

The method we investigate in this paper uses these features of the luminosity distributions to determine the transverse beam widths of the luminous region and to calculate the luminosity. One of the important features of this method is the inclusion of transverse coupling.

The next section of the paper introduces the luminosity formula used to handle transverse coupling. The section following this discusses the method of calculating the luminosity from a set of luminosity distributions and applies the method to a simulated set of distributions. The final section makes some conclusions and lists some additional sources of error which have not been considered in this analysis.

2 LUMINOSITY FORMULA

Without giving the details of the derivation (see [2]), the expression for the luminosity generated by a single proton

* Operated by University Research Association for the United States Department of Energy

0-7803-4376-X/98/$10.00 © 1998 IEEE

and antiproton bunch colliding can be reduced to

$$\mathcal{L} = \frac{N_p N_a f_{\rm rev}}{\sqrt{2\pi}^3 \sigma_z} \int \frac{1}{|\det \underline{\underline{C}}|^{\frac{1}{2}}} \exp(-\frac{1}{2}\underline{\chi_0}^T \cdot \underline{\underline{C}}^{-1} \cdot \underline{\chi_0} - \frac{1}{2}(s - z_o)^2/\sigma_z^2)\, ds. \quad (1)$$

where $\mathcal{L}$ is the total luminosity, N_p (N_a) is the number of protons (antiprotons), $f_{\rm rev}$ is the revolution frequency, and s is the longitudinal position. The integral extends over the entire luminous region and $s = 0$ is located at the center of the detector. The longitudinal bunch widths of the protons and antiprotons are combined into the single parameter σ_z^2 which is equal to the proton and antiproton rms bunch lengths added in quadrature and divided by 2. It should be noted that this expression was derived by assuming the transverse and longitudinal phase space distributions of the proton and antiproton bunches are ideal Gaussians.

As written, Equation 1 has no mention of lattice functions, Edwards and Teng parameters [3], or beam emittances. Instead we use the 4×4 covariance matrix $\underline{\underline{C}}(s)$ which is a measure of the transverse width of the luminous region as a function of longitudinal position s. More explicitly the covariance matrix is

$$\underline{\underline{C}}(s) = \begin{pmatrix} \sigma_x^2 & \sigma_{xy}^2 \\ \sigma_{xy}^2 & \sigma_y^2 \end{pmatrix} \quad (2)$$

where the σ are the rms widths of the luminous region and each of the σ^2 is a quadratic function of the longitudinal position s. In the ideal case with no coupling σ_{xy} would be zero and σ_x (σ_y) is determined from the convolution of the proton and antiproton horizontal (vertical) beam widths. Because $\underline{\underline{C}}(s)$ is a symmetric matrix there are a total of 9 parameters needed to completely specify $\underline{\underline{C}}(s)$.

An important part of Equation 1 is the inclusion of the possibility of proton and antiproton closed orbits which are separated. If there is a difference in the closed orbits the bunches will not collide head-on but instead will pass by each other with some separation and crossing angle. The total separations between the proton and antiproton orbits is given by $\underline{\chi_0}^T = (\Delta x(s), \Delta y(s))$. The final parameter in Equation 1 is the cogging offset, z_0 which is the longitudinal distance between the center of the detector and the position at which the centers of the proton and antiproton bunches collide as they pass by each other.

As expressed in Equation 1 there are a total of 18 parameters ($\underline{\underline{C}}(s)$, $\underline{\chi_0}^T(s)$, σ_z, z_0, N_p, N_a, and $f_{\rm rev}$) needed to calculate the luminosity. In the next section we will show how 15 of these parameters (all except N_p, N_a, and $f_{\rm rev}$) can be determined by making measurements of the luminosity distributions with different orbit separations intentionally introduced.

3 LUMINOSITY DETERMINATION FROM LUMINOSITY DISTRIBUTIONS

The integrand of Equation 1 is the longitudinal luminosity distribution. This can be measured using the experimental detectors in the luminous regions to make event by event vertex reconstructions of the longitudinal position. Intentionally changing the separation of the proton and antiproton closed orbits will change the luminosity distributions as demonstrated in Figure 1. By collecting a set of distributions with a variety of closed orbit offsets it is possible to fit the distributions for most of the parameters in Equation 1.

To determine the sensitivity of the method just described a set of nine simulated luminosity distributions was generated from a given set of lattice parameters and beam emittances. For this particular example the lattice used was calculated by assuming that a low beta quadrupole near the interaction region was rolled by 10 mrad and the resulting global coupling was corrected using the skew quadrupole correction circuits in the Tevatron. (This is similar to a situation that existed in the Tevatron early in Collider Run Ib.) The emittances used for the Monte Carlo generation are typical of Tevatron beam in collider operations. The horizontal and vertical proton (antiproton) emittances were 25π (15π) mm-mrad (95%, normalized) and the rms bunch lengths were 65 cm.

Distribution Number	Δx μm	Δy μm	Δz cm
1	0	0	0
2	+180	0	0
3	−180	0	0
4	0	+140	0
5	0	−140	0
6	+140	+140	0
7	−140	−140	0
8	0	0	+40
9	0	0	−40

Table 1: Orbit separations and cogging offsets introduced for the simulated luminosity distribution measurements. The values are the added separation between the proton and pbar orbit. A positive value indicates that the proton orbit was moved vertically up (or radially out) with respect to the centered orbit.

The distributions were generated with 10000 events divided into bins 2 cm wide. The separations introduced for the 9 distributions are shown in Table 1. These values were chosen since they are close to the maximum separations currently achievable with the electrostatic separators in the Tevatron. The distributions were simulated to include Poisson statistical deviations from the nominal value in each bin. Typically there were about 100 counts per bin in the peaks of the distributions. One of the distributions is shown in Figure 1 as circles with the error bars being the Poisson statistical errors.

These nine Monte Carlo distributions were then fitted simultaneously for 24 parameters, $\underline{\underline{C}}(s)$ (where $\sigma_x^2(s) = \sigma_{x0}^2 + \sigma_{x1}^2 s + \sigma_{x2}^2 s^2$, etc), $\underline{\chi_0}$, z_0, σ_z^2, and 9 scale factors which scale the number of events in the luminosity distributions to the the actual luminosity. (In principle there needs

to be only one overall scale factor but in practice it is simpler to have one scale factor for each distribution. The ratios of the fit scale factors values can then be compared to the ratios of the measured scale factors and used as a consistency check.) Using the fit values of the 24 parameters the luminosity distributions and luminosity can be calculated using Equation 1. In Figure 1 the dashed line is the calculated distribution using the fit parameters.

Fit Parameter	Mean fit value	Std dev. fit value	Actual value
z_0 (cm)	0.07018	0.290	0.0
σ_z^2(cm^2)	2125.0	35.2	2112.5
horz sep (μm)	0.07834	1.29	0.0
horz ang (μrad)	0.3959	1.59	0.0
vert sep (μm)	.004826	1.52	0.0
vert ang (μrad)	-0.3417	1.65	0.0
σ_{x0}^2	7231	253	7129
σ_{x1}^2	2445	377	2389
σ_{x2}^2	26860	2170	25920
σ_{xy0}^2	-2556	231	-2499
σ_{xy1}^2	-1156	365	-1173
σ_{xy2}^2	-7290	1340	-7386
σ_{y0}^2	7000	320	6930
σ_{y1}^2	2468	507	2491
σ_{y2}^2	21340	1960	21300
Scale factor 1	0.007511	0.000256	0.0075
Scale factor 2	0.04768	0.00256	0.0487
Scale factor 3	0.04758	0.00267	0.0487
Scale factor 4	0.02613	0.00109	0.0261
Scale factor 5	0.0261	0.00125	0.0261
Scale factor 6	0.1405	0.00829	0.1444
Scale factor 7	0.1402	0.00861	0.1444
Scale factor 8	0.00928	0.000317	0.0092
Scale factor 9	0.008631	0.000277	0.0086
luminosity	14.5576	0.453	14.7462

Table 2: Average and standard deviation of fit values for 100 simulated data sets compared to actual values for the distributions shown.

To determine statistically accuracy of this method 100 independently generated sets of Monte Carlo distributions were fitted and the mean and standard deviation of the fit values calculated. The results are listed in Table 2 and show that the luminosity can be determined with a 95% confidence level of $\pm 6\%$. The fit value of the luminosity was also systematically 1.3% lower than the actual value although it is not understood why. (Notice also that σ_{xy0}^2 is not zero due to the coupling of the lattice.)

4 CONCLUSIONS

In practice there are a number of difficulties which would add error to these measurements. Among these are the possibilities of detector errors, a smearing of the distributions from finite resolution of the z-vertex, and multiple interactions per crossing which may distort the luminosity distribution as well.

There were also several assumptions in this analysis which if not true will add error. First it was assumed that the intensities of the proton and antiproton bunches were known exactly. The uncertainties in these measurements will add at least several percent error to the calculated luminosity. Second, the formula for the luminosity in Equation 1 also assumes the proton and antiproton bunches are ideal Gaussians. Finally, it was assumed in this analysis that the actual separation introduced in the closed orbits was known exactly. In practice the amount of separation added between the closed orbits may not be known accurately.

Another complication not considered in this paper is the changing beam conditions while the luminosity distributions are being collected. Collecting 10000 events per luminosity distribution for several distributions can take on the order of an hour. During this time the proton and antiproton bunch lengths and transverse emittances are increasing leading to changing beam conditions and luminosity.

It may be possible to reduce the errors on this analysis but this has not yet been investigated. For instance measurements of the bunch lengths to within several percent could be used to further constrain the fits. Finally the choice of orbit separations used in this Monte Carlo (those listed on Table 1) were chosen as an example and were not chosen to optimize the error on the luminosity.

Despite limitations on the accuracy of the luminosity determined by this method, it still may be possible to gain information about the coupling of the lattice from the measurement of the covariance matrix $\underline{\underline{C}}(s)$.

5 ACKNOWLEDGMENTS

I would like to thank Mike Tartaglia and the DZero Luminosity Group for the idea of using luminosity distributions to determine the luminosity. I also thank Mike Tartaglia for his continued interest in this subject (See [4].)

6 REFERENCES

[1] M. Month, "Collider Performance with Ideal Collisions", "Accelerator Division Report 85–1", (1985)

[2] J. Holt, M.A. Martens, L. Michelotti, G. Goderre "Calculating Luminosity for a Coupled Tevatron Lattice" *Proceedings of the 1995 Particle Accelerator Conference*, p. 455, (1995).

[3] D.A. Edwards and L.C. Teng, "Parameterization of Linear Coupled Motion in Periodic Systems" *IEEE Trans. Nucl. Sci.*, vol. NS-20, No. 3, pp. 885–888, June 1973.

[4] M.A. Tartaglia, "Experiments with Separated Beams in Run I at the Tevatron Collider", These Proceedings.

EXCITATION CHARACTERISTICS OF FERMILAB MAIN INJECTOR DIPOLES AND MAGNET ASSIGNMENT TO REDUCE CLOSED ORBIT ERRORS

P.S. Martin and C.S. Mishra
Fermi National Accelerator Laboratory*
Batavia, Illinois 60510

Abstract

The Fermilab Main Injector project is building 344 dipoles, produced from steel with varying magnetic properties. The strategies for assigning dipoles, based upon their strength characteristics, are discussed. The closed orbit errors due to the strength variations are expected to be small in comparison to alignment errors.

1 INTRODUCTION

The Main Injector accelerator [1] will be constructed using 344 new conventional dipole magnets [2-3]. The new magnets consist of 216 6-m dipoles and 128 4-m dipoles. The 6-m dipoles are divided into two types with different styles of electrical and cooling connections, referred to as IDA and IDB dipoles; similar, there are two types, IDC and IDD, of 4-m dipoles. A given location in the lattice can use only one type, i.e. an IDB cannot be used in a location for which an IDA magnet is intended. The goal for dipole strength variations was to have a distribution of all strengths with an rms width of less than 0.10%. If that could be achieved, then the dipoles could be placed randomly in the ring and the closed orbit errors arising from the strength variations would (i) be correctable with the independent trim dipole correctors being fabricated, and (ii) would be comparable to the closed orbit errors arising from misalignments of the quadrupole magnets.

2 DIPOLE STRENGTHS

The dipoles for the Main Injector fall into three categories. First, twelve preproduction dipoles, three of each of the four different magnet types, were built using steel from one vendor (Armco). These were uniform in relative strength, but were about 1% too strong relative to later production. They were subsequently machined [4] to reduce their high-field strength to more closely match the production magnets. The production of the remaining dipoles used steel from another vendor (LTV Steel). The steel used in the early production dipoles had different B(H) characteristics than the later production, [5] and consequently, the first fifty magnets (approximately) were weaker by as much as 0.4% than the remainder of the production. The relative strength at 1.38 T of all the dipoles produced and measured to date are shown in Figure 1. In this plot, the Armco steel preproduction magnets are shown with negative abscissa.

As can be seen from this figure, the dipole strength rose during the first fifty production dipoles up to the nominal level, then remained within the band ±0.12%. The rms of the production dipoles after the first fifty is only 0.04%. The rms of the entire distribution, including the modified Armco steel dipoles, is less than 0.12%. However, the sample is certainly not a Gaussian distribution. While it appears likely that we could easily have endured the effects of randomly placing the dipoles in the ring, the production and installation schedule afforded us ample opportunity to minimize the closed orbit effects by assigning dipoles based upon their strength characteristics.

The sole criterion used in assigning magnets is that in Figure 1, the strength at 1.38 T. This field corresponds roughly to 120 GeV, the energy at which most Main Injector extractions take place, in particular the fixed target program with resonant extraction from the Main Injector. With injection at 8 GeV, the dipole correctors can easily handle rather large strength variations at that energy. Tevatron injection takes place at 150 GeV; it is hoped that by having a good orbit established at 120 GeV, the corrections needed to control the orbit at 150 GeV will be minimal. Other aspects of the dipoles, e.g. field shape, can be found elsewhere [6].

The phase advance per cell in the Main Injector lattice is close to 90°. This permits us to place magnets of the same type, e.g. two IDAs, one cell apart to produce a local orbit distortion with essentially no effect on the closed orbit in the rest of the ring. Orbit calculations are done using a detailed Main Injector lattice and the program TEAPOT. Special handling is obviously required for the preproduction dipoles and the weaker early production dipoles, placing them one cell apart. For the production dipoles, with their tighter distribution of strengths, the only measure taken is to ensure that no two adjacent dipoles have a greater than two standard deviation (of the same sign) strength variation from the mean. This technique has been applied in a series of episodes during the past fifteen months. By the time the FMI ring

* Work supported by the U.S. Department of Energy under contract number DE-AC02-76CH03000..

0-7803-4376-X/98/$10.00 © 1998 IEEE

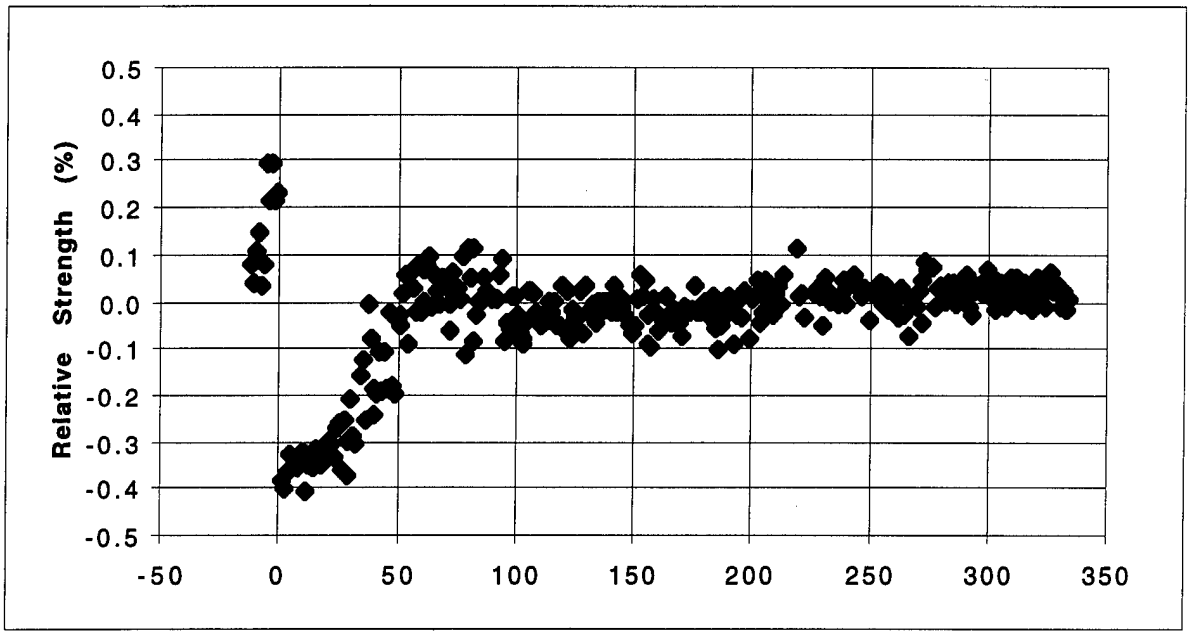


Figure 1. Relative strength of all dipoles produced to date, in approximate order of production. The pre-production dipoles are at the left.

enclosure became available in December, 1995, for the installation of utilities followed by magnet stands and magnets, a large inventory of magnets(~150) had been fabricated and measured. These were assigned and installed during the period February through April, 1996. As additional magnets are fabricated, we wait until thirty to forty magnets are available (about three months of production) and then assign and install them in a period of about one week. At this point in time, 297 dipoles have been assigned to the ring, of which 280 have been installed. Because of the strength variations observed, dipoles have also been assigned as spares, so that single-magnet replacements can be made without serious impact on the closed orbit.

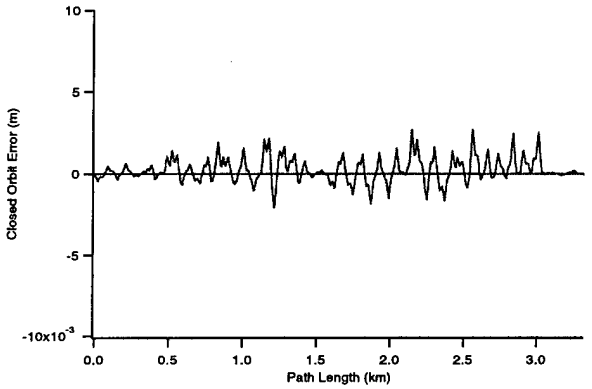


Figure 2. Closed orbit error due to dipole strength variations.

The expected closed orbit distortion resulting from the variations in dipole strength of all the magnets assigned to date is shown in Figure 2. The distortion is less than 3 mm everywhere. The correction dipole magnets being fabricated [7] for the Main Injector have the capability of correcting errors up to 7 mm at 120 GeV, and therefore can easily correct these errors. At commissioning time, closed orbit distortions from alignment errors are expected to be larger than those due to the dipole strength variations.

REFERENCES

1. S.D. Holmes, et al. "Status of the Main Injector and Recycler", these proceedings.
2. B.C. Brown, et al., "The Design and Manufacture of the Fermilab Main Injector Dipole Magnet", EPAC 92, Proceedings of the 1992 European Particle Accelerator Conference (1992).
3. D.J. Harding, et al., "Magnetic Field Measurements of the Initial Fermilab Main Injector Production Dipoles", Proceedings of the 1995, IEEE Particle Accelerator Conference.
4. P.S. Martin, et al., "Modifications To The Excitation Characteristics of FMI Dipoles by Machining", these proceedings.
5. P.S. Martin, et al., "Variations in the Steel Properties and the Excitation Characteristics of the FMI Dipoles", these proceedings.
6. D.J. Harding, et al., "Magnetic Field Measurements of the Initial Fermilab Main Injector Production Dipoles", Proceedings of the 1995 IEEE Particle Accelerator Conference.
7. I. Terechkine, et al., " Air-Cooled Trim Dipoles for the Fermilab Main Injector", these proceedings.

STATUS OF THE FERMILAB FIXED TARGET PROGRAM

C. D. Moore, FERMILAB[1] P.O. Box 500 Batavia, Illinois , U.S.A.

Abstract

Fermilab is in the midst of an 800 GeV fixed target run involving ten external beam lines and the operation of the pbar source for two additional experiments. Details of the preparation are presented with an emphasis on how changes from the last run have impacted the current run. Statistics and graphical representations show the progress toward meeting the goals of the program. An overview is presented of the external (floods....) and internal (machine instabilities ...) challenges encountered during the run.

1 FIXED TARGET GOALS

The main goal of the fixed target program can be succinctly stated: we wanted to increase the intensity by 50% over what we had achieved in the last fixed target run which implied that we wanted to increase the intensity by 1E13 per pulse. In absolute intensity the goal was 3E13/pulse; historically we had trouble running reliably at 1.6E13 and the peak record was 1.80E13. Our new peak intensity record so far is 2.81E13 and we have been able to run reliably at over 2.5E13/pulse which was another goal.

A feature of this run was the presence of a neutrino experiment, E815, requiring high intensity fast spill which had not been done for 9 years. Another set of goals was to provide 20 seconds of good quality slow spill every 60 seconds at 800 GeV. In the past the fast spills had been interspersed within the slow spill and caused interference with the slow spill users. In this run all the fast spills are bunched together at the start of the flattop to provide the 20 seconds of slow spill.

Our final goal was to reliably provide 100 hours of stable running per week.

2 OVERVIEW OF THE RUN

Figure 1 provides an overview of the run. In the beginning there was a melding of three activities : during the daytime there was Main Injector construction near the Booster and 1 TeV testing in the Tevatron, beam was available during the night and part of the weekends. The first goal was to push the beam as far as possible to find out what was broken and to test new devices. As mentioned above, the fast spill was bunched at the beginning and this was made possible by an upgraded extraction system QXR, Quadrupole Extraction Regulator, [1]. There were three components to our being able to place the spill in this manner: QXR upgrade, pulser upgrade, and E815 DAQ. In order to have as long a period of slow spill as possible we wanted to shorten the time between the fast spills. However the experimental data acquisition system could not go below a half second repetition rate, but even at this rate we had to upgrade our pulsed trims in the Switchyard since this was an order of magnitude increase in repetition rate. So an important component of the early startup was the commissioning of the extraction system with the multiple fast spills.

One aspect of the early running was a dedicated 150 GeV alignment run for E815 which utilized 1/3 of the Tevatron as a beam line. This was accomplished during the night time running. After 24 hour/day operation was established on June 14,1996 we quickly got up to around 1E13 but we were plagued with numerous feeder failures in addition to a large scale flooding from a very severe storm. A period of dedicated repairs to the most vulnerable feeders reduced the failures to manageable level.

However, we were still mired at an intensity level of approximately 1.2E13 until a set of measurements and calculations [2] were done that enabled us to increase the extraction step size. This change was made in September and along with the work on dampers in the Booster, Main Ring, and Tevatron [3] enabled the steady increase in intensity up till now. Even with the decrease in losses due to the step size change there was a concern about activating the D0 collision hall which would cause background for the D0 experiment and so a shutdown was made to install additional shielding There was a long shutdown for Christmas and the final two major interruptions to the program were a TeV dipole failure and a site wide power outage.

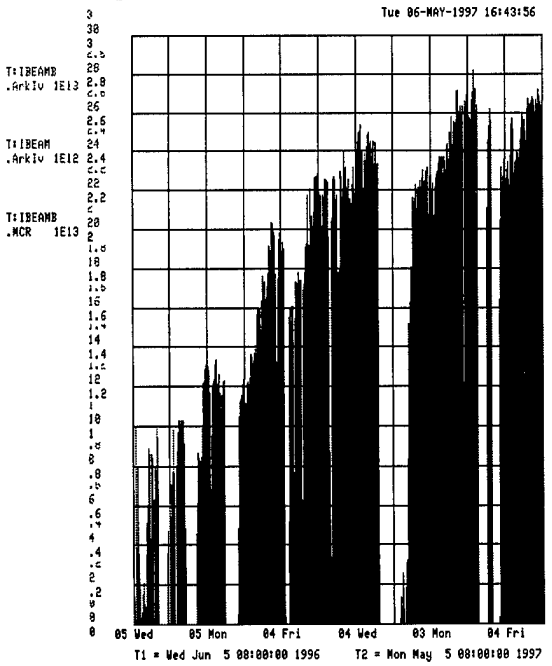


Figure 1: Overview of the Fixed Target Run. Tevatron Intensity from 6/5/96 to 5/5/97.

[1] Operated by University Research Association for the United States Department of Energy

0-7803-4376-X/98/$10.00 © 1998 IEEE

3 RUN SUMMARY

The run has gone well in comparison with our goals and with past runs. Figure 2 shows the integrated hours and the weekly hours and it is apparent that we are doing a reasonable job of providing 100 hours/week.

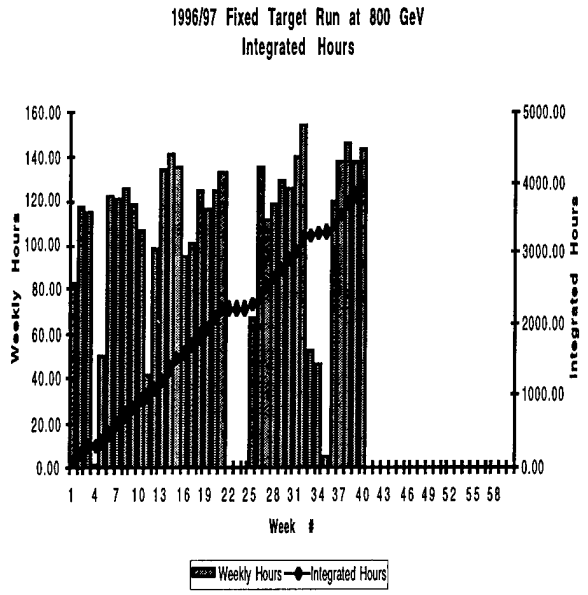


Figure 2: Integrated hours and weekly hours for the 1996/1997 Fixed Target Run.

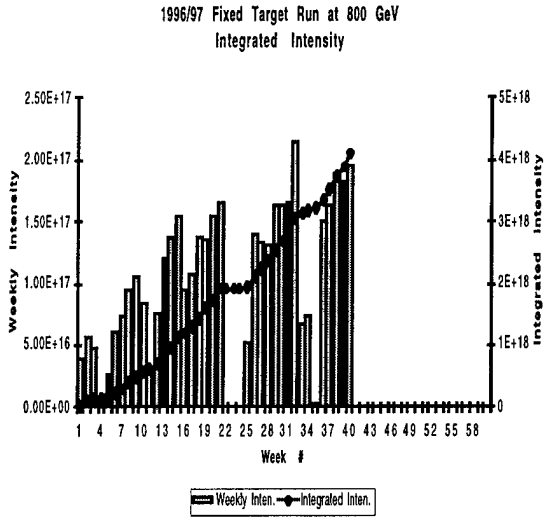


Figure 3: Integrated intensity and weekly intensity for the 1996/1997 Fixed Target Run.

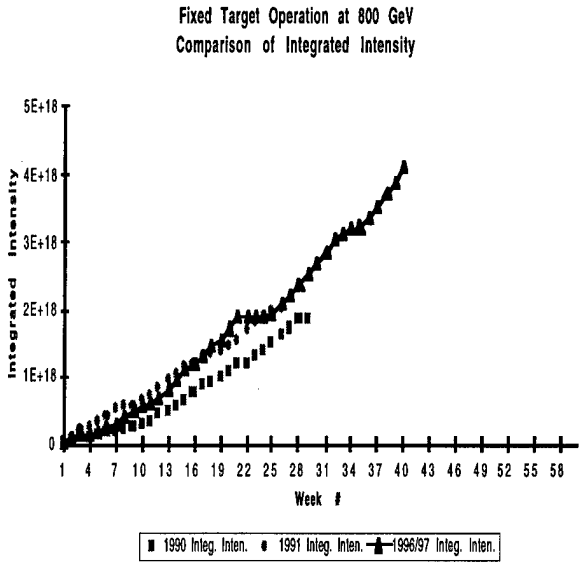


Figure 4: Comparison of integrated intensities.

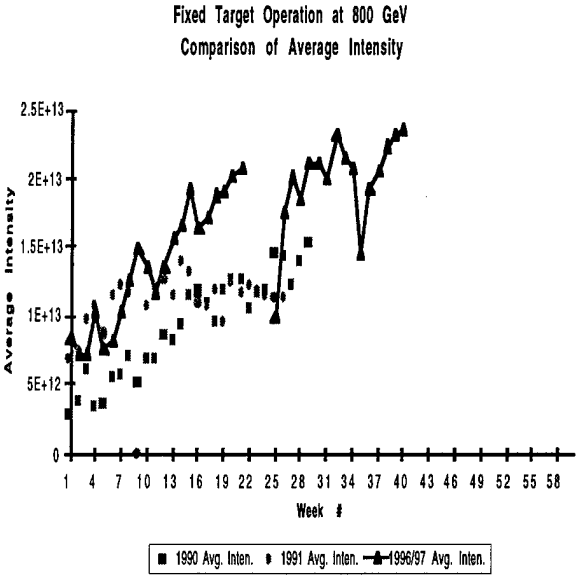


Figure 5: Comparison of average intensity

Gains have been made in the intensities delivered to the experiments. Figure 3 shows the analogous plots for the weekly intensity and the integrated intensity. Figure 4 compares the present run to the two previous runs and the fair comparison should be between the present run and the 1990 run (the 1991 run was a continuation of the 90 run with a hiatus for our shielding assessments and hence we did not make a change from collider operation). The most striking gain has been made in the intensity per pulse. Figure 5 gives a comparison between the current run and the previous runs and it is clear that we have achieved an approximately 50% increase in intensity. It should be noted that we have consistently met the users request since differing experiments have been coming on line during the course of the run.

4 CONCLUSIONS

We are doing well in this run particularly in terms of increased intensity; and we can consider four main ingredients to the success of the run: the E815 target train, the Linac upgrade, dampers, and the step size change.

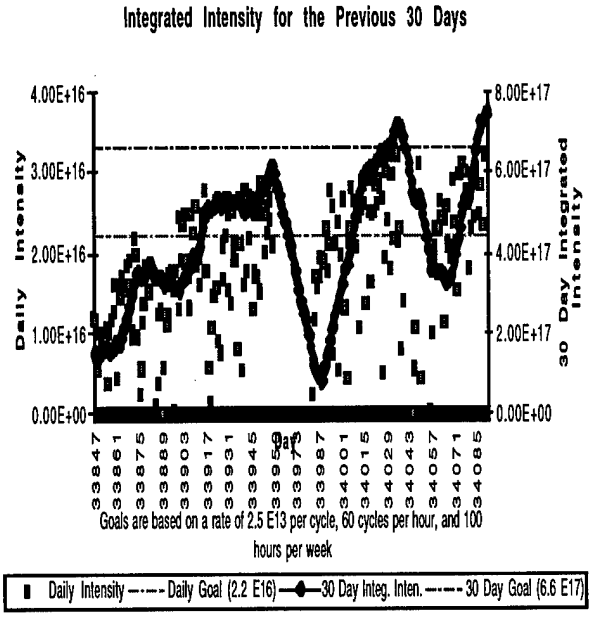
The E815 target train has several positive implications for increasing the intensity for the entire program. A very helpful use of the train is a convenient and useful place to put beam when other experiments go down. This means that there is no ratcheting of intensity and the intensity of the complex can stay high. A reason that we can have this flexibility and not disrupt the program is that we have improved (widened) the shape of the fast pulses so that operationally we can increase the intensity in each pulse (as opposed to adding pulses which would change the timing for everybody else) without greatly increasing the dead time of E815. The QXR upgrade and the Switchyard pulser upgrade imply that we can get rid of the intensity related to the fast spill in the Tevatron quickly and hence get back to the level of intensity that we had run before. However we still have to get the beam through the Main Ring and accelerate in the Tevatron.

The Linac upgrade was the reason that we had set our intensity goals for the run so much higher than previous runs had achieved. This upgrade gives us brighter beams to fit through the Main Ring and its overpasses (prior to the overpasses the Main Ring intensity record was 3.3E13). We want more intensity without increasing the size of the beam so it will fit in the available aperture (transverse, longitudinal, and dynamic), but when we make the beam brighter we increase the interaction of the particles with themselves and with their environment.

A general solution to this problem is to build dampers and of course we have done this before this run, in fact eleven dampers were used for this run that had been built previously [3] for the Booster and Main Ring. However twelve dampers were specifically built for this run [3] for the Main Ring and Tevatron, along with specific modifications [4] to the Tevatron RF to suppress some High Order Modes that had caused problems in the last fixed target run. In addition two anti-dampers were built for spill quality considerations [3].

More intensity means more extraction losses since we resonantly extract utilizing a thin wire septum. Modeling and experimental measurements which verified the modeling indicated that we could increase the step size and since the extraction losses are approximately given by the ratio of the wire diameter to the step size it was expected that the losses would go down. In fact the step size was increased by 50% and the losses in the regions of the extraction septum and the extraction Lambertsons went down by approximately 1/2. In general there was an interactive interplay between the various systems (dampers, antidampers, step size parameters), and between the various machines (Booster, Main Ring, and Tevatron)

The experimenters are interested in spill quality over varying time scales; there is a web site [5] which shows the spill on a short time scale and figure 6 shows our progress in meeting our goal of 2.5E13/pulse, 60 pulses/hour, 100 hours/week over a 30 day average.



5 ACKNOWLEDGMENTS

The success of this run has been due to the dedicated efforts of many people in the Beams Division.

6 REFERENCES

[1] Peter Lucas, private communication.
[2] M. Martens, J. Marriner, and J. Holt, paper 2B7 in this conference.
[3] D. McGinnis, J. Steimal, private communication
[4] D. Wildman, private communication
[5] Peter Kasper, private communication

http://www-focus.fnal.gov/snapshots/spill.html

SLIP STACKING FOR THE FERMILAB LUMINOSITY UPGRADE

S. Shukla, C. Ankenbrandt, D. Capista, I. Kourbanis, J. Marriner, D. McGinnis, J. Steimel and R. Tomlin
Fermi National Accelerator Laboratory, Batavia, IL 60510 USA

Abstract

Increasing the proton intensity available for antiproton production is part of a plan for increasing the luminosity in the Fermilab Tevatron in the near future. We intend to increase the proton intensity using a kind of momentum stacking in the Main Injector called Slip Stacking [1]. We report the status of the effort towards its implementation.

1 INTRODUCTION

According to the current plan for Run II, the 120 GeV protons used in antiproton production will be obtained by transferring one booster batch into the Main Injector at 8 GeV and accelerating it to 120 GeV. We intend to increase the antiproton production rate using Slip Stacking in the Main Injector. This involves stacking two booster batches end to end but with slightly differing momenta, into the Main Injector. The two batches have different periods of revolution and 'slip' relative to each other azimuthally and finally overlap.

The fractional difference in periods of revolution for the two batches is given by

where $\frac{\Delta p}{p}$ is the fractional momentum difference and η is the slip factor. The slip factor is given by

$$\frac{\Delta\tau}{\tau} = \eta\frac{\Delta p}{p} \qquad (1)$$

$$\eta \equiv \frac{1}{\gamma_t^2} - \frac{1}{\gamma^2} \qquad (2)$$

For the MI, $\gamma_t = 21.8$ and at injection, $\gamma = 9.55$. and $\eta = 8.86 \times 10^{-3}$. The duration of a booster acceleration cycle, T = 66.7ms. At injection, the length of a booster batch l = 1.57 μs, and the period of revolution in MI, τ = 11.14 μs. If the two batches are injected 46 MeV apart and allowed to slip, they would overlap completely after half a Booster cycle, i.e., 33 ms.

When they overlap they are captured using a single rf which is the average of the initial frequencies associated with the two batches. The two batches might be moved closer together in momentum if a smaller longitudinal emittance for the final beam is desired. Since the booster and Main Injector acceleration cycles are 66ms and 1.5s respectively, we expect a substantial increase in the pbar production rate, if the process can be completed efficiently.

2 RF MANIPULATIONS

The following is a list of factors that determine the optimum momentum separation between the two batches, initially and just before they are coalesced, and the rf voltages involved.

1) A larger momentum separation reduces the time before the batches can be coalesced.
2) A larger momentum separation requires a larger horizontal aperture.
3) A smaller momentum separation just before the batches are coalesced leads to a smaller longitudinal emittance for the final beam, if the effect of the second rf system is small.
4) The rf buckets for the two batches get more distorted as the separatrices move closer together. The losses become fairly high if the separatrices overlap. So the beams should spend as little time with their separatrices close together as possible before they are coalesced.

The procedure used to find rf curves that would result in a coalesced beam of small emittance containing a reasonably large fraction of the initial beams, is described elsewhere[2]. A set of acceptable rf curves is shown in figures 1a -1d. Figures 1a , 1b, 1c and 1d show the variation, before coalescing, of

1) the rf voltage for either of the two original beams,
2) the bucket height for either of the two original beams,
3) the separation of the frequency of one of the two beams from the mean of the two frequencies before coalescing, and
4) the synchronous phase angle for one of the beams

respectively. The mean of the two frequencies before coalescing is constant through the RF manipulations and is the same as the frequency used for coalescing.

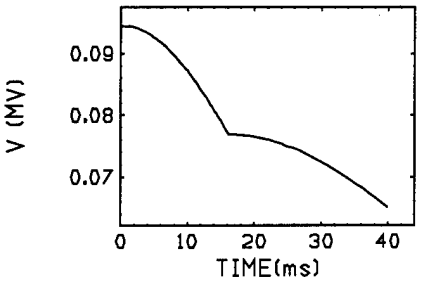


Figure 1a : Variation of rf voltage for either beam.

0-7803-4376-X/98/$10.00 © 1998 IEEE

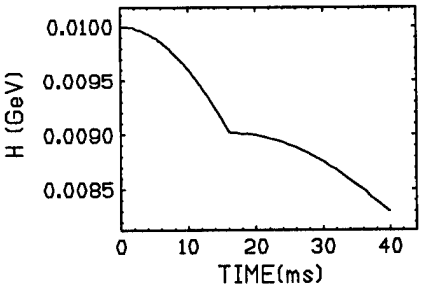


Figure 1b : Variation of bucket height for either rf.

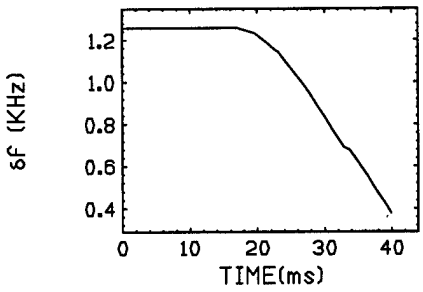


Figure 1c : Variation of the separation of one frequency from the mean of the two frequencies.

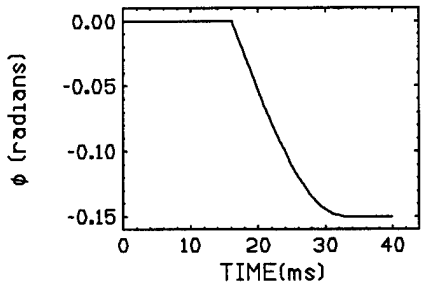


Figure 1d : Variation of the synchronous phase for one of the two beams.

Fig. 2 shows the particle distributions just before coalescing in simulated beams of low intensity subjected to the rf curves depicted in figures 1a-1d. The rf buckets corresponding to the two frequencies just before coalescing are also shown. The two beams are captured with a single rf while they are still accelerating. The efficiency of acceleration and coalescing for a final longitudinal emittance of 0.34 eV-s is 95%. The shape of the final bucket is shown in the figure as the solid line. The dashed curve inside the final bucket is a contour containing 0.34 eV-s of area. The distributions were obtained ignoring all collective effects including beam loading.

At higher intensities, some of the collective effects are expected to become important. We have investigated the longitudinal space charge effect and the effects of beam loading in the rf cavities. We find that the beam loading voltage is high and will have to be compensated for.

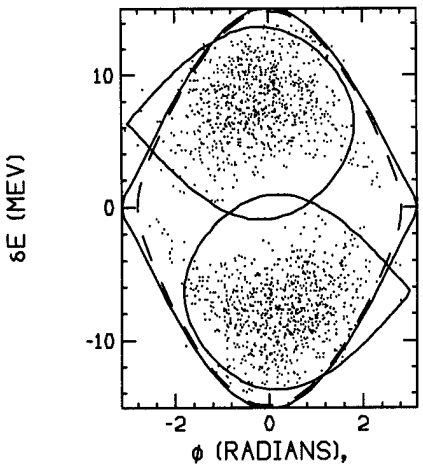


Figure 2: Beam distributions just before coalescing.

3 BEAM LOADING

If the quality factor, Q, is high and the bunch length is short, the cavity voltage V(t) following the passage of a bunch of charge q is given by

$$V(t) = \frac{q\omega_r R}{Q} \; e^{-(\alpha+i)\omega_r t} \qquad (3)$$

where R is the cavity shunt impedance, ω_r is the cavity resonant frequency, and $\alpha=1/2Q$.

In the case that the bunches are spaced by $\tau=2\pi/\omega_r$, the voltage after the passage of n bunches is easily found to be

$$V(n\tau) = \frac{q\omega_r R}{Q} \; \frac{1 - e^{-n\pi\alpha}}{1 - e^{-\pi\alpha}} \qquad (4)$$

We can apply eq.4 to estimate the beam loading voltage. As an example, we consider the case where there are two batches of 84 bunches each in the Main Injector and that the last 42 bunches of the first batch and the first 42 bunches of the last batch overlap and are exactly in phase. We ignore the difference in revolution frequencies of the two batches and the difference between the resonance frequency of the cavity and the revolution frequencies. Under these circumstances, one can use a generalization of eq.4 to estimate the beam loading voltage as shown in fig. 3. The calculation is for a total of 9 cavities with R/Q=100 Ω and Q=5000. The voltage increases when the beam passes through the cavities. During the time that the two beams overlap the voltage increases at twice the rate. When the beam is absent the voltage decays at a rate determined by the time constant α.

Approximately 0.4 ms later the bunches are out of phase and the beam voltage becomes very small.

This estimate of the beam loading voltage indicates that, if uncompensated, the beam loading voltage (1.5 MV) would dwarf the rf voltage (100 kV). Our computer simulations show that beyond bunch intensities of 4×10^9 protons/bunch, the beam loading voltage would result in loss of beam if not dealt with.

At this intensity the beam loading voltage is comparable to the rf voltage.

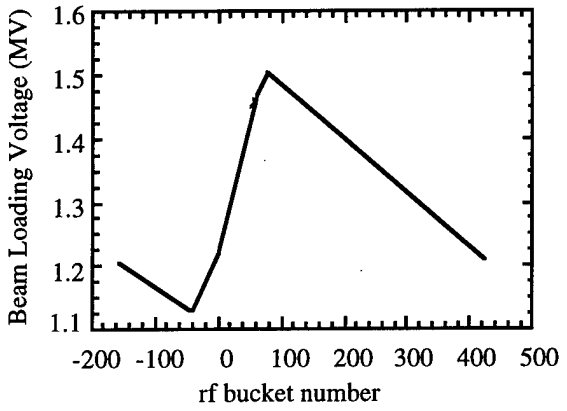


Figure 3. Beam loading voltage

We intend to control the beam loading voltage by:

1. Tuning all cavities to the nominal 8 GeV frequency.
2. Using feedforward on all the cavities. A resistive gap measures the wall current. This current, after being properly scaled, can be applied to the cavity drivers. Based on current Main Ring experience it is expected to achieve a factor of 10 reduction in the effective beam current.
3. Using feedback on all the cavities. A signal proportional to the gap voltage is amplified, inverted, and applied to the driver amplifier. This technique is expected to achieve a factor of 100 reduction (based on previous experience in the Main Ring and results achieved elsewhere).

If all these efforts are successful, beam loading should be reduced sufficiently.

4 CONCLUSIONS

The problems associated with the implementation of Slip Stacking are being studied using computer simulations and beam in the Main Ring. Based on the studies so far, beam loading voltage appears to be the most serious problem, and we are working on solving it. We plan to study the methods of reducing the beam loading voltage mentioned in Section 3 and the effects of the reduced voltage on the beam.

REFERENCES

[1] D. Boussard and Y. Mizumachi, 'Production of Beams with High Line-Density by Azimuthal Combination of Bunches in a Synchrotron', CERN-SPS/ARF/79-11; 1979 IEEE Particle Accelerator Conference (1979).

[2] C. Ankenbrandt, 'Slip-Stacking: A New Method of Momentum Stacking' Fermilab FN-352 (1981).

[3] S. Shukla et al 'Slip Stacking in the Fermilab Main Injector' , 1996 DPF/DPB Summer Study : New Direction for High Energy Physics, June 25 - July 12, Snowmass Colorado, U.S.A.

EXPERIMENTS WITH SEPARATED BEAMS IN RUN I AT THE TEVATRON COLLIDER

M.A. Tartaglia
DZero Collaboration, Fermi National Accelerator Laboratory*, P.O. Box 500, Batavia, IL 60510

Abstract

During the Tevatron collider Run I, a great deal of effort was spent understanding the luminosity at the two colliding detectors. In collaboration with the Tevatron operations group, the DZero experiment recorded data while the colliding beams were intentionally separated by several beam widths in the horizontal and vertical planes. The resulting luminosity profiles contain a great deal of information about the lattice and beam size parameters at the low-beta focus, which can be extracted by fitting in a variety of ways. This paper will review details of these separated beam measurements and present results on Tevatron lattice parameter and luminosity determination.

1 INTRODUCTION

At the start of Tevatron Collider Run 1b there was difficulty diagnosing the state of the machine. The luminosities at two collider detectors did not agree, with the DZero monitor indicating about 25% higher luminosity, and the CDF longitudinal event profile being asymmetric. Following the discovery and correction of a rolled low-beta quadrupole at CDF, the machine performance improved dramatically and luminosity measurements became more consistent, but with DZero showing a 10% deficit relative to CDF. With the search for the top quark in full swing, this difference generated some interest among DZero experimenters to explore whether there might be problems at their collision region.

As the peak luminosity climbed, both luminometers revealed shortcomings. Improved bunch-by-bunch devices were installed at both experiments, and additional scrutiny was given to the luminosity calculations. Ultimately the experiments agreed to about 3%, with that difference now resolved[1] by further work to understand efficiencies and acceptance of the system[2] used to measure the rate of interactions in the DZero collision region. However, the *accelerator-calculated* luminosity (using measured bunch intensities, emittances, and assumed lattice parameters) predicts the detectors should observe about 30% greater luminosity than is seen (assuming a world average total cross section[3]). Precision cross section measurements drive the need for a well determined luminosity, and a suitably precise calculated value (if achievable) would provide a useful cross check to the rate method.

The beams were first separated at DZero to study halo backgrounds and shielding effectiveness: it was observed that interactions still occurred some distance from the crossing point, where the beam widths are large and overlap. This luminosity z-distribution was asymmetric, which set the stage for a series of separated beam tests[4] completed on 4 stores over the course of Run 1b.

2 EXPERIMENTAL METHOD

All scans were performed at the end of a store at relatively low luminosity, about $5 \cdot 10^{30}\ cm^{-2}\ s^{-1}$. The scan sequence was to first separate the beams to an extreme position (e.g., 200 μm) in the horizontal (x) plane, whence DZero data were taken for about 10 minutes, yielding 10K to 45K events; then the separation was changed to a smaller value and data taken again. After completing 2 or 3 data points, the beam separation was brought through zero to repeat the procedure for the same set of separations, but with opposite sign. The same scan procedure was then administered in the vertical (y) plane (with no x separation), and at least one zero-separation point was recorded. The first scan was in x only; in the final test a scan along a diagonal was made in addition to the x and y scans. Three tests occurred during normal $\beta^* = 35\ cm$ operations and one during a week of Tevatron running with $\beta^* = 25\ cm$.

The DZero Level-0 apparatus[2] is constructed of two segmented arrays of fast scintillation counters – situated near the beam pipe on either side of the collision region – and utilizes precise timing for longitudinal collision point "vertex" z-position finding. There are two readout modes: 1) a FASTZ mode (for triggering DZero) which uses a subset of the available counters, has less precise resolution ($\sigma \sim 8\ cm$), and is sensitive to vertices within 100 cm of the detector center; 2) a SLOWZ mode which individually analyzes and records pulse height and time from each counter and provides vertex position resolution of 4 cm for vertices out to 150 cm, flags multiple interactions and rejects halo particles. Initially the DZero online luminosity monitor was based upon a FASTZ ratemeter which averaged over all 6 colliding bunches. The improved monitor devices utilized SLOWZ signal scalers and a precise clock to evaluate a 1-minute rate per bunch, and was commissioned in late Run 1b (only the fourth scan has both FASTZ and SLOWZ luminosity measurements, though all runs have both conditions flagged in the recorded data). Data taking was initiated by a loose coincidence of the two Level-0 arrays, or by a prescaled clock signal (to monitor the exposure duration).

The Level-0 data were histogrammed into vertex z-distributions with bin size equal to the digitizer resolution, 0.75 cm. A typical distribution is shown in Figure 1, which shows single- (SI) and multiple-interaction (MI)

*Operated by University Research Association for the United States Department of Energy under contract DE-AC02-76CH03000

0-7803-4376-X/98/$10.00 © 1998 IEEE

profiles for a 100 μm separation (the MI shape depends strongly on the SI shape). Most of these distributions display asymmetries in the relative peak height, and z-position minima clearly offset from zero in both x and y planes. Some normalization corrections are then applied, to make *luminosity* distributions which can be compared and analyzed: 1) the FASTZ luminosities are corrected (using recorded SLOWZ data) for z-acceptance to 150 cm; 2) the number of recorded events is scaled to account for trigger prescale and exposure duration, then must be adjusted upward slightly to account for multiple interactions (hence, to first order one must know the luminosity!); 3) all distributions and measured luminosities are corrected up for the measured luminosity decay, about 1% per 10 minute data point.

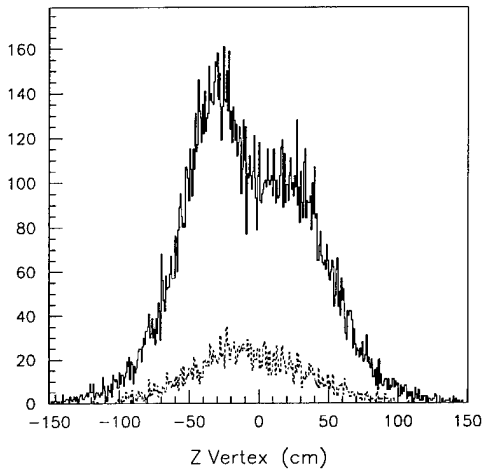


Figure 1: Longitudinal Luminosity Profile for beams separated horizontally by 100 μm. Solid lines are Single Interaction, and dashed lines are Multiple Interaction events.

3 ANALYSIS AND RESULTS

The accelerator-calculated luminosities are evaluated in the framework of an ideal Tevatron, where luminosity $\mathcal{L}$ is described by a linear model, uncoupled in x and y, characterized by 24 parameters (e.g., see [4]). Making the standard assumption of Gaussian transverse and longitudinal bunch shapes, the luminosity distribution $d\mathcal{L}/dz$ can be written

$$\frac{d\mathcal{L}}{dz} = \mathcal{A}\frac{\exp\left\{-\left(\frac{\delta X^2}{2\,\sigma_x^2}\right)-\left(\frac{\delta Y^2}{2\,\sigma_y^2}\right)-\left(\frac{(Z-Z_C)^2}{2\,\sigma_z^2}\right)\right\}}{\sigma_x(z)\,\sigma_y(z)\,\sigma_z}. \quad (1)$$

$\mathcal{A}$ contains the sum over proton and antiproton bunch intensities which, along with the bunch lengths σ_{zp} and σ_{za}, are measured to about 1% [5],

$$\mathcal{A} = \sum_{i=1,6}\frac{N_{ip}N_{ia}f_{rev}}{(2\pi)^{3/2}}. \quad (2)$$

δX and δY are the bunch center to center transverse separations, and z_c is the beam crossing point (with detector center at $z = 0$), which is measured to a few cm by Beam Position Monitor (BPM) timing. Crossing angles are possible and result in z-dependent separations. Expressions for the transverse beam widths result from convolution over bunches, $\sigma_x^2 = (\sigma_{xp}^2 + \sigma_{xa}^2)$, where

$$\sigma_{xp}^2(z) = \beta_x(z)\epsilon_{xp} + \eta_x^2(z)\left(\frac{\delta P}{P}\right)^2, \quad (3)$$

with similar expressions in y. The ϵ_{ij} are emittances, which are related to the "normalized 95%" values measured using flying wires. Note that the beam widths depend only on the sum of proton and antiproton emittances. The (well known) momentum dispersion is $\frac{\delta P}{P}$ whose coefficient $\eta(z)$ is taken to be a linear function of z (nominally *zero* in y). The "beta function" at the low-beta focus is characterized by a length β^* and given by a quadratic function with minimum at z_0,

$$\beta_x(z) = \beta_x^* + \frac{(z - z_{0x})^2}{\beta_x^*}, \quad (4)$$

with a similar expression for terms in y.

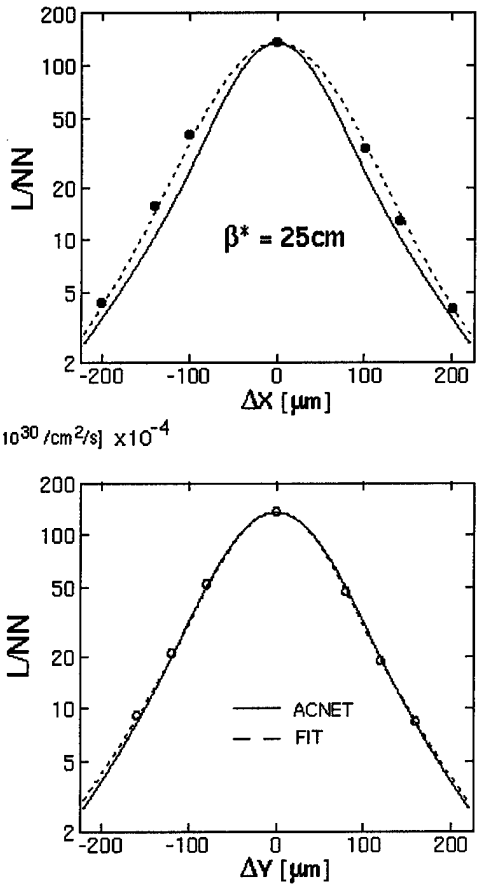


Figure 2: $\mathcal{L}/(N_pN_a)$ versus separation for X and Y scans; the overlayed model calculations use accelerator- (solid line) or fit separated beam- (dashed line) parameters and have been scaled to agree at zero separation.

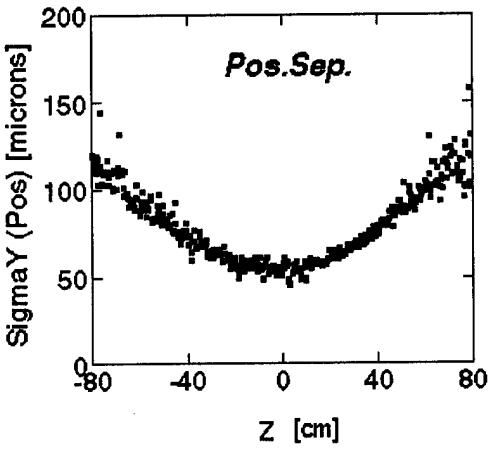


Figure 3: σ_y versus z, overlay of 3 separation ratios from scan 2 positive vertical separations.

We have used several approaches to extract information about the colliding beam optics. First, the behavior of luminosity versus transverse separation *could* be fitted; however, there is no independent determination of the actual separations because BPMs are only accurate to $\sim 20\ \mu m$. Since these profiles were not all symmetric with the sign of separation, one might be concerned about the separator performance; instead we simply compared the resulting profiles and model as shown in Figure 2.

A second way is to try to fit the longitudinal luminosity profiles, $d\mathcal{L}/dz$, to extract parameters independently for the vertical and horizontal scans: there are 4 or 6 separation points in each scan, in each plane, and we find excellent consistency. The separations can be made parameters of the fit and in most cases agree with the nominal separations with about 5 μm error. In all of the scans we find the vertical profiles to be completely consistent with expectations, but the horizontal focus is less sharp than predicted: the fits prefer a larger value for $\beta_x^*, 25\ cm \rightarrow 35\ cm$, and $35\ cm \rightarrow 45\ cm$. It is also possible that the dispersion center is offset from the detector center. We find crossing angles (up to $50 \mu rad$) and focus offsets ($8\ cm$) from zero in both planes in most of the scans. The large number of parameters could be better determined by performing a *global* fit to all of the x and y scans for a given store.

Third, a very useful consequence of Equation (1) is that $\sigma_x^2(z)$ (and $\sigma_y^2(z)$ or $\sigma_{xy}^2(z)$) can be calculated from *the ratio of two z-distributions* recorded with different separations δX_1 and δX_2,

$$\sigma_x^2(z) = \frac{(\delta X_2)^2 - (\delta X_1)^2}{2 \ln\left(\frac{d\mathcal{L}_1}{dz} / \frac{d\mathcal{L}_2}{dz}\right)}. \qquad (5)$$

The σ_i^2 are quadratic functions of z that can be easily fit. The multiple separations of each sign again provide a consistency test which in this case validates the fundamental Gaussian profile assumption, to about 4 σ. In Figure 3 an overlay of three determinations of $\sigma_y vs.\ z$ is shown for one scan. One could improve this analysis by using a larger bin size for better statistics; it may then be possible to get widths of the individual colliding bunches. This last analysis promises to be useful in the more complex case of a coupled lattice, where a general framework has been derived that requires only measurements of $\sigma^2(z)$ along $\{x, y, diag\}$ at the focus to calculate the luminosity[6].

4 CONCLUSIONS

The separated beam technique provides a new method for fast diagnosis of the low beta focal optics, and a tool for precise measurement of machine parameters. Using separated beam scan fitted parameters gives somewhat better agreement with the measured luminosity and transverse profiles than is obtained using accelerator measured emittances and assumed lattice parameters. However the calculated luminosity is still substantially low as can be seen in Table 1. The next step will be to combine these measurements of σ^2 with the covariance matrix technique[6].

Scan	Store	β^* (cm)	Model/Meas. *Accel Params*	Model/Meas. *Fit Params*
1	5224	35	1.31	–
2	5320	35	1.34	1.19
3	5378	25	1.43	1.28
4	5628	35	1.35	1.46

Table 1: Ratios of calculated to measured luminosity for separated beam scan stores.

5 ACKNOWLEDGEMENTS

The author would like to thank Mike Martens and the Fermilab Accelerator Division for their time and help with these studies, and the DZero luminosity group for help recording and processing these data.

6 REFERENCES

[1] J.Bantly, R.Partridge, D.Owen, 'DZero Luminosity Monitor Constant for the 1994-1996 Tevatron Run', Fermilab TM-1995, Feb 1997.

[2] J. Bantly, K. Epstein, J. Fowler, G.S. Gao, R. Hlustick, R.E. Lanou, F. Nang, R. Partridge, L. Wang, and H. Xu, 'The Level-0 Trigger for the DZero Detector', IEEE Trans. on Nucl. Sci. **41**, 1274 (1994).

[3] S.M.Pruss, 'Present Status of $p\bar{p}$ Elastic and Total Cross Section Data', Fermilab TM-1949, October, 1995.

[4] M.Tartaglia, 'Run 1b Tevatron Lattice Parameter Measurements with Separated Beams at DZero', Fermilab TM-1932, May 1997.

[5] E.L.Barsotti, 'A Longitudinal Bunch Monitoring System Using LabVIEW and High-Speed Oscilloscopes', FERMILAB-TM-1908, October 1994.

[6] M.Martens, 'Using Luminosity Distributions to Determine Luminosity in a Collider with a Coupled Lattice', contribution to this conference.

CAPTURE FROM PAIR PRODUCTION AS A BEAM LOSS MECHANISM FOR HEAVY IONS AT RHIC*

B. Feinberg, A. Belkacem, N. Claytor, T. Dinneen, and H. Gould
Lawrence Berkeley National Laboratory
1 Cyclotron Rd., Berkeley, CA 94720 USA

Abstract

Electron capture from electron-positron pair production is predicted to be a major source of beam loss for the heaviest ions at RHIC. Achieving the highest luminosity thus requires an understanding of the capture process. We report measurements of this process at Brookhaven National Laboratory's AGS using 10.8 GeV/nucleon Au^{79+} projectiles on Au targets. Capture from pair production is a process in which the very high electromagnetic field involved in the collision of two relativistic heavy ions results in the production of an electron-positron pair with the capture of the electron by one of the ions. There are many theoretical papers published on capture from pair production with discrepancies between predicted cross sections. The experimental results are compared to theory and to previous experiments at 1 GeV/nucleon. The implications of extrapolations to RHIC energies are presented.

1 INTRODUCTION

At relativistic energies, the capture of electrons by ions (recombination) occurs by the well-understood collisions processes of Radiative Electron Capture (REC) and Non-Radiative Capture (NRC). These processes, which require an electron in the initial state, have cross sections that decrease rapidly with increasing collision energy. REC is the capture of a target electron by the ion with the simultaneous emission of a photon (to balance momentum and energy). NRC is the capture of an electron that is initially bound to a target atom or ion. Until recently, REC and NRC were thought to be the dominant processes for electron capture at all relativistic energies.

The large transient fields produced in relativistic charged particle atomic collisions (no nuclear contact) have long been known to produce electrons through electron-positron pair production [1]. But, in 1984, Gould pointed out that for bare heavy ions, the probability for pair creation with simultaneous capture of the electron from the pair into the K-shell, was significant [2]. The cross section for this "capture from pair production" mechanism has been shown to increase with energy (as does the cross section for producing free electron-positron pairs), and is predicted to be the dominant electron capture mechanism at highly relativistic energies [3]. Since capture from pair production requires no electron in the initial state, it can take place between two bare ions, possibly limiting the lifetime of stored beams of bare heavy ions in relativistic heavy ion colliders.

A number of theoretical papers aimed at calculating the cross sections for electron capture from pair production have been published since 1984 [4]. Different calculational techniques were used for high and low relativistic factor (γ). Therefore agreement at low energies does not assure agreement at high energies. Until recently, no experimental measurement to check the validity of the theoretical predictions at high γ has existed.

In this article we report measurements of electron capture from electron-positron pair production in relativistic heavy ion collisions at highly relativistic energies, and discuss the possible implications for the lifetime of heavy ions in the Relativistic Heavy Ion Collider (RHIC) now being constructed at Brookhaven National Laboratory [5]. The experiments have been performed at the AGS accelerator at Brookhaven National Laboratory, using 10.8 GeV/nucleon bare gold ions (Au^{79+}) incident on thin, fixed targets of Au, and are compared to experiments at the Bevalac accelerator at Lawrence Berkeley Laboratory, using 0.4 - 1.3 GeV/nucleon bare lanthanum ions (La^{57+}) incident on gold targets.

2 EXPERIMENT DESCRIPTION

Figure 1 shows a diagram of the Advanced Positron Spectrometer (APS) used to detect positrons. The Au^{79+} ion passes through a fixed target located inside the APS, described below. In the case of capture from pair production, the electron is created directly bound to the gold ion, changing its charge by one unit to Au^{78+}. The experimental signature is the detection of the positron emitted during the collision, in coincidence with the charge-changed Au^{78+}. The Au^{78+} is magnetically separated from the main beam of Au^{79+} and each charge state is detected by a scintillator-photomultiplier tube detector.

* Supported by the Director, Office of Energy Research, Office of Basic Energy Sciences, Chemical Sciences Division and (BF) Material Sciences Division, U.S. Department of Energy under contract DE-AC03-76SF00098.

0-7803-4376-X/98/$10.00 © 1998 IEEE

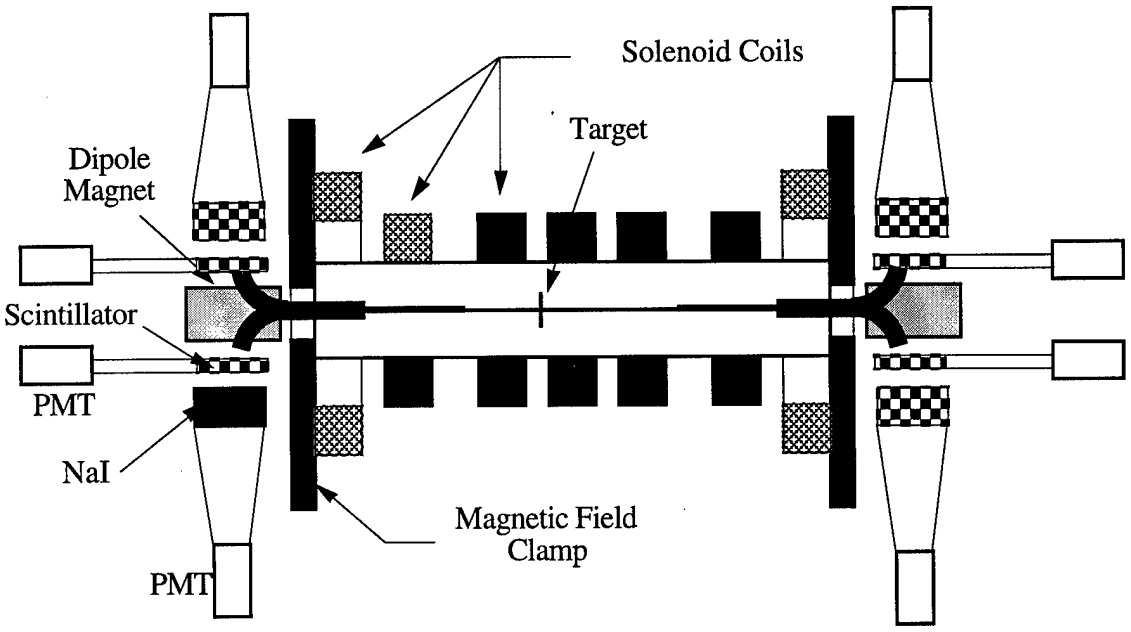


Figure 1 - Schematic diagram of the apparatus (top - sectional view). The solenoid field decreases adiabatically from the center towards the ends causing the particle orbits to grow and their divergence to decrease, allowing them to be swept by the dipole magnets into the detectors. Only one positron detector (and no electron detector) is labeled. The target is located near the center of the solenoid and the heavy ion beam travels horizontally through the apparatus.

The target is placed inside and slightly upstream from the center of the APS. The APS is used to detect and measure the energy distribution and angular distribution of the electrons and positrons emitted from the target. It contains a solenoid magnet in the center and a dipole magnet at each end. The solenoid generates a strong magnetic field (B=0.8 T max.) that adiabatically decreases toward the ends. The field transports the electrons and positrons away from the target, and converts much of the positron (electron) transverse motion into longitudinal motion. The positrons and the electrons are efficiently deflected in opposite transverse directions at each end of the solenoid by the dipoles. There they strike plastic scintillator-photomultiplier tube detectors.

This combination of magnetic fields results in a very high acceptance for electrons and positrons emitted both forward and backward with respect to the beam direction. Without the adiabatically decreasing field, the acceptance of the spectrometer would be very low because most of the positrons, upon reaching the end of the solenoid field, would have a large transverse motion causing them to strike the walls of the apparatus rather than to be deflected into the spectrometer detectors. Tests of the APS using beams and radioactive sources have shown a detection efficiency close to unity for emission angles of up to 75 degrees forward and backward.

The emission angle with respect to the beam direction is measured using the time of flight of the positrons (electrons) through the solenoid. Four plastic scintillator-detectors (see figure 1) are used to detect the positrons (electrons) and to measure their energy and time of flight. The magnetically separated Au^{78+} ion that produced the positron, detected in its scintillator-detector at the end of the beamline, is used for the timing reference.

The dipole magnets that deflect electrons and positrons in opposite directions are used for the initial discrimination between electrons and positrons. However, at 10.8 GeV/nucleon, a large number of knock-on electrons are ejected from the target by collisions with the gold ion. Approximately 3 to 4 electrons with an energy above 100 keV are ejected from a 1 mg/cm^2 gold target for every gold ion, while only one positron from the same target is expected for every 5 x 10^3 gold ions. Roughly two or three per thousand knock-on electrons backscatter from the electron scintillator-detector into the positron scintillator-detector, thus simulating a positron.

To discriminate against these scattered electrons we require the detection of one of the two 511 keV photons that are emitted back-to-back when the positrons annihilate at rest in the plastic scintillator. The 511 keV photon is detected by a NaI scintillator-photomultiplier detector (see figure 1). The detection efficiency of the photon (by the 12.5 cm diameter by 15 cm long active area) NaI detector has been measured to be 30%, with roughly 60% of the photons appearing as a narrow single peak at 511 keV, and the rest as a broad Compton distribution. In our data analysis only the narrow peak is used. This sets the overall efficiency of the APS for the detection of a positron at 18%.

3 RESULTS

We integrate the spectra over the positron energy and angle to obtain the total cross section for capture from pair production. Preliminary results for the total cross section for capture from pair production by a 10.8 GeV/nucleon Au^{79+} on a gold target are 9.2 barns.

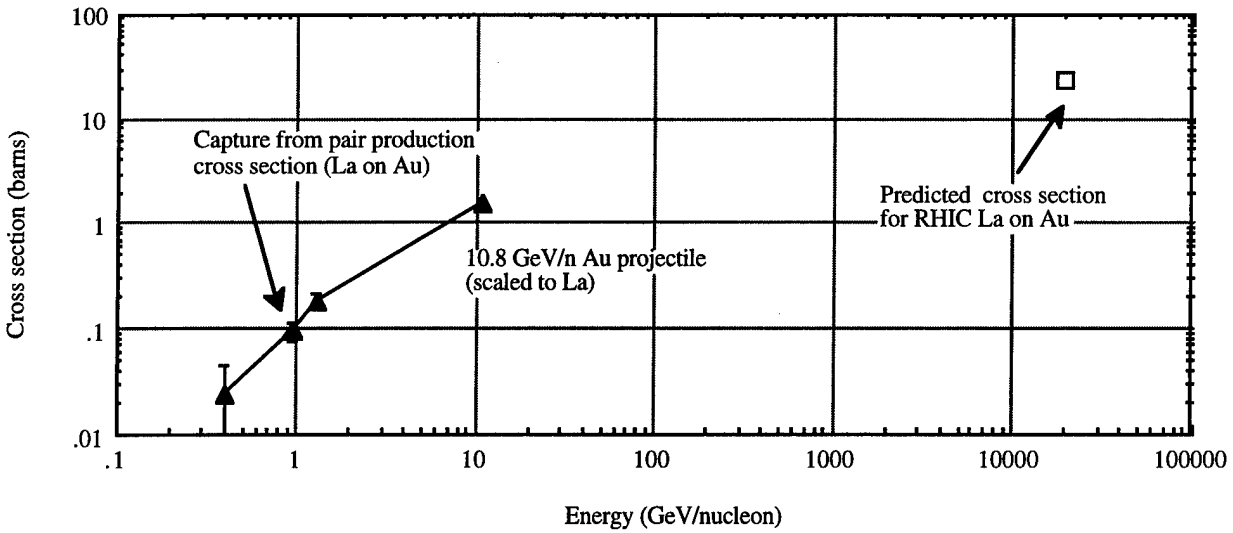


Figure 2 - Graph of capture from pair production as a function of energy. All results are scaled to La on Au, the case for which the most experimental data exists. The triangles represent measured cross sections, while the square point at RHIC energies, scaled to La, is predicted from perturbation theory.

4 DISCUSSION

The preliminary results presented here are in the middle of the range of predictions. These calculations, based on perturbation theory, predict cross sections ranging from 5.7 barns to 12.2 barns [6 - 9].

A convenient way to visualize the cross section for capture from pair production as a function of energy is to scale the collision system to La on Au, where the most experimental results exist [3]. Figure 2 shows the capture from pair production cross section, scaled for a La projectile, as a function of energy. The triangles represent experimental results, scaling the point at 10.8 GeV/nucleon (AGS result) by Z^5 to represent a La projectile rather than a Au projectile. The point for RHIC collider energies is scaled from perturbation theory predictions for Au on Au [10]. A visual analysis of the increase of the experimental cross section with energy indicates that the RHIC predictions are reasonable, but not necessarily assured.

Capture from pair production (resulting in the loss of the charge-changed ion in the collider ring) has been predicted to be the dominant beam loss mechanism for colliding Au + Au beams at RHIC and a significant loss mechanism for lighter ions [5]. If the cross section is an order of magnitude higher than predicted at RHIC energies, then the current after 10 hours will decrease to about 20% of the initial value, instead of 77%, after taking into account intrabeam Coulomb scattering.

Measurements of the cross section for capture from pair production at AGS energies indicate that the high-γ calculations used to predict the loss rate at RHIC are not unreasonable at the low end of their range of validity.

5 ACKNOWLEDGEMENTS

We thank Philip Pile and Joseph W. Glenn III for assistance with the beam optics, David Phillips and David Dayton for timely engineering support, Herman Bartalomy and the entire AGS experimental area support groups for assistance in staging the experiment, and the AGS operators and staff for patience and perseverance in providing the beam tune that made this experiment possible. We thank Harvey Oakley and Robert Aita for providing us with critical equipment and Denise Merkle and Peter Thieberger for assistance in setting up the experiment.

6 REFERENCES

[1] G. Racah, Nuovo Cimento **14**, 93 (1937) and references therein.
[2] H. Gould, Lawrence Berkeley Laboratory Report No. LBL-18593 (1984).
[3] A. Belkacem, H. Gould, B. Feinberg, R. Bossingham, and W.E. Meyerhof, Phys. Rev. Lett. **73**, 2432 (1994).
[4] See references in A. Belkacem, Harvey Gould, B. Feinberg, R. Bossingham, and W.E. Meyerhof, Phys. Rev. Lett. **71**, 1514 (1993].
[5] "Conceptual Design of the Relativistic Heavy Ion Collider - RHIC", BNL Report BNL-52195 pp 117-121.
[6] U. Becker, J. Phys. **B20**, 6563 (1987).
[7] U. Becker, Phys. Rev. **A36**, 4628 (1987).
[8] U. Becker, N. Grün and W. Scheid, J. Phys. **B20**, 2075 (1987).
[9] Baltz, Rhoades-Brown, and Weneser, Phys. Rev. **A50**, 4842 (1994) and A. Baltz, private communication.
[10] C. Bottcher, M.R. Strayer, Phys. Rev. **D39**, 1330 (1989).

NUMERICAL OPTIMIZATION OF COLLIMATOR JAW ORIENTATIONS AND LOCATIONS IN THE LHC

D.I. Kaltchev, M.K. Craddock*, R.V. Servranckx,
TRIUMF, 4004 Wesbrook Mall, Vancouver, B.C., Canada V6T 2A3
J.B. Jeanneret, CERN, CH-1211 Geneva 23, Switzerland

Abstract

The collimation system of LHC will consist of flat collimator jaws distributed along the IR7 lattice with the aim of limiting the maximum combined amplitudes of secondary halo particles (born along the edges of the primary collimators). The code DJ (Distribution of Jaws) computes this amplitude using a quasi-analytic algorithm (no tracking), by which the maximum initial angles are found, corresponding to trajectories escaping all secondary jaws. We report the latest version of DJ, which contains the following enhancements: (1) the orientation of each pair of jaws is a free variable (instead of using only vertical, horizontal, or 45° skew jaws); (2) the minimizing method used is "simulated annealing", which, for our case of a discontinuous function of up to 32 variables, always finds a global minimum. Different initial jaw distributions lead to different final ones, but they all give essentially the same maximum halo amplitude; this seems to depend only on the number of jaws and the lattice parameters, particularly the tune-split. We discuss lattice characteristics found favorable for collimation.

1 INTRODUCTION

The betatron beam collimation system for the LHC will be installed in the IR7 insertion. It will consist of a set of primary collimators, followed by a number of secondary collimators arranged to limit the so-called secondary beam halo produced at the edges of the primaries, thereby protecting the LHC vacuum chamber from scattered particles. Each collimator will be composed of a pair of opposing flat jaws.

In [1] we presented the computer code DJ, which distributes secondary jaws along the IR7 lattice with the aim of minimizing the largest surviving combined amplitude of the halo. We now report some enhancements to DJ and the improved results which they have made possible.

2 DEVELOPMENT OF THE MODEL

2.1 *Varying the jaw angles*

In the code DJ, the production of halo particles is modeled by a set of point-like sources distributed along the borders of the primary jaws (straight lines in the transverse plane). The secondary jaws, assumed to act as black absorbers, are defined by their horizontal tune advance μ_x (within the collimation section IR7) and their rotation angle α around the longitudinal axis.

For a given jaw distribution, a mapping technique is used to isolate the fraction of trajectories escaping all secondary jaws, i.e. those passing between the two opposing jaws of all pairs. For these uncaptured halo particles, the code finds the maximum combined x-y betatron amplitude A_{max} , where $A = (A_x^2 + A_y^2)^{1/2}$ and A_x,A_y are the single-plane transverse invariants. This computation is fast (~1 s) as no tracking is needed. DJ further minimizes A_{max} as a function of the jaw distribution vector $(\mu_{x1}, \mu_{x2}..., \mu_{xN}, \alpha_1, \alpha_2..., \alpha_N)$.

In [1] four types of jaws are used – vertical, horizontal and two skew – with rotation angles $\alpha = 0°$, $90°$, $45°$, $135°$ respectively. In the new version of the code DJ, the angle α is an independent variable, along with the jaw position, and may range over $0° \leq \alpha \leq 180°$; during minimization the jaw positions and angles are varied together. The improvement in A_{max} (expressed in terms of the r.m.s. amplitude σ) is shown in Table 1, for primary and secondary collimators set at 6σ and 7σ respectively. For 12 secondary collimators, allowing α to vary has the same effect as adding 4 more secondaries; for 16 secondaries the improvement is less dramatic.

Table 1:

Number of secondary pairs of jaws	A_{max} discrete α = $0°, 90°, 45°, 135°$	A_{max} $0° \leq \alpha \leq 180°$
12	9.4σ	8.7σ
16	8.6σ	8.4σ

With variable angles, the program module calculating A_{max} for a fixed jaw distribution remains unchanged. However, the minimization of A_{max} with twice as many variables called for some new numerical tools and solutions.

2.2 *Minimization*

During minimization, the locations of the four primary jaws are fixed at maxima of the corresponding beta functions, their angles being: $0°, 90°, 45°$ and $135°$.

The optimization process has been developed in two stages: 1) conventional methods, which allow better insight, but show an unwelcome dependence on the initial conditions, with some runs ending up in local minima, and 2) simulated annealing.

A_{max} is not a smooth function of the jaw-distribution vector, because of screening effects by some secondary

* Also at Dept. of Physics & Astronomy, UBC, Vancouver, Canada.

0-7803-4376-X/98/$10.00 © 1998 IEEE

jaws on others. A step of *finite* length made in any direction of the $2N$-coordinate space may result in unpredictable changes in the indices m, n of the two *maximum amplitude jaws* [1] and correspondingly in A_{max} . However, for small enough increments, the coordinates of the two maximum-amplitude jaws are the only ones whose variables affect A_{max} , so there are only four active variables $\mu_m, \alpha_m, \mu_n, \alpha_n$ (local smoothness).

Downhill-overstep methods [2] are based on the local smoothness of A_{max} . At each iteration, the LMDIF package routine is used with four variables up to the limits of the smoothness interval. After that, a step is made outside this interval, to pick a new pair of active jaws. The step is halved after each unsuccessful iteration (no downhill direction found).

Simulated annealing (SA) – a probabilistic optimization method [3], is a recent technique devised for solving difficult problems involving discontinuous multi-variable functions, but requiring large computing time. The Appendix offers a quick overview of SA in one dimension.

At early stages of minimization, if the percentage of accepted cases rises, then the range over which the code searches for an optimum increases, i.e. the SA algorithm keeps more than one local minimum in sight. As the "temperature" parameter is reduced, downhill moves are less likely to be accepted, more cases are rejected and SA focuses on the global extremum.

In several initial runs, appropriate values were chosen for the most important SA parameters – the initial temperature ($T_0 = 5$) and the temperature reduction factor (0.6). A typical SA run assumed fixed IR7 lattice functions, a sufficiently large number of source points along the edges of the four primary collimators, and 12 to 16 secondary collimators.

With these parameters fixed, SA runs made for random initial jaw distributions always resulted in essentially the same minimum value for A_{max} , as desired. The final jaw distributions, however, were by no means identical, although many were very similar (see §3.2 below). The secondary-halo cross-sections differed correspondingly, having different maximum single-plane invariants A_{xmax} and A_{ymax} (but the same amplitude near the diagonal in (A_x, A_y) space).

If DJ is modified to search only for jaw locations compatible with the rest of the hardware, then the computing time increases unacceptably. The alternative approach was taken of shifting the quadrupoles slightly to free locations at which jaws were needed.

3 RESULTS

Different IR7 tunes were explored for several recent versions of the LHC lattice, and for 16 secondary collimators A_{max} was found to be between 8.4σ and 9.1σ, depending on the lattice setting.

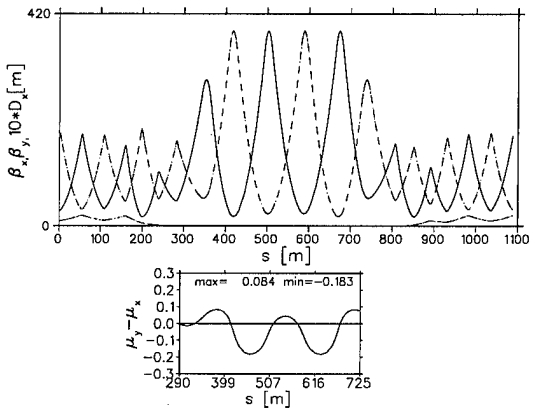


Figure 1: IR7 lattice and tune-split functions for LHC version 4.2, with IR7 quadrupoles tuned for high negative tune split, giving $A_{max} = 9.1\sigma$.

3.1 *Optimum lattice setting*

Optics criteria can be formulated in terms of $\mu_x(s)$ and $\mu_y(s)$ – the horizontal and vertical tune advances along the straight section, with $\mu_x(s_0) = \mu_y(s_0) = 0$ at the first primary collimator ($s_0 = 290$ m), or equally, in terms of the functions $\mu^{\pm} = (\mu_y \pm \mu_x)/2$. The average tune advance μ^+ is roughly proportional to the distance from the first primary: $\mu^+ \propto s - s_0$. Therefore, for a fixed length of the collimation section, the collimation quality can essentially be expressed in terms of the total μ^+ and the tune-split function $\mu^-(s)$.

The advantage of having the tune split vary along the beamline was first suggested, and confirmed by tracking, by Risselada [4]. For the case of circular collimators, initial studies have been carried out [5], aiming to explain the relation between the shape of $\mu^-(s)$ and the collimation quality, and a search for a rigorous theory is under way.

As reported in [1], larger oscillations in $\mu^-(s)$ give lower A_{max} , but we have also found dependence on the sign of μ^-. The figures below show the lattice and tune-split functions of IR7 for two cases recently studied: a tune giving large negative μ^- and $A_{max} = 9.1\sigma$ (Fig. 1), and a tune giving large positive μ^- and $A_{max} = 8.45\sigma$ (Fig. 2). The following tune-split variation gave $A_{max} < 8.5\sigma$:

- almost everywhere positive and close to periodic, with three nearly equal maxima ~ 0.2 each (Fig. 2, bottom);
- one high peak in the middle ~ 0.25 (an abandoned lattice version, not shown).

On the other hand, a tune giving two large negative peaks in μ^- (Figure 1, bottom), gives a somewhat higher $A_{max} = 9.1\sigma$.

3.2 *Optimum collimator phases*

For a lattice optimized purely for collimation, some relation is to be expected between the horizontal and vertical betatron phases of perfectly located collimators. Even in realistic lattices, constrained by additional factors, the SA runs showed that this remains true, favouring certain jaw

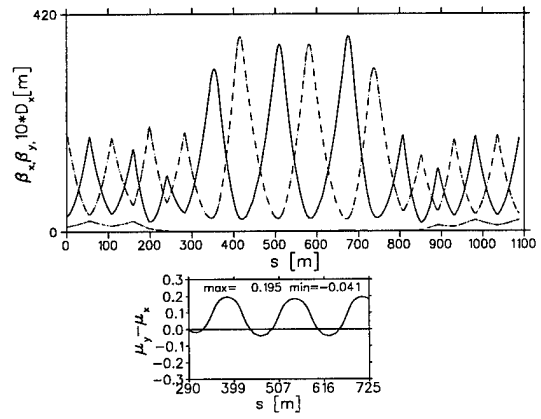


Figure 2: IR7 lattice and tune-split functions for LHC version 4.2, with the IR7 quadrupoles tuned for high positive tune split, giving $A_{max} = 8.45\sigma$.

locations. We also found that μ^+ is a more relevant independent variable than s.

Fifty SA runs were performed for nearly optimum conditions ($A_{max} = 8.45\sigma$) using the lattice shown in Fig. 2. Each run used a randomly generated initial jaw distribution, i.e. random angles and phases for 16 collimators. The values of α were then plotted against μ^+ (Fig. 3) for the resultant 50 jaw distributions, which all give nearly the same value of A_{max}: $8.4\sigma < A_{max} < 8.5\sigma$. The jaw locations tend to cluster near the extreme values of the function $\mu^-(\mu^+)$. On the other hand, for the lattice with $A_{max} = 9.1\sigma$ the pattern is more chaotic (Fig. 4).

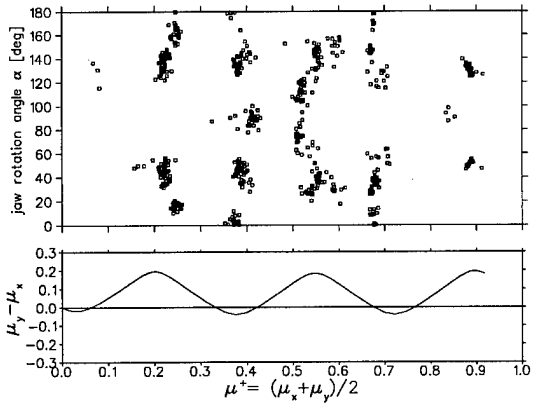


Figure 3: Collimator distributions from 50 SA runs for the lattice shown in Fig. 2 ($A_{max} = 8.45\sigma$) using 16 pairs of secondary jaws with random initial settings. Each point represents the rotation angle and the average betatronic phase μ^+ of one pair.

4 APPENDIX: EXAMPLE OF SIMULATED ANNEALING ALGORITHM IN ONE DIMENSION

In this example, the global minimum of $F(x)$ is searched for, within some interval (x_1, x_2). The user supplies initial

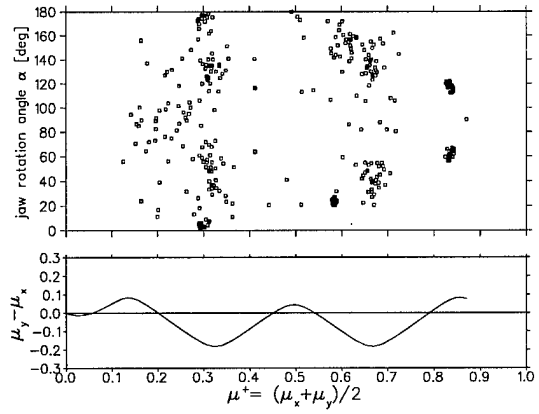


Figure 4: Collimator distributions for the lattice shown in Fig. 1 ($A_{max} = 9.1\sigma$).

values for x ($x_1 < x < x_2$), the step dx and the temperature parameter T ($T > |x_1 - x_2|$).

At each iteration, 20 trial values x_{tri} are generated randomly in the interval $(x - dx, x + dx)$. If a trial value x_{tri} is downhill, i.e. $F(x_{tri}) < F(x)$, then it is accepted and, if $F(x_{tri})$ is lower than its previously lowest value, x_{tri} is recorded as a new optimum. An uphill x_{tri} can also be accepted with probability $P = e^{(F(x)-F(x_{tri}))/T}$ (Metropolis criterion). If the trial x_{tri} is out of bounds, then it is rejected and simply a new x_{tri} is generated in bounds. Each time the trial is accepted, x_{tri} replaces x (the centre x moves, but dx stays). At the end of the iteration, dx is scaled to some new length, which would have produced a roughly equal number of rejected and accepted trials; for instance, dx is increased if too many cases have been accepted.

The temperature is reduced by a factor 0.6 after each 5 iterations. The process is halted if the optimum found remains unchanged during several subsequent temperature cycles.

5 REFERENCES

[1] D. Kaltchev, M.K. Craddock, R.V. Servranckx, J.B. Jeanneret, Optimization of Collimator Jaw Locations for the LHC, Proc. EPAC96 (Barcelona, June 1996), ed. S. Myers et al., (IOP, Bristol, 1996), 1432-4.

[2] D. Kaltchev, M.K. Craddock, R.V. Servranckx, Progress Report on Optimizing Collimator Jaw Angles and Positions with the Code DJ (Distribution of Jaws), TRIUMF design note (in preparation).

[3] A. Corana, M. Marchesi, C. Martini, S. Ridella, Minimizing multi-modal functions of continuous variables with the "simulated annealing" algorithm, ACM Transactions on Mathematical Software Vol. 13, No. 3 (Sept. 1987), 262-280.

[4] T. Risselada, Optical Requirements for an LHC Cleaning insertion with Elliptical Collimators, SL Note 95-67, 1995.

[5] T. Risselada, private communication.

THE IPNS ACCELERATOR 50 MeV AND 500 MeV TRANSPORT LINES*

J. C. Dooling, F. R. Brumwell, G. E. McMichael
Argonne National Laboratory.

Abstract

The Intense Pulsed Neutron Source (IPNS) accelerator delivers up to 500 MeV protons to a depleted uranium target producing spallation neutrons for material science and other research. A 70-80 ns bunch strikes the target at a rate of 30 Hz with an average beam current of 15 μA. The 50 MeV and 500 MeV beam lines transport protons from the Drift Tube Linac (DTL) to the Rapid Cycling Synchrotron (RCS) and from the RCS to the Neutron Generating Source (NGS) target, respectively. Through over 15 years of operation, the accelerator has been highly reliable with the 5 billionth pulse on target recorded March 12, 1997. During this time, IPNS operators have discovered tunes for various parts of the DTL/RCS accelerator allowing for continual improvement in average current delivered to the target; however, in numerous cases this has been achieved by moving significantly away from the original design parameters. A new attempt is being made to analyze the lines and develop computer models that can be used to alleviate some of the undesirable features of the present "best tune." In the 500 MeV line, higher order elements will be included in the modeling with the goal of providing a uniform power density profile at the NGS target. This paper describes features of the present lines, and progress-to-date in analyzing and improving them.

1 INTRODUCTION

The primary components of the IPNS accelerator are a negative ion source, 750 kV DC Cockroft-Walton, 50 MeV DTL, 50 MeV transport line, 450 MeV RCS, and 500 MeV transport line. We concentrate on the two transport lines here. A plan view of the IPNS accelerator is presented in Figure 1. In the 50 MeV line, attention is centered on beam misalignments and what affect they have on RCS transmission. In the 500 MeV line, the beam profile on the target is important: if too small, the high power densities can damage to the target; if too large, protons may miss the target resulting in a reduction in neutron production and an increase in activation.

*This work is sponsored by the U.S. Department of Energy, Contract No. W-31-109-ENG-38.

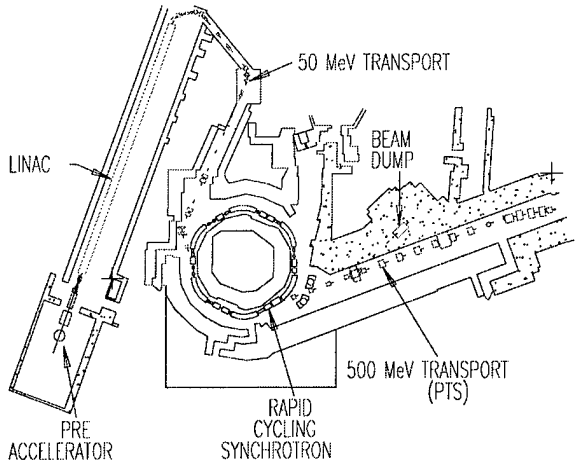


Figure 1: The IPNS Accelerator System.

2 50-MeV LINE

The 50 MeV line includes 8 sector dipoles, 16 quadrupoles, and a number of smaller vertical steering dipoles (VSM). The line is shown schematically in Figure 2. Diagnostics in the 50 MeV line include wire scanners (WS), segmented Faraday cups, toroids, scintillators, and beam position monitors (BPM). Beam positions, sizes, and profiles are analyzed with WSs at twelve locations along the 50 MeV line. BPMs provide real-time displays of beam centroid position. In addition, a segmented Faraday cup and a pair of scintillators also indicate beam size and position. Starting in 1996, a target irradiation area has been established in the 50 MeV line for the production of radio-isotopes for experiments at the Argonne Tandem Linear Accelerator System (ATLAS). The target slugs are relatively small (5 mm, diam.); therefore accurate beam positioning information is required.

A working model of the 50 MeV line was developed using the first-order-optics code, TRACE3D[1] to predict beam size and focusing. It was found that the model does a reasonable job in most sections of the 50 MeV line. For example, near the linac, it was useful in identifying the reversal of x and y axes in WS1. Nevertheless, some discrepancies remain between prediction and WS size data; in addition, WS data indicates some beam profiles are neither uniform nor Gaussian but instead are quite peaked. Beam offsets

0-7803-4376-X/98/$10.00 © 1998 IEEE

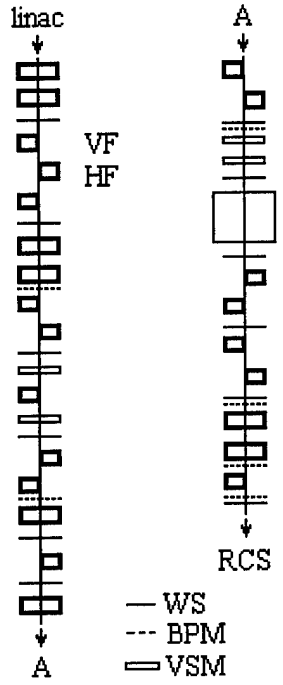


Figure 2: 50 MeV transport line elements

may be responsible for some of the observed nonlinear behavior.

Analysis of a beamline is complicated by beam misalignments. Consider the geometry in Figure 3 showing a circular beam cross section within a

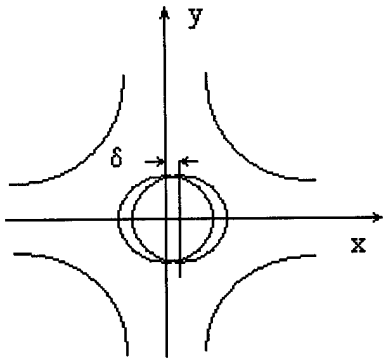


Figure 3: Beam offset geometry in a quadrupole

quadrupole magnet. The beam center is offset from the magnetic center by δ. With respect to the center of the quadrupole, the beam radius may now be expressed as,

$$r_m = \sqrt{r^2 + 2\delta\, r\, \cos\phi + \delta^2}$$

where ϕ is measured from the x-axis. The ϕ-component of field may be written as[2],

$$B_\phi = Cnr^{n-1}\cos\left[n\left(\phi - \phi_r\right)\right]$$

where $C=\mu_o NI/R^n$ and n=2. The results of Fourier transforming both aligned and misaligned profiles are shown in Figures 4 a and b. As expected, a single

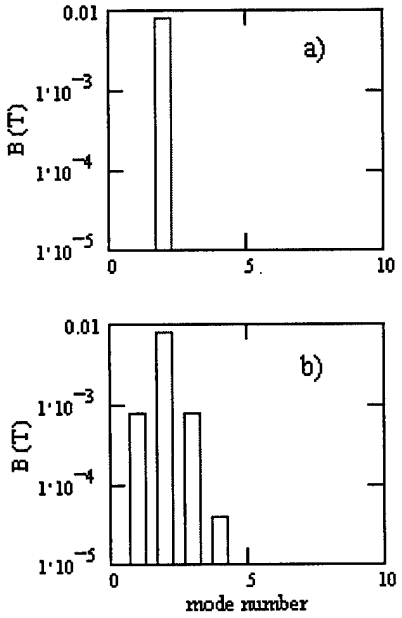


Figure 4: Modal analysis for a) an aligned beam and b) misaligned beam within a quadrupole where R=50.8 mm and δ=1mm.

quadrupole (n=2) mode is evident in the aligned case; however, dipole, quadrupole, sextupole, and octupole modes (as well as higher order components not shown) are predicted for the misaligned beam. An easily observable feature is the dipole steering effect of a quadrupole on a beam that is not on center. This can be used to check beam alignment between diagnostic locations. By varying quadrupole coil current a few percent about the operating point, BPM data from downstream indicates when steering is taking place. Higher order field components can also lead to emittance growth. In the 50 MeV line some emittance growth is tolerable[3]. Δp/p is relatively low from the linac and should be at least 0.5 percent at injection to avoid instability in the RCS. The x and y rms beam emittance out of the linac is measured to be 1.8 π-mm-mrad. Beam emittance is monitored on the 50 MeV line using WS data at three adjacent axial locations[1], each separated by approximately 5 m of drift space. (The transfer functions of two small VSMs are ignored.) Note that this analytical technique combines dispersion with emittance.

An effort was made to reduce beam offsets in the 50 MeV line quadrupoles. Using VSMs and larger sector dipoles, the beam position was made to lie close to the center of the BPMs. (It was not possible to achieve zero BPM offset at all locations.) WS data indicates rms emittances as follows: ε_x=3.76± 0.35 π-mm-mr and ε_y=3.28± 0.32 π-mm-mr. These values are in reasonable agreement with TRACE3D which calculates 4.63 and

2.33 π-mm-mr for ε_x and ε_y through this region of the line. Though steering in some quadrupoles has been substantially reduced, it is still evident in others. Based on these initial results, further beam alignment studies are planned.

3 500-MeV TRANSPORT SYSTEM

The 500 MeV line carries accelerated protons approximately 45 meters from the RCS to the Neutron Generating Source (NGS) target. The line is composed of 2 dipole and 15 quadrupole magnets, not including extraction optics. The beamline is shown schematically in Figure 5. Beam size and position along the line are measured with Segmented Secondary Emission Monitors (SSEMs). A Segmented Wire Ionization Chamber (SWIC), located just in front of the target, provides similar information. Current Toroids provide transmission efficiency. TRACE3D is again used to indicate beam size and focusing along the line. While within the RCS, space charge plays a major role in longitudinal stability; however, after extraction space charge has relativley little effect on the beam. This is significant since it means that space charge can be ignored in multiparticle analysis of the 500 MeV line without loss of accuracy.

4 BEAM UNIFORMITY

By adding nonlinear magnet elements to the 500 MeV line, a more uniform beam profile may be obtained on the NGS target[4]. This modification will be significant, especially if the present RCS current limit can be increased with a proposed second-harmonic rf cavity. At the NGS target, the beam profile is observed to be circular in real space and approximately Gaussian as measured by the SWIC. We are presently developing a particle tracking model to investigate the placement of higher order elements in the 500 MeV line. Incorporating the model shown in Figure 6, the phase space distribution in x-x' space given in Figure 7 is predicted at the NGS target.

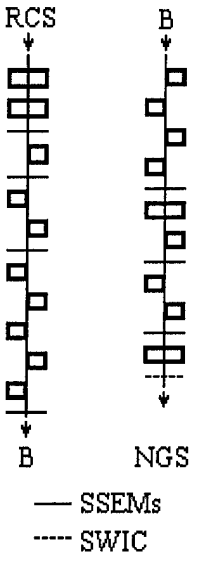


Figure 5: 500 MeV transport line elements

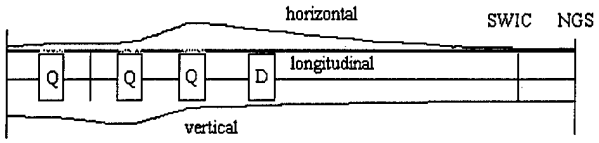


Figure 6: 500 MeV line upstream of the NGS

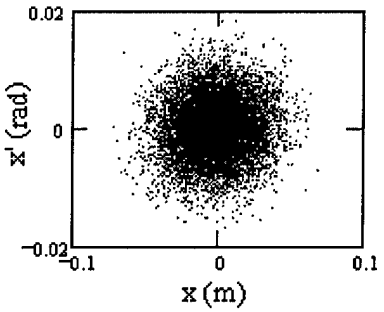


Figure 7: Modeled phase-space distribution at the NGS

ACKNOWLEDGMENT

The authors wish to express their gratitude to other members of the IPNS Accelerator Group for assistance in this effort.

REFERENCES

[1] K. R. Crandall, D. P. Rusthoi, "TRACE 3-D Documentation," LANL Report LA-11054-MS, Los Alamos, August, 1987.

[2]D. A. Edwards, M. J. Syphers, *An Introduction to the Physics of High Energy Accelerators*, Wiley, New York, 1993, p. 228.

[3]Y. Cho, E. A. Crosbie, and H. Takeda, "Determination of the 50 MeV Beam Characteristics," ANL, IAS Note 80-6, July 1980.

[4]B. Sherrill, J. Bailey, E. Kashy, C. Leakeas, "Use of Multipole Magnetic Fields for Making Uniform Irradiations," Nuc. Instr. and Meth., B40/41 (1989), 1004.

H⁻ CHARGE EXCHANGE INJECTION FOR THE NSNS ACCUMULATOR*

L. N. Blumberg and Y.Y. Lee
Brookhaven National Laboratory, Upton, NY 11973

Abstract

A scheme for injection into the FODO cell of the National Spallation Neutron Source(NSNS) Accumulator ring is discussed. A 400 μg/cm^2 carbon foil is chosen for a high stripping efficiency and for heating of the foil consideration. Additional schemes to reduce losses due to nuclear and Coulomb scattering at the foil are discussed. Subsequent loss from magnetic field ionization of the residual H^0 component is estimated to be small comparable to nuclear loss. A method for sweeping and collecting the stripped electrons from the foil is presented.

1 INTRODUCTION

Injection into the NSNS accumulator ring is H⁻ charge exchange process where one can accumulate even on top of occupied phase space. As described in the linac section the beam from the linac is chopped in revolution frequency of the ring insuring there be a gap in the accumulated proton. The injection will take place in one of the dispersion free straight sections just upstream of the center quadrupole which has a large aperture. Because of the dumping scheme of the excited H^0 from the stripping foil the injection shall take place exact radial position where the magnetic field of the quadrupole is 2.43 KG which is exactly 10 cm from the reference orbit. The magnetic field value is important because the electric field felt by the excited H^0 is such that principal quantum number n=4 or less survives the field where n=5 or higher strip immediately. It is working a assumption that the stripping will take place between DC dipole and the quadrupole. However we may consider placing the stripping foil inside of the dipole upstream in order to avoid the effect of fringe field, however it is much more complicated mechanically. A set of 4 pulsing and one fixed field dipole are used to create orbit bump to paint optimum phase space of the injected proton population. The pulsing dipoles are programmed to paint the phase space to reduce the space charge effect of the circulating proton beam. The optimum distribution would be determined later by computer simulation and by experiment. The bump scheme should be able to accommodate a wide range of distribution from uniform phase space density to a so called smoke ring distribution. Likewise a set of four vertical pulsing dipoles are utilized to paint the vertical phase space. The basic scheme of painting the phase space is shown in the fig.1, and the proposed orbit bump is illustrated in fig. 2. Table I lists the location and kick angle of the orbit bumps both for the start and end of the injection process.

* Sponsored by the Division of Material Sciences, U.S. Department of Energy, Under contract DE-AC05-96OR22464 with Lockheed Martin Energy Research Corp. for Oak Ridge National Laboratory.

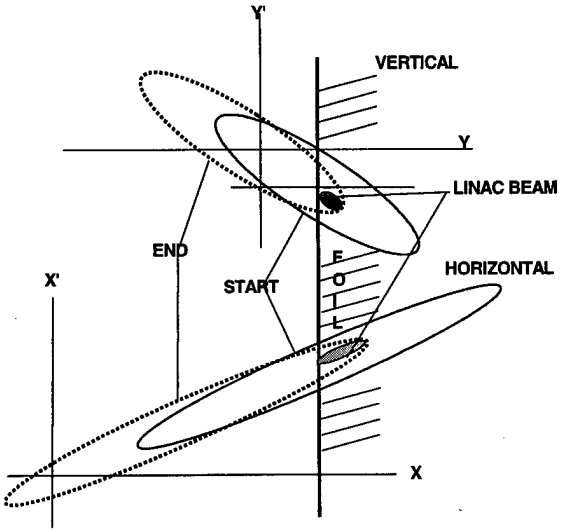


Fig. 1 X and Y injection Phase Space diagram

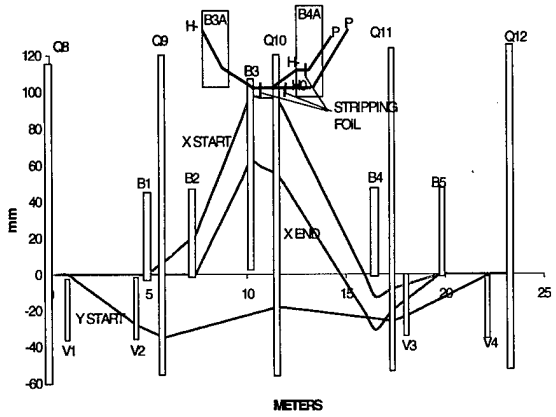


Fig. 2 Schematic Injection Bump Scheme

Table I Injection Bump Kicker Specifications

BUMP	LOCATION#	θ start	θ end
B1	Q_8 + 4.9m	7.75 mr	0.0
B2	Q_9 + 1.6m	17.35 mr	22.1 mr
B3	Q_9 + 4.4m	-27.15 mr	DC
B4	Q_{10} + 4.9m	27,05 mr	24.05 mr
B4A	Q_{10} + 2.0m	177 mr	DC
B5	Q_{11} + 2.4m	-2.67 mr	-7.78 mr
V1	Q_8 + 0.9m	8.0 mr	0.0
V2	Q_8 + 4.4m	-3.0 mr	0.0
V3	Q_{11} + 0.9m	-1.0 mr	0.0
V4	Q_{11} + 4.9m	5.5 mr	0.0

#Distance is from center of the quadrupole to the center of the bend. Q8 through Q11 are quadrupoles in the straight section starting from last quadrupole of preceding arc.

0-7803-4376-X/98/$10.00 © 1998 IEEE

One has to keep the injection loss and subsequent beam loss due to the injection mechanism manageable. There are several injection loss mechanisms. They are 1) the linac beam missing the foil, 2) H^0's emerging from the foil which is a function of the thickness of the foil, 3) H^-'s emerging from the foil which is calculated to be negligible, and 4) circulating beam loss due to Coulomb and nuclear scattering on the foil. The loss mechanism 1) is related to the stripping foil size and one should keep this loss to less than a few percent. This beam loss along with loss due to the mechanism 3) is well known and a controlled dumping of the waste beam is planed. The loss mechanism 4) is directly related to the thickness and number of circulating beam hitting the foil which is proportional to the foil size exposed to the circulating beam. The foil size is chosen such that it provides a compromise between mechanisms 1) and 4). The thickness of the foil is determined by mechanism 2), 4) and foil heating problem described later. Present working plan calls for a foil size of 8 x 4 mm and 400μg/cm^2 thick carbon foil. The bump magnets are programmable to create the best possible distribution of the proton population.

2 DISPOSAL OF UNSTORED PROTONS

The H^- ions which missed the stripping foil and H^0 emerging from the foil should be disposed in proper beam dump. We place a thick stripping foil in the path of the H^0 to convert entire beam to proton. The H^- bent by downstream quadrupole will travel to 10KG septum magnet, and because of the high magnetic field, they will be stripped to neutral hydrogen in the field. We place a thick stripping foil inside the septum to strip them to proton. Placement of the foil will be determined after careful measurement of the magnetic field, and to have median of the proton emerging from the septum to be parallel with the protons from H^0. A rule of thumb estimation place the foil about 12 cm inside the magnet. A set of two quadrupoles placed downstream of the septum focuses the protons to the beam dump downstream.

3 STRIPPED ELECTRON DISPOSAL

The striped electrons from incoming H^- have a momentum 0.923 MeV/c and a magnetic rigidity of 0.003 T-m. The electrons travel with the protons until they encounter a magnetic field. The first magnetic field the electrons encounter is the field of the quadrupole following the foil. The quadrupole has a 0.243 T field at the radial location, which minimizes the halo created by the excited states of H^0. The magnetic fringe field extends to approximately a distance corresponding to its gap height. The electron trajectory become right angle to the proton orbit several centimeters upstream of the magnet yoke and 8 cm outside of the foil location. We place a collection plate parallel to the proton orbit at this location. The final position of the collector plate should be determined by the magnetic measurement of the quadrupole. The collection plate is water cooled as the electron power is expected to be about 1/900 of the proton power (about 1 KW for 1 MW NSNS). One has to minimize the generation for free electrons inside the ring which can cause an instability to the stored protons. The collection plate will be electrically biased so that no secondary electrons, generated by the striped electron striking the plate, escape the plate.

4 FOIL HEATING CONSIDERATION

A carbon foil is used to strip electrons of the H^- beam because of the resiliency and high sublimation temperature of the material. The sublimation temperature of carbon is above 3500 degree K. The foil is heated by the energy deposited by the proton and two accompanying electrons. Since they all have the same velocity, they should have the same energy loss in a given material. There is no data available for what fraction of the energy lost by beam in the material contribute toward heating of the material. At higher energies, the efficiency is estimated to be as low as 30%. However, for our calculations we assume that all the energy loss contributes to the heating of the material. Furthermore, we assume that no heat dissipates by conduction along foil edge and that the black body radiation is the only mechanism which dissipates the heat. For the one megawatt NSNS injection, the linac has effective average current of 18.2 mA in the unnormalized rms emittances of 0.14π mm-mr in both planes. The peak current density at the foil, where the beta-functions are 17 and 5 meters, is about 3800 A/m^2. Temperature at the spot will rise very quickly to the equilibrium where the heat input and the black body radiation become equal. Since the heat input is proportional to the thickness of the foil while the black body radiation is proportional to the surface area, the thicker the foil results in a higher equilibrium temperature. Figure 3 shows the calculated equilibrium temperatures for the effective linac current. In this calculation we assumed the emissivity of the carbon foil to be 0.8. For the linac current assumed for the NSNS injection, up to 400μg/cm^2 carbon foil can survive the injection whereas thicker foil may reach sublimation temperature. In the case where we double the linac current for increased power, we may consider a tandem foil of two 200μg/cm^2 about a cm apart. The foil may lose

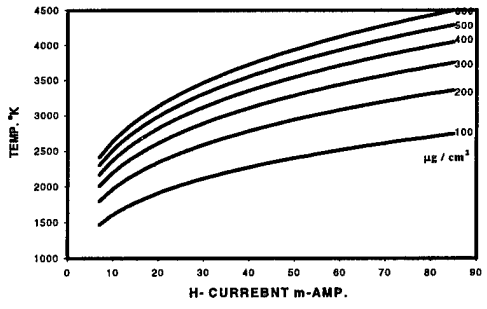


Fig.3 Peak Foil Temperature

some solid angle to radiate the heat, however, they have enough solid angle to radiate and would survive the injection process.

5 CONVERSION EFFICIENCY IN CARBON FOIL

Recently very precise measurements of these cross sections for H^- in carbon have been obtained by Gulley et al. [1] at 800 MeV as

$$\sigma_{-1,0} = (6.76 \pm .09)10^{-19}\ cm^2$$
$$\sigma_{0,1} = (2.64 \pm .05)10^{-19}\ cm^2$$
$$\sigma_{-1,1} = (0.12 \pm .06)10^{-19}\ cm^2$$

In Fig. 4 we have evaluated the fraction of H^0 beam emerging after traversing carbon foil in function of thickness. It is seen that for our choice of 400 $\mu g/cm^2$ the H^0 fraction is $8.19\ 10^{-3}$. It would, of course, be possible to reduce the H^0 fraction by using a thicker foil. However, losses from nuclear interactions and Coulomb scattering would then increase. More serious, the foil temperature will increase with the larger energy deposition from protons traversing the foil. If thinner foils are required by temperature considerations, it is always possible to use several foils in tandem to achieve lower values of the fraction.

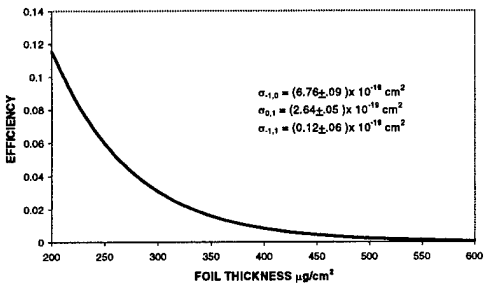


Fig. 4 Fraction of H^0

6 MAGNETIC STRIPPING OF H^0

Hydrogen atoms emerging from the stripper foil are in a distribution of excited states resulting from the stripping reaction $H^- \rightarrow H^0*(n) + e^-$ where n is the principal quantum number. This beam then traverses a quadrupole downstream of the foil, which bends the foil-produced protons back to the equilibrium orbit and the unstripped H^- component out of the ring. However, the neutral atoms can be magnetically stripped in the quadrupole and the resulting protons can contribute to uncontrolled losses downstream when the stripped proton is outside the acceptance ellipse of the ring. Gulley et al.[1] measured the population of H^0 in quantum state n and gives distribution function as $n^{-2.8}$. We have assumed that their results at 800 MeV are valid for a 400 $\mu g/cm^2$ foil at 1 GeV. We estimated the fraction of the excited H^0 decaying in .241T field of downstream quadrupole causing resulting proton to be outside of the horizontal acceptance of the accumulator ring. Using level width evaluated by Damburg and Kolosov [2]. A negligible portion (order 10^{-6}) of the states $n \leq 4$ or $n \geq 6$ decays outside of the horizontal acceptance. Though significant portion of n=5 H^0 decay proton end up outside of the acceptance. The fraction to total protons stored would be $<5x10^{-5}$ of stored protons which is less than our loss criteria of $<10^{-4}$. However, if this portion of loss becomes a problem we have an option of placing the stripping foil inside the gap of upstream dipole to avoid this problem. Since placing the foil inside the gap of a dipole creates significant complication in foil handling mechanism, present working assumption is to place the foil in the field free region between the dipole and the quadrupole.

6 COULOMB AND NUCLEAR INTERACTIONS

The injection process has been simulated with a Monte Carlo program HMININJ which tracks the transverse motion of protons from randomly selected H^- ions through the stripper foil and subsequent turns around the ring. The formulation and source code have been given elsewhere [3]. After a foil traversal the projected horizontal and vertical angles of the proton are modified by a random angle chosen from a multiple Coulomb scattering (MCS) distribution The formulation of nuclear elastic scattering (NES) in HMININJ is analogous to the MCS formulation. The elastic, non-elastic and total cross sections for 1 GeV p+C are taken from Igo, et.al. [4] as σ_e = 112 mb, σ_{ne} = 258 mb, and σ_T = 370 mb respectively. We have chosen beam ellipses of area ε_{BX} ε_{BZ} = 120π mm-mr and acceptance areas $A_x = A_z = 240\pi$ mm-mrad. The average number of foil traversals per proton $<N_t>$ minimized at $<N_t> = 2.43$ when we optimized the injection bump for foil traversal. And the loss out of the ring acceptance due to Coulomb and elastic scattering is also minimum (within statistics for this $N = 10^7$ incident H^- run) at $(2.25 \pm .2)10^{-5}$. For this case we can also evaluate the fractional loss from nuclear non-elastic events using non-elastic cross section = 258 mb, and the fraction is $1.26\ 10^{-5}$, satisfying the NSNS loss criteria. The choice of the foil thickness of 400$\mu g/cm^2$ is based on comparison of losses due to H^0 magnetic stripping against Coulmb and nuclear scattering loss.

REFERENCES

[1] M. S. Gulley, P. B. Keating, H. C. Bryant, E. P. MacKerrow, W.A.Miller, D. C. Rislove, S. Cohen, J. B.Donahue, D. H. Fitzgerald, S. C. Frankle, D. J. Funk, R. L. Hutson, R. J. Macek, M. A. Plum, N. G. Stanciu, O. B. van Dyck, C. A. Wilkinson, and C. W. Planner, Phys. Rev. A53, 3201 (1996).

[2] R. J. Damburg and V. V. Kolosov, Theoretical Studies of Hydrogen Rydberg Atoms in Electric Fields, Chap. 2 in Rydberg States of Atoms and Molecules. R. F. Stebbings and F. B. Dunning, Eds., Cambridge University Press (1983).

[3] L. N. Blumberg and Y. Y Lee, BNL/NSNS Tech. Note 003 (Nov. 1, 1996).

[4] G. J. Igo, J. L. Friedes, H. Palevsky, R.Sutter, G. Bennett, W. D. Simpson, D. M. Corley and R. L. Stearns, Nucl. Phys. B3 (1967) ;181.

THE NSNS HIGH ENERGY BEAM TRANSPORT LINE*

D. Raparia, J. Alessi, Y.Y. Lee, and W.T. Weng
AGS Department, Brookhaven National Laboratory, Upton, NY 11973.

Abstract

In the National Spallation Neutron Source (NSNS) design, a 180 meter long transport line connects the 1 GeV linac to an accumulator ring. The linac beam has a current of 28 mA, pulse length of 1 ms, and 60 Hz rep rate. The high energy transport line consists of sixteen 60^0 FODO cells, and accommodates a 90^0 achromatic bend, an energy compressor, collimators, part of the injection system, and enough diagnostic devices to measure the beam quality before injection. To reduce the uncontrolled beam losses, this line has nine beam halo scrapers and very tight tolerances on both transverse and longitudinal beam dynamics under space charge conditions. The design of this line is presented.

1 INTRODUCTION

In the 1 MW NSNS [1], the High-Energy Beam Transfer line (HEBT) connects the 1 GeV linac [2] to an accumulator ring [3]. A major requirement of all parts of this accelerator is to have low uncontrolled beam losses ($\leq$ 1 nA/m), to allow hands on maintenance. To achieve such low beam losses in the accumulator, the beam must be prepared very carefully before injection. The HEBT not only matches the beam into the accumulator, but also determines the beam quality at injection. The HEBT is equipped with nine sets of beam halo scrapers, and the ratio of aperture to rms beam size is kept greater than 10 throughout the line. The maximum magnetic field in dipoles and quadrupoles is kept less than 3 kG, to keep H^- stripping losses to acceptable levels. In addition, one must maintain very tight tolerances on elements. Fig. 1 shows the HEBT line. Table 1 gives the Twiss parameters at the entrance and exit of the HEBT.

2 FUNCTIONS OF THE HEBT LINE

The HEBT has the following functions, which we have managed to decouple: (a) matching of the beam from the linac into the transport line, (b) momentum selection, (c) momentum compaction, (d) preparation of the beam for injection. In addition, one must characterize the beam out of the linac and before injection, and cleanup any beam halo. We can consider the HEBT as having three sections: Linac-Achromat Matching Section (LAMS), Achromat, and Achromat-Ring Matching Section (ARMS). In addition to the bend to the ring, there is a straight beam line used for linac beam characterization, as shown in Fig. 1. The first four cells (11.4 m/cell) after the linac (LAMS) are used to characterize the linac beam, match beam into the achromat, collimate beam halo, and maintain space for a kicker required in future upgrades. Following this, the six cell long achromat (14 m/cell) provides momentum selection by cleaning up the beam energy halo at the point of maximum dispersion (η_x=8.9m).

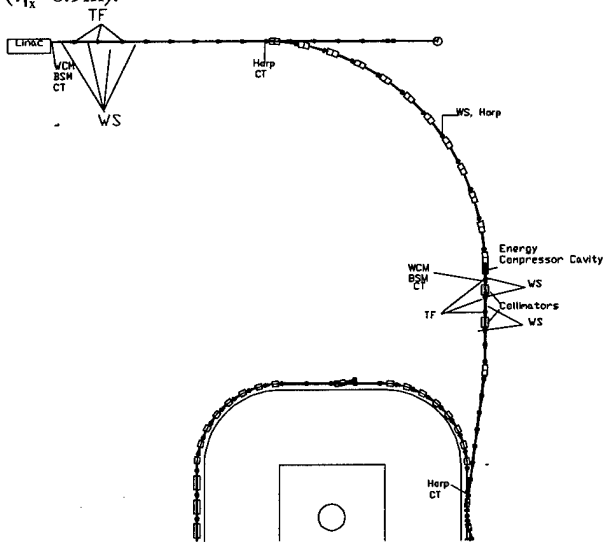


Fig. 1 HEBT layout.

Table 1 Twiss Parameters at the Entrance and Exit of the HEBT for a 1 MW beam.

Twiss parameters	Entrance	Exit (foil)	Units
α_x	0.00	-2.088	
β_x	12.811	17.358	mm/mrad
ε_x	0.70	0.70	π mm mrad
α_y	0.00	0.659	
β_y	9.181	4.20	mm/mrad
ε_y	0.70	0.70	π mm mrad
α_z	0.0005	0.14	
β_z	0.005	0.05	deg/keV
ε_z	1500	1500	π keV deg

The energy compressor cavity is located in the first cell following the achromat (in the ARMS), where the dispersion and its derivative are zero. The remaining six cells (8 m/cell) are used for matching the beam into the accumulator ring, diagnostics, and for beam halo scrapers. Every quadrupole in the HEBT is followed by a small

* Research on the NSNS is sponsored by the Division of Material Science, U.S. Deppartment of Energy, under contract number DE-AC05-96OR22464 with Lockheed Martin Energy Research Corporation of Oak Ridge National Laboratory.

0-7803-4376-X/98/$10.00 © 1998 IEEE

dipole magnet for steering of the beam in the quadrupole focusing-plane. To keep the uncontrolled beam losses low, a study of the required alignment tolerances [4], has led to the following requirements (a) translation errors (x and y) of < 0.1 mm, (b) pitch and yaw of < 0.1 mrad, (c) rotation of < 0.5 deg.

Linac to Achromat Matching Section

The linac has a FDOO lattice with a phase advance of about 19°/cell, and the achromat has a FODO lattice with 60°/cell phase advance. The first two cells (four quadrupoles) of the HEBT provide a smooth transition between the two. To remove any linac beam halo, there are two movable and two fixed collimators located in the 2nd to 5th half-cells in this section. The 6th and 7th half-cells are kept for kickers required in a future upgrade. The space between quadrupoles in the first cell of the HEBT is occupied by beam diagnostics.

Momentum Selection (Achromat)

A 90° achromatic bend starts at the 5th cell of the HEBT line, and finishes in six cells, containing twelve 7.5° dipoles. The total phase advance in the achromat is 360°. A beam energy-halo scraper is located at the middle cell of the achromat, where the dispersion is maximum (8.9 meter). Fig. 2 shows amplitude functions (β_X, β_Y) and dispersion function (η) along the HEBT. The first dipole of the achromat is a switching magnet to provide beam to the straight linac dump.

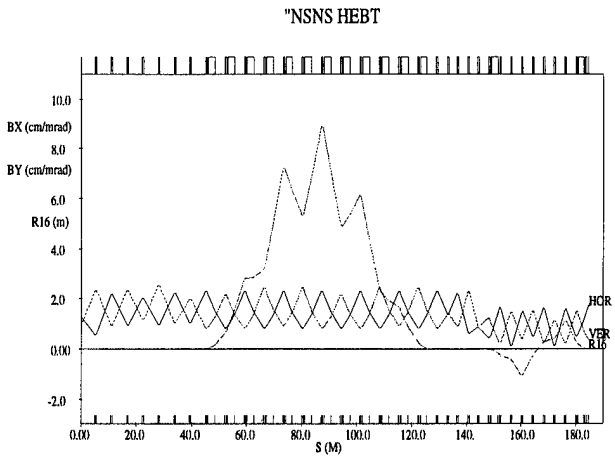


Fig. 2 TRANSPORT output showing the amplitude functions β_X and β_Y, and dispersion function η, along the HEBT.

Momentum Compaction

Momentum compaction is accomplished with a 2.6 meter long, 16 cell, 805 MHz rf cavity with a gradient of 1.375 MV/m. This cavity is similar to the last cavity of linac. The cavity is located in the first half-cell after the achromat (130 m from the linac), where the dispersion and its derivative both have zero values. This location of the cavity can provide the desired momentum spread for a 1 MW (28 mA) beam (see Fig. 3), as well as a 2 MW (56 mA) beam.

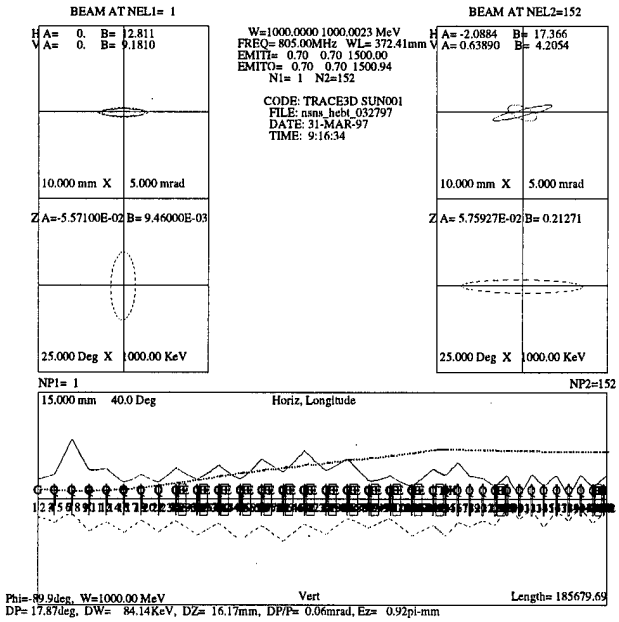


Fig. 3 TRACE3D output for a 1 MW beam.

Achromat to Ring Matching Section

After the achromat, two cells are provided for the diagnostics and beam collimators. At the end of the achromat this line is parallel to the ring straight section, but offset by 10 m, allowing one to have the required "dog leg" for injection into the ring. These bends are necessary to allow the dispersion and its derivative to be zero at the injection stripper foil. As shown in Fig. 2, the dispersion has a minimum and maximum of similar amplitude but opposite sign through the "dogleg". This section has enough quadrupoles to match six variables (four amplitude functions and two dispersion functions). There is no vertical bend and no vertical dispersion. The locations of the dipoles are determined by the injection scheme. Fig. 4 shows the phase space particle distribution at the foil.

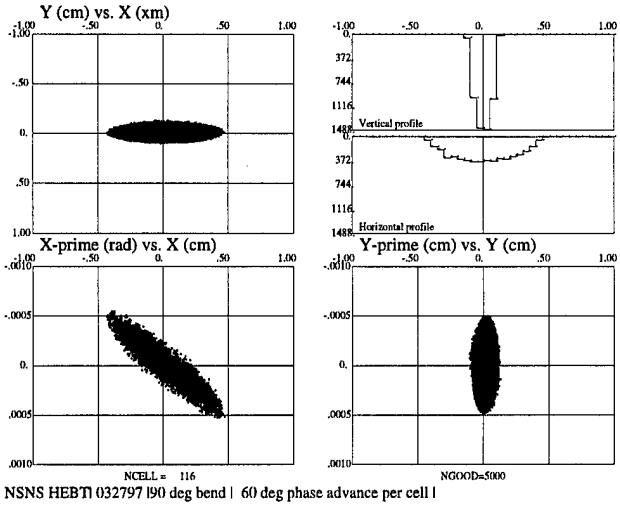


Fig. 4 The phase space and beam size at the injection foil.

Diagnostics

In addition to the straight-ahead linac diagnostic line, one needs enough diagnostic devices spread over the entire HEBT to determine beam losses and beam quality before injection. There is one beam loss monitor per quadrupole and one per dipole, with another 27 left for additional critical locations.

Beam position monitors (x and y) are located near each quadrupole. Harps, which will only be used at low repetition rate due to thermal constraints, will allow beam profile measurements to be made at the entrance to the achromat, middle of the achromat, and entrance to the ring. Using profiles from four crawling-wire profile monitors located between four consecutive quadrupole magnets, one can infer the beam emittance. There will be two of these four-profile units, one at the exit of the linac, and one before the entrance to the ring. Bunch shape monitors (detailed bunch shape), wall current monitors (continuous monitoring of coarse bunch shape), and time-of-flight energy monitors (continuous monitoring of beam energy) will be located at the output of the linac and output of the debuncher cavity (with an additional wall current monitor at the entrance to the debuncher). Finally, current toroids will allow continuous monitoring of beam current at four locations. The diagnostics are shown in Fig 1.

Halo Scraping (Collimation)

There are a total of nine collimators in the HEBT, one for momentum collimation and eight for transverse collimation. Four transverse collimators (2 each in x and y) are located just after the linac, and the other four in a zero-dispersion region just after the compressor cavity. Of these eight collimators, the four horizontal collimators are movable foils, which strip the H^- to H^+, which is then dumped, after horizontal defocusing, in the same dump that is used for fixed vertical collimation [5]. This reduces costs, and has the added advantage of being adjustable in the bending plane. The momentum collimator is located at the maximum dispersion point in the achromat. This scraper is a pair of movable stripping foils in the middle of the bend section, followed by an off-line beam dump for the oppositely bent protons. All collimators are designed to handle 10^{-3} of the beam, but we expect any one to intercept less than 10^{-4}. The configuration for these collimators is shown schematically in Fig. 5.

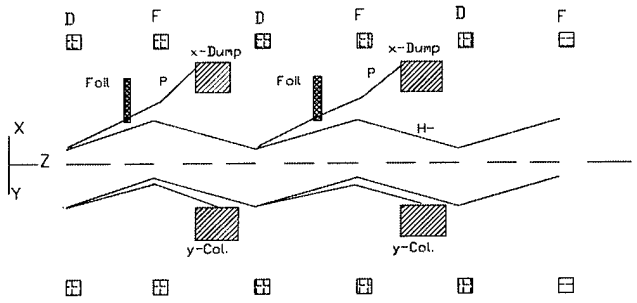


Fig. 5 Schematic of the HEBT collimator configuration

3 SPACE CHARGE AND MOMENTUM SPREAD

The tune depression is defined as $\mu=\sigma/\sigma_0$, where σ and σ_0 are the tune with and without space charge. Table 2 shows these values for different beam currents. The tune depression for the 1 MW and 2 MW cases is almost the same, because the emittance is larger in the 2 MW case. To simulate space charge effects we have used TRACE3D and PARMILA programs. Fig. 3 shows the TRACE3D output for 1 MW. The momentum spread at the exit of the linac is 0.678 MeV for 28 mA. There is no longitudinal focusing in the line until the momentum compression cavity. The momentum spread at the cavity and at the foil for different currents is also shown.

Table 2 Tune Depression and Energy Spread

Current† (mA)	σ	σ_0	μ	ΔE at HEBT Ent. (MeV)	ΔE at Com. Cavity (MeV)	ΔE at Foil‡ (MeV)
0	60	60	1	0.678	0.678	0.678
56	50	60	0.83	0.678	1.494	1.597
112	49	60	0.81	0.743	1.994	2.119

†These currents describe the 1 MW (56 mA) & 2 MW (112 mA) if all the 805 MHz buckets are filled.

‡ Energy Compressor cavity is off.

4 REFERENCES

[1] J. Alonso, "The NSNS Project", these proceedings.

[2]A. Jason, *et al*, "A High Intensity Linac for the NSNS", these proceedings.

[3]W. T. Weng, *et al.*, "Accumulator Ring Design for the NSNS Project", these proceedings.

[4] D. Raparia, *et al.*, "The NSNS High Energy Beam Transport Line", BNL/NSNS Tech. Note #2, Oct. 1996.

[5] H. Ludewig, *et al*, "Collimator Design for the NSNS Accumulator Ring", to be published in ANS Winter Conf., Albuquerque, New Mexico, Nov. 1997.

FIRST OBSERVATION OF THE DEFLECTION OF A 33 TeV Pb ION BEAM IN A BENT SILICON CRYSTAL

C. Biino, M. Clément, N. Doble, K. Elsener, L. Gatignon, P. Grafström,
U. Mikkelsen (CERN, Geneva, Switzerland), A. Taratin (JINR, Dubna, Russia)
S.P. Møller, E. Uggerhøj (ISA, Aarhus University, Denmark)
P. Keppler, J. Major (MPI für Metallforschung, Stuttgart, Germany)

Abstract

For the first time, the deflection of an ultra-relativistic, fully stripped Pb^{82+} ion beam in a bent silicon crystal has been observed. The ions were provided by the CERN-SPS in the H4 beam at a momentum of 400 GeV/c per unit of charge. A 60 mm long silicon crystal, bent over 50 mm to give a 4 mrad deflection angle, was used in this experiment. The measured Pb ion deflection efficiency is comparable to the one obtained with protons at an equivalent ratio of momentum per charge, and is found to be about 15% for a beam with a divergence of 35 microradians (FWHM). The interaction rate observed in a background counter is found to drop when the crystal is well aligned with the beam. This corroborates further the channeling model, which predicts that channeled ions are steered away from regions of high electron densities as well as the nuclei in the crystal.

1 INTRODUCTION

During the past ten years, the deflection of high energy proton beams by planar channeling in bent silicon crystals has been intensively studied and this technique is now being applied routinely at accelerator laboratories around the world [1], [2], [3], [4]. Planar channeling, the steering of particles by the collective fields of crystalline planes, takes place when particles enter the crystal within a small angle (the so-called critical angle) to these planes. For small bending angles, channeling persists throughout the full crystal length.

Apart from the attraction of a bent crystal as a cheap and easy way to extract and split particle beams, it has been astonishing to see how well the channeling models, originally developed for MeV particles, still apply at the highest energies available at proton accelerators today, i.e. up to 900 GeV. Recently, the validity of the models for planar deflection were also tested in a different material, i.e. a germanium crystal, and very good agreement was found [5]. Ions, on the other hand, have hardly been used in connection with bent crystals at accelerators, the only exception being an early test with 53 GeV/c C^{6+} nuclei at Dubna [6], where a deflection efficiency could not be measured. Predictions for bent crystal assisted beam extraction from the heavy ion accelerators in Dubna and Brookhaven are available since a few years [7]. With the availability of the ultrarelativistic Pb ion beam at CERN, it was thus of particular interest to try and deflect such a very high energy beam with a bent crystal.

The fully stripped 33 TeV Pb ions challenge the experimenter further due to the high background (δ-electrons, pions, etc.) observed wherever such ions pass material or, worse, are stopped in a beam-line aperture limitation. Special precaution has therefore to be taken to identify Pb ions in the detectors and to distinguish them from lighter particles with lower charge leading to background events. The high charge state, however, provides one with a very strong signal from Pb ions passing the detectors based on energy loss or scintillation. While many experiments turn to Cerenkov counters for clean Pb ion identification, in the present case standard scintillation counters were used with photomultipliers run at a strongly reduced gain compared to that used for singly charged relativistic particles.

On the other hand, the large number of interaction products from Pb ions passing through material allows to test one of the hypothesis' of channeling theory: Positively charged channeled particles are steered through the crystal at large impact parameters, i.e. away from the lattice nuclei, and channeled ions should thus experience a reduced interaction rate compared to non-channeled ions.

2 EXPERIMENT

The experiment was carried out in the H4 beam line in the North Area of the CERN-SPS. The beam was calculated to be parallel in the vertical plane, in which the deflection by the bent crystal should take place. The experiment was performed in three phases: (a) In order to verify the experimental arrangement and test the detectors, a proton deflection experiment with a 450 GeV/c beam from the SPS was performed prior to the Pb ion run. This test gave confidence that the bent crystal deflected protons as efficiently as expected from the experience acquired over the past years. (b) The $^{208}Pb^{82+}$ ions with a momentum of 400 GeV/c per charge, thus 32.8 TeV/c, were used in a first option with more generous collimator settings, resulting in a wider vertical angular distribution with a FWHM of 50 μrad, very similar to the beam divergence in the proton run. With this beam, the first Pb ion deflection experiment was performed. (c) Finally, the same Pb ion beam, but with more restrictive collimator settings, was found to have a vertical angular distribution of 35 μrad (FWHM), leading to a higher de-

0-7803-4376-X/98/$10.00 © 1998 IEEE

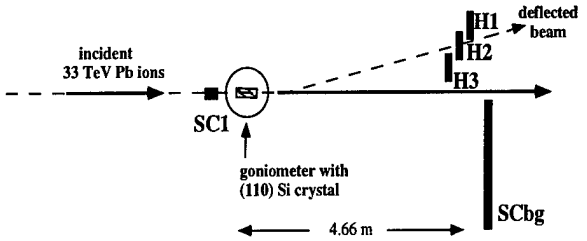


Figure 1: Schematic view of the experimental arrangement. Pb ions are deflected vertically by the bent silicon crystal. Scintillators Sc1 and H1, H2, H3 are tuned to detect Pb^{82+} ions, while SCbg is tuned for background particles.

flection efficiency (see Table 1 below).

The experimental arrangement is schematically shown in Figure 1. The location in the H4 beam, equipped with a goniometer on an x-y translational table, was originally prepared for tests of proton beam splitting in a bent crystal in view of the NA48 CP violation experiment [1]. The crucial movement of the goniometer for the present experiment, i.e. the vertical rotation used to align the (110) planes of the crystal with the beam, has a step-size of 35 μrad, somewhat large compared to the critical angle for channeling at 400 GeV/c/Z momentum, which is $\pm$ 8 μrad, but similar to the Pb ion beam divergence.

The Pb^{82+} ions were steered onto the entrance face of the 1.5 mm thick crystal by aiming at a small scintillator (SC1, 2 mm high, 5 mm thick and 7 mm wide) installed upstream of it. The crystal, 60 mm long in beam direction and 18 mm wide, was bent over 50 mm of its length in a new version of the now 'classical' three-point bending device, which is described in [5]. The resulting bend angle for this experiment was 4 mrad. The deflected Pb ions

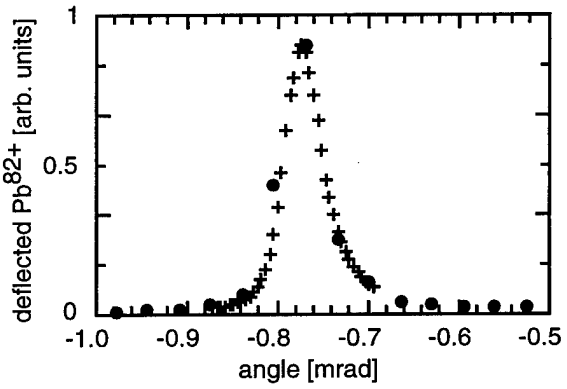


Figure 2: Measurement of the Pb ion vertical beam divergence. Good agreement is found between an angular scan with the crystal (dots) and a scan of the beam angle using steering magnets (+).

were detected in a set of three scintillators ('hodoscope': H1, H2, H3), each 10*10 mm^2 in size and 5 mm thick in beam direction, installed on a motorised support. The central scintillator, H2, overlaps with H1 and H3 by about 2 mm in the vertical (deflection) plane. The high voltage on the photomultipliers of these scintillation counters was reduced and discriminator thresholds adjusted well above the detection level for minimum ionising particles (typical H.T values were -1650 V for protons, -1250 V for Pb ions). An additional scintillation counter (SCbg), 100*100 mm^2 in size and 10 mm thick, was installed outside the beam in order to detect the interactions produced by lead ions passing through the crystal. Thus, its high-voltage was adjusted to a level just below the one used for minimum ionising particles. The beam divergence of the incident Pb ions was determined in two ways: (a) by measuring the intensity of the deflected Pb ion beam for varying goniometer angles, (b) by varying the incident beam angle with a combination of two vertical steering elements (TRIMs), located 42 and 29 meters upstream of the crystal. These magnets allowed to change the incident angle without changing the beam position at the crystal. Typical results for both types of angular scans are shown overlayed in figure 2 for the first experiments with a larger beam divergence. The agreement between the two methods is excellent, and the divergence in this case is found to be 50 μrad (FWHM).

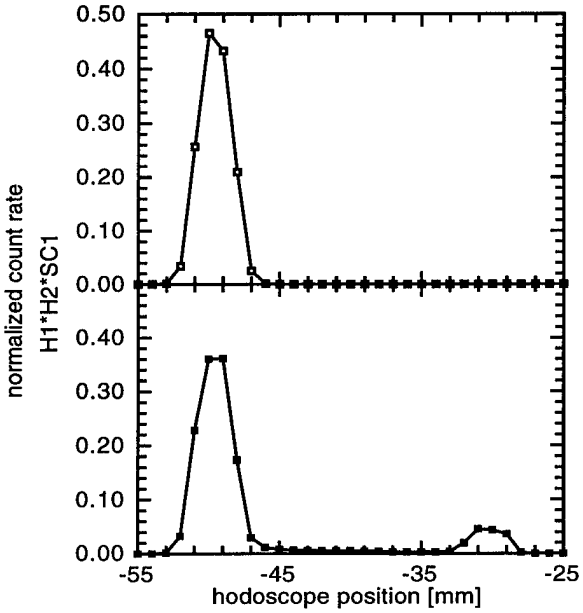


Figure 3: Vertical scan of the hodoscope (stepsize 1 mm) for the more divergent ('wide') Pb ion beam. For a non-aligned crystal (top), the straight beam peak is visible. Its intensity is reduced for the well-aligned crystal (bottom), and an additional peak of upwards deflected Pb ions is visible. (Note: The integrated number of counts is very similar in the two plots.)

3 RESULTS

The undeflected and deflected Pb ions downstream of the crystal can be detected in a given hodoscope scintillator by scanning the hodoscope vertically through the beams. The best position resolution (about 2 mm) in such a scan

is obtained when the coincidence between two overlapping scintillation counters, e.g. H1*H2, is used. The result of such a scan, for the case of the larger Pb beam divergence, is shown in Figure 3. The top of this figure shows the scan for a non-aligned crystal, while the bottom shows the result for a well-aligned crystal. In Figure 4, the same result

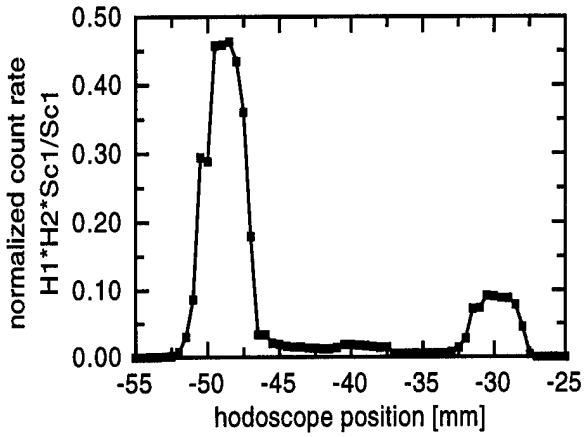


Figure 4: Vertical scan of the hodoscope (stepsize 0.5 mm) for the less divergent ('narrow') Pb ion beam. The coincidence rate in the overlapping counters H1*H2, for ions which passed through SC1, is measured and normalised to the incoming beam rate. The undeflected beam is shown at -49 mm, 19 mm lower than the Pb ions deflected by the crystal. Some ions, visible between the two peaks, were intially channeled and later lost in the bent part of the crystal.

is shown with smaller step-size for the narrow angular distribution of the incident Pb ion beam. Here, the straight and deflected Pb ions are clearly visible, and a region of partially deflected (i.e. initially channeled and then lost) ions can also be seen. Not visible in Figure 3 and 4 is the excellent background rejection of the counters: below the straight as well as above the bent beam, zero counts have been recorded.

Analysing the integrated count rates in such a scan, the deflection efficiency can be deduced as the ratio between the deflected and the incident Pb ions. Results are summarized in Table 1. For the undeflected beam peak, a correction concerning the interactions in the crystal has to be applied to the integral found in the hodoscope scan. The size of this correction in the present case can be estimated from the observation that only 65% of the ions counted in SC1 are detected in SC1*H2, downstream of the crystal, for the non-aligned case (cf. upper part of Fig.3). The remaining systematic errors in the efficiency analysis stem from two sources: (1) The efficiency may be underestimated due to the fact that SC1 is thicker than the crystal (2 vs. 1.5 mm), and the beam is wider than both, FWHM about 3.5 mm. The results presented here have been corrected for this effect. The uncertainty introduced in the efficiencies is estimated to be 1%. (2) The efficiency may be wrongly estimated depending on the cut that is chosen around the bent beam peak in Fig. 3 and 4. (A report comparing the measured deflection efficiencies for Pb ions with those calculated by A. Taratin's simulations is in preparation.)

The observed interaction rate in the 'background' counter SCbg (cf. Fig. 1) is found to drop by about 15% for a well-aligned crystal (at the peak in Fig. 2), i.e. where the largest fraction of Pb ions is channeled and deflected by the crystal. This observation is in agreement with the expectation based on channeling theory: well channeled ions are steered through the crystal far away from the nuclei, and the probability for interactions is thus reduced. The results obtained with the 'background' counter during angular scans will be reported in more detail elsewhere.

Pb beam	divergence	deflection efficiency
'wide' beam	50 μrad	8±2 %
'narrow' beam	35 μrad	14±2 %

Table 1: Measured deflection efficiencies for the 33 TeV Pb ions. Statistical errors are negligible; systematic errors are given. For more details, see text.

4 CONCLUSION

The present experiment has, for the first time, shown the feasibility of deflecting a very high energy, fully stripped Pb ion beam by means of a bent crystal. The experimental results are corroborating the channeling model widely used for protons at energies from MeV to TeV. In addition, the deflection efficiency for these ions is comparable to the one for protons, assuming an equivalent beam emittance and crystal geometry. This is all the more positive as one might have feared a strong loss of ions due to interactions with the atoms in the crystal lattice. The present results can be seen as a first, encouraging step towards extracted ion beams at the Nuclotron (Dubna) and at RHIC (Brookhaven), as proposed by [7].

5 REFERENCES

[1] N. Doble, P. Grafström and L. Gatignon, Nucl Instr. Meth. **B119**, 181 (1996)

[2] R.A. Carrigan, Jr *et al.*, Nucl. Phys. **B163**, 1 (1980)

[3] V.M. Biryukov *et al.*, Physics-Uspekhi **37**, 937 (1994)

[4] K. Elsener *et al.*, Nucl Instr. Meth. **B119**, 215 (1996)

[5] C. Biino *et al.*, CERN-SL/97-05(EA), Phys. Lett. B, in print.

[6] L.I. Belzer *et al.*, JETP Lett., Vol. 46, 381 (1988)

[7] A.D. Kovalenko, A.M. Taratin, E.N. Tsyganov, Preprint JINR E1-92-8, and A.D. Kovalenko *et al.*, JINR Rap. Comm. No.4(72)-1995

ENERGY DEPENDENCE OF CRYSTAL ASSISTED EXTRACTION AT THE CERN SPS

G. Arduini, K. Elsener, G. Fidecaro, M. Gyr, W. Herr, J. Klem*,
U. Mikkelsen and E. Weisse (CERN, Geneva, Switzerland)

1 ABSTRACT

The feasibility of extracting particles from the halo of a circulating proton beam has been successfully demonstrated in an experiment at the SPS. Although most measurements were obtained at an intermediate energy of 120 GeV, more recently we had the opportunity to extract protons from a coasting beam at 14 GeV and 270 GeV, thus exploiting the full available energy range of the SPS. In this report we present a comparison of the measurements at the three energies and a qualitative comparison with the predictions.

2 INTRODUCTION

Beam extraction with a bent crystal depends on parameters that change with the beam energy. Beam diffusion and the resulting impact parameters and angles depend on the beam energy and on the excitation that is used to make the beam particles hit the crystal. When the particles enter the crystal, their interactions are energy dependent. Multiple scattering, critical angle of channeling, and dechanneling in straight and bent parts of the crystal change as a function of beam energy. Consequently, the extraction efficiency for a given extraction set-up depends strongly on the energy of the particles. In the SPS we had the unique opportunity to extract protons at three beam energies: 14 GeV, 120 GeV and 270 GeV. For all energies a beam could be extracted with a good signal to background ratio and extraction efficiencies, extracted beam sizes and angular scan widths could be measured. The crystal properties such as length, thickness and bending radius were designed and originally optimized for an energy of 120 GeV [1] and significant effects are expected for the large energy range available to us.

3 ENERGY DEPENDENCE

3.1 Diffusion process

The impact parameter and angle of a particle intercepted by the crystal depend on the emittance growth of the transverse betatron motion in the halo of the circulating beam. The natural diffusion in the SPS is very slow and an artificial amplitude growth using transverse noise was applied. In our experiment random, transverse kicks were provided by voltage noise between two electrostatic plates [2]. When the noise is uncorrelated and not synchronous with the beam, the average emittance growth per second can be expressed as:

$$\frac{<\Delta\epsilon>}{sec} = \frac{\beta\,\nu_{rev}\,l^2}{2d^2}\cdot\frac{<U^2>}{\gamma^2\,E_0^2} \qquad (1)$$

where β is the transverse beta function at the noise source and ν_{rev} the revolution frequency. Further, $< U^2 >$ is the applied r.m.s. voltage squared between the plates of length l with a distance d between the plates. γ is the relativistic factor and E_0 the proton rest energy. The predicted emittance growth was confirmed by measurements and scales with the energy squared. It has been shown in simulation [2] that the average impact parameter scales approximately linearly with the applied kick strength, and therefore decreases with the beam energy. It is difficult to obtain a fast emittance growth and large impact parameters for the highest energy of 270 GeV.

3.2 Channeling properties

3.2.1 Critical angle

The critical angle scales as $\frac{1}{\sqrt{p}}$ with the momentum p and we find 39.8 μrad for 14 GeV/c, 13.8 μrad for 120 GeV/c, and 9.1 μrad for 270 GeV/c protons in the case of planar channeling in the (110) plane of silicon.

3.2.2 Multiple scattering and multipass extraction

When a proton passes the crystal in the amorphous region or is dechanneled, it experiences multiple scattering and is deflected by a random angle θ with a Gaussian distribution with zero mean value and a width:

$$\theta = \frac{13.6MeV}{\beta cp}\sqrt{\frac{L_{eff}}{X_0}}\left(1+0.038\ ln\left(\frac{L_{eff}}{X_0}\right)\right) \qquad (2)$$

where cp = 120 GeV, $\beta \sim 1$, and X_0 is the radiation length of the crystal ($\sim$ 9.4 cm for silicon). For a particle traversing the full crystal length of 4 cm this angle θ is approximately 66.5 μrad at 120 GeV/c but usually the particles which undergo multiple scattering do not cross the full crystal length but only a small part of it (i.e. L_{eff}, c.f. [3]). It has been shown [4] that the multi pass extraction process plays an important role for extraction from the SPS, i.e. particles traverse the crystal multiple times before they are eventually channeled. The multiple scattering experienced in such a passage determines the impact parameters for further intercepts on the crystal [3]: strong scattering leads to large impact parameters. Due to the strong dependence of the multiple scattering angle on the energy one can expect a strongly changed pattern of impact properties on later encounters of the proton on the crystal. It is also expected that the width of the vertical profiles of channeled particles is increased for lower energies.

* Also: Helsinki Univ. of Technology, Finland

0-7803-4376-X/98/$10.00 © 1998 IEEE

3.2.3 Dechanneling

To be successfully extracted a particle must remain channeled, but interactions with electrons inside the crystal or with the nuclei in the lattice, can lead to dechanneling of initially channeled particles. This dechanneling processes can be approximated by an exponential decrease of the number of channeled particles: $n = n_0 e^{-l/l_0}$ where l_0, called *normal dechanneling length*, is equal to 10.8 cm for [110] silicon planes and 120 GeV/c protons. This parameter scales as $1/p$ with the momentum and becomes a very important factor at 14 GeV/c, leading to a large dechanneling probability P_{dc}. The dechanneling length for 14 GeV/c is only about 1.26 cm, i.e. much smaller than the crystal length and we have to expect that more than 90% of the channeled particles dechannel within the crystal length. The extraction efficiency should therefore be significantly lower than for 120 GeV/c.

4 PREPARATION OF THE SPS

The details of the experiment and the analysis can be found elsewhere [1, 5, 6]. However, a few particularities setting up the SPS for three significantly different energies to get comparable results, deserve some attention. The proton beam is injected into the SPS at a momentum of 14 GeV/c in two batches, one 1.2 seconds after the other, each 10 μs long. Typical tunes during the whole cycle (flat bottom, acceleration and coast) are 26.62 and 26.58 in the horizontal and vertical plane, respectively. Injection oscillations and low frequency instabilities (resistive wall instabilities) are damped by a transverse feedback. A single batch (a few 10^{12} protons) was accelerated (except for the 14 GeV coast) to the target energy. The functions of all the ring power converters were frozen at that point and the injection and the beam dump kickers were inhibited. The damper was active at injection and it was automatically deactivated after a few seconds. In order to damp the resistive wall instabilities during the coast at 14 GeV and therefore guarantee a sufficient lifetime to make the extraction measurement possible, the strength of the octupoles for Landau damping had to be strongly increased (by a factor 2 radially and 5 vertically) as compared to that used for the high intensity fixed target beam (4.5 x 10^{13} protons) at injection. After the initial adjustment of the orbit the RF frequency was switched off and a lifetime of about 4 hours (without crystal) was achieved at 14 GeV. The use of transverse noise or of adequate sextupoles, required for the extraction at higher energy, was not necessary at 14 GeV because of the natural diffusion due to the strong octupolar component and to the spontaneous beam excitation.

5 RESULTS

The experimental procedure such as the alignment of the crystal and details about the angular scans are found in previous reports [1, 5]. Angular scans are performed to align the crystal with the beam envelope and the results of three typical scans for the three energies are shown in Figs. 1 to 3.

5.1 Angular scans and profiles

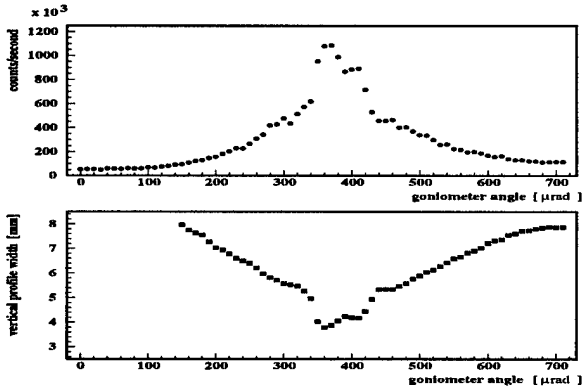


Figure 1: Angular scan and vertical width, 120 GeV

Together with the angular scans we show the width of the vertical profiles. It was already demonstrated [1], that the best alignment of the crystal coincides with a minimum of the vertical width of the extracted beam. This is clearly demonstrated for all three energies.

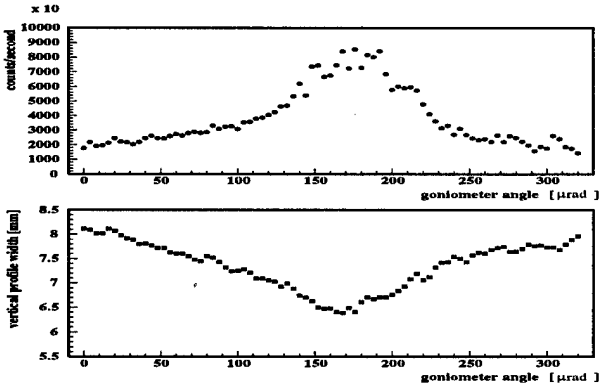


Figure 2: Angular scan and vertical width, 14 GeV

The measured widths of the scans can vary depending on the experimental condition and the type of crystal [1]. This variation is not yet fully understood and is larger than the observable difference between the three energies. The profiles measured with the scintillator hodoscope [1] are shown in Figs. 4 to 6. For 14 GeV, a significant widening of the vertical profiles can be observed and is attributed to a stronger multiple scattering of channeled particles at lower energies.

5.2 Extraction efficiency

The extraction efficiency should be mainly determined by the probability for channeling and the chance for dechanneling. We believe that the "channeling probability" is mainly determined by a multipass process. Although we might expect larger impact parameters for 14 GeV particles, the angular scans show no sign of an increased con-

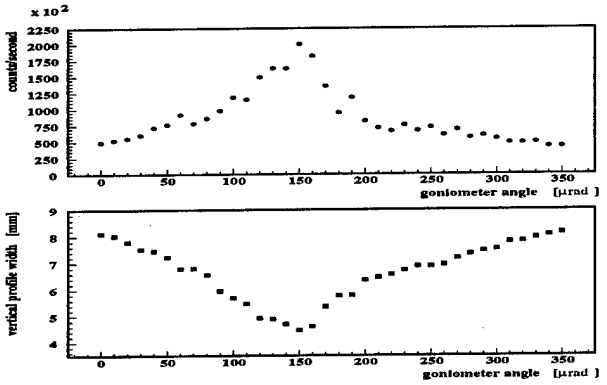


Figure 3: Angular scan and vertical width, 270 GeV

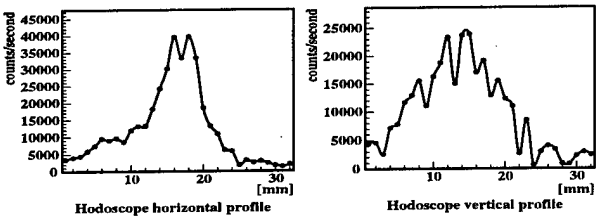


Figure 4: Profiles of extracted beam at 14 GeV

tribution to single pass extraction. For all energies investigated, the multiple scattering in early passes through the crystal is sufficient to increase the impact parameters to values large enough to overcome surface imperfections. Therefore we do not expect the original channeling probability to depend significantly on the energy. The measured widths of the angular scans show also no significantly different behaviour, indicating that the changed critical angle and therefore the angular acceptance play a minor role. Once captured into a channel, the particles can undergo multiple scattering, leading to dechanneling and widening of the profiles. This widening of the profiles should be pronounced in the vertical plane and is clearly observable in Figs. 4 to 6. The increased dechanneling probability for lower energy should significantly affect the extraction efficiency. We define the efficiency of the extraction process as the ratio of the number of extracted particles to the number of particles lost from the circulating beam I_{lost}: $\epsilon_{extr} = \frac{I_{extr}}{I_{lost}}$. The number of extracted particles is determined from a threefold coincidence of trigger scintillation counters and the background from the measured profiles.

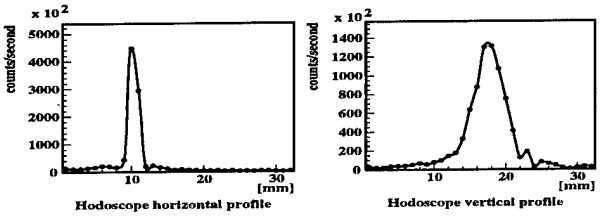


Figure 5: Profiles of extracted beam at 120 GeV

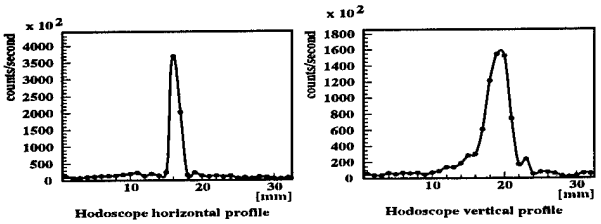


Figure 6: Profiles of extracted beam at 270 GeV

The number of particles lost from the beam is determined from the beam intensity measured with a beam-current-transformer (BCT) and the measured beam life time. For the measurement at 14 GeV, special care had to be taken for the life time measurement: while for the other energies it was correct to assume an infinite life time without the crystal, the natural life time of the beam at 14 GeV was much lower and only about 0.1 to 4 hrs. This natural life time was measured every time and folded into the calculation of the life time reduction due to the crystal. A consequence of the small life time at 14 GeV was that during a measurement the beam intensity changed significantly, thus changing the number of particles intercepting the crystal. This had to be taken into account in the calculation of the efficiency. The result of this analysis is summarized in Tab.1.

Beam energy (GeV)	Extraction efficiency (%)	Prediction simulation (%)
14	0.55±0.3	0.46
120	15.1±1.2	15.1*
270	18.6±2.7	17.7

Table 1: Extraction efficiences at different energies. *Simulation normalized to 120 GeV.

The extraction efficiencies at 120 and 270 GeV are comparable, while the efficiency at 14 GeV is much lower, as expected from qualitative arguments. Also given are the efficiencies predicted from simulation for the three energies. Since the efficiency is usually overestimated in the simulation [3, 5] we have normalized it to the value measured at 120 GeV to study the energy dependence and find excellent agreement with the measurement.

6 REFERENCES

[1] K. Elsener *et al.*, Nucl.Instr.Meth. **B119** (1996) 215.

[2] W. Herr, CERN/SL/92-53 (AP).

[3] G. Vuagnin, CERN/SL/Note 95-24 (AP)

[4] X. Altuna *et al.*, Phys.Lett. **B357** (1995) 671.

[5] J. Klem; PhD Thesis, Helsinki Univ. of Technology (1997).

[6] H. Akbari *et al.*, Phys.Lett. **B313** (1993) 31.

EXTRACTION OF 22 TeV/c LEAD IONS FROM THE CERN SPS USING A BENT SILICON CRYSTAL

G. Arduini, K. Cornelis, K. Elsener, G. Ferioli, G. Fidecaro,
M. Gyr, W. Herr, J. Klem* and E. Weisse
CERN, Geneva, Switzerland

1 ABSTRACT

The extraction of protons from the halo of a circulating beam has been repeatedly demonstrated at the SPS. In a recent experiment a coasting lead ion beam was available at a momentum of 270 GeV/c per charge corresponding to a total momentum of 22 TeV/c per ion and the possibility to extract ultrarelativistic lead ions with a bent crystal could be demonstrated for the first time. We present the experimental challenges, the measurements performed during this experiment and the first results.

2 INTRODUCTION

Extraction of high energy protons from a stored beam with a bent crystal has been demonstrated successfully and with a good extraction efficiency at the CERN SPS [1, 2, 3] and other laboratories [4]. At the CERN SPS it was shown that protons could be extracted for a large range of energies between 14 and 270 GeV and the energy dependence is in good agreement with the expectation [5].

More recently [6] fully stripped lead ions $^{208}Pb^{82+}$ were deflected in a bent crystal in a beam line experiment at the SPS with high efficiency. Encouraged by this result and due to the availability of Pb ions in the SPS we have conducted a short experiment where we stored a lead ion beam in the SPS at a momentum of 270 GeV/c per charge, i.e. a total momentum of approximately 22 TeV/c. Using the standard experimental procedure we obtained Pb ions extracted from the coasting beam with a bent crystal. It is the first time that an ion beam at high energy was handled in this way.

In this paper we shall first describe the setting up of the SPS accelerator as a lead storage ring and discuss the experimental difficulties connected with this high energy and charge per nucleon. We present the results obtained and estimate the extraction efficiency.

3 PREPARATION

3.1 Setting up of the SPS for Pb

The fully stripped lead ion beam is injected in the SPS with a momentum of 13 GeV/c per charge in 4 batches (2 x 10^{10} charges/batch) each 2 μs long. The beam is accelerated to a momentum of 26 GeV/c per charge with a fixed-frequency acceleration technique [7], it is debunched to fill the whole machine (23 μs revolution period) to increase the effective spill length for the experiments and then it is further accelerated to 400 GeV/c per charge, the usual energy of lead ions for fixed target physics. Because of the large emittances of the beam (close to the physical acceptance of the machine, in particular vertically) the control of the orbit, of the tune (QH=26.62 and QV=26.58), of the chromaticity (close to zero in both planes) and of the momentum spread is important all through the acceleration and in particular at low energy. In the preparation of this experiment the above-mentioned corrections were performed and a single batch was injected and accelerated up to 270 GeV/c per charge where all the ring power converters were frozen and the injection and beam dump kicker inhibited. Due to the low intensity no relevant instabilities are observed.

To obtain the desired emittance growth, transverse noise was applied to the beam as in the case for protons [1, 2, 5].

3.2 Setting up of the experiment

The equipment available for this experiment has been identical to the one described for proton extraction in Refs. [1, 2, 3]. The extracted beam, deflected 8.5 mrad by the bent crystal, exits the vacuum chamber and passes three scintillation counters (used in coincidence). The $^{208}Pb^{82+}$ ions are expected to give a very strong signal in these scintillators, at least two orders of magnitude above the one for protons and pions. Thus, the setting up of the corresponding high voltages (HV) on the photomultipliers was done in the following way: First, the crystal was misaligned (no extraction!) and background was observed in the detectors set to the nominal proton HV (e.g. 2450 Volts in SC1). Then, the HV was lowered until the background signal disappeared (2000 V). Finally, in order not to lose any extracted Pb ion signal, the HV was set 50 Volts higher for data taking. Discriminator levels and delays remained untouched. Angular scans, obtained by turning the crystal and observing the coincidence rate SC1*SC2*SC3, show about 20% of background (cf. Figs. 1 a to c). This is a clear indication that the HV was not perfectly tuned for Pb ions - due to lack of time. For the estimates of the extraction efficiency, the same triple coincidence was used in the "steady state" for a well-aligned crystal, and a 20% background subtraction was applied to the extracted beam rate.

The extracted beam profiles were obtained from the luminescent screen (BTV) installed downstream of SC2. This BTV is a standard SPS beam instrument, equipped with various screens of different sensitivity, which can be chosen remotely. The screens are viewed by a CCD camera, and more choice of sensitivity is available due to its diaphragm and gain. For the present experiment, the sensitivity could be reduced dramatically with respect to proton extraction, and very clean profiles practically free of

* Also: Helsinki Univ. of Technology

0-7803-4376-X/98/$10.00 © 1998 IEEE

background could be obtained. These are available either directly on TV screens in the SPS control room or in a digitized form, available at 20 ms intervals, for later evaluation. Typical extracted Pb ion beam profiles are shown in Fig. 2.

4 EXPECTATIONS FOR LEAD IONS

The main difference between lead ions and protons is the high mass and charge state. Both have an impact on the interaction of the ions with its environment, in particular with the crystal. Important for the acceptance for channeling is the critical angle ψ_c which scales with $\sqrt{Z/p}$. For a highly charged ion the relevant parameter is the momentum per charge p/Z and therefore the critical angle for ions is equivalent to the angle for protons at the corresponding momentum of 270 GeV/c, i.e. 9.1 μrad. Protons with a momentum of 270 GeV/c have been successfully extracted from the SPS [5].

Furthermore, the dechanneling scales like Z/p, leading to a dechanneling like for protons of equivalent momentum per charge. Similar arguments hold for the multiple scattering in the crystal and its effects, i.e. widening of profiles and increased impact parameters, should be comparable to protons.

However, due to the dependence of the inelastic nuclear cross-section on the atomic mass A: $\sigma_{in} \propto A^{0.71}$, the losses due to inelastic collisions are strongly increased. Worse, the electromagnetic (Weizsaecker-Williams) breakup cross section is very important for such highly charged, fast ions. As a result, we expect a significant decrease of the contribution of multiple pass extraction to our extraction process.

5 RESULTS

5.1 *Angular scans*

The results of three angular scans can be seen in Figs. 1 a to c. The experimental procedure is similar to the one used for extraction of protons [1, 5]. The three angular scans were taken at different times during the experiment to study the reproducibility. While the widths of the angular scans for proton extraction was difficult to reproduce [1, 5], the limited statistic for Pb ions available at present seems to indicate that the reproducibility is better. Furthermore, after the background of 20 to 25 % is subtracted, the full width half maximum (FWHM) of the scans in Figs. 1 a to c is between 45 and 55 μrad, thus significantly narrower than the ones measured for protons between 14 and 270 GeV/c [5]. One may try to speculate whether these narrower angular scans are due to a suppressed contribution of multiple pass extraction to the total extracted rate, or a reduced phase space acceptance for multiple passes.

5.2 *Extracted beam profiles*

Profiles of the extracted beam were measured with a luminescent screen and the CCD camera, and could be digitized and stored. The results can be seen in Fig. 2. The profiles

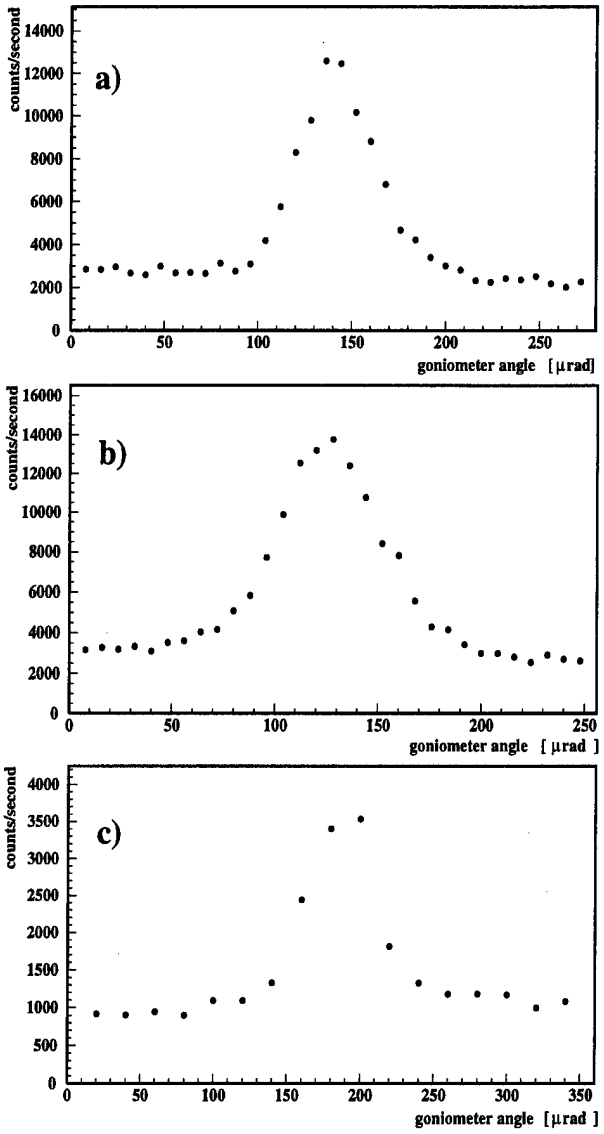


Figure 1: Angular scans, taken at different times to study reproducibility, Pb ions, 270 GeV/c per charge.

are similar to the profiles obtained with the scintillator hodoscope for protons [1, 5].

5.3 *Efficiency*

The efficiency of the extraction process we define as the ratio of the number of extracted particles to the number of particles lost from the circulating beam I_{lost}:

$$\epsilon_{extr} = \frac{I_{extr}}{I_{lost}} \quad (1)$$

The number of extracted ions is determined from a threefold coincidence of trigger scintillation counters SC1*SC2*SC3 and the background estimated from the measured angular scans is subtracted. As mentioned above, the high voltage could not be adjusted to an optimum value

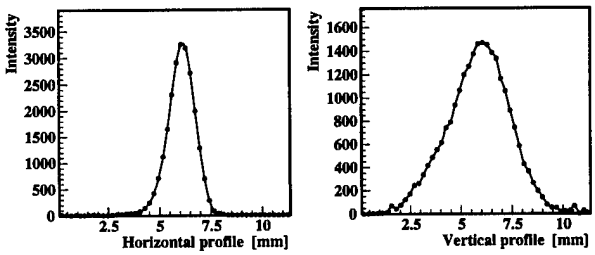


Figure 2: Horizontal and vertical profiles for optimum alignment, Pb ions, 270 GeV/c per charge

for the ions and the error on the number of extracted particles is therefore increased. The number of particles lost from the beam is determined from the beam intensity measured with a beam-current-transformer (BCT) at 19.2 s intervals and thus from the measured beam life time. Due to lack of time, the calibration of both measurements could not be done carefully and the extraction efficiency is therefore less accurate than the ones reported for protons [5]. For the calculation of the efficiency we use rather conservative values and estimate an error on the efficiencies of approximately 35 - 40 %. The results of our efficiency esti-

Beam intensity (10^7 ions)	Beam lifetime (hrs)	Extraction efficiency (%)
13.0	2.2	4.0±1.5
10.0	0.3	10.0±3.5
6.7	1.2	9.0±3.0
5.0	0.04	11.0±4.0
5.0	0.23	5.0±2.0

Table 1: Extraction efficiences for Pb at 270 GeV/c per charge.

mates are given in Tab. 1. For the first four measurements in Tab. 1 the standard U-shaped crystal [1, 5], which was used in most of the experiments with protons, was positioned at a distance of about 10 mm from the closed orbit. For the last measurement an alternative crystal with slightly different properties (miscut) was used at a larger distance of approximately 20 mm from the orbit. Significant differences are not observed between the two types of crystals.

Compared with the measured efficiency from proton extraction at 270 GeV/c which was about 18% [5], the efficiencies for lead are about a factor two smaller, although this comparison is based only on a few measurements made for lead extraction. We show the efficiencies for different values of the noise excitation on the ion beam, i.e. beam lifetimes. As it is the case for protons [1, 5], no clear correlation can be observed and the variation of the efficiencies is even slightly larger than for protons, but with the present precision a clear conclusion cannot be reached.

6 CONCLUSION

We have demonstrated for the first time that fully stripped lead ions $^{208}Pb^{82+}$ can be extracted from a stored SPS beam at a momentum of 270 GeV/c per charge, corresponding to a total momentum of the ions of approximately 22 TeV/c. Care was taken to suppress possible background signals in the detectors. Although the error on the extraction efficiency is substantially larger than for protons, the estimated efficiency reaches values up to 10%. A first analysis indicates that the width of the angular scans may be significantly smaller than for protons, which can be possibly explained by a reduced angular acceptance and could indicate a suppressed multiple pass component of the extraction process.

7 ACKNOWLEDGEMENT

We would like to express our gratitude to Albert Hofmann without whom this experiment would not have become a reality. Only his proposal to use a coasting lead ion beam in the SPS for another experiment and his friendly generosity to make the beam available to us for a few hours made this study possible. We would also like to thank the operations crew of the SPS for their help running the machine in this unusual mode of operation.

8 REFERENCES

[1] K. Elsener *et al.*, Nucl.Instr.Meth. **B119** (1996) 215.

[2] H. Akbari *et al.*, Phys.Lett. **B313** (1993) 31.

[3] X. Altuna *et al.*, Phys.Lett. **B357** (1995) 671.

[4] T. Murphy *et al.*, Nucl.Instr.Meth. **B119** (1996) 231.

[5] G. Arduini *et al.*, Energy dependence of crystal assisted extraction at the CERN SPS Proc. Part. Acc. Conference 1997, Vancouver, May 1997.

[6] K. Elsener *et al.*, First observation of the deflection of a 33 TeV Pb ion beam in a bent silicon crystal Proc. Part. Acc. Conference 1997, Vancouver, May 1997.

[7] X. Altuna *et al.*, The SPS as lead ion accelerator Proc. 5th Eur. Part. Acc. Conference, Sitges, 1996.

GABOR-PLASMA LENS FOCUSING FOR LEBT SYSTEMS*

J. Pozimski, R. Dölling, A. Jakob, P. Groß and H. Klein

Institut für Angewandte Physik, Frankfurt

Abstract

Low energy beam transport (LEBT) of high perveance ion beams suffers from high space charge forces. Spacecharge compensation reduces the necessary focusing force and the filling factor of the lenses and therefrom the emittance growth due to aberrations and inner fields. The use of electrostatic lenses is restricted due to decompensation by the electric fields. On the other side magnetic lenses suffer, for high mass ions, from necessary high magnetic fields and the resulting technical problems. A different approach for a LEBT system is a lens using a static non neutral plasma confined in a magnetic and electrostatic field configuration allowing strong electrostatic focusing together with partial conservation of spacecharge compensation. Modelling of the plasma in a way that lens aberrations are small is very difficult and the underlying theory is not fully understood. New measurements at low residual gas pressure as well as theoretical work and the results of numerical simulations will be discussed.

1 INTRODUCTION

Plasma lenses (using electrostatic or magnetic forces for focusing) have certain advantages compared with conventional lens systems. But so far they suffer from inhomogeneities in the plasma column which lead to beam aberrations and emittance growth. For the Gabor plasma lens (GPL) studies have been started in Frankfurt to investigate theoretically and experimentally the properties of electrostatic plasma focusing.

2 THEORY

Assuming a homogeneous density distribution in the lens the maximum electron charge density the 'classicl limit' is given by the radial enclosure criteria [1]

$$\rho_{e,\max,rad} = \frac{e\varepsilon_0 B_z^2}{2m_e} \qquad (1)$$

neglecting all radial loss processes (i. g. by diffusion) and any longitudinal effects. An first estimation of the restrictions of electron charge density due to longitudinal losses ist given by

$$\rho_{e,\max,long} = \frac{4U_A\varepsilon_0}{r_A^2} \qquad (2)$$

with U_A the anodevoltage and r_A the anode radius, assuming homogeneous lens filling and the minimum potential on lens axis to be zero. Combining both criteria the maximum

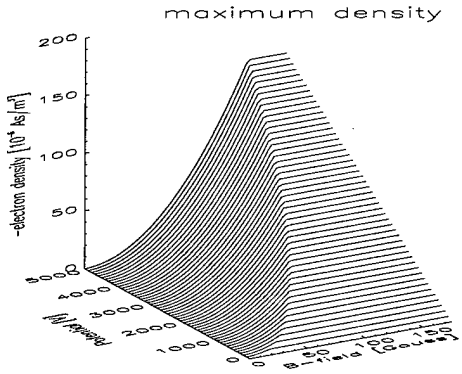


Fig. 1 : Theoretical maximum electron charge density in a Gabor plasma lens as a function of external parameters (Eq. (1)&(2)).

electron charge density as a function of the external parameters is shown in fig. 1. The electron density is a quadratic function of the magnetic field and linear with anode potential. Nevertheless hereby the electron density is overestimated by a factor of 3-5 compared with measurements . This behaviour is well known in literature for similar confined plasmas [2]. Therefore a computer code has been developed to simulate the local electron density in the GPL in a self consistent manner. Longitudinal losses are estimated from the density of Boltzmann distributed electrons at the wall and their thermal velocity. It is further (somewhat arbitraryly) assumed that the mean lieftime of electrons given by this losses equals the thermalization time of the electrons due to collisions. Radial losses caused by diffusion of electrons across magnetic field lines are neglected.

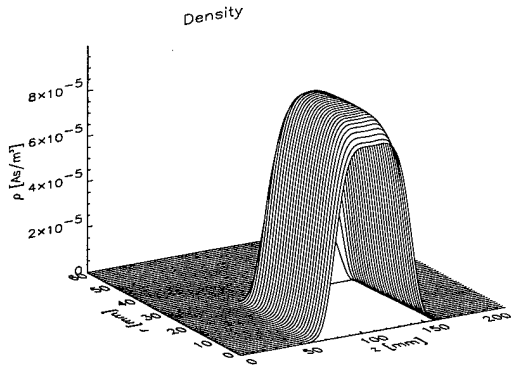


Fig. 2 : Numerically simulated selfconsistent electron density distribution in a Gabor plasma lens (B_z=90*10^{-4} T, U_A=5 kV, I_{loss}=1 μA).

*Work supported by BMBF

0-7803-4376-X/98/$10.00 © 1998 IEEE

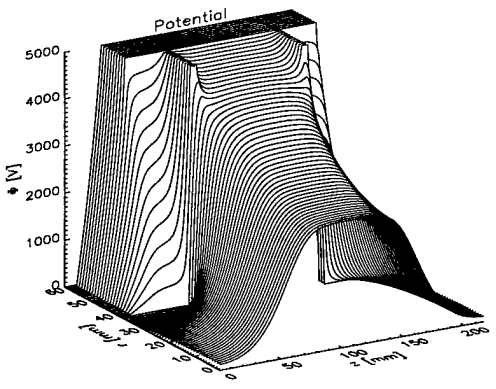


Fig. 3 : Potential distribution corresponding to fig. 2.

3 NUMERICAL SIMULATIONS

Fig. 2 shows the simulated electron density distribution inside the GPL assuming equilibrium state for an anode voltage of 5 kV and the magnetic field of $90*10^{-4}$ T. The longitudinal electron losses result to 1 µA. The electron density on lens center is comparable to the results of the classic theory (Eq. 1). The electrons are longitudinally (due to the temperature and losses) and radially (reaching the classical limit) concentrated on the lens center. Fig. 3 shows the potential distribution inside the lens including the space charge of the electrons. To investigate the behaviour of the electron distribution inside the lens and of electron losses for varried anode voltage and magnetic field strength multiple simulations have been performed. Fig. 4 shows the dependency of the longitudinal electron losses on the electron density on lens axis in equilibrium state. Only for loss rates below 100 µA the electrons can thermalize. For higher electron loss rates (and therfore production rates) the electron density on axis weakly increases. This is due to the fact that the electron loss function is dominated by electron temperature not by electron density. Fig. 5 shows the influence of the anode voltage on the electron density for constant magnetic field. The electron density is in first order

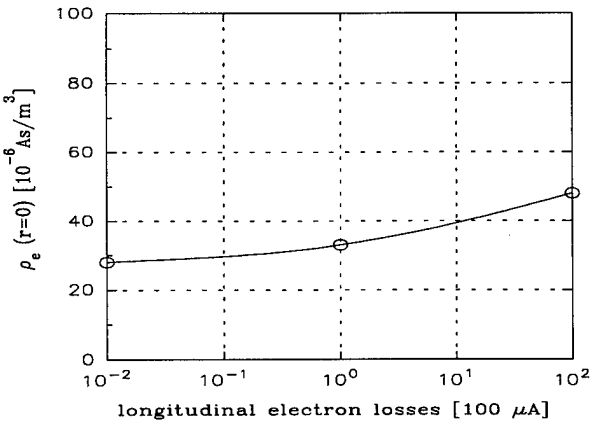


Fig. 4 : Numerical simulated development of electron density in equilibrium state in a GPL as a function of longitudinal electron losses (B_Z=500*10^{-4} T, U_A=5 kV).

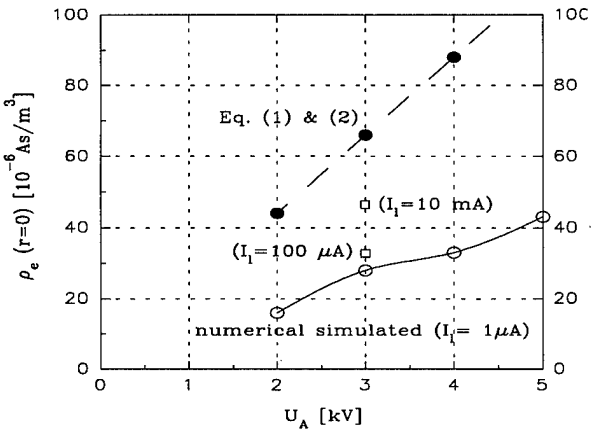


Fig. 5 : Numerical simulated development of electron density in equilibrium state in a GPL as a function of anode voltage (B_Z=500*10^{-4} T, I_{loss}=1 µA)..

approximation linear with the anode voltage (like in the semi classical theory (Eq. (1) & (2))). In contrary the measurements show a slightly underlinear behavior. This can be explained by increasing radial losses due to higher electric fields (diffusion is proportional to E/B). Fig. 6 shows the electron density for fixed anode voltage as a function of the magnetic field. Below a minimum field strength all electrons are radially expelled solely by the action of the external electric field (classical limit). Above the critical field strength the electron density on axis at first drastically rises and then becomes constant. For increasing magnetic field the diameter of the electron cloud and therefore the focusing capabilities are increasing too.

4 MEASUREMENTS

Beam measurements using a LEBT with two solenoids for beam formation have been performed [3,4] at low residual gas pressure (minimizing the effects of electron production and the influence of the space charge of the residual gas ions). The beam was matched parallel with a diameter of appr. 45 mm into the lens. Fig. 7 shows the result of an emittance measurement with the beam focussed to minimum radius at measurement point by the GPL. The

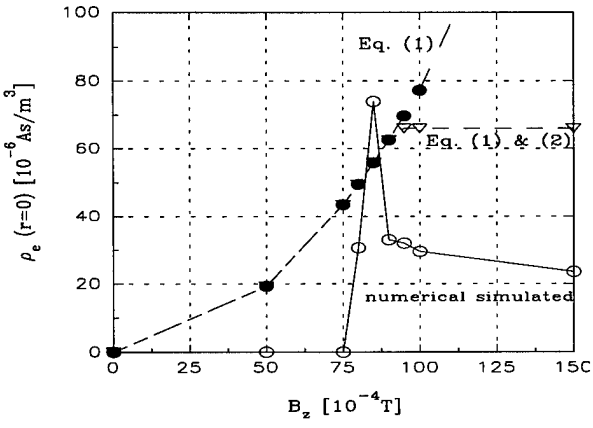


Fig. 6 : Numerical simulated development of electron density in equilibrium state in a GPL as a function of magnetic field strength (U_A=3 kV, I_{loss}=1 µA).

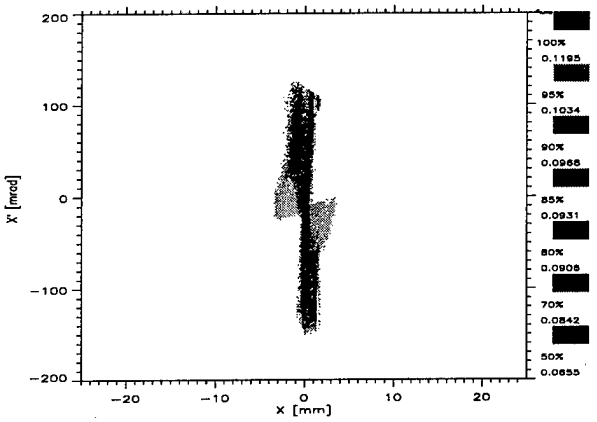


Fig. 7 : Emittance pattern of a He^+ beam (10 keV, 3.6 mA) measured appr. 60 mm behind the GPL (5 kV, 90 *10^{-4} T).

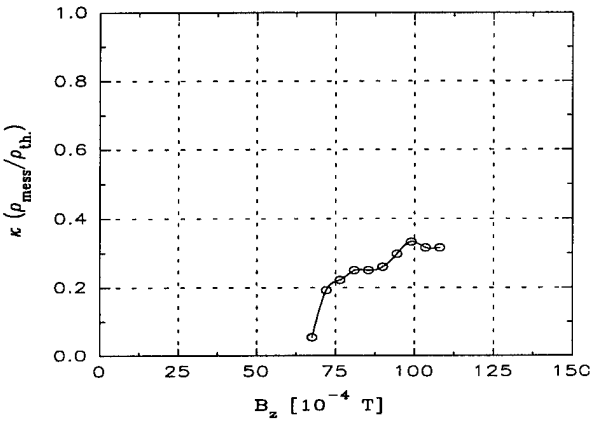


Fig. 9 : Development of filling factor κ as a function of the magnetic field strength (gained by comparison of measured data with classical theory (eq. 1)).

performance of the lens is capable to fulfill the injection requirements of an RFQ. Comparison with a numerical transport simulation (see fig. 8) show that the aberration at low angls are caused by inhomogeneous electron density. κ the quotient of the indirectly measured electron densities and the classical theory as a function of the magnetic field strength (Fig. 9) show similar behaviour compared with the results of the numerical simulations (Fig. 6). Measurements of the degree of compensation show a decrease (from 80 % compensation to 20 %) compared with transport using only magnetic fields. For different external fields the loss channel dominating the behavior of the lens changes and therefrom the compensation degree. The emittance growth variies from 20-300 % dominated by time variing space charge forces due to ion source noise and by radial plasma inhomogenity. The second is mainly influenced by lens geometry and therefore can be optimized through simulation. In a second experiment the LEBT has been modified by inserting to anodes into the solenoids using the two solenoids for delivering the magnetic fields for the GPL. Using Argon as beam ions the modified solenoids show a higher focusing strength with the GPL effect than without. Fig. 10 shows an emittance measurement with an already overfocussed beam (at 2 kV, 120*10^{-4} T) where the solenoids can deliver an parallel beam at maximum field strength only (at 0.6 & 0.8 T).

5 CONCLUSIONS

Measurements have proofed that GPLs are able to focus a positve ion beam of high perveance and medium mass at 10 keV beam energy fullfilling the requirements for injection into a RFQ. The emittance growth is (at optimum external parameters) comparable with magnetic solenoids and for high currents better than conventional electrostic einzellenses. Numerical simulations show an improved quality of transport capability forecast especially for plasma states where radial diffusion processes are neglectible. Experiments are planned with higher masses (Bi^+) at higher energy to investigate the possiblities for an inertial fusion driver LEBT. In a next step the radial diffusion processes will be included into the simulations.

6 REFERENCES

[1] D. Gabor, Nature 160 (1947) 89

[2] D. P. Xi, Physika Scripta 39, 105 (1989)

[3] J. Pozimski et. Al. Proc. LINAC Conf. 1996, Geneva

[4] J. Pozimski , Dissertation in preparation (IAP, 1997)

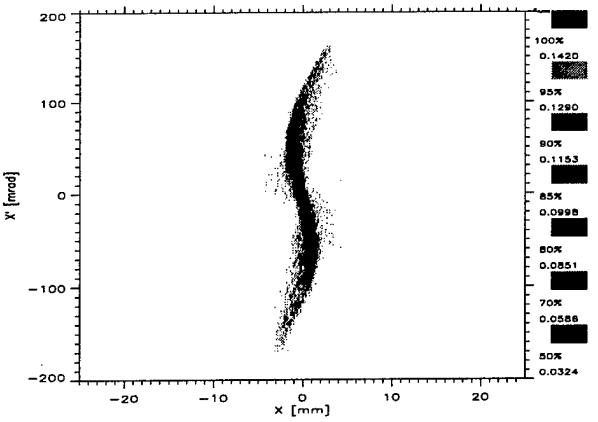


Fig. 8 : Calculated emittance pattern of a He^+ beam (10 keV, 3.6 mA) appr. 60 mm behind the GPL (5 kV, 90 *10^{-4} T) using 10000 particles for transport calculation.

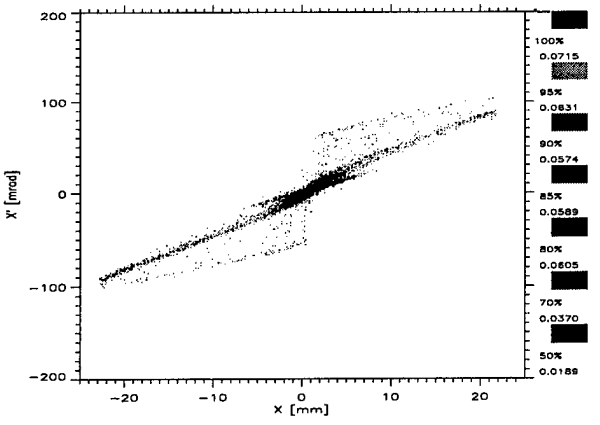


Fig. 10 : Emittance pattern of a Ar^+ beam (10 keV, 400 µA) measured appr. 330 mm behind the second soleniod (used as GPL at 2 kV , 120 *10^{-4} T).

AN IDEAL FOR SELECTION OF SHORT-LIVED PARTICLES BY A FOCUSING CRYSTAL

Valery Biryukov*
IHEP Protvino, 142284 Moscow Region, Russia

Abstract

An experimental technique for selection of the short-lived particles by means of a focusing crystal is proposed. A target (to produce short-lived's) and a focusing crystal are to be arranged so that the crystal traps into channeling mode the particles emerging from the region downstream of the target only. The particles emerging from the target directly, cannot be trapped in the crystal. In this way one can trap the decay products of short-lived particles to carry them out of the background; the trapped beam can be bent, e.g., onto the experimental set up. The technique can handle the particles with decay length $c\tau$ down to few micron. The capabilities of the technique, resolution, and efficiency are analyzed.

1 INTRODUCTION

Short-lived particles such as B-mesons have the lifetimes τ so short that $c\tau$ equals to only $\sim$100–400 μm. Even with relativistic factor of $\sim$100 the mean path before decay for these particles equals only $\sim$1–4 cm. There is no way to handle these particles by a traditional magnet beam optics. The bent-crystal-channeling technique allows to steer the particle beams, bend or focus them, along a few cm path, with equivalent fields on the order of 1000 Tesla and more [1]. Applications of this technique to short-lived particles have been proposed [2,3]. One application—a measurement of the particle's magnetic moment in a bent crystal—was successfully tested in the experiment [4].

2 THE PRINCIPLE

The discussed idea involves a focusing crystal, which can either focus a parallel beam into a point, or perform a reversed process, i.e. trap a beam emerging from a point-like source; both applications have been demonstrated experimentally [1]. Suppose, a target (to produce short-lived's) and a focusing crystal are arranged so that the crystal focal point F is outside of the target (Fig. 1). Only the particles emerging from F can be trapped by the crystal. Then, if some particle decays at F, all the decay products will be trapped. If some particle emerges from the target directly, it is not trapped, unless it passes through F; this consideration sets a "blind spot" B on the crystal face, where one cannot distinguish between the particles of interest and the garbage. The trapped particles can be bent, e.g. onto some experimental set up (bending efficiencies up to 60% have recently been demonstrated [5]).

* E-mail: biryukov@mx.ihep.su

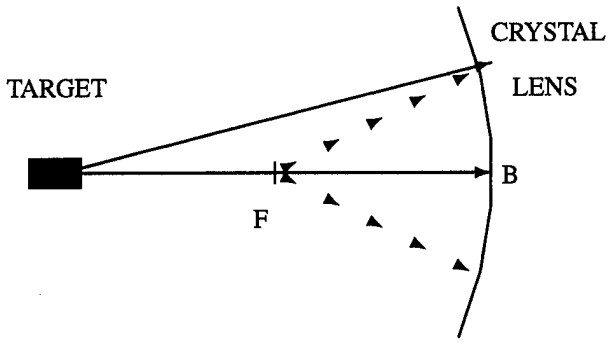


Figure 1: Schematic arrangement of a target, focusing crystal, and the focus F. "Blind spot" is also shown (B).

With the principle understood, let's understand the limitations. Crystal traps a particle if it comes within a Lindhard angle θ_L, which is e.g. $5\mu\text{rad}/E^{1/2}(\text{TeV})$ in Si(110) planes at energy E. Therefore, the focus is not a precise point, but has a transverse size of $\pm\theta_L L$, where the focal length L is as set by the crystal design (e.g. it was 0.5–4 m in the experiment[1]); in Fig. 1, L is the distance between points F and B.

The typical angle θ_D under which the decay products emerge from F, is set by the relativistic factor γ of the parent particle: $\theta_D \simeq 1/\gamma$. Therefore, the longitudinal size of the focal spot equals $\theta_L L/\theta_D \simeq \gamma\theta_L L$. Only the particles emerging from this focal spot of the length $\gamma\theta_L L$ and of the width $\theta_L L$ can be trapped by the crystal (Fig. 2).

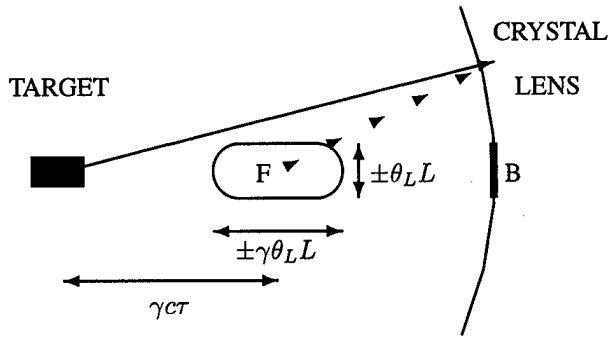


Figure 2: Schematic of a target and the focal spot dimenions. The "blind spot" is shown (B).

A particle with relativistic factor γ and the lifetime τ has

0-7803-4376-X/98/$10.00 © 1998 IEEE

a mean decay path of $\gamma c\tau$. The discussed scheme makes sense only if $\gamma c\tau$ is on the order of or larger than $\gamma\theta_L L$. Hence, our technique can handle particles with $c\tau$ as small as $\theta_L L$. For the short-lived particles (with beauty or charm, or τ-leptons etc.) $c\tau$ varies from 50 to 400 μm. The minimal $\theta_L L$ already obtained in the experiment at 70 GeV was 40 μm [1]. At higher energy E the technique resolution $\theta_L L$ improves like $E^{-1/2}$. Moreover, L is defined by just practical convenience. Again, θ_L can be chosen smaller og bigger from different crystal planes or axes. E.g., using L=0.2 m at 500 GeV gives the minimal resolution of $\sim$1 μm. If one doesn't care on fine resolution for $c\tau$ but wish to increase the focal spot just to increase the working space, this is easy to do by means of greater L.

The angular acceptance of the crystal should be about $\pm 1/\gamma$. The "blind spot" angular range in the crystal center is set by the focal spot transverse size $\theta_L L$ and the target-to-focus distance, about $\gamma c\tau$. The "blind" range is then $\pm\theta_L L/\gamma c\tau$. Its ratio to the crystal angular acceptance, i.e. the crystal inefficiency, equals $\theta_L L/c\tau$. As from above, this inefficiency is on the order of 1%.

We can also estimate the rejection factor for the particles incident beyond the Lindhard angle. They may be trapped in crystal through the scattering processes only, so called feed-in or volume capture. The probability of feed-in as measured at 70 GeV is on the order of 10^{-3}. Therefore only $\sim 10^{-3}$ of the background is not rejected by the crystal and hence mixed up with the "particles of interest".

Unfortunately, a high efficiency trapping and bending has been demonstrated so far for positive particles only. Therefore, a major drawback of the discussed scheme (as well as of any other application of bent crystals) is its restriction to only positive particles produced in a decay.

3 CONCLUSION

The proposed technique can trap the decay products of the short-lived particles and bend them toward an experimental set-up. The rejection factor for the particles produced in the target is $\sim$1000. The technique can handle particles with $c\tau$ down to $\sim$1 μm.

4 REFERENCES

[1] V.Biryukov, Yu.Chesnokov, V.Kotov. *Crystal Channeling and its Application at High Energy Accelerators.* (Springer, Berlin: 1997)

[2] R.A.Carrigan, Jr. in *Relativistic Channeling.* R.A.Carrigan, Jr. and J.Ellison, eds. (Plenum, NY, 1987) p. 339

[3] C.R.Sun in *Relativistic Channeling.* R.A.Carrigan, Jr. and J.Ellison, eds. (Plenum, NY, 1987) p.379

[4] D.Chen et al. *Phys Rev. Lett*, **69**, 3286 (1992)

[5] C.Biino et al., to appear in Phys.Lett. B

AN IDEA FOR STUDYING A MULTIPASS CRYSTAL EXTRACTION BY THE ENERGY LOSS DETECTOR

Valery Biryukov*
IHEP Protvino, 142284 Moscow Region, Russia

Abstract

We consider a proton extraction from accelerator by a crystal equipped with an energy loss detector. The idea is proposed that the energy loss dE/dz deposited in the crystal by a channeled proton may indicate, whether this proton was extracted in the first pass, or in the subsequent passes; this is a key question in the crystal extraction.

1 INTRODUCTION

Because of the abnormally low energy losses shown by channeled protons, the technique of dE/dz detectors built-in in crystals has found wide application in the high-energy channeling experiments. The energy-loss spectrum in aligned crystal is split into the "channeled" and "random" fractions, thus providing a way to distinguish between these two sorts of particle motion (Fig.1).

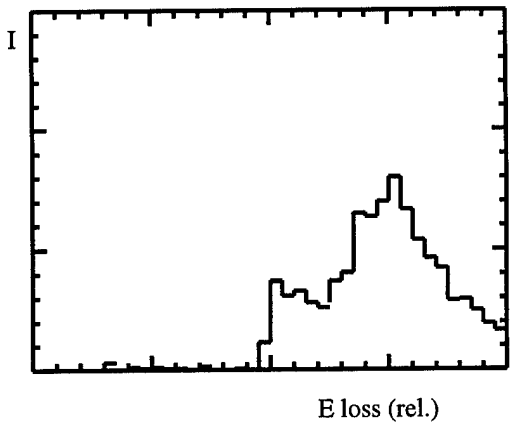


Figure 1: The energy-loss spectrum in aligned crystal of Si(110) simulated for 900-GeV protons with divergence (σ) of 11.5 μrad.

In the crystal extraction experiments, in a diffusion mode, the first passage of protons through the crystal is very close to the surface, at a depth of <1 μm. Then the escape of δ-electrons (knocked out by a channeled proton) from the crystal modifies the dE/dz *deposited* in the crystal, thus making it depend on a depth (impact parameter) b. Hence one may hope to resolve the first pass or multi-passes, observing dE/dz deposition of the extracted protons in a crystal.

* E-mail: biryukov@mx.ihep.su

2 ENERGY LOSS DEPOSITION

The difference between the energy loss and its deposition in the detector is a well-known effect due to the mentioned leakage of the most energetic electrons from the detector. Here this effect is brought to its extreme, going from typical thickness of $\sim$1 mm to <1 μm for the first passage in crystal extraction.

The mean energy loss for channeled particle in the electronic scattering can be written as a function of the position x [1]:

$$-\frac{\mathrm{d}E}{\mathrm{d}z} = \frac{D}{2\beta^2}\left(\ln\frac{2m_\mathrm{e}c^2\beta^2\gamma^2}{I} - \beta^2 - \delta + C(x) + \rho_\mathrm{e}(x)\left(\ln\frac{T_\mathrm{max}}{I} - \frac{T_\mathrm{max}}{2m_\mathrm{e}c^2\gamma^2}\right)\right)$$

where $D = 4\pi N_\mathrm{A} r_\mathrm{e}^2 m_\mathrm{e} c^2 Z_\mathrm{i}^2 \frac{Z}{A}\rho$, and the other notation being standard[2]. Here $T_\mathrm{max} \approx 2m_\mathrm{e}c^2\beta^2\gamma^2$ is the maximal energy transfer to a single electron. $C(x)$ is correction[1].

To calculate the dE/dz deposition in a 1-mm thick Si, one should use $T_\mathrm{max}\approx$1 MeV because the electrons with energy $>$1 MeV have ranges $>$1 mm, and leak out. The practical range l in Si of the electron of T (keV) energy is [2]

$$l[\mu\mathrm{m}] \approx 2.4T\left(1 - \frac{0.9841}{1+0.0030T}\right)$$

For instance, l=1μm corresponds to T=10 keV. With the average $\rho_\mathrm{e}\approx Z_\mathrm{v}/Z\approx$0.3 ($Z_\mathrm{v}$ $\approx$4 is the number of valence electrons), one finds the dE/dz deposition to be reduced by $\sim$15% if one restricts T $<$10 keV instead of 1 MeV. In fact, some energy carried by electrons with 10 keV$< T <$1 MeV may be deposited, while the rest of it escapes. The escape is a random-walk process.

3 SIMULATION

In order to check the discussed idea, the simulation code CATCH [3] was applied. Fig. 2 shows a simulated spectrum for the parallel beam of 900 GeV protons incident on aligned Si(110) crystal. Here T_{max}=1 MeV, corresponding to the proton depth b of order of 1 mm from the crystal surface. As opposed, Fig.3 shows the same spectrum for the protons passing through the crystal at $b \simeq 1$ μm near the surface.

The comparison of Figs. 2 and 3 shows that the reduction of the mean dE/dz signal for the protons extracted with a single pass may be of order 10%, w.r.t. the protons extracted with multi-passes. The width of dE/dz peak for

0-7803-4376-X/98/$10.00 © 1998 IEEE

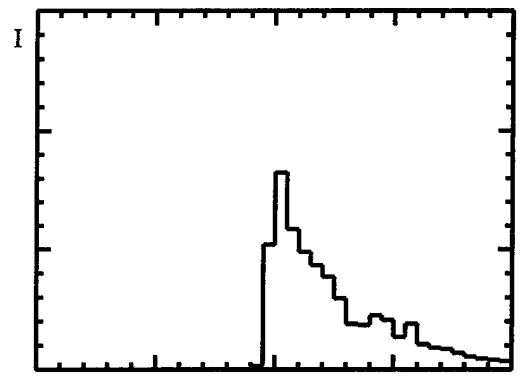


Figure 2: The energy-loss spectrum simulated for a parallel beam of protons in the bulk of Si(110) crystal.

the channeled protons is due to energetic electrons, hence it is greatly reduced for the "low-b" signal. Therefore, if the contribution of the first pass to the extraction efficiency is significant, it should be seen in the dE/dz spectrum. Ideally, this contribution may be sharply peaked, thus even splitting the dE/dz spectrum of extracted protons into the "first-pass peak" and the "secondary-pass peak". If the first-pass signal were easily recognized, this would give a great deal of possibilities for research. By reducing the primary b below 1 μm, one may make the dE/dz signal even more pronounced, thus exploring the crystal at very small depths. Note that dE/dz in the secondary passes depends on the depth also, thus also providing information.

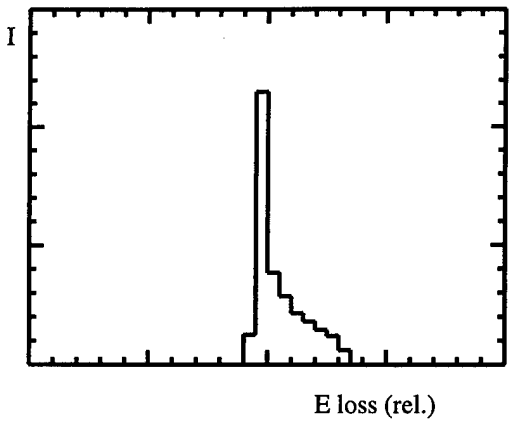


Figure 3: The energy-loss spectrum simulated for parallel protons channeled within 1 μm from the surface of Si(110) crystal.

4 REFERENCES

[1] Esbensen H. et al., Phys. Rev. B **18**, 1039 (1978)

[2] Particle Data Group, Phys. Lett. B **239** (1990)

[3] Biryukov V., Phys. Rev. E **51**, 3522 (1995); **52**, 2045 (1995); **52**, 6818 (1995).

EXPECTED CHARACTERISTICS OF THE NUCLOTRON BEAMS FOR EXPERIMENTAL SETUPS

I. Issinsky, O. Kozlov, V. Mikhailov, P. Rukoyatkin, B. Vasilishin
141980, Laboratory of High Energies
Joint Institute for Nuclear Research, Dubna, Russia

Abstract

The experiments are planned to perform on the external beams of the Nuclotron [1]-[2], require a knowledge of their final characteristics which are determined by the initial ones such as energy range and spread, time structure, envelopes etc., generated inside the accelerator. One of the distinctive features of the Nuclotron is the possibility to extract accelerated beams beginning with an injection energy of 5 MeV/amu up to a maximum of 6 GeV/amu.

1 ENERGY RANGE

The application of the resonance of radial betatron oscillations for extraction of the beam requires a space between its pre-resonance envelope and the septum of a deflecting device. This space is used for the growth of the betatron amplitude. After injection and at the initial stage of acceleration, the beam occupies a considerable part of the aperture. The reserve, chosen in designing in the aperture of the vacuum chamber (for possible great orbit distortions during commissioning and the use of a beam with a larger emittance from the booster in the future), permits one to perform the extraction over the full energy range of the accelerator.

Owing to diminishing the emittance and momentum spread the extraction coefficient is increased with raising the particle energy. However at a maximum beam energy narrowing the dynamic aperture of the accelerator appears, due to iron saturation for high magnetic fields above 1.9 T in the dipoles and 37 T/m in the quadrupoles. The sextupole and octupole components, arising in this case, distort the phase trajectories which enlarge the effective emittance and decrease the extraction coefficient.

Filling the aperture of the vacuum chamber in the straight section where the electrostatic septum is located, is shown in Fig. 1–2. Two cases are more typical: the picture just after the injection at a beam energy of 5 MeV/amu and at 5.5 GeV/amu. The intermediate case for an energy of 200 MeV/amu is also presented.

To avoid beam losses on the septa of the extraction devices under injection, additional currents are introduced in the nearest structure dipoles at this time to make a horizontal orbit bump and to shift the circulating beam to the inner wall of the vacuum chamber. The required additional horizontal space turns out to be enough for beam extraction at the injection energy. In this case, the extraction coefficient has the lowest value due to a larger momentum spread [3] as well as due to the limitations in the vertcal plane of the aperture. The values of the extraction coefficient for these three cases are presented in Table 1.

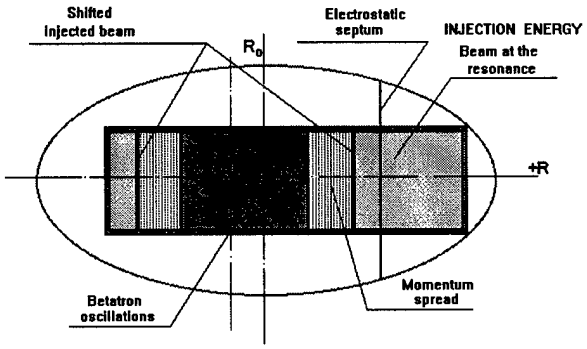


Figure 1: Filling the aperture of the Nuclotron vacuum chamber after the injection at a beam energy of 5 MeV/amu.

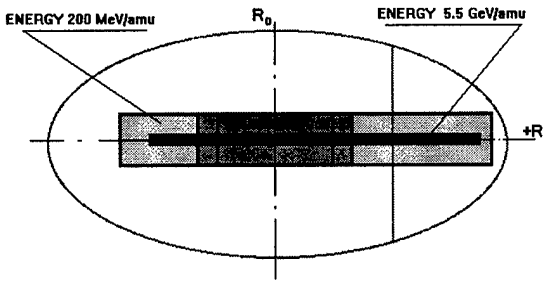


Figure 2: Filling the aperture of the vacuum chamber at a beam energy of 200 MeV/amu and 5.5 GeV/amu.

Table 1: Slow extraction efficiency.

Beam energy	5 MeV/u	200 MeV/u	5.5 GeV/u
Extr.coeff.,%	93	96	98

2 BEAM EMITTANCE

The phase diagrams of particles for the resonance $Q_x = 20/3$ in the Nuclotron for the low and high energy before the essential influence of the third and fourth components in magnetic fields are shown in Fig. 3–4. As seen the full value of the extracted beam emittance is determined by the total momentum spread in the beam and the spectrum of the radial amplitudes. The instantaneous emittance is much

0-7803-4376-X/98/$10.00 © 1998 IEEE

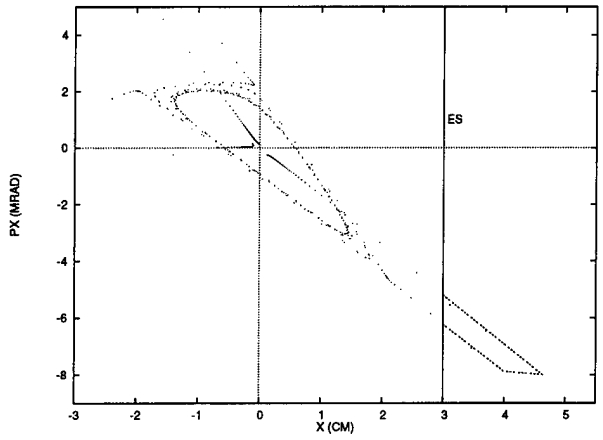


Figure 3: Horizontal phase space at ES during slow extraction at 200 MeV/amu.

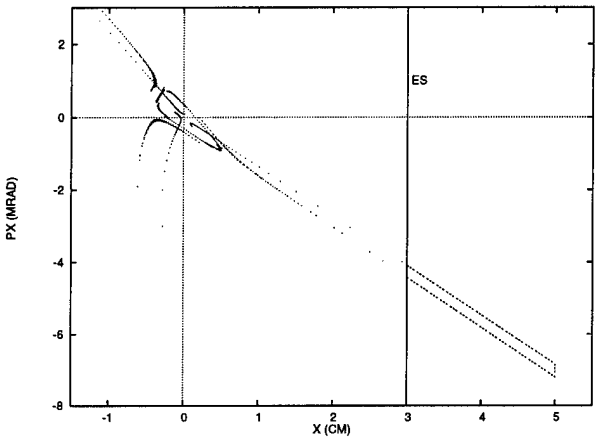


Figure 4: Horizontal phase space at ES during slow extraction at 6 GeV/amu.

smaller than this value since the particles, leaving the separatrix at every instant,have only part of the total momentum spread. The emittance of particles inside the septum gap is correlated in time with their amplitudes and momenta, and therefore it can be decreased by steering the entry or exit angle of particles during the extraction process. The first one can be done by means of bump-magnets, the latter by means of an additional magnet corrector downstream the accelerator exit. This decrease has a limitation connected with a permanent occurrence of particles with different momenta in the gap. The calculated simultaneous momentum spread of particles coming to physical setups, dp/p is equal to $\pm 7 \times 10^{-4}$ and $\pm 2 \times 10^{-4}$ for low and high energies, respectively. The emittance value of the extracted beam in the horizontal plane is 9.5π mm $\cdot$ mrad for the low energy and 2.5π mm $\cdot$ mrad for the high one. Its value in the vertical plane is equal to 20π mm $\cdot$ mrad and 2.0π mm $\cdot$ mrad, respectively.

3 BEAM IN THE TRANSPORT LINES

As the values of emittance indicated above much smaller than the Synchrophasotron one, it allows one to use the existing beam lines in the Main Experimental Hall, actually without changing. Only the head part of the transfer line should be constructed. The expected envelopes of the external beam in the transport channel, obtained from the phase diagrams of Fig. 3–4, are shown in Fig. 5–6.

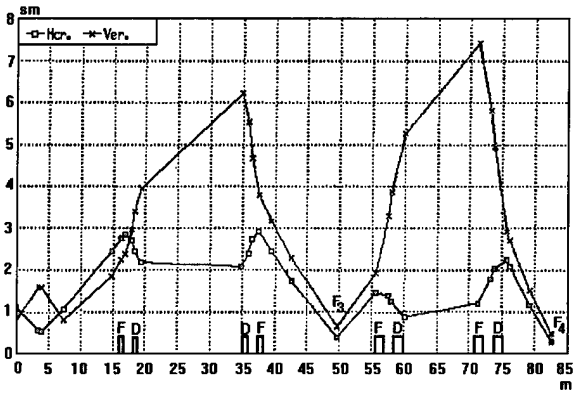


Figure 5: Envelopes of the 200 MeV/amu extracted beam.

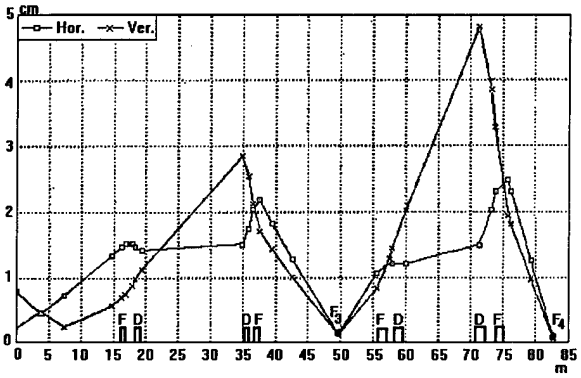


Figure 6: Envelopes of the 6 GeV/amu extracted beam.

4 BEAM TIME STRUCTURE

The main reason of beam inhomogeneity in time is due to ripples in current supplies or parasitic currents in transport cables. The band of these frequencies lies within 50 Hz and several kHz. Large difficulties in suppressing perturbations are caused by high frequencies since an instantaneous current of the extracted beam is determined by the effective derivative of the radial betatron frequency Q_x. It is also more difficult to suppress high frequencies by means of a beam feedback system. The main specific role of this system is to control the beam time macro-structure and particle steering to the targets, since the time homogeneity must be provided with a high stability of supply currents. The

evaluations of the beam time homogeneity coefficient

$$F = \left(\int_0^{T_e} \frac{dN_e}{dt} dt \right)^2 / \left(T_e \int_0^{T_e} \left(\frac{dN_e}{dt} \right)^2 dt \right),$$

where T_e – extraction time, dN_e/dt – extracted beam intensity, allow one to formulate the requirements to the Nuclotron magnet power supply system under slow extraction operating conditions.

Table 2 presents the expected values of the time homogeneity coefficient obtained using the existing power supply system under the flat-top slow extraction operating conditions. (Now this system is used for ramping the magnetic field and providing flat-tops for steering the accelerated beam to the internal target of the Nuclotron.) As can be seen, for a good extraction spill, ripples in the supply system should be reduced at least from 5 to 10 times.

Table 2: Time homogeneity of the external Nuclotron beam with the use of the existing supply system.

W	200 MeV/amu		6 GeV/amu	
T_e,s	1.0	10	1.0	10
F	0.1	10^{-5}	0.95	0.1

5 INTENSITIES OF THE IONS

The works that are being performed on the ion sources [4] , allow one, after completing all the program, to expect a wide set of ions for experiments on the Nuclotron beams (Table 3).

Table 3: Nuclotron external beam intensities, part./sec.

Particles	Sources	Injection from	
		Linac 1997-1998	Linac+Booster Prolonged plans
P	Duoplasm.	$1 \cdot 10^{11}$	$2 \cdot 10^{12}$
D	Duoplasm.	$5 \cdot 10^{10}$	$1 \cdot 10^{11}$
D $\uparrow$	POLARIS	$1 \cdot 10^{8}$	$2 \cdot 10^{9}$
He^{2+}	Duoplasm.	$2 \cdot 10^{9}$	$4 \cdot 10^{10}$
C^{6+}	Laser	$2 \cdot 10^{9}$	$1 \cdot 10^{10}$
O^{8+}	Laser	$1 \cdot 10^{9}$	$5 \cdot 10^{9}$
F^{9+}	Laser	$1 \cdot 10^{9}$	$5 \cdot 10^{9}$
Mg^{12+}	Laser	$2 \cdot 10^{8}$	$1 \cdot 10^{9}$
Ar^{16+}	EBIS	$2 \cdot 10^{8}$	$1 \cdot 10^{9}$
Fe^{24+}	EBIS	$1 \cdot 10^{8}$	$5 \cdot 10^{8}$
Xe^{44+}	EBIS	$2 \cdot 10^{7}$	$1 \cdot 10^{8}$
U^{82+}	EBIS	—	$\sim 5 \cdot 10^{6}$

6 ACKNOWLEDGEMENT

The authors would like to express their thanks to Prof. A.M. Baldin, Dr. A.D. Kovalenko and Dr. A.I. Malakhov for the support and permanent attention to the work on the Beam Extraction System.

7 REFERENCES

[1] A.M.Baldin et.al. IEEE Trans.Nucl.Sci.,NS-30, No.4 1983,p.3247.

[2] S.A.Averichev et.al. 5-th Eur.Part.Acc.Conf., Barcelona,10-14 June, 1996,Vol.3 p.2435.

[3] N.Yu.Kazarinov and V.A.Mikhailov. Efficiency Evaluation of the Slow Extraction. JINR, 9-86-503, Dubna 1986.

[4] Proposals on the LHE JINR Program 1991-95. JINR, R1, 2-89-631, Dubna,1989.

BEAM INJECTION INTO THE NUCLOTRON

V.N.Buldakovsky, V.I.Chernikov, I.B.Issinsky, A.D.Kovalenko, V.A.Mikhailov,
V.A.Monchinsky, S.A.Novikov, M.A.Voevodin, V.I.Volkov
141980, Laboratory of High Energies
Joint Institute for Nuclear Research, Dubna, Russia

Abstract

The system for the single-turn injection of 5 MeV/u heavy ions into the Nuclotron is described. The system comprises a superconducting septum-magnet, kick electric plates, beam diagnostic apparatus and magnet correctors. The septum magnet has an iron yoke. The coil and septum made of a hollow superconductor, are cooled with a two-phase helium flow. The magnetic field is 1T. The electric field and its fall time in the fast kicker are 7 kV/cm and about 100 nsec, respectively. The beam diagnostics are composed of the Faraday cups and multi-wire collector chambers for current and profile measurements over a wide range of intensities. The magnetic correctors in the beam line and the Nuclotron ring are used for injection adjustment.

The system has operated since 1992. The experimental results are presented.

1 INTRODUCTION

The superconducting heavy ion synchrotron Nuclotron [1]-[3] was put into operation in 1992 as a replacement of the 35-year Synchrophasotron. The Nuclotron ring was placed in the cable tunnel at a mark of -3.76 m below the median planes of the Synchrophasotron and the injector (the Alvaretz type linac [4]). The latter accelerates ions with a charge-to- mass ratio of $0.28 < q/A < 0.5$ up to 5 MeV/u and protons up to 20 MeV.

The existing set of heavy ion sources [5]: a duoplasmatron (protons, deuterons, and α-particles), a source of polarized deuterons, a laser source and an electron beam ion source (EBIS) permits us to get ion beams over a wide range of masses.

There are two reasons why the single turn injection was chosen:
– beam pulse durations of the laser source and EBIS are comparable to the time of one turn;
– the minimization of the lattice magnet apertures and cross section sizes allows the power consumption to be decreased substantially. As for the storage of light ions (protons, deuterons and α-particles), we are planing to include booster [6] into the Nuclotron layout.

2 INJECTION LAYOUT

Taking into account the features of the Nuclotron position, the injection scheme was chosen to provide the beam deflection in the vertical plane.

A standard layout of the single-turn injection comprises two main elements: a deflecting septum- magnet and a kicker. In our case, the principal demand to these devices is to have low levels of heat and gas releases. The superconducting septum magnet and kick electric plates obviously satisfy these conditions better than their warm magnetic analogs.

A low level of the magnetic field and a large thickness of the septum allow one to make the coil and septum of the superconducting cable. A traditional magnetic kicker was also substituted by an electric one because of the low magnetic permeability of a ferrite yoke under cryogenic temperature. The cross sections of the septum-magnet and plates were determined by parameters of the injected and circulating beam parameters:

– transverse emittance of the injected beam	30πmm · mrad,
– horizontal emittance of the circulating beam	40πmm · mrad,
– vertical emmitance of the circulated beam	45πmm · mrad,
– relative momentum spread	10^{-3}

The parameters of these devices for the injection of protons and heavy ions with a charge-to-mass ratio of 0.5 are presented in Table 1. A scheme of beam injection is given in Fig.1.

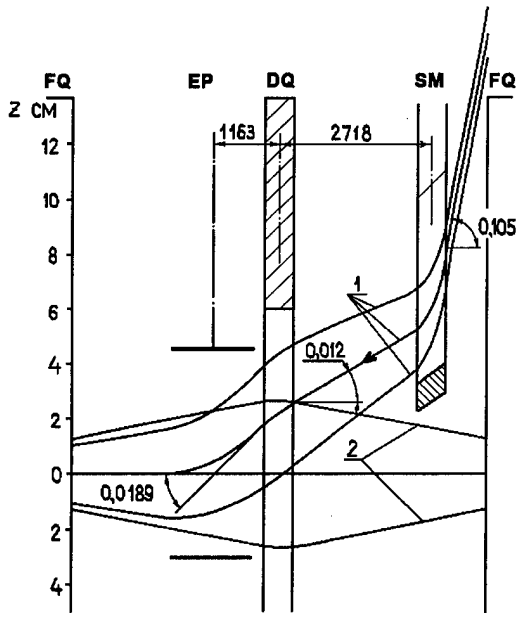


Figure 1: The injection scheme. 1 – injected beam, 2 – circulating beam.

0-7803-4376-X/98/$10.00 © 1998 IEEE

Table 1:

No	Parameters		Ions	Protons
1.	Energy	MeV/u	5	12
2.	Charge-to-mass ratio	q/A	0.5	1
3.	Magnetic rigidity	T · m	0.647	0.649
4.	Electric rigidity	MV	19.95	39.58
5.	Revolution time	μsec	8.152	4.125
6.	Magnetic field in the septum-magnet	T	0.120	0.121
7.	Length of the septum-magnet	m	0.5	
8.	Electric field of the plates	kV/m	250.9	497.7
9.	Length of the plates	m	1.5	

3 SUPERCONDUCTING SEPTUM-MAGNET

The superconducting septum-magnet (Fig.2) comprises a C-shaped iron yoke and a coil . The coil is made of a hollow superconductor and cooled with a two- phase helium flow.

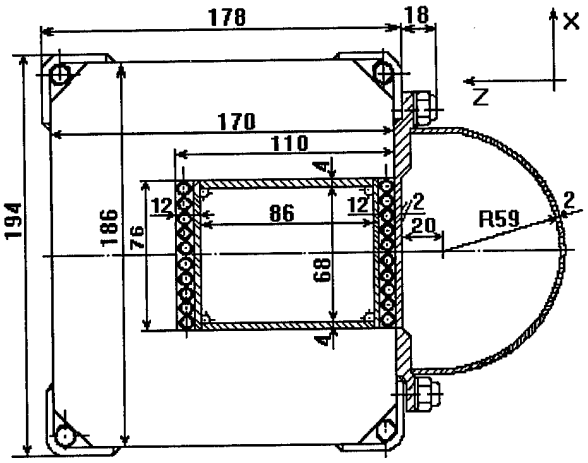


Figure 2: The cross section of the septum-magnet.

The magnetic yoke is made of steel plates (electrotechnical steel E330-A) 0.5 mm in thickness. The plates were compressed at a 6000 kg pressure. The compaction factor of the steel plates was 0.985. For cooling the septum-magnet to cryogenic temperature the four copper tubes 10 mm in diameter were soldered on four external corners of the yoke.

The superconducting coil consists of 300 windings. The superconducting cablec 0.5 mm in diameter twisted 2970 filaments is covered with special lacquer and wounded on a copper-nickel 5 mm diameter tube with a two-phase helium flow inside. The cable consists of 30 isolated superconductors, wounded with a step of 40 mm. The superconducting coil has more than 30 soldered junctions [7] to obtain a successive connection of windings. This connection allows one to increase the number of windings up to 300 and to reduce the current as well as the load in the current lead-ins. The coil has 3 exits to protect it from quenching.

The cryogenic test of the septum magnet has given the following results:

Coil current	(A)	0	70	120	150
Heat releases	(W)	10.6	12.4	14	21

The current septum 21 mm in thickness has two rows of windings, limited by steel plates. They are also used as protection from a beam halo. The septum-magnet in cryostat is shown in Fig.3. The magnetic field measurements were carried out by means of harmonic coils in the warm and cold regimes. The results of these measurements in the areas of the injected and circulating beams are presented in Fig.4.

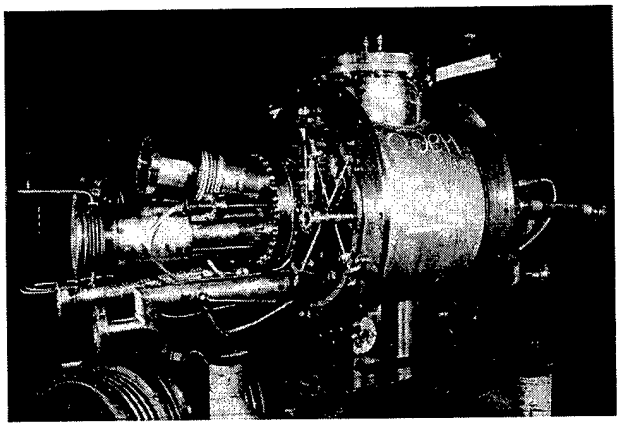


Figure 3: The septum-magnet in cryostat.

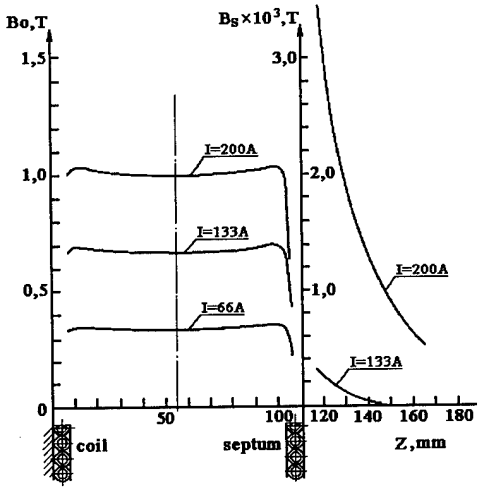


Figure 4: The working and fringing fields in the septum-magnet.

4 KICK ELECTRIC PLATES

A principal scheme and main characteristics of the electric plates are given in Table 2 and Fig.5.

The device of fast voltage removal with a given fall time is the line with distributed parameters: plates as a strip line and a commutating thyratron circuit as a coaxial line. Both lines are matched by wave impedance.

The values of resistance, linked to the thyratron anode circuit, are selected to get a voltage fall smaller than 100 nsec according to the nonperiodic law. A subsidiary scheme was included in the discharge of the high voltage cable.

Table 2:

1.	Nonlinearity of electric field in the working area	$< 1\%$
2.	Voltage on the plates	$(40 + 0.4)$kV
3.	Discharge time	$< 0.1\mu$sec
4.	Rest voltage for 1msec after discharge	$< 2\%$
5.	Total capacity of the potential plate relative to the ground	280 pF
6.	Total inductance	0.4μH
7.	Wave impedance	37.8 Ohm

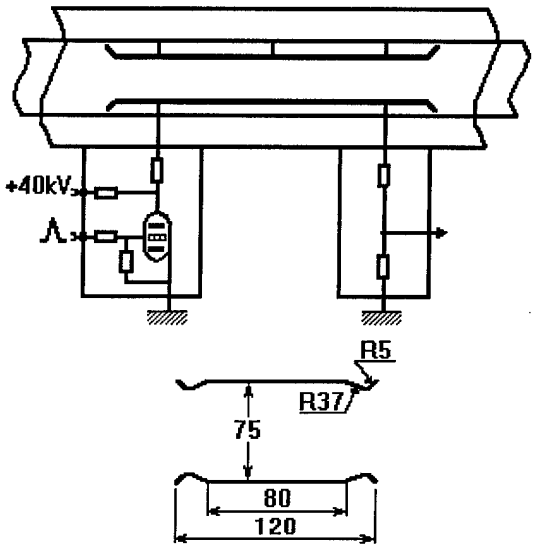


Figure 5: The simplified scheme of the electric plates.

5 DIAGNOSTICS

Faraday cups, beam current monitors, multi-wire collector profilometers, scintillation observation stations and pickup electrodes are used for tunning the injection and first turn of the Nuclotron ring. Intensities of the beams ($> 10^9$) and their profiles are obtained using the collector current profilometers. They are placed at the entrance and exit of the septum-magnet.

The Faraday cup and three collector plates are combined by four observation stations. The sensitivity of the Faraday cups is 10^7 elementary charges/pulse. The transparancy of the first station is about 95%. It is used with another station for the adjustment of the first turn.

Two beam current monitors located in the ring are intended of intensity beam measurements from 0.5 mA and more.

6 CONCLUSION

The first two octants were installed in the tunnel in February,1992, and its cooling down, the 5 MeV/u deuteron injection and transportation through 1/4 of the ring were performed. The total assembly of the Nuclotron was completed in January, 1993, and the first run of cooling and beam circulation were carried out in March 17-26. The first acceleration experiment took place in July, 1993. Then 10 runs were carried out and there were no reclamations for the injection system.

7 ACKNOWLEDGEMENTS

We thank the linac and Nuclotron staffs for fruitful collaboration and assistance.

8 REFERENCES

[1] A.M.Baldin et al. Nuclotron Status Report, IEEE Trans. on Nucl. Sci., 1983, NS-30, p.3247.

[2] I.B.Issinsky et al. Nuclotron Lattice, Proceeding of EPAC'90, Nice, 1990, vol.1, p.458.

[3] A.D.Kovalenko. Status of the Nuclotron, Proceeding of EPAC'94, London, 1994, vol.1, p.232.

[4] A.M.Baldin et al. Upgrades of Nuclotron Injector for Acceleration of Ions with Z/A = 0.28, Proceeding of XVIII Int. Linear Acc. Conf., 1996, Geneva, v. 1, p. 352.

[5] A.N.Govorov et al. Linac LU-20 as Injector of Nuclotron, ibid., p. 349.

[6] I.B.Issinsky, V.A.Mikhailov. Conception of the 200 MeV/u Booster for the Nuclotron, IEEE Part. Acc.Conf., 1991, San Francisko, v.5, p.2886

[7] S.A.Averichev et al. Technology of the Superconducting Winding Production for the Nuclotron Magnets. Proc. of the XIV Acc. Conf., 1994, Protvino, p. 83.

CARBON STRIPPER FOILS USED IN THE LOS ALAMOS PSR

M. J. Borden, M. A. Plum, MS H838, Los Alamos National Laboratory, Los Alamos, N.M., 87545, U.S.A.; I. Sugai, INS, University of Tokyo, Midori-cho, Tanashi-shi, Tokyo 188, Japan

Abstract

Carbon stripper foils produced by the modified controlled ACDC arc discharge method (mCADAD) at the Institute for Nuclear Study have been tested and used for high current 800-MeV beam production in the Proton Storage Ring (PSR) since 1993. Two foils approximately 110 μg/cm^2 each are sandwiched together to produce an equivalent 220 μg/cm^2 foil. The foil sandwich is supported by 4-5 μm diameter carbon fibers attached to an aluminum frame. These foils have survived as long as five months during PSR normal beam production of near 70 μA average current on target. Typical life-times of other foils vary from seven to fourteen days with lower on-target average current. Beam loss data also indicate that these foils have slower shrinkage rates than standard foils. Equipment has been assembled and used to produce foils by the mCADAD method at Los Alamos. These foils will be tested during 1997 operation.

1 CARBON FOIL REQUIREMENTS

The LANL Proton Storage Ring (PSR) currently uses a two-stage stripping process. H ions are first neutralized with a high field electro-magnet, injected into the PSR through the first ring dipole, and then stripped to H^+ (protons) with a carbon stripper foil. The LANSCE Reliability Improvement Project (LRIP), which is now underway, will remove the high field electro-magnet and allow single-stage stripping [1].

Beam losses in PSR have two primary causes. First-turn losses are caused by excited states of H° produced in the injection stripper foil. These particles are lost in the first dipole and quad following the stripper foil and account for loss of about 0.20% of the injected beam. Production of excited states of H° and, therefore, first-turn losses, decrease as the foil thickness is increased. The second mechanism accounts for most of the losses (about 0.25% of injected beam) and occurs because of nuclear and large-angle coulomb scattering of the stored circulating beam in the stripper foil. These losses are distributed around the entire ring.

1.1 Foil requirements prior to the LRIP

Currently the PSR delivers an average proton beam current of 70 μA. Original PSR beam-dump design requirements called for stripper foils 90% efficient. For 800 MeV hydrogen atoms a 200 μg/cm^2 carbon foil is required. Over the past 10 years of operation we have used carbon foils with a range of mass density from 185 μg/cm^2 to 220 μg/cm^2. A 220 μg/cm^2 foil is now preferred because first turn losses are reduced.

The PSR foils are currently 16mm wide and approximately 55mm long. The size of the foil is chosen to minimize scattering losses from interaction with the primary circulating beam and maximize foil lifetime. The foils are slightly larger than the injected beam size of approximately 12mm. This allows for foil shrinkage and hence a longer lifetime. The foil assembly is made up of two foils of nominal thickness 110 μg/cm^2, sandwiched together between glass slides and cut to size with a laser. The laser cut edges partially bond and assist in holding the two foils together. Two aluminum frames are strung with 4-5 μm diameter carbon fibers orthogonally and diagonally. The doubled foil is then glued along one edge to an aluminum frame with a conductive paint. The two aluminum frames are bolted together with the doubled foil suspended between the carbon fiber grids. See Reference 2 and Fig. 1.

1.2 Foil Requirements for LRIP

When LRIP is completed, direct H^- injection and phase space painting (beam bumping) should reduce overall beam losses by a factor of five. The circulating beam will be moved off of the stripper foil during the injection period and the injected beam will be better matched to the circulating beam. These techniques allow use of a smaller width foil with a higher mass density. This will reduce the circulating beam interaction with the stripper foil and decrease the production of H° excited states. A more detailed explanation of ring losses may be found in Reference 2. Calculations have shown that a stripper foil with mass density 400 μg/cm^2 minimizes the sum of the two types of beam loss [3]. The desired average beam current at the completion of the current upgrade is 100 μA. The stripper foils will be mounted in the fashion described above with the exception that the foil holder will be larger to match the new aperture requirements both upstream and downstream of the stripper foil mechanism.

2 TESTING CARBON FOILS IN PSR

Over the past ten years several types of carbon foils have been used in PSR. Foils produced by electron beam evaporation, glow discharge and arc discharge methods have been used. A very detailed lifetime comparison has been made by Sugai, et al. [8]. For comparison Figures 2-3 show the fraction of injected beam lost due to first turn losses for several foils. Note that the first turn losses

0-7803-4376-X/98/$10.00 © 1998 IEEE

decrease rapidly for the commercial foil as the foil curls, shrinks and becomes thicker. However, first turn losses remain nearly flat for mCACAD foils throughout the months that these foils were used, attesting to the superior dimensional stability of this type of foil. A mCADAD foil is now in use which has nearly 6 months of beam interaction. This is an order of magnitude longer than other commercially available foils. Most recently we have been using foils produced at the Institute for Nuclear Study, University of Tokyo.

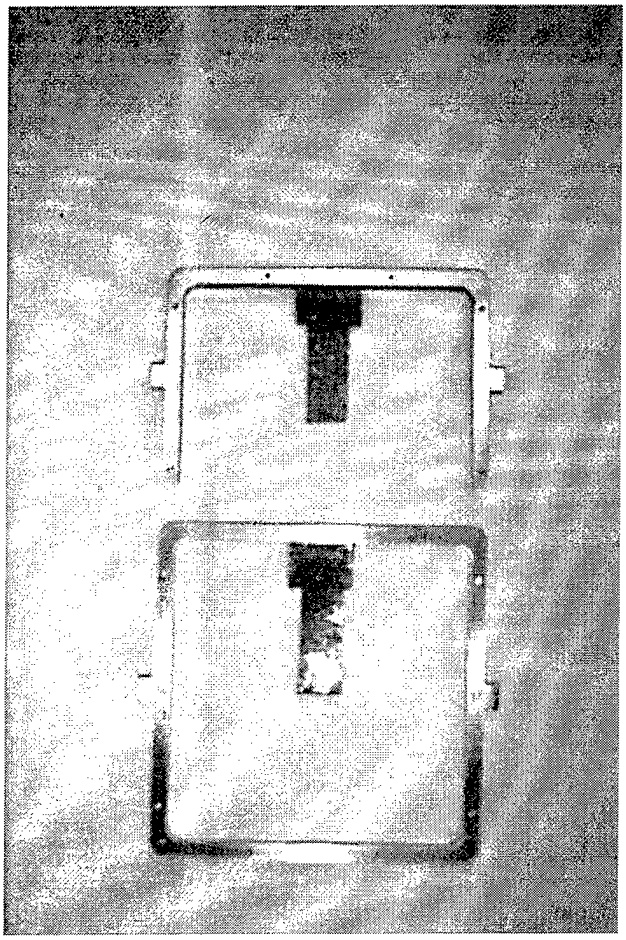


Fig. 1. Aluminum frames with carbon foil and fibers.

2.1 Carbon foils produced at INS

The team at the University of Tokyo has developed a technique for producing carbon foils which have shown lifetimes in excess of an order of magnitude higher than commercially available foils. The foils are produced through an arc evaporation process referred to as modified controlled AC/DC arc discharge method (mCADAD) and is described in detail in references [4-8].

The mCADAD foils are produced by arc evaporating alternating layers of carbon produced with AC and then DC current. The carbon is deposited on clean glass substrates and then annealed to remove residual stresses. The mCADAD technique is only limited in that it is not possible to produce foils with a mass density greater than approximately 130 $\mu g/cm^2$ [8]. Work is currently in progress to improve on this limit. With this limitation a minimum of three foils will be necessary to achieve an equivalent thickness of 400 $\mu g/cm^2$ for the upgraded PSR.

2.2 Foil Production Capabilities at LANL

An evaporation system has been assembled at LANL with Dr. Sugai's assistance which is capable of producing foils with the mCADAD method. The system consists of a large, stainless steel vacuum chamber, cryo-pump, rotating substrate holder, and arc welding, and annealing power supplies, shown in Fig. 4. The electrode holder and annealing furnace can be seen in Fig. 5. The carbon electrode holders are machined from Macor™. Thickness is measured insitu during deposition with an oscillating quartz crystal monitor. Annealing temperatures are measured with type K thermocouples placed in contact with the substrate glass and copper homogenizer.

Carbon foils have been produced with this system using the mCADAD method, and initial testing of these foils with the PSR should be completed this year.

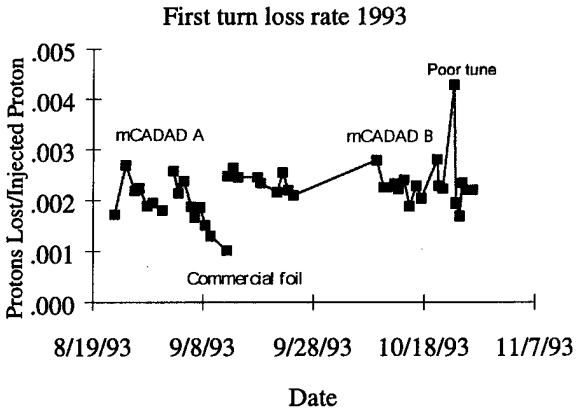


Fig. 2. First turn loss rate 1993.

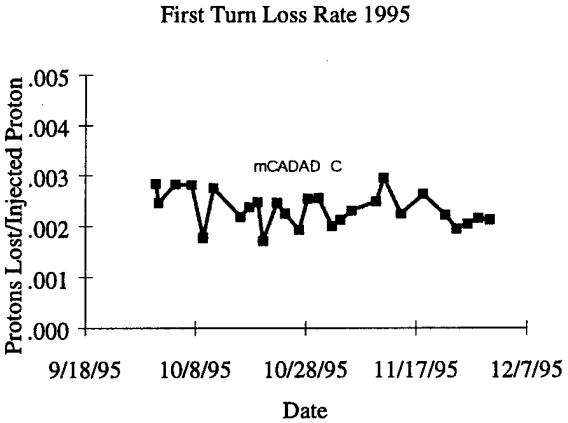


Fig. 3. First turn loss rate 1995.

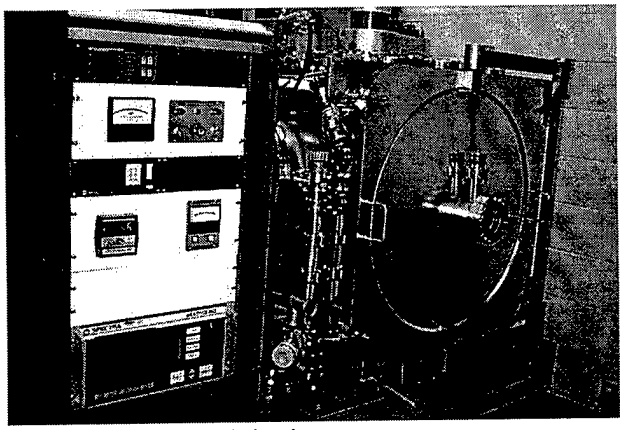


Fig. 4. mCADAD fabrication system.

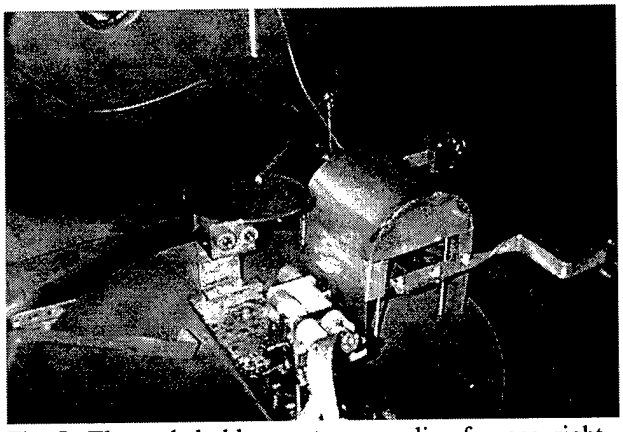


Fig. 5. Electrode holder, center, annealing furnace, right.

3 CONCLUSIONS

Carbon foils produced with Dr. Sugai's mCADAD method have significantly improved the operational performance of the Proton Storage Ring. The decreased shrinkage rates associated with these foils allow the use of smaller width foils, thereby decreasing stored beam losses. Lower beam losses imply that the ring components are less radioactivated and therefore worker radiation exposures are reduced. Because of the long lifetimes of these foils, only a few (3-6) are required during the beam operational cycle, further reducing radiation exposures to maintenance personnel. The mechanical stripper foil mechanism can also be of a relatively simple design, even though the LANSCE operations will be extended to eight months per year.

3 REFERENCES

[1] D. H. Fitzgerald, et al. 'Overview and Status of the Los Alamos PSR Injection Upgrade Project', these proceedings.

[2] M.J. Borden, G.E. Adamson, R.N. Johnson and W.F. Nicaise, Nucl. Instr. and Meth. A 303 (1991) 63.

[3] "Proton Storage Ring Upgrade to Direct H- Injection: Phase II Technical Design Report" Arch Thiessen, editor, Los Alamos, 7/26/96.

[4] I. Sugai, T. Fujino, K. Yamazaki, T. Hattori and M. Ogawa, Nucl. Instr. and Meth. A236 (1985) 576.

[5] I. Sugai, T. Hattori, H Suzuki, H Kinoshita, H. Kator and K. Yamazaki, Nucl. Instr. and Meth. A 265 (1988) 376.

[6] I. Sugai, T. Hattori, H. Muto, Y. Takahashi, H. Kato, and K. Yamazaki, Nucle. Instr. and Meth. A 282 (1989) 164.

[7] I. Sugai, M, Oyaizu, T. Hattori, K. Kawasaki, T. Yano, H. Muto, Y. Takahashi, and K. Yamzaki, Mucl. Instr. and Meth. A 303 (1991) 59.

[8] I. Sugai, M. Oyaizu, H. Kawakami, C. Ohmori, T. Hatorri, K. Kawasaki, M. J. Borden, R. J. Macek, Nucl. Inst. and Meth. A 362 (1995) 70.

LANSCE SHORT-PULSE SPALLATION SOURCE TARGET UPGRADE

J.B. Donahue, G.D. Baker, N.K. Bultman, T.O. Brun, P.D. Ferguson, R.J. Macek, M.M. Njegomir, M.A. Plum, J.E. Roberts, G.J. Russell, and W.F. Sommer
Los Alamos National Laboratory, Los Alamos, New Mexico 87545 USA

Abstract

A project to upgrade the short-pulse spallation source target at the Los Alamos Neutron Scattering Center (LANSCE) is in progress. This upgrade will reduce the target change out time from about a year to about three weeks and permit the proton beam current to be raised to 200 μA. The project includes a new target-moderator-reflector system, a new suite of moderators for four new flight paths, improved auxiliary systems, remote handling capability, and a new crane and service building. The project has also supported calculations and experiments for target neutronics, rod-target thermo-hydraulics, and corrosion-related measurements in a proton beam. The final engineering design is now complete and the project has begun fabrication and procurement. Installation will begin in the fall of this year.

1 INTRODUCTION

The short-pulse spallation target is located at the Manuel Lujan, Jr. Neutron Scattering Center (MLNSC) at the Los Alamos Neutron Scattering Center (LANSCE). The present target is a split (flux-trap) solid cylinder made from a tungsten alloy. [1] The target feeds a liquid hydrogen moderator, a high-resolution water moderator, and two high-intensity water moderators. Each moderator is viewed by three neutron flight paths and their associated instruments. The proton beam is supplied from a storage ring (PSR) which stores 800-MeV protons from the linear accelerator and delivers 250ns-wide pulses at 20Hz. The average current is presently limited to 70μA due to stress limitations in the solid upper target.

The target upgrade is part of a larger project, the LANSCE Reliability Improvement Project, which has the goal of improving the overall availability and productivity of the facility. [2] The goals of the target upgrade are

- Change out of the target-moderator-reflector system (TMRS) insert in three weeks or less
- Provide coupled upper-tier moderators to service four new flight paths
- Increase current capability from the present 70μA (56kW) to 200μA (160kW)
- Preserve the neutronic performance of the existing lower-tier flight paths

When the new target is installed and commissioned in May 1998, we will be able to raise the beam current to over 100μA. The recently-approved SPSS enhancement project, when complete, will allow us to raise the current to 200μA at a repetition rate of 30Hz.

2 SIMULATIONS AND TESTING

The target design process has been guided by extensive computer simulations and engineering tests. We have also benefitted from the APT materials irradiation experiments led by one of us (WFS).

The final design choices were a compromise between neutronic performance, operational reliability, good engineering practice, radioactive materials handling, and waste management considerations.

2.1 TMRS neutronics

The neutronic performance of the TMRS was calculated using the LAHET Code System. [3] These simulations were used to determine the moderator thickness, target material, target thickness, reflector material, reflector thickness, and the choice of coolant. Studies were done for various partial decoupling schemes in the upper tier of moderators and several choices of decoupling materials. The moderator overlap and the flux trap gap were also varied in the simulations. [4,5]

2.2 Target thermo-hydraulics

The LAHET calculations also provided the source term for beam heating in the target. The computational fluid dynamics code FLOW-3D [6] was then used to model the water cooling.

The clad rod bundle target concept was also tested experimentally since it has not been used before in spallation targets. This design was conceived to control the problem of activated corrosion and erosion products contaminating the cooling system and making maintenance operations difficult and possibly limiting the lifetime of the target. The rod bundle target consists of 11.1mm diameter tungsten rods inside 0.25mm-thick Inconel tubes.

The test program consisted of placing the Inconel tubes in a water cooling loop and heating them electrically to simulate the peak heat flux in the target of 142 watts/cm^2. Pitch-to-diameter ratios (p/d) of 1.02, 1.05 and 1.10 were tested. A failed test at p/d=1.05 led us to consider a plate target as an alternative. After a careful analysis and repeat experiments, we determined that the

0-7803-4376-X/98/$10.00 © 1998 IEEE

rod bundle concept will work and has a sufficient thermal margin at 200μA.

2.3 Corrosion measurements in a proton beam

The upgrade project has contributed to the materials irradiation program. Various material samples, including clad and unclad tungsten rod bundles, have been irradiated with a one-milliamp beam of 800-MeV protons. We now have experience with operations and maintenance on tungsten systems and we will soon have measurements of the bulk properties of irradiated materials.

The results from this work are very preliminary but we have been able to make some general observations. After about two amp-hours of operation, corrosion and erosion of tungsten was evident but there were no catastrophic failures. The material still had some strength. The auxiliary water systems were difficult to maintain for unclad tungsten because of activated corrosion products which tended to deposit on fittings and flex lines.

3 HARDWARE DESIGN DESCRIPTION

In order to meet the goal of a three-week replacement schedule, the targets, moderators, and inner reflector are mounted on a single (TMRS) insert. The project will build two inserts, compatible crypt shielding, the outer reflector and a new crane and access building. It will also provide tooling fixtures for assembling future targets and facilities for handling irradiated targets. The target insert is shown in Figure 1.

3.1 Target

The target team has carried two different concepts for the upper target to final design. This is because of concerns with the thermo-hydraulics of rod bundles and the corrosion of bare tungsten. The baseline design is a plate target with seven pure tungsten plates and no cladding. The fall-back design is an Inconel-clad tungsten rod bundle with a pitch-to-diameter ratio of 1.05. The rest of the target insert is designed to be compatible with either choice.

The plate target is preferred for neutronic performance and is simpler to build than a rod bundle. However, the plate target is suceptible to corrosion and the design depends upon the bulk properties of tungsten, such as thermal conductivity and strength. Some of these properties will change with irradiation.

The lower target is not as severly stressed with only 10% of the bulk heating rate as the upper target. It is made from a solid piece of tungsten.

3.2 Moderators

The lower-tier moderators are in flux-trap geometry and fully decoupled. They are designed to give the same

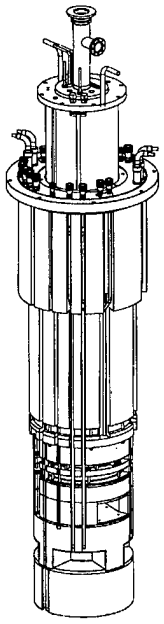


Figure: 1 The TMRS insert. The proton beam enters vertically through the pipe at the top. The openings for the neutron flight paths can be seen near the bottom.

performance as the existing flux-trap moderators. The upper-tier moderators are in backscattered geometry and are partially coupled. Table 1 lists the moderator types and the flight paths that they serve.

Table 1 Moderator types and their associated flight paths.

FP #	Moderator Type	Coupling
1,2,16	high-resolution water	decoupled
3,4,5	high-intensity water	decoupled
6,7,8	high-intensity water	decoupled
9,10,11	liquid hydrogen	decoupled
14,15	water	coupled
12,13	liquid hydrogen	coupled

3.3 Reflectors

The inner reflector is edge-cooled solid beryllium. Since there is no water in the beryllium to capture neutrons, neutronic performance is enhanced and light water can be used for a coolant. The beryllium reflector is 0.25m thick and is attached to the removable TMRS insert.

The outer reflector is lead with embedded stainless steel cooling lines. It has an inner diameter of 0.60m and an outer diameter of 1.14m. It is part of the crypt shielding but it can be removed through the roof using the bridge crane if necessary.

3.4 Materials handling

Safe and efficient methods for handling irradiated components is essential in order to meet the goals of the upgrade. We have the benefit of over twenty years

experience with high-power (one-megawatt) beams and we have developed a substantial remote handling capability.

The target insert is removed and replaced through a special access port in the roof of the target cell. Irradiated targets are pulled directly into a transfer cask using a radio-controlled bridge crane. The transfer cask shields personnel from radiation and controls contamination. Secondary containment is provided by a building over the access port.

Irradiated targets will be taken to the facilities in the high-power beam area for post-mortem testing. We have the option of storing them in special culverts for future use or cutting them up for disposal. There is a new hot cell facility at the CMR building for detailed analysis of irradiated samples. The MONITOR remote handling system will be used for operations in Area A.

4 ACKNOWLEDGEMENTS

The work was supported by the US DoE and DoD. The target team is grateful to Guenter Bauer and Tim Broome for stimulating conversations and good advice.

REFERENCES

[1] G.J. Russell, C.D. Bowman, E.R. Whitaker, H. Robinson, and M.M. Meier, 'LANSCE High-Power Target-Moderator-Reflector-Shield,' ICANS-VIII (November 1985).

[2] R.J. Macek, *et al.*, 'Overview of Progress on the Improvement Projects for the LANSCE Accelerator and Target Facilities', these proceedings.

[3] Richard E. Prael and Henry Lichtenstein, 'User Guide to LCS: The LAHET Code System,' Los Alamos National Laboratory Report LA-UR-89-3014, http://www-xdiv.lanl.gov/XTM/lcs/lahet-doc.html (September 1989).

[4] G.J. Russell, P.D. Ferguson, E.J. Pitcher, and J.D. Court, 'Split-Target Neutronics and the MLNSC Spallation Target System', ICANS-XIII, October 11-14, 1995.

[5] P.D. Ferguson, G.J. Russell, and E.J. Pitcher, 'Reference Moderator Calculated Performance for the LANSCE Upgrade Project,' ICANS-XIII, (November 1995)

[6] FLOW-3D Computer Code, Version 7.0, Flow Science Inc., 1325 Trinity Dr., Los Alamos, NM 87544, 1996.

OVERVIEW OF THE BUMP-MAGNET SYSTEM AT THE LANSCE PROTON STORAGE RING

C. R. Rose, D. B. Barlow, B. Blind, F. Neri, J. F. Power, and P. L. Walstrom
Los Alamos National Laboratory, Los Alamos, NM 87545

Abstract

An upgrade program for increasing the stored beam current in the Proton Storage is presently under way. A part of the upgrade is the design and installation of a four-magnet beam-bumping system used for phase-space painting and minimizing interaction of the stored beam with the injection stripper foil. This paper describes the bump-magnet system including the relevant beam requirements, magnet specifications, power-cable specifications, pulsed-modulator requirements, and beam-tube eddy-current effects. The magnets are ferrite window-frame magnets with saddle windings. The series-pass pulsed modulators are programmable both in rise and fall time as well as amplitude. The peak current can be varied between 50 and 300 A. The pulsed-current rise-time is fixed at 1 ms, and the linear fall-time during which beam is injected into the ring can be varied between 0.5 and 1.5 ms.

1 SYSTEM OVERVIEW

The purpose of the bump-magnet modulator system is to "paint" the injected beam into the storage ring. To do this, four bump magnets are used that have precisely controlled, linear-decaying magnetic fields that move the injected beam into the ring synchronously with the ring-orbit cycle. The beam is bumped in the vertical plane. The maximum field strength in any one magnet is on the order of 500 gauss, and each of the four magnets is pulsed at different field levels with respect to the others. The magnetic field strength of 500 gauss translates roughly to 300 A peak current in the magnets. A simplified view of one modulator/cable/magnet system is shown below in Fig. 1.

The required current waveshape is depicted next to the waveform generator. It has a linear risetime, a flat-top, and a linear decay time. The decay time is variable from 0.5 to 1.5 ms. The amplitude can be varied from 50 to 300 A.

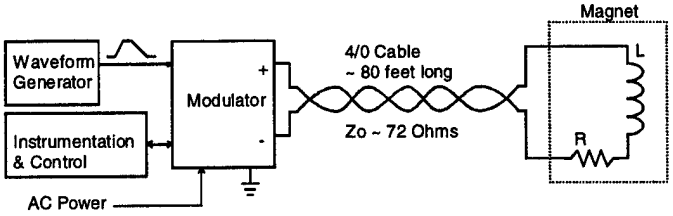


Fig. 1 Block diagram of one bump-magnet system.

2 BUMP MAGNETS

The four bump magnets are fast-slewing small-deflection dipole magnets. In order to minimize design and prototype development costs, a single magnet design is used for all four magnets. This standardized design produces a field strength of 488 gauss (at 300 A) which is sufficient to produce a deflection of 3 mrad for 800 MeV protons. Important magnet parameters are: 30-cm length, 12 cm by 12 cm clear aperture, 16 turns, and 140-μH inductance. A drawing of the magnet is shown in Fig. 2.

Ferrite-yoke magnets were chosen on the basis of their lighter weight, smaller size, and lower overall cost compared to tape-wound-core magnets. A Ceramic Magnetics Inc. MN60 magnetically-soft manganese-zinc ferrite with an initial relative permeability of 6500, a maximum flux density of 0.45 T, and a coercive force of 0.08 oersteds was chosen for the magnet. At this frequency and flux density, the continuous power loss is less than 1 mW/cm^3. When the duty-cycle (about 3% for a typical magnet power cycle) is factored in, the average ferrite power loss is negligible. The magnet yoke is made from four ferrite pieces with steps in two of the pieces to lock the pieces together when pressed by an external

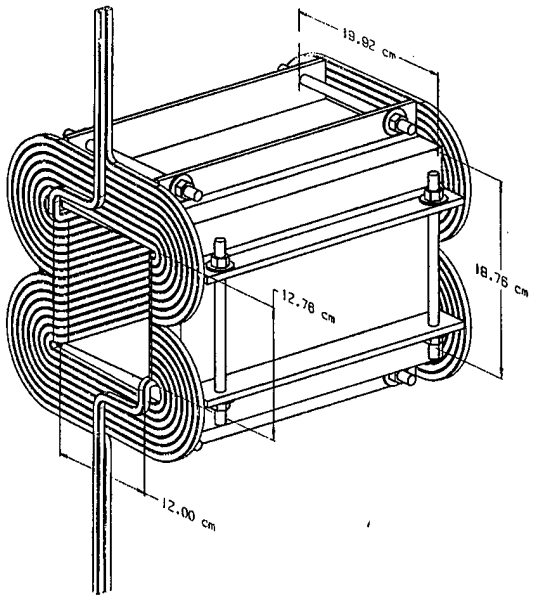


Fig. 2 Diagram of the bump magnet with dimensions.

0-7803-4376-X/98/$10.00 © 1998 IEEE

clamping structure. The magnet windings are single-layer epoxy-potted saddle coils of insulated square copper conductor with a circular internal cooling channel. Resistive power losses in the windings are small enough to be easily removed by air or water cooling.

The largest magnet-related power losses are expected to be in the beam pipe running through the bore of the magnet. Eddy currents in the tube not only cause a power loss but also affect the field within the tube. It is important that the field perturbations be minimized. In the pipe, a characteristic decay time of dipole eddy currents of 15 microseconds or less is allowable. In order to provide a thin-enough wall to minimize the eddy currents and to simultaneously withstand external pressure when the pipe is evacuated, we have chosen to use a 0.2 mm (0.008 in.)-wall 316 stainless-steel formed bellows for the beam pipe within the magnet. The duty-cycle averaged eddy-current power for this pipe is estimated to be about 50 watts at 60 Hz repetition frequency. This amount of power can be removed by natural air convection.

The first of the five magnets (four for installation and one backup) has been fabricated by Everson Electric Company and delivered to Los Alamos.

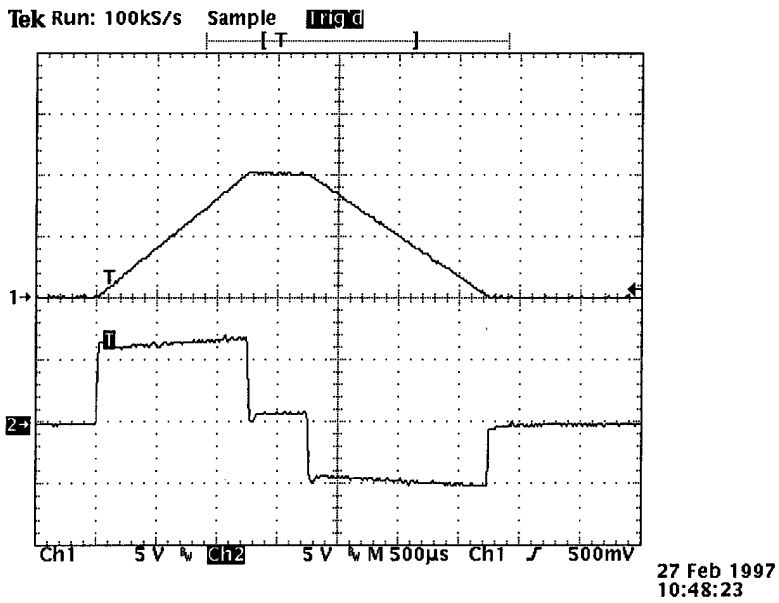


Fig. 3 Actual waveforms of magnet current and voltage across the magnet. Top scale: 30 A/V. Bottom: 10 V/V.

3 MODULATORS

To date, Los Alamos National Laboratory has received one of the five modulators from the vendor, Dynapower Corporation, to be used in the complete bump system. It has been connected to the magnet as shown in Fig. 1 and data taken. In the final system, the peak current of each magnet is independently adjusted while maintaining the same functional shape. In addition, when or if needed (or desired) the waveform of each magnet's current can be slightly adjusted or shaped because each modulator will be controlled by a separate programmable-waveform generator. However, in all cases, the timing of all four modulators will be synchronized. An actual current waveform from the first modulator and magnet pair is shown in Fig. 3. The top waveform is the magnet current, and the bottom waveform is the voltage across the magnet. The leading-edge risetime will be fixed at about 1 ms. The ring injection takes place during the down-trending portion of the waveform. It is this portion that must be accurately and repeatedly controlled to ensure accurate and repeatable beam bumping. Each of the four magnets requires different magnetic-field strengths, and different electric-current values. During the leading edge and flat-top, the magnet is energized and brought to the desired current and field level. The flat-top is a holding period used to synchronize the bump system to the ring injection system from which it receives a timing pulse and begins the down ramp.

4 CONCLUSIONS

At present, there is one operating bump system at Los Alamos from which data has been taken. The first magnet and modulator have been connected together and operated at full current and full repetition rate of 60 Hz. Test data show that the error between the programmed current and actual current is less than one percent at the corners which is twice as good as the specified accuracy, and less than 0.2 percent during the smooth parts of the function. The first bump magnet has been field mapped, and the integral field varied less than one percent across the bore of the aperture. The remaining magnets and modulators are presently on order from the respective vendors and are scheduled for installation during the Fall of 1997.

DESIGN AND SIMULATION STUDIES OF A ONE-TENTH SCALE FINAL FOCUS SYSTEM FOR HEAVY ION FUSION

X. Wu and R.C. York, NSCL, Michigan State University, East Lansing, MI 48824
A. Faltens, D. Judd and E. Lee, LBNL, University of California, Berkeley, CA 94720
Enrique Henestroza, University of California, Davis, CA 95616

Abstract

A scaled test of a final focus lattice for Heavy Ion Fusion (HIF) is planned at LBNL. The test parameters have been set by scaling the length dimensions of the envelope equation by one tenth while maintaining the generalized perveance. The values to be scaled were taken, in large part, to be those of the HIBALL-II final focus system [1]. The tenth-scale test will focus a 120 keV Cs^+ beam to a radial spot size of 0.25 mm. Tracking studies of the tenth-scale system have been performed using a version of COSY INFINITY [2] modified to include a linear space charge force. A description of the planned experimental system, the beam parameters, and simulation results are presented.

1. INTRODUCTION

The HIBALL-II parameters were chosen for scaling since it represents one of the more comprehensive designs of a final focus system for heavy ion fusion. The HIBALL-II final focus system specifies a 10 GeV, 1.25 kA, Bi^+ beam. The beam emittance at the entrance to the final focus system was assumed to be 30 π mm-mrad with a momentum spread $\Delta p/p$ of $\pm 1\%$. Under these conditions, simulations predict a radial beam spot size of 3.5 mm at the final target position. The HIBALL-II lattice consists of two magnetic quadrupole triplets between which are two dipoles. (Note that the dipole elements are not significant relative to the transverse optics [~3° each], and were not included in this analysis.) Shown in Figure 1 are the HIBALL-II lattice and the beam envelopes predicted with a modified version of COSY INFINITY.

The beam envelope equation for a uniform, isolated beam of elliptical cross-section with semi-major and semi-minor axes of a and b respectively, and a beam emittance of ε is given by:

$$\frac{d^2X}{dz^2} = -\frac{B'X}{B\rho} + \frac{\varepsilon^2}{X^3} + \frac{2K}{a(a+b)}$$

Where X is the physical size of the beam envelope and K is the generalized perveance given by:

$$K = \frac{I}{I_0}\frac{2}{(\beta\gamma)^3} \text{ with } I_0 = 31\frac{A}{Z}\times 10^6 \text{ (A)}$$

Following the philosophy of scaling the length dimensions of the beam envelope equation by a factor of 0.1 while maintaining the generalized perveance K, the HIBALL-II parameters result in those given in Table 1 for the tenth-scale final focus experiment [3]. (Note that the momentum spread does not result from scaling, but rather from specific experimental test issues.)

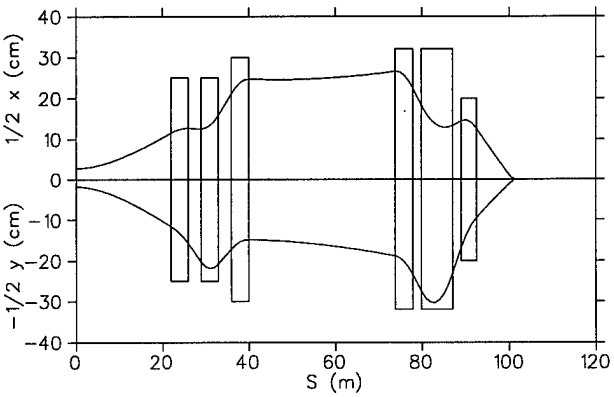


Figure 1. Lattice and beam envelopes of HIBALL-II.

Ion	Cs^+
Energy	120 keV
Beam Current	63 μA
K	1.13×10^{-5}
Emittance	3.0 π mm-mrad
Momentum Spread	±0.2%
Final Radial Beam Size	0.25 mm

Table 1. Tenth-Scale Final Focus Experiment beam parameters.

2. CODE DEVELOPMENT

COSY INFINITY is a beam physics code, which uses differential algebraic (DA) methods to provide systematic calculations of particle trajectories resulting from passage through arbitrary optical elements. Since COSY INFINITY allows the computation of dependencies on system parameters and has the ability to compute and use high-order maps, it was considered an appropriate tool for the analysis of the final focus system. However, the generally available version of COSY INFINITY does not have a provision for the inclusion of the space charge force. The initial effort was to include a simple (linear) space charge force in COSY INFINITY.

Work supported by Department of Energy under contract number DE-AC03-76F00098.

0-7803-4376-X/98/$10.00 © 1998 IEEE

The implemented space charge model assumes a uniform, isolated beam of elliptical cross-section with semi-major and semi-minor axes of a and b respectively, beam current I, and beam Lorentz factors β and γ.

The combined electric and magnetic fields generated by the beam space charge distribution acting on a particle at transverse position (x,y) are given by:

$$E_x = 2F\frac{I}{\beta\gamma^2}\frac{x}{a(a+b)} \quad , \quad E_y = 2F\frac{I}{\beta\gamma^2}\frac{y}{b(b+a)}$$

Where:

$$F = \frac{1}{2\pi\varepsilon_0 c}$$

The potential is then given by:

$$\Phi(x,y) = -F\frac{I}{\beta\gamma^2}\left(\frac{x}{a(a+b)} + \frac{y}{b(a+b)}\right)$$

This space charge induced potential Φ is used in the modified version of COSY INFINITY to calculate the transfer matrices and maps.

3. TENTH-SCALE FINAL FOCUS EXPERIMENT SYSTEM DESIGN

The tenth-scale final focus experiment system will consist of a gun module, a matching section, and the tenth-scale final focus magnetic quadrupole lattice. Figure 2 shows the system configuration of the tenth-scale final focus experiment and the beam envelopes predicted with the modified COSY INFINITY.

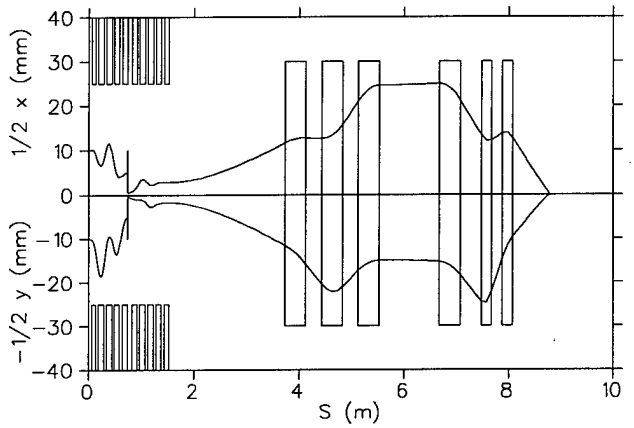


Figure 2. Lattice and beam envelopes of the Tenth-scale Final Focus experiment system.

The gun module consists of the LBNL 120 keV Cs^+ gun and a lattice of five electrostatic quadrupoles followed by a circular aperture. The gun parameters provide for a 6.3 mA beam with an emittance 30 π mm-mrad. To create the beam required for the final focus experiment (63 μA in 30 π mm-mrad), five electrostatic quadrupoles will be used to focus the source image (10 mm radius) to a spot 5 mm in radius at the position of an emittance truncation aperture plate. The emittance truncation aperture will be a circular hole of 0.5 mm in radius. Therefore, the beam current and emittance will be truncated by a factor of 0.01 and 0.1 respectively, providing a beam of 63 μA in 3.0 π mm-mrad.

Following the aperture plate, an additional five electrostatic quadrupoles will be used to match the phase space of the truncated beam to that required for the tenth-scaled final focus lattice. Note that the electrostatic quadrupoles were modeled as hard-edged with the pole voltages symmetric about ground. (Adjacent poles were assumed to have equal and opposite voltages.)

The tenth-scale final focus magnetic quadrupole lattice will use two magnetic quadrupole triplets to focus the 120 keV Cs^+ beam to a radial spot size of 0.25 mm at the target position. The length dimensions and quadrupole settings of the module have been modified slightly from the scaled values of HIBALL-II lattice to reduce the number of quadrupole types required. In addition, the drift space between triplets has been reduced to bring the overall length to 8 m.

4. HARDWARE REQUIREMENTS

A total of 10 electrostatic quadrupoles are required to match the beam phase space from the gun to that required for the tenth-scaled final focus module. The maximum voltage required is 10 kV with a radial aperture of 2.5 cm. The first quadrupole following the gun has an effective length of 0.0762 m with the remainder having an effective length of 0.1016 m. The electrostatic quadrupoles as well as the 120 keV Cs^+ gun have been constructed and successfully operated at LBNL.

For the tenth-scaled final focus module, a total of six of magnetic quadrupoles with a radial aperture of 3 cm and an integrated strength of 2.3 m^{-1} are required for the two triplets. Four of the quadrupoles will have an effective length of 0.4 m and a maximum pole tip field of 1.0 kG. The other two will have an effective length of 0.2 m and maximum pole tip field of 2.0 kG. The quadrupoles are located within existing vacuum tanks and powered with nominal 1.0 ms half-sine, pulsed waveforms. As such, they are easy to modify or reposition, and other configurations could be tried.

5. SIMULATION STUDIES

The system was evaluated by particle tracking using a 5th order map generated by the modified COSY INFINITY. Due to the large intensity reduction (0.01) at the emittance truncation aperture, the tracking was done in two steps; from the gun to the emittance truncation aperture and from the plate to the final target.

For the gun to aperture plate tracking, ten random seeds were used to populate 4,000 particles within an initial transverse phase space of 30 π mm-mrad for each of three momentum values ($\Delta p/p$ = 0 and $\pm 0.2\%$) giving 12,000 particles. Of these 12,000 particles, 165 particles shown in Figure 3 fall within the phase space defined by the 0.5 mm radial aperture. The number of surviving particles

(165) is statistically consistent with that predicted by the 0.01 reduction in beam current (120 particles).

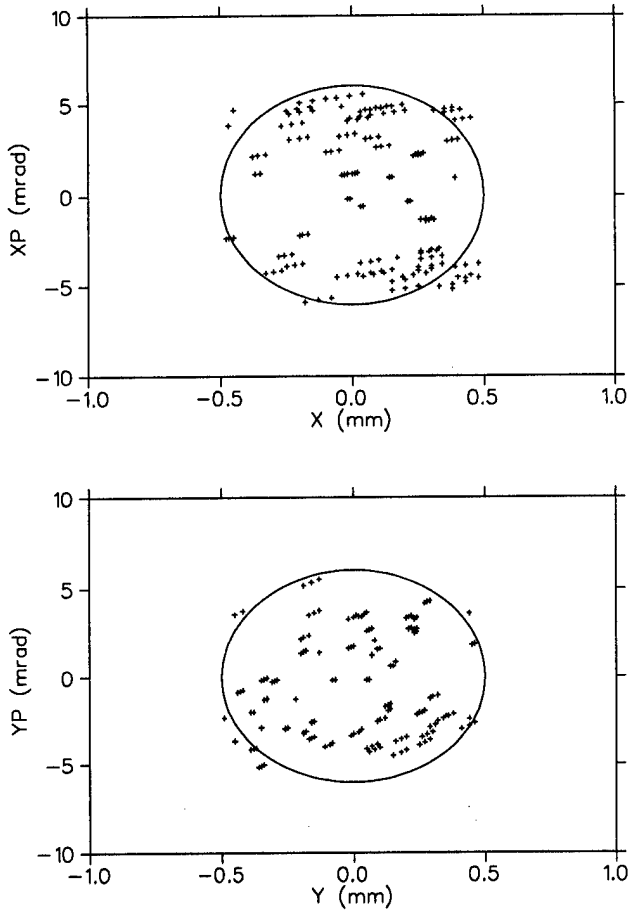


Figure 3. Transverse phase space of surviving particles for the gun to aperture plate tracking.

For the emittance aperture to final target tracking, 400 particles within an initial beam emittance of 3.0 π mm were tracked for each of three momentum values ($\Delta p/p$ = 0 and ±0.2 %) giving 1,200 particles. Figure 4 shows the phase space of these particles at the target position. The real space area at the target position is 0.056 π mm^2 for the case of $\Delta p/p$=0 and 0.069 π mm^2 including particles with momenta of $\Delta p/p$ = ±0.2 %. The final beam spot area at the target position as function of momenta ($\Delta p/p$) is given in Figure 5. For the tenth-scale final focus experiment lattice, the tracking results indicate that the chromatic effects do not generate any significant increase in the final beam spot size, and therefore, higher-order correction will not be necessary.

6. SUMMARY

The Tenth-scale Final Focus design evaluations predict that this test will provide a cost-effective, experimental basis for future full-scale design evaluations.

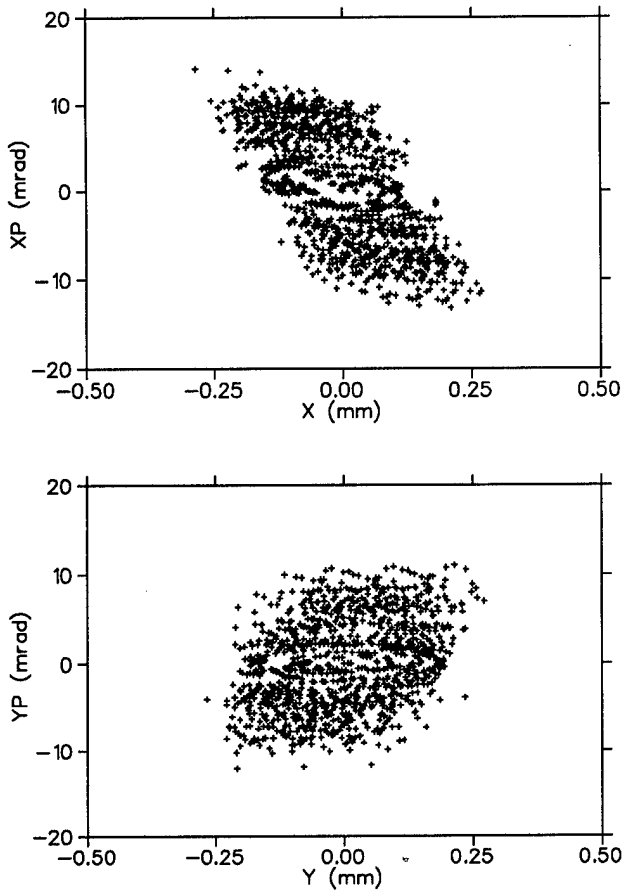


Figure 4. Transverse phase space for particles tracked from the aperture plate to the final target position.

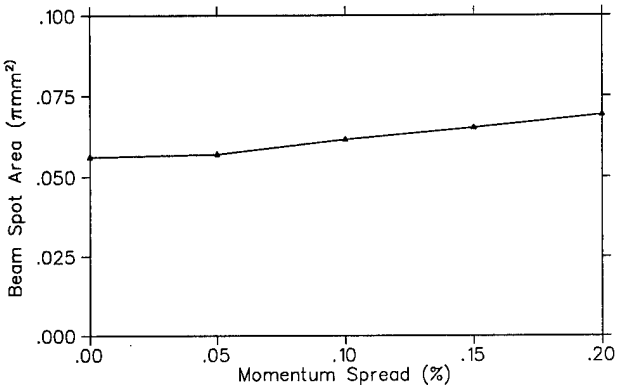


Figure 5. The final beam spot area at the target position as a function of momentum spread.

7. REFERENCES

[1] H. Wollnik, "HIBALL-II, An Improved Heavy Ion Beam Driven Fusion Reactor Study", KfK-3840, Kernforschungszentrum Karlsruhe, 1985.

[2] M. Berz, "User's Guide and Reference Manual for COSY INFINITY", MSUCL-977, Michigan State University, 1995.

[3] E. Lee, et. al. "Workshop on Scaled Final Focus Experiments", HIFAN-831, LBNL, 1996.

TRACKING STUDIES AND PERFORMANCE SIMULATIONS OF THE NSCL A1900 FRAGMENT SEPARATOR

X. Wu, D.J. Morrissey, B.M. Sherrill, R.C. York, and A.F. Zeller
National Superconducting Cyclotron Laboratory, Michigan State University, East Lansing, MI 48824

Abstract

At the National Superconducting Cyclotron Laboratory (NSCL), secondary beams of often short-lived radioactive nuclei are produced by the technique of projectile fragmentation where a primary beam impinges on a thin target to produce a broad spectrum of isotopes with near-beam velocity. As a major element of a recently funded upgrade of the NSCL facility, an increased capacity fragment separator used to select a particular isotope will be constructed. The key features of the new fragment separator include a high rigidity (6.3 T-m) and large acceptance with a solid angle of 8 msr, momentum acceptance of ±3%, and an energy resolution of 0.1%. Tracking studies and machine simulations have been done to verify the optical stability and performance of the lattice. The results of these studies, including simulations of magnet misalignment and magnetic field errors, are presented in this paper.

1 INTRODUCTION

World-wide there are significant physics programs which use ion beams of radioactive species as a unique tool to support research in nuclear structure and nuclear astrophysics research. Two complimentary processes are used to produce the radioactive beams. A technique called Isotope Production On-Line (ISOL) stops a primary, non-radioactive beam in a thick production target. The radioactive species produced are then transferred to an ion source where they are ionized and accelerated to final energy. A second technique called Projectile Fragmentation uses a primary, non-radioactive beam on a thin ($\Delta E/E \bullet 10\%$) production target. In this case, the radioactive species produced have nearly the velocity of the primary beam and a downstream magnetic transport system (fragment separator) is used to select a particular radioactive species. The Projectile Fragmentation technique is used at the NSCL [1,2].

The projectile fragment separator is used to select the specific radioactive species by a two step process. Downstream of the production target, the mixture of primary and secondary ions is selected for Bρ with an aperture system at a high-dispersion point. (See Figure 1.) Since energy loss is proportional to the square of the projectile atomic number, the isotopic selection is achieved by passing the Bρ–selected and dispersed ions through a wedge-shaped energy degrader. The remainder of the separator optics is then used to complete the isotopic separation. The nature and thickness of the production target and the energy degrader, as well as the sizes of the momentum apertures are parameters that are adjusted to control the secondary beam intensity and purity.

2 OPTICS

The fragment separator rigidity requirements are set by the primary beam energy and the fact that even fully stripped neutron-rich ions lighter than the primary beam will require a higher rigidity than that of the primary beam. At the NSCL, the K1200 cyclotron and the capacity of the following beam switch yard have set the design rigidity at 6.3 T-m or ~30% greater than that of the K1200 cyclotron.

In addition, the kinematics of the secondary beam production requires a large solid angle and momentum acceptance to achieve efficient capture of the radioactive species. A small magnification and large dispersion are desirable in the dispersive, horizontal plane (x) to achieve a high momentum resolution for the Bρ selection. A small beam size and resulting larger angular spread are desirable in the vertical (y) plane to minimize the effect of multiple scattering in the energy-degrading wedge used for isotopic separation. The configuration of the planned, A1900 fragment separator is shown in Figure 1. Basic design specifications are given in Table1.

The initial secondary beam emittance at the production target position compatible with the A1900 admittance will be 25 π mm-mrad (0.5 mm x 50 mrad) and 20 π mm-mrad (0.5 mm x 40 mrad) for the horizontal (dispersive) and vertical planes respectively. These values provide the 8 msr solid angle specified in Table 1.

The first-order lattice functions are given in Figure 2. The lattice uses 24 quadrupoles configured in eight triplet packages, and four 45° dipoles in a reverse bend geometry so that the incoming and outgoing beams are coaxial.

Work supported by NSF contract number PHY-952884.

0-7803-4376-X/98/$10.00 © 1998 IEEE

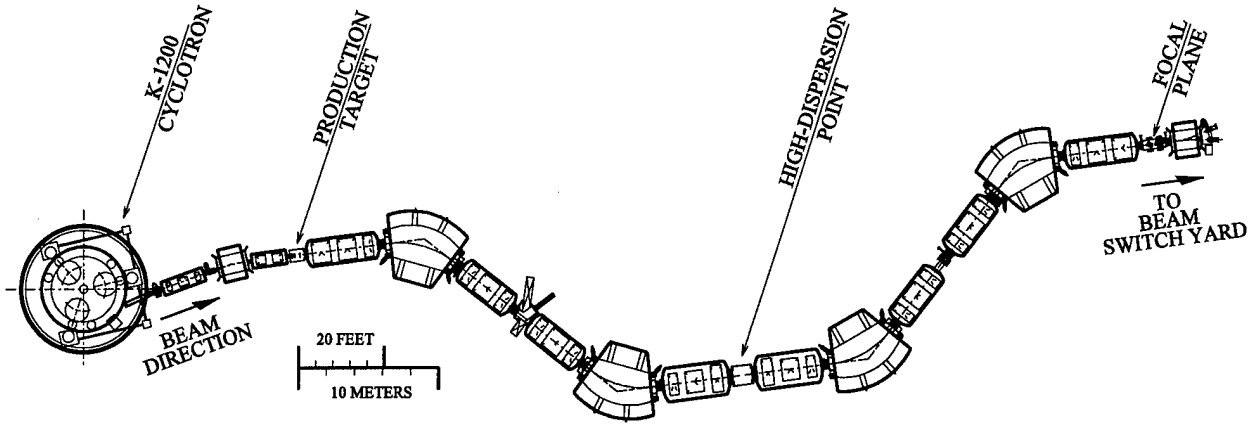


Figure 1. Layout of the proposed A1900 fragment separator.

The overall system (production target to focal plane) is a unit transfer.

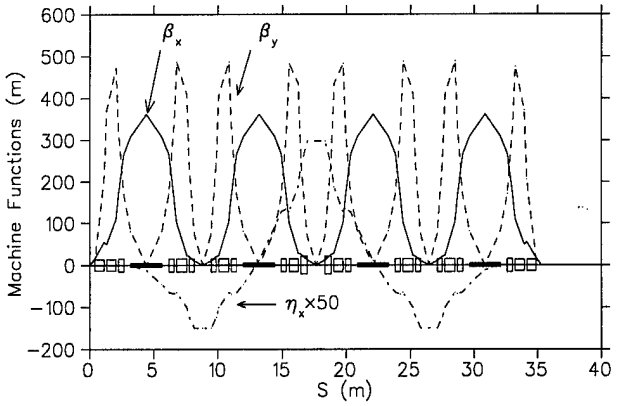


Figure 2. Lattice functions of the A1900.

Parameter	Specification
Solid Angle	8 msr
Rigidity	6.3 T-m
Momentum Acceptance	±3%
Intermediate Image (2)	
Magnification R11/R33	2.04/0.75
Resolving Power*	2915
Dispersion	5.95 m
Focal Plane	
Magnification (R11/R33)	1.0/1.0

Table 1. First-order, A1900 design parameters. *Resolving power = dispersion/(initial spot size x magnification).

3 SIMULATIONS

Since many of the quadrupoles will have a relatively poor aspect ratio (length:aperture = ~2.2:1) a 6th-order map generated by COSY INFINITY [3] was used to evaluate higher-order correction schemes and to track particles to determine transmission, resolving power, beam phase space, and error sensitivity.

The optical properties were evaluated by tracking 3,600 particles consisting of 400 particles uniformly populating the initial phase space for nine momenta values (±3%, ±2.5%, ±2%, ±1%, and 0%). Particle loss was considered at each magnet aperture and the phase space of the surviving particles was evaluated at the lattice mid-point and at the focal plane. Of the phase space delineated (8 msr and $\Delta p/p$ = ±3%), ~94% and ~92% survived to the lattice mid-point and the focal plane, respectively. The energy-degrader isotopic separation was not modeled in these simulations.

Due to the large momentum spread (±3%) and divergence (±50 mrad (x) and ±40mrad (y)) of the secondary beams, the higher-order aberrations are significant. The dominant 2nd-order aberrations are the chromatic terms x|x'δ and y|y'δ. Six families of sextupoles were used to minimize all 2nd-order geometric and chromatic terms. The phase space generated by using the corrected 2nd-order map is given in Figure 3 for the lattice mid-point and Figure 4 for the focal plane. The maximum sextupole magnetic field required was 2 kG. Effort is now underway to provide a similar 3rd-order correction scheme.

Magnet alignment and mispowering errors were evaluated by applying the appropriate errors assuming a Gaussian distribution (±2σ) for each error and using particle tracking to determine the performance degradation as a function of the σ value. A degradation of 5% in the resolution was taken as the criteria for these specifications. As a result, the full-range, misalignment specifications have been set at ±0.5 mm for the transverse positions, ±0.5 mrad angular rotation about the beam axis, ± 5 mm longitudinal position, and ±10 mrad angular rotation about an axis perpendicular to the beam axis. Similarly, the full-scale ripple specifications have been set at $\pm 10^{-4}$ for the dipole and quadrupole and $\pm 10^{-3}$ for the multipole power supplies.

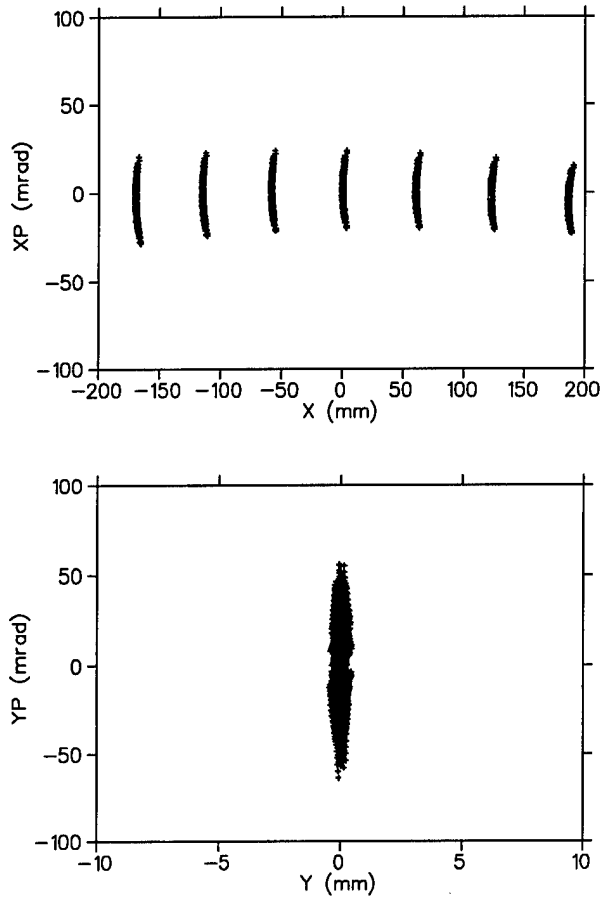


Figure 3. Transverse phase space for particles tracked through the corrected 2nd-order A1900 lattice from target to the high-dispersion mid-point.

4 HARDWARE

Of the 24 quadrupoles, 16 have multipole packages consisting of a sextupole and octupole pair. The half-lattice, symmetric about the mid-point is: (QA-QA-QB^M) - B - (QB^M-QC^M-QB^M) - (QB^M-QC^M-QB^M) - B - (QB^M-QE-QD) where QX represents a quadrupole type, ^{M} denotes those quadrupoles with multipole packages, ( ) delineates the triplet package, and B specifies a bend. Table 2 lists the primary magnetic specifications for the quadrupoles. For all magnets, the magnetic field shapes are determined by the iron configuration and the current coils are superconducting. The dipoles have a length of 2.5 m, a maximum pole-tip field of 2 T, and a good-field region of ±10 cm (x) and ±4.5 cm (y).

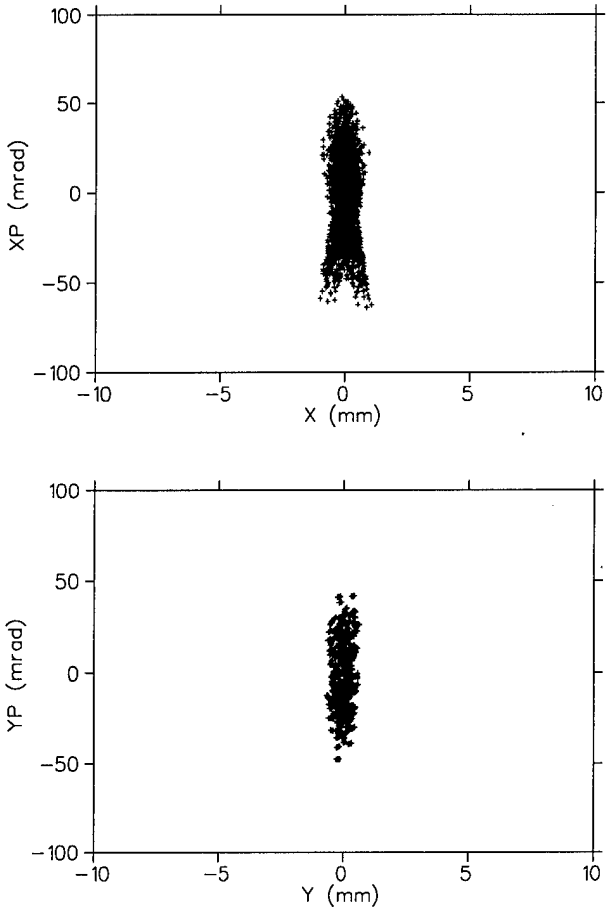


Figure 4. Transverse phase space for particles tracked through the corrected 2nd-order A1900 lattice from target to the focal plane.

Type	#	Effective Length (cm)	Pole Tip Radius (cm)	Warm Bore Radius (cm)	Max. Pole-Tip Field (kG)
QA	4	72.3	13.3	10.0	22.1
QB	12	40.0	15.0	10.0	20.7
QC	4	79.0	15.0	10.0	22.1
QD	2	48.6	21.0	17.0	23.1
QE	2	70.0	15.0	11.6	24.1

Table 2. A1900 quadrupole paramaters.

5 REFERENCES

[1] "The K500⊗K1200 – A Coupled Cyclotron Facility at the National Superconducting Cyclotron Laboratory", July 1994, Michigan State University, East Lansing, Michigan, MSUCL-939.

[2] R. C. York et. al., "Proposed Upgrade of the NSCL", IEEE Particle Accelerator Conference, Dallas, TX, p. 345, (1995).

[3] M. Berz, "User's Guide and Reference Manual for COSY INFINITY", MSUCL-977, Michigan State University, 1995.

MEASUREMENTS ON INJECTION PROPERTY IN HIMAC SYNCHROTRON

K. Noda, M. Kanazawa, E. Takada, A.Itano, S. Sato, and S. Yamada
National Institute of Radiological Sciences, Chiba, Japan
T. Nomura and T. Kohno,
Tokyo Institute of Technology, Kanagawa, Japan
N. Araki,
Hitachi-zosen Corp., Osaka, Japan

Abstract

A multiturn-injection method has been used in HIMAC synchrotron to obtain higher beam-intensity. A total and a partial efficiency of the multiturn injection are measured. The stored beam-intensity and its life-time were considerably decreased above 600 μA of an injection current of alpha ions with 6 MeV/n of the energy, mainly due to the space charge effect on the transverse tune. A dependence of a stored intensity on a vertical tune is investigated, and the tune-shift by the space charge effect is measured.

1 INTRODUCTION

HIMAC (Heavy Ion Medical Accelerator in Chiba) is an accelerator complex dedicated to medical application [1]. Clinical trials have been successfully progressing since June 1994 [2] and the treatments of 230 patients were completed by February 1997.

Heavy ion beams are very suitable for cancer treatment because of its high dose localization and high LET characterisitic. A high irradiation-accuacy has been required in the heavy ion therapy, however, because of the high dose-localization. Therefore, innovative works to realize a high accuarcy treatment are under way: (1) The irradiation gated by respiration of a patient was developed and has been used for a lung or a liver cancer moved along with a respiration [3]. An irradiation dose-rate in this case is maximized at DC beam with a sufficient intensity. (2) A secondary beam course is being constructed in order to treat a cancer around a critical organ by using positron emitter beam such as ^{11}C and ^{19}Ne that can be monitored and verified for dose localization by a positron camera [4]. When a patient is treated by the positron-emitter beams, an intensity of a primary beam is required naturally higher by two order than the treatment by the primary beam.

An extracted beam-intensity from HIMAC synchrotron should be increased by about one order in both cases, because HIMAC accelarater-complex can already deliver higher beam-intensity by about one order compared with the intensity in the present treatment.

In the commissioning stage of HIMAC synchrotron, however, a stored beam-intensity after an rf-capture was considerably decreased above 600μA of an injection current of He^{2+} with 6MeV/n. The space charge effect on transverse tune was suspected and horizontal tune-shift was observed. Therefore, an injection efficiency and a dependence of a stored intensity on a vertical tune are measured as further investigation. The paper reports the preliminary results.

2 MULTITURN INJECTION

A multiturn-injection system of HIMAC synchrotron consists of an electrostatic inflector which separates the horizontal phase-space in an injection beam line from an acceptance of the ring, and four bump magnets which distort the closed orbit. The design parameters of the multiturn injection are summarized in table 1. A septum of the inflector is located at the distance of 65mm from the central orbit in the ring. A collapsing speed of the bump orbit is 1.3mm/turn to obtain a gain of about 20 turn in injecting a beam of 50 turn in the design stage. An efficiency of the multiturn injection is expected at about 40%, because of a shadow of the septum with 0.5mm in thickness and mismatching a dispersion function of the injection beam with that in the injection point of the ring.

Table 1. Parameters in the multiturn injection

(a) Injection Beam Parameters	
Energy T (MeV/n)	6.0
Emittance ε_x (mm mrad)	13.2 π
Twiss parameters β_x (m)	0.33
α_x	0.0
Dispersion func.D_x (m)/ D'_x	0.0/0.0
Momentum spread ΔP/P	0.3% (FWHM)
(b) Ring Parameters at Injection Point	
Hori. tune Q_x	3.75
Twiss parameters β_x (m)	6.59
α_x	1.32
Dispersion func.D_x (m)/ D'_x	2.06/-0.23
Septum thickness (mm)	0.5
Acceptance A_x (mm mrad)	264 π

0-7803-4376-X/98/$10.00 © 1998 IEEE

The injection gain was estimated at about 15-20 turns in a commissioning stage, however, because the transverse emittance of an injection-beam from the injector linac was around 7π mm mrad which was reduced by 50% compared with the design one. Thus, the collapsing speed of the bump orbit is optimized to 0.87mm/turn. As a result, the injection gain is improved to about 30 turns and the stored beam-intensity just after the injection is increased by a factor of about 1.5.

A partial capture-efficiency of the multiturn injection in 1.3mm/turn in the collapsing speed of the bump orbit is also measured by using a chopped injection-beam. A time-width of a chopped beam is about 20μs corresponding to a time period of 4-5 turns in the ring. Figure 1 shows the measurement of partial-efficiency in a 70μA of an injection peak-current, ant also a survival rate after 1s of an rf-capture. The partial capture-efficiency is maximized at around 120μs corresponding to 30 turns of the injection beam in the ring, which is almost consistent with the design. The survival rate after 1s is decreased at later injection-timing, because of reduced a clearance between an acceptance of the ring and an amplitude of the betatron oscillation.

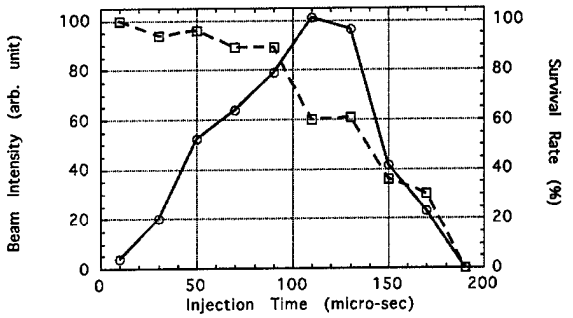


Fig. 1 A partial capture-efficiency just after the rf-capture and the survival rate after 1s. The solid and broken line indicate partial efficiency (arbitrary unit) and the survival rate (%), respectively.

3 SPACE CHARGE EFFECT

The total and the partial capture-intensity in the multiturn injection are almost proportional to the injection-intensity in increasing from 70 to 200μA of the injection peak-intensity. In increasing injection beam-intensity from 200 to 700μA in a peak-intensity, however, the stored intensity after the rf-capture with an adiabatic capture is not proportional to the increasing ratio. The stored intensity is improved by increasing the vertical tune by around 0.1 when the injection-intensity is increased from 200 to 700μA. These results suggest a limit of a stored beam-intensity by a space charge effect.

A dependence of a stored intensity on the vertical-tune is surveyed in the injection peak-intensity of around 100, 300 and 780μA, therefore, because the vertical tune-shift and -spread by the space charge effect are larger by factor of about 5 than the horizontal one in HIMAC synchrotron. The surveyed tune-line in the tune diagram is shown in fig. 2.

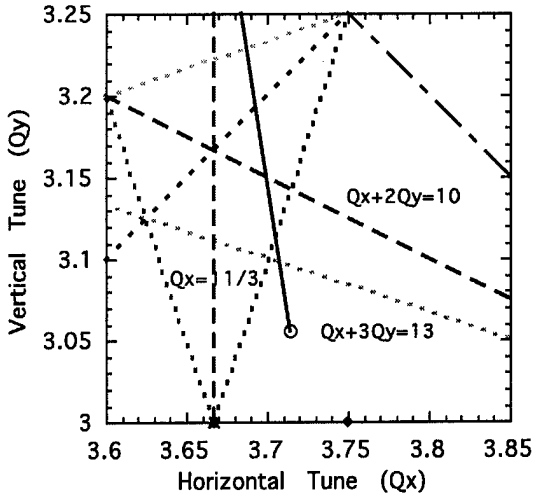


Fig. 2 The surveyed tune-line is indicated by the solid line. The dashed, broken and dotted line are 2nd, 3rd and 4th resonance line, respectively.

The measurement results are shown in fig. 3(a)-(c). These figures show a stored beam-intensity after 0.1s of the injection in setting various Qy while current of focusing quadrupole magnet is fixed to be 3. 689 of the Qx in 3.129 of the Qy. Other than the common fall off due to Qy=3 integer resonance, distinct dips are observed in both cases of rf-on and off. They are caused by the resonance of Qx+2Qy=10 in the cases of 100 and 300μA, while the dip in 780μA by Qx+3Qy=13. The vertical tune-shift depending on the stored beam-intensity is estimated at around $-0.05/10^{11}$(ppp) in a coasting beam, which is almost consistent with Laslett tune-shift. The tune-shift is obtained as follows; In a working point above Qx+2Qy=10 such as (3.685, 3.176), a stored beam is lost by two step in the case of 780μA, as shown in fig. 4. Such a beam-loss is caused by crossing two resonance lines which are Qx+3Qy=13 and Qx+2Qy=10. Tune-shift is gradually decreased by decreasing a stored beam-intensity after the tune-shift is quickly occurred during the multiturn injection period of 300μs. The tune-shift is obtained by calculating the distance along with the tune-shift line between two resonance lines and measuring a stored beam-intensity just before a beam-loss, therefore, in the assumption on a ratio of horizontal tune-shift to vertical one of 5-10 by the space charge effect.

A stored beam-intensity is rapidly decreased after the rf-on with an adiabatic capture, on the other hand, because the tune-shift and -spread is increased by bunching effect which leads a bunching factor to above 2 and vertical chromaticity of -6.0. The tune-shift in the rf-on is also measured by the same way in the coasting beam; Tune-shift is enlarged by factor of 2 compared

with that in the coasting beam, which is consistent with a measurement result of the bunching factor.

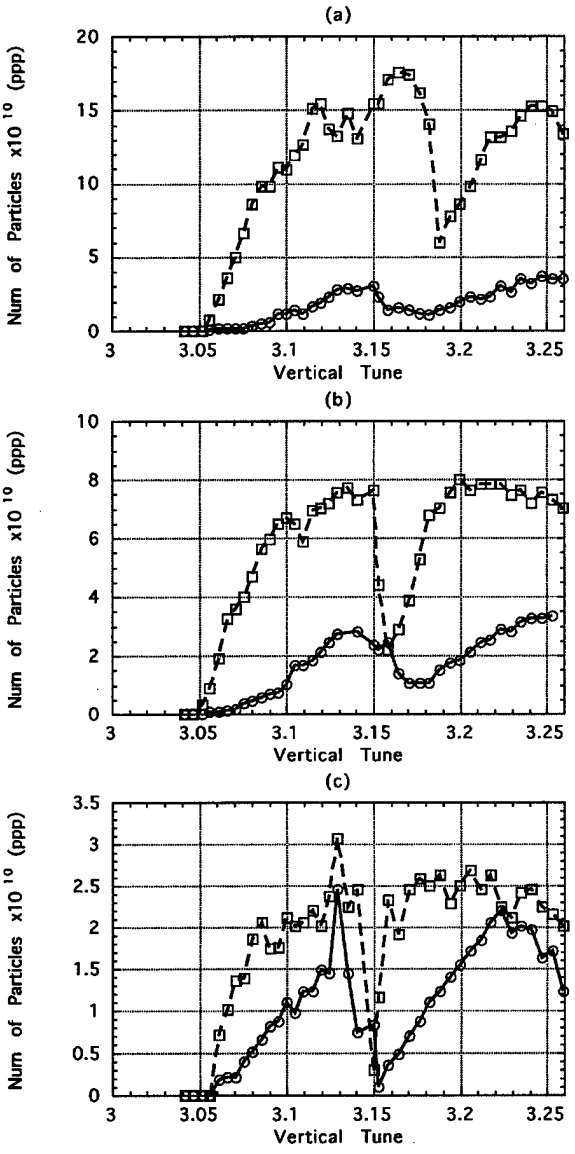


Fig. 3 The dependence of the stored intensity after 0.1s of the injection on the vertical tune. The injection peak current of (a) 780μA, (b) 300μA, and (c) 100μA. The broken and the solid lines indicate the coasting beam (rf-off) and the bunched (rf-on) beam case, respectively.

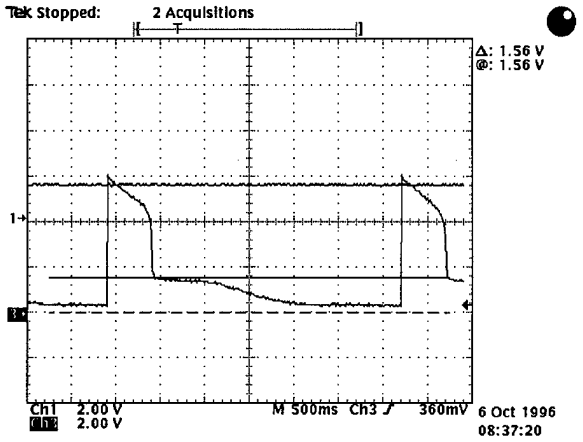


Fig. 4 The time-change of the stored beam-intensity in the injection current of 780μA when the rf is turned off. The working point is (3.685,3.176). The vertical scale corresponds to 6.0×10^{10}ppp/div and the horizontal scale is 500ms/div.

4 SUMMARY

Total efficiency of the multiturn injection is achieved at 45% in just after the multiturn injection. Partial one is maximized at around 30 turns which is basically consistent with the design.

A space charge effect on a transverse tune is investigated by a vertical-tune survey. The tune-shift in a coasting beam is obtained by measuring intensity just before beam loss in crossing two resonance lines and calculating the distance between them. The result is consistent with Laslett tune-shift. A stored beam-intensity is considerably decreased due to enlarged tune-shift and -spread by bunching effect.

5 ACKNOWLEDGEMENTS

The authors would like to express their thanks to the crew of Accelerator Engineering Corp. for their skilful operation of HIMAC accelerator complex. The authors are also grateful to Dr. K. Kawachi and members of the Div. of Accelerator Physics and Engineering at NIRS for helpful discussions. This work has been carried out as a part of Research Project with Heavy Ions at NIRS-HIMAC.

REFERENCES

[1] Y. Hirao et al., HIMAC-Report-001,1192.
[2] S. Yamada, Proc. 1995 PAC, USA, p.9.
[3] K.Noda, et al., Proc. 5th EPAC, Spain, (1996) 2656.
[4] S. Kouda, et al., in these proceedings.

PREDICTED FOIL TEMPERATURES IN THE BROOKHAVEN ACCUMULATOR RING FOR THE NSNS*

Jonathan Duke,Rutherford Appleton Laboratory,Chilton,Didcot,United Kingdom.

Abstract

An investigation has been carried out into the peak equilibrium stripping foil temperatures that could be expected in the 1 GeV NSNS Accumulator Ring proposed by Brookhaven National Laboratory.

A carbon foil is assumed. Computed foil temperature distributions on the foil's surface are presented, as well as the predicted relationships between foil temperature and quantities such as the average number of recirculated proton hits, linac intensity, and foil mass per unit area used.

1 INTRODUCTION

The 1 GeV NSNS accumulator ring has been designed to use H^- injection. In order to ascertain whether the stripping foil would survive under the injection conditions present in the NSNS a computer simulation has been carried out. This is described below.

The foil simulation is based on a rectangular carbon foil , 8 mm wide and 4 mm high. This is a very small foil, and the injected beam spot touches both edges. The foil is modelled as supported only on the top edge. The temperature of the frame is fixed at 295 K . A foil mass per unit area of 400 μgcm^{-2} is chosen, corresponding to a thickness of approximately 2.6 μm for carbon. The H^- beam is centred in the foil, and is modelled with a Gaussian elliptical transverse profile with standard deviations of 1.7548mm in the horizontal direction and 0.8544mm in the vertical direction. Other relevant input parameters are a 1280 turn injection at a repetition frequency of 60 Hz and with a macro-pulse duration of 1.076864 ms. The original planned beam intensity of 1.04×10^{14} ppp would give a target power of 1 MW, but present project philosophy is to do all calculations for the 2 MW case, ie 2.08×10^{14} ppp. Both intensities are simulated.

Injected H^- ions, stripped electrons and recirculating protons scatter in the foil and large temperature rises result from atomic excitations. The initial rate of temperature rise is inversely dependent on the foil specific heat. The temperature reaches a maximum at the end of each injection and the temperature rise in the 60 Hz cycling is limited mainly by radiation, with a small additional contribution from conduction within the foil. Energy losses due to radiation and conduction scale as the fourth and first power of the temperature difference from the surroundings, and are proportional to the foil emissivity and thermal conductivity respectively. Specific heat, emissivity and thermal conductivity are all material and temperature dependent.[1],[2].

With the parameter range covered by this study, a constant peak temperature is reached after a time which varies between three and fourteen beam pulses, this number being inversely related to the energy deposited in the foil.

2 SIMULATION

Heating and cooling of the NSNS foil are simulated in a program based on finite elements, both for time passage and transverse position co-ordinates. A fifty by fifty array of elements is used. Each element is rectangular and the same shape as the foil as a whole. The distribution of recirculating protons on the foil is modelled as uniform. A real distribution from tracking codes will be used in the near future. Since the energy density at the peak of the Gaussian distribution is 3.78 times that at the edge of the foil, (for 400 μgcm^{-2} and 2.5 foil hits) the recirculated distribution has a much smaller effect on the peak temperature than the H^- beam spot. The time distribution of recirculated proton hits is approximated as linearly increasing during each accumulation, in proportion to the size of the accumulated beam. In reality the recirculating proton hits do not have a simple time distribution, but the use of an approximation is justified because a previous study [8] had shown the time distribution chosen to be unimportant. Energy deposited in the foil is calculated using charged particle energy loss data, (both for protons and stripped electrons) and mean H^- and H^0 lifetimes [3],[4],[5]. High temperature estimates for specific heat have been made by scaling normalised Debye curves [6] in both dimensions to give a best fit for published data. The asymptote used for the specific heat at high temperatures is 2125 $Jkg^{-1}K^{-1}$ .The emissivity is assumed constant at 0.80 and the thermal conductivity is approximated by:

$15 + 305958\ T^{-1.3091}$ for $T > 573$ K and

$217.9653 - 0.2233\ T$ for $T < 573$ K.

The effects of different numbers of foil hits and of using a foil of a different thickness are also investigated. By altering independently input parameters such as emissivity, heat capacity, and the energy deposited in the foil by one H^- ion, the variations in foil temperature

* The U.S. National Spallation Neutron Source

0-7803-4376-X/98/$10.00 © 1998 IEEE

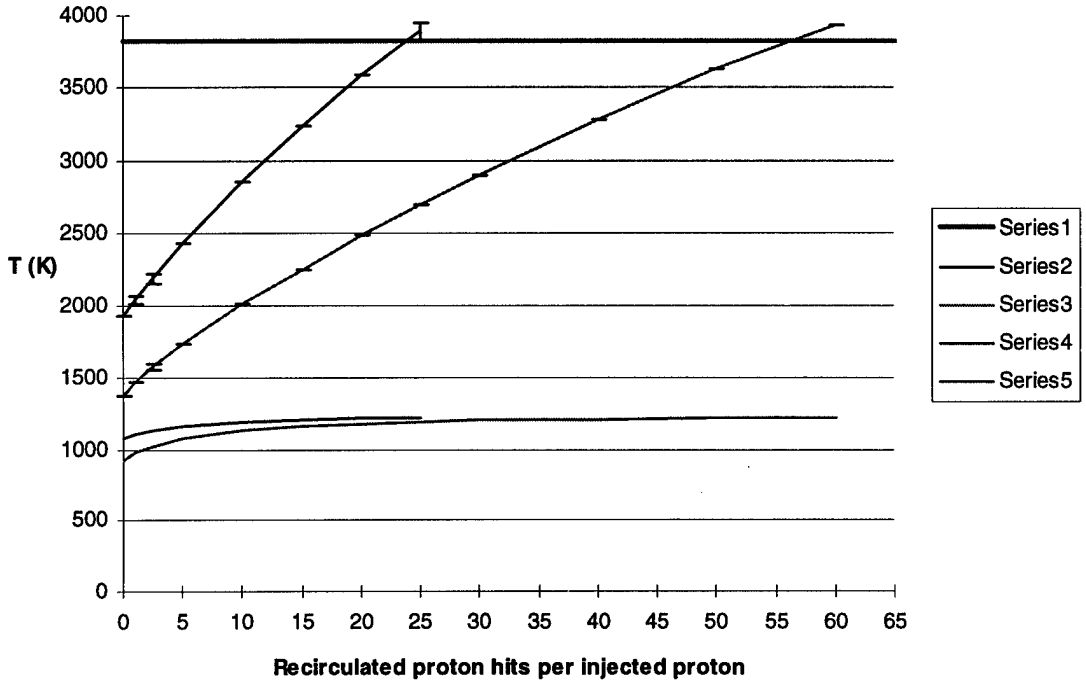


Figure 1. A plot of 400 μgcm^{-2} stripping foil temperatures versus recirculated proton hits.
KEY: Series 1 = Melting point of Carbon
Series 2 = Peak equilibrium temperatures at 2 MW
Series 3 = Peak equilibrium temperatures at 1 MW
Series 4 = Minimum equilibrium temperatures at 2 MW
Series 5 = Minimum equilibrium temperatures at 1 MW

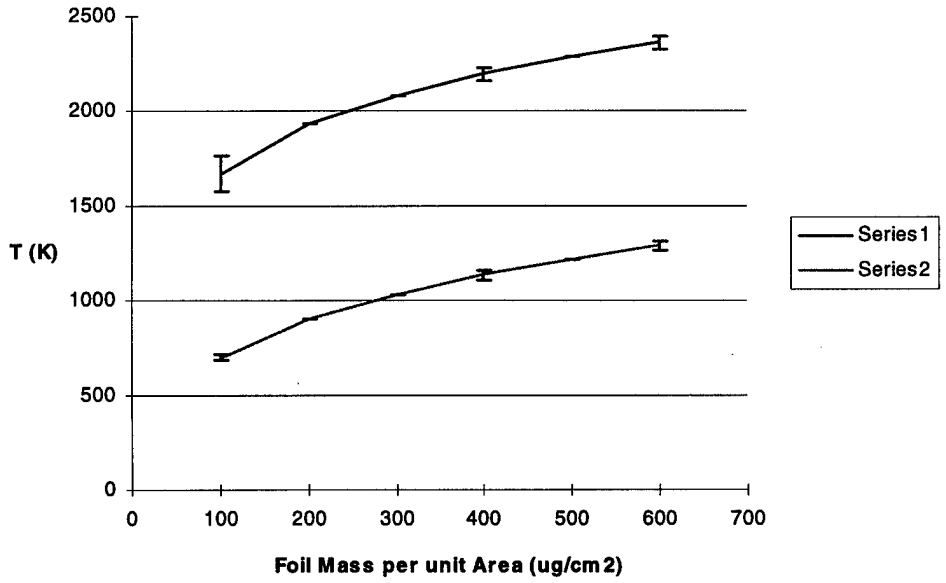


Figure 2. A plot of Carbon stripping foil temperatures versus foil mass per unit area
KEY: Series 1 = Peak equilibrium temperature with 2.5 foil hits per injected proton, at 2 MW
Series 2 = Minimum equilibrium temperature with 2.5 foil hits per injected proton, at 2 MW

caused by the uncertainties in the input conditions are explored For thinner foils, eg 100 μgcm^{-2}, variations in specific heat and deposited energy dominate the total uncertainty , but for thicker foils, eg 400 μgcm^{-2} and above, the variation in emissivity dominates. For 2.5 foil hits, the summed estimated uncertainties in temperatures at the peak of the temperature cycle are:
1 MW: 1.5% 2 MW : 1.6%
Uncertainties in minimum temperatures are:
1 MW: 2.0%. 2 MW : 2.2%

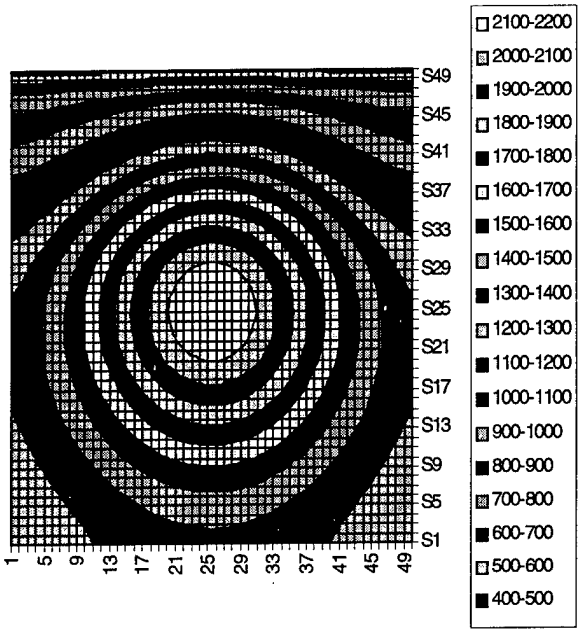


Figure 3. Peak Equilibrium temperature distribution after eight pulses for a 400$\mu g\ cm^{-2}$ foil with 2.5 foil hits per injected proton. (Please note, the foil is actually twice as wide as it is high).

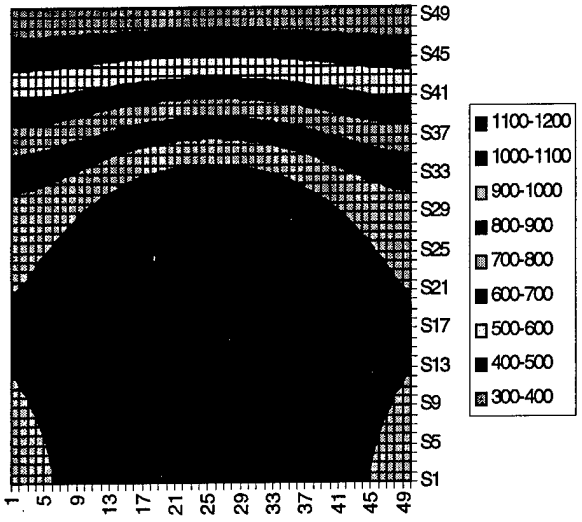


Figure 4. Minimum Equilibrium temperature distribution an instant before the eighth pulse, for the same parameters as in Figure 3

3 CONCLUSION

The peak temperature in the carbon foil, assuming a value of 2.5 recirculated proton hits per injected proton, is 1575 K for 1 MW and 2195 K for 2 MW. These should be compared to the melting point of carbon of 3823 K. Therefore the foil as presently proposed by Brookhaven would be below its melting point, but no account has yet been taken of the stresses caused by the temperature gradients or by constant proton impact.

4 ACKNOWLEDGEMENTS

My grateful thanks go to Dr L.N.Blumberg and Dr Y.Y.Lee, of Brookhaven National Laboratory, for their help with the parameters of the NSNS used in this paper.

REFERENCES

[1] Arthur M. James and Mary P.Lord
'Macmillan's Chemical and Physical Data'
- pub. The Macmillan Press Ltd. 1992
pp. 40,434,438,442

[2] Y.S Touloukian and D.P.Dewitt
'Thermophysical Properties of Mattter -Vol.8-
Thermal Radiative Properties - Nonmetallic Solids'
pub. IFI / Plenum ,New York. 1972 pp. 31,142-3

[3] J.F. Kanni,Kirtland Air Force Base, New Mexico.
Atomic Data and Nuclear Energy Tables-
Proton Range-Energy Tables , 1 keV-10 GeV, p. 219
Volume 27 Numbers 2/3 .Academic Press, 1982.

[4] Subcommittee on Penetration of Charged
Particles and Committee on Nuclear Science
Nuclear Science Series -Report no. 39
'Studies in Penetration of Charged Particles in Matter'
publication 1133 , National Academy of Sciences-
National Research Council, USA. 1964
pp. 232,234,237,146

[5] E.A.Andreev,D.Bohne,V.L.Bychkov and
V.P.Shevelko,GSI Report,
'Stripping of Fast H^- and H_2^+ ions in foils'. pp3&8

[6] Mark W Zemansky and Richard H Dittman
'Heat and Thermodynamics' (sixth edition)
pub. Mcgraw-Hill Book Company. 1981 pp. 309-11

[7] L.N.Blumberg and Y.Y.Lee
BNL/NSNS Technical Note No. 003
'H^- Injection into the 1GeV NSNS Accumulator'
November 1st, 1996

[8] J.P.Duke, EPAC'96 Poster, 'Stripping Foil
Temperatures in the European Spallation Source'.
EPAC'96 proceedings, p2465,Vol 3.

TRANSFER OF A POLARIZED PROTON BEAM FROM AGS TO RHIC

N. Tsoupas*, T. Roser, M. Syphers, A. Luccio,
Brookhaven National Laboratory, Upton, NY 11973
D. Underwood Argonne National Laboratory

Abstract

As part of the RHIC project, the RHIC machine will also be able to accelerate polarized proton beam bunches. The bunches will be extracted from the AGS machine, with kinetic energy T=25 GeV, and transfered into RHIC via the AtR transfer line[1]. When the RHIC machine accelerates polarized protons, it will operate with two full snakes, which define the stable spin direction of a polarized proton beam circulating in each ring, along the vertical. Therefore a polarized proton beam should be injected into the RHIC machine with the stable spin direction along the vertical in order to match that of the RHIC machine. The layout of the dipole magnets of the AtR line[1] creates a dependance, on the injection energy, of the stable spin direction of a polarized proton beam injected into the RHIC machine. In this paper, the study of the stable spin direction (at the RHIC injection point) of a polarized proton beam as a function of the injection energy is presented. A modification of the AtR transfer line, which eliminates this energy dependance (within the range of proton injection energies) of the stable spin direction is also presented.

1 SECTIONS OF THE ATR LINE AFFECTING THE STABLE SPIN DIRECTION OF A POLARIZED PROTON BEAM

Two sections of the AtR line are affecting the stable spin direction of a polarized proton beam during injection into the RHIC machine. The first section, which will be referred to as the "12.5 mrad vertical bend", (Fig. 1) is part of the W-line[1] and is located within the 20° horizontal bend. It starts with the +12.51 mrad vertically pitching magnet which is located midway along the drift space of the second and third combined function magnets[1] and terminates at the exit of the -12.51 mrad vertically pitching magnet located midway along the drift space of the second and third quadrupoles of the W-line.

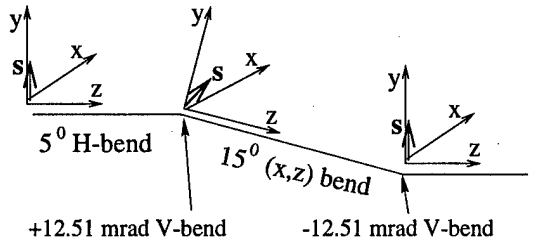


Fig. 1. Diagram of the "12.5 mrad vertical bend".

The second section, which will be referred to as the "3.0 mrad vertical bend", (Fig. 2) is located within the injection section[1] of the AtR line and begins with the 3.0 mrad vertically pitching magnet, followed by a Lambertson septum magnet[2], and terminates at the exit of the RHIC injection kicker[3],[4]. It is for the arrangement of the bending magnets in these two vertical bends, that affects the stable spin direction of a polarized proton beam.

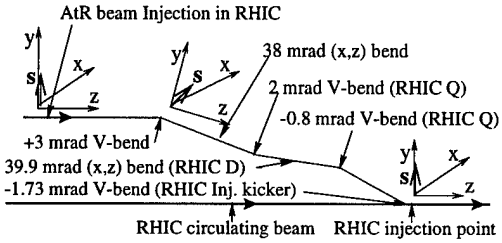


Fig. 2. Schematic diagram of the "3 mrad vertical bend".

2 STABLE SPIN DIRECTION AT RHIC INJECTION POINT

The stable spin direction at the exit of the "12.5 mrad vertical bend" has been calculated[5] earlier. However the inclusion of the partial snake[6],[7] in AGS as well as the redesign of the injection section of the AtR line[1] required new calculations to determine the stable spin direction at the RHIC injection point. Details of the calculations are also presented in Ref[8]. The new items which are included in the present calculations are:

- *A section of the AGS machine (from the center of the straight section C10 of AGS to the H13 fast extraction point)[8] followed by the AtR line[1].*
- *The energy dependance of the stable spin direction[7] of a polarized proton beam circulating in the AGS machine.*
- *The knowledge of the beam ellipsoid in AGS[8].*

The calculations to determine the stable spin direction at the "RHIC injection point" were based on the numerical integration of two equations: the differential equation of motion (Eq. 1) of a charged particle moving in static magnetic and electric fields, and the spin precession equation (Eq. 2) of a particle with magnetic moment in the same electric and magnetic field:

$$\frac{d\mathbf{v}}{dt} = \frac{e}{m\gamma}\left(\mathbf{v}\times\mathbf{B} + \mathbf{E} - \frac{(\mathbf{v}\cdot\mathbf{E})\,\mathbf{v}}{c^2}\right) \qquad (1)$$

$$\frac{d\mathbf{s}}{dt} = \frac{e}{m\gamma}\left((G\gamma+1)\,\mathbf{s}\times\mathbf{B} +\right.$$

* Work performed under the auspices of the U.S. Department of Energy

$$+(\gamma-1)\,G\frac{(\mathbf{v}\cdot\mathbf{B})\,(\mathbf{v}\times\mathbf{s})}{v^2}\Big)+$$

$$+\left(\left(G\gamma+\frac{1}{1+\gamma}\right)\mathbf{s}\times(\mathbf{B}\times v)\,c^2\right) \qquad (2)$$

The simultaneous integration of the (Eq. 1) and (Eq. 2), above, and the required initial conditions which were obtained from the items mentioned above, were performed with a modified version of the RAYTRACE computer code[9] which comes under the name RAYTRACE_SPIN[10].

2.1 *Stable Spin Direction at RHIC Injection Point (AGS Partial Snake Off)*

The vertical component S_y of the stable spin direction, at the RHIC injection point, is shown in Fig. 3 as a function of $G\gamma$. The empty squares are the S_y components of the central trajectory particle. The filled squares are the average vertical spin projection $< S_y >$, as calculated from the distribution of the S_y component of the 1000 injected particles. The error bars are one standard deviation of the vertical spin projection S_y and contains over 90% of the final spin distribution which is not Gaussian and represent a measure of the spread of the stable spin direction at the RHIC injection point. This spread of the stable spin direction at the RHIC injection point is due to the off central trajectory particles which are experiencing the non vertical fields of the various quadrupoles and combined function magnets (dipole plus quad) of the AtR transfer line. The random sampling of the particles was taken from a beam with a normalized beam emittance of 10 π mm mrad for both vertical and horizondal planes, and one standard deviation of the beam momentum spread $\Delta p/p = \pm 0.05\%$. The calculations performed to obtain the results shown in Fig. 3 assumed that the initial stable spin direction was along the vertical. In an actual injection of a polarized proton beam the assumption that the spin direction is along the vertical will not be valid, at least at the range of energies covered by the Fig. 3. This is because of the AGS partial snake[7], the effect of which is discussed next.

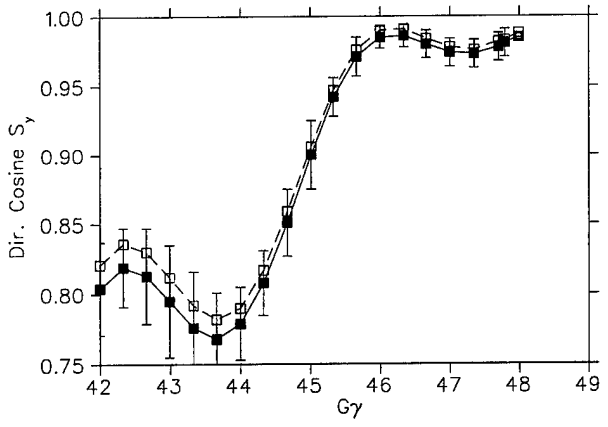


Fig. 3. S_y component of the stable spin direction at RHIC injection point. AGS partial snake off.

2.2 *Stable Spin Direction at RHIC Injection Point (AGS Partial Snake On)*

The vertical component S_y of the stable spin direction at the RHIC injection point when the partial snake in the AGS is on with 5in Fig. 4 as a function of the $G\gamma$. The interpretation of the graph's symbols is similar to the one given in the previous subsection. The results of the stable spin direction as presented in Fig. 4 show that the initial stable spin direction, which is defined by the strength of the partial Snake in the AGS, has a profound effect not only in the spread but also on the average value of the stable spin direction itself at the RHIC injection point.

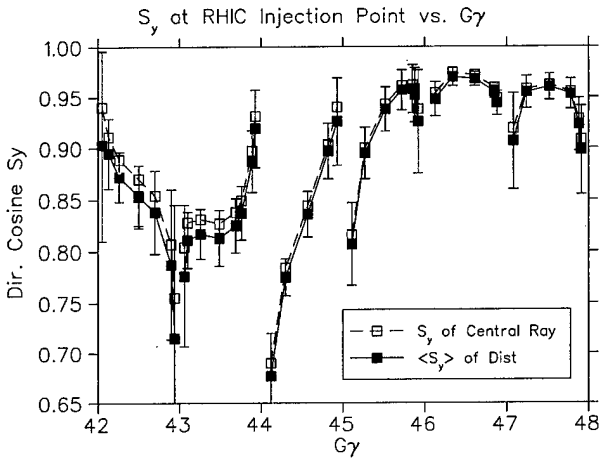


Fig. 4. S_y component of the stable spin direction at RHIC injection point. AGS partial snake on.

3 OPTIMIZATION OF STABLE SPIN DIRECTION WITH INJECTION ENERGY

The preceeding sections suggest that the optimum energy range for injection of a polarized proton beam into RHIC corresponds to values of $G\gamma$ from ~45 to 48. However, it is possible to alter the energy range for optimum polarization transfer of an injected beam into RHIC by employing three additional horizontally bending dipole magnets in the AtR tranfer line. A schematic diagram of the section of the AtR transfer line which includes the three added dipoles, is shown in Fig. 5.

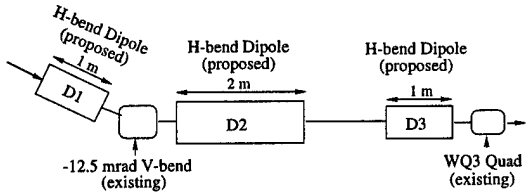


Fig. 5. Diagram of the proposed modification of the AtR transfer line for optimum polarization transfer.

The first of the three proposed dipoles (D1) shown in Fig. 5 is placed in front of the second 12.5 mrad vertically bending magnet of the 20° bend of the ATR line (see Fig. 1). The second dipole (D2) shown in Fig. 5 is to be placed just after the second 12.5 mrad vertically bending magnet

with the center of the third dipole (D3) placed downstream from the center of the (D2) dipole, at a distance equal to the distance of the centers of the (D1) and (D2) dipoles. This dipole arrangement is not dispersive, and will only affect the stable spin direction after the vertical magnet shown in Fig. 5. The beam trajectory will be restored at the exit of the D3 dipole, (Fig. 5) and the beam parameters will be practically the same as before the inclusion of the dipoles. The next two subsections present and discuss the results of the stable spin direction at the RHIC injection point when the three horizontal dipoles D1,D2 and D3 shown in Fig. 5 are excited to 1.5 Tesla and bend the beam right,left,right respectively.

3.1 Stable Spin Direction (AGS Partial Snake Off; AtR Modified)

With the AtR transfer line modified by the insertion of the three dipoles mentioned above, the calculation for the stable spin direction at the RHIC injection point was repeated. The vertical component S_y of the stable spin direction at the RHIC injection point is shown in Fig. 6 as a function of $G\gamma$.

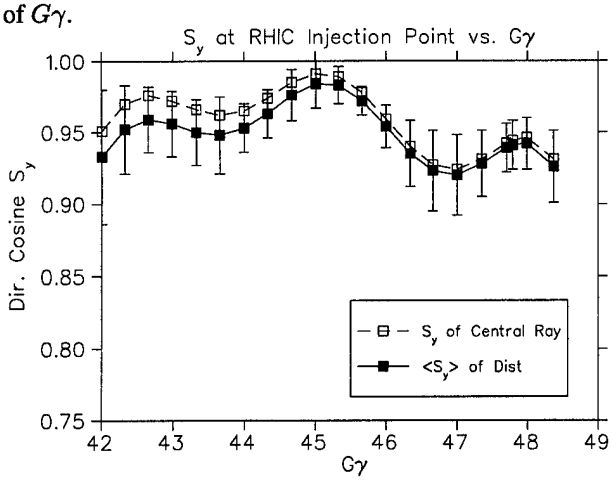


Fig. 6. S_y component of the stable spin direction at RHIC injection point. AGS partial snake off, AtR line modified.

3.2 Stable Spin Direction (AGS Partial Snake On; AtR Line Modified)

In these calculations the AtR transfer line is modified as mentioned earlier, and the AGS partial Snake is turned on at a 9° strength. The vertical component S_y of the stable spin direction at the RHIC injection point when the partial Snake in AGS is on, is shown in Fig. 7 as a function of $G\gamma$.

4 REFERENCES

[1] 'Focusing and matching properties of the AtR transfer line', N. Tsoupas, et, al., BNL, these proceedings.

[2] 'Design and B-Field Measurements of a Lambertson Injection Magnet for the RHIC Machine', N. Tsoupas, E. Rodger, J. Claus, H.W. Foelsche, and P. Wanderer, PAC 1995, p. 1352 (May 1-5 1995), Dallas, TX.

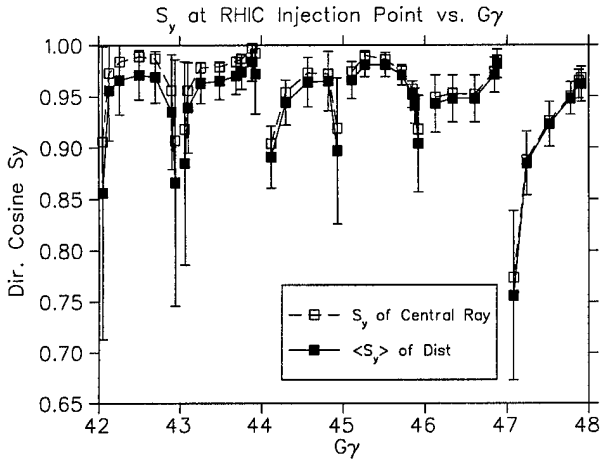


Fig. 7. S_y component of the stable spin direction at RHIC injection point. AGS partial snake on, AtR line modified.

[3] 'The RHIC Injection Kicker', H. Hahn, N. Tsoupas, J.E. Tuozzolo BNL, these proceedings.

[4] 'Beam Injection into RHIC', W. Fischer, H. Hahn, W.W. MacKay, N. Tsoupas, BNL, these proceedings.

[5] S.Y. Lee and E.D. Courant, BNL Technical Note AD/RHIC-63.

[6] T. Roser, AIP Conf. Proc. No. 187, p.1442 (1988)

[7] H. Huang et al., Phys. Rev. Lett. 73, 2982 (1994)

[8] 'Closed Orbit Calculations at AGS and Extraction Beam Parameters at H13', N. Tsoupas, H.W. Foelsche, J. Claus, and R. Thern, AD/RHIC/RD-75.

[9] S.B. Kowalski and H.A. Enge, The ion-optical program RAYTRACE NIM A258 (1987) p407.

[10] N. Tsoupas, BNL, private communication

BEAM INJECTION INTO RHIC

W. Fischer*, H. Hahn, W.W. MacKay, T. Satogata, N. Tsoupas and W. Zhang
Brookhaven National Laboratory, Upton, NY 11973, USA

Abstract

During the RHIC sextant test in January 1997 beam was injected into a sixth of one of the rings for the first time. We describe the injection zone and its bottlenecks. We report on the commissioning of the injection system, on beam based measurements of the kickers and the application program to steer the beam.

1 INTRODUCTION

The beam for the Relativistic Ion Collider (RHIC) is extracted from the Alternating Gradient Synchrotron (AGS), transported through the AGS-to-RHIC transfer line (AtR) and then injected into either the Yellow or Blue ring of RHIC. The AtR comprises the u- and w-line (shared for both rings) and one 90 degree arc for each of the RHIC rings (named x-line for the Blue and y-line for the Yellow ring) [1]. At the end of 1995 u- and w-line were tested with beam [2, 3]. In January 1997, bunches of gold ions were guided through the y-line, injected into a sextant of the Yellow ring and transported to the end of the sextant [4, 5, 6].

At the beginning of the sextant test a vertical corrector magnet(yo5-tv9, next to quadrupole yo5-qf8, see Fig. 1) was powered with 30 A and replaced the injection kickers. It made the initial injection of beam into the sextant easier. Later, when good injection conditions were established, the injection kickers [7] were commissioned. Kicker strength and rise time were measured with beam to ensure that design criteria are met. An injection application program, designed to assist the operator in bringing the incoming beam onto the design orbit, was partially tested.

2 THE INJECTION REGION

There are 6 quadrupoles at the end of the y-line (yq1, ..., yq6, see Fig. 1) providing enough degrees of freedom to match the optical functions of the AtR with those in the ring. After passing the last quadruple triplet (yq4, ..., yq6) the beam is injected into the sextant. The incoming beam lies in a plane about 52 mm above the ring level. A pitching magnet (yp1) provides a 3 mrad downward deflection upstream of the septum magnet ylamb. The beam then passes through the quadrupoles yo5-qf8 and yo5-qd9 and crosses the RHIC reference orbit in the center of the injection kickers yki1-yki4. The four kickers deflect the beam vertically by 1.86 mrad onto the RHIC design orbit.

The iron Lambertson septum magnet ylamb bends the incoming beam by 38 mrad and brings the beam axis into horizontal coincidence with the reference orbit in the sextant. The iron septum magnet will separate the incoming beam from the circulating one. The stray field in the region of the circulating beam is kept below 10^{-4} T by means of a soft iron beam pipe, acting as a magnetic shield. The Corrector-Quadrupole-Sextupole assemblies (CQS) for yo5-qf8 and yo5-qd9 are shortened by leaving out the sextupole corrector. In addition, the beam pipe in yo5-qf8 is slightly bent upwards to give more clearance for the injected beam.

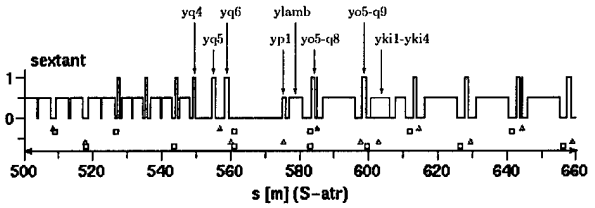


Figure 1: The optical elements in the injection region of the RHIC Yellow ring. Dipole are of height 0.5, quadrupoles are of height 1. The upper (lower) squares show the locations of horizontal (vertical) beam position monitors, the triangles denote orbit correctors. The longitudinal s-position is taken from the beginning of the transfer line.

Tab. 1 lists some optical functions in the injection region. The relatively large vertical beta function in the injection kicker (the maximum in the arcs is 45 m) combined with the small inner beam pipe diameter (41.2 mm compared to 80 mm in the arcs) is a bottleneck for injection.

Table 1: Optical functions in the injection region for the horizontal and vertical plane.

element	pos. [m]	β_x [m]	β_y [m]	D_x [m]	D_y [m]
yq4	549.81	27.98	25.67	1.69	-0.00
yq5	555.70	35.68	43.68	1.84	-0.00
yq6	559.30	12.20	103.12	1.00	-0.00
yp1	575.93	22.86	25.32	-0.55	0.00
ylamb	580.83	38.22	14.50	-0.94	0.02
yo5-qf8	584.35	47.82	11.20	-1.08	0.03
yo5-qd9	599.18	11.18	47.82	-0.83	0.11
yki1	601.68	14.61	37.91	-1.00	0.10
yki2	603.13	17.28	32.79	-1.10	0.10
yki3	604.59	20.44	28.17	-1.20	0.09
yki4	606.04	24.08	24.04	-1.30	0.09

3 INJECTION KICKER MEASUREMENTS

The injection kickers are described in detail in Ref. [7]. There are four injection kickers per ring. The kickers for the Yellow ring were commissioned during the sextant test.

* Work performed under the auspices of the US Department of Energy

0-7803-4376-X/98/$10.00 © 1998 IEEE

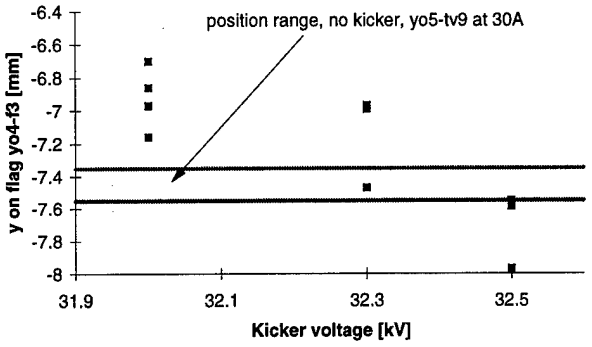


Figure 2: Measurement of the injection kicker strength. The beam was observed on a flag at the end of the sextant. The position on this flag for 3 different kicker strengths is compared with the position when the kicker was replaced by a nearby vertical corrector.

The commissioning consisted of four parts: first, finding the correct timing, second, determining the correct kicker strength, third, measuring the rise time and fourth, recording the shot-to shot stability for multi-bunch extraction. In this case four bunches, 100 ms apart, were injected.

For the first task the kicker current signal was compared with the signal from a beam position monitor close to the injection kickers. The main vertical deflection for the injection still came from the vertical corrector yo5-tv9. The kickers were operated with about 30% of their design voltage to find the delay time with the maximum vertical deflection. The beam response to the kicker was observed on a flag (yo4-f3) some 500 m downstream at the end of the sextant.

Second, the kicker voltage was varied while the beam position was observed on the flag at the end of the sextant. At 32.3 kV (close to the design value of 32 kV) the beam position on this flag was the same as with the vertical corrector next to yo5-tv9.

The rise time limits the number of bunches that can be injected into a RHIC ring. Since the electromagnetic field in the kicker is rather complicated (about 94% of the magnetic and about 6% of the electric field contribute to the kick) only a measurement with beam can give reliable results for the rise time. The following procedure was used to measure the rise time: In a first step the vertical corrector was switched on with the kicker timing far off. Then the kicker timing was changed until a change of the beam position on the last flag was visible. In a second step, the kicker was used fully timed in and the corrector yo5-tv9 switched off. The kicker delay time was varied so long as to see a drop in the maximum beam deviation on the flag. In Fig. 3 this measurement is shown, when all four kickers were used.

However, in kicker current measurements one of the four kickers showed a longer rise time and a reduced flat top value. Therefore, another measurement without this weaker kicker was taken too. The kicker was switched off and the missing strength was again provided by the vertical corrector magnet. Applying a similar procedure as for the first measurement, the measured rise time was clearly below the design value of 95 ns (see Fig. 4). It was found out later, that the different behavior of one of the kickers could be explained by a temperature regulation problem of a thyratron in the pulser circuit for this kicker.

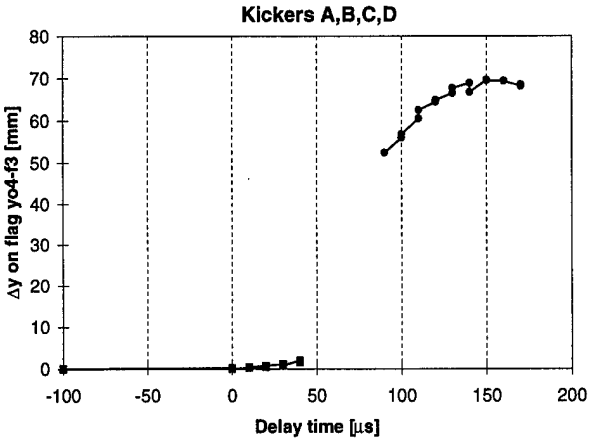


Figure 3: Rise time measurement using all four injection kickers. The beam position was observed on a flag at the end of the sextant. The left part of the curve was measured while the vertical corrector yo5-tv9 was powered at nominal strength; the right part of the curve was measured without it.

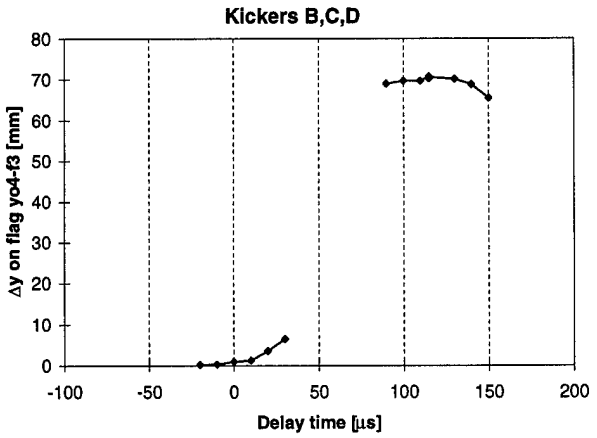


Figure 4: Rise time measurement using only three injection kickers, excluding the "abnormal" one (cf. Fig. 3). The left part of the curve was measured while the corrector yo5-tv9 was powered at its nominal strength; the right part of the curve was measured with 0.25 of its nominal strength.

Fourth, the stability for multibunch injection was measured. In Fig. 5 the horizontal and vertical trajectories in the sextant are shown for 4 injected bunches separated by

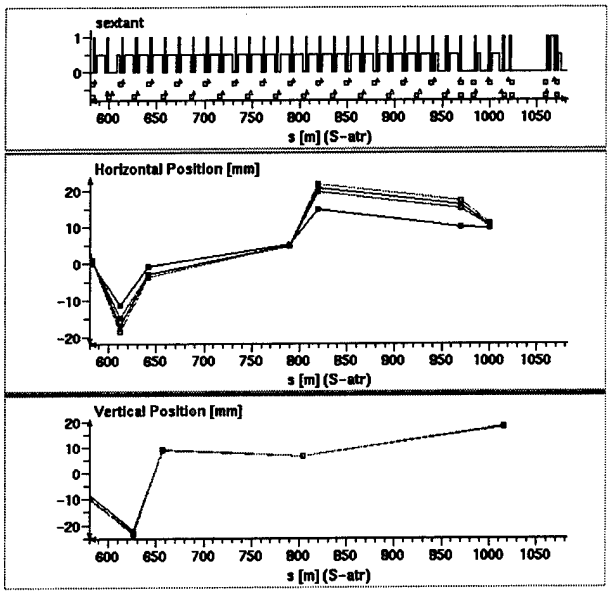


Figure 5: Injection of multiple bunches into the Sextant. Bunches are separated by 100 ms.

100 ms. There is an excellent agreement for the vertical orbits, indicating that there is no performance degradation of the kickers in this mode. The disagreement in the horizontal plane can be attributed to changing horizontal ejection conditions of the AGS.

4 THE INJECTION PROGRAM

The injection tuning program guides the beam from the pitching magnet yp1 through the kicker magnets yki1 through yki4 (see Fig. 1). The horizontal and vertical phase space coordinates at yp1 are constructed from two position measurements in each plane upstream of yp1. The horizontal and vertical phase space coordinates at the kickers are obtained from a pair of beam position monitors in each plane downstream of yki4. From the measured phase space coordinates at the kickers a pair of horizontal and vertical correctors in each plan is set to correct for the deviations. Correctors between yp1 and yk1 can be set manually. The graphical user interface of the program is shown in Fig. 6.

However, the initial steering in the injection region was done with beam loss monitors since the beam position monitors were not available at this time. Later the injection tuning program could be tested only for the horizontal plane and without the injection kickers. A test result is shown in Fig. 7.

5 CONCLUSION

Although there is no ample space for the the beam injection into RHIC, the injection process during the sextant went very well. In addition, the kickers performed as expected, even exceeding the rise time requirements.

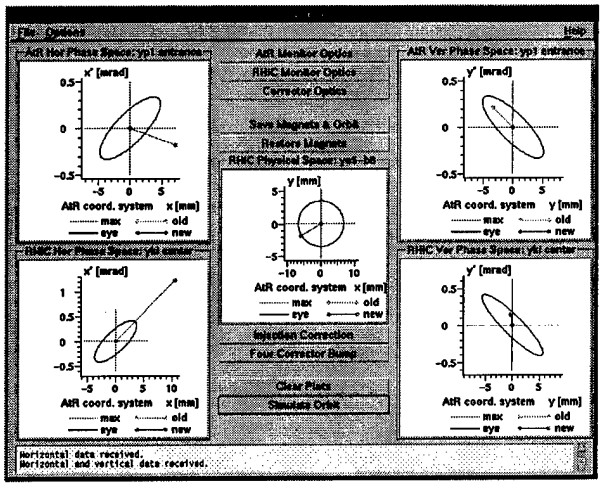


Figure 6: Graphical user interface for the injection tuning program.

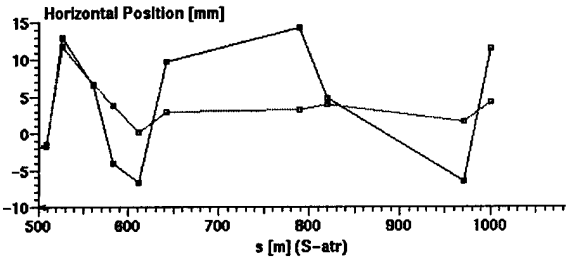


Figure 7: Correction of the horizontal orbit at injection.

6 ACKNOWLEDGMENTS

We are thankful to all engineers, technicians and operator for their support, especially to R. Sanders and J. Touzzolo for the supervision of the construction and installation of the kickers and pulsers.

7 REFERENCES

[1] "The RHIC design manual" Revision of September 1995.

[2] W.W. MacKay, "AGS to RHIC Transfer Line: Design and Commissioning", EPAC proceedings (1996).

[3] T. Satogata, "Physics of the AGS to RHIC Transfer Line Commissioning", EPAC proceedings (1996).

[4] F. Pilat et al., "RHIC Sextant Test – Accelerator Systems and Performance", these proceedings.

[5] J. Wei et al., "RHIC Sextant Test – Physics and Performance", these proceedings.

[6] N. Tsoupas et al., "Focusing and Matching Properties of the AtR Transfer Line", these proceedings.

[7] H. Hahn, J.E. Tuozzolo and N. Tsoupa, "The RHIC Injection Kicker", these prceedings.

THE RHIC INJECTION KICKER

H. Hahn*, N. Tsoupas, and J. E. Tuozzolo,
Brookhaven National Laboratory, Upton, New York 11973

Abstract

Beam transfer from the AGS to RHIC is performed in single-bunch mode. Close spacing of the bunches in the collider requires an injection kicker with a rise time of <90 nsec, suggesting adoption of a travelling wave structure. The required vertical kick of 0.186 T·m is provided by 4 magnets, each 1.12 m long with a 48.4 × 48.4 mm aperture and operated at 1.6 kA. The kicker is constructed as a "C" cross section magnet, in which ferrite and high-permittivity dielectric sections alternate. The dielectric blocks provide the capacity necessary for the nominally 25 Ω characteristic impedance of the travelling wave structure, but impose the practical limit on the peak voltage, and thus current, achievable. Computer studies to minimize local electric field enhancements resulted in a configuration capable of holding ~50 kV, with adequate safety margin over the nominal 40 kV. Equivalent circuit analysis indicated the possibility of lowering the nominal voltage by operating mismatched into 20 Ω terminations without degrading the pulse shape. In this paper, the experience gained in the fabrication of the production units and the results from various single-unit tests and operation of four kickers with beam in the "Sextant Test" are reported.

1 INTRODUCTION

The design of the RHIC injection system was dominated by the requirements of the strength and risetime of the fast kicker. The kicker has to provide a vertical deflection of 1.86 mrad for beams with a $B\rho$ = 100 Tm. The available free space for the four kickers limits their effective length to 1.12 m each. Neglecting any contribution from the electric field, the deflecting magnet field is required to be 415 G inside the beam tube. This leads, with the horizontal aperture of 4.84 cm, to the current requirement of 1.6 kA. The kickers are each powered from a Blumlein pulser which is designed for 50/2 Ω, imposing a characteristic impedance of 25 Ω and a nominal voltage of ~40 kV in the kicker. Injecting beam from the AGS to RHIC is performed by single-bunch transfer into stationary buckets of the acceleration rf system at 24.15 MHz. Transfer of 120 bunches, as intended in a design upgrade, requires filling of every third bucket, spaced 107 nsec apart. The ion bunches are expected to be <15 nsec long, leading to a risetime requirement (1 - 9%) of <90 nsec in deflection or ~45 nsec in current. During the bunch length, the flat top requirement is ±1%, easily achieved with the 100 nsec long pulse. At the end of the injection process, a gap of ~1 μsec will be left to facilitate the beam abort, implying that there is no severe constraint on the fall time.

The risetime requirement suggested the adoption of a transmission line structure. Using a CERN-type "plate-kicker" is the quasi-standard solutio to achieve fast rise times[1]. Replacing its lumped capacitors by high-permittivity ceramic blocks promised to be simpler, more compact, and thus more economical. Following concepts contemplated at SLAC[2, 3], the original design for the RHIC injection kicker was generated by Forsyth, et al.[4]. The kicker R&D program with the results from half-length models demonstrated the viability of this solution. However, it became evident that the specifications for the RHIC kicker are at the limit of what can be expected from this type of kicker; furthermore sharp resonances in the coupling impedance made appropriate design changes imperative[5]. A modified design of the kicker core and the development of special tooling and fabrication procedures then made the production of full-size kickers for operation in the "Sextant Test" possible.

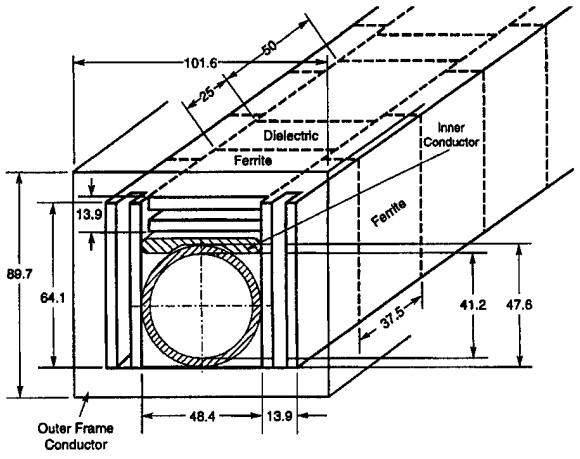


Figure 1: RHIC injection kicker configuration (Dimensions in mm). Only the end blocks are slotted.

2 KICKER CONFIGURATION

The kicker is configured as a "C" magnet with interspersed ferrite[6] and dielectric[7] blocks as shown in Fig. 1. On the top, there are 14 × 1 in. dielectric and 15 × 2 in. ferrite blocks. The field in the ferrite reaches here 2.13 kG at the nominal 415 G in the gap. The ferrite in the sides, although in principle continuous, must be assembled from 1.5 in. long blocks to avoid eddy currents.

* Work performed under the auspices of the U.S. Department of Energy

0-7803-4376-X/98/$10.00 © 1998 IEEE

The design objective of 40 kV across the 1.39 cm thick blocks results in a nominal field of 29 kV/cm. This is below published values, ~60 kV/cm, for similar dielectrics such as sintered titania-rutil[8], or barium titanate[9]. However, the manufacturers of our materials provided no information (or warranty) as to their electric breakdown limits. Thus, prior to their assembly, all incoming blocks were tested in Fluorinert between parallel plates to 60 kV with millisec pulses. The test voltage for the dielectric and ferrite blocks is thus 50% above the nominal design requirement. There is reason to assume, that higher fields can be reached with nanosec pulses, especially in the ferrite where eddy currents play an important role.

The nominal electrical field of 29 kV/cm is also significantly below the reported electric breakdown strengths of epoxy and RTV (~300 kV/cm)[10]. Epoxy is used to form the magnet core consisting of the ferrite/dielectric blocks with the busbar (i.e. the inner conductor), and RTV is used in the final assembly of the core into the frame. However, due to the large ratio of $\epsilon_{diel}/\epsilon_{epoxy} \sim 30$, correspondingly larger fields can exist in an epoxy layer over the dielectric and must be avoided. Prior to its final assembly the kicker core is machine-ground with a diamond wheel to remove any epoxy from the surface and to assure direct contact via an indium layer with the frame.

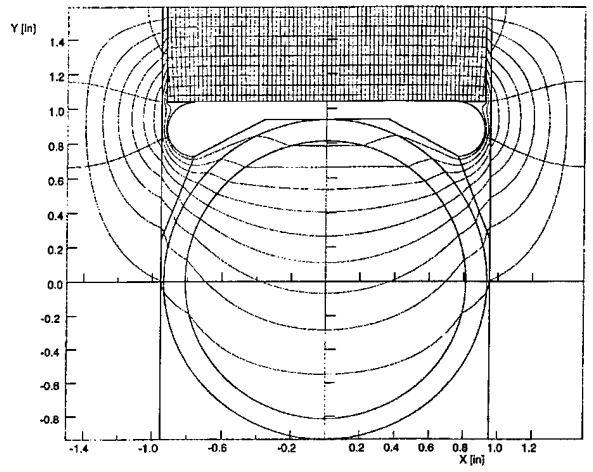


Figure 2: Electric field lines in a cross section at the center of the dielectric blocks.

Searching for a solution which minimizes local field enhancements while retaining a maximum capacitance lead to an extensive experimental and theoretical R&D program. Electrostatic computations using the OPERA-2d program were performed to establish the peak electric fields and their location in the core. The design was optimized by focussing on the geometry of the dielectric block and the details of its contact with the busbar, established by a 4 mil indium layer. The obvious ideal condition is a dielectric block between two infinite parallel plates, but finding the best approximation required numerous computations and their experimental verification by tests on almost a dozen half-length models. Tests were done on magnet cores with dielectric blocks ranging from 1.5 to the original 3 in. width while maintaining the same overall dimensions and busbar geometry. The two-dimensional electric field lines and equipotentials in a cut through the center of the dielectric block is shown in Fig. 2.

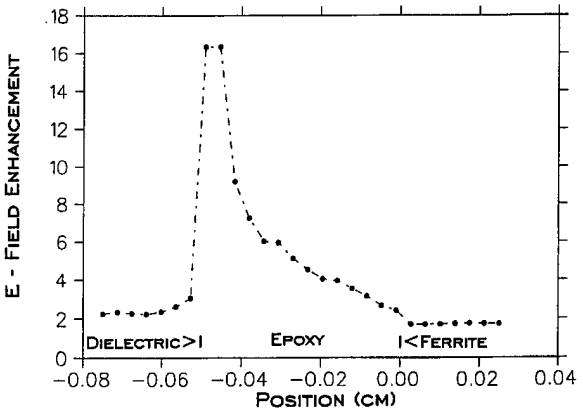


Figure 3: Electric field components on a line in beam direction through the dielectric block (at left), the epoxy layer, and the ferrite block (at right).

The boundary conditions of the time-varying electric components of the TEM mode in the kickers are identical to those of two-dimensional static electric fields. Thus the electrostatic field computations with the OPERA-2 program provide correct results for the pulsed electric fields at the center of the blocks, and a good approximation over a large fraction of the blocks. However, the fields at the ferrite-dielectric interface are three-dimensional and have been addressed by separate computations. The electric field components on a line in beam direction through the blocks at the location of the peak field is shown in Fig. 3. The results confirmed the assumption that the disturbance due to the epoxy layer is highly localized and that the fields are essentially two-dimensional in the blocks. The three-dimensional peak field enhancement in the dielectric blocks of the present design were found to be 3.5 at the corner versus the 2.2 at the center.

3 KICKER PERFORMANCE

As of today, six full-size production kickers have been built. The first four were assembled with MCT-100 blocks resulting in a characteristic impedance of 28.6 Ω. Starting with kicker #5, MCT-125 blocks were used in order to reduce the impedance to ~25 Ω.

Direct measurement of the kicker performance without beam is effectively limited to the current in the termination load and the Blumlein charging voltage, but its value is not rigorously equal to the voltage at the kicker input end. Half-length models were tested at 50 kV for ~1M pulses without degradation, and all production units are

verified to reach the nominal 40 kV. In the Sextant Test, the kicker magnets were terminated with 20 instead of the nominal 25 Ω as a precaution in order to gain safety margin against voltage breakdown. An equivalent circuit analysis substantiated the observation that the current pulse shape is only minimally changed[11]. The measured load current in kicker #5, terminated with 20 Ω is shown in Fig. 4 and with a different time scale in Fig. 5. The mismatch causes an "after-pulse," about 850 nsec after the peak of the deflection, due to a reflected signal returning to the pulser and there being reflected again. The after-pulse, by serendipity, falls between the 4th and 5th beam pulse after the injected bunch, if the design 60-bunch injection is attempted. In any case, the after-pulse falls within the ~1 μsec beam dump gap. Measurements in the Sextant Test with beam confirmed that 1.6 kA (or ~32 kV across the 20 Ω) provide the required deflecting strength with a risetime of <90 nsec[12].

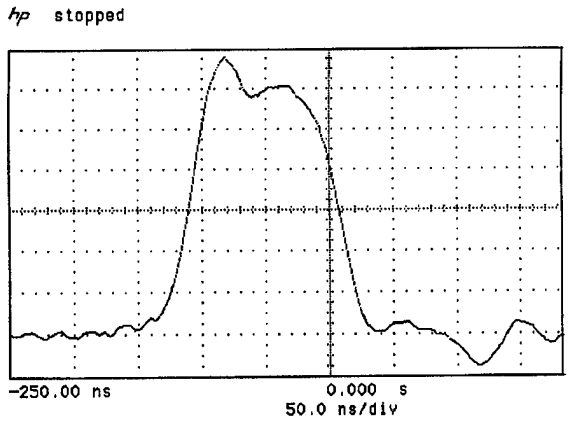


Figure 4: Load current.

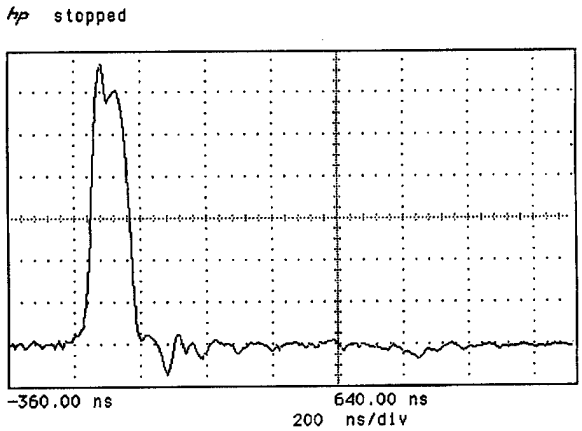


Figure 5: Load current with "after pulse" at 850 nsec.

4 ACKNOWLEDGEMENTS

The authors would like to thank A. Bera, K. Hartmann, C. Rhein, J. Slavik, J. Walsh, A. Wisowaty, and R. Zapasek for their efforts during the R&D program and the manufacturing and testing of the production magnets.

5 REFERENCES

[1] D. Fiander, Proc. 1971 IEEE Part. Acc. Conf., Chicago, Ill., p. 1022.

[2] F. Bulos and A. Odian, Report SLAC-PUB-3453, CN-279 (1984).

[3] R. Cassel (private communication).

[4] E. B. Forsyth, et al, Proc. 1995 Part. Acc. Conf., Dallas, TX, p. 1921.

[5] H. Hahn, N. Tsoupas, J. E. Tuozzolo, BNL Report AD/RHIC/RD-109 (1997).

[6] CMD-5005, Nickel-Zinc ferrite with high permeability and resistivity for use at frequencies up to ~100 MHz and a dielectric constant of ϵ ~10, Ceramic Magnetics, Fairfield, NJ.

[7] MCT-125, Sintered mixture of Magnesium Titanate and Calcium Titanate with high dieletric constant ϵ ~125, Trans-Tech, Adamstown, MD.

[8] Gmelins Handbuch - Titan, vol. 41, p. 250, (Verlag Chemie, Germany, 1951).

[9] B. Ritscher, Valvo Berichte, vol. VIII-4, p. 110 (1962).

[10] F. B. A. Fruengel, "High Speed Pulse Technology," (Academic Press, 1980) vol. 1, p 12.

[11] H. Hahn and A. Ratti, "Equivalent Circuit Analysis" (these proceedings) and BNL Report AD/RHIC/RD-112 (1997).

[12] W. Fischer, et al (these proceedings).

EQUIVALENT CIRCUIT ANALYSIS OF THE RHIC INJECTION KICKER

H. Hahn*and A. Ratti†, Brookhaven National Laboratory, Upton, New York 11973

Abstract

The RHIC injection kicker is built as a travelling wave structure in order to assure the required 95 nsec risetime in the deflection strength. The kicker is constructed from 14 cells, each 7.5 cm long, with alternating ferrite and high-permittivity dielectric sections. The cell structure permits an analysis of the electrical properties of the kicker using lumped L, C, and R circuit elements. Their values are obtained directly from impedance measurements of the full-length kicker, the inductance and shunt capacitance values by measuring the input impedance at 1 MHz with the output shorted and open, respectively. A lossy series resonance circuit in each cell is found to reproduce the measured input impedance of the terminated kicker up to ~100 MHz. The validity of the equivalent circuit was confirmed by comparing the measured output current pulse shape time with that computed by the P-Spice program.

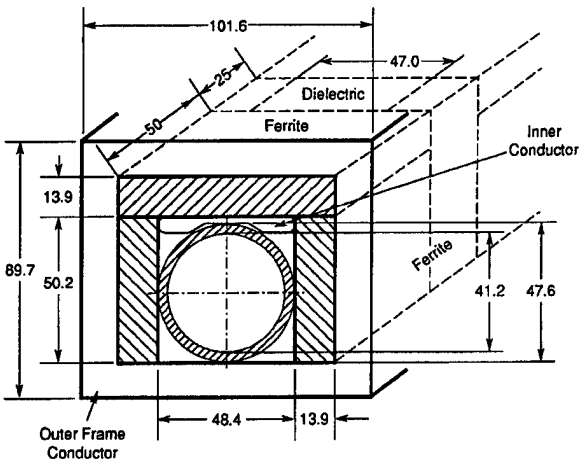


Figure 1: RHIC Injection Kicker Configuration.

1 INTRODUCTION

The RHIC injection kicker was conceived as a transmission line magnet in order to achieve the required rise time of < 95 nsec[1]. The kicker is configured from ferrite and dielectric blocks as a "C" type magnet with its geometry shown in Fig. 1. The deflecting properties of the kicker are dominated by the magnetic field and thus by the geometry and properties of the ferrite blocks. The nickel-zinc ferrite (CMD-5005 by Ceramic Magnetics) has a high permeability and resistivity for use at frequencies up to ~100 MHz. Although in principle continuous at the side, the ferrite must be subdivided to limit eddy current effects. The capacity required to achieve the transmission line behavior is predominantly provided by the dielectric ceramic blocks, a sintered mixture of magnesium and calcium titanate (MCT-125 by Trans-Tech) with high dielectric constant, $\epsilon = 125$, to achieve the characteristic impedance of 25 Ω. The contribution to the capacity from the ceramic beam tube is negligible, and for convenience sake, all kicker measurements were made without it.

The original kicker design was based on an equivalent circuit analysis of a low-pass filter with lumped L and C elements[2]. In a subsequent paper, the kicker was treated as a transmission line with uniform, albeit anisotropic properties in order to establish a better correlation of geometrical with electrical parameters[3]. In an attempt to estimate the current rise time from the low-pass band width, the kicker was treated as a cascaded chain of transmission lines with different characteristic impedances and propagation velocities[4]. Although useful, the simple equivalent circuits presented so far are limited and do not allow a reliable prediction of the kicker performance resulting from engineering changes or from varied operational conditions, such as the mismatched 20 Ω termination used in the Sextant Test. In this paper, an equivalent circuit for a generalized low-pass filter with lumped elements is presented, which was obtained from direct measurements of the kicker. The P-Spice program was then used to simulate the kicker performance and the comparison with experimental data showed fully satisfactory agreement[5].

2 EQUIVALENT CIRCUIT

The RHIC injection kicker is constructed as a low-pass filter with 14 cells, each 7.5 cm long, with alternating ferrite and high-permittivity dielectric sections, thereby approximating a transmission line magnet. The cell structure permits an analysis of the electrical properties of the kicker using an equivalent circuit with lumped L, C, and R elements. Their values are obtained directly from input impedance measurements of the full-size kicker in the frequency range up to ~100 MHz. Discussed here in detail is the production kicker #5, in which the MCT-125 dielectric blocks are used.

The inductance is obtained from the input impedance at 1 MHz with the output port shorted. The total inductance was measured to be 1.59 μH, resulting in 106 nH for each of the 15 series inductors. At frequencies below the λ/4 resonance, 4.757 MHz, the input impedance of the shorted

* Work performed under the auspices of the U.S. Department of Energy
† Present address: LBNL, Berkeley, CA 94720

0-7803-4376-X/98/$10.00 © 1998 IEEE

kicker is given by $Z_{in} = Z_K \tan(\frac{1}{2}\pi f/f_{\lambda/4})$, from which follows the characteristic impedance of the kicker as $Z_K \approx 26\ \Omega$.

The capacitance is obtained from the input impedance at 1 MHz with the output port open. The total capacitance was 1.99 nF, resulting in ~140 pF for each of the 14 dielectric blocks. The measured input impedance of the kicker terminated with the nominal 25 Ω is shown in Fig. 2. The pronounced resonance at 64 MHz can be represented by a lossy series resonance. This resonance is associated with eddy currents in the ferrite side blocks, as established by a series of measurements with side blocks of different lengths. The circuit elements, and in particular the damping resistors, were adjusted to render the strength of the resonances in the open and shorted condition.

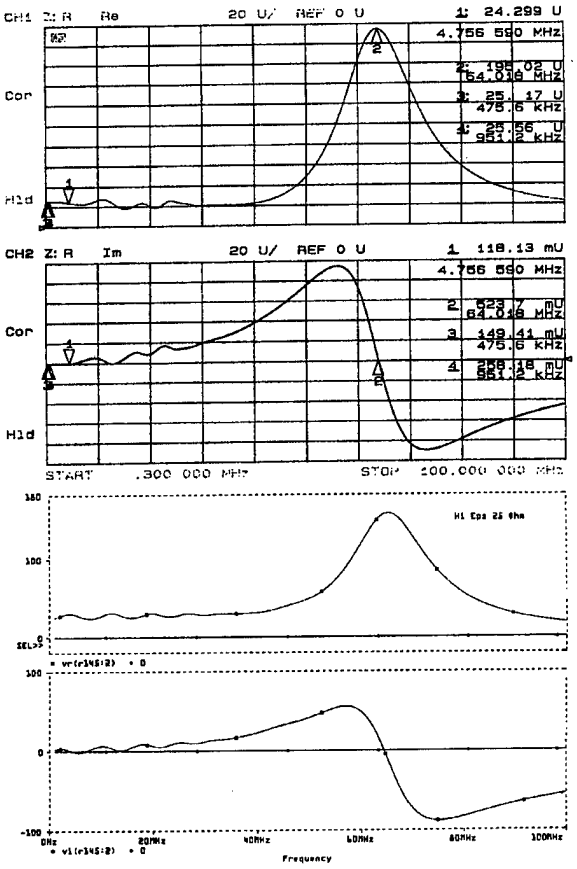


Figure 2: Measured input impedance of kicker with matched output port termination and comparison with P-Spice computations.

Using the equivalent circuit shown in Fig. 3, the P-Spice computed input impedances for the output port terminated in the design 25 Ω are compared with the measured results in Fig. 2. As seen, the agreement is quite satisfactory and establishes the confidence, that dependable predictions of the kicker performance can be made based on the equivalent circuit diagram. Of interest are, for example, the kicker response to a step function voltage, the operation of the kicker with a 20 Ω termination to reduce the voltage requirement, and the estimate of the longitudinal coupling impedance in the frequency range below 100 MHz for which the equivalent circuit is applicable[6].

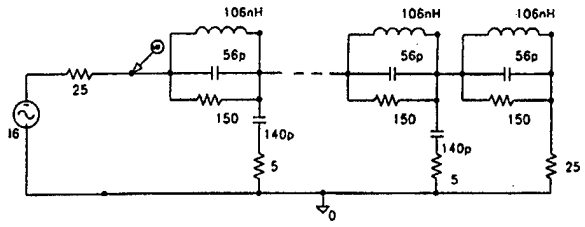


Figure 3: Equivalent circuit of injection kicker. Only 3 of the 14 dielectric capacitors in a full-length kicker are shown.

3 TIME DOMAIN KICKER PERFORMANCE

Having established the equivalent circuit based on measurements in the frequency domain, it is now possible to predict the kicker performance in the time domain by means of P-Spice computations. Measurement of the performance of the kicker without beam is effectively limited to the current in the output load. The charging voltage on the Blumlein pulser can also be measured, but its value is not rigorously equal to the input voltage at the kicker.

The kicker load current in production unit #5 terminated into 25 Ω is shown in Fig. 4 for a ~40 kV pulser voltage, which satisfies the nominal design requirement of 1.6 kA. The measured current is in good agreement with the P-Spice computation. Also shown is the computed "effective kicker current," which renders the rise time of the deflecting force and, neglecting the 3 nsec ion transit time, is obtained by averaging the instantaneous current in the 15 series inductors. The computed rise time of the effective current is ≤100 nsec in full agreement with the Sextant Test beam measurements[7].

The pulse propagation time in the 1.12 m long kicker was directly measured by means of uncalibrated capacitive probes at the input and output ends. The two signals are shown in Fig. 5; by using a single trigger, the propagation time was directly measured to be ~50 nsec, in excellent agreement with the theoretical prediction based on a propagation velocity of $v/c = 0.07$. The measured value is also in agreement with the computed P-Spice predictions as seen in Fig. 5, where the the voltages at the input, at the first dielectric block and at the load are shown.

4 EQUIVALENT CIRCUIT ANALYSIS OF COUPLING IMPEDANCE

The analytical treatment of the kicker coupling impedance at low frequencies, i.e. below ~100 MHz, is instructive but limited and can be complemented with the use of equivalent circuits[6]. An appropriate model seems to be a multi-cell

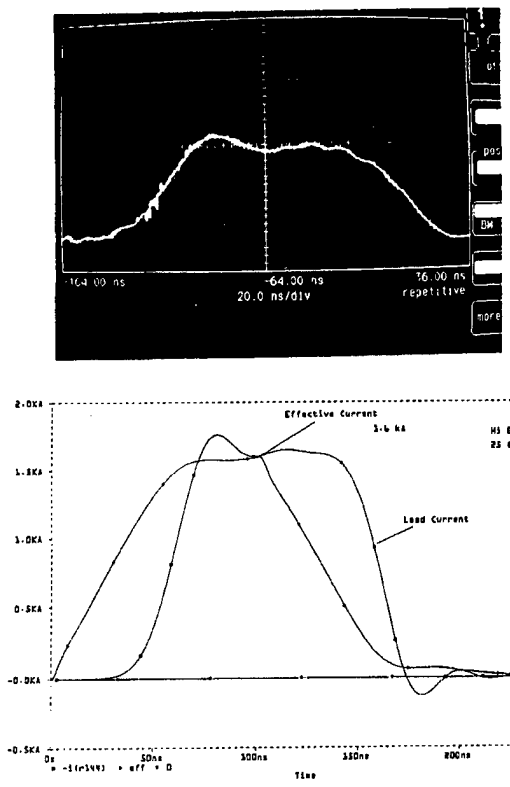


Figure 4: Measured load current at 500 A/division and comparison with P-Spice computed curve. The computed "effective" current represents the average of currents in the 15 series inductors and is an estimate of the time-dependent kicker deflecting strength.

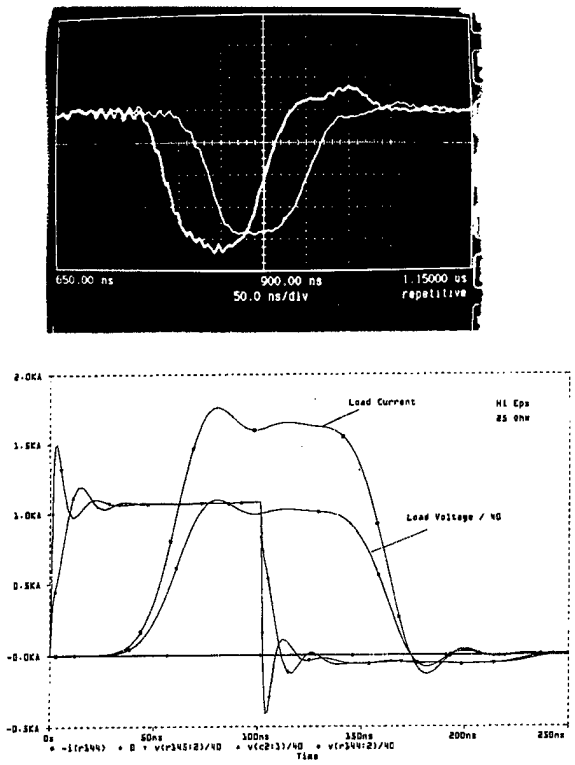


Figure 5: Measured voltage of pulse at input and output end of the kicker. The measured transit time of ~50 nsec is confirmed by the P-Spice computations.

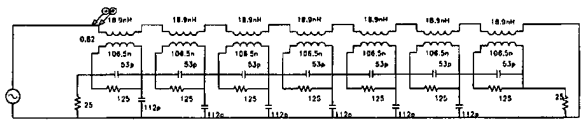


Figure 6: Equivalent circuit representation for the P-Spice computation of the kicker coupling impedance.

section low-pass filter with lumped elements, shown in Fig. 6 for a half-size kicker model. Having established the equivalent circuit of the kicker alone, one can add the beam as a series of magnetically coupled inductors, the values of which are determined from impedance wire measurements $L_B = 18.9$ nH and $\kappa = 0.82$. The coupling impedance computed by the P-Spice program at low frequencies has been compared with the results from the "wire" measurements[6]. The agreement is reasonable considering the possible errors in measurement and the limitations of the model.

5 REFERENCES

[1] H. Hahn, et al, "The RHIC Injection Kicker," (these Proceedings).

[2] E. B. Forsyth, et al, Proc. 1995 PAC, Dallas, TX, p. 1921 (IEEE, 1996).

[3] H. Hahn and E. B. Forsyth, EPAC 94 London, vol. 3, p. 2550.

[4] H. Hahn, BNL Report AD/RHIC/RD-66 (1994).

[5] H. Hahn and A. Ratti, BNL Report AD/RHIC/RD-112 (1997).

[6] H. Hahn and A. Ratti, "The Coupling Impedance of the RHIC Injection Kicker System," (these Proceedings). BNL Reports AD/RHIC/RD-105 and AD/RHIC/RD-111.

[7] W. Fischer, H. Hahn, W. W. MacKay, T. Satogata, N.Tsoupas, and W. Zhang, "Beam Injection into RHIC," (these Proceedings).

A STUDY OF BETATRON AND MOMENTUM COLLIMATORS IN RHIC *

D. Trbojevic, A.J. Stevens, M.A. Harrison, F. Dell, and S. Peggs
Brookhaven National Laboratory, Upton, NY, 11973, USA

Abstract

The Relativistic Heavy Ion Collider (RHIC) has two interaction regions where β^*=1-2m, with large detectors PHENIX and STAR. The transverse and longitudinal emittances are expected to double in size between one to two hours due to intra-beam scattering which may lead to transverse beam loss. Primary betatron collimators are positioned in the ring to allow efficient removal of particles with large betatron amplitudes. We have investigated distributions and losses coming from the out-scattered particles from the primary collimators, as well as the best positions for the secondary momentum and betatron collimators.

1 INTRODUCTION

A primary goal of the Relativistic Heavy Ion Collider (RHIC) is to provide collisions of heavy-ions at six interaction regions (IR). Two IR are designed to be at a β^*=1-2 m to allow for luminosities of the order of L=$10^{27} cm^{-2} s^{-1}$. Two large detectors, STAR and PHENIX, are located at the high luminosity regions. The strong focusing quadrupoles at opposite sides of these two IP-s are the limiting apertures due to the large betatron amplitude functions of the order of $\beta \sim$ 1500 m. There will be collisions between different ion species as well as between polarized protons. The six dimensional emittance of the heavy ion beams is expected to double in size due to intra-beam scattering between one to two hours. Particle amplitudes can also grow due to other effects like beam gas interaction, beam diffusion due to the nonlinear beam dynamics etc. This results in beam loss at limiting apertures at the triplet magnets close to the large detectors. This beam loss created hadronic showers which leads to larger than desirable backgrounds in detectors. To reduce this background it is necessary to scrape the unwanted beam. The primary betatron collimator has to be able to remove particles with large amplitudes. This report studied the distribution of scattered particles from the primary collimators and their propagation throughout the RHIC accelerators. The optimum location for the secondary betatron and momentum collimator are reported.

2 PRIMARY COLLIMATORS

Positions of the primary collimators in the two (*blue* and *yellow*) rings are downstream of the large PHENIX detector at locations with high β value. The efficiency of the betatron collimator depends on the value of the betatron amplitude function. The best possible location is immediately downstream end of the high focusing quadrupoles where $\beta \sim$1000 m. Interaction of the gold ion and proton beams with the collimator target has been performed by using a computer code written by Van Ginneken [1]- [2]. The out-scattered particles were obtained in two steps:
-The betatron amplitude of particles in the ring is increased by a diffusion process based on measurements at the SPS-CERN [3]. The amplitude grows continuously if it reaches amplitudes larger than 4 σ.
The upstream edge of the collimator is set at 5.5 σ with a slope which corresponds to the betatron function slope. The emittance of the heavy-ions (gold) is assumed to be 40 π mm mrad, and 20 π mm mrad for the proton beam. The particles' orbit is tracked through the 0.45 m long collimator. Any orbit which emerges from the collimator without having inelastically interacted creates an initial particle distribution for further studies. Figure 1 represents the initial horizontal phase space of the gold ions orbits at nominal energy of 100 GeV/nucleon scattered from the primary collimator. The angle of the scattered ions is very narrow (as shown in 1).

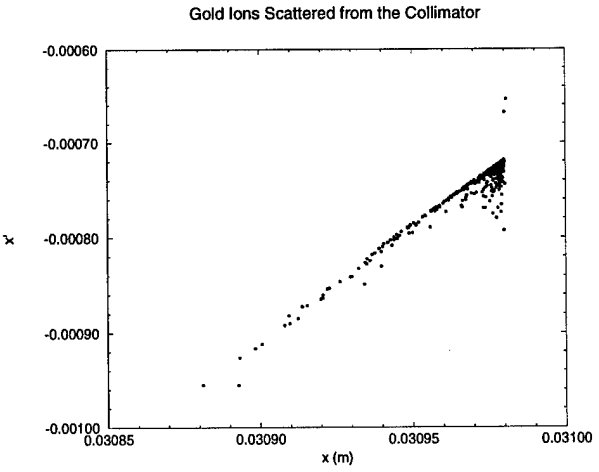


Figure 1: Initial distribution of gold ions scattered from the primary collimator

The momentum distribution of the scattered particles from the collimator shows (see Figure 2) that a large number of particles have momentum offsets much larger than the projected RHIC bucket size at storage $\sigma_p \pm 0.2\%$.

3 PHASE SPACE DISTRIBUTION OF THE SCATTERED PARTICLES

This initial particle distribution was then used as input for the tracking program TEAPOT [4]. The tracking was performed with the systematic and random multipoles within

* Work performed under the auspices of the U.S. Department of Energy

0-7803-4376-X/98/$10.00 © 1998 IEEE

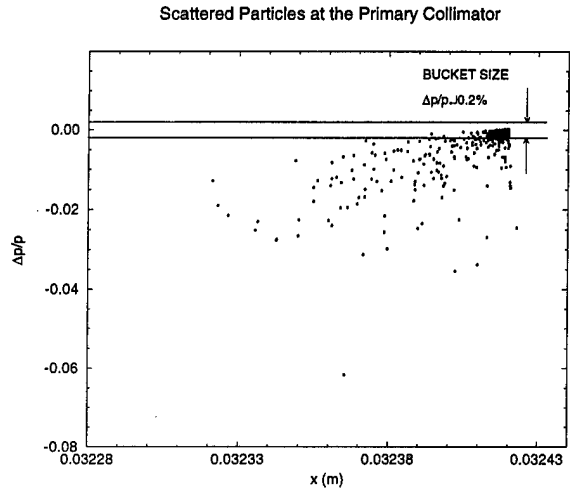


Figure 2: Initial momentum distribution of gold ions scattered from the primary collimator versus horizontal position.

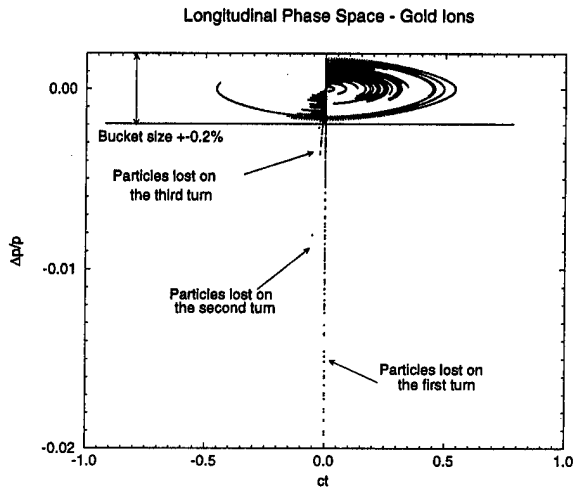


Figure 3: Longitudinal tracking

the quadrupoles and dipoles obtained from the measurement data, at the top energy of 100 GeV/nucleon for gold or 250 GeV for protons and for 256 turns. The misalignment and roll errors were estimated from the surveying data. The rms values for misalignment used for the arc quadrupoles were Δx,y=0.5 mm $\Delta\theta$=0.5 mrad, while from the measurements of the triplet quadrupoles the roll and misalignment errors for the rms values were $\Delta\theta$=0.5 mrad and Δx,y=0.5 mm.

3.1 Longitudinal Phase Space

During tracking the RF voltage was included and the longitudinal motion of the surviving particles was monitored. Particles with momentum offsets within the bucket size limit executed synchrotron oscillations. Particles projections in the longitudinal phase space show in Figure 3 that only particles within the bucket survive. Only few particles, which survived all 256 turns, finished almost one synchrotron oscillation. The phase space, shown in 3, is at the location downstream of the primary collimator.

3.2 Transverse Phase Space Distribution

The transverse positions of the scattered particles on the first turn show that most of the particles with large momentum offsets, are lost around the first bending elements. The particle distributions at different locations are presented in the normalized phase space:

$$\xi = \frac{x}{\sqrt{\beta}} \quad and \quad \chi = x'\sqrt{\beta} + \frac{x\alpha}{\sqrt{(\beta)}} \qquad (1)$$

Locations with the betatron phase differences of $\sim 30^o, 165^o$ with respect to the position of the primary collimator, have been shown to be preferable [5] positions for the secondary scraper. One of the suitable positions (*Q9-D9 in th RHIC lattice*) for the secondary collimator is shown in Figure 4. The phase difference is 165^o.

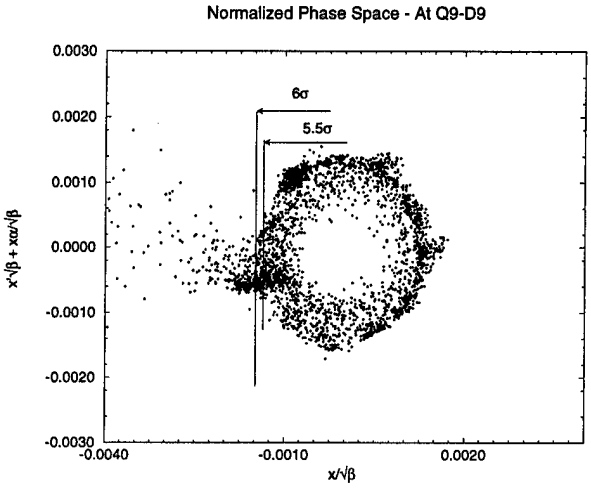


Figure 4: Possible position of the secondary collimator

3.3 Particles' momenta at the secondary scraper

Figure 5 represents projections of the particles positions at the possible secondary collimator but in a different space. The horizontal axis represents particles' momenta, while the vertical axis is chosen for their horizontal positions. This plot shows another advantage of having the secondary scraper at this location. When the secondary scraper is set to a horizontal offset larger than 7σ, particles out of the bucket are eliminated. It should be noted that the dispersion function has a large value at this location.

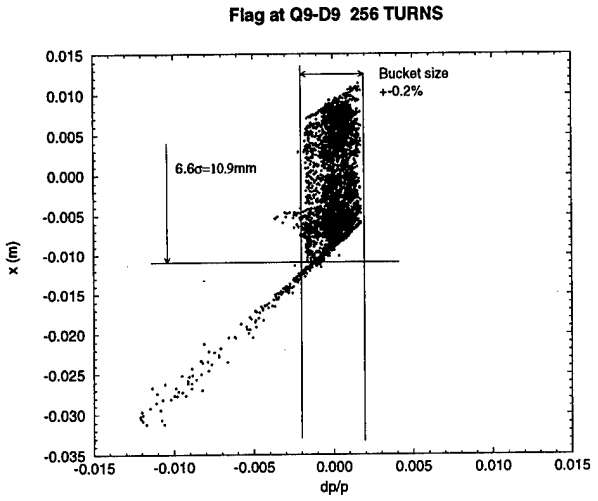


Figure 5: Horizontal positions of gold ions scattered from primary collimator at the secondary collimator with respect to their momenta.

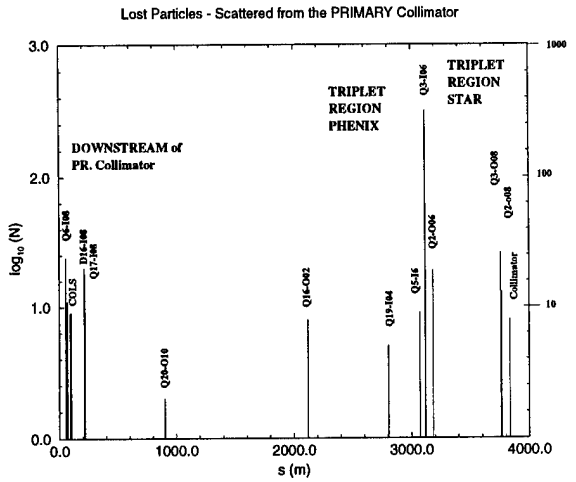


Figure 6: Losses around the ring from the primary collimator

4 BEAM LOSS LOCATIONS IN THE RING

The primary betatron collimators will reduce the background at the RHIC detectors, eliminating particles with the large betatron amplitudes. On the other hand the scattered particles from the primary collimator could influence the background if they get lost upstream of the detectors. At the large detectors with $\beta^* = 1m$ the strong focusing quadrupoles have their effective apertures reduced, due to the large values of the β functions. The losses of the scattered particles from the primary collimator occur at these quadrupoles, as shown in Figure 6. The lost particles are presented on a logarithmic scale. Figure 6 also shows losses at a set of magnets downstream of the primary collimator which are mostly due to the large momentum offset particles. The largest number of lost particles is at the strong focusing quadrupoles.

5 CONCLUSIONS

The primary collimators in RHIC are important for many reasons:

- To remove the beam halo and reduce the background noise for the detectors.
- As a very good tool for beam diagnostics [5]: acceptance measurements, transverse particle distribution of the beam, frequency analysis of the beam loss rate, etc.

A combination of the primary and secondary betatron collimators can be used to remove not only the scattered particles from the primary collimator but also to remove particles out of the buckets. The secondary betatron collimators are effective only if the betatron phase difference between the two scraping stages is correctly chosen. Efficient momentum collimation [6] had already been reported at the same location, as it is the optimum position of the secondary betatron collimator (found in this study). It would be possible to create *macro buckets* with the use of the RHIC 28 MHz cavities to trap the particles outside of the buckets and scrape them [6]. The secondary collimator position determined in this study removes particles with large momentum offsets scattered from the primary collimator. It should be noted that losses from the primary collimators will still be the same in the region between primary and secondary collimators. The spray at the triplets with the high values of β functions exists although it is significantly reduced.

6 REFERENCES

[1] A.Van Ginneken, *Elastic scattering in thick targets and edge scattering*, Physical Review D, Vol. 37, number 11, 1 June 1988, pp.3292-3307.

[2] A.Van Gineken, *ELSHIM, Program to simulate Elastic Processes of Heavy Ions*, BNL-47618, AD/RHIC-100, Informal Report, May 1992.

[3] W. Fischer, M. Giovannozzi and F. Schmidt, "Dynamic aperture experiment at a synchrotron", Phys. Rev. E, Vol. 55, Number 3, p. 3507 (1997).

[4] L.Schachinger and R. Talman, *A Thin Element Accelerator Program for Optics and Tracking*, SSC Central Design Group, Internal Report SSC-52 (1985).

[5] M. Seidel, *The Proton Collimation System of HERA*, Dissertation, DESY 94-103, June 1994, Hamburg 1994.

[6] S. Peggs and G.F. Dell, *Momentum Collimation at Q9*, Report-no:RHIC/AP/78, November 1995

FOCUSING AND MATCHING PROPERTIES OF THE ATR TRANSFER LINE*

N. Tsoupas, W. Fischer, J. Kewisch, W.W. MacKay, S. Peggs
F. Pilat, S. Tepikian, J. Wei
Brookhaven National Laboratory, Upton, NY 11973

Abstract

The AGS to RHIC (AtR) beam transfer line[1] has been constructed and will be used to transfer beam bunches from the AGS machine into the RHIC machine which is presently under construction at BNL. The original design of the AtR line[1] has been modified. This article will present the optics of the various sections of the existing AtR beam line, as well as the matching capabilities of the AtR line to the RHIC machine.

1 THE ATR LINE

The AtR beam transfer line, has been constructed and commissioned[2],[3],[4],[5] by extracting ^{+77}Au beam bunches of momentum 11.2 GeV/c per nucleon, injected from the AGS machine. A schematic layout of the accelerator complex at BNL is shown in Fig. 1. A more detailed diagram of the AtR line is shown in Fig. 2. The AtR line is purposely partitioned into four main sections: U-line, W-line, X- and Y-lines, and the injection sections, one following the X-line and the other the Y-line. This partition facilitates the optical design of the AtR , because each section can be studied independently. A description and the beam optics of each section of the AtR will be discussed next.

1.1 The U-line

The U-line is the first section of the AtR beam line (Fig. 2) which starts at the AGS Fast Extraction Beam (FEB) point[6] H13 and terminates at the entrance of the first magnetic element of the W-line. The U-line has two right bends, one 4.25° made of two A-type dipole magnets[7] modified from a 29 mm gap to 39.6 mm gap, and the other 8° of four C-type combined function magnets[7] (placed in a FDDF arrangement), and thirteen quadrupoles. The U-line has the following functions:

- Match the Twiss parameters at the AGS extraction point[6] H13 (Fig.1) and create an achromatic beam (η_x=0, η'_x=0) at the exit of the 8° bend
- Create a beam waist with low beta function values at the location of a thin gold foil which is placed just upstream of the quadrupole Q6 of the U-line. The gold foil, strips[8] the two K-shell electrons from the ^{+77}Au ions, and other heavier ions.
- Match the Twiss parameters of the line to the ones at the origin of the W-line
- Maintain a reasonable upper limit of the beta functions along the line, so that beam with 95% normalized emittance $\pi\epsilon = 20\pi$ $(mm.mrad)$ will not extend more than half of the available beam tube radius

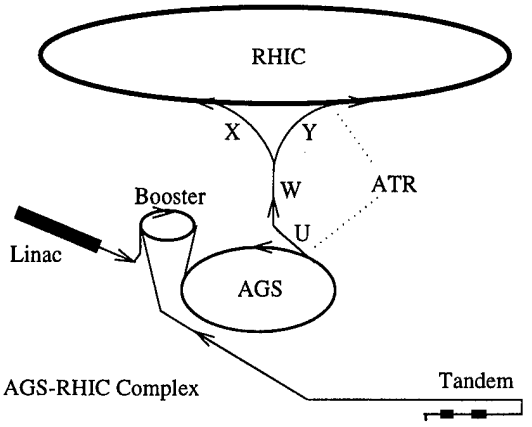


Fig. 1. Layout of the AGS-RHIC complex with the AtR transfer line.

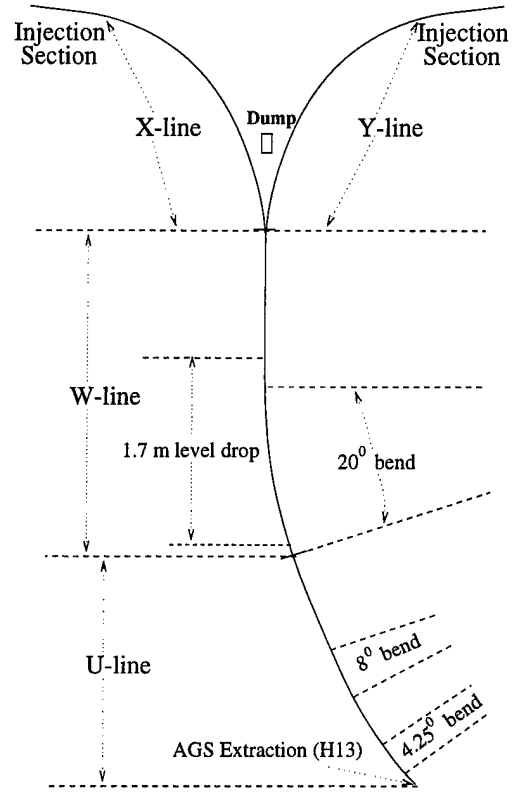


Fig. 2. Layout of the AtR transfer line with the U,W,X,Y lines and Injection sections.

Although the AGS Twiss parameters at the extraction point H13 depend on the extraction conditions[6], the AtR

* Work performed under the auspices of the US DOE

0-7803-4376-X/98/$10.00 © 1998 IEEE

line has the capability to satisfy all constraints mentioned above, over the range that these parameters may vary. The β_x, β_y, η_x, η_y functions of the U-line are shown in Fig. 3.

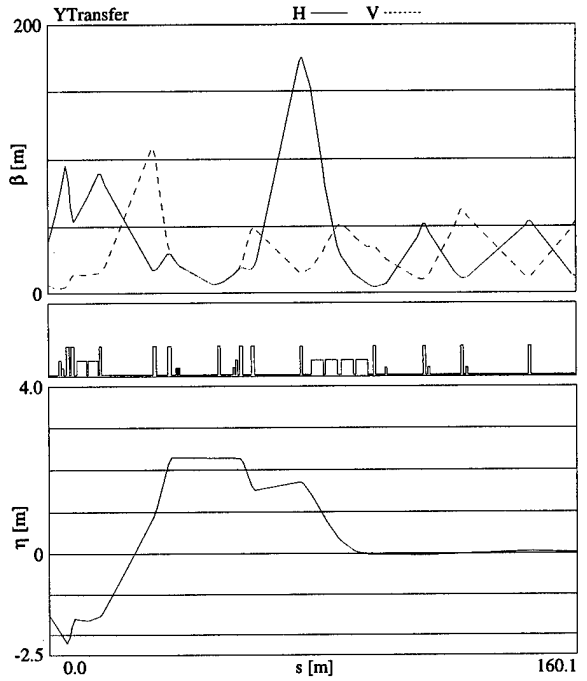


Fig. 3. Beta functions (β_x, β_y), and eta functions (η_x, η_y) of U-line.

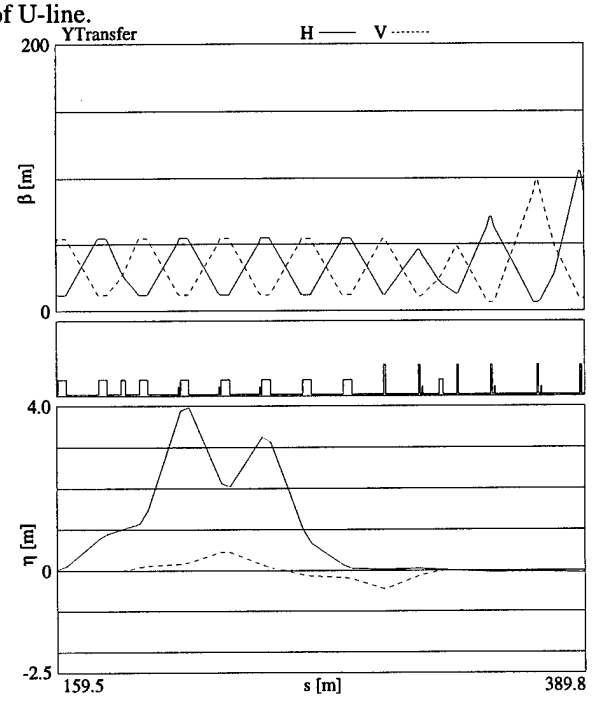


Fig. 4. Beta functions (β_x, β_y), and eta functions (η_x, η_y) of W-line.

1.2 The W-line

The W-line (Fig. 2) consists of eight C-type combined function magnets[7], of 2.5° bend each, followed by six quadrupoles. The eight combined function magnets forming a 20° achromatic horizontal bend are placed in a (F-D) arrangement to make four cells of 90° phase advance per cell. Part of the W-line lies in an incline of 12.51 mrad which lowers the beam elevation by 1.73 m. This level drop is accomplished by two vertical dipole pitching magnets. One, which bends the beam down, is located between the first and second combined function dipoles of the W-line, and the second, which restores the beam to the horizontal level (bend-up), is located between the second and third quadrupoles of the W-line. The beam section between the two pitching magnets is designed to be non- dispersive in the vertical direction, introducing linear beam-coupling which is not significant as far as the first-order beam transport optics are concerned. However, this simultaneous vertical and horizontal bend of the beam turns out to be a concern when polarized protons are to be transported by the AtR[9]. Finally, the quadrupoles of the W- line are tuned to match the Twiss parameters to the those of the X-line and Y-line, discussed next. The optical functions of the W-line are shown in Fig. 4.

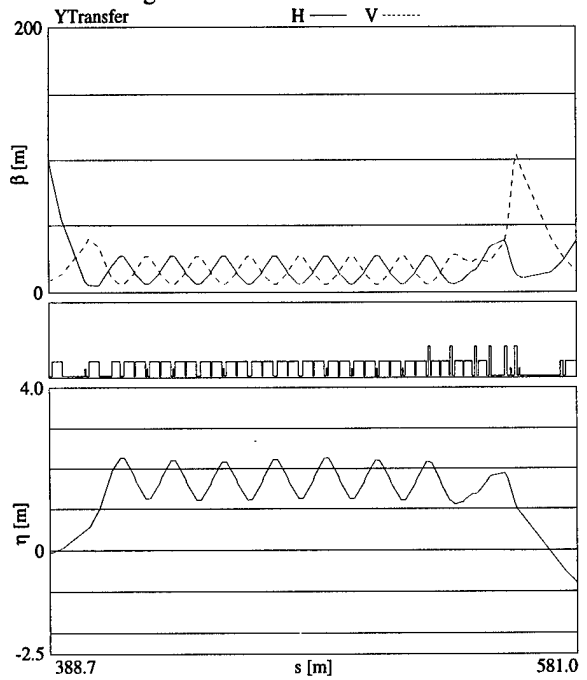


Fig. 5. Beta functions (β_x, β_y), and eta functions (η_x, η_y) of Y-line.

1.3 The X- and Y-lines

At the end of the W-line the AtR line branches into two separate lines, the X- line and the Y-line which transport the beam to the injection point of the Blue (clockwise circulating beam) and Yellow (clockwise circulating beam) ring respectively. The layout of the magnets of the X-line is identical to that of the Y-line apart from the bending direction of the beam due to the dipoles of each line. The first magnet, common to both lines, is a switching magnet which directs the beam to the X or Y line. This is followed by an array of twenty six B-type combined function magnets[7] providing a total beam-bending angle of 74°. All of the combined function magnets are identical in cross-section and length

except, the second magnet, which is shorter. The next 24 magnets are arranged in a regular lattice of six cells. Each cell has four magnets (FFDD) with 90° phase advance per cell. The last part of the (X,Y) line is the Injection section which is discused next. The optical functions of the line are shown in Fig. 5.

2 THE INJECTION SECTION AND MATCHING WITH RHIC

This section of the AtR at the end of the (X,Y)-lines consists of four short C-type combined function magnets[7], a single A-type dipole magnet[7] six quadrupoles, a vertical pitching magnet of 3 mrad bend, followed by a Lambertson septum magnet[10] of 38 mrad horizontal bend. The total beam-bend of the dipoles is 13.5°. The main function of the injection section is to match the beam parameters of the injected beam to the those of the RHIC lattice, which depend on the cell phase advance. Although the original design value of the phase advance per cell for the RHIC machine is 89.3°, a different phase advance per cell may be required when the value of β^* at injection is different from that of the design. For this reason, a study of the matching ability of the injection section, was made over a range of RHIC Twiss parameters corresponding to different phase advances per cell. It was found that, within the range of the strength of the last six quadrupoles, the AtR Twiss parameters can match those of the RHIC lattice from 70° to 130° phase advance per cell. Figure 6 shows the optical functions of the Injection line and part of the RHIC lattice when the phase advance per cell is 100°. Beam emittance growth due to optical mismatch of the AtR line with RHIC has already been simulated[11].

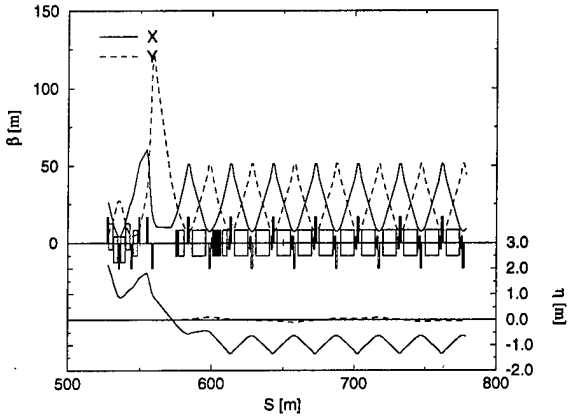


Fig. 6. Beta functions (β_x, β_y), and eta functions (η_x, η_y) of Injection-line and a section of RHIC. The phase advance per cell in RHIC is 100°

3 CONCLUSIONS

The theoretical predictions of the AtR optics and its matching properties to RHIC were presented. Experimental tests[2],[4],[5] performed on the AtR optics showed good agreement with theory. The matching properties of the AtR line were also tested[2][3] and found to aggree well with the theoretical predictions.

4 REFERENCES

[1] 'Beam Transfer from AGS to RHIC" J. Claus and H. Foelsche, BNL RHIC Technical Note 47.

[2] S. Peggs, 'RHIC Status', These Proceedings.

[3] 'RHIC Sextant Test - Physics and Performance' J. Wei et, al. BNL These Proceedings.

[4] 'AGS to RHIC Transfer Line: Design and Commissioning" W.W.Mackay et, al. UPAC 1996, Barcelona Spain.

[5] ' Physics of the AtR to RHIC Transfer Line Commissioning' L. Ahrens et, al. UPAC 1996, Barcelona Spain.

[6] 'Closed Orbit Calculations at AGS and Extraction Beam Parameters at H13' N. Tsoupas H.W. Foelsche, J. Claus, and R. Thern AD/RHIC/RD-75

[7] 'Bending Magnets for the CBA Beam Transport Line' R.E. Thern IEEE PAC 1983 Santa-Fe.

[8] 'Temperature Increase of the Foil Stripping Material in the AGS-RHIC Beam Transfer Line' N. Tsoupas, M.J. Rhoades-Brown AD/RHIC/RD-36

[9] 'Transfer of a Polarized Proton Beam from AGS to RHIC' N. Tsoupas, T. Roser, M. Syphers, A. Luccio BNL D. Underwood ANL These Proceedings.

[10] 'Design and B-Field Measurements of a Lambertson Injection Magnet for the RHIC Machine' N. Tsoupas, E. Rodger, J. Claus, H.W. Foelsche, and P. Wanderer PAC 1995, p. 1352 (May 1-5 1995), Dallas, TX

[11] 'Emittance Growth in RHIC during Injection' W. Fischer, W. MacKay, S. Peggs, and J. Wei BNL RHIC/AP/112

DESIGN ASPECTS RELATED TO THE RELIABILITY OF THE LHC BEAM DUMP KICKER SYSTEMS

J.H. Dieperink, J.-L. Bretin, E. Carlier, L. Ducimetière, G.H. Schröder,
E. Vossenberg, CERN, Geneva, Switzerland

Abstract

The two LHC beam dump kicker systems consist each of 14 pulse generator and magnet subsystems. Their task is to extract on request the beams in synchronisation with the gap in the beam. This operation must be fail-safe to avoid disastrous consequences due to loss of the beam inside the LHC. Only a failing operation of one of the 14 pulse generators is allowed. To preserve this tolerance premature beam dumps are forced immediately after early detection of internal faults. However, these faults should occur rarely in order not to be a source of undesirable downtime of the LHC. The report determines first the level of reliability required for the main components of the system. In particular faults which could cause spontaneously non-synchronised beam dumps are identified. Then, technical solutions are evaluated on failure behaviour. Those having a most likely failure mode which does not cause dump triggers are favoured. These solutions need redundancy and are more complex but have the advantage to be fault tolerant. The design goal can be achieved with a combination of high quality components, redundant signal paths, fault tolerant subsystems, continuous surveillance and check-list validation tests before the start of the injection of beam in the LHC.

1 INTRODUCTION

The LHC beam dump kicker system must be able to safely dump the beam at any stage during the filling, the accelerating and colliding phase, i.e. from the injection energy of 450 GeV up to the top energy of 7 TeV. The circulating beam, with a nominal maximum energy of 334 MJ per ring, must be extracted in one single turn of 89 μs duration [1].

Severe damage can be induced to the LHC, due to full or partial loss of the beam onto machine components. This can happen when no response is given to a request for dumping the beams or when the dump kicker system works incorrectly.

Possible faults can be classified in 3 types as follows:

1. Faults detectable early enough such that a dumping action without risk can be done, e.g. a faulty charging supply with consequence of a slowly decaying stored energy on the capacitor. These faults reduce the availability of the LHC for physics.
2. Faults occurring during the dumping action. These faults can cause damage when occurring coincidentally on more then one subsystem.
3. Faults generating a spontaneous dumping action unsynchronised with the particle free gap in the beam. These faults can result in a quench in the super conducting magnets. However, the overall system is conceived such that no damage occurs.

The required reliability and the preferred fault behaviour of the main components of the dump kicker system have been determined such that the risk for damage to the LHC is minimised and the availability for physics runs is maximised. The study has been restricted to the dump extraction kicker system and its service equipment. The generation of requests and their transmission has not been dealt with.

2 SHORT DESCRIPTION OF THE DUMP KICKER SYSTEM

Figure 1 shows a functional lay-out of the main components of the beam dump extraction kicker system.

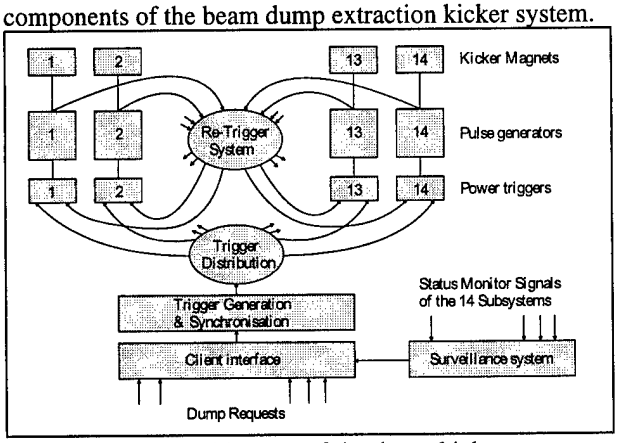


Figure 1. Functional lay-out of the dump kicker system.

The 14 dump *kicker magnets* are powered by 14 *pulse generators* which get the trigger from *power trigger* modules. The *trigger generation and synchronisation* system distributes the trigger requests, from the *client interface*, to the *power triggers* in synchronisation with the gap in the circulating beam. There is a *re-trigger* system, which has the task to detect any spontaneous trigger in one of the pulse generators and to re-distribute this information, as fast as possible, to all remaining pulse generators as trigger pulse. Finally, there is a *surveillance system* which has the task to issue a dump request when a severe fault has been detected.

0-7803-4376-X/98/$10.00 © 1998 IEEE

3 REQUIRED PERFORMANCE

The required performance for safe operation can be summarised as follows:

1. The failure rate of the execution of a request for a beam dump should not exceed 1 failure/10^6 hours.
2. Operation of 13-out-of-the-14 magnet systems is sufficient to dump the beam safely. However, when one out of the 14 systems becomes faulty, the beam must immediately be dumped. The rate of these faults must remain orders of magnitude lower than the rate of normal beam dump requests. The failure rate of the execution of this request should not exceed 1 failure/10^6 hours.
3. A spontaneously generated trigger in one of the systems must trigger immediately all other systems. Therefore the maximum admissible rate of these triggers has been set to less than 1 event/year. The failure rate of this re-triggering process should not exceed 1 failure/10^6 hours.
4. The reliability must be such that the availability of the LHC for physics is not reduced significantly.

4 THE RESULTING REQUIREMENTS

For the estimation of the reliability and the risk of all systems a same failure rate of less than 1 failure/year/subsystem has been assumed. In reality this will not be the case because the complexity of the different systems is rather different. However, it gives the possibility to rank the order of risk that the different systems provide. The following conclusions have been drawn:

- The failure behaviour of the *trigger generation*, the *trigger distribution*, the *re-trigger*, the *power trigger* and the *pulse generator* must be fault tolerant, i.e. a fault should not cause a current pulse in the magnets but should result in unavailability. Hence, redundant equipment must take over the task of an unavailable element.
- The failure behaviour of the *surveillance system* and the *fault detectors* in the whole system must be fault tolerant, i.e. the occurrence of an internal fault must initiate a safe action, which is in most cases a dump request.
- Redundant *power trigger/pulse generator* chains are necessary, otherwise the risk that less then 13 chains work simultaneously is above the required level.
- The more complicated *power trigger/pulse generator* chains have a higher failure rate than the relatively simple *trigger and trigger generation* systems. Every effort in the choice of material must be made to keep this failure rate below 1 failure/year/chain.
- A redundant *normal trigger* system is necessary to meet the requirements.
- A redundant *re-trigger system* is not really necessary but remains recommended.
- Redundant *trigger generation and synchronisation systems* are necessary. To ensure that the beam dump is requested when both systems fail simultaneously, a different third redundant system is needed.
- Non relevant but nevertheless necessary equipment should not have any impact on the availability of the dump kicker system.

5 APPLICATION TO THE HARDWARE

5.1 Prototype pulse generator

The prototype pulse generator, constructed and successfully tested in 1994, is actually composed of two parallel circuits (called A and B) connected to a common power switch. The subdivision is required for reduction of the leakage inductance and the generation of an acceptable pulse shape. Two types of power switches have been tested. A gas switch [2] and recently a solid state switch [3].

5.2 Proposed final generator

To achieve the requirements enumerated in chapter 4 the following choices and additions are proposed:

- The generators will be equipped with solid state switches because the spontaneous discharges in gaseous switches are more likely and lead to faults of type 3 (chapter 1).
- Instead of connecting both subsystems to one power switch, each unit will be equipped with its own switch. Both switches are interconnected such that each takes normally half the current, but is capable to conduct the full current in case of unavailability of its partner.
- Two other interconnections between the two units provide additional fault tolerant behaviour in case of unavailability of other important generator elements.

Figure 2 shows a block diagram of the pulse generator with its power trigger units.

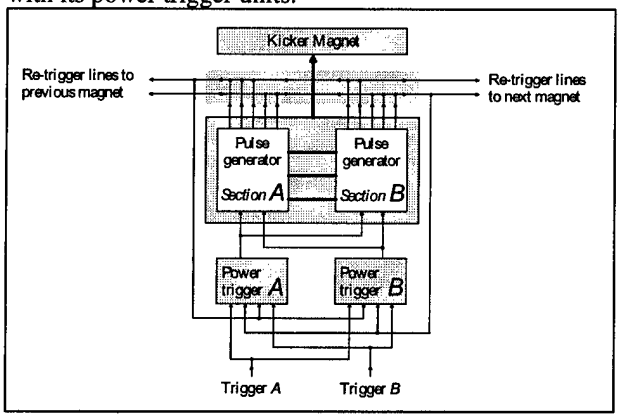


Figure 2. Block diagram of the power trigger/pulse generator/magnet chain.

5.3 Normal trigger and re-trigger system

Figure 3 shows the principle of the re-trigger system whose task is to re-transmit a trigger from one generator as fast as possible to all others.

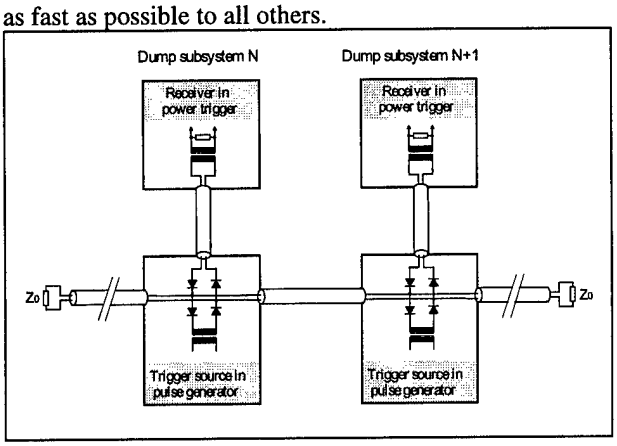


Figure 3. Principle of the re-trigger system.

A chained input/output system has been chosen instead of a star system because it is faster. Each pulse generator has several re-trigger sources originating in the other 13 pulse generators. One trigger source has enough energy to trigger all power trigger modules. Since there is no stored energy in the system itself it is difficult to create spurious triggers, neither can a disconnected cable nor a defective trigger source cause triggers.

The normal trigger distribution system has no constraints on speed and can use the same technology.

5.4 Trigger generation and synchronisation system

Figure 4 shows the principle of the proposed trigger generation and synchronisation system.

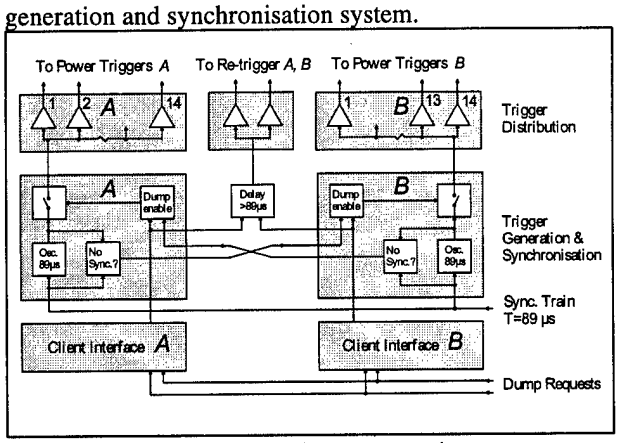


Figure 4: Client interface, trigger generation, synchronisation and distribution

Quartz controlled generators produce continuously dump trigger pulses synchronised with the gap in the circulating beam. Internal distribution of these pulse trains is inhibited until a beam dump is requested. The pulses which pass the inhibit stage are sent via a fan-out system to all power trigger modules. In this way the first pulse after the reception of a dump request will trigger the system. If synchronisation is lost, a synchronised beam dump remains nevertheless possible for several seconds, because of the stability of the quartz oscillator. If the synchronisation of only one of the oscillators fails, a dump trigger is forced by the redundant system. This mechanism reduces the probability of non synchronised dumps to almost zero. Any dump request sends also a dump trigger, delayed by 89 µs, via the re-trigger system to the power trigger modules. This third trigger path guarantees that a beam dump is initiated, even when both principle systems fail.

5.5 Surveillance system

The surveillance system continuously collects status information and makes a beam dump request when a fault appears. It collects also the post mortem information generated by a dump or by a test program which is used to validate the safe operation of the system. Special attention must be paid to the large volume of information needed for these tests. Commercially available PLCs are foreseen to be used for this purpose.

6 CONCLUSION

The reliability study of the extraction kicker systems of the LHC beam dump confirms that most attention must be paid to the high voltage pulse generators and their power switches to assure fault tolerance and availability. It is therefore proposed to employ solid state power switches rather then gaseous switches whose risk of spontaneous breakdown, which would entail spontaneous unsynchronised dumps, is most likely greater. These solid state switches will be doubled to assure fault tolerance and availability.

The stringent reliability requirements impose also the duplication of the auxiliary systems for triggering, synchronisation and surveillance.

Finally a fault tolerant re-trigger system is needed that powers immediately all magnets in case of a spontaneous discharge in one of the generators.

7 ACKNOWLEDGEMENTS

The authors acknowledge the constant interest and support of E. Weisse, leader of the LHC beam dump project.

REFERENCES

[1] The LHC study group, "The Large Hadron Collider", CERN/AC/95-05 (LHC), CERN, (October 1995).

[2] L. Ducimetière, P. Faure, U. Jansson, H. Riege, M. Schlaug, G.H. Schröder, E. Vossenberg, "Pseudospark Switch Develoment for the LHC Extraction Kicker Pulse Generator", LHC Project Report 96-57, CERN, (September 1996).

[3] E. Carlier, L. Ducimetière, U. Jansson, M. Schlaug, G. Schröder, E. Vossenberg, "Solid State Switch Application for the LHC Extraction Kicker Pulse Generator", LHC Project Report 96-57, CERN, (September 1996).

THE CERN PS EAST AREA IN THE LHC ERA

L. Durieu, O. Ferrando, J.-Y. Hémery, J.-P. Riunaud, B. Williams
CERN, CH-1211 Geneva 23, Switzerland

Abstract

Experiments planned at the CERN Large Hadron Collider (LHC) will require a well-equipped test area with low momentum (<15 Gev/c) secondary particle beams. These beams will be used to test some of the LHC detectors components (ALICE, ATLAS, CMS, LHC-B). In addition another recently approved experiment (DIRAC) will be installed in the PS East Area. This experiment will require a primary proton beam of 24 GeV/c to test QCD predictions. In this context, the EHNL project (East Hall New Look) has been launched. The major modifications include (i) an extension of the present area with a primary 24 GeV/c beam line, (ii) a new secondary beam line lay-out with test areas at 3.5, 7, 10 and 15 GeV/c, (iii) an additional irradiation area, (iv) an improved facility for beam sharing between the various users. This paper describes the scope of the project, its new features, the planned facilities and its installation schedule.

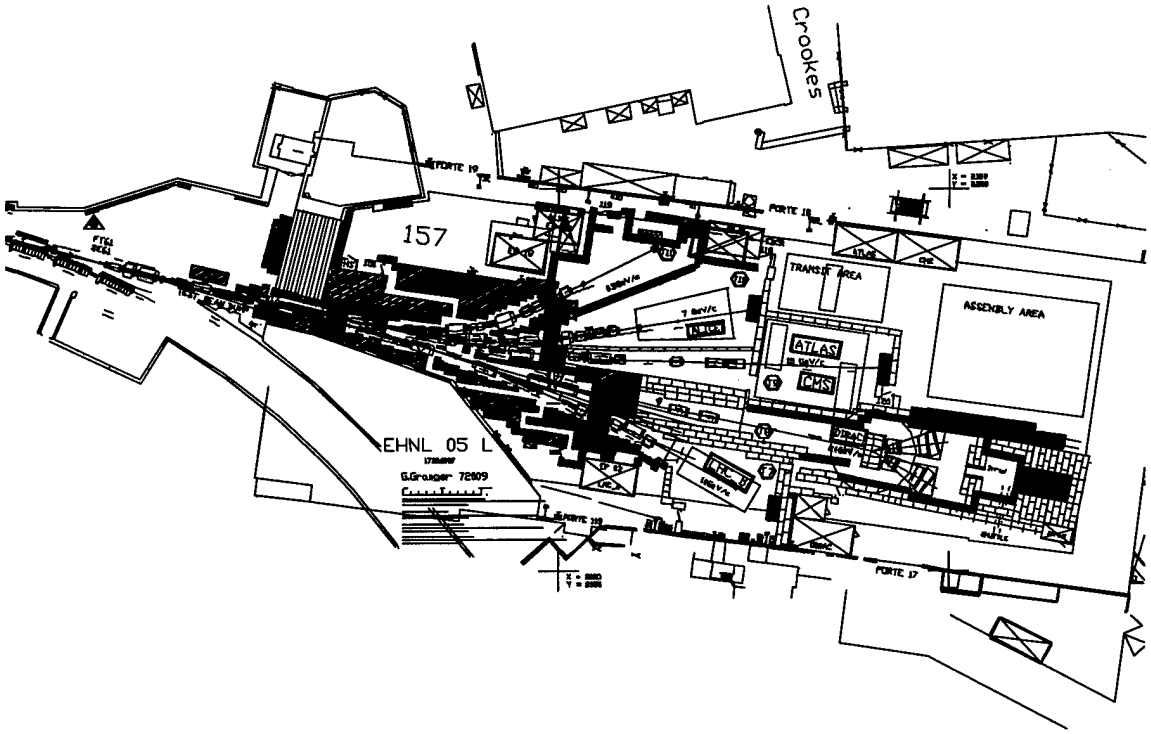
1 INTRODUCTION

Following the approval of the Large Hadron Collider, the planned LHC experiments are now preparing parts of their detectors. Before full scale manufacture and assembly are launched, tests and optimization of these components are needed under adequate beam conditions. Part of these tests require low-energy particle beams and can be performed in the East Hall, either with a primary proton beam provided by the PS or with secondaries produced by the PS beam hitting a target [1]. Merging these needs with the additional request of housing the DIRAC experiment to be running with primary 24 GeV/c protons in the same East Area, led to the decision to carry out a major reshuffling of the PS East Hall under the project name EHNL, for East Hall New Look [2]. This project aims at upgrading and renewing the area for use by physicists before and beyond LHC start-up.

2 SCOPE OF THE PROJECT

The DIRAC experiment [3] will make use of a primary proton beam of 24 GeV/c from the PS delivered by means of a resonant extraction process (300 ms spill) to a new, dedicated channel[4]. This experiment has very stringent requirements on beam quality: very low residual intensity modulation, low beam halo [5], small secondary particles contamination and high geometric stability.

LHC experiments will use secondary particles



General lay out of the new PS East Area Fig 1.

0-7803-4376-X/98/$10.00 © 1998 IEEE

selected in momentum and polarity but not separated by species, produced from a very similar proton beam hitting a target. As at present, there will be 2 targets in the area: one on the undeflected beam of the North branch, feeding 3 secondary channels, T9, T10 and T11, and another one on the beam deflected to the South branch by the splitter magnet, feeding the secondary channel T7. The equipment modules to be tested are up to several cubic meters in volume and the various test places should be able to house them.

The above requirements have imposed the redesign of three of the secondary lines [6] [7] [8] and major modifications in the target area and the switchyard in addition to the new primary channel. The facility, presently covering 2/3 of the building area, will extend to the whole available space.

Downstream of the DIRAC experiment an irradiation facility has been added using the beam catcher upstream the beam dump. It will be used to test the radiation hardness of voluminous (4 x 4 x 2.4 m^3) equipment such as the planned liquid argon calorimeter of ATLAS. The expected rate of secondaries produced by 2 x 10^{11} primary protons/spill imposes quite a massive shielding.

These modifications, undertaken with restricted resources, will make maximum use of existing hardware.

User	Line	Momentum	Particle	Particles/s pill
General use	T11	3.5 GeV/c	secondary	10^6
ALICE	T10	7 GeV/c	secondary	10^6
ATLAS/CMS	T9	15 GeV/c	secondary	10^6
DIRAC	T8	24 GeV/c	primary p	2 x 10^{11}
LHC-B	T7	24 GeV/c	secondary	10^6

Table 1. Users and beam characteristics.

3 NEW FEATURES

In order to allow maximum operational flexibility, most lines will be able to run simultaneously, taking advantage of the PS multi-user feature. While sharing between both secondary targets is achieved, as at present with a septum (splitter) magnet, a laminated switching magnet is used to serve two users with different needs. For cost reasons, switching between the 2 optics will be carried out with the available solid yoke quadrupoles. Preliminary tests have been conducted showing that induced currents can be limited with a suitable current rate of change, giving adequate performance in terms of stability and heating.

Since the completion of the antiproton programme at the end of 1996, the intensive proton cycles from the PS are no longer required for antiproton accumulation. The PS can now feed the East Area with 2 slow extracted spills within a 14.4 s supercycle. Thanks to the PS multi-user facility, each of these 2 spills can be dedicated to different East Area users. For example, while the first one can be used by DIRAC only (as single user), the second one can be shared by all other users or given to any of the North or South branches (see Table 2).

In the PS itself, an additional tuning device will be implemented in the slow extraction process to control the instantaneous extracted intensity and reduce the low-frequency spill modulation as required by DIRAC.

4 PLANNED FACILITIES

These are shown in Fig. 1. with their main characteristics and assigned users described in table 1. For secondary lines, the momentum and intensity quoted are the maximum of the line while for the primary line, they are nominal. Irradiation of small samples as done today close to the south target position will still be possible but will be incompatible with the use of beamline T8.

The secondary lines are based on the double monochromator design and provide full momentum recombination in the user area. Momentum resolution is a fraction of a percent and the momentum is freely adjustable by each experiment up to the maximum.

The beam transport uses a full set of optimised optics to ensure the best possible beam characteristics in the user areas. Two examples are depicted on Fig. 2 and 3.

BEAM LINE	SPLITTER MAGNET ON: All beam within splitter gap and deflected to South branch		SPLITTER MAGNET ON: Beam shared by splitter between North and South (deflected) branch		SPLITTER OFF or Beam outside splitter gap
	Beam to T7	Beam to T8	Beam to T7	Beam to T8	All beam to North (undeflected) branch
T7	Primary p+ or Secondaries < 10 GeV/c	No Beam	Primary p+ or Secondaries < 10 GeV/c	No Beam	No Beam
T8	No Beam	24 GeV/c p+ (unscraped)	No Beam	24 GeV/c p+ (scraped)	No Beam
T9	No Beam		Secondaries < 15 GeV/c		Secondaries < 15 GeV/c
T10	No Beam		Secondaries < 7 GeV/c		Secondaries < 7 GeV/c
T11	No Beam		Secondaries < 3.5 GeV/c		Secondaries < 3.5 GeV/c

Table 2. Possible beam sharing combinations between the 5 East Area beam lines.

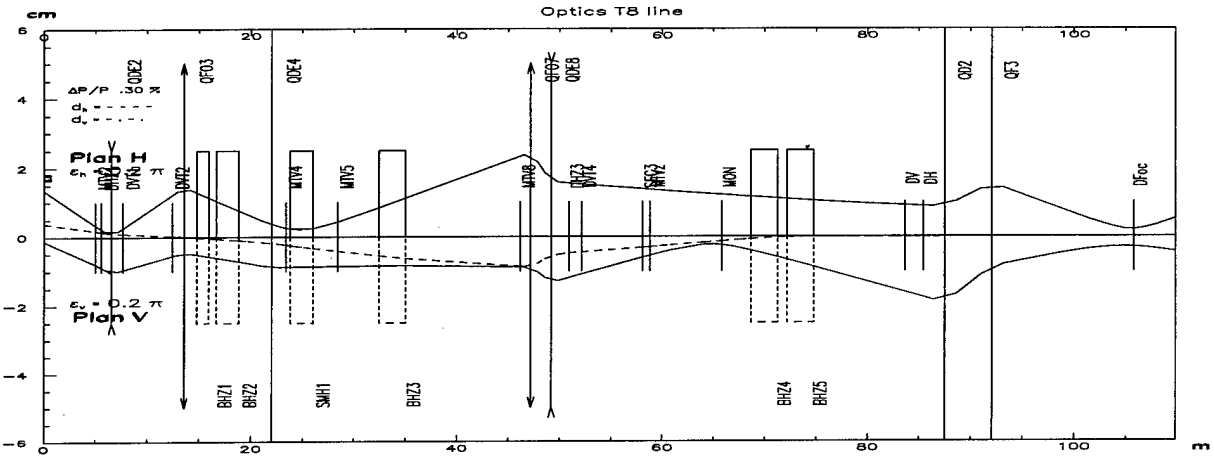


Fig. 2. Beam optics of primary line T8 for the DIRAC experimen

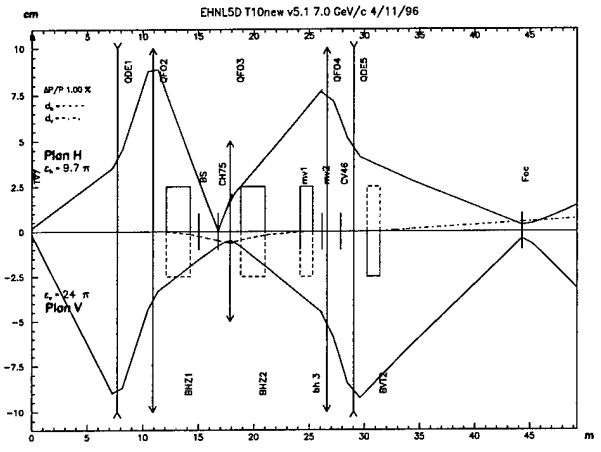


Fig. 3. Beam optics of secondary line T10 for ALICE

5 INSTALLATION SCHEDULE

Installation is planned during a long (9 months) shut-down of the area, starting at the end of September 1997. After dismantling some of the shielding and modifications of the target area and switchyard, transformation of the secondary lines will take place. In parallel, maintenance of recovered elements will be carried out, before their reinstallation. After shielding replacement, during DIRAC installation, the experimental lines will be commissioned and sequentially put back into operation, starting with the least affected line T11 and ending with the new line T8. The whole area coming back again to life in the fall of 1998.

6 CONCLUSIONS

At the end of 1998, after completion of the EHNL project, the CERN PS East Area will house a major physics experiment while providing the physics community with a convenient detector test facility for the years to come. This facility will then be mainly devoted to tests of parts of LHC experiment including the capacity for testing radiation hardness of key components.

7 ACKNOWLEDGEMENTS

We are indebted to many colleagues in the physics teams for fruitful discussions during the global optimization process. People within and outside the PS division who gave pertinent advice on diverse aspects of the project are too numerous to cite here. We express our thanks to all of them for their inappreciable collaboration.

REFERENCES

[1] D.J. Simon (editor), revised by L. Durieu. "Secondary Beams for Tests in the PS East Experimental Area" CERN PS/PA Note 93-21.

[2] J.-Y. Hémery. "EHNL_5 Proposal for the Beam Lines & Areas for Tests and Experiments in the East Hall." CERN PS/PA Note 96-28.

[3] B. Adeva and 61 co-authors. "Lifetime Measurement of $\pi^+\pi^-$ Atoms to Test Low Energy QCD Predictions" CERN/SPSLC 95-1.

[4] O. Ferrando, J.-Y. Hémery. "Design of T8 (DIRAC) for EHNL". CERN PS/CA Note 97-16.

[5] L. Durieu, M. Giovannozzi, J.-Y. Hémery. "Measurement of Beam Halo in FT61S for the DIRAC Experiment." CERN PS/PA Note 96-09.

[6] L. Durieu, O. Ferrando. "Design of T10 (ALICE) for EHNL" CERN PS/PA Note 96-38.

[7] L. Durieu, O. Ferrando. "Design of T9 (ATLAS/CMS) for EHNL" CERN PS/PA Note 96-39.

[8] L. Durieu. "Design of T7 (LHC-B) for EHNL" CERN PS/CA Note, to be published.

PETRA BUNCH ROTATION

Wilhelm Kriens
Deutsches Elektronen-Synchrotron, DESY, Hamburg, Germany

Abstract

The upgrade of the Petra *bunch rotation* scheme for protons will be described. Bunch compression in Petra is necessary for stable longitudinal transfer matching with Hera. The influence of beam loading in Petra has to be taken into account for currents above 50 mA even though a strong fast rf feedback system is installed. Amplitude modulation in a short push-pull cycle is chosen for *bunch rotation* and a bunch length compression factor of 0.7 is established with tolerable distortion.

1 INTRODUCTION

Proton transfer from Petra to Hera at 40 Gev/c with regard to longitudinal phase space matching using a 52 MHz rf system in both machines is somewhat critical [1].

Even with an optical change in Petra [2] (γ_{tr} = 6.2 to 7.9) the rf voltage ratio for matching is rather unfavourable.

$$\frac{(\,h\,|\eta|\,)_{\text{Petra}}}{(\,h\,|\eta|\,)_{\text{Hera}}} \;=\; 7.7 \qquad (1)$$

The voltage in Petra is limited to 150 kV for short term operation. Therefore the voltage in Hera for matching (20 kV) is too low for stable beam injection.

Choosing to operate Hera at 100 kV during injection, requires longitudinal bunch compression by a factor of 0.66.

2 BUNCH COMPRESSION

The first scheme for *bunch rotation* comprised a 180 degree phase jump, a dwell period during which the bunch lengthens, a jump back to the original stable phase followed by about a quarter synchrotron period before beam transfer [3]. Since the transfer is determined from synchronization with Hera, the start trigger for the phase jump is prepared a fixed number of revolution turns before transfer. Although the procedure could be optimized to achieve adequate compression at moderate beam currents, above 50 mA (some 40 % of design) beam loading effects degraded the ideal behaviour. In particular the bunches became distorted during the phase jump.

In order to reduce beam loading effects, amplitude modulation was applied to the rf system inducing quadrupole mode oscillation for bunch compression. For this purpose a voltage controlled attenuator device with small phase deviation is used at low power input. Additionally the time constant of the transmitter gain control had to be increased to pass the modulation. The choice for the modulation cycle depends on the ability of the rf system and was optimized in relation to beam dynamics. The result can be seen from figure 1. A typical bunch in Petra is measured just before *rotation* and in the last turn at transfer.

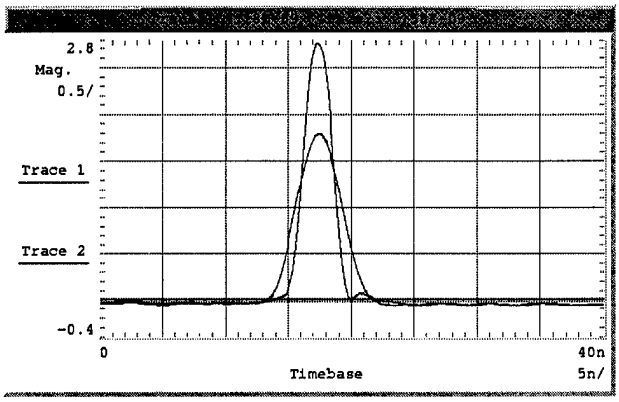


Figure 1: Bunch display just before *bunch rotation* (Trace 1) and the same bunch at extraction time (Trace 2).

2.1 PETRA RF System

Two 52 MHz cavities of the same type with independent power transmitters are installed [4]. Therefore careful phasing for power balancing is necessary to get the required circumferential voltage. In this case the total rf system can be simplified as shown in figure 2 to calculate the beam loading effects.

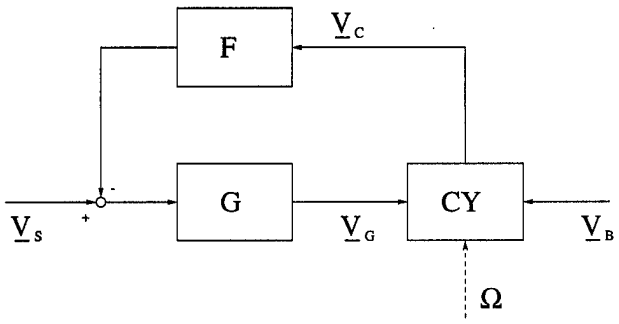


Figure 2: Block diagram of the Petra rf system with G the transmitter gain and F the feedback factor. Voltages $\underline{V}$ are in complex notation. Ω is the detuning value of the cavity CY.

The transmitter forward voltage $\underline{V}_G$ can be expressed in terms of the cavity voltage $\underline{V}_C$ and the beam voltage $\underline{V}_B = \frac{R_0}{2}\underline{I}_0$. From figure 2 we get the relation between the low level input voltage $\underline{V}_S$ and $\underline{V}_C$ directly.

$$\begin{aligned}\underline{V}_G &= \underline{V}_C + i\Omega\underline{V}_C + \underline{V}_B \\ &= (\underline{V}_S - F\underline{V}_C)G\end{aligned} \qquad (2)$$

The detuning value $\Omega = Q_0\frac{\Delta\omega}{\omega}$ has settled prior to *bunch rotation* i.e.

$\underline{V}_B = -i\Omega\underline{V}_{C0}$ and $\underline{V}_{C0} = \underline{V}_{G0}$ with $\varphi_B = 0$.

0-7803-4376-X/98/$10.00 © 1998 IEEE

Introducing the modulation index $\underline{m} = \frac{\underline{V_S}}{\underline{V_{S0}}}$ and assuming $FG \gg \Omega$ ($FG \approx 100$) we get

$$\frac{\underline{V_C}}{\underline{V_{C0}}} = \frac{\underline{m}(1+FG)+i\Omega}{1+FG+i\Omega} \approx \underline{m} \quad (3)$$

$$\frac{\underline{V_G}}{\underline{V_{G0}}} = \frac{\underline{V_C}}{\underline{V_{C0}}}(1+i\Omega) - i\Omega \approx \underline{m}(1+i\Omega) - i\Omega \quad (4)$$

From equation 3 we can see that the cavity voltage is proportional to the input voltage due to the strong fast feedback. Therefore the low level modulator directly controls the cavity voltage as desired but the power transmitter is disturbed by beam loading corresponding to equation 4.

With $V_{C0} = 140\,kV$, $R_0 = 2\,M\Omega$ and 70 mA of average beam current the detuning value is $\Omega = 1$.

If we suppose that the transmitter could deliver a factor of two more power for short term modulation, then 35 mA for phase jump ($\underline{m} = -1$) and 130 mA for amplitude modulation ($\underline{m} = 1.3$) are the beam current limits for operation. Both computer simulations and the reality in Petra has shown that $\underline{m} = 1.3$ is sufficient for bunch compression via amplitude modulation.

2.2 *ESME Simulation*

The ESME computer program [5] was used to optimize the operation mode for amplitude modulation of the cavity voltage. The aim was to get a minimum compression factor for the bunch length with tolerable distortion of the emittance.

Due to the ability of the rf transmitter the simulation is done with a modulation cycle as shown in figure 6. It can be seen that fast ramping of the voltage up and down with twice the synchrotron frequency is the best way to quickly induce shape oscillation. The maximum voltage corresponds to $\underline{m} = 1.3$ and the minimum voltage is found to be symmetric with respect to the starting value.

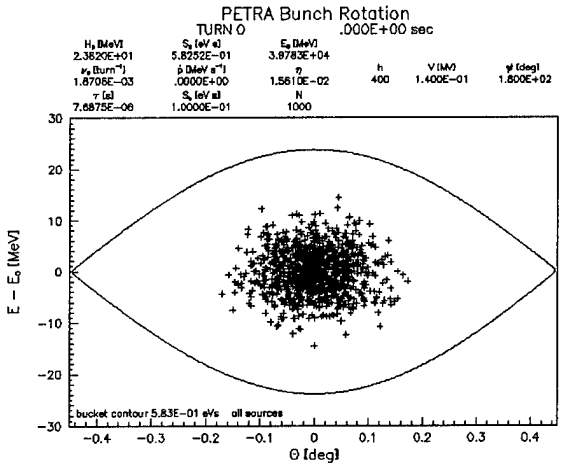


Figure 3: Initial bigaussian Phase Space Distribution.

For the special case of 0.1 eVs emittance and a bigaussian distribution (see figure 3) we get the evolution of the bunch length and the distortion of the emittance turn by turn as seen in figure 7 and figure 8. The optimum timing for beam transfer is at turn 440 after three quarter synchrotron oscillations. Only for rather low emittance more *rotation* cycles are useful. Figure 4 displays the phase space at turn 440 in our special case.

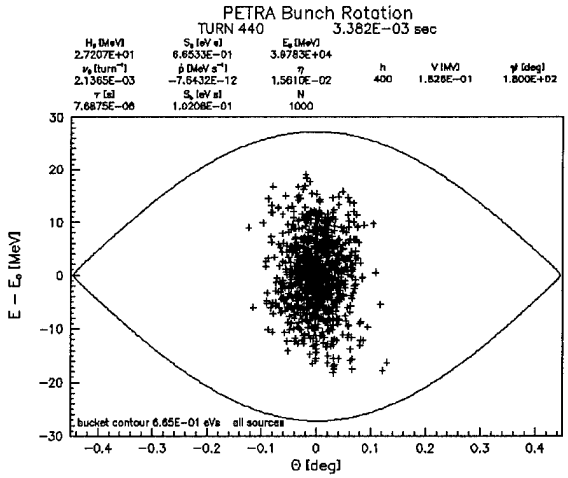


Figure 4: Distribution at Transfer (turn 440).

To illustrate the bunch oscillation more impressively a mountain range display of the bunch length is shown in figure 5.

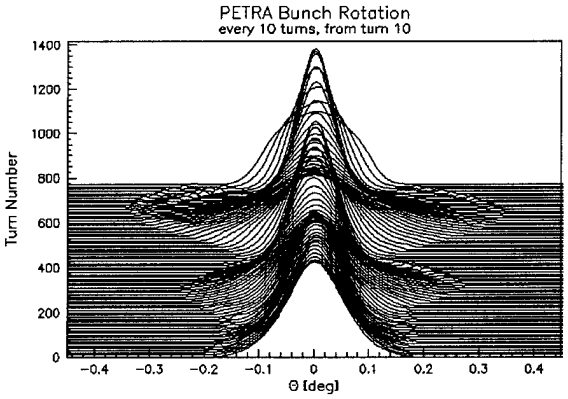


Figure 5: Mountain Range Display of the Bunch length.

Table 1 shows the influence of the initial emittance on the *bunch rotation* based on a bigaussian phase space distribution. Bunch compression fulfills the Hera requirement for stable injection with less than 5 % of distortion.

Furthermore it can be seen from the simulation that the modulation parameters are not very sensitive. Therefore a tuning of these values is not foreseen in the operation control.

Table 1: Compression and Distortion vs initial Emittance.

Emittance	Bunch length	Compression	Distortion
[eVs]	FWHM [ns]	[ ]	[%]
0.04	1.74	0.652	0.2
0.06	2.15	0.646	0.6
0.08	2.49	0.647	1.2
0.10	2.80	0.653	2.1
0.12	3.09	0.668	3.4
0.14	3.33	0.686	5.0
0.16	3.61	0.717	7.4

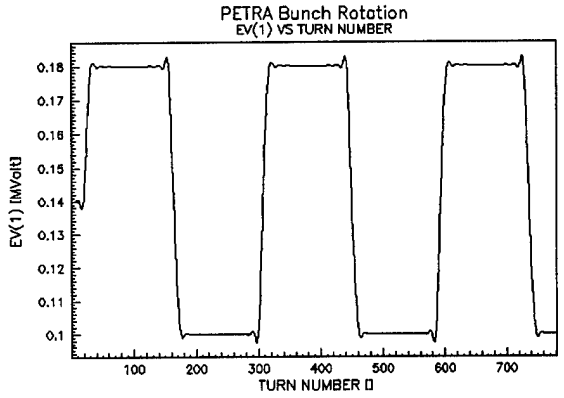


Figure 6: Cavity Voltage Modulation.

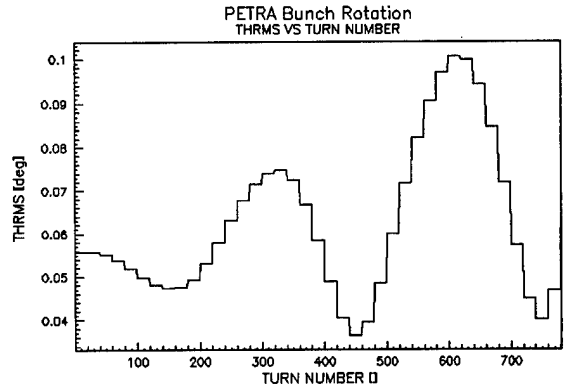


Figure 7: Bunch length (THRMS $\times$ 50 ns $\approx$ FWHM).

3 ACKNOWLEDGEMENT

The author would like to thank U. Hurdelbrink, P. Schmidt and G. Weiberg for technical support and J.R. Maidment for comments regarding the manuscript.

4 REFERENCES

[1] J.R. Maidment, 'HERA-p: Longitudinal Miscellany', Internal Paper, DESY, August 10, 1992

[2] K. Balewski, R. Brinkmann, B. Parker, 'IMPROVED PROTON INJECTION INTO HERA VIA PETRA OPTICS TRICKERY: ARE THE PROSPECTS REAL OR IMAGINARY?', EPAC'96, Barcelona, 1996

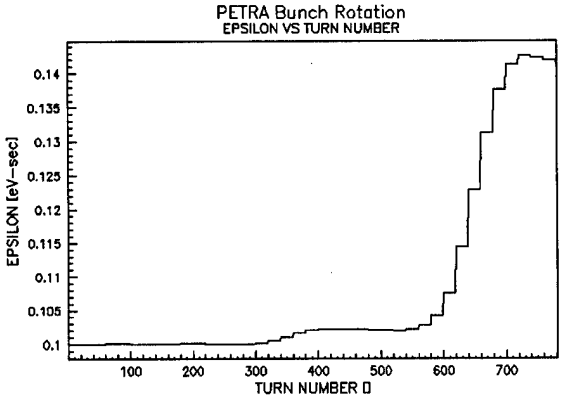


Figure 8: Emittance growth.

[3] G. Wiesenfeldt, 'Untersuchungen zur longitudinalen Strahlanpassung beim Protonentransfer von PETRA nach HERA', Diplomarbeit, Universitaet Hamburg, March 1995

[4] A. Gamp, 'Servo Control of RF Cavities under Beam Loading', DESY HERA 91-09, May 1991

[5] J. MacLachlan, 'User's Guide to ESME v. 8.13', June 30, 1995.

DEVELOPMENT OF A BEAM SWEEPING SYSTEM FOR THE FERMILAB ANTIPROTON SOURCE TARGET

F. M. Bieniosek, Fermilab, Batavia, IL 60510 USA*
O. Kurnaev, A. Cherepakhin, IHEP, Protvino, Russia
John Dinkel, Creative Designs, Inc.

Abstract

Intensity of the incident 120-GeV proton beam on the antiproton production target is scheduled to increase to $5x10^{12}$ protons per pulse. To prevent damage to the target, we plan to spread the hot spot on target with a beam sweeping system. Now under development are rotating-field magnets for installation upstream and downstream of the target. These magnets will deflect the beam in a circular pattern on the target. Peak current of 7 kA and peak voltage drop of 6 kV are expected. The power supply, which is separated from the magnet by a distance of about 10 m, utilizes magnetic pulse compression by saturating inductors to drive the magnets through the long transmission lines.

1 INTRODUCTION

Antiprotons are collected from the interaction of a 120-GeV proton beam with a solid nickel target. The efficiency of collecting antiprotons from the target rises as the size of the proton beam spot on the target is reduced. However at the same time the peak energy deposition on target rises. Estimates of the peak instantaneous energy deposition for the highest intensity achieved to date ($3.4x10^{12}$ protons per pulse) indicate an energy deposition of about 800 J/g. This is above the melting point of copper (about 600 J/g), and close to the melting point of nickel (about 1000 J/g). Under Main Injector conditions (5×10^{12} protons in a 1.6-μs pulse), the spot size will have to be increased to at least 0.25 mm to keep peak energy deposition near current levels. To bring the density of energy deposition with a 0.1-mm spot size down to currently-existing levels, a system to sweep the beam spot on the target will be required[1]. Several upgrades have been proposed for the Main Injector as part of the Tev33 project[2]. These upgrades (*e.g.* slip stacking) will result in increases in proton intensity of factors of 2-4 or more above the initial intensity of 5×10^{12}. Under these conditions sweeping becomes increasingly important, and larger sweep radii are required to restore the antiproton yield to its level at low intensity. The relative yield increase due to the sweeping system is about 15% for a 0.33-mm sweep radius at an intensity of 5×10^{12}, and 50% for a 0.5-mm sweep radius at a proton intensity of 1×10^{13}.

The upstream sweep magnets will be installed at the end of the AP1 beamline. The AP1 beamline transports and focuses the 120-GeV protons from the Main Ring onto the target. A pair of upstream magnets, placed at the downstream end of the AP1 beamline where the toroid M:TOR109 now resides, will sweep the 120-GeV proton beam. This location is near the focal point of the proton lithium lens, which may be used to focus 120-GeV proton beam on target. Antiprotons created in the target are collected by a lithium lens, and deflected by the pulsed magnet into the AP2 beam line for injection into the Debuncher. A single downstream sweep magnet placed in a double module between the collection lens and the pulsed magnet, near the focal point of the collection lens, will redirect the 8 GeV antiprotons exiting the collection lens parallel to the AP2 beamline. The portion of the antiproton flux that is focused by the lithium lens and collected downstream has a diameter of 22 mm. The magnet aperture radially inside the conductors is 28.5 mm.

2 SWEEP MAGNET

The beam sweeping system currently under development traces a 0.33-mm-radius circular pattern on the target over the 1.6-μs proton beam pulse. The magnets have a 2-phase, 4-conductor winding excited by two power supplies that deliver 625 kHz sinusoidal current waveforms in quadrature to generate a rotating dipole field[3]. The magnetic field due to two pairs of current-carrying conductors oriented 90° apart is rotating on axis if the current in the two pairs of conductors is $I_0 cos(\omega t)$ and $I_0 sin(\omega t)$. Figure 1 shows the magnetic field lines as calculated by POISSON at four times in the cycle. Currents to the horizontal and vertical pairs of conductors have a cos(ωt) and sin(ωt) time dependence, respectively.

The local field is itself not sufficiently uniform for use as a sweep magnet. However if the conductors are twisted such that the axial current distribution integrated over the length of the magnet has the distribution $sin\theta$ or $cos\theta$, respectively, the line integral of the field along the beam path is uniform and rotating. A design for the windings is indicated in Figure 2. The windings are in the form of two single-turn circuits placed symmetrically at 90-degree intervals. Each circuit has a twist of 180 degrees over the length of the magnet, such that $z=z_0 sin\theta$, where z_0 is an axial length, for example, half the length of the magnet. If $z_0/r_0 >> 1$ (long, thin magnet), the integrated axial current is distributed as $cos\theta$. The external power-supply connections for the two circuits are indicated respectively by the black and shaded circles. The end rings are

0-7803-4376-X/98/$10.00 © 1998 IEEE

common to the two circuits, and, if the magnet is driven by a bipolar power supply, are at ground potential. This magnet design is simple and mechanically robust. There are no breaks in the windings for power supply leads, and since the voltage is nominally zero at the ends, there is no need to allocate space to provide electrical insulation from neighboring devices in the target station.

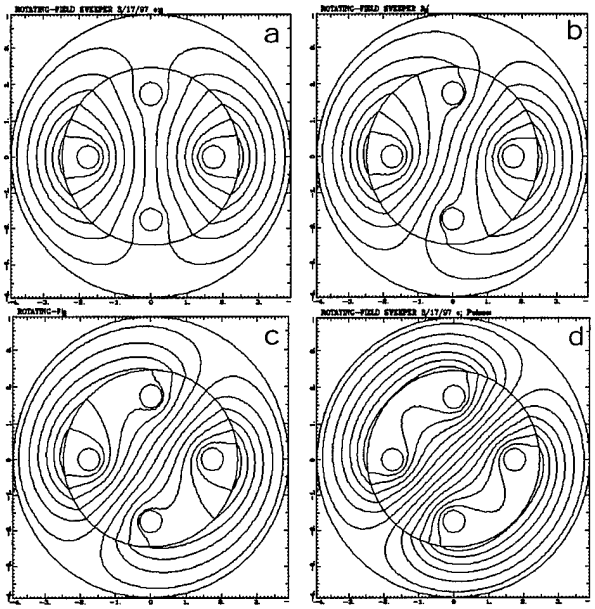


Figure 1. Local magnetic field structure for a 2-phase rotating-field sweep magnet. Field distribution is shown for (a) $\omega t=0$, (b) $\omega t=\pi/12$, (c) $\omega t=\pi/6$, (d) $\omega t=\pi/4$. A magnetic core surrounds the conductors. Dimensions are in cm.

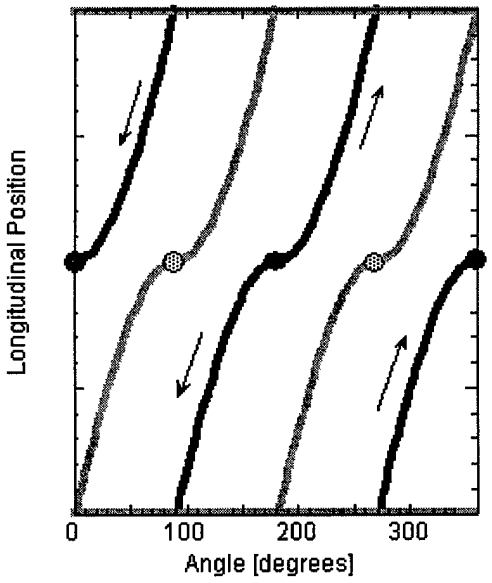


Figure 2. Shape of windings. The black curves represent one circuit, the gray curves represent the orthogonal circuit. Direction of current flow is indicated in one of the circuits.

Three identical magnets will be used, two upstream of the target, and one downstream. The sweeping radius is much smaller than the 2 cm diameter of the lithium collection lens and the aperture of the AP2 beam line. Each magnet is 56 cm long. The deflecting field is 900 G. An air gap is used since the beam is already transported through air from upstream of the target to downstream of the pulsed magnet.

MARS10 and CASIM calculations of energy deposition by hadron and electromagnetic cascades, supported by measurements on the high-voltage test module, show significant heating of iron and ferrite magnet cores downstream of the target. Total heating increases linearly with particle flux, and is a strong function of the radius of the magnet core. Three options for the composition of the magnetic core have been considered in detail.

1. Ferrite. Steady-state temperature rise of the core is determined by thermal conductivity of the material and the rate at which heat is removed at the surface. Because of the poor thermal conductivity and low Curie temperature ($T_c \cong 200°C$), it would be necessary to operate with a large inner-radius (3 cm) core and carefully cool the ferrite. Ferrite would need to be contained in case of cracking due to thermal stress.
2. Iron laminations. A laminated iron core does not have the thermal restrictions of a ferrite core. However very thin (<0.1 mm) laminations are required. Difficulties are expected in preparing and stacking the laminations.
3. Powder cores. The material chosen for the cores on the prototype magnet is 2-81 Mo-Permalloy pressed-powder (MPP). Construction with these cores is simple, and their relatively high thermal conductivity and Curie temperature ($T_c \cong 460°C$) significantly simplify the thermal restrictions compared to ferrites. The thermal stresses are small and can be contained by press-fitting the cores in a nickel housing. Eddy-current losses in the MPP material increase in intense radiation environments[4]. This is not likely to be a major concern, however, since the core is not the dominant loss mechanism in the circuit. A ceramic pipe will provide electrical insulation between the electrical conductors and the cores.

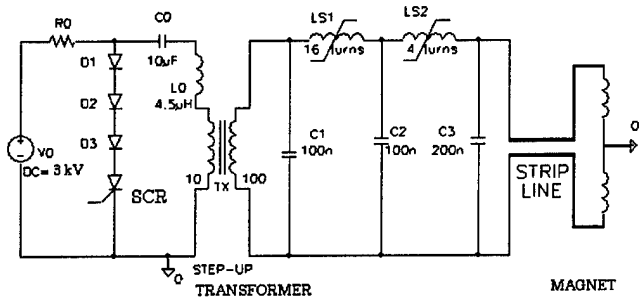
3 POWER SUPPLY

The sweep magnets must be provided with approximately 7 kA at 625-kHz by a power supply located on the floor of the AP0 service building. The current will be supplied through cables over a distance of approximately 10 m into the target vault, and by 2.5 m of strip line through steel shield modules to the magnets at the bottom of the target vault. The power supply circuit diagram is depicted in Figure 3a. Capacitor C3 is connected to the sweep magnet (inductance L3) via the strip line. Pulse compression is used to excite the ringing circuit L3, C3. Two-stage compression with saturated reactors has been chosen, which facilitates transfer of the current pulse to the ringing

circuit, and provides the capability to utilize a SCR switch for resonance charging of first stage capacitor C1 using a 1:10 step-up transformer. The reactors LS1 and LS2 are each composed of three 3.3-mV-sec/turn Metglas cores, wound with 10-μm Kapton insulation. The reactor LS1 has 16 turns and LS2 has 4 turns. The SPICE analysis (Figure 3b) shows that 5 kA peak current, 0.5 μs width is required to oscillate the magnet ringing circuit at 625 kHz with nominal 7 kA amplitude. The peak voltage amplitude at the magnet is 6 kV (3 kV to ground), with 8 kV (4 kV to ground) amplitude at ringing circuit capacitor C3. To achieve this, the first compression stage capacitor C1 should be charged to 17 kV. Taking into account the step-up transformer, the storage capacitor C0 charging voltage is 1.7 kV, the SCR switch peak current is 2 kA and the pulse duration is 15 μs. The power supply is designed to be capable of delivering 80% more current than nominal, for a 30 kV charge, to allow for possible future increase in beam sweeping radius. The magnet current pulse should be synchronized with the extracted beam with an accuracy of less than ±30 ns. Total delay in the power supply circuit, mainly due to the saturated reactors, is 25 μs at nominal current. This delay leads to a requirement on charging voltage stability of 10^{-3}, which is relatively easy to achieve. No other significant source of delay jitter has been observed, when testing a model power supply. The delay in the charging pulse also allows time to disable the Main Injector proton extraction kicker, in case of failure of the sweeping system charging supply.

4 HIGH-VOLTAGE TEST

Ionization of the air by the particle shower downstream of the target will increase the conductivity of the air between the conductors. Electrical losses through the ionized-air path across the gap reduce the Q of the circuit driving the magnet. A dummy test module was installed to measure the leakage current between two conductors symmetrically placed parallel to the beam path. Both the measurement and estimates based on CASIM calculations indicated a current drain between the plates on the order of 100 A, an acceptable amount. The measured leakage current is shown in Figure 4. The current through the air gap turned on rapidly at the beginning of the beam pulse and the gap rapidly opened after the end of the beam pulse. Avalanche ionization of the air is not a problem, as long as peak electric fields are kept well below breakdown levels, i.e. E<10 kV/cm. The test module was instrumented to provide information on heat dissipated and short-term magnetic effects in ferrite and tape-wound magnetic cores caused by the particle shower downstream of the target.



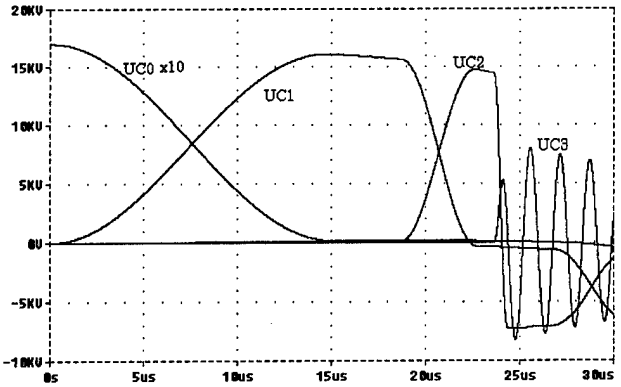


Figure 3. Sweep magnet power supply circuit. (a) SPICE circuit model, (b) voltage waveforms.

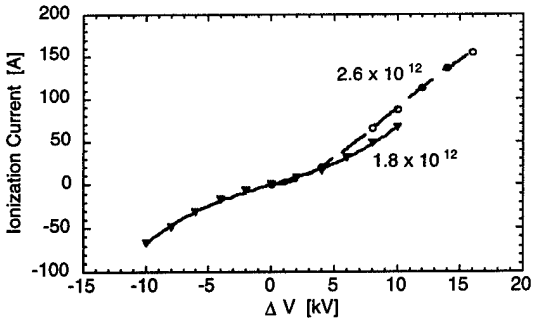


Figure 4. Measured leakage current during beam pulse between a pair of conductors 3-cm wide x 3-cm gap x 24-cm length as a function of voltage drop across the gap. Measurements were taken at two beam intensities.

---

*Operated by the Universities Research Association Inc., under contract with the U.S. Department of Energy.

[1] F. M. Bieniosek, A Beam Sweeping System for the Fermilab Antiproton Source, Fermilab-TM-1857 (1993). F. M. Bieniosek, K. Anderson, K. Fullett, Requirements for a Beam Sweeping System for the Fermilab Antiproton Source Target, Proc. 1995 US Particle Accelerator Conference.

[2] P. P. Bagley, et.al. Summary of the TeV33 Working Group, Proc. 1996 Snowmass Conf.

[3] F. M. Bieniosek, Beam-Sweep Magnet with Rotating Dipole Field, Pbar Note#561 (1996).

[4] C. W. Chen, Magnetism and Metallurgy of Soft Magnetic Materials, Dover, 1977, p. 474.

TEST OF VERY FAST KICKER FOR TESLA DAMPLING RING*

B. I. Grishanov, F. V. Podgorny, Budker INP, Novosibirsk, 630090, Russia
J. Rümmler, DESY, Notkestrasse 85, Hamburg 22603, Germany
V. D. Shiltsev, FNAL † M.S.345, P.O. Box 500, Batavia, IL 60510, USA

Abstract

We describe a very fast kicker with unique combination of high repetition rate and short pulse width. Constructionally, the device is a symmetrical counter traveling wave strip-lin kicker fed by semiconductor high-voltage pulse generator. Experimentally tested kicker has a full pulse width of about 7 ns, 1.4 MHz repetition rate and maximum kick strength of the order of 3 G·m. Recent achievementsin high-voltage semiconductor field-effect-transistors (FET) technology and goal-specific optimization of the kicker parameters allow many-fold increase of the strength, and the kicker can be very useful tool for bunch-by-bunch injection/extraction and other accelerator applications.

1 INTRODUCTION

The TESLA linear $e^+ - e^-$ collider project (see, e.g. [1]) requires that the train of 1130 bunches with total length of 0.8 ms, or 240 km must be stored in a damping ring in a compressed mode with a bunch spacing smaller than in the linac, and then expanded with use of bunch-by-bunc extraction out of the ring. Thus, the circumference of the ring is proportional to the minimum rise/fall time of the ejection kicker used, e.g. 60-ns-kicker yields 20 km long ring, while the circumference of about 2.3 km (the ring in existing PETRA tunnel [2]) requires rise and fall times of the kicker to be less than 7 ns. Some 3 G·m of the kicker strength is needed for the 10 rms bunch size kick amplitude [3]. The pulse spacing must be 0.7 μs.

Many present-day fast kickers are essentially ferrite kickers fed by thyratrons. They enjoy high voltage abilities of thyratrons but can not work effectively with repetition rate above dozen of Hz and can not provide the kick duration less than 50-100 ns. Here we describe a device which operates with one order of magnitude shorter pulses and five orders of magnitude higher repetition rates. Constructionally, the device is a symmetrical counter traveling wave strip-line kicker fed by FET based pulse generator. We present test results of the kicker prototype which fits to the mentioned above requirements.

2 THE KICKER

The counter traveling wave kicker is designed, built and preliminary tested in Budker Institute of Nuclear Physics (Novosibirsk, Russia). High-voltage pulse generator is basedon fast field effect transistor (FET) switch by BEHLKE Electronic GmbH (Frankfurt a.M., Germany). Test measurements with the high-voltage generator were held in October 1996 at DESY (Hamburg, Germany). Details of kicker construction and preliminary test results can be found in Ref.[4].

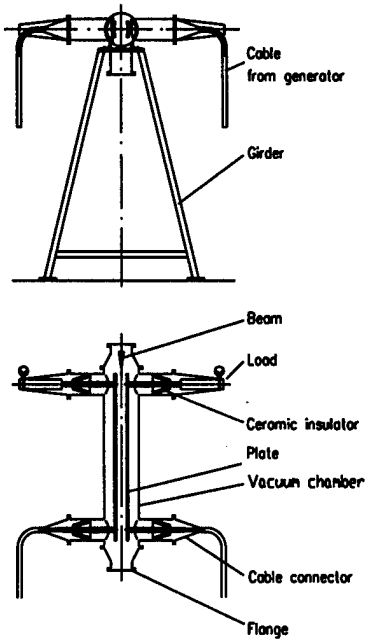


Figure 1: Traveling wave kicker design.

2.1 *Principle of operation*

Fig.1 shows the kicker major parts and construction. Two pulses from generator with negative and positive polarities simultaneously go through connection cables and ceramic insulator inputs into two parallel conducting plates (electrodes). Wave resistance of the electrodes inside the vacuum chamber is tuned to be 50 Ohms. An electro-magnetic wave between the electrodes travels with the speed of light c along in the direction *opposite* to an incoming charged particle beam and produces horizontal kick. Then the pulses pass ceramic outputs (the same construction as the inputs) and in ideal case are fully damped in two 50 Ohms loads. Each load contains an in-built 1:120 attenuator for measurement purposes.

The electro-magnetic field between the plates consists of equal amplitude and perpendicular electric and magnetic components. For ultra-relativistic particles moving alongthe electrodes, the resulting horizontal deflecting force is twice the electric force for the beam traveling in the direction opposite to the pulse propagation direction, and the electric and magnetic components cancel each other for the beam which goes in the same direction as the pulse.

* work is supported by DESY
† Operated by Universities Research Association, Inc., under Contract No. DE-AC02-76CH03000 with the US Department of Energy

0-7803-4376-X/98/$10.00 © 1998 IEEE

2.2 *Time structure of the kick*

Now we consider the time structure of the kick (or deflection angle) produced by the traveling wave kicker. For simplicity, we take a rectangular input voltage pulse $U(t)$ with maximum amplitude of U_m and pulse duration of t_p – see-upper plot in Fig.2. Let us denote $t = 0$ the moment of time when the front of the pulse enters the kicker input. As the beam passes through the oncoming wave, the maximum deflection will be seen by test particles which at $t = 0$ are distanced by doubled kicker length $2l$ from the input end of the device. We will call the corresponding time value of $\tau_g = 2l/c$ as the "kick growth time". The maximum kick lasts over time interval of $t_f = t_p - \tau_g$ which is supposed to be synchronized with the bunch to extract (see lower diagram in Fig.2). Behind that bunch, the amplitude vanishes over the same "kick growth time".

One can make two remarks: firstly, if the pulse duration is less than the growth time $t_p < \tau_g = 2l/c$, then the kicker does not work in full strength; secondly, if the bunch spacing in the storage ring is equal to τ, then the generator pulse duration must be less than $t_p < 2\tau - 2l/c$ otherwise neighbor bunches will be deflected too. As the result, one can conclude, that the duration of the rectangular pulse equal to the bunch spacing $t_p = \tau$ corresponds to maximum kicker strength. The kicker length has to be less than $l < c\tau/2$ because the pulse shape can not be exactly rectangular, besides that, some flat top of the kick is usually required. Again, making numerical example for the TESLA damping ring with $\tau = 7$ ns, we choose $l = 0.5$ m (i.e. $\tau_g = 2l/c = 3.3$ ns $< \tau$) and the pulse FWHA equal 6-8 ns.

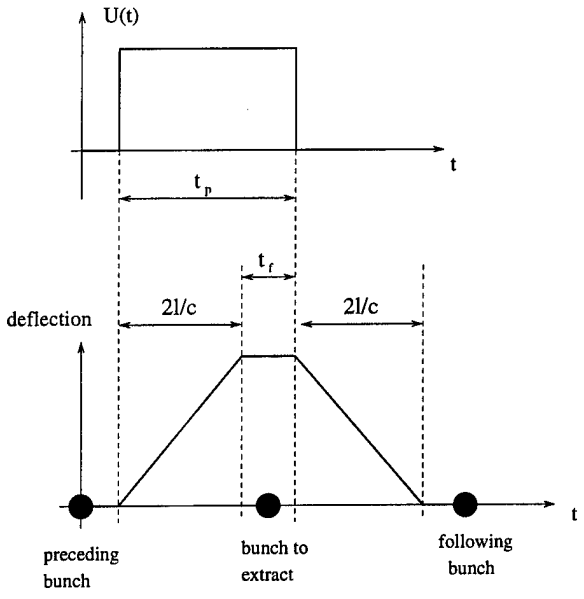


Figure 2: Operation of traveling wave kicker.

2.3 *Construction features*

The kicker is made from materials which are able to work under conditions of "baked-up" high vacuum such as stainless steel, special kind of bronze, ceramics, covar. Copper alloy is used for welding of ceramic insulators. The electrodes are connected to central conductors of ceramic inputs by use of special fixators.

The electrodes are not flat, their shape is optimized in order to achieve homogeneous field and the wave resistance of 50 Ohms. Calculated field non-uniformity is less than 10% over 80% of full aperture of $2A_x \times 2A_y \approx 50 \times 50$ mm^2.

2.4 *Preliminary tests*

Vacuum testing has been done at Novosibirsk INP in accordance to modern requirements on accelerator elements. The whole kicker was heated ("baked") up to 300°C under continuous vacuuming with use of oil-free magneto-discharge pumps. Vacuum of about $1 \cdot 10^{-10}$ Torr was observed after cooling the kicker down to the room temperature.

High voltage test has been done in order to check the kicker electrical performance under high vacuum. 1 ms long, half-sinusoid shape, 15 kV pulses with opposite polarities fed the kicker electrodes through input cables and ceramic inputs at repetition rate of 1 Hz. The loads were taken off the kicker. The test has shown no spark or discharge events over 10 minutes interval.

The kicker element impedances matching was checked with use of low voltage short pulse generator. The reflected signal comes after the main pulse and can be presented in the same oscilloscope record. An amplitude of the reflected pulse serves as an indicator of the matching. During the test with 12 ns long pulse which has 2 ns rise and fall times we found that the reflected pulse has some 5.5% in amplitude mostly due to reflections at the initial pulse fronts.

2.5 *High-voltage pulse generator*

The high-voltage (HV) short-pulse generator is based on the solid state field-effect transistor switch HTS 50-12-UF by BEHLKE Electronic GmbH (Germany). It has been specially designed for HV generators with a short pulse duration and extreme edge steepness, and has a very low jitter and the lifetime typical of semiconductor devices. Major technical parameters of the switch are as follow: maximum operating voltage 5000 V, maximum peak current 120 A, turn-on rise time (10-90% in amplitude) $\simeq$ 1.6 ns, minimum pulse spacing is less than 1 μs, dimensions $89 \times 64 \times 31$ mm^3. Generator provides the necessary time structure of the signal: variable number of pulses in train – from 10 to 1130, pulse spacing – typically 700 ns (frequency of about 1.4 MHz), and the pulse train repetition frequency of 10 Hz.

3 RESULTS

Fig.3 shows about 120 times attenuated outputs of the kicker fed by high-voltage pulse generator. High-precision 500 MHZ bandwidth HP54542A oscilloscope was used for signal recording.

The maximum voltage applied to each plate is about U_m = 2.4kV, the full aperture of the kicker is $2a$ =50 mm and total length l =0.5 m, that yields the kicker strength of S_0 = 3.2 G·m. The pulse shape is close to half-period of sine function with zero-to-zero duration of $t_p \approx 6$ ns. Being installed at the E =3.3 GeV TESLA damping ring such kicker can deflect the positron beam by $\theta_m \approx 30$ μrad, that corresponds to about $\theta\sqrt{\beta\beta_k} \simeq 6$ mm beam displacement at the point with beta function of about β =200 m if the beta function β_k at the kicker is the same.

Reflected pulse amplitude was found to be less than 8% of the initial one. Further reflected pulse reduction needs precise mechanical tuning of the plate convections to the output kicker conductors. Observed pulse-to-pulse amplitude variations were definitely less that 5%, but the stability issue was not studied thoroughly.

As the TESLA damping ring beam extraction requires 1130 pulses spaced by 0.7 microsecond and this pulse train to be repeated 5-10 times a second, we studied the kicker in such conditions.

General conclusion is that the pulse generator works well in this regime. The only problem we observed was monotonically decreasing pulse amplitude with increasing pulse number. As the result the maximum amplitude of, say, pulse number 11 was some 4% less than of the first one. It is known how to work out this effect with use of larger high-voltage storage capacitance in the pulse generator, and we are going to implement this modification. To carry out the mean power maintenance test, we used smaller number of pulses (few dozens) in the train with correspondingly increased repetition rate, and the kicker works well with the design average power of 18 W.

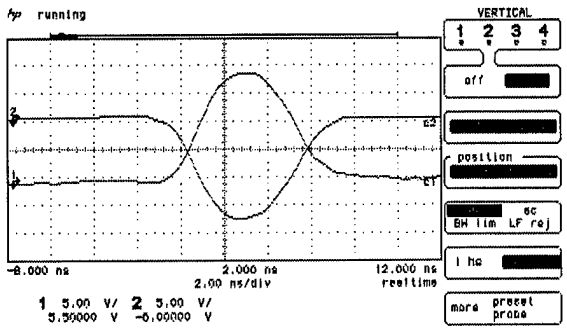


Figure 3: High voltage pulse at both outputs (attenuation 1:120).

4 DISCUSSION AND CONCLUSION

Very fast kicker for accelerator applications was designed, produced and tested in collaboration of Budker Institute of Nuclear Physics (Novosibirsk, Russia), DESY (Hamburg, Germany) and Fermilab (Batavia, USA). We have found that the counter traveling wave kicker with more than 2 kV voltage, 7-8 ns pulse generator produces some 3 G·m deflecting kick strength. The kicker makes possible to work with up to thousand pulses in train with pulse-to-pulse space of 0.7 microseconds, and repetition rate more than 10 Hz. We intend to make further tests and study ultimate kick strength, amplitude stability, ways to reduce pulse reflections and eliminate the decrease of the voltage in long pulse train.

There are some ways to increase the kicker strength. For that one has either increase the maximum voltage U_m, or decrease the device aperture a, or increase the kicker length l. The maximum voltage is limited by FET breakdown in HV switches. Nevertheless, there are existing switches with U_m of about 8-10 kV, while, at the sacrifice of pulse spacing and repetition rate, the voltage can be increased up to 15-25 kV. Usually, there is no large freedom in decreasing the kicker aperture in circular accelerators, nevertheless, for some applications which use single passage tiny beams (e.g. in linacs), the shrinking of a can be useful and possible. Finally, making longer kicker one has to take into account the required kick duration because the traveling wave kicker has intrinsic kick growth time proportional to the length $\tau_g = 2l/c$ which should be less than bunch spacing in accelerator. Thus, fast and strong deflection can be done with use of several short kickers. E.g. the bunch spacing of τ = 20 ns requires the kicker to be sectioned into several parts each of them has to be shorter than $l = \tau c/2 = 3$ m.

All together, one can estimate maximum strength of the fast kicker for accelerator applications – which we think can be realized at the moment – taking the parameters of U_m = 12 kV, $2a$ = 4 cm and total length of l = 10 m, that results in the strength of S_m = 400 G·m. This value indicates that fast traveling wave kickers with semiconductor pulse generators can be widely used at medium- and high-energy accelerators.

5 ACKNOWLEDGEMENTS

We acknowledge useful discussions with J. Marriner, P. Colestock, and C. Jensen (FNAL). Authors are indebted to N. Dikansky (INP), D. Finley (FNAL), R. Brinkmann, R. Kose and D. Trines (DESY) for their steady interest and support of this work. We would like to thank H. Gundel (TU Berlin) for assistance in the pulse generator handling.

6 REFERENCES

[1] R.Brinkmann, Proc. IEEE PAC'95, Dallas (1995), pp.674-676.

[2] V.Shiltsev, DESY Print, TESLA 96-02 (1996).

[3] V.Shiltsev, Nucl. Instr. and Meth. A374 (1996) 137.

[4] B.Grishanov, F.Podgorny, J.Rümmler, and V.Shiltsev, FERMILAB-TM-1990 and DESY Print TESLA 96-11 (1996).

OPTICS AND FIELD ERROR COMPENSATION IN THE FNAL PERMANENT MAGNET 8.9 GEV/C PROTON TRANSFER LINE

John A. Johnstone, FNAL*, P.O. Box 500, Batavia, IL, USA 60510-0500

Abstract

Protons are transported 760 m from the Booster extraction point to injection into the Fermilab Main Injector. Apart from two, comparatively short, specialized optical matching sections the transfer lattice is described by 90° betatron phase advance arc cells and missing-dipole dispersion suppressing cells. This repetative structure, combined with the small average bend per cell makes it feasible to construct this section exclusively from low-field permanent dipoles and gradient magnets. The permanent magnet section is nearly devoid of powered correctors: trajectory control and momentum error compensation is accomplished instead by moving select gradient magnets transversely. Permanent magnets are being used in the transfer line primarily to acquire the manufacturing and operational experience necessary to ensure success of the future FNAL Recycler Ring.

1 INTRODUCTION

Protons extracted from the Booster are transported 756 m for injection into the FMI. The 8 GeV transport line is comprised of three major sections: a matching section between the Booster and the main body of the beamline, which also incorporates the descent from the Booster to Main Injector elevation; a long section of periodic FODO cells; and a final section to match the optics between the beamline's FODO section and the FMI.

As originally designed, the 8 GeV line was to be constructed exclusively from magnets recycled from Main Ring and the present Booster to Main Ring transfer line. This remains true for the optical matching sections at each end of the line. However, in the long arc of repetitive FODO structure all electromagnets (B2 dipoles and 3Q52 quadrupoles) have been eliminated and replaced with permanent magnet dipoles, gradient magnets, and quadrupoles. The design of the permanent magnets used in the 8 GeV line are described extensively elsewhere in these proceedings [1-4].

In addition, unlike its electromagnetic predecessor which had trim correctors assigned to every quadrupole location, trajectory control through the permanent magnet arc will be accomplished largely by gradient magnet movements.

2 PERMANENT MAGNET OPTICS

The transfer line's permanent magnet section extends for 644 m and is constructed from 65 gradient, 45 dipole, and 9 permanent quadrupoles. The relevant magnet parameters are summarized below in Table 1. The available aperture at each magnet is 92.075 x 47.625 mm, corresponding to the interior dimensions of a squashed 3" beampipe.

The long arc section of permanent magnets produces a total bend of 103.45°, with each dipole and gradient magnet bending the trajectory by 1.10°. The first 8 dipoles have reverse bends relative to the remaining magnets in the series, which serves to keep the beam well clear of the existing Anti-Proton complex.

Magnet	#	L (m)	B (kG)	B' (kG/m)
Gradient	65	3.9751	1.4327	4.6562
Dipole	45	2.4638	2.3116	0
Quadrupole	9	0.5080	0	29.1470

Table 1 : Parameters of the permanent magnets used in the 8 GeV line FODO section.

The permanent magnet section is constructed from just three different types of cells. These cells were designed with the intent to replicate as closely as was reasonable the optics and trajectory defined by the earlier electromagnet design. These cells are depicted in Figure 1 below.

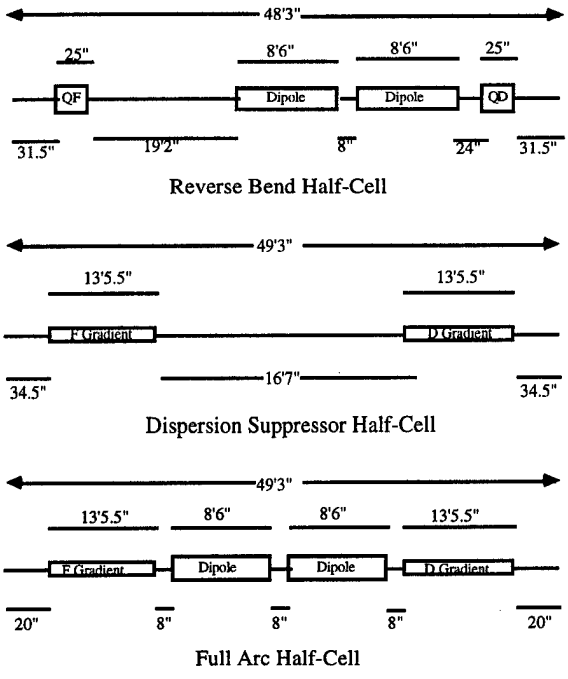


Figure 1 : Physical layout of the 3 permanent magnet cell types in the 8 GeV transfer line (not to scale).

0-7803-4376-X/98/$10.00 © 1998 IEEE

Lattice functions for the entire 8 GeV line from Booster to Main Injector are shown below in Figure 2. The 'reverse bend' section extends from quad Q810 to 814, and the regular long arc runs from 814 through to the first Injector-end powered matching quad at 847.

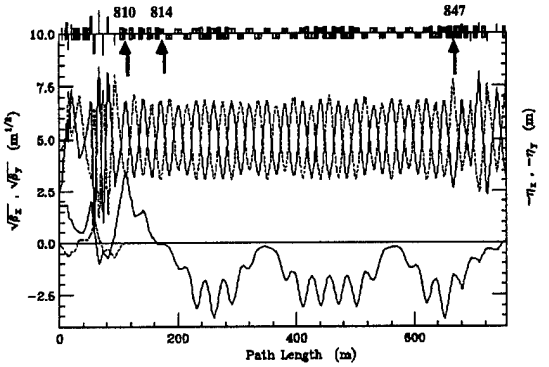


Figure 2 : Lattice functions of the proton 8 GeV line from the Booster to Main Injector.

The 'reverse-bend' section is constructed from two cells, each characterized by 4 permanent dipoles, 4 permanent quadrupoles, and 84° of betatron phase advance per cell. These cells represent a compromise betweeen following as closely as possible the trajectory through the tunnel defined by the earlier electromagnet solution and achieving a smooth optical match to the subsequent long arc of FODO cells.

The regular lattice section is constructed from two types of cells -- regular cells with 4 permanent dipoles plus 4 gradient magnets per cell and missing-dipole dispersion suppressing cells with 4 gradient magnets per cell. Both types of cells have ~90° of phase advance but are not perfectly matched optically. This mismatch is the consequence of intentionally creating additional space in the lattice to accommodate the possible insertion of further diagnostics in the future. As a result dispersion neither reaches precisely zero anywhere, nor is it optimally minimized through the arc. However, horizontal dispersion becomes as small as 0.12 m and does not exceed 3.71 mm, which is acceptable. With a maximum β = 47 m and $\delta p/p$ = 0.2% the transverse beam size is less than ±16 mm for a 40π mm-mr (95% normalized) emittance, which is compatible with the 48 mm (V) x 92 mm (H) aperture of the beampipe. With each dipole and gradient magnet producing 1.10° of bend, the sagitta is only 5.9 mm and 9.5 mm respectively. Again, this is compatible with the available aperture.

3 FIELD ERROR PROPAGATION & COMPENSATION

Every cell boundary in the 8 GeV line has a BPM associated with it and every electric quadrupole in the line also has a recycled Main Ring correction dipole nearby. Additional correctors are located at the entrance and exit of the long arc to provide beam position and angle adjustment.

The main body of the permanent magnet section is nearly devoid of trims, and these are situated with an eye to centering the beam on downstream multiwires rather than for global trajectory control. Instead, as will also be the case in the Recycler Ring, any necessary trajectory corrections will be performed by moving gradient magnets.

The gradient magnets are designed, and installed, with the ability to 'float' transversely on the beampipe by as much as ±1". With this feature the available beam aperture is always determined solely by the beampipe dimensions and is independent of the transverse position of the magnet. The dipole kick due to horizontal translation by an amount δ is:

$$\Delta\theta = \frac{\int B_1 \cdot ds}{B\rho} \bullet \delta = 614 \cdot \mu r/cm$$

A 1 cm magnet displacement therefore translates into a kick ~0.85% of the nominal bend. This is comparable to the strength obtainable from a Main Ring trim ($\Delta\theta$ = 580 μr @ 5A). Fairly modest magnet moves therefore provide significant steering capability. The effect of dipole field errors on the trajectory through the long arc, and the consequent gradient magnet movements required for correction, have been investigated in simulations. Random field error compensation must be addressed by any beamline but, unlike the case with electromagnet transfer lines, systematic dipole field errors (or, equivalently, a systematic beam momentum offset) becomes an important issue for permanent magnet lines.

3.1 Simulation Approximations

Rather than using the true lattice configuration, trajectory error simulations were performed with a lattice constructed from 7 regular plus 12 dispersion suppressor cells to mimic the repetitive optics of the long arc. While results from the simulations should not be sensitive to this approximation, trajectory correction is simplified by being amenable to solution via the canned algorithms intrinsic to MAD [5].

The optics of this approximate lattice are shown in Figure 3. In all following discussions of simulations the beam is assumed to be described by 40π mm-mr emittance (95% normalized) with a momentum spread of $\delta p/p$ = 0.2%.

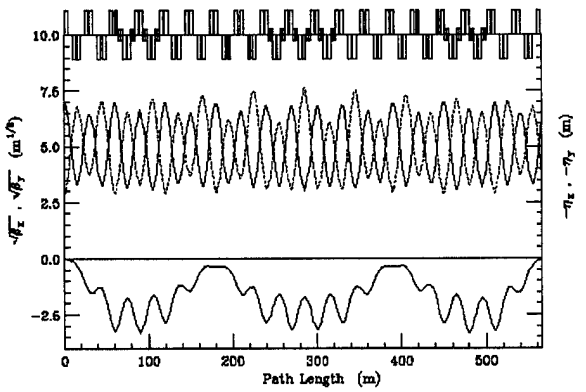


Figure 3 : Lattice functions of the 'approximate' repetitive FODO lattice employed in simulations of error propagation and correction.

3.2 Systematic Field / Momentum Errors

A systematic 1% dipole field error (much larger than any realistic error source imagined) was assigned to each of the 28 dipoles, 38 F-gradient, and 38 D-gradient magnets in the approximate lattice. Figure 4 shows the resulting horizontal beam trajectory and envelope. The solid bars intruding from the top and bottom of the graph indicate the available beampipe aperture. Position and angle of the incoming beam have been optimized to minimize the transverse excursions. The resulting rms displacement of the orbit is $\Delta x(\text{rms}) = 18.5$ mm and, with maximum displacements of $\Delta x(\text{max}) = 31.0$ mm, the beam scrapes at all high dispersion locations.

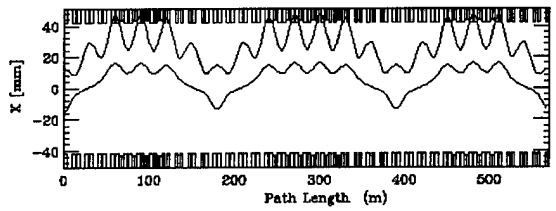


Figure 4 : Horizontal beam trajectory and envelope for a 1% systematic field (or momentum) error.

Figure 5 shows the beam trajectory and envelope after correction. Moving just the F-gradient magnets, 8 by 10 mm, 12 by 7.5 mm, and 18 by 5 mm, the excursion of the beam is dramatically reduced to $\Delta x(\text{rms}) = 1.7$ mm and $\Delta x(\text{max}) = 3.2$ mm.

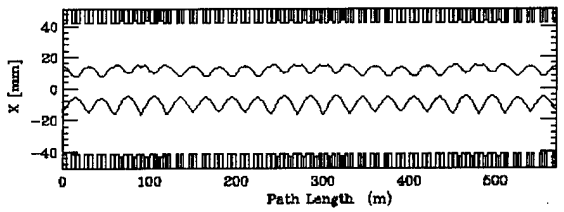


Figure 5 : Horizontal beam trajectory and envelope after moving magnets to correct for the 1% systematic error.

3.3 Random Field Errors

Random field errors can be treated analogously to the systematic errors. Uniformly distributed, random dipole errors in the range ±0.25% were assigned to all 104 magnets in the approximate lattice. The beam trajectory resulting from 20 random generator seeds was calculated. The worst case trajectory, which had an orbit wobble characterized by $\Delta x(\text{rms}) = 3.7$ mm and $\Delta x(\text{max}) = 13.0$ mm, is illustrated in Figure 6 below.

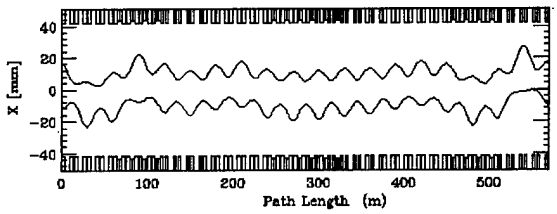
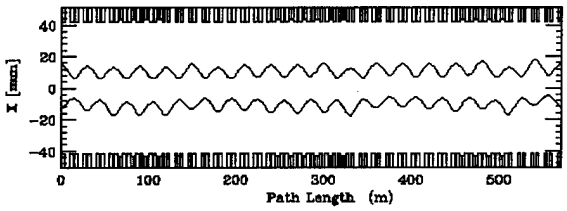


Figure 6 : Horizontal beam trajectory and envelope for the 'worst case' random 0.25% field errors.

It can be seen from Figure 6 that no correction of the orbit is strictly necessary -- there is ample aperture for lossless beam transmission. However, with small adjustments to just 12 of the F-gradient magnets, moving 4 by 1.25 mm, 6 by 1.00 mm, and 2 by 0.5 mm, the trajectory deviation can be reduced to the level achieved for the 1% systematic error case. Figure 7 shows this corrected trajectory, where orbit excursions have now been dropped to $\Delta x(\text{rms}) = 1.2$ mm and $\Delta x(\text{max}) = 3.0$ mm.



.Figure 7 : Trajectory and envelope after compensation for the 0.25% random field errors.

4 DISCUSSION

There are additional sources of error intrinsic to the permanent magnets that have not been addressed here. The two most important of these are probably the field strength variation with temperature and the systematic plus random bend center errors. To a large extent however the adverse effects of these flaws can be eliminated by sorting the magnets prior to installation.

What has been demonstrated by the simulation results presented here is that very large momentum offsets from nominal and/or large field errors can be corrected through fairly modest movements of gradient magnets, without the necessity of separate correction elements.

REFERENCES

[1] 'Permanent Dipole Magnets for the 8 GeV Transfer Line at FNAL', H.D. Glass et al, these proceedings – 2P.12.

[2] 'Stability Tests of Permanent Magnets Built With Strontium Ferrite', H.D. Glass et al, these proceedings -- 2P.13.

[3] 'Permanent Gradient Magnets for the 8 GeV Transfer Line at FNAL', H.D. Glass et al, these proceedings – 2P.14.

[4] 'Hybrid Permanent Quadrupoles for the 8 GeV Transfer Line at Fermilab', S.M. Pruss et al, these proceedings -- 7P32

[5] 'The MAD Program', H. Grote, F.C. Iselin, CERN/SL/90-13(AP).

* Work supported by the U.S. Department of Energy under contract number DE-AC02-76CH03000.

A HIGH INTENSITY BEAM ABSORBER COREBOX FOR THE FERMILAB MAIN INJECTOR ABORT SYSTEM

M. Reichanadter, C.M. Bhat, C. Crawford, P.S. Martin
Fermi National Accelerator Laboratory*
P.O. Box 500, Batavia, Illinois 60510

INTRODUCTION

The beam abort system proposed [1] for the Fermilab Main Injector will extract a proton beam from the accelerator in a single turn (~10μsec) and direct it to an external beam absorber, of which the corebox is the central component. The primary design constraint of the corebox is to absorb an incident proton beam in a safe, efficient manner and transfer its energy to the primary cooling loop of the Abort Core cooling system. Additionally, it is clearly necessary, due to the induced radioactivity in and around the beam absorber, that the corebox be maintenance-free and have a lifetime equal to that of the Main Injector Accelerator, 20 years.

To achieve the above constraints, the corebox design must satisfy three primary aspects; absorb incident and secondary particles such that radiation levels are maintained below PSAR limits [2], efficiently transfer bulk heat to the cooling system, and dissipate mechanical wave propagation resulting from the sudden deposition of beam energy.

1 BEAM ABSORBER DESIGN REQUIREMENTS

The upper bound parameters of a single aborted beam pulse are listed below[2];

beam energy	150GeV
beam type	proton
total kinetic energy	2.4MJ
pulse duration	10 μsec
pulse rate	0.53Hz
#particles/spill	1.00E+14
transverse beam size ($\sigma_x=\sigma_y$) Gaussian beam distribution	0.125cm

With regard to repeated beam aborts and the yearly average beam we have the following specifications[2];

short term continuous operation	1E+14ppp @ 150GeV with a 1.9 sec cycle time for 1 hour duration
average power input	1.28MW
yearly proton flux	2.124E+19p/yr @ 150GeV

* Operated by Universities Research Association, Inc., under Contract No. DE-AC02-76CH03000 with the U.S. Department of Energy.

2 ENERGY DEPOSITION ANALYSIS

Energy deposition due to high energy particle beam interaction within the abort system per proton pulse has been calculated using the Monte Carlo computer code MARS13 which simulates the three dimensional hadron and electromagnetic cascades. The analysis assumes radial symmetry and the energy deposition is calculated on a per grid zone basis. The radial zone size varies from 0.06cm near the beam axis to 2.54cm at the outer perimeter. Along the azimuthal axis, Δz is fixed at 12.20cm.

For a single beam spill, the maximum energy deposition for the corebox materials (carbon, aluminum) and the steel shielding (downstream of the corebox) is shown in the figure below.

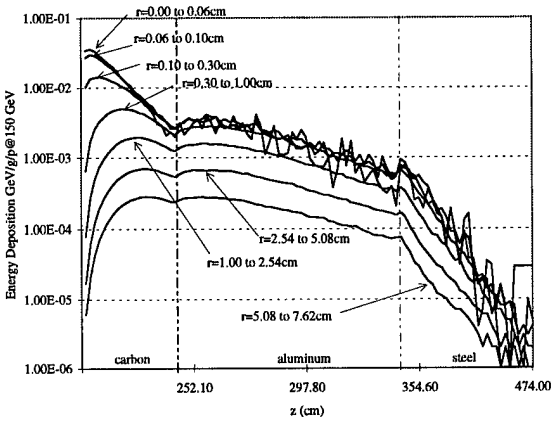


Figure1. Energy deposition in MI Abort Corebox (Mars13).

A summary of the maximum energy deposition values and related temperature increase is shown below.

	Carbon	Aluminum	Steel
energy (GeV/g/p)	3.60E-02	4.11E-03	9.32E-04
energy (J/g)	576.72	65.84	14.93
ΔT (degrees C)	469.00	72.00	33.00

3 COREBOX DESIGN

The Abort Corebox, shown in Figure 2, consists of eight, 12-inch long, 6-inch diameter cylinders of isostatically-molded, fine grain, high purity carbon, which are held in an 11-foot long aluminum water jacket with a light shrinkfit (0.002"). The shrinkfit is necessary to insure good thermal contact between the carbon cylinders and the aluminum water jacket. This design length, 96

0-7803-4376-X/98/$10.00 © 1998 IEEE

inches of carbon, followed by 36 inches of aluminum is sufficient to absorb approximately 800kW (average power) of the beam's total energy, with the remainder deposited in the steel shielding downstream of the corebox. The corebox housing is made of aluminum 6061-T6, a weldable, machinable, moderate strength alloy having good corrosion resistance.

A 0.010" thick titanium window seals and separates the carbon cylinders in an argon environment, to prevent oxidation of the carbon at elevated temperatures. Energy deposition calculations predict that the titanium window will reach a peak temperature of 386.68K in about 45 pulses at 1E+14ppp. The temperature of the carbon cylinders and the aluminum corebox are monitored using high temperature thermocouples (Type J, 0.125" dia.).

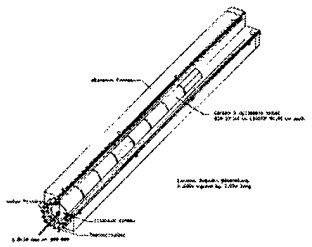


Figure 2. Cutaway isometric of the Abort Corebox

The primary cooling system for the Abort Corebox has a flow rate of 160gpm (Δp=3.8psi) with eight parallel paths through the aluminum section of the corebox. The aluminum surface temperature is approximately 68C, with the ΔT of the water at 16C, and a film coefficient of 10500W/m2-K. Prolonged exposure to beam environments, leading to the production of tritium, require an all-welded system design.

4 THERMAL CONSIDERATIONS

Using the energy deposition values per Main Injector proton pulse as an input, the temperature increase associated with each pulse can be carried out over time, until a quasi-steady state is reached. At this point average power into the abort equals the average power dissipated, and the storage term drops to zero. Separate analysis for the carbon, aluminum and steel were evaluated using the finite element code ANSYS®, with the following assumptions and boundary conditions;

- unsteady, non-linear energy deposition(C,Al)
- energy deposition is in discrete zones (r,z)
- transient, 2-D conduction(r,z)
- ρ = constant, k and c_p = f(T) Ref[3]
- constant temperature boundary at r=7.62cm (C, Al)
- adiabatic boundary on cylinder ends,$\partial T/\partial z$=0 (C,Al)
- natural convection and radiation heat transfer at the Fe boundary r=22.86cm, l=213.36cm
- steady, non-linear energy deposition (Fe only)
- shape factor=1.0, emmissivity=1.0 (Fe only)

Single pulse results of the finite element analysis for the carbon and aluminum predict the highest ΔT values of 456.1 in the carbon and 66.8 degrees C for the aluminum. Average deviation with the MARS13 analysis is less than 5%. Carrying the analysis forward in time, the carbon and aluminum sections reach the quasi-steady state point in about 80 and 25 pulses, respectively, as shown in Figure 3.

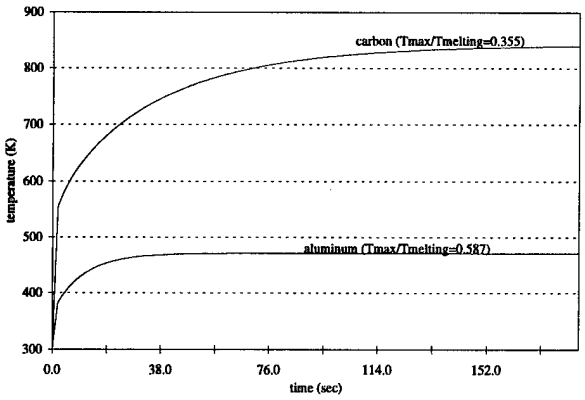


Figure 3. Maximum nodal temperature versus time for the carbon and aluminum sections.

Downstream of the corebox consists of a series of steel shielding slabs 84"high x 84"wide x 121" in length. The total energy (57GeV/p @150Gev) is deposited directly in a single central slab 18"high x 51" wide x 66"in length.

A steady-state solution for the steel was investigated using the first pulse radial and azimuthal energy deposition values averaged over time. Heat transfer from the steel shielding was conservatively modeled as a single right circular cylinder (r=22.86cm, l=213.36cm), using natural convection and radiation at the boundary as the transport mechanisms. The results of this analysis predict the maximum temperature in the slab of 1437K (Tmax/Tmelting=0.807) while transferring 480kW to the surrounding atmosphere.

5 STRESS WAVE CONSIDERATIONS

The deposition of a large amount of beam energy over a few micro-second duration results in rapid material expansion due to high temperatures causing dynamic stresses that propagate through the material at the velocity of sound. Dynamic stress waves can be potentially destructive, if either the incident wave imparted by the beam, or the reflected wave returning from the free surface exceeds the fatigue strength of the material. For a perfectly constrained body under thermoelastic pressure increase due to energy deposition, we have,

$$p = \frac{E}{1-2\nu}\alpha(\Delta T) \quad (1)$$

Where E= the elastic modulus, ν=Poisson's ratio, and α= the linear expansion coefficient. Applying this to the highest energy deposition zones in the carbon and aluminum gives values of 25MPa and 337MPa, respectively. From this conservative estimate we can determine both materials are well below their yield

strength, and assume that only elastic waves are present. The details of the stress waves imparted in the MI Abort carbon and aluminum were investigated using the ANSYS program, using the following assumptions and boundary conditions;

- one-dimensional transverse elastic waves are present
- material is initially at rest, and stress free
- axisymmetric model, at r=0.0cm, deflection=0.0cm
- constrained boundary at r=7.62cm, deflection=0.0cm (carbon only)
- ignore water passages in cross-section (aluminum only)
- linear material properties
- reflection coefficient=100%

For the carbon cylinders, the outer radial boundary is constrained by the shrink fit, resulting in the incident compressive wave being fully reflected as a compressive wave. This returning wave is focused radially on the region surrounding the centerline of the carbon, and returns at the beam axis centerline in approximately 50μsec. Element size chosen for the carbon analysis is 0.5mm (152 elements total), with a wave speed of $c=(E/\rho)^{0.5}$ (≈2600m/s). The time step used to resolve the dynamic wave is 0.065μsec, roughly 1/3 of the ratio Δr/c to ensure stability[4]. Total time for the analysis is 80μsec, which is sufficient for the incident wave to be reflected off the outer boundary and return to the central beam axis. The analysis indicates that the incident beam imparts a compressive radial stress of 9.0MPa (-1300psi), with the returning reflected wave increasing the compressive stress to 10.0MPa (-1450psi), both significantly less than the carbon compressive yield strength of 90MPa, as displayed in Figure 4. Circumferential stresses were found to be equal or lower than the radial stresses.

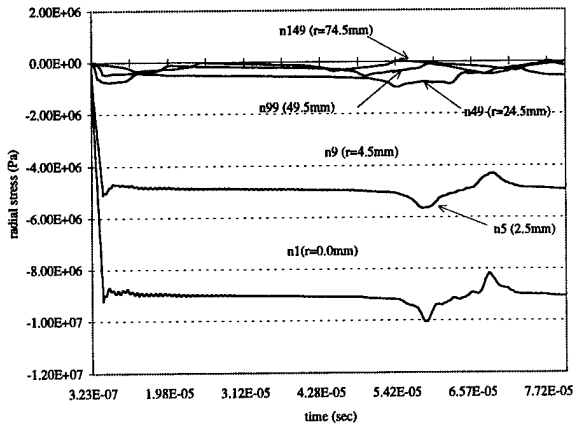


Figure 4. Radial pressure wave resolved for selected nodes in the carbon section of the MI Abort Corebox.

The aluminum section of the corebox was modeled as a square prism with a center to edge distance of 15.24cm. Higher stress peaks are expected in the aluminum section due to a high expansion coefficient. Additionally, the outer edge of the aluminum is a free surface, resulting in a reflected tensile wave, rather than a compressive wave, as in the carbon. Tensile waves can lead to density decrease in the material, and fracture if the tensile strength is exceeded.

Using Δr=0.5mm with 2400 time steps over 75μsec time span ($c=(E/\rho)^{0.5}$≈5100m/s for aluminum), the results of the analysis reveal a radial compressive stress of 49.0MPa (7100psi) from the incident beam. The reflected wave, focused along the centerline of the aluminum, is found to be 67.0MPa (9700psi). This analysis is considered conservative since there was no consideration of the water channels that form a radial pattern through the aluminum corebox. This array of holes will help to disperse the outgoing compressive wave, and diffuse the reflected ingoing tensile wave. The 9700 psi tensile peak, 42% of the aluminum's fatigue strength is considered acceptable. Figures 5 below illustrates the principal stress imparted by the incident and reflected waves.

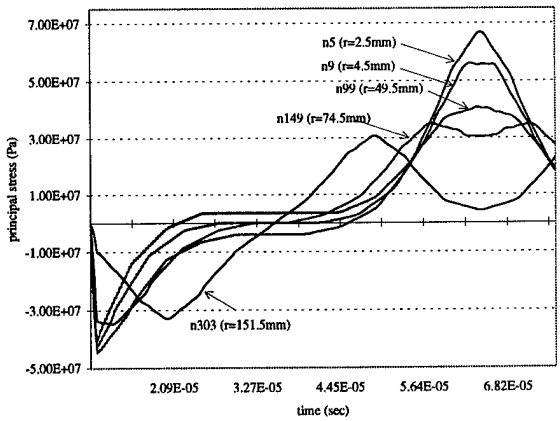


Figure 5. Principal stress wave resolved for selected nodes in the aluminum section of the MI Abort Corebox.

6 ACKNOWLEDGMENTS

We thank K. Anderson, Z. Tang, and the people at ANSYS for helpful discussions on the corebox analysis, J. Bielicki and S. Wesseln for assistance on the presentation of this paper, R. Rauchmiller and R. Dunklin for the assembly of the corebox, and D. Snee and the Fermilab machine shops for their advice in fabrication and assembly.

REFERENCES

[1] 'Fermilab Main Injector Technical Design Book', August 1994.

[2] Bhat, C.M., MI-0086, 'A Design Study of the MI-40 Beam Abort Dump', 1993.

[3] F.P. Incropera and D.P. DeWitt, 'Fundamentals of Heat and Mass Transfer', New York: John Wiley & Sons, 1985.

[4] Z. Tang, "Elastic Waves in a Cylinder under Thermal Shock Loading', Internal Fermilab Memo, 1990.

DIAGNOSTIC OF THE COMPENSATION PROCESS OF ION BEAMS WITH A TIME-RESOLVING ION ENERGY SPECTROMETER

A. Jakob, K. Reidelbach, J. Pozimski, R. Dölling, H. Klein
Institut für Angewandte Physik,Robert –Mayer Str. 2-4, 60054 Frankfurt, Germany

Abstract

Space-charge compensated high-perveance ion beams are of main interest for the injection into RFQ systems. Space-charge compensation enhances the maximum transportable current in low energy beam transport lines which is mainly limited by space-charge forces. The compensation electrons are usually produced by residual gas ionisation. In this case beam pulses reach the final degree of compensation after a certain time. To investigate the compensation processes of a periodically decompensated beam, a time-resolving residual gas ion energy spectrometer was developed. Results of measurements and corresponding numerical simulations will be presented.

1 INTRODUCTION

The residual gas ions (RGI) produced by the interaction of beam ions and residual gas are expelled radially in the beam potential. Under the assumption of neglectable start energy of the RGI, the kinetic energy of the RGI corresponds to the beam potential at the point of production. The RGI energy distribution contains information on the radial beam potential distribution and thereby on the degree of compensation. For the investigation of the build-up time of space-charge compensation a time-resolving RGI energy spectrometer with a single particle detector (channeltron) [1] was used. The time resolution was limited to 2 µs, due to the data acquisition. Self-consistent numerical simulations of the compensated beam [2] have been performed for different electron temperatures and axial densities to match the 10 % base points of the measured spectra. The combination of simulation and measurements allows the determination of beam plasma parameters (electron temperature, electron line charge density and relative charge density of the compensation electrons compared to the beam ions on the beam axis) which are difficult to measure directly.

2 MEASUREMENTS

The rise time of the space-charge compensation of a periodically decompensated DC He^+ (10 keV, 3 mA) ion beam has been investigated. A pulsed voltage (350 V, 500 Hz, 50% duty cycle, rectangular) was provided to an electrode in order to periodically decompensate the ion beam. With the falling edge of the pulse the compensation of the uncompensated beam starts by trapping the produced compensation electrons in the beam potential. Simultaneously the time resolved measurement of the RGI flux passing the energy analyser (at a fixed analyser voltage) [3] begins. This was done for a variety of fixed analyser voltages. Rearrangement of the data gives the energy spectra at different times. The 10% base points of this dynamic energy spectra yield the time dependent potentials of the beam center and the beam edge (Fig. 1).

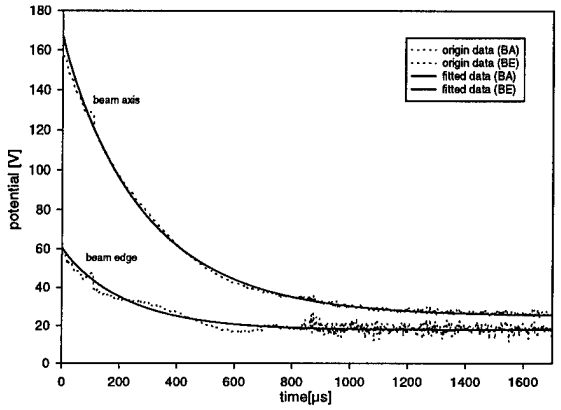


Figure: 1 Temporal development of potentials of beam axis and beam edge and analytical fit.

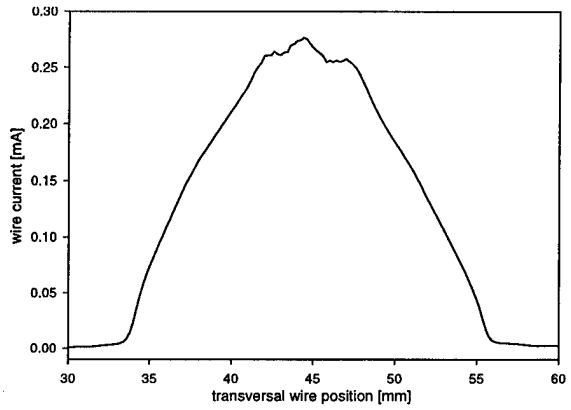


Figure: 2 Projection of beam profile measured with wire scanner.

The projection of the beam ion current density distribution was measured with a wire scanner at a DC beam for different voltages applied at a decompensation electrode. The settings of the focusing magnets were choosen in a way that the corresponding change of beam profile was neglectable. Fig. 2 shows a measurement for a decompensation voltage of 250 V. To receive the needed radial density profile from this measurement it was Abel-

0-7803-4376-X/98/$10.00 © 1998 IEEE

inverted (Fig. 3). It was assumed that the profile of the dynamically compensating beam stayed unchanged as well.

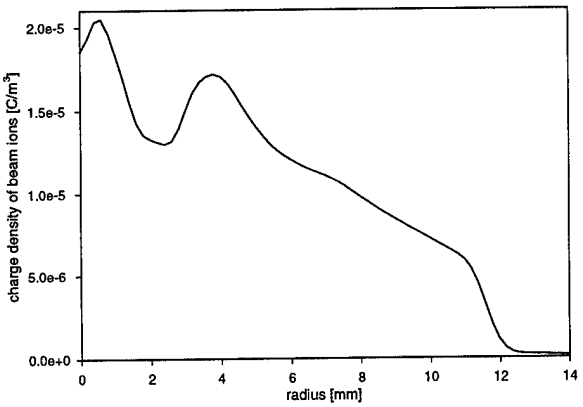


Figure: 3 Radial beam profile gained from Abel-inversion.

3 SIMULATIONS

A self-consistent equilibrium state of the compensated beam can be calculated numerically with radial beam ion density distribution and residual gas density as input data and electron temperature and density at the beam axis as free parameters. A two dimensional multiplicity of appr. 10000 self-consistent states was calculated. From this variety suitable self-consistent states could be choosen for every measured couple of beam axis and beam edge potentials. (A computer code was developed to compare the measured potentials with the potentials calculated by the simulation. The minimum distance between the measured and calculated value in a two dimensional plot (potential of beam center versus potential of beam edge) is determined and the corresponding equilibrium state is choosen.)

The resulting time-dependent evolution of electron temperature, **r**elative electron **d**ensity on beam axis (RD) and **e**lectron **l**ine **c**harge **d**ensity (ELCD) are shown in Figs. 4, 5, 6 (dotted lines). The same procedure was applied to an analytical fit of the original data (full lines). By comparison can be seen that the electron temperature is (only at higher temperature values) critically dependent on fluctuations of the input parameters while RD and ELCD are only weakly affected. Further the temperatures resulting from the simulation are unplausible high at the beginning of the compensation process (first 30 µs) since electrons with kinetic energies exceeding the appr. 100 eV corresponding to the uncompensated beam potential are expected to be lost instantaneously. Both effects are due to the fact that a beam edge potential which is only a little higher than what is compatible with beam axis potential and total charge density profile requires electrons outsides but not insides the beam radius, to be made self-consistent again. In certain limits this can be provided by using higher electron temperatures in the simulation. But for nearly uncompensated beams already little errors of the input parameters can result in unrealistic temperatures.

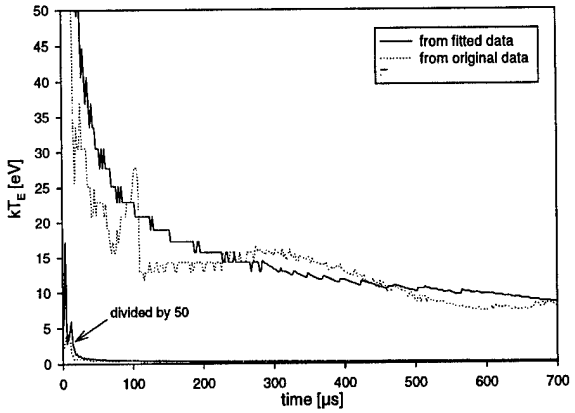


Figure: 4 Temporal development of electron temperature.

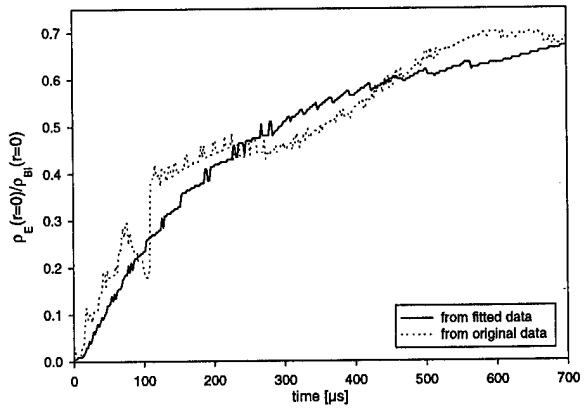


Figure: 5 Relative electron density on beam axis as a function of time.

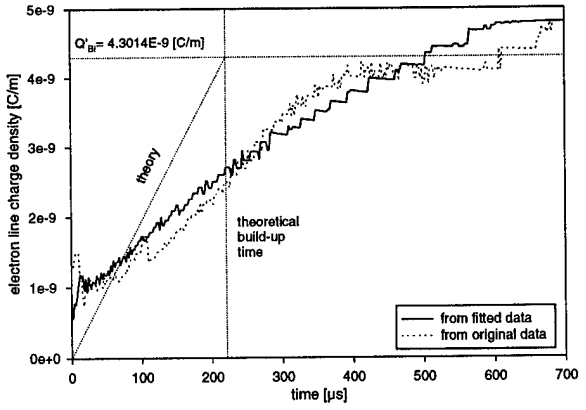


Figure: 6 Electron line charge density as a function of time.

From Figs. 1, 5, 6 can be seen that the build-up of space-charge compensation needs a time of at least 700 µs. The theoretical build-up time is shorter by a

factor of 3. This is plausible because the simple calculation takes no electron losses into account. The build-up of RD and ELCD takes place approximately simultaneously during the first 700 μs, which are actually covered by simulations. This indicates a relatively constant shape of the spatial electron distribution and is consistent with the approximately constant relations of beam axis potential, beam edge potential and electron temperature. In the later stages of the process the quotient of beam edge potential to beam axis potential decreases (Fig. 1) indicating a stronger confinement of the electrons to the inside of the beam and a further cooling of the electrons.

4 FUTURE WORK

The simulations will be extended to the later phases of the build-up process. The beam profile monitor will be replaced by a CCD camera. The CCD camera is an undisturbing diagnostic instrument which might be a big advantage, because secondary electron production is avoided and it allows for a time-resolved measurement of the beam profile. In the following time resolved beam profile measurements will be compared to the RGI spectra. Furtheron the time-resolved RGI measurements will be performed on a pulsed ion beam, instead of a continuous beam with pulsed decompensation. For this investigations the ion source will be pulsed.

REFERENCES

[1] K.Reidelbach et al., GSI-94-10 (1994) 36
[2] J.Pozimski et al., GSI-93-17 (1993) 38
[3] K.Reidelbach et al., GSI-95-5 (1995) 31

DEVELOPMENT OF CRYSTAL EXTRACTION STUDIES AT THE IHEP ACCELERATOR

V.M. Biryukov, V.N. Chepegin, Yu.A. Chesnokov, V.I. Kotov, E.A. Lyudmirskiy,
V.A. Maisheev, E.F. Troyanov, N.K. Vishnevskiy, V.G. Zarucheiskiy
Institute for High Energy Physics, 142284, Protvino, Moscow Region, Russia

Abstract

The crystal extraction of 10^7 proton/s on BEC experimental facility is described. Detailed computer analysis is made to explain the basic experimental results. Future high-intensity efficient extraction using a short crystal is announced.

1 INTRODUCTION

In 1989 at the IHEP accelerator, a crystal extraction of a 70-GeV proton beam onto the experimental set-up PROZA[1] was carried out. As a development of this method, another extraction has been realized onto the experimental set-up BEC[2]. The beam line where BEC is located, was created for formation from an internal target of the beams of negatively charged particles in the energy range of 20-40 GeV (see fig. 1).

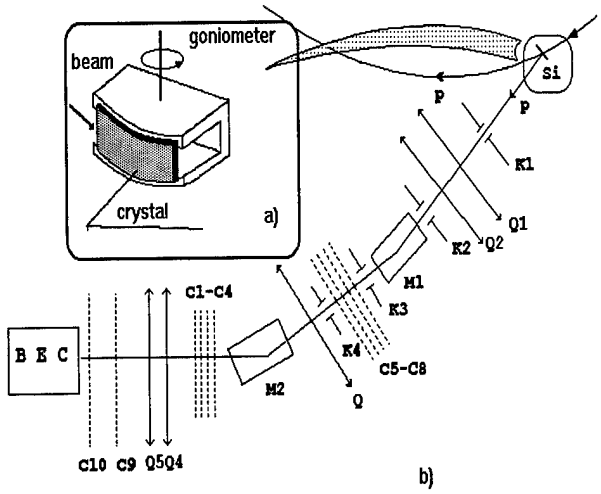


Figure 1: A bent crystal with bending device (a) and schematic of proton extraction onto BEC (b). K is collimators, Q quadrupoles, M magnets, C scintillation counters, p the orbit part, Si the crystal.

Usage in this case of the other methods of extraction of a proton beam is extremely difficult, and requires a significant reconstruction of an initial part of the beam line. Using a bent crystal, its bending angle and position inside a vacuum chamber of the accelerator can be chosen so that the line of the extraction of a proton beam is on the axis of the beam line. An opportunity of extraction into the beam line of negatively charged particles from internal targets is thus saved. The computations of proton trajectories through a nonlinear magnetic field of an accelerator were conducted under the programs FINT and TRAEK[3]. To not restrict the accelerator acceptance, the radial position of a crystal was chosen equal to $\approx$ 50 mm from the axis of the vacuum chamber. To bring protons onto the crystal, a local distortion of a closed orbit was invoked.

For extraction, a Si crystal of orientation (111) with the sizes 85 $\times$ 16 $\times$ 0.5 mm^3, bent on a angle of 89 mrad was used. The goniometer, on which crystal was established, provided its radial translation (coordinate accuracy of 0.1 mm) and turning in a horizontal plane with the step $\approx 80\mu$rad.

Up to 10% of the intensity of an accelerated beam, i.e. up to 10^{11} protons in a cycle, were incident on the crystal. Thus the intensity in the extraction beam line was 10^7 protons in a cycle and, hence, the efficiency of extraction was at the level $\sim 10^{-4}$ (see fig. 2).

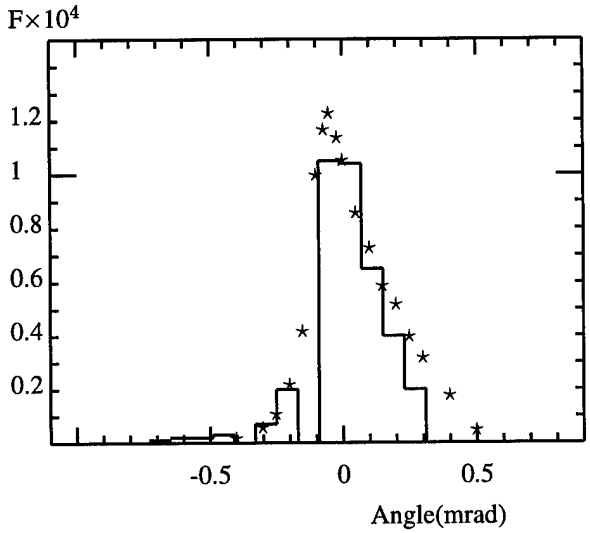


Figure 2: Histogram is the measured dependence of the extraction efficiency on the crystal orientation angle. Points ($\star$) are the simulation results.

The received intensity of protons was quite sufficient for fulfilment of the planned experiment on BEC. The low efficiency of extraction with the help of a crystal, bent on large angle, as simulations show, is connected not only to intensive dechanneling process of particles in such a crystal, but also to essential influence of defects, inevitablly introduced at its manufacturing (destroyed near-surface layer) and bending (twists). The experiment was simulated by the program CATCH [4], which took into account a geometry

0-7803-4376-X/98/$10.00 © 1998 IEEE

of the crystal with distortions and the effects of repeated passage of particles through a crystal. During the passage of particles through a bent crystal lattice, every step ($\sim$1 μm) the local crystal fields and densities of nuclei and electrons were calculated, and the scattering events generated [4]. The lattice of a crystal was considered ideal, however on its surface there could be a nonchanneling layer of the thickness of a few microns [5] ("septum thickness"), the influence of which was investigated in details. In the computation, the geometry of the holder of a crystal (scattering in it) and variable longitudinal and transverse curvatures of a crystal, existing in a geometry of fig. 1, were taken into account. Besides, the crystal twist was taken into account, as a result of which the orientation of atomic planes (111) at the entrance of a crystal becomes a parabolic function of vertical coordinate y. In our case an angle θ of misorientation of the planes (111) is given by the expression $\theta(\mu\text{rad})=20\times y^2$ (mm).

The results of modeling are shown on figs. 2–4. Computed for real conditions of the experiment, the efficiency of extraction dependence on the angle of orientation of a crystal, shown on fig. 2, well agrees with the results of the experiment. Modeling has shown, that the chosen length of a crystal is optimum, while a vertical gap of the holder of 10 mm and accordingly the height of a crystal are not sufficient. Indeed, in experiment the vertical size of undisturbed beam was $\sim$13 mm. Moreover, the inaccuracy of the middle plane at the crystal position is $\pm$5 mm. Therefore the significant part of particles may be lost at the scattering on the holder. If to increase a vertical gap of the holder of a crystal up to 20 mm, the efficiency of extraction increases by 1.5-2 times.

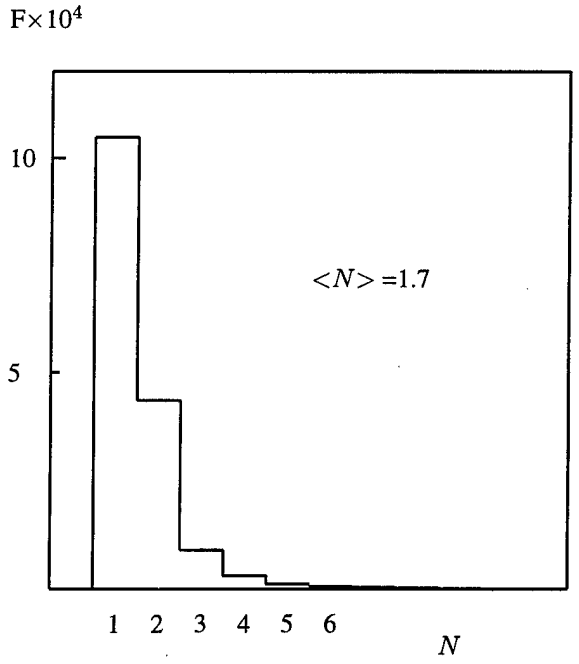


Figure 3: The number of extracted particles extracted by an ideal crystal at the N-th passage through the crystal.

Fig. 3 shows the computed efficiency of extraction by an ideal crystal (no twist, nor near-surface nonchanneling layer) as a function of the number N of particle's encounters with the crystal. The main contribution to efficiency of extraction is from the first passage of particles through the crystal, whereas the contribution of the subsequent passages quickly drops because of a large scattering of nonchanneled particles in a crystal. The average number of passages of a particle through a crystal before a capture into the channeling state, as follows from fig. 3, is only $< N >$=1.7.

The presence of a near-surface nonchanneling layer, which in our case has a thickness of the order 60 μm, and of a twist, changes this picture essentially. If a beam is slowly brought onto a crystal, the primary impact parameter is only a fraction of micron (the speed of this process is $\sim$5 mm/s, the revolution time of a particle in a ring is 5 μs). At such a depth, a particle hits a nonchanneling layer of a crystal and, passing in it the way $\sim$1 cm, scatters by $\sim$50 μrad, that results in a secondary impact parameter at the crystal of $\sim$60 μm. Thus, the presence in the crystal of the nonchanneling layer $\sim$60 μm results in a complete suppression of efficiency of the first passage and partial one of the second passage. Dependence of efficiency of the extraction on a thickness of this layer, with twist and without it, is shown in fig. 4.

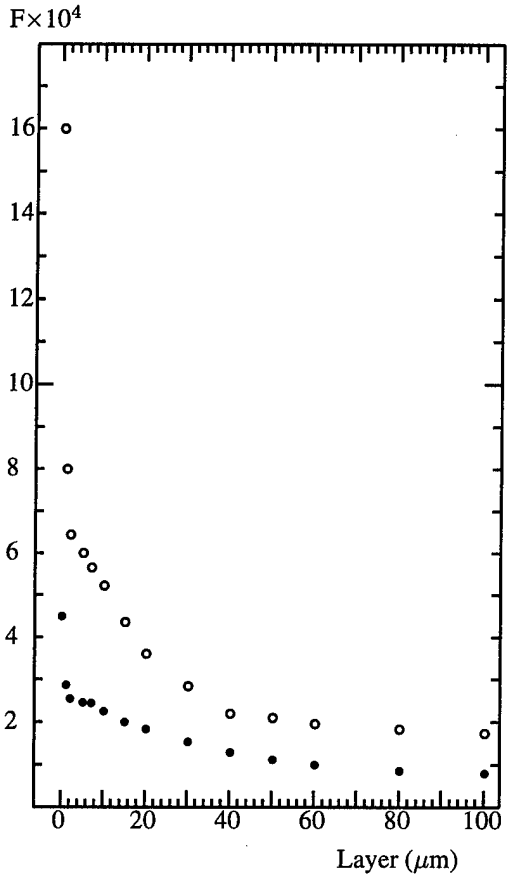


Figure 4: As simulated, the extraction efficiency as a function of the thickness of nonchanneling layer: crystal with twist (•) and without it (o).

From there we see that twist has a large influence on efficiency either. The crystal with an ideal surface and without twist would ensure an efficiency of the extraction one order of magnitude higher than presently.

A radical increase of efficiency of the extraction can be reached by a use of a short crystal, bent on the small angle $\sim$ 1–3 mrad. In a long, strongly-bent crystal the dechanneling losses are almost two orders of magnitude. Besides elimination of dechanneling losses of particles, the gain in efficiency is reached also because of significant reduction of scattering over the crystal length, i.e. respective reduction of the beam divergence at the incidence on a crystal. Thus unlike in a long crystal, another mechanism of the growth of efficiency of the extraction of particles begins to work, related to the increase of the average number of encounters of particles with a crystal. Computations show that at the IHEP accelerator the efficiency of extraction of $\sim$ 20–40 % by means of a crystal of the length of $\sim$5 mm, bent on the angle $\sim$1.5 mrad, can be achieved. Herewith, the extracted intensity may be as high as 10^{11} protons/s. The experiment on realization of such an extraction is in a stage of preparation.

2 REFERENCES

[1] Asseev A.A. *et al.*., Nucl. Instr. and Meth. A **309**, p.1 (1991)

[2] Asseev A.A. *et al.*, XV meeting on accelerators of charged particles, IHEP, Protvino, October 1996, Summaries of the reports, page 78, 1996.

[3] Fedotov Yu., Fronteau J., Keyser R., CERN /DD/CO/67-5, Geneve, 1967

[4] Biryukov V., Phys. Rev. E **51**, 3522 (1995); **52**, 2045 (1995); **52**, 6818 (1995).

[5] Baranov V.I. *et al.*, Proc. of PAC-95 (Dallas) v.**3**, p.1949 (1995)

EFFICIENCY OF THE UNK SCRAPER SYSTEM

I.I. Degtyarev, A.E. Lokhovitskii, I.A. Yazynin
Institute for High Energy Physics
Protvino, Moscow region, 142284, Russia

Abstract

Optimum collimators location and choice of their apertures with the purpose of decreasing the flux of outscattered protons in circle is considered in this paper. The analytical and computer graphic methods are used for solution of this task. Statistical modeling of forming beam process are made for the UNK and sources of lost protons are defined. With the help of the scattered proton traces out from the system and special curves the correct installation of collimators can be defined. The optimum set and efficiency of collimators can be defined by showing collimator jaws on the phase planes in the scraper place. Also the advantages of systems with the scattering target are considered. It is shown, that the losses in the circle are $\sim 0.05\%$ from all scraped protons in the UNK.

1 INTERCEPTING COLLIMATORS

To trap the protons, outscattered from a scraper, collimators installed downstream are used. An optimum location of collimators and displacement them jaws[1-3] can be found from outscattered protons trajectories which are defined by initial coordinates at scraper x, x', $\delta = \Delta p/p$ and magnet structure of the accelerator:

$$x = \sqrt{\frac{\beta}{\beta_0}}(\cos\Delta\psi + \alpha_0 \sin\Delta\psi)(x_0 - \eta_0\delta + \Delta x) + \sqrt{\beta\beta_0}\sin\Delta\psi(x_0' - \eta_0'\delta + \Delta x') + \eta\delta, \quad (1)$$

where α, β - Twiss parameters, η ,η'- dispersion and its derivative, $\Delta\psi = \psi - \psi_0$ - a change of a phase betatron oscillations from scraper, $\Delta x'$ - scattering angle. The parameters with index "0" correspond to scraper location.

In the case of dispersion absence in system $\eta_0, \eta = 0$ for particles, which were on a phase ellipse with maximum coordinate x_0, with appreciation $\Delta x \ll x_0$, the movement equation become more simple:

$$x = x_0\sqrt{\beta/\beta_0}\cos\Delta\psi + \Delta x'\sqrt{\beta\beta_0}\sin\Delta\psi. \quad (2)$$

Let us assume that coordinate of scraper edge $x_0 = m\sigma$, $\sigma = m\sqrt{\varepsilon\beta_0}$, where ε is a beam emittance. Distance from a beam axis to collimator jaw is $x_c = \pm n\sigma_c = \pm n\sqrt{\varepsilon\beta}$, where the mark " + " means the jaw installed at the same side as the scraper from beam and " − ", when any. In this case the collimators intercept particles with amplitude more then $k\sigma$:

$$k^2 = m^2 + (\pm n - m\cos\Delta\psi)^2/\sin^2\Delta\psi. \quad (3)$$

The collimator position, when to trap outscattered particles with minimum amplitude, is defined from(3):

$$\Delta\psi = \pm arccos(\frac{m}{n}) + \pi i, \qquad where \quad i = 1, 2, \ldots .$$

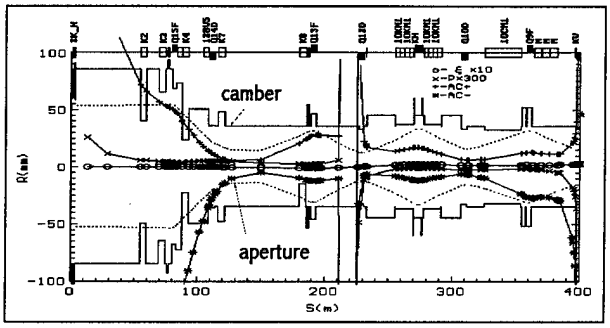


Figure 1: Horizontal plan of SS1,UNK-600

In this case the size of a beam, which not interacting with collimator, coincides with collimator aperture, that is $k = n$. It is desirable to install the collimators as possible closer to the scraper (i=0,1,...), in order not to irradiate the equipment stand between them. The size k is defined by the narrowest place in the accelerator.

The particles escaping from the system may change also a moment. In case of dispersion availability the displacement of outscattered proton may be presented like:

$$x = \widetilde{x} + \delta\xi, \quad (4)$$

$$\xi = \eta - \sqrt{\beta/\beta_0}(\cos\Delta\psi + \alpha_0\sin\Delta\psi)\eta_0 - \sqrt{\beta\beta_0}\sin\Delta\psi\eta_0',$$

where $\widetilde{x}$ - coordinate of escaping particle with equilibrium moment. Consequently it is necessary else to consider such way will be scrape particles with changed moment on the main collimators, and then may define the necessity to install the additional collimators.

In order to reduce of outscattered protons from the system it is necessary to take into account, that their density on the edges of collimators jaws was as small as possible. If we know normalized angular density of protons, scattered by the system target and scraper $\rho_0(x')$, and its intensity I_0, then density of protons on the edge of collimator jaw can be defined as

$$\rho = I_0\rho_0(x') \cdot p(s) \quad , \text{where } p(s) = \frac{1}{\sqrt{\beta\beta_0}\sin\Delta\psi}.$$

Having drawn on plan(fig.1) the curves $Ac = k(s)\sigma$, which define a displacement of collimators jaws, intercepting particles with amplitude of betatron oscillations exceeding $n\sigma$, and knowing distribution function of density on the jaw edge, it is rather simply to define an optimum location and aperture of collimators. The collimators jaws are desirable to install in places with least density p(s) and minimum significance $k(s)$. To trap the protons with changed moment it is necessary to know the dependence $\xi(s)$ (fig.1)

0-7803-4376-X/98/$10.00 © 1998 IEEE

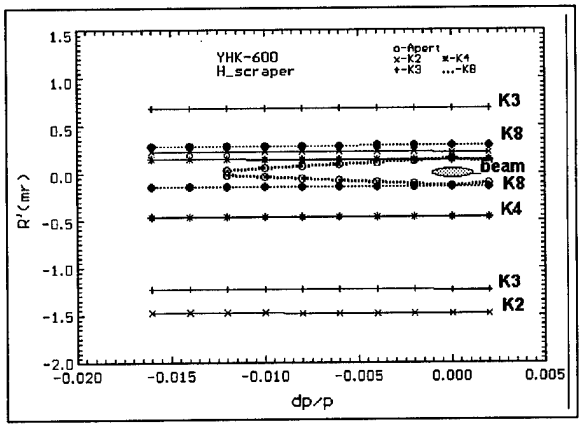


Figure 2: Position of collimator jaws on the phase plane r',p in location of horizontal scraper.

and in places with sufficient size of this function (4) to install additional collimators.

The particles outscattered by a scraper can significantly change deviation in vertical plane and to pass through the hole of horizontal collimators put on the equipment. With the purpose of interception such particles it is necessary to install a minimum two additional collimator jaws in vertical plane. The dispersion in vertical plane in circular accelerator usually is negligible. Therefore at the account of system we shall consider only particles with equilibrium moment:

$$z = z_0(\sqrt{\beta/\beta_0}\cos\Delta\psi+\alpha_0\sin\Delta\psi)+(z_0'+\Delta z')\sqrt{\beta\beta_0}\sin\Delta\psi. \quad (5)$$

For particles with different initial coordinates z_0 there will be the different optimal position of collimators. Let us consider a particle with zero coordinate $z_0 = 0$, that equals to average size of particles coordinates of the whole beam. Such particle at hit on collimator edge will have an angle $z_1' = n\sqrt{\varepsilon/\beta_0}/\sin\Delta\psi_z$.

Maximum coordinate z of betatron oscillations which can have a scattered proton escaping from the scraper $z_0 = m\sqrt{\varepsilon\beta_0}$. That is the maximum amplitude of protons (in vertical plane), which can pass in the accelerator circle, will be $A_z = k\sigma$, where $k^2 = m^2 + (\alpha_0 m + n/\sin\Delta\psi_z)^2/\beta$. So as $\alpha_0 \simeq 0$ in scraper location in UNK-600 $k^2 \simeq m^2 + n^2/\sin^2\Delta\psi_z$. Then the optimum position of such collimators will be in case: $\Delta\psi_z = \frac{\pi}{2} + \pi i$, and the maximum amplitude of vertical betatron oscillations of outscattered protons, that will pass in circle will be $A_z = \sqrt{m^2+n^2}\,\sigma$.

Analogically, as well as in case of radial plane, by drawing curves $Ac(s)$ and $p_z(s)$ on plane, it is possible to define optimum position and aperture of vertical collimators.

In order to visualize the losses process on plan it is possible to draw trajectories of particles leaving from a scattering element with some angles and moments. The places of intersections the consequent trajectories with vacuum chamber or magnet elements define a location of expected losses. For further consideration of system work it is necessary to take into account the collimators as a source of scattered protons.

2 METHOD OF PHASE PLANES

By way of drawing inner edges of collimators jaws on the phase planes in scatterer position(target, scraper, collimator or another equipment) it is possible to define the optimum set and sufficiency of collimators. On the fig.2 the location of jaws and circulating beam on the phase plane x',p is shown. Two-dimensional consideration is possible because the protons leave scraper with the same coordinate x_0. The jaws surfaces are imaged by straight lines, that defined by expression received from (1):

$$x' = x_0' + \frac{x_c - x_0\sqrt{\beta/\beta_0}sin\Delta\psi}{\sqrt{\beta\beta_0}sin\Delta\psi} - \frac{\delta\xi}{\sqrt{\beta\beta_0}sin\Delta\psi},$$

which must be disposed outside of circulating beam region. If in straight section there are not large magnet dipoles, then the lines will be almost parallel to an axe abscissa, since $\xi(s) \sim 0$. If it is necessary to trap the protons with large moment displacement the collimators should be install in normal periods. Then the lines, representing the jaws surfaces, will have slope that proportional to $\xi(s)$. From the picture one can see the duplicating of the jaws, although for the interception of scattered particles in one transverse plane is enough two, that disposed at any sides from circulating beam. The additional collimators are used for protection of the equipment in straight section from the particles are obtained from nuclear reaction and for interception the scattered particles from the main collimators. On the phase plain it is possible to image the narrowest places in accelerator. In our case these are some places of vacuum cambers of normal periods, that are imaged by dotted line. The protons scattered by the system located on the phase plane outside of accelerator aperture between nearest to the beam collimator jaws(K4,K8), which have small vertical amplitude of betatron oscillations, will be lost in the accelerator circle. Knowing distribution of scattered protons it is possible to find losses on the collimators and the equipment by considering them consecutive along downstream.

In view of the fact that dispersion in vertical plane is close to zero it is enough to consider the phase plane z,z'. The edges of collimator jaws will be imaged by straight lines and circling beam - by ellipse(5).

3 ESTIMATION OF LOSSES

There are two main sources of scattered protons which are lost in circle:

- scraper and scattering target;
- main collimators.

The particles escaping from the scraper with big amplitude of betatron oscillations are intercepted by main collimators in radial and vertical planes. The protons pass in the circle with changed moment and put in places with big bend magnets. With decreasing the aperture of collimators the quantity of such particles decreases, but from the increasing the density of protons on the edge jaws the losses in the

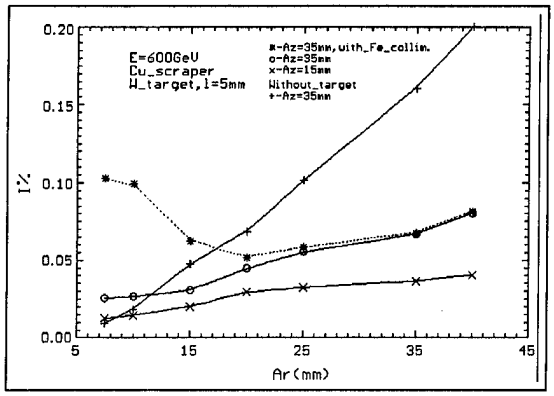


Figure 3: The losses in the circle from main collimators aperture.

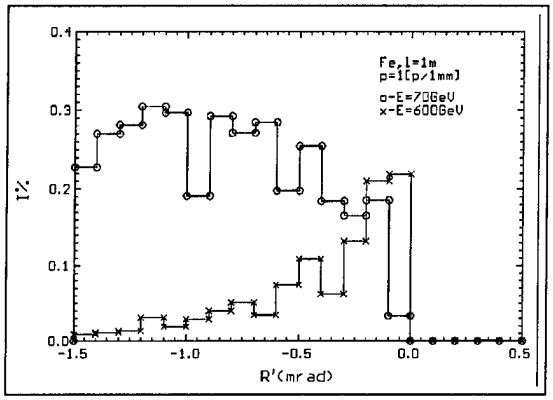


Figure 4: Distributions of the protons scattered by steel collimator for angle.

circle grows. Solid lines show the dependencies with using the collimators of full absorption and dashed line - with using the collimators on the base of iron. In first case with diminution collimator aperture the flux of scattered particles in the circle decreases. In the second case is minimum of losses I ~0.04% when aperture of main collimators are $A_{r,z} = 20 - 25\ mm(\beta = 152\ m)$. By using the system without target such losses will increase twice.

Fig.4 represents calculated distributions of protons scattered by steel collimator on the angle at beam energy 70 and 600 GeV at the density of hitting beam is 1p/mm. From distribution it is visible, that at small energies the flux of scattered protons is more, but fraction of particles that pass in circle is about identical, since even without using of additional collimators particles with scattered angle from $x'_1 \sim 0.1$ to $x'_2 \sim 0.2\ mrad$ will be lost in circle. That is quantity of such particles is possible to estimate $I \simeq 2\Delta x'_c \cdot P_c$, where $\Delta x'_c = x'_2 - x'_1$, and P_c - average angle proton density in this interval.

In order to define the density of scattered protons on the collimator edges it is necessary to know normalized angular density of the protons leaving from the scraper and the target $\rho_0(x')$. Then density can be estimate: $\rho(x) = I_0\rho_0(x')/\sqrt{\beta\beta_0}sin\Delta\psi$, and the size of losses of such particles in circle will be $I = I_0\lambda$, where $\lambda = 2\frac{\Delta x'_c \cdot P_c \rho_0(x')}{\sqrt{\beta\beta_0}sin\Delta\psi}$. For UNK-600 decreasing coefficient will be $\lambda \sim 4 \cdot 10^{-5}$, but with consideration of additional scattered protons on any collimators except main the real coefficient is increased twice. By using the system without target its fraction of losses is doubled. That is the main part of losses in the circle form the protons with change moment. For superconductor accelerators interception of such protons is especially important. In UNK-3000 the additional collimators can decrease a level of losses in circle up to 0.01% from the intercepted halo beam.

4 REFERENCES

[1] M.A.Maslov, N.V.Mokhov, and I.A.Yazynin, SSCL-,SSC Laboratory (1991).

[2] L.Burnod, J.B.Jeanneret, "Beam losses and collimation in the LHC: A quantitative approach", CERN SL/91-39 (EA), LHC Note 167.

[3] P.J.Bryant,E.Klein, "The design of betatron and momentum collimation systems", CERN SL/92-40 (AP), SL Division(1992).

SUBSTANCE CHOICE OF THE SCRAPER SYSTEM ELEMENTS

I.I. Degtyarev, Yu.S. Fedotov, A.E. Lokhovitskii, I.A. Yazynin
Institute for High Energy Physics
Protvino, Moscow region, 142284, Russia

Abstract

In this paper the functioning of scraper system elements at maximum radiation and thermal loads in different regimes of the system's work is considering. Substance choice and design of system elements construction are made with purpose of prevention their thermal,mechanical and radiation destruction. The advantage of using scraper system with scattering target is shown. By simulation of the real scraping process in UNK the maximum heating elements is defined during many circles and at different beam energies. The designed scraper system with W target and Cu scraper can scrape up to 10% of full intensity $6{\times}10^{14}p$ at the energy $E = 70\ GeV$ and up to 1% at $E = 600\ GeV$.

1 INTRODUCTION

One of the main tasks at the design of circling accelerator is engineering reliable and effective scraper system/1/. Apart from optimum configuring of optical structure with purpose of minimization the protons production in accelerator circle and decrease heating and irradiation of system elements and nearby equipment the main meaning for the capacity of work system is the choice of construction substance of target,scraper and collimators that securing long work in condition of large thermal and radiation loads.

The conditions of the thermal load of elements are considered at three possible regimes of system work:
1) stationary regime - slowly scrape the halo beam;
2) to trap particles that are not took in acceleration regime;
3) accident situation - interception the halo beam during the some turns.
At the stationary regime of work the good thermal conductivity λ of the system elements for fast removal heat is important. At the momentary absorption of beam energy by the system for prevention its destruction is needed to choice the substance with big thermal capacity C_p and melting temperature T_{mel} and thermal mechanical stability. The parameters of some considered substance are introduced in table 1.

Table 1

	C_p $\frac{J}{g\times deg}$	ρ $\frac{g}{sm^3}$	λ $\frac{W}{sm\times deg}$	T_{mel} ^oC	L_r mm	$\sim 6L_n$ m
W	0.134	19.34	1.686	3380	3.5	0.6
Cu	0.388	8.93	3.896	1083	14.3	0.9
Al	0.896	2.7	2.093	660	89.	2.4
Fe	0.440	7.88	0.744	1535	17.6	1.0
C	0.670	2.3	0.980	3540	188.	2.4

The basic circuit of a design of a scraper and target U600 is submitted on fig.1. With the purpose of reduction of a thermal heating of a scraper the intercepted protons at first interact with flat scattering target and having changed angular deviation through some turns get on front face of a scraper, having significant impact parameter. For prevention of mechanical destruction of a scraper oving to a nonuniform heating it suppose to make up from blocks, which fasten to frame with gaps $\Delta \sim 2\ mm$ between blocks and frame.

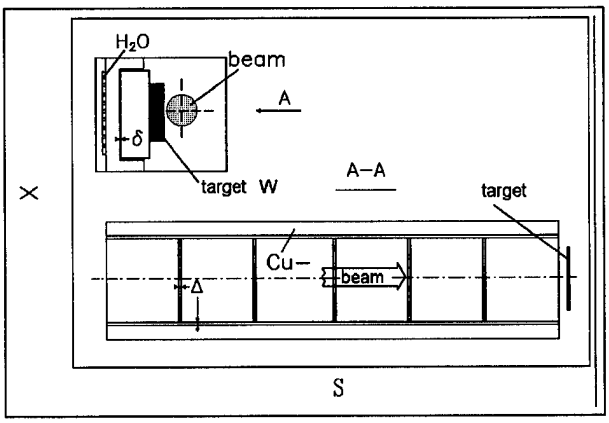


Figure 1: The layout of a scraper.

2 CHOICE OF TARGET SUBSTANCE

At forming the beam by scraper system with scattering target the impact parameter on it is insignificant /2/ and as a result take place the strong heating of its edge that may lead to destruction the substance of target and then self scraper. In case of using the thin target the density of energy deposition in substance is practically constant and weakly depends on the proton energy.

Table 2

	dE/dy $\frac{MeV}{sm}$	α $\frac{1}{deg}$	η $\times 10^6$	η_1	η_2	κ $\frac{sm^2}{s}$	Δt ^oC
W	33.0	4.3	0.84	265	0.21	0.65	800
Cu	18.2	17.0	0.57	206	0.22	1.12	510
Al	6.3	22.9	0.62	253	0.24	0.87	150
Fe	16.5	16.0	0.89	322	0.15	0.22	420
C	5.6	7.9	2.18	974	0.78	0.64	40

The heating of the target can present by process of one-dimensional defusion at presence the heat source:

$$\frac{\partial T}{\partial t} = \kappa \frac{\partial^2 T}{\partial x^2} + p(x,t), \quad where \quad \kappa = \frac{\lambda}{C_p \rho}.$$

0-7803-4376-X/98/$10.00 © 1998 IEEE

In stationary case of scraping process the heat source may be considered as point $p(x,t)|_{x=0} = p_0$, and temperature change will be /3/:

$$T(x,t) = 2p_0\sqrt{\frac{t}{\pi\kappa}}e^{\frac{-x^2}{4\kappa t}} - \frac{p_0 x}{\kappa}(1 - \frac{2}{\sqrt{2\pi}}\int_0^{\frac{x}{2\sqrt{\kappa t}}} e^{-s^2}ds).$$

After closing the process of forming beam with duration t_s the temperature of most heated region of target edge will be: $T = 2p_0 \times \sqrt{\frac{t_s}{\pi\kappa}}$.

If one assumes that the beam distributed for normal law in plane that perpendicular to out plane, then the maximum density of the particles is $Iz_{max} = \frac{I_0}{\sqrt{2\pi}\sigma_z}$, where I_0 - number of scraped particles, and σ_z - r.m.s of the beam in z plane. Since as $p_0 = \frac{I_0\frac{dE}{dy}}{\sqrt{2\pi}\sigma_z C_p \rho t_s}$, the temperature of the most heated region of target edge $T_{max} = \frac{\sqrt{2}I_0\frac{dE}{dy}}{\pi\sigma_z\sqrt{C_p\rho\lambda t_s}}$. That is the maximum heating of the target to decrease with increasing the duration of the forming beam. The maximum intensity of the beam that target can stand is

$$I_m = \eta_1\frac{\pi\sigma_z\sqrt{t_s}}{\sqrt{2}}, \qquad \eta_1 = \frac{T_{cr}\cdot\sqrt{\rho\cdot C_p\cdot\lambda}}{\frac{dE}{dy}},$$

where T_{cr} - temperature of substance destroy. In considering case of slowly heating the T_{cr} practically corresponds to T_{mel}. The coefficient η_1 characterizes the durability property of the target in the stationary regime.

At the accident situation in case of quick beam swelling or orbit displacement the particles during the some turns put to the target. In that case the heating may be considered as momentary and temperature change of the target edge may be defined: $\Delta T = \frac{P_{max}\cdot\frac{dE}{dy}}{\rho\cdot C_p}$, where P_{max} - maximum density of particles during scraping process.

If to approximate the density distribution of the particles on the target in out plane by linear function and to knew the value of impact parameter $\Delta = \sqrt[3]{RV^2}$ /2/, where R - transverse beam size and V - the transverse velocity the beam to the target, one can find the maximum density of protons $P_{max} = I_0/\sqrt{2\pi}\sigma_z\Delta$. Then the maximum intensity of the beam that target can stand in accident situation is

$$I_m = \eta_2\frac{T_{cr}-T_0}{T_{cr}}\sqrt{2\pi}\sigma_z\sqrt[3]{RV^2}, \quad \eta_2 = \frac{T_{cr}\cdot\rho\cdot C_p}{\frac{dE}{dy}}.$$

The coefficient η_2 characterizes the durability property of target in accident regime.

The thickness of the scattering target is chosen with consider of needed scattered angle of the protons for prevention the thermal destroy of the scraper and therefore proportional to radiation length L_r(table 1). With consider the above-mentioned the most suitable substance for making the target is tungsten.

The computer simulation of the beam forming process end energy deposition in system elements was done by codes "SCRAPER"/4/ and "MARS12". Calculated curves

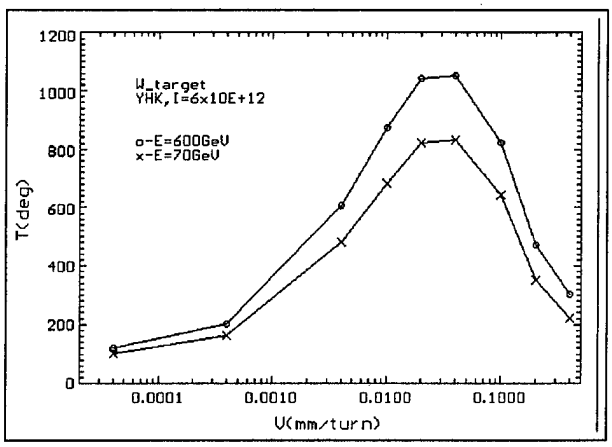


Figure 2: The heating of W target from the transverse velocity of the beam when to scrape 6×10^{12}p.

of the heating of the edge tungsten target from the beam transverse velocity when to scrape the halo beam with intensity $6 \times 10^{12}p$ are shown in fig.2. From there it can be seen that in stationary work regime (V $\sim 4 \times 10^{-5}$ $mm/turn$, during t$\sim$ 2 s) the heating target not exceeds 120° C. During the rest time of acceleration cycle the thermal energy practically completely removes from the target edge. The shape of the curves explained that with increasing the transverse velocity increases intensity of beam interaction with target and enlarges the impact parameter.

The most dangerous regime of system work is possible at fast beam swelling in transverse plane or fast equilibrium orbit displacement. Thus the heating of target during some dozens turns of scraping halo beam (V $\sim 2\times10^{-2}$mm/turn) can reach $\simeq$ 1100° C (fig.2). In that case for protection of accelerator it is necessary to foresee the turn on the beam abort system.

In the regime to trap protons that not took in acceleration the protons drift to scraper with average speed V $\sim 1.5 \times 10^{-2}$ $mm/turn$ during the time $\sim$ 30 mc and simulation of process shows that the temperature of the target edge not exceeds 200° C.

3 CHOICE OF SCRAPER SUBSTANCE

The choice of longitudinal scraper size are made with take into account practically full suppression outscattered protons from back face of absorber. The flux of such protons may be estimated $I = I_o \times e^{-l_s/L_n}$. That is when absorber length l_s in six times exceedes the nuclear length L_n(tab.1), then flux of outscattered protons from back face of absorber will be $\sim 0.2\%$ from intercepted protons.

The values of absorber maximum heating Δt at scraping the halo beam with energy $E = 600$ GeV and intensity $I = 6 \times 10^{12}p$ for some substance are presented in the table 2. It can be seen that maximum part of the beam to its melting $I > 80\% \times I_0$ to absorb graphite absorber.

But its using is practically impossible because of vacuum aggravation and technologically hard production.

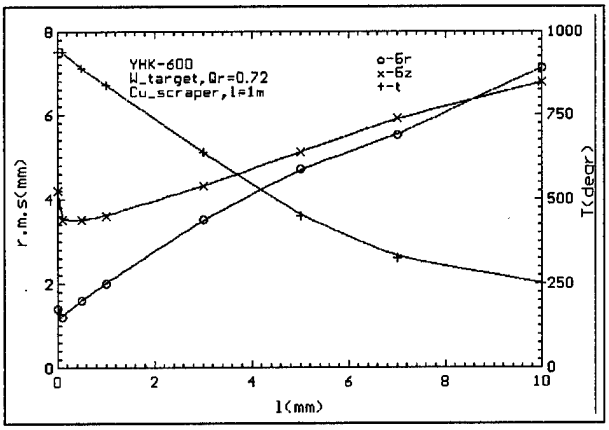


Figure 3: Beam sizes on the absorber and its maximum heating from thickness of the target.

The absorber heating, in view of large impact parameter of protons from them scattering on the target, not depends on regimes of system work, but defined from its energy and intensity. With increased thickness of the target magnifying the beam sizes on the absorber because of increasing the scattered angles of protons and therefore decreasing the maximum scraper heating (fig.3). When intercepted $0.5\%I_0$ the halo beam with the energy 600 GeV by the system without target the maximum momentary heating of copper absorber reaches 1000° C. By using 10 mm tungsten target the heating of most heated region reduces in four times. Such the momentary heating of copper absorber at intercepted 1% of beam with energy 600 GeV (fig.4) and 10% of beam with energy 70 GeV does not exceed 500° C.

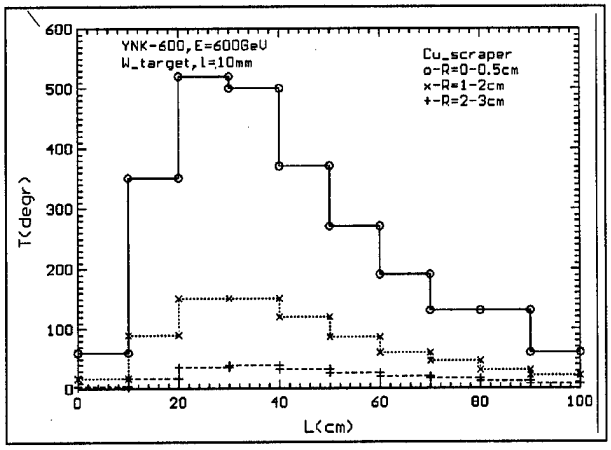


Figure 4: Momentary heating of copper absorber at intercepted 1% of beam with energy 600 GeV.

In case of approximation of the transverse distribution of energy deposition by cosine function, the changing temperature with time is shown by simple expression:

$$T = T_0 e^{-kt} \times cos\frac{\pi x}{2l},$$

where $k = \frac{\kappa\pi^2}{4l^2}$ is the coefficient that characterizes the rate of absorber cooling , l - thickness of absorber. Then the maximum absorber heating will be $T_{max} = T_1(1 + e^{-kt})$, where T_1 is the maximum temperature changing at single intercept of the halo beam. When used cooper blocks with thickness $l_b = 5\ sm$ and the same thickness of the frame(fig.1) like energy absorber the heating enlargement during the many acceleration cycles will be the least from the considers substances: $\Delta T = T_1 e^{-kt} = T_1 e^{-3}$. The additional increase of a heating will occur because of presence thermal resistance between blocks and frame α_1 and between frame and pipes with cooling water α_2:

$$\Delta T = \frac{dQ}{dt} \cdot (\alpha_1 + \alpha_2).$$

Considering above-mentioned facts and technology production, cooper as an absorber substance is chosen. In that case at multiple intercept the halo beam with consideration of machining contacting surfaces not less then 4 precision class and water cooling the temperature of most heated region to enlarge weakly $\Delta t \sim 100°$ C.

The designed scraper system with W target and Cu absorber allows in stationary regime intercepted up to 10% of the beam intensity $6\times10^{14}\ p$ at $E = 70\ GeV$ and up to 1% at $E = 600\ GeV$. In accident case can allow intercept not more then 3% of beam from the possibility of destruction the tungsten scattering target.

4 REFERENCES

[1] M.A.Maslov, N.V.Mokhov, and I.A.Yazynin, "The SSC Beam Scraper System", SSCL-,SSC Laboratory (1991).

[2] I.A.Yazynin, "The impact parameter of the particles at the scraper and ways to increase it", Paper presented at 4-th EPAC,London,27 June,1994.

[3] Y.V.Zeldovich, A.D.Myshkis, "Elements of mathematical physics", p.301,1973.

[4] I.I.Degtyarev, A.E.Lokhovitskii, Yu.S.Fedotov, I.A.Yazynin. "Integrated version of IHEP code system SCRAPER". VI Russian scientific conference on radiation shielding of nuclear installation. Obninsk,1994,v.2,p.25.

RTS&T MONTE CARLO CODE (FACILITIES AND COMPUTATION METHODS)

A.I.Blokhin†, I.I.Degtyarev, A.E.Lokhovitskii, M.A.Maslov and I.A.Yazynin
SRC Institute for High Energy Physics, Protvino, Russia
†SRC Institute of Physics and Power Engineering
(Nuclear Data Center of Russian Federation), Obninsk, Russia

Abstract

The paper describes facilities and computation methods of the RTS&T new Monte Carlo code. This code performs simulations of three dimensional electromagnetic showers development and low energy neutron production and transport in accelerator and in shielding components with a calculation of the isotopes transmutation problem. RTS&T is based on the compilations from ENDF/B-VI, JENDL-3, EAF, FENDL and EPNDL evaluated data libraries to detailed physical processes simulation, and only a few approximations are made. It is possible to use RTS&T complex to solve the critical reactor problem. Combinatorial method of the geometry definition is provided with the program. Recently RTS&T code interface to the ANSYS 4.4 code system has been developed and tested.

1 RTS&T MAIN FEATURES

The code RTS&T (Radiation Transport Simulation and Isotopes Transmutation calculation) was assigned for Monte Carlo simulation of many particle types transport in complex 3D geometries with composite materials and calculation particles fluences and functionals of radiation fields and isotopes transmutation problem as well.

The specific features of RTS&T Code are: basic processes of particles interactions during their passage through the matter are taken into account for the energy range about

1. 10 eV to 10 TeV for photons
2. 0.01 MeV to 10 TeV for leptons
3. 1 MeV to 25 GeV for charged hadrons
4. Thermal region to 25 GeV for neutral hadrons

In RTS&T Code 3D geometry definition is provided with combinatorial (recursivial) method. Complex 3D geometries can be defined to a combination of boxes, cylinders, spheres and etc. More then 15 standard or user–written base shapes and 10 types of the initial radiation source distributions may be defined in this code version.

The secondary particles transport parameters are retained in stack which can be organized according to lexicographical or direct method.

RTS&T Code can be successfully used for verification of non-grouping constant systems was recorded in ENDF-VI format.

2 ELEMENTARY PROCESSES SIMULATION

2.1 Photonic processes

In the current version of RTS&T Code the following photonic processes types are simulated: Photoelectric effect (from K, L_I, L_{II}, L_{III} atomic shells), Rayleigh scattering,Compton scattering, pair production by photons, hadronic interactions of photons (photonuclear effect).

The EPDL evaluated data library[2] of photon-interaction total cross sections, coherent and incoherent scattering form-factors are used in photon transport simulation for the energy range about 10 eV to 100 GeV.

2.2 Charged particles ionization processes

To simulate the ionization processes induced by the charged particles two different models are provided:

1. Continuous energy loss model with δ-ray generation.
2. Continuous energy loss model without δ-ray production and full Landau - Vavilov fluctuations. The density effect correction to the stopping power of matter has been taken account.

Multiple scattering of charged particles was simulated according to Moliere theory. Direct pair production by charged hadrons is included in the calculations as well.

2.3 $e^{\pm}$ discrete bremsstrahlung process

The discrete bremsstrahlung photon energy is sampled from a Seltzer and Berger[4] differential cross section for electron kinetic energy below 10 GeV and Bethe-Heitler cross section above this value. The angular distribution of the emitted photon is sampled according to facilitated form of the double differential cross section[5–6].

2.4 Hadronic processes

2.4.1 High energy hadronic interactions

To simulate the interactions of hadrons and charged pions with the nuclei in kinetic energy range about 20 MeV to 25 GeV intranuclear cascade-evaporation model (Dubna version) was provided. To calculate the distance to the interaction point and simulation of hadronic process type the Barashenkov total cross sections compilation[7] was used. π^0-mesons decay into two photons is simulated according to decay kinematical scheme.

0-7803-4376-X/98/$10.00 © 1998 IEEE

2.4.2 Low-energy neutrons transport

In practice of low-energy neutrons transport calculation the files of evaluated nuclear data present the original constant information, however, they are used not directly but after treatment to multi-group constant systems. In this approach comparison of calculation results with benchmark-experiments allows to test only information obtained after treatment. Then the system mistake supplemented by treatment itself cannot be estimated in principle, since it is indivisible from the system errors of the evaluated data file itself[8].

RTS&T code is based on the *direct* use of ENDF/B-VI[1] evaluated data library to detailed low-energy neutron interactions simulation. The partial neutron-interactions processes simulation is performed according to ENDF/B laws. During constants preparation process linearization and restoration of resolved resonances of neutron cross sections with LINEAR and RECENT ENDF-utilities is made. Data reading and constants preparation procedure was written in the ANSI "C" language.

3 ISOTOPES TRANSMUTATION CALCULATION METHOD

The isotopes transmutation process is described by a system of balance ordinary differential equations. For the isotopes concentration N_i, where $i = 1, M$ (M is the total number of nuclides which to participate in connected transitions) the given system of equations is the following:

$$\frac{dN_i(t)}{dt} = -N_i \cdot \left(\lambda_i + \sum_k \int_0^{E_0^k} \sigma_i^k(E) \cdot \phi^k(E,t) dE \right) + \quad (1)$$

$$+ \sum_{j \neq i} N_j \cdot \left(\lambda_{ji} + \sum_k \int_0^{E_0^k} \sigma_{ji}^k(E) \cdot \phi^k(E,t) dE \right)$$

$$N_i(0) = N_i^0,$$

Where $\sigma_i^k(E)$ - summary cross section of reactions presenting the change of i-th nucleus structure, $\sigma_{ji}^k(E)$ is the partial cross sections of i-th isotopes formation reactions from j-th mother nucleuses under action of particles of grade k with the energy E, λ_i - disintegration constant of the i-th isotopes, λ_{ji} - disintegration constant of the j-th isotopes on the channels were presented to i-th nuclide formation; $\phi^k(E,t)$ is the particles of grade k with the energy E total flux, maximum significance of which is E_0^k. Breaking a period of exposition of a material on a number of temporary sessions with $\phi^k(E,t \cong \phi^k(E)$, we receive from (1) the independent system of equations with constant factors, the analytical decision of which is recorded in a matrix kind:

$$N(t) = N_0 \exp(Ct), C_{ij} = \begin{cases} -(\lambda_i + \sum_k \int_0^{E_0^k} \sigma_i^k(E) \cdot \phi^k(E) dE) \\ \qquad \text{if } i = j \\ \lambda_{ij} + \sum_k \int_0^{E_0^k} \sigma_{ij}^k(E) \cdot \phi^k(E) dE \\ \qquad otherwise \end{cases} \quad (2)$$

where $\exp(Ct)$ is matrix exhibitor:

$$\exp(Ct) = \sum_{s=0}^{\infty} \frac{C^s t^s}{s!}, C^0 = E. \quad (3)$$

We shall note a number of the equation system (1) features:

- Practically at any modes of exposition or endurance of any material the isotopes transmutation process contains both fast and slow making, and the distinction between them can reach 20 and more orders. Such spread of significances of elements of a matrix results to its bad conditionality [$cond(C) \gg 1$] and allows to assume, that a system of equations (1) is "stiff". Correctly the definition of "stiffness" of the equations system requires the calculation of own significances λ of matrix C, that reasonably is a difficult problem for large-size matrixes. Usually for these purposes a ODE system use the following criterion — the system is "stiff" if inequalities are executed:

$$\|C\|_1^{-1} \ll H, \quad |Sp(C)|^{-1} \ll H \quad (4)$$

Where H is the duration of exposition session or endurance, $\|C\|_1$ and $Sp(C)$ is the norm and trace of matrix C respectively:

$$\|C\|_1 = \max_{1 \leq i \leq n} \sum_{j=1}^{n} |c_{ij}|, \quad Sp(C) = \sum_{i=1}^{n} c_{ii} = \sum_{i=1}^{n} \lambda_i.$$

Numerical integration of "stiff" systems any obvious discrete methods (Runge-Kutta, Adams and etc.) results in effect "error explosion" at the chosen step $h \geq \max(\|C\|_1^{-1}, |Sp(C)|^{-1})$.

Given restriction from above on a integration step can result in unreal times of account when connected transitions (chains combined with nuclear reactions of radiation disintegration) contain nuclides with strongly distinguished life-times. Hence, application of standard methods of numerical integration non-stiff systems in an isotopes transmutation problem unacceptably.

- The majority of specialized methods of numerical integration of "stiff" systems of equations are based on implicit discrete methods (Rosenbrok, Kollahan and etc.), which in case of a system with constant factors

require calculations of a return matrix $(E + hC)^{-1}$, where h is the integration step, E – unit matrix. As the overwhelming majority of matrix C elements is considerably less than 1, reference (manipulation) of a given matrix is made with a large error, which grows with an increase of its size and with a reduction of the integration step. Use of arithmetics with a floating point of double accuracy to isotopes transmutation problem solution does not remove this problem (for example, at radioactive disintegration of U^{235} nuclei, $C_{ii} = 3 \cdot 10^{-17}$ and, in case of small h, even the operation of summation the diagonal elements of matrices E and hC already passes on limit of allowable accuracy by use of the 64 bits computers).

The marked specific of an isotopes transmutation problem limits the applicability discrete methods of numerical integration of ODE systems, that makes the their universal settlement circuit unsuitable for construction.

Direct use of the analytical decision (2) at large times and bad conditionality of the matrix C results in unjustified quantity terms at calculation exhibitor and high error. For the decision of a system of equations (1) in RTS&T code the circuit of calculation $\exp(Ct)$ was applied recurrent, which gives satisfactory results even in case of brightly expressed "stiffness" of a equations system (1) in a wide range of intervals of time h.

To construct recurrent of the calculation circuit $\exp(CH)$, where H is the duration of the exposition session, the interval H is broken into a number of any uniform sections h. Then isotopes concentration in each discrete moment of time $t_n = nh$, $n = 0,\ 1,\ ...$ are defined by the formula:

$$N_{n+1} = N_n\ \exp(Ch),\ n = 0,\ 1,\ ... \qquad (5)$$

To the exponential ($\exp(Ch)$) calculating the additional recurrent matrix equation construction is required. Such step h' is chosen, which satisfied to following conditions:

$$h' = \frac{h}{2^K}, \qquad h" \ll \min(\|C\|^{-1}, |Sp(C)|^{-1})$$

where K is any integer value. Having calculated on (3) $\exp(Ch')$, we can find $\exp(Ch)$, applying consistently formulas:

$$\exp(2Ch') = \exp(Ch')\exp(Ch'),$$

$$....$$

$$\exp(2^K Ch') = \exp(2^{K-1}Ch')\exp(2^{K-1}Ch').$$

We shall record these equations as the recurrent matrix equation:

$$\phi_{k+1} = \phi_k^2, \text{ where } \phi_k = \exp(2^k Ch'), \quad k = 0, 1, ..., K-1; \qquad (6)$$

Thus, it is possible to choose so small size h', that high accuracy of representation $\exp(Ch')$ by decomposition (3) with small number of the members (s) is provided no matter how. On the other hand, the use recurrent of equations (5) and (6) for the decision of a system (1) considerably reduces number of steps of integration for the given interval H:

$$H/h = 2^{-K} \cdot H/h',$$

That removes a "large times" problem in any isotopes mixes. Valuation of a relative error of the numerical circuit of the decision of a equations system (1) to be made according to the Runge rule: i.e. results received for the steps $h'(K)$ and $h'/2(K+1)$ are compared.

4 ACKNOWLEDGEMENTS

The contribution to the RTS&T code (geometry description procedures) have been made by O. Lyashenko to whom the autors expresses his cordinal gratitude.

The autors is grateful to Yu. Fedotov for his interest to the work and R. Mukhamadeev (SRC IPPE) for the stimulating discussions.

5 REFERENCES

[1] ENDF-102 Data Formats and procedures for the evaluated nuclear data file ENDF-6. BNL-NCS 44945, July 1990.

[2] D.E. Cullen, M.N. Chen, J.H. Hubbel, S.T. Perkins, E.F. Plechaty, J.A. Rathkopf, and J.H. Scofield. Tables and Graphs of Photon-Interaction Cross Section from 10 eV to 100 GeV Derived from the LLNL Evaluated Photon Data Library (EPDL). UCRL-50400 vol.6, Lawrence Livermore National Laboratory, 1989.

[3] V.V. Varlamov, V.V. Surgutanov, A.P. Chernyaev, N.G. Efimkin. Photo-nuclear library, EPNDL-1, PART2 version MARCH-1996. Private communication.

[4] S.M. Seltzer, M.J. Berger, "Bremsstrahlung spectra from electron interactions with screened atomic nuclei and orbital electrons", NIM B12 (1985) 95-134.

[5] Y.S. Tsai, "Pair production and bremsstrahlung of charged leptons", Rev. Mod. Phys. 46 (1974) 815.

[6] Y.S. Tsai, "Erratum: Pair production and bremsstrahlung of charged leptons", Rev. Mod. Phys. 49, 815 (1977).

[7] V.S. Barashenkov. Cross Section of interaction particles and nuclei with nuclei. Dubna, JINR, 1993.

[8] P.A. Androsenko, A.A. Androsenko, G.V. Bolonkina, S.I. Dubrovina, A.S. Krivtsov, "The experience of direct use of ENDF-B/6 in calculations by the Monte-Carlo method. VI Russian scientific conference on radiation shielding of nuclear installations", Obninsk, 1994.

[9] R. Silberberg, C.H. Tsao "Partial Cross-Sections in High–Energy Nuclear Reactions and Astrophysical Applications", The Astrophysical Journal Supplement Series, supplement number: 220, vol.25, 1973.

[10] R. Silberberg, C.H. Tsao "Spallation processes and nuclear interaction products of cosmic rays", Physics reports, A Review Section of Physics Letters, vol.191, $N6$, August 1990.

[11] "Radionuclides decay channels. Radiation energy and intensity. ICRP Recommendation." v.1–4, Energoatomizdat, 1987.

PERTURBATION OF RELEVANT RESONANCE FOR SLOW EXTRACTION EFFICIENCY INCREASE

N.N.Alexeev, S.L.Bereznitsky, A.E.Bolshakov, ITEP, Moscow, Russia

Abstract

In synchrotron, slow extraction of circulating beam when influenced by non-linear perturbation was analysed both analytically and by computer simulation. It was found that beam loss on the septum may be reduced two times and more if particles distribution in the cross section of kicker magnet is deformed with decapole perturbation of sextupole magnetic field using for resonance excitation. Similar effect is observed for gradient resonance extraction with octupole perturbation. Results of simulation for ITEP PS slow extraction system are presented.

1. INTRODUCTION

The resonance slow extraction of the beam circulating in the synchrotron is impossible without loss of a part of beam that jumping unsuccessfully over a septum. To increase the efficiency of the slow extraction, the septum width has to be constructed as thin as possible. We are considering another way of the beam loss minimisation which is base on the forming the particles distribution in the cross section of the kicker magnet to reduce a portion of scattered particles in the septum of given width. The required deformation of the conventional distribution may be obtained by the relevant resonance perturbation as it will be shown below.

2. FOUNDATIONS OF ANALYSIS

The equation of motion at resonance slow extraction is written usually in the form

$$\frac{d^2\eta}{d\phi^2} + \nu^2\eta = -a\eta^{n-1}\cos(m\phi) \quad , \quad (1)$$

where η, ϕ - Courant-Snyder variables, $\nu=\nu_r+\Delta\nu$ - tune value, n=2 - for gradient resonance, n=3 - for sextupole resonance, $m=n\cdot\nu_r$ - resonance harmonic number. Eq (1) may be rewritten in the co-ordinate system (X,Y) proposed by Krylov-Bogolubov-Metropolsky [1]

$$\eta = X(\phi)\cos(\nu_r\phi) - Y(\phi)\sin(\nu_r\phi)$$

$$\eta' = -(\nu_r+\Delta\nu)\{X(\phi)\sin(\nu_r\phi) + Y(\phi)\cos(\nu_r\phi)\} \quad (2)$$

in the form

$$X' + \Delta\nu Y = \frac{1}{\nu} a\eta(X,Y,\phi)^{n-1}\cos(m\phi)\sin(\nu_r\phi)$$

$$Y' - \Delta\nu X = \frac{1}{\nu} a\eta(X,Y,\phi)^{n-1}\cos(m\phi)\cos(\nu_r\phi) \quad (3)$$

Removing from (3) harmonic addendums and keeping addendums responsible for slow changing of betatron oscillation amplitude we obtain for gradient resonance

$$X' + \Delta\nu Y = \frac{a}{4\nu} Y$$

$$Y' - \Delta\nu X = \frac{a}{4\nu} X \quad (4)$$

and for sextupole resonance

$$X' + \Delta\nu Y = \frac{a}{4\nu} XY$$

$$Y' - \Delta\nu X = \frac{a}{8\nu}(X^2 - Y^2) \quad (5)$$

It follows from Eq.(4) that a rate of oscillation amplitude increases at gradient resonance as

$$R' = R\frac{a}{4\nu}\sin(2\varphi) \quad , \quad (6)$$

where $X=R\cos(\varphi)$, $Y=R\sin(\varphi)$. For sextupole resonance, the rate dependence of amplitude is

$$R' = -\frac{a}{8\nu} R^2\cos(3\varphi) \quad (7)$$

When oscillation amplitudes are big enough, the phase space trajectories are close to the linear separatrix and $\varphi\approx$const.

The particles distribution f(R) in the kicker magnet cross section may be obtained in assumption that the flow of particles to the transverse direction at the beam ejection process is stable and independent of R. In this case

$$R' \cdot f(R) \approx \text{const} \quad (8)$$

and the particles density in the kicker magnet cross section for Eq.(7,8) conditions is decreased with R, so the maximum density value corresponds to the septum co-ordinates.

3. PERTURBED MOTION ANALYSIS

It follows from Eq.(8) that a distribution function f(R) with lower density value at the septum co-ordinates may be obtained by means of corresponding modification of R' function. It may be done for example through the relevant resonance perturbation according, to

$$\frac{d^2\eta}{d\phi^2} + \nu^2\eta = -a\eta^{n-1}(1 - k\eta^2)\cos(m\phi) \quad .(9)$$

where k - factor of resonance perturbation. The rate expressions of oscillation amplitude growth for Eq.(9) conditions are

0-7803-4376-X/98/$10.00 © 1998 IEEE

$$R' = R\frac{a}{4\nu}\left(1-\frac{k}{2}R^2\right)\sin(2\varphi) \qquad (10)$$

and

$$R' = -\frac{a}{8\nu}R^2\left(1-\frac{3}{4}kR^2\right)\cos(3\varphi) \qquad (11)$$

Setting the k factor in Eq.(10-11) to optimum value, one can possible to obtain the required particles distribution f(R) with minimum density value at the septum co-ordinates.

4. RESULTS OF SIMULATION

Analytical analysis was verified by computer simulation for ITEP Proton Synchrotron slow extraction system constructed on simplest scheme with one sextupole lens for resonance excitation and one kicker magnet for particles extraction. Fig.1 shows layout of main components for this system.

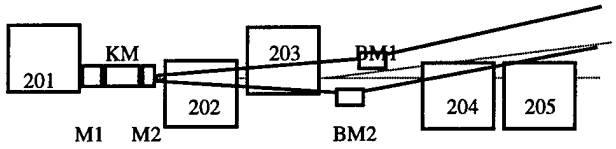


Fig.1 Schematic arrangement of beam ejection system, where K-is kicker magnet with septum, M12 - magnets for local orbit deviation, BM - bending magnets.

The effective thickness of septum is 2 mm and the width of magnetic gap is 4 mm. So the efficiency of beam ejection at conventional sextupole resonance conditions is near to 60%. Summary distribution diagram of particles in the cross section of kicker magnet is shown in fig.2.

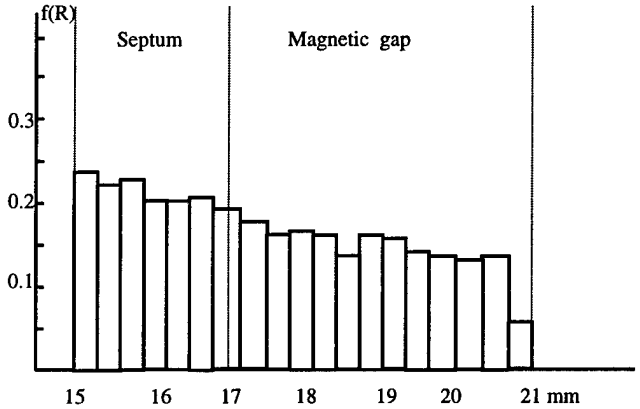


Fig.2. Conventional particles distribution in the cross section of kicker magnet at slow extraction

One can see in this picture that the density slope is close to the $1/R^2$ function as predicted by Eq. (8). and the ejection efficiency is 59%.

Small perturbation of sextupole resonance according to Eq.(9) causes deformation of distribution of interest in that way that the density descends at septum co-ordinates and raises at magnetic gap, but the distribution shortens, so the ejection efficiency goes down. Obvious way to high efficiency is to lengthen the distribution by extension of sextupole resonance. Result of this procedure optimisation is shown in fig.3.

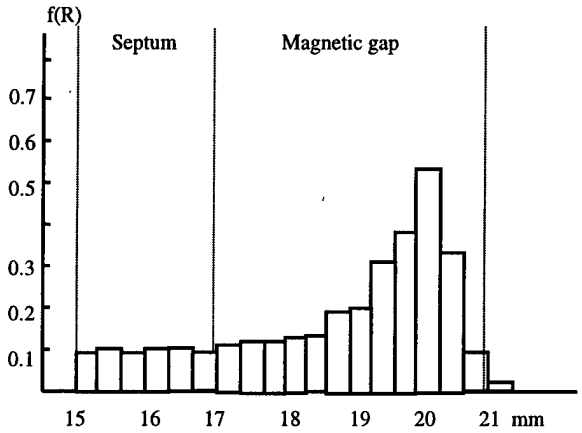


Fig.3. Optimised distribution of particles in kicker magnet cross section at decapole perturbation of sextupole resonance

The particles loss in septum was reduced two times and efficiency of the beam ejection has raised by 20%.

Deformation of distribution shown in fig.3 is a result of the rate amplitude moderation with approach to the septum. In the vicinity of septum the particles are jumping hardly over the obstacle to the distant edge of septum, but at the more distance from the septum, the jumps are further and particles hit the magnetic gap free space.

Fig.4 and Fig.5 show phase space trajectories near unperturbed and perturbed sextupole resonance

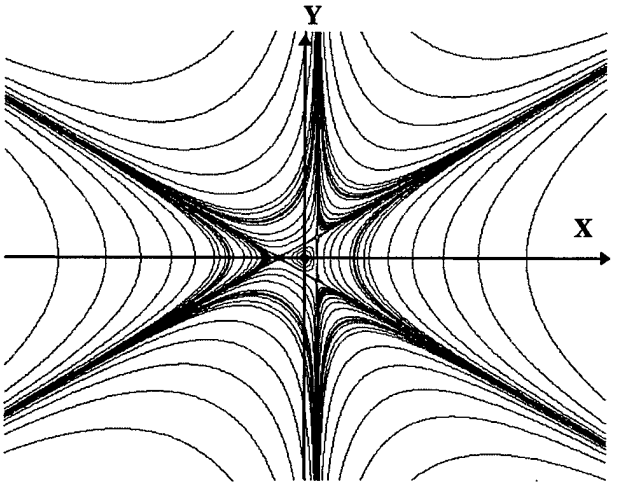


Fig.4. Phase-space trajectories near sextupole resonance

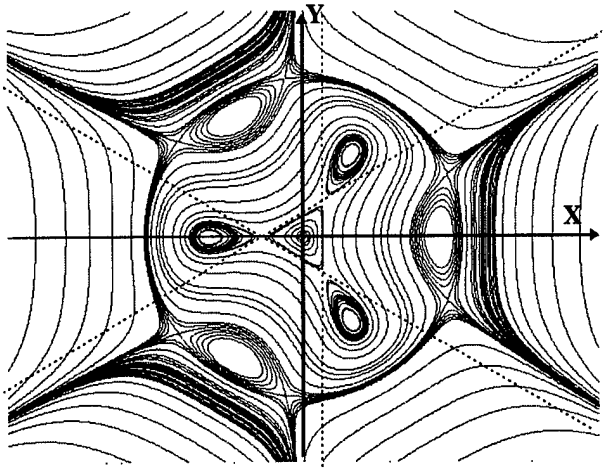


Fig.5. Phase-space trajectories near perturbed sextupole resonance

described by Hamiltonian

$$H=\frac{\Delta\nu}{2}(X^2+Y^2)+\frac{a}{24\nu}X[(X^2-3Y^2)-\frac{3}{4}k\{X^4-3Y^4-2X^2Y^2\}]$$

The open domain of unstable motion around a small triangle shown in Fig.4 is transformed to the ring domain of formally stable motion with fixed points of two levels, shown in Fig.5. The unexcited beam is located in the vicinity of origin, so trajectories streamlining three fixed points of the first level is only occupied. The kicker magnet phase space image is placed near the external side of a fixed point separatrix for the best interception of particle by particle of the whole beam.

Fig.6 and Fig.7 show co-ordinate/angle distribution of the beam in the cross section of kicker magnet for the cases of conventional and perturbed resonance. One can see that the growth of ejection efficiency is accompanied by some swelling of the transverse phase volume. This is a natural fee for the ejected beam intensity increase.

Emittance growth is a serious problem and disadvantage of this method if it can't be compensated by some way. We haven't try to seek minimum emittance conditions but it's clear that the value of emittance growth depends on a betatron oscillation phase shift that happens due to the additional non-linear field component. The value of this phase shift may be regulated by changing some parameters and conditions of slow extraction system. Though there are some complications in theoretical treatment and in the choice of the optimum configuration for ejection system, we expect to get answers for main questions in near future.

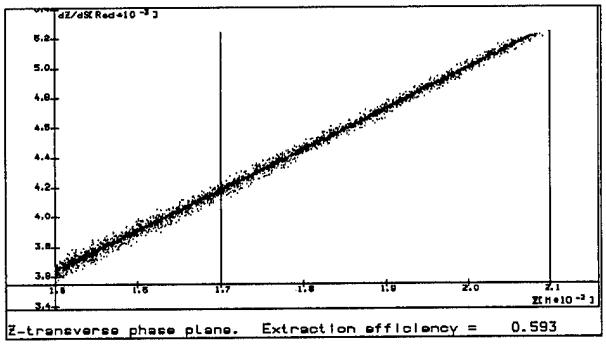


Fig.6. Beam phase portrait for ejection at conventional sextupole resonance

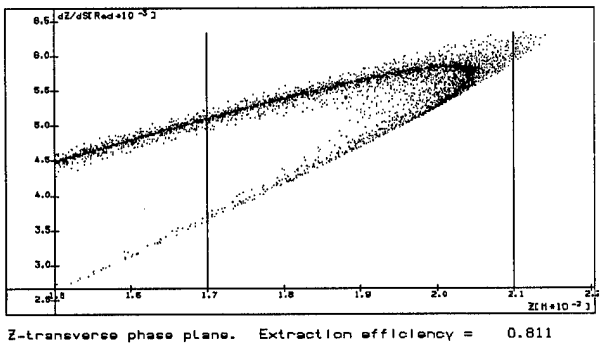


Fig.7. Beam phase portrait for ejection at perturbed sextupole resonance

CONCLUSION

The method of beam loss minimisation at slow extraction based on the relevant resonance perturbation was considered analytically and by computer simulation. It was shown that an ejection efficiency growth may be obtained with the n+2 order perturbation of the n order resonance that using for extraction. The optimum value of perturbation for the maximum gain of efficiency depends on the machine configuration and the initial parameters of the unexcited beam. The problem of ejected beam emittance growth is the subject for future research.

REFERENCES

[1] N.N.Bogolubov, Yu.A.Metropolsky,'Asymptotic Methods in the Non-linear Oscillation Theory', Moscow, 1958.
[2] H.G.Hereward. Proc. Intern. Conf. High Energy accelerators. Dubna 1960, p.690.
[3] Y.K.Kobayashi. Nucl. Instr. and Meth. 83 (1970) 77.
[4] R.Nagaoka. Nucl. Instr. and Meth A302 (1991) 9

BEAM EXTRACTION SYSTEM FOR THE COOLER INJECTOR SYNCHROTRON AT IUCF

X. Kang, G.P.A. Berg, D. Friesel, S. Y. Lee and T. Sloan
Indiana University Cyclotron Facility
2401 Milo B. Sampson Lane, Bloomington IN 47405

Abstract

The Cooler Injector Synchrotron (CIS) being built at IUCF will serve as an injector for the existing IUCF Cooler Ring. The beam extraction from CIS and injection to the Cooler Ring include the the orbit bump, extraction kicker, septum magnet in the CIS ring, the transport beam line, and injection part to the Cooler ring. After extracted from CIS ring with a traveling wave fast kicker (15 mrad) and a Lambertsen septum, beams are transported by the beam line BL9 to the cooler injection point and injected into the cooler ring by a fast traveling wave injection kicker.

1 INTRODUCTION

A Cooler Injector Synchrotron (CIS)[1], nearing completion at IUCF, is designed to provide polarized light ion beams, such as 200MeV proton beams, for the existing Cooler Ring. The CIS beam extraction system is composed of four orbit bumpers, a traveling wave fast kicker and a 12° Lambertsen septum. After extracted from CIS, beams are transported to the Cooler Ring by the beam line BL9, which consists of a suitable set of quadrupoles and dipoles for beam matching at the injection point and two solenoids for spin manipulation. Beams are injected into the Cooler Ring at an angle of 9.4 $mrad$ by a septum and fast traveling wave injection kicker at the injection point. The beam parameters are matched at the injection point horizontally by adjusting the positions the strength of the quadrupoles and vertically by setting a proper conditions of both CIS and Cooler rf systems.

2 BEAM EXTRACTION FROM CIS

As shown in Figure 1, single-turn method is used for the fast beam extraction from CIS. After deflected by the kicker, the beam passes through the region with deflecting field for extraction while the closed orbit passes through the field-free region in the septum. The beam offset at the location of septum x_s must not be less than the half-width of the circulating beam with an allowance for closed orbit distortions and alignment errors plus the half-width of the extracted beam and the septum width. The kicker is often dictated by technology and economics, so it is advantageous to make betatron phase shift between the kicker and septum $\Delta\mu$ closed to $\pi/2$ and β_k large so that δ_k is reduced. The minimum strength of septum depends on how much more angular deflection is needed to take the beam clear of the next machine magnet. However, the deviation of the beam directly from the central orbit provided by the kicker is not big enough for the structure of the septum.

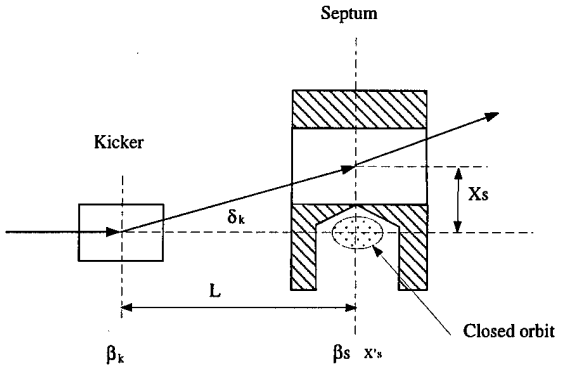


Figure 1: CIS fast extraction structure.

To minimize the cost and strength of the fast kicker, beam bumpers are used to adjust the closed orbit locally closer to the septum. Outside the four bumpers, the closed orbit is still along the CIS central line.

For the CIS extraction, a fast traveling wave kicker[2] is used which can deflect $200MeV$ proton beam at least for an angle of 15 $mrad$ within a cycling time of 90 ns. The deviation of the beam at the septum is only $17mm$ According to the geometry of the septum, totally the beam should have a displacement of $> 40mm$ in order to be extracted from the ring. So before kicking the beam, four bumpers are used to bump the closed-orbit by about 25mm from the central orbit in the vicinities of the septum. Figure 2 shows the closed orbit bump and beam extraction trajectory in the horizontal plane. The beam has a small angle(0.65°) inwards before entering the septum. If the septum is rotated by 3.1°, the field component B_z can correct this angle.

If the traveling wave kicker pulse has some fluctuation before and after the kick, the closed orbit and the extracted beam will be affected slightly near the septum. The simulation results show that the maximum change of the closed orbit due to $\pm 5\%$ pre-pulse fluctuation is less than $\pm 1mm$ and the changes at kicker and septum are even less. The effect of the $\pm 10\%$ kicker top pulse fluctuation(total effect of $\pm 5\%$ pre-pulse and $\pm 5\%$ top pulse fluctuation) is that the beam trajectory has a change of $\pm 1.5mm$ at the first dipole after kicker. The beam positions at kicker and septum change less than $\pm 2mm$.

In the vertical plane, the septum deflects the beam upwards by 12° to let the beam avoid the dipole magnet No. 3 and then deflected back to the horizontal direction by another dipole TPES. After the beam is extracted from CIS, it is 0.77m above the CIS ring plane vertically, as shown in Figure 3.

0-7803-4376-X/98/$10.00 © 1998 IEEE

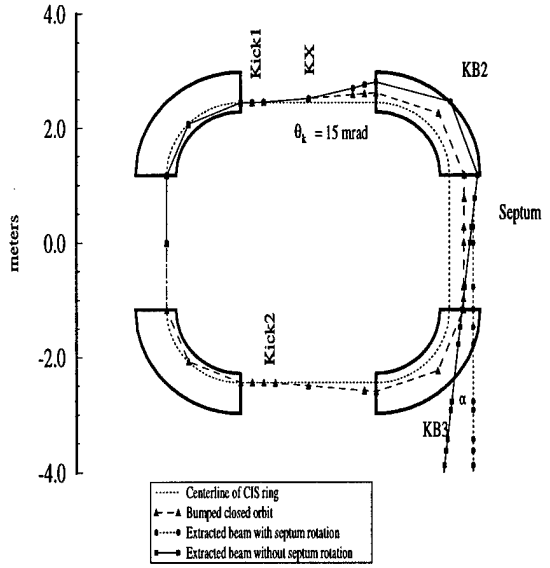


Figure 2: Closed orbit bump and beam extraction from CIS. Note that the orbit deviation are enlarged by 10 times.

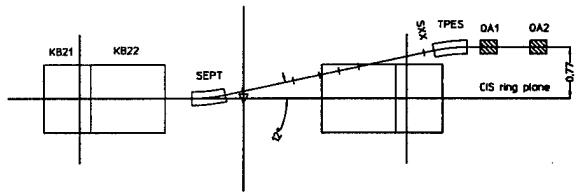


Figure 3: Beam extraction trajectory in the vertical plane.

3 TRANSPORT BEAM LINE BETWEEN CIS AND COOLER

The extracted beam from the CIS ring has emittance of $10\pi mm \cdot mrad$ and momentum spread of 0.15% and is transported from CIS to Cooler by the transport beam line composed of a set of suitable quadrupoles, dipoles and solenoids. Two solenoids SOL1, SOL2 and two dipoles D1, D2 are used for providing proper spin orientation for polarized beam injection for the cooler ring. In order to inject the beam to the cooler properly, both the transversal and longitudinal beam parameters must be matched at the injection point.

The constraints for the transversal beam matching are the field gradients B' of eight quadrupoles from QA1 to QA6, Q99 and Q109, the distance SA12 between the first two quadrupoles Q1 and Q2. After adjusting the above constraints, the beam parameters β functions β_x, β_y, α_x, α_y and dispersion function D_x and D'_x are matched at the injection point of the cooler ring. Table 1 shows the initial and final values of the above constraints. Table 2 shows all the matched parameters. After the matching of the beam parameters, the beam envelope along the beam line must be smaller than the vacuum chamber to avoid beam loss. Figure 4 shows the β functions along the beam line. After the calculation, the horizontal beam envelope is much smaller than the vacuum chamber and the vertical beam envelope is also smaller than the magnet gap, as shown in Figure 5.

Table 1: Constraints for the transversal injection matching.

Parameters	Initial	Final
B'_1	9.9999982	9.9999999
B'_2	-7.2650281	-7.3876488
B'_3	6.6119067	0.9066779
B'_4	-6.5590755	1.1898049
B'_5	2.2938179	6.7237249
B'_6	-2.4567029	-7.1063014
B'_{99}	2.0705442	2.5966974
B'_{109}	-1.2928168	-5.5034685
S_{12}	0.2155292	0.2378493

Table 2: Beam parameters matched at the cooler injection point.

Parameters	Desired	Present	Error
β_x(m)	2.281	3.189	0.908
β_y(m)	1.744	1.599	-0.144
α_x	0.173	-0.486	-0.658
α_y	-0.130	-0.463	-0.333
D_x(m)	-4.180	-5.079	-0.899
D'_x	-0.027	0.053	0.080

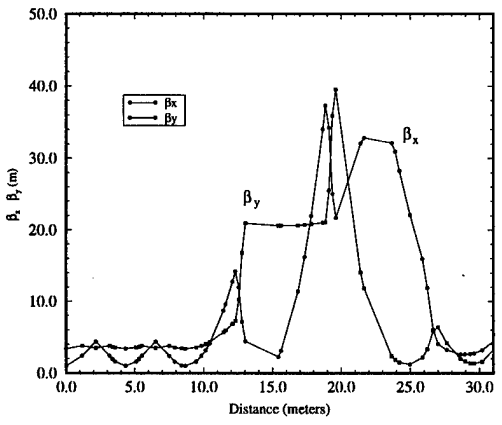


Figure 4: β functions along the extraction beam line.

For the longitudinal beam matching, the ratio of the bucket height and width of the two rings must maintained in order to avoid the bunch dilution during the bucket to bucket transfer from CIS to Cooler,

$$\left|\frac{\hat{\delta}}{\sigma}\right|_{CIS} = \left|\frac{\hat{\delta}}{\sigma}\right|_{Cooler} \quad (1)$$

This condition requires the equilibrium phase space profile

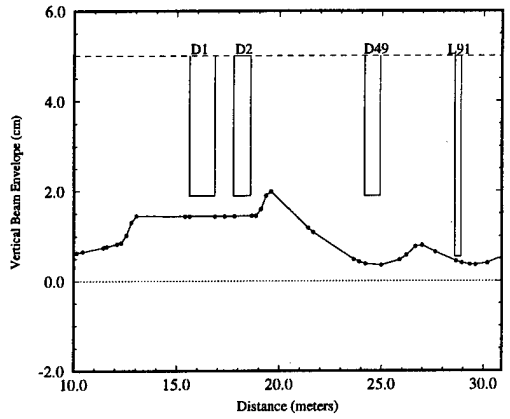


Figure 5: Vertical beam envelope along the beam line.

matching of the rf system

$$\left|\frac{V\cos\phi_s}{h\eta}\right|_{CIS} = \left|\frac{V\cos\phi_s}{h\eta}\right|_{Cooler} \quad (2)$$

which means that the rf system in CIS should reflect a proper longitudinal matching condition.

4 BEAM INJECTION TO THE COOLER

Fast injection method is used for the beam injection into the Cooler upon the modification of the existing beam line BL9. Figure 6 shows the horizontal plane of the injection section.

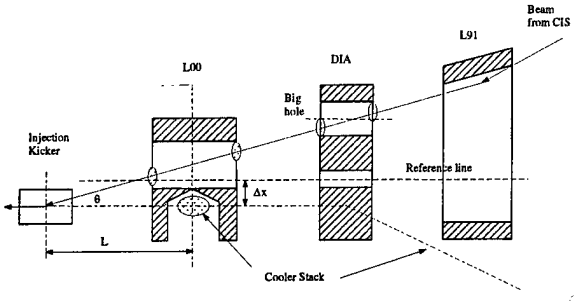


Figure 6: Horizontal plane of the cooler injection section.

In the horizontal direction, Cooler stack is deflected by 3° by DIA and DIB respectively and is bumped close to injection beam near L00 by the existing bumpers in the Cooler Ring. Injected beam from L91 enters the kicker with an angle less then 15mrad and then kicked to the Cooler stack direction by the traveling wave kicker. Vertically, the beam is bent down by a dipole SV2 before entering L91 and flatten at Lambertsen magnet L00.

Based on the existing beam element arrangement, the available space for injection kicker is 1.5m and the center of the kicker should be 2.0m away from L00. In order to pass through DIA and L00, the injection beam must have an angle of $> 16mrad$, which is difficult for a 1.5m long injection kicker to deflect. The solution is to merge the two holes in DIA into one big hole. Then, with an angle of $9.4mrad$, the beam is easily injected into Cooler by the fast kicker which is 2.0m away from L00.

Making two existing holes into one big hole, the strength and quality of the DIA dipole maybe affected. However, the calculation results show that the leaking field in the big hole of DIA is only 12Gs which has a deflection angle of $0.1564mrad$ on the $200MeV$ beam. This effect is negligible.

For each injection cycle, 5 pulses from CIS are injected to the cooler and accelerated to the desired energy. This requires that the rise and fall time of the injection fast kicker is less than 70 ns. The horizontal gap of the injection kicker must be big enough for the beam and the Cooler stack bump. The acceptance of the cooler is $20\pi mm \cdot mrad$ and the dispersion function at the injection point is 1.5m, which gives a beam size of 11mm. The closed orbit needs to be bumped from 8mm to 14mm for the injection. So the total width of the gap should be bigger than 4.3cm.

5 CONCLUSION

Fast extraction method is used to extract the $200MeV$ beam from CIS and fast injection method is used to inject the beam into Cooler Ring. The kicker angles required for the extraction and injection kickers are less than $15mrad$. The $\pm 5\%$ pre-pulse and $\pm 5\%$ top pulse fluctuation of the CIS extraction kicker has small effect on the beam trajectory. Some modifications are needed on the existing beam element arrangement in order to inject the beam into the Cooler properly. Both transversal and longitudinal beam parameters can be matched for the Cooler injection by adjusting parameters of the beam elements and rf systems.

6 ACKNOWLEDGEMENTS

We would like to thank the entire IUCF operation group for their help.

7 REFERENCES

[1] D.L. Friesel and S.Y. Lee, "Status of the IUCF Cooler Injector Synchrotron Construction Project", Proceedings of this conference.

[2] G. P Berg, "CIS Kicker Design Notes".

[3] H. Grote *et al.*, The MAD Program, User's Reference Manual.

[4] A. A. Garren *et al.*, SYNCH, User's Guide, 1993.

[5] P. J. Brant and K. Johnsen, "The Principle of Circular Accelerators and Storage Rings", Cambridge University Press, 1993.

[6] G.H. Rees, "Injection and extraction", Proc. CERN Accelerator School General Physics, GIf-sur-Yvette, 1984, CERN 85-19 (Nov. 1985), 346-57.

INTENSITY ASYMMETRIC MULTIPLE SLOW EXTRACTION AT THE KEK-PS

M.J.Shirakata, K.Marutsuka and H.Sato,
High Energy Accelerator Research Organization
Y.Shoji, Himeji Institute of Technology

Abstract

Intensity asymmetric simultaneous extraction to multiple beam lines at the KEK 12GeV Proton Synchrotron has been performed for physics experiments since the end of 1995. The exctracted beam to one beam line is about 1/100 lower intensity than another. This weak beam has been utilized for the primary beam experiments with stable spill quality.

1 INTRODUCTION

Resonant slow extraction is widely used in existing synchrotrons. Some of them have two extraction lines and simultaneous beam extraction for multiple beam lines are carrying out in order to save the operation time. They are symmetric in resonant phase.

Fig.1 is a schematic drawing of the KEK-PS. The KEK-PS has three beam lines which consist of two slow extraction beam lines (called EP1 and EP2) and one secondary beam line of the internal target (IT). In usual, we extract the beam only to either EP1 or EP2 beam line with parasitic IT beam. Since the EP1 and EP2 beam lines have their own independent extraction system designed for single extraction, they are not symmetric in resonant phase.

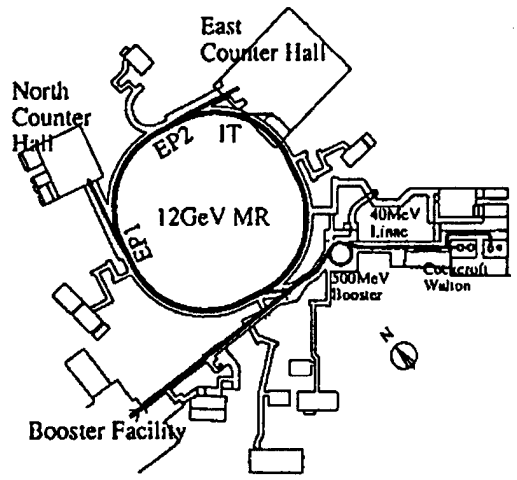


Figure 1: Schematic drawings of the KEK-PS.

The test operation for the double slow extraction was started in 1992, the basic design work was performed[1]. In this case, though much efforts was spent to guarantee the same intensity on the extracted beam both EP1 and EP2 beam lines, it found difficult to utilize them for the physics experiments due to their unstability and large beam losses without building a new extraction system. However the physics committee proposed the intensity asymmetric multiple extraction in late 1995 accompanied with the build of the new branch of the beam line called EP1-B. The EP1-B was designed for very low intensity beam of under 5×10^{10} [ppp]. This new offering required the intensities of EP1, EP2 and IT of about 1:100:10, respectively. The very weak extracted beam is utilized for the experiments on the primary proton beam.

The test operation of the simultaneous multiple beam extraction began to start again with largely asymmetric beam intensity.

Table 1: Expected beam losses.

case 1	case 2	case 3
4 %	5 %	22 %

case 1: EQ1 for EP1 or EQ2 for EP2
case 2: EQ1 for EP2 extraction
case 3: EQ2 for EP1 extraction

2 EXTRACTION SCHEME

2.1 *Double Slow Extraction*

The extraction system of the KEK-PS is designed to utilize the $2\nu_h = 15$ half-integer resonance[2]. The EP1 and EP2 extraction system are almost same. The slow extraction system consists of one perturbing quadrupole magnet called "EQ", one octupole magnet called "OCT" and two electrostatic septa "ESS" and five magnetic septa "septum A to E". The "EQ" is installed in order to produce a half-integer stopband and the "OCT" is to separate unstable phase space region. On the horizontal tune getting closer to the half-integer, the stable region in phase space becomes smaller and beam particles begin to spill out of the accelerator. The beam particles spilled out are consequently shaved by "ESS" and deflected to the beam line by magnetic septa. The extracted beam is controlled by the spill-servo system feeding back the spill intensity[3][4]. The spill-servo system has two inputs. One is the circulating beam intensity just before extraction process and the other is the realtime spill intensity. The spill-servo system controlls the purturbation quadrupole based on these signals in order to keep the spill intensity to the constant.

In double slow extraction, we have two purturbation quadrupoles. Table 1 shows the predicted beam loss during the extraction period in three cases.

Obviously the case 1 which is the ordinary extraction

0-7803-4376-X/98/$10.00 © 1998 IEEE

scheme shows the best extraction performance. Though the case 2 is acceptable, the case 3 is not. This results determines that the using EQ1 is the unique solution for the double slow extraction. In case of the EP2 main channel mode, the EP2 spill intensity feeds back to the EQ1 through the spill-servo system.

2.2 *Internal Target*

The Internal Target(IT) is the oldest system which was applied for the physics experiments in the KEK-PS. The IT system consists of the two bump magnets called "IT-bump", and two target arms including a spare arm. The circulating beam is bended out by IT bump magnets and one target arm is inserted into the beam line during the extraction period. The secondary beam intensity produced through the target is about 1/10 of the primary extracted beam in usual. Unfortunatery, because the IT bump cannot be completely closed due to their series cabling, it can largely affect on the intensity of the weakest beam in case of the multiple extraction.

3 RESULTS

3.1 *Beam Intensity and Spill*

The intensity asymmetric multiple extraction has started in extracting the weak beam to the EP1-B line which is referred as the EP2 main channel mode. The EP1 main channel mode is expected to run in this autumn.

In both cases, multiple extraction has to start the single extraction (very often with IT) using EQ1 purturbation quadrupole magnet. The EP1 main channel mode starts the ordinary EP1 extraction operation. Then turning on the EP2 extraction system with guradually raised bump magnets. Fig.2 shows the extracted beam spills, circulating beam intensity and current of EQ1 magnet of the EP1 main channel mode. Table 2 shows the intensities of extracted beams. In case of the EP1 main channel mode, the interfere on the main spill from the multiple extraction is very small.

Table 2: Beam intensities in [ppp] of each extraction modes.

Timing	EP1 main	EP2 main
P3	2.9e+12	2.8e+12
EP1	2.4e+12	2.0e+10
EP2	2.4e+10	2.0e+12
IT	1.0e+11	3.3e+11

P3: acceleration end corresponding to just before the extraction.

Fig.3 shows those of the EP2 main channel mode. In case of the EP2 main channel mode, firstly the EP2 single extraction tuning utilizing EQ1 is performed and then turning on the EP1 extraction system. The EP2 extracted beam

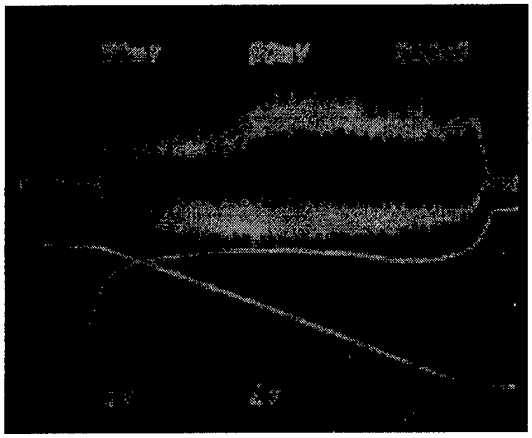


Figure 2: EP1 main mode. Extracted beam spills (EP2 was reversed), circulating beam intensity and EQ1 current.

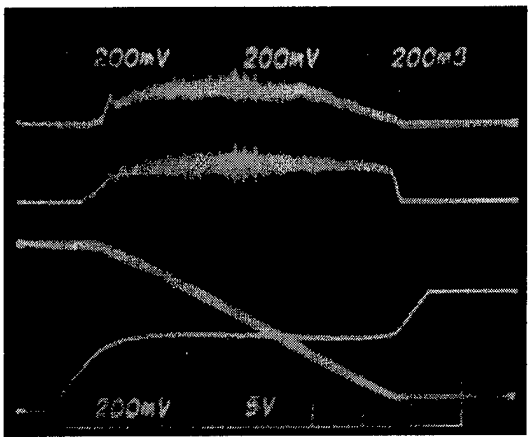


Figure 3: EP2 main mode. Extracted beam spills, circulating beam intensity and EQ1 current.

has a different angle with respect to the ordinary extraction which is achieved by EQ2. Fig.4 and Fig.5 show the beam profile at EP2 after the ESS measured by a single wire profile monitor. The single wire profile monitor consists of the scattering wire and loss monitors. A number of particles corresponding to the beam profile scattered by a wire are detected by a loss monitor placed just behind the wire. Fig.4 is in the normal extraction by EQ2. The island of the center is of the extracted beam profile and the right continent is the coast of the circulating beam. Fig.5 is of the multiple extraction by EQ1. The beam profiles are shifted to the inner of the ring and close each other. The septum A and B have to be moved to the appropriate position on the multiple extraction.

As mentioned in Table 1, the amount of the beam loss with respect to the EP2 extraction utilizing EQ1 is expected to be almost the same as that under the normal operation. However the extraction ratio of the EP2 main channel mode is under 80%. In actual, the beam loss at the EP2 during extraction period became above twice, especially on ESS and Septum A which were the upstream of the extraction

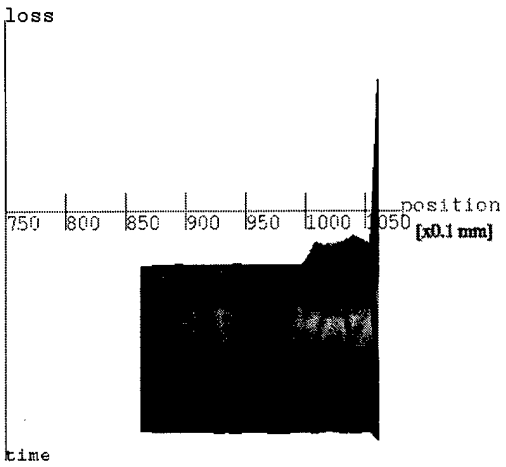


Figure 4: Ordinary extracted beam profile after ESS.

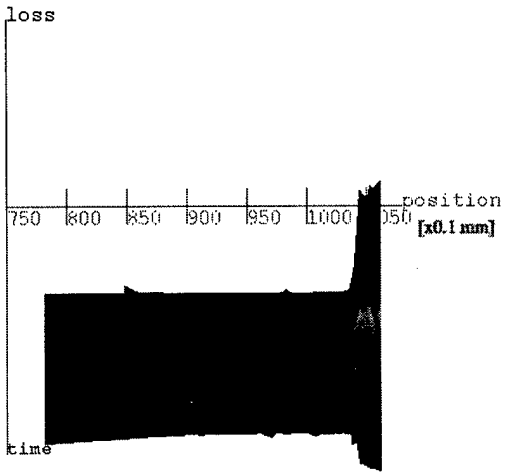


Figure 5: Beam profile of the EP2 main mode after ESS.

septa, according to turning on the EP1 extraction. This comes from the unseperation between shaved beam by ESS and circulating beam as shown in Fig.5. Moreover the inscrutable islands were found in the profile measurements in later runs. This problem has not been solved yet even in the simulation.

3.2 Stability

In the case of the EP2 main channel mode, the stability of the beam intensity and spill structure were monitored.

- December 1995, 2 days (the first try)
- January 1996, 6 days
- February 1996, 8 days
- April 1996, 14 days
- May 1996, 6 days
- October 1996, 8 days

including no IT extraction period

Although the weakest EP1 beam intensity varied in 1.7 to 3.4×10^{10} [ppp] during above period, it could be corrected very easily. Any serious changes on the spill structure did not observed. The multiple extraction has enough stability.

On April 1997, the first try of the EP1 main channel mode has done. Though this test ended in half a day, it seemed to be also very stable.

4 CONCLUSION

The intensity asymmetric multiple beam extraction of 100:10:1 was successed and being applied for physics experiments nowadays as the usual operation. Over the 3 experiments goes at the same time on our three beam lines. This intensity asymmetric multiple beam extraction is our answer to the strong requirements to get more machine time for the physics experiments.

5 REFERENCES

[1] Y.Shoji et al., Proc. of JAERI-Conf 95-021(332-334)

[2] Y.Shoji et al., KEK Report 93-10, Nov., 1993

[3] H.Sato et al., Proc. of the 9th Symp. on Acc. Sci. and Tech., 1993(208-210)

[4] T.toyama et al., Proc. of the 9th Symp. on Acc. Sci. and Tech., 1993(404-406)

PSR INJECTION-LINE UPGRADE*

Barbara Blind and Andrew J. Jason, Los Alamos National Laboratory

Abstract

We describe the new injection line to be implemented for the Los Alamos Proton Storage Ring (PSR) in the change from a two-step injection process to direct H^- injection. While obeying all geometrical constraints imposed by the existing structures, the new line has properties not found in the present injection line. In particular, it features decoupled transverse phase spaces downstream of the skew bend and a high degree of tunability of the beam at the injection foil. A comprehensive set of error studies has dictated the imposed component tolerances and has indicated the expected performance of the system.

1 INTRODUCTION

We are converting to direct H^- injection to reduce the beam losses in PSR and thus allow an increase in beam current from 75 μA to 100 μA, through improved quality of the injected beam and injection painting [1,2].

To make direct H^- injection possible, the injection line must be rerouted to bypass the ring dipole through which the beam is presently injected. This seemingly minor change in geometry, coupled with stringent requirements on the beam at the foil, necessitates changes throughout the line, while the existing tunnel walls place severe restrictions on the layout.

2 PRESENT INJECTION LINE

Figure 1 shows a sketch of the present injection line.

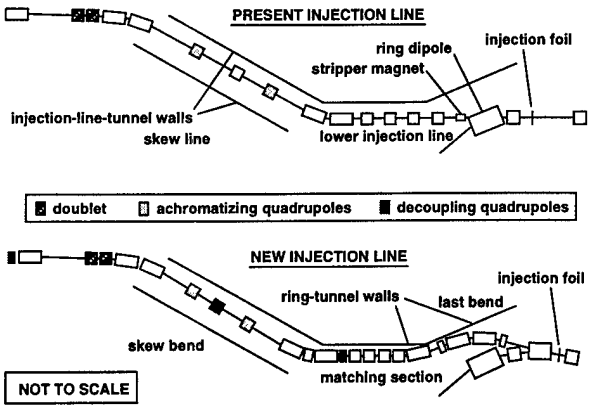


Figure 1. Top view of present and new injection line.

The present injection line consists of a skew line to take the beam from the transverse coordinates of the upstream transport line to those of the ring injection section, and a lower injection line to transport the beam through a stripper magnet, where H^- are converted to H^0, and through a hole in the side of one of the ring dipoles to the injection foil in the ring, where H^0 are converted to H^+.

The skew line contains an S-shaped bend in a 24.36° plane. In beamline order, a 1.5° kicker magnet deflects the beam into the injection line, a doublet provides needed focusing, and an FDF triplet, between two 6.75° dipoles and two −7.5° dipoles, makes the bend achromatic while providing focusing in both transverse planes. The D quadrupole resides at the dispersion crossover, thus decoupling achromaticity from vertical focusing. The skew bend causes downstream transverse linear coupling, leading to an apparent transverse-emittance growth of a magnitude that depends on the input beam and on the focus of the line.

The four quadrupoles in the lower injection line prepare the beam for the stripper magnet, where the vertical beam size must be small because of the narrow gap and the horizontal beam size must be small to minimize the additional horizontal-emittance growth caused by the stripping process. Because of these constraints the injected beam is not matched to the stored-beam parameters.

3 NEW INJECTION LINE

The new injection line consists of a skew bend, matching section and last bend, as sketched in Figure 1.

3.1 Layout

The bend in a skew plane is retained because it is not practical to replace it by separate horizontal and vertical bends. In order to gain space for the matching section, the bend angles of the 6.75° dipoles are increased to 7.5° and a −1.5° dipole is added between the −7.5° dipoles. The 26.86° roll angle of the skew bend is determined by the layout of the last bend.

The matching section is as close to a ring-tunnel wall as possible and is more compact than desirable. It is not possible to push the skew line upstream to gain more space, because it would obstruct access to the injection-line tunnel, as well as get too close to the floor.

The layout of the last bend is essentially fixed by the requirement of dipoles at or below the field-stripping limit of 3.8 kG, with small bend angles, and the presence of the existing PSR elements and ring-tunnel walls.

3.2 Expected Input Beams

The accelerator-output-beam transverse profiles are Gaussian with longer-than-Gaussian tails. These profiles are described well by the sum of two Gaussian distributions. Typically, the "wide-peak beam" (about

* Work supported by the U.S. DOE and DOD

70% of the total beam) and the "narrow-peak beam" (the remaining 30% of the beam) have transverse rms emittances of about 0.08 π-cm-mrad and 0.02 π-cm-mrad, respectively.

The momentum distribution is skewed, with a long low-momentum tail. The momentum deviation of the beam does not exceed about ±0.5%.

3.3 Nominal Beam at Injection Foil

The stored-beam Twiss parameters at the injection foil are $\beta_x = 2.675$ m, $\alpha_x = 0.6180$, $\beta_y = 11.093$ m and $\alpha_y = -1.3894$, with $D_x = 1.456$ m and $D_x' = -0.166$.

We will inject a zero-dispersion beam. For a dispersion-matched injected beam of the assumed momentum distribution, the foil must practically cover all horizontal coordinates to cover the same fraction of the beam as for the zero-dispersion injected beam, resulting in over twice the number of foil traversals.

To establish nominal injected-beam parameters and a preliminary injection point (injected-beam centroid location) at the foil, we chose among the upright injected-beam ellipses based on foil-edge location (as far from the stored-beam axis as possible, to minimize the number of foil traversals) and number of large-emittance stored-beam particles created. For transverse rms emittances of 0.08 π-cm-mrad, the nominal ellipses have rms parameters of $x = 0.10$ cm, $x' = 0.80$ mrad, $y = 0.16$ cm, $y' = 0.50$ mrad.

Through repeated ACCSIM runs, we found the desired injection point, $x_0 = 0.721$ cm, $x_0' = -1.960$ mrad, $y_0 = 2.250$ cm, $y_0' = 3.100$ mrad. For this injection point, the 2-rms injected-beam ellipses touch stored-beam ellipses with emittances of $\varepsilon_x = 3.2$ π-cm-mrad and $\varepsilon_y = 6.3$ π-cm-mrad. Figure 2 shows the transverse phase space at the injection foil. Shown are the 2-rms injected-beam ellipses and the stored-beam ellipses being filled. The foil edges are shown at −2.5 rms of the injected beam.

Horizontally, the foil edge is close to the axis, and there is no advantage in a closed-orbit bump. We will have a vertical closed-orbit bump for injection painting and to minimize the number of foil traversals [1,2].

3.4 Handling of Non-Nominal Injection-Line Input Beams

The injection line was designed with a particular input beam. For all accelerator output beams that have been documented to date, it is possible to restore the nominal injection-line input-beam Twiss parameters with the four quadrupoles immediately upstream of the skew bend. In case the non-nominal input beams are allowed to go through the line, the matching section can then restore the nominal Twiss parameters at the foil.

3.5 Issues Concerning Skew Bend

In order to explain the beam-optics properties of the skew bend, we need to distinguish between transfer-matrix elements in the upright coordinate system (R_{ij}) and in the skew coordinate system (S_{ij}).

The skew bend must again be achromatic, to avoid dispersion-related emittance growth and beam-centroid motion with beam-energy shifts. With two quadrupoles one can set $S_{16} = S_{26} = 0$ downstream of the bend, which automatically results in $R_{16} = R_{26} = R_{36} = R_{46} = 0$.

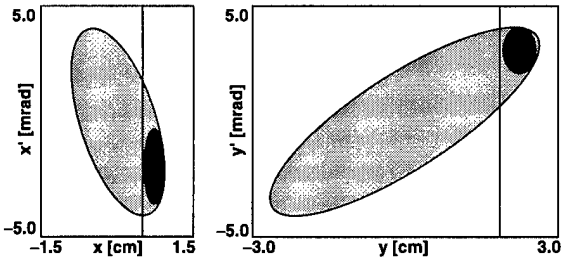


Fig. 2. Horizontal (left) and vertical (right) phase space at injection foil. Shown are the 2-rms injected-beam ellipses (dark shade), the stored-beam ellipses (light shade) and the foil edges (vertical lines).

In order to avoid the transverse linear coupling usually caused by beamlines in a skew plane, the skew bend is tuned so that $S_{11} = S_{33}$, $S_{12} = S_{34}$, $S_{21} = S_{43}$, and thus also $S_{22} = S_{44}$, resulting in a decoupled R matrix ($R_{13} = R_{14} = R_{23} = R_{24} = 0$, $R_{31} = R_{32} = R_{41} = R_{42} = 0$) with two identical diagonal blocks ($R_{11} = R_{33}$, $R_{12} = R_{34}$, $R_{21} = R_{43}$, and $R_{22} = R_{44}$). There is no downstream apparent transverse-emittance growth, regardless of input beam.

The proposed skew-bend design is quite similar to the present configuration (see Figure 1). The doublet provides needed focusing, the two F quadrupoles of the FDF triplet make the bend achromatic, and the D quadrupole at the dispersion crossover provides additional vertical focusing. This latter magnet and two new quadrupoles at zero-dispersion locations, one upstream of the 1.5° kicker magnet and one downstream of the last skew-bend dipole, decouple the line. Tuning for achromaticity and decoupling are independent.

The degree of coupling will be checked with a vertical steerer upstream, and two BPMs downstream, of the skew bend. We should be able to detect coupling that leads to 1% emittance growth.

For each near-nominal setting of the doublet, the skew bend can be made achromatic and decoupled. By measuring the rms beam sizes at strategic points in the line, we will be able to distinguish between the nominal and near-nominal tunes.

3.6 Issues Concerning Matching Section

The matching section has four quadrupoles, which is the minimum required to adjust four beam parameters at the injection foil. The matching-section quadrupoles are in a dispersionless part of the line so that adjusting the focus at the foil does not affect the dispersion at the foil.

The matching section can produce the nominal beam parameters at the foil with the nominal and all expected non-nominal input beams. It can also produce beams that differ in size by ±25% from nominal in either or both planes. These are beams with reasonable foil-edge locations and maximum stored-beam emittances that we will want to check out in trying to establish the optimal tune for the actual input-beam transverse and longitudinal distribution.

3.7 Issues Concerning Last Bend

The last bend contains four dipoles to guide the beam around the ring dipole, and two quadrupoles to make the bend achromatic.

Horizontally, the last bend points at the nominal injection point ($x_0 = 0.721$ cm, $x_0' = -1.960$ mrad), vertically, it is aligned for on-axis injection ($y_0 = 0$ cm, $y_0' = 0$ mrad). The last bend will have two dual-axis steerers. To get to the nominal injection point, no horizontal steering is required, but the steerers have to achieve $\Delta y = 2.250$ cm, $\Delta y' = 3.100$ mrad at the foil, with deflections of about 2.2 mrad and 1.4 mrad, respectively. For on-axis injection, no vertical steering is required, but the steerers have to achieve $\Delta x = -0.721$ cm, $\Delta x' = 1.960$ mrad at the foil, with deflections of about −1.4 mrad and 3.5 mrad, respectively. Horizontal on-axis injection can also be achieved by lowering the currents of the first and third dipole, by about 2.0% and 3.7%, respectively.

3.8 Particle Losses

The apertures will clear at least 6.6 rms of the nominal beam with transverse rms emittances of 0.08 π-cm-mrad and a full momentum spread of ±0.5%. In the skew line and in the matching section, there is no allowance for steering errors, which we attempt to minimize. The aperture of the last bend has an allowance for vertical steering to the injection point and horizontal on-axis injection. Scraping losses in the line thus are expected to be minimal.

Particle losses from field stripping were computed from the relevant formulas [3]. They should be around $1.6 \cdot 10^{-5}$ from all injection-line dipoles and below $2 \cdot 10^{-11}$ from the quadrupoles of the matching section.

3.9 Component Tolerances

A comprehensive study of the relative sensitivity of the line to alignment and field errors of all magnets resulted in tolerances that are readily achievable. To limit steering by individual magnets to 0.3 mrad, we specify dipole rolls below 0.1°, transverse alignment of the skew-bend and last-bend quadrupoles to 0.5 mm and of the stronger matching-section quadrupoles to 0.25 mm, and dipole longitudinal alignment to 1.0 mm. To keep apparent transverse-emittance growth due to individual magnets below 3%, quadrupole rolls should be below 0.1°. The 1.5° kicker magnet is regulated to ±0.2%, causing beam-centroid shifts at the foil to the 0.28-rms injected-beam ellipse, horizontally, and the 0.12-rms injected-beam ellipse, vertically. For an equivalent effect from all other dipoles, the skew-line dipoles will be regulated to ±0.01% and the last-bend dipoles to ±0.002%. To control fluctuations in the injected-beam parameters, the quadrupole power supplies need to be regulated to about 0.1%, with the last matching-section quadrupole requiring 0.01% regulation.

4 PERFORMANCE OF SYSTEM

Beam losses in the injection line should be minimal, even in the presence of the expected magnet errors and imperfections. The performance of the injection line will be judged against the factor-of-nine reduction in foil traversals (to about 35) and factor-of five reduction in ring losses (to about 0.1%) computed for the nominal injected beam.

We simulated beam transport through injection lines with errors and beam injection into the ring. The input beam was Gaussian-distributed, transversely, with rms emittances of 0.08 π-cm-mrad and had a skewed momentum distribution. The central energy was chosen to minimize ring losses. The lowest-energy particle had about −0.537%, the highest-energy particle about 0.330% momentum deviation. The assumed injection-line errors were those that can not be corrected, namely random roll errors, dipole power-supply fluctuations and quadrupole set-point errors to twice the tolerances. Also included were random normal and skew sextupoles to $4 \cdot 10^{-4}$ and normal and skew octupoles to $2 \cdot 10^{-4}$ of the dipole field, and random normal and skew sextupoles and normal and skew octupoles to $2 \cdot 10^{-3}$ of the quadrupole field, at the pole radius. These limits correspond to twice the maximum measured values of the mapped magnets.

The study showed that, for injection lines with errors, the nominal ring losses can be preserved as long as more beam is allowed to miss the foil and go to the H^0 dump. The approach should be to always keep the nominal foil-edge locations and injection point, in which case the number of foil traversals, the nuclear-scattering losses and the scraping losses all remain essentially unchanged.

For tuning the line, the injected-beam rms parameters will be determined, to better than 20% accuracy, with an emittance station near the foil. For the range of beams to be then expected, the nominal ring losses can likewise be preserved by allowing more beam to miss the foil.

REFERENCES

[1] D. H. Fitzgerald, et al., "Overview and Status of the Los Alamos PSR Injection Upgrade Project", proceedings of this conference.

[2] C. R. Rose, et al., "Overview of the Bump-Magnet System at the Los Alamos Proton Storage Ring", proceedings of this conference.

[3] A. J. Jason, et al., Neutralization of H^- Beams by Magnetic Stripping", IEEE Trans. Nucl. Sci. NS-28, No. 3, p. 2704, 1981.

MULTI-PULSE EXTRACTION FROM LOS ALAMOS PROTON STORAGE RING FOR RADIOGRAPHIC APPLICATIONS

H. A. Thiessen, F. Neri, K. Rust, and D. B. Redd, Los Alamos National Laboratory,
Los Alamos, New Mexico 87544

Abstract

In Proton Radiography, one of the goals is a motion picture of a rapidly moving object. The Los Alamos Proton Storage Ring (PSR) in its normal operating mode, delivers a single pulse approximately 120 ns wide (fwhm). In development runs at the PSR, we successfully demonstrated operation of a technique to deliver two pulses, each 40 nsec wide, with adjustable spacing.

1. INTRODUCTION

For radiography of moving objects, two or more pulses with adjustable time spacing are required. The existing Proton Storage Ring (PSR) extraction system is configured to extract the entire beam in a single turn. Two kickers and two kicker modulators fired at the same time perform the normal extraction function. By reconfiguring the two kickers and two modulators, it is possible to obtain two half-sized extraction kicks with adjustable time spacing. In this way, we have extracted two pulses with adjustable relative timing. The setup will be described and experimental results will be presented.

2. SETUP

The basic idea of the setup was to rearrange the existing kickers and modulators of the PSR extraction system as shown in Fig. 1 below.

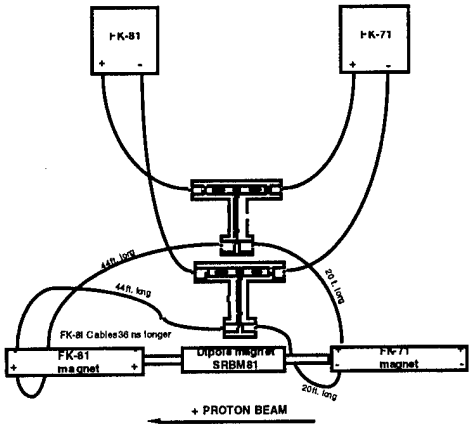


Fig: 1 Arrangement of two kickers and modulators used to deliver two pulses from PSR. In the standard mode of operation, each kicker is excited by a separate modulator.

In this arrangement, one modulator drives two kickers in parallel, but with half the voltage of the standard operation mode. The second modulator is timed to deliver its pulse after adjustable delay. Diodes are used to isolate the two modulators from each other as shown in the circuit of Fig.1. Ideally, the beam responds to the first of the two kicks by moving to a position corresponding to the center of the septum. Approximately 25% of the beam is extracted and 50% of the beam is lost on the septum. When the second kick is applied later, the remaining 25% of the beam is extracted.

3. EXPERIMENTAL RESULTS

In our first experiment (November 24 1996) we ran the PSR with a nominal 30 ns wide injected pulse at 4 Hz. The injection time was limited to 200 microseconds and the repetition rate was limited to 4 Hz to limit the beam injected to 100 nA, well below the normal loss in the PSR, in order to limit activation and minimize risk to components in the event of a spill at a single point. The separation between modulator pulses was limited to the range of 1-10 microseconds by the existing timing system.

At the best operating point found in the first experiment, approximately 83% of the beam was lost, with 10% and 7% delivered in two pulses to the Fast Current monitor in Line D. (The accuracy of our fractional beam calibrations is ± 30%.) Pulse width measured by the fast current transformer in Line-D was 40 ns, consistent with a slight broadening of the 30 ns injected pulse. The observed beams were similar over the range of 1 to 10 microseconds, and nothing was seen that would preclude extending the separation time to 100 microseconds or more. The extracted beams were "clean", showing no side lobes or unwanted spurious pulses. The observed pulse pair is shown in Fig.2.

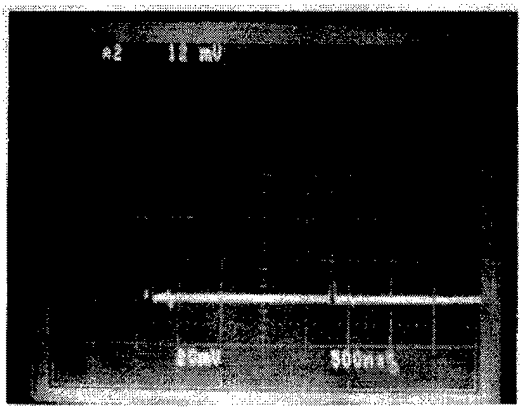


Fig: 2. Observed pulse shape in two-pulse extraction mode from PSR.

0-7803-4376-X/98/$10.00 © 1998 IEEE

The observed beams at the fast current transformer contained approximately 1.6×10^{10} protons per pulse, more than 5x more protons per pulse than available in a batch of 6 micropulses from the linac. (which would have the same time width as the observed pulses at PSR).

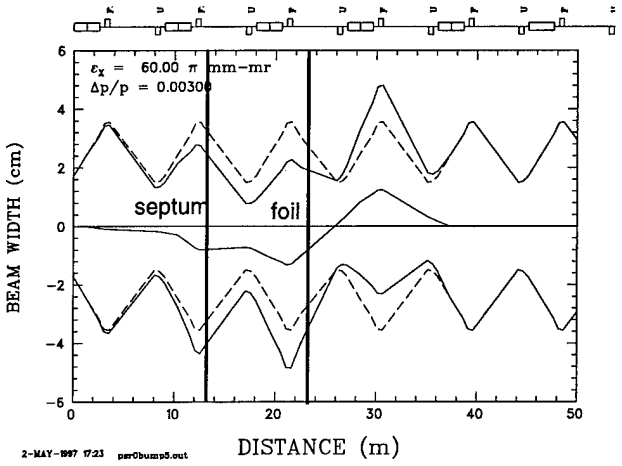


Fig: 3 The closed-orbit bump used in the two-pulse extraction experiments. Two vertical lines show the position of the septum and of the foil. The closed-orbit displacement is -8 mm at the septum, -10 mm, +3 mr at the foil.

In the February 24 1997 experiment, using the bump scheme illustrated in Fig: 3 we increased the efficiency to about 35% of the stored beam. The bump is designed to move the beam closer to the septum and to move the closed-orbit away from the center of the injected beam at the foil. Moving the beam closer to the septum places the center of the beam kicked the first time on the center of the septum. Without the bump, the beam center would be on the inside edge of the septum.

The closed-orbit offset at the foil is designed to produce an hollow beam in phase-space, whose projection in the horizontal direction has two peaks, with a separation of about 10 mm. This reduces the percentage of the beam lost on the septum, when the two pulses have equal intensity. The nominal bump is calculated to be the largest one that does not produce significant beam loss.

The results of the second experiment are shown in Fig. 4. After the first modulator is fired, about 50% of the beam is extracted or lost on the septum. After the next turn, only about 33% of the beam remains in the ring. About 6 turns later, more beam is lost. The remaining 17% stays in the ring until the second modulator is fired. The horizontal fractional tune is close to 1/6, so that the two modulators are fired with a separation that is a multiple of six times the revolution period, or 2.16 μs. We observed that he second modulator had to be fired n×6 or n×6+1 turns after the first, in order to extract the beam. Firing the second modulator on any other turn resulted in a neglegible second extracted beam pulse.

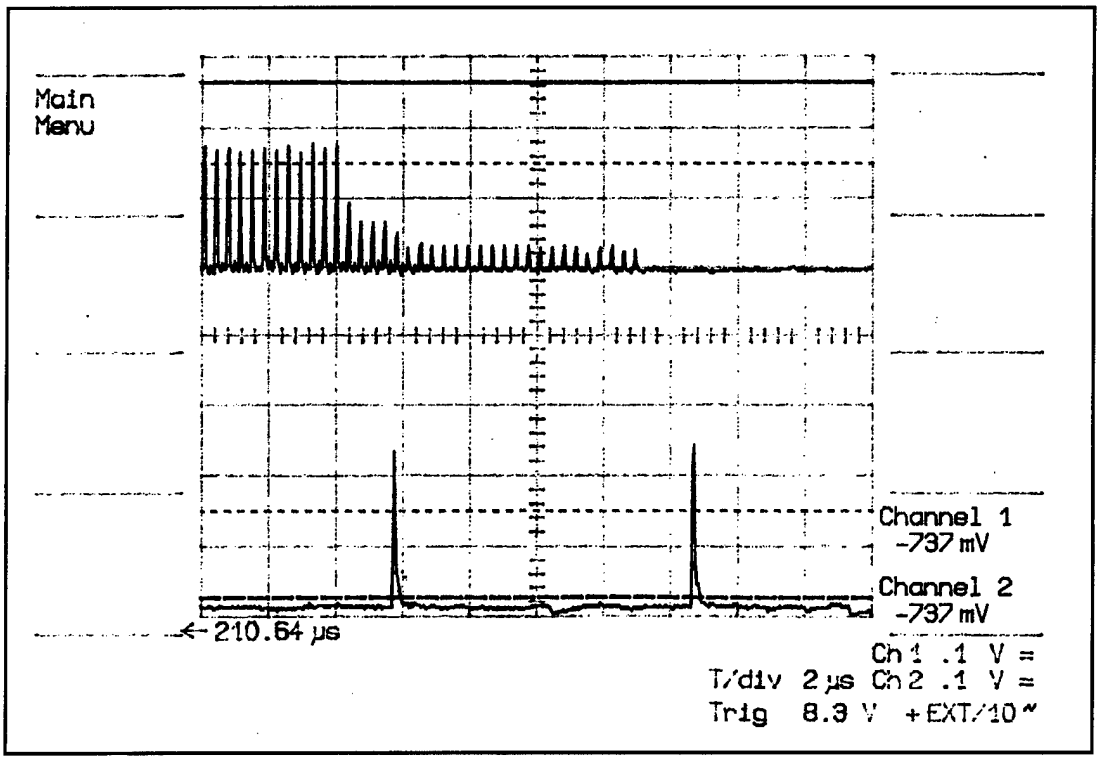


Fig: 4 The top trace shows the ring current from the wall current monitor. The bottom trace is the signal from a fast current transformer in Line-D. One time division is 2 μs. The two modulators are fired 9 μs apart.

With the nominal bump, shown in Fig. 3, most of the beam is lost on the septum, after the first kick. Increasing the bump at the foil (to make the stored beam more hollow) reduces the percentage of the beam lost when the kickers are fired but increases the percentage of beam lost during accumulation. The efficiency is not increased.

The pulses in the extraction line have the same width as the ring current profile. The "tails" noticeable in the two bottom pulses of Fig. 4 are actually due to the line not being correctly terminated. We observed 100% transmission of the extracted pulses to the LANSCE target 1. This means that both pulses fit in the acceptance of the extraction line, even though they are not centered in the extraction channel. Two steerers could be used in the extraction line to correct for this offset for proton radiography experiments. However, as shown in Fig. 5 the two pulse will not completely overlap in phase space, so that a DC steerer cannot exactly correct the offsets of both pulses. Adjusting the tune of the ring away from exactly 1/6 can help correct for this, but to to illuminate the same object with the same spatial distribution on both pulses will not be possible.

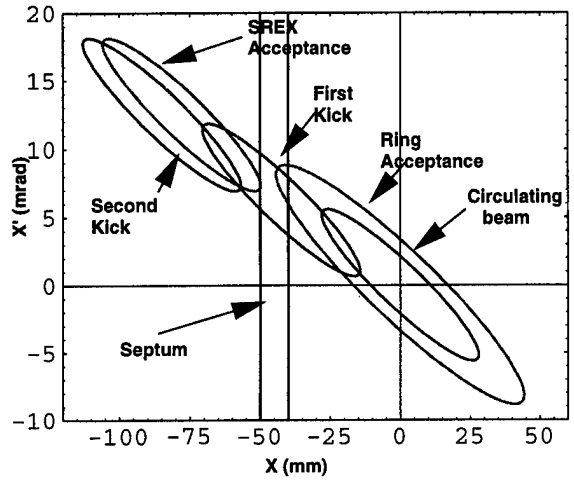


Fig: 5 The phase-space locations of the circulating beam, beam after the first kick and beam after the second kick. The ring acceptance of the ring and extraction line are also shown.

In a future run, we hope to improve the extraction efficiency, extend the injection pattern width, and extend the injection time. Our goals are to increase the available beam in each pulse by a factor of 10-20 with a pulse width of 50 nsec, and demonstrate separation of extracted pulses out to 100 microseconds. After the SPSS enhancement program is complete, it would be possible to generate up to 6 pulses in a nearly arbitrary pattern if a suitable six-pulse modulator were to be developed.

In summary, we have demonstrated the ability to produce from the PSR two pulses, each with a width of about 40 nsec and at least $3x10^{10}$ protons per pulse, an order of magnitude more protons than a train of linac bunches with a similar width. The separation between the pulses can be adjusted from 2 μs up to 100 μs. These pulses could be used for high-resolution freeze-motion radiography of moving objects.

BREMSSTRAHLUNG FROM A NEW TYPE OF TARGET: INCREASED INTENSITY AND AVERAGE ENERGY, AND REDUCED DIVERGENCE

B.Bogdanovich, V.Kudinov, A.Nesterovich, Yu.Pomasan, E.Tsygankov, V.Janenko,
Moscow Physics Engineering Institute, 115 409 Kashirskoe shosse, 31, Moscow, Russia

The purpose of the present work is the study of increase opportunity of electron bremsstrahlung in narrow bodily angle at forward direction.

Main factor, influencing on bremsstrahlung intensity for electron fixed energy and target material, is target thickness. During electron interaction with substance two competitive processes are observed: bremsstrahlung photons' generation, the number of which is increased with growth of thickness, and photons' absorption and scattering in target material. For all target materials there is such thickness (so named "optimum thickness"), at which maximum significance of bremsstrahlung intensity is observed. Optimum thickness for various materials of targets usually satisfies to thickness close to (0.1-0.3) radiating lengths [1,2].

The angular distribution width increase of bremsstrahlung with target thickness growth is stipulated, mainly, electrons multiple scattering in target material.

Therefore one of ways of bremsstrahlung output increase in narrow bodily angle at forward direction can lay in electrons angular divergence reduction.

Such way can be realized by means of beam repeated passage method through the thin target. At this method photons' absorption is practically eliminated, the electrons' energy will be realized completely, i.e. the way, that electrons pass, corresponds to its run, that, in turn, will cause bremsstrahlung output increase.

Characteristic researches of the electrons' bremsstrahlung generated by multiple beam passage through thin target were conducted at experimental stand based on electron linear accelerator with travelling waves. Accelerator (see figure) has following parameters of a accelerated beam: energy 3 - 6 MeV, average current 0 - 60 μA, current pulse duration 0.5-2.0 μs. The beam parameters were received at klystron pulse power about 12 MW.

Electron beam, leaving accelerator, has some angular divergence, therefore narrow directed beam was formed by collimator with 30 mm length and aperture diameter of 8 mm. Aluminium was used as the collimator material. Such choice is connected that aluminium has small bremsstrahlung output energy, that, in turn, permits to provide a small level of background radiation, arising as a result of electrons' interaction with collimator material. Electron beam formed by collimator fell into electron-guide fabricated from iron, which executed a role of the magnetic screen. After electron-guide leaving the electron beam gets into magnetic field. Adjusting magnetic field strength in magnet, it is possible to transform electrons' trajectory in circular orbit. The sizes of the area with uniform magnetic field of this magnet permit to provide circular orbit of electrons with energy 4.5 MeV on the diameter about 120 mm. Maximum magnetic field at median plane of electron beam rotating area was equalled 2830 gauss.

The bremsstrahlung registration expediently to execute under a corner 90° with respect to the beam motion direction in accelerator, since in this direction background minimum level. Such background always takes place in accelerating structure of linac because of small beam waste in it. On this basis target unit is placed on distance, equal quarter of circle length, describing electron orbit, from place of beam entry into magnetic field

Target unit consists from thin aluminium foil by the size 50-20 mm, fixed on ceramic pillar and electrically insulated from the chamber. This construction has allowed to execute beam current control, dropping on the target. The aluminium target thickness makes 100 μm, i.e. ~1.1·10-3 radiative length. The electron energy was defined from passage curve in aluminium, measured with help multi-plate Faraday cylinder. Electron energy has made 4.5 MeV.

Electron current, measured from the conversional target at magnetic field value provided circular electron orbits in the chamber, makes 1μA.

Analyzing received data, it is possible to generalize that use of method of electron repeated passage through conversional target increases bremsstrahlung output in 1.9 times in comparison with use of the optimum thickness target.

REFERENCES

[1] Kovalev V.P. Secondary Radiation of Electron Accelerators.-Moscow, Atomizdat, 1979, 200 pp. (In Russian).

[2] Dickinson W.C. Lent E.M. Calculation of Forward Bremsstrahlung Spectra from Thick Targets. - UCPL - 50 442, 1968.

0-7803-4376-X/98/$10.00 © 1998 IEEE

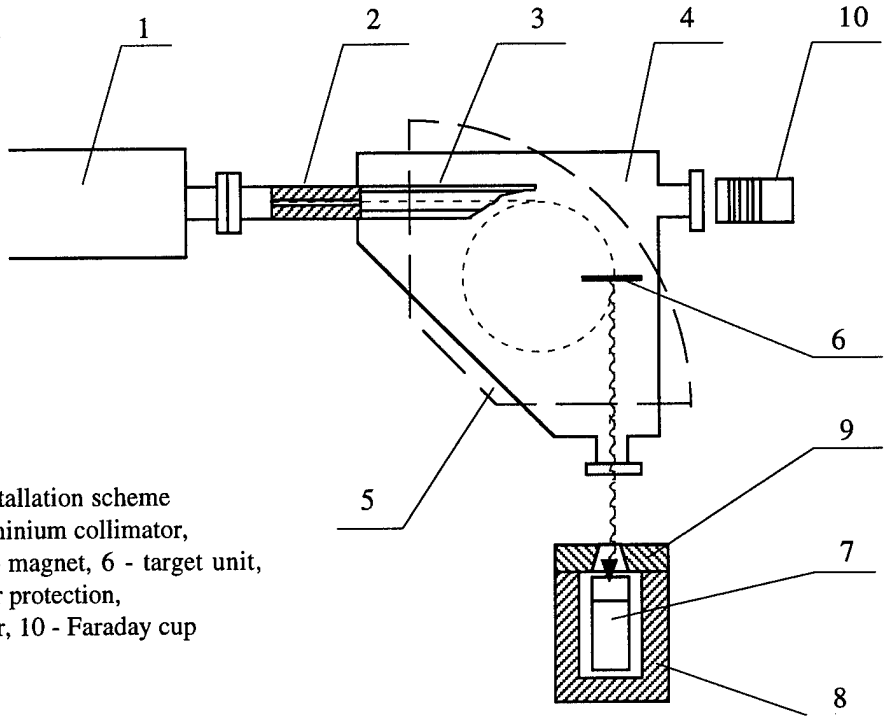


Fig. Experimental installation scheme
1 - accelerator, 2 - aluminium collimator,
3 - magnetic screen, 5 - magnet, 6 - target unit,
7 - detector, 8 - detector protection,
9 - plumbum collimator, 10 - Faraday cup

THERMO MECHANICAL CALCULATIONS OF A CYCLOTRON DEFLECTOR*

J. DeKamp and F. Marti
National Superconducting Cyclotron Laboratory,
Michigan State University, East Lansing, MI 48824, USA

Abstract
We discuss in this paper finite element calculations that simulate the thermal and mechanical effects on the deflector septum of a cyclotron. The energy deposited by the beam is cooled by radiation and conduction to a water cooled plate. The deformation of the septum due to the thermal expansion and electrical pressure is calculated in the model.

1 INTRODUCTION

The experimental program at the NSCL is shifting toward radioactive beams produced by the projectile fragmentation method. An upgrade of the facility is under way with the purpose of increasing the intensity of secondary beams. In the new regime intense primary heavy ion beams (10^{12} ions/sec of Ar at 8 GeV) will be extracted. The extraction process starts with an electrostatic deflector that peels off the last turn from the internal beam. No real separation exists between them, just a lower current density region. Power losses of 400 W will be absorbed and dissipated by the deflector septum. The usual difficulties of cyclotron deflectors are compounded in the superconducting cyclotron case because of the small vertical gaps where the deflector must be placed.

Traditionally, the cyclotrons accelerating high intensity beams have accelerated protons. Some high intensity radioisotope producing cyclotrons accelerate negative H ions and extract the beam by stripping to positive H. The highest intensity cyclotron beams are extracted from the PSI accelerators where intensities higher than 1.5 mA have been achieved [1]. These accelerators are separated sector cyclotrons, where more space is available to include large electrostatic deflectors, and due to their large size the separation between turns is significantly larger than in compact machines like our superconducting cyclotrons.

When the beam is intercepted by the extraction system septum, protons will deposit the energy in a much larger volume than a heavy ion of the same energy per nucleon. For example a 200 MeV proton has a range of 25.8 mm in Tungsten while a 200 MeV/u Ar beam has a 3.3 mm range, see Figure 1. This much shorter range creates unique problems for high intensity heavy ion cyclotrons.

Cyclotron septa have been designed for many years with a V notch in their leading edge to increase the boundary area of the region where the beam deposits the energy [2].

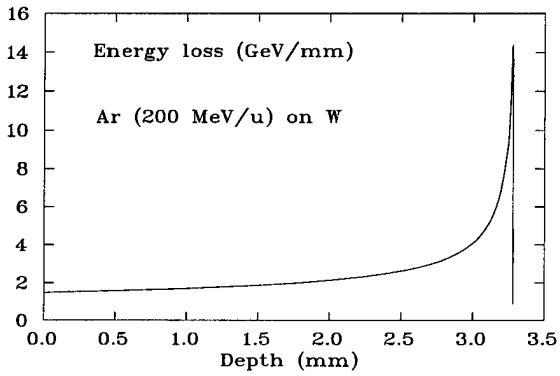


Figure 1 Energy loss as a function of the penetration depth for an 8 GeV Ar ion (200 MeV/u).

2 MECHANICAL DESCRIPTION

The first electrostatic deflector of the K1200 cyclotron consists of three sections approximately 35 cm long, connected with hinges that allow the deflector to adapt to the orbit shape of the different ions being extracted. Most of the losses occur at the entrance edge of the first section [3]. Our calculations are then restricted to this first segment. A cross section of the deflector is shown in Figure 2. The top and bottom plates are made of Cu to assure good thermal conductivity and the bottom one is water cooled. The high voltage electrode is cooled only by conduction through the insulators. The model includes the copper housing but not the high voltage electrode.

The septum is positioned by top and bottom clamps. These clamps can prevent the motion in all directions, or alternatively, provide a sliding guide that allows displacements of the septum, but maintaining some alignment while constraining the angle between the septum and the guides. When the clamps are "loose" the heat transmission to the cooled support housing is decreased.

* Work supported by NSF Grant PHY-95 28844

0-7803-4376-X/98/$10.00 © 1998 IEEE

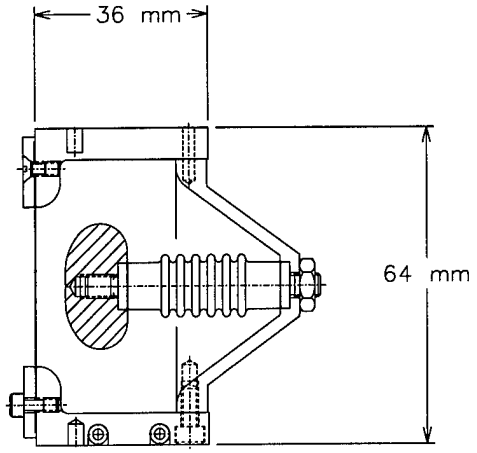


Figure 2 Cross section of the K1200 cyclotron electrostatic deflector. The gap between the septum on the left and the high voltage electrode is 6 mm.

3 THE MODEL

Thermal and mechanical analyses were accomplished using the general purpose finite element analysis (FEA) program COSMOS/M [4] using 3 node or 4 node shell elements for the septum and 8 node solid elements for the housing. All thermal analyses used nonlinear, transient analysis with temperature dependent material properties. Transient analysis was more efficient because of the difficulty in convergence of a static analysis with the high temperatures and gradients present and T^4 radiation dependency.

Mechanical analysis was done on full septa to investigate the effects of pressure on the septum due to electrostatic forces. For thin septa nonlinear dynamic analysis was done because of the relatively large displacements and initial instability of thin materials. For thicker septa linear static analysis could be used. The electric field in the gap (80 kV over 6 mm) will deform the septum, increasing the apparent thickness that the beam will see. We considered first a Molybdenum septum with thicknesses from 0.05 to 0.25 mm, like the septa used in the cyclotron at the present reduced power levels. These calculations showed that if the electric field started on the edge of the septum, the deformations were 0.5 and 0.016 mm respectively. If the electric field is displaced 1 cm away from the edge (extending the septum upstream of the high voltage electrode) the corresponding displacement was reduced to 0.04 mm for the 0.05 thick septum and a 0.12 mm thick septum had a displacement of 0.015. The electric field was then included in the following calculations starting 1 cm from the edge.

Thermal mechanical analysis was then done investigating the effects of both temperature and pressure along with methods to spread the power dumped in the septum over a larger area. The thermal analysis was first performed with the resulting temperature profile loaded into the mechanical problem, accomplished in COSMOS/M by simply specifying a reference temperature and issuing a command to read the calculated temperatures as a load case. Linear static analysis was used for the mechanical analysis. Different boundary conditions were investigated on both the thermal and mechanical analyses.

Radiation cooling from only one side of the septum has been considered. This gives us a more conservative evaluation of the result. The emission toward the high voltage electrode side has been neglected .

4 MATERIALS

Our study was restricted to the two materials that are more likely to succeed in handling the high power: pyrolytic graphite (PG) and tungsten (W). In the past we have used mostly molybdenum as septum material in the cyclotron because the power requirements were lower and the residual radioactivity is less than with tungsten. Pyrolytic graphite is more expensive and more difficult to obtain than Mo or W.

The thermal conductivities of PG and W are shown in Figure 3. The thermal conductivity of PG in the plane parallel to the layers is very much higher than in the perpendicular direction.

An important difference between PG and W is the ion range. For example the 8 GeV Ar ion mentioned above has a range of 3.3 mm in W, but almost 16 mm in carbon. This much lower energy density deposition is a big advantage that favors PG, besides its lower residual radioactivity.

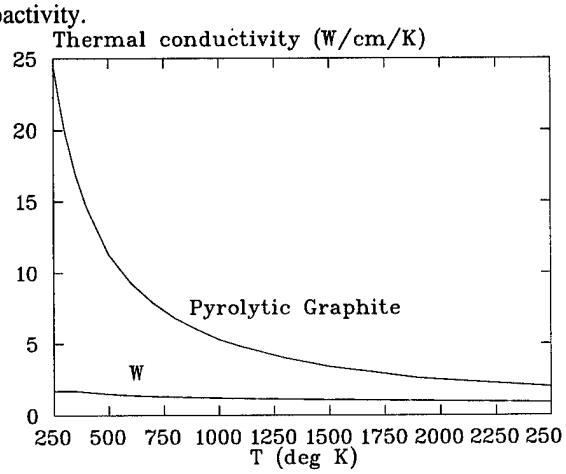


Figure 3 Thermal conductivites of pyrolytic graphite and W used in the COSMOS model.

5 RESULTS

Multiple thermal and mechanical boundary conditions were considered. We have performed all the calculations

with an 8 GeV Ar beam depositing 400 W in a 0.25 mm thick septum. This beam characterizes our worst power deposition case. The power density near the end of the range is 130 W/mm^3 for PG and 510 W/mm^3 for W. A beam height of 4mm was assumed in the calculations.

For a PG septum constrained with both (top and bottom) clamps and good conductivity to the Cu plates the maximum temperature reached 1230 deg. K. We found that the septa buckled significantly under these conditions. The expansion of the material produced a bulging that could reach 2.4 mm. Obviously this is not acceptable, because any small increase of the apparent septum thickness will increase the amount of power deposited on it and increase the problem even more. If we modify the boundary conditions, allowing the septum to "float" inside the guiding clamps, the heat transmission to the cooled Cu plates is decreased but a significant fraction of the heat is still dissipated by radiation and the temperature does not increase significantly. The buckling in this case is reduced to 0.08 mm. A plot of the temperature distribution is shown in Figure 4. The corresponding displacement plot is shown in Figure 5.



Figure 4 Thermal distribution in the pyrolytic graphite septum. Maximum temperature is 1230 deg. K. The beam comes from the right.

The higher thermal conductivity of PG helps to expand the radiation emission area, improving its cooling efficiency. In the case of W we have used a V notch on the leading edge as described in the Introduction. Under this conditions, the W septum reaches a maximum temperature of 2000 deg. K approximately, see Figure 6. This is a very comfortable margin of safety for a melting point temperature of 3400 deg. C.

6 SUMMARY

We have modelled the behavior of the electrostatic deflector in a heavy ion cyclotron, including the forces due to electric fields, temperature dependence of heat conduction coefficients and radiative cooling. The model predicts temperatures of less than 1300 deg K for the pyrolytic graphite septum and of 2000 deg. K for a W septum with a V notch. The deformations calculated do not indicate a serious buckling problem if appropriate support systems are used.

7 ACKNOWLEDGEMENTS

We acknowledge the discussions with the other members of the deflector development group that includes H. Blosser, T. Grimm, P. Miller, D. Poe, G. Stork and R. York.

REFERENCES

[1] U. Schryber et al., 'High Power Operation of the PSI-Accelerators', Proc. of the 14th Intl. Conf. On Cyclotrons and Their Appl., World Scientific, 1995, p. 32.

[2] H.A. Grunder, F. B. Selph and H. Atterling, 'Operating Experience with the Berkeley 88-inch Cyclotron Electrostatic Deflector', Intl. Conf. On Sector-focused Cyclotrons, CERN 63-19, 1963, p. 59.

[3] P. Miller et al., ' Electrostatic Deflector Development', NSCL-MSU Annual Report 1995, p.205.

[4] Structural Research and Analysis Co., California.



Figure 5 Displacement map for the septum in Figure 4. The septum is allowed to move inside the guides. The maximum displacement is 0.08 mm.

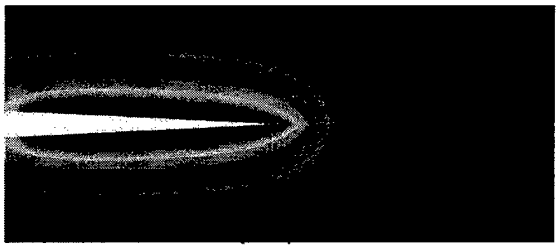


Figure 6 Temperature distribution in a 0.25 mm thick W septum with notch. The beam comes from the left. The maximum temperature is 2000 deg. K.

OPERATION OF CEBAF WITH HEAVY BEAMLOADING

A. Hutton, Thomas Jefferson National Accelerator Facility, 12000 Jefferson Avenue, Newport News, VA 23606, USA

Abstract

CEBAF is a 4 GeV, 200 μA five-pass recirculating superconducting electron accelerator that has been operating for nuclear physics research at full energy since November 95. The beam current has been increased to over 180 μA at 4 GeV with the maximum current in the linac over 900 μA. The superconducting cavities operate in a regime where the beam-induced voltage is comparable to the accelerating gradient. The operational limits and the issues required to maintain stable operation of the 1497 MHz superconducting cavities will be discussed, together with the implications for the other accelerator systems. There are three experimental Halls which can run simultaneously with three interleaved 499 MHz bunch trains and RF separators. Operation with simultaneous beams to two Halls is now routine, and simultaneous three beam operation has been demonstrated. The maximum design current per bunch train (120 μA) has been achieved. Hall B eventually requires beam currents as low as 1 nA (200 pA has been delivered) simultaneous with delivery of up to 200 μA to the other Halls. The required beam current ratio of 10,000 has been achieved; development of 1 nA beam position monitors continues.

1 NOMINAL DESIGN PARAMETERS

CEBAF was designed to accelerate electrons to 4 GeV by recirculating five times through two, 1497 MHz superconducting linacs, each making 400 MeV per pass, with the nominal accelerating gradient of 5 MeV/m. The design maximum current is 200 μA CW (maximum current per linac of 1 mA CW). The current can be split arbitrarily among three interleaved 499 MHz bunch trains, destined for the three experimental Halls A, B & C. A bunch train may be peeled off to any one Hall after each pass using RF separators and septa, while all Halls can receive the maximum energy. Hall B has a large solid angle detector and requires very low currents – down to 1 nA CW in the presence of beams of up to 200 μA CW in the other halls. Most experiments will need polarized beams, initially 35% polarization and later up to 80%. Emittance and energy spread criteria of the beams are very demanding (design goal of 2×10^{-9} m for the 4σ transverse emittance at energies ≥ 1 GeV and an energy spread $>2.5\times10^{-5}$). The emittance goal is met routinely, while the energy spread goal has been obtained, and is approached routinely. Low background conditions are vital, so careful attention must be paid to beam halo.

2 INJECTOR

2.1 Thermionic Gun

The beam from the 100 keV thermionic is sent through a 499 MHz chopper which rotates the beam in a circle of ~1.5 cm radius. Three independent slits are used to individually control the current for the three Halls. The three beams are then recombined, bunched and accelerated to 500 keV, before reaching the first superconducting cavities. This region of the machine is the most susceptible to space charge deformation and has been the extensively modeled with PARMELA. The simulations have been carefully benchmarked against measurements and have been used to establish focusing parameters that minimize space-charge effects. The maximum current that has been accelerated in a single 499 MHz bunch train is 220 μA, comfortably above the required 120 μA.

Over the last year, extensive tuning has been carried out to set up the three simultaneous beams. The major problems encountered were in obtaining the same path length through the choppers for each of the three beams. Without this condition, the bunching for the three beams is different and leads to background at the experiments.

2.2 Three-Beam Operation

The independent currents are set using the chopper slits in the Injector while the energies, or more exactly, the number of passes, is controlled by a set of 499 MHz RF separators, phase locked to the 499 MHz chopper RF system. There is one of these separators in each beamline downstream of the second linac. This enables one beam to be extracted on each of the intermediate passes and all three beams to be separated after five passes. The separators are set up using an air-cored corrector to deflect a single beam and then varying the phase and amplitude of the separator power to exactly re-create the same extraction orbit. This works well; the only remaining hardware is an independent phase reference for setting up an alarm signal for the machine protection system.

Downstream of the RF separators are DC septum magnets to complete the beam separation. These were damaged by the pulsed beam used for set-up and are being updated to improve the cooling.

Operation with two beams is now routine and three beam operation has been demonstrated. The first operation with three simultaneous beams is scheduled for May 15, 1997.

0-7803-4376-X/98/$10.00 © 1998 IEEE

2.3 Polarized Gun

The polarized gun currently installed in the accelerator uses a bulk gallium arsenide cathode illuminated by a 1497 MHz RF gain-switched diode laser operated at 780 nm [1]. The laser makes 510 mW total power or 170 mW per Hall. The combination of laser and cathode can produce a maximum of 1070 μA/Hall per 1% quantum efficiency. The quantum efficiency of the cathode declines initially at a rate dependent on the vacuum conditions, but stabilizes just below 1% and is fairly stable at this level.

The polarized gun was pressed into service on short notice and operated routinely, around the clock for five weeks. Typical currents required for operation were 25 μA CW, and this was obtained with a measured polarization of 36%. The maximum current ever captured in the Injector was 140 μA.

When the Injector is set up correctly, it is possible to change from the polarized to the thermionic gun with no change in RF phases. The rotation of the polarization vector using a Mainz style Z-bend is still somewhat slow, as the solenoids used to perform the rotation also steer the beam. This is currently being improved.

The polarization was measured using a Mott scattering chamber [2] operating at 5 MeV, with four counters at 173°. The counting rate is very low at these extreme backward angles, but we have high currents and the backgrounds are so small that measurements can be made to a precision of better than 1% in less than a minute.

Two techniques were tried to increase cathode lifetime. The optics in the Injector region were carefully optimized to obtain ~100% transmission at low current. Adding a pre-buncher reduces the chopping losses at high currents and, with a higher power amplifier than we currently have, 100% transmission of beams of 120 μA per bunch train should be obtainable. The ability to move the laser spot (300 micron diameter) over an area of the cathode of at least 6 mm diameter, while maintaining the transmission, has been demonstrated successfully.

A technique using atomic hydrogen (produced by RF discharge in low pressure hydrogen) has been extremely successful in cleaning bulk gallium arsenide [3], quantum efficiencies of 10% at 780 nm being regularly obtained. The process has been transferred to MAMI at Mainz where the process was able to recover "dead" cathodes with nearly twice the previous quantum efficiency. This technique is extremely important for high polarization (~80%) strained cathodes where the polarization is a surface, rather than a bulk, process and other cleaning techniques cannot be used on these very thin layers. If this technique can be used for *in situ* cleaning, the use of load-locks for transferring clean cathodes from the laboratory to the accelerator may be avoided.

The lifetime of these cathodes at high currents is the principal focus of further study.

3 SUPERCONDUCTING CAVITY LIMITS

3.1 Characterizing the Cavity Gradient Limits

The accelerating gradient in the linac is limited by many different phenomena, either inherent to the cavities, or due to protection interlocks, or system limitations. The phenomena and operational criteria are as follows:

1 Field Emission – the most important effect, limiting the gradient in 86% of the cavities. The initial criterion was 1 W heat load per cavity, and the operational limit is 1 Rad/hr per cavity, established during tests; the main effect is electrostatic charging of the cold RF window leading to arcing – we interlock a photodiode detecting light from the arc. If the arc is real, it is always accompanied by a waveguide vacuum trip.
2 Waveguide Vacuum: $>10^{-7}$ torr – usually due to an arc, but can be outgassing from excessive reflected power.
3 Quench: 1 MeV/m below the gradient at which quench observed in tests – with this limit, a quench has never been seen during accelerator operations.
4 Beamline Vacuum: $>3\times10^{-9}$ torr – usually due to thermal profile shifts which release adsorbed hydrogen.
5 Q_0 (intrinsic cavity quality factor) $<1.0\times10^{9}$ – affects the cryogenic plant and can be ignored for single cavities.
6 Window temperature: the infrared pyrometer tripped – this is usually due to bad waveguide RF seals, which can cause warm window failures.

Measurements are under way to characterize the applicable limit for each of the 330 superconducting cavities installed in CEBAF. This involves the original cavity acceptance data, and measurements in the tunnel at various beam currents to obtain information about the integrated systems. This data base is currently about 80% complete.

3.2 Helium Processing

The average gradient of the installed superconducting cavities was 7.4 MeV/m (predicted from the cryomodule commissioning data). Every cryomodule (which contains eight cavities) exceeded the design specification of 5 MeV/m. This year, two different approaches were taken to improve the operating performance of the cavities, both carried out *in situ* [4]. The aim was to reduce field emission and arcs using helium processing, and to condition the waveguide in the thermal transition region between the warm and cold RF windows using waveguide vacuum processing.

Helium processing is a well known technique for cleaning cavities in laboratory conditions. A gradient of a few MeV/m is applied to the cavity and low pressure helium gas is bled in to bring the pressure up to $\sim4\times10^{-4}$ torr. These conditions create active field emission, but not an RF discharge. The fields were slowly increased to the gradient limit due to other effects and maintained at this level for as long as the schedule permitted. Most of the improvement was obtained in the first half hour, followed by diminishing returns.

One interesting problem arose in all of the cavities. If the cavity trips off, there is a hard multipacting limit at ~0.7 MeV/m which prevents the RF from being switched back on. This was addressed by using a variable frequency phase lock loop RF system. By approaching the nominal frequency from above, the phase lock loop "jumps" the frequency across the multipacting barrier and the cavity can be switched on [5]. Thereafter, the gradient can be freely varied over the whole range. The effect limited our ability to process cavities in parallel, as a mobile RF system was needed rather than the installed RF equipment. After the helium conditioning was complete, the cavity was warmed up to 20 K, which outgassed the helium that had been adsorbed by the cavity as well as some hydrogen that had built up. There is some evidence that this thermal warm-up alone is beneficial to the cavity.

Operationally, helium processing of two cryomodules can be completed in 24 hours with the tunnel locked up for safety reasons. This is followed by a 16 hour warm-up and cool-down cycle, during which other routine maintenance can be performed. We have now processed 12 of the 41 cryomodules.

3.3 Waveguide vacuum processing

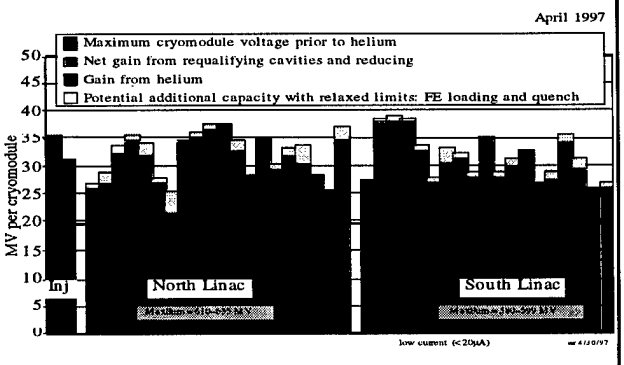
Waveguide vacuum processing is a form of pulsed RF power processing. We use it *in situ* to process the thermal transition region between the warm and cold waveguide windows. Gas is adsorbed in this area, and when the cavity reflected power increases due to cavity mis-tuning (in principle, beam loading can also produce this effect but this has not been observed), the RF wave pattern changes from a standing wave (most power reflected) to a traveling wave (most power transmitted to the beam). Shifting the thermal profile creates outgassing leading to arcing and waveguide vacuum trips.

Low duty factor, pulsed RF power is applied, maintaining the vacuum pressure below 10^{-7} torr. Four waveguides are treated at a time for 4 hours, using the installed RF power sources and specially adapted software. Following this, the waveguide vacuum is usually more stable. In particular, the cavities are more tolerant of mis-tunings, which makes operation easier. We have now processed the waveguide vacuum in 10 of the 41 cryomodules.

It is still unclear whether the vacuum improvement due to 20 K thermal cycling is equivalent to pulsed RF processing or whether there is a qualitative or quantitative difference between the two processes.

Using the two processing techniques, every cryomodule showed improvement (some cavities could not be processed as they were limited by other effects) and an overall gain of 63 MeV was obtained in the two linacs (i.e. 315 MeV for five passes). This includes some gain from relaxed limits. We estimate that continuing this treatment for all of the cryomodules would yield a further 135 MeV (675 MeV for five passes). Figure 1 shows the gains achieved.

Figure 1
Maximum Cavity Voltage per Cryomodule in CEBAF



4 RF/CAVITY SYSTEM PERFORMANCE

4.1 Optimizing RF Systems

Each superconducting cavity is individually fed by a 5 kW klystron with its own low level control module to feed back and stabilize the cavity phase and amplitude. There are 330 of these systems and maintaining each one at optimum performance requires tuning with RF power alone, as well as procedures using the beam. Careful file management is then required to maintain this information.

The cavities are tuned to the correct frequency using the AUTOTUNE program, which also provides an offset angle to normalize the phase angle between the input drive phase and the cavity gradient, compensating for differences in cable lengths and electronic delays. Over time, or under different conditions, the control modules may change and the AUTOTUNE data is no longer valid, so other checks must be made to ensure consistency.

An effective global check is to slew the master oscillator frequency and measure the forward power drawn from each klystron, as the cavity accelerating voltage is maintained constant by the feedback system [5]. An off-line script is then used to look for changes in forward power indicating those cavities whose center frequency is not correct.

A further check can be made using beam loading. The phase of the klystron forward power with respect to the cavity probe signal is monitored as the beam current is turned off and on [5]. Changes indicate that the cavity loading and the klystron drive power are not in phase.

The cavity gradients were calibrated using the beam and compared with the expected values from the measured Q_0 values of the cavity. This consistency check was used to correct calibration and other errors. The gradients are now correct to within 5%. This also provided cross-checks on cavity dissipation, required to compensate the cryogenic loading as a function of gradient.

4.2 Cavity Phase

The phase of the cavity fields with respect to the beam are calibrated using the KREST program. The concept is

simple: move the klystron phase (or more exactly the phase of the cavity probe signal) by ±10°; use the energy feedback system to measure the energy change; and set the phase to equalize the energy change on either side of the nominal phase. The program is used regularly (at least daily) as the phase distribution system is still not sufficiently stable. However, KREST works so well that we can tolerate this lack of stability, at least for now.

The net result of this preparatory work is that we can set the cavity phase and amplitude correctly, independent of gradient and beam current.

4.3 Operating Cavities

The klystron power is limited operationally by lowering the high voltage and by using the modulating anode to minimize the electric power. The klystron filament voltage is used to limit the cathode current to extend the filament lifetime. The parameters are set at the beginning of an experimental run, based on the beam energy and on the total current traversing the cavities (beam current multiplied by the number of passes through the linacs). An overhead of 15% is added to the klystron power to provide headroom for phase and amplitude control.

An off-line computer program is used to calculate the maximum gradient limit of each cavity, given the cavity limitations, the required current in the linacs, and the klystron power limits. The gradient limits are used by the Linac Energy Management (LEM) program in the control room to set up and maintain the linac energy. These programs are being integrated into one package, the Momentum Management System (MMS), which will set the arc magnets as well as the RF systems. The gradient of each active cavity is set proportional to the maximum allowed gradient for the cavity to maintain the accelerating voltage in the linac constant. With a 5% overhead at the start of the run, problem cavities can be taken off-line to extend the time between maintenance periods.

5 LINAC PERFORMANCE

5.1 Preparatory Tests

During breaks in routine beam operation for physics, the gradients of individual cavities were slowly increased to determine the maximum acceptable operating gradient. This required operating sections of the accelerator at full klystron power and was carried out over a period of months, using successive maintenance periods to change the klystron voltage tap settings until each zone had been tested. The maximum gradient was usually limited by the arc rate, and one per hundred hours was considered acceptable initially. These numbers were then used to define the maximum operating gradient.

5.2 High Gradient Operation

The first attempt in May 96 was to set the machine for 1 GeV per turn (corresponding to 5 GeV total, 25% above nominal). All the cavities were simultaneously brought up to their nominal setting. After reducing the gradient in troublesome cavities and allowing them to condition, most (but not all) could be returned to their original setting. After about a shift, the gradients in the linac were adjusted to obtain exactly 500 MeV per linac and pulsed beam was established. The tune was re-checked, the feedback systems were switched on and the gradient calibration was checked with beam.

The 1 GeV run was repeated in December 96 when CW beam was established. Initial set-up of the gradients took many hours due to waveguide outgassing and fixing RF problems. Pulsed beam was set up and apertures were swept to ensure that the optics was properly loaded. 100 μA CW beam was then established and maintained for several hours while working on the RF systems to improve the trip rate.

Following this success, further cavity processing was scheduled, leading to a repeat test. This time, the linacs were set up for 1.12 GeV (40% above nominal). Following approximately the same scenario, 90 μA CW beam was established (limited by the capacity of the beam switchyard dump) and after a 2 hour run, the trip rate was 45/hour – sufficiently good for an accelerator test but not yet good enough for physics. The average gradient of the active cavities was 7.76 MeV/m, compared to the nominal 5 MeV/m.

An interesting effect was observed that had been predicted for some time. The ponderomotive force of the RF fields tends to expand the cavities and the cavity tuner changes to maintain the correct operating frequency. If the cavity trips off at high gradient, the resulting frequency shift can be sufficiently large that the cavity goes out of resonance. This was observed in only a few cavities. The present work-around is to use manual tuning or slow ramping of the gradient to allow the tuner to follow the frequency changes. This works, but is both time-consuming and suffers from mechanical hysteresis of the tuner. A better solution would be to slew the drive frequency in the control module, but this will take some time to develop.

The result of the tests is that first experiments at 5 GeV have been scheduled for November 1997, and we expect to be scheduling experiments at 5.5 GeV next year.

5.3 High Power Operation

The nominal beam current to be divided amongst the three experiments is 200 μA, i.e. 1 μA total current in the linacs with five passes. The beam current is regulated as part of our NEPA (National Environmental Protection Agency) permit and initially we were only permitted to operate up to 180 μA, due to DOE imposed safety limits. The DOE has now granted permission to test the accelerator up to the full current.

We have had a series high power tests, scheduled together with the high gradient runs, as the RF and cavity preparation was the same. The additional problem is to ensure that the beam-loading power vector is aligned with the klystron power vector over the range of beam currents. The strategy adopted was to raise the current to 100 μA and re-check the cavity tunes by sweeping the RF frequency, as described above. After fixing any problem cavities, the current was increased until the trip rate became excessive again, monitoring the klystron drive for evidence of saturation. The RF frequency was again swept and problem cavities addressed. In a series of tests, the current was successfully increased to 180 μA. The final step to reach the maximum current is expected soon.

All the problems encountered were due to system interactions between control module, RF power source, and the cavity, which could all be (somewhat laboriously) addressed. There are no indications that there are any fundamental limitations. The primary difficulty was access to a suitable dump, as the only dumps capable of taking the power (up to 1 MW) are in the experimental Halls and the experimenters are usually either taking data or are taking access for fixing their equipment.

We are now able to schedule multiple Halls with a total current of 200 μA and expect that the availability, after initial conditioning, will be independent of beam power.

6 EXPERIMENTAL CAPABILITIES

6.1 Hall Status

Hall C has been taking data since November 95 at ever increasing current. The maximum power that has been delivered to an experiment is 4 GeV, 120 μA (480 kW) which was achieved with similar availability to any other run. Four experiments completed data-taking and data for 16 theses was obtained. Initially, solid targets were used, but the cryo-target was commissioned in August 96. In the first three months of 97, the detector was re-configured for the t20 experiment and data-taking has commenced.

Hall A started taking beam in April 96 using the electron spectrometer only. A problem with the superconducting coil of the hadron spectrometer delayed two-arm testing until February 97. Commissioning officially ended in April 97 and the first experiment is starting now.

Hall B took first beam in December 96 to evaluate backgrounds and determe whether the low currents required (see below) could be obtained with sufficient stability. A vacuum chamber misalignment was found in the experimental line and instabilities in the RF systems created beam loss. The misalignment has now been corrected and the improvements in the RF tuning that were driven by the high gradient and high power programs are expected to lead to a significant reduction in background for the detector.

As far as the accelerator is concerned, every beamline in the machine has now been successfully commissioned.

6.2 Low Beam Current for Hall B

The range of beam currents required by Hall B is from 1 nA to 1 μA. A version of the Switched Electrode Electronics (developed for the linacs with a current range of 1 μA to 1 mA) was developed to improve the low current capability. The range achieved was from 100 nA to 200 μA and this electronics is installed on beam position monitors in the injector, and is now being installed for the feedback systems and all the experimental beamlines. They were used successfully for the initial phase of Hall B commissioning.

A new type of beam position monitor is being developed for use at the target [6]. It uses resonant cavities, operating on the lowest deflecting mode at 1497 MHz. The expected sensitivity of these monitors is 1 nA.

One important capability has been demonstrated. Currents as low as 200 pA have been produced in the Injector, observed on fluorescent screens in the Hall B beam-line, and used by the detector for stability and background studies. The ability to produce the range of beam currents required has been demonstrated. When the new 1 nA monitors become available, we will be ready to make operation at these low currents a standard operating condition.

It had been expected that the low current beams for Hall B would always need a "witness" beam to allow the feedback systems to lock on. In these studies, it was demonstrated that if a beam with more than a few μA is present on the first turn to enable the energy feedback systems to stabilize the linac energies, then the Hall B beam at any energy would be sufficiently stable. This will be a great help in scheduling multiple Halls.

7 ACKNOWLEDGMENTS

This paper presents an overview of the work of a large group of dedicated people in Jefferson Lab. I would like to thank each and every one for their tenacity and skill, which have resulted in the excellent performance obtained. This work was supported by the U.S. Department of Energy under contract number DE-AC05-84-ER40150.

REFERENCES

[1] M. Poelker: Appl. Phys. Lett. 67, 2762 (1995).
[2] J.S. Price et al.: '5 MeV Mott for rapid, precise electron beam polarization measurements'; Spin 96, Vrije Universteit Amsterdam, 10-14 Sept. 96.
[3] C.K. Sinclair et al.: 'Atomic Hydrogen Cleaning of Semiconductor Photocathodes', this conference.
[4] C. Reese et al: 'Improvement of the Operational Performance of SRF Cavities via in situ Helium Processing and Waveguide Vacuum Processing', this conference.
[5] L. Doolittle: private communication.
[6] R. Ursic and C. Pillar: '1 nA Beam Position Monitoring System', this conference.

PROGRESS ON $\mu^+\mu^-$ COLLIDERS

Robert B. Palmer, Physics Department, Brookhaven National Laboratory, Upton, NY 11973, USA

Abstract

Advantages and disadvantages of muon colliders are discussed. Recent results of calculations of the radiation hazard from muon decay neutrinos are presented. This is a significant problem for machines with center of mass energy of 4 TeV, but of no consequence for lower energies. Plans are outlined for future theoretical and experimental studies. Besides continued work on the parameters of a 4 TeV collider, studies are now starting on a machine near 100 GeV that could be a factory for the s-channel production of Higgs particles. Proposals are also presented for a demonstration of ionization cooling and of the required targeting, pion capture, and phase rotation rf.

1 INTRODUCTION

The first ideas about the use of muon colliders as a potential useful machine for high energy physics were presented by Skrinsky and collaborators[1] and shortly after by D. Neuffer[2]. More recently the concept has further developed and aggressively pursued in a series of collaboration meetings and workshops[3],[4]. A feasibility study of a 4 TeV muon collider was presented at Snowmass[5] and now studies have started of low energy machines of energy range $500 - 100$ GeV.

1.1 Advantages

A muon collider[6] is a class of lepton collider with many of the advantages usually associated with e^+e^- colliders. Unlike protons, the muons are fundamental particles, and when they interact, all the center of mass energy is available for the production of new states.

The possible advantages of muons, compared with electrons, all arise from the formers higher mass. As a result of that:

- Synchrotron radiation ($\propto \gamma^4 \propto m^{-4}$) is suppressed, and, as a result, muons can be accelerated to high energies in circular rings that appear to be much smaller than the linear accelerators needed for electrons.
- Since muon collisions can occur in a ring, the bunches collide with one another many (of the order of 1000) times. In a linear e^+e^- collider they can interact only once.
- Synchrotron radiation (beamstrahlung) is also suppressed as the bunches pass through one another, allowing, in principle, very narrow energy spreads ($\rightarrow$ 0.01 %).
- The cross section for the direct production (s-channel) of Higgs particles ($\mu^+ \mu^- \rightarrow h, A, H$), which is $\propto m^2$ is over 40,000 times higher for muons than electrons.

1.2 Disadvantages

But there are disadvantages, most of which arise from the fact that μ's decay with a life time, at rest, of about 2 μs.

- Because of their short lifetime it is not possible to cool muons by the conventional methods used for antiprotons (stochastic, or electron cooling). These methods are too slow. And because of the muon's high mass, synchrotron radiation cooling is also ineffective. Instead, ionization cooling [7] can be used, but the minimum emittance achievable by this method is not as low as that achieved for antiprotons or electrons.
- Because of their short lifetime, acceleration must be rapid and conventional synchrotrons would be too slow. A single linac would be good but expensive. A linac would thus only be used at the lowest energies. Recirculating linacs would be cheaper for later stages, and fast pulsed magnet synchrotrons might be desirable for the higher energy accelerators.
- As the muons decay in the collider ring, the electrons from the decay enter the beam pipe walls depositing energy and generating radioactivity. A tungsten liner is required to shield this heating from the superconducting magnets used to form the ring. As a result, these magnets must have relatively large apertures.
- Muons decaying as they approach an experimental area will also direct electrons into the experiment, and these too must be shielded by a tungsten cone that extends down towards the vertex. As a result, the solid angle over which the detector can operate is reduced and experiments must live with a relatively high rate of background tracks.
- Another, and at first surprising, problem from the muon decays is that the flux of decay neutrinos can, at high energies, become a significant radiation hazard. This will be discussed in more detail below.

1.3 Neutrino Radiation Hazard

This problem was first pointed out by Bruce King [8] and has since been calculated in detail by Mokhov[9]. The initial discrepancies between these calculations have now been resolved.

The annual doses from this radiation are given by

$$dose \propto E^3/length^2 \propto E^3/depth,$$

0-7803-4376-X/98/$10.00 © 1998 IEEE

where E is the muon beam energy, *length* is the distance from the ring and *depth* is the depth of the ring below the ground. Unless straight sections are kept very short, the radiation is dominated by such sections, each of which generates a highly collimated beams of neutrinos.

We take the dose limit, as by FNAL, at 10 mR/year limit (c.f.: The federal limit is 100 mR/year). Then the 4 TeV design (luminosity $10^{35} cm^{-2} s^{-1}$), without straight sections, would meet the requirement if located at a depth of 250 m. If moderate fields are introduced over all straight sections, and/or the orbits are time varied, then various solutions appear possible, at this energy, without major changes to the concept.

The cubic power law means that colliders below 2 TeV present relatively little difficulty, but those significantly above 4 TeV will have serious problems unless:

- Special locations are chosen; or
- Ways are found to cool the muons to lower emittances than now seem possible with ionization cooling. Friction cooling, cooling in crystal lattices, electron cooling, and optical stochastic cooling are being studied. With lower emittances, the required luminosities could be achieved with lower muon currents and thus less neutrino radiation. A very speculative scenario using optical stochastic cooling[10] would achieve the same luminosity with 1/50 th of the muon current and allow colliders up to 15 TeV (and luminosity over 10^{36}) to meet the dose limits. More work is needed.

2 CONTINUED THEORETICAL STUDIES

A lot of progress has been made on the theoretical design of a 4 TeV, luminosity $10^{35} cm^{-2} s^{-1}$ muon collider[5], but much still needs to be done. The highest priority items are:

- Continued study and simulation of all components of a muon collider, with particular emphasis on the ionization cooling system.
- The studies of a 4 TeV collider must continue. In particular, the neutrino radiation problem needs detailed study such a higher energy example.
- Work is also needed on the parameters of lower energy machines that could serve both as technology demonstrations and colliders aimed at specific physics objectives.

In particular the collaboration is studying machine with an energy near 100 GeV that might serve as a Higgs Factory. The final ring of such a machine would only be built after the existence and approximate mass of a light Higgs is known. The muon collider would then be able to make such a particle via the S-channel and set limits or determine its mass, width and branching ratios far better than either a hadron machine, like the LHC, or an electron machine, like LEP or a linear collider. Upgrades of such a machine to energies of 200 and 400 GeV will also be studied.

Table 1: Parameters of a 4 TeV and 100 GeV c-of-m energy machines

c of m Energy	GeV	4000	100	
p Energy	GeV	30	24	
p's/bunch	10^{13}	2.5	5	
rep x $n_{bunches}$	Hz	30	5	
p power	MW	7	2	
muons/bunch	10^{12}	2.0	4	
collider circ	m	8000	260	
ℓ^* at IP	m	6.5	5	
4 x σ_θ at IP	mrad	3.5	8	
dp/p	%	.12	.12	.01
rms ϵ_n	π mm mrad	50	85	195
β^*	cm	0.3	4	9
σ_z	cm	0.3	4	9
σ_r	μm	2.8	82	180
tune shift		0.04	0.05	0.02
luminosity	$cm^{-2} sec^{-1}$	10^{35}	$5\ 10^{31}$	10^{31}

Tb.1 gives possible parameters of the 4 TeV collider[5] and a 100 GeV "Higgs Factory". In order to minimize the cost, it assumes the use of a proton driver that is an upgraded version of an existing accelerator (in this case the AGS, but it is assumed that similar performance should be possible using upgraded FNAL accelerators). Parameters are given for two modes of operation of the 100 GeV machine:

1. with maximum luminosity, but a relatively large momentum spread; and
2. with momentum spread reduced to 0.01 % for use in precision measurements and S-channel Higgs production, but a somewhat lower luminosity.

3 CURRENT EXPERIMENTAL PROGRAM

Two experiments are now under way:

- The collaboration has joined a BNL nuclear physics experiment E910 that, using a Time Projection Chamber (TPC), is measuring pion production on heavy metal targets at different energies. Data has been taken and is now being analyzed. The results will be essential in establishing a good model of such production and will allow an optimization of the target and capture geometry.
- An AGS accelerator experiment (E932) has been proposed, approved and is scheduled for running in the next few weeks. This experiment will study phase rotation in the accelerator ring, to form the very short proton bunches that our parameters require.

Results from this experiment should indicate if the current parameters are reasonable and what new equipment may be required to achieve them.

4 INITIAL EXPERIMENTAL PROGRAM

It is clear that theoretical studies alone will not establish whether a muon collider is really possible or practical. An experimental program is required. An initial 5 year program is being discussed that would consist of the following items:

4.1 Cooling Demonstration Experiment

The object of this experiment would be:

1. to test the performance of components of the ionization cooling system and establish the technical performance of such subsystems.

2. To compare the performance of these components with computer simulations so that the use of those simulations can be confidently used in the design of the complete system.

It is proposed to build a test facility in which muons from a relatively slow spill beam can be fully characterized (in all 6 dimensions) as they enter and leave a test module. This would be done by the use of counter planes interleaved with spectrometer magnets and rf deflector cavities (see Fig. 1).

The modules that would be tested in this facility would include at least one each of:

- A FOFO Lattice consisting of alternating solenoids surrounding a traveling wave linac with periodic lithium hydride absorbers at the zero axial field nodes. Elements of this type cool in the transverse direction down to modest emittances and would be used for the majority of transverse cooling stages.

- A lattice consisting of one or more current carrying Lithium Rods (lithium lenses) alternating with Linacs. Such a system, being pulsed, is less desirable than the passive FOFO lattice, but has stronger focusing and can cool to smaller emittances. Such elements would be used in the last few transverse cooling stages.

- A lattice with bends and wedges of lithium hydride placed at locations with dispersion to reduce the momentum spread, and thus longitudinal emittance of the muons. Such elements would be interspersed with the above transverse cooling elements.

4.2 Target and RF Demonstration

This experiment, like the cooling, would be performed in stages. A beam is required with the most intense and shortest proton bunches available. The experimental stages would then be:

4.2.1 Phase I (without Solenoid)

Build a target system (probably a liquid metal target) and study shock damage and cooling. Place an rf cavity at different distance from this target and study breakdown in the cavity due to the intense radiation.

4.2.2 Phase II (with Solenoid)

Surround the target with a high field (as near the final proposed 20 T as possible, but, unlike in the real case, it could be pulsed) solenoid to capture the produced pions. Build lower field solenoids to transport those pions to the rf cavity. Study total pion production and capture efficiency, study heat and radiation levels in the solenoid and elsewhere, and study breakdown in a geometry (see Fig. 2) closer to that of the muon collider under study.

4.3 Prototype Pulsed Magnet

A prototype fast pulsed magnet for the final acceleration stage of a 100 GeV machine would be designed and tested. Field precession and time jitter would be determined.

4.4 Prototype SC Magnets

A prototype Nb_3Sn large aperture dipole should be built and tested. It may be noted that the luminosity of a muon ring is inversely to the circumference and thus proportional to the average field in the collider ring. High field is thus of special interest to a muon collider.

A prototype Nb_3Sn large aperture insertion quadrupole is also needed. Field quality is of particular interest for such a magnet.

5 LONG TERM R & D

On a ten year time scale, prior to construction of a First Muon Collider, a more extensive experimental program would be required. But such a program must be conditional on the earlier experimental demonstrations that the basic technical components of a collider can be built.

A major component of this longer term R and D would be a complete demonstration of target, capture, decay channel, phase rotation, and the first stages of cooling of a real high intensity muon bunch. This might form a third phase of the Target and RF Demonstration, discussed above. For this experiment it would be important to achieve, through appropriate accelerator improvements, the actual required proton bunch length and intensity.

This would be a represent a far more realistic demonstration of the required high intensity of muon production and of cooling real, and intense, muon bunches. It would also represent the construction of items that could be used in the First Collider.

Prototype work would also be required on other magnets, rf systems, modulators etc. The definition of such a program would be one of the tasks of the earlier R and D effort.

Initial Cooling Experiment (FOFO)

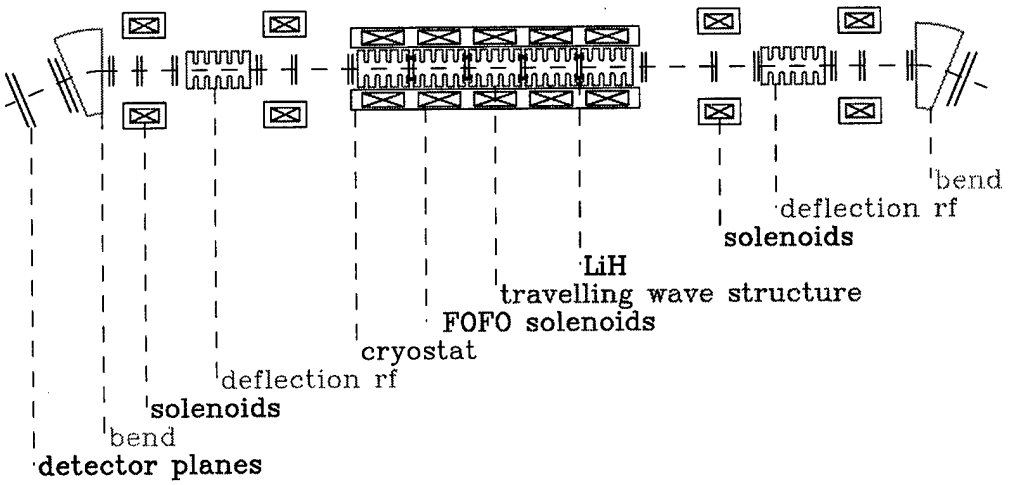


Figure 1: Schematic of the proposed Ionization Cooling Experiment.

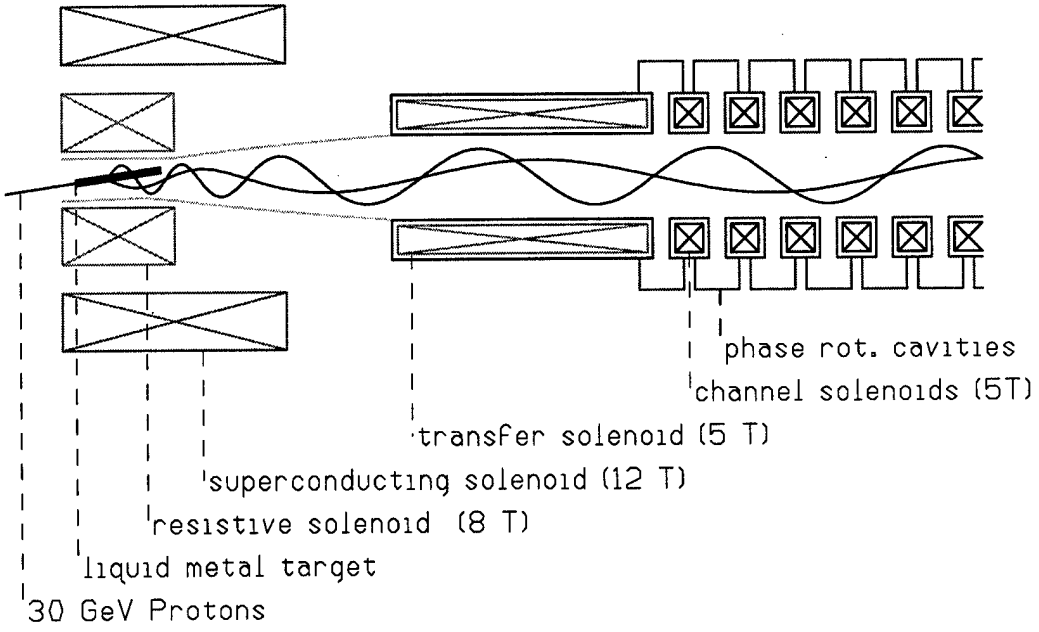


Figure 2: Heavy metal target surrounded by a high field capture solenoid followed by the phase rotation channel.

6 ACKNOWLEDGEMENTS

This work was supported by the U.S. DoE, under Contract No. DE-AC02-76CH00016 and DE-AC03-76SF00515.

7 REFERENCES

[1] V. V. Parkhomchuk and A. N. Skrinsky, Proc. 12th Int. Conf. on High Energy Accelerators, F. T. Cole and R. Donaldson, Eds., (1983) 485; A. N. Skrinsky and V.V. Parkhomchuk, Sov. J. of Nucl. Physics **12**, (1981) 223; *Early Concepts for $\mu^+\mu^-$ Colliders and High Energy μ Storage Rings, Physics Potential & Development of $\mu^+\mu^-$ Colliders. 2^{nd} Workshop*, Sausalito, CA, Ed. D. Cline, AIP Press, Woodbury, New York, (1995).

[2] D. Neuffer, Fermilab Note FN-319, July 1979; Proc. 12th Int. Conf. on High Energy Physics (1983) 481; *Principles and Applications of Muon Cooling*, Part. Acc. **14** 75 (1983)

[3] *Proceedings of the Mini-Workshop on $\mu^+\mu^-$ Colliders: Particle Physics and Design*, Napa CA, Nucl Inst. and Meth., **A350** (1994) ; Proceedings of the Muon Collider Workshop, February 22, 1993, Los Alamos National Laboratory Report LA-UR-93-866 (1993) and *Physics Potential & Development of $\mu^+\mu^-$ Colliders 2^{nd} Workshop*, Sausalito, CA, Ed. D. Cline, AIP Press, Woodbury, New York, (1995); Proceedings of the 9th Advanced ICFA Beam Dynamics Workshop, Ed. J. C. Gallardo, AIP Press, Conference Proceedings 372 (1996).

[4] R. B. Palmer et al., *Monte Carlo Simulations of Muon Production, Physics Potential & Development of $\mu^+\mu^-$ Colliders 2^{nd} Workshop*, Sausalito, CA, Ed. D. Cline, AIP Press, Woodbury, New York, pp. 108 (1995); R. B. Palmer, et al., *Muon Collider Design*, in Proceedings of the Symposium on Physics Potential & Development of $\mu^+\mu^-$ Colliders, Nucl. Phys B (Proc. Suppl.) **51A** (1996); R. B. Palmer and J. C. Gallardo, *Muon-Muon and other High Energy Colliders*, to be published in *Techniques and Concepts of High Energy Physics IX*, edited by T. Ferbel, Plenum Pub. 1997

[5] *$\mu^+\mu^-$ collider, A Feasibility Study*, BNL-52503, FermiLab-Conf-96/092, LBNL-38946, submitted to the Proceedings of the Snowmass96 Workshop. For aupdated information, see the Muon Collider Collaboration WEB page: http://www.cap.bnl.gov/mumu/.

[6] R. B. Palmer, *High Energy Colliders*, submitted to the Proceedings of 250^{th} Anniversary Conference on Critical Problems in Physics, Princeton University, Oct. 31 - Nov. 2, 1996, to be published.

[7] D. Neuffer, *Principles and Applications of Muon Cooling*, Part. Acc. **14** 75 (1983); R. C. Fernow and J. C. Gallardo, *Muon Transverse Ionization Cooling: Stochastic Approach*, Phys. Rev. **E52** 1039 (1995); see also A. N. Skrinsky et al. in ref. [1]

[8] B. King, unpublished report; presentation at the Muon Collider Workshop, LBNL, Feb. 1997 and private communication.

[9] N. Mokhov, presentation at the Muon Collider Workshop, LBNL, Feb. 1997 and private communication.

[10] A. A. Mikhailichenko and M. S. Zolotorev, Phys. Rev. Lett. **71**, (1993) 4146; M. S. Zolotorev and A. A. Zholents, SLAC-PUB-6476 (1994); presentation at the Muon Collider Workshop, Orcas Island, May 17-22, 1997, unpublished and private communication.

PERFORMANCE OF THE CESR HIGH LUMINOSITY INTERACTION REGION

S. Henderson*, Laboratory of Nuclear Studies, Cornell University, Ithaca, NY 14853†

Abstract

In November 1995, the Cornell Electron Storage Ring (CESR) began Phase II operations. The CESR/CLEO Phase II upgrade involved the installation of a silicon vertex detector for the CLEO experiment, and an interaction region optimized for a small-radius (2cm) beampipe and bunch-train collisions at total beam currents of 600 mA. The operating experience of the CESR Phase II Interaction Region is reviewed.

1 INTRODUCTION

The Cornell Electron Storage Ring (CESR) began Phase II Operation in November 1995 following the installation of the Phase II Interaction Region (IR). The Phase II IR was optimized for bunch-train collisions at a finite crossing angle to provide a design luminosity of $6 \times 10^{32}\text{cm}^{-2}\text{sec}^{-1}$. As part of the upgrade project, the CLEO Experiment installed a silicon vertex detector (SVX) [1] around a small-radius beampipe. The detector background shielding system was designed to minimize backgrounds and radiation dose to the silicon detector and associated electronics in the presence of crossing angle collisions at design currents of 300mA e^+ + 300 mA e^-. After an initial commissioning period in which the vacuum system was beam processed, CESR beam currents increased, and the luminosity followed. CESR presently operates [2] at peak colliding beam currents of ~340 mA and a peak luminosity of 4.1×10^{32} $\text{cm}^{-2}\text{sec}^{-1}$. CESR has delivered 3.9fb^{-1} since the Phase II start-up.

2 CESR PHASE II

CESR Phase II exploits an idea put forth by Meller [3] to increase the number of bunches in each beam by colliding the beams at a small horizontal angle ($\theta_c \simeq \pm 2$ mrad). This crossing angle allows "trains" of closely spaced bunches (with minimum bunch spacing of 14ns) to be collided; the angle generates adequate separation of the beams at the nearby parasitic crossings in the IR. The beams follow "pretzel" orbits in the arcs, and are thus separated at each parasitic crossing.

The presence of the crossing angle has several important consequences for the IR design. First, the off-axis beams in the IR quadrupoles generate synchrotron radiation (SR) which must be properly masked, and this masking must in turn be adequately cooled. Second, the crossing angle displaces the beams in the horizontally focussing IR quadrupole, thereby reducing the aperture. Adequate space must therefore be provided for the injected bunch oscillations.

E	5.3 GeV
$\mathcal{L}$	6.0×10^{32} cm^{-2} sec^{-1}
ξ_v	0.03
C	768 m
N_b	27 per beam
I	300 mA per beam
θ_c	2.5 mrad
β_v^*	1.9 cm
β_h^*	1.2 m
η^*	0 m
σ_l	1.8 cm
ϵ_h	0.21 mm mrad
Q_x	10.53
Q_y	9.60

Table 1: CESR Phase II Design Parameters

The CESR Phase II design parameters are shown in Table 1. The design calls for 9 trains per beam and 3 bunches per train for a total beam current of 600 mA. At these currents the expected luminosity is 6.0×10^{32} cm^{-2} sec^{-1}.

3 PHASE II INTERACTION REGION

The IR design had to accomodate competing requirements from the accelerator and the detector. To take full advantage of the precision tracking capability of the SVX, it was important to allow the first tracking layer to be as close to the interaction point (IP) as possible while still maintaining acceptable background levels in the face of a 3-fold increase in beam currents. The SVX readout electronics, the most radiation sensitive component in the IR, were measured [4] to fail at 25-35 krad accumulated dose when powered. (The lifetime dose when unpowered is ~80-100 krad. The detector background design goals were i) SVX layer 1 occupancy $< 1\%$ hits/strip/μsec and ii) SVX dose (when powered) ≤ 20 krad in 3 years. In addition, the SVX temperature stability requirements are $\pm 5°$C.

Meanwhile, the accelerator design requires minimization of HOM-generation and adequate IR aperture for injected bunch oscillations into crossing angle orbits.

The IR design was based largely on simulation of detector backgrounds and radiation dose (described below). We determined that a beampipe radius of 2 cm gave acceptable backgrounds and set the first layer of Si at $r = 2.35$

* Representing the CESR Operations Group

† Work supported by the National Science Foundation

0-7803-4376-X/98/$10.00 © 1998 IEEE

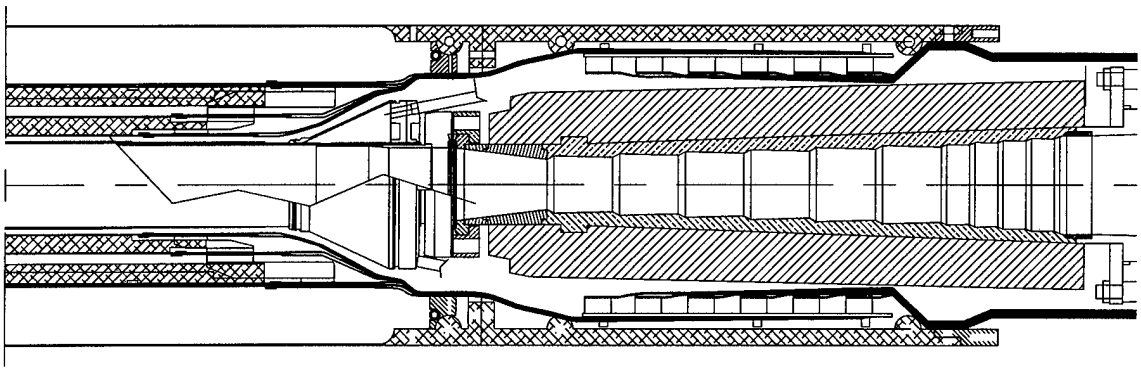


Figure 1: Interaction Region layout from the IP to 52 cm. Starting at the IP and moving radially outward are the Be beampipe (extending to 21 cm), three layers of Si tracking and the carbon fiber support tube. Starting in the middle of the figure and moving outward is the stepped copper SR mask (21-50 cm), tungsten shielding, SVX receiver electronics and carbon fiber housing.

cm. The Phase II interaction region upgrade consisted of installing the following components: i) a 2cm radius beryllium beampipe, ii) the CLEO SVX, iii) the detector background shielding system, iv) IR instrumentation, and v) new vacuum system components within ± 12 m of the IP. In addition, the final focus quadrupoles were modified. The Phase II IR from the IP to 52 cm is shown in Figure 1.

3.1 Interaction Region Optics

A rearrangement (from Phase I) of final focus quadrupoles made for more favorable IR optics [2]. The vertically focussing permanent magnet quadrupole was lengthened, allowing the horizontally focussing IR quadrupole to be moved closer to the interaction point. This reduces the maximum horizontal β in the IR to $\sim$60 m (an improvement over the Phase I optics which had $\hat{\beta}_h \simeq 100$m). Injection performance is improved since the maximum excursion of the injected bunch is reduced at this point. In addition, the physical aperture in the electromagnetic IR quads (Q1 and Q2) was increased by enlarging the pole tip radii, providing an additional $\sim$2 cm of horizontal aperture. These two features improve CESR injection and reduce detector backgrounds during injection.

3.2 Central Beampipe

The central beampipe is a 2 cm outer radius double-walled water cooled beryllium beampipe [5]. The beampipe, manufactured by Brush-Wellman Inc.[1], was assembled from two Be tubes; the inner tube had ribbed supports. A 20 mil gap between Be tubes was provided for coolant flow. Manifolds at each end provide inlets and outlets to four separate cooling channels. Water was selected as the coolant because of its excellent thermal conductivity, capable of dissipating 400W with only 5°C temperature rise.

The inner surface of the Be beampipe was coated with 10μm gold for the absorption of scattered synchrotron radiation. The gold was deposited with a cylindrical magnetron sputtering technique [6]. The total beampipe thickness is 0.6% X_0, half due to the gold coating and half due to Be/H_2O.

Since corrosion of bare Be by ions in water is problematic, a layer of epoxy was applied to all bare Be surfaces by the manufacturer following the gold coating process.

3.3 Detector Background Shielding

The detector shielding system [7] minimizes beam-generated backgrounds arising from two sources: beam-gas interactions (Coulomb scattering and Bremsstrahlung) and scattered synchrotron radiation. Bremsstrahlung interactions result in beam particles which have lost a portion of their energy and which become over bent in dipole magnets and over focused in quadrupoles. Such "lost particles" may be directed into the experimental detector by the IR quadrupoles. In addition, Bremsstrahlung photons are generated and may strike near the IP. Coulomb interactions result in full energy beam particles which have large oscillation amplitudes and may strike the vacuum chamber near the IP.

Synchrotron radiation, generated in the final bend before the IR straight and in the IR quadrupoles due to the crossing angle trajectory, is directed toward the interaction point, and if not intercepted would strike the Be beampipe directly, leading to unacceptably large x-ray fluxes in the inner detectors.

The detector shielding consists of two parts. The detector is shielded from lost beam particles with massive W shielding, chosen for its short radiation length. The detector is shielded from synchrotron radiation by a stepped copper mask with innermost tip radius $r = 1.2$ cm. The mask is profiled in such a way that SR photons strike only the "tips" of the mask, and no flux is received on other surfaces. X-rays striking near the tip may forward scatter into the beampipe and detector, generating background (termed "tipscattering" in this paper). Additionally, x-rays which

[1]Brush Wellman ADC, 34325 Ardenwood Boulevard, Fremont, CA 94555

pass over the innermost tip may strike the back surface of the mask. These photons may interact, producing fluorescent x-rays which strike the beampipe. (This process is termed "backscattering").

The choice of scattering materials and beampipe coating material was based on x-ray scattering Monte-Carlo detector background simulations. In particular, the gold beampipe coating material was chosen because its L absorption edge was found to be a good match to the scattered x-ray flux.

To monitor radiation levels in the IR, the beampipe has been instrumented with 12 PIN diode detectors at each end, sensitive to charged particles, as well as x-rays. The monitoring system is continuously read out and logged, and is used for background tuning purposes.

The detector background simulation predictions for CESR design conditions (600 mA total current; flat 3.5 nTorr pressure profile; 40% CESR duty factor; 15 keV SR threshold) are summarized in Table 2.

Source	SVX layer 1 Occ. % hits/layer/μs	Dose krad/year
SR (tipscattering)	0.007	0.1
(backscattering)	0.001	0.6
Beam-Gas	0.18	8
Total	0.2	9

Table 2: Detector background simulation predictions for CESR design conditions

3.4 *Retractable Radiation Shields*

During CESR injection, the beams are horizontally separated at the interction point, making one of the beams further off-axis in the horizontally focusing IR quadrupole. As a result, large SR fluxes can be generated. Simulations show that SR doesn't directly strike the beampipe, but for added safety, retractable W shields were mounted on the beampipe [9]. The shields are constructed from W foil and have total thickness 200μm. They are remotely actuated, and were designed to close during CESR injection and machine studies.

3.5 *IR Vacuum System*

As part of the Phase II interaction region upgrade new vacuum system components between $\pm$12m from the IP were required. IR Pumping [8] is accomplished in large plenums incorporating massive titanium sublimation pumping (located at $\pm$2m, $\pm$6m and $\pm$10m from the IP).

4 COMMISSIONING AND OPERATIONAL EXPERIENCE

The IR components were assembled in early 1995, and the IR was installed from April-October 1995. CESR start-up began October 29, 1995 and first e^+e^- collisions were obtained November 14. The SVX was turned on during collisions on November 21, 1995. Beam currents were initially limited by detector background levels for the first 2-3 months of operation as the storage ring pressure improved from beam processing. Since this initial start-up period, CESR currents have no longer been limited by detector backgrounds.

Figure 2 shows the dynamic pressure rise (dP/dI) vs. accumulated beam dose measured at the 6 m TiSP chambers, demonstrating the effects of beam processing (and TiSP flashing) since Phase II start-up. For orientation, after the first month $\sim$10 A-hr had been accumulated, and after five months, $\sim$100 A-hr had been accumulated. Now, after $\sim$700 A-hr, typical dynamic pressure rises in the IR are $\sim$0.002 nTorr/mA [8].

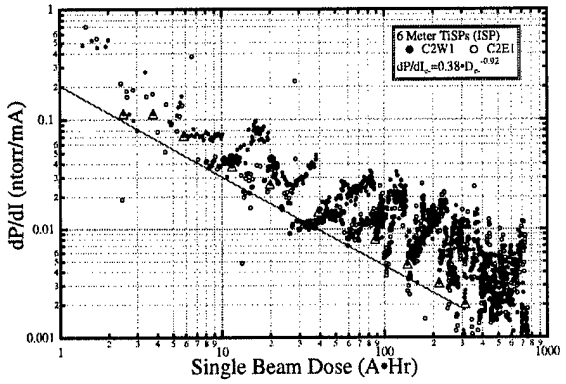


Figure 2: Dynamic pressure rise vs. beam dose for the 6 m TiSP chambers since CESR Phase II start-up.

4.1 *Radiation Levels*

The IR radiation history since Phase II start-up is shown in Figure 3. Nearly 2 krad was logged during the initial 2 month beam processing phase. About 10 krad have been logged since start-up, about half of which was accumulated with the SVX electronics powered. Since CESR beam currents have been nearly constant for the past $\sim$6 months, the radiation has been increasing linearly with time, at a rate of $\sim$8krad/year at peak total currents of $\sim$320 mA ($\sim$4.6 krad/year powered). The accumulated powered dose represents about 20% of the lifetime dose for the SVX readout electronics.

Of the total accumulated dose since Phase II start-up, 63% was delivered during high energy physics data-taking, 17% during CESR Injection, and 20% during other activities, including machine studies.

4.2 *Beampipe Cooling*

The beam-generated heat load on the central Be pipe has been measured [10] by reducing the coolant flow and storing large beam currents, noting the temperature rise. 15-20W was measured at 300mA total current (36 bunches and $\sim$8.3 mA/bunch). The heat load has also been measured

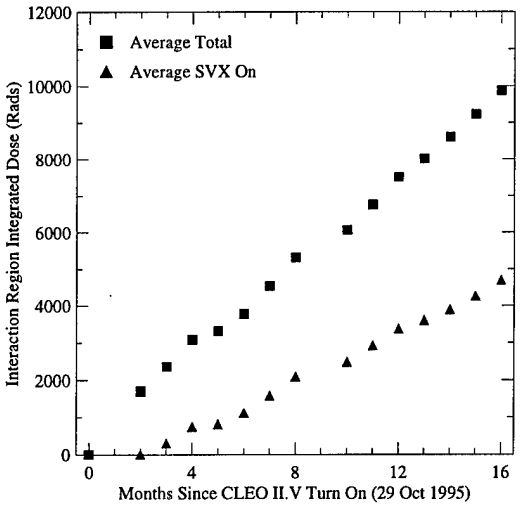


Figure 3: IR radiation history since CESR Phase II start-up.

by noting the temperature rise during data-taking periods, although the heat generated by the nearby SVX detector electronics (~200 W) is a much larger source, making extraction of the small beam-related power difficult. Scaling this heat load to the design current of 600 mA gives at most 80W, well within the design capacity of 400W.

The measured heat loads are consistent with calculated values, given the uncertainties involved. The expected image current heating is ~3W; the HOM power generated in the IR mask structure is ~6W at these beam currents.

5 COMPARISON OF BACKGROUND WITH SIMULATION

A comparison of measured background rates with detector background simulation predictions has been undertaken. Two simulation tools are in use at CESR, one for beam-gas backgrounds and another for SR backgrounds [11]. Each begins with the CESR lattice description, vacuum chamber geometry, and closed orbit and interaction region bump strengths. The beam-gas simulation generates Coulomb and bremsstrahlung interactions throughout the machine and tracks the secondaries, collecting those beam particles and photons that strike near the IP. These particles are used as input to a GEANT-based Monte-Carlo simulation of the detector response. The SR simulation generates photon fluxes from a 2-D description of the beam, and follows their trajectories to vacuum chamber surfaces where fluxes are accumulated. These calculated fluxes are used as input to an x-ray scattering Monte-Carlo simulation, which propagates scattered photons (from Compton scattering, Rayleigh scattering and fluorescence) to the detector where the response is simulated.

5.1 Single Beam Results

We have compared single-beam radiation levels, measured with the beampipe radiation monitoring system, with simulation predictions. For a single beam of 140 mA, the average IR radiation was 0.8 rads/hr, compared with a simulation prediction (including the measured pressure profile and IR bumps) of 0.75 rads/hour (0.25 from SR, 0.50 from beam-gas). Although the agreement for this set of conditions is quite good, other results revealed discrepancies. Namely, the simulation failed to predict the dependence of background rates on the horizontal displacement bump, an IR bump (used to displace the collision point) which is routinely used to optimize background levels.

5.2 Pressure Bump Studies

Preliminary pressure bump studies also revealed disagreement. By introducing calibrated leaks and turning off pumps in different sectors of the machine, the "source-effectiveness" (the contribution of a single source point to detector backgrounds) of different portions of the ring was measured. We observed that only the region from 0-30m from the IP contributes to detector backgrounds; the IP is "masked" from lost-particles generated elsewhere. (This result is predicted by simulation.) In addition, we observed that ~2/3 of the background is generated within 12m from the IP (the IR straight and the nearest dipole) and ~1/3 is generated in the "hard-bend" region (the region 14-40m from the IP which contains stronger bends), a result for which the beam-gas simulation failed to account.

In order to better understand the "hard-bend" contribution to detector backgrounds, a calibrated CO leak was introduced at ~15m from the IP [12]. Different pressure profiles were generated (shown in Figure 4a) by systematically turning off distributed and lumped pumps one-by-one in the hard bend region to obtain a set of 7 pressure conditions. Pressure profiles were calculated (based on available pressure measurements) with a one-dimensional finite element method in which the pumping speed of each pump and thermal outgassing rate are adjusted to obtain the best fit. For each condition, IR radiation levels were measured with a small stored beam current. The IR radiation response for each of the 7 cases, normalized to beam current, is shown in Figure 5 (curve "rad_meas").

Since the beam-gas simulation did not properly account for the hard-bend contribution, another simpler approach was taken. The source-effectiveness *for IR mask strikes* was calculated as follows. At each source location, the range of energy losses which produce trajectories that strike the IR mask (without hitting an aperture between the source point and mask) is calculated. A bremssstrahlung weight is assigned to that location from the bremsstrahlung cross-section integrated over the range of calculated energy-losses. Likewise, a Coulomb weight is calculated by determining the range of scattering angles which lead to trajectories that strike the IR mask. The total weight (bremssstrahlung and Coulomb) is plot-

ted as a function of the source location in Figure 4b (curve "effect_SDH_tot_p2"; relative strength shown on the right axis). This calculated source effectiveness clearly shows two contributions: one lobe from 0-10m, and another from 16-27m.

The calculated source-effectiveness is compared to the measured radiation rates for various pressure profiles, up to a normalization factor, by multiplying the pressure profile times the source-effectiveness. The overall normalization is obtained by choosing two pressure profiles (P2-P3) whose *difference* corresponds to a pressure bump near 20m (shown in Figure 4b, curve "P2_minusP3") which overlaps the predicted source effectiveness. The pressure bump times the effectiveness divided by the measured difference in radiation between the two cases provides the normalization factor. The calculated radiation response for the 7 cases, using this normalization factor, is displayed in Figure 5 (curve "RAD_cal_norm"). The agreement between the measured radiation response and the calculated response is excellent.

These results confirm that there is a significant contribution to backgrounds from the "hard-bend" region, a result explained by a simple calculation of lost particle trajectories and fluxes. Work is underway to reconcile the simple source-effectiveness calculation described here with the full Monte-Carlo simulation.

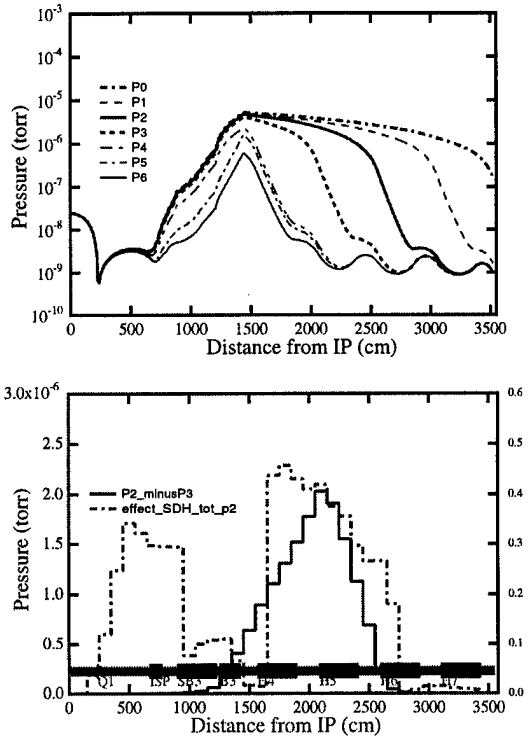


Figure 4: (Top) Pressure profiles for a calibrated CO leak experiment. The leak was introduced at 15m. (Bottom) The calculated source-effectiveness for IR mask strikes is shown (right axis) together with a pressure bump resulting from the *difference* in profiles P2 and P3.

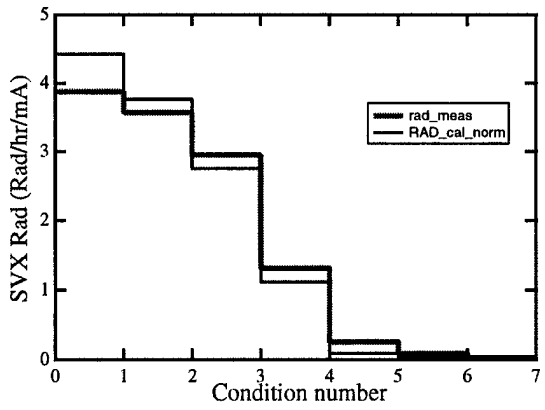


Figure 5: Measured IR radiation response is compared with the calculated response for the 7 pressure profiles shown in Figure 4.

6 CONCLUSIONS

The design and performance of the CESR Phase II Interaction Region has been reviewed. The IR shielding performance is as expected, although detailed features of the background sources are still under investigation. Meanwhile, CESR luminosity continues to improve, having delivered 3.9 fb^{-1} since Phase II start-up [2].

7 ACKNOWLEDGEMENTS

The author would like to thank D. Cinabro, Y. Li and N. Mistry for results presented in this paper.

8 REFERENCES

[1] D. Cinabro, "A Silicon Vertex Detector for CLEO," Proc. XXVI ICHEP (Dallas, TX, 1992) 1727.

[2] D. Rubin, "CESR Status," these proceedings.

[3] R. Meller, Cornell Note CON-90-17, 1990.

[4] J.P. Alexander *et. al.*, NIM **A337** (1993) 171.

[5] Stuart Henderson, "The CLEO-II SVX Water-cooled Be Beampipe," Proc. 8th Meeting of DPF (Albuquerque, NM), World Scientific, (1994) 1480.

[6] Stuart Henderson and Scott Roberts, Cornell CBX-97-15.

[7] S. Henderson, "The CESR-CLEO Interaction Region Upgrade," Proc. XXVI ICHEP (Dallas, TX, 1992) 2022.

[8] N. Mistry, "Massive Titanium Sublimation Pumping in the CESR Interaction Region", these proceedings.

[9] D. Dumas, Cornell CBX-95-106.

[10] D. Cinabro, private communication.

[11] "CESR-B Conceptual Design Report," (1993)

[12] N. Mistry, Cornell CON-97-02.

B-FACTORY INTERACTION REGION DESIGN*

M. Sullivan
Stanford Linear Accelerator Center, Stanford University, Stanford, CA 94039 USA

Abstract

High luminosity B-factories are generally high current (1-3 A) e+e- storage ring accelerators that operate at a center-of-mass energy equal to the mass of the Upsilon (4S) resonance (10.58 GeV). The high beam currents are achieved by storing a large number of bunches (several hundred to several thousand) into each beam. Two designs, the ones located at SLAC and KEK, also have asymmetric beam energies. This imparts a boost to the nearly stationary B mesons formed from the decay of the 4S resonance and allows precision vertex tracking detectors to look for a difference between the decay profiles of the matter and anti-matter B mesons, thereby observing a violation of CP. Bringing the stored beams into collision is one of the major challenges of any B-factory design. In order to achieve high luminosity the beams must be tightly focused. This pushes the final focusing elements close enough to the interaction point to be inside the solenoidal field of the physics detector. In addition, beam-related detector backgrounds from synchrotron radiation and scattered beam particles must be kept below an acceptable level. The major B-factory designs at Cornell University, KEK, and SLAC have all addressed these problems in various ways that depend on specific accelerator design decisions. This paper discusses the accelerator parameters and detector constraints that influence an interaction region (IR) design, as well as how the various IR designs address the challenges posed by a high luminosity B-factory.

1 ACCELERATOR PARAMETERS

Several factors must be balanced in the design of any IR. First, detector backgrounds from the incoming beams, always a concern, must be manageable. But there are several accelerator parameter decisions that strongly affect the design of an IR, and some of these parameter selections are not driven by IR concerns but are the result of other constraints of the accelerator design. Some of the parameters that affect any design of an IR are:

- Beam energies
- β_y^*
- Beam coupling or beam aspect ratio
- Head-on or crossing angle collision
- Beam bunch spacing
- Beam currents
- Beam size and beam emittance
- Beam-Stay-Clear

1.1 The beam energies of a B-factory

For B-factories, the beam energy range is somewhat restricted since all designs have a center-of-mass energy of 10.58 GeV. However, the three B-factory designs use different beam energies. The SLAC, LBNL, LLNL PEP-II design[1,2] has the largest energy asymmetry (9 on 3.1 GeV) while the Cornell CESR-III design[3,4] has symmetric beam energies and the KEK design (KEKB)[5,6] has an intermediate energy asymmetry of 8 on 3.5 GeV. How these beam energy selections affect the IR designs will be discussed in more detail shortly.

1.2 β_y^*

The vertical beta function value (β_y^*) at the interaction point (IP) for all three B-factory designs is small: 1–2 cm. In order to achieve these small β_y^* values the final focusing elements of the beams must be very close to the collision point. All three designs have machine elements within 1 meter of the IP, which places these elements inside the detector magnetic field.

1.3 Beam coupling

The beam coupling or beam aspect ratio at the collision point is another important parameter. Generally, the flatter the beams—vertical over horizontal beam size as small as possible—the easier it is to control synchrotron radiation (SR) backgrounds. This is one reason why round-beam designs are difficult. However, extremely flat beams are also difficult to achieve. The accelerator must be very precisely aligned in order to get the beam coupling much below 2%. All three B-factory designs use a beam coupling of 2-3%.

1.4 Collision angle, bunch spacing and beam separation

At what angle the beams collide plays an important role in designing how the beams are separated. Head-on colliding beams are certainly the most difficult to separate. The beam energies, the distance between beam bunches and the collision angle determine the beam orbit geometry near the IP. Each B-factory design has a different approach in dealing with this aspect of the IR design.

1.5 Large beam currents

To obtain a high luminosity, all B-factories have significantly large beam currents; typically 1-2 A per beam.

*Work supported by U.S. Department of Energy, under contract number DE-AC03-76SF00515.

0-7803-4376-X/98/$10.00 © 1998 IEEE

These large beam currents pose several difficulties for IR designs. Synchrotron radiation power is a distinct concern throughout the accelerator but this is especially true inside or just outside the detector where space is tight and temperatures must be carefully controlled.

The large beam currents also induce I^2R heating losses and higher-order-mode (HOM) losses. These power losses can be quite large and special care must be taken that beam pipes are smooth and conductive throughout the IR. Unwanted cavities in the beam pipe near the IP—almost unavoidable due to the large beta functions and/or the merging of two beam pipes—have HOM absorber material to limit their Q and lower the amount of local resonant heating.

1.6 Beam size and beam emittance

The beam size in the IR influences many aspects of the design. Masking for SR, magnet apertures and beam separation all depend on the size of the beams. The size is determined by the emittance of the beam and the beta functions in the IR. Although the beam emittance is an important IR parameter, the range of this parameter is generally set by other aspects of the accelerator, usually by the circumference of the ring and the design of the lattice for each beam. In some cases, the emittance is increased through the use of wigglers. The beta functions near the IR are usually lower in high emittance accelerators than they are in accelerators that have low emittance in order to keep the beam sizes reasonable. In general, the larger the beam, the more difficult it is to protect the detector from SR; especially the radiation that is emitted from the particles out at a high number of beam sigmas.

1.7 Beam-stay-clear and beam tails

The collision of the two beams induces a disruption in the colliding bunches, which kicks beam particles out to large transverse distances (many beam sigmas) from the beam center and starts to lower the lifetime of the beams. For this reason, as well as to increase accelerator flexibility, the beam-stay-clear (BSC) aperture is usually made as large as possible especially near the IP. In addition, in order to minimize detector backgrounds from lost beam particles, one prefers a beam aperture that gets larger as the beams approach the IP. However, the desire for large beam apertures must be balanced with the need to install masks near the IP for both SR and lost particle backgrounds and the need to keep magnet apertures reasonably sized. The population of particles in these "beam tails" is a major concern in estimating SR background rates. The particles at large transverse distances from the beam center have the best chance of generating photons that can directly strike the detector beam pipe.

2 DETECTOR CONSTRAINTS

The physics detector of a B-factory needs to be as efficient as possible in collecting the interesting physics events. This is the important definition of integrated luminosity—how many physics events are accumulated. Toward this end, the detector imposes some requirements on the accelerator and also complicates the IR by its presence. Some detector needs and constraints are:

- Low backgrounds
- Maximum solid angle for detecting particles
- Smallest possible radius for the beam pipe
- A beam pipe that is as transparent as possible
- A solenoidal detector field of 1–1.5 T

2.1 Low Backgrounds

The beam-related backgrounds, both SR and lost particles, must be kept below a level that allows the detector to operate with minimal impact on detector efficiency. In addition, the radiation levels must also be kept low enough to ensure that detector components have a reasonable (5–10 yr.) lifetime before being damaged. One of the primary ways of keeping the lost beam particle backgrounds low is to have a very low vacuum in the beam pipe upstream of the detector. All B-factory designs ask for a low vacuum in these regions.

2.2 Maximum solid angle

Maximizing the solid angle of the detector means that the space left for accelerator components that are inside the detector is very precious. The beam pipe, supports and magnetic elements must be as compact as possible.

2.3 The detector beam pipe

The beam pipe around the IP needs to have as small a radius as possible to get a precision vertex tracker as close to the collision point as possible. In addition, the beam pipe needs to be as transparent as possible to the emerging physics events and yet be opaque to the SR from the beams. The choice for all three B-factories is a Be beam pipe that is coated on the inside with a high Z material (e.g. Au) to absorb the SR photons.

2.4 Detector magnetic field

The detector has a solenoidal magnetic field with a value in the range of 1-1.5 T. Any accelerator magnets inside the detector field must be either permanent magnet (PM) or superconducting. The detector magnetic field will also steer the beams because the beams are not traveling down the axis of the detector. Each B-factory design has a different approach toward solving these difficulties.

3 B-FACTORY IR DESIGNS

Some of the accelerator parameters that influence the design of the IR and the choices made by the three accelerator designs are listed in Table 1. Comparing B-factory IR designs, we shall see how these parameter selections have influenced each design.

Table 1. Some Parameters of the B-factories

	PEP-II		KEKB		CESR-III	
	e+	e-	e+	e-	e+	e-
E (GeV)	3.1	9.0	3.5	8.0	5.3	5.3
I (A)	2.1	1.0	2.6	1.1	0.5	0.5
β_y^* (cm)	1.5	2.0	1.0	1.0	1.0	1.0
ε_x (nm-rad)	66	49	18	18	251	25
σ(x,y) (mm)	181, 5.4		77, 1.9		388, 11.7	
Coupling (%)	3		2		3	
ξ	0.03		0.05		0.03	
S_h (m)	1.26		0.59		4.2	
# of bunches	1658		5027		45	
θ_c (mrad)	head-on		±11		±2.1	
L ($cm^{-2}sec^{-1}$)	3×10^{33}		1×10^{34}		1.8×10^{33}	

3.1 PEP-II

As stated earlier, PEP-II has the largest energy asymmetry (9 on 3.1 GeV) of the three designs. This permits the design to have head-on colliding beams. The fairly small bunch spacing (1.26 M) means that a strong horizontal bend magnet (B1) must start separating the beams as soon as possible after the beams have collided. This tapered magnet starts at about 21 cm from the IP and separates the beams enough so that the tune-shift at the first parasitic crossing (0.63 M) is small. Immediately following B1 is the vertical focusing quadrupole (Q1) for the low energy beam (LEB). This horizontally defocusing magnet continues to separate the beams. Separation is maximized by superimposing a dipole field over the quadrupole field, which shifts the magnetic center of Q1 to where the high energy beam (HEB) is located. These two magnets are in the detector field and are therefore permanent magnets. The next magnet (Q2) is a horizontally focusing septum quadrupole for the LEB—the HEB travels through a field free region. The following two magnets (Q4 and Q5) are also septum magnets and are the final focusing doublet for the HEB. Figure 1 shows a plan view of the IR for PEP-II. It is important that Q2 be a septum magnet. If it were a shared magnet, with both beams going through it, a large amount of the beam separation gained in B1 and Q1 would be lost.

The rapid separation of the beams by B1 and Q1 generates significantly high-power fans of SR. The SR fan from the upstream Q1 magnet must be masked from the detector beam pipe and the power absorbed by the mask

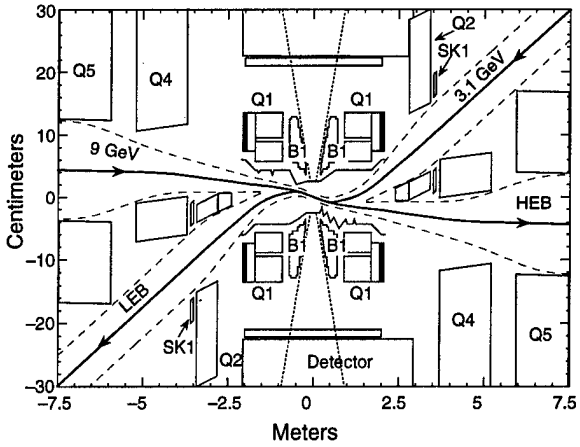


Figure 1. Layout of the interaction region of the PEP-II B-factory. The vertical scale is highly exaggerated. The detector for PEP-II is offset in z by 37 cm in the direction of the HEB.

must be completely removed to maintain a constant temperature for the PM material of B1 and Q1.

The SR fans generated by the HEB as it travels through the B1 magnets are very intense. However, the 49 kW of power in these fans do not strike any nearby surfaces and are absorbed in a dump that starts about 12 m away from the IP in the downstream HEB beam pipe. The primary source of SR background is the photons that scatter to the detector beam pipe from the mask tips. Because of this, the PEP-II design is insensitive to SR from the beam tails. Some care must still be taken to ensure that photons generated by particles in the beam tails do not directly strike the detector beam pipe. Once this is achieved, the SR background rates from beam tail particles are much lower than the background rates produced by the photons that scatter from the mask tips.

The design has no room for a compensation solenoid to help cancel the effects the detector field has on the beam orbits. Instead, the location of the IP is allowed to move vertically. This displacement means that the two beams will receive a vertical kick from Q1 which partially compensates the steering effects of the detector field. In addition, the center of the Q2 and Q4 magnets are also vertically displaced by a few mm to further steer the beams before correctors positioned between Q4 and Q5 can be used to continue correcting the beam orbits. A series of skew quads completes the corrections needed to compensate for the effects of the detector field[7].

The two beams go into separate pipes in the Q2 septum magnet so the beam pipe in front of Q2 and behind Q1 is the largest beam pipe in the IR. This local bulge in the beam pipe can trap HOM energy. Some amount of absorber material (e.g. silicon carbide) will be mounted in this chamber to limit the amount of resonant power trapped in this region.

The HEB travels through two bend magnets located between 22 and 27 m from the IP. The magnet closer to the IP is a low field bend magnet, which minimizes the SR striking the IP region. The magnets sweep out a large fraction of lost beam particles that were produced even farther from the IP. Consequently, the region from these magnets to the IP is the primary source of lost particle backgrounds in the detector for the HEB. The LEB goes through a vertical bend magnet at about 10 m from the IP that is also effective in sweeping out lost beam particles that have been produced further upstream. The PEP-II design calls for a low vacuum in these regions in an effort to minimize lost particle backgrounds. In addition, the PEP-II design includes a graded beam aperture where the aperture gets larger as the beams travel to the IP. This also helps to reduce the background rate from lost particles.

3.2 CESR-III

The accelerator at Cornell is a single storage ring with equal energy beams of 5.3 GeV. The final focus doublet is located close to the IP with the vertical focusing quadrupole made up of two elements. The first is PM material and is positioned very close to the collision point (0.34 m to 0.84 m). The rest of the vertical focusing and all of the horizontal focusing is accomplished by two superconducting quadrupoles (Q01 and Q02). Figure 2 shows a layout of the CESR-III IR.

Cornell has developed a scheme to store many bunches into each beam and still use only one storage ring. Electrostatic plates separate the beams into different orbits around the ring that intersect each other in several places. However, by carefully selecting which rf buckets to fill with charge, they plan to be able to store up to 0.5 A in each beam. In order to get this much current into each beam it is necessary to introduce a small crossing angle of ±2.1 mrads. This allows the beams to be far enough apart at the first parasitic crossing (2.1 m) so that the extra tune-shift is small. The crossing angle introduces some SR due to the bending of the beams in Q01 and Q02, but the power is not high (3 kW) and it is directed nearly forward and should not contribute to detector backgrounds. The small amount of near IR bend radiation means that SR background calculations are dominated by radiation from particles in the beam tails and by upstream bend magnets.

The relatively small circumference of the Cornell ring when compared to the other two B-factories means that it is difficult to get beam emittances that are much below 250 nm-rad for 5.3 GeV beams. This means the maximum β_x value needs to be kept reasonably low in order to keep the x size of the beams manageable. To achieve this, the final focusing elements are close to the IP.

CESR-III has no compensation solenoids. The beams are nearly parallel to and only slightly offset from the detector axis so there is very little beam steering from the detector field. A family of skew quads take out the coupling induced by the solenoidal field.

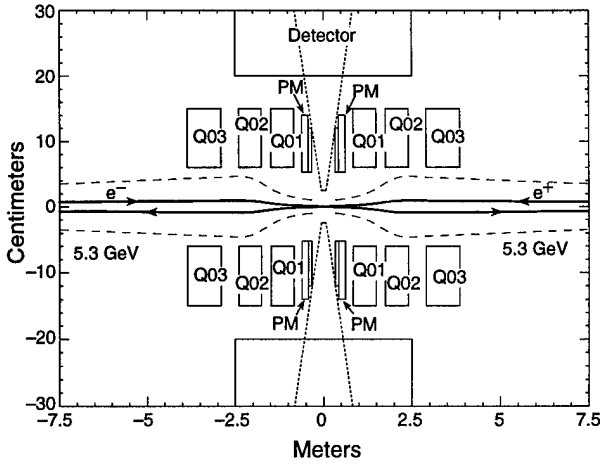


Figure 2. Layout of the CESR-III interaction region. The vertical and horizontal scale are the same as in Fig. 1. The QO3 magnets are not used except for round beam studies.

Since CESR is a symmetric energy accelerator, the masking must be symmetric on either side of the IP. This leads to SR backgrounds that are dominated by photons that strike the inside, or detector beam pipe side, of a downstream mask. These surfaces usually have a fairly large solid angle view of the detector beam pipe so photons that bounce out of these surfaces have a good chance of entering the detector.

The arc magnets begin about 15 m from the IP with the start of a low-field bend magnet. The hard-bend arc magnets are so close to the IP that lost beam particles originating from the start of the arc are swept out into the detector and are a major source of lost particle background. The design asks for a low vacuum pressure in this region.

3.3 KEKB

The B-factory at KEK has beam energies of 8 and 3.5 GeV. This smaller energy asymmetry makes it difficult to collide the beams head-on. This is one reason the KEKB design collides the beams with a crossing angle of ±11 mrads. The large crossing angle helps to separate the beams quickly, which allows the KEKB design to have the smallest bunch spacing (0.6 m) and hence the smallest parasitic crossing (0.3 m). The large crossing angle also helps to separate the beams enough to place the first septum magnets (QC1E) about 3 m of the IP. The design minimizes the bending of the incoming beams, which minimizes the SR that can cause detector backgrounds. This produces an asymmetric lattice design around the collision point (the other two designs have symmetric optics) and concentrates all of the bending of the beams to the downstream side of the IP. The beams are still bent because the first vertically focusing quadrupole (QCS) is

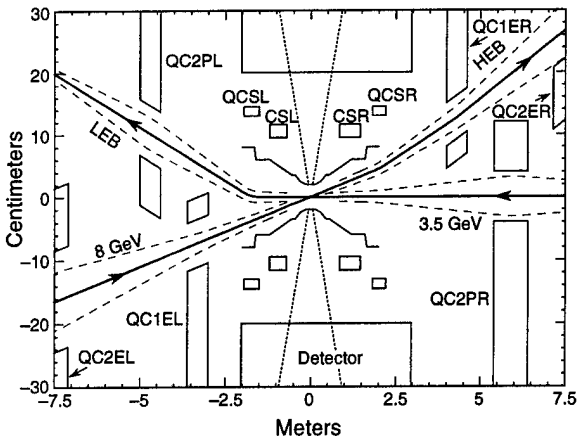


Figure 3. Layout of the KEKB interaction region. The scale matches that found in Figs. 1-2. CSL and CSR are compensating solenoids.

shared. QCS is a superconducting quadrupole and the three remaining quadrupole pairs are normal-conducting septum quads. Figure 3 shows the layout of the KEKB design near the IP.

The cyrostats that contain the QCS magnets also contain compensating solenoids that are positioned inboard of the QCS magnets. These two coils together completely cancel the detector integral B•dl seen by the beams by operating at 2-3 times the strength of the detector field.

The KEK design uses the Tristan tunnel to house the storage rings. This tunnel is the largest of the three designs (3016 m in circumference) and this allows the KEKB design to have small beam emittances. These small emittances have made it possible to use larger beta functions near the IP without making the transverse beam size too large, which in turn allows the final focusing elements to be positioned farther from the IP where the beams more separated. The small emittances make it easier to shield the detector from SR, and it also means that the detector backgrounds from SR are almost entirely driven by the particle density in the beam tails, out at high beam sigma.

KEKB also has a single beam pipe near the IP that splits into two pipes, one for each beam, so there is a local cavity that can trap resonant power. Absorber material will be placed in this cavity to limit the resonant power.

Not bending the beams as they approach the IR, significantly lowers the number of SR photons that can cause background in the detector. However, this also tends to lengthen the amount of beam pipe that must have a low vacuum in order to keep the lost particle background at an acceptable level.

4 SUMMARY

Several accelerator parameters influence IR designs of B-factories. The beam energies, β_y^* values, emittances, coupling values, currents, bunch spacing, and collision angles are all important parameters that affect IR designs. The physics detector also has conditions or requirements that must be included in any design. Low backgrounds, maximum solid angle, a small thin beam pipe, and a large solenoidal field are some of the requirements for a B-factory detector.

Of all of these parameters, the selection of the beam energies probably has the largest single impact. The CESR-III design with symmetric-energy beams has the simplest IR. The focusing elements are naturally shared because both beams are in the same ring. A small non-zero crossing angle is utilized to enable the storing of more beam bunches, which increases the current and hence the luminosity. The other two B-factories (KEKB and PEP-II) have asymmetric beam energies (3.5 on 8 and 3.1 on 9 GeV). The different beam energies mean that each beam is in a separate storage ring and that each beam has separate final focusing elements near the IP. Both designs have one shared quadrupole, the vertical focusing quadrupole of the LEB, which helps to further separate the beams horizontally and allows the next final focus element to be a septum magnet. The KEKB design minimizes SR as a source of background by not bending the incoming beams near the IR. This, with the smaller energy asymmetry and small beam emittances leads the design to a crossing angle of ±11 mrads and to different beam optics on either side of the IP. The PEP-II design has a large enough energy asymmetry to be able to collide the beams head-on. However, in order to get the beams far enough apart at the first parasitic crossing, powerful bend magnets are positioned very close to the IP. The final focus optics are kept symmetric, but this means the shared vertical focusing quadrupole generates significant SR on the incoming side that must be masked and absorbed.

Essentially, all three B-factory IR designs have to address the same problems. The design differences primarily occur when initial accelerator parameters are chosen (beam energies, crossing angle, beam emittances, etc.). These parameter decisions lead to IR designs optimized for the particular choices made.

REFERENCES

[1] "PEP-II an Asymmetric *B* Factory," Conceptual Design Report, CALT-68-1869, LBL-PUB-5379, SLAC-418, UCRL-ID-114055, UC-IIRPA-93-01, June 1993.

[2] M. Sullivan, *et al.*,"Interaction Region Design at the PEP-II *B* Factory," European Particle Accelerator Conference, p. 460 (1996).

[3] D. Rice, "CESR: Steps Toward a B Factory," EPAC, p. 17 (1996).

[4] D. Rubin, "CESR Status and Plans," CBN 95-8 (Cornell LNS note).

[5] "KEKB B-Factory Design Report," KEK Report 95-7.

[6] S. Kurokawa, "The Present Status of the KEKB Project," EPAC, p. 448 (1996).

[7] Y. Nosochkov, *et al.*, "Detector Solenoid Compensation in the PEP-II B-Factory," Particle Accelerator Conference, p. 585 (1995).

HIGH BEAM CURRENT EXPERIMENTS FOR THE KEKB CONDUCTED AT THE TRISTAN ACCUMULATION RING

Y. Funakoshi and K. Akai, High Energy Accelerator Research Organization (KEK),
1-1 Oho, Tsukuba-shi, Ibaraki-ken, 305 Japan

Abstract

Dedicated machine time of about 10 weeks has been devoted to the high beam current experiment by using an electron beam of the TRISTAN Accumulation Ring (AR). In the experiment, we investigated performance of prototypes of RF cavity systems and a bunch-by-bunch feedback system which will be used in the KEKB. We found that the RF cavity systems work very well at the beam current more than 500mA. The bunch feedback system was very effective to suppress the instability. We also made an experiment on the fast ion instability with interesting results.

1 PURPOSE OF THE EXPERIMENT

The KEKB is an asymmetric electron-positron collider aiming at the study of the B meson physics and is now under construction at KEK. Main design parameters of the KEKB are listed in Table1.

	HER	LER
Beam energy	8.0GeV	3.5GeV
Luminosity	$1 \times 10^{34} cm^{-2} sec^{-1}$	
Beta functions at IP β_x^*/β_y^*	0.33/0.01m	
Tune shifts ξ_x/ξ_y	0.039/0.052	
Beam current	1.1A	2.6A

Table 1: Main design parameters of the KEKB

As is seen in the table, one of the most critical issues for realizing its design performance is accumulation of these unusually high beam currents against several obstacles.

One of the major beam current limitations will possibly come from coupled bunch instabilities arising from the fundamental mode and the higher order modes of acceleration cavities and some other sources such as resistive walls. To overcome the coupled bunch instabilities from RF cavities, we have developed two new types of RF cavity systems. One of these is a normal conducting cavity called ARES(Accelerator Resonantly coupled with Energy Storage) and the other is a specially designed superconducting damped cavity. We have also developed a bunch-by-bunch beam feedback system to suppress remaining instabilities.

The main purpose of the present experiment is to investigate whether these RF systems and the beam feedback system do work well under a high beam current. In the beam test conducted at the AR, we could prepare the beam current of 573mA at maximum.

In parallel with these beam tests, we also carried out machine studies on the fast ion instability and other coupled bunch instabilities, which resulted in some interesting information.

2 EXPERIMENTAL SETUP

2.1 AR

The AR was designed and had been employed for the injector of the TRISTAN Main Ring. When the TRISTAN project was terminated in 1995, the main role of the AR was switched to a SOR machine. Main machine parameters are listed in Table 2, including beam parameters used in the experiments. A 2.5GeV linac is used for the injector of the AR. Almost all present experiment was done at this injection energy, although usual SOR operation is done at 6.5GeV.

Particles	electrons
Circumference C	377m
RF frequency f_{RF}	508.58MHz
Harmonic number h	640
Beam energy E_b	2.5GeV
Beam current I_b	573mA(max)
Tune ν_x/ν_y	10.160/10.228
Momentum compaction α	0.0129
Natural chromaticity ξ_{x0}/ξ_{y0}	-14.5/-13.7
Chromaticity corrected ξ_x/ξ_y	~7/7
Radiation loss/turn U_0	0.1458 MeV
RF voltage V_c	0.6~2.5 MV
Synchrotron tune ν_s	0.018~0.036
Natural bunch length σ_l	2.0~0.94 cm
Energy spread $\Delta E/E$	4.40×10^{-4}
Damping time τ_e/τ_β	21.6/43.1 msec
Natural emittance ε_{x0}	43.6 nm

Table 2: Main machine parameters of the AR

The AR has two RF sections in the east and west long straight sections. Originally 4 units of 9-cell RF cavities called APS (Alternating Periodic Structure) were installed in each RF section. In the experiment, these APS type cavities were removed temporarily and the cavities for beam test were installed. The bunch-by-bunch feedback system was installed in the south long straight section.

2.2 ARES

The ARES is composed of three cavities; i.e. an accelerating cavity, a coupling cavity and a storage cavity. The storage cavity is intended to store large energy so that we can decrease the effective R/Q value of the cavity system and mitigate the coupled bunch instability arising from the fundamental mode. We have prepared two different types of the ARES for the beam test. They adopt different schemes for HOM damping of the accelerating cavities. For the first

0-7803-4376-X/98/$10.00 © 1998 IEEE

type of the ARES (ARES95), we adopted a chokemode-type accelerating cavity. The second type of the ARES (ARES96) is equipped with four rectangular waveguides and grooved beam pipes. In addition to these, an accelerating cavity of the ARES95 alone, which we call ARES-A, was installed in the east RF section in order to provide necessary RF voltage.

2.3 SCC

For a superconducting cavity (SCC) of the KEKB, we adopted single-cell structure, since it can reduce the number of HOMs and also minimize the coupler power. For the purpose of HOM damping, beam pipes with large diameters are attached on both sides of the single cell cavity. All HOMs are extracted to the beam pipes and absorbed by ferrite absorbers attached on the inner surface of the pipes. As for an input coupler, we adopted a coaxial antenna type coupler, which is the same type as was used for the TRISTAN Main Ring.

2.4 Bunch-by-bunch Feedback System

Prototypes of both transverse and longitudinal feedback systems were tested in the experiment. The transverse system consists of button electrodes for signal pickup, an analog signal processing system including a long cable delay, two kinds of power amplifiers which cover different frequency regions and stripline electrodes used for kickers. The longitudinal system is composed of button electrodes for signal pickup, a digital signal processing system including a 2-tap FIR filter, power amplifiers and a four cells of series-drift-tube type kicker which is just the same as used in ALS.

3 MACHINE OPERATION

3.1 Schedule

The experiment was done in two periods except some preliminary beam experiments. The first experiment was carried out during the period from July 1st to July 22nd in 1996. In this experiment, we only tested ARES-A and a full system of the superconducting cavity. As for the feedback system, only the transverse feedback in the horizontal direction was tested.

The second experiment was done during the period from October 17-th to December 2nd. In this experiment, two sets of full-set ARES (ARES95 and ARES96) were installed and examined with the beam. In this report, we mainly describe results of the second experiment and mention briefly the first experiment when necessary.

The study time of the second experiment consists of about 7 weeks. For the first 4 weeks of the study, we operated the ARES96 in the west RF section and ARES-A in the east. And for the next two weeks, all normal conducting cavities in the ring were detuned and SCC was operated and studied. For the last week of the study, we operated SCC and the ARES95. In Table 3, we summarize study or operation items and the number of shifts consumed for each item. Here, we mean 8 hours by 'shift'.

Study or operation item	# of shifts
ARES96	16.5
ARES95	4
SCC	20
Feedback	9.5
Fast ion instability	7.5
Multibunch instability	4.5
Other studies	1
SCC warmup	14
ARES95 aging	16.5
Machine tuning	4
Trouble	13.5
Gas desorption from vacuum chamber	19.5
Linac study and maintenance	26

Table 3: The operation statistics in the second experiment

3.2 Preparation of High Current Beam

A crucial mission to the beam operation was to accumulate as high beam current as possible. In the following subsections, we describe experiences on problems which we encountered in the course of the beam operation.

3.2.1 Beam lifetime

Prior to the experiment, we installed lots of devices for the beam test in the ring. Owing to this, vacuum pressure of the ring was rather bad particularly at the beginning of the experiment. In this situation, the beam lifetime which is determined by the collision of the beam with residual gas was very short and the beam current was limited by the balance between the particle loss rate due to the beam life and the injection rate.

To improve this situation, we had to rely on the photo-desorption process of the vacuum chamber induced by synchrotron radiation. For this purpose, we merely circulated the beam without any other studies. The number of shifts used for gas desorption amounted to 19.5 in total. Most of these were concentrated in the beginning of the experiment. The effort to improve vacuum pressure continued until the middle of the experiment when beam lifetime did not limit the beam current anymore.

3.2.2 Coupled bunch instability

In the beam test, we encountered unexpectedly strong coupled bunch instability. Strength of the instability depended on the beam filling scheme. In the experiment, we tried three different kinds of filling schemes, i.e. (1) bunch train scheme, (2) equally spaced multibunch scheme and (3) 4×4 filling scheme.

In the bunch train filling scheme, we tried to inject a beam with a bunch spacing of 2nsec. This bunch spacing is minimum with our RF frequency of 508MHz. We tried three cases for the bunch current; i.e. 1mA/bunch,

2mA/bunch and 4mA/bunch. When we did not use the beam feedback system, the maximum beam current was around 40mA in the case of 2mA/bunch, for example. However, by using the transverse feedback system the total beam current was increased to 320mA. Both the horizontal and vertical feedback were needed to store high current.

The equally spaced multibunch filling scheme was mainly used for the study on the coupled bunch instability itself. Results of the study are summarized briefly in the next section. Also in this mode, large beam current could not be stored without the feedback system.

The bunch train injection and the equally spaced multibunch mode were needed for some study items, such as the study on the fast ion instability or the study on the coupled bunch instability itself. However, other studies required as a high average beam current as possible. To meet this requirement, the optimum beam injection condition has been searched. Through trial and error, we found that we can store more than 500mA with so-called 4×4 injection scheme. In this scheme, we inject four bunch trains which are equally spaced. Each bunch train consists of four bunches and then the total number of bunches in the ring is 16. The bunch spacing in the bunch train is 40nsec which means 20 RF buckets. In addition to this injection scheme, we used relatively high values for corrected chromaticities of 7 both for ξ_x and ξ_y so that we can rely on the head-tail damping.

3.2.3 Heat-up of hardware components

The AR was not designed for a high beam current machine. We paid very close attention to heat-up of hardware components. Particular attentions were paid to the bellows, gate valves and ceramic chambers for pulse magnets or beam current monitors. Temperature sensors were attached on all of these components and temperature was monitored in realtime and recorded with a logging database system together with values of vacuum pressure all around the ring. In the first experiment, we observed conspicuous temperature rise for some ceramic chambers and one of these induced vacuum leakage just before the end of the experiment. Before the second experiment, these were replaced with spares. In the second experiment, the components listed above did not give us any troubles. However, we were troubled with heat-up of the stripline electrodes which were used for beam feedback system in the usual operation and were not used in the experiment. Owing to this heat-up, one of the electrode was deformed to block off the beam motion. We removed all relevant electrodes. Based on the bench test after the beam experiment, we guess that heat-up was triggered by radiation damage of cables which connected the electrodes and dummy loads for power attenuation[1].

4 RESULTS

Results of the experiment for each study item are reported in detail elsewhere[2][3][4][5][6][7] [8][9]. In this report, a very brief summary is given below.

4.1 ARES

The two ARES systems were tested independently to each other; when one ARES was operated, the other ARES was detuned. Most of the study was concentrated on the ARES96, which was considered to be adopted as the normal conducting cavity for KEKB. The ARES96 was operated for about 4 weeks and the ARES95 for 2 days. In order to provide necessary voltage, ARES-A or SCC was also operated together with the ARES.

4.1.1 High power and high current operation

Main RF design parameters for the ARES in KEKB-LER are: 0.5 MV of accelerating voltage which corresponds to a wall dissipation of 155kW, and 350kW of input power with full design current. Prior to the beam experiment both ARESs were successfully tested above 200 kW of the wall dissipation. In the beam test, a beam current of 500mA was stably stored by either of the two ARES cavities operating at 0.5MV together with SCC or ARES-A.

Two input couplers with a disk-type ceramic window were broken at about 70kW just before the beam test. After replaced with a spare, we conditioned it more carefully by having harder interlocks and keeping better vacuum pressure. This coupler was successfully operated up to 200kW during the beam experiment. In a bench test performed after the beam experiment, it was shown that this type of coupler works well with an input power of 430kW.

4.1.2 Fundamental mode behavior under heavy beam loading

Since the ARES is a highly original scheme, its basic characteristics of the fundamental mode with heavy beam loading was carefully studied. We observed behavior of the ARES system with changing beam current, beam fill pattern, relative phase between the ARES and another cavity (ARES-A or SCC) or a voltage ratio of the two cavities. Observed behavior was well reproduced by calculations based on a coupled-resonator model. In particular, following two points are important. First, the movement of the tuners at the accelerating and storage cavities under beam loading was in good agreement with a calculation. It indicates that the frequency detuning of the fundamental mode is reduced as was expected. Second, we observed transient behavior of the power extracted from the damper at the coupling cavity which damps parasitic 0 and pi modes associated with the fundamental mode. The measured responses to a single bunch beam, an equally-spaced beam, and an equally-spaced beam with an ion-clearing gap were pretty well reproduced by simulations. Thus the principles of the ARES theory were experimentally confirmed.

4.1.3 HOM damping and absorbers

The maximum power absorbed by the HOM absorbers was about 6.6kW per cavity for the ARES95 and about 6.4kW

for the ARES96. So far as these power is concerned, there was no problem in HOM power absorption.

The effect of HOMs on the beam was studied by scanning the movable tuners at the accelerating and storage cavities of the detuned ARES with a 100mA single bunch beam. During the tuner scans, there was no indication that the HOMs affected the beam motion. In the other studies during the experiment, we did not see any indication that the HOMs are responsible for the beam instability.

4.1.4 Long-term stability

The ARES96 was operated for about 4 weeks. During this term, we consumed lots of shifts for gas desorption of the vacuum chambers. In some cases, we continuously held overnight a high beam current more than 400mA. Even in such a relatively tough condition, the ARES did work very stably.

4.2 SCC

The SCC was operated for one week in March, two weeks in July and two weeks in November in 1996. Most of the time it was operated at 1.0 - 2.5MV and all other cavities were detuned except for the tuner scan study.

4.2.1 High current and high field operation

The results of the beam tests with the SCC exceeded the world records set by a CESR-B SC cavity tested in the CESR ring as follows. The maximum beam current of 573mA was stored by our cavity operating at 1.2MV. A high current of 350mA was also stored at 2.5MV, which is much higher than the design voltage of 1.5MV for KEKB-HER. The current limitations were not by cavity performances, but by other things such as saturation due to a balance between the beam life time and the injection rate (the case of 1.2MV), or heat-up of ring components (the case of 2.5 MV). The maximum RF power transferred to beam was 160kW with an input power of 270kW. Furthermore, at a bench test performed prior to the beam test, an input coupler was successfully tested up to 850kW.

4.2.2 HOM damping and absorbers

The maximum HOM power absorbed by the ferrite absorbers was 4.2kW. We experienced no degradation of performance of the HOM absorbers during the experiment. The loss factor estimated from the absorbed power is consistent with a calculation at a bunch length of 1.5cm and longer.

Tuner scan was done at the beam current more than 400mA. We could not see any effects of the HOMs on the beam motion. In the tuner scan, we surveyed a frequency range of about 400kHz for the fundamental mode.

4.2.3 Direct RF feedback

The SCC control system was equipped with a direct RF feedback loop. We observed that it was very effective to stabilize the cavity control loops. When we stored 500mA without the direct RF feedback, there was a strong 0-mode coherent synchrotron oscillation. By applying the direct RF feedback, however, the oscillation was suppressed by 10dB and the beam current of 573mA could be stored stably. It mitigated the stability condition for the static Robinson phase instability.

4.2.4 Long-term stability

One critical issue is a trip, which is a discharge caused by condensed gas on cold surface of the SC cavity and the input coupler region. In the first beam test (July), the SCC could not be operated stably due to frequent trips. At that time vacuum condition of the AR was too bad, since we had opened a large part of the ring to install hardware components to be tested. Prior to the second experiment, we took two measures for this; i.e. (1) We increased the number of vacuum pumps from 2 ion pumps to 5 NEG plus 1 ion pump on each side of the SCC. (2) We installed an equipment to supply a DC bias between the inner and outer conductor of the coaxial-type input coupler. In addition to these, we warmed up the SCC to room temperature after the 4 week operation of the ARES96 and before the study of the SCC in order to degas the condensed gas. As things turned out, the frequency of the trips drastically decreased even without the DC bias and stable operation continued for two weeks during the second experiment. We guess that the improvement of vacuum pressure contributed to this. It is estimated that the gas flow rate to the cavity from the ring was reduced by one order by strengthening the vacuum pump power. Then, we could not investigate the effect of the DC bias.

4.3 Beam Feedback System

In the bunch train filling scheme, the transverse feedback was very effective, as is briefly mentioned before. Table 4 shows a summary of the maximum number of bunches stored in this mode depending on the feedback status and the bunch current. H (V) in the table designates the horizontal (vertical) feedback. The bunch spacing was 2nsec for these data.

Bunch current	H:off V:off	H:on V:off	H:off V:on	H:on V:on
1mA	18	20	-	>300
2mA	20	70	20	>170
4mA	25	25	60	>100

Table 4: Maximum number of bunches stored in the bunch train filling scheme.

In the case of 4mA/bunch, we could store 376mA at maximum, while we could not store 100mA without the feedback. The feedback system worked well with this short bunch spacing of 2nsec as well as with longer bunch distances. Damping times of the feedback were measured by employing the memory function of the two-tap FIR filter complex. Results were less than 1msec for the horizontal plane and about 2msec for the vertical direction at the

bunch current of 2mA, which are consistent with expected values from a rough calculation.

On the other hand, we observed a strong coupled bunch motion also in the longitudinal direction. The longitudinal feedback system was effective to suppress the instability, although the feedback gain was not sufficient in some cases. However, the longitudinal coupled bunch instability was not responsible for the beam current limitation. A possible explanation for this longitudinal motion is that it originates from the bellows which do not have an inner shield. There exist about 130 such bellows in the AR.

4.4 Multibunch instability

To investigate the coupled bunch instability, we tried the all RF bucket filling scheme. In this scheme, we filled all of 640 RF buckets with the beam by injecting beam at a very low injection rate, typically in units of 20μA/bunch. This measurement was mainly intended to search high Q modes responsible for the coupled bunch instability. The total beam current was limited at around 20mA with this filling mode. However, no sharp betatron or synchrotron side band was observed at the maximum beam current. What we observed instead were vertical betatron side bands which were broadly distributed in a range of $\pm$20MHz around $n \times f_{RF}$, where n is an integer and f_{RF} the RF frequency. This indicates that the phenomena are related to the ion trapping.

To focus on the ion trapping effect, we made a further study with a symmetrical 64 bunch mode for the sake of the time saving. In this study, we used the transverse feedback system to hold the beam against the instability. We observed what happens when the feedback is turned off. By using the two-tap FIR filter complex again, the transverse positions of every bunch were recorded turn-by-turn for 1640 turns. The data taken was processed by FFT to see the beam spectrum and its time development. We found that the m=12 mode is most unstable at the total beam current of 80mA and the m=13 mode at 110mA, although some broadly distributed modes were excited. These results are qualitatively well reproduced by a calculation based on the 2-beam model. We guess that the beam current limitation in the equally spaced multibunch filling scheme comes from the ion trapping effect from these observations.

The current limitation in the bunch train mode, however, can not be explained by the conventional ion trapping effect, since most of the RF buckets are left unoccupied by the beam and the ions should be cleared during this long gap. A calculation shows that the fastest growth of the coupled bunch instability comes from the resistive walls and its growth time is around 7msec at 500mA if cancellation does not work. However, this growth rate is not enough to explain the maximum current shown in Table 4. It was observed that the beam loss due to the instability was coincident with the beam injection timing. This indicates that the transient effect of the coupled bunch instability should be taken into account. Further study is needed to understand the origin of this current limitation.

4.5 Fast ion instability

In the study, a bunch train of 100 bunches with the 2nsec spacing was stored, which means that only about successive 1/6 RF buckets were filled with electrons. Although we studied two cases for the total beam current of 115mA and 170mA, the two cases gave essentially the same result. We observed that the vertical coupled bunch oscillation was enhanced by introducing a nitrogen gas into the ring. This indicates that the phenomena are ion-related. The oscillation amplitude increased along the bunch train from the head to tail of the train. On the other hand, the oscillation phase decreased along the train. The growth time of the instability was shorter than several msec. These results can be interpreted as the fast ion instability. The total (oscillation) phase shift from the head to tail of the train was about 3 radians, which is consistent with a calculation based on the linear theory within factor 3. Further simulation studies based on more realistic model have been in progress.

5 FUTURE PROSPECTS

The test results encourage us to use the ARES in LER and HER, and the SC cavities in HER by keeping good vacuum environment. In FY1997 we started mass-production of the ARES and the SC cavities.

6 ACKNOWLEDGEMENTS

The authors would like to give thanks to each member of the team for the AR high current experiment. They also thank Profs. S. Kurokawa and Y. Yamazaki for their continuous encouragement and efforts to arrange the experiment. The experiment has been supported also by the KEKB accelerator group.

7 REFERENCES

[1] T. Ieiri: private communications.

[2] N. Akasaka et al.:'Fundamental Mode Characteristics of ARES Cavity under Beam Environment', in these proceedings.

[3] T. Kageyama et al.:'Development of high-power ARES cavities', in these proceedings.

[4] Kobayashi et al.:'HOM Characteristics of the ARES Cavity', in these proceedings.

[5] T. Furuya et al.:'Beam Test of a Superconducting Damped Cavity for KEKB', in these proceedings.

[6] T. Tajima et al.:'Beam Test Results on HOM Absorber of Superconducting Cavity for KEKB', in these proceedings.

[7] M. Tobiyama and E. Kikutani: 'Study of bunch by bunch feedback system in TRISTAN-AR', in these proceedings.

[8] S. Matsumoto et al.:'Experimental study of the ion trapping phenomenon in TRISTAN-AR', in these proceedings.

[9] H. Fukuma et al.:'Experimental Observations of the Ion-related Coupled Bunch Instability in a Bunch Train in TRISTAN AR', in these proceedings.

EXPERIMENTAL STUDY OF THE ION TRAPPING PHENOMENON IN TRISTAN-AR

S. Matsumoto, H. Fukuma, K. Ohmi, M. Tobiyama, E. Kikutani, M. Suetake, K. Satoh, Y. Funakoshi
High Energy Accelerator Research Organization (KEK), Oho 1-1, Tsukuba, Ibaraki, Japan

Abstract

The betatron oscillation of the electron beam in TRISTAN AR was observed in multi-bunch operation in which every a few tens of rf buckets are selected to be filled with beam. Transverse coupled bunch instability was observed and its growth time was measured by utilizing the feedback system. The betatron sideband spectrum were distorted when most of the selected buckets were filled. The conjecture of ion trapping explains the facts that we observed.

1 INTRODUCTION

During the high current operation study in TRISTAN-AR[1], we tried to store beam with full rf buckets (640 bunches) a few times. We found that we could store only $\sim$ 20mA beam current or less, unless we use orbit feedback. At that moment, we observed the vertical beam oscillation whose frequency was $1-\delta\nu_y$, where $\delta\nu_y$ is the fractional part of the vertical tune (~ 0.23). Although this limitation was easily overcame by the feedback, however, we were interested in what gives it. This is the motivation of our study. We suspected this current limitation was coming from the coupled-bunch instability caused by the trapped ions. We identified the unstable modes and measured their growth time. We observed the betatron sideband spectrum to look for a signal of trapped ions on it. In this paper, we will report on these observations and discuss the results based on the conjecture of ion trapping.

The main machine parameters of AR, which are used in this paper, are listed below. The average vacuum pressure was a few $\times 10^{-7}$ Pa.

AR parameters		
Beam energy	$m_e c^2\gamma$	2.5 GeV
RF frequency	$\omega_{\rm rf}/2\pi$	508.58 MHz
Harmonic number	h	640
Revolution frequency	$\omega_{\rm rev}/2\pi$	794.66 kHz
Circumference	C	377.26 m
Horizontal emittance	ϵ_x	43.6 nm
Horizontal tune	ν_x	10.160
Vertical tune	ν_y	10.228

For simplicity, we use the averaged beam sizes which are defined as $\sigma_x = \sqrt{\epsilon_x \bar{\beta}_x} = 510\mu$m, where $\bar{\beta}_x = C/2\pi\nu_x$ is the constant called the *typical value* of the horizontal betatron function. We assume 6% xy coupling and we get $\sigma_y = 125\mu$m. In the followings of this paper, the beam sizes read these constant values.

2 EXPERIMENTS AND RESULTS

In our study, we operated the machine with 64 bunches (equally spaced, every 10 rf buckets) instead of with 640 bunches (to save time for the beam injection). According to the argument of the stability of the linearized motion of ions near the beam orbit, 64-bunch beam can trap all kinds of ions (singly ionized). Suppose the beam consists of n_b identical bunches, which are equally separated from each other (by C/n_b), and each contains N_e electrons. The bunch has the Gaussian distribution both in x and y whose r.m.s. are σ_x and σ_y respectively. The stability criterion of the ion (vertical) motion is

$$\frac{4\pi N_e r_p c}{\omega_{\rm rev} A}\frac{1}{\sigma_y(\sigma_x+\sigma_y)}\frac{1}{n_b} \le 4, \qquad (1)$$

where r_p is the classical proton radius. By using the parameters in the table, the formula is reduced to $I(\mathrm{mA}) \le 0.035\ A\ n_b^2$ where I is the total stored beam current. If $n_b = 64$, all kinds of ions are trapped if $I \le 140$ mA. Since the beam current was at most $I \sim 100$ mA in our study, $n_b = 64$ is enough.

We measured the growth time of the unstable mode by utilizing the transverse feedback system in AR[2]. By the trigger of the feedback off, the data taking was started to record the positions of every bunch turn to turn (for 1640 turns). The stored data was processed by FFT to see the spectrum and its time dependence. See Fig. 1. In this case, the initial beam current was 80 mA. We can see the lower sideband at the frequency $2-\delta\nu_y$ grows up. The growth looks linear rather than exponential. When we start with 110 mA, we found the sideband at $3-\delta\nu_y$ grew up linearly. The summary of our observations is

- $m = 12$ mode is unstable at 80 mA,
- $m = 13$ mode is unstable at 110 mA,
- linear growth.

One possible explanation of this coupled-bunch instability is the resistive wall instability. We estimated its growth time to be a few tens msec or less but this is too slow compared with our observation in Fig. 1. If resistive wall instability occurs, the maximum growth always appears in $m = 11$ mode and this means the sideband at $1-\delta\nu_y$ has always dominant growth. However, this was not true in our observation. The impedance of the rf cavities may also be another source of the instability. However, the impedance calculation shows the rf cavities give very small growth even when we operate the machine with its maximum beam current ($\sim$ 500 mA).

0-7803-4376-X/98/$10.00 © 1998 IEEE

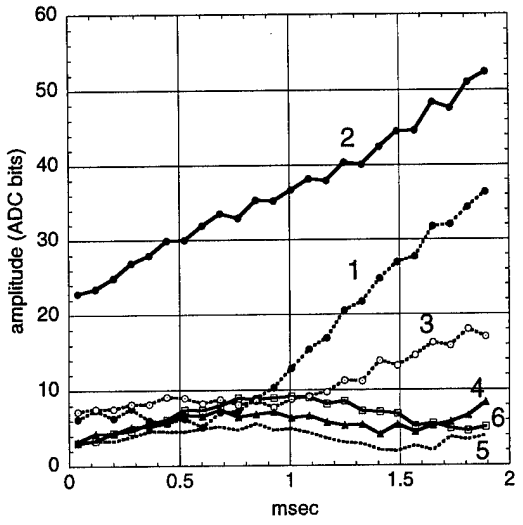


Figure 1: A result of the measurement of growth time. The growth of the betatron lower sidebands, $n - \delta\nu_y$ are plotted for the case $n = 1, 2, \ldots, 6$. We did not find a significant growth at the lower sidebands of $n \geq 4$ nor at all of the upper sidebands. Ordinate is the amplitude of the betatron sidebands and abscissa is elapsed time after the feedback being off. We see $n = 1$ and $n = 3$ sidebands also grow.

We now consider whether the observed mode instability can be induced by ion tapping or not. If the ions are produced and trapped by the stored beam, the transverse motion of the ions and the betatron motion of the beam are coupled. The 2-beam model[3] is the simplest model to describe this coupled oscillating system. In this model, both the beam and ions are uniformly distributed along the ring (they have constant line densities) and their transverse distributions are Gaussian of same dimensions both in x and y (σ_x and σ_y). If the oscillation is small, the transverse oscillation of the ions is $\propto \exp(i\Omega t)$ while the beam oscillates $\propto \exp\{i\,(m\theta - \Omega t)\}$, where m is the transverse mode index of the multiple bunches and $0 < \theta < 2\pi$ is the azimuthal coordinate along the ring. The frequency Ω is the solution to the mode equation[3]

$$\left(\Omega^2 - \omega_i^2\right)\left\{(\Omega - m\omega_{\rm rev})^2 - \nu_y^2\omega_{\rm rev}^2 - \omega_e^2\right\} = \omega_e^2\omega_i^2. \quad (2)$$

The parameters in Eq. (2) are $\omega_i^2 = \lambda_e r_p c^2/A\sigma_y(\sigma_x + \sigma_y)$ and $\omega_e^2 = \lambda_i r_e c^2/\gamma\sigma_y(\sigma_x + \sigma_y)$, where r_e is the classical electron radius and λ_e and λ_i are the line density of the electrons and of the ions along the ring respectively. The former, λ_e, reads $N_e n_b/C$ in our case. We consider only CO^+ since it is expected to be dominant among the ions in the ring.

Eq. (2) has four solutions and two of them can be complex, if $m \geq 11$. The complex solutions imply the system is unstable (2-beam instability). If this occurs, the oscillation grows exponentially. In Fig. 2, the frequency spectra of beam-ion system in the cases of $m = 11$, 12 and 13 are shown. It is notable that our observation of the unstable modes basically agrees with the model predictions on what mode is unstable and on where (how much beam current) it occurs. Note that the model predicts $m = 11$ mode is unstable just above 10 mA. This instability might cause the current limitation that we observed in 640-bunch operation. The oscillation at the sideband $1 - \delta\nu_y$ will grow and this also meets our observation.

However, the growth rate of the unstable modes predicted by the model is the order of μsec, which is extremely fast compared with our observations. Of course, the growth rate by the model is false, because we could stabilize the beam by the orbit feedback, which gives the damping rate about 1 msec. A weak-strong simulation (in which ions are treated by macroparticles while the beam is rigid) on the 2-beam instability indicates that actual growth rate becomes smaller due to the ions decoherence by the nonlinear force by the beam[4]. Since ion decoherence is not included in the 2-beam model and this should be the one reason the model disagrees with our observation of the growth time.

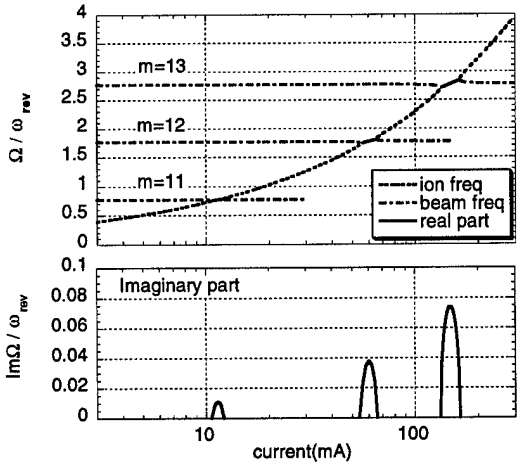


Figure 2: 2-beam instability by CO^+ ions. We assume $\lambda_i/\lambda_e = 1 \times 10^{-3}$. If the solution is complex, both its real and imaginary part are shown. The mode $m = 11$ is unstable in the beam current range from 10 to 12 mA. Similarly, the model predicts $m = 12$ and $m = 13$ modes are unstable from 56 to 64 mA and from 134 to 162 mA respectively.

Next we observed the signal from a button pickup with a network analyzer to see the tune shift due to the ion trapping. We observed the spectrum of a sideband during the injection process. The beam was injected into the 64 buckets sequentially. In Fig. 3, we show three examples of spectrum at $4 - \delta\nu_y$. Compare the spectrum at 20 buckets being filled (top picture) and that at 50 buckets (middle picture). The spectrum became fater and fatter (but the frequency of the peak was almost kept) and finally the spectrum was suddenly distorted like the bottom picture just before the injection was over (at around 60 buckets were filled). We see that the peak of the spectrum is at 2.9856 MHz in the top picture while it is at 2.9843 MHz in the bottom. The

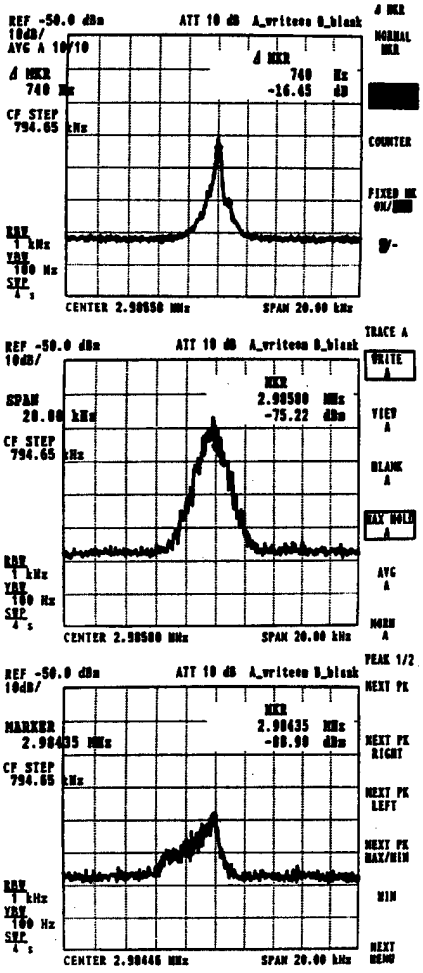


Figure 3: The pictures of the display of network analyzer to observe the spectrum of the betatron sideband at $4 - \nu_y$. Each picture shows the spectrum observed when 20 buckets(Top), 50 buckets(middle), or 64 buckets(bottom) were filled. The span of each picture is 20 kHz. The bunch current was 0.65 mA (42 mA/64 bunches).

peak was shifted by 1.3 kHz by this distortion.

We performed same observations for 32-bunch,16-bunch and 4-bunch operation mode, keeping the total beam current. In the 32-bunch mode (bunch current was $\sim$ 1.3 mA), the spectrum was again changed as in the 64-bunch mode. It is implicative that this occurred when about 30 buckets were filled. In the other operation modes, we didn't see the change. This kind of distorted spectrum was observed in other machine[5]. It is natural to understand this spectrum change is induced by the additional focusing by the trapped ions. We tried to reproduce the "trapped signal", the spectrum like the bottom picture in Fig. 3, by the weak-strong simulation. The result is shown in Fig. 4. A spectrum which looks similar to the trapped signal has been obtained.

Finally, let us estimate λ_i from tune shift by the formula

$$\delta\nu_y \approx \frac{r_e}{\gamma}\frac{\bar{\beta}_y C}{4\pi}\frac{1}{\sigma_y(\sigma_x+\sigma_y)}\lambda_i, \qquad (3)$$

where $\bar{\beta}_y$ is the typical betatron function ($\sim$ 6 m). By Eq. (3), we find the total number of ions in the ring is $\lambda_i C \sim 3.3\times10^8$ if the tune shift is 1.3 kHz. The number of beam electrons is $7.9 \times 10^9\, I(\mathrm{mA})$. In Fig. 3, $I = 42$ mA and we find the ratio λ_i/λ_e is 1×10^{-3}.

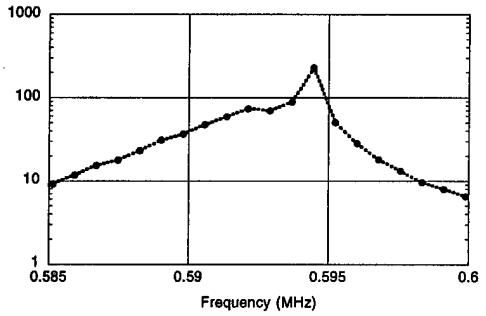


Figure 4: Weak-strong simulation result on the response (the amplitude of forced oscillation) of the beam. The beam is shaken at the frequency near $1 - \delta\nu_y$ sideband. The beam consists of 64 bunches and the beam current is 15 mA.

3 CONCLUSION

The facts we observed here suggest that the trapped ions do exist in the multi-bunch operation in AR. The 2-beam model is useful to understand the mechanism of the instability, however, the numerical simulation is necessary for clarifying the detailed mechanism, since the strong nonlinearity in the ion motion plays a role.

4 ACKNOWLEDGEMENTS

We are grateful to TRISTAN OPERATION GROUP for the support of this experiment.

5 REFERENCES

[1] Y. Funakoshi et al.: 'High beam current experiments for the KEKB conducted at TRISTAN', in these proceedings.

[2] M. Tobiyama and E. Kikutani, 'Study of Bunch by Bunch Feedback System in TRISTAN-AR', in these proceedings.

[3] E. Keil, B. Zotter, CERN-ISR-TH/71-58(1971); D. G. Koshkarev, P. R. Zenkevich, Particle Accelerators **3**, 1 (1972) .

[4] K. Ohmi, KEK Preprint 96-160, to be appeared in Phys. Rev. E **55**.

[5] D. Sagan and A. Temnykh, Nucl. Instr. Meth. A 344 (1994)459.

EXPERIENCE WITH BUNCH TRAINS IN LEP

W. Herr, B. Goddard, E. Keil, M. Lamont, M. Meddahi and E. Peschardt
CERN, Geneva, Switzerland

Abstract

Since 1995 LEP is operated with the new bunch train scheme. This scheme allows head-on collisions of four trains of up to four bunches within a train. The first experience with this new scheme and the problems encountered during the commissioning and the operation are reviewed and discussed. The performance of LEP and the results from dedicated experiments are shown and compared with expectations. The modifications and improvements to allow a successful operation at LEP2 energies are discussed and the performance at energies above 80 GeV is presented.

1 INTRODUCTION

The bunch train scheme for LEP was developed in 1994 [1, 2, 3], and then commissioned operationally in 1995 [4, 5, 6]. The two motivating factors for the scheme were:

- To increase the luminosity at Z° energies by increasing the number of bunches
- To raise the maximum current per bunch in 8 bunches per beam for operation at W energies.

The 8 bunch pretzel scheme [7, 8] was limited, at injection energy, to bunch currents significantly less than the expected 1mA. For operation at 45 GeV this limitation was not a problem since the beam-beam effect limits the bunch current to around 350 μA, which is easily attainable at injection energy with pretzel. However at higher energies, it is desirable to collide much larger intensities and this limitation becomes a problem. It follows that a new scheme should be flexible enough to permit an optimization of the number of bunches and bunch intensity, depending on the constraints and requirements.

The plan was to operate LEP in 1995 with four equidistant trains of bunches in each beam. The number of bunches per train is determined by the maximum length of the train, limited by the separation scheme and experimental constraints [5]. Simultaneously, the scheme was optimized and modified for running at LEP2 energies where eight bunches per beam and higher intensities per bunch were envisaged.

2 CONFIGURATION IN 1995

The 1995 bunch train scheme in LEP used electrostatic separators to provide extended local separation bumps around the interaction points (IP) such that: a) trains of up to four bunches separated by 87 λ_{RF} could be accommodated; b) all bunches in the counter- rotating e^+ and e^- beams were separated at all encounters at injection energy and during the energy ramp; c) bunches in the counter-rotating e^+ and e^- beams were separated at all parasitic encounters at physics energy; d) collisions could take place between e^+ and e^- bunches at the four experimental IPs; e) a vertical 'vernier' bump could be superimposed at these points to allow adjustment of the collision for luminosity optimisation. In each such pit six separators are necessary, since the beams need to be brought into collision at the IP while remaining separated at the parasitic encounters, essentially creating a closed electrostatic 3 "corrector" bump on each side of the IP. The small closed vernier bump was superimposed using two of the separator pairs.

Each of the odd (non-experimental) pits was equipped with four electrostatic separators, to create an extended bunch train bump which separated all e^+ and e^- bunches [2, 6].

The direction of the separation bumps can be chosen freely but since some of the side effects of the bumps, (e.g. dispersion and orbit effects, see later section), can accumulate or cancel depending on the relative direction of the orbit distortion, the directions of the separation bumps were chosen to minimize these effects by a partial compensation.

3 SIDE EFFECTS AND BEAM DYNAMICS

3.1 Vertical dispersion

The vertical separation bumps induce a residual vertical dispersion proportional to the bump amplitude which must be kept as small as possible to avoid an increase of the vertical emittance or the excitation of synchro-betatron resonances in the RF cavities. An insufficient separation however, would lead to other effects, i.e. large beam-beam tune shifts and beam-beam induced orbit effects. This would result in low life-times and reduced luminosity. A compromise has to be found to meet all requirements simultaneously.

3.2 Effects from parasitic beam-beam interactions

Further insight into the side effects of the parasitic encounters can be gained by a first-order calculation, starting with the vertical orbits caused by the electrostatic separator bumps. The vertical orbit kick, $\Delta y'$, the horizontal and vertical beam-beam tune shifts, ξ_x and ξ_y, at a parasitic encounter are given by:

$$\Delta y' = -\frac{2Nr_e}{\gamma d} \qquad \xi_x = \frac{Nr_e\beta_x}{2\pi\gamma d^2} \qquad \xi_y = -\frac{Nr_e\beta_y}{2\pi\gamma d^2} \quad (1)$$

The separation between the beams at the parasitic encounter is d. It is assumed that the vertical r.m.s. beam ra-

0-7803-4376-X/98/$10.00 © 1998 IEEE

dius is much smaller than the separation at the parasitic encounter, $\sigma_y \ll d$; N is the intensity of the opposite bunch, r_e is the classical electron radius, and γ is the usual relativistic factor. Any vertical orbit kick $\Delta y'$ causes a vertical orbit distortion y and a vertical orbit slope y' at any observation point around LEP which are given by the standard equations for the closed orbit and its slope. The closed orbit position and slope of a bunch are obtained by adding the contributions of all parasitic encounters with the bunches of the counter-rotating beam.

In general, different bunches in different trains meet the bunches of the opposite beam at different parasitic encounters. Therefore, different bunches travel on different vertical orbits and have different vertical slopes around LEP. Hence, different vertical collision offsets δy and different slopes $\delta y'$ exist between any two bunches colliding at the head-on interaction points. From symmetry arguments it is evident that, for an ideal machine without imperfections and equal bunch populations, the first bunch of a train has an orbit offset of the same magnitude and opposite sign as the last bunch of the equivalent counter-rotating bunch train. Similar arguments hold for each bunch of a train, resulting in an asymmetric orbit for the bunches along a train. It is easy to remove the average vertical offset by vernier adjustments, but it is impossible to remove the spread in the vertical offset between the bunches. For trains of only two bunches the above mentioned symmetry allows a vernier adjustment to collide both bunches of a train head on, although not on the same orbit.

Not only at the interaction point the orbit of a bunch is changed, the separation at a parasitic encounter is also affected and such a change of separation is not taken into account in the perturbative approach. A self consistent treatment of the problem becomes necessary.

3.3 Self consistent calculation

The first-order calculation mentioned does not include the consequences of the beam-beam interaction at the parasitic encounters. These effects are included in a self consistent computation which is embedded in a computer program `train`[10]. It finds the individual closed orbits of all bunches, as well as their vertical dispersion, tunes and chromaticities. The understanding and evaluation of the side effects via the self consistent calculation was important in understanding some of the limitations of the scheme. The comparison is made for bunch trains of three bunches per train since most of the time LEP was operated with such trains and experimental data is available.

3.3.1 Self consistent orbits

Tab. 1 shows the results of calculations of the separation s_y at the collision point in μm for the three bunches, labelled a, b and c in a typical bunch train in the even-numbered pits. The vertical separation s_y is symmetrical between the leading and trailing bunches in a train as expected. The measurement of the vertical separation between bunches in a train is a by-product of the luminosity optimisation by vernier scans. Fig. 1 shows the results of a typical scan. The difference between the optimal position for families a, b and c gives a measure of the shape of the trains and the width of the scan a measure of the vertical beam size which is significantly larger than the separation between the bunches. A rather good agreement between the calculated and measured results was found [6].

Table 1: Self consistent results for the separation s_y in μm for the three bunches in a train. The bunch current is $I = 0.25$ mA, the beam energy is $E = 45.6$ GeV.

Bunch	IP2	IP4	IP6	IP8
a	1.42	-1.59	1.82	.15
b	.32	.07	.61	2.09
c	1.42	-1.59	1.82	.15

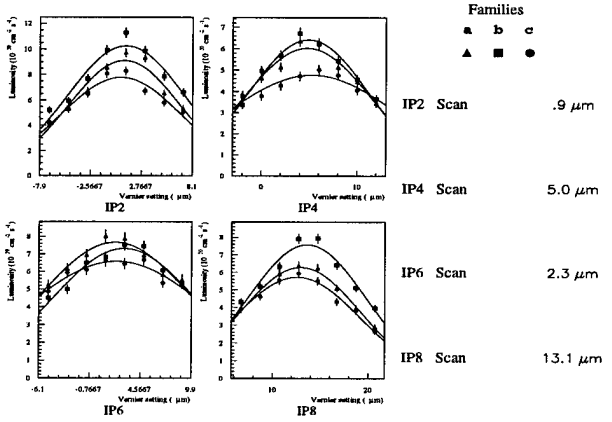


Figure 1: Vertical scans to optimize luminosity and to measure individual orbits

3.3.2 Tune and chromaticity splits

Similar differences between the bunches within a train exist for the tunes, the chromaticities and the dispersion. Typically one finds in the calculation splits up to 0.02 for the fractional part of the tune for bunch currents of 0.5 mA. The chromaticity spread can reach values up to $\Delta Q' \approx 1.0$. These calculations have been confirmed by measurements [6].

4 PERFORMANCE

4.1 Life time

In the original design it was foreseen to operate LEP with four bunches per train, i.e. each individual bunch having three parasitic encounters at each interaction region. The typical separation d at the three encounters in an even insertion are shown in Tab.2. Also shown are the calculated cor-

Table 2: Separation and normalized beam-beam tune shift for parasitic encounters

Encounter	Separation	ξ_x/ξ_y [10^{-3}]
1	10-12 mm	2.7/1.0
2	15-20 mm	0.3/1.5
3	5-7 mm	1.1/7.5

responding horizontal and vertical beam-beam tune shifts at 45.6 GeV and for 0.5 mA bunch current. It can be observed that the encounter farthest from the interaction point experiences a much larger vertical shift, caused by the significantly smaller separation [6]. During the running period when LEP was operated with four bunches per train, frequent life time problems were experienced for the bunches corresponding to this close encounter. As a consequence, it was decided to abandon the fourth bunch and continue the operation with three bunches per train, thus avoiding the encounter with the smallest separation. Furthermore, since the contribution of the 4th bunch to the spreads of the tunes and chromaticities is large, the overall spreads were also reduced. The machine was much easier to operate with these shorter trains and the life-time of all remaining bunches was acceptable [6].

4.2 Luminosity and beam-beam tune shift

When LEP was operated with three bunches per train, the luminosity was not fully up to the expectations and particularly the beam-beam tune shift achieved was lower than was hoped for. Values between 0.025 and 0.030 were the best found during the year. This should be compared with tune shifts of 0.03 to 0.04 regularly obtained with four bunches and the Pretzel scheme with 8 bunches, and with best values of around $\xi_y \approx 0.045$.

It was already demonstrated (Fig.1 and Tab.1) that with 3 bunches per train the bunches do not collide head on. It was believed that the lower beam-beam tune shift was caused by the offset collison. In a dedicated a run with only two bunches per train where all bunches can be collided head on, the beam-beam tune shift quickly reached values above 0.040 with a maximum at 0.045.

5 EXPERIENCE AT LEP2

5.1 Configuration in 1996

Unlike LEP running at 45.6 GeV, LEP2 is not beam-beam limited and it is advantageous to concentrate the available intensity into fewer bunches. While the aim at LEP1 was to increase the number of bunches the main issue at higher energies is to remove the intensity limits at injection and run with a smaller number of bunches. The original scheme was designed that it could operate with any number of bunches between one and the maximum of four per train and the bunch spacing was kept flexible to optimize it for the number of bunches, however fulfilling the constraints dictated by the hardware. For the first runs of LEP2 in 1996, no hardware modifications were necessary on the separation scheme but the bunch spacing was increased to minimize the residual beam-beam effects from unwanted parasitic beam-beam encounters [9]. The chosen spacing of 118 λ_{RF} is compatible with the existing longitudinal feedback system and has a minimum impact on the performance of the orbit measurement system.

5.2 Luminosity and intensity

In 1996 LEP was run at two energies: 80.5 and 86.0 GeV. During most of the year, the total current was limited to rather low values due to RF considerations and therefore the machine was operated with single bunch trains, i.e. four on four bunches. Furthermore, several low emittance lattices were tried [11] with varying success. However a few runs were made with trains of two bunches and the results were very promising. The beam-beam tune shift achieved was the same as for single bunches at equivalent bunch intensities and the resulting luminosity was as expected. The total current was always limited due to the commissioning of the large LEP2 RF system.

In a dedicated experiment [12] the maximum intensity at injection was studied for different RF configurations and no bunch train related problems were found up to intensities above 0.550 mA per bunch, where the intensity could not be further increased due to RF limitations. This is a very promising result for a good luminosity in future runs.

6 REFERENCES

[1] W. Herr; *Bunch trains without a crossing angle*; Proc. 4th workshop on LEP performance, (Chamonix 1994) CERN SL/94-06 (DI) (1994) 323.

[2] C. Bovet *et al.*, *Final report of the 1994 bunch train study group*; CERN SL/94-95 (AP) (1994).

[3] O.C. Brunner *et al.*, Proc. 1995 Part. Accel. Conf. (Dallas 1995) 514.

[4] P. Collier, B. Goddard and M. Lamont, CERN-SL/96-22 (OP), Proc. 5th Eur. Part. Accel. Conf. (Sitges 1996)

[5] C. Bovet *et al.*, *Report of the 1995 bunch train study group*; CERN SL/96-12 (AP) (1996).

[6] B. Goddard *et al.*; *Bunch trains for LEP*; Submitted to Part. Accelerators, CERN SL/97-02 (AP) (1997).

[7] C. Rubbia, Proc. 1st Eur. Part. Accel. Conf. (Rome 1988) 290.

[8] J.M. Jowett, W. Kalbreier and S. Myers, Proc. 2nd Eur. Part. Accel. Conf. (Nice 1990) 403.

[9] W. Herr; *Bunch trains at high energy*; Proc. 6th workshop on LEP performance, (Chamonix 1996) CERN SL/96-05 (DI) (1996) 125.

[10] C. Iselin, private communication.

[11] Y. Alexahin *et al.*, these proceedings.

[12] D. Boussard *et al.*, *More tests on Injection Intensities with Various RF Configurations*; CERN SL-MD Note 233 (1997).

LOW EMITTANCE LATTICES FOR LEP

Y. Alexahin*, P. Beloshitsky*, D. Brandt, W. Herr, J.M. Jowett, M. Meddahi, G. Roy, A. Verdier,
CERN, Geneva, Switzerland

Abstract

In 1997 LEP will enter its third phase and will be operated at energies well above 90 GeV. In order to reach the required luminosities at these higher energies, i.e., to reach the maximum beam-beam tune-shift parameter, an optics with a small horizontal emittance is desirable. Such a lattice must have a dynamic aperture sufficient to guarantee the beam life time. Several lattices with different phase advances per cell have been developed for this purpose and the reasons for these particular choices are explained. The relative merits of these different solutions as well as the experience gained both in dedicated experiments and in using these lattices in regular operation during 1996 are discussed.

1 INTRODUCTION

LEP was originally designed for cell phase advances, $\mu_{x,y}$ of 60° and 90°. At beam energy $E = 45$ GeV, a 90° optics allowed the machine to be operated at the beam-beam limit. Above 90 GeV, this would require larger bunch intensities than can be achieved at present. For flat beams of k_b equal bunches of N particles, the luminosity is

$$\mathcal{L} = \frac{N k_b f_0 \gamma \xi_y}{2 r_e \beta_y^*} \left(1 + \frac{\sigma_y^*}{\sigma_x^*}\right) \qquad (1)$$

where $\gamma = E/mc^2$, f_0 is the revolution frequency, r_e the classical electron radius and ξ_y the usual vertical beam-beam strength parameter. In the absence of horizontal blow-up effects, the RMS horizontal beam size is determined by the emittance, $\sigma_x^* = \sqrt{\beta_x^* \epsilon_x}$, while the vertical size σ_y^* is determined by beam-beam and other effects.

Since $\xi_y \propto N\beta_y^*/(E\sigma_x^*\sigma_y^*)$, a low emittance (high phase-advance) lattice or a lower value of β_x^* allows the beam-beam limit to be reached at high energy with lower intensity.

For flat beams, (1) shows that the luminosity depends only on ξ_y and β_y^*, the vertical beta-function at the interaction point. The luminosity is independent of $\xi_x \propto N\beta_x^*/E\sigma_x^{*2} = N/E\epsilon_x$. However, since ξ_x should itself not exceed a maximum value (presently $\xi_x \lesssim 0.03$ in LEP), it might be necessary to increase ϵ_x when N/E is large enough.

The minimum value, $\beta_y^* \simeq 5$ cm, is determined by the stability of the low beta quadrupoles which produce unmanageable orbit drifts if β_y^* is too small. Accordingly, in order to maximise ξ_y, the only free parameters are ϵ_x, β_x^* and σ_y^*. The vertical beam size σ_y^* is limited by our ability to correct the vertical closed orbit distortion, the betatron coupling and the vertical dispersion at the IPs. The minimum value of β_x^* is limited by the background due to the large value of β_x in QS1 and the correction of the non-linear horizontal chromaticity. Experience in LEP has shown that with $\epsilon_x = 46$ nm, a value of $\beta_x^* \simeq 2$ m produces an acceptable background. Thus, keeping the horizontal beam size σ_x constant in the second, horizontally focusing, quadrupole from the IP (QS1), we see that the minimum of β_x^* scales with ϵ_x, a further advantage of low emittance lattices. Furthermore, since the low beta insertions generate strong chromatic aberrations which have to be corrected by the arc sextupoles, the sextupoles should be arranged in pairs separated by an odd multiple of π. Horizontal phase advances of 90°, 108° and 135° have been considered.

2 SITUATION AT THE END OF 1995

At that time, just before the increase in beam energy from 'LEP1' to 'LEP2', both theoretical work and experimental observations had been accumulated for the three options mentioned above. It was generally agreed that tracking calculations of the dynamic aperture were the best available tools to evaluate the high energy optics. The dynamic aperture of LEP is ultimately limited by the radiative beta-synchrotron coupling instability (RBSC) [1]. However the derivatives of betatron tunes with amplitude are useful indicators [2] that some combination of resonance phenomena and RBSC may limit it sooner. For example, experiments with the $(135°, 60°)$ optics [3, 4] were difficult because of the large horizontal detuning $\partial Q_x/\partial W_x$[1] that rapidly moved the tune towards the integer.

Tracking calculations indicated that, above 90 GeV, the dynamic apertures of both the $(90°, 60°)$ and the $(108°, 60°)$ optics were insufficient, mainly because of the large cross-detuning term $\partial Q_y/\partial W_x$[4, 5]. Instead, a $(108°, 90°)$ optics (with lower $\partial Q_y/\partial W_x$) was recommended for high energy. All predictions of dynamic aperture, including those of larger dynamic aperture for a prototype $(108°, 90°)$ optics, had been tested experimentally [6].

On the other hand, the $(108°, 60°)$ optics had been fully commissioned in machine development and was ready for operation. Similar development for the $(108°, 90°)$ optics would have required a re-cabling of the sextupoles (into 2 instead of 3 SD families) incompatible with the operational $(90°, 60°)$ optics. For 1996, it was therefore decided to operate LEP with a $(108°, 60°)$ optics (at 80.5 and 86 GeV)

* Visitors from PPL JINR, Russia

[1] By convention, these derivatives are quoted with respect to the Courant-Snyder amplitude variables, $W_{x,y}$, equal to *twice* the canonical action variables.

0-7803-4376-X/98/$10.00 © 1998 IEEE

and to complete the development of the $(108°, 90°)$ optics for higher energies.

3 DETUNING WITH AMPLITUDE

The first derivatives of the tunes with respect to amplitude are presented in Table 1 for several LEP optics. Small values are generally better but it should be kept in mind that the tune-variations may become quite non-linear at amplitudes well within the dynamic aperture.

μ_x	μ_y	$\frac{\partial Q_x}{\partial W_x}$	$\frac{\partial Q_y}{\partial W_y}$	$\frac{\partial Q_x}{\partial W_y}$
60°	60°	−0.7	−1.9	−6.5
90°	90°	1.0	0.6	−14.2
90°	60°	1.8	18.7	−28.7
108°	60°	22.4	70.3	−78.7
108°	90°	25.1	16.7	−16.9
108°	36°	19.3	12.3	2.1
102°	90°	11.3	10.2	−16.2
135°	60°	−157.7	7.6	7.6

Table 1: First derivatives of the tunes with respect to amplitude at the closed orbit for various choices of the arc-cell phase advances. The units are $10^3 \mathrm{m}^{-1}$.

From this point of view, the $(60°, 60°)$ optics (used in LEP operation at 45.6 GeV from 1989–91) is an excellent candidate, except that its emittance is too large at high energy. At the other extreme, the very large (negative) $\partial Q_x/\partial W_x$ of the 135°/60° optics ruled it out for operation. Table 1 also shows that all 108° optics have a rather large horizontal detuning in common. With a typical working point $Q_x \simeq 102.25$, this can bring large-amplitude particles onto the imperfection-driven resonance $3Q_x = 307$. As already mentioned, both the $(90°, 60°)$ and the $(108°, 60°)$ optics have a large cross-term $\partial Q_y/\partial W_x$ which is mainly responsible for the insufficient aperture predicted at high energy. The $(90°, 90°)$ optics originally proposed for LEP2 remains a strong candidate. It was dropped from consideration in recent years because $\mu_y = 90°$ is unfavourable for polarization and its emittance is not so small as with $\mu_x = 108°$. Nevertheless calculations show that it has the largest dynamic aperture.

4 LIFETIME AND DYNAMIC APERTURE

As described in detail in previous papers [5, 6, 7], two methods are commonly used to measure the acceptance of LEP:

Kick method: A bunch is given a single kick whose amplitude is increased until about 50 % of the bunch population is lost. The corresponding amplitude is an estimate of the horizontal dynamic aperture and has been compatible with predictions from tracking in all cases studied [7].

Phase space inflation: The horizontal emittance of the beam is increased by reducing the RF frequency (and, consequently, the damping partition number, J_x) until the lifetime reaches a value of one hour. This provides an estimate of the maximum emittance with which the machine can be operated. *If the particle dynamics is essentially linear* (and weakly-damped), direct application of the elementary quantum lifetime formula can be used to estimate the dynamic aperture from this emittance.

Under such conditions, which amount in practice to the absence of strong resonances and "anomalous" non-gaussian beam tails, both methods agree quite well.

Such conditions *do not hold* in, e.g., the $(108°, 90°)$ optics at high energy where the motion is strongly non-linear because of resonances and strong radiation effects. With the kick method, resonances manifest themselves as a partial loss at a certain kick amplitude [5] (corresponding to the location of the high-order fixed points). In deterministic tracking (with "radiation damping" but no quantum fluctuations [1]) of imperfect machines, these amplitudes were found to be stable and are therefore included in the dynamic aperture. At higher amplitudes, the losses decreased before finally rising rapidly at a larger amplitude corresponding to the dynamic aperture.

With the inflation method, it was found in 1996 that the lifetime dropped when the resonance amplitudes were sufficiently populated (usually when they corresponded to about 6σ of the distribution of the beam core). A tentative explanation of the reduced lifetime in terms of enhanced diffusive transport by the resonances has been proposed [8].

Thus, good dynamic aperture is not in itself sufficient to provide good lifetime. It may lead to an over-estimate of the emittance that can be accommodated in the machine, as measured by phase-space inflation.

5 MEASUREMENTS IN 1996

In June 1996, LEP was started up with a $(108°, 60°)$ optics. During the initial period of collisions at 45 GeV (required for the calibration of the detectors), lifetime deteriorated as soon as the bunch intensity exceeded $I_b \simeq 200\,\mu$A. The available aperture was measured and found to be about 20 % smaller than predicted. Given the pressures of time and other conditions unrelated to beam dynamics, the optics was abandoned without actually having been tested at high energy and the "fall-back" $(90°, 60°)$ optics was commissioned. This optics behaved much as predicted and record performance was achieved at 80.6 and 86 GeV.

Towards the end of the period, the sextupoles were recabled and the $(108°, 90°)$ optics was given its first full test. At 45 GeV, similar lifetime problems to those observed with the $(108°, 60°)$ lattice were experienced. It should be noted that, with both 108° optics, it was the first time that LEP was operated with $\xi_y < \xi_x \gtrsim 0.03$. So far, it is not understood whether the observed strong blow-up of the horizontal beam size was related to the absolute value of ξ_x or another mechanism. Apart from these problems

at 45 GeV, the $(108°, 90°)$ optics was used in operation at 86 GeV for the last three weeks of the 1996 period and yielded peak luminosities about 60 % of the best achieved with the $(90°, 60°)$ optics. The main experimental observations can be summarised as follows:

- The maximum ϵ_x measured with the inflation method was about 30 % smaller than predicted and smaller than needed for operation above 90 GeV.
- Third and higher order resonance effects were clearly seen in the beam centroid motion following kicks.
- The missing acceptance was correlated with the presence of enhanced beam tails. Enhanced diffusive transport by the imperfection-driven resonance $3Q_x = 307$ has been invoked to explain the tails [8]. Further resonances are important at larger amplitudes.
- The vertical beam size remained larger than expected from the usual compensation of linear betatron coupling. This anomalous vertical beam size has now been interpreted as a consequence of the proximity of the working point to the synchro-betatron resonance $Q_y - 2Q_s = 96$; it is reproduced in tracking with quantum fluctuations. This feature is much weaker on the $(90°, 60°)$ optics.

These unexpected results have been extensively analysed. The reduced lifetime does not appear to be related to any systematic errors in the model of the machine or the particle dynamics. Systematic non-linear resonances can also be excluded. The only plausible explanation is that the problem is related to the presence of strong resonance islands located at large amplitudes which, in the case of all 108° optics, are easily reached by the particles because of the horizontal detuning with amplitude $\partial Q_x/\partial W_x$. The straightforward behaviour of the $(90°, 60°)$ optics as expected is consistent with this.

6 FUTURE OPERATION

On the basis of the experimental results in 1996, it has been decided to use a $(90°, 60°)$ optics for operation in 1997. At 92 GeV, ϵ_x will be reduced by increasing the damping partition number J_x. However, the motivation for a low emittance lattice remains strong since the latter technique requires more longitudinal dynamic aperture and so reduces the maximum energy attainable with the given RF voltage. As far as low emittance lattices are concerned, three possible counter-measures are presently under study:

Minimize the resonance driving terms (mainly 3rd order). A scheme with some independent sextupoles is under study. A new working point (less sensitive to synchro-betatron resonances) will also be tried.

Reduce the horizontal detuning. A scheme with octupoles is being studied. However, hardware considerations render its implementation impossible before 1998.

An optics with smaller horizontal detuning. Given our present understanding, such a solution seems attractive. As a result of preliminary studies, a $(102°, 90°)$ optics is a very promising candidate. It reduces $\partial Q_x/\partial W_x$ by more than a factor of two (see Table 1) while the related increase in emittance would only be 10 % as compared to the 108° case. Admittedly, such a solution would only be compatible with a single sextupole family in the horizontal plane (hardware constraint) which would not allow β_x^* to be reduced. In fact, a 90° optics (with modified J_x and squeezed β_x^*) would yield a comparable if not better performance than this new lattice. For this reason, a $(90°, 90°)$ solution might regain the attraction it lost in 1993 because of polarization.

7 CONCLUSION

The dynamic apertures of both the $(90°, 60°)$ and the $(108°, 60°)$ optics were predicted to be insufficient above 90 GeV, mainly because of the large cross-detuning term $\partial Q_y/\partial W_x$. Following experimental tests and extensive calculations for imperfect machines in 1995-96, the $(108°, 90°)$ optics was retained as the ultimate candidate for high energy. Operation in 1996 with this optics has shown that the presence of strong imperfection-driven resonances combined with a large horizontal detuning (common to all 108° optics) resulted in the build up of tails which reduce the practical stability region to values lower than required above 90 GeV. Operation in 1997 will resume with a $(90°, 60°)$ optics. Increasing the horizontal damping partition number J_x should reduce the horizontal emittance enough for both background and performance considerations. In parallel, efforts will continue towards developing an improved low emittance lattice. These efforts will be shared between finding cures to the problems of the $(108°, 90°)$ optics (minimize the resonant driving terms and reduce the detuning with amplitude) and developing a new $(102°, 90°)$ optics that could be an attractive alternative from 1998 onwards. In case of difficulties, a $(90°, 90°)$ optics would have to be seriously re-considered.

8 REFERENCES

[1] F. Barbarin, F.C. Iselin, and J.M. Jowett, Proc. 4th European Part. Acc. Conf., London, 1994, p. 193.

[2] S. Kamada, CERN LEP Note 297 (1981).

[3] Y. Alexahin et al.,"Low Emittance Lattice for LEP", Proc. Particle Accelerator Conf., Dallas, 1995.

[4] A. Verdier,"Cross Anharmonicity", AIP Conf. Proc. 344, (1994), p.269.

[5] Y. Alexahin, CERN SL-95-110 (AP) (1995).

[6] J.M. Jowett, et al., "The Dynamic Aperture of LEP at High Energy", Proc. Eur. Part. Acc. Conf, Barecelona, 1996.

[7] F. Ruggiero, "Dynamic Aperture for LEP2", Proc. 5th Workshop on LEP Performance, Chamonix 1995, p.164.

[8] J.M. Jowett, "Non-linear Resonances: Predictions, Effects and Measurements", Proc. 7th Workshop on LEP Performance, Chamonix 1997, p.76.

STATUS AND EARLY COMMISSIONING OF THE PEP-II HIGH ENERGY RING

U. Wienands, E. Reuter, P. Bellomo, A. Fisher, J. Gracia, R. Gray, M. Pietryka, T. Taylor,
V. Bharadwaj, R. Iverson, A. Kulikov, J.T. Seeman, J. Turner, SLAC, Stanford, CA 94309
C. Belser, LLNL, Livermore, CA
M. Zisman, S. Zholents, LBNL, Berkeley, CA

Abstract

The High Energy Ring of the PEP-II B-Factory has been constructed in the PEP tunnel. It is now beginning beam commissioning. This report will address the status of the ring systems and our experience in commissioning the systems as well as the first beam running.

1 INTRODUCTION

The High Energy Ring (HER)[1] of the PEP-II *B*-Factory[2] is a 9-GeV electron storage ring designed for 1 A beam current in 1658 bunches. It has been built at SLAC in the existing PEP tunnel, using mostly existing PEP magnets that have been refurbished. A state-of-the-art copper vacuum system is capable of handling up to 3 A beam current. 5 rf stations with 4 cavities each will deliver up to 14 MV at 476 MHz, sufficient for 1.15 cm bunch length at 1 A beam current.[3] Figure 1 shows a layout of the ring and the ring parameters are given in Table 1. The HER is complemented by the 3.1-GeV Low Energy Ring (LER)[4], which is on a construction schedule roughly one year later than the HER.

Table 1: HER Parameters

Circumference	2199.32	m
Energy	9	GeV
Beam Current	0.99	A
Tunes ν_x, ν_y	24.62, 23.64	
β_x^*,β_y^*	33, 1.5	cm
harmonic number	3492	
Synchr. tune ν_s	0.0049	
Bunch Length	1.15	cm

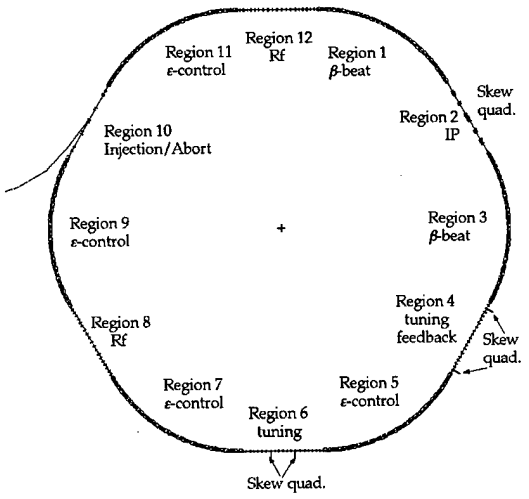


Figure 1: Layout of the High Energy Ring

As of this conference, the accelerator systems for the HER have been installed. A temporary beam pipe is bridging the interaction Region 2, to be replaced with the final vacuum system during installation of the LER. In the meantime, a sophisticated set of background detectors has been installed, thus allowing an early assessment of the backgrounds produced by the HER.

2 SYSTEMS COMMISSIONING

2.1 Magnets and power supplies

In order to provide flexibility in tuning the ring, the magnet system consists of 18 magnet strings that span the whole ring and about 100 locally controlled magnets that are individually powered or in small groups. All magnets have been individually measured and typically have max. $10^{-4}...10^{-3}$ field deviation across the beam-stay-clear aperture. The power supplies and controllers are specified at 10^{-4} accuracy for drift and noise.

Commissioning of this system has been proceeding fairly smoothly. Each supply was first checked in the lab, installed and checked out according to a specified plan with hi-potting and polarity checks preceding initial turn-on of the supplies. The availability of a working control system turned out to be of great help, in fact, checkout of each supply also verified the database entries for the particular magnets involved.

Once checked out, as much long-term testing as possible was carried out. In this way, a sporadic tripping problem of the intermediate supplies was identified and addressed without using any beam time. These runs also confirmed the excellent stability of the system; Fig. 2 shows an example of current variation for a typical supply over about 13 hours.

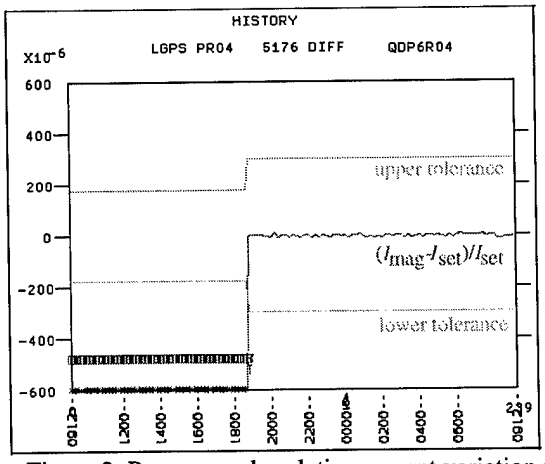


Figure 2: Power supply relative current variation *vs* time

0-7803-4376-X/98/$10.00 © 1998 IEEE

2.2 Vacuum System

Completion and pump-down of the vacuum system proceeded by region. In order to reduce the risk of contamination, installation was done under a constant flow of dry N_2 and using "filtered-air showers." Pump-downs proceeded using cart-mounted turbo pumps for roughing down to the 10^{-6} torr level. Following thorough leak checking the ion pumps were turned on one by one. Pressure in the system is measured by monitoring the pump currents; typically pressures below 10^{-8} torr were achieved after 24 hours as shown in Fig. 3.

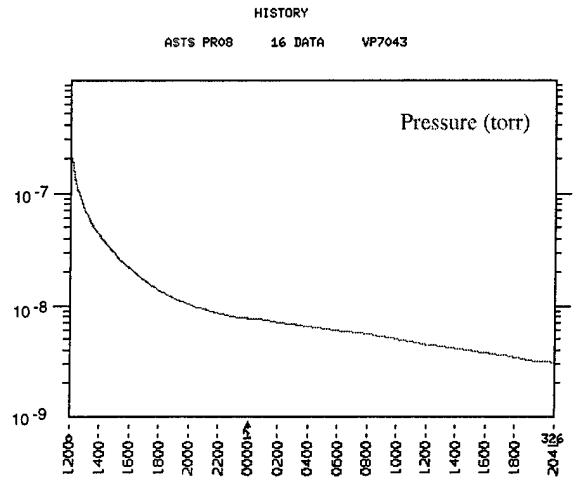


Figure 3: Initial pump down curve for Region 8.

Besides the regular ion pumps there are distributed ion pumps in each arc dipole and NEG pumps in the arc-to-straight transitions as well as in Region 2. These pumps have not yet been activated.

23 Beam Diagnostics

The beam diagnostics system of the HER consists of about 300 button-type beam position monitors (BPM), 100 beam loss monitors (BLM), a dc current transformer, a bunch-current monitor and a synchrotron-light monitor. It is described in detail in another contribution to this conference.[5] The BPM processors are capable of turn-by-turn readout for 1024 turns. Self-calibration and -test capability aids trouble shooting.

The BLM system uses lead-shielded Cherenkov detectors mounted close to the beam line at strategic locations. The processor module is capable of detecting losses over a 10^6 dynamic range by either charge-integrating the PMT output (high losses) or counting pulses (low losses). Each channel can trigger a beam abort if enabled.

2.4 Feedback Systems

Advanced digital broad-band feedback systems have been constructed and installed for both the transverse and longitudinal plane. These are described in detail in other contributions to this conference.[6,7]

3 FIRST BEAM RESULTS

On May 10, 1997, an electron beam was successfully injected and taken through about 1/3 of the ring into a temporary dump located at Region 2. Figure 4 shows a screen photo of the beam spot observed. This has allowed us to begin commissioning of the BPM and the BLM systems as well as assessing the state of the magnet system. Two of the five rf stations are also operational; however, their effect on the beam has not yet been studied.

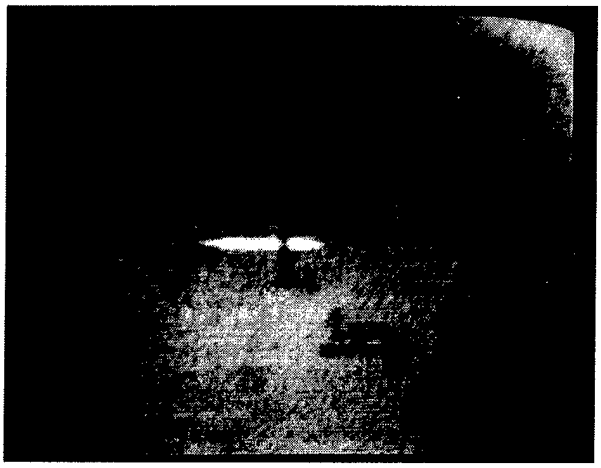


Figure 4: First beam spot observed at the Region 2 dump

3.1 Beam diagnostics

Checkout and timing of the BPM system was the first major task and proceeded fairly smoothly. The timing curves exhibited the expected width of about 40 ns; an unexpected oscillation on top of the distribution was tracked to firmware and corrected. The beam-loss monitors have a gated channel specifically synchronized with the injection timing with a few hundred μs width, these were also timed easily.

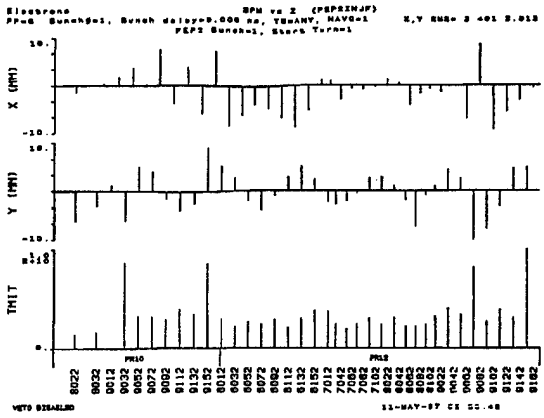


Figure 5: Beam trajectory from injection to Region 2

3.2 Magnet system

The beam was first "parked" on a dump just upstream of the injection region and then injected into the ring using the dc bump magnets only. Once the launch conditions were established the beam made it around the ring to the

dump at Region 2 without using any corrector magnets, indicating the absence of any gross alignment errors. Fig. 5 shows the recorded beam orbit trajectory.

Quadrupole settings were checked in two ways: By recording a difference orbit for two different launch conditions a betatron oscillation was be displayed and compared to the on-line model. The agreement is rather good indicating that the magnet settings are not far off the design values. The dispersion function was determined by taking the difference orbit for beams of different energy; the result showed the dispersion being small in the straight section Region 12 and up to 1.25 m in the arcs; in fair agreement with the model values of 0 (straight) and 1.5 m.

Even though the injection kicker was not required for this run, it was activated and its timing set. Fig. 6 shows a timing curve taken, the kicker rise time was determined to be about 300 ns with a total pulse width of just over 1 μs; in good agreement with the expectation. The kicker field strength was found from R_{12} measurements to be 8-10 Gm/kV, consistent with lab measurements (the uncertainty is due to the still uncertain BPM calibration).

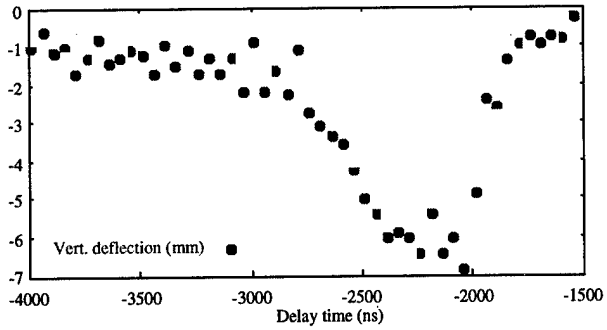


Figure 6: Injection kicker timing curve

3.3 Vacuum system

The vacuum system performed well during the run; beam intensities were still too low to see any significant effect on the gas pressure.

The machine aperture was scanned vertically using the injection bump magnets (which are strong enough to scan the whole aperture of the ring, while individual orbit correctors are not). Fig. 7 shows the result of such a scan; as the transmission drops BLMs downstream of the location of the beam loss show a clear and unambiguous response.

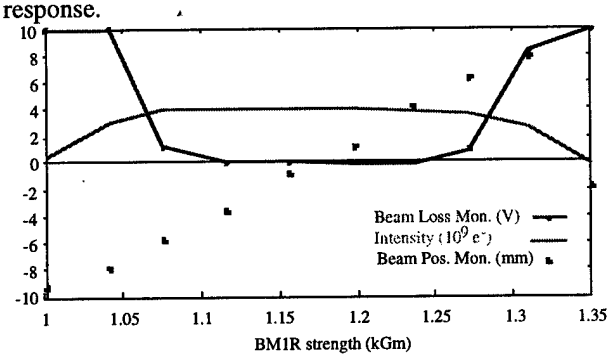


Figure 7: Vertical aperture scan

These scans also provided for a consistency check of the BPM calibration: From the lattice model, the R_{12} coefficients (x/x') from the injection bumps to the point of beam loss were calculated and indicated a vertical aperture of about 45 mm, close to the chamber height of 50 mm. The Figure also shows the reading of a nearby BPM, indicating a maximum excursion of only 10 mm. Since it was already determined that the magnet excitations were roughly correct, this pointed to a calibration error for the BPMs. That was later corroborated by more detailed R_{12} measurements and traced to an omission of a scale factor in the database.

The horizontal aperture was scanned in a similar fashion using the Lambertson septum.

4 SUMMARY AND CONCLUSIONS

With a successful sector test the PEP-II High Energy Ring has entered the commissioning phase. As of the time of the conference the status is as follows:

- Magnet and vacuum system appear to be in good shape with no significant problems uncovered. The alignment of the machine appears to be good.
- Physical aperture of the sector tested is as expected.
- The injection kicker is working and timed in.
- BPM and BLM diagnostics in 1/3 of the ring have been commissioned and appear basically sound.
- Beam trajectories under various conditions indicate that the magnet settings are close to their design values.

5 ACKNOWLEDGMENTS

The commissioning of the HER is done fully integrated with regular SLAC operations. The authors would like to thank the Accelerator Dept. and SLAC Operations for their enthusiastic support, without which our first run would not have been as successful as it was.

Completing the HER installation in time was achieved by a heroic effort of a large number of employees, especially those associated with vacuum work and with installation. Without their dedication the ring would not have been ready for beam commissioning.

REFERENCES

[1] U. Wienands et al., Proc. 1995 Part. Accel. Conf., Dallas, TX, 1995, p. 530.
[2] J.T. Seeman, ibid., p. 486
[3] H. Schwartz et al., ibid., p. 1731, and Proc. EPAC 94, London, July 1994, p. 1882.
[4] M.S. Zisman et al., Proc. 1995 Part. Accel. Conf., Dallas, TX, 1995, p. 533.
[5] A. Fisher et al., these proceedings.
[6] W. Barry et al., these proceedings.
[7] H. Hindi et al., these proceedings

DUAL APERTURE HIGH LUMINOSITY COLLIDER AT CORNELL

D.Rubin, G.Dugan, A.Mikhailichenko, J.Rogers*
Laboratory of Nuclear Studies, Cornell University, Ithaca,NY 14853

Abstract

We describe a very high luminosity electron-positron collider that operates in the Υ_{4s} energy range. Trajectories intersect with a small horizontal crossing angle so that closely spaced bunches collide only at the interaction point. An electrostatic deflector steers the counter-rotating beams into side-by-side vacuum chambers that share a common dipole guide field. The beams also share superconducting RF accelerating cavities. Independent focusing and chromaticity correction is provided by dual aperture superconducting quadrupoles and sextupoles. The machine is installed above the synchrotron injector in the CESR tunnel. The existing storage ring can remain for service as an accumulator or dedicated synchrotron light source. With 3A/beam in 180 bunches, $\beta_v^* = 7mm$, beam-beam tune shift parameter $\xi = 0.06$ and beam energy of 5.3GeV, we anticipate luminosity of $3 \times 10^{34} cm^{-2} s^{-1}$.

1 INTRODUCTION

Luminosity projections for the dual aperture machine are based on straightforward extrapolation of CESR parameters. At present we store trains of bunches in a single ring that collide at a small horizontal crossing angle[1]. We propose to increase the number of bunches, spacing them uniformly rather than in trains, to increase the current in each bunch, decrease β_v^*, and to increase the beam-beam tuneshift parameter. The parameters of the dual aperture machine, and CESR parameters as it operates today, are shown in Table I.

Table I. Dual Aperture Machine

Parameter	CESR	New Machine
Number of SC cavities		10
E[GeV](beam energy)	5.3	5.3
I_{tot}[A](current/beam)	0.16	3.06
n_b(number of bunches)	18	180
I_{bunch}[mA](current/bunch)	9	17
S_b[ns](bunch spacing)	42	14
θ^*[mrad]	± 2.1	± 2.3
β_v^*[mm]	18	7
β_h^*[m]	1	1
σ_l[mm](bunch length)	19	7
$\epsilon_h[10^{-7} m]$	2.2	2
P_{SR}[MW](per beam)	0.176	3.4
V_c[MV](cavity voltage)	6	24
ξ_v	0.04	0.06
L$[10^{33} cm^{-2} s^{-1}]$	0.41	30.2

* Work supported by the National Science Foundation

2 OPTICS AND ORBITS

The trajectories of the beams as they extend from the interaction point to the first dual aperture magnet are shown in Fig. 1. The quadrupole magnets Q1 and Q2 are the same magnets that are being assembled for installation as part of the Phase III upgrade[2]. The 4 meter long separator kicks the beams onto the axes of a dual aperture quadrupole (Q4) 20m from the interaction point, where the beam to beam separation is 81mm. The separator voltage is comparable to that of the horizontal separators now in service in CESR. Note that at distances greater than 2.1m from the IP the separation of the beams is always at least $10\sigma_x$. Bunches can be uniformly spaced every 14ns.

Throughout the rest of the machine the beam trajectories are on the respective axes of the dual aperture quadrupoles. In contrast to present day operation of CESR, where multibunch beams share a common aperture, there are very few parasitic long range interactions in the dual aperture machine. The tunes, orbits, chromaticities, coupling etc., of the beams can be independently manipulated. And nowhere do the trajectories explore the fringe fields of sextupoles, skew quads, or dipole correctors. We expect that this qualitative improvement in the optics will translate to enhanced beam-beam performance.

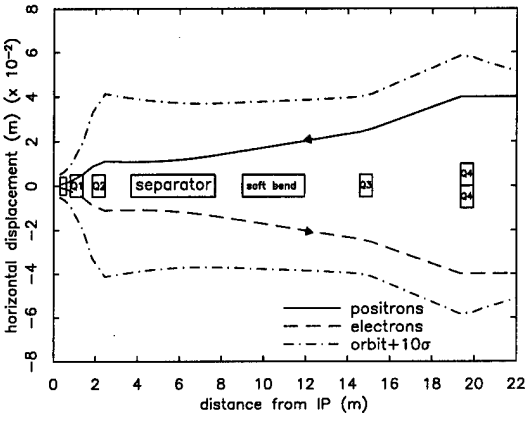


Figure 1: The crossing half angle is $2.3mrad$. The separator kicks the beams $\pm 1.9mrad$. The beams are 81mm apart at the dual aperture quadrupole 20m from the IP.

3 ACCELERATING CAVITIES

The beam current and reduced bunch length are supported by increased RF power and accelerating voltage. With the development a high power, 500Mhz waveguide window, each of the single cell superconducting cavities can deliver 800 kW to the beam at a peak voltage of 3MV. Four superconducting RF cavities will be installed in CESR during the

0-7803-4376-X/98/$10.00 © 1998 IEEE

next year for the Phase III upgrade/citepadamsee. Ten cells are required to store 180, 17mA bunches in each beam with bunch length of 7mm.

In order to obtain the highest accelerating voltage in each beam with the fewest number of cells, both beams circulate through the same set of cavities along parallel orbits that are displaced $\pm 40.5mm$ from the cavity axis. The beam tube radius of the cavities is 120mm. The impedance of the superconducting RF system is very low. Each cell has a large aperture. The R/Q of the higher order modes is low and there is excellent damping. Finally, very few cells are required. It appears that deflecting modes excited by the off axis beams will be tolerable.

4 VACUUM AND IMPEDANCE

The vacuum chamber must be capable of handling large synchrotron radiation heat load, maintaining a long beam-gas lifetime, and must minimize the coupling impedance to avoid beam instability.

4.1 Vacuum system

Synchrotron radiation parameters derived from the overall machine parameters are listed in Table II. The linear and surface power densitites are sufficiently low to allow the use of an extruded aluminum chamber. However, we are considering the use of a formed copper chamber for improved synchrotron radiaton shielding. To withstand the power density in the higher field "hard bend" magnets near the interaction point copper chambers are required. The gas load in the vacuum chamber comes almost entirely from the photodesorption from the chamber walls. If we require a beam-gas lifetime of 3 hours at an ultimate photodesorption coefficient of 2×10^{-6}, the average linear pumping speed in the storage ring arcs must be $230l - s^{-1} - m^{-1}$, as summarized in Table III.

Table II: Synchrotron radiation parameters in arc magnets

Parameter	Value
Beam energy(GeV)	5.3
Current per beam (A)	3.06
Normal bend radius (m)	88
Vertical beam divergence(μrad)	30
Radiation divergence(μrad)	54mm
Total divergence(μrad)	62
Beam chamber radius (mm)	27
Minimum radiation stripe width (mm)	0.135
Maximum linear power density (kW/m)	4.39
Maximum surface power density (W/mm^2)	13.0

Table III: Vacuum parameters in arc magnets

Parameter	Value
Photon emission rate ($s^{-1}m^{-1}$)	2.4×10^{19}
Photodesorption coefficient	2×10^{-6}
Outgassing rate ($s^{-1}m^{-1}$)	4.7×10^{13}
Required beam-gas lifetime (hours)	3
Average pressure (CO_2 equivalent)(Torr)	6.4×10^{-9}
Average linear pumping speed ($ls^{-1}m^{-1}$)	230

The two vacuum chambers must be separate and have circular cross sections where they pass through the dual bore quadrupole magnets. This circular cross section must be maintained through the dipole magnets as well to minimize the coupling impedance. A Ti sublimation pump supplements the distributed ion pumps in the chamber to improve the pumping speed at low pressures. The conductance of the pump slots is well in excess of that needed to maintain the necessary linear pumping speed. The chambers in the quadrupole magnet packages however, must be pumped through their ends with lumped ion pumps. The conductance of the pipe requires that the unpumped region be no longer than 1.3 m. Recent experience with synchrotron light sources [4] indicates that it may be possible to install the chamber without an *insitu* bake, reducing the need for sliding joints, and the associated the coupling impedance.

4.2 Impedance and Stability

The loss factors for critical vacuum chamber components for a bunch length of 7mm are substantial. Total higher order mode power disspated in separators, RF cavities, crotches, scrapers and beam position monitors for a 3A beam is estimated to be nearly 1MW. The beam is predicted to be stable against all single- bunch instabilities and longitudinal coupled bunch instabilities because of the use of very low impedance superconducting RF cavities. The beam will be transversely unstable due to the resistive wall impedance, and will require active feedback of the type currently in use in CESR. The beam is predicted to be stable against the fast ion instability. The photoelectron instability is expected to be weak because of the relatively large bunch spacing.

5 ARC MAGNETS

The arc dipoles will be conventional resistive magnets. The width of the dipoles is sufficient to accomodate both beams, with a beam-to-beam separation of 81mm. Parameters of the magnets are given in Table IV.

Table IV: Dipole magnet parameters

Parameter	Requirements
Number of magnets	140
Magnetic length	3200mm
Field	0.24T
Pole width	300 mm
Gap	65 mm
Good field aperture(0.05%)	135mm X 54 mm
Ampere-turns/pole	6000 A
Current	600 A
Power	10.9 kW

5.1 Quadrupoles, Sextupoles and Correctors

The requirement for closely-spaced dual bore quadrupoles in the two ring symmetric collider arises from the desire to minimize, as much as possible, the separation of the

beams in the two rings. Minimizing this separation allows not only the quadrupoles but also the dipoles to be smaller. This results in less costly and simpler magnets. The limited space available in the existing tunnel for the new rings provides an additional motivation to keep overall dipole and quadrupole cross section small. Furthermore, the difficulties of beam separation as the beams emerge from the interaction region is minimized with a small beam separation. The goal for the beam-to-beam separation in the current design, 81mm, requires a sufficiently high current density that a normal conducting solution for the quadrupoles would have prohibitively large operating costs. Thus a superconducting coil design is the only practical and affordable choice. Table V presents the parameters of the superconducting quadrupoles.

Table V: Quadrupole magnet parameters

Parameter	Requirements
Number of magnets	90
Magnetic length	380mm
Field gradient	10T/m
Pole tip diameter	70 mm
Gap	65 mm
Good field aperture(0.05%)	54
Ampere-turns/pole	6750 A
Current	150 A
Heat leak($4.6°K$ to $300°K$)Power	2W

The quadrupole is shown in Fig. 2. A prototype has been fabricated and tested[5]. The warm bore tube is water cooled. The coil was fabricated from NbTi operating at $4.6°K$. The cryostat contains inner and outer LN_2 shields, and multilayer insulation. The combination of a rectangular coil cross section, and a hyperbolic shape for the iron, assures excellent field quality over the 54 mm diamter aperture. The required field quality has been measured in the prototype.

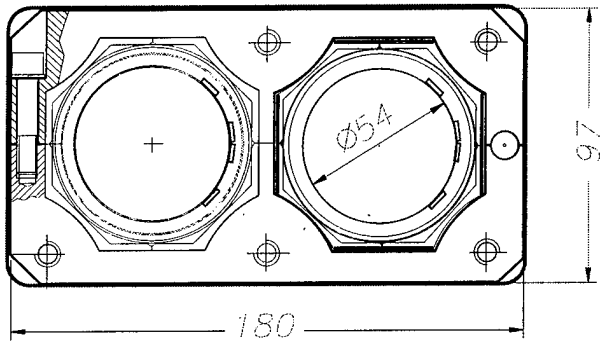


Figure 2: Dual aperture superconducting quadrupole magnet.

Adjacent to each quadrupole will be a sextupole and a dipole corrector. These magnets will also be superconducting, and will be packaged in the same cryostat with the quadrupole. Each quadrupole, sextupole, and dipole corrector in the ring will be separately powered. To reduce the heat leak due to the multiplicity of leads, high temperature superconductor will be used for the current lead transition to room temperature.

An alternative high temperature superconductor (HTS) design is being explored[6].

6 INJECTION

Table VI summarizes the requirements on the injector system. The current performance of the Cornell Linac/synchrotron complex is adequate to satisy the requirements indicated in Table VI, on a charge-per-bunch basis. However, the Linac/synchrotron now accelerates only 14 bunches, not 180, per cycle; so the total current must be increased by a factor of more than 10. There may be some multibunch stability issues which will need to be solved in this mode of operation.

Table VI: Injector requirements (per species)

Parameter	Requirements
Bunches per synchrotron cycle	180
Particles per bunch	2×10^7
Total particles per synchrotron cycle	3.6×10^9
Transfer efficiency	90%
Fill time (minutes) at 60Hz	5
Total particles in storage ring	6×10^{13}

The existing transfer lines from the synchrotron to CESR need to be modified by the insertion of a switching dipole in each line. New transfer lines, starting from this dipole, then bring the beams up to an injection system into the two-ring collider. In this scheme, positron beams can also be transferred from CESR into the two-ring collider.

7 REFERENCES

[1] Rubin,D., session 8W5, these proceedings

[2] Welch,J.,et.al., session 3P17, these proceedings.

[3] Belomestnykh,S.,et.al., session 3P21, these proceedings.

[4] J.Miertusova and F.Giacuzzp, Proc. 1996 European Particle Accelerator Conf., Barcelona (1996) p. 2527

[5] A.Mikhailichenko and D.Rubin, Proc. 1996 European Particle Accelerator Conf., Barcelona (1996) p. 433

[6] G.Dugan, J.Rogers, session 4C.08, these proceedings

BEIJING TAU-CHARM FACTORY DESIGN STUDY

BTCF Design Group, Presented by Y.Z. Wu
IHEP, Chinese Academy of Sciences, P.O. Box 918-9, Beijing 100039, P.R. of China

Abstract

This paper describes recent progress of the design of the Beijing Tau-Charm Factory (BTCF). The main machine goals, parameters, various operation modes, and some hardware systems are reviewed here.

1 INTRODUCTION

A Tau-Charm Factory (TCF) is a high luminosity e^+ e^- collider operating near the J/ψ and τ production threshold, which requires center of mass about 3 to 6 GeV. It has been considered as an unique facility to research some areas of particle physics by the worldwide communities of the high energy physics [1].

The feasibility study of the BTCF was approved in Feb. of 1995. Since then the design study activities have mainly focused on the optimization of the lattice and a preliminary study of key components and systems. The experiences from the existing e^+e^- storage ring colliders, specially from CESR and BEPC provide a firm foundation for BTCF design. Also there is a lot experience that we can use from previous designs of TCF, B-factory and ϕ-factory. Considerable economies can be achieved by siting BTCF nearby BEPC site. The injector system (linac) of BEPC can be used for the injector of the BTCF and there are substantial opportunities to use the hardwares and existing buildings and the other infrastructure for BEPC [2]. The layout of general BTCF is shown in Figure 1.

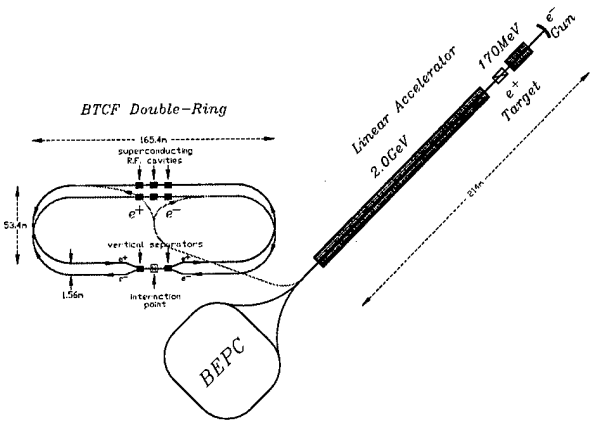


Figure 1: General layout of the Beijing tau-charm factory.

2 GOALS AND PARAMETERS

The BTCF is planned, ultimately, to have three modes of operation. In priority order, they are the high luminosity mode, longitudinal polarization mode and monochromator mode respectively. Accordingly, this design focuses primarily on the high luminosity mode. Preliminary designs for providing polarization and monochromatic operation are included to assure that the basic design is compatible with eventual operation in these modes. The main machine parameters for the high luminosity mode and the monochromator mode are listed in Table 1. The design goals are listed as follows:

- Achieving a peak luminosity $L = 1 \times 10^{33}$ cm^{-2}s^{-1} in a high luminosity mode at a beam energy E = 2.0 GeV.
- Beam energy being adjustable from 1.5 GeV to 2.5 GeV with the potential up to 3.0 GeV being kept.
- Providing the possibility of the operation of the polarization mode and the monochromator mode in the future.
- Maintaining the detector background at acceptable level.
- Keeping high injection efficiency and reliable operation.

3 DESCRIPTION OF THREE MODES

The collider consists of two rings, one above the other, with one IP. Each ring is 53 m wide and 165 m long with a circumference of 385.4 m. The two rings are vertically separated 1.56 m. Each ring can be divided into four main parts: one interaction region (IR) with a beam separation section at each side, the spin rotator sections for the polarization mode, two arcs and an utility region with the injection section at one side. Detailed design of the optics for the operation modes has been discussed in Ref. [3]. The design about IR and background issues can be referred to in Ref. [5]. The beam-beam issue is discussed in [6]. The following is general description for the three operation modes.

3.1 High Luminosity Mode

Electron and positron beams collide at a small horizontal crossing angle which is refered to the crossing angle scheme. This scheme has the advantages that more bunches can be stored and the particles per bunch can be reduced

0-7803-4376-X/98/$10.00 © 1998 IEEE

Table 1: Machine parameters for BTCF including the high luminosity mode and the monochromator mode.

Mode	High Lumi.	Monochr.
Beam energy E (GeV)	2.0	1.55
Circumference C (m)	385.447	385.447
Revolution frequency f_0 (MHz)	0.778	0.778
Crossing angle at IP $2\phi_c$ (mrad)	5.2	0.0
β-function at IP $\beta_x^*/\beta_y^*(m)$	0.66/0.01	0.01/0.15
Dispersion at IP D_x^*/D_y^* (m)	0.00 /0.00	0.00/0.45
Betatron tunes Q_x/Q_y	11.75/11.76	12.21/11.23
Momentum compaction α_p	0.014	0.014
Synch. rad. loss/turn U_0 (keV)	174	67
Damping time $\tau_x/\tau_y/\tau_\epsilon$ (ms)	30/30/15	26/61/90
Natural emittance ϵ_{x0} (nm)	138	36
Vertical emittance ϵ_y (nm)	2.1	5.3
Momentum spread σ_ϵ	5.9×10^{-4}	7.8×10^{-4}
Synchrotron tune Q_s	0.069	0.067
Natural chromaticity Q'_x/Q'_y	-17/-35	-36/-31
Total current per beam I (A)	0.57	0.33
Number of bunches k_b	86	29
Particles per bunch $N_b(10^{11})$	0.54	0.93
Bunch space (m)	3.78	11.97
RF frequency f_{rf} (MHz)	476	476
RF voltage V_{rf} (MV)	6.8	5.0
Natural bunch length σ_l (cm)	0.76	1.0
Beam-beam effect ξ_x/ξ_y	0.044/0.04	0.018/0.015
Luminosity L ($\mathrm{cm}^{-2}\mathrm{s}^{-1}$)	1×10^{33}	2×10^{32}
CM energy spread σ_ω (MeV)	1.7	0.14

compared to the head-on collision at the certain luminosity. There are 86 bunches spaced 3.78 m in each ring for this scheme with the gap of about 15% leaving for ion-clearing. The crossing angle ϕ_c at the interaction point (IP) is chosen as $2\phi_c \leq 0.16\sigma_x^*/\sigma_l$ to avoid the excitation of synchro-betatron resonance according to the CESR experience [4]. This angle is produced by a pair of horizontal bending magnets BHs, each located symmetrically in one side of the IP. The horizontal phase advance between the BH and the IP is π so that the orbit distortion is defined between this two BHs. Certainly, head-on collisions can be obtained if needed and the way is to turn off the BHs.

3.2 *Polarization Mode*

The major energy range of the longitudinal polarized beam required by physics side is around 2.0 GeV and 1.55 GeV. In case of BTCF, the polarization time due to Sokolov-Ternov effect is too long [2] compare to the beam lifetime. The use of asymmetric wiggler to shorten the polarization time causes the significant increase in energy spread. Consequently, the beams must be prepolarized before they are filled into the ring. It is planned that only e^- is prepolarized at begin ing for the design.

The spin rotation scheme(s) is certainly needed to ensure the longitudinally polarization at the interaction point. Three kinds of spin rotator, say, HERA-type mini-rotator, symmetric solenoid spin rotator and Siberian snake, are studied to seek the proper scheme on the BTCF. Briefly, the main difficulty for the mini-rotators each consisting of 3 vertical and 3 horizontal bends is that the vertical emittance produced by vertical bends can not be neglected owing to the large bending angle (about 20° at 2.0 GeV) needed. The vertical emittance can hardly be controlled lower then 10 nm with general arrangement. The more sophisticated arrangement aiming to minimize the vertical emittance needs to split the large dipoles to 2-3 small pieces and to insert quadrupoles in between therefore longer space is required. The Siberian snake is the candidate for low energy polarization scheme on BTCF. However it suffers from the short depolarization time, i.e., about 26 minutes at 1.55 GeV.

The scheme adopted in current BTCF design is symmetric solenoid spin rotator. The rotator in each side of the IR consists of a pair of superconducting solenoid and 2 horizontal dipoles to rotate the spin direction and many quadrupoles for the local coupling compensation and other matching. To reach an applicable polarization level the spin-matching must be applied to suppress the strong depolarization effects even for the perfectly aligned machine. The 'partial' spin-matching by adjusting 25 quadrupole strengthes results in remarkable enhancement in depolarization time (100 minutes) and equilibrium polarization level. Change in helicity can easily be achieved by reversing the field direction of solenoid.

Generally speaking, up to now, the consideration for the longitudinal polarization has significantly changed the layout and lattice of BTCF. The detailed studies [7] suggest that more modifications in ring design are necessary to optimize the performance of polarization operation mode. For instance, a larger circumference(420-450m) is much preferable.

3.3 *Monochromator Mode*

The monochromator mode has been incorporated into design at normal energy of 1.55 GeV with 29 bunches in each ring. The bunch space is 11.97 m with the gap of about 10% for ion-clearing. This mode doesn't affect the layout of the storage ring. Only small variation is needed. In the IR, some qaudrupoles are required to change polarity, and some are required to turn on or turn off. In arc, eight Robinson wigglers are arranged to reduce beam emittance and increase beam energy spread.

4 INJECTION

The BEPC linac system will be upgraded to a full energy injector which will provide the ability to finish the injection in 5 minutes. To this end, the following measures will be taken: (1) upgrading linac energy. An accelerating unit (12 m long) will be added in the end of the existing linac, and meantime 14 new klystrons (65 MW) replace the present 14 klystrons (30 MW); Another option is to use recirculating scheme. (2) Increasing the positron yield rate. A high

current electron gun(10 A) would be developed to increase the electron strength on the e^+ target and the positron target are moved to next station to enhance the bombarding energy of electrons; (3) Increasing the repetition rate from current 12.5 Hz to 25 Hz; (4) adopting the bunch train injection mode.

5 INSTABILITY CONTROL

The beam current limitation and its stabilities are very important issues for the BTCF. To reach the high luminosity, there is high current in storage ring. A great attention must be paid on the effects which the strong current maybe cause.

The criterion of microwave instability gives an impedance threshold requirement at single bunch current of 6.7 mA as $|Z/N|_{eff} \leq 0.51\Omega$. The present estimation for the impedance of ring components including RF cavities, kickers, separators and vacuum chambers indicates that $|Z/N|_0 \sim 0.24\,\Omega$. It seems that a good control of ring impedance can be realized. The bunch lengthening effect due to the longitudinal wakefield has also been investigated with a code [8] developed in KEK. The results show that the bunch length increases about 6%.

The important means to control multibunch instability is to reduce the number and impedance of the high-Q resonant structures in the rings, so that the superconducting cavities would be adpoted. Using of the HOM dampers would reduce external Q value less than 100. Great progress has been made in the design and test of fast feedback system at PEP-II and other labs, which makes it feasible to develop a system for the BTCF to suppress instability as required.

For the Transient Ion Trapping and Beam-Photoelectron Interaction, their mechanisms are being investigated with simulation program developed in KEK, and related machine studies are in progress in the BEPC and other laboratories. Due to the factor that the BTCF has a large beam emittance and less bunch numbers than B factory, it would be expected that these instabilities in BTCF should be much weaker than that in a B-factory.

6 RF SYSTEM

The design requirements of the RF system are mainly based on following considerations: maintaining a short bunch length of less than 1 cm; minimizing the contribution of RF system to the machine impedance.

Single-cell and deeply damped superconducting (SC) cavity with a frequency of 476 MHz is selected in terms of following reasons. First, it has large gradient$\sim$ 10 MV/m. Second, it has large beam pipe and small impedance. The RF voltage is designed at 9 MV in maximum and operated at 6.8 MV with 3 SC cavities per ring. Each cavity delivers 50 KW to the beam.

7 VACUUM

The BTCF storage ring requires that the operating pressure should be $\leq 1\text{x}10^{-9}$ Torr in the arc region and $\leq 5\text{x}10^{-10}$ Torr in the IR.

Total pumping speed of $5.8\text{x}10^4$ L/s with 58 sets of sputter ion pumps and NEG pumps is needed per ring to deal with high thermal load and minimize the photo desorbed gas load. A test with NEG pumps to get the pressure of lower than 10^{-10} Torr has been done, which provides experience to the design of the IR vacuum.

The vacuum chamber will be made of extruded aluminum in the arc and stainless steel in the straight section with the following inner dimensions: 90 mm$\times$60 mm in arc region (H$\times$V); 90 mm$\times$90 mm in utility section; 130 mm $\times$ 130 mm in Q1 and 150 mm $\times$ 150 mm in Q2; The vacuum pipes at bending magnet region consist of two parts: the beam chamber and antechamber in which the copper absorbers are installed to intercept the synchrotron radiation flux. The great attentions has been paid to smoothness of the chamber.

The vacuum system of the BTCF is similar to B-factories and ϕ-factory but not quite as much of a challenge with that of other factories. So their experiences will be incorporated to the BTCF design.

8 SUMMARY

The BTCF with a luminosity of $10^{33}\text{cm}^{-2}\text{s}^{-1}$ at the energy of 2.0 GeV is feasible on a rather conventional basis of multibunch and small crossing angle collision scheme together with a micro-β insertion. To reach such a goal, it is essential to incorporate the advanced experience and the technological achievements of the existing e^+e^- storage ring collider. However, some challenging work for the BTCF still needs to be studied further in optimizing the lattice, the IR design, impedance control, RF design, vacuum design and some problems related to the engineering.

9 REFERENCES

1. Memorandum on the Tau-Charm Factory in the era of B-Factories and CESR, SLAC, Aug. 15-16, 1994.
2. Feasibility Study Report on Beijing Tau-Charm Factory, IHEP-BTCF, Report-02.
3. N. Huang, L.H. Jin, et al, "Lattice Design of BTCF Storage Ring", this proceedings.
4. M. Tigner, Private communication.
5. Y.Z. Wu, Q.L. Peng, "Interaction Region Design for Beijing Tau-Charm Factory", this proceedings.
6. C. Zhang, et al, this proceedings.
7. D.Wang, to be published.
8. K. Oide and K. Yokoya, KEK Preprint 90-10, 1990

AUTOMATED TUNING OF THE ADVANCED PHOTON SOURCE BOOSTER SYNCHROTRON

S.G. Biedron and S.V. Milton
Advanced Photon Source, Argonne National Laboratory
9700 South Cass Avenue, Argonne, Illinois 60439 USA

Abstract

The acceleration cycle of the Advanced Photon Source (APS) booster synchrotron is completed within 223 ms and is repeated at 2 Hz. Unless properly corrected, transverse and longitudinal injection errors can lead to inefficient booster performance. In order to simplify daily operation, automated tuning methods have been developed. Through the use of beam position monitor (BPM) readings, transfer line corrector magnets, magnet ramp timing, and empirically determined response functions, the injection process is optimized by correcting the first turn trajectory to the measured closed orbit. These tuning algorithms and their implementation are described here along with an evaluation of their performance.

1 INTRODUCTION

The Advanced Photon Source (APS), located at Argonne National Laboratory, is a third-generation synchrotron light source facility which consists of a main storage ring with attached beamlines and a powerful, high efficiency injector system. The injector system is comprised of a 400-MeV, 60-Hz positron linac, a positron accumulator ring (PAR), and a 7-GeV, 2- Hz booster synchrotron (booster).

The booster synchrotron accelerates a 400-MeV bunch of positrons to 7 GeV in 223 ms. This bunch is then extracted from the booster and is directed toward the storage ring with the entire process being repeated at a 2-Hz rate. The booster lattice is quite simple and is comprised of forty FODO cells laid out over a circumference of 368 m.

Reliable, efficient operation is of key importance at a synchrotron light facility such as the APS. Diagnosing operational problems and treating them effectively must occur to insure that the users obtain maximum beam time. Automation of processes such as injection tune-up and maintenance insures consistent beam quality and allows operators to quickly set up beam and deliver it to the storage ring for use by the experimenters. This paper will focus on the operation and automated injection tuning methods of the booster.

2 BOOSTER SYNCHROTRON INJECTION TRAJECTORY CONTROL

2.1 General

In an ideal machine under ideal conditions, the closed orbit would be immediately revealed on the first turn; however, due to errors in the injection trajectory, energy, and phase, this is not the case. In the case of trajectory errors, if the measured closed orbits and the first turn trajectories are known, then the correction of first turn trajectory to the closed orbit can be automated. If the beam position trajectory history is known at a region of high dispersion, then a similar process can be applied to the longitudinal plane.

2.2 Transverse and Longitudinal Planes

Through the use of pulsed septum and kicker magnets, the beam arrives in the booster from the transfer line during a single turn on axis injection process. Transverse injection errors result when the voltage-controlled PAR extraction and booster injection pulsed magnets drift slightly over time. This causes the injection trajectory to wander. For reasons of simplicity and accuracy, the PAR-to-booster (PTB) transfer line corrector magnets are used to touch up the incoming injection trajectory with an automated tune-up procedure, rather than attempting to accurately control these pulsed magnets.

Eighty beam position monitors exist around the booster synchrotron, each capable of single-pass measurements in both the vertical and horizontal planes, and each attached to a 64k beam history module. After waiting 1 ms and then averaging 1000 or more turns, the measured closed orbits are revealed. The timing of the BPM system is then adjusted so that the BPMs measure the first turn trajectory. This is then compared to the closed orbit, yielding the error signal for the feedback algorithm.

Due to zero dispersion, the injection trajectory feedback in the vertical plane is inherently much less complex than that of the horizontal and will be discussed first. Using timing changes and the BPM system, two vectors are constructed—one for the closed orbit and one for the first turn. Both assume the form of

$$\mathbf{u}_m = (u_1 , u_2 , ..., u_m). \quad (1)$$

Four horizontal and vertical corrector magnets in the PTB line can be adjusted relative to the behavior of the existing trajectory such that the incoming trajectory will be corrected to the measured closed orbit. To inject automatically onto the closed orbit, two correctors are chosen such that they are separated by approximately 90 degrees phase advance. For each corrector, a beam response is determined at every beam position monitor throughout the booster. These two data sets are then combined into one, giving the desired response matrix. The kick provided to the beam via a corrector k can be represented by θ_k, giving the following matrix equation

$$\Delta \mathbf{u}_m = \Re \, \Delta\theta_n , \quad (2)$$

0-7803-4376-X/98/$10.00 © 1998 IEEE

where $\mathfrak{R}$ is the response matrix found by the method given above and $\Delta\theta_n$ is the vector giving the size of variation of the correctors used. The objective is to reduce $\Delta\mathbf{u}_m$, the error trajectory used for the feedback loop, to zero, describing the situation in which the first turn trajectory matches the measured closed orbit. Singular value decomposition is used to invert the matrix $\mathfrak{R}$ [1]. After inversion,

$$\Delta\theta_n = \mathfrak{R}^{-1}\,\Delta\,\mathbf{u}_m\,, \qquad (3)$$

which reveals the amount the correctors must be adjusted [2]. The calculated currents are then multiplied by a gain factor, and the corrector setpoints are updated by this amount. This process is repeated in a feedback loop until the rms of $\Delta\,\mathbf{u}_m$ is sufficiently small. A gain of 0.5 was empirically determined to maximize the system performance while avoiding instability.

Because longitudinal and horizontal beam motions both appear as positional variations at BPMs located in the non-zero dispersion regions, the longitudinal errors must be corrected before simple correction of the horizontal can begin. The longitudinal injection errors result from slight drifts of the booster dipole magnet ramp or the relative rf phase between the PAR and booster. Phase and energy errors appear 90 degrees out of phase. Upon injection, an energy error, as measured on a turn-to-turn basis at a high dispersion point, assumes a cosine-like form, while a phase error has a sine-like signature. Energy errors are corrected through the adjustment of the start ramp time of the magnet ramping system. Phase errors are corrected by changing the relative phase between the PAR and the booster.

In the longitudinal plane, only one reliable beam position monitor in a high dispersion region need be used. The beam position is recorded over a series of 256 turns and is stored in a beam history module. This number of turns was chosen such that a sufficient number of synchrotron oscillations could be viewed ($Q_s = 4\times10^{-2}$). It is through this data that the energy and phase errors are revealed.

The longitudinal corrections can be approached in a fashion similar to that used for the vertical plane. The required feedback parameters are again empirically determined. The start ramp time and relative phase are adjusted manually to eliminate errors such that only noise remained. Then, the start ramp time is adjusted in a series of five steps relative to the original setpoint, and the slope is determined. Also, the relative phase is adjusted in a series of five steps relative to the original setpoint, and the slope is again determined. Figure 1 exemplifies the results of manual longitudinal tuning in the following order: energy and phase errors eliminated, phase error only (36 degrees), and energy error only (1.25 MeV). Some signal processing is first applied in order to extract only the desired longitudinal motion from the accumulated beam position history. An example of the processed phase error is found overlaid in Figure 2.

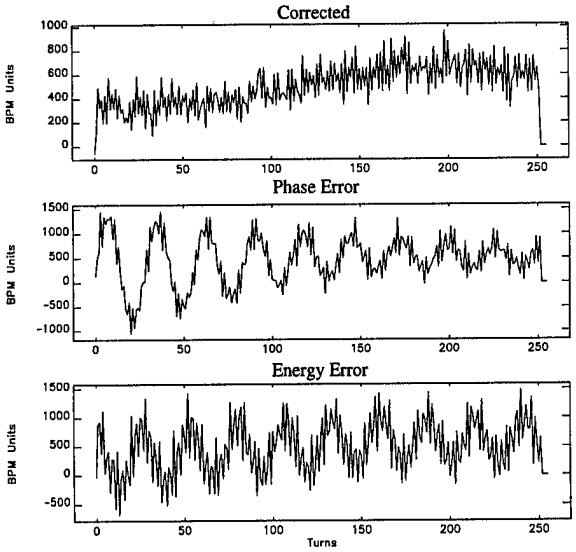


Figure 1: Manual tuning results.

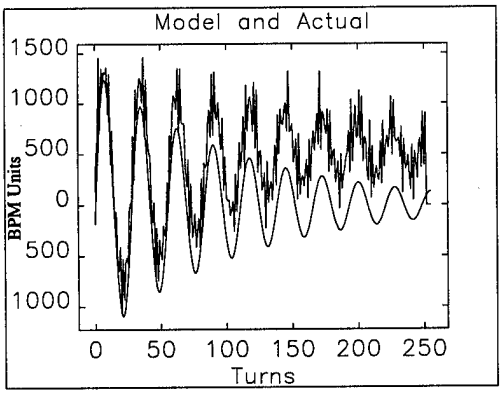


Figure 2: Model and actual phase error.

Regarding correction of the longitudinal errors, a simple method is employed. First, the cosine-like component of the motion is determined. A change in the start ramp time is then made to zero this energy error. The data is then processed on the remaining sine-like component, and a PAR rf system phase change is made to zero the phase error.

With the longitudinal corrected, it is now simple to perform the horizontal correction. This method is quite similar to that used in the vertical plane; however, the dispersion in the horizontal plane adds a small complexity. The revolution freuqency of the booster is adjusted to accommodate the storage ring. This forces the booster to run slightly off-energy and creates a constant off-energy orbit displacement, which must be accounted for and subtracted off the closed orbit measurement to reveal only the betatron closed orbit. This is measured by calculating the average offset of the closed orbit in the horizontal plane and by dividing it by the average dispersion in the booster, i.e.,

$$((dp)/p) = \langle x_E\rangle/\langle\eta\rangle\,. \qquad (4)$$

The energy of the incoming trajectory position offset is then determined at each BPM. This result is subtracted from the measured horizontal betatron closed orbit motion, and the same correction algorithm used in the vertical case is employed.

3 RESULTS

3.1 Vertical Tune-up

Automation in the vertical plane has proved quite effective. Figure 3 shows the rms difference of the closed orbit and the first turn trajectory with the feedback loop off and then switched on. Here, the gain was set to 0.5 which was found to be adequate in that it kept the system from becoming unstable yet still rapidly corrected the vertical trajectory. The vertical feedback system can run indefinitely without becoming unstable.

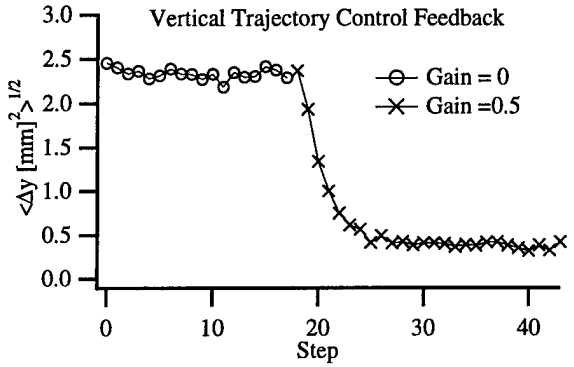


Figure 3: Vertical feedback response.

3.2 Longitudinal Tune-up

Using unity gain in the feedback loop designed for correcting the longitudinal errors proved successful. Both the phase and energy errors were corrected within one iteration. This feedback loop may also be run indefinitely; however, reduction in the gain proves to be slightly less noisy.

3.3 Horizontal Tune-up

The horizontal plane corrected successfully after the longitudinal errors were eliminated; however, if the longitudinal errors are not corrected, the horizontal feedback loop becomes unstable in less than twenty iterations. This is due to the energy and phase offsets of the first turn corrupting the horizontal signal. Figure 4 shows the rms difference of the closed orbit and the first turn trajectory with the feedback loop off, then switched on. As with the vertical, an assigned gain of 0.5 proved successful in that it prevented the system from becoming unstable; however, correction in the horizontal plane it is still not as successful as the results given in the vertical.

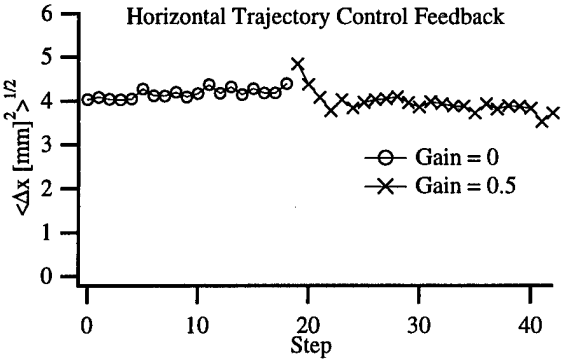


Figure 4: Horizontal feedback response.

4 CONCLUSION

Although this injection tune-up system is in actual fact automated, a graphical user interface, which is currently under development, will provide an easy-to-use system. The automation, however, has proved itself useful by correcting the first turn trajectory in the booster with minimal effort. The vertical was the simplest plane to correct in, thus allowing tests on the automation software to take place, and the automation of the horizontal and longitudinal corrections was built on this knowledge.

5 ACKNOWLEDGEMENTS

The authors would like to thank J. Carwardine for his program *polefind* and K. Evans for his program *getbdeltap*. In addition to many C-shell and Tcl/Tk scripts, various SDDS tools and SDDS-compliant EPICS tools were used [3, 4]. These programs were composed to perform the experiments needed to construct the response matrices and to adjust the currents on the PTB corrector magnets, the relative phase, and the start ramp time, according to the feedback loops.

This work is supported by the U.S. Department of Energy, Office of Basic Energy Sciences, under Contract No. W-31-109-ENG-38.

6 BIBLIOGRAPHY

[1] W. Press, S. Teukolsky, W. Vetterling, B. Flannery, *Numerical Recipes in C*, Cambridge University Press, New York, 1992.

[2] H. Wiedemann, *Particle Accelerator Physics*, Springer-Verlag New York, 1993.

[3] M. Borland et al., "Doing Accelerator Physics Using SDDS, UNIX, and EPICS," *Proc. of ICALEPCS* '95, pp 382-391 (1997).

[4] M. Borland et al., "The Self-Describing Sets Protocol and Toolkit," ibid, pp 653-662.

CONCEPTS FOR A SLOW-POSITRON TARGET AT THE ADVANCED PHOTON SOURCE

E. Lessner and M. White

Argonne National Laboratory, 9700 South Cass Avenue, Argonne, Illinois 60439-4800 USA

Abstract

The Advanced Photon Source (APS) [1,2] linear accelerator beam could be used to produce slow positrons during the hours between the storage ring injection cycles. Initial concepts for the design of a target that is optimized for slow-positron production are discussed, and simulation results are presented. Some possible ways to increase the nominal linac beam power for improved slow-positron production are also discussed.

1 INTRODUCTION

Slow positrons are valuable tools in atomic physics, materials science, and solid state physics research. Slow positrons can be used: 1) to probe defects in metals, as positrons are repelled by ionized atoms and may be captured at vacancies; 2) to study Fermi surfaces through analysis of photons generated by positron/electron annihilation; and 3) to study surfaces and interfaces of materials through analysis of energy losses, diffraction, and reemission of positrons from surfaces or interfaces.

Slow positrons can be emitted by radioisotope sources or they can be obtained by moderating the positrons produced by accelerator beams. Normally, an intense electron beam impinges on a target made of a high atomic number material, such as tungsten or tantalum. Positron production occurs as a result of bremsstrahlung interactions, and the positrons are then moderated by a series of foils that have a negative work-function for positrons. Positrons emitted from the moderator are then captured and transported to an experimental area by electromagnetic fields. The number of positrons that can be delivered to an experiment is a function of the incident beam power, target material and geometry, moderator efficiency, and slow positron capture and transport efficiency.

The APS linac beam could be used to produce slow positrons during the hours between storage ring injection cycles or top-off operations. The linac and some possible ways of increasing its beam power are discussed.

Initial concepts for the design of a target that is optimized for slow-positron production are discussed, and simulation results are presented. We compare the positron yield obtained from simulations of various target configurations for a fixed beam power and energy. Finally, we present an integrated target-moderator concept that will result in a high-intensity slow positron source, when combined with an efficient extraction and transport system.

2 THE APS LINAC

The APS electron linac accelerates 30-ns-long pulses containing 50 nC of charge to an energy of 200 MeV. The resulting 500-W electron beam impinges on a 7-mm-thick water-cooled tungsten target that serves as a positron converter. Pair-produced positrons and electrons are refocused by a 1.5-T pulsed coil and directed into the positron linac where, during normal operation, they are captured and accelerated to 450 MeV. Linac design parameters are listed in Table 1, together with achieved performance values.

The nominal electron beam power of 500 W can be increased for slow positron production purposes by increasing the nominal pulse length of 30 ns and by increasing the effective repetition rate.

The upstream accelerating structure in each linac is directly powered by a 35-MW klystron, while the remaining structures are powered in groups of four by a klystron and SLED (SLAC Energy Doubler) cavity assembly. The SLED cavities can be detuned, thereby allowing the full klystron pulse, nominally 5 μs, to be used. The beam energy with SLEDs detuned but without heavy beam loading was measured to be about 400 MeV. Measurements to determine the maximum accelerated pulse length with reasonable energy spread are scheduled. A new pulser design that allows re-firing of the gun 1 μs after the end of the first beam pulse is under consideration.

The linac repetition rate is limited to 60 Hz by the present modulator's resonant-charging system design; however constant-current power supplies that could also allow a faster rate are presently being tested [3].

Table 1: Linac Performance Summary

	Design	Achieved	Units
Energy on Target	200	240	MeV
Gun Pulse Length	30 ns	> 1 μs	
Current on Target	1.7	> 2	A
Rf Rate	60	60	Hz
e^- Energy Spread	± 8	≤ ± 8	%
e^+ Emittance	≤ 1.2	≤ 1.2	mm mrad
e^+ Energy	450	458	MeV
e^+ Current	8	14	mA
e^+ Energy Spread	± 1	≤ ± 1.6	%

0-7803-4376-X/98/$10.00 © 1998 IEEE

3 TARGET DESIGN SIMULATIONS

We performed computer simulations of several target configurations using the electromagnetic shower code EGS4 [4], in order to optimize the target-moderator design parameters. In the simulations, a pencil beam of electrons is incident perpendicularly to the basis of a tungsten cylinder. The beam power is fixed at 800 W and the incident electron energy is 400 MeV. We examined the positron yield from single-layer targets and multiple-layer targets of varying layer thicknesses. The energy distributions and the divergences of all shower products were analyzed in each case.

Simulations of single-layer target geometries indicate that a tungsten target that is three radiation lengths (Xo) thick (10.5 mm thick) results in the highest positron yield. However, for the same incident beam power and energy, the total positron yield from segmented targets can be significantly higher. The total yield of positrons with energies up to 6 MeV is shown in Figure 1. The yields in the figure are calculated per incident electron and are shown for the optimized single-layer target and for the optimized five-layer target. The single-layer target is three-radiation-lengths thick, and the multi-layer target segments are 1.250-, 0.750-, 0.750-, 0.125-, and 0.125-radiation-lengths thick, respectively.

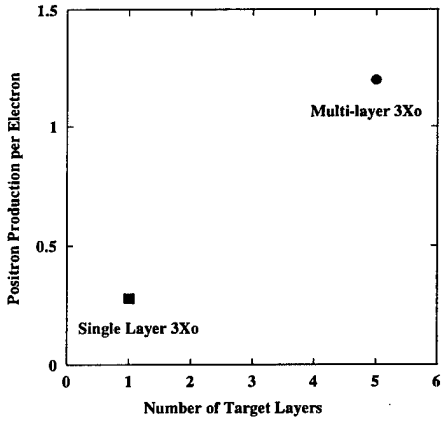


Figure 1: Production, per 400-MeV electron, of positrons with energies in the range $0 \le E_{e^+} \le 6$ MeV, by a single-segment three-radiation-length target and by a five-segment target of the same total effective length.

In Figure 2 we show positron production by each segment of the five-layer target. The yield per incoming 400-MeV electron increases from 0.14 positrons per electron after the first segment to 0.30 after the fourth segment, and decreases slightly to 0.24 after the last segment. Contributions from backscattered positrons are negligible, and are not included in this estimate. Using the numbers above and assuming an average moderator reemission efficiency of 10^{-2} [5], we estimate a total slow positron yield from the target of roughly 10^{10} positrons per second. The final slow positron current at the experiment will, of course, be significantly less as a result of inefficiencies in the capture and transport processes.

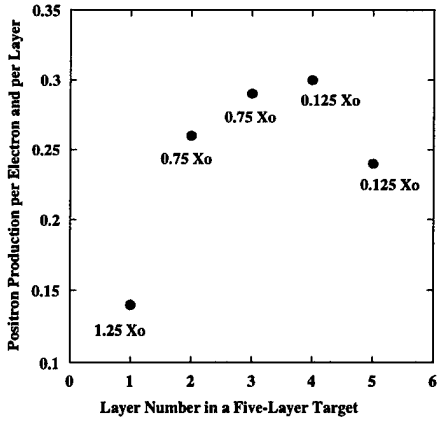


Figure 2: Positron production in the range $0 \le E_{e^+} \le 6$ MeV after each target segment of the optimized five-layer target. The segment thicknesses are indicated under each symbol.

The transverse distributions of positrons generated in the first and last segments are shown in Figures 3(a) and 3(b), respectively. The positron beam divergence increases by a factor of ten between the first and the last target segment, as can be seen in the figures.

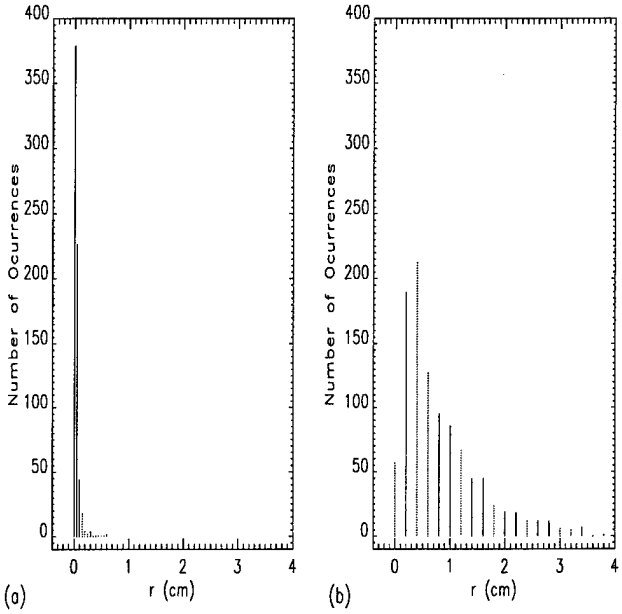


Figure 3: Transverse distributions of positrons with ($0 \le E_{e^+} \le 6$ MeV) generated in the first (a) and fifth (b) segments of the five-layer target.

4 A TARGET-MODERATOR CONFIGURATION

The efficiency of slow positron production depends strongly on the target-moderator geometry. We are developing an integrated tungsten-based target-moderator concept in which the moderator "foils" are machined into the target itself. Figure 4 depicts such a self-moderating tungsten target segment. The reemission percentage of low-energy positrons would be higher if we were to use thinner foils, but thinner foils are difficult to produce and to handle. Our concept uses the electrical discharge machining (EDM) process to machine foils into the target in a simple and straightforward way, thus reducing the manufacturing and handling difficulties. We have shown that foil thicknesses ≥ 125 μm can be machined, and we are continuing to investigate ways to achieve thinner foils.

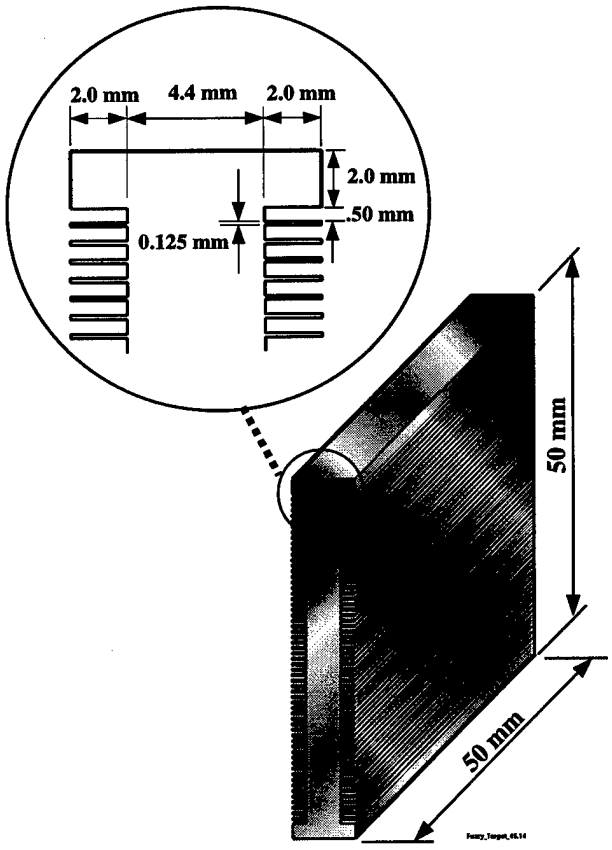


Figure 4: Self-moderating tungsten target segment. Details of the moderator are shown in the insert.

The separation between foils must be optimized for maximum efficiency while still allowing penetration of the electromagnetic extraction fields. We incorporated effects of the electrical extraction fields into our computer simulation, and preliminary tests of the code have been performed. We have not yet simulated the moderating process.

Our studies indicate that the APS linac can be used as a source of slow positrons. An integrated target-moderator concept is now being optimized, and measurements to determine the maximum achievable linac beam power are underway.

5 ACKNOWLEDGMENTS

Work is supported by the U.S. Department of Energy, Office of Basic Energy Sciences, under Contract No. W-31-109-ENG-38. We acknowledge L. Emery (ANL) for the use of his C-program interface to EGS4 and P. K. Job for valuable discussions, K. J. Peterson for drawings, D. Mangra for mechanical assistance, and J. N. Galayda and L. C. Teng for continuing support.

6 REFERENCES

[1] 7-GeV Advanced Photon Source Conceptual Design Report, ANL-87-15, April 1987.

[2] M. White et al., "Construction, Commissioning, and Operation of the Advanced Photon Source (APS) Linear Accelerator," Proc. of the XVIII International Linac Conference, Geneva Switzerland, 26-30 August 1996, pp. 315-319.

[3] R. Fuja et al., "Constant-Current Charging Supplies for the Advanced Photon Source (APS) Linear Accelerator Modulators," these proceedings.

[4] W. R. Nelson, H. Hirayama, D. W. Rogers, "The EGS4 Code System," SLAC-265 (1985).

[5] S. Okada and H. Sunaga, Nuclear Instruments and Methods, B56/57, pp. 604-609 (1991).

ELFE@DESY: SLOW EXTRACTION FROM HERA

M. Gentner, D. Husmann,
Bonn University, Physics Institute, Nussallee 12, 53115 Bonn, Germany
P. Nghiem, J. Payet, A. Tkatchenko,
Laboratoire National Saturne, CE Saclay, 91191 Gif-sur-Yvette Cedex, France

Abstract

The feasibility of the conversion of the HERA electron ring into a pulse stretcher for a 15-25 GeV injector linac has been studied. Such an injector would be available if a linear collider will be built at DESY. The linac pulses will be stretched to a c.w. beam by slow extraction from HERA. This paper describes the proposed extraction scheme and gives estimations of the stretcher performance in terms of duty factor, emittance and energy spread of the stretched beam.

1 THE ELFE@DESY PROJECT

ELFE (*E*lectron *L*aboratory *F*or *E*urope) is proposed as a 15-25 GeV, 30 μA c.w. electron beam facility for nuclear physics experiments[1]. In the past different approaches have been studied to provide such a beam, e.g., a polytron or a recirculating linac[2].

A new approach has been proposed during the conceptual design studies of a DESY linear collider[3]. If a 500 GeV linear collider linac will be installed at DESY, the first section of this linac could be used to inject a 15 to 25 GeV beam into the HERA electron ring. The ring would then act as a stretcher for the short linac pulses (in the case of TESLA the pulses are 800 μs long at a repetition rate of 10 Hz) to create a quasi-continuous beam. Figure 1 shows the schematic layout of this facility.

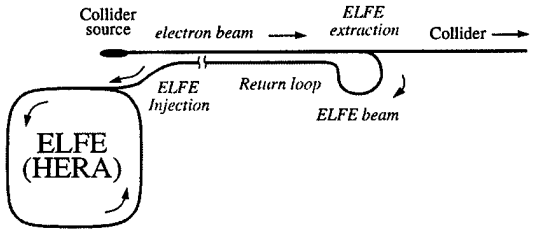


Figure 1: ELFE@DESY schematic layout

The overall feasibility of the conversion of HERA into ELFE@DESY has been discussed in[4]. The main result of that paper is that *ELFE@DESY appears to be feasible*. There are various problems to make the facility work. For example the linac pulses have to be fitted into the HERA circumference, which needs a complex injection scheme.

Furthermore the ring has to be capable to hold currents up to 150 mA to stretch the injected charge to a 30 μA c.w. beam. To counteract the arising collective instabilities a good feedback system has to be installed[5].

And, also very important, a mechanism has to be applied which can ensure the extraction of a constant current from the ring. Details of the extraction mechanism are presented in the following.

2 EXTRACTION METHOD

The extraction methods used in currently operating electron stretchers (which work at energies below 4 GeV) have been checked for their applicability to ELFE@DESY. The two mainly used methods are:

- The stable horizontal phase space area near a betatron resonance is shrinked by ramping the tune towards the resonance in such a way that a constant rate of particles becomes unstable and is extracted.
- A constant rate of particles is pushed out of the RF buckets, for example by RF phase ramps. The particles outside the buckets subsequently loose energy, and with the chromaticity of the ring this energy drift is converted into a tune drift onto a betatron resonance.

In both cases the horizontally unstable particles move along separatrix branches towards an extraction septum. Mostly a sextupole-driven third-order resonance is used where the stable phase space has the shape of a triangle (Fig. 2).[1] During the movement on the separatrix branch the stepwidth increases rapidly, providing a stepwidth sufficiently high to cross the septum with few losses of only 1-2%.

Calculations and simulations show that the energy loss per turn in HERA is too large to enable the use of the second method. The longitudinally unstable particles loose energy too fast, so that they cross the resonant tune with only a small chance of getting extracted in a controlled way. So the extraction method of choice is the tune ramp method.

The disadvantage of the tune ramp method is the dependence of the optics on the ramp. The most obvious effect is the drift of the separatrix branches, which is proportional to the tune shift and results in a drift of the x' coordinates of the extracted particles. This can easily be counteracted by an appropriately ramped dipole near the septum.

Other effects are an alteration of the stepwidth of the particles at the septum, and a change of the chromaticity. These two parameters affect the emittance of the beam during extraction, but in ELFE@HERA the influence is less than 5%.

[1] Sometimes a combination of a second and fourth order resonance is used, but there is no apparent advantage.

0-7803-4376-X/98/$10.00 © 1998 IEEE

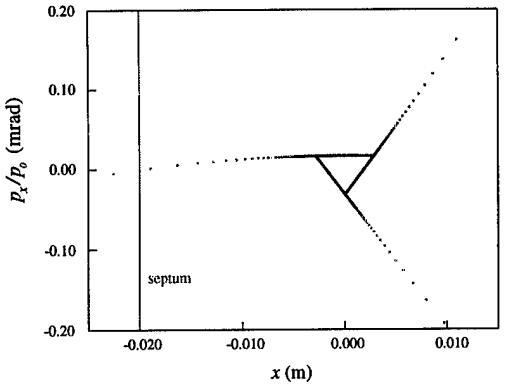


Figure 2: Separatrix triangle (with ELFE@DESY parameters)

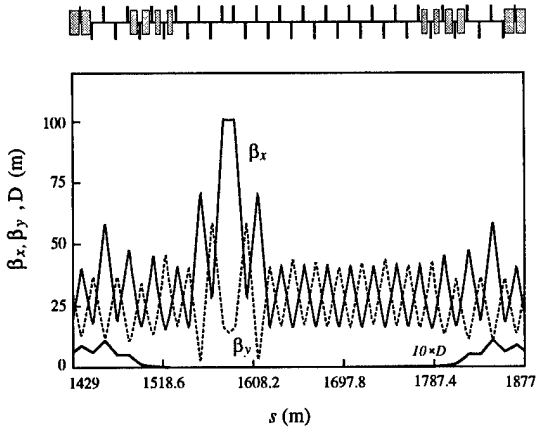


Figure 3: Straight section optics

3 TRANSVERSE OPTICS

To control shape and size of the separatrix area dedicated sextupoles are needed. The effect of a sextupole on the resonance strength scales with $\beta^{3/2}$, so these sextupoles should be placed within regions of high β functions. Likewise, to minimize the influence of the sextupoles needed for chromaticity correction on the resonance the phase advance per cell in the arcs should be near 60°.

For an untilted triangle the phase advance between sextupoles and septum has to be 30° (modulo 120°), and the α function at the septum should be zero. To achieve a small emittance of the extracted beam it is also desired to have vanishing ring chromaticity and a dispersion free beam optics at the septum, e.g. $\xi_x = 0$ and $D(s_{sep}) = D'(s_{sep}) = 0$.

Fortunately in the case of HERA the optics of the straight sections can be tuned nearly arbitrarily. So a beam optics has been designed to fulfil the criteria mentioned above. The betatron tunes, the extraction sextupole strengthes, the optical functions at the sextupoles and the septum, and the horizontal septum position have been chosen to get a step-width at the septum of 4 mm. This value is a good compromise between small emittance and small particle losses on the septum. Figure 3 shows the proposed optics of one straight section.

4 SIMULATION RESULTS

To get an estimation for the achievable performance of the machine in terms of duty factor, emittance and energy spread of the extracted beam a series of tracking simulations has been performed with MAD[6] and BETA. The tracking module of MAD fully includes the influence of synchrotron radiation, which in our case is important.

A small selection of the results is shown in Table 1. In the achromatic case the emittance is very small, but the energy spread is slightly larger than projected in[2]. By tuning the chromaticity the energy spread can be reduced, but then the emittance increases intolerably.

It has been demonstrated that by using an adaptive tune ramp shape control the machine can be emptied nearly completely, and an intensity distribution dependend duty factor of at least 90% can be reached. Taking into account the cycle timing and the filling structure of the ring the overall duty factor is reduced to nearly 80%.

5 ANALYTIC CALCULATIONS

The results of the tracking simulations have been counterchecked with analytic calculations. The emittance of the extracted beam as a function of energy, chromaticity and dispersion at the septum has been succesfully reproduced, as well as the reduction of energy spread by chromaticity change. Details can be found in[7].

The calculations are based on the analytic treatment of sextupole driven third order resonances. Without perturbations unstable particles move along the separatrix branches, in fact they are effectively pushed towards them. By approximating the resulting compression of the outgoing trajectories with exponential functions one is able to compute the effects of perturbing influences which push the particles away from the separatrix branches.

In the case of ELFE@DESY the main perturbation is the stochastic structure of the synchrotron radiation, which creates a random walk of the particles, and synchrotron oscillations in combination with non-zero chromaticity. In the latter case the separatrix branches are displaced periodically, and by the compression effect the particles follow these displacements, but with phase shifts and with smaller amplitudes.

6 SEPTA AND EXTRACTION CHANNEL

The first septum has to be as thin as possible to minimize particle losses. This suggests an electrostatic wire septum. The drawback of an electric septum is that the electrons can only be deflected weakly. Nonetheless with the help of additional magnetic septa it is possible to guide the electrons out of the machine.

Figure 4 shows a solution for the extraction channel with one electrostatic and three magnetic septa. The upper graph

energy [GeV]	horiz. chromaticity	ϵ_x/π (90% of beam) [mm·μrad]	$(\Delta p/p)_{FWHM}$ [10^{-3}]
15	zero	3.75 ± 0.16	1.19 ± 0.05
20	zero	6.76 ± 0.26	1.64 ± 0.06
25	zero	10.06 ± 0.37	2.01 ± 0.07
15	± 10	88.15 ± 3.11	0.92 ± 0.03
15	± 20	117.25 ± 5.23	0.69 ± 0.03
15	± 30	124.45 ± 7.09	0.48 ± 0.03

Table 1: Basic tracking results

shows the trajectory of a particle kicked by the electrostatic septum, whereas the lower graph includes the magnetic septa.

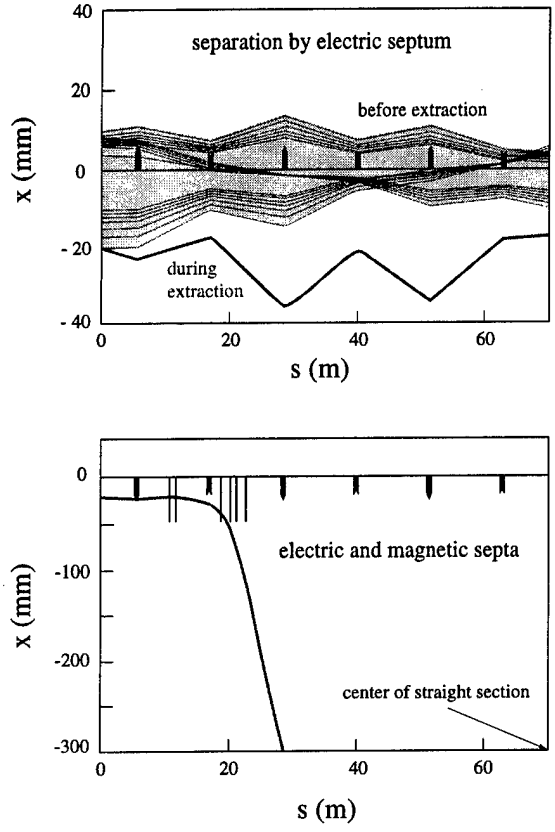


Figure 4: Extraction channel

The extracted beam leaves the ring vacuum chamber 20 m downstream the electrostatic septum. So, there is left a 40 m drift space to the center of the straight section, which should be enough for optical matching to the experimental target.

7 SUMMARY

It appears to be feasible to convert the electron ring of HERA into a stretcher for the pulses of a linear collider linac in the energy range of 15 to 25 GeV. The slow extraction from the ring makes use of a sextupole driven third order betatron resonance controlled by tune ramping. The extraction process has been extensively studied with tracking simulations and analytic models, to get estimations for the duty factor, the emittance and the energy spread of the extracted beam, and to find the optimal operation parameters of the ring.

8 ACKNOWLEDGEMENTS

The ELFE@DESY machine study group consists of R. Brinkmann (DESY Hamburg), P. Bruinsma (NIKHEF Amsterdam), J.-M. DeConto (ISN Grenoble), B. Frois (DAPHNIA-SPhN Saclay), F. Tazzioli (INFN Frascati), Y. Wu (NIKHEF Amsterdam) and the authors of this article. We would like to thank the accelerator physics group at DESY for their help.

9 REFERENCES

[1] P. Hoyer: 'Physics at ELFE', NORDITA-97/25 P, hep-ph/9703462

[2] 'Electron Laboratory For Europe: Accelerator technical proposal', Grenoble 1993, available via J.-M. DeConto, ISN Grenoble, France

[3] R. Brinkmann: 'On a continuous electron beam option at the TESLA and S-Band linear colliders', DESY-TESLA-95-14

[4] R. Brinkmann *et al.*: 'ELFE@DESY: An Electron Laboratory For Europe at DESY', Nuclear Physics A to be published, also part of the DESY linear collider conceptual design report, DESY-97-048, ECFA-97-182

[5] M. Migliorati, L. Palumbo, M. Serio, B. Spataro, F. Tazzioli: 'RF system and related multibunch instabilities issues for the ELFE at HERA stretcher', LNF-97/001

[6] H. Grote, C. Iselin: 'The MAD Program', CERN/SL/90-13 (AP).

[7] M. Gentner: 'Slow extraction - the emittance of the extracted beam', BONN-IR in preparation

BEAM LIFETIME AT THE SRS

H. Owen, CLRC Daresbury Laboratory, Warrington WA4 4AD, UK

Abstract

The beam lifetime in the SRS electron storage ring at Daresbury Laboratory is governed by several processes which vary significantly according to the machine operating mode. A theoretical model of the storage ring has been developed, taking the variable vacuum chamber aperture, dynamic aperture and other effects into account to predict the expected overall beam lifetime. Measurements have been performed to separate the contributions from the different loss processes: Touschek scattering, beam-gas scattering and quantum lifetime effects. Comparison with experiment gives a reasonable agreement with theory in the different operational modes used on the SRS.

1 INTRODUCTION

The 2GeV SRS electron storage ring has delivered synchrotron radiation to users since 1981. In that time, there have been several upgrades, most notably the addition in 1987 of extra quadrupoles to change the lattice from an 8-cell to 16-cell FODO structure to reduce the beam emittance. In addition to the dipole beamlines the storage ring presently includes 2 superconducting wigglers and an undulator; 2 multipole wigglers are planned to be installed in 1998 with reduced vertical apertures [1].

1.1 Lattice Modes

The SRS operates in 2 principal modes. In multibunch mode the lattice is operated with a high radial tune (HIQ) to minimise the emittance. In single bunch operation the Touschek lifetime is maximised by operating with a lower radial tune (LOQ), bringing the working point close to a 2nd-order difference resonance to increase the coupling. Injection from the 600MeV booster synchrotron necessitates ramping to the operating energy of 2GeV. A summary of the lattice properties in the different modes is given in Table 1. Additionally, multibunch operation is performed with both gapped and uniformly filled bunch structures.

Table 1. Lattice properties in HIQ and LOQ modes. Emittances are the theoretical natural values.

	HIQ	*LOQ*
Emittance /nmrad 600 MeV	9	23
2 GeV	104	258
Horizontal Tune Q_x	6.19	4.21
Vertical Tune Q_y	3.37	3.21
Momentum Compaction	0.029	0.058

The 2 working points operating over a range of energies, coupled with the complex aperture profile through the storage ring, makes the modelling and prediction of the beam lifetime complex. In the following sections a simplified machine model is developed which allows a comparison of theory with experiment.

2 APERTURE MODEL

2.1 Introduction

The many modifications to the storage ring have resulted in a complex vacuum chamber profile. In particular, the upgrade to a higher brightness lattice has meant that several vacuum vessels are larger than they need to be, and the usual assumption that dynamic aperture is consistently larger than the physical aperture is not true in the SRS storage ring. This of course has important implications for any theoretical estimates of lifetimes.

2.2 Physical Aperture Model

A simplified model of the storage ring apertures has been adopted to reasonably approximate the real machine whilst making modelling of proposed changes to the physical apertures more straightforward. Broadly speaking, the model breaks the machine up into 4 sections:

1. Dipole vessel
2. D-Quadrupole vessel
3. Straight section vessel
4. F-Quadrupole vessel

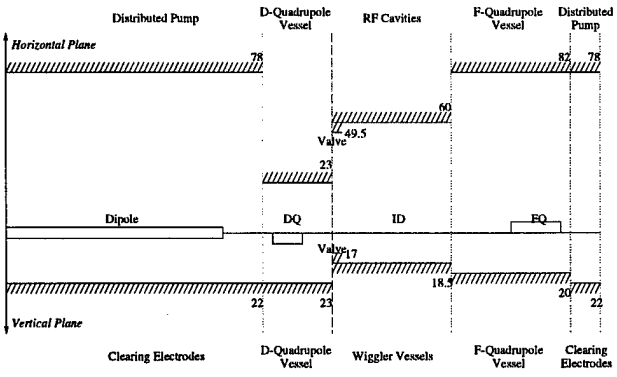


Figure 1. Physical aperture model. The real elements limiting the aperture in each model section are shown for each plane, together with the limiting apertures (given in mm). The positions of the lattice elements are also shown.

The vacuum chamber aperture is assumed to be constant throughout each of these vessels. In addition, a

0-7803-4376-X/98/$10.00 © 1998 IEEE

vacuum valve on the 6T superconducting wiggler further restricts the machine aperture at one point in the machine; the physical model is summarised in Figure 1. In reality, the largest deviation from this model occurs in the insertion device vessels, where there are different components in each straight such as cavities, beam scrapers, undulators etc.

2.3 Dynamic Aperture

Tracking was performed with a MAD model [2] of the lattice in both the ideal case and with realistic error terms deduced from vertical dispersion measurements [3]; typical closed-orbit deviations from errors are consistent with those observed on the real machine With 40 sample sets of errors it is found that the dynamic aperture is approximately 80% of its ideal value in both the HIQ and LOQ lattice modes. Comparing the on-momentum limits with physical aperture confirms that dynamic limits are significant in the horizontal plane (see Figure 2). Vertically, the dynamic aperture exceeds the physical limit throughout the lattice. In most cases the limiting aperture for Coulomb scattering is in the vertical plane, and so the dynamic limit is not relevant.

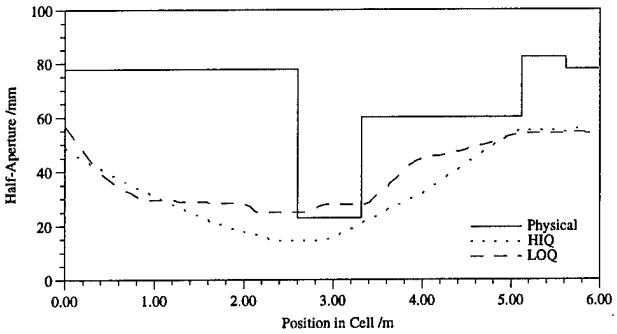


Figure 2. Comparison of physical and dynamic aperture in the horizontal plane in HIQ and LOQ modes. The dynamic aperture is significantly less than the physical aperture in large sections of the machine.

The acceptance limit for off-momentum particles, which determines the Toushek and other gas scattering cross-sections [4], can also come from dynamic limits. Using first MAD to calculate the dynamic momentum acceptance, and then ZAP [5] to calculate the resultant energy aperture, it is found that the dynamic limit is much smaller than the physical limit brought about by the finite lattice dispersion (see Table 2).

Table 2. Physical and dynamic momentum acceptances in the HIQ and LOQ lattice modes.

Mode	*HIQ*	*LOQ*
Physical Limit /%	2.5	1.4
Dynamic Limit /%	0.7	1.1

3 LIFETIME CONTRIBUTIONS

The total beam lifetime is given by the contributions of several effects:

- Beam-beam scattering - Touschek effect.
- Beam-gas scattering from residual gas:
  B - Bremsstrahlung (inelastic) from gas nuclei.
  C - Coulomb (elastic) scattering from gas nuclei.
  I - Inelastic scattering from electrons in residual gas.
  E - Elastic scattering from electrons in residual gas.
- Quantum lifetime limits - this is not significant in the SRS under normal operating apertures.

3.1 Beam Lifetime at 2GeV

3.1.1 Multibunch Lifetimes

At 2GeV the RF voltage of 1.3MV (determined from measurements of synchrotron tune frequency) provides a momentum acceptance of 0.80% in HIQ, meaning that the momentum acceptance is believed to be limited by dynamic effects. The predicted beam-gas lifetimes are shown in Figure 3. At 2GeV the predicted Touschek lifetime is 113 hours with 200mA of uniformly filled beam current (for an emittance coupling of 2.5%); this value changes according to the beam current, the machine coupling and the fill structure. When both Touschek and beam-gas effects are combined in an overall lifetime prediction (using experimental measures of bunch length and fill structure) a reasonable agreement with theory is obtained. An example set of data is given in Figure 4; here the Coulomb scattering component has been varied by changing the limiting vertical aperture with collimators in the storage ring, whilst the other scattering components are constant. The discrepancy may be accounted for if a 30% error in pressure measurement is considered, which is quite reasonable at low pressures.

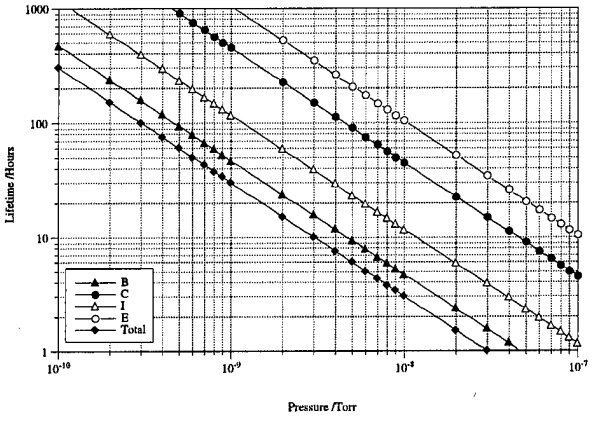


Figure 3. Theoretical beam-gas scattering at 2GeV in the HIQ lattice mode using the physical aperture model. A typical operating pressure in the SRS is around 1nTorr.

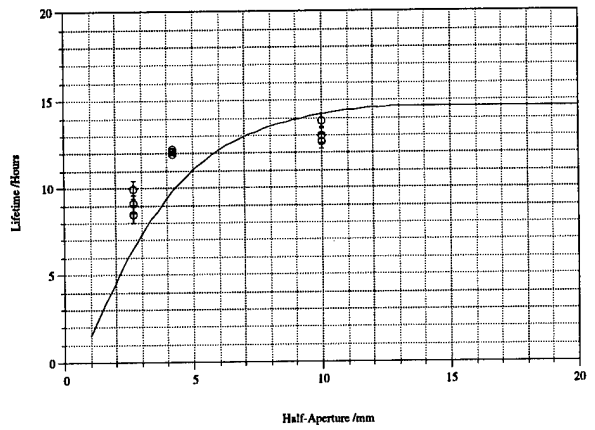


Figure 4. Example of variation of experimental multibunch lifetimes in HIQ with half-aperture at the storage ring vertical collimators. The solid line is the theoretical prediction based upon emittance and pressure measurements.

The increased momentum compaction in LOQ results in a smaller RF acceptance of 0.56%, meaning that the momentum acceptance is RF-limited. The beam-gas scattering contributions are similar to those for HIQ (see above), and varying the vertical aperture with a multibunch beam gives a similar variation of total beam lifetime (see Figure 5).

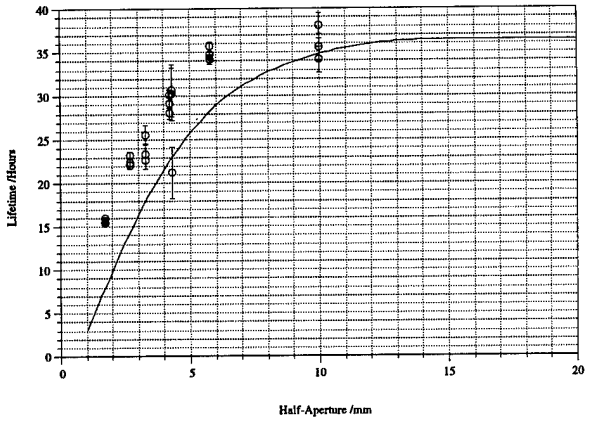


Figure 5. Example of variation of experimental multibunch lifetimes in LOQ with half-aperture at the storage ring vertical collimators. The solid line is the theoretical prediction based upon emittance and pressure measurements.

3.1.2 Single Bunch Lifetimes

With single bunch currents the beam lifetime becomes Touschek-dominated; the RF limit to the momentum acceptance has been confirmed by observing the variation of lifetime with RF voltage in single bunch mode, with a rise from 1.2 to 1.4MV giving ~10% increase in beam lifetime. The variation of the total current-lifetime product with coupling, achieved by varying the distance of the working point from the adjacent 2nd-order resonance, gives a good agreement with calculations of the Touschek lifetime (see Figure 6).

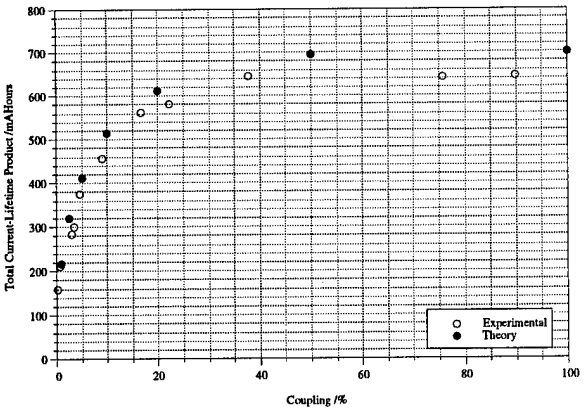


Figure 6. Variation of current-lifetime product with machine coupling for single bunch currents. Theoretical predictions including the gas scattering contribution are also shown.

3.2 Beam Lifetime at 600MeV

At 600MeV in HIQ the RF voltage of 0.4MV gives 1% momentum acceptance, so that dynamic aperture still limits the acceptance. However, even in multibunch the lifetime is strongly Touschek-limited, and with the natural emittance of 9.4nmrad would be around 0.1hours with 200mA of uniform current. This is alleviated by the significant transverse beam blow-up which occurs at 600MeV, which in HIQ corresponds to an emittance around 80nmrad. This raises the Touschek lifetime to around 6 hours; predictions using an increased emittance are consistent with this measurement. A similar phenomenon occurs when injecting at the LOQ working point which helps to maintain the Touschek lifetime in single bunch before energy ramping takes place.

REFERENCES

[1] M.W.Poole and J.A.Clarke, 'Upgrading the Daresbury SRS with Additional Insertion Devices and its Implications for the Storage Ring Layout', *Proc. 5th European Part. Accel. Conf.* p.623, Sitges (1996)

[2] H.Grote and F.C.Iselin, 'The MAD Program', CERN/SL/90-13 (1995).

[3] J.A.Clarke and H.L.Owen, 'Measurement of Vertical Dispersion and Coupling in the Daresbury SRS', *Proc. 5th European Part. Accel. Conf.* p.614, Sitges (1996)

[4] J.LeDuff, *Nucl.Instr.Meth.* **A239**, 83 (1985)

[5] M.S.Zisman, S.Chattopadhyay and J.J.Bisognano, 'ZAP User's Manual', LBL-21270 (1986)

DESIGN OF A DAMPING RING FOR THE SB-LINEAR-COLLIDER PROJECT AT DESY

R. Brinkmann[1], D. Einfeld[2], M. Plesko[3], J. Schaper[2]
[1]DESY, Notkestr. 85, D-22607 Hamburg, Germany
[2]Fachhochschule Ostfriesland, Constantiapl. 4, D-26723 Emden, Germany
[3]J. Stefan Institute, Jamova 39, SLO-1001 Ljubljana, Slovenia

Abstract

For the SB-Linear-Collider project (SBLC) at DESY a redesign of the damping ring has been performed, mainly in order to optimise the dynamic aperture. The lattice of the proposed damping ring has a DBA structure, similar to the 3rd generation light sources ESRF, APS and SPRING-8. The damping ring is build up with 6 superperiods. The straight sections between these periods are used for the injection, ejection and rf-cavities. In turn, each superperiod consists of 6 DBA cells. The straight sections of these cells are used for the installation of the wigglers, which are needed for the damping. With the installation of overall 150 m of wigglers (B_0 = 2 T and λ_0 = 0.2 m) the equilibrium emittances are $\varepsilon_{x,0} = 6.5 \cdot 10^{-10}\ m \cdot rad$ and $\varepsilon_{y,0} = 1.3 \cdot 10^{-11}\ m \cdot rad$ (the corresponding normalised emittances are : $\varepsilon_{x,n} = 3.8 \cdot 10^{-6}\ m \cdot rad$ and $\varepsilon_{y,0} = 7.6 \cdot 10^{-8}\ m \cdot rad$. The damping time results in $\tau_y \leq 3.4$ ms. The dynamic acceptance including misalignment and magnet errors is in the range of $A_x \leq 72\ mm \cdot mrad$ and $A_y \leq 80\ mm \cdot mrad$.

1 INTRODUCTION

1.1 General

High luminosity in linear colliders can only be reached by damping the beam in a so called damping ring before it is accelerated to high energies. For the S-Band-Linear-Collider project (SBLC) at DESY[1] the beam has to be damped to normalised emittances $\varepsilon_{x,n} < 5 \cdot 10^{-6}\ m \cdot rad$ and $\varepsilon_{y,n} < 2.5 \cdot 10^{-7}\ m \cdot rad$ within a time of 19.6 ms corresponding to the repetition frequency of 50 Hz. According to the pulse structure within the linacs (2 μs) the circumference of the damping ring has to be larger than 600 m. The current within one pulse should be 300 mA. In order to reach these parameters the damping ring must have a sufficient dynamic aperture for the injection process and a sufficient lifetime. To meet the requirements on the damping time, damping wigglers have to be introduced. Conventionally, such a ring is realized by a racetrack structure[2][3][4]: two arcs with bends and two long straight sections that accommodate the damping wigglers, injection, extraction and the RF-system. In such a scheme the dynamic aperture is drastically reduced by introducing the long straight sections for the damping wigglers.

In comparison to these design the 3rd generation light sources like ESRF, APS, ALS, ELETTRA[5] etc., have a relatively large dynamic aperture. Investigations at these projects have shown that the installation of insertion devices doesn't reduce the dynamic aperture very much.

1.2 Damping Ring Requirements

The damping of the emittance within a storage ring is,

$$\varepsilon_f = \varepsilon_{inj} \cdot e^{-2t/\tau_D} + \varepsilon_{equ} \cdot (1 - e^{-2t/\tau_D}) \qquad (1)$$

where ε_f is the final emittance, ε_{inj} that one of the injected beam and ε_{equ} is the equilibrium emittance of the damping ring. τ_D is the damping time of the ring and t is the accumulation time within the ring, t = 19.6 ms.

The evaluation of Eq. (1) gives for the damping ring the following requirements: $\varepsilon_{x,n} = 4 \cdot 10^{-6}\ m \cdot rad$, $\varepsilon_{y,n} = 2 \cdot 10^{-7}\ m \cdot rad$, $\tau_D \leq 3.5$ ms.

Here, an emittance dilution budget of 25% from the damping ring to the IP is taken into account. The energy of the damping ring should be in the range between 2.5 and 3.5 GeV. At an energy of 3 GeV the normalised emittance of $4 \cdot 10^{-6}\ m \cdot rad$ translates into an absolute horizontal emittance of $6.7 \cdot 10^{-10}\ m \cdot rad$ which is the domain for a fourth generation light source, about an order of magnitude below existing third generation light sources.

The small emittance of the injected electron beam ($\varepsilon_{x,n} = 1 \cdot 10^{-4}\ m \cdot rad$) results in a relaxed dynamic aperture ($\approx 10\,\pi \cdot mm \cdot mrad$ for the electron damping ring (DR). Quite different is the situation for the positron DR. The emittance of $1 \cdot 10^{-2}\ \pi \cdot mm \cdot rad$ results in a beam size at injection of 5 mm. According to the fast damping ($\tau_D \leq 3.5$ ms) this value will be damped within 3.5 ms down to 1.8 mm. We assume that an aperture of 3 $\sigma_{x,inj}$ = 15 mm should be enough for the positron damping ring, resulting in an acceptance of $20...30\ \pi \cdot mm \cdot mrad$.

2 LATTICE

2.1 Lattice of the base ring

We took as the base of the redesign the lattice of the ESRF[6] and performed the following alterations: 1) Reduction of the circumference from 880 m to 660 m; 2) Decreasing the radius of curvature of the bending magnets in order to enhance the damping; and 3) Changing of the deflection angle from 5.625 degree to 5.0 degree in order to reduce the emittance and increase the number of straight sections from 32 to 36.

0-7803-4376-X/98/$10.00 © 1998 IEEE

2.2 *Introduction of damping wigglers*

Six straight sections are needed for injection, extraction and the rf-system. With an equal distribution of them around the ring we have a sixfold symmetry. The length of a straight section - from quadrupole to quadrupole - is 6 m. With 5 m long wigglers an overall length of 150 m of wigglers can be installed. The maximum magnetic field within the wiggler has been set to 2.0 T and the period length to 0.2 m.

The wigglers have an effect on the damping time, the energy spread and the emittance. The emittance is reduced five-fold, the damping time by a factor of 7.5 and the energy spread increases by 3.1. Including the wigglers the ring has the following parameters:
$\varepsilon_{x,0} = 6.5 \cdot 10^{-10}\ m \cdot rad$, $\varepsilon_{y,0} = 0.13 \cdot 10^{-10}\ m \cdot rad$, τ_ε = 1.67 ms,τ_x = 3.34 ms, τ_y = 3.34 ms.

2.3 *Damping Ring Layout*

The schematic layout of the SBLC-DR is presented in Fig. 1. The DR has a sixfold symmetry and each superperiod consists of five unit cells with two matching sections. The unit cells are the normal DBA-structures with a damping wiggler in the straight section. The matching sections are the places for the injection, ejection and the rf-system. The lattice functions of the superperiod are presented in Fig. 2.

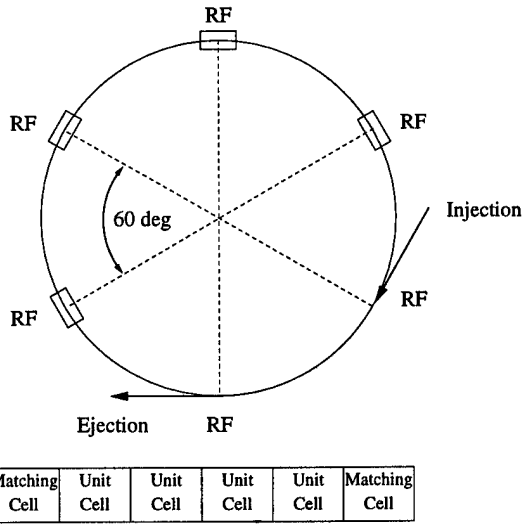


Figure 1: Schematic layout of the SBLC-DR. With a sixfold symmetry. each superperiod consists of five unit cells and two matching sections.

In order to have within the matching sections the same phase advance as within the unit cell one has to introduce in the straight section of the matching section some extra quadrupoles because the wigglers within the straight section of the unit cell perform a focusing in the vertical direction. The dynamic aperture including misalignment and some magnet errors is given in Fig. 3. At injection the aperture is a factor 5 larger as the positron beam size. This is sufficient. The energy acceptance of the DR is larger as 4%.

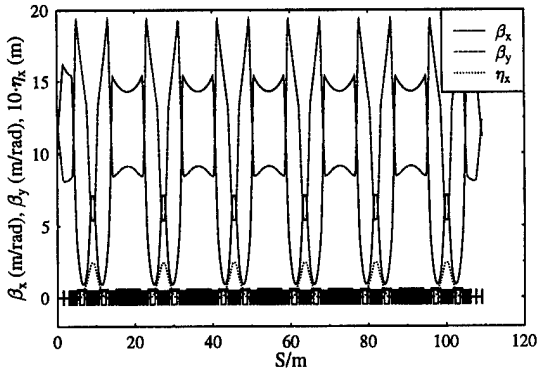


Figure 2: Lattice functions within one superperiod of the SBLC damping ring. Each superperiod consists of the unit cells with wigglers and two matching sections at each side.

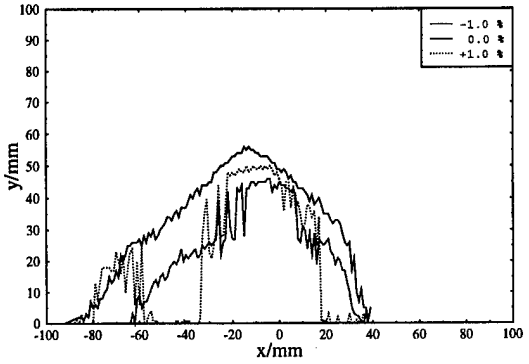


Figure 3: Dynamic aperture of the SBLC-damping ring with field errors $\Delta B/B = 5 \cdot 10^{-4}$ for the bending and $\Delta G/G = 5 \cdot 10^{-3}$ for the quads.

3 ALIGNMENT TOLERANCES AND THE VERTICAL EMITTANCE

The vertical equilibrium emittance is essentially determined by the magnet and beam position monitor (BPM) alignment tolerances and by the orbit correction procedures applied. We used the PETROS computer code to simulate alignment errors and orbit correction procedures. Assuming rms magnet and BPM position tolerances of 50 μm, the MICADO algorithm is applied in several iterations until the quality of the orbit does not improve anymore. From 10 different random seeds of errors we obtain an average vertical normalised emittance of $(1.0 \pm 0.9)10^{-7}\ m \cdot rad$. So the required emittance could just be achieved with the assumed tolerances and standard correction techniques.

4 RF-SYSTEM

The layout of the RF-System is determined by the radiation loss per turn U_0 and the required energy acceptance. For the SBLC-DR U_0 = 3.95 MeV (including the damping wigglers) and the energy acceptance $(\Delta E/E)_{RF}$ should be at least 10 times the energy spread. With an overvoltage factor q = 2 the energy acceptance is 7.2%. There has to be installed an overall voltage of 7.9 MV with a beam power of P_{beam} = 1.2 MW. The number of cavities is determined by the power which can be fed through the input coupler. Currently, both normal or superconducting cavities are being considered. For the ELETTRA normal conducting cavity[7] as well as the HERA superconducting one[8] it is around 110 kW. Hence overall 10 to 12 cavities have to be installed. The CESR superconducting cavity[9] is designed for an input power up to 250 kW. Already achieved have been 150 kW. This means that 5 to 8 cavities have to be installed. The specifications of the CESR cavity are: G = 6 MV/m, V_{RF} = 1.8 MV, $Q_0 = 10^9$, (R/Q = 89 Ω/cell, $Q_L = 2 \cdot 10^5$ and $l_{eff} = 0.3m$). Taking 5 cavities with a gradient of 1.8 MV/cell the overall RF voltage leads to q = 2.6, with an RF energy acceptance of 7.2%. By taking the phase ϕ_s = 22.62 degrees, the synchrotron tune results in $\nu_s = 8.92 \cdot 10^{-3}$, $\Omega_s = 2.55 \cdot 10^4$, f_s = 9.724 kHz.

The bunch length is then, with $\sigma_E/E = 2.2 \cdot 10^{-3}$, equal to σ_z = 4.25 mm.

5 INSTABILITIES

5.1 Single Bunch Instabilities

The microwave instability, sometimes referred to as turbulent bunch lengthening, causes an increase in both the momentum spread and the bunch length of a bunched beam. With I_{aver} = 0.8 mA per bunch, $\alpha = 1.64 \cdot 10^{-4}$, $\sigma_z = 4 \cdot 10^{-3}$ m, $(\sigma_E/E) = 2.2 \cdot 10^{-3}$ and R = 104 m one gets for the broad band impedance a maximum allowed value of $[Z_n/n]$ = 0.3 Ω that would avoid the instability. According to some measurements the contribution of the vacuum chamber at ELETTRA has a value of 0.15 Ω[10]. We assume a similar value here as well. From the measured loss factor of the CESR superconducting cavity[9] a broad band impedance of 0.03 - 0.05 Ω could be determined. With 8 cavities the contribution of the RF-system to the broad band impedance is 0.24-0.4 Ω. From this we can estimate the impedance as : $[Z_n/n]$ = (0.4-0.7) Ω, which is about a factor of two larger than desirable. Taking into account the SPEAR-scaling this value reduces down to 0.06 Ω. So bunch lengthening seems to be avoidable, but not with a large safety margin and further studies of this issue are required.

5.2 Multibunch Instabilities

With 333 stored bunches and a total current of 300 mA, multibunch instabilities are of concern. Stability is guaranteed if $(1/\tau_{\|}) < (1/\tau_{\varepsilon})$. $1/\tau_{\|}$ is the growth rate of the longitudinal coupling bunch instability and τ_{ε} is the damping time of the synchrotron oscillations. Taking a shunt impedance of $R_{s\|}$ = 200 $k\Omega$ (which is typical for a normal conducting cavity) results in a maximum current of 136 mA. The shunt impedances of the HOM's within a CESR superconducting cavity are in the range of 0.1-0.7 $k\Omega$, leading to an instability threshold of I > 380 mA. Hence the coupled bunch instability are of no importance when using superconducting cavities.

There are coupled bunch instabilities in the transverse direction, too. For a transverse impedance of $R_{\perp}$ = 11 MΩ/m (which is typical for a normal conducting cavity) the maximum stored beam within the DR is 4.0 mA. The transverse impedances of the CESR-SC-cavity are smaller than 0.025 MΩ/m leading to a threshold current of 1760 mA. In this case, however, other contributions to the impedance (in particular the resistive wall impedance) may become dominant. Whether or not a feedback system is required, must be determined by more detailed investigations. In any case it should be noted that the issue of multibunch instabilities is significantly relaxed compared to the B-factory rings presently under construction at SLAC and KEK.

6 REFERENCES

[1] Linear Collider Design Report, DESY-97-048

[2] R. Brinkmann, A Study of Low - Emittance damping ring Lattices, DESY M-90-09 (July 1990).

[3] ATF, Accelerator Test facility, Design and Study Report, Internal 95-4 (June 1995).

[4] NCL damping ring, Zeroth-Order Design Report for the next Linear Collider, SLAC, Stanford (1996).

[5] ESRF Foundation Phase Report (February 1987) European Synchrotron Radiation Facility, B.P.220-38043, Grenoble Cedex.

[6] J. Murphy, Synchrotron Light Source DATA Book, BNL/NSLS, BNL 42333, Version 4.

[7] M. Svandrlik *et al.*, The Cure of Multibunch instability in ELETTRA, Proceedings of the PAC 95, Dallas, Texas, USA.

[8] R. Byrns, B. Dwersteg *et al.*, Status of the Superconducting Cavity, Program for HERA, Proceedings of the EPAC 90, Nice (June 12-16, 1990).

[9] S. Belomestnyk *et al.*, Wakefield and HOMs Studies of a Superconducting Cavity Mode with the CESR Beam, Proceedings of the PAC 95, Dallas, Texas, USA.

[10] J.E. Karantzoulis, The Coupling Impedance of the ELETTRA Storage Ring ST/M-TN-()/14 (August, 1990) Sincrotrone Trieste.

KSR AS A PULSE STRETCHER

A. Noda, H. Fujita, M. Inoue, Y. Iwashita, H. Okamoto, T. Shirai, T. Sugimura and H. Tonguu
Nuclear Science Research Facility, Institute for Chemical Research, Kyoto University
Gokasho, Uji-city, Kyoto 611, Japan

Abstract

A pulse stretcher mode of the electron storage ring, KSR, is presented. Such a scheme as includes the extraction system in the same straight section as the injection line is adopted in order to enable coexistence of the stretcher mode with the insertion device. This scheme also has a merit that it can use the same beam dump as the output beam from the electron linac.

1 INTRODUCTION

KSR is an electron storage ring with the maximum energy, circumference and radius of curvature of 300 MeV, 25.6 m and 0.835 m, respectively. It was initially designed as a synchrotron radiation light source [1],[2]. Responding to the recent needs for electron beam of the energy region around 100 MeV with high duty factor, its possibility as an electron stretcher ring has also been studied. The 100 MeV electron beam accelerated by the s-band (2857 MHz) disc-load linac with the maximum duty factor of $2x10^{-5}$ is 3-turn injected and extracted from the ring in ~100 msec by the third-order resonance extraction utilizing transverse RF electric field synchronized with betatron oscillation. Here the repetition rate of 10 Hz is assumed both for the linac and the stretcher ring, KSR. With this stretcher mode enabling duty factor of more than 90 %, the average electron intensity is expected to be improved from $1.2x10^{9}$ per second to $1.5x10^{12}$ per second inspite of the reduction of the peak intensity from $6x10^{15}$ per second to $1.7x10^{12}$ per second [3]. The scheme studied so far, however, had been assuming only tentative use of such stretcher mode before the final use of KSR as a synchrotron light source and the stretcher mode was not compatible with the insertion device. A new arrangement of the extraction system to compromise the insertion device and the stretcher mode is presented in the next section. Then the slow extraction scheme is presented together with the brief design of the extraction equipment. Finally the present status of the KSR is briefly given.

2 LAYOUT FOR KSR STRETCHER MODE

The slow beam extraction channel for KSR stretcher mode is to be installed in the same long straight section as the injection line as shown in Fig.1. The electrostatic septum is to be set 1.809 m downstream from the exit of the quadrupole magnet(QF) just after the RF cavity and the electrode for RF-knockout. The septum magnet is set 0.7 m downstream from the electrostatic septum so as to keep the septum thickness as large as 14 mm with technically reasonable electric field of 60 kV/cm. As the resonance exciter, a single sextupole magnet(SXR) is located after the quadrupole doublet just downstream of the inflector. The contribution of the sextupole magnets for chromaticity correction (SXA and SXB) to the resonance will be cancelled out when the horizontal betatron tune is exactly equal to 7/3 [3]. For real extraction process, the horizontal betatron tune should not coincide with this value in order to form finite size separatrix. The contribution, however, is expected to be small and can be neglected at the lowest order approximation.

3 SLOW EXTRACTION SCHEME

The output beam from the electron linac will be injected by 3-turn injection into the transverse phase space with use of the perturbator (PB) and the beam emittance thus

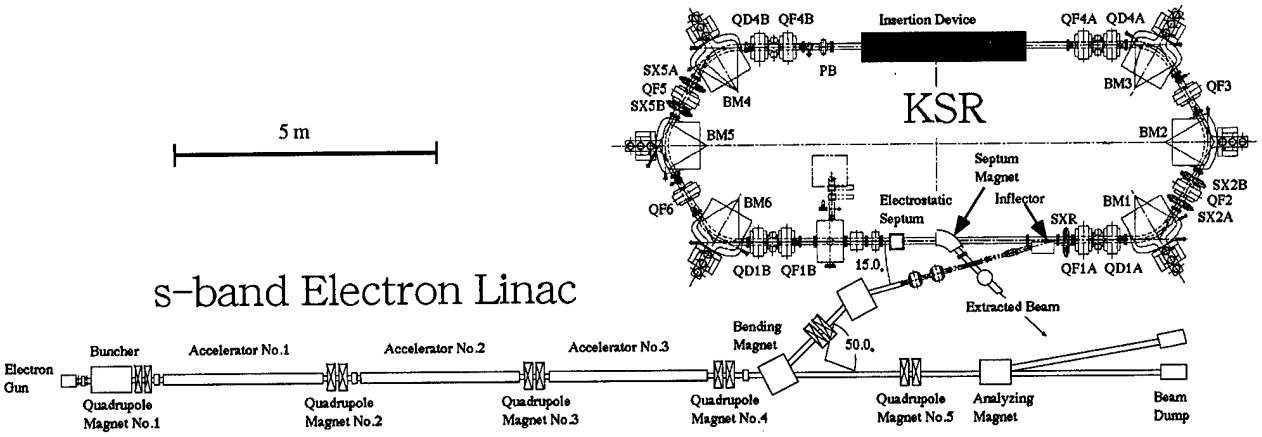


Fig. 1 Layout of the s-band Electron Linac and the Stretcher, KSR

0-7803-4376-X/98/$10.00 © 1998 IEEE

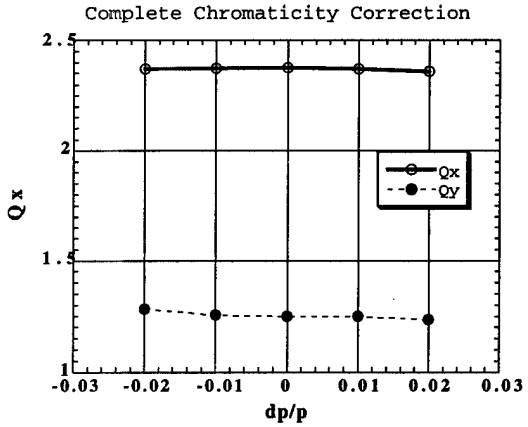


Fig. 2(a) Complete Chromaticity Correction.

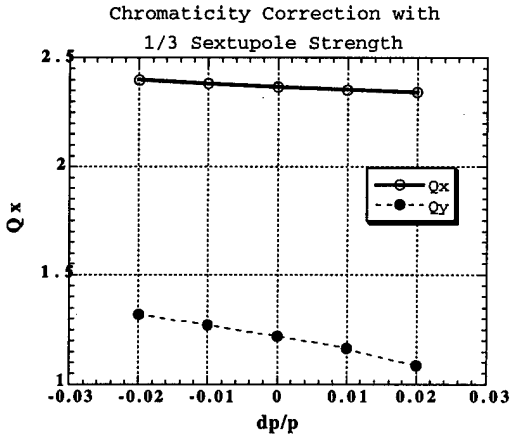


Fig. 2(b) Chromaticity corrected with sextupole magnets with 1/3 strength.

injected is estimated to be 250 πmm•mrad [3]. So we want to extract the beam by expanding the horizontal betatron oscillation amplitude with use of RF knock-out method [4].

3.1 Chromaticity Correction

Complete chromaticity correction so far proposed as shown in Fig. 2(a) assumes usage of rather strong sextupole strength (B"l /Bρ) of -36.0 and 36.5 1/m^2 for SXA and SXB, respectively, where the chromaticities (defined as $\Delta Q/(\Delta p/p)$) in horizontal and vertical directions are calculated to be 0.027 and 0.007, respectively. With this chromaticity correction, it has been found that the extraction beam can almost align at the entrance of the Electrostatic Septum (called as ESS hereafter) when the slow extraction with RF knockout is applied. This situation holds for relatively small momentum spread with the size of a few % as shown in Fig. 3(a). Due to large nonlinearity caused by strong sextupole fields, the situation changes largely for the beam with much larger momentum difference. In addition to this, the extracted beam has the same momentum spread as large as that of the circulating beam.

The sextupole strengths of 1/3 of the above values realize the betatron tunes given Fig. 2(b). Under such chromaticity correction, electron beams with lower momenta than 2% are considered to be stable because their horizontal tunes are much different from the third integer resonance, 7/3. Even for the momentum of 2%, the beam with the amplitude of 0.033 m is also found to be stable as shown in Fig. 3(b) by solid circles. By application of transverse RF electric field which resonates with horizontal betatron oscillation with tune value 2.3406 (corresponding to fractional momentum difference of 2 %), the amplitude of betatron oscillation will increase. The electron with the larger amplitude (0.04 m) will be extracted as shown in Fig. 3(b) by open circles. The merit of this scheme is that the momentum spread of the extracted electron is expected to be smaller because only higher momentum electron around 2% will be extracted. This scheme, however, needs additional beam acceleration scheme described below. More quantitative calculation is needed to give precise value of the momentum spread of the extracted beam.

3.2 Induction Accelerator for Momentum Shift

In order to extract all the circulating beam with the

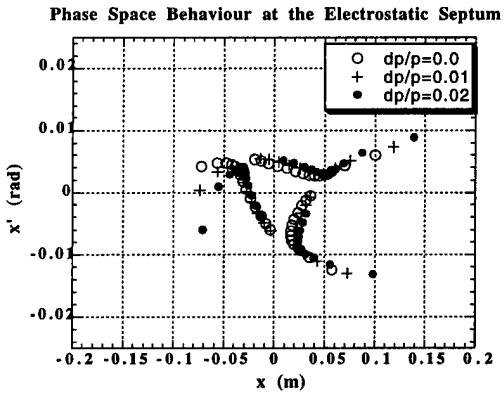


Fig. 3(a) Phase Space Plot of the Extracted Beams with Different Momenta at the Entrance of ESS.

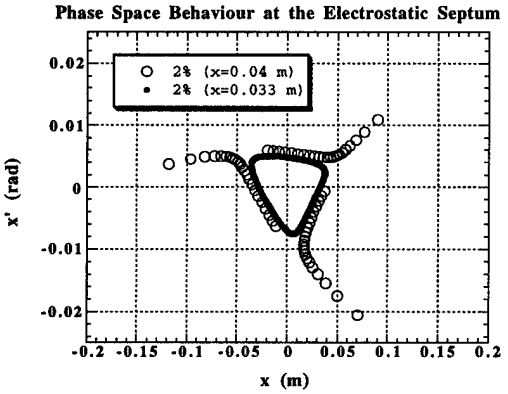


Fig.3 Phase Space Plot of the Electron Beam at the Entrance of the Electrostatic Septum.

scheme described above, the circulating beam should be accelerated in the time interval of 100 msec. For this purpose, we are now thinking about the possibility of utilizing an induction accelerator as used at TSR for laser cooling [5]. We want to accelerate 100 MeV electron as large as 4% in 0.1 second. As the revolution frequency of the electron is 11.67 MHz, necessary acceleration voltage per turn is 3.4 V and flux interval of 0.34 Vs is needed, which seems in the reach of the present technology [5].

3.3 Electrostatic Septum (ESS)

In order to kick out the beam expanded to some amplitude (~0.057 m) and realize the necessary coil space for the succeeding septum magnet, an electrostatic septum with the septum thickness and length of 0.2 mm and 0.3 m, respectively is to be used. The electric field of 60 kV/cm will be applied and the deflection angle of 18 mrad is added to 100 MeV electron. The gap of the ESS is designed to be variable between 10 and 15 mm.

3.4 Septum Magnet (SM)

For the septum magnet located 0.7 m downstream from the end of the ESS, the thickness of 14 mm will be available as septum thickness. With this condition, the magnetic field of 5 kG is attainable although the current density in the septum coil is estimated to be as high as 58 A/mm^2. The septum magnet will be set in the air and the vacuum chamber is installed inside of its gap. From the previous experience at TARN II, the current density up to 78 A/mm^2 has been realized even in the vacuum chamber [6]. For the case of 100 MeV electron, the radius of curvature is 700 mm and the septum magnet will have the curved aperture. It will deflect the extracted electrons as large as 46° with the length of 0.5 m. In Fig. 4, the trajectory of the extracted beam is shown.

4 PRESENT STATUS OF KSR

The precise alignment of the magnets of KSR has already been completed in 1995 and cabling of power line

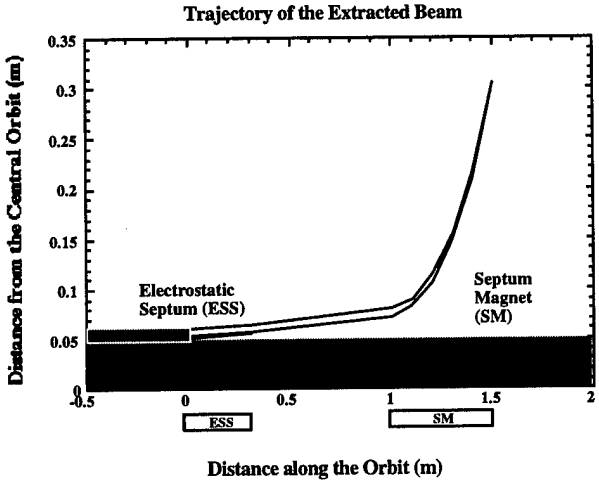


Fig. 4 Trajectory of the Extracted Beam.

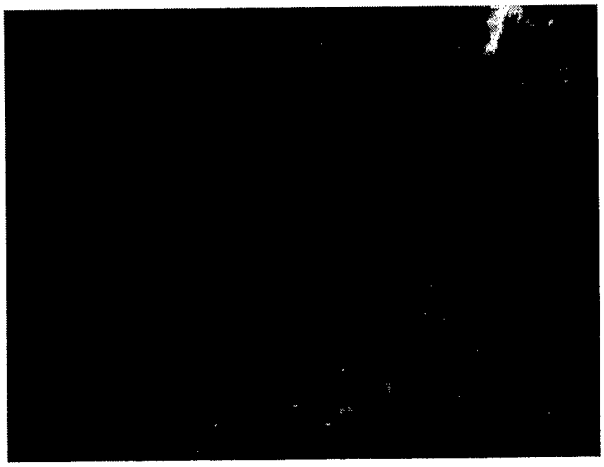


Fig. 5 Overall View of KSR.

and control systems and piping for cooling waters have been finished in 1996. The installation of the vacuum chambers into the magnet sections have also been finished last year. An arc section has been already evacuated and was found to be free from major leak(see Fig. 5).

Within this fiscal year, beam injection into the ring is expected. The construction of the beam injection line and vacuum chambers in the long straight sections are now proceeding. In parallel to this, the construction of the equipment for slow beam extraction has been started so as to use the KSR as an pulse stretcher for the electron-beam radiation-physics.

5 ACKNOWLEDGEMENTS

The authors would like to present their sincere thanks to Dr. M. Seto for fruitful discussions regarding the needs of the stretcher mode from experimental points of view. They are also grateful to Dr. K. Mashiko and Mr. I. Kazama for their cooperation during this work. Their thanks are also due to Nihon Kensetsu Kogyo Co. Ltd. for the cooperation. This work receives financial supports from Grant in Aid for Scientific Research of Ministry of Education, Science, Sports and Culture (Monbusho).

REFERENCES

[1] A. Noda et al.: `Design of an Electron Storage Ring for Synchrotron Radiation'. Proc. of EPAC94, London, United Kingdom, pp645-647.

[2] A. Noda et al.: `Electron Storage Ring, KSR for Light Source with Synchrotron Radiation'. Proc. of 1995 PAC, Dallas, USA, pp278-280.

[3] A. Noda et al.: `Electron Storage and Stretcher Ring, KSR'. Proc. of EPAC96, Barcelona, Spain, pp451-453.

[4] M. Tomizawa et al.: `Slow Beam Extraction at TARN II '. Nucl. Instr. and Meth. **A326** (1993) pp399-406.

[5] Ch. Ellert et al.: `An Induction Accelerator for the Heidelberg Test Storage Ring TSR'. Nucl. Instr. and Meth. **A314** (1992) pp399-408.

[6] A. Noda et al.: `Slow Beam Extraction System of TARN II'. Proc. of EPAC90, Nice, France, pp1263-1265.

ACCELERATOR MODELING AT SPEAR*

G. LeBlanc, MAX-lab, Lund, Sweden/SSRL, Stanford, CA
W. J. Corbett, SSRL, Stanford, CA

Abstract

The response matrix, consisting of the closed orbit change at each beam position monitor (BPM) due to corrector magnet excitations, was measured and analyzed in order to calibrate a linear optics model of SPEAR. The model calibration was accomplished by varying model parameters to minimize the chi-square difference between the measured and the model response matrices. The singular value decomposition (SVD) matrix inversion method was used to solve the simultaneous equations. The calibrated model was then used to calculate corrections to the operational lattice. The results of the calibration and correction procedures are presented.

1 1 INTRODUCTION

The modeling program is based on using a measured response matrix to calibrate a model of the accelerator system. The measured response matrix as a tool for determining the linear optics of storage rings has proven valuable in the past [1-4]. The practical aspects of measuring the matrices at SPEAR and their use as a diagnostic tool are discussed.

1.1 Objectives

The objectives of the SPEAR modeling program are to:

- calibrate models for different configurations of the ring parameters to create an accurate on-line model,
- identify hardware errors and predict and correct beam parameters such as beta functions,
- fine-tune the ring and improve the overall performance of the accelerator,
- isolate the effects of insertion devices on the electron beam and calibrate models for them.

2 MEASUREMENT PROCEDURE

The measurement procedure is time consuming and therefore automated. There are three types of measurements for each attempt at model calibration:

- The response matrix.
- The rms noise level of the BPMs.
- A dispersion orbit.

2.1 The Response Matrix Measurement

The measurements are initially made with a bare lattice. This means shutting off octupoles and skew quadrupoles as well as removing the insertion devices. Once a model is calibrated for the bare lattice, the other elements can be added and modeled.

The measurements are made using a procedure which systematically changes the excitation current of each corrector magnet. For each corrector, the change in the closed orbit is recorded. In the case of SPEAR, there are 31 correctors and 29 BPMs in each plane, which results in a 62 x 58 matrix.

2.2 The BPM noise

The rms noise levels for each of the BPMs is measured by simply taking many orbit measurements with a stable beam. This defines the limit to how well the model matrix can be made to match the measured one.

2.3 The Dispersion Orbit

The dispersion measurement is used to calculate the energy shift associated with each of the horizontal correctors.

3 CALIBRATED PARAMETERS

The calibration of the various model parameters depends upon the effect they have on the response matrix. If the effect is larger than the BPM noise level, it can be calibrated. At present, the following parameters have been calibrated for SPEAR:

- The corrector strengths.
- The BPM gain factors.
- The energy shifts associated with horizontal correctors.
- The quadrupole strengths.

3.1 Corrector strengths

Initially, the corrector strengths are all set to the same value. This provides a means of checking the calibration procedure since there are different types of correctors, which should have different values. The calibrated values can then be compared to the predicted values.

3.2 BPM Gain Factors

The BPM gains are initially set to unity. Once they are allowed to vary, a measure of the spread in gains and a direct indication of whether or not all BPMs are functioning is obtained.

* Work supported in part by Department of Energy Contract DOE-AC03-76SF00515 and Office of Basic Energy Sciences, Division of Chemical Sciences.

0-7803-4376-X/98/$10.00 © 1998 IEEE

3.3 Quadrupole Strengths

The initial model quadrupole strengths need not be very accurate. In the case of SPEAR, there are numerous "fudge" factors which have been introduced in order to obtain a better correlation between model and machine. The calibration procedure described here eleminates these factors.

4 THE CALIBRATION PROCEDURE

The calibration procedure is as follows:

- Measure the response matrix.
- Create a model response matrix.
- Calculate the changes in the model response matrix for the parameters that are to be calibrated.
- Compare the measured and model matrices.
- Calculate the parameter changes that minimize the difference.
- Iterate until the solution converges.

When starting with an un-calibrated model, the number of iterations necessary for convergance can be reduced by calibrating the corrector strengths, energy shifts with horizontal correctors and quadrupole family strengths first. Once this is done, the BPM gains can be added and the individual quadrupole strengths can be calibrated seperately. Experience has shown that five or six iterations usually suffice for convergance of the solution. With several thousand (62 x 58 = 3596) measured data points, it is possible to include many parameters. At present there are 2 x 31 correctors, 2 x 29 BPM gains 50 quadrupole strengths, and 31 energy shifts for a total of 201 calibrated parameters for the bare lattice.

Once a calibrated model is acquired, changes in the parameters can be calibrated. All of the parameters can be left to vary and the measured response matrix from the bare lattice replaced with one measured after the change is made.

5 OBSERVATIONS AND RESULTS

The initial calibrations of SPEAR illuminated the need for a more precise model. The calibration of the bare lattice is now routine.

The results of the very first iterations of the calibration procedure showed that there were two BPMs with gains that differed considerably from the rest. These happen to be older monitors that were known to be problematic. After calibration it is possible to use the information obtained from them scaled with the gain. While the coupling terms of the matrix are not presently being used in the calibration routine, they have shown that there is a BPM that gives an erroneous vertical signal when the horizontal correctors are changed. The cause is still under investigation.

The corrector gains obtained from the first calibrations showed that there was a new corrector that had little or no effect on the beam. This was discovered to be due to the fact that one of the corrector coils was wired wrong and has since been corrected.

5.1 Quadrupole Families

There are seven families of quadrupoles in SPEAR. Each family is powered in series by a single power supply. The calibration of the quadrupole family strength gives a current/quadrupole-strength value which is independent of magnetic measurements made prior to installation of the magnets on the ring. This can then be used to calculate new current settings in order to make any changes. The tunes are not directly used in the calibration routine and are used to confirm that the calibrated values are correct. The individual quadrupole strength calibrations show the spread within families that, while it is not possible to individually set the current, offer a way to simulate beam parameters which are difficult or impossible to measure on the machine.

5.2 Quadrupole Shunt Calibrations

Quadrupole shunts are used on SPEAR for finding the center of quadrupoles and measuring the beta functions [5,6]. A response matrix was measured for a bare lattice and a model was calibrated, and then the shunt was activated and a new response matrix was measured. This matrix was put into the calibration routine and all the parameters were left to vary. The first iteration showed that the calibrated strength of the shunted quadrupole was reduced by a couple percent while the others remained virtually unchanged. This test will be repeated for every quadrupole and the calibrated change in strength with shunts used to refine shunt-based measurements. It also shows that the calibrated differences in quadrupole strengths within a family of the order of a few percent can be trusted. The calibrations done so far have shown that the quadrupoles within a family keep their ordering from strongest to weakest with different current settings as well.

5.3 Beta Function Corrections

The beta functions calculated using the initial calibrated model were not very uniform compared to the design values. A measurement of the beta functions was then made and compared to the calibrated model values. The calibrated current/quadrupole-strength values were then used to calculate new current settings in order to correct the discrepancy. The beta functions were measured and a new model was calibrated. Figures 1 and 2 show the vertical beta functions before and after correction. The stars are measured values and the solid lines are calculated from the calibrated models. Some of the difference between the measurements and the model values is due to the fact that the quadrupole shunts are not all calibrated as yet and the measured values are an average over the length of the quadrupoles.

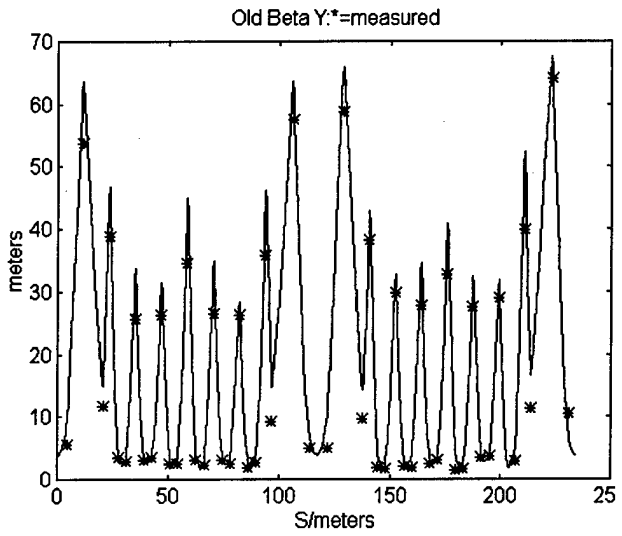


Figure 1: Vertical beta function before correction.

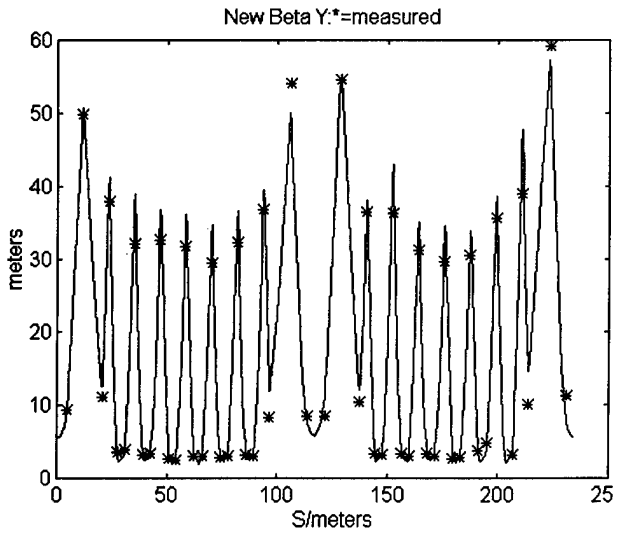


Figure 2: Vertical beta function after correction.

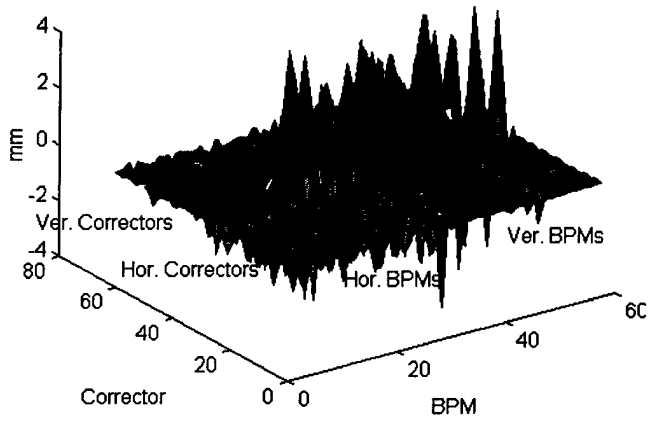


Figure 3: Difference matrix before calibration.

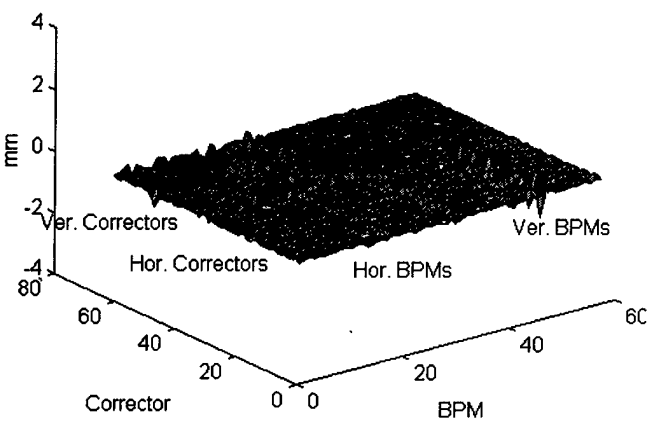


Figure 4: Difference matrix after calibration.

6 CONCLUSIONS

The response matrix calibration method produces a very accurate model of the linear optics of a storage ring. Figures 3 and 4 show the difference between measured and modeled response matrices before and after calibration. Work is in progress to calibrate the effects of insertion devices.Once a calibrated model exists, it is straigthforward to identify and quantify changes to the machine due to installation of new elements or failure of existing ones.

7 ACKNOWLEDGEMENTS

The authors would like to thank Max Cornachia and Mikael Eriksson for their support of this work. James Safranek provided the LOCO [1] code for the calibration routine and many helpful suggestions, and Martin Lee provided stimulating discussion. Heinz-Dieter Nuhn, Bob Hettel and the SPEAR operations staff are gratefully acknowledged for their help in the practical aspects of making the measurements and interpreting the results.

REFERENCES

[1] J. Safranek, Nucl. Instr. and Meth. A388, pages 27-36.

[2] W.J. Corbett, et al, IEEE PAC, Washington, D.C. (1993).

[3] J. Safranek, M. Lee, AIP Conf. Proc., Vol. 315, (1994).

[4] D. Robin, et al, Proc. of 1996 EPAC, Barcelona, (1996).

[5] P. Röjsel, Nucl. Instr. and Meth., A343 (1994) pages 374-382.

[6] W. J. Corbett, AIP Conf. Proc. 390, page 350

STATUS OF THE MAX-II STORAGE RING

G. LeBlanc, Å. Andersson, M. Eriksson, L-J. Lindgren, P. Röjsel and S. Werin
MAX-lab, Lund, Sweden

Abstract

The MAX-II storage ring is a third generation synchrotron light source recently commissioned in Lund, Sweden. A description of the ring is presented along with an evaluation of the performance during commissioning. The status and most recent results of the early stages of operation are also presented.

1 INTRODUCTION

The MAX-II storage ring was designed [1] and built in such a way as to optimize the cost/performance ratio rather than the performance per se. In addition, there were constraints far as space, economy and manpower, which necessitated the use of some novel techniques [2]. The commissioning procedure has proven that these techniques were successful.

2 MACHINE DESIGN

A national committee defined the specifications for the MAX-II ring. The most important ones were:

- An electron energy of 1.5 GeV.
- An emittance of less than 10 nmrad.
- 10 straight sections at least 3meters long for insertion devices.

There were also conditions, which necessitated the following constraints:

- A maximum ring circumference of 100 meters.
- Approximately 40 man-years for design and construction.
- The ever present limited funds.

2.1 Solutions

The idea was to build a very compact machine that would be delivered in blocks. Each block would be one cell of the ring, with vacuum chamber, beam position monitors and magnets mounted on a rigid girder. One main supplier would have the responsibility to deliver the cells and subcontract the various components as necessary. The design specifications were given in terms of mechanical and electrical tolerances rather than ring performance.

2.2 Lattice

The double bend achromat was taken as the starting point for the lattice design. It was known from previous experience with the MAX-I storage ring that allowing finite dispersion in the straight sections would permit a substantial reduction in the emittance. A ten-cell structure would meet the specification of less than 10 nmrad emittance at 1.5 GeV. The ideal position for chromaticity correcting sextupoles is in the middle of the quadrupoles. This combined with the desire for a compact lattice led to the decision to design the sextupoles in the pole profiles of the quadrupoles. A back-leg winding allows for chromaticity correction. An evaluation of the magnets can be found in reference [3]. The machine functions for the unit cell are seen in figure 1.

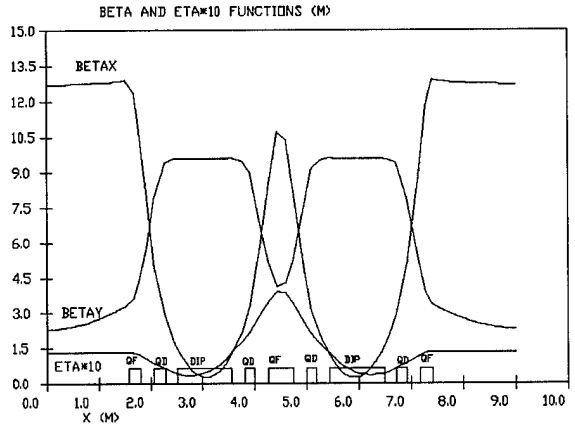


Figure1: MAX-II machine functions.

2.3 Magnets and Girders

The goal was to manufacture the magnets in such a way as to be able to mount them on the girders in well-defined positions, eliminating the need for further adjustment of individual magnets. The girders were fitted with knobs that were machined in a numerical planer. The magnets are built with stamped grooves, which are used to align them on the machined knobs.

The BPMs are also placed on machined knobs, eliminating the risk of movement with the thermal expansion of the vacuum chamber. The stainless steel vacuum chamber is connected to the BPMs with bellows on either side. Otherwise it hangs freely, with strategically placed bellows to allow for thermal expansion.

Once assembled, the girders are aligned using a central reference pillar. Two people can adjust the alignment of the whole ring in two days.

2.4 Injection

The need to be cost efficient led to the existing, 500 MeV MAX-I storage ring, being used as the injector. MAX-I is injected with 100 MeV electrons from a racetrack

0-7803-4376-X/98/$10.00 © 1998 IEEE

microtron, the energy is ramped to 500 MeV, and the beam is extracted in one shot and sent through a transport line before being injected into MAX-II. Several shots are required to fill the ring with the 200 mA design current before the energy is ramped to 1.5 GeV.

3 PRESENT STATUS

The storage ring is performing well and the first synchrotron radiation experiments will be performed soon. The alignment procedure proved to be effective when the first attempt to store a beam was accomplished without the use of corrector magnets.

3.1 Injection

The MAX-I storage ring is functioning well as an injector to MAX-II [4]. It takes a couple of minutes to cycle MAXI from extraction of the beam to injection from the microtron to a stored beam at 500 MeV. The whole process takes approximately 20 minutes, as seen in figure 2. With a circulating current of 200-250 mA in the "injector" we have succeeded in injecting approximately 30mA in each shot into MAX-II. Taking the difference in machine circumference into account, this means an overall efficiency of around 50% where the fast extraction, transfer, injection and capture procedures are included.

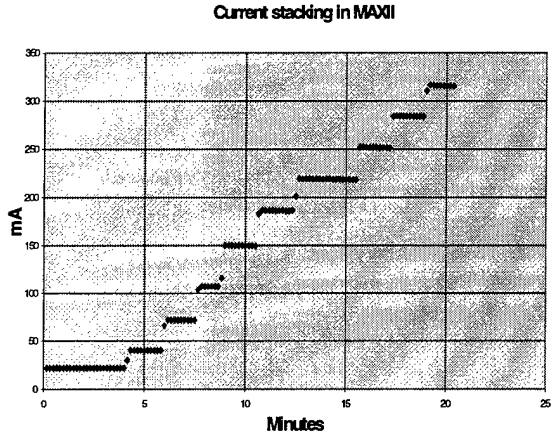


Figure 2: Current Stacking in MAX-II

3.2 Operation

The target and achieved parameters are compared below.

Parameter	Target	Achieved
Energy (GeV)	1.5	1.53
Current (mA)	200	220
Life time (Ah)	2	2*)
Coupling (%)	10	<1
Hor. Emittance (nmrad)	8.8	**)
Beam Long Term Drift (μm)	20	7
Energy Spread	0.07	**)

*) At 5% coupling.
**) To be measured.

3.3 Emmitance Measurements

Emittance measurements have been performed at "zero"- current and 1.5 GeV, where the results show that the nominal horizontal emittance (9 nmrad) is achieved. Choosing different coupling can vary the vertical emittance. At the lowest coupling an emittance of only 20 pmrad has been measured. At nominal currents the coupling can be chosen to about 1% without problem. However, at nominal currents the energy spread of the beam is larger than the natural one.

3.4 Insertion Devices

At present, there are four insertion devices installed on MAX-II. In addition, there is a super conducting wiggler which is being conditioned outside of the ring for installation in the near future. Table 1 gives the parameters of the existing insertion devices.

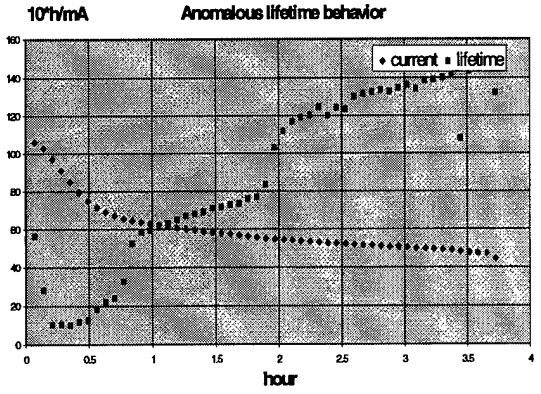
	I311	**I411**	**I511**	**I611**	**I711**
λ_u	66 mm	60 mm	52 mm	244	174 mm
K_{max}	4.50	3.63	2.69	140 *)	29.3
# of poles	77	87	99	1/2 + 1 + 1/2	27
Total length	2.65	2.65	2.65	0.9 m	2.65
Magnet gap	22 - 300 mm	22 - 300 mm	22 - 300 mm	36 mm	22 - 300 mm
Peak field	0.74 T	0.65 T	0.55 T	6 T *)	1.8 T
Type	Hybrid, taper	Hybrid, taper	Hybrid, taper	Super conducting wiggler	Multipole wiggler
Status	In operation	In operation	In operation	Delivered	In operation

*) To be measured

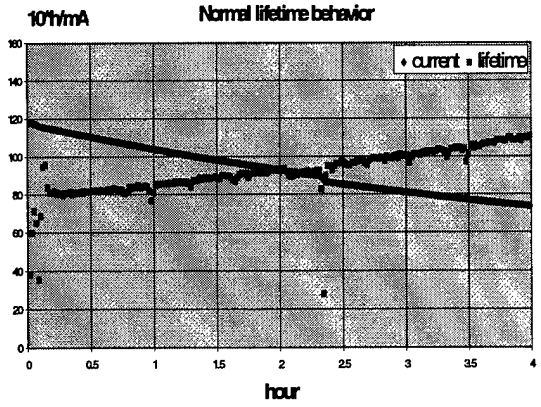
Table 1: Insertion devices for MAX II (May 1997)

4 LIFETIME PROBLEMS DURING COMMISSIONING

After filling the MAX-II ring with about 150 mA and ramping to 1.5 GeV, the lifetime was as expected for the first 10 to 20 minutes. Then suddenly the lifetime dropped to a much lower value, say about one hour. During this drop we did not observe any increased currents in the ion vacuum pumps. However, we did observe an increased radiation level in the extension of one of the short straight sections of a specific cell. After some time with a rapidly decreasing current the lifetime made a rather quick increment of at about the same time scale as the initial decrement. Some hours later we could observe another sharp lifetime increment. These abnormalities are seen in figure 3.



(a)



(b)

Figure 3: Typical current/lifetime maps found a) before and b) after removal of remaining rf-shields.

4.1 Possible Cause

We had previously experienced problems with fingers of the rf-shields in the ring. These shields were installed to smooth the vacuum chamber in all bellow joints. After the first troubles they were dismantled in all cells but two. The rf-shields are made from thin sheets of a beryllium-copper alloy with a melting point at around 900deg/celsius. The sheets are cut finger-like and formed to fit the vacuum-pipe.

The observed radiation increase coincided with the position of the remaining rf-fingers. This led us to the conclusion that they might be responsible for the observed effect. It was previously observed that part of the rf-fingers might loosen from the vacuum chamber wall and even bend into the path of the electron beam. Assuming that this could happen, without fully understanding why, it could happen that such a finger might be hit by synchrotron light. The light would heat up the finger to the melting point, and start to evaporate it. The circulating beam would experience the metal vapor, which explains the reduced lifetime, however the vapor will not reach the ion-pumps.

4.2 Cure

We decided to open up the last two cells and check the rf-fingers and found two melted fingers. We assume that the stepwise rising lifetime corresponds to the two situations when finger 1 and finger 2 stop evaporating. After starting up Max-II again we conclude that the beam lifetime problems have disappeared, and we now see a normal lifetime map.

REFERENCES

[1] Å. Andersson et al., DESIGN REPORT FOR THE MAX-II RING ISRN LUNTDX/NTMX—7019—SE

[2] M. Eriksson, Novel Techniques Used in MAX-II, Proceedings of the Fifth European Particle Accelerator Conference, page 72.

[3] M. Eriksson and L.-J. Lindgren, The MAX-II Lattice Magnets Measurements and Conclusions, Proceedings of the Fifth European Particle Accelerator Conference, page 2198.

[4] Å. Andersson and L.-J. Lindgren, Performance of the MAX-II Injector, Proceedings of the Fifth European Particle Accelerator Conference, page 2494.

HIGH DUTY FACTOR BEAMS EXTRACTED FROM THE MIT-BATES SOUTH HALL RING*

K. Jacobs, R. Averill, S. Bradley, G. Dodson, K. Dow, M. Farkhondeh, S. Kowalski, B. McAllister, D. Tieger, C. Tschalaer, E. Tsentalovich, W. Turchinetz, F. Wang, A. Zolfaghari, and T. Zwart
MIT-Bates Linear Accelerator Center

Abstract

The South Hall Ring at the MIT-Bates Linear Accelerator Center is a combination of pulse stretcher ring to produce high duty factor extracted beams and storage ring for use with internal targets. It is designed to operate at energies from 300 MeV to 1 GeV for nuclear physics experiments. In pulse stretching mode, half-integer resonant extraction is used to convert the <1% duty factor beam from the linac into near CW beam. To date, we have extracted beams with duty factors in excess of 50%, and high throughput efficiencies. The first nuclear physics experiments using extracted beam are planned for the near future. Details of commissioning the ring for extracted beam operation are presented.

1 INTRODUCTION

The MIT-Bates Linear Accelerator Center operates a 1 GeV S-band linac/recirculator used for basic research in nuclear physics. The linac has a maximum duty factor of 1%, with average currents up to 50 μA. With the present interest in coincidence experiments, it is desirable to have a much higher duty factor while maintaining the same average current. To achieve this, we have constructed the South Hall Ring (SHR) at Bates. Operated in pulse stretcher mode, it is designed to convert the pulsed beam from the linac to near CW beam using half-integer resonant extraction. The extracted beam is delivered to the existing external target set-up in the South Hall for use in experiments.

This paper describes the design of the ring and the results of resonant extraction to date.

In addition to operating as a pulse stretcher, the ring can also be operated in a storage mode to provide high average current beam to internal target experiments.

2 DESCRIPTION

Figure 1 shows the layout of the Bates facility, including the ring and the south experimental hall. The ring is 190.204 m in circumference, with a 9.144 m bend

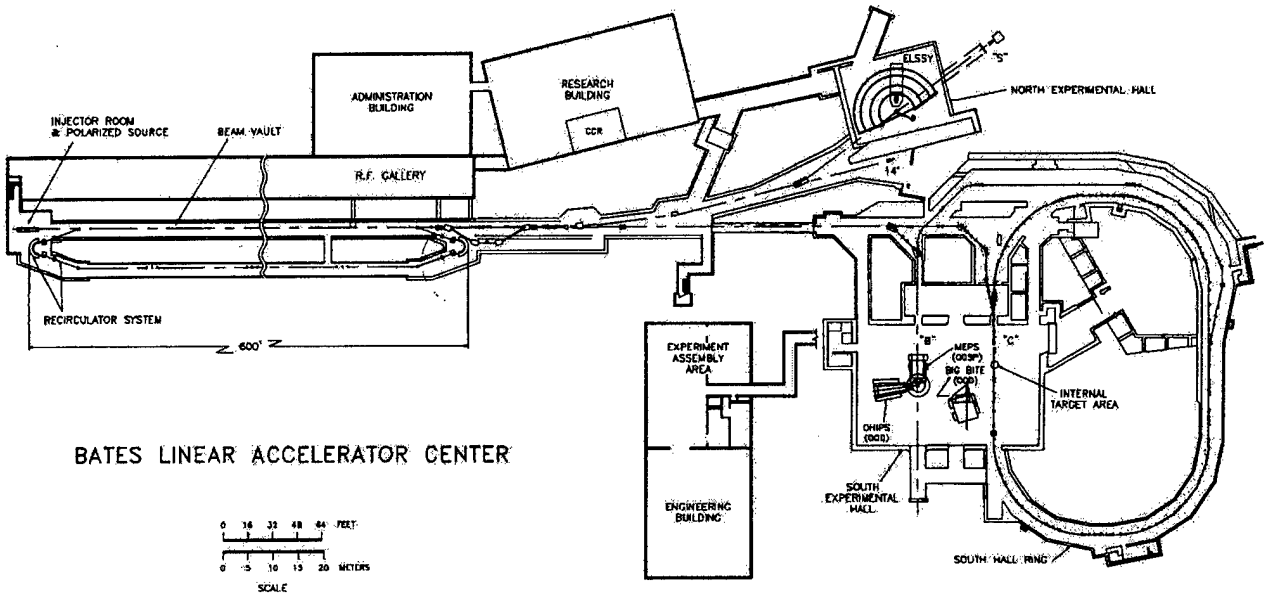


Fig. 1 Layout of the Bates facility, including the South Hall Ring and associated beamlines

.*Work supported by U.S. Department of Energy

0-7803-4376-X/98/$10.00 © 1998 IEEE

radius. It is designed for two-turn injection of 40 mA from the linac, giving 80 mA stored current, operating at a fixed electron energy between 0.3 and 1 GeV. With an injection frequency of 1 kHz and a 1 ms extraction time, the average current delivered to an experiment is designed to be 50 μA. The ring RF frequency is 2.856 GHz, the same as the linac frequency, giving a harmonic number of 1812. Every RF bucket contains charge. An energy compression system located after the linac gives an injected energy spread into the ring of 0.04%.

In extraction mode, the horizontal tune is 7.460. Octupoles are used to divide the horizontal phase space into stable and unstable regions. The beam is injected into the stable region near the separatrix. A ferrite-core ramped quad is then used to move the tune closer to the half-integer resonance. This causes the stable area to gradually shrink resulting in some of the electrons becoming unstable. As an unstable electron's betatron oscillation amplitude increases, it will eventually enter the field of the extraction electrostatic septum and be deflected down the extraction line to the fixed target in the South Hall.

Diagnostics for use in extraction include a DCCT to monitor the current in the ring, another DCCT in the extraction line to measure extracted current, and a Faraday cup located after the South Hall target point, to quantify the extracted charge. The expected precision of the Faraday cup is ±0.1%[1]. A retractable secondary emission monitor (SEM) foil in the extraction line can be used for qualitative duty factor assessment, as well as a measure of the extraction efficiency. For more accurate duty factor measurements, we have implemented a system of particle detectors to monitor the singles and accidental coincidences counting rates[2].

3 RESULTS

We have successfully performed resonant extraction from the ring using both one-turn and two-turn injection. Figure 2 shows the extraction line SEM for extraction of a single, one-turn injection pulse. By integrating the SEM signal to determine the extracted charge, we calculate an extraction efficiency of 86%. A rough estimate of the duty factor, based on observing the SEM signal on different time scales, indicates a duty factor of a few tens of percent. The spike at the beginning of the extraction pulse is, in some cases, due to part of the injected beam lying outside the stable phase space area. In this situation, adjusting the injection trajectory into the ring can eliminate this spike, although this leads to a delay in the onset of resonant extraction with a corresponding reduction in the duty factor.

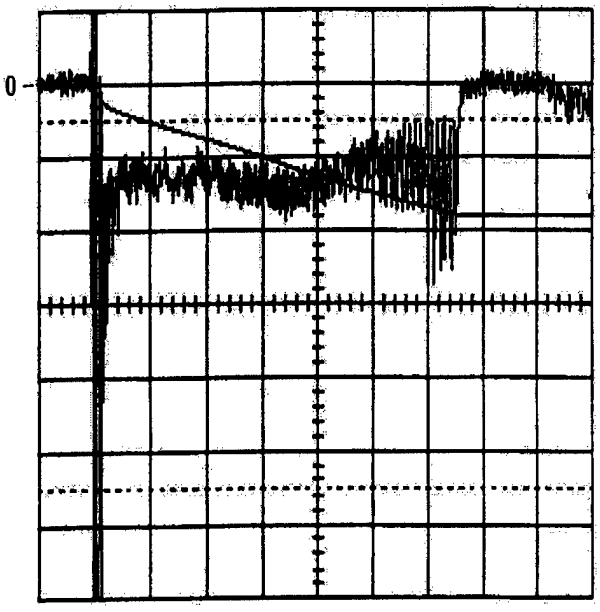


Fig. 2 Extraction of a single pulse from the ring. The vertical scale is 4.2 μa/div, and increasing current is down on the graph. The horizontal scale is 0.2 ms/div. Also shown is the integral of the extracted current.

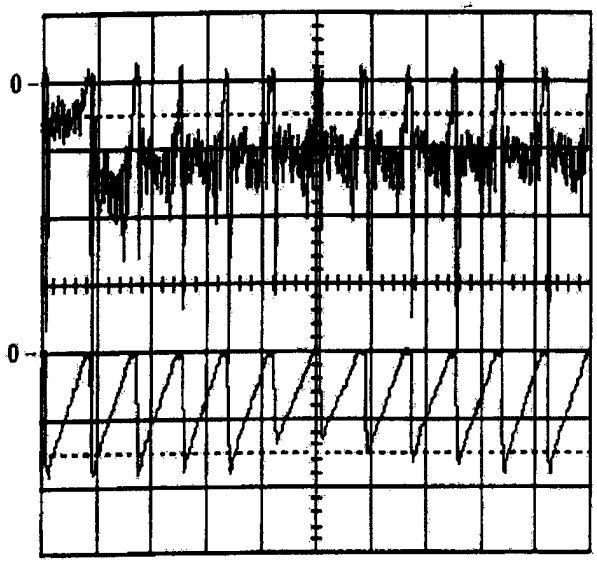


Fig.3 Extraction of a train of pulses injected into the ring at 600 Hz. The upper trace is the extracted current, and the lower trace is the current in the ring. For both traces, increasing current is down. The horizontal scale is 2 ms/div. The average extracted current is a few microamps.

In an effort to fully understand extraction from the ring, it has proven useful to study the ring in storage mode. With stored currents of up to 30 mA, we have achieved 1/e lifetimes of 7 minutes at 750 MeV. This has allowed us to make detailed investigations of various ring properties, including the closed orbit, tunes, and possible ion effects.

To date, extraction at high injection rates, as would be required by a nuclear physics experiment, has not been attempted for more than a brief period of time. Figure 3 shows an example of such extraction. The figure shows the extraction line SEM signal, and the current stored in the ring, for a series of injection pulses occurring at 600 Hz. This is a preliminary example of the sort of quasi-continuous beam we expect to be able to deliver in the near future.

Monochromatic extraction from the ring has also been performed. In this case, the ring RF is turned off, and the chromaticity is adjusted to be negative. (This is most easily accomplished by turning off the sextupoles, and using the natural chromaticity of the ring.) As the electrons lose energy due to synchrotron radiation, their tune gradually increases toward the half-integer resonance, and they are eventually extracted. This extraction technique lacks the flexibility of the extraction process described earlier because the duration of extraction is determined by the beam energy, the spread of electron energies in the beam, and the chromaticity. We do not anticipate using monochromatic extraction in general.

4 SUMMARY

We have demonstrated operation of the South Hall Ring in pulse stretcher mode using half-integer resonant extraction. Good throughput efficiency has been obtained, and rough estimates of the duty factor indicate extracted beams are close to being useable for experiments. More work is planned in both these areas. It is expected that after one more commissioning run, the ring will be ready to deliver extracted beam for use by experiments.

REFERENCES

[1] J. Shaw, R. Averill, S. Kowalski, S. Sarkar, C. Sibley, S. Sobczynski, and W. Turchinetz, "A High Power Faraday Cup to Measure Extracted Beam Current from the Bates South Hall Ring",presentation 8P73, these proceedings.

[2] J. M. Vogt, R. Florizone, "A Duty Factor Monitor for Usewith a Near CW Beam", *Nucl. Instr. and Meth. in Phys. Rev. A* **339**, 425 (1994).

TRANSVERSE KICK IN MISALIGNED TRAVELING WAVE STRUCTURES DRIVEN AT THE FUNDAMENTAL MODE

D. H. Whittum* and H. Henke†
SLAC, Stanford University, Stanford CA, 94309

Abstract

Fabrication errors in traveling wave structures result in non-axissymmetric RF fields that couple to the rf drive at the fundamental mode frequency. We calculate the excitation of the dipole mode and the integrated effect on the beam, using the thin iris and small hole approximation.

1 INTRODUCTION

An advantage commonly claimed for structures with circular symmetry is that the accelerating kick is independent of transverse position, and no transverse deflection results from the fundamental accelerating mode. Here we calculate the correction to this statement resulting from misalignment of the accelerating cells during the fabrication process. The resulting tolerance on fabrication errors is qualitatively different from the well-known limit deriving from the loss in no-load voltage from cell detuning [1]. While the effect is small for conventional accelerator applications, it could be significant for applications requiring low-emittance beams, and for structures of small dimension, where mechanical alignment is difficult.

We consider an n-cell travelling wave structure as a stack of coupled cavities, as illustrated in Fig.1. To calculate the cell-to-cell coupling in the general case,

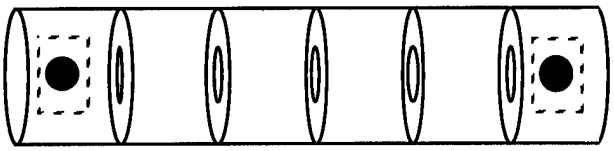


Figure: 1 An ideal, perfectly aligned n-cell structure.

we consider first a mode λ of a closed lossless cell, for which Maxwell's Equations may be expressed as, $\vec{\nabla}\times\vec{E}_\lambda = k_\lambda \vec{H}_\lambda$ and $\vec{\nabla}\times\vec{E}_\lambda = k_\lambda \vec{H}_\lambda$, with normalization of E_λ^2 to unit volume integral. With the introduction of the port coupling the cavity to another cavity, we consider the amplitude of the electric field in mode λ,

$$e_\lambda(t) = \int d^3\vec{r}\ \vec{E}(\vec{r},t)\bullet\tilde{E}_\lambda(\vec{r}),$$

for which Maxwell's Equations may be expressed as

$$\left(\frac{\partial^2}{\partial t^2}+\omega_\lambda^2\right)e_\lambda = -\omega_\lambda c\int_{port}\left(\hat{n}\times\vec{E}\right)\bullet\vec{H}_\lambda\, dA,$$

with $\omega_l=k_\lambda c$. The magnetic field amplitude

$$h_\lambda(t) = \int d^3\vec{r}\ \vec{H}(\vec{r},t)\bullet\tilde{H}_\lambda(\vec{r}),$$

may be computed from $\partial h_\lambda/\partial t = -\omega_\lambda e_\lambda/Z_0$, with Z_0~377Ω. When coupling is magnetic it is convenient to transform the coupling integral to the form,

$$\left(\frac{\partial^2}{\partial t^2}+\omega_\lambda^2\right)e_\lambda = \omega_\lambda Z_0\vec{H}_\lambda(0)\bullet\int_{port}\vec{r}\left(\hat{n}\bullet\frac{\partial\vec{H}}{\partial t}\right)dA.$$

For illustration, consider the case of two right-cylindrical pillboxes operated in the TM_{010} mode. One has, for the unperturbed mode,

$$\vec{E}_{01} = \hat{z}J_0(\beta_{01}r)E_{01},\ \vec{H}_{01} = -\hat{\phi}J_0'(\beta_{01}r)E_{01},$$

where $\beta_{01}=\omega_{01}/c = j_{01}/R$, the cavity radius is R, the length is L, and j_{01}~2.405. The normalization is $E_{01} = \left(\pi LR^2J_1^2(j_{01})\right)^{-1/2}$, with $J_1(j_{01})$~0.5192. In the presence of a centered aperture of radius $a<<R$, the electric field lines are deformed, some terminating on the iris edge, with the result that in the iris there is a tangential electric field [1]

$$\vec{E}_\perp = \frac{1}{\pi}\frac{\vec{r}}{\sqrt{a^2-r^2}}\Delta E_z,$$

where $\Delta E_z = \left(e_{01}^1 - e_{01}^2\right)E_{01}$ is the discontinuity in normal electric field across the closed iris, and e_λ^k is the amplitude of mode λ, in cell #k. Evaluating the port integral, one finds

$$\left(\frac{\partial^2}{\partial t^2}+\omega_{01}^2\right)e_{01}^1 = -\frac{1}{2}\kappa_{01}\omega_{01}^2\left(e_{01}^1 - e_{01}^2\right),$$

* Supported by the DOE Contract DE-AC03-76SF00515.
† On leave from Technische Universität Berlin.

0-7803-4376-X/98 /$10.00 © 1998 IEEE

$$\left(\frac{\partial^2}{\partial t^2}+\omega_{01}^2\right)e_{01}^2=-\tfrac{1}{2}\kappa_{01}\omega_{01}^2\left(e_{01}^2-e_{01}^1\right),$$

with coupling constant

$$\kappa_{01}=\frac{4}{3\pi J_1^2(j_{01})}\frac{a^3}{LR^2}=1.575\frac{a^3}{LR^2}.$$

In the general case of multiple cells, one has a chain of coupled oscillators. Including the perturbation due to wall-losses, one finds that the k-th interior cell satisfies,

$$\left(\frac{\partial^2}{\partial t^2}+\frac{\omega_{01k}}{Q_{wk}}\frac{\partial}{\partial t}+\omega_{01k}^2\right)e_{01}^k=\tfrac{1}{2}\omega_{01k}^2\left(\kappa_{01k-}e_{01}^{k-1}+\kappa_{01k+}e_{01}^{k+1}\right)$$

For a perfectly tuned structure driven at the design frequency ω, the mode amplitude, takes the form, $e_{01}^k=\tilde{e}_{01}e^{-\gamma(k-1)}$, with $\gamma=j\theta+\Gamma$, θ the design phase-advance per cell, and Γ the damping decrement per cell. The accelerating or "no-load" voltage may be expressed as $V_{NL}=\Re\tilde{V}_{01}e^{j\omega t}$, with t the arrival time at the first cell, and

$$\tilde{V}_{01}=\left(E_{01}LT\right)e^{j\varphi/2}\sum_k e^{j(k-1)\varphi}\tilde{e}_{01}^k,$$

with $T=\sin(\varphi/2)/(\varphi/2)$ and $\varphi=\omega L/c$ the transit angle at the drive frequency. By design, travelling-wave structures are operated at synchronism $\theta=\varphi$, so that $\tilde{V}_{01}=\left(E_{01}LT\right)e^{j\varphi/2}\tilde{e}_{01}\left(1-e^{-n\Gamma}\right)\left(1-e^{-\Gamma}\right)^{-1}$. For a constant impedance structure $n\Gamma=\tau$ is the attenuation parameter for the structure.

Next, let us perform a similar calculation for the TM_{110} mode in this geometry. Considering the x-coupled polarization, the mode basis functions are

$$\vec{E}_{11}=\hat{z}E_{11}J_1(\beta_{11}r)\cos\phi,$$
$$\vec{H}_{11}=E_{11}\left(\hat{r}\frac{J_1(\beta_{11}r)}{\beta_{11}r}\sin\phi+\hat{\phi}J_1'(\beta_{11}r)\cos\phi\right),$$

where $\beta_{11}=\omega_{11}/c=j_{11}/R$, $j_{11}\tilde{}3.832$ and the normalization is $E_{11}=\left(\frac{\pi}{2}LR^2J_2^2(j_{11})\right)^{-1/2}$, where $J_2(j_{11})\tilde{}-0.4028$. Near the axis $\tilde{H}_\lambda\approx\frac{1}{2}\hat{y}E_{11}$.

To compute the cell-to-cell coupling of the TM_{110} mode one requires the normal component of the magnetic field in the iris [2],

$$H_z=\frac{2}{\pi}\frac{r}{\sqrt{a^2-r^2}}\Delta H_y\sin\phi,$$

where $\Delta H_y=\frac{1}{2}E_{11}\left(h_{11}^1-h_{11}^2\right)$ is the discontinuity in tangential magnetic field across the conducting boundary in the absence of the port. Evaluating the port integral

$$\vec{H}_\lambda(0)\bullet\int_{port}\vec{r}\left(\hat{n}\bullet\vec{H}\right)dA=\tfrac{2}{3}a^3E_{11}\Delta H_y,$$

and, eliminating h_λ^k in favor of e_λ^k, one finds,

$$\left(\frac{\partial^2}{\partial t^2}+\omega_{11}^2\right)e_{11}^1=\tfrac{1}{2}\omega_{11}^2\kappa_{11}\left(e_{11}^1-e_{11}^2\right),$$
$$\left(\frac{\partial^2}{\partial t^2}+\omega_{11}^2\right)e_{11}^2=\tfrac{1}{2}\omega_{11}^2\kappa_{11}\left(e_{11}^2-e_{11}^1\right),$$

where the coupling constant is

$$\kappa_{11}=\frac{4}{3\pi J_2^2(j_{11})}\frac{a^3}{LR^2}.$$

In the normal development of the subject of dipole modes, it would be natural at this point to extend the formulation to include excitation by the beam in a multi-cell structure. However, our interest is not beam-excitation of dipole modes, but excitation by the externally driven fundamental mode.

2 CELL MISALIGNMENT

We consider next a multi-cell structure with misalignments, parameterized as illustrated in Fig. 2. Depending on the fabrication technique, additional constraints may apply. For example, for the Mark III structure [1], all $c_k\tilde{}0$ to within the straightness of the pipe, and the x_k are roughly independent. For the DDS structure [3], all $c_k\tilde{}x_k$ to the machining accuracy of the cups, while the cell-to-cell offsets are roughly independent. Note that each of these approximate equalities places the emphasis on *post-machining* assembly, where the largest errors occur in practice.

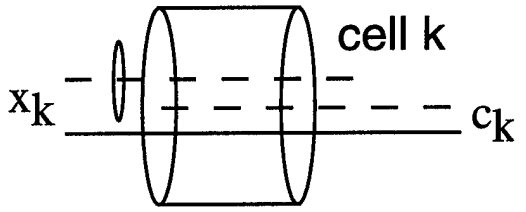


Figure: 2 With respect to a reference axis (solid line), cell k has offset c_k, while the kth iris (on the upstream side of cell k) is offset by x_k from the axis.

To compute the dipole mode excitation in cell k, let us first fix attention on the downstream port. We will work to lowest order in misalignments, neglecting quadrupole and higher modes, and neglecting too the perturbation to the fundamental mode from the dipole

mode. In the absence of a port the discontinuity in tangential magnetic field from the TM_{01} mode alone is

$$\Delta H_y = \tfrac{1}{2} E_{01}\beta_{01}\left([x-c_k]h_{01}^k - [x-c_{k+1}]h_{01}^{k+1}\right).$$

It is the zeroth Fourier component in iris-centered azimuth of this term that determines the normal magnetic field threading the port, and this is just the average over the coupling iris, $\langle \Delta H_y \rangle = \tfrac{1}{2} E_{01}\beta_{01}\left(\varepsilon_k h_{01}^k - \delta_{k+1} h_{01}^{k+1}\right)$, with $\varepsilon_k = x_{k+1} - c_k$, and $\delta_k = x_k - c_k$. The resulting drive term for the kth-cell TM_{11} mode is then

$$\left(\tfrac{\partial^2}{\partial t^2} + \omega_{11}^2\right) e_{11}^k \Big|_{upstream,01} = -\omega_{11}^2 \eta\left(\varepsilon_k e_{01}^k - \delta_{k+1} e_{01}^{k+1}\right),$$

where the coupling constant is

$$\eta = \tfrac{1}{3} a^3 E_{01} E_{11} \beta_{01} = 1.73 \tfrac{a^3}{LR^3}.$$

Including all other perturbations one has

$$\left(\tfrac{\partial^2}{\partial t^2} + \tfrac{\omega_{11-k}}{Q_k}\tfrac{\partial}{\partial t} + \omega_{11-k}^2\right) e_{11}^k = \tfrac{1}{2}\omega_{11-k}^2\left(\kappa_{11k-} e_{11}^{k-1} + \kappa_{11k+} e_{11}^{k+1}\right) - \omega_{11-k}^2 D_k,$$

with

$$D_k = \eta_{k+}\left(\varepsilon_k e_{01}^k - \delta_{k+1} e_{01}^{k+1}\right) + \eta_{k-}\left(\delta_k e_{01}^k - \varepsilon_{k-1} e_{01}^{k-1}\right),$$

As described in the introduction the terms $\tilde{e}_{01}^k$ are known; thus the amplitudes $\tilde{e}_{11}^k$ may be obtained in the frequency domain, with the numerical solution of a tri-diagonal matrix equation. The impulse to an electron enetering the first cell at time t can then be computed from $\Delta p_x = \Re \tilde{P}_{11} e^{j\omega t}$, where ω is the frequency of the drive and the integral of vertical magnetic field yields

$$\tilde{P}_{11} = \tfrac{j}{2}\tfrac{e}{c}\tfrac{\omega}{\omega_{11}} E_{11} L T e^{j\varphi/2} \sum_k e_{11}^k e^{j(k-1)\varphi}.$$

To make some analytic progress, note that it is typically the case that the fundamental mode drive frequency lies in a stop-band for the dipole modes and thus to a good approximation, adjacent TM_{110} excitations are decoupled. Thus $\tilde{e}_{11}^k \approx \tfrac{\omega_{11-k}^2}{\Delta_k} D_k$, with $\Delta_k = \omega^2 - \omega_{11-k}^2 + j\omega_{11-k}\omega / Q_k$. For illustration let us simplify to the case of a constant impedance structure. Suppressing subscripts, and substituting $e_{01}^k = \tilde{e}_{01} e^{-\gamma(k-1)}$, we have

$$e_{11}^k e^{j(k-1)\varphi} \approx \tfrac{\omega_{11-k}^2}{\Delta_k}\eta\left\{\varepsilon_k + \delta_k - \delta_{k+1}e^{-\gamma} - \varepsilon_{k-1}e^{\gamma}\right\}$$

Performing the sum, we have,

$$\tfrac{1}{mc}\tilde{P}_{11} = \tfrac{1}{2}\tfrac{e}{mc^2}\tilde{V}_{01} j \tfrac{\omega_{11}\omega}{\Delta}\eta \tfrac{E_{11}}{E_{01}}\left(\tfrac{1-e^{-\Gamma}}{1-e^{-n\Gamma}}\right) n\xi$$

where,

$$n\xi = \sum_{k=1}^{n-1}\varepsilon_k + \sum_{k=2}^{n}\delta_k - e^{-\gamma}\sum_{k=1}^{n-1}\delta_{k+1} - e^{\gamma}\sum_{k=1}^{n-1}\varepsilon_{k-1}$$
$$= \left(e^{\gamma}-1\right)\left\{\left(1-e^{-\gamma}\right)\sum_{k=2}^{n}\left(x_k - c_k\right) + \left(c_n - c_1\right)\right\}.$$

This phasor ξ is, in magnitude, roughly an average of misalignments over the structure. However, remarkably, for cup-type cells and assuming the first and last cells are centered on the beam-axis, there is no deflection to lowest order in misalignments. For the Mark III-type assembly errors add. We may extract from this result a simple rule of thumb for the maximum deflection Δp for a short ($n\Gamma \ll 1$) structure imparting maximum energy ΔE,

$$\Delta p \approx \tfrac{1}{c}\Delta E \tfrac{\xi}{d},$$

with

$$\tfrac{1}{d} \approx 1.6 \tfrac{a^3}{LR^3}.$$

In this form the result permits simple, practical estimates. For example, taking an 11.4GHz structure, operated in $2\pi/3$-mode, with $a/\lambda \tilde{}0.16$, we find $L \tilde{}0.88$cm, $R \tilde{}1$cm, $a \tilde{}0.42$cm, and $d \tilde{}15$cm. Thus a 1μm average offset between iris and cell center, in a 100MeV accelerating section, can produce a maximum kick of $7\text{x}10^{-4}$MeV/c, or a 0.6 μrad deflection for a 1GeV beam. This kick is reduced to zero as the beam approaches the accelerating crest.

3 CONCLUSIONS

We have quantified a new alignment tolerance on accelerating structures, arising from cross-talk between the fundamental and dipole modes, occuring when cylindrical symmetry is broken due to fabrication errors.

REFERENCES

[1] M. Chodorow, *et al.*, Rev. Sci. Instrum. **26** (1955) pp. 134-204.

[2] J. D. Jackson, **Electrodynamics** (John Wiley & Sons, New York, 1975)

[3] M. Seidel, *et al.*, (these proceedings).

LOW-LEVEL RF SYSTEM DESIGN FOR THE ACCELERATOR TEST FACILITY (ATF) DAMPING RING*

M.G. Minty
SLAC, Stanford, CA 94309, USA
K. Kubo, F. Hinode, S. Sakanaka, J. Urakawa
KEK, Oho, Tsukuba-shi, Ibaraki-ken, 305 Japan

Abstract

The ATF damping ring[1] was built to demonstrate the production of low emittance, high current beams for future linear colliders. To attain high beam currents, multiple high current bunch trains are required. The low-level rf system should be designed to minimize both steady-state and transient beam loading effects in the accelerating cavities. In addition the design should be sufficiently flexible to allow for a variety of beam dynamics tests which require a wide range of beam currents and cavity voltages. The low-level rf system and stability boundaries for reduced power and full power operation are discussed in this paper.

1 INTRODUCTION

Control of the longitudinal beam parameters is just one aspect of many exciting studies to be performed using the ATF damping ring. These include the use of damped cavities[2] for suppression of longitudinal coupled-bunch modes, the use of a sub-rf cavity to compensate for intra-train synchronous phase offsets[3], and beam-loading effect minimization during normal operation using a single-turn beam injection/extraction scheme[1]. Many of the studies planned involve the use of a wide range of beam currents and bunch lengths (i.e., cavity voltages).

2 STABILITY BOUNDARIES

Table 1 shows the operating conditions at the design energy of 1.54 GeV with a full 714 MHz (harmonic number h = 330) rf system (250 kW klystron[1], 4 cavities) for different numbers of bunch trains. The cavity coupling parameter[2] $\beta = 2.4$ corresponds to optimum coupling at full current neglecting higher order mode losses. The variables listed are: the dc beam current I_{dc}, the beam energy E_0, the accelerating voltage V_c, the radiation loss per turn per electron U_0, the higher order mode loss per turn[4] U_h, the synchronous phase[1] ϕ_s, the synchrotron frequency f_s, the longitudinal damping time τ_s, the natural energy spread $\frac{\sigma_\epsilon}{E}$, the bunch length σ_s, the momentum compaction α, the Robinson damping time τ, the total shunt impedance[2] R, the quality factor Q, the cavity fill time (without direct feedback) T_{fill}, the cavity tuning angle (for minimum reflected power) ϕ_z, the overvoltage[3] q, the rf bucket height $\frac{\Delta E}{E}$, the average klystron power $\langle P_g \rangle$, average dissipated power $\langle P_c \rangle$, the average beam power $\langle P_b \rangle$, and the average reflected power $\langle P_r \rangle$.

Parameter	$N_t = 1$	2	3	4	5
I_{dc} [mA]	120	240	360	480	600
E_0 [GeV]	1.54	1.54	1.54	1.54	1.54
V_c [MV]	1.0	1.0	1.0	1.0	1.0
U_0 [keV]	156	156	156	156	156
U_h [keV]	36	36	36	36	36
ϕ_s [deg]	79	79	79	79	79
f_s [kHz]	17.4	17.4	17.4	17.4	17.4
τ_s [ms]	5.5	5.5	5.5	5.5	5.5
$\frac{\sigma_\epsilon}{E}$ [10^{-4}]	6.75	6.75	6.75	6.75	6.75
σ_s [mm]	3.6	3.6	3.6	3.6	3.6
α [10^{-3}]	1.9	1.9	1.9	1.9	1.9
τ [ms]	0.19	0.11	0.13	0.17	0.23
R [MΩ]	7.2	7.2	7.2	7.2	7.2
Q	22100	22100	22100	22100	22100
T_{fill} [μs]	2.90	2.90	2.90	2.90	2.90
ϕ_z [deg]	-26.3	-44.7	-56.0	-63.2	-68.0
q	5.21	5.21	5.21	5.21	5.21
$\frac{\Delta E}{E}$ [%]	1.94	1.94	1.94	1.94	1.94
$\langle P_g \rangle$ [kW]	101	120	140	162	186
$\langle P_c \rangle$ [kW]	70	70	70	70	70
$\langle P_b \rangle$ [kW]	23	46	69	92	115
$\langle P_r \rangle$ [kW]	8	4	1	0	0

Table 1: RF parameters for design operation with 1 to 5, full current bunch trains.

Plots for various operating currents at different number of particles per bunch N_{ppb}, number of bunches per train N_{bpt}, and number of trains N_t are shown in Fig. 1 for the case of a single (top) and five (bottom) bunch trains. The solid curves are contours of constant total dc current. The expected threshold for transient bunch lengthening[1] is shown at $N_{ppb} = 3.5 \times 10^{10}$ assuming a 5 mm bunch length. The vertical lines indicate constraints imposed by the larger of the injection or extraction kicker rise and/or fall times (τ_k):

$$N_{bpt}{}^{max} = [\frac{1}{N_t}(\frac{h}{f_{rf}}) - \tau_k] \times \frac{1}{\tau_{bb}} \qquad (1)$$

where τ_{bb} is the bunch-to-bunch spacing. Assuming τ_k = 60 ns, are shown in Fig. 1(b) a solid vertical line

* Work supported by the Department of Energy, contract DE-AC03-76SF00515

[1] $\cos\phi_s = \frac{U_0+U_h}{V_c}$

[2] $R = \frac{1}{2}\frac{{V_c}^2}{P_c}$

[3] $q = \frac{V_c}{U_0+U_h}$

0-7803-4376-X/98/$10.00 © 1998 IEEE

(τ_{bb}=1.4 ns), and a dashed vertical line (τ_{bb}=2.8 ns). The solid vertical line in Fig. 1(a) corresponds to a maximum kicker flattop time of 180 ns with $\tau_{bb} = 2.8$ ns.

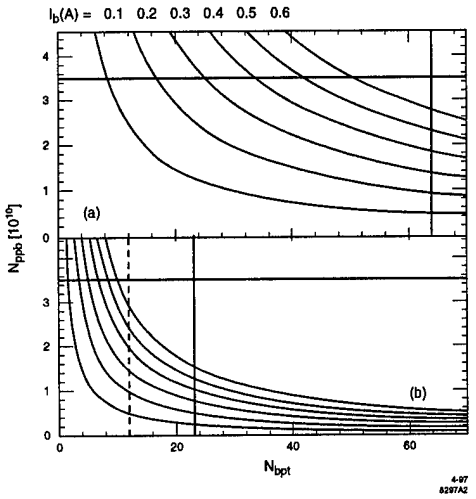


Figure 1: Map of possible fill patterns for the ATF damping ring with a single train (a) and with the design fill of five bunch trains (b).

The parameter space [5] for full current operation at 1.54 GeV is shown in Fig. 2. The horizontal axis is the tuning angle ϕ_z, which is a measure of how far off resonance the cavity is being driven. The open circle designates the design operating point which lies along the line of zero loading angle ($\phi_l = 0$) for minimum reflected power. The shaded region shows a region of instability due to Robinson's high current limit. The region indicated by hatches is accessible as limited by the available klystron output power. In practice, the hatched region may be somewhat reduced, particularly at high currents, if transient loading in the accelerating cavities is not minimized.

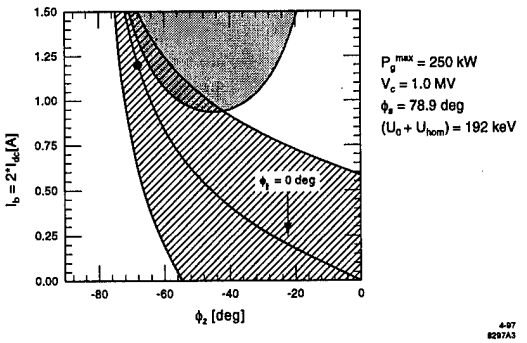


Figure 2: Parameter space for full current operation. Plotted is the beam current ($I_b = 2I_{dc}$) as a function of tuning angle ϕ_z.

Steady-state limitations to the rf beam current (twice the dc beam current) are shown as a function of cavity voltage in Fig. 3. The top two plots are for initial commissioning at reduced power (45 kW) with 2 cavities and a radiative loss per turn of 79 keV at 1.30 GeV and 156 keV at 1.54 GeV. The bottom plot assumes 225 kW available klystron power, 4 accelerating cavities, and a 1.54 GeV beam energy. Shown for zero loading angle are two limits: the maximum klystron output power (circles) and Robinson's high current limit (crosses below the power limit). For experiments requiring both high beam currents and low cavity voltages, direct feedback[6] will be required.

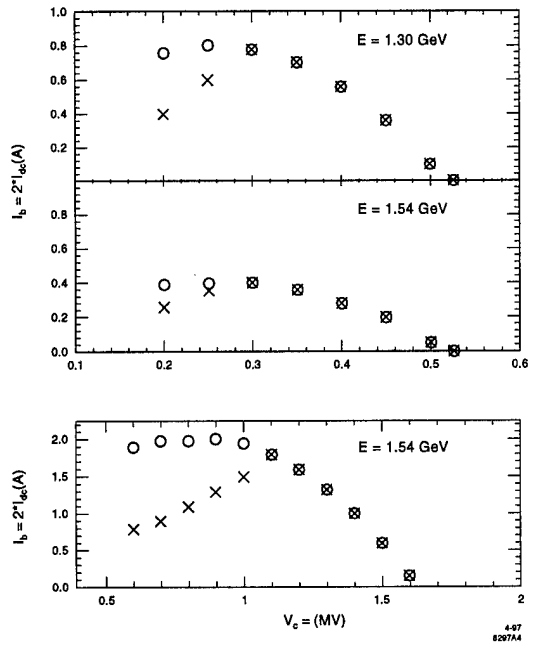


Figure 3: Beam current limits. Plotted is the beam current I_b versus the cavity voltage V_c.

3 LOW-LEVEL RF SYSTEM

The design of the low level rf control system aims towards minimum complexity while satisfying basic requirements. These include compensation for radiation and higher order mode losses, provision of sufficient cavity voltage to ensure an energy acceptance of 1%, regulation of the cavity voltage and beam phase under steady-state operating conditions, and minimization of adverse effects arising from transient beam loading at injection. These requirements should be fulfilled while minimizing the required source power and the power reflected from the cavities.

A block diagram for the low level control system is shown in Fig. 4. In the full rf system, the output of a single 714 MHz klystron is used to power 4 cavities. Conventional isolators are used after the klystron output power has been divided by two. A 1428 MHz master oscillator provides the phase reference for the S-band linac, the damping ring, and the extraction line bunch compressor klystron. The phase of the beam at injection and extraction is varied using phase shifters upstream of the feedback loops. Using the single-turn injection and extraction scheme[1] the injection and extraction phases may not be independently con-

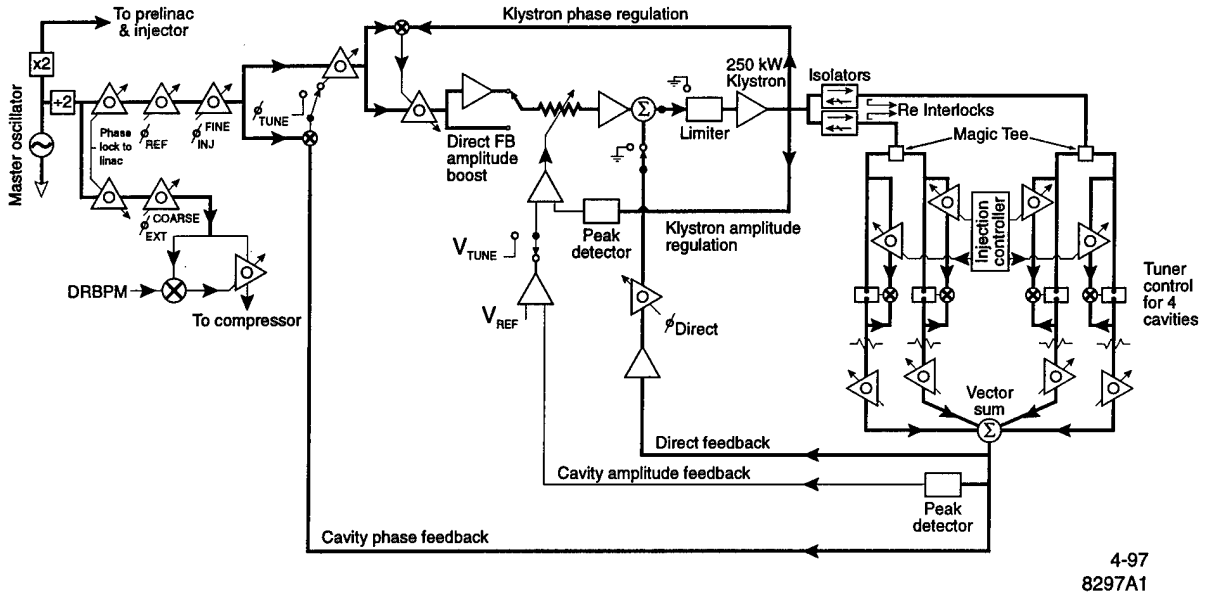


Figure 4: Block diagram of low level rf system.

trolled. In this design, the damping ring rf phase is adjusted for optimum phase at injection; the phase at extraction is therefore fixed. To ensure proper phase in the bunch compressor, the phase of the compressor klystron is adjusted via feedback using a measurement of the beam phase from the damping ring. Conventional feedback loops are used to regulate against changes in the cavity voltage and beam phase. Direct feedback[6] is included to facilitate experiments at low cavity voltage.

4 RAMP TO FULL CURRENT

Due to the proximity of the design operating current to stability boundaries (see Fig. 2), care must be exercised with injection of each bunch train. A suggested injection scheme involves detuning the cavities using the tuner feedback setpoints prior to injection of each train such that after the train has been injected, the average loading angle is zero. The required tuning angle for a train of current ${I_b}^t$ is

$$\phi_z = \tan^{-1}(-\frac{{I_b}^t R_l}{V_c}\sin\phi_s), \qquad (2)$$

where $R_l = \frac{R}{1+\beta}$ is the total loaded impedance. But since the tuning feedback loop measures the loading angle (not the tuning angle), the tuner setpoint required at train t is

$$\phi_l = -\tan^{-1}\frac{({I_b}^{t+1} - {I_b}^t)R_l\sin\phi_s}{V_c + {I_b}^t R_l\cos\phi_s}. \qquad (3)$$

Note that conventional current ramping with a fixed tuner setpoint would result in beam loss at injection of the final bunch train due to the beam loading limit.

Numerical simulations of the complete rf system have shown that transient loading of the rf system may lead to beam loss at the highest operating currents. This may be avoided using either direct feedback or, for better regulation of the cavity voltage and beam phase, by changing the rf phase (in this case by $\Delta\phi = -\phi_l$ from Eq. (3) at injection of a bunch train. The latter option is particularly useful for maintaining a high duty cycle and is described further in Ref. [7].

5 ACKNOWLEDGEMENTS

We gratefully acknowledge E. Paterson, G. Loew, and S. Takeda for their support during for the course of these studies. In addition we thank R. Siemann for insightful discussions.

6 REFERENCES

[1] F. Hinode *et al.*, 'ATF Accelerator Test Facility Design and Study Report', KEK Internal 95-4 (June, 1995).

[2] S. Sakanaka, K. Kubo, T. Higo, 'Design of a HOM Damped Cavity for the ATF Damping Ring', Proc. 1993 IEEE Part. Accel. Conf., Washington, DC (1993) 1027; S. Sakanaka *et al.*, 'Low-power Measurement on a HOM Damped Cavity for the ATF Damping Ring', Proc. 1994 Intl. Linac Conf., Tsukuba, Japan (1994) p. 281, KEK Internal 94-79 (August 1994); S. Sakanaka *et al.*, 'Design of a High-power Test Cavity for the ATF Damping Ring', Proc. 1995 Part. Acc. Conf., Dallas, TX (1995) p. 1788.

[3] K. Kubo, T. Higo, 'Compensation of Bunch Position Shift Using Sub-RF Cavity in a Damping Ring', 1993 IEEE Part. Accel. Conf., Washington, DC (1993) p. 3503.

[4] K. Kubo, private communication.

[5] See, for example, M. Minty and R. Siemann, "Heavy Beam Loading in Storage Ring Radio Frequency Systems", *Nucl. Instr. and Meth. A*, **376** (1996) 301-318.

[6] F. Pedersen, IEEE Trans. on Nucl. Sci., NS-22, no.3 (1975), and NS-32, No. 3 (1985).

[7] M.G. Minty, 'Low-level RF System Design for the Next Linear Collider Damping Rings', these proceedings.

LOW-LEVEL RF SYSTEM DESIGN FOR THE NEXT LINEAR COLLIDER DAMPING RINGS*

M.G. Minty
SLAC, Stanford, CA 94309, USA

Abstract

The design current for the Next Linear Collider (NLC) damping rings is an order of magnitude higher than existing damping rings. As opposed to storage rings, damping rings are required to operate at a high repetition frequency. Transient beam loading is therefore particularly severe. The NLC design[1] calls for a full current fill pattern consisting of up to 4 trains of 90 bunches for a total dc current of 1.2 A. However, using conventional filling techniques, with a rapid current ramp the ring energy acceptance could decrease due to transient loading and the beam might not be captured. In this paper we describe two features of the low-level rf system design. The first avoids any reduction of duty cycle while the second ensures beam capture and regulation of the cavity voltages and beam phase.

1 INTRODUCTION

A critical requirement of the NLC damping ring rf system design is to maintain a high duty cycle (i.e., the damping ring should not limit the repetition frequency). There are three sensible schemes for injecting to full current. The usual approach uses the tuner feedback loops to compensate for detuning caused by the beam. Because conventional tuner movers are slow, however, rapid injection to full current is not possible. The second option involves minimizing the total reflected power by preseting the tuning angle ϕ_z prior to injection of each train such that the loading angle ϕ_l is zero after the train is injected. This scheme is required if the total klystron is power limited[2], but is also slow due to the tuner bandwidth. A faster technique involves one preset of the tuners to ${\phi_z}^*$, which is the tuning angle for zero loading angle at full current, followed by consecutive injection of all bunch trains. Since the reflected power may be substantial, particularly during initial detuning without beam, the magic tee and circulator loads must be designed to absorb high power levels. In the interest of maintaining a high duty cycle the fast injection scheme has been studied for the NLC.

2 HIGH DUTY-CYCLC INJECTION

Simulations have shown that both with and without the tuner preset, the NLC damping ring could not be ramped to full current: the impulse change to the cavity voltage caused by injection of a high current pulse train caused enormous cavity voltage and beam phase oscillations. To correct this problem, direct feedback[3] was considered for correcting these beam-induced transients. However, there are a number of disadvantages introduced by the loop:

- the required gain places a tight tolerance on the total delay (less than 210 ns for an open loop gain of 2.5 for the NLC damping ring) and hence on the delay time in the klystron,
- the required gain may introduce coupled bunch modes that could be supported by the cavity, and
- because the transient is corrected *after* it is detected, residual cavity voltage and beam phase oscillations still persist.

Alternatively, the cavity phase and amplitude may be 'preconditioned'[4] based on knowledge of the incoming charge. Preconditioning is similar to feed-forward, however the incoming charge is *anticipated* rather than measured. In either case, the total cavity current, cavity voltage, and the phase angle between them are held constant during the injection process.

The principle of the injection procedure involves presetting the external references for the cavity voltage V_{ref} and for the input rf phase ϕ_{ref} such that the cavity voltage is unchanged in phase and amplitude at injection. The required preset of the reference voltage is $\Delta V_{ref} = S\Delta I_g$ where S is the transconductance of the klystron and I_g is the generator current:

$$\Delta I_g = \frac{V_c/R + {I_b}^k \cos {\phi_b}^k}{\cos {\phi_b}^k} - \frac{V_c/R + {I_b}^{k+1} \cos {\phi_b}^{k+1}}{\cos {\phi_b}^{k+1}}, \quad (1)$$

where V_c is the total cavity voltage (which is the vector sum of the generator and beam voltages), R is the total, loaded cavity shunt impedance, ${I_b}^k$ is twice the dc beam current for train k, and $\phi_b(k)$ is the synchronous phase angle (measured with respect to the crest of the cavity voltage) with k trains.

The preset for the reference phase is given by

$$\begin{aligned} \Delta\phi_{ref} &= \tan^{-1}\left[\frac{\tan {\phi_z}^* + \frac{{I_b}^k R}{V_c} \sin {\phi_b}^k}{1 + \frac{{I_b}^k R}{V_c} \cos {\phi_b}^k}\right] \\ &- \tan^{-1}\left[\frac{\tan {\phi_z}^* + \frac{{I_b}^{k+1} R}{V_c} \sin {\phi_b}^{k+1}}{1 + \frac{{I_b}^{k+1} R}{V_c} \cos {\phi_b}^{k+1}}\right]. \end{aligned} \quad (2)$$

Here ${\phi_z}^*$ is the tuning angle for at maximum current I_m and desired loading angle ϕ_l at maximum current:

$$\tan {\phi_z}^* = \left(1 + \frac{I_m R}{V_c} \cos\phi_b\right) \tan\phi_l - \frac{I_m R}{V_c} \sin\phi_b. \quad (3)$$

*Work supported by the Department of Energy, contract DE-AC03-76SF00515

0-7803-4376-X/98/$10.00 © 1998 IEEE

Typically the loading angle is zero at maximum current so

$$\phi_z{}^* = \tan^{-1}\left(\frac{I_m R}{V_c}\sin\phi_b\right). \quad (4)$$

The steady-state phasor diagram for the injection process is shown in Fig. 1. Here I_c is the total cavity current, and $I_b{}^k$ and $I_g{}^k$ are respectively the beam and generator currents for train k. The total cavity voltage V_c and total cavity current I_c have contributions from both the beam and the power generator. By presetting the rf amplitude and phase at injection of each bunch train, V_c and I_c are are constant for all bunch trains. As shown in Fig. 1, the cavity tuners are preset to $\phi_z{}^*$ to allow for rapid injection of all bunch trains. The loading angle ϕ_l decreases from $\phi_l = \phi_z{}^*$ with no beam to $\phi_l = 0$ at full current. The time required to reach the steady-state condition depicted is minimized by presetting the rf amplitude and phase (see Eqs. (1) and (2)) at injection of each bunch train.

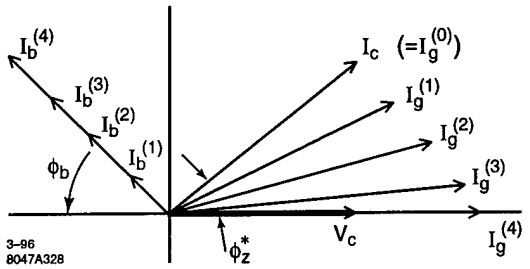


Figure 1: Phasor diagrams for injection. The superscripts (1) through (4) refers to the total number of bunches in the damping ring.

The procedure for ramping to full current is:
1. With beam off, deactivate the tuner loops and detune for $\phi_l = 0$ at maximum current; that is, set the tuner position to $\phi_z{}^*$ (see Eq. 4).
2. Set the external references $V_{ref} = SI_g$ for the desired cavity voltage.
3. Inject train 1.
4. Increment V_{ref} by $\Delta V_{ref} = S\Delta I_g$ and ϕ_{ref} by $\Delta\phi_{ref}$ and inject train 2.
5. Repeat step 4 until all trains have been injected.
6. Reactivate tuner loops. This procedure could be executed at maximum duty cycle so that the total time for injection is of n trains is n cycles, or 22.2 ms at 180 Hz for 4 bunch trains in the NLC damping rings.

In practice, recovery from no beam to full current would require at least 12 cycles (66.7 ms at 180 Hz) due to limitations imposed by the machine protection system (MPS). The envisioned startup sequence[1] is as follows: inject 4 single bunch trains, inject 4 trains of 10 bunches, and inject 4 trains of 90 bunches. Startup procedures under these conditions are given in detail in Ref. [1] for initial commissioning and MPS-compatible injection to full current.

3 SIMULATIONS OF THE HIGH CURRENT RAMP

Numerical simulations were performed using a model containing two (linear) klystrons, two rf cavities, and various feedback loops including realistic nonlinear elements such as time delays and filters. At present the cavity is modeled as a narrow-band resonator so that only beam interactions with the fundamental cavity mode are analyzed. The simulated response of the cavity voltage and beam phase to the injection of the first train is shown in Fig. 2 for three cases: no transient loading compensation (solid), correction with direct feedback using a loop gain of 2.5 (dot-dashed), and correction with presets (dashed, almost flat). The results are summarized in Fig. 3 in which the peak-to-peak cavity voltage and phase oscillations are plotted as a function of train number using direct feedback or using presets. As can be seen, the correction of the beam-transients is substantially improved (by more than a factor of 10) with the rf amplitude and phase presets.

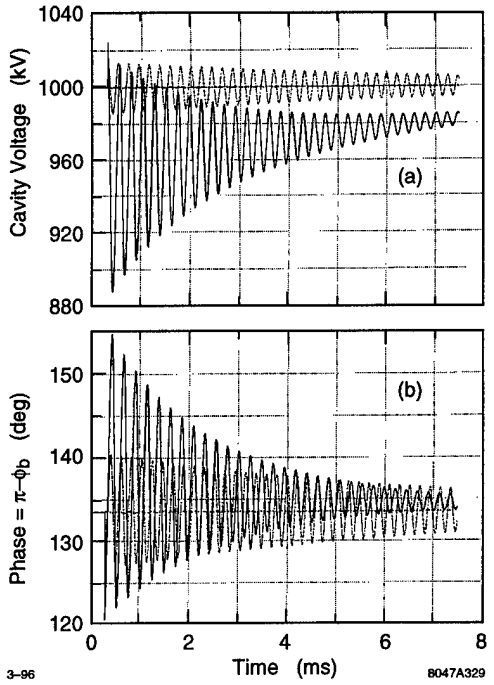


Figure 2: Simulations of injection transients in the cavity voltage (a) and beam phase (b) at injection of the first 0.6A train. There are three curves: uncorrected (largest oscillations), correction with direct feedback (intermediate oscillations), and correction with presetting the rf amplitude and phase (essentially flat).

In Fig. 4 is shown simulation results for the injection procedure outlined above for a zero to full current ramp. The cavity voltage and beam phase preset references as calculated from Eqs. (1) and (2) are also shown along with the required generator and reflected powers. Notice that the Robinson damping time is shorter the higher the current. This is because of the fixed tuning angle. Also worth noting is the decrease in the coherent synchrotron oscillation

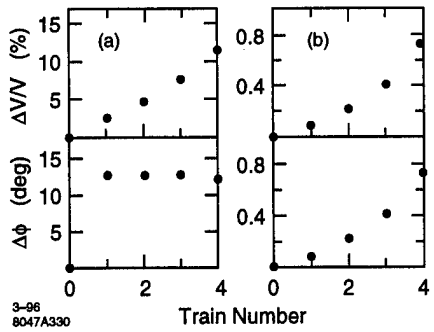


Figure 3: Simulated peak-to-peak variations in the cavity voltage and beam phase as a function of train number. The transients are corrected either with direct feedback (a) or with presets (b). Note the change in vertical scales.

frequency with current; as the beam current is increased the phase of the beam with respect to the generator crest becomes smaller resulting in a reduced restoring force for coherent phase perturbations.

A potential error associated with presetting the phase and amplitude is that the cavity voltage will be regulated to the specified value, V_{ref}; if the incoming charge is of different current than anticipated, then the amplitude feedback loop would regulate to an incorrect voltage. Notice however that Eqs. (1)-(4) may be used in feed-forward, which would require a measurement of the incoming charge. Another complication arises from thermal heating due to synchrotron radiation in the accelerating cavities. Fortunately, the thermal time constant of the cavity is much longer than the time required for the current ramp.

4 SUMMARY

A simple technique is proposed which would allow the high duty-cycle required for the NLC damping ring. One complication is the power dissipation requirements in the circulators and magic tee loads. Fortunately, the total absorbed power is 4 times smaller that of the PEPII[5] loads so it appears managable. Superior cavity voltage and beam phase regulation was predicted by numerical simulations to result from using cavity voltage and rf phase presets (as opposed to using direct feedback). The preset scheme also has the advantage that no additional hardware is required to damp the coupled-bunch modes that would be introduced using direct feedback.

5 ACKNOWLEDGEMENTS

The analyses described were made possible with the kind support of R. Siemann, T. Raubenheimer, P. Wilson, M.C. Ross, and J. Irwin. In particular I thank them for the interesting and illuminating discussions

6 REFERENCES

[1] 'Zeroth-Order Design Report for the Next Linear Collider', NLC Design Group, SLAC-474, LBNL-5424, UCRL-ID-124161, UC-414.

[2] See for example, M.G. Minty, 'Low-level RF System Design for the Accelerator Test Facility (ATF) Damping Rings', Proc. IEEE PAC, Vancouver, BC, Canada (1997).

[3] F. Pederson, IEEE Trans. on Nucl. Sci., NS-22, No. 3 (1975); and NS-32, No. 3 (1985).

[4] M.G. Minty and R.H. Siemann, "Heavy Beam Loading in Storage Ring Radio Frequency Systems", *Nucl. Instr. and Meth. A*, **376** (1996) 301-318.

[5] PEP-II Conceptual Design Report, SLAC-418, LBL-PUB 5379 (June, 1993).

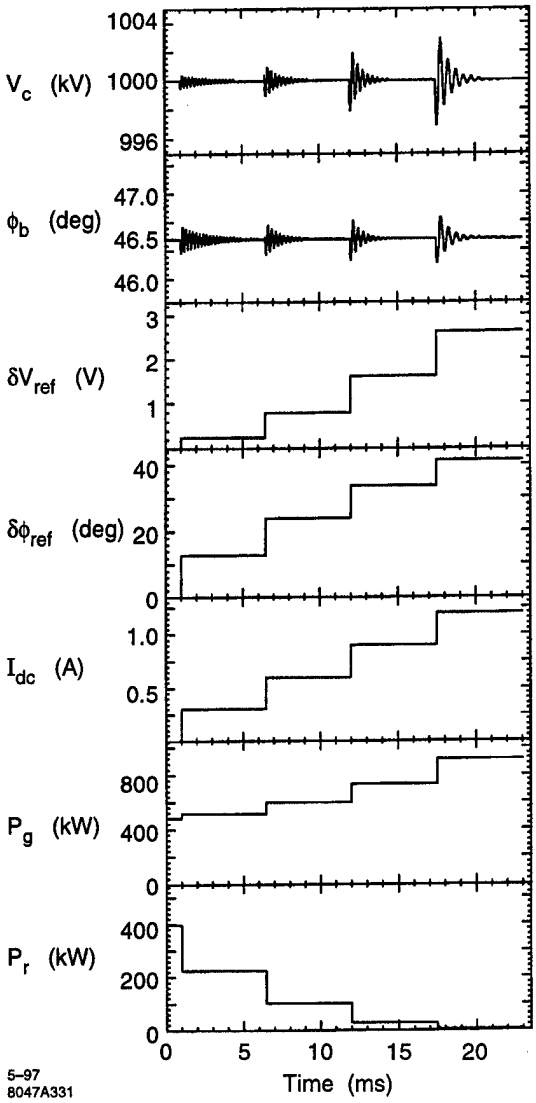


Figure 4: Simulated current ramp from no beam to full current. Plotted are the cavity voltage V_c, the beam phase ϕ_b, the change in reference voltage δV_{ref}, the change in reference phase $\delta\phi_{ref}$, the dc beam current I_{dc}, the generator power P_g, and the reflected power P_r.

CENTROID AND EMITTANCE OF A KICKED BEAM IN RINGS

Chun-xi Wang and John Irwin
Stanford Linear Accelerator Center, Stanford, CA 94025

Abstract

We generalize the existing decoherence theory of a kicked beam to linearly uncoupled 4D transverse phase space. Analytical results for the beam centroid motion as well as beam emittance (i.e., 1st and 2nd order beam moments) are given. We formulate the problem in the language of one-turn map and normal form theory in order to emphasize the approximations used and facilitate further generalizations. We will not discuss the chromaticity decoherence factor, which can be found in the references.

1 BEAM PHASE-SPACE DISTRIBUTION AND NORMAL FORM OF ONE-TURN MAP

After a stored beam is kicked, the beam phase space distribution will filament due to nonlinearities. In order to calculate the beam centroid motion and emittance growth, we need to know the phase-space distribution of the kicked bunch. To obtain this time dependent distribution, we employ the basic rule for transforming a continuous distribution f from one set of variables $\vec{u}$ to another $\vec{v} = \mathcal{T}\vec{u}$, which is:

$$f_{\vec{v}}(\vec{v}) = f_{\vec{u}}(\mathcal{T}^{-1}\vec{v})|J_{\mathcal{T}}| \tag{1}$$

where $J_{\mathcal{T}}$ is the Jacobian of the single-valued transformation $\mathcal{T}$. This rule will be used repeatedly although in most cases it will not be mentioned explicitly. Suppose the initial distribution is $\rho_0(\vec{x})$ and the effect of a kick is to translate the equilibrium distribution from $\langle p\rangle = 0$ to $\langle p\rangle = \Delta x'$ without changing positions, the new phase space distribution obviously is $\rho(x,p) = \rho_0(x, p - \Delta x')$.

The n-th turn phase space distribution $\rho_n(\vec{x})$ depends on the one-turn map $\mathcal{M}$ of the ring, i.e., $\rho_n(\vec{x}) = \rho(\mathcal{M}^{-n}\vec{x})$, where we have used the fact that the Jacobian of the one-turn map equals to 1 due to symplecticity. In general, the map $\mathcal{M}$ could be extremely complicated and numerical tracking is the only way to proceed, even though such tracking is very time-consuming. However, for a normal operating ring, the one-turn map usually has very weak nonlinearity and the tune is placed away from significant resonances. Therefore, it is safe to assume that there is an effective normal form

$$\mathcal{N} = \mathcal{A}^{-1} \circ \mathcal{M} \circ \mathcal{A} \tag{2}$$

for the map of a normal operational storage ring. Now the phase space distribution becomes:

$$\rho_n(\vec{x}) = \rho(\mathcal{A} \circ \mathcal{N}^{-n} \circ \mathcal{A}^{-1}\vec{x}) \tag{3}$$

Since the normal form represents a simple rotation in the normalized phase space $\mathcal{A}^{-1}\vec{x}$, it is much easier to work with this normalized phase space. Using action-angle variables $\vec{J} \equiv \{J_x, \phi_x, J_y, \phi_y\}$, the n-th turn phase space distribution reads:

$$\begin{aligned} \rho_{\vec{J}}(\vec{J}) &= \rho_{\vec{x}}(\mathcal{A} \circ \mathcal{N}^{-n}\vec{J}) \\ &= \rho_{\vec{x}}(\mathcal{A}\{J_x, \phi_x - 2\pi\nu_x n, J_y, \phi_y - 2\pi\nu_y n\}) \end{aligned} \tag{4}$$

In Eq. (4) we only assumed that the single particle motion can be canonically transformed (via a nonlinear map $\mathcal{A}$) into a circular phase space motion with amplitude dependent tunes ν_x and ν_y. To further simplify the calculation, we adopt the following major approximations:

- Take only the leading terms in the normal form $\mathcal{N}$, i.e., consider only the linear tune-shift-with-amplitude terms.
- Drop the nonlinear part of $\mathcal{A}$, i.e., just use the linear Courant-Synder normalization and the well-known action-angle variables $\{J, \phi\}$.

Note that these approximations, especially the last one when nonlinear part of $\mathcal{A}$ is large, may limit the usefulness of the result. In the following, we limit our discussion to the case of linearly uncoupled 4D transverse phase space.

Let us start with a 2D well-damped beam. Due to radiation damping and quantum excitation, the well-known equilibrium distribution is:

$$\rho_0(x,p) = \frac{1}{2\pi\epsilon} e^{-\frac{1}{2\epsilon}(\gamma x^2 + 2\alpha x p + \beta p^2)} \tag{5}$$

where α, β, γ, and ϵ are the Twiss parameters and emittance. Using Eq. (4) and the Courant-Synder normalization matrix $A = \begin{pmatrix} \sqrt{\beta} & 0 \\ -\alpha/\sqrt{\beta} & 1/\sqrt{\beta} \end{pmatrix}$, the action-angle phase space distribution right after a kick becomes:

$$\begin{aligned} &\rho(J,\phi) \\ &\simeq \rho_0\left(\sqrt{2J\beta}\cos\phi, -\sqrt{2J/\beta}\,(\sin\phi + \alpha\cos\phi) - \Delta x'\right) \\ &\simeq \frac{1}{2\pi\epsilon} e^{-\frac{1}{2}\left[2J/\epsilon + 2\sqrt{2J/\epsilon}\,k\,\sin\phi + k^2\right]} \end{aligned} \tag{6}$$

where $k \equiv \sqrt{2\Delta J/\epsilon} = \frac{\beta}{\sigma}\Delta x'$ is a dimensionless quantity that measures the effective kick ΔJ on the action. For the n-th turn, one simply shifts the phase ϕ by $-2\pi(\nu_0 + aJ)n$, where ν_0 and a are the linear tune and tune-shift-with-amplitude.

Now we consider the 4D case with negligible linear coupling between the x and y degree of freedom. The total phase space distribution is a direct product of the distributions in the two 2D subspace. However, there is an extra tune-shift term contributing to the decoherence process

0-7803-4376-X/98/$10.00 © 1998 IEEE

which must be taken into account because, in the 4D case, the tunes reads:

$$\begin{aligned} \nu_x &= \nu_x^0 + a_x J_x + a_{xy} J_y + \cdots \\ \nu_y &= \nu_y^0 + a_{xy} J_x + a_y J_y + \cdots \end{aligned} \tag{7}$$

where a_x, a_{xy}, and a_y are the tune-shift-with-amplitude coefficients. In summary, the 4D phase space distribution of a beam kicked to $\{0, \Delta x', 0, \Delta y'\}$ is:

$$\begin{aligned} & \rho(J_x, \phi_x, J_y, \phi_y) \\ \simeq\ & \frac{1}{2\pi\epsilon_x} e^{-\frac{1}{2}\left(2J_x/\epsilon_x + 2\sqrt{2J_x/\epsilon_x}\, k_x \sin\Phi_x + k_x^2\right)} \cdot \\ & \frac{1}{2\pi\epsilon_y} e^{-\frac{1}{2}\left(2J_y/\epsilon_y + 2\sqrt{2J_y/\epsilon_y}\, k_y \sin\Phi_y + k_y^2\right)} \end{aligned} \tag{8}$$

where all the symbols are subscribed with x and y to indicate the horizontal and vertical planes. $\Phi_x \equiv \phi_x - 2\pi(\nu_x^0 + a_x J_x + a_{xy} J_y)n$ and similar shorthand holds for Φ_y.

2 BEAM CENTROID

Using the phase space distribution of Eq. (8), the centroid motion is simply given by:

$$\begin{aligned} \langle x \rangle &= \langle \mathcal{A}\{J_x, \phi_x, J_y, \phi_y\} \rangle|_{x \text{ component}} \\ &\simeq \langle \sqrt{2J_x\beta_x} \cos\phi_x \rangle \end{aligned} \tag{9}$$

$$\begin{aligned} \langle p_x \rangle &= \langle \mathcal{A}\{J_x, \phi_x, J_y, \phi_y\} \rangle|_{p_x \text{ component}} \\ &\simeq -\langle \sqrt{2J_x\gamma_x} \cos(\phi_x - \frac{\pi}{2} + \arctan\alpha_x) \rangle \end{aligned}$$

where $\langle \cdots \rangle$ means average over phase space distribution. These first moments rely on the integral:

$$\begin{aligned} \langle \sqrt{2J_x} \cos(\phi_x + \phi_0) \rangle &= \int_0^\infty d\,J_x d\,J_y \int_0^{2\pi} d\phi_x d\phi_y \\ & \rho(J_x, \phi_x, J_y, \phi_y) \sqrt{2J_x} \cos(\phi_x + \phi_0) \\ &= k_x \sqrt{\epsilon_x}\, \bar{A} \sin(2\pi\nu_x^0 n + \Delta\bar{\phi} + \phi_0) \end{aligned} \tag{10}$$

where

$$\begin{aligned} \bar{A} &\equiv \frac{1}{1+\theta_x^2} e^{-\frac{k_x^2}{2}\frac{\theta_x^2}{1+\theta_x^2}} \cdot \frac{1}{\sqrt{1+\theta_{xy}^2}} e^{-\frac{k_y^2}{2}\frac{\theta_{xy}^2}{1+\theta_{xy}^2}} \\ \Delta\bar{\phi} &\equiv \frac{k_x^2}{2}\frac{\theta_x}{1+\theta_x^2} + 2\arctan\theta_x + \\ & \frac{k_y^2}{2}\frac{\theta_{xy}}{1+\theta_{xy}^2} + \arctan\theta_{xy} \end{aligned} \tag{11}$$

and $\theta_x \equiv 2\pi a_x \epsilon_x n$, $\theta_{xy} \equiv 2\pi a_{xy}\epsilon_y n$.

In summary, we obtained the centroid motion of a kicked beam in uncoupled 4D transverse phase space as:

$$\begin{aligned} \langle x \rangle &\simeq k_x \sigma_x\, \bar{A} \sin(2\pi\nu_x^0 n + \Delta\bar{\phi}) \\ \langle p_x \rangle &\simeq k_x \sigma_{x'} \bar{A} \cos(2\pi\nu_x^0 n + \Delta\bar{\phi} + \arctan\alpha_x) \end{aligned} \tag{12}$$

Obviously, similar results hold for $\langle y \rangle$ and $\langle p_y \rangle$. Comparing this to the 2D result in Ref. [1, 5], there are extra contributions to the decoherence factor $\bar{A}$ and phase shift $\Delta\bar{\phi}$ due to the new transverse degree of freedom and nonlinear coupling, even when the beam was kicked in one plane only. These modifications are particularly important when considering beam decoherence in the vertical plane, because the horizontal emittance is usually much larger than the vertical one. The effect of non-zero α is also included in Eq. (12) explicitly. For kicks other than the one we have used, the phase and amplitude need to be adjusted to satisfy the initial condition as for a single particle.

3 BEAM SIZE AND EMITTANCE

For many applications, it would be important to know the rms emittance and other second order beam moments as the beam decoheres. The calculation of these moments rely on the following two integrals:

$$\begin{aligned} \langle J_x \rangle &= \frac{1}{\epsilon_x\epsilon_y} e^{-\frac{k_x^2+k_y^2}{2}} \int_0^\infty dJ_x J_x e^{-\frac{J_x}{\epsilon_x}} I_0(\sqrt{\frac{2J_x}{\epsilon_x}}\, k_x) \\ & \qquad \int_0^\infty dJ_y e^{-\frac{J_y}{\epsilon_y}} I_0(\sqrt{\frac{2J_y}{\epsilon_y}}\, k_y) \\ &= \epsilon_x(1 + \frac{1}{2}k_x^2) \end{aligned} \tag{13}$$

and

$$\begin{aligned} & \langle J_x \cos(2\phi_x + \phi_0) \rangle \\ &= -\frac{1}{\epsilon_x\epsilon_y} e^{-\frac{k_x^2+k_y^2}{2}} \int_0^\infty dJ_y\, e^{-\frac{J_y}{\epsilon_y}} I_0(\sqrt{\frac{2J_y}{\epsilon_y}}\, k_y) \\ & \int_0^\infty dJ_x\, J_x\, e^{-\frac{J_x}{\epsilon_x}} I_2(\sqrt{\frac{2J_x}{\epsilon_x}}\, k_x) \cos[4\pi\nu_x n + \phi_0] \\ &= -\epsilon_x \frac{k_x^2}{2} \tilde{A} \cos(4\pi\nu_x^0 n + \Delta\tilde{\phi} + \phi_0) \end{aligned} \tag{14}$$

where I_0 and I_2 are modified Bessel functions,

$$\begin{aligned} \tilde{A} &\equiv \frac{1}{[1+(2\theta_x)^2]^{3/2}} e^{-\frac{k_x^2}{2}\frac{(2\theta_x)^2}{1+(2\theta_x)^2}} \cdot \\ & \frac{1}{\sqrt{1+(2\theta_{xy})^2}} e^{-\frac{k_y^2}{2}\frac{(2\theta_{xy})^2}{1+(2\theta_{xy})^2}} \\ \Delta\tilde{\phi} &\equiv \frac{k_x^2}{2}\frac{2\theta_x}{1+(2\theta_x)^2} + 3\arctan 2\theta_x + \\ & \frac{k_y^2}{2}\frac{2\theta_{xy}}{1+(2\theta_{xy})^2} + \arctan 2\theta_{xy} \end{aligned} \tag{15}$$

Using Eqs. (13)&(14) we obtain:

$$\begin{aligned}&\langle x^2\rangle \\ &= \beta_x\left(\langle J_x\rangle + \langle J_x\cos 2\phi_x\rangle\right) \\ &= \sigma_x^2\left[1+\frac{1}{2}k_x^2-\frac{1}{2}k_x^2\tilde{A}\cos(4\pi\nu_x^0 n+\Delta\tilde{\phi})\right]\end{aligned} \tag{16}$$

$$\begin{aligned}&\langle p_x^2\rangle \\ &= \gamma_x\left(\langle J_x\rangle - \langle J_x\cos(2\phi_x+2\arctan\alpha_x)\rangle\right) \\ &= \sigma_{p_x}^2\left[1+\frac{1}{2}k_x^2+\right. \\ &\qquad \left.\frac{1}{2}k_x^2\tilde{A}\cos(4\pi\nu_x^0 n+\Delta\tilde{\phi}+2\arctan\alpha_x)\right]\end{aligned} \tag{17}$$

$$\begin{aligned}&\langle x\,p_x\rangle \\ &= -\alpha_x\langle J_x\rangle - \sqrt{\beta_x\gamma_x}\,\langle J_x\cos(2\phi-\frac{\pi}{2}+\arctan\alpha)\rangle \\ &= -\alpha_x\epsilon_x(1+\frac{k_x^2}{2})+ \\ &\quad \frac{\epsilon_x}{2}\sqrt{\beta_x\gamma_x}k_x^2\tilde{A}\sin(4\pi\nu_x^0 n+\Delta\tilde{\phi}+\arctan\alpha)\end{aligned} \tag{18}$$

From the first and second order moments, it is easy to get the rms values, such as

$$\begin{aligned}&\sigma_x^{\rm rms}(n) \\ &\equiv \sqrt{\langle x^2\rangle-\langle x\rangle^2} \\ &= \sigma_x\left\{1+\frac{k_x^2}{2}(1-\bar{A}^2)+\frac{k_x^2}{2}[\bar{A}^2\cos(4\pi\nu_x^0 n+2\Delta\bar{\phi})\right. \\ &\qquad \left.-\tilde{A}\cos(4\pi\nu_x^0 n+\Delta\tilde{\phi})]\right\}^{-\frac{1}{2}}\end{aligned} \tag{19}$$

The rms emittance becomes:

$$\begin{aligned}&\epsilon_x^{\rm rms}(n) \\ &\equiv \sqrt{\left\langle(x-\bar{x})^2\right\rangle\left\langle(p_x-\bar{p}_x)^2\right\rangle-\left\langle(x-\bar{x})\,(p_x-\bar{p}_x)\right\rangle^2} \\ &= \epsilon_x\left\{1+k_x^2(1-\bar{A}^2)+\frac{k_x^4}{4}\left[1-2\bar{A}^2-\tilde{A}^2+\right.\right. \\ &\qquad \left.\left.2\bar{A}^2\tilde{A}\cos(2\Delta\bar{\phi}-\Delta\tilde{\phi})\right]\right\}^{-\frac{1}{2}} \\ &\simeq \epsilon_x\sqrt{1+2k_x^2\theta_x^2+k_x^2(1+k_y^2)\theta_{xy}^2+O(\theta^4)}\end{aligned} \tag{20}$$

where $k_x \equiv \sqrt{\frac{2\Delta J_x}{\epsilon_x}}$ and $k_y \equiv \sqrt{\frac{2\Delta J_y}{\epsilon_y}}$. Since both $\bar{A}$ and $\tilde{A}$ decay to 0 as the time increases, it is obvious that $\epsilon_x^{\rm rms} \to \epsilon_x(1+\frac{1}{2}k_x^2) = \langle J_x\rangle$. Note that this is the limit without radiation damping. The beam will finally be damped into the equilibrium state of emittance ϵ_x. The rms emittance of Eq. (20) has a very interesting property: it does not depend on the linear tunes ν_x^0 and ν_y^0. The Taylor expended expression is good for a relatively small number of turns after the kick, where $\theta \propto n$ is small. By switching the subscripts, all expressions apply to the vertical plane as well.

4 ACKNOWLEDGEMENTS

The author would like to thank A. Chao and G. V. Stupakov for helpful discussions. This work is supported by the Department of Energy under contract DE-AC03-76SF00515 and the Applied Physics Department of Stanford University.

5 REFERENCES

[1] R.E. Meller *et al.*, SSC report SSC-N360 (1987).

[2] I.C. HSU, Particle Accelerator (1990) v. 34, p. 43

[3] S.Y. Lee, SSC report SSC-N-749 (1991).

[4] H. Moshammer, Phys. Rev. E 48 (1993) 2140.

[5] M.G. Minty *et al.*, Proceedings of the 1995 Particle Accelerator Conference, p. 3037 (1995).

AN e^+e^- TOP FACTORY IN A 50 + 50 TeV HADRON COLLIDER TUNNEL

J. Norem, J. Jagger, S. Sharma, Argonne National Laboratory, Argonne IL 60439 USA
E. Keil, CERN, CH-1211 Geneva 23 Switzerland
G. W. Foster, E. Malamud, Fermilab, Batavia IL 60510 USA
E. Chojnacki, Cornell University, Ithaca NY 14853
D. Winn, Fairfield University, Fairfield CT 06430 USA

Abstract

We present the parameters of an e+e- collider sized for the tunnel of a 50 + 50 TeV superferric hadron collider[1]. Assuming a diameter of 170 km and a maximum radiated power of 100 MW, this collider should have a maximum energy of 500 - 600 GeV (c.m.) and should be able to produce a luminosity L = 0.9.1033 cm-2sec-1 at a center of mass energy of 360 GeV, (somewhat less at higher or lower energies) which would make it useful for producing top quarks or light Higgs bosons. Design problems include the very low field magnets, synchrotron radiation power, beam stability, and heat removal systems. Preliminary magnet, vacuum chamber and cooling designs are presented along with possible construction techniques, and some costing algorithms. We also consider an ep collider with 70 GeV electrons and 5 TeV protons as an injector.

1 PARAMETERS

We have considered an e^+e^- collider[2] located in the tunnel of a 50 + 50 TeV hadron collider, which could operate at energies sufficient to study $e^+e^- \rightarrow t\bar{t}$ and light Higgs production[3]. If this facility was operated as an ep collider, a c.m. energy of $\sqrt{s} = 7$ TeV could be reached.

The most important parameters of a $t\bar{t}$ factory operating at a beam energy of 180 GeV are shown in Table I. A complete parameter set is on the WWW[4]. We assume a total RF generator power available at the cavity windows of 100 MW, and a superconducting RF system similar to that of LEP operated at a gradient of 5 MV/m. We assume that the collider consists either of a single ring, operated with pretzels and parasitic beam-beam collisions every quarter betatron wavelength, and have adapted phase advance, arc tune Q and number of bunches k accordingly, or of two rings. Wiggler magnets are used to make the horizontal emittance a factor of 10 higher than its equilibrium value without wigglers. The advantage is a smaller value of the synchrotron tune, the disadvantages are a smaller dispersion in the arcs, a possibly smaller dynamic aperture and a larger momentum spread in the beam. We have not checked that the dynamic aperture is large enough.

We assume that the aperture is filled and that the beam power limit is reached at a beam energy of 180 GeV. If we control the beam size such as to remain at the beam-beam limit over a range of energies, the luminosity is proportional to E^2 for $E \leq 180$ GeV, and proportional to E^{-3} for $E \geq 180$ GeV. We increase the phase advance of the arc cells in steps from $\pi/8$ at 100 GeV to $\pi/2$ at 250 GeV. In order to satisfy the pretzel condition, all phase advances are integral fractions of $\pi/2$. We assume that wiggler magnets, installed in wiggler insertions where H has four times the arc value, are used to make the horizontal emittance a factor of ten larger than its equilibrium value without wigglers. Table II shows the proposed variation of phase advances and wiggler excitation. At energies below 250 GeV, the desired beam size can often be reached by more than one combination of phase advance $\mu/2\pi$ and emittance increase F_ε. In Table II, we favor higher values of $\mu/2\pi$ and F_ε in order to restrict the variation of the synchrotron tune Q_s with the energy E. It is indeed possible to achieve the strong variation of the beam radii with E by adjusting the phase advance in steps and using emittance wigglers.

Table I: The Parameters of a Very Large Lepton Collider

Beam energy E /GeV	180
Circumference C /m	531000
Luminosity L /cm^{-2}s^{-1}	9.15E+32
Beam-beam tune shift $\xi_x = \xi_y$	0.03
Beta functions at IP $\beta_x^* : \beta_y^*$ /m	1.0 : 0.05
Beam emittances $\varepsilon_x : \varepsilon_y$ /nm	32.5 : 1.7
Beam radii at IP $\sigma_x^* : \sigma_y^*$ /μm	180 : 9.01
Bunch population N	8.04E+11
Total current / beam I_b /mA	37.2
Number of bunches /beam k	512
Bending radius ρ /m	72628
Injection Energy E_{inj} / GeV	50
Dipole fields $B_{max} : B_{inj}$ /mT	8.3 : 2.3
Phase advance / cell $\mu/2\pi$	0.125
Arc tune Q	258
Cell Length L_p /m	249
Beta functions in arcs $\beta_{max} : \beta_{min}$ /m	488 : 218
Beam radii $\sigma_x : \sigma_y$ /mm	4.3 : 2.8
Synchrotron radiation loss U_s /MeV	1376
Aperture radii $A_x : A_y$ /mm for 10σ	53 : 38
Center of mass energy spread σ_E /GeV	0.26
RF voltage V_{RF} /MV	1616
Total generator power P_g /MW	102

0-7803-4376-X/98/$10.00 © 1998 IEEE

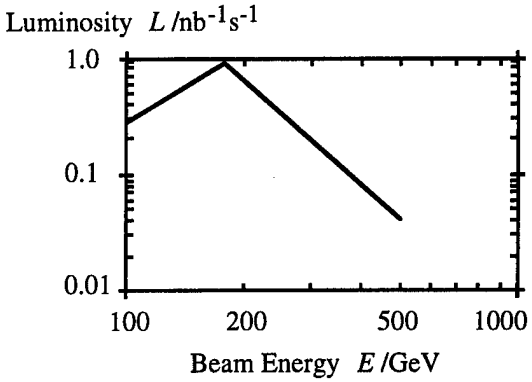


Figure 1, The energy dependence of the luminosity

The aperture limited luminosity is given by the expression $L_a = \pi f k \xi \sigma_x^* \sigma_y^* \gamma^2 / r_e^2 \beta_y^*$, where the revolution frequency $f \propto 1/\rho$, and the number of bunches $k \propto \rho$ if the bunch spacing is fixed by the hardware required to separate the beams, thus L_a is independent of ρ. If power limited, $L_P = (3/16\pi)\xi \rho P / r_e^2 E_e \beta_y^* \gamma^3$, where E_e is the rest mass of the electron and r_e its radius[2]. The maximum luminosity occurs when $L_a = L_P$, and this energy, E_{max}, is proportional to $\rho^{1/5}$. Thus the specific dimensions of the tunnel only weakly affect the operating parameters.

The energy resolution of the collider, σ_E ~0.26 GeV, in the center of mass at the $t\bar{t}$, would be useful for high resolution studies of threshold behavior and may be better than other collider options.

The polarization time is about 19 hours at 180 GeV, and comparable to the typical duration of a physics fill. The tolerance on the closed orbit harmonic at the spin tune is very tight, even with Siberian snakes. Therefore, no useful degree of polarization is expected.

The requirements that all three degrees of freedom are damped by synchrotron radiation imposes constraints on the length of all quadrupoles, as does nonlinear radiation damping [3].

Table II. Luminosity L, proposed phase advances $\mu/2\pi$ in the arc cells, emittance increase factors F_ε with wiggler magnets and circumferential RF voltage V as functions of the beam energy E, (L, I and V are evaluated at the lower end of the energy range).

E /GeV	L /nb^{-1}s^{-1}	$\mu/2\pi$	I /mA	F_ε	V /GV
100→136	0.28	0.0625	21	4→2.2	0.2
136→180	0.52	0.0833	29	5.2→3	0.7
180→250	0.92	0.125	39	10→1	1.8
250→335	0.34	0.25	10	8→1	5.3

2. RF SYSTEM

Table II also shows the total current in one beam I, the luminosity L, and the total circumferential RF voltage V as a function of energy. The total RF generator power at the cavity windows increases proportional to E^5 up to 180 GeV. There it reaches 100 MW, and remains at that value for higher energies by design, although the required voltage continues to rise as E^4. Above 250 GeV, the RF voltage and the length of the RF system, assuming ~6 MV/m, become absurd.

Current technology limits input power to superconducting cavities to about 500 kW. Using a very reasonable gradient of 6 MV/m in a superconducting cell with 0.425 m active length, operating at a synchronous angle of 31.6° and matched at 160 mA beam loading gives 3 cells per cavity for 588 kW input power. Klystrons providing 1.7 MW at 350 MHz determine 3 cavities per klystron and 70 klystrons for 1.4 GV synchrotron loss. This system should benefit from expected improvements in RF coupler and window technology, superconducting gradients and klystron power.

Instabilities related to higher order monopole and multipole modes can be managed by aggressive higher order mode damping techniques, which are available. Coupled bunch longitudinal instabilities, exacerbated by cavity detuning being comparable to the revolution frequency are a concern.

3 MAGNET ISSUES

Since the maximum dipole field required is only 23 mT even for 500 GeV, one could use thin steel laminations separated by large nonmagnetic spacers, as in LEP, and stabilized against thermal expansion with materials like invar. Error fields should be on the order of 4 x 10^{-4} of the dipole fields, and the earth's field is on the order of 0.05 mT, thus it will be necessary to carefully shield this field from the beam, particularly at injection when the dipole field is ~2.3 mT, (assuming E_{inj} = 50 GeV). If the electron ring was used in combination with the hadron ring for e/p collisions, even larger fields from the superferric magnet and return current must be shielded.

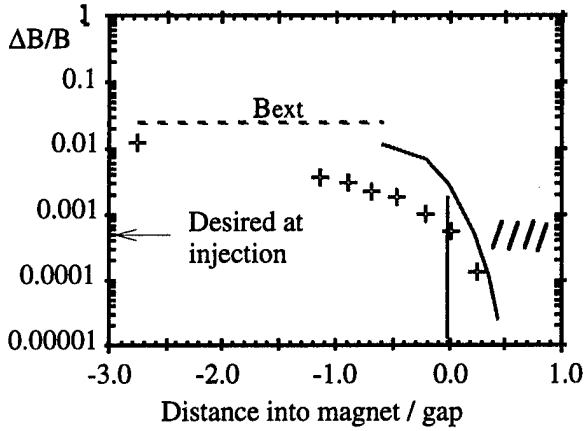


Figure 2, Measured error fields after degaussing, with parametrizations of Brown and Spencer. ΔB/B = (measured field) / (field at injection), which is equivalent to the measured field in mT. The hatched line shows level of residual fields.

In order to evaluate experimentally the degree of shielding one would expect from the normal magnet yoke itself we constructed a prototype of a C magnet from

0.025" laminations spaced by 0.25". This prototype is 0.2 m long and made from magnet laminations cut and glued to make a C magnet with a gap height of 3.81 cm. Measurements were made with a Bartington MAG-01 single axis fluxgate magnetometer. The magnet was degaussed by exciting it at 60 Hz, with slowly decreasing amplitude from 700 A-turns to zero. The results are shown in Figure 2, above, compared with Brown and Spencer[5].

Since the total mass of iron required is ~ 20 kg/m the magnet will rely on an external support structure against mechanical motion and thermal expansion. Possible component dimensions are shown in Figure 3.

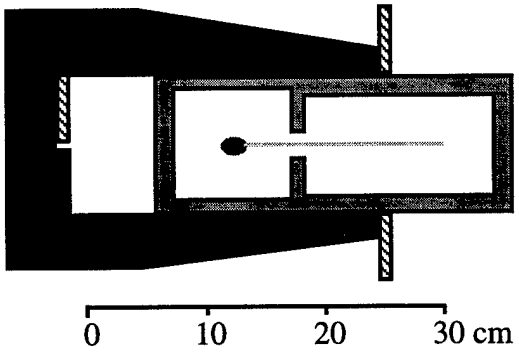


Fig 2. Dipole yoke, 4 conductors and vacuum chamber

4 VACUUM ISSUES

The vacuum system is defined by the comparatively small amount of photoproduced gas per unit length, and the large radius of the ring, which makes the vacuum chamber effectively straight between discrete absorbers. The average photodesorption of gas per meter by synchrotron light is given by $Q_{gas}/m=24.2EI\eta/2\pi R$ [6], where Q_{gas} is the gas load in Torr-L/s, and η is the photodesorption coefficient, roughly 10^{-5}- 10^{-6}. At 180 GeV a pressure of 10^{-9} Torr could be reached with an average pumping speed of ~ 2 $Ls^{-1}m^{-1}$.

We consider a vacuum chamber with a beam channel and a antechannel containing NEG strips, discrete absorbers and ion pumps. The slot impedance is a concern for beam stability. OFHC copper absorbers 0.6m long protruding into the antechannel would protect the vacuum chamber from synchrotron radiation. With discrete absorbers the gas load and ionizing radiation would be localized and handled more efficiently. Each absorber would intercept 19 kW of power with a surface temperature rise of 150 °C. Bulk water temperature rise in the absorber with 4 gpm of water flow would be 18 °C.

Since the machine would be far underground and distances would be large, we have considered sinking the 200 W/m of synchrotron power directly into the rock by taking the cooling water from the synchrotron absorbers through an array of pipes extending from the tunnel. Since the conductivity of rock is low but the specific heat is high, heat tends to be absorbed rather than conducted away. The required power can be absorbed by an array of pipes extending on the order of 3 m in one direction from the tunnel, water in the rock would help heat conduction.

We anticipate sharing a ~3 m diameter tunnel with the hadron collider magnets and a two way railroad, with access points to the surface located far apart.

5 COST MINIMIZATION

The cost of the facility is expected to be dominated by the cost of the tunnel, magnet/vacuum systems and RF. Tunnel costs have been estimated at 1000 $/m from a number of sources[1]. Bending magnet costs for a system of length l should roughly scale like $Bl \propto B\rho \propto E$ for a given magnet cross section, however the very low dipole field permits the use of more compact coil structures which should permit a considerably smaller and lighter stamping than that used in LEP. The RF cost has been roughly estimated at <0.25 $/V, although R&D directed at producing higher gradients could perhaps reduce this.

6 THE INJECTOR: AN ep COLLIDER

The injector for the hadron and e^+e^- colliders would be a proton ring of 3-5 TeV and an electron ring, both with a circumference of 15 - 30 km. If the >1.8 GV, 100 MW rf system for the e^+e^- collider were installed in the injector ring, an energy E_e ~ 80-100 GeV might be obtained. Use of these rings as an ep collider would thus be possible up to $\sqrt{s}$ ~1000 - 1350 GeV. The power to the vacuum chamber, P_{av} ~8 W/mm, can be cooled with simple water channels on the outside circumference.

7 CONCLUSIONS

An e^+e^- collider could be added to a 50+50 TeV low field hadron facility permitting high energy lepton physics as well as ep physics in an integrated facility.

8 REFERENCES

[1] G. W. Foster and E. Malamud *Low-cost Hadron Colliders at Fermilab - A Discussion Paper,* Fermilab TM-1976 June 1996. Updated parameters and referen-ces are located at http://www.ap.fnal.gov/PIPE/.

[2] E. Keil, *Storage Ring Design*, Physics of High Energy Accelerators, Fermilab '81, AIP Conference Proc.#87 (1982), 824.

[3] J. Norem and E. Keil, *1996 Snowmass Workshop Proceedings.*

[4] http://wwwslap.cern.ch/keil/Design/vllc100-500.lis

[5] K. Brown and J. E. Spencer, 1981 Part. Accel. Conf. Washington, D. C. (1981) p2568

[6] *PEP-II, An Asymmetric B Factory,* SLAC-PUB -418, (1993).

TRANSVERSE POLARIZATION BEYOND THE Z ENERGY AT LEP

A. Blondel, M. Böge, E. Bravin, B. Dehning, M. Placidi, F. Tecker, J. Wenninger
CERN

Abstract

Experimental results on transverse polarization obtained at LEP at a beam energy of 50 GeV are shown. The application of the refined orbit correction procedure known as Harmonic Spin Matching, implemented to compensate for depolarizing effects originating from orbit errors and misalignments of the machine elements, is described. Prospects and plans to improve the transverse polarization level at higher energies to extend the range of application of the direct and precise calibration with resonant depolarization are reported.

1 MOTIVATION

At LEP II the W mass should be determined with a accuracy which is 5 to 6 times smaller as the present value[1]. To reach this aim the beam energy has to be known with an accuracy of 15 MeV[1]. The energy calibrations at LEP I were based on the technique of resonant depolarization which is not directly applicable at the LEP II beam energies of about 90 GeV. Energy calibrations with the technique of resonant depolarization will be done at lower energies and the results will be extrapolated to the LEP II beam energy. The extrapolation is based on magnetic field measurements. To ensure a low extrapolation error relative comparisons of magnetic and the resonant depolarization technique calibrations have to be done at several energies. The error on the extrapolation will decrease with an increase of the difference between highest and lowest beam energy were this comparison could be performed. The lowest energy is given by the instruments for the magnetic field measurements and the highest energy by the level of polarization which allows a resonant depolarization calibration.

2 POLARIZATION MEASUREMENTS ABOVE THE Z ENERGY

It gets extremely difficult to achieve a reasonable level of polarization at energies well above the Z energy of 45 GeV (see Section 4). As a step towards higher energies where polarization can be used in order to perform an energy calibration this paper reports on a polarization measurement at 50 GeV in November, 1996 (see Fig. 1). The measurement was performed during a dedicated machine development shift. The solenoids of the experiments were switched off in order to exclude the depolarizing effects introduced by their strong longitudinal fields. For the same reason the bunch train bumps which are used during luminosity operation were deactived. After the application of deterministic and empirical HSM (see Section 5.1) the polarization went up to $\approx$11%.

An attempt to measure polarization at an even higher energy around 55.3 GeV lead to a measured polarization of about 2%. This turned out to be not sufficient for the present polarimeter to perform a proper energy calibration.

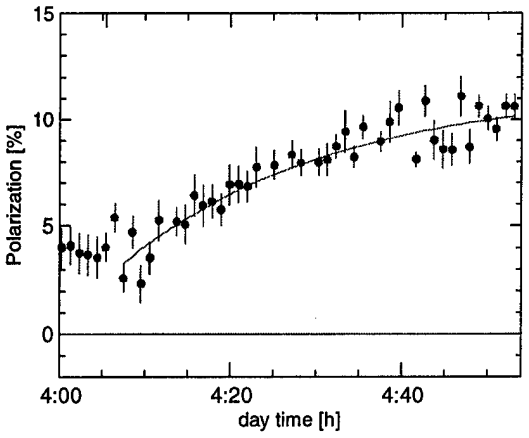


Figure 1: Polarization Measurement at 50 GeV. The rise-time fit confirms $\approx$11% polarization measured by the LEP polarimeter.

3 POLARIZATION IN ELECTRON STORAGE RINGS

The centre of mass spin motion in electric and magnetic field is governed by the Thomas-BMT[2][3] equation:

$$\frac{d\vec{s}}{d\theta} = \vec{\Omega} \times \vec{s},$$

where $\vec{\Omega}(\vec{B}, \vec{E}, \gamma)$ is a function of the fields and energy. θ is the azimuthal coordinate.

In a flat ring with the conditions $\vec{B} \parallel \vec{e_z}$, $\vec{E} = \vec{0}$ and after transformation to a frame which is circulating with the beam, $\vec{\Omega}$ becomes:

$$\vec{\Omega} = \frac{e\vec{B}}{cm\gamma}\frac{R}{2\pi} \quad a\gamma,$$

where the first part is the relativistic cyclotron frequency, R the circumference of the ring and $a\gamma$ the spin tune. a denotes the electron anomalous g factor.

The emission of synchrotron radiation in an electron storage ring can cause spin flip from up to down and vice versa. An asymmetry in the emission rates leads to an exponential polarization buildup with time antiparallel to the direction of the bending field:

$$P(t) = P_\infty(1 - \exp[-t/\tau_p]), \quad \tau_p^{-1} \propto \gamma^5 \oint \frac{1}{\rho^3} d\theta$$

0-7803-4376-X/98/$10.00 © 1998 IEEE

with ρ = modulus of bending radius, the equilibrium polarization $P_\infty = 92.4\%$ for a flat ring and the characteristic buildup time $\tau_p = 360$ min for a ring like LEP at 44.74 GeV. The rise time decreases with the 5th power of the energy. So far depolarizing effects have been neglected. Due to the stochastic change of momentum by photon emission betatron oscillations are excited. Especially in the quadrupoles this leads to additional fields seen by the particle which can act on the spin. As a result spin diffusion and hence depolarization is introduced. This diffusion process is particularly strong when the precession of the spins is synchronous with orbital and energy oscillations, i.e., when the spin resonance condition:

$$a\gamma = m + m_x Q_x + m_y Q_y + m_s Q_s$$

is fulfilled, where Q_x, Q_y, Q_s are the horizontal, vertical and synchrotron tunes, m and $m_{x,y,s}$ are integers.

Under the presence of these depolarizing effects the reachable equilibrium polarization P is given by:

$$P = \frac{P_\infty}{1 + (\tau_p/\tau_d)([a\gamma]^2)} \qquad (1)$$

where τ_d denotes the characteristic time of the depolarization process and τ_p/τ_d depends quadratically on the beam energy in linear approximation. Figure 2 visualizes P as a function of the spin tune $a\gamma$.

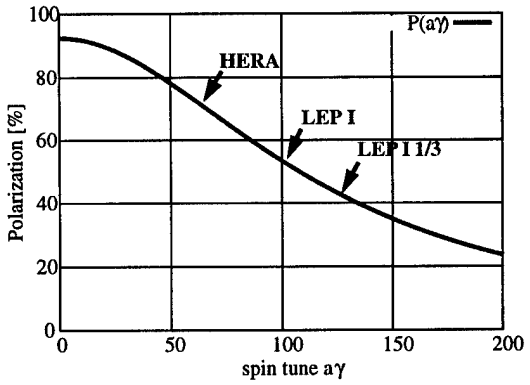


Figure 2: Equilibrium polarization P as a function of the spin tune $a\gamma$.

At high energy and large energy spread not only the first order resonances ($|m_x| + |m_y| + |m_s| = 1$) are important. The synchrotron sidebands ($a\gamma = Q_{x,y,s} + m_s Q_s$) are getting strong and becoming the main limitation of polarization at high energies (see Section 4).

The spin diffusion can be controlled by a proper alignment of the ring elements (especially the quadrupoles) and with a special orbit correction scheme which minimizes the coupling between the orbital and spin motion for a given (but unknown) error distribution of the magnets (see Section 5.1).

4 LIMITATIONS OF POLARIZATION AT HIGH ENERGIES

Synchrotron oscillations with large amplitudes cause a large frequency modulation of the spin tune $a\gamma$. Similar to the mechanism of frequency modulation in RF waves, synchrotron sidebands appear in the spectrum of the spin motion. This leads to sidebands to the linear spin resonances. On the basis of a formalism introduced by Buon[6] and S. Mane[7] the strength of the sidebands can be quantified. The relevant parameter is the modulation index:

$$\alpha = \left(\frac{a\gamma\sigma_e(\gamma)}{Q_s}\right)^2. \qquad (2)$$

The sideband strengths only depend on the strength of the parent resonances and on powers of α. For rings with large energy spreads like

LEP with an relative energy spread $\sigma_e \sim 6.5 \times 10^{-4}$ at 44.7 GeV and with $Q_s = 0.06$ the sideband resonances are strong up to high order (α =1.2). Figure 3 visualizes the rapid change of α with energy for 3 different values of Q_s. It should be noted that α nearly doubles between from 44.7 ($a\gamma$=101.5) to 50 GeV ($a\gamma$=113.5). The most appropriate way to fight these sidebands is the weakening of the driving linear resonances which can be performed using the method of Harmonic Spin Matching.

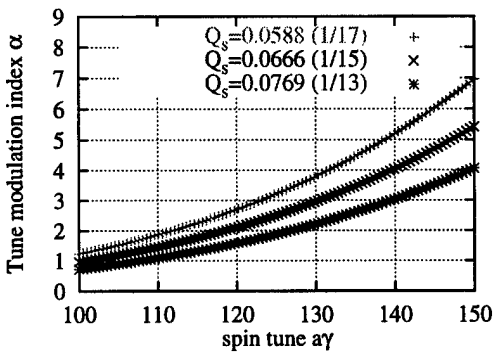


Figure 3: Modulation index α as a function of the spin tune $a\gamma$ for three different synchrotron tunes.

5 METHODS TO RESTORE POLARIZATION AT HIGH ENERGIES

5.1 *Harmonic Spin Matching*

The spin motion can be highly perturbed when the spin precession is in phase with energy (synchrotron) and betatron oscillations, in particular for harmonics of the perturbed orbit close to the actual spin tune. Suggested in 1985[4], Harmonic Spin Matching (HSM) is a method to minimize the spurious tilt of the spin precession axis by compensating the harmonics of the Fourier expansion of the orbit close to a specific value of the spin tune. The method relies on a lengthy procedure for the correction of the orbits, made difficult from the tiny entities of the corrections required,

only monitored by the observation of the effects on the polarization itself (Empirical HSM).

The HSM implementation described in[5] was intended to reduce the drawback caused by the very long polarization time in LEP (≈360 min at 44.7 GeV) and consisted in deriving the amplitude of the correcting bumps for the harmonics of interest directly from the beam position information (Deterministic HSM).

In 1993 the application of this method lead to an improvement of the polarization from ≈15%) to more than 40%[5]. Starting from this level the correcting harmonic amplitudes were varied in steps while recording the polarization level to search for an optimum. The experiment, performed at a spin tune $a\gamma = 101.5$ corresponding to an energy of 44.7 GeV resulted in a polarization level of (57±3)%.

At higher energies with much lower equilibrium polarization (see Fig. 4) one has to improve on the Deterministic HSM just described in order to get near to the polarization maximum. Without any good initial guess it would be very difficult to optimize polarization using Empirical HSM. In fact one can improve on it by applying a "Beam Based Alignment" technique.

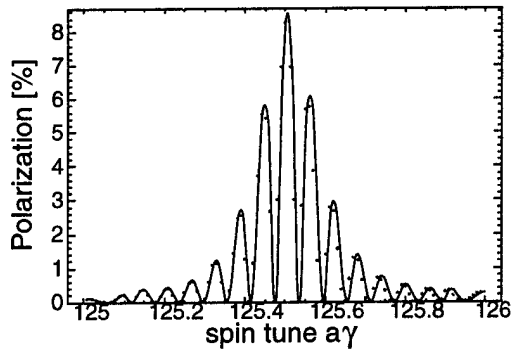


Figure 4: Estimate of the reachable polarization level at 55.3 GeV involving linear spin resonances plus their synchrotron sidebands derived from [8].

5.2 Beam Based Alignment

The technique described in[9] determines the offset between the magnetic axis of a quadrupole and its adjacent beam position monitor. The gradient of the magnet is modulated with low frequencies (a few Hz) and very small amplitudes and the effect on the beam is observed with a high sensitivity pickup. The observed movement of the orbit is minimal when the beam goes through the magnetic centre of the quadrupole. It is shown that the knowledge of these offsets together with the quadrupole alignment data brings the Deterministic HSM very near (80%) to the maximum polarization level which can be achieved with Empirical HSM. Following this argument it was recently decided to equip all vertically focussing quadrupoles in the arcs of LEP with the necessary hardware.

6 CONCLUSIONS

A measured polarization of ≈11% at 50 GeV has been reported. The main aim of the forthcoming studies will be to increase the maximum energy were polarization can be observed in order to reduce the energy extrapolation error at 90 GeV. Beam Based Alignment in combination with Deterministic and Empirical HSM will be used to correct the orbit properly. There are as well ongoing studies on a new dedicated polarization optics which will provide better starting conditions for polarization.

7 ACKNOWLEDGEMENTS

We would like to thank the LEP team for their continous support of our polarization studies.

8 REFERENCES

[1] G. Altarelli, CERN 96-01 (1996).

[2] L. Thomas, Philos.Mag., Vol. 3, p.1 (1927).

[3] V. Bargmann, L. Michel, V.L. Telegdi, Phys. Rev. Letts., Vol.2, p. 435 (1959).

[4] Rossmanith, R. and Schmidt, R., NIM A 236 (1985) 231.

[5] Assmann, R. *et al.*, CERN SL/94-008 (1994).

[6] Buon,J., Proc. 8th Int. Symp. on High Energy Spin Physics, Minneapolis (1988) 963.

[7] Mane, S.R., Phys. Rev. A36 (1987) 105.

[8] Mane, S.R., Nucl. Instr. Meth. A292 (1990) 52.

[9] Tecker, F. *et al.*, This Conference.

TRAPPED MODES IN CESR SLIDING JOINTS

E. B. Anderson and J. Rogers
Laboratory of Nuclear Studies, Cornell University, Ithaca, NY

Abstract

Trapped modes in the sliding joints in CESR were investigated as a possible source of instabilities. To detect these modes, experiments were performed where pairs of bunches of positrons were run through at various spacings. It was hoped that constructive and destructive interference of wake fields would produce varying amounts of heating. Data taking was time consuming, and insufficient numbers of data points could be taken to fit to the wake fields. To help solve this, the frequency of the mode was measured on the bench. A single trapped mode and its profile were observed. The trapped mode has a frequency of 3.59 GHz, just below the TM cutoff of the beampipe. Measurements of the mode were used to predict a shunt impedance of 4.9 ohms. The corresponding loss factor is slightly higher than the total loss factor found in previous time domain measurements[6]. The program ZAP[8] was used to predict an instability threshold of about 2.1 A.

1 INTRODUCTION

A section of waveguide, like a beampipe, has a cutoff frequency below which modes cannot propagate down the guide. If there is an enlargement in part of the guide, a mode can exist there that is unable to propagate in either direction down the waveguide. This "trapped" mode will have a frequency just below the cutoff frequency of the guide if the perturbation is small. The frequencies of trapped modes have been estimated analytically[1, 2]. In this paper, the clear observation of a trapped mode in a CESR sliding joint is described and the consequences to the machine investigated.

2 TWO BUNCH TESTS

In order to search for trapped modes in the sliding joints, a single beam, two-bunch test was undertaken[3]. The first bunch would excite any trapped modes. The second would pass through the fields six to twenty-eight nanoseconds later. This would create varying amounts of heating depending on the phase of the trapped mode when the second bunch passed. Because the time constant for the heating of the sliding joints was around ten minutes, waiting for the temperature to stabilize was time consuming, and only a limited number of data points could be taken.

Because the bunch measurements were made in terms of temperature, a calibration was made to relate the energy lost in the sliding joints to the temperature differences observed. A resistor was lowered into an unused cooling pipe hole on the sliding joint and surrounded by thermally conductive grease. With no current in the accelerator, known currents could be passed through the resistor at a known voltage.

The data from the two bunch tests did not appear to represent a single mode in the joints, but there was insufficient data to fit two modes to the small number of data points. In order to fit this data, an attempt was made to measure the frequency of any trapped modes by making bench tests.

3 BENCH TESTS

In previous experiments[4], two apparently trapped TM_{01} type modes were observed. A Slater perturbation method[5] was used to determine the field profiles of the modes. The results suggested that these peaks were actually the first and second order cavity modes produced by end plates used to terminate the ends of the sliding joint.

The problem of differentiating cavity and trapped modes was then addressed. It was important to be able to separate out the cavity modes, while also terminating the ends of the cavity to clean up the measurement. Sliding electrical shorts were constructed that could be moved freely along the inside of the beampipe. Indium was used between the sliding joint and the beampipe sections in order to improve the conduction at the joints.

The length of the cavity could now be quickly and easily changed. Changing the length caused the cavity modes to move, but any trapped mode would maintain the same frequency. By using this method, an unshifting peak was spotted at 3.5977 GHZ, just below the TM cut-off frequency. In order to establish if this was a trapped mode, the profile was measured using a Slater perturbation method[5] identical to the one used above. The profile observed, shown in Fig. 2, had the characteristic shape of a trapped mode located near the center of the sliding joint. The Q value for the measure mode was at least 1800, and rose close to 2000 when the contact between the beampipe sections was particularly good. Because the actual extensions of the sliding joints in the accelerator varies appreciably, the frequency of the mode was measured as a function of the separation of the bellows plates. The original data was taken with a separation between the bellows plates of 0.83 inches. It can be seen in Fig. 3 that the frequency changes over an approximately 50 MHz range. Notice that the full width at half maximum of an individual peak is about 1.8 MHz, so the separations must be fairly close for the modes in the different sliding joints to interact.

0-7803-4376-X/98/$10.00 © 1998 IEEE

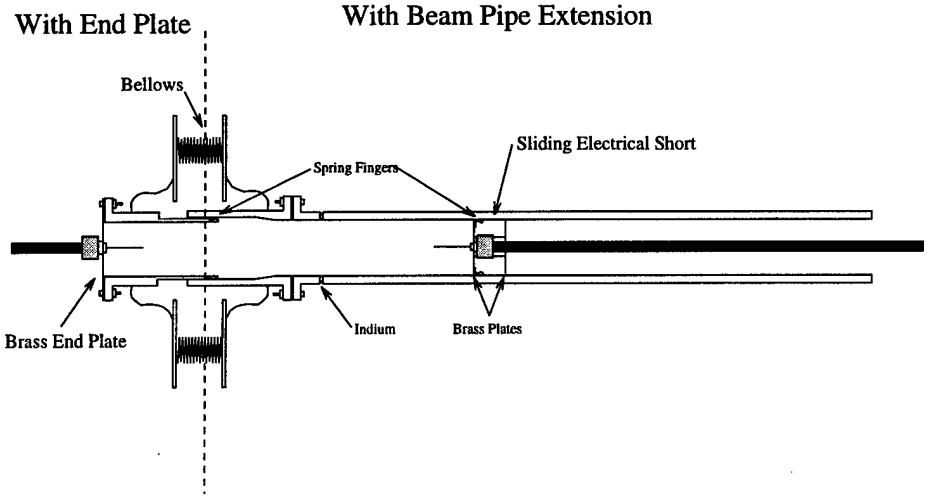


Figure 1: The diagram above shows the brass end plate used in the early bench measurements along with the beampipe section and sliding short used in the later measurements. They are shown together for space and comparison reasons: the sliding short was never used with the brass end plate.

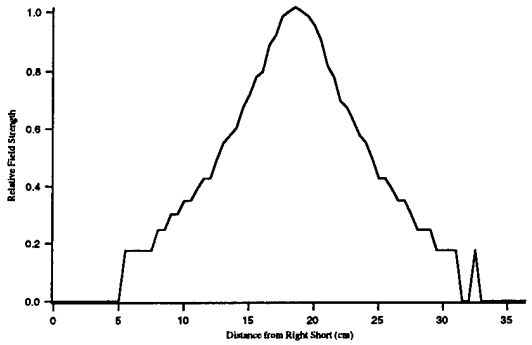


Figure 2: The plot above shows the relative electric field strength of the mode as a function of position.

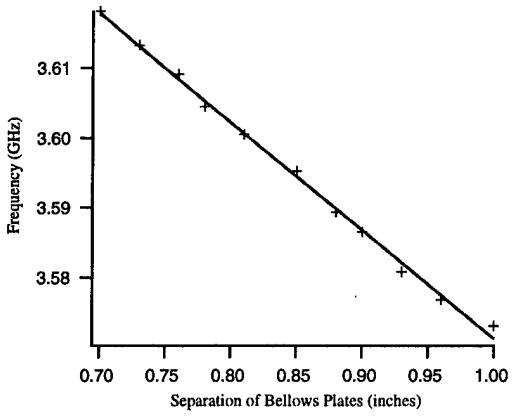


Figure 3: The frequency of the trapped mode changed as a function of the extension of the sliding joint. This is important since the extension of the joints vary greatly around the accelerator.

4 CALCULATION AND COMPARISON

Attempts were made to use the frequency measured above and make a fit to the two bunch test data. The calibration done above had already indicated that the temperature variations expected would be on the order of a degree. Attempts to fit to individual joints seemed dominated by noise, so an average was taken over all of the joints in the machine. There seemed to be a consistent change in temperature between data points. Unfortunately, the fits clearly indicated a very non-physical result for the heating. When the fits were extrapolated to zero bunch spacing, the heating was not a maximum, in fact, it appeared to be near a minimum, which is clearly nonsensical. It seemed clear from the pattern of the points, and the non-physical nature of the fits that could be made, that current variation probably dominated any temperature effect that could be measured.

Knowledge of the relative field profile and the frequency of the mode allowed the calculation of the transit time factor for the mode. The value for this factor was 0.787.

Previous bench measurements[6] had determined an approximate total loss factor for the sliding joint of $3.9\text{x}10^{-3}$ (V/pC) at a bunch length of 1.8 cm. The loss factor due to the trapped mode should depend on bunch length in a Gaussian fashion as shown in Fig. 4. Information about the trapped mode was used to determine its contribution to the total loss factor of the sliding joint. The field configuration in the sliding joint was estimated by using the transverse dependence of the calculated fields of the lowest order TM mode[7] and the longitudinal profile measured above. This field configuration was used to calculate the stored energy in the mode and, thus, the shunt impedance of the mode. This calculation gave a shunt impedance (R/Q) of 4.9 ohms. This impedance relates to a loss factor of $4.2\text{x}10^{-3}$ (V/pC) for the trapped mode in the sliding joint at a bunch length of 1.8 cm. Note that this value is higher than the measured value for the total loss factor,

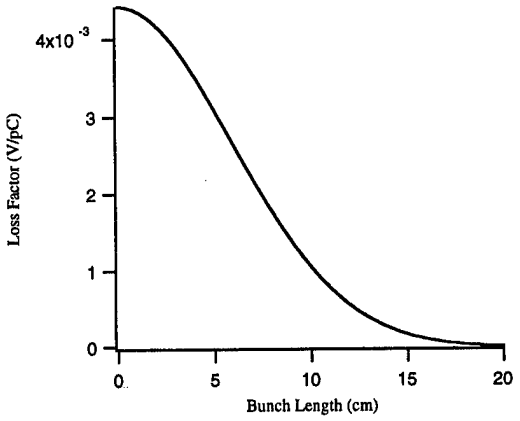


Figure 4: The loss factor due to the trapped mode should depend on bunch length in a Gaussian fashion, as shown above.

which includes all of the modes in the joint. In any case, the high value of the loss factor for the mode suggests that the trapped mode is the dominant source of impedance in the sliding joint.

Analytical estimates of the trapped mode[10] predicted that the mode would be found 21 MHz below the cutoff frequency compared to an experimentally measured difference of about 80 MHz. The predicted shunt impedance was lower, only about 2.1 ohms.

Under normal operating conditions, the loss factor above relates to about 80 eV lost per sliding joint per electron. Because there are one hundred sliding joints in the ring, the total energy loss would be 8 keV per revolution.

The program ZAP[8] was now used to estimate the effects of the trapped mode on beam stability. The program could not deal with the large number of actual sliding joints in CESR. First, as a very rough measure, a simulation was done with a single mode with one hundred times the predicted impedance. This rough test came up with all stable modes under normal operating currents, and an instability did not occur until a current of 2.13 A was used. Next, twenty sliding joints were used, with each having five times the impedance of a single joint. In this test, the there were some Landau damped modes over the entire reasonable current range. Unstable modes appeared at currents of 2.17 A, a value well above current operating conditions.

For tests where more than one mode was used, the frequencies of the sliding joint modes were not assumed to be the same. The distribution of sliding joint extensions in the ring had been sampled previously[9]. Of the hundred sliding joints in the accelerator, the extensions of 31 had been measured. To determine the extension of a random joint, a measured value was selected at random. The extensions were measured to the nearest thirty-second of an inch, but were only measured at one point around the rim of the bellows plates, so significant error was possible. To simulate this uncertainty, a Gaussian deviate of one thirty-second of an inch was added to the randomly selected measured value. Using the measurement discussed above, the extension was translated into a frequency for the trapped mode.

5 CONCLUSION

Trapped modes in the sliding joints were studied to see if they might eventually place a limit on the beam current. Machine studies generated interesting data, but data collection was too time consuming for the number of unknowns involved. Attempts to measure the frequencies using a network analyzer shed doubt on earlier measurements of the mode frequencies, but indicated a trapped mode in the sliding joint at about 3.60 GHz with a Q factor of about 2000. The mode observed predicted a loss factor of $4.2\text{x}10^{-3}$ (V/pC) due to the trapped mode. The loss factor is slightly higher than expected from earlier measurements, but indicates the importance of the trapped mode in the overall impedance of the structure.

6 ACKNOWLEDGMENTS

Special thanks is given to Maury Tigner and Mike Billing for helpful discussion. Thank you to S.S. Kurennoy for his theoretical estimates. The bench studies were completed with the gracious loan of space, equipment, and time from the SRF group here at Cornell.

7 REFERENCES

[1] S.S. Kurennoy, R. Gluckstern, and G. Stupakov. Coupling Impedances of Small Discontinuities: A General Approach. Physical Review E *52*, No. 4, 4354 (1995).

[2] G. Stupakov, and S.S. Kurennoy. Trapped Electromagnetic Modes in a Waveguide with a Small Discontinuity. Physical Review E *49*, No. 1, 794 (1994).

[3] Alexander Temnykh. Wake Field Study Using Two Spaced Bunches, CON95-06.

[4] Murray Tigner. Trapped Modes in the CESR Sliding Joint and Collective Instabilities in PH II and III - a Progress Report, CON93-11.

[5] Edward Ginzton. **Microwave Measurements**, McGraw-Hill: New York (1957).

[6] Mike Billing. Higher power Mode Loss Limitations for Beam Currents in CESR. CBN 84-15 (1984).

[7] Sergei Belomestnykh. Personal Communication.

[8] Michael Zisman, Swapan Chattopadhyay, and Joseph Bisognano. ZAP accelerator physics code.

[9] Maury Tigner. Personal Communication.

[10] Sergey S. Kurennoy. Personal Communication.

CESR Status

D.L.Rubin
for the CESR Operations Group*
Laboratory of Nuclear Studies, Cornell University, Ithaca, NY 14853

1 INTRODUCTION

The Cornell Electron Storage Ring operates with trains of bunches that collide with a horizontal crossing angle of ± 2.1 mrad. CESR has achieved a peak luminosity of 4.1×10^{32} cm$^{-2}s^{-1}$ with a total current of 320 mA and nine two-bunch trains in each beam. The beam-beam tune shift parameter saturates at $\xi_v \sim 0.04$ The current dependence of luminosity and tune shift parameter are shown in Fig. 1 During the 1996 calender year a total of 2.69 fb^{-1} was delivered to the CLEO experiment at center of mass energies on or near the Υ_{4s} resonance, 5.3 GeV/beam. In February 1997, our most recent full month of operation, we logged 443 pb^{-1}. Total current is limited by a multibunch londitudinal instability generated by parasitic modes in the RF accelerating cavities.

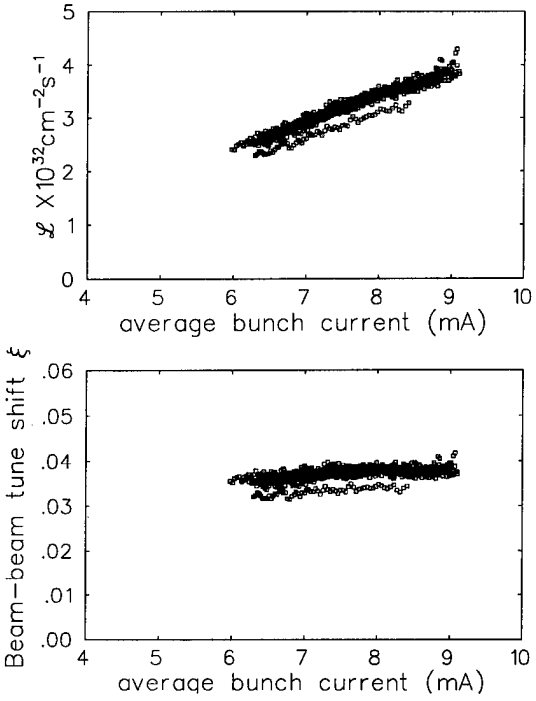


Figure 1: Luminosity and beam-beam tune shift parameter at 5.3 GeV with nine two-bunch trains in each beam. Bunches within each train are 42 ns apart.

2 OPTICS

During an extended shutdown in 1995 to install a silicon vertex detector in the CLEO detector, the interaction region optics were modified to increase the effective aperture for the crossing angle trajectories. Maximum excursion of the separated orbits occurs in the horizontally focusing interaction region quadrupole. By moving the horizontally focusing quadrupole nearer to the interacton point, the peak horizontal β is reduced from 100 m to 70 m. In addition, we increased the physical horizontal half aperture from 70 mm to 82 mm. (At the interaction point β_v^*=18 mm and β_h^*=1.1 m.) With this modification, the limiting aperture is shifted to the diametrically opposite point of the machine. The increased aperture reduces the sensitivity of the detector to particles lost during the injection process and to background associated with colliding beams. The interaction region optics will be modified again when superconducting quadrupoles are installed next year in Phase III of the luminosity upgrade. β-functions as they exist today (Phase II) and as modified for Phase III are shown in Fig. 2.

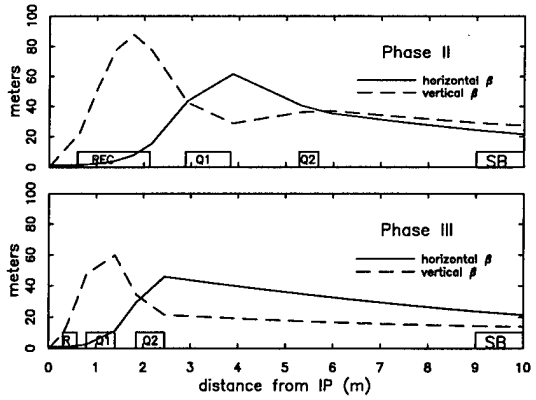


Figure 2: Upper plot indicates optical funtions in IR based on 1.5 m long permanent magnet quadrupole(REC). With installation of superconducting quadrupoles (Q1 and Q2) β_v^* is reduced to 10 mm and peak β as parasitic crossings are reduced to 40 m.

3 CROSSING ANGLE

Four horizontal separators generate a differential closed orbit distortion. The storage ring optics are symmetric with respect to the diameter that includes the interaction point. The separators are arranged in pairs about the symmetry axis with equal but opposite voltages. The differential orbits are antisymmetric with ± 2.1 mrad horizontal angle and zero displacement at the interaction point. The crossing angle provides for separation of the closely spaced bunches at the parasitic crossings near the interaction point.

The quadrupole optics are designed so that the closed orbits minimize the long range beam-beam interaction at the

* Work supported by the National Science Foundation

0-7803-4376-X/98/$10.00 © 1998 IEEE

multiple parasitic crossings in the machine arcs that arise with 9 trains of bunches. The number of trains is constrained by the number of horizontal betatron wavelengths around the ring. The closed orbits are shown in Fig. 3. The horizontal tune is 10.52.

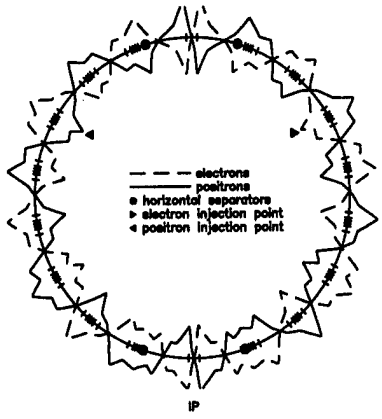


Figure 3: Electrostatically separated, crossing angle orbits can accomodate nine trains. Maximum train length is 56ns corresponding to 5 bunches per train spaced 14 ns apart. Tick marks indicate parasitic crossings that occur with 2 bunches spaced 28 ns apart in each train.

4 INJECTION

Various modifications to the injector and storage ring during and subsequent to the 1995 shutdown have lead to improvements in injection rates.

In the linac the positron converter and pulsed solenoid assembly were replaced. Solenoid misalignment was eliminated. Failed DC focusing solenoids located directly beyond the target were also replaced. Instrumentation was implemented to allow fine tuning of gun pulser delay for compensation of prebuncher loading[1]. A pair of quadrupoles in the synchrotron were relocated to reduce dispersion and increase energy aperture of the accelerator. Injector positron current has increased by a factor a five.

Electrons are injected into CESR after the storage ring is filled with positrons. The electron bunch is injected in the horizontal plane executing betatron oscillations about the closed orbit of the stored electrons. In the reconfigured optics, the effective horizontal aperture in the interaction region is significantly increased. In addition, the closed orbits have been manipulated to increase the aperture in the arcs for the injected bunch, and to increase separation from the counter-rotating positrons at the parasitic crossing points.

Filling rates are 45 mA/minute for positrons and 90 mA/minute for electrons. Twelve bunches are accelerated in each synchrotron cycle. Luminosity and current measured in a 24 hour period is shown in Fig. 4. The length of each run is 75 minutes. The time from the end of one run until the start of the next is 10 minutes.

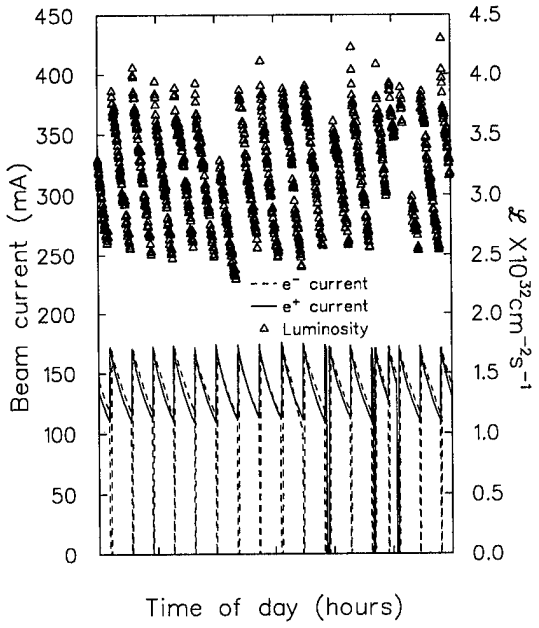


Figure 4: Luminosity and current for 5 February 1997. Integrated luminosity for the day was $23.6pb^{-1}$.

5 CURRENT LIMITS

5.1 *Collective effects*

Instabilities arise in CESR due to distributed ion pump leakage voltage and parasitic cavity modes. Photoelectrons are trapped in the electric field that leaks through the pump slots in the dipole magnets[2]. Trapped electrons resonate with the multiple bunch beams. The effect is dramatically reduced by operating the pumps at 2 kV rather than the nominal 7 kV. Pumping speed is essentially unaffected by the change in voltage.

A broadband horizontal feedback system independently stabilizes bunches spaced as few as 14 ns apart via a stripline kicker. The horizontal feedback permits operation with chromaticity at or slightly less than zero. Dynamic aperture is greater with the weaker sextupoles. A vertical feedback system with similar capability is installed but not yet required in normal operation.

At present total beam current is limited by a longitudinal instability[3]. The instability threshold is sensitive to spacing of bunches within the train. A consequence of our RF numerology is that bunches are necessarily spaced in multiples of 14 ns. Allowed spacings for operation with nine, two-bunch trains include 14 ns, 28 ns, 42 ns, or 56 ns. The 42 ns spacing yields the highest threshold for the instability of about 280 mA in a single beam. Additional dependence of the instability threshold on RF cavity temperature and orbits within the cavities indicates that higher order cavity modes are the relevant impedance. Calculations of instability rise times, based on measured frequency and Q, and computed R/Q of cavity modes are consistent with dependence of thresholds on current and bunch spacing[4].

We have implemented longitudinal feedback based on the signal processing and kicker of the horizontal feedback system. Finite dispersion in the kicker couples horizontal kick to longitudinal motion. The effective longitudinal kick is about 140 V. With the existing feedback the instability threshold is increased to a total current of about 330 mA. Work is continuing to improve the sensitivity of the pick-up to the longitudinal motion and to assemble an amplifier capable of producing a 1400 V kick.

5.2 *Parasitic long range beam-beam effect*

We anticipate increasing the number of bunches in each train from two to three as performance of the longitudinal feedback system permits. With 27 bunches in each beam there are 53 long range parasitic interactions of the counterrotating bunches. There is an observable dependence of various optical functions of one beam, on the current and spacing of bunches within the opposing beam[5]. We find that the long range effect can be compensated but that tuning for best luminosity is very different for single and multiple bunch configurations.

Measurements with a single high current positron beam of multiple bunches, and one or two noncolliding bunches of electrons indicate tolerance to nonlinearities of the parasitic forces. We measure the lifetime of a single two-bunch train of electrons in the presence of 270 mA of 8 two-bunch trains of positrons as a function of total separation amplitude. The bunches of train one of electrons collide with none of the bunches in trains 2-8 of positrons at the interaction point. We find no effect on positron lifetime for separation amplitude of 70% of the maximum consistent with the machine aperture. The measured dependence of required separation as the fourth root of total current suggests an upper limit in excess of 500 mA/beam[6].

5.3 *Electrostatic separators*

There are four horizontal and two vertical separators required to separate the electrons and positrons at all of the parasitic crossing points. Vertical separators one half a vertical betatron wavelength apart displace beams at the crossing opposite the interaction point. Photoelectrons are produced in the synchrotron radiation absorbers. We observed instabilities due to the resulting photocurrents in the vertical separators. Permanent magnets were installed on the absorbers to trap the electrons[7]. The separator plates were biased by increasing the voltage on the negative plate and decreasing voltage on the positive plate to reduce photocurrent from absorber to plates and the instability was eliminated. Although there is no evidence that the performance of the horizontal separators has suffered due to photoelectron emission, permanent magnets have been installed on the absorbers and photocurrent has been reduced.

6 UPGRADE STATUS

Within the next two years, as part of the Phase III upgrade, the CESR RF system and the interaction region optics will be replaced so that we can collide 500 mA/beam with nine trains of as many as five bunches. The four 5-cell room temperature RF cavities will be replaced with four single-cell superconducting cavities[8]. Each of the superconducting cavities will be capable of coupling over 400 kW to the beam. Because of the large open geometry of the superconducting cell, the high gradient and excellent damping of parasitic modes, the effective higher order mode impedance of the superconducting system is about 1/10 of the existing structures. We expect that the threshold for longitudinal instability to correspondingly increase. With processing and operating experience we anticipate attaining total accelerating voltage nearly double that of the existing installation.

During the shutdown for upgrade of the CLEO detector, the interaction region quadrupoles will be replaced with superconducting magnets[9]. The superconducting quadrupoles will be arranged in pairs. There will be a horizontally and vertically focusing magnet in each of two cryostats. A vertically focusing permanent magnet quadrupole will be mounted on the interaction point end of each of the cyrostats[10]. The β-functions, (β_v^*=10 mm, β_h^*=1 m) are shown in Fig. 2 (Phase III). Parasitic crossings occur at 2.1 m, 4.2 m, etc., from the interaction point if the bunches are spaced 14 ns apart. Note that the β-function at the crossing points is 40 m or less, and consequently no greater than at typical crossings in the machine arcs. The near miss in the interaction region will not limit bunch current.

Machine parameters in present operation and anticipated with the installation of superconducting RF and interaction region quadrupoles are shown in the table.

Parameter	Today	Phase III
β_v^*(mm)	18	13
β_h^*(m)	1.1	1.0
Horizontal emittance(mm-mrad)	0.21	0.21
Bunch length(mm)	19	13
Accelerating voltage (MV)	6	12
Number or trains	9	9
Bunches per train	2	5
Bunch spacing	42 ns	14 ns
Total beam current(mA)	160	500
Synch. radiation power(kW) (2 beams)	350	1100
Peak luminosity ($\times 10^{32}$cm$^{-2}s^{-1}$)	4.1	>10.0

7 REFERENCES

[1] Meller, R., *et al.*, session 3W23, these proceedings.

[2] Rogers, J., CBN 95-2 (March, 1995).

[3] Billing, M., session 4P55, these proceedings.

[4] Belomestnykh, S., private communication.

[5] Rubin, D.L., CBN 96-2 (January, 1996).

[6] Temnykh, S., Elog entry 24 (April 29, 1997).

[7] Greenwald, S., session 9P41, these proceedings.

[8] Belomestnykh, S., *et al.*, session 3P21, these proceedings.

[9] Welch, J., *et al.*, session 3P17, these proceedings.

[10] Lou, W., session 2P5, these proceedings.

BEAM-BEAM SIMULATION USING THE UNIFIED ACCELERATOR LIBRARIES

T. Koyama, N. Malitsky and R. Talman
Laboratory of Nuclear Studies, Cornell University, Ithaca, NY 14853 USA

Abstract

Colliding beam experiments at CESR with beams made round by running on the coupling resonance have been performed[1], and runs are planned with the beams made round by Möbius modification[2]. To simulate performance in these configurations stochastic and beam-beam modules have been added to the Unified Accelerator Libraries[3] for use along with pre-existing lattice representation, and map and element-by-element, TEAPOT++ modules. For a realistic CESR lattice containing sextupoles beam-beam performance is simulated.

1 INTRODUCTION

Over the years, many accelerator simulation programs have been developed. These programs, libraries and data formats tend to be inoperable with one another, and major modifications are required for them to work together. To cope with this interoperability issue, the Unified Accelerator Library (UAL) has been designed and developed[3].

The UAL not only gives guidelines to programmers who develop codes in the future but also enables existing "legacy" codes to work seamlessly with other UAL compliant codes. In other words, with one-time-only modifications, old codes can be integrated with other UAL compliants. Due to the UAL, the lifetime of codes is expected to be extended considerably, permitting more emphasis to be placed on design and algorithms.

One of the objectives of this paper is to demonstrate the effectiveness and versatility of the UAL to enable realistic simulation. The other objective is to predict the luminosity of CESR. To achieve the latter, real CESR lattice data is extracted from the CESR database and converted into Standard Machine Format (SMF)[4], and a beam-beam interaction UAL module and a stochastic-damping[5] UAL module have been developed to simulate the essential beam physics.

2 SIMULATION

To simulate colliding beams, one beam is described by an analytical distribution function and the other is described by a large number of macroparticles. As the macroparticles are tracked, self-consistency is achieved by allowing the parameters of the analytic distribution to evolve. A flow diagram of the simulation is shown in Fig. 1.

First, we have to supply input parameters relevent to the CESR operations. These values are either obtained empirically from direct measurements, or from computations of other computer programs, or as control parameters of the

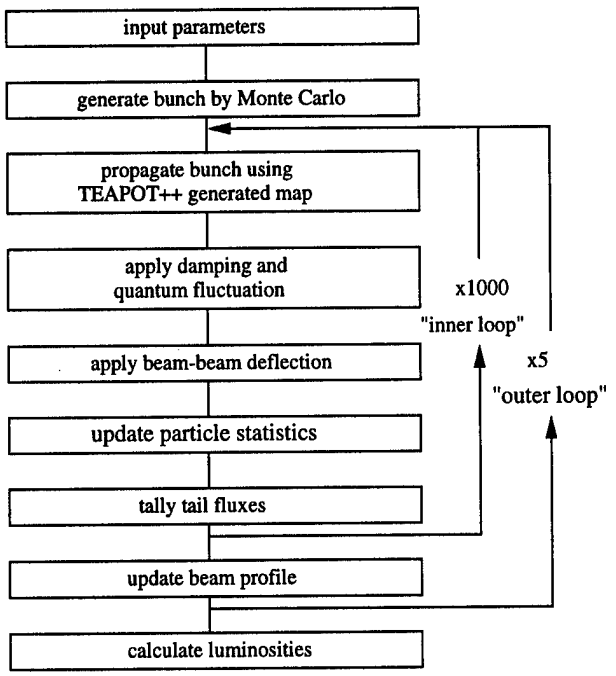


Figure 1: Program flow diagram.

simulation. The empirical ones include values such as energy deviation, damping coefficient, average energy, and bunch length. The computed values include Twiss parameters and the CESR lattice description. The only control parameter we have used so far in this simulation is beam current.

Next, a single bunch with, say 1000, sample particles is Monte Carlo generated in accordance with the input parameters. Parameters of this artifical bunch are preferably in the neighborhood of the "self-consistent" state for faster convergence.

After the bootstrapping processes, the program enters nested loops. The "outer loop", associated with beam evolution, consists of 1000[1] (typically) cycles of "inner loops". In the inner loop, we transport the beam around CESR by the TEAPOT++ generated map, apply damping and quantum fluctuation, apply beam-beam interaction, update particle statistics, and tally tail fluxes of the beam. This whole outer loop cycle is iterated about 5 times until a self-consistent state is reached.

The first process in the inner loop is particle propagation around the CESR lattice. Since the TEAPOT++ element-by-element tracking method is considerably slower than the

[1]The number of cycles should be appreciably larger than the inverse of the damping coefficient to achieve equilibrium

0-7803-4376-X/98/$10.00 © 1998 IEEE

map method, we employed the map method in the simulation. However, this map method has to be checked. To do so, we transported a particle with initial amplitude 1 mm at the interaction point using element-by-element tracking, 6th order map, 8th order map, and 10th order map. The displacements after 5000 turns are tabulated in Table 1. The results show that even 6th order can provide accurate propagation. Since essentially all particles lie within 1 mm from the center at the interaction point as seen in Fig. 3, it is valid to use the map method to transport the particles in the storage ring for faster processing. In particular, we have chosen an 8th order map[2].

method	x	x'	y	y'
track	9.4828478	3.8684952	8.2396275	1.4646015
map6	9.4**904625**	3.8**555656**	8.2**165072**	1.4**473738**
map 8	9.48**31417**	3.868**1267**	8.239**2599**	1.464**3757**
map10	9.4828**516**	3.8684**907**	8.23962**38**	1.464**5996**

Table 1: Displacements of various transporting methods after 5000 turns with initial amplitude 1 mm. x and y are in units of 10^{-4} m, and x' and y' are in 10^{-3}.

Comparison among maps of different orders are tabulated in Table 2. The numbers in the second and the third columns are calculated by fomulas:

$$\sum_{k=1}^{order} \frac{(k+dim-1)!}{k!(dim-1)!} \tag{1}$$

and

$$\sum_{k=1}^{order} \frac{(k+dim-1)!}{k!(dim-1)!}(k-1) \tag{2}$$

respectively[3]. These tables provide information useful for selection of an optimal method and to estimate processing times.

order	generation time	terms	multiplications
6	3 min	923	3829
8	25 min	3002	17590
10	150 min	8007	60633

Table 2: Comparisons among map methods. The times are measured on a system with SPECInt92 ≈200.

Next, damping and quantum fluctuation is applied to a once-circulated bunch. The damping decrement we used so far is 10 times larger than the empirical value for faster convergence. And the amplitude of quantum fluctuation is:

$$\sqrt{12\delta_d}\sigma_0 \tag{3}$$

where δ_d is damping constant. This amplitude is multiplied by a uniformly distributed random number between -1 and 1. The quantum fluctuation is applied in both horizontal and vertical directions with independent random numbers.

After damping and quantum fluctuation, we apply beam-beam deflection to a bunch. The deflection due to the beam-beam interaction is calculated by the formula:

$$\Delta p_x, \Delta p_y = -2r_e\frac{m_e}{E}NC_r\frac{x,y}{r^2} \tag{4}$$

where C_r is a (cumulative) circularly symmetric distribution, r_e is the classical radius of electron, and N is the total number of particles in a bunch. During the first 1000 turns, the beam-beam deflection is calculated with a Rayleigh distribution (which is just a circularly symmetric Gaussian distribution in polar coordinates) with a standard deviation consistent with the input Twiss parameters. However, starting from the second outer loop cycle, a "near-Rayleigh distribution"[4] obtained at the end of previous outer loop cycle is used to calculated beam-beam deflections until the end of the cycle. This corrected beam profile gradually drives the beam into a self-consistent state.

Then, we update the particle distribution statistics and this accumulated data is used to fit the beam profile with an improved "near-Rayleigh probability density function" at the end of every outer loop cycle[5]:

At the end of every inner loop, we take statistics of particles crossing preset boundaries located at 8σ, 10σ, 12σ, and 14σ in phase space, where σ is the initial Courant-Snyder invariant. To prevent multiple counting of particles wandering near boundaries, we put "Schmidt trigger" like buffer layers of $\frac{1}{2}\sigma$ surrounding those boundaries. Those crossing the 14σ boundary are declared lost and are restarted in accordance with the initial parameters. These data are used to estimate lifetimes.

After 1000 inner loop repetitions, we use the collected particle distribution data to fit the beam profile by near-Rayleigh function. The first and the second moments of the distribution are used to calculate power p and σ_{nr} as in the equation (5) by a formula:

$$\frac{\langle r\rangle^2}{\langle r^2\rangle} = \frac{\Gamma^2(3/p)}{\Gamma(2/p)\Gamma(4/p)} \tag{6}$$

and

$$\sigma_{nr} = 2^{-1/p}\frac{\Gamma(2/p)}{\Gamma(3/p)}\langle r\rangle \tag{7}$$

Finally, after the nested loop processes, luminosity of a self-consisted state is calculated from the near-Rayleigh function of the self-consistent state.

[2]Because of synchrotron radiation damping, preservation of symplecticity is not a critical issue.

[3]In our case, $dim = 6$

[4]The corresponding probability density function is:

$$P_{R_p}(r,\sigma_{nr}) = \frac{p}{2^{2/p}\sigma_{nr}^2\Gamma(2/p)}re^{-\frac{1}{2}(\frac{r}{\sigma_{nr}})^p}. \tag{5}$$

This near-Rayleigh function is a generalization of the well-known Rayleigh probability density function.

[5]Data in the database is cleared at the end of each outer loop cycle

3 RESULTS

This whole simulation is repeated for several beam strengths from 1 mA through 28 mA as explained in the previous section. Obtained luminosities are plotted against beam current in Fig. 2. As beam currents increase, deviations from the quadratic single beam curve become large due to beam-beam interaction. The quadratic curve is based on the 1mA point, where the beam-beam effect is insignificant.

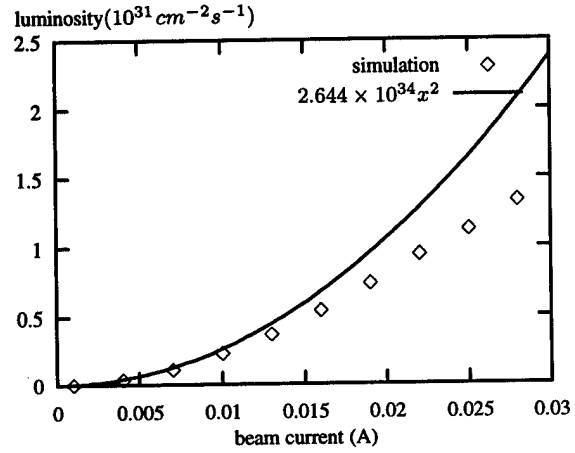


Figure 2: Graph of luminosity versus beam current.

It is also interesting to see how the beam profile evolves as the beam current increases. To see the beam evolution, we have plotted the fitted near-Rayleigh density functions of those self-consistent states in Fig. 3. As can be seen in the figure, tails of the beam profile grow, the peaks move outward, and entire beam profiles are correspondingly lowered somewhat as beam intensity increases.

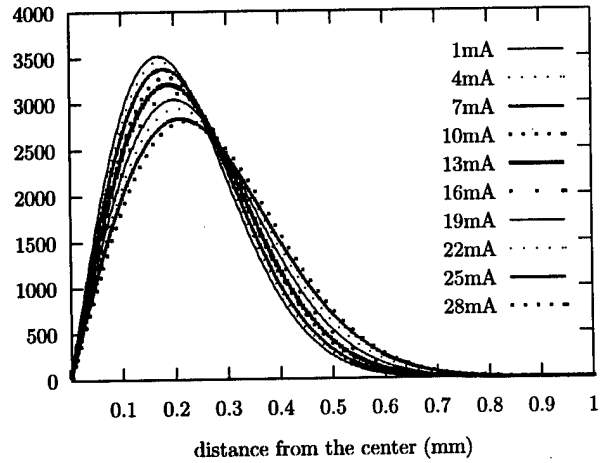


Figure 3: Self-consistent states of various beam currents at $\beta \approx 0.2$ m.

Lifetimes of high beam currents are estimated based only on the final outer loop cycle. This is because most particle loss takes place during evolution to the self-consistent state, but we are only interested in the stability of the self-consistent state. To estimate lifetimes, we fit the plot of emittance versus logarithm of number of boundary crossings with a straight line. This is then extraporated to various aperture sizes from 14σ through 20σ. The result is tabulated in Table 3. These estimates cannot be expected to have absolute values, but their relative significance as other parameters vary is expected to help finding optimal operating conditions.

current	14σ	16σ	18σ	20σ
22mA	10s	10^2s	10^3s	10^4s
25mA	1s	10s	10^2s	10^2s
28mA	1s	1s	10s	10s

Table 3: Estimated beam lifetime for high beam current.

4 PLANS AND PROSPECTS

We intend to develop a method to apply the quantum fluctuation process collectively rather than turn-by-turn as in this simulation. Such a method will enable us to construct a multiple turn map with beam-beam interaction and stochastic-damping process incorporated. Furthermore, a semi-continuous model of the beam may replace the discrete particle model employed in this simulation.

5 REFERENCES

[1] E. Young et al. Collisions of resonantly coupled round beams at the cesr. In *Proceedings to this conference*, (1997).

[2] R. Talman. *Phys. Rev. Lett.*, 74, 1590 (1995).

[3] N. Malitsky and R. Talman. Status of unified acclerator libraries. In *Proceedings to this conference*, (1997).

[4] N. Malitsky et al. A proposed flat yet hierarchical accelerator lattice object model. *Particle Accelerators*, 55, 313 (1996).

[5] E. Young and R. Talman. Design, analysis, and compensation of coupled accelerator lattices. *CESR internal report*, (1997).

INTERACTION REGION DESIGN FOR BEIJING TAU-CHARM FACTORY

Y.Z. Wu, Q.L. Peng
Institute of High Energy Physics, Beijing 918-9, China

Abstract

Beijing τ-charm factory (BTCF) is compatible with three modes of operation: high luminosity mode, longitudinal polarization mode and monochromator mode. It consists of two rings, one above another, with one interaction point (IP). This paper will describe the overall design of the BTCF interaction region (IR). A cryostat which contains an anti-solenoid (A-S), a shield solenoid (S-S), two focusing quadrupoles (Q1, Q2) will be installed at each side of the IP. Design parameters of these iron free superconducting magnets A-S, S-S, Q1, Q2 and the supporting system for these IR magnetic elements will be described. The IR vacuum chamber, the background issues which related to synchrotron radiation and lost particles will be described also.

1 INTRODUCTION

BTCF is a high luminosity collider with large number of bunches, the design of the IR is inherently difficult since two requirements must be satisfied. The beams must be focused to as small size as possible so that the quadrupoles must therefore be close to the interaction point to reduce chromatic aberrations and sensitivity to magnets position errors. The beams must also be separated as near to the IP as possible to minimize the spacing between successive bunches and still avoid unwanted crossings.

The IR configuration design for BTCF gives both accelerator physics and technology challenges:

- keeping the two beams in collision and separating them as close as possible to the IP.
- compatibility with multi-operation schemes and different phases.
- masking for synchrotron radiation and lost particles backgrounds.
- accommodating required machine elements without violating detector stay-clear region.

The design criteria for BTCF IR include the following:

- The IR configuration provides an effective compensation scheme of the high field(1.0T) of detector solenoid.
- All apertures in the IR must be designed for a beam of at least 14σ (uncoupled in the horizontal plane and full coupled in the vertical plane).
- The levels of synchrotron radiation and lost particles in the detector must be sufficiently low.

2 BEAM SEPARATION SCHEME

The geometry of the central drift chamber of the detector has a direct bearing on the IR design. In the present design of the BTCF detector, it requires the accelerator components must fit within a conical space with an opening angle of 18.2^o. The first accelerator component can only approach to within 600 mm on each side of the IP, which follows the forward detectors. The Schematic side view of the detector and together with the IR accelerator components are shown in Fig 1.

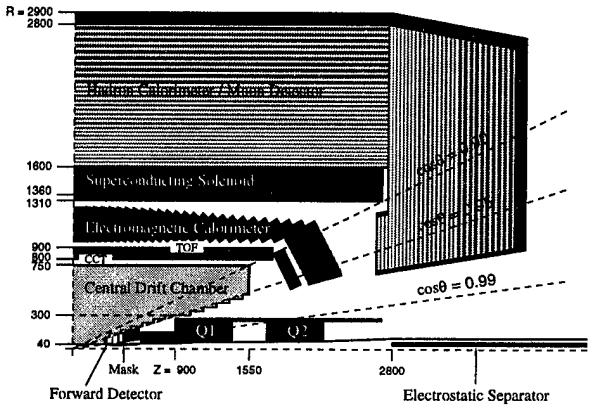


Figure 1: Schematic layout of the detector facility and IR accelerator components.

The IR is designed to be compatible with different modes[1]. Our initial choice is head-on collision or a small crossing angle configuration with flat beams. This configuration is the closest to conventional circular colliders so that the designed luminosity estimates are the most reliable. The monochromator mode will be realized by changing the polarity of the insertion quadrupoles and using additional quadrupoles in the beam separation region.

Figure 2 is the magnet layout of the interaction region. Two iron-free superconducting quadrupoles (Q1, Q2) are used to achieve the micro-beta function at the IP. The maximum field gradients of Q1 and Q2 are respectively 29 T/m and 20 T/m with a length of 0.5 m. An electrostatic separator (ES) with 3.5 m long makes two beams separation about 9 mm at the first parasitic crossing point which is just inside of ES. Two vertical offset quadrupoles QV1 and QV2 are used to further increase beams separation so that a sufficient separation is obtained to install the vertically bending septum magnets while QV1 and QV2 have a function to focus the beams in horizontal plane. Three bending magnets BV1, BV2, and BV3 further finish the beams separation. The last vertical bending magnet BV4 brings the beams back onto horizontal orbit.

0-7803-4376-X/98/$10.00 © 1998 IEEE

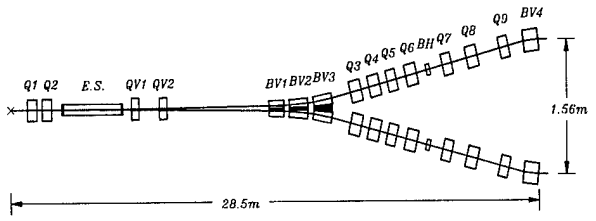


Figure 2: Magnet layout in the interaction region.

3 SUPERCONDUCTING SOLENOIDS AND QUADRUPOLES

The detector superconducting solenoid has a maximum field strength of 1.0 T over a distance of ±2.70 m around the IP. This longitudinal magnetic field causes strong coupling of the betatron oscillations and perturbations of the machine beam optics. To reduce this effect, an A-S and an S-S are used on each side of the IP to compensate the detector field along the beam line[2]. Located at 0.6 m away from IP, A-S with an effective field length of 0.3 m and field strength of 3.0 T compensate the detector field from IP to 0.9 m, and S-S which has a field of 1.0 T and effective length of 1.8 m compensate the detector field from 0.9 m to 2.7 m. Calculation of the magnetic field by combination of these solenoid magnets and the detector solenoid, including effects of iron yoke of the detector, has been done with computer code. The design parameters of the anti-solenoid and the shield solenoid are listed in Table 1.

Table 1: Main parameters of the compensation solenoid.

	A-S	S-S
central field	3.0	1.0 T
current	442.6	86.61 A
max. field on conductor		
with detector field	1.80	1.035 T
no detector field	2.935	1.80 T
store energy	44.58	80.93 KJ
current density	147.5	28.87 A/mm^2
magnetic pressure		
in radial direction	9.8	0.4 MPa
coil IR	100	182 mm
coil OR	120	202 mm
number of turns	1500	11700
effective magnet length	300	1800 mm
body force		
in axial derection	25.42	37.35 KN

Though the strength of the longitudinal attractive forces between the end yoke and the A-S and S-S is somewhat larger, they are within the acceptable level for engineering viewpoints.

Because the S-S screens the Q1 and Q2, the saddle coils of Q1 and Q2 no longer suffer large attractive forces coming from the detector field. The Q1 and Q2 saddle coil end parts should sustain enough radial attractive forces when the S-S does not work. The design parameters of the quadrupoles are listed in Table 2. The design is based on the cos2θ windings that are clamped by stainless collars. The maximum fields of the Q1 and Q2 are all less than 4.0 T, these quadrupoles can be operated in a very wide margin.

Table 2: Main parameters of the quadrupoles.

	Q1	Q2
field gradient	29	20 T/m
effective field length	500	500 mm
current	3096.6	2381.9 A
max field on conductor	3.47	2.98 T
store energy	218.6	150 KJ
induction	22.8	53 mH
coil IR	115	125 mm
coil OR	129	139 mm
number of turns	110	119 /pole

Figure 3 shows the cryostat cross section at the middle of the Q2 quadrupole. Starting with the innermost part, the main components of the cryostat at Q2 are: inner vacuum vessel, inner radiation shield, inner helium vessel (80K), inner helium vessel (4K), Q2 correction coil, Q2 coil, stainless collar, outer helium vessel (4K) for Q2, inner helium vessel (4K) for shield solenoid, shield solenoid correction coil, shield solenoid coil, outer helium vessel (4K), outer helium vessel (80K), outer radiation shield, outer vacuum vessel. The inner and outer diameter of the vacuum vessel of the cryostat at Q2 are 180 mm and 508 mm respectively.

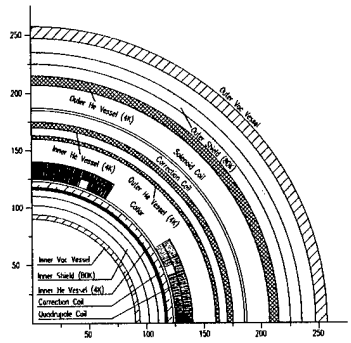


Figure 3: Cryostat cross section at the middle of Q2.

A cryostat will be installed at each side of the IP. They are supplied through a multi-channel transfer line by a comman cryogenic system. Many practical constraints near the IP are considered for designing the cryostat, including small outer diameter, large warm bore, narrow thermal space, sufficient strength to sustain the forces on the magnets, small heat load, easy operation and maintenance.

4 IR VACUUM CHAMBER CONSIDERATION

To ensure adequate quantum life time, the chamber is designed to accommodate at least 14σ. The diameter of the IP vacuum chamber grows up from 80 mm at IP to 120 mm at forward detector, to 140 mm at A-S and at Q1, to 160 mm at Q2.

In order to easily assemble the SC cryostat, the beam pipe is divided into three parts at its different cross section. The first part is over a distance of ±0.60 m around the IP, which ends at the forward of the A-S. The second part begins at the forward of A-S and ends at the backward

of Q1 with the length of 0.8 m. The third part begins at the backward of Q1 and ends at the backward of S-S with the length of 1.3 m. The central section of the first part is a double-walled pipe of pure beryllium with the length of 400~600 mm around IP. The inside wall and outside wall are all 0.5 mm thick with a space of 1 mm between the two walls for helium cooling. The beryllium section around IP is brazed directly to the copper beam pipe that extends outside.

After the first part of the beam pipe has been pushed in and assembled onto the inner surface of the central drift chamber by support pillars at 0.6 m from IP, the forward detector, which has been divided into four sectors(each sector 90°) in order to assemble easily, is then assembled onto the beam pipe at 300-600 mm from IP. Next the second part is assembled on the first part, then the SC cryostat is pushed in along the beam line through a movable table, at last the third part is assembled on the second part through a special flange.

The average pressure of the vacuum chamber will be maintained below 5×10^{-10} Torr by the distributed NEGPs at the upstream of Q1 and Q2. Ti-sublimation pumps(TSP) surrounding the beam pipe at A-S will absorb the large SR power.

5 SUPPORTING SYSTEM

Design of IP suport system is based on these cosiderations: sufficient rigid strength, easy assembly, easy maintenance, and easy alignment. For the accelerator requirement, the whole cryostat of the SC component should be completely buried inside the detector. So the cryostat assembly can only go along the beam line.

The SC cryostat at each side of the IP is supported by a precise table. Controlled by a host computer, the table can be moved along the beam line (Z direction), horizontally (X direction), vertically (Y direction), and can also be rotated around the X and Y axises. During the operation, the mass center of the cryostat is nearly 1.8 m off from the support table which has to remain outside of the detector, so enough rigid strength is needed for cryostat and joints that connect the cryostat and the support table to prevent the shake of the cryostat from earthquake.

Each cryostat has its position monitors for detecting the cryostat X, Y position and its tilt meters for detecting the tilt of the cryostat. For easy alignment of the two cryostats along the beam line, each cryostat has a set of hair cross targets stationed on its top surface. On each endplate of the detector central drift chamber, two glass windows will be installed to allow the surveyors looking through left and right of hair targets on the SC cryostats.

In order to easily access into the inner detector, the detector end yoke is designed to split into two same doors along its central vertical line. When the left and right door of the detector end yoke are opened and moved along X in opposite direction, the support table that loads the 3.5 m long ES is receded about 1.2 m along the beam line and then moved along X direction about 2 m, next disassembled the third part of the beam pipe in order to easily pull out the SC cryostat, then the SC cryostat table can be receded along the beam line.

6 BACKGROUND ISSUES

IR beam-related background includes synchrotron radiation (SR) photons and lost beam particles. SR is produced when beam particles experience transverse accelerations in the magnetic fields of quadrupoles and dipoles. Lost particles are created through Bremsstrahlung and Coulomb scattering on the residual gas molecules inside the vacuum chamber.

According to the computer simulation[3], the SR fans generated from the bending magnet BV1, BV2, BV3, offset quadrupoles QV1, QV2, and electrostatic separator ES mainly strike on the central part of the beam pipe and on the end part of the ES. Lost particles through Bremsstrahlung hit the vacuum chamber between the two ES. Two half-circle shaped masks, made of high Z material such as tantalum and installed inside at upstream of the copper vacuum chamber, are designed to prevent the SR fans from directly striking on the beam pipe. They also are used as masks to intercept the lost particles. A vertically movable mask should be placed between QV1 and QV2 to intercept parts of SR fans from hitting on the ES's. In order to reduce the rate of lost particles, two more movable masks are arranged in vertical direction, one is placed at upstream of BV3 at 17.7 m from IP, another is at 46.55 m from IP. With these masks and movable masks, the IR background can reach better condition than the two B factories[4].

7 SUMMARY

The interaction region of BTCF is described. The beam separation scheme is initiated by two electrostatic separators, two offset quadrupoles and several vertical bending magnets further finish the beam separation. The SC cryostat at 0.9m from IP must be stayed within a limited angle(18.2°) in order to provide maximum amount of the detector solid angle. The SC cryostat that contains superconducting magnets is supported by a movable table which can be moved along the beam line easily. In order to assemble the IR beam pipe easily, it is divided into several parts at its different cross sections. IR background can be reached a relatively better condition by using several masks.

8 REFERENCES

[1] N. Huang *et al.*, "A Preliminary Lattice Design of a Tau-Charm Factory in Beijing", PAC 95.

[2] K. Tsuchiya em et al., "The Superconducting Magnet systerm for KEKB B-Factory", KEK-Preprint 96-45.

[3] D.H. Zhang, "Feasibility Study Report of Beijing τ-charm Factory", IHEP-BTCF Report-03, P95-101.

[4] M Sullivan *et al.*, "Interaction Region Design at the PEP-II B Factory", SLAC-PUB-7206.

STATUS OF THE KEKB PROJECT

Shin-ichi Kurokawa, KEK, High Energy Accelerator Research Organization
1-1 Oho, Tsukuba-shi, Ibaraki-ken, 305 Japan

Abstract

KEKB, KEK B-Factory, is an asymmetric energy, two-ring, electron-positron collider for B-physics, and is now under construction at KEK. Machine study done at the accumulation ring, AR, of TRISTAN, in 1996 showed that HOM-free normal-conducting cavities, called ARES, and superconducting, single-cell, single-mode cavities being developed could be used for KEKB. Fast beam-ion instability was also studied experimentally. Installation of equipment in the tunnel started in February 1997. Commissioning of the machine will start from the upgraded injector linac in May 1998 to the two rings in October 1998. We anticipate beam collision toward the end of the year, which will be followed by the start of physics experiment in early 1999.

1.INTRODUCTION

KEKB[1][2][3] is one of the two B-Factories under construction in the world. Energies of the KEKB rings were set at 3.5 GeV for the positron ring (LER) and 8 GeV for the electron ring (HER). In order to facilitate direct injection into the rings and increase the intensity of positrons, the present 2.5 GeV linac is now being upgraded up to 8 GeV. The positron production taget will be moved from the present 0.2 GeV position to the place where 3.7 GeV electrons hit the target. A new 150 m tunnel is being constructed to accommodate transport lines between the upgraded linac and the KEKB rings.

Two rings of KEKB are housed in the TRISTAN tunnel of 3000 m circumference and installed side by side. At the center of one of the four long straight sections of the tunnel, we have an interaction point, IP, where BELLE[4] detector will be installed.

Even though we try to squeeze βy^* at IP to 1 cm, the design luminosity goal of KEKB, $10^{34}cm^{-2}s^{-1}$, requires high stored currents of 2.6 A at LER and 1.1 A at HER distributed into 5000 bunches. These large currents and large number of bunches oblige us to use special higher-mode free and beam-loading proof accelerating cavities to prevent coupled-bunch instablities. Two types of cavities, normal-conducting ARES cavity and superconduction single-cell, single-mode cavity, SCC, are being developed. We adopt copper vacuum ducts for both rings that can sustain large heat load, have a smaller photo-desorption coefficient and have good self-shielding capability of synchrotron lights.

The most salient feature of KEKB is a finite-angle crossing scheme at IP. Electron beam and positron beam collide at ± 11 mrad. This crossing scheme makes any use of separation dipole magnets unnecessary; the interaction region becomes simple and facilitates the shortest bunch spacing of 0.59 m. Although simulation studies have not shown any degradation of luminosity and significant increase of tails due to synchrobetatron resonances excited by the finite-angle crossing, we are rather prudent and developing crab cavities as a backup system. Orientation of incoming bunches of electrons and positrons is tilted by crab cavities by 11 mrad; the electron and positron bunches collide head-on at IP in the center-of-mass frame.

Figure 1 shows the layout of KEKB, and Table 1 summarizes its parameters.

Table 1 Main Parameters of KEKB

Ring	LER		HER
Energy(GeV)	3.5		8.0
Circumference(m)		3016.26	
Luminosity($cm^{-2}s^{-1}$)		1×10^{34}	
Crossing angle(mrad)		± 11	
Tune shifts		0.039/0.052	
Beam function at IP(m)		0.33/0.01	
Beam current(A)	2.6		1.1
Natural bunch length(cm)		0.4	
Bunch spacing(m)		0.59	
Emittance(m)		$1.8 \times 10^{-8}/3.6 \times 10^{-10}$	
Energy loss/turn(MeV)	0.81†/1.5††		3.5
RF voltage(MV)	5 ~ 10		10 ~ 20
RF frequency(MHz)		508.887	

† without wigglers
†† with wigglers

0-7803-4376-X/98/$10.00 © 1998 IEEE

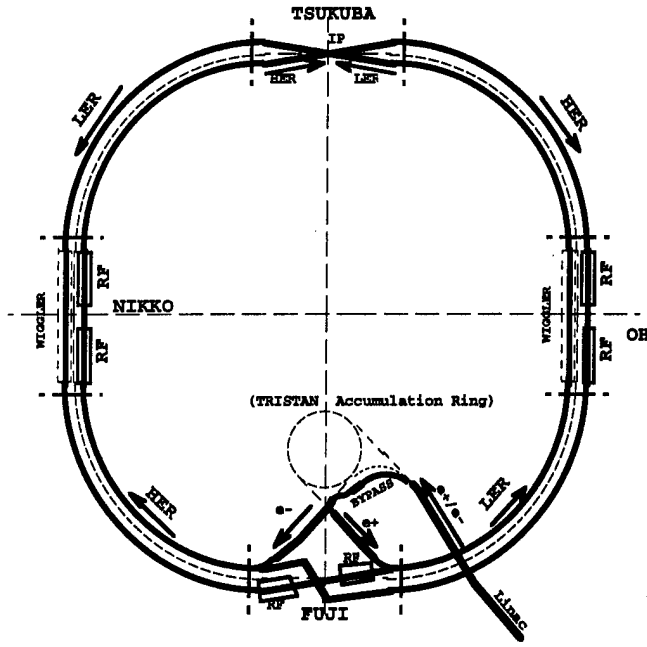


Fig. 1 Configuration of KEKB accelerator system

2. PRESENT STATUS OF CONSTRUCTION

2.1 Magnets and its installation

One thousand and six hundred main magnets and 1700 steering magnets are used at KEKB. Among them 119 dipoles and 313 quadrupoles of HER are refurbished magnets from TRISTAN. Except for small number of correction magnets and special quadrupoles near IP, all magnets have been ordered and delivery of magnets started in December 1996. Magnetic measurement systems became ready in January 1997 and have been in full operation from February. Forty magnets are measured per week.

Since two rings are installed side by side and only 1.1 m is available for transportation of magnets, we made two hovercraft-type transporters. Magnets started in late February 1977. Installation of magnets located at outer side of the tunnel will be installed first by this summer, which will be followed by the installation of magnets at inner side of the tunnel.

2.2 Vacuum system

By 1996 90% of copper vacuum ducts and their components had been ordered to companies. The delivery of the vacuum ducts started in September 1996. Vacuum ducts are baked, leak-checked, filled with dry nitrogen gas and stocked before being installed.

2.3 Interaction region

Basic iron structure of BELLE detector was completed and temporarily moved in to IP in April 1997 for surveying its position with respect to accelerator components. A pair of superconducting final-focus quadrupoles will be installed at both sides of IP inside the detector. One cryostat contains one superconducting quadrupole, one anti-solenoid, one correction skew quadrupole and two steering dipoles. The first full set of these coils have been completed and a test in a vertical cryostat will start soon. The superconducting magnet system will be completed by this summer and in September 1997 a combined test with the BELLE solenoid will begin.

3. CAVITIES AND AR BEAM TEST

In June, July and November 1996, we had a series of dedicated beam tests at the accumulation ring, AR, of TRISTAN[5]. All APS-type normal-conducting cavities were replaced with cavities of KEKB, namely, two ARESs, and one SCC. ARES consists of three cells: an accelerating cell, an energy-storage cell operated in TE013 mode, and a coupling cell that connects the accelerating cell and the energy-storage cell. Two ARESs that were tested differed from each other in that one type of ARES (ARES-95) used a choke-mode type cavity as its accelerating cell and the the other (ARES-96) had an accelerating cell with four wave-guide HOM dampers attached to the side of the cell.

Throughout the beam tests, AR was filled with electrons and operated at 2.5 GeV. We oftained the following results concerning ARES[6]:

(1) We could stably store 500 mA of the total current with both types of ARES operated at 0.5 MV. No serious HOM modes were found to be excited by beams.

(2) Power absorbed by HOM dampers attached to the accelerating cell and that absorbed by a damper attached to the coupling cell agreed well with the design.

(3) Concerning the fundamental RF property such as the detuning frequency, transient response, etc., we did not find any serious disagreement between the experiment and theoretical calculation.

The results we obtained about SCC are summarized as follows[7]:

(1) By the use of SCC operated at 1.2 MV, we could store 573 mA. This current was not limited by the cavity but by the radiation level around AR. No serious HOM modes were excited in SCC.

(2) The maximum accelerating voltage achieved was 2.5 MV that corresponded to the field gradient of 10.3 MV/m.

(3) We encountered rather frequent trips of the cavity in the July run. During summer shutdown we increased the pumping power of ducts close to the cavity and lowered the vacuum pressure by more than one order of magnitude. This worked well: in the November run, we observed almost no trips of the cavity.

(4) SCC has two cyrindrical HOM ferrite absorbers attached to the vacuum ducts at both ends of the cavity. Maximum HOM power absorbed by these absorbers amounted to 4.2 kW, which was very close to the expected value of 5 kW when the cavity is used at HER.

Encouraged by the results of the beam tests, we have decided to use both types of cavities. By the commissioning, we will install 10 ARESs at LER, and 4 SCCs and 12 ARESs at HER.

4. FAST ION INSTABILITY AND PHOTOELECTRON INSTABILITY

The following two new instabilities are expected to be serious at B-Factories.

4.1 Fast ion instability

Even though we have a long enough bunch gap at the electron ring and all ions are cleared during the gap, ions created within a passage of a bunch train excites strong coupled-bunch oscillation in the train. The amplitude of the oscillation grows as the bunch number counted from the head of the train increases. This is the fast ion instability, FII[8].

At AR we studied FII[9]. We stored 100 to 200 electron bunches in AR at 2.5 GeV and observed the spectrum of beam oscillation. If the current was high enough, strong vertical betatron oscillations were observed. After the stored current decreased and the vertical oscillations died out, we injected nitrogen gas in the ring. Strong coupled-bunch oscillations were excited again. The oscillation amplitudes of bunches in the train were registered for 1600 turns on a transient memory system. Analysis shows that the amplitude of the oscillation grows along the bunch train. The phase advance between bunches was consistent with that determinded by the ion oscillation frequency.

4.2 Photoelectron instability

In a positron ring, photoelectrons created by synchrotron lights at the inner surface of the vacuum duct are attracted by the beam. Although electrons are swept out rather quickly (within a few times ten nanoseconds), a stationary distribution of electrons (electron cloud) is established by continuous production and clearing of electrons. Transversely displaced bunches disturb the elctron cloud, which then exerts forces on subsequent bunches. The oscillations of bunches may resonantly couple via the electron cloud and lead to a coupled-bunch instability called photoelectron instability, PEI[10].

There had been only one experiment on the PEI performed at KEK PF[11]. The experiment showed that positron bunches stored at PF ring started to oscillate vertically if the current became larger than a threshold. The spectrum showed a pattern that was similar to that of oscillations excited by a wake field of 10-20 nsec range.

In order to verify the PF experiment and clarify the details of PEI, we conducted a series of experiments at BEPC of IHEP as a joint collaboration beween KEK and IHEP. These experiments clearly confirmed the result of the PF experiment[12]: The vertical betatron oscillations were observed only for the positron beam; The spectrum of the betatron oscillation was distributed around 50 MHz range that indicated that the range of force was 15-20 nsec. The study will be continued in 1997.

5. MILESTONES

We have set the following new milestones taking into account the progress of the construction. See Table 2.

Table 2 Milestones of KEKB

date		Milestones
1994	April	start of construction
1995	July	bidding for LER main equipment
	Dec.	start of dismantling of TRISTAN
1996	Mar.	end of dismantling
	June	bidding for HER main equipment and final focus sperconducting quadrupoles
	July	beam test at AR
	Oct.	beam test at AR
	Nov.	beam test at AR
	Dec.	start of bypass tunnel construction
1997	Feb.	start of installation of magnets
	Oct.	completion of bypass tunnel
1998	May	upgraded linac commissioning
	Oct.	LER and HER commissioning
1999	early	physics run starts

ACKNOWLEDGMENT

The paper summarizes the results of hard works by the members of the KEKB accelerator group; the author is deeply indebted to them.

REFERENCES

[1] KEKB B-factory Design Report, KEK Report 95-7.
[2] S. Kurokawa, Proc. 1995 PAC, p.491.
[3] S. Kurokawa, Proc. 1997 EPAC. p.448.
[4] BELLE TDR, KEK Report 95-1.
[5] Y. Funakoshi, High Beam Current Experiments for the KEKB Conducted at the TRISTAN Accumulation Ring, in these proceedings.
[6] T. Kageyama, et al., Development of High-Power ARES Cavities, in these proceedings.
[7] S. Mitsunobu, et al., Status and Developments of Superconducting Cavity for KEKB, in these proceedings.
[8] T.O.Rauvenheimer and F. Zimmermann, SLAC-PUB-95-6740.
[9] H. Fukuma, et al., Experimantal Observations of the Ion-Related Coupled-Bunch Instability in a Bunch Train in TRISTAN AR, in these proceedings.
[10] K.Ohmi, Phys., Rev. Lett., **75**, 1526 (1995).
[11] M. Izawa, Y. Sato and T. Toyomasu, Phys. Rev. Lett. **74**, 5044 (1995).
[12] Z. Guo, et al., The Experimentation Study on Beam-Phtoelectron Instability in BEPC, in these proceedings.

SIMULATION OF TAIL DISTRIBUTIONS DUE TO RANDOM PROCESSES AND BEAM-BEAM INTERACTION IN KEKB

Eun-San Kim and Kohji Hirata
High Energy Accelerator Research Organization (KEK), 1-1 Oho, Tsukuba, Ibaraki, 305, Japan

Abstract

A simulation that uses a new technique to obtain tail distributions in electron-positron storage rings is applied to KEKB. This program makes it possible to investigate tail distribution in simple and fast simulation technique and shows good agreement with solvable cases. The simulation now includes exact solution for six dimensional beam-beam interaction and several rare random processes. An estimate of the lifetimes for KEKB is also presented.

1 INTRODUCTION

It is important to calculate beam distributions by considering several processes which affect the beam tails. However, it is not always possible to obtain beam distributions by analytical treatments.

D.N. Shatilov developed a method to reduce the CPU time in simulating the beam tail due to scattering by the residual gas[1]. The beam tail is then obtained by considering the contribution of small angle scattering which occurs with a high degree of probability. However, it is not sufficient to consider small amplitude and frequent random processes only when we estimate the beam tail. Thus, we will investigate the beam tails caused by the rare and large amplitude processes from the core.

The aim of this paper is to propose a simple and fast simulation technique for various rare random processes on the beam tails. It is shown that results of this simulation technique show good agreement with solvable cases[2]. We thus expect that this simulation technique is applicable to obtain beam tails in the cases of analytically unsolvable random processes. The beam lifetime are also obtained by counting number of the particles extending beyond energy and transverse apertures.

In Sec. 2 the simulation technique is described and results of the simulation are compared with those of analytically solvable examples. Some applications are given in Sec. 3, and Sec. 4 is devoted to a discussion and conclusions.

2 DESCRIPTION OF SIMULATION TECHNIQUE

As an example, we can consider the case in which an electron loses energy by random processes in a ring. The initial distributions of n macroparticles in the phase spaces are given randomly with specified variances. Each macroparticle i has a particle number (N_i) and p is the probability that an electron undergoes a random process in one turn. Once an electron in a maroparticle undergoes this process, we create a new macroparticle $(n+1)$-th. This new macroparticle has one particle (N_{i+1}=1) and the macroparticle which undergone a random process now has a number of particles $N_i - 1$.

We assume that the variation in the random variable due to a random process is limited to a range between a minimum and a maximum value. The variation in the random variable due to a random process can be obtained by the following way. First, calculate the probability ($P \equiv N_i p$) that a macroparticle undergoes a random process in the ring, and generate one uniform random number ($0 \leq x \leq 1$). If $x < P$, a random process occurs for the macroparticle. Second, generate a uniform random number (ε_1) in the interval between the minimum value (ε_c) and the maximum value (ε_m) and one uniform random number in the interval $0 < y < (\frac{d\sigma(\varepsilon)}{d\varepsilon})_{max}$, and compare y and $(\frac{d\sigma(\varepsilon)}{d\varepsilon})_{\varepsilon=\varepsilon_1}$. Here ε is the energy random variable and $(\frac{d\sigma(\varepsilon)}{d\varepsilon})_{\varepsilon=\varepsilon'}$ is the cross section corresponding to the ε'. If $y < (\frac{d\sigma(\varepsilon)}{d\varepsilon})_{\varepsilon=\varepsilon_1}$, the random variation corresponding to ε_1 is given to an electron. If $y > (\frac{d\sigma(\varepsilon)}{d\varepsilon})_{\varepsilon=\varepsilon_1}$, discard these ε_1 and y, and generate new ε_1 and y until the relation $y < (\frac{d\sigma(\varepsilon)}{d\varepsilon})_{\varepsilon=\varepsilon_1}$ holds.

It is shown that equilibrium distributions are little changed by variations of ε_c of around 0.001% in beam-gas bremsstrahlung. The number of initial macropartices that are used in simulation is 40000. We investigate the present method using design parameters of KEKB, τ_ε=2300, τ_x=τ_y=4600, ν_s=0.01, ν_x=47.52 and ν_y=43.08[3].

The motion of each macroparticle is as follows:

1. Input

We rescale the variables as follows:

$$X = \frac{x}{\sigma_x^o}, \quad P = \frac{\beta^{IP} P_x}{\sigma_x^o}, \quad Y = \frac{y}{\sigma_y^o},$$

$$Q = \frac{\beta^{IP} P_y}{\sigma_y^o}, \quad Z = \frac{z}{\sigma_z^o}, \quad E = \frac{\varepsilon'}{E_o\, \sigma_\varepsilon^o}$$

where $\sigma_{x,y}^o$ and σ_z^o are nominal beam sizes in transverse and longitudinal directions. β^{IP}, E_o, σ_ε^o and ε' ($=E - E_o$) are betatron function at IP, nominal energy, relative energy spread and energy deviation due to a random process, respectively.

2. Random Process

$$E' = E - \frac{\varepsilon'}{E_o \sigma_\varepsilon^o}, \tag{1}$$

0-7803-4376-X/98/$10.00 © 1998 IEEE

where ε' is given by values between the minimum energy and the energy aperture of the beam.

$$P = P - \frac{\theta_x}{\sigma'_x}, \qquad Q = Q - \frac{\theta_y}{\sigma'_y}, \tag{2}$$

where transverse scattering angles $\theta_{x,y}$ are given by values between the minimum angle and the transverse apertures of the beam. $\sigma'_x = \frac{\sigma_x}{\beta_x}$ and $\sigma'_y = \frac{\sigma_y}{\beta_y}$. Here, $\sigma_{x,y}$ and $\beta_{x,y}$ are the transverse beam sizes and betatron functions at the position where the random process occurs, respectively. Equations (1) and (2) can be applied for longitudinal random processes and beam-gas scattering, respectively.

3. Synchrotron and Betatron Oscillations
4. Synchrotron Radiation

On the other hand, the probability that an electron loses energy ε is given by

$$f(\varepsilon) = \frac{1}{\sigma_{tot}} \frac{d\sigma}{d\varepsilon}. \tag{3}$$

When a random proces occurs, then its contribution to equilibrium distribution has the expression

$$\exp[N \int_0^\infty dt \tilde{f}\{Ke^{-dt} sin(\phi + wt)/(E_o \sigma_\epsilon^o)\} - 1], \tag{4}$$

where $\phi = tan^{-1} K_2/K_1$[4]. We assume that the number of synchrotron oscillations during one damping time is very large. We can then replace the synchrotron oscillation by an average over each synchrotron period. A solvable model to obtain the distribution functions in longitudinal and transverse random processes was shown in Refs. [2] and [4].

To show the validity of the simulation technique, we compare the results of the simulation for the cases of beam-gas bremsstrahlung and beam-gas scattering with those of the solvable model.

2.1 Beam-Gas Bremsstrahlung

An electron with energy E_o, which passes a molecule of the residual gas, loses its energy due to the radiation emitted when an electron is deflected. There is a certain probability that a photon with energy u is emitted, producing an electron with energy E', where $E' + u = E_o$. The differential cross section for an energy loss due to bremsstrahlung between E and $E + dE$ is given by

$$d\sigma = 4\alpha r_e^2 Z(Z+1) \frac{\mathrm{du}}{\mathrm{u}} \frac{E'}{E_o} [(\frac{E_o^2 + E'^2}{E_o E'} - \frac{2}{3}) \log \frac{183}{Z^{1/3}} + \frac{1}{9}], \tag{5}$$

where Z, α and r_e denote the atomic number, the fine-structure constant and the classical electron radius, respectively[5].

We assume that one type of molecule uniformly exists in the ring, so that $N = Q\sigma c$, Q=2.65 $\times 10^{20} n P_a$, where σ, c, Q, n and P_a are cross section of the beam-gas bremsstrahlung, velocity of the light, number of gas molecules in a unit volume, number of atoms in each gas molecule and partial pressure of the gas in pascals. Figure 1.(a) shows energy distribution produced from the tracking of synchrotron oscillation, synchrotron radiation and beam-gas bremsstrahlung for a vacuum pressure of 10^{-9} Torr. The dotted lines and square symbols are equilibrium distributions obtained from the simulation and solvable model, respectively. Figure 1.(b) shows energy distribution produced from the tracking of the synchrotron oscillation and synchrotron radiation. It may be inferred that the beam tails in Figs. 1.(a) and (b) are caused by the influence of beam-gas bremsstrahlung.

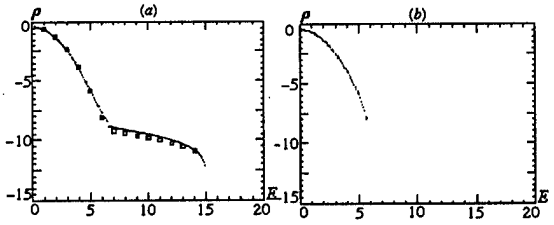


Figure 1: The horizontal axis is E, the energy deviation normalized by the energy spread. The vertical axis represents the distribution in E measured using a logarithmic scale. The number of turns is 230000.

2.2 Beam-Gas Scattering

The cross section of the elastic scattering with an atom is given by Rutherford scattering formula. Figure 2.(a) shows the vertical distribution produced from the tracking of beam-residual gas scattering, betatron oscillation, synchrotron oscillation and synchrotron radiation. Here we considered scattering angle occuring between $8\sigma'_y$ radian and $300\sigma'_y$ radian. The β_y value at the position where the scattering occurs is set to 10 meters. The dotted lines and square symbols show equilibrium distributions from obtained the simulation and solvable model, respectively.

We see from the above two examples that the simulation shows good agreements with the solvable model.

3 APPLICATION

For practical purposes, we consider beam-beam interaction and random processes with a non-uniform density distribution such as beam-beam bremsstrahlung and Bhabha scattering. Transverse beam-beam force is given by Bassetti-Erskine formula[6] and synchro-beam mapping is considered[7].

3.1 Beam-gas Scattering and Beam-Beam Interaction

Figures 2.(b) and (c) show the horizontal and vertical distributions due to beam-residual gas scattering for a pressure of 10^{-9} Torr and beam-beam interaction. It is shown that particle loss is increased by the beam-beam interaction. It is also shown that the vertical tail is caused by the beam-gas scattering rather than the beam-beam interaction.

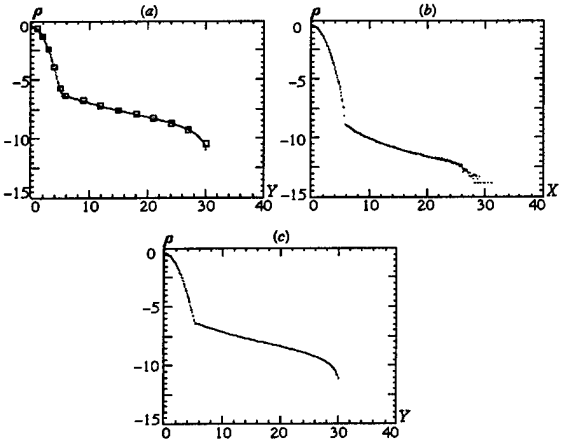


Figure 2: (a) shows vertical distribution due to beam-gas scattering. (b) and (c) show horizontal and vertical distributions due to beam-gas scattering and beam-beam interaction. The horizontal axis is Y, the distance normalized by the nominal vertical beam size. The vertical axis represents the distribution in Y measured using a logarithmic scale. The number of turns is 46000. Horizontal and vertical apertures are assumed to $34\sigma_x^{o\prime}$ and and $30\sigma_y^{o\prime}$ at IP, respectively, where $\sigma_x^{o\prime}=\sigma_x^o/\beta_x^{IP}$ and $\sigma_y^{o\prime}=\sigma_y^o/\beta_y^{IP}$.

3.2 *Random Processes in Longitudinal and Transverse Motions and Beam-Beam Interaction*

Figures 3.(a), (b) and (c) show the horizontal, vertical and longitudinal distributions due to the random processes of Bhabha scattering, beam-gas scattering, beam-gas bremsstrahlung, beam-beam bremsstrahlung and beam-beam interaction. The apertures are limited by $34\sigma_x^{o\prime}$, $30\sigma_y^{o\prime}$ and E=15 in the horizontal, the vertical and the energy directions, respectively. We can see that particle losses are mainly limited by the energy and the vertical apertures.

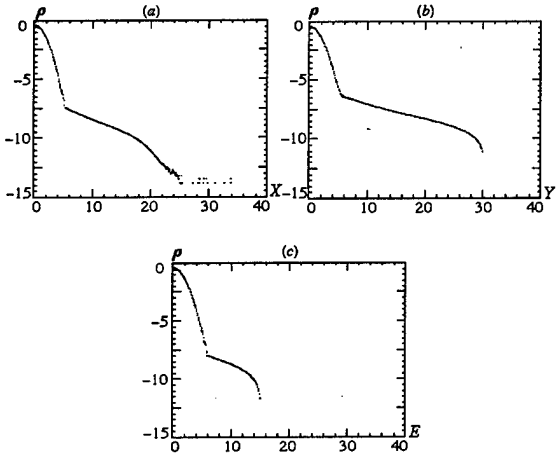


Figure 3: (a) Horizontal, (b) vertical and (c) longitudinal distributions due to longitudinal and transverse random processes and beam-beam interaction after 46000 turns. Pressure in ring is 10^{-9} Torr.

3.3 *Lifetime as a Function of Apertures in KEKB*

Beam lifetimes for bremsstrahlungs and scatterings as a function of energy and vertical apertures are listed in unit of hours below. Horizontal aperture is assumed to $34\sigma_x^{o\prime}$. If

Energy aperture	E=10	E=15	E=20
Beam-Beam Brems.	6.6	7.3	7.8
Beam-gas Brems.	32.4	35.3	37.7
Vertical aperture	Y=$25\sigma_y^{o\prime}$	Y=$30\sigma_y^{o\prime}$	Y=$35\sigma_y^{o\prime}$
Bhabha Scattering	13182	18595	25252
Beam-gas Scattreing	21.8	31.3	42.7

we estimate the lifetime including the beam-beam interaction to four random processes, it gives the lifetime around 5 hours in the aperture limitations of $34\sigma_x^{o\prime}$, $30\sigma_y^{o\prime}$ and E=15 for KEKB. It is shown that particle loss due to the beam-beam bremsstrahlung plays important role on electron beam lifetime for KEKB.

4 DISCUSSION AND CONCLUSION

Two simplifications were employed for our simulation to be valid: first, once a particle undergoes a random process, it does not undergo a random process again. The choice of a too small ε_c reduces the efficiency of this simulation, without giving any contribution to the tail distribution; and large ε_c can result in larger statistical fluctuations. Secondly, we assumed that new macroparticles in longitudinal and transverse directions reach an equilibrium state during two longitudinal and transverse damping times, respectively. This assumption makes it possible to simulate long-term runs.

The tail distributions are obtained by considering only the events of relative large amplitudes in several rare random processes for KEKB. It is shown that the beam-beam bremsstrahlung in KEKB is the predominate random process leading to particle losses.

A new simulation technique for beam tails is presented. This simulation method provides a simple and fast means to obtain the tail distributions due to various random processes in the storage rings. This simulation showed a good agreement with the solvable cases.

On the other hand, if random processes that produce beam tails occur with high probability, this situation requires us to generate more new macroparticles in our simulation. We would thus need more tracking times in this case.

The contribution of small amplitude scattering to the tail can be obtained by the simulation method of D.N. Shatilov. The effect of large amplitude scattering on the tail can be treated by this simulation method.

5 REFERENCES

[1] D.N. Shatilov, INP 92-79, Novosibirsk (1992).

[2] Eun-San Kim, Part. Accel. **56**, 249 (1997).

[3] KEKB B-Factory Design Report, KEK Report 95-7 (1995).

[4] K. Hirata, K. Yokoya, Part. Accel. **39**, 147 (1992).

[5] W.Heilter, The Quantum Theory of Radiation, Oxford Univ. Press (1954).

[6] M. Bassetti and G. Erskine, CERN ISR TH/80-06 (1970).

[7] K.Hirata, H. Moshammer, F. Ruggiero and M.Bassetti, CERN SL-AP/90-02.

HOM HEATING AT THE PEP-II B-FACTORY IR BERYLLIUM VACUUM PIPE *

X. Lin, C.-K. Ng, K. Ko
Stanford Linear Accelerator Center, Stanford University, Stanford, CA 94309

Abstract

The higher-order-mode (HOM) heating of the central beryllium beam pipe in the PEP-II B-Factory interaction region is evaluated. Both single and multi-bunch effects are considered. While single-bunch heating is not an issue, resonant heating due to multiple bunch passages is found to be unacceptable. Modifying the IR configuration around the central pipe has been shown to alleviate this problem. Simulation results indicate that the new design is sufficiently effective in reducing possible resonant heating down to a level that is within existing cooling requirements.

1 INTRODUCTION

The PEP-II interaction region (IR) consists of a central beryllium vacuum pipe connected to incoming beamlines through a series of synchrotron masks which are not collinear and vary in dimensions along the beam axis. Fig. 1 shows the IR geometry in the horizontal and vertical planes. The aspect ratio of the structure is very large; the central pipe length is 40 cm while its radius is 2.5 cm. At one end the masks extend to almost a meter from the interaction point. Since there is only vertical symmetry this long structure is numerically challenging to model. Previous studies have assumed a rotationally symmetric mask geometry for simplicity. This work is aimed towards modeling the full 3D effect of the actual IR geometry.

The set of masks and tapers in the IR raises concerns in regard to the impedance it presents to the beam as well as the joule heating generated by the electromagnetic fields that the colliding beams induce. The design as depicted in Fig. 1 has already incorporated smooth tapers with the first concern in mind. Wakefield calculations show that the IR contribution to the ring impedance is not significant. The concern over joule heating is the subject of this paper and the present analysis seeks to determine whether the additional thermal loading will exceed existing cooling specifications.

2 TRAPPED MODES IN BERYLLIUM PIPE

The wakefields generated by the colliding beams at the masks can be trapped in the beryllium pipe due to the constrictions by the masks at both ends of the pipe. These trapped modes do not play a role in the heating incurred in a single bunch transit. However, in multiple bunch passages, resonant heating can occur if the trapped mode is driven by a beam harmonic and its decay time is long compared with the bunch spacing (high Q). This cumulative heating can lead to thermal loading much beyond what the cooling system can handle. To quantify this effect, the identification and characterization of the trapped modes are essential.

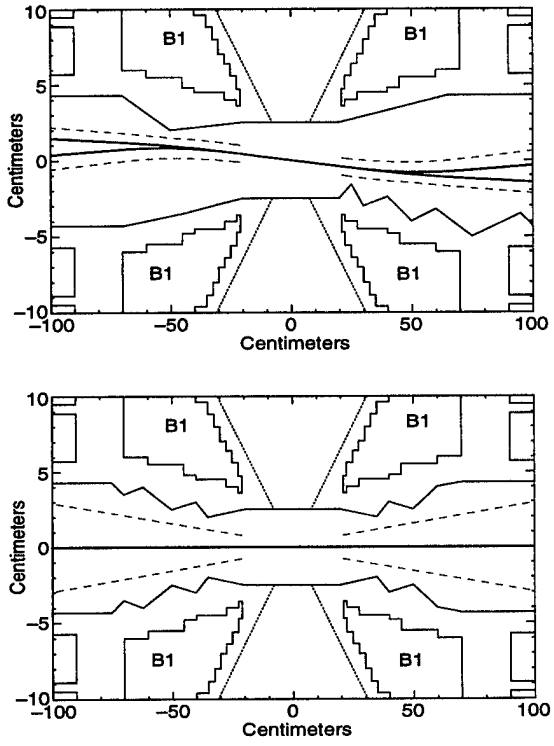


Figure 1: PEP-II IR region: horizontal and vertical plane

Trapped modes are normally best calculated in the frequency domain using cavity codes. These are localized modes below the beampipe cutoff and with low loss (high Q). The central pipe is, in a sense, a quasi-cavity whose beampipes are formed by the masks and tapers that extend out to larger pipes. Seen from the central pipe the beampipe cutoff is effectively changing with distance, first higher then lower as one approaches the larger outer pipes. In this structure some modes can be trapped within the central pipe while others can tunnel through the mask region and propagate in the outer pipes.

Figure 2 sketches the axial electric field of a partially trapped mode. Such a mode would not be determined correctly by a cavity code because there is outflow of energy. Although methods exist that use cavity code data to treat this coupling, they presently cannot handle multiple modes in the external waveguides which is the case here. To circumvent this difficulty we pursue a direct time domain approach in which all the modes are impedance matched at

* Work supported by the Department of Energy, contract DE-AC03-76SF00515.

0-7803-4376-X/98/$10.00 © 1998 IEEE

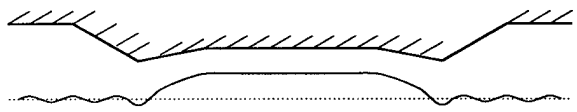


Figure 2: The longitudinal mode pattern in PEP-II IR region

the ends of the larger beampipes.

3 SINGLE BUNCH SIMULATION

The time domain simulation is basically a wakefield analysis whereby one drives a nominal bunch through the structure to find the energy loss and Fourier-transforms the wakefield to obtain the impedance spectrum. For heating calculation, it is further necessary to find the fraction of the energy loss to the pipe wall. We achieve this by monitoring the tangential magnetic field on the wall surface as a function of time (up to 67nsec, 16 bunch spacings). The set of monitors includes 8 locations in the azimuthal direction and 20 in the axial direction. Using this magnetic field data the wall loss can be obtained via perturbation theory. Fig. 3 shows the total heating spectrum within 20 cm of

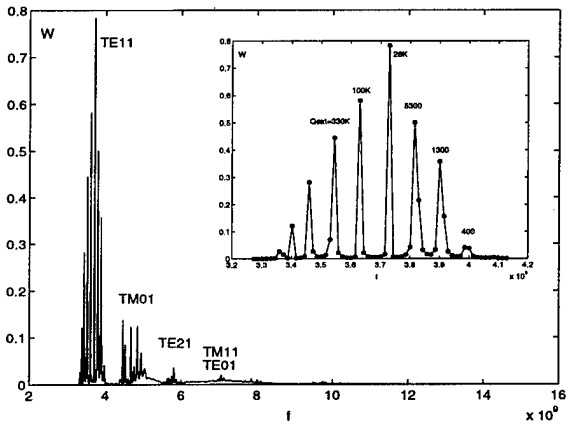


Figure 3: Heat spectrum in the beryllium pipe. The insert lists the Q value of the TE_{11} group of modes.

the IP, which is essentially the beryllium pipe. One can identify the modes by referencing the cutoff frequencies of the central pipe: TE_{11} = 3.5 GHz, TM_{01} = 4.6 GHz and TE_{21} = 5.8 GHz. It is found surprisingly that the dominant modes are from the TE_{11} family. If the IR geometry were treated to be rotationally symmetric (2D) the dominant contributions would have been from the TM_{01} group. TE modes would not be excited by the beam because they have zero electric field along the beam path. However, in the region where the masks intrude into the beampipe in the horizontal plane (right end of the central pipe), The azimuthal symmetry has been broken. The TE modes can have an axial field component and therefore be generated. Fig. 4 shows the dominant mode in the group, TE_{116}, that is well trapped. This is a clear indication that the 3D geometry of the masks is an important effect. Summing all

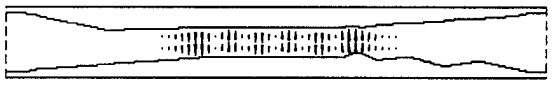


Figure 4: TE_{116} mode pattern

the modes the total heating is calculated to be 9W for a 3A beam.

4 MULTIBUNCH HEATING

When a single bunch passes through IR, it loses energy ΔU_n to the mode n. In the case of a train of bunches passing through IR, each bunch not only interacts with its own wakefield but that of the proceeding bunches[1]. Therefore the energy loss

$$U_n = \Delta U_n\{1 + 2\sum_{l=1}^{\infty} \exp\,[(\frac{-\omega_n * t_B}{2Q_n} + i\omega_n t_B)l]\} \quad (1)$$

contains the summation of all previous wakefield. The factor of 2 comes from the fundamental Theorem of beam loading[2]. The summation at resonance $\omega_n t_B = 2\pi m$, with integer m, is

$$U_n = \Delta U_n \frac{4Q_n}{\omega_n t_B}, \quad (2)$$

when $2Q_n \gg \omega_n t_B$.

In the previous single bunch heating calculation, we have integrated up to T = 67nsec, at which time most low Q modes have been completely damped. However, a few slowly decaying modes are still resonating. Thus, we express the multibunch heating

$$\begin{aligned} P_{multi} &= P_{single}\frac{\int_0^{\infty}\exp(-\frac{\omega t}{Q})}{\int_0^{T}\exp(-\frac{\omega t}{Q})}\frac{4Q}{\omega t_B} \\ &= \frac{P_{single}}{1-\exp(-\frac{\omega T}{Q})}\frac{4Q}{\omega t_B} \end{aligned} \quad (3)$$

to account for finite integration time interval. The mode index n has been dropped to simplify the notation.

Because wakefield calculation requires a much finer mesh and correspondingly more CPU time, a separate MAFIA simulation with a dipole to excite individual modes is performed to calculate the Q_{ext}. A few Q_{ext} values for the TE_{11x} modes are displayed in the insert in Fig. 3. The Q_{ext} of the first 3 modes are so high that we are not able to determine them. Since the metal surface results in a natural Q_0 of 30K, the total Q of TE_{116}, for example, is roughly 14K. From Eq. 3, TE_{116} results in a heating of 4.4 KW if it is on resonance. The other high Q modes contribute even more. The total heating is unacceptable.

5 HEATING REDUCTION

It is seen from Eq. 3 that high Q resonance is highly undesirable. And we have also noticed that the smooth taper, with the aim to reduce the broadband impedance, traps the modes very well. Since wakefield calculation shows that the IR contribution to the ring impedance is not significant, we could use thin irises (See Fig. 5) instead of tapers to increase the tunneling of the trapped mode, thus reduce the Q_{ext}. The vertical mask on the right side is also pushed

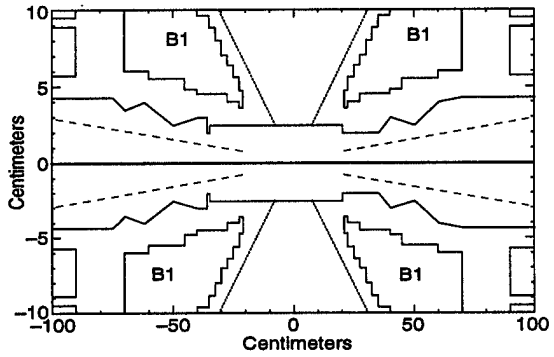


Figure 5: New PEP-II IR region- horizontal plane

in to shield horizontal mask, which induces the dominant TE_{11} contribution. The resulting single bunch heating is shown in Fig. 6. The TE_{11} contribution has been greatly

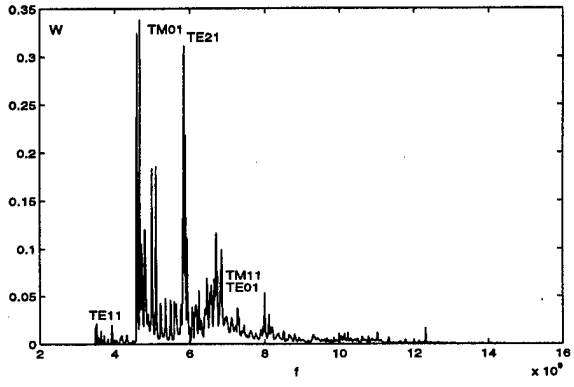


Figure 6: Power dissipation spectrum for new design

reduced at the expense of larger TM_{01} and TE_{21} excitations due to the abrupt geometry change.

We also evaluated the Q_{ext}'s of the modes by the previously mentioned method. Tab. 1 summarizes the multibunch heating if modes are on resonance. The total heating of 242 W assumes a very pessimistic situation where all modes are on the beam harmonics. It is very unlikely because the beam harmonics are 238 MHz apart in the case of nominal 4.2 nsec spacing.

Table 1: Multibunch heating

modes	Q_{ext}	P_{single}	P_{multi}
TE_{111}	3600	0.018	8.32
TE_{112}	1080	0.022	1.38
TM_{011}	4000	0.33	113
TM_{012}	730	0.1	2.58
TE_{211}	8000	0.13	103
TE_{212}	1400	0.32	14.2
Total(W)			242

6 TWO BEAM EFFECTS

For a symmetric mode with respect to IP, its excitation from two colliding e+ and e- beam will be twice as that from a single beam. Correspondingly 4 times the power will be generated. On the other hand, an anti-symmetric mode will have zero excitation (see Fig. 7). Assuming the worst case

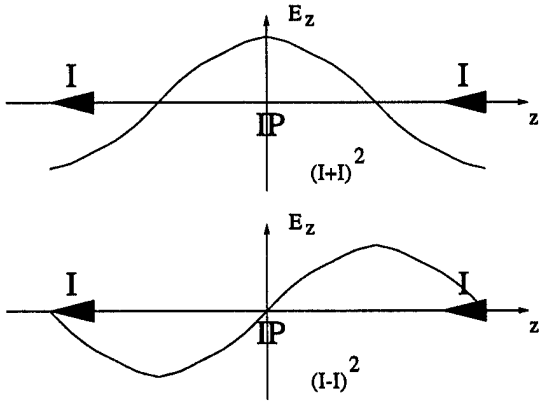


Figure 7: Two head on beams.

scenario with all the modes being symmetric, the HOM heating is $4 \times 242 = 968$W for 3 A beams. In addition to the 30 W image current heating, the total wall heating does not exceed the cooling requirement.

7 CONCLUSION

The PEP-II IR HOM heating has been numerically analyzed. By modifying the synchrotron masks at the ends of the central beryllium chamber, the excitation of TE modes are substantially suppressed and the Q_{ext}'s are greatly reduced. Resonant heating from multibunch on the chamber wall is lowered to within the designed 1 KW cooling capacity.

8 REFERENCES

[1] 'Impedance Study for the PEP-II B-factory', by S. Heifets et al. SLAC-AP-99. March 1995.

[2] 'High Energy Electron Linacs: Applications to Storage Ring RF systems and Linear Colliders' By P. Wilson, SLAC-PUB-2884, Nov. 1991.

THE PEP II INJECTION KICKER SYSTEM

G.C. Pappas, A.R. Donaldson, D. Williams,
Stanford Linear Accelerator Center

Abstract

PEP II or the B Factory consists of two asymmetric storage rings. The injection energy for electrons is 9 GeV, while that for positrons is 3.1 Gev. The bend angle into the high energy ring (HER) is 0.35 m-rad, and the angle into the low energy ring (LER) is 0.575 m-rad. The magnetic length for the HER kicker is 0.85 m, and 0.55 m for the LER kicker. The field produced by the magnet is therefore 123.5 G for the HER, and 132 G for the LER. Each ring has a kicker magnet upstream of the injection line which is used to distort the orbit of the stored beam. An identical magnet downstream of the injection line is used to restore the orbit of the stored beam and inject the incoming beam. The two magnets are driven in parallel by the modulator. The aperture of the magnets is 3.86×3.46 cm (H×V). Therefore the current required to drive the HER is 863 A, while for the LER it is 756 A. The inductance of the magnet is approximately 1.4 μH/m. The current pulse is a critically damped sinusoid with a rise time of less than 300 ns. A kicker system has been designed which can be used for injection of both beams by varying the charge voltage. The modulator uses a conjugate circuit to match the impedance of the magnet, and coupling to the beam chamber.

THE PEP II INJECTION KICKER MAGNET

The PEP II injection and orbit distortion kicker magnets are single turn, H-type magnets, made from blocks of Ceramic Magnetics CMD5005 ferrite. The HER magnet uses 6 C-shaped ferrite blocks which are clamped together with their pole tips facing to form a rectangular aperture. The LER, which is 1/3 shorter, uses only four ferrite blocks. The magnets used for beam abort are identical to the injection kicker magnets[1]. The beam chamber is made from 2.5" inner diameter by 3.0" outer diameter alumina-ceramic pipe, and is coated with 0.3 Ω/square of kovar which was applied by a sputtering process. The length of the ceramic tube is 39.37", resulting in a coating resistance of approximately 1.5 Ω. The bus bars are bonded to the ceramic chamber with indium, and are water cooled to remove the power dissipation of the beam return current in the resistively coated chamber. The ceramic beam chamber supports the weight of the upper bus, and the upper ferrite. EPR rubber is used between the bus bars and the ferrite for mechanical compliance. The ferrite core is then clamped together in an aluminum housing. A cross sectional view of the magnet is shown in Figure 1, while a longitudinal view is shown in Figure 2.

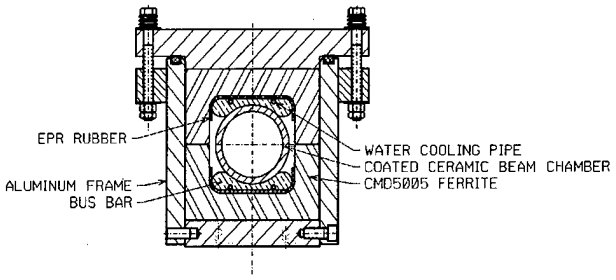


Figure 1. Cross section of the PEP II injection kicker magnet.

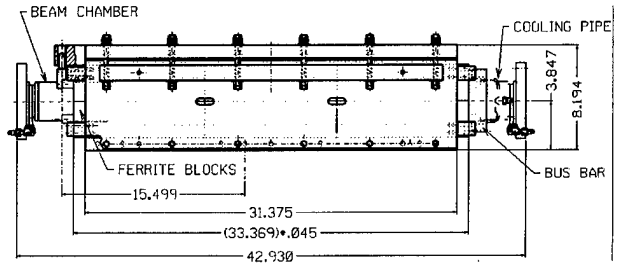


Figure 2. Longitudinal view of the PEP II HER injection kicker magnet.

The electro-magnetic field solver MAXWELL was used to calculate various parameters associated with the magnet. The inductance of the single turn of the magnet was calculated to be 751 nH, the inductance of the beam chamber is 577 nH, and the mutual inductance between the bus bars and the chamber is 556 nH. The capacitance from the bus bars to the aluminum case and the coated chamber is 5 nF. A plot of the field distribution across the middle of the aperture is shown in Figure 3. The driving current for this calculation was 1221 A which results in a magnetic gain of the magnet of 0.139 G/A. The highest electrical field stress point is in the corner where the bus bar separates from the ceramic chamber. The field calculated at this point with a bus bar voltage of 15 kV is 4.7 MV/m. This high field is troublesome, however no electrical breakdown, or corona has been detected in testing.

Work supported by the Department of Energy under contract No. DE-AC03-76SF00515

0-7803-4376-X/98/$10.00 © 1998 IEEE

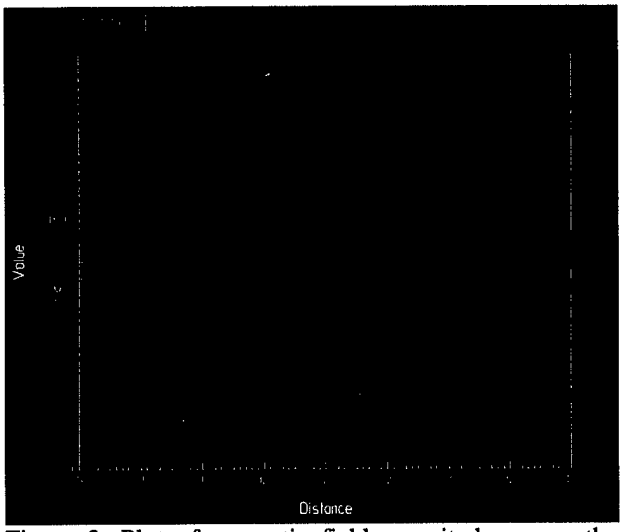


Figure 3. Plot of magnetic field magnitude across the center of the aperture.

The magnet and coated chamber can be modeled as a single turn transformer shown in Figure 4. In this model the bus bar L_1 is replaced with the term L_1-M (90 nH), and the coating inductance L_2 is replaced with the term L_2-M (180 nH), where M is the mutual inductance between the conductors. The resistor is used to model the chamber coating resistance. Using this model it is possible to solve for the effect that the coating has on both the B field rise and fall times, and the peak magnetic field[2]. The results of this analysis are shown in Table 1 for various coating resistances. The nominal rise time for the current pulse was 100 ns for this analysis.

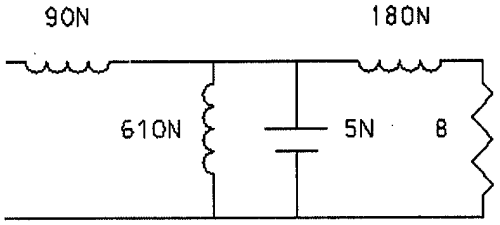


Figure 4. Schematic for single turn transformer model of magnet and beam chamber.

R_c Ω	t μs	B
100	0.3	15.7
0.45	0.34	14.22
0.2	0.38	13.43
0.1	0.44	11.48

Table 1. Pulse rise time and peak B field for various chamber coating resistances.

THE PEP II INJECTION KICKER MODULATOR

The modulator for the PEP II injection system uses a capacitor discharge circuit to form a pulse which has a sinusoidal rise, and an exponential decay. A schematic of the modulator is shown in Figure 5. A 20 kV, Electronic Measurements, Inc. capacitor charging power supply, model 402L, is used for the high voltage source. The switch tube used is a EG&G HY5, single gap, ceramic envelope, hydrogen thyratron.

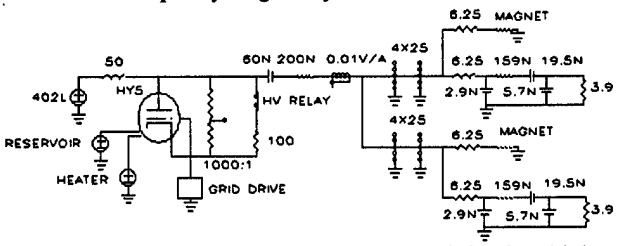


Figure 5. Schematic of the PEP II, HER injection kicker system.

Four parallel lengths of Time Microwave AA8481 cable connect the modulator to the magnet. The impedance of the AA8481 cable is 25 Ω, for a 6.25 Ω connection to the magnets, with the injection kicker magnet and the orbit distortion magnet being driven in parallel. The lengths of the cable runs for the magnets are 189.5 ft for the HER injection kicker, 254 ft for the HER orbit distortion kicker, 478.1 ft for the LER injection kicker, and 260 ft for the LER orbit distortion kicker.

It is possible to use a conjugate circuit in parallel with the magnet which makes the magnet load and matching resistor appear to be purely resistive, and therefore minimize reflections[3]. In the conjugate circuit, the inductors, capacitors, and resistors from the magnet model shown in Figure 4 are replaced with capacitors, inductors, and resistors, respectively. The values of the components in the conjugate circuit can be calculated from the characteristic impedance of the cable, $Z = \sqrt{\frac{L}{C}}$, in the case of the inductor and capacitors, and $R_{con}=R^2/Z$, where R is the resistance of the chamber coating. The modulator, magnet with beam chamber, and the conjugate circuit were modeled in SPICE. The results of this analysis are shown in Figure 6. Here the charge voltage was 15 kV.

OPERATION OF THE HER INJECTION SYSTEM

The HER injection kicker system has been fully tested and installed. Figure 7 shows the magnet current, and the magnetic field integrated over the length of the magnet. The area of the probe used was 1.275×10^{-3} m^2, therefore the field at 1200 A is approximately 149 G, or 124 mG/A.

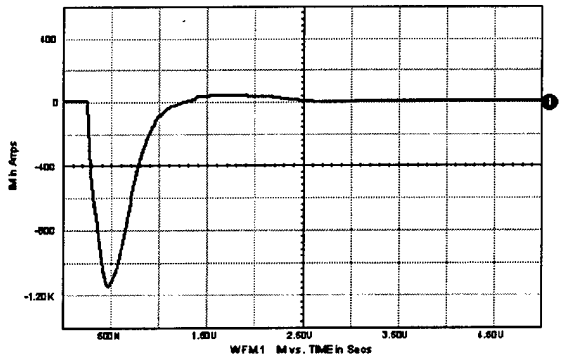


Figure 6. SPICE simulation of the PEP II HER injection kicker system, showing magnet current.

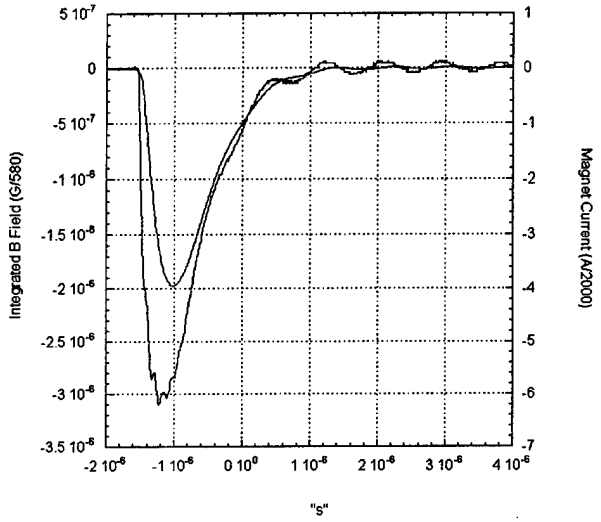


Figure 7. Magnet current and integrated magnetic field.

From Figure 7, it is seen that the rise time of the current pulse is approximately 200 ns, while the rise time of the integrated magnetic filed is approximately 400 ns. This discrepancy is close to that predicted by the analysis shown in Table 1. Several attempts where made to increase the rate of rise of the current pulse. Circuit, and magnet connection inductances were reduced as much as possible. The overall circuit inductance with the magnet shorted was measured to 810 nH. The load, which is made from sixteen parallel, twelve inch long by one inch diameter, cylindrical, Cesiwed, type AS resistors, contribute the majority of this inductance, approximately 500 nH. A new load using disk type resistors with a coaxial return is planned.

In order for the PEP II injection scheme to work properly, the magnetic field in the injection kicker magnet and the field in the beam distortion magnet need to be identical. Because the cable runs to the magnets are different, any reflection from the magnets need to be minimized. Figure 8 shows the magnet currents for the HER injection and beam distortion magnets, and clearly shows that the injection magnet and the orbit distortion magnet are well matched.

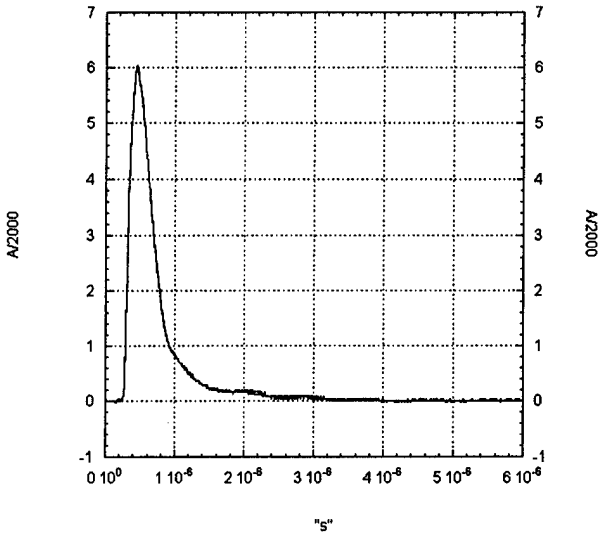


Figure 8. Overlay of HER injection and beam distortion magnet currents.

CONCLUSIONS

A modulator and magnet have been constructed which are capable of providing the pulsed magnetic field consistent with the PEP II injection kicker requirements. Only a proto type modulator has been built and installed for the HER. Two new modulators are currently being fabricated. The system has not been fully commissioned with beam.

ACKNOWLEDGMENTS

The authors would like to thank Dick Cassel, for his encouragement to build a H magnet instead of a C magnet, which leads to a lower induced voltage on the beam chamber. Also thanks to Ed Daly, Hank Atilles, and Mike Robertson for their help with the mechanical design and assembly of the magnet, and Pat Banglos, Joe Olszewski, and John Krzaszczak for their electronic technical support, and installation.

REFERENCES

1. *The PEP II Abort Kicker System*, J. de Lamare, etal, PAC97.
2. *Response of Kicker Magnets with Coatings*, Glen Lambertson, PEPII publication AP96.30.
3. *Fast Kickers for SLC*, G.B. Bowden, SLC, Klystron R&D Technical Note, No. 003.

TARGET OPTIONS AND YIELDS FOR A MUON COLLIDER SOURCE

D. Ehst, Argonne National Laboratory, Argonne, Illinois 60439, USA and
N.V. Mokhov, R.J. Noble and A. Van Ginneken,
Fermi National Accelerator Laboratory, Batavia, Illinois 60510 USA*

Abstract

Efficient production and collection of a large number of muons is needed to make a muon collider viable. Target options are considered to maximize pion yield and to provide target survivability for 8 and 30 GeV primary beams of approximately 10^{14} protons per pulse at 15 Hz. Realistic Monte-Carlo simulations are performed for targets of different configurations and dimensions in a high-field solenoid. Different materials, including liquid metals and coolants, are studied to optimize heat removal.

1 INTRODUCTION

To achieve adequate luminosity in a muon collider it is necessary to produce and collect large numbers of muons. The basic method starts with a proton beam impinging on a thick target (one to two interaction lengths) immersed in a 20 T solenoid followed by a long 5 T solenoid channel which collects muons resulting mainly from pion decay (Fig. 1). The aperture of the 20 T solenoid is assumed to be 7.5 cm so as to give a large transverse phase space acceptance adequate for a transverse momentum $p_\perp^{max} = qBa/2$, where B is the magnetic field, q the particle charge, and a the solenoid radius. The normalized phase space acceptance of this solenoid for pions is $ap_\perp^{max}/m_\pi c = qBa^2/2m_\pi c$. For a 20 T solenoid the momentum acceptance is 0.22 GeV/c, and the phase space acceptance is 0.12 m·rad.

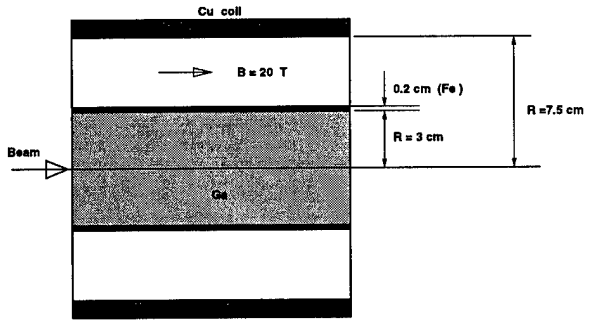


Figure 1: Production target in 20 T solenoid.

Extensive simulations have been performed for pion production from 8 and 30 GeV proton beams on different target materials in a high field solenoid [1, 2]. Solid (carbon, aluminum, copper, tungsten iridium) and liquid (gallium, mercury, lead) targets of different radii (0.4 cm to 3 cm) and thicknesses (0.5 to $3\lambda_I$, where λ_I is nuclear interaction length) have been explored. Values of λ_I are taken from [3].

* Work supported by the U.S. Department of Energy under contract No. DE-AC02-76CH03000.

2 YIELD AND TARGET HEATING STUDIES

For the collection geometry described in the previous section, target composition, length and radius are varied and pion yield is studied using particle production and transport simulation codes. The MARS code [4], developed over many years at IHEP and Fermilab for particle-matter interaction simulations, is used for simulating particle production and transport in thick targets within the solenoid field. The MARS code is also used to study energy deposition in the target and surrounding solenoid. In excess of 90% of all accepted muons are found to be the progeny of pions in the momentum range 0.05 - 1 GeV/c for both 8 and 30 GeV protons.

Materials investigated as target candidates are carbon, aluminum, copper, gallium, tungsten, iridium, mercury and lead. This set spans the Periodic Table and ranges in density from 1.8 to 22.4 g/cm^3. It is found [1, 2] that the pion yield is higher for high-Z materials, but saturates at $Z \geq 29$. At the same time, power dissipation grows rapidly with Z. Analysis shows that for the required beam parameters the only practical materials are those with $Z \leq 31$ (gallium or lighter). Copper and solid carbon have been studied in detail in [1, 2]. Below we concentrate on carbon/water and liquid gallium since they appear to have a desirable combination of thermal and yield properties in the proton energy range of 8 to 30 GeV. The π+K yield in the kinetic energy range from 0.05 to 2 GeV is studied for the above targets in the 20 T solenoidal field.

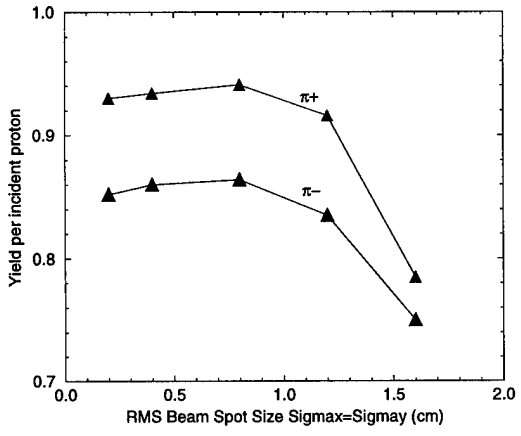


Figure 2: Positive and negative meson yields per 30 GeV proton for gallium target (R=3 cm, L=36 cm) *vs* rms beam spot size σ_x=σ_y.

0-7803-4376-X/98/$10.00 © 1998 IEEE

It is found that pion yields are nearly optimized as long as the target radius R≈2.5σ, where σ is the rms beam spot size, for all target materials and lengths, at both 8 and 30 GeV. For the fixed target radius, the yield is slightly smaller for small beam spot sizes and drops rapidly at $\sigma \geq$ R/3 (Fig. 2).

Figures 3 and 4 show the yield versus target thickness for carbon and gallium targets. The optimal target length is about 1.2 to 1.4 λ_I, but yields vary by no more than 10% over a range of 1 to 2.5 λ_I.

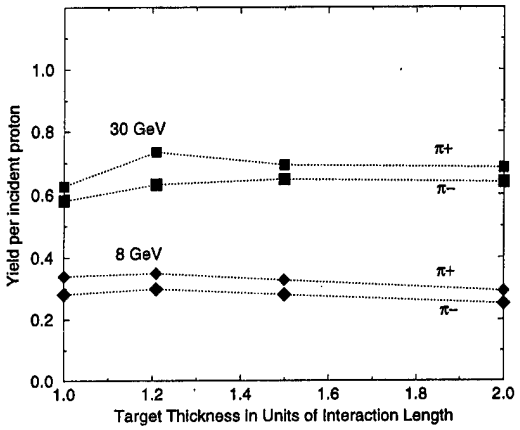


Figure 3: Positive and negative meson yields per one 8 or 30 GeV proton for a target composed of carbon disks (0.704 cm thick) with 0.15 cm water gaps *vs* target assembly thickness. Beam rms σ=0.4 cm. R_C=1 cm, R_{water}=4 cm, λ_C=53 cm, λ_{water}=91 cm.

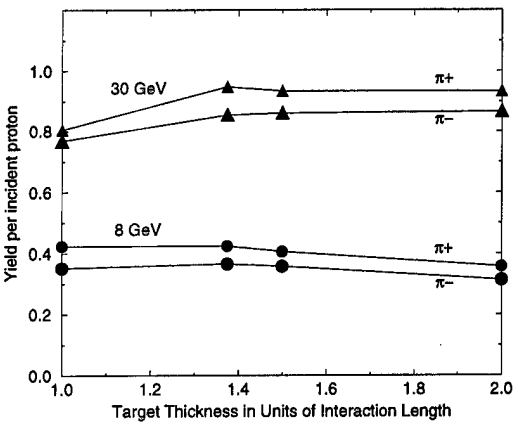


Figure 4: Positive and negative meson yields per one 8 or 30 GeV proton for gallium target (R=3 cm, λ_{Ga}=24 cm) *vs* target thickness. Beam rms σ=0.4 cm.

Beam power deposited in the target varies greatly with composition mainly due to increased electromagnetic shower development in high–Z materials. Because pion yield roughly doubles from 8 to 30 GeV, target heating studies were done using 1.5 × 10^{15} protons per second at 8 GeV and 7.5 × 10^{14} protons per second at 30 GeV to produce the same number of muons per second in the collider. This corresponds to beam powers of 1.9 MW at 8 GeV and 3.6 MW at 30 GeV. Due to the relatively short target lengths, only 5 to 15 percent of the beam power is absorbed by the target.

3 TARGET COOLING OPTIONS

The MARS calculations show the target energy deposition per pion produced increases linearly with target length for lengths more than one interaction length, and so, since the yield maximizes at lengths slightly in excess of one λ_I, the remaining calculations were typically performed for targets of length about 1.3 λ_I. A broad set of liquid targets as well as solid targets with forced cooling are considered. The best coolants include water and low-melting point alloys of gallium. Carbon is the best option for a surface-cooled, solid-cylinder geometry due to its relatively low heating power density. However, a large radius graphite cylinder is needed at these powers in order to have enough surface area for heat transfer to the cooling water which flows through the solenoid bore at 10m/s. There is a film drop ΔT_f = 46°C across the target-coolant interface, so for an inlet temperature of 40°C the water temperature will approach 86°C at some locations.

A core-cooled bar with narrow water channels improves heat transfer for any solid target by increasing the heat transfer surface area. In this geometry, coolant channels may be drilled through the bar. The selected core-cooled design has the target sliced into disks (7 mm thick with a 1.5 mm coolant channel between adjacent slices), and the proton beam passes through the whole stack of these disks. This results in a smaller target radius (2.5 cm for carbon) with a water tank of only 4 cm radius at these beam powers. Water supplied at a flow rate of 19 liter/s is adequate to provide 3 m/s flow across the carbon disks, resulting in a maximum water temperature of about 75°C as shown in Fig. 5. The steady-state maximum disk temperature is about 110°C for both 8 and 30 GeV beams.

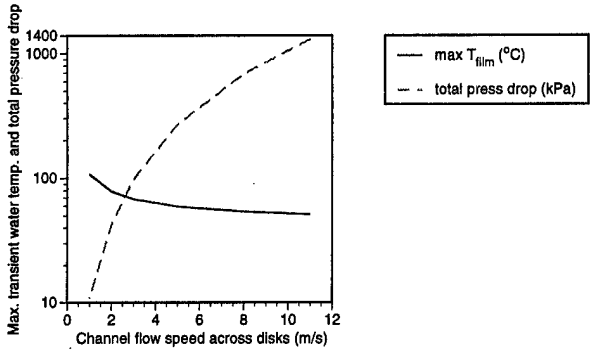


Figure 5: Maximum water temperature and pressure drop in 2.5 cm radius, 69 cm long carbon target for 8 and 30 GeV protons.

A liquid target circumvents the fatigue life limits associated with solid targets at high beam powers. A cylindrical tank of stagnant gallium could be inserted into the solenoid bore and cooled by concentric loops of flowing water, immersed in the liquid metal. This approach eliminates all MHD pressure drops, since the liquid metal is not flowing through the magnetic field. The preferred liquid target option however, is the simplest system: the Ga serves as the coolant as well as the target. In this target geometry, inlet and outlet headers flow the liquid gallium parallel to the solenoid's magnetic field in order to minimize the MHD pressure drops. Within the niobium alloy tank (3 cm radius), the gallium flows a short distance across the magnetic field at a slow speed (less than 0.1 m/s). A volumetric flow rate of 1.2 liter/s is adequate to keep the outlet temperature at 248°C (for the higher power, 30 GeV beam) with a total pressure drop of 176 kPa (see Fig. 6). Extensive experimental work at Argonne has shown that a thin ceramic coating (*e.g.*, 10 μm Al_2O_3) inside the tank will essentially eliminate the MHD portion of the pressure drop (Fig. 6). Alternatively, flow control and MHD pressure reductions are possible by tank geometry modifications and/or electric biasing [5].

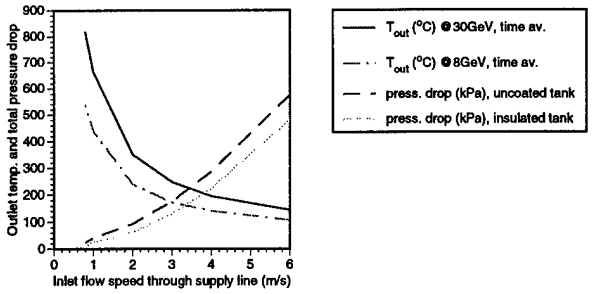


Figure 6: Outlet temperature and pressure drop in a 3 cm radius, 33 cm long liquid gallium target in a metal tank irradiated by 8 and 30 GeV beams.

4 CONCLUSIONS

For a 30 GeV proton driver with 12.5×10^{12} protons/bunch, gallium yields 10.6×10^{12} pions/bunch while graphite yields only 7.7×10^{12} pions/bunch. At 8 GeV, these yields are about a factor of two lower. Using a large beam and target radius (2.5 - 3 cm) reduces the maximum pulsed energy density to 10 J/g in graphite and 20 J/g in gallium, minimizing shock damage. A gallium target is about half the length of a graphite assembly, possibly reducing costs of the high field solenoid. It is desirable to operate coolants at pressures less than 400 kPa to reduce the likelihood of leaks and loss of flow accidents (LOFA). The graphite performance here assumed unirradiated properties, but thermal conductivity, shock and fatigue resistance may deteriorate with beam fluence.

For solid targets water cooling is simplest, but operation near boiling can result in possible overpressure failure with LOFA and water leaks will introduce high vapor pressure (V. P.) coolant to the vacuum. Tritium production and removal must also be considered in water cooled systems. Liquid gallium has several useful properties for high power targetry including a very large temperature margin to boiling (less sensitive to LOFA), extremely low V. P. and low reactivity in air and water. It is also safe to handle. To minimize corrosion, gallium should be kept below 350°C. We have not performed detailed calculations for pressure and flow behavior in high magnetic fields or activation of gallium at high proton fluence. In summary, either water cooled, solid carbon disks or liquid gallium can probably be used as targets in a muon collider source.

5 REFERENCES

[1] N.V. Mokhov, R.J. Noble and A. Van Ginneken, 'Target and Collection Optimization for Muon Colliders', Fermilab-Conf-96/006, 1996, and in 'Beam Dynamics and Technology Issues for μ^+mu^- Colliders', AIP-372, p. 61, 1996.

[2] 'The Muon Collider Feasibility Study', Chapter 4, Fermilab-Conf-96/092, July 1996.

[3] *Review of Particle Properties*, Phys. Rev. *D50*, 1177, 1994.

[4] N.V. Mokhov, 'The MARS Code System User's Guide, version 13 (95)', FNAL–FN–628, 1995.

[5] B.F. Picologlou, C.B. Reed, T.Q. Hua, J.S. Walker, L. Barleon, et al., 'Experimental investigation of MHD flow tailoring for first wall coolant channels of self-cooled blankets', Fusion Technology, v. 15, 1180, 1989.

BUNCH SHORTENING EXPERIMENTS IN THE FERMILAB BOOSTER AND THE AGS

J. Norem, Argonne National Laboratory, Argonne, IL, 60439 USA
C. Ankenbrandt, J. Griffin, C. Johnstone, S. Y. Lee, K. Y. Ng, M. Popovic, Fermilab, Batavia, IL 60510
M. Brennan, T. Roser, J. Wei, D. Trbojevic, Brookhaven National Laboratory, Upton, NY 11973 USA

Abstract

The proton driver for a muon collider [1,2] must be capable of producing 2.5 x 10 13 p/bunch on target (in 4 bunches) in order to reach the design luminosity in the collider ring. Additionally, the bunches are very short, with an rms of only ~1 ns, to match the longitudinal emittance requirements of downstream capture, cooling, and acceleration systems. This criterion along with the high intensity places constraints on the proton driver design which will require both theoretical and experimental verification. This paper will discuss the bunch shortening techniques to be tested experimentally, the impact of longitudinal space charge, and potential instabilities in such an accelerator.

1 INTRODUCTION

There has been great interest in developing high-intensity (~10^{14} protons per pulse) proton sources for neutron spallation sources, hadron factories, and muon colliders. Muon colliders also require rms bunch lengths as short as a nanosecond. Short bunch lengths limit the initial muon longitudinal phase space area, thereby enabling effective collection, cooling, transport, and acceleration, as described in ref [1]. Shorter proton bunches also allow capture of more highly polarized muon beams. This paper describes methods for producing short bunches and the experimental tests which are planned at the AGS and the Fermilab Booster.

Because of the conservation of longitudinal phase-space area, shorter bunches imply larger momentum spreads. For example, a Gaussian bunch with a longitudinal emittance of 1 eV-sec and an rms bunch length of 1 nsec at 8 GeV has a full momentum spread of about ±1.5%. Such momentum spreads are probably tolerable for a short time before extraction in a well-designed lattice.

2 BUNCHING

Bunch rotation has been used at Fermilab and elsewhare as a straightforward way to shorten bunches. In this method, the amplitude of the rf voltage is programmed to induce a rotation of the longitudinal phase space distribution in a stationary bucket. The efficacy of a simple bunch rotation is limited by the fact that the dependence of synchrotron frequency on amplitude in longitudinal phase space causes the distribution to distort into an S shape as it rotates.

Three methods are under consideration to reduce the bunch distortion during bunch rotation. These are: a) separate shears in energy and phase to minimize the motion in phase space required to produce the final bunch, b) augmenting the fundamental rf frequency with harmonic cavities which can cancel the nonlinearities, and c) compensating rotations above and below transition which cancel nonlinear effects.

The use of separate shears in momentum and phase requires that the transition gamma of the machine, γ_t, be changed between the two processes, using new lattices such as the FMC[3]. If necessary, the momentum dependence of the slip factor η of the lattice can be matched to that of the beam. A transition jump is also required in the third method.

Working close to transition has some obvious advantages: the beam is naturally shorter there and more bucket area is available. However, flattoping too close to transition energy should be avoided for two reasons: the synchrotron frequency is very low, so that bunch manipulations take too long; also, as described below, space charge effects below transition can prevent bunching unless they are compensated by inductive inserts[4-7].

3 LONGITUDINAL SPACE CHARGE

Below transition the longitudinal space charge force [4] is defocusing and thus opposes the effect of the rf voltage. Longitudinal space charge can strongly perturb, and perhaps prevent, the bunch rotation required to produce short proton bunches. The voltage produced on a particle in one turn by the longitudinal electric field due to space charge is

$$V_i = -\frac{Rg_0\lambda'}{2\varepsilon_0\gamma^2},$$

where $g_0 = (1+2\ln(b/a))$, b is the vacuum chamber radius and a is the beam radius, λ' is the longitudinal charge density gradient, ε_0 is the permittivity of free space, γ is the relativistic factor and $2\pi R$ is the circumference of the ring. As the bunch is compressed over N turns, an individual particle in a bunch will lose (or gain) an amount of energy, shown in Fig 1, given by

0-7803-4376-X/98/$10.00 © 1998 IEEE

$$U = q\sum_{i=1}^{N} V_i = q\langle V\rangle N = q\langle V\rangle \frac{\Delta\phi_{\max}}{2\pi\eta\,\Delta p/p},$$

where $\langle V\rangle$ is the simple average of the space charge induced voltage per turn, during the compression process, q is the charge and U must be in units like W introduced below. The value of synchrotron phase at the start of the compression is $\Delta\phi_{\max}$, and the expression in the denominator is the phase change per turn for a given slip factor η and momentum offset, $\Delta p/p$, since $\delta\phi_{\text{turn}}/2\pi = \delta f/f = \eta\,\Delta p/p$.

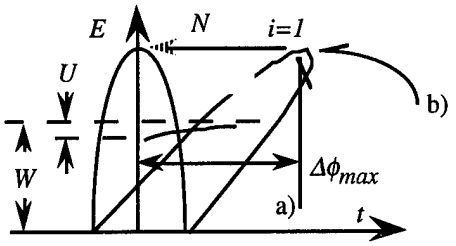


Figure 1, the final stage of bunching.

The complete expression can be written for a triangular bunch more explicitly in terms of the average charge density gradient $\langle\lambda'\rangle$ rather than the average voltage per turn $\langle V\rangle$, after expanding η as

$$U = \frac{qRg_0\langle\lambda'\rangle\Delta\phi_{\max}}{4\pi\varepsilon_0(1-\gamma^2/\gamma_t^2)\,\Delta p/p}.$$

As long as the energy loss by the particle is much less than the initial energy displacement from the center of the bunch, W, distortion of the bunch will be minimal. Thus the condition for bunching is that

$$\frac{U}{W} = \frac{qRg_0\langle\lambda'\rangle\Delta\phi_{\max}}{4\pi\varepsilon_0 W(1-\gamma^2/\gamma_t^2)\,\Delta p/p} < 1.$$

Values for the parameters can be obtained numerically for the AGS and the driver of the muon collider for a bunch compression using widths from FWHM / 2 = 10 ns down to 1 ns, Figure 2. The results show that if the bunching is done too close to γ_t it will proceed slowly and space charge will dominate, however if $|\gamma-\gamma_t|>0.2\gamma$, bunching can proceed.

Since the design of the accelerator enters into this expression as $R/W(1 - \gamma^2/\gamma_t^2)\Delta p/p$, the size of the ring should be minimized, likewise the momentum aperture and the difference between the operating and transition energy should be maximized. (Because the energy offset $W\approx\Delta p$, the momentum spread essentially enters with an exponent of 2). Thus one wants a lattice with an efficient packing factor for dipoles, magnets with a large aperture and the transition energy as far from the beam energy as possible during the final bunch rotation.

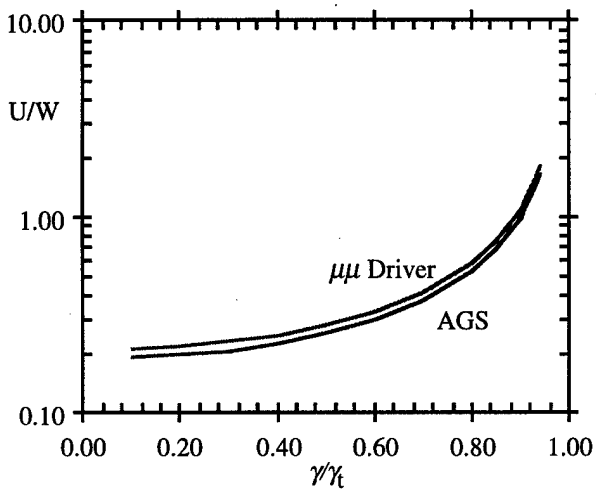


Fig 2. Degree of nonlinearity during bunching.

The third method under consideration, in which transition is jumped before the final bunch rotation, has the potential to put the space-charge voltage to good use to augment the rf bunching voltage. Alternatively, if inductive inserts are used to alleviate longitudinal space-charge effects, the above limitations can be circumvented.

4 OTHER INSTABILITIES

The bunch hitting the target will have a peak current of 1600 - 3200 A, which is significantly larger than is presently seen in synchrotrons. Although this current might be the cause of significant instabilities, the bunch will be stabilized by a number of effects.

The incoherent space charge tune shift

$$\Delta\nu_{inc} = \frac{3r_pN_t}{2AB\beta\gamma^2} \approx 0.2$$

will be large. By introducing Landau damping, this tune spread will tend to stabilize the beam against transverse resistive wall effects.

In synchrotron space, the bunch is stabilized by a large momentum spread. Since the approximate threshold for these instabilities is given by the Keil-Schnell relation

$$\frac{Z_{\|}}{n} = \frac{F|\eta|\beta^2E/e}{I_{pk}}\left(\frac{\Delta p}{p}\right)^2,$$

a constant phase space area would imply $I_{pk}\propto\Delta p/p$ for a vertical bunch, so the threshold $Z_{\|}/n \propto \Delta p/p$. Thus bunches become more stable as they are shortened.

In addition, it is assumed that the current will rise very rapidly in the final stages of bunching, and this period of time will be short relative to the growth time for known resonance effects.

4 EXPERIMENTAL TESTS

Bunch rotation schemes can be tested at both the AGS on high-intensity (~10^{13} p/bunch), long bunches (rms close to 20 ns) and on low-intensity, nanosecond bunches in the Fermilab Booster (~$5x10^{10}$ p/bunch). The longitudinal structure of the beam will be measured using a resistive wall monitor, a fast analog scope with sequential triggering (25 μs rearm rate) and diagnostic software developed at Brookhaven (ref).

With this system, the longitudinal structure of the Fermilab Booster has been explored from injection to just below transition by accelerating to 4 GeV instead of the nominal 8-GeV extraction energy. Although the Booster gradient magnets cannot sustain a flattop, at least a millisecond of data can be obtained with little energy change before extraction. To effect a bunch rotation, the rf cavities can be quickly paraphased in opposite directions which cancels the net rf voltage seen by the beam. A "tumbling" bunch can be observed in Fig. 3 when the rf cavities are paraphased from a net rf voltage of 800 kV to 150 kV. Hardware is presently being developed and tested to unparaphase the rf cavities in order to recapture a shortened bunch.

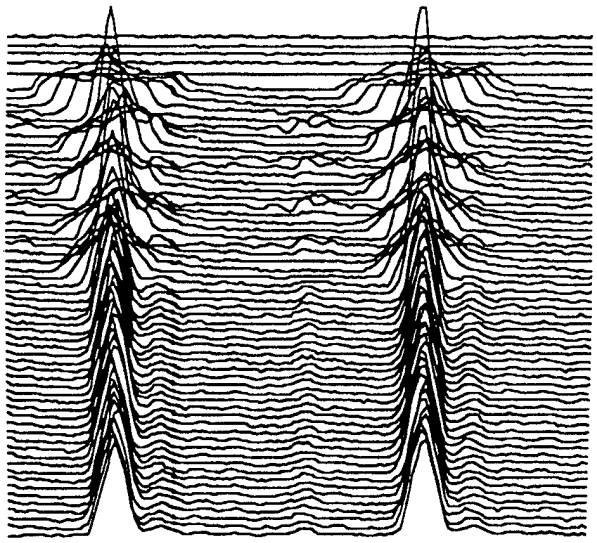


Figure 3. tumbling bunches in the Booster.

In the AGS, the gradient magnets can be programmed to maintain a flattop. During a flattop of 25-GeV kinetic energy, a bunch rotation will be effected using the rf cavities. Other techniques such as firing the γ_t jump system on the AGS to shorten the bunches by the shearing caused in crossing transition (rapidly) will also be investigated.

Expansion of the bunch can be accomplished either by turning down the rf and letting the beam expand in phase or by operating close to transition with the rf fully on, which expands the energy spread. Although the bunch will be truncated by the momentum aperture, rotation to a vertical orientation would then proceed to the extent allowed by longitudinal space charge. Both procedures would be studied as a function of proximity to transition and bunch intensity, with two dimensional reconstruction of bunch density from time dependence of the longitudinal current density.

REFERENCES

[1] The $\mu\mu$ Collider Collaboration, "$\mu\mu$ Collider: A Feasibility Study", J. Gallardo, Ed. BNL-53503, Fermilab Conf 96/092, LBNL-38946 (1996).

[2] J. Norem et al., "The Proton Driver for the μμ Collider", submitted to this conference.

[3] S. Y. Lee, K.Y. Ng and D. Trbojevic, "Minimizing Dispersion in Flexible-Momentum-Compaction Lattices", Phys. Rev. E48, 3040 (1993).

[4] S. Hansen, H.G. Hereward, A. Hofmann, K. Hubner, and S. Myers, "Effects of Space Charge and Reactive Wall Impedances on Bunched Beam", IEEE Trans. Nucl. Sci. NS-22 , No.3, 1381, (1975).

[5] A.M. Sessler and V.G. Vaccaro, "Passive Compensation of Longitudinal Space Charge Effects in Circular Accelerators", CERN 68-1, ISR Div. (1968).

[6] R. Cooper et al., "Passive Compensation of Beam Space Charge by Insertion of Ferrite Inductors", PSR Technical Note 100, Los Alamos Nat'l. Lab. (1982).

[7] J.E. Griffin, "Proton Driver Proposal", Fermilab Internal Note (1996).

THE PROTON DRIVER FOR THE $\mu\mu$ COLLIDER*

J. Norem, Argonne National Laboratory, Argonne, IL, 60439 USA
C. Ankenbrandt, J. Griffin, C. Johnstone, S. Y. Lee, M. Popovic, K. Y. Ng, Fermilab, Batavia, IL 60510 USA
M. Brennan, T. Roser, D. Trbojevic, J. Wei, Brookhaven National Lab, Upton, NY 11973 USA

Abstract

The proton driver for the $\mu\mu$ collider might operate at about 15 Hz and produce four bunches of $2.5{\cdot}10^{13}$ protons/bunch at about 10 GeV (or half that number at 20 - 30 GeV) with an rms bunch length of about 1 nsec. A number of options have been considered to produce these bunches using: a) simple bunch rotation, b) energy slewing near γ_t followed by a fast increase of γ_t which facilitates bunching, and c) change of rf frequency in a ring-to-ring transfer. Flexible Momentum Compaction (FMC), or similar, lattices seem to offer control of γ_t even on short time scales. The large momentum spread, space charge tune shift and rapid bunching would tend to stabilize short, intense bunches, although $I_{pk} \sim 1600$ A. Both active (harmonic cavities) and passive (inductive wall) solutions have been considered to minimize high current beam effects. Magnet and vacuum systems would be similar to other high current designs.

1 REQUIREMENTS

The specifications on the proton driver for a $\mu\mu$ collider follow from the muon bunch parameters desired in the collider and from the capabilities of the systems for muon production, collection, cooling, and acceleration. Designs for these systems have been discussed at length in the "Snowmass Book" [1]. Although there is considerable latitude in the choice of system parameters, it is clear that a high-performance muon collider requires a high-performance proton driver. In general, delivery to the production target at a high repetition rate of a few short, intense proton bunches of moderate energy is necessary. The two parameter sets in Table I, adapted from reference [1], typify the formidable requirements on a proton driver for a 2 TeV x 2 TeV collider with luminosity of order 10^{35} cm^{-2}sec^{-1}. Of course the specifications on the proton driver and/or on the other systems can be relaxed for a less demanding collider, such as a demonstration machine at lower energy and luminosity.

Table I. Typical Proton Driver Requirements

Energy	30	10	GeV
Repetition Rate	15	30	Hz
Bunches	4	2	
protons/bunch	$2.5{\cdot}10^{13}$	$5{\cdot}10^{13}$	
Rms bunch length	1	1	nsec

Except for the short bunch lengths, these beam specifications are similar to those for recently designed medium-energy hadron facilities and spallation neutron sources, and so similar approaches are possible. (The short bunch lengths are needed to keep the initial longitudinal emittance of the muons as small as possible, thereby simplifying their collection and subsequent cooling; shorter bunches also allow production of muon beams of higher polarization.) The need for short bunches can be addressed either by adding systems such as a compressor ring or multiple chicanes downstream of the proton acceleration stage(s) or by integrating the short-bunch requirement into the acceleration stage(s). (A companion paper at this conference presents more detail on bunch-shortening strategies.[2])

2 THREE ALTERNATIVES

Three proton driver designs have been considered. The first two columns of Table II show major accelerator parameters of the first two approaches, a 30 GeV synchrotron loosely based on the AGS and a single 10 GeV synchrotron with a 1 GeV linac injector. These two options were described in the "Snowmass Book" [1], and so they will not be discussed further here. This paper presents a third alternative that has been developed since the Snowmass meeting: an 8 GeV, two-ring complex in which the bunch-shortening strategy is integrated into the design of the two synchrotrons. The last two columns of Table II show major accelerator parameters for the two rings of this latter option.

Table II. Major Synchrotron Parameters

Final Energy	30	10	8		GeV
Booster Energy	3.6		4	4	GeV
Injection Energy	0.4	1		1	GeV
Circumference	1080	580	474	158	m
Tune shift	0.1	0.2	0.4	0.4	
Transition energy	40	10-14	14	7	
RF Harmonic	12	8	84	4	
Long Emittance	4.5	2.5	1	0.5	eV-s
Voltage /turn	4	1.8	0.5	0.2	MV

*Work supported by US Department of Energy under contracts with the respective laboratories.

0-7803-4376-X/98/$10.00 © 1998 IEEE

3 DESIGN OVERVIEW

The design requirements are a challenge for all the accelerators. A design intensity of 10^{14} protons per cycle corresponds to 100 mA x 160 μsec from the linac. Longitudinal tracking including the effects of space charge indicates that efficient capture can be achieved by injecting chopped beam into pre-existing buckets. It is expected that the full energy spread of the 1 GeV H^- injected beam will be reduced to about 1 MeV by a debuncher cavity. Under these conditions the simulations show that the longitudinal emittance per bunch following injection and capture will be about 0.5 eV-s. The small circumference of the first ring helps to keep the longitudinal emittance relatively small.

Transverse space charge effects are serious in both rings. The Laslett incoherent tune shift is limited to the barely tolerable value of 0.4 by the high linac energy of 1 GeV and by large normalized 95% transverse emittances of 200π mm-mrad. In the first ring, the harmonic number of four is chosen to match the desired number of bunches so that every bucket is occupied, thereby keeping the bunching factor favorable to reduce space-charge effects.

The strategy for bunch length reduction calls for a bunch rotation just before extraction from each stage. The rf frequency in the second ring is chosen to be seven times that of the first ring for ease of matching to the longitudinal phase space distribution of the rotated bunch. With a circumference ratio of three, the harmonic number of the second ring is 84; the circumference and harmonic number of the second ring then match those of the Fermilab Booster.

Of course the shorter bunch length exacerbates space-charge effects in the second ring. In fact the transfer energy of 4 GeV is chosen to equalize the Laslett tune shifts shortly after injection in the two rings. After acceleration, another bunch rotation just before extraction from the second ring produces rms bunch lengths of about 1 nsec. Even if the longitudinal emittance has grown by this time to 1 eV-s, the momentum spread after rotation will be only about ±1%, which should be tolerable for a short time in a well-designed lattice.

Transition energies somewhat above the extraction energies are specified for both rings. This not only avoids acceleration through transition but also facilitates the bunch rotation. For the second ring and, if necessary, also the first, flexible momentum compaction lattices [3] can be used to raise the transition energy above the operating range. Such lattices also facilitate rapid variation of the transition energy, as may be useful for some of the bunch-rotation schemes.

4 RF SYSTEMS

In the limited space available, the design is illustrated by a fairly detailed discussion of rf considerations for the critical first ring rather than a more superficial treatment of both rings.

The guide field ramp is resonant at 15 Hz and is linearized by addition of about 15% of second harmonic. The rf frequency varies from 6.64 to 7.43 MHz. The required accelerating voltage $V_{acc} = V \sin \phi_s$ reaches a maximum nearly constant value of 52.7 kV. The rf bucket area is chosen to start at 1 eV-s, twice the expected bunch area, and to grow during acceleration to 1.7 eV-s just prior to extraction. In the case where the beam intensity is sufficiently small so that rf potential well distortion due to beam space charge effects can be ignored, the required rf voltage reaches a maximum value of 104 kV with $\phi_s = 20$ degrees near 8 ms in the cycle. Beyond the maximum, the voltage decreases because the slip factor η decreases as γ approaches γ_t.

At the design intensity, 2.5 x 10^{13} protons per bunch, the rf potential well is distorted seriously by longitudinal space charge effects[4]. In order to develop the required bucket area in the presence of the potential well distortion, the rf voltage must be increased to a maximum value near 146 kV with a corresponding decrease in synchronous phase angle. It may be possible to reduce or eliminate the additional rf requirement by compensating for the space charge induced longitudinal voltage through the introduction into the ring of additional inductance[5.6,7]. This can be done by lining short sections of the beam pipe with ferrite having sufficient bandwidth and relative permeability. The value of the introduced inductance must be reduced during acceleration to compensate for changes in $\beta\gamma^2$. It is proposed to do this by enclosing the ferrite sections in bias current carrying solenoids which are capable of changing the ferrite permeability during acceleration. (A collaboration has been initiated between Fermilab and Los Alamos to make an experimental study of passive compensation of longitudinal beam space charge forces. Several ferrite inductive inserts with bias solenoids are being built at Fermilab. These will be measured electrically at Fermilab and subsequently installed in the Los Alamos Proton Storage Ring for a two day experiment with high intensity beam).

Near 27 ms on the acceleration ramp the rotation period of the ring is about 620 nsec. With 10^{14} protons (16 μC) in the ring the dc current is 26 A. At this point the rf power delivered to the beam, $I_{dc}V \sin \phi_s$, is 1.4 MW. An rf system capable of generating 120 kV and delivering 1.5 MW to the beam over the specified frequency range is indicated. This can be done using ten ferrite loaded rf cavities of standard design. Each rf station (rf cavity,

power amplifier, dc power source, etc.) will be capable of generating 12 kV and delivering 150 kW to the beam.

The rf cavities will be single gap double-ended structures slightly more than 1 m long. Each side of the accelerating gap will be driven directly by a 300 kW power tetrode capable of delivering up to 40 A of rf current. Because of the anticipated very heavy beam loading and the consequent large current capability of the tubes (and the relatively low Q of the system), it may not be necessary to actively tune the cavities to (or near) resonance during acceleration. The beam loading will require that the cavities be tuned above the beam frequency in any case, so the cavities may be tuned to a resonant frequency above the maximum beam rf frequency (thus ensuring Robinson stability) and allowed to remain there. This will require that the tubes deliver substantial "quadrature" current in some cases, which will increase the anode dissipation. It is expected that the dissipation and current capability of the tubes to be used will be adequate to meet these demands.

During acceleration the rf bucket area is adjusted adiabatically such that as the bunches approach extraction energy the bunch longitudinal emittance (assumed here to approach 0.75 eV-s) will extend to $\pm\pi/2$ radians in the quasi-stationary buckets. The required bucket height is ±7.1 MeV and the rf voltage is near 2 kV. At this point, just prior to extraction, the rf voltage is raised suddenly to its maximum value, 120 kV. This raises the bucket height to ±75 MeV. The bunch distribution will rotate to a maximum energy spread ±50 MeV in approximately 75 μs. Even with slight deformation due to synchrotron tune spread the resulting bunch length will be within ±7-8 nsec. This will allow extraction and injection into a second ring where the rf frequency may be as high as 53 MHz.

This bunch rotation process may be subject to several limitations. As the momentum spread of the bunches is reduced near extraction the beam conditions may exceed the Keil-Schnell threshold for self bunching instability (microwave instability). Because the beam is below, but near, transition, the growth rate and the resulting longitudinal emittance blow-up may not be sufficient to rule the procedure out. Secondly, as the bunches are narrowed during rotation the longitudinal space charge voltage will increase dramatically and may limit the desired bunch narrowing. This problem may be mitigated by use of the above mentioned passive space charge compensation scheme. Finally, at the end of rotation the beam momentum spread will reach ±1%, so the ring aperture and that of the extraction channel must be made adequate to accept this rather large momentum spread.

REFERENCES

[1] The $\mu\mu$ Collider Collaboration, "$\mu\mu$ Collider: A Feasibility Study", J. Gallardo, Ed. BNL-53503, Fermilab Conf 96/092, LBNL-38946 (1996).

[2] J. Norem et al., "Bunch Shortening Experiments in the Fermilab Booster and the AGS", submitted to this conference.

[3] S. Y. Lee, K.Y. Ng and D. Trbojevic, "Minimizing Dispersion in Flexible-Momentum-Compaction Lattices", Phys. Rev. E48, 3040 (1993).

[4] S. Hansen, H.G. Hereward, A. Hofmann, K. Hubner, and S. Myers, "Effects of Space Charge and Reactive Wall Impedances on Bunched Beam", IEEE Trans. Nucl. Sci. NS-22 , No.3, 1381, (1975).

[5] A.M. Sessler and V.G. Vaccaro, "Passive Compensation of Longitudinal Space Charge Effects in Circular Accelerators", CERN 68-1, ISR Div. (1968).

[6] R. Cooper et al., "Passive Compensation of Beam Space Charge by Insertion of Ferrite Inductors", PSR Technical Note 100, Los Alamos Nat'l. Lab. (1982).

[7] J.E. Griffin, "Proton Driver Proposal", Fermilab Internal Note (1996).

OPTIMIZATION OF THE TARGET FOR MUON COLLIDERS

H. TAKAHASHI, Y.AN*, X.CHEN* and M.NOMURA
Brookhaven National Laboratory, Upton, NY 11973

Abstract

We analyze the design of the target for pion production and energy deposition for the muon-muon collider using the nuclear cascade codes. Heat removal from high-energy deposition in the target is discussed, together with the use of a target compressed by a laser, or light- and heavy-ions drivers. The latter approach needs further technological development, but it can reduce substantially the energy needed to collect and control the produced muons.

1 INTRODUCTION

To achieve a luminosity of $10^{35} cm^{-2} s^{-1}$ for a 2 + 2 Tev muon-muon collider machine as well as a luminosity of $10^{33} cm^{-2} s^{-1}$ for a 250+250 GeV collider, it is necessary to produce and collect a large number of muons[1]. The basic method presently used starts with a proton beam impinging on a thick target (one to two interaction lengths), followed by a long solenoid which results mainly from the decay of pions. Since a substantially large amount of the energy is deposited to the small target, heat removal from it is one of most important problems in designing the target to efficiently collect pions. The energy cost to collect the secondary particle beam using the high solenoid magnetic field and RF cavity is very high. To reduce the energy cost of producing and collecting the muons which result from the decay of the pions, the approach of using a highly compressed target, which is practiced in inertial fusion, is promising.

2 YIELD OF PIONS

To evaluate the various nuclear cascade codes, we calculated the rate of pions production and energy deposition of a 1-cm-radius target with a radiation length of 1.5, made of carbon or copper,placed in a 28 Tesla solenoid field, into which 8 or 30 GeV protons were injected. We compared the results obtained by the LAHET, GEANT, MARS and ARC codes (Table I)[2],[3],[4]. The positive pion yields from LAHET are almost the same as those from the MARS calculation; however, the negative pion yield for high-energy proton injection is greater than the yield of positive pions. The yield of positive and negative pions by GEANT code are, 1.5 and 2.0 times greater, respectively, than the MARS calculation, and the GEANT code has highest yields.

The large difference among the yield of pions indicated that the presently adopted codes for this analysis are not satisfactory. To capture efficiently the pions produced in the target, data on its momentum distribution is important. The early experiments mostly measured pions with rather large momentum; data for those of less than 300 MeV/c is scarce. New experiments presently are being carried out at the AGS[3]. The cascade models for the production of pions in the HETC code, from which LAHET was derived, do not take into account the detailed resonance reaction above 3 GeV proton energy injection. The hadron cascade model must be improved to give a good evaluation in the medium energy range above this energy.

3 ENERGY DEPOSITION AND ITS REMOVAL

Table II shows the deposition energy calculated by the MARS[2], GEANT, and LAHET codes for the injection of protons with 8 and 30 GeV energies. The MARS calculation is almost same as the GEANT code except for Cu target 30 GeV proton injection, while LAHET produces about 20% less than the others. Energy deposition in the

Table 1 Pion yields from Carbon and Cupper targets.

	Proton Energy	8GeV	8GeV	30GeV	30GeV
	Material	C	Cu	C	Cu
π^+/p	MARS[2]	0.5	0.58	0.91	1.16
π^-/p	MARS[2]	0.41	0.50	0.83	1.05
π^+/p	ARC[3]	0.52	0.62	1.31	1.62
π^-/p	ARC[3]	0.37	0.51	1.15	1.62
π^+/p	GEANT	0.858	0.858	2.184	2.674
π^-/p	GEANT	0.581	0.613	1.857	2.396
π^+/p	LAHET	0.4701	0.588	0.747	1.329
π^-/p	LAHET	0.3646	0.600	0.586	1.630

* Permanant address: Tsinghua University, Beijing 100084, China

0-7803-4376-X/98/$10.00 © 1998 IEEE

carbon target is reduced by increasing the proton energy of injection, but that deposited in the copper target is almost independent of the proton injection energy.

Table 2. Energy deposition in the target. in unit of KW.

Proton Energy	8GeV	8GeV	30GeV	30GeV
Material	C	Cu	C	Cu
MARS	140.	360.	153.	600.
GEANT	143.	376.	153.3	743.7
LAHET	—	303.6	—	493.2

Figure 1 and 2 show, respectively, the distribution of energy deposition in the target of r= 0.~10. mm and z= 0.~20. cm when a pencil beam is injected into the center of copper targets to which solenoid magnetic field of 28 and zero tesla is applied. The figures show that the presence of the magnetic field does not greatly change distribution of the deposition energy. In the case of the carbon target, deposition peaks at about 0.4 interaction length; heavy atom targets, such as Cu and Pb, have a secondary peak appearing at near 0.6 interaction length. The distribution of energy deposition is sharply reduced as radial direction increases.

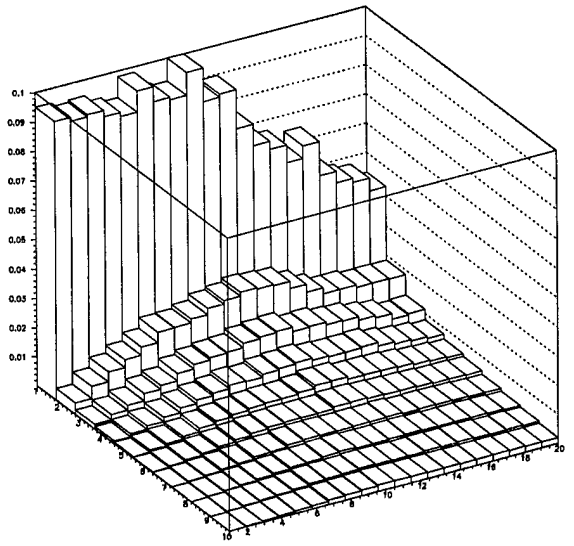


Figure 1: Energy deposition in Cu target with 28 tesla solenoid magnetic field.

Although energy deposition in the copper target is not high enough to damage it by shock waves created by the sudden deposition of energy, efficient heat-removal is required to reduce the stress caused by the increase in temperature. Although copper material has good thermal conductivity, the temperature at the center rises by more than 1250 ^oC above the coolant temperature, and the stress caused by this excessive heat reduces the lifetime of the

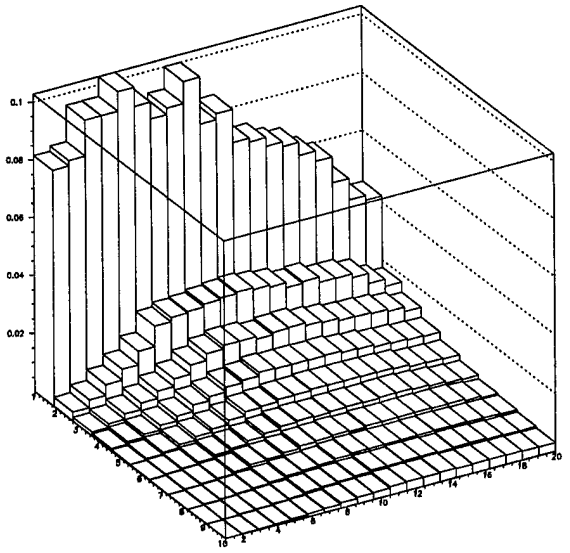


Figure 2: Energy deposition in Cu target without magnetic field.

target above a heat deposition of 8.5 KW power density. Thus, the solid material target must have excellent thermal conductivity. Carbon does not have good thermal conductivity, and so its center temperature is higher than that of the copper material, even when a smaller amount of energy is deposited. When water is used to remove heat, a substantial volume has to go through a 2-cm radius coolant channel connected to the copper target at a velocity of 3 m/sec to get a 50 ^oC decrease. One way to reduce the temperature of the target center is to circulate the liquid, such as H_2O, inside the target even though this reduces pion yield somewhat.

Liquid target materials, such as Hg, Li, and Pb-Bi Eutectic are good candidates for removing heat. Heavy-atom material is more efficient in producing pions, but the specific heat is not very large; the removal of 0.8 MW heat generated in a 1-cm radius target requires a 10 m/sec coolant velocity for Pb coolant, and 3 m/sec for liquid Li coolant.

4 USE OF A COMPRESSED TARGET

The heat-removal problem can be mitigated by increasing the size of the target; however, this makes the phase-space of the produced pions large, so that collecting and cooling the decayed muons becomes more expensive.

It was demonstrated in inertial fusion [5] that the DT pellet could be compressed to about 600 times the liquid density DT target using the 15KJ (1 nano sec, 15 TW) laser beam of Gekko-XII.

When the target material is compressed to M times its original density, the size of all devices controlling the secondary particle can be reduced in inverse proportion to the compression factor of (1/M). For example the 1-cm radius 20-cm long target can be reduced to a 0.001-cm radius and 0.02 cm length target, and the emittance of the sec-

ondary particles of pions created can be reduced by a factor of 1000. The secondary particles with short, low emittance can be effectively controlled by the high-power laser instead of by a radio-frequency electro-magnetic wave, which produces a far smaller electric field strength than the laser and requires a large acceleration cavity for controlling them.

To compress target material heavier than the DT target, more high- driving energy is needed, but it is different from inertial fusion which requires a temperature increase to start the fusion reaction. The compression of our target material does not require an increase in temperature; thus, the required compression energy is much smaller than in practical inertial fusion. In inertial fusion to compress the fusion pellet of radius 0.5 mm requires MW orders of laser driver.

A $10^{18} watt/cm^2$ laser beam-power can create an electric field of $10^9 V/cm$ by using inverse Cerenkov radiation[6]. An extensive study is underway on the acceleration of electrons using a laser with strong intensity, such as a far field approach of inverse free electron laser[7] a plasma acceleration of laser wake field accelerator, two beat wave-beams acceleration[8,9,10]. By modulating a high intensity laser, we might control the secondary particles produced by a high-power accelerator in a similar way as laser acceleration.

By using the RF cavity, the secondary particles produced are confined with a high magnetic field of a few tens Tesla, and the phase rotation cavity is located far from the target area[1]; the bunch of secondary particle beam is elongated during its travel from the point of generation to this cavity, and long cavity is required which has low frequency RF.

When secondary particles are created from a small sized target of high density, the bunch of secondary particles are small in size and can be focussed and controlled directly just after their creation by a strong laser field. The cavity is not needed.

Although to compress the target material initially requires a large amount of energy for driving devices, such as a laser, light- and heavy-ions drivers, the substantial expense of energy required for controlling the secondary particles can be saved. The reduction of the emittance confers a tremendously high cost-benefit advantage.

This approach of using the laser is especially useful for collecting the anti-protons[11] for which ionization cooling can not be used because of its annihilation of anti-protons.

The technology of accelerating a charged beam by laser is still in its infancy, but this technology also should be applied to target technology.

To compress the target material, we can employ a high-z pinch device instead of irradiation by laser, light- and heavy-ions. This suggested approach to compression is much simpler than the others.

5 ACKNOWLEDGEMENTS

The authors acknowledge to Drs. R.Palmer, A.N.Skrinsky, J.Gallardo, H.Kirk, R.Fernow, Y.Zhao, Y.Torun for their valuable discussion ,and to Dr. Woodhead for her editorial work on this paper. This work was performed under the auspices of the U.S.Department of Energy under contract No. DE-AC02-76CH00016, and was partially supported by Power Reactor and Nuclear Fuel Development Corporation.

6 REFERENCES

[1] R.Palmer *et al.* "Muon Collider Design", BNL-62949 (1996). , "Muon Collider" 9th advanced ICFA, Beam Dynamics and Technology Issue for Mu-Mu collider, Beam Dynamics Workshop. Oct.1995, AIP Conf. 372, P.3. Montauk, NY, 1995 Edited by J. Gallardo.

[2] N.V.Mokhov, R.J.Noble and A. Van Ginneken, "Targetry and Optimization for muon colliders" Fermilab-Conf-96/006 & AIP Conf. 372. p.61

[3] D. Kahana and Y.Torun "Analysis of Pion Production Data from E-802 at 14.6 Gev/c using ARC" BNL-61983(1995), and private communication.

[4] H. Takahashi and X. Chen, " An Analysis of Pion Production" AIP Conf. -372, p.87, Montauk (1995).

[5] C. Yamanaka " Advances in inertial Confinement Fusion" OR3.1, ICENES'89, Karlsruhe, 1989.

[6] L.C.Steinhamer and W.Kimura, " Mutistaging & e-beam Trapping in Laser Particle Accelerator, Advanced accelerator Concept, AIP-279, Port Jefferson NY, 1992, Edited by J.Wurtele

[7] C.M. Tang "Report of the working group on Far Field Accelerators", AIP-279, p. 259,

[8] T. Tajima and J.M.Dawson Phys. Rev. Lett. 43 , 267 (1979).

[9] T. Katsouleas " Summary of the working group on Plasma Accelerator' AIP-279. p.371.

[10] A. Fisher, J Gallardo, J. Sandweiss, A. Van Steenbergen , " Inverse Free- Electron Laser Accelerator, AIP-279, p.299.

[11] H. Takahashi, and J. Powell " Multiple Collision Effects on the Antiproton Production by High Energy Proton (100-1000 GeV), Antiproton Science and Technology" The Rand Corporation. Oct 6-9. 1987, p.620.

A LATTICE FOR THE MUON COLLIDER DEMONSTRATION RING IN THE RHIC TUNNEL *

D. Trbojevic, R.B. Palmer, E.D. Courant, J. Gallardo, S. Peggs, S. Tepikian
Brookhaven National Laboratory, Upton, NY, 11973, USA
K.Y. Ng, Fermi National Laboratory

Abstract

The future $\mu^+\mu^-$ *Muon Collider* should have a luminosity of the order of 10^{35} cm^{-2}s^{-1}, an the energy of 2 × 2 TeV. We present here a demonstration machine at a lower energy to test the feasibility of all components involved, which could be placed inside the existing Relativistic Heavy Ion Collider (RHIC) tunnel. The maximum energy of the muons in the RHIC tunnel depends on the maximum attainable field in the dipoles. The maximum energy in the existing RHIC rings for protons is 250 GeV, where the strength of the magnetic field in the dipoles is 3.5 T. A design of the storage ring lattice for a 50 GeV muon demonstration machine is also presented.

1 INTRODUCTION

The *Muon Collider* advantage with respect to an electron collider at high energies is that it could be a circular machine, because of negligible synchrotron radiation (for energies less than 10 TeV). This makes the number of collisions per bunch much larger than 1 in linear electron colliders, and together with a larger mass makes,in principle, a luminosity advantage of a factor of 10^5 for the same size machine. Other components of the muon collider, its feasibility and physics opportunities are presented in reports [1],[2], [3], [4], [5], [6] etc. The muon collider storage ring will have 2 TeV energy μ^+ and μ^- bunches and will provide luminosity of $10^{35}cm^{-2}s^{-1}$. For this luminosity the rms bunch length has to be 3 mm, which defines the β^*=3 mm at IP. *Short* bunches require the collider to be isochronous [7]. In this report lattices for demonstration of the muon collider rings, with muon energies of 250 GeV and 50 GeV, are presented. Parameters for the *demo* machine (Section 1), like transverse and longitudinal emittances, distances of the first quadrupoles to the crossing point, etc. are defined first. Next, possible choices for values of the magnet apertures, lengths, and strength will be presented. The momentum spread of the μ^+ and μ^- beams sets up a limit for the dispersion function excursions. An existing ring and elements of the Relativistic Heavy Ion Collider (RHIC) were used to create a first example (Section 3) of an isochronous storage ring. The RHIC collision parameters and magnet elements were used for the new lattice. Next, a *demo* muon collider storage ring lattice, with 0.5 TeV center of mass energy, is set inside the RHIC tunnel (Section 4). Finally another *demo* machine with a 0.1 Tev center of mass energy is presented (Section 5).

* Work performed under the auspices of the U.S. Department of Energy

2 STORAGE RING PARAMETERS

Muons, μ^+ and μ^-, will be created from the decay of pions π^+ and π^+, made from higher energy protons on a high Z target. Muons, μ^+ and μ^-, will reach the collider storage ring after they have been accelerated and cooled in both longitudinal and transverse phase space. A design of a *demonstration* muon collider storage ring would be at much lower muon energy than the proposed 4 TeV (center of mass energy) machine. The muon six-dimensional emittance, defined as:

$$\varepsilon_{6D} = \varepsilon_x^{Norm}\varepsilon_y^{Norm}\Delta p/p\ \ \sigma_z\ \gamma\beta, \qquad (1)$$

of a lower energy *demo* ring should not be different from the estimated 4 TeV collider emittance (latest prediction $\varepsilon_{6D} = 170 \cdot 10^{-12}\pi$m). A free space parameter *LD*, between the first high focusing quadrupole and the crossing collision point, is defined by the opening angle of the detector. The bunch length defines the β^* at the crossing point. The momentum compaction α ($\alpha = 1/\gamma_t^2$) also depends on the bunch length. Parameters of interest for a lattice design of lower energy storage rings, are presented in Table 1. The bunch lengths in the 200 GeV and 50 GeV *demo* muon colliders, as presented in Table 1, are equal to 10 cm and 16 cm, respectively. Short bunches require the momentum compaction to be adjusted. The maximum of the dispersion function in the lattice design is limited by the large beam momentum spread. Momentum offsets of the incoming muons are estimated to be large ($\Delta p/p = 0.12\%$). If the beam size, resulting from the momentum offset, σ_p, is of the order of the transverse beam size, defined by the betatron function, σ_β, than:

$$D_{max} \leq \sigma/(\Delta p/p). \qquad (2)$$

The muons have a short life time. Products of the muon decay deposit energy in the magnets, requiring shielding of the superconducting magnets. The size of the aperture is reduced and has to be considered in the lattice design. The aperture of the magnets depends on the muon beam size. Parameters like: the shield radius, quadrupole coil

Table 1:

E (TeV)	Δp/p (%)	$\varepsilon(\pi$m)	β^* (mm)	*LD* (m)
4.0	0.12	50 10^{-6}	3	6.50
0.4	0.12	85 10^{-6}	10	4.00
0.2	0.12	108 10^{-6}	13	2.80
0.1	0.12	136 10^{-6}	16	2.00

0-7803-4376-X/98/$10.00 © 1998 IEEE

Table 2:

E TeV	Shield	Coil(cm)	P_t(W/m)	$L(s^{-1}cm^{-2})$
4.0	R=6.0cm	D=8.0	1292	732 10^{32}
0.4	R=4.0cm	D=6.0	431	8.4 10^{32}
0.2	R=3.5cm	D=5.5	431	2.6 10^{32}
0.1	R=3.0cm	D=5.0	431	0.8 10^{32}

diameter, power per length dissipation, and luminosities at four different center of mass muon energies, are presented in Table 2:

3 ISOCHRONOUS RHIC LATTICE

The RHIC collider lattice is three fold symmetrical. It has standard FODO cells in the arcs and six "zero" dispersion anti-symmetric interaction regions (IR) with triplet quadrupoles. Dipoles reach a magnetic field of 3.5 T with 30% quench margin in the arcs. An isochronous lattice is designed by using *flexible momentum compaction* (FMC) modules, as previously presented [8], and magnets of the same size as in the present RHIC machine. Figure 1 shows the betatron functions inside one of the IRs together with one FMC module.

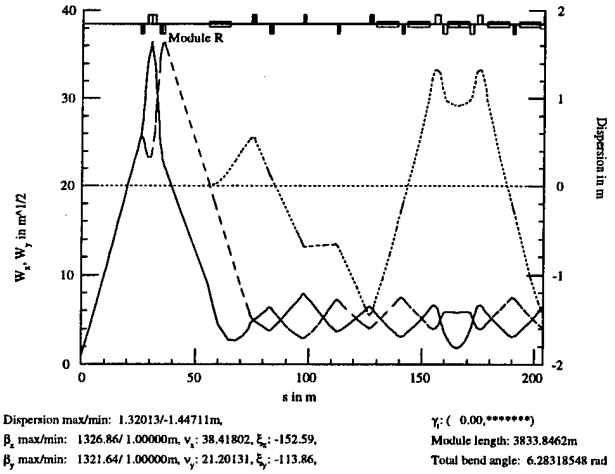


Figure 1: Isochronous RHIC lattice-IR with one FMC module.

4 250 GEV ISOCHRONOUS MUON *DEMO* COLLIDER LATTICE IN THE RHIC TUNNEL

Previous RHIC upgrade parameters at the crossing points, of $\beta^* = 1m$ and $\beta_{max} = 1326$m, are replaced by the 250 GeV *demo* muon collider storage ring of $\beta^* = 10$ mm and$\beta_{max} = 18525$m. The distance between the crossing point and the first quad is estimated to be $LD{\sim}3$ m. The RHIC triplet is replaced by quadrupole magnets optimized for the *demo* muon collider. Figure 2 shows the betatron functions inside one of the IRs together with one FMC module. The FMC module is the same as in the previous example. A dipole, located between the first and the second high focusing quadrupoles, reduces the background of the detector.

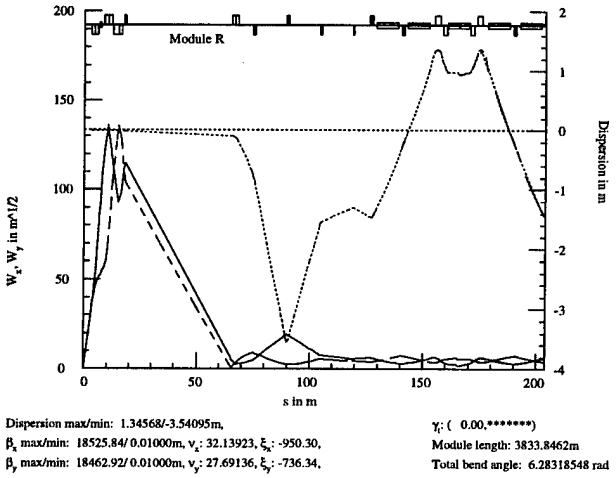


Figure 2: The IR and one FMC module of the 250 GeV isochronous *demo* muon collider lattice in the RHIC tunnel.

5 *DEMO* MUON COLLIDER 50 GEV STORAGE RING

The rms transverse emittance of a 50 GeV on 50 GeV muon storage ring is estimated to be $\varepsilon = 136 \cdot 10^{-6}\pi$m (see Table 1). The beam size is defined as:

$$\sigma = \sqrt{\sigma_\beta^2 + \sigma_p^2} \tag{3}$$

while from the rms transverse emittance:

$$\sigma_\beta = \sqrt{\frac{\varepsilon \beta_{Twiss}}{\gamma\beta}}. \tag{4}$$

The relativistic factor for a muon energy of 50 GeV is $\gamma\beta$=473.22. The rms muon beam momentum width reaching the 50 GeV *demo* collider is estimated to be $\Delta p/p = 0.12\%$. If the maximum value of the dispersion function is D_{max}=2m, the beam size $\sigma_p = D_{max}\Delta p/p = 2.4$ mm. For $D_{max} = 1$m the rms of beam size from the momentum width is a factor of two smaller (σ_p=1.2 mm). If the maximum pole tip field at the quadrupoles is B_{max}=8 T, then estimated gradients are calculated by using the radii equal to 4 σ.

The *demo* muon collider storage ring consists of eight FMC modules, which make the arc part of the machine, and a single interaction region with one crossing point. The FMC module consists of four FODO cells with a π *low beta* section in the middle. Longitudinal dimensions of the magnets inside the FODO cells define the maximum values of the betatron functions. There has to be enough clearance between the wall of the beam pipe, which is reduced due to the shield and the circulating beam. Construction of the FMC module starts by defining a 90^o FODO cell which conforms to the σ_β beam size request. The maximum value of the dispersion function in this FODO cell is defined by the size of the bending angle. As reported earlier [9] the dispersion value in an FMC module is roughly half of the value within the 90^o FODO cell. The length of a dipole in the FMC module is L_d=3.7m. The maximum values of the

betatron functions in the FMC module are β_x=17.1 m and β_y=17.5 m, and for the dispersion function $D_x = +1.38m$ and $D_x = -1.23$ m, as presented in Figure 3. A proce-

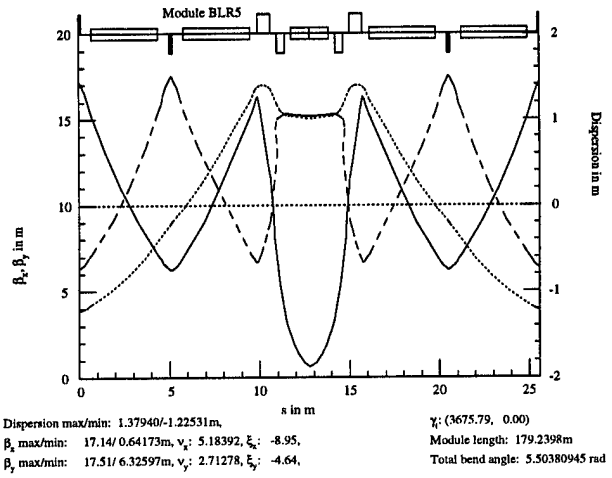


Figure 3: The *Flexible Momentum Compaction Module* of the 50 GeV *demonstration.* storage ring

dure for the interaction region triplet design was previously reported [10]. Table 3 shows the quadrupole gradients and lengths: It is important to note that for experimental back-

Table 3:

QUAD	G (1/m)	Length(m)	β_x (m)	β_y (m)
Q1	-115.0	0.686	597.0	331
Q2	58.34	2.293	2261.3	1140.0
Q3	-58.34	1.646	1083.15	2261.0
Q4	123.0	1.630	135.54	2.03

ground reduction a dipole was installed between the first and the second quadrupoles inside the IR region, and that the quadrupoles on the opposite sides of the crossing point are antisymmetric to balance the chromaticities. The betatron functions of the interaction region together with FMC modules are presented in Figure 4. The circumference of the machine is 263.4 m with an average radius of 42 m. There are eight FMC modules each 25.6 m long, and one straight section-IR 58.5 m long. The chromaticity of the whole lattice is corrected by sextupoles within the FMC modules in the arcs. The second order tune shift induced by the sextupole is small (all $\alpha_{xx}, \alpha_{xy}, \alpha_{yy} \leq 10^4$ m^{-1}).

6 SUMMARY

A progress report on the muon collider *demonstration* machines was presented. First, two examples showed that an isochronous storage ring could be placed inside an existing tunnel (RHIC) with magnets already built. The center of mass energy for μ^+ and μ^- beams in these two rings is 0.5 TeV. If this energy is selected for a *demonstration* machine, the circumference of the new ring could be much smaller than in the examples presented. The two examples of 250 GeV storage rings had a circumference 3833 m because this

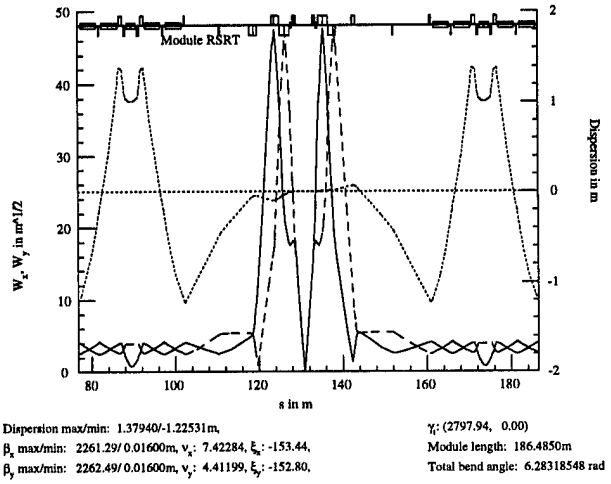


Figure 4: The IR with two FMC modules of the 50 GeV isochronous *demo* muon collider lattice.

is the RHIC circumference. The size of the 0.1 TeV muon collider *demonstration* storage ring is very small (the circumference is only 263 m). More tracking and detector background studies will follow.

7 REFERENCES

[1] R.B. Palmer, "Progress on $\mu^+\mu^-$ Colliders", these proceedings.

[2] D. Trbojevic, J.M. Brennan, E.D. Courant, T. Roser, S. Peggs, J. Norem, C. Johnstone, K.Y. Ng, M. Popovic, "Proton Driver Lattice for the Muon Collider Source with Adjustable Momentum Compaction", these proceedings.

[3] J. Norem, C. Ankenbrandt, J. Griffin, C. Johnstone, F. Mills, A. Moretti, R. Noble, M Popovic, Z Qian, M. Brennan, T. Roser, D. Trbojevic, J. Wei, "The Proton Driver for the $\mu^+\mu^-$ Collider", these proceedings.

[4] D. Neuffer and A.Van Ginneken, "μ-Ionization Cooling Simulation Results", these proceedings.

[5] R.C. Fernow, J.C. Gallardo, R.B. Palmer, "Ionization Cooling using a FOFO lattice", these proceedings.

[6] D. Summers, D. Neuffer, Q.S. Shu, and E. Willen, "Acceleration for the $\mu^-\mu^+$- Collider", these proceedings.

[7] D. Trbojevic, K.Y. Ng, E.D. Courant, S.Y. Lee, C. Johnstone, J. Gallardo, R.B. Palmer, and S. Tepikian, "Design of the Muon Collider Isochronous Storage Ring Lattice", Micro-Bunches Workshop, AIP Press, Conference Proceedings, (1996), pp. 269-278.

[8] S. Y. Lee, K.Y. Ng, D. Trbojevic, "Minimizing dispersion in flexible-momentum compaction lattices", Physical Review E, Vol. 48, Number 4, October 1993, pp. 3040-3048.

[9] D. Trbojevic, K.Y. Ng, and S.Y. Lee, "Is the Momentum Space Optimally Used with the FODO Lattices", Stability of Particles in Storage Rings, Particles and Fields, Series 54, AIP Conference Proceedings No.292, pp. 260-263.

[10] R.B. Palmer et al., "Muon Colliders", in Beam Dynamics and Technology Issues for $\mu^+\mu^-$ Collider, AIP Conference Proceedings 372, American Insitute of Physics, 1996, p.21.

A NORMAL CONDUCTING ACCELERATOR FOR A MUON COLLIDER DEMONSTRATION MACHINE

Y.Zhao, R.Palmer, R.Fernow, J.Gallardo, H.Kirk
Brookhaven National Laboratory, Upton, NY 11973

Abstract

We present a 250 GeV linac arrangement using normal conducting cavities that could be used for a muon collider demonstration machine. One scenario consists of six 200 MHz linacs and rapid cycling pulsed magnets to be installed in a tunnel with six straight sections. The RF parameters of the cavities are given. Another scenario consists of 800 MHz. Also addressed is the possibility of using normal conducting cavities with liquid nitrogen cooling, which has several advantages.

1 INTRODUCTION

The realizability of the muon collider is interesting from both technological and economical points of view. As a first step, a demonstration machine with lower energy is considered. Since the lifetime of muon is short, rapid acceleration is required and thus the RF equipment must take a significant part of the total cost, especially at the final stage, which plays a major role for the energy gain. Superconducting cavity would be desirable in order to save rf power. However, the machine in question will work at a low duty rate, pulse mode, the peak power extracted by the muon beam is 640 kW average (see later). Besides, the muon decay deposits energy all along its path, which may cause trouble to the super-conductivity. Therefore an alternative, normal conducting scheme was investigated [1].

2 BASIC PARAMETERS OF THE DEMONSTRATION MACHINE

Since the muon collider involves lots of new technology, a demonstration machine with reduced energy and luminosity is considered so as to be more realistic. The energy of 250 GeV with intensity of 4×10^{12} muon per bunch is considered. Recently, an even lower energy, which may also be interesting from the point of view of physics, has been proposed. In this paper we concentrate only on the final stage of a 250 GeV + 250 GeV machine. Following is a list of basic parameters related to the RF.

Number of beams	2 (μ^+ and μ^- beams passing same channel)
Number of bunches	2 (1 for each beam)
Muons per bunch	4×10^{12}
Charge per bunch	0.64 C
Repetition rate	2.5 Hz
Current per beam	1.6 μA
Injection energy and γ	50 GeV / γ = 473
Output energy and γ	250 GeV / γ = 2366
Average extracted power	320 kW per beam
Total extracted power	640 kW

It is also of very much concern about the radiation energy, which is produced due to the muon decay and dissipated along its path, including RF cavities. The decay equation is:

$$\frac{dN}{dt} = -\frac{N}{\gamma\tau_\mu} \quad (1)$$

where N is the number of muons, γ is the relativistic factor, and τ_μ = 2.2 μs is the muon lifetime in the rest frame. So the decay (radiation) power, P_d, is:

$$P_d = -\gamma E_{\mu 0}\frac{dN}{dt} = \frac{E_{\mu 0}}{\tau_\mu}N = N\cdot 7.70\times10^{-6}W \quad (2)$$

where $E_{\mu o}$ is the rest energy of muon. Note that the decay power depends only on the number of muons, but is independent of the energy γ. For our basic parameters, the instantaneous radiation is P_d = 30.8 MW per bunch. The total energy will be the integral of time.

3 THE CONCERNS FOR THE RF SYSTEM

1.1 Superconducting or normal conducting

The advantages of superconducting (sc) are saving RF power and possibly higher gradient, which will shorten the acceleration length. However, the minimum average power is 640 kW, while the peak power is three orders higher, so it must work in pulse mode, which complicates the sc system. Besides, the stability in the heavy radiation environment and the capability of handling its heat load are questionable. According to the above data, assuming the accelerating cycling time is 400 μS, then the total radiation power is 61.6 kW on average. Assuming one third is converted to electrons (or positrons for μ^+, the remaining to neutrinos), and that one third of electrons are dissipated at cavity walls, we find the deposit power is 6.8 kW. This is a big load for a sc cryogenic system. The normal conducting (nc) system, on the other hand, requires a much higher rf power, which implies a large amount of capital investment. As an improvement, liquid nitrogen cooling has been investigated. The result is encouraging, and will be discussed later.

1.2 Frequency

The higher frequency can run with higher gradient, less stored energy, more compact and less costly. However,

0-7803-4376-X/98 /$10.00 © 1998 IEEE

the bunch length and transverse emittance will limit the maximum frequency. The availability of power sources is also an important consideration for the frequency choice. In our case, 200 and 800 MHz have been considered. To our knowledge, the largest power available for 200 MHz is with tetrode or triodes only. Triode RCA/Burle 7835 with a maximum long pulse power of 5 MW, and tetrode 4CM25000KG of CPI with a potential power output 7 MW may be the best candidates. For 800 MHz, the klystron Litton L-5859 with peak power of 12 MW would be satisfactory.

1.3 Accelerating Gradient

The gradient must satisfy two criteria. One is related to the muon lifetime, i.e. after acceleration the number of decayed muons must not be significant. This leads us to the expression:

$$\overline{E}_{acc} >> \frac{E_{\mu 0}}{ec\tau_{\mu}} = 0.16MV/m, \qquad (3)$$

where $\overline{E}_{acc}$ is the average gradient throughout the entire muon system [2].

Another criterion is related to the energy drop due to the beam loading, i.e. that energy extracted by the bunch must be much less than the energy stored inside the cavity. It results in the expression:

$$E_{acc} >> q \cdot \tfrac{4\pi}{c}(R/Q) f^2 T^2 \cos^2\phi, \qquad (4)$$

where E_{acc} is the accelerating gradient, q is the charge of the bunch, R/Q the cavity parameter, f the rf frequency, T the transit time factor of the cavity, and ϕ the synchrotron phase. Since the total charge q is rather large, this data is of concern. The energy drop will be addressed later. These criteria suggest applying the highest gradient possible. However, the maximum gradient is primarily limited by the breakdown. The maximum surface electric field on the cavity wall is considered to be no more than 2 times the Kilpatrick criterion[1]. Then one would like to reduce the ratio of maximum surface field to the acceleration gradient (or the gap voltage). A noseless cavity has a lower ratio than a cavity with noses (termed reentrant cavity), and it also has a lower H_{max}, which determines the maximum surface current density. But, noseless cavities have lower R/Q and thus require higher rf power. Therefore, if highest gradient is desirable, one tends to use noseless cavities, as in many super-conducting rf systems, where the power loss is ignorable. If a normal conducting cavity is used and lower rf power is required, then a reentrant cavity is usually better. A compromise is necessary. Table 1 shows a comparison.

1.4 The RF power requirement

Many factors affect the power requirements. The power source must be able to compensate the cavity resistive loss, the energy extracted by the beam, and the energy converted to high order modes (HOM). The finite filling time will require longer pulse length than the real acceleration time. This portion of the energy is reflected from the cavity or dissipated as a pulse tail. The beam-extracted power is 640 kW as mentioned above. HOM losses are generally small, and can be ignored, provided proper depression has been made. The resistive loss is the major part for a normal conducting system. The following equation shows the relation to other parameters.

$$P = \frac{\lambda}{2}\frac{E_{acc}}{T^2\cos^2\phi}\frac{G}{n}\frac{1}{Q(R/Q)}, \qquad (5)$$

where G is the total energy gain of the muons, equal to 200 GV in our case, n the number of cycling turns, and λ the free space wave length. Therefore, increasing Q, number of turns, or frequency will reduce the power requirement, while increasing gradient will increase it. The high R/Q of the cavity is desirable from the above equation. The reentrant cavity usually has higher R/Q, but also has a higher ratio of maximum surface field to the gap voltage.

1.5 Voltage drop and energy drop

In our case the beam loading is very heavy, and the voltage drop can be significant. The voltage induced by the bunch is[2]:

$$V_b = 2Tkq = \tfrac{1}{2}T\omega q(R/Q) \qquad (6)$$

where k is the loss parameter[3],

$$k = \frac{1}{4\alpha} = \frac{V^2}{4W} \qquad (7)$$

α is a cavity shape parameter. The relative energy drop has the exact form as follows:

$$\frac{\Delta W}{W_c} = T\frac{\omega(R/Q)}{V_c}q\cos\phi, \qquad (8)$$

while the relative voltage drop is roughly a half.

$$\frac{\Delta V}{V_c} \approx \frac{1}{2}\frac{\Delta W}{W_c} \qquad (9)$$

The energy stored in the cavity must be much larger than that extracted by the beam in order to avoid instability. The expression (4) is deduced from (8). Moreover, in our scheme both μ^+ and μ^- will pass through the same cavities, while the phase difference between the two bunches varies with the location of cavities. The voltage induced by two beams differs from cavity to cavity. This factor strengthens the above concern. A lower R/Q is beneficial from above equation.

[1] A multiple of 2.5 or 3 may be possible, but not certain.

[2] The formula is in accordance with the definition R/Q = $V^2/\omega W$, which has a factor of 2 difference with another frequently used definition of R/Q.

4 THE 200 MHZ SCENARIO

As a paper study example, we considered using the existing RHIC tunnel at Brookhaven National Lab to house the muon accelerator ring. This ring includes 6 straight sections with length of 283 m for each and a circumference of 3834 m. There would be adequate room for a 250 GeV rapid cycling accelerator. The following parameters were chosen:

Number of cycling turns	40
Energy gain per turn	5 GeV
Linac length	6 X 200 m
Accelerating gradient	4.17 MeV/m
Revolution time	12.77 μS
RF effective pulse length	510 μS

Cavities were simulated by SUPERFISH. Many options were calculated but not optimized yet. Some results are summarized in Table 1.

Table 1

Cavity code #		200A3	200B5	200B8
Shape (w/wo nose)		w	wo	wo
Diameter	cm	96	132	128
Iris (diameter)	cm	15	46	30
$E_{s max}$	MV/m	34.8	11.3	10.6
$E_{smax}/E_{kilpatric}$		2.38	0.77	0.72
H_{max}	kA/m	25.5	17.3	15.4
Total rf power	GW	1.96	3.43	2.79
Average power[3]	MW	2.94	5.15	4.18
Efficiency	%	25.6	14.6	18.0
Energy drop	%	5.59	1.93	2.55

The reentrant cavity needs less power, but the maximum field is higher. The noseless cavity has more potential to increase gradient, but the power will also increase correspondingly. The energy drop is for one bunch only. For two bunches it will be higher. The worst case is that two bunches, μ^+ and μ^-, enter the same cavity at the same time, then the drop will be doubled.

5 THE 800 MHZ SCENARIO

From Equation (5), it is clear that highest frequency is preferable. If it's not restricted to an existing tunnel then a smaller ring with more cycling turns will reduce the power further. We now consider the following parameters:

Frequency	800 MHz
Circumference	2000 m
Cycling turns	60
Revolution time	6.67 μS
RF effective pulse length	400 μS

A cavity is simulated via SUPERFISH and Table 2 summarizes some data with different gradients.

Table 2

Gradient	MV/m	15	10	5
$E_{smax}/E_{kilpatric}$		1.57	1.04	0.52
Linac length	m	222	333	667
Cavity loss	GW	3.57	2.38	1.19
Beam load	GW	0.64	0.64	0.64
Total rf power	GW	4.21	3.02	1.83
Average power[4]	MW	4.44	3.18	1.93
Efficiency	%	15.2	21.2	35.0
Energy drop	%	8.2	12.3	24.6

It shows the power requirement is reduced, even though the gradient is higher and with much shorter linac length, implying a significant cut of cost. However, the energy drop is rather large. A further careful treatment is necessary.

5 LIQUID NITROGEN COOLING

It is well known that the resistivity of metals decreases with decreasing temperature. Although the cryogenic system is usually expensive, liquid nitrogen is not. At NY it costs 5 cents a liter, cheaper than bottle water. The cooling cost is $1.13 per kWhr. At liquid nitrogen temperature, 77K, the conductivity of copper is 7.5 times better than that at room temperature. For beryllium it is 23 times better than that of copper at room temperature. Assuming this condition is applied, then the Q of the cavity will increase 2.7 and 4.8 times respectively. Taking account that the inner surface temperature of the cavity is higher than the coolant, with a beryllium coating applied, the Q can still be 2.7 times higher. The preliminary study shows it will save a lot of rf power and the capital investment.

The challenge is to develop this technology. The concerns are: (1) Does the heat conductivity enable the cavity to reach an adequate low temperature? (2) Does the anomalous skin effect invalidate the estimate? (3) Does the magnetic field surrounding the cavity matter? (4) Is the cost saving for liquid nitrogen really worthwhile? Early studies of the above problems are encouraging.

6 REFERENCES

[1] Y.X. Zhao, 'The rf consideration of 200 MHz normal conducting accelerator for muon collider demonstration machine', Muon-collider cooperation workshop, Oxiford, Mississippi, Jan 17-18, 1997.

[2] 'Muon Muon Collider, A feasibility Study', BNL-52503, Fermi Lab-Conf-96/092, LBNL-38946, July 1996, p.278.

[3] P.B. Wilson: 'High energy electron linacs: Applications to storage ring RF system and linear collider', SLAC-PUB-2884 (Rev) 1991.

[3] With pulse length of 600 μS as taking the rise time into account.

[4] With pulse length of 422 μS.

A RING LATTICE FOR A 2-TEV MUON COLLIDER

C.J. Johnstone*,
Fermilab, P.O. Box 500,Batavia, IL 60510 USA
A. Garren
UCLA Center for Advanced Accelerators, Los Angeles CA 90095, U. S. A.
and Lawrence Berkeley National Laboratory, Berkeley CA 94720, U. S. A.

1 INTRODUCTION

A 2 TeV on 2 TeV muon collider has been proposed [1] with a design luminosity of $10^{35}\,\mathrm{cm}^{-2}\,s^{-1}$. The ring has a circumference of about 8 km, and the muon lifetime at 2 TeV corresponds to approximately 1000 turns before the beam luminosity degrades substantially. The cooling process produces a round beam with a normalized emittance of 50×10^{-5} mrad and 2×10^{12} muons per bunch. The beam's large emittance requires that β^* at the interaction point (IP) must be only 3×10^{-3} m, in order to reach the design luminosity. Due to the hourglass effect, a very short bunch length equal to β^* must be maintained to reach the design luminosity. To prevent the bunch from spreading in time, the momentum compaction factor α must be 10^{-5} [2], or less; that is, the ring must be nearly isochronous.

The small value of β^* leads to very large peak beta values in the final-focus quadrupoles, and unprecedented chromaticities. Correction of the large chromaticities makes for a highly nonlinear Interaction Region (IR). This IR, combined with the isochronicity condition, makes design of a muon collider lattice very challenging. The lattice presented here builds on a base ring design described in a feasibility report, [1], and, more recently, in several muon-collider workshop proceedings [3].

2 LATTICE

The collider lattice must satisfy three major design constraints. The first is an Interaction Region (IR) with an extremely low value of β^* ($\sim$ 3 mm) at the IP, consistant with an acceptable dynamic aperture. This requirement is difficult because the the final-focus quadrupoles need shielding from the high muon-decay backgrounds [4], which reduces their gradients, leading to increased peak β-function values and nonlinear beam dynamics. Second, the ring must be nearly isochronous in order to preserve short 3 mm long bunches with a modest rf system. Third, the corrected chromaticity must be small, so that the momentum dependent dynamic aperture is sufficient. Following is a description of a lattice which meets these requirements.

2.1 *Overview*

The ring has a roughly oval shape, with reflection symmetry about the vertical axis. The lattice has two circular arcs, separated by the experimental insertion and a utility insertion for injection, extraction, and beam scraping. The two arcs are identical; each contains 14 periodic cells or modules. One additional arc module located at the experimental-insertion end of each arc can be perturbed and rematched to allow adjustment of the machine tunes without impacting lattice functions in the rest of the ring. Consequently the ring structure, both geometrically and optically, has a single superperiod, and reflection symmetry about the line joining the centers of the two insertions.

Arc module In order to have very short 3 mm bunches in the 2-TeV muon collider, the storage ring must be quasi-isochronous, which requires that the momentum compaction α be very close to zero. Furthermore, the lattice must be designed so that over the required momentum range, the momentum compaction remains small. Since the experimental insertion has bending regions with positive contributions to α, the contributions of the arcs must be negative.

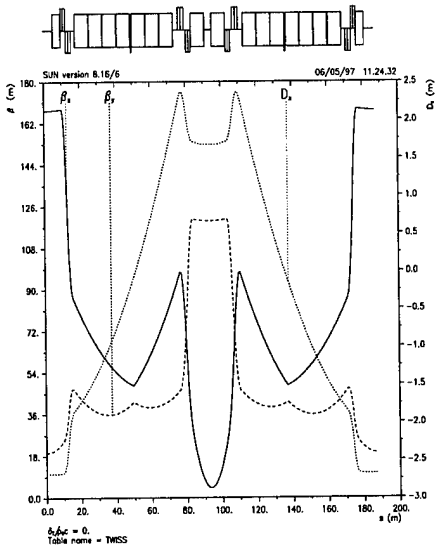


Figure 1: Lattice functions of an arc module (β_x: solid, β_y: dashed, η: dot-dash).

A negative value of α in the arcs is obtained by invok-

* Operated by Universities Research Association, Inc. under contract No. DE-AC02-76CH03000 with the U. S. Department of Energy

0-7803-4376-X/98/$10.00 © 1998 IEEE

ing the approach used in flexible momentum compaction (FMC) modules[5]; where two FODO cells are connected by a matching region with horizontal phase advance of nearly π (low β_x). This drives the dispersion η to a negative value at the ends of the module and makes $\eta_{bends} \sim 0$.

The specific module used for this muon collider lattice (Fig. 1) has been modified by including an insertion with a vertical phase advance of nearly π (low β_y) at the end of the module. This modification has several advantages compared to the standard FMC module. Firstly, the negative dispersion region has been flattened and lengthened so that the value of α is mainly determined by the bends placed in the dispersion plateaus–making it much less sensitive to η', and thus providing a wider range of quadrupole settings and corresponding lattice functions which satisfy the negative or low-α criterion. In fact, α can be tuned with a sensitivity of 10^{-5} to 10^{-7} through the use of paired trim dipoles in these two regions alone; thereby preserving both lattice functions and closure. Over a range in α of -10^{-4} to $+10^{-4}$ the impact on the lattice functions in the rest of the ring is negligible.

Secondly, the vertical phase advance of the module is no longer nearly an integer, but is identical to the horizontal phase advance, 1.5π. This is particularly important, because when the corresponding sextupoles in successive modules are separated by odd multiples of π in both planes, one obtains partial cancellation of their geometrical effects. (The near π vertical phase advance caused off-momentum particles to experience integer-related resonances in the long arc strings when sextupole correctors were on.)

Thirdly, the regions of high-β_x, low-β_y and low-β_x, high-β_y in this arc module are ideal locations for sextupoles for chromatic correction of the arcs and reduction of the variations of α with momentum. A pair of horizontal sextupoles adjacent to the center doublets are especially effective in eliminating the dependence of α on momentum offset. With these two sextupoles the variation of α over the momentum range of $\pm.004$ can be restricted to less than 10^{-6}, cancelling the dependence to approximately third order.

Experimental insertion The design of an insertion with an extremely low-beta interaction region for a muon collider presents a challenge similar to that encountered for the Next Linear Collider (NLC)[6]. The design used here for each half of the symmetric low-beta insertion follows the prescription proposed by Brown[7]; it consists of two telescopes with a chromatic correction section between. Therefore, the experimental insertion consists of three parts: the Final Focus Telescope (FFT) or IR, a Chromatic Correction Section (CCS), and a Matching Telescope (MT). Fig.2 shows the right half of the insertion beginning at the IP. From left to right, the figure shows the FFT, CCS, and MT.

The low beta-function values at the IP are mainly produced by four strong superconducting quadrupoles in the FFT with NbSn coils. Their poletip fields range from 9.5 to 12 T depending on the apertures, which determines the size of the coils and sustainable currents [8]. The first of the four quadrupoles begins 4 m away from the IP, they all have 2-cm thick tungsten liners and are interleaved with tungsten collimators to protect them from the intense backgrounds from muon decay [4].

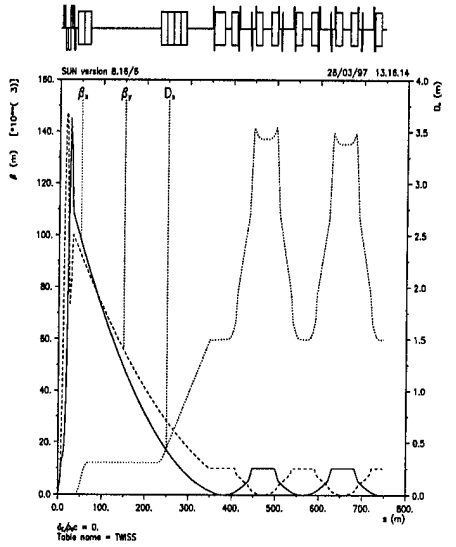


Figure 2: Experimental insertion (half) with 3 mm $\beta*$ values at the IP ($\sqrt{\beta_x}$: solid, $\sqrt{\beta_y}$: dashed, η: dot-dash)

The IR quadrupoles are followed by a pair of 15-m long bucked superconducting dipoles which sweep background particles produced by muon decays away from the IR. A long space follows without quadrupoles but with a substantial length of bending magnets that function to match η and η' from their zero values at the IP into the CCS and to give additional protection of the detector from muon decay products. In this IR design, β_{max} in both planes is 145 km. A more detailed description of the experimental insertion, especially the FFT, can be found in the Snowmass proceedings[9].

The extremely high beta values in the FFT quadrupoles produce large chromaticities, which must be corrected locally with sextupoles. The natural chromaticity of the FFT is -1500 in the horizontal and -2200 in the vertical. The purpose of the CCS is to correct these large first-order chromaticities locally, relatively close to the IP, by using interleaved sextupole pairs. These sextupole pairs are located at positions with large values of the dispersion and of the beta function corresponding to the chromaticity to be corrected by that pair.

In this design, these β values are 10 km in the plane being corrected and $.5 - .7$ m in the opposite plane. The dis-

persion is 3.4 m at the horizontal sextupoles and 1.5 m at the vertical ones. The sextupoles which comprise each pair are separated by betatron-phase intervals of $\phi = \pi$. Additionally, they are located at positions where the phase interval from the IP is an odd multiple of $\pi/2$. The vertical-correction sextupole is closest to the IP, since the vertical chromaticity is the largest.

This sextupole arrangement cancels the second-order geometric aberrations of the sextupoles, which reduces the second order tune shift by several orders of magnitude. The large ratio between the beta functions allows the sextupoles to be interleaved and still maintain the delicate higher-order cancellation. Shortening the chromatic correction section– especially with respect to the number of maxima and minima included for sextupoles– proves to be very important in improving the dynamic aperture. Placement of sextupoles at minima in the plane not being corrected reduces significantly the aberrations arising from sextupole length and cross-plane correlations.

Utility insertion The utility insertion has been specifically designed with high-beta regions to facilitate beam scraping and extraction of unwanted beam, and injection and extraction. A detailed discussion of this insertion can be found in a paper submitted to this conference [11].

3 SUMMARY

Work on improving the experimental insertion at first concentrated on reducing its chromaticity by altering the FFT, but it t proved necessary also to optimize the CCS and and the global phase advance to improve the dynamic aperture. When the peak beta functions in the CCS were lowered from 100 to 50 km, the dispersion raised in the insertion sextupoles, and the working point optimized using the phase trombones, the dynamic aperture increases from 1 to 5 sigma. Further studies indicated that a 10 km version of the CCS with the same final focus structure had an even more improved dynamic aperture due to a much reduced tuneshift with amplitude created by the strong chromatic correction sextupoles.

In a sextupole-dominated ring, as is the muon collider, a global tune of just below the integer or half integer preserves the near π phase advance required on successive passes of beam through strong sextupoles. There appears to be a delicate cancellation of residual nonlinearities on a turn-by-turn basis even when sextupoles are paired with the required π phase difference. The large (negative) tuneshift with amplitude counters the near integer/half integer tune so that particles off the closed orbit are displaced away from and do not cross resonances. Therefore, despite a near ineger tune, the working point is stable and appears to be a characteristic of a sextupole-dominated ring.

The chromaticity must be corrected in order to provide a reasonable momentum aperture; if it is not the sign of the momentum which crosses the integer tune (as determined by the residual chromaticity) is severely clipped. The overall momentum bandwidth of the system is limited by third-order aberrations and residual second-order amplitude-dependent tune shifts. These aberrations arise from small phase errors between the sextupoles and the final quadruplet, and from the finite lengths of the sextupoles. Presently, the entire ring has a dynamic aperture of greater than 5 sigma and a momentum acceptance larger than $\pm.15\%$. The base working design stands to be improved further by raising the dispersion in the utility sections (from .6 m at the sextupoles) and by implementing higher-order correction schemes; as was done in another collider lattice design by K. Oide [10], which has many good features and performance.

4 REFERENCES

[1] '$\mu^+\mu^-$ Collider: A Feasibility Study', The $\mu^+\mu^-$ Collider Collaboration, BNL–52503; Fermilab–Conf–96/092; LBNL–38946, July 1996.

[2] W. Cheng, 'Single Bunch Collective Effects in Muon Colliders', talk presented at Muon Collider Ring and Detector Workshop, Feb. 10-14, 1997, Lawrence Berkeley Laboratory.

[3] Proceedings from the Muon Collider Ring and Detector Workshop, Feb. 10-14, 1997, Lawrence Berkeley Laboratory. Proceedings of the Snowmass Workshop, June-July, 1996.

[4] C.J. Johnstone and N.V. Mokhov, 'Optimization of a Muon Collider Interaction Region with Respect to Detector Backgrounds and the Heat Load to the Cryogenic Systems', Fermilab–Conf–96/366, 1996, and to appear in the Proceedings of the Snowmass Workshop, June-July, 1996.

[5] S. Y. Lee, K. .Y. Ng, and D. Trbojevic, 'Minimizing Dispersion in Flexible-momentum Compaction Lattices', Phys. ReV. E **48**, 3040 (1993).

[6] 'Zeroth-Order Design Report for the Next Linear Collider', The NLC Design Group, LBNL-5424; SLAC-474; UCRL-ID-124161; UC-414, May, 1996.

[7] K. Brown, 'A Conceptual Design of Final Focus Systems for Linear Colliders, SLAC-PUB-4159, (1987).

[8] E. Willens, 'Summary, Superconducting Magnets for a 2-TeV Muon Collider', talk presented at Muon Collider Ring and Detector Workshop, Feb. 10-14, 1997, Lawrence Berkeley Laboratory.

[9] C. Johnstone and A. Garren, 'An IR and Chromatic Correction Design for a 2-TeV Muon Collider', to appear in the Proceedings of the Workshop on New Directions for High-Energy Physics, Snowmass 96, June-July, 1996.

[10] K. Oide, Private communication.

[11] S. Drozhdin, paper submitted to the PAC '97 conference.

5 ACKNOWLEDGEMENTS

The collider design described here is builds upon previous collaboration [1], with Drs. J. Gallardo, K. Y. Ng, R. Palmer, D. Trbojevic and others. For the present work, we want especially to acknowledge the help and advice of Dr. Juan Gallardo on the lattice and Eric Willens and Mike Green on the design of the final-focus quadrupoles.

SHIELDING THE MUON COLLIDER INTERACTION REGION

C.J. Johnstone and N.V. Mokhov*
Fermilab, P.O. Box 500, Batavia, IL 60510, USA

Abstract

One of the most serious technical problems in the design of a 2-TeV muon collider arises from muon decay. With 2×10^{12} muons in a 2-TeV bunch, 2×10^5 $\mu \rightarrow e\nu\bar{\nu}$ decays occur per meter. Immersed in strong magnetic fields, the induced electromagnetic showers deposit about 2 kW/meter in the storage ring; far surpassing the heat load capacity of cryogenic systems. Yet a more problematic background is the intense, highly directional, neutrino flux generated by the decays. This background does not respond to conventional shielding techniques; in fact the total radiation dose from neutrino interactions is worsened in the presence of shielding. The work presented here will discuss methods to reduce or compensate for the severe decay backgrounds and radiation produced in a very high-energy muon collider.

1 INTRODUCTION

There has been strong interest in a high-energy high-luminosity $\mu^+\mu^-$collider project [1] based on the physics potential of such a machine which is beyond or complementary to what can be accomplished at $e^+e^-$and hadron colliders. However, there remain many issues to be examined in such a machine, especially technical ones. One of the most serious technical problems in the design of a muon collider arises from muon decay. With 2×10^{12} muons in a 2-TeV bunch, there are 2×10^5 $\mu \rightarrow e\nu\bar{\nu}$ decays per meter in a single pass through an interaction region (IR), or 6×10^9 decays per meter per second. Both the decay electrons (with an energy of about 700 GeV) and the synchrotron photons emitted by these electrons in a strong magnetic field induce electromagnetic showers in the collider and detector components. Almost 15 MW of power is deposited in the storage ring, or about 2 kW every meter. The resulting heat load to the cryogenic systems and the background levels in the collider detectors exceed the past operational experience and even the upgrade designs at hadron and e^+e^-colliders. In addition, the intense, directed neutrino beam generated is, in itself, a serious issue, perhaps even more so than the high radiation level from electromagnetic showers. Neutrino interactions in the soil intended to shield the collider produce unacceptable radiation levels at large distances. Since earth shielding is unavoidable, techniques have been explored which diffuse neutrino-generated radiation.

Substantial suppression of the induced background levels is critical in the concept of a muon collider and detector [1, 2]. The design of a storage ring and, in particular, an IR in such an environment is a difficult and challenging problem [3]. The merits of different approaches to solving beam-induced energy deposition issues in a muon collider IR are the subject of this paper. Calculations of the particle interactions in the lattice and detector components for a 2 TeV muon beam are performed with the MARS code [4].

2 IR DESIGN PROBLEMS

The MARS studies have shown that the two quadrupoles nearest the interaction point (IP) require a minimum of 6 cm of tungsten. Even with a relaxed $\beta^* = 3$ cm IR lattice [5] a power dissipation in these quadrupoles range from 4 to 13 kW. An acceptable level is about 10 W/m so these values are too high by two orders of magnitude. The second solution, a noncosine theta magnet, does not work for the SC IR quadrupoles. Compared to the early IR design with $\beta^* = 3$ cm, the situation is much worse for a similar IR design with $\beta^* = 3$ mm even with a considered 6-cm thick tungsten liner.

In the IR adding a 6-cm liner increases the difficulty of an already problematic design, since the nonlinear attributes of the IR are strongly correlated with the strength of the final-focus quadrupoles [6]. The beam size at the quadrupole nearest the IP is only 2 cm; therefore, adding 6 cm to the aperture represents a factor of 4 decrease in the quadrupole gradient. The β-functions in the high-beta quadrupoles increase by roughly this factor, feeding an iterative effect: apertures increase further and gradients decrease correspondingly. First-order chromaticity has approximately a linear dependence on the peak β-functions, and increases proportional to the gradient reduction. Nonliearities, particularly those associated with sextupole-based chromatic correction have a much stronger dependence. Higher orders of chromaticity, for example, show an increase of about two orders of magnitude for a factor of two decrease in gradient. Therefore the net effect of a thick liner is to increase dramatically the nonlinear behavior of the IR.

3 REDUCTION OF HEAT LOAD

More recent designs [6] employed strong non-superconducting quadrupoles near the IP (Bitter quadrupoles), to reduce the peak β-function values and distribute the energy more evenly through the IR. The power levels, however, were still unacceptable in two of the SC quadrupoles: over a hundred Watts per meter. At this point it became clear that both active and passive shielding must be designed into the final focus system. The following calculations have been performed using the final focus and chromatic correction section shown in Fig. 1.

* Operated by Universities Research Association, Inc. under contract No. DE-AC02-76CH03000 with the U. S. Department of Energy.

0-7803-4376-X/98/$10.00 © 1998 IEEE

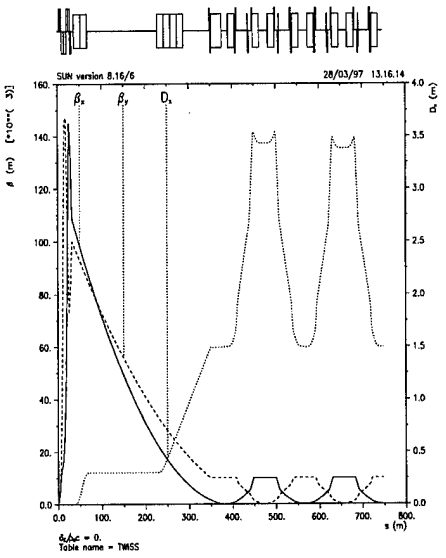


Figure 1: Horizontal (solid line) and vertical (dashed line) β-functions in the $\beta^* = 3$ mm IR lattice. Dot-dashed line shows the dispersion.

To eliminate background particles generated outside of the IR, sweep dipoles were positioned on either side of the final focus [3]. To be effective, the sweep dipoles had to be 15 m long and superconducting with a poletip field of 8.5 T. Additionally, they had to be placed at least 1 m upstream of the elements to be protected. The sweep dipoles removed backgrounds propagating from the long drift preceeding the high-β quadrupoles and from the arcs. In the latest design, a pair of reversed, horizontally-bending dipoles were used in order to restrain the dispersion function through the long IR drift. Otherwise, the dispersion would reach an enormous value at the end of the 150 m drift, which marks the beginning of the chromatic correction module.

In spite of the added dipoles, the heat load remained too high in most of the IR quadrupoles, in particular, the focussing and defocussing pair nearest the IP. Optically, these quadrupoles are the most significant in determining the nonlinear properties of the IR. Passive shielding was then included in the final focus to spread decay electrons (positrons) along the entire region instead of allowing them to hit apertures in the immediate vicinity of the IP. To achieve this tungsten collimators were sandwiched between all quadrupoles. Calculations indicate the collimators should be 15 cm long, with a 4σ aperture in order to fully shadow the SC quadrupoles which have a 5σ aperture. As shown in [3] combined effect of adding dipoles and collimators to the IR allowed the protective tungsten liner of all the SC quadrupoles, including the innnermost ones, to be reduced to 2 cm. Resulting power dissipation in the SC components is shown in Fig. 2 together with the results for the original lattice. One sees a drastic reduction in heat load in most critical components closest to the IP. With the thinner liner the strength reduction of the IR quadrupoles is a factor of 2 compared to the case with no liner, but it is twice as strong as the case with a 6-cm liner. The smaller liner reduced peak β-functions by about factor of two (to 150 km), and first-order chromaticities were correspondingly halved (presently -1500 in the horizontal and -2300 in vertical plane). Second and third order chromaticities fell by almost two orders of magnitude.

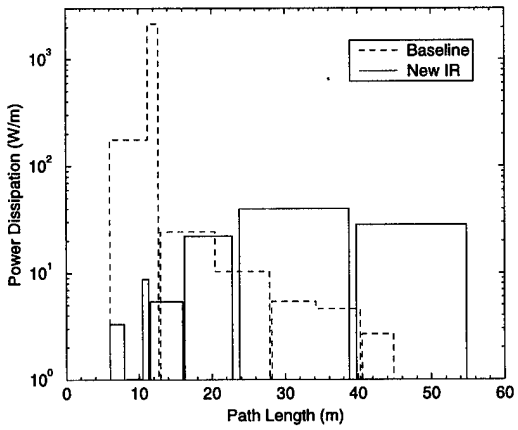


Figure 2: Power dissipation in the IR SC components.

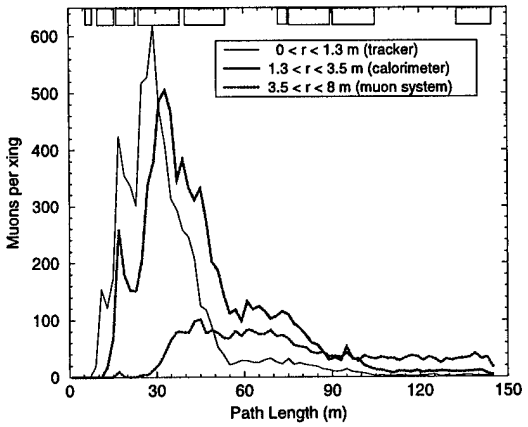


Figure 3: Number of secondary muons coming to three detector regions as a function of distance from IP of 2 TeV muon decays.

4 BACKGROUND REDUCTION

A careful design of the final focus system includes [3]: 1) tapered liner apertures, 2) sweep dipole magnets, 3) tungsten collimators interspersed between quadrupoles, and 4) tungsten collimators inside the detector with the aspect of two nozzles about the IP. Careful attention to the IR and shielding design has reduced the background levels significantly. In the optimum configuration, background fluxes are reduced by an order of magnitude. However, there still remains a serious problem with secondary muons, mainly

Bethe-Heitler pairs $\gamma Z \rightarrow Z\mu^+\mu^-$. Fig. 3 shows the secondary muon background distributions in three detectors caused by 2 TeV muon beam decays along the IR. One can deduce that the region, $15 \leq L \leq 90$ m, from IP is mostly responsible for high muon fluxes in the calorimeter. The results were obtained with thin shielding between the quads and dipoles, but it is clear that thick magnetized shields across the entire tunnel cross section (or even wider) will be required to bring the muon fluxes down. Another promising possibility, also studied using MARS, is the implementation of timing cuts.

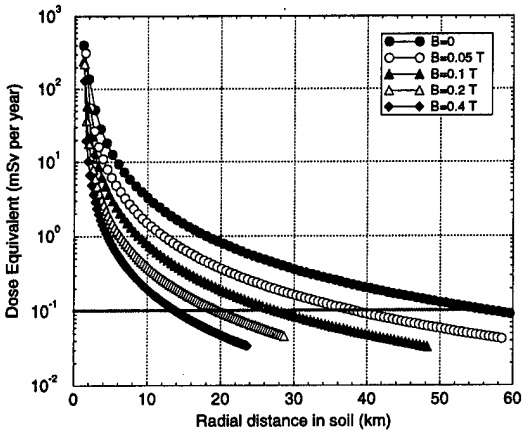


Figure 4: Neutrino induced average dose in the orbit plane *vs* distance in soil from the ring center for five values of the vertical wave field.

5 NEUTRINO

An intense secondary neutrino beam is created from muon decays and significant radiation levels result from neutrino interactions. The dose levels remain high even at very large distances from the collider ring [7]. Ironically, the neutrinos are not a problem in air at same distances; i.e. if the collider is left unshielded. Since the neutrino beam is highly collimated and directional – the intrinsic divergence is only 50 μrad from 2-TeV muon decay – the solution proposed here is to vary the production direction of the secondary neutrino beam. The neutrino beam is already spread in a horizontal disc by the collider dipoles. A vertical wave can be instituted in the collider ring to distribute the radiation and lower the average dose. This vertical wave should be varied in strength and phase over time to really smear the dose. MARS calculations indicate that such a floating vertical wave installed in the arc can be used to mitigate the neutrino flux by more then order of magnitude (Fig. 4). The approximately 8-m arc dipoles can be rolled by 20 mrad to achieve the desirable 200 μrad kick (B$\sim$0.2 T in Fig. 4). To avoid the complication of skewed quadrupoles, net rolls or horizontal magnetic fields are cancelled before entering quadrupoles. That is, the first dipole in a set of three is rolled 10 mrad horizontally, the next double that in the opposite direction, and the last the same amount in the original direction to almost exactly cancel coupling, vertical dispersion and amplitude effects. Reverse rolls and other time-varying changes can be instituted to reduce dose levels in all directions.

6 SUMMARY

The combination of 5σ aperture sweep dipoles and 4σ aperture tungsten collimators reduced not only the heat load in the SC IR elements to acceptable values, but also improved tremendously the performance of the muon collider IR through strengthed quadrupole gradients. The reduction of dissipated power is almost a factor of 2000 in some elements for the same IR design. Operationally, therefore, the beam-induced energy deposition problems in the IR appear to be resolved (if the liners and collimators are kept at room or nitrogen temperature). The backgrounds in the detector with the new IR, although reduced by a factor of 10, still require further work.

The serious problem of neutrino-generated radiation, in principle, appears to be solved by introducing a systematic, time-varying vertical wave in the collider ring to disperse this strongly-directed radiation. The lattice appears to support the concept of a vertical wave through rolled arc dipoles although detailed tracking and error studies need to be done to determine is such a configuration can be supported.

7 REFERENCES

[1] '$\mu^+\mu^-$ Collider: A Feasibility Study', The $\mu^+\mu^-$ Collider Collaboration, BNL–52503; Fermilab–Conf–96/092; LBNL–38946 (1996).

[2] N. V. Mokhov, Nucl. Physics B (Proc. Suppl.), 51A, 210, 1996.

[3] C.J. Johnstone and N.V. Mokhov, 'Optimization of a Muon Collider Interaction Region with Respect to Detector Backgrounds and the Heat Load to the Cryogenic Systems', Fermilab–Conf–96/366, 1996.

[4] N. V. Mokhov, 'The MARS Code System User's Guide, Version 13(95)', Fermilab–FN–628 (1995).

[5] C. J. Johnstone, K.-Y. Ng and D. Trbojevic 'Interaction Regions with Increased Low-Betas for a 2-TeV Muon Collider', in *AIP Conference Proceedings 372 of the 9th Advanced ICFA Beam Dynamics Workshop: Beam Dynamics and Technology Issues for $\mu^+\mu^-$ Colliders*, Montauk, NY, October 15–20, 1995, pp. 178-189.

[6] 'Zeroth-Order Design Report for the Next Linear Collider', The NLC Design Group, LBNL-5424; SLAC-474; UCRL-ID-124161; UC-414, May, 1996. C. Johnstone and A. Garren, 'An Interaction Region and Chromatic Correction Design for a 2-TeV Muon Collider', to appear in the Proceedings of the Snowmass Workshop, June-July, 1996.

[7] N. V. Mokhov and A. Van Ginneken, 'Muon Collider Neutrino Radiation', to be published.

SIMULATION STUDIES OF IONIZATION COOLING

D. Neuffer and A. Van Ginneken
Fermilab, P. O. Box 500, Batavia IL 60510

Abstract

A μ^+-μ^- collider must compress the beam phase-space volume by a factor of ~10^6 to obtain high luminosity, and this beam cooling must occur before μ-decay. In this paper we present simulations of ionization cooling which explore the various conditions needed for cooling to collider conditions. Cooling by large factors is demonstrated and directions toward complete cooling scenarios are discussed.

I. INTRODUCTION

The μ^+-μ^- collider [1, 2, 3] concept relies on ionization cooling to compress the beam phase-space volume to obtain high luminosity. This method has been described by Skrinsky et al.[2] and by Neuffer.[3] In ionization cooling, the beam loses transverse and longitudinal momentum while passing through a material medium, but regains only longitudinal momentum in acceleration cavities. Cooling by large factors requires successive stages of energy loss and reacceleration (20 to 50 stages). In this process the beam will evolve from a large phase-space volume to more compressed forms, and the cooling sections must change to match these. Also since the ionization cooling process does not directly cool the beam longitudinally, the beam must also pass through wedge absorbers at regions of non-zero dispersion to exchange longitudinal and (cooled) transverse phase-space.

The differential equation for rms transverse cooling is:

$$\frac{d\varepsilon_N}{ds} = -\frac{1}{\beta^2 E}\frac{dE}{ds}\varepsilon_N + \frac{\beta_\perp E_s^2}{2\beta^3 m_\mu c^2 L_R E} \qquad (1)$$

where the first term is the frictional cooling effect and the second is the multiple scattering heating term. ε_N is the normalized transverse emittance, E is the μ energy, and $\beta_\perp$ is the betatron amplitude. Similarly an equation for longitudinal cooling (reduction of energy spread σ_E) with energy loss can be written as:

$$\frac{d\sigma_E^2}{ds} = -2\frac{\partial \frac{dE}{ds}}{\partial E}\sigma_E^2 + \frac{d\left\langle \Delta E_{rms}^{\,2}\right\rangle}{ds} \qquad (2)$$

in which the first term is the cooling term and the second is the heating term caused by random fluctuations in energy losses. The longitudinal cooling term is nearly zero, but it can be enhanced by placing the absorbers where transverse position depends upon energy (at nonzero dispersion) and where the absorber density or thickness also depends upon energy, such as in a wedge. In that case the cooling derivative can be written as:

$$\frac{\partial \frac{dE}{ds}}{\partial E} \Rightarrow \left.\frac{\partial \frac{dE}{ds}}{\partial E}\right|_0 + \frac{dE}{ds}\frac{\eta\rho'}{\beta c p \rho_0} \qquad (3)$$

where ρ'/ρ_0 indicates the change in density with respect to transverse position, ρ_0 is the reference density associated with dE/ds, and η is the dispersion (η = dx/d(δp/p)). Increasing the longitudinal cooling in this manner decreases the transverse cooling by the same amount.

In the long pathlength Gaussian-distribution limit, the energy heating term is given approximately by:

$$\frac{d\left\langle \Delta E_{rms}^{\,2}\right\rangle}{ds} = 4\pi\left(r_e m_e c^2\right)^2 n_e \gamma^2\left(1-\frac{\beta^2}{2}\right), \qquad (4)$$

where n_e is the electron density in the material. This expression increases rapidly with higher energy (larger γ).

II. μ-COOLING REQUIREMENTS AND SCENARIOS

The μ-beam at the end of the rf rotation and decay section is expected to be ~300 MeV in energy with an rms energy spread of ~10%, an rms bunch length of ~3m and with a transverse emittance in x and y of ε_T = 0.015 m-rad (normalized). With the presently proposed high-energy μ^+-μ^- collider parameters the rms transverse emittance must be reduced to ~0.00005 at the end of the cooling system (300× smaller). The longitudinal emittance required in the 2×2TeV collider is 3mm bunch length by 3 GeV energy width, (only ~10× smaller). The overall 6-D cooling required is ~10^6. Cooling by these large factors requires a sequence of absorbers interspersed with reaccelerations. This sequence must include dispersion/wedge absorbers for energy cooling, and rf bunching for bunch length control. To minimize transverse heating (see Eq. 1), L_R (the material radiation length of the absorber) must be large, which means a light element such as Li or Be, and $\beta_\perp$ must be small and become progressively smaller as the beam is cooled, which means strong focusing at the absorbers. Scenarios for complete cooling have been developed; detailed simulations are needed to verify and optimize possible scenarios.

III. SIMULATION METHODS

Simulation of particle transport through a cooling section starts from a description of the phase space of the incident muons. To evaluate the cooling progress the kinematic variables of the particles are noted upon crossing some fixed set of planes perpendicular to the central trajectory—including the start and finish of the absorber. For a Hamiltonian formulation, this makes z, the distance along the nominal trajectory, the logical choice of independent variable. The cooling channel may include absorbers of arbitrary composition and dimensions as well as magnetic fields of arbitrary specification. Absorber

0-7803-4376-X/98/$10.00 © 1998 IEEE

material and magnetic field as a function of location are supplied to desired accuracy either by a field map or by an analytical prescription. Except when traversing a field-free void or a void in which the field is simple enough to permit an exact analytic solution, particles are traced through the absorber geometry in a series of small steps—each typically of the order of a few mm.

The physics content of SIMUCOOL is essentially unchanged from that presented in some detail in ref. [5]. Briefly, the main ingredients are: *ionization energy loss* as described by the Vavilov distribution modified for spin one-half particles and with inclusion of an energy threshold above which μ-e collisions are simulated individually, and *multiple Coulomb scattering*, in which an angular threshold is adopted below which it is treated in the Gaussian approximation and above which as coherent individual μ-nucleus scattering events. Lesser contributions (small at the low energies of interest here) such as incoherent Coulomb scattering between muons and nuclear protons, bremstrahlung, e^+-e^- production, and deep inelastic μ-nucleus collisions are also included in the simulations.

Energy loss and multiple scattering are treated as continuous processes and are thus applied during each step of the Monte Carlo which takes place in a material. All other processes, including large energy losses and large angle scattering, are treated event-by-event.

In each simulation a beam of 5000—25000 particles, generated within 6-D gaussian distributions is tracked through absorbers plus through transport and acceleration modules. Beam properties at the end of the transport are calculated and compared with rms equations.

IV. SIMULATION RESULTS

Simulations of ionization cooling have been obtained for a variety of situations corresponding to critical portions of a cooling scenario. The cases which have been explored include the following: absorbers at a β* focus, absorbers within solenoids, Be or Li lens absorbers, and wedge absorbers with cooling over a range of energies from multi-GeV levels to 20-MeV. We discuss some of these below; a more detailed discussion, with more cases, is found in ref. 6.

1. Absorbers in free space

The simplest cooling case is a field-free absorber at a beam focus. A number of these cases have been studied, using a variety of materials, and with beams at momenta from 200 MeV/c to 1.2 GeV/c. Overall very close agreement with rms equations is obtained, and very little particle-loss by scattering to large angles or large δp/p occurs. For example, a 400 MeV/c beam was tracked through 40cm of Be (matched to β*=20cm at the center). With p reduced to 277 MeV/c, the rms emittance is reduced from 0.01 to 0.0077 m-rad while δp_{rms} increases from 8 to 10.4 MeV/c.

Cooling was tracked over a broad range in initial energies, and figure 1 shows energy spread before and after a 20 cm Be rod, showing the increased width as well as the non-gaussian loss pattern with a "Landau tail". Energy straggling increases with increasing energy (see Eq. 4) and becomes too large for p > ~800MeV/c.

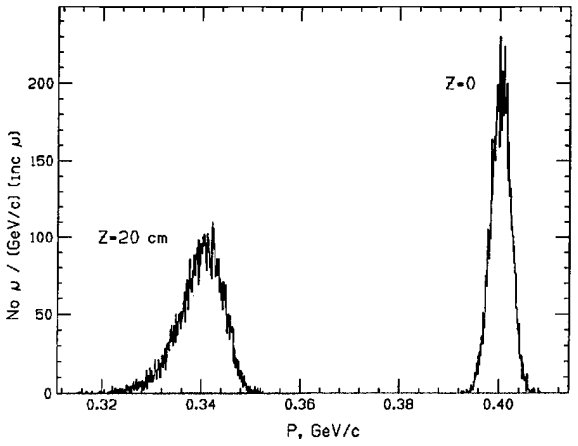


Figure 1: momentum distribution of a beam before and after a 20 cm Be absorber, showing increase in δp, as well as change in distribution shape.

2. wedge absorbers

μ-cooling naturally cools only transversely, and is accompanied by a gradual increase in δp_{beam}. 6-D cooling requires periodic exchanges in phase space, and this can be obtained if the beam is given a non-zero dispersion (position dependence on momentum) and then passes through a wedge absorber, which is placed so that the high-momentum side of the beam passes through more material and loses more energy. The resulting process reduces δp/p while increasing the intrinsic transverse size, thereby increasing ε_T by the same factor.

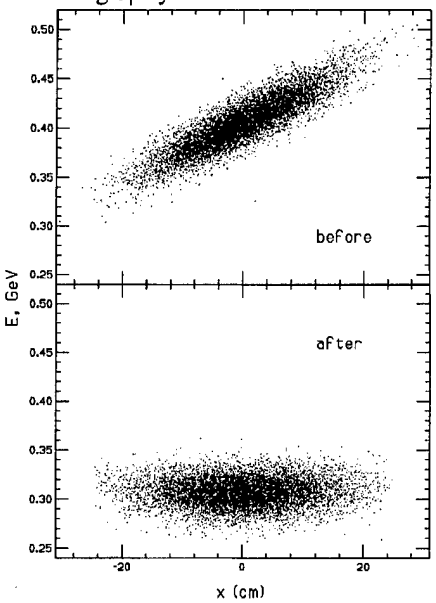


Figure 2. Beam (x-E distribution before and after a wedge + absorber for x-p emittance exchange. Note that δE is reduced by a factor of 2, and dispersion is reduced (1m → ~0).

Wedge absorbers of various materials have been simulated with vaious beam conditions (p, δp_{rms}, ε_T, etc.) and phase-space exchanges in agreement with cooling models have been obtained.

As discussed in ref. 7, the wedge and beam transport can be optically matched to obtain $\eta \cong 0$ at the exit of the wedge. Figure 2 shows simulation results of such a case, in which a hot 400 MeV/c beam with δp_{rms} =7.4%, ε_T = 0.015, at β^* = 0.34m and dispersion η = 1m, passes through a Be wedge + absorber. In the simulation, the energy spread is reduced by a factor of 2 while ε_x is nearly doubled, in agreement with expectations. (ε_y is slightly cooled.) As seen by the reduction in the x-p correlation, the dispersion η is cancelled to ~ zero.

3. Cooling in Be (Li) lens and in Solenoids

From Eq. 1, cooling requires small β^* or strong focusing at the absorbers. This can be most readily sustained if there is strong focusing at the absorber, and this can be obtained if the absorber is itself a focusing lens; i. e., a Li or Be lens, which is a conducting rod carrying a high current (up to ~1MA). Fields up to ~20000T/m can be developed in such rods. Simulations of μ-beam transport within conducting rods are able to obtain excellent cooling, in agreement with the rms equations. The cooling was insensitive to initial conditions and occurs with very large momentum spread (δp_{rms}).

Another suggested method for focusing within absorbers is to place the absorber within a high-field solenoid. Our simulations showed that this was not effective. The difficulty occurs because the solenoid introduces axial motion (angular momentum) into the beam which is damped within the absorber. However on exiting the absorber, the original axial motion is removed, and the beam has a net axial motion which dilutes the (projected) emittance.

4. Multistep cooling

To demonstrate the possibility of cooling by large factors, a beam was transported through a sequence of 8 Be lens. In each of these, momentum loss by a factor of 2 (from 400 to 200 MeV/c) was obtained and followed by reacceleration, while focussing gradients were increased from lens to lens from 30T/m to 2000T/m, matching the decreasing beam size. To control δp_{rms} a set of wedges was placed in the center of the cooling sequence, which reduced δp_{rms} by ~2×. Fig. 3 shows transverse phase-space (p_x, x) at the beginning and at the end of the sequence. Transverse cooling from 0.01 to 0.0004(~25×) and 6-D cooling by ~500× was obtained. Extrapolation to a complete cooling scenario seems possible.

V. DISCUSSION

We have obtained simulations of μ-cooling within absorbers in close agreement with rms equations. These simulations cover the range of conditions which occur within a complete collider cooling scenario, and support μ-cooling feasibility. However the simulations do not yet track a complete scenario, and they do not include a complete representation of the nonlinear beam transports and rf acceleration details. An integrated transport + energy loss simulation is needed, and this integrated code should develop into an optimizing design tool. μ-cooling simulations are also being developed by Fernow, Kirk, MacDonald, Palmer, et al.[8, 9] and their contributions will be essential in developing consistent design tools.

Also, there is as yet no experimental verification of ionization cooling, and cooling experiments in agreement with design calculations will be needed to establish the practicality of the μ-cooling concepts and requirements.

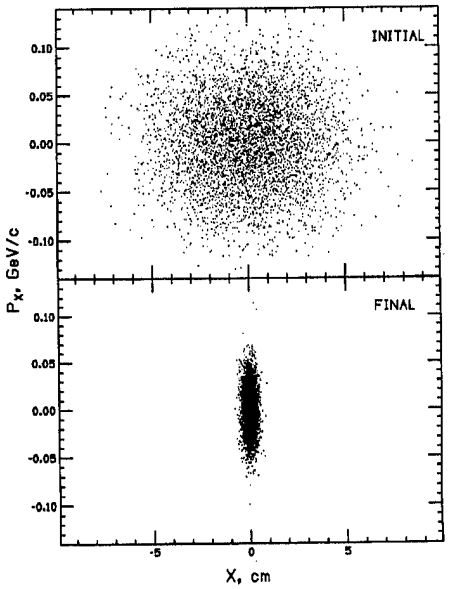


Figure 3: Transverse phase space before and after an 8-rod Be lens cooling system, with wedges for δp control. ε_T is reduced by a factor of 25 and 6-D ε is cooled by 500×

VI. REFERENCES

[1] $\mu^+\mu^-$ Collider - A Feasibility Study, BNL-52503, Fermi-Lab-Conf.-96-092, LBNL-38946 (1996), Snowmass workshop.

[2] A. N. Skrinsky and V.V. Parkhomchuk, Sov. J. Nucl. Physics 12, 3 (1981), E. A. Perevedentsev and A. N. Skrinsky, Proc. 12th Int. Conf. on High Energy Accel., 485 (1983).

[3] D. Neuffer, Fermilab Note FN-319, July 1979, D. Neuffer, Particle Accelerators 14, 75 (1983), D. Neuffer, Proc. 12th Int. Conf. on High Energy Accelerators, 481 (1983), D. Neuffer, Nucl. Inst. and Meth. A350, 27 (1994).

[4] R. Palmer, unpublished (1996).

[5] A. Van Ginneken, Nucl. Inst. and Meth. A362, 213 (1995).

[6] D. Neuffer and A. Van Ginneken, Fermilab Pub-96-451, to be published in Nucl. Inst. and Meth. A (1997).

[7] D. Neuffer, "Phase Space Exchange in Thick Wedge Absorbers for Ionization Cooling," Fermilab Pub-96-140 (1996).

[8] R. Fernow et al., Proc μ^+-μ^- Collider Ionization Cooling Meeting, April 7-8 (1997), BNL (unpublished).

[9] R. Fernow et al., paper 4W.26, this 1997 PAC proceedings.

AN ASYMMETRIC MUON-PROTON COLLIDER: LUMINOSITY CONSIDERATION

V.D. Shiltsev
FNAL*, MS 221, P.O. Box 500, Batavia, Illinois 60510

Abstract

An asymmetric muon-proton collider is proposed as an instrument for possible quark structure search. Energy of proton beam is supposed to be some 5-6 times of muon energy. Estimated luminosity of the collider with two rings – the Tevatron accelerator and μ-ring – is found to be of the order of $10^{33}\,s^{-1}\,\mathrm{cm}^{-2}$.

1 INTRODUCTION

Several proposals of $\mu^+-\mu^-$ and $\mu-p$ colliders were made in recent years (the past and present status of these ideas can be found, e.g., in Ref. [1]). Here we discuss a modification of existing plans of muon facilities which would fit to the requirements of a search for quark structure. This could be an asymmetric muon-proton collider in which the momenta of colliding quarks and muons are roughly the same in value but opposite. This condition will ease the observation of the events with large transverse momentum transfer which involve destruction of quarks or where quark structure may manifest itself. As an example, one can consider 1000 GeV protons of the Tevatron facilities which confine quarks with broad momentum spectra around the mean value of some 160 GeV/c. Therefore, an appropriate muon momentum should be about 100-200 GeV/c. This paper is devoted to brief consideration of the possibilities of such a collider, beam parameters and luminosity of the machine, and comparison with other probable competitive accelerator schemes.

2 BEAM PARAMETERS AND COLLIDER LUMINOSITY

Let us consider possible scheme of the $\mu-p$ collider which consists of two rings. Parameters of the ~200 GeV muon ring are taken from[2] where it is assumed that muon production and acceleration systems can provide $M = 2$ bunches of $N_\mu = 2\cdot 10^{12}$ particles within transverse normalized rms emittance of $\epsilon_{n\mu}$=50 mm · mrad with a rate of f_L=30 Hz. These muons decay in the ring after a characteristic number of turns of $n_s = 300\cdot B[T]$ in the bending field of B in Tesla. Here we will consider $B \sim 6T$ and, therefore, $n_s \sim 2000$.

A good candidate to deliver the beam of protons could be Tevatron. In the upgraded regime of "TeV33"[3] the length of the bunch of E_p=1000 GeV protons will be about σ_z=15 cm, while the number of protons depends on the transverse normalized emittance as $N_p \simeq 10^{11}\cdot\epsilon_{np}[mm\cdot mrad]$. The last relation assumes limiting factors for proton beam population are low-energy space charge effects at injector stages and intrabeam scattering.

Transverse sizes σ^*_μ, σ^*_p of the beams at the $\mu-p$ collider interaction point should be approximately the same, thus, under the condition on beta-functions $\beta^*_\mu \sim \beta^*_p \sim \sigma_z$ we have following relation between transverse emittances:

$$\epsilon_{np} = \left(\frac{\gamma_p}{\gamma_\mu}\right)\left(\frac{\beta^*_\mu}{\beta^*_p}\right)\epsilon_{n\mu}, \qquad (1)$$

here $\gamma_p \approx 1000$ and $\gamma_\mu \approx 2000$ denote relativistic factors of particles.

Taking for definiteness $\beta^*_p = 2\beta^*_\mu = \sigma_z = 15$ cm, we obtain $\sigma_{IP} = \sqrt{\epsilon_{n\mu}\beta^*_\mu/\gamma_\mu} \approx 40\,\mu$m and $\epsilon_{np} = 12.5\cdot 10^{-6}$ m. Consequently, the expected maximum number of protons is $N_p = 1.25\cdot 10^{12}$.

Now we can estimate the luminosity of the muon-proton collider as:

$$L = \frac{f_L n_s N_\mu N_p M}{4\pi\sigma^2_{IP}} \approx 1.3\cdot 10^{33}\ s^{-1}cm^{-2}. \qquad (2)$$

As protons are supposed to live for a long time in the ring, one should consider beam-beam effects. With the parameters mentioned above, the proton tune shift due to opposite muon beam is:

$$\xi_p = \frac{N_\mu r_p}{4\pi\epsilon_{np}} \approx 0.02, \qquad (3)$$

that seems acceptable (here $r_p = 1.53\cdot 10^{-18}$ m is the proton classical radius). The decay of muons leads to changing (reduction) of the shift within characteristic time of 2000 turns, therefore some external stabilization of the proton ring tune probably would be useful.

Beam-beam tune shift for muons is equal to

$$\xi_\mu = \frac{N_p r_\mu}{4\pi\epsilon_{n\mu}} \approx 0.026, \qquad (4)$$

again far away of limiting values ($r_\mu = 1.36\cdot 10^{-17}$ m).

Concluding this section, we would note that the key parameters for the $\mu - p$ collider luminosity are the muon production rate and the muon emittance. As these parameters are presently under detailed study, somewhat "pessimistic" variant II[1] with smaller N_μ, smaller repetition rate of μ production f_L, and larger emittance $\epsilon_{n\mu}$ is considered and put into summarizing Table 1, while high μ-production option is marked as variant I in the Table. For proton beam-beam tune shift estimations with smaller repetition rate f_L, the 'duty factor' of collisions was taken into

* Operated by Universities Research Association, Inc., under contract with the U.S. Department of Energy

0-7803-4376-X/98/$10.00 © 1998 IEEE

Table 1: Two Options of $\mu - p$ Collider

Parameter	I	II
Muon Energy, E_μ, GeV	200	200
Proton Energy, E_p, GeV	1000	1000
μ Intensity, N_μ/bunch	$2 \cdot 10^{12}$	$5 \cdot 10^{11}$
μ Emittance, $\epsilon_{n\mu}$, $10^{-6}\,m$	50	200
Storage turns, n_s	~2000	~2000
μ Pulse rate, f_L	30	10
N bunches (p, μ), M	2	2
Beta at IP β^*_μ, cm	7.5	7.5
β^*_p, cm	15	15
Waist size σ_{IP}, μm	~40	~90
p Emittance ϵ_{np}, 10^{-6} m	12.5	50
p Intensity, N_p/bunch	$1.25 \cdot 10^{12}$	$5 \cdot 10^{12}$
Beam-beam shift ξ_p	0.02	0.0005
ξ_μ	0.026	0.026
Luminosity L, $s^{-1}cm^{-2}$	$1.3 \cdot 10^{33}$	$1.1 \cdot 10^{32}$

account: $< \xi_p > \approx \xi_p(f_L n_s/f_0)$ where $f_0 \simeq 47$ kHz is the Tevatron revolution frequency, and ξ_p is given by Eq. (3). Let us remark also, that inasmuch as beta functions at the interaction point are of the order of bunch length, the "hour-glass" effect can slightly decrease luminosity (by some dozen percents).

3 DISCUSSION

It is interesting to compare the proposed proton-muon collider with other lepton-hadron machines presently under study, namely, possible $e - p$ facilities of LEP+LHC at CERN and TESLA+HERA-p at DESY(Hamburg). Table 2 demonstrates main features of these machines: momenta of quarks ($p_q \sim E_p/6c$) and leptons p_l, maximum momenta transfer $Q \simeq 2\sqrt{p_q p_l}$ (all momenta in GeV/c), and luminosity in $s^{-1}cm^{-2}$.

Table 2: Quark-Lepton Collider Projects

Project	Q	p_l	p_q	$L, 10^{31}$
TESLA+HERA-p	350	250	140	~1.0
LEP+LHC	700	90	1300	1–10
μ–ring+Tevatron	350	200	160	10–100

The TESLA+HERA-p project[4] with use of superconducting linear accelerator of electrons can provide momenta-symmetric quark-lepton collisions, but its luminosity is limited by power of electron beam. The luminosity of the LEP+LHC is somewhat higher and limited by beam-beam instabilities into both beams of electrons and protons, but momenta asymmetry of the order of 15 is not convenient for the experiment. As it is mentioned in the Table 2, the luminosity of the muon-proton collider at FNAL could be the highest one, depending mostly on the μ–production and cooling.

It seems reasonable to consider the proposed $\mu - p$ machine as the first step toward a large scale 4 TeV c.m. energy $\mu^+\mu^-$ collider. With respect to the full-scale set up such a testing facility does not require production of both charge muons, allows large longitudinal emittance of μ-beam and, therefore, gives some freedom in obtaining lower transverse emittance (see in Refs. [1, 2]). Due to ability to operate with μ bunches as long as proton ones, one expects no troubles with single bunch instabilities in the muon ring, and at the same time it could substantially simplify focusing optics of the ring and the interaction region.

Further increase of the $\mu - p$ collider luminosity can be obtained with larger number of bunches M, or with implementation of "traveling focus" regime [4] in order to decrease effective beam sizes at interaction point while bunch length is larger than the value of beta function. Formally speaking, quark-muon luminosity is some 3 times the obtained value, because number of quarks is triple number of protons we used in our estimations.

4 CONCLUSIONS

The asymmetric $\mu - p$ collider with energies of 200 GeV in muon beam and 1 TeV for protons is considered as a tool for quark structure search. The option with intersecting Tevatron accelerator and μ-ring allows to obtain luminosity of the order of $10^{33}\,s^{-1}$ cm^{-2}. The key issues for high luminosity are large number and small transverse emittance of muons, while the muon bunch length can be as large as proton one's. The beam-beam effects are found to give no severe constraints on beam intensities. It was also shown that the proposed scheme has some advantages with respect to other possible lepton-hadron colliders, such as LEP+LHC and TESLA+HERA. The muon-proton collider at FNAL seems to be also a perfect candidate as the first stage of high-energy $\mu^+\mu^-$ facility.

5 ACKNOWLEDGMENTS

I acknowledge valuable comments and corrections done by Dan Green and David Neuffer. Discussions with Reinhard Brinkmann, Joerg Rossbach, Gus Voss (DESY), and Pat Colestock encouraged me to pursue the topic.

6 REFERENCES

[1] AIP Conference Proceedings 352, "Physics Potential and Development of $\mu^+\mu^-$ Colliders", 2nd Workshop, Sausalito, CA (Nov. 1994).

[2] R. Palmer *et al*, "Beam Dynamics Problems in a Muon Collider", BNL - 61580 (March, 1995).

[3] G. Jackson, ed., "Recycler Ring Conceptual Design Study", FERMILAB-TM-1936 (July, 1995).

[4] R. Brinkmann and M. Dohlus, "A Method to Overcome the Bunch Length Limitation on β^*_p for Electron-Proton Colliders", Internal Report DESY M-95-11 (Sept. 1995).

CONTROL OF LONGITUDINAL COLLECTIVE BEHAVIOR IN THE MUON COLLIDER RINGS *

Wen-Hao Cheng, Andrew M. Sessler, William C. Turner, and Jonathan S. Wurtele
Lawrence Berkeley Laboratory
Berkeley, California 94720

Abstract

The longitudinal single bunch collective effects in a Muon Collider [1] ring are theoretically examined. The situation involves an intense bunch, a short bunch, a small momentum compaction, a rather large impedance compared with the stability threshold criterion, and a luminosity life time limited by muon decay to a thousand turns. Qualitative descriptions of stability are given and a scaling law for the instability threshold is derived. Numerical simulation results for the impedance-related instabilities are given for two cases of current interest - a 250 GeV × 250 GeV demonstration machine and a 2 TeV × 2 TeV high energy machine. The results of these simulations are in good agreement with the predictions of the scaling law and show that the longitudinal collective effects are controllable with a proper choice of parameters (viz. rf voltage, rf frequency, linear and non-linear longitudinal chromaticity).

1 LONGITUDINAL BEHAVIOR

A ring with a high degree of isochronicity (i.e. a small slippage factor $|\eta| = |pdC/Cdp - 1/\gamma^2| = 10^{-7} \sim 10^{-5}$, where $\gamma = 1/\sqrt{1-\beta^2}$, p is the particle momentum, and C is the circumference of the ring) is needed to satisfy the requirement of a short bunch with a practical rf system [1]. However, small $|\eta|$ implies small longitudinal Landau damping. Small $|\eta|$ also implies that the static effect of the longitudinal wake force causing potential-well distortion of a beam is important. The longitudinal motion of the beam is one of the main concerns for a muon collider ring [2].

A large number of accelerator parameters enter into the description of longitudinal beam motion. Although each of these impacts the analysis of beam stability, the values of many of them are fixed by considerations that do not involve beam stability, and they are not available for manipulation to improve the beam stability situation. Some examples of the fixed parameters are: beam energy, circumference, peak beam current, bunch length, momentum spread etc.. However, there remain a few free parameters that can be adjusted for longitudinal beam stability. They are: the lowest order and higher orders of the slippage factor, i.e., η_1, η_2, η_3; the supply of rf energy per turn, eV_{rf}; and the wavelength of rf, λ_{rf}. Here, the slippage factor is expaned as $\eta = \eta_1 + \eta_2\delta + \eta_3\delta^2$, where $\delta = dp/p$. In this study, we use multi-particle simulations [3] to search for a workable operation region in the parameter space: $\pm\eta_1, \eta_2, \eta_3, (V_{rf}/\lambda_{rf})$. A key ingredient in these analyses is the choice of broad-band impedance model to describe the electrodynamic interaction of the beam with beam tube discontinuities. In this paper, we use a broad-band ($Q = 1$) resonator model [4]. The ring inductance and resonant frequency of the model are chosen by scaling [5] from the impedance budgets (inductance and loss factor) that have been reported for B factories (PEPII and KEKB). The scaling takes account of differences in circumference, beam tube radius and bunch length and yields an impedance that is representative of the state of the art for smooth beam tubes. To fit the impedance of existing machines scaled to the muon collider rings, we use the paramters of the broad-band resonator model: shunt impedance $R_s(k\Omega) = 18.8$ (2 TeV), $3.1(250GeV)$; $Q = 1$; and the resonant angular frequency $\omega_r = 17$GHz for both rings. The low frequency broad-band impedance of the rings is $|Z_0^{\|}/n| = \omega_0 L = 0.26\Omega$, where ω_0 is the revolution angular frequency and L is the ring inductance. The rf cavity impedance is also included in our simulations. We use Perry Wilson's scaling formula for the longitudinal wake function [6]. Effects of Landau damping, potential-well distortion, nonlinear synchrotron oscillation, longitudinal microwave instability, and also, intensity decrease due to mu-decay, are all included in the simulations. Since the muon storage time is typically only a thousand turns, the system is in a transient state. The choice of storage ring working point will be seen to depend on the tolerance for bunch lengthening and energy spreading during the storage time.

1.1 How isochronous? The value of $|\eta_1|$.

Simulations show that the most suitable values of $|\eta_1^{\mu}|$ (when $\eta_2 = \eta_3 = 0$) are: $\sim 10^{-6}$ for the 2 TeV machine and $\sim 10^{-5}$ for the 250 GeV machine, which for resonable rf voltage gives tolerable bunch centroid drift, energy spread growth, and bunch lengthening, compared to smaller η_1. This is simply because larger $|\eta_1|$ gives faster Landau damping, where the Landau damping rate can be approximated as $\tau_d^{-1} = n\sigma_\omega = n\eta_1\omega_0\sigma_\delta$ [7]. Our simulations show that, the regime of $|\eta_1| \leq |\eta_1^{\mu}|$ freezes the $z-$motion but engenders in the δ-motion a correlated growth of σ_δ which quickly exceeds the lattice momentum acceptance. The regime of $|\eta_1| \simeq |\eta_1^{\mu}|$ smears the wake field-energy correlation and reduces the growth of momentum spread and bunch lengthening. Increasing η_1 further to $|\eta_1| > |\eta_1^{\mu}|$ results in unreasonably large rf voltage (to match the phase space) for acceptable bunch length and momentum spread.

* Work supported by the U.S. Department of Energy under contract No. EDDEFG-03-95ER-40936 and DE-AC03-76SF00098

0-7803-4376-X/98/$10.00 © 1998 IEEE

1.2 *How much rf? The value of V_{rf}/λ_{rf}.*

Since increasing the rf gradient results in improved compenstation of the variation of wake potential across the bunch, the problem of longitudinal behavior in the muon collider rings can be ameliorated by employing a large V_{rf}/λ_{rf}. Furthermore, for a given V_{rf}/λ_{rf}, the value of V_{rf} will be reduced by using a high rf frequency. However, there are two restrictions: (1) width of the rf bucket needs to be large enough, where $\Delta z_{bucket} = \lambda_{rf} >> \sigma_z$; and (2) beam loading due to the rf-cavity impedance cannot be too large, where f_{BL}(=energy-loss per particle per eV_{rf}) is scaled approximately by $1/\lambda_{rf}^2$ [6]. For the cases we have examined we find that a S-band rf (f_{rf} = 3GHz) is a suitable candidate, compromising the requirements of a large V_{rf} slope, a large enough rf bucket width (Δz_{sep} = 10cm $\simeq 33\sigma_z$), and a small enough beam loading factor ($f_{BL} \approx 33\%$, obtained by numerical calculation of the energy loss of a Gaussian beam due to the rf cavity) [6]. Simulations show that one needs approximately 450 MeV of eV_{rf} for the 2 TeV machine and about 25 MeV for the 250 GeV machine to suppress the large excitations of bunch length and bunch energy spread. The requirement for large V_{rf}/λ_{rf} can, alternatively, be achieved by using two rf cavities. One cavity with higher frequency (X-band) provides large rf voltage gradient across the bunch (even if the cavity is overloaded), and the second cavity with lower frequency (S-band) supplies the beam energy lost due to interaction with impedance of the cavities and the ring [8]. Via this scheme, the total V_{rf} needed could perhaps be reduced. Detailed examination is underway.

1.3 *Above or below transition? The sign of η_1.*

Simulations show that operation of the ring below transition $\eta_1 < 0$ produces less bunch-lengthening and energy-spreading than operation above transition $\eta_1 > 0$. A possible explanation is that when $\eta_1 < 0 (> 0)$, the bunch tends to lean backward (forward) due to the potential-well distortion. The bunch tail thus experiences less (more) wake force generated by the bunch head. Consequently, the bunch tail lengthens less (more). Of course, this could depend on the impedance models, bunch length, and how bunch frequency spectrum overlaps with an impedance spectrum. Detailed discussions on the effect of negative η_1 can be found in Ref. [9].

1.4 *Effects of longitudinal chromaticity: η_2.*

The longitudinal chromaticity η_2/η_1 introduces energy dependence into the synchrotron frequency in a way exactly analogous to the energy dedendence of the betatron frequency described by transverse chromaticity. Similarly, the transverse head-tail instability due to the transverse chromaticity has a longitudinal counterpart - the longitudinal head-tail instability (LHT) driven by longitudinal chromaticity. The head-tail instabilities have no stability threshold [10]. Moreover, when $\eta_2 \neq 0$, the rf-bucket is distorted and the phase space acceptance is reduced . The so called "α-bucket" appears when η_2 is larger than some critical value. It is clear that the lattice design should have the value of η_2 minimized to avoid the LHT instability and reduction of longitudinal phase space acceptance.

1.5 *Effects of nonlinear longitudinal chromaticity: η_3.*

It has been shown in a study of the transverse head-tail instability [11], that the nonlinear transverse chromaticity plays role similar to the varying transverse chromaticity (modulated by a synchrotron period), in which an otherwise accumulating head-tail phase is cancelled during the modulation. Similar to its transverse counterpart, the nonlinear longitudinal chromaticity η_3, in contrasted to η_2, does not cause the LHT instability but contributes an incoherent frequency spread that provides Landau damping. Our simulations show that, η_3 can help decrease energy-spreading of the bunch, when $\eta_1 \leq 10^{-6}$ and the synchrotron oscillaton period is longer than the storage time.

1.6 *Effects of beam-beam interaction*

There are two longitudinal effects from the classical beam-beam interaction that could degrade the beam luminosity. The first is the hourglass effect for centered collisions, in which the luminosity decreases when σ_z grows at fixed β^*. This could occur when there is bunch lengthening due to microwave instability, or phase space mismatch. The second is the hourglass effect for longitudinally displaced collisions at the IP (Interaction Point). This could occur when there are bunch centroid shifts due to the potential-well distortion, rf phasing errors or injection timing errors [1]. Control of the bunch length and bunch centroid, described above, is therefore important to prevent these sources of luminosity degradation.

2 SCALING LAW FOR THE LONGITUDINAL STABILITY THRESHOLD

We examine the longitudinal behavior of 250 GeV × 250 GeV and 2 TeV × 2 TeV machines with a scaling law for the impedance threshold. The parameters essential to the scaling of the stability threshold are listed in Table 1. First we examine the scaling law for the energy spread (by using the low current matching condition):

$$\sigma_\delta = \sigma_z(\omega_s/c|\eta_1|) \propto \sigma_z\sqrt{(V_{rf}/\lambda_{rf})/(CE|\eta_1|)}. \quad (1)$$

According to Table 1, we have

$$\frac{\sigma_\delta(0.25TeV)}{\sigma_\delta(2TeV)} = 18.7\sqrt{\frac{(V_{rf}/|\eta_1|\lambda_{rf})\,(0.25TeV)}{(V_{rf}/|\eta_1|\lambda_{rf})\,(2TeV)}}. \quad (2)$$

If we keep the same energy spread for both collider rings, then the rf needed is scaled as

$$\frac{V_{rf}/\lambda_{rf}(0.25TeV)}{V_{rf}/\lambda_{rf}(2TeV)} = \left(\frac{1}{350}\right)\left[\frac{|\eta_1|(0.25TeV)}{|\eta_1|(2TeV)}\right]. \quad (3)$$

The Boussard-modified Keil-Schnell criterion gives us the scaling law for the effective threshold-impedance [4], as $|Z_0^{\|}/n|_{the} \propto (E/e)|\eta_1|\sigma_\delta^2/I_p$. Since $I_p \propto N/\sigma_z$, we have

$$\frac{\left|Z_0^{\|}/n\right|_{the}(0.25TeV)}{\left|Z_0^{\|}/n\right|_{the}(2TeV)} = \frac{1}{6}\left[\frac{|\eta_1|(0.25TeV)}{|\eta_1|(2TeV)}\right]. \quad (4)$$

If we increase $|\eta_1|$ by a factor of 35 for the 250GeV machine, then V_{rf}/λ_{rf} needed (to satisfy the matching condition) becomes a factor of 10 smaller, and $|Z_0^{\|}/n|_{the}$ a factor of 5.83 larger. If the ring impedance of the low energy collider is below this threshold, then the wake voltage no longer dominates the longitudinal dynamics, and the matching condition needs to be approximately preserved. The scaling laws, from Eqs. (1) to (4), are thus self-consistent. Simulations show that the longitudinal behavior of the 250GeV machine is much easier to control.

3 CONCLUSION

Based on an estimate for the impedance and results of multi-particle slmulations, we conclude that the longitudinal behavior in the Muon Collider rings can be controlled to a level that the luminosity will not be significantly degraded. The parameters for the rings are presented in Table 1. Results of simulation for the longitudinal behavior are shown in Figs. 1 and 2.

Beam energy E (TeV)	2	0.25
Muons per bunch N (10^{12})	2	4
Circumference C (km)	8	1.3
Bunch length σ_z (cm)	0.3	0.8
Bunch energy spread σ_δ (%)	0.15	0.15
Slippage factor η_1 (10^{-6})	-2	-70
Longitudinal chromaticity η_2	0	0
Nonlinear long. chromaticity η_3	-0.1	-0.1
RF energy eV_{rf} (MeV/turn)	450	25
RF frequency f_{rf} (GHz)	3	3
RF phase-offset ϕ_{rf} (radian)	-0.32	-0.53
Synchrotron period $1/\nu_s$ (turn)	417.6	262.7

Table 1: Nominal parameters of the Collider Rings and the paramters for the rf and η used in simulations.

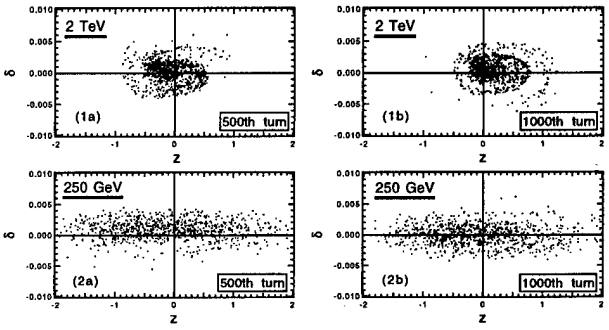


Figure 1: Multi-particle simulation results of the phase space in the (a) $500th$ and (b) $1000th$ turn, for the (1) 2 TeV ring and (2) 250 GeV ring. The initial distribution is bi-Gaussian in the phase space. The effect of mu-decay is included, the rf-cavity impedance and the impedances of a broad-band-resonator model are employed. Parameters used in simulations are shown in Table 1.

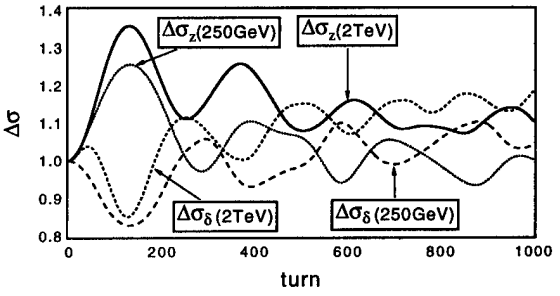


Figure 2: Simulation results of the excitation of bunch length and bunch energy spread for the 2 TeV ring and the 250 GeV ring, where $\Delta\sigma_z = \sigma_z/\sigma_z(0)$, $\Delta\sigma_\delta = \sigma_\delta/\sigma_\delta(0)$. Parameters used in simulations are shown in Table 1.

4 REFERENCES

[1] $\mu^+\mu^-$ *Collider: A Feasibility Study*, BNL-52503, Fermi Lab-Conf.-96/92, LBNL-38946 (1996); $\mu^+\mu^-$ *Colliders, Proc. of the Symposium on Physics Potential and Development of* $\mu^+\mu^-$ *Colliders*, ed. D.B. Cline, Nuclear Physics B (Proc. Suppl.) 51A (1996).

[2] W.-H.Cheng, A.M. Sessler, J.S. Wurtele and K.Y. Ng, Proceedings of the 5th European Particle Accelerator Conference, Barcelona, Vol. 2, p. 1081, June, 1996.

[3] W.-H.Cheng, A.M. Sessler, and J.S. Wurtele, Lawrence Berkeley National Laboratory Report, LBNL-40224 (1997).

[4] A. W. Chao, *Physics of Collective Beam Instabilities in High Energy Accelerators*, (John Wiley & Sons, 1993).

[5] W. Turner, report in preparation, (1997).

[6] P.B. Wilson, Stanford Linear Accelerator Center Report, SLAC-PUB-2884, (1982).

[7] S. Krinsky and L.M. Wang, Part. Accel. **17**, 109 (1985).

[8] Alvin Tollestrup, private communication, (1997).

[9] S. X. Fang, *et al*, National Laboratory for High Energy Physics Report, Tsukuba-shi, KEK Preprint 94-190 (1995).

[10] B. Chen and A. W. Chao, Particle Accelerators, vol. 43(1-2), pp. 77-91,1993.

[11] W.-H.Cheng, A.M. Sessler and J.S. Wurtele, Lawrence Berkeley National Laboratory Report, LBNL-39717 (1996).

RESULTS FROM THE DESY TESLA TEST FACILITY

B. Aune, for the TESLA collaboration
Deutsches Elektronen-Synchrotron DESY
D-22603 Hamburg, Germany

Abstract

The TESLA Test Facility (TTF), under construction at DESY by an international collaboration, is an R&D test bed for the superconducting option for future linear e+/e- colliders. It consists of an infrastructure to process and test the cavities and of a 390 MeV linac. The infrastructure has been installed and is fully operational. It includes a complex of clean rooms, an ultraclean water plant, a chemical etching installation and a ultra-high vacuum furnace. The linac will consist of three cryomodules, each containing eight nine-cell cavities operated at 1.3 GHz. The accelerating gradient should be of at least 15 MV/m, with a Q of $3x10^9$. The injector delivers a beam of 10-15 MeV, it has been installed and commissioned. The first module is in place, a 140 MeV beam is expected in June 97. An overview of the facility and results of the tests are given in this paper.

1 INTRODUCTION

The superconducting option for an electron-positron linear collider of 500 GeV center of mass energy (TESLA) is being studied by an international collaboration [1], in parallel with similar efforts by other groups on various technical solutions.

The TESLA approach uses superconducting structures operating at a frequency of 1.3 GHz with a gradient of 25 MV/m and a quality factor of $5x10^9$ at T=2K. This choice presents advantages for the design of the collider, linked to the low rf frequency and the high AC-to-beam power efficiency of a SC linac. Many well-separated bunches are accelerated in a long rf pulse, the tolerances are relaxed compared to other approaches. Another characteristic of this choice is the low peak rf power needed and the availability of klystrons [2].

The technical challenge of TESLA is to operate a large number of cavities (20000) at very high gradient and to design the linac at a reasonable cost.

The TESLA Test Facility (TTF) is under construction at DESY with major components flowing in from the members of the TESLA collaboration. Its aim is to demonstrate the ability to accelerate a beam with proper qualities through a chain of 24 cavities operating at a field level of at least 15 MV/m and to reach an overall design of cavities, cryostats, couplers and auxiliary systems which leads to costs competitive with the other approaches based on conventional structures.

2 INFRASTRUCTURE AND CAVITY PERFORMANCE

2.1 Cavity processing

Obtaining a useable gradient of 25 MV/m or more in 9-cell cavities requires that one can overcome the field limitations: quenches and field emission. The quench limit is due to heat dissipation in local defects, the solution to the problem is to use very high purity Nb with increased thermal conductivity. The field emission, mainly due to the presence of micron sized particules on the surface , requires extreme cleanliness in the processing and installation of the cavities.

The infrastructure for cavity preparation is composed of a complex of clean rooms (from class 10000 to class 10), a chemical etching facility and ultra-clean water supply. A UHV furnace is used to improve the niobium material properties via heat treatment at 1400 C in presence of Ti gettering. High pressure water rinsing (100 bar) is applied at the last step of cavity preparation.

2.2 Cavity performance

The cavities are first tested in a vertical cryostat in which high peak power processing (up to 1 MW in short pulses) can be applied. Temperature mapping is also available.

After welding of the helium tank and mounting of couplers and tuner, a cold test is performed in a special horizontal cryostat, where the complete accelerating system is tested in the TTF pulsed mode (field flat top of 0.8 ms). The behavior of the couplers, the tuning mechanism and other components are checked before the cavity is installed in the linac.

Twenty cavities have been tested in the vertical cryostat, nine of them in the horizontal one. A complete summary of the tests is given in a separate paper [3].

The specifications for TTF have been exceeded in the majority of these tests. In several cases, a field of 25 MV/m has been obtained in cw mode and up to 30 MV/m in pulsed mode. According to the measurements in the horizontal cryostat, the average field in the first module should exceed 15 MV/m.

0-7803-4376-X/98/$10.00 © 1998 IEEE

3 THE TTF LINAC

The experience gained on the TTF linac will feed directly into the TESLA collider design. There are a number of aspects in which both designs are similar. A detailed description of the linac can be found in [4].

The main components of the linac are: the injector, a first cryomodule housing 8 cavities, a 12 m long warm section in which a bunch compressor will be later installed, two cryomodules connected in series and a diagnostic area. The main parameters of the linac are given in table 1.

Table 1 TTF linac parameters

Energy	390 MeV
Beam current	8 mA
rms energy spread	$2x10^{-3}$
pulse length	0.8 ms
repetition frequency	10 Hz
Accelerating gradient	15 MV/m
Quality factor Qo	$3x10^9$
Heat load at 2 K	86 W
Number of cavities	24
Number of modules	3

3.1 Injectors

The TESLA design values for the beam current will be reached in two stages: the 1st injector delivers 8 mA with a bunch repetition frequency of 216 MHz and a bunch charge of 37 pC, while the 2nd one will give the same current with a frequency of 1 MHz and a bunch charge of 8 nC. In both cases, the rms bunch length is 1 mm.

Injector I delivers a beam of at least 10 MeV. It consists of a thermoionic 250 kV source (40 kV gun followed by an electrostatic column), a 216 MHz (f/6) prebunching cavity and a standard nine-cell SC cavity housed in its own cryostat and powered by a 200 kW klystron. A beam analysis station allows the tuning of the injector linac.

Injector II will be composed of an rf gun followed by the same SC cavity giving a total energy of about 20 MeV. A bunch compressor will be used at this level to obtain the bunch length of 1 mm. Two models of rf gun are under development: one for the full TESLA bunch charge (8 nC) and another one optimized for very low emittance (~1 mm.mr) at reduced charge (1 nC) for FEL experiments. They both use a 1.5 cell 1.3 GHz cavity powered by a 5 MW klystron and a Cs_2Te photocathode. The installation will permit the use of injector I or injector II alternatively.

3.2 Cryomodules

Three cryomodules, each 12.2 m in length, constitute the main body of the linac. Each one contains eight cavities, and a 4 K package including a superferric quadrupole doublet, steerers, a beam position monitor (cylindrical RF cavity, TM110 mode) and a HOM absorber. The liquid helium distribution and cold gas recovery system are incorporated into the cryostat. The cryostat design principle is to make the individual accelerating modules as long as possible and combine them to strings fed by a single cold box. This should result in low static losses (typically 0.2 W/m at 2K) and important cost reduction. The cavities are suspended from the helium gas return pipe which serves as a reference girder. Each cavity is equipped with its own Ti helium vessel welded around it, the beam tubes and the connections for couplers being inside the insulating vacuum.

3.3 Cavities

The 9-cell cavities are made of 2.8 mm, high RRR niobium. In addition to the standard fabrication technique, stiffening rings between adjacent cells have been added in order to reduce the detuning due to radiation pressure. With this technique a detuning parameter of ~1 $Hz/(MV/m)^2$ is obtained. The main parameters of the accelerating cavity are given in table 2.

A tuning mechanism acts on the overall length of the cavity, driven by a stepping motor located in the isolation vacuum. The tuning range is 800 kHz, corresponding to about 10^6 motor steps.

Table 2 Parameters of the TTF cavity

Frequency	1.3 GHz
Number of cells	9
Active length	1.036 m
Cell to cell coupling	1.87 %
Iris diameter	70 mm
Epeak/Eacc	2
R/Q	1010 Ohms
long. loss factor (σ=1mm)	8.5 V/pC
RF power at 25 MV/m	206 kW
External Q	$3x10^6$

3.4 Couplers

Two versions of coaxial input coupler have been developed. The coupler consists of a cold part mounted on the cavity in the clean room and closed by a 70 K ceramic window, and a warm part mounted after the installation of the cavity in the cryomodule. This part contains a coaxial to wave-guide transition and a second ceramic window at room temperature. An adjustment of the coupling by a

factor of 3 around the design value is provided by moving the inner conductor. Flexibility for axial displacement during cooldown of up to 15 mm is achieved via inner and outer conductor bellows.

The HOM couplers are mounted at both ends of the cavity with a nearly perpendicular orientation. A notch filter is incorporated for the fundamental mode rejection. Two types have been developed, a welded version and a demountable one. Both have been tested at high field level during the horizontal cryostat tests and the damping of the most dangerous modes has been measured. The Q's of the dipole modes are sufficiently low for the designed multibunch instability in TESLA.

3.5 RF system

RF power is provided by a 5 MW klystron which can feed 16 cavities. The power distribution is a linear system branching off identical amounts of power for each cavity from a single line by means of directional couplers. Individual three stub wave guide tuners for impedance and phase matching of each cavity provide the possibility of adjustment of phase by ± 30 deg. Individual low power circulators are installed on each cavity.

The low level RF control system must keep the fluctuations of the accelerating field (vector-sum of 16 cavities) to a low level to reduce the uncorrelated contributions to energy spread. The major sources of field perturbations are caused by fluctuations of the resonance frequency of the cavity and by fluctuations of the beam current. A digital feedback system will provide control of the accelerating field [5].

4 STATUS AND RESULTS

All the components for beam acceleration through the first cryomodule (140 MeV) are installed, the first beam is expected at the beginning of June 97.

4.1 Injector

The complete injector has been installed and tested [6]. During this first experiment the accelerating field in the capture 9-cell cavity was limited to 14 MV/m by strong field emission, although in the previous horizontal test a field of 18 MV/m was obtained. High power processing will be applied during the next run. The designed characteristics for the beam have been obtained (table 3) with a very good stability and reproducibility. The analog RF control system has been extensively tested with and without beam [7]. The expected values for amplitude and phase stability have been demonstrated: ± 4.10^{-4} and ± 0.1° peak to peak.

In addition the 12 MeV beam has been used for beam monitors developments: profile and emittance using an OTR station associated with an intensified gated camera, calibration of BPM, beam current measurement and loss monitoring system using toroid transformers.

Table 3 Injector Test Results

	Design	Measured
Beam current	8 mA	8 mA
Energy	> 10 MeV	12 MeV
rms energy spread	100 keV	< 100 keV
pulse length	0.8 ms	0.8 ms
bunch rep rate	216 Mhz	216 Mhz
bunch width (gun)	640 ps	600 ps
rms norm emitt.	5 mm.mr	3-4 mm.mr

4.2 Cryomodule and cryogenic system

The connection and pre-alignment of the string of 8 cavities and the SC quadrupole doublet has been made inside the clean room. The string is then moved on a rail outside the clean room. The complete mounting of the cryomodule has been achieved in 8 weeks, as scheduled. This first module has been equipped with a large number of temperature sensors as well as vibration sensors. Particular care has been taken in the alignment procedure. It has been found that with the present design, an accuracy better than 0.5 mm can be achieved for the cavities, as required from the TESLA specifications. Some improvements will be made for the following cryostat which will permit an accuracy of 0.2 mm. The position of the cavities will be monitored during cool-down and steady state operation with a system of stretched wires and wire position monitors [8], each cavity being equiped with 4 monitors.

The cryogenic system is fully operational, it has been used in routine operation during the injector tests.

4.3 RF system

The existing 5 MW klystron and modulator will be used to power the 8 cavities of the first cryomodule. A new multi-beam klystron is under development by Thomson which will deliver a power of 10 MW with an efficiency of 70%. The first tube is expected by the end of 97, it will be used to power the 24 cavities.

The digital low level RF control system has been extensively tested during experiments in the horizontal cryostat. The design performances of the system have been demonstrated under high field operation where the detuning of the cavity due to Lorentz forces is important. The data acquisition system for amplitude and phase of RF signals based on a 1 MHz sampling, digital in-phase and quadrature detection system has been used during the injector tests to monitor the field stability.

4.4 Beam lines and monitors

The complete beam line from the injector to the high energy beam analysis station is installed and under vacuum. All the components have been vacuum fired and carefully cleaned, the connections in the tunnel being

made under the protection of a local clean room. The pressure in these lines is in the range of 10^{-10} mbar.

The complete beam monitoring system, including data acquisition is installed, some monitors have been tested using the 12 MeV beam from the injector.

5 SCHEDULE AND EXPERIMENTS

5.1 First module, injector I

Starting in June 97 the experimental program with the beam accelerated through the first module includes:

- Measurements of cavity performance in linac environment.
- Cryostat behavior: losses, alignment of cavities.
- RF to beam power transfer: test of the rf control system.
- RF steering effect of couplers by measuring the beam displacement for various rf phases.
- Measurement of dark current.

5.2 Modules 2 and 3, injector II

In 98 will be installed the high charge injector and two more modules, giving an energy of at least 400 MeV. This equipment will permit to evaluate some of the key parameters for the collider design, like:

- HOM power deposited at T=2 K and choice of absorber at intermediate temperature.
- Cavity offset measurement with HOM power on dipole modes.
- short range and long range wakefields evaluation, damping of HOM with beam on axis and off axis.

In 99 an ondulator will be installed to demonstrate the feasibility of a free electron laser operating in the SASE mode. A bunch compressor after the 1st module will reduce the bunch length to 0.2 mm.

5.2 Future plans

For the longer term future, it is planned to double the length of the linac to 1 GeV and to operate a VUV light source yielding a coherent, very bright beam of photons with wavelength tuneable between 20 nm and 6 nm.

The linac extension would be composed of optimized versions of the components of TESLA.

6 CONCLUSION

The first stage of the TTF linac is now finished, the injector has delivered a 12 MeV beam, the beam experiments at the level of 140 MeV will start in June 97. A test set up for the FEL gun will be operated at DESY starting in September 97, the final tests for the TESLA gun are being accomplished at Fermilab. Experiments on free electron laser are schedule for 99.

REFERENCES

[1] The TESLA R&D effort is carried out by a number of institutions which includes IHEP Beijing, TU Berlin, Max Born Institute Berlin, Cornell Univ., Cracow Univ., TH Darmstadt, DESY, TU Dresden, DSM/DAPNIA Saclay, JINR Dubna, Fermilab, Frankfurt Univ., IN2P3/LAL Orsay, IN2P3/IPN Orsay, INFN Frascati, INFN Roma II, INFN Milano, FZ Karlsruhe, INP Novosibirsk, Polish Acad. of Science, IHEP Protvino, SEFT Finland, UCLA Dep. of Physics, Warsaw Univ., Wuppertal Univ.

[2] R. Brinkmann, "Status of the design for the TESLA linear collider", PAC 95, Dallas.

[3] M. Pekeler: "Test results on the 9-cell 1.3 GHz superconducting RF cavities for the TESLA Test Facility Linac", this conference.

[4] D.A. Edwards ed, "TESLA Test Facility Linac Design Report", DESY Print TESLA Rep. 95-01

[5] S. Simrock et al. "Design of the digital RF control system for the TESLA Test Facility", EPAC 96, Sitges

[6] T. Garvey et al., "First beam tests of the TTF injector", this conference.

[7] A. Mosnier et al., "RF control system for the SC cavity of the TTF injector", this conference

[8] A. Bosotti et al., "A Wire Position Monitor System to Control the Cold Mass Movements inside the TTF Cryomodule", this conference

THE SLAC DAMPED DETUNED STRUCTURE: CONCEPT AND DESIGN

Norman M. Kroll,
University of California, San Diego, La Jolla, CA 92093
Stanford Linear Accelerator Center, M/S 26, P.O Box 4349, Stanford, CA 94309

Abstract

The SLAC Damped Detuned Structure (DDS) is an accelerator structure designed to suppress the long range transverse wakefields which limit the performance of high current multibunch accelerators. We discuss the conceptual considerations which have led to its development and discuss the steps involved in arriving at a design.

1. INTRODUCTION

The performance of long pulse train, high pulse current accelerators is limited by long range dipole wakefields. These wakefields distort particle orbits, thereby causing transverse emittance growth and eventually Beam Break Up. The SLAC Damped Detuned Accelerator Structure, the DDS, is being developed in order to mitigate this problem as it occurs for the design parameters of the linacs for the Next Linear Collider, parameters which include an X-band operating frequency with 120 nanocoulomb pulse trains of the order of fifty meters in length, but the concept is applicable to any long pulse train high pulse current accelerator.

2. DESCRIPTION OF DDS 1

The accelerator structures of the presently planned DDS series are composed of a sequence of 204 cells coupled by beam irises and terminated at each end with a matched coupler cell. The structure is driven at 11.424 GHz through the upstream coupler, the downstream coupler is used to provide a matched termination. The cells are uniformly spaced at one third the 11.424 GHz free space wavelength (8.747 mm) and must be dimensioned so as to maintain a uniform cell to cell phase advance of 120 degrees in the accelerating (monopole) mode. This requirement constitutes a constraint which must be respected when individual cell dimensions are varied so as to detune the dipole modes and the manifolds added so as to damp them.

The aim of Gaussian detuning [1] is to replace the narrow band of synchronous modes of each dipole band excited by an offset velocity of light bunch in a uniform structure with a broad band of discrete modes which by virtue of their amplitude and frequency distribution is Gaussian in a smoothed sense. If the frequency distribution were in fact a smooth Gaussian, then the wake function would exhibit a Gaussian decrease with time. The Gaussian is however truncated because the number of participating modes is finite, which imposes a finite frequency width on the Gaussian. Furthermore, since it is composed of a set of discrete modes, the mode amplitude density function is a sum of δ functions in frequency rather than a smooth function. On account of the truncation, the decrease is, on average, less than Gaussian after a time of the order of $\delta f/\left(4\pi\sigma_f^2\right)$, where δf is the frequency width and σ_f the Gaussian width parameter. On account of the discreteness the destructive interference which caused the decrease becomes partially constructive at times of the order of the reciprocal mode separation, leading to a reappearance of the wake. These effects are exhibited in the detuned structure wake shown in Fig. 1.

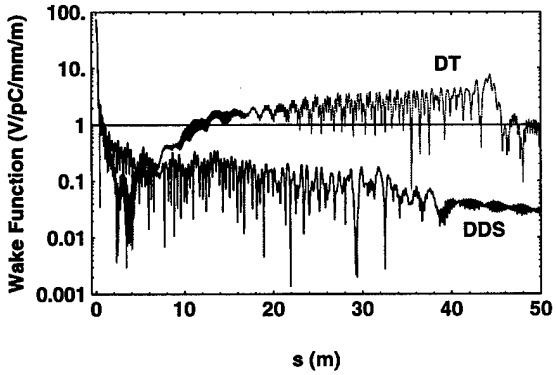


Fig 1: Wake function for DT and matched DDS 1

A careful balance between the Gaussian width σ_f and the frequency spread δf is required to optimize the wake for the first few trailing bunches; the detuned structure of Fig. 1 has δf equal to four times σ_f. With reference to trailing distance, the wake naturally separates into a short range (to be distinguished from the intra bunch wake) and a long range part.

In order to prevent the reappearance of the wake at larger time delays, damping is added to the detuned structure to form the DDS. The damping is provided by four waveguide-like structures equally spaced in azimuth around the accelerator structure and running its full length. In DDS 1, the first realization of the DDS concept, each waveguide is delineated by a rounded rectangular aperture in the disc containing the beam aperture which connects smoothly to a slot extension from the cylindrical wall of the cell. Because of their appearance and because they also serve as pumping manifolds, these structures are typically referred to as manifolds. Also because they are intended to drain dipole

0-7803-4376-X/98/$10.00 © 1998 IEEE

mode energy from the cells and carry it to loads at both ends of the manifolds, their function is manifold-like with respect to dipole mode energy as well.

In addition to the detuning related variation of cell dimensions, the manifold dimensions also vary along the structure to optimize cell to manifold coupling. Cross sections in the cell center and through the aperture disc as well as a perspective drawing are illustrated in [2], along with a cell in perspective (or cup) with the upper beam iris absent. The structure is fabricated by stacking such cups. The terminating loads involve a mitered 90 degree H-plane bend, a 90 degree circular H-plane bend, a taper to standard waveguide, a window, and an external load. Two cells plus the coupler at each end of the structure are not connected to the manifolds to avoid conflict with the load assembly. The end section of the structure plus its load assembly is illustrated in Fig. 2.

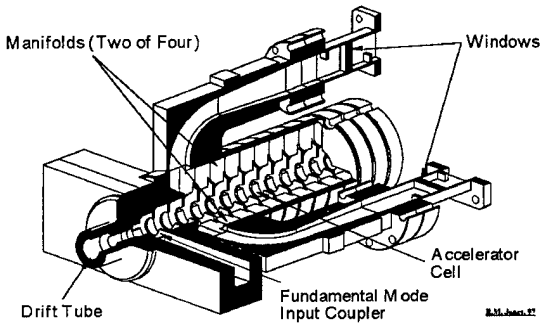


Fig 2: Cross-sectional view of DDS 1

3. QUALITATIVE DESCRIPTION OF DDS DAMPING AND MANIFOLD RADIATION

We begin by examining the properties of a strictly periodic structure formed by stacking a set of identical cells of typical cross section, say cell 106. Figure 3 shows a plot of the frequency of the lowest three modes as a function of phase advance per cell. The dots are points obtained by MAFIA simulation (see comparison to experiment in [3]), and the curves are obtained from an equivalent circuit theory [4,5]. The dashed curves correspond to equivalent circuit theory results obtained by setting the coupling of the cells to the manifold to zero. The large dashes correspond to the lowest two dipole modes of the manifold decoupled structure, the small dashes (fine-line in inset) to the manifold itself. The manifold has the character of a periodically shunted waveguide; only the lowest pass band is shown. One sees from Fig. 3 that the coupling has a significant effect only where the uncoupled curves approach one another, and that typical avoided crossing behavior is exhibited where the uncoupled curves cross (the "crossing point frequency" f_x). Examination of the electromagnetic field patterns shows a clear separation of modes into cell modes and manifold modes except at avoided crossing regions, where they mix. The synchronous mode (at the synchronous frequency f_s where the light line and lower dipole curve cross) is virtually confined to the cell, therefore negligibly damped, and has a strong TM character, which is responsible for its strong coupling to a velocity of light beam.

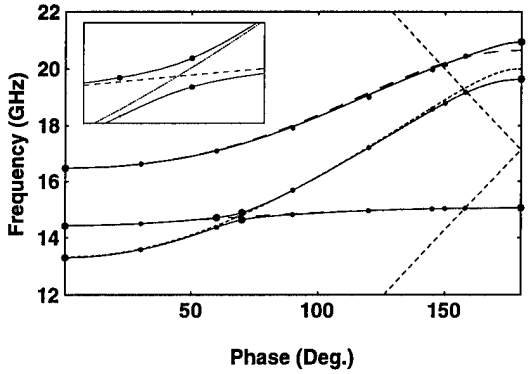


Figure 3: Brillouin Diagram for Cell 106 (Avoided Crossing shown inset)

Much of the behavior of a DDS can be understood by examining the aggregate of the individual cell properties described in the preceding paragraph. Figure 4 is a plot of the zero and π phase advance frequencies, f_x, and f_s all plotted as a function of cell number. The frequency range shown is restricted to the region relevant to the lower dipole mode. We do not discuss the upper dipole band because its contribution to the wake is negligible.

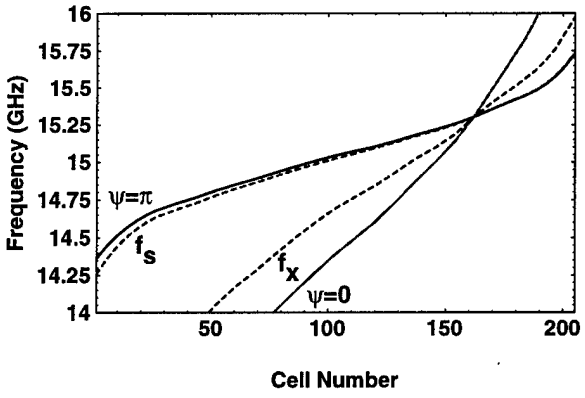


Figure 4: Mode limits, excitation point and damping point as a function of cell number

The curves are based on the uncoupled lower dipole curves (like that shown for cell 106 in Fig. 3) for an assortment of cells. The structure may be thought of as a propagating structure with slowly varying properties. There is a band of frequencies which appear on both phase advance curves. A mode within that band may be thought of as a wave which propagates back and forth between the turning points represented by these phase limits. Such modes are localized within the structure,

being confined to the corresponding range of cells. At frequencies below this band modes are confined to a region between the upstream end of the structure and the cell on the zero phase advance line. Similarly modes at frequencies above this band lie between the cell on the zero phase advance line and the downstream end of the structure. The two phase advance curves cross because the cell to cell coupling changes from forward wave to backward wave for cells on the downstream side of the crossing region, and the modes with frequencies near this crossing are highly localized in the corresponding cells. An offset drive beam excites a mode at frequency f at cells whose f_s approximately coincides with f, and only the modes which have such cells contribute significantly to the wakefunction. Thus the frequency band of the wake function is limited to the band of synchronous frequencies. It is apparent from Fig. 4 that all such modes include cells with crossing frequency close to the mode frequency. Thus we have the following physical picture. A given mode is excited in the neighborhood of its synchronous cells. The excitation propagates back and forth between the zero and pi phase advance cells, passing the crossing point cells on each trip. The energy leaks into the manifold at the crossing point cells thus providing damping.

The confinement of most beam excited modes to the interior of the structure and the extreme localization of some are confirmed in equivalent circuit calculations and for azimuthally symmetric structures by full simulations [6] as well. The correlation of frequency with cell number is demonstrated in fig. 5, and the relation between frequency and cell number which it implies is shown in fig. 6. Because this frequency at a given cell is shifted from the synchronous frequency of that cell, we refer to them as the coupled and uncoupled frequencies respectively. The short horizontal lines in fig 6 represent the number of cells in the localized offsets required to reach the level of the localization peaks shown in fig 5 and, are indicative of the sharpness of the localization. For application of the manifold power spectrum to monitoring beam position and structure alignment see [7, 8]. The following picture emerges of the damping process. To be specific we consider a particular mode, mode 100 at 14.836 GHz. The mode is localized between cells 48 and 148. The drive bunch launches a forward wave around cell 55 which propagates downstream. When it passes cells near 122 it loses power to the manifold, exciting in it a downstream wave. The remaining power is partially reflected at the coupling point and partially reflected at the downstream end of the mode. Only the latter portion contributes to a manifold wave in the upstream direction. In the perturbation theory limit the power coupled out is small and the forward and backward excitations of the manifold are equal. When the coupling to the manifold is large, however, one expects the downstream excitation of the manifold to predominate. Figure 5 indeed shows that the downstream preference occurs for virtually all the important modes, even those for which the relative position of the excitation and damping points are reversed. This reversal occurs only downstream from the point where the curves cross in Fig. 4, where the cell group velocity is negative. The beam induces a wave with forward phase velocity in the cells, but the excitation moves backwards and passes the coupling cell before it is reflected. Its phase velocity is still forward, however, so that it excites a forward wave in the manifold. Thus the expected preference is still downstream. This preference is in fact seen to be very large, one of many results in conflict with a perturbation treatment.

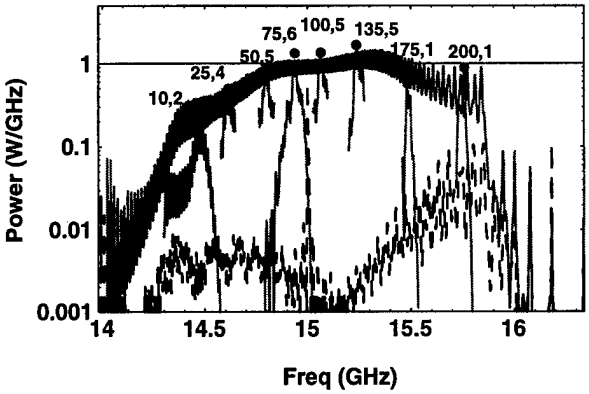


Fig 5: Power spectrum emitted from downstream DDS manifold with the power spectrum of localised offsets overlaid Upstream power spectrum shown dashed.

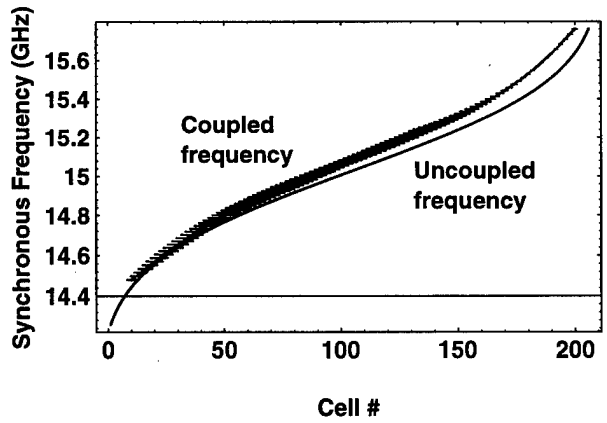


FIG 6: Coupled and uncoupled synchronous frequency vs cell number

4. THE SPECTRAL FUNCTION

The transverse momentum p_t imparted to a charge q_w witness bunch that has passed through an accelerator cavity of length L trailing a charge q_d drive bunch at distance s with offset r_d, both traveling at velocity c, due to the dipole mode excitation left in the cavity by the drive

bunch is expressed in terms of the wake function W(s) via the relation

$$c\,p_t = q_w\,q_d\,r_d\,L\,W(s) \tag{4.1}$$

W(s) is usefully expressed in terms of its spectral function S(f) [5] as follows:

$$W(s) = \theta(s)\int_0^\infty S(f)\sin(2\pi sf/c)\,df \tag{4.2}$$

with

$$S(f) = -4\,\mathrm{Im}\{Z(f - j\varepsilon)\} \tag{4.3}$$

where Z(f) is the wake impedance, ie the Fourier transform of W(s) evaluated just below the real axis. The usually displayed wake envelope function $\hat{W}(s)$ is given by:

$$\hat{W}(s) = \theta(s)\left|\int_0^\infty S(f)\exp(2\pi jsf/c)\,df\right| \tag{4.4}$$

The definitions given here are appropriate to the wake function of a well aligned structure with a uniformly offset drive beam. Wake functions, wake moments, and their associated spectral function representations for more general situations are discussed in [9].

The computation of S from the equivalent circuit representation of the structure is described in [5,10]. In the undamped case S consists of a sum of δ functions generally written in the form:

$$S(f) = 2\sum_p K_p\,\delta(f - f_p) \tag{4.5}$$

where K_p is the kick factor and f_p the frequency of the modes [1]. In order to visualize its form for the undamped case it is useful to replace it by its smoothed version $S_s(f)$, obtained by replacing $\delta(f-f_p)$ by $1/(f_{p+1} - f_p)$ over the interval $[f_p, f_{p+1}]$ and zero otherwise. The behavior of W(s) at the first trailing bunches is well represented by using S_s in place of S. For DDS the spectral function is continuous in the pass bands spanned by the manifolds. The modes are damped in this frequency range, and (by design) the undamped modes outside this range have negligible kick factors. The appearance of S is like a sum of lorentzians reflecting the underlying structure of damped modes and oscillating about the smoothed undamped S_s (Fig. 7). If the structure is well damped, the widths are of the order of the mode separation so that the oscillations are quite gentle and for ideal damping would be barely discernible.

Apropos of the smoothed undamped spectral function S_s, we note that a good representation of the short range wake can also be obtained from an independent cell model, the "uncoupled model", as discussed in [1,11], and equally well from the associated smoothed spectral function, $S_u(f)$, a function which can be obtained without reference to an equivalent circuit. The frequencies and kick factors in the modal sum are simply the synchronous frequencies of the individual cells and their kick factors.

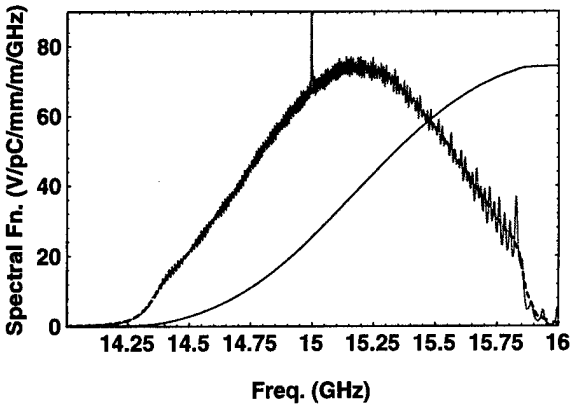


Fig 7: Matched DDS spectral function overlaying smoothed undamped spectral function

5. DESIGN

The design of a DDS begins with the selection of a basic cell-plus-manifold configuration and the dimensions to be varied to shape the detuning and damping profile. As discussed in [12,13] the primary considerations are Q (high) and shunt impedance (high) of the monopole mode, control of intra bunch transverse wakefields, and manufacturability. The manifolds are designed to be single mode in the lower dipole range and cutoff at the accelerator frequency. The pros and cons are discussed in [13], the main advantages, however, are compactness of design, simplification of fabrication, and of analysis. The basic design also includes the cell to manifold coupling configuration. The requirements are adequacy, adjustability, minimal degradation in cell Q, shunt impedance, and pumping efficiency. A combination of openings in the cell walls, slots which intrude into the beam iris, and variation of manifold dimensions have been found to meet the requirements.

The next step in design is selection of a structure profile, *ie* cell parameters as a function of cell number. The procedure for the DDS is very similar to that of the detuned structure described in [11]. It is a two step process. Beginning with a qualitative idea of required detuning width, one designs a set (~11) of fiducial cells. The primary requirement is the tuning of the accelerator mode. This being done one needs the dispersion diagram for the lowest three dipole modes, the determination of the

synchronous frequency f_s, and the kick factor for each of the fiducial cells. A smooth continuous mapping of cell dimensions and kick factors onto f_s is then constructed. The selection of $S_u(f)$ (typically a truncated Gaussian) provides as discussed in [13] an assignment of f_s to each cell and allows one to compute and evaluate the short range wake in the uncoupled model. To proceed further it is necessary to use the dispersion diagrams to establish the circuit parameters of the equivalent circuit theory and to construct smooth continuous mappings of them on to f_s as well. One can then construct S_s, the smoothed undamped but coupled spectral function and again compute and evaluate the short range wake. Should the two differ in detail in an unfavorable way, one could refine the f_s distribution. This procedure was used to design DDS 3&4 from the fiducial cell set of DDS 2 [12,14].

At this stage all the information is at hand to compute the complete damped wake function for matched loads from the full spectral function theory. Examples of the foregoing for matched manifold terminations are shown in Figs 1 and 7. Design of terminations is of course part of the design job. Up to now this has proved to be very important because even quite small reflections seriously degrade the wake. Reflection coefficients for DDS 1 are shown in [3], its highly oscillatory spectral function in Fig 8, and its experimentally measured wake envelope function in Fig. 9.

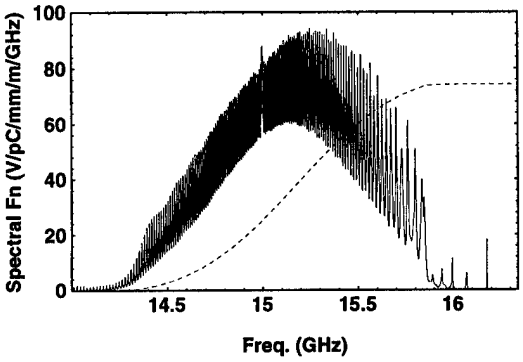


Fig 8: Spectral function for DDS 1 including VSWR of the manifold terminations.

Other examples, with reduced reflections and improved detuning configurations are shown in [12]. In order to optimize the damping profile it would be useful to have two or three sets of our ~11 fiducial cells. Then, using interpolation, one could choose manifold and cell-manifold coupling dimension profiles so as to lead to the smoothest spectral function. While at this stage matching seems to be more important than the damping profile, it is possible that the extreme sensitivity to reflection is related to the manifold being over coupled in the central region, and the contribution of the undercoupled cells at the doownstream end may not be as seriously affected by the reflections.

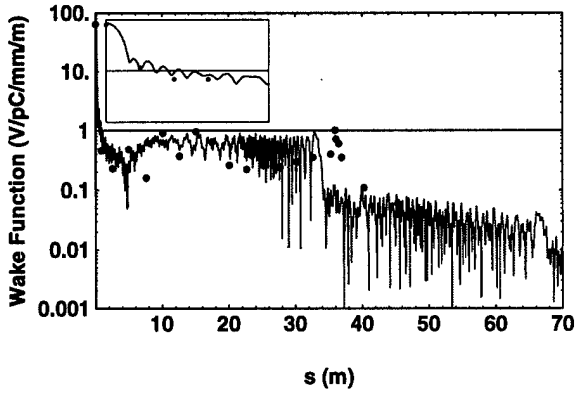


Fig 9: Calculated wake function for DDS 1. The dots indicate experimental data measured in the ASSET experiment. Shown inset is the short range wake function up to two metres.

6. ACKNOWLEDGMENTS

This work is supported by Department of Energy Grant DE-FG03-93ER40759 and Contract DE-AC03-76SF00515. We have benefited greatly from the contributions of the DDS team. Special thanks are due R. H. Miller and R.M. Jones for their contributions to the material presented in this paper and for their assistance in its preparation.

7. REFERENCES

[1] K.L..F. Bane et al, Particle Accels., **42**, p 123 (1993)
[2] K. Ko et al, Proc. PAC95, p 1058 (1995) SLAC-PUB 95-6884
[3] M. Seidel et al, Proc. Linac96, p 653 (1996) SLAC-PUB-7289
[4] RM. Jones et al, Proc EPAC 96, p 1292 (1996), SLAC-PUB-7187
[5] RM. Jones et al, Proc Linac96, p 650 (1996) SLAC-PUB-7287
[6] X-W Zhan & K. Ko, paper 8p94, PAC'97
[7] M. Seidel, Paper 5B3, PAC97
[8] R.M. Jones et al, Paper 3w16, PAC97
[9] RM. Jones et al, Paper 3W15 PAC'97
[10] NM Kroll et al, Recent Results and Plans for the Future on SLAC DDS, Proc 7'th Workshop on Advance Accelerator Concepts, SLAC-PUB-7387 (1996)
[11] K.A. Thompson et al, Particle Accels., **47**, p 65 (1994)
[12] R.M. Jones et al, Paper 3W14 PAC'97
[13] R.H.. Miller et al, Proc Linac96, p 644 (1996) SLAC-PUB-7288
[14] R.M. Jones et al, A Rapid Re-Design Method for the NLC DDS and Phase Stability of the Accelerating Mode: Implementation and Results, NLC-Note #24 April 1997

STUDIES OF BEAM INDUCED DIPOLE-MODE SIGNALS IN ACCELERATING STRUCTURES AT THE SLC

M. Seidel
Stanford Linear Accelerator Center, Stanford University, CA 94309

Abstract

Beam emittance dilution by self induced transverse fields (wakefields) in accelerating structures is a key problem in linear accelerators. To minimize the wakefield effects the beam trajectory must be precisely centered within the structures. An efficient way to achieve this is to detect beam induced microwave signals in the lowest dipole mode band and to steer the beam by minimizing these signals. This paper briefly covers some experiences from SLC S-band structures, but mainly concentrates on results of a wakefield instrumentation scheme applied to a NLC prototype X-band structure and tested with beam in the SLC linac. A beam based in-situ structure straightness measurement is shown as well as results of beam steering experiments based on phase and amplitude detection of two separated modes in the structure. After centering the beam the reduction of the wakefield was demonstrated independently by probing it with a test bunch that is deflected by the residual wakefield at a short distance behind the drive bunch.

1 INTRODUCTION AND BASIC PRINCIPLES

A high energy beam of charged particles that passes through an accelerating structure off-center excites asymmetric electromagnetic fields, to lowest order *dipole modes*, that act back on the beam. These transverse wakefields dominate the beam dynamics in linear accelerators and present the most severe limitation for the preservation of small emittances during the acceleration process. These concerns are important not only for linear colliders but also for industrial or medical applications of linear accelerators. Wakefield effects can be classified as short range effects, ie. fields that deflect the tail of a single bunch on a ps time scale, and long range effects that couple the orbits of consecutive bunches in a train. Both can lead to instabilities and emittance blow up of the beam. An historical example for the performance limiting effects of transverse wakefields is the observation of the *beam-breakup instability* in the SLAC Two-Mile Accelerator in 1966 [1].

Since then several powerful methods for suppressing long range wakefields have been developed. The basic approaches employ detuning and/or damping of the higher order modes (HOM's) that deflect the beam. A frequency spread of the modes is introduced by a specific variation of cell dimensions. It leads to a fast decay of the wakefield in time due to destructive interference of the modes. Damping can be achieved by several methods. In the case of the SLAC *damped detuned structure* [2][3] small slits in the cells couple the HOM's to manifolds that run along the structure and guide them to loads. Another way is to coat the cell irises with a lossy material as in the SBLC design [4]. The so called *choke-mode cavity* [5] employs integrated choke filters on each cell that reflect the fundamental mode but permit a strong damping of the higher modes.

However, the described methods cannot reduce the amplitude of the short range wakefield that is mainly determined by the iris radii of the structure cells and is therefore more or less fixed by the choice of accelerating mode frequency. As a result the wakefield scales roughly as the third power of the frequency [6]. In order to reach high gradients several new collider designs employ high frequency structures that result in enhanced wakefields. The only way to keep short-range wakefields small is to align the beam with micron precision to the electrical center of the structure, thereby preventing the excitation of asymmetric fields. An effective approach is to detect beam induced dipole mode signals directly in the structure and minimize them by moving beam or structure. The technique of using the accelerator structure itself as a beam position monitor (BPM) is being considered in several of the presently proposed linear collider designs. The advantage of this scheme over separate BPM's is that the structure measures the beam position in the only relevant reference frame, namely with respect to the electrical center of the structure. This eliminates the need for conventional structure to BPM alignment on a μm scale.

2 EXPERIENCES WITH THE TEN-FOOT S-BAND STRUCTURE IN THE SLC

The SLC linac consists of roughly 900 ten-foot structures which are operated at 2.856 GHz (S-Band). Typically the vertical emittance blowup in the linac amounts to 100% to 200% and is caused by transverse wakefields. One tries to compensate the wakefield effects by BNS damping and by empirical optimization of long orbit bumps. Otherwise one relies on beam steering using BPM information. There is some evidence from long range wakefield measurements that misalignments between structures and BPM's can occasionally reach mm size levels [7]. The observed emittance growth suggests rms beam-to-structure misalignments of $\approx$ 300 μm. Therefore a more precise method of determining the beam orbit with respect to the electrical center of the structure would improve the performance of the machine considerably. In the SLC runs of 1995/96 several dedicated experiments were carried out to investigate beam induced dipole mode signals in the SLC structures and to evaluate their usefulness for beam steering purposes. For these experiments the signals are detected in the standard SLC waveguide network that distributes the

0-7803-4376-X/98/$10.00 © 1998 IEEE

RF power from the klystron to the input couplers of four structures. The signals were analyzed with crystal detectors that integrate over the whole spectrum, with a spectrum analyzer, and with a down-mixing scheme that allows for amplitude and phase detection in connection with a strip-line BPM signal to provide a beam phase reference. Details are presented in [8]. The most important results and identified problems are summarized here briefly:

- Beam position dependent modes are detected in roughly the expected frequency range 4.1 GHz to 4.4 GHz, however, the detailed mode spectrum is not understood well. A strong signal whose origin is not known dominates the spectrum around 4.210 GHz.
- Signals generated by either horizontal or vertical offsets are not easily distinguished, complicating their interpretation. Horizontally polarized modes will couple to the TE10 mode in the input waveguide. Vertically polarized modes could either couple to the TE20 mode or, after a slight rotation, to TE10 as well. Experimental results indicate that for the same beam offset, horizontally excited signals are 5 to 10 times stronger than vertical ones.
- The input and output couplers introduce intrinsic asymmetries in the horizontal plane that possibly shift the detected center position for certain modes systematically.
- Using both phase and amplitude detection of individual modes a position measurement resolution of 12 μm rms was demonstrated by correlating the signal with BPM data [8]. Fifteen BPM's were used to determine the beam orbit at the structure position for this measurement in the horizontal plane. It remains to be demonstrated that the position of minimum dipole mode excitation indeed coincides with minimum wakefield deflection.

In summary the application of dipole modes for beam steering is difficult in the SLC because the structure has no dedicated ports for HOM's, and, in addition we measure a superposition of signals from four structures. To overcome this problem one has to perform multidimensional scans in both planes, offset and angle to find a global minimum of the signal amplitude. For more detailed studies it is planned to install a special setup in sector 2 that allows to access signals from individual structures.

3 ACCELERATOR STRUCTURE SETUP EXPERIMENT (ASSET)

In August 1996 a prototype NLC structure was installed in the SLC beamline at the low energy end of the linac. The main goals of this experiment were to measure the long-range wakefield suppression in a damped detuned structure (DDS) and to test a *wakefield instrumentation scheme*, based on the above described principles of dipole mode detection. The ASSET facility [9] [10] permits to send two bunches, "drive" and "witness" through the structure at a precisely controlled time separation. The drive bunch consists of positrons, the witness bunch of electrons and their trajectories are separated by a chicane downstream of the structure under test. The drive bunch was dumped immediately whereas the witness travelled down the SLC linac. The wakefield seen by the witness bunch was inferred from the change in its downstream orbit. Basic beam parameters are given in Table 1. The setup is sketched in Fig. 1. The prototype DDS used in the experiment consists of 206 cells and operates in $2\pi/3$ mode at 11.424 GHz (X-Band). The lowest dipole mode band is roughly Gaussianly detuned with a mean of 15.1 GHz and a width of 2.9 %. The damping is provided by coupling the cells to four manifolds that run along the structure. With these features the wakefield amplitude falls below 1 V/pC/mm/m within 1.4 ns and does not recohere above that level afterwards.

	E [GeV]	Q_b [nC]	σ_z [mm]	$\gamma\varepsilon_x/\gamma\varepsilon_y$ [mm mrad]
drive	1.2	3.2...4.8	0.55	30/3
witness	1.2	−2.6	0.55	30/3

Table 1: Beam parameters for the ASSET experiment.

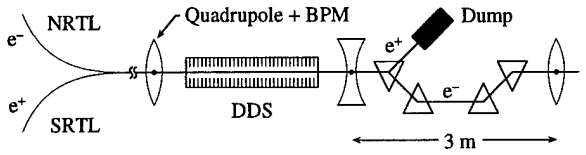


Figure 1: Layout of the ASSET facility.

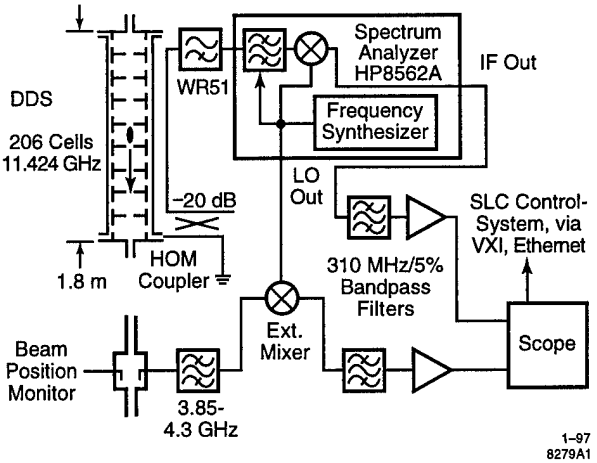


Figure 2: Electronic setup for the detection and processing of the DDS manifold signals.

Besides providing damping the manifolds permit to access beam induced dipole mode signals that origin throughout the structure. The signals from one manifold are processed in the circuit depicted in Fig. 2. With this setup it is possible to measure either the RF power excited by the beam as a function of frequency, or to select a 15 MHz wide slice of the spectrum and determine phase and amplitude of the signal at this particular frequency. In the latter case a broad band BPM signal is used as phase reference in

a second mixer arm. The witness deflection measurement capability of the ASSET setup provides the unique opportunity to center the beam based on dipole signals and to confirm the precision of the alignment independently with the wakefield measurement.

3.1 Beam Based Structure Straightness Measurement

The detuning of the structure results in a longitudinal localization of the beam-structure interaction for certain dipole mode frequencies [11]. Qualitatively this can be understood from Fig. 3 that shows a Brillouin diagram of the phase advance per cell as a function of frequency for five different longitudinal locations in the structure. When the phase advance reaches that of a free space wave it interacts coherently with the beam that moves at nearly the speed of light. The corresponding frequencies can be read from the diagram by determining the crossover of the curve with the *speed-of-light-line*.

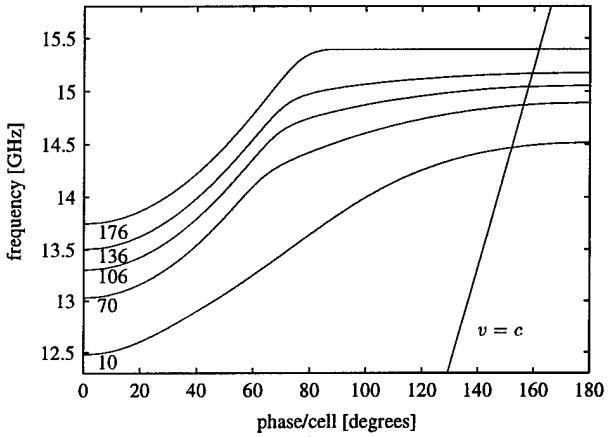


Figure 3: Brillouin diagram for the lowest dipole mode band, for five representative cells in the structure (cell numbers given).

This localization allows one to extract the cell to cell straightness of the structure from the beam induced manifold signals. For this purpose the beam was moved stepwise transversely across the structure and a complete spectrum of the manifold signal was acquired at each step. Then the two dimensional array of dipole mode power P as a function of frequency ν and beam position y was fit slicewise to parabolas:

$$P(\nu_n, y_k) = A_n^2(y_k - y_n^{\min})^2 + B_n^2, \qquad (1)$$

where y_k is the beam position in the k'th step, and A_n, B_n and $y_n^{\min}$ are the parabolic fit parameters for frequency slice ν_n. A measurement is shown in Fig. 4.

Several methods to transform the minimum power positions into cell offsets have been investigated. One possibility is to describe the structure by a *two-band coupled circuit model* and to express the field energy deposited by a passing beam in terms of an eigenfunction expansion of TM-like modes. After minimizing this expression with respect to the beam position one obtains a system of coupled

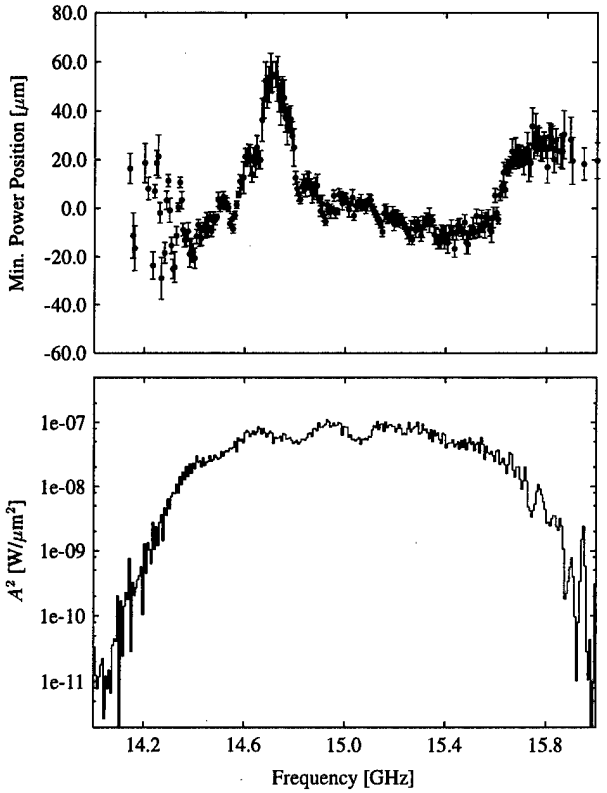


Figure 4: Minimum power positions $y^{\min}$ (upper plot) and fit parameter A^2 from Eq. (1) (lower plot) as a function of frequency for a beam position scan in the vertical plane. Note the zero position in the upper plot is arbitrarily defined.

linear equations that can be solved for the cell positions [12]. A different scheme that takes the manifold damping into account uses a *spectral function method* [11] to predict the beam induced power directly at the manifold ports for any frequency. Again one obtains a set of linear equations after minimizing the power with respect to the beam positions. Simulations indicate that also a simple one-to-one mapping of frequencies to cell positions gives a satisfactory result. A computation of the cell positions using the eigenfunction expansion is shown in Fig. 5 together with a mechanical measurement of the structure. Though the beam based measurement reproduces the basic features in the alignment curve, there are larger differences at the ends. These deviations are probably caused by thermal expansion of the material due to the raised temperature levels in the SLC tunnel. The large vertical displacement after cell 45 is due to slippage during bonding of the structure cells.

A practical application of this beam based straightness measurement is to find large internal misalignments in structures without time consuming surveying. Furthermore the knowledge of the cell to cell alignment permits to compute an optimum trajectory in the structure for minimal emittance growth. Though the excitation of wakefields in a structure with misalignments cannot be avoided in general, it is possible to minimize single bunch effects. We note that

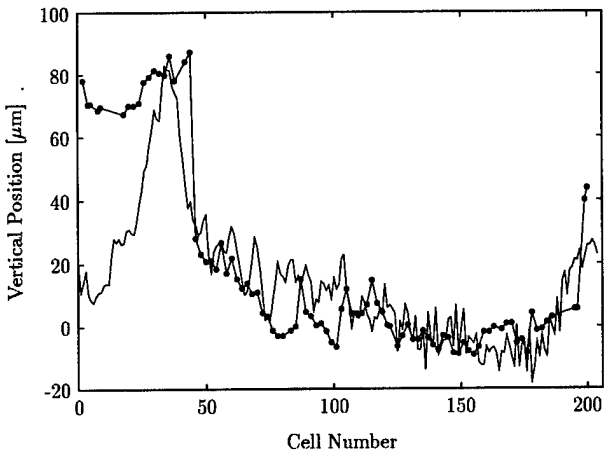


Figure 5: Cell to cell alignment, inferred from the minimum power position measurement (solid line), compared to a mechanical straightness measurement (dots).

the short range kick in cell n for times of the order of the bunch length $t \approx \sigma_z/c \ll \lambda/c$ can be parametrized as [6]:

$$\Delta\theta_n(t) \propto \frac{y_0 + \theta_0 s_n - y_n^{\text{cell}}}{a_n^{3.5}}\, t, \qquad (2)$$

were y_0, θ_0 are beam offset and angle with respect to the structure center and s_n, a_n are the longitudinal position and iris radius of cell n. The emittance growth of the bunch is minimized when the slopes of integrated kick and projected beam displacement at the structure center vanish:

$$\sum_n \Delta\dot{\theta}_n = 0, \quad \sum_n \Delta\dot{\theta}_n s_n = 0. \qquad (3)$$

For known cell offsets the equations (3) can be solved for y_0, θ_0 and determine thereby the optimum trajectory:

$$\theta_0 = \frac{c_1 m_0 - c_0 m_1}{m_0 m_2 - m_1^2}, \qquad y_0 = \frac{c_0 m_2 - c_1 m_1}{m_0 m_2 - m_1^2}$$
$$m_\nu = \sum_n \frac{s_n^\nu}{a_n^{3.5}}, \qquad c_\nu = \sum_n \frac{y_n^{\text{cell}} s_n^\nu}{a_n^{3.5}} \qquad (4)$$

In a large scale linac, however, performing this procedure for each structure will be too time consuming. With straight structures it is sufficient to center the beam at two longitudinal locations as described in the next section.

3.2 *Two Mode Beam Steering and Residual Beam Offset Measurement*

As noted above the ASSET setup provides one the opportunity to center the drive beam in the structure by minimizing dipole mode microwave signals, and to confirm the alignment afterwards by adding the witness beam and measuring its deflection. The kick the witness bunch receives is given by

$$\Delta\theta_y(t) = \frac{eQ_d L_s W_\perp(t)}{E_w} \Delta y_d, \qquad (5)$$

were $L_s = 1.8$ m is the length of the structure, E_w is the energy of the witness bunch, $W_\perp$ the transverse wakefield, Q_d, Δy_d drive bunch charge and offset. Thus the transverse wakefield as a function of time can be inferred by measuring the kick per unit drive bunch offset while varying the distance between the two bunches (Fig. 6). Once the wakefield amplitude is known one can also infer an unknown beam offset from the measured kick. For small beam offsets the transverse wakefield kick will scale down whereas the longitudinal wakefield at 11.4 GHz (beam-loading) stays strong. This can introduce a systematic error for the measurement of the transverse kick due to dispersive trajectory variations. In order to suppress this effect for precise offset measurements the relative timing of the two bunches was varied in three steps at which the 11.424 GHz beam-loading was zero, but the transverse wakefield varied nearly maximally (Fig. 6). Amplitude and phase detection of the dipole mode signal was used for centering the beam (Fig. 7). In order to align the beam both in position and angle, two modes, located near the input and output ends of the structure, were minimized simultaneously by switching the spectrum analyzer back and fourth between two frequencies. This procedure has been performed several times using different frequencies. After each attempt at centering the drive beam, the witness beam was introduced and its deflection was measured ten times at the three bunch distances. The amplitude of the kick oscillation was determined by fitting a sine-function to the three values and then converted into an equivalent drive beam offset.

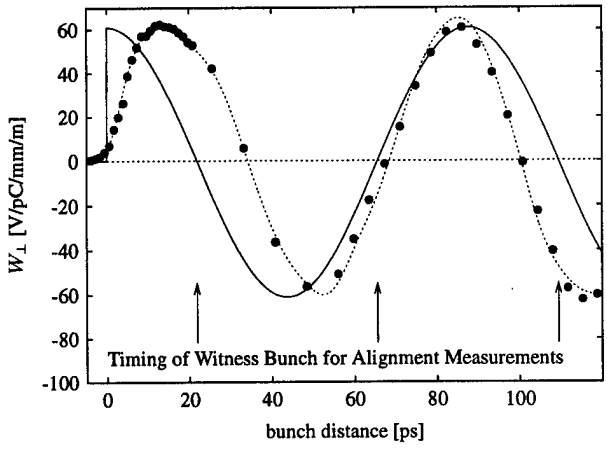


Figure 6: Transverse wakefield inferred from the deflection of the witness bunch for large drive beam offsets as a function of time (dots), a scaled prediction (dotted line) and the expected variation of the fundamental mode component (solid line, arb. units). For alignment measurements the wakefield curve was sampled at the indicated three points.

However, when analyzing the data it became clear that the relative ratios of the three measured wakefield amplitudes did not scale as the expected sine-like curve in Fig. 6. In order to fit the points one has to allow either the frequency of the oscillation to deviate from 15.1 GHz or its

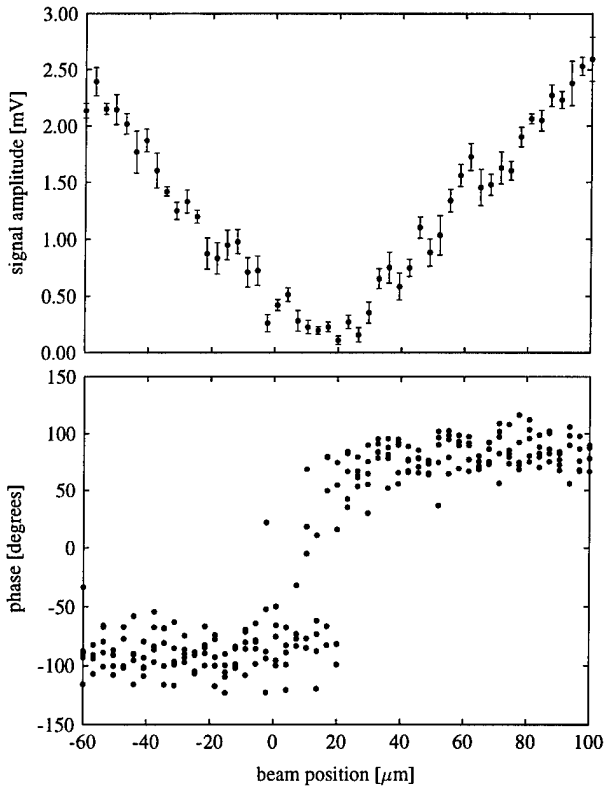


Figure 7: Amplitude and phase of the dipole mode signal at a frequency of 14.9675 GHz as a function of the vertical beam position. For each beam position 5 pulses have been measured. The vertical beam jitter amounts to 15 μm rms.

phase with respect to the bunch crossing to deviate from 0°. Fig. 8 shows the measurement results when we allow the frequency to vary. The pattern of the data could be related to the relatively large internal misalignments in the structure. If the beam is centered on average it will excite modes with opposite signs in different regions of the structure that beat against each other. As pointed out above it is now impossible to avoid the excitation of wakefields for any trajectory. We define the optimum beam position as the point where the slope of the wakefield for $t \rightarrow 0$ vanishes. In our measurements, however, we sample the beating oscillation at only three points and interpret it as a pure harmonic oscillation for which we determine amplitude and frequency. Apparently we observe the inferred frequency going down for small amplitudes, whereas at some point it jumps over to values above 15.1 GHz. The solid line in Fig. 8 is an analytical prediction which is based on the mechanical alignment measurement. This curve exhibits the same qualitative behavior as the measurement but not the observed magnitude. The dashed curve, which fits the data better, assumes in addition a sine-like transverse force at the fundamental mode frequency 11.424 GHz with an amplitude corresponding to 10 μm beam offset. Such a component could be generated by specific cell misalignments although its magnitude has not yet been estimated.

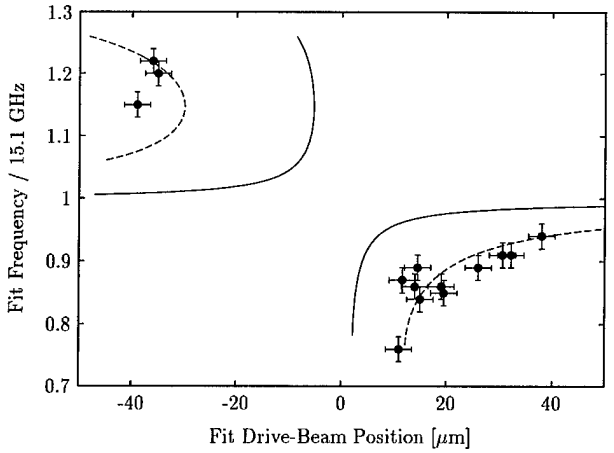


Figure 8: Inferred frequencies and equivalent beam offsets for several trials of centering the drive beam.

4 SUMMARY

Dipole mode based beam steering is a promising technique to control transverse wakefields in accelerating structures. It will be essential to push performance limitations in future low emittance or high current linear accelerators. The comparison of experiences from the SLC and the modern DDS structure shows that dedicated HOM couplers are needed to distinguish both transverse polarizations of the modes. The DDS manifolds permit to access all modes along the structure which makes it possible to perform an in-situ beam based straightness measurement. Using phase and amplitude detection an alignment precision of better than 40 μm has been achieved and verified by measuring the wakefield deflection of a second test bunch.

The author is indebted to C. Adolphsen, R. Assmann, K. Bane, P. Emma, R. Jones, N. Kroll, R. Miller, C. Nantista, T.Slaton, J. Wang, D. Whittum for contributions to the presented results. This work was supported by the Department of Energy, contract DE-AC03-76SF00515.

5 REFERENCES

[1] G. Loew, R. Helm, H. Hoag, R. Koontz, R. Miller, Conf. on High Energy Part. Accel., Yerevan (1969)

[2] R.H.Miller *et al.* Linac 96, Geneva (1996)

[3] N. Kroll, these proceedings

[4] M.Dohlus *et al.* DESY **96-169** (1996)

[5] T. Shintake, Jpn. J. Appl. Phys. **31**, 1567 (1992)

[6] R. Palmer, Ann. Rev. Nucl. Part. Sci. **40**, 529 (1990)

[7] R. Assmann *et al.* these proceedings

[8] M. Seidel, C. Adolphson, R. Assmann, D.H. Whittum, these proceedings

[9] C. Adolphsen *et al.* Phys. Rev. Lett. **74**, 2475 (1994)

[10] C. Adolphsen *et al.*, subm. to Phys. Rev. Lett. (1997)

[11] R.M. Jones *et al.*, these proceedings

[12] M. Seidel *et al.* subm. to Phys. Rev. Lett. (1997)

RESULTS FROM THE SLAC NLC TEST ACCELERATOR[1]

R. D. Ruth, C. Adolphsen, S. Allison, R. Atkinson, W. Baumgartner, P. Bong, V. Brown, M. Browne, G. Caryotakis, R. Cassel, G. Cisneros, S. L. Clark, T. Constant, C. Corvin, T. Dean, J. Eichner, R. Fowkes, R. Fuller, S. Gold, J. Grippe, S. Hanna, H. Hoag, P. Holik, S. Holmes, R. Humphrey, L. Johnson, R. Jones, E. Jongewaard, K Ko, R. Koontz, N. Kroll, T.Lavine, G. A. Loew, R. Loewen, R. H. Miller, J. Minister, V. Nesterov, C. Nantista, J. M. Paterson, C. Pearson, R. Phillips, M. Pietryka, R. Pope, T. Porter, J. Rifkin, W. Roster, M. Seidel, H. Smith, S. Smith, J. Spencer, N. Spencer, D. Sprehn, S. Tantawi, P. Tenenbaum, A. Tillghman, A. Vlieks, V. Vylet, J. W. Wang, P. B. Wilson, Z. Wilson, E. Wright, D. Yeremian, J. Zelinski, C. Ziomek
Stanford Linear Accelerator Center, Stanford, CA 94309

Abstract

The design for the Next Linear Collider (NLC) at SLAC is based on two 11.4 GHz linacs operating at an unloaded acceleration gradient of 50 MV/m increasing to 85 MV/m as the energy is increased from 1/2 TeV to 1 TeV in the center of mass[1]. During the past several years there has been tremendous progress on the development of 11.4 GHz (X-band) RF systems. These developments include klystrons which operate at the required power and pulse length, pulse compression systems that achieve a factor of four power multiplication and structures that are specially designed to reduce long-range wakefields. Together with these developments, we have constructed a 1/2 GeV test accelerator, the NLC Test Accelerator (NLCTA)[2]. The NLCTA will serve as a test bed as the design of the NLC is refined. In addition to testing the RF system, the NLCTA is designed to address many questions related to the dynamics of the beam during acceleration, in particular, multibunch beam-loading compensation and transverse beam break-up. In this paper we describe the NLCTA and present results from initial experiments.

1 INTRODUCTION

The Next Linear Collider Test Accelerator (NLCTA) is a 42-meter-long beam line consisting consecutively, of an injector, a chicane, a linac, and a spectrometer.

The injector is a 150-KeV gridded thermionic-cathode gun, an X-band prebuncher, a capture section, and a preacceleration section. Downstream from the injector we have a magnetic chicane for longitudinal phase-space manipulation, energy measurement and collimation. After the collimation, the average current injected into the linac is comparable to the NLC specification, 1.0 ncoul/1.4 ns.

The NLCTA linac consists of up to six 1.8-meter-long X-band accelerator sections which are designed to suppress the long-range transverse wakefield. These sections are powered by three 50-MW klystrons whose peak power is quadrupled by SLED-II rf pulse compressors. This yields an unloaded acceleration gradient of 50 MV/m so that the maximum energy gain of the beam in the linac is 540 MeV. The NLCTA RF system parameters are listed in Table 1.

Downstream from the linac we have a magnetic spectrometer that can analyze the bunch train after acceleration. A vertical kicker magnet in the spectrometer provides a method for separating the bunches vertically so that the energy and energy spread can be measured along the bunch train. We can also measure the emittance in the spectrometer and in the chicane.

Table 1. NLCTA RF System Parameters

Parameter	Design	Upgrade
Linac Energy	540 MeV	920 MeV
Active Length	10.8 m	10.8m
Acc. Gradient	50 MeV	85 MeV
Inj. Energy	90 MeV	90 MeV
RF Freq.	11.4 GHz	11.4 GHz
No. of Klystrons	4	7
Klystron Power	50 MW	75 MW
Klystron Pulse	1.5 μsec	1.5 μsec
RF Compression	4.0	4.0
Structure Length	1.8 m	1.8 m

In the next few sections we present an overview of the NLCTA, and we conclude the paper with a discussion of results from initial experiments.

2 CONVENTIONAL SYSTEMS

All the conventional systems for the NLCTA are complete. All of the non-RF components in the beam line are installed; this includes magnets, beam position monitors, vacuum system and all shielding and cabling. All of the power supplies are installed and tested and are operated routinely with the NLCTA control system which is an extension of the SLC control system. The thermionic electron gun and all injector solenoids are installed and tested. Presently, the beam line is under vacuum with the two injector structures installed and two of the six linac accelerator structures installed.

[1] Work supported by Department of Energy contract DE-AC03-76SF00515.

0-7803-4376-X/98/$10.00 © 1998 IEEE

3 THE RF SYSTEM

A schematic layout of the NLCTA RF system is shown in Fig. 1. The beam is initially bunched with two pre-buncher cavities at the fundamental frequency of 11.424 GHz. It is then accelerated in two 0.9 m-long RF structures with an unloaded energy gain of 90 MeV. The first of these two injector structures has several low-beta cells to capture the beam optimally. The injector accelerators and prebunchers are powered by a single 50 MW klystron compressed by a factor of 4 by a SLED-II pulse compression system. After the chicane, the linac consists of six 1.8 m-long structures (two presently installed). Each of the first two pairs is powered by a single 50 MW klystron. The final pair of structures and final klystron will use the SLED-II compression system in common with the middle pair of the linac.

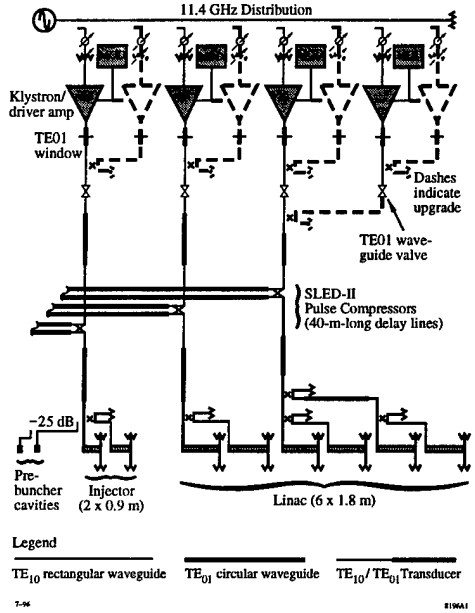


Figure 1. A schematic of the NLCTA rf system

4 KLYSTRONS

The NLCTA (and NLC) specifications call for a 50 MW Klystron operating with a 1.5 μsec pulse length (1.2 μsec for the NLC). Thus far the klystron development effort at SLAC has produced five klystrons that meet or exceed the NLCTA specification [3]. In Fig. 2 you see the output power of the fourth in the series, XL-4. It is a very robust klystron with a very stable output power. As you can see from Fig. 2, XL-4 can produce a 75 MW pulse 1.2 μsec long. Both XL-2 and XL-3 also produce more than the required 50 MW and all of the three klystrons have the required bandwidth to work with the SLED-II compression system. The first XL-4 klystron has been installed on the NLCTA injector modulator and is being used to power the injector of the NLCTA. The second XL-4 klystron has been installed in the first RF station of the NLCTA linac and is presently being used to power the first two accelerator structures of the linac.

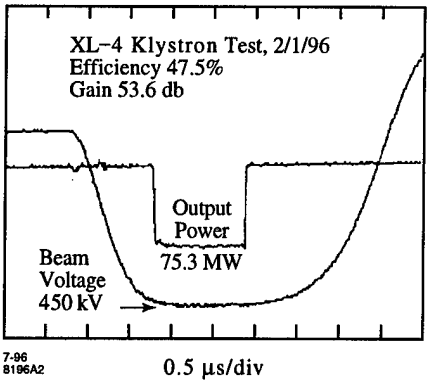


Figure 2. High-Power test of XL-4.

Several more klystrons of the XL-4 type will be produced for the NLCTA. However, the development effort for NLC klystrons has been turned towards the development of a periodic permanent magnet (PPM) focused klystron[4]. This eliminates the focusing solenoid from the klystron which reduces both the capital and operating cost significantly. The initial tests of the first PPM klystron have yielded up to 60 MW with about 60% efficiency. This klystron power exceeds the 50 MW required for the 0.5 TeV NLC.

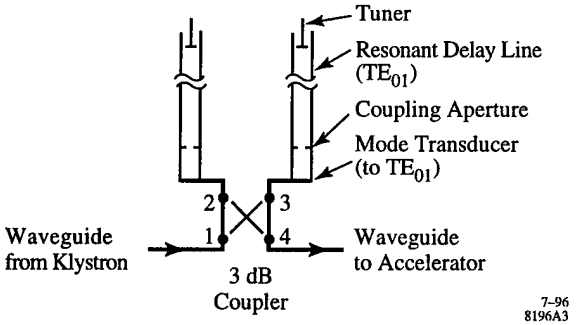


Figure 3. A schematic of the SLED-II rf compression.

5 RF PULSE COMPRESSION

A schematic diagram of the SLED-II compression system is shown in Fig. 3. The klystron power flows through a 3-dB hybrid where it is split to resonantly charge two delay lines. After several round trip times the klystron phase is flipped by 180 degrees, after which the power from the klystron adds to the power emitted from the delay lines to create a compressed pulse of RF power.

In Fig. 4 you see the results of low power and high power tests of the injector SLED-II. The cold tests show the expected pulse compression of four, and the high-power tests follow the cold tests quite closely.

All three SLED-II systems have been installed in the NLCTA, and the injector compression system and the first linac compresion system have been conditioned up to about 180 MW output. The tests of the these two SLED-II systems have shown excellent performance with an overall efficiency that exceeded our expectations.

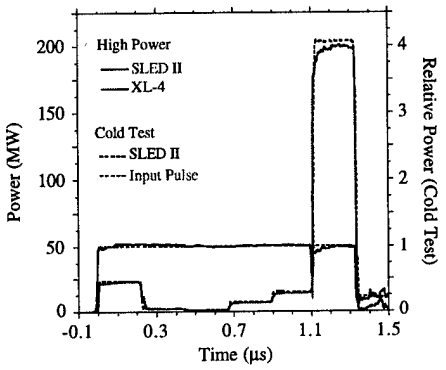


Figure 4. Test of Injector SLED-II system.

6 RF STRUCTURES

The NLC requires accelerator structures that operate reliably with an unloaded gradient of 50 MV/m for the 0.5 TeV collider and 85 MV/m for the 1.0 TeV upgrade. The NLCTA will serve as a model of this upgrade path in that we will begin at the lower acceleration gradient and eventually increase the gradient to the required 85 MV/m (see Table 1).

In addition to the gradient requirement, the NLC structures must be designed to substantially reduce the long-range transverse wakefields that can cause beam breakup. To achieve this reduction we have pursued two basic types of accelerator structures, the detuned structure and the damped-detuned structure. As you can see in Fig. 1, there are a total of eight structures in the NLCTA. The first two are one-half-length detuned structures. The second pair are full-length detuned structures. The third pair are damped-detuned structures; and finally, the last pair will be damped-detuned structures.

6.1 Detuned Structures

In a constant gradient traveling wave structure the irises are tapered to vary the group velocity in order to keep the gradient constant in spite of the loses in the structure. This tapering produces a variation of the frequency of the first dipole mode along the structure length that can be as much as 10%. The detuned structure takes advantage of this by changing the profile of the iris taper in order to create a smooth Gaussian-like distribution of higher-order modes. This leads to a Gaussian like initial decay of the wake field behind the bunch[7]. We have succesfully tested this concept using probe and witness beams in the Accelerator Structure Test Set-up (ASSET) facility in the SLC[8]. There are four detuned structures in the NLCTA.

6.2 High-Power Tests of Structures

During the past several years we have performed many high-power tests of different types of structures[9]. These tests indicate that surface fields up to 500 MV/m can be obtained in copper structures at 11.4 GHz. In power-limited tests, average acceleration gradients in short structures have reached 120 MV/m[10]. The first 1.8 m detuned structure has been high-power tested up to 67 MV/m[11]. Thus far, the injector sections in the NLCTA have been conditioned up to 55 MV/m average accelerating gradient while the first two linac structures have been conditioned up to 45 MV/m.

6.2 Damped-Detuned Structures

In order to further reduce the wakefield and the tolerances, it is necessary to provide some moderate damping for the higher-order dipole modes. To accomplish this we have developed a damped-detuned structure that uses four symmetrically placed manifolds to provide the damping [12]. A schematic of the cell for the structure is shown in Fig. 5. The structure cells are coupled to four waveguides that are formed when the cells are diffusion bonded together. The dipole mode is coupled out to the waveguide where is propagates to the end of the structure to a load. This technique damps the first dipole modes with Qs of about 1000. The signals from the manifold can be used as a beam position monitor to align the structure to the beam.

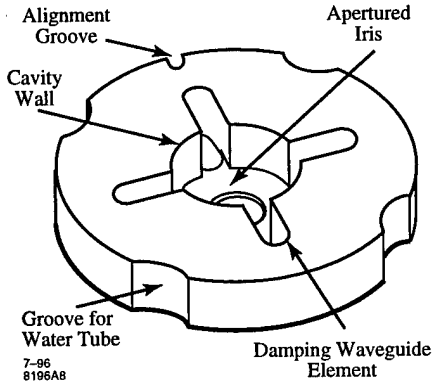


Figure 5. A cell of the Damped-Detuned structure.

The first two damped-detuned structures have been constructed in collaboration with KEK[13,14]. The first of these, DDS1, has been tested in the ASSET facility. The results of the experiment are shown in Fig. 6. The measured long-range transverse wakefield is reduced by more than two orders of magnitude realtive to the short-range wake and agrees well with the theoretical predictions[14,15]. Finally, the modes that are damped have now been shown to yield a sensitive position measurement along the length of the structure[16].

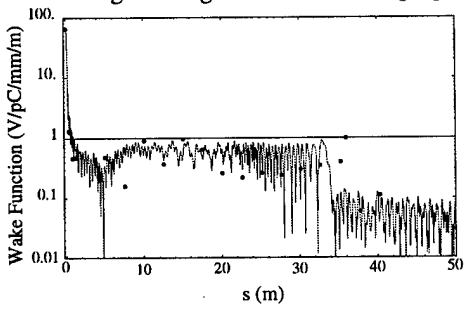


Figure 6. Tests of the Damped-Detuned structure. Points are data while the curve is a theoretical prediction.

7 BEAM LOADING EXPERIMENTS

Presently, we are accelerating beam up to 60 MV in the NLCTA injector and an additional 140 MV in the two installed structures of the NLCTA linac. This yeilds 200 MV in the spectrometer.

The first round of experiments in the NLCTA address the primary goal for beam dynamics studies: to acieve an rms energy spread of 10^{-3} with the NLC beam loading. To accomplish this it is nessesary to tailor the RF pulse for one filling time so that it matches the steady state beam loaded profile for the desired current. All subsequent bunches then serve to keep the beam in the steady state.

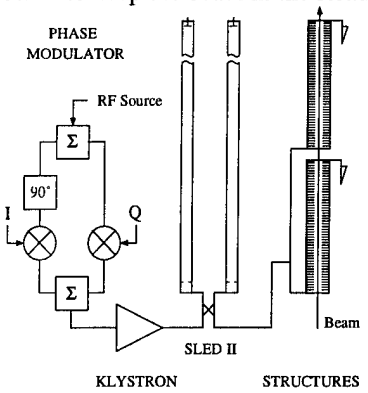


Figure 7. Layout of an RF station including the phase modulator which is controlled by the I & Q inputs.

This profile is closely matched by a simple ramp of the RF amplitude in the output from the SLED-II compression system. To achieve this ramp in the NLCTA we take advantage of the addition of several time bins of RF in the SLED system. By varying the phase in a programmed manner, the resultant RF output from SLED-II can be a linear ramp, or any variation thereof.

A conceptual diagram of the fast phase variation system is shown in Fig. 7. The phase modulator is controlled by I and Q modulators driven by an arbitrary function generator. The phase programming chosen for this experiment is shown in Fig. 8. You see that the resulting ramp of the RF amplitude in the compressed pulse is quite linear.

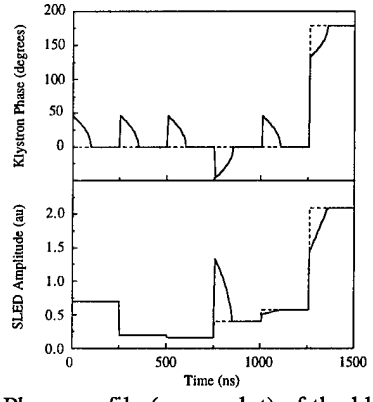


Figure 8. Phase profile (upper plot) of the klystron RF drive and resulting SLED output amplitude (lower plot) for 13% loading (solid line) and no loading (dashed).

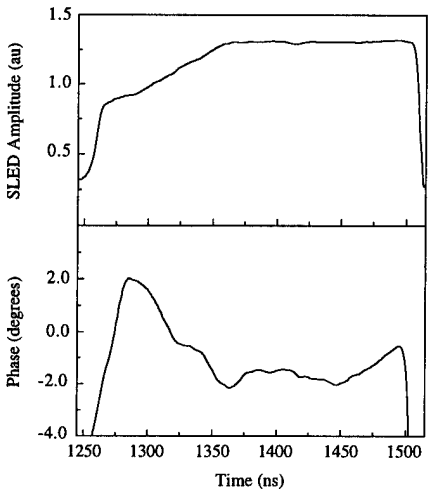


Figure 9. Measured RF amplitude (top plot) and phase (bottom plot) out of SLED when the klystron drive was phased to compensate 13% beam loading.

The measured RF output from the linac SLED-II system is shown in Fig. 9. The amplitude is quite linear while the phase changes over the ramp are about 4 degrees.

In order to measure the effect of this RF profile on the accelerated beam the NLCTA has been equipped with a kicker magnet upstream of the spectrometer magnet which provides a dipole field that ramps linearly in time during the 120 ns bunch train passage. In the plane of the spectrometer profile monitor, the vertical direction is mapped to position within the bunch train while the horizontal position is mapped to the beam energy.

In Fig. 10 you see two cases, one for uncompensated beam loading and one for compensated beam loading. In the uncompensated case, there is a large transient due to the beam loading after which in the upper part of the figure the beam reaches steady state. In the compensated case the transient has been completely compensated yielding a 200 MeV beam with 1/3 A current with a full spread of about 0.3% in relative energy. Therefore, with 1/2 the desired average current for the NLC, it seems to be quite straightforward to compensate all beam loading effects locally along the length of the linac.

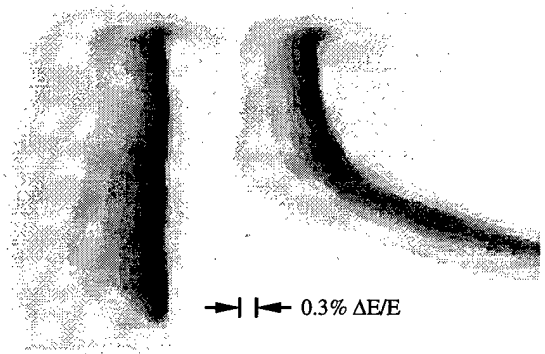


Figure 10. Profile monitor images of the bunch train at the end of the spectrometer.

The kicker magnet has spread the 120 ns train length vertically with head of the train at the bottom. The dispersion generated by the spectrometer bend magnet has spread the electrons horizontally in proportion to their energy with higher energy toward the right. The left image was recorded with 13% loading compensation in the linac and right image with no linac compensation.

9 ACKNOWLEDGMENTS

The installation of the accelerator structures, modulator, and klystron for the third RF station in the NLCTA is taking place during this conference. This marks the end of the NLCTA project, and the beginning of an active experimental program for the NLC. We would like to thank the SLAC Technical Division Directorate and Department Heads for their support during construction and commsioning of the NLCTA.

REFERENCES

[1] Zeroth-Order Design Report for the Next Linear Collider, SLAC Report 474, 1996.

[2] R. D. Ruth *et al.*, "The Next Linear Collider Test Accelerator", SLAC-PUB-6293, in Proc. 1993 Part. Accel. Conf., Washington, DC, 543-545 (1993).

[3] G. Caryotakis, "The X-Band Klystron Development Program at SLAC", SLAC-PUB-7146, in Proc. of the 3rd Int. Wksp. on Pulsed RF Sources for Linear Colliders, Hayama, Japan, 1996.

[4] D. Sprehn *et al.*, "PPM Focused X-Band Klystron Development at SLAC", SLAC-PUB-7231, in Proc. of the 3rd Int. Wksp. on Pulsed RF Sources for Linear Colliders, Hayama, Japan, 1996.

[5] S. G. Tantawi *et al.*, "Performance Measurements of SLAC's X-band High-Power Pulse Compression System (SLED-II)", SLAC-PUB-6775, submitted for publication.

[6] S. G. Tantawi, *et al.*, "The Next Linear Collider Test Accelerator's RF Pulse Compression and Transmission Systems", Proc. of EPAC96, Sitges, Spain and in SLAC-PUB-7247.

[7] K. L. F. Bane and R. L. Gluckstern, "The Transverse Wakefield of a Detuned X-Band Accelerating Structure", SLAC-PUB-5783, Part. Acc. **42**, 123 (1993).

[8] C. Adolphsen *et al.*, "Measurement of Wakefield Suppression in a Detuned X-Band Accelerator Structure", SLAC-PUB-6629, Phys. Rev. Lett. **74**: 1759-1762 (1995).

[9] J. W. Wang *et al.*, "High-Gradient Tests of SLAC Linear Collider Accelerator Structures", SLAC-PUB-6617, Proc. of the 1994 Int. Linac Conf., Tsukuba, Japan, 305-307 (1994).

[10] J. W. Wang *et al.*, "SLAC/CERN High-Gradient Tests of an X-band Accelerating Section", CERN-SL-95-27-RF, SLAC-PUB-6617, in Proc. of 16th IEEE Part. Acc. Conf., Dallas Texas, 1995.

[11] S. Takeda *et al.*, "High Gradient Experiments by the ATF", Proc. of the 1991 Part. Acc. Conf., San Francisco, CA, 2061-2063 (1991).

[12] R. M. Jones *et al.*, "Equivalent Circuit Analysis of the SLAC Damped Detuned Structure", Proc. of EPAC96, Sitges, Spain and in SLAC-PUB-7187..

[13] R. H. Miller *et al.*, "A Damped Detuned Structure for the Next Linear Collider", Proc. of LINAC96, Geneva, Switzerland.

[14] R. M. Jones *et al.*, "A Spectral Method Applied to the Calculation of the Wake Function for the NLCTA", Proc. of LINAC96, Geneva, Switzerland.

[15] C. Adolphsen *et al.*, submitted for publication.

[16] M. Seidel *et al.*, "Microwave Analysis of the Damped Detuned Accelerator Structures", Proc. of LINAC96, Geneva, Switzerland.

KEK / ATF DAMPING RING

Junji Urakawa
High Energy Accelerator Research Organization (KEK)
Oho, Tsukuba-shi, Ibaraki-ken, 305 Japan

Abstract

One of the major challenges in the next-generation electron-positron linear colliders is to produce and control multi-bunch beams with extremely small transverse emittance. The Accelerator Test Facility (ATF) at KEK is a test accelerator that has been built to study the feasibility of production, damping, control and diagnosis of such beams. The facility consists of a multi-bunch capable thermionic gun, bunchers, followed by a 1.54 GeV S-band injector, beam transport and a test damping ring. This paper reports the preliminary results from commissioning and accelerator studies of the test damping ring that has started in January, 1997.

1 INTRODUCTION

Next-generation electron-positron linear colliders, such as JLC [1], must collide multi-bunch trains of electrons and positrons with extremely small transverse and longitudinal emittances. This is an absolutely essential requirement for obtaining the desired collision luminosity. Typically, the beam to be accelerated in a linear collider is a bunch-train which consists of $\sim$ 100 bunches, whose invariant emittance should be $\gamma\epsilon_x \sim 3 \times 10^{-6}$ m and $\gamma\epsilon_y \sim 3 \times 10^{-8}$ m. The bunch length should be $\sim 100\,\mu$m, and a typical bunch intensity should be 1×10^{10} or less.

The ATF (Accelerator Test Facility) project [2] was launched in 1990 as a test facility for investigating the technical feasibility of the low-energy portion of such a linear-collider, which is responsible for producing multi-bunch beams with extremely low emittance. At present the ATF consists of:

- A multi-bunch capable thermionic gun that can produce a bunch train with up to 20 bunches spaced by 2.8 ns with an intensity $< 5 \times 10^{10}$/pulse,
- A 1.54 GeV S-band injector linac equipped with multi-bunch beam-loading compensation system based on the $\pm\Delta F$ scheme [3],
- An injection beam line,
- A 1.54 GeV damping ring, and
- An extraction beam line.

In addition, a variety of beam diagnostic instruments are implemented throughout the facility.

After completing the injector linac, a series of experiments were conducted on producing and diagnosing multi-bunch trains by using the gun, pre-injector and the 1.54 GeV linac, prior to building the damping ring (DR), [4,5]. Construction of the ATF DR was started in November of 1993. The hardware commissioning of the ATF DR began in December of 1996, and the beam commissioning in January of 1997. This paper reports the preliminary results from the commissioning work of the ATF DR and presents the plans for the near-future.

2 DESIGN OF THE DAMPING RING

As mentioned earlier, the beam to be produced at ATF is a multi-bunch beam with up to 20 bunches, whose spacing is 2.8 ns. The ATF DR has been designed to operate at 1.54 GeV and can store up to five such bunch trains. The ring has a race-track shape, consisting of two arc sections and two straight sections. The ring cirumference is 138.6 m.

The target equilibrium emittance is $\gamma\epsilon_x = 5 \times 10^{-6}$ m and $\gamma\epsilon_y = 3 \times 10^{-8}$ m. For this purpose, a special design of a strong-focusing FOBO lattice is implemented using combined-function bending magnets in the arc sections. The two arcs have 36 FOBO cells in total. The horizontal phase advance per cell can be varied from 100° to 160°, leading to the equilibrium horizontal emittance of $\gamma\epsilon_x = 6.6 \times 10^{-6} \sim 4.3 \times 10^{-6}$ m.

The two straight sections are dispersion-free, and they accommodate injection and extraction septa, RF cavities, and 20.4 m of damping wigglers which reduce the radiation damping time by a factor of 1/2. The expected damping time is 9.1 ms, when operated at 1.54 GeV.

The apertures in the injection and extraction septum magnets region are 7 mm vertically and 14 mm horizontally. In the early stage of the beam commissioning a significant beam loss often occurred in this region due to the jitter originating in the linac. The physical apertures in the wiggler section are 12 mm vertically and 24 mm horizontally. The aperture in the arc section is 24 mm diameter and the 5 m long straight section in the ring near the injection and the extraction lines has the physical aperture of 14 mm diameter.

In total 96 sets of beam-position monitors (BPMs) are installed in the DR for measuring the beam orbit in an arbitrary turn. For beam profile measurements, a synchrotron radiation monitor has been installed near the exit point of one of the arc sections. In addition, a "laser-wire" system is under development to measure the profile of several micron sized beam.

As a study machine, the ATF DR has several operation modes in terms of the bunch structure. For example, the number of particles per bunch, the bunches per train and

0-7803-4376-X/98/$10.00 © 1998 IEEE

the trains per ring, and the train spacing can be flexibly chosen under the restriction that the total stored current should not exceed 600 mA due to the limitation of radiation safety requirements and the cooling of the vacuum chamber.

The control system for ATF has been built based on the commercially-available V-system[6]. It allows to implement graphical user interface that lets physicists without the inner knowledge of the hardware system easily operate the device from an X-window terminal.

3 FIRST BEAM COMMISSIONING

The beam commissioning started on Jan. 21. The first beam revolution (two-turns) in the damping ring was observed on Jan. 27. A beam profile in the first turn was measured by synchrotron radiation monitor, and many turns of beam circulation was confirmed on Jan. 30 with a wall current monitor[7]. The effect of the radiation damping was observed on Feb. 15.

As of May 1997, the ATF DR is operating with a beam energy of 0.96 GeV at a repetition rate of 1.56 Hz in a single-bunch mode. The stored beam current is up to 6×10^9 electrons/bunch. The measured beam lifetime is about 50 s, consistent with the estimated Touchek lifetime assuming the ring momentum acceptance of ± 0.5 %.

In the following, we present some highlighting items from the initial commissioning experience of the ATF DR.

3.1 Alignment

The damping ring is built on support girders that are equipped with active position controls for applying the beam-based alignment technique. Full implementation of this system is expected to complete in September, 1997.

One active-girder in the arc section supports one combined bending magnet, two quadrupole and two sextupole magnets. The magnets on each girder have been installed with a relative position accuracy of $\sim 30\mu$m (rms). The girder-to-girder alignment accuracy resulting from the initial installation in January of 1997 is estimated to be $\pm 200\,\mu$m (peak-to-peak). The scatter plot of the x-y setting errors, and distribution of the measured longitudinal setting errors are shown in Figure 1[8].

The closed orbit distortion (COD) has been measured on the stored beam and the COD amplitude was found to be less than ± 1 mm, peak-to-peak. This is consistent with the currently-conceived quality of the transverse alignment.

Conducting beam-based alignment measurements on quadrupole magnets and combined-function bending magnets, and applying the results would significantly improve the alignment accuracy. This work is planned for the near-future run. During the initial run, the alignment of SF sextupole magnets has been quickly checked by observing the dependence of the tune on the strength of SF magnets. It is estimated that the position accuracy of 34 SFs is 120μm (r.m.s.), or better.

When the wiggler magnets are turned-on, the beam is captured by using the rf frequency of 714 MHz, which is

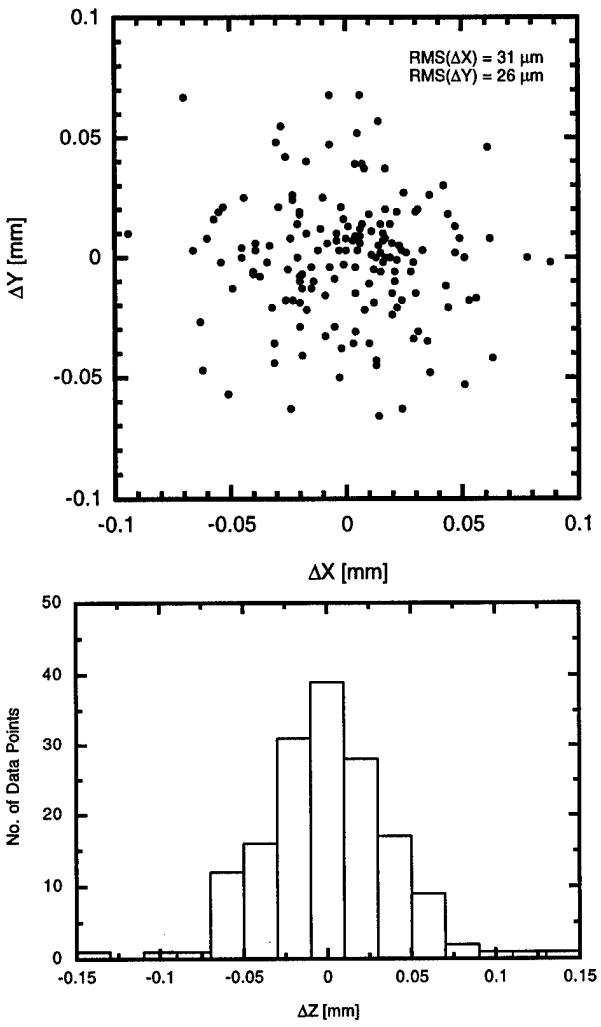


Figure 1: Scattered plot on transverse setting error and longitudinal setting error which were measured on magnets of the ATF 14 active girders using a 3D mobile tracking system

the design value. This indicates that the longitudinal alignment is fairly good, too. When the wiggler magnets are not excited for machine study purposes, the orbit length becomes shorter by 1.95 mm. To cope with this condition, the ring rf frequency needs to be increased by 10 kHz in such cases.

Estimation of COD in the injection septum region is shown in Figure 2. With the use of the energy feedback system (pulse by pulse) for the linac beam, and by applying an optical matching between beam transport and the damping ring, the beam loss in the injection septum region has become negligible.

3.2 BPM Response versus Steering Kick

The beam trajectory in the ATF DR is measured with 96 sets of BPMs. A simple and inexpensive circuit has been developed for signal processing. At present the beam or-

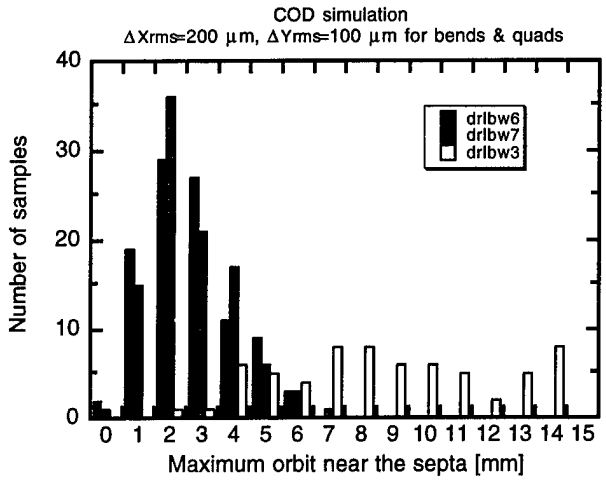


Figure 2: Simulation results of COD in septum region

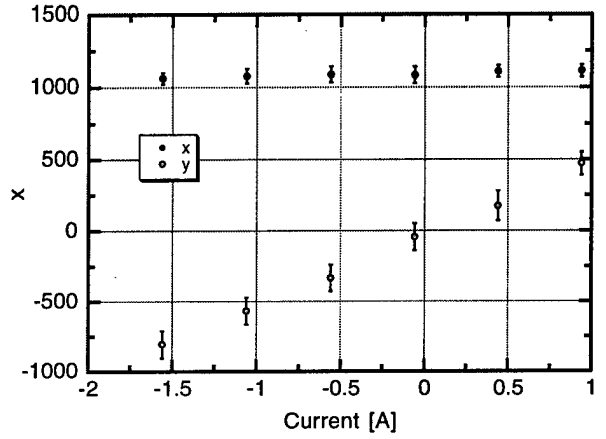


Figure 3: Response of BPM

bit can be measured every 20 ms[9]. The working of the BPM system has been checked by analyzing the response of the measured orbit with respect to perturbations applied by varying the excitation of steering dipole magnets. By comparing the current on the steering magnets and the response of the BPM data in their immediate neighborhood, the BPM resolution was found to be 90μm at 3×10^9 electrons/bunch. Figure 3 shows an example of the response of a BPM right next to the steering dipole magnet whose excitation is varied. There, the excitation current of one of the vertical steering magnet is varied while observing the variation of the beam orbit on a BPM near-by is measured.

3.3 *Field Errors of Quadrupole Magnets*

Field errors of quadrupole magnets in the ATF DR have been studied by creating π-bump orbit perturbations[10]. If no "leakage" orbit distortion is found to be originating from the bump, it indicates an absence of optical errors. If a "leak" orbit distortion is observed, its magnitude is related to the magnitude of focusing field errors in the region where the π-bump is created.

Quadrupole field errors are also estimated by measuring the orbit distortions, which are induced by varying the strength of steering magnets, and comparing them with model calculations[11].

In the initial phase of the study errors of a few % level were found on quadrupole magnets used in the ATF DR. All quadrupole magnets and combined-function bending magnets are equipped with individual trim-coils and small power supplies associated with them. Small quadrupole magnets are installed near the combined bending magnets. By using these trim coils, the overall quadrupole field errors can be reduced to a ~ 0.2 % level.

3.4 *Field Error on Combined and Wiggler Magnets*

For each type of magnets used in the ATF DR, magnetic field measurements were conducted on representative prototype models only. Not all magnets in the ATF DR had their field map data collected, due to the budget constraint and the desire to reduce the production period.

However, provisions are made to allow surveys of magnetic field qualities using the beam. All combined-function bending magnets and major quadrupole magnets have trim windings whose currents can be individually controlled.

It has been found that the combined bending magnets (36 units in total) can be grouped into three families according to their field strength for a given excitation current. A group of six bending magnets has the field strength weaker than the average by 0.86 %, while another group of 15 is stronger by 1.02 %.

In addition, an uncanceled error kick that amounts to 3 mrad was found on the wiggler magnet. To quickly reduce this error, the cabling of the wiggler magnets have been temporarily revised, so that these error kicks form a chicane orbit which roughly cancels the orbit distortion. As a more definitive solution, four horizontal steering magnets will be installed at both sides of the wiggler section during a long shutdown period this summer[12].

3.5 *Beam Size and Damping Time Measurements*

An SR (Synchrotron Radiation) monitor, which is installed near the end of the first arc[13], has been used to study the beam profile and beam damping within the ATF DR. An image spot size of $76\,\mu$m (horizontal) was measured after damping. This corresponds to an actual beam spot size of $45\,\mu$m, when corrections are applied for the diffraction effects and the depth of focus. This horizontal spot size is in rough agreement with the expected value for operation at $\sim$ 1 GeV. Considering the intra-beam scattering effects at 0.96 GeV, β- and η-functions at the light source point of the SR monitor, diffraction effects, the depth of focus, and other issues, very preliminary estimates of on the beam parameters in the first beam commissioning are quoted as:

- Horizontal emittance $\sim$ 2 nm,

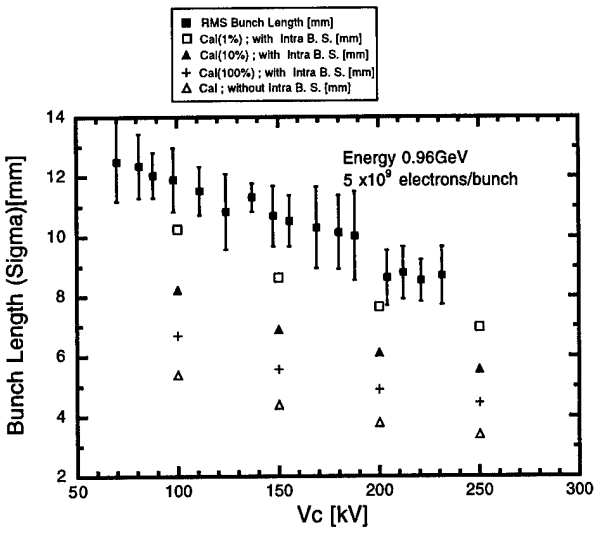


Figure 4: Bunch Length Measurements and Calculation with intra-beam Scattering

- Vertical emittance ~ 0.5 nm,
- Bunch length ~ 9 mm, and
- Energy spread $\sim 6 \times 10^{-4}$ at 0.96 GeV.

At present, the observed vertical size of the SR image is bigger than the expectation by factor 2. Detailed studies on possible set-up errors in the ATF DR as well as plausible systematic errors in the SR monitor optics system are being done. The vertical deformation of the first mirror was found. It enlarges the vertical image size. To measure the beam size directly, new beam instrumentation like the laser wire with a optical cavity in the ring and 5μm carbon wire scanner in the extraction line is necessary.

The damping times have beem measured in cases with the wiggler magnets turned on and off. The horizontal damping time has been measured to be about 40 ms with the wiggler off, and 30 ms with the wiggler on. They are in good agreement with expectations at ~ 1 GeV.

The SR monitor is also equipped with a streak camera which can be used to measure the bunch length. The result of a bunch length measurements is shown in Figure 4, together with the calculated values which takes into account intra-beam scattering effects. This is indicative of effects of potential-well distortion and an x-y coupling (emittance ratio) of several %. Also, synchrotron frequency was measured as function of the cavity voltage, by using a bunch phase monitor. The measurement was found to agree with theoretical values within 1%[14].

4 PROSPECTS

The ATF DR has been operated at the beam energy of 0.96 GeV, limited by the hardware condition of the injector linac until now. The beam energy will be gradually increased up to 1.54 GeV later this year.

For the next few months our focus will be on the development of the beam handling techniques to stably operate the entire ATF complex with a 1.0 GeV beam. The specific work item list includes: transient beam loading at high current beam injection, fast ion instability, beam loading effect due to train gap, nonlinear beam dynamics, intra-beam scattering, long beam tail due to beam-gas scattering, investigation of Touchek lifetime, and so on.

The next-stage beam commissioning will be started on May 20. Beam energy will be increased to 1.3 GeV. Then, a series of precise measurements on the image size, the bunch length, possible field errors and so on will be continued in a single-bunch operation until the summer shutdown. Hardware upgrades for the rf system and multi-bunch operation are scheduled for the next year (1998)[15,16]. Many experiments with the extracted beam from the damping ring are under consideration. Precise measurement of wake-field is also planned at the ATF extraction line next year[17].

5 ACKNOWLEDGMENTS

The author would like to thank Professors H. Sugawara, Y. Kimura, M. Kihara, K. Takata, Y. Yamazaki and S. Kurokawa, for their continuous encouragement and support, and to Profs. Seishi Takeda, S. Kamada and H.Mizuno for in-depth discussions. The collaborations with SLAC, DESY, CERN, BINP(Protvino), PAL, IHEP(Beijing), INP(Novosibirsk), SEFT and LBNL as well as the domestic universities helped make a great advance in the design and the operation of the damping ring. Specially, he would like to thank Professors B. Richter, G. Voss, E. Paterson, G. Loew, W. Namkung, S. H. Wang, D. Trines, In Soo Ko and R. Ruth, Drs P. Clout and E. Tanabe for their continuous encouragement.

The author also would like express his gratitude to all members of the ATF group. Specially, H. Hayano is working on the construction and operation as the key-person of the ATF group, N. Toge reporting on the summary of the beam status for the international collaboration, M. Akemoto working on the RF power supply, T. Naito working on the SR profile monitor, wall current monitor, CT monitors and the timing system, S. Sakanaka on the construction of the RF system, K. Oide on the optics design and operation, K. Kubo working as the leader of the operation group and on the RF low level control, N. Terunuma working on the control system and the vacuum hardware, T. Korhonen working on the active girder system for beam based alignment and the control system, F. Hinode worked on the BPM system, S. Kuroda working on the design of the optics and the operation, Y. Funahashi and N. Sato working on the support stages, M. Takano and S. Araki working on the alignment of the magnets, H. Hirayama and Y. Namito working on the radiation control system.

The students participating in the ATF project from universities; S. Kashiwagi, T. Okugi, M. Kagaya and T. Sakamoto also worked on the construction and operation

of the damping ring.

T. Higo, Shuji Matsumoto, Toshikazu Suzuki , E. Kim, C. Montag, T. Mimashi, T.Tauchi, Y. Kurihara, T. Omori, D. Parkhomtchouk, K. Ishii and F. Tamura contribute as the operation shift leader.

M. Kikuchi, T. Raubenheimer, M. Ross and M. G. Minty contributed to the design of the damping ring in an early stage. It is noted that many collaborators from over-seas joined the first beam commissioning: T. Donaldson and D. Williams worked on the operation of the injection kicker. N. Phinney, M. Ross, K. Jobe and D. McCormick built the beam loss monitor (PLIC) for the first beam tuning and implemented software tools using MATLAB for off-line data analyses. F. Zimmerman, P. Emma and M. Woodley worked on the beam diagnostics to survey errors in the model and the hardware set-up. W. Bialowons and S. Choroba contributed to the damping ring beam operation and hardware diagnosis. T. Lee and M. Kim checked the sensitivity of beam transfer matrices in the ring. E. Gianfelice , J. Choi and K. Kim measured β-function and W. Kriens built a signal processing circuit to measure the synchrotron frequency. S. Morita, K. Wachi, A. Miyamoto and T. Matsui of E-Cube Co. are working on the power supply system, the water cooling system and the alignments. T. Ishi and N. Koizumi of Kanto-Joho Co. are working on the V-system software. Their works are greatly appreciated. The success of ATF damping ring on first beam commissioning is a consequence of the efforts of all the above people. Finally the author acknowledges the useful comments and critical reading of the manuscript offered by N. Toge.

6 REFERENCES

[1] Ed. by N. Toge, "JLC Design Study", KEK Report 97-001, May, 1997.

[2] Ed. by F. Hinode et. al., "ATF Design and Study Report", KEK Internal 95-4, June, 1995.

[3] S. Kashiwagi et.al., "Preliminary Test of $\pm\Delta F$ Energy Compensation System", Proc. of the 18th International Linear Accelerator Conference (Geneva Switzerland), August 1996.

[4] H. Hayano, "ATF Linac Commissioning", Proc. of the 18th International Linear Accelerator Conference (Geneva Switzerland), August 1996.

[5] Seishi Takeda et. al., in these proceedings.

[6] Peter Clout, in these proceedings.

[7] S.Sakanaka et. al., in these proceedings.

[8] M. Takano, private communication.

[9] N. Terunuma, private communication and F. Hinode et. al. in these proceedings.

[10] Shuji Matsumoto and E. Kim, private communication.

[11] K. Kubo et. al. in these proceedings.

[12] E. Gianfelice, ATF Internal Report, ATF-97-14.

[13] T. Naito et. al., in these proceedings.

[14] W. Kriens, ATF Internal Report, ATF-97-15.

[15] M. Minty et. al., in these proceedings.

[16] S.Sakanaka et. al., in these proceedings.

[17] S. Kashiwagi et. al., in these proceedings.

SUPER-ASSET: A TECHNIQUE FOR MEASURING AND CORRECTING ACCELERATOR STRUCTURE MISALIGNMENTS AT THE SLC

F.-J. Decker, R. Assmann, M.G. Minty, P. Raimondi, G. Stupakov
Stanford Linear Accelerator Center †, Stanford University, Stanford, CA 94309 USA

Abstract

Transverse wakefield kicks from misaligned accelerating structures in the SLC linac contribute significantly to emittance growth. If these kicks could be measured directly, it would be possible to align and/or steer the beam to a kick-free trajectory. In the Accelerator Structure Test Facility at SLAC, ASSET [1], the kicks due to a drive bunch are measured with a witness bunch at varying bunch separations. In ASSET, the first bunch is discarded and only the second bunch is measured. Super-ASSET is an extension of this technique where both bunches are accelerated down the entire linac together and a "sum trajectory" of both bunches is measured with beam position monitors (BPMs). The trajectory of the second, kicked bunch can be calculated by subtracting the orbit of the first bunch, measured alone, from the sum trajectory. This paper discusses BPM response issues and the expected resolution of this technique together with alignment and steering strategies.

1 INTRODUCTION

In the SLAC Linear Collider (SLC), misalignments of the accelerating structures may cause transverse wakefield kicks which deflect the tail of the bunch and create emittance growth. In addition to several indirect techniques summarized in the next section, we will discuss here the most direct approach to measure locally the kick of the bunch head to the bunch tail. Two bunches are accelerated down the linac very close together in time, a few wavelengths λ) apart. For e^+ and e^-, possible choices are $\pm\lambda/2$, $\pm 3\lambda/2$, $\pm 5\lambda/2$, . . . so that they are both accelerated. This method probes the short-range wakefields. A perfect wakefield free orbit would produce no kicks for all bunch separations, but the real situation is more complicated. If the linac is not totally straight, the steering kicks of the magnets create dispersion which must be compensated.

2 DIFFERENT TECHNIQUES

Many other alignment techniques have been suggested to reduce emittance growth. After mechanical alignment, beam-based measurements are used to center the beam position monitors (BPMs), quadrupoles, and structures. Most of these techniques rely on assumptions which may not be valid. With the following table we try to give an overview.

Technique	Assumption (BPM, Quad, Acc.)	Achievement
1 Alignment (all)	mechanical,	mechanical
a) initial	electric center	resolution,
b) beam based	change is right	beyond that
2 Steering (B, Q)	B, A offset = 0	BPM reading
a) 1-to-1	Q to B offset = 0	bpm center
b) DF,TBDFS	B offset for $e^{+/-}$	quad center
c) SVD	ave. alignment	less corr. kick
d) ballistic	no elec/mag field	get B offset
e) quad scaling	no elec. kicks	get Q offset
3 Wakefield (A)	wake big effect	signal reading
a) dipole signal	A to signal = 0	S center
b) ΔI or $\Delta\sigma_z$[4]	clean distiction	calc. effect
c)hi order wake	no asym coupler	hi wake center
d) Super-Asset	BPM response	beam-S center
4 Bumps (global)	end result o.k.	smaller emit.
a) oscillations	error within oscil.	minimum
b) local 360°	meas. and corr.	and stable

Table 1: Alignment and emittance reduction techniques (DF [2]: dispersion free, TBDFS [3]: two beam DF steering, SVD: single value decomposition).

3 SUPER–ASSET

The basic idea of Super-ASSET is to measure the wakefield kick from one bunch closely following another. It is necessary to take the first bunch orbit x_1, and subtract it from the "sum orbit" x_Σ of both beams to get the kicked beam orbit x_2:

$$x_\Sigma = (q_1 x_1 + q_2 x_2 f(t)) / q_\Sigma \qquad (1)$$

with $q_\Sigma = q_1 + q_2 f(t)$ and $f(t)$ is the response function of the BPM: $f(t) = 0$ for a large time separation t of the two bunches, and $f(t) = 1$ for $t = 0$.

3.1 BPM Response

The BPM response function $f(t)$ was measured by combining positive ($1.5 \cdot 10^{10}$) and negative ($-1.06 \cdot 10^{10}$) signals in a test setup. Figure 1 shows the result compared with a theoretical response. Since the BPMs are self-triggered by the signal, the sum signal must exceed a certain threshold: $q_1 + q_2 \geq q_{trig}$ ($\approx 2 \cdot 10^9$ particles).

† Work supported by the Department of Energy contract DE-AC03-76SF00515.

0-7803-4376-X/98/$10.00 © 1998 IEEE

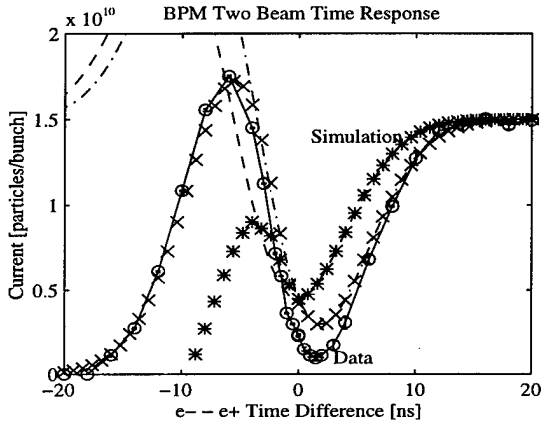


Figure 1: Measured (o) and calculated (*) BPM response. Due to the slow rise time of pulses used in the test setup, the minimum is shifted to +2 ns, which can be also modeled (x). The dashed and dash-dotted lines in the top left, would be the curves, if the BPM were triggered externally and not self-triggered by the beam. The dashed curve is 1.5E10 (1–0.7 $f(t)$).

When superimposing bunches of different sign charge, the BPM resolution can be significantly increased because the measured offsets are normalized to the total beam current, which is small. For example, $4{\cdot}10^{10} - 3{\cdot}10^{10} = 0.4{\cdot}10^{10} = q_\Sigma$, $x_2 = 0$, $x_\Sigma = q_1\, x_1 \,/\, q_\Sigma = 10\, x_1$. The BPM readout will saturate for big offsets, so only ±0.8 mm offsets can be measured rather than the full ±8 mm.

3.2 Wakefield Kicks

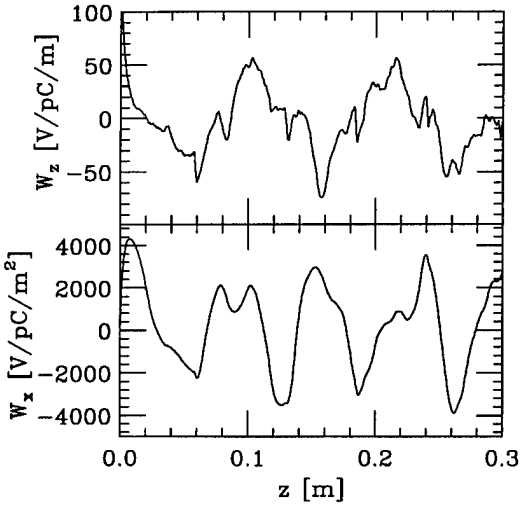


Figure 2: Wakefield of an SLC accelerator structure.

The maximum wakefield of an SLC accelerator structure is about $W_\perp$ = 5 V/pC/mm/m (Fig. 2). Therefore for $N = 5{\cdot}10^{10}$ particles (8 nC), an offset Δx = 1 mm, and a 12 m long structure (L), the transverse kick $\theta_\perp$ is 480 keV / E:

$$\theta_\perp = e\, N\, L\, \Delta x\, W_\perp / E. \qquad (2)$$

This kick will affect the beam differently at different points along the linac depending on the energy E and the betatron function β of the focusing lattice. Averaged over a bunch length of about 1.2 mm the wakefield is only $W_{\perp ave}$ = 1 V/pC/mm/m or 20% of the peak. Table 2 shows the effect of this wakefield at different locations in the linac. At the beginning of the linac (Li02) there is only a 3 m structure between quadrupoles. The region about 500 meters along the linac (Li05) is the most sensitive by a factor of 2.5–3, because the quadrupole spacing becomes large and the energy is still relatively low. Li30 is the end of the linac.

	Li02	Li05	Li30
E [GeV]	1.2	7	46
β_{max} [m]	10	40	50
σ_y' [μrad]	14	3	1
$\theta_\perp$ [μrad]	80 (/4)	14	2
σ_y [μm]	140	115	50
Δy [μm]	200	540	100
ratio=θ/σ'	1.4	4.7	2

Table 2: Effective kick of a 1 mm accelerator structure offset between quadrupoles compared with the angular divergence σ_y' for an emittance of $\gamma\varepsilon_y = 0.45{\cdot}10^{-5}$ m-rad.

3.3 Measurement Sensitivity and Systematic

As seen from the Tab. 2, a 1 mm offset of the beam in a structure would cause an average centroid displacment of 1.4 to 4.7 times σ_y, increasing the projected emittance. To measure these kicks, the difference orbit at two different bunch separations is used, e.g. $\lambda/2$ and $3\lambda/2$, or $3\lambda/2$ and $5\lambda/2$ (λ = 105 mm). The wakefield kick changes sign for different separations, enhancing the sensitivity of the measurement. Wakefield differences of 4 or 6 V/pC/mm/m produce effectively 5 times the offset Δy of table 2 or about 1 mm, 2.7 mm, 0.5 mm for the three locations. A typical measurement with e^+/e^- might be $2{\cdot}10^{10}$ positrons follow by $3{\cdot}10^{10}$ electrons with a difference orbit $x_{\Sigma,diff} = x_{\Sigma a} - x_{\Sigma b} = 3(x_{2a} - x_{2b})$ = 1.2, 3.2, 0.6 mm. The BPM reading is about 0.5 to 3 times the structure offset, indicating that with a BPM resolution of 10–20 μm, one measures the structure offset to about the same resolution. Averaging many readings can further increase the accuracy.

4 FIRST MEASUREMENT

Although the experiment with high current electron and positron bunches has not yet been performed, preliminary tests with two electron bunches were made during the 1997 SLAC fixed target run. A charge of $3.0{\cdot}10^{10}$ in two bunches (λ = 105 mm apart), or of $1.5{\cdot}10^{10}$ in one bunch was accelerated down the linac (Fig. 3).

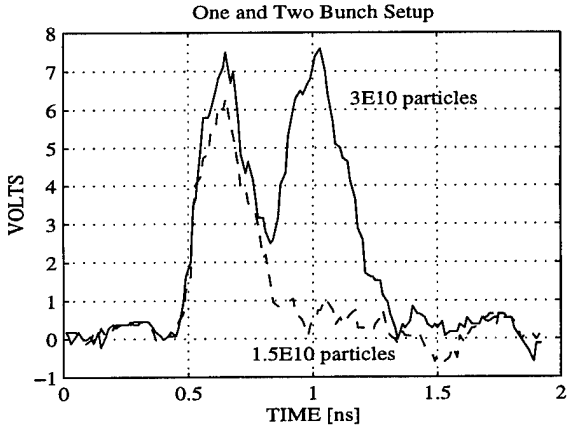


Figure 3: Gap monitor signal of one or two bunches.

The expected kick is much less for this configuration: 2.7 mm in sector 5 becomes 0.8 mm at these currents which is measured as 0.4 mm when the BPMs average two same sign bunches and is further reduced to 0.16 mm because the wakefields are 2 rather than 5 V/pC/mm/m at this separation. A closed bump of 2 mm peak (1.7 mm effective) should produce an oscillation of about 0.27 mm, in good agreement with the measurement (see Fig. 4).

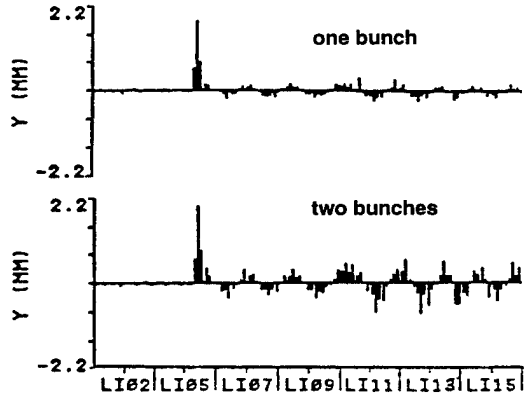


Figure 4: Wakefield kick of a 2 mm bump, top: for one bunch nearly closed, bottom: for two bunches a 250 μm oscillation starts.

5 COMPENSATION METHODS

Once the accelerator structure misalignments are known, there are two basic approaches. First, there is mechanical alignment which may be only practical for a few worst offenders. Second, one may attempt to find an optimal beam trajectory through these misalignments.

Simulations have shown that dispersive emittance growth which is normally 4 times smaller than the wakefield growth may increase dramatically if the beam is steered to the center of the structures to avoid any wakefield kicks. Clearly wakefield and dispersion effects have to be minimized at the same time. This can be done by canceling wakefield and dispersion growth separately over one betatron oscillation (8 correctors for e^+/e^-). One may also try to cancel the growth locally by trading the dispersive kick off against the linear part of the wakefield kick. The method to be used is still under study.

6 SUMMARY

With Super-ASSET, a beam based technique, we should be able to measure and locally correct the biggest source of emittance growth in the SLC linac – the transverse wakefield kicks of the accelerator structures. If successful, this method promises to be useful for future linear colliders, and might relax the tolerances for wakefield dominated designs.

7 ACKNOWLEDGMENTS

We would like to thank D. McCormick for the BPM test stand measurements, J. Turner for the injector setup used in the fixed target run tests, and K. Bane for wakefield computations.

REFERENCES

[1] C.E. Adolphsen et al., *Measurements of Wakefields generated in Accelerator Test Structures Using the SLC,* HEACC'92, Hamburg, Germany, 1992, p 870.

[2] T. Raubenheimer and R.D. Ruth, *A Dispersion-Free Trajectory Correction Technique for Linear Colliders,* NIM, A302, 1991, p. 191-208.

[3] R.W. Assmann et al., TBDFS to be published.

[4] T.O. Raubenheimer, K. Kubo, *A Technique of Measuring and Correcting Emittance Dilutions due to Accelerator Structure Misalignments,* SLAC-Pub-6523, NIM, A370, p 303-311; and SLAC-Pub-6608.

LIMITATIONS OF INTERACTION-POINT SPOT-SIZE TUNING AT THE SLC*

P. Emma, L.J. Hendrickson, P. Raimondi, F. Zimmermann
Stanford Linear Accelerator Center, Stanford University, CA 94309, USA

Abstract

At the Stanford Linear Collider (SLC), the interaction-point spot size is minimized by repeatedly correcting, for both beams, various low-order optical aberrations, such as dispersion, waist position or coupling. These corrections are performed about every 8 hours, by minimizing the IP spot size while exciting different orthogonal combinations of final-focus magnets. The spot size itself is determined by measuring the beam deflection angle as a function of the beam-beam separation. Additional information is derived from the energy loss due to beamstrahlung and from luminosity-related signals. In the 1996 SLC run, the typical corrections were so large as to imply a 20–40% average luminosity loss due to residual uncompensated or fluctuating tunable aberrations. In this paper, we explore the origin of these large tuning corrections and study possible mitigations for the next SLC run.

1 INTRODUCTION

During the last two runs of the Stanford Linear Collider, typical vertical interaction-point (IP) spot sizes at nominal bunch populations ($\sim 4 \times 10^{10}$ particles per bunch) were about 35% larger than expected from the linac emittances, energy spread and IP angular divergences. Recent evidence suggests that a large part of this discrepancy might be attributed to imperfect or inadequate IP spot-size tuning. In this paper, we present some of the evidence and outline possible solutions for the next run.

2 SPOT-SIZE CORRECTIONS

The spot size at the SLC interaction point (IP) is routinely optimized by correcting the most important low-order aberrations, such as waist shift, dispersion and skew coupling, for either beam. The aberrations are corrected by exciting orthogonal linear combinations of quadrupoles and/or skew quadrupoles (so-called 'knobs'), measuring the spot size for different, typically 5–7 knob values, and adjusting each knob to the best value.

Consider one aberration as an example. For different values of the knob correcting this aberration, the convoluted horizontal or vertical spot size of the two beams at the IP is inferred from beam-beam deflection scans [1], i.e., from the measured deflection angle as a function of beam-beam separation. The optimum correction is computed by fitting a parabola to the square of the spot size as a function of the knob value. A correction is applied by setting the knob to the minimum of this parabola. The same procedure is then repeated for another aberration.

A full set of beam-beam based corrections for a total of 10 aberrations (5 per beam: 3 vertical and 2 horizontal) requires about 1 hour of real time, during a large part of which the luminosity is then necessarily mistuned. In addition, often at least one tuning iteration is necessary, in order to achieve typical 'good' spot sizes. On average one correction is applied to each aberration about once per 8-hour shift. A qualititative illustration of the effect of tuning and the spot-size degradation between two tunings is shown in Fig. 1. In the figure, the degradation $\Delta\sigma/\sigma$ (which is added in quadrature to unity) is shown to grow linearly in time. In reality it may increase with the square root of time or, more likely, in some irregular fashion.

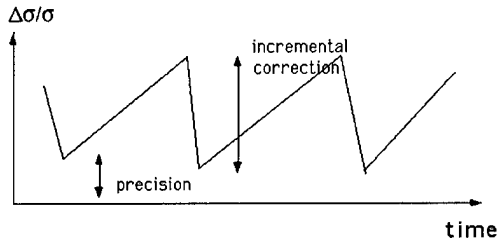


Figure 1: Schematic of tuning effect and spot-size increase between tunings.

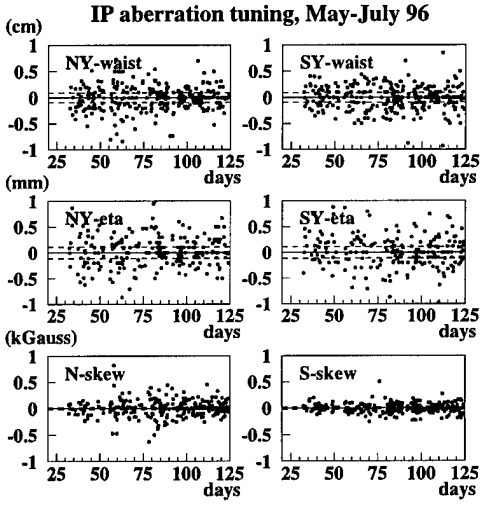


Figure 2: Incremental IP corrections of waist, dispersion and skew coupling during the 1996 SLC run. Shown dotted is the average resolution of an aberration scan as quoted by the SLC control system.

* Work supported by the U.S. Department of Energy under contract DE-AC03-76SF00515.

0-7803-4376-X/98/$10.00 © 1998 IEEE

Figure 2 depicts all incremental corrections to the vertical waist position, dispersion and skew coupling that were applied during the 1996 SLC run. The rms corrections appear to be larger than the typical measurement resolution, indicated by dotted lines.

If an IP aberration is not fully corrected, the spot size will be larger than the nominal value. For the three most critical aberrations, the increase of the vertical spot size $\Delta\sigma$ due to imperfect correction is given by

$$\Delta\sigma_y = \begin{cases} w_y\theta_y^* & \text{for a vertical waist shift } w_y \\ \eta_y\delta & \text{for vertical a dispersion } \eta_y \\ d\,\theta_x^* & \text{for a skew coupling coeff. } d \end{cases} \quad (1)$$

where the spot-size increase $\Delta\sigma_y$ is added in quadrature to the design rms spot size, which in the following is taken as $\sigma_{y0} = 500$ nm.

The relative luminosity degradation due to limited measurement precision ($\Delta\sigma_y/\sigma_{y0}$) for the kth aberration on a single beam is given by the formula $\Delta L/L_0|_{k,p} = 1 - 1/\sqrt{(\Delta\sigma_y/\sigma_{y0})^2_{k,p}/2+1}$, approximately equal to

$$\left.\frac{\Delta L}{L_0}\right|_{k,p} \approx \frac{1}{4}\left(\frac{\Delta\sigma_y}{\sigma_{y0}}\right)^2_{k,p}, \quad (2)$$

where L_0 designates the ideal luminosity without any aberration, the subindex p refers to the precision, and k counts the different aberrations.

To estimate the luminosity loss which is implied by the rms incremental corrections, one has to make assumptions about the evolution of an aberration between two consecutive corrections. Assuming a random walk ($\sim \sqrt{t}$) between tunings, and considering a tuning interval which results in an incremental correction $\Delta\sigma_y/\sigma_{y0}|_{k,i}$ of the kth aberration, the average luminosity loss is $\Delta L/L_0|_{k,i} = 1 - 1/\sqrt{(\Delta\sigma_y/\sigma_{y0})^2_{k,i}/2+1}$, or, again expanding the square root,

$$\left.\frac{\Delta L}{L}\right|_{k,i} \approx \frac{1}{8}\left[\left(\frac{\Delta\sigma_y}{\sigma_{y0}}\right)^2_{k,i} - \left(\frac{\Delta\sigma_y}{\sigma_{y0}}\right)^2_{k,p}\right] \quad (3)$$

where the subindex i indicates that this luminosity loss is inferred from the 'incremental' correction. To avoid double counting, we have subtracted a contribution from the measurement precision. The total luminosity loss due to both precision and incremental changes of all vertical tuning corrections is finally obtained from

$$\left.\frac{\Delta L}{L_0}\right|_{tot} \approx \frac{1}{8}\sum_k\left(\frac{\Delta\sigma_y}{\sigma_{y0}}\right)^2_{k,p} + \frac{1}{8}\sum_k\left(\frac{\Delta\sigma_y}{\sigma_{y0}}\right)^2_{k,i} \quad (4)$$

where in the SLC case, $k = 1, ..., 6$. Additional luminosity loss may arise from the horizontal tuning corrections.

Using the above formula, we can estimate the luminosity loss implied by the incremental corrections in Fig. 2 and by the quoted measurement precision. The results for the various aberrations are summarized in Table 1. A luminosity loss $\Delta L/L$ is equivalent to an increased vertical spot size of $\sigma_y/\sigma_{y0} \sim L_0/L \sim 1/(1-\Delta L/L_0)$, where $\sigma_{y0} \approx 500$ nm is the ideal single-beam spot size. A 38% luminosity reduction due to IP aberration tuning would thus correspond to a vertical spot size of 700 nm, which is remarkably close to the typically achieved good values!

corr. knob	precision	$\Delta L/L$	rms incr.	$\Delta L/L$
waist shift	0.09 cm	6.5%	0.23 cm	28.4%
dispersion	0.11 mm	2.6%	0.22 mm	9.4 %
skew	0.02 kG	0.2%	0.14 kG	10.0 %
total	38%			

Table 1: Quoted scan precision, rms knob increment and estimated luminosity loss from residual low-order vertical aberrations for the 1996 SLC run. The luminosity-loss numbers are relative to a 500-nm single-beam spot size.

3 INTERPRETATION

If the applied corrections reflect real aberration drifts, due to, for example, orbit changes in the final-focus sextupoles, or rf phase changes in the linac etc., one might expect to see correlations in the corrections for different aberrations. In Fig. 3 we plot incremental changes to one knob versus those of another knob (*i.e.*, for another aberration or the other beam) which were coincident within one hour. No correlation between any two knobs is evident, which suggests that the corrected aberration drifts are not real.

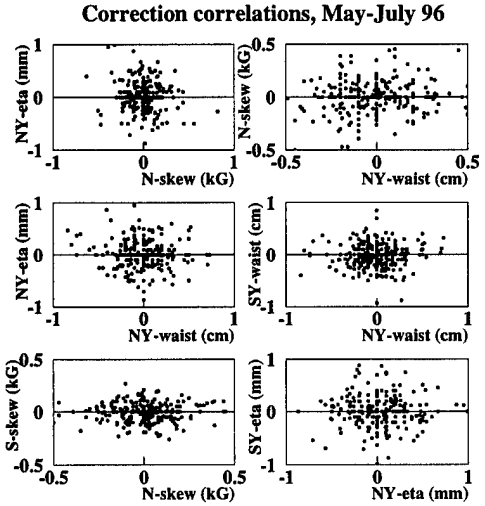


Figure 3: Zero correlation between IP corrections for different aberrations and for the two beams.

To better understand the above findings, we performed hundreds of tuning simulations for waist, dispersion and coupling correction. In all of these simulations the aberration to be tuned was perfectly corrected initially. Then, for each beam-beam based tuning scan we added a random

measurement error

$$\Delta\Sigma_y \approx 0.12\,\Sigma_{y0}\left[\frac{\Sigma_y}{\Sigma_{y0}}\right]^{1/2}, \qquad (5)$$

where $\Sigma_y \equiv \sqrt{\sigma_{y,e-}^2 + \sigma_{y,e+}^2}$ denotes the convoluted spot size of the two beams at the IP, and the subindex 0 refers to the beam size at the minimum of the fitted parabola. In rough agreement with measurements, the error was scaled as the square of the spot size for each step of the scan. The error increases on the wings of the parabola, because, during a tuning scan, when, *e.g.*, the waist is off center, both the IP orbit-jitter correction [2] and the beam-beam scan range are no longer optimal.

The rms correction calculated in this way was 0.19 cm for the waist position, 0.24 mm for the vertical dispersion, and 0.09 kG for the skew coupling. These values are very close to the actual incremental corrections listed in Table 1. This strongly suggests that the quoted scan precicision widely underestimates the actual error, at least by a factor 3–4, and that the IP corrections were completely dominated by the limited resolution of the beam-beam deflection scans!

4 MITIGATIONS

There are two possible approaches to alleviate this situation. First, one may improve the resolution of the beam-beam deflection scans. This could be achieved by a variety of means, such as using better beam-position monitors to correct for orbit variations, optimizing and adjusting the scan ranges (*e.g.*, by expanding the scan range for larger beam sizes), or increasing the scan speed (*e.g.*, by using fewer BPMs or by shifting the waist with upstream quadrupoles and not with the superconducting final triplet).

An alternative approach is to replace the beam-beam deflection scans altogether with a feedback dither technique based on informations from a fast luminosity monitor, in conjunction with fast orbit bumps across the final-focus sextupoles.

The second option is more innovative and also more promising. Here, a knob is varied in some harmonic or random pattern for thousands of pulses (roughly 10 s are needed per 1000 pulses), and the corresponding luminosity signal (radiated-Bhabha scattering events) is recorded.

Suppose the knob setting k, taken as dimensionless, is related to the convoluted IP spot size (inversely proportional to the luminosity) as

$$\Sigma_y = \Sigma_{y0}\sqrt{1 + S\,(k - k_0)^2} \qquad (6)$$

where k_0 represents the residual aberration that we want to correct, and the parameter S is a normalized 'sensitivity'. If the aberration is completely corrected initially ($k_0 = 0$), a knob change by $k = \pm 1$ would reduce the luminosity by a factor $1/\sqrt{1+S}$.

In SLC operation the signal of the luminosity monitor L_m is impaired by a large and fluctuating background contribution, so that its distribution is fairly wide, with an rms spread equal to about 30% of the average signal. If we average over n pulses, the resolution of the luminosity signal should improve as $\Delta L_m/L_m \approx 0.3/\sqrt{n}$. To be conservative, in the following we assume that the spread of the signal is 100%, *i.e.*, we assume $\Delta L_m/L_m \approx 1/\sqrt{n}$.

We denote the average luminosity signal for the three different knob settings $k = -1, 0, +1$ by L_{m-}, L_{m0} and L_{m+}. Fitting $L_m(k)$ to a parabola and assuming $S < 1$ and $k < 1/\sqrt{2S}$, the approximate optimum knob value can be inferred:

$$k_{opt} \approx \frac{L_{m+} - L_{m-}}{4L_{m0} - 2(L_{m+} + L_{m-})}. \qquad (7)$$

If the luminosity is measured over $n/3$ pulses for each of the three knob values, the statistical resolution in centering the knob is $\Delta k/k = \sqrt{3/(2n)}\;(\Delta L_m/L_m)/S$, and the residual luminosity loss from the statistical error is $\Delta L/L \approx S\,(\Delta k)^2/2$ or

$$\frac{\Delta L}{L} \approx \frac{3}{4S}\left(\frac{\Delta L_m}{L_m}\right)^2 \approx \frac{3}{4Sn} \qquad (8)$$

However, the systematic error made by the parabolic approximation in Eq. (7) is for most cases larger than the statistical error, so that the tuning will have to be iterated.

For example, if $S = 0.2$ (5% luminosity loss during the dithering) and using 10000 pulses of data, the statistical accuracy is $\Delta L/L \approx 0.04\%$ for a single knob, or 0.4% for 10 knobs! This is two orders of magnitude better than what has been achieved by aberration tuning with beam-beam deflection scans, but, recognizing additional systematic errors, we aim for an overall improvement by a factor of 3–10.

5 CONCLUSIONS

There is strong evidence that inaccurate IP spot-size tuning is responsible for about 20–40% average luminosity loss over the last 2 SLC runs. For the next run, we will replace the conventional tuning which is based on beam-beam deflection scans by a novel dithering feedback which we expect to be more effective and as much as ten times more precise. This feedback correlates fast orbit-bumps across the final-focus sextupoles with the signal from a fast luminosity monitor.

ACKNOWLEDGEMENTS

The importance and luminosity impact of IP spot-size tuning was first pointed out by John Irwin and Ghislain Roy, for the Final-Focus Test Beam [3].

6 REFERENCES

[1] P. Raimondi, F.J. Decker, IEEE PAC95, p. 2922 (1995).

[2] P. Raimondi, these proceedings.

[3] G. Roy and J. Irwin, Proc. of the 1990 Summer Study on High Energy Physics, Snowmass 1990, World Scientific, p. 743 (1990)

DEVELOPMENT OF C-BAND RF PULSE COMPRESSION SYSTEM FOR e^+e^- LINEAR COLLIDER

T. Shintake, N. Akasaka and H. Matsumoto,
High Energy Accelerator Research Organization, 1-1 Oho, Ibaraki, 305 JAPAN

Abstract

A new type of RF compression scheme was proposed by the authors for the C-band RF system in the e^+e^- linear collider in 1996[1]. This scheme generates a flat pulse output using 3-cell coupled-cavity for the high-Q energy-storage. A cold model cavity was fabricated and tested to test the flat pulse generation. The input RF amplitude is modulated with a scheduled waveform in order to compensate the output power ripple associated with the coupled cavity resonances. The cold model generated a flat pulse compressed with gain G_p of 3.25.

1 INTRODUCTION

A new scheme to compress an RF pulse into a short square high peak-power pulse was proposed by the authors in the course of R&D study for e^+e^- linear collider[2]. Figure 1 shows the schematic diagram. This scheme uses a 3-cell coupled cavity as an RF energy storage. After the filling time, when the input RF phase is flipped by 180 degree, the compressed RF pulse is emitted into the output port and no reflection power backs to the input port because of the 3-dB hybrid coupler same as in the case of SLED. The coupling irises limit the group velocity of the propagating wave inside the 3-cell cavity, and make it like a delay line. Therefore, this scheme is an extension of the SLED-II pulse compressor, which uses a long circular waveguide as a delay line and generates an ideal square output pulse[3]. The irises make the delay line length short, however it causes the frequency dispersion effect in the propagating wave, resulting in a large distortion in the output waveform. To compensate this, we apply the amplitude modulation (AM) on the input RF power into the compressor.

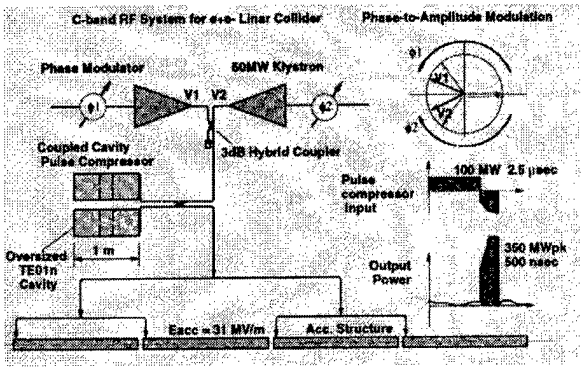


Fig.1 System diagram

Basically, we can do this with one klystron. However, the klystron is non-linear device, that is, the input to output power response is not a linear function, we need a careful compensation to this effect. The klystron will be operated below saturation condition, then the power efficiency will be lowered. In the two klystron configuration shown in Fig 1, the klystrons operate at saturation condition with enough power efficiency. The input RF phase is modulated (PM), and the two output powers are combined in the 3-dB hybrid. The in-phase component (vector sum) goes to the pulse compressor, and the quadrature component (vector difference) is damped in the dummy load. Since the two vectors rotate in the opposite directions, the vector sum always runs on the real axis, and no phase change is came out in the output sum vector. The amplitude of the two vectors is adjusted to the same value with the input RF power knob. The phase modulation pattern will be generated automatically in the self-learning pulse-to-pulse feedback system.

2 DESIGNED COMPRESSION PARAMETERS

In the coupled cavity system, only the $\pi/2$-mode does not generate dynamic phase variation during the transient pulse response. Because the $\pi/2$-mode stays just in the middle of the Brillouin diagram, all vectors of the sideband components associated with the AM modulation rotate symmetrically, and generate a real vector sum same mechanism as the PM-to-AM modulation scheme in Fig. 1.

We studied the pulse response of the delay line by a computer simulation based on the equivalent circuit model. We chose the 3-cell design as the optimum. The simulation predicted the power gain of 3.5 at the pulse-length compression factor of 5, thus the effective power efficiency was 70% (= 3.5/5).

3 COLD MODEL DESIGN

Figure 2 shows the cold model of the RF compressor. One delay line is enough to study the RF pulse compression by detecting the reflection wave using a directional coupler. The input power is fed through a rectangular waveguide, and converted into the circular TE01 mode in the newly developed mode converter, then injected into the 3-cell energy storage cavity. The total cavity length is about 1 m.

0-7803-4376-X/98/$10.00 © 1998 IEEE

Table 1 Cavity parameters. The symbol k stands for the coupling constant between two cavities.

	1st cell	2nd cell	3rd cell
Diameter [mm]	152.60	152.60	152.60
Length [mm]	432.70	144.02	433.42
Mode	TE0,1,15	TE0,1,5	TE0,1,15
Q (analytical)	190 k	85 k	190 k
Q (measured)	181 k	82 k	187 k

	1-2 cell	2-3 cell
Iris Diameter [mm]	43.6	42.4
k (designed)	1.00	0.65
k (measured)	0.95	0.66

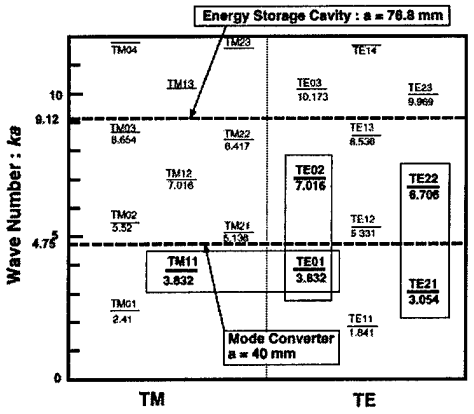


Fig. 3 Mode diagram.

3.1 Energy Storage Cavity

The design and achieved parameters are listed in Table 1. In order to get a higher Q-value and low loss mode, we need to use a copper pipe with a large diameter. We chose the pipe diameter at 152.60 mm, which corresponds to $ka = 9.12$. Since the operating frequency is much higher than the lowest cutoff frequency (1.1 GHz for TE11), there are many unwanted low-Q modes as shown in Fig. 3. We use TE01n mode for the energy storage. To avoid mode mixing, all of the structure in the energy storage cavity was made cylindrically symmetric, which makes no mode coupling to the modes other than TE0n. Additionally, to avoid direct excitation of those mode from the external circuit, we use a mode converter.

From a pulse simulation with the measured coupling constants, the highest attainable power gain is 3.45.

3.2 Cavity Tuning

The $\pi/2$-mode pattern and its resonance frequency is exactly identical to those in the individual cell-mode. We can establish the cell-mode by replacing the neighboring cells with detuned cavities. Since the dimension of the detuned cavity is chosen not to resonate at the target frequency in any mode, no power can leak into the detuned cavity and all field is trapped within the test cell.

We measured the cell-mode using detuned cavities, and machined the cavity length on a turning lathe. Each of the three cavities was tuned to the target frequency. The maximum error was 100 kHz in the 2nd coupling cavity.

3.3 Mode Converter

In order to limit the number of propagation mode inside the circular waveguide, its diameter was chosen as small as 80 mm (see Fig. 3). The four coupling irises generate rotational electric field symmetrically to excite only the TE01 mode. Residual imbalance can generate a small amount of TE21 mode. Computer simulation using HFSS predicted the excitation power of unwanted mode is less than 1%.

RF performance was measured from rectangular waveguide port, attaching a matched load in the circular waveguide port. The measured VSWR was 1.05 for 5 MHz bandwidth.

4 PULSE MEASUREMENT TEST

For this cold model measurement, the input pulse to the cavity was generated by AM modulation with a double balanced mixer. The modulation signal was provided by HP8175A Digital Signal Generator. The input signal was fed into the cavity, then the reflected signal was detected. After fine trimming of the modulation pattern in order to

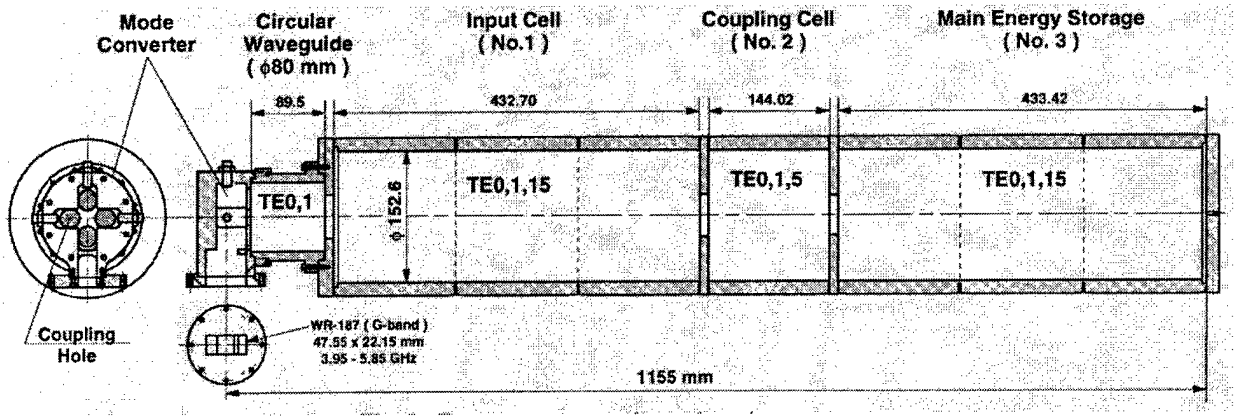
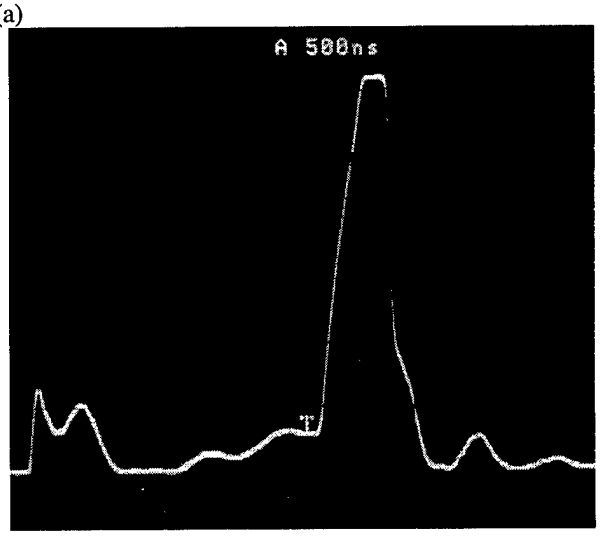


Fig. 2 Energy storage cavity and mode converter.

(a)



(b)

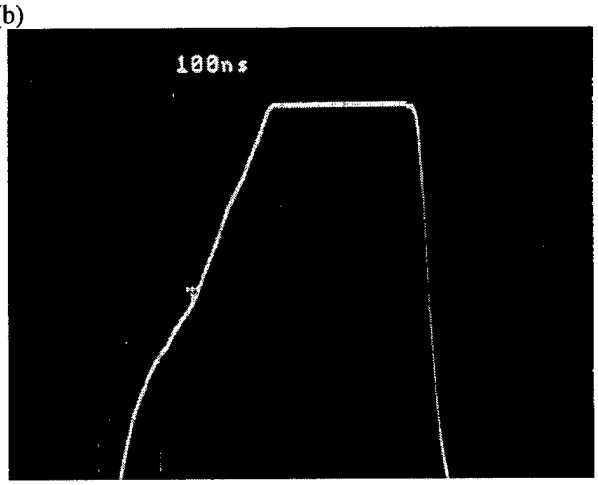


Fig 4. (a) Output pulse. (b) Zoom at the flat top.

obtain the maximum power gain and to make the pulse top flat, the resulting output signal is shown in Fig. 4. At the flat top, the output power is constant within 1%. The measured power gain G_p is 3.25, which is 94% of the expected value of 3.45. Further analysis on the power gain measurement is under way.

5 DISCUSSION

The required tuning accuracy was estimated by the coupled cavity analysis[4]. Thanks to the high stability in $\pi/2$-mode, errors in the cell resonance frequency do not cause large phase or voltage error in the stored field. Therefore, tuning accuracy of the cell-to-cell frequency is not tight. For example, 300 kHz frequency error (the relative frequency error of 10^{-4}, which corresponds to dimension error of 50 μm of cavity length or 15 μm of cavity diameter) on the 3rd cavity cause only 1% amplitude error and 0.06 degree phase error in the 3rd cavity voltage. The leakage power into the 2nd coupling cell is sensitive to the 3rd cavity error. However, the deterioration in the total Q-factor due to this leakage is only 0.67%. Dimension accuracy in a practical machining of a cylindrical cavity on a turning lathe is much better than the error assumed above.

We need to study the error effect due to the brazing process. According to some experience in fabrication of the disk-loaded structure, the resonance frequency shift due to brazing is below 200 kHz at S-band (2856 MHz). Therefore, the brazing will not cause a difficulty.

After the brazing, we will measure the $\pi/2$-resonance using the detuned cavity attaching to the input port, and adjust the screw mounted on the end plate of 3rd cavity to meet the frequency to the right operation frequency of 5712 MHz. The $\pi/2$-mode resonance frequency is simply given by

$$\omega_{\pi/2} = \frac{U_1\omega_1 + U_3\omega_3}{U_1 + U_3},$$

where U_n is the stored energy in the nth cavity. Since the large energy stored in the 3rd cavity, we can adjust the $\pi/2$-mode resonance by tuning the 3-rd cavity frequency. To get phase stability of 3 degrees in the compressed RF pulse, the required frequency accuracy is 8 kHz, and temperature must be kept constant within 0.1 °C. This is the same accuracy level required to the conventional SLED cavity.

6 ACKNOWLEDGMENTS

The authors would like to acknowledge the supports of Prof. Hirotaka Sugawasa, Prof. Yoshitaka Kimura and Prof. Yoshishige Yamazaki to the C-band R&D project.

REFERENCES

[1] T. Shintake and N. Akasaka, "A New RF Pulse-Compressor Using Multi-Cell Coupled-Cavity System", Proc. of EPAC 96, pp. 2146-2148.

[2] T. Shintake et. al., "C-band RF Main Lineac System for e^+e^- Linear Collider at 500 GeV to 1 TeV C.M. Energy", Proc. of EPAC 96, pp. 492-494.

[3] A. Fiebig and C. Schlieblich, "A Radiofrequency Pulse Compressor for Square Output Pulses", Proc. of EPAC 88.

[4] E. A. Knapp, B. C. Knapp and J. M. Potter, "Standing Wave High Energy Linear Accelerators", Review of Scientific Instruments, Vol. 39, No. 7, 1968, pp. 979-991.

BEAM CHARACTERISTICS VERSUS CAVITY MODELS IN CLIC

G. Guignard, CERN,1211 Geneva 23, Switzerland and J. Hagel, Madeira Univ., Funchal, Portugal

Abstract

The luminosity requested for linear colliders with center-of-mass energies exceeding 500 GeV, implies a multibunch operation be considered in order to limit the RF power consumption. In the Compact Linear Collider (CLIC), though the repetition rate is high, a train of at least 20 bunches is necessary to obtain the performance needed for the experiments. Since at high RF frequency the wakefields are large, beam break-up is critical and stability simulations have been carried out for different pre-estimated models of detuned and/or damped cavities. The results obtained give indications about the wakefield level that should not be exceeded along the train, to avoid significant emittance growth. They also show the sensitivity to some specific parameters and the dependence on the scaling of focusing with energy. Eventually, they are used as guide lines for accelerating structure development and as a basis for a possible set of CLIC parameters.

1 INTRODUCTION

In CLIC, studies of multibunch beam dynamics were required since the luminosity requested for the physics implies the use of trains of bunches. For such investigations, analytical models were developed and numerical codes written, that simulate the beam behaviour in the presence of both short- and long-range wakefields [1]. The MBTR code [1] allows one to track simultanously an arbitrary number of bunches. using wakefield Green's functions computed either from the frequency modes or the dependence in the time domain. The bunches are subdivided into slices and the wakefield kicks are then calculated for all possible combinations of pairs of slices j and k, with j smaller than k. Two utility programs MBUNCH and MOVIE help for an efficient use of MBTR. MBUNCH deals with editing the input file, handling the emittance graphs and the output files, running the codes and allowing an automatic optimization of some preselected parameters. MOVIE presents animated graphics of the transverse motion of the slices during acceleration. Off-sets of bars represent the displacements of the slices of each bunch and evolve with the distance s down the linac. The motion of any subset of 5 bunches can be observed simultanously on the screen and instabilities brought into evidence. More recently, a representation of the motion in the phase space of the center-of-charge of every slice of charge has been added [2]. The phase-space oscillations of any subset of 5 bunches can be displayed simultanously, informing on the quality of the focusing constraint. In both cases, a single bunch can also be followed on the monitor. Fig. 1 gives such a picture frozen at $s = 265m$ for a bunch controlled by BNS damping (the head being at the origin).

These tools have been used to investigate the long-range field attenuation necessary to damp the beam break-up. Two models issued from recent design studies and field calculations made for CLIC structures have been retained for the simulations reported below. The first one is a damped structure with radial wave-guides in each cell and the second is a damped-detuned structure with staggered tuning of the cells and reduced damping. Calculations were done with these two models and different beam parameters. The charge was either pushed to the single bunch limit or decreased by a factor two, focusing was increased and scaling with energy optimized on the single bunch stability. Bunch-length was reduced with the charge per bunch. Microwave quadrupoles for BNS damping were used in the high-charge case and momentum spread in the other. BNS-damping was adjusted for minimizing the single-bunch emittance in the presence of misalignments of all linac elements and autophasing condition on minimizing the growth due to a betatron oscillation.

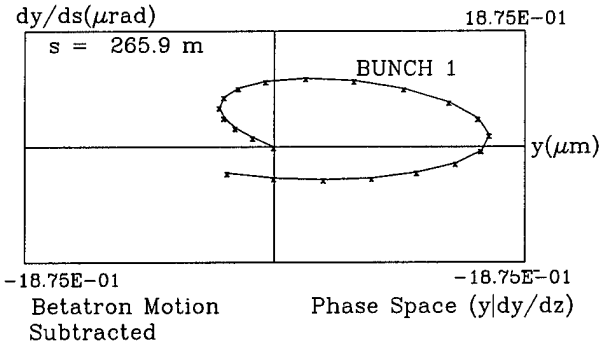


Figure 1: Controled off-sets of bunch 1 in phase space.

2 QUADRUPOLE VERSUS DIPOLE MODE OF SINGLE BUNCH MOTION

Single bunch emittance growth is vanishing if all its slices oscillate coherently in a dipole mode. This can approximately be obtained by a proper setting of RF quadrupoles or energy-spread minimizing the effect of the transverse self-wakefields. It seems evident that the long-range transverse effects of a bunch on a second are dominant when the first bunch is submitted to a dipole mode. These effects should indeed be weaker when the first bunch oscillates with the same amplitude but in a higher coherent mode or incoherently. However, the single bunch emittance increases in the latter case. Taking into account the fact that BNS damping is an efficient method to preserve this emittance and that such a method is not practical in multibunch mode [1], it can be a useful strategy to deviate from a coherent dipole mode in the first bunch. This is in fact what

0-7803-4376-X/98/$10.00 © 1998 IEEE

is happening in the autophasing case.

In this section, the effect on the second bunch of a first oscillating in a quadrupole mode is investigated analytically. Following Ref.1, the equations of motion for a slice of charge with index n in bunches 1 and 2 are given by

$$y''_{1n} + \mu^2/(4\pi^2) y_{1n} = 0 \quad (1)$$

$$y''_{2n} + \mu^2/(4\pi^2) y_{2n} = \mu^2/(4\pi^2)\beta^{3/2}(\theta) \times \frac{q}{E}\sum_{k=1}^{N} y_{1k}(\theta) W^T(z_n - z_k) \quad (2)$$

where θ and y are the usual Courant and Snyder variables, i.e.

$$\theta = \frac{1}{\mu/(2\pi)} \int_0^s \frac{ds}{\beta(s)} \quad (3)$$

and N is the total number of slices. The function W represents the transverse wake potential of bunch 1 acting on bunch 2 and E and q are the bunch energy and the charge of one slice respectively (a constant charge distribution across the bunch is assumed). While the first equation has a trigonometric solution, the second equation is evidently resonant. Keeping only the secular term we obtain:

$$y_{2n}(\theta) = \frac{q_B \alpha_1}{E\mu/\pi} \sigma_n B_0 \theta \sin \mu/(2\pi)\theta \quad (4)$$

where $q_B = Nq$ is the total charge of the bunches and α_1 represents the strength of the lowest dipole mode of the transverse wakes. The n dependent quantity σ_n is given by

$$\sigma_n = \sum_{k=1}^{N} Y_k \cos\left[\frac{\omega_1}{c}(z_{sep} + (n-k)\Delta z)\right] \quad (5)$$

where Y_k are the initial transverse displacements of the slices in bunch 1 , z_{sep} is the separation between the two bunches, Δz is the length of one slice and ω_1 and c are the circular frequency of the dipole wake and the light velocity respectively. In the case of a coherent dipole oscillation of bunch 1, $Y_k = Const. = Y_0$ where Y_0 represents the oscillation amplitude. In the case of a coherent quadrupole oscillation, the first and the last slices oscillation are of the same amplitude but out of phase by π. This is exactly fulfilled by a distribution of the initial conditions such as:

$$Y_k = Y_0 \left[1 - 2\frac{k-1}{N-1}\right]. \quad (6)$$

The relation between the two solutions for bunch 2, valid with the quadrupole mode and the dipole mode respectively, is found to be

$$\rho_n = \frac{y_{2n}^{(Q)}}{y_{2n}^{(D)}} = \frac{\sigma_n^{(Q)}}{\sigma_n^{(D)}} = 1 + \frac{2}{N-1} - \frac{\sum_{k=1}^{N} \frac{2k}{N-1} C_{kn}}{\sum_{k=1}^{N} C_{kn}} \quad (7)$$

with

$$C_{kn} = \cos\left[\frac{\omega_1}{c}\left(z_{sep} + (n-k)\frac{l_b}{N-1}\right)\right] \quad (8)$$

Fig. 2 shows ρ along the second bunch for an increasing number of slices. As can be seen the reduction of the excited amplitudes in bunch 2 when bunch 1 oscillates in a quadrupole mode rather than in a dipole mode is tremendous, namely about 0.4%.

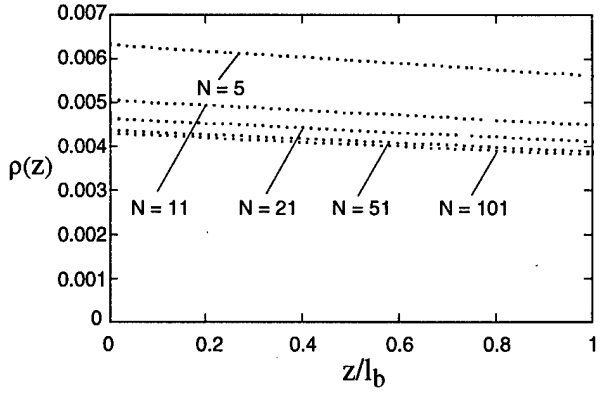


Figure 2: Ratio between oscillation amplitudes caused by a dipole and a quadrupole mode in bunch 1

This result indicates that deviating from a dipole mode in the single bunch should reduce multi-bunch emittance growth along a train of bunches. However, the single bunch emittance will be increased by such a method and one has to find a good balance between these two quantities.

3 WAKEFIELDS FOR DS AND DDS

Studies of accelerating structures for multibunching have been carried out. Three schemes of wakefield reduction have been considered, detuning [3], damping [4] and detuning with additional damping [5]. A detuning scheme does not provide a sufficient level of performance, according to previous simulations [1]. Hereafter are given the simulations required to demonstrate the adequacy of the other two schemes. First, the models of long-range wakefield deduced from the structure studies are briefly described. The short-range wakefields are taken equal to those obtained from the frequency mode analysis of the structure with no field reduction and constant impedance (CIS).

The damped structure (DS) is based on frequency discriminated waveguide damping. Damping waveguides, connected to the outer cavity wall are chosen to have a cut-off frequency above the fundamental but below all higher modes. Time domain MAFIA computations [4] were used to determine the transverse and longitudinal wakefields. A constant impedance structure has been assumed. The initial exponential drop-off of the transverse wakefield is shown on Fig. 3 over a distance of 2m behind bunch 1. The resonance associated with the the cut-off frequency of the waveguide creates a persistent wake at 33 GHz, which becomes dominant beyond this distance and decreases with $x^{-1.5}$. The numerical model for tracking keeps only this persistent component after 2m, with an amplitude at this point which is equal to the value given by the initial drop-

off. For the longitudinal wakefield, all modes beyond the fundamental have been assumed to be reduced by a factor 10, with respect to the modes of CIS.

The damped-detuned structure (DDS) is a detuned accelerating section with low level damping obtained by coupling all cavities to several identical and symmetrically located waveguides (manifolds) which run parallel to the structure and are terminated at each end by matched loads. As for DS, MAFIA computations [5] were performed to determine the wakefields. The roll-off of the transverse wakefields and the effect of damping over a distance of $2m$ behind bunch 1 is also drawn on Fig. 3. In the absence of a dominant persistent wake, the field was calculated over a total distance of 12m (i.e. 40 bunches separated by 30 RF periods). In this design, the attenuation of the longitudinal wakefield was also estimated and the corresponding function of distance included in the tracking. Fig. 3 shows that DDS has been optimized for a bunch separation of 30 RF periods (field reduction of 100 at 0.3m) and the field recoherence in DDS implies higher wakes than in DS after a distance of 1m behind bunch 1.

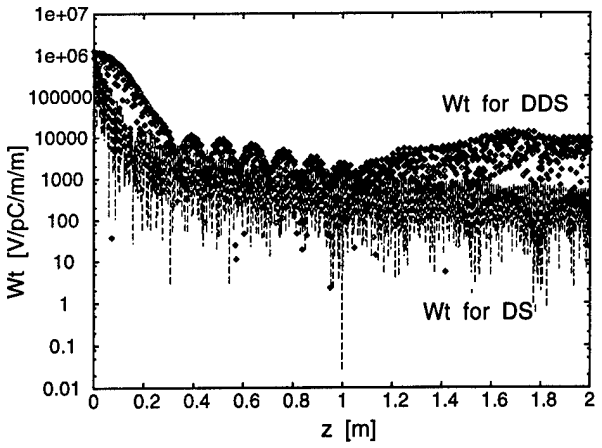


Figure 3: Transverse long-range wakefields.

4 EMITTANCE GROWTH

Tracking simulations were carried out, to compare the merits of the two structures DDS and DS and to check if the wakefield level obtained in these designs at the position of bunch 2 is acceptable for the emittance preservation. Previous calculations [1] indicated that the long-range field should at least be attenuated by a factor 100 at this point, and both designs are achieving this, for a bunch separation of 30 and 15 RF periods with DDS and DS, respectively. Tracking with a small number of bunches confirmed that this requirement is about right. However, for a long train made of 20 bunches or more (beam loading being compensated), it came out that a maintained decay of the long-range field as in DS is a strong advantage in preventing beam break-up by propagation of an instability.

Results depend strongly on the beam parameters and on the assumptions made. It was established that raising the focusing by a factor 2 with respect to the nominal case (1996 parameters) successfully limited the blow-up of the effective emittance. In addition, the emittance growth was found to be sensitive to small variations of the scaling of focusing with energy: the scaling of the quadrupole strength was varied for a given set of misalignments, while the scaling of the cell length was not modified. These two elements were introduced in the simulations. BNS damping was first optimized for single bunch blow-up in the presence of misalignments and off-sets all along the linac (BNS). It was then adjusted either for the blow-up of the whole train or for minimizing the (dipole mode) effect of a betatron oscillation (autophasing). Cases with a charge per bunch of $8 \cdot 10^9$ and a bunch length of $160\mu m$ (1996 parameters) and then $4 \cdot 10^9$ and $60\mu m$, respectively, were computed; the latter aiming at a substantial reduction of the wakes. Results related to 500 GeV linacs (with a gradient of 100 MV/m) are given in Table 1, for the two structures, the two BNS conditions and the two beam characteristics defined above, and different train lengths.

N_e	n_b	DDS (BNS)	DDS (Auto)	DS (BNS)	DS (Auto)
$8 \cdot 10^9$	20	47/24000	216/3742	47/269	216/236
$4 \cdot 10^9$	40	7/1809	30/68	7/15	30/39
$4 \cdot 10^9$	45	26/4580	145/280	26/35	145/170

Table 1. Relative emittance growths (single-/multi-bunch) in % with DDS and DS structures, two BNS conditions and misalignments of $5\mu m$ for the first two cases and of $10\mu m$ for the last.

The conclusion from these results is threefold: a field attenuation by 100 at one bunch separation is required, a further and continuous reduction of the wake behind the exciting bunch is preferable (clear advantage of DS over DDS), and autophasing reduces beam break-up at the expense of the single bunch emittance. The latter is in agreement with the inference of the analysis summarized in Section 2 and results show that the use of DS would allow a compromise between single- and multi-bunch optimization of the emittance preservation.

5 REFERENCES

[1] G.Guignard, J.Hagel, Multibunch Emittance Preservation in CLIC, Proc. 5th EPAC , Sitges, Spain, 1996.

[2] G.Guignard, J.Hagel, Letter to the Editor, ICFA Beam Dynamics Newsletter, No. 13, April 1997.

[3] I. Wilson, W. Wuensch, Multibunch studies for CLIC, CERN-SL/93-20(DI), 1993.

[4] M.Dehler, I.Wilson, W.Wuensch, CLIC Waveguide Damped Accelerating Structure Studies, CERN/PS 96-39 (LP), 1996.

[5] M.Dehler *and 5 co-authors*, Design of a 30 GHz Damped Detuned Accelerating Structure, in this Conference.

LIGA FABRICATION OF mm-WAVE ACCELERATING CAVITY STRUCTURES AT THE ADVANCED PHOTON SOURCE (APS)

J.J. Song, S. Bajikar, Y.W. Kang, R.L. Kustom, D.C. Mancini, A. Nassiri, and B. Lai
Advanced Photon Source, Argonne National Laboratory, Argonne, IL 60439
A.D. Feinerman, Univ. of Illinois at Chicago, Microfabrication Laboratory, Chicago, IL 60607
V. White, Univ. of Wisconsin at Madison, Center for X-ray Lithography, Madison, WI 53706

Abstract

Recent microfabrication technologies based on the LIGA (German acronym for Lithographe, Galvanoformung, und Abformung) process have been applied to build high-aspect-ratio, metallic or dielectric planar structures suitable for high-frequency rf cavity structures. The cavity structures would be used as parts of linear accelerators, microwave undulators, and mm-wave amplifiers. The microfabrication process includes manufacture of precision x-ray masks, exposure of positive resist by x-rays through the mask, resist development, and electroforming of the final microstructure. Prototypes of a 32-cell, 108-GHz constant-impedance cavity and a 66-cell, 94-GHz constant-gradient cavity were fabricated with the synchrotron radiation sources at APS and NSLS. This paper will present an overview of the new technology and details of the mm-wave cavity fabrication.

1 INTRODUCTION

All new concepts for proposed accelerators such as next-generation linear colliders or muon colliders require substantial advances in the area of the rf technology. For example, to maintain a reasonable over-all length at high center-of-mass energy, the main linac of an electron-positron linear collider must operate at a high accelerating field gradient. Scaling accelerating structures to significantly higher frequencies could provide higher field gradient as proposed by P.B. Wilson [1].

The new micromachining technology, known as LIGA, consists of deep-etched x-ray lithography (DXRL), electroplating, and micro-molding. The microfabrication processes have been developed by W. Ehrfeld and co-workers to the degree that sub-millimeter actuators, motors, and gears can be built with great accuracy and a high aspect ratio [2]. Electric field levels as high as 50 MV/m and magnetic field levels of 1 T have been achieved with components. This technology could offer significant advantages over conventional manufacturing methods in such areas as precision fabrication and mass production.

The idea of applying these techniques to develop rf cavities for mm-wave linacs [3], undulators [4], free-electron lasers [5], and mm-wave amplifiers originated at Argonne National Laboratory in 1993. A meter-long structure with similar accuracy that also provides channels for vacuum pumping, adequate cooling, and focusing elements for beam dynamics can be built. Major challenges of the DXRL techniques are: fabrication of the wafers into three-dimensional rf structures, alignment and overlay accuracy of the structures, adhesion of the PMMA on the copper substrate, and selection of a developer to obtain high resolution. Efforts have been directed toward meeting these challenges.

2 MM-WAVE STRUCTURES

Due to DXRL's ability to maintain precise tolerances, it is ideally suited for the manufacture of rf components operating at frequencies between 30 GHz and 300 GHz. The first two structures fabricated were a 32-cell, 108-GHz constant-impedance cavity and a 66-cell, 94-GHz constant-gradient cavity. A 32-cell, 108-GHz constant-impedance cavity is a planar accelerating structure; its linac application has been investigated thoroughly, and its parameters are shown in Table 1. In changing from a typical cylindrical symmetrical disk-like structure to a planar accelerating structure, there is less than 5% loss in shunt impedance and Q-value. For a practical micro-linac application 10 MV/m is chosen in the accelerating gradient, but the accelerating gradient is not limited to that when the rf system is operational in the pulse mode with less repetition rate.

Table 1: The rf Parameters of a 32-Cell, 108-GHz Constant-Impedance Cavity

Frequency	f	108 GHz
Shunt impedance	R	312 MΩ/m
Quality factor	Q	2160
Operating mode	TW	$2\pi/3$
Group velocity	v_g	0.043C
Attenuation factor	α	13.5 m^{-1}
Accel. gradient	E	10 MV/m
Peak power	P	29.1 kW

For a constant-impedance planar structure, the double-periodic structures with confluence in the π-mode designs were considered. The $2\pi/3$-mode operation in these structures can give high shunt impedance, group velocity, and low sensitivity on dimensional errors. More detailed descriptions such as rf simulation using the MAFIA computer code and the thermal analysis related to this structure can be found in Refs. [6, 7].

The constant impedance structure is simple and can be easily fabricated, but may not be the best for accelerator applications, especially due to the difficulty of heat removal in the microstructure. In a constant-impedance

0-7803-4376-X/98/$10.00 © 1998 IEEE

structure, the concentration of heat at the structure input can limit the high power rf operation of the structure. To have higher shunt impedance of the structure, the thickness of the irises between the cells must be small (say $< 0.1\lambda$). However, heating imposes a limit in this case; heating at the center of the irises limits the maximum input power. Successful heat removal and uniform heat loading throughout the structure are important for optimum performance of the mm-wave accelerating structure.

The constant-gradient linear accelerating structure has been used in many present accelerators due to its higher energy gain and better frequency characteristic. The constant-gradient structure has higher shunt impedance and more uniform power dissipation, and is less sensitive to frequency deviations and beam break-up when compared to the constant-impedance structure. The control of cell-to-cell coupling in the side-coupled structures can be made to realize the constant-gradient planar structures.

The one limiting factor in the micromachining process is that the planar structure has to have uniform indentations on a planar wafer. Using microfabrication technology, it is more difficult to realize a constant-gradient structure than a constant-impedance structure. Changing the group velocity along the structure while keeping the gap and cell depth dimensions constant is difficult. Since the structure needs to be manufactured on a planar wafer, adjusting the cell width and length with a constant depth within the structure is necessary. A constant-gradient structure can be realized with a cut in the iris between the adjacent cavity cells along the beam axis in each half structure. Figure 1 shows the constant-gradient structure with cuts in the irises and its rf parameters are summarized in Table 2.

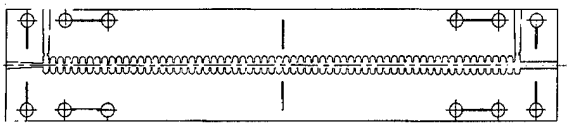


Figure 1: The 66-cell, 94-GHz constant-gradient cavity.

Table 2: 94-GHz Linac/rf Parameters

Parameter	Symbol	Value
Beam energy	E_o	50 MeV
Avg. beam current	I_b	1 mA
Frequency	f	94-GHz
Field gradient	E	10 MV/m
Mode of operation	TW	$2\pi/3$
No. of cavities	N	66
Structure length	l	7 cm
rf power	P	29.1 kW

3 FABRICATION

The simplified version of the DXRL process is shown in Fig. 2. It consists of making an x-ray mask, preparing a sample and x-ray exposure, developing, and electroplating the structure. In DXRL, the requirements imposed on the resist materials, resist coating process, and development are much different from the thin resist layers. No dissolution of unexposed positive resist is allowed during development, and good adhesion of the high-aspect ratio resists structure to the copper substrate is essential. In addition, the microstructures must have high mechanical stability and low internal stresses to prevent stress corrosion during exposure and development. Also, the resist material must be compatible with the electroplating process.

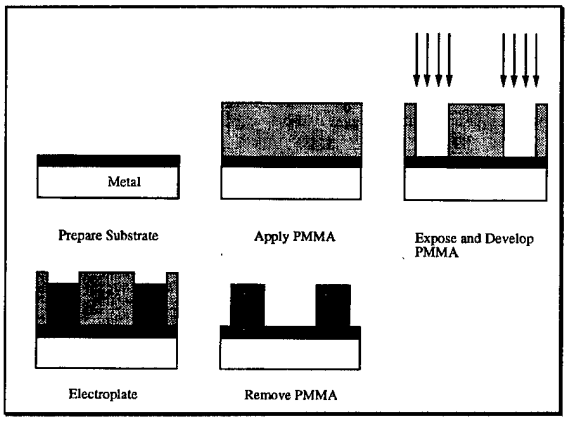


Figure 2: Simplified DXRL process.

DXRL with high-energy synchrotron radiation allows resists up to 1000 μm thick to be fabricated with submicron accuracy. A high-accuracy DXRL mask was made by means of an intermediate mask--that is, in two steps. The first step was the photolithography. A plating base of Ti/Au 75/300 Å was used for the e-beam writer and then 3μm Au was plated on the intermediate mask. The second step used soft x-ray lithography at the Center for X-ray Lithography in Stoughton, Wisconsin (1-GeV Aladdin). For the DXRL mask, 45-μm Au was plated over a 300-μm Si wafer where the x-ray was exposed and removed. To observe the high depth-to-width aspect ratio in the final product, micron range structures were patterned on the DXRL mask [8]. To avoid alignment problems and x-ray fluorescence, these two steps were done on the same sample substrate without a physical gap.

Poly-methylmethacrylate (PMMA), up to 1-mm thick, was used as a positive resist. The copper substrate was diamond-finished to have a flatness of 1 μm over 4 inches. Then either an oxide film was grown to one micron thick or an equally thick Ti coating was deposited in order to promote better adhesion to the copper substrate. Through these processes, the flatness of the copper surface is maintained but still rough enough to give a good adhesion to the PMMA sheet (the roughness of less than 0.1 μm) [9].

When the PMMA film was cast onto the copper substrate, it was then annealed at various temperatures 110 - 170_ C for one to three hours [10]. The NSLS (National Synchrotron Light Source) beamline X-26C and the APS

2-BM-A beamline were used to expose the sample. The transmitted x-ray intensity was calculated based on the APS bending magnet parameters and is plotted in Figure 3. The ratio of the top dose to the bottom dose for the 1-mm-thick PMMA is about 1:1. During the exposure, the sample was enclosed in a He-purged housing with a Kapton window, and the sample holder baseplate was water-cooled. The first platinum mirror with a grazing angle of 0.15° was used to cut off all the high energy x-rays above 40 keV as shown in Figure 3. More information on the APS 2-BM beamline for the DXRL can be found in Ref. 11.

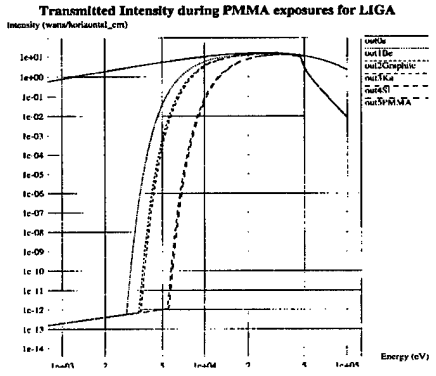


Figure 3: Transmitted x-ray intensity during PMMA exposures for DXRL at APS, energy (eV) vs. intensity (W/cm^3).

Two different developers were used in the developing process. The first developer was a mixture of 60% vol 2-(2-butoxy-ethoxy) ethanol, 20% tetrahydro-1, 4-oxazine, 5% 2-aminoethanol-1, and 15% DI water [12]. The allowed dose range was 3 to about 10 kJ/cm^3. Below the threshold the crosslinked resist could not be dissolved, and above this range damage to the resist can occur from production of gases in the PMMA. The second developer was methyl-iso-butyl ketone (MIBK) diluted with 2-propanol.

After developing the microstructure, copper can be electroplated to the positive resist and the surface can be diamond-finished. The final electroplated structure for the prototype of the 108-GHz constant-impedance cavity structure is shown in Figure 4.

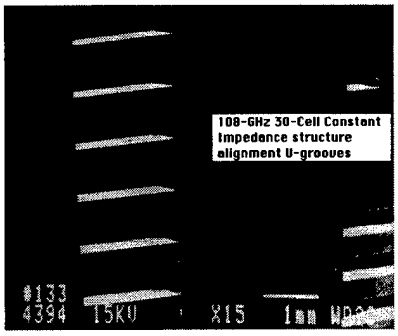


Figure 4: SEM picture of the 108-GHz constant-impedance cavity structure.

4 SUMMARY AND FURTHER WORK

- To get a size-controllable structure, details of both the developing process (for example, use of ultrasonic cleaning) and electro-plating process (pulse mode operation) has to be optimized.
- Two mirror-imaged fabricated structures for the 108-GHz constant-impedance cavity are being aligned ready for network measurement.
- The metallurgical study of the copper-electroplated sample, recently done by C. Pearson at SLAC, shows that the level of oxygen in the sample appears to be too high, one has to improve the electroplating process for vacuum/high power rf.
- The bead-pull measurement setup for the LIGA-fabricated mm-wave cavity structures is underway.

5 ACKNOWLEDGMENTS

This work was supported by the U.S. Department of Energy, Office of Basic Energy Sciences, under Contract No W-31-109-ENG-38. We would like to thank B. Bonivert at SNL and A. Farvid at SLAC for the copper-electroplating work; S. Sutton and G. Shea for the beam time on the X-26C beamline at NSLS; and J. Galayda, Division Director of the Accelerator Systems Division, and G. Shenoy, Division Director of the Experimental Facilities Division at APS, for their support and encouragement. Many thanks to F. Decalro, A. Rehmani, K. Kim, and B. Popek for their technical assistance.

REFERENCES

[1] P.B. Wilson, SLAC-PUB-7263, Oct. (1996).
[2] W. Ehrfeld and D. Muechmeyer, Nucl. Instr. and Methods in Physics Res., A203, p. 523 (1991).
[3] Y.W. Kang et al., Proc. of the 1993 Particle Accelerator Conference, p. 549 (1993).
[4] J.J. Song et al., SPIE-Micromachining and Microfabrication '96, Austin Texas, V2888 (1996).
[5] A. Nassiri et al., IEEE, International Electron Device Conference, Washington DC, p. 169 (1993).
[6] Y.W. Kang et al., Proc. of the 1995 Particle Accelerator Conference, p. 640 (1995).
[7] P. Matthews, and A. Khounsary, private communication.
[8] J.J. Song et al., "X-ray Mask Fabrication for Synchrotron Radiation Lithography at the Advanced Photon Source (APS)," presented to SRI, Argonne, IL, Aug. 4-7, 1996.
[9] F.J. Pantenburg et al., "Adhesion problems in deep-etch X-ray lithography caused by fluorescence radiation from the plating base," Microelectronics Eng., V23, p. 223 (1994).
[10] H. Guckel et al., MEMS 1991, Nara, Japan, January, 1991.
[11] B. Lai et al., SPIE-Micromachining and Microfabrication'96, Austin Texas, V2888 (1996).
[12] E.W. Ehrfeld et al., J. Vac. Sci. Technol, B6 (1), 178 (1988).

DESIGN AND FABRICATION OF A TRAVELING-WAVE MUFFIN-TIN ACCELERATING STRUCTURE AT 90 GHZ †

P.J. Chou, G.B. Bowden, M.R. Copeland, H. Henke*, A. Menegat, and R.H. Siemann
Stanford Linear Accelerator Center, Stanford University, California 94309

Abstract

A prototype of a muffin-tin accelerating structure operating at 32 times the SLAC frequency (2.856 GHz) was built for research in high gradient acceleration. A traveling-wave design with single input and output feeds was chosen for the prototype which was fabricated by wire electrodischarge machining. Features of the mechanical design for the prototype are described. Design improvements are presented including considerations of cooling and vacuum.

1 INTRODUCTION

The cavities of high gradient accelerating structures in the 90 GHz frequency range have millimeter dimensions. Micromachining is more suitable for the fabrication of mm-scale structures than conventional machining. Therefore, a rectangular geometry of the muffin-tin design[1] was chosen. Various fabrication techniques have been reviewed[2] with the conclusion that wire electrodischarge machining(EDM) and deep x-ray lithography(LIGA)[3] were the most promising candidates.

To test wire EDM as a fabrication technique and to gain experience in measuring RF properties of 90 GHz structures, a 7-cell traveling-wave prototype with a single-feed, vertical-coupling input/output scheme was built. This first prototype was used for low-power RF measurements only[4]. The absolute dimensional tolerance required for 90 GHz structures is under 3 μm. A test cut with key features of the design was performed prior to the fabrication of the finished prototype.

Cooling and vacuum were not included in the prototype design. To reduce the need for tight dimensional tolerances and improve the compatibility with cooling and vacuum, a second generation design is contemplated and described in this paper.

2 DESIGN AND FABRICATION OF THE FIRST PROTOTYPE

Figure 1 depicts the sketch of the accelerating cavities. The dimensional parameters in [mm] are: 2a=0.788, 2b=2.364, t=0.263, g=0.831, w=2.364, and d=1.049.

Figure 2 shows the mechanical design of the prototype prior to the assembly. A laminated design with power coupling in the vertical direction was used. The structure is divided accordingly into five layers from top to bottom: input waveguide taper(*a*), coupling iris for input(*b*), muffin-tin cavity structure(*c*), coupling iris for output(*d*), and output waveguide taper(*e*). The linear waveguide taper matches standard WR10 waveguide(2.54 mm × 1.27 mm) to the input coupler(2.54 mm × 0.831 mm); it has a transition length of 10 mm which causes only 1% conversion loss. Each layer is registered by precision alignment pins in two diagonal reference holes. The most critical alignment is between the coupling iris and the coupler cavity. A 5 μm misalignment there could increase the VSWR significantly. Since the coupling irises and coupler cavities are in different layers, this poses a great challenge on the alignment technique.

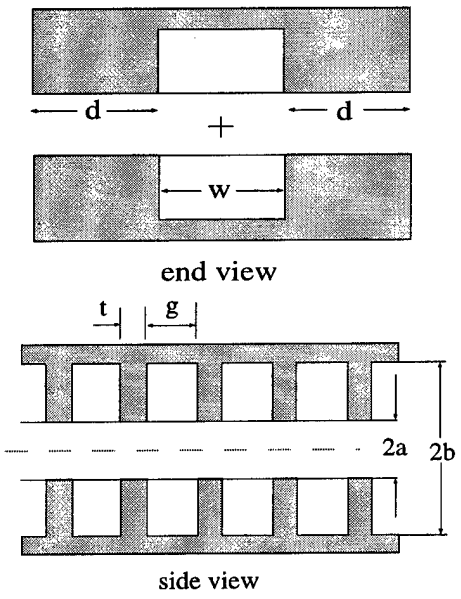


Fig. 1: Sketch of muffin-tin accelerating structure.

The pumping slot and beam pipe were cut through both sides of the middle piece, c in Fig. 2. The width of the beam pipe was chosen to be 1.4 mm in order to prevent leakage of the TM_{11} accelerating mode. Since this prototype will only be used for RF cold tests, the finished structure is just clamped with screws and belleville washers.

Figure 3 shows the cross section of the input coupler sliced along the xy plane. Because of the single-feed input/output scheme, a shallow well with dimensions equal to the coupling iris was used to symmetrize the electromagnetic fields. Without this well, the RF power could leak out through the beam pipe or pumping slot. The geometry of the input/output coupler was designed to obtain a VSWR less than 1.1 and a 1 GHz flat bandwidth centered around the operating frequency[4].

† Work supported by Department of Energy contract DE-AC03-76SF00515.

*Permanent Address: Technical University Berlin, EN2, Einsteinufer 17, D-10587 Berlin, Germany.

0-7803-4376-X/98/$10.00 © 1998 IEEE

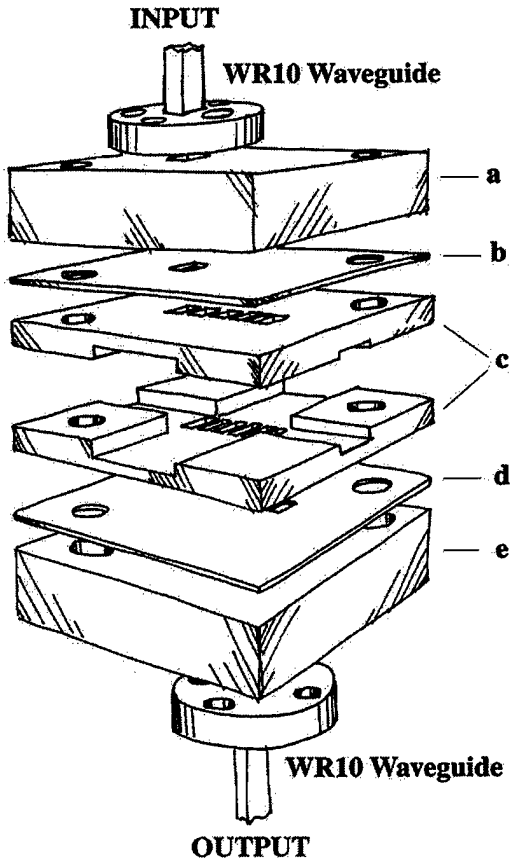


Fig. 2: The mechanical design of the first prototype prior to the assembly.

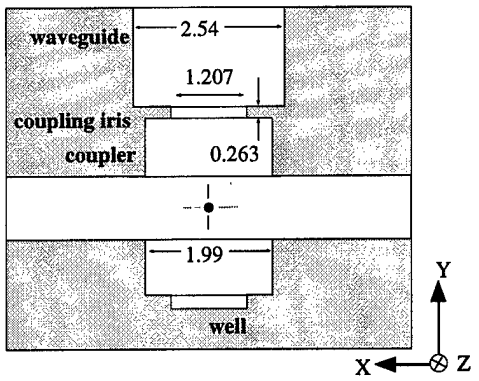


Fig. 3: The cross section of the input coupler sliced along the xy plane. Note that the width of the end cells is w= 1.99 mm as compared with w= 2.364 mm for the other cells.

To assess the machining accuracy provided by wire EDM, a test piece which contains key features such as reference holes, pumping holes, and cavity cells, was fabricated and evaluated by a Leitz coordinate measuring machine which has a measurement accuracy of ±0.5 μm. This test piece was cut on a AGIECUT 150 HSS wire EDM using a 4 mil brass wire at Ron Witherspoon, Inc.. The design of this test piece is depicted in Fig. 4.

The deviation of nominal centers of cavities was within 1 μm, and the variation of sizes of cavities was less than 2.7 μm. The center of pin hole at the upper right corner was off by 3.5 μm in z and 0.3 μm in x direction. The distance between two pin holes are 38 mm in z and 39 mm in x respectively. The results from the test cut seem encouraging. The above results suggest that the fabrication error might be dominated by the accuracy of alignment and assembly of all constituent layers.

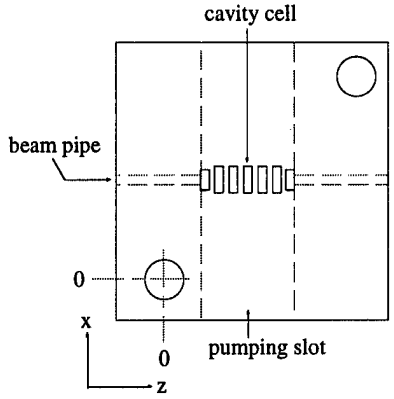


Fig. 4: The schematic sketch of test piece. The reference zero is the center of the pin hole at the bottom left corner.

The RF evaluation of the complete first prototype is presented in P.J. Chou et al. submitted to this conference[4].

3 THE SECOND GENERATION DESIGN

The desire to improve compatibility with cooling and vacuum and relax the tight requirement on layer to layer alignment leads us to the design depicted in Fig. 5. The structure will be divided into four layers. The key parts are layers a and b. The RF power will be coupled into the structure from the horizontal direction. The matching devices used to reduce the reflection of incident power will be integrated into the same layer with the cavity cells. From the results of previous test cuts, we are more confident in the machining accuracy provided by EDM than in the alignment technique. The sketches for layer a and b are shown in Figs. 6 and 7 respectively. The matching devices have the same height as the cavity cells. This one height level design will make technique LIGA[3] a possible candidate for fabrication. Besides wire EDM technique, sinker EDM could also be used to fabricate the structure.

From the standpoint of RF design, the horizontal coupling scheme is better than the vertical coupling scheme used in the prototype in Fig. 2. The vertical coupling scheme could induce a TE_{10} mode which can leak out through the beam pipe or pumping slot if the electromagnetic field is not properly symmetrized for a single-feed design. This is why we have a narrow beam pipe(1.4 mm) in the prototype. From the standpoint of wake fields, we would like to have a wider beam pipe. The horizontal coupling scheme will allow us to use a wider beam pipe without worrying about power leakage. The basic principles are the same as those of a magic T[5].

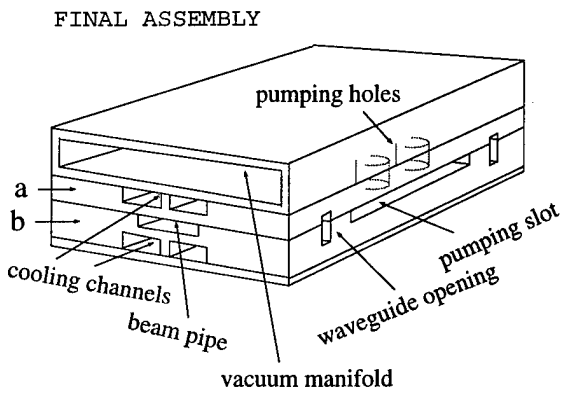


Fig. 5: Sketch of the 2nd generation design. Vacuum and cooling channels are included.

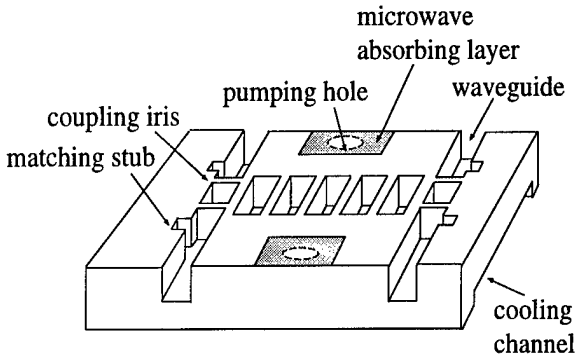


Fig. 6: Sketch of layer a — the top half of the structure.

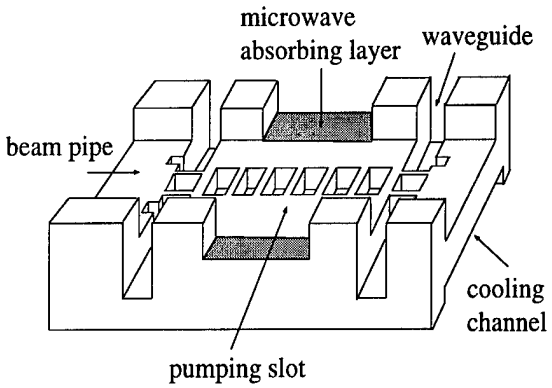


Fig. 7: Sketch of layer b — the bottom half of the structure.

4 ENGINEERING ISSUES OF THE SECOND GENERATION DESIGN

Simplified models were used to estimate some basic characteristics of the cooling and vacuum. A flat duct carrying water at high velocity is used. The duct is assumed to have an infinite width. The higher the water flow velocity, the higher the heat transfer up to the point where water flow erodes the metal and the water cavitates(boils) where it is forced around corners or over edges. As a practical limit, a flow velocity of 600 cm/sec is used. For a 10 °C temperature gradient between the metal wall and 600 cm/sec fluid velocity, the heat transfer was calculated to be 50.5 watts/cm^2 in a 2 mm high duct. An estimate of the average heating due to the RF power dissipation on the wall was made with the following parameters: E= 300 MV/m, r_s= 250 MΩ/m, RF pulse length= 40 ns, repetition rate= 150 Hz, structure width= 4 mm. The average heating per unit area was estimated to be 25 watts/cm^2.

Vacuum has been estimated to be around 10^{-10} Torr for a 1mm × 10 mm rectangular duct that is more or less continuously connected to the structures. The estimate assumes only outgasing from temperature rise due to average RF power. The flux of outgasing from the accelerator structure itself due to pulse heating of peak RF power would have to be added in. The pulse heating problem is currently under experimental investigation[6].

5 SUMMARY

We have presented the design concepts, results of mechanical test cuts, and discussions on various engineering issues for 90 GHz accelerating structures. Cooling and vacuum do not seem to be major problems. Fabrication issues do not seem to be an obstacle.

6 ACKNOWLEDGMENT

The authors would like to thank Ron Witherspoon, Inc. in Campbell, California for many helpful discussions.

7 REFERENCES

[1] H. Henke et al., internal report ANL/APS/MMW-1, Argonne National Lab. (1993).
[2] P.J. Chou et al., SLAC-PUB-7339, to be published in the Proceedings of the 7th Workshop of Advanced Accelerator Concepts.
[3] E.W. Becker et al., Microelectronic Engineering **4** (1986) 35-56.
[4] P.J. Chou et al., "RF Measurements of a Traveling-Wave Muffin-Tin Accelerating Structure at 90 GHz", in this proceedings.
[5] R.E. Collin, Foundations for Microwave Engineering (McGraw-Hill, New York, 1966), p. 283.
[6] D. Pritzkau et al., "Experimental Study of Pulsed Heating of Electromagnetic Cavities", in this proceedings.

WAKEFIELD DYNAMICS IN QUASI PERIODIC STRUCTURES

A. Novokhatski* and A. Mosnier
CEA/DSM, CEA-Saclay, F-91191 Gif-sur-Yvette Cedex, France

Abstract

The behavior of longitudinal wakefields of very short bunches, excited in in multicell accelerating structures has been studied. Computations were performed in structures proposed for future linear colliders (like TESLA, SBLC and NLC) for bunch lengths down to 50 micrometers. The loss factor, which gives the global energy loss of the bunch, and the profile of the wake function, which is of major interest for bunch energy spread calculations, have been carefully studied. A strong modification of wakefields along the finite train of multicell cavities was clearly found for short bunchlengths. In particular, the wakes induced by the bunch, as it proceeds down the successive cavities, decrease in amplitude and become more linear around the bunch center, with a profile very close to the integral of the charge density. The loss factor per unit length, decreasing also with the number of cavities, becomes independent of bunchlength for very short bunches and goes asymptotically towards a finite value in the permanent regime. However, any break in periodicity (or multi-periodicity) will spoil the wake distribution and hence tends to increase the wakefield amplitude.

1 INTRODUCTION

The wakefields, excited by very short bunches in accelerating structures, are of major concern in the design of new projects for Linear Colliders and X-ray Free Electron Laser, because they can give rise to large energy spreads and transverse emittance growths. Up to now, wakefields calculations had been performed for single TESLA cavities[1]. They showed dramatic bunchlength dependence, scaling approximately inversely with square root of bunchlength. For the TESLA linac and especially for the SASE FEL mode[2], such wakefield behaviors could lead to relatively large uncompensated energy spreads. It is worthwhile noting that the ratio of iris radius over the bunch length, the relevant parameter for wakefield studies, is about 50 for the TESLA linac and even 700 for the SASE FEL parameters. Some analytical and qualitative results (see, for example[3]) predict the behavior of fields induced by short bunches in a single cavity and periodic structure. Unlike long bunches, wake potentials for very short bunches scale inversely with the square root of distance and become infinite at vanishing distance for a single cavity, whereas they are bound for periodic structures. It is then of outstanding importance to know when a chain of cavities behaves like a periodic structure or like a single cavity. The three regions, single cavity, transient and permanent regime were studied by means of numerical simulations on different structures. The results on the train of TESLA cavities will only be presented here. Unfortunately, conventional time-domain codes need very tiny mesh sizes to cope with the very high frequency part, generated by short bunches, leading to unreasonable long CPU times and poor accuracy[4]. For successful numerical wakefield calculations, a time-domain code, called NOVO, was then especially developed for very short bunches by one of the authors. For solving Maxwell's equations in time domain, the finite-difference method with improved characteristic of the dispersion curve in the region of minimum critical wavelength was used[5]. Lastly, an 'universal' analytical expression, valid for periodic structures, has been compared to the numerical results. We found that the couple of adjustable parameters, are very smooth functions of the exact geometry for multi-periodic structures like TESLA.

2 SINGLE-CELL APPROACH

Starting from the TESLA cavity, which is composed of 9 cells, we consider the single-cell approximation, where the different cells of a cavity are assumed independent. For relatively long bunches, this approximation is justified and can help in understanding the wakefunction evolution with bunchlength. Two parameters can be used to describe the "smallness" of the bunch length: the aperture radius a and s_0, which is defined for a cell with gap length g as $s_0 = a^2/2g$. In the case of a single cell with simple rectangular shape, for the distances smaller than the aperture radius $s < a$, it is possible to derive a good analytical estimation of the point-like wakefunction[6]

$$w(s) = \frac{Z_0 c}{a\pi^2}\{\frac{s+g}{\sqrt{s(s+2g)}}F(\frac{\sqrt{s(s+2g)}}{a}) - F(\frac{s}{a})\}$$

where the function $F(x)$ is given by

$$F(x) = \begin{cases} (2/x)\arcsin(x/2) & \text{if } x \le 2 \\ (\pi/x) & \text{if } x > 2 \end{cases}$$

The bunch wake potential $W(s)$ induced by a Gaussian bunch with a bunchlength σ = 0.5 mm passing through a TESLA-like cell, approximated by a rectangular shape (a=35 mm, g=90 mm and b=103.3 mm), has been calculated from the convolution of the above wakefunction formula with the bunch charge density and from time-domain simulations. Both results are shown on Fig. 1 and are in very good agreement. For much shorter bunches, when $s << s_0$ (s_0 = 5.3 mm for the TESLA cell), the well known result of K. Bane and M. Sands[3] can be found again from the above expression

$$w(s) = \frac{Z_0 c}{2\pi^2}\frac{1}{\sqrt{s_0 s}}$$

*Permanent address: Budker Institute of Nuclear Physics, 630090 Novosibirsk, Russia

0-7803-4376-X/98/$10.00 © 1998 IEEE

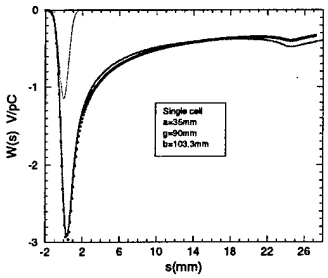


Figure 1: Wake potential for a rectangular TESLA-type cell: numerical (circles) and analytical results (solid lines).

For a single cell, the wakefunction (bunch wake potential) varies inversely as the square root of the distance (bunchlength). A slight discrepancy between numerical simulations and theoritical scaling with bunchlength was found in bell-shaped cells like the TESLA cavity, and can be explained by the following. The more the bunch is short, the less the fields penetrate the elliptical iris region. We can define an "equivalent gap", which grows (from 88 to 100 mm) when the bunch shortens (from 1 to 0.1 mm).

3 MULTI-CELL APPROACH

Whereas the field pattern around the bunch is assumed unchanged before and after its travel through a cell in the single-cell approximation (the total energy loss in multicell structures would be then simply the sum of the losses in the individual cells), this assumption is not any more valid for short bunches. For example, the electric force lines left by the bunch in the exit beam tube of a single-cell cavity are represented on Fig. 2 for two bunchlengths σ = 2 mm and σ = 100 μm. The electric force lines are almost radial for the longer bunch, as they were before the cell, whereas a lot of lines lie horizontal and do not touch the wall of the beam tube in the vicinity of shorter bunch. The next cell will then be excited by the bunch of "extended length" and the radiation energy will be smaller than in the previous cell. After several cells, the electric force lines in the iris region reach a "steady-state regime", as if they were induced by an equivalent longer bunch. The number of cells N needed to achieve this periodic behavior depends on the bunchlenth σ : the more the bunch is short, the more the number of cells must be large. It be estimated from a simple geometrical model of the radiation process for a structure of period L : $N > a^2/2\sigma L$. Time domain simulations were performed

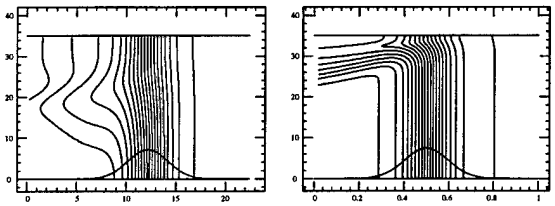


Figure 2: Electric force lines of the bunch field just after one TESLA cell for σ=2 mm (left), σ=0.1 mm (right)

on a periodic structure, consisting of regular TESLA cells. Fig. 3 shows the loss factor per unit length for a bunchlength of 0.2 mm as a function of the number of involved cells and converges to a finite constant value after a large enough number of cells (steady-state).

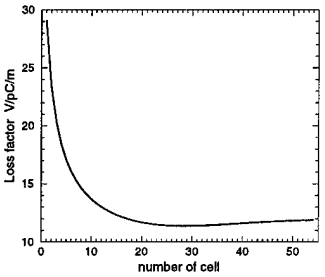


Figure 3: Loss factor vs number of cells in a chain of regular TESLA cells (σ = 0.2 mm).

In the region of very short bunches, the loss factor does not nearly depend on the bunchlength and is given by $k = Z_0 c/2\pi a^2$. However, more than 50 cells are needed to achieve the stabilization of the wakefunction. It was found that for any periodic structure, the wake potential can be very well described by the following expression, as suggested by K. Bane[7]

$$w(s) = \frac{Z_0 c}{\pi a^2}((1+\beta)\exp(-\sqrt{\frac{s}{s_0}}) - \beta)$$

The parameter β is 0.16 and $s_0 = a^2/2L$.

Figure 4 shows wake potentials, calculated for the 0.2 mm long bunch for different number of cells (from the sixth to the tenth 9-cell regular TESLA cavity, as well as the analytical expression. A very good agreement is clearly observed : from the head to about one σ after the bunch center with a fast convergence of the wakes and at the tail with damped oscillations of the wakes around the analytical curve.

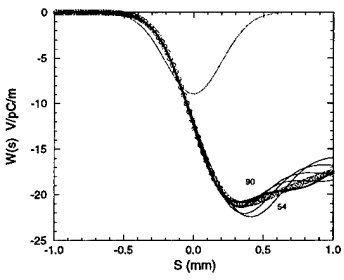


Figure 4: Wake potentials induced in cell numbers 54, 63, 72, 81, and 90 (dark line) and the analytical expression (circles) in the periodic TESLA structure (σ=0.2mm).

4 MULTI-PERIODIC STRUCTURE

If the multi-cell approach gave a good estimation of the wakes induced in periodic structures, the TESLA linac is far from being purely periodic. It is in fact a multi-periodic

structure : a first elementary period is the regular bell-shaped cell, a second one is the 9-cell cavity, connected to a beam tube and a third one is the module, housing 8 cavities and a different connecting tube. In addition, some extra effects, like the larger tube diameter with respect to the iris aperture, must be taken into account. When the bunch leaves a cavity and enters the drift tube, some field must be created to fill in the space enclosed between the two different radii of 35 and 39 mm. First, wake potentials were calculated for a TESLA module, housing eight 9-cell cavities and beam tubes. The successive wake potentials, induced in each of the individual cavities and their beam tube, are shown on Fig. 5 (left) for a bunch of length σ = 0.2 mm. In the same way, the wake potentials, calculated for the periodic structure, composed of regular TESLA inner-cells, and without spacing between cavities are reproduced on Fig. 5 (right) for comparison. We note that the shapes are identical, but with larger amplitudes per cavity in the real multi-periodic TESLA structures. For the multi-periodic

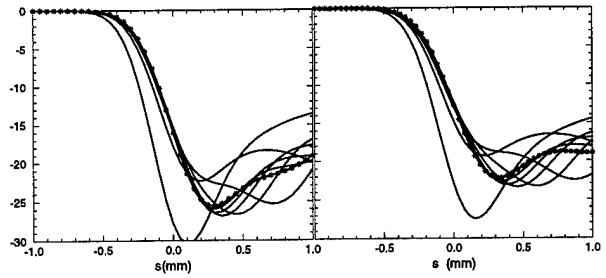


Figure 5: Wake potentials induced by each of the cavities (σ=0.2mm) in first real TESLA module (left) and in periodic structure composed of regular cells (right).

structure, we found that the wake potential per unit length can be described by the same previous expression, valid for the periodic structure, but with two additional parameters

$$w(s) = A\frac{Z_0 c}{\pi a^2}((1+\beta)\exp(-\alpha\sqrt{\frac{s}{s_0}}) - \beta)$$

The parameters $A = 0.94$, $\alpha = 1.33$ and $\beta = 0.18$ were found from the fit of the loss factors, computed for different short bunches. The wake potentials induced in the last 8th cavity of the module are plotted on Fig. 6, as well as the analytical results for two bunchlengths, 0.2 mm and 0.05 mm. We can note that the steady state is practically achieved for the 0.2 mm long bunch, but a larger number of cavities is needed for the shortest 0.05 mm bunch. However, in the reality, the spacing between the last cavity of a module and the first one of the next module will be larger than the standard spacing (3 rf half-wavelengthes) between two successive cavities. The bi-periodicity is broken again and as a result, the wakefields will be reinforced. This effect can be observed on Fig. 7. At the left side, the wake potentials for a 0.05 mm bunch are drawn for each of the eight consecutive cavities in a first module. It is worthy to note the amplitude, decreasing with the cavity index. At the right side, they are drawn for the next 9th cavity, with a same

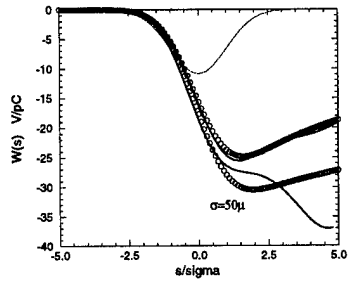


Figure 6: Wake potentials in the 8th cavity of the TESLA module for (σ=0.2 mm and σ=0.05 mm) and analytical results (circles).

standard spacing (as if it belonged to the previous module) and with the real additional spacing between two modules.

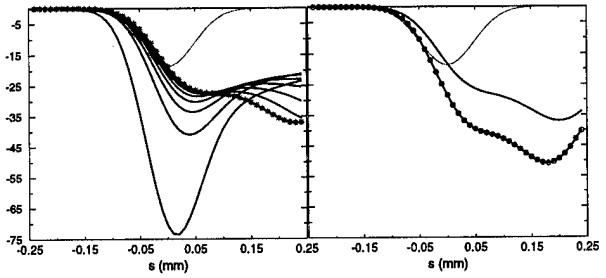


Figure 7: Wake potentials in the 8 cavities of a module (left) and in a 9th cavity (right), with standard spacing and with real spacing (circles)

5 ACKNOWLEDGEMENT

The authors are grateful to K. Bane, A. Sery and O. Napoly for fruitful discussions, as well as to R. Brinkmann, J. Rossbach and R. Wanzenberg for their interest into this study.

6 REFERENCES

[1] A. Mosnier, "Longitudinal and Transverse Wakes for the TESLA Cavity", TESLA report 93-11, DESY Print (May 1993).

[2] J. Rossbach, "New linac based FEL projects using bright electron beams", Proc. of XVIII Intern. Linac Conference, Geneve (August 1996).

[3] Special Issue "Impedance beyond cutoff", Particle Accelerators, Vol.25, Num 2-4 (1990).

[4] Z. Li and J. Bisognano, "On the Importance of Fourth Order Effects on Wakefield Calculations For Short Bunches", Proc. of the 1995 Part. Acc. Conf., Dallas (May 1995).

[5] A.V. Novokhatski, to be published.

[6] A.V. Novokhatski "On the estimation of the wake potential for an ultrarelativistic charge in an accelerating structure", Preprint INP 88-39, Novosibirsk (1988).

[7] K. Bane, "The short range NLC wakefields", NLC-Note 9 (February 1995).

A STATISTICAL APPROACH TO ANALYSE EFFECT OF MISALIGNMENTS AND CORRECTION ALGORITHMS IN HIGH-ENERGY LINACS

S. Fartoukh, CERN, 1211-Geneva 23, Switzerland

Abstract

This paper presents a new and general tracking method capable of analysing, in a statistical way, the dipole wakefield effects on a high-energy charged-particle beam.

1 EQUATION OF MOTION

We consider an electron bunch travelling along a line containing magnetic quadrupoles and RF structures. We note s the longitudinal coordinate along the line, and z, a relative position within the bunch ($z > 0$ at the bunch tail). We will assume the beam to be fully relativistic so that the longitudinal distribution of particles $\rho(z)$ is completely rigid along the $\hat{s}$ axis. For a slice of charge at a relative position z inside the bunch, we note $\delta x(s,z)$ the transverse position (horizontal or vertical) of its centre of gravity, $x(s,z) = \delta x(s,z) + \tilde{x}(s,z)$ the position of any particle within the slice, and $\gamma(s,z)m_ec^2$ its energy (thus, $\tilde{x}$ describes the betatron motion in the presence of acceleration). Then, the fundamental dynamics relation, projected on the transverse and longitudinal planes, gives [1]:

$$\begin{cases} x''(s,z) + \gamma'(s,z)/\gamma(s,z)\, x'(s,z) + k(s,z)\, x(s,z) \\ = \dfrac{e^2/m_ec^2}{\gamma(s,z)} \displaystyle\int_{-\infty}^{z} W_T^{\delta}(z-z^*)\, \rho(z^*)\, \delta x(z^*)\, dz^* \end{cases} \quad (1)$$

$$\gamma'(s,z) = e/m_ec^2 \left(G_{RF}(s,z) - e\int_{-\infty}^{z} \rho(z^*)\, W_L^{\delta}(z-z^*)\, dz^*\right)$$

Here, W_L^{δ} and W_T^{δ} are the longitudinal and transverse delta-function wake potentials, $k(s,z)$ [m^{-2}] is the quadrupole strength seen by the slice z and $G_{RF}(s,z)$ [V/m] represents the accelerating field along the line[1]. Summing Eq. 1 over all the particles of the slice z, we obtain the equations verified by $\delta x(s,z)$ and $\tilde{x}(s,z)$:

$$\begin{cases} \delta x''(s,z) + \gamma'(s,z)/\gamma(s,z)\, \delta x'(s,z) + k(s,z)\, \delta x(s,z) \\ = \dfrac{e^2/m_ec^2}{\gamma(s,z)} \displaystyle\int_{-\infty}^{z} W_T^{\delta}(z-z^*)\, \rho(z^*)\, \delta x(z^*)\, dz^* \end{cases} \quad (2)$$

$$\tilde{x}''(s,z) + \gamma'(s,z)/\gamma(s,z)\, \tilde{x}'(s,z) + k(s,z)\, \tilde{x}(s,z) = 0 \quad (3)$$

Eq. 3 is the the well-known Hill equation and the classical theory of the beam matrix and R matrix, not reported here, can be applied in order to track the "$\tilde{x}$-envelope" of each slice all along the line[2]. Eq. 2 has no analytical solution in the most general case and its numerical treatment is presented hereafter.

[1] $G_{RF}(s,z) = 0$ and $k(s,z) = G_q(s)e/(\gamma(s,z)mc)$ in quadrupoles, $G_q(s)$ [T/m] being the step function which describes the quadrupole gradient within the line; $G_{RF}(s,z) = G_{RF}\cos(\omega_{RF}z/c - \phi_{RF})$ and $k(s,z) = 0$ in RF structures.

[2] In this model, we see that the motion of $\tilde{x}$ is totally independent of the one of δx; this would not be the case anymore if, for instance, we had taken into account the quadrupole mode of the wakes.

2 GENERALISED R-MATRIX

By splitting the bunch into n_s slices of thickness Δz, we can write the integro-differential equation 2 as a vectorial differential equation of order one and dimension $2n_s$:

$$\mathcal{X}'(s) = \mathcal{A}(s) * \mathcal{X}(s) \quad (4)$$

where $\mathcal{X}(s) = [\delta x(s,z_1), \delta x'(s,z_1) \ldots \delta x(s,z_{n_s}), \delta x'(s,z_{n_s})]$ and where $\mathcal{A}$ is the following $2n_s \times 2n_s$ matrix:

$$\mathcal{A} = \begin{pmatrix} A_1^0 & 0 & \ldots & 0 \\ A_{21} & A_2^0 & \ldots & 0 \\ \vdots & \vdots & \ddots & \vdots \\ A_{n_s1} & A_{n_s2} & \ldots & A_{n_s}^0 \end{pmatrix} \text{ with } \begin{cases} A_i^0 = \begin{pmatrix} 0 & 1 \\ -k(s,z_i) - \dfrac{\gamma'(s,z_i)}{\gamma(s,z_i)} & \end{pmatrix} \\ A_{ij} = \begin{pmatrix} 0 & 0 \\ \Delta z \rho(z_j) W_T^{\delta}(z_i - z_j) & 0 \end{pmatrix}. \end{cases}$$

The solution of the previous equation can be written as $\mathcal{X}(s) = \mathcal{R}(s) * \mathcal{X}(0)$, where $\mathcal{R}(s)$ is a $2n_s \times 2n_s$ matrix that we call "generalised R-matrix in the presence of wakefield" and which verifies the matricial differential equation:

$$\mathcal{R}'(s) = \mathcal{A}(s) * \mathcal{R}(s) \text{ with } \mathcal{R}(0) = \mathbf{Id} \quad (5)$$

We can easily see that, like the $\mathcal{A}$ matrix, $\mathcal{R}$ is a lower triangular 2×2 block matrix: the diagonal blocks R_{ii}^0 describe the motion of the slices z_i without any wakefields ($R_{ii}^{0\prime} \overset{5}{=} A_i^0 * R_{ii}^0$) whereas the lower blocks R_{ij}, $i > j$, testify to the interaction between the slices z_i and z_j due to the transverse wake. Certainly more complicated than a classical tracking, this method has nevertheless the advantage of a very practical computation of the beam line sensitivity to the displacements of its components (next section).

3 BEAM LINE SENSITIVITY

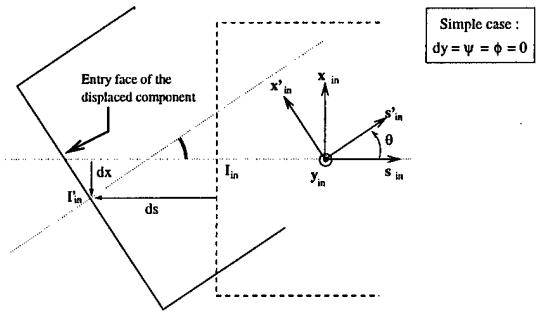


Figure 1:

Here, we are interested in the effects of transverse misalignments of the beam line components. Assuming the elements to be totally rigid objects, their position along the

0-7803-4376-X/98/$10.00 © 1998 IEEE

line can be defined by six parameters (see Fig. 1); first, we execute a global translation of the component, then, three rotations, leaving invariant the middle point of the displaced entry face of the component (I'_{in} in Fig. 1):

- the horizontal, vertical and longitudinal displacements dx, dy and and ds respectively.
- the rotation θ around the actual vertical axis, $\hat{y}_{\text{in}}$ in Fig. 1, or yaw angle, the rotation ϕ around the newly defined horizontal axis, $\hat{x}'_{\text{in}}$ in Fig. 1, or pitch angle, the rotation ψ around the newly defined longitudinal axis or roll angle.

We will forget here the "longitudinal alignment errors", ds and ψ, which do not create any transverse offset[3]. Then, we consider a component of length L with the misalignments dx and θ, and we suppose that the beam goes into the component (abscissa s_0) with the initial conditions $\mathcal{X}(s_0)$; using the previous section, we can compute the beam offset at the component exit ($s_1 = s_0 + L$) in the following way:

$$\mathcal{X}(s_1) = \mathcal{R}(s_0 \rightarrow s_1)\left(\mathcal{X}(s_1) + \mathcal{X}_{\text{in}}(dx,\theta)\right) + \mathcal{X}_{\text{out}}(dx,\theta)$$

where $\mathcal{X}_{\text{in}}(dx,\theta) = -[dx,\theta,\ldots,dx,\theta]$ and $\mathcal{X}_{\text{out}}(dx,\theta) = [dx + L\theta,\theta,\ldots,dx + L\theta,\theta]$ refers to the change of coordinate at the component entry and at the component exit respectively. Thus, at any abscissa s_f, we can estimate the line sensitivity relative to the misalignments of any of its components; for instance, for a yaw angle θ_i of the element number i, we obtain:

$$\partial_{\theta_i}\mathcal{X}(s_f) = \mathcal{R}(s_i + L_i \rightarrow s_f)\left(\Theta_{\text{out}}(L_i) + \mathcal{R}(s_i \rightarrow s_i + L_i)\,\Theta_{\text{in}}\right)$$

with $\Theta_{\text{in}} = -[0,1\ldots0,1]$ and $\Theta_{\text{out}}(L_i) = [L_i,1\ldots L_i,1]$. Finally, in the same way, we can obtain all the response coefficients of the line, concerning the initial offset (angle and position) of the bunch.

4 CORRECTION ALGORITHMS

The simplest alignment methods are based on a correction of the bunch centre-of-charge deviation measured at one or several beam position monitors (BPM) within the line by moving the quadrupoles transversely. More recently, new correction schemes have been proposed, based on the simultaneous minimisation of trajectory deviations and trajectory differences linked to variable quadrupole settings or linked to variable bunch charge or bunch length [2]. However that may be, all these correction techniques have in common the following fact: they all come down to the minimisation by moving quadrupoles of a certain function Φ which depends quadratically on measurements of trajectory deviations. Then, it can be shown [3] that after this minimisation the vector $\mathcal{X}(s_f)$ (containing the positions and angles of the n_s slices at the line output) does not depend anymore on the quad misalignments before correction but only and in a linear way on the errors of the line[4], that we write in the formal following way:

$$\mathcal{X}(s_f) \overset{\text{def}}{=} M_{er}\, dX_{er} \tag{6}$$

where dX_{er} is a stochastic vector containing the "errors of the line" and where M_{er} is a $2n_s \times N_{er}$ matrix which depends on the focusing lattice (via the response coefficients) and on the choice of the correction algorithm (via the choice of the function Φ).

5 STATISTICAL BEAM RESPONSE IN TERM OF EMITTANCE GROWTH

From now on the rest of the paper, the notation $<\mathcal{Q}>_{er}$ will represent the average of the quantity $\mathcal{Q}$ over the statistic distribution of the "errors", compared to the same notation, without suffix, referring to an average over the longitudinal particle distribution $\rho(z)$. So, we suppose that the vector, $\mathbf{m_{er}} \equiv <dX_{er}>_{er}$, and the covariance matrix, $\Gamma_{er} \equiv <dX_{er}{}^{\text{T}} dX_{er}>_{er} - \mathbf{m_{er}}{}^{\text{T}}\mathbf{m_{er}}$, are known quantities which depends on the pre-alignment scheme[5].
For the sake of simplification, we will assume $\mathbf{m_{er}} = 0$. By using Eq. 6, we can compute the average and the covariance matrix of the vector $\mathcal{X}(s_f)$ at the line output:

$$\begin{aligned} \widetilde{\mathbf{m}} &\overset{\text{def}}{=} <\mathcal{X}(s_f)>_{er} &&= M_{er}\,\mathbf{m_{er}} = 0 \\ \widetilde{\Gamma} &\overset{\text{def}}{=} <\mathcal{X}(s_f)^{\text{T}}\mathcal{X}(s_f)>_{er} &&= M_{er}\,\Gamma_{er}{}^{\text{T}} M_{er} \end{aligned} \tag{7}$$

Nevertheless, for reasons which will appear later, we prefer to define the symmetric matrix $\Gamma_{\substack{1\le i\le 2n_s \\ 1\le j\le 2n_s}}$ by:

$$\begin{cases} \Gamma_{2i-1,2j-1} = \Delta Q_{ij}\left\langle(\delta x(z_i) - <\delta x>)(\delta x(z_j) - <\delta x>)\right\rangle_{er} \\ \Gamma_{2i,2j} = \Delta Q_{ij}\left\langle(\delta x'(z_i) - <\delta x'>)(\delta x'(z_j) - <\delta x'>)\right\rangle_{er} \\ \Gamma_{2i-1,2j} = \Delta Q_{ij}\left\langle(\delta x(z_i) - <\delta x>)(\delta x'(z_j) - <\delta x'>)\right\rangle_{er} \\ 1\le i\le n_s,\ 1\le j\le n_s,\ \text{where } \Delta Q_{ij} \overset{\text{def}}{=} \Delta z\sqrt{\rho(z_i)\rho(z_j)}, \\ <\delta x> = \sum_{n=1}^{n_s} \Delta z\,\rho(z_n)\delta x(z_n) \text{ and } <\delta x'> = \sum_{n=1}^{ns} \Delta z\,\rho(z_n)\delta x'(z_n) \end{cases}$$

which can be easily computed from $\widetilde{\Gamma}$ and $\rho(z)$.
The beam matrix of the whole bunch at the line output is then given by: $\mathcal{S} = \begin{pmatrix} <x^2> & <xx'> \\ <xx'> & <x'^2> \end{pmatrix}$ where the notations used are explained hereafter.

- $< x^2 >$ is the RMS value of the transverse beam extension at the line output. Since the motions of $\tilde{x}(z)$ and $\delta x(z)$ are uncorrelated (Section 1), we have:

$$<x^2> = \int dz\,\rho(z)\left[(\sigma_x^2(z) + (\delta x(z) - <\delta x>)^2\right]$$

[3]For flat beams, the roll angle ψ, coupling both transverse planes, may become critical for the emittance growth in the plane where the beam dimension is the smallest, but, actually, it is not yet implemented in the method.

[4]From now on the rest of the paper, by "errors of the line", we will always refer to the structure and BPM misalignments, to the BPM and correction resolution, and to the initial conditions of the different trajectories considered in the correction algorithm.

[5]Here, we will only consider static misalignments of the structures, resulting from the linac pre-alignment strategy; then, we suppose that the characteristic time required to apply the correction remains very small compared to the characteristic period of the machine vibrations (ground motion).

where $\sigma_x(z)$ represents the transverse size (RMS value) of the z-slice at the line output.

- In a similar way, and with evident notations, we have:

$$<x'^2> = \int dz \rho(z) \left[\sigma^2_{x'}(z) + (\delta x'(z) - <\delta x'>)^2\right]$$
$$<xx'> = \int dz \rho(z) \left[\sigma_{xx'}(z) + (\delta x(z) - <\delta x>)(\delta x'(z) - <\delta x'>)\right]$$

Thus, we can write the matrix $\mathcal{S}$ in the following manner:

$$\mathcal{S} = \Sigma_0 + \begin{pmatrix} \sum_{n=1}^{n_s} X_{2n-1}^2 & \sum_{n=1}^{n_s} X_{2n-1}X_{2n} \\ \sum_{n=1}^{n_s} X_{2n-1}X_{2n} & \sum_{n=1}^{n_s} X_{2n}^2 \end{pmatrix} \quad (8)$$

where Σ_0 is the beam matrix at the line output, assuming no error within the line[6], and where X is the $2n_s$-dimensional vector defined by:

$$\begin{cases} X_{2n-1} = \sqrt{\Delta z \rho(z_n)}\left(\delta x(z_n) - <\delta x>\right), & 1 \le n \le n_s \\ X_{2n} = \sqrt{\Delta z \rho(z_n)}\left(\delta x'(z_n) - <\delta x'>\right), & 1 \le n \le n_s \end{cases} \quad (9)$$

the covariance matrix of which is the matrix Γ previously defined. Finally, the RMS emittance is defined as usual by:

$$\epsilon\left(X\right) \stackrel{\text{def}}{=} \sqrt{\det\left(\mathcal{S}\right)} \quad (10)$$

In order to go further in the computations, we are forced to make the following assumption: we assume the vector X_{er} to be Gaussian, so that the vector X becomes also Gaussian[7]. Hence, the knowledge of Γ permits the complete description of the statistical distribution ρ_X related to the vector X:

$$\rho_X\left(X\right) = \frac{1}{(2\pi)^{n_s}\sqrt{\det(\Gamma)}} \exp\left(-\frac{1}{2}{}^{\mathrm{T}}X\Gamma^{-1}X\right) \quad (11)$$

The first and second moment of the emittance distribution are then:

$$\begin{aligned} <\epsilon>_{er} &= \int_{\mathbf{R}^{2n_s}} \epsilon(X)\,\rho_X(X)\,dX \\ <\epsilon^2>_{er} &= \int_{\mathbf{R}^{2n_s}} \epsilon^2(X)\,\rho_X(X)\,dX \end{aligned} \quad (12)$$

The second moment is easy to compute, since the function $\epsilon^2(X)$ is a polynomial in X of degree 4. For the computation of the first moment, a direct estimation by numerical integration is of course out of question (the computation time growing exponentially with $2n_s$). In fact, we are able to reduce this integral to a 2-dimensional integral (independently of n_s) and, under these conditions, we can compute it numerically [3].

If now, we note $N(\epsilon)$, the percentage of machines which give, a final single-bunch emittance lower than ϵ, we have:

$$N(\epsilon) = \int_{\epsilon(X)\le\epsilon} \rho_X(X)\,dX = \int_{\mathbf{R}^{2n_s}} \Theta\Big(\epsilon - \epsilon(X)\Big)\rho_X(X)\,dX$$

where Θ represents the Heaviside step function. Thus, by definition of the density ρ_ϵ, we have:

$$\rho_\epsilon(\epsilon) \stackrel{\text{def}}{=} \frac{dN}{d\epsilon}(\epsilon) = \int_{\mathbf{R}^{2n_s}} \delta\Big(\epsilon - \epsilon(X)\Big)\rho_X(X)\,dX \quad (13)$$

where δ is the Dirac distribution. Unfortunately, no solution was found permitting the estimation of this distribution in the most general case. Indeed, we have to approximate $\epsilon(X)$ by its development at the second order in the coefficients of the vector X. In other words, we assume that a perturbation regime has been reached, for which the non-constant part of the function $\epsilon(X)$ becomes small, when averaging over the distribution of the beam line errors, in such a way that the moments of order greater than two can be neglected. Thus, we write:

$$\epsilon(X) = \sqrt{\det(\Sigma_0)}\left[1 + \frac{1}{2}{}^{\mathrm{T}}X\Gamma_0^{-1}X\right] + \circ(X^4) \quad (14)$$

where Γ_0 is the following 2×2 block diagonal matrix:

$$\Gamma_0 \stackrel{\text{def}}{=} \begin{pmatrix} \Sigma_0 & 0 & \dots & 0 \\ 0 & \Sigma_0 & \dots & 0 \\ \vdots & \vdots & \ddots & \vdots \\ 0 & 0 & \dots & \Sigma_0 \end{pmatrix} \quad (15)$$

Finally, with this approximation, we obtain [3]:

$$\rho_\epsilon(\Delta\epsilon/\epsilon) = \frac{1}{2\pi}\int_{-\infty}^{\infty} dk\, \exp\Big(ik(\Delta\epsilon/\epsilon)\Big)\left(\prod_{p=1}^{2n_s}(1+ik\lambda_p)\right)^{-\frac{1}{2}}$$

where $\Delta\epsilon/\epsilon \stackrel{\text{def}}{=} \Big(\epsilon - \sqrt{\det\Sigma_0}\Big)/\sqrt{\det\Sigma_0}$ and where λ_p, $1 \le p \le 2n_s$, are the $2n_s$ eigenvalues of the matrix $\Gamma\Gamma_0^{-1}$.

6 CONCLUSION

Starting from a given probability law for the misalignments of the beam line components, a given trajectory correction scheme, and a given focusing lattice, the method computes the statistical distribution laws of certain quantities relative to the beam itself. Therefore, the power of this new approach lies in the fact that it can generate, in one single passage, statistical results which could be reproduced by a classical tracking program, but in a much more tedious way (several runs on several beam lines with randomly generated misalignments).

7 REFERENCES

[1] A. Chao, B. Richter, C.-Y. Yao, *Nucl. Inst. Meth.*, **178** (1980) p. 1.

[2] T.O. Raubenheimer, K. Kubo, *Nucl. Inst. Meth.*, **A370** (1996) p. 303.

[3] S. Fartoukh. A Statistical Approach to Analyse the Efficiency of BNS Damping and Correction Algorithms in Linear Colliders. CERN/PS 97-06 (LP) (1997).

[6] $\Sigma_0 = \sum_{n=1}^{n_s} \rho(z_n)\,\Delta z\, R^0_{n,n}\,\Sigma_{in}(z_n)\,{}^{\mathrm{T}}R^0_{n,n}$ where $\Sigma_{in}(z_n)$ is the beam matrix of the slice z_n at the line input and $R^0_{n,n}$, the diagonal block (n,n) of the generalised R-matrix of the whole line, which is also the classical 2×2 transfer matrix describing the motion of the slice z_n without any wakefield (Section 1).

[7] X depends linearly on the vector $\mathcal{X}$, Eq. 9, which depends linearly on the vector X_{er}, Eq. 6.

EMITTANCE DILUTION IN 1 AND 5 TeV 30 GHz LINEAR COLLIDERS

G. Guignard, T.O. Raubenheimer, D. Schulte
CERN, 1211 Geneva 23, Switzerland

Abstract

In this paper, we describe the single and multi-bunch sources of emittance dilution in the linacs of both 1 and 5 TeV center-of-mass energy linear colliders. The linacs operate at high rf accelerating gradients with a frequency around 30 GHz. At this high accelerating frequency, the wakefields are very strong and we discuss the BNS damping and correction procedures as well as the alignment and construction tolerances that are required to preserve the transverse emittance. Finally, because the collider must operate with long bunch trains, we consider the multi-bunch emittance dilution for a few cases where either the long-range transverse wakefield is damped or it is decreased by a combination of weak damping and detuning.

1 INTRODUCTION

In this paper, we discuss the emittance dilutions in linacs for linear colliders with center-of-mass energies (cms) between 1 and 5 TeV. The 5 TeV collider is based upon the design described in Refs. [1, 2] while the 1 TeV version is similar to the CERN Compact LInear Collider (CLIC)[3] although using slightly different parameters which have been optimized to reduce the effect of the transverse wakefields. The primary beam parameters for both cms energies are listed in Table 1.

Center-of-mass energy [TeV]	1	5
Luminosity $[10^{33} cm^{-2} s^{-1}]$	10	100
Part. per bunch (N) $[10^{10}]$	0.4	0.3
Bunches per train (n_b)	45	200
Bunch spacing (Δt) [ns]	0.5	0.5
Bunch length (σ_z) [μm]	50	35
Emit. from DR ($\gamma\epsilon_{x/y}$) $[10^{-8}]$	100 / 5	40 / 0.5
Emit. at FF ($\gamma\epsilon_{x/y}$) $[10^{-8}]$	125 / 10	50 / 1

Table 1: Beam parameters for 1 and 5 TeV colliders

In both cases, the accelerators are based on 30 GHz rf power. This relatively high rf frequency allows for much higher acceleration gradients *without* significantly more severe alignment tolerances[2, 4]. Even though the wakefields are much stronger in the high frequency structures, this scaling arises because the optimized charge and bunch length are much smaller and thus the *effect* of the wakefields and the required tolerances are comparable to those in lower frequency designs.

The primary sources of emittance dilution that we considered are due to misalignments, both static and time-varying, of the accelerator sections, quadrupoles, and BPMs. Simulations were performed using the codes LIAR[5] and MBTR[6] which differ slightly in the models utilized but give similar results. In the next sections, we first describe the linacs that were studied and then discuss the single bunch dilutions, the multi-bunch beam break-up and emittance dilution, and finally, the jitter and stability issues.

2 LINAC DESIGNS

The loaded accelerating gradient is 100 MV/m in the 1 TeV case while it is twice that in the 5 TeV design. Both designs have an injection energy of 10 GeV and the linacs are constructed from standard FODO arrays. In addition, the lattice cell lengths and beta functions, for the 1 and 5 TeV cases, scale roughly with the beam energy to the powers 0.4 and 0.5 and are arranged into 5 or 6 separate sectors, respectively. The linac parameters are listed in Table 2 and the vertical beta function in the 5 TeV design is shown in Fig. 1.

Center-of-mass energy [TeV]	1	5
Loaded acc. gradient (G) [MV/m]	100	200
Beam loading	15.7	12.3%
Total linac length [km]	8.1	15.8
Active/total length	65%	80%
Initial energy [GeV]	10	10
Init. cell length [m]	6.6	7.2
Approx. energy scaling	0.4	0.5
Average rf phase (ϕ_{rf})	$-13°$	$-5°$
Energy overhead for BNS	2%	1%

Table 2: Linac parameters for 1 and 5 TeV colliders

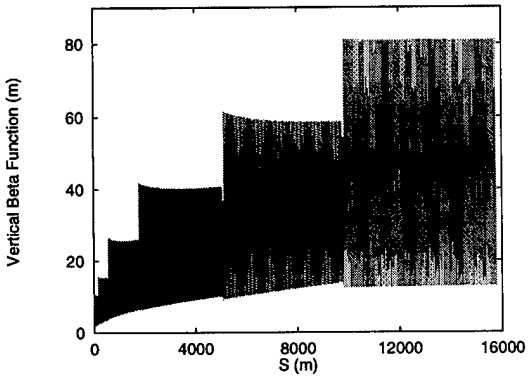


Figure 1: β_y in a linac of the 5 TeV collider.

In most sectors, the phase advance per cell starts at roughly 90° ~100° and then slowly decreases, reducing the variation of the energy spread required for 'autophasing'[7] which is used to control the single bunch beam break-up. In the 1 TeV case, this required energy spread is roughly 0.8% rms while it is about 0.4% rms in the 5 TeV case. Finally, the average rf phase required to achieve a final relative energy spread of 0.8% full width is -13° and -5° for the two cases while the energy overhead required to vary the rf phases and implement the autophasing is roughly 1~2%.

0-7803-4376-X/98/$10.00 © 1998 IEEE

3 SINGLE BUNCH DILUTIONS

The primary single bunch emittance dilutions are due to the transverse wakefields and the non-zero beam trajectory that arises from quadrupole and BPM misalignments. As listed in Table 3, we have assumed tolerances of 10 μm random misalignments of the accelerator structures and 2 μm alignment between the quadrupoles and the BPMs; the initial quadrupole alignment is not important. These values are similar to those used in the NLC design[8] and would be attained using beam-based alignment. Specifically, the accelerator structures could be aligned to the beam trajectory by measuring the beam induced dipole mode power and the quadrupole-to-BPM alignment could be determined by varying the quadrupole strengths; more details on the alignment techniques can be found in Ref. [8].

Center-of-mass Energy [TeV]	1	5
Tolerance on quadrupoles [μm]	100	100
Tolerance on rf struc. [μm]	10	10
Tol. on BPM-to-quad [μm]	2	2
Correction procedures	1-to-1	1-to-1 & ϵ-bumps
Single Bunch $\Delta\epsilon_y/\epsilon_y$	45%	33%
Full Train $\Delta\epsilon_y/\epsilon_y$	46%	37%
Emittance Budget	100%	100%

Table 3: Tolerances for 1 and 5 TeV colliders; the 1 TeV version only uses 1-to-1 trajectory correction while the 5 TeV collider also requires the use of emittance bumps similar in concept to those used in the SLC.

With these tolerances and correcting the trajectory with the simple 1-to-1 method, we find ~50% vertical emittance growth in the 1 TeV design and ~200% growth in the 5 TeV case. While with the 1 TeV parameters, the emittance dilution after the 1-to-1 trajectory correction is acceptable, this is not the case at 5 TeV and thus some additional form of emittance correction has to be considered.

3.1 Emittance Correction

There are a number of possible emittance correction techniques. In this paper, we describe a global correction technique where emittance tuning 'bumps' are varied to minimize the emittance at emittance diagnostic stations located along the linacs; a similar technique is routinely used at the Stanford Linear Collider (SLC) to reduce the vertical emittance dilution from roughly 1000% to about 100%[9]. In our case, the emittance tuning bumps are constructed from pairs of accelerator structures which are separated by 90° in betatron phase and are located upstream of the diagnostic stations. The results of simulations are shown in Fig. 2 where five sets of bumps reduce the emittance dilution from roughly 190% to about 35%. Finally, results using an alternate technique, where the phase advance along the linac is varied by small changes in the quadrupole strengths, are describe in Ref. [10]; here, a similar six-fold reduction was also found.

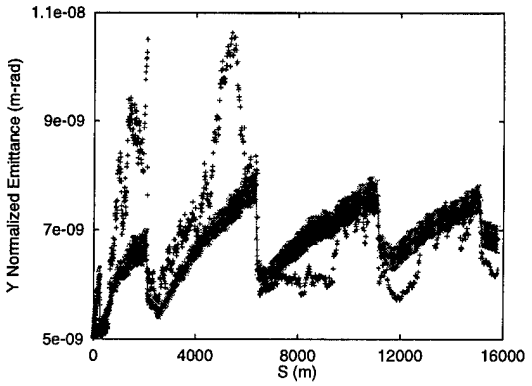


Figure 2: Simulation of emittance growth versus distance in 5 TeV linac after correction using 5 pairs of movable accelerator structures to minimize the emittance at the emittance diagnostic stations; the line is the average of 40 different error distributions with error bars to denote the variation while the crosses are the results from one of the 40 cases.

4 MULTI-BUNCH DILUTIONS

Multi-bunch beam break-up will limit the bunch-to-bunch spacing. In these high energy linacs, the amplitude of the long-range transverse wakefield is reduced by 'detuning' the dipoles modes so that there is a spread in mode frequency and/or by damping the wakefield directly. In either case, the wakefield decays rapidly with time. Thus, the threshold for multi-bunch instabilities, which is proportional to both the bunch charge and the wakefield, is extremely sensitive to the bunch separation.

We have calculated the emittance dilution that arises from an injection trajectory error versus the bunch separation assuming a wakefield calculated by scaling the NLC DDS accelerator structure[8] to 30 GHz. The dilution remains roughly equal to the single bunch dilution until the bunch separation is reduced to 10~12 rf buckets where the beam break-up becomes significant. Similar results are found using the wakefield for the CLIC damped structure[11] but the CLIC DDS accelerator structure[12] does not perform as well at the shorter bunch spacing because it was optimized for a bunch spacing of 30 buckets.

If the multi-bunch beam break-up is small, the multi-bunch emittance dilutions are also usually small when compared to the single bunch emittance dilutions. Assuming the tolerances described in the previous section, we find that this is true for both the 1 and 5 TeV cases; as listed in Table 3, the dilutions with a full bunch train are very similar to the single bunch dilutions.

5 JITTER AND STABILITY

One of the big liabilities in a large linear collider is the sensitivity to vibration and drifts. We can separate the motion into three regimes: motion due to ground waves which tends to be highly correlated, high-frequency motion which is essentially random from magnet-to-magnet (jitter), and slow drifts where the elements perform random-walk type movements.

5.1 *Correlated Ground Motion*

At low frequencies ($f \lesssim 10$ Hz), where the wavelength is long compared to the betatron wavelength, the correlated ground motion has little effect on the beam; the beam simply follows the ground contour. In addition, the trajectory feedback systems further reduce the sensitivity to the low frequency motion. Calculations, based on measurements at SLAC[8], show that, in the worst case, the induced beam motion would be less than 5% of the beam size.

5.2 *Jitter*

The jitter tolerance, to limit the beam motion to 25% of the beam size due to uncorrelated magnet vibration, is 4.5 nm in the 1 TeV design and 1.2 nm in the 5 TeV design; the reduction is primarily due to the smaller beam sizes in the higher energy case. This imposes tight, although not unreasonable, tolerances on the man-made or 'cultural' vibration; measurements at the ALS in Berkeley and the FFTB at SLAC have observed roughly 1 nm difference between quiet conditions where the magnet motion is simply due to ground motion and noisy conditions where all systems where operational. If necessary, additional stabilization could be provided by using either active or passive damping.

5.3 *Drifts*

Slow drifts of the accelerator components are frequently described with the 'ATL' relation[13] which assumes that the magnet positions along the linac perform a random walk in both time and separation. In this case, the expected difference in transverse position between any two locations will vary as $\langle \Delta y^2 \rangle = A \star T \star L$ where T is the time between successive measurements, L is the distance separating the two locations, and A is a coefficient that depends on the geological conditions of the surrounding environment. For our calculations, we use a coefficient A=$5 \times 10^{-7}\, \mu^2/s/m$. This is larger than values measured in the FFTB tunnel at Stanford Linear Accelerator[14] but is smaller than measurements at some other laboratories.

In the 1 TeV case, the emittance dilution increases by roughly 50% after 30 minutes which is similar (50% faster) to the NLC design. The dilution increases roughly 3 times faster in the 5 TeV case as is illustrated in Fig. 3. This suggests that, in the 5 TeV case, the beam trajectory should be re-steered (using 1-to-1 correction) every 5 minutes to constrain the time-averaged dilution to roughly 15%. Alternately, a similar correction procedure could be implemented as a slow steering feedback loop. In either case, there should be minimal luminosity impact.

6 ACKNOWLEDGEMENTS

The determination of the beam parameters for these cases has evolved from many discussions with J.P. Delahaye and I. Wilson. In addition, one of us (T.R.) would like to thank the members of the PS Division and the CLIC group for their generous hospitality during the last year.

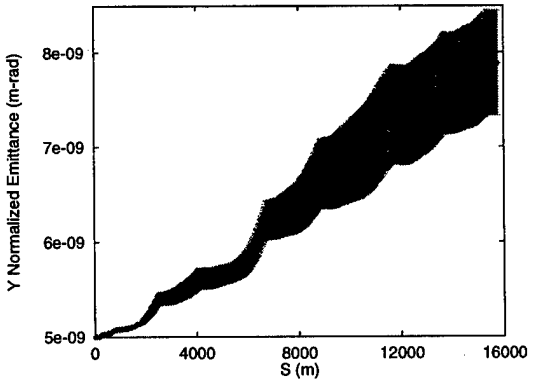


Figure 3: Simulation of emittance growth versus distance in the 5 TeV linac due to ATL motion after 10 minutes with coefficient $A = 5 \times 10^{-7}$; the simulation includes seven feedback stations that constrain the beam trajectory along the length of the linac and the results are the average of 40 different seeds with error bars denoting the variation.

7 REFERENCES

[1] P. Chen *et al.*, "A 5 TeV Linear Collider on the NLC Site", *Proc. of 1996 DPF/DPB Snowmass Meeting* (1996).

[2] J.P. Delahaye *et al.*, "A 30 GHz 5 TeV Linear Collider", *submitted to these proceedings.*

[3] CLIC is a 0.5~1 TeV e^+e^- linear collider design using 30 GHz rf and operating as a Two-Beam Accelerator where a low energy 'drive' beam is used to generate the rf.

[4] J.P. Delahaye *et al.*, "Scaling Laws for e^+e^- Linear Colliders", Clic–Note–333 (1997).

[5] R. Assmann *et al.*, "LIAR—a simulation code for LInear Accelerator Research", *Proc. of the 1996 Linac Conf,* Geneva, Switzerland (1996).

[6] G. Guignard *et al.*, "Multibunch Emittance Preservation in CLIC", *Proc. of the 1996 Eur. Part. Acc. Conf.,* Sitges, Spain (1996).

[7] V. Balakin, *Proc. 1988 Workshop on Linear Colliders,* SLAC–report–355 (1989) p. 55.

[8] NLC ZDR Design Group, "A Zeroth Order Design Report for the Next Linear Collider", SLAC Report–474 (1996).

[9] J.T. Seeman, F.J. Decker, I. Hsu, "The Introduction of Trajectory Oscillations to Reduce Emittance Growth in the SLC Linac", *Proc. of 15th Int. Conf. High Energy Acc.,* Hamburg, Germany (1992) p. 879.

[10] G. Guignard *et al.*, "Beam Characteristics versus Cavity Models in CLIC", *submitted to these proceedings.*

[11] M. Dehler *et al.*, "CLIC Waveguide Damped Accelerator Structure Studies", *Proc. of the 1996 Linac Conf.,* Geneva, Switzerland (1996) p. 734.

[12] M. Dehler *et al.*, "Design of a 30 GHz Damped Detuned Accelerating Structure" *submitted to these proceedings.*

[13] V. Shiltsev, "Space-Time Ground Diffusion: the ATL Law for Accelerators," *Proc. of the 4th Int. Work. on Acc. Align.,* Tsukuba, Japan (1995).

[14] R. Assmann *et al.*, "Beamline Stability Measurements with a Stretched Wire System in the FFTB," *Proc. of the 1996 Linac Conf,* Geneva, Switzerland (1996).

A LOW EMITTANCE LATTICE FOR THE CLIC DAMPING RING

J.P.Potier, CERN, CH-1211 Geneva 23, L.Rivkin, PSI, CH-5232 Villigen

Abstract

Damping rings with very small normalized equilibrium emittance and short damping times are required to deliver trains of bunches with a high repetition rate for the high-luminosity linear colliders. Using analytic expressions for the equilibrium emittance as a function of deflection angle per dipole, as well as the expression for the Twiss parameters providing the minimum emittance, a strategy to stay close to this minimum is described. In order to get as close as possible to the optimum Twiss parameters values, a quadruplet lattice with high horizontal phase advance is introduced. Finally, this approach is illustrated for the particular case of the CLIC damping ring and the resulting performance is described.

1 INTRODUCTION

The electron-positron linear colliders at high energy, requiring high luminosity, are all based on a high collision rate using beams of very small dimensions at the interaction point. These small beam dimensions require strong focusing in the final focus, as well as very small transverse emittance beams. Such small emittance will possibly be reached with high brightness electron guns presently under development, but is impossible to reach directly with the positron sources that have emittance three or more orders of magnitude higher. Therefore, for the positron beam, a damping ring facility will be necessary.

Most of the damping rings proposed nowadays are based on the Theoretical Minimum Emittance lattice (TME) in which the Twiss functions β_x and D_x are minimum in the middle of the bending magnet. The simplest example is a combined function bending magnet with a defocusing gradient and surrounding focusing quadrupoles to produce the appropriate Twiss functions. Such a lattice was proposed [1] for the CLIC damping ring. This ring was designed for the working energy of 3 GeV in order to get enough damping, but due to the strong chromaticity correction sextupoles, it suffered from a severe detuning versus emittance and from a great sensivity of the transverse dynamical acceptance to misalignment errors.

In this paper, using analytic expressions of the equilibrium emittance as a function of the deflecting angle per dipole, as well as the expression for the Twiss parameters corresponding to the minimum emittance, an expression for the emittance of the de-tuned lattice is proposed and a strategy to stay as close as possible to the minimum is developed, keeping the dispersion as high as possible, in order to limit the strength of the chromaticity correction sextupoles. A main damping ring based on this approach is then derived providing beam characteristics fulfilling, without any wigglers, the 500 GeV/c CLIC injector complex requirements [2]. The corresponding parameter list for this damping ring is summarised in Table 2.

2 MINIMUM EMITTANCE LATTICE

The transverse equilibrium beam emittance of a ring working at an energy E, composed of dipole magnets of length L and deflection angle θ, can be expressed as a function of the optics parameters in the middle of the bending magnet α, β, D, D'. After integration of the synchrotron integrals, using the approximation of small bending angle, the emittance is [3].

$$\varepsilon_{x0} = \frac{C_q E^2}{J_x}\frac{I_5}{I_2} = \frac{C_q E^2}{J_x}\left[\begin{array}{l} \dfrac{\gamma D^2 + 2\alpha\cdot D\cdot D' + \beta D'^2}{L}\cdot\theta \\ -\left(\dfrac{\alpha\cdot D' + \gamma\cdot D}{12}\right)\cdot\theta^2 \\ +\left(\dfrac{\beta}{12\cdot L} + \dfrac{\gamma\cdot L}{320}\right)\cdot\theta^3 \end{array}\right]$$

where $C_q = 1.468\cdot 10^{-6}\left[\dfrac{\mathrm{m}}{\mathrm{GeV}^2}\right]$. As is well known, this expression is minimum for $\alpha_{opt} = D'_{opt} = 0$ i.e. the optical and dispersion functions are symmetric with respect to the middle of the bending magnet and

$$\beta_{opt} = \frac{L}{2\cdot\sqrt{15}},\quad D_{opt} = \frac{L\cdot\theta}{24},\quad \varepsilon_{x0} = \frac{C_q\cdot E^2}{J_x}\cdot\frac{\theta^3}{12\sqrt{15}}$$

For the de-tuned lattice, still preserving the symmetry, the emittance blow-up $\varepsilon/\varepsilon_{opt}$ can be expressed using the normalised values $\beta_r = \beta/\beta_{opt}$ and $D_r = D/D_{opt}$

$$\varepsilon_r = \frac{5}{8}\cdot\left[\frac{D_r^2}{\beta_r} - \frac{2\cdot D_r}{\beta_r}\right] + \frac{9}{2}\cdot\left[\frac{1}{4\cdot\beta_r} + \frac{\beta_r}{9}\right].$$

The family of curves for different values of constant blow-up ranging from 2 to 128 in the β_r, D_r diagram is shown using logarithmic scales in Figure 1.

For a given emittance blow-up, the maximum of $D_r = f(\beta_r)$ curve is chosen, where

$$\beta_{rmx} = \varepsilon_r \text{ and } D_{rmx} = 1 + \frac{2}{\sqrt{5}}\cdot\sqrt{\varepsilon_r^2 - 1}.$$

0-7803-4376-X/98/$10.00 © 1998 IEEE

The curve representing the position of these maxima is also shown in Figure 1.

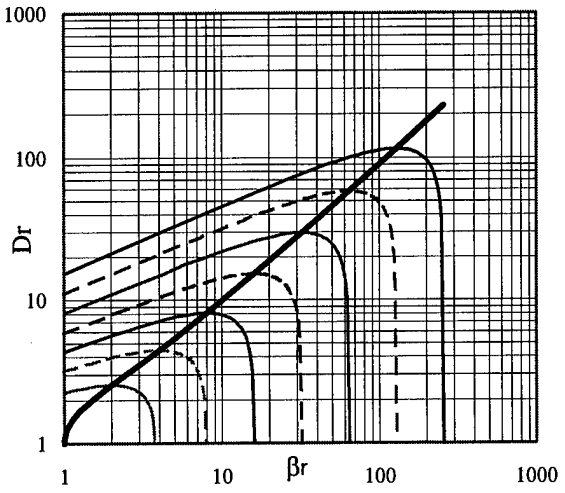


Figure 1 Dispersion versus beta function for a given emittance detuning and dispersion versus emittance for a maximum dispersion and a given emittance detuning

3 CHOICE OF THE LATTICE PARAMETERS

3.1 Bending field and design energy

In the CLIC injector complex [2], one train of 1 to 10 bunches is injected and extracted at a repetition rate, f_r from 1210 to 2400, but a number of trains k, are concurrently circulating in the damping ring in order to leave a larger time for damping $T = k/f_r$. The present design is based on trains of 10 bunches, spaced by 20 cm, at a repetition frequency f_r of 1800 Hz.

The damping ring circumference C is chosen to accommodate the k trains, with enough separation between them to allow for the rise and fall of the injection and extraction system l_k. In the case of a fast kicker, l_k is 7.5 m (25 ns). Using a particular combination of fast kickers and RF kickers, the time separation between the bunch trains, l_s, can be reduced down to $l_k/2$ (12.5 ns) [4]. If n is the number of damping time necessary to damp the incoming emittance the reduced damping time

$\tau_r = \frac{\tau_{x,y}}{C}$ has to satisfy the condition $\tau_r \le \frac{1}{n \cdot l_s \cdot f_r}$

As shown in [5], the round beam produced by the positron injector is first pre-damped in a collector ring with large transverse and longitudinal acceptances during $5\,\tau_{x,y}$ and then damped in the main damping ring (MDR) during $4\,\tau_{x,y}$. Under these conditions, with $\tau_r \le 37$ μs/m, the beam emittance at extraction will not be larger than the equilibrium emittance by more than 10%. This value, which depends on the bending field and on the design energy, can be written as

$$\tau_r = \frac{2.54 \cdot 10^{14}}{J_x \cdot B \cdot E^2}$$

with $J_x = 1$ as the bending magnet will have no gradient. In order to maximise the damping, keeping the normalised emittance low, the highest possible field in the bending magnet is chosen while staying far from saturation, B around 1.5 T, and then E from the above equations is E= 2.15 GeV/c.

3.2 Twiss functions in the middle of the bending magnets needed to produce the design emittances

Taking into account the emittance blow-up between the ring exit and the interaction point, the normalised transverse emittances at the output of the main damping ring have to be $\gamma\varepsilon_x = 2.5 \cdot 10^{-6}$ radm, $\gamma\varepsilon_y = 0.04 \cdot 10^{-6}$ radm with a bunch length σ_z = 18 mm. We have chosen to use a low emittance detuning value ε_r = 3.7 to use the TME lattice efficiently with D_r = 4.2 close to the maximum on the detuning curve and β_r = 4.4 (see figure 1). The number n_B of cells can be worked out from the optimum equilibrium emittance and the emittance detuning, resulting in n_B = 60 and a dipole magnet length L = .5 m.

4 QUADRUPLET TME LATTICE

In order to provide the low dispersion and beta values in the middle of the dipole magnet, it will be flanked on each side by a defocusing quadrupole followed by a focusing quadrupole. The corresponding lattice is shown in Figure 2.

Parameter	Symbol	Units	TME lattice
Momentum	E	GeV/c	2.15
Deflection per cell	θ	dg	6.0
Momentum compaction	α_p	10^{-3}	0. 29
Normalised equilibrium emittance	$\gamma\varepsilon_n$	10^{-6} radm	2.56
Normalised damping time	τ_r	10^{-6}s	37
Horizontal phase advance per cell	μ_x	2π	0.445
Vertical phase advance per cell	μ_y	2π	0.217
Emittance detuning $\varepsilon/\varepsilon_{opt}$	ε_r	-	3.7
Dispersion in the middle of the bending	D	mm	9.4
β in the middle of the bending	β	m	0.292
β detuning	βr	-	4.42
Dispersion detuning	D_r	-	4.19

Table 1: Main characteristics of the CLIC TME lattice

The main characteristics of a ring built of 60 cells are shown in Table 1. The values found are in good agreement with the analytical calculation made above.

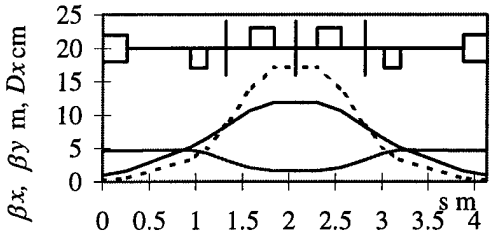


Figure 2: Twiss functions for the TME lattice providing an emittance detuning of 3.7

5 MAIN DAMPING RING DESIGN

Each damping ring arc consists of five TME quadruplet cells and two dispersion suppressers, that utilise half of a regular bending magnet. The arcs are separated by short straight sections equipped with quadrupole triplets to get $\alpha_{x,y} = 0$ and a small β_x in the middle. These short straight sections can house a damping wiggler. An arc is represented in Figure 3.

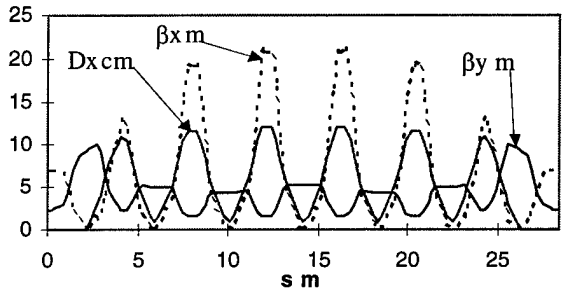


Figure 3: Arc of the CLIC main damping ring including short straight sections

The ring is made up of two halves, 5 arcs each, and two long straight sections with π phase advance in each plane. These straight sections are inserted symmetrically, one for the RF cavities the other for the injection and extraction systems. The chromaticity is corrected by two families of sextupoles in the regular cells, and the 4 other families in the dispersion suppresser and in the straight sections.

The dynamic acceptance has been studied in the ring without the long straight sections. The closed orbit is corrected to 50μm, using position monitors (assumed resolution 25 μm) located at each sextupole, with the correcting dipoles located at the same positions. The dynamic acceptance is more than $6.5*10^{-6}$ radm without errors. In this case, de-tuning versus the emittance in the aperture is less than 0.005 in the horizontal plane and 0.003 in the vertical plane at 10 % coupling. In presence of errors, at full coupling, with *dP/P* within ± 0.5% and position errors up to 50μm, the dynamic acceptance is $4.0*10^{-6}$radm.

As the bunch distance is a multiple of 0.2 m the RF frequency of the accelerating cavity will be 1.5 GHz with a voltage of 1 MV providing enough Touschek life-time. The parameters of the main damping ring are in Table 2.

Parameter	Symbol	Units	MDR ring
Momentum	E	GeV/c	2.15
Number of cells	-	-	60
Ring length (without straight sections)	L	m	283
Normalised equilibrium emittance	$\gamma\varepsilon_n$	10^{-6} radm	2.5
Emittance detuning $\varepsilon/\varepsilon_{opt}$	ε_r	-	3.8
Damping partition numbers	$J_{x,y,z}$		1,1, 2
β detuning	βr		4.4
Dispersion detuning	Dr		4.2
Normalised damping time	τ_r	10^{-6}s	37
Bending magnet field	B	T	1.47
Horizontal / vertical tunes	$\mu_{x,y}$	2π	31.2/13.3
Horizontal/vertical chromaticities	μ_y		-107 / -21
Momentum compaction	α_p	10^{-3}	0.24
Dynamical acceptance in +/- 1%	A_{dyn}	10^{-6} radm	4.0
Rms displacement errors	σ_{misal}	μm	50
RF frequency	f_{rf}	GHz	1.5
RF voltage	V_{RF}	MV	1.0
Energy loss per turn	U_0	MV	0.39
Bunch length	σ_z	mm	1.8

Table 2: Characteristics, of the main damping ring adapted to the CLIC requirements using the TME lattice

CONCLUSIONS

Using an analytic approach, a damping ring working close to the theoretical minimum emittance has been designed fulfilling CLIC's requirements. As the CLIC bunch train length and repetition rate are evolving, this approach will be used to adapt the parameters and possibly introduce wigglers, to adapt to the new requests.

REFERENCES

[1] J.P. Delahaye, J.P. Potier, Reverse Bending Magnets in a Combined-Function Lattice for the CLIC Damping Ring, CERN/PS 89-21 (LP), PAC, Chicago 1989.

[2] R. Bossart, H. Braun, F. Chautard, M. Comunian, J.P. Delahaye, J.C. Godot, I. Kamber, J.H.B. Madsen, L. Rinolfi, S. Schreiber, G. Suberlucq, I. Wilson, W. Wuensch, CLIC - Test Facility Developments and Results, CERN/PS 95-11 (LP), PAC, Dallas, 1995

[3] L.C. Teng , LS-17 1985, ANL-FNAL

[4] J.P. Delahaye and J.P. Potier, A Novel Injection and Extraction Scheme for Short Bunch Separation in Accelerator Rings, CERN/PS 94-15 (LP), EPAC, London, 1994

[5] J.P.Delahaye, An Injector Complex for the Main Beams of the CERN Linear Collider, CERN/PS 94-14 (LP), EPAC, London, 1994

NULLING EMITTANCE MEASUREMENT TECHNIQUE FOR CLIC TEST FACILITY

P. Tenenbaum*, H.H. Braun, F. Chautard
CERN, CH-1211 Geneve 23, Switzerland

Abstract

In order to test the principle of Two-Beam-Acceleration (TBA), the CLIC Test Facility utilizes a high-intensity drive beam of 640 to 1000 nC to generate 30 GHz accelerating fields. To ensure that the beam is transported efficiently, a robust measurement of beam emittance and Twiss parameters is required. This is accomplished by measuring the beam size on a profile monitor, while scanning five or more upstream quadrupoles in such a fashion that the Twiss parameters at the profile monitor remain constant while the phase advance through the beam line changes. In this way the beam size can be sampled at different phases while a near-constant size is maintained at the profile monitor. This eases many of the difficulties of such measurement devices, especially those associated with limited dynamic range. In addition, the beam size is explicitly constant for a matched beam, which provides a "nulling" measurement of the match. Details of the technique, simulations, and results of the measurements are discussed.

1 INTRODUCTION

The CLIC Test Facility (CTF) was constructed in order to demonstrate the validity of the two-beam acceleration (TBA) scheme proposed for CLIC, and to gain real-world experience with such a scheme in an accelerator environment. The CTF consists of a pair of linacs constructed side by side: a Drive Beam, which accelerates a high charge electron beam to roughly 50 MeV and injects same in to a line of 30 GHz CLIC Transfer Structures (CTS); and a Probe Beam which accelerates a low charge to roughly 40 MeV and injects same into a line of 30 GHz CLIC Accelerating Structures (CAS). Energy is removed from the Drive Beam via the CTS and transferred to the CAS. The final energy of the Probe Beam after acceleration in the CAS is expected to be 320 MeV[1].

In order to generate the required accelerating fields in the Probe Beam, the Drive Beam will consist of 48 bunches of 14-21 nC, for a total charge on each RF pulse of up to 1 μC[2]. Such high charges imply serious issues of wakefields, beam loading, and beam size, especially since the beam is required to pass through the CTS region in which the aperture is 15 mm diameter. In order to pass through such small apertures, the normalized rms emittance of the Drive Beam train cannot exceed 200 mm.mrad, corresponding to a limit of 1000 mm.mrad for the entire beam[3].

In order to ensure that such tolerances are met, it is necessary to have some means of measuring the emittance of the Drive Beam, which can then be used to tune charge, orbits, RF phases, for example, until the limits above are met.

In an accelerator of the sort described above, the traditional method of emittance measurement is the so-called "quad scan" technique: the beam is focused to a waist on a profile monitor, and the beam size at the monitor is measured as a function of the strength of an upstream quadrupole. This allows reconstruction of the beam phase space at the upstream face of the scanned quadrupole[4]. In the case of the CTF Drive Beam line, such an arrangement is not optimal for several reasons. First, the small aperture of the CTS mandates that all waist points in the beamline be reserved for RF cavities, not profile monitors, and the waists are difficult to shift. Second, the dynamic range demanded by the quad scan technique is difficult to achieve: because the beam size must be modulated by a factor of $\sqrt{2}$ for good resolution of the parameters, quad scans tend to have poor signal-to-noise performance when the beam is large (at the scan extremes), and saturation when the beam is small (at the center of the scan). Third, the profile monitor of choice in the CTF is a combination Transition/Cerenkov Monitor (TCM): an extremely small beam with the high charge and energy parameters described above is likely to damage the TCM. For these reasons a traditional quad scan was contraindicated, and a different technique had to be devised.

2 NULLING EMITTANCE TECHNIQUE

The principal requirement of an emittance measurement technique is that the beam size be measured at different betatron phases, to allow reconstruction of the beam matrix at a single point. Consequently it is possible to imagine a technique in which only the betatron phase is varied, and the beam parameters at the profile monitor remain constant.

This is the basis of the measurement method used on the CTF Drive Beam. Given the design Twiss parameters at a "treaty point" in the line (β_0, α_0), the design parameters at a downstream profile monitor (β_f, α_f), and the design phase advance ν, the strengths of the intervening quads are varied such as to alter the phase advance but still result in the same final beam parameters.

If the beam is not perfectly matched at the treaty point, some modulation of the beam size will occur during the scan; for a perfectly matched beam, no modulation will occur (as opposed to a quad scan, in which modulation occurs under all beam conditions). Thus, for a reasonably-well matched beam, the adjustment of profile digitization

* Current Address: SLAC, Stanford University, Stanford, CA, USA

0-7803-4376-X/98/$10.00 © 1998 IEEE

and filtering remains valid over the entire scan range, and a large beam size can be maintained on the profile monitor at all times. The technique can be thought of as "nulling" in that a perfectly matched beam experiences no modulation in the measured size, and thus the technique has maximum sensitivity when the tunable parameter (mismatch) is near its minimum.

2.1 *Calculation of Quadrupole Strengths*

In this measurement, there are four parameters which are held constant – β_x, β_y, α_x, and α_y – while one parameter is varied, specifically the betatron tune in the measurement plane (the tune in the non-measured plane was not constrained). This requires 5 quadrupole magnets in all. In the CTF Drive beam, six magnets (arranged in 2 triplets) were varied for emittance measurements, and the extra degree of freedom allowed greater scanning ranges. The quad strengths for each scan were generated by the lattice-fitting facility of DIMAD [5], since the quad strengths vary nonlinearly as a function of tune, as shown in Fig. 1. The total range of betatron phase allowed by quad strength limitations was 108° in the horizontal and 72° in the vertical.

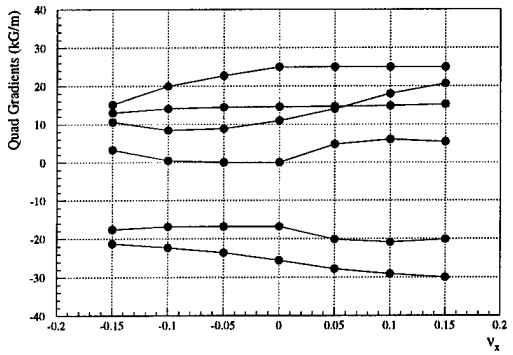


Figure 1: Quadrupole strengths required for ν_x scan.

2.2 *Calculation of the Beam Matrix*

Calculation of the incoming beam matrix follows the traditional emittance measurement formalism. Given an incoming sigma matrix $\sigma^{(0)}$ and a sigma matrix at the profile monitor $\sigma^{(p)}$, the relationship between $\sigma_{11}^{(p)} \equiv (\sigma_x^{(p)})^2$ and $\sigma^{(0)}$ is:

$$\begin{aligned} \sigma_{11}^{(p)} &= R_{11}^2\sigma_{11}^{(0)} + 2R_{11}R_{12}\sigma_{12}^{(0)} + R_{12}^2\sigma_{22}^{(0)} \\ &= r_1s_1 + r_2s_2 + r_3s_3, \end{aligned} \quad (1)$$

where we have defined shorthand variables r_j and s_j to denote transport and beam terms, respectively, of Eq. 1. At each step of the scan the beam size is measured and $\sigma_{11}^{(p)}$ calculated; the R matrix from the input to the screen is calculated from the quad strengths. A least-squares solution to Equation 1 satisfies the matrix equation

$$a = Bc, \qquad \text{where}$$

$$\begin{aligned} a_j &= \sum_i \frac{r_j(i)\sigma_{11}^{(p)}(i)}{\delta^2(i)}, \\ B_{jk} &= \sum_i \frac{r_j(i)r_k(i)}{\delta^2(i)}, \\ c_k &= s_k, \end{aligned} \quad (2)$$

where (i) denotes the values on the ith step of the measurement and $\delta(i)$ is the measurement error on $\sigma_{11}^{(p)}(i)$. The matrix in Eq. 2, a 3 x 3 symmetric matrix, can easily be inverted analytically to yield a solution for the terms of $\sigma^{(0)}$.

2.3 *Simulation of Emittance Scans*

Emittance scans were simulated using DIMAD to track 1000 particles through each step of the emittance scan. Because DIMAD's tracking engine is second-order, this allowed examination of distortions to the fit arising from chromaticity in the quadrupoles between the treaty point and the profile monitor. Table 1 shows the results of the simulation, with monochromatic beam parameters, beam parameters from the sigma matrix of the tracked particles (1% rms energy spread) at the end of the line, and fitted parameters (assuming 10% resolution of the profile sizes). Note that the distortions due to chromaticity are small (deviations of second column from first column), and fitted values agree within errors.

Table 1: Results of simulation studies of Nulling Emittance Technique.

Parameter (unit)	1st Order value	2nd Order value	Fitted value
$\gamma\epsilon_x$ (mm.mrad)	18.4	18.4	18.1 ± 1.4
β_x (m)	0.945	0.986	1.01 ± 0.09
α_x	-1.129	-1.186	-1.19 ± 0.13
$\gamma\epsilon_y$ (mm.mrad)	18.4	19.0	19.4 ± 3.0
β_y (m)	2.691	3.045	3.06 ± 0.6
α_y	-0.600	-0.699	-0.72 ± 0.27

3 RESULTS OF EMITTANCE MEASUREMENT

Early tests of the nulling emittance measurement technique resulted in poor fits and, frequently, imaginary emittances in the vertical plane. Further investigation revealed that both of these pathologies were improved by reducing the strength of the final quadrupole in the fits by roughly 20% at all magnet currents. It was subsequently discovered that the final quad was in fact of a different design from the others, and was weaker than other CTF quads by design. Because the final quad's current-vs.-gradient performance

was uncertain, the scans were redesigned to leave the final quad at zero field (its design strength in the 1996 CTF optics).

Another pathology observed in early tests was that at certain points in the scan the beam size would increase to fill the profile monitor, while for most of the points the beam size varied smoothly. Upon examination it was seen that the scan region which produced well-behaved spot sizes was the region in which all quad strengths were varied monotonically and by increments small compared to their overall strengths, the so-called "perturbative" region of the scans. Magnet scans were re-configured to use only the perturbative regions, resulting in a reduction in the total phase shift available. However, the S/N performance of the system (determined by repeating the scan 3 times and forming an average and rms of the 3 measurements at each point) was seen to be better than expected, and thus the reduction in phase shift did not compromise the fit quality unacceptably. The cause of the discontinuous beam size behavior is not known.

A final oddity observed was that consecutive measurements of the beam emittance would result in inconsistent fits, while the data appeared to be qualitatively similar from one fit to the next. It was determined that on each fit, one point (consisting of 3 beam sizes averaged together) would have a much smaller variance than the other points (as little as 1 μm, while all other points were closer to 20 μm). Because a different point in each scan would be anomalous in this fashion, the low-variance points would pull the fits out of agreement. This was corrected by adding an error of 10 μm in quadrature with the measured variance. This would preserve the overall relative weighting of points but prevent the fits from being pulled in the fashion described. Figure 2 shows a horizontal emittance scan, with the measured data (points) and fit (lines) superimposed.

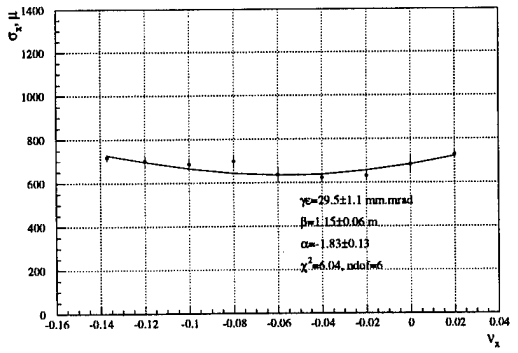


Figure 2: Example of emittance measurement in CTF.

Using the measurement technique as described above, the CTF Drive Beam single- bunch emittance was measured at different bunch charges (2 to 4 nC) and source laser spot sizes (0.7 to 2 mm diameter). Normalized emittances varied from 30 to 50 mm.mrad in the horizontal, and 35 to 70 mm.mrad in the vertical.

4 SYSTEMATIC ERRORS

There are several possible sources of systematic error which can affect the emittance measurement:

- A profile monitor scale factor of up to 2%, based on pixel calibration asymmetries
- A 5% error in determination of absolute energy, based on comparing 2 methods of measurement
- magnet scale factors up to 1% and offsets up to 1% of maximum strength.

The first two errors were studied analytically, while magnet errors were studied via a Monte Carlo simulation. The results of these studies are summarized in Table 2, and compared to systematic errors.

Table 2: Relative contributions of statistical and systematic errors.

Name	Value (typ.)	Stat. error	Scale error	Energy error	Magnet error
$\gamma\epsilon_x$	30-50	5-7%	4%	25%	10%
β_x	1.4	5-7%	0%	5-7%	2-3%
α_x	-1.5	0.2	0.0	0.15	0.03
$\gamma\epsilon_y$	36-70	10-15%	4%	25%	15%
β_y	2.5	10-15%	0%	10-15%	10-15%
α_y	-1.0	0.3	0.0	0.2	0.15

5 CONCLUSIONS

The Nulling Emittance measurement technique is a viable method for measuring beam parameters in environments where the standard quad scan is not available. In the CTF Drive Beam, good statistical resolutions have been achieved for all beam parameters. Some systematic errors (particularly beam energy error) require improvement.

6 ACKNOWLEDGEMENTS

The authors would like to thank M. Comunian, for writing the original emittance acquisition software used in CTF.

7 REFERENCES

[1] CLIC Study Group. *CTF2 Design Report* (CLIC Note 304/CERN PS 96-14(LP) (1996)) 5.

[2] *CTF2 Design Report*, 11.

[3] *CTF2 Design Report*, 29.

[4] Ross, M.C. *et al. Procedings of the 1987 IEEE Particle Accelerator Conference* (1987) 725.

[5] Servranckx, R.V. *et al. Users' Guide to the Program DIMAD*, SLAC Report 285 (Stanford University/SLAC (1990) 23.

A 30 GHz 5-TeV LINEAR COLLIDER

J.P. Delahaye†, G. Guignard†, J. Irwin‡, T.O. Raubenheimer†, R.D. Ruth‡, I. Wilson†, P.B. Wilson‡
† CERN, 1211 Geneva 23, Switzerland ‡Stanford Linear Accelerator Center, California, USA

Abstract
We present parameters for a linear collider with a 3 to 5 TeV center-of-mass energy that utilizes conventional rf technology operating at a frequency around 30 GHz. We discuss the scaling laws and assumed limitations that lead to the parameters described and we compare the merits and liabilities of different technological options including rf power source, accelerator structure, and final focus system design. Finally, we outline the components of the collider while specifying the required alignment and construction tolerances.

1 INTRODUCTION

Over the last decade, there has been an extensive effort in developing designs for a 0.5 to 1 TeV center-of-mass energy (cms) $e+e-$ linear collider[1]. At this time, many of these designs are well advanced and have moved to the stage where detailed engineering is being performed and much of the required technology has been, or is being, demonstrated in dedicated test facilities. Thus, it seems timely to look to the next stage in linear collider development.

In the past, there have been a number of studies of very high-energy linear colliders; for example Ref. [2]. More recently a working group at 1996 DPF/DPB Snowmass meeting was dedicated to the study of a 5 TeV e^+e^- collider and this group concentrated mostly on advanced acceleration and collision techniques[3]. In this paper, we will continue a discussion, that was started in Ref. [4], on the possibility of a 3 to 5 TeV e^+e^- linear collider based on relatively conventional rf power with a frequency around 30 GHz and having a luminosity ($\mathcal{L}$) of $10^{35}\mathrm{cm}^{-2}\mathrm{s}^{-1}$.

The rf frequency is similar to that studied as part of the Compact LInear Collider (CLIC) project. The relatively high rf frequency was chosen because it allows for much higher acceleration gradients *without* significantly more severe alignment tolerances[5]:

$$y_{tol} \sim \sqrt{\Delta\epsilon/\epsilon}\, G^{1/2}/\omega^{7/16} \qquad (1)$$

where $\Delta\epsilon/\epsilon$ is the relative emittance dilution, G is the gradient, and ω is the frequency. Even though the wakefields are much stronger in the high-frequency structures, this scaling arises because the optimized charge and bunch length are much smaller and thus the *effect* of the wakefields and the required tolerances are comparable to that in lower frequency designs. We believe that the primary difficulty presented by the higher frequency choice is the present lack of high power rf sources.

In the following sections, we will first discuss the constraints imposed by the beam-beam interaction, then we will describe the determination of the collider parameters and, finally, we will estimate the impact that these parameters have on the various subsystems of the collider.

2 BEAM-BEAM INTERACTION

The primary difficulty when considering a very high energy e^+e^- collider is the beam-beam interaction at the collision point (IP). Because the beams must be very dense to provide useful $\mathcal{L}$, they have very strong electro-magnetic fields. These fields have two primary effects: first, they cause the particles to radiate beamstrahlung photons which induces a large energy spread, smearing the $\mathcal{L}$ spectrum, and, second, e^+e^- pairs can be produced in the strong fields creating a potential background source.

Two approaches have been or are being investigated to avoid these problems: the muon collider[6], where the relatively massive particles are far less sensitive to the beam-beam forces, and charge compensation, where the beam fields are compensated by co-moving beams or plasma return currents.

Unfortunately, both of these solutions also have significant difficulties. Thus, in this paper, the approach is to optimize the parameters of a conventional e^+e^- linear collider to maximize the amount of $\mathcal{L}$ close to the full cms energy while accepting a substantial smearing in the lower energy $\mathcal{L}$ spectrum. The $\mathcal{L}$ spectrum can be parameterized in terms of Υ, a measure of the field strengths, n_γ, the average number of photons radiated per particle, and δ_B, the energy loss due to the beamstrahlung[7]:

$$\Upsilon \approx \frac{5}{6}\frac{r_e^2\gamma N}{\alpha\sigma_z(\sigma_x+\sigma_y)} \quad n_\gamma \approx \frac{2r_e\alpha N}{\sigma_x+\sigma_y}\frac{1}{\sqrt{1+\Upsilon^{2/3}}} \qquad (2)$$

$$\delta_B \approx \frac{5}{4}\frac{\alpha\sigma_z\Upsilon^2}{\lambda_c\gamma}\frac{1}{(1+(1.5\Upsilon)^{2/3})^2} \qquad (3)$$

where r_e, α, and λ_c are the classical electron radius, the fine structure constant, and the Compton wavelength and γ and N are the beam energy and the number of particles per bunch.

Now, in general, the width of the $\mathcal{L}$ spectrum is described by δ_B but the amount of luminosity at the full cms energy $\mathcal{L}_{100\%}$ is a function of n_γ:

$$\mathcal{L}_{100\%} \approx \mathcal{L}_0\frac{(1-e^{-n_\gamma})^2}{n_\gamma^2} \qquad (4)$$

where $\mathcal{L}_0$ is the luminosity of the collider which scales as n_γ when $\Upsilon \ll 1$ and $n_\gamma^{3/2}$ when $\Upsilon \gg 1$.

At cms energies of roughly 1 TeV, the collider parameters can be chosen so that the effects on the $\mathcal{L}$ spectrum are relatively insignificant. In particular, Υ can be kept around 0.3, where the radiation effects can still be described classically, n_γ is close to 1, and δ_B is around 10%. In this regime, the luminosity at full cms energy scales as $\mathcal{L}_{100\%} \sim (1-e^{-n_\gamma})^2/n_\gamma$ which peaks at an n_γ of 1.26.

Unfortunately, it is difficult to attain similar parameters at higher energies. In particular, because Υ is proportional to the beam energy, Υ will have a value that exceeds 1 and, in practice, is the order of 10. In this regime, δ_B is essentially proportional to n_γ and the luminosity at full cms

0-7803-4376-X/98/$10.00 © 1998 IEEE

energy is $\mathcal{L}_{100\%} \sim (1-e^{-n_\gamma})^2/\sqrt{n_\gamma}$; this is roughly constant for n_γ between 1.6 and 3.5 with a peak at $n_\gamma = 2.34$.

3 PARAMETER DETERMINATION

The parameters of a linear collider are inter-related in a complex manner making their straightforward determination difficult. In the following, we present the principal arguments that lead to the values listed in Table 1. First, we consider issues in the IP region. A straightforward extrapolation from the 1 TeV collider designs shows that to gain an order of magnitude in $\mathcal{L}$ without significantly increasing the beam power, and thereby the ac power consumption, requires decreasing the vertical spot size. The vertical spot size is limited by three effects: the optics, the beam emittances, and beam jitter.

Center-of-mass Energy [TeV]	3	5
$\mathcal{L}$ (with pinch) $[10^{33} cm^{-2} s^{-1}]$	113	125
$\mathcal{L}$ (with FF dilution) ($\mathcal{L}_0$)	90	100
$\mathcal{L}$ within 5% of cms energy	46	44
$\mathcal{L}$ Enhancement (H_D)	1.8	1.8
Num. photons/particle (n_γ)	1.6	1.7
Beamstr. param. (Υ)	6	13
Part. per bunch (N) $[10^{10}]$	0.3	0.3
Emit. at DR ($\gamma\epsilon_{x/y}$) $[10^{-8}]$	40 / 0.5	40 / 0.5
Emit. at FF ($\gamma\epsilon_{x/y}$) $[10^{-8}]$	50 / 1	50 / 1
IP beta funct. ($\beta^\star_{x/y}$) [mm]	8 / 0.10	8 / 0.10
IP beam size ($\sigma^\star_{x/y}$) [nm]	39 / 0.70	31 / 0.54
Bunch length (σ_z) [μm]	35	35
Bunches per train (n_b)	200	200
Bunch spacing (Δt) [ns]	0.5	0.5
Rep. rate (f_{rep}) [Hz]	96	60
Loaded gradient (G) [MV/m]	150	200
Beam loading [%]	14.8	12.3
Total linac length [km]	24	30
Structure length [cm]	63	70
Shunt impedance [MΩ/m]	87.5	87.5
rf $\rightarrow$ beam eff. [%]	27.3	21.7
ac $\rightarrow$ rf eff. [%]	45	45
ac power [MW]	235	330

Table 1: Parameters for 3 and 5 TeV colliders.

Ground motion measurements at SLAC have shown that, if the final doublet magnets are anchored firmly to the ground, the natural seismic motion will cause the beam centroids to jitter by less than 0.3 nm at the IP[8]; in the NLC design, these anchors are constructed from optical interferometers and piezo-electric movers. We will assume this sets a lower limit on the spot size. Given additional constraints from the final focus optics as well as the emittance generation and preservation, we have assumed a minimum vertical spot size of 0.5 nm; this is roughly 10 times smaller than that in the 1 TeV NLC and CLIC designs.

Now, given this vertical spot, the horizontal and vertical emittances are constrained by the 'Oide' effect where synchrotron radiation in the final FD doublet leads to chromatic dilution of the spot. Assuming a doublet with apertures roughly $\frac{1}{2}$ that in the NLC design, the smaller apertures are possible because the beam sizes are also smaller in the FD, the Oide effect limits the emittances to:

$$\gamma\epsilon_x \lesssim 80 \times 10^{-8}\,\text{m-rad} \qquad \gamma\epsilon_y \lesssim 1 \times 10^{-8}\,\text{m-rad}\,. \quad (5)$$

Next, we have chosen to limit n_γ, which constrains the ratio N/σ_x, to the lower end of the range discussed in the previous section, *i.e.*, around 1.6. This provides the largest *fractional* contribution of $\mathcal{L}_{100\%}/\mathcal{L}_0$ while still maximizing the absolute value of $\mathcal{L}_{100\%}$. In this case, the $\mathcal{L}$ within 5% of the cms energy is about 45% $\mathcal{L}_0$ which is the same percentage as that in the 1 TeV NLC design.

Finally, the desired luminosity determines the total beam power. For the 3 TeV collider, the luminosity is scaled with E^2 as desired by the physics while for the 5 TeV parameters the same $\mathcal{L}$, as assumed by the Snowmass working group studying 5 TeV colliders[3], namely $10^{35}\text{cm}^{-2}\text{s}^{-1}$, has been chosen.

At this point, we need to consider constraints from the linacs. First, to attain optimal rf-to-beam efficiency, we must consider trains of bunches that are long compared to the accelerator structure fill time. Second, to prevent beam break-up, the spacing between these bunches is limited by the decay of the transverse wakefield. Given the wakefield of the present CLIC structure design[9] or that of an NLC DDS structure scaled to 30 GHz, the minimum bunch spacing that could be considered is about 12 rf buckets. We have chosen a spacing of 15 rf buckets or 0.5 ns at 30 GHz; this differs significantly from the assumption in Ref. [4].

Next, the gradient is determined from conflicting requirements between the beam dynamics, which are easier with high gradients, the collider length, and the rf-to-beam efficiency, which is greater for low gradients. In this frequency regime, the maximum gradient is not thought to be limited by rf breakdown but instead by heating and the associated fatigue. A straightforward calculation would suggest that 200 MV/m is possible although this will need to be verified with detailed tests. In these parameters, we have chosen to minimize the collider length and thus assumed a loaded gradient of 200 MV/m for the 5 TeV parameters and 150 MV/m for the 3 TeV parameters.

Finally, the bunch charge and length need to be determined and, again, there is a trade between increasing the rf-to-beam efficiency, reducing the effect of the transverse wakefield, and controlling the energy spread induced by the longitudinal wakefield. The optimal scaling[5]

$$N \sim G\omega^{-3/2} \qquad \sigma_z \sim G^{-1}\omega^{-5/8} \quad (6)$$

leads to a bunch length that we felt was too small (15 μm) and thus we limited the bunch length to 35 μm, about 100 times smaller than in the damping rings. We then limited the bunch charge to keep the energy spread required for 'autophasing', a standard method of controlling the single bunch beam break-up, to less than 1%. This results in a smaller beam loading and a lower rf-to-beam efficiency, but keeps the transverse emittance dilution acceptable.

The final parameters are listed in Table 1 for both 3 TeV and 5 TeV cms energies; in both cases, the injection systems are assumed to be similar and thus the beam parameters are similar. It should be noted that we have included

substantial emittance and IP spot size dilution based on tolerances similar to those in the CLIC and NLC designs.

4 COLLIDER SUBSYSTEMS

4.1 RF Power

Attaining an acceleration gradient of 200 MV/m requires 480 MW of rf power in each accelerator structure. This power could be generated using the CLIC Two-Beam Accelerator (TBA) concept, the Relativistic-Klystron TBA[10], or advanced klystrons, such as a sheet-beam or cluster klystron, with rf pulse compression[11]. All of these sources are expected to have efficiencies between 45 and 55%, but, of course, all require extensive R&D; we have assumed 45% in our parameter list.

4.2 Injector Complex

The e^- and e^+ sources are expected to be relatively simple. The required charges and beam currents are significantly lower than in the NLC design and thus the sources could be similar. Of course if desired, the conventional positron source could be complemented using a helical undulator after the IP to generate polarized positrons.

The damping rings are required to produce beams with emittances that are a factor of 6~8 smaller than those from the NLC rings. To do this, one could use a pre-damping ring (similar to the present NLC rings) to perform most of the damping and then a ring with half the bending field but twice as many cells to obtain the final emittances. In this case, the alignment tolerances and the effect of intrabeam scattering will be similar to that in the NLC rings.

Finally, attaining the bunch length of 35 μm will require compressing the bunch length by two orders of magnitude. This is thought to be possible but care must be taken to minimize the longitudinal nonlinearities and the emittance growth due to coherent synchrotron radiation.

4.3 Linac Dynamics

There are three primary issues in the linacs which are described in greater detail in Ref. [12]. First, the bunch spacing is limited by the multi-bunch beam break-up as described earlier. Next, we have assumed alignment tolerances of 10 μm on the accelerator structures and 2 μm on the BPM-to-quadrupole alignment which are similar to the values in the NLC and CLIC designs and are thought to be attainable using beam-based techniques. With these tolerances, the vertical emittance dilution is about 200% after 1-to-1 trajectory correction. Emittance bumps, like those used very effectively in the SLC to reduce the vertical emittance dilution from roughly 1000% to 100%, should reduce the dilution to roughly 50%; this is half of the 100% that is budgeted. Finally, because of the very small beam emittances, the linac and beam delivery systems are sensitive to motion of the quadrupoles. This limits the strength of the focusing system in the linac and requires the use of slow cycling trajectory correction feedback[12].

4.4 Final Focus and Interaction Region

In the final focus and interaction region, we have assumed parameters similar to those of the NLC and CLIC final focus systems, leading to a β_y^* that is significantly larger than the limit imposed by the bunch length. This choice was made for two reasons. First, with the emittances determined by the Oide limit, these beta functions lead to spots that are consistent with the limits from the measured ground motion. Second, for a given optics and tolerances, the length of the final focus system scales linearly with the beam energy[13] which, for the same tolerances, already implies a length of 3 to 5 km per side.

The other difficulty that arises with these high energy parameters is the large number of coherent e^+e^- pairs that are produced when $\Upsilon \gtrsim 1$. Fortunately, these pairs are emitted with small transverse momenta and thus can be removed from the IP with a strong solenoidal field. In addition, by adding a small toroidal component to the solenoidal field, the particles can be directed out the beam exit ports, preventing the pairs from interacting with any material until well outside the detector.

5 CONCLUSION

In this paper, we have studied the feasibility of a 3 to 5 TeV e^+e^- linear collider. Although much work is still required before completing a design and experience gained with a 0.5 to 1 TeV linear collider will further optimize the parameters, this preliminary study shows that a 'conventional' e^+e^- linear collider is a viable candidate for a multi-TeV experimental physics facility.

6 ACKNOWLEDGEMENTS

Work supported in part by the Department of Energy, contract DE-AC03-76SF00515.

7 REFERENCES

[1] G.A. Loew *et al.*, "International Linear Collider Technical Review Report", SLAC Report–471 (1996).

[2] R.B. Palmer "Prospects for High Energy e^+e^- Linear Colliders", *Annu. Rev. Nucl. Part. Sci.*, **40:** 529 (1990).

[3] S. Chattopadhyay et al., "Advanced Accelerator Technologies: A Snowmass '96 Subgroup Summary," *Proc. of 1996 DPF/DPB Snowmass Meeting,* (1996).

[4] P. Chen *et al.*, "A 5 TeV Linear Collider on the NLC Site", *Proc. of 1996 DPF/DPB Snowmass Meeting,* (1996).

[5] J.P. Delahaye *et al.*, "Scaling Laws for e^+e^- Linear Colliders", Clic–Note–333 (1997).

[6] $\mu^+\mu^-$ Collider Collaboration, "$\mu^+\mu^-$ Collider: A Feasibility Study", BNL–52503 (1996).

[7] P. Chen, "Differential Luminosity under Multi-Photon Beamstrahlung", *Phys. Rev. D,* **46:** 1186 (1992).

[8] NLC ZDR Design Group, "A Zeroth Order Design Report for the Next Linear Collider", SLAC Report–474 (1996).

[9] M. Dehler *et al.*, "CLIC Waveguide Damped Accelerator Structure Studies", *Proc. of the 1996 Linac Conf.,* Geneva, Switzerland (1996) p. 734.

[10] See Appendix A of Ref. [8].

[11] P.B. Wilson *et al.*, "RF System for a 30 GHz 5 TeV Linear Collider Based on Conventional Technology", *submitted to these proceedings.*

[12] G. Guignard *et al.*, "Emittance Dilution in 1 and 5 TeV 30 GHz Linear Colliders", *submitted to these proceedings.*

[13] F. Zimmermann *et al.*, "Optimization of the NLC Final Focus System", *Proc. of the 1995 Part. Acc. Conf.,* Dallas, TX.

SIMULATION OF GROUND MOTION INDUCED BEAM JITTER IN THE SBLC MAIN LINAC

C. Montag*
DESY, Notkestrasse 85, D-22607 Hamburg

Abstract

To keep the two beams of linear colliders in collision, the beam offset with respect to each other should be significantly below the beam size. To investigate the effect of ground motion on the beam trajectory, a ground motion simulation algorithm has been developed. This code models measurements taken at various laboratory sites and pays special attention to coherence properties of ground motion. Additionally, possible stabilization feedback algorithms are included. The code can be adapted to a broad range of vibration spectra and coherence properties. As a specific application, beam jitter in the main linac of the S-band Linear Collider SBLC has been investigated. The resulting rms beam jitter of $\sigma_y \approx 1.3$ μm corresponds to a luminosity degradation of only 1%. The jitter can be reduced to about 0.45 μm using active stabilization of quadrupole vibrations. This indicates that, with respect to ground vibration, there is significant luminosity upgrade potential for SBLC.

1 GROUND MOTION SIMULATION MODELS

To simulate ground motion, two complementary algorithms have been developed[1]. Both of them can be adapted to practically any measured ground motion power spectra and coherence. The first one is based on digital filters shaping white noise random signals in order to get a realistic spectrum and correlation properties, while the second one employs fast Fourier transformations to compute ground motion signals in the time domain from the power spectra of absolute ground motion and the coherence spectra.

1.1 The filter-based model

The power spectrum $P_{\mathrm{tot}}(\omega)$ of ground motion can be roughly approximated as

$$P_{\mathrm{tot}}(\omega) = \frac{B}{\omega^4}, \tag{1}$$

while the power spectrum of uncorrelated ground motion of two points at a distance L is described according to the ATL rule[2] as

$$\rho(\omega, L) = \frac{A \cdot L}{\omega^2}. \tag{2}$$

Since $P_{\mathrm{tot},n}(\omega) = P_{\mathrm{corr},n}(\omega) + P_{\mathrm{uncorr},n}(\omega) = P_{\mathrm{tot}}(\omega)$, with $P_{\mathrm{corr},n}(\omega) \geq 0$ and $P_{\mathrm{uncorr},n}(\omega) = \rho(\omega, L_n) \geq 0$ being the power spectra of the correlated and the uncorrelated motion of the nth magnet with respect to the $(n-1)$th at distance L_n, we get

$$\rho(\omega, L_n) \leq P_{\mathrm{tot},n}(\omega) \tag{3}$$

for all n. Therefore, Eq. (2) has to be modified for $\omega \geq \omega_0 = \sqrt{B/(A \cdot L)}$[3].

Application of a first order lowpass filter with cutoff frequency ω_0 to the total motion signal of the nth magnet with power spectrum $P_{\mathrm{tot},n}(\omega)$ leads to[1]

$$\begin{aligned} P_{\mathrm{corr},n+1}(\omega) &= \left|\frac{\omega_0}{s+\omega_0}\right|^2 \cdot P_{\mathrm{tot},n}(\omega) \\ &= \left|\frac{\omega_0}{s+\omega_0}\right|^2 \cdot \frac{B}{\omega^4}, \end{aligned} \tag{4}$$

with $s = i\omega$ being the Laplace variable. The uncorrelated part of motion of the $(n+1)$th magnet with respect to the nth one results from applying a first order highpass filter to a second, independent signal with the same power spectrum $P_{n+1}(\omega) = B/\omega^4$[1]

$$P_{\mathrm{uncorr},n+1}(\omega) = \left|\frac{s}{s+\omega_0}\right|^2 \cdot P_{n+1}(\omega). \tag{5}$$

In the low-frequency limit, we get

$$\lim_{\omega \to 0} P_{\mathrm{uncorr},n+1} = \frac{A \cdot L_{n+1}}{\omega^2}, \tag{6}$$

which reflects the ATL rule.

As can be shown, $P_{\mathrm{corr},n+1} + P_{\mathrm{uncorr},n+1} = P_{\mathrm{tot},n+1} = B/\omega^4$, while the resulting coherence $|\gamma|$ can be calculated as[1]

$$\begin{aligned} |\gamma| &= \sqrt{\frac{P_{\mathrm{corr},n+1}}{P_{\mathrm{uncorr},n+1}} \Big/ \left(1 + \frac{P_{\mathrm{corr},n+1}}{P_{\mathrm{uncorr},n+1}}\right)} \\ &= \sqrt{\frac{\omega_0^2}{|s|^2 + \omega_0^2}}. \end{aligned} \tag{7}$$

To get a more realistic power spectrum, the experimental data obtained at DESY were fitted as

$$\begin{aligned} P_{\mathrm{tot}} &= \left|\frac{B}{\omega^4}\right| \\ &+ \left|\frac{4.225 \cdot 10^{-14}}{s^2}\right| \mathrm{m^2Hz} \\ &+ \left|\frac{7 \cdot 10^{-6}}{s^2 + 9.425\,\mathrm{Hz} \cdot s + 246.74\,\mathrm{Hz}^2}\right|^2 \mathrm{m^2Hz^3} \\ &+ \left|\frac{7 \cdot 10^{-7}}{s^2 + 0.528\,\mathrm{Hz} \cdot s + 0.774\,\mathrm{Hz}^2}\right|^2 \mathrm{m^2Hz^3}, \end{aligned} \tag{8}$$

* now at KEK, Tsukuba, Japan

0-7803-4376-X/98/$10.00 © 1998 IEEE

which in the low-frequency limit is dominated by the B/ω^4 term, leading to an ATL-like behaviour of the uncorrelated motion (Eqs. (5) and (6)).

The power spectrum and coherence measured in the HERA tunnel correspond to $A = 4 \cdot 10^{-6}\ \mu\mathrm{m}^2/(\mathrm{m} \cdot \mathrm{sec})$ and $B = 3 \cdot 10^{-2}\ \mu\mathrm{m}^2 \cdot \mathrm{Hz}^3$[4, 5]. Figure 1 shows the resulting power spectra of absolute and relative motion of two magnets at a distance of L=30 m.

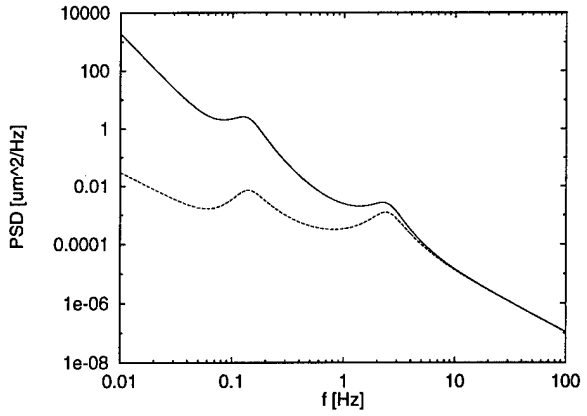


Figure 1: Power spectra (PSD) of absolute (solid line) and relative (dashed line) motion of two magnets at L=30 m distance for $A = 4 \cdot 10^{-6}\ \frac{\mu\mathrm{m}^2}{\mathrm{m}\cdot\mathrm{sec}}$ and $B = 3 \cdot 10^{-2}\ \mu\mathrm{m}^2 \cdot \mathrm{Hz}^3$[1].

1.2 The FFT-based model

To compute the time-dependent motion signals at various points s_k along a straight line, the corresponding amplitude spectrum $P_a(\omega)$ has to be multiplied by a phase factor function $\exp[i(\omega t + \phi_k(\omega))]$ and inversely Fourier transformed. As can be easily shown, this leads to perfectly correlated signals $x(t)$ and $y(t)$ at any two points s_x and s_y for any arbitrarily chosen initial phase functions ϕ_x and ϕ_y,

$$|\gamma(\omega)| = \left| \frac{\Phi(\omega) \cdot \exp[i(\phi_x(\omega) - \phi_y(\omega))]}{\Phi(\omega)} \right| = 1. \qquad (9)$$

On the other hand, averaging over all neighbouring points s_k, s_{k-1} separated by the same distance L leads to[1]

$$\begin{aligned} |\gamma(\omega)| &= |\langle \exp[i(\phi_k(\omega) - \phi_{k-1}(\omega))] \rangle| \\ &= |\langle \exp[i \cdot \Delta\phi_k] \rangle|, \end{aligned} \qquad (10)$$

with $0 \le |\gamma(\omega)| \le 1$. For a gaussian distribution of $\Delta\phi_k$ with mean value $\mu = 0$ and variance σ^2, and for a large number of points, this results in a coherence [1]

$$\begin{aligned} |\gamma| &= \left| \lim_{K\to\infty} \frac{1}{K} \sum_{k=1}^{K} \exp(i \cdot \Delta\phi_k) \right| \\ &= \exp\left(-\frac{\sigma^2}{2}\right). \end{aligned} \qquad (11)$$

To compute signals with a desired correlation $\gamma(\omega)$, the phases $\phi_k(\omega)$ for the motion signal at the location s_k are calculated from those at the point s_{k-1} according to

$$\phi_k(\omega) = \phi_{k-1}(\omega) + \Delta\phi_k(\omega), \qquad (12)$$

with $\Delta\phi_k(\omega)$ being normally distributed with rms value $\sigma = \sqrt{-2\ln(\gamma(\omega))}$ and mean value μ=0.

Having once defined the coherence for a certain distance L_0, the coherence for any distance L results automatically according to

$$|\gamma(L)| = \exp\left(-\frac{L}{L_0}\frac{\sigma^2(L_0)}{2}\right). \qquad (13)$$

The coherence measured in the HERA tunnel can be approximated by[1]

$$\begin{aligned} |\gamma(6\,\mathrm{m})| &= \exp\left(-\frac{0.08}{2\pi}\cdot\omega\right) \\ &+ \frac{0.0028\cdot\omega}{\sqrt{(\omega_m^2-\omega^2)^2 + (2\cdot\delta\cdot\omega_m\cdot\omega)^2}} \\ &+ \frac{1.05\cdot\omega}{\sqrt{(\omega_c^2-\omega^2)^2 + (2\cdot\delta\cdot\omega_c\cdot\omega)^2}}, \end{aligned} \qquad (14)$$

with

$$\omega_m = 2\pi \cdot 0.14\,\mathrm{Hz}, \qquad (15)$$

$$\omega_c = 2\pi \cdot 2.5\,\mathrm{Hz}, \qquad (16)$$

$$\delta = 0.2. \qquad (17)$$

2 THE LINAC LATTICE

The S-band lattice is composed of FODO cells with constant phase advance $\mu = 90°$. Since the accelerating sections between the quadrupoles consist of identical units of l=6 m length, the scaling of the β-function is chosen as a stepwise function of the energy to approximate a $\beta \propto \sqrt{E}$ scaling[6]. Figure 2 shows the scaling of the β-function of this lattice.

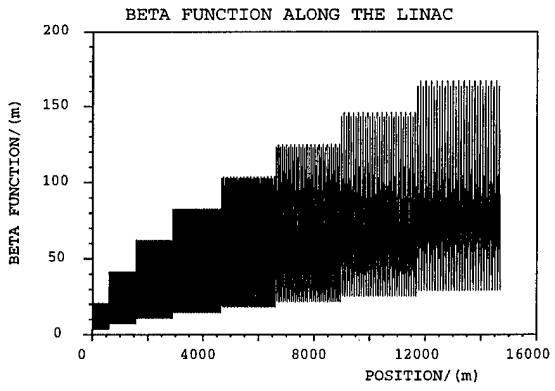


Figure 2: β-function scaling chosen for the SBLC main linac.

3 SIMULATION RESULTS

Both ground motion simulation algorithms described above have been used to determine ground motion induced beam jitter in the SBLC main linac. At the end of the main linac, a beam based correction system has been assumed which corrects the position of each bunch train by subtracting the value measured at the previous one. This can be described by the transfer function[1]

$$H(s) = 1 - \exp(-sT_0), \tag{18}$$

where $s = i\omega$ and T_0 are the Laplace variable and the time between consecutive bunch trains, respectively.

Using the FFT-based simulation algorithm, the rms beam jitter was determined to be approximately 1.3 μm. This can be significantly reduced to about 0.45 μm applying an active stabilization system to reduce quadrupole vibrations[7], with a transfer function shown in Fig. 3.

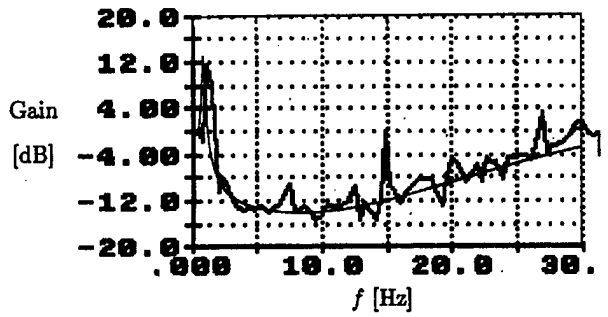


Figure 3: Measured feedback gain (thick line) of the active stabilization system in the frequency band from 0 to 30 Hz. The smooth thinner curve shows the theoretical transfer function used for the simulation[7].

From the rms beam jitter σ_y, the resulting luminosity $\mathcal{L}$ in terms of the nominal luminosity $\mathcal{L}_0$ can be expressed as

$$\mathcal{L} = \mathcal{L}_0 \cdot \exp\left(-2\frac{\sigma_y^2}{4\sigma_{\text{beam}}^2}\right), \tag{19}$$

with $\sigma_{\text{beam}} = 9.1$ μm being the rms beam size at the end of the main linac. The obtained values correspond to luminosity degradations due to beam offset of 1% without and 0.1% with active stabilization, respectively.

Furthermore, the effect of the proportionality constant A on the luminosity was simulated using the filter-based algorithm (see Fig. 4). The rms beam jitter at $A = 4 \cdot 10^{-6}$ $\mu\text{m}^2/(\text{m} \cdot \text{sec})$, the value obtained at HERA, is 1.7 μm without and 0.9 μm with active stabilization (Fig. 4). This is in good agreement with the results obtained using the FFT-based model.

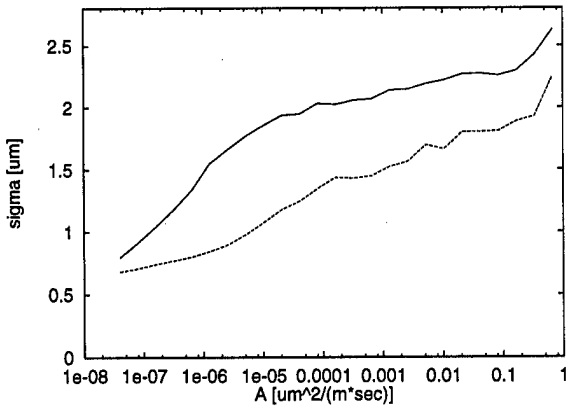


Figure 4: Resulting rms beam jitter as a function of the proportionality factor A in the ATL rule. The solid line represents the rms jitter amplitude resulting from pure ground motion, while the dashed line shows the corresponding value with active stabilization.

4 REFERENCES

[1] C. Montag, Active Stabilization of Mechanical Quadrupole Vibrations in a Linear Collider Test Facility, Ph.D thesis, DESY 97-030.

[2] B.A. Baklakov *et al.*, Investigation of Seismic Vibrations for Linear Collider VLEPP, Sov. Phys. ZhTF., Vol. 63, No. 10 (1993) (in Russian)

[3] A. Sery, O. Napoly, Influence of Ground Motion on the Time Evolution of Beams in Linear Colliders, Phys. Rev. E 63 (1996).

[4] V. Shiltsev *et al.*, Measurements of Ground Vibrations and Orbit Motion at HERA, DESY HERA 95-06.

[5] R. Brinkmann, J. Rossbach, Observation of Closed Orbit Drift at HERA Covering 8 Decades of Frequency, Nucl. Instr. Meth. A 350 (1994).

[6] S-Band Linear Collider SBLC Conceptual Design Report, DESY 97-048 and ECFA 97-182.

[7] C. Montag, Active Stabilization of Mechanical Quadrupole Vibrations for Linear Colliders, Nucl. Instr. Meth. A 378 (1996).

THEORETICAL STUDY OF POWER RELATIVISTIC AMPLIFIERS FOR ELECTRON BEAM BUNCHING *

E.A. Perelstein, L.V.Bobyleva, A.V. Elzhov, V.I. Kazacha, Joint Institute for Nuclear Research,141980, Dubna, Russia

Abstract.

Two schemes of electron-positron linear colliders with energy in the TeV range based on the two beam accelerator (TBA) concept are being studied now [1,2]. In a TBA the first accelerator-driver produces a high current electron beam. The beam must be bunched along all collider length..There are some schemes for generating of such high-intensity drive beam bunches. One of the schemes for generating of high-intensity drive beam bunches was tested in [3], where the Choppertron used transverse velocity modulation of a beam. Another idea for generating drive beam is to use the bunching in the free electron laser (FEL) [4]. It was shown in [5,6], that a high degree of bunching can be rather easily achieved in a short FEL amplifier.In [7,8,9], the first direct observation of the bunching of a relativistic electron beam, produced by a high power FEL interaction, was presented..

This work is devoted to the computer simulation and comparison of the bunching of a relativistic electron beam produced by a FEL and by a travelling wave tube (TWT). The calculation results of the electron beam bunching in the FEL are also compared with the experimental results in [7,8]. With the help of rather simple model it is shown that one can obtain the electron beam bunching in the TWT at a shorter length than in the FEL because the space gain in the TWT is higher than in the FEL.

1 BEAM BUNCHING EQUATIONS

The following equations describe the self-consistent spatial problem of the movement of a relativistic electron beam in a microwave electromagnetic field, which can be used both for a TWT and for a FEL in the Compton regime:

$$\frac{d\gamma_j}{dZ} = -\kappa a_s \sin\psi_j, \quad (j = 1, 2, \ldots, M)$$

$$\frac{d\theta_j}{dZ} = \frac{1}{\beta_{\|j}} - \frac{1}{\beta_{ph}}, \quad \frac{da_s}{dZ} = \eta < \sin\psi_j >$$

$$\frac{d\varphi}{dZ} a_s = \eta < \cos\psi > \qquad (1)$$

Here M is the number of electrons (macroparticles), γ_j is the j^{th} electron energy $E_j = m_0c^2\gamma_j$ units of $E = m_0c^2$; m_0 is the electron rest mass, c is the light velocity, $Z = z\omega_0/c$ is the dimensionless longitudinal coordinate, and ω_0 is the microwave frequency. The value θ_j is the phase of the j^{th} electron relative to the electromagnetic field; φ is the phase of the microwave complex amplitude ($\hat{a} = a_s e^{i\varphi}$), $\psi_j = \varphi + \theta_j$ is the total ponderomotive phase. The brackets in the equations (1) denote an average over the bucket. The value $a_s = eE_s/m_0\omega_0 c$ is the dimensionless amplitude of the microwave electric field, E_s is the amplitude of the microwave electric field.

The parameter κ is the microwave coupling coefficient. Its value depends on the type of used device. The parameter $\eta = \left(\frac{I_b}{I_A}\right)\cdot\frac{2k}{N}$, the constant $I_A = m_0c^3/e \cong 17$ kA; N is the norm of the electromagnetic wave[10]; $\beta_{\|j}$ is longitudinal electron velocity and β_{ph} is the microwave phase velocity.

2 SIMULATION OF BUNCHING PROCESS IN FREE ELECTRON LASER

To obtain the system of differential equations for simulation of the bunching process in a FEL with a helical wiggler we have used the corresponding equations [10,11], taking into account the effective frequency shift ω_p connected with the plasma wave in a beam. It is similar to the accounting of a plasma wave in the resonance condition in [7,8]. Finally we get:

$$\frac{dw_j}{dZ} = \kappa_{1j} a_s \sin\psi_j \qquad (j = 1, 2, \ldots, M)$$

$$\frac{d\theta_j}{dZ} = -\frac{(k_w + k_s)\cdot c}{\omega_0} + 1 + \frac{\omega_p}{\omega_0\beta_z} + \frac{1 + a_w^2 + a_w a_s \cos\psi_j}{2\gamma_0^2(1-w_j)^2},$$

$$\frac{da_s}{dZ} = \eta_1 < \frac{\sin\psi_j}{1-w_j} >, \frac{d\varphi}{dZ} a_s = \eta_1 < \frac{\cos\psi_j}{1-w_j} >, \quad (2)$$

where $\kappa_{1j} = \frac{a_w}{2\gamma_0\gamma_j} = \frac{\kappa_0}{1-w_j}$. Here $w_j = 1 - E_j/E_0$ is the relative change of the j^{th} electron energy; $k_w = 2\pi/\lambda_w$; λ_w is the wiggler period; k_s is the axial wavenumber for the waveguide resonance mode inside

* This work was supported by ISF, grant No. JLD100 and by Russian FBR, grant No.96-02-17395.

0-7803-4376-X/98/$10.00 © 1998 IEEE

the wiggler; γ_0 is the electron initial energy; β_z is the longitudinal dimensionless velocity of the resonant particle, determined from the relations: $\beta_z = \sqrt{\beta_0^2 - \beta_\perp^2}$, $\beta_\perp / \beta_z = a_w / \gamma_0$; $k_0 = a_w / 2\gamma_0^2$ and $\omega_p = \sqrt{\frac{4\pi n_e e^2}{m_0}} \cdot \frac{1}{\gamma_z \gamma^{1/2}}$ is the relativistic plasma frequency,: n_e is the electron beam density and $\gamma_z = 1/\sqrt{1-\beta_z^2}$. The parameter $a_w = eB_w\lambda_w / 2\pi m_0 c^2$, where B_w is the wiggler magnetic field amplitude. The coefficient $\eta_1 = \left(\frac{I_b}{I_A}\right) \cdot \frac{2\kappa_0 \gamma_0}{N}$.

For our simulation we used the electron beam and FEL parameters from [7,8]: electron beam energy ~2.2MeV, electron current inside the wiggler ~ 500 A, electron beam radius ~ 0.5 cm, wiggler period 12 cm, wiggler field B_w = 1.1 kG, microwave frequency $f_0 = 3.5 \cdot 10^{10}$ Hz (H_{11} mode). In [7,8] the initial microwave power of 10 kW was injected into the circular waveguide in the H_{11} mode. The corresponding microwave electric field amplitude $a_s \cong 4.4 \cdot 10^{-4}$. Then we obtain the following parameter values: $\kappa_1 \cong 0.022$, $\eta_1 = 2.5 \cdot 10^{-4}$, (the norm of wave $N = N_{11} \cong 24.3$ in our case). We define the bunching parameter B in the same manner as in [7]: $B = |\langle e^{i\psi} \rangle|$.

We also simulated the initial energy spread in the electron beam with the help of 2000 electrons which had been distributed in 40 phase points from $\theta = 0$ through $\theta = 2\pi$ and in every point 50 electrons had the gaussian distribution upon the relative energy with dispersion σ.

Fig.1 shows the results of the calculations of the FEL microwave power and their comparison with the results obtained in [7,8]. To take into account the wiggler adiabatic entrance in [7,8], we suppose the exponential power growth to start at 48 cm from the wiggler beginning. This point corresponds to zero length in Fig.1. As one can see from Fig.1, these results are in a rather good agreement. Comparing the distribution of the microwave power along the wiggler obtained experimentally in [7,8], one can draw a conclusion that the difference observed between the maximum microwave power and the calculated one for monoenergetic beam in ~10 times may be partially caused by the initial energy spread in the electron beam.
Fig.2 shows the calculated spatial evolution of the bunching parameter B. The vertical lines in Fig.2 correspond to the time dependence meassurements of the correspond to the time dependence meassurements of the bunching parameter along the beam [7]. The regular wiggler part ends at the length approximately equal to 170 cm. Our further along the wiggler calculations are not sufficiently correct. So comparing the obtained curve corresponding $\sigma = 5\%$ and the experimental results one can suppose that the low experimental bunching parameters in [7] (B ~0.1) were due to the beam energy

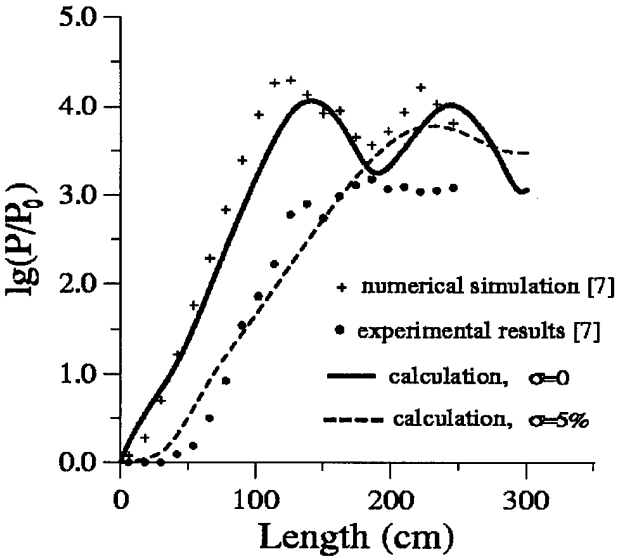


Figure: 1 The FEL microwave power versus the interaction length.

spread influence. The maximum bunching is reached in the region of maximum micromave power values.

3 SIMULATION OF BUNCHING PROCESS IN TRAVELLING WAVE TUBE

To simulate the electron beam bunching in a TWT amplifier based on the corrugated waveguide, we used the following system of differential equations:

$$\frac{dw_j}{dZ} = \kappa_2 a_s \sin\psi_j, \quad (j = 1, 2, \ldots, M)$$

$$\frac{d\theta_j}{dZ} = \frac{1 - w_j}{\sqrt{(1-w_j)^2 - \gamma^{-2}}} - \frac{1}{\beta_{ph}}, \qquad (4)$$

$$\frac{da_s}{dZ} = \eta_2 < \sin\psi_j >, \quad \frac{d\varphi}{dZ} a_s = \eta_2 < \cos\psi_j >,$$

where $\kappa_2 = \frac{\pi l_0}{\gamma_0 d}$, l_0 - is the corrugation amplitude and d is the corrugation spatial period [12]. The parameter η_2 is the following: $\eta_2 = \left(\frac{I_b}{I_A}\right) \cdot \frac{2k_2\gamma_0}{N_{01}}$, where N_{01} is the norm of E_{01} type wave in the TWT.

We chose the following electron beam and E_{01} type electromagnetic wave parameters for our simulation:-electron beam energy ~2.2 MeV, electron current inside the TWT~ 500 A, electron beam radius ~ 0.5cm, microwave frequency $f_0 = 17 \cdot 10^9$ Hz (λ ~ 1.76 cm), initial microwave power in TWT=10 kW. The parameter d value was found from the dispersion curve of the corrugated wave guide having l_0 = 1mm,

radius ~1.8 cm and when β_{ph} ~ 0.982. The dispersion curve was calculated with the help of the code URMEL. In our case

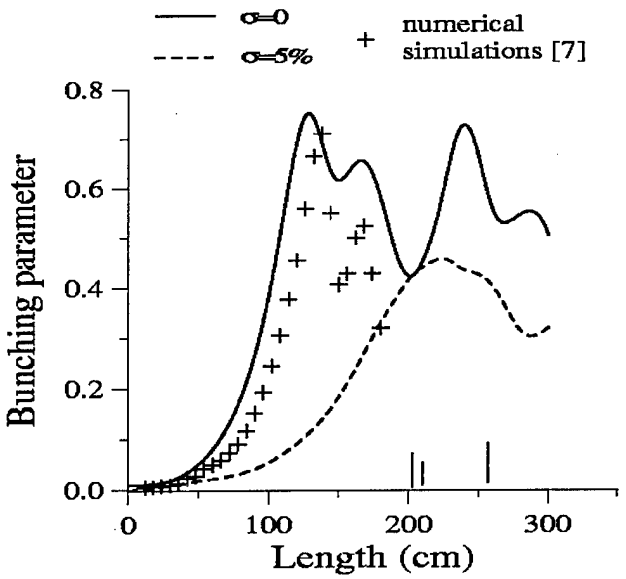


Figure: 2 The FEL bunching parameter versus the interaction length.

d was ~5.8 mm; $\kappa_s d = \frac{2\pi}{3}$. Then we have $\kappa_2 \approx 0.102$ and $\eta_2 \approx 3.2 \cdot 10^{-3}$ (the norm of wave $N_{01} \sim 10$). For the initial microwave power ~ 10 kW in the TWT the corresponding dimensionless amplitude of the microwave electric field $a_s \sim 6.8 \cdot 10^{-4}$.

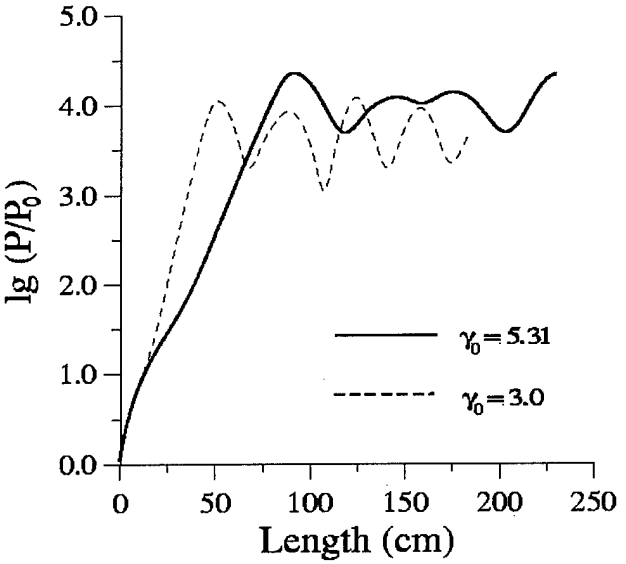


Figure: 3 The TWT micrrowave power versus the interaction length.

Fig.3 represents the calculated evolution of the microwave power as a function of the interaction length along the TWT. The two curves correspond to the initial electron beam energy 2.2 MeV and 1 MeV.

One can also see from Fig.3 that the bunching length in the TWT decreases essentially when the initial beam energy is diminished. The dependence of the microwave power at the TWT exit on the energy spread (2.2 MeV) is rather weak. This dependence becomes sufficient when the initial electron beam energy decreases down to 1 MeV. As one can see from Fig.1 and Fig.3, the bunching length of the electron beam with energy 2.2 MeV in ~ 1.5 times less in the TWT than in the FEL. The energy spread in the bunches is larger in the TWT than in the FEL.

4 CONCLUSIONS

Our simulations showed that a high degree of bunching of the electron beam having the energy in the range 1 - 2 MeV can be rather easily achieved in a short travelling wave tube.

The electron beam (2.2 MeV, 500 A) bunching occurs in a TWT at the distance in ~1.5 times shorter than in a FEL. It is connected with the fact that the space gain in the TWT is much higher than that in the FEL. But the bunch energy spread is larger in the TWT than in the FEL. The bunching effect depends weakly on the initial energy spread in the TWT and greatly in the FEL.

The TWT bunching efficiency decreases with the initial electron beam energy increase. Thus the TWT may be efficiently used for the electron beam bunching in the energy span 1 MeV through 2 MeV when the TWT length may be made of 0.5 m through 1 m.

REFERENCES

[1] A.M. Sessler, Proc. Workshop on the Laser Acceleration of Particles, eds. C. Yoshi and T. Katsouleas, AIP Conf. Proc. 91 (1982), p. 154.

[2] W. Schnell, CERN-LEP-RF/86-27 (1986); CERN-LEP-RF/88-59 (1988).

[3] G.Fiorentini, T. Houk and C. Wang, UCRL-JC-111391, Livermore (USA, 1993).

[4] W.B. Colson and A.M. Sessler, Annu. Rev. Nucl. Part. Sci., v. 35, (1985), p. 25.

[5] H.D. Shay, R.A. Ryne, S.S. Yu and E.T. Scharlemann, Nucl.Instrum. Methods, A304 (1991), p. 262.

[6] J. Gardelle, J. Labrouche and P. Le Taillander, Phys. Rev. E, v. 50 (1994), p. 4973.

[7] J.Gardelle, J. Labrouche and J.L. Rullier, Preprint CESTA/4 (1996).

[8] J. Gardelle et al., Preprint CESTA/5 (1996).

[9] J. Gardelle, J. Labrouche and J.L. Rullier, in: the Proc. of EPAC 96 (Sitges(Barcelona), 10-14 June 1996), v.1, p.298.

[10] N.S. Ginzburg and A.S. Sergeev, Zh. Tekhn. Fiz., v. 61 (1991), p. 133.

[11] A.M. Sessler et al., Nucl. Instr. Methods, A 306 (1991), p. 592.

[12] V.L.Bratman et al., in: Relativistic High- Frequency Electronics, ed. A.V. Gaponov-Grekhov (IAPAS USSR, Gorky, 1979), p. 249.

EMITTANCE DILUTION AND MAGNET DESIGN FOR THE TTF FEL SECOND BUNCH COMPRESSOR

I.N.Ivanov , S.I.Kukarnikov, A.Yu.Molodozhentsev , V.A.Petrov, V.Ph.Shevtsov,
Laboratory of Particle Physics,
Joint Institute for Nuclear Research
Dubna, Moscow region, 141980 Russia and
T. Limberg, M. Marx,
DESY, Notkestrasse 85, 22603 Hamburg, Germany

Abstract

This paper presents results of investigation of the transverse emittance dilution in the TTF FEL bunch compression system. The requirements for the bending magnet field of the dipole magnets of the second bunch compressor are determined. The dipole magnet design for the bunch compression system is performed. The dipole magnets are optimised to obtain minimum transverse emittance dilution.

1 INTRODUCTION

The TTF FEL second bunch compressor consists of four identical bending magnets to change the longitudinal rms bunch size from 0.8 mm to 0.25 mm at the energy of 144 MeV [1]. Main parameters of the dipole magnet for the second bunch compression system should be the following [2] :

- C-type magnet with the aperture gap no less than 2 cm;
- the good field region should be no less than 20 cm in horizontal direction and ±1 mm in vertical direction;
- dipole magnetic field component should be variable from 2808.712 Gs till 3753.616 Gs for different values of the bending angle which should be between 17÷23 degrees [1];
- length of the bending magnet 50 cm.

The main peculiarity of the bunch compression system is the following. Each particle of the bunch moving in transverse magnet field spends time determined by own energy and bending magnet field value. The magnet field is not uniform in a working region caused by the magnet field errors which can be presented as some quadrupole and sextupole magnet field components. In this case calculation of the time should be made accurately to investigate longitudinal and transverse particle motions.

2 TRANSVERSE EMITTANCE DILUTION

Using the special algorithm [2] the special program is made to investigate emittance dilution due to quadrupole magnet field component in the bending magnets of the second TTF FEL bunch compression system. This results is checked by the PARMELA program. And as the next step, the transverse emittance dilution due to sextupole component of the bending magnet field is estimated by the PARMELA program.

2.1 Transverse emittance dilution due to the quadrupole component of the magnet field

To estimate transverse emittance dilution due to quadrupole component of the bending magnet field of the 2nd bunch compression system one can use the developed program. The particle bunch can be presented as some slices in the transverse direction. Each slice has the own energy. The energy of the slices are in the range 144±0.720 MeV (σ=0.005). The transverse coordinates and velocities of the particles in the slice are generated to get the microcanonical distribution.

The initial bunch parameters are the following:
σ_z=0.08 cm, σ_E=0.005; E_s=144 MeV;
ε_n=1 π.mm.mrad or 2 π.mm.mrad;
β_x=15.0 m, β_y=8.0 m, $\alpha_x=\alpha_y=0$, where σ_z are the rms longitudinal beam size, σ_E is the energy dispersion, ε_n is the normalized emittance.

Figure 1 presents the relative emittance dilution $D\varepsilon_x = (\varepsilon^{exit} - \varepsilon^{initial}) / \varepsilon^{initial}$ as a function of the average quadrupole component in the working region of the dipole magnet $\langle g \rangle = \left\langle \frac{1}{B_0} \frac{\partial B_y}{\partial x} \right\rangle$ for the dipole magnet field 2968.617 Gs for the different initial emittances.

The transverse emittance dilution may be estimated by the PARMELA program also. The emittance for the system with an ideal bending magnet field is constant before and after the bunch compressor for the developed program. Unfortunately, using the PARMELA program one can get this result with 1...2% accuracy.

Comparison of the obtained results with the data, obtained by the PARMELA code shows a good coincidence of the results. To analyse the transverse emittance dilution using the PARMELA program the particles of the bunch are generated randomly in a four dimensional transverse hyperspace with uniform phase and random energy (input6).

0-7803-4376-X/98/$10.00 © 1998 IEEE

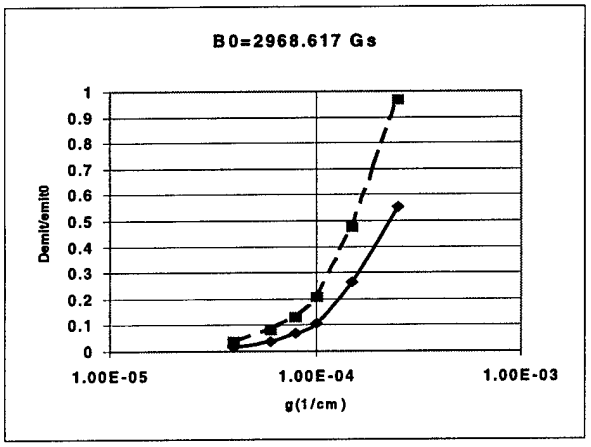


Figure 1: The relative emittance dilution as a function of the quadrupole component of the bending magnet field for different initial values of the normalized transverse emittance : 1pi mm.mrad- the dashed line, 2pi mm.mrad - the solid line. The dipole magnet field is 2968.617 Gs.

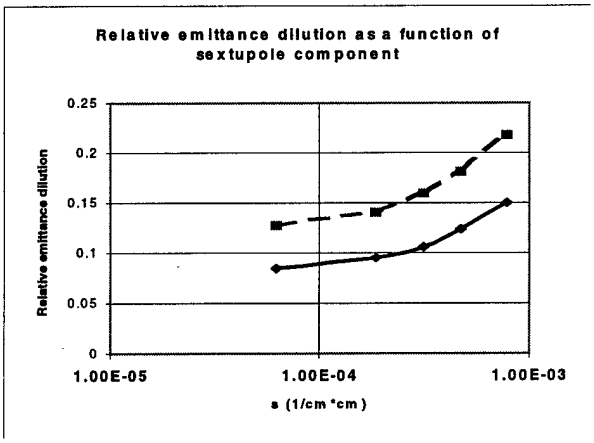


Figure 2: The relative emittance dilution as a function of the sextupole field component of the bending magnet for different initial values of the normalized transverse emittance : 1pi mm.mrad- the dashed line, 2pi mm.mrad - the solid line.

The initial parameters are the same as mentioned above. The obtained result corresponds to the emittance with the 90% of the particles. To present the bunch 1000 particles are used. To include the quadrupole field component in the bending magnet the magnet can be presented as "short" bending magnets. Between the "short" dipole magnets the quadrupole and sextupole lenses can be installed to model the "real" magnet field of the magnet with dipole, quadrupole and sextupole components. Length of the lenses should be small.

2.2 *Transverse emittance dilution due to the sextupole component of the magnet field*

To estimate the emittance dilution caused by the sextupole magnet field component in the bending magnet, the PARMELA program is used. In this case the quadrupole component is fixed and get from the previous calculations. Figure 2 presents the relative emittance dilution as a function of the sextupole field component of the bending magnet field for the dipole magnet field value of 3200 Gs. The quadrupole field component is g=5.0e-5 (1/cm) that corresponds to the 9.5% emittance growth of the 1 π.mm.mrad beam without the sextupole field component . To estimate the influence of the sextupole component for the another initial condition the extra calculation is made for the 2 π.mm.mrad beam with the quadrupole component g=7.5e-5 (1/cm) that corresponds to the 8.5% emittance growth. One can see from Figure 2 that to get the emittance growth about 15% in the 2nd bunch compression system the average sextupole field component should be about (2÷5)e-4 ($1/cm^2$).

3 DESIGN OF THE DIPOLE MAGNET

3.1 *Definition of the main parameters of the magnet*

For the 1 π.mm.mrad initial normalized emittance and the emittance dilution in the second bunch compression system about 15% the relative quadrupole component $g = \frac{1}{B_0}\frac{\partial B_y}{\partial x}$ of the magnetic field in the working region should be $4.0 \cdot 10^{-5}$ (1/cm) and the average sextupole component $5.0 \cdot 10^{-4}$ ($1/cm^2$). Then the dipole magnet design is performed to get the field quality in the working region for the emittance dilution less than 15%.

When the aperture of the magnet is much smaller than the length of the magnet and a radius of curvature is bigger than the magnet's length the ends of the magnets constitute only a small fraction of the investigated field seen by a beam and the fact that the fields in the ends are three-dimensional can be ignored. Magnet calculations are made by the POISSON and the OPERA-2D codes.

To simplify installation of the vacuum chamber and the magnetic field probes the C-type dipole magnet should be used [3]. These magnets will be installed vertically along the TTF accelerator. Unfortunately, this type of dipole magnet has some magnetic field gradient to the inner coil for the field in the 0.2÷0.4 T. The value of this gradient is constant in the working region for the range of the bending magnet field of the TTF bunch compression system. Magnetic field distribution is a function

of permeability of the magnet material. To investigate the influence of the material on the magnetic field quality the different permeability tables are used which are the internal tables of the POISSON and the OPERA programs.

3.2 Optimization of the dipole magnet

To decrease the field gradient of the C-type dipole magnet in the working region one can use special trimming the poletips. For this the poles of the magnet should have some converging angle to the external coil to escape the quadrupole component of the field in the working region. Optimization of the pole shapes should be done after the magnet measurements. The correction angle of the magnet poles is a function of the type of the material. Figure 3 demonstrates the relative magnetic field distribution before (the solid line) and after (the dashed line) correction of the converging angle for permeability table that is the internal table of the OPERA-2D program.

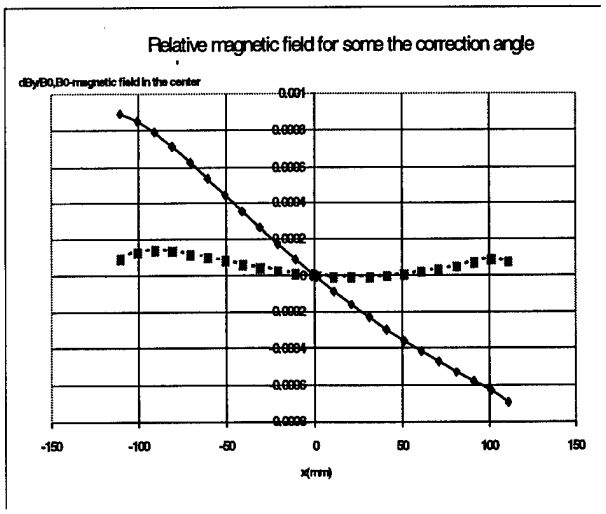


Figure 3: The relative magnetic field distribution before (the solid line) and after (the dashed line) correction of the converging angle of the poles.

3.3 Technical description of the dipole magnet

The steel 1010 with a carbon content less than 0.13% is planned to use for manufacturing of the magnet yoke. The yoke sizes have been optimized to provide the working region about 200 mm, sufficient durability of the yoke under influence of the magnetic field force and to reduce a quadrupole component of the magnetic field in the working region. To minimize the pole width and the power supply the gap height should be as small as possible. The gap size, determined by the beam tube dimensions, is equal to 20 mm. The poles should be made to separate from the yoke of the magnet, to install and swap of the magnet coils and to simplify the pole surface processing.

The final surface processing of the magnet poles should be carried out after the magnet measurement to minimize the quadrupole component in the working region.

After this processing the magnetic field accuracy has to be about 0.05% for the flux density 3753.62 Gs. To optimize the edge field the pole-end pieces are installed. The profile of the pole-end pieces should be determined after the magnetic field measurements. The correction coils will be used for the magnetic field tuning.

REFERENCES

[1] T. Limberg, H. Weise, A. Molodozhentsev, V. Petrov: The bunch compression system at the TESLA Test Facility FEL, DESY PRINT, September 1995, TESLA-FEL 95-04.

[2] I. Ivanov, A. Molodozhentsev, V. Petrov, V. Shevtsov: Emittance Dilution in the TESLA FEL Second Bunch Compression System, DESY PRINT, August 1996, TESLA-FEL 96-11.

[3] I. Ivanov, S. Kukarnikov, T. Limberg, M. Marx, A.Molodozhentsev, V. Petrov, V. Shevtsov: Magnet Design for the TESLA FEL Second Bunch Compression System, DESY PRINT, September 1996, TESLA-FEL 96-12.

POSSIBILITY OF PRECISE WAKEFIELD MEASUREMENT AT ATF EXTRACTION LINE

S. Kashiwagi
Department of Accelerator Science, School of Mathematical and Physical Science,
The Graduate University for Advanced Studies
1-1 Oho, Tsukuba, Ibaraki 305, Japan
H. Hayano, T. Higo, K. Kubo, K. Oide, K. Takata, S. Takeda, N. Terunuma, and J. Urakawa
High Energy Accelerator Research Organization
1-1 Oho, Tsukuba, Ibaraki 305, Japan

Abstract

Measurement of wakefield is planned at the Extraction Line from the Damping Ring of ATF, Accelerator Test Facility at KEK. In this experiment, 'residual' long-range transverse wake field excited by multi-bunch beam will be measured, and will be compared with theoretical calculation of wakefields with cell-to-cell misalignment. The residual wakefield which is induced by cell-to-cell misalignment of structure. Because the multi-bunch beam from the Damping Ring is expected to be stable and extremely low emittance, we can measure a small transverse kick of 10 nrad by using 500 nm resolution BPMs and optimized optics of the extraction beam line.

1 INTRODUCTION

In the linac of the KEK JLC design [1], the bunch train which is 85 bunches of 7.2×10^9 electrons and 1.4 ns bunch spacing. In this multi-bunch design it is important to control the long-range transverse wakefields generated in the accelerating structures of the linac. The transverse modes of the accelerator cavities cause the multi-bunch beam break-up instability. As of today, a variety of structure schemes have been developed to reduce (detune or damp) the effect of dipole wakefields. One is the detuned structure (DS) in which the dipole modes will be canceled by spreading the frequencies of the relevant modes in the structure [2]. Another scheme, such as the damped-detuned structure (DDS) is being studied at SLAC [3]. A heavily-damped or a medium-damped structure based on the choke-mode structure has also been developed recently [4]. In the choke-mode structure, all of the higher-order modes are heavily damped.

The wakefield can be calculated by existing computer programs within certain limitations. So it is important to compare the result of the theoretical calculations with measurement using real beam. Until now, measurement of the wakefield suppression have been made on X-band detuned structure (DS) at Argonne's Advanced Accelerator Test Facility (AATF) [5] and detuned damped structure (DDS) at ASSET [6]. In ASSET, the measurement of wakefields was performed by using two bunches (electrons and positrons) which were injected into the system with individual control of the bunch timing and intensity. This experiment measured wakefield which was proportional to beam offset.

Our plan is to do the measurements of wakefields at KEK in the diagnostics section of the extraction line from the ATF damping ring (Figure 1). This damping ring is designed to generate extremely low emittance and stable multi-bunch beam. Using this low emittance beam, the measurement with high sensitivity will be expected. The purposes of this experiment are the measurement of the residual wakefield which is induced by cell to cell misalignment of structure, when beam goes through the average center of the structure and single bunch blow up will be minimized. It is important to check theoretical calculation of transverse wakefield with cell to cell misalignment. The superposition effect of long-range transverse wakefield excited by multi-bunch beam will also be compared with the result of theoretical calculation.

2 TRANSVERSE WAKEFIELD MEASUREMENT

2.1 Long-range transverse wakefields

The key requirement of this measurements is that its sensitivity to the long-range transverse wakefield is below the tolerance on the wakefield strength in the KEK JLC design. It is difficult to characterize the limit on wake function. However, the criterion of wakefield strength that emerge from recently studies is less than 1.0 MV/nC/m^2 at each bunch location assuming r.m.s. misalignment of about 10 μm [7]. When the beam offset to the structure center is 10 μm and wake function per unit length for 1.3m-long structure with its cells perfectly parallel to the beam is 1.0 MV/nC/m^2, the transverse kick amounts to 25.4 nrad/structure assuming the bunch charge and the beam energy are 3 nC and 1.54 GeV, respectively.

Furthermore, if the cell-to-cell misalignment is comparable to the offset of the beam with respect to the structure, the effect of the misaligned cells cannot be ignored and it becomes important to study the effective kick from the cell misalignment in the structure.

0-7803-4376-X/98/$10.00 © 1998 IEEE

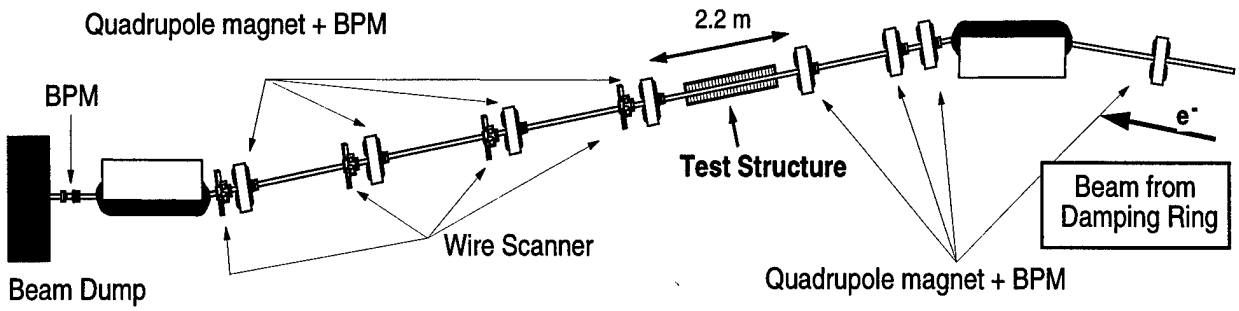


Figure 1 Layout of the ATF extraction line

2.2 Layout of Extraction Line and Measurements

The layout of the extraction line is shown in Figure 1. The measurement of wakefields will take place at the latter half of the extraction line. This linear region is diagnostics section and is dispersion free. The structure will be installed before the diagnostics section and will be mounted on a remotely controllable support. All quadrupole magnets are equipped with internal high resolution beam position monitors (BPMs). These are stripline type, because these have to measure a bunch-by-bunch beam positions. Some wire scanners located at the diagnostics section.

Firstly the Twiss parameters at the test structure and measurement points are optimized. Then single bunch blow-up by beam position jitter at the structure will be minimized by moving the test structure using the active mover support and observing beam profile using the wire scanners. Finally bunch-by-bunch beam positions are measured by BPMs downstream of the structure. The monitors for individual bunches with 2.8 ns bunch spacing have been developed at ATF 80 MeV pre-injector [8][9].

2.3 Optics

Let Twiss parameters of the structure position (S_1) be α_1 and β_1, and those at the position of the BPM to measure transverse kick (S_2) be α_2 and β_2. The transfer matrix from the structure to the measurement point is given by

$$R(s_1/s_2)=\begin{pmatrix} R_{11} & R_{12} \\ R_{21} & R_{22} \end{pmatrix} = \begin{pmatrix} \sqrt{\frac{\beta_2}{\beta_1}}(\cos\psi+\alpha_1\sin\psi) & \sqrt{\beta_1\beta_2}\sin\psi \\ -\left[\frac{(1+\alpha_1\alpha_2)\sin\psi+(\alpha_2-\alpha_1)\cos\psi}{\sqrt{\beta_1\beta_2}}\right] & \sqrt{\frac{\beta_1}{\beta_2}}(\cos\psi-\alpha_2\sin\psi) \end{pmatrix} \quad \text{---(1)}$$

where ψ is phase advance from S_1 to S_2. R_{12} should be big to detect small transverse kick by long-range wakefields in the structure. Beam size at the BPM ($\sqrt{\varepsilon\beta_2}$) should be small for the resolution of measurement, while beam size at the structure ($\sqrt{\varepsilon\beta_1}$) should also be small for minimizing the effect of short-range wakefield induced by beam position jitter. To get the big R_{12}, β_1, β_2 and phase advance from S_1 to S_2 should be optimized.

2.4 Sensitivity

Define the sensitivity at the BPM to measure transverse kick of long-range wakefields as follows.

$$ROS = \frac{Beam\ offset\ by\ long-range\ wakefield}{\sqrt{(net\ beam\ size)^2+(beam\ size\ blowup)^2}} = \frac{\Delta y_{long}}{\sqrt{(\sigma_{y2})^2+(\Delta y_{short})^2}} \quad (y: vertical\ direction) \quad \text{----(2)}$$

This ROS is the ratio of the beam offset by long-range transverse wakefields to the beam size at the BPM. When the value of ROS is big, this measurement will be easy. Here, beam offset by long-rang wakefield (Δy_{long}), the net beam size (σ_{y2}), beam size blow-up by beam jitter and short-range wakefield (Δy_{short}) are given by

$$\Delta y_{long} = R_{12}(s_1/s_2)\times\Delta y'_{long}$$
$$\sigma_{y2} = \sqrt{\varepsilon\beta_{y2}} \quad \text{---------} \quad (3)$$
$$\Delta y_{short} = R_{12}(s_1/s_2)\times\Delta y'_{short}$$

where $\Delta y'_{long}$, $\Delta y'_{short}$ and ε are kick angle by long-range and short-range wakefield at the structure and emittance of beam at BPM, respectively. We assume that all bunches in a pulse have the same injection error, and ignore bunch-by-bunch jitter. From these equations and transfer matrix from S_1 to S_2, ROS is independent of β_2. And optimum β_1 which make ROS maximum is derived from bunch charge, beam energy, beam position jitter and strength of short-range wakefield at the structure. When single bunch wakefield is assumed as $W_T(s)\approx 2\sigma_z\cdot 1.3\times 10^{20}[V/C/m^3]$ [10], the optimum β_1 is given in the case of two particle model by

$$\beta_1 \approx \left[\frac{\Delta y_{jitter}}{\sigma_y}\cdot\frac{q}{2}\cdot W_T(2\sigma_z)\cdot\frac{L}{E}\cdot\sin\psi\right]^{-1} \quad \text{---------} \quad (4)$$

where Δy_{jitter}, σ_y and σ_z are the position jitter at the structure, the vertical and longitudinal beam size at the structure, respectively. Maximum ROS is given by

$$ROS_{\max.} = \frac{\Delta y'_{long}}{\sqrt{2\varepsilon_y \cdot \frac{\Delta y_{jitter}}{\sigma_y} \cdot \frac{q}{2} \cdot W_T(2\sigma_z) \cdot \frac{L}{E}}} \quad \text{--------- (5)}$$

when $\sin\psi$ is equal to 1, i.e. phase advance from S_1 to S_2 is $\pi(n+1/2)$ (n: integer).

The beam position jitter at the structure contributes to the error on the signal measurement. Extremely low emittance of ATF's (ε_{ny}=30 nm) and stable beam has an advantage in getting a high sensitivity. However, our long bunch length (σ_z=5 mm) has a disadvantage from the effect of the short-range transverse wakefields on the measured bunch motions. To minimize this effect, length of the witness bunch should be as small as possible.

2.5 Resolution of measurement

To measure much smaller transverse kicks by long-range wakefield, the beam offset at BPM due to the transverse kicks must be larger than the resolution of BPM. For example, let the transverse kick ($\Delta y'_{long}$) be 10 nrad, and the extracted beam from the damping ring has the following parameters in Table 1.

Table 1 : ATF design parameters

Beam energy	E	1.54	GeV
Bunch charge	q	3.0	nC
Particles/bunch	N	1-3	10^{10}
Bunch spacing	t_b	2.8	ns
Bunches/train	N_b	10-60	
Bunch length	σ_z	5.0	mm
Horizontal emittance	ε_{nx}	4.3-5.1	μm
Vertical emittance	ε_{ny}	30	nm

The beam position jitter at structure is assumed to be $0.1\sigma_y$. In this case, ROS_{max} is equal to 5.4×10^{-3}. For the resolution of BPM is 0.5 μm, β_2 has to be larger than 425 m which means vertical beam size 65 μm at the BPM. A design of the beam optics which satisfied the above requirements was actually done, as shown in Figure 2. The resolution of BPM is also realistic value with 2.8 ns bunch spacing [11].

Even in the case that the pulse-to-pulse or bunch-by-bunch beam jitters are larger than the resolution of BPM and cannot be ignored, by measuring the orbits of all bunches in a pulse at the same time in diagnostic section, this measurement is free from the problem of the beam position jitter. Then we can still measure the much smaller transverse kick by residual wakefield.

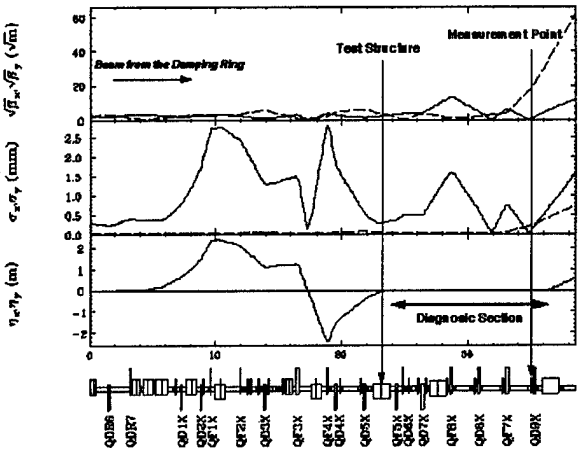


Figure 2 Optics of the ATF extraction line

3 CONCLUSIONS

At the ATF extraction line, the precise transverse wakefields measurements will be able to perform using extremely low emittance beam, high resolution BPMs and optimized optics of the extraction beam line. The experimental study of wakefields in an accelerating structure with cell-to-cell misalignment will be performed with using ATF multi-bunch beam.

4 ACKNOWLEDGEMENTS

The authors would like to acknowledge the continuous encouragement of Professors H. Sugawara, Y. Kimura and M. Kihara. We would like to express our thanks to all the member of the ATF group for their useful discussion.

REFERENCES

[1] JLC Design Study Group, "JLC Design Study Report," to be published.
[2] M. Yamamoto, "Study of Long-Range Wake Field in Accelerating Structure of Linac," KEK Report 94-9, 1995
[3] H. Deruyer et al., "Damped and Detuned Accelerator Structures," Int. Linear Accelerator Conf. Albuquerque, USA, 1990, and SLAC-PUB-5322, 1990
[4] T. Shintake et. al., "HOM-Free Linear Accelerating Structure for e+e- Linear Collider at C-Band," Proc. Part. Accel. Conf. and Int. Conf. High Energy Accel., Dallas, USA, 1995 and KEK Pre-print 95-48.
[5] J. Wang et. al., "Wakefield Measurements of SLAC Linac Structure at the Argonne AATF," SLAC-PUB-5498 (May 1991)
[6] C. Adolphsen et. al., "Measurement of Wakefield Suppression in a Detuned X-Band Accelerator Structure," SLAC-PUB-6629 (August 1994)
[7] K. Kubo, Private communication.
[8] H. Hayano et. al., "An 80 MeV Injector for ATF Linac," 17th Int. Linac Conf. (Linac94) Tsukuba Augast (1994)
[9] T. Naito et. al., "Bunch by Bunch Beam Monitor for ATF Injector Linac," 17th Int. Linac Conf. (Linac94) Tsukuba Augast (1994)
[10] K. Yokoya, Private communication.
[11] H. Hayano et. al., "Submicron Beam Position Monitors for Japan Linear Collider," Proc. of 16th Inte. Linac Conference(1992)

BEAM-BASED MONITORING OF THE SLC LINAC OPTICS WITH A DIAGNOSTIC PULSE[1]

R.W. Assmann, F.J. Decker, L.J. Hendrickson, N. Phinney, R.H. Siemann,
K.K. Underwood and M. Woodley
Stanford Linear Accelerator Center, Stanford University, Stanford CA 94309

Abstract

The beam optics in a linear accelerator may be changed significantly by variations in the energy and energy spread profile along the linac. In particular, diurnal temperature swings in the SLC klystron gallery perturb the phase and amplitude of the accelerating RF fields. If such changes are not correctly characterized, the resulting errors will cause phase advance differences in the beam optics. In addition RF phase errors also affect the amplitude growth of betatron oscillations. We present an automated, simple procedure to monitor the beam optics in the SLC linac routinely and non-invasively. The measured phase advance and oscillation amplitude is shown as a function of time and is compared to the nominal optics.

1 INTRODUCTION

The SLC linac is subject to large variations of its optics. Most of those variations occur on a day-night basis and are strongly correlated with the outside temperature. A diagnostic pulse was first implemented in 1995 [1] and then used extensively during the 1996 run in order to monitor the behavior of the SLC optics.

We distinguish between the *machine* and the *beam optics*. The former is defined by the magnet strengths and the design beam energy, while the latter describes the multi-particle behavior of the beam in the presence of strong wakefields. The diagnostic pulse measures the beam optics. The variations in beam optics that are shown in this paper are caused by two different mechanisms.

1. The beam energy along the linac is not constant. As some of the 300 klystrons switch on and off, the local beam energy changes while the final beam energy is kept constant. The lattice strength in SLC is adjusted in order to minimize this effect. In addition, the accelerating gradient at a single structure can vary due to undetected errors.

2. The transverse beam dynamics in the SLC linac is dominated by wakefields. Wakefield effects cause both a change in phase advance and the amplification of betatron oscillations. The wakefield effects on the optics depend on beam current, RF phases, bunch length and bunch distribution. Any change in those parameters will change the beam optics. For a detailed description of the multi-particle beam dynamics see [2].

2 IMPLEMENTATION

In standard SLC operation electron bunches are sent down the linac with a rate of 120 Hz. The sophisticated timing and triggering system of the SLC allows one to automatically kick selected pulses with 5 Hz, measure the induced betatron oscillations and dump them at the end of the linac. The positrons are not affected. In 1996 the SLC diagnostic pulse used 10 pulses every 15 minutes. The loss in integrated luminosity is negligible. The 1996 implementation was restricted to the vertical plane of electrons. It is illustrated in Figure 1.

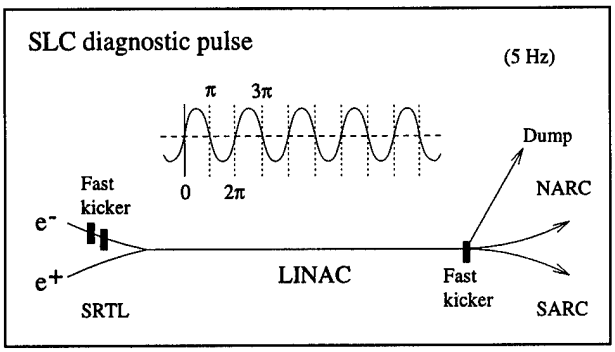


Figure 1 Schematic illustration of the SLC diagnostic pulse implementation.

The data was processed with two different methods. A simple online algorithm fitted the locations where the betatron oscillations crossed the zero axis (zero-crossing method). The phase advance is determined in 180 degree intervals and is almost independent of the knowledge of the optical functions. The method is simple, fast and robust. The average of two initial phases were saved into history plots that allowed tracking of the stability of the phase advance for a number of different regions in the linac. In this simplified model the amplitude of the oscillations was defined as the maximum BPM amplitude between zero-crossings.

A more complete analysis was suggested in [3]. This algorithm was implemented into the online analysis during the 1996 run and was used for the offline analysis presented in this paper. A complete description can be

[1] Work supported by the Department of Energy, contract DE-AC03-76SF00515

0-7803-4376-X/98/$10.00 © 1998 IEEE

found in [4]. Here we merely outline the principle. For a single measurement, the diagnostic pulse acquires two betatron oscillations (x_1,x_1') and (x_2,x_2') with different initial phases. The same **R**-matrix transports both betatron oscillations from the initial point "0" to all downstream locations "i":

$$\left(x_1, x_1'\right)_i = \mathbf{R}\cdot\left(x_1, x_1'\right)_0 \quad \text{and} \quad \left(x_2, x_2'\right)_i = \mathbf{R}\cdot\left(x_2, x_2'\right)_0$$

This allows reconstruction of the full **R**-matrix. Assuming that the single-particle Twiss functions apply locally, the **R**-matrix is then transformed into normalized coordinates. The two main observables, phase advance ψ and normalized amplitude A, are then obtained as:

$$\psi = \arctan\left(\frac{R_{12}}{R_{11}}\right) \quad \text{and} \quad A = \sqrt{\det(\mathbf{R})}\cdot\sqrt{\frac{E}{E_0}}$$

The amplitude is corrected for adiabatic energy damping. Without wakefields, A is equal to one along the whole length of the linac. BNS damping aims at keeping A close to one in the presence of wakefields [4]. In addition, the beam Twiss functions β and α can be determined from the diagnostic pulse data.

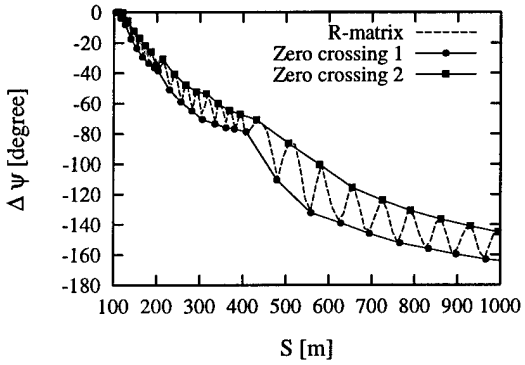


Figure 2 Phase advance difference with respect to the machine optics along the SLC linac (simulation). The "zero crossing" results are compared to the result of the R-matrix algorithm.

The results for the phase advance from the two methods are compared in Figure 2. As expected, the results agree very well. The average of the two "zero-crossing" results gives an accurate measure of the beam phase advance. The total oscillation swing in the R-matrix result in Figure 2 is a measure of the beta mismatch over all possible initial phases.

3 STABILITY

The phase advance and the normalized oscillation amplitude were monitored for the whole 1996 run, from March to August 1996. A major goal for those measurements was to identify the temperature dependent day-night stability problems affecting the SLC performance. As soon as the outside temperature began to rise in May, large day-night variations were observed indeed. Figures 3 and 4 show the measured beam phase advance and normalized oscillation amplitude on May 11th for two periods called "day" and "night". The "night" period contains data from 1:12am to 5:31am, while the "day" period contains data from 12:14pm to 14:38pm.

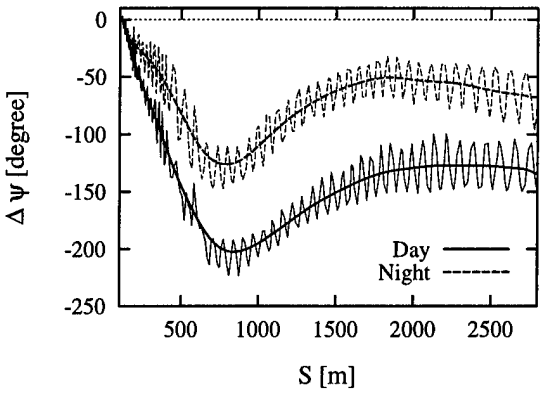


Figure 3 Measured beam phase advance difference in the SLC linac with respect to the machine optics during day and night of May 11th, 1996

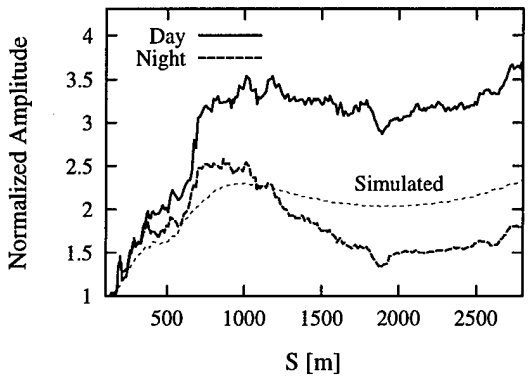


Figure 4 Measured normalized oscillation amplitude in the SLC linac during day and night of May 11th, 1996.

It is seen that the beam optics changes from day to night. The total phase advance varies by up to 100°, while the normalized amplitude changes by almost a factor of 2. The beam-based emittance optimization for the SLC linac is heavily affected by those changes.

Once the beam signature of the day-night variation was measured with the diagnostic pulse it could be traced to an uncorrected temperature-dependent variation of the RF phase synchronization system in the linac [5,6]. A simple model was developed that simultaneously explained several outstanding stability problems in the SLC linac. For more details see [5].

Figures 5 and 6 show the variations in phase advance and normalized amplitude before and after a temperature correction was applied to the phase distribution system (on day 191). Day-night variations in the beam optics were significantly reduced.

4 ABSOLUTE ERRORS

The measured multi-particle beam optics can be compared to the expectations. Detailed simulations were

performed with the LIAR computer program [4]. The simulations used the measured quadrupole settings, the actual SLC beam energy and the measured beam profile and current, to the known accuracy.

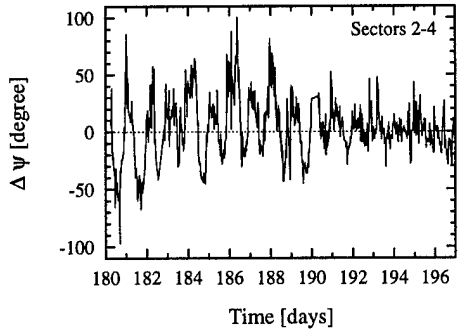


Figure 5 Measured variation of the beam phase advance in sectors 2-4 from June 28th to July 16th.

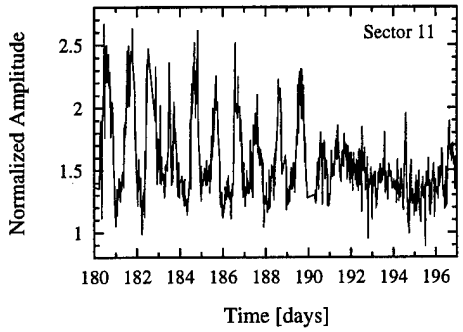


Figure 6 Measured normalized amplitude in sector 11 from June 28th to July 16th.

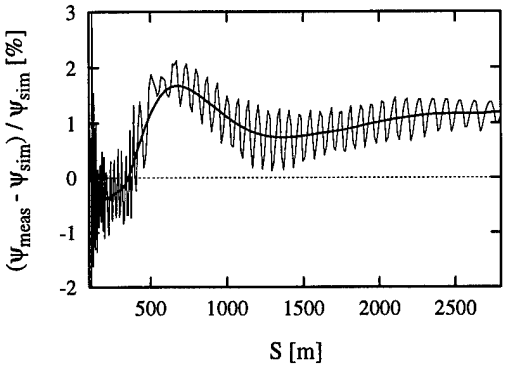


Figure 7 Relative difference between measured and simulated beam phase advance along the SLC linac on the night of July 31st.

Figure 4 compares the measured normalized amplitude to the simulation result. The amplitude at night shows reasonably good agreement with the expectation. Figure 7 shows the relative difference in phase advance between a measurement on July 31st and the simulation. The agreement between the measurement and the simulation is at the 1-2% level. Taking into account uncertainties in the longitudinal beam profile, the RF phases, etc. this agreement is remarkably good.

It is important to point out that the diagnostic pulse also allows one to locate large setup errors. An example is shown in Figure 8. The phase advance changes by about 130° when a klystron early in the linac is switched off.

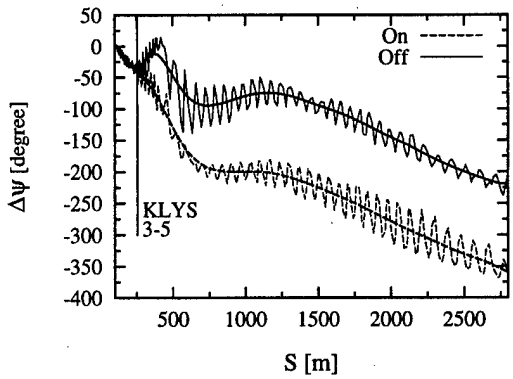


Figure 8 Measured phase advance before and after switching off a klystron in the beginning of the linac. The lattice was not rescaled.

5 SUMMARY

A diagnostic pulse was developed and used successfully in the SLC linac for monitoring and checking of the multi-particle beam optics. The measured signature of large day-night variations in the beam optics indicated a solution to a long outstanding stability problem for the SLC. The measured beam phase advance was shown to agree on the 1-2% level with detailed simulations of the multi-particle beam dynamics. In addition, the normalized oscillation amplitude shows very good agreement within its measured stability. The diagnostic pulse also provides a valuable tool to find large errors in the klystron and optics setup. It will provide an essential tool in the operation of future linear colliders.

ACKNOWLEDGEMENTS

We would like to thank W. Spence for his help and important contributions.

REFERENCES

[1] F.-J. Decker et al, "Diagnostic Beam Pulses for Monitoring the SLC Linac". PAC95, Dallas, May 1995, p. 2646.
[2] R. Assmann, "Beam Dynamics in the SLC". These proceedings.
[3] W. Spence, unpublished note, August 1995.
[4] R. Assmann et al, "LIAR - A Computer Program for the Modeling and Simulation of High Performance Linear Accelerators". SLAC-AP 103.
[5] F.-J. Decker et al, "Beam-Based Analysis of Day-Night Performance Variations at the SLC Linac". These proceedings.
[6] R. Akre, "SLC Interferometer System and Phase Distribution Upgrades at the SLC". These proceedings.

OBSERVATION OF DARK-CURRENT SIGNALS FROM THE S-BAND STRUCTURES OF THE SLAC LINAC[1]

R. Assmann, F.J. Decker, M. Seidel, R.H. Siemann, D. Whittum
Stanford Linear Accelerator Center, Stanford University, Stanford, CA 94309

Abstract

It is well known that the electromagnetic fields in high-gradient RF structures can cause electron emission from the metallic structure walls. If the emitted electrons are captured and accelerated by the accelerating fields so-called "dark-current" is induced. Dark-currents have been measured and studied for various RF structures. In this paper we present measurements of RF induced signals for the SLC S-band structures. For nominal gradients of 17 MV/m it is shown that the dark-current can be strong enough to significantly reduce the signal-to-noise ratio of the SLC beam wire scanners. We also show results from RF measurements in the dipole band. The measurements are compared to more direct observations of dark-current and it is tried to connect the results to possible effects on the accelerated particle beam.

1 INTRODUCTION

Accelerating, high-gradient RF structures are known to generate significant dark-current [1]. The generation and strength of dark-current has been studied experimentally and theoretically in a number of previous publications [1,2,3,4]. Though some quantitative understanding on the strength of dark-currents and its dependence on structure design, cleanliness, gradient, and other parameters has been achieved, it has proved to be hard to quantify the effects on the accelerated beam.

We consider dark-current for the SLC linac. The beam energy (> 1.19 GeV) is high compared to the energy of the dark-current electrons gained within a girder with four or two structures (< 0.220GeV). Due to the large energy
disparity, the dark-current is then almost completely lost after the first quadrupole [4]. The dark-current does not propagate down the linac and only local effects are important. These can be twofold:

1. Generation of background for local diagnostic devices.
2. Beam deflections due to possible azimuthal asymmetry in the dark current distribution.

The first nuisance is observed in the SLC linac on a regular basis and results locally in a limitation of maximum accelerating gradient for certain RF structures in the SLC linac. Possible beam deflections due to asymmetric dark-current have not been observed directly so far. They provide, however, a possible mechanism to explain observed growth in "beam jitter" along the SLC linac [5]. This mechanism, if strong enough, could generate unacceptably large beam jitter in future linear colliders like the NLC, SBLC or JLC. In this paper we describe attempts to indirectly assess possible effects on the beam by simultaneously measuring the dark-current and RF induced dipole mode signals from the structures.

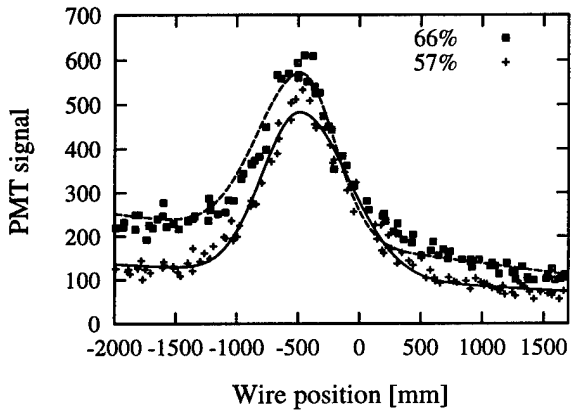


Figure 1 Example of transverse beam profile measurements with two different drive settings of the upstream klystron. The background was almost halved when the klystron drive was reduced from 66% (squares) to 57%.

2 SLC WIRE MEASUREMENTS

RF induced dark-currents can disturb important beam measurements. Among the most crucial diagnostic devices in SLC are the wire scanners that allow a full reconstruction of the beam emittance at different locations in the linac. A thin wire is moved through the beam and produces scattered electrons. The number of scattered electrons is proportional to the beam intensity at the actual location. A measurement of the number of scattered electrons as a function of wire position then reveals the transverse beam profile.

The scattered electrons are detected with a Photo-Multiplier Tube (PMT) that is located downstream of the moving wire. If dark-current electrons hit the PMT they produce a background to the beam-induced signal. The signal-to-noise ratio is reduced and the measurement is

[1] Work supported by the Department of Energy, contract DE-AC03-76SF00515.

0-7803-4376-X/98/$10.00 © 1998 IEEE

distorted. Figure 1 shows an example where the dark-current induced background was reduced by lowering the drive of an upstream klystron.

Occasionally the dark-current induced background can completely "hide" the beam-induced signal in the SLC linac. As a consequence, the maximum accelerating gradient for certain structures must be limited such that dark-current induced background for the wire measurements is avoided. For the study that follows we used the PMT signals as a qualitative measure of dark-current in the RF structure.

3 RF INDUCED DIPOLE-MODE SIGNALS

An asymmetric, not centered current can excite a dipole mode in RF structures. It was shown that beam-induced dipole mode signals correlate well with the centroid position of a particle beam in the RF structure [6]. Here we describe measurements of purely RF induced signals in the dipole-mode frequency range (DM). The setup of dipole-mode measurements for the SLC is described in [6].

In order to study the nature of the observed dipole-mode signals, we simultaneously studied RF induced dipole-mode and PMT (compare above) signals. The experimental layout is sketched in Figure 2. We mainly considered C-Band signals at 4.064GHz and 4.210 GHz. The RF induced DM (without beam) produced a signal that was about 60 times smaller than that from a bunch with $3.5 \cdot 10^{10}$ electrons and a 50-100μm offset in the structures.

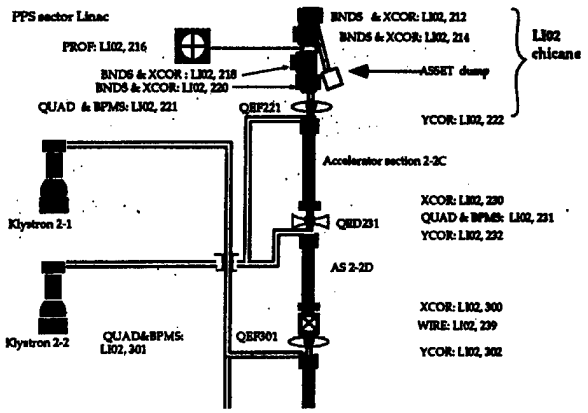


Figure 2 Layout of the experimental setup. The dipole-mode signals were measured at the input couplers of Klystron 2-2. The PMT signals were measured at the location of WIRE LI02, 239.

4 MEASUREMENTS

RF-induced PMT and C-Band ("DM") signals were measured simultaneously for different klystron parameters. The parameters of interest are:

1. *Beam voltage*: Voltage of the klystron beam.
2. *Klystron delay*: Changes delay and width of RF pulse. If small, then the klystron produces no RF power.
3. *RF tuning*: Tuning of the SLED cavities.

As a first test the klystron beam voltage was changed. Figure 3 shows the measured PMT and C-Band signals for the different settings. The results are summarized in Figure 4. As expected for dark current, the PMT signal shows a strong dependence on the beam voltage. However, the C-Band signal shows only little change.

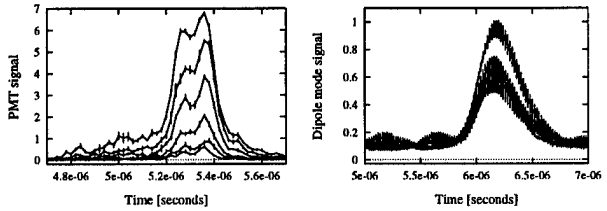


Figure 3 PMT (left) and C-Band (right) signals for different beam voltage settings of klystron 2-2.

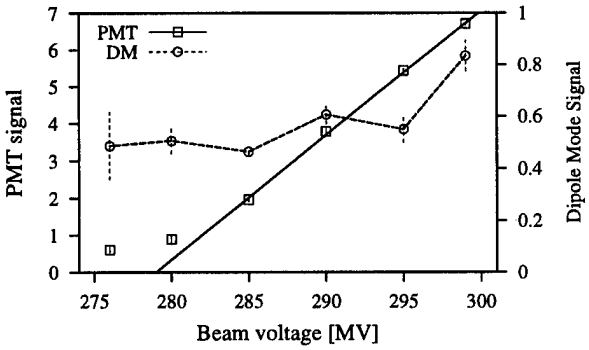


Figure 4 Summary of the results from Figure 3. The PMT signal shows a strong dependence on the klystron beam voltage, while the DM signal does not.

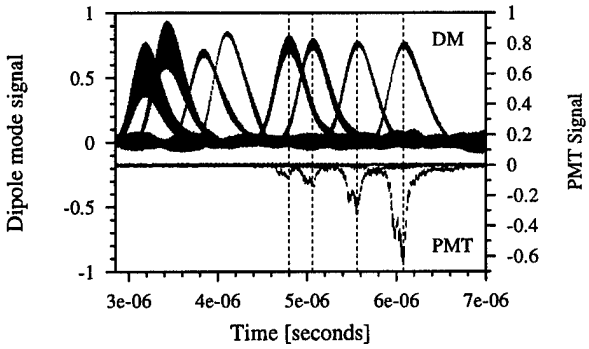


Figure 5 C-Band signals (top) and PMT signals (bottom) for different klystron delays.

The arrival times of both signals follow the klystron delay. This is shown in Figure 5. For small delays the beam voltage drops (measured but not shown here) and the PMT signal vanishes. The C-Band signal becomes unstable (fluctuates between nominal value and zero: large error bars) but does not vanish.

It was also tried to correlate the variations in the PMT and the Beam voltage signals. The correlation for 35 consecutive measurements is shown in Figure 6. There is either no correlation or the correlation is hidden by measurement noise.

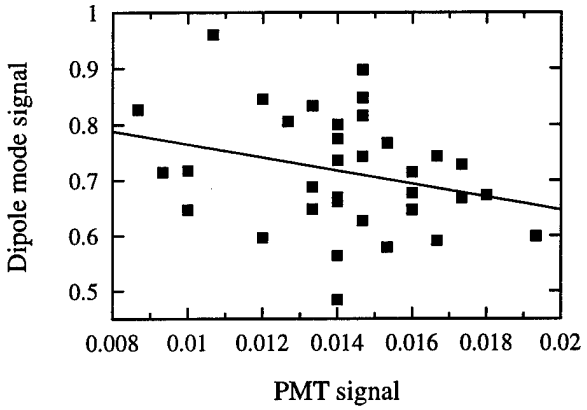


Figure 6 Correlation between C-Band and PMT signal.

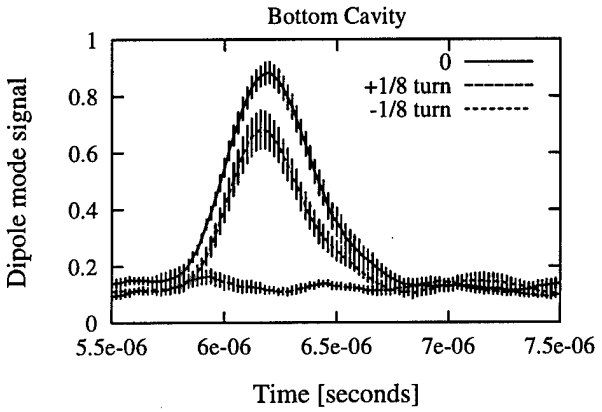


Figure 7 Sensitivity of C-Band signal against tuning of the bottom cavity.

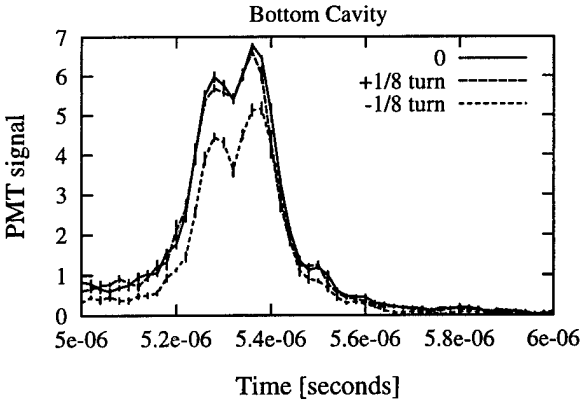


Figure 8 Sensitivity of PMT signal against tuning of the bottom cavity.

Finally we changed the tuning of the SLED cavities. As shown in Figure 7, the C-Band signal was eliminated by a small change in the tuning screw of the bottom cavity. At the same time the PMT dark current signal did not change significantly, indicating that the accelerating RF voltage and the associated dark current did not change.

5 CONCLUSION

Dark current in the SLC S-band structures is observed with the photo-multiplier tubes of the wire scanners. We studied the dependence of the PMT signals on several klystron parameters and found the expected qualitative behavior.

We also observed RF-induced C-Band signals. These signal were about 60 times smaller than the dipole mode signal from a bunch with $3.5 \cdot 10^{10}$ electrons and a 50-100μm offset in the structures. We performed measurements at 4.064GHz and 4.210 GHz for varying klystron parameters. The C-Band signal showed a very different behavior compared to the PMT signal. Its strength did not depend strongly on the beam voltage in the structure or the klystron delay, as did the PMT signal. A minor change in the tuning of a klystron cavity was sufficient to eliminate the C-Band signal. At the same time the klystron beam voltage and the PMT dark current signal remained essentially unchanged. We could adjust the klystron such that we either had a C-Band *or* a PMT signal. Both signals, generated from the same klystron, apparently are caused by different physical mechanisms.

There is a strong indication that the C-Band signal is generated in the upstairs klystron and not in the RF structure. Because the signal is relatively large, it could affect the beam if it was transported into the downstairs RF structure. We can very roughly estimate that the observed variation in the C-Band signals is equivalent to an rms quadrupole jitter of less than 10 nm. Further studies are needed to get a better quantitative understanding of the strength and importance of klystron-generated RF signals.

6 ACKNOWLEDGEMENTS

We thank M. Ross, R. Akre and the SLC RF group.

REFERENCES

[1] G.A. Loew and J.W. Wang: "Field Emission and RF Breakdown in Copper Linac Structures". Proc. XIV Int. Conf. on High Energy Acc., KEK, Japan, August 22-26, 1989.
[2] H. Matsumoto: "Dark Currents". KEK 96-120.
[3] J. W. Wang et al: "SLAC/CERN High Gradient Tests of an X-Band Accelerating Section". CERN-SL-95-27 RF.
[4] N. Akasaka: "Dark Current Simulations in High Gradient Accelerating Structure". KEK 96-65.
[5] C. Adolphsen et al:
[6] M. Seidel, C. Adolphsen, R. Assmann and D. Whittum: "Detection of Beam-Induced Dipole-Mode Signals in the SLC S-Band Structures". These proceedings.

OBSERVATION AND ANALYSIS OF STATIC DEFLECTIONS FROM TRANSVERSE LONG-RANGE WAKEFIELDS IN THE SLC*

R.W. Assmann, F.J. Decker, P. Raimondi, T.O. Raubenheimer
Stanford Linear Accelerator Center, Stanford University, Stanford, CA 94309

Abstract

In the SLC main linac a train of three bunches is accelerated. The leading positron bunch is followed by two bunches of electrons. When the positron bunch passes off-axis through the RF structures, it excites dipole modes in the structures, for example long-range transverse wakefields which deflect the subsequent electron bunches. Although the magnitude of the deflections is small one can infer the deflections by measuring the trajectory difference while changing the spacing between the positron and electron bunches. Knowing the positron trajectory the misalignments of the accelerating RF structures with respect to the BPM's can be calculated. We present measurements from the SLC linac and discuss the data analysis and errors.

1 INTRODUCTION

A charge that is accelerated in the SLC linac excites transverse wakefields if it is misaligned with respect to the center of an RF structure. Figure 1 shows the calculated transverse wakefield $W(z)$ that is excited in an SLC S-Band structure of length L_0 from a charge Q_1 with offset δy. A charge Q_2 at position s with energy $E_2(s)$, that follows the first charge with distance Δz, then experiences a wakefield deflection

$$\theta(s) = W(\Delta z) \cdot \frac{e\,Q_1 L_0(s)}{E_2(s)} \cdot \delta y\,. \qquad (1)$$

The unknown beam to structure offsets δy are caused by unavoidable alignment errors and are the cause for severe emittance dilutions in the SLC linac[1]. If they were determined accurately then the optimization and stabilization of the SLC beam emittances could be improved.

Transverse wakefields are usually distinguished into short-range wakefields that act within a bunch and long-range wakefields that act from one bunch to the next. Both are generated from beam to structure offsets. However, it is important to note that differently from the short-range case, long-range wakefields remain only in the first third of a structure and decohere afterwards. We are going to show how to determine the beam to structure offsets from long-range wakefields. In the presence of large internal structure misalignments those offsets will differ somewhat from the ones important for short-range wakefields.

The SLC beam consists of three bunches: 1) a positron bunch, 2) an electron bunch, and 3) an electron bunch for positron production. Here we consider the first two

* Work supported by the Department of Energy, contract DE-AC03-76SF00515.

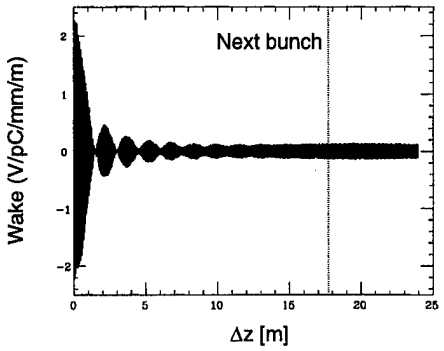


Figure 1: Transverse wakefield as a function of distance Δz for the SLC S-Band structures. The nominal bunch spacing is indicated by the dotted line.

bunches. The electron bunch witnesses the transverse long-range wakefields from the leading positron bunch. With Eq. (1) it is seen that a change in Δz changes the wakefield deflection θ. For a single structure and if Δz is changed in many steps the wakefield can be mapped out and the beam to structure offset is determined. Here we consider many superimposed errors and only a few possible settings for Δz. Assuming that the wakefield function is known, a single change in bunch spacing then allows to calculate the beam to structure offsets from the measured change Δy_2 in the trajectory of the second bunch:

$$\Delta y_2(s) = \int_0^s ds' R_{12}(s,s') \cdot \Delta\theta(s') \qquad (2)$$

$$= \int_0^s ds' R_{12}(s,s') \cdot \frac{eQ_1 L_0(s')}{E_2(s')} \cdot W_0 \cdot f_\phi(s') \cdot \delta y(s')\,. \qquad (3)$$

The long-range wakefield function $W(\Delta z)$ for SLC is dominated by a 4140 MHz mode and can be approximated with good accuracy by $W_0 \cdot f_\phi(s')$ where $W_0 \approx 0.13$ V/pC/mm/m and

$$f_\phi(s') = \cos\left[\phi_d(s') - \Delta\phi + \phi_0\right] - \cos\left[\phi_d(s') + \phi_0\right]\,.$$

The change in distance Δz is expressed through an offset $\Delta\phi = \Delta z/7.2\text{cm} \cdot 360°$ in the long-range wakefield phase. ϕ_0 is the nominal phase between the second bunch and the long-range wakefield. The analysis is slightly complicated by the fact that the long-range dipole-mode frequencies of the SLC S-Band structures have been adjusted by a technique called "dimpling". This was done in order to avoid beam breakup with continuous beam operation in the SLAC linac. The "dimpling" is taken into account

0-7803-4376-X/98/$10.00 © 1998 IEEE

by a phase offset ϕ_d that is a function of position s and takes the values 0°, 45°, and 90° for the modes 4140 MHz, 4142 MHz and 4144 MHz. Figure 2 illustrates the dipole mode frequencies for all structures in the SLC linac.

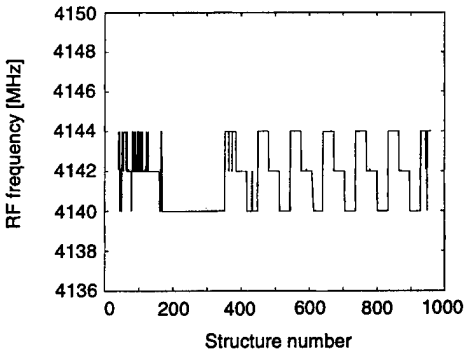


Figure 2: Dipole mode frequencies for the SLC S-Band structures. The effect of "dimpling" is illustrated.

All terms in Eq. (3) can be measured or calculated except the beam to structure errors $\delta y(s)$. This allows to solve for $\delta y(s)$. Note, that due to the energy dependence in Eq. (3) the sensitivity of the method changes widely along the linac. The wakefield deflections at injection energy are almost a factor of 50 stronger than the deflections at the end of the linac. A part of this difference is compensated by stronger focusing in the beginning of the linac.

2 MEASUREMENTS

The fundamental mode of the SLC S-Band structures is 2856 MHz. The corresponding wavelength is 0.35 ns which defines an RF bucket. In order to change the bunch spacing between the positron and the first electron bunch, the positrons were not moved while the timing of the electron bunch was moved in two steps of 1 RF bucket. The corresponding changes in $\Delta\phi$ are 160° and 320°, allowing for a significant change in the phase factor $f_\phi(s)$ and the measured electron trajectory.

The measured trajectory change from a 1 bucket movement of the first electron bunch is shown in Fig. 3. The positron trajectory remained unchanged within its stability. Measurements were done repeatedly with 1 and 2 RF bucket changes for the electrons. Each measurement was calculated from three online measurements, each the average of 30 beam trajectories. The spread within the three average measurements was used to determine the systematic measurement error to be roughly 20 μm.

3 ANALYSIS

Starting from Eq. 2 the problem to be solved is

$$R_{12} \cdot \alpha = b\,, \tag{4}$$

with b being the array of BPM measurements Δy_2, α the array of wakefield deflections θ and R_{12} the relevant transport matrix. Note that for most of the linac, kicks from four

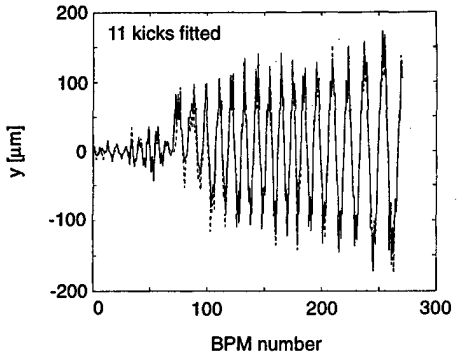


Figure 3: Measured change Δy_2 in the electron trajectory due to moving the electron bunch 1 RF bucket (10.5 cm) closer to the positrons. The measurement (solid) is compared to a fit (dashed) for 10 wakefield deflections and an average offset of all structures (compare next section).

structures between neighboring BPM's are lumped together into a single effective kick.

For the data analysis we used the method of singular value decomposition (SVD). SVD factorizes $R_{12} = U \cdot S \cdot V^T$ with $UU^T = 1$ and $VV^T = 1$. The matrix S is diagonal with the diagonal elements W_i sorted in descending order. A number W_i indicates something like the effectiveness of a combination of kicks to change the trajectory. Putting a "threshold" on W_i will force the solution to use the most effective combinations of kicks and the RMS kick of the solution is reduced. Unphysical kick combinations can such be avoided. This is illustrated in Fig. 4. The solution is obtained as $\alpha = VS^{-1}U^T m$ with the error $(\delta\alpha)^2 = \left(V^T/W\right)^2$. The knowledge of the error $\delta\alpha$ allows to iterate the result while disregarding the most insignificant kicks with large relative errors. In Fig. 5 it is shown that about 15 kicks are sufficient to explain the measured data within its resolution. The agreement between the fit and the measurement is illustrated in Fig. 3 for just 11 kicks. Though some differences are left, the data is well explained within its resolution and possible errors in the used optics R_{12} model. The data also allows to determine the phase ϕ_0 between the electron bunch and the long-range wakefield. Figure 6 shows that a minimum fitted χ^2 is obtained for $\phi_0 \approx 15°$.

For the final results, the 1 and 2 bucket data sets were fitted simultaneously. The structure misalignments were calculated from the fitted wakefield kicks and the results were compared to conventional survey data. We drew the following conclusions:

1. The measured trajectory changes can be explained within the noise of the measurement by 15-20 large structure misalignments with an RMS of 1.5 mm. In addition an average offset of $\approx$120 μm of all structures is needed to explain the data.

2. Due to the limited stability and BPM resolution, it

is difficult to resolve single errors. The errors are lumped together into a few large ones.

3. The LRWF results depend on the model used for the wakefield optics. We obtained consistent results with a modified model.

4. There is no strong correlation between misalignments found by long-range wakefield and survey measurements. However, large offsets from the long-range wakefield analysis tend to coincide with problems in the survey. About 25 out of 263 survey measurements (about 10%) have large uncertainty errors. Assuming no correlation with the LRWF results, we would expect that about 2 out of 20 LRWF kicks coincide with the survey problems. However, we find 7 coincidences that might indicate real problems.

5. Twelve out of twenty large misalignments obtained from the long-range wakefield analysis occur at the end of a sector (instrumentation section).

4 SUMMARY

During the 1994/1995 run transverse long-range wakefields were studied in the SLC. Changing the distance between the e^- and $^e+$ bunches, the static wakefield kicks from the leading positrons on the electrons were changed and the corresponding change in the electron trajectory was measured. A significant change in the electron trajectory was indeed observed, indicating several large transverse structure offsets in the SLC. A detailed data analysis was done for the vertical plane.

Though limited in their accuracy, the long-range wakefield analysis pointed to the instrumentation sections at the end of linac sectors as the likely locations of large structure misalignments. Because the regular lattice is interrupted there, traditional alignment and survey methods are limited in their accuracy, explaining the possibly large misalignments. Also, an average structure offset of about 120 μm is needed to explain the measured electron trajectory.

The available signal to noise ratio from the long-range wakefield measurements is not large enough to resolve all important structure errors with the required accuracy. Within the available resolution, errors are lumped together into a few large kicks. Although sufficient for a steering minimization, the accuracy is not sufficient for a mechanical realignment of the RF structures. A related approach[2] to determine the structure alignment with a better signal to noise ratio has been proposed and will be tested in the SLC linac during the 1997 run.

5 REFERENCES

[1] R. Assmann, "Beam Dynamics in SLC", These proceedings.

[2] F.J. Decker *et al.*, "Super-ASSET: A Technique for Measuring and Correcting Accelerator Structure Misalignments at the SLC", These proceedings.

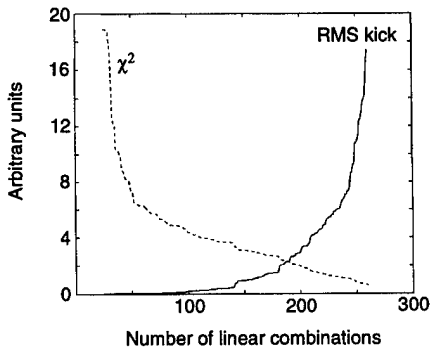


Figure 4: The χ^2 and the RMS kick found by SVD as a function of the number of linear combinations that are included into the solution. The χ^2 can be greatly reduced with just a few kick combinations. If too many combinations are included, unphysically strong kicks are introduced that reduce the χ^2 only slightly.

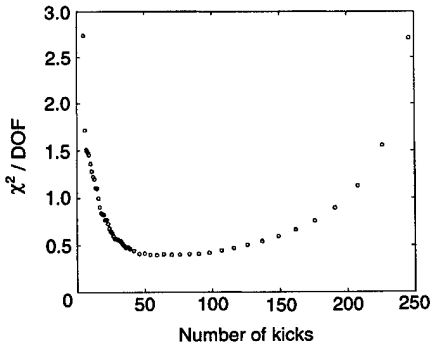


Figure 5: The χ^2 per degree of freedom as a function of the number of kicks that are included into the solution. About 15 kicks are sufficient to obtain a χ^2/DOF of 1.

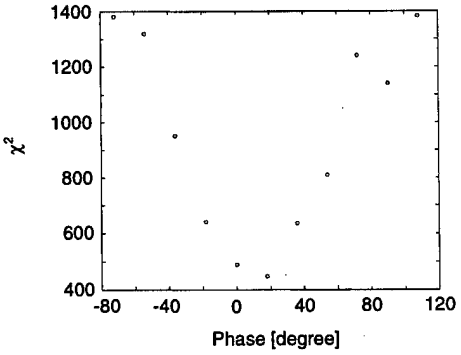


Figure 6: The phase ϕ_0 between the electron bunch and the long-range wakefield is indicated by a minimum χ^2 of the fitted solution.

BEAM-BASED ANALYSIS OF DAY-NIGHT PERFORMANCE VARIATIONS AT THE SLC LINAC

F.-J. Decker, R. Akre, R. Assmann, K.L.F. Bane, M.G. Minty, N. Phinney, W.L. Spence
Stanford Linear Accelerator Center†, Stanford University, Stanford, CA 94309 USA

Abstract

Diurnal temperature variations in the linac gallery of the Stanford Linear Collider (SLC) can affect the amplitude and phase of the rf used to accelerate the beam. The SLC employs many techniques for stabilization and compensation of these effects, but residual uncorrected changes still affect the quality of the delivered beam. This paper presents methods developed to monitor and investigate these errors through the beam response. Variations resulting from errors in the rf amplitude or phase can be distinguished by studying six different beam observables: betatron phase advance, oscillation amplitude growth, rms jitter along the linac, measurements of the beam phase with respect to the rf, changes in the required injection phase, and the global energy correction factor. By quantifying the beam response, an uncorrected variation of 14° (S-band) during 28°F temperature swings was found in the main rf drive line system between the front and end of the linac.

1 INTRODUCTION

Since the SLC now produces flat beams with emittances as low as $\gamma\varepsilon_y = 0.2*10^{-5}$ m-rad at the end of the linac, stability of the hardware has becomes increasingly critical. Slow variations coming from day-night temperature swings make it difficult to maintain the best emittances. It has previously been shown that the largest variations are caused by the accelerating rf system, but it was unclear whether the amplitude (A) or the phase (ϕ) of the rf was varying. An earlier paper [1] described sources of amplitude variations, while this paper concentrates on the more serious effect of rf phase variations. In particular, beam-based measurements were used to distinguish between the two (A, ϕ). First we discuss the stability requirements, then the beam-based signals and simulations, and finally the primary problem source, the main drive line which distributes the rf synchronization.

2 STABILITY REQUIREMENT

If the linac alignment and beam orbit were perfect, the requirements for rf stability would be relaxed. Changes in longitudinal phase space parameters (energy, phase, bunch length, and energy spread) would not couple into the transverse phase space. Improved alignment is clearly desireable (see [2]). In reality there are transverse offsets and the resulting wakefields must be canceled at the SLC by compensating orbit bumps [3]. Typically a bump spans about six betatron wavelengths. An initial emittance of $1.0*10^{-5}$ m-rad without bumps can be reduced to $0.2*10^{-5}$ m-rad. To control transverse jitter, the SLC uses BNS [4] damping which introduces a large energy spread in the beam. This causes the wakefield cancelling bumps to be very sensitive to energy and phase changes. An energy change of 1%, or a phase change of 1.5° over the region of the bump can change the phase advance by 22°. This disturbs the wakefield-tail cancellation and generates an emittance growth of $\Delta\varepsilon = (1.0 * \sin 22°) =$ 0.4 m-rad. Similar effects occur if the energy gain of one klystron (out of 30) is unknown to 30%.

3 BEAM BASED SIGNALS

After stabilizing the rf amplitudes [1], it was recognized that there were still large daily variations in the betatron phase advance of the beam, as measured by oscillation data taken automatically with a diagnostic pulse [5, 6] (Fig. 1).

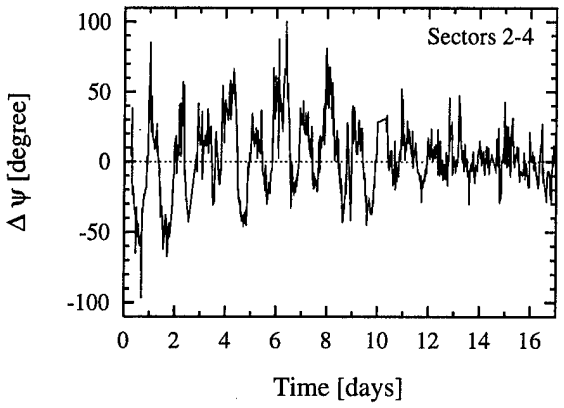


Figure 1: Diurnal betatron phase advance variation. The overall phase measured from the beginning of the linac to this point is 2800°, so a -100° phase change corresponds to 3.5% energy gain. After day 10 it was compensated.

To distinguish between rf amplitude and phase as the source of the drifts, additional diagnostics were required. Table 1 summarizes the observables used.

† Work supported by the Department of Energy contract DE-AC03-76SF00515.

0-7803-4376-X/98/$10.00 © 1998 IEEE

Indications	Variation	Reasons
global energy correction	+1.5%	A, ϕ
betatron phase advance	at 500 m: –100°	A, ϕ
injection phase	e^-: +7°, e^+: +4°	ϕ, cable
oscillation amplitude growth	50%	ϕ
transverse rms jitter	100%	ϕ
beam phase monitors	Li2: 7°, L28: –7°	ϕ, cable

Table 1: Beam parameters studied and possible causes (A: rf amplitude, ϕ: rf phase, cable: cable length). The amount of the variation is the day/night ratio, or for phases the day minus night difference.

The global linac energy correction accounts for the integrated sum of all energy errors. A 1.5% diurnal change corresponds to 1.5% more or less spare energy available. If this were due to rf amplitude changes, it could not explain the 100° phase advance change (equivalent to 3.5% of the energy) measured after 500 meters of linac.

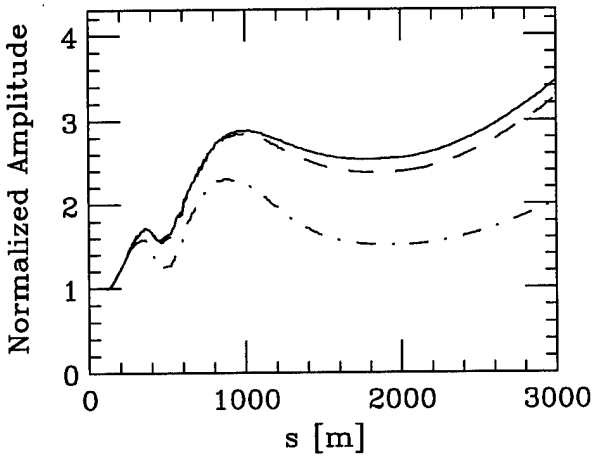


Figure 2: Simulated amplitude growth factor along the linac (solid) compared with 2% energy reduction (dashed) or +3° phase variation (dash-dotted).

An indication that phase variations were dominant came from simulations of the amplitude growth of betatron oscillations which showed a different sensitivity to energy or phase variation (Fig. 2). For a single particle, the amplitude growth factor of an oscillation scales as $(\det(R)\, E/E_0)^{1/2}$, where R is the effective matrix of the beam transport elements including wakefields and E/E_0 is the energy normalization. For a BNS damped beam, the energy spread will cause the amplitude to decrease through filamentation. In the presence of transverse wakefields, the tail of the bunch is excited to even larger amplitudes than the head and the amplitude grows. Oscillation amplitudes were found to change by up to 50% between day and night (see Fig. 3). Similar behavior was observed in the rms of the transverse beam jitter measured by the feedback systems located along the linac. The jitter changed as much as 100% diurnally. If the source of the jitter is constant, this indicates that the BNS damping has become weaker.

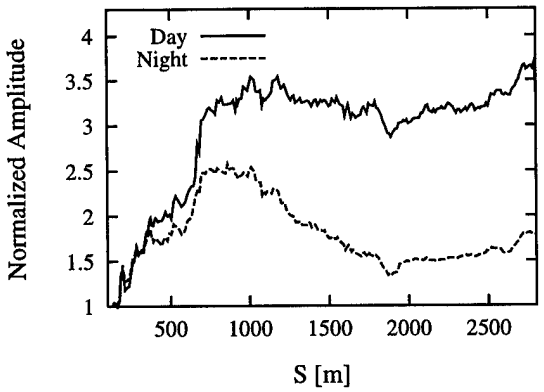


Figure 3: Measured oscillation amplitude growth factor plotted versus location in the linac for day and night. At 1000 m the variation is 50% larger in mid-day (3.6/2.4).

Another indication of these problems was given by monitors which measure the beam phase with respect to the rf near the beginning and end of the linac. A diurnal difference of ±7° (or 14° over the whole linac) was seen (Fig. 4). In principle this change could be due to measurement systematics such as cable length changes. However, the simulations below indicated that the observed variation was consistent with the other measured effects.

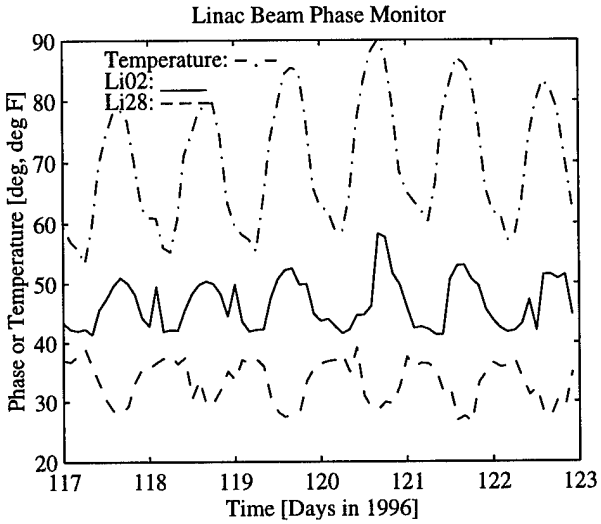


Figure 4: Beam phase in sector 2 and 28 and outside temperature showing an anticorrelation and a phase variation of 7°. The temperature swing during that period was about 28°F daily.

4 SIMULATIONS

Simulations were performed to understand if the various observations were consistent with the hypothesis of a 14° phase variation of the main drive line that synchronizes the linac rf. The simulation assumed an ideal energy profile with a BNS configuration of 22° for the first 700 meters and –16.5° for the rest of the linac at night. If the phase length changed by 14° during the day, the initial BNS phase would decrease by 7° (to 15°) and

the final phase would increase by 7° (to –9.5°). These variations weaken the BNS damping and provide less suppression of beam jitter. With weaker BNS phases, the beam is closer to the crest of the rf and the total energy available is larger. The beam energy at the end of the linac is held constant by feedback but the error is reflected in the global energy correction required. If one calculates the energy gain for the weaker daytime BNS phases (from cos 15° to cos (–9.5°)) and compares it to the ideal night value, there is an energy discrepancy of 1.4% (see Fig. 5). This is consistent with observed behavior.

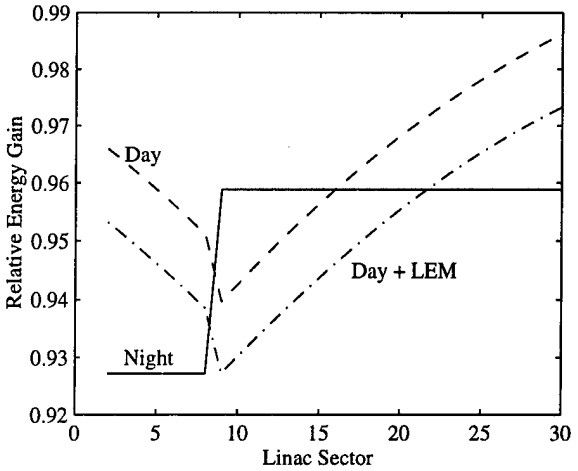


Figure 5: Relative energy gain along the linac for different main drive line conditions: At night the energy gain per sector is reduced by the cos (22°) and cos (–16.5°), while during the day it varies along the length of the linac by a factor between cos (15°) and cos (–9.5°). The third curve shows the day curve scaled down by 1.4% to reflect the effect of the global energy feedback which holds the mean energy constant.

5 MAIN DRIVE LINE

The main drive line (MDL) which synchronizes the linac rf phases was found to be a major source of the observed sensitivity to diurnal temperature variations. The phase length of the MDL is affected by external temperature and barometric pressure variations. This length is monitored by an interferometer [7] and a feedback system then adjusts the linac rf phases to correct for the measured length changes. The various diurnal effects described here indicated that temperature variations of the MDL were not fully compensated by the interferometer feedback. An additional ad hoc temperature correction was applied to alleviate the symptoms while the true source of the error was being investigated. This correction effectively doubled the feedback response to temperature change (see day 124 in Fig. 6), and it successfully reduced the diurnal variation in the beam parameters discussed (see day 10 in Fig. 1). Further investigations of and improvements to the rf hardware are discussed in another paper [8].

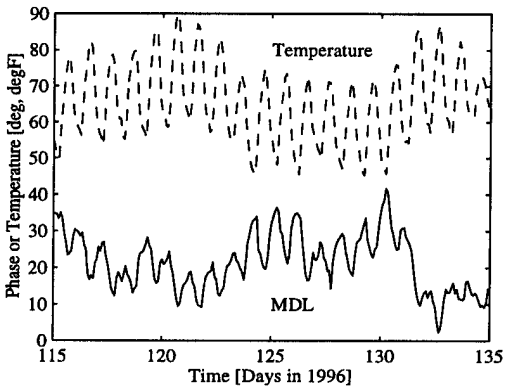


Figure 6: MDL interferometer phase versus time. The phase length may vary by up to 30° with barometric pressure swings, and up to 15° with diurnal temperature cycles. Before the correction at day 124, only half of the temperature dependence, about 7°, was being compensated.

6 SUMMARY

Diurnal variations of linac energy profile were traced to uncorrected phase length changes in the main drive line which synchronizes the rf. The residual phase variation of up to 14° was compensated by applying an additional temperature correction while the true source of the error was investigated.

7 ACKNOWLEDGMENTS

We would like to acknowledge many valuable discussions and insightful suggestions from M. Breidenbach, M. Ross, and the SLAC RF group.

REFERENCES

[1] F.-J. Decker, R. Akre, M. Byrne, Z.D. Farkas, H. Jarvis, K. Jobe, R. Koontz, M. Mitchell, R. Pennacchi, M. Ross, H. Smith, *Effects of Temperature Variation on the SLC Linac RF System,* PAC95, Dallas, May 1995, p. 1821.

[2] F.-J. Decker, R.W. Assmann, M.G. Minty, P. Raimondi, G. Stupakov, *Super ASSET: A Technique for Measuring and Correcting Accelerator Structure Misalignments at the SLC,* PAC97, Vancouver, May 1997.

[3] J.T. Seeman, F.-J. Decker, and I. Hsu, *The Introduction of Trajectory Oscillations to Reduce Emittance Growth in the SLC Linac,* XV Int. Conf. on HEAccel., Hamburg, Germany, 1992, p. 879.

[4] V.E. Balakin, A.V. Novokhatskii, V.P. Smirnov, *VLEPP: Transverse Beam Dynamics,* 12th Int. Conf. on High Energy Accel., FNAL (1983) 119.

[5] F.-J. Decker, M. Stanek, H. Smith, T. Fang, *Diagnostic Beam Pulses for Monitoring the SLC linac,* PAC95, Dallas, May 1995, p. 2646.

[6] R.W. Assmann, F.-J. Decker, L.J. Hendricksen, N. Phinney, R. Siemann, K.K. Underwood M.D. Woodley, *Beam-Based Monitoring of the SLC Linac Optics with a Diagnostic Pulse,* PAC97, Vancouver, May 1997.

[7] R. Keith Jobe, H. Schwarz, *RF Phase Distribution Systems at the SLC,* PAC89, Chicago, May 1989.

[8] R. Akre, *SLC Interferometer System and Phase Distribution Upgrades,* PAC97, Vancouver, May 1997.

LONGITUDINAL PHASE SPACE SETUP FOR THE SLC BEAMS

F.-J. Decker, K.L.F. Bane, M.G. Minty, P. Raimondi,
Stanford Linear Accelerator Center †, Stanford University, Stanford, CA 94309 USA
R.L. Holtzapple, LNS, Cornell University

Abstract

The longitudinal phase space distribution of the SLC beams is affected by many different machine parameters and constraints. By using a technique of over-compression [1] in the ring to linac transfer line, a small energy spread of 0.12 % can be achieved at the end of the linac for a bunch length of 1.2 mm (σ). In the final focus a small energy spread is desirable to reduce emittance dilution due to chromatic effects. Optimization of the bunch length is also important as a longer bunch of 1.2 mm can contribute up to 40 % luminosity enhancement due to disruption. If there is a correlated energy variation along the bunch, for example due to mistuning of the optimal rf phase with respect to the beam, the bunch will be further compressed as it passes through the SLC Arcs. The resulting bunch can be too short to produce the desired disruption enhancement, but will radiate more beam-strahlung during collisions giving a false indication of higher luminosity. This paper discusses the interplay of these issues from the damping ring to the interaction point.

1 GOALS AND PROBLEMS

The longitudinal phase space is setup to give a small energy spread for the limited band-pass [2] at the interaction point (IP) and to give no reason for luminosity weighted polarization [3]. No energy spread also helps to have no compression in the arcs to get a long bunch length at the IP. This gives luminosity enhancement due to disruption, when the hour-glass effect due to a large angular divergence is not yet limiting. – A long bunch in the linac experiences bigger transverse wakefield kicks, and a correlated energy spread would help stability (BNS-damping). Due to beam loading from the first bunch (positrons) to the second one (electrons), the accelerator structure should only be partially filled (off the PSK energy peak) to have the same energy for both bunches. This costs energy overhead and leads to a setup with a shorter positron bunch, which is further off the rf crest getting less energy. Short bunches give more beam-beam background at the IP, and have more low and high energy tails, which create other background along the way.

2 INITIAL CONDITIONS AND HIGHER ORDERS

The bunch length in the damping ring depends strongly on the beam current. Based on the data in [4] a 10 % in current changes the bunch length by 5 %. The dependence of the bunch length on the gap voltage is weaker at high current (fourth-root) than at low current (square root) [4]. At high current and high gap voltage a higher than expect bunch length is seen, which could be due to the microwave instability (saw-tooth) [5]. The measured energy spread varies from 0.080 % at low current to 0.092 % at $4 \cdot 10^{10}$ particles per bunch. The expected spread at low current is close to 0.071 %. There should be no dependence on gap voltage, except from the microwave instability. Increasing the gap voltage from 750 to 950 keV, the energy spread changes from 0.089 to 0.094 % at $4 \cdot 10^{10}$. The bunch length is strongly distorted by the potential well in the damping ring. The asymmetry factor is $A = (\sigma_h - \sigma_t) / (\sigma_h + \sigma_t) = -0.4$ at $4 \cdot 10^{10}$, which means that for $\sigma_z = 7.5$ mm, the head has a $\sigma_h = 4.5$ mm (40 % less) while the tail has a $\sigma_t = 10.5$ mm. The centroid is $1.6\, A\, \sigma_z = -4.8$ mm shifted from the peak.

There are several higher order effects in the RTL, which are utilized to obtain the smallest possible energy spread with no energy tails at the end of the linac. These include:

2.1 Higher Order Dispersion

The T_{566} term is about $1.5\, R_{56} = -900$ mm, which means that higher and lower energy particles in the RTL are bent backwards (late), which is the right direction (sharp rise). This term can not be varied easily without a lattice design change. Figure 1 shows the 1, 2, and 3 sigma contour lines of the compression and the resulting linac bunch distribution.

2.2 Non-linear rf curvature

A similar effect can be achieved by decelerating the centroid of the beam in the compressor cavity using a phase offset.

2.3 Bunch Precompression in the DR

With bunch pre-compression [6] a quadrupole mode oscillation without phase oscillations is induced by successive application of two changes to the gap voltage. While advantageous for increasing the beam current, the advantages of bunch over-compression for bunch shaping are somewhat reduced. Interestingly [7] pre-compression of the bunch does not flip the asymmetry in the longitudinal beam distribution in the damping ring.

After the damping ring (DR) the bunch is asymmetric, it gets on the non-linear rf curve of the compressor, and after the ring-to-linac (RTL) beam line the bunch is over-compressed (S-shape). This gives a linac distribution with about two times ($N/2$) sharper edges than a Gaussian.

2.4 Sawtooth Instability

The sawtooth instability of the new damping ring [5] is visible as bursts in a 180 kHz signal and as ±3 % changes

† Work supported by the Department of Energy contract DE-AC03-76SF00515.

0-7803-4376-X/98/$10.00 © 1998 IEEE

in the wings of the beam distribution at about 20 % peak height (quadrupole mode). This causes the linac bunch length to change by about 10 % causing additional transverse jitter, which was observed for the positron beam [8]. Techniques to control the time of occurrence of this instability have partially successful to date, yet will be studied further.

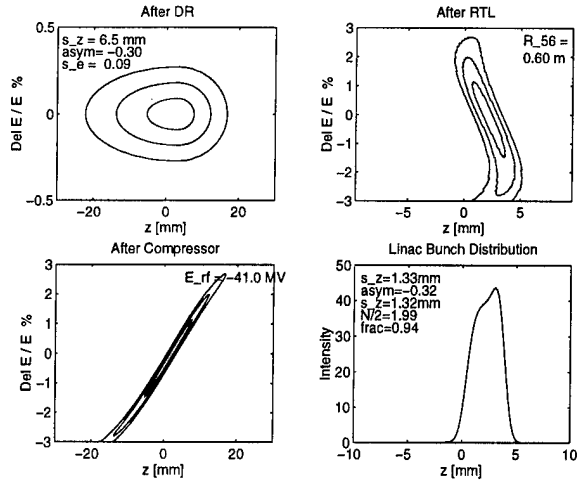


Figure 1: Bunch Compression Setup.

3 LONGITUDINAL PHASE SPACE TRANSPORT

The bunch length is usually adjusted using bunch compression and control of the injection phase into the linac to obtain the smallest energy spread at the end of the linac. With a typical bunch charge of $4 \cdot 10^{10}$ particles, the 7 mm bunch length [4] from the damping ring (DR) is compressed to 1.2 mm. Since 1993, the compressor cavity has been operated at a 1.4 times higher voltage in order to shape the longitudinal particle density distribution by over-compression. The goal of bunch shaping is to produce a very steep leading edge of the distribution which compensates [9] for the slope of the net voltage in the linear accelerator structures. The cancellation results in a minimum energy variation across the bunch (Fig. 2).

The SLC arcs have a compression term R_{56} = 150 mm, which means that a correlated energy spread of 0.3 % would compress the bunch from 1.2 mm to 0.75 mm. If the correlation is not linear, but stronger in the core (as for the 1 mm Gaussian bunch distribution of the SLC design) the compression is even more, the 1 mm SLC-design beam at $5 \cdot 10^{10}$ would be totally compressed. To avoid additional compression in the arcs, the smallest possible incoming energy spread must be maintained. The IP bunch length sensitivity on linac injection phase is about ±20 % per degree. A small energy spread gives nearly no compression (Fig. 3).

At the interaction point (IP) the beams encounter strong beam-beam focusing forces. If the bunch length is of the order of the focal length, the luminosity may be enhanced. Up to 40 % disruption enhancement, at 100 Z/hour, is expected [10,11,12] with 1.0 mm bunch length, $4 \cdot 10^{10}$ particles per bunch. However, in tuning for high luminosity, there may be conflicting requirements.

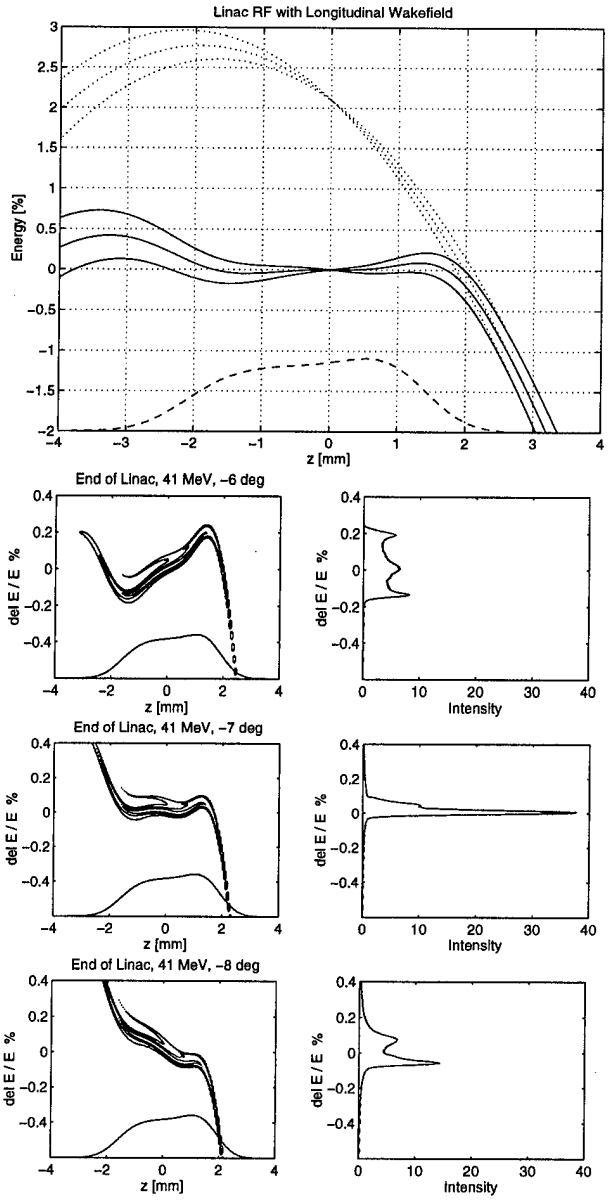


Figure 2: Energy–z correlation for different linac phase.

For example, with a very short bunch and no enhancement, the radiated beam-strahlung is higher. Detectors sensitive to beam-strahlung may therefore be difficult to interpret.

Small phase changes of ± 1° influence the energy–z correlation which changes the IP bunch length by 20%. The beam distribution is generated by over-compression. The lower plots show the energy distribution on the right.

The beam has to get the right bunch length and distribution in the RTL, so the longitudinal wakefield and the rf-curvature cancel each other to get a small energy spread, so that there is no further compression in the ARC.

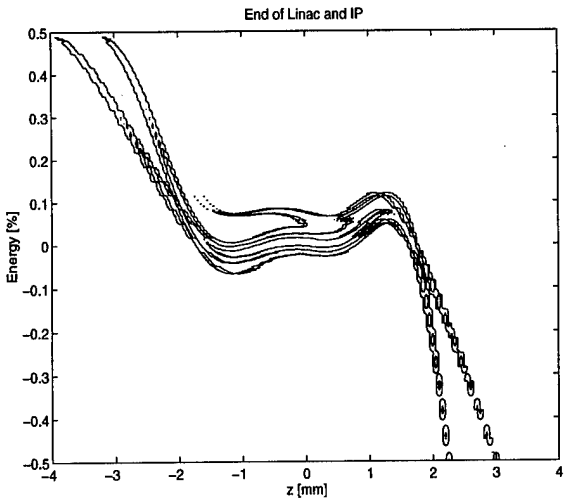


Figure 3: Setup for no ARC compression.

4 EQUAL BUNCH ENERGY

The two bunches in the linac can be adjusted by different means in energy, energy spread, and bunch length. The leading bunch, the positrons, produce via beam loading a change in energy gain (relative to the next pulse of electrons) of about 1.2 % at $4 \cdot 10^{10}$. This energy difference is compensated by adjustment of the time of the phase flip in the energy doubling, SLED (see Fig. 4). Due to finite available energy, however, this time cannot be arbitrarily set. It is difficult therefore to maintain positrons of large bunch length. This area needs further research since the positron bunch length was too short during the last run.

Equal energies are obtained by putting both beams, which are 60 ns apart, off the peak of the PSK energy curve to compensate the beam loading. At high current the beam loading of the positrons is so high that the offset would cost lots of energy, which makes it necessary to use other methods (like short bunch and off the rf crest).

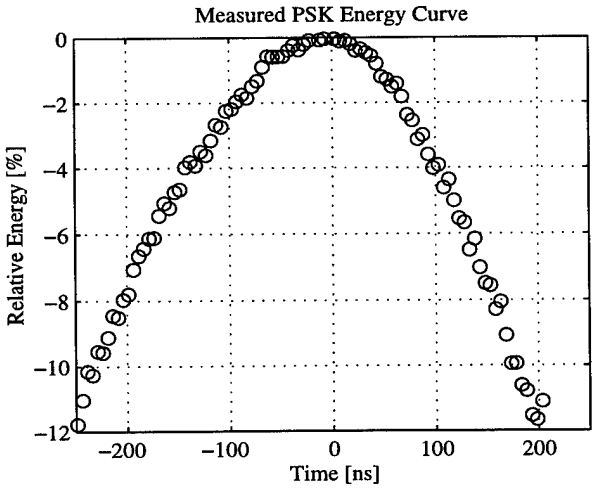


Figure 4: Equal electron – positron energies.

5 SUMMARY

To get the desired long bunch length at the interaction point (IP), the following has to be right:

1. compressor strength 2. linac phase

to get the smallest possible energy spread at the end of the linac. Positron bunches might get shorter to get less energy due to the right rf phase (for energy spread), to compensate for more energy due to the beam loading and rf fill-time of the accelerator (PSK).

6 ACKNOWLEDGMENTS

We would like to thank F. Zimmermann, who is very concerned about the bunch length at the IP and will measure it [13].

REFERENCES

[1] F.-J. Decker, R. Holtzapple, T. Raubenheimer, *Over-Compression, a Method to Shape The Longitudinal Bunch Distribution for a Reduced Energy Spread,* LINAC94, Tsukuba, Aug. 1994, p. 47.

[2] N. Toge et al., *Chromaticity Corrections in the SLC Final Focus,* PAC91, San Francisco, 1991, p. 2067.

[3] F.-J. Decker, J.T. Seeman, *Luminosity Polarization Correlation in the SLC,* EPAC, London, June 94.

[4] R. Holtzapple, Ph.D. Thesis, SLAC-487, 1995.

[5] K. Bane et al., *High Intensity Single Bunch Instability Behavior in the New SLC Damping Ring Vacuum Chamber,* PAC95, Dallas, TX, 1995.

[6] M.G. Minty et al., *Operation and Performance of Bunch Pre-Compression for Increased Current Transmission at the SLC*, PAC97, Vancouver, 1997.

[7] K.L.F. Bane, M.G. Minty, A.W. Chao, *Simulations of Bunch Pre-Compression at High Currents in the SLC Damping Ring,* PAC97, Vancouver, 1997.

[8] F.-J. Decker et al, *Higher Order Beam Jitter in the SLC Linac,* Linac96, Geneva, 1996, p 143.

[9] G.A. Loew, J.W. Wang, *Minimizing the energy spread within a single bunch by shaping its charge distribution,* IEEE, Vol. NS-32, No. 5, 1985, p 3228.

[10] P. Chen, *Grand Disruption: A possible Final Focusing Mechanism for Linear Colliders*, SLAC-Pub-3823 (1986), Part. Accel. 20 (1987), p. 171.

[11] P. Raimondi, P. Chen, F.-J. Decker, *Disruption Effects on the Beam Size Measurement,* PAC95, Dallas, May 1995.

[12] K.L.F. Bane, P. Chen, F. Zimmermann, *Beam-Beam Simulations with Non-Gaussian Distributions for SLC and SLC-2000,* PAC97, Vancouver, 1997.

[13] F. Zimmermann et al., *An RF Bunch-Length Monitor for the SLC Final Focus,* PAC97, Vancouver, 1997.

DYNAMIC FOCUSING SCHEMES FOR LINEAR COLLIDERS*

J. Irwin†, SLAC, 2575 Sand Hill Road, Menlo Park, CA, USA

Abstract

By using the intense fields of a demagnified bunch as a final lens, one can greatly simplify and shorten the conventional final focus and collimation systems of linear colliders. In the dynamic focusing schemes described here, the lens bunches enter the interaction region through separate beamlines. Design details and constraint equations for such focusing schemes are developed for future high energy linear colliders.

1 INTRODUCTION

1.1 Motivation

This study was motivated by the observations that the beam delivery system for the next linear collider (NLC) [1], consisting of a final focus sytem, a big bend, and a collimation system, has a length one-half the length of the main accelerating system length, and that this beam delivery length will grow roughly as the center-of-mass energy to the 3/2 power. Since the length of linear colliders built on the crust of a round earth are limited in length to around 200 km, this scaling law becomes a serious obstacle to building linear colliders with greater than 5 TeV c.m. energy.

1.2 An ideal focusing system

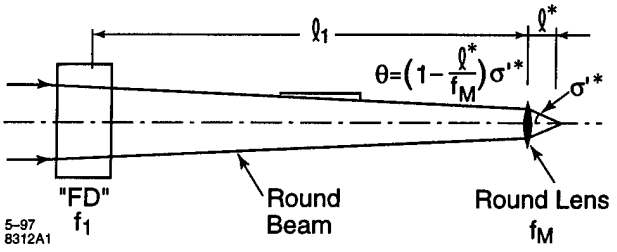


Figure 1. A schematic of an ideal final focus system. A very strong lens is placed 3 mm from the IP. The total length is about 2 m.

Figure 1 shows an ideal final focus system. FD labels a conventional final doublet where the beamsize is only modestly enlarged over its typcial vaues in the linac. The total length, from the final doublet to the IP, is a couple of meters. It is supposed that there is a very strong lens, not much larger than the beam, located a couple of millimeters from the IP. This has the advantage that the chromaticity, ℓ^*/β^* would be so small (about 20) that no chromatic correction is needed, and the sensitivity to errors would be small for similar reasons. Furthermore since the beam is not blown up, there is no need for a collimation system or a big bend. In other words the system of fig. 1 can replace an entire beam delivery system. The problem is how to manufacture the small powerful lens.

1.3 The Dynamic focusing idea

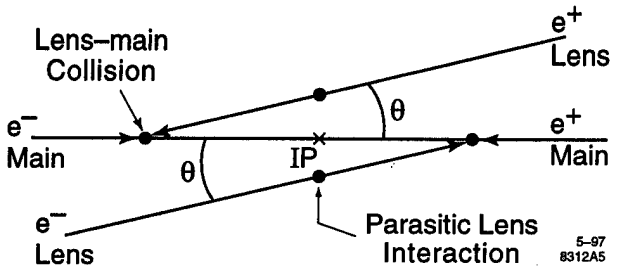


Figure 2. The dynamic focussing scheme for implementing the ideal final focus system.

Figure 2 shows a situation in which the small lens of fig. 1 is created by a secondary beam. The study of such a system will be the subject of this paper.

1.4 Relationship to superdisruption

The idea of using the strong fields of a particle bunch to focus beams has been attributed to D. Leith and discussed under the title superdisruption [2, 3]. These efforts were largely directed at achieving stronger focusing (smaller IP β functions), and implementation schemes were limited to consideration of two closely-spaced bunches traveling in the same beamline. With dynamic focusing the main intention is to simplify the beam delivery systems, and lens beams are imagined to have much lower energy and enter the interaction region through a second dedicated beamline.

2 LINEAR COLLIDER IP PARAMETERS

Any discussion of ideas for future linear colliders must pay attention to the constraints imposed by interaction point (IP) considerations.

†Work supported by the Department of Energy, contract DE-AC03-76SF00515.
*Work initiated during program New Ideas for Particle Accelerators, Institute for Theoretical Physics, Santa Barbara, CA, 1996

0-7803-4376-X/98/$10.00 © 1998 IEEE

2.1 The main IP constraint equations

The three principal IP constraint equations are the luminosity equation, the disruption constraint, and the beamstrahlung constraint. We write the luminsoity equation as $F \equiv 4\pi \frac{L E_B}{P_B} = \frac{NH}{\sigma_x \sigma_y} = \frac{NH\varsigma}{\sigma_y(\sigma_x+\sigma_y)}$ where we have introduced a quantity F , a rationalized flux specified by luminosity, beam energy and beam power. H is the enhancement factor. $\varsigma = 1 + \frac{\sigma_y}{\sigma_x}$, has been introduced for convenience, and equals 1 for flat beams and 2 for round beams.

The vertical disruption constraint equation is crucial because if the beam is not charge compensated there is a kink instability which limits the disruption to about 15, and for charge-compensated beams there is an instability in the charge separation which limits the disruption to about the same value. It is interesting that these two constraint conditions already determine σ_z.

By introducing appropriate variables, the beamstrahlung equation can be solved analytically to give $N/(\sigma_x+\sigma_y)$ as a function of γ/σ_z. The result can be written

$$\frac{25\alpha r_e}{12 n_\gamma}\frac{N}{(\sigma_x+\sigma_y)} = \eta\left(\frac{2 n_\gamma \lambda\!\!\!^{-}_e}{5\alpha}\frac{\gamma}{\sigma_z}\right)^{1/2}$$

where η is a factor greater than 1 which goes to 1 rapidly for large γ/σ_z. Even with charge compensation, which will be valid only to some fractional extent, one must heed a beamstrahlung constraint equation.

One can now solve for σ_y and N.

$$\frac{1}{\sigma_y} = \frac{1}{c_1 \eta}\left(\frac{D_y F}{n_\gamma^3 H \varsigma}\right)^{1/2} \quad \text{and} \quad N = \frac{\eta^2 c_1^2 n_\gamma^3 \varsigma}{D_y}\frac{\sigma_x}{\sigma_y}$$

where c_1 is a constant about equal to 8000. The only free parameter is the aspect ratio at the IP. The Oide condition can be used to determine the required normalized emittance. The β^* thusly determined is fairly constant with energy and has a value near 100 μm.

3 DYNAMIC FOCUSING PARAMETERS

3.1 Cromaticity condition

The chromticity $\xi_y = \frac{\ell^*}{\beta_y^*}$ of the lens-beam lens is chosen to be about 20, so for β^*=150 μm, ℓ^*= 3 mm. The chromaticity is also the demagnification from the lens-beam lens to the IP.

3.2 Lens beam charge per bunch

For a charge $\bar{N}_Q$ in a uniform disk of radius R_Q $\frac{1}{\ell^*} = \frac{2\bar{N}_Q r_e}{\gamma_M R_Q^2}$. This condition yields

$$\bar{N}_Q = N_{Q_0}\frac{R_Q^2}{2\sigma_M^2} \quad \text{where} \quad N_{Q_0} = \frac{(\gamma\varepsilon_M)}{r_e}\xi_y$$

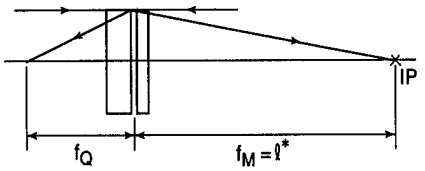
The fraction of the main beam not incident on the uniform disk will be $\exp(-\frac{R_Q^2}{2\sigma_M^2})$. To limit this quantity to 2%, the exponent would have to be about -4. Furthermore, if one assumes that 50% of the beam is outside the uniform disk, then the total charge in the lens will be about 6 times N_{Q0}. For the NLC emittance, the total charge comes out to be a workable 4 10^9.

3.2 Uniform lens distributions

Concerning the production of uniform bunches we remark that there exists a phase-space density function, $\rho \propto 1/\sqrt{R^2 - r^2}$ where $r^2=x^2+x'^2+y^2+y'^2$, which produces a uniform distribution This is hollowed-out in the center and singular at R=r. Nevertheless one can try to approximate this distribution at low energy. Nonlinear elements in the lens-beam final focus system can shape the distribution at the IP phase.

3.3 Pinch effect

Figure 3 shows the lens beam colliding with the main beam. Each beam focuses the other. The ratio of the focal lengths can be detemined to be a power ratio:



5-97 8312A4

Figure 3. The lens beam, moving to the left, is pinched by the main beam moving to the right..

$\frac{f_M}{f_Q} = \frac{\gamma_M N_M}{\gamma_Q N_{Q_0}}$. The luminosity loss due to the change in focal length will be about $\frac{\Delta L}{L} \approx \frac{2}{15}\left(\frac{f_M}{f_Q}\frac{\sigma_z}{\beta_M^*}\right)^2$. To have a low-power lens beam, one must have a very short main-beam bunch length.

4 MAIN CONCERNS

4.1 Parasitic crossing effects

The most challenging situation can be seen in the multibunch geometry of fig. 4, where the beams are separated by a distance $\ell^*\delta\theta$. The parasitic kick can be expanded into multipoles. The dipole kick can be corrected by steering, and the quadrupole kick by adjusment of matching into the interaction region. Even

the sextupole term could be compensated. But suppose we take it as uncompensated and let it define a limit on the beam separation. The resulting equation is $\delta\theta \geq \frac{5}{9}\frac{N_Q}{N_{Q_0}}\frac{\gamma_M}{\gamma_Q}\sigma^*_M$. At the NLC, with a divergent angle of about 30 μr, the limit on δθ is about 1 mr. The parasitic crossing is not a limiting problem.

4.2 Motion of lens

Again referring to the geometry of fig. 4, if θ_L is small, then the focal points as the lens beam travels through the main beam will lie along a vertical line. This is exactly what is required to crab the main beam. If θ_L is non-zero, it must be small compared to the diagonal angle of the main beam. As pointed out in the pinch effect, the main beam must be very short, so the diagonal angles are quite large. Lens motion should not be a problem.

4.3 Multibunch instability

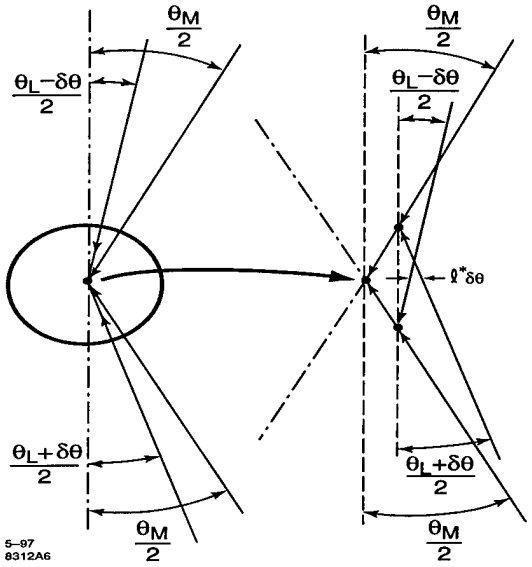


Figure 4. The incoming beam geometry required for multiple-bunch beams.

To facilitate multiple-bunch beams we must have both the main beams and the lens beams enter and exit in separate beam lines with a crossing angle. The required geometry is shown in fig. 4. Because the energy of the lens beam is contemplated to be smaller, one obtains a limit $\frac{\theta_M + \theta_L}{2} \geq \sqrt{\frac{\gamma_M}{\gamma_L}}\,\bar{\theta}_M$ where $\bar{\theta}_M$ is the usual lower limit on θ_M arising from multibunch considerations. This limit establishes the bound on γ_L/γ_M. $\bar{\theta}_M$ depends weakly on energy.

4.4 Jitter

The jitter of the lens beam is a serious problem, because the lens determines the focal point for the main beam. With the demagnifications assumed, the lens beam jitter would have to be less than 1%. If in fact such a small jitter were achieved, one could contemplate a head on δθ=0 operation. Then the head-on lens-lens collision would align the main-main collision if the focal length of the lens-lens collision is twice ℓ^*. The jitter limit in this case comes from distortion due to the misaligned lens-lens collision. See ref. [2]. The jitter limit for this case is about 6%.

5 EXOTICA

It is interesting to contemplate whether one can bypass the Oide limit with dynamic focusing. For the geometries we have described the Oide limit is not changed. But one can contemplate long-bunch lens beam schemes which approach the adiabatic focusing scheme [5]. It seems that appropriate lens beams could be prepared, but the effects of the parasitic crossing reappear and have not been fully analyzed.

6 SUMMARY

For energies greater than 10 TeV cm, beam delivery system lengths become unmanageable. Dynamic focusing is an alternative solution if micron length bunches can be produced and accelerated. Lens beam jitter must be held to a few percent. IP parameters are improved from the ability to have round beams at the IP. For NLC parameters one could achieve $\sigma_y = \sigma_x = 20$ nm, $\gamma\varepsilon = 10^{-6}$ rad-meter, and $N = 5\ 10^9$. Furthermore the collimation system, the big bend and the final focus system are all but eliminated. For $\sigma_z = 2$ μm the lens beam to main beam power ratio is 1/30. An energy ratio of 25 is permitted by the multibunch instability.

7 ACKNOWLEDGMENTS

I would like to thank the leadership of the Institute of Theoretical Physics, Santa Barbara, for hosting a session on accelerator physics, and its marvelous staff for providing a delightful atmosphere in which to work. I thank A. Dragt, V. Telnov, P. Chen, K. Thompson, K. Oide, F. Zimmermann, M. Ross and K. Bane for encouragement and helpful conversations.

REFERENCES

[1] Zeroth-order design report for the Next Linear Collider, SLAC-Report 474 (1996)
[2] R. Palmer, 'Super disruption and its use in linear colliders', SLAC-PUB-3688 (1985)
[3] J. Irwin, Final focus and beam alignment in TeV electron-postron colliders using particle bunches as lenses, AIP Conf. Proc. 156, 531 (1986)
[4] P. Chen, K. Oide and A. Sessler, 'An adiabatic focuser', Part. Accel. 31, 7 (1990)

THE SHORT-RANGE WAKEFIELDS IN THE SBLC LINAC

K.L.F. Bane, Stanford Linear Accelerator Center, Stanford, Ca., USA
M. Timm, T. Weiland, THD, Schloßgartenstr. 8, 64289 Darmstadt, Germany

Abstract

The short–range longitudinal and transverse wakefields of a point charge in the SBLC linac are obtained using a modal summation technique. Simple functional fits to these wakes are given, which can be used as Green functions in beam dynamics simulations of bunches. These results, however, are valid only after the beam has traversed a critical number of cells N_{crit}. Using time domain computations with Gaussian bunches we have obtained results that are consistent with N_{crit} varying as $\alpha a^2/(L\sigma_z)$, with a the iris radius and L the period length of the structure, σ_z the bunch length and α a constant on the order of 1. For the loss per cell to reach to within a few per cent of the asymptotic value we find that $\alpha \sim 0.5 - 1.0$.

1 INTRODUCTION

In the S-Band Linear Collider (SBLC) project[1] long trains of short, intense bunches of electrons and positrons are each accelerated through 16 km of linac to 250 GeV before colliding at the interaction point. The accelerating structure is a disk-loaded, constant gradient structure consisting of 180 cells. Each bunch is Gaussian, with rms length $\sigma_z = 300$ μm, which is short compared to the iris radius a: $\sigma_z/a \sim .025$ (for FEL operation it is even shorter: $\sigma_z/a \sim .0021$). For a single cavity with beam tubes the longitudinal high frequency impedance varies with frequency as $\omega^{-1/2}$, implying that the longitudinal wakefield of a short bunch varies as $\sigma_z^{-1/2}$[2]. For a periodic structure the longitudinal high frequency impedance (real part) varies as $\omega^{-3/2}$, and the wakefield per cell of a bunch approaches a constant value as $\sigma_z \to 0$[3, 4]. For a structure consisting of a finite number of repeating cells with beam tubes the wake of the first cell is the same as the single cell result and the wake per cell asymptotically approaches that of the periodic result as the beam progresses down the structure. For a Gaussian bunch the number of cells needed for the periodic solution to be valid, N_{crit}, is given by[3, 4]

$$N_{crit} = \frac{\alpha a^2}{L\sigma_z} , \qquad (1)$$

with L the structure period length and α a constant of proportionality on the order of one.

In this report first a frequency domain approach is used to obtain the short–range longitudinal (monopole) and transverse (dipole) wakefields in a periodic, SBLC-like structure. Then time domain calculations are performed to test the validity of Eq. 1, and to find α. More details can be found in Ref. [5].

2 THE ASYMPTOTIC WAKEFIELDS

In the SBLC linac the cell dimensions vary within a structure, but only gradually. We first find the wakes for 5 purely periodic models, with cell dimensions similar to 5 representative cells of the actual SBLC structure. For our 5 representative cells we take cells 1, 45, 90, 135, and 180 for which a is 1.1 cm, 1.225 cm, 1.35 cm, 1.475 cm, and 1.6 cm, respectively. Note that the cell length $L = 3.33$ cm, iris thickness $t = 5.3$ mm, and cavity radius $b \approx 4$ cm. The wakes of the 5 models are then averaged to give the wakefields representing an entire structure.

To obtain the longitudinal wakefield of a periodic structure we use the computer program KN7C[6] to obtain the synchronous frequencies and loss factors of lower monopole modes. We approximate the high frequency contribution to the impedance using the so-called Sessler-Vainsteyn optical resonator model[6], a model that has also been applied, for example, to the SLC[7] and the NLC[8]. The real part of the impedance (assuming t/L is small) becomes[8]

$$R_z(\omega) = \sum_{n=1}^{N} \pi k_n \delta(\omega - \omega_n) + \frac{2Z_0 j_{01}^2}{\pi L \zeta^2} \times \qquad (2)$$
$$\times \frac{\sqrt{\nu}+1}{(\nu + 2\sqrt{\nu} + 2)^2} \Theta(\omega - \omega_N) \quad \omega > 0 ,$$

with k_n the loss factor and ω_n the frequency of the n^{th} mode, $Z_0 \cong 377\ \Omega$, $j_{01} \cong 2.41$ the first zero of the Bessel function J_0, $\zeta \cong 0.824$, $\nu = 4a^2\omega/(c\bar{L}\zeta^2)$, with c the speed of light and $\bar{L} = \sqrt{L(L-t)}$; $\Theta(x) = 0$ for $x < 0$, 1 for $x > 0$. Fourier transforming $R_z(\omega)$ we obtain the longitudinal wakefield:

$$W_z(s) = \sum_{n=1}^{N} 2k_n \cos\frac{\omega_n s}{c} + \frac{Z_0 c j_{01}^2 \bar{L}}{\pi^2 a^2 L} \times \qquad (3)$$
$$\times \int_{\nu_N}^{\infty} \frac{\sqrt{\nu}+1}{(\nu + 2\sqrt{\nu} + 2)^2} \cos\left(\frac{\zeta^2 \bar{L} s \nu}{4a^2}\right) d\nu ,$$

with $\nu_N = 4a^2\omega_N/(c\bar{L}\zeta^2)$. The transverse (dipole) wakefield is obtained in the analogous manner, but using the computer program TRANSVRS [9] to obtain the dipole mode frequencies and loss factors.

For the longitudinal case we have found, for each of the 5 representative structures, ω_n and k_n for all modes up to 75 GHz (about 250 modes) using KN7C. Comparing, at the higher frequencies, the binned modal contribution to the Sessler-Vainsteyn part of Eq. 3 we find good agreement, to within 10%. Then substituting into Eq. 4 we obtain the wakefields shown in Fig. 1 (the solid curves). The values

0-7803-4376-X/98/$10.00 © 1998 IEEE

at the origin, which should equal [4] $W_z(0) = Z_0 c/(\pi a^2)$ (= 198 V/pC/m for cell 90 dimensions), are 4–5% low, indicating some calculation error. The average of the 5 representative wakes (with the wakes of cell 1 and 180 weighted by half) is given by the dashed curve in Fig. 1. Finally, a fit to the average wake, given by

$$W_z = 200.(V/pC/m) \cdot \exp\left[-0.77(s/mm)^{\frac{1}{2}}\right] , \quad (4)$$

is shown by the dots in Fig. 1.

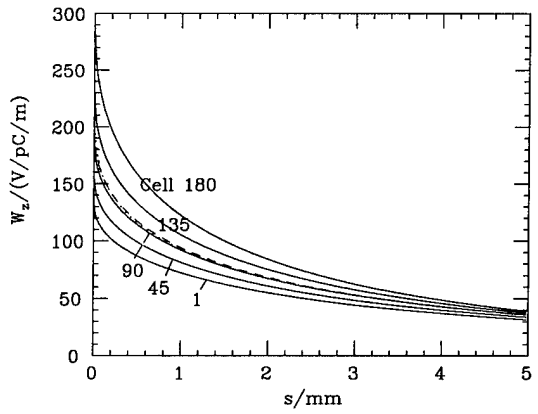


Figure 1: The longitudinal wakefield of representative cells in the SBLC structure (solid curves). The dashes represent the average, the dots the model fit, Eq. 4.

For the transverse case modes up to 68 GHz (about 350 modes) were calculated. Comparing, at the higher frequencies, the binned modal contribution to the Sessler-Vainsteyn part of the impedance we again find good agreement. The transverse wakefields for the 5 geometries are shown in Fig. 2 (the solid curves). In this case the slope at the origin should equal[8] $W_x'(0) = 2Z_0 c/(\pi a^4)$ (= 2.17 V/pC/mm^2/m for cell 90); our numerical results agree to within 2% in all cases. The average wake is given by the dashed curve in Fig. 2. A fit to the average wake, given by

$$W_x = 4.10(V/pC/mm/m) \cdot \left[1 - \left(1 + 1.15[s/mm]^{\frac{1}{2}}\right) \exp\left(-1.15[s/mm]^{\frac{1}{2}}\right)\right] , \quad (5)$$

is indicated by the dots.

3 TRANSITION TO THE ASYMPTOTE

To test the validity of Eq. 1 for N_{crit} (and the applicability of the asymptotic solutions) and to find α, at least for the longitudinal case, we have performed a series of MAFIA[10] time domain calculations. We have obtained the per cell loss factor k_{tot} of short Gaussian bunches of various lengths in structures consisting of a finite number of cells with infinitely long beam tubes. Although the SBLC structure is a constant gradient structure, for simplicity, we use only identical cells, with the dimensions of cell 144 in the real structure, for which $a = 1.20$ cm. The bunch

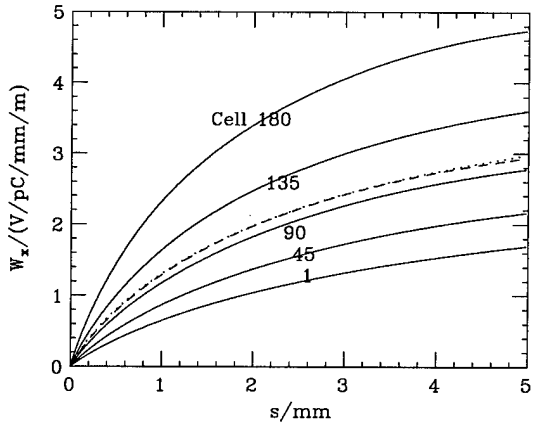


Figure 2: The transverse (dipole) wakefield of representative cells in the SBLC structure (solid curves). The dashes give the average, the dots the model fit, Eq. 5.

lengths vary from $\sigma_z = 0.1$ mm, 0.3 mm, 0.5 mm, and then in 0.25 mm steps up to 4 mm; the number of cells vary from $N_{cell} = 1$ to 10. A very fine mesh is used (*e.g.*, $\sigma_z = 0.1$ mm, $N_{cell} = 10 \Rightarrow 65 \times 10^6$ meshpoints) in order to obtain good accuracy.

The per cell loss factor k_{tot} is plotted as function of σ_z in Fig. 3 (the results are connected by lines). The results are bounded by two curves representing the single cell solution, given by the Lawson diffraction model [2]:

$$k_{tot} = \frac{\Gamma(1/4) Z_0 c}{4\pi^{5/2} a} \sqrt{\frac{g}{\sigma_z}} , \quad (6)$$

with $\Gamma(1/4) \cong 3.63$ and g the cavity gap (*i.e.*, $L - t$), and the periodic solution:

$$k_{tot} = \frac{L}{2\sqrt{\pi}\sigma_z} \int_0^\infty ds\, W_z(s)\, e^{-\frac{s^2}{4\sigma_z^2}} , \quad (7)$$

with W_z given by Eq. 4. For bunch lengths larger than about 2 mm the loss per cell is independent of the number of cells. For shorter bunches we note that the single cell results approach the single cell asymptotes, as the bunch length decreases. Also, for a given bunch length, as the number of cells increases, the loss per cell asymptotically approaches the periodic structure curve, however, with a slight systematic offset (which is not understood). Note that for a finite number of cells, as the bunch length becomes ever shorter the loss again varies as $\sigma_z^{-1/2}$.

To determine N_{crit} we first calculate the differential loss factor for each cell from the MAFIA data, κ_n, defined as the total loss factor for an N_{cell} cell structure minus that of an $N_{cell} - 1$ cell structure, which we then convert into a function of cell number through cubic spline interpolation (see Fig. 4). In Fig. 4 we note that for $\sigma_z = 0.1$ mm the curve decreases throughout the range; for the longer bunch lengths it is rather constant throughout the range. For the intermediate bunch lengths, however, κ_n begins by decreasing gradually, and then levels off for high cell number.

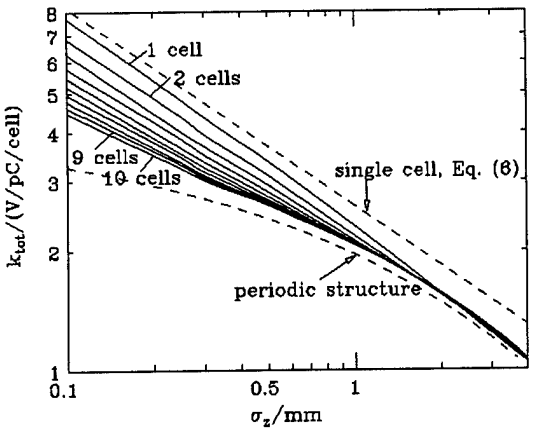


Figure 3: The loss factor $k_{tot}(\sigma_z)$ obtained by MAFIA for a Gaussian bunch in a structure consisting of a finite number of cells (1-10) Also shown are the single cell (Eq. 6) and the periodic structure loss factor.

Upon careful inspection one notices that for these curves there is also a slight ($\sim$ 3%) dip before the curve reaches the final, asymptotic value. In Fig. 5 numerical errors probably account for the slight anomalies that we see in the high end of the curves for short bunches; nevertheless, the general trend of these curves is still correct.

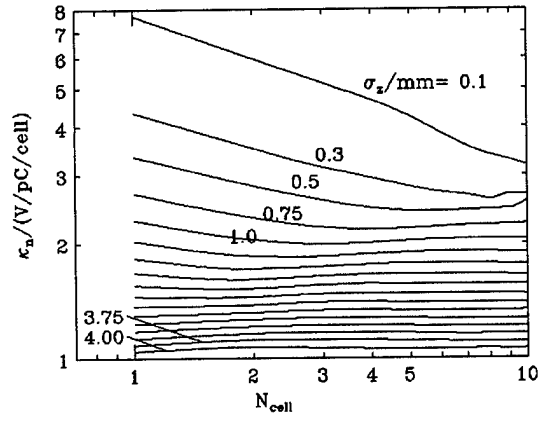


Figure 4: The differential loss factor of cell N_{cell}, κ_n, for various bunch lengths, as obtained by MAFIA (the results are connected by smooth curves).

Let us consider 3 different criteria that result in a κ_n that is within a few percent of the asymptotic value: (1) the point in the curve, before the dip, where κ_n reaches the same value as the asymptote, (2) the dip position, and (3) the position (after the dip) where the curve reaches to 98% of its asymptotic value. The $\sigma_z = 0.1$ and 0.3 curves, as well as those for which $\sigma_z \geq 2.0$ mm, are not included; as asymptote we take the value of κ_n at $N_{cell} = 8$. The results are shown in Fig. 5, with case 1 given by the x's, case 2 by the diamonds, and case 3 by the +'s. Fitting the data to a power law (N_{crit} as a function of σ_z) we obtain as exponent -1.06 in the first case and -0.85 in the others. However, given the accuracy of the calculation, we can say that the results are consistent with the -1 power dependence of Eq. 1. As for the coefficient α, when fitting to Eq. 1 we obtain 0.5, 0.7, and 1.0 for cases 1, 2, and 3, respectively. In summary, to obtain an average loss at the end of a finite length, repeating structure that is within a few percent of the average loss in the truly periodic structure the critical number of cells needed is given by Eq. 1, with $\alpha \sim 0.5 - 1.0$.

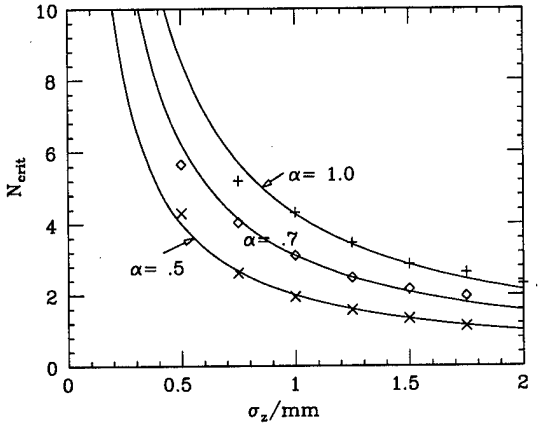


Figure 5: $N_{crit(\sigma_z)}$ is obtained from Fig. 4 following 3 different criteria (discussed in the text). The curves are fits to Eq. 1, taking, $\alpha = 0.5, 0.7, 1.0$ respectively.

4 REFERENCES

[1] T. Weiland: "Design Study of a 500 GeV Linear Collider", Proceedings of the 1990 Linear Accelerator Conference, Albuquerque, LA12004-C, Los Alamos, p. 792.

[2] See Dôme, *IEEE Trans. Nucl. Sci.* **NS-32**, 2531 (1985); in *Part. Acc.* **25** (1990) see articles by S. Heifets and S. Kheifets (p. 61), K. Bane and M. Sands (p. 73), J. Lawson (p.107).

[3] S. Heifets and S. Kheifets, *Phys. Rev. D* **39**, 960 (1989).

[4] R. Gluckstern, *Phys. Rev. D* **39**, 2780 (1989).

[5] K.L.F. Bane, M. Timm, T.Weiland, DESY M-97-02 Internal Report (January 1997).

[6] E. Keil, *Nucl. Instr. Meth.* **100**, 419 (1972).

[7] K. Bane and P. Wilson, Proceedings of the 11th Int. Conf. on High Energy Accelerators, CERN (Birkhäuser Verlag, Basel, 1980), p. 592.

[8] K. Bane, SLAC-NLC-Note 9, February 1995, and in "Zeroth–order Design Report for the Next Linear Collider," SLAC Report 474, p. 367 (May 1996).

[9] K. Bane and B. Zotter, Proceedings of the 11th Int. Conf. on High Energy Accelerators, CERN (Birkhäuser Verlag, Basel, 1980), p. 581.

[10] The MAFIA collaboration, "User Guide," CST GmbH, Darmstadt, Germany.

DESIGN OF A 30 GHZ DAMPED DETUNED ACCELERATING STRUCTURE

M.Dehler[†], R.M.Jones[‡], N.M.Kroll[‡], R.H.Miller[‡], I.Wilson[†] and W.Wuensch[†]

[†]PS Division, CERN, Geneva, Switzerland; [‡] Stanford Linear Accelerator Center, California, USA

Abstract

Within the framework of the SLAC/CERN studies of 30 GHz linear colliders, an attempt has been made to scale as closely as possible the existing X-band NLC damped detuned accelerating structure to 30 GHz. A simple scaling was not possible because of mechanical and RF constraints. The 30 GHz design has 101 cells and a minimum aperture of 3.4 mm. In order to obtain acceptably small values for both the single-bunch transverse wakefield and the long-range multibunch wakefield a relatively large non-linear variation of the iris thickness was introduced in addition to the iris diameter variation. The resulting wakefield has a short-range value of 1290 V/pC/mm/m and a long range value below 10 V/pC/mm/m.

1 INTRODUCTION

RF frequencies around 30 GHz are being considered for both the Compact LInear Collider (CLIC) and the 3-5 TeV e+e- linear collider studies [1,2] to allow operation with high accelerating gradients (100-200 MV/m). In order to reach the required luminosities these machines have to be operated with multiple bunches per rf pulse. There is therefore a common requirement for a 30 GHz multibunch accelerating structure. Because of the large amount of design and experimental verification (ASSET) work that has been invested by SLAC in their X-band Damped Detuned Structure (DDS) it was decided to see to what extent this structure could be scaled to 30 GHz.

The basic approach was to scale as closely as possible, the existing SLAC X-band design but taking into account mechanical and RF constraints specific to 30 GHz. Some design choices have been biased in favour of the existing CLIC parameters (8×10^9 particles per bunch, a bunch spacing of 30 rf cycles (1 ns) and a loaded accelerating gradient of 100 MV/m) which require a transverse wakefield reduction to about 1% at the second bunch and thereafter at least a linearly decreasing level [3]. Although this structure was designed essentially around the CLIC parameters, a parallel aim of the work was to investigate the general potential of the DDS for use with other 30 GHz linac parameters.

2 STRUCTURE GEOMETRY

The basic 30 GHz cell/manifold configuration is the same as that of the X-band DDS (Figure 1). Two cells at both ends of the structure are not coupled to the manifold to allow space for the output manifold bends. All cell and manifold dimensions are approximately scaled 11 GHz values except the minimum iris thickness which was limited to 0.5 mm to have sufficient mechanical stiffness, and the minimum iris diameter which was limited to 3.4 mm to avoid an excessive short range transverse wakefield level. The number of cells for this DDS design has been reduced to 100 cells from the 200 of the X-band structure. This was done to maintain a near optimum RF to beam efficiency for CLIC multibunch parameters and to restrict the maximum accelerating gradient to less than about 150 MV/m (corresponding surface field of about 400 MV/m).

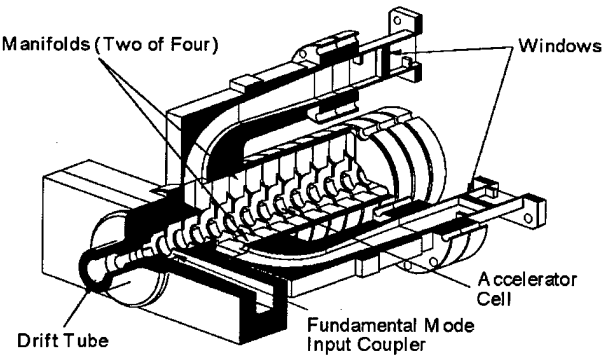


Figure: 1 The basic DDS configuration

3 MICROWAVE DESIGN AND ANALYSIS

The basic design approach is to add a light amount of damping to a detuned structure by coupling the cells to four parallel waveguide manifolds. The three stages of the rf design procedure are (i) analysis of the lowest dipole mode behaviour using an uncoupled cell model (all higher dipole modes are assumed to be detuned by an iris thickness variation) (ii) analysis of the behaviour of the two lowest dipole bands using a coupled cell two-band model (iii) spectral function analysis of the

0-7803-4376-X/98 /$10.00 © 1998 IEEE

detuned structure with manifold coupling. Details are given in references [4,5,6].

The maximum iris diameter was limited to 4.7 mm to obtain a small separation (150 MHz) between the first dipole pass band and the operating frequency. This results in a total detuning bandwidth for uncoupled cells of 8.4% (3.2 GHz). The truncated gaussian detuning distribution was chosen to have a σ=1.56 % (0.6 GHz) to give a roll-off level of about 1% after a time of 30 fundamental RF cycles (the CLIC bunch spacing), and a minimum long range transverse wakefield level (the X-band DDS was optimised for a 16 RF cycle roll-off time).

In the coupled cell analysis it was found that modes with relatively high kick factors were concentrated in the last two cells which were not coupled to the manifold and were therefore not damped (Figure 2). This occurred because a relatively large minimum iris diameter was chosen to minimise the single bunch wake, and consequently the position where the fundamental dipole band changed from a forward wave to a backward wave, with the group velocity going through zero, was close to the end of the structure (in cell 99 of 101 cells). By using a sine-like (0-90°) iris thickness to diameter dependency rather than a linear one, these high kick modes are spread out and extend into damped cells.

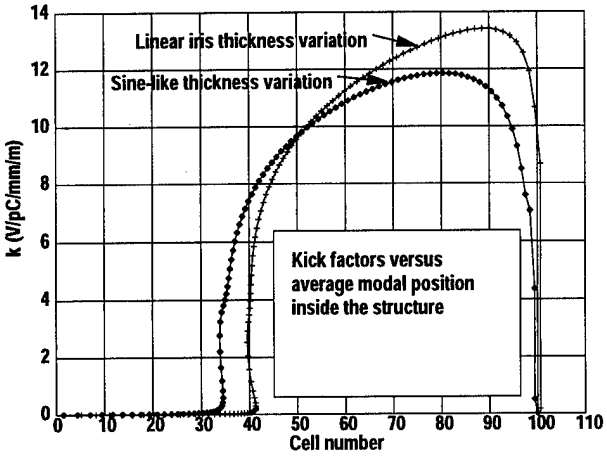


Figure: 2 Kick factors as a function of cell number

One of the main design aims is to maximise the time before recoherence occurs, this is proportional to the inverse frequency separation of the modes. The largest separation, and therefore the shortest time, occurs in the high frequency tail of the gaussian distribution where the previously mentioned undamped high kick modes are localised. Using a sine-like iris thickness distribution rather than a linear one increased the recoherence time significantly (see Figures 3 and 4). After the initial roll-off, the wakefield level for this purely detuned structure stays well above 10 V/pC/mm/m, which is unacceptable for the CLIC parameters [3]. The coupled cell kdn/df (kick factor x modal density) distribution is shown in Figure 3. Although the coupled cell detuning bandwidth is larger than the uncoupled one, the σ is smaller resulting in a longer roll-off time (see Figure 5).

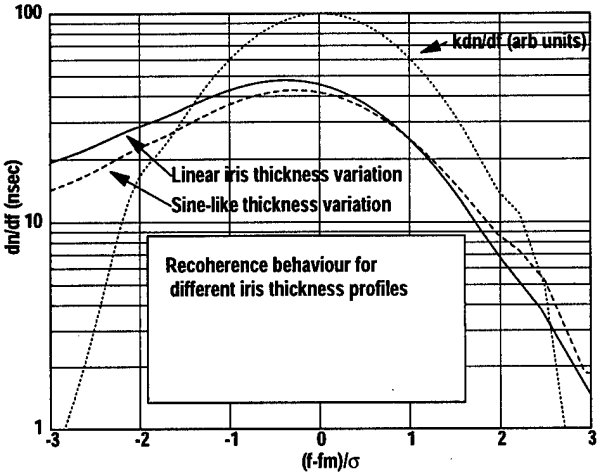


Figure: 3 The modal contributions to the wake

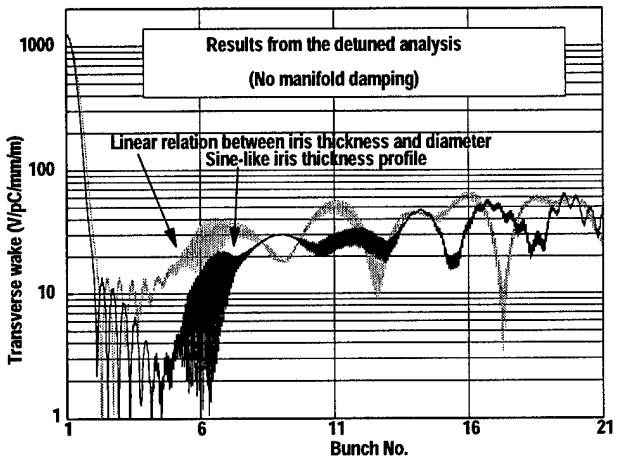


Figure: 4 The transverse wakefield calculated using a double band model but without damping manifold

As in the X-band structure, the dimensions of the damping manifold and the distance between manifold and cell (coupling strength) vary along the length of the structure. The main structure dimensions taking into account the cell/manifold coupling are given in Table 1.

Table 1 Main structure dimensions (input - output)

Cell diameter	8.68 - 8.12 mm
Iris diameter	4.66 - 3.40 mm
Iris thickness	0.50 - 1.10 mm
Manifold height	2.0 mm
Manifold width	4.38 - 4.21 mm
Manifold / cell spacing	+0.09 to -1.10 mm

Including the effect of the damping manifold using the spectral function method of analysis [6] modifies the kdn/df distribution. The effect of the damping manifold is to give a finite Q to the modes (previously assumed to be delta functions) causing them to overlap and produce a continuous but rippled spectral function - see Figure 5.

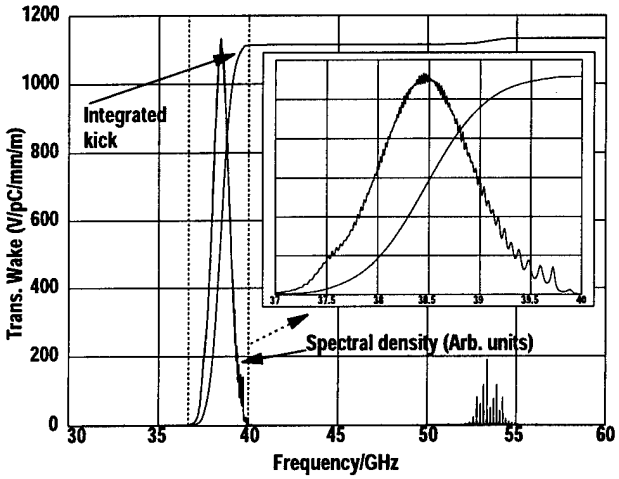


Figure: 5 Spectral function for cell/manifold coupled structure

The resulting transverse wake function is given in Figure 6. The long-range wake level is just below 10 V/pC/mm/m. The 40 V/pC/mm/m wake at the second bunch (1ns) is somewhat higher than that required for CLIC. This level can almost certainly be reduced by redesigning the structure to have a larger σ for the frequency distribution although this would probably increase the long range wakefield level. Increasing the number of cells to 150 would certainly improve the long range transverse wakefield performance. The manifolds are assumed to be perfectly terminated, however analyses made on the X-band structure have shown that the wake is seriously degraded by small termination mismatches.

Table: 2 The theoretical fundamental mode characteristics (input - output)

< Quality factor Q >	3900
Q	4450 - 3700
< Shunt impedance R / Q >	25 kΩ/m
R/Q	21.8 - 28.3 kΩ/m
< Group velocity v_g / c >	7 %
v_g / c	13.3 - 3.6 %
Number of cells	101
Fill time	18 ns

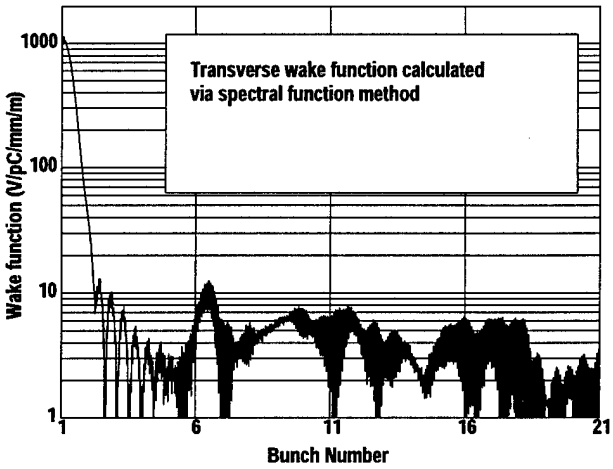


Figure: 6 The final 30 GHz DDS transverse wakefield

The steady state beam loaded voltage along the length of the DDS structure is shown in Figure 7.

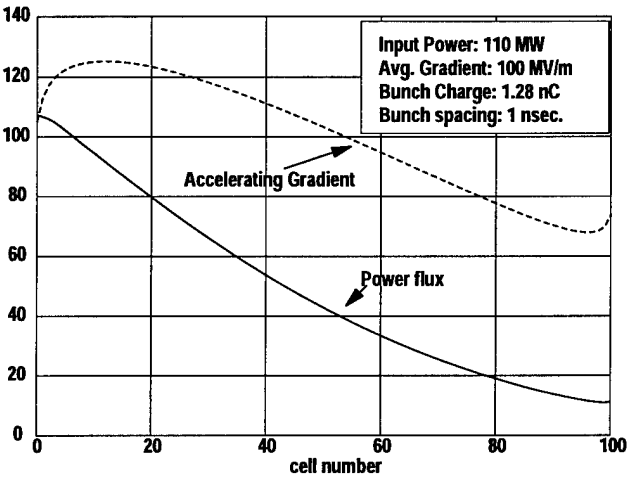


Figure: 7 The steady state beam loaded voltage

REFERENCES

[1] H.Braun and 10 co-authors: 'CLIC-A Compact and Efficient High Energy Linear Collider', PAC95, Dallas, May 1995.

[2] J.P. Delahaye and 6 co-authors: 'A 30 GHz 5-TeV Linear Collider', these proceedings.

[3] G.Guignard, J.Hagel: 'Beam characteristics versus Cavity Models in CLIC', these proceedings.

[4] R.H. Miller and 20 co-authors: 'A Damped Detuned Structure for the Next Linear Collider', Proc. Linac96, Geneva, 1996.

[5] K. Bane, R. Gluckstern, 'The Transverse Wakefield of a Detuned X-band Accelerator Structure', Particle Accelerators , Vol. 42, p 213 (1993).

[6] R.M. Jones , K. Ko, N.M. Kroll and R.H. Miller: 'A Spectral Function Method Applied to the Calculation of the Wake Function for the NLCTA', Proc. Linac96, Geneva, 1996.

ANALYSIS OF HOM INTERACTION BETWEEN CAVITIES BY MULTIMODAL S-PARAMETER MEASUREMENTS

H.-W. Glock, F. Marhauser, P. Hülsmann, M. Kurz, H. Klein
Institut für Angewandte Physik der Johann Wolfgang Goethe-Universität Frankfurt am Main
Robert Mayer-Straße 2-4, D-60054 Frankfurt/M., Germany

Abstract

Accelerating cavities exchange HOM power through interconnecting beam pipes in case of signal frequencies above the cut-off of their propagating waveguide modes. This may lead either to improved HOM damping or - in the case most severe - to unwanted phase coherence of fields to the beam. Therefore the knowledge of the scattering properties of a cavity as a line element is needed to analyse all kinds of RF cavity-cavity interaction. Since there is a lack of measurement tools capable to provide a multidimensional scattering matrix at a given frequency point, we have been developing a method for this purpose. It uses a set of 2-port S-parameters of the device under test, embedded in a number of geometrically different RF environments. The application of the method is demonstrated with copper models of TESLA cavities.

1 INTRODUCTION

Usually the spectra of beam-excited fields contain significant parts above the RF cut-off of several waveguide modes of the beam pipe. Therefore one has to be concerned about the effects caused by the RF-interaction of the beam line elements: it may for example increase the damping of resonant cavity modes by stronger coupling to absorbing elements, it allows for resonant fields localised between different beam pipe insertions or it may introduce signal paths delayed by multiple reflection to - in the worst case - particle velocity. Either of these situations is covered within a description in terms of transmission and reflection properties of the beam line's elements with respect to their interconnecting planes, i.e. their scattering (S-) parameters. Since the interaction is not restricted to the fundamental mode, but includes a - frequency dependent - number of waveguide modes, the multidimensional matrix of the S-parameters (see sect. 2) is necessary and sufficient to characterise a line element in any environment. Thus we have been developing an experimental method, allowing for multidimensional S-matrix measurement in a waveguide setup. Since its first presentations [1,2] we adopted an improved evaluation scheme which minimizes the overall error. It is demonstrated in the case of two modes for a device measurement and three modes for a calibration of an adaptor at single frequency points.

2 THEORY

The S-matrix of an adaptor (A, B in Fig. 1) with one coaxial line (index 0) and n modes propagating in the waveguide port may be written as:

$$\hat{\underline{\underline{A}}} = \left(\begin{array}{c|ccc} A_{00} & A_{01} & \cdots & A_{0n} \\ \hline A_{01} & A_{11} & \cdots & A_{1n} \\ \vdots & \vdots & \ddots & \vdots \\ A_{0n} & A_{1n} & \cdots & A_{nn} \end{array}\right) = \left(\begin{array}{c|c} A_{00} & \vec{A}^{T} \\ \hline \vec{A} & \underline{\underline{A}} \end{array}\right) \qquad (1)$$

Herein the scalar A_{00} describes the reflection at the coaxial port, $\vec{A}$ the coupling from the coaxial line to each waveguide mode and $\underline{\underline{A}}$ the reflection at the waveguide flange, that may couple every mode to each other. The matrix is symmetric due to the reciprocity of the device. Like in the single mode case, the problem of determining the properties of a device splits into the calibration step - i.e. determination of the adaptors, which connect the device to an ideal network analyzer - and the measurement once the adaptors are known. Considering the number of unknowns (10 for two modes at two waveguide ports) it becomes clear that a single measurement with two completely known adaptors, which gives three numbers (two reflection, one transmission quantity), not provides sufficient information. Thus one has to use different pairs of known adaptors for a number of subsequent device measurements. To keep the calibration effort as small as possible we take two adaptors and then combine them with various delay line lengths (Fig. 1). In the same manner we use a short and different delay line lengths (which are the only reliable broadband waveguide standards of easy making) to calibrate the two adaptors.

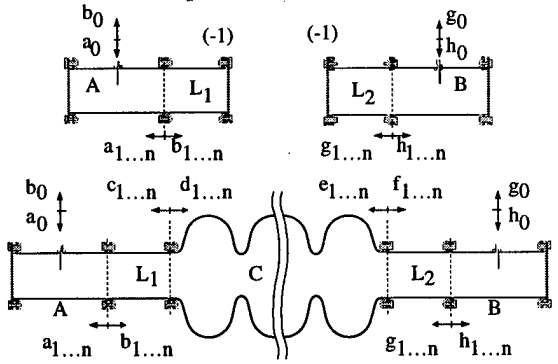


Figure 1: Schematic drawing of setups used for adaptor calibration with delayed shorts and for measurement. Small letters denote the signals at all connection planes, index 0 corresponds to the coaxial line.

If we consider a setup with two adaptors A and B, a test device C and two connecting waveguides with lengths L_1 and L_2 (Fig. 1), we are able to write down all signals, related by S-matrices:

0-7803-4376-X/98/$10.00 © 1998 IEEE

$$\begin{pmatrix} b_0 \\ \vec{b} \end{pmatrix} = \begin{pmatrix} A_{00} & \vec{A}^T \\ \vec{A} & \underline{\underline{A}} \end{pmatrix} \begin{pmatrix} a_0 \\ \vec{a} \end{pmatrix}, \quad \begin{pmatrix} g_0 \\ \vec{g} \end{pmatrix} = \begin{pmatrix} B_{00} & \vec{B}^T \\ \vec{B} & \underline{\underline{B}} \end{pmatrix} \begin{pmatrix} h_0 \\ \vec{h} \end{pmatrix}$$

$$\begin{pmatrix} \vec{a} \\ \vec{d} \end{pmatrix} = \begin{pmatrix} 0 & \underline{\underline{E}}(L_1) \\ \underline{\underline{E}}(L_1) & 0 \end{pmatrix} \begin{pmatrix} \vec{b} \\ \vec{c} \end{pmatrix}, \quad \begin{pmatrix} \vec{e} \\ \vec{h} \end{pmatrix} = \begin{pmatrix} 0 & \underline{\underline{E}}(L_2) \\ \underline{\underline{E}}(L_2) & 0 \end{pmatrix} \begin{pmatrix} \vec{f} \\ \vec{g} \end{pmatrix}$$

$$\begin{pmatrix} \vec{c} \\ \vec{f} \end{pmatrix} = \begin{pmatrix} \underline{\underline{C}}_{11} & \underline{\underline{C}}_{12} \\ \underline{\underline{C}}_{12}^T & \underline{\underline{C}}_{22} \end{pmatrix} \begin{pmatrix} \vec{d} \\ \vec{e} \end{pmatrix} \qquad (2\text{ a-e})$$

All the submatrices are (n x n)-dimensional. For the waveguide of length L and the phase constants γ_j holds:

$$\underline{\underline{E}}(L) = \begin{pmatrix} e^{-\gamma_1 L} & 0 & 0 \\ 0 & \ddots & 0 \\ 0 & 0 & e^{-\gamma_n L} \end{pmatrix} \qquad (3)$$

Using an additional abbreviation

$$\begin{pmatrix} \underline{\underline{H}}_{11} & \underline{\underline{H}}_{12} \\ \underline{\underline{H}}_{12}^T & \underline{\underline{H}}_{22} \end{pmatrix} = \begin{pmatrix} \underline{\underline{E}}(L_1) & 0 \\ 0 & \underline{\underline{E}}(L_2) \end{pmatrix} \begin{pmatrix} \underline{\underline{C}}_{11} & \underline{\underline{C}}_{12} \\ \underline{\underline{C}}_{12}^T & \underline{\underline{C}}_{22} \end{pmatrix} \begin{pmatrix} \underline{\underline{E}}(L_1) & 0 \\ 0 & \underline{\underline{E}}(L_2) \end{pmatrix}$$

and with respect to the fact, that the complete setup is just a coaxial line - two port with a (2 x 2)-S-matrix

$$\begin{pmatrix} b_0 \\ g_0 \end{pmatrix} = \begin{pmatrix} \Gamma_1 & T \\ T & \Gamma_2 \end{pmatrix} \begin{pmatrix} a_0 \\ h_0 \end{pmatrix} \qquad (4)$$

one finds after elimination of all signal quantities ([1]):

$$\begin{pmatrix} \Gamma_1 & T \\ T & \Gamma_2 \end{pmatrix} = \begin{pmatrix} A_{00} & 0 \\ 0 & B_{00} \end{pmatrix} + \\ + \begin{pmatrix} \vec{A}^T & 0 \\ 0 & \vec{B}^T \end{pmatrix} \begin{pmatrix} \underline{\underline{H}}_{11} & \underline{\underline{H}}_{12} \\ \underline{\underline{H}}_{12}^T & \underline{\underline{H}}_{22} \end{pmatrix} \left[1 - \begin{pmatrix} \underline{\underline{A}} & 0 \\ 0 & \underline{\underline{B}} \end{pmatrix} \begin{pmatrix} \underline{\underline{H}}_{11} & \underline{\underline{H}}_{12} \\ \underline{\underline{H}}_{12}^T & \underline{\underline{H}}_{22} \end{pmatrix} \right]^{(-1)} \begin{pmatrix} \vec{A} & 0 \\ 0 & \vec{B} \end{pmatrix} \qquad (5)$$

We shall refer to (5) as the "complete model". It can be rewritten using

$$(\underline{1} - \underline{\underline{M}})^{(-1)} = (\underline{1} + \underline{\underline{M}} + \underline{\underline{M}}^2 + \underline{\underline{M}}^3 + \ldots) \qquad (6)$$

(we skip the discussion of the mathematical conditions)

$$\begin{pmatrix} \Gamma_1 & T \\ T & \Gamma_2 \end{pmatrix} = \begin{pmatrix} A_{00} & 0 \\ 0 & B_{00} \end{pmatrix} + \\ + \begin{pmatrix} \vec{A}^T & 0 \\ 0 & \vec{B}^T \end{pmatrix} \begin{pmatrix} \underline{\underline{H}}_{11} & \underline{\underline{H}}_{12} \\ \underline{\underline{H}}_{12}^T & \underline{\underline{H}}_{22} \end{pmatrix} \sum_{j=0}^{\infty} \left[\begin{pmatrix} \underline{\underline{A}} & 0 \\ 0 & \underline{\underline{B}} \end{pmatrix} \begin{pmatrix} \underline{\underline{H}}_{11} & \underline{\underline{H}}_{12} \\ \underline{\underline{H}}_{12}^T & \underline{\underline{H}}_{22} \end{pmatrix} \right]^j \begin{pmatrix} \vec{A} & 0 \\ 0 & \vec{B} \end{pmatrix} \qquad (7)$$

as a geometric matrix series. This expansion is useful as well as an approach for the numerical solution of (5) with a set of measurement data as for its physical interpretation. We are going to use an approximation for the right hand side of (7), that contains only the terms of order j=0 and j=1. This will be called "reduced model". To simplify discussion, we restrict ourselves to the calibration step, which is a special case of (5) (set all elements of C to 0 except the upper left block which is the negative identity). Then the complete model is:

$$\Gamma_1(L_1) = A_{00} - \vec{A}^T \underline{\underline{E}}^2(L_1) \left[\underline{1} + \underline{\underline{A}}\, \underline{\underline{E}}^2(L_1) \right]^{(-1)} \vec{A} \qquad (8)$$

and its reduced version reads like:

$$\Gamma_1(L_1) \approx A_{00} - \vec{A}^T \underline{\underline{E}}^2(L_1)\, \vec{A} + \vec{A}^T \underline{\underline{E}}^2(L_1)\, \underline{\underline{A}}\, \underline{\underline{E}}^2(L_1)\, \vec{A} \qquad (9)$$

Evaluating this for two modes (10) shows that each term describes a possible signal path from initial incidence to final detection. Thus the arithmetic derivation of (5) ((7) resp.) is just a summation over all paths, written very compact.

$$\Gamma_1(L_1) = A_{00} - \left(A_{01}^2\, e^{-2i\gamma_1 L_1} + A_{02}^2\, e^{-2i\gamma_2 L_1} \right) + \\ + \left(A_{01}^2\, A_{11}\, e^{-4i\gamma_1 L_1} + A_{02}^2\, A_{22}\, e^{-4i\gamma_2 L_1} + \right. \\ \left. + 2\, A_{01}\, A_{02}\, A_{12}\, e^{-2i(\gamma_1+\gamma_2) L_1} \right) - \cdots \qquad (10)$$

In order to find the S-parameters of C (A, B resp. during calibration), a set of equations (5) ((8) resp.) with measured data inserted has to be solved. This is done by an iteration scheme, which significantly improves the results compared with the approximative approach [1,2]. The latter one remains as a first step of the method, used to find initial values in the following way: Neglecting all higher orders of internal reflection but the first, $\Gamma_1(L_1,L_2)$ (and similar T, Γ_2) is a linear combination of length oscillations with well known wavenumbers (left column) and amplitudes with simple dependencies on S-parameters, listed here for the easiest case (10):

1	A_{00}	$\Rightarrow A_{00}$
$e^{-2i\gamma_1 L_1}$	$-A_{01}^2$	$\Rightarrow \pm A_{01}$
$e^{-2i\gamma_2 L_1}$	$-A_{02}^2$	$\Rightarrow \pm A_{02}$
$e^{-4i\gamma_1 L_1}$	$A_{01}^2 A_{11}$	$\Rightarrow A_{11}$
$e^{-4i\gamma_2 L_1}$	$A_{02}^2 A_{22}$	$\Rightarrow A_{22}$
$e^{-2i(\gamma_1+\gamma_2) L_1}$	$2 A_{01} A_{02} A_{12}$	$\Rightarrow \pm A_{12}$

Thus the amplitudes and consequently the S-parameters are found explicitly from the solution of an overdetermined system of equations like (10) with Γ taken from the set of experiments with different L. Although the S-parameters found in this manner seemed to resemble the measured system behaviour quite well [1,2], consistency tests and experiments simulated numerically (sect. 3) showed, that the S-parameters, especially if weakly contributing, may carry intolerable errors. The reason was found to be the influence of higher orders of internal reflection, neglected so far. Therefore their contribution has to be incorporated, which is done by iteration. Again, transform (8) using (6), but keep all higher reflection degrees - again as a geometric series - together with Γ on the left hand side:

$$\Gamma + \left(\vec{A}^T \underline{\underline{E}}^2\, \underline{\underline{A}}\, \underline{\underline{E}}^2 \left[\underline{1} + \underline{\underline{A}}\, \underline{\underline{E}}^2 \right]^{-1} \underline{\underline{A}}\, \underline{\underline{E}}^2\, \vec{A} \right) = \\ = A_{00} - \vec{A}^T \underline{\underline{E}}^2\, \vec{A} + \vec{A}^T \underline{\underline{E}}^2\, \underline{\underline{A}}\, \underline{\underline{E}}^2\, \vec{A} \qquad (11)$$

The expression in brackets is easily evaluated for given S-parameters and corrects the measured Γ for the higher reflection degrees, of course on an approximative base. Then the reduced model on the right is fitted as before to the left hand side, which gives new S-parameters. The procedure is repeated until the variation of the S-parameters vanishes, which corresponds to the best approximation of the *complete* model to the measured data. All considerations demonstrated for the calibration step (starting from (8)) can be transferred to the measurement (5).

3 SIMULATED EXPERIMENTS

In order to test the procedure a 3-mode set of S-parameters of two adaptors A, B and a device C was generated to evaluate (5) for a typical set of 18 x 18 different

combinations of L_1, L_2. This was taken as "measured" input. Tab. 1 shows 4 (of 21) parameters of C; first the true value originally invested, the initial value found by the fit-method and the result of the 4th iteration step. Although there are significant errors of some of the fit-values the iteration shrinks them within a few iterations dramatically. The overall error, defined as the value sum over the deviations between iteration result and truth of all 21 parameters is displayed in Fig. 2 for each iteration step.

4 MEASUREMENT SETUP AND EXAMPLES

The various delay line lengths have been realized by building two adaptor systems sliding in two fixed waveguides. Their design is not critical (beside the supression of transverse polarizations) since they have to be calibrated anyhow. They are driven by stepping motors with spindles that allow for a nominal position resolution of 6.25 µm and a shift of 0.35 m. The RF equipment consists of a HP8753C-6 GHz-network analyzer, connected with the adaptors using phase-stabilized flexible RF cables. The components are computer controlled. The adaptors and the test device are insulated to reduce thermal drifts.

A typical result of an adaptor calibration is shown in Fig. 3. It was found at 4.50 GHz with three propagating modes (TE_{11}, TM_{01}, TE_{21}) in a 78 mm diameter circular waveguide. Fig. 4 demonstrates that the input reflection $\Gamma(L)$ (line) of the adaptor calculated with these S-parameters fits the measured dots very well. Fig. 5 gives an example for results of a device measurement.

5 CONCLUSION AND OUTLOOK

A method that expands network analyzer functionality in the regime of multimoded waveguides has been successfully demonstrated for up to three non-degenerated propagating modes. It provides all information needed to describe the behaviour of a given waveguide insertion at an arbitrary frequency point (or a spectrum of them). Thus it allows to predict the RF properties of every chain of known insertions, which is important not only for accelerator sections with respect to (HOM-) fields but for all waveguide applications with excitation of more than the fundamental mode. Further investigation will be spent in the resolution of (esp. polarizational) degenerated modes in order to expand the method's range of applications.

SUPPORT

Work supported by DESY and BMBF; contract 060f359.

REFERENCES

[1] H.-W. Glock, P. Hülsmann et. al.: Energy Propagation through the TESLA Channel: Measurements with Two Waveguide Modes (TESLA-Rep. 96-07), DESY, June 1996

[2] H.-W. Glock, F. Marhauser et. al.: Measurement of HOM-Propagation through Cavity Chains in Terms of S-Parameters, Proc. 18th Int. Linear Accelerator Conf., Geneva, 26-30 Aug. 1996, pp. 716

Parm.	Truth	First Fit	4th Iteration
c[1, 1]	0.1445 + 0.1334 I	0.3185 - 0.2865 I	0.1445 + 0.1334 I
c[2, 2]	-0.1162 - 0.1434 I	-0.4127 - 0.1202 I	-0.1161 - 0.1434 I
c[2, 6]	0.04041 - 0.06209 I	0.04047 - 0.06113 I	0.04041 - 0.06209 I
c[5, 6]	0.2104 - 0.09209 I	0.1841 - 0.1167 I	0.2104 - 0.09192 I

Tab. 1: Sample S-parameters in simulated experiment

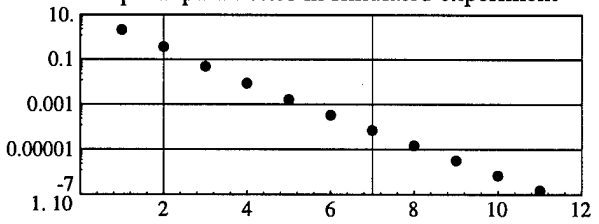


Fig. 2: Value sum of error of all S-parameters over iteration number. First point is result of fit procedure and used as start value.

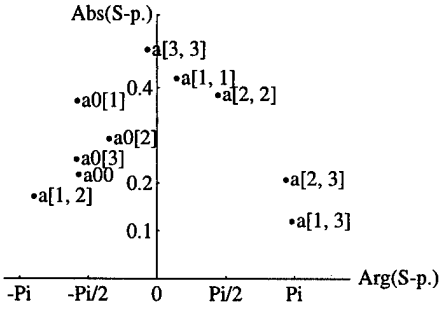


Fig. 3: Typical S-parameter of adaptor, found at 4.5 GHz

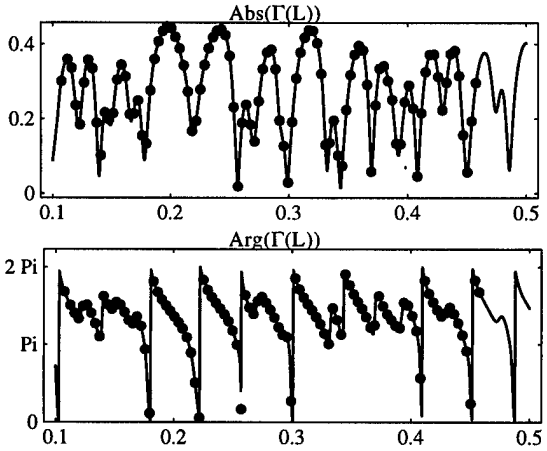


Fig. 4: $\Gamma(L)$, calculated from the S-parameters in Fig. 3 (line) and measured (dots)

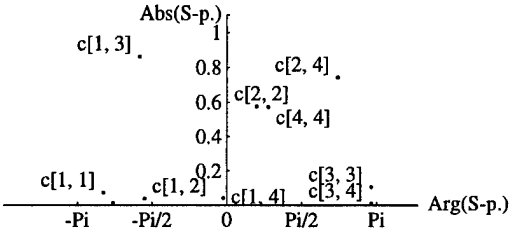


Fig. 5: Example set of S-parameters of a TESLA 9-cell copper cavity, found at 3.50 GHz with comparably high transmission in both modes (c[1,3], c[2,4]).

THE 36-CELL STRUCTURE – CALCULATIONS AND EXPERIMENTS

P. Hülsmann, W.F.O. Müller and H. Klein,
Institut für Angewandte Physik, Universität Frankfurt am Main, Germany
U. van Rienen and T. Weiland,
Theorie Elektromagnetischer Felder, Technische Hochschule Darmstadt, Germany

Abstract

The wake field effects in accelerator sections for future linear colliders will be reduced either by damping, by detuning or a combination of both. In the case of the DESY S-Band Test Facility [1] it is foreseen to employ two higher order mode (HOM) damped cells within a detuned stack of undamped ones. In order to obtain optimal performance by use of single cell dampers a design was derived by applying numerical tools. To understand the behaviour of such a damper cell in a detuned structure, a damper cell was build and inserted in a strongly detuned 36-cell S-Band structure. This structure was investigated by bead pull measurements. The predictions of MAFIA field calculations were compared to experimental results.

1 INTRODUCTION

The S-Band 500 GeV Linear Collider Study SBLC foresees about 5000 constant gradient (cg) acceleration structures of 180 cells with a loaded gradient of 17 MV/m. It considers a bunch train of 333 bunches with a spacing of 6 ns from bunch to bunch. To achieve a high luminosity any cumulative beam break up along the bunch train has to be avoided. Wakefield effects driven by HOMs are one of the primary sources of emittance growth. Consequently, the suppression of these HOMs is a very crucial point in all actual linear collider designs. The major interest of calculations was focused on the modes of the first dipole band since they cause the severest deflecting effects, but also the 3^{rd} and 6^{th} dipole passband need to be studied.

Calculations for the SBLC structure were carried out with ORTHO [2] for a somewhat simplified 180-cell structure with 30 landings. One of the main results was that not only the first π-like dipole modes influence the beam dynamics but about 140 modes! A major part of these deflecting modes is trapped inside the cg structure, that is without contact to the end cells.

Since the phenomenon of trapped HOMs in tapered waveguides was neither theoretically nor experimentally well known and has a strong influence on the design of damping schemes further HOM investigations have been started: A test structure was designed with the goal to have a structure which is easy to measure, easy to manufacture, which is computable with different numerical methods (MAFIA, URMEL–T, ORTHO, COM) without geometric approximations, and which shows the clear appearance of trapped modes.

Performing RF-measurements on long structures is severely limited by the appearance of mode overlap. Therefore a relatively short structure had to be chosen. In order to get a both mechanically and thermally stable structure a massive design was chosen. For low mechanical tolerances a simple geometry was designed. The structure has a very strong linear tapering of the iris, constant outer radius and twice as thick irises as the original SBLC structure. Comparisons of numerical calculations and measurements without damping system [3], gave a good agreement in resonance frequencies and the field distribution. Further the clear appearance of trapped modes was found for several modes [4]. Calculations for the damped system have also been done, and have been compared with measurements.

2 THE TEST SETUP

The structure, made of standard OFHC copper, consists of 36 cells clamped together by truss rods. The cell geometry is similar to the one chosen for the SBLC, except for the iris thickness which is 10 mm instead of 5 mm. The iris openings were evenly tapered from 40 mm diameter at the beginning to 20 mm at the end.

For the measurements of the damped structure we have inserted a sheet of paper covered with graphite in cell #18. This damping material could be inserted without demounting of the structure. It is only a model for test purposes that represents a damping unit like a wall slotted cell with four rectangular waveguides attached. This method avoids the influence of changed electrical contacts due to the reassembling on the measured Q-values. Proper alignment is ensured by laying the structure on top of an optical bench. The field measurements were performed using a modified nonresonant bead pull technique [5], [6], [7]. Data is taken by a HP8719c network analyser for 801 discrete positions along several paths parallel to the cavity axis.

3 SIMULATION WITH DAMPING SHEET

The simulation of the 36-cell structure with a very thin (about 1.5 μm) damping sheet in cell #18 is practically not possible with discretization methods since it is not possible to mesh accurately enough within reasonable storage demands. Therefore other methods were necessary to get quantitative theoretical results for the damping effect. In case of small losses it is well known that the field distribution does not change considerably compared with the loss free case. Then it is reasonable to use the field distribution of the loss free case to calculate the power loss by means of perturbation theory. As the measurement improved [4] the undisturbed field distribution may be used to calculate the damping effect for the 36-cell structure.

0-7803-4376-X/98/$10.00 © 1998 IEEE

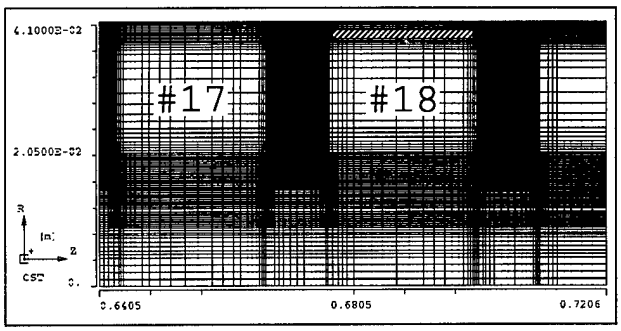


Figure 1: Three cells out of the 36-cell structure. Cell #18 with the damping material (hatched).

Practically this was done with MAFIA in the following way: First a loss free field calculation was executed for the original 36-cell structure. In a second calculation a thin sheet with a different material number was inserted in cell #18, as shown in figure 1. The hatched area near the outer wall of cell #18 is the graphite. Even though a rather coarse mesh would lead to a perfect approximation of the structures shape[1] preceding studies showed that smaller step sizes near all edges resulted in much better agreement for the frequencies obtained in measurement respective simulation while the field distribution agrees already well enough for a coarse, quasi equidistant mesh. The frequency is very sensitive to an appropriate discretization and an appropriate bead [3].

During the solution of the eigenvalue problem this material as well as all walls of the structure are treated as perfect conductors. Afterwards, in the postprocessing all wall material gets the conductivity of copper $\sigma = 5.8 \cdot 10^7$ S/m while the sheet in cell #18 gets a lower conductivity.

At this point some approximations are necessary since the sheet has to be thicker than the original one from the measurements. The reasons are that each material should be discretized with at least two steps in each coordinate direction and that the quotient of largest to smallest step size should be kept within reasonable limits in order to limit the condition number of the matrix of the eigenvalue problem. Therefore the material sheet which represents the very thin graphite sheet got a conductivity of $\sigma = 5.0 \cdot 10^6$ S/m instead of graphite's conductivity of $\sigma = 1.25 \cdot 10^5$ S/m.

After calculating the total stored energy W_{tot} and the wall losses[2] P_{wall} the quality factor Q may be determined [8] for a mode with frequency ω by

$$Q = \omega \cdot \frac{W_{tot}}{P_{wall}} . \qquad (1)$$

Finally the frequency shift caused by the damping sheet in cell #18 is obtained by (2) neglecting second order terms.

$$\frac{\delta\omega}{\omega_0} = \frac{1}{2Q} \qquad (2)$$

1. i. e. vanishing geometric error
2. by power loss method

4 THE MEASUREMENT METHOD

The method applied is a variant of the nonresonant bead-pull technique as described elsewhere [9]. In the measurements we are only interested in the longitudinal component of the electric field, because it is sufficient to indicate the effect of the damper cell. Thus we used a dielectric needle (Al_2O_3, $\varepsilon_r = 9.2$) as bead. This ceramic bead was 6 mm long and 1 mm in diameter. A lumped circuit representation of the resonator combined with Slaters formula [10] leads to the electric field:

$$E^2 = \frac{P_{wall}}{\alpha} \cdot \frac{(1 + k_1 + k_2)^2}{2\omega \cdot \sqrt{k_1 k_2}} \cdot |\Delta s_{21}| \qquad (3)$$

5 RESULTS

For the measurements the bead was calibrated in a TM_{010}-pillbox for the longitudinal perturbation constant ($\alpha = 9.34 \cdot 10^{-20}$ Asm^2/V). Since the measured modes were of dipole type the bead pull measurements were performed off-axis with a distance of 7 mm to the structures axis. For the measurements we have chosen several modes of the first dipole passband which have significant field strength at the damper position (cell #18) since a considerable damping effect could only be expected in this case.

In a tapered structure trapped modes always change their phase shift from cell to cell from 0 to π. To investigate the influence of the damper position, we have chosen mode A with the π-end, mode B with the $\pi/2$-part and mode C with the 0-end at the damper position. Additionally all modes between A and C have been measured (see figure 2). The results are summarized in table 1.

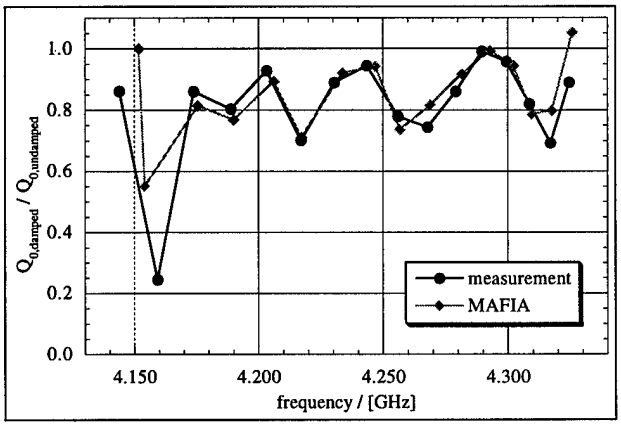


Figure 2: Comparison of calculated and measured damping effect (reduction of Q_0).

As mentioned above, the damper was realized by a sheet of paper covered with graphite (thickness 1.5 µm, conductance of graphite = $1.25 \cdot 10^5$ 1/Ωm). First the sheet was pressed to the inner wall of cell #18 in order to have a symmetric damper and relatively weak damping effect (damper on surface). Additionally the damping effect was increased by moving the sheet some mm towards the iris, since the

electrical field increases in this direction (damper in cell). The results of simulations are presented in table 2. It must be mentioned, that Q-values calculated by the simulations are always higher than those derived by measurements. This is caused by HF-contacts between adjacent copper cells.

To compare the results from measurements and calculations, damping effect versus frequency is plotted for both in figure 2. As can be seen there the agreement is mostly excellent, except the first two modes on the left. These two modes proofed to be very sensitive on the position of the π-like end. Already a small disturbance moves the position to the next cell. Thus this discrepancy was expected.

Table 1: Measurement results

f_0 [GHz]	$Q_{0,undamp.}$	$Q_{0,damped}$	$Q_{0,d.}/Q_{0,und.}$
4.143,830	10,353	8,927	0.862
4.159,260	10,264	2,507	0.244
4.173,972	10,464	9,002	0.860
4.188,848	10,157	8,161	0.803
4.203,234	10,193	9,454	0.928
4.217,087	11,291	7,919	0.701
4.230,494	10,848	9,646	0.889
4.243,603	10,997	10,389	0.945
4.256,029	10,490	8,181	0.780
4.267,888	11,174	8,319	0.744
4.279,207	11,185	9,621	0.860
4.289,655	11,447	11,350	0.991
4.299,424	11,396	10,923	0.958
4.308,621	11,757	9,640	0.820
4.317,108	11,918	8,244	0.692
4.324,609	12,112	10,764	0.889

6 CONCLUSION

From former measurements a strong influence on mode geometry was expected [11]. But weak damping as well as strong damping has not changed the mode geometry significantly. The damping effect is evenly distributed over all phase shifts.

The black line in figure 2 represents the measurement results for the Q-reduction. The results of the MAFIA calculations are plotted as gray line. For all modes, except the first two ones, an excellent agreement was found. Thus one may say that the numerical representation of the damper was successful.

Table 2: Results from MAFIA-calculation

f_0 [GHz]	$Q_{0,undamp.}$	$Q_{0,damped}$	$Q_{0,d.}/Q_{0,und.}$
4.151,653	13,650	13,645	1.000
4.154,160	12,552	6,936	0.553
4.175,661	12,641	10,291	0.814
4.189,950	12,736	9,785	0.768
4.206,170	12,839	11,478	0.894
4.217,273	12,947	9,205	0.711
4.233,617	13,066	12,032	0.921
4.246,928	13,185	12,426	0.942
4.256,809	13,308	9,809	0.737
4.268,974	13,436	10,972	0.817
4.281,471	13,570	12,449	0.917
4.292,834	13,699	13,596	0.992
4.302,226	13,833	13,064	0.944
4.309,774	13,962	10,984	0.787
4.317,561	14,094	11,269	0.800
4.325,724	14,229	14,953	1.051

7 REFERENCES

[1] N Holtkamp: "The S-Band Linear Collider Test Facility", this conference

[2] U. van Rienen: "Higher Order Mode Analysis of Tapered Disc–Loaded Waveguides using the Mode Matching Technique", Particle Accelerators, Vol. 41, pp. 173 - 201, 1993

[3] M. Kurz et al.: "Higher Order Modes in a 36-Cell Test Structure", 5th EPAC, Barcelona, 1996

[4] W.F.O. Müller, P. Hülsmann, M. Kurz, C. Peschke, H. Klein, U. van Rienen, T. Weiland, M. Dohlus: "Measurements and Numerical Calculations on Higher Order Mode Dampers"; Proceedings of the XVIIIth International Linac Conference, Geneva (Switzerland), Aug. 1996

[5] C.W. Steele: "A Nonresonant Perturbation Theory", IEEE Trans. MTT-14 (2), pp. 70-74, 1966

[6] P. Hülsmann, M. Kurz, H. Klein: "Experimental Determination of Field Strength and Quality Factor of heavily damped Accelerator Cavities", Electronics Letters, Vol. 27 No. 19, pp. 1727-1729, 12.09.1991

[7] M. Kurz: "Untersuchungen zu mikrowellenfokussierenden Beschleunigerstrukturen für zukünftige lineare Collider", thesis, Frankfurt, 1993

[8] T. Weiland: "High Precision Eigenmode Computation"; Particle Accelerators, Vol. 56, pp. 61-82, 1996

[9] B. Krietenstein et al.: "The S-Band 36-Cell Experiment", Particle Accelerator Conference and International Conference on High-Energy Accelerators, Dallas (Texas), 1995

[10] L.C. Maier, J.C. Slater: "Field Strength Measurements in Resonant Cavities", Journal of Applied Physics, 23 (1), 1952

[11] M. Dohlus et al.: "S-Band HOM-Damper Calculations and Experiments", Particle Accelerator Conference and International Conference on High-Energy Accelerators, Dallas (Texas), 1995

(work supported by DESY / Hamburg and BMBF under contract 06of359)

SEARCH FOR TRAPPED MODES IN TESLA CAVITIES

F. Marhauser, H.-W. Glock, P. Hülsmann, M. Kurz, H. Klein
Institut für Angewandte Physik der Johann Wolfgang Goethe-Universität Frankfurt
Robert Mayer-Straße 2-4, D-60054 Frankfurt/M., Germany

Abstract

In resonant cavities which are connected via beam pipes fields usually tend to propagate with shrinking wavelengths. Nevertheless there may also exist some non-propagating resonant modes („trapped modes") in the frequency range above the beam-pipe cut-off with relative high shunt impedances which are strongly localised in the inner part of a accelerating structure. Due to their field distributions these trapped modes can hardly be coupled to dampers at the ends of the cavity and therefore could have dangerous effects to beam dynamics. Their detection is very difficult, if one considers that they are embedded in a spectrum of several hundred resonant modes. We therefore started to search trapped modes in a 9-cell copper TESLA cavity. The principles of our method and results from measurements are presented in this paper.

1 INTRODUCTION

For the next generation of electron-positron linear colliders with initial center of mass energies of 350...500 GeV luminosities above 10^{33} $cm^{-2}s^{-1}$ are required [1]. High luminosities correlates with small transverse beam emittance, so that any kind of beam instabilities has to be controlled to avoid emittance growth. One major cause for emittance dilutions in a high energy linear accelerator are wakefields, which are excited by the bunches itself traveling through the accelerating structure. These wakefields could act back on the exciting bunch itself (Single Bunch Breakup) or on all following bunches (Multibunch Beam Breakup) which would be more and more deflected. Especially for superconducting structures with high quality-factors, these wakefields could strongly affect beam dynamics. To preserve the emittance along the whole accelerator, dangerous Higher Order Modes (HOMs) caused by wakefields have to be damped or/and the structure has to be detuned. Differently from long stacked structures with damped cells within the structure [2], the TESLA HOM-damping scheme foresees two couplers attached to both sides of a 9-cell cavity and a single absorber between an 8-cavity module [3]. If HOM-power propagates it can be diminished by the HOM-dampers, but there also may exist some trapped modes which are strongly localised within the cavity. Due to their vanishing field distributions to the ends of the cavity, no strong coupling to the dampers is possible, so they might have considerable influence to the beam dynamics. Therefore we made measurements with a TESLA copper 9-cell cavity following the basic interest to find such trapped modes in the high frequency range.

2 THE MEASUREMENT

2.1 *The Test Setup*

To measure a frequency spectrum in transmission we coupled in the RF-power with an antenna fed through a small hole in the middle plan of the sixth cell of the cavity and coupled out ditto with a second antenna with about 30° distance from the first. The antennas were fixed with the help of brass bases mounted on the surface of the cavity. Hollow waveguide pipes of 78mm diameter and a length of 0,5m were flanged on both sides of the cavity and models of two HOM-couplers and a input coupler were assembled between the cavity and the waveguides. Necessary for the measurement method each pipe was equipped with a movable short, driven by a stepping motor, provide for different boundary conditions. For perturbation measurements we fed a nylon thread through the holes on the axis of the shorts. We used a spherical dielectricum as bead in order to perturbate transversal and longitudinal fields in like manner. Data is taken by a HP8719C network analyzer. The network analyzer and the stepping motors are controlled via GPIB with a computer, using LABVIEW™ and *Mathematica*™ to work up output files.

2.2 *Method*

Compared to propagating modes trapped modes should be less affected by variing the peripheral boundary conditions at the waveguide flanges, due to their vanishing field distributions to the ends of the cavity; thus we started to measure the transmission spectrum in a range of 4...8.2 GHz for several positions of the shorts. By overlaying the measured data, remaining pikes in a spektrum indicate transmission signals (S_{21}) not affected by variing the peripheral boundary conditions. This means low coupling to the waveguide pipes, which is one criterion for trapped modes. Hence, we went in our most stable parts of the spectrum for a bead-pull measurement to confirm whether there are localised modes or not (so far we make no statements about the shunt impedances of the trapped modes). The field measurements were performed using a non-resonant bead-pull method, assuming that for small perturbations holds $E^{\wedge 2} \sim |\Delta S_{21}|$ [4,5].

2.3 *Results*

The following pictures (see fig. 1 and fig. 2) show two measured spectra for different combinations of positions of the stepping motors altogether overlayed in each picture.

0-7803-4376-X/98/$10.00 © 1998 IEEE

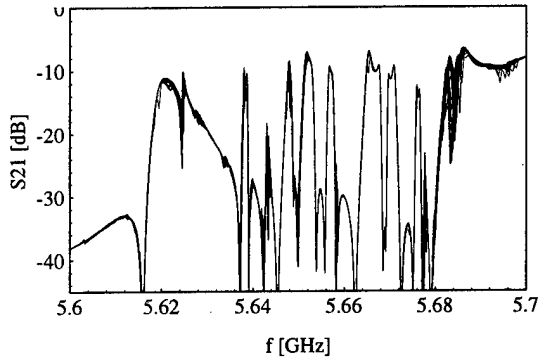


Figure 1: Transmission S_{21} in dependence on frequency for 16 different boundary conditions (f = 5.6...5.7 GHz) .

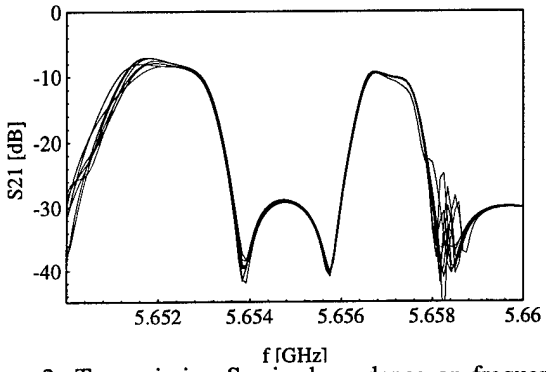


Figure 2: Transmission S_{21} in dependence on frequency for 9 different boundary conditions; zoomed region of fig.1 (f = 5.65...5.66 GHz) . Bead-pull measurements were made at frequencies around the pikes.

The first figure shows a measurement in the frequency range of 5.6...5.7 GHz, where we found some regions with remaining pikes, independent on the positions of the shorts. We examined this regions properly and found some very distinct pikes which are shown in Figure 2.

For perturbation measurements we proceeded in the same manner like we did for the spectral measurements, i.e. measure with different positions of the shorts and overlay measured data (at a given frequency). For all measurements we took 401 positions along the structure and 9 different boundary conditions, moving the shorts along almost the maximum lengths of the waveguide pipes. For some special frequencies located around the pikes, imaged in fig.2, we made bead-pull measurements, to investigate wether fields are concentrated within the inner part of the cavity. Figure 4 shows our result for a frequency of 5.6524 GHz. To get information about the location of the single cavity cells, refer to fig.3, where results of a bead-pull measurement for the accelerating π-mode of the TESLA cavity at 1.3003 GHz is shown (we index cell 1 to 9 from left to right). If we compare both figures, we observe no field distribution at the end cells but in the inner cells, i.e. a trapped mode. Notice the steep decrease of coupling from cell 8 to 9. We also found a localised mode in the adjacent pike at a frequency of 5.6572 GHz (see fig. 5).

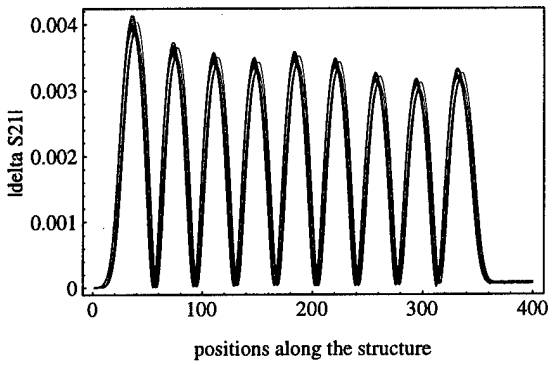


Figure 3: Bead-pull measurement at the accelerating π-mode f=1.3003 GHz of the TESLA cavity; pikes give location of the single cells.

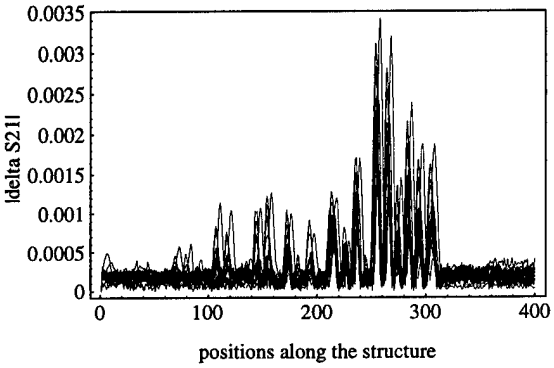


Figure 4: Bead-pull measurement at f=5.6524 GHz.

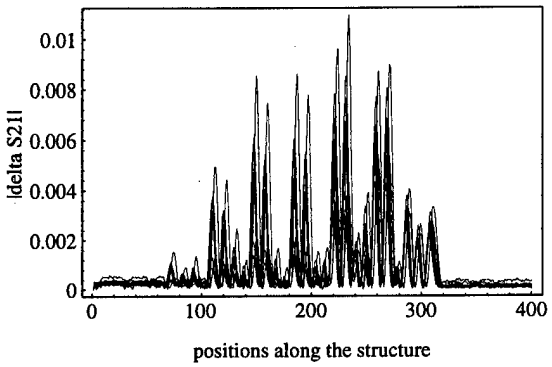


Figure 5: Bead-pull measurement at f = 5.6572 GHz.

In fig. 7 one of the mostly occuring examples of a proof to the contrary is demonstrated, where a spectral measurement (see fig. 6) still shows a pike hardly influenced by the positions of the shorts at 7.4167 GHz, though the field distribution is not localised and strongly dependent on the boundary conditions. Finally in fig. 9 another localised field distribution, found at the frequency of 8.1727 GHz, is displayed (refer to the corresponding spectral measurement illustrated in fig. 8).

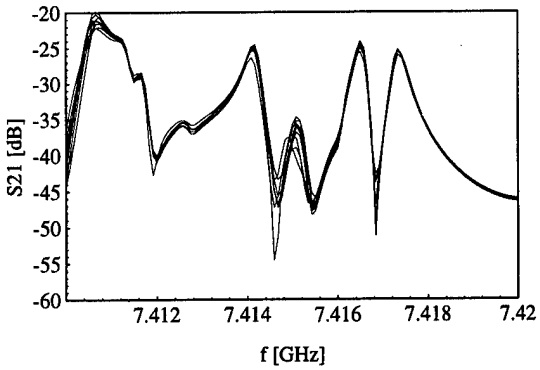


Figure 6: Transmission S_{21} (f = 7.41...7.42 GHz).

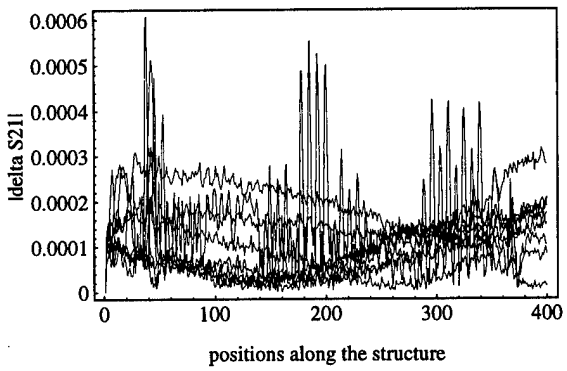


Figure 7: Bead-pull measurement at f = 7.4167 GHz.

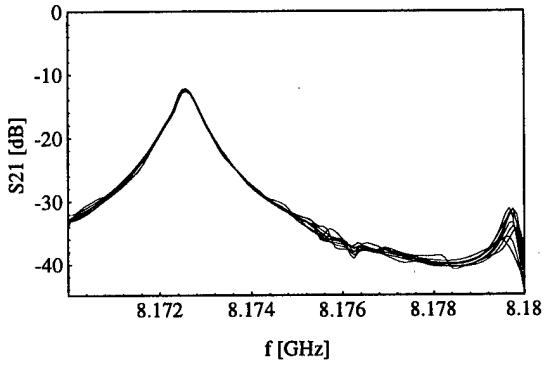


Figure 8: Transmission S_{21} (f = 8.17...8.18 GHz).

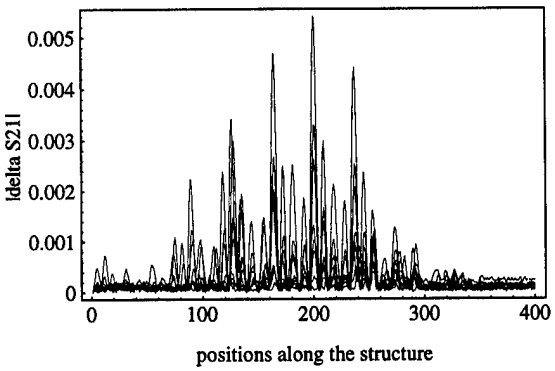


Figure 9: Bead-pull measurement at f = 8.1727 GHz.

2.4 Accuracy

Since the fundamental cut-off frequency of the waveguide pipe (d=78mm) appear at 2.254 GHz (TE11-Mode), the field distribution for the accelerating mode of the cavity at 1.3003 GHz vanishes exponentially in the waveguide pipes. Hence, only very small influences of boundary variations should appear in fig. 4. The amount of remaining fluctuations comes mainly from thermal drifts, we tried to avoid as far as possible by covering the structure with polystyrene, mechanical tensions and oszillations of the bead, provoked from movements of the stepping motors itself or other mechanical excitations.

On the other hand the influence of the antennas, fed in the sixth cell, change its resonant character due to the changed geometrie and hence can lead to the effect of trapped modes which would not be the behaviour of the hollow cavity itself. For further investigations we are going to take remedial measures by variing the depth of the antennas or couple into one of the adjacent cells to prove whether the trapped modes found remain localised.

3 CONCLUSION

In cavities without dampers in the inner part of the structure trapped modes can hardly be damped and hence can strongly affect beam dynamics, especially if they are superconducting. We recently started to search for trapped modes in a copper TESLA cavity. Up to now we found three of them in the frequency range of 4...8.2 GHz. From our experience they occur very rarely but the existence of more than the ones shown cannot be excluded. So far we have no results about shunt impedances of the trapped modes, so that further investigations have to be done.

4 REFERENCES

[1] R. B. Palmer:"Prospects for High Energy e^+-e^- Linear Colliders, SLAC-PUB-5195, Stanford 1990

[2] W.F.O. Müller, P. Hülsmann, M. Kurz, C. Peschke et al. :"Measurements and Numerical Calculations on Higher-Order-Mode-Dampers within a Stack of 36 detuned S-Band-Cells", Proceedings of the XVIIIth International Linac Conference, Geneva (Suiss), 1996

[3] D.A. Edwards (Ed.):"Tesla Test Facility Linac", Design Report (TESLA-Rep. 95-01), DESY, Hamburg March 1995

[4] P. Hülsmann, M. Kurz, H. Klein:"Experimental Determinition of Field Strength and Quality Factor of heavily Damped Accelerator Cavities", Electronic Letters, Vol. 27 No. 19, pp. 1727-1729, 12.09.91

[5] M. Kurz:"Untersuchungen zu mikrowellenfokussierenden Beschleunigerstrukturen für zukünftige lineare Collider", thesis, Frankfurt am Main, 1993

5 SUPPORT

(work supported by DESY/Hamburg and BMBF under contract 06of359)

DEVELOPMENT OF C-BAND (5712 MHz) HIGH POWER WAVEGUIDE COMPONENTS

H. Matsumoto, T. Shintake, N. Akasaka, KEK High Energy Accelerator Research Organization, 1-1 Oho, Tsukuba, Ibaraki, 305, Japan and H. Baba, A. Miura, Nihon Koshuha Co., Ltd., 1119 Nakayama, Midori-ku, Nakayama, Kanagawa, 226, Japan

Abstract

High Power waveguide components at C-band (5712 MHz) frequencies have been developed for a main linac of e^+e^- linear collider range of 300-500 GeV C.M. energy. 350 MW of maximum rf power has to be transmitted through the waveguide components. An EIA-WR187 (W: 44.55 mm, H: 22.15 mm and t: 4 mm) type sized conventional rectangular waveguide was chosen to reduce transmission loss to about the same order of magnitude as with existing S-band waveguide. The thickness of the wave guide was fixed to make for easy machining, and assembling for the brazing process.

A vacuum waveguide flange of unisex type with a simple shape was successfully developed. A Beth-hole type coaxial coupler, E- and H-corner, directional coupler, vacuum pumping port, 3-stub tuner, viewing port and phase shifter were successfully developed all with input VSWRs of less than the 1:1.1.

1 INTRODUCTION

For an e^+e^- linear collider with a center of mass energy of 300 to 500 GeV, the main linac will use some 2040 rf acceleration units [1]. Each unit is comprised of two 50 MW klystrons, two modulator power supplies, one rf compression system of a new design, the waveguide system, four choke-mode type damped accelerating structures and their supporting girder. The total component count is extremely large and no laboratories have any experience yet in the operation of so many accelerator devices. Thus, it is very clear that the preeminent considerations are to make the system simple, highly reliable, of higher efficiency and lower cost.

In the C-band main linac, a maximum rf power of 350 MW has to be transmitted through the waveguide system to drive the accelerating structures with 32 MV/m. The high voltage break-down is dominated by the total rf voltage between metallic surfaces in the waveguide. The waveguide impedance at C-band takes on similar values at S-band. Therefore, the gap voltages in C-band waveguide need not take higher value than the S-band. According to some experience at S-band frequency, power levels of 350 MW should not cause any difficulty for stable operation. At the C-band frequency of 5712 MHz, there are two choices for waveguide size: one is EIA-WR187 (3.93-5.85 GHz), the other is EIA-WR159 (4.9-7.05 GHz). EIA-WR187 which has an inner cross section of 44.55 mm wide and 22.15 mm high was chosen over the larger waveguide because it can have an rf power transmission loss close to that of existing S-band waveguide. The theoretical rf transmission losses in rectangular waveguides of EIA-WR187 (at 5.712 GHz) and EIA-WR284 (at 3 GHz, 72.1 × 34.0 mm) are –0.032 dB and –0.021 dB, respectively. Fortunately the C-band main linac can use conventional rectangular type waveguide pipe. Further, the C-band high power rf system does not require any special components. Thus, it should be producible at the same reliability and cost as S-band.

However, there is no standard for C-band high power waveguide components, especially as high a peak rf power as 350 MW in vacuum. Thus, many components will have to be developed, but most of the design work will be straightforward without any particular limitations. Figure 1 shows a photograph of the directional coupler.

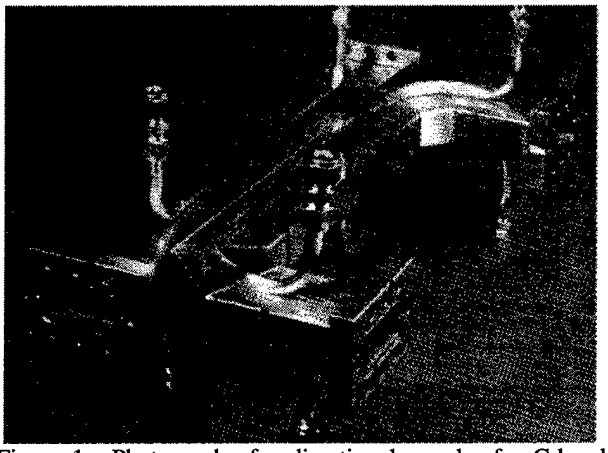


Figure 1: Photograph of a directional coupler for C-band frequencies.

This paper will describe the design concept and performances of wave guide components.

2 WAVEGUIDE COMPONENTS

2.1 Rectangular waveguide pipe

The raw materials of the waveguide use high quality OFHC (Oxide-Free High Conductivity) copper with a purity of > 99.96%, because one of the main reasons for rf breakdown is poor quality inner surfaces – insufficient purity of the raw copper material and it cleanness. Table 1 lists the chemical compositions of the copper material.

The rectangular waveguide is made by a cyclic extrusion process the first step to make a thick circular pipe from a copper bar, which is then gradually formed to shape by 7 more cycles of the pulling processes.

Table 1: Chemical compositions of copper. (%)

Pb	Zn	Bi	Cd	Hg
<0.005	<0.0001	<0.001	<0.0001	<0.0001
O_2	P	S	Se	Te
<0.001	<0.0003	<0.01	<0.001	0.001

0-7803-4376-X/98/$10.00 © 1998 IEEE

A 3 m length was chosen as the unit length of the waveguide so that dimensional accuracy could be maintained. Also a 4 mm waveguide thickness was chosen to allow using a common jig to join each element in the brazing process. Typically a dimensional accuracy of <±0.1 mm and a surface roughness in the range of ~0.13-0.23 μm (rms.) at the center cross section of the waveguide is obtained. From the results of some experiments at S-band, it is clear that there will be no problem in actual operations at high peak rf power.

2.2 Waveguide vacuum flange

In this work, one of the important goals was to make a standardized waveguide vacuum flange. This important component has to serve in two roles as both an rf seal and a vacuum seal. Further, the most commonly occurring problems such as discharge breakdown and vacuum leak often happen near the flange gasket. A new type unisex waveguide flange has been developed to increase reliability and reduce cost; it comes from a modified DESY type S-band flange as shown in figure 2 [3]. As can be seen in the figure, the gasket edge has a simple shape for easy machining and the optimum compression forces produces zero gap at the outside of the flange. The loss in flatness between the flange and gasket along the inside wall is within 50 μm when there is zero gap in the outer wall between the flanges.

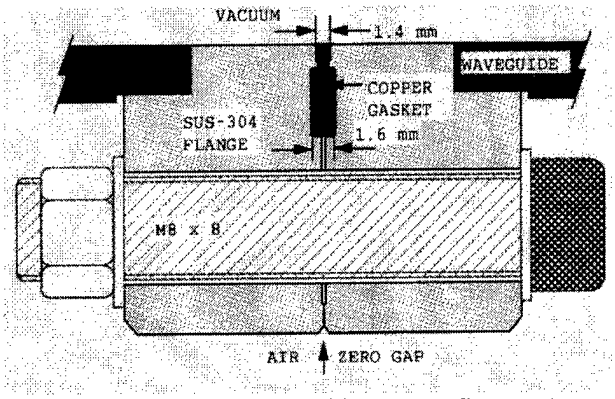


Figure 2: Unisex type waveguide vacuum flange. An expanded view of part of the gasket edge.

2.3 RF Window

The lifetimes of existing high peak power klystrons are typically at most around 4×10^4 hours on average; failures are caused mostly by broken rf window ceramics and insulation breakdown of the electron guns. In the C-band linear collider, more than 4000 klystrons will be used for the two main linacs. Thus, klystron replacement work has to be done without interrupting accelerator operation. It should be also noted that the aging process of an accelerating structure takes roughly one day, once the vacuum is broken. In order not to compromise the operational efficiency, a need arises for rf-windows that allow replacing klystrons without opening the accelerator vacuum system.

2.3.1 Ceramic material

There are three important technologies to make robust alumina ceramic for the high peak power rf windows: (1) use high quality alumina powder which has a fine grain size of <0.8 μm with 99.99% of purity, (2) eliminate the voids inside the ceramic even those whose sizes are on the order of a few micro-meters, and (3) use low rf loss sintering binder materials. Micro-voids between the ceramic grain boundaries and large amounts of Magnesium (Mg) are the main reasons for the discharge breakdown problem in high peak power rf windows [3]. For our work, a Hot-Isostatic-Pressing process was used to eliminate the micro-voids resulting in a reduction from 3.8% to less than the 0.5% by volume weight. The Mg in the sintering binder was successfully reduced to 0.06% by volume weight.

2.3.2 Structure of the window

A pill-box shaped traveling-wave rf window was designed for the 50 MW C-band klystron; it will be used for the two rf windows connected at each output port. The window has a diameter of 57 mm, length of 72.85 mm and a 3.85 mm thick ceramic disk. The design was made to have no TE22 or TE51 resonance modes at 5.712 GHz. For this design, the most important considerations were in reducing the electrical field strength at the window ceramic disk by choosing a traveling-wave structure, and the use of very high quality ceramic disks. Figure 3 shows the electrical field distributions in steady state and the frequency response of the rf window.

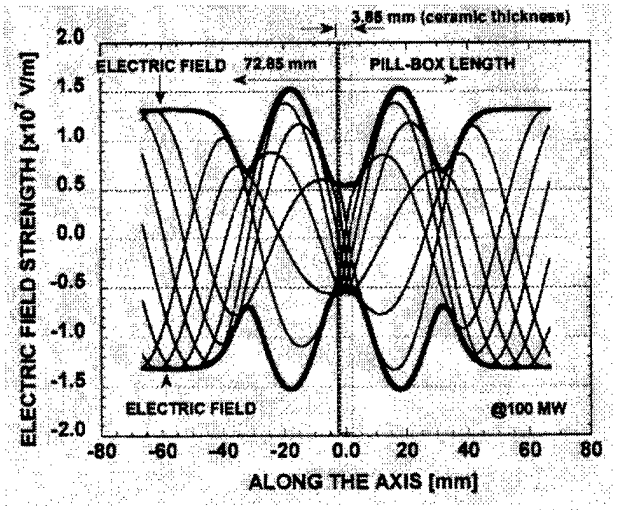


Figure 3: Electrical field strength. Two thick solid lines shows the electrical field strength along the axis.

As can be seen in the figure, the envelopes of the electrical field strength are reduced just at the ceramic disk. The frequency bandwidth where the reflection coefficient is 0.1 or less is 500 MHz as shown in figure 4. These characteristics will be good enough for the 50 MW klystron. Thus from the R&D results at S-band frequency, it will be good enough to apply 50 MW of peak rf power at C-band.

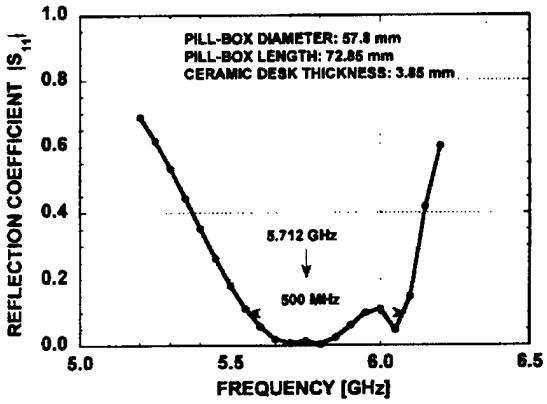


Figure 4: Frequency bandwidth of traveling-wave type pill-box window.

2.4 Traveling wave resonator

The design and fabrication of a Traveling Wave Resonator (TWR) is very useful in developing the key technologies for unknown, variable frequencies, because it is composed of several necessary high power waveguide components such as a directional coupler, a phase-shifter, a stub tuner, a pair of the Beth-hole couplers, two vacuum pumping ports, two viewing ports, E- and H-corners. The parameters of our TWR are shown in Table 2.

Table 2: C-band TWR parameters

Physical size	166 cm × 75 cm
Resonant loop length	~300 cm
Number of wavelengths	48 at 5.712 GHz
Input coupler ratio	-12 dB
RF power gain	12.3 dB
One-way loss in loop	0.11 dB
Variable phase shifter range	±180° at 5.712 GHz
5 elements stub tuner range	$\Gamma < 0.13$ at any phase

This TWR was designed with no specific upper peak rf power handling capability, but it had to be operational at a minimum peak rf power of 150 MW. To guarantee the performance of the rf window in the TWR, the window has to operate even with an overload condition of three times higher than the actual operational output power from klystron. For the moment, 5 MW of rf power will be fed to the TWR from a 5 MW klystron that was received from SLAC. In this case, the rf window of the C-band klystron will test the rf power up to 85 MW, that will be good enough to check the performances of the rf windows for the 50 MW klystron.

In general, the upper limit of rf power handling capability of the TWR would be set by breakdown in one of the tunable components such as the phase-shifter, or the 5 elements of the sub-tuner or the gasket of the vacuum flange [4]. Most TWRs use a variable phase-shifter consisting of a pair of movable multistage choke short plungers with a 3 dB hybrid coupler which usually has rectangular cross section. Thus, the movable choke short plungers have to be aligned to the same gaps with less than a 1 mm error on both horizontal and vertical over the full stroke, that is very hard work even at the S-band frequency. Therefore, it was decided to try to use a circular waveguide (TE11 mode) for the pair of movable shorting plungers as shown in figure 5.

Using circular waveguide will reduce the difficulties in fabrication as well as increase the breakdown limit. The phase shifter has 360° of tuning range with an input VSWR within the 1:1.1. The rf pickup monitor used is based on the Beth-hole type directional coupler with a demountable structure. The vacuum seal between waveguide and coupler head used a ceramic disk (t: 1.5 mm and ϕ: 24 mm) with a metal o-ring gasket, it does not require any brazing process. The other components have already been done by this time. High power operation of the TWR will be started beginning in June 1997.

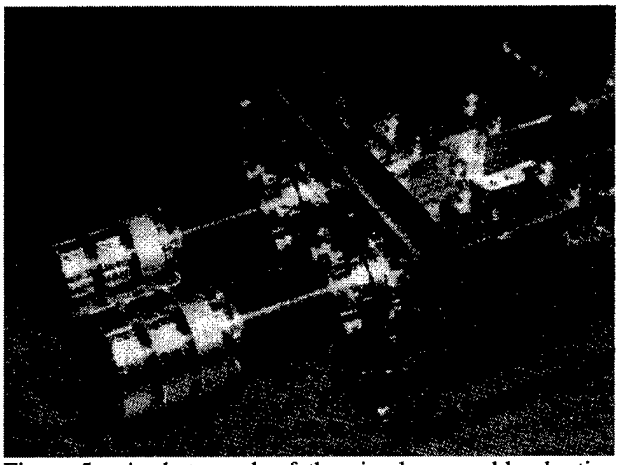


Figure 5: A photograph of the circular movable shorting plungers.

3 CONCLUSIONS

C-band high power waveguide components were successfully developed with a very conventional rectangular waveguide which further does not require any special structure. It was confirmed that the unisex waveguide vacuum flange is very useful to make the system simple as well as to reduce the cost. Thus, the total system cost would be reduced as compared with an existing S-band frequency accelerator with same reliability criterion.

4 REFERENCES

[1] T. Shintake, *et al.*, 'C-band main linac rf system for e^+e^- linear collider of 0.5 to 1.0 TeV C.M. energy', Linear Accelerator Conference 1996, p184-186

[2] N. Holtkamp, DESY, private comments at 1995

[3] A. Miura and H. Matsumoto, 'Development of an S-band rf window for linear colliders', NIM-A334(1993)341-352

[4] W.R. Fowkes, *et al.*, 'High power rf window and waveguide component development and testing above 100 MW at X-band', Linear Accelerator Conference 1992, p184-186

DEVELOPMENT OF C-BAND 50 MW PULSE KLYSTRON FOR e^+e^- LINEAR COLLIDER

T. Shintake, N. Akasaka, H. Matsumoto, KEK High Energy Accelerator Research Organization and
Y. Ohkubo and H. Yonezawa, Toshiba Co., Japan

Abstract

Hardware R&D for the C-band (5712 MHz) RF system was started as a KEK research program for the e^+e^- linear collider project in 1996[1]. In order to achieve 500 GeV C.M. energy at the e^+e^- collision within 25 km site length, the C-band system requests 4080 tubes of 50 MW pulse klystron, which drives the accelerating gradient 32 MV/m at the full beam current. The first 50 MW class klystron at C-band was designed and fabricated (named Toshiba E3746).

1 INTRODUCTION

The e^+e^- linear collider is a large scale machine. In the main linacs for 500 GeV C.M. stage, we use more than 8000 accelerating structures, 4000 klystrons and pulse modulators. Therefore, the system must meet the following demands.

(1) High reliability.
(2) Lower construction cost.
(3) Simple.
(4) Reasonable power efficiency.
(5) Easy to operate.

Above list provides main guide-line and boundary conditions to our design work. Among the design parameters, the choice of the drive rf frequency plays most important role concerning the total system performance as well as the hardware details. We proposed C-band as the best frequency[1]. Reasons are

(1) Fabrication tolerance of the accelerating structure is not so tight. The straightness tolerance is 30 μm for 1.8 m long structure.

(2) RF pulse length to be generated from a klystron is about 2.5~3.0 μsec. HV pulse power supply for the klystron is easy to generate this pulse length, and we can use a conventional line-type modulator.

(3) Klystron can be made as an extension of existing S-band klystrons.

The item (3) will be discussed in the next section in detail.

2 CHOICE OF MAIN PARAMETER

To do optimum design of a high-power klystron, we scaled operating parameters of the existing S-band klystrons to the C-band frequency. Generally speaking, design of the high-power klystron becomes harder at higher frequency bands, and its power rating becomes lower. C-band frequency is twice higher than S-band, thus we have to limit the design target of the output power lower than the existing S-band tubes. To keep the same level of tube reliability or even better, we laid two boundaries.

(1) Gun Voltage

Use the same level or even lower gun voltage than the most reliable klystrons at S-band. We believe that in the pulsed power klystrons, possibility of HV breakdown in gun region, or idler cavities and the output gap, is a sensitive function of the beam voltage. From the experience on Toshiba E3712-klystron (80 MW, 375 kV), or SLAC 5045-klystron (50 MW, 350 kV), we chose the gun voltage around 350 kV.

Lower voltage design needs higher beam current. The power conversion efficiency tends to be lower in a higher beam current klystron due to the space charge force acting on bunch. We took the reliability issue as the first priority than the power efficiency in our design.

(2) Beam energy per pulse ($VI\tau$)

From a view point of the power handling in a tube, it is reasonable to limit the total beam injection energy lower than a certain amount. If a part of the high power beam collides to the drift-tube wall or an interaction gap, and the power density is high enough, the copper material can be melted or vaporized, it resulting in HV breakdown in the output gap or other high-field regions. Since the drift tube diameter scales as inverse of the rf frequency, the $VI\tau$ energy scaling becomes

$$VI\tau \propto D^2 \propto \omega^{-2}$$

From the operational experience in S-band klystrons, we found the safety value for C-band klystron as 300~400 J/pulse. The HV pulse length to be applied is 3.5 μsec, and the power efficiency is 45 %, the safety level of the peak power at C-band becomes 50 MW.

Table-1 shows the design parameter and target performance.

Table-1. Main Parameter of E3746 klystron.

Parameter		Unit
Frequency	5712	MHz
Output Power	50	MW
Beam Voltage	350	kV
Beam Current	317	A
Microperveance	1.5	$A/V^{1.5}$
Gain	> 50	dB
RF Pulse Width	Max. 3	μsec
Pulse Repetition	100	pps

0-7803-4376-X/98/$10.00 © 1998 IEEE

3. ELECTRON GUN

To maintain a long lifetime, it is better to keep the maximum loading of the cathode emission lower than 10 A/cm^2. Assuming the power conversion efficiency as 45 %, and gun voltage 350 kV, the required beam current becomes 320 A. Therefore, the minimum required cathode area is 32 cm^2, or a diameter of 64 mm. We use a cathode diameter of 74.5 mm, then the average cathode loading becomes a quite safe value of 6.3 A/cm^2.

Using the computer simulation code EGUN, the gun geometry was optimized to obtain a laminar flow with desired beam envelop.

The designed parameters are listed in Table-2. The maximum electric field is 22.1 kV/mm, which is same level as that in S-band klystrons such as the SLAC 5045 or Toshiba E3712.

In order to eliminate a diode oscillation associated with a high-Q resonance in the small gap around the cathode element[2], we made the volume of the cylindrical pocket as small as possible.

Table-2 Electron Gun Parameter

Parameter		unit
Microperveance	1.5	$\mu A/V^{1.5}$
Cathode Diameter	74.5	mm
Cathode Loading (average)	6.3	A/cm^2
Type of Cathode	Dispenser Scandate	
Focused Beam Diameter	10	mm
Beam Area Convergence	56:1	
Electric Field on Anode	22.1	kV/mm
on Whenelt	21.7	kV/mm

4. DRIFT-TUBE AND BEAM FOCUSING

Larger size of the drift-tube makes the electron gun design easier and focusing field lower, but it makes danger against spurious oscillation due to positive feedback loop driven by propagating or trapped mode inside the drift-tube. To chose the drift-tube diameter, we basically scaled from S-band tube.

Table-3 summarizes the drift-tube parameter. We use 15 mm diameter at upstream and 16.3 mm at downstream. The Bessel function $J_0(ka)$ value is close to 1.0, which means the interaction gap can keep good coupling to the beam[3].

As listed in the table, the TE11 cutoff frequency at downstream is lower than the operating frequency. In principle, TE11 mode does not interact with a beam in a smooth beam pipe, but it can create a small coupling impedance at a transition of beam pipe or an interaction gap, which sometimes causes a parasitic oscillation in a high current klystron. To avoid this type of oscillation, an rf damper (a small piece of stainless-steel pipe) was inserted at the beam pipe transition taper.

This klystron uses a solenoid focusing. The perfect Brillouin field is 1.13 kG to focus the beam of 10 mm diameter. To maintain beam stability we apply 2.6 kG maximum at upstream, and 2.4 kG at downstream.

Table-3 Drift-tube and Focusing Parameter

Parameter		1st~3rd cavity	4th~5th cavity	
Drift Diameter	2a	15	16.3	mm
Beam Diameter	2Rb	10	10*	mm
Wave Number	ka	0.90	0.97	
Bessel Function	J0(ka)	0.81	0.78	
Cutoff Frequency	TE11	5.86	5.39	GHz
	TM01	7.65	7.04	GHz
	TM11	12.2	11.22	GHz
Brillouin Field	Bz	1.13		kG
Focusing Field	Bz	2.6	2.4	kG

5. INTERACTION CAVITIES AND BEAM SIMULATION

E3746 is a five cavity klystron: the input, 2 gain cavities, the penultimate and the output cavity, whose parameters are listed in Table-4. To optimized those parameters, we used FCI (Field Charge Interaction 2+1/2 PIC code). Example result of the simulation is shown in Fig. 1. FCI said the expected output power is 49.1 MW and the power efficiency is 44.3 %.

Table-4 Interaction Cavities

	Type	Frequency (MHz)	Q	R/Q (Ω)
Input	Reentrant	5712	350	67.3
2nd	Reentrant	5725	2000	62.5
3rd	Nose-less[3]	5738	2000	57
4th	Nose-less	5847	2000	64.2
Output	Nose-less	5712	27.5	79

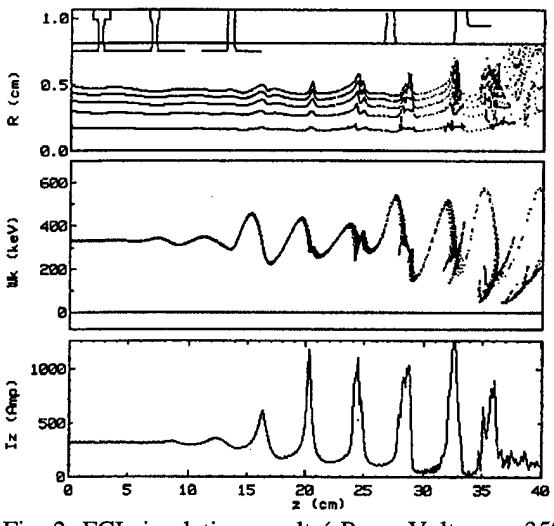


Fig. 2 FCI simulation result (Beam Voltage = 350 kV, Beam Current = 317 A, Drive Power = 250 W, Output Power = 49.1 MW, Power Efficiency = 44.3 %).

6. OUTPUT GAP

6.1 Output Gap Impedance

The output gap extracts the rf power from the beam, as a reaction the beam is decelerated by the rf field. To make the power efficiency maximum, we need to design the output gap at the impedance matching condition. From the equivalent circuit analysis, the optimum impedance is given by

$$Z_{opt} = (R/Q)Q_L = \frac{V_c}{MI_{\omega 1}} = \frac{V_{deceleration}}{M^2 I_{\omega 1}} \quad (1)$$

$V_{deceleration}$ is the beam deceleration voltage, which is usually close to the beam voltage: $V_{deceleration} = 0.8 \sim 0.9 V_{DC}$. $I_{\omega 1}$ is the rf current on the beam, which takes 1.5 or higher value right before the output gap, and it decays inside the output gap. As an average, we assume $I_{\omega 1} = 1.1 \sim 1.3 \cdot I_{DC}$. M is the coupling constant, in our case $M = 0.62$. From eq. (1), the optimum impedance becomes 1.7 ~ 2.3 kΩ. Togather with the FCI simulation, we decided the impedance at 2.2 kΩ.

6.2 Output Structure Design

Figure 2 shows the output structure, which has two output arms, they are combined again at the external circuit after two ceramic rf-windows. The rf-window is so called the traveling-wave type, newly developed as a part of C-band waveguide R&D[4].

The external-Q was determined by the Slater's method on the MAFIA 3D simulation, and the iris size was decided to meet the desired value. According to the *R/Q* calculation, there is always some ambiguity in estimating the stored energy in the cavity, because some field leaks into the waveguide, and we can not clearly define the cavity volume. We solved this problem by recognizing the total system of the output cavity and waveguide as a coupled cavity system. It has 0- and π-modes according to those phase. We calculate the shunt impedance in each mode. According to the coupled cavity model, the intrinsic shunt impedance of the gap is simply given by

$$(R/Q)_{cav} = (R/Q)_{0-\text{mode}} + (R/Q)_{\pi-\text{mode}}.$$

Using this method, the shunt impedance was determined to be 79 Ω, then the cavity impedance becomes 2.18 kΩ.

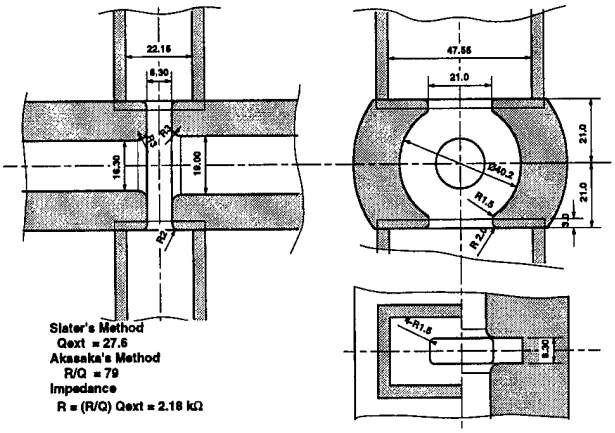


Fig. 2 Output Structure.

7 HIGH POWER TEST AND FUTURE R&D

The high power test is scheduled in June 1997. For the next step, we will try to replace the output cavity by a 3-cell traveling wave output structure[5], in which the field gradient becomes almost half of the single gap design. Additionally, we use the Choke-Mode Cavity[6] in the traveling-wave output structure to damp all of the higher order modes.

7 ACKNOWLEDGMENTS

The authors would like to acknowledge the supports of Prof. Hirotaka Sugawasa, Prof. Yoshitaka Kimura and Prof. Yoshishige Yamazaki to the C-band R&D project.

REFERENCES

[1] T. Shintake et. al., "C-band RF Main Linac System for e^+e^- Linear Collider at 500 GeV to 1 TeV C.M. Energy", Proc. of EPAC96, pp.492-494.

[2] U. Becker et. al., "Simulation of Scillation in High Power Klystrons", Proc. of EPAC96, pp.1274-1276.

[3] T. Shihtake, "Nose-Cone Removed Pillbox Cavity for High-Power Klystron Amplifiers", IEEE Trans. Electron Devices, Vol.38, No.4, April 1991

[4] H. Matsumoto et. al., "Development of C-band (5712MHz) High Power Waveguide Components", contributed to this conference.

[5] T. Shintake, "Recent Status of FCI: PIC Simulation of Coupled-Cavity Structure", Proc. of Linac96, pp.181-183

[6] T. Shintake, "The Choke Mode Cavity", Jpn. J. Appl. Phys. Vol. 31(1992) pp. L1567-L1570

INPUT COUPLER DESIGN FOR C-BAND ACCELERATING STRUCTURE

C. Suzuki, Nagoya University, Department of Physics, Nagoya, 464-01, Japan,
N. Akasaka and T. Shintake, KEK , 1-1 Oho, Tsukuba, 305, Japan

Abstract

To increase an electric field symmetry in a coupler cavity, a very simple structure of two-iris coupler cavity was proposed by H. Matsumoto in 1994. MAFIA 3D code is useful to simulate Slater's tuning curve method, which is used to determine the dimensions of the coupler cavity such as iris aperture and cavity diameter. It was find that MAFIA simulation results show that two-iris method will realize a good symmetrical electric field with very simple structure as well as no difficulties for fabrication. This type of double feed coupler will be used for Choke-mode type damped accelerating structure at C-band (5712 MHz) and rf-gun for linear collider.

1 INTRODUCTION

An e^+e^- linear collider such as energy range of 0.5 to 1 TeV C.M. will require very high luminosity of several times of $10^{33}/cm^2/s$ necessary for physics experiment. Multi-bunched beam operation will be essential to obtain such high luminosity. Thus, it is very important to accelerate a low emittance beam in a main linac to achieve a nano-meter size beam at collision point. However, this is not easy because of the wake field power that accumulates in the accelerating structure.

Choke-mode damped structure at C-band frequency was proposed by T. Shintake in 1992, that will positively eliminate the wake field in the structure [1]. An S-band Choke mode structure was tested up to the maximum accelerating gradient of 50 MV/m with beam loading in 1994 at KEK-ATF (Accelerator Test Facility) with no problem [2].

The field asymmetry due to the coupling iris can be a serious problem. It will kick the beam during passage through the coupler cavity even if the beam is aligned to the cavity axis, leading to the emittance growth.

To eliminate the field asymmetry in the coupler cavity, two-iris coupler came back again at several laboratories such as DESY, KEK, and SLAC with different feeding methods [3,4,5]. An original idea was proposed at SLAC when they planed the two mile linear accelerator, but there has been no actual application until recently years.

In 1994, two-iris coupler cavity, such as shown in figure 1, was proposed by H. Matsumoto to apply the accelerating structure and rf-gun. As can be seen in the figure, its structure is very simple and it requires no additional equipment such as a power divider. It was tested up to the accelerating gradient of 60 MV/m without any problem at S-band frequency [6]. It is very clear that important considerations on the design of coupler cavity is not only the field symmetry but the simplicity of the structure, because no laboratories have any experience on more than 8000 accelerating structures in one accelerator.

This paper will describes the design procedures of the coupler cavity for C-band Choke-mode structure using the Slater's tuning curve method with MAFIA 3D code.

2 C-BAND ACCELERATING STRUCTURE

The main parameters of the accelerating structures for the C-band linear collider at the energy of 500 GeV C.M. are listed in table 1 [6]. The short-range wake-field is a strong function of the beam aperture ($2a$), approximately proportional to $a^{-3.5}$ [7]. To prevent the single-bunch emittance growth, relatively large beam aperture is chosen compared to conventional structures. The average $2a$ (16 mm) allow alignment tolerance of 30 μm, which can be achieved with conventional fabrication techniques of the disk loaded structure. Two 50 MW klystrons with an rf-compression system is planned to generate the accelerating gradient of 31 MV/m (including beam loading) at the beam aperture. The two-iris coupler was designed according to these parameters.

Table 1: Parameters for accelerating structure.

Frequency	f_0	5712	MHz
Phase shift per cell	βD	$3\pi/4$	
Field distribution		C.G.	
Number of cells		91	Cell
Active length		1.8	m
Quality factor	Q	9950	
Average shunt impedance	Rs	53.1	MΩ/m
Attenuation parameter	τ	0.53	
Filling time	t_f	286	nsec
Groupe velocity up-stream	v_g/c	0.035	
down-stream		0.012	
beam aperture up-stream	$2a$	18.2	mm
down-stream		13.1	
Inner diameter up-stream	$2b$	44.7	mm
down-stream		42.5	

3 DESIGN OF COUPLER CAVITY

3.1 Concept

Figure 1 shows the coupler cavity and the 1st regular cavity. Two irises are located on opposite sides of the caivty at vertical direction in the figure, connected to the

0-7803-4376-X/98/$10.00 © 1998 IEEE

narrow wall of a J-shaped rectangular waveguide. The dimension of the J-shaped waveguide is determined as follows: (1)The width is chosen so that the phase length between the two irises is $2\lambda_g$. (2)The radius is set as large as possible to minimize the internal reflection. (3)The height is the same as the iris to allow accurate fabrication. A standard rectangular waveguide EIA-WR-187 (47.55x22.15 mm) is used to feed the rf power.

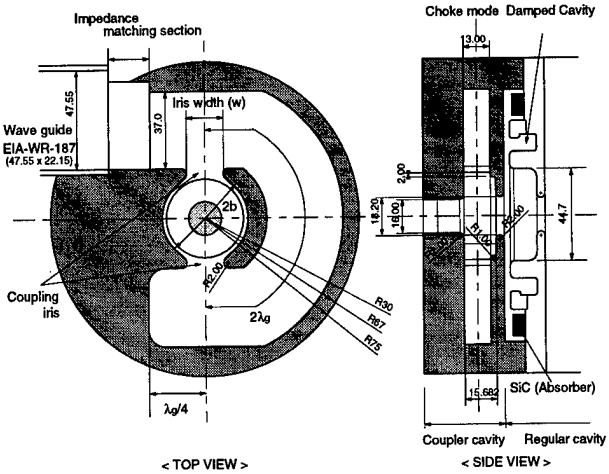


Figure 1: Cross sections of C-band accelerating structure.

A simplified equivalent circuit model of the two-iris coupler is shown in figure 2. This type of coupler uses the conventional impedance change along waveguide [5]. The suceptances iB_1 and iB_2 correspond to the irises. The length between the two irises is chosen as $n\lambda_g$ (n=1,2,3...), and the length from the short end to the second iris is $m\lambda_g/4$ (m=1,3,5...). Then the impedance of the short end seen from the irises become infinite. Finally, when the loss of transmission line between iB_1 and the short end is negligible this system can be modified to a simle parallel circuit and the same power is fed into the cavity from the two irises.

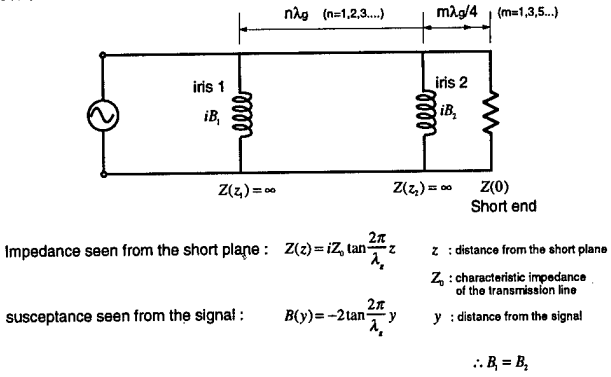


Figure 2: Simplified equivalent circuit model of two-iris coupler.

3.2 Design parameter for coupler cell

According to the equivalent circuit analysis on the coupled-cavity model [8], resonant frequency f_c is given by

$$f_c = f_0\left(1+\frac{1}{2}k\cos\beta D\right),$$

where f_0 is the rf-frequency (5712 MHz) and k is the coupling constant between the input coupler cavity and the 1st regular cavity. The external Q (Q_{ext}) is expressed as

$$Q_{ext} \approx \frac{\beta D}{v_g / c}.$$

Using these equations and table 1, coupler cavity parameters are calculated as listed in table 2, where k was given by the relation $v_g / c = \frac{1}{2}k\beta D\sin\beta D$.

Table 2: Parameters for coupler cavities.

		Input	Output
Frequency (MHz)	f_c	5627.2	5682.9
External Q	Q_{ext}	67.3	196
Coupling constant	k	0.0420	0.0144

4 DESIGN WORK OF COUPLER CAVITY

The dimensions of the coupler cavity was determined by 3D-MAFIA code to obtain the target values of f_c and Q_{ext}. First, the guide wavelength was set to $2\lambda_g$ at 5712 MHz adjusting the waveguide width. Next, the coupling iris width (w) and inner diameter ($2b$) were determined by Slater's tuning curve method.

4.1 Waveguide width

To obtain the guide wavelength of $2\lambda_g$ at 5712 MHz, the resonant frequency of the waveguide was calculated by changing the waveguide width. The geometry used in the calculation is shown in figure 3. From this calculations, determined width is 37.0 mm. In this case the attenuation is as small as 0.06 dB/m. To confirm the absence of internal reflection, the resonant frequencies under the electric and magnetic boundary conditions were compared. Their differences was within 10 MHz, which indicates that no critical reflection occurs.

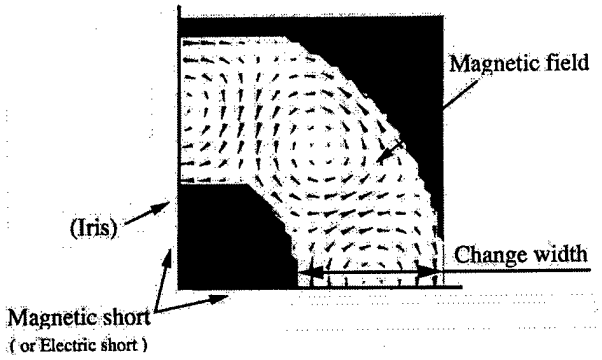


Figure 3: Geometry used in waveguide calculation by MAFIA. The arrows indicate the magnetic field under magnetic boundary condition.

4.2 Resonant frequency and external Q

The Slater's tuning curve method was used to determine f_c and Q_{ext} [9]. In this theory, external Q is related to the frequency change of the resonance according to the distance between the center of iris and short end. The geometry used in the calculation is shown in figure 4. The differential coefficent $dd/d\lambda g$ of the tuning curve takes its maximum value at f_c. The external Q (Q_{ext}) is calculated from $dd/d\lambda g$ at f_c. The calculated values of f_c and Q_{ext} for various w and $2b$ are shown in figures 5 and 6. The solid and dashed lines in figure 7 show the relation between $2b$ vs w with f_c=5627.2 MHz and Q_{ext}=67.3, respectively. The cross point of the two lines gives the design values of $2b$ and w. The result is as follows: $2b$ is 41.55 mm, and w is 18.0 mm.

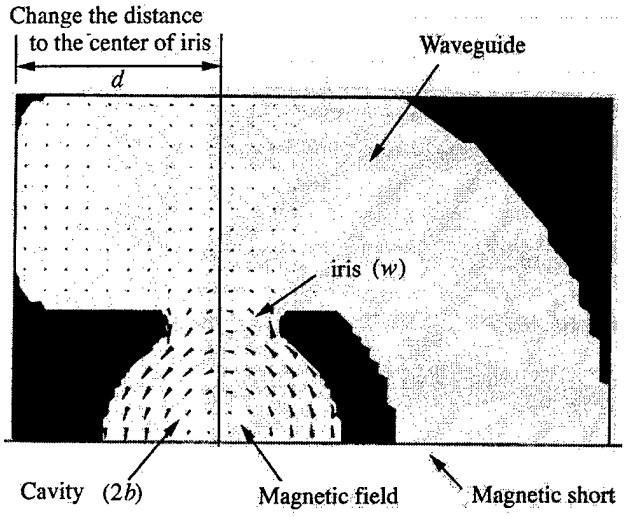


Figure 4: Cross section of the geometry used in Slater's tuning curve method in the plane normal to the beam axis. The whole geometry consists of the coupler cavity, waveguide, beam pipe, and half of 1st regular cavity.

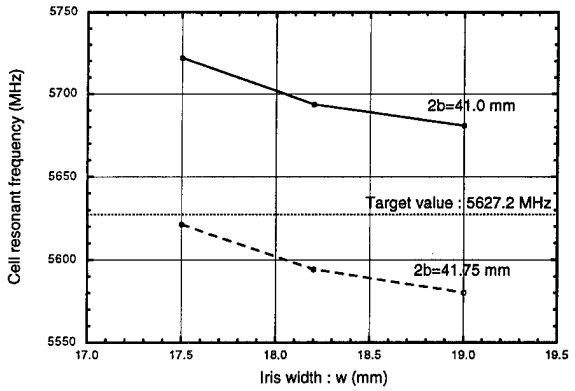


Figure 5: Resonance frequency of coupler cell.

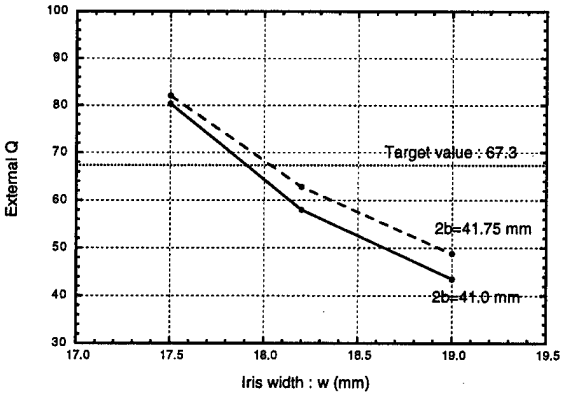


Figure 6: External Q of coupler cell.

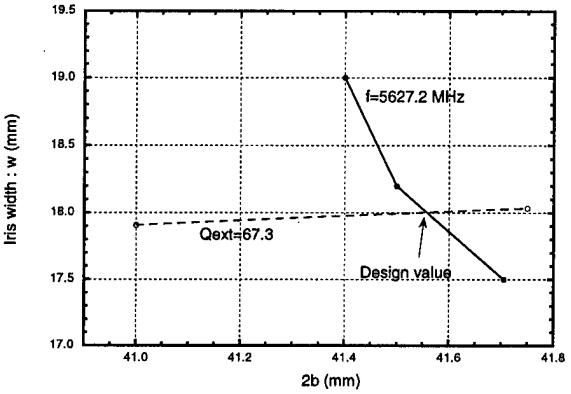


Figure 7: Determination of coupler dimensions

5 SUMMARY

The target value of f_c and Q_{ext} of coupler cell was given by equivalent circuit analysis. The coupler dimensions $2b$ and w were determined so that f_c and Q_{ext} take the target values using Slater's tuning curve method with MAFIA. More detailed calculation including the output coupler will be done. Final values of $2b$ and w will be determined precisely with the cold model test.

6 REFERENCES

[1] T. Shintake, 'The choke Mode Cavity', J. Appl. Phys. Vol. 31, 1992.

[2] T. shintake et al., 'High Power Test of HOM-Free Choke-Mode Damped Accelerating Structure', 1994 Linear Accelerator Conference.

[3] H. Deruyter et al., 'Symmetrical double input coupler development', 1992 Linear Accelerator Conference.

[4] N. P. Sobenin et al., 'DESY linear collider acelerating section coupler', 1994 International Linac Conference.

[5] K. Watanabe et al., 'Double-feed coupler for the linear collider', 1996 International Linear Accelerator Conference.

[6] H. Matsumoto et al., 'C-band choke mode accelerating structure for the linear collider', KEK preprint 96-70, July, 1996.

[7] K. Kubo et al., 'Alignment Issues for C-band Linear collider', KEK preprint 96-66, July, 1996.

[8] T. Shintake, private note.

[9] J. C. Slater, Microwave Electronics.

DEVELOPMENT OF CHARACTERIZATION TECHNIQUES FOR X-BAND ACCELERATOR STRUCTURES

S.M. Hanna, R.J. Loewen, H.A. Hoag, R.H. Miller, R.D. Ruth, J.W. Wang
Stanford Linear Accelerator Center, Stanford University, CA 94304 USA.

Abstract

The recent effort to develop accelerator structures for the Next Linear Collider (NLC), requires an accompanying development of accurate and efficient techniques to characterize these structures at different phases of development. At SLAC, we have been developing different microwave techniques to: verify predictions from computer simulations in the design phase, to insure that the machined cells are within the design tolerances, and finally, to confirm overall RF performance of the completed structure. For this final test, a semi-automated system was built to implement the bead-pulling technique under traveling-wave conditions. This technique maps the phase and amplitude of the axial electric field along the structure.

1 INTRODUCTION

At SLAC, we have built six (6) accelerator sections for the NLC Test Accelerator (NLCTA), [1]. These are nearly constant gradient structures employing Gaussian detuning as means of suppressing the transverse wakefields by varying the physical dimensions of successive cells. Four of these sections are Detuned Structures (DS). The other two are of the Damped Detuned Structure (DDS) type [2]. In these sections, further suppression of wakefields is done through damping of dipole modes excited by the beam. This is accomplished by means of four rectangular slots or manifolds equally spaced in azimuth around the cell and running the full length of the structure.

The DS sections include two 0.9m-long injector sections, and two 1.8m-long accelerator sections. In these four sections the assembly was done through brazing using copper/gold alloys. Variations in the braze fillet required fine tuning of individual cells after assembly.

The two 1.8m-long DDS sections were assembled using diffusion bonding, requiring no tuning. However, the existence of the manifold slots in the cell proper disturbs the azimuthal symmetry. Therefore, the design process included accurate frequency measurements of short stacks of sample cells. The data from these measurements were used to finalize the dimensions predicted from computer simulations.

In this paper, we discuss some of the techniques we use to characterize the above structures. In Figure 1, we outline the series of tests we have implemented to support different development phases of the accelerator sections from the design phase, through manufacturing, and finally, testing of the complete accelerator section.

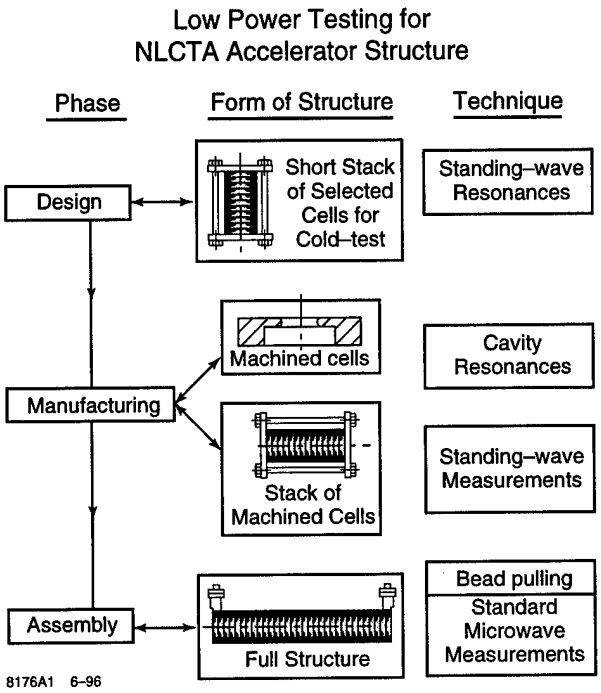


Figure 1. Outline of low-power microwave tests performed on NLCTA accelerator structures.

2 TESTS SUPPORTING DESIGN PHASE

During the design phase of DDS I, the accuracy of the simulation was tested by fabricating five (5) short stacks for cells 10, 70, 106, 156, and 196. Each stack consisted of five cells and two half cells of like dimensions. On-axis probes measure the accelerating mode frequency. Results of these measurements were used to refine the dimensions of the 204 cells of the structure predicted by computer simulation.

Off-axis, E-field probes in the manifolds are used to excite and detect dipole modes, while loop-type H-filed probes in the manifold are used to excite and detect manifold modes. Coupling between cell dipole modes and manifold modes can thus be characterized. Measured frequencies were found to agree well with the simulation. In Figure 2, we show the results of measurement (as compared to computer simulation) of the dispersion curves of the first and second dipole modes and the manifold mode in cell 106 of the DDS I section.

0-7803-4376-X/98/$10.00 © 1998 IEEE

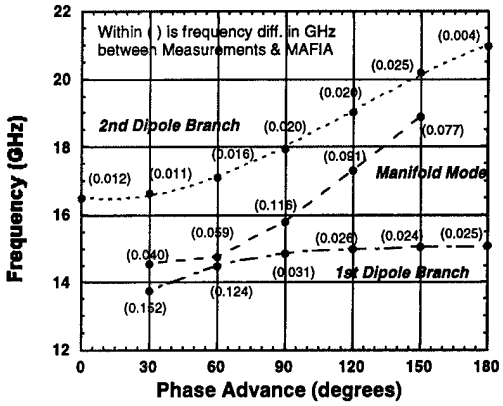


Figure 2. Measured dispersion relation for cell 106 of DDS I as compared to theoretical calculations.

3 TESTS DURING MANUFACTURING PHASE

3.1 Microwave QC of Cells

In all of the NLCTA structures, the diameter of each cell (2b), the thickness of its iris (t), and the diameter of its aperture (2a), all vary progressively from cell to cell. The goal is to detune the dipole modes and prevent short range cumulative build up of wakefields, while maintaining quasi-constant gradient characteristics of the fundamental accelerating mode [2]. To verify the regularity of machining of successive cells, we measured the resonant frequency of the individual cells using a setup for microwave quality control (QC), [3].

By plotting the inverse of the measured frequency versus the cell diameter, one obtains a straight line fit which is a convenient way of verifying the (2b) cell dimension. Results of measurement of 204 cells for DS II structure are depicted in Figure 3.

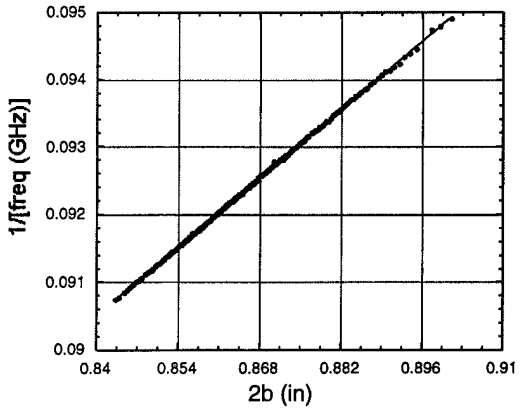


Figure 3. Measured 1/frequency versus cell diameter and the linear fit.

3.2 Tuning DS Sections

The four detuned structures were brazed and required tuning of the cells in the subassemblies. This is to correct for any deviations in the volume of the cells due to brazing. A stainless steel plunger is progressively pulled through the structure from the center of one cell to the next. The resulting phase shift is measured using an HP8510 Network Analyzer at the frequency corresponding to the operating frequency of 11.424 GHz and corrected for room temperature and dry N_2 under atmospheric pressure. Pushing or pulling the cylindrical walls of the cells affects the impedance match from cell to cell for the accelerating mode. Time-domain reflectometery (TDR) measurements are used to check on the matching as the tuning process progresses. The use of both frequency-domain and time-domain capabilities of the network analyzer proved effective in tuning the structure while monitoring the effect on the structureís match. In Figure 4, we show results of typical time-domain measurements during tuning. The reduction in reflection is apparent as more cells are tuned.

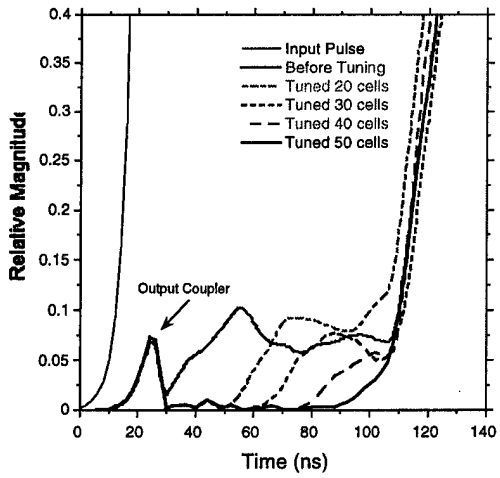


Figure 4 Results of time-domain reflection measurements at different tuning stages of DS II.

4 FULL STRUCTURE CHARACTERIZATION

Each of the completed accelerated sections was finally checked using a semi-automated system of bead-pull [3,4]. The technique implemented is based on traveling-wave perturbation [5]. Figure 5 shows a schematic for our bead-pull system. A small metallic cylindrical bead is attached to a thin nylon string along the axis of the vertically-mounted accelerator section. The position of the bead is determined by the position of the carriage moving on a lead screw driven by a stepper motor. The computer which controls the motor also collects and processes the reflection coefficient data (S_{11}) from the

microwave network analyzer which was operated in the fast acquisition mode. The measurement time is typically 3 minutes. The field perturbation introduced by the bead located at a given position can be modeled as a reactive discontinuity in a transmission line. The susceptance associated with this discontinuity is proportional to the energy perturbation, and hence to the square of the field at this location.

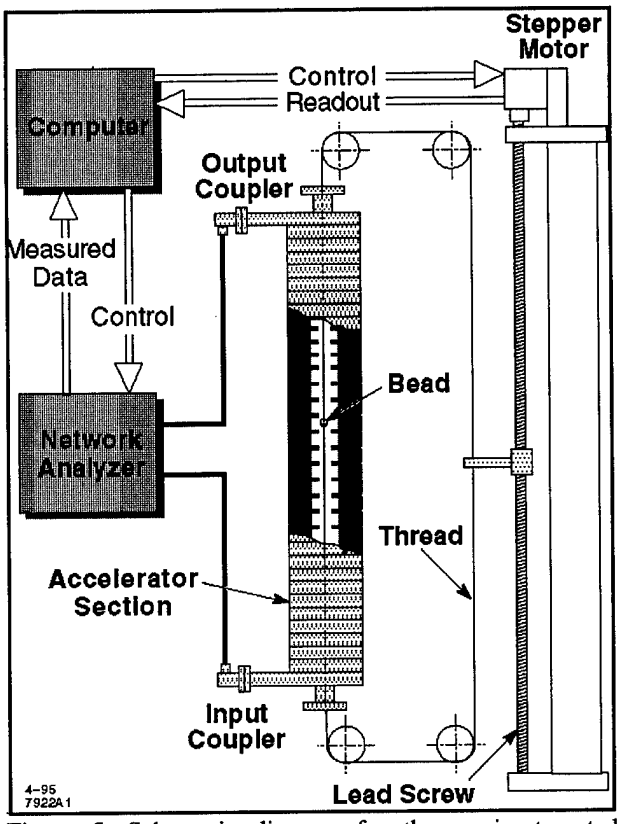


Figure 5. Schematic diagram for the semi-automated bead-pull test setup.

Using the bead-pull system shown schematically in Figure 5, we tested the 6 NLCTA accelerator the sections. We used a stainless steel cylindrical bead of diameter d_b=0.625 mm and a length l_b=1mm supported on a monofiliment nylon string of diameter d_s = 0.145mm. The measurements were made at frequencies corrected for the nylon string, the room temperature and dry N_2. The variation in the reflection from the bead as it is pulled along the axis of each structure traces the hypotrochoid function. This trace can be predicted theoretically for a given longitudinal electric field, E_z based on its space harmonics. Our previous work, [4] showed good agreement between theory and experiment. The electric field E_z can be obtained as the square root of the measured complex reflection coefficient (S_{11}). Measured E_z field for the DDS II section is shown in Figure 6. The three-fold symmetry of the accelerating $2\pi/3$ mode is manifested clearly.

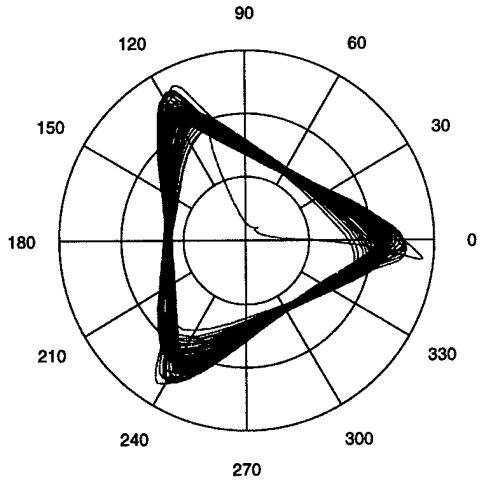


Figure 6. Phasor of the electric field along the axis of the DDS II accelerator section.

5 ACKNOWLEDGEMENTS

We thank K.Ko for the computer simulation data provided. This work is supported by Department of Energy contract DE-AC03-76SF00515.

REFERENCES

[1] R. D. Ruth, "Results from the SLAC NLC Test Accelerator," in these proceedings

[2] R. H. Miller, et al., "Damped Detuned Structure for the Next Linear Collider," Proc. of the XVII International Linear Accelerator Conference, pp 644 - 646.

[3] S. M. Hanna, et al., "Microwave Cold-Testing Techniques for the NLC," Proceedings of the EPAC ë 96, pp 2056-2058.

[4] S. M. Hanna, et al., "A Semi-Automated System for the Characterization of NLC Accelerating Structures," Proceeding of the 1995 Particle Accelerator Conf., pp 1108-1110.

[5] K. B. Mallory and R. H. Miller, "On Nonresonant Perturbation Measurements," IEEE Trans. On Microwave Theory and Techniques, Vol. MTT-14, No. 1966, pp 99-100.

HIGH-GRADIENT CAVITY BEAT-WAVE ACCELERATOR AT W-BAND

D. H. Whittum, H. Henke†, and P. J. Chou*,
SLAC, Stanford University, Stanford CA, 94309

Abstract

Pulsed rf heating is a fundamental limit on high-gradient acceleration in copper structures. Reduction of pulsed heating is favored by a short exposure time for the copper; yet in conventional accelerators, efficiency requires an exposure time of order a cavity fill time. At W-Band, the cavity beat-wave transformer concept permits efficient energy transfer to resonant accelerating modes on a sub-nanosecond time-scale. We re-examine this acceleration scheme as it appears at W-Band, with attention to drive beam dynamics.

1 INTRODUCTION

High energy physics today is limited by the accelerator, and little else. The most severe limit arises due to accelerating gradient, for machines of arbitrarily great dimension are not supportable by society. However, it is impossible to conceive of an electron collider operating with a gradient of, say, 1GeV/m, relying on known collider concepts and technology. Inventions are required.

For the linac proper one must account for *trapping*, *breakdown*, and *pulsed heating*. Trapping refers to the acceleration from rest of field-emitted electrons in the structure. The gradient G, and wavelength λ, may be related to the trapped fraction F, by means of the binding field expression [1], with the result,

$$G\lambda = 3.2MV\left\{1-\sin\left[\pi\left(F-\tfrac{1}{2}\right)\right]\right\}^{-1}.$$

Breakdown is a phenomenological problem at present, but it does exhibit a clear pulse length dependence. For a pulse length equal to the natural fill-time of a travelling wave structure with attenuation parameter τ~1, experience at S and X Band is consistent with a limit on electric field [2],

$$E_{br} \approx 25\tfrac{MV}{m} f^{1/2}\left(1+2.7f^{3/8}\right),$$

where f is the rf frequency in GHz. Pulsed heating refers to the sudden deposition of heat, by Ohmic loss, in the conducting structure. For a pulsed temperature rise ΔT,

$$G\left(\tfrac{GeV}{m}\right) = 0.25\left(\tfrac{\Delta T}{40°K}\right)^{1/2}\left(\tfrac{f}{91.4GHz}\right)^{1/4}$$

for an idealized rectangular pillbox cells, in a constant gradient structure with attenuation parameter τ=1, and pulse length equal to a fill time. These scalings are depicted in Fig. 1. Also seen are gradients achieved to-

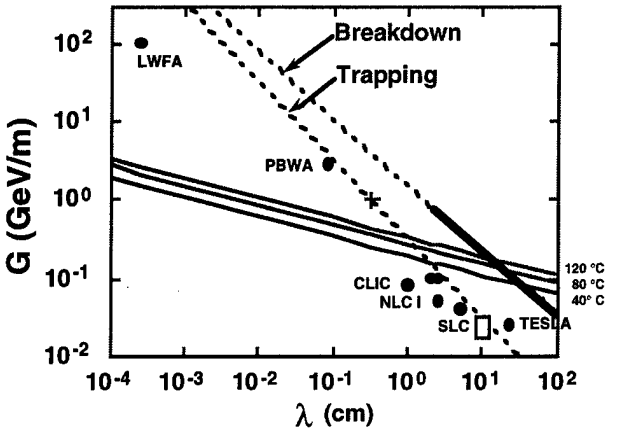


Figure: 1 Current state of the art in high-gradient accelerator research.

date, versus accelerator wavelength. Overlaid are the trapping condition, an extrapolation of known breakdown scalings, and curves of constant pulsed temperature rise. The fit to empirical breakdown results extends only over the solid portion of the curve. Also shown are recent results for the Laser Wakefield Accelerator (LWFA) [3] and the Plasma Beat-Wave Accelerator (PBWA) [4]. Points corresponding to the 0.5TeV collider concepts are also depicted [5]. Shown but not labelled are DESY S-Band, NLC II, VLEPP, and KEK C-Band. The block marked "SLC" extends from 20MV/m as for a typical structure, to 40MV/m as for certain higher gradient structures on the linac.

These scalings imply that *high-gradient* requires *short-wavelength*. For a 1 GeV/m linac, interest begins in the *W-Band*, 75-110GHz. We have added a cross-mark in Fig. 1 as a helpful landmark, corresponding to 1 GeV/m. The corresponding frequency is close to 91.4GHz (3.3mm), the 32nd harmonic of the SLC fundamental frequency, 2.856GHz.

The curves of pulsed temperature rise make clear too, that such a linac will suffer severe pulsed heating, and the conventional travelling wave structure we have taken as our paradigm, will surely fail short of 1 GeV/m.

† On sabbatical from Technische Universität Berlin.
* Supported by the DOE Contract DE-AC03-76SF00515.

0-7803-4376-X/98/$10.00 © 1998 IEEE

To be sure, it is yet an open question exactly what cyclic pulsed temperature rise a structure can withstand, and this is the subject of ongoing research [6]. It should also be emphasized that the technology of handling high mm-wave power does not yet extend to the 150-200 MW level one would require to establish GeV/m gradients. Based on experience at longer wavelengths, one would expect to find serious problems with field emission. Field emitted current density takes the form,

$$J\left(\frac{A}{m^2}\right) \approx 6\times 10^{-11}(\beta E)^{2.5}\exp\left(-\frac{6.2\times 10^4}{\beta E}\right),$$

with E the theoretical surface field in MV/m, and β a phenomenological "field-enhancement factor" typically 50-100, depending on the state of the surface (composition, cleanliness, finish) [7]. Such a field enhancement would result in explosive emission at GeV/m gradients, and would be unacceptable. At the same time, there is experimental evidence that field emission is inhibited on short, ns time-scales [8], and this is encouraging insofar as the natural fill time for a W-Band structure is on the order of 10ns.

2 CBWA CONCEPT

This problem of pulsed heating can be solved in principle by a radically different acceleration technique, first proposed by Henke [9]. The concept is of the two-beam type and promises the high-efficiencies often discussed in connection with such schemes. It is depicted in Fig. 2, consisting of two beamlines, and two side-coupled cavities. The coupling between the two cavities, for the case of isolated resonances, may be characterized by the beat-period T_B.

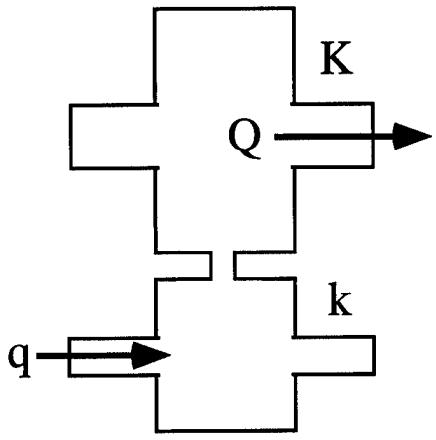


Figure: 2 One period of a CBWA, consisting of two beamlines and two side-coupled cavities.

A drive bunch of charge Q_b passing through the drive cavity will deposit energy $W=KQ_b^2$ in the fundamental mode, characterized by loss-factor K. Total energy loss, all modes considered will be larger by a factor $B>1$. The corresponding average deccelerating voltage in the drive cavity is $V=KQ_b$. In a time $T_B/4$, this energy will appear in the accelerating cavity, characterized by loss factor k, corresponding to a no-load accelerating voltage, $v=2(kK)^{1/2}Q_b$. The transformer ratio is then $R=v/V=2(k/K)^{1/2}$. This energy subsequently reappears in the drive cavity, and can be extracted by a second drive bunch, modulo higher mode losses and wall losses in a beat period.

To evaluate these scalings additional ingredients are required. Given the desired wavelength for operation (3.3mm) geometry constrains k to at most ~32V/pC, and a more conservative value, including reduction due to beam ports would be 13V/pC. Finally, pulsed heating in the drive cavity requires that the decelerating voltage not be too large. We will take R~5. Assuming cavities spaced at 1/3 of a wavelength, one arrives at the parameters indicated in Table 1. The problem with the concept is clearly indicated in the last row: an enormous drive charge is required. From the point of view of single-bunch beam dynamics, this is *untenable*.

Table 1 Example Parameters for a W-Band CBWA

Parameter	Value
Drive Cell Loss Factor K	2 V/pC
Drive Cell *[R/Q]*	14 Ω
" per unit length	13 kΩ/m
Accelerating Cell *[R/Q]*	90 Ω
" per unit length	82 kΩ/m
Peak Accelerating Gradient	1 GeV/m
Avg Decelerating Gradient	200 MeV/m
Drive Cell Avg Voltage V	220 kV
Drive Charge Q_b	110nC

Thus despite any attractive features of the concept, it is clear that the first and most important flaw is stability of the drive beam. To attempt to repair the transverse dynamics, one can split the drive charge up, employing a bunch train. To hold pulsed heating to 200°K, one needs a quarter-beat period of 300ps. Thus at most 30 W-Band periods are available for the drive bunches, and one requires a bunch charge of 5nC. We consider next the transverse stability of such a bunch train.

3 DRIVE-BEAM DYNAMICS

From the foregoing discussion it is clear that the beat-wave accelerator requires an intense drive beam to propagate through mm-dimension apertures. Having required the drive beam to interact strongly with the fundamental mode of the structure, one suspects it will obligingly find other modes of the structure to drive. For the longitudinal wake, one's concerns may be allayed to some degree by the enlarged beam aperture presumed by the lower *[R/Q]* of the drive structure. The transverse

wake, however, requires special attention. While the low *[R/Q]* is favorable for transverse wake reduction, the drive beam charge is quite high, and one must consult the details of the scalings for beam break-up to assess the viability of the concept. The beam centroid ξ satisifies,

$$\left(\frac{\partial}{\partial z}\gamma\frac{\partial}{\partial z}+\gamma k_\beta^2\right)\xi=\int_0^\tau d\tau'\,\frac{I_b(\tau')}{I_0}W(\tau-\tau')\xi(\tau',z),$$

with I_b the beam current, and I_0~17kA. We take as a model wakefield a single dominant, damped mode,

$$W(\tau)=W_0\sin(\Omega\tau)\exp\left(-\frac{\Omega\tau}{2Q}\right).$$

The wakefield amplidute takes the form, $W_0=\hat{w}\omega^3/c^2$, where the dimensionless amplitude $\hat{w}$~1 for a closed pillbox, and diminishes as the beam-port is widened.

Treating the drive beam current waveform as constant, and assuming strong-focusing, asymptotic growth for an initial offset ξ_0 takes the form [10],

$$\frac{\xi}{\xi_0}\approx 0.2\frac{A^{1/2}}{\Omega\tau}\exp\left(A-\frac{\Omega\tau}{2Q}\right),$$

with exponent,

$$A=\left(\frac{z\tau}{\gamma k_\beta}\frac{I_b}{I_0}W_0\right)^{1/2}.$$

If the Q for the dipole mode is sufficiently low, such that $\tau>\tau_{sat}=zW_0Q^2/\gamma k_\beta\Omega^2$ asymptotic growth is a maximum at $\tau=\tau_{sat}$, scaling as $\xi_{sat}/\xi_0\approx 0.3e^{A'}/QA'^{1/2}$ where the exponent is $A'=zW_0Q/2\gamma k_\beta\Omega$. These scalings are quite harsh for a drive beam charge in the range of 110nC. For example, even with an extremely low Q~2, a high drive beam energy ~1GeV, and a modest range z~100m, and assuming an extremely low wakefield amplitude, $\hat{w}\approx 0.1$, one can hold the saturated growth to $\xi_{sat}/\xi_0\approx 14$ only by means of a very short betatron period, $\lambda_\beta\approx 2\pi/k_\beta\approx 10cm$. Such strong focusing is not out of the question, for example, with ion-channel guiding. While other cures are available [10], the research emphasis for such a concept is clear: single-bunch wakefield analysis for a large aperture geometry, one that implements very strong damping of multibunch wakefields, and, if exotic focusing mechanisms are to be avoided, then detailed design and analysis of small aperture magnets for mm-wave structures, along the lines of the work by Hill [11].

4 CONCLUSIONS

The cavity beat-wave transformer permits efficient use of rf in strongly coupled (high *[R/Q]*) accelerating structures, while limiting the time to which copper is exposed to high fields, to the range of several hundred ps. This cannot be accomplished in a conventional travelling wave structure, constrained by the fill time and bandwidth product. In the limit of 100's of ps exposure time, pulsed temperature rises can be held to below 200°K. It is an open question whether such heating is acceptable [6,7]. At the same time, the beat-wave concept suffers, as all two-beam concepts do, from the need for an intense drive beam, and the attendant problems for the drive beam dynamics.

REFERENCES

[1] M. Chodorow, *et al.*, Rev. Sci. Instrum. **26** (1955) pp. 134-204.

[2] A.E. Vlieks, *et al.*, *Breakdown Phenomena in High-Power Klystrons*, SLAC-PUB-4546, presented at the XIIIth International Symposium on Discharges and Electrical Insulation in Vacuum (Paris, June, 1988). P.B. Wilson (private communication).

[3] The Rutherford Appleton Lab LWFA work made use of a 25TW, 0.8ps laser pulse with peak intensity 10^{19}W/cm^2, producing an inferred plasma density of 10^{19}cm^{-3}, and 10^7 44MeV electrons of ~5mm-mrad normalized emittance. The inferred gradient was 100GV/m.

[4] C.E. Clayton, *et al.*, Phys. Rev. Lett. **70** (1994) 37, and Phys. Plasma **1** (1994) 1753. The UCLA PBWA work made use of a 0.2TW, 1ns laser pulse with peak intensity of 10^{14}W/cm^2, in a 10^{16}cm^{-3} plasma. It produced up to 28MeV electrons for an inferred gradient of 2.8GV/m.

[5] *International Linear Collider Technical Review Committee Report*, G. A. Loew and T. Weiland, eds, (July 1995) SLAC-R-95-471.

[6] D. Pritzkau, *et al.*, these proceedings.

[7] G. A. Loew and J. W. Wang, *RF Breakdown Studies in Room Temperature Electron Linac Structures*, SLAC-PUB-4647, presented at the XIIIth International Symposium on Discharges and Electrical Insulation in Vacuum (Paris, June, 1988).

[8] F. Villa and A. Luccio, *Test of a High-Gradient Low-Emittance Electron Gun*, June 1996 (Laser and Particle Beams, *to be published*).

[9] H. Henke, *Cavity Beat-Wave Transformer for a Two-Beam Accelerator*, CERN-LEP-RF/88-55

[10] D.H. Whittum, *et al.*, Phys. Rev. A **46** (1992) 6684.

[11] M. Hill, *A Study of a Planar Six-Wire Quadrupole Magnet Design*, TET-Note-96/08, Technische Universität Berlin (1996).

MINIMIZING RF SYSTEM COSTS IN A LINEAR COLLIDER BY AN OPTIMIZED CHOICE OF BEAM AND STRUCTURE PARAMETERS

R.M. Jones and P. B. Wilson
Stanford Linear Accelerator Center, Stanford, CA 94309

Abstract

In the design of future linear colliders it will be important to reduce the cost of the RF system by minimizing the total number of major system components (klystrons, modulators and pulse compression systems). In this paper we develop a procedure for performing this minimization by varying appropriate accelerating structure and beam parameters while maintaining a constant luminosity, AC "wall-plug" power and net beam-loaded accelerating gradient. Results for both standing-wave and traveling-wave accelerator structures are presented, including the plane-wave transformer and more conventional disk-loaded structures having cells with shaped (as opposed to purely cylindrical) outer boundaries and irises.

1. INTRODUCTION

The process for choosing the parameters of a linear collider proceeds in two, roughly separable, stages. First, given energy and luminosity goals, limitations on final focus optics, and limitations imposed by beam-beam effects such as beamstrahlung and pair production, the bunch dimensions and charge are chosen. Next, the rf accelerating gradient, number of bunches (related to the rf pulse length) and repetition rate are chosen, consistent with the desired luminosity and a reasonable ac "wall-plug" power. Alternatively, in a well-known optimization technique, the accelerating gradient is allowed to vary, and a balance is struck between length-related and power-related costs to find the gradient and associated ac power which minimize the total cost. This optimization is very loose, since the cost coefficients entering into the equation are only approximately known, and further, cost variations about the minimum are second order. In the case of a linear collider, there are further social and political constraints on both the allowable ac power and total collider length. In this paper we assume that both the allowable ac power and accelerator length (or loaded accelerating gradient for a given final energy) have already been fixed by these considerations.

Having fixed the luminosity, the accelerator length and the ac power, the primary goal in the following analysis will be to minimize the rf system cost by adjusting the accelerating structure parameters (primarily the field attenuation parameter, τ) and the beam parameters (spacing between bunches and number of bunches) to minimize the number of rf system components: klystrons, modulators and pulse compression/rf power distribution systems. The analysis is applied to the parameters of the 11.4 GHz, 1 TeV NLC linear collider design as outlined in the Zero-Order Design Report (ZDR [1]).

2. TRAVELING-WAVE STRUCTURES

The NLC 1 TeV design is based on an unloaded gradient of 85 MV/m, a beam loading gradient of 21.5 MV/m (bunches with a charge of 1.1×10^{10} electrons spaced 16 λ, or 1.4 ns, apart) and an on-crest loaded gradient of 63.5 MV/m. The required rf power of 145 MW/m is provided by a binary pulse compression system with a power gain of 3.5 driven by four 75 MW klystrons and delivering 1,040 MW to 7.2 m of accelerating structure (four 1.8 m sections). The power provided by this "power unit" of 4 klystrons, 2 modulators and one pulse compression system is assumed to be fixed in the following analysis. The loaded gradient is given for the NLC detuned accelerating structure [2] by:

$$G_L = 55.5 = (\alpha\rho)^{1/2}\left(1-e^{-2\tau}\right)^{1/2}(96.3) \; - \; \rho N\left(\frac{1}{2}-\frac{\tau e^{-2\tau}}{1-e^{-2\tau}}\right)\left[(141.7)/\Delta T\right] \qquad (2.1)$$

Here α is the relative power per unit length, normalized to 145 MW/m. It is inversely proportional to the separation between power units, and directly proportional to the total number of power units in the linac. The quantity ρ gives the relative shunt impedance, compared to 79MΩ/m for the center cell in the NLC structure design; N is the bunch charge, normalized to 1.1×10^{10}; and ΔT is the separation between bunches in ns (which must be an integer multiple of the damping ring rf period of 1.40 ns). The numerical constants are in MV/m.

Equation (2.1) gives the dependence of the unloaded and beam loading gradients on the attenuation parameter τ for a constant gradient accelerating structure. The field profile for the Gaussian detuned NLC structure differs somewhat from a true constant gradient; moreover, the structure parameters vary considerably along the length of the structure (the shunt impedance varies by about ± 20%). Therefore, the constants in the square brackets are adjusted to give the unloaded and beam loading gradients obtained from an exact calculation. The effective shunt impedances for the unloaded and beam loading gradients

0-7803-4376-X/98/$10.00 © 1998 IEEE

are 78.2 MΩ/m and 80.5 MΩ/m respectively for τ = 0.51). In spite of the approximation underlying Eq. (2.1), we expect that it will adequately represent scaling as function of τ to the precision needed for the optimization proceedure to be carried out here.

A further complexity in Eq. (2.1) is that the effective unloaded gradient is reduced by off-crest operation necessary for BNS damping, by an overhead allowance for feedback and by an allowance for stations off for repair. A reduction factor of 0.91, contained in the 96.7 MV/m constant, takes this overhead into account. The effective loaded gradient is then 55.5 MV/m for $\alpha = \rho = N = 1$, ΔT = 1.4 ns and τ = 0.51. This effective gradient is conserved in this analysis.

For the 1 TeV NLC design given in the ZDR, a luminosity of $1.1 \times 10^{34}/cm^2/sec$ is obtained for a train of 90 bunches spaced 1.4 ns apart. The bunch train length is therefore 125 ns. For a structure filling time of 100 ns, and allowing 15 ns for rise time due to phase switching, the rf pulse length is 240 ns. To keep the ac power constant, the quantity $(T_p/240\ ns)f_r\ \alpha$ must be conserved where f_r is the pulse repetition rate (120 Hz in the NLC design). To keep the luminosity constant, the quantity $N^2 n_b f_r = 10,800$ must also be conserved. As a further consideration, we must allow for the possibility that the Q of the structure can change following design improvements. The time constant of the NLC structure is 195 ns, and the filling time is then T_F = (195 ns) τ Q_r where Q_r is the improvement factor compared to Q = 6980. The beam pulse length is $\Delta T(n_b - 1)$. Putting these considerations together, to conserve both ac power and luminosity:

$$\alpha f_r\left[195\tau Q_r + \Delta T\left(\frac{10,800}{f_r N^2} - 1\right) + 15\right] = 28,800 \qquad (2.2)$$

The quantity in square brackets is the total pulse length, $T_p = T_F + T_{beam} + 15$ ns. For specific values of ΔT, f_r, Q_r and ρ, the quantity N_r can be eliminated between Eqs. (2.1) and (2.2) to obtain $F(\alpha, \tau) = 0$. This can be evaluated to find the value of τ which gives the minimum value of α.

The above procedure has been carried out for six cases: bunch spacings of 1.4, 2.8 and 4.2 ns with repetition rates of 60 and 120 Hz. The minimum values of α for these cases are shown in Table 1, together with corresponding values of τ, N and N_b at α_{min}, for the standard NLC structure with ρ = 1, Q_r = 1 (denoted by NLC-1 in the Table). Recently, changes in the geometry of the individual cells in the NLC structure have lead to a 20% improvement in shunt impedance (ρ = 1.2) and higher Q (Q_r = 1.12). The Q has been increased by making the outer cell wall elliptical in longitudinal cross-section, and the r/Q has been improved by giving these iris a tear-drop shape with a slight bulge. Results of the minimization procedure for these new parameters are shown as NLC-2 in Table 1.

3. STANDING-WAVE STRUCTURES

The minimization procedure described above can also be applied to standing-wave structures. Based on a normalizing shunt impedance of 79 MΩ/m, the expression analogous to Eq. (2.1) for a standing-wave structure is

$$55.5 = \frac{2\beta^{1/2}}{1+\beta}(\alpha\rho)^{1/2}(97.2) - \frac{\rho N}{1+\beta}[(139)/\Delta T] \qquad (3.1)$$

where β is the cavity coupling coefficient. A reduction factor of 0.91 is again included in the constant 97.2 MV/m to allow for the required overhead.

An advantage of a standing-wave structure is that beam loading compensation is exact if the beam is switched on at time $T_s = T_F \ln(1/b)$, where b is the ratio of the beam loading gradient to the on-crest unloaded gradient,

$$b = 0.651\left(\frac{\rho}{\alpha\beta}\right)^{1/2}\frac{N}{\Delta T} \qquad (3.2)$$

The beam pulse length is again given by $T_b = (n_b - 1)\Delta T$, and to preserve the luminosity $N^2 n_b f_r$ = 10,800. Analogous to Eq. (2.2), to conserve ac power and luminosity

$$\alpha f_r\left\{\frac{195\,Q_r}{1+\beta}\ln\left[1.536\left(\frac{\beta\alpha}{\rho}\right)^{1/2}\frac{\Delta T}{N}\right]\right\} + \alpha f_r\left\{\Delta T\left(\frac{10,800}{f_r N^2} - 1\right) + 15\right\} = 28,800 \qquad (3.3)$$

The quantity in the curly brackets is the rf pulse length in ns. Again, N can be eliminated between Eqs. (3.1) and (3.3) to obtain $F(\alpha, \beta) = 0$, which can be solved for minimum α as a function of β for various values of ΔT, f_r, ρ and Q_r. This minimization has been carried out for several standing-wave structures. First, if we assume the NLC structure is converted to a π-mode structure (denoted as PMS) with the same average beam aperture as the center cell of the TW structure, but with fully rounded outer cell boundary, we obtain [3]: ρ = 1.00, Q_r = 1.50. A second interesting structure is the plane wave transformer (PWT) structure proposed by D. A. Swenson [4]. If the iris aperture radius of this structure is opened up to 4.7 mm, the r/Q is expected to decrease by about 40% to 3.8 kΩ/m. This is about 35% of the value for the NLC structure. The scaled Q of the PWT is 44,500. The introduction of this support rods is expected to reduce this

substantially (by about 25%) to 33,000. Thus the high shunt impedance, 132 MΩ/m (ρ = 1.67), comes principally from the large increase is Q (Q_r = 4.73). This has the disadvantage of making the filling time and rf pulse length longer. Minimum values of α, together with associated values of β, N, n_b and T_p, are shown in Table 2 for the PMS and PWT structures for various values of f_r and ΔT.

4. DISCUSSION

From the first entry in Table 1, it is seen that the parameters as given in the ZDR for the NLC-1 structure (τ = 0.51, N = 1, n_b = 90 and t_p = 240 ns) are close to optimum. However, it has recently been realized that by increasing the bunch spacing to 2.8 ns the beam loading could be reduced, allowing a reduction in the unloading gradient and a corresponding decrease in the number of power units required for the linac. The parameters presently under consideration are based on using six 1.8 m NLC-2 structures per power unit (giving α = 0.66) together with τ = 0.54, N = 1.0, n_b = 82 and T_p = 362 and a relative luminosity of 0.91. These values are not too different than the optimum parameters given in the third row of Table 1. The luminosity could be regained by a slight increase in bunch charge. The τ parameter is too low, but it cannot be increased without reducing the structure group velocity, which leads to an unacceptable increase in dipole wakefield. A modest further reduction in α could be made by increasing ΔT to 4.2 ns, but at the expense of higher N (enhancing both wakefields and beam-beam effects), a longer klystron pulse length (equal to 4 T_p), and a still greater optimum τ. All of the 60 Hz solutions, while giving a modest reduction in α, lead to unacceptably long klystron pulse lengths.

In the standing-wave case, the PMS structure gives results which are closely comparable to the traveling wave, NLC-2 results; possibly this structure should be given further consideration. The slight reduction in α offered by the PWT structure is offset by the mechanical complexity of this structure and the difficulty in cooling the irises.

5. ACKNOWLDEGMENTS

Work supported by the US Department of Energy under contract DE-AC03-76SF00515.

6. REFERENCES

[1.] The NLC Design Group, "Zeroth-Order Design Report for the Next Linear Collider", SLAC-474, Stanford Linear Accelerator Center (May 1996).
[2.] *Ibid.*,Sec. 8.2.
[3.] V. Srinivas, SLAC; private communication.
[4.] Donald A. Swenson, "The Plane Wave Transformer Linac Structure", Proceedings of the 1988 European Particle Accelerator Conference (EPAC 88), p. 1418.

Table 1: Minimum α and Associated Parameters for two NLC Traveling-Wave Structures

ΔT (ns)	f_r (Hz)	α_{min} NLC-1	α_{min} NLC-2	τ NLC-1	τ NLC-2	N NLC-1	N NLC-2	n_b NLC-1	n_b NLC-2	T_p(ns) NLC-1	T_p(ns) NLC-2
1.4	120	0.99	0.87	0.47	0.45	0.96	0.88	98	116	243	274
1.4	60	0.84	0.75	0.67	0.62	0.77	0.72	305	350	570	639
2.8	120	0.74	0.64	0.67	0.64	1.17	1.07	65	75	325	372
2.8	60	0.65	0.57	0.91	0.86	0.96	0.89	195	228	734	837
4.2	120	0.65	0.56	0.79	0.76	1.35	1.23	49	60	372	429
4.2	60	0.58	0.51	1.06	1.01	1.11	1.03	145	171	826	950

Table 2: Minimum α and Associated Parameters for two Standing-Wave Structures

ΔT (ns)	f_r (Hz)	α_{min} PMS	α_{min} PWT	β PMS	β PWT	N PMS	N PWT	n_b PMS	n_b PWT	t_p(ns) PMS	t_p(ns) PWT
1.4	120	0.82	0,87	2.79	5.77	0.85	1.12	124	71	291	277
1.4	60	0.73	0.60	2.34	3.38	0.70	0.69	371	376	655	800
2.8	120	0.64	0.60	2.15	3.91	1.07	1.34	78	50	375	402
2.8	60	0.58	0.44	1.86	2.48	0.89	0.85	230	248	821	1079
4.2	120	0.57	0.50	1.90	3.27	1.25	1.54	57	38	420	477
4.2	60	0.53	0.39	1.67	2.15	1.03	0.98	168	186	910	1239

ADVANCED DAMPED DETUNED STRUCTURE DEVELOPMENT AT SLAC

R.M. Jones[†‡], N.M. Kroll[†‡], R.H. Miller[†],R.D.Ruth [†], & J.W.Wang[†]
†Stanford Linear Accelerator Center, M/S 26, P.O. Box 4349, Stanford, CA 94309
‡University of California, San Diego, La Jolla, CA 92093

Abstract

The first damped detuned accelerator structure, DDS 1, has been built, tested in the ASSET experiment, and installed in the NLCTA. The planning and construction of a series of further structures, incorporating some modifications, is under way. DDS 2, 3, and 4 all incorporate the same basic design as DDS 1. The manifold design for the last 5 % of the downstream end of the structure has been modified to accommodate improvements in the manifold loads. Calculations based on the spectral function method indicate, on average, a factor two or better reduction in the long range wake. Modest modifications in the distribution of geometrical detuning parameters along the structure which, according to calculations based on spectral function theory, significantly improve the short range wake will be incorporated in DDS 3 and 4. The basic cell configuration will be redesigned in DDS 5 with the intention of improving shunt impedance as well as incorporating further improvements in the wake.

1 INTRODUCTION

The NLC Accelerator Structures group at SLAC is engaged in three simultaneous processes: 1) optimizing the design of NLC Accelerator Structures, 2) learning how to fabricate them within satisfactory dimensional tolerances including the straightness tolerance, and 3) manufacturing structures for the NLC Test Accelerator. The schedule realities of these three goals have led to a process of making incremental changes in the design which were compatible with the fabrication schedule. The NLC beam parameters have evolved, going from a pulse train of 10 bunches with 1.4 ns spacing to 90 bunches with a 1.4 ns spacing, and now will change to 82 bunches with a 2.8 ns spacing.

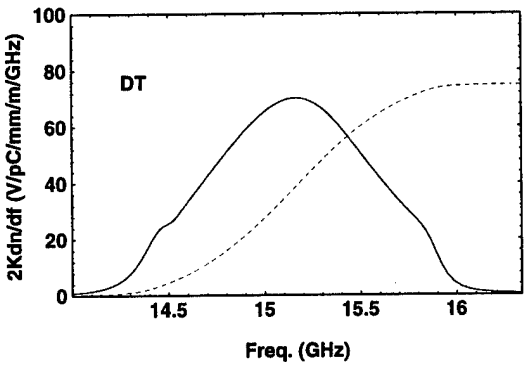
2 DETUNING

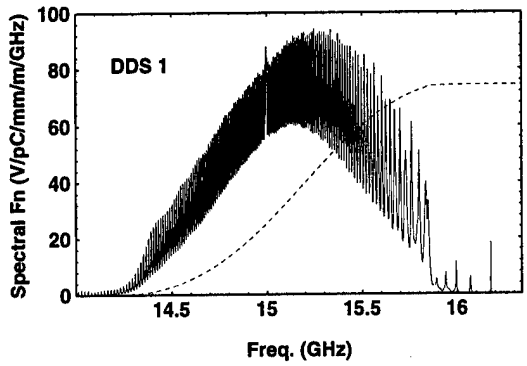
The first two NLC developmental accelerator sections were the Mark 1 and Mark 2, detuned sections which were identical in design except for minor dimensional corrections. All of the NLC structures discussed here are 1.8 meters long with 206 cells (including the couplers) and are designed to operate with a $2\pi/3$ phase advance per cell in the accelerating mode. The dipole modes in the Mark 1 and 2 structures were undamped, except for copper losses. These structures were designed to be approximately constant gradient with the dipole mode frequencies adjusted to have a gaussian density distribution by varying the iris radius a, and the disk thickness t. The resulting gaussian density distribution of the lowest dipole band had σ_f = 2.5% about a center frequency of 15 MHz. The full frequency spread was 10% with the gaussian distribution truncated at $+/-2\sigma_f$. The effect of the gaussian detuning of the Mark 1 was measured by Adolphsen [1]. The measurements showed that the wake fields fell by a factor of about 70 to below 1 Volt/pC/mm/m by the time that a second bunch arrived 1.4 ns after the drive bunch. To get an equivalent fall off in 1.4 ns with damping would require a Q of 12 for the dipole modes. However, while the Gaussian distribution is very effective in achieving a destructive interference which produces a rapid fall off at short times, because there are a finite number (206) of discrete modes, they begin to constructively interfere again after times inversely proportional to the separation between modes. The build up of the wake field due to this reappearance of constructive interference can be seen in the wakefield plot for the detuned (DT) structure at the top of Fig. 2.

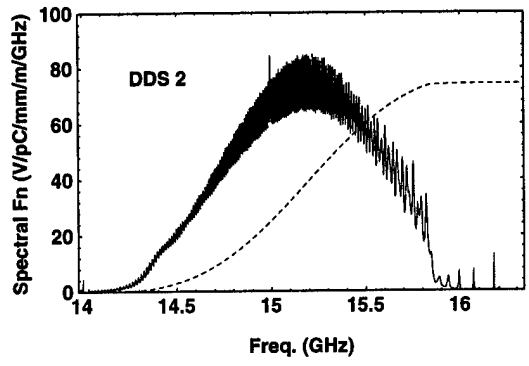
3 DAMPED DETUNED STRUCTURES

DDS 1 was the first of our manifold damped detuned structures. DDS 1,2,3, and 4 have 4 rounded rectangular damping manifolds arranged at 90 degree intervals in azimuth around the accelerator cells. Each manifold is a single mode, TE_{10}, waveguide with its wide dimension in the radial direction, so that the E fields are in the azimuthal direction. The small dimension of the manifolds is 5 mm along its full length. The wide dimension (radial direction) of the manifolds tapers from 11 mm at the input end of the structure to 9.8 mm at the output end. Each manifold couples to every cell except the first 3 (counting the couplers) at each end by means of a rectangular coupling hole which is 5 mm in the azimuthal direction and about 7 mm long. The coupling is controlled by tapering the wide dimension of the manifolds and by controlling the distance of the manifolds from the outer wall of the accelerator cells. In DDS 1 through 4, the coupling was chosen in an attempt to achieve a loaded Q of about 1000 for all the modes in the lowest dipole band which interact strongly with the beam. The loaded Q of 1000 was chosen to produce a damping time of 20 ns. We didn't realize that only the more widely spaced modes which contribute to the early rise in the wakefields need a Q of 1000. The Q of each mode should be such that the bandwidth of the mode is

0-7803-4376-X/98/$10.00 © 1998 IEEE







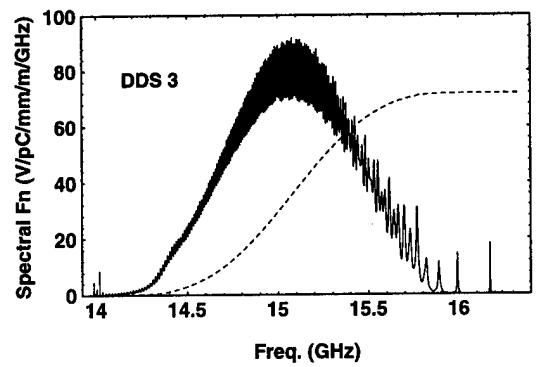
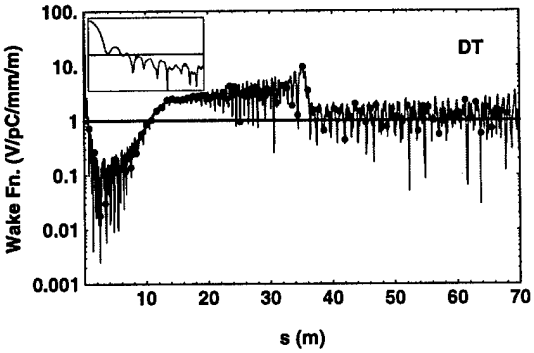
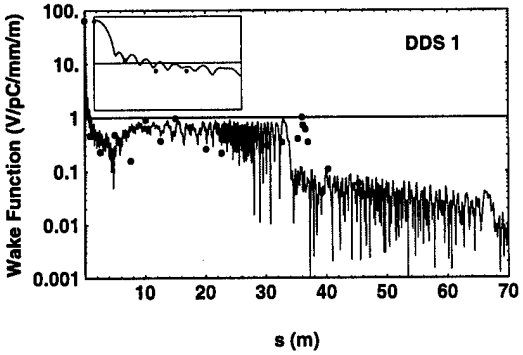
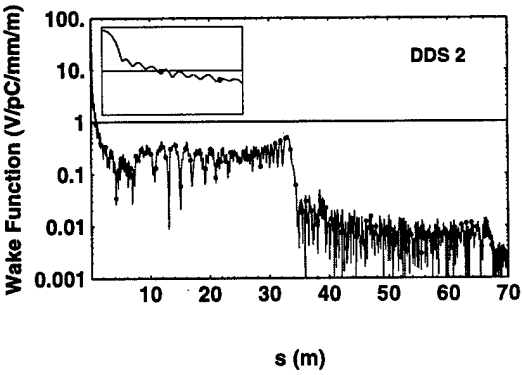


Fig 1: Shown uppermost is twice the kick factor weighted density function (2Kdf/df) for the DT (damped detuned) structure. The succeeding curves are of the spectral function for DDS 1, DDS 2 and DDS 3 The significant improvement in the matching to the HOM loads for DDS 2 reduces the amplitude of the oscillations of the spectral function. DDS 3 uses similar HOM couplers and loads as DDS 2 but the cells have been redistributed using a recently developed mapping function method . The integral is dashed.







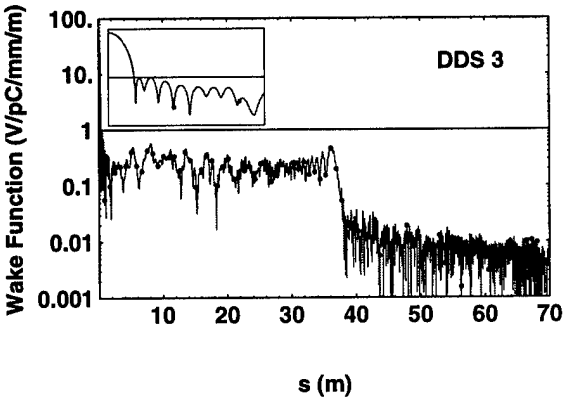


Fig 2: Shown uppermost is the wake function for the DT structure. The succeeding curves are of the wake function for DDS 1 (HOM couplers included and ASSET data points), DDS 2 and DDS 3. The dots in DDS 2 and DDS 3 indicate the position of the 82 bunches placed 2.8 ns apart. The long range wake for DDS 1 is improved over the DT structure by an order of magnitude or more, the medium and long range wake for DDS 2 by a factor of 3 over DDS 1, with further improvement of the short range wake for DDS 3.

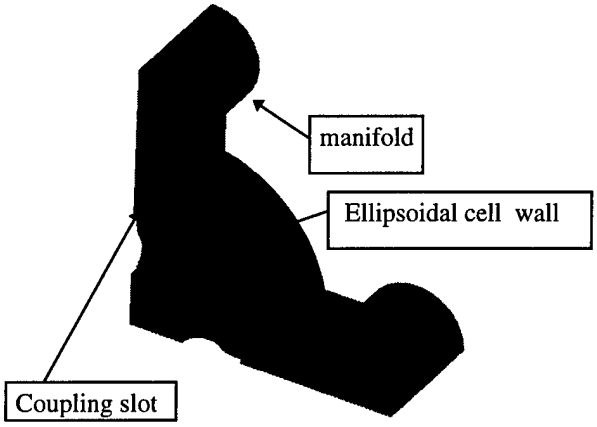


Fig 3: Interior of 1/4 of improved Ellipsoidal Cell.

roughly equal to its frequency separation from it nearest neighbors. This transforms the impedance distribution from 200 delta functions to a fairly smooth gaussian in the frequency domain. Since the mode density varies continuously across the distribution, the Q of the modes should also vary. There were two more significant problems in the design of DDS 1: 1) The manifold terminations were not well matched; 2) the coupling changed the gaussian distribution somewhat and exacerbated the effect of the truncation of the gaussian, particularly at about 15.8 Ghz. This is apparent in the spectral function [2] for DDS 1 and 2 in Fig 1, and causes an increase in the wakefields for the first few meters for DDS 1 and 2 as seen in Fig 2. The terminations for the manifolds DDS 1,2,3, and 4 consist of H plane mitered bends to bring the manifolds out from the structure followed by H plane radiused bends, tapers up to WR-62 rectanqular waveguide, alumina windows and commercial waveguide loads. The VSWR of mitered bends at the output end rose to about 2.0 at the low frequency end of the band, and the VSWR of the windows used on DDS1 rose to 2.0 at the high frequency end.

For DDS 2 the mitered bend on the output end was redesigned and new windows were purchased so that the VSWR is about 1.1 across the center 1 GHz of the band, and rises to 1.2 at the band edges. The improvement in the calculated spectral function and a resultant improvement of a factor of about 3 in the wakefield from about 7 to about 35 meters from DDS 1 to DDS 2 is evident in Fig 1 and 2.

For DDS 3 and 4 the gaussian distribution has been modified to reduce the effect of the truncation at +/- 5%. Using the same range of cell parameters as in DDS 1 and 2, the density distribution has been changed to obtain a symmetric kick factor weighted gaussian density function, Kdn/df with $\sigma_f = 2.125\%$ truncated at +/- 2.35 σ_f. As can be seen in Fig 1 & 2, this significantly reduces the truncation step at the high frequency end of the spectral function and hence significantly lowers the wakefield for the first few meters.

4 DDS 5 AND 6: ELLIPSOIDAL CAVITIES

In the fall of 1996 a program was started to improve the efficiency of the RF system of NLC. The changes in the cell design which raise the shunt impedance about 20% and the related changes in the RF system and its parameters which combined give a 33% reduction in the RF power required for NLC are described in Ref [3] and [4], respectively. The conceptual shape of the interior of the new ellipsoidal cavities is depicted in Figure 3. The round TE_{11} manifolds were chosen because they are easier to fabricate, and improve the vacuum conductance. The outer surface of the cells is an ellipsoid of revolution rather than a right circular cylinder as in DDS 1,2,3 & 4. The ellipsoidal outer surface gives about a 10% improvement in shunt impedance by increasing the Q. The rest of the improvement comes from shaping the disk with a gentle ellipsoidal bulge near the beam hole. The ellipsoidal outer surface significantly reduces the coupling produced by a hole between the manifold and the cavity, so we have added a thin (1.5mm) radial slot in the disk to enhance the coupling. This slot interupts the azimuthal currents in the TM_{11} like dipole mode producing a displacement current across the slot which couples strongly to the TE_{11} mode in the manifold. The slots in the disk will not extend further than 3.5 mm in from the cell maximum diameter, which is roughly half the distance to the beam hole and is also close to the thinest part of the disk, the surface electric fields are well down from their maximum. This slot depth gives a cell to manifold coupling which is about 60% stronger than the couplings for previous structures.

The long range behavior of the wake function could be improved substantially more by improving the match of the terminations. For this reason, and to simplify the mechanical design, internal loads will be considered for future DDS designs.

5 ACKNOWLEDGEMENTS

We wish to thank the many people at SLAC, KEK, and LLNL who have participated in this program. This work is supported by Department of Energy contract DE-AC03-76SF00515 and DE-FG03-93ER40759.

REFERENCES

[1] C.Adolphsen *et al.* Phys. Rev. Lett. **74**:2475, 1995.
[2] R.M.Jones *et al.*, 'A Spectral Function Method ...' SLAC Pub 7287, Proc. Linac96, Geneva, 1996.
[3] V.Srinivas *et al.*, 'Optimizing Cell Contours...', Paper 3W13, this conf.
[4] R.M.Jones, P.B.Wilson, Paper 3W12,This conf.

SPECTRAL FUNCTION CALCULATION OF ANGLE WAKES, WAKE MOMENTS, AND MISALIGNMENT WAKES FOR THE SLAC DAMPED DETUNED STRUCTURES (DDS)

R.M Jones†, N.M. Kroll†‡ & R.H. Miller†

†Stanford Linear Accelerator Center, M/S 26, P.O Box 4349, Stanford, CA 94309

‡University of California, San Diego, La Jolla, CA 92093

Abstract

Transverse wake functions so far reported for the SLAC DDS have been limited to those caused by uniform offset of the drive beam in a straight perfectly aligned structure. The complete description of the betatron oscillations of wake coupled bunches requires an array of wake functions, referred to as moments in [1]. Modifications of these arrays induced by structure misalignments are also of interest. In this paper we express the array elements in terms of a spectral function array. Examples are given based upon DDS1.

1. INTRODUCTION

Adolphsen [1] has pointed out that an analysis of transverse wakefield coupled multibunch motion in a FODO array requires an array of wake functions instead of the single function usually defined. Oide [2] has emphasized the need to compute these wake functions and also to measure them where possible. The offset wake function, which we here designate by W_{00} instead of the usual W, gives the angular deviation $\Delta\theta$ of a witness bunch trailing a uniformly offset drive beam at a distance s that has passed through a structure of length L_s via:

$$\Delta\theta = (q_w\, q_d\, L_s/E)\, W_{00}(s)\, r_d \qquad (1.1)$$

Here q_w and q_d are the charges of the witness bunch and drive bunch respectively, r_d the drive bunch offset, and E the witness bunch energy. As a result of betatron motion through the FODO array, however, the drive bunch motion may be at an angle with respect to the structure axis. Choosing the structure center as the fiducial point from which to define the offset we expect an additional angular deviation $\Delta\theta$ proportional to θ_d, the drive beam angle, which we express as:

$$\Delta\theta = (q_w\, q_d\, L_s/E)\, W_{01}(s)\, (L_s/2)\, \theta_d, \qquad (1.2)$$

the total being the sum of (1.1) and (1.2). Furthermore, for sufficiently large L_s one cannot neglect the effect of the wake induced offset of the witness beam on its betatron motion. This leads us to define two more elements of the wakefield array (called the moment array in [1]), W_{10} and W_{11} via:

$$\Delta x = -(q_w\, q_d\, L_s/E)\, W_{10}(s)\, (L_s/2)\, r_d - (q_w\, q_d\, L_s/E)\, W_{11}(s)\, (L_s/2)^2\, \theta_d. \qquad (1.3)$$

For consistency with our treatment of the drive beam, Δx is defined with respect to the center of the structure by projecting the angle and displacement on emergence from the structure back to its center, assuming rectilinear motion. Expressions for the above array elements based upon the independent oscillator model, a model in which W_{10} and W_{01} are equal, are given in [1]. Finally we note that structure misalignments generate offset patterns of the drive beam different from those discussed above. Some are of a sufficiently general nature (*eg* bowing) that it is useful to define wake functions for them as well (we designate the bowed case by W_{02} and W_{12}). The same general methods which we will apply here apply to more irregular cases such as those discusssed in [3], and for each such case there are two functions that need to be computed, one for $\Delta\theta$ and one for Δx.

2. SPECTRAL FUNCTIONS FOR THE WAKE FUNCTION ARRAY

The extension of the formalism introduced in [4] is straightforward although, as we shall see, some elements of the array require spectral function integrals involving both the sine and cosine of $(2\pi sf/c)$ instead of merely the sine as is the case for W_{00}. The wake function W_{00} is in the equivalent circuit theory expressed as:

$$W_{00}(s) = \sum_{n,m=1}^{N} w_{nm}(s) \qquad (2.1)$$

where $(q_w\, q_d\, L_s/E)w_{nm}$ is the angular kick experienced by the witness bunch at cell n due to a unit displacement of the drive bunch at cell m. Hence the angular kick received by the witness due to a set of displacements $d\chi(m)$ at cell m is:

$$\Delta\theta = (q_w q_d L_s/E) d \sum_{n,m=1}^{N} w_{nm}\chi(m) \qquad (2.2)$$

The various W_{0x} referred to above are determined by specification of the dimensionless $\chi(m)$, with an

0-7803-4376-X/98 /$10.00 © 1998 IEEE

appropriately defined length scale d. To obtain the displacement associated with the above we write (2.2) as:

$$\Delta\theta(s) = \sum_{n=1}^{N} \delta\theta_n \tag{2.3}$$

Then:

$$\begin{aligned} \Delta x &= L_s \sum_{n=1}^{N} \delta\theta_n \left(\tfrac{N-n}{N-1} - \tfrac{1}{2}\right) \\ &= -\tfrac{1}{2} L_s \sum_{n=1}^{N} \delta\theta_n \left(\tfrac{2n-N-1}{N-1}\right) \end{aligned} \tag{2.4}$$

Comparing with eq. (1.3), we see that

$$W_{1x} = \sum_{n,m=1}^{N} w_{nm} \chi_1(n) \chi(m) \tag{2.5}$$

where $\chi_1(n)$ = (2n-N-1)/(N-1). For the angle wake the displacement of the drive bunch at cell m is just $(L_s/2)\theta_d\chi_1(m)$ so that comparing with eq. (1.1), (1.2) and (1.3) we have the general form:

$$W_{ij} = \sum_{n,m=1}^{N} w_{nm} \chi_i(n) \chi_j(m) \tag{2.6}$$

where i, j equals zero or one, and χ_0 equals one .

For a bowed structure the displacement of the drive bunch at cell m is given by d $\chi_2(m)$ where d is the span of the bow and χ_2 is given by:

$$\chi_2(m) = [(2n-N-1)/N-1)]^2 - 1/3 \tag{2.7}$$

In parallel with the W_{ij} array we require a wake impedence array Z_{ij}. Since the wake impedance is simply the fourier transform of the wake function, we have for the array:

$$W_{ij}(s) = \int Z_{ij}(f - j\varepsilon) \exp[2\pi j s / c(f - j\varepsilon)] df \tag{2.8}$$

where ε is a positive infinitesimal quantity, and we write the impedences schematically as:

$$Z_{ij}(f) = \sum_{n,m=1}^{N} \kappa_{nm}(f) \exp[2\pi j L f / c(n-m)] \chi_i(n) \chi_j(m) \tag{2.9}$$

where L is the structure period. It will be sufficient for our purposes to specify the needed properties of κ_{nm}. More detailed information is given in [4]. The κ_{nm} are four valued analytic functions of f with branch points on the real axis located at the propagation band edges of both ends of the manifold. The cuts connecting the four sheets are on the real axis wherever either end of the manifold is propagating. The segments where both ends of the manifold are nonpropagating are called gaps. The integral in eq. (2.8) is carried out on the physical sheet, a sheet on which κ_{nm} has no singularities except poles and branch points on the real axis and vanishes at infinity. κ_{nm} also satisfies the symmetry relations:

$$\kappa_{nm}(f) = \kappa^*_{nm}(f^*) = \kappa_{nm}(-f) = \kappa_{mn}(f) \tag{2.10}$$

with f, f* and, -f all on the physical sheet. An important consequence of these relations is that κ is real on the gaps; the real part is continuous and the imaginary part changes sign across the cuts.

To proceed to the spectral function representation it turns out that one must split Z (and correspondingly W) into even and odd parts thus:

$$\begin{aligned} Z^e_{ij}(f) &= \sum_{n,m=1}^{N} \kappa_{nm} \cos[2\pi L f / c(n-m)] \chi_i(n) \chi_j(m) \\ Z^o_{ij}(f) &= \sum_{n,m=1}^{N} \kappa_{nm} \sin[2\pi L f / c(n-m)] \chi_i(n) \chi_j(m) \end{aligned} \tag{2.11}$$

with:

$$Z_{ij} = Z^e_{ij} + jZ^o_{ij} \tag{2.12}$$

The expressions for W_e and W_o are reduced to spectral function form by making use of the fact in that in general the precursor term θ(s)W(-s) is negligeably small [4]. Noting that the Fourier transform of $W^{e,o}(-s)$ is just ±, respectively, that of $W^{e,o}(s)$ except that it is evaluated just above the real axis instead of below, we are led to write:

$$W^{e,o}_{ij} = \theta(s)\left[W^{e,o}_{ij}(s) \mp W^{e,o}_{ij}(-s)\right] \tag{2.13}$$

$$W_{ij} = W^e_{ij} + W^o_{ij} \tag{2.14}$$

These lead to integrals over positive frequency cuts and sums over positive frequency poles as in [4]. We find

$$\begin{aligned} W^e_{ij} &= \theta(s) \int S^e_{ij} \sin[2\pi L f / c(n-m)] df \\ W^o_{ij} &= \theta(s) \int S^o_{ij} \cos[2\pi L f / c(n-m)] df \end{aligned} \tag{2.15}$$

$$S^{e,o}_{ij}(f) = -4\,\mathrm{Im}\left\{Z^{e,o}_{ij}(f - j\varepsilon)\right\} \tag{2.16}$$

Pole terms are included in the spectral functions as δ functions as in [4].

We note that the even wake functions vanish (by construction) at zero s as expected from causality while the odd ones do not. Some sense of the importance of the precursor term can be obtained by comparing the wake envelope functions of the even and odd parts at zero s.

3. EXAMPLES OF SPECTRAL FUNCTION AND WAKE FUNCTION ARRAY ELEMENTS

We conclude by presenting a number of examples of the spectral function array elements and their associated wake envelope functions. These are useful for assessing the relative importance of the various components. It should be recognized, however, that the envelope functions cannot be combined linearly.

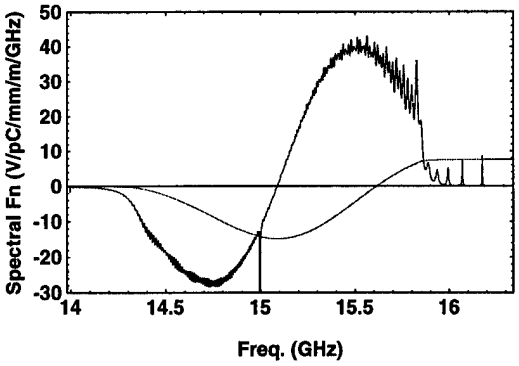


Fig 1: Even spectral function, W_{01}^{c} associated with the sine wake function, and its integral for a matched HOM coupler with a beam transiting a DDS at an angle

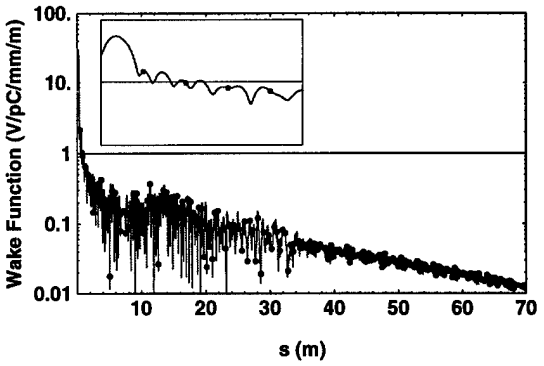


Fig 2: Sine wake envelope function resulting from the spectral function of fig 1.

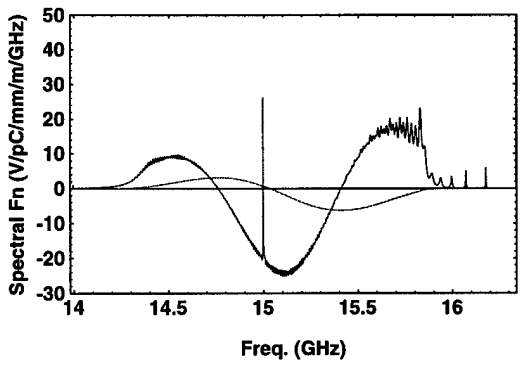


Fig 3: Even spectral function, W_{01}^{c} for matched HOM coupler with a bowed DDS.

For any given situation the wake functions themselves must be linearly combined and the result put in envelope form if desired. In general, it is our experience that the cosine wake terms are far smaller than the sine wake terms, and they are especially small as s vanishes, consistent with the expectation that precursor terms are small. Since W_{01} and W_{10} differ only in the sign of these otherwise equal cosine terms, they are very nearly equal.

Illustrated in fig 1. is the spectral function corresponding to Z_{01} for a beam travelling through the DDS at an angle. The features of the W_{00} are evident, namely under-coupled modes in the upper frequency end.

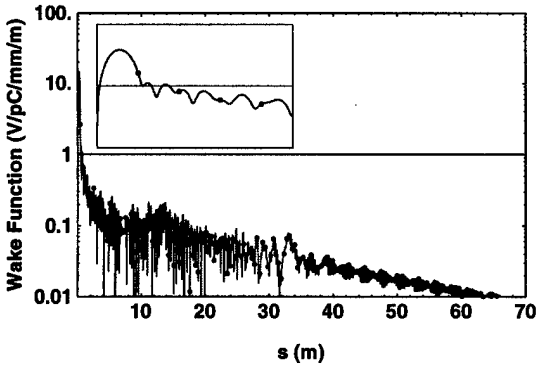


Fig 4: Sine wake envelope function for a bowed DDS

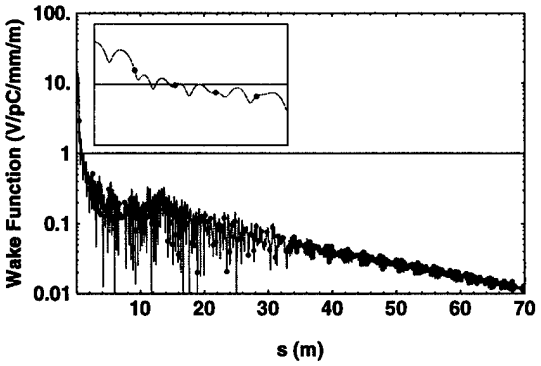


Fig 5: Sine wake envelope function corresponding to S_{11} for a beam travelling at an angle through the DDS

4. ACKNOWLEDGMENTS

This work is supported by DOE grant number DE-FG03-93ER40759[‡] and DE-AC03-76SF00515[†].

4. REFERENCES

1. C. Adolphsen, Proceedings of HEACC'92, Int J. Mod. Phys. A (Proc Suppl.) **2B**, p 867 (1993)

2 K. Oide, unpublished, SLAC/KEK workshop Nov 1996.

3 R.M. Jones, et al, Analysis and Application of Microwave Radiation from the Damping Manifolds of the SLAC Damped Detuned Structures (DDS), Paper 3W16 in this conference.

4 R.M. Jones et al, 1996, Proc. LINAC96 p 650 (1996) SLAC-PUB-7287

ANALYSIS AND APPLICATION OF MICROWAVE RADIATION FROM THE DAMPING MANIFOLDS OF THE SLAC DAMPED DETUNED STRUCTURES (DDS)

R.M. Jones†, M. Seidel†, N.M. Kroll†‡, R.H. Miller†,
C. Adolphsen†, K.L.F. Bane, R.D. Ruth†, and J. Wang†
†Stanford Linear Accelerator Center, M/S 26, P.O Box 4349, Stanford, CA 94309
‡University of California, San Diego, La Jolla, CA 92093

Abstract

The power spectrum emerging from the damping manifolds of a DDS provides valuable quasi-local information on the displacement of a drive beam from the axis of individual cells, where the displacement may be due to beam offset, small cell misalignment, or a combination of the two. The degree of localization and the indexing of frequency to cell number is determined directly from the spectral function theory. Examples for specific DDS designs will be presented. These relations can be used to determine geometrical misalignment patterns.

1. INTRODUCTION

The damped detuned structure (DDS) is a detuned accelerator structure [1] to which four waveguide like structures have been attached in an azimuthally symmetric manner. These "waveguides", called damping manifolds by convention, are extended along the length of the accelerator structure and are coupled to all cells except 3 at either end. These damping manifolds are intended to perform three functions: 1. provide moderate damping of dipole modes excited by an offset drive beam by conducting their energy to loads at the end of the structure, 2. serve as pumping manifolds for the accelerator cells, and 3. provide via the power spectrum of radiation from the ends of the manifolds, beam position and structure alignment information [2]. In this paper we focus on the third of the above and in particular extend the preliminary analysis reported in [3] on power spectrum localization and its application to the determination of structure misalignment from power spectrum measurements. The appliction of manifold radiation to beam positioning is discussed in [4] and [5].

2. THE MANIFOLD POWER SPECTRUM AND ITS RELATION TO OFFSET LOCATION

In the independent cell model (often referred to as the uncoupled model) [1] one treats the cells as independent entities which respond in a narrow band about their synchronous frequencies to an offset velocity c particle. Thus the appearance of a frequency band in the power spectrum of the manifold radiation is associated with offsets at the cells which respond at frequencies within that band. The underlying idea behind this model is the expectation that the structure in the vicinity of a particular cell is sufficiently like a uniform structure based upon that cell that the concept of the cell synchronous frequency is applicable. Since the establishment of synchronism must involve several cells, one expects even in the independent cell model that the association of cell location with radiation frequency must have some width. In this section we apply the equivalent circuit theory, including detuning, damping, and manifold reflections to a determination of this relation.

The power spectrum for a beam with uniform offset δx is proportional to P(f) given below by [3]:

$$P_u(f) = \delta x^2 f \sin\phi(f) \left| A(f) / (1 + R(f)) \right|^2 \qquad (2.1)$$

Here $\phi(f)$ is the manifold phase advance function, R(f) the reflection amplitude, and A(f) the manifold excitation amplitude for unit offset [6] all evaluated at the terminating manifold section, and f is the frequency. This function computed for DDS 1 is shown in Fig. 1 and compared with the results from the ASSET experiment [4].

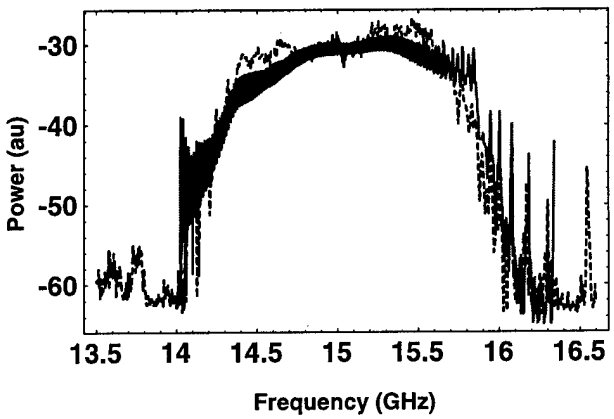


Fig 1: Power spectrum radiated to the downstream HOM coupler: experimental values are shown dashed and those calculated from circuit theory are indicated by the solid curve.

0-7803-4376-X/98/$10.00 © 1998 IEEE

In the equivalent circuit theory both the cell and manifold amplitudes are linearly related to the excitations at the individual cells so that instead of defining A(f) for uniform offset we write $A(f)=\sum u_n(f)\delta x_n$ or with $M_n(f)=\sqrt{f\sin\phi(f)}\,u_n(f)/(1+R(f))$:

$$P_u(f)=\left|\sum M_n(f)\delta x_n\right|^2 \qquad (2.2)$$

The $u_n(f)$ may be determined from the procedure outlined in [3]. To apply (2.2) to the localization problem we set $\delta x_n=\delta x$ for a set of adjacent cells n-r to n+r and zero elsewhere and compute the power spectrum. The result for a representaive set of central cells is shown in Fig. 2. The pair of integers above each sharp peak in the figure give the central cell number n on the left and the span specifier r on the right. The number r is determined by requiring it to be the smallest number which gives a peak equal in amplitude to that obtained by applying δx to all of the cells. Because r is a small integer, this criterion is not met exactly, but the figure indicates how well it is met. We call the central frequency of the peaks the coupled synchronous frequency of the central cell.

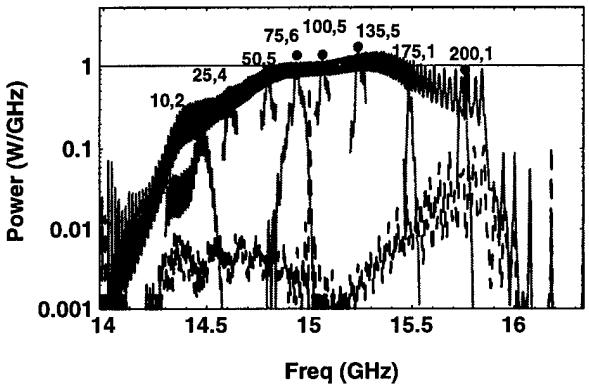


Fig 2: Power spectrum emitted from the downstream DDS manifold illustrating the narrow frequency bands emitted by localized offsets. The pairs of numbers above each peak indicate the central cell and the span specifier (see text) of the localized offsets.

The curve of the coupled synchronous frequency in Fig. 3 is a fit to the points determined in Fig. 2; the horizontal bars represent a fit to the span. The synchronous frequencies of the independent cell model (called "uncoupled") are shown for comparison, and one notes a shift, small, but significant for locating misalignments. The span 2r+1 varies from three to thirteen cells and is largest at frequencies where the mode are most extended. Almost all the (damping suppressed) modes of DDS 1 are standing waves terminating within the structure, but their extension varies from one or two cells to over a hundred. For the more extended modes the excitation region is well localized within the mode.

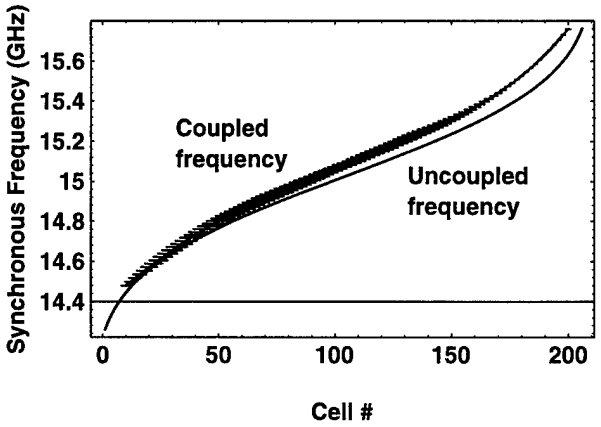


Fig 3: Illustration of the deviation of the synchronous frequency from the uncoupled one due to cell-to-cell detuning. The short horizontal lines indicate the extent to which cell offsets may be localized by frequency.

3. BEAM-BASED STRUCTURE ALIGNMENT

In fabricating the first DDS a number of cell misalignments occurred, the worst being 60 microns at cells 45 to 46. This is illustrated in Fig. 4 in which the second and third of the three mechanical measurements performed using a CMM (coordinate measuring machine) are plotted. The third measurement was performed after the ASSET experiment. However, it is evident that the absolute value of the jog at cell 45 is similar to data set 2. Indeed the main difference between the two data sets is an angular shift, a translational offset, and a bend.

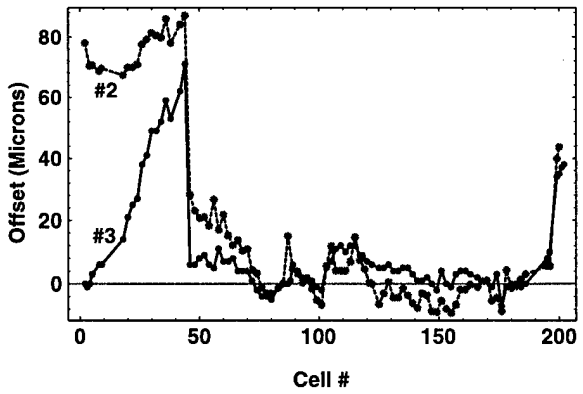


Fig 4: Two set of mechanical alignment data: measured before the ASSET experiment (data set 2) and after the completion of the experiment (data set 3)

A beam based alignment measurement carried out during the ASSET experiment is reported in [5]. The measurement, performed by stepping the beam transversely across the structure, provided a complete power spectrum at each step. From this data one obtains the beam position which minimizes the power at each frequency and generates the curve of minimum power position versus frequency given in [5]. A curve of minimum power position versus cell number can be

obtained by identifying the frequency with the coupled synchronous frequency given in Fig. 3 as a function of cell number. One can then relate this measurement to structure misalignment by assuming that when the power is minimized at a particular coupled synchronous frequency that the beam is centered on the cell to which that frequency belongs. The cell offsets obtained in this way (i.e. remapping) are, after translational and angular adjustment, compared to the two sets of CMM data in Figs. 5 and 6. The adjustments are legitimate because the position and tilt of the beam relative to the axis of the CMM measurements is not known.

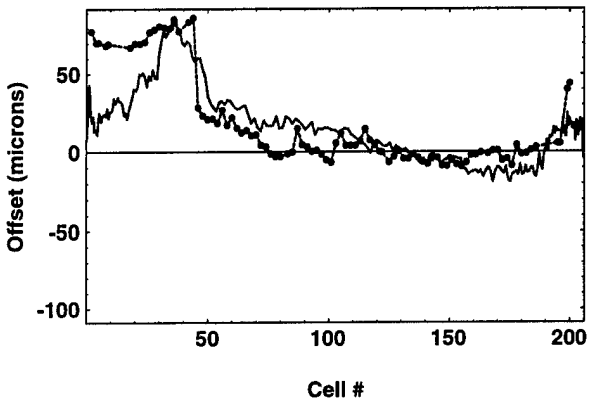


Fig 5: Comparison of the CMM data set # 2 versus the ASSET power minimization position data remapped from frequency to cell number (see text).

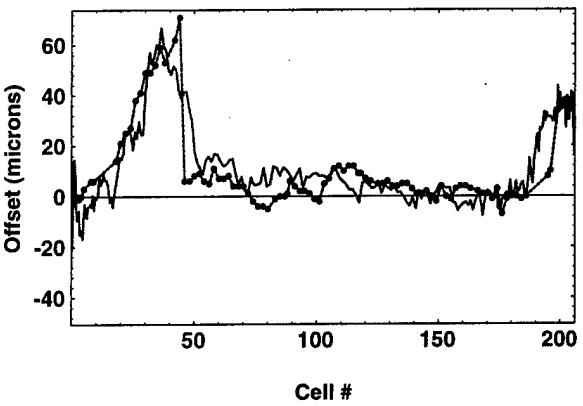


Fig 6: Comparison of the CMM data set # 3 versus the ASSET power minimization position data remapped from frequency to cell number (see text).

The minimum power position X(f) can also be linearly related to the mechanical offsets by writing δx_n in Eq. (2.2) as X(f) - x_n where x_n is the mechanical offset of the n'th cell and minimizing (2.2) with respect to X(f). In terms of 295 discrete frequencies f_n for which the measurements were made one finds:

$$X(f_m) = \sum_n K_n(f_m) x_n \qquad (3.1)$$

where:

$$K_n(f) = \mathrm{Re}\left\{\sum_m M_m^*(f) M_n(f)\right\} \Big/ \left|\sum_m M_m(f)\right|^2 \qquad (3.2)$$

It is thus a set of linear equations for 295 power minimization positions in terms of 206 offsets. The determination of the $X(f_m)$ from a set of x_n is straightforward and reported in [3]. For comparison with the remapping method described above, however, one needs to determine the cell offsets from the minimum power positions. Equation (3.1) is solved for the x_n by employing the pseudo (ie Moore-Penrose) inverse, based upon the singular value decomposition of $K_n(f_m)$ regarded as a 295 x 206 matrix. The result obtained (after stabilization by application of a tolerance criterion on the singular values and Savitzky-Golay filtering on the output) is shown in Fig. 7, where it is compared to that obtained by remapping. The agreement is satisfactory, but there is no evidence that the pseudo inverse method improves the delineation of abrupt offset changes. Thus for the present at least we consider the remapping method to be preferred, both because it is simpler and because it does not involve uncertain numerical procedures.

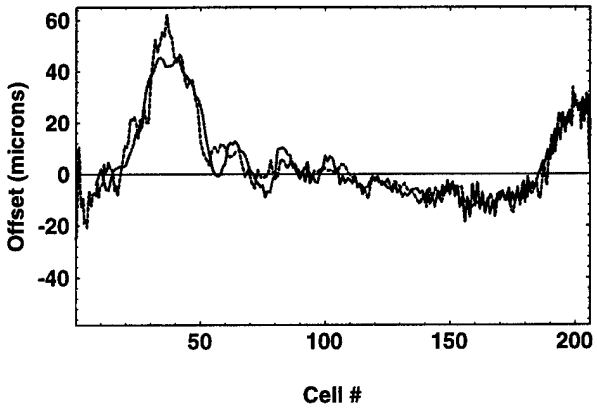


Fig 7: Cell offsets computed by the pseudo inverse method(solid curve) compared to those computed by remapping as in Figs. 5 and 6 (dashed curve).

4. ACKNOWLEDGMENTS

This work is supported by DOE grant number DE-FG03-93ER40759[‡] and DE-AC03-76SF00515[†]. We have benefited greatly from discussions at the weekly structures meeting at SLAC, where these results were first presented and thank all members of the group.

5. REFERENCES

[1] K. Bane et al, Part. Accel. **42**, p 123 (1993)
[2] N. Kroll et al, AIP Proc. 335, p 777 (1994)
[3] R.M. Jones et al, Analysis ... Manifold Radiation ..., Proc. 7'th Workshop on Advanced Accelerator Concepts,
[4] M. Seidel et al, Proc. Linac96 p 653 (1996)
[5] M. Seidel, Studies .. of Dipole Mode .., 5B3 Pac'97
[6] R.M. Jones et al, Proc. EPAC 96, p 1292 (1996)

SPOTSIZE STABILIZATION STUDIES FOR THE TESLA BEAM DELIVERY SYSTEM

A. Sery
Branch of the Institute of Nuclear Physics, 142284 Protvino, Moscow region, Russia

Abstract

Studies of the ground motion induced spotsize growth in the interaction region of the TESLA linear collider and some tools to recover are presented here. Analytical results are given and compared with simulations by particle tracking. Performance of different procedures, such as orbit correction, adaptive alignment and knob scan, studied by tracking simulations, is reported.

1 INTRODUCTION

The main parts of the TESLA Beam Delivery System[1] are the Collimation Section, Tuning and Diagnostic Section and the Final Focus Sytem (Fig. 1). It is the BDS where the most important tolerances on transverse misalignments of focusing elements are located.

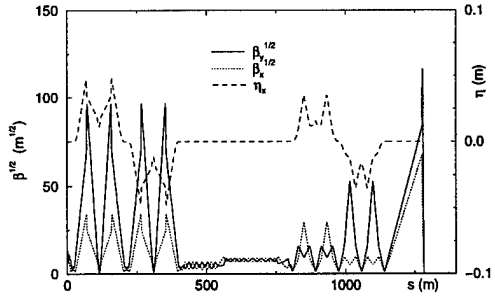


Figure 1: Optics of the TESLA Beam Delivery System[1].

Ground motion is one of the main sources that will produce, after certain time, an intolerable value of misalignments resulting in reduction of luminosity via the beam offset and distortion at the Interaction Point. The fast orbit feedback, which is possible for TESLA due to uniquely long bunch separation, will cure the beam-beam offset. We will concentrate therefore only on the spotsize stabilization.

When the beamline is affected by ground motion only (no correction applied yet), the free evolution of the beam spotsize can be evaluated analytically using the ground motion spectrum $P(\omega, k)$ and the corresponding spectral response functions, determined in linear approximation[2]. This analytical treatment is incorporated into the "FFADA" program[3]. The analytical results provide quite helpful information on the critical time scales, however the question "whether the linear approximation is sufficient?" should not be forgotten.

Semi-analytical methods, appeared recently, are able in some cases to evaluate efficiency of a correction in linear collider. The generalized spectral approach[4] can give clear analytical expression for several correction method applied to a regular linac. The method proposed in[5] is more general and may be of great help if fully developed. However, when a correction is applied to a BDS to stabilize the spotsize, simulations must be used to determine the procedure performance since such procedures may be quite complex and the focusing structure is very irregular.

2 FREE EVOLUTION OF THE BEAM

Since the critical time scales are quite large for the beam size growth, it is sufficient to consider only the diffusive "ATL" ground motion[6]. The motion assumed to have the same coefficient A in both horizontal and vertical planes. Neighboring elements (such as quadrupole – sextupole pairs or the final doublet) were assumed to be placed on the same support. The beam parameters used in simulations were: 250 GeV/beam, $\varepsilon_x = 2.8 \cdot 10^{-11}$ m, $\varepsilon_y = 5 \cdot 10^{-13}$ m, $\beta_x^* = 25$ mm, $\beta_y^* = 0.7$ mm, $\sigma_E = 10^{-3}$. After the beam tracked through the misaligned beamline, the offset was removed and the average beam matrix elements, for example $\sigma_{xy} = \overline{xy}$, were computed. Tracking was performed then with different seeds that gave the rms beam matrix $\langle \sigma_{xy}^2 \rangle^{1/2}$. It was convenient to normalized it to the nominal values in the point of observation: $\langle \sigma_{xy}^2 \rangle_n^{1/2} = \langle \sigma_{xy}^2 \rangle^{1/2} / \sqrt{\sigma_{xx0}\, \sigma_{yy0}}$.

Let us first consider only the the FFS part of the BDS. The analytically found dispersion, waist shift and coupling (which the spot size growth is determined by) versus the $A \cdot T$ coefficient are presented on Fig. 2 in comparison with the tracking results. One can see that the linear approximation and tracking are in perfect agreement for the FFS part of BDS. If one assumes $A = 10^{-5}$ μm^{2}s^{-1}m^{-1} then the critical time scale for 2% luminosity loss is about 200 s for the FFS part of the TESLA BDS.

However, when the complete TESLA BDS was studied by tracking, much faster spotsize degradation has been found (Fig. 3). The terms like yy', yx' and yx of the normalized beam matrix, which were proportional to $A \cdot T$ that indicates on nonlinear effects, have shortened the resulting

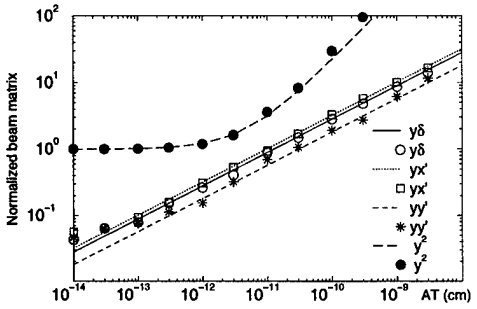


Figure 2: Elements of the normalized rms beam matrix σ_n for the FFS part of the TESLA BDS versus AT. Linear model prediction (lines) and tracking results (symbols).

0-7803-4376-X/98/$10.00 © 1998 IEEE

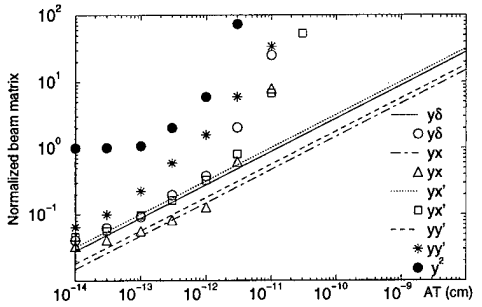


Figure 3: Elements of the normalized beam matrix σ_n for the complete TESLA BDS versus AT. Linear model prediction (lines) and tracking results (symbols).

critical time scale by about one order of magnitude. This time is still quite large with respect to the repetition rate, nevertheless, allowing safe operation of the collider.

The reason for this nonlinearity has been found to be the vertical misalignment of quadrupoles located in maxima of betatron function in the IP-phase part of the collimation section. Since these quadrupoles are in phase with the IP one could expect that they have little effect on the IP beam size. However, misalignments of these quadrupoles produce a vertical beam offset in sextupoles of the Chromatic Correction Section (CCSY). If the matrix between paired sextupoles in CCSY is not perfectly $M = -1$, then the beam distortion at IP will appear.

Assuming that the vertical misalignment of the quadrupole in IP-phase collimator is y_c the following expression for the element of the normalized beam matrix in the IP can be finally deduced:

$$(\overline{yy'})_n = 6K_2^2\,K_1^2\,R_{12}\,\beta_c\,\beta_s^2\,y_c^2$$

where β_c is the maximum of the vertical betatron function in the IP-phase collimation section, β_s is the vertical betatron function in CCSY sextupoles, K_2 is the strength of CCSY sextupoles, K_1 is the strength of quadrupoles in the IP-phase collimation section, R_{12} is the matrix element between paired sextupoles in CCSY. The latter cannot be much smaller than the length of CCSY quadropoles or sextupoles, in our case $R_{12} \approx 1$ m. The 2% luminosity loss criterion gives $y_c \lesssim 0.1$ μm for our parameters, much tighter than the value given by the linear approximation.

3 CONTROLLED EVOLUTION

Different procedures may be used to prevent the beam size growth in the IP of a BDS. We consider here the orbit correction à la "one-to-one", the adaptive alignment[7] and tuning by knob scan[8]. All these procedures have their advantages and disadvantages. So, a proper combination of these or other techniques should be used to provide reliable luminosity stabilization.

Finding the proper combination of algorithms requires to know performance of each individual procedures. In particular, one needs to know influence of Beam Position Monitor resolution (the effect of BPM offset is not considered in the paper) and capability of a procedure to struggle against the increase of misalignments driven by ground motion.

The beam dispersion growth can be found analytically if the first two procedures are applied to a regular FODO linac[4]. The qualitative dependence of the beam dispersion when the "one-to-one" orbit correction is applied

$$\langle\eta^2\rangle \propto (\sigma_{\rm bpm}^2 + A\,T\,L)\,N \;+\; A\,\Delta T\,L\,N^3$$

where N is the number of quadrupoles in the linac, L is the quadrupole spacing, T is the time since the moment of perfect alignment, ΔT is the time interval between successive corrections, $\sigma_{\rm bpm}$ is the BPM resolution. From the other hand, if the adaptive alignment is applied, we have

$$\langle\eta^2\rangle \propto (\sigma_{\rm bpm}^2 \;+\; A\,\Delta T\,L)\,N^3$$

We see the obvious fact that for the "one-to-one" orbit correction the beam dispersion grows with time, since the algorithm does not realign quadrupoles, in contrast to the adaptive alignment where the beam dispersion does not increase with time. From the other hand, the influence of the BPM errors is more severe for the adaptive alignment since a single BPM error produce the trajectory offset in all downstream quadrupoles, while only three quadrupoles will have the trajectory offset for a single error for the "one-to-one" orbit correction.

For a irregular focusing system, such as the BDS is, the dependencies given above are valid too, but the quantitative answer may be obtained only by simulations. The results are shown in Fig. 4 and Fig. 5.

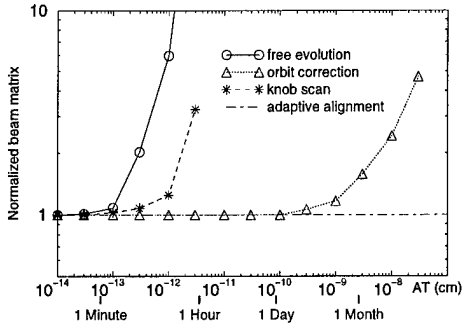


Figure 4: Normalized vertical beam size $(\sigma_{yy})_n$ for the TESLA BDS versus AT for different procedures applied solely. The second axis assumes $A = 10^{-5}$ μm^{2}s^{-1}m^{-1}.

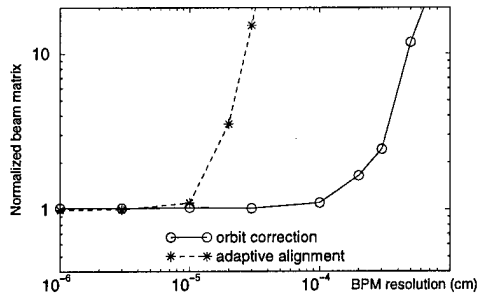


Figure 5: Normalized beam size $(\sigma_{yy})_n$ for the TESLA BDS versus BPM resolution for the orbit correction and for the adaptive alignment.

For the orbit correction simulations we used several monitor-corrector pairs. The monitors are two plane BPM, they are located in all critical places, mainly in maxima of beta functions, at the face of each sextupole, at the face of the final doublet. Correctors are located at the proper place (with respect to the betatron phase) upstream to the corresponding monitor. Simulations assumed that the perfectly aligned line were available at the beginning that gave possibility to store the "gold orbit" to be recovered by the orbit correction after the beam line misaligned.

For the adaptive alignment simulation both the original formula[7] and the one corrected for thick lenses[10], which gave much better but still not quite satisfactory results, were tried. We had to use finally the algorithm which starts from the same conditions as[7] but does not make any simplifying assumptions on the focusing structure. These conditions are the following: a) if three neighboring quadrupoles aligned to the same line but the incoming beam has an offset at the face of the first quadrupole then the displacement applied to the central quadrupole by the algorithm is zero; b) the same but the incoming beam has an angle; c) if the central lens misaligned by Δx the algorithm should move it back by the value $C\Delta x$ where C is the coefficient which control convergence. All the necessary transfer matricis were assumed to be known. The algorithm worked well for the BDS. However, if applied to the beamline with too high misalignments, it diverges because the orbit offset in the CCS sextupoles introduces coupling of x and y planes, which the algorithm assumes independent. Applying the orbit correction before the adaptive alignment will cure the problem.

The knobs used in simulations were the displacements of paired sextupoles of CCSX and CCSY similar as in[9]. The sextupoles can be moved in horizontal or vertical plane, symmetrical or antisymmetrical, in certain relevant range, orthogonally affecting on the IP beam matrix:
in CCSY, horiz., symm., range 2 μm, affect on $\sigma_{yy'}$
in CCSX, horiz., asymm., range 3 μm, affect on $\sigma_{x\delta}$
in CCSY, vert., symm., range 2 μm, affect on $\sigma_{yx'}$
in CCSY, vert., asymm., range 5 μm, affect on $\sigma_{y\delta}$.
These knobs were scanned with step digitized by range$/N_s$, to maximize the luminosity, which was assumed to be permanently measured. The value $N_s \approx 20$ was found to give good results. The knobs located in the tuning section of the BDS, which control all the linear coupling terms at the FFS entrance, were also used in simulations.

We see that the orbit correction is able to stabilize the luminosity during about one week with quite feasible BPM resolution (about 0.5 μm). The adaptive alignment is able to keep the beam size forever if continiously repeated but the required BPM resolution is 10 times higher (50 nm). One should note here that if the orbit correction will be applied after the adaptive alignment, the BPM resolution of the latter should not be already as high. Formally, for the regular linac $\sigma^2_{\rm bpm} \lesssim AT_{121}L$ is required where T_{121} is the time until the orbit correction is able to recover ground motion influence. The value $\sigma_{\rm bpm}$ will be a few μm in our case and might be limited by other effects not considered here (beamline walking out, etc.). The performance of the knob scan procedure is relatively modest since the linear knobs are not able to help when the distortion produced also by non-linear beam matrix elements. This procedure is an additional remedy, therefore.

Would the choice be limited by these three procedures, the following combination could be used. Normal BDS operation will be done with the orbit correction only. The knob scan procedure will be done a few times per week, in vivo. After about one months the adaptive alignment can be applied to recover the smooth beam line. For this the experiment should stop. Of course, another combination as well as other methods of orbit correction and beam based alignment can be used, it will be studied further.

4 CONCLUSION

The IP spotsize growth induced by the diffusive ground motion has been studied by simulations and analytically in the linear approximation. The linear approximation was found to be in perfect agreement with the tracking results for the FFS part of the BDS, while much faster beam degradation caused by nonlinear effects has been found when the complete BDS was studied. The resulting critical time scale is still quite large with respect to the repetition rate, nevertheless, to ensure safe operation of the collider.

The possible spotsize stabilization strategy for the TESLA BDS is to work only with the simple orbit correction, à la one-to-one, performing knob scan procedure several times per week. With this strategy a beam based realignment of all focusing elements will be required only about each month.

5 ACKNOWLEDGEMENT

I am grateful to R. Brinkmann, S. Fartoukh, A. Mosnier, O. Napoly, and N. Walker for a fruitful collaboration.

6 REFERENCES

[1] TESLA Conceptual Design Report, DESY 97-048 (1997).

[2] A. Sery, O. Napoly, Phys. Rew. E. **53**, 5323 (1996).

[3] O. Napoly, B. Dunham, in Proc. of EPAC 94, London, p. 698 (1994).

[4] A. Sery, A. Mosnier, DAPNIA/SEA/96-06, CEA Saclay (1996) to be published in Phys. Rev. E.

[5] S. Fartoukh, CERN/PS 97-06, CLIC Note 323 (1997).

[6] B. Baklakov, P. Lebedev, V. Parkhomchuk, A. Sery, A. Sleptsov, V. Shiltsev, INP 91-15; Tech. Ph. **38**, 894 (1993).

[7] V. Balakin, in Proc. of Workshop on Next Generation Linear Collider LC91, Protvino (1991).

[8] N.J.Walker, J. Irwin, M. Woodley, in Proc. of PAC 93, Washimgton (1993).

[9] NLC Zeroth Order Design Report, SLAC-474 (1996).

[10] V. Alexandrov, V. Balakin, A. Lunin, in Proc. of the Linac 96 Conference, p. 255, Geneve (1996).

PRE-ALIGNMENT OF CLIC USING THE DOUBLE-WIRE METHOD

W.Coosemans and H.Mainaud, CERN, 1211 Geneva 23, Switzerland.

Abstract

The pre-alignment and active control method for the Compact Linear Collider (CLIC) is described. Two new types of instruments are used in this system - a biaxial Wire Positioning System (WPS) which uses a stretched wire as the spatial reference, and a capacitive three axes Tilt Meter System (TMS). The instruments, and the way they are used with the well-known Hydrostatic Levelling System (HLS) are described.

1 INTRODUCTION

Transverse alignment tolerances of about 10μ (rms) are required for the Compact LInear Collider (CLIC) [1] in order to limit the emittance blow-up due to transversely deflecting wakefields to reasonable values. An active alignment system using precision micromovers is proposed to achieve these tight tolerances. The length of each CLIC linac for the 500 GeV centre-of-mass machine is about 4 km. Since the CLIC scheme is a two-beam scheme, each linac in fact comprises two parallel linear accelerators about 550 mm apart. The accelerating structures and beam position monitors of each linac are supported by precisely pre-aligned V-blocks sitting on SiC girders. The ends of two adjacent girders are connected by swivel-joint link rods to a common platform which is driven by three remote-controlled 0.1 μm resolution stepping motors (Fig.1). The inter-girder articulation points are 1.41 m apart. The quadrupole supports are independent of the girder supports and are driven by five identical stepping motors. The quadrupole support platforms are located above the girders.

2 GENERAL DETAILS OF THE METHOD

Aligning the linac in this case means aligning the articulation points of the girders, and the magnetic components. One linac has about 2780 girders and 400 magnetic components.

The standard deviation on the relative position of three consecutive intersection points or three consecutive magnetic components must be less than 5 μm. To obtain this result and to monitor continuously the geometry of the linacs, it is planned to use a technique known as the "double-wire method".

This involves stretching parallel rows of wires parallel to the axis of the linacs. The wires overlap half way along their own length and form a geometric reference network for the alignment and monitoring operations. The articulation points of the girders and the magnetic components are fitted with sensors which use the wires as their reference.

Three types of measuring instrument are foreseen:

a) the hydrostatic levelling system (HLS), which has already been fully described and widely used;
b) the tilt measuring system (TMS), a new instrument currently under development which measures, to a precision of the order of 0.1μrad, angles and accelerations along two horizontal axes, and accelerations along the vertical axis;
c) the two-axis wire positioning system (WPS).

3 WIRE POSITIONING SYSTEM (WPS)

The WPS is an instrument that measures, along two axes and to a precision of the order of one micron, the distance between its mechanical axis and a stretched wire (Fig.2).

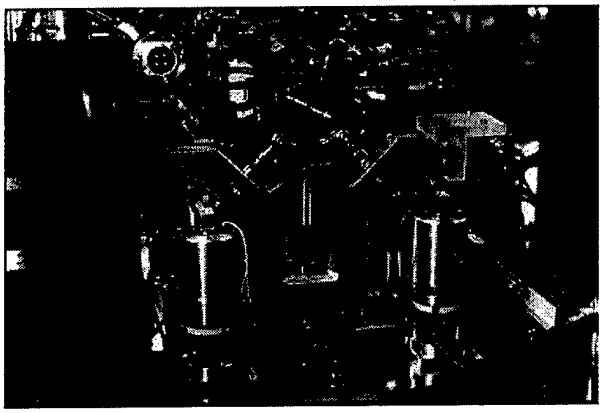


Figure 1: Inter-girder connection

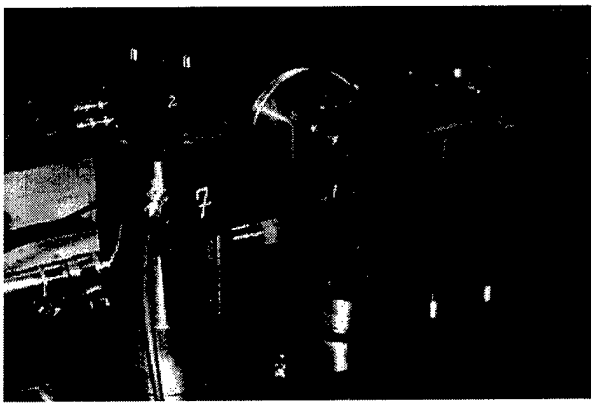


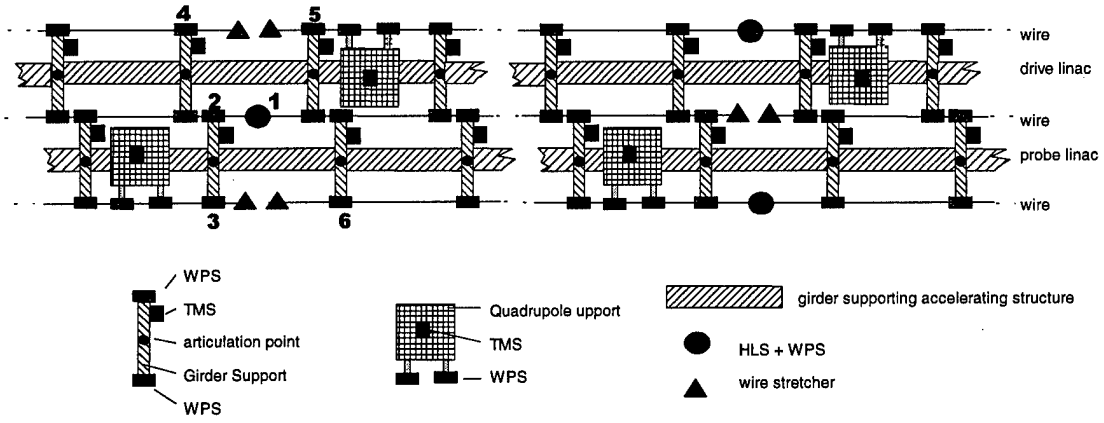
Figure 2: WPS + HLS + Tensioner

0-7803-4376-X/98/$10.00 © 1998 IEEE

The technique used is capacitive measurement. The sensor and its target, the wire, form a variable capacitor. The measurement range along the two axes is ± 5 mm. For this range, the instrument delivers a voltage of 0 to 10 V per axis. The WPS has the form of a rectangular parallelepiped (46x46x70 mm), it has two opposite electrodes per axis this gives a good signal linearity (the most linear zone is around the mechanical centre of the sensor) and also eliminates any symmetrical cross-sectional variations of the reference wire. To install the wire, the instrument opens diagonally with a horizontal sensor and a vertical sensor in each half. Two pins are provided for the precise re-assembly of the two parts. The maximum error after this operation is 2 μm. The sensor consists of passive metal and ceramic components. If necessary the electronics can be located some tens of metres away for protection against radiation and the effects of magnetic fields. The electronic sensor assembly is very stable. Measurements taken over several days under laboratory conditions have shown variations of only 3 μm. Although the inherent capacitance of the cable connecting the sensor to the electronics is several orders of magnitude greater than the capacitance of the sensor this is not in this case detrimental due to the use of the special total shielding technique. The only constraint is that the electronics are adjusted for a given cable length.

Since the instrument is both stable and reproducibile it can be reliably calibrated. It was found that all the instruments have a nearly identical calibration curve, this is a direct result of the manufacturing precision. The calibration curves have a highly linear central zone (± 1 mm) and an outer zone of reduced linearity. The prototype sensors do have a defect, however, namely that the electrical zero does not correspond to the mechanical zero and varies for each sensor. Deviations of up to 50 μm have been observed. This defect will be corrected in the next batch of sensors. Once that has been done, it will be possible to use all the sensors with the same calibration curve; the maximum precision of ± 1 μm will naturally only be obtained in the highly linear zone. Outside this zone the deviations may be as much as 50 μm.

Figure 3 : Clic alignment : schematic plan view



3 THE WIRE

The wire used is actually a twisted wire made out of very strong low density carbon-fibres to minimise deflections. It conducts electricity sufficiently well to allow capacitive measurements.

The characteristics of the wire are as follows:

- apparent average diameter: 0.32 mm
- weight of 100 m of wire: 8.522 g
- deduced density: 1.06 kg/dm^3
- elastic limit: approximately 9 kg
- mass of counterweight used: approximately 6 kg.

The drawback of this wire is that in the long term some fibres eventually break and cause non-symmetric cross-sectional differences which distort the measurement. To eliminate this drawback, a method of impregnating the wire that will only cause a slight variation in the linear weight is being developed.

To be able to consider the wire as a reference it is vital to have a precise model of the stretched wire in the vertical plane under a given load. For a 60 m carbon fibre wire tensioned with 6 kg, a change in deflection of 1 μm may be obtained by modifying (i) the counterweight by 1 g (ii) the wire length by 3 mm (iii) the position of the WPS by 2 mm in the zone where the wire has its maximum slope, or by 27 cm in the horizontal part (iv) the linear weight by less than 0.01 g. It is actually the linear weight which, with a very slight variation, has the greatest impact. As it is impossible to know this value precisely, it will be necessary during the calculations to consider the linear weight as an unknown and to introduce other parameters, namely the heights of the ends and the mid-point of the wire.

A series of experiments has been conducted to determine the catenary of the wire with great accuracy. These measurements were carried out using a system that combined the HLS and WPS (as shown in figure 2). Once the catenary of the wire had been determined, the theoretical shape was calculated using the known parameters: length of the wire, dead weight, an estimated value of the linear weight of the wire and the heights of the ends and the mid-point of the wire. Comparison of measured and calculated values resulted in a standard deviation of less than 5 μm.

5 DOUBLE WIRE METHOD APPLIED TO CLIC

For the reference metrology of CLIC, the technique involves stretching wires approximately 60 m long from end to end on either side of the linacs. There are three rows of wires, of which one is common to both linacs. The wires in each row overlap. The wire attachments of one row are located at the mid-point of the wires in the opposite row. The ends of the girders are fitted with two wire positioning systems precisely located with respect to the articulation point. These instruments determine the position of the articulation point with respect to the wires and define the distance between two wires. The quadrupoles have two sensors which are on the same wire (see figure 4).



Figure 4: Quadrupole support

The points where the wires are fixed are deliberately chosen not to be the points that have to be aligned. The wire is fixed at one end and has a counterweight attached to the other. It passes over a knife-edged pulley which keeps it tensioned to a precision of 10^{-5} N. The model assumes that the ends of the wires are at the longitudinal mid-point of the sensors fitted to the end of the girder closest to where the wires are really fixed. To model the wire in the vertical plane, the heights of the ends and the mid-point of the wire have to be determined. The mid-point height (point 1 in figure 3) is simply measured using the combined HLS-WPS system shown in figure 2. Measurement of the ends could be done in the same way but is in fact done in the following more complicated way to minimise the number of HLS-WPS systems used. Since the WPS unit (point 2 in figure 3) is 100 cm at most from the next nearest HLS the height of point 2 can be calculated from point 1without significant error using the theoretical model. The height of point 3 is then determined from point 2 using the tiltmeter reading. A similar strategy is adopted to determine the heights of points 4,5 and 6 from the height of point 1.

6 ALIGNMENT OF CLIC TEST FACILITY (CTF)

It is planned to install the instruments and support systems described in this paper in CTF2 in June 1997. A pre-assembly of two of the 30 GHz modules is shown in figure 5. This will be a unique occasion to test this system in a working accelerator environment and should produce valuable information for further developments.

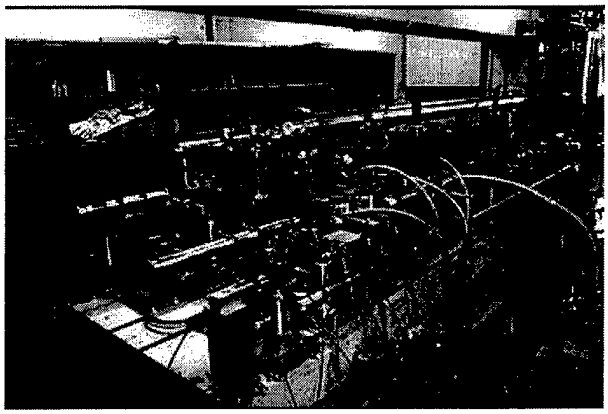


Figure 5: Pre-assembly of CTF2 30 GHz modules

7 CONCLUSIONS

The WPS has been shown to be a very good metrology instrument, and a stretched wire can be used as a two axis spatial reference. As for the double-wire method, some simulation work has been done. Preliminary results have reinforced our belief that the method is valid for the alignment of CLIC, but a great deal of work remains to be done before our study is complete.

REFERENCES

[1] H.Braun and 10 co-authors: 'CLIC-A Compact and Efficient High Energy Linear Collider', PAC95, Dallas, May 1995.

[2] W. Coosemans, H. Mainaud, "Métrologie linéaire : écartométrie biaxiale et fil tendu", CERN, CLIC Note No 326, Septembre 1996.

[3] The firm Fogale Nanotech, "Sensors and actuators for alignment of large machine components", 190 Parc Georges Besse, 30000 Nimes, France

A MULTI-DRIVE BEAM SCHEME FOR TWO-BEAM ACCELERATION IN A TEV LINEAR COLLIDER

R. Corsini, J.P. Delahaye. C. Johnson, A. Millich, A. Riche,
CERN, CH 1211 Geneva 23, Switzerland

Abstract

The Compact Linear Collider (CLIC) study of an e+/e- linear collider in the TeV energy range is based on Two-Beam Acceleration (TBA) in which the overall RF power needed to accelerate the beam is extracted from high intensity relativistic electron beams, the so-called drive beams. Due to the high beam power, acceleration and transport of the drive beams in an efficient and reliable way is specially challenging. An overview of a potentially effective scheme is presented. It is based on the generation of trains of short bunches, accelerated in low frequency c.w. superconducting cavities, stored in an isochronous ring and combined at high energy by funneling before injection by sectors into the drive linac. The various systems of the complex are discussed as well as the beam dynamics all along the process. An original method has been specially developed to stabilize such an intense beam during deceleration and RF power production in the drive linac.

1 INTRODUCTION

The 65 MW of RF power at 30 GHz for e+/e- acceleration up to 1 TeV c.m. in CLIC [1] is provided by high-current relativistic electron beams (the drive beams). The conversion of drive beam energy into RF power is made by means of low impedance resonant structures (CLIC transfer structures, CTS). The power is then fed into the accelerating structures (CLIC accelerating structures, CAS) of the two main linacs (e+/e-), running in parallel with the drive linacs.

Each one of the two drive linacs is divided in 10 sections of ~ 600 m length, powered by different drive beam pulses, providing 136 GW of peak power for 50 GeV acceleration of the main beam. The main and drive linacs are composed of many short modules, whose layout is depicted in Fig. 1.

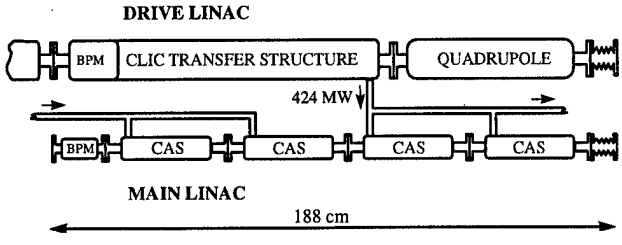


Figure 1. Main-drive linac module.

In such scheme one CTS feeds four CLIC accelerating structures (CAS). In this paper the following set of CAS and CTS parameters are considered:

		CTS	*CAS*	
R/Q	=	100 Ω/m	25 kΩ/m	shunt impedance
l	=	1.33 m	0.39 m	effective length
Q	=	4750	3500	quality factor
v_G	=	0.41 c	0.065 c	group velocity

With the given parameters the required peak RF power per CAS is 106 MW, and the pulse duration is 50 ns. The RF pulse is generated in the CTS by a drive beam pulse composed of 560 bunches, spaced by 3 cm.

The total charge per pulse is 5.6 μC, with a charge per bunch increasing from 5.3 nC to 11.4 nC in the first 20 ns and staying constant for the rest of the pulse, in order to obtain the desired RF pulse shape for beam loading compensation of the main beam. The CTS is a traveling wave structure composed of a cylindrical chamber of 10 mm radius coupled by longitudinal slits to four teeth-loaded rectangular waveguides.

The structure has been optimised [2] using the code MAFIA, in such a way as to obtain the desired coupling and group velocity, while keeping the transverse wakefields to a minimum level (~ 1 V/pC/mm/m). In order to control the transverse instability of the drive beam during RF power production, damping of the dipole mode is foreseen by slits located at 45° in the chamber and terminated with loads.

2 DRIVE BEAM GENERATION

Several schemes for the CLIC drive beam generation are at present under study [3,4]. In the solution described here [5], short bunch trains are generated using photocathode rf guns, accelerated in superconducting structures and then combined with the correct spacing. In this way the global beam loading is distributed in time over all the repetition period, allowing its compensation by power refill of the accelerating structures. A long collector ring (20 km) is used to store the bunches as they are accelerated. The bunches are compressed to their final length only after extraction from the ring. In this way the isochronicity requirements are relaxed, and the resistive wall effect in the ring is minimised. A smaller ring (the combiner ring) is used for the final recombination of the bunches at the right spacing.

0-7803-4376-X/98/$10.00 © 1998 IEEE

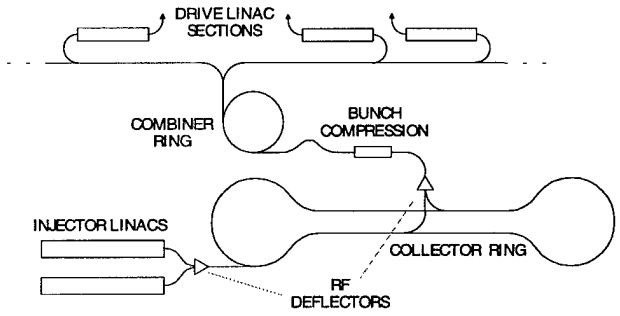


Figure 2. Drive beam generation complex layout.

In Fig. 2 a schematic layout of the drive beam generation complex is depicted. Initially, 2 × 160 trains composed of 35 bunches each are generated in two photoinjectors and accelerated up to 1.8 GeV in two 612.5 MHz superconducting linacs in push-pull configuration. The bunches in a train are spaced by 48 cm and have an rms length of 5 mm. This is repeated with the repetition rate of the main linac (700 Hz). A total of 1.83 GV of cavities at fundamental plus 45 MV cavities at 612.5 MHz ± ε to provide beam loading compensation along the train will be installed. The train to train beam loading is compensated by power refilling of the structures in between the passage of the 160 trains. The necessary RF power at 612.5 MHz is 70 MW, the power per meter of structure being 390 kW/m.

The trains are then combined two by two using a transverse RF deflector at the same frequency as the linacs, halving the distance between bunchlets. The trains are then injected into the collector ring using simple magnetic kickers. The ring is of dog-bone shape, and the two long straight sections (~ 10 km each) can be located in the same tunnel as the main and drive beam.

The end bends are composed of two 360° arcs with the same radius (125 m) needed for the main beam bends, and could be in the same tunnels as well.

After 1.4 ms the whole ring will be filled. When the last train is injected, the ring is emptied. Every second train is ejected by magnetic kickers in two different locations of the ring, at 10 km distance, and each train couple is recombined in a transverse RF deflector operating at 612.5 MHz.

The bunches are then compressed in length by RF (170 MV, 2.5 GHz, superconducting) + magnetic chicanes down to an rms length of 0.6 mm.

The trains are combined four by four in the combiner ring (270 m long), in order to obtain 20 trains of 560 bunches at 3 cm distance. The injection into the ring is made using two transverse RF deflectors at 2.5 GHz that creates a time dependent local deformation of the equilibrium orbit [6]. When all of the four trains are combined, they are extracted by a magnetic kicker, and the whole cycle is repeated for the next four. The 20 long trains so obtained are alternately switched in the two drive linacs.

The longitudinal beam dynamics has been evaluated all along the drive beam generation complex, in order to ensure that the final parameters (bunch length and energy spread) will allow the beam transport and power production in the drive linacs.

The longitudinal wakes and RF curvature in the injector linac, the radiation losses, the resistive wall effect, the space charge and the non-isochronicity in the collector ring are included in the calculation.

The rms energy spread along each bunch train after beam loading correction is very small (~ $6 \cdot 10^{-4}$). The single bunch energy spread at the exit of the injector linac is determined by the combined effect of the longitudinal wakefields and of the RF curvature and is of the level of 0.26 %.

In order to minimize the phase errors between bunchlets introduced in the magnetic chicane by the energy fluctuations between bunchlets, a 180° two-stage compression system is planned to be used [7]. In such a case, the phase error between bunches in a train can be kept to less than ± 1 degree. The final bunch length is 0.6 ± 0.02 mm rms as desired, while the total energy spread is limited to 6 %, which appears to be acceptable for transport to the drive linac.

3 THE DRIVE LINAC

The drive beam must be transported along the drive linac keeping the losses to a minimum, since even a small fraction of the drive beam power can give rise to an unacceptable local temperature increase [8].

The problem is complicated by the huge energy spread that the drive beam bunches develop along the linac (the first bunches of the train remain approximately at the 1.8 GeV injection energy, while the last bunches reach a minimum energy of ~ 200 MeV, see Fig. 3) and by the transverse wakefields in the CTSs. The drive beam focusing is based on variable strength FODO cells.

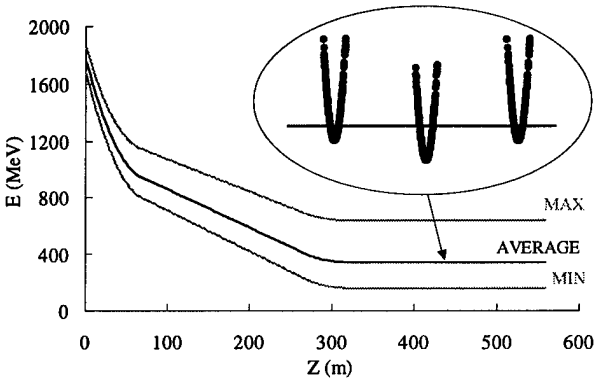


Figure 3. Energy profile along a drive beam pulse at the end of a drive linac section. The energy distribution within three subsequent bunches of the steady state part is also shown.

The initial quadrupole gradient is decreased along each linac section as the bulk of the drive beam pulse loses energy, thus keeping the full energy range in the stable region of betatron phase advance.

In order to control the transverse beam break-up, a certain amount of damping of the dipole mode in the CTS is necessary. On top of that, a novel method [9] (tuned decoherence damping, TDD) has been devised to control the instability during deceleration. An energy modulation is introduced in the train in such a way that odd bunches have a few percent energy difference with respect to the even bunches, as shown in Fig. 3. This essentially decreases the instability growth rate by damping coherent oscillations between adjacent bunches. The lattice parameters and the TDD amount can be optimised depending on the beam parameters using simulation codes that include the wakefields, specially developed for this purpose [9, 10]. In the case considered here, an energy difference of about 5 % is the optimum value; it could be introduced in the drive beam before injection using 40 MV of 5 GHz cavities.

The results of a typical simulation are shown in Fig. 4. Without wakefields (100% structure damping), the beam envelope is controlled all along the section and explodes afterward when the FODO becomes unstable for the lowest energy part of the beam. In the case of no or insufficient CTS damping, the transverse wakefield instability arises very soon, while the use of 30% damping of the dipole mode between subsequent bunches (100 ps) and of decoherence damping allows the instability to be controlled up to the end of the section.

The CTS rms misalignment is assumed to be 50 μm in this simulation, while the rms quadrupoles misalignment is 5 μm. Such values can in principle be obtained by applying a beam based one-to-one alignment algorithm to a witness drive beam pulse, but assumes a very good stability (< 5 μm) of the quadrupole magnetic center.

The use of a dispersion-free algorithm for the drive linac prealignment has been investigated, and while it gives better results for the trajectories without wakes, the simulation results including wakefields show a bigger beam blow-up. Studies on pre-alignment methods that can relax the required precision and improve the operability are under way.

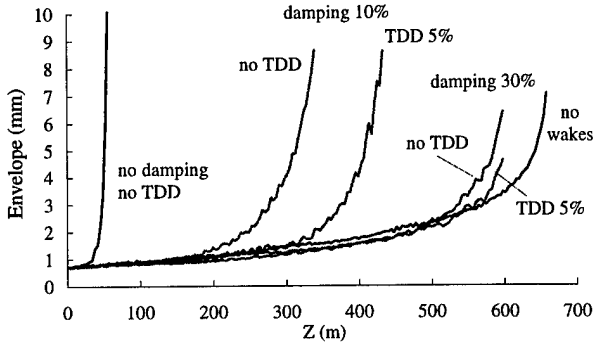


Figure 4. Drive beam envelope along a drive linac section for different hypothesis. The initial integrated quadrupole strength is 5 T, decreasing to a final value of 0.6 T at the end of the section (600 m).

4 CONCLUSIONS

A method has been described for the generation of the CLIC drive beam based on recombination of bunch trains at high energy. Such a method could provide a very good efficiency of ~ 40% (wall plug to RF) for 30 GHz power production. In spite of the unusually high power, the drive beam generation and acceleration are pretty conventional. The splitting in sections of the drive linac allows to keep the power in each drive beam at the acceptable value of 7 MW and makes the scheme easily extendable. The main drawbacks are the necessary gymnastics in beam storage and combination, and the relatively high CTS impedance, resulting in an increased transverse instability. As can be seen in Fig. 4, the drive beam stability is on the edge of the wakefield limit, and a critical issue will be the amount of damping which can be introduced in the CTS.

Experimental tests with beam are under way in the CLIC Test Facility, equipped with modules similar to the ones depicted in Fig. 1, although the CTS and drive beam parameters are somewhat different.

REFERENCES

[1] H. Braun, R. Corsini, J.P. Delahaye, G. Guignard, C. Johnson, J. Madsen, W. Schnell, L. Thorndahl, J. Wilson, W. Wuensch and B. Zotter, "CLIC - a Compact and Efficient High Energy Linear Collider", CERN-SL-95-26 (1995).

[2] A. Millich, "Parameters of the CLIC Transfer Structure for the Alternative Drive Beam Generation Scheme", CLIC Note 332 (1997).

[3] R. Corsini, "The Drive Beam Generation for Two Beam Accelerators", Proceedings of the 7th Workshop on Advanced Accelerator Concepts, Lake Tahoe, 1996 and CLIC Note 330 (1997).

[4] L. Thorndahl, "Push-pull Linac Pairs to Generate Two Drive Beams for CLIC Multibunch Operation", Proceedings of the 18th International Linear Accelerator Conference, Geneva, 1996, CERN/PS 96-38 (LP) and CLIC Note 317 (1996).

[5] R. Corsini, "The Collector Ring Method for Drive Beam Generation", CLIC Note 331 (1997).

[6] J.P. Delahaye, J.P. Potier, "A Novel Injection /Extraction Scheme for Short Bunch Separation in Accelerator Rings", CERN/PS 94-15 (LP) and CLIC Note 229 (1994).

[7] T. Raubenheimer, private communication.

[8] C.D. Johnson, P.K. Kloeppel, "Examination of the CLIC Drive Beam Pipe Design for Thermal Distortion Caused by Distributed Beam Loss", CLIC Note 328 (1997).

[9] C.D. Johnson, "Tuned Decoherence Damping Applied to the CLIC Drive Linac", CLIC Note 329 (1997).

[10] A. Riche, "Beam Dynamics in Drive Linacs", CLIC Note 334 (1997).

ANALYSIS OF A SYMMETRIC TRIPLET AND ITS APPLICATION TO RING INSERTIONS

T. d'Amico, G. Guignard, CERN, 1211 Geneva 23, Switzerland

Abstract

It is interesting to study the matching capability of a triplet for a large range of parameters and to cover all the possible solutions. Fully analytical treatments can be used for this purpose, when working with the thin lens approximation. Closed solutions and the conditions in which they exist are described for the special case of triplets with a symmetric geometrical arrangement. They define all possible matchings, which correspond to the requests or limits on the Twiss parameters that are specified, and then define the range of values that are obtainable for the betatron functions. Numerical extension to thick lenses gives the complete solutions for the retained cases. Applications are presented on insertion and lattice problems, with emphasis on the design for a possible isochronous ring that is part of the injection chain of the CLIC drive beam.

1 INTRODUCTION

The design of a new type of isochronous ring for the injection chain of the CLIC drive beam [1] needs a matching section between two adjacent isochronous cells. The purpose of this section is twofold. First the betatron function at the entrance and at the exit of it should have the same value and its slope should be equal and opposite. Second the total phase advance including the isochronous cell should be $n\pi/m$ where n and m are small integers, in order to minimize the geometrical aberrations. The symmetry of the betatron function leads quite naturally to choose a symmetric lattice for the matching section. We selected a symmetric triplet for its compactness and because it provides the required degrees of freedom. Several authors [2-7] have obtained analytical solutions in the thin-lens approximation for different configurations of quadrupole multiplets which are more general than a simple symmetric triplet. Their number of free variables is different from the six degrees of freedom of the transfer matrix and implies extra constraints or a mismatch factor [8]. In addition the adaptation of the analytical development of the general triplet to the symmetric case is cumbersome and does not take advantage of the lattice symmetry in an easy way.

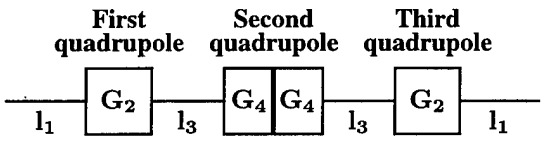


Figure 1: Schematic of a symmetric triplet

A geometrically symmetric triplet as shown in Fig.1 has four free variables (the two drift lengths l_1, l_3 and the magnetic gradients G_2, G_4 respectively of the first and half of the second quadrupole). It can easily be proved [9] that the diagonal elements of the transfer matrix for each plane are equal. Thus the number of independent values which can be fixed by selecting the Twiss parameters at the entrance and at the exit of the triplet is also four. The number of solutions is finite and does not depend upon additional assumptions. This observation has convinced us that a specific study would be useful not only for the design of an isochronous ring but also to explore, in an exaustive way, all the existing solutions for a more general matching problem. A particularly interesting one is related to the experimental insertions of collider rings such as the LHC. Triplets are indeed conveniently used to match the double waist at the interaction point to the rest of the lattice on either side.

2 COMPATIBLE BETATRON FUNCTIONS FOR A SYMMETRIC TRIPLET

The equality of the diagonal elements of the transfer matrix for each plane forces an important constraint on the betatron function in that plane at the entrance and at the exit of a symmetric triplet. Neglecting the special case when the phase advance is an odd multiple of π we may distinguish two situations. The first one which can be called a mirror symmetry triplet occurs when the betatron function has equal values and its derivative has opposite values, the phase advance being a free parameter. This is the case of interest for building up an isochronous module which may be chained up to form a ring. An example is shown in Fig. 2. The second configuration occurs when the betatron function has different values at each end of the symmetric triplet with its derivatives being free parameters. This generality is limited by the fact that the phase advance can no longer be freely chosen and is given by :

$$\cot\mu = \frac{\beta_2\alpha_1 + \beta_1\alpha_2}{\beta_1 - \beta_2}$$

where α_1, β_1 and α_2, β_2 are the Twiss functions at the entrance and exit of the triplet (see Fig. 1) respectively. Thus we have the choice only between two phase advances which differ by π. The more general case, which will be called a matching triplet can be of interest in several types of insertion. Its application to a collider final focus, where a round beam at the interaction point is matched to the standard periodic FODO cell, has been studied. An example is given in Figs 3 and 4.

0-7803-4376-X/98/$10.00 © 1998 IEEE

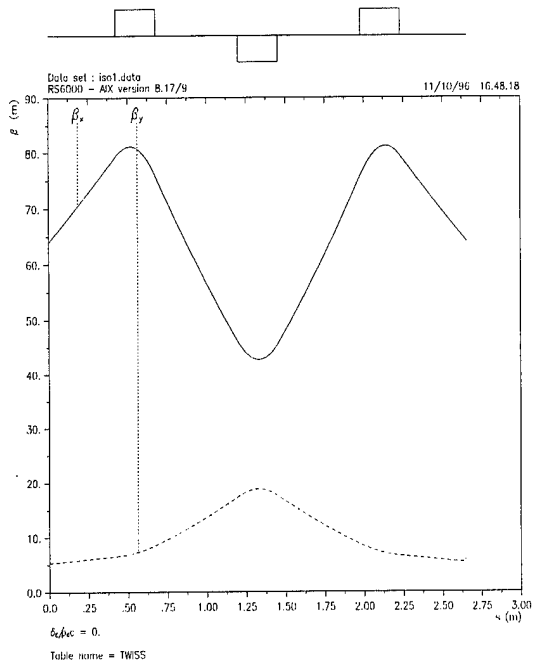


Figure 2: Horizontal and vertical β-functions of a symmetric triplet which inverts the slopes of these functions.

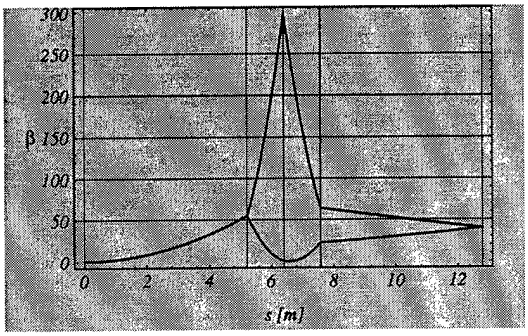


Figure 3: Hor. and vert. β-functions of the first solution of a symmetric triplet which transforms a round beam with a waist into a round beam with opposite divergences.

3 DETERMINATION OF THE FOUR PARAMETERS OF A SYMMETRIC TRIPLET

In the thin lens approximation, the transfer matrices for the horizontal and vertical planes can be expressed as functions of the two drift lengths l_1, l_3 and the quadrupole strengths $g_2 = K_2 l_q, g_4 = K_4 l_q$ where l_q is the quadrupole length and K_2, K_4 are the normalized gradients. To further simplify the problem the corresponding elements in each plane can be combined by taking half the sum and half the difference of those in the first column (only two elements in each transfer matrix are actually independent). Thus we obtain the following system of equations:

$$\begin{cases} c\ell_1 + \ell_3^2 g_2 g_4 = a \\ d\ell_1 + \ell_3(g_2 + g_4) = b \\ \ell_3 g_2(g_2 + 2g_4) = c \\ \ell_3^2 g_2^2 g_4 + g_2 + g_4 = d\,, \end{cases} \tag{1}$$

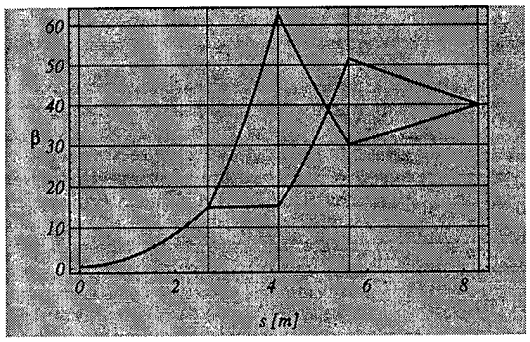


Figure 4: Hor. and vert. β-functions of the second solution of a symmetric triplet which transforms a round beam with a waist into a round beam with opposite divergences.

where a, b, c, d are defined by:

$$a = (t_{h,11} + t_{v,11} - 2)/4\,, \quad b = (t_{h,11} - t_{v,11})/4$$

$$c = (t_{h,21} + t_{v,21})/4\,, \quad d = (t_{h,21} - t_{v,21})/4\,.$$

where $t_{h,nm}$ and $t_{v,nm}$ are the elements of the horizontal and vertical transfer matrices respectively. The full analysis of (1) can be found in [9]. Neglecting the very special cases when either $c = 0$ or $c = \pm d$ and assuming $bc - ad \neq 0$, the general solution of (1) is given by :

$$\begin{aligned} \ell_1 &= \frac{1}{c^2 - d^2}\Big[(bc - ad)z - (bd - ac)\Big] \\ g_2 &= \frac{c^2 - d^2}{(bc - ad)(1 - z^2)} \\ \ell_3 &= \frac{(bc - ad)(1 - z^2)}{z(c^2 - d^2)} \\ g_4 &= \frac{z^2(d - cz)}{1 - z^2} \end{aligned}$$

where z is a solution of the cubic equation

$$z^3 - \frac{2d}{c}\,z^2 + z + \frac{d^2 - c^2}{c(bc - ad)} = 0\,.$$

Of course only real values of z chosen such that the corresponding drift lengths are positive, should be retained.

4 APPLICATIONS

The motivation of the study was to obtain the parameters of the matching triplet between two isochronous modules providing given phase advances in the two planes. The betatron function and its derivative were determined by the isochronous module while the phase advances were chosen in such a way that the total phase advances for the periodic cell were $\pi/3$ in the horizontal plane and $3\pi/2$ in the vertical plane. Thus every three cells in the horizontal plane and two in the vertical plane, kicks due to field errors may cancel out. This is a typical application of mirror symmetry and the results are quite good (Fig. 2). A second interesting

application is the matching from an interaction point to the standard FODO lattice. This would be schematically the case in circular colliders such as LHC when are neglected the constraints imposed on the value of the first drift length. At the interaction point, the values of the betatron functions in the two planes are equal and relatively small ("low β") while their derivatives are null. At the exit to the triplet it is assumed that the betatron functions in the two planes cross each other with opposite slopes. Thus,

$$\beta_{h,1} = \beta_{v,1} = \beta_1 \, , \alpha_{h,1} = \alpha_{h,2} = 0$$

$$\beta_{h,2} = \beta_{v,2} = \beta_2 \, , \alpha_{h,2} = -\alpha_{h,1} = \alpha_2$$

The horizontal and vertical transfer matrices are

$$T_h = \pm 1/\alpha_0 \begin{bmatrix} \alpha_2 & \beta_1 - \beta_2 \\ \gamma_1 - \gamma_2 & \alpha_2 \end{bmatrix}$$

$$T_v = \pm 1/\alpha_0 \begin{bmatrix} -\alpha_2 & \beta_1 - \beta_2 \\ \gamma_1 - \gamma_2 & -\alpha_2 \end{bmatrix}$$

where $\alpha_0 = \sqrt{\beta_1\gamma_2 + \beta_2\gamma_1 - 2}$ and $\gamma_1 = 1/\beta_1$, $\gamma_2 = (1 + \alpha_2^2)/\beta_2$. It is possible to show [11] that two and only two sets of triplet parameters satisfy these transfer matrices if we neglect a difference of π in the corresponding phase advances. The only condition is that α_2 should not be zero or equal to $\sqrt{(\beta_2 - \beta_1)/\beta_1}$. These two sets of parameters are given by:

$$\begin{aligned} a) \quad l_1 &= \tfrac{\alpha_2 z_{r,1} + \alpha_0}{|\gamma_1 - \gamma_2|} \\ g_2 &= \tfrac{\gamma_1 - \gamma_2}{\alpha_2} \tfrac{1}{1 - z_{r,1}^2} \\ l_3 &= 2l_1/z_{r,1}^2 \\ g_4 &= \tfrac{\alpha_2 z_{r,1}^3 g_2}{2\alpha_0} \end{aligned}$$

where $z_{r,1}$ is the (only) real solution of the cubic equation $z^3 + z + 2\alpha_0/\alpha_2 = 0$

$$\begin{aligned} b) \quad f &= 1/g_2 = \tfrac{\alpha_2}{\gamma_1 - \gamma_2} \\ l_1 &= |f/\alpha_2| \sqrt{\alpha_0(\alpha_0 + |\alpha_2|)} \\ l_3 &= |f| \sqrt{1 + |\alpha_2/\alpha_0|} \\ g_4 &= -g_2/2 \, . \end{aligned}$$

This treatment has been included in the package *BeamOptics* developed using the Mathematica language [10]. When l_1 is imposed the approach described here can be extended by adding a drift of free length at the exit of such a symmetric triplet. It is then possible to examine the behaviour of important quantities such as the length of this drift and the maximum value reached by the betatron functions inside the triplet; and this according to the variation of the triplet parameters in a predefined range, and to specific constraints on the betatron functions at the end of the added drift. Two cases have been investigated : waist in one plane and equal values of the betatron function with opposite slopes. All the possible solutions can be determined for canonical triplets ($g_4 = -g_2$), general symmetric triplets and even triplets where the third quadrupole strength is slightly modified. This study was applied to insertions of LHC type and provided interesting results on the ranges of acceptable triplet parameters [11].

5 CONCLUSIONS

It has been shown that in the thin lens approximation a geometrically symmetric triplet is a structure simple enough to be handled analytically and yet powerful enough to be applied to several interesting and quite different lattices. The method provides in a direct way all the existing solutions permitting a complete study of the required lattice. Existence conditions can only be made explicit in special cases but readily constructed as an abacus whenever needed. It can be shown [9] that the extension to thick lenses is easily obtained by solving a system of two nonlinear equations functions of the normalized gradients K_2, K_4. Of course such results are obtainable also by standard numerical matching programs although they may have difficulties in converging if not conveniently guided. Moreover their use is cumbersome and time consuming when included in a chain of specific codes written in other languages. The thin lens approximation obtained by the method described here is an excellent starting point for such algorithms.

6 REFERENCES

[1] T.E. d'Amico, G. Guignard, 'First-order design of a new type of isochronous arc', CERN SL/95–120, 1995.

[2] E. Regenstreif, 'Phase-space transformations by means of quadrupole multiplets', CERN 67–6, 1967.

[3] G. Wüstefeld, R. Maier and B. Simon, 'The analytical lattice approach for the ring design of BESSY II', Proc. First European Part. Accel. Conf. (EPAC), Rome, 1988.

[4] B. Zotter, 'Calculation of the parameters of a quad triplet from the transfer matrices', CERN/ISR–TH/73–43, 1973.

[5] B. Autin, E. Wildner, 'Applications of symbolic techniques to structural beam optics', Proc. Fifth European Part. Accel. Conf. (EPAC), Sitges (Spain), 1996.

[6] O. Napoly, 'Thin lens telescopes for final focus systems', CERN/LEP–TH/89–69, CLIC Note No. 102, 1989.

[7] P.J. Bryant, K. Johnsen,'The principles of circular accelerators and storage rings', (Cambridge University Press, 1993).

[8] P.J. Bryant, private communication.

[9] T. E. d'Amico, 'General treatment of a matching quadrupole triplet which is symmetric around its median plane', CLIC Note 322, January 1997.

[10] B. Autin, T. d'Amico, V. Ducas, M. Martini, E. Wildner, 'Analytic lattice design with BeamOptics' Proceedings of this Conference.

[11] T. E. d'Amico, G. Guignard, 'Constraints in the use of a symmetric triplet for the LHC low β insertion ', to be published.

THE S-BAND LINEAR COLLIDER TEST FACILITY AT DESY

M. Schmitz for the SBLC study group
Deutsches Elektronen Synchrotron (DESY), Notkestraße 85, D-22603 Hamburg, GERMANY

Abstract

The S-Band Linear Collider Test Facility under construction at DESY serves as a test bed for the essentiell hardware to build a large scale e^+e^- linear collider based on a 3GHz accelerating rf and having a center of mass energy of at least 500GeV. Besides the injection system at the beginning and a beam analysis area at the downstream end, the central part of the test facility consists of two modular units similar to those to be installed in a S-Band Linear Collider (SBLC) tunnel. The key-questions of Higher Order Mode (HOM) excitation, measurement, damping and feedback on the alignment of the accelerating structure as well as the quadrupole position have to be answered in order to manage the most crucial aspect of a 15km linear accelerator, namely the beam stability. The final layout of this test facility and the performance of the present setup including the first accelerating section fed by a 150MW klystron will be presented.

I. INTRODUCTION

Since 1991 a study group investigates the feasibility of a large S-Band Linear Collider (SBLC). Although S-Band accelerators are used in a lot of laboratories, the demands for a SBLC are not simple extrapolation from any existing accelerator. Therefore a R&D program started in 1992 to build up a S-Band Test Facility at DESY, in which the crucial aspects for a SBLC design can be investigated experimentally:

- Design, construction and operation of an injection system that is capable to produce bunchtrains that fulfill the SBLC demands (see section II).
- Development, operation and improvement of a high peak power rf-source, i.e. klystron and modulator as well as other high power components, like rf-windows and loads (see section III).
- Elaboration of a reliable concept to keep the HOM-effects below a tolerable limit determined by emittance growth. In this context measurement and damping of HOM's as well as straightness and alignment of the accelerating structure has to be mentioned (see section IV).
- Development of suppression techniques fighting ground motion and vibration (see section V).

The general layout of this test facility is shown in figure 1 and its main parameters are listed in table 1. Delivered by an injector the beam will be accelerated by 2 modular units similar to those as being proposed for the SBLC. One module consists of 2 travelling wave sections (β=1, $2\pi/3$-mode, 17MV/m) of 6m length each, that are driven by one 150MW/3μs klystron connected to a 375MW peak power modulator. In addition the downstream end of each accelerating section is completed with correctors, one screen and a focussing triplet accomodating a stripline type beam position monitor. Before being dumped at the end of the 40m long test facility the quality of the 400MeV beam will be analyzed using a spectrometer beamline including an OTR screen.

energy at full current	400	MeV
injector energy	≈4	MeV
length of bunchtrain	≥2	μs
number of bunches	1-250	
bunch to bunch separation	8, 16 or 24	ns
particles per bunch	1.5, 3.0 or 4.5	$10^{10}e^-$
current in bunchtrain	≥300	mA
normalized rms-emittance	$\approx 100 \cdot 10^{-6}$	π m rad

Table 1: Main parameters of the S-Band test linac

In the present status the beamline ends downstream of the 1. acc. section behind the focussing triplett. Except for a 4-cell travelling wave structure (TWB1), which is quite important for the process of bunching the injector is completely built up and delivers beam to the first acc. section. Since the first half of this section is surrounded by solenoids, it can not be mounted on the regular girder containing the micro-movers (see section IV). Therefore the concept of beam-based-alignment is not applicable for this section anyhow and thus a 5.2m long section similar to the regular 6m section (see table 3) has been placed there. The additional space will accomodate a kicker by which means the excitation of HOM's can be provoked in the following 3 regular 6m sections. From this point of view the 1.acc. section can also be regarded as belonging to the injection system. Results of the beam operation with this present setup are described in the next section.

II. INJECTOR AND BEAM OPERATION

The injector, combining high bunchcharge with short interbunch spacing, was designed by means of EGUN and PARMELA calculations [1]. The pulses of desired charge in a train of adequate timestructure are generated at a 90kV thermionic gun and compressed by means of two standing wave subharmonic bunchers SHB1

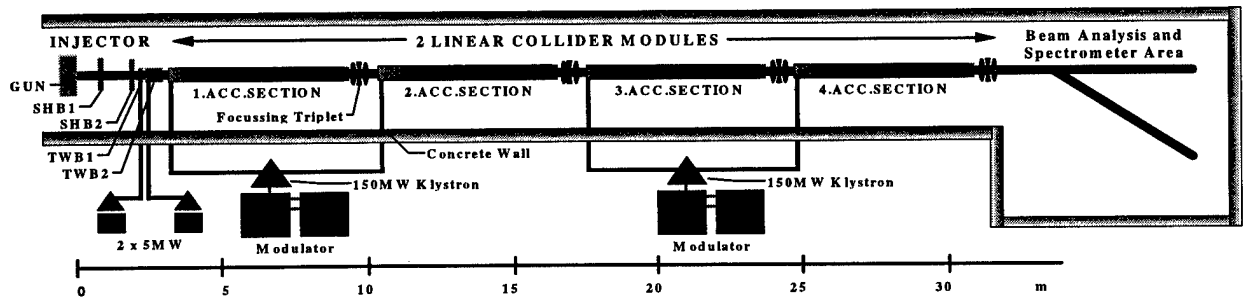


Figure 1: General Layout of the S-Band Test Facility

0-7803-4376-X/98/$10.00 © 1998 IEEE

(125MHz/34kV) and SHB2 (500MHz/36kV) as well as two S-Band travelling wave structures TWB1 (β=0.6, 4cells, $2\pi/3$, 7MV/m) and TWB2 (β=0.95, 16cells, $8\pi/9$, 12MV/m). Two 5MW klystrons will be used to supply TWB1 and TWB2 individually. In order to achieve a gradient of 12MV/m at the available power of 5MW while maintaining a large iris aperture, the group velocity of TWB2 is only 0.4%·c. Therefore the $8\pi/9$-mode was chosen. Starting with a 90kV gunpulse carrying 12nC ($7.5 \cdot 10^{10} e^-$) in a FWHM-bunchlength of 2.5ns, PARMELA simulation predicts an overall compression to a pulselength shorter than 10ps with more than 95% transmission. Since both TWB's also serve for acceleration the kinetic energy at the output of the injector is expected to be about 4MeV.

Starting in april 1995 with a short beamline dedicated for commissioning of the bunchtrain production at the gun, a longer beamline including both SHB's investigated their bunching performance from autumn 1995 to end of june 1996 [2]. The present setup started its operation in autumn 1996. It includes the first accelerating section and the whole injector complex except for TWB1.

The gun produces 2μs long bunchtrains with 8ns, 16ns or 24ns interbunch spacing. The gunpulses carry at least 7nC ($4.4 \cdot 10^{10} e^-$) in a FWHM length of typically 2.2ns. Their normalized rms-emittance measured 60cm downstream of the gun was 3π·mm·mrad compared to the PARMELA prediction of 6.8π·mm·mrad. From the same simulations 200ps long pulses are expected after compression with both SHB's. Bandwidth limited by the wallcurrent monitor 300ps long signals and a transmission better than 85% were observed. This is valid for every bunch of the train, since a feedforward-system compensates beamloading effects at both SHB's. In the final stage TWB1 sitting at the longitudinal focal point determined by the operation of both SHB's and having a phase velocity of 0.6·c will guarantee a clean capture of these pulses.

However TWB1 is still missing while TWB2 is already at its final position. In order to be captured at TWB2 having a phase velocity of 0.95·c, the 90keV pulses have to be accelerated at SHB2 while SHB1 still operates around zero crossing. From a 6.8nC ($4.25 \cdot 10^{10} e^-$) gunpulse about 5nC ($3.12 \cdot 10^{10} e^-$) can be found downstream of TWB2. In that optimized case SHB2 raises the average beamenergy by 36keV while its amplitude was 52kV which gives a phase of about 50° wrt. the beam. Finally 4.8nC ($3 \cdot 10^{10} e^-$) have been accelerated through the 1. acc. section of 5.2m length. From a 8μm-Al foil mounted ≈1.5m behind this section Optical Transmission Radiation (OTR) has been detected and a profile of the beam can be seen. Measuring the displacement of the beam at the OTR-screen introduced by a correction coil results in a beam momentum of 100MeV/c (±15%), corresponding to an accelerating gradient of 19MV/m. Taking the 5.2m section parameters from table 3 this gradient compares fairly well with the measured input power of 58MW.

Besides the information on the beam profile, the OTR will be used for energy and bunchlength measurement. In the first case its angular distribution has to be analyzed, while in the second case the frequency spectrum of the infra-red part of the coherent OTR needs to be measured. Both experiments just started commissioning their setup.

III. MODULATOR AND KLYSTRON

Since modulators and klystrons contribute significantly to the total cost of a linear collider, as much peak power as possible has to be produced with a single device. In 1993 a R&D program together with SLAC, the Technical University of Darmstadt, PHILIPS (Hamburg) and DESY started to construct and operate two 150MW/3μs/50Hz klystrons. Accompanied by 2D and 3D simulations [3] to optimize the overall layout, in 1994 the first and in 1995 the second klystron having a slightly modified output circuit geometry and improved HOM damping in the drift tube was built and tested at SLAC meeting the requirements as can be seen in table 2.

	Design	#1	#2	
beam voltage	535	527	508	kV
μ-perveance	1.79	1.78	1.80	$A/V^{1.5}$
output power	150	153	150	MW
pulse length	3.0	≥ 3.0	≥3.0	μs
efficiency	40	43	45	%
gain	≥50	56	57	dB

Table 2: Parameters of both 150MW klystrons

Similar to the one at SLAC to test the 150MW klystron at full power and 60Hz, two PFN-type modulators for the test facility are built at DESY. They consist of 4 lines in parallel resonantly charged up to 50kV within 17ms via a charging choke. A current of 16kA is supplied into the primary of a 1:23 pulse transformer when discharging the PFN by switching two thyratrons. Maximum ratings of the modulator are 535kV and 700A [4].

The first unit of modulator and klystron has been installed in the test facility and was successfully commissioned at 150MW/3μs/50Hz with the same performance as during the SLAC tests (see table 2). The second unit will be commissioned soon.

Since November 1996 one output arm of the 150MW klystron#1 has been connected to the 1. acc. section while the other still works on a load. Presently, after about 400h of beam operation and conditioning, the section can be operated with an 1.5μs long rf-pulse of 60MW (i.e. 120MW of klystron power) at 25Hz repetition.

IV. ACC. SECTION AND HOM-HANDLING

The accelerating section is of constant gradient type operating in $2\pi/3$-mode, with a continuous taper of the group velocity along its whole length of 6m. HOM handling to avoid emittance dilution due to single- and multibunch instabilities together with simple construction techniques to reduce the costs for mass production are the main topics to be investigated. The HOM handling concept requires HOM-damping, adequate section detuning as well as a certain straightness and alignment of the section. Assuming an average Q-value of the HOM's of 4000 (natural ≈13000) and the SBLC bunchcharge of 1.8nC (6ns interbunch spacing) the total accuracy of alignment and straightness of the 6m section has to be ≤50μm rms. In that case beam dynamics calculations predict an emittance growth of about 20% for a 15km long linac.

Since there are a lot of trapped modes in long travelling wave structures, external dampers would have to be coupled to the section at many positions, which is neither reasonable nor cost saving. Instead of that internal damping by sputtering a thin (20μm) steel layer onto the iris showed a Q-reduction of the HOM by a factor of 5, while the fundamental Q changes only by 5%. This layer withstood an iris tip field of 28MV/m in a high power standing wave test resonator without any degradation.

Nevertheless one or two cells will be equipped with HOM couplers to measure the beam induced power which is correlated to the average excentricity of the beam axis wrt. the section. This signal has to be minimized (beam based alignment) when driving the micromovers that are mounted below the section girder. The girder as shown in fig. 2 must not deteriorate the straightness of the section, mounted on top of it, even with temperature transient around it. Therefore it is constructed from a tube (448mm dia.) that is totally thermal insulated. The movers, one on each end of the girder can operate between ±1.5mm with a step size of 150nm (see figure 2).

	Linac II	SBLC	
length of section	5.2	6	m
attenuation	0.5-0.6	0.55	neper
group velocity	3.3-1.2	4.1-1.3	%·c
filling time	750	790	nsec

Table 3: Parameters of the accelerating sections for LINAC II and SBLC

In the process of replacing old sections of the LINAC II (the e^+e^- injector linac at DESY) 5.2m long sections having comparable parameters (see table 3) were built at DESY. While the straightness tolerance is easily met after the vertical inductive brazing of typically 1m long pieces, which have a measured rms deviation of typically 20μm, the horizontal braze of the complete 5.2m section has shown deviations of up to 1mm. They have been decreased down to 100μm rms by a recently developed straightening procedure, and will achieve the target value of 30μm after commissioning of an improved straightening device constructed for this reason.

Up to now five 5.2m sections have been assembled, tuned and high power tested at DESY. One of them is installed in the test facility as 1. acc. section and 3 are operating in the LINAC II continuously without difficulties.

Other major technical developments being made so far are a very compact symmetric high power input coupler [5] and the collinear load [6]. The collinear load absorbs the remaining rf-power over the last eight cells of the section while still accelerating the beam. Such a load avoids a second high power coupler (costs), represents no obstacle for the inductive brazing coil, is perfectly symmetric (no transverse kicks due to field asymmetries) and absorbs any higher order mode touching the end of the section.

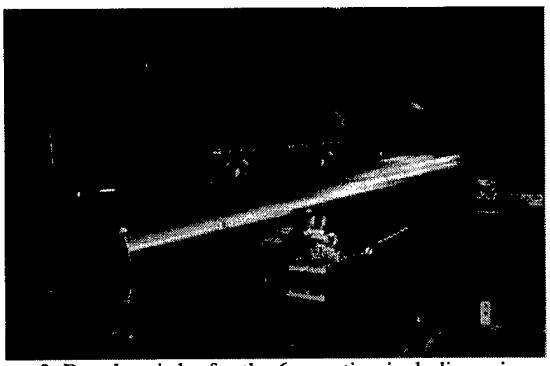


Figure 2: Regular girder for the 6m section including micro movers (short piece of structure on top to demonstrate the full assembly)

The first 6m section equipped with symetric high power couplers, iris coating, internal load and 2 HOM couplers (one at the front end and one almost at 2/3 of the section length) will be installed on the regular girder in the test linac end of May this year.

V. GROUND MOTION AND VIBRATION

Any kind of quadrupole motion within the frequency range of 2-30Hz can hardly be damped either in a passive manner or with beam based feedback techniques. Therefore ground motion detectors (geophones and accelerometers) have been tested and further developed [7]. Each quadrupole in the test facility will be equipped with such a detector to feed back on the vertical quadrupole position via piezo movers. Attenuation of amplitudes up to 14dB within this frequency range has been achieved and corrects the vertical rms quadrupole motion down to the 20nm range.

In addition a simple and stiff concrete support with mechanical resonances well beyond 100Hz has been built for the quadrupole to avoid any externally driven excitation. To decouple the vibration introduced by water flow within the coil windings of the quadrupole, the coils are mounted on a separate aluminium support within the quadrupole yoke. This support can be mounted separately to the floor.

VI. ACKNOWLEDGEMENT

I would like to thank all the members of the collaboration from the different institutes and countries for their contributions. The significant progress which has been made during the last 5 years is based on the enthusiasm of the people involved and the willingness of the management to encourage this work.

VII. REFERENCES

[1] M. Schmitz, A.D. Yeremian, "The Injector for the S-Band Test Linac at DESY", Proc. of the 1994 International Linac Conference, Tsukuba, Japan, 21-26 August 1994

[2] M. Schmitz, "Performance of the first Part of the Injector for the S-Band Test Facility at DESY", Proc. of the 1996 International Linac Conference, Geneva, Switzerland, 26-30 August 1996

[3] M. Dohlus et al, "Comparison of CONDOR, FCI and MAFIA Calculations for a 150 MW S-Band Klystron with Measurements", Proc. of the 1995 P.A.C., Dallas, Texas, 1-5 May 1995

[4] S. Choroba et al., "A 375MW Modulator for a 150MW Klystron at the S-Band Linar Collider Test Facility at DESY", Proc. of the 1996 International Linac Conference, Geneva, Switzerland, 26-30 August 1996

[5] V.E. Kaljuzhny et al, "Design and Performance of a Symmetric High Power Coupler..", DESY-M-94-11, 1994, Internal Report

[6] J. Haimson, "Collinear Termination for High-Energy Particle Linear Accelerators", PATENT-US-3264515, Aug 1966. 7pp.

[7] C. Montag, "An active mechanical Stabilization System for Linear Collider Quadrupoles to compensate fast Ground Motion", Proc. of the 1996 International Linac Conference, Geneva, Switzerland, 26-30 August 1996

AN ASYMMETRIC LINAC-RING COLLIDER FOR BARYON TIMELIKE FORM FACTOR MEASUREMENTS WITH EXISTING HIGH ENERGY STORAGE RINGS

P.Patteri and R.Baldini, INFN-LNF, I00044 Frascati, Italy and
C.Bini, INFN-Roma I, Roma, Italy

Abstract

It is considered the possibility of using a positron storage ring like CESR and a low emittance, high duty cycle electron linac or a CW racetrack microtron of 100-200 MeV to realize an asymmetric collider providing a luminosity L~10^{30} $cm^{-2}s^{-1}$. A suitable linac can be based on the superconducting modules developed for the TESLA Test Facility (TTF) at DESY or for CEBAF at TJ Laboratory. The microtron option can be developed similarly to the existing first 2-stage of the Mainz microtron or based on the studies for the RTM of NIST/LANL in late 80's.

1 INTRODUCTION

The energy range of the existing e^+e^- storage rings no longer spans the $p\bar{p}$ and $n\bar{n}$ pair production threshold with adequate luminosity to improve the statistics and data quality of the old experiment. Quite unexpected results from the FENICE experiment [1], which measured the neutron e.m. form factor from the reaction $e^+e^- \rightarrow n\bar{n}$, are pushing for a new e^+e^- collider at c.m. energy around the baryon pair threshold. Besides the low cross sections, an additional difficulty in these measurements is due to the low kinetic energy of the emerging particles. In order to overcome the difficulty of detecting the low energy neutron coming from the $n\bar{n}$ pair nearly at rest in the laboratory frame, as in a symmetric storage ring, an asymmetric collider has been considered.

Such a a machine could be based on an existing high energy storage ring, e.g. CESR at energy ~5÷8 GeV, where an intense positron beam is stored, and a low energy electron beam at an energy ≤200 MeV. The range of electron energy E_e for head-on collision with a positron beam of energy E_p providing invariant mass $\sqrt{s}$ is given by

$$s = 4E_pE_e. \qquad (1)$$

The center-of-mass energy range between the $n\bar{n}$ threshold and $\sqrt{s}$=3.1 GeV as a function of the electron energy E_e is shown in fig. 1 for two different values of E_p. The invariant masses corresponding to the baryon pair thresholds and the J/ψ mass are also shown.

Crucial parameters of the electron accelerator are the beam emittance, which must be comparable with that of the storage ring, and the average current which, although ~10^3 times lower than the stored current, is nevertheless very high when compared to typical linac currents. A linac in the injection chain around a storage ring cannot provide such a beam quality, but the required performances are achieved at some linac based FEL facilities. The bunch separation in the linac beam must be an integer multiple of that between the bunches stored in the ring and the rf systems must be phase-locked to ensure the stability of the collision point.

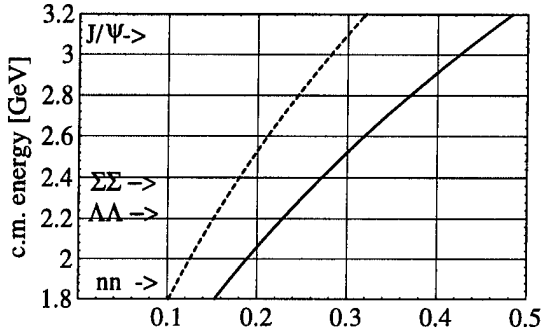


Figure: 1 Invariant mass vs. electron beam energy in head on collision with the stored positron beam of energy 5.3 GeV (continuos line) and 8 GeV (dashed line).

In order to improve the statistical accuracy with respect to FENICE by at least an order of magnitude in a reasonable running time a new collider must provide a luminosity L>10^{29} $cm^{-2}s^{-1}$. Comparing this value with the luminosity L~10^{33} $cm^{-2}s^{-1}$ expected at CESR after planned upgrade to raise the storable current to 500 mA the goal should be attainable with I_{av}>50 μA. This current can be obtained either by a 5 mA, 1% duty cycle sc linac or by a CW machine.

Electron beam polarization would provide a valuable tool to help to disentangle the contribution to the neutron form factor due to the magnetic part G_M and the electric part G_E.

2 THE LUMINOSITY OF A LINAC-RING COLLIDER

The luminosity of an head-on linac-ring collider is given by

$$L = \frac{n_e n_p f_c}{4\pi\sigma_x\sigma_z} \qquad (2)$$

where n_e and n_p are respectively the electron and positron bunch population, f_c is the collision frequency, given by the stored bunch frequency f_b times the linac duty cycle δ. The beam sizes σ_x, σ_z are defined by the

0-7803-4376-X/98/$10.00 © 1998 IEEE

ring lattice and energy and it is assumed that the linac beam sizes can be matched to those of the ring. As far as the "geometrical" coefficients in the denominator of eq.(2) is concerning, it is best to run the ring at the lowest as possible energy E_p, because $\sigma \propto E_p$. However this implies higher sensitivity of the storage ring to beam-beam perturbation and higher electron beam power in the dump. Increasing the ring energy, and therefore decreasing the linac energy to satisfy eq.(1), has similar effect on the linac and ring beam sizes owing to opposite energy dependence

$$\sigma_{linac} = \sqrt{\beta_{x,z} \varepsilon^{(n)}_{linac} / E_e}\ ,\ \sigma_{ring} = \sqrt{\beta_{x,z} \varepsilon^{(n)}_{x,z_{ring}} E_p^2}$$

where $\varepsilon^{(n)}_{linac}$ and $\varepsilon^{(n)}_{ring}$ are respectively the linac and ring normalized emittance. It is worthwhile noting that a reduction of E_e implies a reduction $\propto E_e^2$ of the rf power in the linac accelerating structures: by trading off between the peak power and the duty cycle it is possible in principle to compensate for the luminosity reduction at higher ring energy by increasing the linac duty cycle.

2.1 Machine parameters

A luminosity estimate has been carried out assuming the values experimentally achieved at CESR in the old operating mode [2] which stored 112 mA in 7 bunches. The parameter set is listed in table I.

Table I - Main parameter of the storage ring

Machine parameter	value	unit	Note
Energy E_p	5.3	GeV	
Hor. emittance $\varepsilon_{SR,x}$	$1.2\ 10^{-8}$	m rad	@ 1.0 GeV
Hor.-vert.coupling k	0.015		
Positron/bunch n_p	$2.5\ 10^{11}$		@ 112 mA
Bunch spacing s_b	300	ns	
Horiz. opt. funct. β_x^*	1.0	m	
Vert. opt. funct. β_z^*	$18\ 10^{-3}$	m	
Beam size σ_x	574	μm	
Beam size σ_z	10	μm	
Damping time t_x, t_z	26.9	ms	
Damping synchr. t_e	13.4	ms	

The parameters referring to the electron beam, listed in table II, are based on experimental data or design specifications at the TESLA Test Facility at DESY [3]. These values are comparable with the performances achievable by industrial grade sc technology (see for instance the CEBAF project for a FEL based industrial application of sc technology [4]), so they are a reliable basis for the estimate of the collider performances.

The specifications of the TESLA Test Facility linac are of course suited to linac-linac collider operation, therefore some features which could provide a boosting of performances as a linac-ring collider have not been considered; for instance the R&D privileges higher accelerating gradient to get a shorter linac instead of a longer macropulse.

The luminosity attainable with the parameters listed in table I and table II is 1.7 10^{29} $cm^{-2}s^{-1}$.

Table II - Main parameter of the linac

Machine parameter	value	unit	Note
Energy E_e	0.16	GeV	@ $n\bar{n}$ th.
Length L	45	m	
Emittance $\varepsilon^{(n)}_{linac}$	$1.0\ 10^{-8}$	m rad	@1 GeV
Horiz. opt. funct. b_x^*	5.0	m	@ $n\bar{n}$ th.
Vert. opt. funct. b_z^*	$1.5\ 10^{-3}$	m	@ $n\bar{n}$ th.
Macropulse current I_m	8	mA	
Particles/bunch n_e	$1.8\ 10^{10}$		
Bunch frequency f_b	3.333	MHz	
Pulse duration T_{on}	1.0	ms	
Repetition rate f_r	10	Hz	
Duty cycle δ	0.01		

2.2 Improvements and Limiting Factors

The macropulse linac current limit requires that $n_e f_b$=constant; however, a reduction of linac pulse frequency implies a corresponding increase of n_p so that at constant current both in the ring and linac beam $L \propto f_b^{-1}$. The corresponding luminosity as a function of the number of bunches stored in CESR is shown in fig. 2.

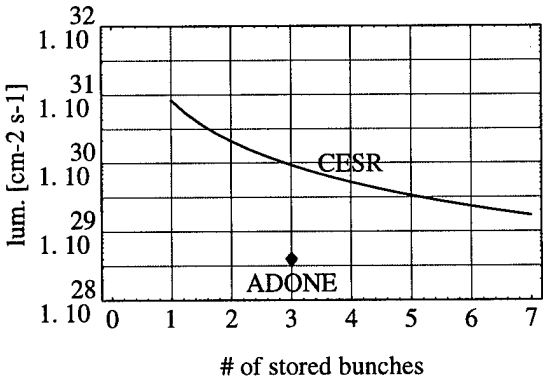


Fig. 2 - Luminosity vs. number of stored bunches in CESR at 112 mA (continuous line). The luminosity achieved at ADONE for the FENICE experiment is shown for comparison.

A limit to the bunch density of the colliding beams is given by the beam-beam perturbation characterized by the linear tune shift parameter ξ_i; the experimental data from all the existing storage rings indicate that a bunch density limit corresponding to ξ_{max}~0.05 cannot exceeded. In the case of a linac-ring collider this limit apply of course only to the stored positron beam. The maximum values of ξ for the cases in fig. 2 are ξ_x=0.032 and ξ_z=0.033. It is to note that this perturbation affects the stored beam with a low duty cycle, so that the damping can restore the initial beam condition before the

next linac macropulse. The average effect on the beam should be not higher than that due to an equivalent ξ_{eq} given by the previous ξ weighted by the duty cycle plus the damping times: $\xi_{eq,i}=\xi_i\ f_r\ (T_{on}+\tau_i)$. The resulting values are well below the range $0.02<\xi_{meas}<0.04$ measured at CESR in a variety of conditions [5]. Probably the single bunch density will be limited by the longitudinal instability before the previous limit applies; it should depend strongly on the planned upgrade of the rf and feedback systems.

These considerations applies if I_{av} is provided by a pulsed beam with $\delta \leq 0.01$. Of course a trade off as large as possible between n_e and f_b is desirable since this relaxes the ring specifications and reduces the perturbation of the stored beam. Moreover, the increase of the current up to 500 mA is achievable mainly increasing the number of the stored bunches.

3 THE MICROTRON OPTION

The average current could be obtained by a low current CW machine like a small storage ring or a racetrack microtron. In this case the beam beam perturbation on the positron beam is reduced by a factor $1/\delta$ and a corresponding increase in luminosity, at constant ξ, could be obtained by squeezing the beam size by the same factor at the interaction point. However, in the case of a low energy storage ring the perturbation affecting the stored beam is likely to be intolerable; although this option deserves a better insight, it is presently rejected because the short lifetime of the perturbed beam is expected be an intense source of background.

The CW racetrack microtron option has no such a limitation since it provide a disposable beam. Moreover the footprint of the microtron is small and can be easily allocated at some distance from the ring. The transport line can be optimized for the best collision point layout without ring lattice constraints. If the perturbation on the stored positron beam could be made negligible, parasitic operation becomes possible as an alternative to dedicated operation largely increasing the running time of the experiment.

The existing machines providing $I_{av} \sim 100\ \mu A$ use normal conducting accelerating modules, which make them simpler and cheaper with respect to a superconducting based accelerator. The suppression of higher order modes excited by recirculating beams was considered the major drawback of the sc structures at the time of their construction; in the meanwhile wide experience has been gained in this field so the feasibility of a superconducting CW microtron deserves a better consideration now. Recent operation of the TTF 10 MeV capture section at 8 mA indicates that a 200 MeV, 20 passes machine providing 400 μA is conceivable.

The performances of the operating Mainz RTM [6] and of the IASA machine [7], derived from the discontinued NIST/LANL FEL program, are listed in table III for comparison.

Table III - Parameter list of existing or planned RT microtrons providing Iav > 100 μA

RTM machine	**Mainz**	**IASA**	**unit**
Energy max	185	247	MeV
Average current	107	100	μA
Injection energy	14	42	MeV
Gain per turn	3.2	8.5	MeV
# of recirculations	51	25	
Energy width	36	--	keV
Emittance	$14\ 10^{-9}$	--	π m rad
Magnet spacing	~ 6	8.6	m

4 CONCLUSION

The construction of a dedicate electron accelerator for one specialized and time limited experiment could seem expensive. However the electron beam quality is very high and it can be easily exploited for up-to-date experiments in different fields, such as FEL or γ production for solid state or nuclear physics, by Compton or Thomsom scattering, thereby largely improving the cost/productivity ratio.

The performances achieved in the past by CESR and those expected by a TTF-like linac allow to design a linac-ring collider providing a luminosity more than an order of magnitude better than the luminosity for the FENICE experiment with boosting in the laboratory frame further improving the effectiveness of the experiment. Potential upgrading of both the linac and the storage ring performances should provide safe margins to easily reach the goal of luminosity $L = 10^{30}\ cm^{-2}s^{-1}$.

REFERENCES

[1] A.Antonelli et al., Proc. LEAP 96
[2] D.L.Rubin, L.A.Schick, Proc. PAC 91 (1991) 144.
[3] TESLA Test Facility - Conceptual Design Report, TESLA Report 95-1, DESY 1995
[4] G.R.Neil et al., Nucl. Instr. and Meth. A358 (1995) 159
[5] L.A.Schick, D.L.Rubin, Proc. PAC 91 (1991) 470.
[6] H.Euteneuer et al., Proc. EPAC 94 (1994). 506
[7] A.Karabarbounis et al, Proc. EPAC 96 (1996) 560

MOPA FEL SCHEME AS A SOURCE OF PRIMARY PHOTONS FOR GAMMA-GAMMA COLLIDER TESLA AND SBLC

E.L. Saldin, E.A. Schneidmiller
Automatic Systems Corporation, 443050 Samara, Russia
M.V. Yurkov
Joint Institute for Nuclear Research, 141980 Dubna, Moscow Region, Russia

Abstract

This report presents description of the free electron laser system to be the source of primary photons at Lnear Collider TESLA/SBLC [1].

1 INTRODUCTION

The project of a Linear Collider is under development by the international TESLA collaboration [1]. In addition to studying e^+e^- physics, it is planned to organize the second interaction region for studying $\gamma\gamma$ and γe collisions. Gamma-quanta will be produced by means of Compton bacscattering of laser photons on the electron beam from the main accelerator [2]. To provide high conversion efficiency, the peak laser power should be not less than 300 GW. Time structure of the laser operation should be identical to that of the main accelerator. The laser pulses should be synchronized precisely with respect to the electron pulses with accuracy of about one picosecond. It is likely that the laser should be tunable, so as an optimal wavelength range depends on the collider energy. Finally, to provide a more reach program of physical experiments, the laser should provide a possibility to steer the polarization of the laser light. All these requirements make the problem of the laser for gamma-gamma collider to be not trivial, especially for the TESLA project [1, 3, 4].

Potential features of a free electron laser (FEL) allow one to consider it as an ideal source of primary photons for a gamma-gamma collider. Indeed, FEL radiation is tunable and has always minimal (i.e. diffraction) dispersion. The FEL radiation is totally polarized: circularly or linearly for the case of helical or planar undulator, respectively. A driving accelerator for the FEL may be a modification of the main linear accelerator, thus providing the required time structure of laser pulses. The problem of synchronization of the laser and electron bunches at the conversion region is solved by means of traditional methods used in accelerator techniques. FEL amplifier has potential to provide high conversion efficiency of kinetic energy of the electron beam into coherent radiation. At sufficient peak power of the driving electron beam the peak power of the FEL radiation could reach the required TW level.

The idea to use the FEL as a laser for gamma-gamma collider has been proposed in ref. [5]. More detailed study of this idea has shown that the problem of construction of free electron laser can be solved using Master Oscillator – Power Amplifier (MOPA) scheme with the driving accelerator for the FEL amplifier constructed on the same basis as the main accelerator for a linear collider [6, 7, 8, 9]. At present an option of an FEL as a laser for gamma-gamma collider is studied for different projects. While there exist different FEL configurations, an amplifier configuration has definite advantages for application in the gamma-gamma collider schemes [9]. The choice of specific technical solution depends on the parameters of the linear collider project. For instance, for the VLEPP, CLIC, JLC and TESLA projects it has been considered to use MOPA FEL scheme [3, 4, 10, 12, 13].

Designers of NLC project consider an FEL scheme using induction linac and chirped pulse amplification technique [14, 15].

2 FEL PARAMETERS

In the present study of the Linear Collider Project it has been accepted to use MOPA FEL scheme as a source of primary photons for gamma-gamma collider (see Fig. 1). Such a choice fits well to both TESLA and SBLC options. In this scheme the optical pulse from Nd glass laser ($\lambda = 1$ μm, 1 MW peak power) is amplified by FEL amplifier up to the power of about 500 GW (see Table 1). The driving beam for the FEL amplifier is produced by the linear rf accelerator identical to the main accelerator, but with lower accelerating gradient due to higher beam load. It is important that the requirements to the parameters of the FEL driving electron beam are rather moderate and can be provided by injector consisting of gridded thermoionic gun and subharmonic buncher.

Table 1 presents the main parameters of the FEL amplifier and the driving accelerator. It is seen from Fig. 2 that

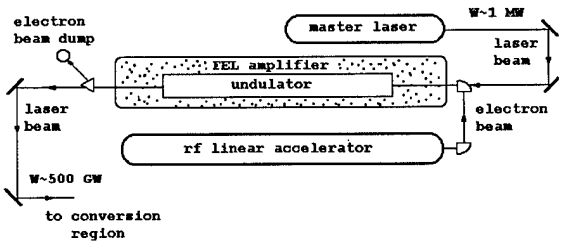


Figure 1: MOPA FEL configuration for a gamma-gamma collider

0-7803-4376-X/98/$10.00 © 1998 IEEE

Table 1: Parameters of the FEL amplifier

Electron beam*	
Electron energy	2 GeV
Peak beam current	2.5 kA
rms energy spread	0.2 %
rms normalized emittance	$2\pi \times 10^{-2}$ cm rad
rms bunch length	1 mm
Undulator	
Undulator type	Helical
Undulator period (entr./exit)	15 cm/ 12.9cm
Undulator field (entr./exit)	10.2 kG/ 11.9 kG
Length of untapered section	17 m
Total undulator length	60 m
Radiation	
Radiation wavelength	1 μm
Input power	1 MW
Output power	500 GW
Flash energy	2.3 J
Efficiency	10 %

*Time diagram of the accelerator operation is identical to the time diagram of the main accelerator.

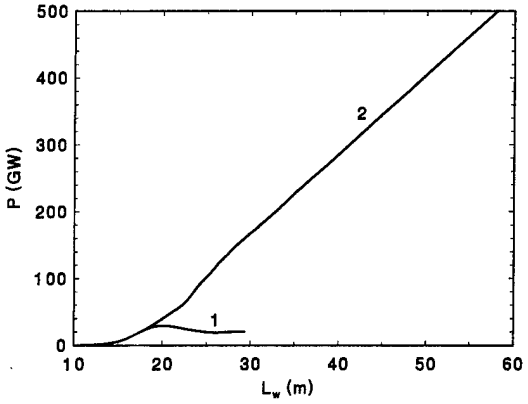


Figure 2: Output power of the FEL amplifier versus undulator length (curve 2). Curve 1 corresponds to untapered undulator.

500 GW level of output power is achieved at the undulator length of about 60 m. Total flash energy in the laser pulse is about of 2 J.

Using FEL amplifier allows one completely exclude transmitting optical elements and deliver the laser beam to the conversion region using several reflections from metallic mirrors which are rather stable to the laser radiation damage. This can be done when vacuum systems of the FEL amplifier and linear collider are combined. The first reflection mirror can be installed at a distance about several tens of meters after the exit of the undulator when the laser beam expands to the size about several centimeters from

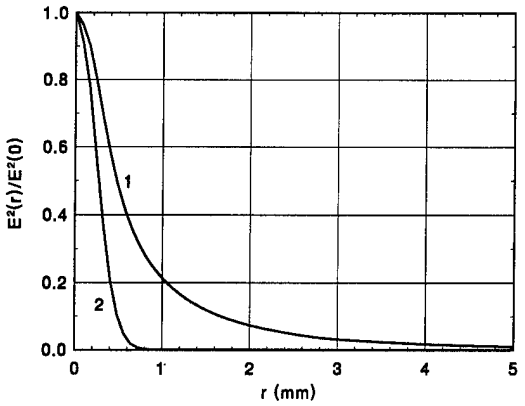


Figure 3: Radial distribution of the radiation power density (1) at the undulator exit and the electron beam current density (2).

initial size of few millimiters (see Fig. 3).

To reduce the cost of the laser system, only one free electron laser can be used. This scheme operates as follows. The FEL is installed only in one branch of the linear collider. When the laser bunch passes the focus of the conversion region, it is not dumped but is directed to the optical delay line which provides a delay time equal to the time interval between the bunches. Then it is focused on the electron beam of the opposite branch of the linear collider. Of course, this configuration provides colliding gamma-beams with the second micropulse of the collider. Nevertheless, the number of microbunches is equal to several hundreds, so it will not result in significant reduction of the integral luminosity.

3 FUTURE PERSPECTIVES

The present design has been limited with an approach which can be realized at the present level of accelerator and FEL technique. The main reserve to improve the FEL performance is to increase its efficiency which will allow to decrease the requirements to the value of the peak electron beam power. The perspectives of the FEL efficiency increase are on the way of using multi-stage FEL amplifier with diaphragm focusing line (see Fig. 4) [16, 17]. The principle of operation of this FEL scheme consists in the storing of the energy in a single laser pulse amplified by a sequence of electron bunches. This scheme has evident perspectives for the TESLA project due to a large bunch spacing. Preliminary study shows that the energy of the driving electron beam could be reduced to the value of several hundreds of MeV and the value of the peak current could be reduced by several times. The beam load in accelerator will be also reduced approximately by a factor of 3 due to higher FEL efficiency about of 30 %.

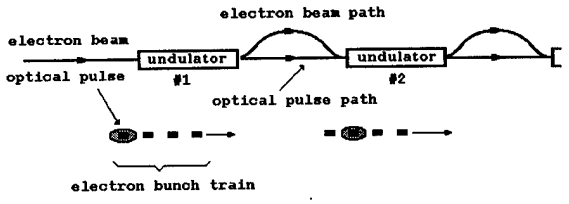


Figure 4: The scheme of multi-stage FEL amplifier. One optical pulse is amplified by a sequence of electron bunches. The peak power of the output radiation exceeds by a factor of N (number of amplification stages) the peak output radiation power of traditional single pass FEL amplifier.

4 ACKNOWLEDGMENTS

We are grateful to R. Brinkmann, N. Holtkamp, V. Telnov, D. Trines and A. Undrus for many useful discussions.

5 REFERENCES

[1] "Conceptual Design of a 500 GeV e+e− Linear Collider with Integrated X-ray Laser Facility" (Editors R.Brinkmann, G. Materlik, J. Rossbach, A. Wagner), DESY 97-048, Hamburg, 1997.

[2] I.F. Ginzburg et al., Pis'ma v ZhETF **34**(1981)514, Preprint INF 81-50, Novosibirsk (1981), in Russian.

[3] E.L. Saldin, V.P. Sarantsev, E.A. Schneidmiller, Yu.N. Ulyanov and M.V. Yurkov, Preprint DESY 94-243, DESY, Hamburg, 1994.

[4] E.L. Saldin, V.P. Sarantsev, E.A. Schneidmiller, Yu.N. Ulyanov and M.V. Yurkov, Nucl. Instrum. and Methods **A361**(1995)101.

[5] A.M. Kondratenko, E.V. Pakhtusova and E.L. Saldin, Dokl. Akad. Nauk **264**(1982)849, Preprint INF 81-130, Novosibirsk (1981), in Russian.

[6] E.L. Saldin, V.P. Sarantsev, E.A. Schneidmiller and M.V. Yurkov, Proceedings of the Second Workshop "Physics at VLEPP" (June 2-4, 1992, Protvino, Russia), Vol. 2. p. 96, in Russian.

[7] E.L. Saldin, V.P. Sarantsev, E.A. Schneidmiller and M.V. Yurkov, Proceedings of the XIII Conference on Charged Particle Accelerators (October 13-15, 1992, Dubna, Russia), Vol. 1. p. 36, in Russian.

[8] E.L. Saldin, V.P. Sarantsev, E.A. Schneidmiller and M.V. Yurkov, Preprint JINR E9-94-70, Dubna, 1994.

[9] E.L. Saldin, V.P. Sarantsev, E.A. Schneidmiller and M.V. Yurkov, Nucl. Instrum. and Methods **A339** (1994)583.

[10] V.A. Alexandrov, V.E. Balakin, E.A. Kushnirenko, A.A. Sery, N.A. Solyak and M.V. Yurkov, Photon linear collider 100 × 100 GeV based on the VLEPP physics and technology, Proc. LC 93 Workshop, SLAC, Stanford, October, 1993.

[11] E.L. Saldin, V.P. Sarantsev, E.A. Schneidmiller, Yu.N. Ulyanov and M.V. Yurkov, Proceedings of the Sixth International Workshop on Linear Colliders LC95 (March 27-31, 1995, Tsukuba, Japan), KEK Proceedings 95-5, August 1995, Vol. III, p.1919.

[12] S. Hiramatsu, S. Hashimoto and Y. Ishida, Nucl. Instrum. and Methods **A355**(1995)133.

[13] R. Corsini and A. Mikhailichenko, Proceedings of the Sixth International Workshop on Linear Colliders LC95 (March 27-31, 1995, Tsukuba, Japan), KEK Proceedings 95-5, August 1995, Vol. III.

[14] K.-J. Kim, M. Xie and A.M. Sessler, Nucl. Instrum. and Methods **A375**(1996)523.

[15] Zeroth-Order Design Report for the Next Linear Collider, Appendix B, LBNL-PUB-5424,SLAC Report 474, UCRL-ID-124161 (May 1996).

[16] E.L. Saldin, V.P. Sarantsev, E.A. Schneidmiller, Yu.N. Ulyanov and M.V. Yurkov, Preprint JINR E9-94-237, Dubna, 1994.

[17] E.L. Saldin, V.P. Sarantsev, E.A. Schneidmiller, Yu.N. Ulyanov and M.V. Yurkov, Nucl. Instrum. and Methods **A361**(1995)317.

[18] W.M. Fawley, Nucl. Instrum. and Methods **A375**(1996)550.

A CONVENTIONAL READ-OUT ELECTRONICS FOR THE BUTTON-TYPE BPM IN THE ATF DAMPING RING

F. Hinode, J. Urakawa, KEK, Oho 1-1, Tsukuba, Ibaraki, 305 Japan and
Y. Yoribayashi, Hoshin Electronics Co. Ltd., Hatanodai 5-4-3, Shinagawa, Tokyo, 142 Japan

Abstract

A conventional read-out electronics for button-type beam position monitor (BPM) has been developed for the KEK ATF (Accelerator Test Facility) damping ring[1]. This electronics system is used in early stage of beam commissioning in the damping ring. The system can measure the beam orbit by single pass processing of bunch train, have the resolution of about 10 μm, and is reliable. It is also desirable that it is low cost because of a requirement of several hundreds of circuit channels. The system consists of charge-sensitive ADCs and clipping modules. The clipping module employs a clipping technique, which clips the bipolar signal from a BPM to integrate the signal charge. It is also useful for strip-line type BPM because of the enrichment of low frequency component. The design and test results with a beam operation are reported.

1 INTRODUCTION

To achieve as small an emittance as possible is one of critical issues to obtain a high luminosity in the linear collider, as well as to achieve a high acceleration efficiency and a strong final focus. Future linear colliders, such as JLC, require a very small vertical emittance, typically $\varepsilon_{ny} = 30$ nm. A damping ring, the most feasible method for obtaining such a tiny emittance, is a fundamental part necessary to ensure the high performance of a linear collider. An ATF damping ring is one of those machines which is devoted to verifying and to demonstrating the tiny emittance of JLC. The damping ring has a race track shape and the lattice has a symmetry of a 180 degree rotation. There are four wiggler magnets and RF cavities or kicker magnets in an each straight section.

To achieve such a low-emittance beam we must correct the dispersion of the orbit, which is small ($\eta < 2$ mm) in the long wiggler section of the damping ring. A precise measurement of the dispersion is indispensable. Usually, the actual dispersion is obtained by comparing each closed-orbit distortion under the conditions of different RF frequency ($\Delta f_{RF} \sim 10$ kHz). For this reason, the requirement for the resolution of the BPM is less than $5\mu m$. Furthermore, the impedance of the components, such as the vacuum chamber, can be the source of a single-bunch instability which could degrade the beam quality. To avoid such an instability, the total longitudinal impedance must be less than about 0.2Ω. The results of wake-field calculations indicate that the impedance is very small on the electrode of the button-type compared with the directional-coupler type. We therefore selected the button-type electrode for the BPM. The detail about BPM chamber is described in[2].

2 SYSTEM OVERVIEW

We developed a conventional read-out electronics system, which feature is a single-path monitor, enough position resolution, flexibility, simple and low cost. To measure the beam orbit with only one-passage of the beam is desirable for well understanding of the beam status; damping, stability, etc. To be a single-path monitor is also very important especially in the first stage of beam commissioning, because we have no screen monitor in the damping ring. In the ATF damping ring, the beam operation is performed with single or multi-bunch beam. In the case of the multi-bunch beam, the bunch spacing is 2.8 nsec and the number of bunches is about 20. Those bunches form a bunched train and the maximum number is five trains which can circulate in the damping ring. It is favorable to measure the position of each bunch in a bunched train, however, it is very hard to satisfy this requirement with the above many conditions in same time. Therefore we did not take into account of this point for the present system. We tried to construct the whole system to be quite simple taking into account of the flexibility and maintainability.

Figure 1 shows BPM system for the ATF damping ring.

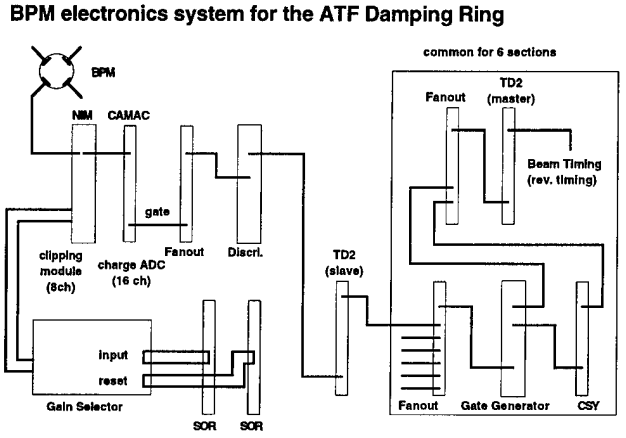


Figure 1: Schematic diagram of the BPM system.

There are 96 button-type BPMs in the damping ring totally, and which belong to three kinds of types. One type of button BPMs are mainly used in the two arc sections of the race track ring, which has a cylindrical shape of inner diameter of 24 mm. The second type is used in the two wiggler sections which has a race track shape, and the third one is in a septum section, which has a cylindrical shape of inner diameter of 14 mm. These 96 BPMs are divided into six sections with respect to the beam line, i.e. two straight sections and 4 quarters of 2 arc sections. These BPMs can measure the position in a same time. The same time means

0-7803-4376-X/98/$10.00 © 1998 IEEE

to measure the same turn signal of a circulating beam. The signal cable length in each section is adjusted taking into account of time of flight to detect the same turn beam by a common trigger signal.

Each section has several units, which consist of clipping modules, charge-sensitive ADCs and a discriminator. Master timing signal from common timing system is adjusted to the beam injection by a master TD2 module and distributed to six sections. The timing adjustment for each section is done by a slave TD2 module. The another turn signal can be easily measured in same time by remote control of the delay timing of the master TD2. And also if we need, arbitrary turn orbit can be measured for each section independently by remote control of the delay timing of the slave TD2. The four signals from each BPM are processed by clipping module, which clips the bipolar signal in order to integrate the charge by charge-sensitive ADC. Figure 2 shows the circuit of clipping module.

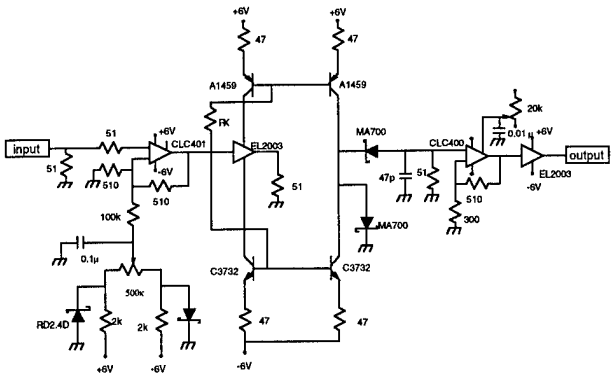


Figure 2: Circuit of CL mini-card in the clipping module.

The clipping module is a NIM type module and highly condensed to mount eight channels, so that one clipping module can process signals for two BPMs. One channel of the clipping module consists of a low-pass (100 MHz) and a band-pass filter (30 MHz), amplifiers and a clipping mini-card. For the first two amplifiers inside the clipping module, which gain can be changed corresponding to the signal level. Inside the clipping mini-card, bipolar signal is clipped by a shot-key barrier type diode, MA700/A (V_F=0.4 V, @I_F=1 mA). The output signal from clipping module is then digitized by the charge-sensitive ADC, which has 16 channels with 14 bit inside a CAMAC one width module.

3 PERFORMANCE OF THE ELECTRONICS

The preliminary electronics test was carried out at a test bench. Test signal was generated by differentiation of a short width rectangular pulse from a pulse generator (Hewlett Packard), and then fed into clipping module. Output linearity of the clipping module was checked with this test signal. Because of the diode feature in the clipping mini-card, the clipping module doesn't have good linearity. Fig. 3 shows the result of output linearity. The horizontal axis is an input signal level (arbitrary unit) changed by an attenuator. The solid line shows a linear fit for the central region.

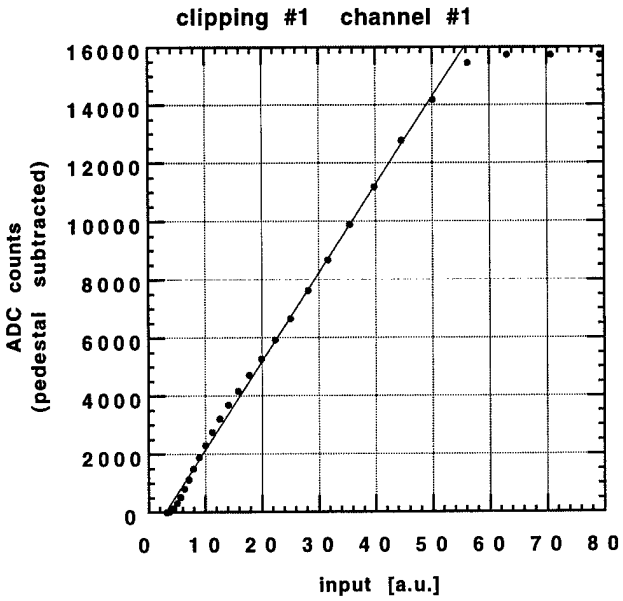


Figure 3: Output linearity of clipping module.

Although this linearity will be improved by a circuit modification, presently the nonlinearity is corrected by a software on the position calculation.

The performance of electronics was checked by using a HP pulser. The input signal which simulated a BPM signal was split into two channels of a clipping module as a centered beam. The position is calculated by $X = k * (Va - Vc)/(Va + Vc)$, where Va and Vc were ADC counts after pedestal subtracted and linearity corrected. Conversion coefficient $k = 6388$ μm was used. In order to estimate a resolution, 50 measurements were made during each signal amplitude and the standard deviation was taken as a resolution. Figure 4 shows the measured resolution of the electronics system. Equivalent beam charge was normalized by an actual beam signal. If beam charge of 2×10^{10} particle/bunch is achieved, the position resolution of about 10 μm will be realized. If more resolution is required, averaging will be taken over several turns.

The position resolution was also demonstrated by using a wire method at a test bench. Test pulse was fed into the 50 μm tungsten wire, and a BPM was moved by x-y mover with respect to the wire. Figure 5 shows the measured wire position as a function of the mover position with 50 μm step. Though the signal shape was not exactly same as the beam one because of miss-match into the thin wire, the measured position could be easily distinguishable with less than 100μm resolution.

Since the first beam commissioning in January 1997, the ATF damping ring is successfully operated with single bunch beam of about 3×10^9 particles per bunch. Although this beam intensity is much smaller than the designed one, which is mainly limited by the efficiency of the beam trans-

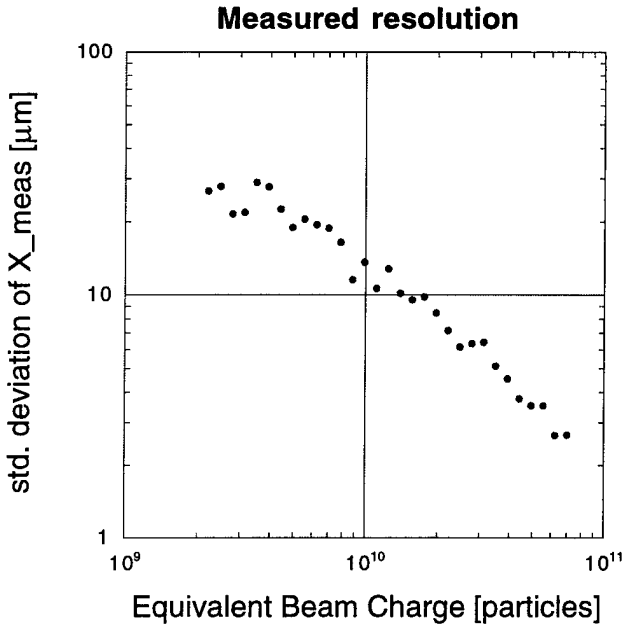


Figure 4: Measured resolution of the electronics. 50 times position measurements. (electronics only)

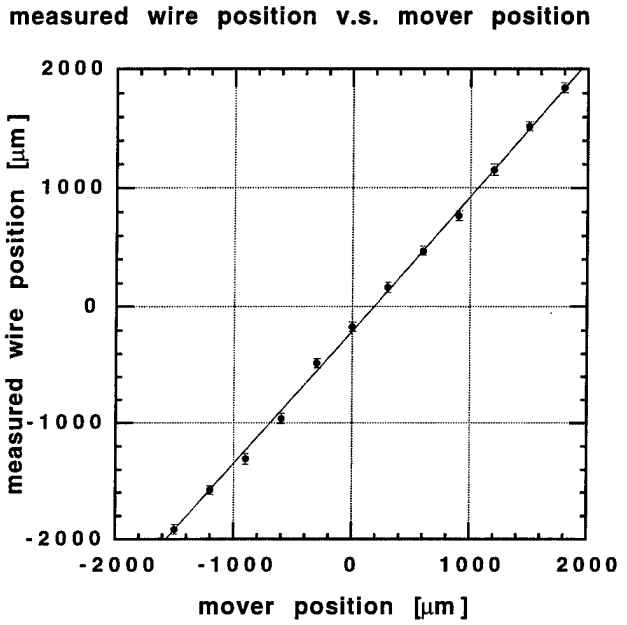


Figure 5: Measured wire position by the BPM pickup. 50 times position measurements.

port, the BPM signal is clearly observed except for some BPMs. Faults of these BPMs are caused by an insufficient signal level and a large noise from a kicker magnet. Figure 6 shows the measured position response to the position calculated from steering magnet currents. The result shows large standard deviation due to the beam jitters, however, the mean position is quite consistent with the position calculated from steering magnet current.

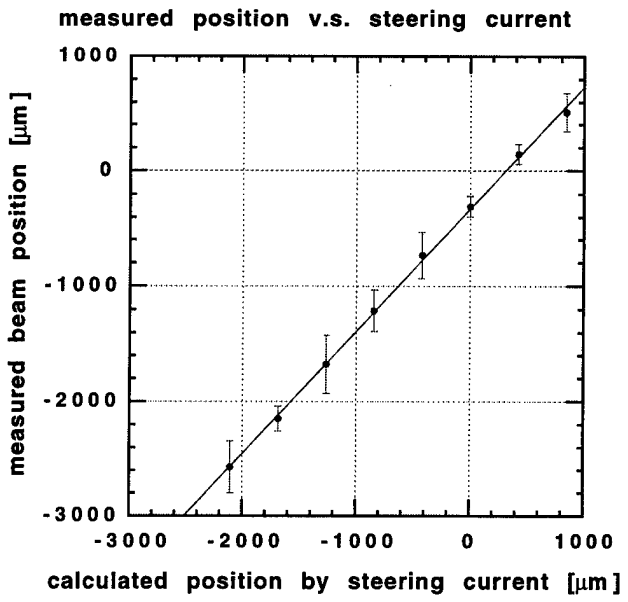


Figure 6: Measured position response to the steering magnet. 100 times position measurements.

4 SUMMARY

A conventional read-out electronics for button-type BPM has been developed. Nevertheless the quite low beam intensity, the damping ring was successfully commissioned with this BPM system. This system has still some points to be improved, however, preliminary result shows the resolution of 90 μm with the beam intensity of 3×10^9 particles as a one-path monitor. As increase the beam intensity, the performance will be improved.

5 ACKNOWLEDGEMENTS

We wish to thank Profs. Y. Kimura and K. Takata for their support to our work. We also acknowledge much help and support given by the ATF collaboration team and by E-CUBE corporation during the development and the preparation of the BPM system. Specially, M.Ross's team from SLAC contributed to the improvement of the BPM system.

6 REFERENCES

[1] "ATF Design and Study Report", KEK Internal 95-4 (1995).

[2] F. Hinode et al., KEK Preprint 95-55 (1995).

DESIGN STUDY OF COOLING WATER SYSTEM FOR A LARGE SCALE LINEAR COLLIDER

H. Matsumoto, Shigeru Takeda, Yasunori Takeuchi, M. Yoshioka, KEK, High Energy Accelerator Research Organization, 1-1 Oho, Tsukuba, Ibaraki 305, Japan, N. Holtkamp, Deutsches Electronen-Synchrotron, DESY, Notkestrasse 85, 22603, Hamburg, Germany, J. S. Oh, Pohang Accelerator Laboratory, 125, Pohang, Kyungbuk, 790-600, Korea

Abstract

A distributed cooling water system was designed for a large scale linear collider. It consists of a large number of small cooling water units and several main cooling systems. One small unit is installed for each RF unit of the main linac. The heat removed from the accelerator is transferred from the small unit to the main cooling system through a heat exchanger and moved to a cooling tower outside the accelerator tunnel. The fine temperature control is carried out in each small unit by utilizing waste heat from klystrons and a small electric heater. A prototype unit was made and has shown that the temperature of cooling water can be controlled within ±0.03°C.

1 INTRODUCTION

The next generation linear collider with the c.m. energy of 200~500 GeV is the most suitable machine to unveil the mystery of the origin of mass, to understand the symmetry breaking mechanism in the standard theory and to determine the direction of the physics beyond the standard theory. Thus, an early construction of the linear collider corresponding to the LHC is the world-wide issue. In order to realize this requirement, a linear collider using C-band frequency (5.712 GHz) for the main acceleration is proposed [1], since the straightness tolerance for the accelerating structure is 30 μm which is achievable with the conventional technology and the klystron and its power supply can be also fabricated with the conventional technology. In the system design of such a large scale linear collider, the cooling water system is one of the important elements which affects the reliability and cost of the whole system and a structure of the accelerator tunnel. A design study of the cooling water system has been carried out to reduce the mechanical vibration due to the fast water flow in the main water pipe, isolate the pressure between the main cooling system and accelerator components and reduce the cost of main pipe not to make sacrifices for the reliability and a distributed cooling water system is investigated [2]. A test by using a prototype model has been carried out to prove the temperature stability.

2 C-BAND LINEAR COLLIDER AND THE COOLING WATER SYSTEM

The overall parameter of the C-band linear collider is given in Ref. 3 and a schematic diagram of one unit in the main linac RF-system is shown in Ref. 1. The design luminosity is $6.6\infty10^{33}/cm^2/s$ and the length of the linac for electron and positron is 13 km. In the RF unit, accelerator components to be cooled with water can be classified into two groups such as (1) four 1.8 m-long choke-mode type accelerating structures which have an accelerating gradient of 40 MeV/m(nominal) and 31 MeV/m (loaded), a coupled cell type RF-pulse compressor, a waveguide system, and two 50 MW klystrons and (2) klystron focusing magnets, RF windows of the klystron and klystron modulators, and a quadrupole magnet. The groups (1) and (2) require fine and rough temperature control, respectively. Total number of the unit in the two main linacs amounts to 2040 and the total wall plug power is 150 MW. Since the total length of the two linacs is about 26 km, the cooling water system is divided into 26 sub-systems in order to reduce the unit length to 1 km. An average density of the dissipated power in the tunnel is 5.8 kW/m, most of which is cooled with water. The other part of the dissipated power including the power loss in the cable, lighting etc. is 0.5~1 kW/m, which have to be moved out of the tunnel with an air conditioner.

3 CONCEPTUAL DESIGN

Requirements for the cooling water system of the linear collider are summarized as follows:
(1) the temperature of cooling water for accelerating structure must be controlled better than ±0.05°C,
(2) the system should not cause vibration to the accelerator components which is larger than 20 nm in the frequency region above 1 Hz [4], and
(3) the diameter of main water pipes should be as small as possible.
The items (1) and (2) are required by the stable operation of the linear collider. The litem (3) is related with the construction cost and the tunnel design.

To satisfy these requirements, we adopt a distributed cooling water system in which many small cooling water units are distributed along the linacs, one cooling unit for each RF unit, and one large cooling water system (Main cooling water system) is installed for each 1 km-section to receive the heat from small units and to move it out of the tunnel. As the fine temperature control is carried out in each unit, rather rough temperature control (±2.5°C) is enough for the main system.

A schematic diagram of the small cooling unit is shown in Fig. 1. The temperature control is carried out in two stages: coarse and fine. The coarse control is done

0-7803-4376-X/98/$10.00 © 1998 IEEE

using waste heat. A part of hot water from the load, such as klystrons, is led to the inlet port of the pump through the valve V2 and mixed with cold water from the tank. Valves V1 and V2 are controlled by single controller to act as one 3-way valve. These valves are controlled so that the temperature at T0 is kept constant which is slightly lower than the final temperature at T2. Some water is led from here to the group (2) components (see Sec. 2). The rest of water enters the next section where the fine control is carried out by the electric heater 2. Then, it is supplied to the group (1) components. The heater 1 is installed as auxiliary heat source which is used at start-up or break down of the RF.

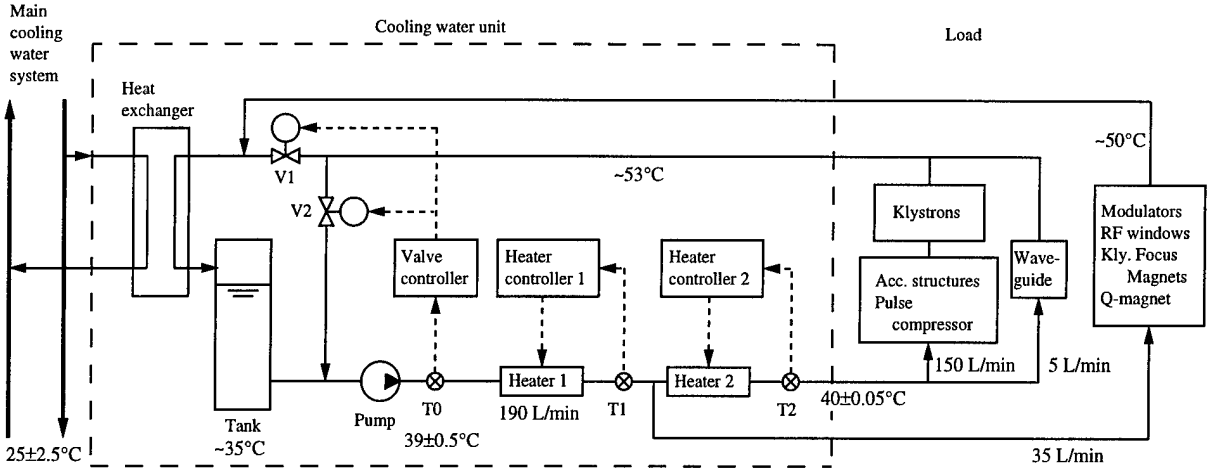


Fig. 1 Blockdiagram of the cooling unit.

4 PROTOTYPE OF THE UNIT

A prototype of the cooling unit has been made and is used at the magnetic measurement station of the KEKB project [5]. The maximum flow rate and the maximum heat load of the prototype unit are 50 l/min and 50 kW, respectively. Figure 2 shows a block diagram of the unit.

Water temperature of the main cooling system is usually maintained at about 25°C and its temperature control is rather coarse (±3°C). Therefore, we have to introduce the present unit. The difference of the two units (Fig. 1 and Fig. 2) is that the prototype unit has chiller unit while the unit of Fig. 1 does not. This is because the water temperature to be fed to the magnets must be maintained at about 28°C even in summer where the temperature of main cooling system may be above 30°C.

Cooling power of the chiller unit is discretely controlled (0-50-100%) and the water temperature of the buffer tank is cooled to 15-20°C. Cooling water is supplied to magnets by pump2. The method of temperature control is the same as described in Sec. 3: coarse control using waste heat and fine control by the electric heater. The target temperature at T1 is 27°C, lower than the final temperature of 28°C by 1°C. As shown in Fig. 3, althoug the temperature of the main cooling water changes ±3°C, the water temperature at T2 is maintained at 28.2±0.02°C, the stability of which is considerably better than the target value of ±0.05°C.

5 CONCLUDING REMARKS

We have designed the distributed cooling water system in which one small cooling water unit is installed for each RF unit. The water temperature in the unit is coarsely controlled by the direct mixing of hot water heated by the klystrons and cold water from the buffer tank. Then the fine control is carried out by the small electric heater. The prototype of the unit was constructed. It shows that the water temperature can be controlled within ±0.05°C by the present method. In the next step, we will pursue better operation parameters to minimize the power consumption. The life and reliability of parts are also important issues to be pursued, because it depends on them whether this method can be adopted by the linear collider or not.

6 ACKNOWLEDGMENTS

The authors thank Dr. T. Shintake of KEK for valuable discussion and suggestions. They also acknowledge the help of Dr. K. Egawa and Dr. M. Masuzawa of KEK, Mr. Y. Kanazawa of ATC CO., LTD, and Mr. M. Hirata of Taiyo Valve MFG. CO., LTD. in the construction and temperature measurement of the prototype unit.

REFERENCES

[1] Shintake et al., "C-band RF Main Linac System for e+e- Linear Collider at 500 GeV to 1 TeV c.m. Energy", EPAC 96.
[2] Frank-R. Ullrich,"Temperature stabilisation of the accelerating structure", LINAC96.
[3] Yokoya et al., "C-band Linear Collider with C.M. Energy 500 GeV to1 TeV", EPAC96
[4] Shigeru Takeda et al., "Ground Motion Studies for Large Future Linear Colliders", this conference.
[5] S. Kurokawa, "Status of the KEKB Project", this conference

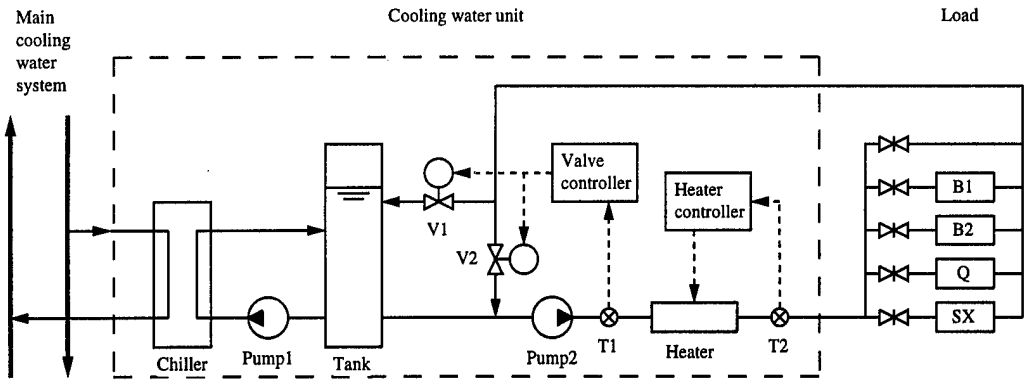


Fig. 2 Block diagram of the prototype cooling water unit.
B1, B2: Bending magnets, Q: Quadrupole magnet,
SX: Sextupole magnet.

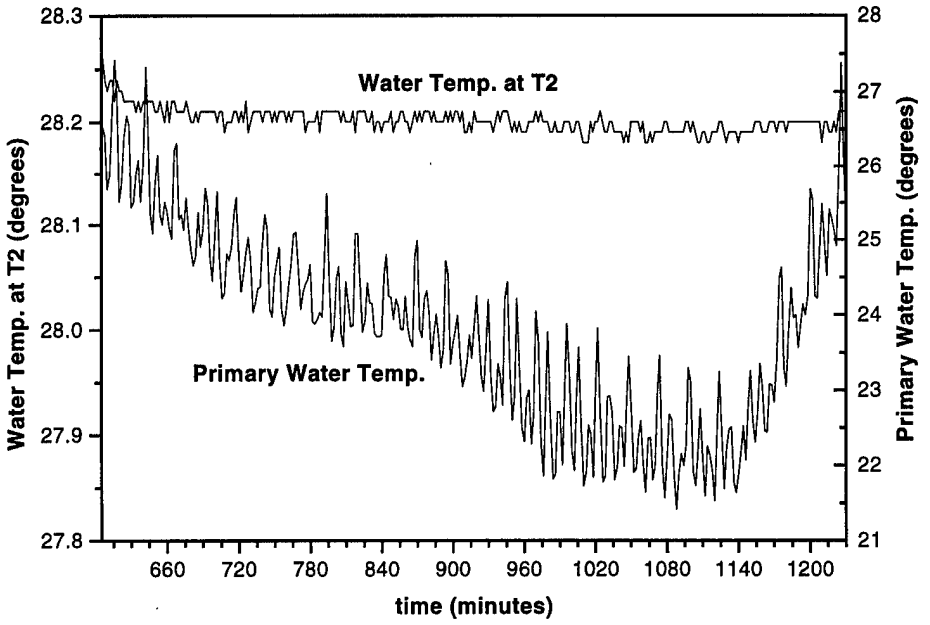


Fig. 3 Water temperature in the prototype coolingwater unit.

SR MONITOR FOR THE ATF DAMPING RING

T. Naito, H. Hayano, N. Terunuma, J. Urakawa, Y. Hashimoto, M. Muto
High Energy Accelerator Research Organization (KEK)
Oho, Tsukuba-shi, Ibaraki-ken, 305 Japan
T. Okugi, Tokyo Metropolitan University, Japan

Abstract

The ATF Damping Ring (ATF DR) aims to demonstrate the technical feasibility of a low-energy part of next-generation electron-positron linear colliders by producing an electron bunch train with extremely small emittance. To diagnose the beam profile and radiation damping there, a synchrotron radiation (SR) monitor which uses visible light has been designed and built. This paper presents the system configuration of this SR monitor and the preliminary results from the initial beam commissioning.

1 INTRODUCTION

The ATF aims to serve as a prototype accelerator complex of a low energy part of a next-generation linear collider, which is responsible for producing a multi-bunch electron beam with extremely small emittance. The design parameters of the ATF DR include: beam energy = 1.5 GeV, beam current = 600 mA max, bunch population = $(1 \sim 3) \times 10^{10}$/bunch, repetition rate = 25 Hz. The target equilibrium beam emittance is: $\epsilon_{nx} = 5.1$ μm, $\epsilon_{ny} = 30$ nm, ϵ_{nz} =12 mm [1]. The beam commissioning of the ATF DR began in January of 1997 in a single-bunch operation ($3 \sim 6 \times 10^9$ e / bunch) with a beam energy of 0.96 GeV, and a reptition rate of 1.5 (or 0.8) Hz.

An SR monitor which uses visible light was prepared as one of the tools for measuring the transverse beam size and the bunch length. The system features: (1) a fast gate camera to distinguish the SR images turn-by-turn and bunch-by-bunch, (2) a retractable reference target for calibrating the image focus point, (3) a mechanical shutter in the SR beam line to prevent deformation of the first mirror due to the thermal stress caused by the SR power deposit, (4) a double-sweep streak camera for observing variations of the bunch length during the damping process.

Major portions of the hardware and software were prechecked at the INS 1.3 GeV electron synchrotron [1], before installing them in the ATF DR. At the ATF DR the system functioned flawlessly from the beginning, and successfully observed the first beam circulating in the DR.

2 APPARATUS

2.1 *Optical System*

Figure 1 shows the layout of the optical system. The source point is located 270 mm downstream of the entrance edge of a bending magnet (bending radius = 5.73 m) at the end of the west arc. The first mirror, made of aluminum-coated copper, reflects the SR light by 90° upward. After reflected by the second mirror and passing through the first lens (f = 1000 mm), the SR light is divided into two paths: one is fed to a fast gate camera after a second lens (f = 40 mm), the other to a streak-camera through a mirror and a second lens (f = 80 mm). The maginification ratio of the optical system for the fast gate camera is 1.17. At the entrance of the streak camera, the SR light is collimated with a slit (30 μm wide), corresponding to a 14 ps (FWHM) offset for our measurement.

When the beam is absent,by inserting the reference target at the source point with an air-actuator mechanism, several illuminated patterns (1 mm square and 0.4 mm rectangles) can be observed with the optical system.This is used for calibration of the magnification ratio and focusing.

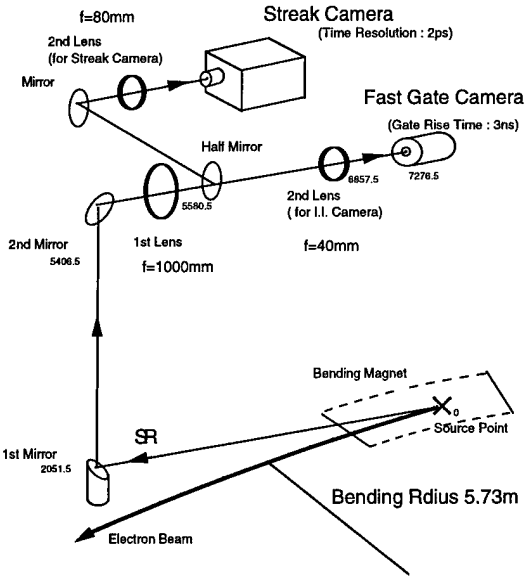


Figure 1: Layout of the optical system.

2.2 *Fast Gated Camera*

A fast gate camera (Hamamatsu, C2925) is used to observe an image with very short gate width with good light amplification. Its main parameters are given in Table 1. Since the minimum bunch separation expected in the ATF DR is 2.8 ns, the camera can discriminate SR signals on a turn-by-turn and bunch-by-bunch basis by appropriately selecting the gate timing and width.

2.3 *Streak Camera*

A double-sweep streak camera (Hamamatsu, C5680) is used to measure the variation of a bunch length during the

0-7803-4376-X/98/$10.00 © 1998 IEEE

Table 1: Main parameters of the fast gate camera.

Gate width	3 ns $\sim$ 100 μs
Gate jitter	less than 200 ps
Repetition frequency	10 kHz
Luminous gain	7000 ft-L/ft-C
Sensitive wavelength	160 $\sim$ 840 nm
Extinction ratio	1.6×10^{10}

damping process. The vertical sweep in the streak image gives the bunch length information, while the horizontal sweep gives the bunch images at specified time intervals. Several tens of streak images are, thus, acquired in a same frame. The main parameters of the streak camera are given in Table 2.

Table 2: Main parameters of the streak camera.

Vertical sweep unit	
streak time	0.2 ns $\sim$ 50 ns
resolution	better than 1.5 ps
repetition rate	10 kHz max.
Horizontal sweep unit	
sweep range	100 ns $\sim$ 100 ms
Sensitive wavelength	400 $\sim$ 900 nm
MCP gain	3000 max.

3 DIAGNOSTICS

3.1 Transverse Beam Profile

The transverse beam profile at a selected turn is measured by appropriately setting the gate timing of the fast gate camera [2]. An example of the observed image profile is shown in Figure 2. This measurement is repeated at different gate times to diagnose the transverse beam damping. The beam size as function of time ($\sigma(t)$) is expressed by

$$\sigma^2(t) \propto \epsilon(t) = \epsilon_i e^{-2t/\tau} + \epsilon_e(1 - e^{-2t/\tau}), \qquad (1)$$

where ϵ_i is the initial emittance at injection, ϵ_e the equilibrium emittance, and τ the damping time. Figure 3 shows the measured σ^2 as function of the store time. Table 3 compares the measured damping time with expectations assuming an emittance coupling of 1%. The measured horizontal beam size has contributions from the dispersion at the SR emission point, namely,

$$\sigma_x^2 = \epsilon_x \beta_x + (\eta_x \Delta p/p)^2. \qquad (2)$$

With design values of $\eta = 48$ mm and $\Delta p/p = 9.2 \times 10^{-4}$, the correction amounts 44 μm. The measured image size in the equilibrium condition is known to be enlarged by a diffraction effect ($\sim$ 21μm) and a focusing depth effect [3, 4]. Their contributions require careful analyses.

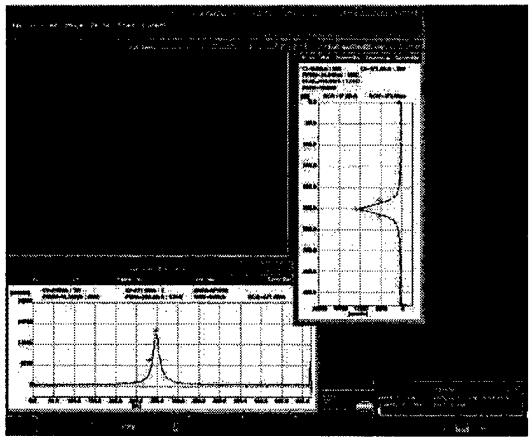


Figure 2: An example of the observed beam profile.

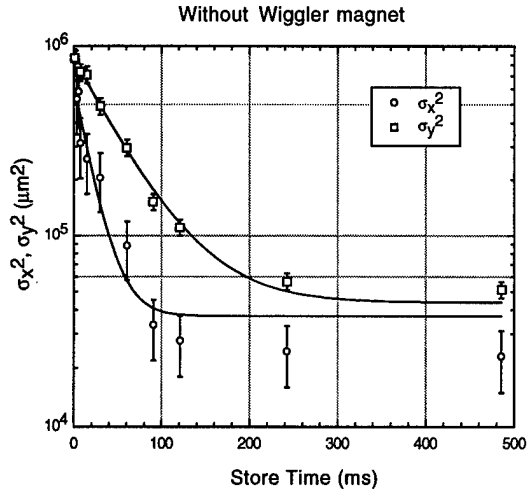


Figure 3: Result from a damping time measurement.

3.2 Bunch Length

The trigger signals for the streak camera are generated based on the revolution frequency. Measurement of the bunch length immediately after injection requires a pretrigger with a large lead-time (80 ms), which, is difficult to create without jitters with the present circuit. A new trigger circuit the jitter-free high-precision pretrigger, based on a digital delay circuit, is under development.

An example of the streak image is shown in Figure 4. The damping of the bunch length is illustrated in Figure 5. The measured and expected bunch length damping times are summarized in Table 3.

4 SR BEAM CHOPPER

Deformation of the first mirror due to the thermal stress cause by the SR light is a concern. The SR power on the mirror surface is estimated to be 10 W/mm^2 for a stored beam current of 600 mA. Copper has been chosen as the material of the mirror for advantages of thermal conductance. Some efforts against the deformation have been

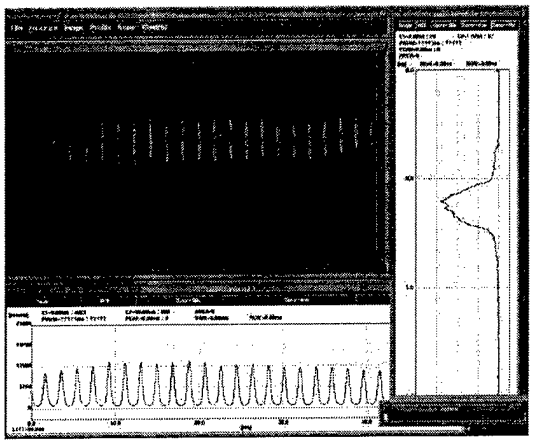


Figure 4: An example of the observed streak image.

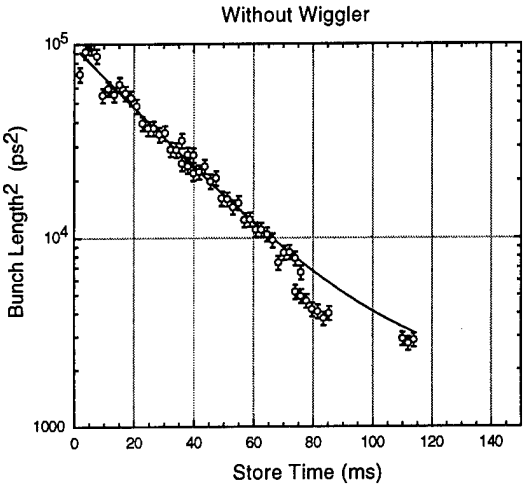


Figure 5: Measurement of the damping of the bunch length.

Table 3: Comparison of the measured and calculated values of the image/beam sizes and damping times.

	Measurement	Calculation
σ_x	76.4 μm	45.2 μm
σ_y	113 μm	7.9 μm
σ_z	41.6 ps	25.5 ps
Damping time (wigglers off)		
τ_x	36 ± 12 ms	46.8 ms
τ_y	100 ± 10 ms	68.5 ms
τ_z	54 ± 2 ms	44.6 ms
Damping time (wigglers on)		
τ_x	29 ± 2.4 ms	30.0 ms
τ_y	58 ± 10 ms	39.7 ms
τ_z	no meas.	56.3 ms

made or planned at other facility [5, 6]. To further reduce the SR power on the first mirror, an SR beam chopper system has been built, whose layout is shown in Figure 6. By driving the shutter at 0.1 Hz, the SR power on the mirror surface can be reduced to 0.1 W/mm^2. In this case, according to calculations with ANSYS, the expected deformation is reduced from $\sim$ 1μm to $\sim$ 20 nm. The performance of the system has not been verified, since up to now the ATF DR has been operated at a small store current ($\sim$0.5 mA).

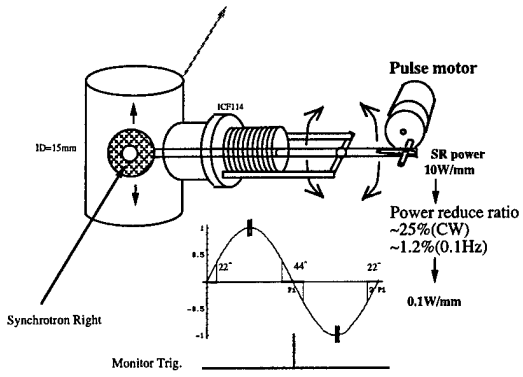


Figure 6: Layout of the SR beam chopper.

5 SUMMARY

An SR monitor system has been designed and built for the ATF DR. The first data set was successfully collected during the initial beam commisioning of the ATF DR. Some discrepancies have been found between the measured image size parameters and calculations. Studies are in progress on diagnosing possible errors in the SR monitor optics system as well as possible set-up errors in the ATF DR.

6 ACKNOWLEDGMENTS

We would like to express our gratitude to Professors M. Kihara and K. Takata for their continous encouragement. We wish to thank Dr. S.Kamada for conducting detailed calculations on the photon distributions and for useful dicussions. We also wish to thank the ATF operation group for their support.

7 REFERENCES

[1] Ed. by F. Hinode, et al., "ATF Design Study Report," KEK Internal 95-4, June 1995.

[2] M. Minty, et al., "Using a Fast-Gated Camera for Measurements of Transverse Beam Distributions and Damping Times," SLAC-PUB-5993, Nov., 1993.

[3] A. Ogata, "On Optical Resolution of Beam Size Measurements by Means of Synchrotron Radiation," Nucl. Instr. and Meth., vol. A391 (1991) 596.

[4] A. Hofman, et al., "Optical Resolution of Beam Cross-section Measurements by Means of Synchrotron Radiation," Nucl. Instr. and Meth., vol. A203 (1982) 483.

[5] T. Mitsuhashi, et al., "A Construction of Optical Beam Profile Monitor for High Brilliance Configuration of the Photon Factory," Proc. of EPAC (1996).

[6] "Optical Beam Diagnostics," ESRF / MAC-19/13a.

STATUS OF 1.54 GeV ATF LINAC

Seishi Takeda, H. Hayano, M. Akemoto, T. Naito, H. Matsumoto, J. Urakawa,
K. Oide, N. Terunuma, K. Kubo, F. Hinode, T. Korhonen, Y. Funahashi, S. Araki,
High Energy Accelerator Research Organization (KEK), Oho 1-1, Tsukuba, Ibaraki 305,
S. Kashiwagi, The Graduate University of Advanced Studies,
T. Okugi, Faculty of Science, Tokyo Metropolitan University,
S. Kagaya, T. Sakamoto, Department of Applied Physics, Tohoku-Gakuin University,
M. Takano, Faculty of Science, Toho University

Abstract

Accelerator Test Facility (ATF) consists of a 1.54 GeV S-band linac, a beam transport line, a damping ring and an extraction beam line. A beam commissioning of the linac was performd in November 1995. A single bunch and multi-bunch beam were accelerated up to 1.43 GeV at the end of the beam transport line. The beam experiments on high-gradient acceleration, structure BPM and multi-bunch energy compensation were performed after the beam commissioning. The operation of the linac was suspended from April 1996 for the construction of the damping ring. The operation of the linac was restarted from December 1996, and the beam commissioning of the damping ring was carried out in January 1997.

1 INTRODUCTION

The 1.54 GeV ATF linac is designed to accelerate multi-bunch of electrons for the injection to a low-emittance damping ring. However, the ATF linac is designed not only as an injector of the damping ring but also as a test-stand for the linear collider technology such as multi-bunch acceleration, high gradient acceleration, beam loading compensation and instrumentations.

The required specification of the linac is as follows: A multi-bunch consists of a train of 20 bunches with a bunch spacing of 2.8 ns and a bunch population of 2×10^{10} electrons. The maximum energy spread of 90 % of multi-bunch electrons is 1.0 % full width, and the normalized emittance at the end of the linac is less than 3×10^{-4} m·rad (1σ).

Table 1 shows the specification of the 1.54 GeV ATF linac. The construction of the linac was completed except some improvements of rf system in order to obtain the design specification of the linac.

2 80 MEV PRE–INJECTOR LINAC

A 200 kV thermionic electron gun consists of an EIMAC Y646-E or Y796 grid-cathode assembly. A train of 20 pulsed-beam with a pulse width of 1 ns FWHM and 2.8 ns pulse spacing is produced from the gun by applying an rf-voltage to the grid. Each pulse beam contains more than 2×10^{10} electrons. The buncher section consists of two 357 MHz subharmoinic bunchers (SHB) and a 2856 MHz travelling wave buncher. A high current multi-pulse beam produces a cumulative loading voltage in the SHB cavity, which distorts the cavity voltage. A small induced voltage and high generator voltage provide a small phase shift caused by successive bunches. Therefore, low R/Q cavities, which reduce the beam-loading voltage are utilized. The bunching and transmission rate were checked by using the PARMELA simulation code. The resultant bunch length was less than 12 ps (FWHM), even after 20 bunch loading with greater than an 87.3% transmission rate. However, the present 5 kW solid-state amplifiers are not sufficient in order to compress a pulse beam to short bunch length without long tail. The bunch with long tail increases energy spread and results in the beam loss in a linac. Two 25 kW amplifiers are now in under fabrication to obtain the sufficient bunching in the SHB cavities.

A Type-E3712 klystron produces 100 MW peak power of 1.0 μs pulse duration for the travelling buncher and a 3 m-long accelerating structure. The peak power of 5 MW divided from the klystron is supplied to the buncher, and that of 60–95 MW is supplied to a 3 m-long constant gradient accelerating structure.

The bunch-by-bunch beam instrumentations are installed in the 80 MeV pre–injector linac. These ae composed of amorphous core monitors, wall current monitors, phosphor screen monitors, button BPMs, optical transition radiation (OTR) monitors and a wire scanner. The bunch length is observed by an OTR monitor and a streak camera. The emittance of the bunch is evaluated from the beam size observed by an OTR monitor combined with the Q-magnet. The emittance of each bunch is also measured by a wire scanner with fast-gate gamma detection.

3 RF SYSTEM

At the ATF linac, nine Toshiba-E3712 klystrons and two SLAC-5045 klystrons are used for the rf system. A type-E3712 klystron is used for the 80-MeV pre–injector descrived above. The accelerating section consists of eight tpe-E3712 klystrons. Each klystron is connected to two accelerating structures via a SLED cavity and operated in the long-pulse mode to produce a rectangular pulse waveform of 80 MW rf peak power in 4.5 μs pulse duration. At 3.5 μs after feeding into the SLED cavity, the rf phase is made to reverse during a 1.0 μs pulse duration. The extracted rf peak power from the SLED cavity is multiplied to 400 MW. Terefore, an accelerating structure is driven at 200 MW of peak power. When the pulse front of non-rectangular rf

0-7803-4376-X/98/$10.00 © 1998 IEEE

Table 1: Required specification of the 1.54 GeV ATF linac.

Beam energy for DR	1.54 GeV
Energy spread	
(Full Width of 90%beam)	<1% (each bunch at 1.54 GeV)
Total length	85 m (from gun to linac end)
Accelerating structure	$2\pi/3$ mode, constant gradient
Total length	3 m
Total number	16
Accelerating field	
Maximum peak	52 MV/m
Nominal	33 MV/m
RF frequency	2,856 MHz
Feed peak power	200 MW/structure
Klystron	
Klystron peak power	80 MW/klystron
Pulse length	4.5μs
Total number	8
Pulse compression	Two-iris SLED
Power gain	5.0 (average)
S-band pre–injector	
Beam energy	80 MeV
Number of bunches	20
Bunch population	2.0×10^{10}
Bunch separation	2.8 ns
Bunch length (FWHM)	<10 ps
Normalized emittance	$<3\times10^{-4}$rad m (1σ)

waveform reaches an output coupler, the accelerating field distributes from 38 MeV/m to 52 MeV/m along the structure. The design accelerating gradient of 33 MeV/m can be achieved at 65 MW of average peak power. Seven klystron modulators in the accelerating section are connected to a 25-kV common HV power supply with HV common-bus. Three of them were designed to reduce a size of modulator. Self-healing type capacitors with long lifetime are utilized to decrease the size of pulse-forming networks. This capacitor consists of a metalized film with thin Zn-electrodes (300 Å in thickness) which form a series of microscopic capacitors. The case volume is less than third of the conventional type of capacitor.

Two 5045 klystrons are operated in a short-pulse mode to produce a rectangular rf pulse with peak power of 50 MW in 1.0 μs pulse duration. These klystrons produce the 2856±4.32727 MHz rf frequencies for the energy-compensation system.

4 ACTIVE ALIGNMENT SYSTEM

The support tables of the accelerator section of the linac have an active mover mechanism and wire-position sensors to align linac components with a tolerance less than 20 μm r.m.s. The 91 m-long wires are stretched in both sides of the linac from the gun to the end of the linac. One end is fixed to the pre–injector stage, which does not have an active mover mechanism, and the other end is stretched by tension weights of 33.5 kg. Each position sensor consists of a pair of induction coils electrically connected in series, and mounted on a vertically movable offset stage fixed at a support stage. The center position of a pair of induction coils is pre-calibrated on the calibration stand. The sensors are installed at four corners of the support table for Q-magnets and beam monitors, and accelerating structures. The wire position is detected by a synchronous detection of the signal from the differential coils using a 60-kHz, 100-mA AC current on the wire. The resolution of the position sensor is 2.5μm. The dynamic range of the sensors is ±2.5 mm, which is determined by the gap length between two induction coils.

The linac support tables are machined with an accuracy of less than ±10μm. The left side of the support table has a reference line parallel to the beam axis. The accelerating structures, Q-magnets and beam monitors are aligned to the reference line with an accuracy of less than ±10μm. Each sensor installed on the left side of the linac has two pairs of induction coils to detect the vertical and horizontal positions from the wire. These sensors are aligned along the sag of the wire with a vertical offset. Therefore, the reference line is aligned in a straight line. Each sensor installed on the right side of the linac stages has a pair of induction coils for measuring only the vertical position. As a result, the support tables are vertically and horizontally aligned with an accuracy of less than 20μm r.m.s. The experiment of structure BPM has been carried out by using active alignment system of an accelerating structure.

5 ±ΔF ENERGY-COMPENSATION SYSTEM

In the damping ring, the variation of bunch spacing is not acceptable. The energy compensation system by using four dipole magnets is not applicable, since the variation of bunch spacing is not acceptable in the damping ring. The proposed ±Δf energy-compensation system is a new idea to compensate the multi-bunch energy by keeping the bunch separation synchronized with the rf frequency. When a multi-bunch pass through an accelerating structure driven at an rf frequency which is slightly larger or smaller than the fundamental frequency, the multi-bunch would be obtained a different energy gain caused by the phase shift. The energy spread of a multi-bunch can be compressed to a small value required by the damping ring. The compensation energy depends on the position of electrons in a bunch, since the bunch has a bunch length and the compensating field has a slope of the part of sinusoidal wave. If the bunch is compensated by both a negative slope and a positive slope, the effect of the slope is canceled and the bunch would be accelerated or decelerated by a flat-top field. The system has high flexibility for bunch populations from zero to 4×10^{10} electrons/bunch by adjusting the rf power of klystrons. The advantages of the ±Δf ECS system are as follows: simple system, high flexibility, highly efficient compensation, and without any effect to the single-bunch beam-loading.

The system in the ATF linac comprises two klystrons and two 3 m-long accelerating structures designed at two different rf frequencies. In order to simplify the timing system,

the rf frequency deviation was chosen to be 4.32727 MHz, which is twice a damping ring revolution frequency, and is also the 660th subharmonic frequency of the 2856 MHz fundamental frequency. Therefore, an accelerating structure is driven at 2856+4.32727 MHz while another accelerating structure is driven at 2856−4.32727 MHz. The maximum peak power from the klystron is 50 MW at a 1.0μs pulse duration. One unit of the system can compensate an 80 MeV energy difference among the multi-bunch. Therefore, the system can compensate an energy difference of 160 MeV at the maximum among the multi-bunch. The maximum compensated beam-loading is estimated to be about 10 %.

Figure 1 shows the multi-bunch energy spread with and without ECS. The observation of the beam energy was performed by using BPM installed after a bending magnet of the transport line. The multi-bunch signal from the BPM was observed by a digital oscilloscope of 1 GHz bad width. The effect of the ECS is successfully demonstrated in the cases of 10 bunches with a bunch population of 4×10^9 electrons and 20 bunches with that of 7×10^9 electrons. The energy spread among bunches could be reduced to $\pm0.5\%$ peak to peak. Figure 2 shows the single bunch energy spread with and without ECS.

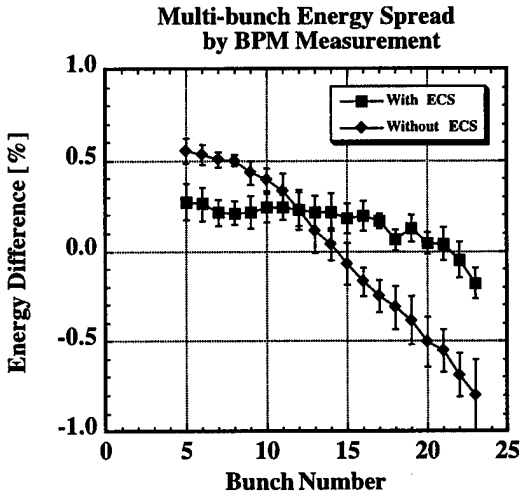


Figure 1: Multi-bunch energy spread with and without ECS.

6 INSTRUMENTATION

The beam-diagnostic system, except for the position monitor is installed in the linear accelerator in order to measure the characteristics of each bunch in a multi-bunch. The beam current is measured by an amorphous core current transformer(CT) and wall current monitors(WCMs). The beam profile (transverse and longitudinal) is measured by optical-transition radiation monitors(OTRMs). The beam-profile measurement of each bunch is performed by using a fast gate camera and OTR monitors. The beam emittances of each bunch is measured by a wire scanner(WS) and a gated photo multiplier tube(GPMT). These monitors have

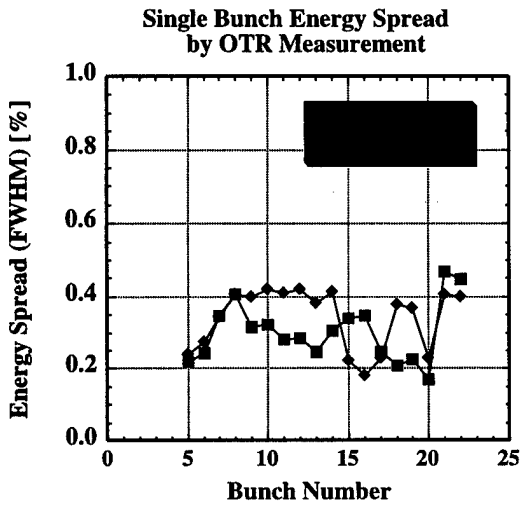


Figure 2: Single bunch energy spread with and without ECS.

the capability of multi-bunch measurements and were described in the pre–injector section.

7 TROUBLE SHOOTING OF THE LINAC

After restarting linac-operation for the beam commissioning of the ATF damping ring, it was found that the prefire in the tyratron tubes during a DC-charge to a pulse-forming network produces an over voltage to the thyratron tube. The source of the over voltage is a resonance between the high capacity DC power-supply connected to seven klystron modulators and a pre-fired modulator. In order to avoid the damage of the thyratron tubes, the seven klystron modulators were forced to operate at lower voltage. Therefore the output rf power from seven klystrons were limited to 30–35 MW, and then the beam energy was limited to 1.0 GeV. The protection circuit to decrease the resonant voltage and an interlock system were installed in the DC power supply and modulators. After that the beam energy could be increased to 1.44 GeV. After rf processing of SLED cavities and accelerating structures, the beam energy would be increased to 1.54 GeV.

8 ACKNOWLEDGEMENTS

The authors would like to express our thanks to Professors Y. Kimura, M. Kihara, K. Takata and Y. Yamazaki for their continuous encouragement and support.

9 REFERENCES

[1] H. Hayano: 'ATF Linac Commisioning', Proceedings of the 18th International Linear Accelerator Conference (held at Geneva, August, 1996).

[2] S. Kashiwagi et. al.: 'Preliminary Test of $\pm\Delta f$ Energy-Compensation System', Proceedings of the 18th International Linear Accelerator Conference (held at Geneva, August, 1996).

DESIGN OF A 1-MV INDUCTION INJECTOR FOR THE RELATIVISITIC KLYSTRON TWO-BEAM ACCELERATOR

D. E. Anderson, S. Eylon, S. Lidia, L. Reginato, D. Vanecek, S. Yu,
Lawrence Berkeley National Laboratory, Berkeley, CA 94720 USA,
T. Houck, G. A. Westenskow,
Lawrence Livermore National Laboratory, Livermore, CA 94550 USA
E. Henestroza, University of California, Davis, CA 95616 USA,

Abstract

A Relativistic Klystron Two-Beam Accelerator (RK-TBA) is envisioned as a rf power source upgrade of the Next Linear Collider. Construction of a prototype, called the RTA, based on the RK-TBA concept has commenced at the Lawrence Berkeley National Laboratory. This prototype will be used to study physics, engineering, and costing issues involved in the application of the RK-TBA concept to linear colliders. The first half of the injector, a 1 MeV, 1.2 kA, 300 ns induction electron gun, has been built and is presently being tested. The design of the injector cells and the pulsed power drive units are presented in this paper.

1 INTRODUCTION

A Lawrence Berkeley National Laboratory (LBNL) and Lawrence Livermore National Laboratory (LLNL) collaboration has been studying rf power sources based on the Relativistic Klystron Two-Beam Accelerator (RK-TBA) concept for several years [1, 2]. The collaboration has prepared a preliminary design study for a RF power source suitable for the NLC [3]. This RF power source, referred to as the TBNLC, is comprised of subunits, each approximately 340 m in length with 150 extraction structures generating 360 MW per structure. The number of subunits is dependent on the power requirement for the collider, e.g. 76 subunits are required for a 1.5-TeV collider. A test facility, called the RTA, has been established at LBNL[4] to verify the analysis used in the design study. The primary effort of the facility is the construction of a prototype TBNLC subunit that will permit the study of technical issues, system efficiencies, and costing. In this paper, we will discuss the development of the RTA electron source and it's pulsed power system, which has recently been constructed and is now undergoing testing.

2 INDUCTION ELECTRON GUN

An illustration of the 1-MV, 1.2-kA induction electron source is shown in Figure 1. The cores are segmented radially to reduce the individual aspect ($\Delta r/\Delta z$) ratios with each core driven separately at about 14 kV. The lower aspect ratio reduces the variation in core impedance during the voltage pulse simplifying the pulse forming network (PFN) design. We chose a constant radius insulator design. This design increased the METGLAS[5] core volume by about 10%, but the added cost was recovered in reduced insulator and fabrication costs. Figure 2 is a photograph of the completed cathode-half of the gun undergoing initial pulsed power tests. Currently, the cathode-half gun is being used to test various insulator configurations. The test results will be incorporated into the RTA's induction accelerator design.

A novel feature of the gun design is the insulator. We are doing high voltage testing with a single, 30 cm ID, PYREX[6] tube for the insulator with no intermediate electrodes. The average gradient along the insulator at

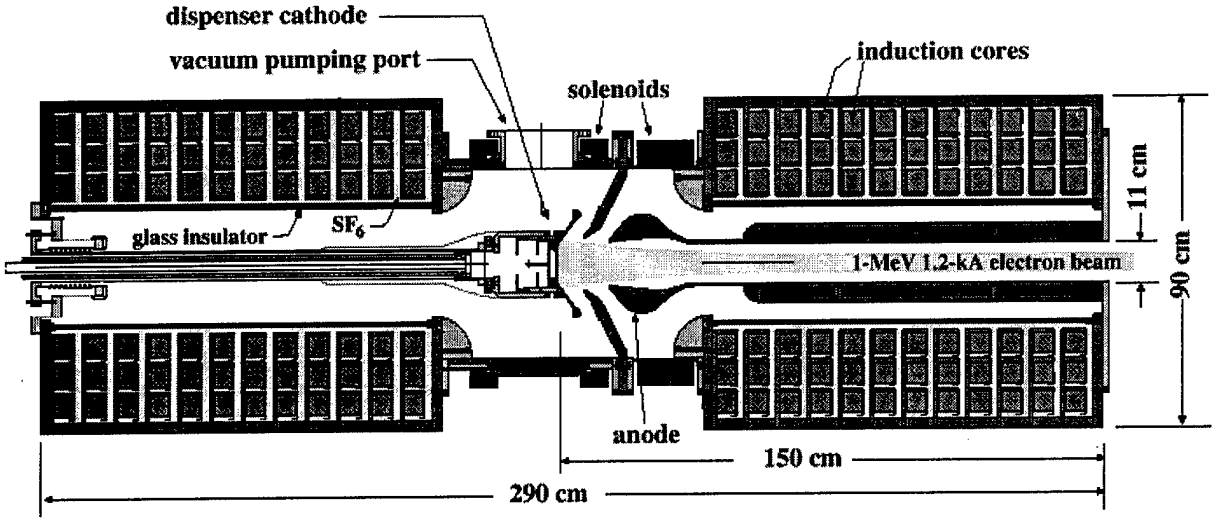


Figure 1. Illustration of the RTA gun, a 1.2-kA, 1-MeV induction electron source.

0-7803-4376-X/98/$10.00 © 1998 IEEE

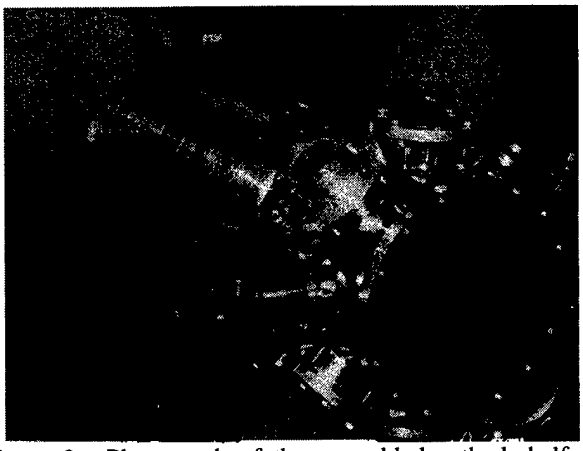


Figure 2. Photograph of the assembled cathode-half of gun. The cathode will be located within the pumping spool. Flange for the anode-half of gun is blanked off.

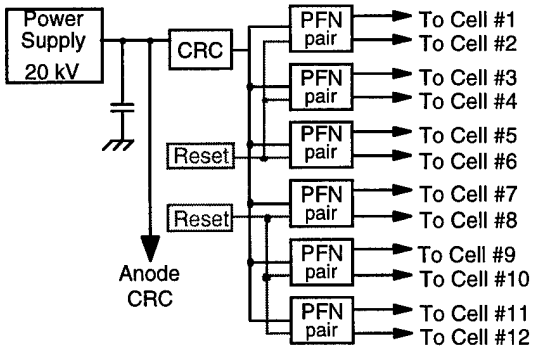


Figure 3. Block diagram of the pulsed power system for the cathode half of the RTA gun.

the operating voltage of 500 kV is about 5.1 kV/cm. Maximum fields at the triple points, the intersection of insulator, vacuum, and metal, is less than 3.5 kV/cm. Maximum surface fields in the cathode half of the gun are about 85 kV/cm. The maximum field is about 116 kV/cm on the anode stalk. The rationale for using PYREX is to explore methods of reducing the costs of induction injectors. PYREX is significantly less expensive than ceramic, and additional savings are realized by avoiding intermediate electrodes. Since there is additional risk associated with this approach, our design allows for the addition of intermediate electrodes and/or substitution of a ceramic insulator with minimal impact to schedule or expense. However, the initial high-voltage tests on the cathode-side insulator are encouraging.

3 PULSED POWER SYSTEM

The pulsed power system will consist of a 20-kV Energy Storage Bank Charging Power Supply, 6-kJ Energy Storage Bank, two Command Resonant Charging Chassis, 24 Switched Pulse Forming Networks, and four Induction Core Reset Pulsers, half of which is shown in Figure 3. A photograph of one PFN is shown in Figure 4. Each PFN will drive a single 3-core induction cell. A sample pulse for a single cell with a 40 Ω resistor simulating beam loading is shown in Figure 5.

Segmenting the core in the induction cell and driving the individual core segments avoids a high-voltage step-up transformer. This reduces the developmental effort needed to achieve a "good" flattop pulse (minimal energy variation) with fast risetime and improves the efficiency of the overall pulsed power system. Our system of low-voltage PFNs driving multiple core induction cells is similar to the system envisioned for the extraction section in the TBNLC design. For the core material, we choose METGLAS alloy 2605SC instead of the 2714AS, the preferred material for the TBNLC, due to the larger inner diameter gun cores. In the RTA gun configuration, the larger flux swing of 2605SC was of greater importance

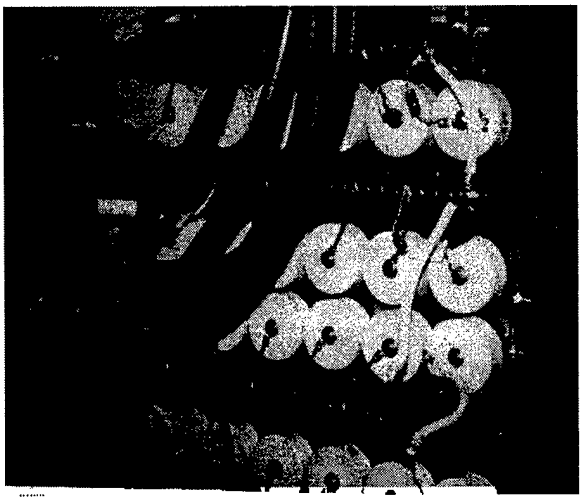


Figure 4. Photograph of single PFN used for driving a gun induction cell. The PFN is comprised of multiple LC stages charged to about 28 kV and uses thyratron switching.

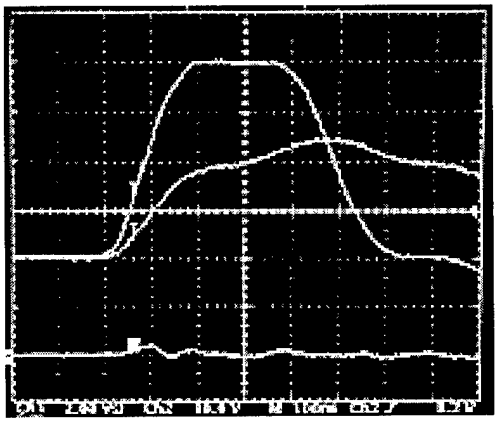


Figure 5. Oscilloscope trace of pulsed gap voltage applied to a single induction cell. Top trace is voltage (10 kV/div) and middle trace is current (4 kA/div). Time scale: 100 ns/div.

than the lower loss per unit volume of 2714AS. The RTA extraction section will use 2714AS to permit an accurate measurement of the pulsed power system efficiency expected for the TBNLC.

Design of the switched PFNs follows easily from published METGLAS core loss data[7]. For the RTA induction cells, a flux swing of 2.6 T in 400 ns (FWHM) results in a magnetization rate of 6.5 T/μs. At this rate, a loss density of 1800 J/m^3 translates into 30 J lost in a cell with 16.7x10^3 cm^3 of 2605SC METGLAS. For a cell input voltage of 14 kV applied for 400 ns, these losses require that 5900 A be supplied to the three radial cores. An additional 3600 A is required to supply beam current (1200 A x 3 cores/cell), resulting is a total current of 9 kA. The required drive impedance is then 1.5 Ω, which is provided by the PFN module shown in Figure 3.

Achieving the fast risetime necessary to minimize the volt-seconds required for the injector cores presented a challenge. Budget constraints coupled with the large availability of EEV CX1538 thyratrons from the ATA program at LLNL made these tubes an attractive option. However, their poor time rate of current change (4 kA/μs rating) made them questionable for this application, which requires about 40 kA/μs. A variety of techniques were tried to decrease the risetime. In a 1.5 Ω system, stray circuit inductances must be maintained at or below 100 nH to achieve a 10-90% risetime of 150 ns. This was accomplished by placing the thyratron between two current sheets connecting the PFN output to the output cables. The ionization time of the thyratron was substantially reduced by applying a 1-2 A pre-pulse to the keep-alive grid 300-400 ns prior to the arrival of the main control-grid pulse. Despite all these improvements, ceramic thyratrons, such as the Triton F-130, may have to be used in the final injector system to overcome excessive stray inductances and capacitance.

An area of concern is the consistency of the METGLAS cores. Several core materials were tested at the RTA Test Facility to establish a data base for design studies. However, this testing did not address the issue of consistency between cores of the same material. We now have a data base including the 38 cores of METGLAS alloy 2605SC used in the construction of the cathode-half of the gun. Figure 6 shows the energy loss per unit volume for these cores extrapolated to a magnetization rate, dB/dt, of 5 T/μs. The cores used 20 μm thick 2605SC layers with MYLAR insulation and achieved an average packing fraction of 76%, minimum of 72% and maximum of 78%. The cores had a radial thickness of 5.8 cm with an inner radius of 19 cm, 27 cm, or 35 cm. The small, medium, and large cores in Figure 6 refer to the different inner radii. The three horizontal lines represent the average loss per volume for the respective core sizes. The smaller the core radius, the higher the loss per volume, as shown in the figure. However, total loss per core for the 38 cores was approximately the same with no significant dependence on core size.

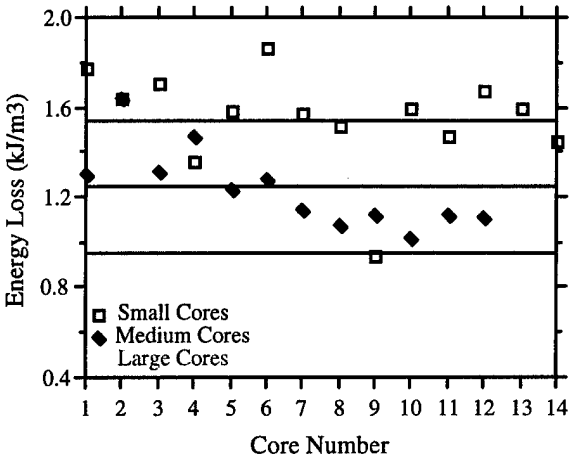


Figure 6. Test results for the METGLAS alloy 2605SC cores.

The standard deviation in loss per volume for the small and medium cores was 14% and the large core was 29%. However, by matching the cores, the standard deviation for a three core cell was reduced to 4%. If the core losses vary sufficiently, it becomes necessary to tailor individual PFNs to adjust for the different cell loads. For a large relativistic klystron, matching cell cores should permit acceptable energy loss variation.

3 ACKNOWLEDGMENTS

The work was performed under the auspices of the U.S. Department of Energy by LLNL under contract W-7405-ENG-48, and by LBNL under contract AC03-76SF00098. We thank Andy Sessler and Swapan Chattopadhyay for their support and guidance and thank Wayne Greenway, William Strelo, and Bob Candelario for their excellent technical support.

REFERENCES

[1] Sessler, A.M. and Yu, S.S., "Relativistic Klystron Two-Beam Accelerator," *Phys. Rev. Lett.* **54**, 889 (1987).

[2] Westenskow, G.A., and Houck, T.L., "Relativistic Klystron Two-Beam Accelerator," *IEEE Trans. on Plasma Sci.*, **22**, 750 (1994).

[3] Yu, S., et al, "Relativistic-Klystron Two-Beam Accelerator Based Power Source for a 1 TeV Center-of-Mass Next Linear Collider Preliminary Design Report," LBNL LBID-2085.

[4] Houck, T.L., and Westenskow, G.A., "Prototype Microwave Source for a Relativistic Klystron Two-Beam Accelerator" *IEEE Trans. on Plasma Sci.*, **24**, 938 (1996).

[5] Registered name of Allied-Signal, Inc.

[6] Registered name of Corning Glass Works.

[7] Smith, C.H., and Barberi, L., "Dynamic Magnetization of Metallic Glasses," in Proc. of the 5th. IEEE Int'l Pulsed Power Conf., 1985.

EFFICIENCY ISSUE IN C-BAND KLYSTRON-MODULATOR SYSTEM FOR LINEAR COLLIDER

J.S. Oh, M.H. Cho, W. Namkung, T. Shintake[1], H. Matsumoto[1], K. Watanabe[2], and H. Baba[3]
PAL/POSTECH, Pohang, Kyungbuk, 790-784, Korea
[1]National Laboratory for High Energy Physics, Tsukuba, 305, Japan
[2]Laboratory of Nuclear Science, Tohoku University, Sendai, 982, Japan
[3]Nihon Koshuha Co., Ltd, Yokohama, 226, Japan

Abstract

A C-band (5,712MHz) RF system for an e+e- linear collider at 500 GeV center-of-mass energy requires total 4,080 units of 50 MW pulse klystrons and matching 111 MW peak-power modulators for two main linacs. An initial design value of the wall plug power for the entire RF system is 150 MW with 2.5 μsec RF pulse width and 100 Hz pulse repetition rate. A detailed circuit analysis shows that it is possible to get the overall RF system efficiency of approximately 24 %, or equivalent to 210 MW wall plug power. This includes 85 % DC high voltage charging efficiency using compact inverter power supplies, and 70 % pulse efficiency using 3.5 μsec pulse length (ESW) with less than 1 % flat top ripple, and auxiliary powers for thyratron heater, klystron heater, focusing magnet, pulse transformer reset, and etc.

1 INTRODUCTION

An e+e- linear collider at 500 GeV C.M. energy is a very large scale machine of which total length is around 20 km. There are many general requirements for this system such as high reliability and availability, reasonable power efficiency, lower construction cost, simple and easy maintenance, easy and flexible operation.

This paper analyzes the power consumption and efficiency of a C-band RF system for an e+e- linear collider at 500 GeV C.M. energy. This system has total 4,080 units of klystrons (50 MW peak) and modulators (111MW peak) for two main linacs[1].

2 SYSTEM DESCRIPTION

Table 1 shows specifications of a C-band RF system including a klystron and a modulator. A modulator produces 3.5 μsec (ESW, Equivalent Square Wave) pulse with 111 MW peak power. The flat-top portion of 2.5 μsec with ripple less than 1% is utilized to generate 50 MW RF power by a klystron with 45 % conversion efficiency. Fig. 1 is a simplified circuit diagram of the modulator. The HV inverter power supply provides DC high voltage generation with 0.5% fine regulation of PFN charging voltage without de-Qing system. It also has a feature of command charging. This makes the system simple, modular, and reliable. A PFN is a 16-stage Guillemin E-type LC network. There is no thyrite to present the low inverse voltage required for the thyratron deionization in the EOLC circuit due to the command charging scheme of the inverter power supply.

Table 1: Specifications of a C-band RF system.

Klystron (E3746)		
Operating frequency	5712	MHz
Peak output power	50	MW
Repetition rate	100	pps
Efficiency	45	%
Perveance	1.53	$\mu A/V^{1.5}$
Gun voltage	350	kV
Beam current	317	A
RF pulse length	2.50	μsec
Modulator		
Peak output power	111	MW
Average output power	38.9	kW
HV pulse length	3.50	μsec (ESW)
Peak switching current	4758	A
PFN charging voltage	46.7	kV
PFN impedance	4.91	Ω
Stored energy in PFN	389	Joule
PFN cell number	16	

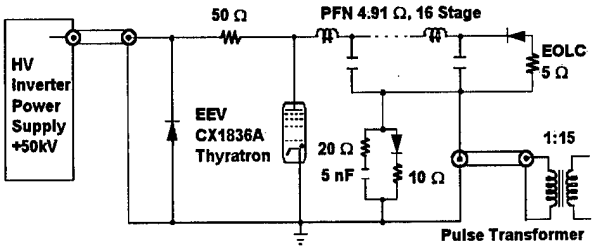


Figure 1: Circuit schematic of a C-band modulator.

3 DEFINITION OF EFFICIENCY

Fig. 2 is a block diagram of power flow for a pulsed RF system. It shows the power conversion flow and corresponding efficiencies of each sub-system. A charging system with P_{AC}, input power supplies P_{DC}, charging power to PFN of a pulsing system. A pulsing system produces P_{PULSE}, pulse power which is the flat-top portion of a pulse. Then a klystron utilizes it to generate RF power, P_{RF}. A P_{AUX}, auxiliary power includes the solenoid coil power for klystron magnet, heater powers for thyratron and klystron, a core reset power for a pulse transformer, a cooling fan power, and so on. η_C, η_P, and η_K represent efficiencies of each sub-system. Table 2

0-7803-4376-X/98/$10.00 © 1998 IEEE

is the list of essential efficiencies.

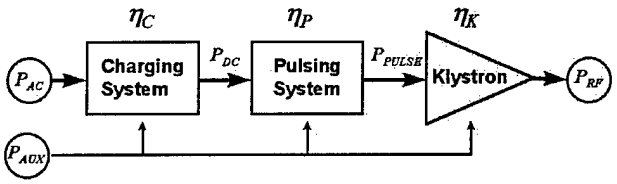


Figure 2: Power flow and efficiencies of an RF system.

Table 2: Definition of efficiencies.

$\eta_C = P_{DC} / P_{AC}$	; Charging Efficiency
$\eta_P = P_{PULSE} / P_{DC}$	; Pulsing Efficiency
$\eta_K = P_{RF} / P_{PULSE}$	; Klystron Efficiency
$\eta_M = P_{PULSE} / P_{AC}$	; Modulator Efficiency
$\eta_{KM} = P_{RF} / P_{AC}$	; Klystron-Modulator Efficiency
$\eta_{RF} = P_{RF} / (P_{AC} + P_{AUX})$	; RF System Efficiency

4 RISE TIME ANALYSIS

A charging system has an efficiency of 85 % specified by the vendor of the inverter power supply. The efficiency of a klystron is given by the design value of 45 %. A pulse efficiency depends on the detail design parameters of the pulsing system including a pulse transformer and a klystron. The rise time of a pulsing system including a pulse transformer and a klystron load for a matched PFN can be described by following equations;

$$T_r = f(\sigma)\,((L_W + L_L)(C_D + C_L))^{0.5}$$
$$f(\sigma) = 2\sigma(m/(m+1))^{0.5}(0.255 - 0.256\,\sigma + 0.537\,\sigma^2)$$
$$\sigma = (\gamma m + 1/\gamma)/(2(m(m+1))^{0.5})$$
$$m = R_L / R_G$$
$$\gamma = Z_T / R_L$$
$$Z_T = ((L_T + L_W)/(C_D + C_L))^{0.5}$$

where $f(\sigma)$ is a fitting function to give the rise time from 10 % to 90 % of maximum pulse height, L_L is the leakage inductance of a pulse transformer, L_W is the wiring inductance of a system, C_D is the distributed capacitance of a pulse transformer between primary and secondary coils, C_L is the distributed load capacitance of a system including the klystron, R_L is the klystron load impedance, R_G is the PFN generator impedance. Z_T is the transformation impedance of the pulse transformer including L_W and C_L, and m is the matching parameter between the PFN and the klystron. γ is the impedance matching parameter between the transformation system and the klystron.

For a lumped PFN modulator with given total distributed capacitance and total leakage inductance, the optimum value of $f(\sigma)$ for generating good waveforms is 1.74 with σ of 0.78, γ of 1.58, and m of 1.05. A good waveform means that it has a minimum rise time with less than 2 % overshoot. A larger γ gives a slow rise time and a smaller γ makes the large overshoot with ringing. It is important to keep the optimum γ, and minimize distributed capacitance and leakage inductance to get the minimum rise time with good waveforms. A wiring inductance of 1 μH of the pulsing system at the primary side with 15 step-up ratio of the transformer gives 225 μH inductance at the secondary side. This inductance corresponds to the minimum rise time of 0.22 μs with γ of 1.58. Fig. 3 is the analyzed result of distributed capacitances using DENKAI in the pulse tank including the klystron assembly. The right-half of the figure shows potential lines in the region of the klystron tube and between the coils of the pulse transformer in the tank. The calculated values of capacitance are presented at the left-half of the figure. Total distributed capacitance in the tank except the capacitance between the coils is 115 pF. If the capacitances between the corona ring and other structures not included in this estimation is added to the result, it becomes approximately 120 pF. This capacitance corresponds to the minimum rise time of 0.39 μs with γ of 1.58. So the large distributed capacitance in the pulse tank is more limiting parameter for the pulse rise time in the case of the C-band RF system.

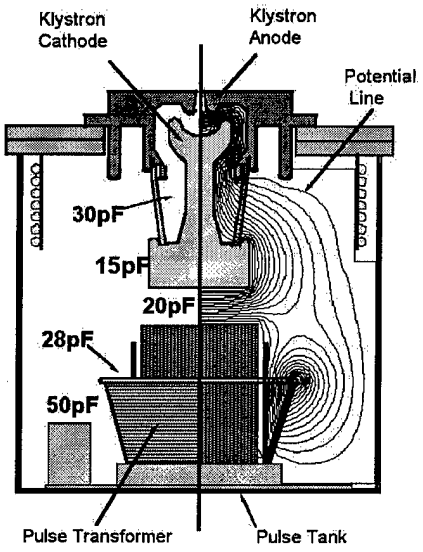


Figure 3: Distributed capacitance and potential lines in the pulse tank with E3746 klystron.

Table 3: Parameters of the C-band pulse transformer.

Turn Ratio	15
Primary turns	3
Leakage inductance (μH)	1.60
Stray capacitance (nF)	6.33
Shunt Inductance (mH)	0.36
Core Resistance (Ω)	411
Droop (%)	2.39
Overshoot (%)	1.96

The primary consideration of the transformer design is to keep the capacitance low between primary and secondary coils, for example under 30 pF to make the rise time of less than 0.5 μs and guarantee the flat-top width of 2.5 μs. Typical parameters of the pulse transformer at the primary side are summarized in Table 3. Total inductance

and capacitance including transformer parameters are 499 μH and 164 pF which give the rise time of 0.47 μs.

5 POWER DISTRIBUTION ANALYSIS

The simulated klystron voltage waveform with its expanded view using PSPICE is shown in Fig. 4. The expanded view shows 2.5 μs flat-top with ripples less than 1 % which results the phase shift of 5.68° of the klystron RF output. Analyzed power distribution of a C-band klystron-modulator system is described in Table 4. Total 51.4 kW is required to generate 12.5 kW RF power with 100 Hz operating condition. The beam power of 15.3 kW is dumped to a collector of a klystron within the portion of flat-top. This loss caused by the conversion inefficiency of the klystron is 30 % of the total power. Wasted pulse power includes all the losses which are not contributed to make RF power from the stored energy of the PFN. The loss during rise and fall time is 10 kW which includes stored energies in the leakage inductance and the distributed capacitance, and electron beam power delivered to the collector during this time interval. This is the main loss in the pulse modulator, which is 19.5 % of the total power. The magnetizing loss of 0.9 kW means the stored energy in the shunt inductance of the pulse transformer which is finally dissipated at the tail clipper. The solenoid coil power of the klystron magnet is assumed just as 3 kW but it still takes main part of the auxiliary power.

Table 4: Power distribution of a C-band system.

Total Power = 51,371 W		
1. RF Power	12,488	(24.3%)
2. Wasted Beam Power	15,263	(29.7%)
3. Wasted Pulse Power	12,071	(23.5%)
4. Charging Loss	7,072	(13.8%)
5. Aux. Power	4,477	(8.7%)
Wasted Pulse Power		
a. Rise/Fall Time Loss	9,991	(19.45%)
b. Magnetizing Loss	929	(1.81%)
c. Thyratron Loss	416	(0.81%)
d. Eddy Current Loss	463	(0.90%)
e. RC Snubber Loss	272	(0.53%)
Aux. Power		
a. Klystron Magnet	3,000	(5.84%)
b. Thyratron Heater	567	(1.10%)
c. Cooling Fan	450	(0.88%)
d. Klystron Heater	316	(0.62%)
e. Core Bias	100	(0.19%)
f. Thyratron Reservoir	44	(0.09%)

6 EFFICIENCY

Table 5 shows the efficiencies of the each sub-system of the C-band klystron-modulators. The pulse efficiency of 70 % is mainly limited by distributed capacitance in the oil-filled pulse tank. It is difficult to improve the pulse efficiency using the standard method. Since a net RF system efficiency is 24 %, the total AC wall-plug power of 210 MW will be consumed to generate the total RF power of 51 MW using 4,080 units of a klystron-modulator system.

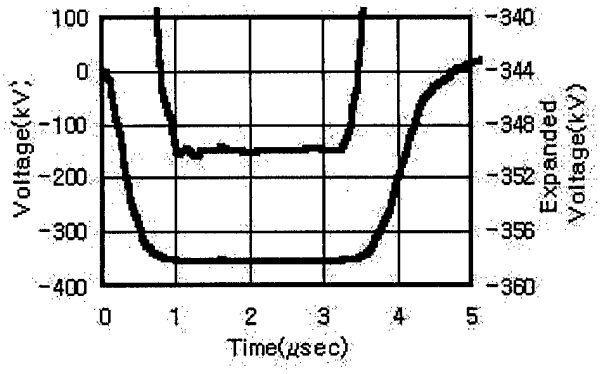


Figure 4: Simulated klystron voltage waveform.

Table 5: Efficiencies of the C-band system.

Charging Efficiency	85.0 %
Pulse Efficiency	69.8 %
Klystron Efficiency	45.0 %
Modulator Efficiency	59.3 %
K-M Efficiency	26.7 %
RF System Efficiency	24.4 %

7 CONCLUSIONS

A net RF efficiency of the C-band system is estimated to be 24 %, and this requires total AC wall-plug power of 210 MW. The charging efficiency of 85 % can be improved up to 90 % through the trade-off design of the inverter power supply. The pulse efficiency of 70 % is almost optimized. If the PM-AM modulation method of the C-band system[2] allows the 2-3 % tolerance of the flat-top ripple, it can be improved up to 75 %. The klystron efficiency of 45 % is the most flexible parameter in the RF sub-systems. It could be raised up to 60 %. Then it is expected to get a net RF efficiency of 35.4 %, and total AC wall-plug power demand can be lowered to 144 MW.

REFERENCES

[1] Shintake, et al., C-band Main Linac RF System for e+e- Linear Collider of 0.5 To 1.0 TeV C.M. Energy, Proc. 18th International Linear Accelerator Conference, Geneva, Switzerland, August 26-30, 1996.

[2] T. Shintake and N. Akasaka, A New RF Pulse-Compressor Using Multi-Cell Coupled-Cavity System, Proc. 5th European Particle Accelerator Conference, Sitges, Barcelona, Spain, June 10-14, 1996.

SLAC ACCELERATOR OPERATIONS REPORT: 1995-1997*

R. Erickson, C.W. Allen, S. Anderson, W. Linebarger, M. Stanek,
Stanford Linear Accelerator Center, Stanford, CA 94309 USA

Abstract

Operational statistics for the linear accelerator programs at SLAC are presented, including run-time records for SLC and the fixed-target programs. Also included are summaries of reliability and maintenance-related statistics.

1 PROGRAM CHRONOLOGY

The SLAC linear accelerator programs and hardware reliability statistics for January 1992 through March 1995 were presented in Reference [1]. This paper extends that analysis through April 1997, for the periods of linac operation summarized in Table 1. Scheduled off times in this table were relatively long periods needed for major installations and upgrades. Time periods when the accelerator was off for holidays are not listed.

ESA runs were periods when polarized electrons were delivered to fixed-target experiments E154 and E155 in the End Station A experimental hall. The ESA run in 1995 was the first to use the A-Line transport system following its upgrade to full 50 GeV capability, and is described in greater detail in Reference [2]. The FFTB runs were periods of low repetition rate (30 Hz) operation in which damped electrons were delivered to the Final Focus Test Beam facility for experiment E144. SLC machine development included extended periods of pre-run system turn-on, new system commissioning, and experiments to characterize and improve the performance of various accelerator systems. SLD logging refers to periods of SLC operation dedicated to producing Z particles with the SLD detector on and recording data.

During the period from August 12 to 19, 1996, the primary beam was delivered to ASSET, a station in the linac tunnel downstream of the damping rings used for testing prototype accelerator structures. This program, which was intended to develop the testing facility as well as to test an actual prototype structure, was essentially a week of continuous tuning and machine studies. The ASSET test, while considered very successful, is not discussed further in this paper because of its short duration and because it offers little additional insight into the overall reliability of the accelerator facility.

In addition to the primary programs discussed in this paper, a parasitic electron beam was operated for parts of May and June, 1996, during the SLD run. This beam, which was generated by converting bremsstrahlung radiation from linac collimators when the SLC was operating, had no adverse impact on the primary program and is not reflected in the statistics presented below. The goal of this program was to characterize the parasitic electron beam, including measuring the achievable flux and energy range, for use in future applications.

Time period	Program
1 Apr 95 - 10 Sep 95	Scheduled off. Rebuild A-Line. Install PEP e^- inject transport line.
11 Sep 95 - 30 Sep 95	Check out / turn on at 30 Hz.
1 Oct 95 - 30 Nov 95	ESA run - E154.
10 Dec 95 - 23 Dec 95	FFTB run - E144.
2 Jan 95 - 10 Feb 96	SLC machine development.
12 Feb 96 - 31 Mar 96	NDR fire and recovery.
1 Apr 96 - 31 Jul 96	SLD logging.
1 Aug 96 - 12 Aug 96	FFTB run - E144.
19 Aug 96 - 3 Feb 97	Scheduled off. Prepare for fixed target program. Install PEP positron inject transport line.
4 Feb 97 - 28 Feb 97	Turn on, commission A-Line and PEP e^- inject line.
1 Mar 97 - 30 Apr 97	ESA run - E155.

Table 1. SLAC program chronology April 1995 through April 1997.

2 TIME ACCOUNTING

Time accounting records were kept by the accelerator operators, who recorded the number of hours devoted to each of the categories in the first column of Table 2 at the end of each eight hour shift. The experimental runs summarized in this table included only the time periods dedicated to logging data in the indicated detector and excluded pre-run turn on and commissioning time. The run periods began when the accelerator and the detector were ready to begin production data collection and continued until the detector was scheduled to shut down. The SLC/SLD program in 1996 was originally scheduled to begin in February; however, a fire in the north damping ring vault delayed this program while repairs were made, and useful luminosity was not delivered to the SLD detector until April. For purposes of this paper, we have taken April 1 as the scheduled starting date and have not included the time period in February and March 1996 in computing the run statistics presented below.

* Work supported by Department of Energy contract DE-AC03-76SF00515.

0-7803-4376-X/98/$10.00 © 1998 IEEE

	ESA 95	FFTB 95	SLD 96	FFTB 96	ESA 97
Exp't Logging	70%	54%	45%	60%	63%
Machine Develop.	1%	5%	12%	3%	3%
Alternate Program	4%	3%	3%	5%	7%
Tuning	8%	7%	14%	10%	5%
Unsched. Down	10%	24%	23%	16%	11%
Sched. Off	7%	8%	3%	6%	11%
Total Hours	1465	336	2927	288	1463

Table 2. SLAC primary linac program run time accounting 1995-1997.

The "experiment logging" category is defined as the time when a suitable beam (or colliding beams) was available to the scheduled experiment, and the detector equipment was active and recording data. Machine development in Table 2 included brief (<1 day) interruptions to data logging, usually dedicated to measuring accelerator system parameters and implementing improvements. The extended periods of scheduled machine development work listed in Table 1 are not included here. Alternate programs were brief tests or experiments scheduled on short notice when the primary program could not be carried out as planned. This typically happened when some accelerator subsystem critical to the primary program was undergoing repairs while other accelerator systems, such as the injector system and the electron damping systems, were operating normally. During the ESA runs, most of the alternate program time was used for testing and commissioning the new PEP electron injection transport line.

Tuning is defined as any time when no specific hardware or software systems were known to be malfunctioning, yet the beam properties did not meet the requirements of the scheduled program. Typically this was the time spent by operators and accelerator physicists measuring and correcting beam parameters. Unscheduled down time was logged when a system or component failed, rendering the beam unusable for either the main experiment or an alternate program. Scheduled off represents planned interruptions to the primary experimental program, typically for maintenance and minor upgrades or for adjustments to existing systems. The extended scheduled off periods shown in Table 1 are not included here, nor are holiday periods.

The improvements in beam polarization achieved in 1993 - 94 proved invaluable for the programs in the time period reported here. The polarization delivered to the ESA experiments was typically 82 to 83 percent. The polarization delivered to the SLD experiment was slightly degraded by the more complex transport system (including the SLC electron damping ring and arc), but was typically 73 to 79 percent at the collision point. During the 1996 SLC run, approximately 52 thousand Z particles were recorded by the SLD detector. This corresponds to an average luminosity of 39.6 Z's per hour, although the peak luminosity improved over the course of the run, and at times reached 100 Z's per hour.

3 HARDWARE RELIABILITY

Hardware availability, defined here in terms of time when the accelerator hardware is not broken, is a measure of the overall reliability of the accelerator systems needed to carry out the accelerator program. The hardware availability, mean time to failure, and mean time to repair are listed in Table 3 for each of the major accelerator programs. These quantities are defined as follows:

Availability = 1- (Downtime / Scheduled Operating Hours).
Mean Time To Failure (MTTF) = Sched hrs / # of Failures.
Mean Time To Repair (MTTR) = Downtime / # of Failures.

	Availability	MTTF	MTTR
SLC 1993	82.8 %	7.7	1.3
SLC 1994	80.7 %	8.5	1.6
SLC 1996	79.0 %	10.7	2.2
ESA 1993	93.3 %	12.7	0.9
ESA 1995	92.0 %	21.2	1.7
ESA 1997	89.4 %	10.9	1.2
FFTB 1995	83.6 %	15.6	2.6
FFTB 1996	83.7 %	16.0	2.6

Table 3. SLAC hardware reliability summary.

Hardware failures as defined in this section are those failures that noticeably interrupt or impede a scheduled running program and do not require testing or inspections to locate. As these data indicate, the hardware availability was consistently better during ESA and FFTB operation than during SLC operation. This was mainly because the ESA and FFTB programs required only electrons (no positrons) and thus required fewer active devices. SLC and ESA data from Reference [1] for 1993 and 1994 are also included for comparison.

The availability values are significantly higher than the experiment logging values in Table 2. For the SLD program, this difference arises primarily because of the substantial time required to tune the SLC and to carry out the machine development activities needed to meet performance goals. For the ESA experiments, the difference is due almost entirely to the time lost when the targets were unable to accept the beam. Experiments E154 and E155 both used sophisticated polarized targets that required frequent attention for maintenance and processing, sometimes scheduled, and sometimes not. The time when the targets were unavailable is counted under a combination of the other categories in Table 2. During target interruptions to E155, the PEP injection line was tested (alternate program), the linac pulse length was stretched (machine development), and safety systems were tested and certified in preparation for SLC and PEP operations (scheduled off).

4 ACKNOWLEDGMENTS

We gratefully acknowledge the contributions of the many engineers and technicians who maintained the accelerator facilities under a demanding schedule, and especially the staff of the Accelerator Operations group for their round-the-clock attention to SLAC's accelerator program.

REFERENCES

[1] 'SLAC Accelerator Operations Report: 1992-1995', R. Erickson, C.W. Allen, T.K. Inman, W. Linebarger, and M. Stanek, SLAC-PUB-95-6895, May 1995. Presented at *16th IEEE Particle Accelerator Conference* (PAC 95) *and International Conference on High Energy Accelerators*, Dallas, Texas, 1-5 May 1995.

[2] 'First Operation of the Upgraded SLAC A-Line', R. Erickson, S. Anderson, A. Baker, S. DeBarger, T.K. Inman, R. Iverson, H. Smith, and M. Stanek, SLAC-PUB-95-7177, October 1996. Presented at the *Fifth European Particle Accelerator Conference* (EPAC96), Barcelona, Spain, June 10-14, 1996.

A COMBINED $\Delta T + \Delta F$ BEAM LOADING COMPENSATION SCHEME FOR POWER SAVING *

Zenghai Li, Roger Miller, David Farkas, Tor Raubenheimer, Huan Tang and Dian Yeremian
Stanford Linear Accelerator Center, Stanford University, Stanford, CA 94309

Abstract

The NLC low frequency (S and L band) rf linacs are heavily loaded by a beam of about 130 ns in macropulse length (90 bunches) and a current up to 2.75 Amps. Beam loading generates a large energy spread along the bunch train. For these linacs, the bunch train is much shorter than the filling time of these linac structures, and the energy of the beam drops approximately linearly with time during the pulse as a result of beam loading. For such a case, there are two natural choices for beam loading compensation, ΔT (which achieves compensation by injecting the beam before the accelerator structure is full) and ΔF (which compensates by having some accelerator sections at $f_0 \pm \Delta F$). There are, however, disadvantages with these methods: non-local compensation in the ΔF method (except using many short ΔF sections) and low efficiency in the ΔT method due to short filling time and amplitude modulation required for compensation. In this paper, we will discuss a combined $\Delta T + \Delta F$ method. In this scheme, the filling time of the structure is optimized for ΔT compensation for phase-I operation. In phase-II operation, ΔF sections are used to compensate the extra 50% beam loading due to higher current. Simulations have shown that up to 30% of power can be saved by using this method.

1 INTRODUCTION

The NLC [1] S-band L-band linacs are heavily loaded by a beam of about 130 ns in macropulse length (90 bunches) and a current up to 2.75 Amps. Energy compensation is required in order to obtain a small energy spread along the bunch train. The pulse length of the bunch train in these accelerators is much shorter than the reasonable filling times of the structures which are in turn shorter than the ringing time, $2Q/\omega$, for the structure. In this situation, the energy of the beam will drop approximately linearly with time during the pulse as a result of beam loading. For this case there are two natural choices for beam loading compensation: 1) ΔT (early injection and amplitude modulation), i.e., inject the beam before the structure is full and modulate the amplitude of the input power to produce a slope in the acceleration voltage that cancels the beam loading; 2) ΔF, i.e., having one or more accelerator structures running at a frequency 1 to 2 MHz above or below the nominal frequency and roughly in phase quadrature from the accelerating phase. Thus the beginning of the pulse can be decelerated by the off frequency section(s), while the end of the pulse is accelerated.

* This work was supported by the U.S. Department of Energy, under contract No. DE-AC03-76SF00515.

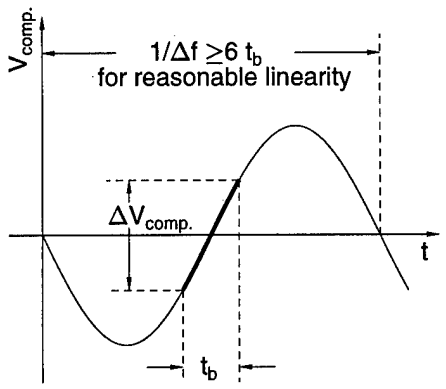


Figure 2.1: Compensation voltage $V_k(t)$ of a ΔF section.

The seven S-band and four L-band low rf frequency linacs in the NLC complex each accelerates a different beam current. For example, in phase-I operation, current in the S-band e^+-drive linac is 1.5-A while in the e^--prelinac is 1.0-A. Further more, the currents will be 50% more in phase-II operation. This requires the compensation schemes to be capable of compensating beam loading of wide range of beam currents. Both ΔF and ΔT schemes have been proven to be effective with NLC operation parameters [2]. However, there are advantages and disadvantages with the ΔF and ΔT methods. While the ΔF scheme has high efficiency (for high currents), it yields a poor energy spectrum along the accelerator. The ΔT scheme, on the other hand, gives a good energy spectrum, but is low in efficiency for high beam currents. To solve the problem, we present, in this paper, a hybrid approach using $\Delta T + \Delta F$. Under high beam loading conditions, compensation is distributed between ΔT and ΔF. Both ΔT and ΔF are operated to compensate a lower beam current, which improves the efficiency (ΔT) and reduces energy spread (ΔF). The machine parameters used in this paper are for the present design. They may evolve in the future.

2 ΔF COMPENSATION

In an compensation accelerator section powered by rf at a frequency $F_0 \pm \Delta F$, the bunches see a field which appears to vary with the difference frequency ΔF as shown in Fig.2.1. If the beam pulse length satisfies the relation $t_b \leq \frac{1}{6\Delta F}$ and is phased as shown, the energy gain will vary quite linearly with time.

The frequency offset ΔF of the compensation sections need to be chosen between the requirement of compen-

0-7803-4376-X/98/$10.00 © 1998 IEEE

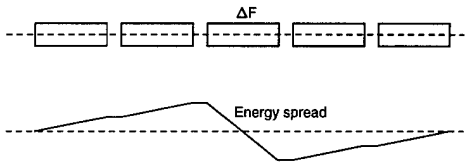


Figure 2.2: Energy spread in an accelerator module with ΔF compensation in the middle.

sation power ($\propto 1/\Delta F^2$) and the residual energy spread ($\propto \Delta F^2$). We have chosen a ΔF (1.4 MHz for S-band) such that the phase spread of the bunch train in the ΔF section is about 60^0. The maximum compensable beam loading voltage in this case is equal to the maximum acceleration of the ΔF section. With 25% maximum beam loading at nominal operation, one ΔF section can compensate beam loading of a module of four regular sections.

Within each module, with the ΔF section in the middle, the beam energy spread reaches half of the compensation voltage of a single off-frequency section as shown in Fig. 2.2. The compensation section then over corrects by a factor of two which reverses correlation of energy with time during the pulse. In order to maintain a small enough energy spread to achieve an acceptable emittance growth it appears necessary to distribute the power from one klystron running off frequency to a number of short accelerator sections, so that each correction is acceptably small. However, the high power microwave distribution system to many short ΔF compensation sections becomes unreasonably complicated and expensive. In addition to non-localness of ΔF compensation, the residual energy spreads (difference between the sine and "linear" beam loading curves) of all modules in an accelerator have the same distribution along the bunch train and they add up.

3 ΔT COMPENSATION

The way ΔT compensation works is shown in Fig. 3.3 in which the voltage $V_k(t)$ produced by a step function rf pulse is plotted as a function of time for a traveling wave linac section. Also plotted is the beam induced voltage $V_b(t)$. The resultant sum of $V_k(t)$ and $V_b(t)$ is plotted for the case where the beam is turned on before the linac structure is full.

For SLED-I driven structures, the input power to the structure decreases exponentially [3]. As a result, the slope of the acceleration voltage decreases with time. To compensate at high beam currents in the NLC, it is preferable to used a reasonably short filling time. In addition, the power profile needs also be modulated to change the slope of the acceleration voltage, which enables to compensate beam loadings of different currents. The advantage of ΔT compensation is that the compensation occurs in every accelerator section, so that the energy spectrum can be good through out the linac, thus minimizing emittance growth from dispersion and chromatic effects. In addition, the amplitude modulations in different modules of an accelerator is independent and the residual energy spread can be made random. The residual energy spread ΔE at the end of the accelerator will be $\sqrt{N}\Delta E_{module}$. The relative energy spread is proportional to $1/\sqrt{N}$.

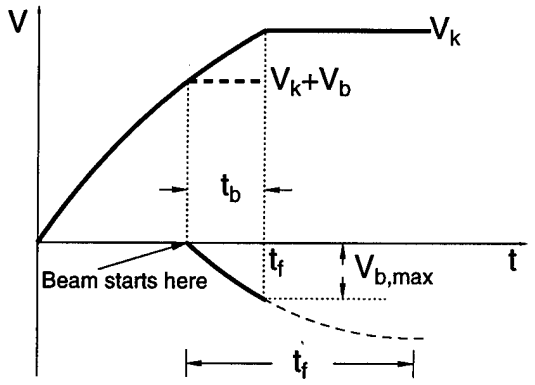


Figure 3.3: ΔT beam loading compensation using early injection.

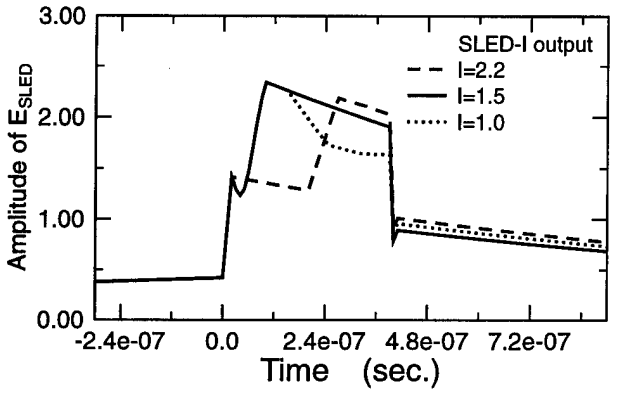


Figure 3.4: SLED-I wave forms for compensating 1, 1.5, and 2.2-A beam currents using ΔT compensation scheme.

For 1.5-A current with optimized filling time, the efficiency of ΔT is comparable to ΔF. For 1- and 2-A currents, the efficiency is about 30% lower due to amplitude modulation, Fig. 3.4.

4 HYBRID $\Delta T + \Delta F$ APPROACH FOR POWER SAVING

Low efficiency with ΔT compensation is mainly due to amplitude modulation of the SLED output. One can improve the efficiency of the ΔT compensation scheme by optimizing the filling time of the structure for each given beam loading current to avoid amplitude modulation. It is effective at relatively low beam currents, fails at high beam currents where the filling time of the structure would become too short. For the later case, a compromise can be found between energy spectrum and efficiency by combining ΔT and ΔF. With the combined scheme, the filling time of the structure is optimized to compensate a lower

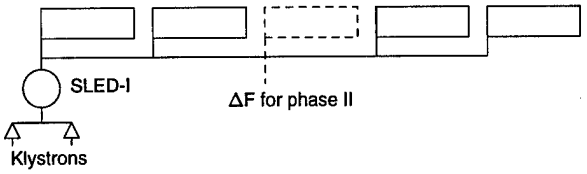


Figure 4.5: A sketch of $\Delta T + \Delta F$ compensation scheme.

Table 4.1: ΔT and $\Delta T + \Delta F$ results for the NLC prelinacs

	Phase-I	Phase-II
Current (A)	1.0	1.5
E_{accel}/module (MeV)	310 (244)	305 (254)
$\Delta E/E_{accel}$	1.1×10^{-3} (3.2×10^{-4})	9×10^{-4} (1.1×10^{-5})
$P_{\Delta F}$/module (MW)	0.0	5
P saved	38%	30%

beam current using ΔT, and ΔF sections are used to compensate the extra beam loading when operating at high currents. In this case, the ΔF section compensates only a small fraction of total beam loading, non-localness of ΔE is less a problem. A sketch of an accelerator module with $\Delta T + \Delta F$ compensation is shown in Fig. 4.5.

In the NLC, The current in phase-II is 50% more than in phase-I. With the combined $\Delta T + \Delta F$ concept, it is natural to optimize the filling time of the structure for ΔT compensation for phase-I. In phase-II, ΔF sections are used to compensate the extra beam loading, which is only 30% of the total phase-II beam loading.

A comparison between ΔT and hybrid $\Delta T + \Delta F$ in power requirement is shown in table 4.1 for the S-band prelinacs operating in phase-I and phase-II. The numbers in parentheses are for pure ΔT compensation. More than 30% of power can be saved with the hybrid approach in both phase-I and II operations for the prelinacs. Similar results were found for other NLC low rf linacs with the $\Delta T + \Delta F$ approach.

5 SUMMARY

In this paper, we have discussed the advantages and disadvantages of using ΔT and ΔF beam loading compensation schemes in term of efficiency and local energy spectrum for SLED-I driven disk-loaded waveguide structures. Compromise between efficiency and energy spread was found by using a hybrid $\Delta T + \Delta F$ approach. With the NLC S-band prelinac parameters, over 30% of power can be saved by using the hybrid scheme as compared with pure ΔT scheme (filling time optimized for 1.5-A current). Similar power saving can be obtained for other low rf frequency lincas in the NLC complex.

6 REFERENCES

[1] Zeroth-order design report for the Next Linear Collider, LBNL-PUB-5424, SLAC Report 474, UCRL-ID-124161, 1996.

[2] Z. Li and *et al*, "Beam Loading Compensation for the NLC Low Frequency Linacs," SLAC-PUB-7429, March 1997.

[3] Z. D. Farkas and *et al*, "SLED: A Method of Doubling SLAC's Energy," SLAC-PUB-1453, March 1974.

NEUTRAL BEAM COLLISIONS AT 5 TEV

D. H. Whittum and R. H. Siemann[1]
Stanford Linear Accelerator Center, Stanford University, Stanford CA, 94309

Abstract

At 5 TeV center-of-mass energy, collective effects are a prominent feature of electron-positron collisions, contributing to backgrounds and energy-spread, and suggesting a practical limit on the charge per bunch. To circumvent such collective phenomena we examine collision of neutral beams, with particular attention to the effect of mismatch and instability.

1 INTRODUCTION

The exploration of high-energy physics has progressed over the last 50 years only by continuous and inspired invention [1]. Today, blessed with a surfeit of predictions for the 5 TeV frontier [2], we are unable to reach the energy required. The problem, for linear colliders is this: to reach high luminosity with a reasonable site power we must produce *small* beams in collision. However, small beams interact collectively and pinch each other [3].

As a particle encounters the oncoming beam at the interaction point, its trajectory is bent and it radiates "beamstrahlung" photons, with a spectrum characterized by the parameter

$$\Upsilon = 1.1\times10^{2}\frac{\gamma N_b r_e^2}{(1+R)\sigma_y\sigma_z},$$

the ratio of average photon energy to incident electron energy. Here r_e = 2.82x10^{-13} cm is the classical electron radius and N_b is the number of particles per bunch. The quantity $R = \sigma_x/\sigma_y$ is the aspect ratio of the beam at the IP, σ_x and σ_y are the rms spot sizes in collision, σ_z is the rms bunch length, and $\gamma=E_{CM}/2mc^2$ is the Lorentz factor for an electron.

It is instructive to parameterize the collider scalings by Y. We abbreviate $W = \sigma_z\Upsilon / r_e\gamma$. The average fractional energy loss of an electron in collision is given by [4]

$$\delta \approx 6.6\times10^{-5} W\Upsilon\left[1+(1.5\Upsilon)^{2/3}\right]^{-2}.$$

The number of particles per bunch is

$$N_b \approx 8.5\times10^{-3} W\left(\frac{\sigma_y}{r_e}\right)(1+R),$$

and the bunch crossing rate may be expressed in terms of luminosity

$$f \approx 2.1\times10^{4}\frac{L\sigma_T}{W^2}\frac{R}{(1+R)^2},$$

where σ_T ~ 6.7x10^{-25}cm^2 is the Thomson cross-section. Site power P may be expressed as

$$P \approx 3.5\times10^{2}\frac{mc^2\gamma}{\eta}\frac{L\sigma_T}{W}\left(\frac{\sigma_y}{r_e}\right)\frac{R}{1+R}$$

where η is the efficiency of conversion of wall-plug energy to beam kinetic energy. Finally, the colliding beams serve to focus each other with focal length ~σ_z/D_y, where the disruption parameter is

$$D_y = 1.7\times10^{-2}\frac{W^2}{\Upsilon}\left(\frac{\sigma_y}{r_e}\right)^{-1}.$$

Center-of-mass energy, luminosity and site power constrain all variables as functions of δ and Y (and R). Additional restrictions should be considered with care; we tentatively consider the following: (1) control energy resolution in collision: $\delta < 0.1$ (2) control backgrounds: $\Upsilon < 0.2$. If we accept these constraints as equalities, all parameters, but R, follow directly. For example, at 5 TeV center of mass energy, a useful event rate requires luminosity of order L ~ 10^{35}cm^{-2}s^{-1}. Perceived operating costs limits P to, let us say, 500 MW. With δ = 0.1 and Υ = 0.2 one finds W ~1.6x10^4, β_y~σ_z~0.1cm, D_y~1.5x10^3, and other parameters as in Table 1.

Table 1 Naive collider scalings at 5 TeV.

$\sigma_y \approx 5\times10^{-7}\eta\left(1+\frac{1}{R}\right)$cm
$f \approx 1.4\times10^{6} R(1+R)^{-2}$ Hz
$N_b \approx 5\times10^{8}\eta(1+R)$
$\varepsilon_{ny} \approx 1\times10^{-7}\eta^2\left(1+\frac{1}{R}\right)^2$ m − rad

The relatively long bunch length has implications. For a linac operating with a pure sinusoidal accelerating waveform (*i.e.*, a conventional linac), the bunch length constrains the linac wavelength to $\lambda \sim 53\sigma_z/\delta^{1/2}$, where δ is the percent rms energy spread for the beam. The momentum bandwidth of the final focus system [5] constrains δ. For example δ ~ 0.2% implies a linac operating at S-Band or longer wavelengths. Gradients are

[1] Supported by DOE Contract DE-AC03-76SF00515.

0-7803-4376-X/98/$10.00 © 1998 IEEE

limited at long wavelengths due to breakdown and trapping [6] and even at a gradient of 50 MeV/m, the linac complex would occupy 100 km. These numbers could be relaxed, with non-interleaved chromatic correction, or harmonic rf energy spread compensation, or with a breakthrough in the understanding of breakdown. Regardless, the disruption parameter is sufficiently large that the beams would be violently unstable in collision.

One way out of this dilemma is to relax the constraint on Y, and accept and deal with the copious pair production that would result. In this case, one could contemplate a machine at wavelengths of cm, gradients as high as 200 MeV/m, and a linac 25 km long. There is a second alternative, and this is the subject of the present work.

2 NEUTRAL BEAM COLLISIONS

We consider luminosity production by collision of two neutral beams, each consisting of two co-propagating e^+ and e^- beams. We put aside the issue of initial state tagging. Parameters we have in mind are $\sigma_x=\sigma_y \equiv \sigma_r \sim 2$ nm, $\beta_y \sim 220$ μm, $\varepsilon_{nx} = \varepsilon_{ny} \sim 1\text{x}10^{-7}$ m-rad, $f \sim 550$Hz, $eN_b \sim 2$nC. Corresponding two-beam parameters are $\delta \sim 1$, $Y \sim 3\text{x}10^4$, $\eta \sim 1\%$. As a check of consistency, we take note of the Oide limit [7], arising from synchrotron radiation in the final focus,

$$\frac{\sigma_y}{r_e} \approx 3.6\left(\frac{\varepsilon_{ny}}{r_e}\right)^{5/7} F^{1/7}, \quad \frac{\beta_y}{r_e} \approx 9.3\gamma\left(\frac{\varepsilon_{ny}}{r_e}\right)^{3/7} F^{2/7},$$

where the function F depends on the optics, and is of order unity. The bunch length is subject to $\sigma_z \le \beta_y$, and the uncompensated disruption parameter $D_y \sim 1.4\sigma_z(\mu\text{m})$.

We consider next, what collective limits arise in this system. As noted by Balakin and Solyak[8] and Rosenzweig *et al* [9] neutralized beams in collision suffer from a charge separation instability. A minute deviation from neutrality is amplified as the like-charge beams repel each other. This effect needs to be evaluated quantitatively, and a strong-strong, multi-particle simulation has been written for that purpose. The following section describes that simulation and the work that has been done to date to verify it.

3 INSTABILITY OF NEUTRAL BEAMS

We employ a particle-in-cell simulation based on a three dimensional grid with charge allocation by area weighting in the transverse plane, and solution of Poisson's equation in the transverse plane. The transverse algorithm is described in references [10, 11], and is best suited for approximately round beams which is the case of interest. The modification of previous work for this paper is that the simulation has been made strong-strong by splitting the beams into a number of slices longitudinally. For the results reported in this paper the azimuthal bin size was $\pi/8$, the radial bin size was $0.01\sigma_r$ and there were 16 longitudinal slices, with 10^5 particles/slice/beam.

The charge separation instability can be solved analytically (see next paragraphs) for uniform charge density beams with the assumption that the beam radius is constant through the collision, and the simulation has been tested by comparing results with this analytical solution.

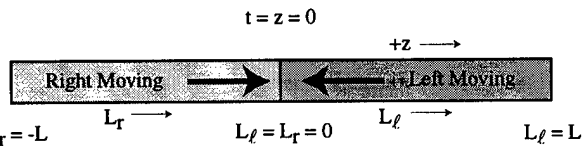


Figure 1: Configuration and coordinates for the calculation. L_r and L_ℓ are right-handed coordinates that move with the beams. The figure is drawn at the start of the interaction.

Let R_r and R_ℓ denote the transverse separations of the beams moving to the right and left, respectively. The equations of motion, derived from Gauss' Law for uniform beams, are

$$\frac{d^2\vec{R}_\ell}{dt^2} = \frac{8c^2D}{L^2}\vec{R}_r; \quad \frac{d^2\vec{R}_r}{dt^2} = \frac{8c^2D}{L^2}\vec{R}_\ell$$

where L is the full length of the beams, D is the disruption given by

$$D = \frac{r_e N_b L}{\gamma\sigma_r^2},$$

and σ_r is the beam radius. Let L_r and L_ℓ denote coordinates that move with the bunch as shown in Fig. 1. The equations of motion can be rewritten in terms of L_r and L_ℓ as

$$\frac{\partial^2}{\partial L_r^2}\vec{R}_\ell(L_\ell, L_r) = \frac{2D}{L^2}\vec{R}_r(L_\ell, L_r),$$

$$\frac{\partial^2}{\partial L_\ell^2}\vec{R}_r(L_\ell, L_r) = \frac{2D}{L^2}\vec{R}_\ell(L_\ell, L_r).$$

These equations can be solved by Laplace transformation. For example, the equation for the Laplace transform of R_r with respect to L_r is

$$\tilde{r}_r(L_\ell, p) = \tilde{r}_{r0}\cosh\left(\frac{2DL_\ell}{L^2p}\right) + \frac{L^2p}{2D}\tilde{r}'_{r0}\sinh\left(\frac{2DL_\ell}{L^2p}\right)$$
$$+ \int_0^{L_\ell} dx_\ell \sinh\left(\frac{2D(L_\ell - x_\ell)}{L^2p}\right)\left\{\vec{R}_{\ell 0} + \frac{1}{p}\vec{R}'_{\ell 0}\right\},$$

where p is the Laplace transform variable and the subscripts "0" denote initial values.

For the specific case where the centroids of the right moving beams are offset from each other by 2Δ, $\vec{R}_{\ell 0} = \vec{R}'_{\ell 0} = \vec{R}'_{r0} = 0$; $\vec{R}_{r0} = 2\Delta$. Substituting into the above equation

$$\tilde{r}_r(L_\ell, p) = \frac{2}{p}\Delta \cosh\left(\frac{2DL_\ell}{L^2 p}\right).$$

which can be inverse transformed after expanding the cosh in a Taylor series to give

$$\frac{1}{2\Delta} R_r(L_\ell, L_r) = 1 + \sum_{n=1}^{\infty} \left(\frac{1}{(2n)!}\right)^2 \left(2D \frac{L_\ell}{L} \frac{L_r}{L}\right)^{2n}.$$

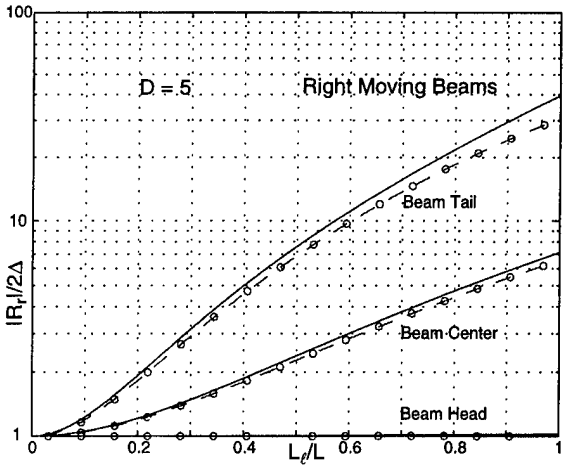


Figure 2: Centroid separation normalized to the initial offset for the right moving beams that were initially offset. The circles are from the simulation, and the solid curve is the analytical result.

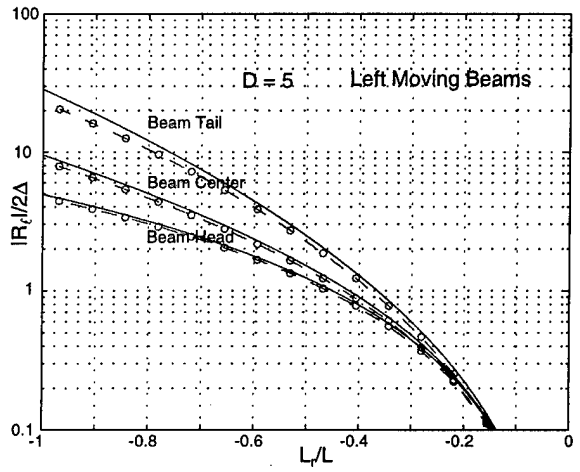


Figure 3: Centroid separation normalized to the initial offset for the left moving beams that were not offset initially. The circles are from the simulation, and the solid curve is the analytical result.

The separation of the left moving beams for this case is

$$\frac{1}{2\Delta} R_\ell(L_\ell, L_r) = \frac{1}{2D}\left(\frac{L}{L_\ell}\right)^2 \sum_{n=1}^{\infty} \frac{1}{(2n)!} \frac{1}{(2n-2)!} \left(2D \frac{L_\ell}{L} \frac{L_r}{L}\right)^{2n}.$$

Note that the last two equations are exact solutions.

These two equations can be compared with simulation results. Figures 2 and 3 show the results for the case of for $D = 5$ and $2\Delta/\sigma_r = 0.05$. The simulation and calculation are in good agreement. We consider this to indicate that the simulation is correct and can be used to study tolerances for realistic situations including Gaussian profiles and unequal charges.

4 CONCLUSIONS

Collision of neutral beams permits operation in a region of IP parameter space that, for simple e+e- collisions would correspond to Y, $\delta >> 1$. With neutral beams much larger emittances, higher bunch charges, and shorter wavelength linacs may be contemplated. Control of 2.5 TeV neutral beams in collision are likely to require an uncompensated disruption parameter $D < 10$, and a correspondingly short bunch length.

We have developed and tested a simulation that can be used to make quantitative estimates of tolerances in neutral beam collisions.

REFERENCES

[1] Robert N. Cahn and Gerson Goldhaber, **The Experimental Foundations of Particle Physics** (Cambridge University Press, Cambridge, 1989)

[2] *Proceedings of the 1996 DPB/DPFWorkshop on New Directions for High Energy Physics* (AIP, New York, *to be published*).

[3] R. Hollebeek, Nucl. Instrum. Meth. **184** (1981) 33; G. Bonvicini, *et al.*, *Phys. Rev. Lett.* **62** (1989) 2381.

[4] P. Chen and V. Telnov, *Phys. Rev. Lett.* **63** (1989) 1796.

[5] K. Brown, *Conceptual Design of Final Focus Systems for Linear Colliders*, in **Fontiers of Particle Beams**, M. Month and S. Turner (eds.), Lecture Notes in Physics (Springer-Verlag, New York, 1988) pp. 481-494.

[6] D. Whittum, H. Henke and P. J. Chou (*these proceedings*).

[7] K. Oide, *Phys. Rev. Lett.* **61** (1988) 1713.

[8] V. E. Balakin and N. A. Solyak, *Proc XIII International Conference on High Energy Accelerators*, Novosibirsk, USSR, 1986J. B.

[9] Rosenzweig, B. Autin and P. Chen, *Proc 1989 Lake Arrowhead Workshop on Advanced Accelerator Concepts.*

[10] S. Krishnagopal and R. Siemann, *Phys Rev Lett* **67**, 2461 (1991).

[11] B. Podobebov and R. H. Siemann, *Phys Rev E* **52**, 3066 (1995).

RF SYSTEM FOR A 30 GHz, 5 TEV LINEAR COLLIDER BASED ON CONVENTINONAL TECHNOLOGY[1]

P. B. Wilson, T. Raubenheimer and R. D. Ruth
Stanford Linear Accelerator Center, Stanford, CA 94309

Abstract

In order that it may be built within a reasonable length and with reasonable ac power consumption, a 5 TeV linear collider must employ an accelerating gradient and rf frequency which are both higher than for present 1 TeV collider designs. The required peak rf power per meter, which will also be higher than for 1 TeV designs, can be provided either by relatively conventional rf technology or by a two-beam scheme such as that proposed for CLIC. In this paper the first alternative, a 30 GHz rf system employing microwave tube power sources together with rf pulse compression, is described which produces an accelerating gradient on the order of 200 MV per meter. Limitations on the peak power that can be obtained from conventional klystrons as a function of frequency are discussed; it is found that such klystrons are only marginally adequate as a power source at 30 GHz. Several alternative rf sources, such as multiple-beam klystrons, sheet-beam klystrons, gyroklystrons and annular-beam ubitrons are described which are capable of providing the required power, after pulse compression, of about 600 MW per meter.

1. INTRODUCTION

Initial parameter sets [1],[2] have been developed for a linear collider with a center-of-mass energy of 5 TeV, a luminosity on the order of $1 \times 10^{35}/cm^2/sec$, and an operating frequency in the 30-34 GHz range. To keep the length of the collider linac within reasonable bounds (on the order of 30 km), the operating gradient must be about 200 MV/m. Several potential problems immediately come to mind. First, can a gradient of this order be substained without rf breakdown, and even below the breakdown threshold, will field emission lead to unacceptable rf processing time or possibly to arcing, gas bursts and surface degredation during operation? Concerning the breakdown threshold, the results of Loew and Wang [3] extrapolated from X-band to 30 GHz indicate a breakdown surface field on the order of 1100 MV/m (corresponding approximately to an accelerating gradient of 450 MV/m) for pulses two or three microseconds in length. For pulse lengths on the order of 100 ns, as contemplated for a 30 GHz collider, the breakdown threshold should be considerably higher. Problems due to field emission tend to escalate above the dark current capture threshold gradient, which scales linearly with frequency. Experience with accelerating structures at S-band and X-band indicates that, using appropriate machining, cleaning and vacuum techniques, the structures can process and operate with satisfactory levels of field emission at gradients of at least 1-1/2 times the dark current capture gradient, or 240 MV/m at 30 GHz.

Before starting on a detailed design of a 5 TeV, 30 GHz linac operating at a loaded gradient of 200 MV/m, we need to ask whether a machine with these parameters can operate at a reasonable repetition rate with a reasonable ac wall plug power. The ac power for a machine with a gradient G, pulse length T_p, active length L_A, repetition rate f_r and rf system efficiency η varies approximately as $P_{ac} \sim f_r G^2\lambda^2 T_p L_A/\eta$. Assuming that the pulse length varies in proportion to the structure filling time ($\sim\lambda^{3/2}$), and that the gradient is scaled as $G \sim \omega_{rf}$, the ac power then scales as $P_{ac} \sim f_r E_{c.m.}\lambda^{3/2}/\eta$. In scaling from the 11.4 GHz NLC design at 1 TeV to a 5 TeV collider at 30 GHz, the unloaded gradient will increase from 85 MV/m to 225 MV/m if $G \sim \omega$ scaling is followed. The factor $\lambda^{3/2}$ decrease the ac power by a factor of 4.3, almost balancing the five-fold increase in energy. Thus at a repetition rate of 120 Hz and a scaled pulse length of 60 ns, the ac power would remain nearly constant. In the design to follow, the pulse length will actually be about twice this, making it necessary to reduce the repetition rate to 60 Hz.

The peak power per meter required to drive the accelerating structure scales approximately as $P_m \sim G^2\lambda^{1/2}$. For $G \sim \omega$ scaling, this becomes $P_m \sim \omega^{3/2}$. The NLC structure requires 145 MW/m for an unloaded gradient of 85 MV/m. This scales to 615 MW/m for a gradient of 225 MV/m at 30 GHz. A third question is, are rf sources available (or possible) which, together with a reasonable rf pulse compression system, can supply this peak power with a reasonable spacing between sources? The remainder of this paper will be devoted to answering this question.

2. BASIC RF-RELATED PARAMETERS

Table 1 gives basic rf parameters for a 30 GHz, 5 TeV collider for two accelerating structure designs.

[1] Work supported by the U.S. Department of Energy under contract DE-AC03-76SF00515.

0-7803-4376-X/98/$10.00 © 1998 IEEE

Table 1
RF Parameters for two Structure Designs

	Str. A	Str. B
Group Velocity/c	.067	.075
Structure Length (m)	0.70	0.75
Filling time T_F(ns)	35	33
Q	3500	4590
$T_0 = 2Q/\omega$ (ns)	37	49
$\tau = T_F/T_0$	0.95	0.68
Shunt Impedance(MΩ/m)	87.5	125
Unloaded Gradient (MV/m)	228	232
Loaded Gradient (MV/m)	200	200
Peak Power/meter (MW/m)	700	580
Power per Structure (MW)	490	435
Power per Klystron (MW)	74	66
Pulse Length at Str. (ns)	140	138
Pulse length at Kly. (μs)	1.12	1.10
AC Power (MW)	340	280

Structure A, having a shunt impedance of 87.5 MΩ/m, is a design developed[2] by the CLIC group at CERN. Dipole-mode damping is achieved by heavy coupling to external loads. Structure B is scaled from the current design for the NLC damped detuned structure having a shunt impedance of 95 MΩ/m at 11.424 GHz (group velocity = 0.05c). Scaling this to 30 GHz, opening up the iris to make $v_g/c = 0.075$ (to give lower wakefields and allow a longer structure length), and derating the shunt impedance r by –8% (5% in Q and 3% in r/Q) to allow for possible additional damping, results in a shunt impedance of about 125 MΩ/m. The beam loading current is based on a train of 200 bunches spaced 0.5 ns (15 λ) apart, each with a charge of 3×10^9 electrons. Including a 5% overhead allowance for feedback, etc., and assuming two 10 GeV injectors, the active length of both main linacs is 26.15 km. The pulse length includes a 5 ns rise time allowance. In calculating the ac power, an rf system efficiency of 45% is assumed: klystron, 60%; modulation efficiency (assuming a gridded tube), 91%; pulse compression efficiency, 82.5%.

At this gradient and pulse length, there is potentially serious problem with pulse heating at the copper surface, estimated be about 150°C. The yield strength in copper is exceeded at a pulse temperature rise on the order of 40°C [4]. However, the extent to which this surface damage might degrade the rf surface resistance is not clear; an experiment is underway at SLAC to measure the effects of pulse heating with a temperature rise of several hundred degrees on a demountable surface in an X-band cavity [5].

Finally, it would highly desireable to reduce the ac power by increasing the rf system efficiency above 45%. A reasonable goal might be: klystron, 65%; klystron modulation, 95%; pulse compression, 85%; system efficiency 52.5%. This would reduce the ac power by 15%.

3. RF PULSE COMPRESSION

The use of rf pulse compression to enhance the peak power output from the rf source becomes more important as the rf frequency increases and the power output capability of microwaves tubes tends to decrease. Several pulse compression schemes have the capability in principle of providing a peak power enhancement of 6.6, as assumed here, with reasonable efficiency. Current efforts at SLAC are being directed toward a so-called Delay Line Distribution System (DLDS) scheme in which the power from eight klystrons is combined to feed four groups of accelerating sections, each for a time equal to one-fourth of the klystron pulse length. In this scheme, power is directed to accelerating sections upstream (toward the gun), and the beam return time serves to reduce the delay line length by a factor of two. Applied to the present 30 GHz parameters, the klystron pulse length would be 4 × 140 ns = 560 ns, and there would by 30 m of delay line per meter of accelerating structure (compared to 9m/meter for the NLC design).

An alternatively possibility is a BPC (Binary Pulse Compression) system using loaded delay lines consisting of a series of 5–10 high Q energy storage cavities. Such a system having a compression ratio of 8 and a power gain of 6.6 (82.5% efficiency) is assumed for the parameters in Table 1. Although possible in concept, design details for such a system remain to be worked out.

4. RF POWER GENERATION AT 30 GHZ

There are two basic limitations on the power that can be generated by a conventional round-beam klystron. First, it is well known that the electronic efficiency of a klystron depends on the microperveance, defined as $K_\mu = (I_b/V_b^{3/2}) \times 10^6$. An expression that fits recent simulations at SLAC is: $\eta = 0.75–0.17K_\eta$. To achieve an efficiency of at least 65%, the microperveance must be less than about 0.6. The output power at a beam voltage of 500 kV would than be less than about 68 MW. From Table 1, this marginally meets the klystron power requirement for the two cases shown.

A second limitation on klystron power is related to the area of the electron beam, which does depend on wavelength. To achieve good coupling to the longitudinal rf fields in the output gap, the radius of the beam should not be larger than about λ/8. If the beam radius exceed this, then electrons on the beam axis and electrons at the edge of the beam will see a substantially different rf gap voltage, and efficiency will suffer. Next, the beam area at the cathode can be larger than the beam area in the drift region by a factor A_c, the area convergence ratio. This ratio is limited by aberrations in the gun optics, transverse emittance, alignment tolerances, etc. A good measure of these effects is the convergence half-angle, which is related to the f-ratio of conventional optics. In practice, it is found that the convergence half-angle is limited to about 40°, corresponding roughly to f 0.6.

Because of the dynamics of space-charge-limited electron flow in the gun region, the gun focal length and hence the area convergence ratio depends on the perveance. By plotting A_c vs K_μ for a variety of gun designs with a convergence half angles of 35^0–40^0, the points can be crudely fit (within a factor of two or so) by [6] $A_c \approx 150/K_\mu^2$. A further limitation is the acceptable cathode loading current per square centimeter, I_A. Putting these factors together, the output power is

$$P_k \approx \eta V_b I_A A_c \pi(\lambda/8)^2 . \qquad (1)$$

If $A_c(K_\mu)$ as specified above is inserted in this and the result equated to $P_k = \eta K V_b^{5/2}$, an expression is obtained for the maximum allowable perveance:

$$K_\mu = 194 I_A^{1/3} \lambda^{2/3} / V_b^{1/2} . \qquad (2)$$

Taking I_A = 10 A/cm^2, λ = 1.0 cm and V_b = 560 kV, then K_μ(max) = 0.59 with a corresponding efficiency of 65% and output power of 68 MW. By coincidence, this is just the efficiency and output power specified above. At shorter wavelengths the perveance would have to be lower and the output power less (although the efficiency would be somewhat higher).

The bottom line is that it should be marginally possible to build a klystron at 30 GHz which has good efficiency (65%) and an output power or the order of 65 MW. To obtain this or higher power from a more coservative power source, there are several possibilities. For example, three or four lower perveance beams can be packaged together in the same vacuum envelope. Such a multibeam klystron having common rf cavities but separate PPM-focused beams has indeed been proposed [7].Klystrons using a sheet beam, which is essentially equivalent to many round beams in parallel, are capable (in simulations) of producing 150 MW at 34 GHz with good efficiency [8]. It is well known that gyroklystrons are also capable of producing high power at high frequency. At the University of Maryland, a coaxial-circuit gyroklystron frequency-doubled from 17 to 34 GHz has been designed which produces an output power of 150 MW at a simulated efficiency of 42% [9]. A single-stage depressed collector can increase the efficiency to 56%.

Another annular-beam device capable of delivering high power output at high frequencies is the Ubitron (FEL) proposed by McDermott et. al. [10]. Using a TE_{01}-mode coaxial cavity and a PPM wiggler, it produces a simulated output power of 250 MW at 11.4 GHz with an efficiency of 50%. It should still be capable of producing a high output power when scaled to 34 GHz.

REFERENCES

[1] P. Chen et al., "A 5-TeV c.m. Linear Collider on the NLC Site"; to be published in the 1996 Workshop on New Directions for High Energy Physics (Snowmass 96), Snowmass, Colorado, June 25–July 12, 1996.

[2] J. P. Delahaye et al., "A 30 GHz 5-TeV Linear Collider"; paper 8W-18, this conference.

[3] G. A. Loew and J. W. Wang, "RF Breakdown studies in Room Temperature Electron Linac Structures", SLAC-PUB-4676, SLAC, Stanaford University (1988).

[4] R. Siemann, Internal Report ARDB-12, SLAC, Stanford University (1996).

[5] R. Siemann, private communication.

[6] R. Phillips, SLAC, private communication.

[7] G. Caryotakis, SLAC prive communication.

[8] D.U.L. Yu, J. S. Kim and P. B. Wilson, "Design of a High Power Sheet-Beam Klystron", in *Proceedings of the Workshop on Advanced Accelerator Concepts, Port Jefferson, New York*, 1992 (AIP Conference Proceedings 279, 1993), pp. 85-102. Also J. S. Kim, private communciation.

[9] G. Saraph, University of Maryland, private communication.

[10] D. B. McDermott et al., "Periodic Permanent Magnet Focusing of an Annular Electron Beam and its Application to a 250 MW Ubitron FEL"; submitted to *Physics of Plasmas* (1996).

PERFORMANCE ISSUES, DOWNTIME RECOVERY AND TUNING IN THE NEXT LINEAR COLLIDER (NLC) *

F. Zimmermann, C. Adolphsen, R. Assmann, K. Bane, D. Burke, F.J. Decker, P. Emma, R. Helm, L. Hendrickson, S. Hertzbach ‡, J. Irwin, H. Jarvis, P. Krejcik, M. Minty, N. Phinney, P. Raimondi, M. Ross, J. Spencer, H. Tang, P. Tenenbaum, K. Thompson, D. Walz, A.D. Yeremian
Stanford Linear Accelerator Center, Stanford University, CA 94309, USA
‡ University of Massachusetts, Amherst, USA

1 INTRODUCTION

The Stanford Linear Collider (SLC) is the only linear collider in the world. One of the primary operational limitations encountered at the SLC is the need to constantly tune up all the different subsystems, *i.e.*, injectors, damping rings, linac, arcs and the final focus. The tuning involves, for example, the optimization of the interaction-point (IP) spot size [1], and the minimization of the linac emittances. The latter are determined by a delicate balance of beam orbit, rf phases and wakefields, which is very sensitive to perturbations, such as temperature or bunch-length changes.

The preservation of a tuned-up state is difficult, as illustrated by Fig. 1 and Table 1. Figure 1 shows the average normalized (or specific) luminosity as a function of daytime for the 1996 SLC run. We observe steady luminosity increases during the day and swing shifts as well as clear drops at the 8-am and 4-pm shift changes. The latter are presumably the result of reduced attention and/or of different tuning strategies. The highest luminosity is achieved during owl shift (from 0 to 8 am), with a peak value reached around 5 am. In Table 1, we present the fraction of time

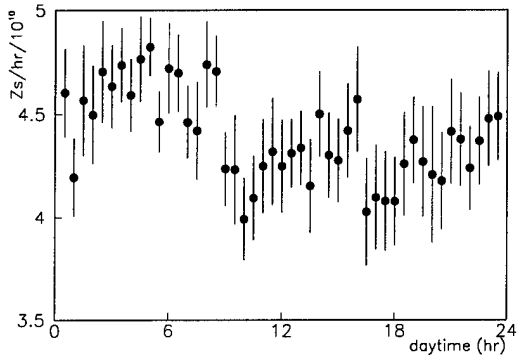


Figure 1: The diurnal luminosity during the 1996 SLC run. Shown is the luminosity normalized to 10^{10} particles per bunch. The actual luminosity would be ~12 times higher. A rate of 1 Z/hr is equal to about 10^{28} cm^{-2} s^{-1}.

during which the SLC luminosity exceeded a certain minimum value. The table shows that the highest luminosity was achieved over less than 20% of the time, with remarkably similar numbers for the last two SLC runs.

* Work supported by the U.S. Department of Energy under contract DE-AC03-76SF00515.

Luminosity	1994/95	1996
$L > 10$ Zs/hr	56 %	57 %
$L > 30$ Zs/hr	42 %	50 %
$L > 40$ Zs/hr	27 %	34 %
$L > 50$ Zs/hr	15 %	18 %

Table 1: Fraction of time (not including overall downtime) during which a certain luminosity was exceeded in the 1994/95 and 1996 SLC runs.

2 PERTURBATIONS, TUNING AND RECOVERY

The SLC experience suggests that tuning and stabilization will be very important also for the NLC.

Magnet displacements due to ground motion or temperature changes could reduce the NLC luminosity, by steering the beams out of collision or by increasing the IP spot size. The most critical magnets are those in the final-focus system. In Ref. [2], it was shown that ground motion does not significantly impact the luminosity, because, first, it is highly correlated and, second, an orbit feedback can correct the accumulative effect of a small random component. The main sources of temperature variation in the NLC final focus are synchrotron radiation and energy loss at beam-pipe transitions, which both cause a local power deposition of about 1–3 W. A proper design will ensure that, for this heat load, the magnet temperature changes by less than 0.02 K over a few seconds or by less than 1 K over 15 minutes. In this case, fast and slow orbit feedback loops can maintain orbit and spot size, provided the offsets of the beam-position monitors (BPMs) are sufficiently stable over the above time periods. FFTB experience has demonstrated that this is possible. Since most of the tuning and stabilization is based on beam information, *e.g.*, BPM readings, the largest perturbations to the tuned-up accelerator are scheduled or unscheduled downperiods without beam.

We, thus, distinguish three types of tuning: 1) continuous tuning under normal operating conditions (*i.e.*, which has to be performed regularly to compensate for slow drifts of the rf phases, BPM readings, or power supplies), 2) recovery from a one-hour down time (DT) where the accelerator was in a stand-by mode, and 3) recovery from a 24-hour repair opportunity day (ROD) with access, repair work and major temperature changes. Tables 2 and 3 illustrate this classification for the NLC final-focus system. Table 2 presents a list of recovery steps and recovery times after a down period. Only the time spent on tuning is listed, and no time for actual repair work is included. Table 3 com-

0-7803-4376-X/98/$10.00 © 1998 IEEE

recovery from	t_{DT} [min]	t_{ROD} [min]
check BPM polarity & offset	NA	5
activate orbit feedbacks	5	5
close FF collimators	0	0
feedb. & orbit for 90 bunches	5	5
match incoming dispersion	NA	5
measure FF emittances	5	5
coupling corr. & beta-match	0	0
turn on & phase crab cavity	NA	5
establish collisions	2	2
turn on detector	NA	5
correct IP aberrations	5	5
total	22	42

Table 2: Performance recovery times of the NLC final focus after a 1-hr down time (DT) and after a 24-hr repair day (ROD).

procedure	t [min]	T [hr]	$\Delta L/L$ [%]
multi-bunch steering	0.5	0.08	0
dispersion (x&y)	0.12	0.25	0.8
waist (x&y)	0.12	0.25	0.8
skew1 (x'y')	0.06	0.25	0.4
IP divergence	0.017	1	0
skew sexts. (x'^2y', y'^3)	0.12	1	0.2
skew2 (xy')	0.06	1	0.1
skew3 (x'y)	0.06	1	0.1
multi-bunch y-disp.	0.06	8	0.03
multi-bunch waist x& y	0.12	8	0.03
adjust FF main collimators	5	24	0.35
orbit resteering	60	100	0.25
BPM align. & offsets	30	170	0.1
sext. (x'^3, $x'y'^2$)	0.12	170	0
chrom. x& y	0.12	170	0
chrom. skew ($x'y'\delta$)	5	170	0.05
2nd order y-disp.	0.6	170	0.01
crab angle (xz')	—	170	0
match inc. dispersion	5	170	0.05
total			3.27

Table 3: Continual tunings procedures in the NLC final focus: required time t, tuning period T, and estimated luminosity impact $\Delta L/L$.

piles the continuous tuning procedures and their estimated impact on luminosity.

Similar analyses have been performed for the other NLC subsystems. The results are summarized in Table 4, which shows that the recovery time of each subsystem is on average 15 minutes after a short down period and about 40 minutes after a ROD. Therefore, the tune-up of the entire NLC takes about 2 or 6 hours, respectively. In addition, there is a luminosity loss due to continual tuning of roughly 20%.

3 MARKOV MODELS

The overall availability A_{NLC} of the NLC is the product of the availabilities of the electron and the positron system: $A_{NLC} = A_{e+} \times A_{e-}$. For an overall availability of 90%, the availabilities $A_{e\pm}$ must be 95%. Both the electron and positron system can again be subdivided into 8 distinct subsystems. To assess the availability A_{e-} (or A_{e+}), we have

subsystem	t_{DT} [min]	t_{ROD} [min]	$\Delta L/L$ [%]
systemwide	—	15	—
injectors	4	45	2.5
damping rings	16	64	2.4
compressors	15	70	3.2
main linac	17	45	4.6
collimation	25	25	4.3
IP switch/b. bend	10	15	0.9
final focus	22	42	3.3
extraction line	9	21	0
total	118	342	21.2

Table 4: Recovery times and luminosity reduction due to continual tuning for all NLC subsystems.

developed a simple Markov model [3], consisting of 9 different states (see Fig. 2). The 0th state means the beam is brought to the IP. The other 8 states refer to a failure in one of the 8 subsystems. For example, in the 8th state the injector is off. Each subsystem is characterized by three parameters: a failure rate λ_i describing the frequency at which this subsystem fails, its tuning recovery time τ_i, and an average repair time ϵ_i. The recovery from a failure of the ith subsystem proceeds at a rate $\mu_i = 1/(\sum_{j\le i}\tau_j + \epsilon_i)$.

Ignoring multiple subsystem failures, the NLC Markov model consists of 9 equations:

$$dA_i/dt = \lambda_i A_0 - \mu_i A_i = 0 \quad (i = 1, ..., 8) \quad (1)$$

$$1 = A_0 + \sum_{i=1}^{8} A_i \quad (2)$$

where A_i denotes the probability that the system is in state i, and A_0 is the availability A_{e-} or A_{e+}. Equation (1) describes transitions between state 0 and state i. The total time derivative was set to zero, since we are interested in the steady state solution. Equation (2) is a normalization condition, which ensures that at any given time the system is in one of the states. Solving Eqs. (1) and (2) yields the availability A_0. Introducing the total failure rate $\bar{\lambda} = \sum_{i=1}^{8}\lambda_i$ it is

$$A_0 = 1/(1 + \bar{\lambda}\bar{\tau}) \quad (3)$$

where $\bar{\tau}$ represents an effective recovery time for the entire ($e+$ or $e-$) system.

In general, the availability A_0 is a function of three 8-component vectors: $A = A(\vec{\lambda}, \vec{\tau}, \vec{\epsilon})$. In the following we assume, for simplicity, that all 8 subsystems have the same repair and recovery time ($\epsilon_i = \epsilon$, $\tau_i = \tau$).

As for the failure rates λ_i, two special cases are of interest. First assume that each subsystem has the same failure rate $\lambda_i = \lambda$. Then $\bar{\lambda} = 8\lambda$ and $1/\bar{\mu} = ((\sum_{i=1}^{8} i\tau)/8 + \epsilon)$, *i.e.*, the effective recovery time is the sum of the average tuning recovery time and the repair time. The resulting availability is $A(\epsilon, \lambda, \tau) = 1/(1 + 36\lambda\tau + 8\lambda\epsilon)$.

In the second case, we choose the individual failure rates such that the failures of all subsystems have equal luminosity impact. This implies $\lambda_i(i\tau + \epsilon) = \text{constant}$, or $\lambda_i = \lambda(8\tau + \epsilon)/(i\tau + \epsilon)$ for all i, where λ now denotes

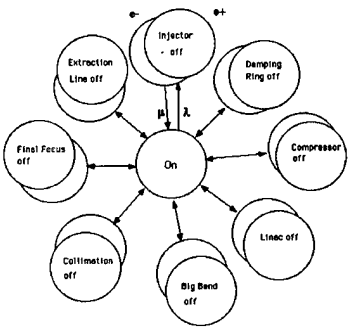


Figure 2: Markov model of the NLC. 'OFF' indicates a failure of the respective subsystem.

the failure rate of the injector ($i = 8$). The availability is given by Eq. (3), using $\bar{\lambda} = \sum_{i=1}^{8} \lambda_i$ and the effective recovery time $\bar{\tau} = \tau_8$ determined from the recursion relation

$$\tau_{i+1} = \tau_i + ((i+1)\tau + \epsilon - \tau_i)\lambda_{i+1} / \sum_{j=1}^{i+1} \lambda_i \qquad (4)$$

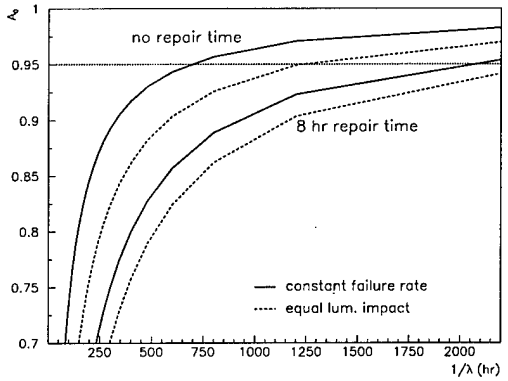


Figure 3: Availability $A_{e\pm}$ versus $1/\lambda$ for an individual recovery time $\tau = 1$ hr, two different repair times ϵ and two different assumptions on failure rate scaling.

Figure 3 shows that, assuming a subsystem recovery time of $\tau = 1$ hr, an availability $A_{e\pm}$ of 95% is achieved if each subsysten fails less often than once per month for zero repair time, or less often than once every 3 months, if the average repair time ϵ is 8 hours.

To benchmark our mathematical description of a linear collider against an existing accelerator, a similar analysis was performed for the SLC. Figure 4 illustrates the greater complexity of the SLC model, which arises because the electron and positron beam share a common linear accelerator, and electrons are used for positron production.

We consider two different models for the individual SLC subsystem recovery rates. In the first model (I), we assume as before that all τ_i are equal. In the second model (II), we postulate, somewhat arbitrarily, a 7 times longer recovery time for the last subsystem ('IP') *i.e.*, $\tau_0 = 7\tau$, which has the effect of weighting the downstream end of the machine more strongly. The recovery times for all other subsystems are still taken as equal to τ. Thus, neglecting the repair time, only two parameters are left: the subsystem failure rate λ (assumed to be equal for all subsystems) and the subsystem recovery time τ.

In the 1996 SLC run, there was a hardware failure or interruption about once every 2.5 hours. As a measure of the SLC or 'IP' availability, we take the fraction of time where both beams were actually in collision: about 57%. Using the total failure rate and the measured availability, we can deduce the subsystem recovery time τ. We attribute the total failure rate uniformly to all 10 SLC subsystems, *i.e.*, $\lambda = 1/25\ \mathrm{hr}^{-1}$, and find the recovery time τ for which the predicted availability equals 57%. This time is 30 or 10 minutes for the two different models, respectively.

Predicted and actual beam availabilities for different SLC subsystems are compared in Table 5, where the prediction is the sum $\sum_{i \le j} A_i$, describing the probability that the beam is delivered either to the jth or to any downstream subsystem, and the actual beam availability was estimated by the time fraction for which beam was present. While the data appear to favor models with a longer recovery time for the last subsystems (model II), they would also be consistent with upstream systems being tuned over extended periods of time.

In conclusion, our approach to describe the tuning states of a linear collider by a Markov model looks very promising. In the future, the model presented here should be extended so as to include information about other beam parameters, *e.g.*, emittances, energy and bunch lengths, and it should be further developed to understand the impact of multiple subsystem failures.

subsystem	May 96	model I	model II
e− damping ring	0.94	0.90	0.93
e+ damping ring	0.82	0.76	0.82
e− arc	0.89	0.78	0.83
'IP'	0.57	0.57	0.57

Table 5: Comparison of actual beam availability for various SLC subsystems with that predicted by two different models; the recovery-time τ was adjusted to give equal IP availability.

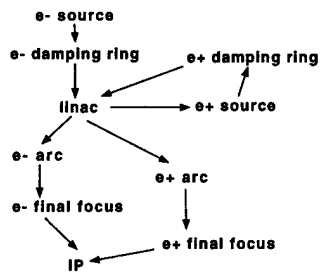


Figure 4: Markov model of the SLC

4 REFERENCES

[1] P. Emma, L.J. Hendrickson, P. Raimondi, F. Zimmermann, "Limitations of Interaction-Point Spot-Size Tuning at the SLC", these proceedings (1997).

[2] J. Irwin and F. Zimmermann, EPAC96, p. 516 (1996).

[3] See, for example, Roger D. Leitch, Reliability Analysis for Engineers, Oxford Science (1995).

CHANNELING AND TIME EVOLUTION OF LASER WAKES AND ELECTRON ACCELERATION IN A SELF-MODULATED LASER WAKEFIELD ACCELERATOR EXPERIMENT

A. Ting, C.I. Moore,[1] K. Krushelnick,[2] H.R. Burris, C. Manka,[3] R. Fischer, M. Baine,[4]
E. Esarey, R.F. Hubbard, and P. Sprangle

Plasma Physics Division, Naval Research Laboratory, Washington DC 20375

Abstract

Large amplitude plasma wakefields produced by a high power laser pulse in an underdense plasma were studied in a self-modulated laser wakefield accelerator (SM-LWFA) experiment. A pump-probe coherent Thomson scattering (CTS) technique was used and the lifetime of the wakefield was measured to be less than 5 psec. A plasma channel was observed to form in the wake of the pump laser pulse. The trailing probe laser pulse was observed to be guided by this channel for about 20 Rayleigh lengths. High energy electrons (up to 30 MeV) have been measured using a magnetic spectrometer. Highly non-linear plasma waves were also detected using forward Raman scattering diagnostics and were observed to correlate with the electron signals.

Significant progress has been made in recent years [1] using laser–produced plasmas as a medium for accelerating electrons to high energies. In the Laser Wakefield Accelerator (LWFA) [2], a high intensity laser pulse is focused into an underdense plasma with a pulse duration, τ_L, close to the electron plasma period (i.e., $\tau_L \sim 2\pi/\omega_{pe}$ where ω_{pe} is the electron plasma frequency). Large amplitude plasma waves (wakefields) are generated with strong longitudinal electric fields and relativistic phase velocities which are capable of accelerating injected electrons. For laser powers approaching or exceeding the relativistic self-focusing threshold (i.e., $P > P_c = 17\,(\omega_0/\omega_{pe})^2$ GW; where ω_0 is the laser frequency), it is not necessary to match the pulse duration to the plasma period. At laser powers for which $P \geq P_c$ and $\tau_L > 2\pi/\omega_{pe}$, the laser envelope undergoes an instability and becomes "self-modulated" at the plasma frequency [3, 4]. This effect resonantly enhances the creation of wakefields and allows use of higher electron densities and generates stronger accelerating fields [5]. Recent experiments in this Self-Modulated Laser Wakefield Accelerator (SM-LWFA) regime have measured the production of high energy electrons where the source of accelerated particles was either background electrons from the target plasma [6-9] or electrons injected into the interaction region from an adjacent laser-produced plasma [10]. Direct observations of wakefields in the conventional LWFA configuration were recently reported using interferometric techniques, in which the spatial and temporal waveforms of the wakefield were measured [11].

In order to obtain high final energies of the accelerated electrons in a LWFA, it is necessary that the laser propagates long distances at high intensity in the plasma. This implies that the laser pulse must be "guided" for distances significantly greater than the vacuum diffraction length (Rayleigh range), which is typically less than a hundred microns if the beam is tightly focused. Guiding of intense laser pulses in plasmas has been demonstrated by a variety of mechanisms. Laser light with intensities of up to 5×10^{15} W/cm^2 has been channeled in a 3 cm waveguide structure created by the hydrodynamic expansion of a preformed plasma [12] and intensities of 10^{16} W/cm^2 have been propagated for up to 3 cm in evacuated glass capillary waveguides [13]. In addition, a preformed plasma generated by a capillary discharge has been used to guide 10^{16} W/cm^2 laser pulses [14]. For laser pulses above the critical power for relativistic optical guiding, self–channeling of laser pulses in plasmas has been experimentally observed [15,16] and has been the subject of extensive theoretical examination [1,3-5, 17,18]. Self-focusing of intense laser pulses in plasmas can also be enhanced by the expulsion of plasma electrons (cavitation) produced by the extreme ponderomotive force of a focused laser pulse [18].

Large amplitude relativistic plasma waves generated in the SM-LWFA have axial accelerating electric fields with extremely high gradients (~100 GeV/m) [5]. The phase velocity of the plasma wave is approximately equal to the group velocity of the laser pulse (~c), and hence, these plasma waves are very suitable for high energy particle acceleration. Nakajima *et al.* [10] have observed high energy electrons (~17 MeV) being accelerated in a SM-LWFA experiment where ~1 MeV electrons were injected. Coverdale *et al.* [6] and Umstadter *et al.* [8] have observed 2 and 5 MeV accelerated electrons respectively from self-trapping of background plasma electrons. Recent SM-LWFA experiments by Modena *et al.* used a 25 TW laser pulse to drive nonlinear wakefield plasma waves in a helium plasma resulting in the capture and acceleration of background plasma electrons to 44

0-7803-4376-X/98/$10.00 © 1998 IEEE

MeV [7]. Their experiments showed a broadening of the anti-Stokes lines in the forward Raman scattering (FRS) spectrum concurrent with the onset of high energy electron production at approximately 7 TW. This broadening and high energy electron production was attributed to the onset of wavebreaking.

The SM-LWFA experiments at the Naval Research Laboratory (NRL) were performed using a Ti:Sapphire/Nd:Glass CPA laser system (λ = 1.054 μm) which generates 400 fsec pulses with an energy of 800 - 1200 mJ (P = 2 - 3 TW). The beam was focused with an f/3 off-axis parabolic mirror into a 3 mm diameter hydrogen or helium gas jet. The gas jet was used to reduce the effects of ionization induced defocusing [19] which may occur during interactions in static-filled gas chambers. The focal spot radius measured in vacuum was 4.5 μm which corresponds to a vacuum Rayleigh length of 60 μm.

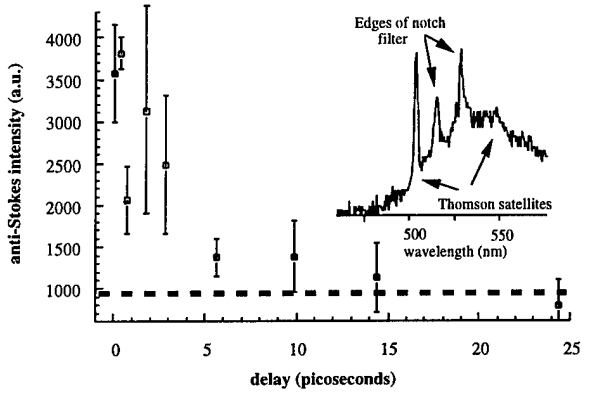


Figure 1: Evolution of electron satellites from zero-degree coherent Thomson scattering. The background level is shown by the dashed line. Data are not shown for pump-probe delay times less than zero since blueshifting of the probe laser spectrum saturates the detector for early times. Insert is a typical spectrum (anti-Stokes at 506 nm, Stokes at 550 nm).

The plasma electron density was measured to be n_0 = 1-1.5x10^{19} cm^{-3}. For a plasma density of $n_0 = 10^{19}$ cm^{-3}, the critical power is P_c = 1.8 TW, and the plasma wavelength is $\lambda_{pe} = 2\pi c/\omega_{pe}$ = 10 μm. Hence, $P \geq P_c$ and $c\tau_L \sim 12\ \lambda_{pe}$, which are necessary for operation in the SM-LWFA regime.

A pump-probe experimental arrangement was used to monitor the temporal characteristics of the high intensity laser produced plasma [20]. Approximately 10 % of the main beam was frequency doubled (to 527 nm) by a 1 cm thick KD*P crystal for use as the probe. The probe pulse timing was varied relative to the pump using an optical delay line. The spatial overlap of the two beams was accomplished by alignment to a series of apertures prior to the off-axis parabolic mirror, which focused the probe beam at f/6 and the pump beam at f/3, and by observation of scattered light in the focal region. Temporal synchronization was achieved by examining the probe frequency. When the probe arrived before the pump, the probe frequency was blue shifted [21]. Otherwise the frequency was unshifted. This measurement resulted in synchronization to better than 1 psec.

Directly forward scattered light was recollimated by a parabolic mirror, while radiation scattered at off-axis angles was collected by a single lens and imaged onto the slit of a 0.25 m Czerny-Turner spectrometer. The interaction was also monitored by transversely imaging Thomson scattered laser light on a CCD positioned at 90 degrees to the laser axis.

Coherent Thomson scattering (CTS) of the probe laser pulse was used to measure the temporal behavior of the wakefields. Coherently scattered light has a wave vector $\mathbf{k}_{sc}$ and a frequency ω_{sc} that satisfy the Bragg scattering conditions of frequency and wavenumber matching. For electron plasma waves with ω_{pe} and $\mathbf{k}_{pe}$, the conditions require $\omega_{sc} = \omega_l \pm \omega_{pe}$ and $\mathbf{k}_{sc} = \mathbf{k}_l \pm \mathbf{k}_{pe}$, where ω_l is the frequency and $\mathbf{k}_l$ is the wave vector of the probe laser. The plasma wakefields in an SM-LWFA have relativistic phase velocities, $v_\phi \sim c$, such that they are capable of accelerating electrons to high energies. For correct matching of $\mathbf{k}$ vectors, both the probe and the Thomson scattered light must therefore propagate in the same direction as the relativistic plasma wave (i.e., pump, probe, and scattered light propagating collinearly). The majority of the 527 nm probe light was not scattered and was blocked before the slit of the spectrometer by a notch filter in the beam path. However, the Thomson scattered electron plasma satellites of the probe light (shifted by ω_{pe}) are positioned beyond the edges of the absorption band of the notch filter and detected by the spectrometer. The principal result in this configuration was the observation of these plasma satellites for about 5 psec after passage of the pump laser (see Figure 1). The full width at half maximum (FWHM) of the wakefield lifetime is ~2 psec which is similar to the wakefield lifetime measured by similar techniques reported by LeBlanc *et al.* [22]. As shown in the insert in Figure 1, the anti-Stokes line was typically more intense than the Stokes line, perhaps indicating that the $\mathbf{k}$-vectors of the electron plasma waves in the wakefield are primarily in the forward direction [23]. These measurements confirmed the generation of wakefields with $v_\phi \sim c$ [24].

The probe pulse was also observed to be affected by the formation of a plasma channel. The propagation of the probe pulse was monitored by imaging the Thomson scattered emission at 90 degrees to the laser propagation direction onto a CCD through a 527 nm filter ($\Delta\lambda$ = 5 nm). When only the probe pulse was injected into the gas jet, very little Thomson scattered emission was observed even though a plasma was created. However, if both pump and probe pulses were incident simultaneously on the gas jet, a bright image of scattered probe light was observed in the region where the pump beam was channeling, *i.e.*, over the width of the gas jet or approximately 20 Rayleigh lengths. This emission is

probably caused by coherent Thomson scattering of the probe laser from ion acoustic waves generated in the turbulent decay of the large amplitude plasma waves in the wakefield [20]. This emission was observed even as the temporal separation between the pump and probe laser pulses was increased by more than the laser pulse width (see Figure 2). In fact, the brightness of the Thomson scattered image from the probe reached a maximum approximately 15 psec after passage of the pump pulse. Thomson scattered emission from the probe continued for pump-probe delays of more than 40 psec before decreasing significantly. The guided intensity was $5x10^{16}$ W/cm^2 with a transmission efficiency of approximately 75%.

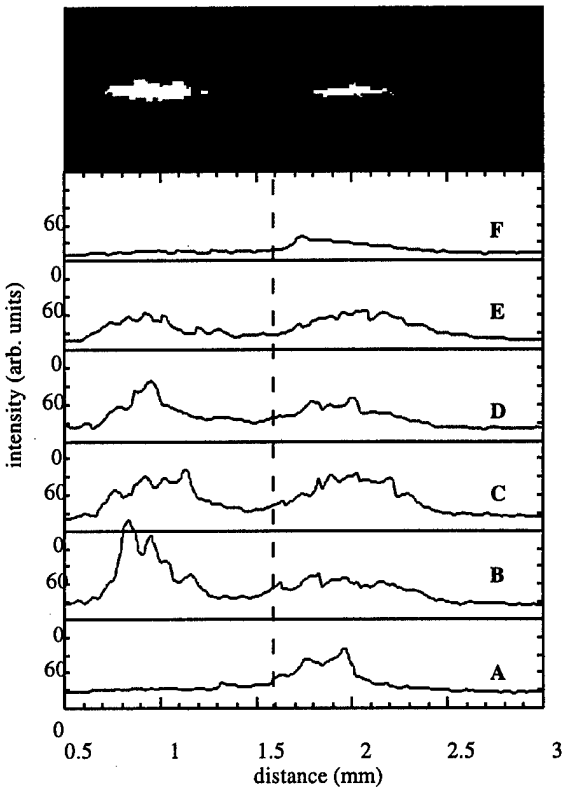


Figure 2: Thomson scattering images of interaction of picosecond probe beam (527 nm) for various delay settings between pump and probe beam in hydrogen gas jet. A) 0, B) 6, C) 14, D) 22 E) 30, F) 46 psec (propagation from right to left). Typical CCD image (Δt = 19 psec) shown at top. Dashed line indicates approximate position of vacuum focus (centered in gas jet).

The "guiding" of the probe pulse is most likely due to formation of a plasma channel in the wake of the pump pulse due to charge displacement effects. As the pump expels electrons by the ponderomotive force, the space charge force on the ions starts a slow radial expansion of the plasma away from the pump laser axis. This expansion causes a density depression on axis and forms a plasma channel capable of guiding the following probe pulse. The observed time scales for formation and decay of the channel are consistent with a simulation and analytical calculations of this hydrodynamic expansion.

Electron measurements and Raman scattering measurements of the pump were also performed. Raman scattered laser light at 40° to the laser axis was imaged on the entrance slit of a spectrometer to measure the relative wakefield amplitude and linearity. An inline spectrometer configuration measured the energy distribution of electrons accelerated from the background plasma. The electron spectrometer consisted of an electromagnet for electron deflection and a plastic scintillator directly coupled to a photo-multiplier tube (PMT) for electron detection. The electromagnet used a 0 to 2500 Gauss magnetic field in a field region 5.5 cm long. Graphite and carbon shielding were arranged with a small gap centered on the laser axis which allowed only high energy electrons with less than an 8° deflection in the magnet to strike the scintillator. Electrons with lower energies were deflected more than 8° and dumped in a graphite block to minimize x-ray production. This inline spectrometer configuration therefore detects all electrons above a cutoff energy which is determined by the magnetic field strength and the maximum acceptance angle of the gap in the shielding (8°).

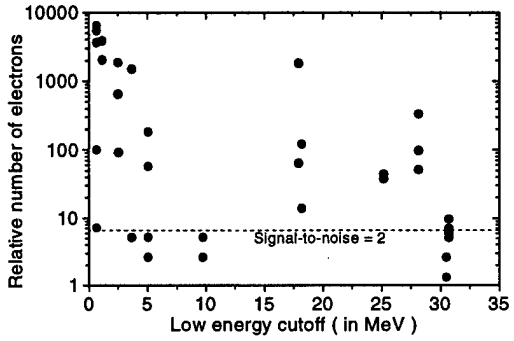


Figure 3: The relative number of electrons above the cutoff energy of the spectrometer. A signal-to-noise level greater than 2 (dashed line) represents a clearly discernible signal from electrons striking the scintillator.

An energy scan is shown in Figure 3. This is raw data showing the electron signal at a range of cutoff energy settings (1-30 MeV). The data points are the total relative number of electrons above the energy specified on the x-axis. The large fluctuations are believed to be shot-to-shot fluctuations caused by the highly non-linear growth of the plasma waves from the self-modulation and the forward Raman instabilities which are seeded from noise. The source of the background accelerated electrons may also contribute to the large fluctuations. A possible source of the background accelerated electrons other than from wavebreaking is the interaction of backward Raman scattered light with the laser wakefield [25, 26].

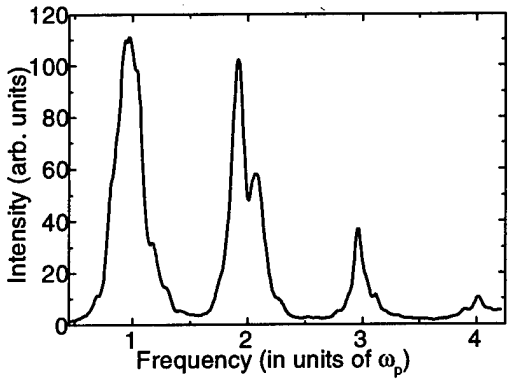


Figure 4: Typical Raman scattering spectrum.

Concurrent with electron measurements we examined the spectrum of Raman scattered light. A typical spectrum is shown in Figure 4 where the strong non-linearity of the plasma wave is obvious from the presence of comparable intensity harmonics in the spectrum [6-8]. Also important is the absence of line broadening in any of the measured spectra. For example, the width of the 1st order anti-Stokes line shown in Figure 4 is the same as those we observed in the linear plasma wave regime (where only the 1st order anti-Stokes line is observed). This indicates that although the wave has steepened, it has not begun to break as was observed by Modena *et al.*. and Umstadter *et al.* at higher powers [7, 8].

The correlation of 2nd order anti-Stokes signal to electron production has been studied. For these experiments, the electron spectrometer measured the number of electrons with greater than 1 MeV of energy. For each laser shot the electron number and forward Raman scattering spectrum were recorded. The 2nd order anti-Stokes signal vs. electron signal is shown in Figure 5. A strong correlation between 2nd order anti-Stokes and electron signal was observed. This perhaps indicates that electrons are only accelerated from the background plasma as the plasma wave becomes non-linear.

Coherent Thomson scattering of a picosecond probe laser was used to measure the time evolution of plasma wakefields produced by a high intensity laser pulse in an underdense hydrogen or helium plasma in the SM-LWFA configuration. Large amplitude plasma wakefields are observed to last for approximately 5 psec.

A plasma channel was observed to be formed behind the relativistically self-guided, subpicosecond, high power pump laser pulse in the gas jet plasma. The channel is probably produced from the radial expulsion of plasma ions due to charge separation created in the displacement of plasma electrons by the large ponderomotive force of the laser. A trailing, frequency doubled probe laser pulse is observed to be guided throughout the length of this channel for about 20 Rayleigh lengths.

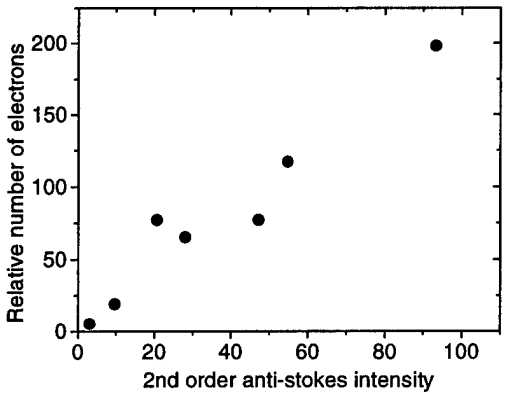


Figure 5: The correlation between the 2nd order anti-Stokes signal and the number of high energy (>1 MeV) electrons.

High energy electrons (up to 30 MeV) have been measured using a high sensitivity detector — a scintillator coupled to a PMT. Highly non-linear plasma waves have been detected using forward Raman scattering as a plasma diagnostic and a correlation between the non-linear plasma waves and electron signal has been observed.

[1] *Omega-P, Inc., New Haven, CT*

[2] *Laboratory for Plasma Studies, Cornell University, Ithaca, NY 14853*

[3] *R.S.I., Inc., Alexandria, VA*

[4] *University of California at San Diego, La Jolla, CA 92093*

ACKNOWLEDGMENTS

The authors would like to thank J. Grun, and A. Fisher for useful discussions and L. Daniels and K. Evans for technical assistance. This work was supported by the Office of Naval Research and the U. S. Department of Energy.

REFERENCES

[1] E. Esarey, P. Sprangle, J. Krall, and A. Ting, IEEE Trans. Plasma Sci. **PS-24**, 252 (1996).

[2] T. Tajima and J. M. Dawson, Phys. Rev. Lett. **43**, 267 (1979); P. Sprangle, E. Esarey, A. Ting, and G. Joyce, Appl. Phys. Lett. **53**, 2146 (1988).

[3] P. Sprangle, E. Esarey, J. Krall, and G. Joyce, Phys. Rev. Lett. **69**, 2200 (1992).

[4] T. M. Antonsen and P. Mora, Phys. Rev. Lett. **69**, 2204 (1992); N. E. Andreev, L.M. Gorbunov, V.I. Kirsanov, A.A. Pogosova, and R.R. Ramazashvili, JETP Lett. **55**, 571 (1992); W. B. Mori, C. D. Decker, D. E. Hinkel, and T. Katsouleas, Phys. Rev. Lett. 72, 1482 (1994); E. Esarey, J. Krall, and P. Sprangle, Phys. Rev. Lett. **72**, 2887 (1994).

[5] J. Krall, A. Ting, E. Esarey, and P. Sprangle, Phys. Rev. E **48**, 2157 (1993); E. Esarey, P. Sprangle, J.

Krall, A. Ting, G. Joyce, Phys. Fl. B **5**, 2690 (1993).

[6] C. A. Coverdale, C. B. Darrow, C. D. Decker, W. B. Mori, K. C. Tseng, K. A. Marsh, C. E. Clayton, and C. Joshi, Phys. Rev. Lett. **74**, 23, 4659 (1995).

[7] A. Modena, Z. Najmudin, A. E. Dangor, C. E. Clayton, K. A. Marsh, C. Joshi, V. Malka, C. B. Darrow, C. Danson, D. Neely, and F. N. Walsh, Nature **377**, 606 (1995); 100 MeV electron detection recently reported by E. Clayton at 7th Workshop on Advanced Accelerator Concepts, Lake Tahoe, CA, Oct. 12-18 1996, Amer. Inst. Phys., NY.

[8] D. Umstadter, S.-Y. Chen, A. Maksimchuk, G. Mourou, and R. Wagner, Science **273**, 472 (1996).

[9] C.I. Moore, K. Krushelnick, A. Ting, C. Manka, H.R. Burris, R. Fischer, M. Baine, E. Esarey, P. Sprangle, and R. Hubbard, *Proc. AIP Conf.*, 7th Workshop on Advanced Accelerator Concepts, Lake Tahoe, CA, Oct. 12-18 1996, Amer. Inst. Phys., NY.

[10] K. Nakajima, D. Fisher, T. Kawakubo, H. Nakanishi, A. Ogata, Y. Kato, Y. Kitagawa, R. Kodama, K. Mima, H. Shiraga, K. Suzuki, K. Yamakawa, T. Zhang, Y. Sakawa, T. Shoji, Y. Nishida, N. Yugami, M. Downer, and T. Tajima, Phys. Rev. Lett. **74**, 4428 (1995).

[11] J. R. Marques, J.P. Geindre, F. Amiranoff, P. Audebert, J.C. Gauthier, A. Antonetti, and G. Grillon, Phys. Rev. Lett. **19**, 3566 (1996); C. W. Siders, S.P. Le Blanc, D. Fisher, T. Tajima, and M.C. Downer, Phys. Rev. Lett. **19**, 3570 (1996).

[12] H. M. Milchberg, T.R. Clark, C. G. Durfee III, T.M. Antonsen, P. Mora, Phys. Plasmas **3**, 2149 (1996).

[13] S. Jackel, R. Burris, J. Grun, A. Ting, C. Manka, K. Evans, and J. Kosakowskii, Opt. Lett. **20**, 1086 (1995).

[14] A. Zigler, Y. Ehrlich, C. Cohen, J. Krall, and P. Sprangle, J. Opt. Soc. Am. B **13**, 68 (1996); Y. Ehrlich, C. Cohen, A. Zigler, J. Krall, P. Sprangle, and E. Esarey, Phys. Rev. Lett. **77**, 4816 (1996).

[15] A. B. Borisov, A.V. Borovskiy, V.V. Korobkin, A.M. Prokhorov, O.B. Shiryaev, X.M. Shi, T.S. Luk, A. McPherson, J.C. Solem, K. Boyer, and C.K. Rhodes, Phys. Rev. Lett. **68**, 2309 (1992); A. Sullivan, H. Hamster, S.P. Gordon, R.W. Falcone, and H. Nathel, Opt. Lett. **19**, 1544 (1994); P. Monot, T. Auguste, P. Gibbon, F. Jakober, G. Mainfray, A. Dulieu, M. Louis-Jacquet, G. Malka, and J.L. Miquel, Phys. Rev. Lett. **74**, 2953 (1995).

[16] K. Krushelnick, A. Ting, C.I. Moore, H.R. Burris, E. Esarey, P. Sprangle, and M. Baine, Phys. Rev. Lett. **78**, 4047 (1997).

[17] P. Sprangle, C.M. Tang, E. Esarey, IEEE Trans. Plasma Sci. **PS-15**, 145 (1987).

[18] G. Z. Sun, E. Ott, Y.C. Lee, and P. Guzdar, Phys. Fluids **30**, 526 (1987); W. B. Mori, C. Joshi, J.M. Dawson, D.W. Forslund, and J.M. Kindel, Phys. Rev. Lett. **60**, 1298 (1988); P. Sprangle, A. Zigler, and E. Esarey, J. Appl. Phys. **58**, 346 (1991); G. Bonnaud, H.S. Brandi, C. Manus, G. Mainfray, and T. Lehner, Phys. Plasmas **1**, 968 (1994); K. Krushelnick, A. Ting, A. Fisher, C. Manka, H.R. Burris, and E. Esarey, Phys. Rev. Lett. **75**, 3681 (1995); C. Decker, W.B. Mori, K.C. Tzeng, and T. Katsouleas, Phys. Plasmas **3**, 2047 (1996).

[19] P. Monot, T. Auguste, L.A. Lompre, G. Mainfray, and C. Manus, J. Opt. Soc. Am. B **9**, 1579 (1992); W. P. Leemans, C. E. Clayton, W.B. Mori, K.A. Marsh, P.K. Kaw, A. Dyson, C. Joshi, and J. M. Wallace, Phys. Rev. A **46**, 1091 (1992).

[20] A. Ting, K. Krushelnick, C.I. Moore, H.R. Burris, E. Esarey, J. Krall, and P. Sprangle, Phys. Rev. Lett. **77**, 5377 (1996).

[21] W. Wood, C. Siders, and M. Downer, Phys. Rev. Lett. **67**, 3523 (1991); E. Esarey, G. Joyce, P. Sprangle, Phys. Rev. A **44**, 3908 (1991).

[22] S.P. Le Blanc, M.C. Downer, R. Wagner, S.Y. Chen, A. Maksimchuk, G. Mourou, and D. Umstadter, Phys. Rev. Lett. **77**, 5381 (1996).

[23] D.M. Villeneuve, H.A. Baldis, J.E. Bernard, and R. Benesch, J. Opt. Soc. Am. B **8**, 895 (1991).

[24] F. Martin, T. W. Johnston, and E. Ebrahim, Phys. Rev. Lett. **55**, 1651 (1985); C. E. Clayton, C. Joshi, C. Darrow, and D. Umstadter, Phys. Rev. Lett. **55**, 1652 (1985).

[25] Bertrand, A. Ghizzo, S.J. Karttunen, T.J.H. Pattikangas, R.R.E. Salomaa, and M. Shoucri, Phys. Rev. E **49**, 5656 (1994); Bertrand, A. Ghizzo, S.J. Karttunen, T.J.H. Pattikangas, R.R.E. Salomaa, and M. Shoucri, Phys. Plasmas **2**, 3115 (1995) .

[26] R. F. Hubbard, P. Sprangle, E. Esarey, A. Ting, H.R. Burris, C.I. Moore, and K. Krushelnick, Bull. Amer. Phys. Soc. **41**, 1602 (1996).

INVERSE FREE ELECTRON LASER ACCELERATOR DEVELOPMENT

A. van Steenbergen*, National Synchrotron Light Source Department, and
Juan C. Gallardo, Physics Department, Brookhaven National Laboratory, Upton, NY 11973, USA

Abstract

The theoretical study of Inverse Free Electron Lasers (IFEL) as a potential mode of electron acceleration has been pursued at Brookhaven National Laboratory(BNL) for a number of years. As part of this program a proof-of-principle experiment with a single module accelerator unit has been recently successfully carried out. The IFEL accelerator made use of the 40 MeV linac beam and high power CO_2 laser beam of the Accelerator Test Facility (ATF), at BNL, in conjunction with a fast excitation , tapered period, wiggler. Basic aspects of the design of this single module IFEL accelerator will be presented, together with the experimental results of $\Delta E/E$ as a function of the IFEL parameters. Comparison with analytical and 1,3-D numerical simulations clearly establish the IFEL character of the electron - EM wave energy exchange, permitting thereby scaling to higher laser power magnitude and acceleration gradients. In addition, planned near term IFEL accelerator development will be indicated, incorporating the use of the IFEL as a beam prebuncher preceding a Inverse Cherenkov Accelerator, and the use of two IFEL modules in cascade in order to more realistically test the feasibility of a multi-module IFEL accelerator.

1 INTRODUCTION

The Free Electron Laser (FEL) uses a beam of relativistic electrons passing through a transverse, periodic , magnetic field (the *undulator*) to exchange energy with the coaxial propagating EM radiation field.[1] The FEL operates in such a manner that there is net energy transfer from the electron beam to the radiation field. Alternatively, net energy transfer from the radiation wave to the electrons is similarly possible. This concept, of using the FEL mechanism to effectively accelerate electrons, now called the Inverse-Free-Electron-Laser (IFEL) accelerator, is due to R. Palmer.[2] The basic principle of the IFEL accelerator is *identical* to that of the FEL, except that, in order to maintain resonance for optimum energy transfer, *tapering* of the undulator period length or its magnetic field is an added requirement. Early studies of IFEL[3, 4], clearly detailed the beam energy limitations of the IFEL accelerator, mainly related to synchrotron radiation energy loss at higher electron beam energies, and also uncovered possible favorable applications of the IFEL as a front end structure for alternative, non-conventional, accelerators. This has been the objective of recent BNL studies [5,6], aimed at the optimization of the IFEL as a high gradient, single-module, accelerator cell as a first step toward a compact multi-module electron accelerator of maximum electron energy of a few GeV. IFEL proof-of-principle experiments have been carried out elsewhere, using a moderate power CO_2 laser source[7] and using a low power FEL with radiation wavelength of 1.65 mm as the driving beam [8]. More recently, experimental results of a single module IFEL, operating with a 1-2 GW CO_2 sapphire waveguide constrained laser beam and uniquely designed tapered period wiggler were reported.[9]

The theoretical description of IFEL interaction has been given by a number of authors. Here, we follow the basic formalism given in CPZ[4], with the further assumption that electron energy loss effect due to synchrotron radiation emission is taken to be zero and that the laser beam attenuation due to absorption by the accelerating electrons is negligible. The latter assumption is abandoned in further detailed treatment and, following KMR[10] a self consistent system of Lorentz equations for the electrons and the wave equations for the input laser field is used, to form the basis of both 1-D and 3-D IFEL computer simulations. With this the parameters for the, first experimental phase, IFEL single module test, were developed. This, together with the parameterization of beam wiggler and CO_2 guide, is given in section 2, below. First phase experimental results, together with IFEL simulation program results are presented in section 3, and a discussion of near term IFEL accelerator objectives is given in section 4.

2 IFEL EXPERIMENTAL ARRANGEMENT

Approximate analytical expressions, as derived in CPZ, together with the results of the 1-D simulation, were used to initially parameterize a single IFEL accelerator module. The parameters of the e- beam,[11] CO_2 laser beam[12] and IFEL wiggler are summarized in Tb.1; a schematic of the experimental configuration is given in Fig.1. For IFEL

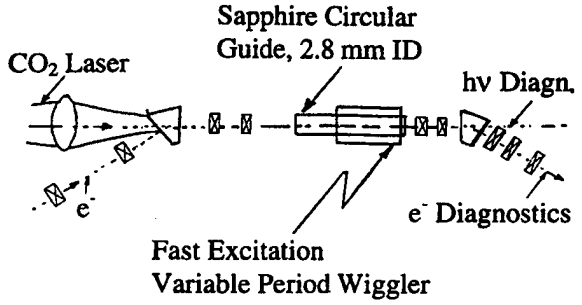


Figure 1: Schematic of the experiment configuration.

* The authors wish to acknowledge the participation of J. Sandweiss, M. Babzien, J-M. Fang, K. Kusche, R. Malone, I. Pogorelsky, X. Qiu, T. Romano, J. Sheehan, J. Skaritka, X-J Wang as coinvestigators in the IFEL accelerator development.

0-7803-4376-X/98/$10.00 © 1998 IEEE

Table 1: IFEL first phase parameters.

e- beam	Injection Energy	40.0	MeV
	Exit Energy	42.3	MeV
	<Accel.Field>	4.9	MV/m
	Current, nominal	5	mA
	N(bunch)	10^9	e-
	I(max.)	30	A
	$\Delta E/E(1\sigma)$	$\pm 3 \times 10^3$	
	Emittance (one σ)	7×10^8	m rad
	Beam radius	0.3	mm
Wiggler	Wiggler Length	0.47	m
	Section Length	0.6	m
	Period Length, λ_w	2.9–3.1	cm
	Wiggler Gap	4	mm
	Field max.	10	kG
	Beam oscill.,a1/2	0.16-0.2	mm
CO_2 Laser	Power, W_λ(Laser)	10^9	Watts
	Wavelength, λ	10.6	μm
	Max.Field, E_o	0.78×10^3	MV/m
	Guide Loss, α	0.05	m^{-1}
	Field Attenuation	0.26	dB/sect.
	Pulse,(FWHM)	220	ps
	A_o	1.53×10^3	m^{-1}
	r_o (L_w/2)	1.0	mm

acceleration, it is necessary to maintain synchronism between the propagating electron beam and radiation wave, hence it is necessary to *taper* the wiggler. This can be accomplished by varying either the wiggler parameter K_w, the period length, λ_w or the maximum wiggler field, B_w . The choice is restricted by the maximum practical wiggler field and the minimum wiggler period length. It has been shown that, at low energy, maximum rate of acceleration, averaged over the full accelerator length, is obtained for a constant wiggler field accelerator.[5] Hence, for the IFEL accelerator of relevance here, the use of a period length tapered wiggler has been adopted. Although such a wiggler structure could be constructed using permanent magnets, the requirement of a specific period length taper would be costly and also difficult to subsequently change, in case higher laser power becomes available. Instead, for the present objective, a novel design fast excitation electromagnetic wiggler has been adopted[13, 14] which permits ready variation of the wiggler period length taper. This wiggler consists of stackable, geometrically alternating substacks of identical ferromagnetic (Vanadium Permandur [VaP]) laminations, in ($\frac{\lambda_w}{4}$) thickness substacks, separated by nonmagnetic laminations. Maximum achievable wiggler field, B_w, results from using conductive material for the nonmagnetic laminations, so that the induced fields from the eddy currents uncouple the wiggler *up* field from the *down* field. These *field reflectors* significantly enhance the maximum achievable field on axis.

A significant step towards design simplification of the single module IFEL accelerator, is the use of an extruded single crystal dielectric circular waveguide for the transmission of the CO_2 radiation wave into the IFEL interaction domain. The design benefited from the pronounced progress that has been made in recent years in the development of waveguides for low loss transport of high power CO_2 laser beams. The type of guide adopted here for the objectives of the IFEL accelerator is the hollow-core dielectric guide, for which the core has a refraction index (vacuum, n=1) greater than the refraction index of the wall dielectric material ($n_{\text{clad}} < n_{\text{core}}$), resulting in solid fiber-like, low loss, behavior. As reported by Harrington and Gregory[16], a particularly favorable dielectric, with $n < 1$, for hollow guide CO_2 transport is Al_2O_3, either in the form of single crystal (SC) Sapphire or polycrystalline Alumina. As shown by Mercatelli and Schmeltzer(MS)[17], the attenuation constant, for the low order modes, is approximated by :

$$\alpha_{11} = (u_{11}/2\pi)^2(\lambda^2/2a^3)Re[(\nu^2+1)/(\nu^2-1)^{1/2}] \quad (1)$$

where α, the attenuation coefficient, is defined by $P(z) = P(0)e^{-2\alpha z}$, $\nu = n - jk$ is the refractive index for the cladding material, [note, at $10.6\,\mu m$, $n = 0.67 - j0.03$], a is the circular guide radius, $2\pi/\lambda$ is the free space propagation constant and $u_{n,m}$ is the modal constant. For the fundamental mode, EH_{11}, $u_{1,1} = 2.406$. For the next low order mode EH_{12}, the modal constant equals 5.52, implying significantly greater attenuation for the CO_2 transport per unit guide length , hence reduced mode mixing, which is favorable for the present application. Various guide configurations were tested at low laser beam power with the beam focused to a Gaussian waist with adjustable radius at the entrance to the guide. For the 2.8 mm ID guide a laser power attenuation factor was measured of 0.2 dB/m. This is larger than predicted by the MS theory, but satisfactory for the IFEL accelerator application. Optimization of the coupling of the Gaussian mode laser beam into the desired EH_{11} propagating mode in the sapphire dielectric guide was done with the adoption of a entry matching cone and variation of the laser beam entry diameter. For optimum laser power transfer, a beam to guide aperture ratio of 0.74 is indicated theoretically[18] and was found to be valid experimentally. The CO_2 laser beam is directed through a ZnSe window into the coaxial $h\nu - e-$system, propagating as a free-space mode, to the circular dielectric waveguide. With deliberation, the dielectric guide was taken to be 0.6 m. in length, whereas the accelerator module length (wiggler length) was set at 0.47 m. This was done, together with the use of the guide entry cone, to approximate a mode matching section, enhancing thereby the mode purity in the IFEL module proper.

Beam transport from the exit of the linac to the e-diagnostic flag is designed to yield a dispersion free IFEL interaction region with a vertical betatron amplitude equal to the natural wiggler betatron amplitude of $\beta_x = 0.17$ m. The IFEL e-acceleration is measured by means of a momentum spectrometer with adjustable local dispersion magnitude ($0.0 < \eta_p < 3.0$ m), using a phosphor screen-vidicon camera-spiracon frame grabber.

3 IFEL EXPERIMENTAL RESULTS

In order to establish unambiguously correct overlap, both time wise and spatially, of the 300 ps CO_2 and 5 ps e^- beams, an observable interaction effect is an experimental necessity. To this end, therefore, the IFEL 1-D simulation code was used to yield the e- momentum distribution for the case of pronounced phase incoherence. The results suggested that, also in that case, the photon-e^- interaction would be measurable, so that synchronization could be established. With optimized matching of the e- beam and

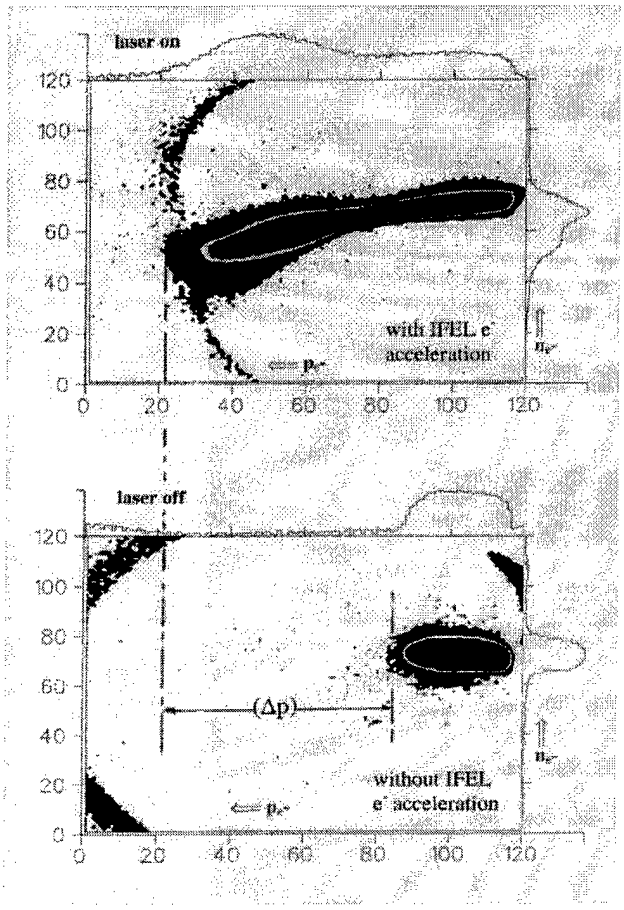


Figure 2: Momentum spectrum of the unaccelerated and IFEL accelerated beam. E(e^-=34.2 MeV, B_w=0.82 T, λ = 2.9 − 3.1 cm, W_l =0.8 GW, $\Delta p/p = 2.2\,\%$.

CO_2 laser beam to the IFEL interaction region, optimization of the time synchronization of both beams, and correct interlacing of the lower repetition rate CO_2 laser pulse with the higher repetition rate e- beam pulses, e- IFEL acceleration was established. An example of the momentum spectrum of the unaccelerated and accelerated electrons is given in Fig.2, where the beam intensity distribution is shown versus $\sqrt{\beta_x \epsilon_x} + \eta_p \Delta p/p$, with the spectrometer optics adjusted so that $\eta_p \Delta p/p >> \sqrt{\beta_x \epsilon_x}$.

Optimization of the IFEL effect and exploration of parameter space, with variation of the electron beam injection energy, CO_2 laser power and wiggler maximum magnetic field magnitude was carried out in several consecutive runs, the results of which established the unambiguous signature

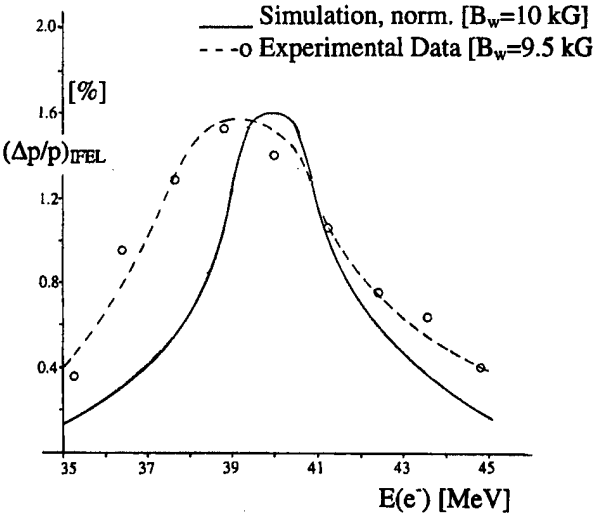


Figure 3: Relative energy gain $\Delta p/p$. vs. E with B_w, W_l fixed.

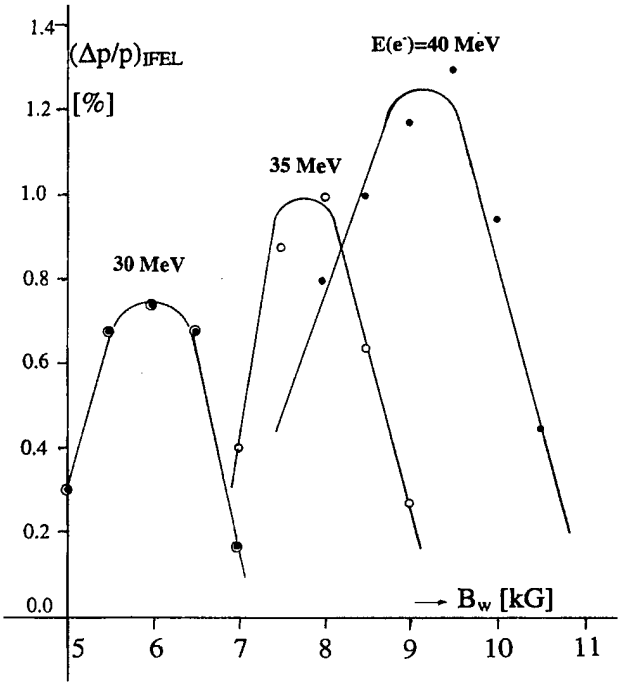


Figure 4: Relative energy gain vs. B_w with E and W_l fixed.

4. In Fig.3 the relative energy gain $(\Delta p/p)_{\mathrm{IFEL}}$ vs electron beam energy E for B_w and W_l constant, is shown, both as derived from the 1-D model simulations and as obtained experimentally, and in Fig.4 the relative energy gain vs B_w, for three beam energy values and W_l constant, is plotted. Although not shown in these figures, a maximum of $\Delta p/p = 2.5\%$ was measured with the parameters E_e = 40 MeV, B_w = 10 kG and W_l = 1 GW.

The approximate IFEL design equation[4] is:

$$\frac{d\gamma}{dz} = A\frac{K}{\gamma}f(K)\sin\psi \qquad (2)$$

with $\psi = (k + k_w)z - kct$ and where the normalized laser electric field is $A = (e/mc^2)(1/R_o)\sqrt{\pi W_l Z_o}$, $K = (eB_w\lambda_w)/(2\pi mc) \approx 2.7$ is the wiggler parameter, $f(K) \approx 0.38$ is a correction factor due to the linear polarization of the wiggler, $Z_o = 377\Omega$, R_o is the waveguide radius and k, k_w are the radiation and wiggler wavevectors, respectively. The resonance condition leads to: $\lambda = 0.5\lambda_w/\gamma^2(1 + K^2/2)$. The relative energy gain of the electron beam in a wiggler of length L_w is:

$$\Delta\gamma/\gamma = (\Delta p/p)_{\rm IFEL} = A(K/\gamma^2)f(K)\sin\psi_r L_w \qquad (3)$$

where ψ_r is the resonance phase. The experimental results, as shown in Fig.3, agree well with the results obtained from the numerical simulations, with laser power W_l = 1 GW and the maximum wiggler field B_w = 10 kG, in $(\Delta p/p)$ magnitude normalized to the maximum experimental value. The experimental results given in Fig.4 also are in good agreement with precalculated values using the resonance condition, i.e. the observed B_w values for $(\Delta p/p)_{\rm MAX}$ are B_w = 9.2 kG (40 MeV), 7.7 kG (35 MeV), 6.0 kG (30 MeV), yielding the λ_w values 3.06 cm, 3.05 cm and 3.11 cm, respectively, well within the design taper of the actual wiggler of $2.89 > \lambda_w > 3.14$ cm. With the present spectrometer, the energy gain could be measured with good accuracy due to the sharp intensity fall-off of the high energy edge of the non-accelerated particles. A quantitative intensity ratio of the accelerated to unaccelerated beam could not be obtained due to the extended low energy edge of the unaccelerated beam. This limited the ability to measure the bucket size and leakage for comparison with model predictions and therefore, the value of the synchronous phase angle ψ_r could not be unambiguously established. Analytically, ψ_r and $\Delta\gamma/\gamma$ as a function of laser power W_l and wiggler parameters are given by:

$$\begin{aligned}\sin\psi_r &= \frac{3k}{16k_w}\frac{K}{Af(K)L_w}\left[\left(\frac{\lambda_w(L)}{\lambda_w(0)}\right)^2 - 1\right] \\ \Delta\gamma/\gamma &= 2\sqrt{\frac{Kf(K)A}{k(1+K^2/2)}}\Gamma(\psi_r) \qquad (4)\end{aligned}$$

These equations permit to calculate the moving bucket[10] parameter $\Gamma(\psi_r)$ and its maximum energy extent $\Delta\gamma/\gamma$. For the experimental value $\Delta\gamma/\gamma = 2.5\%$, it is found : $\psi_r = 34°$ in reasonable agreement with the optimal 45° and a laser power of W_l = 2.7 GW which is larger than the 1 GW estimated experimentally. In conclusion, the IFEL acceleration of a 40 MeV electron beam by $\Delta E/E = 2.5\%$ with a 1 GW CO_2 laser and a tapered wiggler with peak field on axis of 10 kG has been confirmed. Agreement with the model predictions is satisfactory, permitting the scaling of anticipated results to higher laser power.

4 IFEL ACCELERATOR OBJECTIVES

Present IFEL operation is limited to a maximum laser power of $< 2 - 3$ GW. With the objective of high energy gradient acceleration, high CO_2 laser power will be employed, initially at the 100 MW level, but with a longer term objective of 1 TW laser power. Hence, laser power damage to the dielectric guide wall is of concern. Assumed parameters are W_l = 1 TW, Effective Guide Cross Section $= 5.210^{-6}$m^2, or P/area= $2.10^{13}W/cm^2$. Assuming lowest order mode transport only with the radial power density distribution approximated by a cosine function, and coaxial correct guide entry and transport, P/area at the guide wall is a factor of 10^6 smaller, hence the power density at the wall equals $\approx 210^7 W/cm^2$. For the present parameters, in a pulsed operating mode, this is a tolerable power density for the sapphire dielectric.

Table 2: IFEL two-module accelerator.

		M-I	M-II	
e beam	$E_{initial}$	40	76.7	MeV
	E_{exit}	76.7	106.3	MeV
Wiggler	Length	0.51	0.47	m
	λ_w	3.12-4.72	4.72-5.79	cm
	B_w	1	1	T
CO_2 laser	Power	100	100	GW
	pulse	10	10	ps
	Synchr. ϕ_r	50	50	°
	E_{MAX}	7.8	7.8	GV/m

Near term further development of the IFEL accelerator concept will incorporate two approaches: **First**, the construction of a second VaP fast excitation wiggler - sapphire guide IFEL interaction region, for incorporation into a two accelerator modules IFEL accelerator, to test realistically a synchronized multi-module IFEL accelerator sequence and aim, with the above cited CO_2 laser developments, at a 100 MeV IFEL linac. The conceptual layout of this accelerator is shown in Fig.5 and the preliminary parameters are given in Tb2. Early results of IFEL particle transport simulation is given in Fig.6. Clearly, structure phase synchronization and minimization of bunch dilution in the inter cavity drift space demand appropriate, high resulution, bunch time measurement. The beam bunching factor produced by the IFEL interaction was measured using Coherent Transition Radiation (CTR).[19] **Second**, in a joint developmental approach with the STI Inverse Cherenkov Accelerator (ICA) experiment[20], use of the IFEL accelerator as a synchronized prebuncher for the IC accelerator in an IFEL-ICA buncher-accelerator sequence. Particle IFEL transport simulation has also been carried out for this application, as given in Fig.7, clearly evidencing the potential of the IFEL system to serve as a prebuncher for alternative modes of particle acceleration.

5 ACKNOWLEDGEMENTS

The authors acknowledge the technical support of I. Ben-Zvi and the staff of the ATF. This work was supported by the Advanced Technology R & D Branch, Division of High Energy Physics, U.S. DoE, DE-AC02-76CH00016.

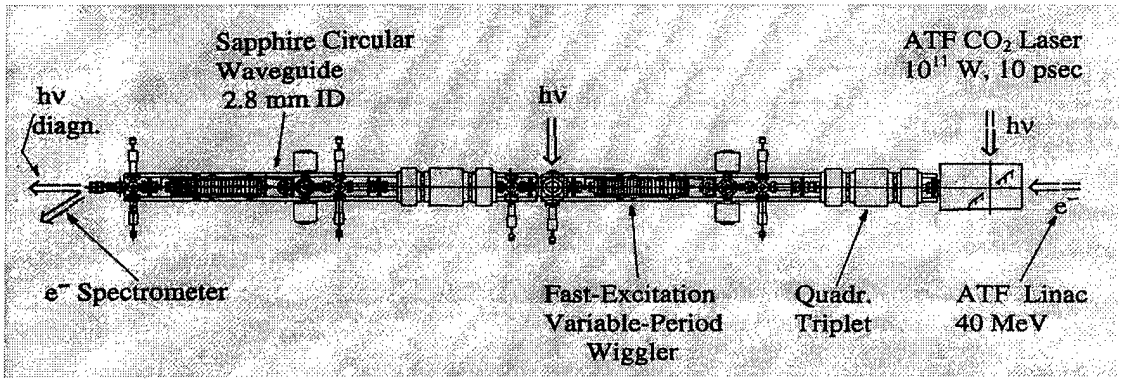


Figure 5: IFEL two-module accelerator.

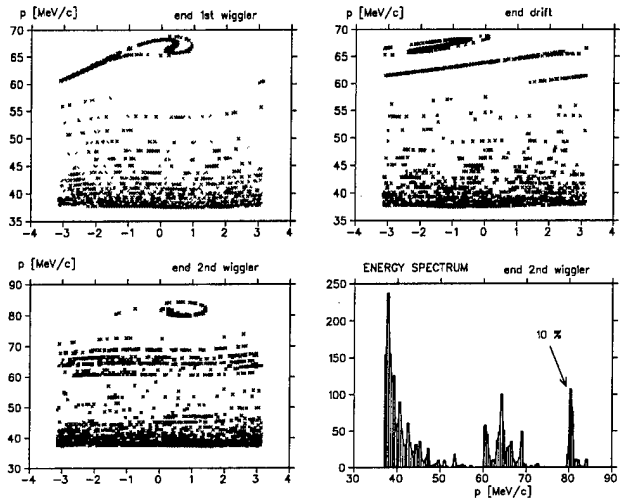


Figure 6: IFEL two-module accelerator simulation.

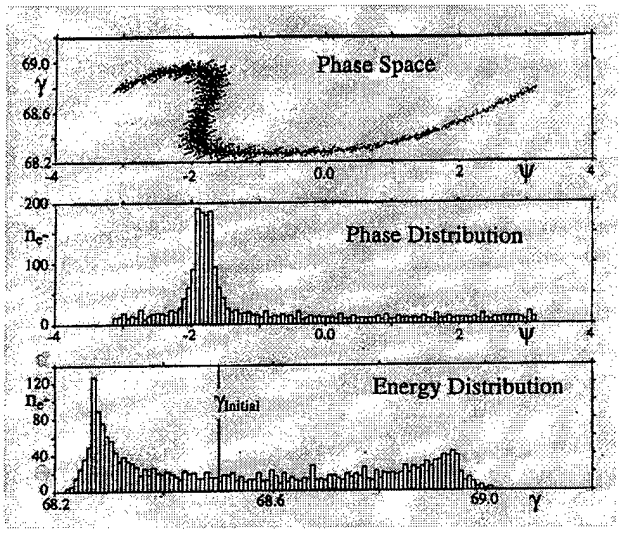


Figure 7: Prebuncher simulation for the combined IFEL-ICA experiment. E=35 MeV, W_l=0.1 GW.

6 REFERENCES

[1] J. Madey, J. Appl. Phys. 42, 1906, 1971.

[2] R. Palmer, J. Appl. Phys. 43, 3014 ,1972.

[3] C. Pellegrini, P. Sprangle,W. Zakowicz, Proc. of the XIII Int.Conf. on High Energy Accelerators, p.473, 1983.

[4] E. Courant, C. Pellegrini, W. Zakowicz, Phys.Rev. A32, 2813, 1985.

[5] A. Fisher, J. Gallardo, J. Sandweiss, A. van Steenbergen, *Inverse Free Electron Laser Accelerator*, Proc. Adv. Accel. Concepts, Port Jefferson, NY, AIP 279, p.299, 1993.

[6] A. Fisher, J. Gallardo, A. van Steenbergen, J. Sandweiss, *IFEL Accelerator Development*, Nucl. Instr. Meth. A341, 1994.

[7] A. Amatuni et.al., Particle Accelerators 32, 221, 1990.

[8] I. Wernick and T. C. Marshall, Phys. Rev. A46, 3566 ,1992.

[9] A. van Steenbergen, J. Gallardo, J. Sandweiss, J. Fang, M. Babzien, X. Qiu, J. Skaritka, X-J. Wang , Phys. Rev. Let., Vol.77, 2690, 1996.

[10] N. Kroll, P. Morton, M. Rosenbluth, QE 7, 89, 1979.

[11] I. Ben-Zvi, Proc. Adv. Accel. Concepts, Port Jefferson, NY, AIP 279, 590, 1993.

[12] I. Pogorelsky, Proc. Adv. Accel. Concepts, Port Jefferson, NY, AIP 279, 608, 1993.

[13] A. van Steenbergen, Patent Application 368618, June 1989 (Issued Aug. 1990).

[14] A. van Steenbergen, J. Gallardo, T. Romano, M. Woodle, Proc. PAC, IEEE NS, May 1991.

[15] A. Fisher, J. Gallardo, A. van Steenbergen, J. Sandweiss, J. Fang, *IFEL Development*, AIP Conference Proceedings 335, editor P. Schoessow, AIP Press, 1995.

[16] J. Harrington, C. Gregory, Optics Letters 15, 1990.

[17] E. Marcatili, R. Schmeltzer, Bell System Techn. J., 43, 1783, 1964.

[18] K. Laakmann, W. Steier, Applied Optics, Vol.15, No.5, 1976.

[19] Y. Liu, X. J. Wang, M. Babzien, D. Cline, J-M. Fang, J. Gallardo, K. Kusche, I. Pogorelsky, J. Skaritka, A. van Steenbergen, *Experimental Results for IFEL Acceleration Micro-Bunching Measurement by CTR*, submitted to the Proc. of this Conference.

[20] W. Kimura, I. Pogorelsky, Y. Liu, K. Kusche, A. van Steenbergen, J. Gallardo, J. Sandweiss, D. Quimby, M. Babzien, *Inverse Cerenkov Acceleration using an IFEL Prebuncher*, submitted to the Proc. of this Conference.

EXPERIMENTAL OBSERVATION OF IFEL MICRO-BUNCHING USING COHERENT TRANSITION RADIATION

Y. Liu and D.B. Cline, University of California, Los Angeles, CA 90095
X.J. Wang, M. Babzien, J.M. Fang, J. Gallardo, K. Kusche, I. Pogorelsky,
J. Skaritka, A. van Steenbergen, Brookhaven National Laboratory, Upton, NY 11973

Abstract

Electron beam bunching in the optical wavelength was observed experimentally for the first time at the Brookhaven Accelerator Test Facility(ATF) using the Inverse Free Electron(IFEL) accelerator. The micro-bunched electron beam has been studied by measuring the coherent transition radiation (CTR). We have experimentally observed a quadratic dependency of the CTR signal with the charge of the electron beam and the observation distance.

1 INTRODUCTION

One of the major challenges in laser accelerator research is to generate an electron beam with a bunch length shorter than the half of the laser wavelength for efficient acceleration and small energy spread. Several techniques[1, 2] were proposed to produce micro-bunched electron beam for laser accelerator applications. A UCLA-BNL collaboration recently has experimentally demonstrated electron beam micro-bunching on the order of a few microns using the IFEL accelerator[3]. Operating the IFEL as a laser accelerator buncher has several advantages. Since IFEL does not involves any medium, such as plasma based laser accelerators, there is negligible electron beam quality degradation. Secondly, there is natural synchronization between the IFEL buncher and laser accelerator since the same laser will be used for both bunching and acceleration. We will first briefly discuss the coherent transition radiation properties, then the experimental setup will be described. The experimental result will be presented in the second half of the report.

2 COHERENT TRANSITION RADIATION

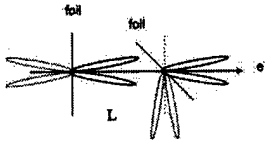
Coherent transition radiation is a collective effect of transition radiation produced by a large ensemble of electrons being in phase with each other. The intensity of photon radiated is highly enhanced and the total radiation distribution becomes[4]

$$\frac{d^2U}{d\omega d\Omega} = [N + N(N-1)F(\omega,\theta)]\,\frac{d^2u}{d\omega d\Omega}\,|_{single}\,, \quad (1)$$

where

$$F(\omega,\theta) = \left|\int\int\int f(r,z)\exp(-i\vec{k}\cdot\vec{x})d^3x\right|^2 \quad (2)$$

is a bunching factor, containing information about the electron distribution. The coherent effect scales like N^2 compare to the incoherent part, which scales linearly with the electron number, N. For a single foil case the CTR angular distribution has been estimated by J. Rosenzweig, et al[5].



$$F(\omega,\theta)=\left|\iiint g(r)h(z)\exp\left(-i\vec{k}\cdot\vec{x}\right)\left[1+\exp\left(-i\varphi_1-i\varphi_2\right)\right]d^3x\right|^2$$

$$\varphi_1=\frac{ikx}{\beta}(1-\beta\cos\theta) \qquad \varphi_2=\frac{ikL}{\beta}(1-\beta\cos\theta)$$

Figure 1: Two-foil configuration. First one generates a forward CTR and redirected by a second foil; the second foil generates backward CTR.

For a two-foil configuration (Figure 1), the first foil is perpendicular to the electron beam direction, contributing a forward CTR, and the second foil is at 45^0 to the electron beam direction, contributing a backward CTR. The individual electrons distributed on the second foil will have an additional phase difference $\varphi(x, L)$ relative to the electron on the first foil.

The phase difference is given by

$$\begin{aligned}\varphi(x,L) &= \varphi_1(x) + \varphi_2(x,L) \\ &= \frac{kx}{\beta}(1-\beta\cos\theta) + \frac{kL}{\beta}(1-\beta\cos\theta), \quad (3)\end{aligned}$$

where L is the separated distance between the two foils. Following the same treatment for a single foil, the two-foil CTR photon angular distribution is expressed as follow:

$$\begin{aligned}\frac{dN_{ph}}{d\theta} \approx\ & \frac{\alpha\beta^2}{8\sqrt{\pi^3}}\left(\frac{k_r\sigma_z}{\pi}\right)\left(\pi\frac{Nb_n}{k_r\sigma_z}\right)^2\left(\frac{1}{n}\right)\frac{\sin^3\theta}{(1-\beta\cos\theta)^2}\times \\ & \left\{\exp\left[-\left(\frac{nk_r\sigma_r}{\beta}\right)^2(\beta\sin\theta-\beta\cos\theta+1)^2\right]+\right. \\ & \exp\left[-(nk_r\sigma_r\sin\theta)^2\right]+ \\ & 2\exp\left[-\frac{1}{2}\left(\frac{nk_r\sigma_r}{\beta}\right)^2(\beta\sin\theta-\beta\cos\theta+1)^2\right]\times \\ & \exp\left[-\frac{1}{2}(nk_r\sigma_r\sin\theta)^2\right]\times \\ & \exp\left[-\left(\frac{L}{2\beta\sigma_z}\right)^2(\beta\cos\theta-1)^2\right]\times \\ & \left.\cos\left[\left(\frac{nk_rL}{\beta}\right)(\beta\cos\theta-1)\right]\right\}. \quad (4)\end{aligned}$$

From the above equation we see that the total CTR intensity is produced by two individual CTR sources plus their interference in the far region.

0-7803-4376-X/98/$10.00 © 1998 IEEE

3 EXPERIMENT SETUP

In the current condition the maximum charge delivered to the IFEL wiggler at ATF is up to 300pC. The space charge effect on the IFEL self-bunching can be ignore[6]. The basic experimental setup can be described as follows. A target (a component to generate CTR) is mounted inside a 6-way cross. The 6-way cross serves as a small vacuum chamber and is able to move along the beam path to find the optimum bunching position during the measurement. Thus, the 6-way cross connected with a pair of bellows is inserted into the beamline. This allows the target to travel back and forth along the e^- beam path without disturbing the vacuum environment. The radiation is transported from the chamber through a ZnSe window and a IR lens into a collecting system, collected by a parabolic mirror and focused into a detector (Figure 2). The detector, liquid Nitrogen cooled, is sensitive to wavelengths from 1.1μm to 5.5μm with $1 \times 1\text{mm}^2$ sensitive area; it is located 60cm away from the target chamber and is well shielded by lead bricks. A HeNe laser is used for optical alignment and parabolic mirror rotation monitoring. For convenience, all components including the target chamber are assembled on a translated stage (movable table) driven by a digitized remote-controlled stepping motor. This allows the whole diagnostic system to travel along the e^- beam path for a maximum distance of 40cm .

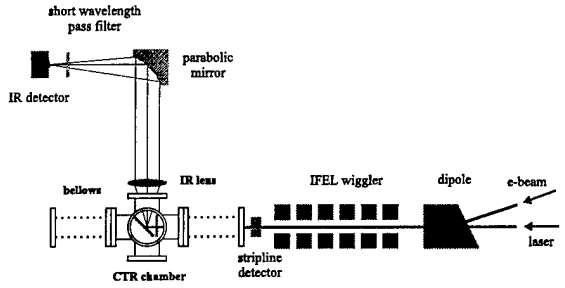


Figure 2: Schematic of the micro-bunching diagnostic setup for the IFEL experiment.

Such a design keeps the optical alignment from changing when the target is moved. A stripline detector is placed between the upstream bellows and the exit of the wiggler to provide the total e^- beam charge information before it strikes the target. The output amplitude of the stripline detector is proportional to the total charge (eN), where e is the electron charge and N is the number of electrons. Control and data collection are performed at the ATF control room.

4 EXPERIMENTAL RESULTS

The wiggler magnetic field steering effect on the e^- beam was investigated by using a high sensitivity CCD camera to look at the optical transition radiation emitted from the surface of the foil (target). When the wiggler magnetic field (B) is strong, which matches with a high energy e^- beam, the e^- beam is strongly focused and steered away from the target. The situation is greatly improved after an additional steering magnet is placed right after the exit of the wiggler. Backgrounds were studied during the CTR measurement. There are three types of backgrounds. 1) x-rays generated by the e^- beam scattering. 2) broad bandwidth radiation produced the CO_2 laser when it passes through the sapphire waveguide in the wiggler. 3) incoherent transition radiation combined with the coherent transition radiation. The backgrounds were measured under the same conditions as the CTR measurement, except that the laser electric field has no spatial overlap with the e^- beam (by changing relative timing delay), which ensures that there is no acceleration (no bunching). Thus, all combined three backgrounds are measured. However, the total background amplitude is much smaller than the CTR intensity amplitude (Figure 3).

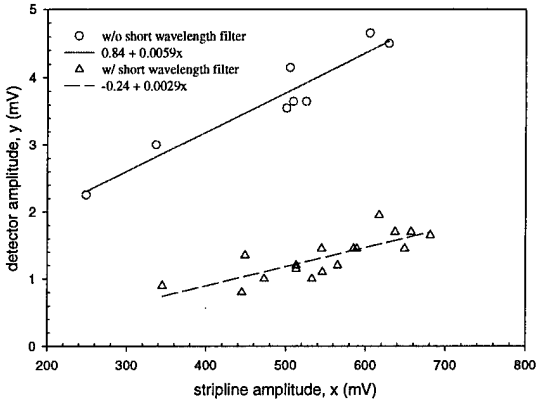


Figure 3: The circles represent the background taken without a short wavelength pass filter. The uptriangle is with the filter.

The CTR intensity amplitude as a function of the e^- beam charge was measured. The results are plotted in Figure 4. Since the cutoff wavelength of the liquid Nitrogen cooled Indium Antimonide (InSb) detector is at 5.5μm and the detected CTR intensity is relatively strong, this shows that the microbunch length should be less than 5.5μm. Furthermore, a short wavelength pass filter having a cutoff wavelength at 2.6μm was placed in front of the detector. The background and CTR data are plotted in Figure 5. At such a short wavelength region, the detector efficiency drops to less than 50%, but the CTR is still detectable. This is definite proof that the bunch length is much shorter than 5μm and close to the fourth harmonic wavelength.

Last, the micro-bunch length change as a function of its drifting distance is examined by positioning the target at different locations (Figure 6). The distance is defined from the wiggler exit to the target position. As predicted, after optimum bunching distance the microbunched electrons start to debunch (bunch length increase) and results in the CTR intensity amplitude decrease. The experimental data

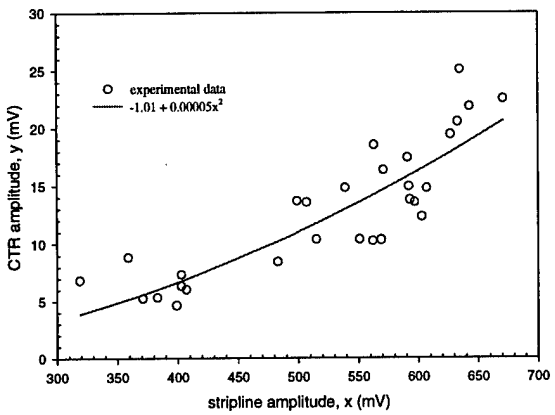


Figure 4: The total CTR intensity amplitude as a function of the total number of electrons. The stripline detector output amplitude is proportional to the total charge (eN).

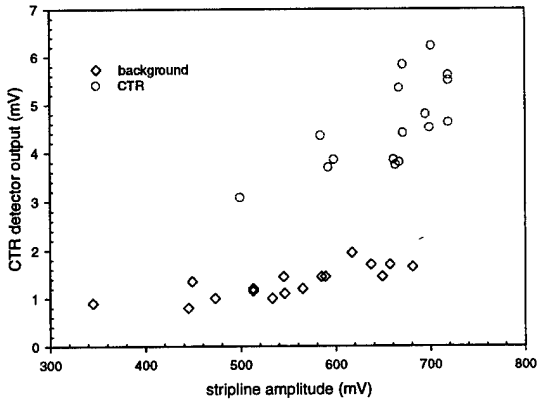


Figure 5: The detected CTR intensity amplitude is well above the background amplitude at short wavelength region. A short wavelength pass filter is used during the measurement.

shown in Figure 6 reasonably agree with the model prediction. The simulation results[7] show that the optimum microbunch length (FWHM) is less than 2μm.

Note, only the debunching process was studied. This is due to the following facts: (1) space-charge may affect the self-bunching process even when the charge density is not very high. This may lead to the bunching distance being longer than the debunching distance. (2) The target traveling distance is about 40cm, which may not be long enough for the present condition.

5 SUMMARY

We have measured for the first time the CTR from $< 5\mu$m microbunches. The experimental results show that the ATF IFEL wiggler is capable of producing very short bunches at the several micron level. An experiment to stage two IFEL

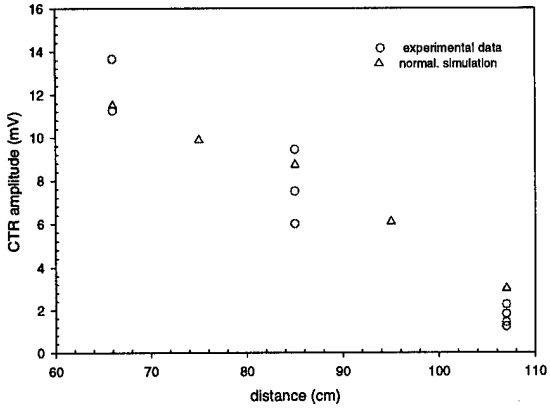


Figure 6: The CTR intensity changes as a function of debunching distance. The circle is the experimental data and the uptriangle is the normalized simulation results.

sections or combine an IFEL section with an ICA section to demonstrate 100MeV acceleration are in preparation and look very promising.

6 ACKNOWLEDGEMENTS

We thank the staff of the ATF at Brookhaven National Laboratory, especially I. Ben-Zvi for his encourage and help, B. Cahill, B. Harrington and M. Montemagno for their technical support. We acknowledge helpful discussions with J. Rosenzweig and E.B. Blum. This work was supported in part by DE-FG03-92ER40695 and DE-AC02-76CH00016.

7 REFERENCES

[1] L.Serafini, *IEEE Trans. on Plasma Sci.*, Vol.**24**, No. 2, 421 (1996).

[2] T.C. Katsouleas et al, *IEEE Trans. on Plasma Sci.*, Vol.**24**, No. 2, 443 (1996).

[3] A. van Steenbergen, J. Gallardo, J. Sandweiss, J-M. Fang, M. Babzien, X. Qiu, J. Skaritka, and X.J. Wang, *Phys. Rev. Lett.* **77**, 2690 (1996).

[4] E.B. Blum, U. Happek and A.J. Sievers, *Nucl. Instr. Methods in Phys. Res.* **A307**, 568 (1991).

[5] J. Rosenzweig, G. Travish, and A. Tremaine, *Nucl. Instr. Methods in Phys. Res.* **A365**, 255 (1995).

[6] Y. Liu, D.B. Cline, X.J. Wang, M. Babzien, J.M. Fang, and V. Yakimenko, "Micro-bunching Diagnostics for the IFEL by Coherent Transition Radiation" in *Proceedings of the Advanced Accelerator Workshop*, Lake Tahoe, CA, 12-18 October 1996.

[7] J. Gallardo, "1D IFEL simulation code including space charge".

ACCELERATION FOR THE $\mu^+\mu^-$ COLLIDER

D. Summers, Dept. of Physics, University of Mississippi–Oxford, University, MS 38677 USA,
D. Neuffer, Fermi National Accelerator Laboratory, Batavia, IL 60510 USA,
Q.–S. Shu, Thomas Jefferson National Accelerator Facility, Newport News, VA 23606 USA, and
E. Willen, Brookhaven National Laboratory, Upton, NY 11973 USA

Abstract

We discuss possible acceleration scenarios and methods for a $\mu^+ - \mu^-$ collider. The accelerator must take the beams from ~100 MeV to 2 TeV energies within the muon lifetime ($2.2 \times 10^{-6} E_\mu/m_\mu$ μS), while compressing bunches of $\sim 10^{12}$ muons from m to cm bunch lengths. Linac, recirculating linac, and very rapid-cycling synchrotron approaches are studied. Multiple recirculating linac approaches are matched to the muon lifetime and appear readily feasible. Rapid-cycling approaches require innovations in magnet designs and layouts, but could be much more affordable.

1 INTRODUCTION

For a $\mu^+\mu^-$ collider [1], muons must be rapidly accelerated to high energies while minimizing the kilometers of radio frequency (RF) cavities and magnet bores. Cost must be moderate. Some muons may be lost to decay but not too many. As the muon energy increases and the bunch length decreases, higher frequency, higher gradient RF cavities may be used to reduce cost.

2 100 MEV → 2 GEV USING RF = 2 GV

This is the initial acceleration of cooled muons. The bunch length decreases from 2 m to 20 cm. A single pass 2 GV linac is used. The RF frequency increases from 10 to 100 MHz from entrance to exit. 93% of the muons survive.

3 2 GEV → 25 GEV USING RF = 2.5 GV

This is the first recirculating ring and has 2.5 GV of 100 MHz RF [2]. A superconducting magnet with 10 bores, each with a different fixed field, is used to pass the muons through a pair of linacs 10 times. The design is similar to the TJNAF in Virginia. 92% of the muons survive.

4 25 GEV → 250 GEV USING RF = 6 GV

This stage uses a single ring of fast ramping $cos\,\theta$ dipoles [3]. Thin stranded copper conductor is used at room temperature to achieve a 4 Tesla field. The low duty cycle is exploited to keep the I^2R losses reasonable. 6 GV of 350 MHz RF is distributed around the ring and accelerates the muons from 25 GeV to 250 GeV in 40 orbits. 85% of the muons survive.

5 250 GEV → 2 TEV USING RF = 25 GV

For the final stage we consider two 2200 m radius hybrid rings [4] of fixed superconducting magnets alternating with iron magnets ramping at 200 Hz and 330 Hz between full negative and full positive field. Muons are given 25 GV of RF energy (800 MHz) per orbit. The RF is divided into multiple sections as at LEP, so that magnetic fields and energies will match around the rings. The first ring has 25% 8T magnets and 75% ±2T magnets and ramps from 0.5T to 3.5T during 54 orbits. The second has 55% 8T magnets and 45% ±2T magnets and ramps from 3.5T to 5.3T during 32 orbits. The packing fraction is taken as 70% in each ring. Acceleration is from 250 GeV/c to 2400 GeV/c and requires a total of 86 orbits in both rings; 82% of the muons survive.

Table 1: Fast ramping $cos\,\theta$ dipole parameters.

Coil inner radius	2 cm
Magnet length	10 m
Field	4 Tesla
Current	29.5 kA
Stored Energy	160 kJ
Inductance	370 μH
Coil Resistance	19 000 $\mu\Omega$
Ramp time, 10% to 90%	360 μS
Power Supply Voltage	31.2 kV
Storage Capacitance	340 μF
I^2R magnet heat per cycle	9400 J
Magnet temperature rise per cycle	0.13 ^{0}C
Power into magnet @ 15 Hz	141 kW
Number of Dipoles for a ring	144
Total power @ 15 Hz	20 MW

$$\text{SURVIVAL} = \prod_{N=1}^{86} \exp\left[\frac{-2\pi R m}{[250 + (25\,N)]\,c\tau}\right] = 82\% \quad (1)$$

Consider the power consumption of an iron magnet which cycles from a full -2T to a full +2T. First calculate the energy, W, stored in a 2T field in a volume 6 m long, .03 m high, and .08 m wide. μ_0 is $4\pi \times 10^{-7}$.

$$W = \frac{B^2}{2\mu_0}[\text{Volume}] = 23\,000 \text{ Joules} \quad (2)$$

Next given 6 turns, an LC circuit capacitor, and a 250 Hz frequency; estimate current, voltage, inductance, and capacitance. The height, h, of the aperture is .03 m. The top and bottom coils may be connected as two separate circuits to halve the switching voltage.

0-7803-4376-X/98/$10.00 © 1998 IEEE

$$B = \frac{\mu_0 NI}{h} \quad \rightarrow \quad I = \frac{Bh}{\mu_0 N} = 8000 \text{ Amps} \quad (3)$$

$$W = .5\,L\,I^2 \quad \rightarrow \quad L = \frac{2\,W}{I^2} = 720\,\mu\text{H} \quad (4)$$

$$f = \frac{1}{2\pi}\sqrt{\frac{1}{LC}} \quad \rightarrow \quad C = \frac{1}{L\,(2\pi f)^2} = 560\,\mu\text{F} \quad (5)$$

$$W = .5\,C\,V^2 \quad \rightarrow \quad V = \sqrt{\frac{2W}{C}} = 9000 \text{ Volts} \quad (6)$$

Now calculate the resistive energy loss, which over time is equal to 1/2 the loss at the maximum current of 8000 Amps. The 1/2 comes from the integral of cosine squared. A six-turn copper conductor 3 cm thick, 10 cm high, and 7800 cm long has an I^2R power dissipation of 15 kilowatts.

$$R = \frac{7800\ (1.8\,\mu\Omega\text{-cm})}{(3)\,(10)} = 470\,\mu\Omega \quad (7)$$

Now calculate the dissipation due to eddy currents in this conductor, which will consist of transposed strands to reduce this loss [5–7]. To get an idea, take the maximum B-field during a cycle to be that generated by a 0.05m radius conductor carrying 24000 amps. This ignores fringe fields from the gap which will make the real answer higher. The eddy current loss in a rectangular conductor made of square wires 1/2 mm wide with a perpendicular magnetic field is as follows. The width of the wire is w.

$$B = \frac{\mu_0 I}{2\pi r} = 0.096 \text{ Tesla} \quad (8)$$

$$P = [\text{Volume}]\frac{(2\pi f B w)^2}{24\rho} \quad (9)$$

$$= [.03\ .10\ 78]\,\frac{(2\pi\ 250\ .096\ .0005)^2}{(24)\,1.8\times 10^{-8}} = 3000 \text{ watts}$$

A similar calculation shows that the cooling water tube losses due to eddy currents can be held to 1200 watts. The tubes must be made of a high resistivity material such as 316L stainless steel.

Table 2: Soft magnetic material properties [8].

Material	Composition	ρ	B Max T	H_c Oe
		$\mu\Omega$-cm		
Pure Iron [9]	Fe 99.95, C .005	10	2.16	.05
1008 Steel	Fe 99, C .08	12	2.09	0.8
Grain–Oriented	Si 3, Fe 97	47	1.95	.1
NKK Super E-Core	Si 6.5, Fe 93.5	82	1.8	
Supermendur [10]	V 2, Fe 49, Co 49	26	2.4	.2
Hiperco 27 [11]	Co 27, Fe 71	19	2.36	1.7
Metglas 2605SC	Fe 81, B 14, Si 3	135	1.6	.03

Eddy currents must be reduced in the iron not only because of the increase in power consumption and cooling, but also because they introduce multipole moments which destabilize beams. If the laminations are longitudinal, it is hard to force the magnetic field to be parallel to the laminations near the gap. This leads to additional eddy current gap losses [12]. So consider a magnet with transverse laminations as sketched in Fig. 1 and calculate the eddy current losses. The yoke is either 0.28 mm thick 3% grain oriented silicon steel [13] or 0.025 mm thick Metglas 2605SC [14, 15]. The pole tips are 0.1 mm thick Supermendur [10] to increase the field in the gap [16].

$$\text{P(3\% Si–Fe)} = [\text{Volume}]\frac{(2\pi f B t)^2}{24\rho} = 27 \text{ kw} \quad (10)$$

$$= [6\,((.42\ .35) - (.20\ .23))]\,\frac{(2\pi\ 250\ 1.6\ .00028)^2}{(24)\,47\times 10^{-8}}$$

Similar calculations for the eddy current losses in a Metglas yoke and in Supermendur pole tips yield much lower values, 75 and 210 watts, respectively.

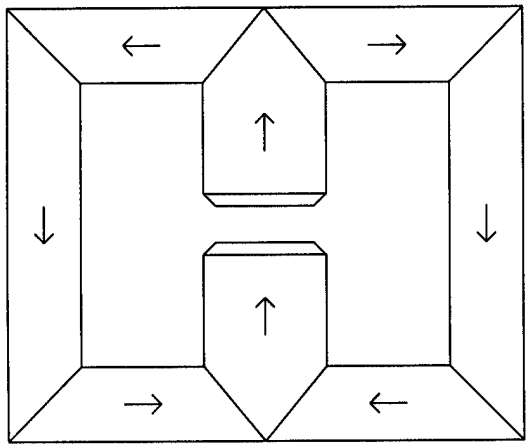


Figure 1: A two dimensional picture of an H frame magnet lamination with grain oriented 3% Si–Fe steel. The arrows show both the magnetic field direction and the grain direction of the steel. Multiple pieces are used to exploit the high permeability and low hysteresis in the grain direction [17]. If Metglas 2605SC is used for the yoke, multiple pieces are not needed, except for the poles. The pole tips are an iron–cobalt alloy for flux concentration exceeding 2 Tesla.

Eddy currents are not the only losses in the iron. Hysteresis losses, $\int \mathbf{H}\cdot d\mathbf{B}$, scale with the coercive force, H_c, and increase linearly with frequency. Anomalous loss [9] which is difficult to calculate theoretically must be included. Thus I now use functions fitted to experimental measurements of 0.28 mm thick 3% grain oriented silicon steel [18], 0.025 mm thick Metglas 2605SC [14], and 0.1 mm thick Supermendur [18].

$$\text{P(3\% Si–Fe)} = 4.38\times 10^{-4}\,f^{1.67}\,B^{1.87} \quad (11)$$

$$= 4.38\times 10^{-4}\,250^{1.67}\,1.6^{1.87}$$

$$= 10.7 \text{ w/kg} = 49 \text{ kw/magnet}$$

Table 3: Magnet core materials.

Material	Thickness (mm)	Density (kg/m^3)	Volume (m^3)	Mass (kg)
3% Si–Fe	0.28	7650	0.6	4600
Metglas	0.025	7320	0.6	4400
Supermendur	0.1	8150	0.01	90

$$\begin{aligned} \text{P(Metglas)} &= 1.9\times10^{-4}\, f^{1.51}\, B^{1.74} \qquad (12)\\ &= 1.9\times10^{-4}\, 250^{1.51}\, 1.6^{1.74}\\ &= 1.8 \text{ w/kg} = 7.9 \text{ kw/magnet} \end{aligned}$$

$$\begin{aligned} \text{P(Supermendur)} &= 5.64\times10^{-3}\, f^{1.27}\, B^{1.36} \qquad (13)\\ &= 5.64\times10^{-3}\, 250^{1.27}\, 2.2^{1.36}\\ &= 18 \text{ w/kg} = 1.6 \text{ kw/magnet} \end{aligned}$$

Table 4: Power consumption for a 250 Hz dipole magnet.

Material	3% Si–Fe	Metglas
Coil Resistive Loss	15 000 watts	15 000 watts
Coil Eddy Current Loss	4200 watts	4200 watts
Total Core Loss	50 600 watts	9500 watts
Total Loss	69 800 watts	28 700 watts

In summary, a 250 Hz dipole magnet close to 2 Tesla looks possible as long as the field volume is limited and one is willing to deal with stranded copper and thin, low hysteresis laminations. Total losses can be held to twice the I^2R loss in the copper alone, using Metglas.

The 1925 ramping dipoles which are required consume 56 megawatts when running. Given a 15 Hz refresh rate for the final muon storage ring [1], the average duty cycle for the 250 → 2400 GeV/c acceleration rings is 6%. So the power falls to 4 megawatts, which is small.

6 REFERENCES

[1] $\mu^+\mu^-$ *Collider: A Feasibility Study*, Juan C. Gallardo, editor, BNL–52503, Fermi Lab–Conf.–96/092, LBNL-38946 (18 June 1996) 481 pages.

[2] Q.–S. Shu, D. Neuffer, and S. Simrock, *Design of Three Re–Circulating Superconducting RF Accelerating Systems for a 4-TeV Muon Collider,* Proceedings, PAC'97, Vancouver, BC (12–16 May 1997) 9C.08.

[3] E. Willen, *Pulsed Dipole Magnets for the Muon Collider,* Proceedings, New Directions for High Energy Physics, Snowmass, CO (25 June – 12 July 1996).

[4] D. J. Summers, *Hybrid Rings of Fixed 8T Superconducting Magnets and Iron Magnets Rapidly Cycling between -2T and +2T for a Muon Collider,* Proc., New Directions for High Energy Physics, Snowmass, CO (25 June – 12 July 1996).

[5] H. Sasaki, *Magnets for Fast–Cycling Synchrotrons,* Invited talk at International Conference on Synchrotron Radiation Sources, Centre for Advanced Technology, Indore, India (3–6 February 1992); KEK 91-216 (March 1992).

[6] A. J. Otter, *A Prototype for the Booster Dipole,* TRIUMF, TRI-DN-89-K18 (February 1989).

[7] Alan J. Otter, *LAMPF Type Stranded Magnet Cable,* TRIUMF, TRI-DN-88-K12 (December 1988).

[8] *Metals Handbook, Properties and Selection of Metals,* Vol. 1, 8th Edition, American Society for Metals (1961).

[9] Chih-Wen Chen, *Magnetism and Metalurgy of Soft Magnetic Materials,* Dover Publications (1986).

[10] Arnold Engineering Company, 300 North West Street, Marengo, IL 60152.

[11] Carpenter Technology, 101 W. Bern St., Reading, PA 19603.

[12] W. O. Brunk and D. R. Walz, *A New Pulse Magnet Design Utilizing Tape Wound Cores,* 7th Natl. Part. Accel. Conf., Washington (12–14 March 1975) 1548; SLAC–PUB–1551 (March 1975) 4 pages.

[13] Producers of electrical steels include Armco, Allegheny Teledyne, and Warren Consolidated Industries in the United States; Kawasaki Steel, Nippon Steel, and NKK in Japan; AST in Italy; Thyssen in Germany; European ES in the U.K.; and Ugine ACG in France.

[14] Allied Signal, Amorphous Metals Division, 6 Eastmans Road, Parsippany, NJ 07054.

[15] Magnetics, Division of Spang & Company, 900 East Butler Road, Butler, PA 16003.

[16] R. A. Early, J. K. Cobb, and J.E. Oijala, *Design Calculations and Measurements of a Dipole Magnet with Permendur Pole Pieces,* IEEE Part. Accel. (1989) 351; SLAC-PUB-4883 (March 1989) 3 pages.

[17] P. Schwandt, *Comparison of Realistic Core Losses in the Booster Ring Dipole Magnets for Grain–Oriented and Ordinary Lamination Steels,* TRIUMF-DN-89-K31 (Apr 1989).

[18] Wm. T. McLyman, *Magnetic Core Selection for Transformers and Inductors,* Marcel Decker, ISBN 0-8247-1873-9 (1982).

Table 5: 4 acceleration stages; 60% $\mu^\pm$ survival overall.

	Linac	10 Bore SC Magnet	Cu $\cos\theta$ Magnet	Iron & SC Magnets
E(GeV)	0.1→2	2→25	25→250	250→2000
RF(MHz)	10→100	100	350	800
N(turns)	1	10	40	86
RF(GV)	2	2.5	6	25
Length(km)	0.4	0.36	2.3	14
τ(ms)	0.0013	0.012	0.307	4.0
μ Bunch(cm)	200→20	6	2	1
μ Survival	93%	92%	85%	82%

RESULTS OF BLOWOUT REGIME PROPAGATION EXPERIMENTS OF AN ELECTRON BEAM IN A PLASMA

N.Barov[1], M.Conde[2], W. Gai[2] and J.B.Rosenzweig[1]
[1]Dept. of Physics and Astronomy, UCLA, 405 Hilgard Ave., Los Angeles, CA 90095
[2]Argonne National Laboratory, 9700 S.Cass Ave., Argonne IL 60439

I. INTRODUCTION

When a tightly focused electron beam propagates in an underdense plasma (beam density greater than the plasma electron density, $n_b > n_0$), the plasma electrons are expelled radially by the space-charge of the beam, forming an ion channel which in turn provides a uniform, linear focusing force on the beam. When the beam is short ($\sigma_z < 2k_p^{-1}$), making it suitable as a driver for plasma wake-field acceleration (PWFA)[3], requirements on the beam properties (current, eminence and energy) to achieve ion channel self-focusing become more difficult to satisfy[10]. If the beam is initially β-matched to the focusing gradient, that is, the β-function is initially equal to $\beta_{eq} = \sqrt{\gamma / 2\pi r_e n_0}$, where σ_r and ε, are the rms transverse beam radius and emittance, the transverse distribution in the body of the beam is nearly stationary, while that near the head expands radially. The loss in beam density near the head associated with this expansion further retards the plasma electron response and causes the pinch point (where sufficient focusing gradient develops) to move backwards in the beam frame. The fast relaxation distance for these beam head dynamics is roughly $4\beta_{eq}$, or 5 cm for our experimental conditions, which is less than half of the plasma length, $L_p = 12$ cm.

The present experiments were motivated by the proposed use of the underdense regime as the basis for a PWFA[8] (the blowout regime) which is very attractive in terms of drive and accelerating beam guiding, in that when a plasma-electron free ion column is formed, the focusing force in this region is linear and the acceleration gradient is independent of radius.

II. EXPERIMENTAL SETUP

The plasma chamber used in the experiments is shown in Fig. 1, with 14.5 MeV electron pulses derived from the Argonne Wakefield Accelerator (AWA)[14] entering from the left. Beam diagnostics immediately upstream of the plasma chamber include an energy spectrometer, an emittance measurement system, an integrating current transformer (ICT) and Faraday cup to measure Q, a phosphor screen and at the focal point of the β-matching solenoid, an optical transition radiation (OTR) screen to obtain transverse beam profile images.

The plasma is created by a DC hollow cathode arc discharge, running at 55 V and 40 A, with Ar gas fed between concentric tantalum tubes. The (approximately 25% ionization fraction) plasma density, which is in the region of $n_0 = 1.15 \times 10^{13}$ cm^{-3}, is mapped with a cylindrical Langmuir probe (calibrated with a 140 GHz microwave interferometer), and found to be within 10 percent of the peak value over the nominal plasma length, $L_p \cong 12$ cm, with a steep initial ramp near the cathode tip. The half-maximum point, located 9 mm downstream of the cathode, is 12.25 cm away from the diagnostic-filled anode.

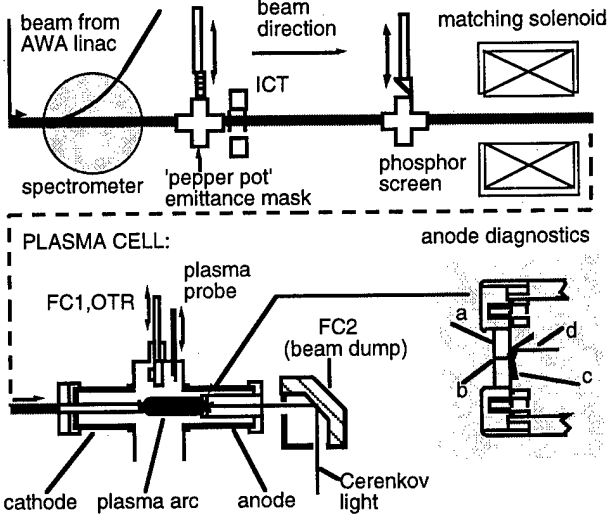


Fig. 1 Diagnostics beamline and plasma cell (shown without the plasma radial confinement solenoid). The anode diagnostics include (a) tungsten collimator with (b) 1 mm wide slit, (c) 500 μm thick quartz Cerenkov radiator, and (d) mirror and outgoing light.

III. EXPERIMENTAL RESULTS

The bunch charge Q was measured for every shot using the nondestructive integrating current transformer (ICT). Prior to this, the small fraction of charge scraped at the cathode assembly aperture must be quantified with simultaneous measurements with the ICT and FC1, the Faraday cup following the cathode. The focal spot size near the waist of the β-matching solenoid was measured with the OTR screen at FC1. Some of these profiles deviated significantly from the cylindrical symmetry assumed in the simulations; the shots characterized by an ellipse with an aspect ratio higher than 2:1 (25% of the population) were discarded. The remaining images were tested for peak intensity as well as for fractional integrated intensity inside a test radius of 0.28 mm. A symmetric Gaussian with $\sigma_x = \sigma_y = \sigma_r$, having the same integral defines an effective radius, which was found to be nearly independent of Q, with mean value of $\sigma_r = 284 \pm 24$ μm. The presence of shots

0-7803-4376-X/98/$10.00 © 1998 IEEE

with mild eccentricities causes the effective Gaussian profile to underestimate the peak beam density, predicting n_b / n_0=2.0 at 14 nC (this assumes a 25 psec FWHM bunch length). The actual value from the peak intensity in the image data is n_b / n_0=2.0 and 2.5 at Q=7 and 14 nC, respectively. The plasma is therefore well underdense at beam input for all experimental conditions. The beam divergence $\sigma_{x'}$ and bunch length were measured using the anode diagnostics, including a 1-mm wide (and 4 mm deep) tungsten slit aperture followed by a 0.5 mm thick Cerenkov emitter inclined 12 degrees to the beam direction. The light is sent to either a CCD camera for time-integrated imaging or to the 2 psec resolution streak camera. The beam charge after collimation by the slit aperture is measured at the Faraday cup following the anode, FC2. The beam divergence $\sigma_{x'}$, is sampled by recording the transverse profile along the slit after it has drifted $\cong$12cm, and fitting a Gaussian. The beam divergence is 18.5 mrad at 14 nC and decreases linearly to 15.5 mrad at 7 nC, yielding $\varepsilon_n = 149$ and 130 mm-mrad and initial β_i=1.52 and 1.74 cm, for high and low charge, respectively. The b-function in these cases is only slightly mismatched to the ion focusing $\beta_{eq} = 1.25$ cm. The input bunch length is measured by refocusing the beam on the anode, with the Cerenkov light analyzed using a Hammamatsu C1587 streak camera; the bunch length is found to be 25 ± 3 psec FWHM.

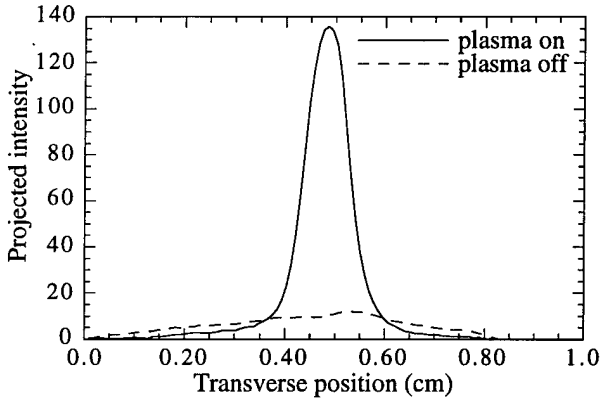


Fig. 2 Transverse beam profile after collimation, from digitized CCD camera image of Cerenkov light.

After the beam is collimated, the transmitted charge Q_{tr} is recorded on the downstream Faraday cup FC2. With plasma focusing, a substantial fraction, $\eta = Q_{tr} / Q$, of the initial charge ought to be transmitted through the slit, serving as an independent measure of the beam radius. With the plasma arc on, the downstream Cerenkov profile, as shown in Fig. 2, displays a narrow, intense peak as a result of ion focusing. The x-projected FWHM of a typical case (Fig 5) is 0.9 mm, 40% broader than at the start of the plasma, but consistent with the radial spreading at the beam head predicted by simulations, and markedly different than the no-plasma background. As the beam's transverse centroid jitter is significant on the scale of the slit aperture, shots with the y-peak too close to one of the aperture edges were rejected. The values of η selected in this way for an initially matched ($z_0 = 0$) case are displayed in Fig. 3 along with the results of simulations, as explained below. The low-η data points, especially at low Q, are thought to result from beam conditions differing from cylindrical symmetry, one possibility being a beam with a double-peaked y-profile starting from irregular initial conditions. Some of the spread in the data also undoubtedly comes from fluctuations in the initial beam aspect ratio, which give rise to quadrupole as well as monopole beam motion.

The simulation results given in Fig. 3 use the plasma fluid code NOVO[7], modified to include a super-particle representation of the beam electrons as described in [9]. The results of this code have been benchmarked against an electromagnetic particle-in-cell (PIC) code; the calculation of transmission efficiency is nearly the same, being smaller in NOVO by 4%, and so NOVO was employed for this analysis because of its speed. The calculations use 8000 beam particles, initialized to a thermal distribution derived from the measured beam size and divergence.

A more detailed view of the underlying dynamics is offered by the time-resolved streak camera analysis. These images contain information only about longitudinal and horizontal profiles, as measured in a 20 μm vertical strip in the center of the slit aperture. The beam was determined to be adequately vertically centered in this measurement by requiring $\eta \geq 0.45$. A streak image obtained in this way is shown in Fig. 4, displaying the predicted flaring of the distribution outward at the beam head.

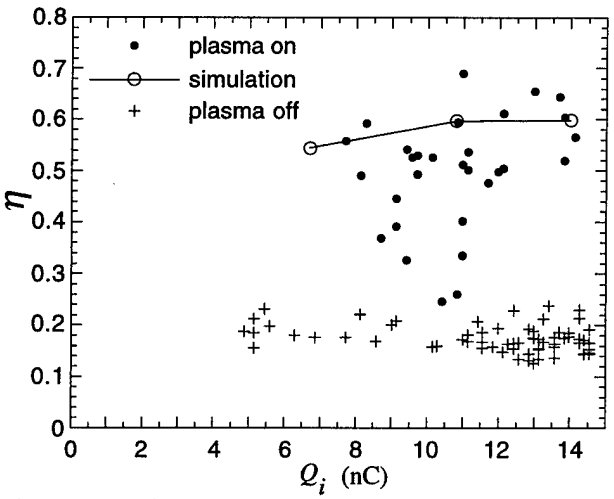


Fig. 3 Transmission data and simulations for an initially nearly β-matched case.

Each image that was analyzed further was sliced into short (5.7 psec) t-sections, and for every t-slice the integrated (in x) intensity, and a measure of the beam width defined by the region $-x_{1/2} \leq x \leq x_{1/2}$ containing half the integrated intensity were determined. The results of this analysis for 10 images within narrow input charge window ($10.2 < Q < 11.8$ nC) were summed to produce a composite picture of the beam distribution,

shown in Fig. 5, along with the accompanying rms error and PIC simulation results, analyzed to give beam width as a function of t-slice. The experimental data and PIC simulations clearly display a profile flared at the beam head due to radial expansion, as well as a beam core which is nearly matched and slightly larger, $\sigma_r \cong 370\ \mu m$, than at input. The simulation's agreement with the data is quite good, with a notable deviation in that the experimental results show less pronounced beam head expansion. This may be due to the assumption of a beam with a thermal input transverse phase space, which is not strictly correct for a photoinjector-derived beam, where the emittance of a single t-slice of the beam is smaller than the full beam[16].

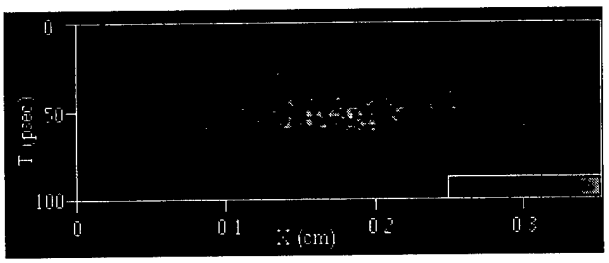


Fig. 4. Streak camera image of plasma exit beam profile.

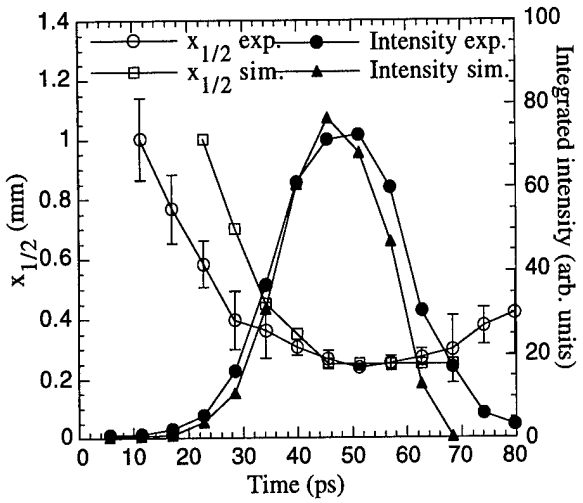


Fig. 5 Time-slice dependence of beam intensity and half-width, from experiment (exp.) and PIC simulation (sim.).

IV. CONCLUSIONS AND FUTURE WORK

In conclusion, short intense relativistic bunches, of the kind available from rf photoinjectors, have been observed, through integrated and time-dependent imaging, as well as collimator transmission, to effectively self-guide in an underdense plasma over many times the initial β-function. Picosecond-resolution measurement of transverse beam size displays the trumpet-shaped beam head predicted by simulations and analysis[10,11]. The simulations are in good quantitative agreement with the beam sizes and transmissions obtained from experiment, with deviations arising from the approximations involved in the simulation model of the beam.

In the next round of experiments, starting June '97, we plan to use a very similar set of experimental conditions to demonstrate high gradient acceleration in a PWFA, by measuring the energy changes of a witness beam propagating in the wake-field of the more intense drive bunch. The beam diagnostics developed for the present work, together with recent improvements to the AWA facility ($\cong$18 ps FWHM bunch length for Q=90 nC [18]), will greatly facilitate the measurement of high-gradient wake-fields. The peak acceleration gradient predicted for this experiment is in the range of 80 to 150 MeV/m, much higher than an earlier experiment at the AWA[9], which yielded 4 - 10 MeV/m. To measure this, we plan, like in the earlier experiment, to generate the witness beam in the same photocathode cavity as the drive beam[9], but additionally to time-resolve the final energy distribution of both beams using the streak camera. This strategy is necessary to overcome the 'shadow' effect occurring when the drive and witness beams overlap in energy.

ACKNOWLEDGMENTS

The authors would like to thank E. Colby, A. Murokh, P. Schoessow and J. Simpson for aid and advice along the way. This work supported by U.S. Dept. of Energy grants DE-FG03-93ER40796 and W-31-109-ENG-38, and the Alfred P. Sloan Foundation grant BR-3225. A more detailed account of this work has been submitted to Physical Review Letters under the title "Propagation of Short Electron Pulses in a Self-formed Ion Channel".

REFERENCES

[1] W.E. Martin, *et al, Phys. Rev. Lett.* **54**, 685 (1985).
[2] P. Chen, *et al, Phys.Rev.Lett.* **54**, 693 (1985), J.B.Rosenzweig, *et al., Phys.Rev.Lett.* **61**, 98 (1988).
[3] G.Hairapetian, *et al, Phys.Rev.Lett.* **72**, 1244 (1994), H. Nakanishi, *et al., Phys.Rev.Lett.* **66**, 177 (1991).
[4] B.N.Breizman, T.Tajima, D.L.Fisher, and P.Z.Chebotaev (unpublished).
[5] J.B.Rosenzweig, *et al., Phys.Rev.A* **44**, R6189 (1991).
[6] N. Barov, *et al., Proc. 1995 Particle Accelerator Conference,* 631 (IEEE, 1995).
[7] N. Barov and J.B.Rosenzweig, *Phys.Rev. E* **49**, 4407 (1994).
[8] J. Krall, *et al., Phys. Fluids B* **1**, 2099 (1989).
[9] J. Krall and G. Joyce, in *Advanced Accel. Concepts* p.505 (AIP Conf. Proc. 335, 1995).
[10] P. Schoessow, *et al., Proc. 1995 Particle Accelerator Conference,* 976 (IEEE, 1996).
[11] X. Qiu, *et al., Phys.Rev.Lett.* **76**, 3723 (1996).
[12] J.Power, *et al.: Proc. of the 7th Workshop on Advanced Accelerators*, Lake Tahoe, CA (1996)
[13] M.E.Conde, et al.,These proceedings.

FEMTOSECOND ELECTRON BUNCHES FROM COLLIDING LASER PULSES IN PLASMAS

E. Esarey, R.F. Hubbard, W.P. Leemans,* A. Ting, and P. Sprangle
Beam Physics Branch, Plasma Physics Division, Naval Research Laboratory, Washington DC 20375

Abstract

An injector and accelerator is analyzed that uses three collinear laser pulses in a plasma: a pump pulse, which generates a large wakefield ($\geq$ 20 GV/m), and two counterpropagating injection pulses. When the injection pulses collide, a slow phase velocity beat wave is generated that injects electrons into the fast wakefield for acceleration. Particle tracking simulations in 1-D with injection pulse intensities near 10^{17} W/cm^2 indicate the production of high energy electrons with bunch durations as short as 3 fs, energy spreads as small as 0.3%, and densities as high as 10^{18} cm^{-3}.

1 INTRODUCTION

Plasma-based accelerators [1] may provide a compact source of high energy electrons due to their ability to sustain ultrahigh electric fields E_z on the order of $E_0 = cm\omega_p/e \simeq n_0^{1/2}[\mathrm{cm}^{-3}]$ V/cm, where $\omega_p = (4\pi n_0 e^2/m)^{1/2}$ is the plasma frequency and n_0 is the plasma density. Accelerating fields of 10-100 GV/m have been generated over distances of a few mm [2-4] in both the standard [5] and self-modulated [6,7] regimes of the laser wakefield accelerator (LWFA). The characteristic scalelength of the accelerating plasma wave is the plasma wavelength $\lambda_p = 2\pi c/\omega_p$, which is typically $\leq$ 100 μm. Although several recent experiments [3,4] have demonstrated the self-trapping and acceleration of plasma electrons in the self-modulated LWFA, the production of electron beams with relatively low momentum spread and good pulse-to-pulse energy stability will require injection of ultrashort electron bunches into the wakefield with femtosecond timing accuracy. These requirements are beyond the current state-of-the-art performance of photo-cathode radio-frequency electron guns.

Recently an all-optical method for injecting electrons in a standard LWFA has been proposed [8]. This method (referred to as LILAC) utilizes two laser pulses which propagate either perpendicular or parallel to one another. The first pulse (the pump pulse) generates the wakefield, and the second pulse (the injection pulse) intersects the wakefield some distance behind the pump pulse. The ponderomotive force $F_p \sim \nabla a^2$ of the injection pulse can accelerate a fraction of the plasma electrons such that they become trapped in the wakefield, where $a^2 \simeq 7\times 10^{-19}\lambda^2[\mu\mathrm{m}]I[\mathrm{W/cm}^2]$, $\lambda = 2\pi c/\omega$ is the laser wavelength, and I the intensity. Simulations, which were performed for ultrashort pulses at high densities ($\lambda_p/\lambda = 10$ and $E_z/E_0 = 0.7$), indicated the production of a 10 fs, 21 MeV electron bunch with a 6% energy spread. However, high intensities ($I > 10^{18}$ W/cm^2) are required in both the pump and injection pulses ($a \simeq 2$). An all optical electron injector would be a significant step in reducing the size and cost of a LWFA.

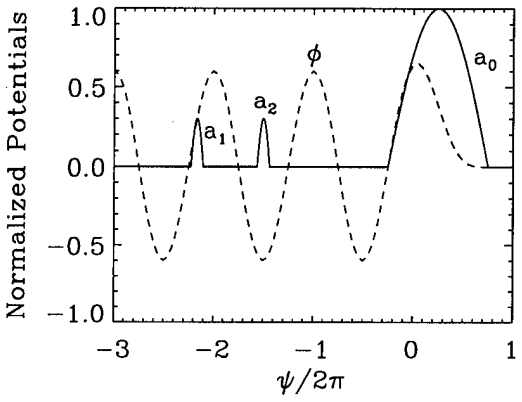


Figure 1: Profiles of the pump laser pulse a_0, the wakefield ϕ, and the forward a_1 injection pulse, all of which are stationary in the $\psi = k_p(z - v_{p0}t)$ frame, and the backward injection pulse a_2, which moves to the left at $\simeq 2c$

In the following, a colliding pulse optical injection scheme for a LWFA is proposed and analyzed that uses three short laser pulses: an intense pump pulse (denoted by subscript 0), a forward going injection pulse (subscript 1), and a backward going injection pulse (subscript 2), as shown in Fig. 1. The frequency, wavenumber, and normalized intensity are denoted by ω_i, k_i, and a_i ($i = 0, 1, 2$). Furthermore, $\omega_1 = \omega_0$, $\omega_2 = \omega_0 - \Delta\omega$ ($\Delta\omega \geq 0$), and $\omega_0 \gg \Delta\omega \gg \omega_p$ are assumed such that $k_1 = k_0$, and $k_2 \simeq -k_0$. The pump pulse generates a fast ($v_{p0} \simeq c$) wakefield. When the injection pulses collide (some distance behind the pump) they generate a slow ponderomotive beat wave with a phase velocity $v_{pb} \simeq \Delta\omega/2k_0$. During the time in which the two injection pulses overlap, a two-stage acceleration process can occur, i.e., the slow beat wave injects plasma electrons into the fast wakefield for acceleration to high energies. It will be shown that injection and acceleration can occur at low densities ($\lambda_p/\lambda \sim 100$), thus allowing for high single-stage energy gains, with normalized injection pulse intensities of $a_1 \sim a_2 \sim 0.2$ ($\sim 10^2$ less intensity than required by the LILAC scheme). Furthermore, the colliding pulse concept offers detailed control of the injection process: the injection phase can be controlled via the position of the forward injection pulse, the beat phase velocity via $\Delta\omega$, the injection energy via the

* Lawrence Berkeley National Laboratory, Berkeley CA 94720

0-7803-4376-X/98/$10.00 © 1998 IEEE

pulse amplitudes, and the injection time (number of trapped electrons) via the backward pulse duration.

2 ANALYSIS

The colliding pulse injection mechanism will be analyzed in 1-D with the plasma wave and laser fields represented by the normalized scalar $\phi = e\Phi/mc^2$ and vector $a = eA_\perp/mc^2$ potentials, respectively. The axial component of the normalized electron momentum $u_z = p_z/mc = \gamma\beta_z$ obeys $du_z/dct = \partial\phi/\partial z - (2\gamma)^{-1}\partial a^2/\partial z$, where $\gamma = \gamma_z\gamma_\perp$, $\gamma_\perp = (1+a^2)^{1/2}$, and $\gamma_z = (1-\beta_z^2)^{-1/2}$. This can be written in terms of the phase of the electron with respect to the wakefield $\psi = k_p(z - v_{p0}t)$, i.e.,

$$\frac{d^2\psi}{d\tau^2} = \frac{(1-\beta_z^2)}{\gamma}\frac{\partial\phi}{\partial\hat{z}} - \frac{1}{\gamma^2}\left(\frac{\partial}{\partial\hat{z}} + \beta_z\frac{\partial}{\partial\tau}\right)\frac{a^2}{2}, \qquad (1)$$

where $k_p = \omega_p/c$, $v_{p0} = c\beta_{p0}$ is the wakefield phase velocity, $\hat{z} = k_p z$, $\tau = \omega_p t$, and $\beta_z = d\psi/d\tau + \beta_{p0}$.

The effects of three waves will be considered: a plasma wakefield $\phi = \hat{\phi}(\psi)\cos\psi$, and a forward and a backward injection laser pulse, both of the form $a_i = \hat{a}_i(z - v_{gi}t)(\sin\theta_i e_x + \cos\theta_i e_y)$. Here, $\theta_i = k_i z - \omega_i t$ and the amplitudes $\hat{a}_i$ and $\hat{\phi}$ are assumed to be slowly varying compared to the phases θ_i and ψ. Also, k_i and ω_i satisfy $k_i = \sigma_i\omega_i(1 - \omega_p^2/\omega_i^2)^{1/2}$, where $\sigma_1 = 1$ and $\sigma_2 = -1$, which implies a group velocity $v_{gi} = c\beta_{gi} = c^2k_i/\omega_i$ ($v_{p0} = v_{g0} = v_{g1}$). Furthermore, $a^2 = \hat{a}_1^2 + \hat{a}_2^2 + 2\hat{a}_1\hat{a}_2\cos\psi_b$, where $\psi_b = \theta_1 - \theta_2 = \Delta k(z - v_{pb}t)$ is the beat phase, $v_{pb} = c\beta_{pb} = \Delta\omega/\Delta k$, and $\Delta k = k_1 - k_2 \simeq 2k_0$.

In the absence of the injection pulses, electron motion in the wakefield is described by the Hamiltonian [9] $H_w = \gamma - \beta_{p0}(\gamma^2 - 1)^{1/2} - \phi$, where $\phi = \phi_0\cos\psi$. The boundary between trapped and untrapped orbits is given by the separatrix $H_w(\gamma,\psi) = H_w(\gamma_{p0},\pi)$, where $\gamma_{p0} = (1-\beta_{p0}^2)^{-1/2}$. The minimum momentum of an electron on the separatrix is given by $u_{min} \simeq (1/\Delta\phi - \Delta\phi)/2$, where $\Delta\phi = \phi_0(1+\cos\psi)$, assuming $\gamma_{p0}\Delta\phi \gg 1$ and $\beta_{p0} \simeq 1$. In particular at $\psi = 0$, $u_{min} = 0$ for $\phi_0 = 1/2$, which means that an electron that is at rest at the phase $\psi = 0$ will be trapped. The background plasma electrons, however, are untrapped and are undergoing a fluid oscillation with a momentum $u_f \simeq -\phi$ ($\phi^2 \ll 1$). Hence, at $\psi = 0$, the plasma electrons are moving backward with $u_f \simeq -\phi_0$, which is far from the trapping threshold.

The beat wave leads to formation of phase space buckets (separatrices) of width $2\pi/\Delta k \simeq \lambda_0/2$, which are much shorter than those of the wakefield (λ_p), thus allowing for a separation of time scales. In particular, it can be shown that both the transit time $2\pi/\Delta\omega$ of an untrapped electron through a beat wave bucket and the synchrotron (bounce) time $\pi/(\hat{a}_1\hat{a}_2)^{1/2}\omega_0$ of a deeply trapped electron in a beat wave bucket are much shorter than a plasma wave period $2\pi/\omega_p$. Hence, on the time scale in which an electron interacts with a single beat wave bucket, the wakefield can be approximated as static.

In the combined fields, the electron motion can be analyzed in the local vicinity of a single period of the beat wave by assuming that the wakefield electric field $E_z = -k_p^{-1}E_0\partial\phi/\partial z \simeq E_{z0}$ is constant. The Hamiltonian associated with Eq. (1) is given by

$$H_b \simeq \gamma - \beta_{pb}\left[\gamma^2 - \gamma_\perp^2(\psi_b)\right]^{1/2} + \epsilon\psi_b, \qquad (2)$$

where $\epsilon = E_{z0}k_p/E_0\Delta k$ is constant and $\gamma_\perp^2 = 1 + \hat{a}_1^2 + \hat{a}_2^2 + 2\hat{a}_1\hat{a}_2\cos\psi_b$. When $\epsilon = 0$, the phase space orbits are symmetric with respect to ψ_b. In terms of the normalized axial momentum, the maximum and minimum points on the separatrix are given by $u_{bm} \simeq \beta_{pb}\gamma_{bp}(1 + 4\hat{a}_1^2)^{1/2} \pm 2\hat{a}_1\gamma_{pb}$, where $\gamma_{pb} = (1-\beta_{pb}^2)^{-1/2}$ and $\hat{a}_1 = \hat{a}_2$ is assumed. When $\epsilon \neq 0$, the separatrix distorts into fished-shape islands. In particular, when $\epsilon < 0$ ($\epsilon > 0$), the "fish tail" of the separatrix opens to the right (left).

A scenario by which the beat wave leads to trapping in the plasma wave is the following. In the phase region $-\pi/2 < \psi < 0$, the plasma electrons are flowing backward, $u_f = -\phi_0\cos\psi < 0$, and the electric field is accelerating, $E_z/E_0 = \phi_0\sin\psi < 0$. Here $\epsilon < 0$ and the beat wave buckets open to the right. Consider an electron that is initially flowing backward and resides below the beat wave separatrix. Since the separatrix opens to the right, there exists open orbits which can take an electron from below to above the beat wave separatrix. Such an electron can acquire a sufficiently large positive velocity to allow trapping and acceleration in the plasma wave. These open phase space orbits, which provide the necessary path for electron acceleration, can exist when the beat wave resides within $-\pi/2 < \psi < 0$.

An estimate for the threshold for injection into the wakefield can be obtained by considering the effects of the wakefield and the beat wave individually and by requiring (i) the maximum energy of the beat wave separatrix exceed the minimum energy of the wakefield separatrix, $u_{bmax} \geq (\Delta\phi^{-1} - \Delta\phi)/2$, and (ii) the minimum momentum of the beat wave separatrix be less than the plasma electron fluid momentum, $u_{bmin} \leq -\phi$. These two conditions imply that the beat wave separatrix overlaps both the wakefield separatrix and the plasma fluid oscillation, thus providing a phase-space path for plasma electrons to become trapped in the wakefield. For a given wakefield amplitude ϕ_0, conditions (i) and (ii) imply the optimal phase location $3\phi_0\cos\psi \simeq 3^{1/2} - 2\phi_0 - 2\beta_{pb}$ and threshold amplitude $6\hat{a}_1 > 3^{1/2} - 2\phi_0 + \beta_{pb}$ of the injection pulse, where $\phi_0^2\cos^2\psi \ll 1$, $\hat{a}_1^2 \ll 1$, and $\beta_{pb}^2 \ll 1$ were assumed. For example, $\phi_0 = 0.6$ and $\beta_{pb} = 0.05$ imply $\psi = -1.3 - 2\pi j$ and $\hat{a}_1 > 0.11$.

3 SIMULATION

To further evaluate the colliding laser injection method, the motion of test particles in the combined wake and laser fields was simulated by numerically solving Eq. (1). At $\tau = 0$, the forward (backward) pulse profile $\hat{a}_1$ ($\hat{a}_2$) is a half-period of a sine wave with maximum amplitude

a_{1m} (a_{2m}), centered at $\psi = \psi_1 < 0$ ($\psi_2 > 0$), with length L_1 (L_2). Test particles are loaded uniformly from $\psi = 0$ to $\psi = \psi_{max}$ with $d\psi/d\tau = -\beta_{p0}$ (initially at rest) and pushed from $\tau = 0$ to $\tau = \tau_{max}$. Also, $\hat{\phi} = \phi_0 \left[1 - \exp(-\psi^2/\pi^2)\right]$ for $\psi \leq 0$.

To validate the analytical predictions for the trapping thresholds, a "near threshold" case was simulated with $\omega_1/\omega_p = 100$, $\omega_2/\omega_p = 90$, and $\phi_0 = 0.6$, which for $\lambda_1 = 2\pi c/\omega_1 = 1$ μm implies $n_0 \simeq 10^{17}$ cm^{-3} and $E_z = 0.6E_0 \simeq 19$ GV/m. Also, $a_{1m} = a_{2m} = 0.3$ (1.2×10^{17} W/cm^2), $L_1 = L_2 = \lambda_p/8$ (42 fs), $\psi_1 = -13.6$ and $\psi_2 = 21.4$ (chosen so the beat wave and test particles overlap). After a propagation distance of $\tau_{max} = 300$ (0.48 cm), trapped electrons were observed with a bunch length $L_b = 6.3$ μm (21 fs) with 60% of the electrons are contained within 66 MeV $\pm$8%. The fraction f_{tr} of those particles which encounter the beat wave that become trapped was $f_{tr} \simeq 30\%$. A numerical optimization of the parameters was also performed to determined the trapping threshold. The optimal phase for injection (which minimizes the value of a_{1m} required for trapping) was found to be $\psi_1 = -13.8$, in good agreement with theory. Furthermore, trapping was observed for $a_{1m} > 0.17$, somewhat higher than the analytical prediction (0.11). Additional simulations indicate that trapping occurs when the center of the $L_1 = \lambda_p/8$, $a_{1m} = 0.3$ pulse is located within $-14.2 \leq \psi_1 \leq -13.5$. This implies that the forward pulse must be synchronized to the wake with an accuracy < 37 fs, which is not a serious constraint and can be relaxed somewhat by using a longer forward pulse.

More dramatic results can be obtained by moving the position of the injection pulse slightly forward and increasing both duration and amplitude of the injection pulses (in comparison to the previous "near threshold" example). As an example, a simulation was performed with $\psi_1 = -12.6$, $a_{1m} = a_{2m} = 0.5$, $\phi_0 = 0.7$, $L_1 = L_2/4 = \lambda_p/4$, $\omega_1/\omega_p = 100$, and $\omega_2/\omega_p = 85$ ($\lambda_1 = 0.85$ μm, $\lambda_2 = 1$ μm, and $\lambda_p = 85$ μm). After a distance of $\tau_{max} = 100$ (0.14 cm), the results are quite dramatic: a bunch duration of 2.9 fs was obtained due to natural compression provided by the axial electric field, with a mean energy of 27 MeV and a standard deviation in energy of 0.32%. The trapping fraction is $f_{tr} \simeq 19\%$ and the bunch density is $n_b = 1.8 \times 10^{18}$ cm^{-3}. Furthermore, in this run, the trapped electron are injected into and remain within a phase region of the wakefield that is both accelerating and focusing.

The bunch density is $n_b \simeq f_{tr} n_0 L_z/L_b$, where $L_z \simeq (L_1 + L_2)/2$ is the length of plasma that encounters the overlapping pulses. Assuming that the 1-D results hold for a pump laser of radius r_0 implies a total number of trapped electrons $N_b \simeq f_{tr} n_0 L_z \pi r_0^2$, e.g., $N_b \simeq 7.7 \times 10^9$ for Fig. 4 with $r_0 = 40$ μm. Note that N_b can be increased by increasing n_0, r_0, a_{1m} (via f_{tr}) and, in particular, L_z by increasing the duration of the backward pulse L_2. The ratio of N_b to the theoretical beam loading limit N_0 [10] is $N_b/N_0 = f_{tr} k_p L_z E_0/E_z$, which can easily approach unity. For N_b near N_0, however, space-charge effects become important and a self-consistent simulation is required.

In summary, a method has been proposed and analyzed for injecting plasma electrons into a large wakefield using two colliding laser pulses. Simulations of test electrons in prescribed 1-D fields indicate the production of relativistic ($\geq$ 25 MeV) electrons with bunch durations as short as 3 fs, energy spreads as small as 0.3%, and densities as high as 10^{18} cm^{-3}.

4 ACKNOWLEDGEMENTS

The authors acknowledge the assistance of C. Schroeder and P.B. Lee. This work was supported by the Department of Energy and the Office of Naval Research.

5 REFERENCES

[1] For a recent review, see E. Esarey et al., IEEE Trans. Plasma Sci. **PS-24**, 252 (1996).

[2] J.R. Marques et al., Phys. Rev. Lett. **76**, 3566 (1996); C.W. Siders et al., Phys. Rev. Lett. **76**, 3570 (1996); A. Ting et al., Phys. Rev. Lett. **77**, 5377 (1996); S.P. LeBlanc et al., Phys. Rev. Lett. **77**, 5381 (1996).

[3] K. Nakajima et al., Phys. Rev. Lett. **74**, 4428 (1995); C. Coverdale et al., Phys. Rev. Lett. **74**, 4659 (1995); A. Modena et al., Nature **377**, 606 (1995); D. Umstadter et al., Science **273**, 472 (1996).

[4] A. Ting et al., Phys. Plasmas **4**, 1889 (1997).

[5] T. Tajima and J.M. Dawson, Phys. Rev. Lett. **43**, 267 (1979); P. Sprangle et al., Appl. Phy. Lett. **53**, 2146 (1988); L.M. Gorbunov and V.I. Kirsanov, Sov. Phys. JETP **66**, 209 (1987).

[6] P. Sprangle et al., Phys. Rev. Lett. **69**, 2200 (1992); T.M. Antonsen and P. Mora, Phys. Rev. Lett. **69**, 2204 (1992); N.E. Andreev et al., JETP Lett. **55**, 571 (1992); E. Esarey et al, Phys. Fluids B **5**, 2690 (1993).

[7] E. Esarey, J. Krall, and P. Sprangle, Phys. Rev. Lett. **72**, 2887 (1994); W.B. Mori et al., Phys. Rev. Lett. **72**, 1482 (1994); N.E. Andreev, V.I. Kirsanov, and L.M. Gorbunov, Phys. Plasmas **2**, 2573 (1995).

[8] D. Umstadter, J.K. Kim, and E. Dodd, Phys. Rev. Lett. **76**, 2073 (1996).

[9] E. Esarey and M. Pilloff, Phys. Plasmas **2**, 1432 (1995).

[10] T. Katsouleas et al., Particle Accelerators **22**, 81 (1987).

THE ARGONNE WAKEFIELD ACCELERATOR: UPGRADE SCENARIOS AND FUTURE EXPERIMENTS

W. Gai, M. Conde, R. Konecny, X. Li, J. Power, P. Schoessow and J. Simpson
Argonne National Laboratory, Argonne, IL 60439, USA

Abstract

The Argonne Wakefield Accelerator is presently operational and nearing completion of its initial dielectric structure- and plasma-based experimental program. In this paper a number of possible future improvements and directions for the AWA are discussed including photocathode source upgrades, laser pulse and beam shaping options, multiple drive bunch generation, and novel wakefield device measurements. Plans for a 1 GeV demonstration wakefield accelerator will be presented.

1 INTRODUCTION

Generating and accelerating high charge and short electron beams have been one of the areas of study for the Argonne Wakefield Accelerator. So far, AWA has demonstrated the capability of producing 100 nC, 20 — 30 ps (FWHM) electron beams at 14 MeV. This unprecedented performance was obtained using a novel half cell photocathode gun cavity and two standing wave iris-loaded linac sections [1,2]. The AWA machine has reached its design goal and has been used for dielectric wakefield [3] and plasma [4] experiments. The initial results are encouraging. Achieving higher gradients in wakefield experiments would require the drive electron pulse to be even shorter and have a lower emittance. Another requirement for both high gradient and sustained wakefield acceleration is that a pulse train of electron bunches with the same high charge and short length must be used [5]. In this paper, we describe near term and future experimental plans using the existing facility and present proposed upgrade plans for the AWA, including: a) A new gun design which when used with one of the existing AWA linac cavities will produce 100 nC, 1.2 mm (4 ps) rms, 400 mm mrad normalized emittance and 17 MeV electron beams; b) Multiple pulse operation with trains of 20—40 40 nC pulses using laser photocathode based technology or a novel high current micropulse gun (HQMG); c) Upgrade of the AWA drive linac to 100 MeV with the capability of accelerating 20 — 100 electron pulses at 40 nC/pulse. We discuss the impact of these upgrades and propose a scheme to demonstrate 1 GeV beam acceleration using dielectric wakefield acceleration technology.

2 NEAR TERM AWA PROJECTS

Although the primary thrust of this report involves possible upgrades to the facility itself, it is important to mention planned areas of research in the near term which will use the existing AWA facility.

- Study the beam generation, formation and emittance growth in the high current linac.
- Study methods to longitudinally shape the drive beam, in particular to generate a triangular profile. This will be used to demonstrate transformer ratio enhancement in both plasma and structure wakefield experiments [6].
- Continuation of the plasma wakefield experiment in both linear and non-linear regimes.
- Dielectric wakefield transformer.

The dielectric wakefield transformer [7] is of particular interest as offering the best candidate technology for practical high energy acceleration. Briefly, the wakefield generated by a drive bunch in a low impedance dielectric structure is coupled to a high impedance dielectric structure. The rf pulse experiences both transverse and longitudinal compression in the high impedance device. High net acceleration can be realized if a train of 10—20 drive bunches is used.

Initial experiments will use a single drive bunch with the goal of observing the gradient step-up and studying optimal coupling between the two structures. Based on the performance of the AWA drive linac, we expect to produce a gradient of 80 - 100 MeV/m at a transformer ratio of 5. Some relevant work on designing efficient rf coupling to dielectric structures is found in [14].

3 PHOTOCATHODE GUN UPGRADES

Rf photocathode technology has experienced tremendous growth since its first invention[8]. To date, most rf PC sources were developed to produce low charge but high brightness beams as injectors for FELs and other applications[9]. In order to achieve high gradient wakefield acceleration, we have designed, fabricated and commissioned a high current (100 nC, 20 — 30 ps) half cell L-band gun with two additional linac sections [1]. However, the present gun was designed with the constraint that only 1.5 MW rf power would be initially available at the AWA. Thus the gun was designed with high shunt impedance and with output energy of 1.5 MeV.

0-7803-4376-X/98/$10.00 © 1998 IEEE

The present gun was designed to operate with a peak photocathode field of 92 MV/m. During initial tests the interior of the gun was damaged by a vacuum window failure while under full rf power. Although the gun is reaching its design goals, depression of the photocathode field by dark current emission limits further performance improvement. Reaching and exceeding 10 kA will require a new gun cavity.

One option is to build a copy of the high current gun cavity with improved surface preparation and conditioning procedures. We are presently collaborating with SSRC (Taiwan) to duplicate our current gun design. We plan to use the dielectric coating technology developed by FM Technologies, which would enhance the rf surface field on the cathode and minimize the dark current (by a factor of 100), thus reducing the electron pulse length.

Another possibility is to implement an improved gun design. In this section, we show that a new design philosophy making use of 10 MW or more rf power available for the drive gun can produce the desired performance improvement for the AWA drive beam.

1—1/2 Cell Design

The choice for this new gun design is Brookhaven type [10] 1—1/2 cell as shown in Figure 1. Although the beam will have lower emittance if one chooses a multi-cell gun cavity, the rf power requirements will be excessive. There have been designs of relatively high charge L-band guns at APEX[11] and TTF[12], but they produce relatively long beams with moderate charges (<10 nC). Magnetic compression is then used after the gun to produce short

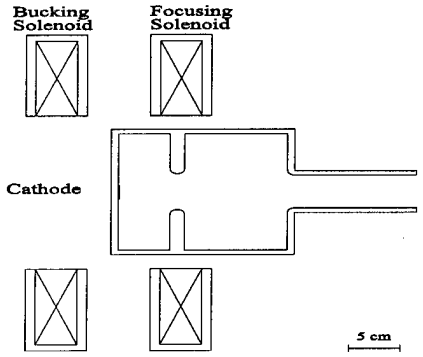


Figure 1. Schematic of proposed 1—1/2 cell drive gun for the AWA upgrade.

bunches. In our case we require much higher charges with the pulse length remaining short (<10 ps). The key to designing a high charge short pulse electron gun is the use of a high photocathode electric field. The computer codes SUPERFISH and PARMELA were used to model cavity fields and beam dynamics respectively. In Figure 2, we show the effect of the peak surface electric field on the rms bunch length and emittance. At 100 MV/m surface field along with other optimized parameters, one can achieve σ_z = 1.2 mm (4 ps) and ε_N = 400 mm mrad.

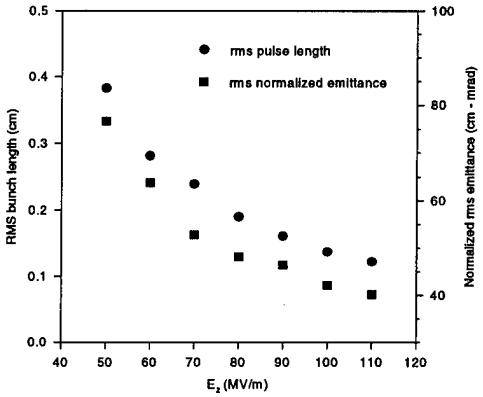


Figure 2. Pulse length and emittance vs E_z (with optimized solenoid design)

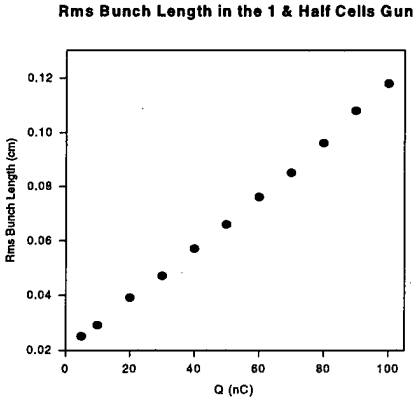


Figure 3. σ_z vs charge in the 1—1/2 cell gun.

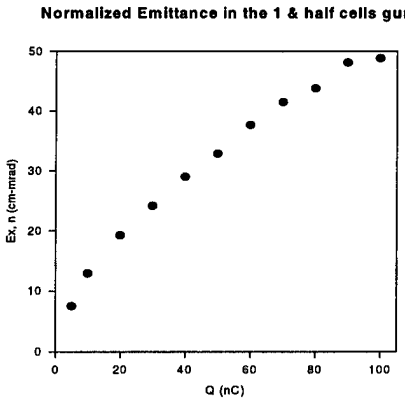


Figure 4. Transverse emittance vs charge

For the 100 nC beam case, the rms pulse length is 1.2 mm and normalized emittance is in the range of 300—400 mm mrad. This is a great improvement over the existing AWA gun design (σ_z = 3 mm, and ε_N=800 mm mrad).

The use of a single AWA linac tank operated at 10 MW in conjunction with the new gun will produce a drive

beam energy of 15—20 MeV with electron bunch parameters as above. Numerical simulations indicate that with these parameters the drive beam could generate wakefield gradients in excess of 1 GeV/m in plasma with density of 7×10^{13} cm^{-3}. For dielectric structures, the reduced emittance and bunch length will permit 100 MV/m gradients to be attained for collinear drive-witness geometries. This second generation AWA high current gun builds upon our experience with the original high current gun and pushes the technology frontier further into this previously unexplored region of photocathode source parameter space.

4 MULTI-PULSE UPGRADE OPERATION

As discussed in section II, operation of the dielectric wakefield transformer at high gradients over extended distances requires the use of a long pulse train drive beam (20—40 pulses of 40 nC each). One way to achieve this mode of operation at the AWA is to use a laser pulse train to generate the electron pulse train. We have obtained a laser pulse splitter which will provide 16 pulses with 760 ps spacing (i.e. one rf period at 1.3 GHz). Thus if sufficient laser power is available, this will enable us to study the technical challenges associated with production and acceleration of multi-pulse high current beams using rf photocathode methods.

Another way to generate bunch trains is to replace the photoinjector with the high current micropulse gun currently under development by FM Technologies[13]. This gun will produce up to 40 nC bunches with rms pulse length of 10 ps. The advantage of this gun is that the beam produced is very stable and repeatable compared to laser photocathode techniques. It eliminates completely the need for the laser and the complications of beam splitting optics. The rf gun designed in the section III can be modified to be used as an injector post acceleration cavity for the micropulse gun. A preliminary study shows that this technology can produce up to 4 MeV beam with the emittance and pulse length preserved as in the case of the new photoinjector design described above.

5 LINAC UPGRADE TO 100 MEV DRIVE BEAM/ 1 GEV WAKEFIELD ACCELERATOR

In order to demonstrate wakefield acceleration concepts at high energy, one needs to increase the drive beam energy. As indicated by our previous study, higher drive beam energy leads to higher wakefield gradients over longer acceleration distances [5]. The AWA Linac design has demonstrated high current electron beams (100 nC) with relative low momentum spread (< 10%) and emittance (600 mm mrad rms normalized). Thus we anticipate the same linac cavity design will be used to accelerate the drive beam to the desired energy, simply by the addition of five new linac cavities and three new rf stations.

For a 1 GeV wakefield accelerator demonstration, one needs to operate the 100 MeV drive linac in multipulse mode (20 pulses/rf macropulse each with 40 nC charge). The dielectric wakefield transformer described above would then provide the additional 1 GeV of acceleration [3].

6 SUMMARY

The AWA facility has attained its challenging design goals and is presently in the midst of its experimental program. A number of performance improvements requiring significant machine upgrades are under consideration. We have described several AWA upgrade scenarios and plans: rf photocathode gun upgrades, multiple pulse operation and linac energy upgrades. We have shown a practical scheme using a dielectric step-up transformer and upgraded AWA machine to accelerate a beam to 1 GeV using wakefield technology.

7 ACKNOWLEDGEMENT

This work is supported by DOE, High Energy Physics Division, Advanced Technology Branch under the contract No. W-31-109-ENG-38.

REFERENCES

[1] P. Schoessow *et. al.*, Proceedings of Particle Accelerator Conference, p976-978., 1995
[2] M. Conde *et. al.*, in this Proceedings
[3] P. Schoessow *et al.*, in this Proceedings
[4] N. Barov *et. al.*, in this Proceedings and submitted to Phys. Rev. Lett. (1997)
[5] W. Gai *et al*, Phys. Rev. E, **55**, 3, p3481, (1997)
[6] K. Bane *et al.*, IEEE Trans. Nucl. Sci., NS-32, 3524 (1985)
[7] E. Chojnacki *et al.*, Proceedings of 1993 Particle Accelerator Conference, pp. 2557-2559.
[8] J. Fraser *et al.*, IEEE Trans. Nucl. Sci., NS-32,p.1719 (1985)
[9] C. Travier, in AIP Proceedings, No. **335**, p57 (1994)
[10] K. Batchelor et al, Proc. of EPAC 541 (1990)
[11] B. Carlsten *et al.*, Proceedings of Particle Accelerator Conference, p.985., 1995
[12] E. Colby *et al.*, Proceedings of Particle Accelerator Conference, p967.,1995
[13] F. Mako *et. al.*, these Proceedings
[14] W.Gai, R.Konecny, J.Simpson, these Proceedings

EXTERNALLY POWERED DIELECTRIC LOADED WAVEGUIDES AS ACCELERATING STRUCTURES

Wei Gai, R. Konecny and J. Simpson
Argonne National Laboratory, Argonne, IL 6039, USA

Abstract

There have been numerous studies examining the use of dielectric materials in accelerating structures in the past. Such studies and related experiments generally concluded that dielectric losses, with the resulting high power requirements, and field breakdown problems made such devices not very attractive. However, development of high dielectric constant, low loss materials plus new demands for emittance preserving acceleration warrant a new look at the idea. In this paper, we discuss reference parameter designs for S-band and X-band structures and show that dielectric loaded guide may now be practical and have certain advantages over conventional iris loaded structures. Preliminary experimental test results of X-band dielectric devices are reported.

I INTRODUCTION

The proposed use of rf driven dielectric based structures for particle acceleration can be traced to the early 50's [1]. Since then, numerous studies have examined the use of dielectric materials in accelerating structures. Such studies and related experiments generally concluded that high dielectric losses with the consequent high power requirements, and field breakdown problems made such devices unattractive compared with conventional copper cavity. However, recent development of high dielectric constant ($\varepsilon \sim 20$ -40), low loss materials (Q~ 10,000 - 40,000) [2] plus new demands for emittance preserving acceleration warrant a new look at the idea [3,4].

Some potential advantages of the dielectric loaded structures are:

- Simplicity of fabrication - the device is little more than a tube of dielectric surrounded by a conducting wall cylinder. This can be a great advantage for high frequency (10 Ghz) structures compared to conventional structures. Also the relatively small diameter of these devices facilitates placement of quadrupoles around the structures.
- Reduced single bunch beam break-up (BBU) - the lowest frequency deflecting mode is almost always lower than that of the acceleration mode.
- Simple reduction of coupled bunch - bunch effects - it has been shown that it is relatively straightforward to build deflection damping into dielectric structure so that very large absorption (I. e. 250 dB/m) of all but TM_{0n} modes can be obtained [5].

Potential problems for dielectric loaded structures are charge accumulation from beam halo, surface breakdown and thermal heating. Whether these problems are fatal or not can only be answered through experiments.

In this paper, we discuss reference parameter sets for both S- and X-band structures and show that dielectric loaded devices may now be practical and have certain advantages over conventional iris loaded structures. Preliminary experimental test results of X-band dielectric devices are reported here in section 5.

II A TRAVELLING WAVE DIELECTRIC LOADED ACCELERATING STRUCTURE

The dielectric travelling wave accelerator has simple geometry. Considering a cylindrical structure partially filled with dielectric material (ε) with inner radius a, outer radius b and conducting wall on the outside. There are also two ports on the side for RF coupling purposes, as shown in Figure 1. The axial electric fields inside the structure can be solved for exactly as

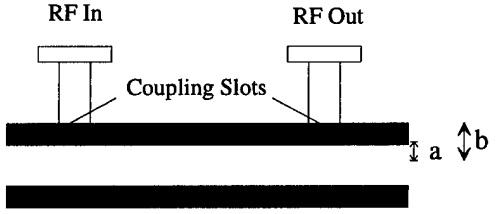


Figure 1. Schematic diagram of a dielelectric loaded travelling wave accelerator.

$$E_z^{(1)}(\omega,r,z,t) = E_0 I_0(kr) e^{i(k_z z - \omega t)}$$
$$E_z^{(2)}(\omega,r,z,t) = [B_1 J_0(s_1 r) + D_1 N(s_1 r)] e^{i(k_z z - \omega t)} \quad (1)$$

Here E_0, B_0 and D_1 are the field amplitudes in the region 0 (vacuum) and 1 (dielectric) respectively and are related by boundary conditions,and

$$k^2 = \frac{\omega^2}{c^2}(1-\beta^2)$$
$$s^2 = \frac{\omega^2}{v^2}(\beta^2\varepsilon - 1) \quad (2)$$

where $\beta c = v = \omega/k$ is phase velocity of the wave travelling inside the tube. Therefore β determines the synchronism of the wave and the accelerated particles. By properly choosing a, b and ε, one can adjust phase velocity accordingly. Thus this proposed scheme works not only for electron acceleration which typically has high phase velocity, but also for low phase velocity

0-7803-4376-X/98/$10.00 © 1998 IEEE

particle acceleration, such as required for heavy ions. The transverse electric field can be written as

$$E_r = \frac{i}{\frac{\omega}{v}(\beta^2\varepsilon - 1)}\frac{\partial E_z}{\partial r} \quad (3)$$

and the magnetic field $H_\phi = \varepsilon E_r$ everywhere inside the tube. By matching the boundary conditions at a and b (E_z and D_r continous), all the fields components can be calculated accordingly.

The stored energy per unit length U in the tube is the sum of contributions from both vacuum and dielectric regions, and can be expressed as

$$U = U_{in} + U_{out}$$
$$= \sum_{0,1}\pi\int(\varepsilon\varepsilon_0 E^2 + \mu_0 B^2)rdr \quad (4)$$
$$= E_0^2 u$$

where u is a geometric factor which solely depends on the structure geometry and dielectric constant. For a given RF power, the axial electric field in the center region of the tube can be expressed as

$$E_0 = [\frac{P}{u\beta_g c}]^{\frac{1}{2}} \quad (5)$$

where v_g is the group velocity. The dielectric loss per unit length is then found from:

$$\eta = \frac{2\pi\delta\int U_{out}}{v_g(U_{out} + U_{in})} \quad (6)$$

The electric fields in the vacuum region described by equation 1 and 3 have very interesting chraracteristics. When $k \to 0$, *i.e.*, the phase velocity of the wave is c, E_z is constant in r. This implies that there are no focusing and de-focusing forces for a relativistics particle travelling inside the vacuum chamber. This is critical for emittance preserving in the Linear Accelerator, particularly for the high brightness electron gun development.

III DESIGN FOR S- AND X- BAND LINAC STRUCTURES

There were proposed schemes using S-Band dielectric structures in the last several years [3,4]. In the past, the dielectric materials available have the characteristics of relatively small ε (<10) and relative high loss tangent (δ > 10-4). However, recently dielectric materials with ε > 20, δ < 10-4 and with DC breakdown voltage > 10 MV/m have become commercially available [2]. In this section, we show several design parameters with different dielectric constants and loss tangents. We compare our design results with SLAC S-band and NLC X-band conventiona cavity designs. Although both SLAC and NLC designs were for constant gradients, we could certainly taper the dielectric tubes to achieve a constant gradient acceleration structure. But we believe that a constant impedance structure would show the same characteristics as constant gradient and a fair comparison can be made.

a. S band structures

We have developed a self consistant computer code to calculated the properties of the dielectric travelling wave structures. The following table summarises the results for two possible dielectric S-band structures. As shown in this table, the group velocity is much higher than SLAC cavity although HEM11 is lower.

Table I: DLG Reference Design for S - Band

Scheme		I	II
Material		MgCaTi	BaTi
ε (diele. const.)		20	35
Loss tangent δ		10^{-4}	$3x10^{-5}$
Inner Radius a		0.5 cm	0.5 cm
Outer Radius b		1.20 cm	1.09 cm
HEM11		2.304 GHz	2.71 GHz
Shunt Imped.		10 MΩ/m	7.4 MΩ/m
group velocity		0.05 c	0.028 c
Attenuation		0.6 dB/m	0.36 dB/m
Power (10MV/m)	required	20 MW	13.6 MW

b. 11.4 GHz structures

We have also considered two possible designs for X-band structure (11.4 Ghz). Unlike the case in S-band, the group velocity for the NLC design is in the range from 0.03 c ~ 0.04c [5]. Thus dielectric loaded structure is having a comparable shunt impedence and group velocity as indicated in the table below.

Table II: DLG Reference Design for X - Band

Material		MgCaTi	BaTi
ε (diele. const.)		20	35
Loss tangent δ		10^{-4}	$3x10^{-5}$
Inner Radius a		0.3 cm	0.3 cm
Outer Radius b		0.456 cm	0.416 cm
HEM11		9.96 Hz	10.2 GHz
Shunt Imped.		37 MΩ/m	47 MΩ/m
group velocity		0.057 c	0.035 c
Attenuation		1.2 dB/m	1.1 dB/m
Power (10MV/m)	required	2.73 MW	2.02 MW

As shown above, one of the common characteristics of all the structures is that the frequency of HEM11 (first deflection mode) is lower than that of the acceleration modes. Because the deflection force is a function of sin(kz), this implies a very different and improved conditions for single bunch BBU problem compared to conventional structures where the HEM11 is always a higher in frequecy than the acceleration mode TM01.

IV DAMPENING HIGHER ORDER MODES IN THE DIELECTRIC STRUCTURES

Unlike conventional disk loaded accelerator, non axial symmetric mode dampening can be achieved easily by cutting some longitudinal slots in the conducting wall. The deflection modes are non-axisymmetric hybrids containing both axial electric and magnetic fields. These hybrid modes are comprised of all six cylindrical field components and will require both azimuthal and axial surface currents on the outer conductor. If the outer conductor is segmented to allow only axial surface currents, the deflection modes will not be confined and will be radiated beyond the outer wall. If this outer region is filled with rf absorbing material, the deflection modes will be highly attenuated. Test on the bench and with electron beam at AATF [6] have shown that 200 dB/m attentuation can be achieved easily.

V CONSTRUCTION AND TEST OF AN 11.4 GHZ PROTOTYPE DIELECTRIC STRUCTURES

We have constructed a 11.4 GHz dielectric loaded travelling wave accelerating structure using dielectric from TransTech, with dimensions of $a = 2.9\ mm$, $b = 4.59\ mm$ and dielectric constant of 20. The length of the structure is 10 cm. This is a comparable structure as in the Type I of the Table 2.

It is also important to emphasize that efficient rf coupling to dielectric structures is required for wakefield step-up transformers. The results obtained here are directly applicable to the optimized design of the coupled wake tube device experiments planned for the AWA [6].

The RF coupling scheme we used here is similiar to conventional disk-washer RF cavities (Side coupled). Impedance matching of the coupling slotsis more difficult in the high ε dielectric case because the outer radius of the dielectric tube is much smaller than the waveguide. By careful adjustment of the coupling slots and monitoring the S-parameters using an HP8510C network analyzer, we have achieved reflection S11< - 28 dB and S21 > -1.8 dB @ 11.45 Ghz as shown in the Figure 2 and 3 respectively.

We have also tested a standing wave dielectric structure with an RF side coupled port. We achieved following S11< - 30 dB @ 11.39 Ghz. The loaded Q from this measurement is 5000, which is in agreement with the manufacturer's specification.

We plan to continue engineering studies of this accelerating structure with improved RF coupling and mechanical fixture to allow operation in vacuum. With 100 MW power, we can test this structure at 60 MV/m gradient. We are planning to perform the high power tests using the X-band rf system at SLAC/NLCTA.

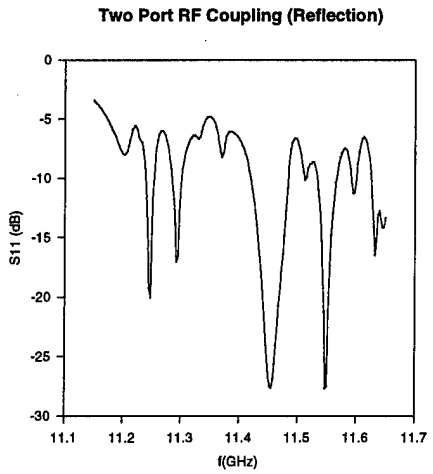


Figure 2. S11 of the optimally coupled waveguide results.

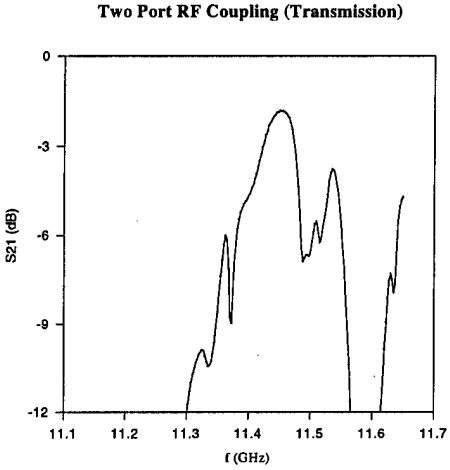


Figure 3. S21 for the optimally coupled wave

In summary, we have studied the dielectric loaded waveguide as a viable alternative for the accelerating structures. We have shown that this structure can be competitive, particularly with the higher frequency demand for the future high energy machine. Some pratical issue can only be answered through careful experimental studies and new materials development. This work is supported by DOE, High Energy Physics Division under contract No. W-31-109-ENG-38.

REFERENCES

[1] G. Flesher and G. Cohn, AIEE Transactions, 70, 887 (1951)
[2] Trans-Tech., Catalog, 5520 Adamstown, Adamstow, MD 21710
[3] J. Simpson, ANLHEP-WF 174, (1992)
[4] T. B. Zhang et. al., in Proceedings of 7th Advanced Accelerator Worksop, (1996).
[5] SLAC repor 474, 1996
[6] E. Chojnacki et al, J. Appl. Phys. 69,6257 (1991)

HIGH GRADIENT DIELECTRIC WAKEFIELD DEVICE MEASUREMENTS AT THE ARGONNE WAKEFIELD ACCELERATOR

P. Schoessow, M. Conde, W. Gai, R. Konecny, J. Power, and J. Simpson
Argonne National Laboratory, 9700 S. Cass Ave. Argonne IL 60439

Abstract

The Argonne Wakefield Accelerator (AWA) is a facility designed to investigate high gradient wakefield acceleration techniques. Wakefields are excited using a drive beam produced by a 14 MeV high current photoinjector-based linac. A second photocathode gun generates a 4 MeV witness beam which is used as a probe of the wakefields in the device under test. The delay of the witness bunch with respect to the drive bunch can be continuously varied from -100 ps to >1 ns. The drive and witness bunches propagate along collinear or parallel trajectories through the test section. A dipole spectrometer is then used to measure the energy change of the witness beam. The complete wakefield measurement system has been commissioned and wakefield experiments using dielectric structures are underway. Initial experiments have focused on collinear wakefield device geometries where the drive and witness bunches traverse the same structure. For attaining very high gradients we will construct and study step-up transformer structures in which the rf pulse generated by the drive beam is compressed transversely and longitudinally.

1 INTRODUCTION

Research on dielectric loaded structures as high energy wakefield accelerators has been proceeding for some time [1]. These devices possess some obvious advantages:

- Simplicity of fabrication.
- Parasitic wake control and suppression. The HEM_{11} mode is in general lower in frequency than the TM_{01} accelerating mode [2], providing greater tolerance to the beam breakup instability than conventional structure based accelerators. Multibunch beam breakup effects can also be controlled with a simple mode suppression scheme [3].
- Adaptability to a two-beam (transformer) configuration [4]. In this technique the wake generated by multiple drive bunches in a low impedance dielectric structure is coupled into a high impedance structure. This provides a transformer ratio enhancement as well as simplifying the staging of the drive and witness beams.

There are also potential difficulties with dielectric devices:

- Breakdown limits at high fields.
- Charging from intercepted beam halo.
- Radiation damage effects on dielectric properties.

Initial experiments at AATF [5] concentrated on understanding the low-field regime. One of the primary goals of the AWA program is to study the physics of dielectric wakefield structures at high gradients with the emphasis on developing techniques useful for high energy accelerators. We report here the results of our initial experiments on collinear drive-witness beam geometry, and describe planned experiments with transformer structures.

2 WAKEFIELD MEASUREMENT SYSTEM

The AWA has been described in detail elsewhere [6,7]. In brief, the facility consists of a unique high current photoinjector and linac which generates the drive beam, a second high brightness photoinjector which produces the witness beam, beamlines to transport drive and witness beams through the wakefield device under test, and a magnetic spectrometer to measure the change in energy of the witness beam from the wakefield of the drive beam.

The drive beam intensity is monitored using an integrating current transformer immediately upstream of the test section. The length of the drive beam can be measured using an aerogel Cherenkov radiator which can be inserted into the beamline. Light produced in the radiator is then transported to a streak camera.

The drive and witness guns share a common laser system. A portion of the laser pulse is split off and directed through an optical trombone before being transported to the witness gun to adjust the delay between the two beams. At the same time the phase of the rf driving the witness gun is varied to maintain a constant laser injection phase.

The witness beam is detected at the 60° port of the spectrometer using a phosphor screen and intensified CCTV camera. The energy acceptance of the spectrometer is ±165 keV; for all but the lowest gradient device measurements the spectrometer current was adjusted to center the witness beam on the phosphor as the delay was varied. The spectrometer current was then recorded for each delay setting as a measure of the wake potential for that delay.

3 DIELECTRIC DEVICE MEASUREMENTS

Initial experiments were performed using simple collinear dielectric structures. These devices were fabricated from borosilicate glass which has a dielectric constant ≈4 and is known from measurements at the AATF to be resistant to charging.

0-7803-4376-X/98/$10.00 © 1998 IEEE

3.1 15 GHz device delay scan

The wake potential for a 15 GHz structure (inner radius a=5 mm, outer radius b=7.7 mm, length=11 cm) was mapped out in detail. For this measurement only a modest drive beam charge (11 nC/pulse) was used. The bunch length was not measured but was estimated to be about 10 ps rms. The witness gun delay was increased in 5 ps steps (later in the run changed to 10 ps increments) from 0—400 ps. The image of the witness beam spot on the phosphor screen downstream of the spectrometer was digitized at each delay setting and saved to disk for offline analysis.

Figure 1 shows the accelerating gradient as measured from the energy change of the centroid of the witness beam as a function of the delay. The largest energy change corresponds to a gradient ≈2 MeV/m.

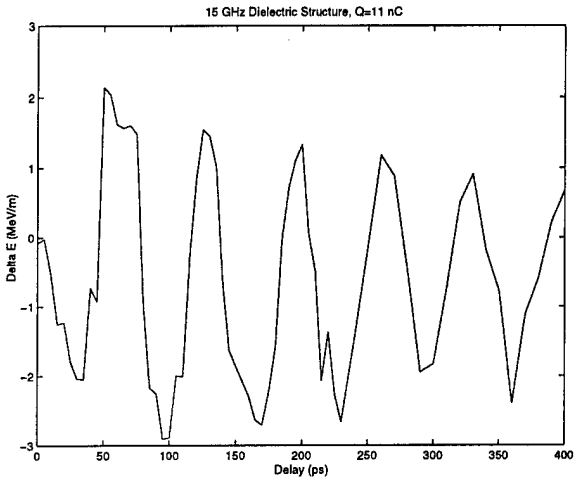


Figure 1. Longitudinal wakefield as measured from centroids of the witness beam energy distribution for 15 GHz dielectric structure.

Additional optimization of the laser injection phase and beamline magnet settings resulted in a gradient of 7 MeV/m with 20 nC drive beam intensity. This agrees well with calculations assuming σ_z=2.5 mm (8.3 ps).

3.2 20 GHZ device—gradient vs drive charge and bunch length

In order to increase transmission of the drive beam through smaller (higher impedance) wakefield devices, a quad triplet was located upstream of the wakefield device. The improved optics allowed up to 40 nC drive charge/pulse to be transmitted through a 3 mm radius aperture 10 cm in length. At these intensities background from X-rays and secondary electrons from drive beam scraping caused problems for witness beam detection. After careful radiation shielding and with improved beam monitoring the background became manageable.

A 20 GHz device (a=2.9 mm, b=5.0 mm) was used to study wakefield effects as a function of drive beam intensity and length. The drive beam current was gradually increased by removing neutral density filters in the laser transport line for the drive gun. The beam transport lines were retuned to give maximum transmission for each drive beam intensity. At each point the gradient (maximum witness beam energy change) was measured, along with the drive bunch length.

Drive charges for this experiment were in the 5—25 nC/pulse range. Rms drive bunch lengths were found to vary from 6 ps at 5 nC to 20 ps at 25 nC. This increase in bunch length resulted in a rolloff in the observed wakefield gradient with drive charge as shown in Figure 2. The Figure also shows the predicted gradient if the

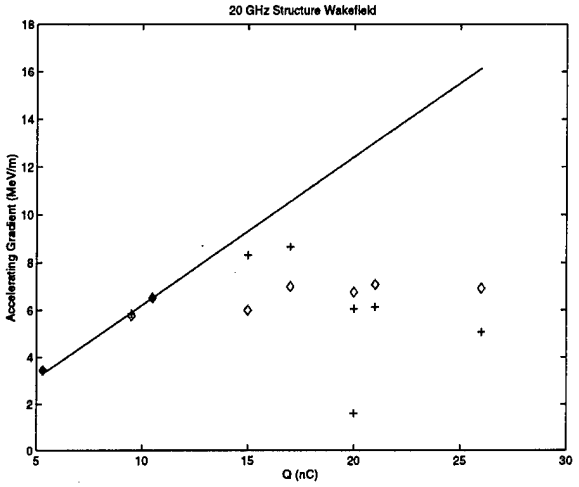


Figure 2. Wakefield gradient vs charge for 20 GHz structure. Diamonds: AWA measurements. Straight line: predicted gradient based on 10.5 nC measurement. Crosses: predicted gradient based on 10.5 nC point and measured bunch length at each charge.

length of the drive bunch had not increased with charge, and also the predicted gradient based on the expected $exp(-k^2\sigma^2/2)$ scaling with bunch length. The scaled gradient generally reproduces the trend of the data.

According to the latest results from beam characterization/optimization experiments [7], where rms bunch lengths of 3 mm at 50 nC have been attained, a gradient of 25 MeV/m should be possible. It is important to point out that at the present time the observed accelerating gradient is > 7 MeV/m, i.e. **larger by a factor of > 10 than the maximum gradients obtained in the earlier AATF experiments** [5].

4 WAKEFIELD TRANSFORMER EXPERIMENTS

The next wakefield experiments planned for the AWA include the demonstration of dielectric step-up transformers. A 15.6 GHz device was chosen for the initial measurement because of its potential for producing high gradients while being well matched to the present performance of the AWA wakefield measurement system. Table I shows two possible configurations for a 15.6 GHz transformer experiment. Transformer ratios of 4-5 can be obtained. Techniques for efficient coupling of rf into dielectric structures have been developed [9]; these

results are directly relevant for the fabrication of transformer structures.

The AWA wakefield measurement system also possesses the capability of transporting the witness beam parallel but at a transverse offset with respect to the drive beam; in fact this mode of operation should greatly simplify data taking since the 4 MeV witness and 14 MeV drive beam no longer need to be transported through the same beam optics upstream of the test section. Thus direct measurements of the gradient and transformer ratio will be possible. The drive bunch parameters shown in Table 1 correspond to beams presently available at the AWA. Initial measurements will use a single drive bunch to verify rf coupling between structures and demonstrate a transformer ratio >2. A laser beam splitter system has been obtained for multiple drive bunch measurements.

5 DISCUSSION

Wakefield acceleration in dielectric structures has been studied at gradients significantly higher than demonstrated previously. At 7 MeV/m no sign of dielectric breakdown was observed. Despite a large intercepted beam from missteering during tuning and halo, charging of the borosilicate glass dielectric was not found to be a problem.

The AWA is well along in attaining its performance goals in terms of drive beam current transported through a wakefield device. The initial experiments demonstrate that the technology of dielectric wakefield structures is a very promising one for use in high energy accelerators.

6 ACKNOWLEDGEMENT

This work is supported by the Department of Energy, Division of High Energy Physics, under contract W-31-109-ENG-38.

REFERENCES

[1] R. Keinigs et al., Part. Accel. **24** 223 (1989)
[2] M. Rosing, W. Gai, Phys. Rev. **D42** 1829 (1990)
[3] E. Chojnacki et al., J. Appl. Phys. **69** 6257 (1991)
[4] E. Chojnacki et al., Proc. 1991 Particle Accelerator Conference, p. 2557-2559
[5] W. Gai et al., Phys. Rev. Lett. **61** (2756) 1988
[6] W. Gai et al., Advanced Accelerator Concepts, Lake Tahoe CA 1996, S. Chattopadhyay ed. (in press).
[7] M. Conde et al., these Proceedings
[8] W. Gai et al., these Proceedings
[9] W.Gai, R. Konecny, J. Simpson, these Proceedings

	Stage I	Stage II (option 1)	Stage II (option 2)
Inner radius a (mm)	5	1.5	1.5
Outer radius b (mm)	8.1	2.38	2.7
Dielectric constant ε	3.0	35	20
Charge/ pulse (nC)	40		
rms bunch length (mm)	2.5		
Wake amplitude/ acceleration gradient (MV/m)	16.2	79	65
Number of drive pulses		20	20
Transformer ratio		4.9	4
Energy gain (MeV)		79	108

Table 1. Parameter sets for two possible 15.6 GHz wakefield transformers.

ENHANCED IFEL PERFORMANCE USING A NOVEL WIGGLER

Z. Parsa
Brookhaven National Laboratory, Upton NY 11973

T.C.Marshall
Department of Applied Physics, Columbia University, New York City 10027

Abstract

In the conventional inverse free electron laser (IFEL), electron acceleration is done via the interaction of an intense laser beam and a wiggler with a sinusoidal field variation. We have studied the effect on IFEL performance using a wiggler that creates a nearly square-wave periodic field pattern [1,2]. A novel numerical technique is described which models this wiggler [1]. We find stable orbits and an improvement in IFEL acceleration gradient, resulting in a gain in energy by as much as a factor of two (equivalent to four times the laser power), when compared with the conventional IFEL with a sinusoidal field wiggler [3]. In an experiment, the magnetic field can be synthesized by running a conventional ferromagnetic wiggler into saturation.

1 INTRODUCTION

The inverse FEL (IFEL) uses the principal of stimulated absorption to accelerate a beam of electrons passing through a wiggler using a source of high intensity electromagnetic waves. The first IFEL experiment was reported in 1991 using a 750kV electron beam that was prebunched by, and powered by, a millimeter-wavelength FEL [4]. Recently, acceleration of a 40MeV beam to 42MeV was reported [5] using a GW C02 laser beam; the bunching of this beam is being studied [6] preparatory to injecting the electron output from the IFEL into another laser accelerator. These experiments used wigglers that provided a sinusoidal field variation, either as a circularly polarized- or dipole- type field, as did previous theory [3]. Results from experiment were interpreted by codes which also used sinusoidal field variation in the wiggler. Although the latter is a logical choice for the IFEL, and is readily fabricated, it turns out that it is not the most effective way to use the magnetic field capabilities of the wiggler for electron acceleration; furthermore it is an approximation to the physics. In this paper we discuss another case, the square-wave wiggler – which, although non-physical, suggests a simple modification of present IFEL experiments which should yield improved performance [1,7].

Of course, an actual wiggler cannot be truly sinusoidal [8], nor can a square-wave field variation be realized. However, it is possible to develop a strong nonlinearity of the sinusoidal pattern in a ferromagnetic wiggler by operating the device into the field regime where the material becomes saturated. The square wave pattern is therefore a limiting case [1]. On the other hand, the interpretation of data from IFEL experiments using codes based on sinusoidal field patterns may result in errors, depending on how closely the actual field pattern approximates a sine wave. In what follows, we present a theory [1,2,7] and results from numerical simulation which models a non-physical square wave wiggler, and then generalize the treatment to include realizable sinusoidal wigglers afflicted with a high degree of non-sinusoidal nonlinearity [1]. In the limit of the square wave, we find an improvement in accelerating gradient by a factor of two.

2 THEORY – SQUARE WAVE MODEL

We consider the motion of an electron under the action of a linearly polarized laser electromagnetic field and an applied transverse magnetic field of the wiggler (B_w) in the form of a square wave. The wave and the particles move in the z-direction, and the components of relativistic motion are:

$$\begin{cases} \frac{d}{dt}(m\gamma v_z) = e\beta_x E_{x0}\sin\phi + e\beta_x B_w f(\phi) & (1) \\ \frac{d}{dt}(m\gamma v_x) = e(1-\beta_z)E_{x0}\sin\phi - e\beta_z B_w f(\phi) & (2) \end{cases}$$

where $E_x = B_y = -E_{x0}\sin\phi$, $\phi = k(ct - z)$, the applied magnetic field of the wiggler is $B_0 f(\phi)$, and $f(\phi)$ us a unit square wave that switches sign at odd numbers of $\pi/2$ and $f(0) = -1$. Integrating (2), and taking Λ_w to be the wiggler period,

$$m\gamma v_x = \frac{eE_{x0}}{kc}\cos\phi - \frac{eB_w}{c}\int^{\phi} dt v_z f(\phi)$$

$$\int^{\phi} dt v_z f(\phi) = \int^{\phi} dz f(\phi) = \frac{\Lambda_w}{4} g(\phi) \quad \text{and} \quad g(\phi)$$

$$g(\phi) = -\frac{8}{\pi^2}\sum_{n=1}^{\infty}\frac{1}{n^2}\sin\frac{n\pi}{2}\sin n\phi$$

$$v_x = \frac{eE_{x0}}{kc}\cos\phi - \frac{eB_w\Lambda_w}{4mc^2\gamma} g(\phi) \quad \text{and}$$

$$mc^2\frac{d\gamma}{dt} = ev_x E_{x0}\sin\phi = \frac{(eE_{x0})^2}{2kc}\sin 2\phi - eE_{x0}\frac{eB_w\Lambda_w}{4mc^2\gamma} g(\phi)\sin\phi$$

Neglecting the $\sin 2\phi$ term in the energy equation, we find $d\gamma/dt \sim (2/\pi)(\Lambda K/\gamma)$ with K the wiggler parameter; which is about twice the result for a planar sinusoidal wiggler.

0-7803-4376-X/98/$10.00 © 1998 IEEE

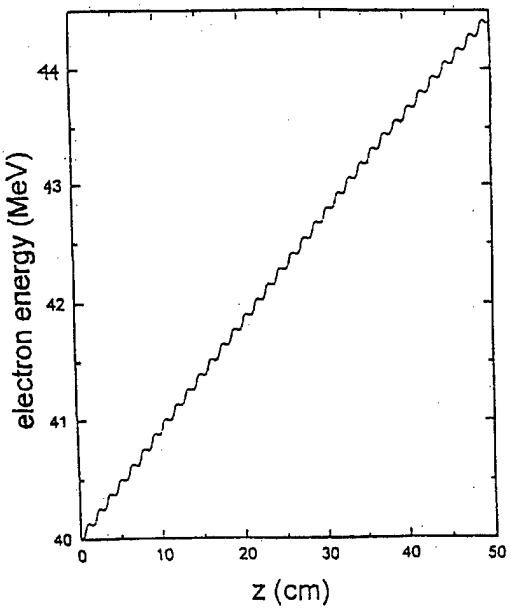


Figure 1a

In Figure 1a and 1b we show a computed example for the case of the recent Brookhaven experiment which reported ~2MeV increase on a 40MeV input beam due to the IFEL [5]. Taking their design (see Table I, loc. cit.), but with a square-wave wiggler, one finds in Figure 1a that the energy increase is about twice that obtained or expected in that experiment. The orbit of the electron in the transverse direction (Figure 1b) is stable, but non-sinusoidal: this results from the fact that dPx/dt is a square wave, and Px is therefore piecewise linear and $x(z)$ is piecewise quadratic. In fact, the reason that the square-wave wiggler performs better is that the electrons experience the high field values over a much larger fraction of their orbit, and so are accelerated more. Other simulations, taking more ambitious parameters for the wiggler and the laser, bear out this result. Since the IFEL accelerating gradient is almost linear in laser field, an improvement in gradient by two is equivalent to four times the laser power.

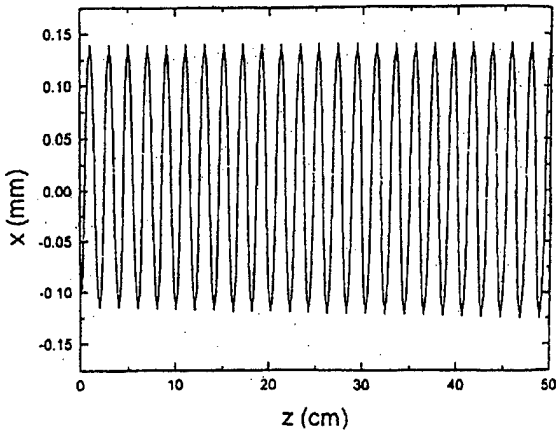


Figure 1b

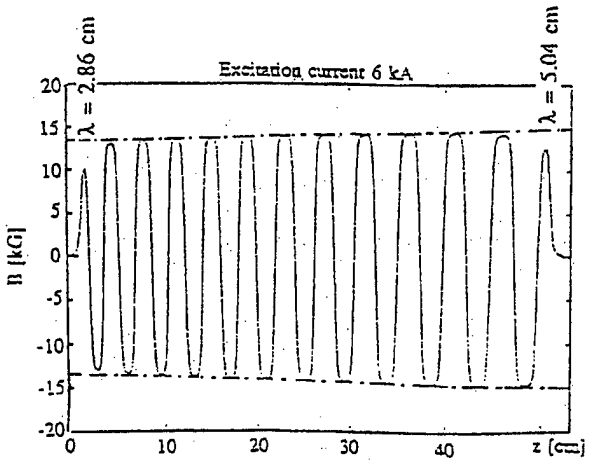


Figure 2: The Brookhaven fast excitation wiggler [9]

3 THEORY – REALIZABLE WIGGLER

The present Brookhaven wiggler, which is made partly of ferromagnetic material, will show pronounced non-sinusoidality if pushed to higher field values (see Figure 2 [9]) than the 10kG used in the past run [5]. Taking this as motivation to study a more realistic case than the square wave, the IFEL equations were cast in terms of a wiggler function that was modeled as a "multiple sine" function. One can consider a function

$$\sin(\sin(\sin(\ \ldots\ldots\ldots(\sin z) = yN(z)$$

where the repeated sine operation introduces a non-sinusoidal flattening of the wiggler field, such as observed [1,7].

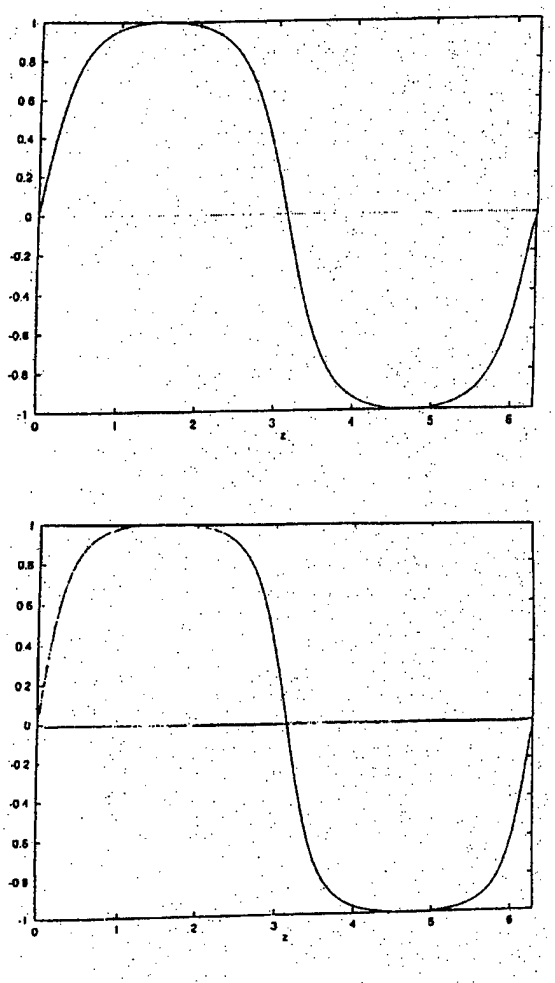


Figure 3: $yN(z)$, multiple sine function of order N: above, Fig. 3a, $N = 10$; below, Fig. 3b, $N = 20$.

In Figure 3a we show a case of a multiple-sine function of order ten, and in Figure 3b, or order 20. In the former case, the energy gain of the sinusoidal wiggler (multiple sine of order one), and in the latter, by 60%. Thus, we look forward to the operation of the IFEL in the regime where the ferromagnetic elements of a typical dipole wiggler become saturated, and the wiggler profile exhibits flattening. One might expect this to become possible with only minor changes in the wiggler design or construction, and therefore the improvement of energy gain is achieved in a painless way. If the departure from wiggler sinusoidality is not large, this study points out the need for careful characterization of the wiggler field so that accurate comparison with theory using codes that model the wiggler correctly can be made. In the present experiment [5], the wiggler effect may not stand out because the difficulty of measuring the CO_2 laser power permits some latitude in interpreting the acceleration result.

4 REFERENCES

[1] Z. Parsa, "An Inverse FEL with a Square Wave Wiggler [IFELSW]", An Experimental Proposal to the ATF Steering Committee (sec. 1-4), October 30, 1996 (ITP96-Report); Z. Parsa, "Square Wave Wiggler IFEL", (Sec. 5), Addition to proposal for IFELSW, November 20, 1996 (ITP96-Report).

[2] Z. Parsa and M. Pato, "IFEL Acceleration with a Square-Wave Wiggler", conference proceedings "New Modes of Particle Acceleration: Techniques and Sources", AIP Press (1997)

[3] E.B. Courant, C. Pellegrini, and W. Zackowitz, Phys. Rev. A32, 2813 (1985)

[4] I. Wernick and T.C. Marshall, Phys. Rev. A46, 3566 (1992)

[5] A. van Steenbergen, et al., Phys. Rev. Lett. 77, 2690 (1996)

[6] Y. Liu et al., paper 3'C003 of this meeting

[7] Z. Parsa, "Improved NAIBEA and IFEL", in abstracts (APS log no 5933) for the Joint April APS/APT meeting, Washington DC 1997

[8] S.Y. Park et al., J. Appl. Phys. 53, 1320 (1982)

[9] CAP/ATF Meeting Report, December 1995 [Brookhaven]

EMERGING TERAWATT PICOSECOND CO_2 LASER TECHNOLOGY AND POSSIBLE APPLICATIONS IN ACCELERATOR PHYSICS

I.V. Pogorelsky and I. Ben-Zvi, NSLS, BNL, Upton, NY 11973, USA

Abstract

The first terawatt picosecond (TWps) CO_2 laser is under construction at the BNL Accelerator Test Facility (ATF). TWps-CO_2 lasers, having the order of magnitude longer wavelength than the well-known table-top terawatt solid state lasers, offer new opportunities for the strong-field physics research. For processes based on electron quiver motion, such as laser wakefield acceleration (LWFA), the advantage of the new class of lasers is due to a gain of two orders of magnitude in the ponderomotive potential for the same peak power. The large average power capability of CO_2 lasers is important for the generation of hard radiation through Compton back-scattering of the laser off energetic electron beams, as well as for other applications. Among them are: LWFA modules of a tentative electron-positron collider, γ-γ (or γ-lepton) collider, a possible "table-top" source of high-intensity x-rays and gamma rays and the generation of polarized positron beams.

1 EMERGING TWps-CO_2 LASER TECHNOLOGY

An important physical parameter that enables generation and amplification of picosecond laser pulses is the gain spectral bandwidth.

Methods to produce picosecond and sub-picosecond CO_2 laser pulses have been developed. One of them is semiconductor optical switching [1]. Using this method, subpicosecond slices out of a multi-nanosecond CO_2 laser output may be produced using conventional mode-locked solid-state laser.

Pressure broadening of the CO_2 gain spectrum at ~10 atm into a 1 THz wide quasi-continuum permits amplification of 0.5 ps laser pulses. Note that gas lasers are free from optical nonlinearity. This permits direct amplification of multi-terawatt λ=10 μm laser beams without a sophisticated pulse chirping technique which is necessary for terawatt solid state lasers.

For a τ_L=1 ps pulse propagating in a 10-atm amplifier, the estimated small-signal gain is 3-4%/cm and the extractable specific energy is ~20 mJ/cm^3. Taking into account that the total discharge volume may exceed 10 *l*, the possibility of extraction of as much as 100 J of energy in a picosecond pulse from a reasonably compact CO_2 laser amplifier looks realistic. However the damage threshold of the output window that is at the level of 0.5 J/cm^2. For an optical window of the ~100 cm^2 size, the extractable energy is 30-50 J which still permits ~30 TW peak power at a 1-ps laser pulse duration.

Thus, to attain terawatt peak power, a ~10-atm, ~10-*l* CO_2 amplifier is required. To maintain a uniform discharge under such conditions, the following requirements should be satisfied: a) strong penetrating preionization, b) ~1 MV voltage applied to the discharge, and c) the energy load of several kilojoules deposited in a relatively short, ≤300 ns, time interval. The first laser with such parameters is under construction at the Brookhaven ATF.

Fig.1 shows the principal optical diagram of the ATF TWps CO_2 laser system. The 1 MW, 100 ns pulse produced by a 1-atm CO_2 laser oscillator is sliced at a semiconductor switch controlled by the picosecond Nd:YAG laser. The high power will be attained via regenerative amplification and four additional passes through the preamplifier followed by three passes in the 10-atm, 10-*l* final amplifier with the beam expansion to its full 10-cm aperture [2].

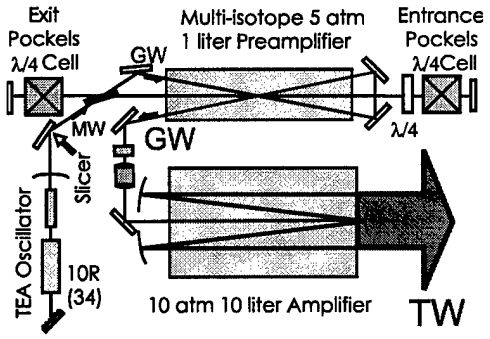


Figure 1: Optical diagram of the ATF TWps-CO_2 laser

The ATF laser, besides its role in user's experiments, will serve as a test bench for proof-of principle evaluation of the TWps-CO_2 technology for such strong field physics applications as high-gradient laser accelerators and high-intensity Compton x-ray sources. For that purpose, ATF also provides a high-brightness 50-MeV electron beam from a photocathode RF linac synchronized within subpicoseconds to the CO_2 laser pulse.

2 LASER WAKEFIELD e^--e^+ COLLIDER

Progress in the exploration of particle interactions relies upon the development of a new-generation of accelerators on a TeV energy scale. One of the prospective approaches is a linear e^--e^+ collider based on a high-gradient laser acceleration. The enthusiasm that drives research in this area is based on ultra-high electric fields attainable upon the tight focusing of terawatt laser beams.

0-7803-4376-X/98/$10.00 © 1998 IEEE

This may permit reduction of the accelerator length by orders of magnitude.

Among the known laser acceleration techniques, the laser wakefield acceleration (LWFA) [3] is considered as the most promising. The LWFA method is based on the ponderomotive charge separation and a relativistic wake formation when a short laser pulse propagates in underdense plasma. The amplitude of the accelerating field, E_a, due to the charge separation in a plasma wave is

$$E_a[V/cm] = \left(a^2/\sqrt{1+a^2}\right)\sqrt{n_e}\left[cm^{-3}\right], \quad (1)$$

where n_e is electron density in plasma, and a is the dimensionless laser vector-potential

$$a = eE_L/mc\omega = 0.3E_L[\mathrm{TV/m}]\lambda[\mu\mathrm{m}]. \quad (2)$$

From Eqs.(1) and (2) we see that $E_a \propto \lambda^2$ for $a<<1$ and $E_a \propto \lambda$ for $a>>1$. This is due to the stronger ponderomotive potential of plasma electrons oscillating in a lower-frequency electromagnetic field. There are still tradeoffs to attain higher E_a with short-wavelength lasers via tighter laser focusing and using higher n_e. The analysis of two options to build the 2.5 TeV multi-stage plasma-channeled LWFA linac using CO_2 or a solid state lasers is presented in Table 1. Both design options are aimed to attain a luminosity $\Lambda=10^{35}$ cm^{-2}s^{-1} [4] defined as

$$\Lambda = N_e^2 \zeta f / 4\pi\sigma_\perp^2, \quad (3)$$

where N_e is the number of particles per bunch, ζ is a number of bunches per train, f is the linac repetition rate, and $\sigma_\perp$ is the e-beam cross-section at the interaction.

The parameters entering Table 1 are chosen according to the following prime considerations:

1. The 50 TW peak laser power foreseeable with state-of-the art laser technology, and the laser pulse duration - close to the experimentally demonstrated minimum.
2. The plasma channels are filled with a 100% ionized hydrogen at the density $0.5n_e$. The normalized emittance of the electron beam at 2.5 TeV due to gas scattering described by Highland formula [5] is:
$$\varepsilon_n[m.rad] \approx 3\times10^{-15}\left(n_e\left[cm^{-3}\right]/E_a^2[MeV/m]\right). \quad (4)$$
3. The channel length for every accelerator stage is $\sim 30z_0$, where $z_0 = \pi r_L^2/\lambda$ is the Rayleigh length. A 20 cm long evacuated dead space is assumed between the accelerating channels. Note that optics of the same focal length are used for both lasers.
4. The maximum number of particles per bunch is calculated under the condition that space charge field of the electron bunch does not effect the wakefield structure: $N_e \le n_e\left(c/\omega_p\right)^3$.

We see that both design approaches illustrated in Table 1 demonstrate the LWFA capabilities to attain the desired 2.5 TeV electron energy in a compact multi-stage accelerator. However, the calculated requirements to the laser driver for two cases are essentially different.

Table 1. Prospective Multi-Stage 2.5 TeV LWFA

Laser Parameters		
Laser wavelength, λ [μm]	10	1
Energy [J]	50	5
Pulse length, τ_L [ps]	1	0.1
Power, P [TW]	50	50
Focal spot radius, r_L [μm]	300	30
Laser field, E_L [TV/m]	0.4	4
Dimensionless laser strength, a	1.3	1.3
Repetition rate. f [kHz]	0.2	20
Average power [kW]	10	100
Wakefield Parameters		
Plasma density, n_e [cm^{-3}]	3×10^{15}	3×10^{17}
Plasma wavelength, λ_p [μm]	600	60
Acceleration gradient, E_a [GeV/m]	4.5	45
Pump depletion length [cm]	280	28
Phase detuning length [cm]	230	23
Assumed channel length [cm]	100	10
Energy gain per stage [GeV]	4.5	4.5
Collider Parameters		
Electrons/bunch. N_e	3×10^9	3×10^8
Number of bunches per pulse, ζ	3	3
ε_n due to gas scattering [m.rad]	4×10^{-7}	4×10^{-7}
$\sigma_\perp$ at β^*=5 μm focus, [Å]	7	7
Luminosity, Λ [cm^{-2}s^{-1}]	10^{35}	10^{35}
Bunch repetition rate, ζf [kHz]	0.6	60
Number of stages	555	555
Total length [m]	666	166

With the 1-μm laser, the short τ_L results in a proportionally small λ_p and N_e. Then, in order to satisfy the high luminosity requirement, the laser repetititon rate and, hence, the average output power increase quadratically. This becomes orders of magnitude beyond any reasonable expectation for picosecond solid state laser technology and does not fit into the anticipated wall-plug power limits. On the contrary, the parameters specified for the 10-μm laser look achievable for TWps-CO_2 lasers.

Another potential advantage of using a longer period plasma wave is the ease in producing the injected electron bunch which is short enough to fit inside the small portion of the wake period thus ensuring the good beam quality (small energy spread and emittance). For example, at τ_L=1 ps and the resonance plasma wavelength λ_p=600 μm the desirable electron bunch duration is $\tau_b \le 200$ fs. Contemporary photocathode RF guns tend to approach these requirements. In particular τ_b=370 fs electron bunches of 2.5×10^8 electrons, $\Delta p/p = 0.15\%$, and ε_n=0.5 mm.mrad. have been demonstrated with the ATF photocathode RF gun [6].

3 X-RAY AND GAMMA SOURCES BY COMPTON SCATTERING OF CO_2 LASER BEAMS

By Compton scattering of the laser photons from the TeV electron beam, a high brightness TeV photon beam can

be created. It opens an opportunity to study a variety of interaction processes by colliding e^-, e^+ and γ beams in any combination and at independently controlled polarization.

The expression for the maximum gamma photon energy for Compton backscattering is

$$\hbar\omega_\gamma = \left(x/x+1\right)E_e, \qquad (5)$$

where E_e is the electron energy, and $x = 4E_e\hbar\omega/m^2c^4$. At $x>>1$, $\hbar\omega_\gamma \approx E_e$. For CO_2 laser, $x>1$ at $E_e>0.5$ TeV.

A requirement to the laser wavelength for the $e^\pm \Rightarrow \gamma$ converter is set by rescattering of gamma photons on the laser beam into pairs through the reaction $\gamma+\lambda \Rightarrow e^-+e^+$. This occurs when when $\omega\omega_\gamma > m^2c^4/\hbar^2$. Based on this condition the optimum laser wavelength is derived:

$$\lambda[\mu m] = 4.2E_e[TeV] \qquad (6)$$

Then, the laser with λ=10.5 μm becomes the optimum choice for the 2.5 TeV collider.

For τ_L=1 ps, probability of the $e^\pm \Rightarrow \gamma$ conversion,

$$\chi = \sigma_c \mathbf{E}_L/\hbar\,\tau_L c^2, \qquad (7)$$

where σ_c=1.9×10^{-25} cm^2 is the Compton scattering cross-section, reaches unity at the laser pulse energy $\mathbf{E}_L \approx 1$ J [7].

The laser pulse repetition rate should match that of the e^-e^+ collider. The TWps-CO_2 laser technology is envisioned to provide the laser source delivering picosecond pulses of a 1 J energy at a several kW of average power to satisfy the requirements of the γ-γ collider. Relatively compact ~10 *l* discharge, high-pressure, fast-flow CO_2 lasers operating at a ~100 Hz repetition rate may serve this purpose when the energy stored in the laser medium is extracted at the wall-plug efficiency approaching 10% by a train of a hundred pulses of a 1 ps length each following at a ~1 ns period. A feasibility of building a solid state laser operating in a similar regime has been considered in Ref. [8].

Lasers may be used also in polarized positron sources for e^-e^+ collider. Here, the backward Compton scattering serves as an intermediate process followed by pair production on a target or via rescattering on laser photons. Polarization of the produced particles is easily controlled by the input laser beam. Picosecond CO_2 lasers are the optimum choice for this application as well due to the high average power and having ten times more photons per joule than solid state lasers. The projected positron source for the Japan Future Collider at KEK [9] will employ a hundred 1.5 kW CO_2 lasers with 150 Hz repetition rate and 50 ps pulse duration. This project appears to become the biggest utilization of CO_2 lasers in fundamental science.

Synchrotrons equipped with wiggler magnets are the sources of x-ray fluxes at a level of 10^{18} photon/sec. According to another approach to a relatively compact high-brightness x-ray generator called laser synchrotron source (LSS), the laser beam acts on relativistic electrons as an electromagnetic wiggler with a period 10^4-10^5 times shorter than the magnetic undulator. Thus, LSS produces proportionally higher energy photons than a conventional synchrotron source operating at the same e-beam energy. Therefore, LSS permits significant downsizing of the electron accelerator.

A combination of a high-gradient LWFA with LSS opens up the possibility of a compact wakefield LSS operating in x-ray and gamma regions. Table-top LSS, generating peak x-ray flux orders of magnitude above conventional synchrotron light sources, may be realized at the ATF using the 5-TW CO_2 laser and a 5 MeV photocathode electron gun (see Table 2) [7].

The ATF laser, designed for proof-of-principle experiments, is limited to the 0.1 Hz repetition rate. The above mentioned possibility of a high repetition rate multi-pulse TWps-CO_2 lasers makes it possible for ~10 kHz compact LSS to approach the time-averaged photon flux of conventional synchrotron light sources.

Table 2. Design Parameters for Table-Top LSS

LWFA	
Electron Energy [MeV]	5
Bunch Charge [nC]	0.1
Bunch Duration FWHM [fs]	300
Laser Peak Power [TW]	4
Laser Pulse Duration [ps]	3
Plasma Density [cm^{-3}]	3.5×10^{16}
Channel Radius [μm]	60
Channel Length [cm]	4
Acceleration gradient [GV/m]	6
Energy Gain [MeV]	50-250
LSS	
Laser Peak Power [TW]	1
Laser Pulse Duration [ps]	3
Laser Focus Radius [μm]	30
Tunable X-ray Photon Energy [keV]	4.7-1000
X-ray Pulse Duration [fs]	300
X-ray Photons per Pulse	3×10^9
X-ray Peak Flux [photons/s]	10^{22}

REFERENCES

[1] P.B. Corkum, *IEEE J. Quant. Electron.*, **QE-21**, 216 (1985)

[2] I.V. Pogorelsky, *et al*, "The First Terawatt Picosecond CO_2 Laser...", *Proceedings of 7th Advanced Accelerator Concepts Workshop*, Lake Tahoe, CA, October 12-18, 1996, to be published

[3] T. Tajima and J.M. Dawson, *Phys. Rev. Lett.*, **43**, 267 (1979)

[4] S. Chattopadhyay, *et al.* 1996 "A Laser Collider at 5 TeV...", *7th Advanced Accelerator Concepts Workshop*, Lake Tahoe, CA, October 12-18, 1996, AIP Proceedings, to be published

[5] V.L. Highland, *Nucl. Instr. & Methods in Phys. Res.*, **129**, 497 (1975)

[6] X.J. Wang, X. Qui, and I. Ben-Zvi, *Phys. Rev., E* **54**, R3121 (1996)

[7] I.V. Pogorelsky, "Ultra-Bright X-Ray and Gamma Sources...", submitted to *Nucl. Instr. & Methods in Phys. Res.* (1997)

[8] C.E. Clayton, N.A. Kurnit, and D.D. Meyerhofer, *Nucl. Instrum. & Methods in Phys. Res.*, **A355**, 121 (1995)

[9] T. Okugi, *et al.*, *Jpn. J. Appl. Phys.* **35**, 3677 (1996)

[10] S.V.Bulanov, *et. al.*, *IEEE Trans. on Plasma Sci.*, **24**, 393 (1996)

HIGH ENERGY-GAIN LASER WAKEFIELD ACCELERATION

K. Nakajima[1,4], M. Kando[2], H. Ahn[4], H. Dewa[4], H. Kotaki[4], F. Sakai[4],
S. Kondoh[4], H. Nakanishi[1], T. Ueda[3], M. Uesaka[3], T. Watanabe[3], and A. Ogata[1]
[1]High Energy Accelerator Research Organization (KEK), Tsukuba, Japan,
[2]Institute for Chemical Research, Kyoto University, Uji, Japan,
[3]Nuclear Engineering Research Laboratory, The University of Tokyo, Tokai, Japan,
[4]Japan Atomic Energy Research Institute, Tokai, Japan

Abstract

The laser wakefield electron acceleration up to 300 MeV has been observed in an underdense plasma driven by a 2 TW, 90 fs laser pulse synchronized with 17 MeV RF linac electron injector at 10 Hz. The electron acceleration was enhanced at a density higher than the resonant density due to gas ionization and self-channeling effects. The wakefield excitation has been confirmed by measuring the electron density oscillation of the plasma wave with the frequency domain interferometer.

1 INTRODUCTION

We report here demonstration of laser wakefield acceleration (LWA)[1] of an externally injected electron beam by a 2 TW 90 fs laser pulses in a plasma created in a gas-filled chamber. A large energy gain (~300 MeV) was attained, partly owing to self-channeling of a laser in a plasma and partly owing to larger acceleration gradient than the prediction of a linear. Large blue shift was observed in the laser spectrum in a dense plasma, but no trace of the Raman scattering was found. These facts suggest a new mechanism of LWA using a laser power well below the critical power of the relativistic self-channeling[2], given by $P_c = 17(\omega_0^2/\omega_p^2)$ GW with ω_0 being the laser frequency and ω_p, the plasma frequency. A frequency domain interferometer certified the density oscillation in the laser wakefield[3].

2 LASER WAKEFIELD ACCELERATION

The LWA has great potential to produce ultra-high-field gradients of plasma waves excited by intense ultrashort laser pulses[1, 4]. The wakefield results from the ponderomotive force exciting the plasma wave with the frequency $\omega_p = \sqrt{4\pi e^2 n_e/m_e}$ in a plasma with an ambient electron density n_e. The maximum amplitude of an axial wakefield is achieved at the plasma wavelength $\lambda_p = \pi\sigma_z$, where σ_z is a temporal $1/e$ half-width of the pulse. Assuming Gaussian beam propagation of the laser pulse at the peak power P in an underdense plasma ($\omega_0 \gg \omega_p$), a peak amplitude of the accelerating wakefield is

$$eE_z = \sqrt{\frac{\mu_0}{\pi\epsilon_0}}\frac{P}{m_e c^2}\left(\frac{\lambda_0}{\lambda_p}\right)\left(\frac{k_p\sigma_z}{2Z_R}\right)\exp\left(-\frac{k_p^2\sigma_z^2}{4}\right),$$

where λ_0 is the laser wavelength, $k_p = 2\pi/\lambda_p$ and $Z_R = \pi R_0^2/\lambda_0$ is the vacuum Rayleigh length, R_0 is the spot radius at the focus. The maximum energy gain is given by $\Delta W = eE_z L_{ac}$ with the acceleration length L_{ac}.

In a homogeneous plasma, however, diffraction of the laser propagation limits the laser-plasma interaction distance to $L_{ac} \sim \pi Z_e$, where Z_e is the effective Rayleigh length. For the resonant plasma density, $n_e = 1/\pi r_e \sigma_z^2$ where r_e is the classical electron radius,

$$\Delta W_{\max}[\mathrm{MeV}] \sim 850 P[\mathrm{TW}]\lambda_0[\mu\mathrm{m}]/\tau_0[\mathrm{fs}] \times (Z_e/Z_R),$$

where $\tau_0 = 2\sqrt{\ln 2}\sigma_z/c$ is the FWHM pulse duration. Note that the maximum energy gain is independent of a focal spot size of laser pulses for Gaussian propagation if $Z_e = Z_R$. Optical guiding has been proposed[5] in order to exceed this limit. Our recent experiments using intense femtosecond laser pulses report that a self-channeling has been observed under the critical power of the relativistic self-focusing[6].

3 EXPERIMENTAL SETUP

We have constructed the LWA test facility consisting of the T^3 laser system and the electron beam injector[8]. The Ti:sapphire T^3 laser system based on the chirped-pulse amplification at $\lambda_0 = 790$ nm produces output pulses compressed by a grating to 90 fs with an energy of > 200 mJ or a peak power of > 2 TW at the repetition rate of 10 Hz. We used the 2856 MHz RF linac as an electron injector to produce a 17 MeV single bunch beam with a 10 ps FWHM pulse duration containing ~ 1 nC at the repetition rate of 10 Hz.

In our experimental setup, focusing optics and the injection electron beamline were installed in the vacuum chamber filled with He gas. Laser pulses were focused with f/10 off-axis parabolic mirror with a focal length of 480 mm. The measured focal spot radius was 13 μm. An electron beam from the injector is brought to a focus in the chamber with the FWHM beam size of 0.8 mm through a beamline consisting of a triple focusing magnet and a permanent quadrupole triplet. The RF linac and the beamline are separated with a 20 μm thick titanium window from the interaction chamber to maintain ultrahigh vacuum in the electron injector. Since the multiple scattering of electrons at this window causes emittance blow-up, a collimator slit is installed at the downstream of the window to reduce the beam emittance. The beam collimation reduced an electron charge to ~100 pC per pulse. Only the electrons injected

0-7803-4376-X/98/$10.00 © 1998 IEEE

to the diameter less than a half laser spot size would be trapped and accelerated by the wakefield. An electron pulse was synchronized to laser pulses with the phase locked control of the mode-locked oscillator. The phase locked loop maintains synchronization of the oscillator repetition period (79.33 MHz) with every 36th RF period of the linac (2856 MHz). A streak camera with a time resolution of 200 fs measured a timing jitter between the laser pulse and Cherenkov radiation from the electron beam. Synchronization between the two pulses was achieved within the rms jitter of 3.7 ps.

The energy of accelerated electrons was measured with the magnetic spectrometer consisting of a dipole magnet and an array of 32 scintillation detectors. Injected electrons undergoing no acceleration were swept out of the detectors by the spectrometer magnet following a permanent quadrupole doublet. The spectrometer covered the energy range of 10~300 MeV. The energy calibration of the spectrometer was made by varying the magnetic field to measure a 17 MeV electron beam from the RF linac.

The timing between laser and electron pulses was adjusted by changing a phase delay of the reference RF to the phase locked loop so that streak images of two pulses were overlapped. After a He gas was filled in the acceleration chamber, fine adjustment of overlapping two spots of laser and electron beams was carried out within 50 μm. Two sets of pulse height data of the scintillator array were taken with pump laser pulses and without them as a background. A net pulse height proportional to the number of electrons accelerated was obtained from subtracting the data without the pump pulses from the data with them. The number of electrons was estimated to be ranged from 2 to 4 per ADC count for all detectors.

4 EXPERIMENTAL RESULTS

In the acceleration experiment the gas pressure of He was scanned from 1 Torr to 300 Torr. Figure 1 shows the pressure dependence of energy gain spectra of electrons accelerated by the laser peak power of 1.8 TW. The maximum energy gain up to 300 MeV was obtained. When the electron pulse preceded the pump laser pulse, no acceleration of electrons was observed. Accelerated electrons visibly appeared as the electron pulse was delayed. No accelerated electron was observed at a delay of 1 ns. We have tried to observe the self-trapping of plasma electrons due to wakefield, without the electron beam injection, increasing the gas pressure up to 760 Torr. No electrons with energies higher than ~1 MeV were however observed. It implies that the ultrashort laser pulses of 100 fs do not excite the stimulated Raman instability and resultant large amplitude wakefields.

The side scattered laser light from the plasma region were imaged onto a CCD camera through a 10 nm FWHM interferential filter to measure the laser intensity distribution. Fig. 2 shows an intensity profile of the scattered light projected onto the propagation axis at various gas pressures. The lineout width of the scattered light proportional to the laser intensity gives a good estimate of the acceleration length. The acceleration field gradient was obtained from the measured maximum energy gain and the FWHM length of the scattered light lineout equal to $2Z_e$. Figure 3 shows the peak accelerating gradient for the laser peak powers of 0.9 TW and 1.8 TW as a function of the gas pressure of He. The data indicate a good agreement with theoretical prediction based on the linear fluid model below 10 Torr, assuming the focal spot radius of 13 μm. However, they show that the acceleration occurs even at much higher pressures than a plasma wake resonance. Recent particle-in-cell simulations elucidate that a large amplitude wakefield can be excited by self-modulation at the front of a laser pulse in rapidly ionizing plasmas[2]. In Fig. 3 the acceleration gradient jumps to ~15 GeV/m above 20 Torr for 1.8 TW. Above this pressure of 20 Torr, it was also observed that the length of the lineouted laser light turned out constant, ~1 cm. These phenomena suggest that self-channeling accompanied by the electron density depletion may take place above 20 Torr.

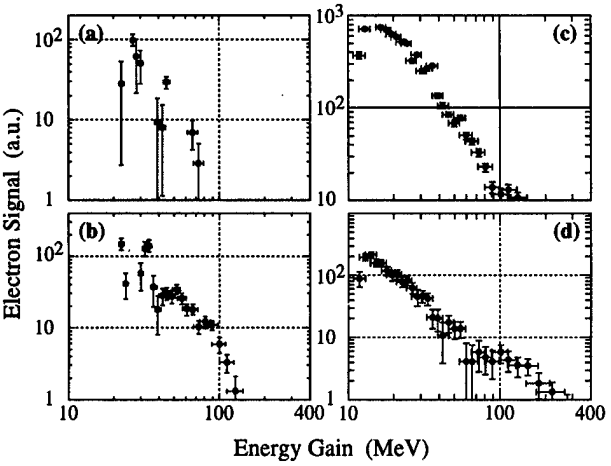


Figure 1: Energy gain spectra of accelerated electrons for a) 3.4 Torr, P=0.9 TW, b) 20 Torr, P=0.9 TW, c) 2 Torr, P=1.8 TW, and d) 20 Torr, P=1.8 TW.

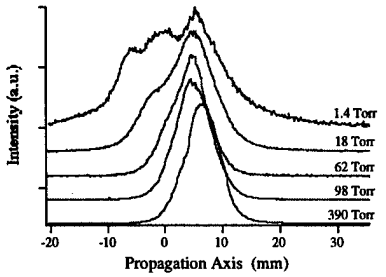


Figure 2: The lineouts of the side scattered laser light at various He gas pressures for P=2.5 TW.

The onset of self-channeling is also inferred from the spectra of the forward scattered laser light shown in Fig. 4. At the low pressure of 1 Torr, only a small blue-shift was observed as the laser intensity increases. When the pressure turned out to be as high as 20 Torr, however, a drastic blue-

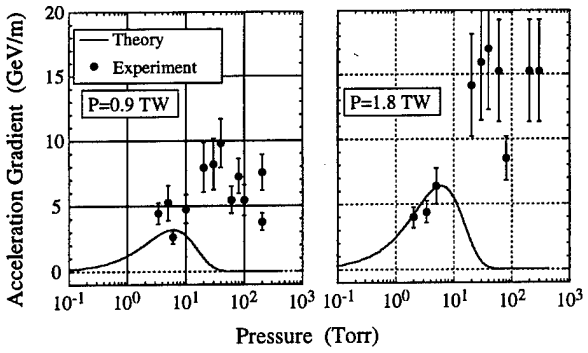


Figure 3: The peak accelerating field gradient deduced from the maximum energy gain and the acceleration length. The solid curve shows theoretical expectation for the spot radius $R_0 = 13$ μm.

shifting of the laser light was induced above 0.5 TW. As the peak power increased to more than 2 TW, a whole spectrum of the incident laser pulse at 790 nm was shifted to 750 nm. It has been known that a large amount of the self-phase modulation results from a long distant self-channeling[7]. In our experiment we have not observed red-shifting nor forward Raman scattering.

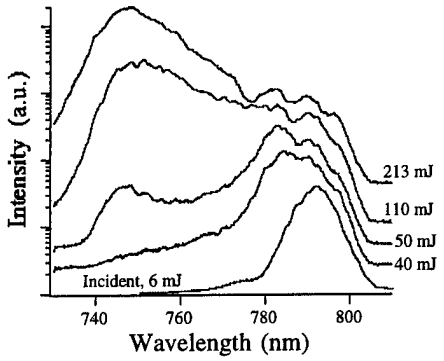


Figure 4: Forward scattered spectra measured in a He gas of a) 1 Torr and b) 22 Torr as the laser pulse energy increases.

In order to make confirmation of wakefield excitation, we measured the plasma oscillation with the frequency-domain interferometer[3]. Figure 5 shows the electron plasma wave measured at 2 Torr at the pump peak power of 1 TW. The frequency of the density oscillation is deduced to be 1.7×10^{13} rad/s from the measured period of the density oscillation, while the plasma frequency is 2.1×10^{13} rad/s assuming a fully ionized plasma at 2 Torr. A frequency decrease of the plasma wave results from nonlinear wakefield excitation. The density perturbation was $\delta n/n_e \sim 10\%$ corresponding to the longitudinal wakefield of ~3 GeV/m. This measured amplitude is in good agreement with the accelerating wakefield theoretically expected.

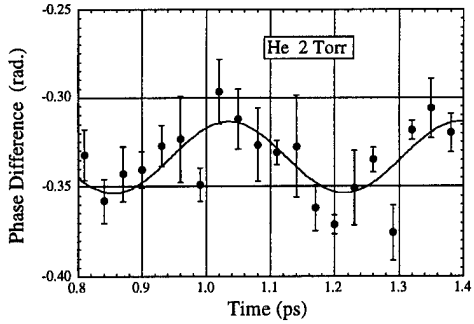


Figure 5: Measurement of the plasma density oscillation excited by a 1 TW pump power in a He gas of 2 Torr. The solid curve shows a fit of the plasma wave with oscillation period of 360 fs.

5 CONCLUSION

We have carried out electron acceleration by wakefields in a static He plasma excited by a 2 TW, 90 fs T^3 laser synchronized with the 17 MeV RF linac electron beam injector at the repetition rate of 10 Hz. We have observed high energy electrons accelerated up to 300 MeV by the wakefield of ~15 GeV/m excited over a few cm long underdense plasma. Acceleration enhancement at higher pressures than the resonant pressure may be elucidated from the pulse self-modulation due to ionization and self-channeling of the laser pulse in a plasma. These effects must help to achieve an efficient electron acceleration up to the higher energy than 1 GeV. A direct measurement of the electron density oscillation by the frequency domain interferometry verified that the wakefield excitation is consistent with the results of acceleration experiments.

6 REFERENCES

[1] T. Tajima and J.M. Dawson, Phys. Rev. Lett. **43**, 267 (1979); P. Sprangle *et al.*, Phys. Rev. Lett. **53**, 2146 (1988).

[2] S. Kato, Y. Kishimoto, and J.K. Koga, to be published in Proc. Int. Conf. on Plasma Physics (ICPP 96), Nagoya (1996).

[3] J.R. Marquès *et al.*, Phys. Rev. Lett. **76**, 3566 (1996); C.W. Siders *et al.*, Phys. Rev. Lett. **76**, 3570 (1996).

[4] K. Nakajima *et al.*, Phys. Rev. Lett. **74**, 4428 (1995); A. Modena *et al.*, Nature **377**, 606 (1995).

[5] E. Esarey *et al.*, Phys. Fluids B, **5**, 2690 (1993).

[6] M. Kando *et al.*, to be published in AIP Conf. Proc..

[7] A. Braun *et al.*, Opt. Lett., **20**, 73 (1995).

[8] K. Nakajima, Phys. Plasmas, **3**, 2169 (1996).

FOCUSING OF RELATIVISTIC ELECTRON BUNCHES AT THE WAKE-FIELD EXCITATION IN PLASMA.

Ya. B. Fainberg, N. I. Ayzatsky, V. A. Balakirev, A. K. Berezin, A. N. Dovbnya, V. I. Karas', V. A. Kiselev, V. A. Kushnir, A. F. Linnik, V .V. Mitrochenko, V. D. Stepin, I. N. Onishchenko, A. P. Tolstoluzhsky, V. V. Uskov

Abstract

Analytical and numerical investigations of the trajectories of probing beam electrons in a two dimensional wake-field, generated in a plasma by a dense bunch of relativistic electrons with Gaussian longitudinal and transverse distributions of density have been carried out. Based on the calculations of probing beam deviations, the diagnostic instruments are developed for the parameters of experiments conducted at NSC KIPT. The diagnostic instruments include an electron gun generating a $10keV$ electron beam with a current of $10\mu A$ and $2mm$ in diameter, which passes through the chamber of interaction and falls on the collector of $10mm$ diameter. The collector (screen) is placed in front of the first plate of a microchannel amplifier which consists of three microchannel plates (MCP) with sizes between 20 and $30mm$. The $3kV$ voltage was applied to each plate. The total amplification of MCP amplifier is 10^4 to 10^5 depending on the number of particles incident on the first plate. As a result of probing beam deviations due to the excited wake-field, the electrons fall on the first plate of the amplifier and are registered by its anode located behind the third plate. The calculated probing beam deviations and the amplification attained with the MCP amplifier permit one to detect and investigate the electrical wake-fields excited by a sequence of relativistic bunches (number of particles in a bunch is $2 \cdot 10^9$, energy is $14MeV$) in a plasma of $10^{11} - 10^{13}cm^{-3}$ density . The intensity of the fields registered by this technique is no less than $2kV/cm$.

1. INTRODUCTION

Measurements of HF-electric oscillations in a plasma is the currently central problem. So, high-intensity HF-fields are excited in a plasma during penetration of intense laser pulses and relativistic electron bunches. Such fields can be used for acceleration of charged particles [1]. For successful experimental realization of charged particle acceleration in a plasma it is nessary to elaborate simple and reliable methods of electric-field measurements in the plasma. This paper proposes such a method that is based on using a probing electron beam and microchannels plates [2]. This diagnostics is alternative to the well-known methodical procedure of plasma wake-field investigation using a streak-camera [3]. By way of example we consider the proposed method for measurements of wake-fields excited by a sequence of relativistic electron bunches.

2. SPATIAL STRUCTURE OF PLASMA WAKE-FIELDS

Let us determine the spatial distribution of wake-fields in a plasma excited by a relativistic electron bunch. We shall consider the bunch with Gaussian longitudinal and transverse profiles:

$$\vec{j}_0 = j_m e^{(-t_1^2/t_b^2 - r^2/\sigma_r^2)}\vec{z}. \tag{1}$$

where $\vec{j}_0$ is the current density of the bunch, $j_m = I_0/\pi\sigma_r^2$ is the maximum current density, I_0 is the peak current, $t_1 = t - z/c$, t_b is the bunch duration, σ_r is the transverse size of the bunch, $\vec{z}$ is the unit vector along the bunch motion, z, V are the longitudinal and radial coordinates, c is the light velocity in vacuum. We neglect the difference between bunch and light velocities, this is quite justified in the case of ultra-relativistic limit consideration.

The axial bunch of current density (1) excites in a plasma the electromagnetic field whose components are described by the expressions:

$$E_z = -\frac{4I_0}{\sigma_r^2\omega_p}\Pi_{\parallel}(\eta)Z_{\parallel}(\tau) \tag{2}$$

$$E_r = -\frac{4I_0}{\sigma_r^2\omega_p}\Pi_{\perp}(\eta)Z_{\perp}(\tau) - \frac{4I_0}{\sigma_r^2\omega_p}\Pi_{\perp}(\eta)e^{(-\tau^2/\tau_b^2)}. \tag{3}$$

$$H_{\varphi} = \frac{4I_0}{\sigma_r^2\omega_p}\Pi_{\perp}(\eta)e^{(-\tau^2/\tau_b^2)}. \tag{4}$$

Here $\tau = \omega_p(t - z/c)$, $\eta = \omega_p r/c$, ω_p is the plasma frequency,

$$\begin{aligned}
\Pi_{\parallel}(\eta) &= K_0(\eta)\int_0^{\eta} I_0(\eta_0)e^{(-\eta_0^2/\eta_b^2)}\eta_0 d\eta_0 + \\
&\quad I_0(\eta)\int_{\eta}^{\infty} K_0(\eta_0)e^{(-\eta_0^2/\eta_b^2)}\eta_0 d\eta_0, \\
\Pi_{\perp}(\eta) &= -\partial\Pi_{\parallel}/\partial\eta \\
Z_{\parallel}(\tau) &= \int_{-\infty}^{\tau} e^{(-\tau_0^2/\tau_b^2)}\cos(\tau - \tau_0)d\tau_0, \\
Z_{\perp}(\tau) &= \int_{-\infty}^{\tau} e^{(-\tau_0^2/\tau_b^2)}\sin(\tau - \tau_0)d\tau_0,
\end{aligned}$$

$\tau_b = \omega_p t_b$, $\eta_b = \omega_p\sigma_r/c$.

0-7803-4376-X/98/$10.00 © 1998 IEEE

At large distances behind the bunch $(z-\tau) >> \sigma_z^2, \sigma_z = c\tau_b$ being the longitudinal bunch size, the wake-field has the form of a harmonic wave with electric field components

$$E_z = -\frac{4\sqrt{\pi}\tau_b I_0}{\sigma_r^2 \omega_p} e^{-\tau_b^2/4} \Pi_{\parallel}(\eta) \cos\tau \qquad (5)$$

$$E_r = -\frac{4\sqrt{\pi}\tau_b I_0}{\sigma_r^2 \omega_p} e^{-\tau_b^2/4} \Pi_{\perp}(\eta) \sin\tau \qquad (6)$$

As it follows from expressions (2)- (6) the longitudinal component of electric field E_z is described by the function $\Pi_{\parallel}(\eta)$, and the transverse components E_r and H_φ are determined by the function $\Pi_{\perp}(\eta)$.

3. PROBING ELECTRON BEAM DYNAMICS IN WAKE-FIELDS

In the proposed method, a nonrelativistic probing electron beam is injected perpendicularly to the direction of relativistic bunch motion (longitudinal axis z) at a distance from the axis (impact parameter). The electric wake-field intensity is determined by the value of beam particles deflection for the given length L (base). For simplicity we neglect the transverse size of the probing beam, assuming it infinitely thin. As the probing beam injection continuously occurs in the periodic HF-field with components (5), (6), then in the plane being perpendicular to $x = L$ the thin probing beam depicts closed curve.

The probing beam particle dynamics in the axial wake-field (5- 6) is described by a set of equations of motion that take the following forms in the Cartesian coordinate system

$$\begin{aligned}
U_x \frac{dU_x}{dX} &= -\epsilon \frac{X}{\eta} \Pi_{\perp}(\eta) \sin\tau, \\
U_x \frac{dU_y}{dX} &= -\epsilon \frac{Y}{\eta} \Pi_{\perp}(\eta) \sin\tau, \\
U_x \frac{dU_z}{dX} &= -\epsilon \Pi_{\parallel}(\eta) \cos\tau, \\
\frac{d\tau}{dX} &= \frac{1}{\beta_0 U_x}(1 - \beta_0 U_z), \\
\frac{dY}{dX} &= \frac{U_y}{U_x},
\end{aligned} \qquad (7)$$

where $\vec{U} = \vec{V}/V_0$ is the dimensionless velocity, V_0 is the initial velocity of the probing beam, $(X, Y, Z) = (\omega_p/c)(x, y, z)$ are the dimensionless Cartesian coordinates, $\beta_0 = V_0/c$, $\epsilon = \frac{4\sqrt{\pi} I_0 \tau_b}{\beta_0^2 \eta_b^2 I_A} e^{-\tau_b^2/4}$ is the dimensionless wake-field amplitude, $I_A = mc^3/e = 17kA$ is the Alfven current.

The set of equations (7) was solved by numerical methods for the following parameters of the plasma, relativistic electron bunch and probing beam: plasma density $n_p = 2 \cdot 10^{11} cm^{-3}$,
plasma frequency $\omega_p = 2.5 \cdot 10^{10} s^{-1}$,
transverse size of a bunch $\sigma_r = 7 \cdot 10^{-2} cm$,
longitudinal size of a bunch $\sigma_z = 7 \cdot 10^{-1} cm$,
bunch current $I_0 = 12A, 24A, 36A$,
corresponding wake-field amplitude $\epsilon = 19.5, 39, 58.5$.

Simulation was performed for 100 particles uniformly distributed in input phases relative to the wake wave $2\pi > \tau_0 > 0$, τ_0 is the initial phase value.

If the bunch current increases or the number of bunches grows, then the maximum displacement of probing electrons becomes greater. So, for a single bunch of $36A$ or for 3 bunches with a $12A$ current in each bunch the displacement increases up to $2.1cm$.

4. EXPERIMENTAL FACILITIES

For intensity measurements of the wake-field excited in a plasma by short bunches of relativistic electrons we have elaborated diagnostic facilities based on the displacement of a $10keV$ probing electron beam current between 10 and $50\mu A$, and $2mm$ diameter, which was produced in a three-electrode electron gun. This beam passed across the interaction chamber perpendicularly to the axis of relativistic bunch motion. The choice of probing beam energy was dictated by the fact that the time of flight of the probing electron over the wake-field excitation zone ($\sim 1cm$) should be commensurable with a half of the excited wave period (for $n_p = 10^{11} cm^{-3}$ $T/2 \sim 150ps$). The scattering of probing electrons in the plasma due to elastic collisions is not essential. Indeed, the collisional length of probing electrons with the chosen energy is greater than the interaction region $l_e = V_e \nu_e = 100cm$, where $\nu_e^{-1} = \frac{2.5 \cdot 10^4}{\Lambda/10} \frac{T_e^{3/2}}{Z n_p}$ is the collision frequency, V_e is the electron velocity, $T_e \simeq 3eV$ is the plasma temperature, $n_p = 10^{12} cm^{-3}$ is the plasma density, Λ is the Coulomb logarithm, Z_e is the plasma ion charge.

According to the calculations presented above, we have constructed the facilities for measuring the excited wake-field intensity. At about $3kV/cm$ the probing beam of $10kV$ should be displaced by $0.1cm$ in the interaction region. With the base length $L = 11cm$ to the registration place the probing electrons are displaced by $1cm$. This geometric configuration was modelled by using two deflecting plates fed by pulse voltage.

As a registration system for deflected probing beam an MCP amplifier [2] was used. It consists of three rectangular plates, each of $20 * 30mm$ size and $1mm$ thickness, with holes of $15\mu m$ in diameter and a structure step of $17.4\mu m$. A voltage of $3kV$ was applied to the current-carrying planes of the plates. Behind the third plate a collector was placed.

The signal from the collector was sent to the oscillograph through the emitter follower. The rate of amplification was 10^4 to 10^6 depending on the number of electrons incoming to each hole of the first plate. The amplifier has an individual vacuum pump, because the pressure in the amplifier chamber should be lower than $10^{-6} torr$.

Before the first plate of the amplifier there was a cop-

per circular collector of $10mm$ diameter that registered the probing beam current. Being deflected by the excited wake-field the probing electrons get to the first plate, and after amplification the current is registered by the main collector. With the availability of a sectional collector the magnitude of probing beam displacement can be measured, and hence, the intensity of the excited wake-field can be evaluated.

5. CONCLUSIONS

The plasma wake-field diagnostics consisting of a probing electron beam and microchannel plates for current registration is proposed. For the same experimental arrangement the topography of excited wake-field has been obtained and evaluated. The trajectories of probing electrons in this field have been studied. Experimental facilities have been elaborated that allow one to measure the wake-field intensity of several kV per cm, excited by a relativistic bunch of $15MeV$, $12A$, by using the probing beam of $10keV$ energy and 10 to $50\mu A$ current.

This work was supported in part by Project STCU N298.

6. REFERENCES

[1] P.Chen, J.M. Dawson, R. Huff, T. Katsouleas Phys. Rev. Lett. , **54**, 692(1985).

[2] C.J. Armentrout Rev. Sci. Inst. **5**, 1179(1985).

[3] K.Nakajima, A. Enomoto, N. Kobayashi et al. Nucl. Inst. and Methods in Phys. Res. **A292**, 12(1990).

EXPERIMENTAL OBSERVATION OF ELECTRON BEAM FOCUSING THROUGH PLASMA LENSES*

R. Govil, S. J. Wheeler, W. P. Leemans, Ernest Orlando Lawrence Berkeley National Laboratory, University of California, Berkeley, CA 94720, USA.

Abstract

A comprehensive experimental study of focusing of relativistic electron beams with overdense and underdense plasma lenses is being conducted at the Beam Test Facility at LBNL [1]. Short (15ps rms) electron bunches, from the 50 MeV LBNL Advanced Light Source injector are transported through laser produced plasmas. The electron beam spot size and divergence at the plasma lens is adjusted using quadrupoles. The plasmas are 1-5 cm long with densities of 10^{13} -10^{14} cm^{-3}. By changing the laser intensity and shape, the plasma density and profile can be controlled. This allows for exploration of both the charge and current compensation regimes, by changing the ratio of the plasma wavenumber, k_p, to the electron beam size, σ_r. Experimental results on the production of plasma through two-photon UV ionization and electron beam diagnostics have been presented earlier [2]. Here we present results from experimentally observed plasma focusing for overdense lenses in charge and current compensation regimes. Detailed interferometric results from the production of highly overdense plasmas are also discussed.

1 INTRODUCTION

The next generation of colliders require tightly focused beams with high luminosity. To focus charged particle beams for such applications, a plasma focusing scheme has been proposed [3]. Plasma lenses can be overdense (plasma density, n_p, much greater than electron beam density, n_b) or underdense ($n_p < 2n_b$). In overdense lenses the space-charge force of the electron beam is canceled by the plasma and the self magnetic force causes the electron beam to pinch. The focusing gradient is non-linear, resulting in spherical aberrations. In underdense lenses, the self-forces of the electron beam cancel, allowing the plasma ions to focus the beam. Although for a given beam density, a uniform underdense lens produces smaller focusing gradients than an overdense lens, it produces better beam quality. The underdense lens focusing strength can be increased by tapering the density of the plasma for optimal focusing [4]. The underdense lens performance can be enhanced further by producing adiabatic plasma lenses to avoid the Oide limit on spot size due to synchrotron radiation by the electron beam [5].

The plasma lens experiment at the Beam Test Facility (BTF) is designed to study the properties of plasma lenses in both overdense and underdense regimes. In particular, important issues such as electron beam matching, time response of the lens, lens aberrations and shot-to-shot reproducibility are being investigated.

2 EXPERIMENTAL SETUP

The Beam Test Facility (BTF) uses the ALS injector which provides 50 MeV electron beam with a charge of 1-2 nC in 15 ps long bunches. The unnormalized emittance is 0.2 - 0.5 mm-mrad. The BTF line is equipped with a wide range of diagnostics including integrating current transformers for charge

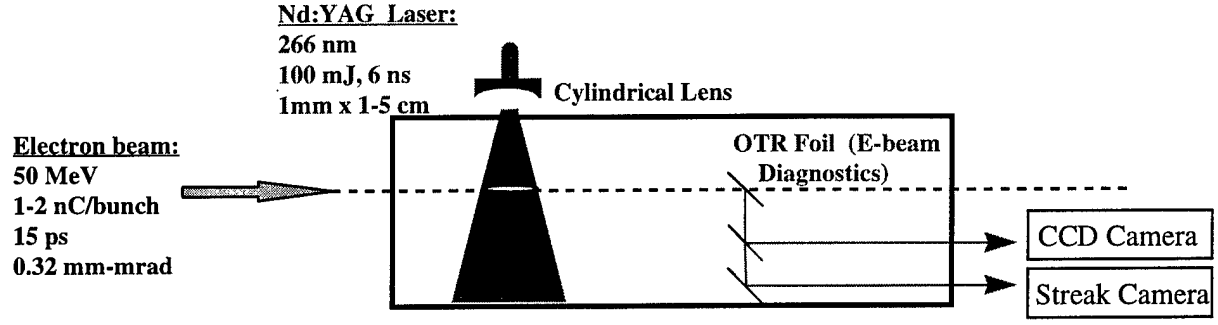


Figure 1. Layout for the plasma lens experiment. The laser is brought to a line focus at the position of the e-beam. Backward OTR is collected for electron beam diagnostics and imaged on to CCD and Streak cameras.

* Work supported by the Director, Office of Energy Research, Office of High Energy Physics and Nuclear Research, High Energy Physics Division, U.S. Department of Energy under Contract No. DE-AC03-76SF00098.

0-7803-4376-X/98/$10.00 © 1998 IEEE

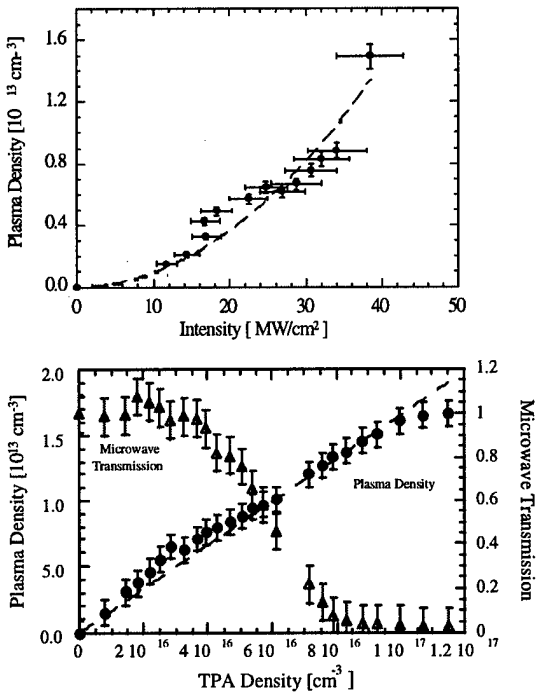


Figure 2. Plasma density (solid dots) scales quadratically with laser intensity and linearly with TPA density. The hollow triangles represent the transmitted microwave signal strength.

measurement, high bandwidth BPMs, fluorescent screens, and optical transition radiation (OTR) diagnostics [6].

The electron beam is focused into a plasma chamber that is separated from the ultra-high vacuum beam line by an 8 μm thick Kapton window. Plasma is produced in tripropylamine (TPA) vapor through two-photon ionization using a 266 nm laser beam. The ionizing laser beam enters the plasma chamber at right angles to the electron beam. The laser is brought to a line focus at the position of the electron beam. The plasma length is adjusted by changing the laser focusing and the density is controlled through the TPA fill pressure and laser intensity.

3 PLASMA PRODUCTION

For ionizing the vapor, 1064 μm radiation from a Nd:YAG laser is frequency quadrupled to provide 6 ns long 266 nm pulses. The two-photon ionization process can be expressed as,

$$n_p = \alpha \frac{n_0 I^2 \Delta t}{h\nu}, \qquad [1]$$

where n_p is the plasma density [cm^{-3}], n_0 is the neutral gas density [cm^{-3}], I is the laser pulse intensity [W/cm^2], Δt is the laser pulse length [s], and $(h\nu)$ the photon energy [Jsec]. Here all the other constants have been absorbed in α, the two-photon ionization coefficient [cm^4/W].

To achieve plasma lengths on the order of a few centimeters, the laser beam is defocused horizontally using a cylindrical defocusing lens (Figure 1). To maintain the laser intensity (and therefore, the plasma density), the beam is focused in the vertical direction.

The plasma density is measured through microwave interferometry at 94.3 GHz described previously [2]. The microwave signal is launched transversely to the plasma sheet. The plasma density is calculated by measuring the relative microwave phase shift introduced by the plasma. Since the plasma densities are close to critical density for microwave beam absorption, a two-channel in-quadrature measurement technique [7] is used to compensate for absorption effects. For plasmas with thickness comparable to collisionless skin-depth, this technique allows super-critical plasma densities to be measured. The plasma density was measured as a function of neutral gas fill pressure and laser intensity as shown in Figure 2. The two-photon ionization coefficient, α, was measured to be 2.5×10^{-29} W/cm^4. Plasma densities up to 2×10^{14} cm^{-3} were measured using this technique. At this density the transmitted microwave amplitude was only 3% of the initial amplitude, in agreement with calculations.

3 ELECTRON BEAM DIAGNOSTICS

The electron beam is diagnosed using optical transition radiation that is produced by a charged particle at it passes through a boundary between two media with different dielectric constants. The radiation contains information about the size, divergence and energy of the source charged particle beam.

A five micron thin nitrocellulose foil coated with

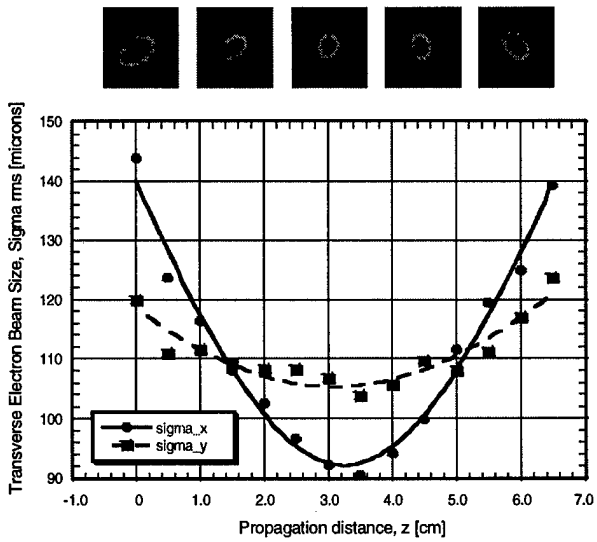


Figure 3. Measurement of beam size through OTR at various positions along the direction of propagation. The solid and dashed lines represent the best fit through the transverse beam size, σ_{rms}, along the x-axis and y-axis, respectively.

high reflectivity aluminum is inserted in the electron beam path. When the beam passes through the foil, it emits transition radiation, which is imaged onto a CCD camera. The OTR foil is mounted on a motorized stage. As the stage is moved along the trajectory of the electron beam, a direct measurement of the beam size as a function of propagation distance is obtained (Figure 3). To study the temporal dynamics of the plasma lens, OTR is imaged to a streak camera with 2ps resolution [2].

4 ELECTRON BEAM FOCUSING BY BEAM-INDUCED PLASMAS

A relativistic electron beam passing through a gas can collisionally ionize the gas. The density of the plasma, n_p, produced by the e-beam is given by,

$$n_p = \left|\frac{dE}{dx}\right| \frac{N_b \sigma_z \rho_m}{E_{th}}, \qquad [2]$$

where dE/dx is the stopping power of electron beam [eVcm^2/g], N_b is the electron beam density [cm^{-3}], σ_z is the electron bunch length [cm], ρ_{gas} is the mass density of background gas [cm^{-3}], and E_{thresh} is the ionization threshold of the gas [eV]. For BTF parameters, this corresponds to a plasma density of approximately 10^{11} - 10^{12} cm^{-3}. Since the plasma is produced by the electron beam, the spatial profile of the plasma follows the evolution of the electron beam and is calculated to be: $n_p(z) = n_{p\max}\beta_0 / \sqrt{\beta_0^2 + s^2}$, where s=z-ct and β_0 is the minimum value of the electron beam beta function in the plasma. The plasmas produced through electron beam ionization are underdense. The focusing strength of an underdense plasma lens is given by $K = 2\pi r_e n_p / \gamma$, where r_e is the classical electron radius, γ the electron beam energy and n_p the plasma density.

Figure 4 shows the measured electron beam size as a function of propagation distance inside the plasma chamber. In vacuum, the beam size at the waist is measured to be 130 μm. As the neutral gas pressure is increased, the beam ionizes the vapor, and is focused by the resulting plasma to 100 μm.

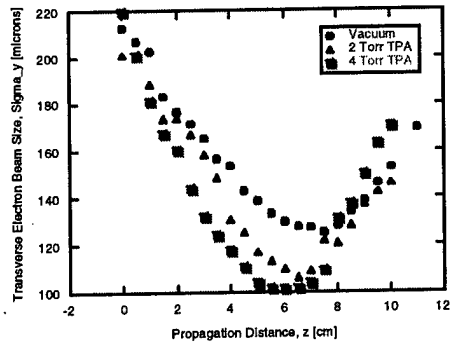


Figure 4. Measured electron beam focusing by beam-ionized plasma for various neutral gas densities.

5 ELECTRON BEAM FOCUSING BY OVERDENSE LASER PRODUCED PLASMAS

The laser beam is temporally and spatially aligned with the electron beam. The electron beam size as a function of propagation distance is measured with and without the laser beam (Figure 5). When the laser beam is turned on to produce plasma, the electron beam is focused to a smaller spot size. A corresponding increase in electron beam peak intensity is measured using OTR. The strength of focusing is found to depend strongly on electron beam beta function matching into the plasma.

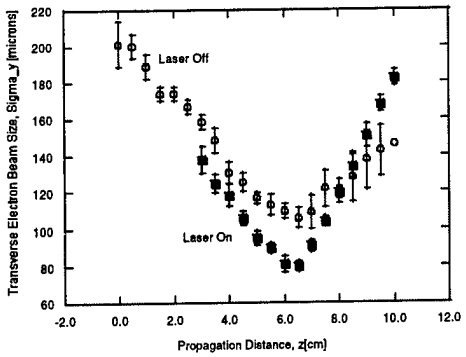


Figure 5. Measured electron beam focusing by laser-produced plasma. When the laser is turned on, the laser produced plasma focuses the electron bunch to a smaller spot size.

6 CONCLUSION

The 50 MeV electron beam from the ALS injector has been focused through plasma lenses at BTF. Electron beam focusing by beam induced plasmas has been studied using optical transition radiation diagnostics. Laser produced overdense plasmas have been observed to focus the electron beam. Both types of lenses show strong dependence on e-beam beta function matching. Currently, highly overdense plasmas are being studied to observe return current cancellation. Detailed simulations are being conducted for comparison with theoretical predictions and temporal dynamics of plasma lenses is being experimentally investigated.

REFERENCES

[1] W. Leemans et al., Proc. 1993 Part. Accel. Conf., 83 (1993).
[2] R. Govil et al., Proc. 1995 Part. Accel. conf., 776 (1995).
[3] P. Chen, Part. Accel. 20, 171 (1987).
[4] T. Katsouleas, et al., Proc. 1992 Adv. Accel. Workshop (1992).
[5] P. Chen, et al., Phys. Rev. Lett. 64, 1231 (1990).
[6] M. de Loos et al., Proc. European Part.Accel. Conf. (1994).
[7] W. Barry, private communication.

DRIVING LASER PULSE EVOLUTION IN A LASER WAKEFIELD ACCELERATOR[†]

P. Volfbeyn, P. B. Lee, J. S. Wurtele, W. P. Leemans, Ernest Orlando Lawrence Berkeley National Laboratory, University of California Berkeley, Berkeley, CA 94720, and G. Shvets, Princeton Plasma Physics Laboratory, Princeton, NJ 08543

Abstract

A numerical study of the coupling between a high intensity laser pulse and a plasma wake is presented, in the context of laser wakefield acceleration in a hollow channel. One dimensional self-consistent equations are derived and numerically solved to provide a more detailed description of the laser pulse evolution for the case of propagation in a uniform plasma. The model obtained provides a simple method for inferring the plasma wake characteristics from measurement of changes in phase and amplitude of the driving laser pulse.

1 INTRODUCTION

Laser driven plasma accelerators, based on the excitation of extremely high longitudinal electric fields with phase velocity close to the speed of light [1] has received much theoretical and experimental attention for nearly two decades. A survey and comparison of different methods for laser acceleration and summaries of experimental and theoretical progress can be found in references [2] - [5]. In this paper we focus on the resonant Laser Wakefield Accelerator (LWFA), in which an ultra-short laser pulse ($\omega_p \Delta t \approx \pi$, where Δt is the laser pulselength , $\omega_p^2 = \frac{4\pi n e^2}{\gamma m_0}$, n is the local plasma density, γ is the relativistic Lorentz factor, e and m_0 are the charge and the rest mass of the electron) is used to excite a plasma wave via the ponderomotive force from the gradient in the laser pulse intensity.

Diffraction limits acceleration length, and hence the final energy of an accelerated charged particle in the LWFA to about one Rayleigh range. Laser guiding in plasma channels has been proposed as a means to extend the acceleration length. The index of refraction of a plasma with density n can be approximated by $\eta \approx 1 - \frac{\omega_p^2}{2\omega^2}$, where ω is the laser frequency. Similar to an optical fiber, a plasma channel can provide optical guiding if the index of refraction peaks on axis. This requires a density profile that has a local minimum on axis. Guiding of laser pulses with moderate intensities (around 10^{15}W/cm^2) over distances in excess of 20 Rayleigh ranges has been demonstrated experimentally [6].

For acceleration purposes, excitation of large amplitude plasma waves requires laser intensities on the order of 10^{18} W/cm^2 (for a laser wavelength ~1 micron). At such high intensities the index of refraction of the plasma is modified by its interaction with the laser pulse through relativistic effects as well as through a plasma density modulation arising from the excited plasma wave. The interaction with plasma affects both longitudinal and transverse properties of the laser pulse, which, in turn, leads to changes in the coupling between the laser pulse and the plasma as well as in properties of the accelerating plasma wave. These issues are important for evaluation and optimization of the efficiency of LWFA designs. In this paper a one dimensional (1-D), nonrelativistic analytic model of the driving pulse evolution and supporting simulation results will be presented, with emphasis on the effects of energy depletion, longitudinal laser pulse shape distortion, and changes in the group velocity and center wavelength of the pulse.

As in conventional fiber optics, the transverse characteristics of the laser beam are determined by the transverse profile of the guide, i.e. the plasma density profile. There are two main types of channels that have been considered in the literature, the parabolic channel and the hollow channel. The parabolic channel has a cylindrically symmetric, parabolic density profile with minimum density on axis. It is usually assumed that the plasma wake in a parabolic channel is purely electrostatic or, equivalently, that the channel size is large compared to the plasma wavelength [3], [7]. The hollow channel refers to a cylindrically symmetric step plasma density profile, where the density inside the channel is zero, and the wall thickness is much less than a plasma wavelength.

A hollow channel is particularly favorable for the propagation of a high quality electron beam. It supports a single electromagnetic plasma wave mode and can be designed to support only one guided laser mode [3], [8]. This suppresses the laser hose instability [3], [7]. Full control over the profile of the channels remains a major experimental challenge and density profiles are typically neither parabolic nor hollow. The transverse fields of the plasma wave excited in an arbitrary profile channel have not been found analytically [3], [9], although much pro-

[†] Work supported by the US Department of Energy contracts FDDEFG-03-95ER-40936 and DE-AC03-76SF00098.

0-7803-4376-X/98/$10.00 © 1998 IEEE

gress has been made in numerically determining the electromagnetic plasma wake modes [10]. In what follows the analysis for the hollow channel case is presented. A similar treatment would be applicable to a channel with an arbitrary transverse plasma density profile, provided that the plasma wake fields were known.

In Sec. 2 the 1-D equations to model the evolution of the laser pulse in the plasma are derived and numerical solutions of these equations is presented. Conclusions and discussion comprise Sec. 3.

2 SELF-CONSISTENT EVOLUTION OF THE LASER PULSE

To study the effect of pump depletion on the driving laser pulse we start with the wave equation:

$$\nabla \times \nabla \times \vec{a}_0 + \frac{1}{c^2}\frac{\partial^2 \vec{a}_0}{\partial t^2} = \frac{4\pi e}{mc^3}\vec{J}. \qquad (1)$$

In the limit that the longitudinal velocity of the electrons remains much smaller than the speed of light and the transverse size of the laser pulse is much larger than the wavelength, the transverse canonical momentum of an electron moving in the laser fields is conserved; so that if the electrons are initially at rest $\gamma V/c = -a_0$, where V is the electron velocity, and $\gamma = 1/\sqrt{1-V^2/c^2}$. The transverse current density then is J=-nea$_0$c and

$$\frac{4\pi e}{mc^3}J = -\frac{\omega_p^2}{c^2}a_0. \qquad (2)$$

Assuming the vector potential is purely transverse, a transversely homogeneous plasma, and a plane laser wave and performing a change of variables $z = z, \xi = z - ct$ transforms Eq. (1) into

$$\frac{\partial^2 a_0}{\partial z^2} + 2\frac{\partial^2 a_0}{\partial z \partial \xi} = k_p^2 a_0. \qquad (3)$$

Using $a_0 = be^{-i\Phi}$, where b is real and a slow function of z and ξ, and Φ is also real and a slow function of z, (while Φ has fast variations in ξ), the real part of Eq. (3) becomes

$$-\frac{\partial \Phi}{\partial(kz)}\frac{\partial \Phi}{\partial(k\xi)} = \frac{\chi}{2}, \qquad (4)$$

and the imaginary part is

$$\frac{\partial}{\partial(kz)}\left(b\frac{\partial \Phi}{\partial(k\xi)}\right) = -\frac{\partial \Phi}{\partial(kz)}\frac{\partial b}{\partial(k\xi)}, \qquad (5)$$

where equations were made dimensionless by dividing both parts by the wave number of the laser, k^2, and treating ω_p/ω as a small quantity, Eqs. (4) and (5) contain only the lowest order in ω_p/ω terms. Also, the quantity $\chi = k_p^2/k^2$ was introduced.

To simulate the effects of the laser pump depletion self-consistently we start with an expression for the plasma density modulation [14], obtained under assumption that the perturbation is small compared to the unperturbed density, $\delta n/n_i << 1$,

$$\frac{\delta n}{n_i}(\xi) = \frac{b^2(\xi)}{4} + k_{pi}\int_{\xi}^{\infty}\sin(k_{pi}(\xi-\xi'))\frac{b^2(\xi')}{4}d\xi' \quad .(6)$$

The right hand side of Eq. (4) can be rewritten as

$$\frac{\chi}{2} = \frac{\omega_{pi}^2}{2\omega^2}\left(1 + k_{pi}\int_{\xi}^{\infty}\sin(k_{pi}(\xi-\xi'))\frac{b^2(\xi')}{4}d\xi'\right) \quad (7)$$

to the lowest order in b^2, where the relativistic correction to the plasma frequency was taken into account.

The evolution of the amplitude b and frequency $\frac{\partial \Phi}{\partial \xi}$ of a laser pulse as it propagates in a plasma has been obtained by integrating Eqs. (4) and (5) numerically. Fig. 1 shows the longitudinal profile of the driving laser pulse vector potential and the relative change in the refractive index of the plasma, corresponding to the plasma wake.

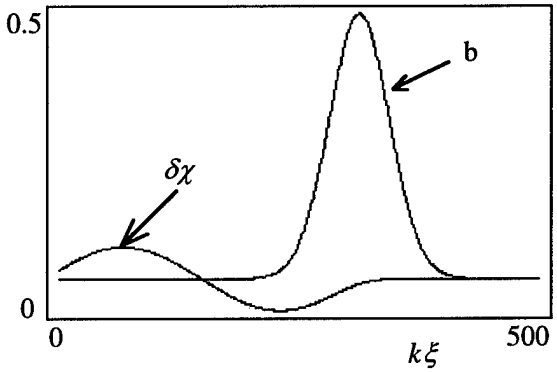


Figure 1. The amplitude of the laser pulse vector potential, b, gaussian pulse shape with the pulselength calculated to maximize the coupling to the plasma wake, and the plasma oscillation, $\delta\chi$, from Eq. (7). Plotted as function of distance from the head of the laser pulse, $k\xi$.

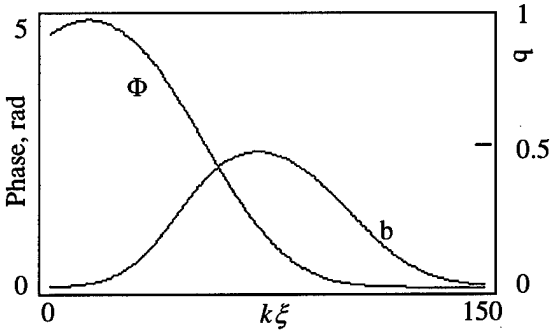


Figure 2. The amplitude of the laser pulse vector potential, b, and the phase, Φ, as a function of $k\xi$ after propagating for one dephasing length. Calculated by integrating Eqs. (4) and (5) numerically with χ calculated from Eq. (7), with $\omega_p/\omega_0 = 1/50$, a laser pulse with a gaussian pulse shape with the pulselength

calculated to maximize the coupling to the plasma wake, and amplitude $a_0 = 0.5$.

It is because different parts of the laser pulse experience different values of the index of refraction, the laser pulse develops a temporal phase chirp. In Fig. 2, b and Φ are shown as functions of ξ after the laser pulse propagated a distance $z=L_{deph}$.

The frequency spectrum of the laser pulse is redshifted and widened (Fig. 3a) resulting in a change in the laser pulse-shape (Fig. 3b).

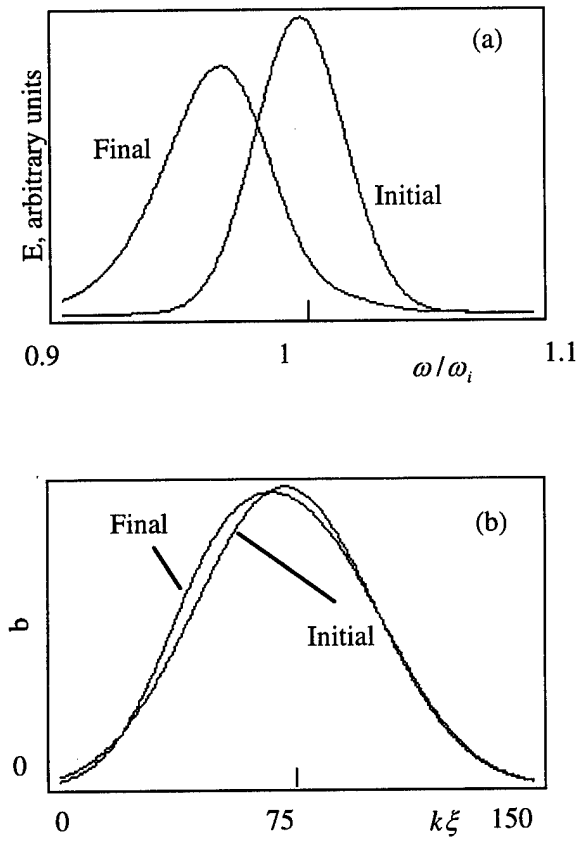


Figure 3. a). Spectrum of the laser pulse (unnormalized, arbitrary units) before and after propagating for one dephasing length. b). The amplitude of the laser pulse vector potential, b, before and after propagating for one dephasing length. Calculated by integrating Eqs. (4) and (5) numerically with χ calculated from Eq. (7), with $\omega_p/\omega_0 = 1/50$, a laser pulse with a gaussian pulse shape with the pulselength calculated to maximize the coupling to the plasma wake, and amplitude $a_0 = 0.5$.

The amplitude of the plasma wake remained nearly constant during the interaction.

3 CONCLUSIONS

A set of 1D equations for the evolution of a driving laser pulse in a homogeneous plasma was derived. The equations were solved numerically. The solutions demonstrated spectral red-shifting of the laser pulse. For realistic parameters, the shift in spectrum is quite pronounced. Measurement of the time resolved amplitude and phase of the driving laser pulse should supply valuable information about the plasma wake. The observed increase in the coupling strength supports the idea of trying to increase efficiency of a single stage accelerator by depleting the laser pulse energy, before dephasing terminates the acceleration.

REFERENCES

[1] T. Tajima and J.M. Dawson, "Laser electron accelerator", Phys. Rev. Lett., vol. 43, 267, (1979); Tajima, T. "Laser accelerator for ultra-high energies", Proc. 12th Int. Conf. on High-Energy Accelerators, Edited by: F. T. Cole and R. Donaldson, Batavia, IL, USA: Fermi Nat. Accelerator Lab, p. 470, 1983.

[2] E. Esarey, P. Sprangle, J. Krall, and A. Ting, "Overview of Plasma Based Accelerator Concepts", IEEE trans. on Plasma Science, v. 24, no. 2, p. 252, 1996.

[3] G. Shvets, "Interaction of intense lasers with plasmas", Ph.D. dissertation, MIT, 1995.

[4] C.E. Clayton, K. A. Marsh, A. Dyson, M. Everett, A. Lal, W. P. Leemans, R. Williams, and C. Joshi, Phys. Rev. Lett. 70, 37 (1993).

[5] N. E. Andreev, L. M. Gorbunov, V. I. Kirsanov, A. A. Pogosova, and R. R. Ramazashvili, "Resonant excitation of wakefields by a laser pulse in a plasma," JETP Lett., vol. 55, no. 10, pp. 571-576, 1992.

[6] C. G. Durfee III and H. M. Milchberg, Phys. Rev. Lett. 71, 2409 (1993).

[7] G. Shvets and J. S. Wurtele, "Instabilities of short pulse laser propagation through plasmas", Phys. Rev. Lett., vol. 73, p. 3540, 1994.

[8] T.C. Chiou, T. Katsouleas, C. Decker, W. B. Mori, G. Shvets, J. S. Wurtele, "Laser wakefield acceleration and optical guiding in a hollow plasma channel", Phys. Plasmas, vol. 2, pp. 310-318, 1995.

[9] G. Shvets , J. S. Wurtele, T. C. Chiou, and T. C. Katsouleas, "Excitation of Accelerating Wakefields in Inhomogeneous Plasmas", IEEE trans. on Plasma Science, v. 24, no. 2, p. 351, 1996.

[10] B. A. Shadwick, G. Shvets, J. S. Wurtele, Bull. Am. Phys. Soc., v. 41, p.1601.

[11] S. V. Bulanov, I. N. Inovenkov, V. I. Kirsanov, N. M. Naumova, and A. S. Sakharov , "Nonlinear depletion of ultrashort and relativistically strong laser pulses in an underdense plasma", Phys. Fluids B 4 (7), July 1992.

[12] J. M. Rax and N. J. Fisch, "Nonlinear relativistic interaction of an ultrashort pulse with a cold plasma", Phys. Fluids B, vol. 4, pp. 1323-1331, 1992.

[13] W. Horton and T. Tajima, "Pump depletion in the plasma-beat-wave accelerator", Phys. Rev. A, vol.34, (no.5):4110-19, Nov. 1986.

[14] W.P. Leemans, C. W. Siders, E. Esarey, N. E. Andreev, G. Shvets, and W. B. Mori, "Plasma guiding and wakefield generation for second generation experiments", IEEE trans. on Plasma Science, v. 24, no. 2, p. 331, 1996.

LASER ACCELERATION IN VACUUM WITH AN OPEN IRIS-LOADED WAVEGUIDE*

Ming Xie, Lawrence Berkeley National Laboratory, Berkeley, CA 94720, USA

Abstract

An open iris-loaded waveguide structure is considered for laser acceleration of highly relativistic particle in vacuum. Complete characterization of all eigenmodes are given in analytical form for the structure. In particular the dominant radially polarized TM mode is evaluated in detail for laser acceleration. The entire parameter space is searched and it is found that below the laser damage threshold of the structure an acceleration gradient around 1 GV/m can be obtained over a phase slippage length of 10s of cm with TWs laser in the wavelength range from 1 to 10 μm.

1 INTRODUCTION

The Open Iris-Loaded waveguide Structure (OILS) considered in this paper is made of a series of equally spaced thin screens each having a circular aperture. It differs from the usual iris-loaded linac structure in the following aspects: first of all it does not have side walls thus called an open structure; secondly all its characteristic dimensions i.e., radius of the aperture (a) and separation between the adjacent apertures (L), are much larger than laser wavelength (λ). As a result the eigenmodes of the structure are determined dominantly by diffraction. Recently, Pantell [1] presented a calculation of the longitudinal field component in the structure using the numerical method of Fox-Li [2] and discussed the possibility of laser acceleration. But, soon after that Pantell [3] claimed that an additional fast axial phase oscillation absent from the Fox-Li's original calculations [2] was found and thus concluded that the structure is not suitable for laser acceleration.

However the claimed fast phase oscillation does not exist. The numerical method of Fox-Li is not an appropriate approach to this problem. To demonstrate net energy gain for a test particle, the field everywhere along the trajectory needs to be calculated. The kernel of the Fresnel integral used in Fox-Li's method becomes increasingly fast oscillatory for the field at locations close to the diffracting aperture, causing the integral extremely cumbersome to calculate and prone to various sources of numerical and systematic errors. To avoid the numerical difficulties fully analytical approach is taken in this paper.

2 EIGENMODES OF THE OPEN WAVEGUIDE

Starting from source free Maxwell Equations in vacuum, we seek axially symmetric, radially polarized TM mode of the form: $\mathbf{E}(r,z,t) = \mathbf{E}_r + \mathbf{E}_z, \mathbf{H}(r,z,t) = \mathbf{H}_\varphi$. All other types of modes can be obtained following the same procedures. For fields with $\exp(-i\omega t)$ dependence, each component satisfies the scalar Helmholtz wave equation, $\nabla^2\Phi + k^2\Phi = 0$, where $k = \omega/c$. Under the conditions $L \gg \lambda$ and $a \gg \lambda$, the wave equation can be further reduced to a parabolic equation

$$\nabla_t^2\Psi + 2ik\frac{\partial\Psi}{\partial z} = 0\,, \qquad (1)$$

where $\Phi(r,z) = \Psi(r,z)\exp(ikz)$, $\Psi(r,z)$ is the envelope slowly varying in z, and ∇_t^2 is the transverse Laplacian.

For open waveguide without side walls it is convenient to solve first for the radial component. With $\Phi = E_r(r,z)$, Eq.(1) becomes

$$\frac{\partial^2\Psi}{\partial r^2} + \frac{1}{r}\frac{\partial\Psi}{\partial r} - \frac{1}{r^2}\Psi + 2ik\frac{\partial\Psi}{\partial z} = 0\,. \qquad (2)$$

This is the equation with azimuthal mode number $m = 1$, and its solution may be labeled as $\Psi_{1n}^{(r)}(r,z)$, where n is the radial mode index, and the superscript indicates the mode is radially polarized. The radially polarized mode is a linear superposition of two degenerate, orthogonal linearly polarized modes $\Psi_{1n}^{(x)}(r,z)\sin(\varphi)$ and $\Psi_{1n}^{(y)}(r,z)\cos(\varphi)$.

Our goal is to solve Eq.(2) for the eigenmodes in an OILS. This problem is shown to be equivalent to finding the eigenmodes in a Fabry-Perot optical resonator with two circular plane mirrors of radius a, separated by a distance L [2]. Under appropriate boundary conditions, Vainshtein [4] obtained solution of the eigenmodes to all orders inside such a resonator. Once E_r is solved, all other field components can be determined directly through Maxwell equations. With all spatial-temporal dependence explicitly included, the solution reads:

$$E_z = E_a J_0(k_r r)\exp[i(k_z z - \omega t)]\,, \qquad (3)$$

$$E_r = -i(k_z/k_r)E_a J_1(k_r r)\exp[i(k_z z - \omega t)]\,, \qquad (4)$$

$$H_\varphi = E_r/Z_{TM}\,, \qquad (5)$$

$$k_r = \frac{\nu_{1n}}{a[1+\eta(1+i)/M]}\,, \quad k_z = k - k_r^2/2k\,, \qquad (6)$$

where $M = \sqrt{8\pi N}$, N is Fresnel number defined as $N = a^2/\lambda L$, $\eta = -\zeta(1/2)/\sqrt{\pi} \approx 0.824$, $\zeta(z)$ is Riemann's Zeta function, $Z_{TM} = (k_z/k)Z_0$, Z_{TM} is the impedance of TM wave, Z_0 is the vacuum impedance, ν_{1n} is the nth zero of Bessel function satisfying $J_1(\nu_{1n}) = 0$, and E_a is peak acceleration gradient. It should be noted that as a result of slowly varying envelope approximation, the modes are characterized by, $|k_z| \sim k$ and $|k_r| \ll k$. The solution is more accurate at small diffraction loss per cell, or equivalently when $N \gg 1$, which happens to be the regime favorable for laser acceleration, as will be discussed later.

* This work was supported by the U.S. Department of Energy under contract No. DE-AC03-76SF00098.

0-7803-4376-X/98/$10.00 © 1998 IEEE

3 ACCELERATOR CONSIDERATIONS

In this section, we exploit properties of the $TM_{1n}^{(r)}$ mode, and derive necessary formulas and scaling laws for the evaluation of OILS as an acceleration structure.

3.1 General Characteristics and Formulas

For convenience, let's introduce a complex quantity $\alpha \equiv \alpha_r + i\alpha_i = ik_r^2/2k$, and from Eq.(6) we have

$$\alpha_r = \frac{4\nu_{1n}^2\eta(M+\eta)}{L\left[(M+\eta)^2+\eta^2\right]^2}, \tag{7}$$

$$\alpha_i = \frac{2\nu_{1n}^2 M(M+2\eta)}{L\left[(M+\eta)^2+\eta^2\right]^2}. \tag{8}$$

The $\{z,t\}$ dependence for all field components becomes

$$\{E_z, E_r, H_\varphi\} \sim e^{i[(k-\alpha_i)z-\omega t]-\alpha_r z}, \tag{9}$$

and power flow through the waveguide is simply

$$P(z) = P_0 e^{-2\alpha_r z}, \tag{10}$$

$$P_0 = \frac{\pi a^2 |k_z/k_r|^2 E_a^2}{Re(Z_{TM})}\int_0^1 |J_1(k_r a\rho)|^2 \rho d\rho. \tag{11}$$

As seen from Eqs.(9,10), the mode is characterized by a phase velocity, $v_p = \omega/(k-\alpha_i)$, larger than c, and a power attenuation due to diffraction loss at the apertures. However, for sufficiently large N both phase slippage per cell, $\phi_c = \alpha_i L$, and fractional power loss per cell, $\alpha_c = 2\alpha_r L$, can be made as small as desired, as seen from Eqs.(7,8). Let's define a slippage length, $L_s = \pi/\alpha_i$, over which an acceleration phase slippage of π is experienced by a highly relativistic particle ($v \approx c$) moving along the z-axis. The energy gain of the test particle traversing a slippage length thus can be calculated as

$$\Delta W_s = eE_a\int_0^{L_s} \sin(\alpha_i z)e^{-\alpha_r z}dz = eE_a L_s T_s, \tag{12}$$

where T_s is a reduction factor due to a full π phase slippage and the attenuation of the acceleration field over a slippage length, given by

$$T_s = \frac{1+e^{-(\alpha_r/\alpha_i)\pi}}{\pi[1+(\alpha_r/\alpha_i)^2]}. \tag{13}$$

Two other figures of merit, the shunt impedance per unit length Z_L and the Q factor, are given here for comparison with traditional microwave acceleration structures

$$Z_L = \frac{|E_z(r=0,z)|^2}{-dP/dz} = \frac{E_a^2}{2\alpha_r P_0}, \tag{14}$$

$$Q = \frac{\omega U}{-dP/dz} = \frac{\pi}{\lambda\alpha_r(v_g/c)} \approx \frac{\pi}{\lambda\alpha_r}, \tag{15}$$

where U is the field energy per unit length given by $U = P/v_g$, and v_g is the group velocity very close to c.

Another important concern for high gradient acceleration by a waveguide is surface field on the structure which is limited by damage threshold. For OILS, we define an edge field by $E_e = |E_r(r=a, z=0)|$, and it can be shown that the condition $E_e > E_a$ always holds.

3.2 Weak Diffraction Limit and Scaling Laws

Before going to the exploration of OILS performance over design parameter space using the general formulas provided in Sec.(3.1), it is instructive to look at more transparent weak diffraction limit and scaling laws for several important performance parameters. We will consider the dominant radial mode with $n = 1$ and $\nu_{11} = 3.832$. Keeping only the leading term while taking the limit $N \gg 1$, we have

$$\frac{E_a}{E_e} \longrightarrow \frac{\sqrt{N}(\lambda/a)}{\sqrt{\pi\eta}\,|J_0(\nu_{11})|} \approx 1.7\sqrt{N}(\lambda/a), \tag{16}$$

$$L_s \longrightarrow \frac{4\pi^2 a^2}{\nu_{11}^2\lambda} \approx 2.7\,a^2/\lambda = 2.7\,N\,L, \tag{17}$$

$$\alpha_s \longrightarrow 1 - e^{-\eta\sqrt{2\pi/N}} \approx 1 - e^{-2.1/\sqrt{N}}, \tag{18}$$

$$\Delta W_s[\mathrm{MeV}] \longrightarrow 2.9\sqrt{N}\,a[\mathrm{mm}]\,E_e[\mathrm{GV/m}], \tag{19}$$

$$I_{av}[\mathrm{PW/cm^2}] \longrightarrow 1.7\times10^{-4}NE_e^2[\mathrm{GV/m}], \tag{20}$$

$$\frac{I_e}{I_{av}} \longrightarrow \frac{(\nu_{11}\eta)^2}{4\pi N} \approx 0.79/N, \tag{21}$$

where α_s is the fractional power loss per slippage length, I_{av} is the laser intensity averaged over waveguide cross section at $z = 0$, thus the required laser power is given by $P_0 = \pi a^2 I_{av}$, and I_e is the laser intensity at the edge of aperture. Also we have $T_s \to 2/\pi$, and with $\Gamma = k - \alpha_i$,

$$v_p = \frac{\omega}{\Gamma} \approx \frac{c}{1-\frac{1}{2}\left(\frac{\nu_{11}\lambda}{2\pi a}\right)^2}, \tag{22}$$

$$v_g = \frac{d\omega}{d\Gamma} \approx \frac{c}{1+\frac{1}{2}\left(\frac{\nu_{11}\lambda}{2\pi a}\right)^2}. \tag{23}$$

The most important characteristics of OILS as a potentially attractive structure for laser acceleration is revealed by Eq.(16). It is shown that the ratio of acceleration to edge (surface) field is enhanced from the usual scaling for all near field accelerations [5], λ/a, by a large factor, $\sqrt{N}$. As a result, substantial acceleration gradient can be obtained on the axis with a favorable intensity scaling, Eq.(21), even though the boundary is hundreds of wavelengths away.

4 PERFORMANCE EVALUATION

With the parameter definitions and general formulas given in Sec.(3.1), we are now ready to evaluate OILS performance. It is noted that there are only four independent parameters and they are chosen for convenience to be $\{\lambda,\ E_e,\ a/\lambda,\ N\}$. We are interested in only a few discrete wavelengths where bright sources are available, in particular at 1 and 10 μm. The maximum tolerable edge field

E_e is determined by laser damage threshold, which can often be set at a constant value given laser wavelength and material of the structure. It can be inferred from the experimental data [6] that 10 GV/m seems to be a reasonable upper limit for E_e at $\lambda = 1\mu$m. Thus we are left with only two independent parameters $\{a/\lambda,\ N\}$ to vary, all dependent parameters can therefore be conveniently visualized in contour plots.

Shown in Fig.(1-3) are the peak acceleration gradient, energy gain per slippage length, and the required laser power, respectively, for $\{\lambda = 1\mu\text{m}, E_e = 10\text{GV/m}\}$. Four examples including $\{\lambda = 10\mu\text{m}, E_e = 5\text{GV/m}\}$ cases with more complete listing of performance parameters are given in Table 1. All these results can be readily scaled to other parameter regime of interest according to the scaling laws given in Sec.(3.2).

Table 1. Example Cases of Acceleration Parameters

CASES	IA	IB	IIA	IIB
$\lambda(\mu\text{m})$	1	1	10	10
a(mm)	0.5	0.25	1	0.5
L(mm)	1	0.125	2	1
N	250	500	50	25
E_a(GV/m)	0.54	1.5	0.6	0.84
ΔW_s(MeV)	227	161	100	35
L_s(cm)	69	17	28	7.2
P_0(TW)	34	17	7.1	0.92
I_{av}(PW/cm^2)	4.3	8.6	0.23	0.12
I_e(TW/cm^2)	13	13	3.3	3.3
ϕ_c(degree)	0.26	0.13	1.3	2.5
$\alpha_c(\%)$	0.019	0.0067	0.2	0.56
$\alpha_s(\%)$	12	8.8	25	33
Q(10^6)	33	12	0.62	0.11
$Z_L(\text{M}\Omega/\text{m})$	0.045	0.25	0.049	0.14
T_s	0.62	0.62	0.59	0.58
E_e(GV/m)	10	10	5	5

5 CONCLUSIONS

I have presented a systematic evaluation of laser acceleration inside an OILS assuming well established eigenmode. Analysis of planar and rectangular structures can be carried out parallel to what's done here. The scaling laws derived from the powerful analytical approach of Vainshtein have both revealed the simplicity of the acceleration mechanism and uncovered some surprisingly favorable characteristics of such a diffraction dominated structure. However I have not touched upon such critical issues as wakefield, beam loading, and ways to couple laser power in and out of the structure without significantly degrading acceleration performance. But, I do want to point out in passing that the axicon scheme used to generate radially polarized laser beam for the inverse Cherenkov laser acceleration experiment [7] appears to be an interesting candidate for OILS mode injection. Further investigation on this and other critical issues will be presented in a forthcoming paper.

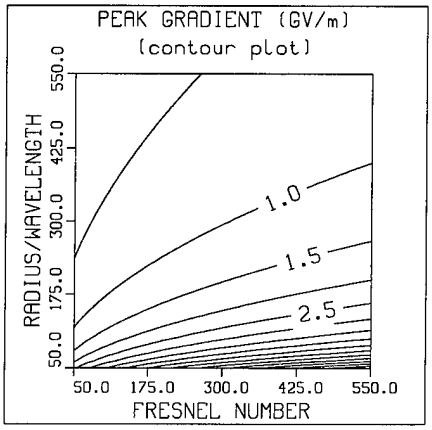


Figure 1: E_a vs. $\{N, a/\lambda\}@\lambda = 1\mu\text{m}, E_e = 10\text{GV/m}$.

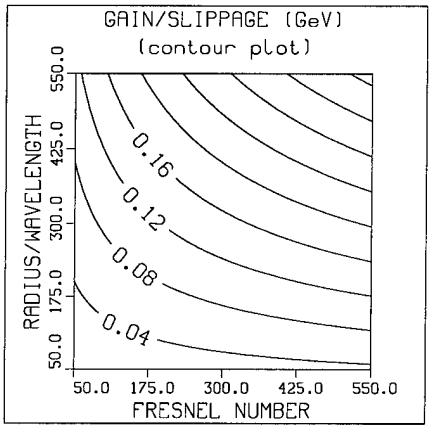


Figure 2: ΔW_s vs. $\{N, a/\lambda\}@\lambda = 1\mu\text{m}, E_e = 10\text{GV/m}$.

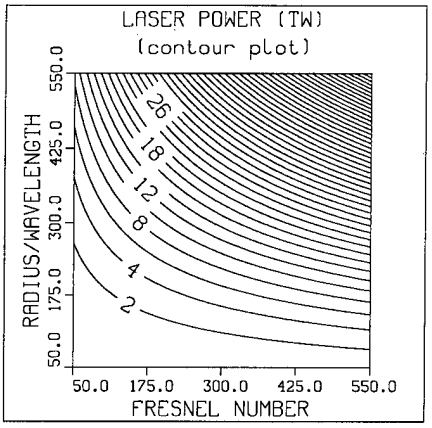


Figure 3: P_0 vs. $\{N, a/\lambda\}@\lambda = 1\mu\text{m}, E_e = 10\text{GV/m}$.

6 REFERENCES

[1] R. Pantell, talk presented at FEL conference, August,1996.

[2] A. G. Fox and T. Li, Bell System Technical J., 40(1961)453.

[3] R. Pantell, private comm. at AAC workshop, October,1996.

[4] L. A. Vainshtein, Soviet Physics JETP, 17(1963)709.

[5] R. B. Palmer, AIP Conference Proceedings, 335(1995)90.

[6] B. C. Stuart, el al., Phys. Rev. Lett., 74(1995)2248.

[7] W. D. Kimura, et al., Phys. Rev. Lett., 74(1995)546.

ION CYCLOTRON RESONANCE ACCELERATOR

T.L. Grimm, C.T. Ramsell, and R.C. York
National Superconducting Cyclotron Laboratory
Michigan State University
East Lansing, MI 48824

Abstract

The Ion Cyclotron Resonance Accelerator (ICRA) is ideally suited for the production of radioisotopes or neutrons. The general theory of the ICRA and the designs of and simulation results for a proof-of-principle, one MeV ICRA and a 10 MeV ICRA for isotope or neutron production are presented.

1. INTRODUCTION

The Ion Cyclotron Resonance Accelerator (ICRA), based on the operating principles of cyclotrons and gyrotrons, should provide beam suitable for the production of radioisotopes for positron emission tomography (PET) or neutrons for material research at a fraction of the cost of the cyclotrons or linacs presently used in these applications. In addition, the ICRA technique holds the potential for higher intensities and energies, as well as for the acceleration of heavier ions.

In a cyclotron, the accelerated particles are axially confined in a solenoidal magnetic field and accelerated azimuthally. In a gyrotron, the energy of a dc electron beam is converted into microwaves in a resonant cavity within a solenoidal magnetic field. The inverse process of electron acceleration by an rf-driven gyrotron structure has also been demonstrated [1].

The ICRA extends cyclotron resonance acceleration to ions by using a magnetron rf structure operating at a harmonic of the cyclotron frequency and a superconducting solenoid. Gyrotron structures use waveguide modes on the order of a wavelength, and hence would be too large at the low frequencies required for ions. However, since a magnetron rf structure is basically a lumped circuit, it can be much smaller than a wavelength [2]. The combination of a magnetron rf structure and the high magnetic fields (>5T) of a superconducting magnet, provide an rf structure which can be placed in a solenoid of reasonable diameter.

Unlike many accelerators, the beams produced in an ICRA will range in energy from that injected to the peak accelerated energy (E_p). However, for the applications discussed, all energies above $E_p/2$ will be productive. Beam extraction is inherently simple in the ICRA since all beam drifts axially through the solenoid to the target position where it can be isolated from the accelerator mitigating maintenance and radiation shielding issues.

Because a compact, superconducting solenoid does not require any steel, the ICRA could be light (<2 tons) and hence portable making it possible for the radioisotope or neutron source to be shared by several institutions or used in the field.

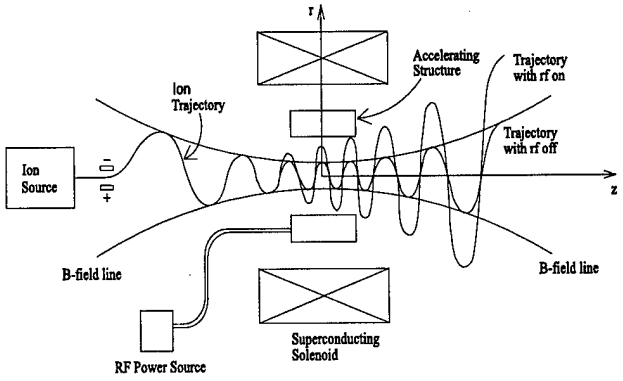


Figure 1 Components of an ICRA.

2. GENERAL THEORY

The main elements of an ICRA, shown schematically in Figure 1, are an ion source, superconducting solenoid, accelerating structure, microwave source, and target system. The beam is extracted from the ion source along a magnetic field line and then electrostatically deflected onto the injection orbit such that most of the beam's velocity is perpendicular to the magnetic field ($v_\perp$). A comparatively small velocity component parallel to the solenoidal magnetic field ($v_\parallel$) causes the beam to drift through the accelerating structure. Within the solenoid, the beam gyrates at the cyclotron frequency, $\omega_c=qB/\gamma m$, where B is the local magnetic field, γ is the relativistic mass factor, q is the ion charge and m is the ion rest mass. The velocity perpendicular to the magnetic field can be written, $v_\perp=r\omega_c$, where r is the beam's radius of curvature.

The beam is accelerated in the magnetron structure by the rf electric field transverse to the constant magnetic field. A four gap magnetron structure is shown in Figure 2. A first-order estimate of the accelerating voltage is obtained by assuming a magnetron cavity consisting of a

0-7803-4376-X/98/$10.00 © 1998 IEEE

hyperbolic fin structure with 2n vanes. In this case, the potential, V, for $r<r_0$ can be written as:

$$V = V_t \left(\frac{r}{r_0} \right)^n \cos(n\theta) e^{i\omega_{rf} t}$$

where V_t is the peak rf voltage at the cavity wall, r_0 is the cavity wall's inner radius, n is the azimuthal mode number of the cavity and ω_{rf} is the rf frequency.

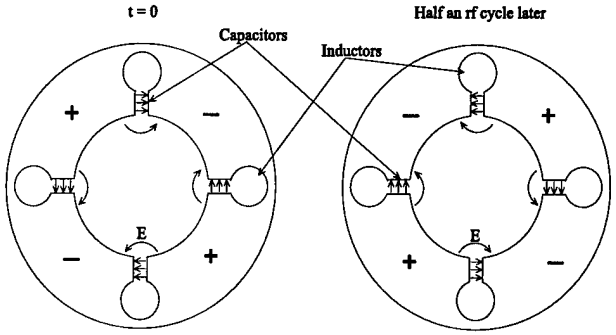


Figure 2 ICRA Magnetron Accelerating Structure.

The resonance condition requires a harmonic relationship between the ion's gyration and the rf frequency ($\omega_{rf} = n\omega_c$). With this condition, the kinetic energy gain across a single gap is given by:

$$K_{gap} = \frac{\pi}{4} e V_0 \left(\frac{r}{r_0} \right)^n$$

where $V_0 = 2V_t$ is the total rf voltage swing in the cavity. The number of turns, N_t, through which the ion is accelerated as it drifts through the cavity depends on the drift velocity, the active cavity length, l, and the cyclotron frequency by:

$$N_t = \frac{l}{v_{\parallel}} \frac{\omega_c}{2\pi}$$

Since the largest energy gains result from maintaining the beam as close to the cavity wall as possible, $K_{gap} \sim (r/r_0)^n$, it is desirable that the cavity radius increase with the beam's orbit radius.

3. DESIGN

A one MeV ICRA was designed as a proposed prototype to provide the basis for concept demonstration, experimental verification of the three-dimensional simulation code, and determination of critical design parameters such as rf voltage, perpendicular and parallel injection velocities, and magnetic field requirements. The prototype would provide a sound basis for the development of a design for a 10 MeV, 50 μA proton ICRA suitable for PET isotope production or neutron source for material research.

Detailed simulations, which tracked particles from the ion source to the target position, were done using the computer codes RELAX3D developed at TRIUMF [3] and a modified version of Z3CYCLONE developed at the NSCL [4]. These codes are well-tested and have been used successfully to design the central regions of the superconducting cyclotrons in operation at the NSCL [5,6].

3.1 One MeV ICRA

Detailed simulations of injection, acceleration, and extraction of a finite emittance beam in a realistic magnetic field were done for the one MeV ICRA. Table 1 provides a synopsis of the parameters chosen.

A significant design parameter is the choice of the solenoidal magnetic field value. In general, the accelerating structure dimensions scale as $1/\omega_{rf}$, and hence, the required magnet bore is inversely related to both the magnetic field and the rf harmonic number. Therefore, a higher magnetic field requires a smaller magnetic field volume reducing the solenoid cost. Existing NbTi superconducting solenoids have peak field values of 8 T and warm bores of 20 cm. Larger magnetic fields and warm bores would require substantially more expensive technology. (For a solenoidal field of 8 T, proton beams of 1 and 10 MeV have radii of 1.8 cm and 5.7 cm respectively.) Simulations predict acceptable performance with a magnetic field variation of 0.5% ($B_z/B_{z0}=0.995$) over the length of the accelerating structure.

The injection geometry simulated placed the ion source in a region of low magnetic field ($B_z=0.6$ T) where the turn spacing and orbit diameter are relatively large. The ion source was aligned with the magnetic field and placed at a potential of 51 kV. The electrostatic bend was modeled as two flat plates 0.8 cm wide, spaced 1.2 cm apart, and operating at ±11 kV. A 4th harmonic rf frequency ($\omega_{rf} = n\omega_c$) was chosen since rf sources for 488 MHz are readily available, and the cavity size is compatible with manufacturing techniques and a 20 cm warm bore. The active cavity length was 10 cm and would be made of OFHC copper by an EDM process. The estimated power required to drive the cavity at the specified voltage is about 430 watts with an additional 380 watts of rf power required to accelerate the beam.

The results of these simulations, given in Figure 3, show that 10% of an initial 2 π mm-mrad (unnormalized) beam will be accelerated to >0.5 MeV with about 12% of the particles lost on the inner surface of the accelerating structure. The remaining beam with <0.5 MeV is delivered to the target system. A high current density proton source such as a duoplasmatron with a current of ~2 mA would produce 200 μA of accelerated beam (>0.5 MeV) [7]. Further optimization is possible since it was found that the simulated acceptance of the one MeV ICRA was substantially larger than 2 π mm-mrad. The

capture efficiency could be increased, for example, by making the injected beam radial dimensions 2-3 times larger than simulated.

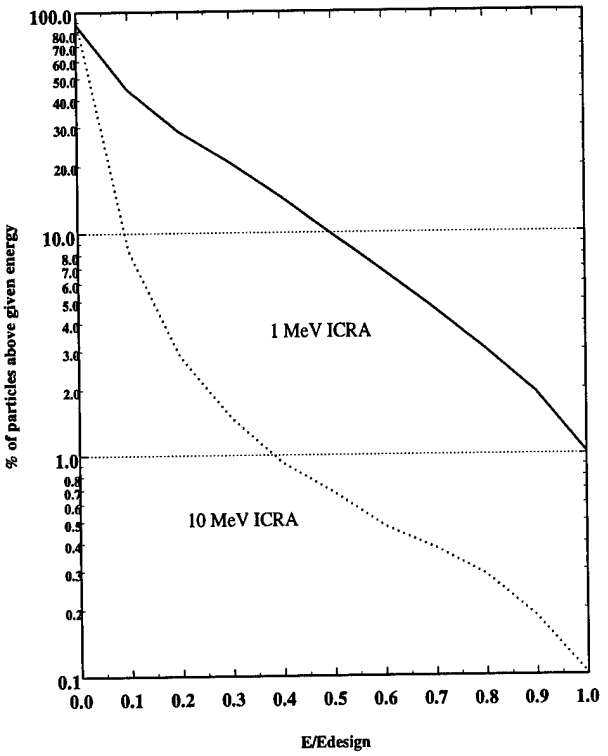


Figure 3 Output beam intensity vs. energy for a one MeV ICRA (solid line) and a ten MeV ICRA (dashed line).

3.2 Ten MeV ICRA

A preliminary, 10 MeV ICRA design was developed in large part by scaling the one MeV ICRA parameters as shown in Table 1. The peak accelerating voltage of 70 kV resulted in an electric field of 190 kV/cm in the gaps. A worst-case field enhancement leads to a peak field of <380 kV/cm, which is well below the Kilpatrick criterion for this frequency regime [8].

Gun-to-target particle tracking was performed as explained for the one MeV ICRA. Assuming an initial phase space of 2 π mm-mrad and beam current of 2 mA, simulations predict that 13 μA of beam would be accelerated to 5-10 MeV as shown in Figure 3. Though less than the design goal of 50 μA, this intensity is encouraging since even at the 13 μA level such a device would be appropriate for the production of PET radioisotopes or neutrons for material research. Design optimization strategies which will be explored include, among others, optimizing and/or increasing the injected phase space, increasing the injection energy to increase the beam brightness, reducing the number of turns, increasing the interaction length, and reducing the solenoidal magnetic field.

Design Energy	1 MeV	10 MeV
Magnetic Field	8 T	8 T
Cavity Length	10 cm	25 cm
RF Frequency	488 MHz	488 MHz
RF Power	<1 kW	8 kW
Cavity Voltage	16 kV	70 kV
Source Current	2 mA	2 mA
Source Voltage	51 kV	54 kV
Beam Perpendicular Energy at Cavity Entrance	44 keV	46 keV
Cavity ID at Entrance	1.1 cm	1.2 cm
Cavity ID at Exit	4 cm	12.2 cm
Number of Acceleration Turns	11	40
Accelerated Current	200 μA	13 μA
Beam area on Target	2.3 cm^2	16 cm^2

Table 1 Design parameters and simulation results for one and ten MeV ICRAs.

4. REFERENCES

[1] H.R. Jory and A.W. Trivelpiece, Charged Particle Motion in Large-Amplitude Electromagnetic Fields, J. of Applied Physics, **39**, 7, p. 3053-3060, (1968).

[2] R.S.H. Boulding, The Resonant Cavity Magnetron, D. Van Nostrand Co. Inc., (1952).

[3] H. Houtman and C Kost, Proc. of the Europhysics Conference, Co Accelerator Design and Operation, Springer Verlag, Lect.Notes in Physics 215, Berlin, p.93-103 (1983).

[4] Z3CYCLONE Version 4.0 Instruction Manual, MSU NSCL Accelerator Group (1993).

[5] F. Marti, J. Griffin, and V. Taivassalo, Design of the Axial Injection System for the NSCL Cyclotrons, IEEE Transactions on Nuclear Science, **NS-32**, 5, p.2450-2452, (1985).

[6] S.L. Snyder and F. Marti, Study and Redesign of the NSCL K500 Central Region, Proc. of the 1995 IEEE Particle Accelerator Conference, p. 375-377, (1995).

[7] T. Dolan, Fusion Research, Pergamon Press, p.226, (1982).

[8] W.D. Kilpatrick, Criterion for Vacuum Sparking to Include Both RF and DC, University of California Radiation Laboratory, UCRL-2321, (1953).

STIMULATED DIELECTRIC WAKEFIELD ACCELERATOR‡

T-B. Zhang,* J.L. Hirshfield,*,§ T.C. Marshall,† and B. Hafizi*
*Omega-P, Inc., New Haven CT, 06520
§Department of Physics, Yale University, New Haven CT 06511
†Department of Applied Physics, Columbia University, New York City 10027

Abstract

A dielectric-lined waveguide can be built that supports multi-mode, nearly non-dispersive propagation; wherein a superposition of TM_{0n} wakefields is shown to result in highly peaked axial electric fields localized on each driving bunch in a periodic sequence. This allows stimulated emission of wakefield energy to occur at a rate which is much larger than the coherent spontaneous emission from a single driving bunch of equal charge. This mechanism can make possible design of a stimulated wakefield accelerator that appears to have the potential of providing an acceleration gradient for electrons or positrons in the range of 50-100 MeV/m, taking a driving bunch charge of a few nC. We present calculations for such wakefields, and give an example with acceleration of a 30 MeV test bunch to 155 MeV in a 2-D dielectric waveguide 200 cm in length, using ten identical 2.0 nC/mm drive bunches.

1 INTRODUCTION

In the dielectric wakefield accelerator [1 - 5], a dielectric--loaded waveguide supports wakefields induced by the passage of an electron bunch of high charge number (the driving bunch). If a test bunch of low charge number is injected at a suitable interval after the driving bunch, it can move in synchronism with the wakefields and experience net acceleration [1-3]. Wakefield acceleration by multiple driving bunches has also been investigated both theoretically and experimentally [4,5]. In this paper, we analyze both spontaneous and stimulated wakefield emission in a waveguide from a train of driving bunches [6]. The multi-mode structure of the wakefields, and stimulated emission from the train of driving bunches, are shown to allow generation of high wakefield acceleration gradients, without need for bunches of exceptionally high charge.

The particular waveguide analyzed here enjoys two uncommon virtues: (a) Many waveguide modes can participate in wakefield formation; this leads to coherent superposition, with a net wakefield amplitude that can be larger than the amplitude of the lowest mode. (b) The near-periodic character of the wakefield allows constructive interference of field amplitudes from successive bunches.

A train of moderate-charge driving bunches is employed for the build-up of an intense wakefield. The bunches are assumed to be identical, and each bunch is injected to move initially with near-synchronism in the net wakefield of prior bunches. The stimulated emission from each trailing bunch can greatly exceed coherent spontaneous Cerenkov emission from a bunch moving alone. It is the spontaneous Cerenkov wakefield emission of one bunch plus the stimulated Cerenkov emission from a train of succeeding bunches that build up a substantial wakefield amplitude.

2 WAVEGUIDE GEOMETRY AND MODES

The model analyzed here is simplified to bring out the essential physics. Thus a two-dimensional waveguide is considered, in which two parallel slabs of dielectric are separated by a small vacuum gap, and in which the outer surfaces of the slabs are sheathed in a lossless conductor. The relative dielectric constant $\kappa = \varepsilon/\varepsilon_o$ is assumed to be independent of frequency. The geometry is depicted in Fig. 1, and all quantities are taken to be independent of y.

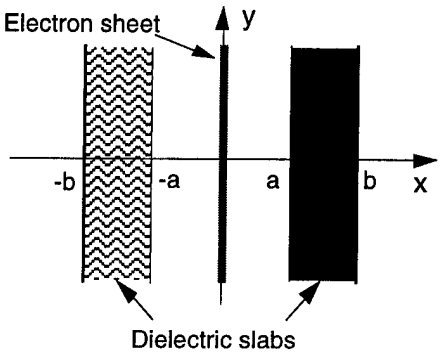


Fig. 1. Geometry for the 2D dielectric-lined waveguide.

The dispersion relation for modes having an axial electric field E_z in this geometry is found to be

$$p_m \tanh(k_m a) = \kappa k_m \cot\left[p_m (b-a)\right], \qquad (1)$$

where $k_m = \omega_m / c\beta\gamma = p_m \Big/ \gamma\sqrt{\kappa\beta^2 - 1}$, $\beta = v/c$, $\gamma = \left(1-\beta^2\right)^{-1/2}$, k_m is the (evanescent) transverse wavenumber in the vacuum, and p_m is the (real) transverse wavenumber in the dielectric. All the modes have the same phase velocity $v_{ph} = v$. Only the TM^x mode, also known as LSM modes [7], has an axial electric field; this is the mode considered here. It is noted that one can have eigenfrequencies with nearly equal spacing, since $p_m(b-a) \to (n+1/2)\pi$ as $\kappa \to \infty$. As $m \to \infty$ the asymptotic eigenfrequency spacing approaches

‡This research was supported by the US Department of Energy, Division of High Energy Physics.

0-7803-4376-X/98 /$10.00 © 1998 IEEE

$\Delta\omega = \pi c\beta\left[(b-a)\sqrt{\kappa\beta^2-1}\right]^{-1}$. The wakefield is more strongly peaked and more nearly periodic in $z-vt$ as the eigenfrequency spacings become more nearly equal. Preliminary study indicates that similar wakefields can be generated in cylindrical dielectric-lined waveguide.

3 NEARLY-PERIODIC WAKEFIELD

The wakefield induced by an electron sheet bunch can be obtained by expanding in orthonormal modes the solution of the inhomogeneous wave equation. For a Gaussian sheet bunch of length Δz, one finds [6]

$$E_z(x,z,t) = -E_0 \sum_{m=0}^{\infty} \frac{f_m(x)}{\alpha_m} e^{-(\omega_m \Delta z/2v)^2} e^{-i\omega_m z_0/v} \tag{2}$$

where $f_m(x) = \dfrac{1}{\sin p_m(b-a)}$

$$\times \begin{cases} \cosh k_m a \sin p_m(b+x), & -b \le x \le -a \\ \cosh k_m x \sin p_m(b-a), & -a \le x \le a \\ \cosh k_m a \sin p_m(b-x), & a \le x \le b \end{cases} \tag{3}$$

and $z_o = z - vt$; α_m is the normalizing constant. In Eq. 2, $E_o = -Ne/2\varepsilon_o a$ is a measure of the Coulomb field of the bunch. Eq. 2 has been evaluated for a waveguide with a = 0.30 cm, b = 1.147 cm, κ = 10.0, Δz = 0.3 cm, $-Ne$ = Q = -2 nC/mm, and γ = 60.0. A relative dielectric constant of κ = 10.0 is close to the value of 9.6 for alumina. For these parameters, E_o = -37.7 MV/m. In this case, modes up to m = 12 in Eq. 2.are significant in evaluating the wakefield. The first frequency interval is

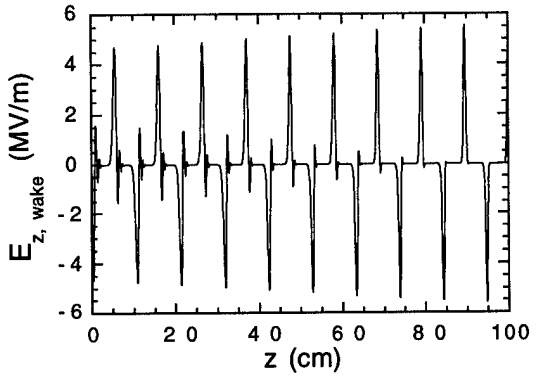


Fig. 2. Spontaneous wakefield from a -2 nC/mm, 30 MeV sheet bunch after it has traveled 100 cm left-to-right in the 2D waveguide depicted in Fig. 1.

5.70 GHz, while the asymptotic interval $\Delta\omega/2\pi$ is 5.88 GHz; eigenfrequency intervals differ by at most 3.1%. The computed spontaneous wakefield pattern of a single bunch is shown in Fig. 2 for $0 \le z_o \le 100$ cm. The wakefield peaks are seen generally to alternate in sign; to each be relatively concentrated in z_o; and to have a period of 10.5 cm, corresponding to the vacuum wavelength at 2.856 GHz, i.e. half the asymptotic frequency interval $\Delta\omega/2\pi$. The peak values of E_z for the first wake are -5.57 and +5.54 MeV/m, and later wakes develop oscillatory precursors. Consideration of only a few modes gives an incomplete wakefield.

4 BEAM DYNAMICS AND SIMULATION

A single-bunch wakefield as shown in Fig. 2 leads to a a drag field on a bare bunch that can be obtained from the energy flow into the fields [6]; here one finds E_{drag} = 1.18 MV/m. Now, when a second bunch is introduced into the waveguide at the first peak of the first bunch wakefield, it can be decelerated by up to 1.18 + 5.54 = 6.72 MV/m, the sum of the second bunch's bare drag field associated with spontaneous emission, plus the wakefield of the first bunch; this produces additional stimulated emission. Second bunch deceleration of 6.72 MV/m is 5.7 times that of a bare bunch. The second bunch adds its wakefield energy to that of the first bunch, for which we find the combined wakefield to be 14.33 MV/m. Successive amplitude enhancements from incremental addition to the net wakefield energy continues so long as synchronism is maintained between bunches and peak wakefields. This conceptual notion has been examined with greater accuracy in a numerical simulation. Particles in each 3.0-mm long bunch are injected each 350 psecs (10.5 cm) near the peak of the cumulative wakefield from all prior bunches. The initial energy of each bunch is chosen as about 30 MeV (γ= 60.0 and $v_o \approx c$).

In Figs. 3a, 3b and 4 are shown the results of injecting a test bunch of low charge into the accelerating phase of the wakefield set up by the passage of ten prior driving bunches in a structure 100 cm in length. The initial energy of the test electrons is also 30 MeV. No beam loading by the test bunch is taken into account. Fig. 3a shows the buildup of the wakefield from the ten driving bunches, while Fig. 3b shows locations of the electrons to be accelerated in the test bunch, which enter behind the tenth drive bunch at the accelerating phase, after the first drive bunch has gone 100 cm. As the drive bunches

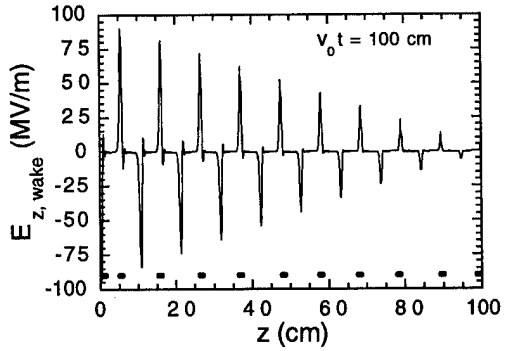


Fig. 3a. Cumulative wakefield set up by ten identical successive bunches, at the time the first bunch has moved 100 cm along the waveguide. The positions of the bunches are indicated by the heavy dots at the bottom.

proceed through the 100 cm long waveguide, the energy of the test electrons increases. In Fig. 4 we plot the energy of typical drive bunch electrons, as well as of the test electrons in bunch #11. After $v_o t$ = 200 cm, the 100 cm train of drive bunches has moved fully out of the wave-guide, and the test electrons are also ready to emerge. Their energy has been increased to γ = 200, which represents an average gradient of about 70 MV/m. The later drive bunches show energy depletion and, indeed by $v_o t$ = 120 cm, they decrease to an energy so low that there is first a slippage off the wakefield maximum, followed by a further slippage into the following accelerating phase, after which the drive bunch energy begins to increase again. As a result, the maximum wakefield is eroded downstream. Reflection of wakefields at the waveguide exit is neglected.

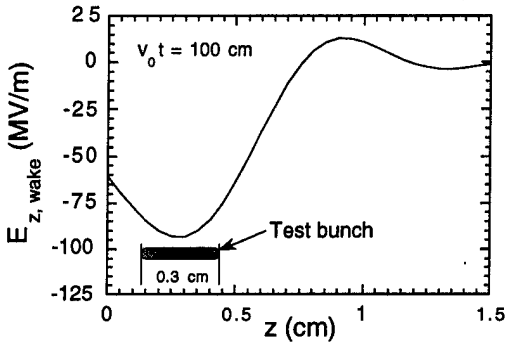


Fig. 3b. Location of the test bunch (bunch 11) in the accelerating wakefield near the entrance of the accelerator.

From the results shown in Fig. 4, it is apparent that one should endeavor to remove driving bunches from the system after their energy has fallen so much that they slip into the following accelerating phase. In Fig. 5, we show a result obtained from a 200 cm dielectric structure, where the ten drive bunches are assumed to be deflected out after traveling 100 cm, i.e. before their energy falls too low. (Discussion of means for achieving such a removal of the driving bunches is beyond the scope of this paper.) We find that the energy of the test bunch particles increases steadily to 155 MeV after traversing the system. This compares favorably with the case when the drive bunches stay in for the full 200 cm, where the test particles reach an energy of only 135 MeV. In another case, the energy of drive bunches does not fall below 3 MeV; no slippage was observed; six bunches survive to z = 65 cm; and the test electrons reach 126 MeV at $v_o t$ = 200 cm.

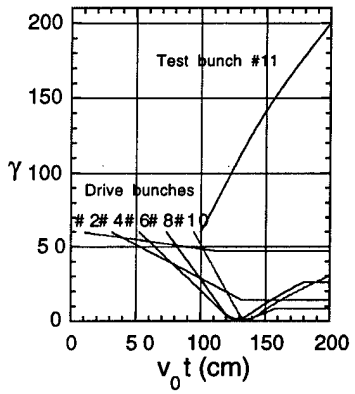


Fig. 4. History of the energy of selected drive bunches, and of the test bunch #11, up to the time the test bunch just emerges from the waveguide.

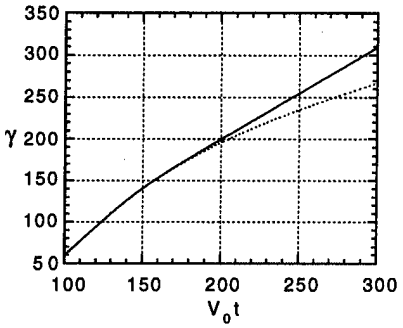


Fig. 5. Energy of test electrons versus $v_O t$ for two cases. Dotted line is the case shown in Fig. 4, but carried out for a 200 cm long structure, and the bunches are left in the system its entire length. Solid line is the case where drive bunches are removed after traveling 100 cm.

5 CONCLUSIONS

A planar two-dimensional dielectric-lined waveguide is shown to be capable of supporting a large number of modes with nearly equal phase velocities. The waveguide can be designed so that these velocities are nearly equal to the velocity of a train of moderate charge drive bunches in a sheet beam. As a result, strongly-peaked cumulative wakefields can arise through stimulated emission that builds up from bunch to bunch. For ten 30 MeV driving bunches of 2 nC/mm each, an axial acceleration gradient of up to 70 MV/m is predicted, as compared with 5.6 MV/m for a single bunch of equal charge. A means for separating spent drive bunches from their wakefields is found to be necessary to avoid re-absorption of wakefield energy by driving bunches that slip into trailing accelerating zones. Acceleration of electrons and positrons to high energy appears feasible using a multi-stage, non-colinear, multi-bunch wakefield accelerator, based on the single-stage mechanism discussed in this paper.

6 ACKNOWLEDGMENT

Suggestions by A. Ganguly are gratefully acknowledged.

7 REFERENCES

[1] K.-Y. Ng, *Phys. Rev.* D **42**, 1819, (1990).
[2] M. Rosing and W. Gai, *Phys. Rev.* D **42**, 1829 (1990).
[3] W. Gai, et al., *Phys. Rev. Lett.* **61**, 2756 (1988).
[4] R. D. Ruth, et al., *Particle Accelerators* **17**, 171 (1985).
[5] I. N. Onishchenko, et al., *Proc. 1995 PAC*, pp. 782-3.
[6] T-B. Zhang, et al., *Phys. Rev.* E (to be published).
[7] R. E. Collin, *Field Theory of Guided Waves*, ch. 6, (IEEE Press, New York, 1991).

BEAM SLICING WITH LASERS AND PLASMAS FOR HIGH-TRANSFORMER-RATIO PLASMA WAKEFIELD ACCELERATION

G. Shvets and P. Stoltz
Princeton Plasma Physics Laboratory

Abstract

A novel method of "slicing" electron beams – Laser-Plasma Scissors (LPS) is suggested. Generation of the sharp-edged beams for high-transformer-ratio plasma wakefield acceleration (PWA) is considered numerically and analytically. Slicing, high-transformer-ratio acceleration, and beam loading are studied numerically, using a one-dimensional code which treats plasma as a linear medium and electron beams as a collection of macroparticles. A tentative design of a multi-stage PWA with laser slicing is presented. Other applications of LPS include generation of ultra-short bunches for sychrotron radiation.

1 INTRODUCTION

Because of the very high electric field it can sustain, plasma has been proposed [1] as a medium for high-gradient particle acceleration. Plasma waves can be excited by relativistic electron bunches [2, 3] in a plasma wakefield accelerator (PWA) or by intense laser pulses [1] in a laser wakefield accelerator (LWA). In this paper we describe the possibility of shaping the driving electron bunch (in the PWA scheme) by the laser pulse, in presense of the plasma. This shaping may lead to high ratio of energy transfer between from the driving to the accelerating beam. A straw-man design of a high-efficiency, multi-stage TeV electron-positron collider, based on this scheme, is presented.

Electron drivers offer several advantages over laser drivers, including (i) long interaction distance due to low emittance (ii) high repetition rates (a megahertz or higher) of rf photocathode guns (iii) possibility of recovering the unused beam energy by sending the beam through an rf cavity.

Unfortunately, the fundamental wake theorem [2, 4] limits the transformer ratio – the peak accelerating field E_+ experienced by the accelerated electrons over the average decelerating field $\langle E_- \rangle$ acting on the driving electron bunch – to less than 2 for symmetric bunches. This makes the total length of the conventional acceleration necessary to produce the driving beams very large. The transformer ratio might be increased by utilizing shaped driver bunches [3] with a slow rise in density and an abrupt termination over a distance smaller than a collisionless skin depth of the plasma $k_p = \omega_p/c = \sqrt{4\pi e^2 n_0/m}$. Novel approaches to beam slicing have to be used to produce such an abrupt termination. In this paper we propose to use an ultra-short intense laser pulse, co-propagating with the electron beam through the plasma, to induce energy variation in a small slice of the electron beam. A magnetic chicane (or simply a magnetic bend) can then be used to scrape off the affected slice, thereby creating a sharp edge in the beam density, and splitting it into two bunches.

A novel configuration of PWA is suggested, in which the leading driving bunch excites the wake; it is followed by the accelerating (witness) bunch, which is accelerated with high transformer ratio; the trailing driving bunch "cleans up" the wake, left behind the leading driving bunch and the accelerating bunch. Limits on per-stage acceleration, acceleration efficiency, and the transformer ratio of this scheme are studied analytically and numerically. Tentative parameters for a multi-stage high transformer-ratio PWA, with energy gain of about 400MeV per stage, are presented.

High transformer ratio in a PWA can be achieved by shaping the driving e-beam. For example, if the beam density is a Gaussian, with a sharp termination at the peak density, i.e. $n_b(\zeta) = n_{b0} \exp(-\zeta^2/2\sigma_z^2)$ for $\zeta < 0$ and $n_b(\zeta) = 0$ for $\zeta > 0$, the ratio between the peak *accelerating* field behind the bunch and the peak *decelerating* field at $\zeta = -\sigma_z$ is approximately equal to $T \approx 11.0\sigma_z/\lambda_p$. To slice the beam we consider a laser-plasma scissors (LPS) configuration. For simplicity, consider a short flat-top laser pulse, of duration exactly equal to the plasma period $2\pi/\omega_p$,.co-propagating through the plasma with a longitudinally Gaussian electron beam of duration $\sigma_z \gg \lambda_p$. Such a laser pulse has an important property of leaving no plasma wake behind it. While in practice flat- top laser pulses may not be obtainable, a combination of, two Gaussian pulses separated by half of a plasma wavelength, may be utilized to reduce the wake behind the pulses.

Neglecting the electron self-wakes, find that electrons at $\xi < 0$ and $\xi > \lambda_p$ are unaffected by the wake, while the electrons at $0 < \xi < \lambda_p$ are modulated in energy. Assuming linear response of the plasma, i.e. $a_0^2/2 \ll 1$, the peak longitudinal field of the wake is estimated as $eE_z = a_0^2/2[\mathrm{GeV/m}]\sqrt{n_p/10^{14}\mathrm{cm}^{-3}}$. Assuming that the interaction length is limited by laser diffraction to twice the Rayleigh length, the energy change of the beam electron at the wake phase $\phi = \omega_p(t - z/c)$ is given by $\Delta E = 2\pi e E_z \sin\phi w^2/\lambda_0$. In practical units,

$$\Delta E\,[MeV] \approx \frac{14.0 \sin\phi U_L\,[\mathrm{J}]\lambda_0\,[\mu]}{n_p/(4\times 10^{17}\mathrm{cm}^{-3})}, \qquad (1)$$

where U_L is the laser energy. After the plasma section, electron beam can be passed through a magnetic bend with a scraper, thereby removing beam electrons which were subjected to the wake. The final result of these manipulations is an electron beam consisting of two half- Gaussian parts, with a λ_p-long hole between them.

To verify these ideas numerically, a one-dimensional code was developed. The philosophy behind the code is

0-7803-4376-X/98/$10.00 © 1998 IEEE

Table 1: Parameters for a 0.4 GeV per stage high-transformer-ratio PWA with laser-plasma slicing

Drive beam energy	γmc^2	100 MeV
Laser Energy	U_L	1.0 J
Pulse duration	τ_L	160 fs
E-beam current	I_b	2.0 kAmp
E-beam radius	r_b	50 μ
E-beam emittance	ϵ_n	2 πmm mrad
E-beam density	n_b	6.0×10^{15} cm^{-3}
Bunch length	σ_z	1.0 psec
Plasma density	n_p	$4 \cdot 10^{17}$ cm^{-3}
Accelerating gradient	W_z	1.0 GeV/m
Final energy	$\gamma_f mc^2$	0.5 GeV
Length of slicer	L_{sl}	50.0 cm
Length of accelerator	L_{acc}	0.25 cm
Rayleigh length	Z_r	0.75 cm
Beam divergence length	Z_D	25.0 cm
Dephasing length	Z_{deph}	200 cm
Peak EER	η	0.2

that in a viable plasma-based accelerator plasma dynamics should remain linear. However, the full nonlinear dynamics of the driving beam needs to be modeled. Laser pulse is asumed non- evolving in the code. This is justified by our assumption that the interaction distance does not exceed a Rayleigh length. Thus, every beam particle excites a sinusoidal plasma wave and moves in a combined wake field of (i) laser pulse and (ii) all other beam electrons ahead of it.

We simulated propagation of electron beam+laser pulse through 2.5mm of plasma using parameters from Table 1. Electron phase space is shown in Fig. 1.

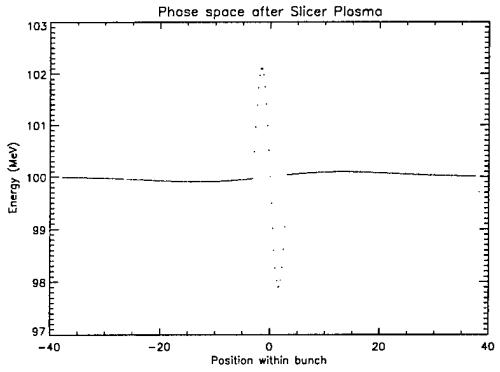


Figure 1: Electron phase space at the end of the laser-plasma scissors.

To simulate the effect of the magnetic chicane we removed all the beam electrons with energies differing from the initial energy (100MeV) by at least twice the energy change of an electron at $\zeta = \pm\sigma_z$. As a result, a split-beam driver is generated, which can now be injected into the plasma for high transformer ratio high efficiency plasma wakefield acceleration.

With the possibility of beam-slicing established, one can envision a multi-stage Tev-scale accelerator, based on a concept of plasma wakefield acceleration. A single stage of such an accelerator consists of 5 sections: (1) RF photocathode gun (2) laser-plasma scissors (3) magnetic chicane (4) plasma-wakefield accelerator (5) energy recovery rf cavity. Sections (1) and (5) can be combined so that the same RF cavity performs the functions of energy recovery from stage N and rf injector into stage $N+1$.

Below we calculate how much energy accelerating electrons gain inside section (4). Assume that the overall length of the plasma is approximately equal to twice the distance over which the cross-section of an unfocused beam doubles, $z_D = \gamma r_b^2/\epsilon_n$ (thereby neglecting plasma focusing). The peak accelerating gradient in *overdense* plasma $n_p > n_b$ can be estimated as

$$W_z[\mathrm{GeV/m}] \approx \frac{(n_b/10^{14}\mathrm{cm}^{-3})}{(n_p/10^{14}\mathrm{cm}^{-3})^{1/2}}. \qquad (2)$$

Simple scaling can be derived for the total gained energy:

$$\frac{\Delta E_{acc}}{E_{drive}} \approx \frac{12Q[\mathrm{nC}]}{\epsilon_n[\mathrm{mm\ mrad}]}\frac{\lambda_p}{\sigma_z}, \qquad (3)$$

where ΔE_{acc} is the energy gained by the accelerating electron, E_{drive} is the energy of the driving beam electron, Q is the total charge of the driving beam.

As Eq.(3) indicates, the single-stage energy gain of accelerating electrons *decreases* as the the bunch length increases. On the other hand, the transformer ratio *increases* as the bunch length increases, according to

$$\frac{\Delta E_{acc}}{\Delta E_{drive}} \approx \frac{3.3\pi\sigma_z}{\lambda_p}. \qquad (4)$$

Beam length (in units of λ_p) determines the peak energy extraction ratio $\eta = \Delta E_{drive}/E_{drive}$, thereby fixing the transformer ratio T and fractional energy extraction per stage η:

$$T \approx \frac{11.0}{\eta^{1/2}}\left(\frac{Q[\mathrm{nC}]}{\epsilon_n[\mathrm{mm\ mrad}]}\right)^{1/2}, \qquad (5)$$

$$\frac{\Delta E_{acc}}{\Delta E_{drive}} \approx 11.0\eta^{1/2}\left(\frac{Q[\mathrm{nC}]}{\epsilon_n[\mathrm{mm\ mrad}]}\right)^{1/2} \qquad (6)$$

Note that the fraction of energy the driver beam loses on average is $\bar{\eta} \approx 0.5\eta$. Extracting a large fraction of the driver beam energy per stage increases the energy gain per stage, but has a disadvantage of decreasing the transformer ratio. Present day emittance compensated photoinjectors are, in principle, capable of delivering electron beams with $Q[\mathrm{nC}]/\epsilon_n[\mathrm{mm\ mrad}]$ of order unity [5]. If, for example, a 100 MeV drive beam is used, and $\eta = 1/4$ of its energy is spent on exciting the plasma wake, transformer ratio $T = 22$ can be achieved, with single-stage acceleration $\Delta E_{acc} \approx 0.4$GeV. This is confirmed by the numerical simulation. The phase space of the driver and test electrons after the accelerator stage are shown in Fig. 2, where 2.0

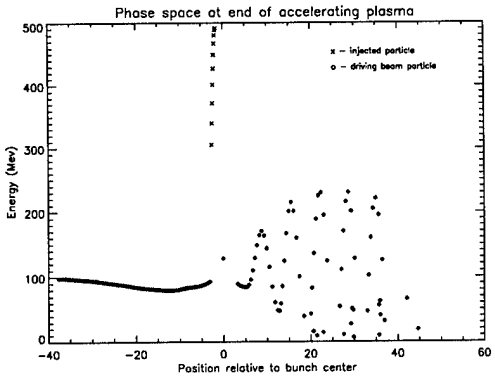


Figure 2: Electron phase space at the end of the laser-plasma scissors.

nC of driver beam are used to accelerate about 2.0 pC of injected electrons from 100 MeV to 500 MeV. An important feature of the proposed split-beam PWA configuration (two half-Gaussian beams, separated by a plasma wavelength) is that the second half of the drive beam picks up some of the wake energy, left behind by the first half of the drive beam. To compare such a configuration with a more conventional one, utilizing a single shaped electron bunch, in Fig. 3 we plotted the fraction of the energy remaining in the first half of the driver beam (diamonds) and in the entire beam (triangles) as a function of the distance along the accelerator. The advantage of using a split beam is evident: more beam energy can be recovered in section (5) (less than a percent of the initial beam energy is left behind the bunches).

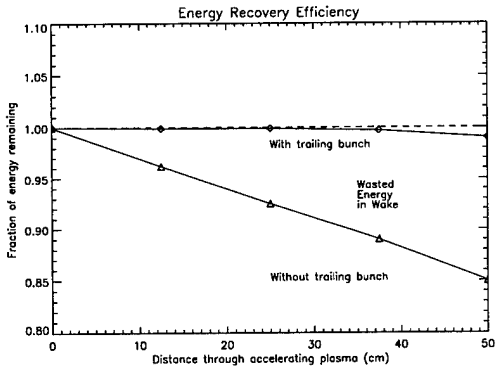


Figure 3: Fraction of energy remaining in leading half of driver bunch (diamonds) and in both halves (triangles) as a function of acceleration distance.

To investigate the efficiency of particle acceleration and the effect of beam loading we simulated the accelerating section (4) using witness beams of five different charges. The acceleration efficiency defined as

$$\eta_{acc} = \frac{\sum_{j=1}^{N_{inj}} \Delta\gamma_j mc^2}{\sum_{i=1}^{N_{drive}} -\Delta\gamma_i mc^2} \qquad (7)$$

is shown in Fig. 4, which indicates that an optimal beam loading exists for which the acceleration efficiency can be as high as 70%. Incidentally, the energy recovery deteriorates with the increased beam loading, and about 2.8% of the total drive beam energy is wasted in the wakes left behind (for the optimal beam loading case). At the same time, energy spread of the trailing half of the drive beam increases, making efficient energy recovery in an RF cavity problematic.

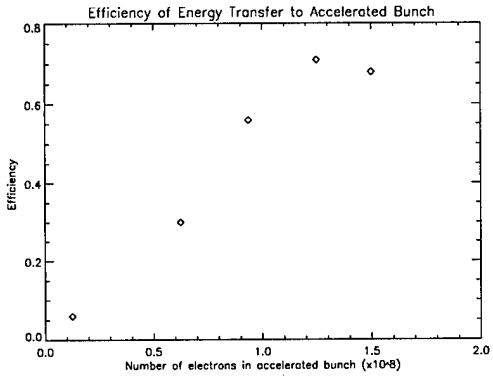


Figure 4: Acceleration efficiency η_{acc} as a function of beam loading.

In conclusion, we suggested and numerically demonstrated the possibility of beam slicing with ultra-short laser pulses and plasmas (laser-plasma scissors). One of the applications of this beam slicing technique is a high-transformer-ratio, high-efficiency multi-stage particle accelerator. The high transformer ratio is achieved by slicing a long beam on a scale shorter than plasma wavelength while the high efficiency is achieved by splitting the beam into two bunches, separated by a plasma wavelength. Future work will extend the present one-dimensional analysis to three dimensions.

This work was supported in part by the U. S. DOE under Contract No. DE-AC02-76-CHO3073. One of us (G. S.) acknowledges enlightening conversations with Professor J. S. Wurtele.

2 REFERENCES

[1] T. Tajima and J. M. Dawson, *Phys. Rev. Lett.* **43**, 267 (1979); L. M. Gorbunov and V. I. Kirsanov, Zh. Exp. Teor. Fiz. **93**, 509 (1987) [Sov. Phys. JETP **66**, 290 (1987)]; C. Joshi, W. B. Mori, T. Katsouleas, *et al.*, Nature, **311**, 525 (1984).

[2] R. D. Ruth, A. Chao, P. L. Morton, and P. B. Wilson, Part. Accel. **17**, 171 (1985).

[3] K. L. F. Bane, P. Chen, P. B. Wilson, IEEE Trans. Nucl. Sci. **32**, 3524 (1985).

[4] A. W. Chao, in *Physics of High Energy Particle Accelerators (SLAC Summer School, 1982)*, AIP Conf. Proc. No. 105, ed. by M. Month (AIP, New York, 1983).

[5] J. Rosenzweig and E. Colby, in *Advanced Accelerator Concepts (Fontana, WI 1994)*, AIP Conf. Proc. No. 335, p. 724, ed. by P. Schoessow (AIP, Woodbury, New York 1995).

RF MEASUREMENTS OF A TRAVELING-WAVE MUFFIN-TIN ACCELERATING STRUCTURE AT 90 GHZ †

P.J. Chou, G.B. Bowden, M.R. Copeland, H. Henke*, A. Menegat,
D.P. Pritzkau, and R.H. Siemann
Stanford Linear Accelerator Center, Stanford University, California 94309

Abstract

A measuring system at the table-top scale was developed for RF measurements of a muffin-tin accelerating structure operating at 32 times the SLAC frequency (2.856 GHz). Both perturbation and non-perturbation methods are employed to characterize the RF properties of a muffin-tin structure. Conventional bead pull measurements are extended to millimeter wavelengths. Design of the measuring system and preliminary results of RF measurements are presented.

I. INTRODUCTION

A relatively low cost, fully automated measuring system which is capable of measuring both the phase and amplitude of microwave signals in the 90 GHz frequency range was constructed. A precision platform for bead pull measurements was also constructed in order to characterize the RF properties of a traveling-wave muffin-tin accelerating structure at 90 GHz[1]. The measuring system was built by combining standard RF measuring equipments and some home-built components together. All equipment and data acquisition are controlled by a PC running with the commercial software package LabVIEW®. A support fork mounted on a 1-dimensional optical translation stage was built to hold a tiny fiber used in the bead pull measurements. The movement of the fiber was controlled by a servo motor driven translation stage with a 1 μm resolution. Preliminary results and ideas for further improvement are presented.

II. HOME-MADE MM-WAVE VECTOR NETWORK ANALYZER

The block diagram of the W-band vector network analyzer is depicted in Fig. 1. The mm-wave power is generated by multiplying the frequency of a Hewlett Packard (HP) 8673D microwave source with a HP 85100W ×5 mm-wave frequency multiplier. The resultant mm-wave power goes through two directional couplers (reference: Hughes 45326H-1120 and signal: Hughes 4532641-1320) and some WR10 waveguides and then is fed into the test structure.

W-band signals from the directional couplers are mixed down to an intermediate frequency, f_{IF} = 835.216 MHz, using HP 11970W waveguide mixers. The local oscillator (LO) frequency is multiplied by ×18 in the waveguide mixers before mixing, so the first stage LO frequency is in the 5 GHz range. This LO frequency is changed when the W-band frequency is changed to keep f_{IF} constant. The signals are amplified by 40 dB with Q-Bit QBS 135 narrowband, low noise (Noise Figure < 1 dB) amplifiers and then mixed down to audio, 16 kHz, using an EM Research SLS-849-ER-01 phase locked loop as the second stage LO. The outputs of the second stages of mixing are low-pass filtered.

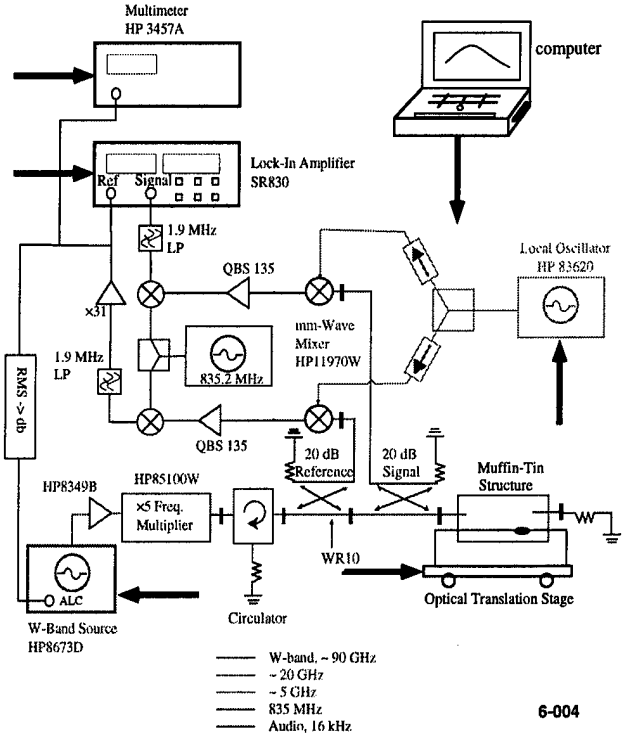


Fig. 1: Block diagram of mm-wave vector network analyzer configured for reflection measurements.

The processed output of the first directional coupler, the reference coupler, is amplified with a ×31 audio amplifier and then used in several ways: i) it is measured with an HP 3457A multimeter; ii) it is the reference input for an Stanford Research Systems SR830 lock-in amplifier; and iii) it is converted to dB to level the HP 8673D microwave source.

The processed output of the signal coupler is connected directly to the signal input of the lock-in amplifier which measures i) the amplitude of the signal at the frequency of the reference input and ii) the phase between the reference and signal inputs. A key to the phase measurement is balanced splitting of the first stage LO output.

† Work supported by Department of Energy contract DE-AC03-76SF00515.

*Permanent Address: Technical University Berlin, EN2, Einsteinufer 17, D-10587 Berlin, Germany.

0-7803-4376-X/98/$10.00 © 1998 IEEE

For transmission measurements, the signal coupler is connected to the output port of the test structure (Fig. 2). This is done rather than connecting the waveguide mixer directly because it allows use of the same calibration intercepts (see below).

Calibrations of the reference and signal arms were performed using an HP 437B power meter and HP W8486A power sensor. A typical setup is shown in Fig. 3. Measurements showed that the reference and signal voltages, measured in dBV, were linear in the power in dBm with intercepts, K, that are a function of frequency

$$\text{Voltage(dBV)} = \text{Power(dBm)} + \text{K}.$$

The intercepts vary by ~ 1 dB over the frequency range from 85 to 95 GHz, and the frequency dependence was reproducible when measurements were taken several weeks apart during a time when the analyzer was taken apart and reassembled several times (Figs. 4 and 5). There was a systematic change of 0.24 dB in the intercept of the reference channel during this time. We suspect that the ×31 amplifier is drifting and plan to replace this home-built amplifier with a high quality commercial one.

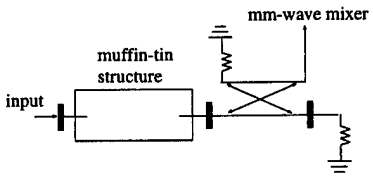


Fig. 2: Configuration for the transmission measurements.

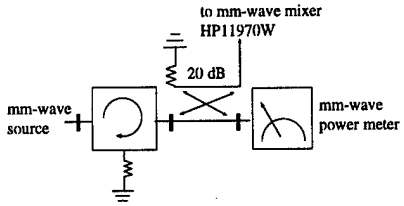


Fig. 3: Configuration of the calibration measurements.

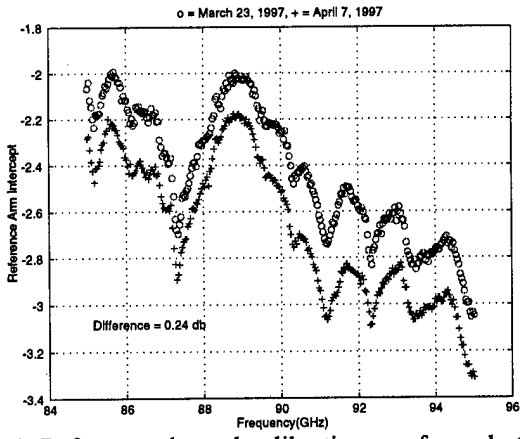


Fig. 4: Reference channel calibrations performed at two different times.

III. PRELIMINARY RESULTS OF RF MEASUREMENTS

The 7-cell muffin-tin structure[1] was designed with the computer code MAFIA[2]. The reflection and transmission coefficients are shown in Figs. 6 and 7 respectively. Note that only 4 cavity cells were used in the simulation.

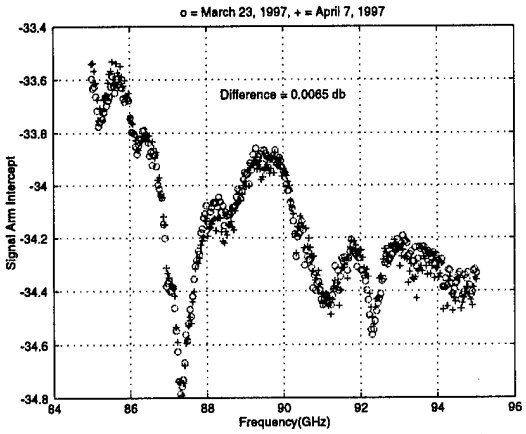


Fig. 5: Signal channel calibrations performed at two different times.

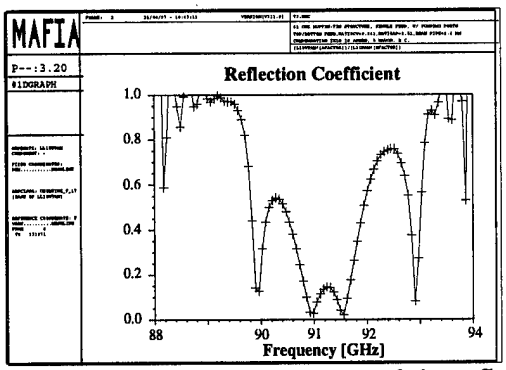


Fig. 6: Simulated frequency response of the reflection coefficient.

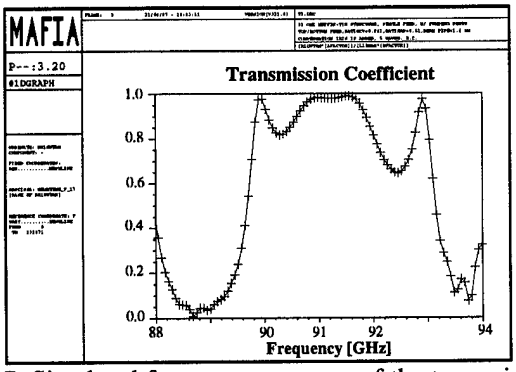


Fig. 7: Simulated frequency response of the transmission coefficient.

The measured reflection and transmission coefficients are depicted in Fig. 8. The measured frequency response is in good qualitative agreement with the simulation except for the magnitude of the transmission coefficient. The sum of the squares of the reflection coefficient and the transmission coefficient is shown in Fig. 9. From energy conservation, we expect the sum to be one. There

is some unexpected power loss in the passband. Roughly 50% of the input power is accounted for. We repeated the measurement with the beam pipe and pumping slot closed, and only a few percent change was observed. We suspect that the surface roughness of the structure may be the cause. Experimental investigations are underway to understand this extra power loss.

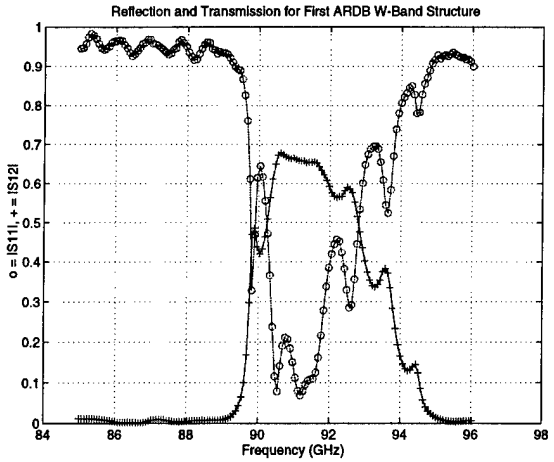


Fig. 8: The measured frequency response of the reflection coefficient for a 7-cell structure.

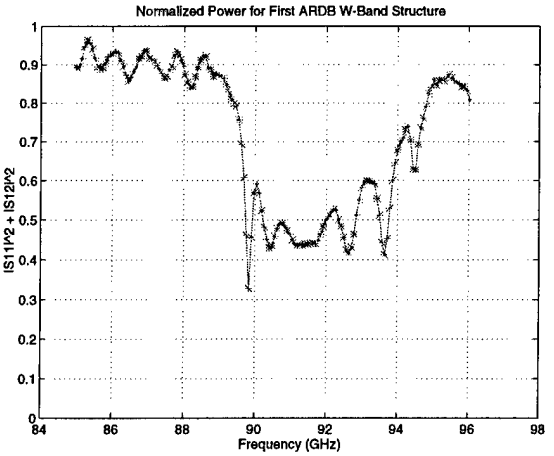


Fig. 9: The sum of the square of the reflection coefficient and the transmission coefficient.

For a traveling-wave structure, the accelerating field along the longitudinal axis of the structure has the following expression:

$$E_z(z) = |E(z)|\, e^{-j\theta(z)}$$

where $\theta(z)$ is the phase advance along the structure. In non-resonant perturbation measurements[3], a perturbing object was placed inside the accelerating structure and the reflection coefficient at the input port was measured. The difference between the unperturbed input reflection coefficient S_{11}^{0} and the perturbed reflection coefficient S_{11}^{p} provides information on both the amplitude and phase of the accelerating field:

$$\Delta S_{11}(z) = a|E(z)|^2\, e^{-2j\theta(z)}$$

where a is a constant depending on the input power level and the shape of perturbing object.

For bead pull measurements, a nylon string with a diameter around 50 μm was threaded through the side pumping slot and moved along the longitudinal direction. Figures 10 and 11 depict the preliminary results of the measured amplitude and phase at 91.392 GHz along the 7-cell traveling-wave structure.

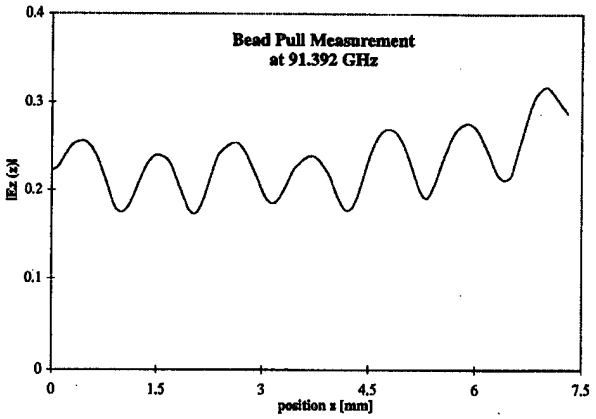


Fig. 10: The measured amplitude(in arbitrary units) of the accelerating field along the structure.

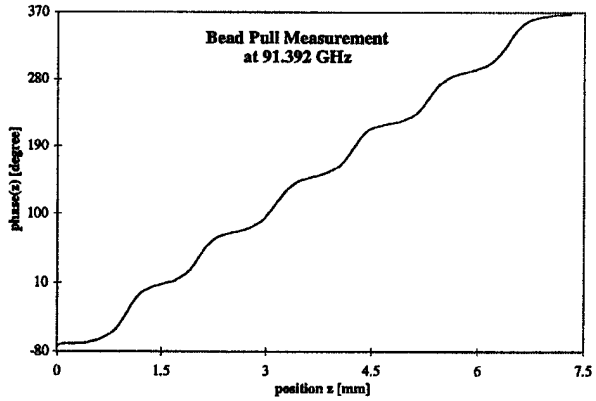


Fig. 11: The measured phase advance(in degrees) of the accelerating field along the structure.

IV. ACKNOWLEDGMENT

The authors would like to thank N.M. Kroll, R.H. Miller, C.K. Ng, and J.W. Wang for many helpful discussions.

V. REFERENCES

[1] P.J. Chou, et al., "Design and Fabrication of a Traveling-Wave Muffin-Tin Accelerating Structure at 90 GHz", in this proceeding.

[2] The MAFIA Collaboration, F. Ebeling et al., MAFIA User Guide, 1992.

[3] K.B. Mallory and R.H. Miller, IEEE Trans. Microwave Theory and Tech., **MTT-14** (1966) 99.

DESIGN AND MODEL SIMULATIONS OF INVERSE CERENKOV ACCELERATION USING INVERSE FREE ELECTRON LASER PREBUNCHING

W. D. Kimura,[*] M. Babzien,[†] I. Ben-Zvi,[†] D. B. Cline,[‡] R. B. Fiorito,[‡‡] J. R. Fontana,[§] J. C. Gallardo,[†] S. C. Gottschalk,[*] P. He,[‡] K. P. Kusche,[*†] Y. Liu,[‡] R. H. Pantell,[**] I. V. Pogorelsky,[†] D. C. Quimby,[*] K. E. Robinson,[*] D. W. Rule,[‡‡] J. Sandweiss,[††] J. Skaritka,[†] A. van Steenbergen,[†] and V. Yakimenko.[†]

[*]STI Optronics, Inc.; [†]Brookhaven National Laboratory; [‡]University of California at Los Angeles; [§]University of California at Santa Barbara; [**]Stanford University; [††]Yale University; [‡‡]Naval Surface Warfare Center

Abstract

An experiment to use an inverse free electron laser (IFEL) to prebunch at optical wavelengths the electrons entering into an inverse Cerenkov accelerator (ICA) is being prepared at the BNL Accelerator Test Facility (ATF). The design and simulations for this experiment are presented. Microbunches on the order of 2 microns in length separated by 10.6 microns are predicted. Under the anticipated ATF conditions, space charge effects should not be an issue. Minimizing bunch smearing is an important design issue also discussed.

1 BACKGROUND

1.1 Inverse Cerenkov Acceleration (ICA)

Inverse Cerenkov acceleration (ICA) [1] uses a gas (e.g., H_2) to slow the phase velocity of the laser light to enable matching the electron velocity. Phase matching is satisfied when the laser light intersects the *e*-beam at the Cerenkov angle θ_c, where $\theta_c = \cos^{-1}(1/n\beta)$, n is the refractive index of gas and β is the electron velocity divided by c.

The present ICA experiment is located at the BNL Accelerator Test Facility (ATF) where acceleration has been routinely observed since the experiment's first operation in 1995 [2]. It features an axicon-focused, radially-polarized laser beam geometry developed by Fontana and Pantell [3] as depicted in Fig. 1.

1.2 Inverse Free Electron Laser (IFEL)

The inverse free electron laser (IFEL) at BNL [4] uses an 47-cm long electromagnet wiggler to provide phase-matching with the laser light. The laser light travels through a circular sapphire waveguide down the center of the wiggler as depicted in Fig. 2. Note, the BNL IFEL wiggler has been designed for easy modification if necessary.

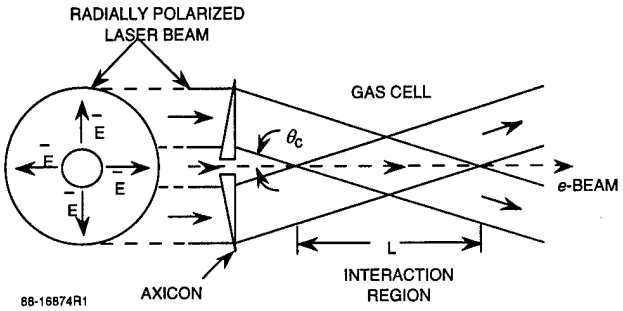


Figure 1: Schematic of basic ICA geometry used in experiment at the ATF [from Ref. 1].

1.3 Motivation for Combining ICA and IFEL Experiments

In the current ICA and IFEL experiments, the 10-ps long electron bunch is much longer than the ~300 ps CO_2 laser pulse. Consequently, electrons intersect the laser light over all phases resulting in both acceleration and deceleration of particles. For efficient acceleration, the electrons must be prebunched into microbunches that are a fraction of the laser wavelength in duration (e.g., for 10.6 μm light, the microbunch length should be ~1-2 μm). These microbunches can then be accelerated as a group by intersecting them at the proper phase with the light wave.

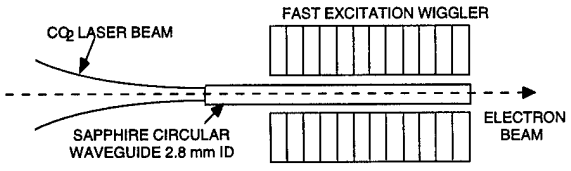


Figure 2: Schematic of basic BNL IFEL geometry.

The present ICA and IFEL experiments modulate the electron energies; thereby, creating these microbunches. An IFEL is a better prebuncher than an ICA device because it does not suffer from scattering of the electrons off the gas molecules. On the other hand, an ICA device scales in energy more favorably than an IFEL

0-7803-4376-X/98/$10.00 © 1998 IEEE

because it does not suffer from synchrotron radiation losses. Gas scattering effects also diminish greatly at high *e*-beam energies.

Hence, the experiments are being combined where the IFEL and ICA devices will be used as a prebuncher and acceleration stage, respectively. The ultimate goal of this combined experiment is to demonstrate 100 MeV of net energy gain.

A conceptual design of the ICA/IFEL experiment is shown in Fig. 3. The drive laser is the ATF CO_2 laser that is capable of delivering 5-10 GW to the gas cell. It is being upgraded to eventually deliver up to 1 TW. The electrons leave the ICA stage where their energies are measured with a spectrometer.

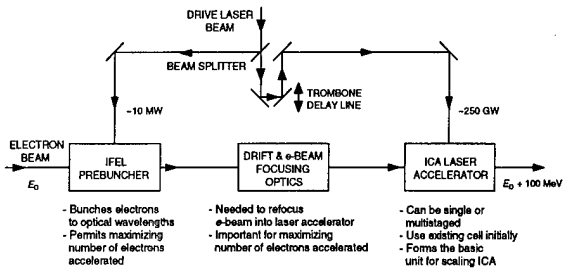


Figure 3: Conceptual design for ICA/IFEL experiment.

2 INTEGRATED MODEL DEVELOPMENT

In order to design and predict the performance of this combined experiment, existing Monte Carlo computer models of the IFEL and ICA were combined into an integrated model. The IFEL model calculates the energy modulation induced on the initial electron distribution. A ray-tracing model of the drift region computes the microbunching resulting from the induced energy spread, including bunch smearing effects due to finite emittance and path length differences through the quadrupole system used for refocusing the beam into the ICA cell (see Fig. 3). The ICA code is used to simulate the acceleration of the prebunched beam in the ICA gas cell, including relevant effects such as laser focusing and electron scattering from the phase matching gas.

2.1 IFEL Design Analysis

Table I lists the IFEL baseline parameters including the typical ATF *e*-beam characteristics entering the IFEL.

IFEL simulations indicate that a uniform 47-cm wiggler with period ≥3.3 cm is suitable over a 40-65 MeV range. The distance between the IFEL and ICA devices is ≈2 m and is constrained by space limitations. To achieve optimum bunching at this distance for a 50 MeV beam requires a modest ~5 MW of laser power to the IFEL. However, the initial energy spread must be much less than the induced energy spread of 1.2%.

The IFEL sensitivity study established other maximum allowable error tolerances: Laser power fluctuations <±50%, energy detuning <±1%, e-beam energy jitter <0.25% p-p, and wiggler current jitter <0.9% p-p.

Table I. IFEL Baseline Parameters

Parameter	Baseline Value
Wiggler	
Length, L_w	47 cm
Period, λ_w	3.33 cm
Peak field, B_0	1.04 T
Wiggler parameter, K	3.23
Energy taper, $\Delta\gamma/\gamma_r$	0%
Laser Beam	
Wavelength, λ_L	10.6 μm
Power, P_L	5 MW
Electron Beam	
Energy, E	50 MeV
Energy spread, $\Delta\gamma/\gamma$	0.25% FWHM
Normalized rms emittance	2π mm-mrad
Matched beam Twiss parameters at wiggler exit	$\beta_x = 0.6$ m $\beta_y = 0.245$ m $\alpha_x = -1$ $\alpha_y = 0$

2.2 Drift Region Analysis With Bunch Smearing

Table II lists the drift region baseline parameters. The primary focusing element in this drift region is a triplet consisting of three 20-cm quadrupoles.

Table II. Drift Region Baseline Parameters.

Parameter	Baseline Value
Overall Drift Length, L_D	1.97 m
Separation between quadrupoles	5.2 cm
Distance from end of triplet to ICA cell	38 cm
Magnetic field gradients	25.5 kG/m -45.5 kG/m 34.0 kG/m
Twiss parameters at ICA cell	$\beta_x = 0.065$ m $\beta_y = 0.095$ m $\alpha_x = 0.1$ $\alpha_y = 0.1$
e-Beam diameter at ICA cell (90% of particles)	154 μm × 186 μm

Using these drift region baseline parameters, the effects on bunch smearing as a function of *e*-beam initial energy spread and emittance are shown in Fig. 4.

This indicates that base widths of order 3 μm (implying bunch widths <2 μm FWHM) are obtainable for initial energy spread ≤ 0.25% and emittance ≤ 2π mm-mrad, which are values obtainable on the ATF.

2.3 ICA Performance Prediction

The microbunched beam is lastly sent through the ICA model whose baseline parameters are listed in Table III.

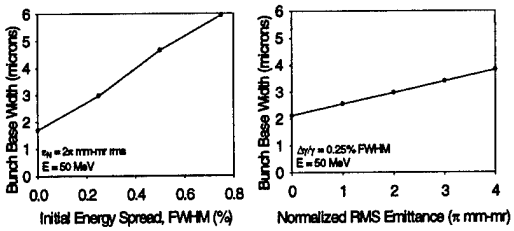


Figure 4. Microbunch base width vs. initial energy spread and emittance.

Table III. ICA Baseline Parameters.

Parameter	Baseline Value
Cerenkov angle, θ_c	20 mrad
Interaction length, L	20 cm
Hydrogen gas pressure, P	1.9 atm
E-beam window thickness	2.1 μm (diamond)

The predictions of the baseline integrated model for a 600 GW laser beam delivered to the ICA gas cell are given in Fig. 5.

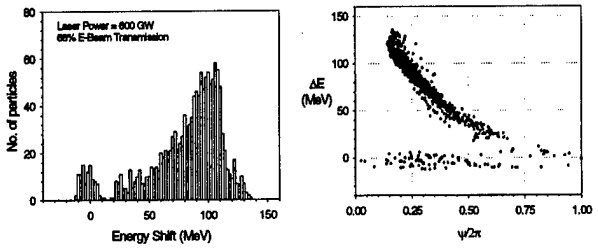


Figure 5. Model prediction of electron energy and phase-space for 600 GW laser beam driving ICA cell.

Notice that a significant number of the 50-MeV electrons have been trapped and accelerated around the 100 MeV point. From the phase diagram it is clear the electron energy spread is caused by particles distributed over phase. Sending these electrons through additional acceleration stages should help reduce this phase spread, thereby narrowing the energy spread.

3 OTHER DESIGN ISSUES

3.1 Space-Charge Effects

Space-charge effects will become a more serious issue at these extraordinarily small microbunch dimensions. Earlier PARMELA simulations [5] indicate that space-charge effects will tend to broaden the microbunch size by ~10% for the ATF conditions. Further PARMELA analysis is being performed to more fully understand when space-charge effects become significant.

3.2 Measurement of Microbunch Characteristics

Conventional diagnostics cannot measure the bunch length of the 2-μm microbunches. We have been examining using coherent transition radiation (CTR) as a means for detecting the degree of microbunching. Recent CTR experiments at the ATF have successfully detected the IFEL-generated microbunches [6]. We are also examining a novel modification of the basic CTR device that may permit a more direct estimation of the bunch length.

4 CURRENT STATUS AND FUTURE PLANS

As of May 1997, the ICA experiment has been moved downstream from its original location to make room for the IFEL and triplet. We are awaiting delivery of the quadrupoles before finishing the installation of the IFEL during the autumn of 1997.

First experiments will be to test the IFEL and prebunching only. Next the combined ICA/IFEL system will be run at relatively low laser power (e.g., 5 GW). The primary goal of these tests will be to demonstrate rephasing of the laser light with the microbunches and subsequent acceleration. Later much higher laser peak power (e.g., ~300-600 GW) will be delivered to the ICA cell to achieve the amount of acceleration predicted in Fig. 5. Issues such as possible laser damage of the gas cell optics must be addressed at these high laser powers.

5 CONCLUSIONS

The combined ICA/IFEL experiment will be one of the first to demonstrate acceleration of laser-generated microbunched electrons. It will examine issues of microbunch preservation and rephasing with the laser light. It will also address engineering issues related to accelerating fsec-long bunches.

6 ACKNOWLEDGEMENTS

This work was supported by the U.S. Department of Energy, Grant Nos. DE-FG06-93IR40803, DE-AC02-76CH00016, DE-FG03-92ER40695, and DE-FG03-90ER40545.

REFERENCES

[1] J. A. Edighoffer, W. D. Kimura, R. H. Pantell, M. A. Piestrup, and D. Y. Wang, "Observation of Inverse Cerenkov Interaction Between Free Electrons and Laser Light," Phys. Rev. A **23**, 1848-1854, (1981).

[2] W. D. Kimura, G. H. Kim, R. D. Romea, L. C. Steinhauer, I. V. Pogorelsky, K. P. Kusche, R. C. Fernow, X. Wang, and Y. Liu, "Laser Acceleration of Relativistic Electrons Using the Inverse Cerenkov Effect," Phys. Rev. Lett. **74**, 546-549 (1995).

[3] J. R. Fontana and R. H. Pantell, "A High-Energy, Laser Accelerator for Electrons Using the Inverse Cherenkov Effect," J. Appl. Phys. **54**, 4285 (1983).

[4] A. van Steenbergen, J. Gallardo, J. Sandweiss, J-M. Fang, M. Babzien, X. Qiu, J. Skaritka, and X.J. Wang, "Observation of Energy Gain at the BNL Inverse Free-Electron-Laser Accelerator," Phys. Rev. Lett. **77**, 2690 (1996).

[5] A. Bogacz, FNAL, private communication.

[6] Y. Liu, D. B. Cline, X. J. Wang, M. Babzien, J. M Fang, and K. P. Kusche, (in these proceedings).

THE NEPTUNE FACILITY FOR 2nd GENERATION ADVANCED ACCELERATOR EXPERIMENTS

C. E. Clayton[a], C. Joshi[a], K. A. Marsh[a], C. Pellegrini[b], and J. Rosenzwieg[b]
[a]Department of Electrical Engineering, [b]Department of Physics
University of California at Los Angeles, 405 Hilgard Avenue, Los Angeles, CA 90095

ABSTRACT

The NEPTUNE Laboratory, under construction at UCLA, will be a user facility for exploring concepts useful for advanced accelerators. [1] The programmatic goal for the laboratory is to inject extremely high quality electron bunches into a laser-driven plasma beat wave accelerator (PBWA) [2] and explore ideas for extracting a high quality $\Delta E/E < 0.1$, $\varepsilon_n < 10\ \pi$ mm-mrad), high energy (100 MeV) beam from a plasma structure operating at about 1 THz and about 3 GeV/m. The lab will combine an upgraded MARS CO_2 laser and the state-of-the-art SATURNUS RF gun and linac. [3] The new MARS laser will be about 1 TW (100 J, 100 ps), up from 0.2 TW (70 J, 350 ps). This allows for doubling the spot size at the IP and quadrupling the interaction length while still driving gradients of 3 GeV/m. The SATURNUS gun will be upgraded to the Brookhaven 1.6 cell design. [4] A novel, multi-cell Plane-Wave Transformer (PWT) RF gun is also under development. [5] A sync-pumped, sub-ps dye laser is available to directly produce ultrashort electron pulses (1/5 of an accelerating bucket). Part of the research program will be devoted to studying pulse compression [6] and phase-locking techniques at these ultrahigh frequencies and diagnosing microbunches generated by such structures. [7] Finally, shaped electron pulses will be studied for the electron driven Plasma Wakefield Accelerator (PWFA) concept.

1 INTRODUCTION

In the previous 10 years, many experiments have demonstrated the "proof-of-principle" of high-gradient laser- or electron-beam-driven plasma accelerators. [1] In fact, accelerating gradients as high as hundreds of GeV/m have been inferred in the high-density laser/plasma experiments. [9] But for applications to high energy physics (HEP), the main question regarding plasma accelerators is no longer will if they work in principle but rather, what can plasma accelerators deliver in terms of beam quality and numbers of electrons per bunch. We refer to experiments of this type as "second generation" plasma accelerator experiments which begin to deal with the structural aspects of the plasma accelerator and its control. These experiments will take place in the new NEPTUNE Laboratory currently being outfitted with electron and laser beam apparatus. The new lab is essentially the combination of two separate state-of-the-art facilities at UCLA: namely the MARS Laser Laboratory where the 0.2 TW CO_2 MARS Laser has been used for a series of PBWA experiments and the SATURNUS Accelerator Laboratory where an extremely high brightness RF gun and PWT linac has been used in plasma lens [10] and FEL experiments [11]. The contents of these two labs are being upgraded and combined.

In this paper we will briefly describe the changes being made to the MARS Laser and to the SATURNUS beamline to improve their respective performance levels.

2 MARS LASER UPGRADE

The purpose of this upgrade is two-fold. First, a means of synchronizing the CO_2 pulse, and hence the accelerating structure, to the electrons from the photocathode is required Secondly,. more laser power is needed to drive plasma waves over a longer interaction length. The former is accomplished through a new "front-end" to the laser while the second latter is primarily accomplished using a new preamplifier prior to the large-aperture final amplifier.

2.1 The Front End

In the prior configuration of the MARS laser, a technique called Optical Free Induction Decay (OFID) was used to generate sub-100 psec pulses to inject into the amplifier chain. This passive, experimentally simple technique was adequate since the electron source was a pulsed X-band magnetron driven linac. There was no control over the startup phase of the magnetron so no attempt was made to phase-lock the micropulses from the linac to the peak of the PBWA as it grew in time. The 107 psec separation of the micropulses was short enough to ensure that some electrons would interact with the PBWA on most shots, [2] although the probability of hitting the peak amplitude of the PBWA in time was < 1 in 10 shots.

The fix is to use active optical switching of the CO_2 oscillator pulse, using the same 1 μm wavelength, 70 psec pulse from Nd:YAG laser to both switch out a 100 psec CO_2 pulse and, after pulse compression down to 3 psec and frequency converting into the UV, to liberate the electrons from the photocathode. The 1 μm pulse can act as a switch for the 10 μm CO_2 pulse by forming a

0-7803-4376-X/98/$10.00 © 1998 IEEE

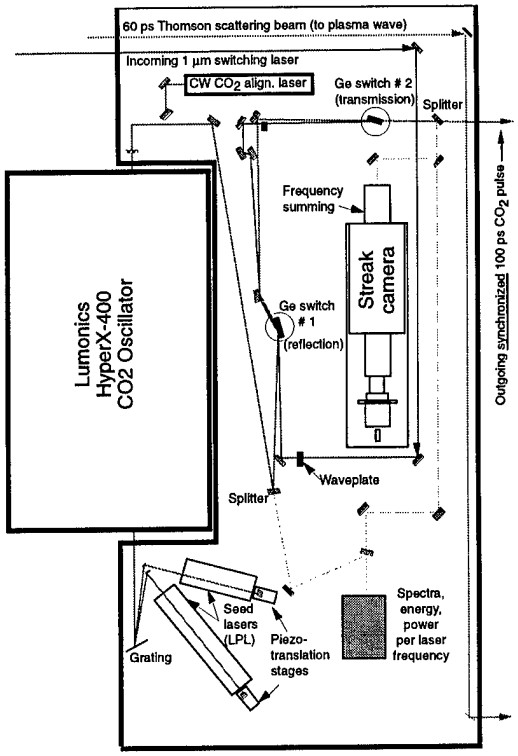


Figure 1: Schematic of the front end of the upgraded MARS laser.

transient solid-state plasma on two pieces of germanium set at Brewster's angle for the CO_2. This technique, know as semiconductor switching, is currently used at the ATF at Brookhaven. Now, by simply translating an optical delay line, one can ensure that the few psec electron bunch from the photocathode will always interact with the peak fields of the PBWA, approximately 60 psec after the CO_2 beam reaches the interaction point.

Another dramatic improvement, already tested and ready for implementation, is to uses a 3-mirror oscillator cavity for generating the required 2-frequency pulse for the beat wave. Essentially, each frequency will have its own cavity by using a grating to send the two frequencies to two separate rear mirrors as shown in Fig. 1. The two cavities share the same energy-storage gain section (a TEA laser) but have individual low-pressure (seeding) lasers (LPL). This eliminates gain competition since each cavity is separately seeded with the appropriate laser frequency and both can extract energy from the TEA laser. This will stabilize the shot-to-shot ratio of the two frequencies.

2.2 *CO_2 Preamplifier*

The old MARS laser used a one atmosphere, double-passed preamp followed by a 2.5 ATM, triple-passed power amplifier. Most of the pulse stretching (3 ×) of the original sup-100 ps OFDI pulse occurred in this preamp. The new laser will use a 10 ATM preamp run in the "regenerative amplifier" mode. Now, pressure-broadening will support the short pulse. In this mode, the pulse is electrooptically switched into an optical cavity containing the gain medium and after about 10 round trips, the pulse is switched out with no degradation of the pulse shape and duration. Also, due to the large number of passes of the preamp, the power is high enough that the final, now 3 ATM, large aperture amplifier need only be double-passed to achieve the 1 TW goal. Making fewer passes on the 3 ATM section will ensure that the pulse will remain short.

3 SATURNUS BEAMLINE

The Saturnus photoinjector has recently been decommissioned following successful running for SASE FEL[11] and high brightness beam dynamics[12,13] experimentation. Most of the Saturnus beamline, rf and control hardware has been transferred from its previous location in the Physics Dept. to the Neptune Laboratory. In order to bring the injector on line as expeditiously as possible, we have made a few important improvements in its design, and developed needed new facilities and diagnostics.

3.1 *The photoinjector and LINAC*

The injector itself presently consists of 1.5 cell BNL rf gun, with a plane wave transformer[3] (PWT) linac, run in an emittance compensation mode. Before recommissioning, we will incorporate a new rf photocathode gun, the next-generation 1.625 cell BNL/SLAC/UCLA gun[4], which, with additional improvements we have made on our emittance compensation solenoids, should yield state-of-the-art emittance performance at Neptune when run at over 100 MV/m peak on-axis field. The PWT linac, which is a very high Q device, is being accommodated at Neptune by the development of a longer pulse rf system (5 μsec, vs. the present 3 μsec rf flat-top) in order to completely fill the linac and, along with the improved gun extend the energy range of the injector from 14.5 to 17 MeV.

3.2 *The beamline*

The beamline itself will be augmented by the introduction of a chicane compressor[6], as shown in Fig. 2, which can be employed to create ultra-short beams for injection into the PBWA experiment, and ultra-high current beams for driving high gradient plasma wake-field acceleration (PWFA) experiments in the blow-out regime[14]. As a PBWA injector, the photoinjector/chicane complex has the desirable effect of suppressing the timing jitter (caused by the injection laser jitter) between the electron emission and the rf wave. The properties of the beam predicted by PARMELA simulations in the various modes of operation discussed are shown in Table 1.

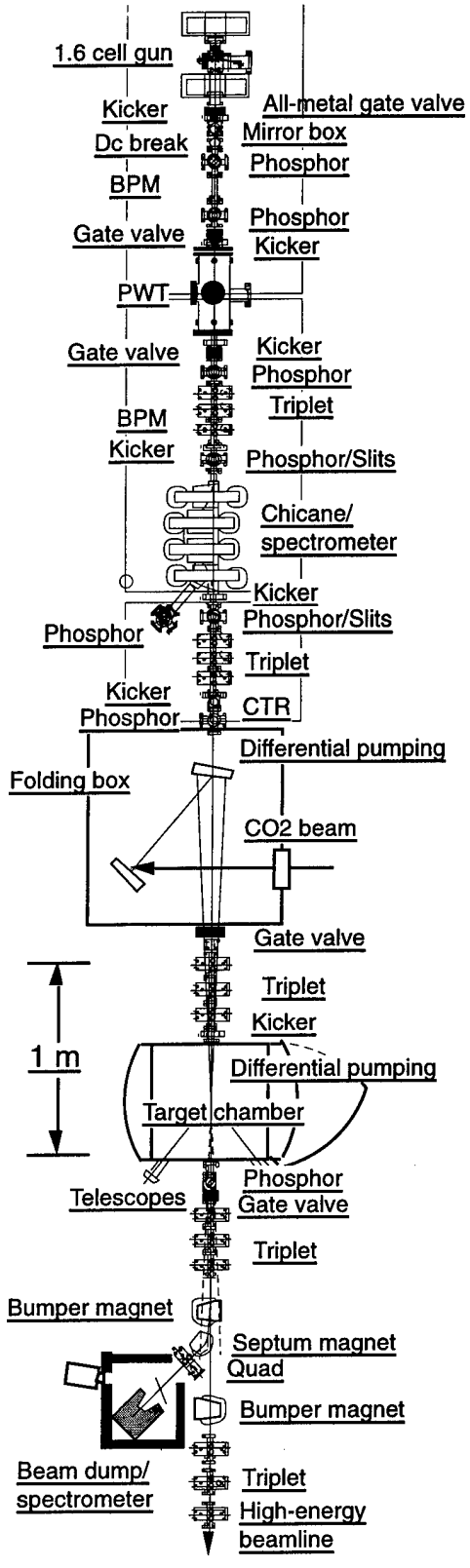


Figure 2: Schematic of the new beamline and PBWA experimental area. The "Folding box" contains a mirror with a small hole to facilitate bringing the electrons collinear with the two-frequency laser.

Mode	High Q	Low Q	High Q (compr.)	Low Q (compr.)
Q	1 nC	015 pC	8 nC	15 pC
σ_z	1 mm	300 μm	130 μm	42 μm
ε_n	1 mm-mrad	.06 mm-mrad	50 mm-mrad	0.2 mm-mrad

Table 1. Predicted performance of the Saturnus photoinjector at Neptune for various modes of operation.

The beam diagnostics for the photoinjector yield on-line information on beam energy (spectrometer, kicker scans), emittance (pepper pot/slit system), charge (integrating current transformer - ICT - Faraday cups, BPM sum signal), beam profile and position (phosphor and transition radiation screens, BPM difference signals) and bunch length (coherent transition radiation - CTR - and streak camera). The longitudinal diagnostics are the most challenging, in that we must diagnose beam structure well below 1 psec at Neptune. This is to be accomplished by CTR, for both macrobunch[c] and microbunch[h] structure, by autocorrelation, and spectral measurements, respectively. All diagnostics and beamline processes are controlled by a Power Macintosh running LabVIEW 4 which directs a GPIB local network (CAMAC crates/modules, digital oscilloscopes, etc.).

3.3 PWT LINAC

A new injector for Neptune, which is an integrated gun/linac of 11.5 cells based on the PWT structure, is now under construction by a UCLA/Duly Research collaboration[5]. This device will produce 20 MeV emittance compensated electron beams with the potential to create 50 μm long bunches without pulse compression. It is planned to perform SASE free-electron laser experiments using short beams created by both this injector and using the compressor in a 2 m long 100 period, 6 kG undulator. These experiments will clarify the role of slice emittance and emittance growth in bends as they apply to the FEL gain process.

4 ACKNOWLEDGMENTS

This work was supported by DOE Contract No. DE-GF03-92ER40727.

5 REFERENCES

[1] See, for example, IEEE Trans. on Plasma Sci., **24** (special issue).
[2] A. Lal *et al.*, to appear in Phys. Plasmas and references therein.
[3] R. Zhang, *et. al., Proc. of the 1995 Part. Accel. Conf.*, 1102 (1995).
[4] D.T. Palmer, *et al.*, these proceedings.
[5] D.U.L.Yu, *et al.*; J.B. Rosenzweig, *et al.*, both these proceedings.
[6] J.B. Rosenzweig, *et al., IEEE Trans. Plasma Sci.* **24,** 409 (1996).
[7] J.B. Rosenzweig, *et al., NIM A* **365**, 255 (1996).
[8] P. Chen *et al.*, Phys. Rev. Lett. **56**, 1253 (1986).
[9] A. Modena *et al.*, Nature **337**, 606 (1995).
[10] G.Hairapetian *et al.*, Phys. Rev. Lett. **72**, 2403 (1994).
[11] M. Hogan, *et al.*, these proceedings, also submitted to *PRL.*
[12] S. Reiche, *et al.*, these proceedings, also to appear in *PRE.*
[13] A. Murokh, *et al.*, submitted to *NIM A.*
[14] J.B. Rosenzweig, *et al., Phys. Rev. A* **44**, R6189 (1991).

OPTICAL BUNCHING OF RELATIVISTIC ELECTRONS FOR INJECTION INTO A GeV PLASMA BEATWAVE ACCELERATOR

D. Gordon, C.E. Clayton, W.B. Mori, and C. Joshi, University of California, Los Angeles, Los Angeles, California 90095
T. Katsouleas, University of Southern California, Los Angeles, California 90089

Abstract

A proposed GeV plasma beatwave accelerator (PBWA) requires a high power 1 μm laser running on two frequencies. The vacuum interaction between such a laser and a relativistic electron beam is one mechanism whereby the electrons can be bunched such that when injected into the PBWA they occupy only small regions of phase situated at the peaks of the accelerating field. This is exactly what is required to obtain a high quality beam from the accelerator. We outline the details of this scheme.

1 INTRODUCTION

In another publication [1], we describe a mechanism whereby a two-frequency laser beam modulates the axial momentum of a copropagating relativistic electron beam via the vacuum interaction between the two. The momentum modulated electrons can subsequently be bunched by a drift space or a magnetic compression device. The resulting beam is ideally suited for injection into a plasma beatwave accelerator (PBWA) [2] where the plasma wave is driven by the same two-frequency laser that was used to bunch the injected particles. Because the bunching is driven by the same pump that drives the plasma wave, the periodicity of the plasma wave and the injected electron bunches would be identical. Hence, the injected electrons would occupy small regions of phase situated at the peaks of the accelerating field, and a nearly monoenergetic beam would emerge from the plasma.

In Ref. [1], we presented an example of the above process wherein a 2.5 TW CO_2 laser modulates the momentum of a 16 MeV electron beam. A chicane compressor was proposed as the bunching element since a drift space would have been too long in light of space charge effects. However, this example was chosen only because it reflects the realities of the PBWA experiments that are likely to be carried out in the next few years. In fact, the technique of optical bunching described in Ref. [1] would lend itself better to the proposed GeV PBWA [3] which employs a 14 TW 1 μm laser. In this case, the perturbation to the axial momentum of the electrons is sufficiently large so that a short drift space suffices to compress the electrons. This simplifies experimental realization of the scheme.

2 OPTICAL BUNCHING

The mechanism of optical bunching described in Ref. [1] works as follows.

Any real laser beam contains an axial electric field. This field becomes smaller as the Rayleigh length becomes larger. This relationship is exactly balanced in the sense that the work done on a particle by the axial field does not change when the Rayleigh length is changed. In other words, the instantaneous force can only be increased by losing interaction length, and can only be decreased by gaining interaction length. If the interaction between the laser and the particle takes place over many Rayleigh lengths, it follows that the axial fields can never be dismissed simply by focusing the laser more gradually.

The effect of the laser's axial electric field on a copropagating electron beam is profound. Without this field, all the forces on the electrons would vary rapidly at the optical frequency and would average to zero when integrated over all time. With the axial field, however, a slowly varying force arises which allows for the possibility of making a net change to the momentum of the electron even after an infinite interaction time. The slowly varying force arises because of the phasing between the transverse and axial electric fields. These two conspire such that an electron is always pushed slowly away from best focus. In the case of a single frequency laser, this repulsion would integrate to zero since it would be the same on either side of the optical waist. In the case of a dual frequency laser, however, a slowly varying interference pattern is introduced which causes the impulse delivered on either side of the waist to be different. A net energy change can then occur.

In order for the above mechanism to work, a number of requirements must be met. Let the Lorentz factor of the electons be γ. The average wavenumber of the two laser lines is k, and the wavenumber difference is Δk. The radius of the laser waist is w_0, while the Rayleigh length is z_0. The peak normalized vector potential of the laser is a_0.

It is required, first of all, that the electron be highly relativistic ($\gamma>>1$). This assures that the velocity, and hence the rate of slippage through the optical cycles, remains approximately constant. In order that forces varying at the optical frequency be dismissed from consideration, it is required that the electron slip through many optical cycles for each cycle of the beat envelope. That is,

0-7803-4376-X/98/$10.00 © 1998 IEEE

$$\Delta k / k << 1 \qquad (1)$$

Similarly, the electron must slip through many optical cycles while passing through the focal region. The exact expression of this requirement turns out to be subtle, depending on the geometric mean of k and Δk:

$$\gamma^2 << z_0 \sqrt{k \Delta k} / 2 \qquad (2)$$

At the same time, the electrons must slip through only a small fraction of the beat envelope while passing through the focal region. That is,

$$\gamma^2 >> z_0 \Delta k / 8\pi \qquad (3)$$

Finally, the intensity of the laser must not be too high. This prevents electrons from being lost radially during their transverse quiver motion. We have,

$$a_0 << k w_0 / \gamma \qquad (4)$$

If all these requirements are met, it is shown in Ref. [1] that the energy of a constant stream of electrons is sinusoidally modulated by the laser. In mks units, the normalized energy perturbation is expressed as

$$\delta\gamma = -\frac{1}{8\gamma}\left(\frac{e}{mc^2}\right)^2 \eta P \frac{\Delta k}{k} \sin(\Delta k z) \qquad (5)$$

where $\eta = 377\ \Omega$ is the impedance of free space and P is the average power in the beat pattern. The modulated beam will reach a longitudinal waist after propagating a distance given by

$$L = \frac{4\pi}{\eta P}\left(\frac{mc^2}{e}\right)^2 \gamma^4 \frac{k}{\Delta k^2} \qquad (6)$$

provided space charge forces are negligible.

3 APPLICATION TO THE GEV PBWA

The design of the GeV PBWA proposed in Ref. [3] is summarized as follows. A large amplitdue plasma wave is driven by a Nd:glass laser running on the 1.05 μm and 1.06 μm lines. The laser achieves 14 TW in 4 ps via chirped pulse amplification, and is focused into a gas jet to a 100 μm radius spot where a plasma is formed via multiphoton ionization. A photoinjector driven RF linac generates a beam of 10 MeV electrons which are injected into the plasma wave and accelerated. The emittance of the 10 MeV electron beam is given as 0.5π mm-mrad, but this is a conservative estimate. We assume here that the intrinsic uncorrelated energy spread on the electron beam is much less than 1%. This is not unusual for a photoinjector driven RF linac.

For these parameters, $\Delta k/k$ is about 0.01, so the condition (1) is easily met. The remaining conditions depend on the f-number of the laser beam which has yet to be specified for the vacuum interaction. Suppose w_0 = 50 μm (z_0 = 8 mm). Then the conditions (2) and (3) become

$$z_0 \Delta k / 8\pi << \gamma^2 << z_0 \sqrt{k \Delta k} / 2 \quad \Leftrightarrow \quad 18 << 441 << 2325$$

which is acceptable. In fact, in Ref. [1] it was found numerically that the upper bound on γ^2 is really higher than equation (2) suggests. Condition (4) requires that a_0<<15. For the spot size being considered, a_0=0.4 so this requirement is easily met.

Assuming all the available laser power is used for the vacuum interaction, equation (5) gives the depth of modulation of the electron energy ($\delta\gamma/\gamma$) as 5.4%. This is well beyond the intrinsic energy spread on the beam. According to equation (6), a beam thus modulated will reach a longitudinal waist after propagating a distance L = 22 cm. Assuming no space charge, the maximum compression ratio should approach the limit for a beam with a sinusoidally correlated velocity disribution. This limit is approximately seven [4].

Once a compressing electron bunch is generated, it must be properly injected into the plasma wave. Both the laser and the electrons must be refocused a distance L from the vacuum interaction. Given the size of typical electron lenses, it might be desirable to increase L either by using a stiffer electron beam or less laser power for the vacuum interaction. This might also be desirable from the standpoint that a small L corresponds to a large energy spread which will lead to chromatic aberration in the final electron lens.

One possible injection scheme is shown in Fig. 1. Here, a single laser beam is split into two parts. The first part is focused by an off-axis parabola (OAP) through a small hole in a second OAP. The second OAP focuses the second part of the laser beam into the plasma. Not shown are two quadropole triplets. The first, located between the two OAP's, focuses the electrons into the hole of the second OAP where the vacuum interaction with the laser modulates the electron momentum. The second is beyond the second OAP and focuses the electron beam into the plasma where the acceleration process occurs.

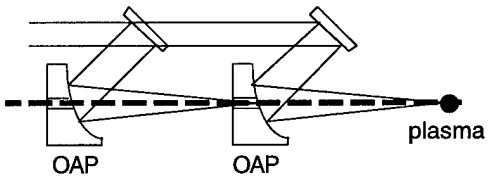


Figure 1: Schematic of the GeV Experiment. The dotted line represents the electron beam while the solid lines represent the laser.

We note here that an aperture placed some distance from the vacuum interaction will eliminate the non-

compressing ("negatively chirped") portions of the modulated electron beam [1].

The laser power required for the vacuum interaction is determined from the distance between the second OAP and the plasma. That is, the power is selected to bring the electrons to a longitudinal waist after propagating that distance. This distance must be rather long since Ref. [3] calls for a very gradual focus of the laser into the plasma. In particular, a distance of at least one meter would be needed in order to make the laser reasonably large on the second OAP. A distance of one meter corresponds to 3 TW of laser power on the first OAP, which would perturb the energy of the electrons by 1%.

The only remaining questions are how much charge can the electron bunches carry, and is a 1% energy spread sufficiently small so that the electrons can be tightly focused into the plasma. These questions are addressed via numerical calculation.

4 NUMERICAL CALCULATIONS

The effects of space charge and chromatic aberration are examined using the computer code TRACE3D. The model commences at the first OAP where it is assumed the electrons have already been perturbed by the laser. The electrons are initialized at a 50 μm waist with an emittance of 0.5π mm-mrad. The longitudinal phase space is approximated by a line segment drawn from (90°,9.875 MeV) to (-90°,10.125 MeV), where 360 degrees of phase corresponds to 111 μm. These electrons are propagated through a 50 cm long drift space, followed by a quadropole triplet, followed by a 47 cm long drift space. The effective length of each quadropole in the triplet is 3 cm, and each pair is separated by 2 cm. The field gradient in the outer quadropoles is 0.927 kG/cm, while the gradient in the inner quadropole is 1.700 kG/cm.

When the beam current is zero, the electrons will of course compress to zero pulse length. When the initial current is 10 A, the longitudinal waist is about 20° wide and occurs at the end of the second drift space, where we assume the plasma is located. The energy spread there is reduced to about 30 keV. Transversely, chromatic aberration in the triplet increases the horizontal emittance to 1.09π mm-mrad, while the vertical emittance increases to 0.65π mm-mrad. Because of this, the beam size at the plasma is about 100 μm x 200 μm, somewhat larger than desired (the electrons should stay inside the laser). However, as mentioned above, the initial emittance of the beam might actually be much better than the 0.5π mm-mrad assumed in this calculation, in which case the final spot size could be made smaller. In addition, the longitudinal bunching guarantees not only that electrons will see the peak accelerating field, but also that they will see the focusing fields of the plasma wave. Chromatic aberration, then, does not appear to be a major problem.

5 CONCLUSIONS

We have presented a practical scheme whereby electrons can be injected into a GeV plasma beatwave accelerator such that they are confined to within 20° of phase from the peak accelerating field of the plasma wave. The average current of the injected beam is 10 A, while the peak current after bunching is 90 A. These numbers might be improved by considering more sophisticated electron optics. If an achromatic focusing system is devised, a larger energy perturbation could be applied to the electrons in which case they would more readily overcome space charge repulsion as they compress. Considering a lower emittance electron beam might also be helpful.

6 ACKNOWLEDGEMENTS

This work was supported by DOE grant DE-FG03-92ER40727.

REFERENCES

[1] D. Gordon *et. al.*, to be submitted to Phys. Rev. E.
[2] T. Tajima and J.M. Dawson, Phys. Rev. Lett. **43**, 267 (1979).
[3] C. Joshi *et. al.*, Comments on Plasma Physics and Controlled Fusion **16**, 65 (1994)
[4] T. Katsouleas, private communication. Actually, it was found numerically in Ref. [1] that a compression ratio of 10 is attainable, suggesting that the velocity perturbation contains harmonics favorable to compression.

LASER ACCELERATION IN VACUUM

J.L. Hsu, T. Katsouleas
University of Southern California, Los Angeles, CA 90089-0484
W.B. Mori
University of California, Los Angeles, CA 90024
C. B. Schroeder, J.S. Wurtele
Lawrence Berkeley National Laboratory, Berkeley, CA 94720

Abstract

This paper explores the use of the large electric fields of high-brightness lasers (e.g., up to order TV/cm) to accelerate particles. Unfortunately, as is well known, it is difficult to couple the vacuum field of the laser to particles so as to achieve a net energy gain. In principle, the energy gain near the focus of the laser can be quite high, i.e., on the order of the work done in crossing the focus $\Delta\gamma = \sqrt{\pi} eEw \sim 30 MeV\sqrt{P/1TW}$, where P is the laser power. In order to retain this energy, the particles must be in the highly nonlinear regime (Vosc/c >>1) or must be separated from the laser within a distance on the order of a Rayleigh length from the focus. In this work, we explore the acceleration and output energy distribution of an electron beam injected at various angles and injection energies into a focused laser beam. Insight into the physical mechanism of energy gain is obtained by separating the contributions from the longitudinal and transverse laser field components.

I. INTRODUCTION

The rapid development of high-brightness lasers leads us to re-examine the interaction of electron beams with vacuum focused lasers. For example, PetaWatt 1μm lasers are nearly available. For such lasers, the electric fields at focus will approach a TV/cm. There has been considerable previous work on this topic, so the limitations to energy gain via a linear interaction are by now well known[1]. This paper is concerned with the highly non-linear regime (normalized quiver velocity $eE/m\omega c >> 1$) where a net energy gain is possible. Here, we present preliminary numerical results of the net energy gain, energy spread and angular spread that may be expected by injecting an electron beam at various angles into a focused PetaWatt-class laser. The goal of the simulation is to determine the net work done on a relativistic electron as it propagates through a laser focal zone. Insight into the physical mechanism responsible for the energy gain is obtained by separating the contribution from the longitudinal and transverse field components.

II. ALGORITHM

For a linearly polarized, cylindrically focused Gaussian beam propagating in the +z direction, the field (for y=0) components are[2]

$$E_x = E_0 \frac{w_0}{w} \exp\left(-\frac{r^2}{w^2}\right)\cos\phi$$

$$E_z = 2E_0 \frac{w_0}{w}\frac{x}{kw^2}\exp\left(-\frac{r^2}{w^2}\right)\left(\sin\phi - \frac{z}{z_0}\cos\phi\right) \quad (1)$$

$$B_y = E_x$$

with the phase

$$\phi = kz - \omega t + \frac{r^2 z}{w^2 z_0} - \tan^{-1}\left(z/z_0\right) \quad (2)$$

where w_0 is the spot size, w is the laser field radius at position z, $z_0 = \pi w_0^2/\lambda$ is the Rayleigh length, and k is the free-space wave number of the laser.

The numerical algorithm is straightforward. Given the initial velocity of this particle, then the EM force can push this electron into a new position with a new velocity after a small time step by using the Time Center Leap Frog method[3].

The maximum energy gain from the acceleration[4] can be evaluated and compared to analytic estimates. The approximate value is given by estimating maximum work done by the laser field when the electron crosses the laser beam:

$$\begin{aligned}\Delta\gamma^{max} &\approx \int_{-w}^{+w} \vec{E}\cdot d\vec{r} \\ &\approx \sqrt{\pi}\cdot w_0 \cdot E_\perp + \int E_z dz \\ &\approx 30 MeV\sqrt{P/1TW}\end{aligned} \quad (3)$$

where P is the laser power in units of TW. For example, if we have a 100 TW laser, then the maximum energy gain is no more than 300MeV. In the following section, we use the model just described to analyze three specific laser acceleration geometries: one is injecting electrons at a small incident angle; the second is coaxial injection; and the third is injecting down the axis of the two crossed laser beams.

III. SIMULATION RESULTS

1. Small Incident Angle Injection:

In Fig.1, the x-z plot shows a laser beam propagating from z = -72000 μm to z = +72000 μm in the z direction.

0-7803-4376-X/98/$10.00 © 1998 IEEE

An electron is injected from the left bottom corner where z = -72000 μm crossing the laser beam with a small incident angle θ. For the parameters used in the example: the laser wavelength λ is 10.6 μm, which corresponds to a CO_2 laser, in order to compare to parameters of UCLA CO_2 laser experiment. The laser waist width w is 200 μm; the normalized laser amplitude, $eE_0/m\omega c \equiv aa$, is 0.4; the initial electron energy γ is 32; and the electron incident angle *theta* is 0.04 rad. The energy of the electron γ is plotted versus the propagating direction z from -72000 μm to +72000 μm and shown in the bottom side. We can see from the γ-z plot that γ increases and decreases as the particle slips in phase behind the light wave, finally reaching the same value as its initial energy. In this example, *aa* is not large enough to induce nonlinear effects, so no net energy gain results, as expected from the Lawson-Woodward theorem[1].

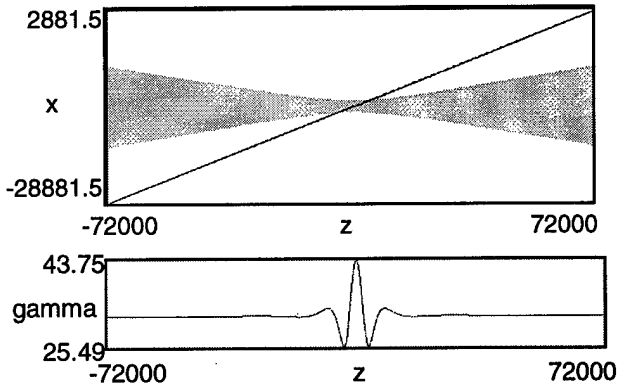


FIGURE 1. Particle trajectory and (below) particle energy (γ) vs. z for aa=0.4.

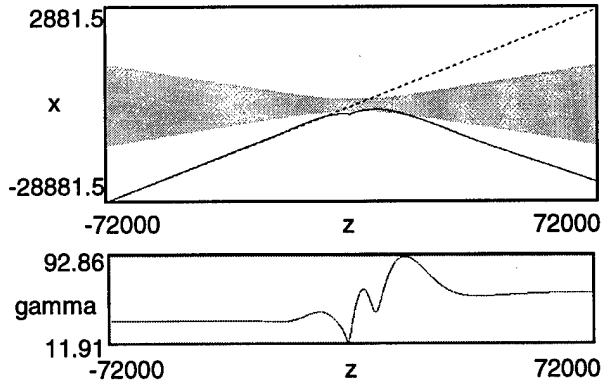


FIGURE 2. Particle trajectory and (below) particle energy gain vs. z for aa = 4. γ increase from 32 to 59.4 (dotted line shows the incident direction for this electron).

In the second example (Fig. 2), we increase *aa* from 0.4 to 4, which means that the laser power is 100 times that of the first one. From the (lower) γ-z plot in Fig. 2, we see that there is a net increase in the energy γ due to the interaction. The final energy at the point z = 72000 μm depends on the initial phase of the electron injection into the laser fields. In this example, the maximum $\Delta\gamma$ in a particular initial laser phase is near 27.4; that is 5% of the maximum value we estimated using the work done by the laser in equation (3).

2. Coaxial Injection:

Before considering the coaxial injection into focused laser beams, consider the movement of electrons in infinite plane waves. The exact solution for an electron moving in an infinite plane wave can be expressed as a drifting "figure eight". Using a large beam waist w in our simulation program approximates the plane wave limit; the trajectory of an electron in Fig.3 exhibits similar behavior to the exact solution in an infinite plane wave.

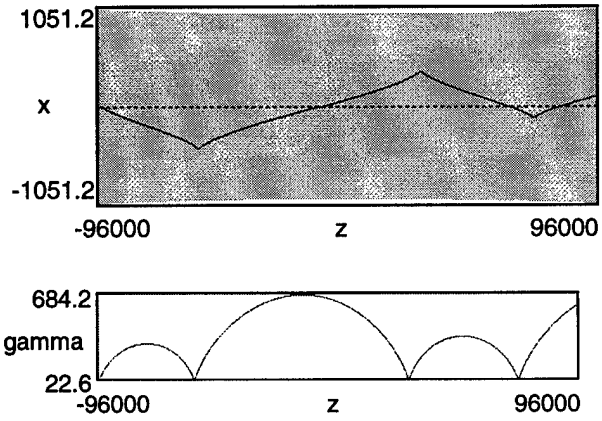


FIGURE 3. Particle trajectory and (below) γ-z plot for coaxial injection with large laser waist.

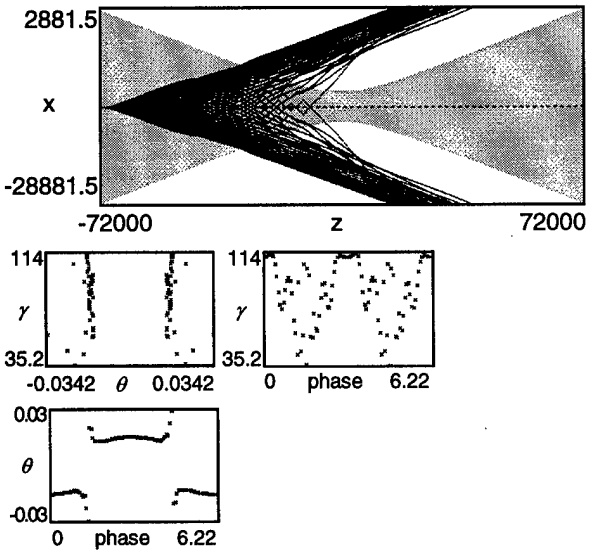


FIGURE 4. Particle trajectories for 100 initial laser phases from 0 to 2π and insets: final γ vs. initial laser phase, final γ vs. outgoing angle θ, θ vs. initial laser phase.

When the laser beam is focused to small spot size w, the trajectories of coaxially injected electrons are quite different. The trajectories of coaxially injected electrons with initial laser phases distributed from 0 to 2π are shown in Fig.4. The initial energy for the electrons is $\gamma =$ 32, and the *γ-theta* plot (the first inset) shows the final γ measured at the point z = 72000 μm versus different outgoing angle *theta*. As the second inset (γ-phase plot) shows, at the injection phases of 0 and π the final energy is relatively insensitive to injection phases (over approximately 1.7 radians or 27% of the full laser wavelength). Therefore, particle injection at these phases will result in better output beam quality (i.e., small energy spread and emittance growth). By Comparsion the runs we have done with injection at a small angle, were very sensitive to the injection phase.

Based on the results of Fig.4, it appears that a 100TW laser could be used to accelerate a micro-bunch (1.4 μm or 14% of the bucket) of cold electrons from 16MeV to 26MeV with an energy spread of 0.4MeV and emittance growth of $\varepsilon_x \approx 1$mm-mrad. The maximum energy gain in this example is only 3.8% of the maximum value from equation (3). By raising γ to 64 (not shown), we could increase the energy gain to 9.1%, but the particles with highest energy were from a very small region of initial phases (2% of the bucket).

In order to separate the effects of transverse and longitudinal fields in the acceleration process, we turn off the longitudinal field and find the interaction with the transverse field only. We observe that the electron trajectories are considerably altered by the presence of the Ez field, even though we found that the $\int E_z dz$ contribution to net energy gain was much smaller than the $\int E_\perp dy$ term for our examples.

3. Crossed Beam Injection:

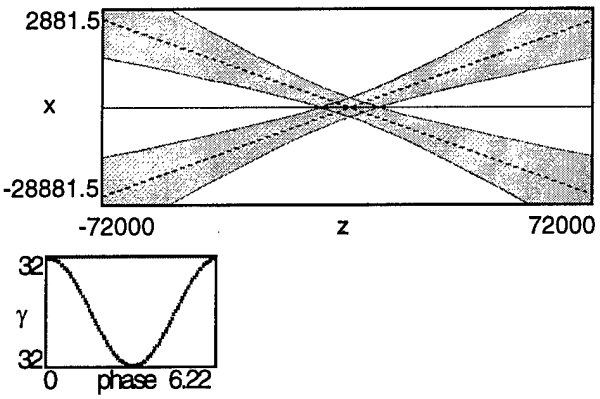


FIGURE 5. Numerical simulation showing no energy gain for any injection phase in two crossed lasers (dotted lines show laser beam axes).

A laser geometry that has received attention is the case of two gaussian laser beams crossed at a small angle with respect to the axis of electron injection[5,6]. The advantage of this geometry is that the transverse electric and magnetic fields will cancel on axis, leaving only the axial electric field to accelerate the particles. Fig.5 shows the simulation results of electrons injected at various initial laser phases on axis into the crossed beams which are positioned at an angle of 0.04 rads with respect to the electron beam. As the inset shows, there was no net energy gain for any initial laser phases. This result can be explained by realizing that by arranging the geometry such that there is only an electric field along the direction of motion, we have eliminated the nonlinear forces which are necessary for laser acceleration in vacuum. This is consistent with the results of P. Sprangle et al.[7]

IV. CONCLUSION

The simulation results show that net energy gain can be extracted from a single laser via nonlinear interactions. The nonlinear energy gain comes from the transverse fields; while the longitudinal field affects the path of electrons but does not increase their energy gain. If initial injection energy and angle and laser amplitude are chosen properly, large scattering spread angle can be avoided. For further research, characteristics of the outgoing electron beam with respect to the injected beam emittance need to be investigated. Other acceleration schemes, such as axicon focused lasers[5], or standing wave acceleration in two counterpropagating lasers[8] are also of interest for further simulations with this code.

V. ACKNOWLEDGMENTS

Work supported by US Department of Energy DOE - AC#DE - FG03 - 92ER40745. The assistance of R. Kinter and D.Gordon in coding the numerical model is gratefully acknowledged.

VI. REFERENCES

[1] P.M. Woodward, *JIEE 93*, 1947, p.1554.
[2] R. Guenther, *Modern Optics*, (Wiley, New York 1990), p.336.
[3] C.K. Birdsall and A.B. Langdon, *Plasma Physics via Computer Simulation*, (McGraw-Hill, NY 1985).
[4] W. Mori and T. Katsouleas, in *Advanced Accelerator Concepts.* AIP Conf. Proc. **No. 335**, (AIP, NY 1994), p.112.
[5] L. Steinhauer et al, in *Advanced Accelerator Concepts,* AIP Conf. Proc. **No. 335**, (AIP, NY 1994), p.131.
[6] C. M. Haaland, Optics Comm. **114,** 280 (1995).
[7] P. Sprangle, Optics Comm. **124**, 69 (1996).
[8] C. Barty, private communication.

A PROPOSAL FOR A 1 GeV PLASMA-WAKEFIELD ACCELERATION EXPERIMENT AT SLAC[1]

T. Katsouleas, S. Lee, *USC*, Los Angeles, CA 90089-0484
S. Chattopadhyay, W. Leemans, *LBNL*
R. Assmann, P. Chen, F.J. Decker, R. Iverson, T. Kotseroglou, P. Raimondi,
T. Raubenheimer, S. Rokni, R.H. Siemann, D. Walz, D. Whittum, *SLAC*
C. Clayton, C. Joshi, K. Marsh, W. Mori, G. Wang, *UCLA*

Abstract

A plasma-based wakefield acceleration (PWFA) experiment is proposed that will accelerate parts of an SLC bunch by up to 1 GeV/m over a length of 1 m. A single SLC bunch is used to both induce wakefields in the one meter long plasma and to witness the resulting beam acceleration. The proposed experiment will explore and further develop the techniques that are needed to apply high-gradient plasma wakefield acceleration to large scale accelerators. The one meter length of the experiment is about two orders of magnitude larger than other high gradient PWFA experiments and the 1 GeV/m accelerating gradient is roughly ten times larger than that achieved with conventional metallic structures. Using existing SLAC facilities, the proposed experiment will allow the study of high gradient acceleration at the forefront of advanced accelerator research.

I INTRODUCTION

The energies of most interest for high energy physics today have reached the multi-TeV level. Linear colliders offer the only possibility to access this energy regime with e+e- collisions. Practical limitations on the size and the cost of linear colliders can only be overcome if the acceleration per unit length is significantly increased. By replacing the metallic walls of conventional structures with "plasma-walls" many limitations are avoided and very high gradients can be achieved. A recent laser-driven plasma wakefield acceleration (PWFA) experiment has measured an accelerating gradient of 100 GeV/m[2].

Although plasma-based experiments have shown impressive advances in their accelerating gradients, they are quite short, extending over only a few mm. This proposal aims at demonstrating high gradient acceleration in a 1 m long plasma cell. Plasma modules of this length would be well suited for building a future linear collider. The intended use of the existing SLAC linac for the proposed experiment limits the achievable gradient to about 1 GeV/m. Though not as high as achieved by other plasma-based experiments, this gradient is much larger than in any metallic structure. It would be the first time that plasma-based structures accelerate particles by 1 GeV.

The basic idea for the proposed experiment is to use a single SLC bunch to both excite the plasma wakefield (head of the bunch) and to witness the resulting acceleration (tail of the bunch). For many reasons, the SLC beam is the ideal driver for a plasma acceleration test. It has high energy; it is very stiff and is not subject to distortion or depletion over the length of the experimental section proposed here. In addition, neither the driving particles nor the accelerated particles will significantly phase slip over the length of the experimental section. All of these factors suggest the possibility for a clean test of plasma wakefield acceleration and the opportunity to make detailed comparisons to theoretical models.

The experiments proposed here will assess the viability of wakefield transformers based on beam-driven plasmas. By designing flexibility into the plasma source and/or drive bunch length, we will be able to explore some of the most important phenomena. Specifically, we can measure the transformer ratio (i.e. the decelerating and accelerating fields within the bunch), transverse focusing fields, and the dependence of the gradient on plasma density, bunch length, beam and plasma radius. Furthermore, increasing the plasma density or bunch length will enable a first test for electron hose instability[3]. A secondary benefit of the proposed experiment will be the opportunity to explore the new physics and technology issues associated with particle beam rather than laser drivers.

	PWFA	Standard SLC
Bunch intensity	3.5-4.0 10^{10} electrons	3.5-4.0 10^{10} electrons
Bunch length	0.6 mm	0.6-1.1 mm
Rate into the FFTB	10 Hz	1 - 120 Hz
$\gamma\varepsilon_x$ at LI02	-	30 mm-mrad
$\gamma\varepsilon_y$ at LI02	-	3.5 mm-mrad
Transv. rms jitter at LI30	< 50 μm	50% of spot size
$\gamma\varepsilon_x$ at IP-1	60 mm-mrad	45 mm-mrad
$\gamma\varepsilon_y$ at IP-1	15 mm-mrad	8 mm-mrad
σ_x at IP-1	< 100 μm	23 μm at 1.0 10^{10}
σ_y at IP-1	< 100 μm	37 μm at 1.0 10^{10}

Table 1. Comparison of beam parameters for the PWFA experiment and SLC standard performance at 46.6 GeV.

We propose to place a meter-long plasma of appropriate density in the path of the SLC beam at IP-1 of the FFTB[4, 5]. The beam parameters needed for the proposed experiment are routinely achieved during standard SLC operation (see Table 1). Most important are a beam intensity of between 3.5 to 4×10^{10} electrons and a suitable bunch length (σ_z = 0.6 mm) and shape. Normalized emittances and transverse beam jitter are not critical and can be significantly larger than the standard SLC values at 46.6 GeV.

0-7803-4376-X/98/$10.00 © 1998 IEEE

In order to minimize the impact and cost of the proposed experiment we plan for parasitic running at 10 Hz during PEPII[6] operation. PEPII will already accelerate the linac beams to 30 GeV for positron production. We avoid additional costs for the maintenance and operation of the RF in the last third of the linac by only requiring 2-3 sectors of acceleration downstream of the positron extraction point. The additional acceleration is needed in order to maintain efficient BNS damping and a small final energy spread. The beam energy in the FFTB will be 30 GeV. Minor modifications in the dumpline transport will allow safe operation of the FFTB with a high current 30 GeV beam.

The development of the different parts of the experiment is well under way. The proposed plasma cell has been built at UCLA and is presently being tested. The beam-induced plasma wakefields have been modeled at USC. The transport of the SLC beam into the FFTB, through the plasma cell and into the beam dump has been modeled carefully at SLAC. Finally, the appropriate beam diagnostic has been specified based on the extensive experience at SLAC and LBNL. We believe that all critical components needed for a successful experiment are in place.

The proposed experiments are envisioned to take place in stages. The first stage will simply place a meter-long plasma of appropriate density in the path of the SLC beam near the end of the FFTB. We expect the head of the bunch to be decelerated by about 0.2 GeV while tail particles are accelerated by up to 1 GeV. The resulting change in energy distribution, will be detected by a time-resolved energy measurement with a streak camera. The wakefield will be diagnosed in detail by subtracting the energy distribution signals with and without the plasma. The second set of experiments proposed here will vary the plasma density, plasma length, and/or beam bunch length to test scaling laws for wake amplitudes and electron hose instability.

We can envision a rich physics program of follow-on experiments not proposed here. Some of these include tests of beam shaping to demonstrate the possibility of high transformer ratios[7], the use of a separate witness beam with a variable delay to fully probe the wakefields[8], the guiding of laser beams with the SLC beam in a plasma over hundreds of Rayleigh lengths[9] and the outcoupling of the plasma wakes as a unique high-power 100 GHz source[10]. We also note that the peak accelerating gradient in the experiment is expected to increase from 1 GeV/m to 2.5 GeV/m if the SLC RMS bunch length can be reduced from 0.6 mm to 0.4 mm. The successful completion of the experiments proposed here will undoubtedly provide a major impetus to advanced accelerator research as well as contribute to fundamental understanding of plasma and beam physics.

In the remainder of this paper we present sample simulations supporting the design of a 1 GeV experiment, and briefly describe the plasma source and beam diagnostic.

II SIMULATIONS

Sample results of a 2-1/2D PIC simulation in cylindrical geometry using the code MAGIC are shown in Figure 1. The parameters correspond to the expected experimental beam and plasma parameters. In Figure 1 the plasma density is 2.1 x 10^{14} cm^{-3} and the beam distribution corresponds to the 36 MV compressor setting of the NRTL bunch compressor (ref.). Figure 1a shows the real space of the plasma electrons in which blowout and crossing of streamlines are clearly visible. Figure 1b is a snapshot of the longitudinal wakefield 6 mm into the plasma. The peak accelerating field is 1 GeV/m.

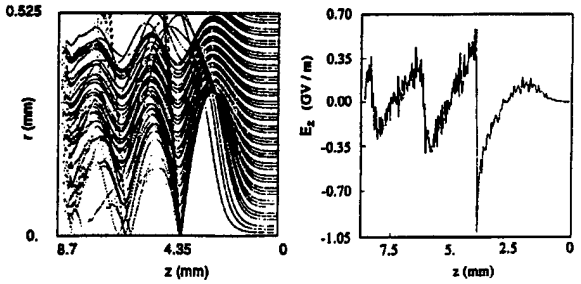


Figure 1. MAGIC PIC simulation of plasma wake for SLC beam (36 MV compressor setting) and plasma density 2.1 x 10^{14} cm^{-3}. (a) Real space r - z of plasma electrons; (b) axial electric field E_z.

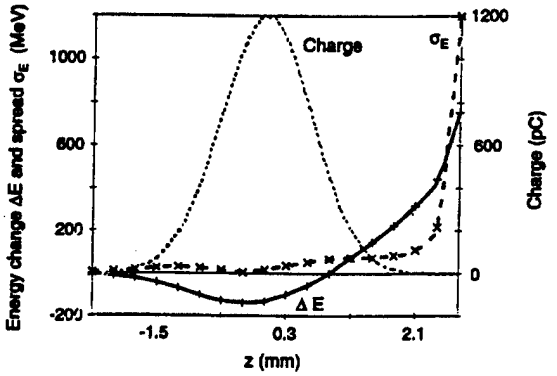


Figure 2. Simulated change of energy (solid line) and absolute energy spread (dashed line) of 1 ps slices along the bunch. This calculation was done for the same parameters as Figure 1 (plasma density of 2.1 x 10^{14} cm^{-3}). The two curves summarize the signature of plasma-wakefield acceleration as expected to be measured with the proposed diagnostic setup. The charge distribution is indicated by the dotted line.

We simulate the experimental observables in Fig. 2. Here we show the beam charge and the simulated beam energy change and beam energy spread in 1 ps intervals as they would be resolved by the streak camera in our transition radiation diagnostic. Even though some particles in the simulation gain over 1 GeV, the 1 ps window captures particles on either side of the acceleration peak. As a result, the energy change of the center of the last ps bin shown is roughly 800 MeV with a spread of 1200 MeV. Note that decelerating and accelerating fields within the bunch are well resolved with 1 ps diagnostic intervals.

As seen in the simulations in Figure 1a, the head of the drive beam rapidly blows out the plasma electrons leaving a positive ion column in the beam path. In this case, the transverse wake on the main body of the beam is particularly simple and takes the value given by a uniform positive cylinder of charge density n_0: $W_r = 2\pi n_0 e^2 r$. This corresponds to an effective quadrupole focusing strength (in both planes) of

$$W_r / r = 960\pi \text{ Tesla/m} \times (n_0/10^{14}\text{cm}^{-3})$$

The variation in the transverse focusing strength along the bunch in a PIC simulation is shown in Figure 3 (at $r = 1\sigma = 75$ μm). From this we see the time-dependent focusing rising at the head then asymptoting to the theoretical valueabove (6400 T/m for this case).

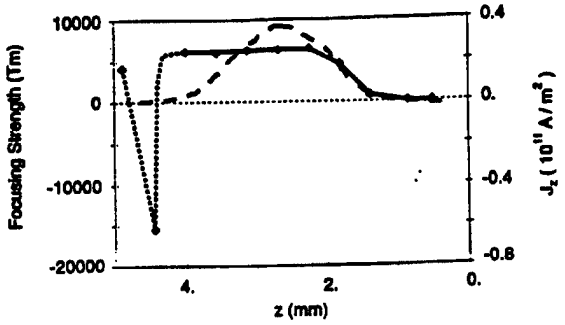


Figure 3. Focusing strength $-(E_r - B_\varphi)/r$ (solid) and axial current J_z (dotted) vs. longitudinal position z for the PIC simulation of Figure 2. Note that there is an important defocusing peak in the far tail of the bunch. Its width is unconstrained within the binning used for this simulation. However, it occurs only after the peak accelerating field. The axial current shows the longitudinal bunch distribution.

The effect of the plasma focusing on the beam optics is shown in Fig. 4. It is seen that the spot sizes with and without the plasma cell are almost identical for certain plasma densities (corresponding to an integer number of betatron oscillations in a one-meter long plasma).

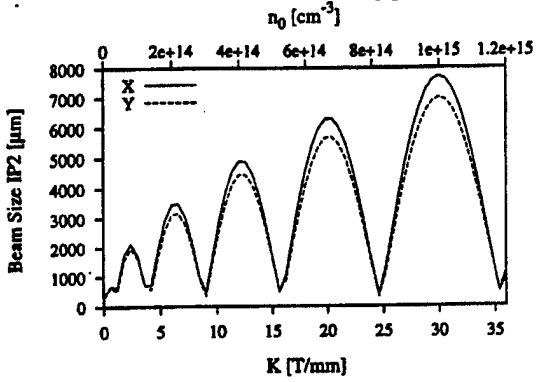


Figure 4. Calculated horizontal and vertical spot sizes at IP-2 *for a 1 ps slice* with 0.3% relative energy spread. The beam size is plotted as a function of plasma density.

III PLASMA SOURCE

The required plasma densities between 2×10^{14} and 1×10^{15} cm^{-3} can be obtained by photo-ionizing lithium atoms ($E_i = 5.9$ eV). The vapor pressure required for this range of densities is 10 to 30 mTorr, which can be obtained at temperatures between 550 and 600°C, Such meter long lithium vapors have been produced at these and far higher (Torr-range) pressures in heat pipes for atomic physics and spectroscopy experiments[11].

IV BEAM DIAGNOSTICS

We propose to use time resolved transition radiation to diagnose the beam. The energy of the transition radiation is calculated to be comparable to the synchrotron light intensity that was used for SLC measurements. The intrinsic resolution of the camera for SLC measurements is 0.85 psec, and taking into account chromatic effects the total resolution is $\sigma = 1.0$ psec.

The vertical deflection Δy due to an acceleration of 100 MeV is

$$\Delta y = D_y \frac{\Delta E}{E} = 0.33mm$$

which should be easily measurable. The energy change between the decelerated head and the accelerated tail of the bunch is shown in Figure 2 to be about 400 MeV for particles within 2.5 sigma of the longitudinal distribution. The maximum acceleration of 800 MeV for a 1 ps slice will show itself as a large offset (~2.5 mm) and a large vertical beam size (~4mm) due to the large induced energy spread (1.2 GeV).

It will be possible to measure the longitudinal wakefield along the bunch in detail. These measurements will enable direct comparisons to the plasma theory and simulations.

REFERENCES

[1] 1-GeV Beam Acceleration in a One Meter Long Plasma Cell. By R. Assmann et al. SLAC-PROPOSAL-E-157, Apr 1997. 51pp.

[2] C. E. Clayton et al, K. Nakajima et al. To be published in Proc. Adv. Accelerator Concepts Workshop, Lake Tahoe, 1996 (AIP, NY 1997), S. Chattopadhay (Ed.).

[3] D. H. Whittum, W. H. Sharp, S. S. Yu, M. Lampe, and G. Joyce, *Phys. Rev. Lett.* **67** pp. 991-994, 1991; M. Lampe, G. Joyce, S. P. Slinker, and D. H. Whittum, *Phys. Fluids B* **5**, pp. 188-1901, 1993.

[4] V. E. Balakin et al, "Focusing of Submicron Beams for TeV-Scale E+ E- Linear Colliders", *Phys. Rev. Lett.* **74** pp. 2479-2482, 1995.

[5] M. Berndt et al, "Final Focus Test Beam: Project Design Report", SLAC-0376, Mar 1991.

[6] "PEP-2: An Asymmetric B-Factory." Conceptual design Report, SLAC-418, 1993.

[7] P. Chen, J. J. Su, J. M. Dawson, K. L. F. Bane and P. B. Wilson,"Energy Transfer in the Plasma Wakefield Accelerator", Phys. Rev. Lett. **56**, p. 1252, 1986.

[8] J. B. Rosenzweig et al, "Experimental Observation of Plasma Wakefield Acceleration", Phys. Rev. Lett. **61**, 98, 1988.

[9] G. Shvets and T. Katsouleas, private communication. The displacement of plasma electrons by the SLC beam increases the refractive index on the beam's axis and enables guiding of the laser light.

[10] J. Yoshii, C. H. Lai, T. Katsouleas, C. Joshi, W. B. Mori, "Cerenkov Radiation from Magnetized Plasma Wakes", submitted to Phys. Rev. Lett., 1997.

[11] C. R. Didul and F. B. Hulles, Rev. Sc. Inst., A2, 1779 (1971).

APPROXIMATE ANALYTICAL DESCRIPTION OF THE UNDERDENSE PLASMA LENS

A.Ts. Amatuni
Yerevan Physics Institute, Alikhanian Brother's St. 2, Yerevan 375036, Republic of Armenia

Abstract

The perturbative approach for describing the underdense plasma–ultrarelativistic electron bunch system is developed,using the ratio $\frac{n_0}{n_b}$ as a small parameter (n_b-bunch,n_0-plasma electron densities). It is shown that in the zero and first approximations for the ultrarelativistic bunch case the role of positive ion column is negligible ($\sim O(\gamma^{-2})$, where γ_0 is the Lorentz factor of the bunch) for the arbitrary bunch length. Focusing of the electron bunch emerged in the first approximation of the perturbative procedure as a result of the plasma electrons redistribution.Focusing gradient and strength for ultrarelativistic,flat,uniform and short bunch are obtained and compared with the previous results, which differs drasticaly from the obtained ones. The plasma chamber conducting walls effect on focusing force is considered by the method of images, adopting the diffuse scattering of plasma electrons on the walls. Effect is small, when the plasma chamber width is much larger than that of bunch.

1 INTRODUCTION

Plasma focusing devices,being compact,simple and effective elements are promissing for obtaining electron (positron) beams of very small spot size, requested for future high energy linear colliders.Theoretical predictions and investigations of the plasma lenses in overdense ($n_b < \frac{1}{2}n_0 \equiv n_p$) and underdense ($n_b > \frac{1}{2}n_0, n_b$-bunch electron density,$n_0$-cold neitral plasma electron density),performed last decade and were supplemented by experimental tests,carried out at ANL, Tokio University-KEK and UCLA for overdense plasma lens regime.

The theoretical treatment of the overdense plasma lens,performed in linear approximation,using ratio $\frac{n_b}{n_0}$ as a small parameter,is more or less complete,at least in the frame of the cold plasma and rigid electron bunch approximations.

The existing theoretical approaches to underdense plasma lens are phenomenological by nature.

It seems,that more detailed description of the underdense plasma lens is needed,in particular, taking into account the program for the future experimental investigations, which include underdense regime too.

Using the ratio $\frac{n_0}{n_b} \ll 1$ as a small parameter,and developing the subsequent perturbative approach for the description of the underdense plasma lens,it is possible to achieve,at least the same level of the understanding of the focusing phenomenon in underdense regime as that of overdense plasma lens case.

2 PERTURBATIVE APPROACH FOR UNDERDENSE PLASMA LENS

Consider the flat electron bunch with the vertical dimension $2b$,which is assumed much smaller than horizontal dimension $2a$; longitudinal dimensions,which are arbitrary,are $2d$.The bunches of such a geometry are suitable for future high energy linear electron-positron colliders.

Bunch electrons uniform density is n_b and bunch is considered as ultrarelativistic and rigid one.Plasma electrons density is $n_0 \ll n_b$,plasma is neutral,cold and with the immobile ions.

The geometry of the bunch,which moves in lab system through the plasma with constant velocity v_0,allows to consider the electric and magnetic fields components as follows:

$E_x = 0, E_y, E_z \neq 0; B_x \neq 0, B_y = B_z = 0$

All physical quantities of the problem are considered as a functions of the arguments y and $\tilde{z} = z - v_0 t$ only (steady state regime).Introduce the dimensionless arguments $y', \tilde{z}' = k_b y, k_b \tilde{z}; t' = \omega_b t, \omega_b^2 = \frac{4\pi e^2 n_b}{m}, k_b = \frac{\omega_b}{c}$,and dimensionless variables $E'_{y,z} = (\frac{\omega_b mc}{e})^{-1} E_{y,z}; B' = (\frac{\omega_b mc}{e})^{-1} B_x;$

Define the generalized plasma electron velocities as

$V_y = \frac{v_{ey}}{v_0 - v_{ez}} = \frac{\beta_{ey}}{\beta - \beta_{ez}}, \beta = \frac{v_0}{c}, \beta_{ez,y} = \frac{v_{e,zy}}{c}$, $V_z = \frac{v_{ez}}{v_0 - v_{ez}} = \frac{\beta_{ez}}{\beta - \beta_{ez}}$

and generalized plasma electron density as

$N = \frac{n_e}{n_b}(1 - \frac{v_{ez}}{v_0}) = \frac{n_e}{n_b}(1 - \frac{\beta_{ez}}{\beta}), \frac{n_e}{n_b} = N(1 + V_z)$,

(BTFCh transformations [1]).

Adopting the condition $\frac{n_e}{n_b} \ll 1$,decompose the quantities in question in the following series:

$$\begin{aligned} N &= \epsilon N_1 + \epsilon^2 N_2 + \ldots \\ V_z &= V_{z0} + \epsilon V_{z1} + \epsilon^2 V_{z2} + \ldots \\ V_y &= V_{y0} + \epsilon V_{y1} + \epsilon^2 V_{y2} + \ldots \\ E_{y,z} &= E_{y,z0} + \epsilon E_{y,z1} + \epsilon^2 E_{y,z2} + \ldots \\ B &= B_0 + \epsilon B_1 + \epsilon^2 B_2 + \ldots \end{aligned} \quad (1)$$

where $\epsilon = \frac{n_0}{n_b}$ (in what follows ϵ^n is included in subsequent quantities N_n, V_{nz} and so on)

In the zero order approximation from

$$\begin{aligned} B_0 &= -\beta E_{y0}, \\ E_{z0} &= -\frac{1}{\gamma^2}\frac{\partial \phi_0}{\partial z}, E_{y0} = -\frac{\partial \phi_0}{\partial y} \\ \frac{1}{\gamma^2}\frac{\partial^2 \phi_0}{\partial z^2} &+ \frac{\partial^2 \phi_0}{\partial y^2} = \begin{cases} 1, & |z| \leq d, |y| \leq b, \\ 0, & |z| > d, |y| > b; \end{cases} \end{aligned} \quad (2)$$

0-7803-4376-X/98/$10.00 © 1998 IEEE

In the first order approximation continuity equations have a form:

$$-\frac{\partial N_1}{\partial z}+\frac{\partial N_1 V_{y0}}{\partial y}=0 \qquad (3)$$

and Coulomb law:

$$\frac{\partial^2 E_{z1}}{\partial z^2}+\gamma^2\frac{\partial^2 E_{z1}}{\partial y^2}=\frac{\partial}{\partial z}\left(\frac{n_0}{n_b}-\gamma^2 N_1-N_1 V_{z0}\right); \qquad (4)$$

The focusing force is

$$\begin{aligned} f_y &= -e(E_y+\beta B)=f_{y0}+f_{y1}+..., \qquad (5)\\ f_{y0} &= -e(E_{y0}+\beta B_0)=-e\gamma^{-2}E_{y0},\\ f_{y1} &= -e(E_{y1}+\beta B_1)\equiv -eW_{y1}. \end{aligned}$$

In the first approximation

$$\frac{\partial W_{y1}}{\partial \tilde{z}}=\frac{\partial E_{z1}}{\partial y}, \qquad (6)$$

which is an analog of the Panoffsky-Wenzel relation;remember that in (6) $\tilde{z}=z-v_0 t$. Differentating (4) over y and then integrating it over $\tilde{z}$, taking into account relation (6) and that

$\frac{\partial}{\partial y}\left(\frac{n_0}{n_b}-\gamma^2 N_1-N_1 V_{z0}\right)\rightarrow 0$ when $y\rightarrow\pm\infty$,we have

$$\frac{\partial^2 W_{y1}}{\partial \bar{z}^2}+\frac{\partial^2 W_{y1}}{\partial y^2}=\frac{1}{\gamma^2}\frac{\partial}{\partial y}\left(\frac{n_0}{n_b}-\gamma^2 N_1-N_1 V_{z0}\right) \qquad (7)$$

where $\bar{z}\equiv\gamma\tilde{z}$.

In what follows, consider the ultrarelativistic bunches,when $\gamma\gg 1$; then $f_{y0}\sim O(\gamma^{-2})$ and in right hand side of (7) it is possible to leave only the term $-\frac{\partial N_1}{\partial y}$. So for the sought quantity W_{y1} we need N_1 from eq. (3).Entered in (3) V_{y0} must be found from eqs. of motion for the fields in zero approximation.It is evident,from eq. (7),that the role of the noncompensated positive ions (the term on the right hand side of eq. (7), proportional to $\frac{n_0}{n_b}-N_1(1+V_{z0})$),is negligible in ultrarelativistic limit ($\sim O(\gamma^{-2})$).

3 ZERO ORDER APPROXIMATION

In the zero order approximation it is necessary to find from (??) E_{0y}, E_{0z} for the flat bunch moving in vacuum.

The approximate results for $\gamma\gg 1$ are the following:

$$E_{y0}\approx -y\left(1-\frac{2bd}{\pi\gamma(d^2-z^2)}\right)=-y+O(\gamma^{-1}) \qquad (8)$$
$$-b\le y\le b, -d<z<d;$$

$$E_{y0}\approx -b\left(1-\frac{2dy}{\pi\gamma(d^2-z^2)}\right)=-b+O(\gamma^{-1}) \qquad (9)$$
$$\gamma d\gg y\ge b, -d<z<d;$$

when $|z|\ll d$ the expression (9) is valid for $\gamma d\le y\le b$.

$$E_{y0}\approx -\frac{2\gamma db}{\pi y} \qquad (10)$$
$$y>\gamma d\gg b, -d\le z\le d;$$

$$E_{y0}\approx -\frac{2dby}{\pi\gamma z^2} \qquad (11)$$
$$z\gg d, \gamma d\gg b, -b\le y\le b;$$

The next problem in zero approximation is the definition of the generalized velocities V_{y0}, V_{z0}.When $\gamma\gg 1$,and bunch length is short enough $d'\ll 1, (d'=k_b d)$ it is possible to drop out in eqs. of motion the terms proportional to $|V_{z0}|^2\ll|V_{z0}|$ and to $|V_{y0}|^2\ll|V_{y0}|$. Taking into account that in the considered case $|E_{y0}|\gg|E_{z0}|$ the approximate solutions for the boundary condition $V_{y0}=0, V_{z0}=0$, when $z=d$ are:

$$\begin{aligned} V_{y0} &= \sinh\left(|E_{y0}|(d-z)\right)\simeq|E_{y0}|(d-z), \qquad (12)\\ V_{y0}(-y) &= -V_{y0}(y),\\ V_{z0} &= \cosh\left(|E_{y0}|(d-z)\right)-1\simeq\frac{1}{2}|E_{y0}|^2(d-z)^2, \end{aligned}$$

where E_{y0} is given by (8-10)and $V_{y0}\rightarrow 0, V_{z0}\rightarrow 0$ when $y\rightarrow\pm\infty$. For the short ($d\ll 1$) bunches from (12) follows that $|V_{z0}|\ll|V_{y0}|$.

4 FOCUSING FORCE IN THE FIRST ORDER APPROXIMATION

Using eq. (3) in the first approximation and eq. (12) for V_{y0} it is possible to find $N_1(y,z)=N_1(-y,z)$ by the method of characteristics. The plasma electrons redistribution function $N_1(y,z)$ has a crest at distances $y_{cr}\approx\frac{2\gamma d}{\pi}\gg b$, conditioned by bunch electric field E_{0y}, exponentialy rising with y at $|y|<y_{cr}$ and has a power fall at $|y|\gg y_{cr}, |y|\rightarrow\infty$

For $\gamma\gg 1$ in eq. (7) we get an approximate solution

$$W_{y1}=-\frac{1}{2\pi}\int d\bar{z}'\int dy'\frac{\partial N_1(y',\bar{z}')}{\partial y'} \qquad (13)$$
$$\ln\left[(y-y')^2+(\bar{z}-\bar{z}')^2\right]^{1/2}.$$

The domain of the integration in (13) is defined by the condition $\frac{\partial N_1(y,z)}{\partial y}\neq 0$,i.e. it is $-\infty<y<+\infty, -\infty<z\le d$,because for $z>d$, $N_1=\frac{n_0}{n_b}$. For $z<-d$ let us assume $N_1(z,y)=N_1(-d,y)$ up to some $-z_0<-d$ where considered steady state regime changes to (nonlinear) wake wave (and later on the uniform distribution of the plasma electrons with $N_1=\frac{n_0}{n_b}$).

For the estimates,it is possible to use approximate expression, which follows from (13):

$$W_{y1}\approx\frac{8}{\pi}yd^2\alpha(z)\frac{n_0}{n_b}, \quad \alpha(z)\sim 1 \qquad (14)$$

Focusing force (14) is the result of the long-range redistribution ($y\sim y_{cr}\approx\frac{2}{\pi}\gamma d$) of plasma electrons caused by

ultrarelativistic bunch electric field E_{0y} (8,9,10), which is practicaly non-screened in the case of underdense plasma. Hence the question is arised on the effect of the walls of the plasma chamber.

The problem can be solved by the method of images in the model of a plasma chamber as a flat plasma layer inside the two conducting planes with distance 2g in between. Adopting diffuse scattering of plasma electrons on the planes, the results of such a consideration can be formulated as following: $g \gg \gamma d \gg b$ the effect of plasma walls on focusing force (14) is negligible; when $\gamma d \gg g \gg b$ the decrease of quantitative factor in (14) takes place.

5 DISCUSSION

The expressions for the, focusing gradient and stregth are subsequently

$$G = \frac{W_{1y}}{y} = \frac{128\alpha(z)er_e}{\pi}(n_b n_0)d^2, \qquad (15)$$
$$K = \frac{eG}{\gamma mc^2} = \frac{128\alpha(z)r_e^2 d^2}{\gamma\pi}(n_b n_0),$$

The expressions (15) differs from the previous results,which for the flat, electron bunch and underdense plasma are ($r_e = e^2/mc^2$ is the electron classical radius):

$$G = \frac{W_{1y}}{y} = 4\pi n_0 e, K = \frac{4\pi r_e n_0}{\gamma} \qquad (16)$$

These expressions are based on the understanding the focusing phenomenon as caused by the positive charge of the ion column,which exists inside and behind the moving electron bunch, because the considered bunch blows out the plasma electrons.

As it follows from the presented consideration (7), the net focusing effect of the ion column,caused by noncompensated positive charge $\frac{n_0}{n_b} - N_1(1 + V_{z0})$, is proportional to γ^{-2} and is negligible in our approximation $\gamma \gg 1$,compared to focusing effect of the plasma electrons redistribution,described by eqs. (13) and (14).The presence of the factor γ^{-2} in the part of the net (electric plus magnetic) focusing force,which caused by ions,is a result of magnetic compesation of the subsequent focusing electric field in lab frame,where electron bunch moves with the velocity v_0 and unperturbed parts of plasma are at rest. Compensating magnetic field is caused by noncompensated positive ions "current", which propogate with the velocity v_0,equal to the velocity of the electron bunch and at $\gamma \gg 1$ cancels the focusing action of the subsequent electric field.The physical reason for that - the exposed positive ions column effectively "moves" in plasma along with the moving electron bunch with the velocity of it.When bunch blows out the plasma electrons,it uncower new forward parts of the partialy noncompensated ion column and this "motion" of the revealed positive ions charge,i.e. subsequent current,generated compensating magnetic field.

The physical interpretation can be based also directly on the displacement current,entered in the Maxwell eq. through the term $\beta\frac{\partial E_{z1}}{\partial z}$.Ions ahead of the bunch are completely compensated by plasma electrons,inside the bunch ions charge is only partially compensated,so exists the change of electric field component with $\tilde{z} = z - v_0 t$, which generates subsequent compensating magnetic field.

All above mentioned general physical arguments are valid for the relativistic bunches with arbitrary length and charge distribution.Assumptions adopted in the present work (short enough relativistic bunch with the uniform charge distribution) allows us to perform analytical calculations (14).

Unfortunately the condition $k_b d \ll 1$ ($d' \ll 1$,short bunches) does not permit to use expression (15) for focusing strength for the flat beams of the FFTB. In that case $n_b = 7,7 \cdot 10^{18} cm^{-3}$ and $2,8 \cdot 10^{18} cm^{-3}$ and $k_b = 5,2 \cdot 10^5 cm^{-1}$ and $k_b = 3,1 \cdot 10^5 cm^{-1}$ consequently, $d = 2,3 \cdot 10^{-2} cm$ and $k_b d = 1,2 \cdot 10^4 \gg 1$ and $0,7 \cdot 10^4 \gg 1$.

Using the short bunches,nevertheless it is possible to obtain sufficiently strong focusing gradients.For example, let $k_b d = 0,1$.Then $d = 10^{-5}\left(\frac{3 \cdot 10^{19}}{n_b}\right)^{1/2}$, $G = 15 \cdot 10^{-11} n_0$ and if $n_0 \approx 10^{17} cm^{-3}$ as in FFTB case,$G \approx 15 \frac{MG}{cm}$.In order to fullfil the condition $\frac{n_0}{n_b} \ll 1$, n_b must be e.g.,equal $10^{18} cm^{-3}$,then $d = 5 \cdot 10^{-5} cm$.

Probably the medium and long bunch cases can be treated by computational methods only.Presented analytical approximate description of the short bunch case can be used then as a physical guide and programmes testing example.

It will be interesting to test experimentaly the predictions for focusing gradient and strenght,particularly,the dependense of these quantities on n_b and d.

6 AKNOWLEDGEMENTS

Author would like to thank A.M. Sessler,who pointed out my attention on the plasma lens concept,for the careful reading preliminary versions of the manuscript,the numerous useful suggestions and criticism.Author is indebted to S.S. Elbakian,A.G. Khachatryan,J.S. Wurtele and S.G. Arutunian for attention, discussion and valuable comments.

I am obliged to G. Amatuni for the significant help in preparing the manuscript for publication.

7 REFERENCES

[1] B.N.Breizman,T.Tajima,D.Fisher,P.Z.Chebotaev preprint Inst for Fusion Studies, Univ. of Texas at Austin,(1993)

SELFACCELERATION OF ELECTRONS IN ONE-DIMENSIONAL BUNCHES,MOVING IN COLD PLASMA

A.Ts. Amatuni
Yerevan Physics Institute, Alikhanian brothers st.2,Yerevan 375036, Republic of Armenia

Abstract

Nonlinear dynamics of the one-dimensional ultrarelativistic bunch of electrons,moving in cold plasma,is considered in multiple scales perturbative approach.A square root of the inverse Lorentz factor of the bunch electrons is taken as a small parameter.Bunch electrons momenta is changed in the first approximation.In the underdense plasma and for the model example of the combined bunch the selfacceleration of the bunch electrons can be remarkable.

1 INTRODUCTION

Nonlinear wake waves exitation in overdense plasma by relativistic electron (positron) one-dimensional bunches,when it is possible to obtain an exact analytical solution,was considered in [1]-[7].The bunch assumed as a given one (rigid bunch approximation) in the most of these work.

The buck influence of the exited plasma wake on electron bunch was considered numericaly in [7],[8].Some attempts of the analytical treatment of the problem have been performed in [8]-[12].

Langmuir already noticed, that the beam, which has passed the plasma column, contains a significant portion of electrons with the energies higher than the initial energy of the beam. In the recent times various groups (see e.g. [11]-[13]) also observed experimentally the effect of the selfacceleration.

In the present work the problem of the plasma back nonlinear influence on the driving one-dimensional electron bunch is treated by the method of multiple scales [16].The bunch is ultrarelativistic and the square root of the inverse Lorentz factor of the bunch $\epsilon \equiv \gamma_0^{-1/2} \ll 1$ is taken as a small parameter.

It is assumed that the bunch-plasma interaction takes place by two stages. First one is the formation of the stationary plasma wake field,generated by the rigid bunch and the second stage is the influence by this field on the momenta of the bunch electrons and wake field itself.This assumption is valid,when $\gamma_0 \gg 1$.Indeed,the time τ_s needed for the formation of the stationary wake in a plasma with density n_0,generated by the electron bunch with the density $n_b, n_b/n_0 < 1/2 - \Delta, \frac{1}{8}\gamma_0^{-2} \ll \Delta < 1/2$,is $\tau_s \sim \omega_p^{-1}, \omega_p^2 = 4\pi e^2 n_0/m$.The time required for the change of the bunch electrons momenta p_0 is $\tau_p \sim p_0/eE_0$ where E_0 is the electric field inside the bunch.In the overdense ($\frac{n_b}{n_0} < 1/2$) plasma $E_0 \leq \frac{mc\omega_p}{e}$;in the underdense ($\frac{1}{2}n_0 \ll n_b$) plasma $E_0 \leq \frac{mc\omega_p}{e}(\frac{n_b}{n_0}\gamma_0)^{1/2}$,[5]. Hence in the overdense plasma $\tau_s/\tau_p \leq \gamma_0^{-1} \ll 1$,and in the underdense plasma $\tau_s/\tau_p \leq (\frac{n_b}{n_0})^{1/2}\gamma_0^{-1/2} \ll 1$.(For some special values of $\frac{n_b}{n_0} \simeq 1/2$ these conditions can change the form or even violate).As in [5] consider the flat electron bunch with the infinite transverse dimensions,longitudinal length d and initial homogenious charge density n_b,moving in the lab system with the initial velocity v_0 through neutral cold plasma with the immobile ions.

In the work [17] it was shown that when the beam is traversing the semiinfinite plasma after a few plasma wave lengths transient effects dissipate and stationary wake field regime is established in coinsideness with the abovementioned estimate. In what follows this moment is taken as an initial one,$t = 0$,and the future development for $t > 0$ of the bunch -plasma system is considered.

2 FORMULATION OF THE PROBLEM

The considered electron bunch -cold plasma system is described by the hydrodynamic equations of the motion,continuity equations for charge densities and currents for the bunch and plasma electrons,and Maxwell equation (Coulomb law) for the electric field.

Dimensionless variables and arguments are introduced:

$$\begin{aligned} t' &= \omega_p t, z' = k_p z, \omega_p^2 = \frac{4\pi e^2 n}{m}, k_p = \omega_p/c, \\ E &= \frac{mc\omega_p}{e}E', n'_e = \frac{n_e}{n}, n'_b = \frac{n_b}{n}, \beta_e = \frac{v_e}{c}, \\ \rho_e &= \frac{p_e}{mc}, \rho_b = \frac{p_b}{mc\gamma_0}, \beta_b = \frac{v_b}{c}, \gamma_0 = (1-\beta_0^2)^{-1/2} \end{aligned} \quad (1)$$

where $p_e, v_e, n_e; p_b, v_b, n_b$ are the momenta,velocity and density of the plasma and bunch electrons subsequently,n is a normalizing constant,which is suitable to choose $n = n_0$ for overdense plasma and $n = n_b$ for underdense plasma cases,$\beta_0 = v_0/c$ is the initial velocity of the bunch electrons in the laboratory system.

The equations,which describe the considered problem are:

$$\begin{aligned} \frac{\partial \rho_e}{\partial t} &+ \beta_e \frac{\partial \rho_e}{\partial z} = -E \\ \frac{\partial \rho_b}{\partial t} &+ \beta_b \frac{\partial \rho_b}{\partial z} = -\frac{1}{\gamma_0}E \\ \frac{\partial n_e}{\partial t} &+ \frac{\partial}{\partial z}(\beta_e n_e) = 0 \\ \frac{\partial n_b}{\partial t} &+ \frac{\partial}{\partial z}(\beta_b n_b) = 0 \\ \frac{\partial E}{\partial z} &= n_0 - n_e - n_b \end{aligned} \quad (2)$$

Eqs. (2) are written in dimensionless variables (1) and prime is omitted.Considering the ultrarelativistic

0-7803-4376-X/98/$10.00 © 1998 IEEE

bunch,introduce a small parameter $\epsilon^2 = 1/\gamma_0$,and all variables,entering in (2),let be a functions of the fast $\tilde{z} = z - \beta_0 t$ and slow $\tau = \epsilon t, \zeta = \epsilon z$ arguments.According to the multiple scale method [16],all variables,entered in (2),are developed in the following serieses:

$$\begin{aligned} \rho_e &= \rho_{e0}(\tilde{z}) + \epsilon\rho_{e1}(\tilde{z},\zeta,\tau) + \cdots, \\ \beta_e &= \beta_{e0}(\tilde{z}) + \epsilon\beta_{e1}(\tilde{z},\zeta,\tau) + \cdots, \\ \rho_b &= \rho_{b0} + \epsilon\rho_{b1}(\tilde{z},\zeta,\tau) + \cdots, \\ \beta_b &= \beta_{b0} + \epsilon\beta_{b1}(\tilde{z},\zeta,\tau) + \cdots, \\ n_e &= n_{e0}(\tilde{z}) + \epsilon n_{e1}(\tilde{z},\zeta,\tau) + \cdots, \\ n_b &= n_{b0} + \epsilon n_{b1}(\tilde{z},\zeta,\tau) + \cdots, \\ E &= E_0(\tilde{z}) + \epsilon E_1(\tilde{z},\zeta,\tau) + \cdots. \end{aligned} \quad (3)$$

In (3) $\rho_{b0}, \beta_0, n_{b0}$ are the constants connected with the initialy rigid electron bunch and differs from zero, when $0 \leq \tilde{z} = z - \beta_0 t \leq d$. The functions $\rho_{e0}(\tilde{z}), \beta_{e0}(\tilde{z}), n_{e0}(\tilde{z}), E_0(\tilde{z})$ are the solutions of the steady state (stationary) problem,and are obtained in [1],[3],[5].Derivatives in (2),according to the multiple scales method are given by

$$\frac{\partial}{\partial t} = -v_0\frac{\partial}{\partial\tilde{z}} + \epsilon\frac{\partial}{\partial\tau}, \quad \frac{\partial}{\partial z} = \frac{\partial}{\partial\tilde{z}} + \epsilon\frac{\partial}{\partial\zeta} \quad (4)$$

Decompositions (3) correspond to the above mentioned main assumption,which,as it was seen,is valid for the ultrarelativistic bunch.

The following steps are evident– decomposition of the eqs. (2),using (3) provides the sequence of the guasilinear equations,describing the steady state regime as a zero approximation and in the next approximations-the back influence of the generated electric field on initialy rigid electron bunch and on wake wave itself.

3 SOME RESULTS

1. The change of the bunch electron momenta (in usual units) arise in the first approximation and is

$$\rho_{b1} = -eE_0(\tilde{z})t\gamma_0^{1/2} \quad (5)$$

i.e. bunch electrons traversing underdense plasma decelerate ($E_0(z) \geq 0$); in the bunch traversing overdense plasma electrons from the head part of the bunch decelerated, electrons from the rear part-accelerated ($E_0(z) < 0$). Hence the bunch traversing overdense plasma contracted around the point $z_0 = d - \frac{\lambda}{2}$ (λ - plasma nonlinear wave length), and bunch traversing underdense plasma-expands. The front of the bunch moves with the velocity v_0 in lab system. The end of the bunch d_0, which initialy ($t = 0$) was at $\tilde{z} = 0$ in overdense plasma case (contruction) for $t \geq 0$ is

$$d_0(t) = -\frac{t^2}{2\gamma_0^3}E(0) - \frac{t^3}{2\gamma_0^4}E^2(0) + \frac{t^4}{2\gamma_0^5}E^3(0) + \cdots \quad (6)$$

i.e. the change of the bunch length is by the order of magnitude $\sim \gamma_0^{-3}$

2. Only forth order corrections to plasma electrons momenta, plasma electron density and electric field are differ from zero and are proportional to γ_0^{-2}. It means that rigid bunch approximation for plasma wake wave characteristics is valid for ultrarelativistic case up to terms proportional to γ_0^{-2} for the time interval $t \leq \omega_p^{-1}\gamma_0^{1/2}$.

3. The large enough accelerating fields can be obtained in combined bunch, which consists from the first part with charge density $n_b^{(1)} \gg 1/2n_0$ (underdense regime) and second part with charge density $n_b^{(2)} \ll 1/2n_0$ (overdense regime). Then first bunch generates large (but decelerating) electric field, second bunch invert the sign of this field on the back side of the bunch, and selfacceleration of electrons from rear side of the bunch can take place, with acceleration gradient $G \sim \gamma_0^{1/2}$.

4 AKNOWLEDGEMENTS

Author is indebted to M.L. Petrosian,S.G. Arutunian,S.S. Elbakian, A.G. Khachatrian,E.V. Sekhpossian for helpful discussions,suggestions and comments.

5 REFERENCES

[1] Amatuni A.Ts.,Magomedov M.R.,Sekhpossian E.V., Elbakian S.S. Physika Plasmi **5**,85(1979) (Sov. J. Plasma Physics **5**,49(1979)).

[2] Ruth R.D.,Chao A.W.,Morton P.L.,Wilson P.B. Part. Acc. **17**,171,(1958).

[3] Amatuni A. Ts.,Sekhpossian E.V.,Elbakian S.S. Physica Plasmi **12**,1145,(1986).

[4] Rosenzweig J.B. Phys. Rev. **58**,555,(1987).

[5] Amatuni A. Ts.,Sekhpossian E.V.,Elbakian S.S.,Abramian R.D. Part. Acc. **41**,153,(1993)

[6] Bilikmen S.,Nasih R.M. Physica Scripta **47**,204,(1993).

[7] Bazylev V.A., Golovin V.V.,Tulupov A.V., Schep T.J., van Amersfoot Proc. EPAC-94,London,1994.

[8] Balakirev V.A., Sotnikov G.V.,Fainberg Ja.B., Physica Plasmi **22**,165,(1996).

[9] Rukhadze A.A.,Bogdankevich L.S.,Rosinsky S.E.,Rukhlin V.G. "Physics of High Current Relativistic Beams", Atomizdat,M. 1980 (in Russian)

[10] Kovtun R.I.,Rukhadze A.A. JTEP **58**,1709,(1970)

[11] Kovalenko V.P.,Pergamentshik V.M.,Starkov V.N., Physika Plasmi,**11**,417,(1985)

[12] Amatuni A. Ts.,Sekhpossian E.V.,Elbakian S.S. Proc. XIII Int. Conf. on High Energy Particles Acc.,Novosibirsk,v.1,p. 175, (1987)

[13] Nezlin M.V. "Beam Dynamics in Plasma", Energoizdat M., 1982

[14] Fainberg Yu.B. Physica Plasmi **11**, 1398, (1985)

[15] Berezin A.K., Kiselev V.A., Fainberg Yu. B. Ukrainen Physical Journal **24**, 94, (1979)

[16] Nayfeh A.H. "Perturbation Methods" ch. 6, J. Willey and Sons Inc., 1973

[17] Mtingwa S.K. FNAL report,FN-452,0104.000 April,1987

GENERATOR-INVERTOR-DAMPER SYSTEM OF ELECTRON (POSITRON) BUNCHES MOVING IN COLD PLASMA.

A.Ts. Amatuni, S.G. Arutunian, M.R. Mailian
Yerevan Physics Institute, Alikhanian Brothers' St. 2, Yerevan 375036, Republic of Armenia

Abstract

It is shown that high accelerating gradient can be obtained in a specially constructed system of electron (positron) bunches, moving in cold plasma with definite density. These combined bunch systems do not generate the wake fields behind and can pass through the plasma column in a periodic sequence. The consideration is carried out numericaly and analyticaly in one dimensional approach, (which can be applied to finite system when its transverse dimensions are larger than plasma wave length). The possibilities of the experimental tests by measuring the predicted energy gain are discussed on the examples of Argonne Wakefield Accelerator and induction linac with typical parameters.

1 INTRODUCTION

In the work [1], which is based on the previous results [2] used as a zero order approximation, nonlinear dynamics of the one-dimensional non rigid ultrarelativistic bunch of electrons, moving in the cold plasma, is considered by multiple scales perturbative approach. Square root of the inverse Lorentz factor of the bunch electrons is taken as a small parameter.

In the first approximation of multiple scales method, the change of the momentum of the bunch electrons is given by $\triangle p_b = -eEt$, where t is a acceleration (deceleration) time interval which, due to applicability of the multiple scales method, is $t \leq \omega_p^{-1}\gamma^{1/2}$.

The essential restriction on the acceleration rate in the considered cases comes from the steady state assumption, adopted in [1]. If plasma electrons momenta in the wake field behind the first dense relativistic bunch, exciedes same critical value, allowed by steady state assumption, the plasma electron density behind the bunch turn out to be negative, which probably means that wake wave breaking limit is achieved. Restriction on the plasma electrons momenta inside the bunch automatically restricts the maximum value of the generated electric field.

In the present work the proper combination of the $(e^{\pm})$ bunches is proposed, which is constructed in such a way, that it does not generate the wake fields behind the combined bunch at all. The plasma electrons momenta, inside the combined bunch being negative, remains in the allowed domain and their maximum value is restricted only by the total momentum conservation low. The maximum of the subsequent electric field then also can be large enough.

The combined bunch in the considered case consists (at least) of three parts:first one is a relativistic negative particles bunch, with density $n_b^{(1)} \gg \frac{1}{2}n_0$, which generates inside the bunch strong electric field, which brakes the bunch particles (generator). The second bunch is a low density bunch $n_b^{(2)} < \frac{1}{2}n_0$ (it can be negative or positive particles bunch), which inverts (invertor) the sign of the electric field generated by the first bunch. The third bunch (dumper) with the parameters, which can coincide with that of the first one, provided on its rear part the zero values of electric field and plasma electrons momenta, coincided with the same values on the front of the first bunch. It means that plasma behind the system of bunches remains unperturbed and no wake field is generated.

Acceleration of the particles of the rear part of the second and of the third bunches, where electric field is negative, will take place. The goal of the following calculations is to estimate the maximum possible values of the acceleration parameter.

2 PHASE PLANE IMAGES OF THE COMBINED BUNCHES.

Consider a plane rigid electron bunch with the infinite transverse dimensions and length $[0, d]$ along the z-axis. Velocity of the bunch in the lab system is $v_z = v_0 \quad (\beta = \frac{v_0}{c})$, plasma is cold with the immobile ions. The charge density of the plasma electrons is n_b;the case, when $n_b > \frac{1}{2}n_0$ called underdense regime, $n_b < \frac{1}{2}n_0$-overdense regime.

Equation of plasma electrons motion can be written in steady state approximation as:

$$E = -\frac{d\Phi}{d\tilde{z}} \equiv -\Phi', \Phi \equiv \sqrt{1+\rho_e^2} - \beta\rho_e \qquad (1)$$

and continuity equation for plasma electrons and Coulomb law give the equation for Φ:

$$\Phi'' - \beta\gamma^2\Phi(\Phi^2 - \gamma^{-2})^{-1/2} = \alpha - \gamma^2 \qquad (2)$$

Eq. (2) has an "energy" integral

$$\mathcal{E} = \frac{1}{2}\Phi'^2 + \gamma^2[\Phi - \beta(\Phi^2 - \gamma^{-2})^{1/2}] - \alpha\Phi, \qquad (3)$$

where $\alpha = n_b/n_0$, and dimensionless arguments and functions are introduced:

$$t' = \omega_p t, z' = k_p z, \omega_p^2 = \frac{4\pi e^2 n_0}{m}, k_p = \frac{\omega_p}{c},$$

$$E = \frac{mc\omega_p}{e}E', n_e' = \frac{n_e}{n_0}, n_b \equiv \alpha = \frac{n_b}{n_0}, \rho_e = \frac{\rho_{ez}}{mc},$$

$$\beta = \frac{v_0}{c}, \beta_e = \frac{v_{ez}}{c}, \gamma = (1-\beta^2)^{-1/2}, \tilde{z} = z' - \beta t'$$

(in what follows the prime is ommited)

0-7803-4376-X/98/$10.00 © 1998 IEEE

The integral (3) allowed to interpret equations (1-3) as equations for the point with unit mass with the "coordinate" Φ and "velocity" Φ' moving in the potential $U = \gamma^2\left[\Phi - \beta\left(\Phi^2 - \gamma^{-2}\right)^{1/2}\right] - \alpha\Phi$. The negative values of $\alpha = \frac{n_b}{n_0}$ correspond to the bunch of positive charged particles, positive α corresponds to the bunch of negative charged particles. For $\alpha < 0, \gamma^{-1} \leq \Phi \leq 1$ and $\Phi \geq 1$for $\alpha > 0$. Boundary conditions, when $\tilde{z} = d$, are $\Phi = 1$ and $\Phi' = 0$. For $\alpha < 0$ the motion is always periodic, it is also periodic for $0 \leq \alpha \leq 1/2$, and non periodic for $\alpha > 1/2$ [2].

Phase plane trajectories can serve to construct the phase portraits of the combined bunches, moving in cold plasma. In the case, when wake field is absent, it must be represented by a closed loop, starts (and accomplished) from the boundary condition $\Phi = 1, \Phi' = 0$ on the phase plane. An example of such a loop is presented on Fig. 1. The loop on Fig. 1 starts from the point 0 : $\Phi = 1, \Phi' = 0$ ($\rho_e = 0, v_e = 0, E = 0$, when $\tilde{z} = d$) and the curve OA represents the motion of the bunch of negative charged particles (generator) $\alpha^{(1)} = 10$, when at the rear side of the bunch very strong positive electric field $E_0 = -\Phi'$ can be generated. Taking this point as a new boundary conditions for the second bunch of positive charged particles (invertor), the trajectory is turned to the point B, where electric field is zero and then to the point A' where the field $-E_0$ is obtained. From point A' to the point 0 the trajectory described the motion of the third bunch of the negatively charged particles (damper) on the rear side of which the initial boundary conditions exist. It means that no wake field excites and the plasma behind the third bunch remains unperturbed. As a consequence, the above mentioned restriction on the value of the field E_0, which arouse from the condition of the stability of the wake field, is removed. This is not only the

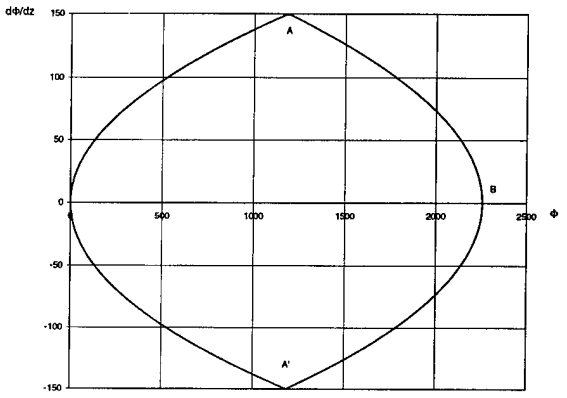


Figure 1:
condition for the applicability of steady state regime for the

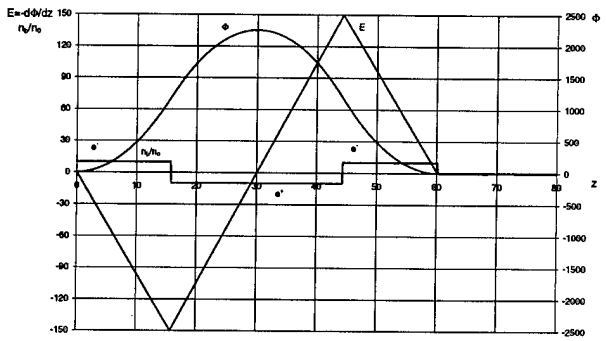


Figure 2:

description of the zero order approximation in the multiple scales approach, but also open the possibility to repeat more than once the procedure, sending the next combined bunches into the unperturbed by previous bunches plasma.

The Lorentz factor of all three bunches in the presented case is, of course, the same $\gamma = 100$, and

$$\alpha^{(2)} = -\frac{n_b^{(2)}}{n_0} = -10, \alpha^{(3)} = \alpha^{(1)} = \frac{n_b^{(3)}}{n_0} = 10.$$

The total length of the positron bunch is $28.57\frac{\lambda_p}{2\pi}$ and lengths of the first and third electron bunches are $\sim 15.77\frac{\lambda_p}{2\pi}$ each.

On Fig. 2 the potential Φ, electric field $E = -\frac{\partial\Phi}{\partial\tilde{z}}$ and ratio $\frac{n_0}{n_b}$ as functions of $\tilde{z}$ are presented. It is evident that positrons of the first part of the second bunch, where $E > 0$, can be accelerated as well as all electrons of the third bunch ($E < 0$). The similar picture may be obtained by construction of the combination of three bunches with negatively charged particles (electrons). The role of the bunch-invertor may play also the plasma itself ($n_b^{(2)} = 0$). The charge distribution inside the bunches can be nonuniform.

3 ANALYTICAL APPROACH. PROPOSED EXPERIMENTAL TEST

In this section the results of the exact analytical solutions of eq. (2) for the combined bunch with the uniform charge distributions inside the constituting bunches are presented.

The possible largest plasma electron momenta inside the first bunch in the considered case differs from that found in by wake wave breaking limit [2] and can be estimated from momentum conservation (see also [1]),

$$n_b^{(1)}\beta\gamma d^{(1)} \geq \int_0^{d_1} \rho_e(\tilde{z})n_e(\tilde{z})dz \approx \frac{n_0|\rho_0|d_1}{4} \quad (4)$$

For the estimate in (4) the expression for n_e, approximated by linear one in interval from $n_e = n_0$ at $p_e = 0$ up to the value $n_e = \frac{n_0\beta}{1+\beta}$ for large ρ_e [2].

From (4), $1 \ll |\rho_0| \leq 4n_b^{(1)}\gamma$, and corresponding electric field from is $|E_0| = 2\left(n_b^{(1)}\right)^{1/2}|\rho_0|^{1/2} \leq 4n_b^{(1)}\gamma^{1/2}$

As it was shown in [1] the change of the bunch electron momenta $\triangle p$, in the first approximation in ordinary units is

$$\triangle p_b = eE_0 t \leq 4\frac{n_b^{(1)}}{n_0}mc\gamma = \frac{4n_b^{(1)}}{n_0}p_b; \quad t \leq \omega_p^{-1}\gamma^{1/2} \tag{5}$$

. The accelerating gradient is

$$G = \frac{c\triangle p_b}{el} \approx 4\sqrt{n_0\gamma}\left(\frac{n_b^{(1)}}{n_0}\right)\frac{V}{cm} \tag{6}$$

The lengths of the first and third electron bunches are:

$$d_1 = d_3 \leq \frac{\lambda_p}{\pi}\gamma^{1/2}\left(\frac{n_b^{(1)}}{n_0}\right)^{1/2}, \quad \lambda_p = \frac{2\pi c}{\omega_p};$$

The length of the second electron bunch is

$$d_2^e \leq \frac{8\lambda_p}{\pi}\gamma^{1/2}\left(\frac{n_b^{(1)}}{n_0}\right), \quad n_b^{(2)} \ll n_0 \ll n_b^{(1)}$$

The length of the second positron bunch is:

$$d_2^p \leq \frac{4\lambda_p}{\pi}\gamma^{1/2}, \quad \bar{n}_b^{(2)} = n_b^{(1)} \gg n_0;$$

The lengths of bunches, increases as $\sim \gamma^{1/2}$, so it seems that the bunches must be from high current accelerators with the energies up to tens of Mev. Even at these energies maximal acceleration gradient is high enough, it can exceed the acceleration gradient of the ordinary linacs by a several orders of magnitude.

Consider the experimental possibilities of proof-of-principle experiment on existing accelerators. It seems that Argonne Wakefield Accelerators (AWA) [3], which accelerates very dense bunches, is suitable for above mentioned propose.

For the existing experimental parameters of AWA:$d_1 = 0,5cm, d_2 = 23cm$, total charge of bunch 70nC, $n_b^{(1)} = 1.4 \cdot 10^{14}cm^{-3}$ results of the numerical calculations, are shown on Fig. 3. The role of bunch-invertor plays the plasma column, with density n_0 as a free parameter, which was been chosen from the necessity to invert the field, produced by the first bunch, in such a way, that the succesive bunch, with the same parameters as the first one, moving at fixed (by RF-frequency) distance from the first one, $d_2 = 23cm$, will be able to dump the field to zero. The sought density of plasma n_0 was found equal to $n_0 \approx 1.17 \cdot 10^{13}cm^{-3}, \lambda_p = 0.973cm, n_b/n_0 = 11.95$. Then the maximum value of the accelerated electric field is equal to $E_{max} \approx 100MV/cm$, and $E < 0$ on the rear part of the second (third) bunch. So about the half of the electrons of the second (third) bunch, as it can be seen from Fig. 3, can be accelerated during the time $t \sim \omega_p^{-1}\gamma^{1/2}$ up to energy $\mathcal{E}_f \approx 70MeV$. Plasma remains practically unperturbed

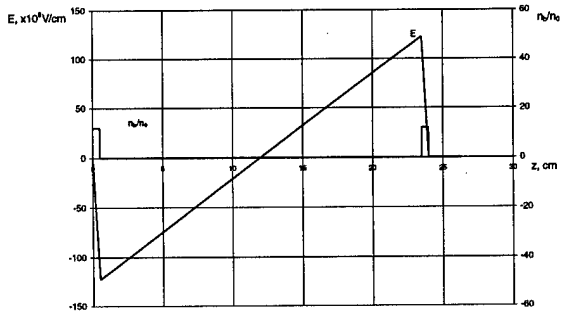


Figure 3:

after the passage of the first and the second bunches, so it is possible to inject the next couple of the bunches and also obtain acceleration, again leaving the plasma behind the bunches in practically unperturbed state and so on. In the considered case of AWA the diameter of the bunch is $D = 0.1cm \leq \frac{c}{\omega_p} = \frac{\lambda_p}{2\pi} = 0.15cm$, so for the existing parameters of AWA predictions of 1-D nonlinear theory can be valid [4]

Another possibility to check the predicted effect is based on the use of induction linacs with the typical parameters.

4 AKNOWLEDGMENTS

The authors are very thankful to all participants of the YerPhI Seminar on "New Methods of Acceleration" for useful discussion and comments. The work was supported by ISTC and Minatom of RF.

5 REFERENCES

[1] Amatuni A.Ts. Preprint YerPhI-1473(10)-96, Yerevan, (1996) e-print:http://xxx.lanl.gov/ps/acc-phys/9609003, present Proceedings

[2] Amatuni A.Ts., Sekhpossian E.V., Elbakian S.S., Abramian R.D. Part. Acc. **41**, 153, (1993)

[3] Simpson J.D. "Argonne New Wakefield Facility" Proc. HEACC-92, Hamburg, 1993

[4] Mori W.B., Katzouleas T., Proc. EPAC-90, Nice, June 12-16, 1990, v. I, p.603.

PERFORMANCE OF THE ADVANCED PHOTON SOURCE

Glenn Decker
Advanced Photon Source, Argonne National Laboratory
9700 South Cass Avenue, Argonne, Illinois 60439 USA

Abstract

The Advanced Photon Source (APS) positron storage ring is a 100-mA, 7-GeV, third-generation x-ray synchrotron radiation source which began operation in March 1995. Since that time, significant progress on beamline construction and commissioning has taken place, with many of the x-ray user beamlines in operation. Operational design goals which have been met or exceeded include < 8.2-nm-rad emittance, > 10-hour lifetime, > 90% availability, > 100-mA average current, > 5-mA single-bunch current, < 10% uncorrected coupling, 8-mm full vertical apertures for insertion devices, and ultra-stable orbit (< 4.5 μm rms vertically, 17 μm horizontally). Progress beyond these design goals and a report on development plans, including top-up operation (injection with x-ray beamline shutters open), are presented.

1 INTRODUCTION

The APS storage ring achieved first stored beam with extracted light on March 26, 1995 and was formally dedicated on May 1, 1996. The ring was officially declared operational for user beam by the Department of Energy on August 8, 1996. Ten insertion device (ID) and six bending magnet (BM) beamlines are now operational with six additional beamlines undergoing commissioning. Eighteen of the planned twenty-one insertion devices are now in place. Table 1 lists the relevant APS storage ring characteristics. The APS storage ring lattice, shown in Figure 1, is a double bend achromat Chasman-Green design.

Table 1: APS Storage Ring Characteristics

Energy (GeV)	7.0
Number of superperiods	40
Circumference (m)	1104
Harmonic number	1296
RF frequency (MHz)	351.93
Critical energy (keV)	19.5
Energy loss/turn (MeV)	6.9
Vertical full aperture (mm)	8
Horizontal tune	35.2
Vertical tune	14.3
Synchrotron tune	0.0072
Horiz. beam size at insertion device source point (μm rms)	325
Vertical beam size at insertion device source point (μm rms)	86
Straight sections available for IDs	35
Straight Section Length for IDs (m)	5.2

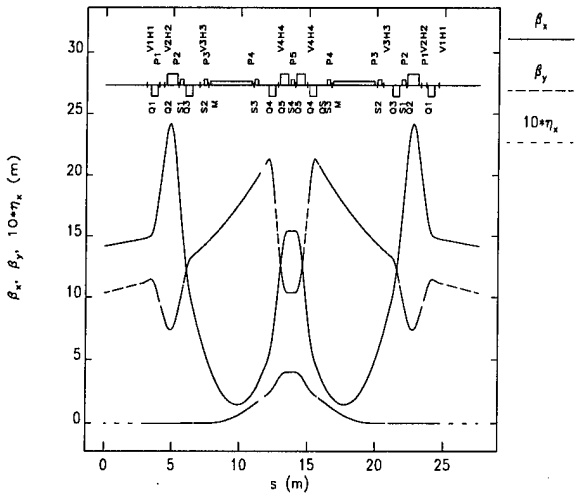


Figure 1: Lattice drawing for the APS storage ring.

2 PERFORMANCE SUMMARY

Table 2 contains APS performance parameters, indicating both design values and best performance to date.

Table 2: Summary of APS Storage Ring Performance

	Design	Achieved
Total current (mA)	100	164
Single bunch current (mA)	5	18.1
Stored beam lifetime (Hr)	> 10	> 30
Emittance (nm-rad)	8.2	7.6 ± 0.8
Horiz. - vert. coupling	< 10%	< 3%
Natural bunch length (ps rms)	17.6	< 29
Bunch length @5 mA (ps rms)	52	52
Vertical beam stability (μm rms 1-50 Hz)	< 4.5	< 4.0
Horizontal beam stability (μm rms 1-50 Hz)	< 17.	< 17.
User x-ray beam availability	> 90%	87%
Avg. vacuum at 100 mA (nT)	< 1.0	0.8

3 OPERATIONS

Regular user runs began in late 1995. Since that time, operation has normally consisted of 3-week user runs interleaved with 3-week-long maintenance periods used mostly for completion of beamline front-end hardware. With the imminent completion of in-tunnel hardware, the relative proportion of user time to maintenance is expected to increase. Shown in Table 3 are availability data for the last six operational periods. At the APS availability does

0-7803-4376-X/98/$10.00 © 1998 IEEE

not include injection and orbit correction time at the beginning of each fill.

Table 3: APS Operations Statistics

Run Number	Scheduled User Time (Hours)	X-ray Availability	Amp-Hours
96-5	250.0	65.9%	12.7
96-6a	255.3	69.1%	14.2
96-6b	268.6	83.2%	16.9
96-7	250.0	58.8%	8.6
97-1	342.9	74.0%	18.8
97-2	236.7	79.7%	15.1

The availability over the course of a run has been observed in general to increase with time, so that the second half of a 3-week run contains significantly fewer unplanned beam dump events. This result is perhaps to be expected and provides an argument for longer runs, which will be pursued following completion of front-end installation work. Also, it should be noted that the "best" availability quoted in Table 2 is for the second half of run 97-2, in comparison to Table 3 which gives the run averages. The largest contributor to unplanned beam dumps in 1997 have been rf system interlock trips, and efforts are focusing on this area in particular, with reliability and availability budgets defined in general for all hardware systems.

4 BEAM CURRENT AND LIFETIME

Operationally, the storage ring is filled to just over 100 mA on a routine basis. While the accelerator components are generally designed from an engineering standpoint to withstand up to 300 mA, the ID front-end photon shutters presently limit operation to 100 mA. Because the insertion device gaps can be closed to 10.5 mm, the APS undulator A, for example, is capable of generating a peak heat flux in excess of 150 W/mm^2, 30 meters from the source point. Further engineering upgrades are under consideration to facilitate operation above 100 mA.

During a studies period in July 1996, a maximum 164 mA was stored in the storage ring with insertion device gaps open. The limitation was essentially due to the fact that only three of the four 4-cavity rf stations were operational at the time. Poor vacuum was evidenced near pulsed magnet ceramic vacuum chambers, which has since been traced to a poor conductive interior coating that resulted in heating in the presence of large peak current [1]. These chambers have since been replaced. During the same time frame, a single-bunch current of 18.1 mA was achieved, making use of large positive chromaticity. These studies were performed using electrons. During the maintenance period which followed, the facility was changed over to positrons, with no impact on operation; however, these efforts have not been repeated since that time due to increased focus on reliability and beam stability work.

The APS injector supplies single bunches to the storage ring at 7 GeV. Given the large harmonic number, a large variety of fill patterns is possible, with an associated variation in beam lifetime. As few as 42 bunches provide lifetime in excess of the 10 hour/100 mA design goal, but this can be increased by more than a factor of three by going to a 206-bunch fill pattern. Due to the small emittance, the machine is Touschek limited for bunch currents in excess of about 1 mA, below which the Touschek lifetime becomes comparable with the gas scattering lifetime. The Touschek effect becomes even stronger when considering a reduction in the vertical/horizontal coupling; the ring typically runs uncorrected, with coupling in the 3 to 4% range.

The limitation on gas scattering lifetime comes from ring vacuum, specified to be less than 1 nTorr at 100 mA. As can be seen from the average ring ion gauge data shown in Figure 2, the ring has cleaned up nicely in the past year from natural photodesorption [2].

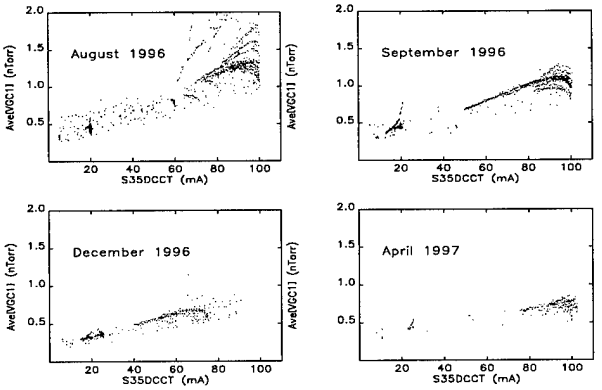


Figure 2: Vacuum vs. beam current and time.

5 EMITTANCE

In early 1996, the first comprehensive study of emittance using insertion device light was conducted on beamline 1-ID [3]. Measurements of beam size and angular divergence resulted in a horizontal emittance value of 7.6 ± 0.8 nm-rad, consistent with the design value of 8.2 nm-rad total emittance and 3% coupling.

Dedicated x-ray imaging capability for the purpose of particle beam diagnostics is available via an x-ray pinhole camera on beamline 35-BM, and is used during operations, with beam size and position process variables logged routinely. This system presently has 1:1 magnification and 60 micron (H) by 40 micron (V) resolutions, with a beamline extension planned to increase magnification by a factor of four. This beamline additionally provides information on beam energy spread due to dispersion at the source point.

A high-resolution imaging station received first light in March of 1997 on beamline 35-ID and is also dedicated to particle beam diagnostics. A special-purpose undulator with 198 periods of 1.8-cm length has a radiation cone angle of only 2.6 μrad in the fundamental, which is less

than the positron beam divergences. Initial divergence measurements ($\sigma_{x'}$ = 21 μrad and $\sigma_{y'}$ = 4.9 μrad) performed at 65 mA stored beam current in May 1997 indicate a vertical coupling of 3.7 ± 0.4% and an emittance of 6.6 ± 0.6 nm-rad (using the theoretical β_x, β_y in the straight; see Table 4 in Ref. 4).

6 BUNCH LENGTH

Associated with the beamline 35-BM is a split ultraviolet/visible light pick-off mirror and optical transport line which can be used both for low-resolution imaging and streak camera bunch-length measurements [5]. In addition to bunch lengthening (Fig. 3), this diagnostic has been used to observe the head-tail instability under reduced chromaticity conditions. Analysis of longitudinal loss factor and transverse impedance can be found in Ref. 6.

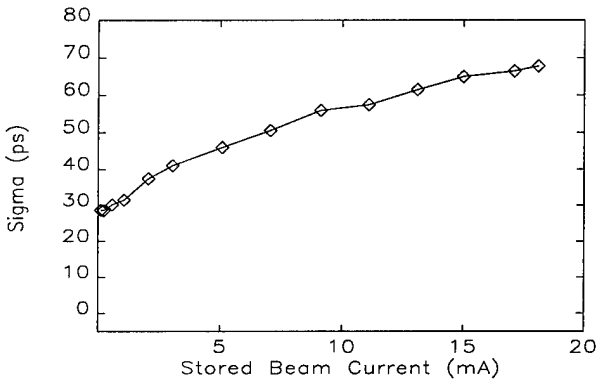


Figure 3: Bunch length vs. current, single bunch.

7 ORBIT STABILITY AND CONTROL

The specification for orbit stability at the APS is that the beam's rms centroid motion should not exceed 5% of its size at beamline source points. For insertion devices, this amounts to 4.5 microns rms vertically and 17 microns rms horizontally in position, and 0.45 microradians rms vertically and 1.2 microradians rms horizontally in angle.

It should be noted that the design 10% coupling is used in deriving these stability criteria. Even though it is possible to reduce the vertical beam size significantly by decoupling the machine, full advantage of the resultant increase in brightness cannot be realized until submicron beam stability can be achieved. Additionally, the reduced Touschek lifetime becomes another limitation on small coupling operation.

It should also be noted that the above stability criteria have been stated without reference to frequency bandwidth. Typically the band of interest to x-ray users extends from very low frequency, i.e., daily variations, up to about 10 Hz, depending on the type of experiment being performed. For many experiments, motions faster than this mimic an increased emittance with associated reduced x-ray flux.

Beam position is measured at 360 stations around the ring circumference using capacitive pickup electrodes. Turn-by-turn position information is collected using amplitude-to-phase conversion rf receivers at each station. Hardware and software averaging is used to obtain submicron resolution readbacks. Orbit correction is effected using up to 317 combined-function horizontal/vertical steering corrector magnets. Of these, 38 have thin wall chambers in their bore, providing correction bandwidth capability above 100 Hz.

Orbit correction software uses a severely under-constrained singular value decomposition (SVD) algorithm, using 40 of 317 possible correctors [7, 8], but a maximum number of beam position monitors (BPMs). A unique "despiking" algorithm is used, which replaces BPM readbacks having unphysical offset shifts by the average of neighboring units. The effect of this is that the algorithm focuses on long spatial wavelength (i.e., physical) orbit motions, ignoring to a large extent the unit-to-unit systematic errors in the BPM electronics. Corrections are written to the corrector magnets every 5 to 10 seconds. Local beamline steering is generally performed at user request only.

A major difficulty in assessing long-term orbit stability is the absence of an absolute reference. At the APS, the most accurately believed beam position measurement is derived from x-ray beam position monitors located at bending magnet beamline front ends, which are sensitive to vertical beam motions. At the 5-micron scale, the long-term (several hour) beam motion characteristics as seen by the x-ray monitors have significant variations compared to the rf beam position monitors. Intensity-dependent offsets in the rf electronics are typically of order 20 microns over a 10-hour fill. Even after compensating for this, examples of what appears to be real beam motion on the rf BPMs at bending magnet source points are not seen on the x-ray monitors. A 7-micron peak-to-peak half-hour period motion read back on the rf BPMs in sector 1 that is correlated with air temperature variations is not present on either of the bending magnet x-ray BPMs in that sector. One possible explanation is that the vacuum chamber is moving locally in response to tunnel temperature changes, but the correction algorithm is insensitive to this owing to the great statistical advantage of using large numbers of BPMs to correct only long spatial wavelength motions. The x-ray BPMs are mounted on specially designed thermally isolated and vibration damped supports, whereas the rf pick-up electrodes are mounted on chambers supported from the magnet girders but mechanically isolated from the magnets themselves. Determining the systematics associated with both the rf and x-ray beam position monitors at the few-micron scale is a major effort in the coming year.

In addition to the "slow" software orbit feedback, a real-time closed orbit feedback system is being commissioned during studies periods and will be released for user operation sometime this summer [9]. This system has access to 320 of the 360 beam position monitors and makes use of the 38 high-bandwidth correction magnets in its global implementation, writing to them at a 1-kHz rate.

A summary of the status of APS orbit stability, over nearly ten decades of frequency, from 3×10^{-5} Hz to 135 kHz, is shown in Figs. 4 and 5. Displayed is the power spectral density averaged over 40 beam position monitors located at insertion device source points. The effect of the real-time closed orbit feedback system is clearly shown. The slow orbit feedback and BPM offset compensation was active for all of the data sets shown and is responsible for the spectral lines located near 0.1 Hz.

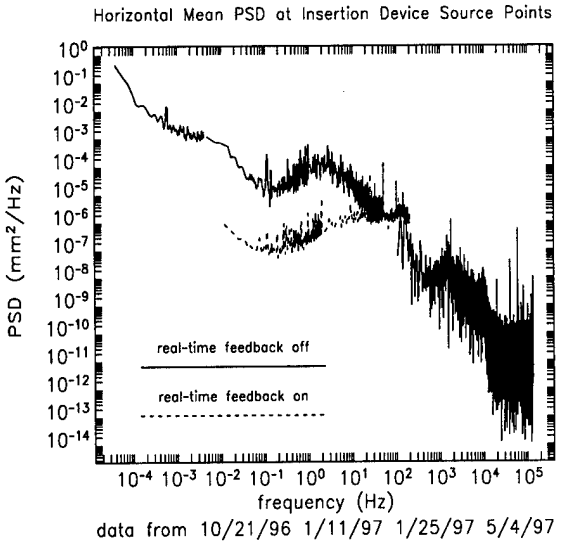


Figure 4: Horizontal spectrum with and without feedback.

Also visible in Fig. 4 are spectral lines at 5.5×10^{-4} Hz (air temperature variations), 25, 50, and 100 Hz (traced to a malfunctioning quadrupole power supply, since repaired), and approximately 1.7 kHz, the synchrotron tune. Lines at 20, 40, and 60 kHz are associated with the pulse-width-modulated power supplies used on nearly all storage ring magnets. Similarly, in Fig. 5 can be seen the 2 Hz injector repetition rate in addition to the 5.5×10^{-4} Hz line.

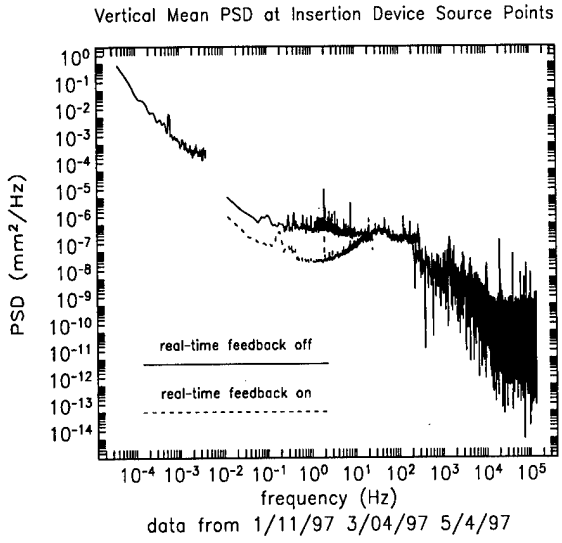


Figure 5: Vertical spectrum with and without feedback.

As stated in Table 2, the orbit stability specifications are met without correction in the band from 1 to 50 Hz. Unfortunately, a very significant contribution to beam motion lies outside this band. The real-time feedback system, when configured to correct dynamic effects only, eliminates the horizontal broadband peak between 0.1 and 10 Hz, extending the band where specification is met down to 10 mHz on the low end. The slow feedback system allows stability criteria to be met at frequencies below this.

In addition to improving orbit stability, the fast feedback system provides an extremely powerful tool for identifying noise sources. By analyzing spectra of the setpoints being written to correction elements, it is in principle possible to localize noise sources to within the spacing of the correctors or better. This type of analysis has occurred before using off-line techniques, and in fact was used to locate a sextupole power supply which was oscillating at 6.5 Hz using EPICS for real-time data acquisition. The possibility of performing this type of analysis in real time up to 500 Hz, and perhaps even generating an alarm when a noise source arises, is an exciting prospect indeed. Early indications are that this will be realizable.

The unique requirements of a synchrotron light source, in particular the extreme emphasis on orbit stability and control, has made possible some unique observations. Shown in Figure 6 is a plot of horizontal beam position averaged over the 40 high dispersion points around the ring. A 25-micron peak-to-peak diurnal variation is clearly seen. This effect was first observed at LEP [10] using polarimeter-based beam energy measurements, and is in fact a geometric effect associated with earth tides. Owing to the small momentum compaction and tight measurement resolution at APS, one can directly observe variations in the ring's orbit circumference resulting from astronomical phenomena.

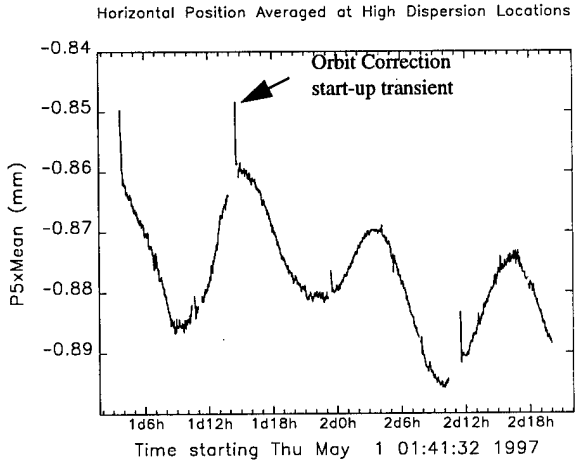


Figure 6: Data showing diurnal ring circumference change.

8 STORAGE RING DEVELOPMENT PLANS

Primary areas where improvements or upgrades are planned in the near future at APS are reliability and availability, orbit stability, and top-up operation. Reliability is a measure of the probability that the ring will be available for a specified time after a user walks in the door and is typically measured in terms of the mean time to an unscheduled beam dump. Availability, on the other hand, is simply the ratio of actual up time to scheduled up time. Both hardware and software upgrades are underway to improve both availability and reliability. Improved electronics cooling, re-design of key machine protection system interlock components, and an rf waveguide switching upgrade [11, 12, 13] are underway on the hardware front, and more sophisticated software alarming and improved software procedures [14] are rapidly becoming available.

Improvements in beam stability are similarly tied to both hardware and software upgrades. The insertion device vacuum chambers have integral to their design two dedicated sets of increased-sensitivity capacitive pick-up electrodes at each end. When these chambers were installed, electronics from neighboring stations were simply relocated to the insertion device pickups. An ongoing upgrade is the procurement of narrow-band switched-receiver electronics [15] for the insertion devices and the relocation of electronics back to their original configuration. While they have nowhere near the bandwidth of the existing electronics as exhibited in Figures 4 and 5, the new receivers should facilitate greatly enhanced long-term stability characteristics at the ID source points. These new electronics will be tied to the real-time orbit feedback system. The software for both real-time and long-term orbit correction is continuously being evaluated for improved characteristics. When submicron beam stability is achieved, a subsequent increase in brightness through lattice modifications and reduced coupling will follow.

Given that the APS has its own dedicated on-energy injector, one special operating mode being actively investigated is called "top-up." This can be simply understood as injection with user x-ray shutters open, for the purpose of regulating stored beam current. This user beam mode has the advantage of alleviating beam-intensity-related systematic errors affecting user experiments. Using existing hardware, it appears feasible to regulate stored beam down to the 0.1% level (i.e., 0.1 mA out of 100 mA total). Improvements in the injector portion of the facility, injection efficiency in general, and beam diagnostics should make it possible to push this to the 0.01% level.

A key safety element necessary for top-up is a modification to the ring access control interlock system used for personnel safety. The worst-case scenario occurs if a storage ring main dipole magnet were to short out during injection with shutters open. This could conceivably direct the injected charged particle beam down a user beamline. If, however, one insists on the presence of stored beam prior to enabling injection in top-up mode, it can be shown that it is impossible for this failure scenario to occur. A reliable top-up beam current monitor for inclusion in this logic is under development.

To gauge the effects of injection beam losses during top-up operation, radiation measurements have been performed on the experiment hall floor while missteering the beam to scrape on the 8-mm-aperture insertion device chambers with safety shutters both open and closed. Preliminary results look promising.

9 CONCLUSIONS

In its first year of operation, the Advanced Photon Source has met all of its design performance goals and is well on the way to providing reliable, ultra-stable beam for its user community. Planned upgrades in brightness, including top-up operation, together with improvements in beam stabilization and injection efficiency will provide state-of-the-art x-ray beams into the next century.

10 ACKNOWLEDGMENTS

This work is a culmination of the efforts of virtually all members of the APS Accelerator Systems Division together with the assistance and support of key members of its sister division, Experimental Facilities.

Work supported by the U.S. Department of Energy, Office of Basic Energy Sciences, under Contract No. W-31-109-ENG-38.

11 REFERENCES

[1] C. Doose et al., "In Situ Measurement of Ceramic Chamber Conductive Coating Quality," these proceedings.

[2] J. Noonan, "APS Storage Ring Vacuum System Performance," these proceedings.

[3] E. Gluskin, APS-XFD, private communication.

[4] B.X. Yang et al., "Status of the APS Diagnostics Undulator Beamline," these proceedings.

[5] A. H. Lumpkin, B.X. Yang, "Time Resolved Imaging of Electron and Positron Beams at APS," these proceedings.

[6] N.S. Sereno et al., "A Potpourri of Impedance Measurements at the Advanced Photon Source Storage Ring," these proceedings.

[7] L. Emery, M. Borland, "Advancements in Orbit Drift Correction in the Advanced Photon Source Storage Ring," these proceedings.

[8] M. Borland, "Applications Toolkit for Accelerator Control and Analysis," these proceedings.

[9] J. Carwardine et al., "Commissioning and Performance of the APS Real-Time Orbit Feedback System," these proceedings.

[10] M. Placidi, "Absolute Beam Energy Measurements in e^+e^- Storage Rings," AIP 390, Proceedings of the Seventh Beam Instrumentation Workshop, Argonne, IL (1997).

[11] D. Horan et al., "Design and Construction of the Advanced Photon Source 352-MHz RF System Switching Control," these proceedings.

[12] Y.W. Kang et al., "Reconfigurable High-Power RF System in the Advanced Photon Source," these proceedings.

[13] A. Nassiri et al., "An Overview and Operation of the Advanced Photon Source 352-MHz RF Systems," these proceedings.

[14] M. Borland, "The Procedure Execution Manager and Its Application to Advanced Photon Source Accelerator Operation," these proceedings.

[15] K. Unser, "New Generation Electronics Applied to Beam Position Monitors," AIP 390, Proceedings of the Seventh Beam Instrumentation Workshop, Argonne, IL (1997).

IMPROVING AND EXTENDING PERFORMANCE AT SYNCHROTRON RADIATION FACILITIES *

A. Jackson, Advanced Light Source Center, E. O. Lawrence Berkeley National Laboratory
University of California, Berkeley, CA 94720 USA

Abstract

Synchrotron radiation facilities around the world have now matured through three generations. The latest facilities have all met or exceeded their design specifications and are learning how to cope with the ever more demanding requests of the user community, especially concerning beam stability. The older facilities remain competitive by extending the unique features of their design, and by developing novel insertion devices. In this paper we survey the beam characteristics achieved at third-generation sources and explore the improvements made at earlier generation facilities.

I. INTRODUCTION

Dedicated synchrotron radiation user facilities have been part of the global research landscape for more than thirty years. Some of the more venerable ones, like SSRL in the USA. the SRS in the UK, HASYLAB in Germany, and the Photon Factory in Japan (to name but a few), continue to produce forefront scientific results. In order to maintain their competitiveness, most of the older facilities have graduated through a series of upgrades; for example, by increasing beam energy ranges and current capabilities, reducing beam emittances, incorporating novel insertion devices, and so on. The more recent facilities based on the so-called third-generation light sources face different challenges. The expectations of these machines were initially downgraded from their linear-model design values because of uncertainties related to intra-beam scattering, momentum acceptance, single- and multi-bunch instabilities, and dynamic aperture. However, the new machines soon attained beam parameters that are very close to the linear-model predictions. Users quickly learned to utilize the higher brightness photon beams, and now beam stability, on the scale of microns, over time scales from milli-seconds to many hours, are being demanded – and met.

The content of this paper is compiled from information provided to the author from existing facilities. I have attempted to be faithful to that information, and apologize for any discrepancies that may have crept in through poor interpretation or (more likely) insufficient research on my part.

*This work was supported by the Director, Office of Energy Research, Office of Basic Energy Sciences, Material Sciences Division, U.S. Department of Energy, under Contract No. De-AC03-76SF00098.

II. THREE GENERATIONS OF SYNCHROTRON LIGHT SOURCES

Synchrotron light sources have been arbitrarily divided into three generations. The first is meant to describe facilities that were parasitic on machines that were built for a different purpose – high energy physics (HEP). Examples of such facilities are Tantalus (Wisconsin, U.S.A.), and DCI (Paris, France). "Second-generation" describes accelerators that were purpose-built as dedicated synchrotron radiation facilities, such as the SRS (Daresbury, UK), and the Photon Factory (Tsukuba, Japan). The third-generation sources are also dedicated facilities, but designed to give orders of magnitude more photon beam brightness by taking advantage of the development of long undulators. Requirements of these machines include long straight sections, typically 6 m or more between magnets, and low emittance beams, typically less than 10 nm-rad.

Unfortunately, many machines do not fit nicely into these categories! For example, SSRL (Stanford, USA), is based on the SPEAR storage ring, which was built as a colliding beam facility for HEP, placing it squarely into the first generation. However, SSRL developed into a dedicated facility, SPEAR has some very long straight sections, and SSRL has pioneered the utilization of wigglers and undulators, which surely raises it's "status" to at least second generation. Similarly, Super-ACO (Paris, France), and NSLS (Brookhaven, U.S.A.), have many undulator beamlines, albeit from somewhat shorter straight sections, utilizing beams with emittances somewhat larger than those defined above! So where do they fit? We will not pursue this question further. Arbitrarily, we will call the "new" facilities those that include the ESRF (Grenoble, France), and the other "third-generation" designed sources that were built thereafter – all others are "older".

III. PERFORMANCE AT THE OLDER FACILITIES

Almost all the older facilities have upgraded their capabilities since they were first commissioned. Those described below should be regarded as representative, since it is impossible, in a paper of this length, to list all the improvements that have been made to all the facilities throughout the world.

(a) Stanford Synchrotron Radiation Laboratory (SSRL) is a dedicated facility based on the former e^+e^- colliding beam storage ring SPEAR. This facility has gone through several upgrades: First the lattice was changed to eliminate the collision optics (mini-β_y), used in the HEP program, and to reduce the natural emittance from 0.47 μm-rad (at 3.0 GeV) to 0.13 μm-rad [1]. In the

0-7803-4376-X/98/$10.00 © 1998 IEEE

process, the chromaticity correction scheme was modified to give a larger dynamic aperture. An associated benefit to eliminating the mini-β sections was a significant reduction in quadrupole strengths in the straight sections which, in turn, led to a reduction in a diurnal variation in the global closed-orbit. The closed-orbit stability has been improved further (by a factor of ≈ 5) by a global feedback system that operates in both planes, and a local system that operates for particular beamlines in the vertical plane. The net result is an orbit stability of around 100 μm (horizontal) by 80 μm (vertically). The facility has built a dedicated injection system (linac and booster synchrotron), so that SSRL operations are essentially independent of SLAC operations. Currently, SSRL operates with 2, 8-pole electromagnetic wigglers; 3 permanent magnet hybrid wigglers, and an elliptical polarizing undulator. Future upgrade plans include full energy (3 GeV) injection, and a major lattice rebuild to further reduce the emittance.

(b) The Synchrotron Radiation Source (SRS) was the first of the purpose-built synchrotron radiation facilities for the utilization of x-rays. This facility was designed in 1974, before the impact of undulators, and the requirement for low emittance, was recognized. In fact the "emittance" (at ≈ 0.5 μm-rad at 2 GeV) is not even mentioned in the 1975 design report – though it is implicitly included in the calculated beam sizes. The SRS was, and still is a generator of flux, rather than brightness. Soon after it's inauguration in 1981, a 5 T superconducting wiggler was added to the lattice that pushed the radiation spectrum to a critical energy of ≈ 16 keV. This was soon followed by an undulator. In 1987 a lattice rebuild was instituted that doubled the periodicity of the FODO lattice structure, and reduced the emittance to 0.1 μm-rad, significantly improving the performance of the undulator, and the flux that could be focused onto small samples, for example in protein crystallography experiments. Recently a second wiggler with a peak field of 6 T was added. Together, these three insertion devices service 15 user stations, for a total of 40. However, this is far from the end of the story. Despite having filled all the space around the circumference, the SRS has embarked on a scheme [2] to relocate accelerator components around the ring (including all four accelerating cavities) in order to free up space for two new multi-pole wigglers – each 1.2 m long, with 10 poles, producing a maximum field of 2 T. This funded project extends the useful life of the SRS well into the next millennium! The Daresbury Laboratory also has a fully developed proposal, not yet funded, for a third-generation x-ray source called DIAMOND [3].

(c) Following closely on the heals of the SRS, came the Photon Factory (PF) which has parameters very similar to the SRS (energy = 2.5 GeV, emittance = 0.13 μm-rad). Over the past 15 years the main upgrades to the facility have been in the development of undulators, with many novel concepts being designed, built, and implemented for users. Currently there are six insertion devices in the ring, one of which – "the revolver" – has 4 separate undulators capable of serving one beam line, two that operate in either wiggler or undulator modes, and one that can provide elliptically polarized radiation. Right now the PF is in the middle of a long shut down for an extensive lattice refit that will push the beam emittance down to 27 nm-rad, and increase the photon brightness from it's many undulator sources by an order of magnitude [4]. Prior to this shutdown, the PF replaced two RF cavities with ones designed to damp higher-order cavity modes (See Figure 1). With these cavities in operation, no serious beam instabilities were observed during normal (400 mA) multi-bunch operation. So, on the last shift before the shut down, the current was pushed, without instability problems being observed, until the RF tripped on a reverse power interlock, at a current of 773 mA. The PF looks forward to bringing the accelerators back into operation for users sometime this autumn.

Acceleration frequency(MHz)	*500.0*
Shunt imedance(MΩ)	*6.8*
Unloaded Q-value	*39,000*

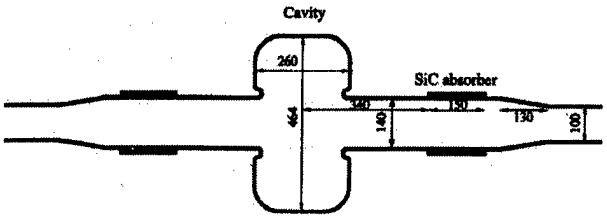


Fig. 1. HOM-Damped Cavity for the PF

(d) A unique feature of the BESSY facility, in Berlin, is it's utilization by the Physikalisch-Technische Bundesanstalt (PTB) as a primary radiation source standard in the VUV and soft x-ray range of the electromagnetic spectrum. This requires a precise knowledge of many machine parameters, in particular the electron energy. To this end, the accelerator physicists at BESSY have developed and implemented two techniques for measuring the energy, one based on resonant depolarization, the other on Compton back-scattering of laser photons [5] (See Figure 2). The latter has been used to measure not only the beam energy (to an accuracy of ≈ $1:10^4$), but also the energy spread, and the momentum compaction factor.

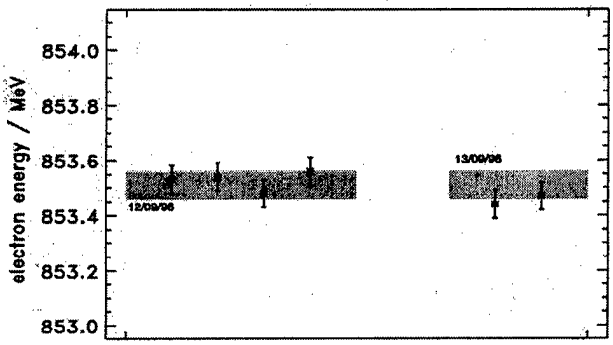


Fig. 2. Electron energy measured by resonant spin depolarization ( ) and by Compton back scattering

(e) The Aladdin facility, in Wisconsin, was originally conceived as an 800 MeV facility, but now operates for one-third of it's time; i.e., 8 hours/day, at 1 GeV. The facility has 29 beamlines, including one undulator line. Six bend magnet beamlines are dedicated for x-ray lithography, a program that has seen tremendous growth at the facility, and one beamline to the emerging technology of micro-machining. In the immediate future, two new undulators and their beamlines will be commissioned, to be followed by a high resolution beamline being financed by Canadian institutions. An electromagnetic undulator has been built and is at the field mapping stage, to be installed at the end of the year. Active accelerator tuning, including quadrupoles and steering magnets, will be implemented with the new undulators, to maintain tune and orbit stability as the undulators are manipulated by the users. The global orbit feedback system currently in use maintains the closed-orbit to within $\pm$ 5 μm against slow (< 0.2 Hz) perturbations.

(f) The Super-ACO facility, in Paris, is based on an 800 MeV, 39 nm-rad emittance positron storage ring that has eight 3.5 m long straight sections. The alternate straights have zero and 1 m dispersion. The facility operates 23 beamlines, with 4 undulator sources, an asymmetric hybrid wiggler, and has the only ring-based FEL facility in the world that is routinely operated for users [6]. The ring is also routinely operated in a "two-bunch" mode, where each bunch is filled to 120 mA, and the beam lifetime is reduced by only a factor of two (to $\approx$ 3 hr) from the nominal 400 mA 24-bunch operation. A recent upgrade replaced the old 100 MHz cavities with 500 MHz designs, which will lead to shorter bunches for the timing experiments, and increase the FEL gain. SuperACO is also one of the few rings that is filled directly from a linac, that can produce either electrons or positrons at the full operating energy. This made it an ideal facility to study the "sudden micro beam-loss" phenomenon that plagued many electron accelerator facilities in the eighties. The accelerator physicists were able to show that the effect was due to the trapping of photo-ionized dust particles in the vacuum chamber – thereby ending years of debate as to the mechanism of this difficult-to-study effect.

(g) The National Synchrontron Light Source (NSLS), on Long Island, operates two storage rings at it's facility, the 800 MeV VUV ring, and the 2.5 GeV X-Ray ring. Here we will concentrate on the X-Ray ring, which has eight zero-dispersion straight sections, each 4.5 m long, and an emittance of 0.1 μm-rad. The major improvements in accelerator operations include a dramatic reduction in the vertical emittance, from 2 nm-rad (i.e., an emittance ratio of only 2%) down to 0.1 nm-rad, a value comparable to those found at third-generation sources. Tests have also been successful in reducing the natural emittance to 45 nm-rad; this will become the routine operating option once improvements to the analog global-orbit feedback system have been implemented. Other improvements include increases in energy (to 2.6 GeV), current (from 200 to 450 mA), and beam stability. The latter has benefited from an increase in the number of beam position monitors (BPMs) by a factor of two (to 16). This enabled the analog vertical closed-orbit feedback system to utilize 8, rather than 6, harmonics in the correction algorithm, and improved the long-term vertical orbit stability by a factor of 3 – down to about 3 μm (See Figure 3). Similarly, drift in the horizontal closed orbit has been reduced to around 2 μm, by using both harmonic feedback and a newly developed digital system. Unfortunately, this correction is with respect to the BPMs, which are not stable themselves to this accuracy. With the improved vertical emittance and beam stability, comes the opportunity to investigate small gap insertion devices. This work started in 1994 with the installation of a variable aperture vacuum chamber and small period undulator [7], and a report on the more recent developments is given in these proceedings [8].

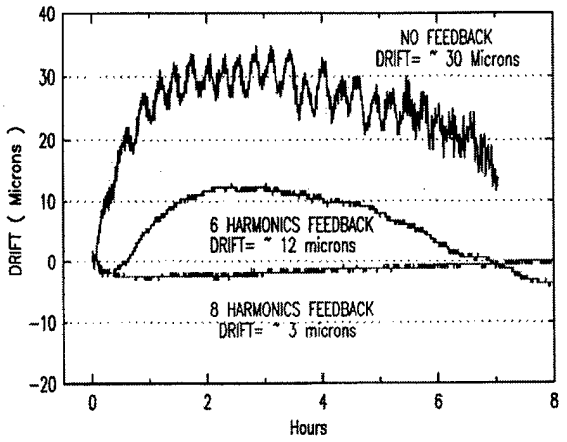


Fig. 3. Stabilization of the vertical orbit in the NSLS X-Ray Ring using the harmonic correction algorithm

IV. PERFORMANCE OF THE THIRD-GENERATION LIGHT SOURCES

The third-generation sources are divided into two broad categories: the lower energy storage rings ($\approx$ 2 GeV) optimized to produce high brightness beams in the VUV and soft x-ray regions of the spectrum, and the higher energy rings (around 7 GeV) optimized for harder x-rays. Currently there are 5 low energy operational facilities (ALS, SRRC, ELETTRA, PLS, and MAX-II) with many more in the construction or design phases; and 3 high energy rings operational, or soon to be operational (ESRF, APS, and SPRING-8). The first of the new sources, ESRF, was commissioned in 1992. These facilities have benefited greatly from the lessons learned at the older facilities, and as a consequence reached their design goals soon after start-up. How then has the performance of these machines been improved and extended?

In all cases the first response has been in beam motion stabilization – in the frequency range from dc to synchrotron and betatron oscillation frequencies. The requirements on beam motion are typically quoted as a fraction, in the range 5-10%, of the beam size. With vertical beam sizes reaching the level of 10 μm, this

implies beam stability at the level of ≈ 1 μm – a very severe constraint to provide over periods of many hours.

The faster motion, introduced by instabilities driven by vacuum chamber and cavity impedances have been cured via several different avenues: tuning of the higher-order modes in the cavities; utilizing bunch fill patterns emittance coupling. However, in the case of the lower energy storage rings, reduced vertical emittance is offset by the reduction in beam lifetime, caused by the Touschek effect, so the gains are not as apparent.

The ALS also has a proposal to upgrade three of the 36 lattice bend magnet with short superconducting

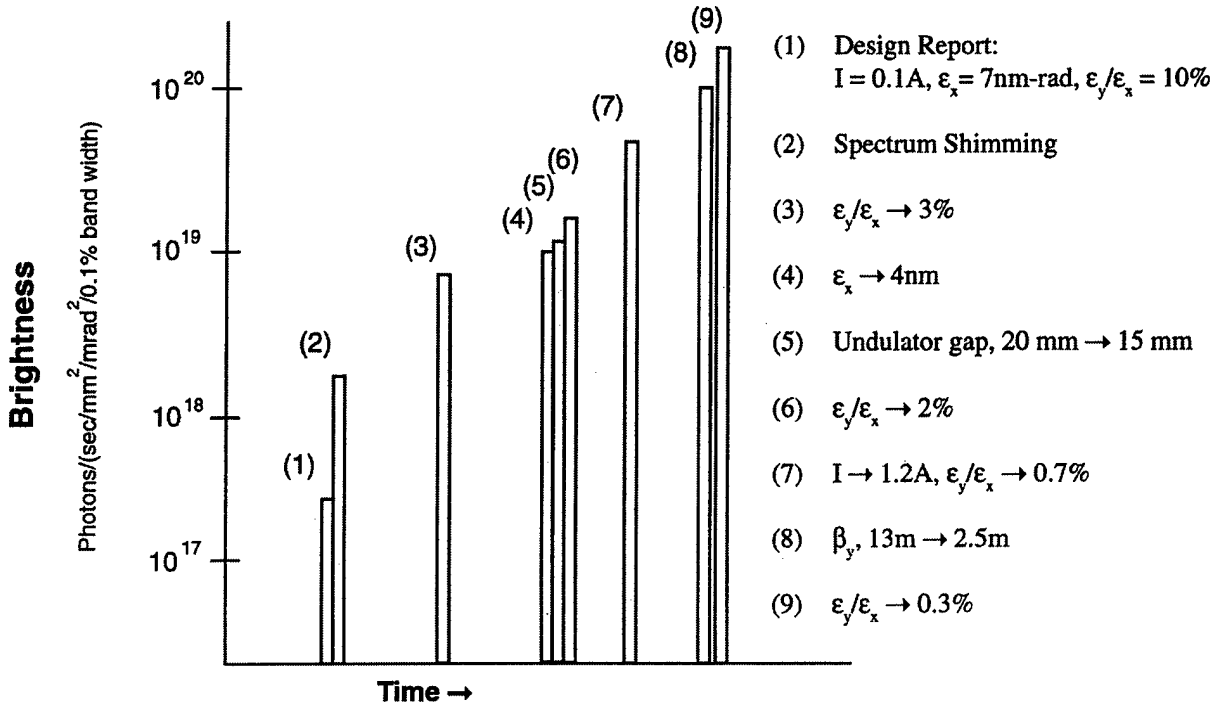


Fig. 4. Improvements in ESRF Brightness from 1992 to Present

that induce frequency differences from bunch-to-bunch; and by utilizing feedback. Slower motion, caused by ground motion, temperature changes, residual fields in undulator magnets, etc., has been either eliminated at the source [9], or through feedback systems. By these means, beam stability has been brought under control at all the operational facilities, to the stringent levels demanded by the users.

At the ESRF, other improvements have been implemented. The current has been increased from 100 to 200 mA, the natural emittance has been reduced from 7 to 4 nm-rad, the emittance coupling reduced from 10% to below 1%, and the vertical beta function reduced to better match the electron emittance aspect ratio to the photon emittance. Together, these improvements have increased the brightness of the undulator radiation from the original specification of 5×10^{17} photons/ (sec.mm^2.mrad^2.0.1% bandwidth) to a value of over 10^{20} – an improvement of more than two orders of magnitude in brightness [10] (See Figure 4). And there are plans to extend this yet further – not bad for a machine that is only in it's fifth year of operation.

The other facilities have also increased their beam brightness' over those originally quoted, mainly by achieving the natural beam emittances expected from simulations, and like the ESRF, operating with lower magnets operating at up to 5 T. This could provide white light x-ray beams to as many as 18 user hutches.

V. SUMMARY

Over the past few decades, synchrotron radiation facilities around the world have accumulated a well deserved reputation for producing high quality science from accelerators that have been almost continually upgraded. The third-generation facilities owe much to their predecessors in understanding the dynamics of tightly focused electron beams, their interactions with their environment, and in developing the technologies necessary to generate the extremely bright beams of radiation being demanded by the user community. They, in turn, are taking this knowledge base yet further, in order to improve their own performance and to provide guidance for the next generation of facilities. The future of synchrotron radiation is indeed bright – and getting brighter.

VI. REFERENCES

[1] J. Safranek and H. Wiedemann, "Low-Emittance in SPEAR", 1991 IEEE Particle Accelerator Conference, San Francisco.

[2] J.A. Clarke and M.W. Poole, "Upgrading the Daresbury SRS with Additional Insertion Devices and its Implications for the Storage Ring Layout", 1996 European Particle Accelerator Conference, Sitges, Spain.
[3] V.P. Suller, et al, "Updated Plans for DIAMOND, a New X-Ray Light Source for the UK", PAC'95, Dallas, TX, pp 180-182.
[4] H. Kobayakawa, private communication.
[5] R. Klein, et al., "Beam Diagnostics at the BESSY I Electron Storage Ring with Compton Backscattered Laser Photons: Measurement of the Electron Energy and Related Quantities", Nuclear Instruments and Methods in Physics Research A 384 (1997) 293-298.
[6] M.E. Couprie, et al., "First Use of the UV SuperACO FEL : Fluorescence Decays and Conformational Dynamics of the NADH Coenzyme", Rev. Sci. Instrum., 65, 1485 (1994).
[7] P.M. Stefan et al., "Small Gap Undulator Experiment on the NSLS X-Ray Ring", PAC'95, pp 2435-2437.
[8] P.M. Stefan et al., "Insertion Device Development in the X13 Straight of the NSLS X-Ray Ring", these proceedings.
[9] R. Keller, et al., "Orbit Stability of the ALS Storage Ring", these proceedings.
[10] J-M. Filhol, et al., "Status Report on the ESRF", these proceedings.

BEAM-BASED MODELING AND CONTROL OF STORAGE RINGS

J. Safranek
National Synchrotron Light Source, Brookhaven National Laboratory, Upton, NY 11973

Abstract

Analysis of the measured orbit response matrix is a powerful technique for debugging the linear optics of storage rings. The orbit response matrix is the change in orbit at the beam position monitors (BPMs) with changes in steering magnet excitation. Results will be presented from a computer code called LOCO (Linear Optics from Closed Orbits) [1] that has been used to analyze the response matrices from several synchrotron light sources including the ALS, NSLS VUV, NSLS X-Ray, and SRRC storage rings. The analysis accurately determines the individual quadrupole magnet gradients as well as the gains of BPMs and the calibrations of the steering magnets. The coupling terms of the response matrix such as the shift in vertical orbit from horizontal steering magnets can be included in the analysis to give the role of the quadrupoles, BPMs and steering magnets. The LOCO code can also be used to find the changes in quadrupole gradient that best compensate for gradient errors from insertion devices and sextupoles. In this way the design periodicity of the linear optics can be restored.

1 INTRODUCTION

When a storage ring is first commissioned, the resulting optics invariably differ to some extent, often significantly, from the design. Achieving maximum performance, whether it be small beam size, small coupling, maximum lifetime, or maximum dynamic aperture, requires understanding and removing or compensating the source of the optics perturbations. This is particularly important in storage rings pushing the limits of accelerator performance such as third generation light sources, damping rings, and high energy physics factories.

The orbit response matrix is a good place to start when trying to debug a storage ring optics. The response matrix contains a large number of accurate data points reflecting the magnetic gradients of the ring. For example, in the NSLS X-Ray Ring, the response matrix contains 8640 data points with a noise level better than 1 μm.

The computer code LOCO was developed using ideas from reference [2] to determine the individual magnet gradients using the measured response matrix. It has been used to calibrate several storage rings [1, 3, 4, 5, 6, 7, 8], and work is in progress with several others. The emphasis of this paper will be the improvements made to the storage rings as a result of applying LOCO, but first a brief summary of the method and accuracy of the analysis will be given.

2 METHOD

For a more detailed discussion of the method and error analysis, see [1].

2.1 *Characterizing linear optics*

The measured, M_{meas}, or model, M_{mod}, orbit response matrix is defined as

$$\begin{pmatrix} \boldsymbol{x} \\ \boldsymbol{y} \end{pmatrix} = M_{\mathrm{meas,mod}} \begin{pmatrix} \boldsymbol{\theta}_x \\ \boldsymbol{\theta}_y \end{pmatrix}, \qquad (1)$$

where $\boldsymbol{x}, \boldsymbol{y}$ is the shift in orbit at the BPMs for some change in steering magnet strengths $\boldsymbol{\theta}_x, \boldsymbol{\theta}_y$.

The parameters, such as quadrupole gradients, in a model such as MAD [9] of the storage ring are varied to minimize the χ^2 difference between the model and the measured response matrices.

$$\chi^2 = \sum_{i,j} \frac{(M_{\mathrm{mod,ij}} - M_{\mathrm{meas,ij}})^2}{\sigma_i^2}, \qquad (2)$$

where σ_i is the measured noise level for the i^{th} BPM.

When fitting an uncoupled model, the parameters varied include the magnet gradients, the BPM gains, the steering magnet calibrations, and the electron energy shifts from changing horizontal steering magnets. When a horizontal steering magnet strength is changed there is an electron energy shift proportional to the dispersion at the steering magnet. Because there is no direct way to measure the dispersion at the steering magnets, $\frac{\Delta E_i}{E}$ is a fit parameter.

When fitting a coupled model, the coupling parts of the response matrix (i.e. the shift in vertical orbit from horizontal steering magnets) are included in the fit data, and additional fit parameters such as quadrupole, BPM, and steering magnet role are varied.

To minimize the number of parameters fit to a measured response matrix, if possible, some magnet gradients are set to zero before measuring the first matrix. For example, the insertion devices are opened, and the sextupoles are turned off, for those storage rings where beam can be stored without sextupoles. The matrix measured without insertion devices and sextupoles is analyzed to calibrate the gradients in the quadrupoles. After measuring this matrix, the sextupoles are turned on and the response matrix is remeasured. For fitting this second matrix, the quadrupole gradients are fixed at the values arrived at from analyzing the first matrix, and the gradients in the sextupoles are fit. Then a third matrix is measured with the insertion devices closed. In this way an accurate model of the full storage ring is derived.

0-7803-4376-X/98/$10.00 © 1998 IEEE

2.2 *Error analysis*

Once LOCO has arrived at a set of magnet gradients for a storage ring, it is natural to ask how accurately these gradients represent the real gradients in the storage ring. The error bars on the fit gradients due to the propagation of random orbit measurement error are fairly straightforward to calculate. Simply measure many consecutive response matrices, analyze each independently, and see how much the fit gradients vary from matrix to matrix. This was done for the NSLS X-Ray Ring analysis, and the variation in the quadrupole gradients for different response matrices was only .04% rms.

This, however, is only a lower bound on the uncertainty in the fit gradients, because it does not include systematic error. With effort, it is possible to reduce the systematic error to the point that, after fitting, the measured and model response matrices agree to very nearly the noise level of the BPMs, but with a system as complex as a storage ring it is practically impossible to completely eliminate systematic error.

With the inevitable and unpredictable systematic error, it is necessary to make additional independent measurements of the fit parameters and of other optics parameters such as tunes, beta functions and dispersion to confirm that the fit model does accurately represent the storage ring. Many such measurements have been made [1, 4], and the results indicate that the LOCO analysis can produce a model that does represent the actual storage ring to very nearly the accuracy determined by random error alone.

2.3 *Restoring design periodicity*

Section 2.1 described a method of applying LOCO to determine the gradient errors in each magnet. This section will describe applying LOCO to find those quadrupole power supply settings that best compensate for these errors and restore the design periodicity.

First, use LOCO as described in section 2.1 to generate a model with the correct BPM gains, steering magnet calibrations, and energy shifts. Then set all the model gradient errors such as gradients in insertion devices and sextupoles to zero. Refit the response matrix varying only those gradients that can be varied independently in the storage ring. For example, if some set of quadrupoles are powered by a single power supply, then gang the model gradient for that set in the fitting. The resulting gradients will show some break in periodicity that best reproduces the break in periodicity of the real ring. If opposite changes are applied to the storage ring, a periodic lattice is restored as close as possible. In essence, the storage ring is adjusted to maximize the periodicity of the response matrix.

3 APPLICATIONS

3.1 *X-Ray Ring horizontal emittance reduction*

LOCO was originally written in order to understand the distortion of the measured horizontal dispersion, η_x, in the NSLS X-Ray Ring [1, 3]. The dispersion in the dipole magnets is critical in determining the horizontal emittance. A synchrotron light source requires minimum emittance to maximize the source brightness, so it was important to understand and correct the η_x distortions.

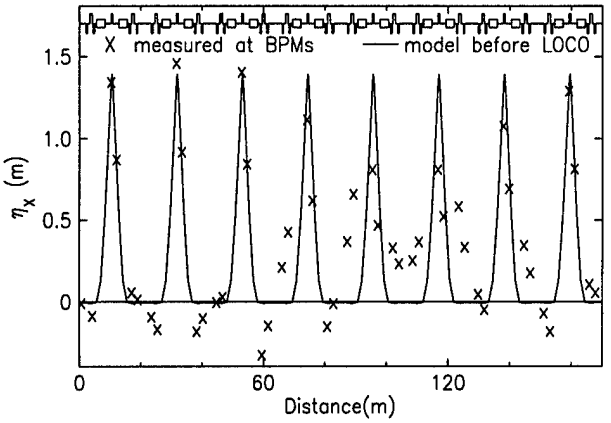


Figure 1: Before applying LOCO in the X-Ray Ring, the measured η_x differed significantly from the model.

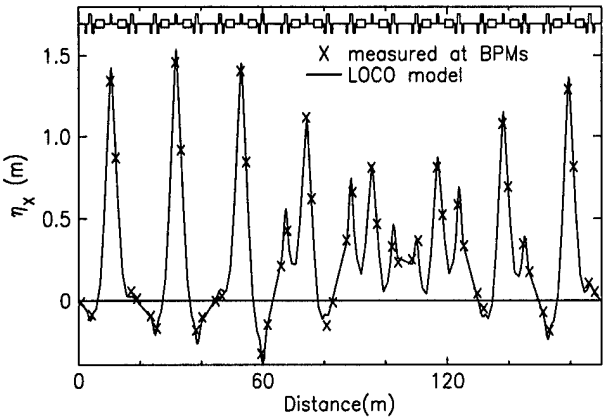


Figure 2: After the model was fit to the measured response matrix, the model also accurately predicted the measured η_x.

Fig. 1 compares the measured horizontal emittance compared to the model prior to applying LOCO. Clearly η_x differed significantly from the design 8-fold periodicity. Fig. 2 shows the measurement compared with the model fit by LOCO to the response matrix. The fit model revealed that the source of the η_x distortion was primarily gradients in the sextupoles due to horizontal offsets of the closed orbit from the sextupole magnetic centers. The sextupoles are located on either side of the single quadrupole between the dipoles. In order to correct for the gradient errors from the sextupoles, trim supplies were installed on the single quadrupoles in each of the eight superperiods. (Changing the orbit in the sextupoles was not an viable option, because it would have required realigning the synchrotron radiation beamlines.)

With the quadrupole trim supplies powered to restore the periodicity of η_x and using LOCO as a guide in setting the quadrupole family gradients, we were able to implement a new low emittance lattice design in the X-Ray Ring [10]. Fig. 3 illustrates the performance improvement achieved. The smaller horizontal profile resulted in increased source brightness.

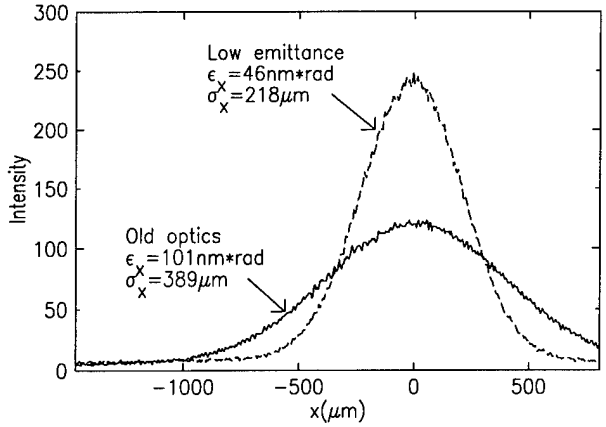


Figure 3: The reduction in X-Ray Ring horizontal beam profile as measured by an x-ray pinhole camera.

3.2 *ALS injection improvement*

LOCO was used to analyze the optics at the ALS to determine the source of the large vertical beta-beating that had been observed even with all insertion devices open. For detailed discussion of the work at ALS, see [4] and [6]. The fit model showed the expected beta-beats (see Fig. 4), and indicated that large variations in the gradients of the vertically focusing quadrupole family was the cause of the optics distortion. This quadrupole family has separate power supplies for each of the 24 magnets. Subsequent measurement of the currents from each power supply confirmed that the supplies were not regulating to specification and that LOCO had accurately predicted the variation from magnet to magnet (see Fig. 5).

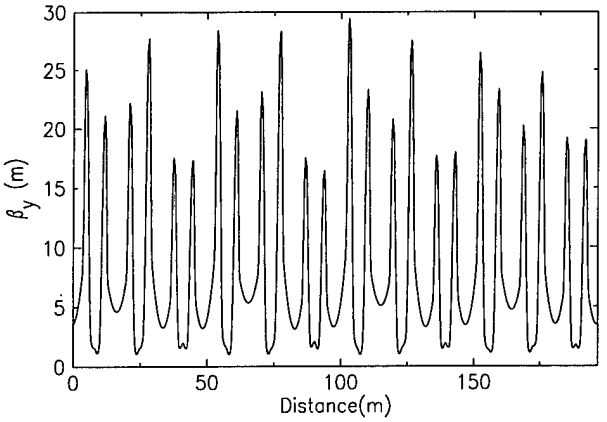


Figure 4: ALS vertical beta before correction with LOCO.

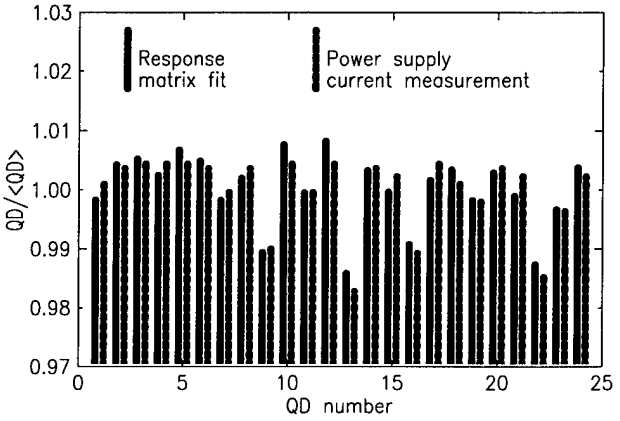


Figure 5: The variation in the fit gradients in the 24 QD quadrupoles agreed with the subsequent measurement of the current to each QD.

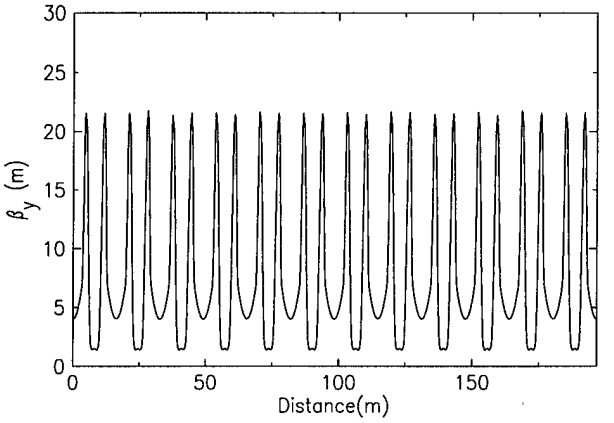


Figure 6: ALS vertical beta after correction with LOCO.

LOCO was then used as described in section 2.3 to restore the periodicity of the optics. Fig. 6 shows β_y of the model fit to the measured response matrix after restoring periodicity. Injection efficiency with the new optics improved by about a factor of two, presumably due to increased dynamic aperture with the periodic optics.

3.3 *VUV Ring lifetime improvement[5]*

The VUV Ring had also been known for some time to have large errors in both β_x and β_y. Two of the four dispersion-free straight sections in the VUV Ring have insertion devices. The vertical focusing of the insertion devices breaks the design four-fold periodicity, so the quadrupoles in the insertion device straights were put on separate power supplies to provide the capability of restoring the periodicity of the β-functions. Nonetheless, measurements indicated large beating of the β-functions. LOCO was used to find the gradient in each quadrupole, each sextupole, and the vertical focusing strength of each insertion device. The resulting model showed that the optics that had been used for operations had distortions of the β-functions of as much as

±35 and ±25 percent horizontally and vertically (see Fig. 7).

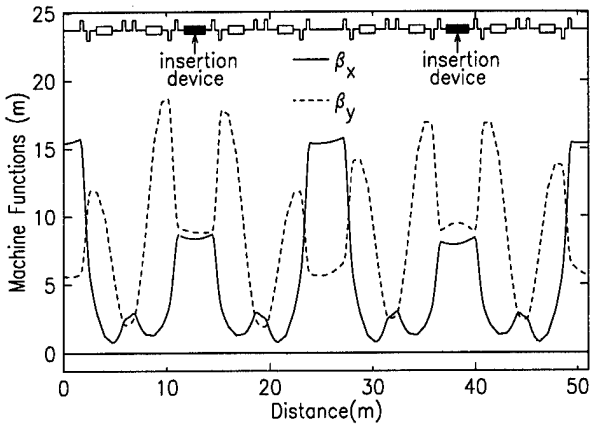


Figure 7: The β-functions in the NSLS VUV Ring did not have the design four-fold periodicity.

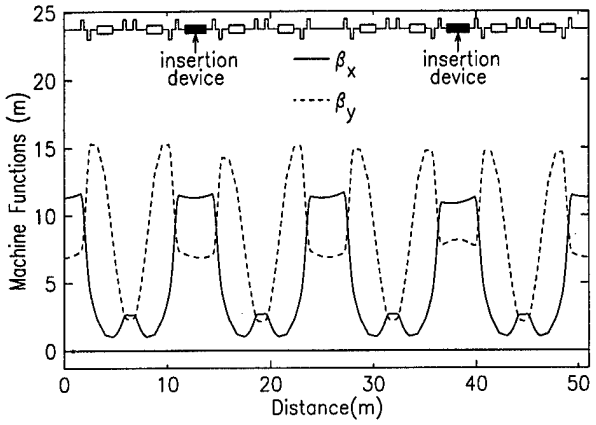


Figure 8: LOCO was able to find a set of quadrupole strengths that very nearly restored the design periodicity of the VUV Ring despite the strong vertical focusing of the insertion devices.

LOCO was then used as described in section 2.3 to restore the periodicity of the optics. Fig. 8 shows the β-functions of the model fit to the measured response matrix after restoring periodicity. The strong vertical focusing effect of the second insertion device is evident from the negative second derivative of β_y in that insertion device straight section. Despite this strong perturbation to the optics, a solution was found which very nearly restored the design four-fold periodicity of the β-functions. When this solution was implemented, the measured beam lifetime increased by 18% while both the measured horizontal and vertical emittances decreased by a few percent.

3.4 *SRRC orbit steering improvement*

The LOCO analysis of the SRRC showed that the storage ring optics is quite close to design with no large gradient errors [7]. The analysis, however, did reveal large variations in the gains of the BPMs as well as some mis-wiring of steering magnets (two magnets were wired backwards and two others had their power supplies swapped). The BPM gains varied from BPM to BPM by a factor of 3 horizontally and 2 vertically. Figs. 9 and 10 show the measured horizontal dispersion before and after correcting for the BPM gain errors derived by LOCO. Much of the apparent distortion in the measured dispersion in Fig. 9 was caused by gain errors in the BPMs.

Both the steering magnet mis-wiring and BPM gain errors were subsequently corrected, resulting in improved orbit control.

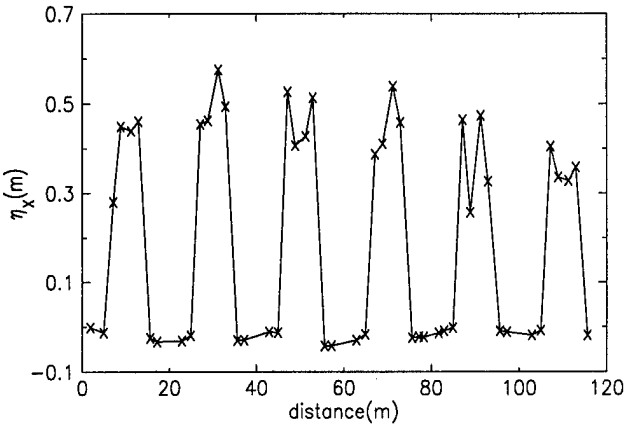


Figure 9: Measured η_x at SRRC without BPM gain error correction.

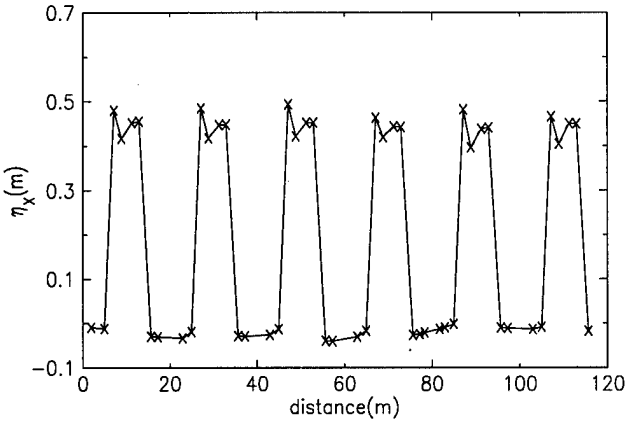


Figure 10: Measured η_x at SRRC after correcting for the BPM gain errors derived by analyzing the response matrix.

3.5 *X-Ray Ring coupling correction*

The coupling terms (i.e. the shift in vertical orbit with horizontal steering magnets) were included in the analysis of the X-Ray Ring response matrix. The result was fitted values for the skew gradients in each quadrupole and sextupole as well as the rotational alignment of each steering magnet and BPM. The steering magnet and BPM alignment data has been used to improve the X-Ray Ring coupling correction algorithm. The coupling correction algorithm uses the

shift in vertical closed orbit with horizontal steering magnets as a measure of the horizontal to vertical betatron coupling [11]. The skew quadrupoles are adjusted to simultaneously minimize these orbit shifts as well as the vertical dispersion. This algorithm proved quite successful, but it suffered from the limitation that some of the measured vertical orbit shift was not due to coupling, but was a result of steering magnet and BPM roles. Once these roles were determined by LOCO, that part of the measured vertical orbit shift could be removed. In this way the skew quadrupoles were set to only remove the part of the orbit shifts associated with skew gradient errors.

Fig. 11 shows the measured vertical profile before and after applying this coupling correction technique.

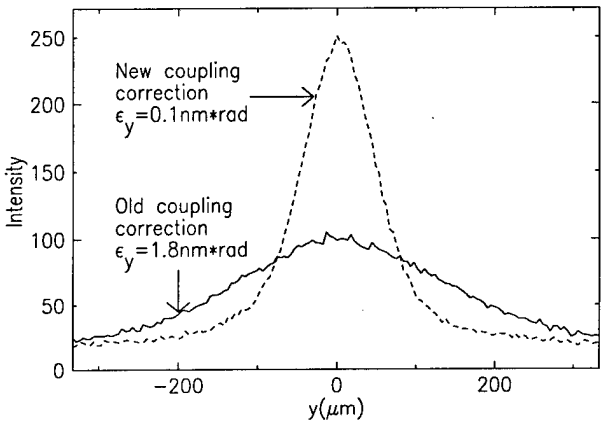


Figure 11: The reduction in X-Ray Ring vertical beam profile as measured by an x-ray pinhole camera.

4 CONCLUSION

Results from NSLS, ALS, and SRRC have shown that the accurate optics model that can be derived from analyzing the measured orbit response matrix can be a valuable tool for maximizing storage ring performance.

5 ACKNOWLEDGEMENTS

I would like to thank Jeff Corbett, Sam Krinsky, Martin Lee, and David Robin for stimulating discussions during the development of LOCO.

The applications of the LOCO code summarized in this paper were the result of collaborations with David Robin, Greg Portmann, Hiroshi Nishimura, and Alan Jackson at ALS with Chin-Cheng Kuo, Peace Chang, and K.T. Hsu at SRRC, and with Steve Kramer at NSLS.

This work was performed under the auspices of the U.S. Department of Energy.

6 REFERENCES

[1] J. Safranek, 'Experimental Determination of Storage Ring Optics Using Orbit Response Measurements', Nucl. Instr. and Meth. A388, (1997) pg. 27.

[2] W.J. Corbett, M.J. Lee and V. Ziemann, 'A Fast Model-Calibration Procedure for Storage Rings', Stanford Linear Accelerator Center, SLAC-PUB-6111, May, 1993.

[3] J. Safranek and M.J. Lee, 'Calibration of the X-Ray Ring Quadrupoles, BPMs, and Orbit Correctors Using the Measured Orbit Response Matrix', *Proceedings of Orbit Correction and Analysis in Circular Accelerators Workshop*, AIP Conf. Proc. No. 315, (AIP, New York, 1994), 128–136.

[4] D. Robin, J. Safranek, G. Portmann and H. Nishimura, 'Model Calibration and Symmetry Restoration of the Advanced Light Source', *Proceedings of the 1996 European Particle Accelerator Conference*.

[5] J. Safranek and S.L. Kramer, 'Experimental Calibration of VUV Ring Optics', *These proceedings.*

[6] D. Robin, J. Safranek, W. Decking, and H. Nishimura, 'Global Beta-beating Compensation of the ALS W16 Wiggler', *These proceedings.*

[7] C.C. Kuo, J. Safranek, H.P. Chang and K.T. Hsu, 'Experimental Calibration of SRRC Lattice Optics', *These proceedings.*

[8] G. LeBlanc and W.J. Corbett, 'Accelerator Modeling at SPEAR', *These proceedings.*

[9] H. Grote and F.C. Iselin, The MAD Program, Version 8.1, CERN/SL/90-13, June 17, 1991.

[10] J. Safranek, 'A Low Emittance Lattice for the X-Ray Ring', *Proceedings of the 1995 IEEE Particle Accelerator Conference*, 266-268.

[11] J. Safranek and S. Krinsky, 'Plans to Increase Source Brightness of NSLS X-Ray Ring', *Proceedings of the 1993 Particle Accelerator Conference*, 1491-1493.

STATUS OF THE HIGH BRILLIANCE SYNCHROTRON LIGHT SOURCE BESSY - II*

E. Jaeschke for the BESSY II Project Team†, BESSY, Rudower Chaussee 5, Geb. 15.1, D-12489 Berlin, Germany

Abstract

The High Brilliance Synchrotron Light Source BESSY II under construction at the WISTA Science and Technology Park at Berlin-Adlershof has by now passed major milestones with the completion of the injector complex. On April 3rd, 1997 a 50 MeV electron beam was stored on a stable orbit in the 10 Hz booster synchrotron. As all magnets and most of the other necessary hardware have successfully passed acceptance tests installation of the 240 m DBA storage ring in 16-fold symmetry has started. Stored beam is expected for the 2nd quarter of 1998. The paper describes the present status of the project.

1 INTRODUCTION

The High Brilliance Synchrotron radiation facility BESSY II [1] is a 3rd generation light source in the vacuum ultraviolet to soft X-ray range. Based on a very flexible 16 cell DBA lattice the 240 m circumference ring provides long dispersion free straight sections with alternating high and low horizontal beta functions for up to 14 insertion devices. The projected emittance at 1.7 GeV will be 5 nm rad. Various types of undulators, wigglers and superconducting wave length shifters (WLS) under construction or already finished will provide synchrotron radiation with brilliance values exceeding $3*10^{18}$ [photons/sec/(mm mrad)^2 /0.1%BW] for undulators. Performance is optimized for the spectral range from VUV to soft x-ray while harder radiation with excellent quality is available at the superconducting devices. So once fully operational BESSY II will be a very versatile and valuable tool equally well suited for fundamental research and industrial application. Commissioning of the light source will start July 1998 and regular user operation will be available from 1st of January 1999.

2 BUILDINGS

After two and a half years of civil engineering the buildings for BESSY II are basically finished. Figure 1 gives an aerial view of the facility as of April 1997.

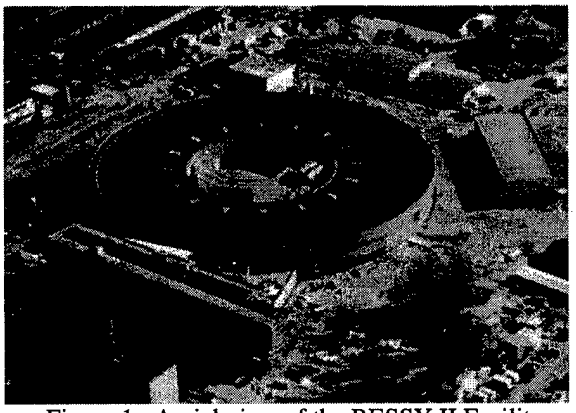


Figure 1: Aerial view of the BESSY II Facility

The 120 m diameter hall houses the accelerators, the experimental area and "non-noisy" infrastructure installations on all together 12000 square meters. To control possible vibrations from cultural noise the experimental area and the storage ring tunnel share a heavily steel reenforced monolytic concrete plate of 60 cm thickness as foundation. Extreme care was taken in compressing the sand and gravel soil under the plate. The synchrotron tunnel as well as most of the technical equipment are situated on a separate plate to have an efficient decoupling. Vibration measurements done in the storage ring tunnel and the experimental hall with all infrastructure equipment (pumps, compressors, air conditioning, etc.) and the White circuits of the synchrotron running showed vibration amplitudes typically less than 100 nm in the frequency range of 1 to 60 Hz.

* Funded by the Bundesministerium für Bildung, Wissenschaft, Forschung und Technologie and by the Land Berlin.

† M. Abo-Bakr, W. Anders, B. Bauda, R. Bakker, J. Bahrdt, T. Becker, R. Bender, T. Bergl, N. Bergel, T. Birke, R. Brühl, K. Bürkmann, B. Dittmann, V. Dürr, H. Dreßler, J. Eigel, F. Falkenstern, D. Faulbaum, J. Feikes, W. Gericke, T. Görgen, M. V. Hartrott, K. Hennig, H.G. Hoberg, S. Horn, S. Khan, A. Knoch, J. Kolbe, D. Krämer, S. Küchler, B. Kuner, B. Kuske, P. Kuske, J. Kuszynski, T. Knuth, R. Lange, K. Ludwig, M. Loßmann, B. Martin, M. Martin, S. Mhaskar, T. Mayer, D. Müller, I. Müller, R. Müller, K. Ott, H. Prange, J. Rahn, F. Radecke, D. Richter, H. Rüdiger, L. Scanu, T. Schneegans, E. Schmitz, , G. Schindhelm, D. Schüler, K. Seliger, D. Simmering, U. Strönisch, L. Schulz, B. Thamm, S. Vogt, E. Weihreter, G. Wüstefeld.

0-7803-4376-X/98/$10.00 © 1998 IEEE

3 COMMISSIONING OF THE SYNCHROTRON

The full energy 10 Hz rapid cycling booster synchrotron [2] of 96 m circumference has a FODO lattice in 16 fold symmetry. Figure 2 is a view onto the completed machine.

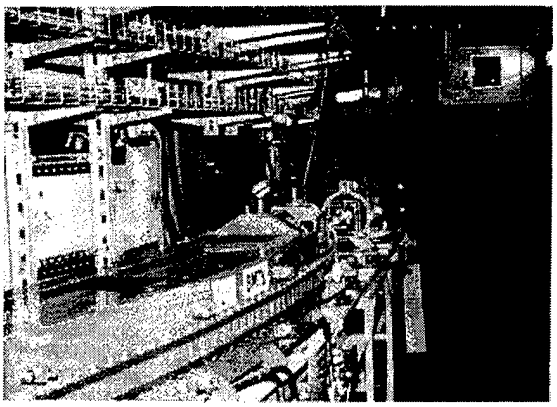


Figure 2: The completed BESSY II synchrotron.

The magnet system [3] manufactured at the Budker Institute of Nuclear Physics, Novosibirsk was installed in mid 1996 just after the tunnel had been handed over by the construction company. After completion of the vacuum system in late October and the installation of power supplies, rf-system, kickers and septa, a first beam from the 50 MeV race track microtron could be injected on April 3rd . Immediately after injection tests had started a signal of a stably stored electron beam could be detected from a strip line monitor with no orbit corrections applied at all. (See Fig. 3)

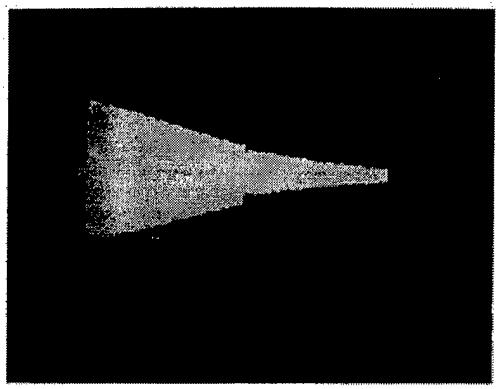


Figure 3: Strip line signal of the first stored 50 MeV electron beam in the synchrotron on April 3rd 1997. Two injections 100 ms apart are visible

The oscilloscope picture shows that electrons are circulating for 100 ms before stopped when the next bunch is injected from the race track microtron. After applying orbit correction beam life time is now approximately 4 minutes corresponding to a vacuum pressure of P = 8 10^{-8} HPa. Energy ramping as the next milestone up to the final value of 1.9 GeV is under preparation.

4 STATUS OF THE STORAGE RING

Parallel to the commisssioning of the booster synchrotron work on the storage ring is progressing well aiming for a first stored beam mid of 1998. The first of the 16 achromats has been assembled already. (See figure 4)

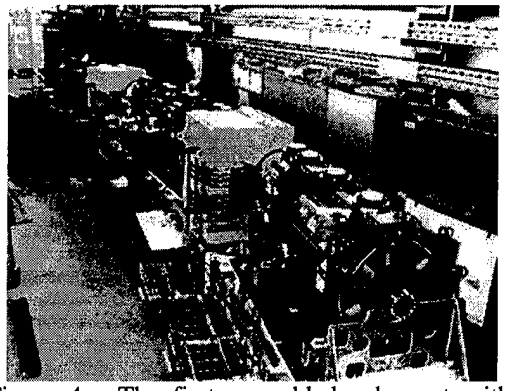


Figure 4: The first assembled achromat with multipole lenses preadjusted on 3 girders and the two dipole magnets inbetween located on individual stands.

4.1 Storage Ring Magnets

For all magnets of the storage ring (144 quadrupoles, 112 sextupoles and 32 dipoles) magnetic measurements have been done in house as for example mapping of the dipole fields and determination of the multipole coefficients for the quadrupoles and sextupoles. The data were used for sorting of magnets [4] in order to minimize the integrated field errors. While the closed orbit amplitudes can be reduced to 0.5 mm rms by proper positioning of the dipoles, (see figure 5) , the ß-beat is decreased from 60% to about 1% by sorting the quadrupoles. Sextupole field errors turned out to be insignificant to reduction of dynamic aperture thus these magnets are positioned without sorting.

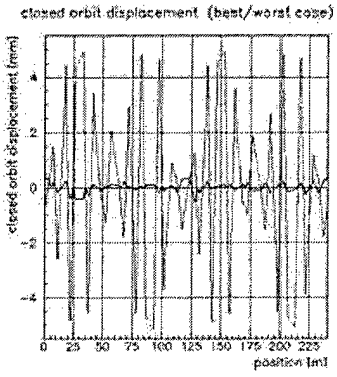


Figure 5: Closed orbit distortion for best/worst sorting

4.2 Vacuum System

The vacuum chambers for the storage ring manufactured from DIN 4429 steel with explosion

bonded copper liners as radiation absorbers are already available in sufficient numbers for installation. Figure 6 shows a special outlet chamber following dipole-1 in an achromat.

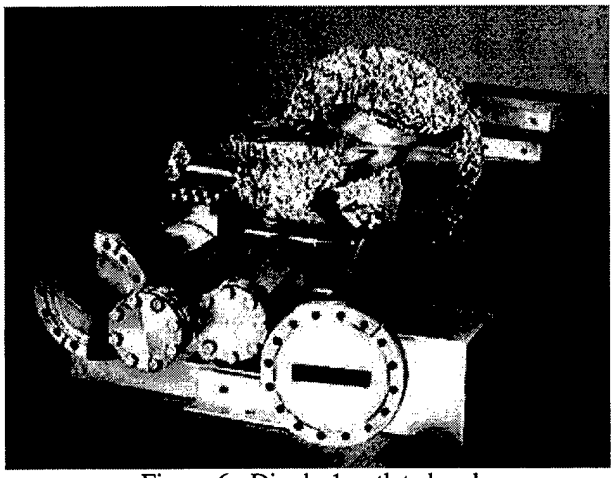


Figure 6: Dipole-1 outlet chamber

4.3 RF-System

The BESSY II rf-system consists of 4 DORIS type 500 MHz single cell resonators fed by individual 75kW clystron transmitters. All transmitters are in house and are presently commissioned.

4.4 Control System

The control system [5] based on the EPICS standard has proven its power by successfully running in all parts of the accelerator complex commissioned up to now. Figure 7 shows the control panel for the microtron injector.

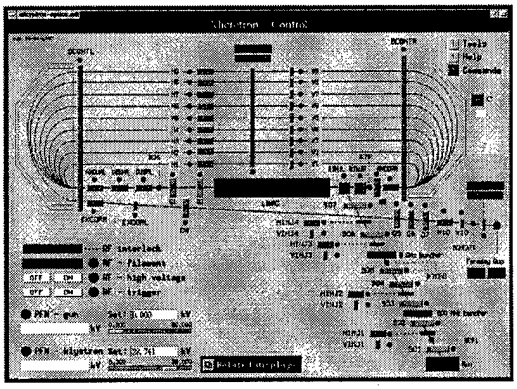


Figure 7: EPICS control panel of the race track microtron

4.5 Insertion Devices

Offering 14 straight sections BESSY II is optimized for insertion devices (IDs) . So various IDs are under construction at Berlin-Adlershof. U180, an electromagnetic device covering the spectral range from 25 to 1900 eV is on the test bench, while the hybrid undulator U49 (see Figure 8) has just been completed. It will deliver radiation with a brilliance of $3x10^{18}$ [photons/sec/(mm mrad)^2/0.1%BW] at about 300 eV.

A 6T WLS presently operating at BESSY I for LIGA applications will cover the range 6 to 50 keV.

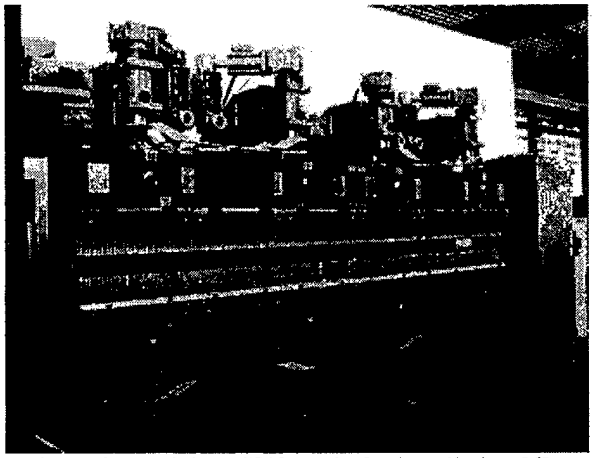


Figure 8: Undulater U49 ready for installation [6]

5 ACKNOWLEDGEMENTS

The author gratefully acknowledges help and advice of many colleagues from accelerator laboratories world wide and enthusiastic and skillful work of the BESSY staff.

REFERENCES

[1] E. Jaeschke, D. Krämer, B. Kuske, P. Kuske, M. Scheer, E. Weihreter, G. Wüstefeld, *Lattice Design for the 1.7-GeV Light Source BESSY II,* Proceedings of the 1993 Particle Accelerator Conference,Washington, D. C. , 1993, p. 1474

[2] M. Abo-Bakr, W. Anders, K. Bürkmann, V. Dürr, W. Gericke, M. v.Hartrott, H. Hoberg, E. Jaeschke, T. Knuth, D. Krämer, B. Kuske, P. Kuske, M. Martin, R. Müller, J. Rahn, D. Richter, T. Schneegans, L. Schulz, G. Wüstefeld, E. Weihreter, I. Chertok, G. Kraynov, S. Michailov, B. Sukhina, M. Tuinov, *The BESSY II Booster Synchrotron,* Proceeding of the 5th EPAC, Barcelona, 1996, p. 527

[3] T. Knuth, D. Krämer, E. Weihreter, I. Chertok, S. Michailov, B. Sukhina, *The Magnet System for the BESSY II Injector Synchrotron,* Proceedings of the 1995 Particle Accelerator Conference, Dallas , 1995 p. 1316

[4] M. Abo-Bakr, G. Wüstefeld, *Sorting of Magnets for the BESSY II Booster and Storage Ring* , Proceeding of the 5th EPAC, Barcelona, 1996, p. 1314

[5] J. Bergl, B. Kuner, R. Lange, I.Müller, R. Müller, G. Pfeiffer, J. Rahn, H. Rüdiger, , *Embedded Controllers, Field Bus and a Modular IO Concept: Central Elements of BESSY II Controls,* this conference

[6] J. Bahrdt, A. Gaupp, G. Ingold, M. Scheer, *Status of the Insertion Devices for BESSY II,* Proceeding of the 5th EPAC, Barcelona, 1996, p. 2535

CANADIAN LIGHT SOURCE PROPOSAL

L.O. Dallin and D.M. Skopik, Saskatchewan Accelerator Laboratory,
University of Saskatchewan, 107 North Road, Saskatoon SK, Canada S7N 5C6

Abstract

The storage ring for a 2.9 GeV Canadian Light Source has been designed. The lattice is composed of twelve compact DBA cells resulting in a ring that is 148 meters in circumference with twelve drifts of 4.5 meters for the inclusion of insertion devices. The emittance is less than 20 nm-rad, resulting in radiation brightness competitive with other "third generation" sources. Details of orbit correction, beam stability and lifetime and the effect of insertion devices have been investigated. The RF requirements have been defined and preliminary magnet designs have been done.

The light source will operate with full energy injection and the injection scheme has been fully defined. Injection includes a 300 MeV linear accelerator, low energy transfer line, booster synchrotron and high energy transfer to the storage ring. With this configuration it will be possible to operate the storage ring with beam currents up to 500 mA, resulting in a source of very intense light over a broad range of photon energies. For example, with a state of the art undulator, it will be possible to produce 20 keV photons with a brightness close to 10^{18} photons/s/mm^2/mrad^2/0.1% bandwidth.

1 INTRODUCTION

Since the creation of the Canadian Institute for Synchrotron Radiation (CISR), in 1990, Canadian synchrotron radiation (SR) users and accelerator physicists have been actively involved in designing and promoting a light source that would satisfy the needs of most users. After several workshops involving the Canadian user community, it was decided that Canada required a source comparable to present third generation machines, capable of operating at a beam energy of 2.5 GeV. To keep the costs as low as possible design efforts concentrated on producing a lattice which was as compact as possible while keeping a large number of straight sections for insertion devices.

In May, 1996, an international peer review committee chose the Saskatchewan Accelerator Laboratory as the site for the Canadian Light Source (CLS). This committee recommended that the beam energy be increased to 2.9 GeV in order to accommodate hard X-ray users. A proposal incorporating this recommendation [1] was submitted to the Natural Sciences and Engineering Research Council (NSERC) which unanimously endorsed the peer review results and recommended that the CLS be built and located at SAL. We are optimistic that funding will be forthcoming in the near future.

The increase to 2.9 GeV was accomplished with a minor modification to the lattice and by upgrading the injection booster. This "final" design will be discussed below.

2 LATTICE

The CLS requires a machine with brightness comparable to existing "third generation" machines, with ten straight sections available for the inclusion of insertion devices (IDs). At the same time it is desirable to keep the machine as small as possible to keep the overall cost low. Both the triple bend achromat (TBA) and double bend achromat (DBA) were initially considered. For a given machine circumference the TBA has lower emittance, but the DBA, with its smaller cell size, can accommodate more straight sections. In the lattices studied [2,3], the DBA had better dynamic aperture, which would improve operations at higher currents. Consequently, the DBA cell structure was chosen to produce a compact design.

To produce photons of energy up 20 keV with high brightness, the CLS will operate with beam energies up to 2.9 GeV. At this beam energy the dipole field strengths are approaching 1.5 T. To have straight sections available for injection and for RF cavities, the total number of cells is twelve.

To create a compact cell structure, only three families of quadrupoles are used in each cell. For additional focusing, a gradient was introduced into the dipole magnets. This gave four focusing parameters to optimize the cell parameters. These parameters were adjusted to create the desired horizontal and vertical tunes, ν_x and ν_y; the horizontal betatron amplitude, β_x, in the ID sections; and the horizontal dispersion, η_x. During this process the lengths of the quadrupoles were adjusted so that the maximum pole tip field did not exceed 5 kG.

To reduce the emittance of the lattice, the requirement that the cell be an achromat was relaxed and some dispersion was introduced into the straight sections. During the optimization, the vertical betatron function, β_y, in the straight sections was allowed to float, but the final value resulted in a favourable amplitude. Finally the dipole gradient was "frozen", leaving three free parameters to adjust the two tunes and either β_x or η_x.

To control the chromaticity of the lattice, two sextupole magnets are included between the two dipole magnets. The resulting lattice is shown in Figure 1a where a half cell is shown. The complete cell is obtained by reflective symmetry about the centre of the sextupole on the right. The machine functions for a complete cell are shown in Figure 1b, with the dipoles and quadrupoles shown schematically below.

Some important parameters for the CLS are given in Table 1. The ring circumference of 147.377 m is small for a low emittance lattice operating at 2.9 GeV, resulting in savings in construction cost while still providing a bright source of photons up to x-ray energies from 10 possible ID locations. An earlier version of this lattice [4], with 3.5 meter

0-7803-4376-X/98/$10.00 © 1998 IEEE

straights, was only 127 m in circumference. The DIMAD [5] input for the present lattice is given in Appendix I.

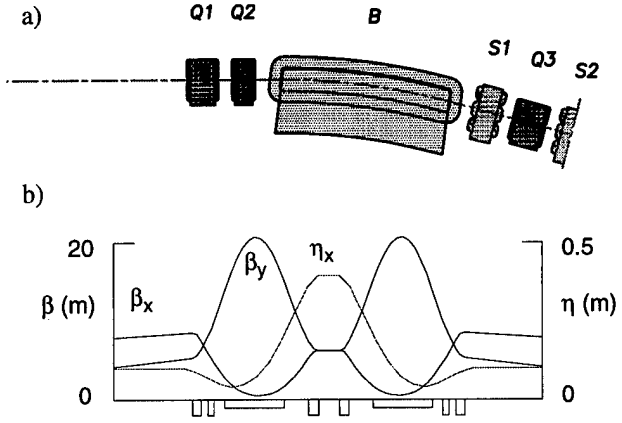


Figure 1 a) Physical layout of one half cell. b) Machine functions for one full cell.

Table 1. CLS machine parameters

Circumference	m	147.377	
Periodicity		12	
Optics			
ν_x (tune)		10.22	
ν_y		3.26	
Straights		12	
length	m	4.5	
β_x (betatron amplitude at centre)	m	8.0	
β_y	m	4.2	
η_x (dispersion)	m	0.15	
RF Cavity			
frequency	MHz	476	
voltage	MV	2.25	
E (energy)	GeV	1.5	2.9
B_{dipole}	Tesla	0.771	1.490
Total Rad. Power	kW @500 mA	35	482
Rad. Power/m	kW/m (dipoles)	0.86	11.81
ε_x (emittance)	nm-rad	4.4	16.3
δ (energy spread)	%	0.060	0.115
Bunch length (full)	ps	43	74

The optimization of both the brightness and critical energy for the CLS lattice is shown in Figure 2. Brightness and critical energy are plotted for several third generation sources now in existence. For the sources shown, brightness increases proportional to the machine circumference. The CLS is especially well optimized for critical energy, especially among the smaller machines. The values shown assume the same ID on each machine, operating at the same beam current and normalized to Spring-8 = 1. The CLS parameters are those given in this paper. For the other machines, parameters are taken from reference [4], with the exception that the ALS is evaluated at 1.9 GeV. For the ESRF the high β straights were considered. The ESRF lattice also has low β straights optimized for short IDs.

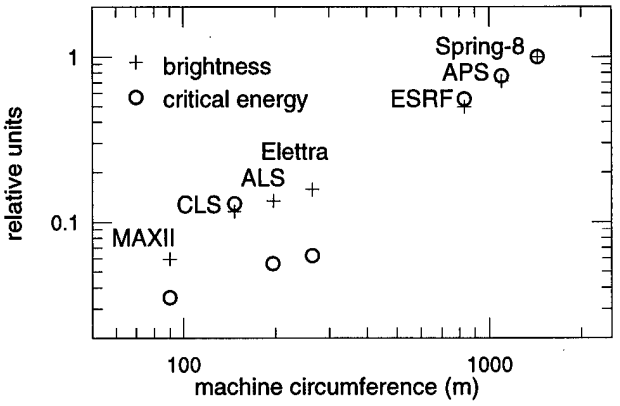


Figure 2: Relative brightness and critical energy vs machine circumference.

The tunability of the lattice was checked by changing the transverse tunes by ±1 , while keeping the dispersion fixed. This is done by varying the three families of quadrupoles. The lattice is stable over all combinations of retuning, but the beam size is optimum for the nominal tunes given in Table 1.

The effects of possible dipole gradient errors were also checked. This showed that systematic errors up to 5% in the dipole gradient and random errors up to 2% are tolerable.

The horizontal betatron amplitude, β_x, in the centre of the straights is as small as possible while maintaining enough amplitude for horizontal injection. The horizontal beam size, $\sigma_x = (\varepsilon_x\beta_x + \delta^2\eta_x^2)^{1/2}$, is 18% smaller than for the lattice tuned for no dispersion in the straights. The vertical size is 26% smaller.

The RF frequency was chosen to be one-sixth of 2856 MHz, the frequency of the existing 300 MeV linac injector. The voltage of 2.25 MV is adequate for Touschek lifetimes of over 80 hrs at 2.9 GeV.

Magnets, including septa and kickers, have been designed with parameters comparable to elements at existing facilities. The ALS design report [2] was especially helpful. Similar to the ALS design, sextupole magnets will have windings so they can be used as both horizontal and vertical orbit correctors. At this time, the possibility of using back leg windings on one family of quadrupoles (Q1) is being investigated. With this set-up there will be five horizontal and three vertical correctors per cell.

3 INJECTION SYSTEM

Injection into the CLS will be done with a full energy booster. The layout of both rings is shown in Figure 3. Injection into the booster will be from the existing 300 MeV electron linac at the Saskatchewan Accelerator Laboratory. The linac is located in a vault which will be 6.5 m below the level of the booster.

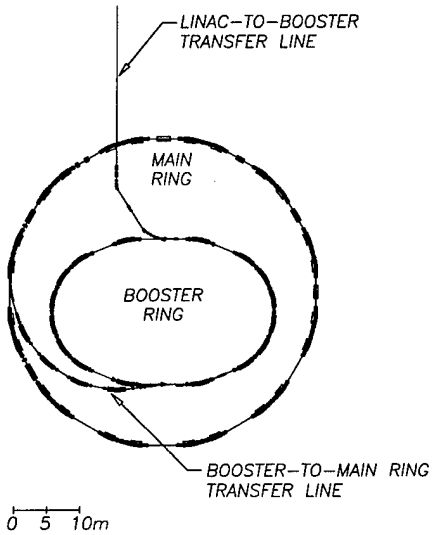


Figure 3: Layout of main ring, booster and transfer lines.

To allow time to ramp injection and extraction kickers, a 126 ns pulse train will be injected into the booster, filling 60 out of 144 buckets. Successive pulse trains will be stacked in the main. ring filling 180 of 234 buckets. Accounting for transmission efficiencies throughout the injection process, 15 mA of current should be injected into 60 buckets of the main ring during each injection cycle. To reach circulating currents of 500 mA, 97% of the beam in the ring must be retained during each cycle. Analyses [6] of beam instabilities indicate that 500 mA of current will introduce no bunch lengthening or emittance growth. At these currents, however, a few coupled bunched modes may need to be suppressed.

4 RADIATION CHARACTERISTICS

For an initial compliment of beamlines, six IDs and five bend magnets will be in service on the CLS. The IDs have been selected to cover a broad range of photon energies and brightness or flux. They include a single pole superconducting wiggler at 5.1 T, a 15 pole wiggler at 1.4 T, and four undulators with periods ranging from 3.6 to 19.2 cm. The undulators are all about 3 m long.

The ideal brightness curves for the IDs and the bend magnets (dipoles) are shown in Figure 4. All are for 2.9 GeV operation except where indicated. The beam size has been evaluated at the center of the straight sections for the IDs and at the centre of the bend magnets for those curves. For the undulators, harmonics up to n = 5 have been evaluated. The K values for the undulators range from K = 1 to K = λ_u, where λ_u is in cm. This results in a minimum gap of 9 mm for the 3.6 cm undulator assuming neodymium-iron permanent magnets.

Also shown in Figure 4 is a curve for a 2.0 cm undulator which shows promise in producing high brightness ($\rightarrow 10^{18}$) at photon energies up to 20 keV. For this curve an undulator length of 4 m was used and odd harmonics up to n = 15 included. At K = 2 the gap size is 5 mm. The ideal curve will be somewhat diminished by the energy spread of the electron beam in the ring as well as imperfections in undulator construction. Simulations using the measured fields of an existing undulator (N =70, λ_u = 3.3 cm) and a lattice similar to the CLS show that the n = 13 harmonic can be reduced to about 20% of its ideal value. If the same efficiency can be achieved with a 4 m ID and considering an operating current of 500 mA, a brightness of about one tenth of the plotted value can be expected.

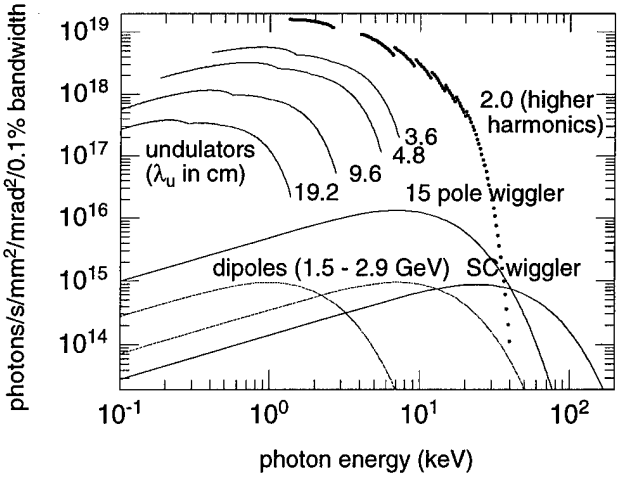


Figure 4: Brightness curves for CLS.

5 REFERENCES

[1] Canadian Light Source, The Proposal for Construction of a National Synchrotron Light Source for Canada, September, 1996 (SAL).

[2] 1-2 GeV Synchrotron Radiation Source. Conceptual Design Report, LBL PUB-5172 Rev. (1986)

[3] A. Andersson, et al. Design Report for the MAX II Ring, MAX-lab, University of Lund, ISSN 0284-1258 (1992)

[4] J. Murphy, Synchrotron Light Source Data Book, Version 4, BNL 42333, May, 1996.

[5] R.V. Servranckx, "USERS' GUIDE TO THE PROGRAM DIMAD", TRIUMF-DN -93-K233

[6] M. Zisman, S. Chattopadhyay and J. Bisognano, "ZAP User's Manual", LBL-21270 ESG-15.

APPENDIX I

Dimad input file:

```
TITLE
CLS
D1:DRIFT,   L=2.24071
D2:DRIFT,   L=0.2
D3:DRIFT,   L=0.3
D4:DRIFT,   L=.3
D5:DRIFT,   L=.2
D6:DRIFT,   L=.2
S1:SEXTUPOLE, L=0.2,K2=-44.341435,APERTURE=.035
S2:SEXTUPOLE, L=0.1,K2=64.73617638,APERTURE=.035
Q1:QUADRUPOLE,L=0.25,K1=2.25622,APERTURE=.035
Q2:QUADRUPOLE,L=0.17,K1=0.435394,APERTURE=.035
Q3:QUADRUPOLE,L=0.28,K1=2.23194,APERTURE=.035
HC:SBEND,L=1.7,ANGLE=0.2617994,E1=0.1308997, &
E2=.1308997, K1=-.46454, HGAP=.025,FINT=0.5
HCELL:LINE=(D1,Q1,D2,Q2,D3,HC,D4,S1,D5,Q3,D6,S2)
CELL:LINE=(HCELL,-HCELL)
RING:LINE=(12*CELL)
```

THE TESLA FREE ELECTRON LASER

J. Rossbach, for the TESLA FEL collaboration
DESY, Notkestrasse 85, D22603 Hamburg, Germany

Abstract

The TESLA Free Electron Laser (FEL) makes use of the high electron beam quality that can be provided by the superconducting TESLA linac to drive a single pass FEL at wavelengths far below the visible. To reach a wavelength of 6 nanometers, the TESLA Test Facility (TTF) currently under construction at DESY will be extended to 1 GeV beam energy. Because there are no mirrors and seed-lasers in this wavelength regime, the principle of Self-Amplified-Spontaneous-Emission (SASE) will be employed. A first test of both the principle and technical components is foreseen at a photon wavelength larger than 42 nanometers.

With respect to linac technology, the key prerequisite for such single-pass, high-gain FELs is a high intensity, diffraction limited, electron beam to be generated and accelerated without degradation. Key components are RF guns with photocathodes, bunch compressors, and undulators. The status of design and construction as well as both electron and photon beam properties are discussed.

Once proven in the micrometer to nanometer regime, the SASE FEL scheme is considered applicable down to Angstrom wavelengths. This latter option is particularly of interest in context with the construction of a linear collider, which requires very similar beam parameters. The status of conceptual design work on a coherent X-ray user facility integrated into the TESLA Linear Collider design is briefly sketched.

1 INTRODUCTION

Most of the information humans receive from their environment are provided by photons. Thus it is not surprising that also for research in natural sciences photons, ranging from radio frequencies to hard γ-rays, provide the most important tool to study nature. For the photon range beyond the narrow optical spectral window up to the hundred keV γ-regime synchrotron radiation has provided over the past thirty years an increase in flux and brightness by more than ten orders of magnitude. The development of storage ring designs with special magnetic components, called wigglers and undulators, over the past twenty years has led to third generation machines specially designed for synchrotron radiation research.

Most recent successes in accelerator development concerning linear accelerators have opened the route to a new jump in photon source quality. X-ray lasers coupled to linear accelerators can possibly provide coherent X-rays with true laser properties through very long undulators. Although such a source of coherent laser-like X-rays would have many applications and the search for such a device has occupied many scientists, a practical solution to this problem has not yet been realized. To be an efficient research tool, such a source would have to provide stable intensities with short pulses and repetition frequencies similar to what is found in optical lasers. Exactly this seems to be possible by using the so-called self amplified spontaneous emission process SASE.

The basic principle [1] makes use of the fact that an electron beam of sufficient quality, passing a long undulator magnet, exponentially amplifies an initially existing radiation field, if the photon wavelength λ_{ph} matches a resonance condition determined by undulator parameters and the beam energy:

$$\lambda_{ph} = \frac{\lambda_u}{2\gamma^2}(1 + K^2) \qquad (1)$$

Here, γ is the electron energy in units of its rest mass, λ_u is the undulator period, K is the undulator parameter, and a helical undulator is assumed. Coherent, stimulated emission is achieved because a bunch density modulation of the electron beam at the optical wavelength builds up during the passage of the bunch through the undulator.

If the desired wavelength is very short, one can, instead of providing the "initially existing radiation field" by a conventional laser, consider the undulator radiation radiated spontaneously in the first part of the undulator as an input signal, see Fig. 1. This principle of Self-Amplified-

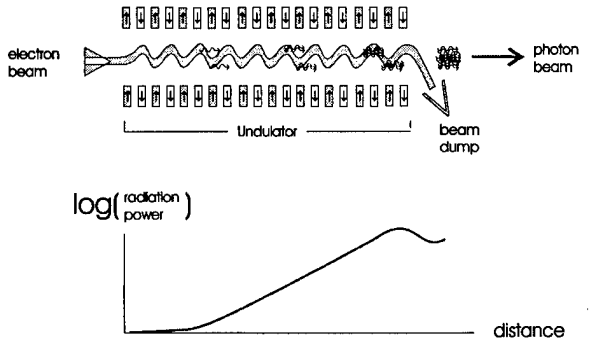


Figure 1: Schematic Diagram of a Single-Pass Free Electron Laser (FEL) operating in the Self-Amplified-Spontaneous-Emission (SASE) mode.

Spontaneous-Emission (=SASE) [2], [3] also does not require the optical cavity resonator normally used in multi-pass, longer wavelength FELs and can hence, in principle, deliver light with wavelength in the Angstrom regime. Compared to state-of-the-art synchrotron radiation sources, one expects a transversely fully coherent beam, larger average brilliance, and, in particular, a pulse length of about

0-7803-4376-X/98/$10.00 © 1998 IEEE

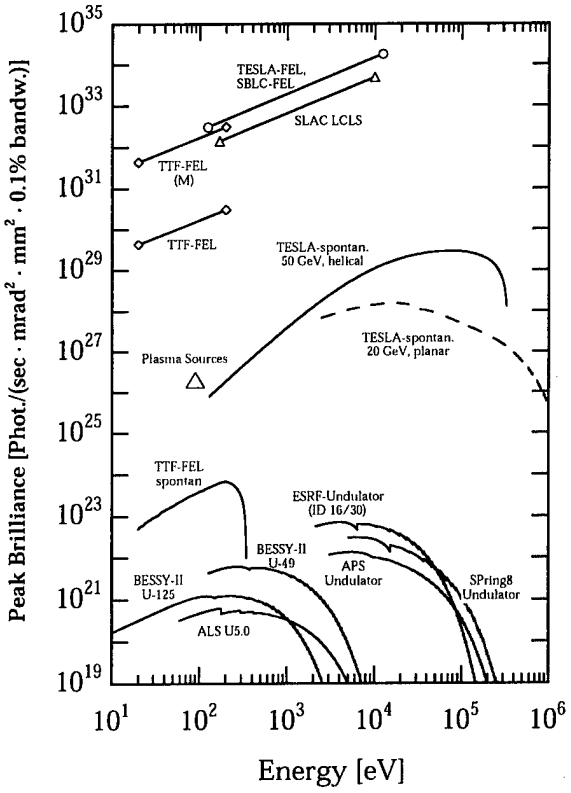


Figure 2: Spectral peak brilliance of X-ray FELs based on SBLC and TESLA linear colliders, together with that of third generation synchrotron radiation sources and the LCLS Free Electron Laser project discussed at SLAC, Stanford, USA [8]. For comparison, also the spontaneous spectra of two XFEL undulators are shown. The peak brilliance of state-of-the-art plasma lasers is also noted.

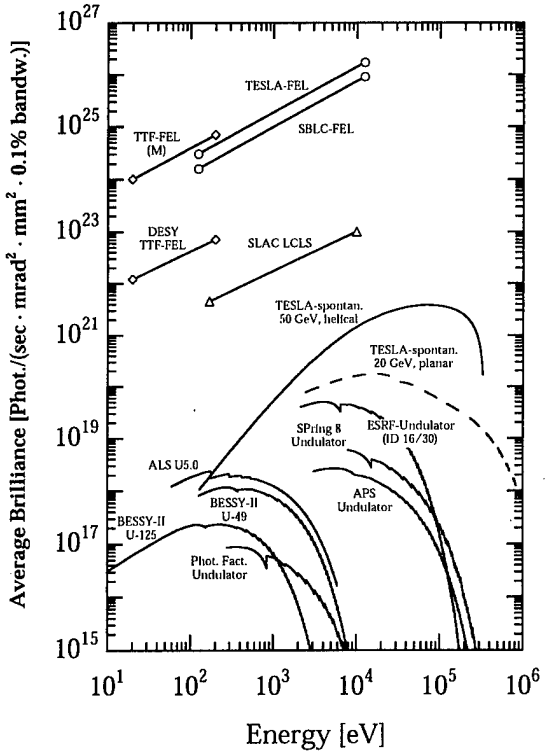


Figure 3: See Fig. 2, but spectral *average* brilliance values are shown.

200 fs FWHM with eight or more orders of magnitude larger peak brilliance, see Figs. 2 and 3. The peak power is in the range 1 – 100 GW. The average brilliance is significantly larger than for the LCLS device proposed earlier[8] mainly because TESLA accelerates a bunch train of ~10000 bunches at a rate of 5 Hz, i.e. the mean repetition rate is much higher. As the SASE FEL is completely independent of atomic excitation levels, it can be tuned over a wide range of wavelengths.

If, according to technical restrictions, undulator periods in the order of few centimeters are assumed, Eq.1 indicates that multi-GeV electron energies are required to achieve photon wavelengths in the Angstrom regime. This goes in parallel with the large energy gain needed in order to sufficiently reduce the beam emittance provided by the injector. Therefore, the electron accelerator required for an X-ray FEL will be a major investment. Also, construction, commissioning and operation of such a device needs a considerable staff of well-trained experts. Last but not least, a large laboratory site will be needed to accommodate the various user facilities. It was concluded, that it will be most attractive to combine an X-ray FEL facility into a linear collider installation [4], and that this will be possible without serious mutual interference.

2 THE TESLA CONCEPT

The different linac concepts considered by linear collider study groups mainly differ with respect to the choice of RF frequency [5]. Roughly speaking, higher RF frequencies offer a higher accelerating gradient, i.e. a shorter tunnel length, at the price of reduced power efficiency and larger beam energy spread. In contrast, low frequency linacs (down to 1.3 GHz for the superconducting TESLA linac) promise very good beam quality, because each electron bunch extracts only a small fraction of the large energy stored in the big cavity volume (small wakefield effects, see section 5). For an X-ray FEL, the highest priority is electron beam quality and large average beam current, while high accelerating gradient might be of minor importance. Finally, it is attractive for many users if a large variability in pulse timing can be offered. In this respect, the TESLA linac again offers an advantage, because a large variety of timing patterns can be realised due to the very large duty cycle of 1%. Thus, for FELs there is a clear preference for low frequency linacs. A Conceptual Design Report on such a combined laboratory has been worked out by the international TESLA collaboration [9]. This paper also discusses

a normal-conducting linac version based on conventional S-band technology (3 GHz), called SBLC.

It is understood that the challenging goal of an 1 Å FEL cannot be achieved within a single step. Thus, a SASE proof-of-principle experiment will be installed at the TESLA Test Facility (TTF), called TTF FEL Phase 1, see Fig. 4. Based on three TESLA accelerating modules, 390 MeV beam energy will allow to reach a photon wavelength of λ_{ph}=42 nm. First operation is scheduled for 1999. A more detailed description and the status is given in Ref. [6].

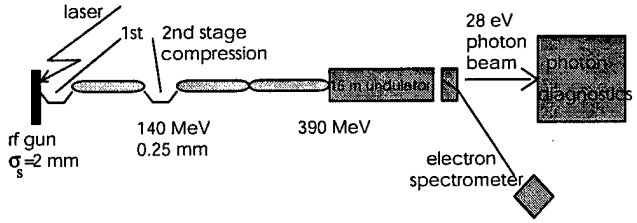


Figure 4: Schematic diagram of the TESLA Test Facility installation including the Phase 1 SASE FEL components.

As a second phase, an energy upgrade to 1 GeV has been approved which will bring the wavelength down to 6 nm in the first harmonic. Besides testing SASE in the soft X-ray regime, an attractive physics program has been identified for this installation [7], covering applications ranging from magnetic materials research and various pump-and-probe experiments to photochemistry and X-ray microscopy of biological samples. In the following sections, design and status of key TTF FEL components are discussed.

3 ELECTRON SOURCE

The transverse coherence condition imposes a tight requirement on the transverse emittance ε_t of the electron beam [10]:

$$\varepsilon_t^n \leq \frac{\gamma\lambda_{ph}}{4\pi} \quad , \tag{2}$$

ε_t^n is the normalized emittance. For λ_{ph}=6 nm, γ=2000, Eq.2 requires $\varepsilon_t^n < 1\pi$mm mrad. Actually, this condition is not very strict, but the saturation length significantly increases if ε_t^n is larger. Thus, we aim at $\varepsilon_t^n = 1\pi$mm mrad for the rms electron emittance of a 1 nC bunch charge from an RF electron gun [11], and we allow for a factor of 2 in emittance dilution during longitudinal bunch compression and acceleration up to 1 GeV, see Table 1.

Compared to state-of-the-art, space-charge compensated, RF photoinjectors [12], the TESLA gun has to provide a longer bunch train and smaller emittance. The laser developed [13] provides an intensity stability of a few % and will be delivered to DESY in summer 1997. Neodymium doped Yttrium-Lithium Fluorid (Nd:YLF) has been chosen as the active medium since it combines a small thermal lensing effect with a high induced emission cross section and a relatively long fluorescence lifetime (480 μs). A pulse train with the desired spacing is selected from the bunches in a pulse train oscillator working at 36 MHz by means of Pockels cells. The light pulses are amplified in a linear low gain amplifier chain and then quadrupled in frequency. Relay imaging techniques in combination with spatial filtering is used to produce a radially uniform intensity profile.

To gain in emittance, any asymmetries in the RF field have been avoided in the design. Since previous calculations have revealed an emittance contribution of more than 1 π mrad mm for a conventional asymmetric input coupler, a symmetric input coupler has been developed. Fig. 5 shows a schematic layout of the gun and the coupler. At present, most components have been built or are under construction. An Aluminum model has successfully been tested to verify the coupler and cavity geometry.

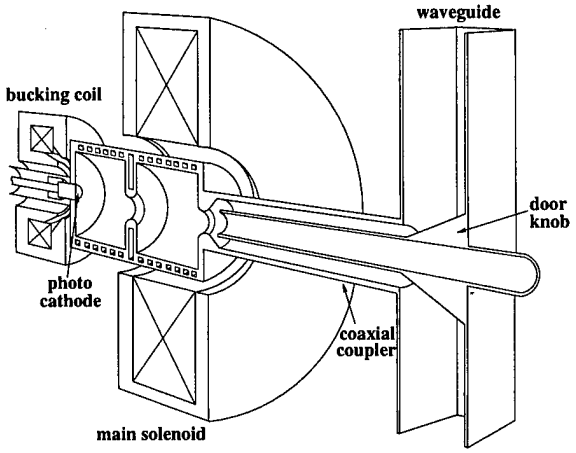


Figure 5: Cross sectional view of the RF gun (schematic) with the gun cavity, the cathode plug, the main solenoid and the bucking coil, and the coaxial input coupler. The RF is coupled from the rectangular waveguide via a door knob transition into the coaxial line and the cavity. The electrons leave the gun through the inner conductor.

4 BUNCH COMPRESSION

In order to achieve laser saturation within a single passage, XFELs require electron pulse currents of few kiloamperes. Because of space charge effects, such high currents cannot be generated directly from the RF gun cathode without blowing up the transverse emittance. Instead, a 7 ps long, 120 A beam is produced, accelerated, and longitudinally compressed by a factor of 20. This compression takes place in several steps at different energies. Bunch compressors are beamline sections which longitudinally compress the bunch using path length differences in a magnetic chicane. This is a well established technique, but has not yet been realized with extremely brilliant electron beams. Although simple in first-order theory, the physics of bunch compression becomes very challenging if collective effects like space charge forces [14],[15] and wakefields (see next section) are taken into account. Especially emittance conservation is then a critical issue [16].

Table 1: Parameters of the FEL at the TESLA Test Facility (TTF) (phases 1 and 2) and at the TESLA Linear Collider.

Linac Parameters	Unit	TTF FEL Phase 1	TTF FEL Phase 2	TESLA X-ray FEL
gradient for XFEL operation	MV/m	10-15	10-15	10-25
linac repetition rate f_{rep} for XFEL	Hz	10	10	5
bunch length (rms)	fs	800	160	80
bunch spacing	ns	93	93	93
number of bunches per train		11315	11315	11315
bunch train length	μs	1050	1050	1050
bunch charge	nC	1	1	1
normalized emittance at undul. entrance	π mrad mm	2	2	1
longitudinal emittance	keV mm	166	50	27
RF duty cycle	%	1	1	0.5
FEL Parameters				
typical saturation length	m	<14	<27	50 - 100
undulator period length	mm	27.3	27.3	5 - 7
undulator K-parameter (planar)		1.27	1.27	4.1 - 5.6
photon wavelength range (1st harmon.)	nm	> 42	> 6	0.1 - 10
peak photon beam power	GW	0.2	3	60 - 280
number of photons per bunch	10^{12}	100	40	10 - 500
typical photon beam divergence (rms)	μrad	100	30	1
typical photon beam diameter (rms)	μm	70	55	20

5 ACCELERATION

Each of the superconducting acceleration modules of the TESLA Test Facility provides a nominal acceleration of 120 MeV. For a more detailed desciption and the status, see Ref. [6]. With respect to FEL performance, a specific issue are the wakefields, because even for TESLA with its big cavity volume, the energy distribution inside each bunch is distorted or even dominated by longitudinal wakefields if the bunches are compressed to 50 μm rms bunchlength (phase 2). Analytical and numerical investigations have shown that the longitudinal wake potential accumulated over one TESLA module is close to the analytic solution of a point charge in an infinitely long periodic structure [18], see Fig. 6.

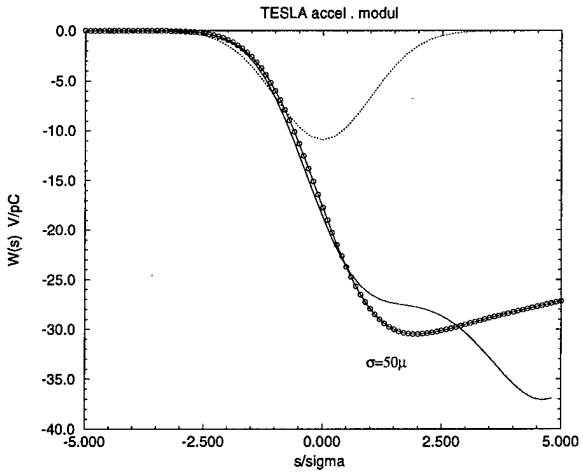


Figure 6: Wake potentials in the 8th cavity of a TESLA cryo-module for an rms bunch length of 0.05 mm and analytical approximation (circles). From Ref. [18].

6 UNDULATOR

The undulator is the most prominent FEL specific component. It has two functions: It has to provide the sinusoidal magnetic field so that the FEL process can take place, and, in order to keep the beam-size small over the whole undulator length, the undulator has to be combined with a superimposed periodic quadrupole lattice. The design for the TTF FEL is based on a planar hybrid permanent magnet undulator [19], see Table 1. It will be fabricated in modules 4.5 m long each, see Fig. 7. Between these modules and inside the 12 mm undulator gap a number of high resolution beam position monitors will be placed to ensure that the overlap between electron beam and photon beam stays within the specified tolerance of approx. 10 μm [20]. The undulator is using four additional magnets per halfperiod to provide focusing, see Fig. 8. A 220 mm long prototype has been built and tested, and two 1 m long prototypes are presently under construction.

7 PHOTON BEAM PROPERTIES

The prediction of photon beam parameters of short wavelength FELs is based on both an elaborate theory and various computer codes (for references, see [7] - [10]). Table 1 contains only few numbers on the expected FEL performance. The values quoted should be used as a guideline only, since there is no experimental experience yet in this wavelength regime. There is a radiation property that is specific to SASE FELs called superradiant spik-

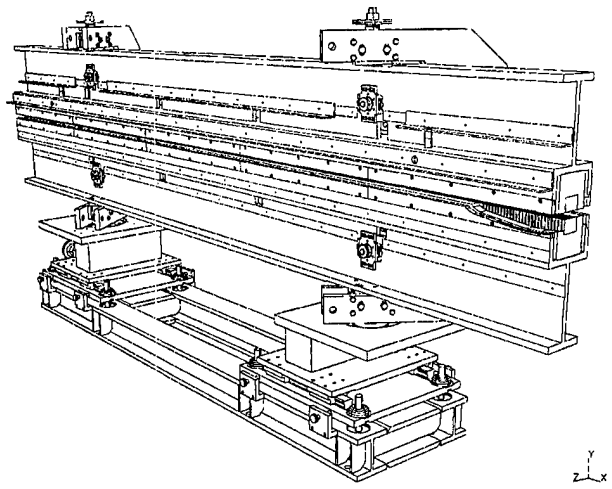


Figure 7: 3-D view of one undulator module for the VUV-FEL at the TTF. From Ref. [9].

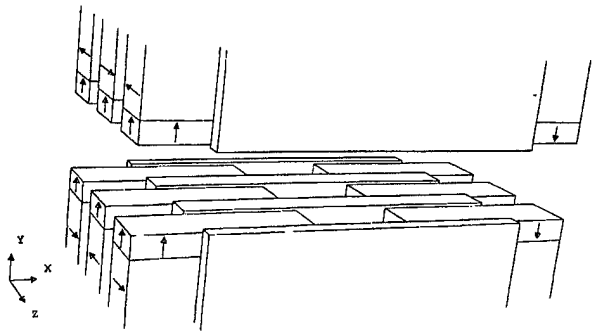


Figure 8: Perspective view of $1\frac{1}{2}$ periods of the TTF FEL undulator which combines undulator field and strong focusing. From Ref. [19]. The small pole pieces with magnetization perpendicular to the gap plane provide the focusing field.

ing [21]. Due to the statistical character of the start-up from noise, the FEL radiation intensity is not homogeneously distributed along the pulse length but concentrated within ultrashort pulses as long as the cooperation length. This length is typically about 1000 times the photon wavelength, i.e. much shorter than the bunch length. There is no phase correlation between these spikes, so the spike length reflects the longitudinal coherence of the radiation. The photon statistics has been shown to be that of completely chaotic polarized radiation [22]. A two-stage FEL scheme has been devised to considerably reduce the bandwidth [23]. In Figs. 2, 3 its performance is referred to by the index (M).

8 REFERENCES

[1] J.M.J. Madey, *Stimulated Emission of Bremsstrahlung in a Periodic Magnetic Field*, J. Appl. Phys. **42** 1906, 1971

[2] A. M. Kondratenko, E. L. Saldin, *Generation of Coherent Radiation by a Relativistic Electron Beam in an Ondulator*, Part. Accelerators, **10**, 207, 1980.

[3] R. Bonifacio, C. Pellegrini, L.M. Narducci, *Collective Instabilities and High-Gain Regime in a Free Electron Laser*, Opt. Cummun. **50**, No. 6 , 373, 1984.

[4] R. Brinkmann, et al., *An X-Ray FEL Laboratory as Part of a Linear Collider Design*, Proc. 1996 FEL Conf., to be Published in Nucl. Instr. Meth. A , 1997.

[5] G. A. Loew (ed.), *International Linear Collider Technical Review Committee Report*, SLAC-R-95-471, 1995.

[6] B. Aune, *Results from the DESY TESLA Test Facility, this conference*

[7] T. Åberg, et al., *A VUV Free-Electron Laser at the TESLA Test Facility at DESY, Conceptual Design Report*, DESY Print TESLA-FEL 95-03, 1995.

[8] H. Winick, et al., *A 2-nm - 4-nm Linac Coherent Light Source (LCLS) Using the SLAC Linac.* SLAC-PUB-6185, May 1993. 3pp. Presented at 1993 Particle Accelerator Conference (PAC 93), Washington, DC, 17-20 May 1993.

[9] R. Brinkmann, G. Materlik, J. Rossbach, A. Wagner (eds.), *Conceptual Design of a 500 GeV e+e- Linear Collider with Integrated X-ray Laser Facility*, DESY 1997-048 and ECFA 1997-182

[10] See e.g.: W.B. Colson, C. Pellegrini and R. Renieri (eds.), *Laser Handbook*, Vol.6, North-Holland, 1990

[11] J. Fraser and R. Sheffield, NIM **A 250** 71, 1986

[12] J.E. Clendenin, Proc. 18th Linac Conf., 298, Geneva, 1996

[13] I. Will, P. Nickles, W. Sandner, *A Laser System for the TESLA Photo-Injector*, internal design study, Max-Born-Institut, Berlin 1994.

[14] Ya. S. Derbenev, et al., DESY Print TESLA-FEL 95-05, 1995.

[15] E. L. Saldin, E. A. Schneidmiller, M. V. Yurkov, DESY Print TESLA-FEL 96-14, 1996.

[16] M. Dohlus, T. Limberg, *Wake Fields of a Bunch on a General Trajectory Due to Coherent Synchrotron Radiation*, this conference

[17] R. Tatchyn, et al. , Proc. PAC93, Washington, 1993.

[18] A.N.Novokhatski and A.Mosnier, *Short Bunch Wake Potentials for a Chain of TESLA cavities*, DAPNIA/SEA-96-08, 1996.

[19] J. Pflüger, Y. M. Nikitina, B. Faatz, T. Teichmann, *The undulator system for the VUV-FEL at the TESLA Test Facility*, Proc. 1996 Intl. FEL Conference, Rome, 1996, to be published.

[20] B. Faatz, J. Pflüger, Y.M. Nikitina, *Study of the Undulator Specification for the VUV-FEL at the TESLA Test Facility*, Proc. 1996 Intl. FEL Conference, Rome, 1996, to be published.

[21] R. Bonifacio, et al., Phys. Rev. Lett. **73** 70, 1994.

[22] E. L. Saldin, E. A. Schneidmiller, M. V. Yurkov, DESY Print TESLA-FEL 97-02, 1997.

[23] J. Feldhaus, et al., *Possible Application of X-ray Optical Elements for Reducing the Spectral Bandwidth of an X-ray SASE FEL*, Proc. 1996 Intl. FEL Conference, Rome, 1996, to be published.

RECENT RESULTS OF THE COMMISSIONING OF THE DELTA FACILITY

J. Friedl, DELTA GROUP, University of Dortmund, Institute for Accelerator Physics and Synchrotron Radiation, Emil Figge Straße 74B, 44221 Dortmund, Germany

Abstract

The DELTA storage ring facility, consisting of a 100 MeV LINAC, the booster storage ring BoDo and the 1.5 GeV main storage ring, is under commissioning since fall '94. All accelerators are in operation. DELTA includes all features of a 3rd generation light source, but in contrast to a user source this facility is mainly devoted to the test and development of components for future accelerators. The second main goal of the facility is to drive short wavelength Free-Electron-Lasers. Furthermore, special beam conditions for single user experiments and local syncrotron radiation users will be provided. This paper presents the recent results of the commissioning of the facility and first measurements of spontaneous synchrotron radiation emitted from the FEL-undulator FELICITA I.

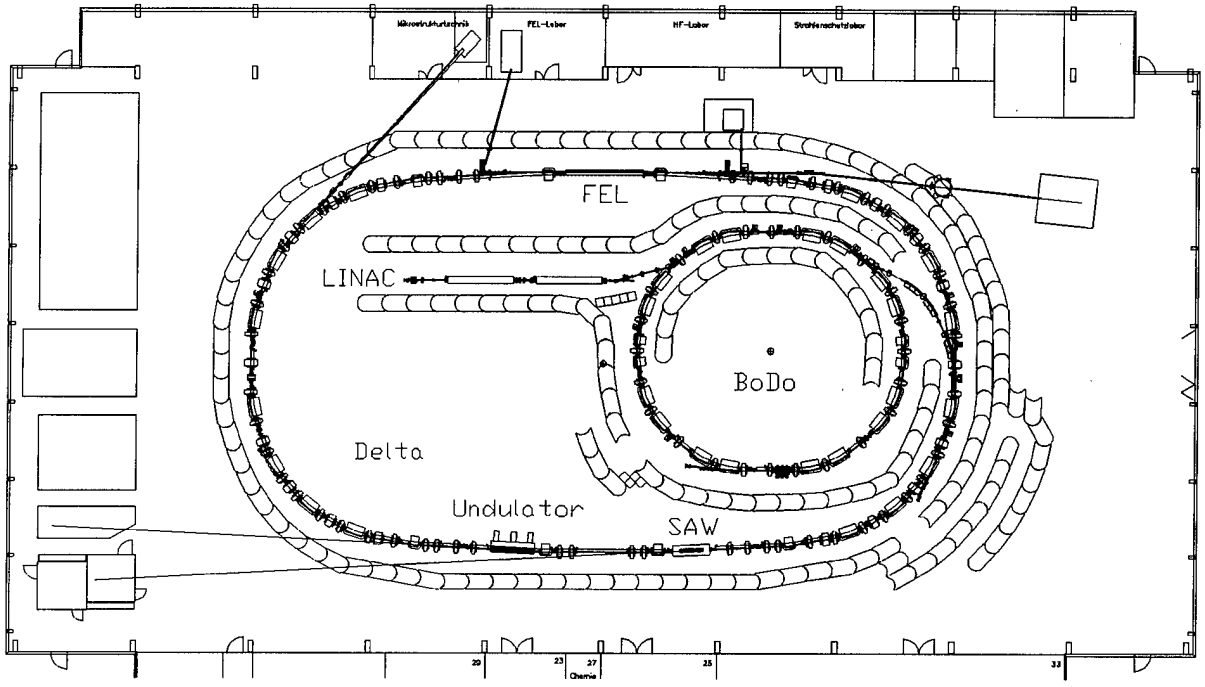


FIG. 1 THE DELTA STORAGE RING FACILITY

1 INTRODUCTION

The **D**ortmund **E**lectron **T**est **A**ccelerator facility DELTA is designed as a 3rd generation light source with beam energies up to 1.5 GeV [1,2]. It consists of a 100 MeV LINAC [3], the full energy booster storage ring BoDo and the main storage ring (Fig. 1). The facility is designed as a test bench for machine components and Free-Electron-Laser (FEL) development. Furthermore, it will also provide local users with synchrotron radiation. Both applications will take 50% of the beam time.

A short wavelength FEL [4] in the northern straight section is under commissioning simultaneously with the storage ring. A **S**uperconducting **A**symmetric **W**iggler (SAW- 3 ports) [5] and a hybrid undulator (period length 55 mm; 1.5 keV photon energy; 1 port) for the 2nd long straight section are under construction. Beside the use of the radiation from these insertion devices up to 5 synchrotron radiation beam lines from bending magnets are possible. One of these ports is already equipped with a beamline designed for micromechanics [6].

0-7803-4376-X/98/$10.00 © 1998 IEEE

2 COMMISSIONING STATUS

2.1 The Linear Accelerator

The S-band LINAC is a modified reconstruction of the old LINAC of the University of Mainz, Germany. Its design energy is 100 MeV, but due to limitations of the old hardware, especially of RF components, the maximum energy is presently about 67 MeV. The thermionic 50 keV triode electron gun produces a beam current of 2 A within a 15 ns pulse. To provide effective bunching with an energy of 4.5 MeV the buncher (LAL design) requires about 2 MW of RF power. With the present setup, using a 10 dB coupler to split up 10 MW RF power from the first klystron (one arm of Thomson F2042) to the first accelerating structure and the buncher only 750 kW remains for the buncher, yielding a reduced transmission of 30%. Parmela calculations have shown the ability of 70% transmission within 2% energy spread only by increasing the RF power for the buncher. The short term solution is to use the old klystron, but with a second transmission line providing the design power at the buncher. First results from this modification are expected in July 97. On a longer timescale the change to a new klystron type (Thomson TH2100; 35 MW) is planned to reach the design values for the RF power in all structures, and thus the design energy and transmission.

2.1 BoDo, The Booster Dortmund

The full energy booster BoDo was designed not only as an injector for the DELTA storage ring but also to serve as a test bench for low energy injection and accumulation. Therefore, it is constructed as a ramped storage ring. A 3 kicker system of the slotted pipe type [7] is used to inject into a FODO-lattice. For accumulation studies the kicker PFN can produce a 1 μs flat top current pulse with a fall time smaller than 1 BoDo revolution (168 ns). Currently an on orbit injection scheme with 2 kickers and a sinusoidal half wave pulse (t_p=340ns) is used.

The shortest possible acceleration cycle to reach the maximum energy is 5.6 s. During the acceleration all quadrupoles and dipoles run computer controlled current functions, to compensate for individual hysterises and dynamics. At the present state of commissioning a 960 MeV energy ramp with 6.4 s cycle duration is mainly used. The beam current at the top is about 4 mA and the particle loss is about 50% during the energy ramp. During the cycle the RF power is ramped from 20 W at injection to 2kW for beam energies higher than 400 MeV. Up to now a maximum energy of 1.4 GeV has been achived.

A closed orbit beam bump, produced by additional coils on three main dipoles, is used to prepare the beam for extraction. The extraction kicker is a double kicker of the slotted pipe type with a rise time of less then one BoDo revolution (168 ns).

2.3 Transfer Line Between BoDo and DELTA Main Ring

As the transfer line from BoDo to the DELTA main ring has to be compact, pulsed dipole magnets with a field exitation of 1.5 T for 1.5 GeV energy are used. The pulse length for the 2π pulse is 100 ms. Without special shielding stray fields act on the stored beam of the main ring. Therefore, a magnetic shielding is under construction.

2.4 The Main Storage Ring DELTA

The main storage ring has a racetrack shaped triplett lattice. At 1.5 GeV the design emittance is 1.1 10^{-8} mrad. The ring provides two superstraights of nearly 20 m each. Concerning space for matching insertion devices up to 14 m length are possible. This feature is essential for future FEL development. At present 2 additional dipoles are used to split up each of these sections into 3 straights. This allows for the use of up to 3 insertions per superstraight.

The main ring operation started in June '96 with a high emittance commissioning optics shown in Fig.2. Small values of the chromaticity allowed to start without sextupoles.

Currently beam currents up to 52 mA have been stored in a train of 6 bunches at 0.96 GeV. The typical lifetime is about 1 hour at 20 mA. The chromaticity is corrected to +2 using two families of sextupoles. With the integrated NEG and ion getter pumps [8] the beam loaded average vacuum pressure is about 10^{-7} Pa.

Table:1 lists the actual and design performance of the comissioning for BoDo and the main storage ring

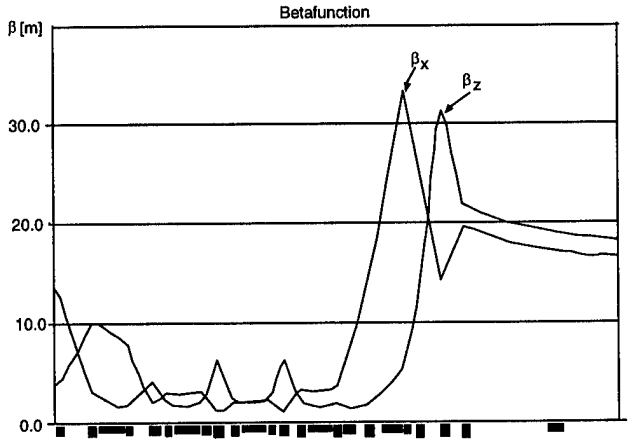


Fig. 2 β-functions of the commissioning optics for the DELTA storage ring

3 THE STORAGE RING FEL FELICITA I

Simultanously with the commissioning of DELTA first tests of the FELICITA I FEL hardware have started [9]. The electromagnetic undulator with 25 cm period and 4.875 m total length was tested with beam in both possible operation modes. By changing the excitation of 2 central periods it is possible to switch online between

the undulator mode and the optical klystron mode and vice versa without loosing the stored electron beam. The distance between the FEL-cavity mirrors is 14.4 m providing operation with 1, 2 and 4 bunches in DELTA. With energies ranging from 300 MeV to 1 GeV wavelengths from 2 μm down to 200 nm should be available. First tests of the magnet at 650 MeV and at maximum undulator K-value produced a spontanous spectrum shown in Fig.3. Maximum excitation of the dispersive section yields the spectrum of the fundamental of the optical klystron shown in Fig.4 [10]. Besides small changes of the vertical tune the influence on the stored beam was neglectable. The energy spread of the electron beam calculated from these measurements is in a good agreement with the theoretical values.

BoDo	*Actual*	*Design*
Optics	FoDo	FoDo
RF Power [kW]	0.01 - 4	30 (max)
Energy [MeV]	67 - 1400	50-1500
hor. Emittance [mrad]	$< 3x10^{-7}$@1GeV	$1.6x10^{-7}$@1GeV
Av. Current [mA]	3-5	5
Cycle Time [s]	6.4 (<1 GeV)	5.4 (<1.5GeV)
Lifetime [h]	>3	1.5
Main Storage Ring		
Optics	Triplet	Triplet
RF Power [kW]	10	60
Energy [MeV]	960	300-1500
hor. Emittance [mrad]	$7.5x10^{-8}$ **	$5.3x10^{-8}$
Av. Current [mA]	52	100
Lifetime [h]	1 (@20 mA)	10
Bunchlength [ps] P_{RF}=3.5kW	65 (0 A extrapolated)	60 (@ 960 MeV)

**: optical measurement

Tab. 1 Some parameters of BoDo and the main storage ring with the commissioning optics.

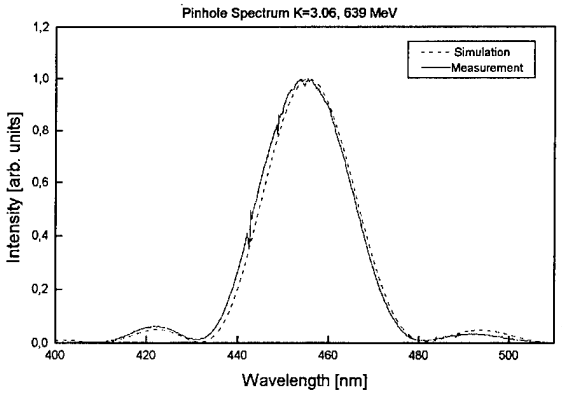


Fig. 3 Comparison of the spectrum of the undulator at 639 MeV and maximum excitation of the undulator section. The Simulation is based on a Hall-Probe Measurement.

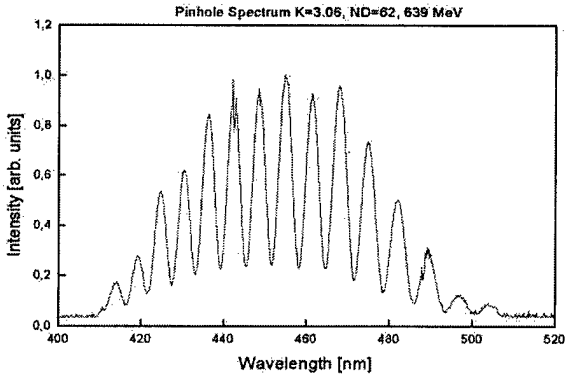


Fig. 4 Measurement of the OK-spectrum at 639 MeV and maximum excitation of the undulator section and the dispersive section.

4 CONCLUSION

During the ongoing commissioning process, DELTA is heading for the design current of 100 mA. As soon as this goal has been reached with the commissioning optics, the machine will be switched to its design low emittance optics with $\varepsilon_x = 5x10^{-9}$ mrad (1GeV). After the commissioning of the optics at 1 GeV, the machine will be run at 1.5 GeV. Simultaneously to the progress of the facility, the first experiments are starting. At the end of 1997 it is expected, that DELTA has reached its main design goals.

REFERENCES

[1] DELTA Group, 'Status Report', University of Dortmund, 1990 (unpublished).

[2] K. Wille et al, *'Initial Experience with DELTA'*, Proc. 1996, EPAC, Vol. 1, 95, 1996.

[3] G. Blokesch et al, *'The Injector LINAC of the DELTA-Facility'*, Proc. 1996 EPAC, Vol. 1, 834, 1996

[4] D. Nölle et al, *'DELTA, A New Storage-Ring-FEL Facility At The University of Dortmund'*, NIM, A296, (1990), 263-269.

[5] M. Negrazus et al, *'SAW - A Superconducting Asymmetric Multipole Wiggler at the DELTA Storage Ring'*, Proc. 1996 EPAC, Vol. 3, 2576, 1996.

[6] M. Körfer, *'Aufbau einer Bestrahlungsapparatur für die Röntgentiefenlithographie'*, PHD-Thesis, Dep. Physics of the University of Dortmund (in preparation)

[7] G. Blokesch et al, *'A Slotted Pipe Kicker For High-Current Storage Rings'*, NIM, A338, (1994), 151 - 155.

[8] B. Hippert et al, *'The DELTA Vacuum System'*, Proc. 1996 EPAC, Vol. 1, 364, 1996.

[9] A. Geisler et al, *'Experience On The Operatoin Of The 2-in-1 Electromagnetic Undulator Of FELICITA-I'*, NIM, A375, (1996), 445-447.

[10] T. Schmidt, *'Aufbau des FEL Experiments FELICITA-I im sichtbaren und ultravioletten Spektralbereich am Speicherring DELTA'*, PHD-Thesis, Dep. Physics of the University of Dortmund Apr. 1997 (unpublished).

INSERTION DEVICE DEVELOPMENT IN THE X13 STRAIGHT OF THE NSLS X-RAY RING

P. M. Stefan, S. Krinsky, C.C. Kao, G. Rakowsky, O. Singh, L. Solomon
NSLS, Brookhaven National Laboratory

Abstract

On the NSLS X-Ray Storage Ring, the X13 straight section and beamline have been used for insertion-device-related R&D since 1990. We will describe three important projects: The Prototype Small-Gap Undulator (PSGU), the In-Vacuum Undulator (IVUN), and the Time Varying Elliptically Polarized Wiggler (EPW). The PSGU has successfully operated with a vertical aperture of only 3 mm, with minimal reduction in electron beam lifetime. The EPW has successfully run during regular user operations while switching at either 2 Hz or 100 Hz, with no adverse effects on other experiments. The IVUN project is a collaboration between NSLS and Spring-8, and installation is scheduled for May 1997.

1 SMALL GAP UNDULATORS

The PSGU [1,2] combines a short-period (16 mm) undulator magnet and a variable-aperture vacuum chamber to produce high-brightness undulator light with a higher photon energy in the fundamental than would otherwise be possible in the 2.5 GeV X-Ray Ring. Photons from the PSGU have been used to develop a coherent x-ray beam for X-ray Photon Correlation Spectroscopy (XPCS). A coherent beam of $3x10^9$ photons/sec at 3 keV (4.1Å) was produced through a 10 μm pinhole.

The long low-β straight sections of the NSLS X-Ray Ring (such as the X13 straight) are particularly well-suited for small-gap insertion devices. The stored electron beam focuses to a minimum dimension both in the vertical and in the horizontal at the center of the long straight. The PSGU is installed in the center of the straight section, and is quite short. The minimum-aperture-region of its variable vacuum chamber is 390 mm long, and the undulator magnet arrays are 320 mm long. In the regions closest to the electron beam, the PSGU vacuum chamber is thinned to 1 mm. The magnet arrays are in air, located just outside the thinned vacuum chamber. The magnet gap is always at least 3 mm greater than the vertical aperture of the vacuum chamber for the electron beam.

One of the most important studies conducted with the PSGU measured the reduction in the electron beam lifetime as the variable vacuum chamber aperture was reduced. The results are illustrated in Figure 1. The lifetime was essentially unaffected to a full aperture of 4 mm, but then started to decrease. In a practical sense, an aperture of about 3 mm is operationally acceptable, since the overall lifetime reduction is small.

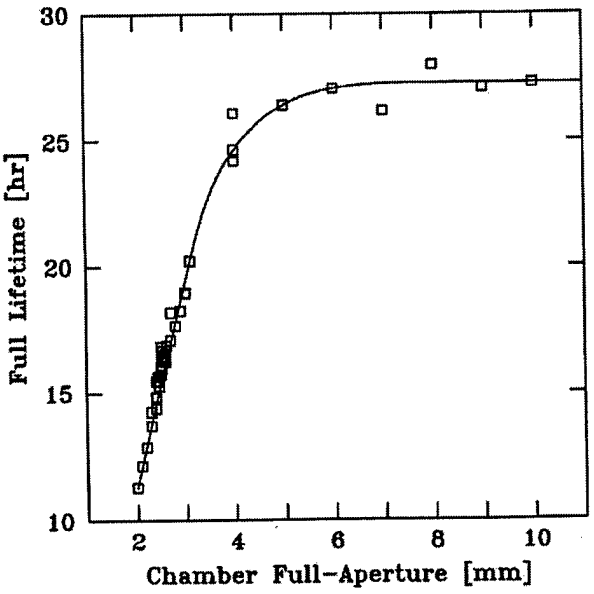


Figure 1: Stored beam lifetime as a function of the electron beam aperture presented by the PSGU vacuum chamber, at 220 mA. The line drawn is a guide for the eye.

0-7803-4376-X/98/$10.00 © 1998 IEEE

In order to take full advantage of the ability to run with a 3 mm aperture, we are pursuing an in-vacuum undulator project (IVUN). This is a logical extension of the PSGU, with the variable vacuum chamber eliminated, and the undulator magnet arrays placed directly in the storage ring vacuum. For IVUN, the magnet gap and the corresponding electron beam aperture are very nearly the same dimension. A comparison between the parameters of the PSGU and IVUN is presented in Table 1.

Table 1. PSGU/IVUN Comparison

	PSGU	IVUN
Period	16 mm	11 mm
NominalMagnet Gap	6.0 mm	3.3 mm
Corresponding Max. Beam Aperture	3.0 mm	3.0 mm
Peak On-Axis Field	0.623 T	0.678 T
$h\nu_{1\,out}$, ($\lambda_{1\,out}$)	2.77 keV (4.48 Å)	4.64 keV (2.67 Å)

The IVUN design goal is for a photon output at 4.6 keV (2.7 Å) in the fundamental, with high flux at the second and third harmonics, at a magnet gap of 3.3 mm. Experiments spanning the whole spectrum of synchrotron-light applications, from spectroscopy and diffraction to microscopy and scattering, can benefit from this high-brightness, high-flux source. In addition, the electron beam characteristics of the X-Ray Ring allow IVUN to produce good second-harmonic intensity on-axis, at just over 8 keV, with a half-intensity bandwidth of over 2 keV. IVUN is being built in a collaboration between the NSLS and the Japanese SPring-8 Project. Our collaborators at SPring-8 worked on the first successful in-vacuum undulator and are fabricating the 11 mm-period magnet arrays for IVUN. When installed in the X13 straight section, IVUN will replace the PSGU,which is now situated at the center of the straight. Studies are planned to begin in the Summer of 1997.

2 TIME VARYING ELLIPTICALLY POLARIZED WIGGLER

The Time Varying Elliptically Polarized Wiggler (EPW) [3] produces elliptically-polarized light on axis, with the sense of rotation of the field vectors, i.e. the helicity, alternating at up to 100 Hz. The EPW, as originated by Yamamoto and Kitamura [4], consisted of permanent magnet wigglers with crossed fields capable of generating circularly polarized radiation with higher harmonics on the wiggler axis. In our device, the horizontal permanent magnet structure has been replaced by an AC electromagnet wiggler, in order to modulate the helicity. The EPW was built in a collaboration between the NSLS, the APS at Argonne National Lab, and the Budker Institute of Nuclear Physics at Novosibirsk. Usable fluxes of photons are available from 100 eV to 10 keV, with the measured degree of circular polarization exceeding 50%. Such a source is extremely useful for circular dichroism studies of both magnetic materials and materials with natural optical activity. The stable alternation of the helicity, at frequencies up to 100 Hz, is an extremely powerful aspect of the source. This allows gating or lock-in techniques to separate the responses of the sample to opposite helicities. When a lock-in amplifier is used, any steady-state or background signals are summarily removed from the start, since the lock-in only detects the signals which follow the EPW reference signal

The EPW was installed in December 1994, commissioned during Spring 1995 at an operating frequency of 2 Hz, and became operational subsequently [5]. Utilizing trim coils at the wiggler ends and the high-precision orbit measurement system of the NSLS X-Ray Ring, the residual orbit motion was reduced to a level below 0.5 μm [6]. No adverse effects on other experiments have been observed. The degree of circular polarization of the radiation from the wiggler was characterized by making Magnetic Circular Dichroism (MCD) measurements using the X13A soft-x-ray beamline [7]. For values of the vertical deflection parameter, K_x, of 1.2 and 1.6, the MCD effects at the Fe $L_{2,3}$ edges indicated a degree of circular polarization of 60% and 75%, respectively, in good agreement with calculated values. Experimental programs based on the device, including MCD, Natural Circular Dichroism, and Resonant Magnetic Scattering, have also started. As an example, very small MCD effects near the Cr $L_{2,3}$ edges were observed in a series of Co-Cr alloys (a promising candidate for a high-density perpendicular magnetic recording medium) by a collaboration of the Naval Research Laboratory, AT&T, and the NSLS [8]. From these results, the Cr in the alloys was found to be polarized, and the induced Cr moment aligned anti-ferromagnetically with respect to that of the neighboring Co. These results also showed that MCD effects much smaller than 1% can be easily detected with the EPW, as illustrated in Figure 2. To fully utilize the EPW, a new soft x-ray spherical grating beamline and a double-crystal x-ray monochromator are being constructed, and will be operational in fiscal year 1997. Operations are now underway utilizing the EPW switching at 100 Hz and 2 Hz, and commissioning at 23 Hz is underway.

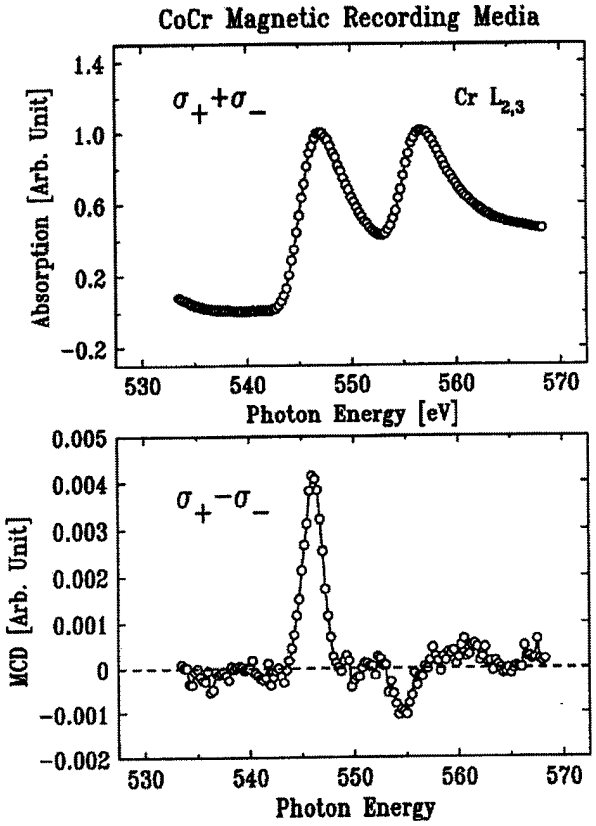


Figure 2: Magnetic Circular Dichroism (MCD) effects near the Cr $L_{2,3}$ edges in a series of Co-Cr alloys [8]. From these results, the Cr in the alloys was found to be polarized, and the induced Cr moment aligned anti-ferromagnetically with respect to that of the neighboring Co. The MCD effect illustrated is much smaller than 1%.

3 ACKNOWLEDGEMENTS

Work performed under the auspices of the U.S. Department of Energy under contract DE-AC02-76CH00016.

4 REFERENCES

[1] P.M. Stefan, L. Solomon, S. Krinsky and G Rakowsky, Proc. 1991 Part. Accel. Conf., San Francisco, CA, p. 2542, (1991).

[2] P.M. Stefan, S. Krinsky, G. Rakowsky and L. Solomon, Proc. 1995 Part. Accel. Conf., Dallas, TX, p. 2435, (1995).

[3] A. Friedman, S. Krinsky and E. Blum, "Polarized Wiggler for NSLS X-Ray Ring: Design Consideration", Informal Report, BNL 47317, (1992); E.Gluskin, et al., Proc. 1995 Part. Accel. Conf., Dallas, TX, (1995).

[4] S. Yamamoto and H. Kitamura, Japan J.of Appl. Phys., 26, p.L1613, (1987).

[5] S. Krinsky, and C.-C. Kao, Synchrotron Radiation News, 8, 38, (1995).

[6] O. Singh, S. Krinsky, P.M. Ivanov and E.A. Medvedko, Proc. 6th Int. Synch. Rad. Instrum. Conf., Argonne, IL, October 1995.

[7] K.J. Randall, Z. Xu, E. Gluskin, I. McNulty, R. Dejus, S. Krinsky, O. Singh, C.-C. Kao, E.D. Johnson, C.T. Chen, and G. Meigs, J. Electron Spectroscopy and Related Phenomena, 80, 433, (1996).

[8] K.M. Kemner, V.G. Harris, V. Chakarian, Y.U. Idzerda, W.T. Elam, C.-C. Kao, Y.C. Feng, D.E. Laughlin, and J.C. Woicik, J. Appl. Phys. 79, 5345, (1996), Proceedings of the 40th Annual Conference on Magnetism and Magnetic Material Nov. 6-9, 1995 Philadelphia.

OPERATION OF FIR-AND UV-FEL FACILITIES AND FEL BEAM SHARING TO USER'S ROOMS AT THE FELI

T. Tomimasu, S. Okuma, K. Wakita, T. Takii, E. Oshita, K. Wakisaka and H. Tongu
Free Electron Laser Research Institute, Inc. (FELI), 2-9-5, Tsuda-Yamate, Hirakata, Osaka 573-01, Japan

SUMMARY

Four FEL facilities FEL-1, FEL-2, FEL-3 and FEL-4 achieved lasing at FELI in Oct. 1994, in Feb. 1995, in Dec. 1995 and in Oct. 1996, respectively. Two IR facilities FEL-1 and FEL-2 are open for users to supply several MW-level FELs covering the wavelength range of 1-20μm every other week. The maximum average power of the IR-FEL is 2W. Total operation time in 1996 was about 2400 hours. The visible- and UV-facility FEL-3 has broken the world record for the shortest wavelength oscillation of linac-based FELs with a thermionic gun up to 0.278μm. The FEL beams are delivered from the optical cavities to the diagnostics room and four user's rooms (eighteen stations) through the pipe lines using fan-shaped mirrors with a 90°-opening angle.

INTRODUCTION

The FEL facility consists of an S-band, 165-MeV electron linac with a thermionic gun, beam transport (BT) lines and four FEL facilities FEL-1, FEL-2, FEL-3 and FEL-4 as shown in Fig. 1. Each FEL facility consists of an undulator, an optical cavity and an optical pipeline. FEL-1, FEL-2 and FEL-3 were designed in 1993 and 1994 to cover the wavelengths from 0.3μm to 22μm. FEL-4 was designed in 1995 to cover the wavelengths from 20μm to 80μm.

The 165-MeV linac consists of the 6-MeV injector [1] and seven ETL type accelerating waveguides [2]. The seven accelerating waveguides with a length of 2.93m is of linearly narrowed iris type to prevent beam blow up (BBU) effects at high peak current acceleration.

The injector is composed of a 120-kV thermionic triode gun, a 714-MHz prebuncher, a 2856-MHz standing wave type buncher and focusing solenoids. The axial field keeping the beam radius constant is calculated from the K-V equation.

The gun with a dispenser cathode (EIMAC Y646B) usually emits 500-ps pulses of 2.3A at 22.3125MHz or at 89.25MHz. The grid pulser was manufactured by Kentech Instruments, Ltd., U.K. These pulses are compressed to 60A10ps by the prebuncher and the buncher.

The electron beam of the FELI linac consists of a train of several picosecond micropulse repeating at 22.3125MHz or at 89.25MHz. The train of the micropulse continues for 24μs (macropulse). The repetition rate of the macropulse is 10Hz or 20Hz.

Our rf sources are a 714-MHz klystron (1VA88R, 15kW for 20-Hz, 24-μs flat top pulses) for the prebuncher and two 2856-MHz klystrons (E3729, 25MW for 20-Hz, 24-μs flat top pulses per each) for the buncher and seven accelerating waveguides.

The latter klystrons are based on a E3712 klystron, used for 80-MW, 4-μs pulse operation, modified for 25-MW, 24-μs pulse operation [3] [4]. The modulator for the klystron 1VA88R uses MOS-FET modules [5]. However, the modulator for the E3729 klystron consists of 4 parallel networks of 24 capacitors and 24 variable reactors, and it has a line-switch of an optical thyristor stack. The flatness of our klystron modulator for E3729 is 0.067% at 24-μs pulse operation [6]. The 24-μm pulse operation of these modulators were very successful for lasing at visible-and UV-range.

LASINGS AT FIR-,MIR-,VISIBLE-AND UV-RANGE

The operation of the FELI facility was begun in May 1994. The electron beam size and position are always monitored and controlled to pass through the center of accelerating waveguides using screen monitors installed at the inlet and outlet of every accelerating waveguide and quadrupole magnet. Further, using five screen monitors installed in the S-type BT line [7] for each FEL facility, the beam size and position are adjusted along the axis so as to pass through the center of a narrow vacuum chamber inside each undulator.

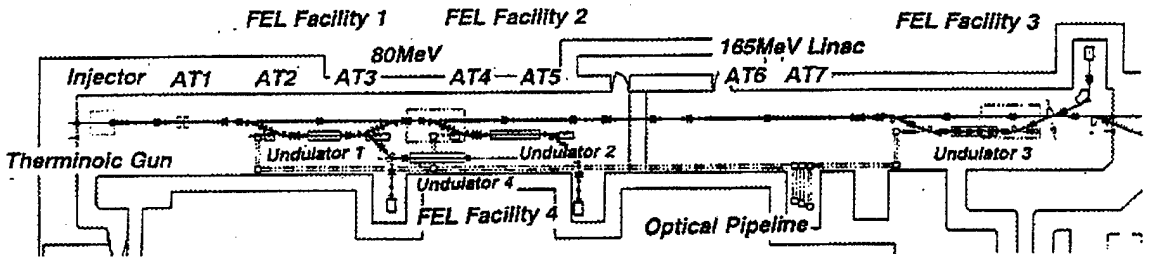


Fig. 1 Layout of 165-MeV linac, S-type BT linacs and four FEL Facilities

0-7803-4376-X/98/$10.00 © 1998 IEEE

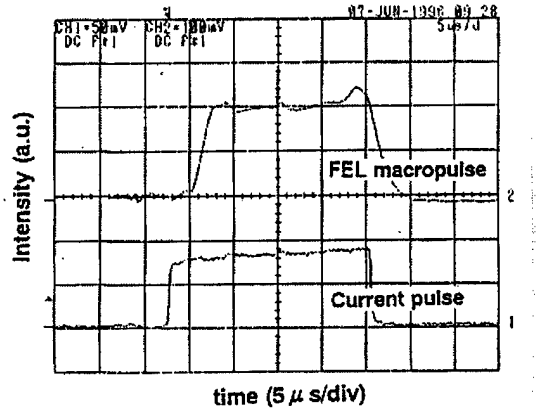


Fig. 2 7.5m FEL macropulse shape and electron current pulse shaped

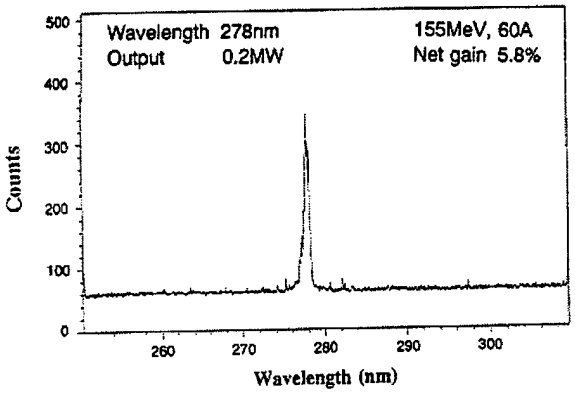


Fig. 3 0.278m FEL spectrum

The beam emittance was measured using three Al-foil OTR beam profile monitors installed in the undulator vacuum chamber. The two profile monitor emittance measurement method is used for its simplicity and short time for data acquisition. The normalized emittance ε_n of a 144-MeV, 60-A electron beam is estimated to be 26π mm mrad [8]. Each Al foil has a 1-mmϕ aperture. The S-type BT line can focus about 80-90% of the electron beam to pass through the aperture.

Each optical cavity is a 6.72-m long Fabry-Perot cavity which consists of two mirror vacuum chambers [9].

The FEL oscillation experiment was begun at FEL-1 (5-22μm) in August and succeeded in lasing at 5-7μm in Oct. 1994 [10]. Fig. 2 shows a 7.5-μm FEL macropulse shape measured with an HgCdTe detector and electron current pulse shape measured with a button monitor [11]. FEL-2 (1-6μm) and FEL-3 (0.23-1.2μm) achieved lasing at 1.88-3.1μm in Feb. [12] and at 0.339-0.353μm and in Dec. 1995, respectively [8].

It has been said that no lasing at ultraviolet wavelengths can be achieved by using an electron linac with a thermionic gun from the wavelength limit due to optical diffraction, because of beam emittance growth in the bunching process from the thermionic gun to the linac. Therefore, the FELI linac was carefully designed to reduce the emittance growth in the bunching process and FEL-3 has broken the world record for the shortest wavelength oscillation up to 0.278μm on June 6, 1996. Fig. 3 shows a 0.278μm FEL spectrum.

Experimental verifications of gain estimates given by Dattoli, et al. [13] and of the criteria on the electron beam quality and wavelength limit due to photon diffraction given by Sprangle, et al. [14] are given by our data on visible- and ultraviolet-FEL oscillations [15].

Peak interacavity power is about 1GW at 0.6μm.

FEL-asist radiation damage to the downstream multilayer mirror was observed after about fifty hours oscillation. Irradiated radiation dosage to multilayer mirrors in optical cavity 3 is estimated to be 0.3 MGray for fifty hours irradiation with thermoluminescence dosimeters (TLDs) [16].

FEL-4 (20-80μm) including a 2.7-m long Halbach type undulator (λu =8cm, N=30) and a 6.72-m long optical cavity was installed at the 33-MeV beam line, downstream of FEL-1 in Dec. 1996. The FEL beam is delivered from the downstream optical cavity to the user's rooms through the pipeline of FEL-2.

First lasing at 18.6μm was achieved on Dec. 26, within ten hours operation. FEL-4 achieved lasing at 18.6~40μm in Jan. 1997 [18].

FEL BEAM QUALITIES

The FEL micropulse structure depends on the electron micropulse and macropulse structures, the detuning effect of the optical cavity, and the small signal gain of the undulator.

The electron beam of the FEL consists of a train of several picosecond pulses (micropulses) repeating at 22.3125MHz, or to 89.25 MHz although the results presented in this paper were all taken at the lower frequency. To estimate the electron micropulse duration, the optical transition radiation induced by the electron micropulse was measured with a streak camera. The train of micropulses continues for 24μs (macropulse) and repeats at 20Hz. The usual FEL micropulse duration is determined by the detuning effect of the optical cavity and is shorter than half of the electron micropulse duration (bunch length) of several picosecond. The detuning effect on visible-and ultraviolet-FEL micropulse duration was measured with the streak camera. The FEL micropulse duration varies from 2.7ps to 0.9ps according to the detuning.[19]

The FEL peak and average powers of FEL-1 are 6MW and 0.2W at 7.5μm, respectively, at the outlet of Au-coated front mirror with 1-mm aperture. The FEL peak power of FEL-2 is 2MW at 1.88μm at the 0.5-mm aperture of Au-coated mirror and those of FEL-3 are 1.8MW at 0.35μm and 4.7MW at 0.6μm at the multilayer mirror. Fig. 4 shows the average FEL powers measured at each front mirrors as a function of wavelength.

Experimental data on the wavelength dependence of $\Delta\lambda/\lambda$ agree with the estimated valules calculated from $\Delta\lambda/\lambda=(1/\pi)\sqrt{\lambda R/N\sigma_z}$, where N is the number of undulator periods and σ_z is the standard deviation of the electron bunch length.

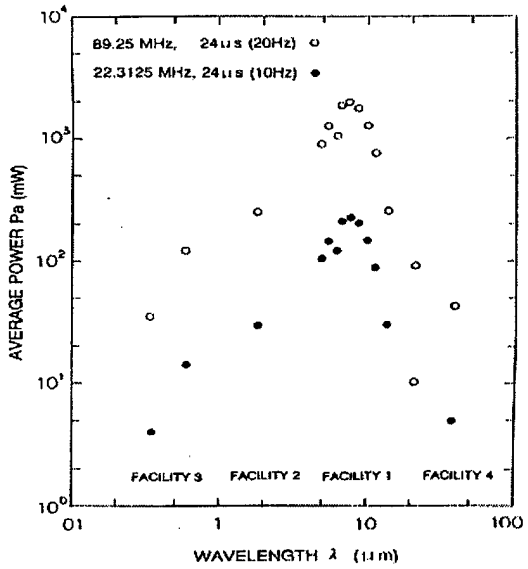


Fig. 4 Average powers vs wavelength

FEL BEAM SHARING FOR USER'S ROOMS

The FEL beams are delivered from the optical cavities to the diagnostics room and four user's rooms (eighteen stations) on the third floor through the optical pipes as shown in Fig. 5 [20]. Since Oct. 1995, FEL-1 was open for FEL users for two days a week. Since the end of Oct. 1996, FEL-1 and FEL-2 are open for users every other week. Total operation time in 1996 was about 2,400 hours.

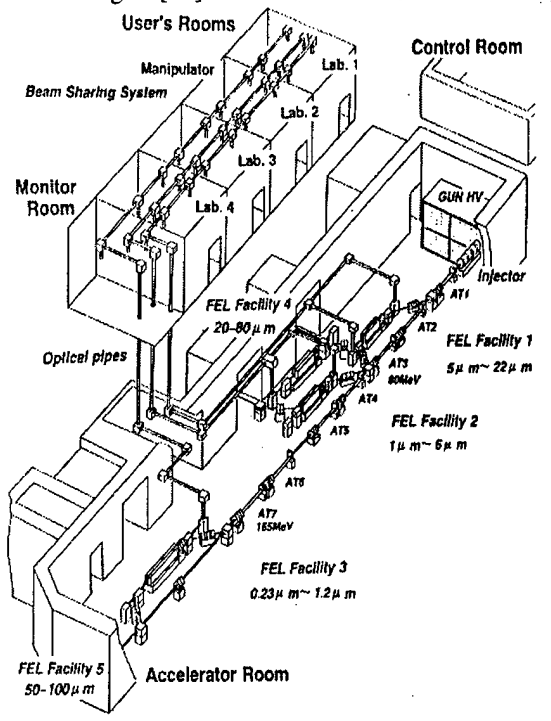


Fig. 5 Bird's eye view of FEL facilities and user's rooms of the FELI

The FEL beam extracted from the narrow aperture becomes thick and round due to diffraction and is delivered to the diagnostics room and four user's rooms. The FEL power and spectrum are always monitored with a fan-shaped mirror [21] at the diagnostic room and the linac control room.

The thick and round FEL beam is suitable for simultaneous FEL beam sharing to the diagnostics room and the user's stations, using fan-shaped Au-coated mirrors. The opening angle of the fan-shaped Au-coated mirror can change the sharing ratio of delivering FEL average power to the diagnostics room and the user's rooms. For the present FEL diagnosis, a quarter of the round FEL beam is shared using a fan-shaped mirror with a 90°-opening angle. Two manipulators were installed in Lab. 2. Each can focus the FEL beam to a 0.1-mmϕ MIR-FEL spot size inside of 3-m diameter working area.

REFERENCES

[1] T. Tomimasu, et al., Nucl. Instr. Meth., A358 (1995) ABS11
[2] T. Tomimasu, IEEE Trans., NS-28, No. 3 (1981) 3523
[3] Y. Morii, et al., Proc. 9th Symp. on Accelerator Sci. and Tech. (KEK, ug. 25-27, 1993) p. 225
[4] Y. Ohkubo, et al., Proc. 20th Linear Accelerator Meeting (FELI, Osaka, Sept. 6-8, 1995) p. 72
[5] S. Abe, et al., Proc. 19th Linear Accelerator Meeting (JAERI, July 20-22, 1994) p. 225
[6] E. Oshita, et al., IEEE Proc. PAC'95 (Dallas, May 1-5, 1995) 1608
[7] Y. Miyauchi, et al., Ref. 3, p. 416
[8] T. Tomimasu, et al., Nucl. Instr. Meth., A383 (1996) 337.
[9] K. Saeki, et al., Nucl. Instr. Meth., A375 (1996) 10
[10] T. Tomimasu, et al., Ref. 6, p. 257
[11] A. Zako, et al., Proc. 2nd Asian Symp. on FEL (Novosibirsk, June 13~16, 1995) p. 57
[12] A. Kobayashi, et al., Ref. 9, p. 317
[13] G. Dattoli, et al., IEEE J. Quantum Electron., QE-20 (1984) 637.
[14] P. Sprangle, et al., Nucl. Instr. Meth., A331 (1993) 6.
[15] T. Tomimasu, to be published in Nucl. Instr. Meth. A.
[16] K. Wakisaka, et al., to be published in Nucl. Instr. Meth. A.
[17] T. Takii, et al., to be published in Nucl. Instr. Meth. A.
[18] T. Takii, et al., Proc. AFEL'97 (FELI, Hirakata, Jan. 1997) p.75
[19] K. Wakita, et al., Ref. 18, 1997 p. 87
[20] T. Tomimasu, et al., Ref. 9 p. 626
[21] S. Okuma, et al., Ref. 9 p. 654

STIMULATED TRANSITION RADIATION IN THE FAR-INFRARED

Chitrlada Settakorn, Michael Hernandez and Helmut Wiedemann
Applied Physics Department, Physics Department and Stanford Linear Accelerator Center,
Stanford University, Stanford, California 94309 *

Abstract

Stimulated transition radiation is generated by recycling coherent far-infrared light pulses of transition radiation in a special cavity. The cavity length is designed to be adjustable. At specific intervals the light of a previous bunch coincides at the radiator with the arrival of a subsequent bunch. In this situation, the external electromagnetic field stimulates the emission of higher intensity transition radiation. It is expected that the extracted energy from the cavity will be about 17 times more than would be possible without recycling.

1 INTRODUCTION

Electromagnetic radiation can be produced over a wide spectrum from radiowaves to hard x-rays through a variety of physical effects. Specifically, electron beams can be used to produce coherent or incoherent radiation. Coherent radiation is emitted when particle density fluctuations or modulations exist on the scale of the radiation wavelength. Such density modulations are used to produce microwaves in, for example klystrons, or shorter wavelength radiation from free electron lasers. In this paper we present a new way to produce broadband coherent far-infrared radiation from relativistic electron beams. The principle combines the emission of coherent radiation from electron bunches with the stimulation of such radiation by an external field with the source of the external field being the radiation emitted by an earlier electron bunch.

At the **S**tanford **U**niversity **S**hort **I**ntense **E**lectron source (SUNSHINE) high intensity electron bunches of sub-picosecond duration are produced from an rf-gun and a bunch compressor[1]. At wavelength equal and longer than the electron bunch length coherent radiation can be produced with an intensity scaling like the square of the number of electrons per bunch. With typical electron populations the intensity of such coherent radiation exceeds that of incoherent radiation by a factor of 10^8 or more. Since the shortest electron bunch lengths that can be directly produced are of the order of tens to hundreds of μm's the coherent radiation emitted falls into the far-infrared(FIR) spectral regime. This is the wavelength range where no readily available high intensity sources exist except for a few free electron lasers.

Coherent radiation can be produced, for example, in form of synchrotron, Cherenkov, Smith-Purcell or like in the case of the SUNSHINE experiment in form of transition radiation. Transition radiation (TR) is generated when a charged particle passes through an interface between media with different dielectric constants[2]. The most effective transition occurs at the interface from vacuum ($\varepsilon_1 = 1$) into metal ($\varepsilon_2 \rightarrow \infty$). At the SUNSHINE facility a thin aluminum foil is employed to serve as the radiator. This foil is tilted by 45° with respect to the electron path and the backward TR is emitted at 90° with respect to the beam axis for easy separation from the electron beam through a polyethylene window. The total spectral energy W radiated per unit solid angle is

$$\frac{d^2 W}{d\omega\, d\Omega} = \frac{r_e mc^2 \sin^2\theta}{\pi^2 c\,(1-\beta\cos^2\theta)^2}.$$

where θ is the emission angle with respect to the electron beam axis. The radiation intensity vanishes along the beam axis and increases to a maximum at $\theta = 1/\gamma$. The total spectral radiation energy per electron becomes

$$\frac{dW}{d\omega} \approx \frac{2\, r_e mc^2}{\pi\, \beta\, c} \ln\gamma$$

after integration over a 2π half space.

Of this total radiated energy 51.2% can be collected within an acceptance angle of $\theta = 0.245$ rad in the set up described here. The single electron TR spectrum is uniform up to very high frequencies and folds with the spectrum of the electron bunch which is the Fourier transform of the particle distribution called the form factor. For sub-picosecond electron bunches of the SUNSHINE facility the form factor is close to unity for wavelength down to about 100 μm and the available spectral energy is for example $dW/d\omega = 3.73\times10^{-19}$J-s for $N_e = 6\times10^8$ electrons per micro bunch. The spectral radiance exceeds that of black body radiation by several orders of magnitude due to its efficient collimation in the forward direction. Furthermore, the radiation is broad band, coherent, polarized and of sub-picosecond, Fourier transform limited duration.

2 STIMULATED TRANSITION RADIATION

A possible way to further increase the intensity of this coherent FIR TR is to stimulate the emission process with an external electromagnetic field. To obtain stimulated transition radiation (STR), we recycle the TR from one bunch by mirrors such that the radiation pulse arrives back at the radiator just in time when another electron bunch arrives there as well [3]. The recycled radiation pulse serves now as an external field $\mathbf{E}_{ex}$. In case of perfect temporal coincidence with the arrival of an electron bunch this external field adds to the spontaneous TR field $\mathbf{E}_{sp}$ emitted from the electron bunch for a combined radiation field $\mathbf{E}_{sp}+\mathbf{E}_{ext}$. Since the radiation

0-7803-4376-X/98/$10.00 © 1998 IEEE

intensity is proportional to the square of the field we get from this electron bunch an extra radiation energy of

$$\Delta\varepsilon = |\mathbf{E}_{sp}+\mathbf{E}_{ext}|^2 - |\mathbf{E}_{sp}|^2 - |\mathbf{E}_{ext}|^2 = 2\mathrm{Re}(\mathbf{E}_{sp}\mathbf{E}_{ext}^*).$$

The extra energy is the stimulated radiation which is due to the work done by the external field on the electrons [3]. STR has been observed at SUNSHINE.[3,4] by measuring the radiation intensity as a function of the cavity length. STR is observed at cavity lengths matched to the stimulating condition. In the absence of stimulation, the total radiated power from all bunches would be independent of the cavity length. As visible in Fig.1, the radiation intensity increases whenever the cavity path length is an integer, half integer, third integer etc. multiple of the electron bunch distance. In case of fractional integers the radiation pulse has to travel twice, three and more times through the cavity before it meets another electron bunch at the radiator.

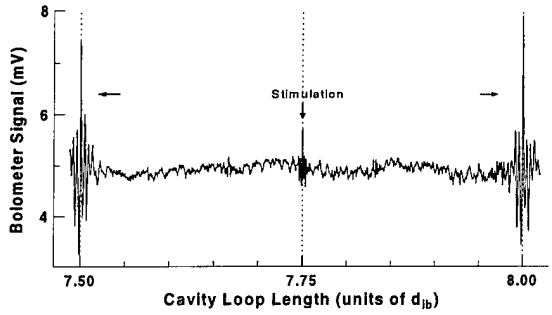


Figure:1 The STRdetuning scan[4,5]

3 OPTICAL CAVITY FOR STR

First let us consider a lossless cavity with a total round trip path length d equal to the distance Δ between adjacent electron bunches. The first electron bunch generates TR at the radiator and the forward radiation of intensity $|\mathbf{E}|^2$ travels through the cavity to arrive back at the radiator at the same time with another electron bunch. The total intensity is now $|\mathbf{E}+\mathbf{E}|^2 = 4|\mathbf{E}|^2$ producing an extra energy $2|\mathbf{E}|^2$. Interaction with the third electron bunch, the energy of the radiation increase to $|2\mathbf{E}+\mathbf{E}|^2 = 9|\mathbf{E}|^2$. The field in the cavity builds up until the last (N-th) electron bunch arrives at the radiator with the radiation energy scaling proportional to N^2. At SUNSHINE, for example, N=3000 and one would expect an increase of the instantaneous radiation intensity by a factor of 3000^2 and an increase by a factor of 3000 in the total number of photons per pulse.

If the cavity length is mΔ, the radiation pulse arriving at the radiator after one round trip will meet the m^{th} subsequent bunch. For a train of N electron bunches per pulse, the radiation energy in the cavity then scales like $m(N/m)^2|E|^2$ with m independent radiation pulses in the cavity. Since the optical cavity is composed of several reflectors, there exist unavoidable losses and the intensity of STR can be greatly diminished. This makes it imperative to use mirrors of maximum reflectivity.

For the purpose of generating STR, a cavity as shown in Fig.2 has been studied and constructed. The cavity is composed of a metallic foil as the TR generator(R) and several reflectors(F,P1,P2,M). Although it is important to minimize the number of mirror to decrease losses, the cavity requires a specific mirror arrangement. Due to the divergent nature of TR from the radiator, one cannot use a flat mirror to recycle the radiation back to the radiator. After separating the radiation from the electron beam by a 45° thin metallic reflector(F), two parabolic mirrors(P1, P2) are required to generate a parallel beam for path length adjustment and a correct polarization condition of the recycled radiation at the radiator. The focal points of P1 and P2 are aligned to the center of R and flat mirror(M). In the cavity we insert a beam splitter(BS) to extract some of the radiation field while the rest remains circulating in the cavity.

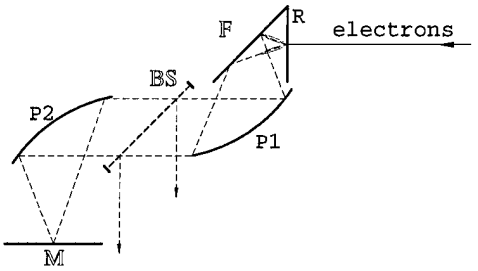


Figure:2 The schematic of STR cavity.

Based on the electron beam parameters at SUNSHINE, the efficiency of the optical cavity can be calculated. The SUNSHINE facility produces electron pulses at 10-20 Hz each containing a train of 3000 bunches at an energy of 28 MeV. Each bunch has an effective length of 180 μm and includes up to 6×10^8 electrons. From the form factor we derive a spectrum for the STR ranging from 100 - 1000 μm. The cavity path length is adjustable within $\Delta \le d \le 8\Delta$, where Δ=10.5cm.

As described earlier, the intensity of STR in a lossless cavity is $(N^2/m)|E|^2 = 1.28\times10^6|E|^2$. Considering reflection losses, we define α as the remaining fraction of field after one round trip being equal to the product of the reflectance from all reflectors. The radiation intensity in the cavity after a train of N electron bunches pass through the radiator becomes

$$|\mathbf{E}_{cav}|^2 = |\mathbf{E}+\alpha\mathbf{E}+\alpha^2\mathbf{E}\ldots+\alpha^M\mathbf{E}|^2 = |\mathbf{E}|^2(1-\alpha^{M+1})/(1-\alpha), \quad (1)$$

where M is the nearest integer less than (N-1)/m. From (1) we conclude that the reflectivity of metal surfaces will ultimately determine the losses in the optical cavity. Reflectance calculation for gold surfaces based on Drude's model[5] shows that the reflectance can be better than R=0.995 for FIR, approaching unity for longer wavelengths. At λ=200μm the reflectance of a gold surface is 0.996407 and for 8 reflections per round trip α=0.971615. The radiation intensity in the cavity reaches a maximum in a short fraction of the beam pulse limited only by radiation production and overall losses.

The extracted radiation is determined by the reflection coefficient(r) of BS and can be only a small fraction of the cavity energy since it adds to the losses in the cavity. The fraction of the cavity field after passage through BS is αt, where t is the transmission coefficient of BS satisfying $|t|^2+|r|^2=1$. The amount of radiation coupled out of the cavity must be chosen carefully. If too much radiation is being extracted the cavity field cannot build up to significant intensity. Conversely, if too little radiation is extracted, the cavity field builds up to higher values, however it is not available to the user. The optimum extraction efficiency must be determined.

The STR energy in each micro pulse obtained from the cavity in units of spontaneous TR from one electron bunch is shown in Fig.3 as a function of r of BS assuming constant r and t within the spectrum of interest.

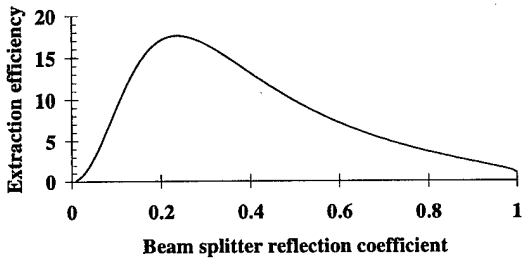


Figure:3 Radiation extraction efficiency as a function of beam splitter reflection coefficient.

It becomes obvious that maximum extraction efficiency is reached for r=0.24 which is equivalent to extracting 5.76% of the cavity energy per pass. Including all losses, the radiation energy after p bunches pass through the radiator can be written as

$$|E_{out}(p)|^2 = |E|^2|r|^2\alpha_0^2\begin{cases}\left[\dfrac{1-(\alpha t)^{\lfloor p/m\rfloor+1}}{1-\alpha t}\right]^2 & 0\le p<N\\ \left[\dfrac{(\alpha t)^{\lceil (p-N)/m\rceil}-(\alpha t)^{\lfloor p/m\rfloor+1}}{1-\alpha t}\right]^2 & p\ge N\end{cases}$$

Here, α_0 and α are the remaining fraction of the field from the radiator to the BS and for one round trip in the cavity, respectively. The symbol $\lceil\ \rceil$ and $\lfloor\ \rfloor$ are round up and round down operations. Fig.4 shows the available radiation energy in units of spontaneous TR as electron bunches pass through the cavity for an optimized BS reflection coefficient R=0.24. The total STR energy per macropulse is $5.07\times10^4\ |E|^2$ .The gain compared with radiation from a single pass of 3000 electron bunches is 16.91.

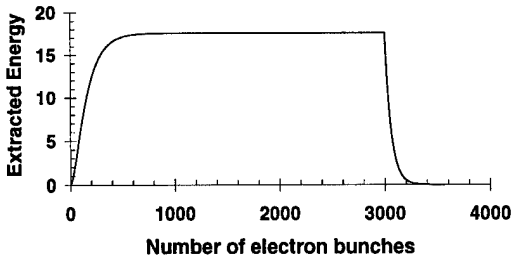


Figure:4 The available radiation for R=0.24.

4 STR INTENSITY

The STR radiance greatly exceeds that of black body radiation as shown in Fig.5. The width of the spectrum can be extended toward short wavelength as it becomes possible

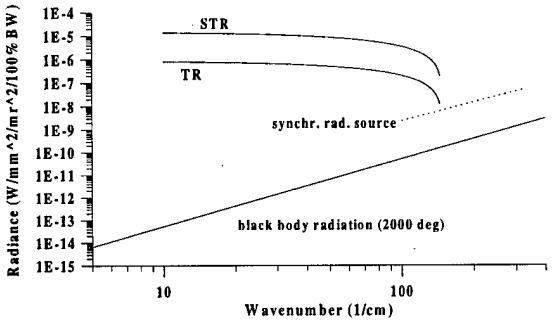


Figure:5 STR radiance

to reduce the bunch length further. Between 100 μm and 1000 μm STR exceeds black body and synchrotron radiation by 3 to 8 orders of magnitude. Furthermore the radiation is polarized and comes in subpicosecond Fourier transform limited pulses.

REFERENCE

[1] P. Kung, D. Bocek, H. Lihn, H. Wiedemann, Phys. Rev. Lett.**73**(1994)967

[2]V.L. Ginzburg and V.N. Tsytovich, *Transition Radiation and Transition Scattering*, (Adam Hilger, Bristol, 1990)

[3] H.-C. Lihn, *Stimulated Coherent Transition Radiation,* Ph.D. thesis (Stanford University, Stanford, CA,. 1996)

[4] H.-C. Lihn, D. Bocek, M. Hernandez, P. Kung, C. Settakorn, H. Wiedemann, Phys. Rev. Lett. **76**: 4163(1996)

[5] H.E. Bennett and J.M. Bennett , *Optical Properties and Electronic Structure of Metals and Alloys*, edited by F. Abeles (North-Holland, Amsterdam, 1996)

* work supproted by DOE Contract No. DE-AC03-76F00515

MEASUREMENTS OF HIGH GAIN AND NOISE FLUCTUATIONS IN A SASE FREE ELECTRON LASER*

M. Hogan, S. Anderson, K. Bishofberger, P. Frigola, A. Murokh, N. Osmanov[◆], C. Pellegrini, S. Reiche[†], J. Rosenzweig, G. Travish, A. Tremaine, A. Varfolomeev[◆]

UCLA Department of Physics and Astronomy, Los Angeles, California

Abstract

We report measurements of large gain for a single pass Free Electron Laser operating in Self Amplified Spontaneous Emission (SASE) at 16 μm starting from noise. We also report the first observation and analysis of intensity fluctuations of the SASE radiation intensity in the high gain regime. The results are compared with theoretical predictions and simulations.

1. INTRODUCTION

The measurements have been done using the Saturnus linac [1], consisting of a 1 1/2 cell BNL photocathode RF gun, and a PWT accelerating structure [2], followed by a beam transport line and a 1.5 cm period, 0.75 Tesla peak field, Undulator Parameter of 1, 40 period undulator built at the Kurchatov Institute [3], [4]. The undulator provides focusing in both planes. The linac operates at 5 Hz, with 2.5 μs long macropulses, and one 13 MeV electron bunch per macropulse. Steering magnets control the beam trajectory and align the beam in the undulator, slits measure the emittance [5], an Integrating Current Transformer (ICT) and Faraday cups measure the beam charge, and phosphor screens measure the beam transverse cross section. The beam can be propagated straight through the undulator, or bent through a momentum analyzer to measure the energy and energy spread.

The radiation produced by the undulator is focused by mirrors to a copper doped germanium detector cooled at liquid helium temperature. The detctor can measure the radiation produced by a single electron bunch and has a response time of about 5 ns, while our electron pulses are typically 4 to 6 ps long. The detector has been calibrated and the linearity of its response measured using the 10 picosecond long radiation pulses from the Firefly FEL at the Stanford Subpicosend FEL Laboratory. The noise level in the detector and its associated electronics is of the order of 10 mV. A detector signal of 20mV corresponds to 10^7 photons at.

The experiment is done with an undulator of fixed length by changing the electron bunch charge from a low value (0.2nC), where we expect no or small amplification, and observe only spontaneous radiation, to a large value (0.6 nC) where we expect to see amplified spontaneous radiation. We produce one electron bunch, send it through the undulator, and measure the pulse charge and the intensity of the infrared radiation. This is repeated many times to accumulate statistics. We then repeat the experiment blocking the infrared radiation to measure the noise level due to background X-rays. The charge is measured non destructively with the ICT.

When changing the electron bunch charge other beam parameters (energy spread, emittance, pulse length, and beam transverse radius in the undulator) also change. Since all these quantities are important to understand the amplification and fluctuation properties, they have been measured independently as a function of charge. The energy spread changes from about 0.08 to 0.14% rms, when the charge changes from 0.2 to 0.58 nC, putting an upper limit to the rms bunch length of 0.64 to 0.84 mm, corresponding to a peak current (I) of 38 to 83 A. The normalized rms emittance changes from about 8 mm mrad at the lowest charge of about 0.2 nC to about 10 mm mrad at 0.58 nC. Beam losses in the 4mm inner diameter beam pipe, which can produce an X-ray background in our detector, were less than the resolution of our diagnostics. Beam transport and the IR signal were maximized with the beam focused to a spot size of about 0.4 mm (FWHM) at the undulator exit and about three times larger at the entrance.

In an FEL the undulator radiation emitted by the electron beam has a wavelength $\lambda=\lambda_u(1+K^2/2+\gamma^2\theta^2)/2\gamma^2$ where λ_u is the undulator period, K the undulator deflection parameter, θ the angle with respect to the beam axis, and γmc^2 the beam energy. The FEL theory shows that the radiation intensity can grow exponentially along the undulator axis, z, as $I_{rad}\sim\exp(z/L_g)$. In the simple 1D theory [6], [7] neglecting diffraction and slippage, the gain length (L_g) is proportional to the ratio of the beam peak current to the beam cross section, Σ, raised to the power 1/3.

2. GAIN

The gain is evaluated by comparing the SASE with the spontaneous (non amplified) undulator radiation which is linearly proportional to the charge in the bunch. Another effect which can increase the radiation intensity above the spontaneous undulator radiation level is coherent spontaneous emission, which gives an intensity proportional to the bunch form factor and to the square of the charge. Since our bunch is 1.5 - 2 mm long and our wavelength is 16μm, we expect this term to be small. Further, our intensity measurements at low charge, where we expect no FEL amplification, agree within the errors with the calculated spontaneous undulator radiation, with no discernible contributions from coherent spontaneous emission. The undulator infrared radiation (IR) is measured in the forward direction, within a solid angle Ω corresponding to an angle θ=7.7 mrad defined by the exit window of the beam line, and over all photon frequencies transmitted to the detector. The detector has a peak sensitivity between 2 and 32 μm. The KrS5 beamline exit

---

[◆]RRC Kurchatov Institute, Moscow, Russia

[†]DESY, Hamburg, Federal Republic of Germany

*Work supported by DOE Grant DE-FG03-92ER40793

0-7803-4376-X/98/$10.00 © 1998 IEEE

window and detector window attenuate wavelengths shorter than 0.6 μm and longer than 30 μm, but have a transmission of 70% for wavelengths in between. Hence, we integrate the intensity over the undulator spectrum within Δf=2-30 μm and over Ω defined by the exit window.

The signal we expect from non amplified spontaneous radiation within Ω and Δf after reduction for the windows attenuation, is evaluated using undulator radiation formulas. The energy in a single IR pulse is calculated to be 4.9×10^{6} eV, or about 8×10^{-13} J at 0.2 nC. The detector noise including its' amplifier is of the order of 10 mV, so we expect a signal to noise ratio of about 1 at 0.2 nC. X-rays hitting the detector have been minimized with lead shielding, measured while blocking the IR radiation, and have a mean value of 18 mV over our charge range. A typical background measurement is shown in Fig. 1.The almost constant X-ray background between 0.2 to about 0.6 nC indicates that the X-rays are mainly due to distributed background in the detector area, produced by the dark current from the electron source, and not to beam losses through the undulator.

ICT noise corresponds to a mean charge of 7 pC with a standard deviation of 2.3 pC. The measured IR intensities have been divided in bins, corresponding to a charge interval of +/- 2.5% of the central charge value. A distribution of IR intensities for the case of an average charge of 0.56 nC is shown in Fig.1. For each charge interval we accumulate 100 events or more, determine the mean IR intensity and the standard deviation, then subtract the mean X-ray background. The mean IR intensity and standard deviation is ploted vs. charge in Fig. 2, where we have also plotted the calculated undulator radiation intensity, reduced by the windows attenuation. Again, our calculation does not include coherent spontaneous radiation, but our observations are consistent with this contribution being negligible. At 0.6 nC the measured intensity is about 2.5 times the calculated spontaneous intensity,thus showing SASE.

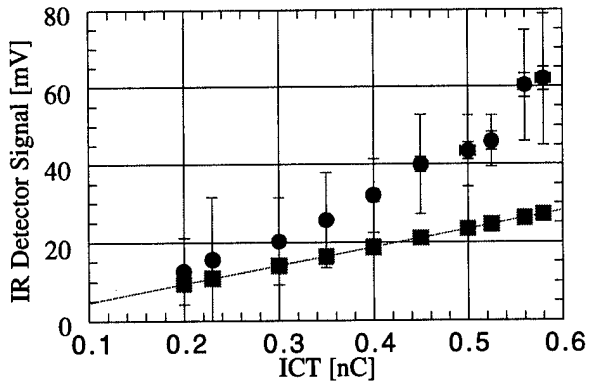


Fig. 2 IR radiation intensity vs. charge. The vertical bars are the standard deviation for the intensity fluctuations due to starting from noise. For comparison, the effect of beam charge and transverse beam size uncertainties is 4 mV at 0.56 nC. The lower line is the calculated spontaneous emission intensity.

The IR intensity in Fig. 2 contains photons in the third harmonic and outside the coherent solid angle Ω_c, a region where the FEL gain is very small compared with the gain in the first harmonic and within Ω_c. To establish the FEL gain for the coherent first harmonic we have measured at the lowest charge of 0.2 nC, the intensity of the third harmonic and the change in intensity when reducing the solid angle to Ω_c. The third harmonic has been measured using a CAF2 filter that does not transmit radiation above 10 μm; the filtered intensity was ~5/12 of the total intensity. The ratio of the intensity within the coherent solid angle, Ω_c and in the total solid angle, Ω, has been measured to be ~1/2 using an iris near the beamline exit window to reduce the solid angle. We have used this experimental information to evaluate the intensity in Ω at the third harmonic, plus that of the first harmonic outside Ωc. These radiation components can be extrapolated linearly with charge (if we assume that they are not amplified), and subtracted from the measured value leaving only the first harmonic within Ω_c. The result, along with the calculated value for the spontaneous first harmonic within Ω_c, is plotted in Fig. 3. The ratio of the first harmonic intensity, 42.7 mV, measured at a charge of 0.58 nC, to the extrapolated spontaneous first harmonic at the same charge, 7.5 mV, is about 5.6.

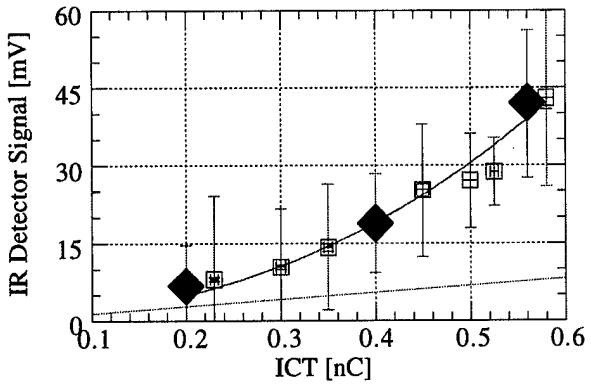


Fig. 3 First harmonic coherent IR vs. charge. The vertical bars are the standard deviaion for the intensity fluctuations due to starting from noise. For comparison, the effect of beam charge and transverse beam size uncertainties is 4 mV at 0.56 nC. The lower line is the calculated spontaneous emission intensity. The curve fit to the data is IR = 1.85 x $ICTexp(4.4ICT^{1/3})$. The three diamonds at 0.2, 0.4, 0.6 nC are the results of simulations with the code Ginger, normalized to fit the data point at 0.2nC.

The first harmonic experimental points in Fig. 3 are fitted with a curve of the form:

$$I=\alpha Q\exp(\Gamma(Q/\Sigma)^{1/3}) \qquad (1)$$

which gives an intensity proportional to the charge (Q) for low beam brightness, when we expect to recover the spontaneous radiation limit, and growing exponentially with $Q^{1/3}$ for large electron beam brightness, as one would expect from a 1-D FEL theory [6], [7]. The fit gives an exponent of 3.7 at 0.58 nC indicating that at the largest charge we have about 3.7 power gain lengths in our system. The value of the FEL parameter ρ for the beam and undulator used in this experiment is ρ ~0.01, and the gain length evaluated from this value in the 1-D theory is about 7 cm. When including 3-D effects but no slippage this increases to about 11 cm. The larger gain length we observe is due

to the slippage, defined for a bunch length σ_z as $\lambda N_u/\sigma_z$, which is of order one. The code Ginger [8], which includes both 3D effects and slippage, has been used to simulate three cases: 0.2. 0.4, and 0.58 nC (38, 64, and 83A), while keeping the same beam transverse cross sections. The results have been normalized to fit the experimental point at 0.2 nC to take into account experimental effects like the attenuation from the windows. The normalized results are shown in Fig. 3 and fit the data well.

3. FLUCTUATIONS

We observe output intensity fluctuations due to starting from noise. In the case of no gain the IR power will scale linearly with charge, and does not depend on other beam parameters. When there is gain, a change in charge, Q, will lead to a change in output power which we can evaluate using (1). A maximum gain of 5 would give a maximum change in the IR intensity of 4% for $\Delta Q/Q$= +/- 2.5%. The beam transverse area, Σ, at the undulator exit has been observed to change by about +/-10%. Since the gain changes as $\Sigma^{-1/3}$ in the exponent, we can expect a change in IR intensity of ~5%. The combined error due to uncertainties in Q and Σ is +/-6.4%. The much larger power fluctuations, due to starting from noise, are about 34% at 0.56 nC and 39% at 0.58 nC. Following the work of [9], [10], [11] the intensity fluctuations are expected to follow a distribution with a relative standard deviation given by $M^{1/2}$, where M is qualitatively the number of degrees of freedom, or modes in the radiation pulse: $M=(T/\tau_c)(\Omega/\Omega_c)$. T is the time over which the radiation is measured, $\tau_c=(\lambda/c)(\Delta\lambda/\lambda)$ the correlation time, and Ω , Ω_c the solid angles already discussed. Since in our experiment most of the radiation is in the first harmonic we evaluate $\Delta\lambda/\lambda$ to be approximately $1/N_u$, giving $\tau_c \cong$ 2ps. The time T is given in our experiment by the electron pulse length, which at the largest charge is about 2 mm (FWHM) or about 6.6 ps. The value of M is then $M \cong 8$ giving an expected width of the fluctuations of about 35%. A Gamma Probability Distribution Function with M=11 fits the IR intensity at high charge (shown in Fig. 4) and give a relative standard deviation of 30%. Although this value of M is somewhat larger than that given by the simple expression above, it is still in qualitative agreement with the data. A more complete analysis of the data, using a convolution of the X-ray background and IR intensity distributions, will be presented in a future publication.

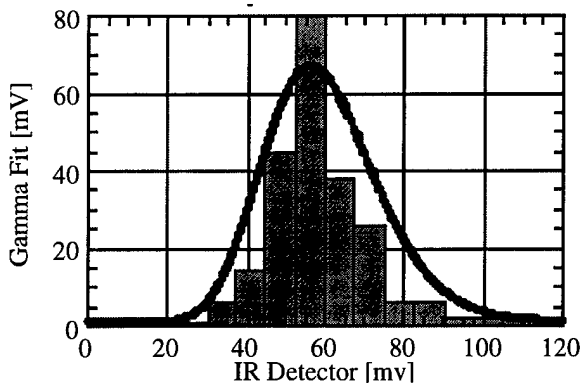


Fig. 3 Distribution of IR Detector Signals for a mean charge of 0.52 nC +/- 5% fitted with a Gamma Probability Distribution Function corresponding to M = 11.

To summarize, we have observed amplification of the spontaneous radiation, with an increase of the first harmonic intensity by 600% over the spontaneous intensity. We have also observed for the first time the intensity fluctuations of the output amplified radiation. Analysis of the data shows a good agreement with the analytic theory of SASE, the 3D time dependent Ginger simulations, and the experimental results.

4. ACKNOWLEDGMENTS

We wish to express our gratitude to the many people who, with their help, have made this experiment possible, in particular Herman Winick, Massimo Cornacchia, Rich Sheffield, Todd Smith, Glen Westenskow,and Ilan Ben-Zvi.

5. REFERENCES

[1] S.C. Hartman et al., Nuclear Instruments and Methods {A340}, 219 (1994)
[2] R. Zhang, C. Pellegrini, and R. Cooper, "Study of a Novel Compact Standing Wave RF Linac", in course of publication in Nuclear Instruments and Method.
[3] A.A. Varfolomeev, S.N. Ivanchenkov, and A.S. Khlebnikov, Nuclear Instruments and Methods {A318}, 813 (1992).
[4] A.A. Varfolomeev, Yu. P. Bouzouloukov, S.N. Ivanchenkov, and A.S. Khlebnikov, N.S. Osmanov, S.V. Tolmachev, Nuclear Instruments and Methods {A359}, 85 (1995).
[5] J. Rosenzweig et al., Nucl. Instr. Methods {A 341}, 379 (1994).
[6] R. Bonifacio, C. Pellegrini, and L. Narducci, Optics Comm.. { 50} 373 (1984).
[7] K.-J. Kim, Nucl. Instr. and Meth. {A250}, 396 (1986).
[8] W. M. Fawley, Private Communication.
[9] M.C. Teich, T. Tanabe, T.C. Marshall and J. Galayda, Phys. Rev. Lett. {65}, 3393 (1990).
[10] R. Bonifacio, et al, Phys. Rev. Lett. {73}, 70 (1994)
[11] E.L. Saldin, E.A. Schneidmiller, and M.V. Yurkov, "Statistical properties of Radiation from VUV and X-ray Free Electron Laser", DESY rep. TESLA-fel 97-02, (1997).

USE OF JEFFERSON LAB'S HIGH AVERAGE POWER FEL AS A THOMSON BACKSCATTER X-RAY SOURCE

G. A. Krafft, TJNAF, 12000 Jefferson Ave., Newport News, VA 23606

Abstract

Recently, workers from Berkeley have measured Thomson forward scattered X-rays at the ALS injector. The average power of their device was limited by, among other things, the repetition rate of the high power laser. In order to achieve high average power, it is natural to investigate the possibility of backscatter from the recirculating optical pulses in Jefferson Lab's CW IRFEL, now under construction. Photon brightnesses of order 10^7 photons/(sec mm^2 mrad^2) will be produced at this facility, with a spectrum extending up to 7 keV in energy, in the present operating mode. A near-term upgrade to 75 MeV yields about 30 keV photons with similar brightness. In the longer term, the UV upgrade of our device could potentially produce 4 MeV photons with substantially higher brightness. Scaling laws for such configurations are given and these three cases are presented in detail.

1 X-RAY LUMINOSITY

In the Berkeley work [1], and in the current work, the primary purpose of the experiments is to produce short-time-duration pulses. Such pulses may be produced by scattering a short IR laser pulse at ninety degrees to a 45 MeV electron beam that has been focussed transversely to a small spot size, or by 180 degree scattering off a very short bunch. A distinguishing feature of the IRFEL at Jefferson Lab is its relatively short bunch duration of 1 psec rms; the radiation pulse distribution mirrors the "micropulse current" distribution of the beam in time.

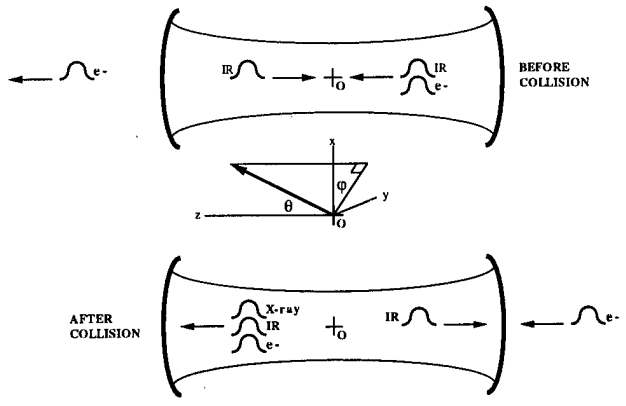


Figure 1: Scattering Geometry

In Fig. (1) the general geometry is presented. The micropulse separation is chosen to be equal to the optical cavity length; two optical pulses are circulating in the optical cavity. Before the collision, overlapping optical and electron pulses move downstream, and an optical pulse moves upstream. After the collision, overlapping optical, electron, and high energy photon pulses move downstream, and again, the scattered pulse continues upstream. There are clearly $f = c/l$ collisions per unit time, where c is the velocity of light and l is the optical cavity length. To get the total power, the total energy transferred into high energy photons in one collision should be estimated.

To analyze a single collision, recall that the total number of scattered X-rays is a Lorentz invariant quantity, as is σ, the total scattering cross section in the rest frame of the electrons [2]. Now $\Phi_e^\mu = J^\mu/e$ is a 4-vector, where J^μ is the usual current density 4-vector, whose time component is the number density of electrons. Likewise $\Phi_p^\mu = (n_p, n_p\beta_p)$ is the 4-vector describing the photon flux. Clearly, N_s, the number of scattered photons is proportional to both n_p and n_e, and d^4x is Lorentz invariant. Consequently N_s must be expressed as

$$N_s = \int \Phi_{p\mu}\Phi_e^\mu \sigma d^4x$$

$$= \int (1 - \beta_p \cdot \beta_e) n_p(x,y,z,t) n_e(x,y,z,t) \sigma d^4x.$$

If the distributions are separable, $n_p(x,y,z,t) = n_p(x,y)I_p(z+ct)$, $n_e(x,y,z,t) = n_e(x,y)I_e(z-\beta ct)$, where I_p, I_e are unit normalized and where $n_p(x,y)$ and $n_e(x,y)$ are the transverse number distribution of the low-energy photons and electrons respectively, the above integral simplifies to

$$N_s = \int n_p(x,y) n_e(x,y) \sigma_T dx dy.$$

The total Thomson scattering cross section, $\sigma_T = 8\pi r_e^2/3$, is the cross section for the process of interest, $\beta = v_z/c$ is the usual relativistic velocity, and r_e is the classical electron radius. Specializing to the case of overlapped Gaussians of the same *rms* size σ, one obtains

$$N_s = \frac{N_p N_e}{4\pi\sigma^2}\sigma_T$$

where N_p is the number of low-energy photons and N_e is the number of electron scatterers. One defines a "luminosity"

$$L = f\frac{N_p N_e}{4\pi\sigma^2}$$

which defines the intensity generated by the scattering geometry. Such a quantity may be used to evaluate the geometry, much as the usual definition of luminosity is used in

0-7803-4376-X/98/$10.00 © 1998 IEEE

particle physics. Typical values fall in the 10^{33} cm^{-2}sec^{-1} range, for the types of devices that we will consider. Also note that as N_p tends to be proportional to N_e in an FEL oscillator geometry, luminosity can scale as rapidly as N_e^2 (i. e., as the beam current squared) if the electron and photon beam sizes remain the same as the current is changed. To estimate the total X-ray power multiply $L\sigma_T$ by the energy of a typical photon.

2 PROPERTIES OF THE RADIATION

Next, the properties of the backscattered radiation are discussed. As in figure 1, laboratory quantities are referred to a coordinate system with z-axis in the beam direction. The x-axis is taken to be in the (vertical) polarization direction of the circulating laser pulse. The y-axis, into the paper, completes the right-hand set. The origin of the coordinate system is the point of collision; standard polar coordinates θ and ϕ are used to describe the direction of the backscattered radiation. A beam-fixed primed frame is also used, with unit vectors in the same directions as in the laboratory system, and with similar polar coordinates θ' and ϕ'. The beam relativistic factors are $\beta = v_z/c$ and $\gamma = 1/\sqrt{1-\beta^2}$. The energy of the low-energy photons in the laboratory frame will be denoted E_0.

In the beam frame, the upshifted energy of the photons $E' = \gamma(1+\beta)E_0$ is much less than the electron rest energy, and the scattering may be described by the Thomson scattering cross section [3],

$$\frac{d\sigma'_T}{d\Omega'} = \frac{d\sigma'_{T\|}}{d\Omega'} + \frac{d\sigma'_{T\perp}}{d\Omega'}$$

where

$$\frac{d\sigma'_{T\|}}{d\Omega'} = r_e^2 \cos^2\theta' \cos^2\phi'$$

is the scattering into the polarization parallel to the plane of scattering,

$$\frac{d\sigma'_{T\perp}}{d\Omega'} = r_e^2 \sin^2\phi'$$

is the scattering into the polarization perpendicular to the plane of scattering, and r_e is the classical electron radius. The total cross section is $\sigma_T = 8\pi r_e^2/3$, with 3 times the intensity in the perpendicular polarization than in the parallel polarization. These cross sections are used to calculate the total number of photons produced per collision in a given solid angle

$$\frac{dN_{s\|}}{d\Omega'} = \frac{N_p N_e}{4\pi\sigma^2}\frac{d\sigma'_{T\|}}{d\Omega'}$$

$$\frac{dN_{s\perp}}{d\Omega'} = \frac{N_p N_e}{4\pi\sigma^2}\frac{d\sigma'_{T\perp}}{d\Omega'}$$

Now, the distribution must be translated back into the laboratory frame. The scattering angles transform as

$$\cos\theta' = \frac{\cos\theta - \beta}{1-\beta\cos\theta}$$

$$\phi' = \phi.$$

The cross sections are converted by noting that the total number of scattered photons must be Lorentz invariant. Therefore

$$\frac{d\sigma}{d\Omega}(\theta,\phi) = \frac{d\sigma'}{d\Omega'}(\theta'(\theta),\phi'(\phi))\frac{d\Omega'}{d\Omega},$$

and so

$$\frac{d\sigma_{T\|}}{d\Omega}(\theta,\phi) = r_e^2\left(\frac{\cos\theta-\beta}{1-\beta\cos\theta}\right)^2\frac{\cos^2\phi}{\gamma^2(1-\beta\cos\theta)^2}$$

$$\frac{d\sigma_{T\perp}}{d\Omega}(\theta,\phi) = r_e^2\frac{\sin^2\phi}{\gamma^2(1-\beta\cos\theta)^2}.$$

These cross-sections have the characteristic opening angle of $1/\gamma$ for the majority of the scattered radiation.

The total intensity is calculated by multiplying the number of scatters per collision by the collision frequency and photon energy. In general, the energy of the back-scattered photons is

$$E = \gamma^2(1+\beta)(1+\beta\cos\theta')E_0 = \frac{(1+\beta)E_0}{1-\beta\cos\theta},$$

and the scattering intensity, in power per unit solid angle, is

$$\frac{dP_{\|}}{d\Omega} = L\frac{(1+\beta)E_0}{1-\beta\cos\theta}\frac{d\sigma_{T\|}}{d\Omega} \qquad (1a)$$

$$\frac{dP_{\perp}}{d\Omega} = L\frac{(1+\beta)E_0}{1-\beta\cos\theta}\frac{d\sigma_{T\perp}}{d\Omega}. \qquad (1b)$$

Alternatively, these results are obtained from the standard synchrotron radiation integrals; I have not been able to find these expressions in such a simple form in the extant literature.

The obvious generalization of Eqs. (1) to include nonzero electron and optical beam angles is to convolve over the (unit normalized and zero centered) relative angle distribution of the two beams. The generalization to include finite pulse effects is also straightforward:

$$\frac{dP_{\|}}{d\omega d\Omega} = \frac{fc}{4\pi^2}|\tilde{E}(\frac{\omega(1-\beta\cos\theta)}{(1+\beta)})|^2\frac{d\sigma_{T\|}}{d\Omega}$$

$$\frac{dP_{\perp}}{d\omega d\Omega} = \frac{fc}{4\pi^2}|\tilde{E}(\frac{\omega(1-\beta\cos\theta)}{(1+\beta)})|^2\frac{d\sigma_{T\perp}}{d\Omega},$$

where $\tilde{E}(\omega) = \int E(t)e^{i\omega t}dt$ is the Fourier transform of the incident electric field of the low-energy photons. As there are about 40 oscillations in the micropulse, the energy spread in the emerging radiation is about 2% at each observation angle. The maximum energy of the scattered photons, at $\theta = 0$, is

$$E_{max} = \gamma^2(1+\beta)^2E_0 \approx 4\gamma^2E_0.$$

	Phase I	Phase II	Phase III	Berkeley	NRL	APS	Units
E_{beam}	42	75	200	50	50	6000	MeV
$E_{photons}$	6	70	3800	30 (90°)	47	10-100	keV
$E_{0photons}$	0.21	0.8	6.2	1.5	1.2	NA	eV
f	37.5 M	37.5 M	37.5 M	2	1 k	0.1-1 G	Hz
σ_x	500	400	200	50	50	300×90	μm
σ_t	1000	1000	1000	100	1000	20,000	fsec
q	135	135	135	(0.05)1300	1000	NA	pC
N_p	8.0×10^{15}	3.4×10^{15}	5.4×10^{14}	2.4×10^{17}	1.0×10^{19}	NA	
L	8.1×10^{37}	5.3×10^{37}	2.1×10^{37}	6.2×10^{33}	2.0×10^{39}	NA	$m^{-2}sec^{-1}$
Brightness	2.2×10^{7}	7.2×10^{7}	5.2×10^{8}	2.4×10^{5}	7.8×10^{10}	5×10^{19}	$mm^{-2}mrad^{-2}sec^{-1}$

Table 1: X-ray source parameters for various backscatter sources

3 RESULTS

The accelerator parameters of Jefferson Lab's IRFEL (IR Demo) project are given in another contribution to this conference [4]. Table 1 presents the expected X-ray brightness from the IR Demo project (Phase I), and two potential upgrade projects: a near-term upgrade to 75 MeV yielding about 1 μm radiation circulating in the FEL (Phase II), and a longer-term upgrade to 200 MeV yielding UV light in the FEL (Phase III). For comparison purposes, the reported performance in the Berkeley measurements, a design patterned on early Naval Research Laboratory (NRL) work on this topic [5], and from a typical high energy storage ring, the Advanced Photon Source (APS), are also given.

Compared to the Berkeley proposal, the Phase I IRFEL at Jefferson Lab will produce photons at a rate 10000 times higher, although the average brightness is only a factor of 100 times higher. The difference is entirely due to the difference in luminosity. The advantages of the Berkeley proposal, namely higher N_p and smaller focussed spot size, are more than made up for by the much higher repetition rate of the IR Demo proposal. Because the IRFEL will normally operate in two-bunch mode, no additional hardware is needed to generate the Thomson scattered X-rays. Because the electron beam and optical beam are guaranteed to overlap (the electron beam is producing the optical beam after all!), many of the alignment and timing issues important in the 90° scattering geometry vanish.

Compared to storage rings designed to produce light or X-rays, the total fluxes are of modest average power. However, the pulse length of the emerging radiation is equal to the micropulse length, which can be very short for a linac beam. The bunch length reported above was from the current design parameters, driven somewhat by IRFEL commissioning needs. An opportunity exists to try to further reduce the bunch length. Given the rather modest charge-per-bunch of 135 pC in our designs, compression to several hundred fsec may be possible, and will be explored.

4 CONCLUSIONS

In this paper formulas are given which completely describe the backscattered radiation for 180° Thomson scattering. These results are applied to analyze a possible X-ray source based on the CW FELs being built/planned at Jefferson Lab. Even though the total brightness is not competitive with that generated by synchrotron light sources, to obtain short pulses ($\sigma_t < 1$ psec) of X-rays, such an arrangement is probably superior. In turn, analyzing the short X-ray pulses may provide an excellent bunch-length diagnostic, particularly because the time of arrival of the X-rays will be known to better than 1 psec. The additional hardware needed to pursue this type of research at Jefferson Lab consists of X-ray handling and diagnostic equipment.

5 ACKNOWLEDGEMENTS

The author would like to thank K. Kim of the Berkeley laboratory for discussing the results at Berkeley with him, and for discussing why such a device might be interesting. G. Neil of Jefferson Lab was helpful with references to previous work in this field, and C. Bohn and H. F. Dylla provided encouragement to pursue this work. This work supported by U. S. DOE Contract No. DE-AC05-84ER40150.

6 REFERENCES

[1] Schoenlein, R. W., *et. al.*, Science, **174**, 236 (1996).

[2] Landau, L. D., and Lifshitz, E. M., *Classical Theory of Fields*, 4th Edition, Section 12.

[3] Jackson, J. D., *Classical Electrodynamics*, 2nd Edition, Section 14.7.

[4] Bohn, C. L., these Proceedings.

[5] Sprangle, P., Ting, A., Esarey, E., and Fisher, A., J. Appl. Phys., **72** 5032 (1992).

ADVANCES IN ORBIT DRIFT CORRECTION IN THE ADVANCED PHOTON SOURCE STORAGE RING

L. Emery M. Borland
Advanced Photon Source, Argonne National Laboratory
9700 South Cass Avenue, Argonne, Illinois 60439 USA

Abstract

The Advanced Photon Source storage ring is required to provide X-ray beams of high positional stability, specified as 17 μm rms in the horizontal plane and 4.4 μm rms in the vertical plane. We report on the difficult task of stabilizing the slow drift component of the orbit motion down to a few microns rms using workstation-based orbit correction. There are two aspects to consider separately—the correction algorithm and the configuration of the beam position monitors (BPMs) and correctors. Three notable features of the correction algorithm are: low-pass digital filtering of BPM readbacks; "despiking" of the filtered orbit to desensitize the orbit correction to spurious BPM readbacks without having to change the correction matrix; and BPM intensity-dependent offset compensation. The BPM/corrector configuration includes all of the working BPMs but only a small set of correctors distributed around the ring. Thus only those orbit modes that are most likely to be representative of real beam drift are handled by the correction algorithm.

1 INTRODUCTION

The mathematics of orbit correction is covered extensively in the literature. In this paper, we discuss the application of these well-known ideas in a realistic situation with non-ideal and possibly malfunctioning BPMs. We also discuss practical issues such as how many BPMs and correctors to use, and mention potential pitfalls.

The main problems we encountered in orbit drift correction are the dependence of rf BPM electrical offset on bunch train intensity and on bunch uniformity within the detected bunch train. The range of offset variation for individual BPMs is actually several times the stability specification (see below), requiring use of compensation schemes to estimate the true orbit from the BPM system data. The intensity-dependent offset variation is largely reproducible and is regarded as a systematic error that can be taken into account. The bunch train uniformity dependence of offset is more difficult to quantify and is considered an error that is randomized at every fill. In addition, we developed a way to handle intermittent bad BPM data without interrupting correction and having to remove the BPM from the correction matrix.

The positron beam in the Advanced Photon Source (APS) storage ring must be stable to 5% of its size. The specified limit on rms orbit motion at the insertion device (ID) source points and the actual uncorrected orbit motions are given in Table 1. Slow motion is seen by the user as an unwanted beam steering, while the fast motion is seen as an unwanted emittance growth.

Table 1: Orbit Motion Specification and Measurements in Various Frequency Ranges

	x β_x = 15 m	y β_y = 10 m
stability specification	17 μm	4.5 μm
slow motion (10^{-4} - 10^{-2} Hz)	18 μm	5 μm
slow motion after correction	2 μm	2 μm
"fast" motion (10^{-2} - 50 Hz)	17 μm	6 μm

The uncorrected orbit drift rms amplitude has not been uniform in all running periods, but it has reached values as high as those listed in Table 1. As the data show, the workstation-based orbit correction handles the slow motion quite effectively, but can do nothing about the fast motion. A real-time orbit feedback system has been designed and tested to reduce the orbit motion up to 50 Hz [1,2]. The latter system should be ready for operations soon. However, since it may encounter difficulties at low frequencies due to some of the problems discussed below, it is anticipated that the workstation-based system will continue to be used to correct orbit drift.

The correction system is implemented on a Unix workstation with Tcl/Tk interfaces and simple SDDS-compliant toolkit programs that communicate with our EPICS control system. The flexibility of this system, which has been described elsewhere [3], has allowed us rapid turnaround in orbit correction implementation changes.

2 GENERAL CONSIDERATIONS

There are a number of issues that are common to any orbit correction algorithm. Orbit correction consists of reading BPM data from the control system and processing this data so that it reflects as much as possible the real orbit with the appropriate frequency components. This involves correcting systematic errors and, if needed, averaging over time or filtering. This set of values is a vector that is multiplied by a correction matrix (in our case a corrector-BPM response matrix that is inverted using SVD). The result is a vector of corrector strength changes that is then applied, typically after multiplication by a dimensionless "gain" factor that is between 0 and 1.

Generally, the algorithm waits an interval after making a change before repeating the whole operation. It is

0-7803-4376-X/98/$10.00 © 1998 IEEE

desirable to make orbit corrections as frequently as possible so that any orbit change can be acted upon as soon as possible. However, the frequency of correction is always limited by practical considerations. In our case, it is limited by the response time of the correctors in reaching their full setpoint value, the need to wait sufficient time for the BPMs to settle to new readbacks, the need to wait for averaging of BPM readbacks, and the response time of the control system. A conservative wait time of 5 seconds guarantees that the new orbit has settled.

As mentioned above, the gain is the fraction of the correction to be applied at every iteration. Given that the correction matrix (whether from a model or experiment) is never known exactly and that the BPMs are not perfectly precise, it is necessary to use a gain lower than 1 for the orbit to converge to the target orbit. Of course, the speed of the correction is reduced by the factor of the gain. We typically use gain factors of 0.4.

3 ORBIT DATA PREPARATION

Proper preparation of the orbit data proved critical to the success of our system. Some of the algorithms we used are new or specific to APS systems.

3.1 Low-Pass Filtering

Low-pass filtering provides sampled BPM data in the frequency band of interest. If the sampled BPM data contain frequencies above half the sampling frequency, the orbit correction will be effectively injecting noise into the lower frequency band. In our system a 2048-turn running average of the orbit position is produced by low-level digital hardware and is made available to local CPUs at a 10 Hz rate. This data is processed by the local CPUs through a one-pole digital filter of a time constant of 10 s. Although the time constant was not optimized in a systematic way, it was made consistent with the correction interval. Its value was selected initially to provide a readback with an rms variation much less that the orbit drift amplitude that we wanted to eliminate.

3.2 Despiking

Under-determined orbit correction (i.e., orbit correction employing fewer singular values than BPMs) effectively "fits" a free betatron oscillation through the many BPMs between correctors. This fitting does more harm than good when an individual BPM suffers a sudden offset shift while no real orbit drift occurred. A conventional orbit correction algorithm will generate an unwanted orbit bump of the opposite sign to the offset change and will minimize the rms of the apparent orbit error in the area. Other linear methods (e.g., best corrector or bump methods) also intrinsically do betatron oscillation fitting and hence exhibit the same behavior.

Since sudden offset shifts are a problem with the APS BPMs, a "despiking" filter is applied to the set of BPM data to smooth out obviously bad data. This filter uses information from neighboring BPMs to test the validity of the data from each BPM. If the reading for any BPM differs from the average of its C nearest neighbors by more than a chosen threshold T, the reading is replaced by the average of its R nearest neighbors. Several passes of the filter may be applied. This stage of the processing is a nonlinear operation, and distinguishes it from the conventional linear correction. The average value of the neighbors may not be the actual orbit value at the suspect BPM, but the reasonable and lower-valued guess allows the orbit correction to proceed without creating an unwanted bump.

During a user store at APS, we use a despiking threshold T of 20 μm, compare to C=36 nearest neighbors, replace suspect points with the average of R=4 nearest neighbors, and employ two passes of the filter. Figure 1 shows an example of despiking of an orbit readback that has obviously bad data.

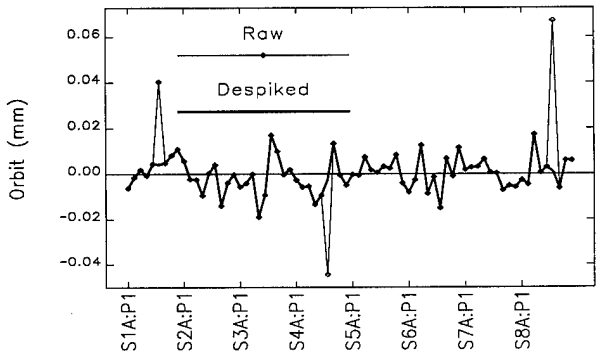


Figure 1: Raw and despiked orbit data for part of the ring.

Another approach to bad BPM data would be to ignore it altogether. This is impractical, as it requires a time-consuming recomputation of the inverse response matrix. It is very efficient to replace the suspect BPM value with another value rather than simply ignoring the BPM in the correction.

3.3 Offset Compensation

In general all BPM systems suffer to some degree from electrical offset variation with bunch train intensity and bunch pattern. For a fixed-bunch pattern, the offset variation as the current decays is in principle reproducible. A measurement of the intensity-dependent offset for all BPMs can be performed and the resulting data used to adjust the BPM readbacks during a user store. The measurement consists of scraping down the beam over a period of about 10 minutes while the orbit correction is running, while simultaneously reading BPM data at short intervals. Typically, we do many such experiments and choose the one that gives the cleanest result. The variation for each BPM is fit with a quadratic as a function on intensity and used to create a look-up table for offset adjustments.

Figure 2 shows offset data for some BPMs from the look-up table. The sum signal of a selected BPM is used as a measure in intensity. At the beginning of a store, the intensity is maximum, and the offset adjustment is necessarily zero for all BPMs.

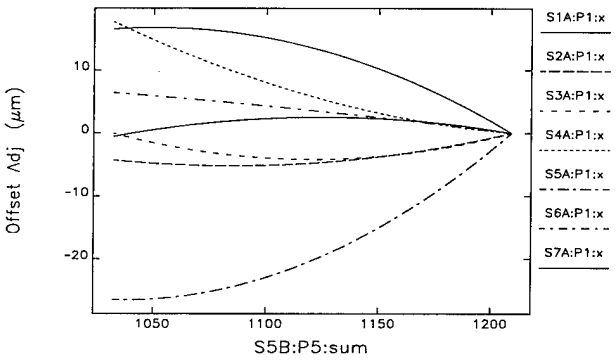


Figure 2: Fitted offset data for some BPMs.

4 BPM/CORRECTOR CONFIGURATION

4.1 Global Orbit Correction

The correction configuration refers to the set of BPMs and correctors used in the correction matrix. In addition, the number of singular values used in the SVD inversion procedure should be considered part of the configuration. We have optimized our orbit drift correction for the case of several weak sources.

In such a case, we expect a smooth-looking orbit composed of a few harmonics near the tune value. While the latter is true in the case of larger individual sources, an orbit kink is present at such a source. This makes the orbit hard to correct unless one of the correctors of the configuration happens to be very near the source.

The correction configuration is comprised of all working BPMs and relatively few correctors. We use as many BPMs as possible in order to reduce the importance of any individual BPM readback. This also increases the effectiveness of the despiking filter mentioned above.

Since we are correcting many small, distributed sources, we use relatively few correctors distributed around the ring: two correctors for each sector that is equipped with an ID, and one in sectors with no IDs. We kept all the singular values in the matrix in order to have the selected correctors acting independently and as locally as possible. The two correctors in each ID sector are particularly good at compensating the ~20 μm global orbit perturbation that occurs from opening or closing the ID. Here, the orbit very close to the ID is not maintained completely. However the local orbit should have been locally steered earlier with the gaps closed. Thus repeatedly closing the ID gap with global orbit correction running should return the X-ray beam to the previously steered position.

Using many more BPMs than correctors and the implied fitting of the despiking orbit has the additional effect of controlling the X-ray beam positions better that the noise level of the rf BPMs in the frequency range of the orbit drift correction [4].

The nonreproducibility of the uniformity of the bunch train contributes to the fill-to-fill orbit variability. To alleviate the problem one can reinject bunch trains until one of sufficient uniformity is obtained. In addition, one can restore the corrector setpoints at the end of the previous fill and run a global correction on the new fill. The global correction is expected to correct any real orbit drift that may occur in the time between the fills and de-emphasize the offset change of individual BPMs. The effectiveness of this procedure is evaluated using bending magnet source X-ray BPMs readbacks over several fills.

A local source of orbit drift will cause the nearby correctors active in the global correction to move in a highly correlated manner. Searching for correlated correctors is expected to aid in locating unknown sources.

4.2 Local Steering

Local orbit bumps are occasionally applied to adjust the position of the X-ray beam at the end of an X-ray beamline. In practice, bump coefficients derived from a lattice model or measured response matrix do not produce an exactly matched bump, particularly in a machine with strong nonlinearities. Our solution is to create an orbit correction configuration using two BPMs on either side of the source point and 40 others distributed evenly around the ring. Two pairs of correctors on each side of the source point provide steering. The resulting 4×42 correction matrix is very over-constrained. While the first iteration of the local correction will be unmatched to whatever degree the bump coefficients are inexact, subsequent iterations will correct for this.

5 ACKNOWLEDGMENTS

We thank F. Lenkszus and K. Evans for the programming work they contributed to orbit correction. We thank J. Galayda for several insights into orbit correction.

This work was supported by the U.S. Department of Energy, Office of Basic Energy Sciences, under Contract No. W-31-109-ENG-38

6 REFERENCES

[1] J. Carwardine, K. Evans, "Evaluation of the Global Orbit Correction Algorithm for the APS Real-Time Orbit Feedback System," these proceedings.

[2] J. Carwardine, G. Decker, K. Evans, A. Hillman, F. Lenkszus, R. Merl, A. Pietryla, "Commissioning and Performance of the APS Real-Time Orbit Feedback System," these proceedings.

[3] M. Borland, "Applications Toolkit for Accelerator Control and Analysis," these proceedings.

[4] G. Decker, "Performance of the APS Storage Ring," these proceedings.

INVESTIGATION OF OPEN-LOOP BEAM MOTION AT LOW FREQUENCIES AT THE APS

S. H. Kim, G. Decker, C. Doose, D. Mangra, and R. Merl
Advanced Photon Source, Argonne National Laboratory
9700 South Cass Avenue, Argonne, Illinois 60439 USA

Abstract

Sources of transverse beam motion in the APS storage ring have been investigated for ground-motion- and water-system-induced vibrations of the magnet and vacuum systems, and for power supply ripple. The displacement of magnets in a bandwidth of 4-30 Hz have been reduced significantly by inserting viscoelastic damping pads between the girder supports and pedestals, and by welding the magnet cooling headers to the ceiling of the storage ring tunnel. Current ripple on magnet power supplies was identified as a source of horizontal beam motion. Beam motion was measured without the closed-orbit feedback system activated. At β_x=15.4 m and β_y=10.4 m the rms beam motion in the 0.02-30 Hz band was 22.7 μm and 6.3 μm in the horizontal and vertical planes, respectively. A few narrow-band structures of the horizontal beam motion spectrum in the 1-4 Hz band have to be investigated further to identify the sources.

1 INTRODUCTION

The tolerances of the rms beam motion in the storage ring (SR) of the Advanced Photon Source (APS) [1] are to be less than 4.4 μm and 17 μm in the vertical and horizontal planes, respectively, in a bandwidth of 4-50Hz.

In the horizontal or vertical planes, the transverse beam motions or time-dependent closed-orbit distortions at position s in the SR due to a kick $\Delta\theta(s_k,t)$ at position s_k may be expressed as [2]

$$\Delta x_c(s,t) = \frac{\sqrt{\beta(s)}}{2\sin\pi\upsilon}\sum_k \Delta\theta(s_k,t)\sqrt{\beta(s_k)} \cdot \cos[|\psi(s)-\psi(s_k)|-\pi\upsilon], \quad (1)$$

where $\beta(s)$ and $\beta(s_k)$ are the beta functions at s and s_k, respectively, ψ is the betatron phase, υ is the betatron tune of the SR. The kick at s_k may be expressed in general as a Fourier series:

$$\Delta\theta(s_k,t) = \sum_j \frac{(\Delta B l)_{kj}}{B\rho}\cos(\omega_{kj}t+\theta_{kj}). \quad (2)$$

Here $B\rho$ = 23.349 T·m is the beam rigidity corresponding to 7.000 GeV, and ω_{kj} is the angular frequency of the j-th kick at s_k.

When the transverse beam motions are superimposed to the beam offset for a single bunch of a beam in the SR, the beam signal to an rf beam position monitor (BPM) located at s is

$$f(s,t) = \sum_{n=-\infty}^{\infty}\delta\left(t-n\frac{2\pi}{\omega_r}\right)[\Delta x(s)+\Delta x_c(s,t)], \quad (3)$$

where ω_r is the angular revolution frequency, $\Delta x(s)$ is the offset of the transverse beam position, and $\Delta x_c(s,t)$ is the time-dependent transverse beam motion of Eq. (1). The frequency spectrum of Eq. (3) is as follows:

$$F(s,\omega) = \omega_r\sum_{n=-\infty}^{\infty}\left\{\Delta x(s)\delta(\omega-n\omega_r)+\frac{1}{2}\sum_{kj}|\Delta x_c(s,\omega_{kj})|[\delta(\omega-n\omega_r-\omega_{kj})+\delta(\omega-n\omega_r+\omega_{kj})]\right\}, \quad (4)$$

with $|\Delta x_c(s,\omega_{kj})|$ as the spectral amplitude of the beam motion, which will be shown as a sideband to the offsets of the beam position. Major sources of time-dependent kicks in the SR are the effective dipole field due to the displacement of quadrupole magnets (quads), power supply current ripple, induced field due to eddy currents in the vacuum chamber, and mechanical vibrations.

Displacement of the quads for the strong-focusing lattice of the SR causes a relatively high amplification factor of the beam motion. Random uncorrelated quad motions of rms displacement Δx_q result in rms beam motion of amplitude $17.2\beta^{1/2}\Delta x_q$, and the amplification for random girder motion is $7.4\beta^{1/2}\Delta x_{girder}$, where β at the insertion device source point is 14.2 m [3].

2 MECHANICAL VIBRATIONS

The vibration modes of the quad girders are dominated by a horizontal bending mode with lowest resonance frequency of approximately 10-11 Hz. The quad motion had a peak displacement of 210 nm at 10.2 Hz and an integrated rms displacement of 320 nm in 4-54 Hz.

In order to reduce the quad displacement, vibration damping pads were inserted between the wedged jack supports and the pedestals [3]. The damping pads are made of two layers of 0.15-mm-thick Anatrol-217 visco-elastic material and three layers of 1.6-mm-thick stainless steel plates. The damping pads were easily inserted below the jack supports with minimal impact on the girder alignment. The damping pads reduced the peak displacement by a factor of three and the resonance frequency was shifted downward a few Hz in general. The total rms displacement was reduced by a factor of two. After three successive simulated alignments to shear the pads up to 0.75 mm, no appreciable changes in Q-value at the resonance

0-7803-4376-X/98/$10.00 © 1998 IEEE

frequency have been observed. Besides the ground-motion-induced displacements, the cooling-water headers induced magnet displacements. Figure 1 shows measurements of the rms displacements for sector 10 after welding the water header to the ceiling of the SR tunnel and an unwelded sector 9. The vertical axis in Fig. 1 denotes horizontal rms displacement calculated for the 4-50 Hz band. Along the horizontal axis the measurement times are shown at the bottom, and the on/off status of the cooling water for the magnet and vacuum chamber are shown on the top. The data indicate that the impact of the vacuum chamber cooling water on the girder vibration is minimal. The magnet cooling water, on the other hand, increases the quad vibration by more than a factor of two, regardless of whether the headers were welded or not. The welds reduced the quad rms displacement from about 130 nm to 90 nm. The ratios of the displacements between the quads and pedestals, however, are not significantly different for the welded and unwelded headers.

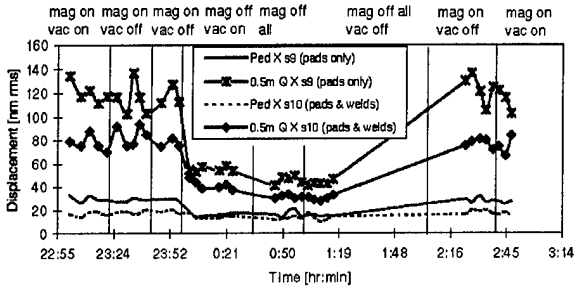


Figure 1: Displacements (rms in 4-50 Hz) of two quads and two pedestals with and without welding of the magnet cooling water headers. The on/off conditions of the cooling water for the magnets and vacuum chambers are shown on top.

To further investigate the impact of the welds when the cooling water was on, coherences of the vibrations between the quads and pedestals were measured; the data in the 6-11 Hz band are shown in Fig. 2(a). For the girder in the welded sector, the quad rms displacement was 44 nm compared to 106 nm for the one in the unwelded sector. At the same time the coherence for the unwelded case was lower, as shown in Fig. 2(b), which indicates that the water header contributed more than half of the vibration when the headers were not welded. The headers were welded as a test in two sectors; it was decided not to weld the whole ring due to cost vs. benefit.

3 MEASUREMENTS OF BEAM MOTION

Low-frequency beam motions in the SR were measured using a Hewlett Packard 89440A Vector Signal Analyzer [4] which obtains the frequency spectrum of the beam signal from rf BPMs [5]. The periodicity of the output signal from a BPM module is one-half the revolution frequency, $\omega_r/2$. This is due to the fact that beam positions are measured with a 180° phase shift on alternate turns for removal of systematic offsets. The amplitude of the signal

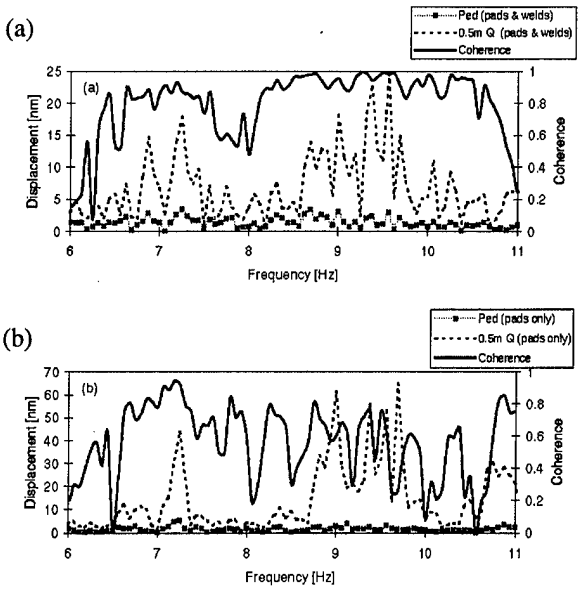


Figure 2: Coherence of the vibrations between the quads and pedestals (a) with and (b) without the welds. Without the welds the coherence is low, but the rms displacement in 6-11 Hz is 106 nm compared to 44 nm for the welded case.

at $\omega_r/2$ is the average position offset of the beam, $\Delta x(s)$ in Eq. (4), relative to the geometric center of the four buttons. Low-frequency beam motion corresponding to $|\Delta x_c(s,\omega_{kj})|$ produces an amplitude modulation of the position offset signal and appears as sideband to the $\omega_r/2$ "carrier."

Figure 3 shows a typical horizontal and vertical beam motion spectra measured at a position of β_x=15.4 m and β_y=10.4 m in sector 12 in a bandwidth of ±30 Hz with a frequency resolution of 0.1 Hz. The magnitude of the beam offset signal at $\omega_r/2$=135.774 kHz (f = 0 in Fig. 3) is not shown in the figure. The horizontal rms beam motion in a bandwidth of 1-30 Hz was 33.1 μm with its major contribution in 1-4 Hz. For the vertical beam motion the rms value in the band 1-30 Hz was less than 5 μm. Only a few of the narrow-band structures in the spectra could be reproduced. When averaged from the measurements of 40 BPMs (one in each sector) at the same β_x and β_y, the rms beam motions were 22.7 μm and 6.3 mm in the horizontal and vertical directions, respectively.

In order to correlate the beam motion with that of a magnet, the beam motion was measured while a quad girder in sector 19 was being displaced with a "shaker." The spectra of horizontal displacements for the AQ4 quad on the girder and the beam motion in an adjacent sector are shown in Fig. 4. The girder has a resonance frequency at approximately 10 Hz and the shaker has its own resonance frequency around 14 Hz. The amplification of beam/quad displacements is approximately two. This data and Fig. 3 indicate that horizontal beam motion due to a 1-μm quad displacement from a single girder vibration near 10 Hz would be difficult to detect.

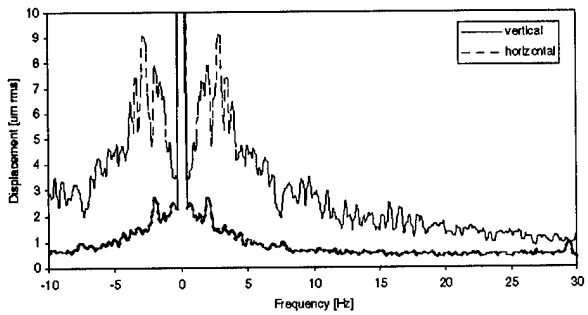


Figure 3: Horizontal and vertical beam motion spectra measured at a position of β_x=15.4 m and β_y=10.4 m with a frequency resolution of 0.1 Hz. The magnitude of the beam offset at 135.774 kHz (f=0 in the figure) is not shown.

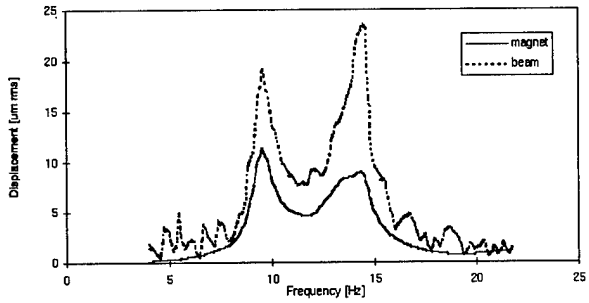


Figure 4: Correlation of a quad displacement in sector 19 and beam motion in sector 20 both in the horizontal direction. The quad girder was displaced using a shaker.

4 CURRENT RIPPLE

Statistics of current fluctuations for quads, sextupoles, and correctors were computed from 100 current samples, and some of those power supplies were measured in the frequency domain to identify the ripple spectrum responsible for the beam motion spectrum in certain bandwidths. A sextupole magnet power supply had current ripple of 0.2 A near 6.5 Hz. After modification of the power supply, the horizontal beam motion near that frequency was reduced from 21.9 μm to 8.5 μm [6]. The direct vertical field-integral for the magnet at the current ripple of 0.2 A should be less than 0.8×10^{-8} T·m within 1 mm of the magnetic axis. However, the ripple sextupole field due to the current ripple induces a considerable amount of eddy current in the aluminum vacuum chamber, which in turn induces a vertical field inside the chamber. The main contribution of the eddy current comes from the higher field at the larger aperture of the magnet. It should be noted that the direct and induced fields are out of phase. At the ripple current the induced field-integral was approximately 0.25×10^{-4} T·m, which is an expected field strength for a beam motion of 10-20 μm.

5 CONCLUSION

By inserting viscoelastic damping pads between the girder supports and pedestals, and by welding the magnet cooling headers to the ceiling of the storage ring tunnel, the displacements of magnets induced by the vibrations in the floor and water system were reduced by more than a factor of two. Current ripple of a sextupole magnet was identified as a source of beam motion. The average rms beam motion at β_x=15.4 m and β_y=10.4 m was 22.7 μm and 6.3 μm in the horizontal and vertical planes, respectively, in the band 0.02-30 Hz. Narrow-band structures of the horizontal beam motion spectrum, most of them not reproducible, have to be further investigated, the 1-4 Hz band in particular.

6 ACKNOWLEDGMENTS

The authors gratefully acknowledge J. Galayda for his encouragement and direction of the work and L. Emery for his helpful discussions on beam motion induced by current ripple. This work was supported by the U.S. Department of Energy, Office Basic Energy Sciences, under Contract No. W-31-109-ENG-38.

7 REFERENCES

[1] J. N. Galayda, "The Advanced Photon Source," Proc. 1995 PAC, IEEE 95CH35843, 4 (1996).

[2] M. Sands, "The Physics of Electron Storage Rings: An Introduction," SLAC-121 (1970).

[3] G. Decker, Y.G. Kang, S. Kim, D. Mangra, R. Merl, D. McGhee, and S. Sharma, "Reduction of Open-Loop Low Frequency Beam Motion at the APS," Proc. 1995 PAC, IEEE 95CH35843, 303 (1996).

[4] The explicit reference to a particular product does not imply that other vendors might not be able to supply equivalent products.

[5] E. Kahana, Y. Chung, A.J. Votaw, and F. Lenkszus, in *Beam Instrumentation Workshop*, Santa Fe, NM 1993, AIP Conference Proc. 319, 201 (1994).

[6] S. Kim, G. Decker, C. Doose, R. Hogrefe, D. Mangra, R. Merl, and S. Milton, "Investigation of low-frequency beam motion at the Advanced Photon Source," *Rev. Sci. Instrum.*, 67(9) 1996 (CD-ROM).

EXPERIMENTAL CALIBRATION OF VUV RING OPTICS

J. Safranek and S.L. Kramer*
National Synchrotron Light Source, Brookhaven National Laboratory, Upton, NY 11973

Abstract

The individual quadrupole gradients, undulator focusing, beam position monitor (BPM) gains, and orbit steering magnet calibrations in the NSLS VUV Ring were determined by analyzing the measured orbit response matrix with the computer code LOCO[1] (Linear Optics from Closed Orbits). The measured orbit response matrix is the change in orbit at the BPMs with changes in steering magnet excitation. The analysis showed beta function distortions of $\pm 35\%$ and $\pm 25\%$ horizontally and vertically. The design periodicity of the optics was restored by adjusting the quadrupole gradients to restore the periodicity of the response matrix. This lead to an increase of about 18 percent in the beam lifetime at 500 mA with a slight (3 and 7 percent) decrease in both the horizontal and vertical electron emittances as determined from the beam sizes measured using a synchrotron light monitor.

1 INTRODUCTION

The VUV Ring is an 800 MeV storage ring at Brookhaven National Laboratory that has been producing synchrotron radiation for experiments since 1983. The storage ring magnet lattice has the Chasman-Green lattice [2, 3], a design that has been subsequently adopted by many of the third generation light sources.

The lattice consists of four super periods, each with a dispersion-free straight section (for injection, RF cavities and two insertion devices) and a double-bend achromat having a quadrupole doublet that provides the achromatic focusing (QAs). The dispersion-free straight sections have a symmetric pair of horizontally focusing quadrupoles (QFs) and horizontally defocusing guadrupoles (QDs). The magnet layout is shown at the top of Figure 1. This design should produce linear optics with a four-fold periodicity, if within each of the three quadrupole types, the individual magnets have the same gradients. This periodicity is broken primarily by the focusing effects of the two insertion devices, but also by field gradient errors from quadrupole magnet construction tolerances and orbit offsets in sextupoles, which contribute a linear focusing effect on the beam. To better control the periodicity breaking due to the insertion devices, the QFs and QDs in each of these straight section were seperately powered. The calibration of the gradients in these seperately powered quadrupoles provides another source of periodicity breaking, even with the undulators removed from the ring. The total number of independent focusing parameters is determined by the seven quadrupole powers supplies that control the gradients in the seven families of quadrupoles (3-QFs, 3-QDs and 1-QAs).

Despite the additional power supplies, optics measurements indicated that the β-functions varied significantly from the design 4-fold periodicity. This break in periodicity of the lattice functions degrades the performance of the ring from the design. The work described in this paper was undertaken to better understand the sources of the break in periodicity and derive the settings for the quadrupole power supplies that best restores the design optics.

2 OPTICS ANALYSIS

The VUV Ring optics were characterized by analyzing the measured orbit response matrix with the computer code LOCO [1]. The orbit response matrix, M, is defined as

$$\begin{pmatrix} \boldsymbol{x} \\ \boldsymbol{y} \end{pmatrix} = M \begin{pmatrix} \boldsymbol{\theta}_x \\ \boldsymbol{\theta}_y \end{pmatrix}, \tag{1}$$

where $\boldsymbol{x}$, $\boldsymbol{y}$ are the shift in closed orbit at the BPMs for a change in steering magnet excitation $\boldsymbol{\theta}_x$, $\boldsymbol{\theta}_y$. LOCO adjusts the parameters of a computer lattice model (in this work we used a MAD [4] model) in order to minimize the χ^2 difference between the model, M_{mod}, and measured, M_{meas}, response matrices.

$$\chi^2 = \sum_{i,j} \frac{(M_{\mathrm{mod,ij}} - M_{\mathrm{meas,ij}})^2}{\sigma_i^2}, \tag{2}$$

where the σ_i are the measured BPM rms noise levels. For the VUV Ring analysis, we used a model with no coupling between horizontal and vertical planes. We did not use the coupling terms in the response matrix (e.g. the shift in vertical orbit when changing horizontal steering magnets). Only the normal gradients in the quadrupoles were fit. The VUV Ring has 24 BPMs that read in both the horizontal and vertical planes. Sixteen horizontal and 16 vertical steering magnets were used to measure the response matrix, so a total of 768 data points were used in the statistical fit.

In order to minimize the number of parameters used in the fit and thus maximize the accuracy of the fitted magnetic gradients, the response matrix was first measured with all sextupoles turned off and all insertion devices open. The parameters varied to fit this response matrix included the individual gradients in the 24 quadrupoles, the dipole gradient, the horizontal and vertical gains of the 24 BPMs, and the calibrations of the 32 steering magnets. In addition, the energy shifts associated with changing the 16 horizontal

* Work performed under the auspices of the U.S. Department of Energy

0-7803-4376-X/98/$10.00 © 1998 IEEE

steering magnets were varied in the fit. When a horizontal steering magnet is changed, there is a shift in the electron energy and an associated shift in the closed orbit proportional to the dispersion. This shift is not included in the model. To account for this, an orbit shift proportional to the measured dispersion was added to the model response. The proportionality constant for the dispersion was fit, and the fit result is the energy shift for each horizontal steerer. In all, 121 parameters were used to fit the 768 data points in the response matrix. After the fit, the measured orbit response matrix differed from the model by 2.2 μm rms compared to the measured BPM rms noise level of 1.6 μm.

Then the sextupoles were turned on and the response matrix was measured again. This second matrix was used to calibrate the gradients in the sextupoles. Response matrices were also measured after closing each of the insertion devices. These were used to calibrate the vertical focusing associated with each insertion device.

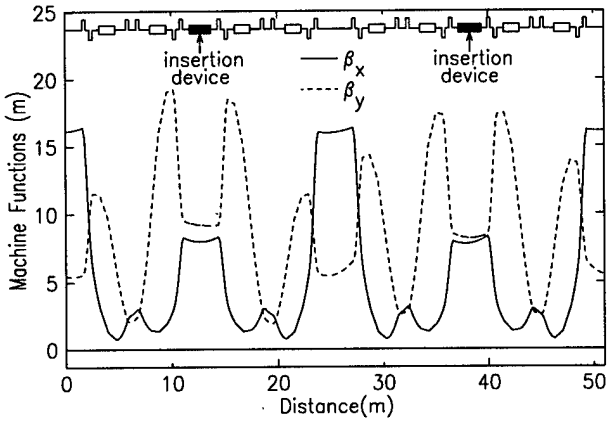


Figure 1: The β-functions in the NSLS VUV Ring calculated by LOCO as described in Section 2, before the periodicity restoration described in Section 3 was applied.

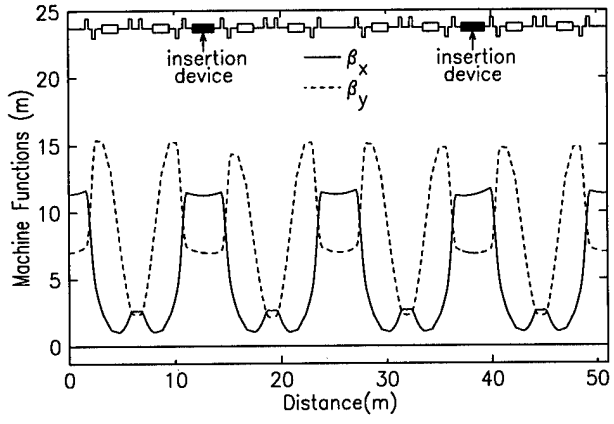


Figure 2: The β-functions in the NSLS VUV Ring calculated by LOCO as described in Section 2, after the periodicity restoration described in Section 3 was applied.

In this way we arrived at a complete model of the VUV Ring focusing optics. Figure 1 shows the β-functions for this model. This model was measured with the maximum focusing effect (smallest gap and maxiumum strength parameter, K= 7.6) for the second insertion device (at the right hand end) of the lattice. The effect of this insertion device on the vertical β-function is clearly seen when compared to the weaker insertion device (K$\approx$1) at the left hand end of the lattice. As had been expected, the distortions from the periodic design were large (up to $\pm$35% horizontally and $\pm$25% vertically). The injection straight section had been observed to have an increased radiation loss during injection with the insertion device gap closed, consistent with the larger β_x predicted by LOCO in this region.

3 PERIODICITY RESTORATION

Section 2 described a method for determining a model of the individual gradient errors in each of the VUV magnets - the quadrupoles, sextupoles, and insertion devices. In this section we present a method for finding those quadrupole power supply settings that compensate for these errors and restore the design periodicity. The method has also been used successfully at the ALS [5]. The algorithm is similar to orbit correction, where one does not usually try to find the specific dipole errors that caused an orbit shift. Instead one trys to find the changes in orbit steering magnet excitation that would best reproduce the orbit shift, then applies just the opposite steering magnet changes to cancel the orbit shift.

In this case we model the break in four-fold periodicity by the gradient difference between the quadrupole families (one gradient for all quadrupoles with a common power supply) that best reproduces the measured response matrix. We look at the variation in the gradients between the three different QF families and between the three different QD families. Then we adjust the power supplies in the ring so that the fit gradients for the three QF families are the same and the three QD families are the same. In this way, the quadrupole power supplies are adjusted to maximize the periodicity of the measured response matrix.

The response matrix was measured with insertion devices closed and sextupoles on, the normal operating condition for the ring. Then we first performed the analysis described in Section 2 on this matrix, in order to fix the calibrations of the BPMs, the steering magnets and the energy shifts of the horizontal steering magnets. Then we took as a "model" of the storage ring a lattice with zero gradient errors in the sextupoles and insertion devices and with no individual quadrupole gradient errors (i.e. all quadrupoles in each family have the same gradient). The χ^2 difference between the model and measured response matrix was minimized by varying only the 7 quadrupole family gradients. If the fitted values for the gradients in the 3-QF and 3-QD families differ, this means they could be changed to improve the periodicity of the response matrix. Then the power supply current, I_i, for each of the three QF and QD

families was changed as follows:

$$(I_i)_{new} = (I_i)_{old} \frac{< K >_{QF}}{K_i}, \qquad (3)$$

where K_i is the fitted gradient for the i-th QF family and $< K >_{QF}$ is the average of the K_i over the individual quadrupoles in all the QF families. The power supply currents were similarly corrected in the 3-QD families. The current in the one QA family power supply was not changed, since it already had the required periodicity in the "model".

The changes predicted by Equation (3) were applied to the 3-QF and 3-QD power supplies in the VUV ring and the linearity of the change in the quadrupole field gradients (assumed in Eq. (3)) were verified using the available high precision Hall probe installed in one magnet of each quadrupole family. The resulting lattice had its response matrix measured and analyzed using the non-periodic model of the ring as described in Section 2. The calculated β-functions resulting from this new lattice of VUV ring are plotted in Figure 2. The resulting distortions from the four-fold design periodicity are greatly reduced: $\pm 3\%$ horizontally and $\pm 4\%$ vertically. The larger vertical periodicity breaking resulting from the large periodicity breaking of the vertical focusing effects of the two very different insertion devices.

4 IMPROVEMENT IN THE VUV RING PERFORMANCE

Several properties of the VUV Ring operation were improved with the increased four-fold periodicity obtained from the changes in Section 3. Measurement of the transverse profile of the beam with a focused synchrotron light monitor, showed a 3% and 7% reduction in the horizontal and vertical emittances, respectively. This resulted from the reduction in the larger variations of the β_x in the dipole magnets and the skew quadrupoles in the original lattice compared to the restored periodicity lattice. Despite this decrease in transverse emittance, the lifetime of the beam increased at all currents, as shown in Figure 3. This increase was about 15% at 850 mA and increased to about 18% at 550 mA. Calculations of the Touschek scattering lifetime with the program ZAP[6], using the calculated β-functions and the measured emittance showed an increase of 50 to 65% in the lifetime coming mostly from the reduction in the β_x in the long straight sections without insertion devices. This prediction was observed by comparing the radiation loss rate in detectors installed in these straight sections, which measured a 62 to 68% reduction in loss rate depending on current after the periodicity restored lattice was implemented. The difference of the total lifetime improvement from this loss rate could be due to changes in gas scattering partial lifetime due the increase in the β_y in parts on the ring.

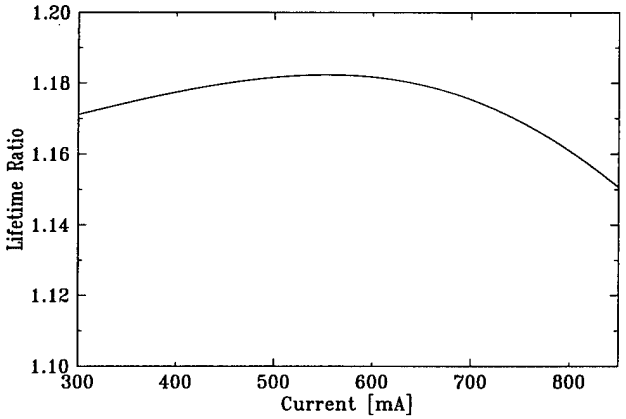


Figure 3: The measured increase in beam lifetime versus current after the periodicity restoration relative to before restoration.

5 CONCLUSION

Measurement of the the actual lattice properties of the the VUV Ring at NSLS yielded a model of the periodicity breaking of the focusing optics in the Ring. This model made it possible to predict a method of restoring the four-fold periodicity of the lattice functions. Changing the focusing optics as predicted by this model yielded significant improvement in beam lifetime while at the same time making slight reductions of the measured beam emittance. This improvement was attributable to the reduction of the peak to peak variations of the ring β-functions.

6 REFERENCES

[1] J. Safranek, 'Experimental Determination of Storage Ring Optics Using Orbit Response Measurements', Nucl. Intr. and Meth. A388, (1997), p. 27.
'Beam-based modeling and control of storage rings', these proceedings.

[2] R.Chasman,G.K.Green and E.M.Rowe, "Preliminary Design of a Dedicated Synchrotron Radiation Facility", IEEE Trans. Nuc. Sci.,NS-22,p1765 (1975).

[3] "Proposal for a National Synchrotron Light Source", BNL-50595, (1977).

[4] H. Grote and F.C. Iselin, "The MAD Program, Version 8.1", CERN/SL/90-13, June 17, 1991.

[5] D. Robin, J. Safranek, W. Decking, and H. Nishimura, 'Global Beta-beating Compensation of the ALS W16 Wiggler', *These proceedings.*

[6] M.S.Zisman, et.al., "ZAP User's Manual", LBL-21270, (1986).

STATUS REPORT OF THE ESRF

JM Filhol, L. Hardy, ESRF, Avenue des Martyrs, BP 220, 38043 Grenoble Cedex, France

Abstract

The ESRF is now in full routine operation with nearly 30 beamlines taking X-ray beam and opened to external Users. The performances of the Machine have been steadily improved during the last year : increase of the intensity up to 200 mA, reduction of the vertical emittance, lowering of the vertical β in the straight sections, reduction of the undulator minimum gap, all of these resulting in a significant gain on the achieved photon brilliance. In parallel to this net improvement, the routine operating standards have been largely improved with a Mean Time Between Failures larger than 40 hours and an availability better than 94 % over the 5000 hours of beam scheduled in 1996. In addition, the versatility of the Machine has been enlarged with an increasing number of operating modes so as to better satisfy the different Users' requirements (multibunch mode, single bunch mode, 16 bunch mode and various hybrid modes).

1 INTRODUCTION

The ESRF was the first of the third generation high energy synchrotron radiation sources to start User operation in 1994. The 10 years construction phase will end in 1998 with the completion of the last of the 30 ESRF beamlines. Today 27 beamlines (including 5 Collaboration Research Group beamlines) are open to the Users, and during the year 1996, a total of 518 experiments were carried out during 6563 shifts (of 8 hours) by 1777 external Users.

2 PERFORMANCES

Brilliance

At the same time the ESRF was starting User operation, a lot of developments were undertaken to increase the brilliance available to these Users [1]. The present situation is summarised in table 1.

Parameters	Units	FPR Design Goal	Routinely served in USM (April 1997)	Medium term objectives *
Current	mA	100	200	200
Associated lifetime	hours	8	50	60
Lifetime @ 100mA	hours	8	80	100
Horizontal Emittance ε_x	10^{-9} m.rad	6.2	4	3
Vertical Emittance ε_y	10^{-12} m.rad	620	40	10
ID minimum gap	mm	20	16	11
Brilliance @ 1• 1.6m undulator	ph/s/mm²/mrad² /0.1%Bwidth	$6\ 10^{17}$	$2.1\ 10^{19}$ (low βz)	$8.3\ 10^{19}$ (low βz)
Brilliance @ 1• 5m undulator	ph/s/mm²/mrad² /0.1%Bwidth	$2\ 10^{18}$	$8.8\ 10^{19}$ (low βz)	$3.8\ 10^{20}$ (low βz)

* End of 1997

Table 1 : Evolution of the brilliance at the ESRF.

Position stability

For the beamlines to fully benefit from this high brilliance, an excellent beam position stability has to be provided and figures less than 10% of beam sizes and divergences are routinely achieved thanks to the automatic closed orbit correction running every 5 minutes. With the very small vertical emittance, the required vertical position stability starts to be at the limit of the feasibility (a few μm) and all sources of errors or drifts have to be minimised [2]. To reduce the fast fluctuations of the vertical beam position, which exceed the 10% specifications, a fast AC position feedback is being developed. The goal is to reduce the amplitude of the beam oscillations in the vertical plane in the frequency range from 0.1 Hz to 100 Hz. The strategy will consist in applying a global correction over the full machine and not several local corrections on each ID straight section. This system will rely on 16 dedicated electron BPM's (located in the straight sections) and 16 fast steerer magnets. It will be controlled by a central DSP board communicating with local DSP boards via fast data links operating at a 44 kHz frequency.

Lifetime

After several years of operation, the ring vacuum vessels (stainless steel) have been fully conditioned and the average dynamic pressure is about 2.10^{-9} mbar at I=200 mA. Such a low pressure corresponds to a very large gas scattering lifetime. In fact, even on a 6 GeV machine, the main limitation of the lifetime comes from Touchek scattering due to the increased density in the bunch volume. This explains the moderate lifetime (8 hours) in single bunch and 16 bunch modes, but also shows up in multibunch mode, due to the high intensity (200 mA) and the low coupling (1%), A significant increase in lifetime was obtained at 200 mA by increasing the number of circulating bunches thereby reducing the current per bunch: From 40 hours in 1/3rd filling the lifetime jumped to more than 50 hours in 2/3rd filling, at 200 mA. When lengthening the bunch train, the machine gets more sensitive to HOMs developing in the RF cavities and this was overcome by a careful temperature control of these cavities [3]. An efficient way to increase the Touchek lifetime is to enlarge the energy acceptance. By moving the injection septum away from the stored beam (from 13 mm to 19 mm), a net gain of several hours was achieved on the lifetime in 16 bunch (from 7h up to 11h). However, a larger gain was expected and investigations are being pursued to enlarge the present ± 3% energy acceptance.

0-7803-4376-X/98/$10.00 © 1998 IEEE

3 OPERATION AT THE ESRF

Since 1993, when the beam was delivered for the commissioning of the first beamlines, until 1997, the number of hours dedicated for the Users (the User Service Mode) has been progressively increased: from 2984 hours in 1993 to 5359 hours in 1997. The ultimate goal is to deliver 6000 hours per year in USM, which should be reached before the year 2000. Throughout these years, our guidelines were always to improve the reliability of the Machine, its meantime between failures whilst increasing the beam performances. Four years after the first USM shift, we can state that these three goals have been met. In 1996, only 3% of the operation time was lost due to failures, the remaining 97% being composed of the time for the refills (2.5%) and the delivery (more than 94%). Not only is the availability important but the meantime between failures (MTBF) which is of major interest for the Users. This figure which was only 13 hours in 1994 has now been increased to more than 41 hours in 1996, i.e. 3 times better. The mean duration of one failure is now about one hour. These good results are not a matter of chance. Many actions have been undertaken to improve the reliability of the Machine, among others:

- Preventive maintenance on the water circuitry: a lot of beam losses occurred due to cooling interlocks following the blocking of some magnet cooling pipes by metallic dust circulating in the water circuits. Since 1995 when the preventive maintenance policy was initiated, very few failures have been recorded as far as this piece of equipment is concerned.
- High Quality Power Supply (HQPS): the Grenoble area is subject to violent storms during the summer the consequence of which are severe drops on the electrical mains resulting in beam losses. Since summer 1995, ten units (1 MW each) have been operational to take over any electrical mains drop. The HQPS has been operating for more than 1 year now and the conclusions to be drawn are very positive. Over the full year 96, more than 220 drops recorded on the input electrical mains have been smoothed, avoiding beam trips with all their possible direct and indirect consequences. It is clear that the very significant improvement in Mean Time Between Failures described above can be, for a large part, attributed to the unperturbed primary power delivered by the HQPS. At the same time this has enabled intrinsic faults in equipment to be clearly distinguished from actual outside perturbations. Moreover, the absolute low harmonic pollution engendered by the HQPS on site means that all power converters will have increased lifetimes.
- Radio-frequency system : Since May 1995, the machine has been running with 2 klystrons each of them feeding 2 cavities. The main advantage lies in the fact that each klystron works far below its designed maximum power thus reducing the rate of trips. The switching from 1-transmitter to 2-transmitter mode together with an efficient work of reduction of the sensitivity to EMC noises of the RF plants have resulted in a doubling of the MTBF of this touchy equipment. In order to increase the available accelerating voltage and to provide more flexibility to the RF operation, a third RF plant feeding 2 extra cavities will be commissioned and put into operation this year.

Super Spare Power Supply

Although power supply failures are rare, they can last a long time when they occur (replacement of a transformer or another major repair). To avoid a loss of time in these situations, a Super Spare Power Supply was built. Its role is to supply any magnet power supply which would fail. Furthermore a switching board was recently installed: it allows any magnet family from the Super Spare Power Supply to be supplied within less than one hour.

	1994	1995	1996	1997
USM scheduled hours	3800	4752	5193	5359
USM delivered hours	3372	4412	4901	5090*
Availability (%)	88.7	92.8	94.3	95 *
Time lost for refills (%)	2.7	2.9	2.4	2.5 *
Time lost for failures (%)	8.6	4.2	3.2	2.5 *
MTBF (hours)	13.5	21.5	41.2	> 40*

* expected

Insertion devices

The ESRF was designed to be essentially an Insertion Device based source. Out of the 28 available straight sections, 25 are already equipped with 1, 2 or 3 ID segments (1.6 m long), which can be either planar or helical undulators, or wigglers [4]. The very large variety of ID types enables experiments to be carried out simultaneously at X-ray energies ranging from 500 eV (on beamlines equipped with windowless front-ends) up to 500 keV (from a superconducting wiggler). 12 straight sections are equipped with 5m long 15mm high stainless steel vacuum vessels devoid of pumping, which authorises a 16mm minimum gap. We are presently developing 5m long 10mm high ID vacuum vessels which will enable the gap of the insertion devices to be closed down to 11mm. These stainless steel vessels will be copper plated so as to minimise their contribution to the impedance of the machine. Following the reduction of the vertical β function, 2 prototypes of 10mm high 2m long vacuum vessels were installed and successfully tested on the machine. The first 5m long 10mm high vessel will be installed during the summer of 97.

Beamline Front-Ends

There are presently 25 front-ends transmitting X-ray beam from insertions devices, and 6 from bending magnets. 6 ID front-ends are windowless. On some wiggler front-ends the total power in the X-ray beam can reach 15kW, whilst the power density approaches 750

W/mm^2 (normal incidence at 10m from the source) with 2 phased undulators at a 16mm gap. A specific carbon filters-Beryllium window assembly was developed which enables the transmission of such a high power density. To preserve the X-Ray beam coherence, some beamlines have been equipped with polished Be windows and sometimes with diamond filters. A noticeable point to be mentioned is the slightly increasing meantime between failures of the front-end equipment despite the increasing number of beamlines (and of front-ends) since 1994.

4 BEAM MODES

As a consequence of the great variety of experiments which are carried out at the ESRF, various filling patterns of the electron beam are now served to the Users. The Users community is divided into two parts, those who need a maximum intensity with the longest lifetime whatever the filling pattern is, and those who need a time-structured mode (for nuclear scattering or structural biology for instance). For the first part of the Users community, the machine is operated in multibunch mode (either 'one third' or 'two third' filling modes) at 200mA.

For the second part of the community, time structured modes have been developed. The single bunch mode is now delivered at an intensity of 15mA (with a 5 hours lifetime). A transverse feedback is under development and should enable higher intensity to be reached.

	2/3 filling	Single Bunch	16 bunch	Hybrid mode
Max. intensity (mA)	200	15	90	200
Associated Lifetime (hours)	50	5	8	30
% of time in operation	55 %	5 %	25 %	15 %

Modes routinely delivered at the ESRF

The 16 bunch mode was first developed as a compromise for all the Users and is still delivered now (25% of the shifts). The maximum intensity of 90mA is mainly limited by the overheating and consequent outgassing of the RF liners of the vacuum chamber. An R&D program on the RF liners is in progress to increase the maximum intensity.

To maintain the same brilliance per mA, the beam is delivered with the same low emittances (ε_x=4nm.rad and ε_z=40 pm.rad) in these modes which explains the associated moderate lifetime.

More recently, various hybrid modes have been developed to better satisfy the community of Users. They consist in a one third filling bunch train (typically 180mA) with one or several isolated bunches regularly spaced in the opposite gap (typically 5mA per bunch). Despite the fact that everyone can find their advantages in these hybrid modes, the drawback of these exotic modes is the reduced lifetime (30 hours) which is mainly driven by the lifetime of the single bunches and also the longer dead time for the refill (about 25 minutes instead of a couple of minutes for the other modes).

For the filling of the Storage Ring in single bunch, 16 bunch or hybrid modes, the Linac produces short pulses with a 2ns FWHM. It has been optimised in order to achieve an initial purity in the 10^{-3} range in the SR. Then a cleaning process is applied which consists in exciting the parasitic bunches in the vertical plane so as to kill them on a scraper.

The bunch purity (relative intensity of the parasitic bunches compared to the main bunch) is measured by an X-ray avalanche photodiode installed in the tunnel which has an excellent dynamic range (better than 10^8) and a good time resolution (10^{-6} at 2.8 nsec of the main bunch). The quality of all the time-structured modes is very high since a bunch purity better than 10^{-7} is routinely delivered.

Jitter free streak camera

A collaboration contract was signed in 1996 with the CUOS (Centre for Ultra-Fast Optical Science) in Michigan for the development of a state of the art streak camera. This streak camera, which will have a resolution less than 1 pico-second in accumulation mode, will be triggered by an ultra-short laser pulse (300 femto-second) in order to eliminate the jitter. The laser pulses will also be produced synchronised to the X-ray pulses with a jitter of much less than the width of the X-ray pulse. This set-up will demonstrate that even with a 100 pico-second X-ray pulse, it is possible to probe events on the sub pico-second scale.

5 SHORT TERM GOALS

The ESRF objective is to further develop its high potential while maintaining the excellence of its operation standards. The following major goals have been set for 1997:

- 5400 hours of scheduled USM time.
- An increased rate of availability with an objective of 95% (the last % is the most difficult to achieve).
- The commissioning of a third RF plant (transmitter) together with 2 additional cavities.
- The installation of a few 10 mm high insertion device vacuum vessels.
- A reduction of the horizontal emittance: A new version of the optics giving 3nm.rad (instead of the present 4) is being studied.
- A reduction of the coupling down to values in the 0.3% range, which is extremely challenging.
- A fast global AC position feedback which will operate in the vertical plane, using electron beam position monitors.

REFERENCES

[1] A. Ropert, L. Farvacque : `Lattice-related brilliance increase at the ESRF`. PAC97.

[2] L. Farvacque et al : `Beam centre of mass stability` ESRF internal report, Jan 96

[3] O. Naumann, J. Jacob : `Fractional filling induced Landau damping of longitudinal instabilities at the ESRF`. PAC97

[4] J. Chavanne, P. Elleaume, P. Van Vaerenbergh : 'Recent developments of Insertion Devices at the ESRF'. PAC97

LATTICE RELATED BRILLIANCE INCREASE AT THE ESRF

A. Ropert, L. Farvacque, ESRF, BP 220, F - 38043 Grenoble Cedex

Abstract

The ESRF brilliance is currently being increased by more than two orders of magnitude with respect to the original design target value of 1018 photons/sec/mm2/mrad2/0.1% relative bandwidth by acting on the stored beam current, the refinement of the insertion device technology and beam emittances. This paper will review the lattice-related contribution to the on-going improvements of the initial performances in brilliance of the source: modifications in the tuning of the basic Chasman-Green lattice enabling the reduction of the horizontal emittance from the design 7 nm down to 4 nm, strategy to control the coupling below 1 %, optimization of the beta functions in the insertion devices. This already brought a factor of 30 in brilliance. The potential for a further improvement in the brilliance by a factor of ten will be described.

1. INTRODUCTION

Brilliance is the figure of merit the most referred to for third generation light sources. At the ESRF, the initial brilliance performance has been upgraded by a factor of 100 by acting on the different parameters entering into the brilliance formula:

$$B = \frac{I}{\kappa \varepsilon_x^2} f(E, g, B)$$

- the stored beam current I has been increased from 100 mA to 200 mA by overcoming the HOM limit thanks to the partial filling of the circumference and to the detuning of the HOMs by temperature control of the cavities.

- on the insertion device side (gap g, field B), spectrum shimming techniques have pushed the highest useful undulator harmonic and increased the brilliance at all harmonics. Undulator gaps have been decreased from 20 mm down to 15 mm which allows a gain of a factor of 2 in brilliance in the fundamental via the associated reduction of the undulator period. Thanks to the reduced vertical beam stay-clear affordable with the new lattice optics, new insertion devices will have a gap of 11 mm.

- lattice-related parameters (the horizontal emittance ε_x and the coupling factor $\kappa = \frac{\varepsilon_z}{\varepsilon_x}$) have been significantly reduced with respect to the design values. This, together with a better matching of the optical functions at the source points, has brought an improvement in brilliance of a factor of 30, i.e. the major part of the quoted figure of 100.

2. REDUCTION OF THE HORIZONTAL EMITTANCE

In the Double Bend Achromat lattice used at the ESRF, the small emittance is achieved by lowering the horizontal β function inside the bending magnets, thus generating unacceptably high β values in the focusing structure outside the bending magnets and leading to large chromaticities, higher sensitivity to errors and reduced dynamic apertures. Our design value of 7 nm resulted from a compromise between these different effects [1].

In order to achieve a lower emittance nevertheless, a new version of lattice settings with a distributed dispersion has been implemented and has now been operated for 2 years. By detuning the quadrupoles in the achromat, the dispersion pattern is more balanced inside the bending magnets where the emittance is created [2]. This strategy enabled almost a factor of 2 to be gained on the horizontal emittance from 7 nm down to 4 nm. This gain is almost entirely transferred in brilliance increase since the non-zero dispersion combined with the internal beam energy spread contributes to the beam size in the straight sections very slightly.

3. COUPLING CONTROL

The X-ray pinhole camera [3] enables the photon beam emittances and accordingly the electron beam emittances to be permanently measured. Two of these devices are installed on different bending magnets. Their results are in good agreement, thus confirming the extremely low vertical emittance achieved at the ESRF. Since the image made with the second camera has a significant contribution from energy spread, it also provides an accurate diagnostic of the electron energy spread.

In comparison with initial objectives of a 10 % coupling, dramatic progress was made and the coupling routinely decreased to 1 %.

Until January 1996, the correction of coupling was based on the cancellation of the 2 coupling resonances $\upsilon_x - \upsilon_z = 25$ and $\upsilon_x + \upsilon_z = 48$ close to the working point ($\upsilon_x = 36.44$, $\upsilon_z = 11.39$) [4]. This was performed by using 2 pairs of skew quadrupole correctors for each resonance in order to adjust the amplitude and the phase of the correction while moving the tunes to the resonances. The residual coupling of 1 to 2 % obtained is due to other resonances which look difficult to minimize via the single resonance method.

The installation of an additional set of 8 skew

0-7803-4376-X/98 /$10.00 © 1998 IEEE

quadrupoles now allows more advanced corrections [5]:

- measurement of the coupled response of the machine to steerer excitation and minimization of the cross-talk terms
- minimization of the spurious vertical dispersion

This procedure results in routinely achieved values of less than 1 % in all operating modes (as shown in Figure 1 during a two-week period alternating hybrid, single bunch, 16 bunch modes) and record values of 0.5 %.

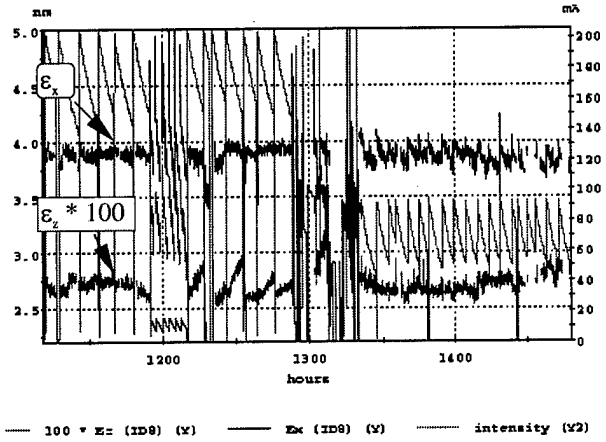


Figure 1

At this stage, the reduction of the vertical dispersion (given the small initial values as shown in Figure 2) does not give a noticeable improvement in coupling. However, the induced radiation in the presence of vertical dispersion will start to play a role when further refining the correction algorithm in order to achieve the future goal of an 0.3 % coupling. This upgrade also requires the discrepancy between modeling and calibration experiments on the effect of a single skew quadrupole to be clarified.

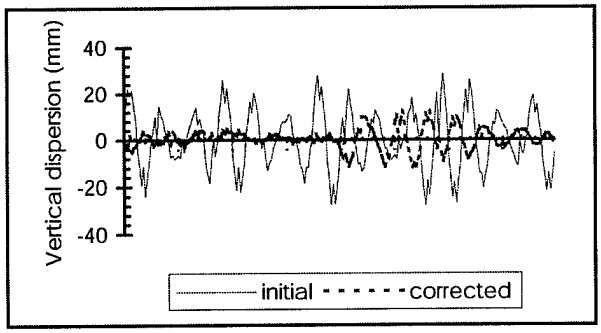


Figure 2

4. WINNING OVER DIFFRACTION WITH β

With the original 7 nm lattice and 10 % coupling, the brilliance of the photon beams was essentially dictated by the emittances of the electron beam. This is no longer the case with the presently achieved 40 pm vertical emittance, as shown in Figure 3. The effective dimensions result from the convolution of the electron beam emittances and the photon beam emittance associated with the single electron which can be expressed as $\varepsilon_R = \frac{\lambda}{2\pi}$ (λ being the wavelength of the radiation). For a given value of ε_R and ε_z (vertical electron beam emittance), the minimum photon beam emittance is obtained for a perfect matching ($\beta_z = \beta_R$, with $\beta_R = \frac{L}{\pi}$ and L being the length of the undulator) as illustrated in Figure 4. This corresponds to β_z = 1.59 m or β_z = 0.53 m, depending on the number of 1.6 m long insertion device segments (3 or 1), emitting at 14 keV. When the matching is imperfect, the reduction of the effective brilliance which would be only 12 % with 10 % coupling reaches 55 % with 1 % coupling. Any further reduction of the vertical emittance would be impaired by a greater relative reduction of the brilliance.

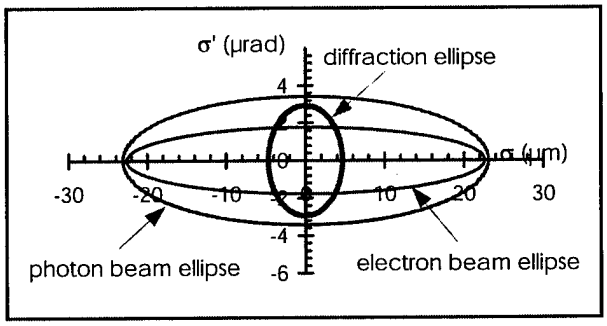


Figure 3

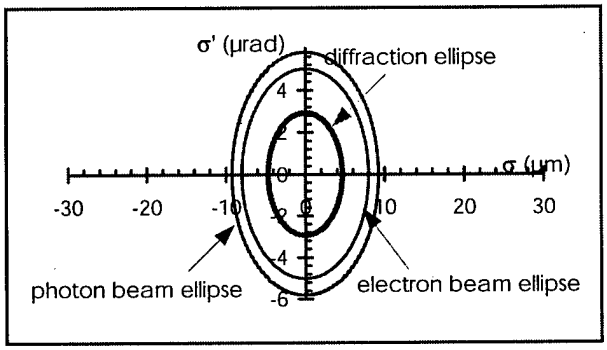


Figure 4

Going to β_z values of the order of 0.53 m looks very difficult to achieve in terms of machine tuning. Also given the parabolic increase of the β_z value at the 5 m undulator edge, the reduction of the insertion device gap from the present 15 mm to 11 mm would be inhibited. Since the tendency at the ESRF is to evolve towards the installation of 3 insertion device segments per straight section, β_z = 1.59 m would provide a perfect matching. However, other constraints (such as the evolution of the actual beam size of the X-ray beam drifted 30 m downstream the source point or beam position stability considerations) favour β_z values of the order of 2.5 m, which in terms of brilliance reduction is negligible in the case of 3 installed segments. In this new version of the optics [6] used in User Service Mode since November 1996, the vertical β in the undulator straight sections is

therefore decreased from 13 m down to 2.5 m, thus leading to an increase of the vertical tune by three integers, from 11.39 to 14.39 (Figure 5).

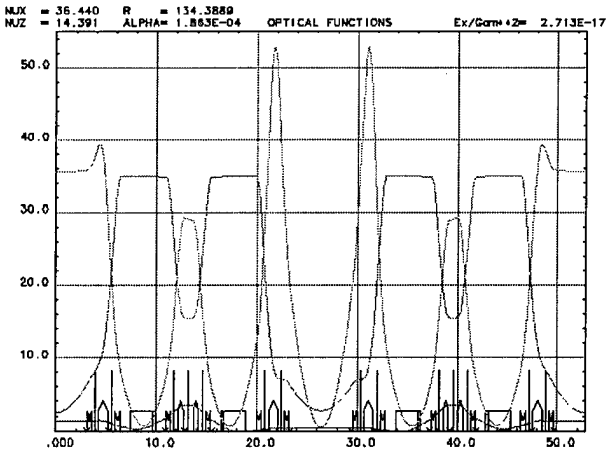


Figure 5

Reducing the vertical β was also a prerequisite for decreasing the insertion device gaps. Thanks to the smaller electron beam vertical sizes in the straight sections, beam scraping on the reduced beam stay-clear ID vacuum vessels (± 4 mm inner aperture) is less severe and consequently the beam gas scattering lifetime reduction and Bremsstrahlung emission on the beamlines minimized. Comparative studies with the high β and low β optics (Figure 6) show that a minimum beam stay-clear of 5 mm can now be accepted instead of 7 mm for the same 20 % reduction in beam lifetime. Two 2 meter long, 8 mm high vacuum vessels are now installed without significant impact on the lifetime. The first 5 meter long, 8 mm high vacuum vessel will be installed next summer.

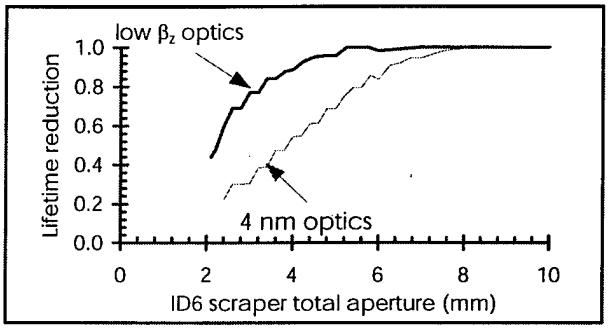


Figure 6

The low β_z optics also has other potential advantages:

- the reduced sensitivity to insertion device chamber wall impedance enables a relaxed chromaticity to be used in all filling modes. This is particularly visible in single bunch mode where the intensity threshold is strongly chromaticity dependent. The required vertical chromaticity (ξ_z = 0.67 instead of 0.9 for the high β_z optics) favours the obtaining of a larger energy acceptance and longer lifetimes.

- the reduced sensitivity to insertion device field imperfections minimizes the possible effects induced by gap changes such as modification of the coupling or orbit distortions.

- the beam at a cross-over tolerates larger scattering angles, therefore the lifetime is less sensitive to the vacuum in the insertion device straight sections.

5. FUTURE PLANS

The significant evolution of the lattice since the design stage with even stronger focusing and larger non-linearities via the chromaticity compensating sextupoles reinforces confidence in further possibilities of reducing the natural horizontal emittance. Tests on a new optics providing a 3 nm emittance will be initiated very soon. This upgrade, together with the reduction of coupling and the operation of 11 mm gap insertion devices will push the ESRF in the 10^{21} range in brilliance which is the maximum achievable figure with the present generation of storage rings.

The possibility of provoking dissymmetry of the electron beam horizontal envelope in the high β insertion device straight sections while operating the lattice with a non-zero alpha function in the straight section such that the emitted photon beam would focus about 30 m downstream the beamline at the sample location is also under consideration [7]. For a number of beamlines, the resulting increase in flux at the sample would be superior to a gain by a factor of 10 in brilliance. Necessary hardware allowing an assymmetrical powering of the quadrupoles of the straight section triplets is being purchased and the scheme will be tested first in one straight section during the second half of 1997.

6. REFERENCES

[1] A. Ropert, " The ESRF lattice", ESRF-SR/LAT-86-05

[2] L. Farvacque, J.L. Laclare, A. Ropert, P. Nghiem, J. Payet, A. Tkatchenko, H. Tanaka, "Possible retuning of the ESRF storage ring lattice for reducing the beam emittance", EPAC94

[3] P. Elleaume, C. Fortgang, C. Penel, E. Tarazona, "Measuring beam sizes and ultra small electron emittances using an X-ray pinhole camera", J. Synchrotron Radiation (1995)

[4] A. Ropert, "Strategy for the correction of resonances", ESRF-1-94/Theory

[5] L. Farvacque, "Horizontal / vertical coupling", 4th Workshop on European Synchrotron Light Sources, Trieste (1996)

[6] A. Ropert, "The low β_z lattice", ESRF-3-97/Theory

[7] P. Elleaume, "Optimization of the β function in the IDs", 10th ICFA Workshop, Grenoble (1996)

VUV AND SOFT X-RAY LIGHT SOURCE "NEW SUBARU"

A. Ando, S. Amano, S. Hashimoto, H. Kinosita, S. Miyamoto,
T. Mochizuki, M. Niibe, Y. Shoji, M. Terasawa, T. Watanabe,
Laboratory of Advanced Science and Technology for Industry,
Himeji Institute of Technology, 2167 Shosha, Himeji, Hyogo 671-22, JAPAN

Abstract

The main facility of the New SUBARU project is the 1.5 GeV electron storage ring which is under construction at the SPring-8 site in Harima Science Garden City. The first beam commissioning from the SPring-8 LINAC is scheduled at the end of March, 1998. The aim of new SUBARU is to promote industrial activities in the local area (Hyogo prefecture) and to develop experimental investigations for new light sources.

1 INTRODUCTION

An 1.5 GeV electron storage ring for the light source in the region of VUV and soft X-ray is under construction at the SPring-8 site using the LINAC as an injector. The project team for new SUBARU between HIT and SPring-8 has been organized to establish the SR research complex in SPring-8. The storage ring has two very long straight sections (LSS,14 m each) comparing its small circumference (~119 m). Two LSS's are initially used for a 11-m long undulator (L-U) and an optical klystron(FEL), and two short straight sections (4m each) for an 2.3-m undulator (S-U) and an 8-T super conducting wiggler (SC-W). The natural emittance @ 1.5 GeV is 67 nm because the total number of main dipole magnets is 12. The maximum brilliance is expected as $10^{18}(photons/sec/mm^2/mrad^2/0.1\%bw)$. Considering complemenarity to the most brilliant light source in the world, SPring-8, new SUBARU aims to produce a short pulse of radiation. New ideas using such as laser-electron interaction or for beam cooling will be also tested in this ring. The main purpose of the project are as follows. (1) Research and development towards new light sources such as (a) a small and low cost source in the region from VUV to soft X-ray, (b) strong ring FEL and coherent soft X-ray, (c) very short light pulses and (d) beam cooling to obtain very small emittance and enery spread in a small ring. (2) Application for industry and biomedical such as (i) micromachining, (ii) investigation for new material and (iii) X-ray microscopy. The project has also a 15-MeV LINAC for FEL (named as LEENA)[1]. The expected brilliance and enery region is shown in Fig.1. The energy region of ~0.1eV to ~50 keV will be totally covered.

2 STORAGE RING

The main parameters of the ring are summarized in Table 1. The characteristics are (1) quasi-isochronous and/or variable momentum compaction facter α_p between ± 0.001, and (2) 14-m-LSS's. The ring has a hexagon shape and the unit structure is a double bend achromat cell with two 34-deg. bending magnet(BM) and one invert BM at the middle. The typical envelope functions are shown in Fig.2. The excitation strength of quadrupoles for various α_p is shown in Fig.3. The HOM damped cavity with SiC duct developed and used at INS-SOR and PF[2] is installed.

Table 1: Main parameters of new SUBARU storage ring.

Fundamentals		
Injection energy	1	GeV
Operation energy	1.5	GeV
Stored current	< 500	mA
Circumference L	118.716	m
Revolution period	0.396	μ sec
Revolution freq.	2.525	MHz
Harmonic No.	198	
RF frequency	500	MHz
Betatron Tunes	6.21/2.17	
Chromaticity (ξ)	-19/-7.5	
α_p	0.001	
Straight sections	4m	$\times 4$
	14m	$\times 2$
Operation parameters	**1. 5**	**GeV**
Natural emittance (1σ)	67	nm
Coupling	10	%
Bending field	1.55	T
Critical photon	0.53	nm
	2.33	keV
Radiation loss/ Turn	176	keV
Damping time		
Longitudinal	3.42	msec
X/Y	6.56/6.73	msec
Energy spread	0.072	%
RF voltage	> 250	kV
Bucket height	> 0.83	%
Synchrotron tune	0.0021	
Bunch length ($1\sigma_t$)	26	psec
Touschek life	> 10	hrs

2.1 *Bunch Length*

The natural energy spread is calculated as $\sigma_\delta \simeq 4.8 \times 10^{-4}E$ where E is energy of electron beam measured in GeV and the bunch length is given by $\sigma_t \simeq 2.3 \times$

0-7803-4376-X/98/$10.00 © 1998 IEEE

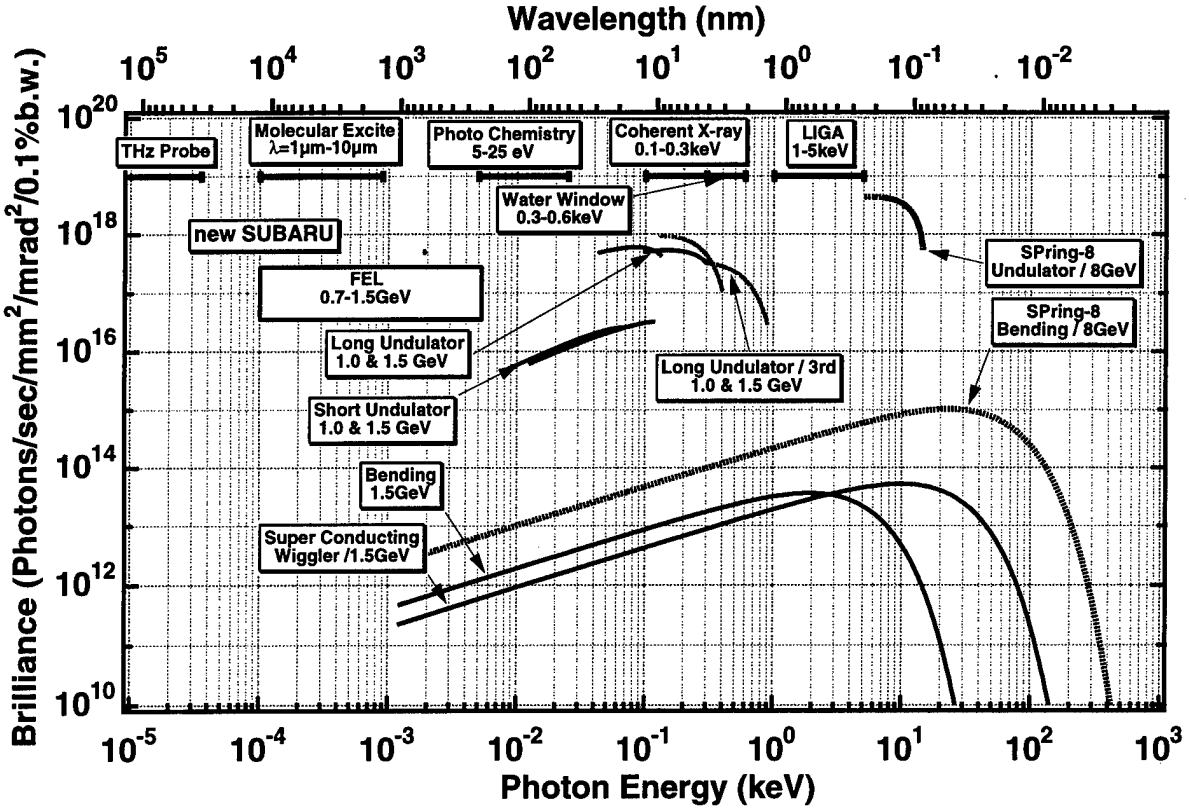


Figure 1: Expected brilliance of new SUBARU project compared with SPring-8.

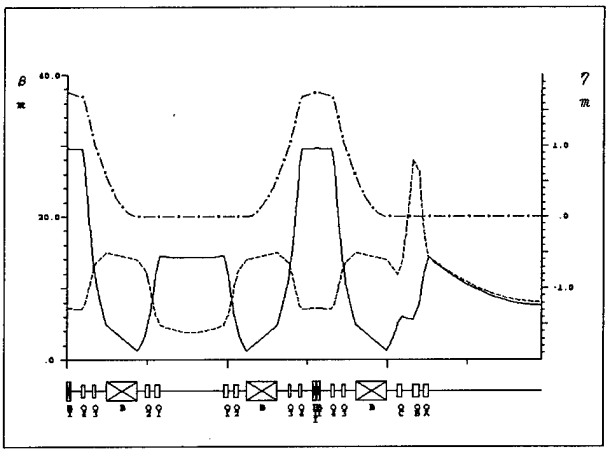


Figure 2: Twiss parameters of the quadrant for $\alpha_p \simeq -0.001$. Real line: β_x, broken:β_y, dotted:dispersion(η).

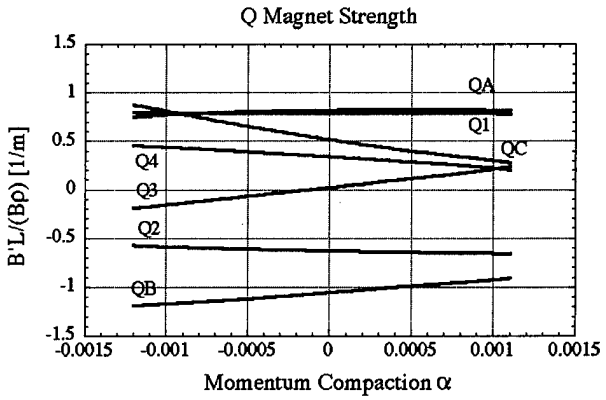


Figure 3: Strength of quadrupoles (QM) for various α_p. (Q1,Q2 : main QM, Q3, Q4 : adjusting QM for η, QA, QB, QC : matching QM for LSS).

$10^{-8}(AE)^{1/2}\sigma_\delta(sec)$ where $|\alpha_p| = A\times 0.001$, because the RF voltage can be always higher than 250 kV. On the other hand the energy spread would become more large due to microwave instability. Supposing the Keil-Schnell criterion is applicable, σ_δ and σ_t become twice of the natural values at $\simeq$ 4 mA/bunch for $A = E$ =1 and $|Z/n| = 0.1(\Omega)$, which is almost the same result by ZAP. To reach $\sim$3 psec of σ_t is one of the goals of the accelerator R&D.

2.2 *Sextupole Correction*

The control of higher order terms in momentum compaction facter is very important in a very small α_p or isochronous ring. As the second order islands in synchrotron oscillation appear at[3],

$$\delta_\pm = \{-\alpha_2 \pm (\alpha_2^2 - 4\alpha_1\alpha_3)^{1/2}\}/(2\alpha_3),$$

where revolution period is expanded as,

$$\Delta T/T = \alpha_p \delta = \sum_k \alpha_k \delta^k,$$

the guide line for the free oscillation from these islands in the region of $|\delta| \leq 1\%$ becomes, $(1)|\delta_\pm| > 0.1$, *or* $(2)\alpha_2^2 - 4\alpha_1\alpha_3 < 0$, *or* $(3)|\alpha_3/\alpha_2| < 0.1(\alpha_1 \simeq 0)$, $|\alpha_2/\alpha_1| < 0.1(\alpha_3 \simeq 0)$. (In this paper α_p and η(momentum slipping facter) are treated as the same value.) Then the equations for correction are,

$$d\xi_x/dg_j = (\beta_x D)_j/(4\pi),$$

$$d\xi_y/dg_j = -(\beta_y D)_j/(4\pi),$$

$$d\alpha_2/dg_j = -D_j^3/(2L),$$

$$dA_{n,p}/dg_j = (2^{1/2}8\pi n)^{-1}[\beta_x^{3/2} g \cdot exp\{i(p\theta + nQ_x)\}]_j,$$

$$dB_{1,q}/dg_j = (2^{1/2}4\pi)^{-1}[\beta_x^{1/2}\beta_y g \cdot exp\{i(q\theta + Q_x)\}]_j,$$

$$dB_{\pm,r}/dg_j = (2^{1/2}8\pi)^{-1}[\beta_x^{1/2}\beta_y g \cdot exp\{i(r\theta + Q_\pm)\}]_j,$$

where $\xi = \Delta\nu/\delta$, ν is a tune of betatron oscillation, β and D are the envelope function and momentum dispersion, L is the circumference of a ring, $g = l(\partial^2 B_y/\partial x^2)/B\rho$ and the suffix j means the j-th sextupole. p, q and r are integers which satisfy $n\nu_x = p$ ($n = 1$ or 3), $\nu_x = q$, and $\nu_x \pm 2\nu_y = r$, θ is the azimuthal angle of the ring, $Q_a = \psi_a - \nu_a\theta, (a = x$ or $y)$, ψ_a is the phase advance of betatron oscillation and $Q_\pm = Q_x \pm 2Q_y$. Instead of the last three equations for resonance driving terms, so-called Collins' distortin function[4] should be carefully controlled. In new SUBARU, these are $A_{1,}$, $B_{1,6}$ and $B_{-,2}$ and 5 families of 50 sextupoles seem enough for the correction.

3 INSERTION DEVICE AND BEAM LINE

Table 2 summarizes the ID's where λ_u, N are the length and the number of period, g and L_u are the gap height and the total length. W is the covered region of photon wave length and B is the brilliance $(photons/sec/mm^2/mrad^2/0.1\%bw)$. S-U, L-U and SC-W mean the short undulator, long undulator and superconducting wiggler, repectively. Comments on this table are a) critical photon energy and b) 0.5~0.7 GeV operation of electron beam. As seen in the table, the K values of undulators are almost higher than 1 and the harmonics will be positively used (see Fig.1).

3.1 FEL / Optical Klystron

The main aims of the hardware development in FEL are to obtain lasing in the wave region less than 200 nm and high average power in μm region. The storage ring will be operated mainly at 0.5 ~ 0.7 GeV, because the simple calculation gives gains more than a few tens percent at the peak current of 10 A including energy widening. Normal conducting magnets are used for the undulators and dispersive section, and the length of one period is selected by changing current connection. The phase slipping number is optimized at each wave length between 7 and 71. The distance between the mirrors, of which radius is ~13 m, is one fourth of the ring circumference.

Table 2: Main parameters of new SUBARU ID's.

Type	S-U	L-U	SC-W	FEL
$\lambda_u(mm)$	76	54	350	160 /320
N	30	200	1	32.5/16.5 ×2
g(mm)	25~ 58	25~ 44.5	30	40
K	1.3~ 5.3	0.8~ 2.5	262	1.7~ 12
L_u(m)	2.3	10.8	0.7	5.2×2
W(nm)	8.1~ 149	1.4~ 29	0.1~ 0.23[a)]	200~ 12000[b)]
B	4×10^{16}	10^{18}	7×10^{13}	

3.2 Beam Line

There are 4 beam lines (BL) from ID'S and 9 BL's from BM at the bending point of 10 degrees. Table 3 shows the present category in discussion.

Table 3: Beam lines in discussion.

Purpose	Source	Energy(keV)
EUVL	BM	0.08~0.3
LIGA	BM	3
Holography & coherence	L-U	0.08~0.3
Materials creation	BM	< 1
Photo-active materials	BM	< 1
Light source R&D	FEL	0.006
X-ray microscope	L-U/S-U	0.3~0.6
Topography	SC-W	> 2
Optical elements R&D	BM	0.05~1

In this year two BL's are constructed for EUVL (extreme ultra-violet lithography) and LIGA.

4 REFERENCES

[1] T.Mochizuki *et al.*, "First Lasing of LEENA Free Electron Laser at LASTI", Proc. 18th International Free Electron Laser Conference, Rome, August 1996.

[2] M. Izawa *et al.*, Rev. Sci. Instru. **66**, 1910 and 1926 (1995)

[3] A. Ando and K.Takayama, IEEE Trans. Nucl. Sci. **NS-30**, 2604 (1983)

[4] A. Ando, Paricle Accelerators **15**, 177 (1984)

A SHORT PULSE X-RAY GENERATION VIA THOMSON SCATTERING OF ULTRASHORT LASER PULSES BY RELATIVISTIC ELECTRON BEAMS

K. Nakajima, H. Nakanishi, A. Ogata,
KEK, Tsukuba, Ibaraki, Japan 305,
H. Kotaki, H. Ahn, H. Dewa, M. Kando, S. Kondoh, F. Sakai,
JAERI, Tokai, Ibaraki, Japan 319-11,
T. Watanabe, T. Ueda, M. Uesaka,
NERL, The University of Tokyo, Tokai, Ibaraki, Japan 319-11

Abstract

Short pulsed X-rays were experimentally generated by 90° Thomson scatterings of 2 TW, 90 fs laser pulses by 17 MeV electron beams. Synchronization between the laser pulses and electron beams were achieved within a few ps. A 100 fs X-ray pulse will be generated via backward Thomson scatterings from a 100 fs electron bunch made by a bunch compression chicane. A high peak power, high brightness, high repetitive laser synchrotron radiation source consisting of counter-colliding laser and electron storage rings is proposed.

1 INTRODUCTION

A compact, narrow bandwidth, ultrashort pulses of hard X-rays have basic and industrial applications in a number of fields, such as solid-state physics, material, chemical, biological and medical sciences. An ultrashort pulse X-ray source will allow measurements of time resolve atomic motion providing important information about the material properties, chemical and biological reactions on ultrafast time scales. The present high-brightness hard X-ray sources have been developed as third generation synchrotron light sources based on large-scale high energy electron storage rings and magnetic undulators. Recently availability of compact terawatt lasers referred to as table-top-terawatt (T^3) lasers based on chirped pulse amplification arouses a great interest in the use of lasers as undulators of which a period is $\sim 10^4$ shorter than the conventional undulator. This feature of laser undulators allows the use of $\sim$ 100 times less energetic electrons to generate X-rays of a particular wavelength. The laser undulator concept using T^3 lasers makes it possible to construct an attractive compact synchrotron radiation source which has been proposed as a laser synchrotron radiation source (LSRS)[1].

In order to generate an ultrashort X-ray pulse, we attempted 90° Thomson scattering experiments, where a femtosecond laser pulse interacts with a relativistic electron beam at 90°[2]. In this configuration the X-ray pulse length is determined by the transit time of the laser pulse across the electron beam waist as long as the laser pulse length is much shorter than the electron bunch length. It is, however, essential to achieve an exact timing between the laser pulse and the electron pulse. Experiments were carried out by using a T^3 laser delivering laser pulses of 90 fs duration with the peak power of 2 TW and a 17 MeV electron beam of 10 ps bunch length produced from the RF linac synchronized with laser pulses at the repetition rate of 10 Hz.

If the electron pulse duration is as short as a femtosecond, head-on collisions of laser pulses with the electron beam should generate femtosecond X-ray pulses through backscattering. The head-on configuration can produce twice higher energy photons than the 90° configuration as well as the higher photon intensity. In this scheme a difficulty in timing between laser and electron pulses can be relaxed as long as a spatial overlapping of two beams can be accomplished. In order to test the backward Thomson scattering to generate femtosecond X-ray pulses, we prepare the picosecond photocathode injector and the bunch compression chicane in the electron linac.

As an example of a practical high-brightness quasi-monochromatic, high repetitive ultrashort hard X-ray source, we propose a compact synchrotron radiation source consisting of counter-colliding laser and electron storage rings where the compressor and the stretcher for both beams are installed. A conceptual design is discussed for providing high peak power as well as high average power comparable to the present conventional synchrotron light source.

2 X-RAY GENERATION VIA THOMSON SCATTERING

When a laser beam interacts with an electron beam at an angle ϕ, Thomson scatterings of relativistic electrons in the laser undulator field generate frequency up-shifted radiation with the peak frequency given by

$$\omega_X = \frac{2\gamma^2(1-\cos\phi)}{1+a_0^2/2}\omega_0, \qquad (1)$$

where γ is the Lorentz factor of the electrons, ω_0 the incident laser frequency and a_0 the undulator strength or the normalized vector potential of the laser field given by $a_0 \sim 0.85 \times 10^{-9} I^{1/2}[\mathrm{W/cm^2}]\lambda_0[\mu\mathrm{m}]$ for the peak intensity I in units of W/cm^2, the laser wavelength $\lambda_0 = 2\pi c/\omega_0$ in

0-7803-4376-X/98/$10.00 © 1998 IEEE

units of μm. For the $\phi = 90°$ configuration, the maximum radiation photon energy is

$$E_X[\text{keV}] = \hbar\omega_X = 9.5 \times 10^{-3} \frac{E_b^2[\text{MeV}]}{\lambda_0[\mu\text{m}](1 + a_0^2/2)}, \quad (2)$$

where E_b is the electron beam energy. The radiation wavelength is $\lambda_X[\text{Å}] = 12.4/E_X[\text{keV}]$. In the head-on configuration with $\phi = 180°$, the maximum photon energy turns out to be twice as high as the $\phi = 90°$ configuration. The angular distribution of radiation with the spectrum $\lambda \geq \lambda_X$ is within a cone of half angle, $\theta = (1/\gamma)\sqrt{(\lambda - \lambda_X)/\lambda_X}$.

2.1 90° *Thomson scattering*

Assuming the Gaussian temporal and spatial distributions of both the electron and laser beam with the transverse and longitudinal beam sizes of σ_x and σ_z and the laser transverse and longitudinal laser beam sizes of σ_w and σ_L, the rms pulse length of the X-ray radiation is obtained from

$$\sigma_X = \frac{\sigma_z\sqrt{\sigma_x^2 + \sigma_w^2 + \sigma_L^2}}{\sqrt{\sigma_z^2 + \sigma_x^2 + \sigma_w^2 + \sigma_L^2}}. \quad (3)$$

The number of photons per pulse within the spectral width $\Delta\omega/\omega$ is given by[2]

$$\Delta n = \frac{113 N_e J \lambda_0}{\sqrt{(\sigma_x^2 + \sigma_w^2)(\sigma_z^2 + \sigma_x^2 + \sigma_w^2 + \sigma_L^2)}} \frac{\Delta\omega}{\omega}, \quad (4)$$

where N_e is the total number of electrons per bunch, J the laser pulse energy in Joules, and λ_0 and the beam sizes are measured in μm.

2.2 *Backward Thomson scattering*

In the head-on configuration x-rays are generated toward the direction of the electron beam propagation. It turns out that the x-ray pulse length is determined primarily by the electron pulse duration, i.e. $\sigma_X = \sigma_z$. The number of photons per pulse within the spectral width $\Delta\omega/\omega$ is obtained from[1]

$$\Delta n = 4 \times 10^3 \frac{N_e J}{Z_R[\mu\text{m}]} \frac{\Delta\omega}{\omega}, \quad (5)$$

where $Z_R = \pi r_0^2/\lambda_0$ is the Rayleigh length, r_0 the spot radius of the Gaussian laser profile and $r_0 \sim r_b$ is assumed with the electron beam radius r_b.

3 EXPERIMENTS AT 17 MEV LINAC

Experiments of X-ray generation through Thomson scattering are made by the use of the 17 MeV electron linac and the T^3 laser system[3]. The Ti:sapphire T^3 laser system based on the chirped-pulse amplification at $\lambda_0 = 790$ nm produces output pulses compressed by a grating compressor to 90 fs with an energy of > 200 mJ corresponding to a peak power of > 2 TW at the repetition rate of 10 Hz. The electron beam is delivered from the 2856 MHz RF linac to produce a 17 MeV single bunch beam with a 10 ps FWHM pulse duration at the repetition rate of 10 Hz. An electron pulse is synchronized to laser pulses with the phase locked control of the mode-locked oscillator. The phase locked loop maintains synchronization of the oscillator repetition period (79.33 MHz) with every 36th RF period of the linac (2856 MHz). We measured a timing jitter between the laser pulse and Cherenkov radiation from the electron beam with the streak camera with a time resolution of 200 fs. Synchronization between two pulses was achieved within the rms jitter of 3.7 ps.

The setup for the 90° Thomson scattering experiment is shown in Fig. 1.

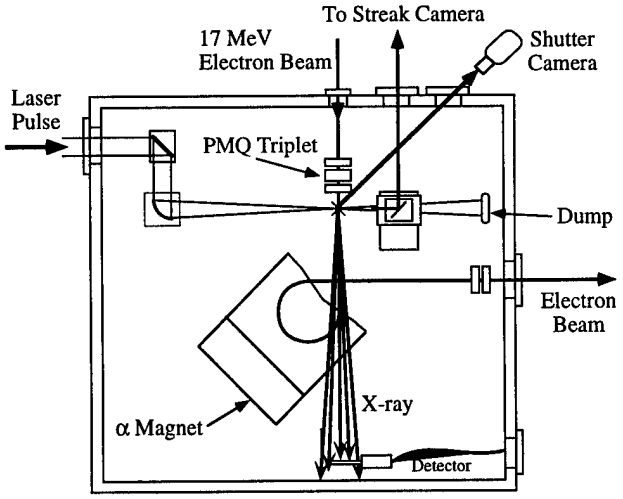


Figure 1: The experimental setup for 90° Thomson scattering.

Laser pulses were focused with f/10 off-axis parabolic (OAP) mirror with a focal length of 480 mm. The electron beam from the linac is focused by a permanent quadrupole (PMQ) triplet in the chamber. Since the electron beam spot size was 480 μm, the X-ray pulse duration of 1.6 ps was expected. The linac was separated with a 50μm thick titanium window from the interaction chamber to maintain ultrahigh vacuum in the linac. The incident electron beam was swept off with the α magnet at a bending angle of 270°. The X-ray radiation was detected by a scintillator with the 1×6 cm^2 sensitive area to be coupled to the photomultiplier tube. Plenty of the bremsstrahlung background was generated from the titanium window and the upstream beam line. In order to subtract the background signal, two sets of X-ray signals were taken with laser pulses and without them as the background. The signal was averaged over 500 to1000 shots to reduce a signal fluctuation. A net signal height proportional to the X-ray flux was obtained from subtracting the background signal from the signals with interaction. Fig. 2 shows the net X-ray signals observed as the timing between laser and electron pulses was scanned.

In order to test ultrashort pulse X-ray generation by the backward Thomson scattering in the head-on configuration, the bunch compression chicane is installed in the beam line

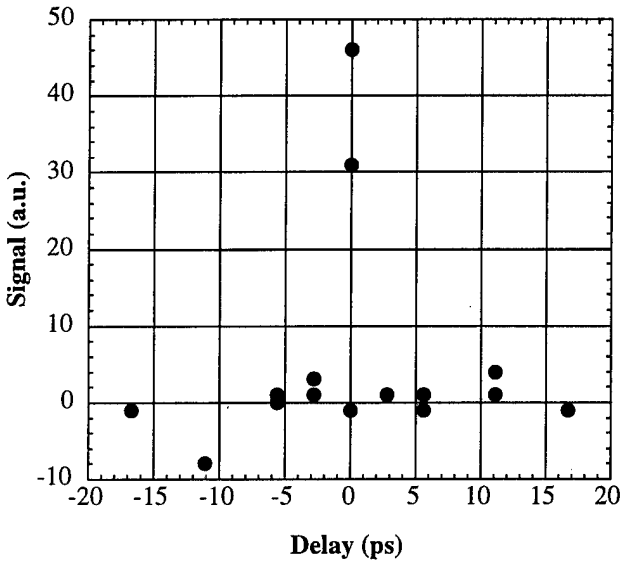


Figure 2: X-ray signals observed as a function of the time delay between laser and electron pulses.

following the linac to produce the pulse duration of $\sim$ 100 fs. The present thermionic electron gun is replaced by the photocathode RF gun which can provide a small normalized emittance of $\sim$ 1πmm-mrad and the electron pulse duration of 1 ps. Estimates of experimental parameters are summarized in Table 1.

Table 1: Parameters of X-ray generation experiments.

Laser beam	
Wavelength	790 nm
Peak power	2 TW
Pulse energy	0.2 J
Pulse duration	90 fs
Focal spot radius	50μm
Electron beam	
Energy	17 MeV ($\gamma = 33$)
Pulse duration	100 fs
Charge/pulse	1 nC
Beam radius	50μm
X-ray pulse	
Photon energy	7 keV ($\lambda_X = 1.8$ Å)
Pulse duration	100 fs
Number of photons	$5 \times 10^7 (\Delta\omega/\omega = 0.1)$
Collection angle (2θ)	2×9 mrad

4 LASER SYNCHROTRON RADIATION

Consider that LSRS is composed of a compact electron storage ring and a storage ring of laser pulses with the low gain amplifier to compensate the power loss due to X-ray radiation. Ultrashort intense X-ray pulses can be generated by the head-on interaction between ultrashort electron and laser pulses made through the pulse compressors for both beams at the interaction region. After passing through the interaction, both pulses are stretched in the other section of the ring to avoid beam instabilities or damages in the optical components. This system will allow both a high peak power and a high average power operations of LSRS in a compact size. Table 2 summarizes design parameters of LSRS performance[1].

Table 2: A design of laser synchrotron radiation.

Laser pulse parameters	
Wavelength	0.8μm
Pulse energy	1 J
Peak power	10 TW
Pulse duration	100 fs
Spot radius	50μm
Rayleigh length	1 cm
Repetition rate	10 MHz
Electron pulse parameters	
Energy	150 MeV
Peak current	100 kA
Average current	100 mA
Pulse duration	100 fs
Beam radius	50μm
Revolution frequency	10 MHz
X-ray pulse parameters	
Photon energy	530 keV max.
Pulse duration	100 fs
Peak photon flux	2.5×10^{23} photons/s
Peak brightness†	2×10^{20}
Peak radiation power	3.6 GW
Average photon flux	2.5×10^{17} photons/s
Average brightness†	2×10^{14}

† photons/s mm^2 mrad^2 0.1 % BW

5 CONCLUSION

A short pulse X-ray generation was observed by the 90° Thomson scattering of 2 TW, 90 fs laser pulses from the 17 MeV electron beam. A femtosecond X-ray pulse is efficiently generated via the backward Thomson scattering with the electron pulse compression. A compact, high peak power, high brightness laser synchrotron radiation source is proposed to provide attractive features comparable to a large storage ring based synchrotron light source.

6 REFERENCES

[1] E. Esarey, P. Sprangle and A. Ting, NIM **A 331**, 545 (1993).

[2] K.-J. Kim, S. Chattopadhyay, C.V. Shank, NIM **A 341**, 351 (1994).

[3] K. Nakajima, Phys. Plasmas, **3**, 2169 (1996).

ANKA-STATUS OF THE 2.5 GeV SYNCHROTRON LIGHT SOURCE AT FORSCHUNGSZENTRUM KARLSRUHE

D.Einfeld, A. Hagestedt[1], E.Huttel, A.Krüssel, H.O.Moser, F.Perez[2], M.Plesko[3], R.Rossmanith, J.Schaper, R. Simon, R.Steininger, D.Tommasini[4], S.Voigt
Forschungszentrum Karlsruhe, POB 3640, D-76021 Karlsruhe, Germany
[1] Fachhochschule Ostfriesland, Constantiapl. 4, D-26723 Emden,Germany
[2] Lab. Sincrotro Barcelona-IFAE, Campus UAB, E-08193 Bellaterra, Spain
[3] J.Stefan Institute, Jamova 39, SLO-1001 Ljubljana,Slovenia
[4] Sincrotrone Trieste, Padriciano 99, I-34012 Trieste, Italy

Abstract

ANKA, a 2.5 GeV synchrotron light source will be built within the next three years at the Research Centre Karlsruhe, Germany. This source is dedicated to the fabrication of microstructures (LIGA-technique) and X-ray analysis. With four double-DBA structures, a magnetic field of 1.5 T and a circumference of 110.4 m, an emittance of 39 $nm \cdot rad$ can be reached. ANKA has four long (6 m) straight sections for the installation of insertion devices. Additional four short (2.2 m) straight sections host the injection scheme, four ELETTRA-type cavities (two cavities per section) and one short insertion device. The RF power will be provided by two 250 kW klystron. The pre-acceleration will be done with a 22-50 MeV linac or microtron. As injector a 500 MeV booster synchrotron with a repetion rate of 3 to 10 Hz is foreseen. The ramping from 0.5 GeV to 2.5 GeV will be done in around one minute.Eleven out of thirty-two available bending magnet radiation ports will be equipped with beam lines in the first phase.

1 INTRODUCTION

Fabrication of microstructures by X-ray deep lithography (XRDL), galvanoforming, and plastic molding (German acronym LIGA) has made its way from Forschungszentrum Karlsruhe to many labs throughout the world. ANKA is designed to satisfy the needs of XRDL as well as of X-ray analysis, in particular, of microstructures. Industrial demand of service in both fields will play a major role for ANKA [1]. After the approval of ANKA in March 1996 a redesign of the storage ring has been done and the design of the main components has been finished. At present, a call for tender for the main components (injector, magnets, power supplies, vacuum-system, and rf-system) is under way and it is assumed that the first contracts for the production of some components can be placed in June 1997. According to the time schedule the first beam should be stored at the end of 1999.

2 LATTICE OF THE ANKA STORAGE RING

As mentioned in earlier papers [2],[3], the lattice of ANKA is a double DBA-structure with a fourfold symmetry. The leading design principles were to build a light source which

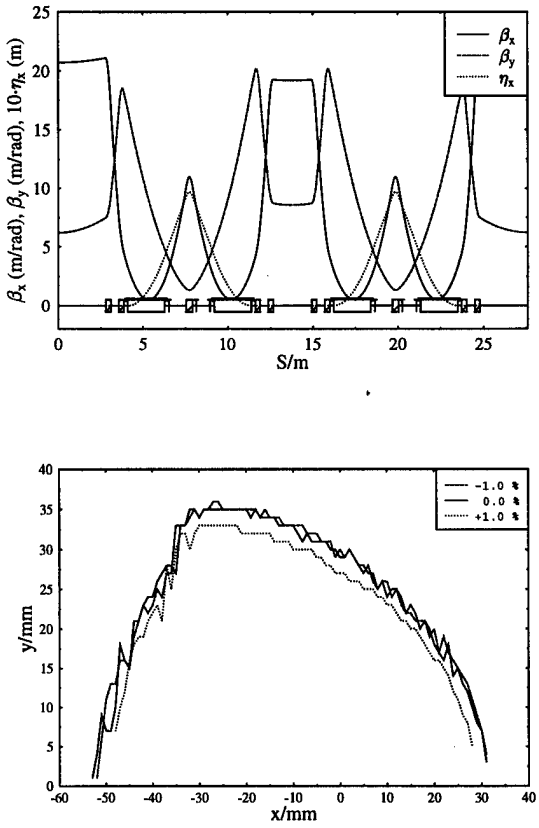


Figure 1: Behaviour of the machine functions within one quadrant of the ANKA storage ring: a) Upper figure: optics A with achromatic arcs, b) Lower figure: dynamical aperture of the ring.

is relatively small and has a low emittance; two conditions which are usually in contradiction. The original design contained only four straight sections of 5.6 m length each, one of which was used up for injection. To get more space for insertion devices, a redesign was made, increasing the circumference to 110.4 m. ANKA now has four long straight sections (6 m) and four short straight sections (2.2m). The layout of the storage ring is presented in fig. 2. The long straight sections are foreseen for insertion devices with the possibility to insert some more quadrupoles for getting a mini-beta section [4] in a later stage. The short straight sections will be used for the injection, for the in-

0-7803-4376-X/98/$10.00 © 1998 IEEE

Table 1: Main parameters of ANKA for both optics. * Upgrading at a later time.

Achromatic structure		DDBA	
Number of unit cells	4		
Nominal energy (GeV)	E	2.5	
Circumference (m)	C	110.4	
Beam current (mA)	I	200 (400*)	
Coupling factor	c	0.02	
Betatron tunes	(Q_x/Q_y)	7.10/3.15	
Nat. energy spread	dE/E	$9.1 \cdot 10^{-4}$	
Version		η=0.0	$\eta \neq 0.0$
Emit. $(nm \cdot rad)$	$\varepsilon_x/\varepsilon_y$	73/1.5	39/0.8
Nat. chromaticity	ξ_x/ξ_y	-17.3/-7.7	-16.7/-7.6
Mom. com. factor	α	$0.81 \cdot 10^{-3}$	$0.91 \cdot 10^{-3}$
Beta func. (m/rad)			
– straight sections	β_x/β_y	20.0/7.00	18.0/7.00
– bending magnets	β_x/β_y	0.56/12.4	0.55/10.6
– Maximum value	β_x/β_y	20.4/19.6	18.5/19.8
Disp. funct. (m)			
– straight section	η_{ss}	0.00	0.50
– bending magnet	η_{bm}	0.11	0.12
Source Size (mm)			
– straight section	σ_x/σ_y	1.2/0.10	0.95/0.07
– bending magnet	σ_x/σ_y	0.23/0.13	0.18/0.09

stallation of the four rf-cavities (two cavities in one section) and a short insertion device.

The machine functions within one quadrant are presented in fig.1. At the working point $Q_x = 7.10/Q_y = 3.15$ the conventional DBA-lattice (optics A - fig. 1a) results in an emittance of 73.4 $nm \cdot rad$. By decreasing the strength of the quadrupole within the dispersive section one gets an optics with a distributed dispersion function (optics B). The minimum of the dispersion is now in the bending magnets, which leads to an emittance of 39 $nm \cdot rad$. The lattice can be shifted from one optics to another by keeping the working point constant. Because the dynamic aperture is larger for optics A (presented in fig 1b) than for optics B, it is planned to accumulate the beam and ramp the energy from 500 MeV to 2.5 GeV with optics A and switch to optics B at nominal energy. The main parameters for both structures are given in table 1.

3 COMPONENTS OF THE STORAGE RING ANKA

3.1 Magnets

The first design of the ANKA magnets has been presented at the EPAC 96 [5]. During the redesign of the bending magnets the pole profile has been changed in order to get to higher fields. Now it should be possible to run the magnets with a maximum field of 1.65 T. The nominal field is 1.5 T. For the quadrupoles and the sextupoles only the pole shape has been changed in order to have parallel coils, which should be cheaper for the production.

3.2 Vacuum System

The vacuum chamber with a height of 32 mm and a width of 70 mm will be made of stainless steel. An in situ bake out is not foreseen. Most of the synchrotron radiation will be absorbed by discrete absorbers (two per bending magnet) in ante chambers. Here 500 l/s and 300 l/s diode pumps will be installed. The pumping will be done with a total nominal pumping speed of 18800 l/s and 13000 l/s, respectively, at 10^{-9} mbar. Pressure profile calculations show that the foreseen pumping speed should be sufficient to obtain a pressure of $3 \cdot 10^{-9}$ mbar, necessary to get a lifetime of more than 12 h. More details of the vacuum system are presented in a seperated paper of this conference [6].

3.3 RF System

The rf system consists of four cavities and two 250 kW klystrons. With an installation of a rf power of 500 kW it is possible to accelerate a beam of 400 mA with an overall cavity voltage of 3.2 MV. This leads to an overvoltage factor of q = 5 with an energy acceptance of 2 % for the klystrons. A power supply with 50 kV and a current of 16 A is needed. Within this scheme the input has to stand a power of 120 kW. The intention is to use the cavities and the input couplers designed at ELETTRA[7]. A test performed recently at DESY showed that the ELETTRA input coupler can withstand a power of more than 130 kW.

3.4 Injector

The injector at ANKA consists of a 20 - 50 MeV preaccelerator, a 500 MeV booster synchrotron and the two transfer lines. As preaccelerator a microtron or linac can be used. For the booster synchrotron we investigated both a weak focusing and a strong focusing machine. Both types have some advantage and disadvantages. They are discussed in a separated paper [8] at this conference. For the ANKA project it is foreseen to buy the whole injector as a turn key machine from industry.

3.5 Control System

The design of the ANKA control system [9] is based on standard industry components. A minimum number of different hardware interfaces will be allowed. PCs are used as consoles and servers. The operating system is Windows NT. Graphical applications will be implemented in Java in order to fully benefit from Internet and WWW products and technologies. Communications, run-time databases and objects will be supported by the control system platform TACO [10] that has been developed by the ESRF. Currently, several field buses, which will connect PCs to controlled equipment, are being investigated. As of now, preference is given to LonWorks. Both TACO and LonWorks have been evaluated and proven to meet the needs of ANKA.

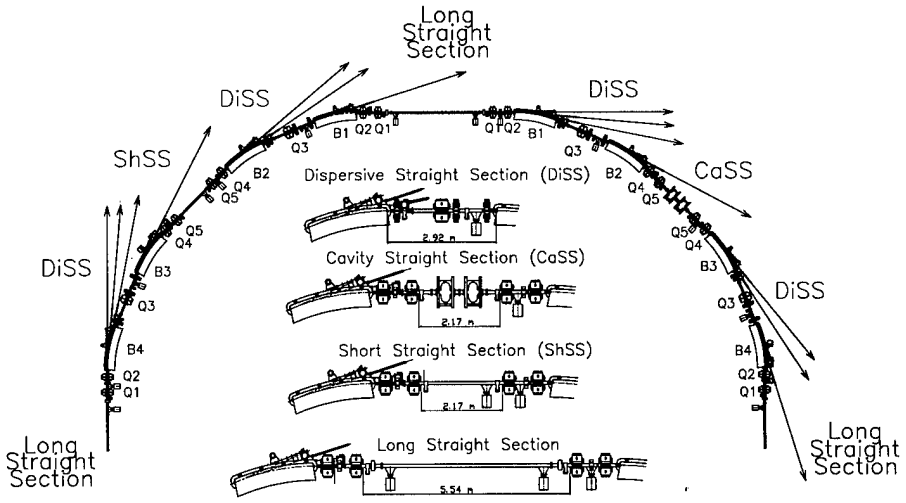


Figure 2: Layout of half of the storage ring ANKA.

Table 2: The beamlines to be built in first phase of ANKA

	Method	Industrial application
1-3	X-ray deep lithography	Microfabrication
4	Absorption, diffraction	Catalysts, chemical analysis, electrochemistry
5	Diffraction	Macromolecular crystallography, powder & single crystal diffraction
6	XUV spectromicroscopy	Mesoscale microscopy, absorption spectroscopy of light elements
7	(F)IR spectro- & micro-scopy	Chemical analysis
8	Fluorescence	Trace analysis (wafer)
9	Topography	Crystal quality (wafer)
10	SAXS, Tomography	Polymers, morphology of irregular structures
11	Roentgenography	Stress & strain, morphology, texture

3.6 Beamlines

11 beamlines, as presented in table 2, are planned to be built in the first phase. They cover X-ray deep lithography in the framework of LIGA technology and related methods in microfabrication, and include important analytical methods.

4 REFERENCES

[1] H.O. Moser, D. Einfeld, R.Steininger, Vorschlag zum Bau einer Synchrotronstrahlungsquelle (ANKA) im Forschungszentrum Karlsruhe zur Foerderung der industriellen Nutzung von Mikrofertigung und Analytikverfahren, Forschungszentrum Karlsruhe, 22 September 1995

[2] H.O. Moser et al, ANKA, a Synchrotron Light Source for Microstructure Fabrication and Analysis, Proceedings PAC 95, May 1-5, Dallas, Texas

[3] D.Einfeld, J.Schaper, F.Iazzourene, H.O. Moser, Lattice and Dynamical Behavior of the Light Source ANKA, Proceedings EPAC 96, Sitges (Barcelona), 10-14 june 1996

[4] U.Bandow, D.Einfeld, T.Hezel, H.O.Moser, R.Rossmanith, J.Schaper, Calculation of the Dynamic Aperture in the ANKA Storage Ring with a High-field Wavelength Shifter, Proceedings EPAC 96, Sitges (Barcelona), 10-14 June 1996

[5] D.Einfeld, A.Kruessel, D.Tommasini, Magnet Design for the Synchrotron Light Source ANKA, Proceedings EPAC 96, Sitges (Barcelona),10-14 June 1996

[6] E.Huttel, D.Einfeld,The Vacuum System of the Synchrotron light Source ANKA, this conference

[7] ELETTRA, Conceptional Design Report, Sincrotrone Trieste, Padriciano 99, I 34012 Trieste

[8] D.Einfeld, F. Perez, R.Rossmanith, R.Walther, The ANKA Booster Synchrotron, this conference

[9] S. Avsec, B. Jeram, G. Mavric, M. Plesko, M. Smolej, Designing the Control System of ANKA, this conference.

[10] A. Goetz et al., TACO: An object oriented system for PC's running Linux, Windows/NT, OS-9, LynxOS or VxWorks, presented at the PCs and Particle Accelerator Control (PCaPAC) Workshop, DESY Hamburg, 1996.

SPATIAL COHERENCY OF THE SYNCHROTRON RADIATION AT THE VISIBLE LIGHT REGION AND ITS APPLICATION FOR THE ELECTRON BEAM PROFILE MEASUREMENT

Toshiyuki MITSUHASHI, Institute of Materials Structure Science, High Energy Accelerator Research Organization, Oho, Tsukuba, Ibaraki, 305 Japan

Abstract

A spatial coherenceies of SR beam at visible light region were measured both σ and π-polarized components at Photon Factory. A wave-front division type polarized interferometer was designed and constructed for this experiment. Interferograms were observed clearly in the vertical direction. π phase difference of the interference fringe was observed between interferograms corresponding to σ and π-polarized components. Degree of spatial coherence was measured and by means of the van Citterut-Zernike's theorem, a vertical beam profile was obtained by the Fourier transform of the degree of spatial coherence.

1 INTRODUCTION

The measurement of profile of the object by means of spatial coherency was known as the Van Cittert-Zernike's theorem[1]. It is well known that A. A. Michelson was measured the angular diameter of stars by this theorem [2]. Recent developments in the accelerators, according to the reducing the beam emittance, the beam size becomes very small (few ten microns). The problem to observe such a small beam profile becomes as a same problem as in the measurement of angular diameter of the stars. In this time, for the purpose to measure the beam profile, I applied profile measurement of the object by means of spatial coherency. At first, basic investigation of the spatial coherence of synchrotron light in the visible light region has been performed. In the second, by means of the van Citterut-Zernike's theorem, the electron beam profile in the vertical direction was obtained by Fourier transform of the degree of spatial coherence.

2 INTENSITIES OF INTERFEROGRAMS BY THE SYNCHROTRON RADIATION IN THE VEERTICAL PLANE

In the vertical plane, elliptical polarity of the Synchrotron radiation is opposite against the medium plane of the electron beam orbit. Therefore, it is expected that π phase difference in the phase of interferogram corresponding to σ and π-polarized components. Disturbances U of the synchrotron light are written by[3];

$$u_\sigma = A_0 \frac{\eta}{(1+\theta^2)^{\frac{1}{2}}} K_{\frac{2}{3}}(\eta)$$

$$u_\pi = A_0 \frac{\eta\theta}{(1+\theta^2)} K_{\frac{1}{3}}(\eta)$$

for σ and π-polarized components. Where θ denotes observation angle and K denotes the second order Bessel function. Divided the wave front of the light beam into two beams against the medium plane of the electron beam orbit, then coupled again to make the interferogram, the intensity of the interference fringe is given by;

$$I_\sigma = (a_1^2 + a_2^2)\left\{1 + \frac{2a_1a_2}{a_1^2 + a_2^2}\cos(\delta)\right\}$$

$$I_\pi = (a_1^2 + a_2^2)\left\{1 + \frac{2a_1a_2}{a_1^2 + a_2^2}\cos(\delta + \pi)\right\}$$

where δ denotes optical pass difference in phase. a_1 and a_2 denote amplitude of the light beams corresponding to two optical pass of the interferometer. The phase term of the interferogram of π-polarized components is shifted by π from the phase term of σ -polarized components.

3 DESIGN OF THE INTERFEROMETOR

A wave-front division type tow beam interferometer by the use of polarized quasi-monochromatic rays was designed and constructed. A schematic drawing of the interferometer is shown in Fig.1. A double slits assembly was applied for dividing the wave-front. The distance between the tow slits can change continuously from 5mm to 80mm. A dichroic sheet polarizer was used to select σ or π-polarized component. The extinction rate of this filter for one component to the other is 10^{-4}. This filters can be rotated by 360° around the optical axis of the interferometer. A band-pass filter of 10nm bandwidth at 700nm was used to obtain a quasi-monochromatic ray. A diffraction limited doublet-lens having a diameter of 80mm and a focal length of 1000mm was used as an objective lens of the interferometer. The obtained interferogram is measured by a CCD (Plinix,TM765) and an image processor (Spiricon,LBA-100A).

0-7803-4376-X/98 /$10.00 © 1998 IEEE

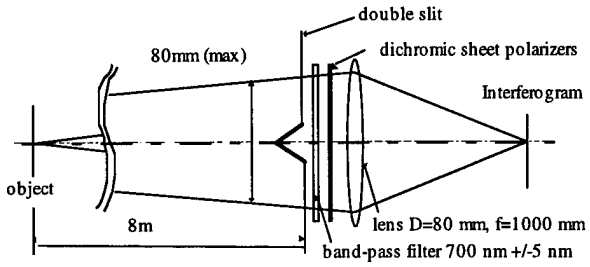
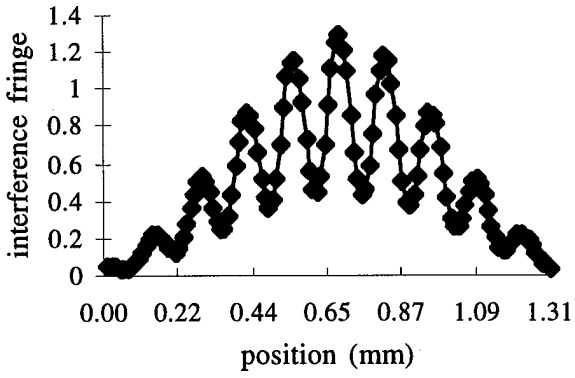


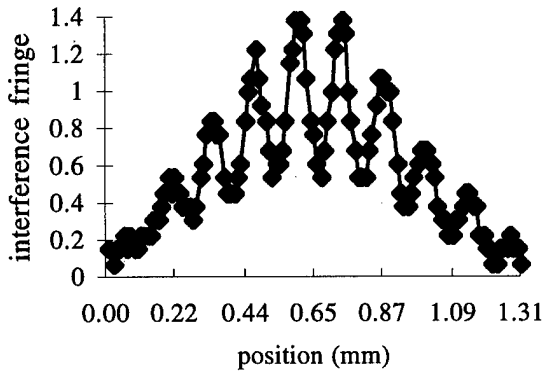
Fig.1 design of interferometer

4 EXPERIMENTAL RESULTS OF SPATIAL COHERENCY OF THE SYNCHROTRON RADIATION

Interferograms were measured both σ and π-polarized components of the synchrotron light at the optical laboratory 2 of BL-27 in the Photon Factory. Examples of observed intereferograms corresponding to σ and π-polarized components are shown in Fig.2.



a) interferogram by s -polarized components.



b) interferogram by p-polarized components.

Fig.2 results of interferograms for σ and π-polarized components. The distance of double slit is 5 mm.

Comparing these two interferograms, the phase of the interference fringe is shifted by π.

The absolute value (visibility) and phase of complex degree of spatial coherence was measured by changing the distance of the double slit from 5mm to 15mm. Results are shown in Figures 3 and 4. As in Fig.3, the visibility is almost zero at the distance of double slit of 15mm. Its means beam profile has no more higher spatial frequency parts of Fourier component.

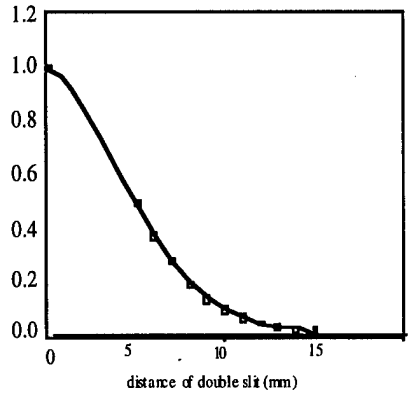


Fig.3 Absolute value of the complex degree of spatial coherence

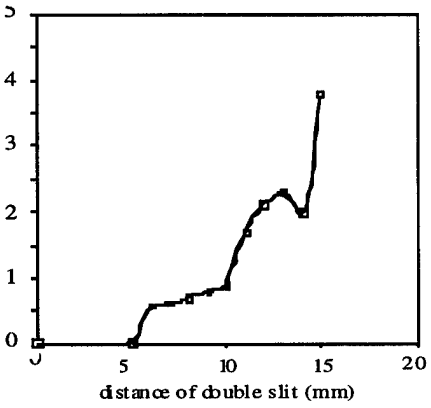


Fig.4 Phase of the complex degree of spatial coherence vertical axis is phase in radian

5 VERTICAL BEAM PROFILE

According to the van Citterut-Zernike's theorem, the profile of object was obtained by Fourier transform of the complex degree of spatial coherence. Let f(Θ) denotes beam profile as a function of angular diameter Θ and γ(D) denotes the complex degree of spatial coherence, γ is given by the Fourier transform of f as follows;

$$\gamma(D) = \int f(\Theta)\exp(-ikD\Theta)d\Theta$$

$$= C(D) + iS(D)$$

where C(D) denotes Fourier cosign transform of f(Θ) and S(D) is Fourier sin transform of F(Θ). Then interferogram is given by;

$$I(\Theta) = 1 + |\gamma(D)| \cos\{kD(\Theta + \varphi)\}$$

$$\varphi = \tan^{-1} \frac{S(D)}{C(D)}$$

Therefore, from the data of the absolute value and phase of the complex degree of spatial coherence , we can obtain the beam profile by the Fourier transform. A result of the beam profile is shown in Fig.5.

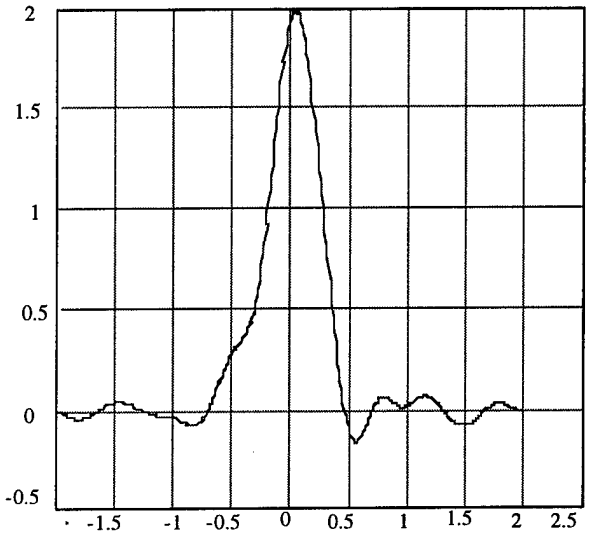


Fig.5 The beam profile obtained by a Fourier transform of the complex degree of coherence.

A least square beam size s through a second order moment is 214 μm.

According to the phase term of complex degree of spatial coherency, the beam profile has a asymmetric distribution. This asymmetry in the distribution curve is mainly caused by a deformation of the extraction mirror for SR light. A large astigmatism term was observed by the in situ measurement of the surface flatness of the mirror [4],[5]. As same technique as in the noise elimination processing in the Fourier transform of the electric signal, it is possible to eliminate asymmetric part of the Fourier components of complex degree of spatial coherency. As most easy way to do this process, we try to neglect Fourier sine transformation. The result is shown in Fig.6.

Compare with Figures 5 and 6, the asymmetric part caused by deformation of the mirror was completely eliminated. The least square beam size in Fig 6 is 202 μm. This technique is very useful for the elimination of unknown effects (asymmetric terms of the wavefront aberration) of the optical components between the object and the image plane. As demerits, we cannot use this technique for 1. optical system has a symmetric wave front error such as spherical aberration, 2.beam has asymmetric distribution.

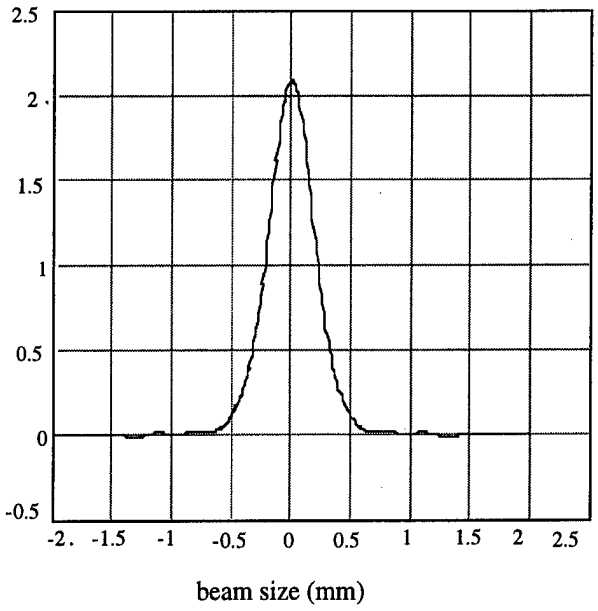


Fig.6 The beam profile obtained by a Fourier cos transform

6.CONCLUSIONS

A spatial coherenceies of SR beam at visible light region were measured both σ and π-polarized components. A phase difference of π in the interference fringes corresponding to σ and π-polarized components was observed. The Complex degree of spatial coherency was measured and by means of the van Citterut-Zernike's theorem, a vertical beam profile was obtained by the Fourier transform of the complex degree of spatial coherence. An asymmetry of the distribution curvature caused by a deformation of optical mirror was observed. This effect was eliminated by neglecting the Fourier sin transform.

7.ACKNOWLEDGMENTS

The author thank to Mr. Takeuchi of Tsukuba University for him help in experiments.

REFERENCES

[1] M. Born and E. Wolf, "Principles of Optics" p508,PERGAMON PRESS,(1980).
[2] A. A. Michelson,Astrophsyc.J51,257,(1920).
[3] A. Hofmann and F. Meot. Ncl. inst. and Meth.203,483(1982).
[4] T. Mitsuhashi and M.Kato,Proc.5th European Particle Accelerator Conf.1669,(1996).
[5] N. Takeuchi, T. Mitsuhashi, M. Itoh and T. Yatagai, somewhere in this proceedings.

LONGITUDINAL BEAM TRANSFER FUNCTION DIAGNOSTICS IN THE ALS *

John Byrd
Lawrence Berkeley Laboratory, One Cyclotron Road, Berkeley, California 94720

Abstract

We describe the technique of longitudinal beam transfer function (BTF) for measuring several properties of longitudinal oscillations in a electron storage ring such as the synchrotron frequency, radiation damping time, and bunch length. The technique takes advantage of the Gaussian distribution of longitudinal oscillation amplitudes within the bunch at very low current and the dependence of synchrotron frequency on amplitude. Results of measurements made at the Advanced Light Source (ALS) are presented.

1 INTRODUCTION

Beam transfer function (BTF) diagnostics are used in almost all storage rings for measuring the betatron and synchtrotron frequencies. In the simplest case, a swept frequency drive excites either betatron or synchrotron oscillations while a beam signal is observed on a spectrum analyzer. In other applications, BTF techniques have been used[1, 2, 3] for measuring beam impedance and feedback loop stability. We describe in this paper an application of the BTF technique for use in an electron storage ring for making measurements of the distribution of synchrotron frequencies within a single bunch at low beam current. By taking advantage of the Gaussian distribution in the energy spread within the bunch resulting from the quantum nature of the emission of synchrotron radiation and the sinusoidal RF voltage, we can use the measurements to derive a relatively precise measure of the nominal synchrotron frequency, the longitudinal radiation damping rate, and the bunch length. Although these parameters can be measured using other techniques, the BTF method has the advantage of being relatively simple and inexpensive, and typically uses equipment that is either already available in the control room or easily assembled. The BTF technique can potentially be used to study the effects of short range wakefields and the longitudinal beam dynamics of more complicated situations such as double RF systems and low momentum compaction.

In general, the BTF is defined as the ratio of the driven beam response to the external excitation at a given frequency. In practice, either an network or FFT analyzer is used to supply a swept frequency or noise excitation to the beam via either a stripline kicker or RF cavity and the beam response is measured through a pickup. For the cases discussed in this paper, we excite longitudinal oscillations by phase modulating the voltage in the fundamental mode of an RF cavity and measure the synchrotron oscillations by detecting the phase of a beam pickup signal relative to a fixed reference phase or by measuring energy oscillations at a point of dispersion in the lattice. It is also assumed throughout the paper that the amplitude of synchrotron oscillations is small enough that the motion can be described as linear.

Section 2 discusses the longitudinal beam distribution and gives a physical interpretation of the transfer function for a Gaussian distribution. Section 3 presents the measurements performed at the ALS.

2 BEAM TRANSFER FUNCTION FOR A GAUSSIAN DISTRIBUTION

The energy distribution in an electron bunch in a storage ring is Gaussian, resulting from the balance of the quantum excitation from synchrotron radiation emission and radiation damping[4]. It can be shown that the phase space density distribution to second order is given by

$$\psi_0(\hat{\tau}) = \frac{1}{2\pi\sigma_\tau^2} e^{-(\hat{\tau}^2/2\sigma_\tau^2)} \tag{1}$$

where $\hat{\tau}$ is the oscillation amplitude and σ_τ is the RMS bunch length, both in units of time. The nonlinearity of the sinusoidal RF voltage results in a synchrotron frequency dependent of the amplitude of phase oscillation of the form

$$\omega_s(\hat{\tau}) = \omega_{s0}(1 - \mu\hat{\tau}^2) \tag{2}$$

where

$$\mu = \frac{\omega_{RF}^2(1 + \frac{5}{3}\tan^2\phi_s)}{16} \approx \frac{\omega_{RF}^2}{16} \tag{3}$$

where ϕ_s is the synchronous phase angle. For most cases, the effect of ϕ_s can be ignored.

The combination of the distribution of oscillation amplitudes and synchrotron frequency as a function of amplitude yields a unique distribution of synchrotron frequencies within the bunch for a given bunch length. As described below, the natural spread in frequencies leads to Landau damping of coherent oscillations.

Given the distribution, the BTF can be found by solving the Vlasov equation for a small perturbation of the phase space distribution at the excitation frequency and integrating to find the first moment of the distribution. This approach is identical to that used in finding the stability conditions of coherent instabilities. Equivalently, the BTF can be found by calculating moments of the distribution in response to an impulse excitation in the time domain and making a Fourier transform on the result. The time domain

* This work was supported by the Director, Office of Energy Research, Office of Basic Energy Sciences, Materials Sciences Division, of the U.S. Dept. of Energy under Contract No. DE-AC03-76SF00098.

0-7803-4376-X/98/$10.00 © 1998 IEEE

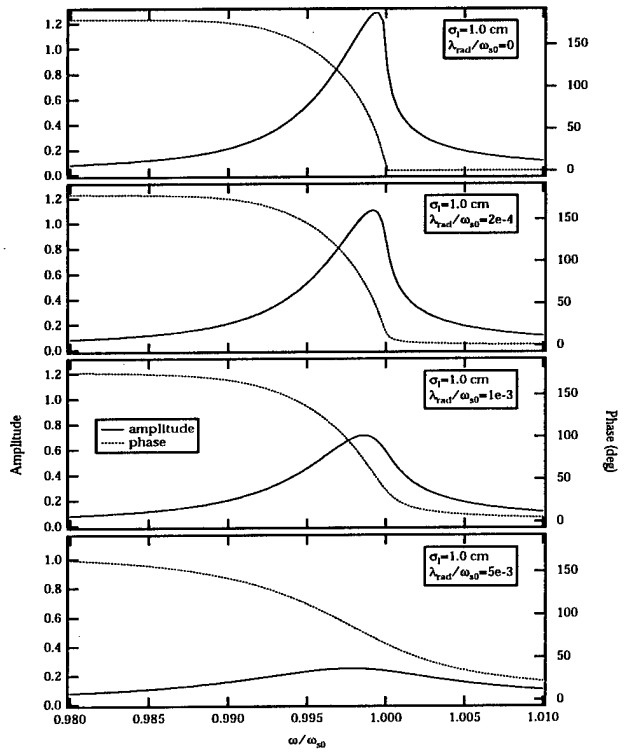


Figure 1: Calculated BTF for a 1 cm RMS bunch length as a function of increasing radiation damping.

impulse response has been calculated[5] and can be shown to give the same result as the Vlasov approach for infinitesimal excitation. The BTF can be expressed in terms of a dispersion integral given by[6]

$$I(\omega_m) \propto \int_0^\infty \frac{\hat{\tau}^2 d\hat{\tau}}{\omega_m - \omega_s(\hat{\tau})} \frac{\partial \psi_0}{\partial \hat{\tau}}. \qquad (4)$$

where ω_m is the angular modulation frequency. Radiation damping is included by making the synchrotron frequency complex as given by

$$\tilde{\omega}_s = \omega_s + j\lambda_{rad} \qquad (5)$$

For a Gaussian distribution in oscillation amplitude, the dispersion can be expressed in terms of the exponential integral[7], given by

$$I(x) \propto 1 - xE_1(x)e^{-x} \qquad (6)$$

where $x = \frac{8(\omega_{s0} - \omega - j\lambda_{rad})}{\omega_{s0}\omega_{rf}^2\sigma_\tau^2}$.

The amplitude and phase of the BTF is plotted for several values of the bunch length as a function of increasing radiation damping in Figures 1a-d. For convenience, we have used the convention that the phase goes from 180 to 0 degrees passing from far below the nominal synchrotron frequency to above. Consider the case of no radiation damping ($\lambda_{rad} = 0$) shown in Figure 1a. When the external excitation frequency is greater than the zero–amplitude synchrotron frequency, the phase of the beam response does

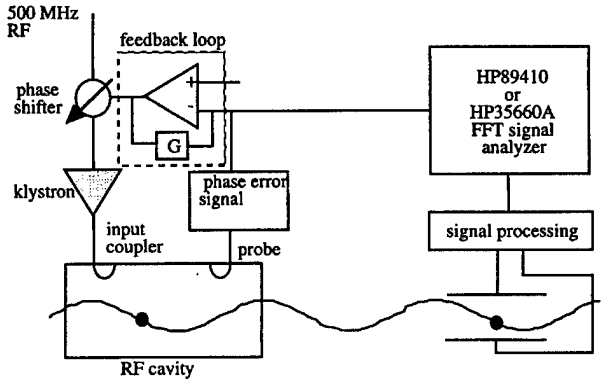


Figure 2: General setup for longitudinal BTF measurements.

not vary with frequency because all of the electrons within the bunch are being driven above their resonant frequency. When $\omega_m < \omega_{s0}$ and the external excitation frequency is within the spread of incoherent frequencies, some of the particles in the bunch are being driven resonantly, some below resonance, and some above resonance and thus there is a net phase shift between the drive and the response. When the external excitation frequency is far below the synchrotron frequency, all electrons have again the same phase response. Neither the amplitude and phase response are symmetric in frequency because the distribution of synchrotron frequencies with oscillation amplitude is not symmetric. Also note that the peak amplitude response does not occur at the nominal synchrotron frequency but slightly below.

For nonzero radiation damping as shown in Figures 1b-d, the response of individual electrons now have a natural width. This tends to smear the response of the distribution of synchrotron frequencies. As the width due to radiation damping approaches the width of the distribution of synchrotron frequencies, the response becomes much more like the Lorentzian shape expected from a damped harmonic oscillator.

3 BEAM MEASUREMENTS

The setup for measurement of the BTF is shown in Figure 2. We excited longitudinal oscillations by phase modulating (PM) the RF voltage. This was achieved by injecting the modulation signal as an error signal in the RF phase control feedback loop.

Synchrotron oscillations were detected using the phase detector for an existing longitudinal coupled–bunch feedback system[8]. This detector passes the sum of the signal from four capacitive button BPMs (beam position monitors) located at one point in the ring through a 4–tap comb filter with a center frequency of 3 GHz ($6 \times F_{rf}$). The sum of the four button signals is not sensitive to the transverse position of the beam. The signal is demodulated to baseband through a double balanced mixer using a 3 GHz local oscillator derived from the 500 MHz master oscillator. Detection at the sixth RF harmonic increases the sensitivity

to phase oscillations compared to detection at the RF frequency and is also near the frequency of maximum pickup impedance of the BPMs. Because of the relatively short bunch length in the ALS, the 3 GHz component of the beam signal is reduced very little compared to the 500 MHz component.

The sensitivity required for the detection of the synchrotron oscillations depends somewhat on the storage ring parameters. For example, to obtain the most accurate results, we found that it was important to excite the synchrotron oscillations with an amplitude at least two orders of magnitude less than the natural bunch length in order that the oscillations remained quasilinear. Therefore, measurements with shorter bunch length require greater sensitivity. We indepently verified the amplitude of PM in the cavity by measuring the spectrum of PM sidebands present on a cavity probe signal with no beam. Also, to avoid conversion of PM to amplitude modulation, the frequency of the RF cavity was tuned to on resonance with the RF drive frequency for all measurements. For the conditions of these measurements, the variation of the cavity response over the bandwidth of the measurement was negligible.

An HP89410 FFT signal analyzer was used as the source and receiver for the signal for both measurements. We found that for a given level of excitation, a better signal/noise ratio could be achieved using a bandwidth limited noise source than for a swept frequency excitation. In principle both approaches yield the same results. In order to avoid the influence of collective effects on the bunch shape, all of the measurements presented here were made at the lowest single bunch current possible which still gave a reasonable signal level. We used a bunch current of 100-300 μA, well below the threshold for any instabilities and low enough that potential well distortion is negligible.

Shown in Figure 3 are BTFs measured at various beam energies and synchrotron frequencies. Each result is fit to the functional form given in Eq.6. The width of the amplitude response is due in roughly equal parts to the radiation damping and the spread of synchrotron frequencies and thus the BTF is much more symmetric. We independently measured the bunch length with a streak camera with values shown in parentheses in the figure for comparison. Although the agreement for the values of the bunch length is good, it is less precise for the case when the decoherence rate and the radiation damping rate are comparable. If the interest is in measuring bunch length, the BTF technique would be limited to relatively long bunches.

4 CONCLUSIONS

The BTF is a relatively simple method for measuring the incoherent spread in synchrotron frequencies in a single bunch. With a careful analysis, the small amplitude synchrotron frequency, the longitudinal radiation damping rate, and the bunch length can all be inferred from this measurement. The precision of the measurement depends primarily of the value of the radiation damping rate compared with the incoherent spread in synchrotron frequencies. The measurement of the bunch length is more precise when $\lambda_{rad} < \Delta\omega_s$ and vice versa for measurement of the radiation damping time.

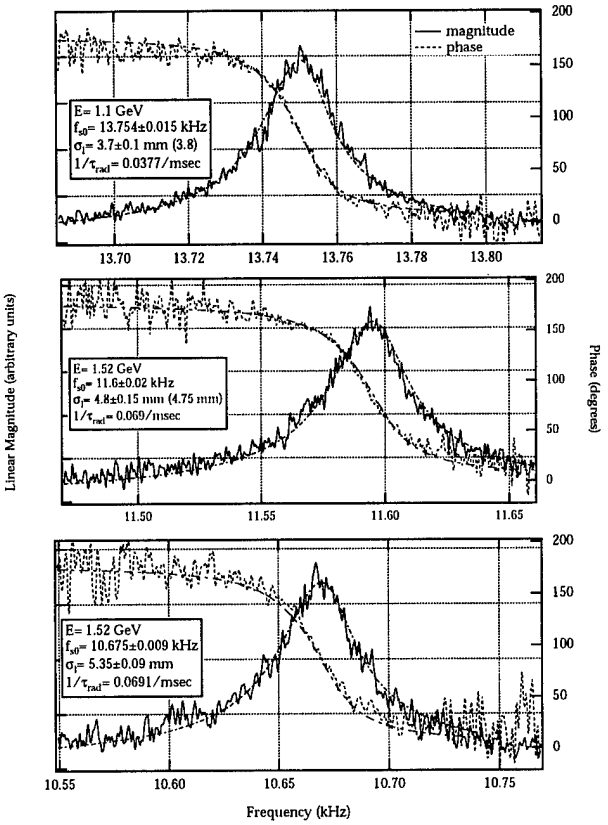


Figure 3: Results of BTF measurements at ALS for several energies and nominal bunch lengths. The fit values for the synchrotron frequency, bunch length, and damping rate are shown for each case. Bunch lengths measured using a streak camera are shown in parentheses for comparison.

We are hopeful that this technique can be used for measuring the effects of distortions of the phase space distribution due to instabilities or other effects. We would like to thank the the ALS operations group for assistance with the measurements.

5 REFERENCES

[1] D. Mohl, A. M. Sessler, Proc. 8th Int. Conf. High Energy Accel., p. 334.

[2] A. Hofmann, B. Zotter, Proc. 1977 PAC., p. 1487.

[3] J. M. Jowett, et. al., Proc. 1987 PAC., p. 726.

[4] M. Sands, **SLAC-121**, 1970.

[5] H. Moshammer, NIMA **323**, 553 (1992).

[6] J. M. Byrd, submitted to *Particle Accelerators*.

[7] M. Abromowitz and I. A. Stegun, "Handbook of Mathematical Functions", Dover (1965), p. 228.

[8] J. D. Fox, et. al., Proc. 1996 EPAC

CONTROLLING THE VERTICAL MODE COUPLING INSTABILITY WITH FEEDBACK IN THE ADVANCED LIGHT SOURCE

J. M. Byrd[†*], W. Barry[‡]
[†]ALS Acc. Physics Group, [‡]Beam Electrodynamics Group, Center for Beam Physics
Lawrence Berkeley National Laboratory, Berkeley, CA 94720

Abstract

We present the results of experiments to control the mode coupling instability in the vertical direction using a feedback system. Presently, we can raise the instability threshold from ~20 mA to 35 mA. The maximum current threshold is reached when the feedback is operated in a resistive mode.

1 INTRODUCTION

The transverse mode coupling instability (MCI) has been studied for some time[1, 2]. In a simple physical picture of the instability, transverse oscillations of the head of a bunch resonantly drive oscillations of the tail through the short range transverse wakefield. The constant interchange of the bunch head and tail via synchrotron oscillations prevents buildup of the oscillations and allows them to damp. However, when the growth time of the tail oscillations becomes comparable to the synchrotron period, the bunch motion becomes unstable, resulting in a dramatic increase in the emittance. This can cause sudden beam loss or a limit to the bunch current.

A normal mode analysis of the instability expresses the bunch motion as a series of modes. The lowest modes are the dipole and head–tail, known respectively as the m=0 and ±1 modes. The oscillation frequency of the m=±1 modes appear as upper and lower sidebands of the m=0 mode. The typical instability occurs when the frequency of the dipole mode (m=0 mode) shifts downward as a function of current and coincides with the $m = -1$ mode as illustrated in a calculation using the MOSES code shown in Figure 1. As the m=0 and m=-1 modes become mixed there is a rapid increase in the growth rate with current.

For the present vacuum chamber configuration of the Advanced Light Source (ALS), the MCI is observed in the vertical direction with a single bunch current of ~20 mA. For a typical multibunch filling pattern, the single bunch current does not exceed 1-2 mA and thus the instability is currently of interest only to users who require high single bunch current. However, as small vertical gap (10 mm) vacuum chambers have been installed in straight sections to accommodate insertion devices, we have observed a decrease in the MCI threshold. So far, two small gap sections have been installed and the threshold has dropped by ~25%. The prospect of further vacuum chamber modifications has prompted further interest in studying the effect.

*This work was supported by the U.S. Department of Energy under Contract Nos. DE-AC03-76SF00098 and DE-AC03-76SF00515.

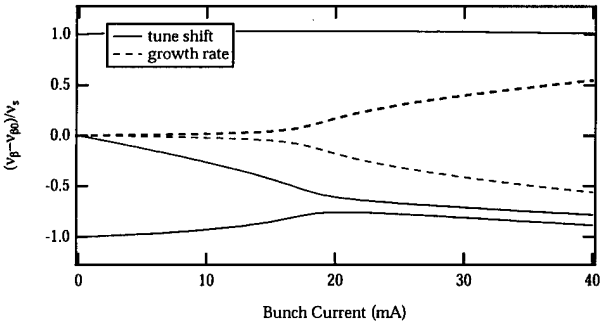


Figure 1: Example calculation of mode coupling instability using the MOSES code. The solid lines show the tune shift of the m=0,±1 modes. The dashed lines show the growth (and damping) rates of the coupled modes above threshold.

Transverse feedback (TFB) has been used to control the MCI in the past[3, 4, 5, 6, 7]. For these experiments, the TFB has been operated in both resistive and reactive modes. In the resistive mode, the TFB acts only to damp or antidamp coherent betatron oscillations. In reactive mode, the TFB shifts the coherent betatron frequency either up or down but does not actively damp coherent oscillations. For avoiding MCI, the FB in reactive mode is adjusted such that the slope of the downward frequency shift with current of the m=0 mode is reduced, thus reducing the coupling to the m=-1 mode and delaying the onset of the instability. Typically, the TFB can be adjusted to have any combination of resistive and reactive components. Experimentally, both modes have had some success in raising the threshold but there is no clear evidence indicating an optimal configuration or a clear theoretical understanding of the interaction of the instability and the TFB.

We have recently begun experiments to control the MCI with TFB in the ALS. Our studies employ a TFB system designed for damping coupled bunch oscillations. We modified the system slightly for use with high single bunch currents as described in the next section. Experimental results and conclusions are given in sections III and IV. General parameters of the ALS are given in Table 1. A summary of measurements of single and multibunch collective effects is given elsewhere[8, 9].

2 TRANSVERSE FEEDBACK SYSTEM

A schematic diagram of the ALS TFB system is shown in Figure 2. Detailed description of the system in given elsewhere[10]. The x, y moments of the bunch are detected

0-7803-4376-X/98/$10.00 © 1998 IEEE

Parameter	Description	Value
E	Beam energy	1.5 GeV
C	Circumference	196.8 m
f_{rf}	RF frequency	499.654 MHz
σ_ϵ	RMS $\delta E/E$	7.1e-4
h	Harmonic number	328
α	momentum compaction	1.594e-3
Q_s	Synchrotron tune	0.0075
σ_ℓ	RMS bunch length	4.5 mm
$Q_{x,y}$	Betatron tunes (x,y)	14.28, 8.18

Table 1: Nominal ALS parameters.

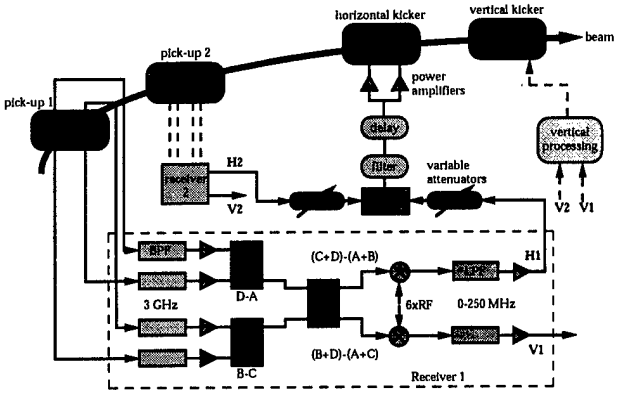


Figure 2: Block diagram of transverse FB system. The system is identical for horizontal and vertical directions.

at two points in the ring, with nominal betatron phase differences (modulo 2π) of approximately 65 and 245 degrees in the x, y directions. The beta functions at the two pickups are equal. The two signals can be combined in any proportion. This signal passes through a single turn notch filter to remove the DC orbit offset and is then delayed the appropriate amount and amplified with a 150 W solid state amplifier. The kicker is a single plate of a pair of stripline kickers. The other plate is used independently for driving betatron oscillations for tune measurements.

The detection of the transverse moment ($I\Delta x$) rather than the position (Δx) makes the TFB gain linearly dependent on current. The summing of the signals from two pickups allows the FB signal to have an arbitrary phase with respect to the betatron oscillation, allowing arbitrary combination of resistive and reactive components in FB. Ordinarily, the FB is adjusted to be purely resistive, maximizing the damping rate.

The TFB system as shown in Figure 2 is intended for damping transverse coupled bunch instabilities for a minimum bunch spacing of 2 nsec and is not optimized for damping high current single bunches. For our experiments in damping the MCI, we modified the system by attenuating the input signal to the receiver by 20 dB in order to not saturate the front end electronics at high single bunch current. A 26 dB gain preamplifier was also inserted immediately before the high power amplifier for some of the

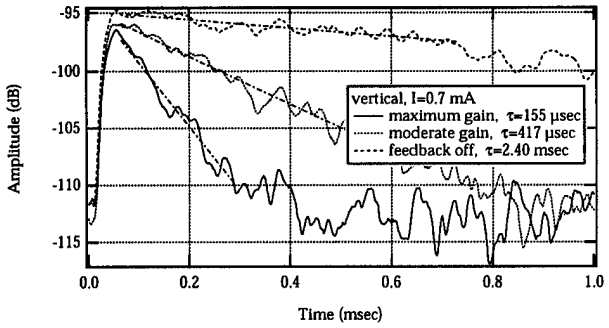


Figure 3: Vertical transients for several settings of FB gain for single bunch current of 0.7 mA. Transients are expected to be 10-20 times faster with the preamplifier in the FB loop.

data shown below. Only the vertical FB loop was closed during the experiments.

We characterized the damping rate of the TFB by measuring directly measuring the transient response of the vertical betatron oscillations in response to an impulse excitation. We can generate a small amount of vertical kick using the pulsed horizontal kicker magnets used for injection. We used a spectrum analyzer tuned to a vertical betatron line in tuned receiver mode. Shown in Figure 3 are several vertical damping transients for high, moderate, and zero FB gain for a single bunch current of 0.7 mA. These measurements were made in the nominal configuration of the FB system with no preamplifier and no front–end attenuation. The damping rate with no FB is dominated by head–tail damping from the small positive chromaticity of the lattice.

Unfortunately, we have not yet succeeded in making damping rate measurements for the conditions used in the MCI studies because of a drop in the signal/noise as we increase the resolution bandwidth of the spectrum analyzer to accommodate the faster damping rates. However, if we scale the measured damping rate by the expected increase in gain used in the MCI studies, we expect damping times on the order of 15-50 μsec, faster than the synchrotron period of 90 μsec. We are currently working to directly measure the damping rate of the FB for very high gain operation.

3 RESULTS

To date we have used TFB in two conditions to control the VMCI. In the first, the FB was configured as described in the previous section except without the preamplifier. As the bunch current surpassed the instability threshold, the FB gain and phase were empirically adjusted to maximize the stable threshold. The maximum stable single bunch current was 27 mA. An example of the spectrum of a vertical monitor signal is shown in Figure 4. The signal spectrum without FB above the MCI threshold for a bunch current of 22 mA is shown on the left and the spectrum with FB on at the same current is shown on the right. In both cases the

signal is excited using a tracking generator driving the vertical kicker plate not used by the FB. At this bunch current, the $m = 0$ mode signal has shifted from the zero current betatron frequency at the center of the frequency span to nearly 3/4 the synchrotron frequency. The $m = -1$ signal appears at the synchrotron sideband and does not depend on external excitation. The signal at the zero–current vertical betatron tune is not understood but may correspond to a radial mode. When the vertical FB loop is closed, the $m = -1$ mode signal dissappears and the $m = 0$ signal is depressed. The vertical beam size also returns to the nominal size as observed on the transverse beam size monitor.

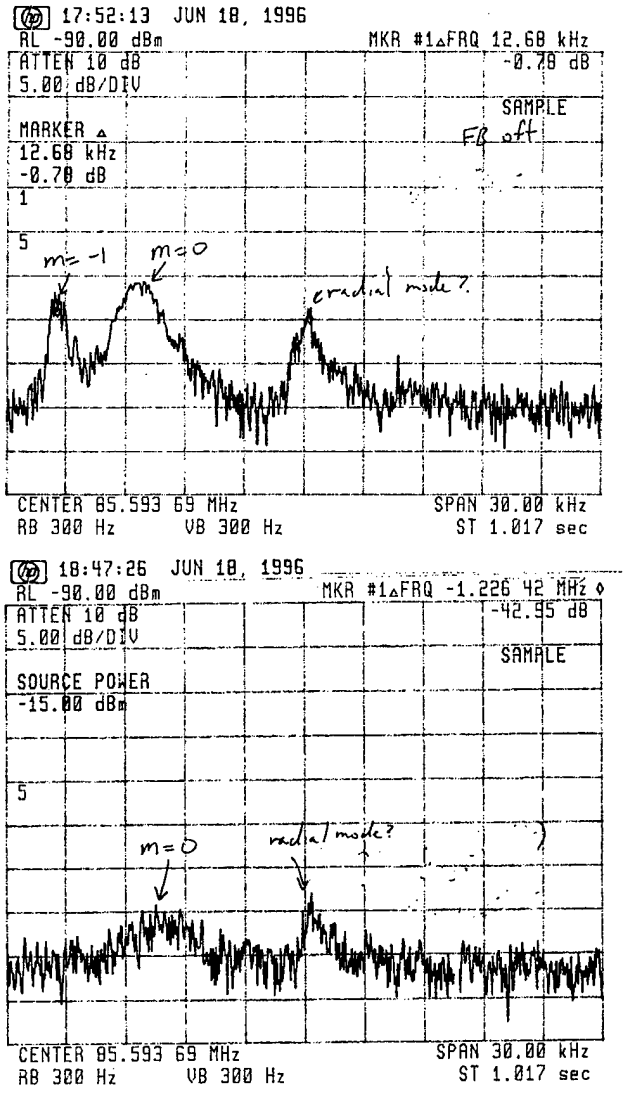


Figure 4: Spectrum of vertical monitor signal just above threshold (I=22 mA.) The left plot is with FB off and right with FB on. The $m = -1$ mode signal dissappears with FB on and the $m = 0$ signal is depressed. The signal at the zero current vertical betatron tune is not understood but may correspond to a radial mode.

Unfortunately we were not able to directly measure the FB phase and determine the combination of resistive and reactive FB. However, measurements of the tune shift with current for the case of FB on and off are identical, indicating that the FB was in a resistive mode.

In the second configuration, a preamplifier was added before the power amplifier. In this configuration, the maximum stable bunch current was 37 mA. Unfortunately, it was not possible to measure the betatron tune above ~6 mA because the strong FB damping depressed and broadened the signal below the noise floor of the spectrum analyzer. However, tune shift measurements below 6 mA with and without FB are identical, indicating that the FB phase appears to be purely resistive.

We are currently trying to understand the reason for the current limitation with FB. We believe the limit results from the maximum FB voltage available.

4 CONCLUSIONS AND ACKNOWLEDGEMENTS

We have used TFB in the resistive mode to damp the MCI in the vertical plane and raised the instability threshold from ~20 mA to 37 mA. Future plans include measurement of the threshold with TFB as a function of FB phase, development of beam transfer function measurements to directly measure FB gain and phase.

5 REFERENCES

[1] R. Kohaupt, *DESY 80/22*, 1980.

[2] K. Satoh, Y. Chin *NIM 207*, pp. 309-320, 1983.

[3] S. Myers *Stabilization of the fast head–tail instability by feedback, Proceedings of the 1987 PAC*, May 1987, p. 503.

[4] S. Myers *Transverse feedback and LEP performance, Proceedings of the 1992 EPAC*, July 1992, p. 66.

[5] V. V. Danilov, E.A. Perevedentsev, *Feedback system for elimination of the transverse mode coupling instability, CERN SL/92–38 (AP)*,Sept. 1993.

[6] J. L. Revol, E. Plouviez *Diagnostics and equipment for single bunch operation at ESRF, Proceedings of the 1994 EPAC*, July 1994, p. 1506.

[7] M. M. Karliner, et. al., E.A. Perevedentsev, *Feedback system for elimination of the fast head–tail instability at storage ring VEPP–4M, Proceedings of the 1996 EPAC*,June 1996.

[8] J. Byrd, R. Holtzapple, B. Pedobedov, *Single Bunch Collective Effects in the ALS, Proceedings of the Micro Bunches Workshop, AIP 367*, p. 236, 1995.

[9] J. Byrd, W. Barry, J. Corlett, J. Fox, D. Teytelman *Observations of collective effects at the Advanced Light Source*, to appear in *Proceedings of the 1995 Workshop on Collective Effects in B–Factories*, KEK, June 1995.

[10] W. Barry, J. Byrd, J. Corlett, G. Lambertson, C. C. Lo *Transverse coupled-bunch feedback in the ALS, Proceedings of the 1994 EPAC*, July 1994.

COMMISSIONING OF THE ADVANCED LIGHT SOURCE DUAL-AXIS STREAK CAMERA*

J. Hinkson, R. Keller, and J. Byrd
Lawrence Berkeley National Laboratory, University of California, Berkeley, California 94720, U.S.A
A. Lumpkin
Advanced Photon Source, Argonne National Laboratory, Argonne, IL 60439

Abstract

A dual-axis streak camera, Hamamatsu model C5680, has been installed on the Advanced Light Source photon-diagnostics beam-line to investigate electron-beam parameters. During its commissioning process, the camera has been used to measure single-bunch length vs. current, relative bunch charge in adjacent RF buckets, and bunch-phase stability.

In this paper we describe the visible-light branch of the diagnostics beam-line, the streak-camera installation, and the timing electronics. We will show graphical results of beam measurements taken during a variety of accelerator conditions.

1 THE SOURCE OF LIGHT

The Advanced Light Source (ALS) is a 1-2 GeV, third-generation synchrotron light source which has been in operation since 1992. One bend magnet beam-line [1] off the storage ring is devoted to beam diagnostics. Silicon mirrors deflect the visible portion of the photon beam to an optical bench. Recently a Hamamatsu streak camera system was installed to view the visible light and provide temporal information on the electron beam bunches.

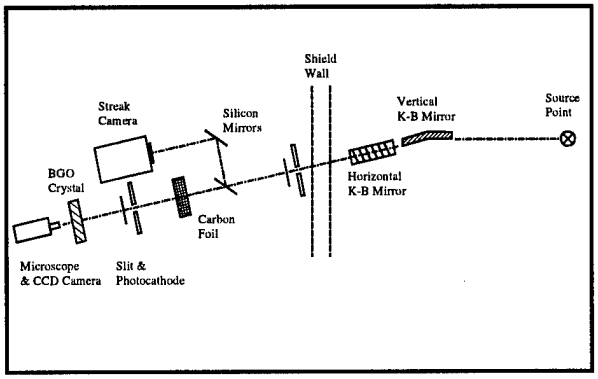


Figure 1. Schematic of diagnostics beam-line.

2 THE CAMERA SYSTEM

The streak camera and optical hardware are installed on a small optical bench above the beam line. The camera system consists of a Hamamatsu C5680 streak camera fitted with an M5679 dual time base extender unit and an M5675 synchroscan unit. The streak tube S20 photo cathode operates over wavelengths from visible to UV. The camera output is RS-170 video. The camera input optics (A1974) have an effective f number of 1.2, a magnification of 1:1, and spectral transmittance from 400 to 900 nm. Other accessories include an M5676 fast single sweep unit, an M5677 slow single sweep unit, a C1097 trigger delay unit, and a C4547 streak trigger unit. All measurements for this paper were taken with the synchroscan unit.

2.1 Camera Synchronization

The synchroscan module deflects the streak tube beam with RF sine waves on the deflection plates. At the ALS the synchroscan frequency is 124.9 MHz (¼ the cavity RF) which falls between the manufacturer's range of 75 to 165 MHz. The ALS synchroscan RF is derived from the storage ring RF master oscillator. In order to minimize timing jitter the RF is filtered in a cavity (Q = 1000) before being divided by four. The ring orbit clock (SROC, 1.523 MHz) is re-synchronized with the RF at the beam line racks. System jitter measured with an Tektronix 11801B sampling oscilloscope is less than 4 ps rms.

The synchroscan module is driven continuously. The maximum triggering rate for the dual axis module is 10 Hz. Triggers for this unit are derived from the C4547 streak trigger unit which reduces the SROC trigger to 10 Hz. A Stanford Research DG535 delay generator is used to delay the dual-axis triggers to permit measurement of a desired bunch or series of bunches.

The longest sweep range for the synchroscan module is 1.4 ns, approximately 1/6 of the 124.9 MHz sine wave duration. The fastest sweep range is 150 ps. The dual sweep axis module time range is from 100 ns to 100 ms.

3 MEASUREMENTS

3.1 Bunch Length

Single bunches ranging from 1 to 20 mA average current were circulated in the ALS. Fig. 3 shows the measured rms bunch length and the shift in synchronous phase as the bunch current was increased. To determine phase shift two bunches were stored at any time. One bunch was weak and taken as the phase reference as current in the other bunch was increased.

0-7803-4376-X/98/$10.00 © 1998 IEEE

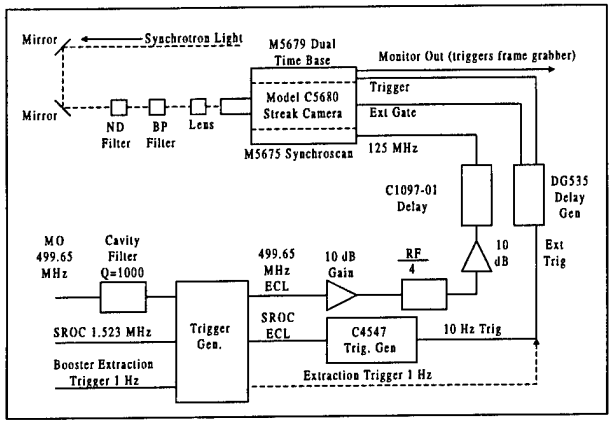


Figure 2. Streak camera block diagram.

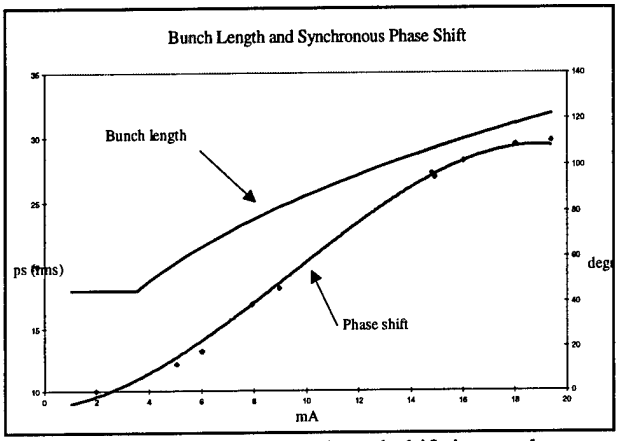


Figure 3. Single bunch length and shift in synchronous phase. The bunch length curve is fitted to experimental data. The phase shift curve is a polynominal fit to data shown.

3.2 Beam Damping

The ALS has bunch-by-bunch damping systems to suppress longitudinal and transverse coupled-bunch instabilities. The dramatic effect of longitudinal damping is seen in the following two figures.

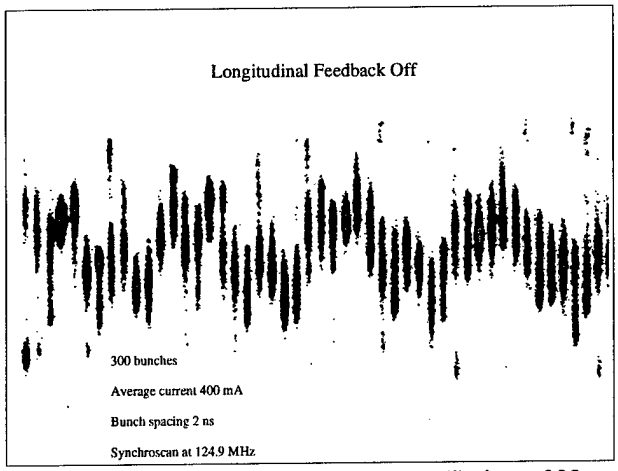


Figure 4. Damping off. Vert. = 1 ns. Horiz. = 200 ns. Bunch spacing = 2 ns. Every other bunch is shown.

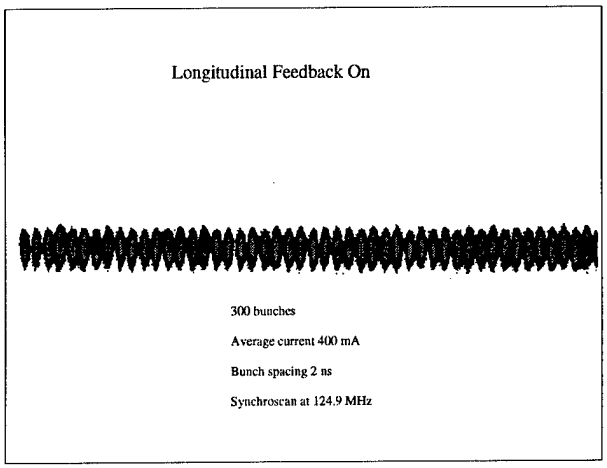


Figure 5 Damping on. Vert. = 1 ns; Horiz. = 200 ns. Bunch spacing = 2 ns. Every other bunch is shown.

3.3 Camera Resolution and Dispersion

Accurate measurements of electron bunch length require good focus of the syncyrotron light spot on the streak tube photocathode and understanding of chromatic dispersion in optical elements and space charge effects in the streak tube. For our bunch length measurements we achieved a vertical spot size of 4.3 channels, which, on the 600 ps streak range, yields time resolution of 5.4 ps. (On the fastest range, 150 ps, this focus yields 1.3 ps resolution.) The factory reports chromatic dispersion of 0.05 ps per nm at 620 nm in the A1974 input optics. At 488 nm where our measurements were made we take the dispersion to be about 0.1 ps per nm. With the shortest bunches we measured 13 ps reduction in FWHM by placing a 488 nm bandpass filter with 10 nm bandwidth in the optical path. Measurements of space charge effects were attempted over five decades of light intensity without a bandpass filter. We observed a 10% increase in FWHM of a 50 ps bunch as neutral density filters were removed and the microchannel plate intensifier (MCP) gain was decreased from its maximum value. These measurements were made during a production run at 1.9 GeV with 300 bunches and damping systems working. It is thought that bunch length remained constant during the measurements. It is worth noting that repeated measurements at fixed settings resulted in about 10% changes in FWHM. Clearly, many more measurements must be made to fully characterize our streak camera system.

3.4 Potential Well Distortion

The effects of potential well distortion in the bunch profile are apparent above 2 mA. This is due primarily to inductive and resistive broadband impedance in the storage ring vacuum chamber.

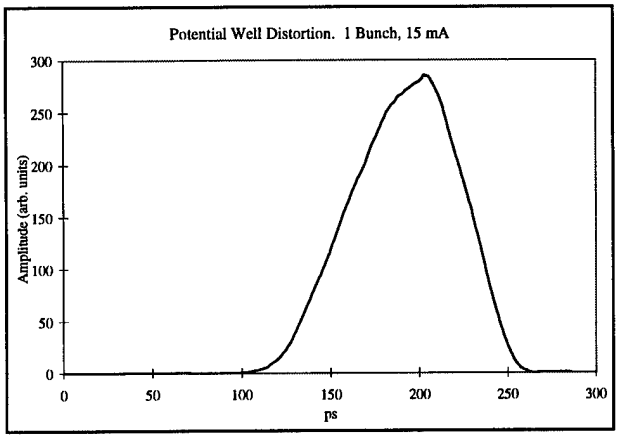


Figure 6. High current bunch showing distortion.

3.5 Bunch Purity

The ALS injector electron gun is modulated at 124.9 MHz providing bunches at 8 ns intervals. The gun may be gated to provide a single bunch. If the gun timing is not adjusted properly a weak bunch may be accelerated and corrupt the purity of the desired single bunch. Also improper settings of gun bias allow dark current to be accelerated in the linac. Charge from a single bunch in the storage ring may migrate to a following RF bucket 2 ns away. Attempts were made to measure single bunch purity in the storage ring with the streak camera.

Of the three sweep modules the synchroscan module offers the highest dynamic range for light intensity measurement. Because the camera sweeps at the same rate as electron gun modulation it is easy to see another bunch 8 ns away. By adjusting MCP gain and light intensity for maximum performance, one may examine a streak image on a log plot and see another bunch weaker by a factor of about 1000. For this measurement the dual axis scan is used. Finding a weak bunch 2 ns away is more difficult. The camera is adjusted for optimum perfomance with the strong bunch using single axis scanning. Then the 124.9 MHz RF is adjusted in phase exactly 2 ns. This has the effect of gating the streak tube although the strong light is still striking the photocathode. Again, a dynamic range of about 1000 to 1 is obtained. To satisfy ALS single-bunch users we will require a better bunch purity measurement technique. Components of a single-photon counting system have been obtained for more rigorous measurements This system is not yet operational. In addition, we will require a method to knock out unwanted bunches when they are detected.

4 CONCLUSION

The streak camera has proven to be a very powerful tool for examination of the ALS electron beam temporal characteristics. Recently the camera has been used to study non-linear longitudinal dynamics in the presence of cavity RF phase modulation [2].

5 ACKNOWLEDGEMENT

*This work was supported by the Director, Office of Energy Research, Office of Basic Energy Sciences, Materials Sciences Division, of the U.S. Department of Energy, under Contract No. DE-AC03-76SF00098.

REFERENCES

[1] R. Keller, T. Renner, D. Massoletti, 'Electron Beam Diagnostics Using Synchrotron Radiation at the Advanced Light Source', Proceedings of the 7th Beam Instrumentation Workshop, Argonne National Laboratory May 1996, Published in AIP Conference Proceedings No. 390, pp 240

[2] J. Byrd, et. al. 'Nonlinear Longitudinal Dynamics Studies at the ALS' these proceedings.

ALS-N – A CANDIDATE FOR A NEXT-GENERATION SYNCHROTRON LIGHT-SOURCE

A. Jackson, J. Byrd, W. Decking, M. Howells, R. Keller, C.H. Kim, D. Massoletti,
H. Nishimura, D. Robin, H. Zyngier,
E.O. Lawrence Berkeley National Laboratory, 1 Cyclotron Road, Berkeley, CA 94720 *

1 INTRODUCTION

Judging from the experiments currently being pursued at the ALS, there is already a compelling case to be made for considering a future synchrotron radiation source that has a higher beam brightness than the third-generation facilities. For example, a large, and growing fraction of the ALS scientific program is based on soft x-ray microscopy experiments in materials science. Currently these experiments use high-brightness undulator radiation, on beam lines that are already oversubscribed. Dedicated beam lines from bend magnet sources would be useful for these techniques if the source brightness could be pushed to $\approx 2 \cdot 10^{16}$ photons/(s $\cdot$ mm^2 $\cdot$ mrad^2 $\cdot$ 0.1%b.w.), i.e., a factor of 20-100 higher (depending on wavelength), than currently available at the ALS. Another growing class of experiments uses microfocused beams for microanalysis, microdiffraction, microEXAFS, microXPS, and microNEXAFS. These are classic brightness experiments, but even at the high ALS brightnesses, require long exposure times. Finally there is a requirement to get to $\approx$ 2 keV in the fundamental peak of the undulator spectrum, to access most transition-metal L-edges, and the rare-earth M-edges. This could be achieved with a machine energy of 2.5-3.0 GeV. An alternative strategy is to go to smaller gaps with a shorter period undulator – which is compatible with lower emittance beams [1].

With this incentive we have begun studies of a storage-ring based source of soft x-rays. We are concentrating on machines with an energy of 2-2.5 GeV, and a circumference of $\approx$ 350-400 m, with the ultimate goal of building such a machine on the site of the Bevatron at LBNL. We will address the following questions in this paper: can a lattice be generated with these constraints, plus have a natural emittance of $\approx$ 0.5 nm-rad, and have sufficient dynamic aperture; can the emittance be maintained under the influence of intrabeam scattering (IBS); what is the Touschek lifetime?

Other considerations are beam stability and cost. Part of our thinking is to build an inexpensive machine. To this end we are borrowing an idea from the FNAL recycler ring [2] to use permanent magnets for most of the lattice. With the small aperture anticipated for the ring (around 20 mm horizontal x 10 mm vertical full widths), such magnets could be relatively small and inexpensive. Further, the magnets would be of light weight, therefore have a relatively inexpensive mounting system, and have no low-frequency vibrational modes. Another advantage is that the magnets have no power requirements (maybe a little for trims), and therefore do not require cooling water. Cooling water and air temperature variations have been the source of many motion problems in the ALS [3].

* This work was supported by the Director, Office of Energy Research, Office of Basic Energy Sciences, Materials Sciences Division, of the U.S. Department of Energy, under Contract No. DE-AC03-76F00098

2 LATTICE DESIGN

The primary goal for the lattice design of ALS-N is to reach an horizontal emittance of $\epsilon_x \approx 0.5$ nm-rad at 2 GeV while the ring fits on the Bevatron site at the Berkeley. This restricts the circumference to $\approx$ 350-400 m. For optimal use of the more or less rectangular site, a racetrack-shaped ring is considered. It consists of two $\approx 120^o$ arcs, and dispersion-free straight sections which are separated by weak bending magnets.

2.1 *Theoretical minimum emittance*

The horizontal equilibrium emittance is given by

$$\epsilon_x \approx \frac{\gamma^2}{J_x \rho} < H >_{dipole} \qquad (1)$$

where J_x is the horizontal damping partition number, ρ is the bending radius of the dipole, and $< H >$ is the function

$$H = \frac{1}{\beta_x}(\eta_x^2 + (\alpha_x \eta_x + \beta_x \eta_x')^2) \qquad (2)$$

averaged over the dipole. $\beta_x, \alpha_x, \eta_x, \eta_x'$ are the usual optical functions and their derivatives. It has been shown [4] that the theoretical minimum emittance is reached if the horizontal beta- and dispersion-functions reach their minimum in the center of the bending magnets, with the following values:

$$\beta_{x,min} = \frac{1}{2\sqrt{15}} L \qquad \eta_{x,min} = \frac{L^2}{24\rho^2} \qquad (3)$$

The horizontal emittance is then:

$$\epsilon_{x,min} \approx \frac{\gamma^2}{J_x \rho} \frac{1}{12\sqrt{15}} \rho \theta^3 \qquad (4)$$

where θ is the bending angle of the dipole; $\epsilon_{x,min}$ then depends solely on the bending angle and the damping partition number.

0-7803-4376-X/98/$10.00 © 1998 IEEE

Since the dispersion-function has a minimum in the middle of the bending magnet, lattices built with this strategy do not provide dispersion-free straight sections as the Chasman-Green lattices do. The dispersion-induced emittance in the middle of a straight section ($\alpha = \eta' = 0$) is given by

$$\epsilon_\eta = \frac{(\eta_x \delta)^2}{\beta_x} \quad , \tag{5}$$

where δ is the relative energy spread. Thus the gain in horizontal emittance is partly compensated by an enlargement of the beam size due to dispersion.

Several synchrotron radiation source lattices have been worked out [5] [6] following the theoretical minimum emittance strategy.

2.2 *The arc cell*

The main contribution to $< H >_{dipole}$ and thus to the emittance of the storage ring comes from the bending magnets in the arcs. A compact low-emittance arc is obtained by placing a combined-function bend-magnet at the position of the defocusing element in a FODO cell. This leads to a minimum of the horizontal beta- and dispersion-functions in the middle of the dipole, which is a requirement for small emittance. Furthermore a combined-function magnet reduces the emittance even more by increasing the horizontal damping partition number J_x.

The phase advance per cell is 90^o horizontally and 60^o vertically, thus allowing for a sextupole scheme with cancelation of the first-order driving-terms after 3 cells. The cell length and dipole strength are chosen to give a compact arc and the desired emittance of $\epsilon_x \approx 0.5$ nm-rad. This is far away from the theoretically minimum achievable value but gives moderate focusing and phase advance per cell. The total cell length is 2.3 m. The dynamic acceptance for this cell is rather large ($A_x \approx A_y \approx 50$ mm-rad for $\delta p/p \pm 3\%$).

2.3 *The insertion-device straight sections*

The insertion-device sections contain only a small fraction of the bending magnets of the storage-ring. Their contribution to the natural emittance is small and so one does not have to put much emphasis on getting a low-emittance lattice in this part of the ring. On the other hand, the insertion-device straight sections should have zero or very small dispersion to prevent enlargement of the source size due to energy spread in the beam. With equation 5 and the assumptions $\delta \approx 1 \cdot 10^{-3}$, $\beta_{x,straight} \approx 3$ m, the dispersion in the straight should be smaller than ≈ 0.02 m in order not to contribute more than 20% to the overall beam-size. Either a double-bend (DBA) or a triple-bend achromat (TBA) structure, including combined function magnets with weak bending (2.5^o bending angle per magnet), fulfills these requirements. Because of the weak bending in these cells, the dispersion function stays small and thus the sextupoles for the chromatic correction have to be strong. This leads to a very small dynamic acceptance for these cells. Sextupole arrangements to overcome this problem are being investigated.

2.4 *The complete ring*

The two parts of the storage ring are connected by matching sections. Due to the degeneration of symmetry from several tens down to two, the dynamic acceptance collapses. A more complicated sextupole distribution may overcome this problem. Another solution would be a machine made of identical cells, which however would not fit so well into the existing site. Up to now, a storage ring constructed out of 52 FODO cells and 18 DBA cells gives the best performance. A footprint of the machine on the Bevatron site is shown in figure 1; the main machine parameters are summarized in table 1.

The magnet aperture will be decreased to values of ≈ 10 mm best-field diameter. These small magnets can be built with standard permanent-magnet technology to achieve the fields and gradients given in table 1 [7].

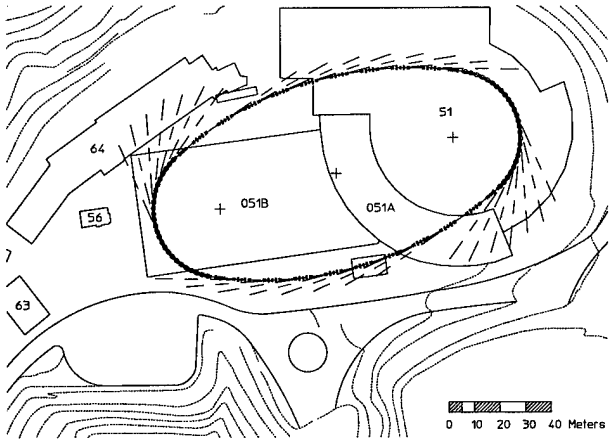


Figure 1: Footprint of ALS-N on the Bevatron site. The straight-section beam lines are 40m long.

Table 1: Main parameters of ALS-N

Energy	2 GeV
Circumference	380 m
Natural emittance	$5.5 \cdot 10^{-10}$ m-rad
Natural energy spread	$8 \cdot 10^{-4}$
Momentum compaction	$6.7 \cdot 10^{-4}$
Tunes x,y	33.18, 23.73
Chromaticities x,y	$-46, -76$
Number of free straights	16, each 5 m long
β_x, β_y in straight	3 m, 3.2 m
β_x, β_y in arc bend	0.8 m, 4 m
Max. current	400 mA
Bending magnet	$l = 1.0$ m, $B_y = 0.585$ T, $\partial B_y/\partial x = 12$ T/m
Strongest Quadrupole	$\int \partial B_y/\partial x = 10$ T
Strongest Sextupole	$\int \partial^2 B_y/\partial x^2 = 160$ T/m

3 BEAM SIZE AND LIFETIME

The electron density of a next-generation light-source will be one order of magnitude higher. The beam lifetime will be short due to Touschek scattering and the beam emittance will grow due to intrabeam scattering. The deleterious high-intensity effects can be considerably mitigated by increasing the bunch-length using well-known techniques such as adding a third harmonic cavity. These high-intensity effects were studied using a modified ZAP code [8]; the results are summarized in table 2.

Coupling between the vertical and longitudinal motion is an important factor. For smaller coupling the vertical beam size shrinks and the intrabeam scattering rate increases, which in turn increases the horizontal and longitudinal beam sizes. Higher RF voltage decreases the bunch length and increases the intrabeam scattering rate which in turn increases the transverse beam size. The microwave instability tends to increase the energy spread and the bunch length. Since the threshold for the microwave instability only depends on the peak current, adding a third-harmonic cavity greatly increases the threshold current I_{MWI}. Table 2 gives lifetime and emittance with and without a third-harmonic cavity and with different values for the initial emittance-coupling $\kappa = \epsilon_y/\epsilon_x$. The energy acceptance was assumed to be 3 %, given by the RF-bucket height.

Table 2: Lifetime and emittance of ALS-N at low and maximum current with and without a third-harmonic cavity.

Current [mA]	ϵ_x [nm-rad]	κ %	τ [h]	σ_L [mm]	$\frac{\Delta E}{E}$ %	I_{MWI} [mA]
≈ 0	0.55	3		5.2	0.8	6.4
400	1.05	3	2.9	7.0	1.1	6.4
400[a]	0.8	3	6.4	19.5	0.97	260
400[b]	0.95	1	4.4	19.5	1.0	260

[a] third-harmonic cavity
[b] third-harmonic cavity

4 BRIGHTNESS

The brightness expected from insertion devices and bend magnets is plotted in figures 2 and 3 in comparison to the ALS. The values are calculated up to the 7th harmonic for undulators with 5 cm (U5) and 2 cm (U2) period length and a peak field of 1 T. The storage-ring current is 400 mA, and the coupling ϵ_y/ϵ_x is assumed to be 1%. The dipole radiation is calculated for a normal lattice-dipole and a special high-field dipole ($B = 5$ T) at a location with small beta-functions.

5 SUMMARY

We have begun an investigation of a next-generation light-source, and shown that a factor of 10-100 increase in photon brightness from undulators can be achieved in the soft x-ray energy range. Both the electron emittance and bunch length suffer significantly from the effects of IBS at a beam current of 400 mA. Though this caps the achievable beam brightness, there is a favorable increase in Touschek lifetime. The brightness from bend magnets is also increased, to the level that it starts to become interesting for soft x-ray microscopy. With specially tailored optics at the bend magnet sources, the photon brightness could be increased by another order of magnitude.

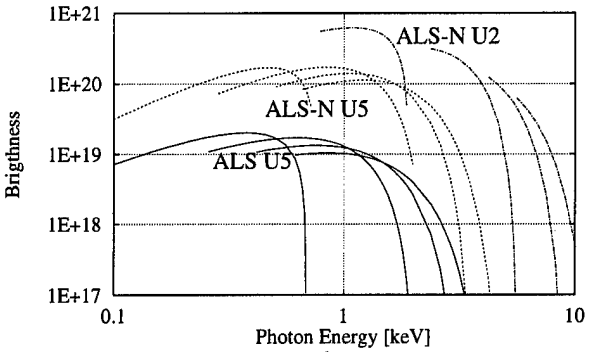


Figure 2: Brightness $[\frac{\text{photons}}{(\text{s}\cdot\text{mm}^2\cdot\text{mrad}^2\cdot 0.1\%\text{b.w.})}]$ from insertion devices at the present ALS and the ALS-N.

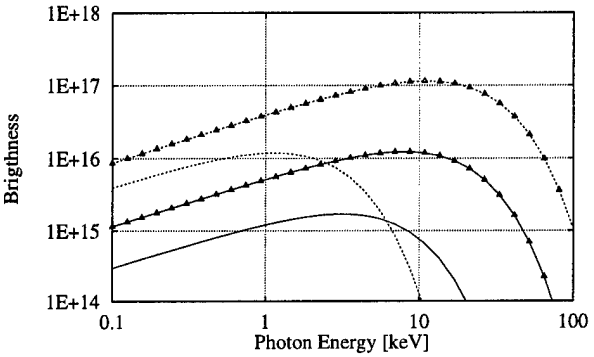


Figure 3: Brightness $[\frac{\text{photons}}{(\text{s}\cdot\text{mm}^2\cdot\text{mrad}^2\cdot 0.1\%\text{b.w.})}]$ from lattice bend magnets and high-field bend magnets (triangles) at the present ALS (solid lines) and the ALS-N (dashed lines).

6 REFERENCES

[1] P.M. Stefan, et al., 'Small Gap Undulator Experiments the NSLS X-Ray Ring', PAC 95, Dallas.

[2] G.W. Foster, et al., 'Permanent Magnet Design for the Fermilab Main Injector Recycler Ring', PAC 95, Dallas.

[3] R. Keller, H. Nishimura, 'Orbit Stability of the ALS Storage Ring', this conference.

[4] S.Y. Lee, and L. Teng, 'Theoretical Minimum Emittance Lattice for an Electron Storage Ring', PAC 91, San Francisco.

[5] D. Einfeld, M. Plesko, and J. Schaper, 'A Low Emittance Optics for a Pure Insertion Device Lattice', EPAC 94, London.

[6] D. Einfeld, J. Schaper, and M. Plesko, 'A Lattice Design to Reach the Theoretical Minimum Emittance for a Storage Ring', EPAC 96, Barcelona.

[7] R. Schlueter, private communication.

[8] C.H. Kim, 'A modified ZAP code for Calculating Initial Value Problems and effects of third Harmonic Cavities', this conference.

TRANSFER FUNCTIONS FOR THE ALS LATTICE MAGNETS*

R. Keller, Advanced Light Source Center, E. O. Lawrence Berkeley National Laboratory
University of California, Berkeley, CA 94720 USA

Abstract

The primary purpose of the magnetic measurements performed on the ALS storage-ring lattice-magnets was to ascertain their compliance with the strict tolerances established for this third-generation synchrotron light source. In the course of the data evaluation, a novel approximation method has been developed that leads to four-parameter representations of all magnet transfer-functions, and includes saturation and residual field effects. These transfer functions were used to change the standard working point of the ALS storage ring at 1.5-GeV beam energy from the upper to the lower hysteresis branches, and later to ramp the ring energy from 1.5 GeV to the maximum design value of 1.9 GeV in one uninterrupted process that did not require any intermediate tune correction. Likewise, predicted magnet set values for 1.0-GeV conditions were applied and very closely led to the standard betatron tunes.

1 INTRODUCTION

This paper is concerned with characterizing the integrated fundamental strengths of the ALS [1] lattice magnets in the form of analytical expressions. There are six families of ALS lattice magnets, i.e. bend magnets with substantial gradient producing a defocusing quadrupole component; three families of quadrupoles proper; and two families of sextupoles. During the storage-ring construction-phase, the relative spread of fundamental strengths within each of the six families was the parameter by which the placement of individual magnets along the ring was to be judged; conveniently the spreads turned out to be low enough for all three quadrupole families and the bend magnets to allow arbitrary positioning, but the two sextupole families required insertion of customized current shunts to narrow their spread.

To ascertain the fundamental strengths, and also to obtain reasonable interpolation values between the measured excitation points for energy ramping purposes, the original magnetic measurement data which showed relative errors in the order of 2×10^{-3} had to be smoothed. Furthermore, the ever present drive to push an accelerator's performance beyond the original design limits led to the question how the strengths of the lattice magnets could be extrapolated beyond the highest excitation conditions so far explored, representing an electron beam energy of 1.9 GeV. Analytical approximations are very convenient for both purposes, but the important problem is which type of functions to use for the approximations in order to best represent the magnet properties.

Magnet strengths are commonly expressed using transfer functions,

$$F = T \times I \qquad (1)$$

where F is the integrated fundamental strength, $F = \int B_y \, dz$ for a dipole, $F = \int (B_r/r) \, dz$ for a quadrupole, etc.; T the transfer function value (assumed to be constant); and I the excitation current. This representation, however, is too simple to take into account seemingly minor effects which are quite relevant for third-generation light-sources with relative strength tolerances of 10^{-3} and below. Therefore a more complicated class of functions was developed in the course of this work to represent magnet strengths under varying excitation conditions. The essential features of these new magnet transfer functions are that they allow to distinguish between the two hysteresis branches; are constant at low excitation values; are free of turning points over their entire range; accurately represent the measured saturation effects; and do not fall off too steeply beyond the highest measured excitation-current value. It is worthwhile noting that simple polynomial approximations do not fulfil most of these conditions. On the other hand, even the best transfer function expressions still require the magnets to be be given a well-defined history of excitation that unambiguously defines a working point on either the upper or the lower hysteresis branch.

2 ELEMENTS OF TRANSFER FUNCTIONS

In deriving magnet transfer functions from measured data, one can distinguish three zones of the excitation curve, F(I), dependent on whether 1), residual field effects are dominant, 2), the excitation curve is linear, and 3), saturation effects begin to show, see Fig. 1. In this paper the expression hysteresis is being used rather loosely because none of the magnets has ever been brought to full saturation and the magnetization direction was never reversed for any of them. The maximum excitation currents applied during the magnet measurement activities, however, were nearly equal to the ones that are now being applied in day-to-day conditioning after their installation in the storage ring. Therefore the measured excitation curves can be regarded as truly representative of the actual magnet operation conditions, and we use the term hysteresis loop for the two branches of the excitation curve that are followed when running the current between zero, the power-supply imposed limit, and back again to zero.

*This work was supported by the Director, Office of Energy Research, Office of Basic Energy Sciences, Material Sciences Division, U.S. Department of Energy, under Contract No. DE-AC03-76SF00098.

0-7803-4376-X/98/$10.00 © 1998 IEEE

2.1 Residual field effects

The basic assumption about residual field effects made here is that the two branches of the hysteresis curve are linear and parallel to each other at low currents. A look at the corresponding diagram, Fig. 1, suggests that in this case we can unify the two branches into one curve that starts at the origin if we substitute the actual excitation current I with an effective current $I_{eff} = I \pm I_c$ where I_c, the coercive current, is subtracted to represent the lower hysteresis branch and added for the upper branch. Equ. (1) then reads:

$$F_{u,l} = T \times (I \pm I_c). \qquad (2)$$

where the indices u and l stand for upper and lower branch. In the following formulae, these two indices are left out for the sake of simplicity, and the distinction between the two branches is implied by the ± sign only.

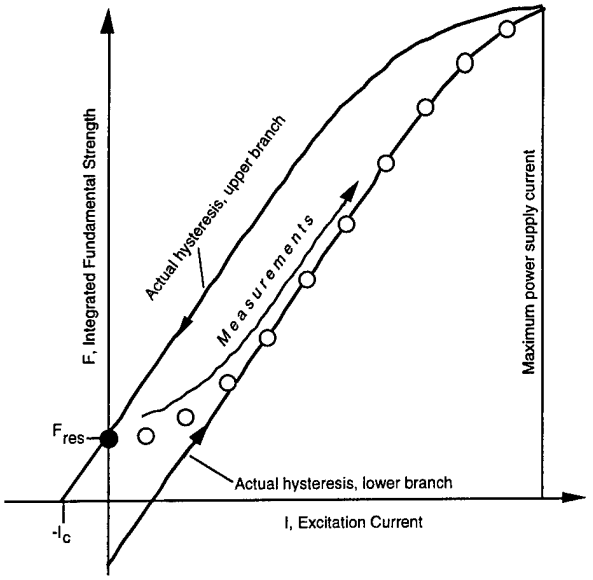


Figure 1. Schematic of a hysteresis loop with magnet measurement data, $F_{i,meas}$ (open circles). Residual field and saturation effects are exaggerated in this illustration.

In the case of the ALS, the original ten excitation measurements had been taken after completing three unipolar conditioning loops with current settings rising from zero, see Fig. 1; and this fact makes it more complicated to derive a value for the coercive current without direct measurement, even more so because the residual fundamental strength, F_{res}, was not recorded either. The way followed here consists in extrapolating the linear part of the measured excitation curve back to zero strength, thereby determining $-I_c$ and F_{res}, and then reducing all data points $F_{i,meas}$ in a graded manner:

$$F_{i,red} = F_{i,meas} - 2\,F_{res} / \exp\{I_i / (C\,I_c)\} \quad [1 \le i \le 10] \qquad (3)$$

The constant C in the exponential damping term on the right hand side of Equ. (3) is found by empirical optimization, iterating the evaluations of I_c and F_{res} to minimize the standard deviation for all available, reduced measurement points. The actual values for F_{res} and C are only needed for determination of the constant part of the transfer function, T_{lin}; once this term is known the sign of I_c is the one parameter that allows to distinguish between upper and lower branch of the hysteresis curve. For the ALS lattice magnets, the optimization was performed empirically on spreadsheets, at first determining individual best values of F_{res} and C for all magnets of one family following a strict standard-deviation optimization and then again, trying to keep the individual values close to the averages for the entire family while allowing the standard deviations to slightly exceed the absolute minimum values.

2.2 Saturation effects

ALS lattice magnets typically show a few percent saturation at excitations corresponding to 1.9-GeV beam energy, and this drop is significant in view of the tolerance band of 10^{-3} relative strength for each magnet type. To represent saturation, Equ. (2) is modified by introducing a denominator,

$$F = \frac{T_{lin}\,(I \pm I_c)}{1 + \left(\frac{I \pm I_c}{I_s}\right)^A} \qquad (4)$$

and now contains four parameters in addition to the excitation current I as independent variable. The former transfer function T is now called T_{lin} to emphasize that in terms of Equ. (1) it represents the linear part of the excitation curve only.

The evaluation of all five transfer function parameters (including the damping factor C) for every individual magnet is performed in iterations, optimizing residual field and saturation effects in separate loops. After preliminary parameters for each member of one magnet family are established the exponent A and the damping parameter C are averaged for the entire family, and new iterations are performed for each magnet to find the definitive values of the other parameters.

3 ACTUAL TRANSFER FUNCTIONS

An example of a calculated transfer function is given in Fig. 2. In addition to the transfer function calculated according to the formalism developed in the preceding section, the figure displays a "raw transfer function" obtained by simply dividing measured integrated fundamental strengths by the excitation currents, without regard for residual field effects. The low-current part of this curve (broken line) represents the transition from the upper to the lower hysteresis branches.

A list of the averaged calculated transfer function parameters in terms of Equ. (4), as derived from the original measurements [2] for the ALS lattice magnets, is given in Table 1. Note that all entries in the third column are given as integrated flux density values, in units of [T m] divided by the excitation current in [A] and by a nominal radius of

0.03 m elevated to the $(n-1)^{th}$ power, where n = 1 refers to a dipole, n = 2 to a quadrupole, and n = 3 to a sextupole.

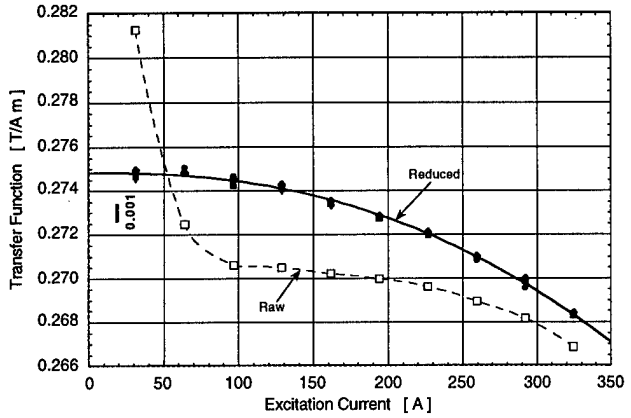


Figure 2. Transfer function for sextupole #10, bold line, evaluated in terms of Equ. (4); the full symbols represent five series of measurements after data reduction. The open symbols represent one of these series before reduction, calculated by dividing the measured fundamental strengths by the corresponding excitation currents according to Equ. (1).

Table 1.
Transfer-Function Parameters for the ALS Lattice Magnets

Type	n	T_{lin} [$T A^{-1} m^{2-n}$]	I_c [A]	A	I_s [A]
B	1	0.001312	3	5.73	1739
QFA	2	0.01722	2.56	3.1	2250
QF	2	0.05292	0.661	2.8	604
QD	2	0.02875	0.711	4.3	353
SF	3	0.2742	2.767	2.4	1548
SD	3	0.2744	2.844	2.4	1542

4 APPLICATION OF TRANSFER FUNCTIONS

The list of transfer function coefficients of all lattice-magnet families underwent a first critical test when the working points had to be moved from the upper hysteresis branch to the lower one, in view of future energy ramping. Ramping of the storage ring magnets is necessary for all energy levels significantly above 1.5 GeV because this is the design energy-limit of the booster synchrotron that injects beam into the storage ring. The working-point conversion on the base of the predicted set values went smoothly and required only very minor corrections to recover the standard betatron tune values.

To actually ramp the storage ring energy from 1.5 to 1.9 GeV a finely-spaced table of set values (128 steps corresponding to 3 MeV energy increase each) was computed. For every step, Equ. (4) was inverted with a "regula falsi" method to find the proper excitation-current set-values, separately for each magnet family. The variations of the betatron tunes that occurred during the ramping [3] without applying any corrections are displayed in Fig. 3; they correspond to maximum transfer function errors of 8×10^{-4} and 7×10^{-4} for the QF or QD families, respectively, if the total error were ascribed to one of these families only. With the generated ramping tables, the ALS storage-ring energy can now be changed from 1.5 to 1.9 GeV in 64 seconds, without any appreciable loss in beam current.

For operation at 1.0 GeV ramping is unnecessary, and one series of set values has been computed using the entries in Table 1. To fully recover the customary working point at this energy after the calculated magnet current values had been applied, only the QF magnet-family set-currents had to be raised by 0.24%; for all other magnets the calculated values could be used unchanged.

The success in predicting correct set values for all lattice-magnet families under a variety of conditions confirms the validity of the approach developed here. The reader should be warned, however, that the expression for the saturation term in Equ. (4) is valid only as long as the saturation current, I_s, is much larger than the highest applied actual excitation current, I_{max}. This is the case for all magnets discussed in this paper.

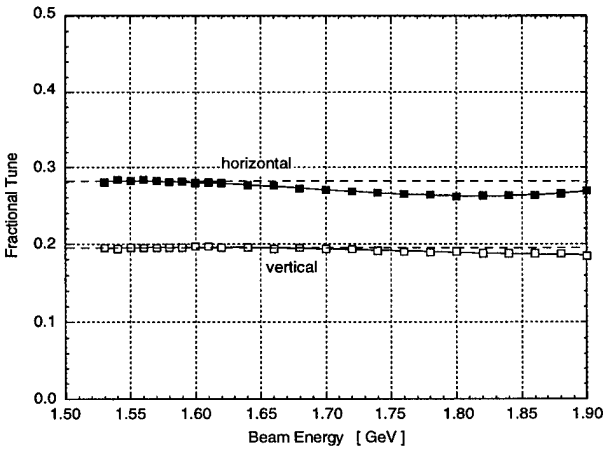


Figure 3. Fractional betatron tunes measured while ramping the storage ring energy with precalculated magnet set values. The full standard tune values at 1.5 GeV are 14.282 (horizontal) and 8.192 (vertical), respectively, as indicated by the straight, broken lines.

5 ACKNOWLEDGMENTS

R. Alvis deserves credit and thanks for diligently processing and plotting the magnet data over and over before the final results as presented here were achieved. Thanks are also due to K. Halbach and A. Jackson for many helpful discussions and to F. Iazzourene, ELETTRA Trieste, for reviewing the employed algorithms and pointing out an inconsistency.

6 REFERENCES

[1] "1-2 GeV Synchrotron Radiation Source, Conceptual Design Report," LBL Pub. 5172 Rev., LBL Berkeley, 1986.
[2] Measurements performed at LBL Berkeley under the guidance of J. Tanabe, D. Nelson, and M. I. Green, 1991.
[3] The code for the control-system application that executed the ramping table was written by H. Nishimura, LBNL Berkeley, unpublished work (1995).

ORBIT STABILITY OF THE ALS STORAGE RING.*

R. Keller, H. Nishimura, and the Stability Task Force,† Advanced Light Source Center
E. O. Lawrence Berkeley National Laboratory, University of California, Berkeley, CA 94720 USA

Abstract

The Advanced Light Source (ALS) storage ring [1], a synchrotron light source of the third generation, is specified to maintain its electron orbit stable within one tenth of the rms beam size. In the absence of a dedicated orbit feed-back system, several orbit-distorting effects were investigated, aided by a new interactive simulation tool, the code TRACY V. The effort has led to a better understanding of the behavior of a variety of accelerator subsystems and in consequence produced a substantial improvement in day-to-day orbit stability.

1 INTRODUCTION

The ALS electron storage ring [1] is a third-generation light-source with very tight electron orbit tolerances. During user runs, the orbit should not vary by more than 1/10 the rms beam size in any of the straights, amounting to 20 μ horizontally and 2 μ vertically. Stability requirements this tight would normally require an orbit-feedback system, but over the nearly four years of storage-ring operation such a system has not yet been implemented at ALS, mostly because of Beam-Position Monitor (BPM) motion associated with the complex mechanical design of the ALS vacuum chambers and girders that each span an entire arc section, see Fig. 1. It is easy to imagine that the BPMs that are installed in the vacuum chamber and whose signals would be used for orbit feedback would follow the thermal distortions and mechanical vibrations of the vacuum chamber and therefore compromise the quality of the orbit correction.

On the other hand, the need for better control of the photon source-point locations increased with the degree of sophistication the users applied to their end stations, most notably with the increased spatial resolution required by microscopy experiments. For this reason a task force was established that had the mandate to improve the ALS orbit stability by about a factor of ten and thus meet the original specifications.

The diagnostics applied to the stabilization problem can be grouped into four classes: direct and indirect orbit monitors such as the electron BPMs and readout from a photon-beam feedback-system; precision dial indicators, linear potentiometers and inclinometers; temperature monitors for air, water, and storage-ring girders; and, last but not least, the simulation code TRACY V [2]. This code was upgraded and amended several times in the course of these investigations to better represent the influence of lattice magnet strengths and location variations of the electron orbit.

From the beginning, the task force concentrated on investigations of thermal effects for two reasons: thermally

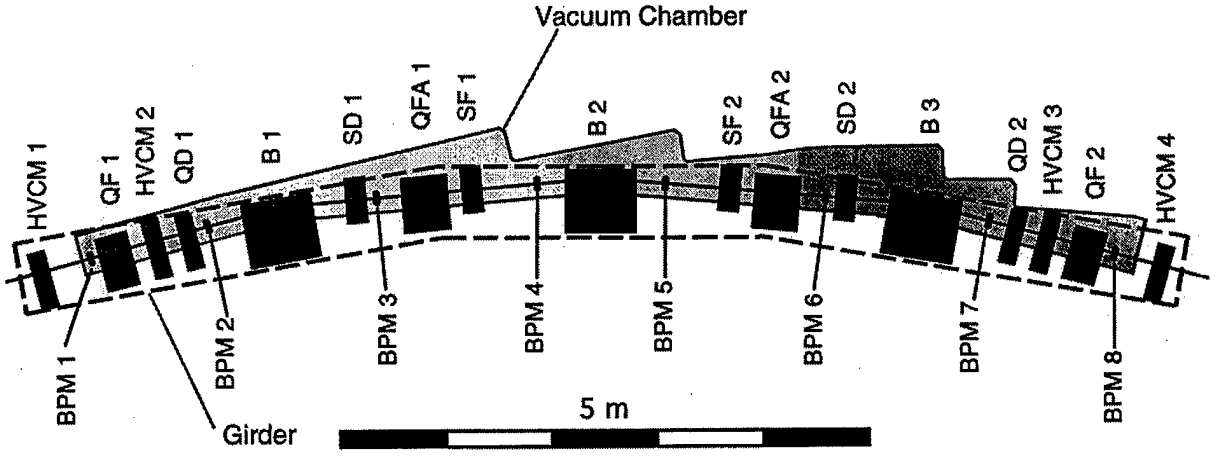


Figure 1. One out of twelve storage-ring arc sections showing outlines of girder, vacuum chamber, lattice and corrector magnets, and locations of the beam-position monitors (BPM).

*This work was supported by the Director, Office of Energy Research, Office of Basic Energy Sciences, Material Sciences Division, U.S. Department of Energy, under Contract No. DE-AC03-76SF00098.

† A. Biocca, M. Chin, B. Feinberg, K. Fletcher, T. Henderson, J. Hinkson, M. Howells, Z. Hussain, A. Jackson, G. Krebs, D. Massoletti, R. Miller, E. Moler, A. Paterson, J. Pickrell, G. Portmann, W. Thur, T. Warwick, and J. Wunderlich.

0-7803-4376-X/98/$10.00 © 1998 IEEE

induced deformations of the girders had caused poor convergence of the survey/alignment cycles [3] when the lattice magnets were put in place during the construction phase of the storage ring; and secondly, a vertical orbit oscillation with a 15-min. period had been completely eliminated by keeping the cooling water temperature of the ALS magnets constant within ±0.1°C [4]. On several occasions, however, other causes of orbit distortions were discovered and successfully eliminated.

2 TRACY V

The simulation code TRACY V is a "virtual machine" representing the ALS storage ring, written in Borland Delphi2 for Windows NT. The code calculates and displays many machine functions, such as linear optics functions and the closed orbit for a given set of magnet parameters; it also includes analysis tools for measured data. A Graphical User Interface provides flexibility in the modes of usage and display of results. With the exception of dynamic aperture calculations the response to user input is automatic and almost instantaneous.

In the context of orbit stability investigations, TRACY V furnished closed-orbit calculations for given sets of lattice-magnet strengths and misalignment values, and for combinations of corrector strengths. The computations are based on measured and adjusted sensitivity matrices that describe the response of the BPMs to changes in each individual corrector. For analysis of actual orbits, TRACY V can be linked to either archived data or to programs that capture BPM data on-line. Orbit correction can be performed using the local-bump, most-effective corrector, and singular-value decomposition methods. Misalignment values for lattice magnets can be set either individually or in a special ganged mode where the horizontal misalignment of all magnets on one girder progressively increases from the locations of the QFA magnets, see Fig. 1, to the QF magnets at the ends. An example of a closed-orbit distortion caused by this kind of girder deformation is given in Fig. 2.

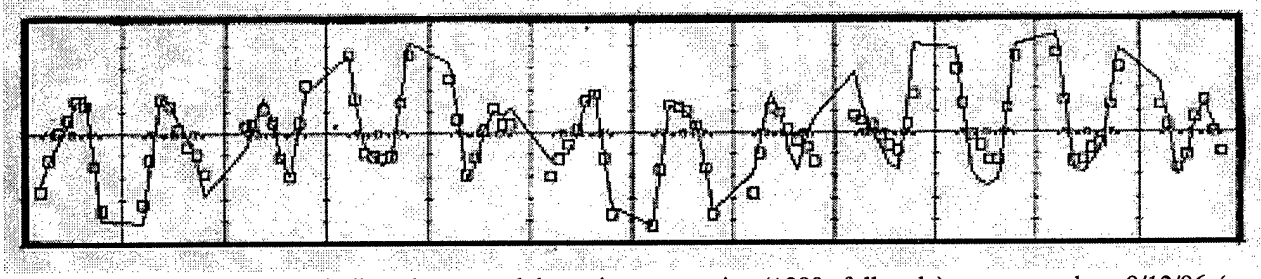


Figure 2. Horizontal closed-orbit distortion around the entire storage ring (±200μ full scale) as measured on 9/12/96 (open symbols) and simulated by TRACY V (continuous line), assuming a progressive girder deformation of up to 31 μ.

3 TYPICAL ORBIT DISTORTIONS

The storage-ring orbit is continuously being monitored by a set of new BPMs that are installed at both ends of most of the straights and termed ID-BPMs to distinguish them from the arc BPMs shown in Fig. 1. The ID-BPMs are inherently more sensitive and less beam-current dependent than the arc BPMs because they use one common amplifier chain only, in a multiplexing mode [5]. Archived ID-BPM data taken over a 12-hour period are displayed in the ALS control room [6] and give a very good indication of the orbit stability. An example of these signals, recorded at the end of summer 1996 before the work described here began, is given in Fig. 3.

Of the phenomena displayed in Fig. 3, the step change indicated by the asterisk is certainly the most intriguing. Its investigation stimulated the development of TRACY V to accommodate the effect of girder deformations, and in a dedicated experiment where a girder was locally heated by a hot-air gun, dial indicators mounted on the girder showed in fact several instantaneous position shifts of up to 16 μ. Later on, however, a step change was unambiguously correlated with the movement of one of the two building cranes. In another experiment it was shown that the perturbation of the magnetic field across a storage-ring straight, induced by the presence or absence of the crane, was associated with the orbit distortion and could be simulated by exciting two corrector magnets, one at the location from where the crane was leaving and one where it went. The second building crane showed similar effects, and once known they were eliminated administratively by regulating the use of the cranes.

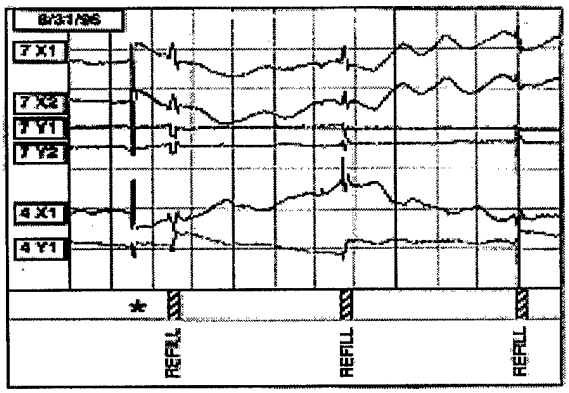


Fig. 3. Horizontal (X) and vertical (Y) ID-BPM signals from sectors 4 and 7, taken on 8/31/96. Grating units correspond to 150μ, vertically, and 1 hour, horizontally. The illustration shows 1-hour oscillations, long-term drift, and a 10-min. step change (marked by an asterisk at the bottom). Signals have no validity during refill times.

4 AIR TEMPERATURE STABILIZATION

After ascertaining in experiments that the hourly orbit oscillations were associated with air temperature changes of about 1°C and corresponding girder temperature changes of 0.2°C these distortions could substantially be reduced by a series of improvements to the system of 9 independent air-handling units that supply chilled air to the storage-ring tunnel. The changes included using temperature sensors with 0.1°C sensitivity, relocated to the outer perimeter of the storage ring; averaging their readout to regulate all air-handling units with identical set values; and forcing the tunnel air to move in a spiralling pattern upstream by directing the outlet heads of the air-handling units and deploying four additional fans on the tunnel floor. These improvements also cured most of the long-term drift problems seen before.

Another type of orbit distortions manifested itself as four-hour, 100-μ humps on the ID-BPM display. Two causes were identified to contribute to these phenomena, one associated with the switchover between two water chillers of different size that supply the air-handling units during nighttime and daytime, respectively, and the other one originating in the enhanced water flow of a building air-conditioning system that utilizes the same chillers. These effects were eliminated by using the larger of the chillers as a default and reducing the water flow through a bypass in the air-conditioning unit.

The striking improvement in orbit stability obtained after resolving all these issues is shown in Figs. 4 and 5.

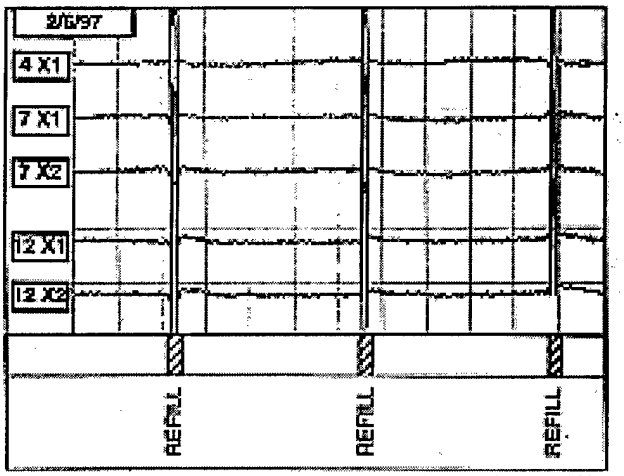


Figure 4. Horizontal ID-BPM signals observed on 2/6/97 after substantially improving the temperature-stabilization. Grating units 150μ, vertically, and 1 hour, horizontally.

5 ADDITIONAL EFFECTS AND OUTLOOK

One other flavor of orbit distortion, a step change without apparent return, used to occur about 30 minutes before a refill of the storage ring was planned. It turned out that this effect was caused by the excitation of the last two of the four dipole magnets in the booster-to-storage-ring (BTS) injection line. Even though these magnets are located about 1.5 m away from the storage ring, their fringe fields are strong enough to perturb the stored electron beam. This problem can again be solved administratively.

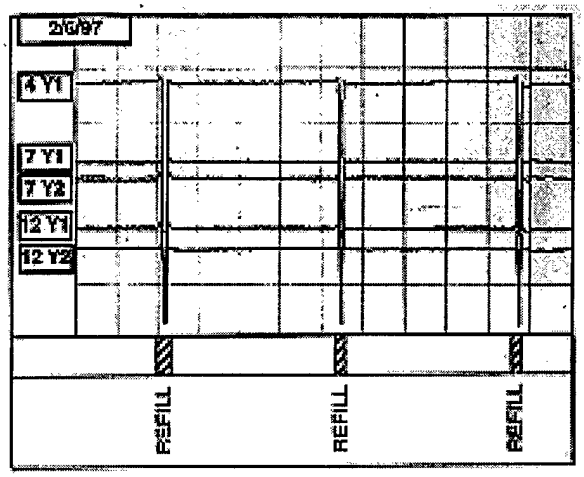


Figure 5. Vertical ID-BPM signals observed on 2/6/97 after substantially improving the temperature-stabilization. Grating units 150μ, vertically, and 1 hour, horizontally.

Last, but certainly not least, it should be mentioned that the ALS orbit is heavily affected by the changing magnet fields when insertion-device gaps are opened or closed. This effect is suppressed by applying corretive set values to the steerer magnets in a feed-forward mode [7].

With all these measures, ALS has reached an impressive level of orbit stability, even exceeding the tight specifications mentioned at the beginning. The reduction of temperature variations in the tunnel to ±0.1°C also largely reduces the arc vacuum-chamber deformations and in this way leads to much more stable arc-BPM positions. This eliminates one of the major obstacles for the implementation of an orbit feedback system, and such a system could now be developed to reach even better orbit stability, below ±1 μ vertically.

6 ACKNOWLEDGMENTS

We would like to thank R. Alvis for carrying out numerous simulations using TRACY V in the course of this work. Thanks are further due to the ALS operators for their engagement and help in all phases of the investigations.

7 REFERENCES

[1] "1-2 GeV Synchrotron Radiation Source, Concept. Design Rept.," LBL Pub. 5172 Rev., LBL Berkeley (1986).
[2] H. Nishimura, "Accelerator Modelling and Control Using Delphi on Windows NT," Proc. Int. Workshop on Controls for Small and Medium-Scale Accelerators, KEK Tsukuba, 1996 (in print).
[3] R. Keller, Proc. 3rd Int. Workshop on Accelerator Alignment, p. I/29-36, Annecy, France (1993).
[4] A. Jackson, "Operational Experiences at the Advanced Light Source," Rev. Sci. Instr. 67(9) (1996).
[5] J. Hinkson and K. Unser, "Precision Analog Signal Processor for Beam Position Measurements in Electron Storage Rings," Proc. 2nd Europ. Workshop on Beam Diagnostics and Instrumentation for Particle Accelerators, Travemünde, Germany (1995).
[6] Computer application written by J. Pusina, LBNL Berkeley (1996).
[7] G. Portmann, unpublished work, LBNL Berkeley (1994).

TUNE-SPLIT EFFECTS AT THE ALS STORAGE RING*

R. Keller, Advanced Light Source Center, E. O. Lawrence Berkeley National Laboratory
University of California, Berkeley, CA 94720 USA

This paper is concerned with operational characteristics of the Advanced Light Source (ALS) storage ring, a synchrotron light source of the third generation that is capable of operating between 1.0 and 1.9 GeV beam energy. Even though the magnetic properties of its lattice magnets appeared to be very well understood an anomaly was observed with the measured betatron tunes when the working point of any of the three quadrupole families or the bend magnets was switched from the upper to the lower hysteresis branch. In no case was it then possible to recover the standard horizontal and vertical tune values simultaneously at any given excitation current; either one was considerably off normal when the other one was set to the proper value. The nature of this so-called "tune-split effect" was investigated, and the solution to the problem is presented here, together with an outlook on consequences for operational scenarios resulting from this effect.

1 INTRODUCTION

The ALS electron storage ring [1] is designed to operate between 1.0 and 1.9 GeV beam energy. Its betatron tunes have to be kept constant during operation within 5 kHz to maintain the radiation source-points in stable positions. This implies that the integrated fields of the bend and quadrupole magnet families, see Fig. 1, have to be held within about 0.03%; and therefore these magnets are subjected to a standardized conditioning procedure which guarantees the proper fields at nominal current set-points. In the case of ALS, a single conditioning loop from zero to maximum excitation current and then down to the nominal set point was used at first for all lattice-magnet families. This loop represents the fastest way to achieve well-defined working points after bringing the magnets as far into saturation as the power supplies would allow, and it establishes the working points on the upper hysteresis branches.

This simple conditioning procedure worked very well during the initial operation phase, but it soon became clear that it was not optimal in several regards. With the available 1.5-GeV synchrotron injector, the storage ring has to be ramped up to reach 1.9 GeV energy, and this process by definition shifts the magnet working points to the lower hysteresis branches. Furthermore, the requirement to retune at least some of the quadrupoles to compensate for tune changes when insertion-device gaps are being varied [2] imply that the concept of well-defined working points on either one of the hysteresis branches might have to be given up entirely.

2 CONDITIONING AND HYSTERESIS EFFECTS

Operation of the ALS storage ring requires very precise stability and working-point reproducibility for all lattice magnets to always maintain the one beam orbit that provides the customary source point locations to the light-source users. Therefore the ALS magnets undergo a specific conditioning process that defines their history of excitation and always leads to the same working points, on the same branch of the hysteresis loops when setting the magnet currents to nominal values. It is very impractical, however, to check the effectiveness of the conditioning routine with actual

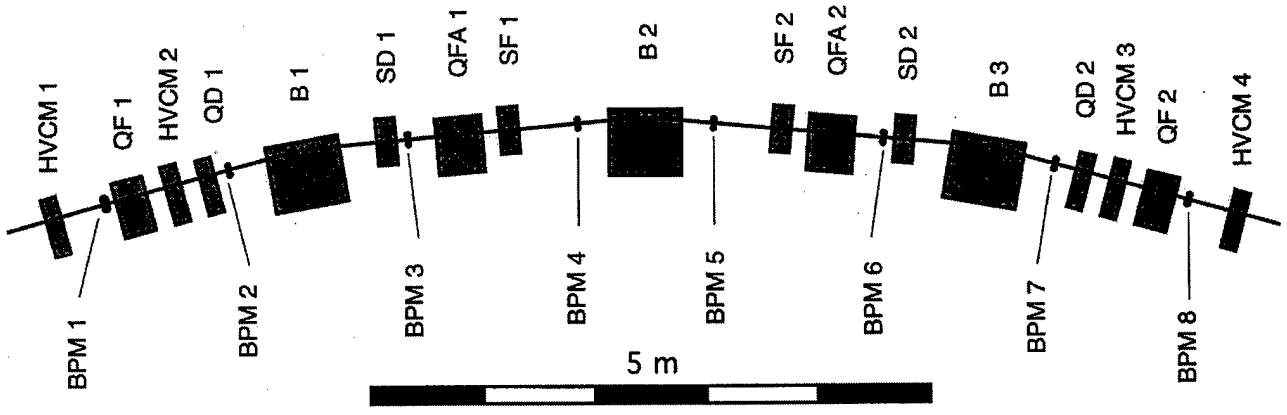


Figure 1. ALS storage-ring lattice showing one out of twelve arc sections. HVCM, horizontal and vertical corrector; QF, focusing quadrupole; QD, defocusing quadrupole; QFA, second focusing quadrupole; B, bend magnet; SF, focusing sextupole; SD, defocusing sextupole. BPM, beam-position monitor. The bend magnets have gradients generating a defocusing quadrupole. All magnets are open towards the outside of the ring (C-type yokes) to avoid intercepting synchrotron radiation.

*This work was supported by the Director, Office of Energy Research, Office of Basic Energy Sciences, Material Sciences Division, U.S. Department of Energy, under Contract No. DE-AC03-76SF00098.

0-7803-4376-X/98/$10.00 © 1998 IEEE

field measurements. Instead, the horizontal and vertical betatron tune values of the machine are taken as indicators of global magnet-field reproducibility. The relative resolution of tune measurements amounts to 5 kHz or 0.003 tune units and corresponds to about 3×10^{-4} relative change in the total focusing strength of a quadrupole family.

The concept of hysteresis generally would imply that for a given magnet there should be two working points where the integrated fundamental fields are exactly equal, one point on the lower branch of the hysteresis loop and one on the upper branch, at properly reduced excitation current, see Fig. 2. This assumption did not hold true, however, when the working points of the ALS lattice-magnets had to be moved from the upper hysteresis branches, where they had been during the commissioning and early operation phases of the storage ring, to the lower branches in order to allow ramping of the beam energy from 1.5 to 1.9 GeV. For a variety of reasons such as power supply limitations, time consumption, and unnecessary increase of radiation losses at higher energies it is totally unfeasible to bring the magnets back to the upper hysteresis branches for a beam energy of 1.9 GeV.

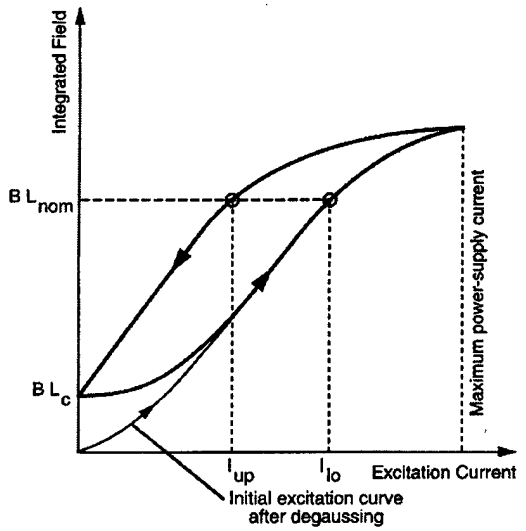


Figure 2. Schematic of the effective hysteresis loop described when using a unipolar power supply. Two excitation current values, I_{lo} and I_{up}, respectively, generate the same (nominal) integrated field value B L_{nom} when operating the magnet on either the lower or the upper hysteresis branch. The magnitudes of hysteresis-loop width, saturation effects at higher current, and coercive field value, BL_c, are exaggerated in this schematic for illustration purposes.

With any of the quadrupole or gradient magnet families, the change between hysteresis branches gave rise to an abnormal behavior of the ring, here termed 'tune-split effect:' with rising excitation of one of these families one betatron tune value could be set to its nominal value at a certain current, but the other one was still far off, and when the magnet current was raised somewhat more the second tune reached its nominal value, but now the first one was significantly off. The tune-split effect as found with the QFA family is demonstrated in Fig. 3.

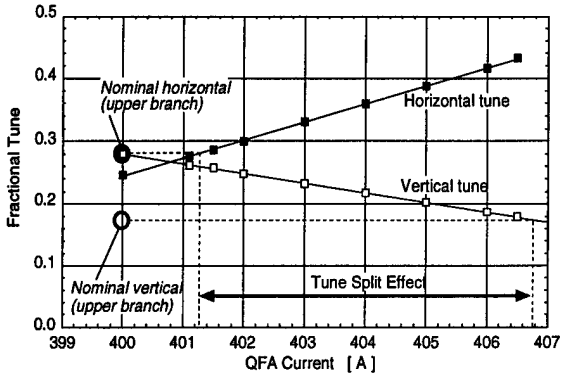


Figure 3. Tune-split effect. Measured fractional betatron tune values are shown as a function of the QFA excitation current, after changing the working point from the upper to the lower hysteresis branch. The machine reaches the nominal vertical tune at significantly higher excitation current than the nominal horizontal tune.

3 QUANTIFICATION OF TUNE-SPLIT EFFECTS

Tune split effects occurred with all three quadrupole families and with the gradient magnets; to a lesser degree even with the two sextupole families. To quantify these effects, the difference in the excitation currents, where either the horizontal or the vertical nominal tune is obtained, is taken and expressed as a percentage of the mean of both currents. Linear approximations to the measured data are used to identify these currents as accurately as possible. Results are given in Table 1.

Table 1. Tune-split effects found with ALS lattice-magnets.

Magnet Type	Rel. Tune Split [%]	Core Length [m]	Split/Length [% / m]
B	2.35	0.807	2.9
QFA	1.38	0.470	2.9
QF	0.60	0.318	1.9
QD	0.35	0.168	2.1

The data in Table 1 demonstrate that the tune-split effect found with quadrupole-type magnets varies monotonically, if not quite linearly, with the core length of the magnet type in question, even when including the bend magnets that in essence represent the inner halves of true quadrupole magnets. This trend points to a residual-field effect which would be stronger the more iron-dominated a magnet is.

4 EXPLANATION OF TUNE-SPLIT EFFECTS

Tune-split measurements performed at one tenth of the customary ramping speed gave identical results, leading to the exclusion of dynamics hypotheses such as eddy-current effects or enhanced residual magnetization because of fast current reversal. The pertinent clue was then obtained from local Hall-probe measurements on two of the four pole pieces

of one QFA magnet with high-resolution, differential readout [3].

The magnet was conditioned and left in its standard excitation state on the upper hysteresis branch at nominal current. After changing the current to zero and then back to nominal, a 15-G change in the difference value of the two probe readings was recorded. This field difference can readily be explained by closer examining the remnant excitation of the magnet back leg [4]. Those flux lines that pass through the back leg have quite different total lengths inside the iron, depending on whether they connect the outer or the inner pole pair, as illustrated in Fig. 4. Flux densities associated with these two kinds of flux lines are about inversely proportional to the line lengths, and therefore a net magnetization effect results which creates a dipole magnet field in the free space between the two upper and the two lower poles. When the magnet is brought from the upper to the lower hysteresis branch the back leg magnetization is subject to a hysteresis effect as well, amounting to the 15-G difference measured.

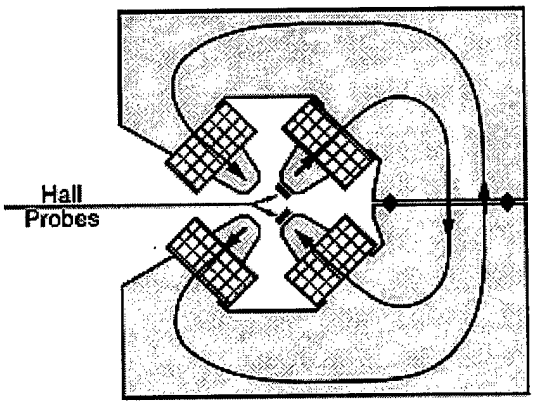


Figure 4. Cross section of an ALS quadrupole. Of the flux lines, only the ones passing through the back leg are drawn.

The dipole field resulting from the C-shape of the magnet yoke, superimposed on the main quadrupole field, is equivalent to a pure quadrupole field whose center of symmetry is shifted horizontally. This is a well-known feature of C-shaped magnets and had been quantified for each of the installed ALS quadrupoles during the original magnetic measurements [5], leading to individual positioning corrections for all these magnets. What had not been recognized at that time was that the magnitude of these shifts changes as the magnets are brought from one hysteresis branch to the other.

Once the idea of hysteresis-induced dipole fields is accepted, deriving a convincing explanation for the observed tune-split effects is straightforward. The dipole fields inside the quadrupole gaps give small kicks to the beam, and in consequence the beam is offset from its ideal path when it passes through the sextupoles in the ring, leading to a change in the total focusing strength. A tracking study was undertaken to investigate this effect for the case of the QFA quadrupole family [6]. In this study, 0.1-mrad kicks were applied to the standard beam at all QFA locations, and as a result the betatron tunes changed by +0.057 and +0.042 in the horizontal and vertical directions, respectively. From Fig. 3 one can read that at 403.5 A excitation current, the tunes are shifted from their nominal values by +0.064 and + 0.048, respectively. A comparison of orbit distortions measured when the QFA family was brought to the lower hysteresis branch with simulated distortions from the same theoretical study likewise shows a remarkable agreement.

In the case of the bend magnets, a similar reasoning as followed for the quadrupoles, again involving different lengths of the flux lines in the return yoke depending on where on the pole faces they start and end, leads to the conclusion that even parallel-faced C-shaped dipoles have a considerable quadrupole component [7]. If this quadrupole component then has a different hysteresis width than the main dipole component the observed tune shifts upon switching between hysteresis branches could be readily explained.

5 OUTLOOK

After deriving a convincing explanation for the observed tune-split effects the first consequence for operating the ALS storage-ring was to painstakingly follow established conditioning procedures for all lattice magnets. Secondly, because of the ramping option, the working points of all lattice-magnets were changed to the lower hysteresis branches. As a third consequence, even minute downward set-point corrections were prohibited.

But one effect cannot be tackled in this way, and that is the change of vertical betatron tunes caused by variations of the insertion-device gap widths. Installation of back-leg windings on all quadrupole magnets would be the best solution to this problem. Luckily it is not necessary to compensate the bend magnets for tune-split effects because they would not take part in a local tune-compensation scheme anyway.

6 ACKNOWLEDGMENTS

Thanks are due to Alan Jackson and Klaus Halbach for many discussions that contributed to uncovering the roots of the tune-split effect. It is also a pleasure to express my gratitude towards the ALS operators for their help in carrying out the tune measurements and the Hall-probe investigations of the QFA magnet.

7 REFERENCES

[1] "1-2 GeV Synchrotron Radiation Source, Conceptual Design Reptort" LBL Pub. 5172 Rev., LBL Berkeley (1986).
[2] D. Robin, H. Nishimura, and J. Safranek, "Global Beta-beating Compensation of the ALS W16 Wiggler," these conference proceedings (1997).
[3] Measurements performed together with J. Hinkson and M. Chin (1994)
[4] K. Halbach, LBL Berkeley, private comm. (1994).
[5] Measurements performed at LBL Berkeley under guidance of J.Tanabe, D.Nelson, and M. I. Green (1991).
[6] L. Schachinger, LBL Berkeley, unpubl. work (1994).
[7] G. E. Fisher, "Iron Dominated Magnets," SLAC-PUB-3726, SLAC Stanford (1985).

A CODE FOR CALCULATING THE TIME EVOLUTION OF BEAM PARAMETERS IN HIGH INTENSITY CIRCULAR ACCELERATORS*

C. H. Kim
Accelerator and Fusion Research Division, E. O. Lawrence Berkeley National Laboratory
University of California, Berkeley, California 94720

Abstract

Beam emittances in a circular accelerator with a high beam intensity are strongly affected by the small angle intrabeam Coulomb scattering. In the computer simulation model we present here we used three coupled nonlinear differential equations to describe the evolution of the emittances in the transverse and the longitudinal planes. These equations include terms which take into account the intra-beam scattering, adiabatic damping, microwave instabilities, synchrotron damping, and quantum excitations. A code is generated to solve the equations numerically and incorporated into a FORTRAN code library. Circular high intensity physics routines are included in the library such as intrabeam scattering, Touschek scattering, and the bunch lengthening effect of higher harmonic cavities. The code runs presently in the PC environment. Description of the code and some examples are presented.

I. INTRODUCTION

For many years ZAP code [1] has been widely used for calculating equilibrium beam properties in high intensity circular accelerators. The code is conveniently menu-driven by an extensive inventory of menus such that the user need not have any programming skills.

In dynamic situations such as in synchrotrons, calculation of the evolution of beam parameters in a self-consistent manner in time is important. The vertical beam size is calculated self-consistently by the balancing of the damping rate with coupling and intrabeam scattering (IBS), such that the emittance ratio may be higher than the coupling ratio when intrabeam scattering is strong. The equilibrium beam parameters can be calculated naturally by letting the time run for a few damping times.

Modularization is recommended in modern programming. It is a way of unleashing the power of the routines and procedures by making them available (reusable) to other programs written by other users (client). The routines should be made as simple as possible (no fat).

Some parts of the ZAP subroutines such as the routines for calculating IBS time constants and for Touschek lifetime are used in the present FORTRAN library. New routines such as for calculating the bunch lengthening effect of third harmonic cavities are also added to the library.

Many modern accelerators demand higher beam intensities and low emittances. We found the code useful for evaluating high intensity low emittance circular accelerators such as the one contemplated for a next generation light source [2]. Our calculation showed that addition of a third harmonic cavity significantly reduces beam emittance blow up due to intrabeam scattering and at the same time increases beam lifetime.

A basic description of the code is given in section II. Some calculations are compared with measurements in section III. The modified version is particularly fast and convenient for varying certain parameters and studying how other parameters change. One such example is given in section IV.

II. THE TIME DEPENDENCE

In the present model we used the following three equations to calculate the evolution of beam parameters in time:

$$\frac{d\varepsilon_x}{dt} = -\frac{1}{\tau_x^{SR}}\left(\varepsilon_x - \frac{1}{1+\kappa}\varepsilon_x^{nat}\right) - \frac{1}{\beta\gamma}\frac{d(\beta\gamma)}{dt}\varepsilon_x + \frac{1}{\tau_x^{IBS}}\varepsilon_x \qquad (1)$$

$$\frac{d\varepsilon_y}{dt} = -\frac{1}{\tau_y^{SR}}\left(\varepsilon_y - \frac{\kappa}{1+\kappa}\varepsilon_x\right) - \frac{1}{\beta\gamma}\frac{d(\beta\gamma)}{dt}\varepsilon_y + \frac{1}{\tau_y^{IBS}}\varepsilon_y \qquad (2)$$

$$\frac{d\varepsilon_L}{dt} = -\frac{1}{\tau_L^{SR}}\left(\varepsilon_L - \varepsilon_L^*\right) - \frac{1}{\beta\gamma}\frac{d(\beta\gamma)}{dt}\varepsilon_L + \frac{1}{\tau_L^{IBS}}\varepsilon_L \qquad (3)$$

where ε_x, ε_y and ε_L are the horizontal, vertical, and longitudinal emittances, τ^{SR} are the radiation damping times, ε^{nat} are the natural emittances, κ is the coupling coefficient, and τ^{IBS} are the intra-beam scattering (IBS) time constants [3].

* This work was supported by the Director, Office of Energy Research, Office of Basic Energy Sciences, Materials Sciences Divisions, of the U. S. Department of Energy under Contract No. DE-AC03-76SF00098

0-7803-4376-X/98/$10.00 © 1998 IEEE

For low intensity storage rings the beam emittances are determined by the synchrotron damping and the quantum excitations [4]. which are included in the first two terms in the parenthesis on the RHS of equations (1), (2), and (3). In this case the emittances reach the equilibrium (natural) state in a few damping times, where the final emittance ratio between vertical and horizontal emittances is κ. The third term represents adiabatic damping or growth when the beam energy changes. In dynamic situations the vertical emittance is "driven" by the actual (not the natural) value of the horizontal emittance as shown in the second term in the parenthesis of equation (2). For low intensity, ε_L^* in equation (3) is interpreted as $\varepsilon_L^* = (\sigma_p^{nat}\ \sigma_L^{nat}) = \varepsilon_L^{nat}$, where σ_p^{nat} is the natural energy spread and σ_L^{nat} is the natural bunch length.

For high intensity circular accelerators, the intrabeam scattering (IBS) represented by the fourth (the last) terms is important. In the final equilibrium state, damping is balanced by quantum excitations and growths due to IBS.

If the intensity is above the threshold for the microwave instability (MWI) the energy spread and the bunch length increase above the natural values. In the present model this increase is treated in the same way as the quantum excitations and the value of ε_L^* in equation (3) is interpreted as $\varepsilon_L^* = (\sigma_p^{mwi}\ \sigma_L^{mwi}) = \varepsilon_L^{mwi}$.

Equations (1), (2), and (3) are coupled nonlinear equations, with τ^{IBS} depending on the beam emittances. A program is written to solve them numerically and is included in the Circular-High Intensity Physics Code library.

Most of the ZAP subroutines are rewritten into smaller modules and incorporated into the code library.

III. TESTS

The code was tested by comparing the calculated beam parameters with the measured beam parameters in the following two experiments.

In the first experiment, electrons are cooled in the ALS booster synchrotron [5] in which the 50 MeV electrons were injected into the booster, accelerated to 650 MeV and cooled for about 330 msec, decelerated to about 200 MeV, and extracted. The calculated emittances agreed well with the measurements within the experimental errors.

In the second experiment, the ALS storage ring beam sizes were measured at the diagnostics beam line [6]. Beam size should grow with current as a result of IBS and more rapidly at lower energies where IBS is stronger. The beam size at the source point was measured indirectly by measuring the spot size of synchrotron radiation on a scintillator screen. Measurements were done at two beam energies, 1100 MeV and 1522 MeV. The results are summarized in Figures 1 an 2.

Figures 1 and 2 shows that beam sizes are larger at higher currents compared to the zero current beam sizes. Beam size grows more rapidly for 1100 MeV beam.

Measurement and calculation errors may come from several systematic and random sources. Systematic errors may be caused by the optical distortion in the diagnostics beam line, saturation in the target, calculation of the magnification, calculated lattice functions, etc., and estimated to be about ± 10%. Random errors errors from unknown sources appear to be about ± 10%. Calculated beam sizes agree with the measured values within the experimental error.

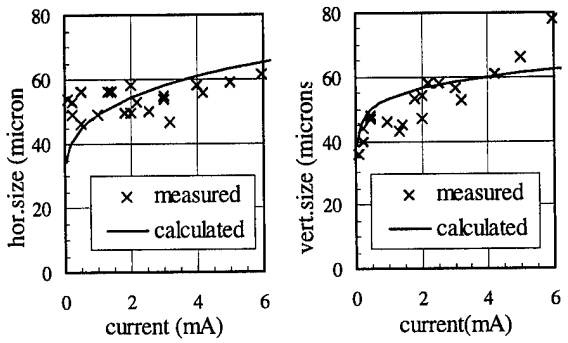


Figure 1. Measured and calculated beam sizes in the ALS for beam energy of 1100 MeV. Coupling was assumed to be 3 %.

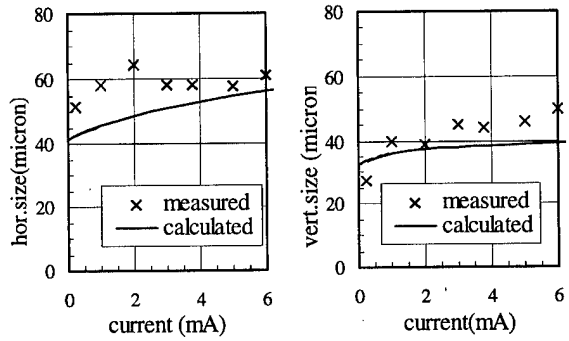


Figure 2. Measured and calculated beam sizes in the ALS for beam energy of 1522 MeV. Coupling was assumed to be 1.5 %.

The source point and the coupling were used as fitting parameters for calculating the beam sizes. The source point is the point where the beam line meets tangent to the electron orbit in the bending magnet. We achieved the best fitting if we assume that the source point is at 5.2 meters from the center of the straight section where β_x=0.39 m, β_y=20.6 m, and η_x=0.030 m. The source point could move as much as 5 cm if the orbit moved by 10 milliradians, which could give us better fittings for the two energies. However, it is not likely that we will have such a large orbit distortions in ALS [7]. The coupling were assumed to be 3 % for 1100 MeV and 1.5% for 1522 MeV in the calculation. Coupling in ALS is thought to be caused by magnet misalignments and orbit distortions. The

orbit at 1100 MeV had a larger closed-orbit distortion which can explain why the coupling is larger at this energy.

IV. AN EXAMPLE

In order to illustrate the capability of the code we present the following example where the variation of beam parameters were studied as functions of the coupling coefficient. Parametric dependency studies can be done conveniently in "DO-LOOPs". Subroutines, such as the IBS routine, can be called in a do-loop repeatedly while other parameters can be varied systematically.

In the present example, the coupling coefficient was varied in a do-loop while in each do-loop the time is let run for a few damping times to calculate the equilibrium emittances, bunch length, and the lifetime for each value of the coupling. This calculation also serves a practical purpose for improving the ALS beam brightness by reducing the coupling. The calculation results are summarized in Figures 3 and 4.

The calculation was done for the normal ALS operating condition with beam energy 1522 MeV, current 400 mA, and the number of bunches 288. The beam current is just below the measured microwave instability threshold of 2 mA per bunch [8]. The half bucket height was assumed to be 2.67 % and $\nu_s = 0.0076$.

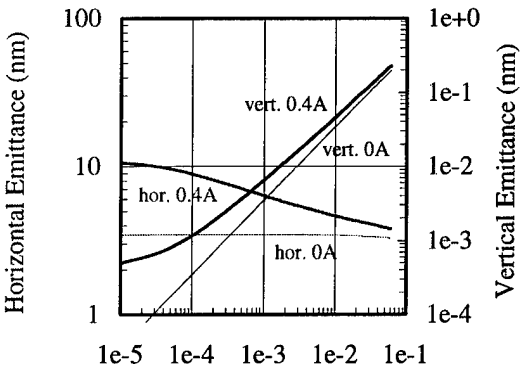


Figure 3. Horizontal and vertical emittances are plotted as functions of the coupling coefficient. The differences between the zero current and the 400 mA plot are due to the intrabeam scattering.

Some physics can also be learned. As the coupling coefficient becomes very small ($\kappa < 0.1$ %), the vertical emittance decreases until the IBS rate becomes large enough to balance the radiation damping rate. The increased intrabeam scattering rate will, in turn, cause the horizontal emittance and the bunch length to grow dramatically and reduce the beam lifetime as shown in Figures 3 and 4.

If there was no coupling (only a theoretical possibility), beam parameters equilibrated at the following values: $\varepsilon_x = 1.1 \times 10^{-8}$ m -Rad, $\varepsilon_y = 4.2 \times 10^{-13}$ m - Rad, $\sigma_L = 6.0$ mm, and $\sigma_p = 0.0009$, vertical tune shift = 0.011, and a beam lifetime of 40 minutes

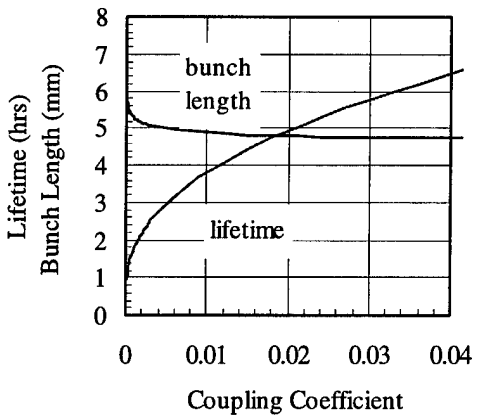


Figure 4. Bunch length and beam lifetime as functions of the coupling coefficient.

V. SUMMARY

A FORTRAN code library for circular high intensity physics is created which is used for calculating evolution of beam parameters in time in a self-consistent manner in the presence of strong intrabeam scattering. We have compared the calculated values using the library with experimentally measured values with good results.

The code runs in the PC environment using FORTAN90 in the Microsoft Development Studio©.

REFERENCES

[1] M. S. Zisman, S. Chattopadhyay, and J. J. Bisognano, Lawrence Berkeley National Laboratory Report, LBL-21270 (1986)

[2] J. Byrd, W. Decking, M. Howells, A. Jackson, R. Keller, C. Kim, D. Massoletti , H. Nishimura, D. Robin, and H. Zyngier, in these proceedings

[3] J. Bjorken and S. Mtingwa, Particle Accelerators, Vol. 13 pp.115-143(1983)

[4] See, for instance, D. A. Edwards and M. J. Syphers, "An Introduction to the Physics of High Energy Accelerators", John Wiley & Sons (1993)

[5] A. Zholents, M. Fahmie, J. Johnson, C. Kim, K. Luchini, D. Massoletti, C. Timossi, J. De Vries, in these proceedings

[6] R. Keller, T. Renner, D. J. Massoletti , Proc. of the 7th Beam Instr. Workshop (1996).

[7] Hiroshi Nishimura, Private Communications

[8] John Byrd, et. al., Proc. of the Microbunches Workshop, BNL, 236 (1995)

MEASUREMENT OF STORAGE RING MOTION AT THE ADVANCED LIGHT SOURCE*

Gary F. Krebs, E.O. Lawrence Berkeley National Laboratory, Berkeley, California 94720, U.S.A.

Abstract

The mechanical stability of the Advanced Light Source storage ring is examined over a period of 1.5 years from the point of view of floor motion. The storage ring beam position monitor stability is examined under various operating conditions.

1 INTRODUCTION

The Advanced Light Source (ALS) at the E.O. Lawrence Berkeley National Laboratory is a third generation synchrotron x-ray source[1]. The ALS, shown schematically in Figure 1, has a 50 MeV LINAC and a 1.5 GeV booster and 2.1 GeV storage ring.

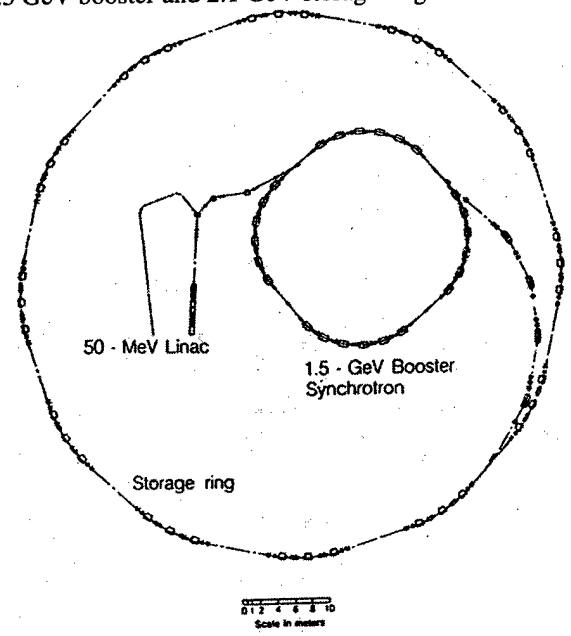


Figure 1: The ALS accelerators system

To produce a stable and bright electron beam, long term mechanical alignment and stability of the magnets over the 200 m circumference storage ring must be maintained. In order to track the electron beam, a system of over 100 Beam Position Monitors (BPM) are mounted in the storage ring vacuum chambers. Characteristics of the storage ring motion and vacuum chamber BPM motion have been measured and are presented in this paper.

2 STORAGE RING MOTION

To accomplish accurate alignment of the storage ring magnets, a reference network of 36 monuments was created. The monuments are imbedded in an 18 inch thick concrete floor. The angles and distances between monuments are measured with theodolites and mekometers, respectively, to determine their coordinates relative to an arbitrary chosen origin. Magnet positions around the 12 sectors of the storage ring are then referenced and aligned to the monuments. Some 200 storage ring magnets are mounted on a system of 12 moveable sector girders such that after initial alignment on the girder, future storage ring alignment can be achieved by aligning the girders alone.

Since September 1995 storage ring monument elevation surveys have been carried out nearly every month in an effort to characterize floor, and hence nearby, magnet/girder motion. Monument elevations were measured with 30 μm accuracy. The changes in elevation of the 36 storage ring monuments are shown in Figures 2a-2d from the period September 1995 to March 1997. We find the storage ring monuments have dropped in elevation as much as 1.2 mm in sectors 6 and 7, see Figure 2d. Over the period represented in Figure 2a-d, a great deal of floor loading has occurred. Insertion devices weighing 30 tons each, were added to the storage ring in sectors 9 and 5 in 5/94 and 4/96, respectively. In Figure 2a,2d we observe a characteristic drop followed by a rise in monument elevations during the rainy winter months. In Figures 3a-3d the average of each sectors three monuments elevations is shown over the same time period. Sectors 10 and 11 are the most stable sectors as shown in Figure 3d. Operationally, the storage ring requires smoothness magnet-to-magnet to function optimally. Since the magnets were aligned on their girders relative to their ideal position to within 150 μm and remain stable, what remains is to maintain girder-to-girder smoothness as floor motion occurs. Figure 2a-d

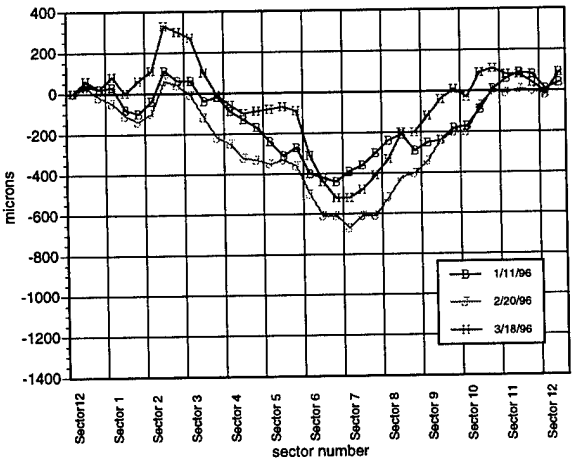


Figure 2a: Elevation changes around the storage ring

* This work is supported by the Director, Office of Energy Research, Office of Basic Energy Sciences, Material Sciences Division of the U.S. Dept. of Energy, under Contract No. DE-AC03-76SF00098.

0-7803-4376-X/98/$10.00 © 1998 IEEE

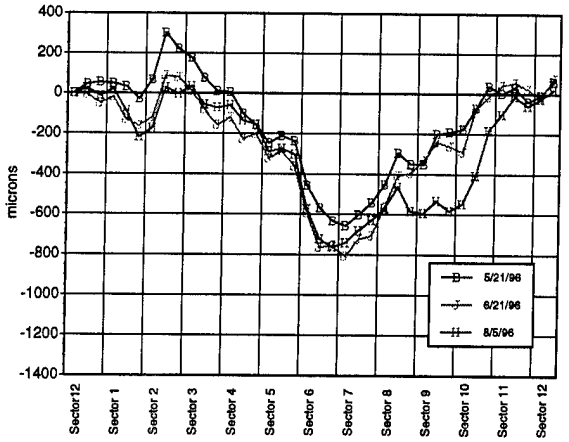


Figure 2b

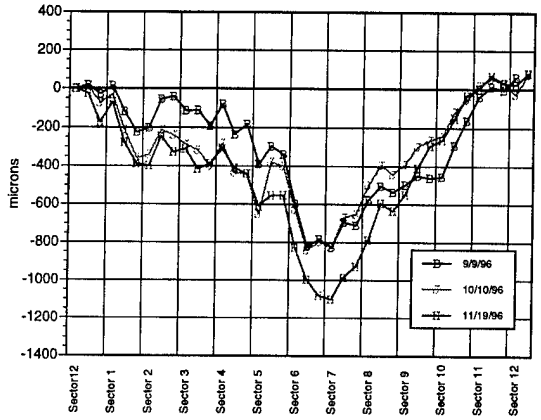


Figure 2c

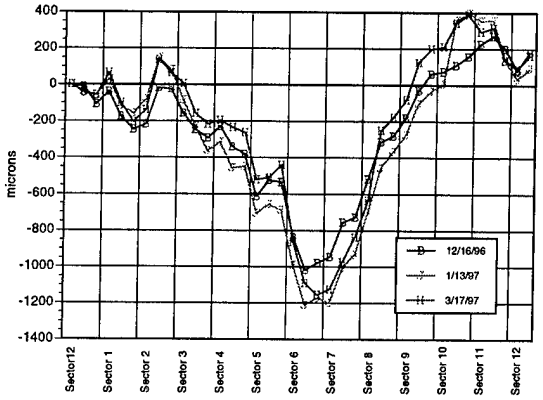


Figure 2d

shows the smoothness monument-to-monument and, by extension, girder-to-girder to be typically better than 100 μm. A system of beam position corrector magnets around the storage ring can correct for girder-to-girder misalignments up to a few hundred microns. As the beam corrector magnet field limits are approached, the storage ring must be realigned.

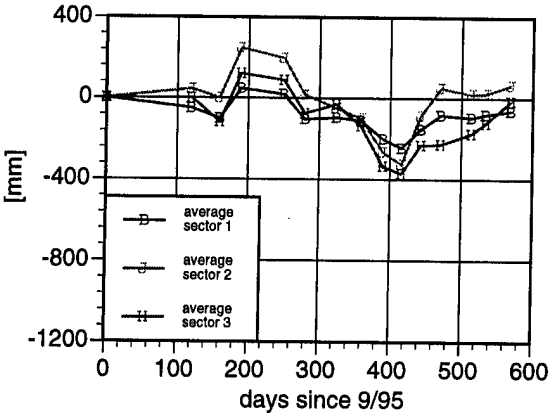


Figure 3a

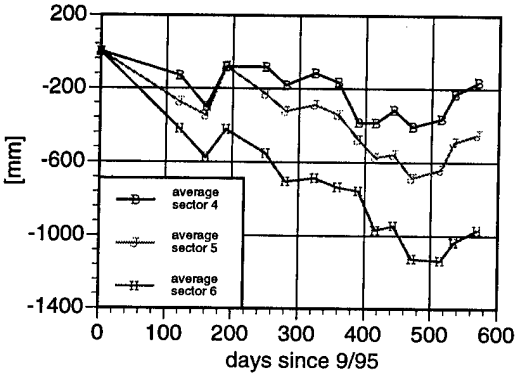


Figure 3b

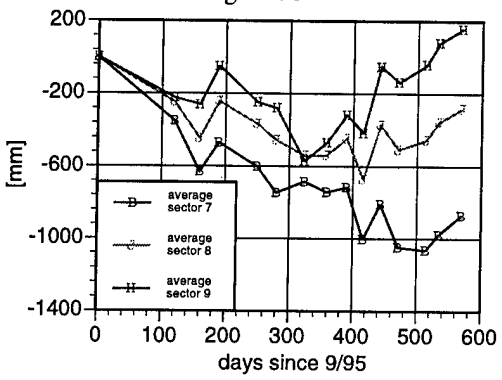


Figure 3c: Elevation changes at the storage ring

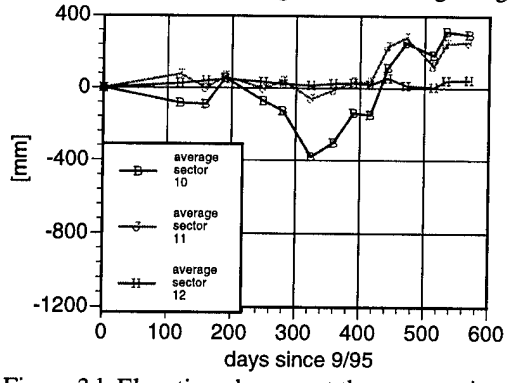


Figure 3d: Elevation changes at the storage ring

3 BEAM POSITION MONITOR MOTION

The BPM allow accelerator operators to track the electron beam through the magnet lattice, make corrections and compare the electron beam location to various influences and models. Beam stability is affected by many different parameters. Here at the ALS we have found such things as overhead crane usage, earthquakes and air temperature stability inside the storage ring tunnel to be some of the influences effecting the trajectory of the electron beam[2]. In addition to real motion of the electron beam, there is also 'false beam motion' that occurs when the BPM themselves move. Since the BPM are assumed fixed in location, this effect appears as beam motion. The BPM are located inside the storage ring vacuum tanks which are mounted in an overconstrained mode directly to the sector girders. Measuring the motion of the BPM relative to the girder was carried out using 1 μm precision dial indicators[3]. The motion occurs due to heating of the vacuum chamber from synchrotron light and stray electrons. Figure 3 shows the motion the BPM undergoes during routine operation of the storage ring. A typical storage ring cycle lasts about 4 hours and begins with filling the ring to about 400 ma of electrons. During this process heating of the vacuum tank is at its maximum. Over the cycle period, the electrons decay down to about 200 ma. At this point the heating is at a minimum. The temperature change produces maximum 15 μm horizontal and 8 μm vertical position changes in the BPM location. Aside from the initial filling process, the change in BPM position is about 4 μm/hr horizontally and 1 μm/hr vertically. The effect is clearly seen in Figure 4 where a 24 hour time period is covered and 3 fills or cycles of the storage ring occur.

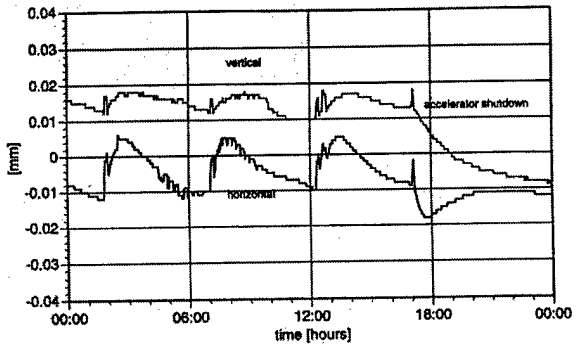


Figure 4: Vacuum chamber position change fill-to-fill

The baseline for this heating and cooling cycle is affected by the air temperature inside the storage ring tunnel. Temperatures inside the tunnel are usually maintained to within ± 0.5 °C. (Changes in temperature inside the storage ring tunnel affect the length and orientation of the storage ring and produce real beam motion which is far larger (100-500 μm) than this effect. At the end of a weekly operation cycle as the storage ring is routinely shut down for preventive maintenance, we see the horizontal and vertical positions relative to the girder change as much as 30 μm. When the machine is brought back on, a similar motion occurs in the opposite direction. This stabilization period typically lasts about 8 hours. Electrically the BPM are considered to be repeatable to £5 μm[4]. However, such inherent electrical accuracy may be unnecessary when the mechanical stability of the BPM is far larger.

4 CONCLUSIONS

Monitoring the alignment of third generation synchrotron storage rings is important in order to maintain a high quality electron beam. Periodic realignments are typically required approximately every 24 months at the ALS. In determining the electrons position in the storage ring many factors affect the repeatability of the BPM. Mechanical stability due to electron beam effects are important when considering the overall accuracy of the ALS storage ring BPM system.

ACKNOWLEDGMENTS

I would like to thank the survey and alignment crew at the ALS: Bill Baldock, R. DeMarco, A. Gavidia, R. Armstrong, D. Jones and H. Meyer. Special thanks go to Bill Baldock whose help was crucial in collecting the dial indicator data for this study.

REFERENCES

[1] 1-2 GeV Synchrotron Radiation Source (conceptual design report) LBNL Pub. 5172

[2] Orbit stability of the ALS storage ring.R.Keller et al. PAC Vancouver, 1997

[3] Mitutoyo digimatic indicator 543-523A

[4] Private communication with Jim Hinkson, ALS.

MEASUREMENT OF THE RADIATION INCIDENT ON ALS NdFeB PERMANENT MAGNET INSERTION DEVICE STRUCTURES AND A DETERMINATION OF THEIR LIFETIME*

Gary F. Krebs and Michael Holmes
E.O. Lawrence Berkeley National Laboratory, Berkeley, California 94720, U.S.A.

Abstract

Measurements of the radiation incident on ALS insertion device NdFeB permanent magnet structures were carried out using thermoluminescence dosimeters. A plastic scintillator gamma telescope was utilized to unravel the various contributions to the integrated dose. Magnet lifetimes were calculated for various operational conditions.

1 INTRODUCTION

The Advanced Light Source (ALS) [1] at the Lawrence Berkeley National Laboratory is a third generation electron accelerator that produces photons in the 10 eV-10 keV range. The descriptive "third generation" is given to light sources with low beam emittance incorporating insertion devices to produce extremely bright x-ray beams. The ALS is composed of a 50 MeV LINAC, a 1.5 GeV booster and a 1.9 GeV storage ring. The 200 m circumference storage ring has 12-fold symmetry and 10 available straight sections for insertion devices. Presently, the ALS storage ring has five insertion devices in operation (two more to be added in 1997-8) whose magnetic structures are fabricated from NdFeB permanent magnets. These devices have anywhere from 38 to 178 alternating North -South poles on either side of a vacuum chamber. Near the storage rings electron beam the radiation level is mainly due to γ brehmsstrahlung [2]. Since the x-ray brightness produced by the insertion devices will degrade with loss of magnetization, the stability of the permanent magnets to radiation exposure is of paramount importance. A number of studies have been carried out to measure the change in magnetic properties of NdFeB[2-10] and SmCo[2,4-6] due to radiation exposure. We have exposed over 400 thermoluminescence dosimeters (TLD) under various beam conditions to determine the magnitude of γ-radiation incident on the insertion device permanent magnets and have utilized a gamma telescope to help unravel the source of the integrated dose measured by the TLD.

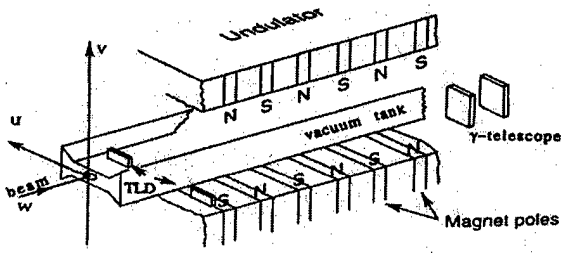


Figure 1: ALS insertion device showing coordinate system, vacuum tank, TLD and γ-telescope

2 MEASURING THE RADIATION DOSE

In this study we used TLD composed of $Li_2B_4O_7$. The TLD were calibrated using a ^{137}Cs irradiator over the range 0.04 Gy to 120. Gy[11]. The dose measured by a TLD reader[12] was consistent with the dose given the TLD by the ^{137}Cs source to within 7 %. TLD were placed on top of the storage ring insertion device vacuum chamber and on the bottom poles of the insertion device, see Figure 1. Two types of insertion device vacuum chambers with different vertical gaps are utilized in the ALS storage ring. The vertical distances from ideal beam center to the inside surface of the vacuum chambers are 5 mm and 9.5 mm for the small gap and large gap chambers, respectively. (Horizontal clearances are much larger.) For the small gap vacuum chambers, the TLD were located 7 mm above and 95 mm below beam center. The position above the vacuum chamber corresponds to the location of the insertion device permanent magnets during a typical running mode while at the highest magnetic field. The position of the TLD below the vacuum chamber corresponds to the location of the permanent magnets at maximum gap during the refilling phase of the storage ring.

3 RESULTS

Table I lists the integrated dose received by a series of TLD placed along the length of the insertion device vacuum chamber (small gap) above and below the electron trajectory. The coordinate system u,v,w is shown in Figure 1 where the origin is taken to be the entrance to the vacuum chamber. The irradiation occurred over 26.679 amp-hours with an electron energy of 1.5 GeV.

* This work is supported by the Director, Office of Energy Research, Office of Basic Energy Sciences, Material Sciences Division of the U.S. Dept. of Energy, under Contract No. DE-AC03-76SF00098.

0-7803-4376-X/98/$10.00 © 1998 IEEE

Table I: TLD doses at 1.5 GeV

TLD #	u [mm]	v [mm]	w [mm]	Dose [Gy]
1	0	7	70	35
2	0	7	236	133
3	0	7	390	**134**
4	0	7	550	112
5	0	7	710	109
6	0	7	870	98
7	0	7	1030	104
8	0	7	1350	102
9	0	7	1590	111
10	0	7	1990	134
11	0	7	3110	123
12	0	7	3430	123
13	0	-95	236	31
14	0	-95	390	38
15	0	-95	550	38
16	0	-95	710	48
17	0	-95	1350	42
18	0	-95	1990	49
19	0	-95	3111	**55**
20	0	-95	3430	52
21	100	7	550	39
22	-20	120	390	2
40	0	-95	390	9.0
41	0	-95	710	10
42	0	-95	1990	10
43	0	-95	3430	17
44	-20	120	390	5

At 1.5 GeV, the highest doses measured on the TLD for the insertion device gap closed position were typically 134 Gy for a period of one week (26.667 amp-hours). In the insertion device gap open position, the highest doses measured were about 55 Gy.

Shown in Table 2a,b are the doses received at an electron energy of 1.9 GeV for 24.7 amp-hours and for 4.7 amp-hr, respectively.

Table 2a: TLD doses at 1.9 GeV (24. 7 amp-hr)

TLD#	u [mm]	v [mm]	w [mm]	Dose [Gy]
23	0	7	70	17
24	0	7	390	**124**
25	0	7	870	109
26	0	7	1590	119
27	0	7	1990	102
28	0	7	3430	102
29	0	-95	390	38
30	0	-95	710	**45**
31	0	-95	1990	34
32	0	-95	3430	43
33	-20	120	390	0.2

Table 2b: TLD doses at 1.9 GeV (4.7amp-hr)

TLD#	u [mm]	v [mm]	w [mm]	Dose [Gy]
34	0	7	70	6.0
35	0	7	390	72
36	0	7	870	39
37	0	7	1590	24
38	0	7	1990	25
39	0	7	3430	68

At 1.9 GeV, the highest doses measured on the TLD for the insertion device gap closed position were typically 124 Gy for a period of one week (24.7 amp-hours). In the insertion device gap open position, the highest doses measured were about 45 Gy.

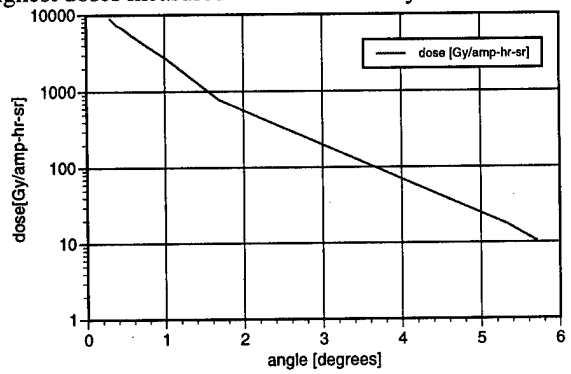


Figure 2: Dose at various positions inside the insertion device

From inspection of Table 2a and Table 2b it can be seen that the dose received by the TLD does not scale directly with amp-hours. This is because the dose received also depends on the number of storage ring fills occurring for each integrated irradiation as well as the electron beam emittance. During the electron ring 10-15 minute refilling process a much higher dose/min. is collected by the TLD than during the normal 240 min. running period. Figure 2 shows a typical relationship between the normalized dose recorded on a TLD versus angle to the TLD (measured relative to the insertion device vacuum chamber entrance). The dose has been normalized to amp-hours-steradians.

A series of experiments were also carried out with one insertion device that uses a large gap vacuum chamber. We found the radiation incident on the permanent magnets of the large gap chamber insertion device was approximately 100-120 times less than for the small gap chambers due to the larger minimum gap available to the magnets.

To determine the contribution to the integrated dose from the running period and the refilling period separately, we utilized a gamma telescope. This telescope was composed of two scintillator photomultiplier 'paddles' whose output signals, when in coincidence with each other during a 10 ns gate, produce a single signal count. The scintillator was 0.25 in. thick x 2 in. x 2 in. NE 102 plastic and the photomultiplier tube RCA 8575.

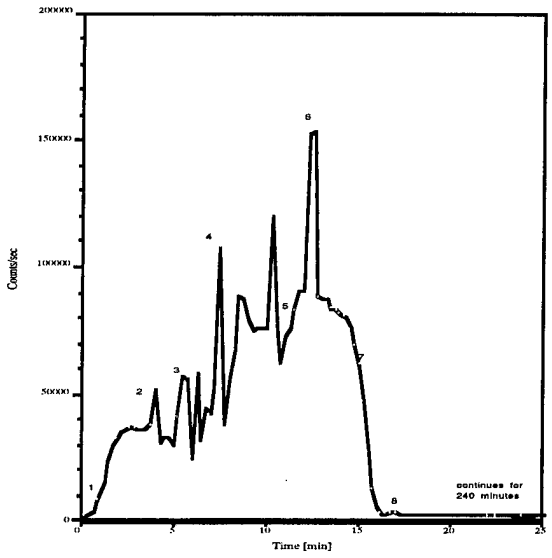


Figure 3

1.Insertion device gaps open
2.Ramp 1.5 to 1.9 GeV
3.Injection process begins
4.Beam stacking
5. Ramp from 1.9 to1.5 GeV
6.Running mode begins
7. Insertion device gaps closed
8. Beam lines opened

We were able to place the telescope about 10 cm from the electron beam in horizontal plane as shown in Figure 1.

We recorded the number of coincidence counts during the electron ring filling process and running period as shown in Figure 3. We found the average ratio (counts during refilling/counts during running) for the full running and refilling periods was 1.0 when running 1.5 GeV electrons but rose to 2.5 when running 1.9 GeV electrons. As shown in Figure 3, part of the contribution from the refilling process occurs when the energy of the stacked electrons were ramped from 1.5 GeV to 1.9 GeV.

Since the insertion device gaps at the ALS are always opened during the refilling process, and if we assume the insertion device gaps are fully closed during normal running, the actual dose seen by the permanent magnets when running in the 1.5 GeV mode is about

134 Gy/wk(1/2)+55 Gy/wk (1/2) ≈ 95 Gy/wk.

For 1.9 GeV electrons the average ratio resulted in a dose of

124 Gy/wk (1/3.5)+45 Gy/wk (2.5/3.5) ≈ 68 Gy/wk.

Previously, an estimate of the useful lifetime of the ALS insertion devices magnets was based on a loss of magnetic remanence of 0.5% [7]. This loss was found to occur when the magnets were subjected to a dose equivalent of $8.5X10^4$ Gy. The number $8.5X10^4$ Gy is a worst case value with an error estimated at 25%. Making various operational assumptions a useful magnet lifetime was calculated to be about 85 years. Several assumptions made in determining that lifetime, though reasonable at the time, are now know to be incorrect. If we estimate the storage ring is in operation 37 weeks/year, the lifetime, T, of the insertion device magnets under current operating conditions is about:

at 1.5 GeV,

$T_{1.5} = 8.5X10^4$ Gy / [(37wk/yr)*(95 Gy/wk)] = 24.2 yr.

at 1.9 GeV,

$T_{1.9} = 8.5X10^4$ Gy / [(37wk/yr)*(68 Gy/wk)] = 33.8 yr.

If the gaps are closed during storage ring injection, the lifetime would be only about 17 years and 18.5 years for 1.5 GeV and 1.9 GeV operation, respectively. This result points clearly to the need for fully opening the ALS insertion device gaps during the short refilling period in order to minimize the radiation incident on the permanent magnets. In addition, when beam dumping is required, the insertion device gaps should also be opened to minimize the radiation damage to their magnets. Improving operation conditions, such as increasing the injection efficiency may further mitigate the radiation damage and increase the lifetime of the insertion devices.

ACKNOWLEDGMENTS

I would like to thank Egon Hoyer for his useful suggestions. Thanks go to Greg Jones and the dosimetry office who carried out calibrations and processed the TLD at the LBNL Radiation and Analytical Measurements Laboratory.

REFERENCES

[1] 1-2 GeV Synchrotron radiation Source July 1986, Lawrence Berkeley Laboratory Pub. 5172-rev.

[2] J. Plueger, G. Heintze, and I. Vasserman, Rev. Sci. Instrum. **66** , 2 (1995).

[3] J. R. Cost, R. D. Brown, A. L. Giorgi and J.T.Stanley, IEEE Trans. Magn. **MAG-24**, 3 (1987).

[4] J. R. Cost, R. D. Brown, A. L. Giorgi and J.T.Stanley, Mater. Res. Soc. Symp. Proc. **96**, 321 (1987)

[5] K. Boockman, H. Liehr, W. Rodewald, E. Salzborn, M. Schlupp, and B. Wall, J. Magn. Mater. **101**, 345 (1991).

[6] 6P. Colomp, T. Oddolaye, and P. Elleaume, ESRF Report MACH-ID 83-09.

[7] W. V. Hassenzahl, T. M. Jenkins, Y. Namito, W.R.Nelson, and W. P. Swanson, Lawrence Berkeley Laboratory Report LBL-27808, 1989

[8] William P. Swanson, Lawrence Berkeley Laboratory unpublished report, 1988

[9] A. F. Zeller, Eleventh International Workshop on Rare-Earth Magnets and Their Applications, Pittsburg, PA, October, 1990.

[10] Bernhard Kulke and James Palomar, Lawrence Livermore National Laboratory note RM 88-16, March 1988.

[11] Greg Jones LBNL Radiation & Analytical Measurements Laboratory internal report Jan 16, 1997. Cs source: Shephard Cs Irradiator model 81.

[12] Panasonic TLD Reader model UD-710A.

GLOBAL BETA-BEATING COMPENSATION OF THE ALS W16 WIGGLER

D. Robin *†, J. Safranek*‡, W. Decking*†, and H. Nishimura*†
†Lawrence Berkeley National Laboratory, Berkeley, CA 94720
‡Brookhaven National Laboratory, Upton, NY 11973

Abstract

The W16 wiggler is the first wiggler and highest field insertion device to be installed in the ALS storage ring. When the gaps of the W16 wiggler are closed, the vertical tune increases by 0.065 and the vertical beta function is distorted by up to $\pm 37\%$. There are 48 quadrupoles in the ring whose fields can be adjusted individually to restore the tunes and partially compensate the beta-beating. In order to adjust the quadrupole field strengths to accurately compensate the focusing, it is necessary to have a method to precisely determine the beta-beating. In this paper we compare measurements of the induced beta-beating using two methods: measuring the tune dependence on quadrupole field strength and fitting a lattice model with measured response matrices. The fitted model also allows us to predict quadrupole field strengths that will best compensate the beta beating. These quadrupole field strengths are then applied and the resultant beta-beating is measured.

1 INTRODUCTION

The W16 wiggler is a high field insertion device that produces intense X-ray radiation for the study of protein crystology[1]. The wiggler has 19 periods each 16 cm in length—thus the name W16. The peak magnetic field strength, B_0, of the wiggler is dependent upon the vertical gap between the poles which can be mechanically adjusted from a maximum gap of 210 mm ($B_0 \approx 0$ T) to a minimum gap of 14 mm ($B_0 = 2$ T). For the most part, when in use, the wiggler will be set to 14 mm and when not in use and also during injection it will be set to 210 mm.

The W16 causes vertical focusing. When closed to its minimum gap of 14 mm, it is the strongest focusing insertion device in the ring. This has several deleterious effects. The first effect is that the vertical focusing increases the vertical betaton tune by 0.065, shifting the tunes relative position to the coupling resonance which causes the vertical emittance and thus the vertical beam size to change. The second effect is that the focusing produces an oscillatory distortion of the vertical beta-function that is as much as $\pm 37\%$ of the "unperturbed" beta-function. Due to this "beta-beating", the vertical beam size changes by as much as $\pm 17\%$ from its nominal size. The third effect is that the vertical focusing perturbs the ring's natural 12-fold symmetry causing many previously suppressed structural resonances to become excited [2]. These resonances can shorten the beam lifetime, limit the "stable" region of the the tune plane and alter the beam size and shape[2, 9].

Previous theoretical studies [3, 4, 5] have examined the effect of the wiggler and undulator focusing on the dynamics of the electron beam. The conclusion of these studies can be sumarized as follows: The focusing of the wiggler can not be locally compensated in the ALS. However, there exist 48 quadrupoles (24 QF and 24 QD) whose fields can be independently adjusted in order to partially compensate the wiggler focusing. Unfortunately, even with all these quadrupoles, it is still not possible to completely compensate all the focusing effects simultaneously. In particular one study [5] showed if the quadrupoles are adjusted to minimize the beta-beating, than the dynamic aperture shrinks. Nevertheless from an operational standpoint, compensating the beta-beating is a desirable condition if the resulting dynamic properties of the ring are acceptable.

To effectively compensate beta-beating in practice it is necessary to have a way to experimentally measure the effect of the wiggler, predict how the quadrupoles should be adjusted, and then experimentally confirm that the compensation has been achieved. In this paper we present a method for compensating the wiggler and its realization for the W16. This is also being used for Brookhaven National Laboratory's VUV ring [6, 7]. We show that the beating is reduced from $\pm 37\%$ to less than $\pm 10\%$ everywhere with the exception of 10 meters on either side of the wiggler. We also show that beta-beating as determined by fitting orbit response matrices is in very good agreement with measurements of the beta-beating made by varying individual quadrupole fields and measuring the change in the tune.

2 METHOD AND RESULTS

To compensate beta-beating in the ring we rely upon fitting a magnetic lattice model (COMFORT[8]) to measured orbit response matrix data using the code LOCO [6]. The orbit response matrix (sometimes called the sensitivity matrix), R, relates changes in steerer magnet currents to changes in the orbit at the beam position monitors (BPM). Parameters in the model, quadrupole gradients, BPM gains, corrector gains, and so on, are adjusted to minimize the difference, in a least squares sense, between measured orbit response matrix and one generated by the model. The general method for fitting measured response matrices is described in more detail in other papers[6, 9, 10].

2.1 *wiggler gap open*

Figure 1 outlines the steps we take to globally compensate the beta-beat. First the machine model is calibrated

* This work was supported by the Director, Office of Energy Research, Office of Basic Energy Sciences, Materials Sciences Division of the U.S. Department of Energy, under Contract No. DE-AC03-76SF00098

0-7803-4376-X/98/$10.00 © 1998 IEEE

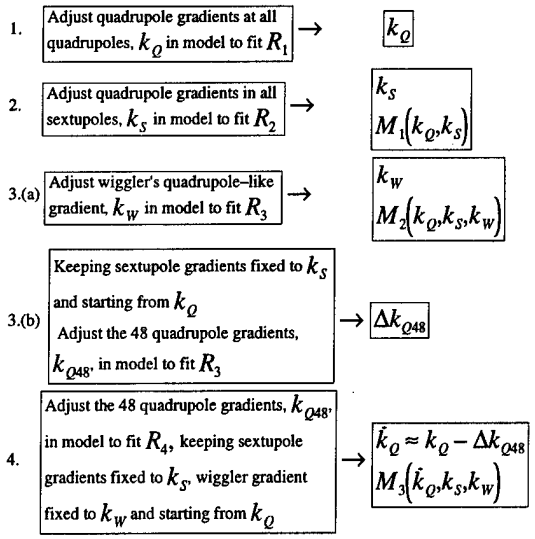


Figure 1: Steps necessary to measure and fit the beta-beating with measured orbit response matrices.

in the case where the gap is at 210 mm. This is done in two steps. The first step is to measure and fit an orbit response matrix, R_1, with the sextupole magnetic fields set to zero (step 1 in Figure 1). The matrix is fit and the individual quadrupole gradients, k_Q, are determined. The second step is to turn the sextupole magnets on and remeasure the response matrix, R_2. Sextupoles have a quadrupole gradient that is proportional to the orbit offset in the sextupole. So this second response matrix is fit by adjusting quadrupole gradients, k_S, placed at the location of the sextupoles (step 2 in Figure 1). Now a calibrated model, $M_1(k_Q, k_S)$, for the machine exists.

With this calibrated model, the beta-function can be computed at any position around the ring. The solid line in Figure 2 is a plot of relative deviation (in percent) of the vertical beta-function in the real machine from the beta-function in an ideal machine, $\Delta\beta_y/\beta_y$. As the figure indicates, the beta-beating is very small—less than $\pm 2\%$. (This small beta-beating is a result of earlier work with LOCO [9] where normal lattice errors were compensated.)

An independent measurement of the beta-beating is made by changing the field of the 24 QD magnets one-by-one while simultaneously measuring the change in the betatron tune. The change in tune is proportional to the change in field multiplied by the beta-function[11],

$$\Delta\nu_{yi} = \frac{\beta_{yi}}{4\pi}\Delta k_{li}, \qquad (1)$$

where $\Delta\nu_{yi}$ is the change in the vertical betatron tune due to the ith QD quadrupole, β_{yi} is the vertical beta-function at the ith QD quadrupole, and Δk_{li} is the change in the ith QD quadrupole's integrated field strength. The result of this measurement is plotted as crosses (+) in Figure 2. The two beta-beating measurements agree to within a few percent.

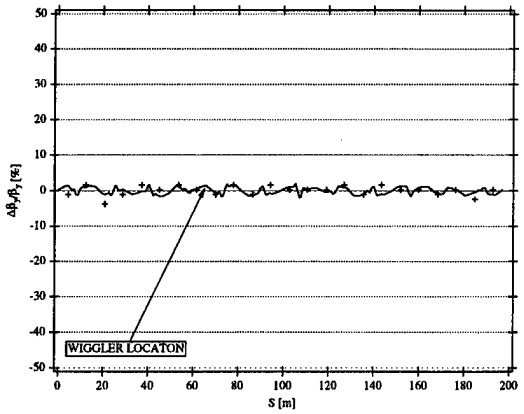


Figure 2: Relative vertical beta-beating verses longitudinal position in the case where the wiggler gap is opened.

2.2 *wiggler gap closed*

Next the gap of the wiggler is closed and a new orbit response matrix, R_3, is measured. This new matrix is fitted in two different ways. The first fit is to determine the induced beta-beating of the wiggler (step 3(a) in Figure 1). This is done by including a thin-lens model of the wiggler in the lattice model and adjusting its field strength, k_w, to fit R_3. The resulting beta-beating is calculated and plotted in Figure 3. As seen in Figure 3, the beating is as large as $\pm 37\%$. The beating has a cusp at the location of the wiggler and oscillates at twice the tune (ν_y=8.18). The tuneshift measurements are also plotted (+) and again there is good agreement.

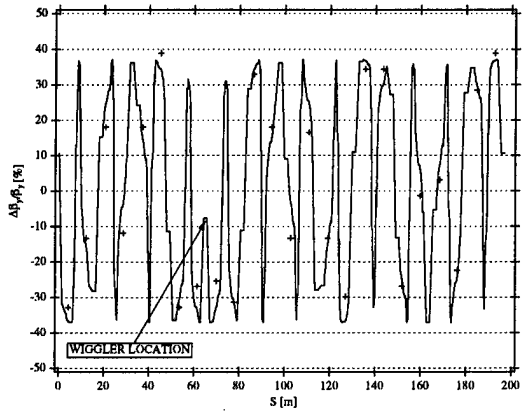


Figure 3: Relative vertical beta-beating verses longitudinal position in the case where the wiggler gap is closed.

2.3 *compensation of the wiggler*

Now it is necessary to determine how the quadrupoles need to be adjusted in order to best compensate the beta-beating. In particular the objective is the following: When the wiggler gap is at 14 mm and the quadrupoles are adjusted, the resulting measured orbit response matrix, R_4, should be as similar as possible to the orbit response matrix measured

before the quadrupoles were adjusted and the wiggler gap is at 210 mm, R_2. This is done in the following way (step 3(b) in Figure 1). Starting from $M_1(k_q, k_s)$, LOCO fits R_3 by adjusting the gradients of the 48 quadrupoles instead of the wiggler. Now one has a new calibrated model of the ring without the wiggler where Δk_{Q48} has been added to the initial gradients,k_Q, in order to simulate the focusing effects of the wiggler. Therefore to compensate the focusing of the wiggler, one needs to subtract Δk_{Q48} from k_Q in order to best restore the matrix, R_2.

The fit resulted in quadrupole changes shown in Figure 4. There are two quadrupoles, QD7 and QD10, that have the much larger gradient changes than the others. These quadrupoles are not immediately next to the wiggler which is located between QD8 and QD9 but are the next nearest QDs.

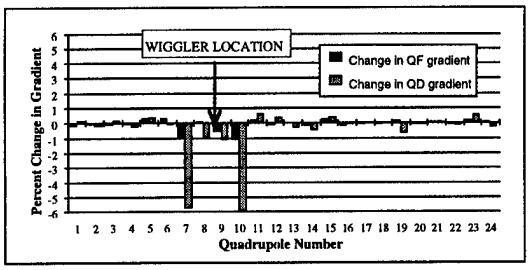


Figure 4: Experimentally determined quadrupole changes that will minimize the beta-beating generated by the wiggler $-\Delta k_{li}/k_{li}$.

The quadrupole magnets are adjusted by $-\Delta k_{li}$ and a new response matrix, R_4, is measured with the gap at 14 mm. Then R_4 is fit by adjusting the 48 quadrupoles and a new calibrated model is created (step 4 in Figure 1). The resultant beta-beating is displayed in Figure 5.

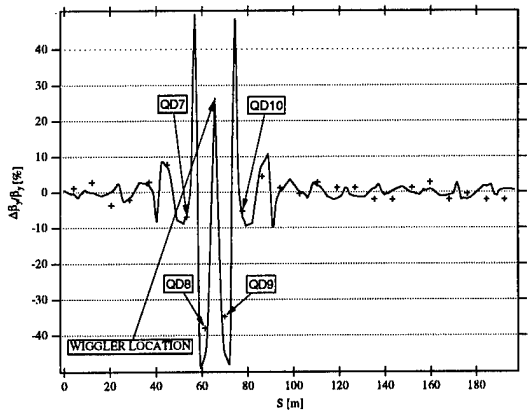


Figure 5: Relative vertical beta-beating verses longitudinal position in the case where the wiggler focusing is compensated.

From the plot one sees that the beta-beating is less that $\pm 10\%$, with the exception of ± 10 m on either side of the wiggler where the distortion is $\pm 50\%$. In other words the beta-beating is large between QD7 and QD10 and small outside.

The reason that we are unable to eliminate the beta-beating between QD7 and QD10 has to do with the difference in phase advance between the wiggler and QD8 and QD9 which is $\Delta\phi(s) = \pm 43°$. In general, if there is a change in gradient, Δk_l, then the resultant beta-beating is [11]

$$\frac{\Delta\beta_y(s)}{\beta_y(s)} = \frac{\Delta k_l \beta_y(\bar{s})}{2\sin(2\pi\nu_y)} \cos(2\Delta\phi(s) - 2\pi\nu_y)). \qquad (2)$$

where s is the longitudinal coordinate. Because the beta-beating oscillates at $2\phi(s)$ these quadrupoles are at $2\Delta\phi(s) = \pm 86°$ away in beta-beat phase. Since the phase is so close to $2\Delta\phi(s) = \pm 90°$ from the wiggler they are orthogonal and thus virtually useless for correcting the wiggler generated beta-beat. The next quadrupoles QD7 and QD10 which have a betatron phase advance of $\Delta\phi(s) = \pm 200°$ to the wiggler are not orthogonal and can effectively correct the beta-beat.

3 CONCLUSION

We presented the results for measuring the beta-beat from the W16 wiggler. Without correction the induced beta-beating by the wiggler is as large as $\pm 37\%$. With correction the beta-beat is reduced to less than $\pm 10\%$ everywhere except in the immediate vicinity of the wiggler. In all cases the beta-beating as determined by the calibrated model is in good agreement with the measured tuneshifts.

4 REFERENCES

[1] E. Hoyer and R. Schlueter, ALS Light Source Note LSME 633

[2] D. Robin, G. Krebs, G. Portmann, and A. Zholents, Proceedings of the 1995 Particle Accelerator Conference, 2789 - 2791 (1995)

[3] A. Jackson, E. Forest, H. Nishimura, and M. Zisman, Proceedings of the 1989 Particle Accelerator Conference, 1752-1754 (1989)

[4] M. Zisman, LBL report 26392 (1988)

[5] J. Bengtsson and E. Forest, AIP Conference Proceedings No. 255, 229-233, (1991)

[6] J. Safranek, Nuclear Instruments and Methods, **A 388**, 27 - 36 (1997)

[7] J. Safranek and S. Kramer, "Experimental Calibration of the VUV Optics", to be published in these Proceedings.

[8] M. P. Woodley et al, SLAC PUB Number 3086 (1983)

[9] D. Robin, J. Safranek, G. Portmann, and H. Nishimura, Proceedings of the 1996 European Accelerator Conference, 971-973 (1996)

[10] W. Corbett, D. Robin, J. Safranek, and V. Ziemann,"Debugging Real Accelerators", to be published in Particle Accelerators (1997)

[11] See for instance, M. Sands, SLAC PUB Number SLAC-121 (1970)

CROSSED ELLIPTICAL POLARIZATION UNDULATOR

Shigemi Sasaki, Ross Schlueter, and Steve Marks
Lawrence Berkeley National Laboratory
1 Cyclotron Road, Berkeley, CA 94720

Abstract

The first switching of polarization direction is possible by installing two identical helical undulators in series in a same straight section in a storage ring. By setting each undulator in a circular polarization mode in opposite handedness, one can obtain linearly polarized radiation with any required polarization direction depending on the modulator setting between two undulators. This scheme can be used without any major degradation of polarization degree in any low energy low emittance storage ring.

1 INTRODUCTION

There are increasing demands among the synchrotron radiation users for utilizing not only the circularly polarized radiation, but also the linearly polarized radiation with fast switching of polarization directions.

An elliptical polarization undulator (EPU) is planned to be installed in the storage ring of Advance Light Source (ALS) [1]. Similar devices are also planned for other third-generation synchrotron radiation facilities. Those devices have a capability of generating both circularly polarized radiation and linearly polarized radiation by mechaninally changing the magnet phases. However, it is very difficult to change the polarity quickly due to the magnet motion mechanism. One possible solution to achieve the fast switching of polarization direction is to install two identical EPUs in series with an electromagnetic modulator in a same straight section of storage ring. The concept of crossed undulator was originated by Kim in order to produce various polarization states including elliptical polarization with two planar undulators [2]. A similar approach is used for analyzing a crossed EPU.

Assume the first EPU is set in a circular polarization mode with right-handedness, and the second is set in the mode with left-handedness. If an electron passes through the system of two EPUs with the setting mentioned above, the polarization vector of radiation is written as :

$$\varepsilon = \frac{1}{\sqrt{2}}\left(\varepsilon_{-} + e^{i\phi}\varepsilon_{+}\right). \qquad (1)$$

Here ε_{-} (ε_{+}) is the complex orthogonal unit vector of left (right) handed circular polarization [3]. The combination of right hand circular polarization and left hand polarization with the phase difference ϕ results in a linear polarization. The direction of polarization depends on ϕ. For example, the polarization direction is horizontal (vertical) when ϕ equals to zero (π).

As described in ref. 2, the phase ϕ can be changed by changing the path length of the electron between the two undulators. An electromagnetic modulator can be used for the rapid change of phase [4].

2 ANALYSIS

Figure 1 is a schematic drawing of the proposed system. The system consists of two identical EPUs, one of which is set in a opposite magnet raw phase from the other. For simplicity, the magnetic field of each undulator is assumed to be perfectly helical and the field of a single period (λ_M) modulator is assumed to be sinusoidal.

Let's assume that the first undulator EPU1 is set in a right hand circular polarization mode, and the second undulator EPU2 is set in the oposite. The wavelength of fundamental radiation peak in the forward direction is

$$\lambda = \frac{\lambda_u}{2\gamma^2}\left(1 + K^2\right), \qquad (2)$$

where λ_u is the magnetic period length, $\gamma = E/mc^2$, and

$$K = eB_0\lambda_u/2\pi mc = 93.4B_0[\mathrm{T}]\lambda_u[\mathrm{m}]. \qquad (3)$$

Here, B_0 is the magnetic field, e and m are electron charge and mass, respectively.

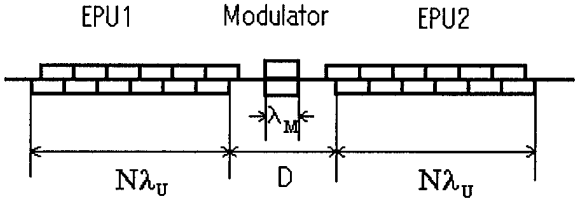


Figure: 1 Schematic drawing of the crossed EPU.

In this system the phase ϕ in Eq. 1 is:

$$\phi = \frac{2\pi}{\lambda}\left(N\Delta L + \Delta L_M + \frac{D}{2\gamma^2}\right). \qquad (4)$$

0-7803-4376-X/98/$10.00 © 1998 IEEE

Here, ΔL is the path difference between an electron and a photon in the undulator, ΔL_M is that in the modulator, and D is the distance between two undulators, respectively. Since the fields are helical in undulator and sinusoidal in modulator, one can obtain the phase ϕ using the relation in Eq. 2 as follows:

$$\phi = \frac{\pi}{\lambda\gamma^2}\left\{N\lambda_u\left(1+K^2\right)+\lambda_M\left(1+K_M^2/2\right)+D\right\}$$

$$= 2\pi\left\{N+\frac{\lambda_M\left(1+K_M^2/2\right)+D}{\lambda_u\left(1+K^2\right)}\right\} \qquad (5)$$

Here,

K_M=93.4B_M[T]λ_M[m], (6)

where B_M is the peak magnetic field of modulator. In order to change the phase, one has to change the distance D mechanically or change K_M^2 by changing the magnetic field of modulator.

3 DEGREE OF POLARIZATION

In an actual storage ring, electron beam has a finite emittance so that some electrons in the beam travel with angular divergence and energy deviation. If the angular distribution of electrons is Gaussion, the mean square phase deviation is written as:

$$\left\langle(\Delta\phi)^2\right\rangle = \left\langle\left(\phi-\langle\phi\rangle\right)^2\right\rangle$$

$$= \left(\phi_0\frac{\sigma_\lambda}{\lambda}\right)+2\left(2\pi\eta\frac{\gamma^2\sigma_\theta^2}{1+K^2}\right)^2, \qquad (7)$$

where $\sigma_\lambda^2 = \left\langle(\Delta\lambda)^2\right\rangle$, $\sigma_\theta^2 = \left\langle\left(\theta^2\right)\right\rangle$, ϕ_0 is the ideal phase given by Eq. 5, and

$$\eta = N+\frac{\lambda_M+D}{\lambda_u}. \qquad (8)$$

By using Eq. 7, the degree of resulting polarization is [2]:

$$P = 1-\frac{\left\langle(\Delta\phi)^2\right\rangle}{2}$$

$$= 1-\frac{1}{2}\left(\phi_0\frac{\sigma_\lambda}{\lambda}\right)^2-\left(2\pi\eta\frac{\gamma^2\sigma_\theta^2}{1+K^2}\right)^2 \qquad (9)$$

As one can see from Eq. (9), the degree of polarization decreases when σ_λ is large due to the large energy spread of electron or large band width of monochromator. However, the degradation is much serious due to the third term in Eq. (9). Therefore, this scheme cannot be used for high energy or high emittance storage ring.

4 EXAMPLES

The Advanced Light Source (ALS) is a low emittance, low energy storage ring. It is operated at an electron energy 1.5 GeV, and the natural emittance is 4 nm-rad. The beam divergence in a straight section for insertion device is 1.9×10^{-5} rad. The energy spread of electron beam is smaller than 1×10^{-3}.

An EPU which will be installed in ALS has the period length of 5 cm, and the number of period N is 37. The achievable maximum K value is 2.5. If we construct the proposed system with two identical EPUs in a same straight section of ALS, η in Eq. (8) is 40 by assuming $\lambda_M = \lambda_u$ and $D = 2\lambda_u$. In our case, the second term in Eq. (9) is negligibley small. Therefore, the polarization is witten as:

$$P \approx 1-\left(80\pi\frac{\gamma^2\sigma_\theta^2}{1+K^2}\right). \qquad (10)$$

In table 1, parameters of example system and the resulting polarization are listed.

Table 1

ALS and EPU parameters		
E[GeV]	1.5	
σ_θ[rad]	1.9×10^{-5}	
σ_λ/λ[%]	0.08	
N	37	
λ_u[cm]	5.0	
λ_M[cm]	5.0	
K	1.0	2.5
λ[nm]	5.8	10.15
ε[eV]	214	122
P[%]	84.7	98.8

The degree of polarization is 98.8% at assumed maximum K value of this system.

5 DISCUSSIONS AND CONCLUSIONS

A proposed crossed EPU system can be used in photon energy ranges below 200 eV with reasonably high polarization degree. Although this system can be used above 200 eV by selecting a K value smaller than 1, the degree of polarization decreased rapidly when K approaches to zero. For the purpose of higher polarization degree in lower photon energy range, a longer magnetic period length and smaller number of period are recommended. It can be achieved with the cost of reduction of peak brightness.

An advantage of the proposed device is that one can obtain a purely monochromatic radiation with no higher harmonics on axis. The reason is that the radiation from each undulator is a circularly polarized radiation with no higher harmonics.

A fast switching of polarization direction can be achieved by using an electromagnetic modulator. Alternating switching between horizontal and vertical

polarization may be useful for investigating the property of surface or interface of material. One can also used a circularly polarized radiation by setting both EPUs in the same helicity mechanically.

Utilization of two EPUs with a modulator as a crossed EPU is proposed for generating a linearly polarized radiation with the fast switching capability and no higher harmonic contamination in the spectrum. This scheme is usefull in any third generation low energy (<2 GeV) storage ring.

ACKNOWLEDGEMENTS

Authors thank K.-J. Kim for helpful discussions with him. This work was supported by the Director, Office of Energy Research, Office of Basic Energy Science, Material Science Division, U. S. Department of Energy, under Contract No. DE-AC03-76SF00098.

REFERENCES

[1] S. Marks, C. Cortopassi, J. DeVries, E. Hoyer, R. Leinbach, Y. Minamihara, H. Padmore, P. Pipersky, D. Plate, R. Schlueter, A. Young, these Proceedings.
[2] K. J. Kim, Nucl. Instrum. Meth. **219** (1984) 425.
[3] J. D. Jackson, Classical Electromagnetics, Second Edition (John Wiley and Sons, Inc., New York, 1975, p275).
[4] R. Savoy, K. Halbach, in Proc. of the 1991 IEEE Particle Accelerator Conference, page 2718.

ACCELERATOR CONTROL SOFTWARE CONSTRUCTION BASED ON SOFTWARE OBJECT COMPONENTS*

C. Timossi, H. Nishimura, Lawrence Berkeley National Laboratory, Berkeley, CA 94720, USA

Abstract

We will be presenting the results of a recent effort on the use of software object components for software construction for the Advanced Light Source control system [1]. Components are written for Win32 for low-level access both to the current control system and to EPICS [2] Channel Access, and for higher level physics tools. We will discuss the merit of the component-based approach based on our experience with several examples.

1 BUILDING ACCELERATOR APPLICATIONS

Much work has been done at the ALS to provide object oriented class libraries for both control of the machine and for modeling and simulation of machine behavior [3]. As new devices are added to the accelerator and the current control system begins it's migration to EPICS, some weaknesses of continuing to build applications, especially new graphical applications, using these libraries has become apparent.

There is a trend in the industry, both in operating system and application design, towards component based architectures such as Microsoft's Component Object Model [4] and Sun's JavaBeans [5]. We feel that there are clear benefits in following this trend for the construction of accelerator applications. As a test, we built new components and migrated parts of existing class libraries to components using them to build several applications.

2 COMPONENT SOFTWARE

The goal of using component based software construction is to enable rapid development of applications, especially graphical applications, from pre-assembled components while allowing the developer the broadest choice in development tools. A *component* is distinguished from a subroutine or class library, in the way it makes itself available to its client (container). A component can make much more information about itself available at run time in a language independent way. The exact way that this information is published is dependent on the component architecture, but usually involves some process of registration with the operating system. The type of information that becomes available to the client is the component's methods and method signature (parameters), its attributes, and which types of events it can handle (sink) and can generate (source). The creation of such a component is more complicated than the creation of a subroutine or class library due to the need to conform to the architecture. What is gained from the effort is the ability to build applications using a wide variety of existing development tools that conform to the architecture. The containing application will have full access to the component and may also let itself be driven from the component.

2.1 Win32 components

Though component standards such as Sun's JavaBeans promise platform independent components, we restrict ourselves to the Microsoft Win32 platforms (Windows NT and Windows 95) for two reasons. First, it is the dominant platform at the ALS and second, there are wide variety of development tools for building components and containers.

Components on Win32 platforms conform to the Component Object Model (COM). The process of component registration follows these steps: a component's interface is specified using an Object Definition Language (ODL) in which each interface is tagged with a globally unique identifier (GUID), then the ODL is compiled to produce a *type library*, which, along with the executable for the component, is registered with the operating system. Once registered, a variety of tools can view the component's interface.

2.2 ActiveX Controls

An ActiveX *control* is a type of a COM component that implements a defined set of interfaces. The applications or development tools that use them are called *containers*. We find that these controls are the most useful in application construction because of the many third-party software packages that serve as Active X containers. In particular, we are using Borland's Delphi 2 and Microsoft Visual BASIC 5 development tools for building applications that contain our controls.

Controls can have rich graphic content, such as the one developed to display a tune-plot, or they have just be invisible helper controls such as the ones implemented to access accelerator data.

A control has the ability to serve as a 'source' or 'sink' of events, either system events, such as mouse movement, or user defined events.

* This work was supported by the Director, Office of Energy Research, Office of Basic Energy Sciences, Material Sciences Division, U. S. Department of Energy, under Contract No. DE-AC03-76SF00098

0-7803-4376-X/98/$10.00 © 1998 IEEE

3 EPICS CHANNEL ACCESS CONTROL

Since a major source of accelerator data is generated by control system processors running the EPICS software, a low level component that handled channel access (CA), the network protocol for EPICS, was an obvious first choice.

3.1 Channel Access monitors

A channel access client application can ask a server to send updated data for a particular *process variable* (PV) whenever that variable changes by a significant, user defined, amount. This mechanism is called placing a monitor on a variable. We wanted a control that would allow the user to enter a PV name, would monitor the PV, and would fire events to the container when a new value was detected.

3.2 Control architecture

The control was built with Visual C++ and the Active X Template Library (ATL), a Library of C++ templates for implementing COM objects with minimal overhead. The control is linked to a Dynamic Link Library, ca.dll, that we ported for Win32 to handle the channel access protocol.

When the control is placed on the container, a property sheet is used to enter the name of the PV to be monitored. When the first PV monitor object is created, a *pend thread* is created to listen for monitors and to call the object's handler when a change occurs in the PV. The handler then fires a *CaFloatMonitorEvent* to the container which will usually handle it by updating some graphic element. Since ca.dll is not thread-safe, a mutex semaphore is used to avoid conflicts between the pend thread and other CA routines.

3.3 Beam Position Monitor application

An application was built using Visual Basic 5 that displays the digital values of 16 of the BPMs in one section of the ALS Storage Ring. In addition, a third party control, Pinnacle Publishing's Graphics Server, was used to display a line plot of the data. This application illustrates the usefullness of combining controls from various sources into a final application.

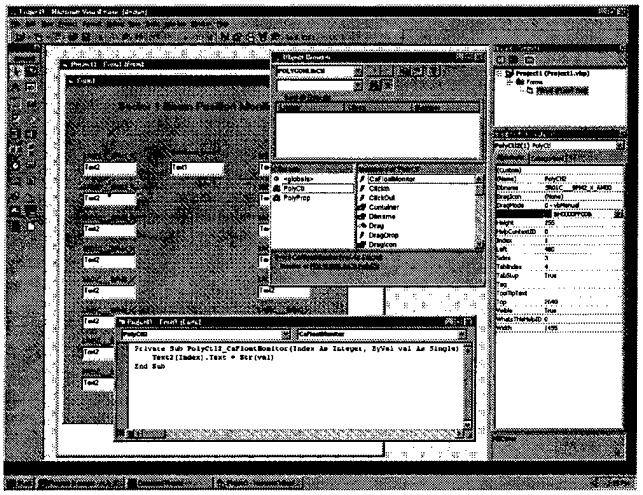


Fig 1. BPM display construction with Visual Basic

4 ACCELERATOR PHYSICS CONTROLS

4.1 Existing Class Libraries

There are two class libraries in wide use at the ALS: Goemon and TracyLiB for modeling and DMM96 [3] for online control. These libraries were implemented in both C++ and Object Pascal/Delphi. Moving their functionality to an ActiveX Control, written in Microsoft Visual C++, allows them to be maintained in one language and still be used by applications written in either language.

4.2 Modeling and Simulation

For the development of TracyV [6], a visual and interactive machine simulator for the ALS, a version of Goemon, called TracyLib, was developed in Delphi2 to ease graphic application development. ActiveX Controls have been developed to implement the more flexible Goemon and yield the graphics capability of TracyLib that can be used in both Delphi2 and Visual C applications.

4.2.1 Tune Diagram and BPM Display Controls

There is a set of graphs, such as tune diagrams, beta and dispersion function diagrams and dynamic aperature display, commonly used in modeling and simulation. ActiveX controls have been implemented for use at the ALS that show a tune diagram and a BPM display, that can be used directly in an active X container. Fig. 2 shows an example of a local bump emulation assembled on a Visual Basic form.

4.2.2 Smatrix and Local Bump Controls

An Smatrix-based method for orbit control is in use at the ALS as described in a previous paper [7]. The Smatrix component encapsulates a sensitivity matrix and its manipulation routines, that can be used for both orbit

control and machine diagnostics and characterization studies.

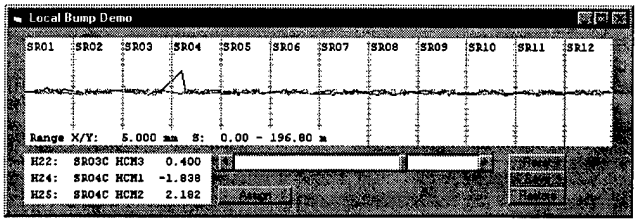


Fig.2. BPM display control showing a local bump emulation.

The local bump component implements local orbit bump using three steering magnets. This component is evolving into a general orbit control component by implementing other algorithms such as the most-effective corrector method and the singular-value decomposition method.

4.3 Machine Control

A subset of the DMM96 library is being supported as a collection of ActiveX controls built using MFC. Instead of mirroring the class structure of the existing C++ class library, components have been implemented that 'wrap' a group of classes that are used by application programs.

5 CONCLUSIONS

Components, such as ActiveX controls for Win32 systems, are still difficult to construct even with the new tools available. Once they are constructed, however, they allow efficient and rapid graphical application development using very different environments, such as Delph2 and Visual Basic 5.

REFERENCES

[1] S. Magyary, et al.,"The Advanced Light Source Control System",Nuclear Instruments and Methods in Physics Research A293 (1990) p36-43

[2] L.R. Dalesio, et al.,"EPICS Architecture", ICALEPCS 91, KEK Proceedings 92-15, (1992)pp.278-282., Dalesio,L., et al. "The Experimental Physics and Industrial Control System Architecture, ",ICALEPCS,Berlin, Germany,Oct.18-22,1993.

[3] H. Nishimura, "Taking an Object-Oriented View of Accelerators," IEEE 95PAC, 95CB35843(1996)2162

[4] Microsoft Corporation and Digital Equipment Corporation, "The Component Object Model Specification", Draft Version 0.9, October 24, 1995

[5] Sun Microsystems, "JavaBeans 1.0", Dec. 4, 1996

[6] R. Keller, H. Nishimura, et al.,"Orbit Stability of the ALS Storage Ring", 97PAC

[7] H. Nishimura, L. Schachinger and H. Ogaki, "Orbit Control at the ALS Based on Sensitivity Matrices",IEE 95PAC, 95CB35843(1996)2247

MODIFICATION OF THE ALS BOOSTER SYNCHROTRON FOR AN EXPERIMENT ON OPTICAL STOCHASTIC COOLING *

A. Zholents, M. Fahmie, J. Johnston, C. Kim, K. Luchini, D. Massoletti, and J. de Vries
Accelerator and Fusion Research Division,
E.O. Lawrence Berkeley National Laboratory, Berkeley, CA 94720

Abstract

Modifications to the Booster synchrotron of the Advance Light Source of the Lawrence Berkeley National Laboratory have been made in preparation for a test of the Optical Stochastic Cooling in a single pass beam line, planned for installation in the extraction area of the synchrotron. Electron beam acceleration to 650 MeV, synchrotron radiation cooling at 650 MeV, and deceleration to 200 MeV have been demonstrated. Measurements have been made of the beam horizontal and vertical emittances and beam energy spread in the beam extracted from the synchrotron at 200 MeV and 250 MeV and compared with computer simulation results.

1 INTRODUCTION

The work that we are going to describe in this paper was done in preparation for a test of the optical stochastic cooling scheme[1],[2] in a single pass beam line[3]. We propose to build a new beam line in the extraction area of the ALS Booster synchrotron, where we will include a bypass lattice similar to the lattice that could be used in the cooling insertion in a storage ring. The design of this beam line is being presented in an accompanying paper at this conference[4]. The ALS Booster synchrotron will provide electrons for the test beam line. It is idle all the time between injection cycles into the ALS and, thus, is available as a source of electrons for a new beam line. The layout of the experimental area, showing several Booster synchrotron magnets, the existing beam transport line from the synchrotron to the ALS, and a schematic of a proposed new beamline, is shown in Fig. (1).

For an experimental test of the optical stochastic cooling we need a beam energy of only 200–250 MeV.[1] But there are specific requirements for the quality of the beam. Simulations performed in[4] show that the relative beam energy spread $\sigma_e < 10^{-3}$, the horizontal emittance $\epsilon_x < 1.5 \times 10^{-7}$ m·rad, and the vertical emittance $\epsilon_y < 6 \times 10^{-8}$ m·rad are required for a successeful test. In order to reach the desired beam quality, we did a number of modifications to the Booster that we describe in this paper. We also did computer modeling of the beam characteristics in the Booster in the modified mode of operation and measured their actual performance. All of these results are described in the paper.

* Work supported by DOE under Contract DE-AC03-76SF00098.

[1] The lower energies are preferable for this experiment since the electron radiation in the visible part of spectra is used.

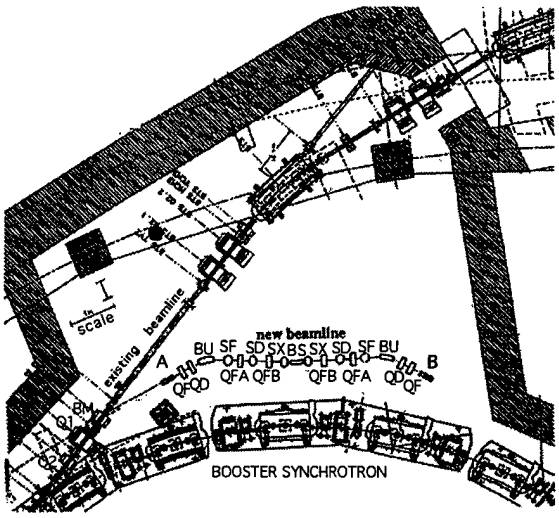


Figure 1: The layout of the extraction area of the ALS Booster synchrotron showing several Booster synchrotron magnets, the existing beam transport line and a schematic of a proposed new beamline.

2 MODIFICATIONS TO THE BOOSTER

In order to get a good quality beam extracted from the Booster at the energy 200–250 MeV, we modify the energy ramp profile. Namely, we ramp the Booster beam energy up from 50 MeV to ~650 MeV, allowing the beam time to stay at this energy, and then ramp the beam energy down to ~200 MeV. The goal of this proceedure is to cool the beam emittance and energy spread by using synchrotron radiation damping at the energy of 650 MeV.

The modification to the energy ramp was accomplished by selecting a particular output current ramp shape of the bend magnet power supply. An arbitrary wave form generator was used to provide an input voltage to the bend magnet power supply that resulted in the desired shape of the output current. The quadrupole, sextupole and steering magnet power supplies just follow the bend magnet ramp. To ensure no losses of the beam current in the modified ramp, special attention was paid to a smooth transition from the up ramp to the flat top and from the flat top to the down ramp. However, some extra variations to the output current at the flat top were intentionally induced. The control system interprets any period of level ramp that exceeds 25 ms as the end of the ramp and resets tables used to control the RF ramp profile and to correct tracking of focusing magnets with the bend magnet. In order to avoid this, we simulated some activity at the flat top by inserting just enough

0-7803-4376-X/98/$10.00 © 1998 IEEE

slope in the field. Figure (2) shows the oscillograms of the waveform shape of the bend magnet power supply output current, amplitude of the RF voltage and the beam current.

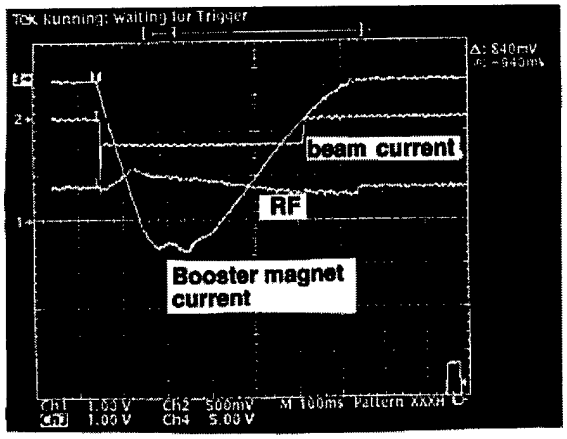


Figure 2: The oscillograms of the wave form shape of the bend magnet power supply output current, amplitude of the RF voltage and the beam current.

Booster extraction energy is controlled by a 'gauss clock'. It processes the output of a pickup coil in one of the bend magnets and triggers many of the functions in the Booster. Extraction is triggered when the field reaches a value corresponding to the desired energy. Initial efforts to use this system to track the down ramp result in unacceptable energy jitter. We decided that we would continue to use it for the up ramp functions, but would base extraction timing on the measurement of the output of the precision transductor that measured bend magnet current. The timing system was modified to begin the extraction cycle when the current fell through the setpoint of a precision comparator.

All modification were made in a such way that typically it takes approximately 10 minutes to switch from the default mode of operation to the modified ramp.

3 COMPUTER MODELING

The electron cooling process in the ALS Booster synchrotron being considered in the present paper includes effects due to the adiabatic damping, intrabeam scattering, and microwave instability, in addition to the synchrotron radiation damping, and the quantum fluctuation excitations. The electron energy varies as shown in Fig. (3a) from 50 MeV at injection, to about 650 MeV at the flat top where electrons are cooled for about 180 msec (or 330 msec), and decelerated to below 200 MeV. Damping time of betatron oscillations, τ_d, at 650 MeV is ~120 ms; damping time of synchrotron oscillations is twise as short. Figure (3b) shows how the calculated vertical emittances corresponding to the two configurations, as in Fig. (3a), vary with energy during the accelerating and the decelerating phases. (The horizontal emittance and the energy spread behave similarly). The flat top of 330 msec is long enough for horizontal emittance to cool to the minimum possible emittance at 650 MeV, but not for the vertical emittance. A flat top of about 500 msec is required for the vertical emittance to reach the minimum emittance (this configuration is not shown in Fig. 3a).

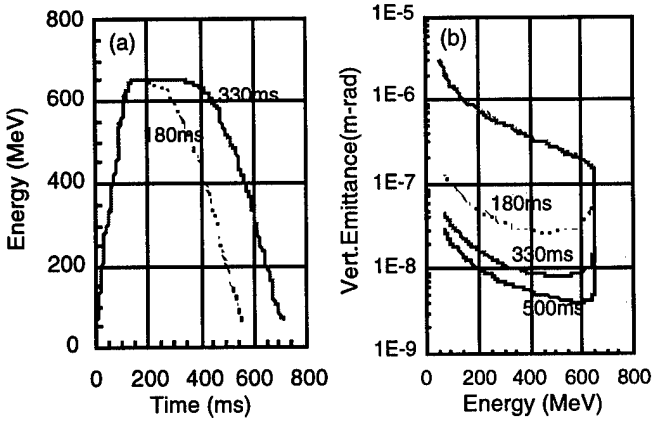


Figure 3: (a) shows the two ramping configurations where the dotted line represents a 180 msec flat top ramp and the solid line a 330 msec flat top configuration, (b) shows how the calculated vertical emittances corresponding to the two configurations as in (a) vary with energy during the accelerating phase (upper part of the curves) and the decelerating phase (lower part of the curves).

The plots in Fig. (3b) and other numerical results presented below were obtained by using the computer program described in[5]. This program was purposely written to consider the evolution of the beam energy spread and the beam emittances in electron synchrotrons and storage rings under the influence of the various effects listed in the beginning of this section. The calculations were made for initial beam parameters taken to be equal to those measured after electron beam acceleration in the 50 MeV injector linac: (i) injected beam intensity of $\sim$ 2 mA (this is above the microwave instability threshold for beam energies up to 1 GeV); (ii) the normalized rms beam transverse emittance of 1.5×10^{-4} m·rad for both horizontal and vertical planes; (iii) the energy spread of 1% and bunch length of 4.5 mm. Initial longitudinal and transverse beam parameters usually are not perfectly matched to the booster acceptance, resulting in transient oscillations which eventually damp in a few damping times at the flat top. In present simulations these oscillations are ignored because, practically, they do not affect final results. Additionally, the coupling coefficient was used as a parameter for fitting the measured horizontal and vertical emittances with the model, and a good fit was obtained at ~10% coupling.

Numerically, we studied the relative importance of the intra-beam scattering (IBS) and the microwave instability (MWI) in the booster by comparing the following computer simulations for 330 msec flat top ramp configuration: (i) zero intensity; (ii) 2 mA beam with IBS included, but not MWI; (iii) 2 mA beam with IBS and MWI included. The results are summarized in Table 1.

Table 1 shows that when IBS was added to the model the normalized horizontal emittance was increased by 25%

Table 1: Summary of the three computer simulations. Energy spread and normalized horizontal and vertical emittances are listed as the electrons are cooled at 650 MeV and decelerated to 350, 300, 250, and 200 MeV.

0 mA	$\sigma_{\Delta_E/E}$	ϵ_H m·rad	ϵ_V m·rad
350	2.9E-4	2.95E-5	6.86E-6
300	3.1E-4	2.88E-5	6.78E-6
250	3.4E-4	2.84E-5	6.70E-6
200	4.0E-4	2.81E-5	6.64E-6
2 mA+IBS			
350	3.4E-4	3.44E-5	7.07E-6
300	3.7E-4	3.44E-5	6.96E-6
250	4.3E-4	3.47E-5	6.89E-6
200	5.1E-4	3.52E-5	6.83E-6
2 mA+IBS+MWI			
350	7.7E-4	3.10E-5	6.93E-6
300	8.4E-4	3.05E-5	6.84E-6
250	9.4E-4	3.03E-5	6.75E-6
200	11.0E-4	3.02E-5	6.72E-6

and beam energy spread by 30% at 250 MeV point. When MWI was also included, then IBS became weak as a result of more than 100% increase of the beam energy spread due to the MWI. The vertical emittance is not fully damped and so mostly affected by the flat top length.

4 EXPERIMENTAL RESULTS

With the first energy ramping configuration (180 msec flat top) beam parameters were measured at two energy points 250 MeV and 213 MeV. With the second energy ramping configuration (330 msec flat top) beam parameters were measured only at 250 MeV. Measurements of the beam parameters were performed with a quadrupole scan, i.e., by extracting the beam from the booster and observing the variation of the beam profile at the beam profile monitor as a function of the strength of the quadrupole located upstream of the monitor.

As a bench mark test of the measurement technique we measured the beam parameters for the normal mode of operation with beam extracted at 1.5 GeV. The measurement results and comparison with the calculated values for four experimental configurations are summarized in Table 2.

Our measured values are systematically larger than those calculated. Possible sources of discrepancy are the thermal diffusion of images on the scintillator used as the beam profile monitor and deviations of the beta and dispersion functions from their theoretical values. It is likely that our measurements overestimate real emittances, but, taken even as they are measured, the beam emittances and the beam energy spread satisfy a requirement of the beam quality needed for a test of Optical Stochastic Cooling.

Table 2: Measured and calculated beam parameters for the four experimental configurations described in the text.

	Measured	Calculated
Energy 213 MeV, flat top time 180 ms		
ϵ_H, [m·rad]	$1.6 \times 10^{-7} \pm 26\%$ a)	0.9×10^{-7}
ϵ_V, [m·rad]	$9 \times 10^{-8} \pm 20\%$	4.8×10^{-8}
$\sigma_{\Delta E/E}$	$1.5 \times 10^{-3} \pm 26\%$	1.1×10^{-3}
Energy 250 MeV, flat top time 180 ms		
ϵ_H, [m·rad]	$1.25 \times 10^{-7} \pm 22\%$	0.8×10^{-7}
ϵ_V, [m·rad]	$6 \times 10^{-8} \pm 10\%$	4.1×10^{-8}
$\sigma_{\Delta E/E}$	$\leq 7 \times 10^{-4}$ b)	9.3×10^{-4}
Energy 250 MeV, flat top time 330 ms		
ϵ_H, [m·rad]	$1.1 \times 10^{-7} \pm 18\%$	6.2×10^{-7}
ϵ_V, [m·rad]	$6 \times 10^{-8} \pm 12\%$	1.4×10^{-8}
$\sigma_{\Delta E/E}$	$\leq 7 \times 10^{-4}$	1.1×10^{-3}
Energy 1.5 GeV		
ϵ_H, [m·rad]	$2.5 \times 10^{-7} \pm 20\%$	1.6×10^{-7}
ϵ_V, [m·rad]	$2 \times 10^{-8} \pm 12\%$	1.5×10^{-8}
$\sigma_{\Delta E/E}$	7×10^{-4}	6.4×10^{-4}

a) Statistical error.

b) Measurements were not sensitive to the beam energy spread below this value.

5 CONCLUSION

Modifications to the ALS Booster synchrotron were done in order to reduce emittance and energy spread in the beam extracted from this accelerator at low energy. Then, actual measurements were performed and the horizontal beam emittance of 1.1×10^{-7} m·rad , vertical beam emittance of 6×10^{-8} m·rad, and relative beam energy spread of 7×10^{-4} were found. A computer model produced similar results. Our conclusion is that this accelerator can provide a beam of the required quality for an experiment on Optical Stochastic Cooling in the new beam line.

We are grateful to S. Chattopadhyay, J. Hinkson and A. Jackson for interest in this work and useful discussions. The friendly assistance of the ALS Operations Staff for the emittance measurements is greatly appreciated.

6 REFERENCES

[1] A. Mikhalichenko and M. Zolotorev, Physical Review Letters, v.71, 25, (1993) 4146.

[2] M. Zolotorev and A. Zholents, Physical Review E, v.50, N4, (1994) 3087.

[3] S. Chattopadhyay *et al.*, Preprint, LBNL-39788, (1997).

[4] A. Zholents *et al.*, *Design and Analysis of a Bypass Lattice for Optical Stochastic Cooling*, this conf.

[5] C.H. Kim, *A Modified ZAP Code for Calculating Initial Value Problems and Effects of Harmonic Cavities*, this conf.

COMMISSIONING AND OPERATION OF THE BRAZILIAN SYNCHROTRON LIGHT SOURCE

A.R.D. Rodrigues[†], R.H.A. Farias, M.J. Ferreira, G.S. Franco, L.C. Jahnel, Liu Lin, A.C. Lira, R.T. Neuenschwander, C. Pardine, F. Rafael, A. Rosa, C. Scorzato, C.E.T. Gonçalves da Silva[‡], A. Romeu da Silva, P.F. Tavares, D. Wisnivesky‡ and A. Craievich[§]
Laboratório Nacional de Luz Síncrotron, Campinas, Brazil

Abstract

The Brazilian National Synchrotron Light Laboratory, LNLS, operates a 1.37 GeV electron storage ring with a 120 MeV injector Linac. Commissioning of the storage ring at low energy started on May 1996 and now, an year later, we can store 120 mA at 120 MeV and ramp more than 75 mA to 1.37 GeV. A summary of the latest commissioning results and a description of the present operational performance of the LNLS Synchrotron Light Source facility is presented.

1 INTRODUCTION

The Brazilian National Synchrotron Light Laboratory, LNLS, sponsored by the National Council for the Development of Science and Technology (CNPq), operates a 1.37 GeV electron storage ring with a 120 MeV injector Linac. Commissioning of the Linac started in December 1995 and after almost simultaneous completion of all sub-systems on April 1996, commissioning of the storage ring at low energy started on May 1st. The first stored beam was observed a month later, on May 30. Some weeks later we could capture a current of 3 mA (after one damping time, or 10 s) with the one-shot on-axis injection. The off-axis accumulation process (with 3 kickers producing a closed bump) was still very difficult and the accumulated current saturated at about 0.3 mA. Our efforts at this time split roughly into two main tasks: accumulation at 120 MeV and energy ramping. While energy ramping evolved quickly with a rather systematic approach, accumulation turned out to be much more challenging. The first stored beam at 1.15 GeV was observed in July 96 but only in October have we succeeded in accumulating 20 mA at 120 MeV. The quality of the magnets allowed us to extend the planned 1.15 GeV operating energy to 1.37 GeV. This is the usual operating energy since October 96. Since then the accumulated current both at injection and operating energies increased steadily with small adjustments in many parameters and hardware improvements, such as an increase in the gun pulse length to allow operation in the beam-loading steady state regime (where energy dispersion is small). At present (May 97) we can store 120 mA at 120 MeV with about 90 seconds lifetime for an average pressure of about 7 x 10^{-10} Torr. The lifetime is limited by elastic scattering on the residual gas. At 1.37 GeV we can store more than 75 mA with 1.5 hour (instantaneous) lifetime. As the current decreases to 20 mA, the lifetime reaches 3.5 hours. A more relevant figure of merit for the lifetime (as far as users are concerned) is the time it takes for the current to fall to 1/e of its initial value. This is about 2.2 hours.

Table I shows the specified and achieved values of the main performance parameters. Fig. 1 compares the flux expected from the nominal machine parameters with the flux obtained from the achieved machine parameters.

Table I: Specified and achieved performance parameters.

Parameter	Specified	Achieved	
Energy	1.15	1.37	GeV
Current	100	75	mA
Lifetime	7	2.2	hours

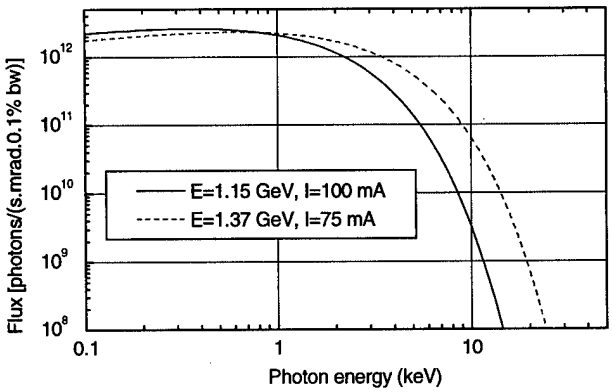


Figure 1: Comparison between the flux expected from the specified and achieved machines.

2 THE LNLS SYNCHROTRON LIGHT SOURCE

The LNLS Synchrotron Light Source [1,2,3,4,5,6,7,8] is composed of a low energy injector Linac, a transport line and the UVX storage ring. The Linac is a standard SLAC-type, with four 3 m long accelerating sections which are powered by two 25 MW klystrons reaching a maximum energy of 125 MeV. The RF frequency is 2856 MHz. The Linac is being operated at a repetition rate of 0.5 Hz, gun pulses of 4 μs in length and gun currents varying from 0.5 to 1.7 A. Beam loading effects are very noticeable and have a large impact on the current pulse length and shape at the end of the transport line. By adjusting gun current, synchronism and RF phases, the pulse at the end of the transport line has been optimized both for higher charge

[†] Also at Instituto de Física de São Carlos, Universidade de São Paulo.
[‡] Also at Instituto de Física Gleb Wataghin, Universidade Estadual de Campinas.
[§] Also at Instituto de Física, Universidade de São Paulo.

0-7803-4376-X/98/$10.00 © 1998 IEEE

per pulse and lower energy dispersion. At present, we get typically pulses of 150 to 200 ns and 100 to 140 mA (current in the macro pulse), of which about 40 % is accepted by the storage ring.

The storage ring consists of 6 double-bend achromatic arcs, with a circumference of 93.2 m (311 ns). The 12 dipoles operate at 0.15 T at 120 MeV injection energy and 1.67 T at 1.37 GeV operation energy. There are 36 quadrupoles, 18 sextupoles and 29 orbit correctors. The theoretical emittance for the standard operation mode is 99.8 nm.rad at 1.37 GeV and the nominal tunes are ν_x=5.27 and ν_y=2.17.

The beam diagnostic system of the storage ring includes 24 stripline type beam position monitors, a betatron and synchrotron tune measurement system, a visible light beam line for transverse and longitudinal beam profile measurement, a beam current monitor (DCCT) and beam scrapers for aperture measurements.

The 476 MHz RF frequency is a sub-multiple of the Linac frequency.

2 COMMISSIONING RESULTS

2.1 Low Energy Injection and Accumulation

In order to optimize (and in fact make possible) accumulation at 120 MeV, we have performed a thorough scanning of the tune space looking for points of higher beam lifetimes. The best machine working point has found to be very close to the integer resonance, ν_x=5.05 and ν_y=2.09. With the present beam lifetime at low energy (90 s) the Linac pulses are injected every 2 seconds, about a fifth of the radiation damping time.

The three kicker parameters have also been scanned to find the optimum compromise between higher injected charge and smaller current loss per Linac pulse. In order to guarantee that the kicker bump is local, beam lifetime (with the kicker bump on) was maximized as a function of relative kicker strengths and timing.

Since the first successful accumulation of 20 mA in October 96, the accumulated current has increased continuously mainly due to adjustments in the injector, which increased the current and decreased the beam energy spread at the end of the transport line. Also, improvements in the injector stability (with reduction of energy drifts and fluctuations) were essential to allow optimizations in the storage ring parameters to take place. Other adjustments and hardware developments were important as well, such as reduction in the quadrupoles power supply ripple and reduction of leakage field from the septum magnets by addition of magnetic shielding, The average pressure is also improving slowly with washing with high energy photons. At the moment of this writing we can accumulate 120 MeV at 120 mA. The injected current varies from 20 to 30 mA per pulse depending on the injector state and it takes about 15 to 20 pulses to reach the saturation current.

Further improvements of the accumulated current are expected with the upgrade of the injector energy to 170 MeV, and the replacement of the present DC septum by a thinner pulsed septum.

2.2 Ramping Process

Energy ramping from 120 MeV to 1.37 GeV can be optimized for minimum loss during ramp by setting up intermediate configurations with corrected orbits and tunes and varying ramping speed, energy steps and RF gap voltages at different energies. The beam losses occur mainly at the very beginning of the ramp (up until 300 MeV) and are probably mainly due to the excitation of large amplitude longitudinal oscillations as well as the poor lifetime.

The machine working point is kept close to integer resonance (ν_x=5.05, ν_y=2.09) up to 500 MeV, after which it is brought to the nominal value of ν_x=5.27 and ν_y=2.17 at 1.37 GeV. Ramping takes about 4 minutes.

Eddy current effects on the magnetic fields have visible effects on the orbit and tunes during the ramp. An off-line correction of these effects (using saved parameters during ramping) have been implemented in the intermediate configurations.

The ramping efficiency varies according to the initial accumulated current, being less efficient for higher currents. For 120 mA the present ramping efficiency from 120 MeV to 1.37 GeV is 64%. 90% of the losses occur from 120 to 300 MeV.

2.3 Beam Characterization

The machine has been characterized at injection and operation energies. Betatron and dispersion functions show good agreement with theoretical values. The chromaticity can be corrected by setting the sextupoles to calculated values. The results are shown in figures 2 to 4. At 120 MeV, the beam horizontal size, as seen and measured on a synchrotron light monitor, is compatible with the expected from intrabeam scattering effects whereas the vertical size is larger than predicted from coupling effects. At 1.37 GeV, the measured beam emittance - 98 nm.rad - (from beam size measurement and knowledge of betatron functions) is very close to the nominal value. This is another indication that we have a reliable model for the machine first order optics. The small coupling measured at 1.37 GeV (smaller than 0.3%) attests a careful alignment procedure for the magnets.

2.4 Orbit Correction

Orbit correction algorithms can be applied successfully both at low and high energies. At high energy (1.37 GeV) the machine optics model can be derived either from the implemented quadrupole strengths or by fitting the strengths to reproduce the measured tunes. At low energy, however, the fitted model is required. This is expected since remnant field contributions cause the excitation curves to be less precise at low energy. Localized beam bumps using 3 correctors have also been produced either to move the photon beam in an experimental station or to scan the vacuum chamber aperture during commissioning.

Orbit reproducibility from fill to fill is better than 60 μm and long term orbit drifts can be kept below ± 30 μm by means of an automatic periodic correction.

2.5 *Observation of ion trapping*

Ion trapping effects have been observed as a vertical expansion of the beam seen in the synchrotron light monitor when excitation by kickers are produced. The enlarged beam persists even when the excitation is turned off. The beam can be made flat again by applying appropriate voltages to the clearing electrodes. This effect has been observed for energies up to 900 MeV, where the present maximum kicker excitation is needed.

BEAMLINES STATUS

Seven beamlines have been built in parallel with the synchrotron light source: X-ray absorption fine structure XAFS, Soft X-ray Spectroscopy (SXS), Small Angle Scattering (SAXS), X-ray Optics (XRD), Protein Crystallography and two VUV beamlines with thoroidal grating (TGM) and spherical grating (SGM) monochromators, respectively. The SAXS and XAFS beamlines are operational and the others are been commissioned. Access by external users should start in July 1997.

CONCLUSIONS

The LNLS synchrotron light source has been commissioned and achieved most of its specified performance figures. Further improvements in the stored beam current are expected to be achieved when the injector energy is upgraded to 170 MeV, whereas beam lifetime should improve as the vacuum pressure decreases with washing by synchrotron radiation photons. Even with present parameters the photon flux delivered by the source is above the specification over most of the harder photon spectrum.

The machine operation reliability is increasing. From January to April 1997, 500 hours were scheduled for user's shifts. The machine was not operational during about 10% of this time. This percentage falls to 2% if we take only the last month. In the same period of 4 months, 675 hours were dedicated to commissioning sessions and 150 hours to maintenance or improvement of the equipment.

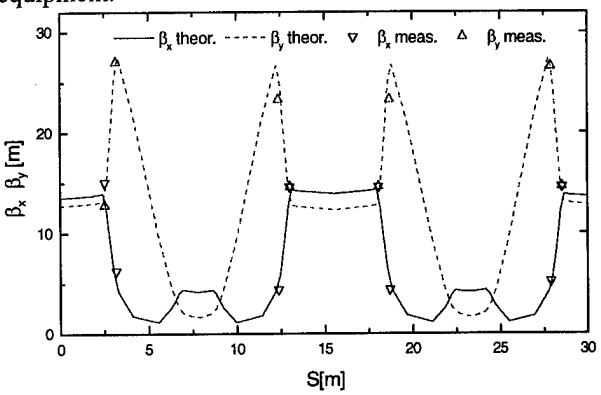


Figure 2: Theoretical and measured betatron functions.

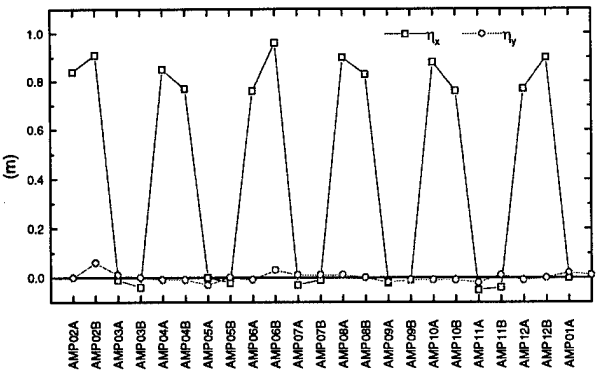


Figure 3: Horizontal and vertical dispersion functions for E=1.37 GeV. Theoretical value at even BPMs is 0.90 m.

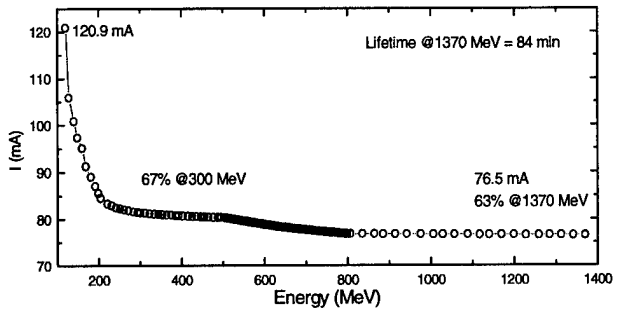


Figure 4: Beam current decay during energy ramping.

REFERENCES

[1] R.H.A.Farias et al 'Optical beam diagnostics for the LNLS synchrotron light source', these proceedings.
[2] R.H.A.Farias et al 'Orbit measurement and correction in the LNLS synchrotron light source', these proceedings.
[3] R.H.A.Farias et al 'Ramping efficiency studies in the LNLS synchrotron light source', these proceedings.
[4] A.R.D.Rodrigues et al 'Pulsed septum for the LNLS injector', these proceedings.
[5] D.Wisnivesky et al 'Operation of the LNLS storage ring RF system', these proceedings.
[6] D.Wisnivesky et al 'Upgrading of the LNLS injection system', these proceedings.
[7] D.Wisnivesky et al 'Commissioning and first year operation of the LNLS magnets power supplies', these proceedings.
[8] M.J.Ferreira, 'LNLS Vacuum System Commissioning', these proceedings.

CURRENT STATUS OF THE LSB PROJECT

M. Muñoz[†], LSB-IFAE, UAB, 08193 Bellaterra, Barcelona, Spain

Abstract

A summary of the current status of the LSB project is given..

1 INTRODUCTION

The LSB project (Laboratori del Sincrotró de Barcelona) [1] has the responsibility for the design and eventual construction of a Spanish synchrotron radiation light source.

Following a survey of user requirements in 1995 [1], the following priorities emerged:

- The spectrum of the synchrotron light must extend to X-Rays of intermediate energy [up to 20 keV].
- The source dimensions must be as small as possible in both the vertical and horizontal planes.
- The accelerator should run with a long lifetime (at least 24 hours) and be free of beam instabilities.
- The design should be conservative enough to guarantee that the specifications are achieved, but susceptible to future upgrades.
- The straight sections should be as long as possible.

With these considerations, as well as cost, in mind, the design [2,3] has converged to the following parameters:

- Energy 2.5 GeV.
- Bending field 1 T.
- 12 Cells.
- TBA structure with gradient in the bending magnets.
- Injection at nominal energy.

This design will offer a critical energy of 4.2 keV and an emittance under 10 nm-rad.

2 THE LATTICE

Figure 1 shows the layout of one of the 12 cells of the machine. Some notable features are:

- Achromatic cell.
- 2 families of sextupoles used for chromaticity correction. A third family, normally set to zero strength, is provided to compensate for possible non-linear effects.
- 2 families of quadrupoles are used to select the working point.

The working point (14.3, 8.2) has been chosen to provide a good dynamic aperture, a relatively low emittance (ε_x~8.5 nm-rad) and the potential for good coupling control.

Figures 2 and 3 show the optical functions and the dynamic aperture respectively.

8 BPMs and correctors are used per cell. Some of the correctors are integrated in the sextupoles. Simulations carried out with various codes (e.g. MAD, Tracy2, Racetrack) including a realistic set of errors show a good that a good stability of the beam (maximum closed orbit distortions of the order of 0.15 mm) and a coupling of the order of 2-3% can be achieved.

Table 1 lists the most important parameters of the machine.

Table 1: Parameters of the machine.

Lattice type	TBA	
Energy	2.5	[GeV]
Number of Cells	12	
Cell Length	20.987	[m]
Circumference	251.844	[m]
Current	250	[mA]
Length of ID sections	7.31666	[m]
Emittance	8.48	[nm]
Coupling	5%	
Horizontal Emittance	8.08	[nm]
Vertical Emittance	0.40	[nm]
Energy Spread	$8.61*10^{-4}$	
Energy Lost per Turn	0.42	[MeV]
τ_x	6.67	[ms]
τ_y	10.03	[ms]
τ_ε	6.71	[ms]
α_p	$1.9*10^{-3}$	
Q_x	14.30	
Q_y	8.20	
ξ_x	-24.6	
ξ_y	-24.6	
ε_c	4.20	[keV]

[†] On behalf of the LSB design team.

0-7803-4376-X/98/$10.00 © 1998 IEEE

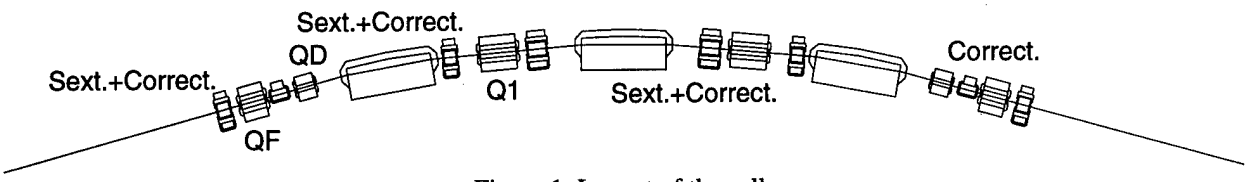


Figure 1: Layout of the cell.

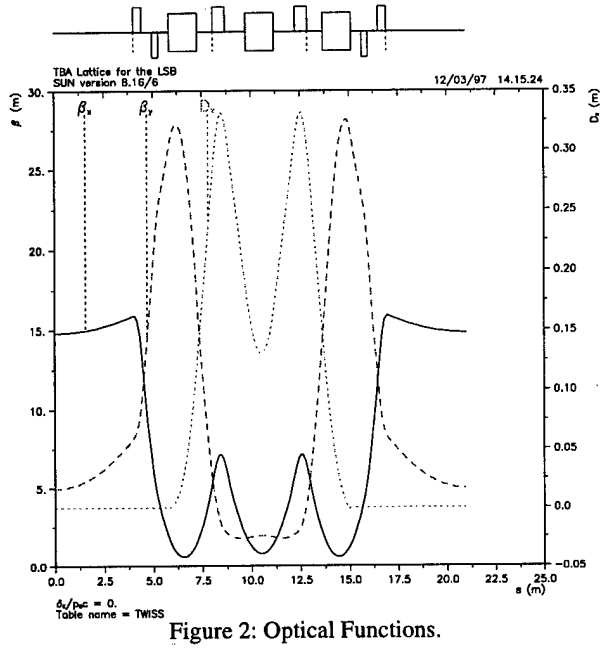


Figure 2: Optical Functions.

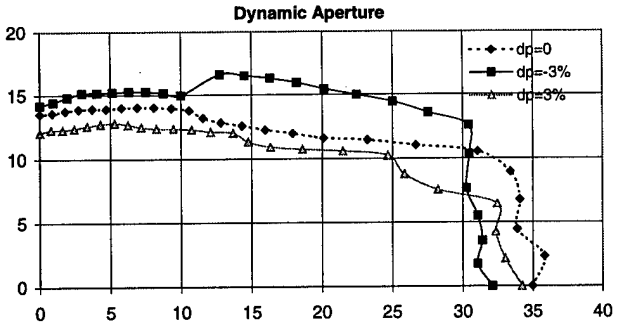


Figure 3: Dynamic aperture.

3 VACUUM SYSTEM AND LIFETIME [4]

Assuming an average vacuum pressure with beam of 10^{-9} mbar, the contributions to the lifetime in the multibunch mode of operation have been calculated to be:

Process	Lifetime [h]
Touschek	55
Bremsstrahlung	96
Coulomb	300
Elastic	6145
Inelastic	213
TOTAL	27

These values fulfil the design goals.

The conceptual design of the vacuum chamber is finished. It consists of two vacuum vessels for the achromat region. The first of these vessels covers from the first bending to the entry of the second, and the second vessel extends from the second to the third bending. A detailed engineering design of the chamber is currently underway.

4 RF SYSTEM [5]

The RF system will be distributed, with 4 cavities placed along the ring, at the ends of some of the straight sections. Bell shaped cavities, operating at a frequency of 500 MHz, with a total voltage of 2.6 MV, and allowing a maximum beam current of 500 mA, will be used. This system offers the potential to increase the energy of the machine to 3 GeV.

5 MAGNETS [6]

The design of quadrupoles, sextupoles and bending magnets is finished. The construction of a prototype bending magnet has started. Delivery is expected in October 97. Simultaneously, a laboratory for the testing of magnetic structures is being commissioned. In addition to the testing of the prototype bending magnet, we anticipate the development of prototype insertion devices.

6 INSERTION DEVICES

Following from the users specifications, we have selected a number of generic insertion devices. Currently, we are considering 2 undulators and 3 multipole wigglers. The parameters defining this insertion devices are given in table 2, whilst figures 4 and 5 show the predicted performance. These insertion devices will cover the know needs of the current user community.

Table 2: Parameters of the Ids.

Name	λ_u [cm]	Poles	Gap [cm]	k	Field [T]
U44	4.4	136	2	2.3	0.57
U73	7.3	82	2	5.7	0.83
W80	8	75	2	8.3	1.11
W120	12	50	2	15.7	1.4
W150	15	40	2	22.4	1.6

The detailed study of the effect of these insertion devices in the machine is being carried out at present. First results shows that the diminution of the dynamic

aperture generated by the multipole wigglers can be compensated by restoring the correct phase advance in the corresponding straight section.

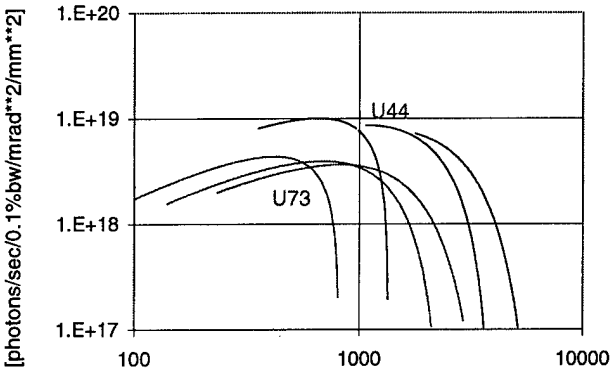


Figure 4: Undulator spectra.

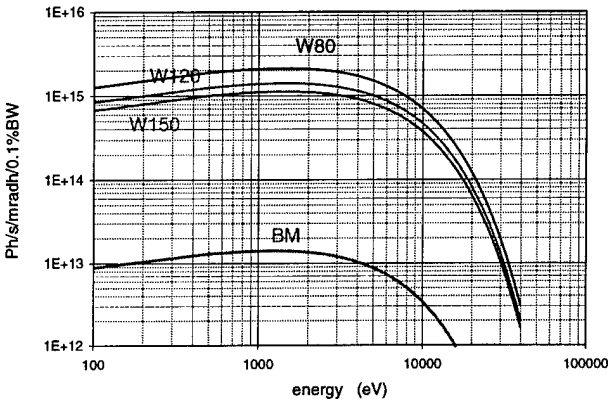


Figure 5: Wiggler and bending spectra.

7 POSSIBLE UPGRADES

The design provides for some possible future upgrades, for example:

- The energy of the machine can be increased up to 3 GeV, increasing the critical energy to 7.3 keV, as both the magnet and the RF systems can support this upgrade with ease.
- Insertion of a third family of quadrupoles in pairs of straight sections will allow further reduction of the vertical size of the beam, thus enabling the use of undulators with smaller gaps. These could provide first harmonic with a higher energy than those currently designed.
- The possibility exist to replace some of the central bending magnets with superconducting magnets, thus providing the potential for experiments in the region of very high energy X-Rays (e.g. 40 keV).

8 CURRENT STATUS

A detailed design report, and a request for full construction funding, will be submitted to the relevant authorities by the end of this year (1997). A decision on how to proceed is expected by early 1998.

ACKNOWLEDGEMENTS

The author acknowledges the information and help provided by his colleagues at the LSB.

REFERENCES

[1] J. Bordas, *The Spanish Project for a Synchrotron Laboratory at Barcelona (LSB)*, Proceeding of EPAC 1996.
[2] M. Muñoz , *Linear Lattice for the LSB Storage Ring*, Proceeding of EPAC 1996
[3] M. Muñoz, X. Queralt, *Study of the Non-linear Behaviour of Particles and the Effect of IDs in the LSB Storage Ring*, Proceeding of EPAC 1996
[4] M.J. Vicente, *Vacuum System and Lifetime for the LSB Storage Ring*, Vacuum, to be published.
[5] F. Pérez, *A Proposed RF System for the LSB Storage Ring*, Proceeding of EPAC 1996
[6] M. Pont , *Magnet design for the LSB Storage Ring*, Proceeding of EPAC 1996.

STATUS OF THE SOLEIL PROJECT[1]

J.-L. Laclare*, M.-P. Level*, P. Bosland°°, P. Brunelle°, R. Chaput°, S. Chel°°, M. Corlier°, G. Flynn°, M. Juillard°°, X. Hanus°°, C. Herbeaux°, A. Loulergue°°, J.-L. Marlats°, A. Mosnier*, A. Nadji*, J. Neel°°, P. Nghiem*, S. Palanque*, J. Payet°°, P. Peaupardin°, J.-P. Pénicaud°°, M. Sommer°, A. Tkatchenko°°, M. Tkatchenko°°, M.-A. Tordeux°

*Projet SOLEIL, DRIF CNRS, Av. de La Terrasse, Bât. 5, 91198 Gif sur Yvette, France
°LURE, Centre Universitaire Paris-Sud, Bât. 209 A, 91405 Orsay Cedex, France
°°CEA Saclay, 91191 Gif sur Yvette

Abstract

With the goal to be prepared for a start of construction in January 99, the SOLEIL project was recently reviewed. The main characteristics have been confirmed while some options have been revised. The preinjector is now a 100 MeV electron linac installed together with the Booster inside the storage ring. The storage ring energy is increased to 2.5 GeV in order to meet the new user's requirements on the brilliance ($B>10^{18}$) around 10 keV. Optics were reoptimised with an emphasis on the energy acceptance so as to obtain large Touschek lifetime. New designs of vacuum chamber and magnetic elements are in progress and a new type of superconducting cavity with heavily damped HOM's at 353 MHz is being prototyped.

1. INTRODUCTION

From many discussions with potential users on the performances of SOLEIL [1] in all its specific energy photon domain (5 eV-100 KeV) as well as in the different operating modes (multi-bunch mode for high brilliance, few-bunch mode for temporal structure and FEL) it has been decided to increase the energy of the Source from 2.15 to 2.5 GeV.

All the accelerators (Linac, Booster, Storage Ring) have been reoptimised and detailed designs of the major components are underway.

2. STORAGE RING

2.1. Main characteristics and Performances

In order to achieve a better complementarity with the ESRF and in particular to satisfy the demand of high brilliance around 10 keV ($B>10^{18}$) two solutions were considered :

- Short period minigap undulators.
- Increase of the energy of the electron beam.

The first proposition implies an undulator of 1.6 cm period with a 4 mm gap which leads to a poor beam gas lifetime penalizing all the beamlines. Top off injection is then compulsory to restore the beam and ensure satisfying operation.

The alternative is less risky, since the performance specifications are obtained (see below) with a 3.4 cm period undulator with a 15 mm gap (instead of 20 mm for the standard undulator at 2.15 GeV). As a result, the beam gas lifetime (behaving like $\gamma^2 g^2$) is preserved and the Touschek lifetime is increased ($\gamma^{5/2}$).

New lattices were optimised, keeping the same ring circumference [2]. Comfortable dynamic apertures even at large energy deviation (up to 6 %) are obtained for all proposed operating points. Table 1 gives the main characteristics of the storage ring and the new typical operating point.

Table 1.a. Main characteristics of the ring.

Energy (GeV)	1.5/2.5
Circumference (m)	336
Lattice cell type	DB
Nb of cells ; nb of superperiods	16 ; 4
Straight section length	14mx4+7mx12
Dipole : nb, field (T) (2.5 GeV)	32 ; 1.56
Quad.: nb, max grad. (T/m), [nb fam.]	160; 21; [8]
Sext. : nb, max str. (T/m^2), [nb fam.]	112; 320; [8]
Rad. loss/turn (keV) (2.5 GeV)	645+155[ID]
RF freq. (MHz); Max peak volt. (MV)	353 ; 4
Harmonic nb	396

Table 1.b. Typical operation point.

Emittance (nm.rad) ε_x	3.1
Energy (GeV)	2.5
Betatron tunes ν_X, ν_Z	18.28, 8.38
Synchrotron tune ν_S	$5.1\ 10^{-3}$
Momentum compaction α	$4.76\ 10^{-4}$
Energy spread σ_ε	$9.24\ 10^{-4}$
Damping times (ms) τ_s, τ_x, τ_z	4.33, 8.66, 8.66
Natural bunch length (mm), σ_l	4.1
V_{RF} (MV) for $\varepsilon_{RF} = 6$ %	3.8
Natural chromaticities (ξ_x, ξ_z)	- 3.03, - 2.68

When Touschek collisions with large energy deviation occur in dispersive sections they induce large betatron oscillations. The study was made taking into account the non linear chromatic orbit as well as energy variation of the optical functions [3]. The results show that, for SOLEIL, Touschek lifetime is still limited by physical aperture and RF acceptance. A vacuum chamber

[1] Work supported by CNRS, CEA, MENESR.

0-7803-4376-X/98/$10.00 © 1998 IEEE

horizontal dimension of 70 mm is chosen as a compromise between improved lifetime and reasonable RF and magnetic system design. In the vertical plane, the dimension of 25 mm retained for the arcs and triplets has been determined by beam gas scattering in the insertion devices (the 15 mm minimum gap implies a 13 mm vacuum chamber height which corresponds to 25 mm in the dipole). The Touschek effect should also be considered in this plane when transverse coupling is not negligeable. The lifetime increases roughly linearly with the coupling up to around 10 %, then saturates and decreases beyond 80 %. The total lifetime for the 2 main expected modes of operation (2.5 GeV, ε_x = 3.1 nm.rad) are :

1) High brilliance with 500 mA($\kappa^2 = 0.01$), τ = 17 h.
2) Temporal structure with 9 × 10 mA ($\kappa^2 = 0.1$), τ = 18 h.

Remarks :

- Beam gas scattering is calculated for 10^{-9} Torr dynamic pressure at 500 mA.
- Touschek lifetime is calculated for the natural bunch length (s_l = 13 ps). If bunch lengthening occurs as we expect (s_l (10 mA) = 24 ps), lifetime becomes 25 h.

Fig. 1 shows the brilliance calculated in the first operating mode from the bending magnets and several types of insertion devices, covering the full energy range from 5 eV to 100 keV. Notice that brilliance is around 10^{19} à 10 keV (meanwhile, we have to correct this value by taking into account the energy spread of the beam which reduces the brilliance by a factor 3.6 for the 13th harmonic). For the lowest energy (5 eV), one can get the same brilliance as at 2.15 GeV, but at the price of a factor 2 increase in dissipated power, which nonetheless remains reasonable (140 W and 200 W respectively for U70 and U50).

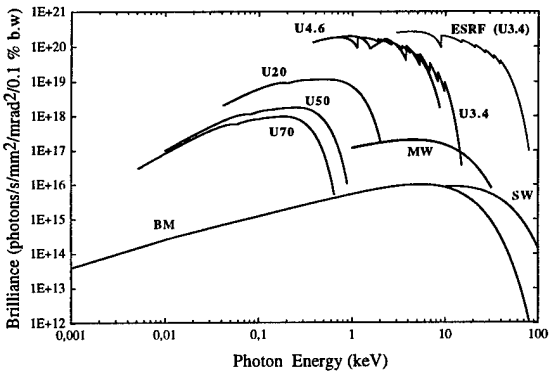


Fig. 1. Typical brilliances for SOLEIL. Comparison with some ESRF sources.

2.2. Technical studies

Magnetic and vacuum systems were reviewed as a whole taking into account the presence of vacuum pumps in the quadrupoles and a minimum clearance between vacuum chamber and the poles allowing micro transverse displacement of the vessel neccessary for BPM mechanical stability. Fig. 2 shows the quadrupole and vacuum chamber cross section and Table 2 gives dipole and quadrupole main characteristics. Although the standard optics need only 8 families, the 160 quadrupoles will be powered by individual power supplies. The question of whether in situ bake-out should be incorporated in the design is still under discussion and test are in progress on a beam line of DCI dedicated to PSD measurements at LURE [4]. Nevertheless, a very thin bake-out system (printed circuit, glass fiber or air and aluminium foil) less than 2 mm thick is being studied in order to allow a 170° bake-out.

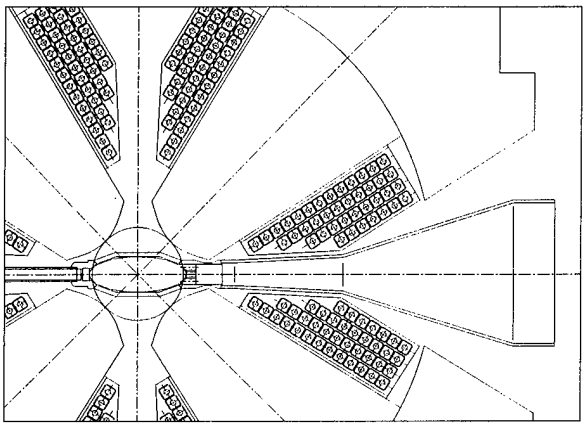


Fig. 2. Quadrupole and vacuum chamber cross section.

Table 2. Main dipole and quadrupole characteristics.

	Dip.	Quad.
Gap or bore Ø (mm)	37	66
Strength max	1.7 T	21 T/m
Nb of families	1	8
Nb of power supplies	1	160
Total power (kW)	245	720
U (V), I (A)	490/500	18/250
Good field region (mm)	± 20	± 30
Homogeneity : required	10^{-3}	$3\ 10^{-3}$
computed	$4\ 10^{-4}$	$1.5\ 10^{-3}$
Reproducibility	$1\ 10^{-3}$	10^{-3}

From the beginning of the SOLEIL project, a superconducting cavity based on the general principles of the Cornell monomode cavity (large beam-tubes, ferrite dampers) has been considered. R&D program which involves collaboration with other European laboratories, in particular CERN and ESRF is now set up and a new design at 353 MHz is being investigated [5]. It consists of a pair of single-cell cavities linked by a large beam pipe, such that the coupling is very weak for the fundamental mode, but very strong for the HOMs. After the optimization of the cavity shape, beam pipe opening and length, the simulations show that harmful HOMs can be sufficiently damped to ensure absolute beam stability for SOLEIL by classical dampers without ferrite in the vacuum chamber. The construction of a prototype is underway.

3. INJECTOR

3.1. Linac ELIOS

A new 100 MeV electron Linac was studied. The main parameters are shown below :

S band Linac, f = 2 998.55 MHz
Energy : 100 MeV ± 5 MeV, $\Delta E/E < \pm 1.5$ %
Repetition rate : F_r = 10 Hz (see below)
Beam power : ≈ 2 watts
Emittance : 10^{-6} m.rad at 100 MeV

Two operating modes are forseen :

- Few pulses (1 to 3) of 2 ns durations separated by 125 ns for temporal structure modes.
- A 300 ns macropulse duration modulated at 353 MHz for multibunch operation.

The total accelerated charges are respectively of 1 nC (1 W) and 3 nC (2 W) while the gun intensity peak varies from 180 mA to 30 mA. In both modes the storage ring filling time is ≤ 1 min. The linac is composed of the following elements : triode gun (90 kV, 250 mA), prebuncher (10 kV, 200 W), buncher (SW, 15 MeV, 5 MW) focalised by a solenoid, 2 accelerating sections (TW, 2 π/3) 3 m long of 45 MeV each. The sections are powered by two klystrons (35 MW operating at 24 and 18 MW) and two modulators (80 MW, 25 MW HF). This choice ensures an excellent reliability since it will be possible to still deliver beam in case of a major component failure.

3.2. Booster

The booster accelerates the 100 MeV electron beam to full energy of 2.5 GeV. The optics chosen is a FODO structure, with fourfold symmetry and missing magnets in order to have zero dispersion in the straights. The main characteristics are given in Table 3.

Table 3. Booster main characteristics.

Energy (GeV), injection/ejection	0.1/2.5
Emittance (injected, ejected)	10^{-6}/2.5 10^{-7}
Orbit length (m)	142.78
Dipoles : nb ; l (m) ; gap (m)	24 ; 2.17 ; 0.032
Field (T) : min, max	0.04 ; 1
Quad. : nb ; l (m) ; bore radius (m)	40 ; 0.4 ; 0.030
Maximum gradient (Tm^{-1})	11
Betatron tunes	6.30 ; 5.30
Max optical functions $\beta_x = \beta_z$ (m)	13.2
Natural chromaticities $\xi_x = \xi_z$	-1.4
Momentum compaction α	3.32 10^{-2}
RF : frequency (MHz), V_{max} (MV)	352.75 ; 1.1

The injection repetition rate has been reviewed and the advantages and drawbacks of 1 Hz and 10 Hz cycle were compared. It turns out that beam dynamics is much easier at 10 Hz : no energy spread problem in the linac, no high peak current in the linac and the booster, easier crossing of the resonances during the faster energy ramping in the booster, safety margin for a fast injection in the two operating modes. The investment cost is higher (resonant H.V. power supplies in addition to DC instead of ramped power supplies) but will be compensated by lower operation cost (only circuit losses have to be delivered by the mains). The 10 Hz repetition rate was then adopted.

The transfer beamlines as well as the injection/ejection have also been studied. Fig. 3 shows the general layout of the accelerators and the experimental hall.

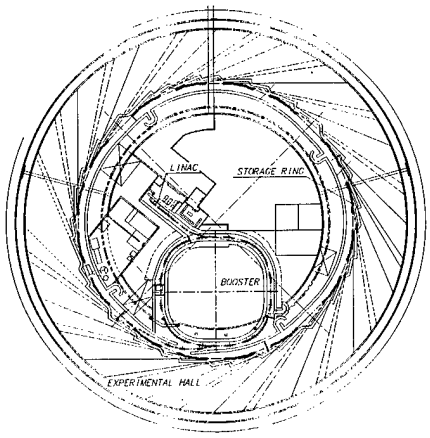


Fig. 3. General layout of SOLEIL.

4. CONCLUSION

The new nominal energy 2.5 GeV offers better performances at high photon beam energy and better electron beam dynamic behaviour with acceptable consequencies in the low energy domain.

New improvements have been obtained in optics and Touschek lifetime as well in the design of HOM suppressors in superconducting cavities. In all technical designs special attention is paid to reliability and low operation cost.

5. REFERENCES

[1] M.-P. Level et al., "Status of the SOLEIL Project", Proceed. EPAC 96, Vol. 1, p 670.

[2] P. Nghiem et al., "Optics for SOLEIL at 2.5 GeV", this conference.

[3] A. Nadji et al., "Energy Acceptance and Touschek Lifetime Calculations for the SOLEIL Project", this conference.

[4] P. Marin et al., "In situ"/No "in situ" bake out for future SR sources measurements on a test stainless steel chamber at DCI", to be published.

[5] A. Mosnier et al., "Design of a Heavily Damped Superconducting Cavity for SOLEIL", this conference.

A PLAN OF SYNCHROTRON LIGHT SOURCE FOR MEDICAL APPLICATIONS AT NIRS

M. Torikoshi, M. Endo, M. Kumada, K. Noda, S. Yamada and K.Kawachi
National Institute of Radiological Sciences, 4-9-1 Anagawa, Inage, Chiba 263, Japan

Abstract

We are designing a synchrotron light source dedicated to medical applications including an intravenous coronary angiography for practical uses at a hospital. The synchrotron light source system is required to be compact for installation in a limited space of the hospital. The system is also required to be operated easily as medical diagnostic devices. For the energy subtraction coronary angiography, required design parameters of a storage ring are circumference of about 45 m, 1.8 GeV electron energy and a stored beam currents of 400 mA. A multipole wiggler with superconducting coils is considered to be one of key devices to realize a required high photon intensity. A microtron with higher energy than that of commercially obtainable ones could be a good candidate of an injector for downsizing the whole system. Two optional beam lines are planned to be used for clinical diagnoses, and other beam lines of bending magnets are prepared for biology, physics, and other experiments to support the clinical diagnoses. We report the design of the compact system for the medical uses.

1 INTRODUCTION

Medical applications of synchrotron radiation have been researched at various synchrotron light source facilities in the world. Intense monochromatic X rays provided by the synchrotron light sources take many advantages on X ray imaging and medical diagnoses. A coronary angiography is one of well studied techniques, and has been clinically applied to examinees at HASYLAB[1] and KEK[2].

The applications are researched mainly in the facilities which have storage rings of electron energy more than 2 GeV. Because most medical applications require not only high energy X rays, but also intense photon flux compared with basic researches, such as a structural biology. High energy and large current storage rings are necessary for satisfaction of the both conditions. Compact rings dedicated to the coronary angiography were proposed in a few papers[3,4]. But the compact ring for the medical applications is not well studied in comparison with those for idustrial applications.

Our plan is motivated by a heavy ion radiotherapy which has been being carried out with carbon beams at NIRS since 1994[5]. More precise heavy ion irradiation can be achieved with help of a monochromatic X ray CT scans. Because the CT scans with the monochromatic X ray make a treatment planning of the heavy ion radiotherapy more accurate by giving more precise CT-values. Conventional X ray tubes cannot produce enough photon flux to provide with intense monochromatic X rays. Another new techniques studied at NSLS[6] on a mammography and a bronchography are expected to give better quality images which help to find out cancers at early stages. Strongly focused X ray sources are able to make magnification of X ray radiography larger than the conventional one, so microscopic investigations is possible on examinees. There are many options of the medical applications, but, of course, they must be developed in complement with many other medical fields.

We mention here estimation of the photon flux for the medical applications and the basic design, and show its layout.

2 ESTIMATION OF PHOTON FLUX

Intravenous coronary angiography using synchrotron radiation is a powerful and non-invasive diagnostic method for finding out the coronary heart disease. This technique is one of the best studied method in the medical applications. It has also many common techniques with other diagnoses, and requires intense photon flux compared with the other applications. At these backgrounds we took the energy subtraction coronary angiography as the start point of the design.

Photon flux for the coronary angiography was estimated with conditions as follows.

1) Two dimensional animation of 30 frames per second.
2) Exposure area is at least 150 mm × 150 mm.
3) Each frame is produced by subtraction of two images taken at a higher energy X ray exposure and a lower one with respect to a K-edge energy of a contrast agent, respectively.
4) Exposure time of each image is less than 2 ms, and an interval time between two exposures is less than 5 ms.
5) At least 50 % stricture of a coronary artery can be clinically recognized.
6) Concentration of the contrast agent is more than 20 % at the coronary arteries.

The first condition is as same as the conventional angiography. The third one is necessary to avoid artifacts from the image due to cardiac impulses. The last condition is a case of catheter injection of the contrast agent from a central venous. Iodine is clinically used as a contrast agent, which has K-edge at an energy of 33.17 keV. The calculated photon flux is 1.8×10^{15} photons/sec/15 mrad with 0.3 % band width of 33 keV at 20 cm water equivalent body thickness. Higher energy photons have an advantage of less exposure dose on an

0-7803-4376-X/98/$10.00 © 1998 IEEE

examinee because of low absorption rate. Gadolinium could be a good candidate of the contrast agent of the angiography, which has the K-edge at 50 keV. We calculated the flux at 8×10^{14} in case of the Gd with the same conditions. The Gd is used as the contrast agent for MRI, but so far the concentration is too low to use for the angiography. Nevertheless it is worth taking the new contrast agent into consideration for the design. Rough estimations of photon flux for the other applications, the large magnification X ray radiography and monochromatic X ray CT scan, preliminarily showed that flux was order of 1 or 2 less than those of the angiography. It means that about 2×10^{15} photon flux is supposed to cover the amount of photon required by other medical applications we will try in future.

3 DESIGN AND LAYOUT OF THE LIGHT SOURCE

3.1 Design parameters and Layout

We studied a few cases to search suitable design parameters as listed in Table 1. We took a space limitation into the consideration of the design. So the dimension of the ring is limited less than 15×15 m^2.

Table 1 Design parameters

Items	*Designed values*	
Beam energy	1.8	GeV
Beam intensity	400	mA
Circumference	44.8	m
Bending magnet	8	
bending angle	45°	
radius	1.33	m
maximum magnetic field	4.5	T
Beam emittance	4.9×10^{-7}	m·rad
Energy loss per turn (total)	1200	keV
RF frequency	508	MHz
RF voltage	2.0	MV
Microtron		
beam energy	300	MeV
peak current	10	mA
Multipole wiggler	2	
number of pole	9	
maximum magnetic filed	8	T
period length	400	mm

The system layout is shown in Figure 1. The main ring has no booster ring for preacceleration, but has a microtron as an injector. The ring has four free straight sections for insertion devices as well as for injection device and acceleration RF cavities. There are two beam lines from the insertion devices and a few lines from bending magnets.

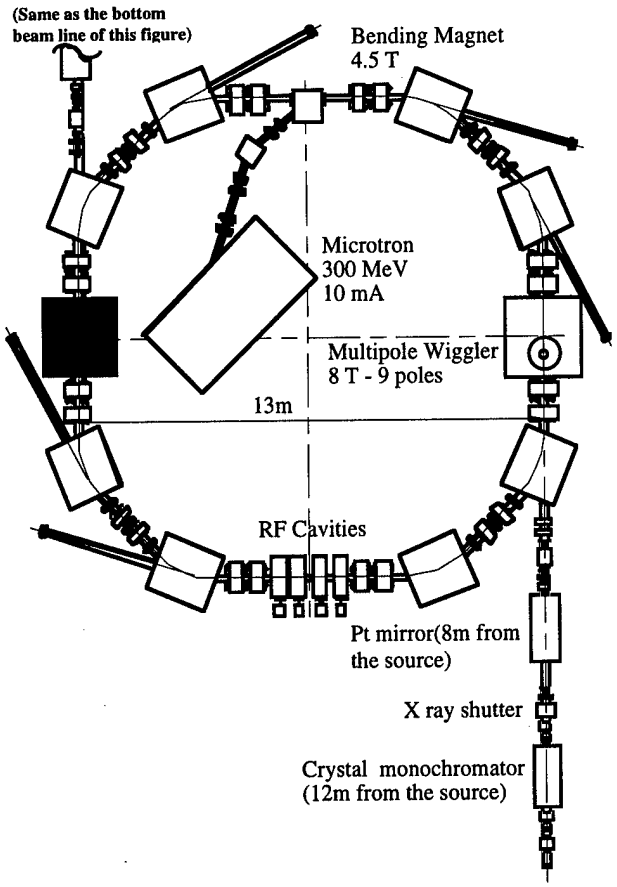


Figure: 1 System layout of the compact synchrotron light source for the medical applications.

3.2 Injector and Ring

A race-track microtron is preferred over a linear accelerator because of the space limitation. In this design 300 MeV microtron through 21 recirculations with 10 mA current was studied. The microtron is operated in L-band microwave instead of S-band for stable operation and higher stored energy. According to a numeric simulation, beam transportation efficiencies are almost 100% when the emittance of injected beams from an electron gun is less than 50π mm·mrad. The final beam conditions are chosen to be 0.1π mm·mrad emittance and ±1% momentum resolution to meet ring injection conditions

The ring consists of eight superconducting bending magnets to reduce the circumference. The bending magnets and quadrupole magnets form a double bend achromatic lattice and make a dispersion free at the straight sections. Superconducting multipole wigglers give strong magnetic field at the straight sections. Their edge effect changes the beam tunes during raising up their excitation currents. The strength of quadrupole magnets have to be continuously varied to keep the tunes constant following the wiggler excitations. QF and QD at both sides of the wiggler are operated independently with another QF and QD in order to keep β_y function symmetry with respect to the wiggler. The operating point is

$\nu_x=\nu_y=3.25$. There are three sextupole magnets between a pair of bending magnets to correct a chromaticities.

When the wigglers are operated, the beam emittance will become 0.5π mm·mrad due to radiation dumping. The maximum beam size is estimated 2.4 mm × 0.8 mm in the wiggler magnets. A quantum life time is more than 100 hours when the RF peak voltage is more than 1.9 MV. Touchek life time is more than 100 hours at 1 A of 1.8 GeV operation. A life time due to collisions with the residual gases in the ring is about 50 hours under an average pressure of 1.3×10^{-7} Pa.

Thermal loading can be a serious problem in case of the compact ring. The energy loss is 700 keV/turn at the bending magnets and 500 keV/turn at the wigglers. Power density can be estimated about 8.4 kW/cm^2 at the bending sections. In the wiggler magnets the radiation horizontally fans out 84 mrad, so parts of the power dissipate on the side wall of the beam ducts. Some special structured beam duct which has thermal dumper and effective cooling system is necessary at the bending magnets. The thermal loading of the wigglers can be reduced by widening lateral size of the beam ducts.

3.2 Insertion device and photon flux

The multipole wiggler is an essential component to obtain high photon flux. Design of the wiggler depends on design of the ring, and vice versa. We studied some cases to determine the designs of the wiggler and the ring under conditions of enough photon flux and less contamination of higher harmonic components of 33 and 50 keV which deteriorate image qualities.

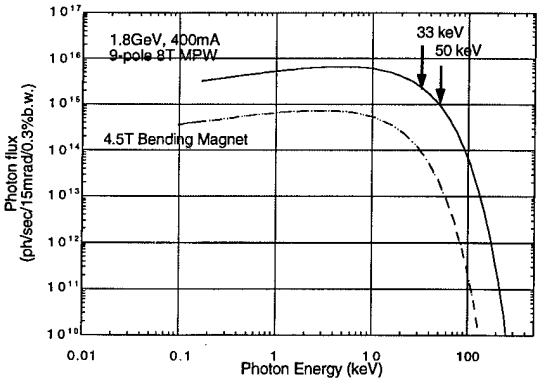


Figure: 2 Photon flux spectra produced by the 8T, 9-pole multipole wiggler and the bending magnet.

We put a limitation of the contamination of third harmonics at 5 %. The wiggler has 9-pole with period length is 400 mm and maximum field 8 T, that gives a critical energy ε_C=17.2 keV at 1.8 GeV ring operation. The flux of 33 keV X ray is 2.2×10^{15} photons/sec within 0.3% band width and 15 mrad, and 1×10^{15} photons at 50 keV. The third harmonics is about 3.5 % and 0.5 % of the amounts of 33 keV and 50 keV photon, respectively. Energy spectra of the photon flux produced by the wiggler and the bending magnet at the full electron energy are shown in Figure 2.

3.3 Beam lines for medical use

There are two beam lines from the multipole wigglers for clinical uses, and a few lines from the bending magnets for basic researches and developments of new technique.

Large silicone crystal of (311) as a monochromator generates X rays with a few tenth % energy resolution with asymmetry reflection. It broaden the beam vertically to 150×150 mm^2 wide at the examinee position. Another mirror is installed upstream of the monochromator to remove the higher harmonic components to less than 0.1 %. In this design, the transmission efficiency is less than 60 % for 33 keV X ray. Introduction of a parabolic mirror should be taken into the consideration to cover wider solid angle than 15 mrad.

4 SUMMARY

The light source designed here is applicable to the higher energy angiography using the gadolinium contrast agent. It meets to a tide of using higher energy photon in the medical application to give the low exposure dose. But there are some technical problems to be solved, such as thermal loading. This design should be elaborated more to overcome the problems and to realize the stable operation with the long lifetime for the clinical use.

5 ACKNOWLEDGEMENTS

We should like to thank Dr. Hyodo at KEK for important information on their beam line for the angiography and Dr. Garren at LBL for valuable discussion on the lattice design of the ring.

REFERENCES

[1] Dix. W-R: `Intravenous coronary angiography with synchrotron radiation', Prog. Biophys. Molec. Biol. 63, 159(1995).

[2] Y. Sugishita, S.Otsuka, Y. Itai, T. Kakeda, M. Ando and K. Hyodo: `Synchrotron radiation coronary angiography and its application', Abstracts of 10th. meeting of the Jap. Soc. for Synchrotron Radiation. Research, pp.1,(1997).

[3] H. Wiedemann, M.Baltay, R Carr, M. Hernandez and W. Lavender: `A compact radiation suorce for digital subtractive angiography', Nulc. Instrum. Methods A347,515(1994).

[4] Y. Oku, K. Aizawa, S. Nakagawa, M. Ando, K. Hyodo, S. Kamada and H. Shiwaku: `Conceptual design of a compact electron storage ring system dedicated to coronary angiography', Proc. of the 1993 IEEE PAC, Vol.2, 1468.

[5] S. Yamada: `Commissioning and performance of the HIMAC medical accelerator', Proc. of the 1995 IEEE PAC, Vol.1 pp.5.

[6] W. Thomlinson: `Current status and perspectives of synchrotron radiation in medicine', Proc. of Int. Conf. on Applications of Physics in Medicine and Biology, Trieste, Italy 1996.

OPERATIONAL STATUS OF POHANG LIGHT SOURCE

J. Choi, T. Lee, M. Kwon, J. Y. Huang, S. H. Nam, M. Yoon, M. H. Cho, I. S. Ko, and W. Namkung
Pohang Accelerator Laboratory, POSTECH, Pohang 790-784, Korea

Abstract

The PLS, a 2-GeV dedicated electron synchrotron light source, has been in normal operation mode for users since September 1995. It consists of 2-GeV electron linear accelerator, which works as a full energy injector, and a storage ring. The linac is 150-m long and has 42 accelerating sections. The storage ring has a 12-cell TBA type lattice with 4 rf cavities. The construction of PLS was started in 1988, and the installation was completed in August 1994. From then until December 24, 1994, which we call the first commissioning phase, we succeeded in stacking the 2-GeV electrons up to 300-mA in the storage ring. After baking out the vacuum chamber, the second commissioning was performed from April to July 1995. In 1996, the user beam time reaches about 2,800 hours among 4,800 hours of the accelerator operation time. We present the current operational status of PLS in this paper.

1 INTRODUCTION

The PLS, a third generation light source, consists of a 2-GeV linac and a storage ring [1]. The project started in 1988 and the construction was completed in 1994.

1.1 Linac

The PLS linac is working as a full energy injector to the storage ring. It consists of 11 klystrons and modulators, 10 pulse compressors, 42 accelerating structures including those for the preinjector.

The 1-ns long output electron beam from the 80-kV e-gun passes through the bunching system. The prebuncher is a reentrant type, standing-wave cavity, and the buncher is a travelling structure with four cavities including the input and output coupler cavities. The beam is compressed into three micro-bunches. This bunched beam passes through 42 accelerating structures and get the 2-GeV energy from microwaves of 2,856 MHz in the structures. The required accelerating gradient of the main linac is at least 15.8 MV/m. Considering one or two klystrons as stand-by, it requires an accelerating gradient of 17.8 and 19.8 MV/m, respectively. In order to achieve this accelerating gradient, we adopt high power klystrons of 80-MW maximum output and SLAC-type pulse compressors with TE015 operation mode. In addition, we require the RF pulse length at least 4 ms for a higher energy multiplication factor from pulse compressor cavities.

The beam transport line (BTL) for connecting the storage ring and the linac consists of 5 bending magnets, 24 quadrupoles, 5 vertical correctors and 8 horizontal correctors. The 2-GeV electron beam leaving the linac is bent to 20 degrees horizontally by two bending magnets toward the injection area of the storage ring. After the beam travels about 65-m behind the end of the linac, it is bent upward to the beam plane of storage ring which is 6-m higher than that of the linac.

1.2 Storage ring

The PLS storage ring lattice is a triple bend achromat structure with 12 superperiods and 280.56-m circumference. Each superperiod has a mirror symmetric configuration. Each half superperiod contains six quadrupoles; three in the dispersive section and three in the non-dispersive section.

Since the completion of its construction in 1994, the PLS storage ring underwent the commissioning in two phases; the first one from September 1 to December 23, 1994 and the second one from April 4 to July 21 1995. The maximum current reached to more than 300-mA at 2- GeV during the phase I commissioning. However, the beam lifetime was less than 50 minutes at 100-mA because of poor vacuum. During the machine shut-down from January to March 1995, which was between the two commissioning periods, all the chambers were baked out. When the phase II commissioning started, the beam lifetime was 2 hours at 100-mA, and at the end of the commissioning, it reached to 10 hours at 100-mA. The total dose attained during this commissioning was about 114 ampere hours.

On September 1, 1995, the PLS finally opened for user service mode. However, on October 19, there was water leakage from the flange in No.1 sector, and we could not supply the beam to users for 40 days. Total beam storage time during 1995 was 3,329 hours. From September to December in 1995, the beam was stored for 1,944 hours. In this period, the beam was available to users for 1,142.4 hours, and the average beam availability to users was 64%. If the vacuum failaure from the water leakage be excluded, the availability would be about 95% [2].

2 STATUS, STUDY AND ACTIVITIES

As the main subject of the beam physics study, both the conventional ion trapping and the new Fast Beam-Ion Instability have been studied. For analytic study, the theory of two beam instability is applied. Even though this linear theory cannot describe the instability growth

0-7803-4376-X/98/$10.00 © 1998 IEEE

correctly, it can properly describe the beginning stage of the instability.

As of December 1996, the accumulated operation time of the linear accelerator after the start of the commissioning in 1994 is about 7,960 hours. Until then, the total accumulated high voltage run-time of the linac klystron-modulator system has reached average 23,460 hours per module, and the average accumulated klystron heater time reached 23,746 hours. We expect more than 30,000 hours of the tube lifetime because the operation power level is approximately 65-80% of the rated power level. The operating time of 1996 is 6,432 hours and the availability is increased to 94% from 85% in 1995 [3]. The improvement of the availability is due to the modification of heater circuits not to be interrupted by the instant unnecessary heater power interruption in case of the momentary klystron vacuum change which is recoverable almost immediately.

The vacuum system of the PLS linac performed with average loaded microwave energy of 45.3 GJ per module in 1996. The average pressure was maintained about at 1.1 $x10^{-8}$ Torr in the klystron gallery under the high power microwave loadings of average 54 MW peak power per module with 4.1 ms pulse width and 10 Hz repetition rate. With 45°C cooling water supply, the outgassing rate of the system has been about $9.0x10^{-13}$ Torr·l/sec·cm^2. The residual gas consists of mostly hydrogen (62%) with minor molecules of H_2O, Ch_2OH, CO, C, N, and O_2. A total of 26 faults with 20 hours of the down time in the vacuum system appears to have MTBF (Mean Time Between Failure) of 181.8 hours and the system availability of 99.5%.

Most activities of the storage ring control system engineers have been devoted to the development of the machine diagnostics programs and the beamline control programs. They include the development of the data acquisition system for the X-ray fluorescence microprobe beamline and the upgrade of the existing data aqcuisition system as well as the development of the required console computer software.

The R&D and upgrade activities of the beam diagnostics system are focused on the longtime analysis of the closed orbit data, beam-based alignment (BBA) of the quadrupole magnet-BPM pairs [4,5], development of the transverse feedback system [6], and the construction of a diagnostic beamline.

In January 1996, the vacuum pressure of storage ring was $(1\sim3)x10^{-9}$ Torr at 100 mA of beam current. And the specific pressure rise due to the photon induced desorption was about $2x10^{-11}$ Torr/mA. The pressure rise is still decreasing and it reaches to $(4\sim6)x10^{-12}$ Torr/mA in December 1996 [7].

3 OPERATION STATUS

At the normal operation period, such as user beam time, beam line alignments and the storage ring tuning, electron beams are injected into the storage ring three times a day.

From January 8 to June 23, 1996, seven shifts were planned and performed for user beam times. Each shift consists of a ten-day run in user service mode and a two-day turn-off for the maintenance followed by a two-day run for machine study. For this period, the total planned machine operation time is 2,640 hours, in which 1,819 hours are assigned to users. Among the scheduled beam time for users, 1,715.23 hours have been practically devoted to users which corresponds to 94.3% of the availability.

The machine was shut-down from February 16 to March 10 to install a new front-end for the X-ray lithography beamline owned by LG Semicon. Also, we had the regular summer shut-down in July and August for system improvements and regular preventive maintenances.

After the shut-down, the user experiments resumed in September with five public beamlines. Two of them received their first users. Seven user shifts were scheduled until the end of 1996. Of the 1,416 hours of this beam time, 1,338 hours were actually provided. It corresponds to 94.5% of availability. Tables 1 and 2 summarize the results of beam operations during the user service modes of operation in 1996 and 1997.

Table 1. Summary of user service mode I

Run	Period	Planned	Supplied	%
96-1	1/8~1/26	423h 58m	401h 45m	94.8
96-2	2/5~2/12	264h	257h 36m	96.9
96-3	3/27~4/4	195h 26m	185h 52m	95.1
96-4	4/10~4/21	264h	252h 48m	95.7
96-5	5/1~5/9	192h	174h 08m	91.0
96-6	5/15~5/23	192h	167h 07m	92.1
96-7	6/12~6/23	288h	275h 58m	93.7
96-8	9/11~9/22	288h	265h 25m	94.2
96-9	9/30~10/15	360h	335h 23m	95.0
Sum		2467h 24m	2316h 02m	93.8

Table 2. Summary of user service mode II

Run	Period	Planned	Supplied	%
96-10	10/18~11/7	192h	184h 44m	96.7
96-11	11/13~11/20	192h	185h 53m	97.9
96-12	11/27~12/4	192h	183h 24m	97.4
96-13	12/3~12/16	192h	173h 09m	92.6
97-1	1/11~1/19	216h	199h 05m	92.2
97-2	1/25~2/3	240h	226h 36m	94.4
97-3	4/5~4/14	240h	222h 15m	93.7
Sum		1464h	1376h 06m	95.0

4 MACHINE UPGRADE

During the 1996 summer shut-down, a couple of major reinforcements have been added to the system for greater stability and reliability.

In the linac, optical cables were installed for timing system upgrade and the klystron heater interlock circuit has been modified, so that klystron and thyratron could be stable even in the case of instantaneous power failure. Also, the thermal shield blanket was installed for the microwave main drive line, which is made of copper tube (coaxial line) and was found responsible for the unstable beam energy drift caused by the automatic intermittent circulation of air.

In the storage ring, several suspect points of the vacuum chamber have been scrutinized and rebaked while some new devices were installed for performance enhancement; a kicker for the transverse feedback system, and new coils for the four quadrupole magnets damaged last January by interlock failure.

One more RF station was added to the storage ring. Total four cavities powered by independent power source, TV klystron, provide 240 kW of RF power, which is enough to store 400-mA of beam current at 2.0-GeV [8].

5 BEAMLINES

In 1996, three more beamlines have been installed and the total number of beamlines becomes 6. There is one more beamline for the beam diagnostics which was installed in 1996. All of them are bending magnet beamlines as listed in Table 3.

Table 3. Working beamlines

Beamline	Areas of Research	Year of Installation
Whitebeam	X-ray Microprobe	1996
Photoemission	Surface Science	1994
NIM	Atomic & Molecular Science	1995
EXAFS	Chemical	1996
X-ray Scattering	Engineering	1994
Lithography	X-ray Diffraction Semiconductor (LG)	1996

During the first half of 1996, total 34 experiments have been conducted using the three operational beamlines (photo-emission, NIM, and X-ray scattering beamlines). In the last four months from September to December, a total of 35 experiments have been conducted at five beamlines.

6 FUTURE PLAN

In the year 1996, there was no big change in the PLS beam state. Most parameter values were maintained without any significant change. But, it does not mean that the PLS is in a stable and fully tuned state. Rather we would like to say that it reached a phase I; the PLS is capable of storing a stable beam of 100 ~ 130 mA with lifetime more than 10 hours, and major lattice parameters are reasonably close to the design values [2]. We should make a transition to phase II, in which it is possible to store a stable beam of a few hundred mA with a lower emittance, and the machine itself is fully understood.

To achieve this phase and to serve the reliable photon beams to the users, we have some machine upgrade plans. Among them, the installation of beam position monitors in the linac and BTL for energy feedback system, beam based alignment, and the installation of longitudinal feedback system are included.

Adding to these, the installation of the 12th klystron-modulator module is being under progress and the U7 undulator is ready for its installation. As for the beamlines, SAX and X-ray diffraction beamlines are expected to be installed in 1997.

7 ACKNOWLEDGEMENTS

The authors thank to PAL staff for their hard work, and to POSCO and MOST for their commitment and endorsement to the PLS project.

REFERENCES

[1] Design Report of Pohang Light Source (revised ed.), Pohang Accelerator Laboratory, 1992.
[2] M. Yoon, et. al., "Operation Status of the PLS Storage Ring," Proc. of 1996 European Particle Accelerator Conference, Barcelona, Spain.
[3] W. Namkung, et. al., "Operational Status of PLS 2-GeV Linac," Proc. of 1996 European Particle Accelerator Conference, Barcelona, Spain.
[4] J. Y. Huang, et. al., "Beam-Based Offset Calibration of PLS BPM," in these proceedings.
[5] S. H. Nam, et. al., "High Current Shunt Regulator for Quadrupole Magnets in PLS 2-GeV Storage Ring," in these proceedings.
[6] J. Y. Huang, et. al., "The Transverse Beam Feedback System in PLS," in these proceedings.
[7] C. D. Park, et. al., "Operation Experiences for PLS Vacuum System," in these proceedings.
[8] M. Kwon, et. al., "Operational Characteristics of RF system Affecting PLS Beam Stability," in these proceedings.

ELETTRA PERFORMANCE AND UPGRADES

C. J. Bocchetta, D. Bulfone, F. Daclon, G. D'Auria, A. Fabris, R. Fabris, M. Ferianis, A. Galimberti, F. Iazzourene, E. Karantzoulis, M. Lonza, C. Pasotti, C. Rossi, C. Scafuri, M. Svandrlik, L. Tosi, R. Visintini, R. P. Walker, F. Wei, A. Wrulich and D. Zangrando
Sincrotrone Trieste, 34012 Trieste, Italy

Abstract

The present status of the ELETTRA synchrotron radiation light source is given. Of importance to the User community is the brightness and the stability of the source. Recent improvements to the machine, completed or in progress, allow a further increase of the performance values. These upgrades include modifications to increase the current and/or beam energy, improved compensation of insertion device effects, orbit feedback and the control of multibunch instabilities.

1 PRESENT STATUS

The present organisation of machine operation periods follows that of last year [1], namely, three to four week round the clock operation followed by a one to two week shutdown period. The facility during 1997 will operate for a total of 6168 hours of which 5064 will be dedicated to User experiments. The uptime of the machine for the past calendar year was 93.6%, an improvement compared to the previous year which was 91.5%. The major source of downtime still remains external disturbances on the electrical line from thunderstorms or otherwise and accounted for 24% of all downtime.

At present the facility is providing photons from five insertion devices and one bending magnet. The total number of beamlines active at the time of this conference is ten with additionally four under construction. This autumn will see the installation of an electromagnetic elliptical wiggler, a collaboration between BESSY and MAX-lab [2]. The device is an open sided structure and utilises electromagnets for the generation of both horizontal and vertical fields allowing both wiggler and undulator modes of operation. It can switch its fields in a trapezoidal manner between 0.1 to 1.0 Hz and sinusoidally from 10 to 100 Hz. Four new insertion devices, up to 2.2m in length, have been approved for construction, see [3] for further details. These devices, for which installation is foreseen in 1998, are elliptical undulators (APPLE-II types) providing photons which cover the range 10 to 2000 eV.

A new low gap insertion device vacuum chamber is under construction and will be installed in August this year. The chamber made of stainless steel has an internal aperture of 15 mm and externally 17 mm. The novel feature of this chamber is the absence of pumping along it's length, thereby simplifying it's fabrication. A cross-section is shown in figure 1. In addition a new bending magnet chamber is being studied, made of aluminium, for the new helical insertion devices. These will have larger vertical radiation slots to accommodate the increased vertical divergence of the radiation from the new devices.

This year saw the full implementation of the operations task manager program "One Button Machine" [4]. It is a UNIX based tool that spawns, communicates and controls the logical flow of the pre-defined operations required for a machine refill. The program reduces to the theoretical minimum the preparation time for a refill. Modules are presently being included to perform the ramping and final insertion device settings before consignment of control to the Users.

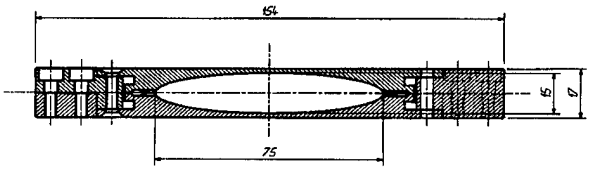


Figure 1: Cross-section of vacuum pump free insertion device chamber.

2 INCREASING THE CURRENT/ENERGY

The routine 250 mA current already exceeds the design current of 200 mA at 2.0 GeV. The main limitation at the facility to fully exploit the flexibility of ELETTRA and operate at even higher currents is the thermal load on the vacuum chamber due to synchrotron radiation. The main obstacle for an increase of current and/or energy is the thermally induced mechanical stress on the vacuum gaskets of the beam position monitors (BPM's) downstream of the bending magnets. Already in 1994-95 additional cooling was installed which gave noticeable improvement in vacuum and thermal stability. The BPM monitor, however, still suffers from thermal stress because of the difficulty in providing additional cooling to the body of the monitor. In view of this, composite gaskets of steel/copper have been designed and are being installed. The installation takes one week per achromat and all gaskets will be upgraded by summer 1997. This will permit an increase of current to 300 and it is expected to 350 mA. Alternatively the machine energy may then be increased to 2.35 GeV with a current of 200 mA which would generate the same heat load as 350 mA at 2.0 GeV. The higher energy is beneficial in improving the Touschek lifetime and helps in combating multi-bunch instabilities. The radio frequency system would limit the current at this higher energy at about 250 mA.

0-7803-4376-X/98/$10.00 © 1998 IEEE

3 COMPENSATION OF INSERTION DEVICE EFFECTS

Insertion devices are the principle sources of bright photon beams in ELETTRA. To minimise the effect of gap changes the devices are fabricated to the highest standards. Notwithstanding the fact, however, that the magnetic field integrals are measured and minimised to the lowest possible levels given by present day methods and even utilising the most sophisticated techniques in pole shimming, residual field errors persist which disturb the closed orbit. To compensate this effect correction coils or rotating blocks (for the wiggler) are used. A lookup table is utilised for the compensation. Recently the correction method has been improved and also takes into account the simultaneous compensation of horizontal and vertical effects which arise through the non orthogonal magnetic fields used in the compensation of some devices. The technique has been automated to provide the fastest characterisation allowing rapid confirmation, and if needed adjustment, for new machine files. The method gives a factor of five improvement over the previous correction scheme. The maximum closed orbit displacement relative to the beam size at the source point is 1.1% horizontally and 6.7% vertically for an effective emittance coupling of 1%. This is sufficient to allow User control of the insertion devices. Work is terminating for the complete implementation on all insertion devices which will permit experimental Users to control their devices in May 1997. The present level of correction is at the limit of the BPM resolution and method will be upgraded to incorporate information from the photon BPM's. This in combination with the local orbit feedback system will provide substantial beam stability for the Users.

4 LOCAL ORBIT FEEDBACK

Transverse orbit stability is essential to guarantee the maximum exploitation of the brightness of a light source. The amount of beam degradation observed by an experimental User depends on the frequency of the disturbance compared to the speed of the measurement. With increasing data acquisition rates from beamline experiments it is essential that a fast orbit stabilisation system be employed. At ELETTRA the sources of disturbance are primarily due to thermally induced mechanical movement of the chamber, to insertion device manipulation (both slow effects) and fast spurious signals at 50 Hz and multiples thereof due to the mains. Extensive tests have so far failed to pinpoint the source of the latter disturbance. In view of this the fast local orbit feedback utilising digital controllers and signal processors has been implemented to locally combat all the above mentioned effects at the insertion device source points [5]. The high frequency component has been successfully eliminated using a dedicated harmonic suppressor. Figure 2 shows the reduction in noise level for the lower frequencies. The system will be implemented on all insertion device beam lines by the end of summer 1997. The foreseeable use of the system will be to isolate beamlines from external disturbances. The known effects, however, of insertion device gap changes producing fictitious orbit displacements (due to the presence of bending magnet radiation) may limit the use to fixed gaps and rely on insertion device compensation as described in section 3 for gap/monochromator scans. Studies are presently being completed to evaluate this effect as a function of gap. A foreseeable development would be the use of electron BPM's as the monitors for the system [6].

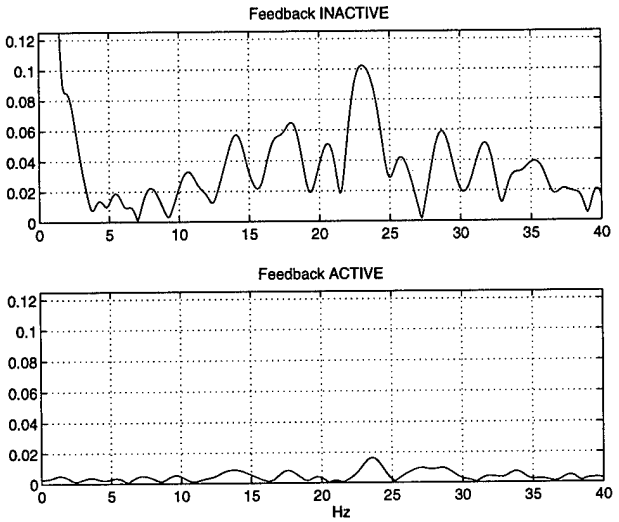


Figure 2. Results of local orbit feedback at ID_6 in compensating low frequency disturbances.

5 COMBATING MULTIBUNCH INSTABILITIES

Longitudinal and in particular transverse multibunch instabilities degrade machine brightness. The effects vary from a blow-up of the longitudinal bunch dimensions to transverse jitter and partial to total beam loss. As has been described elsewhere ELETTRA utilises temperature tuning of the cavities for mode shifting [7]. This method, however, becomes more laborious and possibly impossible to use as the stored beam current increases. In view of the planned increase in current adjustable higher order mode frequency shifters (HOMFS's) are being installed in all four cavities [8]. The work started in late summer 1996 will terminate by the end of 1997. The first results performed last year are very promising and showed an improvement in shifting both the longitudinal and transverse modes. Figure 3 illustrates the behaviour of transverse coupled bunch modes in cavity S9 as a function of cavity temperature at a beam energy of 2.0 GeV and 250 mA stored current. The first diagram shows the distribution of the most prominent modes before installation of the adjustable HOMFS. The broad transverse mode complicated matters during ramping of the beam from the injection energy to the final operating value of 2.0 GeV. The instability led to partial or total beam loss during the ramp. The second figure shows the distribution after installation of the adjustable HOMFS in this cavity which allowed a careful tuning and shifted the dangerous mode out of the temperature working window. A complete characterisation of the machine with all cavities having the HOMFS's will take place in the later part of this year. The characterisation will be performed with the higher

stored current and based on these results a decision will be made as to whether or not a longitudinal multibunch feedback system will be implemented.

To allow rapid evaluation of the best position for the HOMFS's a system of mode measurement with beam has been implemented. The system operated from a UNIX environment can perform a complete scan of the 432 modes in 10 minutes.

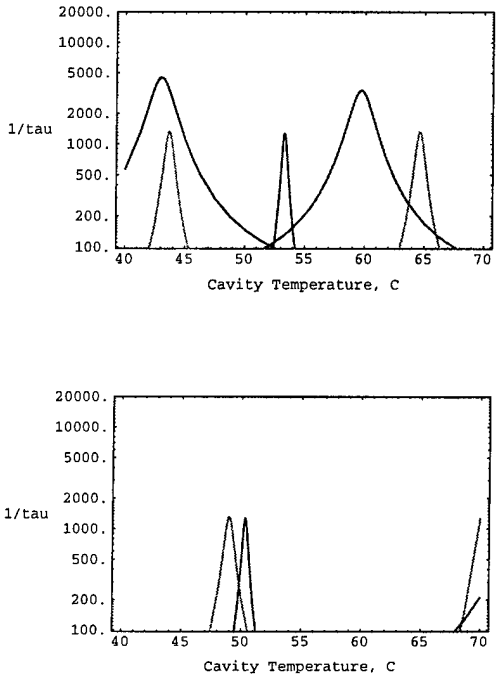


Figure 3: The shifting of horizontal transverse coupled bunch modes with a adjustable HOMFS on cavity S9. 2.0 GeV, 250 mA. Before installing the adjustable frequency shifter (upper graph) and after (lower graph).

6 FUTURE OUTLOOK

With the operation of the facility at higher currents the control of dangerous transverse coupled bunch modes becomes more difficult. Therefore to guarantee the best possible conditions for experiments a transverse multibunch (bunch by bunch) feedback system is being actively studied and developed. The installation date is foreseen for 1998. For what regards orbit stability and in view of the increasing number of future bending magnet beam lines a global feedback system will be studied to enhance the already existing slow feedback which currently operates at a high control level to compensate the slow thermal drifts of the orbit.

Apart from the newly approved devices the possibility of building a short period (22 mm) in vacuum device is being evaluated [3]. This device will have a tentative operational gap of 7mm.

To compensate the increased effect of Touschek scattering associated with the higher currents and/or denser bunches a study programme has been launched with the task of evaluating the impact of installing a super conducting radio frequency cavity for compensating the energy loss of the Touschek scattered particles. The study will also examine the feasibility of installing additional sextupole magnets into the ring which would be required to improve the transverse off-momentum energy acceptance. In addition a re-optimisation of the existing harmonic sextupoles will be performed to see the impact of lessening the compensation of the geometric aberrations in favour of an increased off-momentum aperture. Associated with this study will be the examination of an alternative method to improve the beam lifetime through the use of a super conducting higher harmonic cavity. This would provide a longer Touschek lifetime by lengthening the bunch. In this case the time structure of the beam would be altered and special machine periods would then be dedicated to Users requiring short bunches for experiments.

REFERENCES

[1] C. J. Bocchetta, "Operational Experience with ELETTRA", Proc. 5th European Particle Accelerator Conference, Sitges, (1996), 76.

[2] R. P. Walker, et al., "Design of an Electromagnetic Elliptical Wiggler for ELETTRA", These Proceedings.

[3] R. P. Walker, "Operation of Insertion Devices in ELETTRA and Plans for Future Devices", These Proceedings.

[4] D. Bulfone, et al., "Automating ELETTRA Operation with "One Button Machine"", These Proceedings.

[5] C. J. Bocchetta, et al., "First Operational Results with the ELETTRA Fast Local Feedback System", These Proceeding.

[6] E. Plouviez and F. Uberto, "A Fast Local Feedback System to Correct the Beam Position Deviation in the ESRF Storage Ring", Proc. 5th. European Particle Accelerator Conference, Sitges, (1996), 1872.

[7] M. Svandrlik, et al., "The Cure of Multibunch Instabilities in ELETTRA", IEEE Proc. Particle Accelerator Conference, Dallas, (1995), 2762.

[8] M. Svandrlik, et al., "Improvements in Curing Coupled Bunch Instabilities at ELETTRA by Mode Shifting after the Installation of the Adjustable Higher Order Mode Frequency Shifter", These proceedings.

BEAM DENSITY MANIPULATIONS IN THE ELETTRA STORAGE RING

C. J. Bocchetta, A. Fabris, F. Iazzourene, E. Karantzoulis, M. Svandrlik, L. Tosi, R. P. Walker and A. Wrulich
Sincrotrone Trieste, 34012 Trieste, Italy

Abstract

Low energy third generation light sources, such as ELETTRA, are lifetime limited by Touschek scattering. In principle an improvement of the lifetime can be obtained by increasing the emittance coupling or by increasing the longitudinal bunch dimensions, however, both methods have an adverse effect on the light quality. The trade off between lifetime and light quality in ELETTRA is discussed and spectral measurements for various scenarios are presented.

1 INTRODUCTION

One of the main difficulties facing third generation light sources is the low lifetime associated with the low emittance of these machines. The lifetime restriction arises from an enhancement of the Touschek effect, an effect which involves large angle intra-beam Coulomb collisions, and is evidenced in low emittance machines because of the higher density of the bunches. Increasing the lifetime without compromising the quality of the light is one of the desired goals in machine operation. There are several techniques for the improvement and involve either an increase in the storage ring particle acceptance or a reduction in the particle density. The former can be performed by increasing the dynamic aperture for off-momentum particles which must be done both longitudinally and transversely. The longitudinal acceptance increase may be performed by increasing the radio-frequency voltage applied to the beam. The method is costly and may involve upgrading the rf plant and/or the power feed-through to the cavity, or the installation of additional cavities and plant units. New methods have recently been proposed to increase the rf voltage by including in the ring a super conducting cavity operating at zero phase providing voltage only for those particles which have suffered an energy loss, either through a Touschek event or gas Bremsstrahlung. Increasing the transverse off-momentum acceptance is more complicated for an existing machine since the placement of additional sextupoles will require space which is generally hard to find. For machines in the development stage new lattices are being designed providing more than four percent energy acceptance [1].

The second technique for an improvement of the Touschek lifetime is to reduce the bunch density. Apart from increasing the number of bunches for a given current, the density reduction may be performed in either the transverse or longitudinal plane. However, this is in conflict with the goal of modern light sources and compromises the quality of the light, since increasing the transverse bunch dimension will reduce the brightness and lengthening the bunch will spoil the time structure and may enhance energy spread contributions. Transversely, the natural coupling of the machine may be increased either with skew quadrupoles or by operating on the coupling resonance. Longitudinally the bunch may be lengthened by a higher harmonic cavity [2] with precautions being taken not to increase the energy spread of the beam.

2 CONDITIONS IN ELETTRA

ELETTRA, which is Touschek limited in the longitudinal plane, at present operates with an effective accelerating voltage of 1.76 MV. This provides an overall lifetime (including gas scattering) of ~10 hrs at 250 mA under the conditions of reduced longitudinal multibunch instabilities (LMBI), see below. Going to the maximum voltage of 1.96 MV gives little improvement and increases the overall lifetime to 11.4 hrs. As to increasing the number of bunches in the ring a small improvement may be performed by going to 100% filling rather than the 80-90% currently used. This, however, would increase the likely-hood of ion trapping effects and generally gives a noisier beam. The method chosen to increase the lifetime is to operate with a controlled amount of longitudinal multi-bunch instability. The instability leads to a bunch dilution in the longitudinal plane as described in ref [3]. The control is performed by temperature tuning of the cavities with additional control being given by the adoption of Higher Order Modes frequency shifters [4] for operation at higher currents. The excitation can be varied from no modes being excited to full excitation. An intermediate regime corresponding to reduced longitudinal multibunch instabilities (LMBI) is characterised by coherent coupled bunch oscillations of a few degrees. The effective beam energy spread in this case is determined by the oscillation amplitude. The lifetime, however, is fully Touschek dominated since the bunch suffers little dilution. To obtain a bunch dilution the bunch has to perform larger oscillations which then Landau damp. The resulting average energy spread has to be evaluated taking into account the damping time in the longitudinal plane. Estimates indicate that the increase in the rms energy spread is two to three times the natural value of 8×10^{-4}. In addition to increasing the lifetime this mode of operation also helps in combating the strong transverse modes.

3 MEASUREMENTS

Experiments were performed on two beamlines and spectra were recorded under various operating conditions to estimate the effect of choosing to increase the lifetime via longitudinal bunch dilution. There are essentially three distinct ways to manipulate the lifetime at

0-7803-4376-X/98/$10.00 © 1998 IEEE

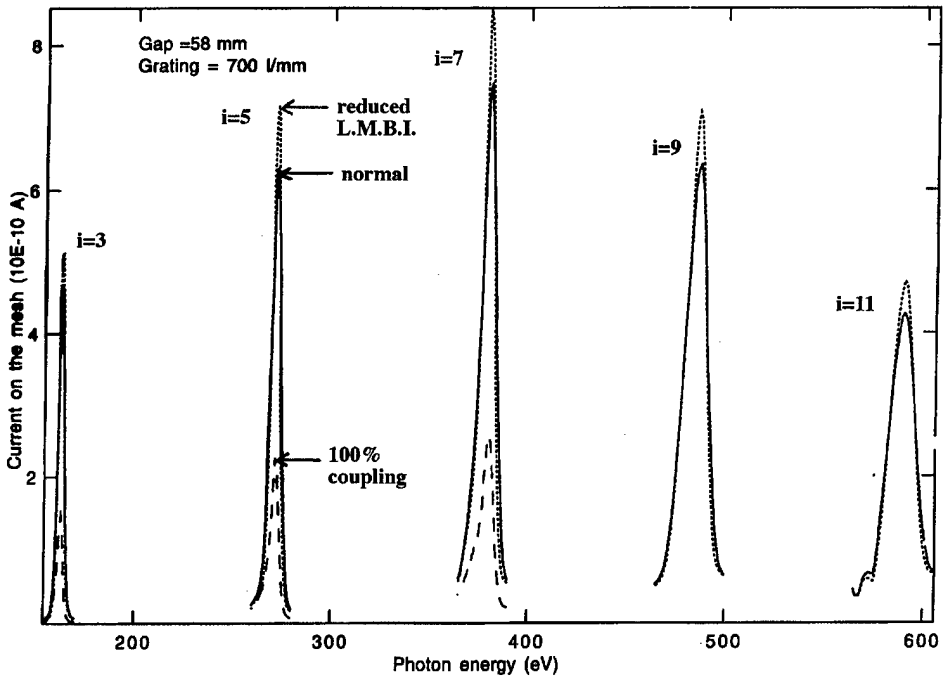


Figure 1: Line spectra taken on the ID_3, VUV beamline as a function of the different methods to increase the beam lifetime. Spectra shown refer to reduced longitudinal multibunch excitation, normal operating conditions (x2 increase in energy spread) and 100 % coupling.

ELETTRA. These are (a) controlled use of longitudinal multibunch excitation, (b) compensation or not of the spurious vertical dispersion and (c) excitation of the coupling resonance to increase the vertical beam size. The spurious dispersion, horizontal and vertical, affects the emittance by altering the equilibrium between quantum excitation and radiation damping. Additionally the dispersion alters the beam size via the energy spread of the beam. This effect is relevant to both planes and is particularly important when coupled bunch instabilities are driven by the cavity higher order modes. The spurious dispersion is most damaging in the vertical plane, and given the low geometric coupling accounts for most of the vertical beam dimension if not corrected. The natural coupling has been measured to be 0.1% (Δf_{min} of 6kHz) and the uncorrected vertical dispersion can have a peak rms values of up to 3.5 cm. The amount of effective emittance coupling as a function of vertical dispersion can be found in ref [5] and shows that an rms dispersion of 1.5 to 0.3 cm will change the dispersion caused coupling from 1.0 to 0.05%. The correction has been described elsewhere [5] and final rms values of 3 mm have been attained. Table 1 shows the lifetime for these three conditions. In the table a reduced LMBI condition corresponds to the description given in the preceding paragraph, whereas normal vertical dispersion has been taken to be 1.0 cm and the reduced dispersion as 3 mm rms. We note that the lifetime can be varied by a factor of five.

The lifetime is composed of gas scattering effects (elastic and inelastic) and the Touschek effect. To compute the Touschek contribution under stable beam conditions the bunch length has been taken to have the nominal value of ~18 ps at 250 mA for 80% filling (harmonic number of 432). The bunch length at this current is below the microwave instability threshold (the measured longitudinal broadband impedance |Z/n| is below 0.7 Ω). From fitting the lifetime contributions to the measured data results in an estimate for the bunch length or energy spread increase of a factor of two when operating under normal conditions.

	LMBI	Vertical Dispersion	Coupling	τ[hrs]
1	reduced	reduced	normal	6.7
2	reduced	normal	normal	10.3
3	normal	normal	normal	20.0
4	reduced	normal	maximum	30.0
5	normal	normal	maximum	36.5

Table 1: Lifetime as a function of controlled longitudinal multibunch instability (LMBI), spurious vertical dispersion and coupling. (250 mA, 2.0 GeV)

Figure 1 shows the effect on the undulator line shapes for the three cases examined on the VUV beamline (ID_3: period of 12.5 cm, N=36). The findings can be summarised as follows: exactly on the coupling resonance (reduced LMBI) for ID_2 a 10-15% reduction in intensity is observed whereas for ID_3 a reduction of 70% is noted and the noise level is greatly increased (the latter beamline uses an 20 μm entrance slit while the former does not). Going from a situation with reduced LMBI to normal LMBI operating conditions gives a reduction in intensity of 16-28% for ID_2 and a reduction of 10-13% for ID_3.

4 PHOTON COHERENCE

An important parameter is the fraction of coherent radiation emitted from an undulator. Diffraction limited effects are most noticeable at long wavelengths. Figure 2 shows the coherent fraction of emitted radiation for different horizontal to vertical emittance couplings in ELETTRA as a function of photon energy. The greatest effect, as expected, is found in the vertical plane. A summary is given in table 2. From these results we see that increasing the vertical emittance is not an attractive option. Table 3 shows the reduction in intensity as a function of energy spread for the two beamlines in consideration. We note a small overall effect on the results for the first few harmonics under consideration.

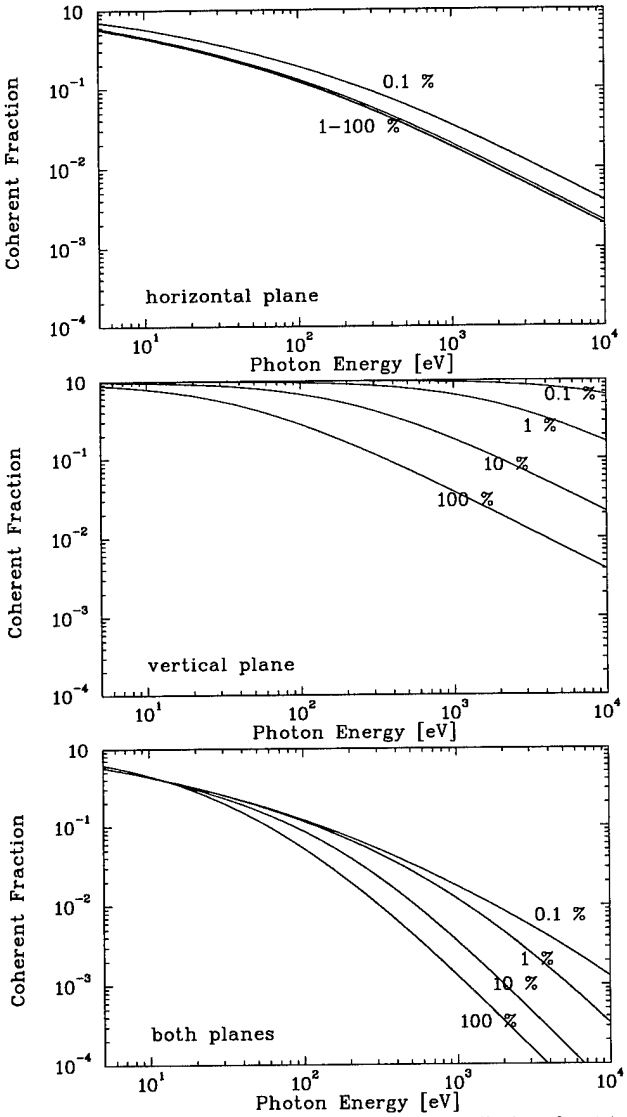


Figure 2: Coherent fraction of undulator radiation for (a) the horizontal plane, (b) the vertical plane and (c) the combined effect.

Photon Energy [eV]	Diffraction Limited to a Coupling of
10	100%
100	10%
1000	1%

Table 2: Extent of diffraction limit (within 20-30%) as a function of coupling.

Harmonic	ID_2 (N=81)	ID_3 (N=36)
1	-4%	-1%
3	-23%	-7%
5	-35%	-16%

Table 3: Theoretical reduction in intensity due to doubling the beam energy spread (worst case, zero emittance on axis).

5 CONCLUSIONS

These preliminary results indicate that increasing the bunch length and the associated energy spread by means of controlled residual coupled bunch excitation gives acceptable reduction of undulator flux whilst doubling the lifetime. Increasing the lifetime by increasing the vertical dimension by operating on the coupling resonance gives too great a reduction in flux and intensity and additionally results in the production of noisy spectra. In view of future developments to increase the stored current and to combat the consequently enhanced coupled bunch instabilities options to provide adequate Touschek lifetime using other methods are being actively pursued [6]. These involve the use of bunch lengthening techniques using a higher harmonic cavity (super conducting) or the installation of a super-conducting cavity for additional rf acceptance (without bunch lengthening) as described above. The choice will be based on the feasibility of increasing the transverse off-momentum acceptance.

6 ACKNOWLEDGEMENTS

The authors thank the VUV and Esca-microscopy personnel for their assistance in the measurements.

REFERENCES

[1] e.g., Proc. 5th European Particle Accelerator Conf., Sitges, (1996), 670 and 685.

[2] R. Biscardi, et al., Nucl. Instr. and Methods, A366, (1995), 26.

[3] A. Wrulich, et al., Proc. 5th. European Particle Accelerator Conference, Sitges, (1996), 1108.

[4] M. Svandrlik, et al., "Improvements in Curing Coupled Bunch Instabilities at ELETTRA by Mode Shifting after the Installation of the Adjustable Higher Order Mode Frequency Shifter", These proceedings

[5] R. Nagaoka, Proc. 5th. European Particle Accelerator Conference, Sitges, (1996), 980.

[6] C. J. Bocchetta, et al., "ELETTRA Performance and Upgrades", These Proceedings.

IDEAS FOR FAST ACCELERATOR MODEL CALIBRATION*

J. Corbett and G. LeBlanc†
Stanford Linear Accelerator Center, Stanford/SSRL, CA 94309
†MAX-Lab, Lund, Sweden/Stanford Linear Accelerator Center

Abstract

With the advent of a simple matrix inversion technique, measurement-based storage ring modeling has made rapid progress in recent years. Using fast computers with large memory, the matrix inversion procedure typically adjusts up to 10^3 model variables to fit the order of 10^5 measurements. The results have been surprisingly accurate. Physics aside, one of the next frontiers is to simplify the process and to reduce computation time. In this paper, we discuss two approaches to speed up the model calibration process: recursive least-squares fitting and a piecewise fitting approach.

1 CONVENTIONAL APPROACH

Some of the first accelerator model fitting routines were based on numerical adjustment of model parameters to make simulated orbit perturbation data match the measured data [1]. Originally known as the 'GOLD' method [2], model calibration concentrated on one section of the lattice at a time. With the GOLD method, the operator first identified parts of the lattice where the model agreed with the measured data. The next step was to vary model parameters near any discontinuities until the model-simulated trajectories matched the measurements. The power of the GOLD method is twofold: (1) hardware errors are quickly identified, and (2) once the model fields are found optical parameters can be predicted throughout. The same technique can applied to both perturbation orbit and absolute orbit measurements.

'Multi-track fitting' increases the accuracy of the result. With multi-track fitting, a set of orbit perturbations made by different dipole kicks provides many self-consistent constraints for the analysis. In effect, with each new trajectory the particle beam makes an independent probe of the spatial field structure of the lattice. Multi-track fitting was initially carried out with RESOLVE [3], a graphical interface program where the operator can interactively adjust parameters to find model and/or hardware errors.

*work supported in part by Department of Energy Contract DE-AC03-76SF00515 and Office of Basic Energy Sciences, Division of Chemical Sciences.

In the limit, multi-track fitting can include the complete corrector-to-bpm response matrix with many parameters in the model declared as variables.

Unfortunately, the number of operations required to set-up the calculation, the computation time, and interpretation of the results become unwieldy in a graphical interface environment.

To speed up the process, the problem was linearized and statistically correlated solutions were found by matrix inversion in a dedicated code [4]. As with many system identification problems, the non-linear aspect was accommodated by iterative re-expansion around the operating point.

The matrix inversion procedure evolved into a powerful tool that can accurately predict quadrupole strengths, BPM gains, corrector gains, and a variety of other model parameters [5-8]. Although the linearization technique is robust and accurate, the turn-around time required to make the measurements, calculate hundreds of closed orbits, and then invert the matrix can be many hours.

In the following sections, we describe ideas for reducing the model calibration turn-around time. The goal is to predict the model soon after the measurements become available.

2 RECURSIVE LEAST-SQUARES

In order of increasing complication, some of the more useful accelerator model calibration procedures are:

I. Fit single orbits to verify corrector and bpm operation.

II. Fit single quadrupoles or families in-plane.

III. Fit quadrupoles, correctors, bpms in-plane.

IV. Fit quadrupoles, correctors, bpms, coupled-plane.

Depending on the objectives of the analysis, one or more of these procedures might be adequate. For large calculations, it is worthwhile to minimize the number of correctors and bpms needed to realize an accurate fit. Eliminating redundant measurements reduces the time to calculate the closed orbits and to invert the sensitivity matrix.

One way to speed up the process would be to employ a recursive least-squares algorithm. With

0-7803-4376-X/98 /$10.00 © 1998 IEEE

recursive least-squares, a 'batch' of data is initially processed to arrive at preliminary least-squares answer [9]. Subsequent data is used to update the previous model estimate iteratively. For storage ring model calibration, this translates into choosing a subset of orbit perturbations from the response matrix (with appropriate corrector phases) to yield an initial estimate for the model. Each new set of orbit data is then used to update the previous solution on an iterative basis.

In a fast on-line system, the model calculations of the perturbed orbits could be carried out in parallel with the initial measurements. Once a sufficient block of data is acquired, the model is fit with a set of variables chosen by the operator. The new model is used to calculate the next set of closed orbits while more measurements made. Depending on the goal of the analysis, subsequent iterations could include more subtle model variables.

3 PIECEWISE FITTING

In this section, we return to the original 'GOLD' notion of piecewise model calibration, but apply the linearized response-matrix fitting technique. Instead of adjusting many model parameters to agree with the measured response matrix around the entire storage ring, suppose we want to analyze only a part of the ring, the IP or an insertion device for instance. Data is acquired in the same way as before, namely, kick the beam with corrector magnets and measure the beam deflection.

For this application, however, fewer measurements are needed since only a subset of the model parameters are variable. Furthermore, the time required to calculate trajectories from the perturbed model, and the time required to invert the sensitivity matrix is reduced. The main difference is that (similar to the GOLD method) each section of the storage ring is treated like a transmission line.

Mathematically, the procedure becomes clear if we compare to the closed-orbit response matrix method. In that case, the Taylor expansion of the response matrix '**C**' is

$$\mathbf{C}_{measure} = \mathbf{C}_{model} + (\partial \mathbf{C}/\partial \mathbf{k})_{model} \cdot \Delta \mathbf{k} + \ldots \qquad (1)$$

The column vector of expansion variables, $\Delta\mathbf{k}$, is nominally a set of quadrupole strengths, but corrector gains, BPM gains, energy shifts or other model parameters can be added [5,8]. Any increase in the number of variables will expand the dimensions of the problem. Collecting known quantities in Eq. 1, the

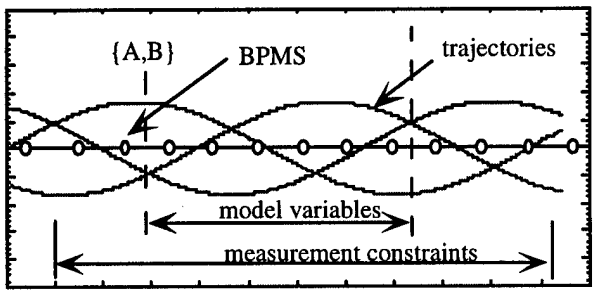


Figure 1: Schematic Piecewise Fitting

parameter vector $\Delta\mathbf{k}$ is found by least-squares inversion of the sensitivity matrix $(\partial \mathbf{C}/\partial \mathbf{k})_{model}$.

Piecewise model calibration proceeds similarly. Expressed in terms of linear transport equations, the displacement $\Delta\mathbf{x}$ of a single trajectory propagates as

$$\frac{\Delta \mathbf{x}}{\Delta \theta} = \mathbf{A}\mathbf{R}^{11} + \mathbf{B}\mathbf{R}^{12} + \ldots \qquad (2)$$

where {A , B} are the cosine- and sine-like components of each trajectory. The column vectors $\{\mathbf{R}^{11}, \mathbf{R}^{12}\}$ are elements of the linear transport matrix evaluated along the beamline.

If we Taylor expand the **R**-matrix elements about the nominal quadrupole strengths, we get an equation for each trajectory:

$$\left(\frac{\Delta \mathbf{x}}{\Delta \theta}\right)_{measure} = \mathbf{A}[\mathbf{R}^{11}{}_{model} + (\partial \mathbf{R}^{11}/\partial \mathbf{k})_{model} \cdot \Delta \mathbf{k}] + \mathbf{B}[\mathbf{R}^{12}{}_{model} + (\partial \mathbf{R}^{12}/\partial \mathbf{k})_{model} \cdot \Delta \mathbf{k}] + \ldots \qquad (3)$$

In this form, $\mathbf{R}^{11}$ and $\mathbf{R}^{12}$ contain model values for elements of **R**-matrix, and the calculated matrices $\partial \mathbf{R}^{11}/\partial \mathbf{k}$ and $\partial \mathbf{R}^{12}/\partial \mathbf{k}$ contain the sensitivity terms. Although it is desireable to solve for $\Delta\mathbf{k}$ directly, the initial conditions $\{A, B\}^{\dagger}$ and the column vectors $\{A\Delta\mathbf{k}, B\Delta\mathbf{k}\}$ appear as the variable parameters for each trajectory.

To reduce the dimensions of the problem, and to constrain the solution vector $\Delta\mathbf{k}$, an iterative approach is possible:

I. Solve for {A , B} from Eq. 2 for each trajectory, then

II. Solve for $\Delta\mathbf{k}$ from Eq. 3 with initial conditions {**A** , **B**} as determined in Step I, i.e., solve for $\Delta\mathbf{k}$ from

$$\frac{\Delta \mathbf{x}}{\Delta \theta} - \mathbf{A}\mathbf{R}^{11} - \mathbf{B}\mathbf{R}^{12} = (\partial \mathbf{R}^{11}/\partial \mathbf{k} + \mathbf{R}^{12}/\partial \mathbf{k}) \cdot \Delta \mathbf{k} \qquad (4)$$

---

†With transmission line fitting, the 'beam' can be propagated in either direction, e.g., the initial conditions {A ,B} can be located on the right in Fig. 1.

for all trajectories simultaneously. As with the closed orbit case, BPM, corrector, coupling, and energy variations can be added to the parameter vector $\Delta\mathbf{k}$.

The approach of iteratively solving for the initial 'launch' conditions $\{\mathbf{A}, \mathbf{B}\}$ and then the model parameters $\Delta\mathbf{k}$ is used routinely in RESOLVE [10] analysis (and independently suggested by S. Prabhakar). Other numerical solutions are possible. The difference here is the linearization step that facilitates the analysis.

4 SUMMARY

Two ideas are presented with the intention of speeding up measurement based model calibration for on- line applications. The first method, recursive least-squares analysis, is similar to the method used in practice today, but explores the possibility of 'updating' the solution as new data becomes available without re-analyzing the entire data set.

The second method draws on concepts used before closed-orbit analysis became available, namely piecewise model calibration. Relative to closed-orbit model calibration for an entire storage ring, piecewise analysis involves

- less calculation time for perturbed trajectories,
- fewer BPMs and correctors, and
- fewer variable model parameters.

In practice, once a corrector is kicked the full (closed) orbit can be recorded, but only a section of the accelerator is analyzed at any one time. The model fitting can be 'propagated' along a transmission line, around a storage ring, or focus on a specific region of the accelerator. The time savings for piecewise fitting is derived from elimination of closed orbit calculations (only the coefficients $\mathbf{R}^{11}(s)$ and $\mathbf{R}^{12}(s)$ are needed), and inversion of a smaller sensitivity matrix. After adjusting IP optics in a large collider, for instance, a quick check of quadrupole strengths is possible without analysis of the entire storage ring.

5 ACKNOWLEDGEMENTS

Multi-track analysis originated with Martin Lee, leading to RESOLVE. Volker Ziemann performed the first test of linearized analysis, James Safranek extended the method to where it stands today, and David Robin has made many contributions to its application. Max Cornacchia, Mikael Eriksson, Alan Jackson, Sam Krinsky, and Ron Ruth are gratefully acknowledged for allocating research time in sometimes uncertain directions.

6 REFERENCES

[1] M. Lee, J. Sheppard, M. Sullenberger, Europhysics Conference on Computing in Accelerator Design and Operation, Berlin (1983).

[2] M. Lee, et al., Europhysics Conf. on Control Systems for Experimental Physics, Villiars, Switzerland (1987).

[3] M.J. Lee, et al, International Conference Cum Workshop on Current Trends in Data Acquisition and Control of Accelerators, Calcutta, India (1991).

[4] W.J. Corbett, V. Ziemann, M. Lee, IEEE PAC, Washington, D.C. (1993).

[5] J. Safranek, M. Lee, AIP Conference Proceedings, Vol. 315, (1994).

[6] D. Robin, et al, Proc. of 1996 EPAC, Barcelona, Spain (1996).

[7] W.J. Corbett, D. Robin, J. Safranek and V. Ziemann, LHC96 Workshop, Montreaux, Switzerland (1996).

To appear in *Particle Accelerators*.

[8] J. Safranek, NIM (A), Vol. 388, No. 1&2 (1997).

[9] See, for instance, G.F. Franklin, J.D. Powell, M.L. Workman, 'Digital Control of Dynamic Systems', Addison-Wesley (1990).

[10] W.J. Corbett, M.J. Lee and Y. Zambre, Proc. 3rd EPACS, Berlin (1992).

THE SPEAR RF CAVITY CHARACTERIZATION AT STANFORD SYNCHROTRON RADIATION LABORATORY*

Sanghyun Park *and* James J. Sebek
Stanford Synchrotron Radiation Laboratory
SLAC MS 69, P.O.Box 4349, Stanford, California 94309

Abstract

At the SPEAR storage ring, the 3 GeV stored beam is driven by a five-cell π-mode standing wave cavity operating at 358.54 MHz. The frequency tuning and the field balance between the cells are feedback controlled by movable tuners at the end cells. Another cavity of the same type in the ring can be powered for higher beam currentin the future, but it is presently in a standby mode as a backup system. This idle cavity is also used to suppress the beam instability by manually positioning the tuners. For the purpose of cold tests, one PEP-I cavity is being prepared for the RF measurements.

1 INTRODUCTION

At Stanford Synchrotron Radiation Laboratory (SSRL), a 3.0 GeV electron beam is stored in the SPEAR, which stands for Stanford Positron Electron Accumulator Ring and built originally for high energy research in electron-positron collision, to provide bright X-rays for the users at 10 beamlines. At the top of the fill the stored beam current reaches 100 mA, diminishing to about 50 mA when it is dumped for a refill 24 hours later. As an indication of the quality of the photon beam delivered, the intensity at every beamline is monitored.

A pair of photoelectric probes, made of tungsten tip and placed symmetrically at either side of the beam center, develops photoelectric voltage roughly proportional to the photon intensity at the center. The difference is used to steer the beam, and the sum is proportional to the stored electron beam current. Occasionally, however, the sum voltage shows spikes or bistable oscillations. From the users' point of view, this noise must be minimized by all means for them to do accurate measurements.

At the accelerator side, there are several factors that force the system to deviate from the designed way of performance such as higher order modes in the cavity initiated by the circulating beam, and fluctuations in cavity temperature mainly due to limits in cooling regulation. The stored beam current, photon intensity, cavity temperature as measured at one out of five cooling channels, and the positions of the two tuners #1 and #5 are shown below over a 2-hour period that includes 35-minute beam noise activities as seen at the beamline 10.

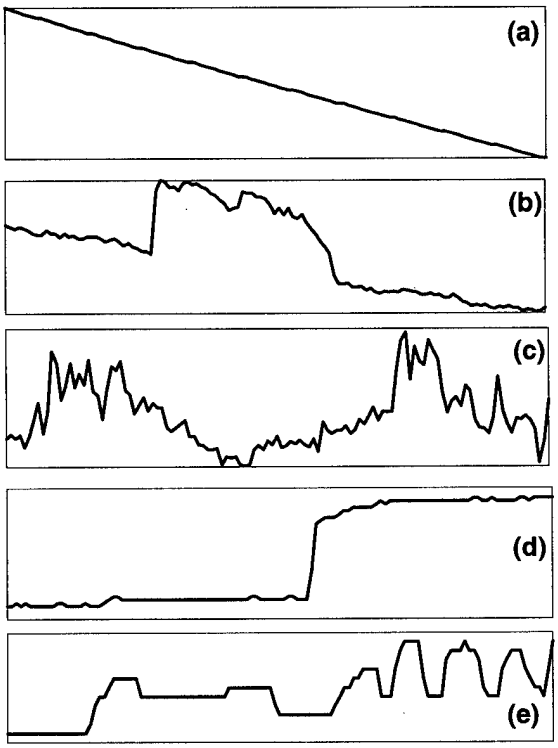


Fig. 1 Typical system performance over a two-hour period (horizontal axis) that includes a 35-minute beam noise. **a** beam current (96.2 to 90.6 mA), **b** Beamline 10 sum (0.13V span, 1.47V min.), **c** cavity temperature (between 48.4 to 48.9 deg C), **e** tuner #1 position (0.34 mm span), **f** tuner #5 position (0.11 mm span). All scales are linear.

From the figure above, it is clear that the stored beam current follows $\sim(1+t/\tau)^{-1}$ dependence even when the beamline 10 sum is jumped to its higher level, returning to the normal value about 30 minutes later. Without any loss

* Work supported by Department of Energy Contract DE-AC03-76SF00515.

0-7803-4376-X/98/$10.00 © 1998 IEEE

of the beam, there is no discernable precursor detected in any data channel. It is noticeable that the period of noise coincides with a dip in the cavity temperature, and the noise subsides as the tuner number 5 makes a large excursion. In recent years, there are more data acquisition channels being added to the system for engineering and environmental diagnostics. Further details will be given in the later sections.

2 CONVENTIONAL CONTROL

There are a number of five-cell cavities currently in use worldwide mostly operating at 352 MHz. One such system is the PEP-I, now being replaced by single-cell based PEP-II for the B-factory at SLAC. Other examples are ESRF and LEP where the two tuners are placed in cells 2 and 3, instead of 1 and 5 at PEP-I and SPEAR.
The SPEAR cavities are scaled version of the PEP-I, and most low level RF and control/monitoring electronics are derived from the PEP-I design.[1] Despite the minor difference in operating frequencies, there are still many features that are common to the two systems.

At the SPEAR RF cavity, each cell is equipped with an RF probe, which indicates the accelerating field strength at the power level of 50 dB down from the driving RF power fed to the third cell. There are five voltages overall from the cavity; V_1 to V_5. The difference $\Delta = V_5 - V_1$ is used for differential movements of the tuners 1 and 5 so that $\Delta=0$. The sum $\Sigma = V_1 + \ldots + V_5$ is the readback voltage for the gap voltage set. As the gap voltage is raized from 0 to a set voltage of 1.6 MV or so in the absence of any beam, about 100 kW of RF power is dissipated at the wall. As a result, the temperature difference between the inlet and return ports of the cooling water channels are also raised to a value determined by the power dissipation along the cooling channel, and by the inlet temperature. As the electron bunches are injected up to100 mA, an additional 0.75 kW/mA is needed to make up for the beam loading.

The probe signal from the cell 3, across the high power RF input coupler, is also used as a reference for feedback control of the RF phase. Throughout the system, the control and monitoring circuitry is blind to any higher order mode. In fact, every detector is preceded by a low pass filter with the cutoff frequency at
400 MHz.

3 INSTABILITIES

During the startup period following a shut down for maintenance lasting two to three months, the system reveals higher ring vacuum pressure and shorter beam life time. Since the beam current needs to be 50 mA or higher to deliver useful photon beams to the users, the ring is filled twice or even three times a day until the ring vacuum is stabilized and the beam lifetime reaches
25 hour or so. As the lifetime is inversely proportional to the beam current, the vacuum quality defined as the product of the two is roughly a constant over many days, improving on a time scale of weeks.

The noise and fluctuations of the photoelectric detector voltage mentioned earlier are more frequent in this early phase of the startup. Even many months into the user run, sporadic occurences of this phenomena is noticeable to the users. A fine adjustment of tunes, slight changes in manually set gap voltage, and repositioning of tuners at the idle cavity are the routine counter measures for stabilization.

As the ring is filled and some 40 bunches of electrons pass through the idle cavity, the wakefields are picked up by probes. After the filtering and amplitude detection, the sum of all five signals is registered as a gap voltage. Again, only fundamental frequency component of the fileds is registered. Without altering this gap voltage, a small change in tuner position (fraction of a millimeter out of a 10 cm full range) results in a big variation of the tune space and the beam quality.

Recently it has been noticed that the brief beam noise that last only a few minutes occurs once a day, typically right after the sun rise. Considering the fact that relatively long (over 30 feet) waveguide is directly exposed to the sun, and the RF cables are not shaded either, the cause may well be thermal effect from the environment.

So far most of the efforts to maintain the noise-free beam have been based on empherical know how. And part of the justification for this study of the old cavities is to explore the parameter space in RF mode structure as a function of externally controlable variables. The other part the goal is to address the physics and engineering issues centered on the use of the five-cell cavities at higher beam current with increased gap voltage to serve more synchrotron radiation users at additional beamlines with insertion devices in the future.

4 REVISITING THE OLD CAVITIES

At the time when the five-cell standing wave cavities were designed and built, the accelerator physics infra-structure was such that test equipment or computer codes were not powerful enough to provide details of the field structure or beam dynamics.

As a national user facility that delivers beams 24 hours each day interrupted only by injection that lasts about 20 minutes, the access to the SPEAR cavities is extremely limited, whether it's active or idle. One alternative is to

monitor the cavities with the beam on. Especially during the machine physics sessions, any desired number of bunches can be stored and one can afford to lose any or all of the beam over the course of machine exploration.

The raw signal from the cavity probe is coupled out before it reaches the low pass filter of the system. The insertion loss of the wide band directional coupler is compensated for by raising the detector gain, leaving the high frequency probing transparent to the rest of the system. A computerized data taking is presently under way to evaluate the effect of tuner positions on the beam behavior and high frequency components of the wakefields.

Still another option is to work on the cavity itself offline. The PEP-I cavity, decommissioned and surplused, was lifted to the SSRL booster building, with all of ancillary items attached to it still intact. Although the working frequency of the PEP-I cavity is 352 MHz, about 6 MHz below the SPEAR frequency, the basic structure is almost identical to the other. While it is not possible to run the electron beam through, one finds freedom in other areas. For example, there are eight RF ports available; one at the high power input coupler following the waveguide-to - coax adaptor, two on axis, and five RF probes. Any one port can be used for the reflection measurements, and any two can be selecterd for the transmission.

A modestly priced vector network analyzer is readily available. It has a frequency range of 0.3MHz to 3.0GHz and its dynamic range is about 70dB, which can be complemented by adding a wide band amplifier at each port. While a preamplifier that drives klystron can output up to 25 watts, its bandwidth is rather limited to about 400 MHz. For the study of higher order modes going up to 1.5GHz, a one-watt output amplifier covering the whole bandwidth of the network analyzer, commercially available off the shelf, can be modulated by a fast rising (less than 10ns) pulses for a time domain measurement.

Preparation is under way to make the tuner drive mechanism programmable. The electric probes have also been made to launch and detect test waves alng the cavity axis. Since there is no high power involved, wall dissipation and raised temperature distribution can be simulated by passing independently temperature contolled water through five separate water channels at very low flow rate. By placing adequate thermal shielding around the cavity, the accosiated electrical power requirement is minimal.

5 IMPLICATION TO THE UPGRADED SYSTEM

Unlike a case where a light source is designed with little constraint on machine parameters, the SPEAR has its circumference very much fixed. Although it is true that a small change may possibly be accommodated, the existing beamline locations dictate the geometry, and thus the RF frequency. Presently, the Booster[2] and the SPEAR have the circumference ratio of 4 to 7, and the SPEAR harmonic number is 280. If the frequency needs to be changed, both rings will have to be modified as well. Unless there is a compelling reason yet to be found, keeping the present frequency is the least expensive proposition. [3]

While many single-cell cavities are currently in use, or being planned at various installations, the standard design at either 500MHz or 476MHz is not entirely compatible with the SSRL system in straightforward way. One other drawback of the single-cavity system is that it has low shunt impedance. In the case of PEP-II low energy ring with 3.1MeV beam energy, which is quite comparable to the case of SPEAR, and more than 2000mA of beam current, the energy loss per turn is still lower as compared to the SPEAR when all the spaces for insertion devices are fully utilized. Yet, the low energy ring of PEP-II takes 3 MW of RF for its 6 cavities, whereas the fully loaded SPEAR with two five-cell cavities needs less than 600kW.

Once the measurements described above are made, the quantitative data will be utilized for the better simulation in system design and beam dynamics. With the data on optimal settings of tuner positions, for example, the latest version of MAFIA code may be beneficially used to elucidate the details of the field structure. Along with non-invasive measurements taken from the SPEAR cavities, both active and idle, the conclusion will me drawn as to the suitability of the present five-cell cavities for the upgraded beam parameters.

REFERENCES

[1] M.A. Allen , and R. McConnell, private communications

[2] J.N. Weaver, *et al.*, PAC91, p. 769

[3] R.O. Hettel, *et al.*, these proceedings

SPEAR III – A BRIGHTER SOURCE AT SSRL*

R. Hettel, R. Boyce, S. Brennan, J. Corbett, M. Cornacchia, W. Davies-White, A. Garren, A. Hofmann, C. Limborg, Y. Nosochkov, H.-D. Nuhn, T. Rabedeau, J. Safranek†, H. Wiedemann
Stanford Synchrotron Radiation Laboratory, SLAC, Stanford, CA 94309

Abstract

By replacing the magnets and vacuum chamber for the 3 GeV SPEAR II storage ring, the natural emittance of the machine can be reduced from 130 to 18 nm-rad and the stored current can be raised from 100 to 200 mA with a 50 h lifetime. This configuration increases focused photon flux for insertion device beamlines by an order of magnitude and the photon brightness for future undulators would exceed 10^{18} at 5 keV. Due to a higher critical energy, the photon flux in the 20 keV range for bending magnet beamlines increases by more than two orders of magnitude. We present preliminary SPEAR III design study results and plans to implement the facility upgrade with minimal downtime for SSRL users.

1 INTRODUCTION

For the last 25 years the SPEAR storage ring has served both the high energy physics (HEP) and synchrotron radiation (SR) scientific communities, first as SPEAR I operating at a maximum energy of 2.4 GeV, and then as SPEAR II (1974), operating at up to 3.5 GeV. In 1990 SPEAR II became a dedicated 3 GeV, 100 mA light source with beam injected from a newly commissioned booster synchrotron. To this day, the SPEAR septum magnet limits the injection energy to 2.37 GeV and energy ramping to the 3 GeV user configuration is required. While other studies were made to reduce SPEAR emittance in the 1970s and 80s [1,2], the addition of a third injection kicker enabled a practical alteration the FODO lattice magnet settings in 1991 that reduced the emittance from ~500 nm-rad used for HEP to 130 nm-rad [3]. Alternative lower emittance lattices, which require new magnets and vacuum chamber, have since been considered and proposed [3,4]. These studies are now being extended for the 3 GeV, 200 mA low emittance SPEAR III proposal.

SPEAR II has eighteen magnet girders and eighteen straight sections. Seven straight sections are presently used for ~2 m insertion devices (IDs) and four more are available for future IDs, including one of the two long interaction region (IR) straight sections that could accommodate up to 17 m of ID. Four beamlines have bending magnet sources.

SPEAR III upgrade goals include:

- Reduce natural emittance to 18 nm-rad
- Increase stored beam current to 200 mA
- Achieve high lifetime at 200 mA (~50 h)
- Achieve high beam stability
- Maintain existing beamline alignment
- Create more long straight sections (~4 m)
- Inject at 3 GeV
- Maintain high operational reliability
- Reduce operating power costs
- Limit conversion downtime to <6 months
- Permit future upgrade possibilities

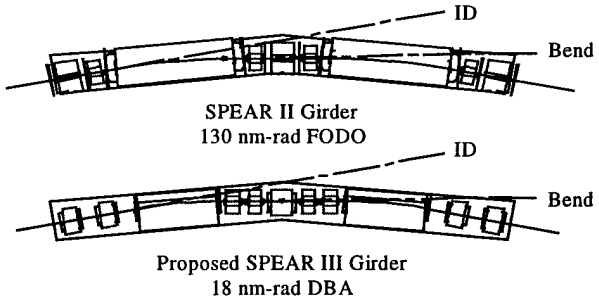


Figure 1: Magnet girders for SPEAR II and III

The basic upgrade plan is to replace the SPEAR II magnets with new magnets on the existing girders in a double bend achromat (DBA) configuration, leaving SR source points and beamline alignment virtually unchanged (Fig. 1). The four magnet girders flanking the two long IRs will be moved closer to the interaction points to increase the lengths of four straight sections from 2.7 m to 4.2 m while reducing the IR straight length to 12 m. The two existing RF cavities can be moved to the West IR (or an adjacent straight section) to create two new ID sites. The vacuum chamber will be replaced with a smaller aperture chamber rated for 500 mA to permit future higher current operation. A key aspect of the upgrade strategy is to limit the conversion period to one long downtime of six months (or less) together with normal two month shutdowns in order to minimize the impact on user programs. In the following sections we discuss photon and electron beam properties for SPEAR III and present preliminary design plans for beamline and accelerator systems.

* work supported in part by DOE Contract DE-AC03-76SF00515 and Office of Basic Energy Sciences, Division of Chemical Sciences

† presently at the NSLS, BNL.

0-7803-4376-X/98/$10.00 © 1998 IEEE

2 SPEAR III PHOTON BEAMS

2.1 Photon Beam Properties

For a broad range of experiments, focused flux density (photons/sec/mm^2/0.1%BW), or the number of photons one can fit through a small aperture at the sample, is a more important beam parameter than brightness (photons/sec/mm^2/mrad^2/0.1%BW). The reduced beam size and increased current and critical energy of SPEAR III (Table 1) result in an order-of-magnitude increase in focused flux density for ID beamlines, and a two order-of-magnitude increase for bend magnet lines, making them comparable to SPEAR II ID lines (Fig.2). A 4 m undulator in SPEAR III could produce a brightness of $>10^{18}$ in the 5 keV range, and $>10^{17}$ in the 10 keV range.

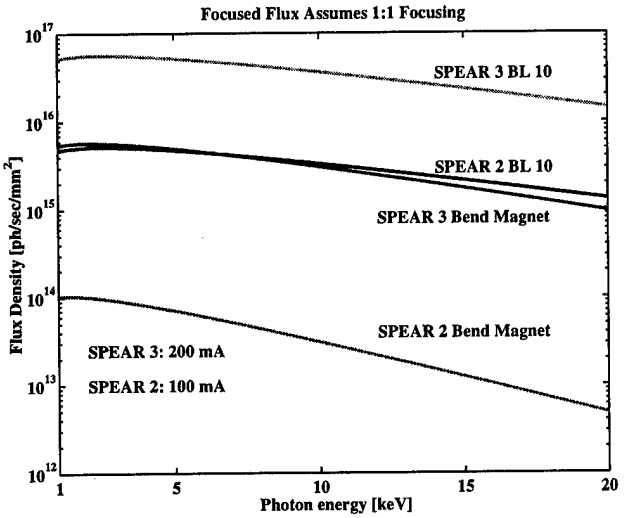


Figure 2: Flux densities for bend and wiggler (BL10) lines for SPEAR II and III.

2.2 Beamline Upgrades

SPEAR III provides two challenges for photon beamlines: (1) increased power loading on masks, slits and windows, and (2) the need for enhanced beamline optical performance in order to fully exploit beam source improvements. All beamline masks and windows will be upgraded for 200 mA operation; few changes are anticipated for ID beamlines built in recent years. Replacement components will utilize concepts developed for SSRL's newest and most powerful beamline 11 which develops a 4.5 kW/mrad^2 peak power density. Monochromators and mirrors on most ID lines will be replaced with versions using cooling technologies developed for third generation SR sources, which include pinpost and LN-cooled Si monochromator crystals, and internally and side clamp-cooled Si mirrors. Where possible, optics upgrades will extend beamline capabilities, for example, by changing mirror cutoff energies or optics acceptances.

	SPEAR II	SPEAR III
Current	100 mA	200 mA
Natural emittance	130 nm-rad	18 nm-rad
H-V coupling	1%	1%
Energy spread	.00074	.00087
Momentum compact.	.015	.0012
Nat. chromaticity (x,y)	-12, -14	-20, -20
Betatron tunes (x, y)	7.18, 5.28	14.75, 5.85
Critical energy	4.8 keV	7.1 keV
Lifetime at max. curr.	~30 h	~50 h
Average ring pressure	1 nTorr	1 nTorr
Beam sigma (x,y) – ID	1.85,.05 mm	.51,.04 mm
Beam sigma (x,y)-bend	.72,.18 mm	.16,.04 mm

Table 1: Machine parameters for 3 GeV SPEAR II and SPEAR III (approximate).

3 LATTICE

The 12.8 m bending radius SPEAR II FODO lattice will be replaced with an 8.38 m bending radius DBA lattice in SPEAR III. Since the new lattice is constrained by girder, ID and beamline locations, as well as by the RF-determined path length of 234.12 m, options for the numbers and placement of magnets are limited. The most conservative option uses separated function magnets with doublet quadrupoles and four sextupoles per cell (Figs. 1,3). Additional quadrupoles are placed in the long IRs for tune and optics control. Detailed study and optimization of this lattice is in progress. A combined function lattice that would increase arc straight section lengths by up to 0.5 m and reduce the horizontal beta functions in them by a factor of two is also being considered. A reduced horizontal beta is desired by users because of the smaller focused beam size, but it makes injection more difficult and may reduce the Touschek lifetime.

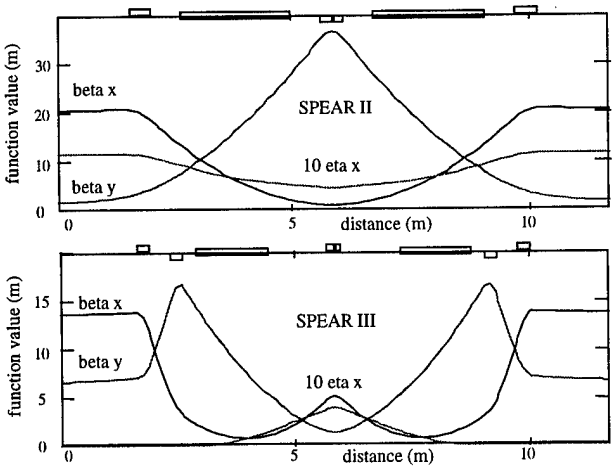


Figure 3: Lattice functions for SPEAR II and III cells.

4 COLLECTIVE EFFECTS AND LIFETIME [5]

The two SPEAR II 5-cell RF cavities will be used initially for SPEAR III. These cavities have numerous high order mode resonances, necessitating longitudinal and transverse feedback systems to damp multibunch beam instabilities. Computed instability thresholds are below 10 mA, assuming zero chromaticity and the overlapping of synchrotron sidebands with HOM resonances. A future upgrade possibility, especially if the stored current is increased beyond 200 mA, is to install single-cell, mode-damped cavities to reduce or eliminate the need for feedback.

The broadband impedance of the ESRF was scaled to the SPEAR circumference to yield |Z/n| = ~2.5 ohms and a Q=1 resonance centered at 30 GHz. This impedance will initiate a turbulent regime at 0.6 mA. Bunch lengthening and widening coefficients will be 1.9 and 1.5 respectively for a 2.8 mA single bunch current (200 mA in 70 out of 280 RF buckets).

A 70 h Touschek lifetime has been computed assuming a 3% momentum acceptance, 2.7 MV RF voltage, and 200 mA in 70 bunches. This value can be increased by filling the same current in more buckets (i.e. a factor of 4 increase for the maximum 280 bunches) or by using a bunch lengthening cavity.

A 100 h Coulomb scattering lifetime has been calculated for an N_2-equivalent pressure of 0.25 nTorr and a minimum vertical full aperture of 12 mm in one ID chamber. The bremsstrahlung lifetime is 300 h assuming a 3% momentum acceptance.

The total 200 mA lifetime is 36 h for 70 bunches and 60 h for 280 bunches.

5 ACCELERATOR COMPONENTS

5.1 Vacuum System

The girder vacuum chambers will be designed to accommodate smaller magnet gaps and higher SR power loads. The chamber cross section has ~36x90 mm inner dimensions. Many of the existing straight section chambers will be kept, including those for the IDs, kicker magnets, and some diagnostic components. Tapered transitions from new to old chambers will be required in some cases to reduce impedance. RF-shielded bellows elements will be designed to minimize parasitic mode losses. Beamline front end masks and absorbers will also be upgraded for higher SR power.

To maximize beam lifetime, we seek an average ring pressure of order 1 nTorr. An antechamber design with discrete photon absorbers would achieve this goal and maximize chamber stability under varying SR power load. Since an antechamber design may be more costly and may necessitate more expensive C-core or Collins-type magnets, we are also considering a narrow chamber design. Since absorbed SR power may cause this chamber to move, beam position monitor modules would need decoupling bellows and stable supports to reduce transverse motion to the 10 μm level as requred by the orbit stabilizing system.

5.2 Magnets and Supports

The preliminary separated function SPEAR III lattice requires 36 dipoles (50 mm gap), 94 quadrupoles (70 mm bore diameter), and 72 sextupoles (80 mm bore diameter), and 54 pairs of horizontal and vertical correctors. The operating field for the 1.5 m, 10.6° dipoles will be 1.19 T at 3 GeV. Quadrupole gradients are ~20 T/m at 3 GeV. Sextupole strengths are on the order of 300 T/m^2. These field designs will permit 3.5 GeV operation with acceptable core saturation. A C-core dipole accommodates the SR beamline exit chamber. It has not been determined if open-core quadrupoles and sextupoles will be needed.

The new magnets will be mounted on existing 10 m concrete girders, each of which is now supported by three piers sunk 1.5 m into the ground. These girders have a rotational oscillation mode at ~5 Hz about the long axis that could be stabilized with a fourth support. The magnets will be mounted on the girders using kinematic struts. New girders will be installed for the four repositioned magnet cells flanking the IRs.

5.3 Injection

The booster synchrotron and booster-to-SPEAR transport lines will be upgraded for 3 GeV injection. A new septum magnet will be needed for the higher injection energy and the reduced displacement between incoming and stored beams (~15 mm). The three existing vacuum-core kicker magnets will be reused.

A possible future upgrade is to move the injection point to a long straight section unsuitable for beamline use and to install shorter ferrite-core kickers. This would liberate two arc straight sections and the second 12 m IR straight section for IDs.

6 ACKNOWLEDGMENTS

The authors are indebted to A. Bienenstock and B. Richter for supporting this work; to H. Winick for his encouragement; to J. Arthur, R. Carr and R. Tatchyn; and to the SSRL engineering and design groups.

REFERENCES

[1] A. Garren, M. Lee, P. Morton, "SPEAR Lattice Modifications to Increase Synchrotron Light Brightness", SPEAR Pub. 193, 1976.

[2] L. Blumberg, J. Harris, R. Stege, J. Cerino, R. Hettel, A. Hofmann, R. Liu, H. Wiedemann, H. Winick, Proc. of 1985 IEEE PAC, 3433.

[3] J. Safranek, Ph.D Thesis, Stanford Uiversity, 1991.

[4] W. Davies-White, H. Wiedemann, "SPEAR Upgrade Program", SSRL internal report, Jan. 8, 1997.

[5] A. Hofmann and C. Limborg, "Beam Instabilities in SPEAR III", SSRL internal report, April 11, 1997.

EXPERIMENTAL CALIBRATION OF SRRC LATTICE OPTICS

C.C. Kuo, J. Safranek[+], H.P. Chang, K.T. Hsu
Synchrotron Radiation Research Center
No 1. R&D Rd VI, Hsinchu Science-Based Industrial Park, Hsinchu, Taiwan, R.O.C.
[+]NSLS, Brookhaven National Laboratory, Upton, New York

Abstract

The linear optics of the TLS (Taiwan Light Source) storage ring at SRRC (Synchrotron Radiation Research Center) have been experimentally determined using the measured orbit response matrix. The storage ring with insertion devices open was found to have small beta beating with the linear optics very close to the design. The analysis revealed some incorrect wiring of the orbit steering magnets and significant variation in the gains of BPMs. Both of these problems were subsequently corrected. Analysis of the orbit response matrix data also can be used to correct beta beating caused by the insertion devices

1 INTRODUCTION

Since the commissioning of the TLS at SRRC in April 1993, it has operated for 4 years[1-3]. The 1.3 GeV electron beam is injected from the booster synchrotron to the storage ring, and the energy is normally ramped up to 1.5 GeV in the storage ring started from September 1996. The lattice structure of the storage ring has six periods, each 20 m long. One period consists of a 6-m long straight and a combined function triple bend achromat. In all there are 48 quadrupoles and 24 sextupoles. The emittance of the lattice at 1.3 GeV is 1.9 10^{-8} m-rad. Each integrated sextupole strength is about 10 m^{-1}. The beam closed orbit can be corrected down to a level of 100 to 200 μm rms with respect to the ideal orbit, based upon the beam position monitor readings. However, the real center could be different from these values partially due to the electronics offsets of the BPMs and partially the alignment errors. At the sextupole position, this offset creates quadrupole fields, and the linear optics is thus distorted. The symmetry of the linear optics is then broken. To determine the lattice optics precisely, the computer code called LOCO (Linear Optics from Closed Orbits) developed by one of the authors, J. Safranek, was used to analyze the orbit response matrix associated with the steering magnets[4]. The analysis provided best fit values for the gradients in the individual quadrupoles and sextupoles as well as the BPM gain errors and steering magnet calibration errors. The measured BPMs gain errors were consistent with subsequent measurements made using a test signal.

2 METHOD

For a storage ring of known magnet strengths, one can calculate the orbit response matrix. The LOCO program reverses this process and calculates the magnetic field gradients from the measured orbit response matrix. Adjusting the gradients in the model until the model calculated response matrix is best fit to the measured one, we can obtain the real machine gradient distribution.

The COMFORT or MAD [5] accelerator optics program can be used to calculate the model response matrix. The measured and model response matrices are defined by

$$\begin{pmatrix} x \\ y \end{pmatrix} = M_{\text{meas,mod}} \begin{pmatrix} \theta_x \\ \theta_y \end{pmatrix} \tag{1}$$

where θ_x, θ_y is a change in the orbit steering magnets and x, y is the resulting change in electron orbit. The model parameters in the program are varied to minimize χ^2 defined as

$$\chi^2 = \sum_{i,j} \frac{(M_{\text{meas,ij}} - M_{\text{mod,ij}})^2}{\sigma_i^2} \equiv \sum_{i,j} V_{k(i,j)}^2 \tag{2}$$

where the sum is over the 62 orbit steering magnets (30 horizontal and 32 vertical) and the 96 BPMs (48 horizontal and 48 vertical). The σ_i are the measured noise levels for the BPMs. In this study, we ignored the coupling terms for the transverse planes such that only the normal terms of the gradients were fitted. The vector $V_{k(i,j)}$ has 2976 elements for the uncoupled response matrix in this study. Because the response matrix is not a linear function of the quadrupole gradient, LOCO must be iterated until it converges to the best set of parameters, i.e., the best gradient distribution.

In the fitting of the response matrix, the energy shifts due to the horizontal corrector in the dispersion region is also included, i.e., a term $\frac{\eta_{xi}\eta_{xj}}{\alpha_c L_0}$ is considered in the M_{model}. The kick size was usually of a size to create an orbit distortion of 1 mm rms so as to have good noise-to-signal level and eliminate the nonlinear effects in the BPMs.

0-7803-4376-X/98./$10.00 © 1998 IEEE

3 QUADRUPOLE MAGNET ERROR

We stored the beam current in the SRRC storage ring first with sextupole magnet turned on to correct chromaticities of the lattice and then turned off the sextupole magnet power supplies. In both cases, we performed the measurements of the orbit response by changing the individual correctors. We averaged the BPM data from database 100 times per measurement. Except a few malfunctioning BPMs, we achieved a BPM noise level of 1 μm. However, the BPM gains varied quite significantly and the fitted gain errors were checked with testing electronic signals. The results were in good agreement.

The closed orbit could be corrected down to several hundred microns rms for the normal users operation. Due to construction errors the alignment of the sextupole magnets were not as accurate as quadrupoles of which alignment errors were 0.15 mm rms. The systematic position errors at the BPMs also gave extra orbit offsets at sextupole locations. To remove the gradients generated from the sextupole offsets, we first analyzed the case without powering sextupoles.

The fit of the quadrupole gradients showed that quality of the SRRC magnets is very good. The following tables shows that the rms variation in the fit gradient for the four quadrupole families. Also shown is the rms variation in gradients according to the magnetic measurements.

Table 1: Variation in fit and measured gradients within each family.

Quadrupole family	rms variation from average	
	fit	magnetic measurements
1	.26 percent	.06 percent
2	.07 percent	.03 percent
3	.30 percent	.07 percent
4	.14 percent	.04 percent

The larger variation in the fit gradients is probably due to systematic errors in the fitting associated with variation in the dipole gradients. In the fitting it was assumed that the dipole gradients are all exactly same. The variation in real dipole gradients results in variation in the fit quadrupole gradients. Including the individual dipole gradients as fit parameters showed that the orbit response matrix was insufficient to accurately calibrate both the individual dipole gradients and the gradients of the quadrupole adjacent to the dipoles. It results in an increase of both gradients errors in the fit. This means that the variations of the quadrupole gradients is smaller than can be resolved with the orbit response matrix analysis.

As shown in Fig. 1, the analysis showed that the distortion of the beta function was very small in the case that the sextupoles were turned off. When the sextupoles were on, the orbit offsets created gradients and the betatron functions were distorted as given in Fig. 2. The beta distortion was about ±4.5 percent and ±8 percent in the horizontal and vertical plane, respectively.

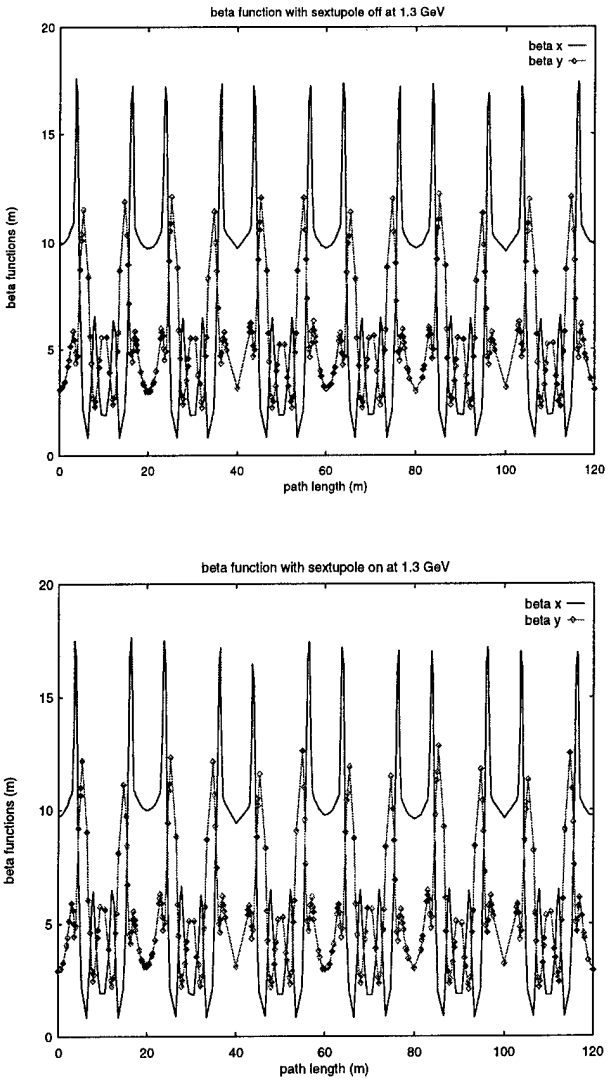


Figure 1, 2: The fit betatron functions in the cases with and without sextupoles at 1.3 GeV.

The beam energy is usually ramped up to 1.5 GeV after 1.3 GeV injection and the sextupole strengths are increased. It showed the beta beat was larger at 1.5 GeV (shown in Fig. 3).

In the presence of perturbations from the insertion devices, the vertical beta beat becomes larger if the perturbations are not compensated. Fig. 4 shows the effect of the wiggler magnet (1.8T, 25 poles). Correction of the beta beats of the SRRC storage ring will be possible once we have independent quadrupole trims which are presently being installed.

4 BPM CALIBRATION

We found significant variations in the calibrations of the BPMs. They varied in the horizontal plane by a factor of 3 from 1.946 to 0.665, and by a factor of 2 vertically from

1.830 to 0.791. This caused the errors in the closed orbit correction to some extent. Figs. 5 and 6 show the measured horizontal dispersion without and with correction for the fit gain errors. Much of the apparent distortion in the measured dispersion in Fig. 5 was caused by gain errors in the BPMs.

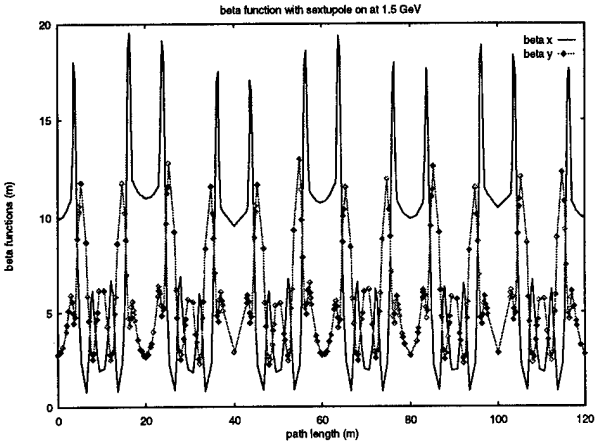


Figure 3. The beta functions at 1.5 GeV with sextupole on.

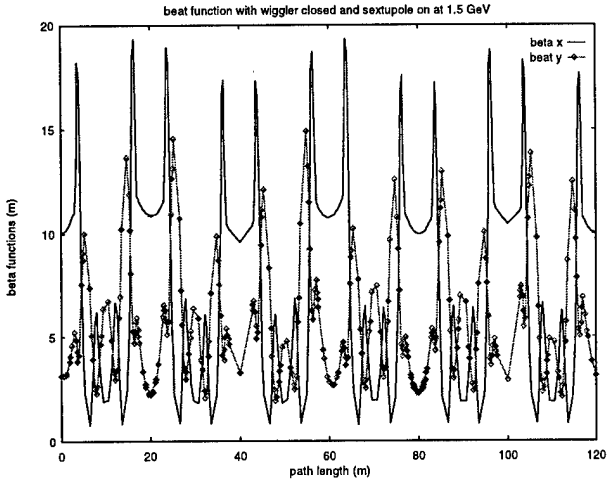


Figure 4: The betatron functions at 1.5 GeV with the wiggler magnetic gap closed.

5 CONCLUSION

Analysis with the LOCO code demonstrated that the SRRC lattice optics distortion is very small in the case when insertion devices are open and sextupoles are turned off. The accuracy of the SRRC quadrupole magnet gradients is very good. The parameters fit by LOCO were in good agreement with the measured results. The presence of the sextupole magnets and/or insertion devices generated beta beating. Further work to correct the betatron distortion can be undertaken when individual quadrupole power supplies are available. Using LOCO, we also observed the miswiring of correctors which was consequently corrected.

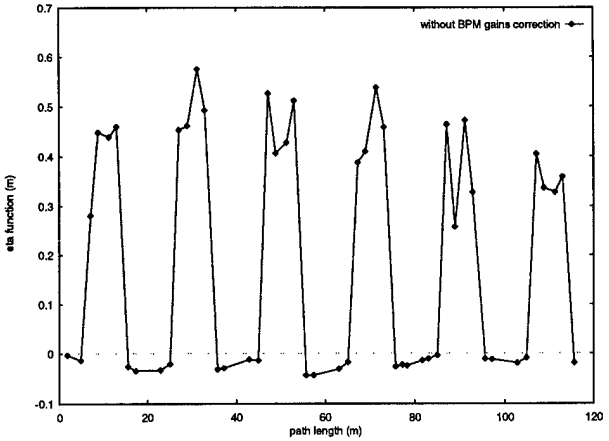


Figure 5: The dispersion without BPM gain error corrections.

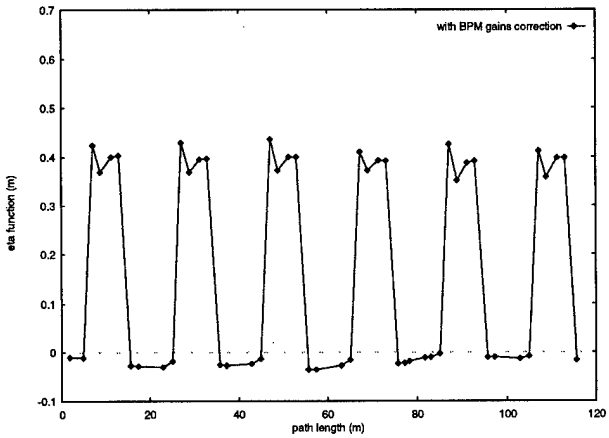


Figure 6: The dispersion function with BPM gains correction.

6 REFERENCES

[1] E. Yen, '*Present Status of SRRC*', 1993 IEEE PAC Conf. Proc., p. 1460.

[2] Y.C. Liu, '*The Status of SRRC*', 1994 EPAC Conf. Proc., p. 110.

[3] C.C. Kuo, *et al.*, '*The Performance of the SRRC Storage Ring and Wiggler Commissioning*', 1995 IEEE PAC Conf. Proc., p. 582.

[4] J. Safranek, '*Experimental Determination of Storage Ring Optics Using Orbit Response Measurements*', **Nucl. Inst. Meth A**, Vol. 388, No. 1&2, p. 27-36, 1997.

[5] H. Grote and F.C. Iselin, '*The MAD Program*', Version 8.0, CERN/SL/90-13, 1991
M.D. Woodley *et al.*, '*Control of Machine Function, or Transport Systems*', SLAC-PUB-3086, March 1983.

PRELIMINARY STUDY OF THE WAVELENGTH SHIFTER EFFECT IN SRRC STORAGE RING

J. C. Lee
Synchrotron Radiation Research Center

Abstract

The possibility of installing a superconducting wavelength shifter was discussed in SRRC. After surveying and comparing, magnet of one full strength pole and two half strength poles, with peak field of 7.5 tesla, was chosen for the feasibility study. Due to the space constraint, the wavelength shifter will not installed in the straight section middle. This paper reports the perturbation on lattice of the chosen wavelength shifter and the restoring from its perturbation. Effect on the ring is also investigated form the dynamic aperture point of view.

1 INTRODUCTION

The SRRC storage ring is dedicated for the VUV and soft X-ray research. It was operated at 1.3Gev while it is upgraded to 1.5 GeV for the routine operation. For higher photon energy applications, a wavelength shifter (WLS) was proposed to install in the ring. Under the constraint of available space, parameters for WLS were discussed. This paper reports the feasibility of the discussed situation in 1996. In this study, one full strength pole and two half strength poles with the maximum field of 7.5 tesla are assumed for the WLS. That means the WLS is a superconducting wiggler. Table 1 summarized the WLS parameters used in the study.

Table 1: The assumed WLS parameters

Maximum field strength	7.5 T
Number of poles	1 full strength
	2 half strength
Pole length	0.244 m
Location:	
(from Q1 edge to WLS center)	0.87 m

Figure 1 illustrates the relative location and spacing of quadrupoles and WLS in the section in which the WLS installed. The quadrupoles are used to match the beta-function to the desired values at the matching points. From figure 1 the WLS is not installed at the middle of straight section, i.e doesn't locate at the symmetry point. Hence the beta-function will be strongly disturbed and would not be symmetry w.r.t. WLS center. The photon flux from WLS and from 1.24 tesla bending magnet at 1.3 GeV are compared and shown in figure 2. The increasing of photon energy by WLS is clearly illustrated in the figure. The critical energy is governed by

$$\varepsilon_c(KeV) = 0.665 * E^2(GeV) * B(T) \qquad (1)$$

Therefore the critical energy will be increased from 1.394 KeV, emitted from 1.24T bending magnet(1.3GeV), to 8.429 KeV at 1.3 GeV and to 11.222 KeV at 1.5 GeV as WLS is installed in the ring.

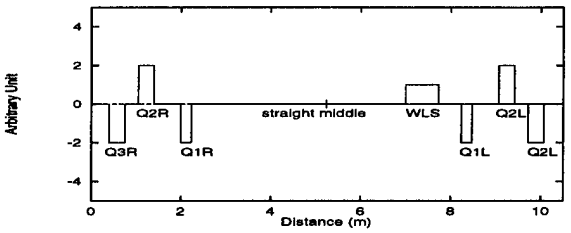


Figure 1: Schematic layout of quadrupoles and WLS in the straight section.

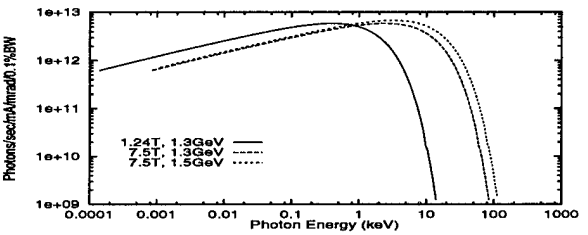


Figure 2: Comparison of photon flux between different magnetic field.

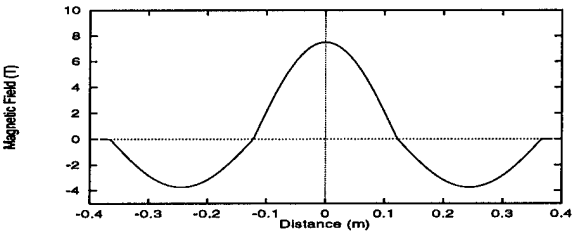


Figure 3: Magnetic field profile of WLS along the ideal trajectory.

2 FIELD INTERPRETATION

The WLS field in the ideal beam trajectory is represented by half sinusoidal function for each pole. Figure 3 shows the field profile along the WLS axis for the study. The field profile is symmetrical and has a zero field integral such that the exit angle equals the entrance angle. The second integral is also zero for this profile arrangement. Form of the WLS field is that of K. Halbach expression. Following the same trick of reference 1, the WLS field is approximately written by

0-7803-4376-X/98/$10.00 © 1998 IEEE

$$B_y = B(m)sin(K_p(z-(m-1)A_p/2))(1+ \{(K_py)^2/2! + (K_py)^4/4!\}) \quad (2)$$

where B(m) is the peak field for each pole with B(1)=B(3)=-B_0/2, B(2)=B_0 and B_0=7.5 tesla.

The term outside the braces contributes to the linear perturbation due to the WLS and the terms within the braces are the intrinsic non-linear field of WLS which contribute to the non-linear perturbation. In order to perform the beam dynamics calculation the linear part of WLS field, as defined in equation (2), is cut into a series hard edged rectangular dipole magnets to model the additional vertical focusing. Before the study, method of the series dipole approach was verified first. The code MAD8[2] was used to do this checking by comparing the theoretical vertical tune shift[3,4] due to one assumed wiggler field with the simulated results of which the wiggler field is approximated by a series dipoles. Results of these two approaches are consistent within the acceptable level.

3 BETA FUNCTION MATCHING AND TUNE COMPENSATION

Before the matching, the perturbation of WLS on linear optics was first investigated. Compared with the original ones, as shown in figure 4, the perturbated optical function is illustrated in figure 5. It is obvious that the vertical beta function was strongly distorted and enhanced to big values at some locations and the symmetry of the vertical beta function is also broken. Vertical tune is shifted from the design one of 4.13 to 4.277. As expected, the horizontal beta function and eta function are not affected by the WLS field.

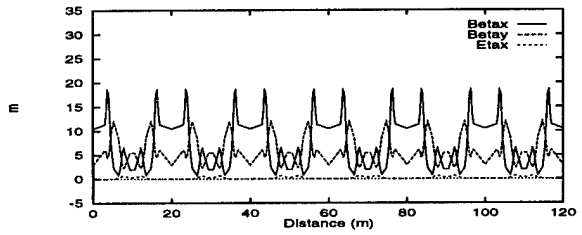


Figure 4: Unperturbated optics functions.

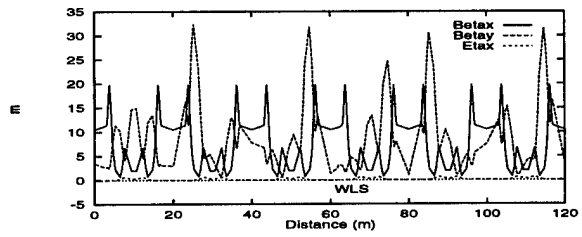


Figure 5: Perturbated optics functions by WLS.

By using the dipole model approximation and chosing the proper cutting[1], the beta matching and retunning from the WLS perturbation was performed by using MAD8. The quadrupoles within the WLS section are used to match the beta functions to the design ones at the matching points. Since the WLS doesn't insert at the middle of straight section, the symmetry point, the matched optics would not be symmetrical w.r.t. the symmetry point. This indicates the matched quadrupoles within the WLS section need to be tunned independently. Figure 6 shows the matched optics. It is clear that the optics is almost restored to the original ones outside the WLS section except those within the WLS section. The vertical beta function is also reduced to the acceptable value. With this matching the optics conditions will almost keep at design sets outside the WLS section and the perturbation on optics is mainly localized within the WLS section. The setting of quadrupoles within the WLS section for the cases with and without matching are listed in table 2.

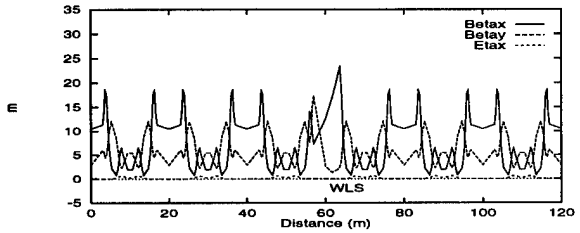


Figure 6: Matched optics functions from the WLS perturbation.

Table 2: Quadrupole settings in the WLS section with and without matching

Quadrupole	Design (m^{-2})	Matched (m^{-2})
Q1R	-1.50815	-2.34859
Q2R	2.87048	2.93744
Q3R	-1.15592	-0.05415
Q1L	-1.50815	-0.000189
Q2L	2.87048	1.88955
Q3L	-1.15592	-1.61765

As beta functions are matched, the tune shifts a little bit from the design one. Two quadrupole families, Q2 and Q3, outside the WLS section are chosen to restore the tune. After retunning, setting of Q2 family changes from 2.87048 m^{-2} to 2.850635 m^{-2} and Q3 family shifts from 1.15592 m^{-2} to -1.061488 m^{-2}. The Twiss functions slightly shifts from the matched optics and would not give big effect.

4 DYNAMIC APERTURE TRACKING

The dynamic aperture tracking study was performed 1000 turns at the WLS center by running RACETRACK[5]. Matched lattice with the linear WLS field, which is treated by a series rectangular dipole as described in section II, was tracked first. Figure 7 shows the tracking results compared with the aperture of the bare lattice. From figure 7,

the vertical aperture is reduced about 42% and no reduction in the horizontal as the linear WLS field included only. For the non-linear WLS field, as shown within the brace of equation (2), it is integrated for each cutting and is taken as ordinary multipole field. The tracking study was then performed with the matched and retunned lattice by including the non-linear WLS field and the measured (or the specified) multipole errors of dipole, quadrupole and sextupole magnets, as listed in table 3. Since the sextupole multipole errors will effect as quadrupole components and give tune shift as there is a closed orbit distortion, setting of Q2 and Q3 families are tunned a little bit to restore tune again. No significant strength changing of Q2 and Q3 family was found. The chromaticity is also corrected to zero in the study. Figure 8 shows the tracking results with the considered conditions. From figure 8, the horizontal aperture is reduced about 43% to 20.5mm (averaged). Compared with the original physical aperture of 20mm in horizontal, it is also big enough. The vertical aperture is reduced further only by 5%.

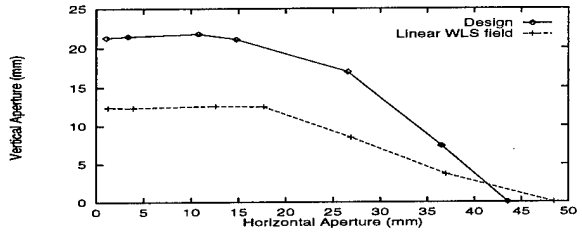


Figure 7: Comparison of dynamic aperture at the WLS center with the linear lattice considered only.

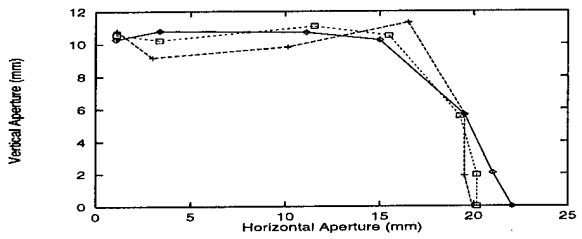


Figure 8: Dynamic aperture tracking of three random runs at the WLS center with the matched and retunned lattice and with multipoles in magnets considered.

From above study, it indicates the vertical aperture reduction is mainly coming from the linear WLS field but not from its non-linear parts. Above tracking study also indicates the WLS do have impact on the dynamic aperture.

5 DISCUSSION

Due to the space consideration the WLS won't be installed at the middle of straight section. For this arrangement the perturbation from WLS will become bigger than that the WLS inserted at the straight section middle. Compared with other rings, the maximum WLS field to the beam energy ratio for the proposed WLS in SRRC is quite large.

Table 3: Integrated multipoles in magnets used in the study

Magnet Type	order	systematic	random
Dipole			
	$4(m^{-1})$	0.0	0.00122
	$6(m^{-2})$	0.0657	0.033
	$8(m^{-3})$	3.06	1.1
	$10(m^{-4})$	-72.4	36.2
Quadrupole:			
	$4(m^{-1})$	0.0	0.0013
	$6(m^{-2})$	0.005	0.01
	$8(m^{-3})$	0.277	0.05
	$10(m^{-4})$	0.0	17.71
	$12(m^{-5})$	1307	265
Sextupole:			
	$18(m^{-8})$	3005617(SF)	
	$18(m^{-8})$	-13836572(SD)	

Hence the impact of WLS on the beam will be more serious than other rings. Nevertheless, the WLS effect is reduced by matching beta-function and restoring the tune. From above dynamic aperture tracking results , it is found the vertical aperture is mainly reduced by the linear WLS field. As the non-linear field of the WLS and of the ring magnets included, the dynamic aperture at the WLS center is reduced further to 10.5mm(V)x20.5mm(H) (averaged). For the original chamber in the straight section, it is elliptical shape with inner cross section of 38mm(V)x40mm(H). This indicates the tracked vertical aperture is smaller than the original physical aperture. Hence a reduction of beam lifetime would be expected from the aperture limitation point of view.

6 REFERENCES

[1] Dan Y. Wang, F. C. Younger and H. Wiedemann, Incorporation of a 5T Superconducting Wiggler in the MLI Model 1.2-400 Synchrotron Light Source, 1991 IEEE PAC.

[2] Hans Grote and F. Christoph Iselin, The MAD Program Version 8.1 (User's Reference Manual), CERN/SL/90-13(AP).

[3] Lloyd Smith, Effect of Wigglers and Undulators on Beam Dynamics, ESG TECH NOTE-24, 1986.

[4] M. H. Wang, P. Chang, J. C. Lee, C. C. Kuo and C. S. Hsu, Wiggler Effects on the Beam Dynamics of the SRRC Lattice, SRRC/BD/IM/91-05.

[5] A. Wrulich, RACETRACK version ssc/AUG 86.

OPERATIONAL EXPERIENCE AT SRRC

Y.C. Liu, J.R. Chen, K.T. Hsu, C.C. Kuo, W.K. Lau,
G.H. Luo, R.C. Sah, T.S. Ueng,
Synchrotron Radiation Research Center (SRRC)

Abstract

The Taiwan Light Source (TLS) is a synchrotron radiation facility that has operated for the past four years at SRRC. At this time, the operating energy has been increased from 1.3 GeV to 1.5 GeV, and the beam lifetime is 9 hours at a current of 200 mA. The monthly uptime is normally more than 90%, and the orbit stability better than 5 micrometers. Both transverse and longitudinal instabilities have been observed, and the corresponding feedback systems have been constructed. The transverse feedback system is in routine operation. A fast orbit feedback system is capable of restricting orbit errors to within 10 micrometers, even in the presence of strong orbit perturbations such as insertion-device gap changes.

1 ACCELERATOR OPERATIONS

During 1996, the TLS operating energy was increased from 1.3 GeV to 1.5 GeV, thereby greatly increasing the flux of x-rays, especially for photon energies greater than 1 keV. The beam lifetime is now 9 hours or more at a current of 200 mA. During typical user operations, the vertical emittance coupling is increased to a few percent to increase the vertical beam size and the beam lifetime.

The light source is normally scheduled to operate 24 hours per day, five days per week, for synchrotron radiation users and for machine studies. The operation of the light source has been very reliable, and monthly beam availability has normally exceeded 90%. Long shutdowns are occasionally scheduled - for upgrades, maintenance, repairs, and holidays. For example, user operations were interrupted for 9 weeks in March and April of 1997, in order to install and to commission the U5 undulator and 18 new quadrupole power supplies (which provide independent control of pairs of quads in the storage ring). At the same time, the power-supply control system was upgraded, so that the storage-ring energy can now be ramped from 1.3 GeV (the injection energy) to 1.5GeV, in only a few seconds.

There are three insertion devices installed in the storage ring: W20, U10, and U5. The U9 undulator will be completed in 1998. Additional insertion devices are under development or are being considered, including an elliptically-polarizing undulator (EPU) and a superconducting magnet (wiggler or bend magnet) to address the needs of the x-ray user community.

Four photon beamlines are in routine operation for users, and a major beamline construction program is in progress. A total of 15 photon beamlines are expected to be operational by early 1998.

2 BEAM INSTABILITIES AND CURES

Coherent beam oscillations due to transverse coupled-bunch instabilities have been observed since the commissioning of the storage ring. Up until 1995, these instabilities were suppressed by increasing the sextupole-magnet strengths to provide large positive chromaticities. Unfortunately, this method of beam stabilization had two serious drawbacks. First, variations in the filling pattern required changes in the sextupole strengths and thereby led to orbit changes of up to 100 μm. Second, the high sextupole-magnet strengths reduced the dynamic aperture and the beam lifetime.

In October of 1995, a transverse feedback system was put into operation [1]. This broadband, bunch-by-bunch transverse feedback system consists of transverse-oscillation detectors, notch filters, baseband quadrature processing circuitry, power amplifiers, and kickers. It successfully controls a large number of transverse coupled-bunch modes, and the orbit stability and beam lifetime have been improved by operating at (constant) lower sextupole-magnet strengths.

The transverse beam instabilities can be observed using a synchrotron-radiation profile monitor. When the transverse feedback system is turned on, the beam is seen to be stabilized, and its effective vertical size is reduced to less than 100 μm. Reducing the beam size in this way results in a shorter beam lifetime, showing the importance of Touschek scattering in the TLS.

Longitudinal instabilities have also been observed. For now, the dangerous higher-order modes are reduced or shifted away from the beam modes by tuning each cavity using an additional tuner and by using precision control of the cavity temperature. Also, a longitudinal feedback system is under construction and will be completed in 1998.

3 ORBIT STABILITY AND FEEDBACK SYSTEMS

An extremely stable electron beam must be provided at any third-generation synchrotron-light source, because electron-beam motion degrades the effective brightness of the photon beams. Sources of beam perturbations have been identified and suppressed at the Taiwan Light Source, so that at this time the electron beam is intrinsically very stable. The short-term beam motions are less than 5 μm, and the long-term beam drift is less than 20 μm. However, a significant remaining source of

0-7803-4376-X/98/$10.00 © 1998 IEEE

beam perturbations are the insertion devices, which create orbit changes when their magnetic gaps are adjusted.

A digital global feedback system (DGFB) has been developed to suppress orbit changes caused by insertion-device adjustments and by other low-frequency beam motions.[2] The beam-response matrix is experimentally measured, and this matrix is then used in making orbit corrections by the singular-value decomposition method. Eddy currents in the vacuum chamber limit the field penetration, so that the correction bandwidth is now 20 Hz horizontally and 80 Hz vertically. Operational experience with the DGFB system shows that orbit motions can be kept within ±10 μm, even during insertion-device gap changes.

The intrinsic beam stability is so good that a global feedback system may not always be needed. Under some operating conditions, a local feedback system may be able to suppress beam perturbations at their very sources. Such a local system is currently under development, and its hardware will be integrated with that of the global feedback system.

4 STORAGE-RING PARAMETER OPTIMIZATION

A careful program to study the actual tuning of the storage ring, followed by the correction of any residual errors found, can improve the performance of high-precision synchrotron light sources. With the collaboration of James Safranek of NSLS, the machine-error-finding program LOCO [3] was used experimentally to measure the linear optics of the TLS - and the BPM gain errors, as well. The rms variations in the quadrupole-magnet strengths, within each family of quads, was found to be only a few tenths of a percent. This result is in general agreement with the results of earlier magnetic measurements.

Figure 1 shows the measured betatron functions during 1.3-GeV operation with the sextupole magnets on. Horizontal offsets of the beam in the sextupoles cause focusing errors and a small "beta beat," about 4.5 percent horizontally and 8 percent vertically, measured beta distortion. We anticipate that the recently-installed independent power supplies for quadrupole-magnet pairs can be used to correct these minor lattice errors.

5 UPGRADE PLANS

The operation of the Taiwan Light Source has matured over the past few years. Accordingly, an increasing focus is being placed on machine upgrades and improvements, in contrast to routine operations. That is, more effort is being expended to improve the performance of the machine and to increase its reliability for user operations.

Planning for light-source upgrades is an ongoing process, involving physics studies, workshops, and engineering designs. By its very nature, it will evolve and be clarified over a period of time. Nevertheless, considerable effort has been expended in planning for machine and building upgrades, primarily for the next two or three years. A summary of this plan is as follows:

1997 plans:

- Digital global feedback loops.
- Noise suppression and upgrade of the "core" area.
- Design studies of a superconducting wiggler and a superconducting bend magnet.
- Upgrade of the RF laboratory.

1998 plans:

- Passive Landau cavity to increase bunch length and beam lifetime.
- Longitudinal feedback system.
- Local orbit feedback loops.
- Integration of injector controls with storage-ring controls.
- Start replacement of storage-ring gate valves with all-metal-seal gate valves.
- Utilities upgrades.

1999 plans:

- Increased laboratory and office space.
- A third RF system for the storage ring, to permit operation at up to 450 mA.
- Dedicated diagnostic photon beamline.
- Control system upgrades.

Other efforts to improve machine reliability include a program of failure analysis and a related spare-parts program. Furthermore, planned reorganizations will streamline the operation and maintenance of the TLS, in order to increase the overall efficiency of the accelerator effort.

6 CONCLUSIONS

During the past four years, the operation of the Taiwan Light Source has been significantly improved, in terms of beam energy, beam lifetime, and beam stability. Also, plans have been developed to further enhance the performance and reliability of this light source. These plans are designed to carry SRRC forward to significantly improved accelerator performance in support of an aggressive research program at the beginning of the next millennium.

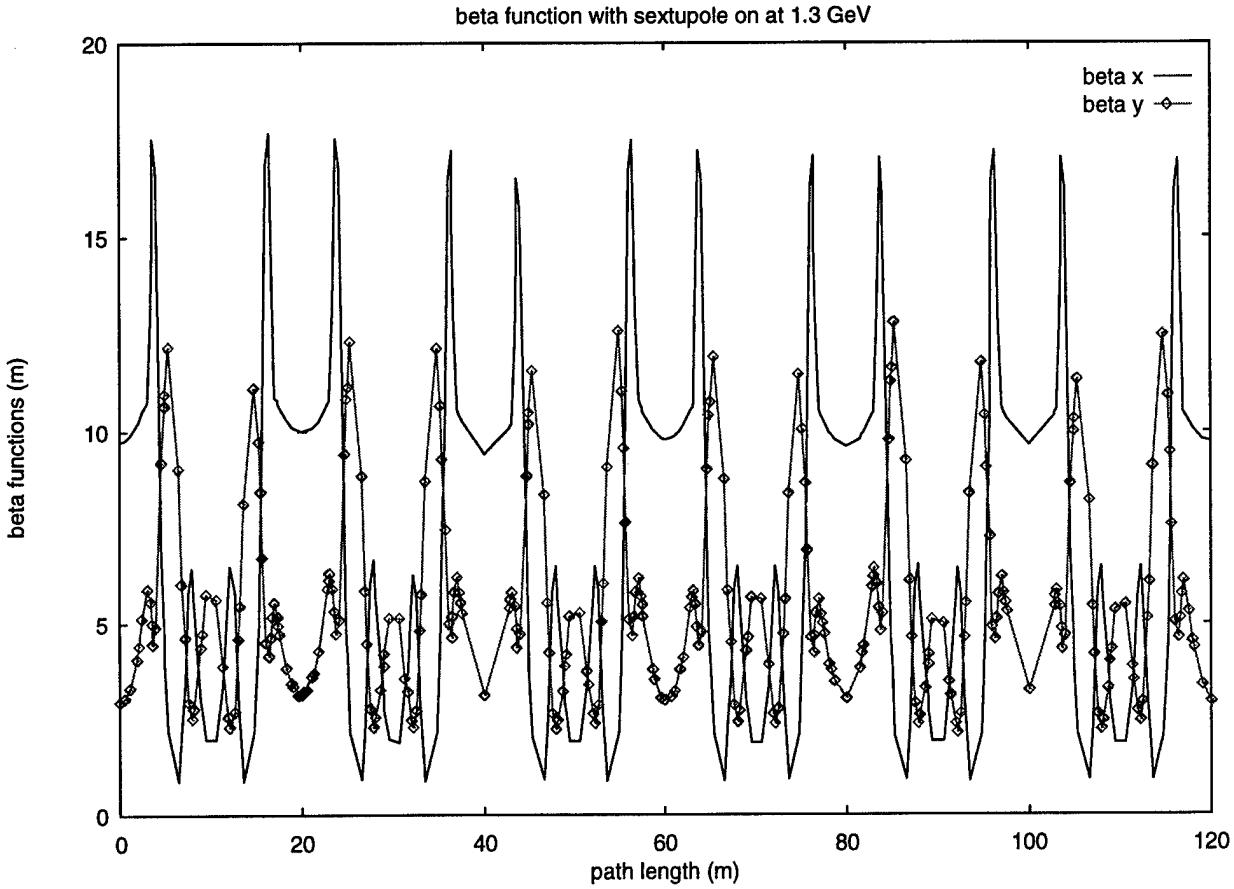


Figure 1: Measured betatron functions with sextupoles on at 1.3 GeV.

7 REFERENCES

[1] "Performance of the Transverse Coupled-Bunch Feedback System in the SRRC," K.T. Hsu, C.C. Kuo, C.H. Kuo, K.K. Lin, T.S. Ueng, W.T. Weng, EPAC 96, p.1920-1921, 1996.

[2] "Fundamental Architectures of the Digital Global Orbit Feedback System for SRRC Storage Ring," C.J. Wang, K.T. Hsu, G.J. Jan, C.H. Kuo, K.T. Pan, T.S. Ueng, EPAC 96, p. 1923-1925, 1996

[3] J. Safranek, *'Experimental Determination of Storage Ring Optics Using Orbit Response Measurements'*, **Nucl. Inst. Meth A**, Vol. 388, No. 1&2, p 27-36, 1997.

ANALYZING THE RELATIONSHIP BETWEEN THE BEAM LIFE TIME AND AVERAGE GAS PRESSURE

Gwo-Huei Luo, Glory Lin, C.C. Kuo, John Chiang, Y.J. Hsu,
D.H. Lee, R.C. Sah, SRRC, Hsinchu, Taiwan, ROC, and
Ian C. Hsu, National Tsing-Hua University, Taiwan, ROC

Abstract

For a low-energy third-generation synchrotron storage ring like Taiwan Light Source (TLS), the beam life time is a critical issue to determine the future expansion and design criterion of the insertion devices. The beam life time also affects the routine operation of the beam energy, from 1.3 GeV to 1.5 GeV has been successfully operated, which could increase the beam life time. There were various ways and experiments that have been carried out at TLS to investigate dominating factors of the beam lifetime. The dominating factor of beam life time was intra-beam scattering at 1.3 GeV. From various operation experiences of 1.5 GeV, the dominating factor of overall beam life time is changing. A simple algorithm is setup to interpret the relation between residual gas pressure and beam lifetime using archived data during 1.5 GeV normal operation.

1 INTRODUCTION

There are several well known factors [1] that will cause the store beam with finite lifetime. The major issues that affect the beam lifetime include: 1) elastic or inelastic scattering on the residual gas, ions, and electrons reside in the vacuum chamber, 2) scattering with the particles that confined within the same rf bucket, 3) energy loss due to synchrotron radiation emission, 4) beam instability due to the energy coupling between interrupted surface of vacuum chamber and stored beam. Some of these effects will interact with stored beam coherently and causing sever beam lost. Some will only affect individual particle motion, each particle ignoring the history of other particle. During a light source users' shift, a dedicated synchrotron light source will provide a stable and high brightness beam. The major issues on lifetime will be confined to gas scattering and Touschek lifetime. The ZAP [2] offers a good analysis tool to estimate the gas and Touschek lifetime under certain assumptions and known structure of a storage ring. There are also several papers [3,4,5] that have discussed and measured the lifetime at TLS, which is using various methods and different conditions to estimate the Touschek and gas lifetime. The conditions of the storage ring is changing from time to time. The insertion devices, the physical aperture of vacuum chamber, the operation energy, and beam current will have influence on the estimation of beam lifetime. We will utilize a very simple algorithm and an interesting phenomena to deduct the gas lifetime at 1.5 GeV beam energy.

2 THE PHENOMENA OF HOLIDAY EFFECT

An interesting phenomena has been found which was related to the beam lifetime vs. beam current during the machine startup right after holiday. Figure 1 shows two typical start shifts for users beam time. The first shift of the two typical cases indicates a shorter beam lifetime compared to the second users' shift. The injection, operation, filling pattern, working point, beam energy, and the chromaticities are all identical for the first two shifts of same day except the vacuum condition. The only uncontrolled parameter that causes a shorter beam lifetime is the residual gas adhere on the surface of chamber and bases pressure. We will try using the residual gas pressure as the only free parameter that affects the beam lifetime, then estimates the Touschek and gas lifetime.

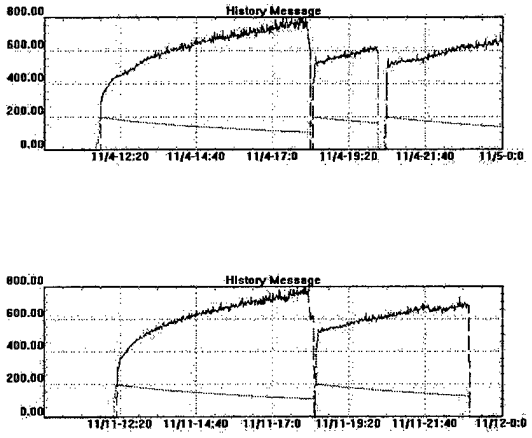


Figure 1. The beam current and lifetime vs. time. These data were taken during the first and second users' shift after a holiday machine shutdown.

The machine is scheduled to shutdown 36 hours for normal maintenance without venting any chamber once

0-7803-4376-X/98/$10.00 © 1998 IEEE

a week. From our judgment, the residual gas will deposit several layers on the clean surface of vacuum chamber during the normal maintenance. The first injection after maintenance will give out a lot of gas by photo-desorption. It is offering a good opportunity to analysis relation between beam lifetime and gas pressure without interrupt the normal operations.

The normal operation conditions are set as: 1.5 GeV beam energy, 200 mA beam current, 800 kV RF gap voltage, multi-bunch operation. The photon beam stability is maintained within .5% peak-to-peak variation which is determined by a 50 α m pin-hole detector. The filling pattern is set to be nearly identical for two different users' shifts. This gives us the same Touschek effect during the two shifts. The only effect on the beam lifetime will come from the vacuum pressure.

3 ANALYSIS OF THE ARCHIVED DATA

The beam lifetime, beam current, and average pressure were recorded on archived data. Figure 2 shows the beam lifetime vs. the beam current. The lower lifetime curve represents the first injection shift. The upper lifetime curve represents the second injection shift. A hyperbolic regressions method is used to have a best fit for the measured results. The correlation between the measured data and fitting curve is strong for the 4th order fitting. Hence, we can write

$$\tau^{-1}(I) = a_1 I + a_2 I^2 + a_3 I^3 + a_4 I^4 + O(I^5).$$

Figure 3 shows the average pressure vs. the stored beam current. The upper curve of average pressure represents the first injection shift with higher vacuum pressure. The lower curve of figure 3 represents the second injection shift. The average gas pressure as function of the beam current will be fit by polynomial regressions to have a best fit of the measure data points. We have

$$P(I) = P_0 + \lambda_1 I + \lambda_2 I^2 + \lambda_3 I^3 + \lambda_4 I^4 + O(I^5)$$

where P_0 is the bases pressure. As a well known calculation for the overall beam lifetime,

$$\tau_T^{-1} = \tau_{Touschek}^{-1} + \tau_{Gas}^{-1}$$

If two users' shift with the same filling pattern, we can assume the Touschek related lifetime are identical. The subtraction results of the inverse lifetime between the first and second shift will proportion to the difference of induced gas pressure. This leads to

$$\tau_{T1}^{-1} - \tau_{T2}^{-1} = \alpha (P_1 - P_2)$$

where α is a constant depend on the beam current, P_1 and P_2 are the pressure at the same current for the first and second shift, respectively. The proportional constant can be solved, so as the lifetime of Touschek related lifetime, and the gas lifetime for two different users' shifts. Figure 4 shows the calculated intra-beam scattering related lifetime and gas lifetime of first users' shift. The dominate factor of beam lifetime at the winter of 1996 is gas scattering.

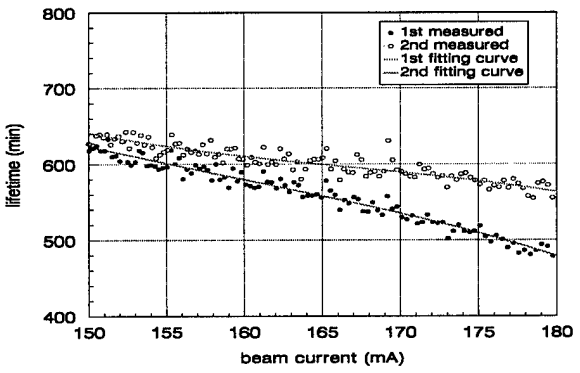


Figure 2. The measured data for the beam lifetime vs. beam current, a hyperbolic fitting curve and the interpolation line is drawn.

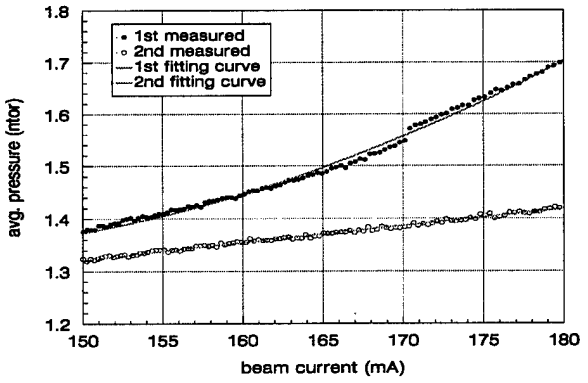


Figure 3. The measured data for the average pressure vs. beam current, the polynomial fitting curve and the interpolation line is drawn.

4 DISCUSSION

For most dedicated synchrotron radaition source, the structure of lattice and hardware are changing from time to time. It is necessary to have frequent check of beam parameters to maintain in a ultimate performance of a storage ring. Here, we offer a simple method to

check the lifetime dominate factors. From the calculated results, the Touschek lifetime strongly depends beam current. For high current and multi-bunch operation mode, the bunch lengthening effect will enter the calculated Touschek lifetime which makes the lifetime longer than expected. Using the simple algorithm to analysis archived data, it seems to us that the calculated gas related lifetime is a dominate factor for the TLS during the winter 1996 period. The improvement of the vacuum pressure will improve the beam lifetime a little bit.

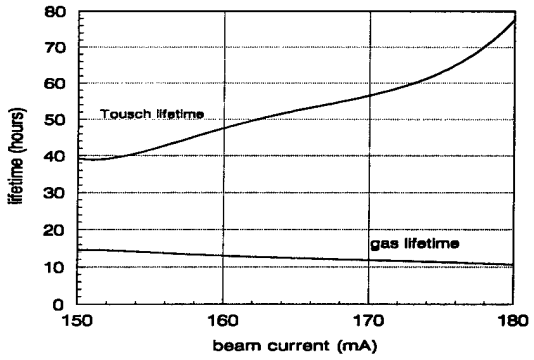


Figure 4. Using the method discussing at section 3 with the interpolation function of beam lifetime and vacuum pressure, the calculated Touschek like lifetime is over 40 hours, the gas lifetime is over 10 hours.

.

5 REFERENCES

[1] J. LeDuff "Current and Current Density Limitations in Existing Electron Storage Rings", NIM, A239, 1985, 83-101

[2] M.S. Zisman, et al., "ZAP User's Manual",1986, LBL-21270, EG-15

[3] Ian C. Hsu, et al., "The beam lifetime studies by two special schemes", EPAC, 1996, 1458-1460

[4] C.C. Kuo et.al., "Beam lifetime investigations at SRRC", EPAC, 1996, 697-699

[6] "SRRC design handbook", SRRC, 1991

THE 1.5 GEV OPERATION PARAMETERS AND PERFORMANCE AT SRRC

Gwo-Huei Luo, Peace Chang, K.T. Hsu, Jenny Chen,
C.C. Kuo, Y.K. Lin, R.C. Sah, and Y.C. Liu
SRRC, Hsinchu, Taiwan, ROC

Abstract

The storage ring at SRRC is highly promising as an ultra-violet to soft x-ray radiation source for use in basic research and industrial applications. Energy ramping of the storage ring can push the critical photon energy to the edge of hard x-ray. The tune drifting, during the ramping procedure, is expected and should be minimized such that the beam can survive through the ramping process. The betatron frequencies and the ramping function of magnets were carefully monitored in order to avoid the betatron tunes cross fatal resonance line. A successful ramping results and lattice parameters were measured and discussed in this paper. The measured photon flux increased by six to seven folds at the x-ray beam line. Life time reaches 9 hours of 200 mA beam current.

1 INTRODUCTION

The storage ring at SRRC is a source of ultra-violet to soft x-ray radiation for scientific research and industrial applications. The energy ramping from 1.3 GeV to 1.5 GeV increases the photon flux and brightness in the UV and soft x-ray region, and will also push the critical photon energy closer to hard x-ray.

In order to accommodate users with 1.3 GeV and 1.5 GeV operations, SRRC selected the energy ramping project as the highest priority. Since the booster at Taiwan Light Source (TLS) can not inject electrons into the storage ring with energy higher than 1.3 GeV without significant modification of booster and transport line system. The most cost effective way to increase the stored beam energy is to ramp the energy of the storage ring. Energy ramping of stored electrons requires nearly synchronous control of the main storage ring magnets. The seven families of magnets have different properties, making the tracking of the energy ramping difficult.

SRRC hoped to utilize the energy ramping from 1.3 GeV to 1.5 GeV for increasing the photon flux and brightness at x-ray regime. The estimated brightness [1] variation vs. the photon energy for the bending magnet and wiggler device is shown in Fig. 1 with 1.3 and 1.5 GeV beam energy. As a well known phenomena, a shorter wavelength allows for a smaller feature to be observed and written. The potential research area for higher photon energy include general x-ray users, micro-machining, microscopy, lithography and LIGA applications. A successful ramping program also provides a highly effective tool for the machine physicist to examine the machine performance under different electron beam energies, for examples using different energy to estimate the beam lifetime, radiation hazard analysis and energy calibration for the various detectors etc.

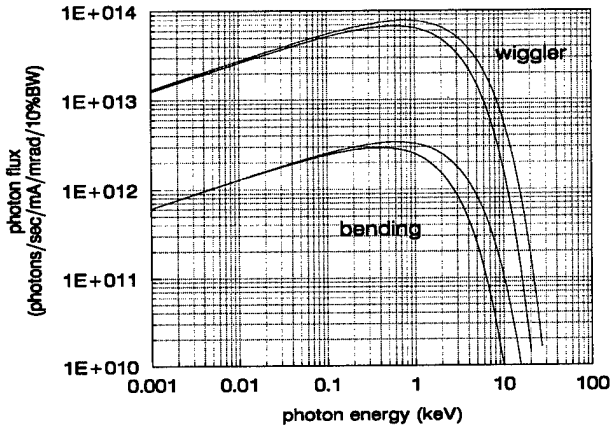


Figure 1. Calculated photon flux vs. photon energy for bending magnet and wiggler at 1.3 GeV and 1.5 GeV beam energy.

The short term approach of increasing the stored beam energy at TLS is using the nominal energy injection from booster, 1.3 GeV, with synchronized or asynchronized ramping of magnets field at the storage ring. However, for a long term planning or in preparing a mini-undulator operation with the necessity of frequent injection, a full energy injection from booster is the long term option to make top-up injection a feasible option.

2 RAMPING AND EXPERIMENT

2.1 Preparing the Storage Ring

Preparation tasks for the energy ramping project include the program coding, temperature measurement of magnets, the stability and capability test of magnet power supplies at high current, and preparation of an interlocking system. The currents of dipole and quadrupole magnets were driven to the maximum capacity of power supplies. Critical temperature of the magnet interlocking system was set at 60°C. If any of

0-7803-4376-X/98/$10.00 © 1998 IEEE

the thermal sensors at magnets sense that the temperature exceeds the 60 ℃ limit, the interlocking system interrupts the power supplies to protect the magnet from overheating. This system also protects the vacuum chamber from overheating as well. Several radiation survey meters are also placed around the storage ring to continuously monitor the radiation dosage. Each of the two RF transmitters can deliver 60 kW power to the cavities. According to the power loss estimation, the two transmitters can drive the 1.5 GeV electron beam at beam current as high as 300 mA if beam instability and beam loading problem are not of concern. The radiated power, due to the increase of beam energy, increases by a factor of 68%. Notably, the thermal loading of mirrors along the beam line estimated by the designer is well within the safety margin.

2.2 Beam Behavior during Energy Ramping

Two sets of stripline type beam-position-monitor (BPM), which can pick up a broad-band signal induced by the electron beam, have been installed at the storage ring. Successively analyzing the beam position at fixed BPM can yield information reading of the electron beam's betatron frequency and the bunch distribution of the electron beam. A carefully monitored betatron frequency and ramping function of magnetic setting can prevent the betatron tunes from crossing the resonance line, thereby inducing beam loss during the acceleration. We attempt to maintain the working tune at a constant level. The tune drifting during the ramping procedure should be minimized to allow the beam to survive through the ramping process[2]. During the ramping process, there is no significant beam loss except the scattering loss. A ramping down procedure has also been performed.

The control system of the storage ring power supplies was modified by using AI/AO interface, recently. This will eliminate the handshaking and waiting response time for each GPIB device. Instead of GPIB interface, the AI/AO interface enhances the reading and setting speed which makes the ramping process be completed within 30 seconds. A further shortening of the ramping time is possible, but it is not a critical issue for a storage ring operation.

2.3 Measurement of Beam Parameters

The simulations of beta function, dispersion function, and chromaticities were performed using MAD [5] as major tool. The measurement of the beta function has been carried out which is shown in Fig. 2. The measurement results shows very good agreement with theoretical prediction. A measurement of dispersion function also has been carried out by varying RF frequency and taking the orbit difference to determine. During the normal operation, chromaticities are set to slightly positive in order to suppress instability.

The basic parameters of 1.5 GeV lattice for the electron beam at TLS was listed at Table 1 [3,4,5].

Table 1. The beam parameters for 1.5 GeV operation

Nominal energy	1.5 GeV
Natural beam emittance	2.56×10^{-8} rad m
Radiation loss per turn (dipole)	128.1 keV
Critical photon energy	2.14 keV
photon flux (at critical energy)	2.40×10^{12} (photons/s/mrad, 10% BW, mA)
betatron tune	7.18/4.13
bunch length (RF@800KeV)	9.2 mm

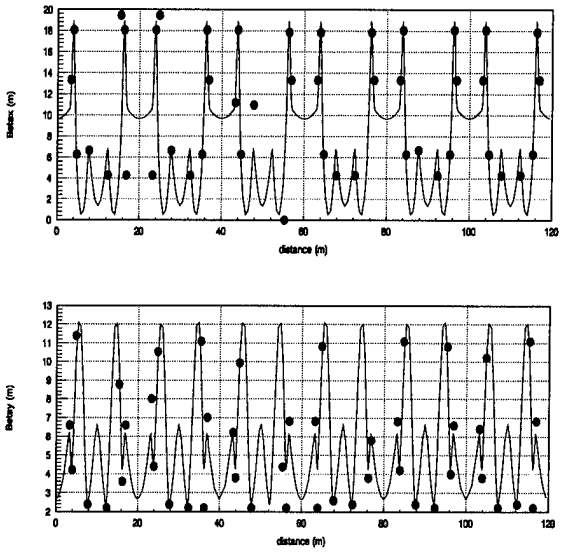


Figure 2 The measured beta function in x-direction and y-direction around the storage ring and compared with theoretical data.

During the users' shift, some long term effects was analyzed by the archived data. From the measurement, the beam lifetime will increase by a factor of 40-50%. The photon stability, which was measured at one of white light beam line using a 50 ℃m pinhole to detect the beam vibration in vertical direction, can be maintained within 0.65%. The close-orbit-distortion in x and y-direction indicated a very good reproducibility.

The variation of photon flux ratio was measured at wiggler and x-ray beam line as shown in Figure 3. Figure 3 shows that the variation of photon flux ratio depends on the photon energy. The higher the photon energy, the larger the photon flux ratio. The betatron tune frequencies converged after three times of 1.3 to

1.5 GeV magnets setting cycling as shown in Figure 4. A normal operation includes the three cycles of magnets setting process to prepare the magnets and eliminate the tune shift. A formal testing of the ramping project to monitor the long term effect which can not be observed during the machine study shifts.

3 SUMMERY

The largest benefit of the energy ramping program for VUV users is the prolong lifetime. 1.5 GeV operation increased the beam lifetime by 40%. The beam lifetime at 1.5 GeV with insertion devices gaps closed is 9 hours compared to 6 hours at 1.3 GeV. The photon stability, which was measured at a focusing white light beam line using a 50 ℃m pinhole to detect the beam vibration in vertical direction, can be maintained within .65%. The closed-orbit-distortion in the transverse directions indicated a very good reproducibility. A ramping loop was also established where the beam can be decelerated from 1.5 GeV to 1.3 GeV and current can be "topped-up" before ramping back to 1.5 GeV.

The improvement in photon flux was measured at wiggler and x-ray beam lines which indicated the flux increased by a factor of two to ten, depending on the photon energy.

4 ACKNOWLEDGMENT

The authors would like to thank all the members in Light Source Division, Instrumentation Development Division , Radiation and Operation Safety Division and Beam Line Division. The support from these divisions makes this experiment possible and quick transform this research project into a normal operation process. The authors would also express great thanks to Prof. Ian C. Hsu and Prof P.K. Tseng for suggestions and valuable discussions. The appreciation also goes to Dr. W.T. Weng, BNL, for his long term support and advice.

5 REFERENCES

[1] H. Winick and S. Doniach, "Synchrotron Radiation Research," Plenum Press, New York, 1980, p11-25 .

[2] G.H. Luo, etc. "Measurement of Lattice Parameters during the Energy Ramping at Storage Ring", EPAC, 1996,

[3] H.Kung, C. Travier and C.C. Kuo, "Emittance Calculation for a TBA Storage Ring," SRRC Internal Memo, SRRC/BD/1987-04.

[4] H. Wiedemann , "Particle Accelerator Physics," Springer-Verlag, New York, 1993.

[5] H. Grote, F.C. Iselin, "Methodical Accelerator Design," CERN report, CERN/SL/90-13 (AP)

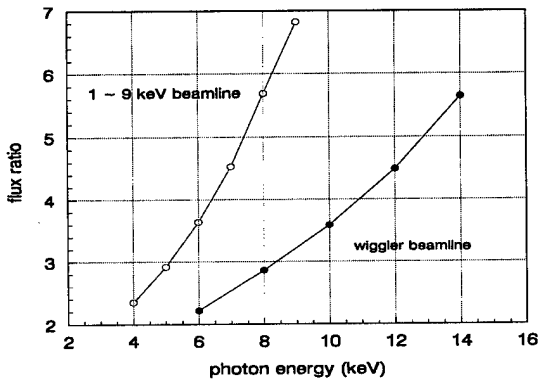


Figure 3. The measurement results of photon flux ratio, the ratio of photoelectron current at 1.5 GeV and 1.3 GeV, vs. photon energy at wiggler beam line and general purpose x-ray beam line.

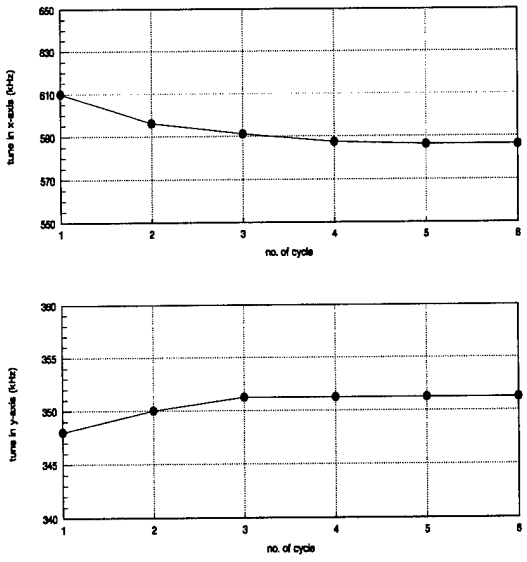


Figure 4. The measured betatron frequency as function of the cycling times, the x-axis is the numbers of cycles between 1.3 GeV and 1.5 GeV lattice setting.

A LATTICE FOR THE FUTURE PROJECT OF VUV AND SOFT X-RAY HIGH-BRILLIANT LIGHT SOURCE

Hiroyuki Takaki, Tadashi Koseki, Norio Nakamura, Yukihide Kamiya
Synchrotron Radiation Laboratory, The Institute for Solid State Physics (ISSP),
The University of Tokyo, Tanashi, Tokyo 188, Japan,

Yukinori Kobayashi
Photon Factory,
National Laboratory for High Energy Physics,
Tsukuba, Ibaraki 305, Japan
and
Toshiya Nagatsuka
Hitachi-Zosen Corporation.

Abstract

Presented in this paper is a lattice for a third-generation VUV and soft X-ray light source, which is a future project of the University of Tokyo and is being designed in close collaboration with the Photon Factory of KEK. The storage ring has an energy of 2 GeV, a circumference of about 400 m, an emittance of about 5 nm•rad, four 14.3 m *"long"* straight sections and twelve 7.0 m *"semi-long"* straight sections for insertion devices. Three different optics were studied in the same lattice configuration. It was proved that this lattice configuration has large flexibility and the basic optics has a sufficiently large dynamic aperture.

1 INTRODUCTION

The University of Tokyo has a future project to construct a third-generation VUV and soft X-ray light source in Kashiwa[1]. The "third-generation" light source is characterized by the low emittance and the long straight sections for insertion devices. To realize these characteristics, a Double Bend Achromat (DBA) lattice was adopted for our storage ring.

Since it is preferable to have small beam size divergence for undulators, the basic optics has high betatron functions at the long straight sections ("high-beta mode").

Two optional optics were also designed in the same lattice configuration. One is "hybrid mode" where the betatron functions are less than 2 m ("low-beta") at the RF-cavity in order to increase the threshold current of the coupled-bunch instabilities. This mode also enables to place wigglers instead of undulators, because the RF-cavity occupies only one of four "low-beta" long straight sections and it is important to have small beam size for wigglers. Another one is "very low emittance mode" which dose not hold the achromatic condition of DBA.

In following sections, we report the lattice configuration and these optics.

Table 1: The element lengths of the *Normal Cell* and the *Long Cell*.

*1: the center of the 7 m *"semi-long"* straight section.
*2: the center of the 14.3 m *"long"* straight section.

Normal Cell		Long Cell	
Element	L [m]	Element	L [m]
*1	–	*2	–
	3.50		7.156667
Q1	0.40	Q1L	0.40
	0.20		0.20
SF1	0.15	SF1L	0.15
	0.20		0.20
Q2	0.60	Q2L	0.60
	0.20		0.20
SD1	0.15	SD1L	0.15
	0.20		0.20
Q3	0.40	Q3L	0.40
	0.50		1.00
B	1.30	B	1.30
	0.90		0.90
Q4	0.60	Q4	0.60
	0.20		0.20
SF0	0.20	SF0	0.20
	0.80		0.80
SD0	0.20	SD0	0.20
	0.20		0.20
Q5	0.40	Q5	0.40
	0.20		0.20
SD0	0.20	SD0	0.20
	0.80		0.80
SF0	0.20	SF0	0.20
	0.20		0.20
Q4	0.60	Q4	0.60
	0.90		0.90
B	1.30	B	1.30
	0.50		0.50
Q3	0.40	Q3	0.40
	0.20		0.20
SD1	0.15	SD1	0.15
	0.20		0.20
Q2	0.60	Q2	0.60
	0.20		0.20
SF1	0.15	SF1	0.15
	0.20		0.20
Q1	0.40	Q1	0.40
	3.50		3.50
*1	–	*1	–

0-7803-4376-X/98./$10.00 © 1998 IEEE

2 LATTICE CONFIGURATION

The storage ring consists of 16 DBA cells with a circumference of 388.45 m. Each cell has two long straight sections for insertion devices at both ends. The number of these long straight sections are 16. Four of them are 14.3 m long and twelve of them are 7 m long. The 14.3 m "*long*" straight sections are arranged to be four-fold symmetry. A cell with 7 m "*semi-long*" straight sections at both ends is called *Normal Cell* and a cell with the "*long*" straight section at one end is called *Long Cell* (see Table 1). The lattice configuration of the *Long Cell* is the same as that of the *Normal Cell* except for the three quadrupole magnets (Q1L, Q2L, Q3L), two sextupole magnets(SF1L SD1L) and the drift space between B and Q3L.

3 HIGH-BETA MODE

The basic optics is a "high-beta mode", where horizontal and vertical betatron functions are around 10 m at the long straight sections. The betatron and dispersion functions in a quadrant of the storage ring is shown in Fig. 1. In this figure, both ends represent the center of the "*long*" straight sections. The fundamental parameters

Table 2: Fundamental parameters of the storage ring in the "high-beta mode"

Energy	E [GeV]	2.0
Lattice type		DBA
Superperiod	Ns	4
Circumference	C [m]	388.45
Semi-long straight section		7.0m x 12
Long straight section		14.3m x 4
Natural emittance	ε_{x0} [nm•rad]	5.10
Energy spread	σ_E/E	6.66×10^{-4}
Momentum compaction	α	6.87×10^{-4}
Horizontal tune	ν_x	18.84
Vertical tune	ν_y	9.55
Horizontal natural chromaticity	ξ_x	-47.78
Vertical natural chromaticity	ξ_y	-18.45
Horizontal damping time	τ_x [msec]	24.17
Vertical damping time	τ_y [msec]	24.25
Longitudinal damping time	τ_z [msec]	12.14
Revolution frequency	f_{rev}[MHz]	0.771759
RF voltage	V_{RF} [MV]	1.4
RF frequency	f_{RF} [MHz]	500.1
Harmonic number	h	648
Synchrotron tune	ν_s	0.007
Bunch length	σ_z [mm]	4.04
RF-bucket height	$(\Delta E/E)_{RF}$	0.028

Table 3: The condition of random errors (r.m.s.)

Quadrupole alignment error	0.1 mm
Sextupole alignment error	0.1 mm
Dipole tilt error	5×10^{-4} rad
Quadrupole tilt error	5×10^{-4} rad
Sextupole tilt error	5×10^{-4} rad
Dipole filed error	5×10^{-4}
Quadrupole filed error	5×10^{-4}
Sextupole filed error	5×10^{-4}

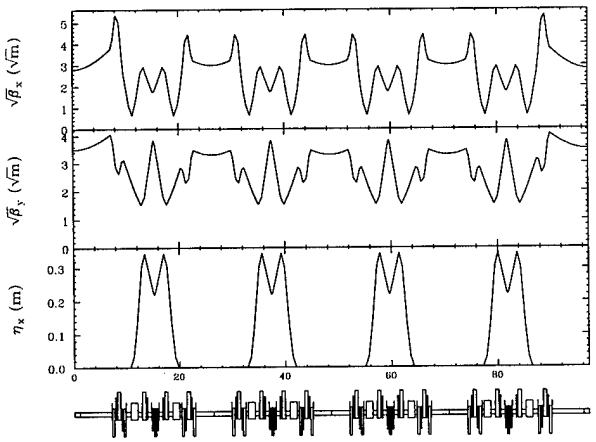


Fig. 1: The "high-beta mode" optics in the quadrant of the storage ring.

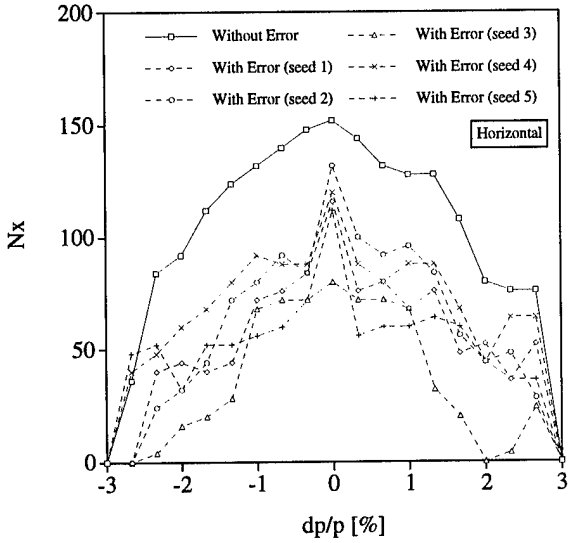


Fig. 2-a: The horizontal dynamic aperture versus momentum deviation in the "high-beta mode".

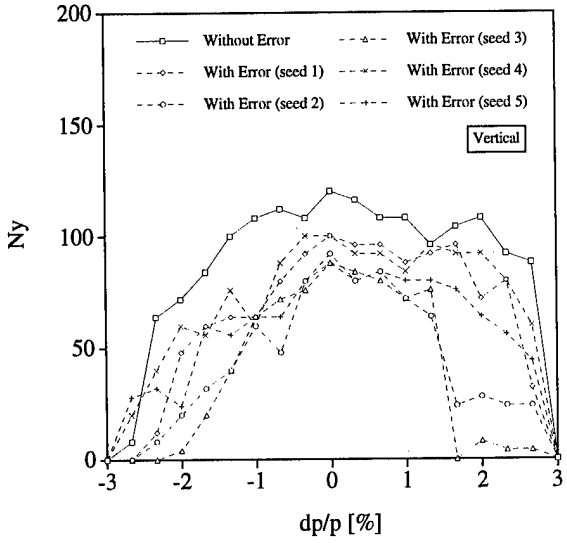


Fig. 2-b: The vertical dynamic aperture versus momentum deviation in the "high-beta mode".

of the storage ring are shown in Table 2. The natural emittance is 5.10 nm•rad. We have used SAD[2] code for the calculation.

The horizontal chromaticity of the ring is -47.78 and the vertical one is -18.45. The chromaticity is corrected by using chromatic sextupoles (SF0, SD0) located in the dispersive region of the cell. The strengths of these sextupoles are 498 [T/m^2] for SF0 and –392 [T/m^2] for SD0, while the design limit of the sextupole strength is 600 [T/m^2]. These chromatic sextupoles may reduce the dynamic aperture. In order to obtain a dynamic aperture as large as possible, the harmonic sextupoles (SF1, SD1, SF1L, SD1L) has been incorporated in the dispersionless region of the lattice. The dynamic aperture should be larger than the half width of the vacuum chamber (40 mm) horizontally and lager than the half height of the vacuum chamber (8 mm) vertically. A wide momentum aperture is also required to obtain a long Touschek lifetime.

By optimizing the harmonic sextupoles, we obtained Nx ≈ 150 and Ny ≈ 130 for the dp/p (momentum deviation) = 0 as shown in Fig. 2 (solid line), where Nx and Ny are the amplitude normalized by $\sqrt{\beta_x\,\varepsilon_{x0}}$ and $\sqrt{\beta_y\,\varepsilon_{x0}}$ respectively. The horizontal dynamic aperture is 68 mm and the vertical dynamic aperture is 28 mm at the center of the "*semi-long*" straight section. Here, the dynamic aperture is defined as the stable region in which a particle can revolve the ring over 1000 turns.

The effect of the field and alignment error of magnets were also studied. The condition of random errors (r.m.s.) are listed in Table 3. After C.O.D. correction using 128 BPM and 256 steering magnets (128 for horizontal and 128 for vertical), the dynamic apertures were calculated for five different cases in Fig. 2 (dashed line). On average, we obtained Nx ≈ 100 and Ny ≈ 90 for dp/p = 0. In the large dp/p region, some cases have rather small dynamic apertures. It is caused by the large relative displacements (five or six times the standard deviation) of the neighboring magnets. We expect to reduce a such displacement by using a scheme of the grouping alignment of magnets.

4 HYBRID MODE

In order to increase the threshold current of the coupled-bunch instabilities caused by the RF-cavity, some modifications for the betatron functions was made. In this optics, both horizontal and vertical betatron functions are less than 2 m at one of "*semi-long*" straight sections in the quadrant of the ring (see Fig. 3), where the RF-cavity is placed.

The dynamic aperture for this mode is rather small in comparison with the "high-beta mode" and sensitive to the magnet alignment error. To obtain the same performance as "high-beta mode", the quadrupole and sextupole alignment errors should be kept down to 0.05 [mm]. For this mode, we need the further study.

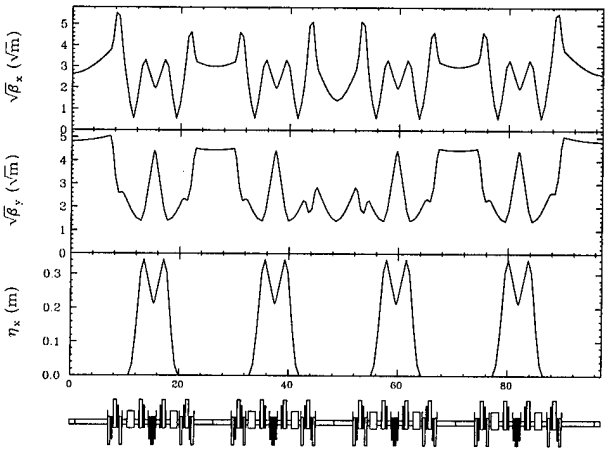


Fig. 3: The "hybrid mode" optics in the quadrant of the storage ring.

Table 4: Fundamental parameters of the storage ring in the "hybrid mode"

Natural emittance	ε_{x0} [nm•rad]	4.46
Horizontal tune	ν_x	18.84
Vertical tune	ν_y	11.55
Horizontal natural chromaticity	ξ_x	-61.43
Vertical natural chromaticity	ξ_y	-27.61

Other parameters are as same as those listed inTable 3.

5 VERY LOW EMITTANCE MODE

In this optics, the lattice configuration (shown in Table 1) is also not changed. The emittance reduction is made by breaking the achromatic condition of the DBA. The minimum achievable natural emittance is 1.0 nm•rad for our lattice configuration theoretically. This "very low emittance mode" is now under study. So far, the natural emittance is obtained around 2.5 nm•rad.

REFERENCES

[1] Y. Kamiya *et al.*, "A Future Project of VUV and Soft X-ray High-Brilliant Light Source in Japan", Proceedings of European Particle Accelerator Conference (London) 1994, p639.

[2] SAD is developed by KEK accelerator group.

WAVEFRONT DISTORTION MEASUREMENT OF A SR EXTRACTION MIRROR FOR THE BEAM PROFILE MONITOR USING SHACK-HARTMANN METHOD

N. Takeuchi,[1] T. Mitsuhashi,[2] M. Itoh[1] and T. Yatagai[1], [1]Institute of Applied Physics University of Tsukuba, Tennodai, Tsukuba, Ibaraki, 305 Japan[2]Institute of Materials Structure Science, High Energy Accelerator Research Organization, Oho, Tsukuba, Ibaraki, 305 Japan

Abstract

The wavefront measurement technique using the Shack - Hartmann wavefront sensor has been developed for measurement of wavefront distortion of a SR extraction mirror for the beam profile monitor at Photon Factory. The instrument consists of a multi-lens array (8x8 array, 250 μm pitch and focal length of 4.5 mm), a beam expander (20:1), an image relay lens system (1:1), a He-Ne laser (633 nm) and a digital CCD camera. To analyze positions of focal spot on the CCD in 1/10 of the pixel size, the wave front sensor can measured to be λ/30. A dynamic range of the wavefront sensor was designed 12.6 μm max. Performance of the wavefront sensor was tested with an optical flat. With this wavefront sensor, a wavefront error caused by surface deformation of the SR extraction mirror was measured at Beamline 27 of Photon Factory. The correction of the measured wavefront distortion is also described.

1 INTRODUCTION

The beam profile monitor based on an imaging of the synchrotron radiation (SR) will give a visible beam profile, which greatly improves the efficiency of the operation of the accelerators. In this monitor , the visible SR beam is extracted from the accelerator ring by a mirror, then the SR beam guided into a focusing system to making an image of stored electron beam in the accelerator ring. We use a water-cooling mirror made of beryllium as a extraction mirror [1]. The mirror will be deformed by not only a mechanical stress but also a thermal expansion caused by absorption of X-rays in the spectrum. The deformation of the Be-mirror introduce a wavefront error (often more than few λ(λ=633 nm) and it makes a blurred beam image. To correct the blurred image, it is necessary to measure the wave front error caused by the deformation of the Be-mirror. The measured wavefront error is used to calculate the point spread function (PSF). The PSF is the intensity distribution that would result from imaging a point source. The beam profile is then estimated from the correlation of images and PSF by a deconvolution process. We have several methods to measure the wavefront error such as interferometer technique. The interferometer is generally very sensitive to grand vibrations. The Be-mirror is fixed in the accelerator and is not insulated from the grand vibration. In this time, we apply the Shack-Hartmann wavefront sensor [2] because of this sensor can measure a mean wavefront error under having a grand vibration.

In this time, a Shack-Hartmann wavefront sensor was designed and constructed for a measurement of wave front error caused by a deformation of the Be-mirror. We corrected the blurred beam image by the use of deconvolution technique. This investigation was performed at beamline-27 in Photon Factory, High Energy Accelerator Research Organization.

2 WAVEFRONT SENSOR

To measure the wavefront distortion of Be-mirror, we designed and constructed the Shack-Hartmann wavefront sensor. The sensor consists a multi-lens array (a number of lenses distributed in matrix) and a detector (like a CCD camera) and is based on geometrical optics. The principle of the Shack-Hartmann wavefront sensor is shown in Fig. 1.

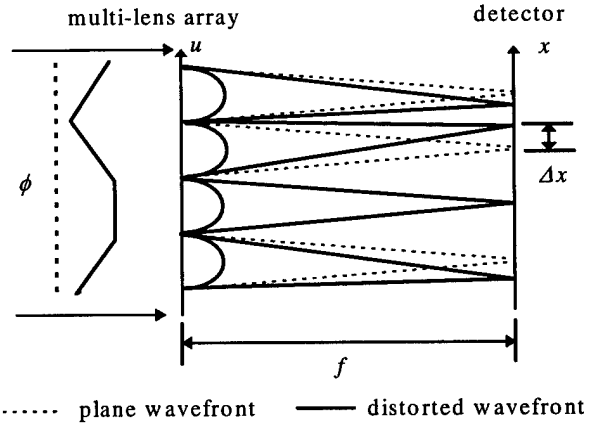


Fig. 1 principle of Shack-Hartmann wavefront sensor

The wavefront comes into a multi-lens array and it is divided by each lenslet. In the multi-lens array's focal plane, the image spot of each lenslet is shifted by a quantity proportional to the local slope of the wavefront. When a wavefront ϕ comes into a lenslet, if we measure a spot displacement in the focal plane as Δx, the corresponding slope measurement is

$$\frac{\partial \phi}{\partial \phi} = \frac{2\pi \Delta x}{\lambda f} \qquad (3)$$

0-7803-4376-X/98/$10.00 © 1998 IEEE

where f is the focal length of the each lenslet and λ is the wavelength of detected light. The spot image is recorded by the detector in the multi-lens array's focal plane. The position of the each spot image is calculated by a centroiding algorithm. This measurement determines the mean slope of the wavefront on subaperture of lenslet, in perpendicular directions. To integrate the gradient in perpendicular direction we reconstruct the phase ϕ from its gradients using the least-square fitting algorithm.

The layout of the Shack-Hartmann wavefront sensor is shown in Fig. 2. The instrument consist of a multi-lens array (8x8 array, 250 μm pitch and focal length of 4.5 mm), a image relay lens system (20:1), an image relay lens system (1:1), a He-Ne laser (λ=633 nm) having a collimator system and a digital CCD camera (Electrim, EDC-1000M, 324x242 pixels, 10x10 μm each pixel). The image of Be-mirror is transfer on the multi-lens array by the use of the image relay lens system (20:1). Because of the focusing length of the lenslet is only 4.5 mm, the focal plane image of the multi-lens array is again transferred on the CCD by the use of the image relay lens system. This image on CCD is captured by a computer and analyzed. In this system, we can measure the root mean square spot displacement by 1/10 of the pixel, then the corresponding sensitivity is λ/30 (λ=633 nm).

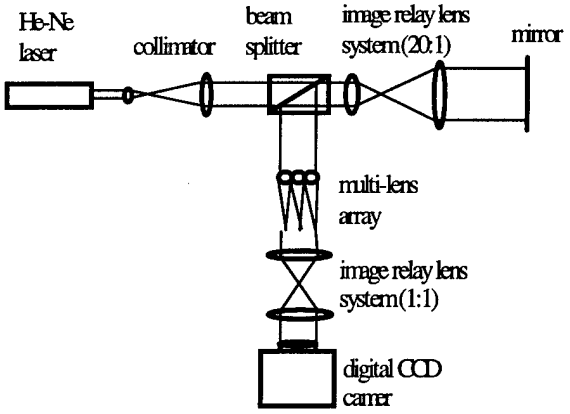


Fig. 2 the system of the Shack-Hartmann wavefront sensor

3 PERFORMANCE OF SHACK-HARTMANN WAVEFRONT SENSOR

We tested the performance of the Shack-Hartmann wavefront sensor using an optical flat (surface quality λ/20) and a gimbal mirror holder having a micrometer. We tilt the optical flat and measure the tilt of wavefront. A result of measured wavefront is shown in Fig.3. The flatness of wavefront from Fig.3 is λ/20. Result of angular response of the sensor is shown in Fig.4. The scattering from the linear line is 0.03 mrad in maximum. The precision of the ginbal holder is about 0.04 mrad, so small scattering from linear line is mainly due to this precision. A dynamic range of the Shack-Hartmann wavefront sensor is 12.6 μm max.

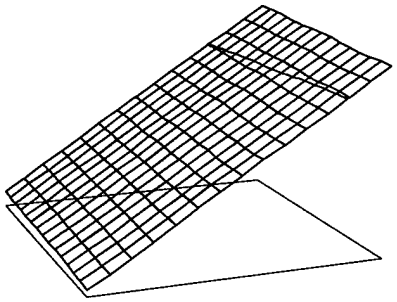


Fig. 3 A result of wavefront by the Shack-Hartmann wavefront sensor. Flatness of the wavefront is less than λ/20. The side length of the 3-dimensional plot is 35 mm.

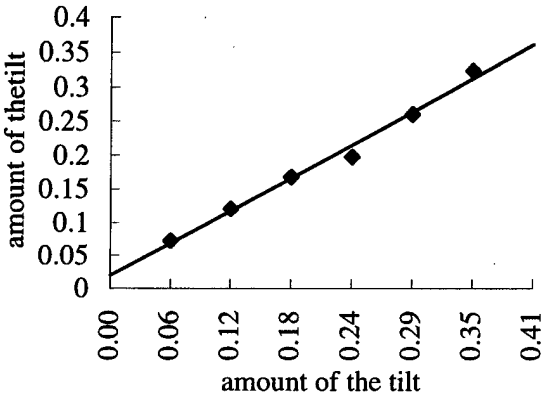


Fig. 4 Angular response of the Shack-Hartmann wavefront sensor

4 MEASUREMENT OF THE WAVEFRONT ERROR

We measured a wavefront error caused by surface deformation of the Be-mirror using Shack-Hartmann wavefront sensor. A result of the measurement is shown in Fig. 5.

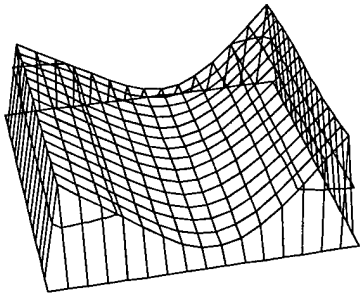


Fig. 5 The surface deformation of the Be-mirror. The side length of the 3-dimensional plot is 35 mm.

The Be-mirror was deformed to cylindrical way in the horizontal about 2 μm peak to valley (this deformation

was caused by baking process). The side length of the 3-dimensional plot is 35 mm.

5 OBSERVATION OF THE BEAM IMAGE

The optical image of the beam is produced by a diffraction limited focusing system [1]. To obtain the PSF caused by the deformation of the Be-mirror and finite aperture of the entrance pupil of the focusing system at the balanced astigmatism point, the propagation of the wavefront error is calculated by a computer code ZEMAX. A result of the PSF is shown in Fig. 6.

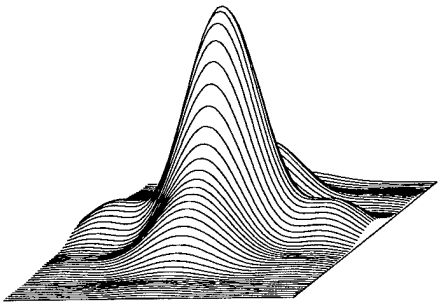


Fig. 6 The PSF at the balanced astigmatism point. The side length of the 3-dimensional plot is 96 μm.

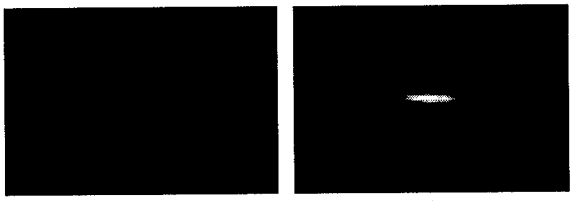
The rms width of the central peak of the PSF are 13 μm in vertical and 15 μm in horizontal. The image of the beam is given by a convolution of the PSF and geometrical image. The observed image of the beam as shown in Fig. 7 (a) is given by a convolution of the PSF (Fig. 6) and the geometrical image. The rms beam size from the beam image are 96.5 μm in the vertical and 280 μm in horizontal. Considering the conjugation ratio of 0.148, the rms width of PSF is almost same size as in the beam size. Therefore, to observe the original beam size, it is necessary to deconvolute the raw image by the PSF. In the present time, Wiener inverse filter [3] was applied. In the spatial frequency domain, the convolution integral is represented by

$$G(u,v) = H(u,v)F(u,v) + N(u,v) \qquad (2)$$

where G denotes a two dimensional Fourier transform of blurred image, H is thought of as inverse filter (two dimensional Fourier transform of PSF), F is a two dimensional Fourier transform of original image, and N is as a two dimensional Fourier transform of noise term in the image. The Wiener inverse filter H_w in equation (2) is given by

$$H_w(u,v) = \frac{H^*(u,v)}{|H(u,v)|^2 + \dfrac{\phi_n(u,v)}{\phi_f(u,v)}} \qquad (3)$$

where the asterisk indicates the complex conjugate of H. ϕ_n is the power spectra of the noise and ϕ_f is the power spectra of the signal. In the present time, the observed image was taken at the balances astigmatism point, we neglect asymmetric components of the obtained PSF as shown in Fig. 6, and use a Gaussian approximation as the PSF. To perform the deconvolution process, we use the computer code Hidden Image which has the maximum entropy deconvolution method. A result of the deconvolution is shown in Fig. 7 (b). The rms beam size from this beam profile are 59.4 μm in the vertical and 231 μm in the horizontal.



(a) (b)

Fig. 7 A beam image of the Photon Factory. The ring energy is 1 GeV and the beam current is 1 mA. (a), The observed image of the beam; (b), the beam image after deconvolution process.

6 CONCLUSION

The Shack-Hartmann wavefront sensor for the measurement of wavefront error was designed and constructed. The deformation of the Be-mirror was measured within λ/30. We have analyzed aberration of the focusing system including the deformation of the Be-mirror in the Fourier optical manner, and obtained PSF at the balanced astigmatism point of the focusing system. By the use of obtained PSF and beam profile image, we applied the image restoration method. After the image restoration process, we obtained a beam size 59.4 μm in vertical and 231 μm in horizontal. The performance of the Shack-Hartmann wavefront sensor is enough to measure the wavefront error of SR beam.

7 ACKNOWLEDGMENTS

We thank K. Nakama (Nippon Sheet Glass Co. , Ltd.) for multi-lens array.

REFERENCES

[1] T. Mitsuhashi, Proc. 5th European Particle Accelerator Conference, SITGES (Barcelona), 1669, (1996).
[2] J. G. Allen, A. Vankevics, D. Wormell, L. Schmutz, 'Digital wavefront sensor for astronomical image compensation', Proc. SPIE, Vol. 739, 124-128, (1987).
[3] A. Rosenfeld and A. C. Kak, 'Digital Picture Processing', Academic Press, Inc. (1976)

INSTABILITY ANALYSIS OF AN ACTIVE HIGHER-HARMONIC CAVITY

R. A. Bosch
Synchrotron Radiation Center, University of Wisconsin-Madison
3731 Schneider Drive, Stoughton, WI 53589

Abstract

A radiofrequency system with an active higher-harmonic ("Landau") cavity may prevent coupled-bunch instabilities and increase the bunch lifetime of an electron storage ring. However, the equilibrium phase and Robinson instabilities must be avoided. An algorithm is presented for evaluating an active Landau cavity, and applied to the electron storage ring, Aladdin.

1 INTRODUCTION

An active radiofrequency (RF) cavity with resonant frequency near a harmonic of the fundamental RF cavity may increase Landau damping of synchrotron oscillations and increase the bunchlength [1, 2], thereby suppressing coupled-bunch instabilities and increasing the Touschek lifetime. However, the equilibrium phase and Robinson instabilities must be avoided. To evaluate an active Landau cavity, we present an algorithm similar to that for a passive (unpowered) Landau cavity [3]. The algorithm is applied to the electron storage ring, Aladdin [4]. We use the notation of Sands [5].

2 ANALYSIS ALGORITHM

Consider an electron storage ring where the fundamental RF cavity and active Landau cavity are each operated in the "compensated condition" [5] with the generator current in phase with the voltage. We consider a Landau cavity which is operated to maximize the bunchlength by eliminating the quadratic and cubic terms of the synchrotron potential. The control systems which maintain the compensated condition and maximum bunchlength are assumed to be slow compared to the phase oscillation period [5].

We assume that the coupling between each cavity and its RF amplifier, as well as any fast RF feedback to compensate beam loading, may be represented by a resistor in parallel with the cavity impedance. The effect of this resistance is characterized by an equivalent RF-coupling coefficient [6, 7].

The following values must be input to the algorithm: V_{T1}: peak RF voltage in Cavity 1; Q_1^o: unloaded quality factor of Cavity 1; R_1^o: unloaded impedance of Cavity 1 at resonance (one-half of the "accelerator definition" of shunt impedance); β_1: RF-coupling coefficient for Cavity 1; α: momentum compaction; T_o: revolution period; ω_g: generator angular frequency; E: electron energy; σ_E: electron energy spread; I: average beam current magnitude; V_s: synchronous voltage; ν: harmonic number of Cavity 2; Q_2^o: unloaded quality factor of Cavity 2; R_2^o: unloaded resonant impedance of Cavity 2; β_2: RF-coupling coefficient for Cavity 2; τ_L: longitudinal radiation damping time; $Z(\omega_{C.B.})$: parasitic impedance driving coupled-bunch oscillations; and $\omega_{C.B.}$: parasitic mode angular frequency.

Let ω_1 be the resonant frequency of Cavity 1, $Q_1 = Q_1^o/(1+\beta_1)$ the loaded quality factor, $R_1 = R_1^o/(1+\beta_1)$ the impedance at resonance, and ϕ_1 the tuning angle, defined by $\tan\phi_1 = 2Q_1(\omega_g - \omega_1)/\omega_1$. This tuning angle is the same as that used by Sands [5], and the negative of that used by Wilson [6]. Robinson oscillations depend upon the angles $\phi_{1\pm}$ which obey $\tan\phi_{1\pm} = 2Q_1(\omega_g \pm \Omega - \omega_1)/\omega_1$, where Ω is the Robinson angular frequency.

Cavity 2 has resonant frequency ω_2 near $\nu\omega_g$, where ν is its harmonic number. $Q_2 = Q_2^o/(1+\beta_2)$ is the loaded quality factor, $R_2 = R_2^o/(1+\beta_2)$ is the impedance at resonance, and ϕ_2 is its tuning angle, given by $\tan\phi_2 = 2Q_2(\nu\omega_g - \omega_2)/\omega_2$. Robinson oscillations involve the angles $\phi_{2\pm}$ which obey $\tan\phi_{2\pm} = 2Q_2(\nu\omega_g \pm \Omega - \omega_2)/\omega_2$. For both cavities, the tuning angles are defined with the loaded value of Q.

Let Ω denote the real Robinson angular frequency, α_R the Robinson damping rate (negative for growth), and $e > 0$ the electron charge magnitude. Our algorithm proceeds as follows:

1. Calculate ψ_1 and ψ_2, the equilibrium phase angles of the bunch center in Cavities 1 and 2, and V_{T2}, the peak voltage in Cavity 2. By our convention, a phase angle equals zero for a bunch at the voltage peak. Neglecting the small difference between the synchronous phase and that of the bunch center, the assumption that the quadratic and cubic synchrotron potential terms vanish gives [3]:

$$V_{T1}\sin\psi_1 + \nu V_{T2}\sin\psi_2 = 0 \tag{1}$$

$$V_{T1}\cos\psi_1 + \nu^2 V_{T2}\cos\psi_2 = 0. \tag{2}$$

The energy of an electron at the synchronous phase is unchanged by a revolution around the ring:

$$V_s = V_{T1}\cos\psi_1 + V_{T2}\cos\psi_2 \tag{3}$$

Simultaneous solution of eqs. (1) – (3) yields:

$$\psi_1 = \cos^{-1}\left(\frac{V_s}{(1-\frac{1}{\nu^2})V_{T1}}\right) \tag{4}$$

$$\psi_2 = \tan^{-1}(\nu\tan\psi_1) - 180^\circ \tag{5}$$

$$V_{T2} = -V_{T1}\frac{\sin\psi_1}{\nu\sin\psi_2} \tag{6}$$

0-7803-4376-X/98/$10.00 © 1998 IEEE

If eq. (4) cannnot be solved with ψ_1 between 0 and 90 degrees, then there is no equilibrium phase.

2. Calculate the quartic coefficient of the effective synchrotron potential, $U(t) = at^2 + bt^3 + ct^4 + ...$, where t is the time displacement from the synchronous time. Neglecting the difference between the synchronous phase and that of the bunch center gives [3]:

$$c = -\frac{\alpha e \omega_g^3}{24 E T_o}(V_{T1}\sin\psi_1 + \nu^3 V_{T2}\sin\psi_2) \qquad (7)$$

3. Calculate the bunchlength. In a quartic confining potential, the charge distribution is [8, 9]: $q(t) = k\exp(-t^4/t_o^4)$. The rms bunchlength, $\sigma_t = t_o/1.72$, obeys [8, 9]:

$$\sigma_t = 0.69(\frac{U_o}{c})^{1/4} \qquad (8)$$

where $U_o = \frac{\alpha^2}{2}(\frac{\sigma_E}{E})^2$ is the "filling height."

4. Determine the form factors. In a quartic confining potential, the Cavity 1 form factor obeys:

$$F_1 = \frac{\int_{-\infty}^{\infty}\cos(\omega_g t)\exp(-t^4/t_o^4)dt}{\int_{-\infty}^{\infty}\exp(-t^4/t_o^4)dt} \qquad (9)$$

The Cavity 2 form factor, F_2, obeys the same formula with $\omega_g \rightarrow \nu\omega_g$.

5. Calculate the tuning angles of Cavities 1 and 2 for operation in the "compensated condition" [5]:

$$\phi_1 = \tan^{-1}(\frac{2F_1 I R_1}{V_{T1}}\sin\psi_1) \qquad (10)$$

$$\phi_2 = \tan^{-1}(\frac{2F_2 I R_2}{V_{T2}}\sin\psi_2) \qquad (11)$$

6. Determine if the dipole longitudinal coupled-bunch instability may be expected. Neglecting Landau and radiation damping, the coherent frequency of the dipole coupled-bunch mode in a quartic synchrotron potential obeys [9]:

$$\Omega_{C.B.}^2 = i(\delta\Omega_o)^2 \qquad (12)$$

where, for resonant interaction with a cavity mode:

$$(\delta\Omega_o)^2 = \frac{eI\alpha}{ET_o}F_{\omega_{C.B}}^2\omega_{C.B.}Z(\omega_{C.B.}). \qquad (13)$$

Here, $F_{\omega_{C.B.}}$ is the form factor at $\omega_{C.B.}$, given by eq. (9) with $\omega_g \rightarrow \omega_{C.B.}$. Landau damping is overcome provided that [9]:

$$|\,\Omega_{C.B.}\,| > 0.6\Delta\omega_s \qquad (14)$$

where, $\Delta\omega_s \equiv \omega_s(t_o)$ is a measure of synchrotron frequency spread, and $\omega_s(t_o)$ is the synchrotron frequency for oscillations of amplitude $t_o = 1.72\sigma_t$. Because the frequency is proportional to amplitude in a quartic potential:

$$\Delta\omega_s \equiv \omega_s(t_o) = \omega_s(1.72\sigma_t) = 1.72\omega_s(\sigma_t) \qquad (15)$$

where [8, 9]:

$$\omega_s(\sigma_t) = 1.17(U_o c)^{1/4} \qquad (16)$$

Therefore, Landau damping is overcome when:

$$|\,\Omega_{C.B.}\,| > (0.6)(1.72)(1.17)(U_o c)^{1/4} \qquad (17)$$

To include the effect of radiation damping, we subtract the damping rate τ_L^{-1} from $\mathrm{Im}(\Omega_{\mathrm{C.B.}})$:

$$\Omega_{C.B.} = [i(\delta\Omega_o)^2]^{1/2} - i\tau_L^{-1} = \frac{\delta\Omega_o}{\sqrt{2}} + i(\frac{\delta\Omega_o}{\sqrt{2}} - \tau_L^{-1}) \qquad (18)$$

We use the following criteria for the coupled-bunch instability: First, $\delta\Omega_o/\sqrt{2} > \tau_L^{-1}$ is required to overcome radiation damping. Second, Landau damping is overcome provided that eq. (17) is obeyed, where radiation damping is included in $\Omega_{C.B.}$ by using eq. (18).

7. Determine if the equilibrium phase instability will occur. Stability is assured if [3]:

$$F_1 V_{T1}\sin\psi_1 + \nu F_2 V_{T2}\sin\psi_2 >$$

$$R_1 F_1^2 I\sin 2\phi_1 + \nu R_2 F_2^2 I\sin 2\phi_2 \qquad (19)$$

8. If the previous inequality is satisfied, calculate the Robinson frequency, Ω, which obeys [3]:

$$\Omega^2 = \frac{e\alpha\omega_g}{T_o E}\{F_1 V_{T1}\sin\psi_1 - \frac{R_1 F_1^2 I}{2}(\sin 2\phi_{1-} + \sin 2\phi_{1+})$$

$$+\nu F_2 V_{T2}\sin\psi_2 - \frac{\nu R_2 F_2^2 I}{2}(\sin 2\phi_{2-} + \sin 2\phi_{2+})\} \qquad (20)$$

This calculation requires iteration; we start by evaluating the RHS with zero beam current.

9. Neglecting radiation damping, the Robinson damping rate obeys [3]:

$$\alpha_R = \frac{4\alpha e I}{ET_o}[F_1^2 R_1 Q_1 \tan\phi_1 \cos^2\phi_{1+}\cos^2\phi_{1-}$$

$$+F_2^2 R_2 Q_2 \tan\phi_2 \cos^2\phi_{2+}\cos^2\phi_{2-}]. \qquad (21)$$

To include radiation damping, we add the quantity τ_L^{-1} to the above value of α_R. If the result is positive, the Robinson mode is stable. If not, the Robinson mode will be unstable provided that Landau damping is overcome, for which we use a criterion appropriate for a quartic synchrotron potential:

$$(\Omega^2 + \alpha_R^2)^{1/2} > 0.6\Delta\omega_s. \qquad (22)$$

We evaluate a Landau cavity by performing the above algorithm for a sequence of values of ring current (I) and Cavity 2 RF-coupling (β_2). Steps 1–4 are independent of I and β_2, so only Steps 5–9 need be repeated.

3 APPLICATION

The above algorithm was applied to the fourth harmonic cavity at the electron storage ring, Aladdin. For analysis of the coupled-bunch instability, we considered a parasitic mode impedance of $Z(\omega_{C.B.}) = 0.01$ MΩ at $\omega_{C.B.} = 6.28$ GHz. Input parameters are: V_{T1}: 80 kV, Q_1^o: 10000, R_1^o: 0.65 MΩ, α: 0.0335, T_o: 2.96x10^{-7} s, ω_g: 318 MHz, E: 800 MeV, σ_E/E: 4.8x10^{-4}, V_s: 17.4 kV, ν: 4, Q_2^o: 22700, R_2^o: 1.4 MΩ, and τ_L: 13.8 ms.

For all values of I, β_1, and β_2, the Landau cavity peak voltage, V_{T2}, is 19.5 kV, $\psi_1 = 76.6°$, and $\psi_2 = -93.4°$. The bunchlength, σ_t, is 603 ps, versus 271 ps in the absence of a Landau cavity. Because the Touschek lifetime is approximately proportional to the bunchlength, we expect the Touschek lifetime to increase by a factor of ~ 2.2 with the active Landau cavity.

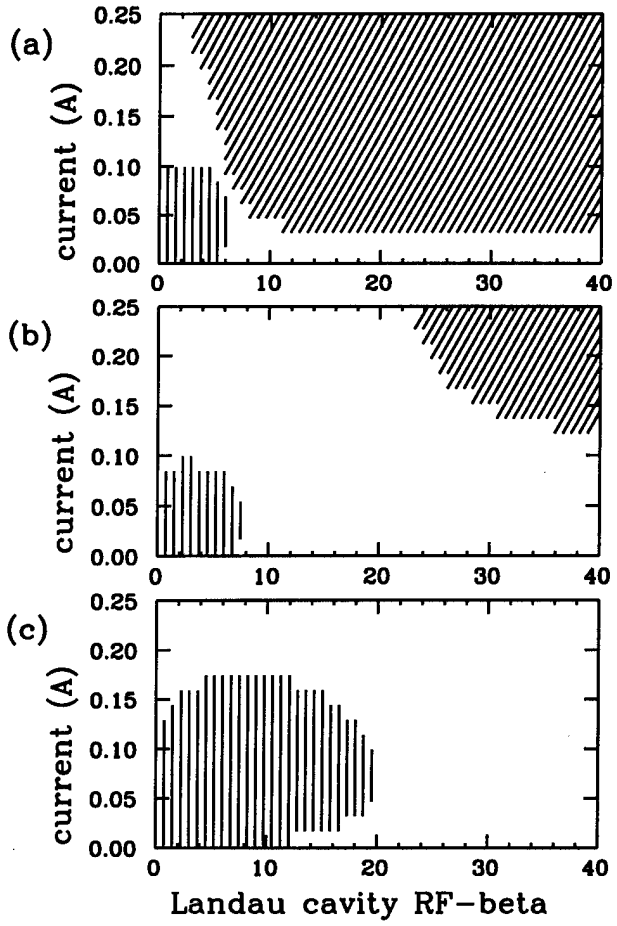


Figure 1: Instabilities are predicted for a range of ring currents (I) and active Landau cavity RF-coupling values (β_2), for the electron storage ring, Aladdin. | : Robinson instability. / : equilibrium phase instability. (a) $\beta_1 = 0$. (b) $\beta_1 = 2$. (c) $\beta_1 = 8$.

Stability plots are shown for three cases: $\beta_1 = 0$ in Fig. 1(a), $\beta_1 = 2$ in Fig. 1(b), and $\beta_1 = 8$ in Fig. 1(c). The coupled-bunch instability is suppressed for the range of ring current (I) and Landau cavity RF-coupling (β_2) shown: $0 < I < 0.25$ A, $0 < \beta_2 < 40$. For small values of I and β_2, the Robinson instability occurs, while the equilibrium phase instability occurs at large values of I and β_2. For $\beta_1 = 0$, there is no value of β_2 giving stable operation for the range of ring current shown. For $\beta_1 = 2$, values of β_2 between 8 and 23 ensure stable operation for $0 < I < 0.25$ A, while for $\beta_1 = 8$, values of β_2 exceeding 20 give stable operation.

4 SUMMARY

An algorithm has been developed to evaluate instabilities in an electron storage ring with an active higher-harmonic cavity. For the electron storage ring, Aladdin, an active fourth-harmonic cavity with appropriate RF feedback is expected to suppress coupled-bunch instabilities and to increase the bunchlength and Touschek lifetime by a factor of ~ 2.2.

5 ACKNOWLEDGMENTS

The author thanks E. Weihreter for suggesting this research topic and many helpful discussions. I would also like to thank C. S. Hsue, K. Kleman, and W. S. Trzeciak. This research was supported by NSF grant DMR-95-31009.

6 REFERENCES

[1] E. Weihreter, A. Gaupp, H. G. Hoberg, W. D. Klotz, P. Kuske, H. Lehr, R. Maier, G. Mülhaupt, IEEE Trans. Nucl. Sci. **NS-32,** 2317 (1985).

[2] Y. Miyahara, S. Asaoka, A. Mikuni, and K. Soda, Nucl. Instrum. Meth. **A260,** 518 (1987).

[3] R. A. Bosch and C. S. Hsue, Part. Accel. **42,** 81 (1993); see also Proc. 1993 PAC, p. 3369 (1993).

[4] M. A. Green, D. L. Huber, E. M. Rowe, and B. Tonner, Rev. Sci. Instrum. **63,** 1582 (1992).

[5] M. Sands, Institut National de Physique Nucleaire et de Physique des Particules, Rapport technique 2-76, 3-76, 4-76 (1976).

[6] Perry B. Wilson, "High Energy Electron Linacs: Applications to Storage Ring RF Systems and Linear Colliders," SLAC-PUB-2884 (1982) and in AIP Conference Proceedings No. 87 (AIP, NY, 1982).

[7] R. A. Bosch, SRC-137 (1994), Synchrotron Radiation Center, University of Wisconsin-Madison.

[8] A. Hofmann and S. Myers, CERN ISR-TH-RF/80, and in *Proc. 11th Intern. Conf. on High Energy Accelerators,* CERN (Birkhäser, Verlag, Basel, 1980) p. 610.

[9] S. Krinsky and J. M. Wang, Part. Accel. **17,** 109 (1985).

ALADDIN, PRESENT AND FUTURE*

W. S. Trzeciak and SRC Staff, 3731 Schneider Dr., Stoughton, WI, 53589-3097, USA

Abstract

The Synchrotron Radiation Center (SRC) at the University of Wisconsin-Madison operates a 1 GeV electron storage as the synchrotron radiation source, Aladdin. Operation at 800 MeV (200 mA) or 1 GeV (180 mA) is the standard for the user experimental periods. The present status of the ring will be discussed. Improvement of the stored beam lifetime by implementation of a fourth harmonic rf cavity, ring corrections for a high field permanent magnet undulator, and the global orbit control system will be presented. Future plans for Aladdin include the installation of two electromagnetic undulators (one already undergoing magnetic field measurement), full implementation of an infrared beamline, and a 120 kV electron gun for the Aladdin microtron injector.

1 ALADDIN STATUS

Aladdin is a 1 Gev electron storage ring [1] dedicated to synchrotron radiation. It is operated under contract to the National Science Foundation by the University of Wisconsin, Madison. It has been in operation since 1985, and, in many respects, it performs at the level of third generation synchrotron radiation sources.

1.1 Ring Operations

A typical week begins with a 5-day period, each day of which is divided into four user shifts with 12 hours for operation at 800 MeV and 8 hours for 1 GeV. The remaining four hours per day, from 8 am to noon, are used mostly for user beam time at 800 MeV, but are available for special uses by prior arrangement at a scheduling meeting held each Monday at noon. Each user shift begins with ring injection that lasts about 20 minutes. Weekends are available for special beams such as low current (nanoamp) beams used for calibration experiments, ring maintenance, or for making up unscheduled down time. Three such user weeks in succession comprise a "quantum", and represent the smallest block of time that an experiment can be given. Approximately nine times each year, a single week is set aside for: major ring hardware upgrades; maintenance that may require more than several hours and could be delayed until one of these machine weeks; and accelerator studies.

1.2 Aladdin at 800 MeV

While Aladdin is a 1 GeV storage ring, most of the operating time for user beams is at 800 MeV with dedicated shifts from noon to 6 pm, and 6 pm to midnight during the normal user weeks. Most beams start out at about 200 mA and have a current-lifetime product of about 950 mAh. The stored beam lifetime, would be lower were it not for regular use of the harmonic cavity (see § 1.5). Typical measured source sizes from the bending magnets are $\sigma_x = 480$ μm, and $\sigma_y = 91$ μm, whereas calculated source sizes at the middle of undulators in the middle of long straight sections are $\sigma_x = 849$ μm, and $\sigma_y = 63$ μm.

1.3 Aladdin at 1 GeV

Usual 1 GeV beams during users weeks are from midnight to 8 am, 5 days per week. The main users of the higher energy flux are the X-ray lithography and MEMS (MicroElectroMechanical Systems) programs. Currents are kept below 180 mA to limit the synchrotron radiation power delivered to the vacuum chamber. The current lifetime product is about 1150 mAh. Typical measured source sizes from the bending magnets are $\sigma_x = 560$ μm, and $\sigma_y = 160$ μm, whereas calculated source sizes at the middle of undulators in the middle of long straight sections are $\sigma_x = 1061$ μm, and $\sigma_y = 79$ μm.

1.4 Beamlines

Figure 1 shows a schematic layout of Aladdin. There are 29 active beamlines One of the active beamlines makes use of the original, pure permanent magnet, LBL/SSRL undulator that was installed on Aladdin in 1986 [2]. Another undulator beamline that utilizes a commercially built permanent magnet device is the source for a plane grating monochrometor (PGM) beamline [3,4]. This undulator and beamline will cover the photon energy range of 8 eV on the fundamental to 240 eV on the 5th harmonic. The commissioning of this line is nearly complete, and users are expected in several months. An electromagnetic undulator [4] is also installed on the ring, and its beamline is nearing completion. A new high resolution beamline built for the Canadian Synchrotron Radiation Facility (CSRF) is being installed.

* Work supported by the NSF grant DMR-95-31009.

0-7803-4376-X/98/$10.00 © 1998 IEEE

The Center for X-ray Lithography (CXrL) has 6 beamlines for its own use. There is one beamline dedicated to MEMS work, and a new beamline is used for biofluorescence experiments by the Aladdin Biofluorescence Center (ABC).

The newest beamline is an infrared (IR) line that utilizes the edge radiation [5,6] of a dipole magnet. During the commissioning of this line it became clear that 60 Hz (and its harmonics) noise and 720 Hz noise from the main dipole power supply were seriously compromising the full utility of the line. Most of the 60 Hz noise was found to be coming from user power transformers. After relocating the transformers the 60 Hz spectral component of the radiation was reduced by almost an order of magnitude. A source of the 720 Hz beam noise has been identified as the large filter choke, located 60 cm from the electron beam orbit, in the dipole power circuit. This choke will soon be moved and should further reduce beam noise.

1.5 Recent Operational Enhancements

A global feedback system has been operational since mid 1996. Prior to the implememntation of the system, the slow drift of the stored beam would be as much as 100 μm over a user beam fill. With the global feedback system active, typical orbit drifts, as measured at the source points in the dipoles, are kept within ±5 μm against slow perturbations (≤0.2 Hz). This system is now always used during user beams.

One aspect of using such a system is that the beam stability is tied directly to the long and short term positional stability of the beam position monitors (BPM's) themselves. In Aladdin the BPM's are placed in a continuous section of vacuum chamber that includes a quadrupole doublet and a dipole. The BPM's are located in the quadrupole part of the section. Because of construction tolerances, many of the chamber sections are in contact with the quadrupole poles, and they shift in position as the quadrupoles are powered. Section 2.2 discusses the steps being taken to stabilize the BPM's.

An rf cavity [7] running on the 4th harmonic of the main rf system is used to lengthen the bunch and, hence, the stored beam lifetime. The bunch length is almost doubled, going from σ_s = 425 ps to 800 ps, increasing the lifetime by 80%. An added bonus of harmonic cavity usage is the almost complete absence of coupled bunch instability [8]. The cavity is powered and can keep the bunch length constant from full ring currents down to about 40 mA.

The radiation source for the PGM beamline is a permanent magnet undulator [4]. The undulator itself has 9 steering coils to correct the vertical and horizontal orbits through the device. These corrections are programmed, via a lookup table keyed to the undulator gap (field), to straighten the orbit through the device. A measure of the resulting improvement was that the fifth harmonic flux increased from 70% to more than 90% of its theoretical value. An additional skew quadrupole winding is used to correct coupling caused by the undulator as a function of gap. By shunting some current around four of the ring quadrupoles (two upstream and two downstream of the undulator) the lattice functions can be corrected so that the maximum tune shifts are $\Delta\nu_x \leq 0.0001$ and $\Delta\nu_y \leq 0.0007$ for any gap of the undulator. The shunted currents are also keyed to the undulator gap. In conjunction with the global feedback, over the entire operational range of the undulator, the maximum vertical closed orbit variation at other source points around the ring is ±5 μm, and the maximum throughput variation observed by other beamline users is about 1.5%. This throughput variation is the result of source size variation, an expected result of $\beta_y(s)$ for vertical and also some ε_x variations due to the incomplete lattice function correction. Since some users require throughput variations ≤0.1%, the lattice correction scheme will need to be improved.

2 FUTURE PLANS

2.1 Insertion Devices

An electromagnetic undulator will be installed on Aladdin in the fall. This undulator, combined with a normal incidence monochromator, will cover the photon energy range of 8 eV to 40 eV. A second electromagnetic undulator is planned, probably to be installed in late 1998.

2.2 Ring Upgrade

A major effort is underway to understand the sources of noise in the stored beam and to implement measures necessary to increase beam stability. During the fall of 1997 large sections of the main ring vacuum chamber will be replaced. The design of the new sections will address some long standing difficulties of operation. The principal benefit will be the decoupling of the chamber that passes through the quadrupole doublets from the chamber that fits in the dipole gap by means of a newly installed bellows. The quadrupole chamber, which contains the BPM's, can then be firmly attached to bedrock via the quadrupole stands, and not subject to motion and stress resulting from dipole section movement, thus optimizing beam stability. A second modification of the new chamber is the addition of separate ion clearing electrodes. The present BPM's are also used as clearing electrodes. The electronics necessary to isolate the ion clearing high voltage (up to 1200 V) from the stripline beam signal is not conducive to high resolution beam position measurements. The new BPM's are more robust, able to withstand baking and synchrotron radiation heating with negligible distortion.

As mentioned in Section 1.4, a program to rid the beam of noise from power line frequencies and its harmonics is well underway. The next most likely place to clean up power line noise is in the main ring rf system. After that each subsystem will be carefully evaluated to determine its contribution to any beam noise.

A new 120 kV electron gun line is designed and will be built as the replacement injector for the Aladdin microtron. The new gun will have a gridded structure so that it can be modulated at the 50 MHz frequency of the main ring rf system. This will allow efficient filling of the rf buckets, and include the possibility of filling various bunch patterns. The high voltage is necessary to ameliorate beam size growth due to space charge forces, a problem with the present 35 KeV gun.

REFERENCES

[1] D. L. Huber, et al, 'SRC: Current activities and plans for the future', Nuclear Instruments and Methods in Physics Research A 347 (1994) 49-51.

[2] M. A. Green, et al, 'FIRST UNDULATOR OPERATION AT SRC', Nuclear Instruments and Methods in Physics Research A 266 (1988) 91-95.

[3] R. Reininger, et al, 'Vacuum untraviolet high-resolution and high-flux beamline for the Aladdin storage ring', Review of Scientific Instruments, 66 (2), February 1995, 2194-2196.

[4] F. C. Younger, et al, 'Two new insertion devices for Aladdin', Nuclear Instruments and Methods in Physics Research A 347 (1994) 98-101.

[5] R. A. Bosch, 'Long-wavelength radiation along a straight-section axis in an electron storage ring', Nuclear Instruments and Methods in Physics Research A 386 (1997) 525-530.

[6] R. A. Bosch, et al, 'Infrared radiation from bending magnet edges in an electron storage ring', Proceedings of SRI '95, RSI 67 (1996) 3346 (K).

[7] K. J. Kleman, 'A Bunch Lengthening Cavity for Aladdin',Proceedings of the 1995 Particle Accelerator Conference, Pg. 1785.

[8] R. A. Bosch and C. S. Hsue, 'Suppression of Longitudinal Coupled Bunch Instabilities by a Passive Higher Harmonic Cavity',Particle Accelerators, 42, 81 (1993).

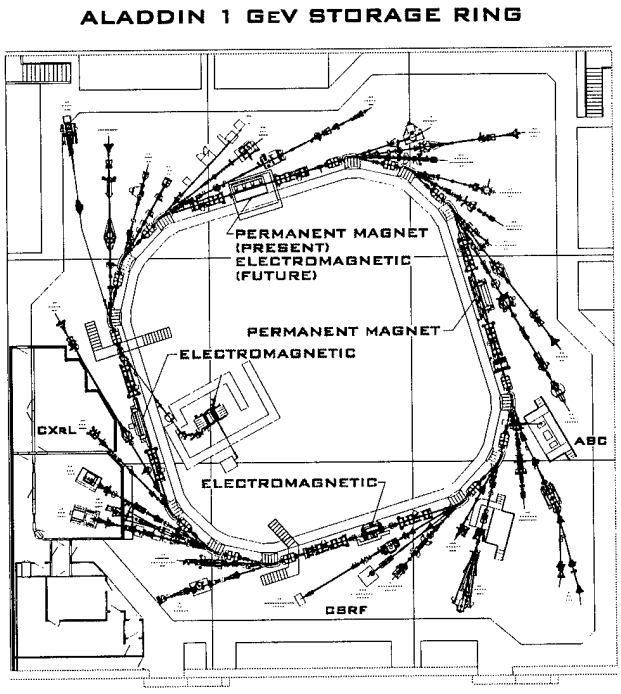


Figure 1: Aladdin plan view: present and future undulators; several user program areas, i.e. CXrL, CSRF, ABS.

AN ALTERNATIVE LATTICE DESIGN FOR A COMPACT LIGHT SOURCE RING

A. A. Garren*, and M. A. Green**
* UCLA Center for Advanced Accelerators, Los Angeles CA 9009
** Lawrence Berkeley National Laboratory, Berkeley CA 94720, USA

Abstract

A 26 meter circumference 1.5 GeV electron storage ring, designed to deliver x-rays with a critical energy of 10.4 keV, and has been proposed for the UCLA campus. This ring has twelve 6.9 T superconducting dipoles grouped in pairs. Each pair bends the beam sixty degrees. The quadrupoles and sextupoles are conventional. The alternative ring design presented in this report would have twelve separate 6.9 T superconducting dipoles that bend the beam thirty degrees each. Although this ring would have a larger circumference (about 36 meters) and more focusing elements, it would have a smaller emittance and consequently it would be a brighter source of x rays. As with the smaller ring, the focusing elements would be conventional. The x-ray power from the alternative ring delivered to the users is expected to be much higher than that from the smaller ring.

1 BACKGROUND

UCLA has proposed to build an ultra compact light source (UCS) on the campus. The electron storage ring produces synchrotron light within 6.9 T bending magnets. It would have an energy of 1.5 GeV and a circumference of 26 meters[1,2]. The compactness of the ring is achieved by pairing the 30 degree bending magnets to form six bending stations. Synchrotron light is extracted from the downstream dipole. The synchrotron light from the upstream magnet is absorbed by the downstream dipole vacuum chamber. The beam current in the machine is limited by the amount of synchrotron radiation that can be absorbed by the downstream magnet and its vacuum chamber. The compact storage ring has a race track structure about 10.8 meters long by about 5.5 meters wide.

Each arc in the baseline machine consists of six 30 degree superconducting dipoles, four conventional room temperature quadrupoles and six conventional sextupoles. The dipoles are grouped in three pairs; each pair share a common cryostat. Conceptually, the arcs of the ring are built up of three cells, where the outer two cells are truncated beyond the two dipoles. The beam emittance of the ring is entirely determined by the arc lattice. The baseline ring has two different straight section between the two arcs. One side of the race track has seven quadrupoles with short straight sections between them. This region will contain RF Cavities. The other side of the race track has eight quadrupoles, one 1.6 meter long space and two 0.8 meter long spaces. This side of the race track will be used for injection. A schematic representation of the baseline UCS ring is shown in Figure 1

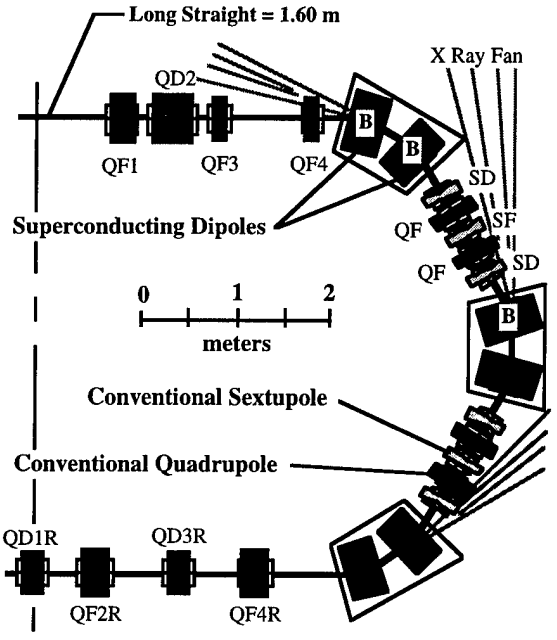


Figure 1 A Schematic Representation of Half of the Baseline UCLA Ultra Compact Light Source

2 THE ALTERNATIVE RING DESIGN

The design of the alternative ring is driven by the desire to extract the synchrotron radiation from all of the dipoles so that beam current can be increased and more x-rays can be sent to more users. There is also a desire to reduce machine emittance so that the vacuum chamber throughout the ring can have the same cross-section. As a result, the quadrupoles and sextupoles would all have the same aperture. The number of types of quadrupoles would be reduced to two and there would be only one type of sextupole. The reduced emittance lead to a smaller beam size in the dipoles and brighter x-ray beams.

The alternative ring has six identical 6 meter long cells. Thus the periodicity of the machine is six as compared to one for the baseline ring. Each of the six cells contains two 30 degree superconducting dipoles. Each cell has a 1.34 meter long drift space (between two quadrupole doublets) and a section that contains all of the chromaticity sextupoles. The sextupoles surround QF3 focusing quadrupole, which forces the dispersion to be zero in the long straight section. The dipoles have parallel faces that provide vertical edge-focusing.

The ring has six 1.34 meter long drift spaces. Three adjacent long straight sections can be used for injection (one for the septum and two for kickers that are three quarters of a betatron wave length from the septum in the horizontal direction. One or two of the other long

0-7803-4376-X/98/$10.00 © 1998 IEEE

straight sections can be used for RF cavities. This leaves one or two straight sections that can be used for insertion devices. The x-rays from the insertion devices would travel through the downstream dipole. The insertion device x-rays would be at the edge of the x-ray fan from the downstream dipole. Figure 2 shows a schematic representation of half of the alternative compact light source storage ring.

The x-ray fan shown in figure 2 represents about half of the x-rays produced in each of the bending magnets. The quadrupoles are assumed to be of the figure of eight type. This type of quadrupole is open along the mid-plane to allow for the passage of x-rays to the user. By using quadrupoles and sextupoles that are open on the mid-plane, 70 to 80 percent of the x-ray fans can be transmitted to the users.

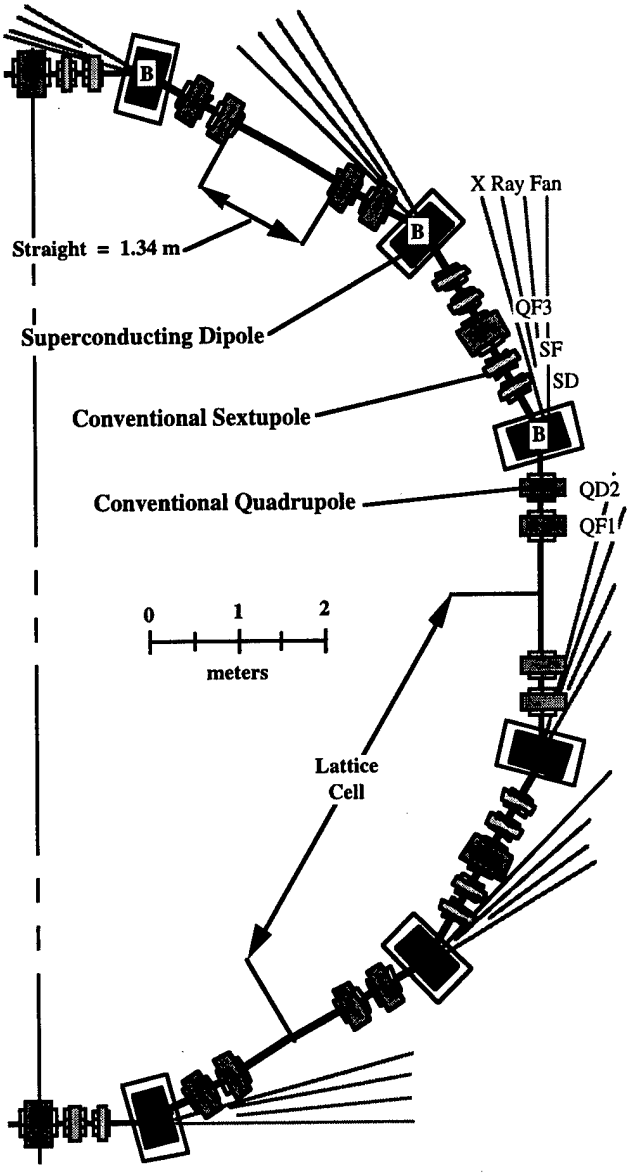


Figure 2 A Schematic Representation of Half of the Alternate Compact Light Source Ring

Table 1 A Comparison of the Lattice Parameters for Two 1.5 GeV Compact Light Source Rings

PARAMETER	Baseline Ring	Alternative Ring
Maximum Energy (GeV)	1.5	1.5
Injection Energy (GeV)	0.1	0.1
Max. Beam Current (mA)	50	100
Ring Circumference (m)	26.0	36.0
Bend Radius (m)	0.7257	0.7257
Dipole Length (mm)	380	380
Dipole Induction* (T)	6.984	6.894
x-ray Critical Energy* (keV)	10.4	10.4
Number of x-ray Stations	6	12
Extracted x-ray Power* (kW)	15.4	61.6
x-ray Brightness** (MWm^{-2})	0.51	1.71
Number. of Long Straights	1	6
Long Straight Length (m)	1.60	1.34
Machine Periodicity	1	6
Number of Cells	6	6
Number of Bend Stations	6	12
Number of S/C Dipoles	12	12
Dipole Pole Width (mm)	180	176
Dipole Cold Gap (mm)	40	40
Number of Quadrupoles	23	30
Quadrupole Dia. (mm)	Variable	33.2
Number of Sextupoles	12	24
Sextupole Dia. (mm)	Variable	33.2
Horz. Op. Emittance* (nm)	2110	309
Vert. Op. Emittance* (nm)	234	34
Horizontal Tune	3.17	4.42
Vertical Tune	2.57	2.38
Horizontal Chromaticity	-2.22	-5.24
Vertical Chromaticity	-5.24	-7.40
Max. Horizontal Beta (m)	3.09	5.62
Max. Vertical Beta (m)	6.66	5.54
Max. Dispersion (m)	1.29	0.62
Energy Loss per Turn* (MeV)	0.62	0.62
RF Voltage (MV)	2.5	1.2
RF Frequency (MHz)	500	500
Energy Spread (parts in 1000)	1.52	1.52
Bunch Length* (mm)	30	8.1
Horz. Damping Time* (ms)	0.41	0.57
Vert. Damping Time* (ms)	0.42	0.58
Energy Damping Time* (ms)	0.21	0.30
Quantum Lifetime (s)	2.2×10^{8}	$>1 \times 10^{10}$

* at the full design energy of the machine
** at full design energy and 5 meters from the dipole

3 DISCUSSION

Table 1 compares the lattice parameters for the baseline ring and the alternative design. Both machine have a maximum energy of 1.5 GeV and an injection energy of 0.1 GeV. A microtron is assumed for the injector for both cases. The beam current in the baseline case is limited by heating due to x-rays from upstream dipole of the dipole pair in the vacuum chamber of the second dipole. The Alternative ring design has no such limitation. With correction, the beam current in the

alternative machine might be increased a factor of two or three. The increased periodicity results in an emittance that is a factor of seven lower than the base line case. As a result, the beam aperture of all of the dipoles and quadrupoles is reduced by almost a factor of two. The quadrupoles and the sextupoles can all have the same design aperture. As a result, there are two types of quadrupoles and one type of sextupole. All of the quadrupoles in the ring can have the same cross-section. Twenty-four quadrupoles are 200 mm long while the other six are 300 mm long. All of the twenty-four sextupoles are 100 mm long. All of the quadrupoles and sextupoles have a pole induction that is less than 0.6 T. As a result, the magnets should track very well during the acceleration phase of the storage ring operation.

The dipoles in the alternative ring are not much different from the baseline ring case. The proposed dipoles for the ring are similar in design to magnets proposed by P. Vobly INFN Novosibirsk[3,4,5]. The horizontal aperture of the dipole is dominated by sagita and the x-ray fan out of the upstream part of the dipole. A conservative dipole design calls for a cold pole width of 176 mm. If the good field region of the dipole covers 90 percent of the pole width, the beam position can be shifted and the pole width reduced to 155 mm. The cold gap of the dipole did not change from the baseline case (despite reduced beam emittance) because the vacuum chamber inside the dipole has been designed to be identical to the vacuum chamber in the other elements, in order reduce the impedance. If a different vacuum chamber dimension was used in the dipole, the magnet cold gap could be reduced from 40 to 32 mm. The cost of the dipoles is driven by the pole width.

The energy loss per turn is 0.62 MeV per turn for both rings. The RF voltage for the alternative ring is lower than for the baseline case. The bunch length for the baseline case is 30 mm, compared to 8.1 mm for the alternative lattice. It is assumed that one would use two 500 Mhz RF cavities to provide the needed RF voltage and power for the light source. The increased x-ray power extracted from the alternative machine is due to an increase in the beam current and the fact that the x-rays are completely extracted from all twelve dipole magnets. Since the x-ray power is not limited by cooling, the extracted x-ray power will continue to increase with increased beam current. The increased brightness of the alternative ring is due to a combination of increased beam current and reduced beam size in the dipole magnet, due to a lower emittance.

For both rings, 10 percent coupling between the vertical and horizontal emittances is assumed. The alternate ring, with constant aperture dipoles, quadrupoles and sextupoles, permits the beam to be fully coupled and still maintain a 15 sigma margin around the beam within the dipoles. The margin for the beam in the QF1 quadrupole would be 11 sigma. The margin in all other elements would be 15 sigma. In most respects, the alternative ring design is more conservative than the baseline case. In both cases, the dipoles are expected to operate at about 88 percent of their design critical current when the machine operates at its design energy.

The dynamic aperture, measured in uncoupled sigmax units and fully coupled sigmay units, is about 20 sigma, which corresponds to about 30 mm. The tune variation is within 0.01 for relative momentum deviation of ±2 percent.

4 CONCLUSIONS

The alternative machine appears to be a better machine at its design energy than the baseline machine. The x-ray brightness and the amount of x-ray power available to the experimenter could be as much as an order of magnitude higher for the alternative ring operating at high beam currents. The alternative ring has the potential to serve more users with brighter x-ray beams.

The major problem with the alternative ring design is its size. The circular alternative ring is approximately 12 meters in diameter, compared to the 6 by 11 meter race track baseline ring. The increase in size may or may not reflect negatively on the cost of the machine. However, since the alternative design uses a large number of identical elements, its cost may not be greater than that of the baseline ring. More engineering is needed in order for the cost either ring to be accurately cost estimated. The alternative ring design has not been optimized. It is quite possible that the alternative ring can be made smaller without affecting performance. Further work should be done to design a ring using the alternative ring lattice that has a circumference from 32 to 33 meters.

ACKNOWLEDGMENTS

The authors acknowledge discussions they have had with D. B. Cline and J. J. Kolonko of the UCLA Center for Advanced Accelerators. This work was performed with the support of the Office of High Energy and Nuclear Physics, United States Department of Energy under contract numbers DE-AC03-76SF00098.

REFERENCES

[1] A. A. Garren, D. B. Cline, M. A. Green, et al. "A 1.5 GeV Compact Light Source with Superconducting Bending Magnets," Proceedings of the 1995 Particle Accelerator Conference, p 119, IEEE Publications, New York (1995)

[2] D. B Cline, A. A. Garren, M. A. Green, et al. "A Compact-High Performance Damping Ring Using High Magnetic Field Bending Magnets," Proceedings of the 1995 Particle Accelerator Conference, p 520, IEEE Publications, New York (1995)

[3] G. N. Kulipanov, N. A. Mezentsev, L. G. Morgonov, et al, "Development of a Superconducting Compact Storage Rings for Technical Purposes in the USSR," Rev. Sci. Instrum. **63** (1) p 731 (1992)

[4] M. A. Green and D. Madura, "Design Parameters for a 7.2 Tesla Bending Magnet for a 1.5 GeV Compact Light Source," IEEE Transactions on Magnetics **MAG-32**, No. 4, p 2081, (1996)

[5] M. A. Green, A. A. Garren, E. M. Leung, et al. "A Superconducting Bending Magnet System for a Compact Synchrotron Light Source," Advances in Cryogenic Engineering **41**, p 367, Plenum Press, New York (1996)

PLANNED OPTICAL DIAGNOSTICS FOR THE APS LOW-ENERGY UNDULATOR TEST LINE

A. H. Lumpkin, W. J. Berg, and B. X. Yang
Advanced Photon Source, Argonne National Laboratory
9700 South Cass Avenue, Argonne, Illinois 60439 USA

Abstract

At the Advanced Photon Source (APS), an alternate configuration of the injector linacs (low-energy undulator test line) using an rf gun as the source is projected to provide low, normalized emittance electron beams ($\varepsilon_n \sim 5\pi$ mm mrad). In order to characterize such beams, the present intercepting Chromox screens with limited spatial resolution and temporal response are being complemented by optical transition radiation (OTR) screens at selected positions in the beamline to provide sub-100 μm spatial resolution and sub-ps response times. Both gated cameras and streak cameras will be used to measure the beam properties. Additionally, coherent transition radiation (CTR) and diffraction radiation (DR) based techniques will be evaluated. These beam characterizations will support self-amplified spontaneous emission (SASE) scaling experiments.

1 INTRODUCTION

An increased interest in diffraction-limited light sources for the next generation sources and the implementation of prototype or scaling experiments has been evident since the Fourth Generation Light Source Workshop held in Grenoble in January 1996 [1]. At the Advanced Photon Source (APS), a research and development effort had been underway for several years [2, 3, 4] to use the injector linacs with a low-emittance electron beam source. More specifically, an rf thermionic gun would be used for injection into the 100-to 650-MeV linac subsystem based on the existing 200-MeV electron linac and 450-MeV positron linac. The low, normalized emittance beams ($\varepsilon_n \approx 5\ \pi$ mm mrad) require an upgrade to the existing Chromox viewing screens for characterization of beam transverse size and bunch length. We are in the process of installing optical transition radiation (OTR) screens at selected positions in the beamline to provide sub-100 μm spatial resolution and sub-ps response times [5, 6]. In order to compensate for the reduced brightness of this conversion mechanism, both gated, intensified cameras and streak cameras will be used to measure the beam properties. Initial tests with beam at 650 MeV have been done with a charge-injection device (CID) camera. Additionally, the feasibility of using coherent transition radiation (CTR) and diffraction radiation (DR) based techniques will be evaluated. The diagnostics will be used to characterize, optimize, and monitor the bright beams needed to support self-amplified spontaneous emission (SASE) scaling experiments at $\lambda \sim 120$ nm and a beam energy of 400 MeV as described separately [7].

2 EXPERIMENTAL BACKGROUND

The APS facility's injector system uses a 250-MeV S-band electron linac and in-line S-band 450-MeV positron linac. The electron gun is a conventional thermionic gun in standard operations. For the alternate configuration, an rf thermionic gun, designed to generate low-emittance beams (<5 π mm mrad) and configured with an α-magnet, injects beam just after the first linac accelerating section [4]. Then both in-line linacs can be phased to produce 100-650 MeV electron beams when the positron converter target is retracted.

The rf-gun projected, normalized emittance is orders of magnitude lower than the conventional gun and correspondingly much smaller beam spot sizes ($\sigma_{x,y} \approx 100$ μm) result than from the conventional gun. The standard intercepting screens are based on Chromox of mm-thickness and with a 300-ms decay time [8]. Previous experiences on the Los Alamos linac-driven free-electron laser (FEL) with a low-emittance photoelectric injector (PEI) support the applicability of optical transition radiation screens in this case [9]. A summary of beam properties is given in Table 1. Initial tests of a Ti foil used as an OTR screen at a beam energy of 650 MeV are described in the next section.

Table 1: APS Linac Beam Properties in the Low-emittance Mode (rf Gun)

rf frequency (MHz)	2856
Beam energy (MeV)	100-650
Micropulse charge (pc)	350
Micropulse duration (ps)	3-5 (FWHM)
Macropulse length (ns)	30
Macropulse repetition rate (Hz)	1-20
Normalized emittance (π mm mrad)	~5 (1 σ)

3 BEAM CHARACTERIZATIONS

A general description of the proposed techniques for beam characterization is given in Ref. 2. A subset of those based on optical techniques and now in the installation and testing stage are presented here.

0-7803-4376-X/98 /$10.00 © 1998 IEEE

3.1 Transverse Characterizations

Although beam position monitors are also planned using the stripline pickup technology, the transverse beam sizes and profiles are key to evaluating the beam emittance and its preservation throughout the accelerator and transport lines.

At the 50-MeV station, two additional OTR screens are being installed. Although their axial spacing is less than 1 meter, beam quality will be initially checked at this point using the two-screen beam size measurement technique as well as the beam size versus quadrupole-field strength scan technique.

Another key station is at the end of the linac in the transport line, nominally the 650-MeV station. At this point an optical transport line is being installed to bring the OTR light to an optical table outside of the linac tunnel. This table will provide an experimental base for measurements with a gated, intensified charge-coupled device (ICCD) camera (Stanford Computer Optics, Quik-05A). With the microchannel plate (MCP)-based shutter, 5-ns-wide samples from the beam macropulse are possible. The gain factor of the MCP also allows for imaging of defocused spots during a quadrupole field scan for an emittance measurement. The tests of these cameras have already been done on the APS positron accumulator ring (PAR) and the booster synchrotron using synchrotron radiation from ~1 nC charge passing through a dipole.

An initial test of OTR source strength has been done using 1-3 nC of beam in a macropulse from the conventional gun and at energies of 580 and 650 MeV. Since the Ti foil was placed over only the lower half of the Chromox screen at this station, the e-beam could be steered and focused on the Chromox first, and then steered downward to the OTR foil. Figure 1 shows a sample beam image, and Fig. 2 shows the horizontal and vertical profiles with Gaussian fits. Focused spots (~2 mm, FWHM) were readily imaged with the CIDTEC CID camera operating in the X2 gain position with 3 nC in a macropulse. However, normal transport conditions usually have a large spot size at this location and are seen much more readily with the Chromox screen. This baseline measurement supports the OTR screen choice.

The PAR bypass transport line provides a unique opportunity with its 10-m drift space to perform a three-screen emittance measurement. As shown in Fig. 3, the center screen is 5 m from the two end ones. Relay optics will bring the images to a lead-shielded ICCD camera. A fourth screen will be used for OTR interferometer experiments in conjunction with the center screen.

3.2 Longitudinal Characterizations

Since longitudinal beam brightness is related to evaluations of SASE gain, the measurement of bunch duration and profile are also critical in this program.

At the 50-MeV station, one of the OTR screens and one part of the beamline cross will be configured to send

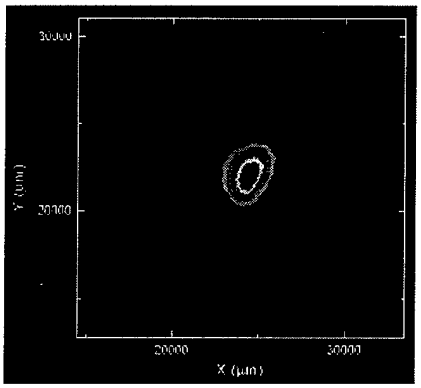


Figure 1: One of the first OTR images of APS linac beam at 650 MeV and ~3 nC in a macropulse from the conventional thermionic gun. A two-frame average was used to improve the statistics.

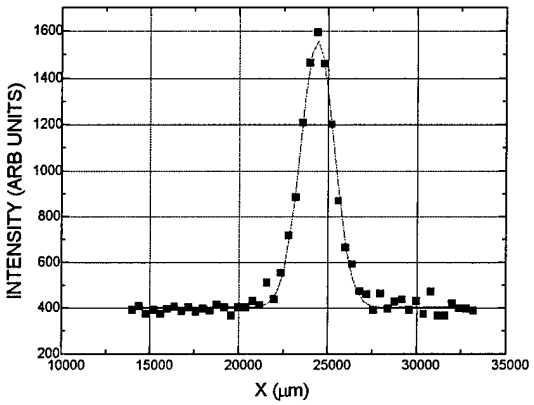


Figure 2: Horizontal profile for the OTR image in Fig. 1. The solid line is a Gaussian profile fit to the data. The beam sizes are about 1 mm (1σ).

the far-infrared (FIR) coherent transition radiation that will be generated by the few-ps or mm-long bunches to a FIR Michelson interferometer. An optical autocorrelation technique will be evaluated as a bunch duration diagnostic [10].

A baseline technique will be based on a Hamamatsu C5680 dual-sweep streak camera viewing the incoherent OTR signal from the 650-MeV station. The transport of OTR to the optics table outside the tunnel will facilitate these experiments. The most likely vertical sweep plug-in will be a synchroscan unit phase-locked to 119.0 MHz, the 24th subharmonic of the 2856 MHz frequency. Low-jitter of the synchronous sum of beam bunches will be advantageous in dealing with the very low charge in a single micropulse. Because the S-band micropulse spacing is much smaller than the 119.0-MHz period, the sequence of micropulses will best be displayed using the dual-sweep technique. This particular 119.0-MHz unit has been successfully phase-locked to an rf source at the Duke Storage Ring FEL facility which is injected by an S-band linac [11]. At APS, a low jitter countdown circuit has been built

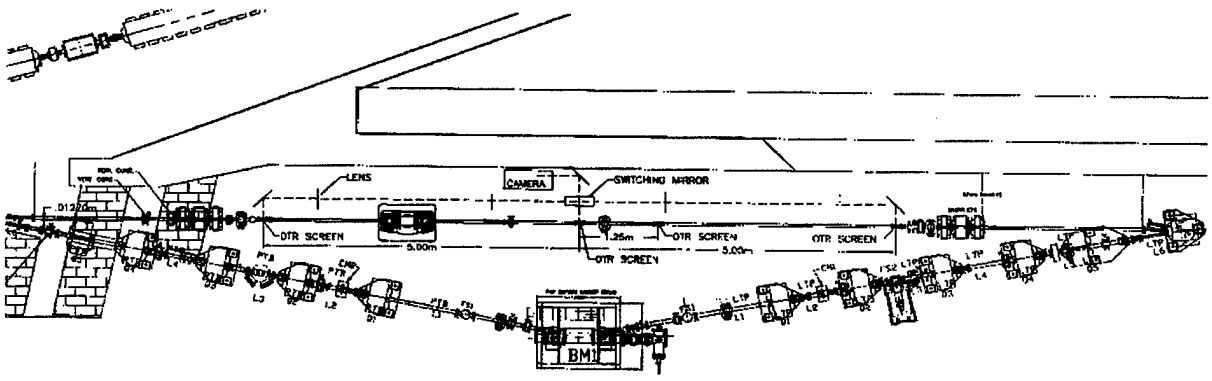


Figure 3: Schematic drawing of the three-screen emittance measuring station at the bypass area to the positron accumulator ring. The 10-m drift space with $B_{x,y}$ ~5 m will allow reasonable rotation of the phase space. A beam waist will be produced on the center screen location.

using Motorola ECLIN PS logic to generate the 24th subharmonics. It has been tested with a 0.7 ps (rms) jitter pulse generator, and the total jitter was observed to be 1.1 ps. Bandpass filters on the output result in a clean 119.0-MHz sine wave to be used with the synchroscan unit [12].

In the two cases above, an intercepting OTR foil is used. For nonintercepting bunch-length measurements, coherent DR is a possible way to extend the Michelson interferometer technique to a nonintercepting category [13, 14]. In the streak camera case, a bend in the transport line, a special few-period diagnostics wiggler, or the final prototype wiggler for the SASE experiments are possible nonintercepting sources of optical radiation for a bunch-length measurement.

4 SUMMARY

In summary, the adjustments of optical diagnostic techniques to low-emittance beams are well underway in the APS linac. Tests of some techniques have already been done with alternative particle beam sources, e.g., OTR, gated cameras, and the synchroscan (119.0 MHz) streak camera. Further tests will be done with the conventional injector, and the initial tests with rf-gun injected beam are expected in the coming months of 1997.

5 ACKNOWLEDGMENTS

The authors acknowledge the foresight of John Galayda (Accelerator Systems Division) in keeping the options open for an undulator test line and Marion White for linac studies time for the OTR tests. This work was supported by the U.S. Department of Energy, Office of Basic Energy Sciences, under Contract No. W-31-109-ENG-38.

6 REFERENCES

[1] Proceedings of the Workshop on Fourth Generation Light Sources, Grenoble, France, January 22-25, 1996, J. Laclare (Ed.)

[2] A. H. Lumpkin, S. Milton, and M. Borland, "Proposed Particle-Beam Characterizations for the APS Undulator Test Line," *Nucl. Instr. and Methods* A341, pp. 417-421 (1994).

[3] A. H. Lumpkin et al., "Diagnostics for the APS Undulator Test Line," Proc. of the Fifth Beam Instrumentation Workshop, Santa Fe, NM, Oct. 20-23, 1993, *AIP Conf. Proc.* 319, pp. 211-219 (1994).

[4] M. Borland, "An Improved Thermionic Microwave Gun and Emittance Preserving Transport Line," Proc. 1993 Particle Accel. Conference, Washington, DC, May 17-20, 1993.

[5] D. W. Rule, R. B. Fiorito, A. H. Lumpkin, R. B. Feldman, and B. E. Carlsten, *Nucl. Instr. and Methods* A296, p. 739 (1990).

[6] A. H. Lumpkin, R. B. Fiorito, D. W. Rule, D. Dowell, W. C. Sellyey, and A. R. Lowrey, *Nucl. Inst. and Methods* A296, p. 150 (1990).

[7] S. V. Milton et al., "The Advanced Photon Source Low-Energy Undulator Test Line," these proceedings.

[8] M. White and A. Lumpkin, private communication, Feb. 15, 1997.

[9] Alex H. Lumpkin, "Advanced, Time-Resolved Imaging Techniques for Electron Beam Characterization," Proc. of the 1990 Workshop Accelerator Instrumentation, Batavia, IL, Oct. 1-4, 1990, AIP No. 229, p. 151, and references therein (1991).

[10] H. C. Lihn et al., *Phys Rev.* E 53(b), p. 6413 (1996).

[11] A. H. Lumpkin et al., "Initial Application of a Dual-Sweep Streak Camera to the Duke Storage Ring OK-4 Source," these proceedings.

[12] R. Laird and F. Lenkszus, Argonne National Laboratory, private communication, April 1997.

[13] W. Barry, "Measurements of the Sub-picosecond Bunch Profiles Using Coherent Transition Radiation," Proc. 1996 Beam Inst. Workshop, Argonne, IL, May 6-9, 1996, AIP Conf. Proc. 390, p. 173 (1997).

[14] Y. Shibata et al., *Phys Rev.* E 52, p. 6787 (1995).

INITIAL APPLICATION OF A DUAL-SWEEP STREAK CAMERA TO THE DUKE STORAGE RING OK-4 SOURCE

A. H. Lumpkin and B. X. Yang
Advanced Photon Source, Argonne National Laboratory
9700 South Cass Avenue, Argonne, Illinois 60439 USA

V. Litvinenko, S. Park, P. Wang, and Y. Wu
Duke University FEL Laboratory, Durham, North Carolina 27708 USA

Abstract

The visible and UV spontaneous emission radiation (SER) from the Duke OK-4 wiggler has been used with a Hamamatsu C5680 dual-sweep streak camera to characterize the stored electron beams. Particle beam energies of 270 and 500 MeV in the Duke storage ring were used in this initial application with the OK-4 adjusted to generate wavelengths from 500 nm to near 200 nm. The OK-4 magnetic system with its 68 periods provided a much stronger radiation source than a nearby bending magnet source point. Sensitivity to single-bunch, single-turn SER was shown down to 4 μA beam current at λ = 450 nm. The capability of seeing second passes in the FEL resonator at a wavelength near 200 nm was used to assess the cavity length versus orbit length. These tests (besides supporting preparation for UV-visible SR FEL startups) are also relevant to possible diagnostics techniques for single-pass FEL prototype facilities.

1 INTRODUCTION

It is well-established that two critical factors in successfully starting a free-electron laser (FEL) in an oscillator configuration are the gain (strongly dependent on peak current or particle beam charge density) and the synchronism of the orbit length and the resonator cavity length. Recently, in a collaborative effort between Duke University and the Advanced Photon Source (APS), the first dual-sweep streak camera images were taken of the output radiation of the Duke optical klystron version 4 (OK-4) installed in the 1-GeV storage ring [1]. These data were used to address directly the issues of the observed bunch length as a function of single-bunch current and rf cavity gap voltage. For the available rf fields a reasonable operating condition for adequate FEL gain was identified. Additionally, the key aspect of ring orbit length versus the resonator round trip time was actually done with λ = 195 nm radiation outcoupled from the resonator, a wavelength shorter than the existing 240-nm FEL lasing record. The usefulness of these key measurements was confirmed as first lasing experiments were successful a few weeks later, although at 350-400 nm [2]. These experiments in a sense are extensions of techniques demonstrated on a linac-driven visible FEL in the late 1980's [3].

2 EXPERIMENTAL BACKGROUND

The Duke storage ring and OK-4 have been described elsewhere [1,2] and key parameters are listed in Table 1. Operating energies from 0.25 to 1.0 GeV are possible. In this case the linac injection energy was about 270 MeV and beam could be stored there or ramped slowly upward in energy to 500 MeV. A key practical detail involved the rf frequency of 178.547 MHz which is a subharmonic of the linac's s-band at 2856 MHz. To use the synchroscan streak plug-in at 119.0 MHz, the 24th subharmonic of 2856, a special circuit was built at Duke that was phase-locked to the 178.5 MHz [4]. The OK-4 total length of 68 periods was also critical to performing the very low (sub-0.1 mA) current measurements.

Table 1: Summary of Parameters of the Duke Storage Ring and OK-4 (see Ref. 1)

Parameter	Design Value
Storage Ring	
Operating energy (GeV)	0.25-1.0
Ring circumference (m)	107.46
Revolution freq. (MHz)	2.789
rf frequency (MHz)	178.547
Beam current, A	0.1
Peak current, A	80-130
Horizontal emittance (m-rad)	18×10^{-9}
Vertical emittance, m-rad	1×10^{-9}
Bunch length (σ, ps)	33
OK-4 Parameter	
Undulator length (m)	3.40
Period (m)	0.10
Peak magnetic field (kG)	0.0-5.8
Buncher length (m)	0.34
Magnetic field (kG)	0-12

As shown schematically in Fig. 1, the SER was initially picked off by a retractable mirror positioned upstream of the cavity mirror. Mirrors and/or beam splitters were also used to bring the cavity's outcoupled radiation to the APS streak camera. A monochromator that is

0-7803-4376-X/98 /$10.00 © 1998 IEEE

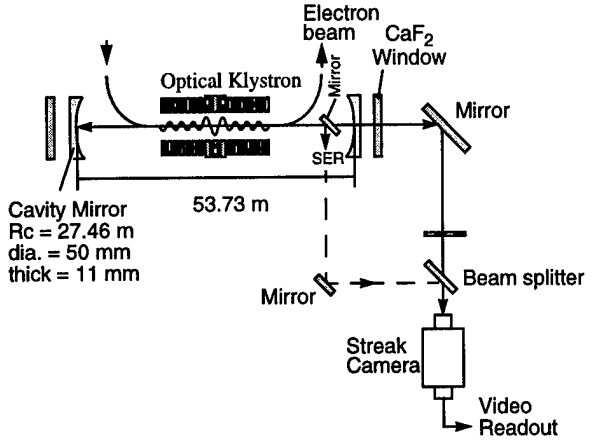


Figure 1: Schematic of the resonator set-up on the Duke OK-4 storage ring FEL. A pick-off mirror inserted just upstream of the cavity mirror allows the sampling of the SER for each pass of the electron beam.

not pictured was used to verify the operational wavelengths generated by the OK-4. The Hamamatsu C5680 dual-sweep streak camera was generally run with the vertical sweep in synchroscan mode and the horizontal sweep time selected for 10 μs, 50 μs, 1 ms, or 50 ms. With the revolution frequency in the ring of 2.78 MHz, single-bunch, turn-by-turn data could readily be attained.

It also should be noted that the nominal operating range of the S-20 photocathode streak tube with the UV-transmitting input optics is from 200 nm to 800 nm [5]. However, there is a rapid decrease in transmission of UV light through this input optics as one approaches and goes below $\lambda = 250$ nm. This practical effect in detector sensitivity was a key part of our tests, and why we originally looked at SER in the 400-500 nm regime in dual-sweep and then used synchronous averaging at $\lambda = 200$ nm.

3 EXPERIMENTAL RESULTS

3.1 Bunch Length

Initial tests on beam imaging were done with the bending magnet source, but we quickly moved on to the much stronger OK-4 source. A 450 × 40 nm bandpass filter rejected most of the bending magnet's white radiation. A representative example of a dual-sweep streak image at $\lambda = 450$ nm, beam energy $E_B = 500$ MeV, rf gap voltage $V_{rf} = 150$ kV, and beam current $I_B = 1.62$ mA is shown in Fig. 2. The vertical axis is the fast time axis with about 800 ps of the 1000-ps range displayed, and the horizontal sweep covers 10 μs. Each vertical image comes from a single pass through the OK-4. The selected fifth image's temporal profile has a calculated duration of 162 ps (FWHM). For comparison purposes, Fig. 3 then shows a similar image but with a higher gap voltage $V_{rf} = 500$ kV and lower current $I_B = 0.19$ mA. The measured bunch is much shorter at 60 ps (FWHM) or 25 ps (σ).

Figure 4 summarizes a series of measurements of bunch length with a variation of rf gap voltage and nominally for the low current regime (0.10-0.14 mA) and a ten times higher current regime (1.0-1.8 mA). It is noted that the plotted values are based on the preliminary analysis using the Hamamatsu MAC-TA algorithm which finds the peak intensity and then searches for the two half-maximum intensity points. Generally, there are ten beam images per file and two files were saved per parameter set. We are using the data from a single image, and plan to do further analysis on the actual profile shape as compared to a Gaussian shape. Based on available rf power, the 500 kV gap voltage with a few mA average current resulted in 5-10 A peak current. This latter value was calculated to have adequate gain for lasing experiments [2].

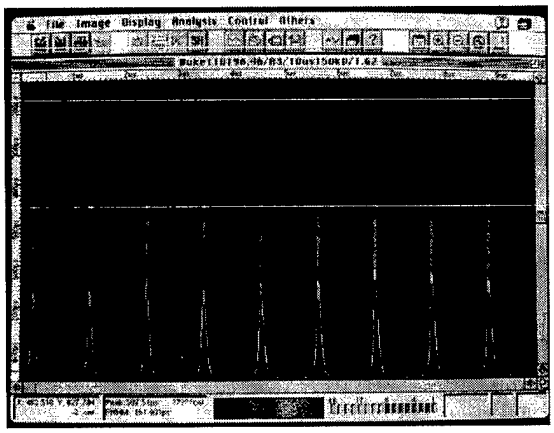


Figure 2: Dual-sweep streak camera image of the SER from the OK-4 at $\lambda = 450$ nm and for a beam energy of 500 MeV. The vertical sweep covers 800 ps while the horizontal axis is 10 μs. These are single-bunch data taken turn by turn. The measured bunch length at 150 kV rf gap voltage and $I_B = 1.6$ ma is 160 ps (FWHM).

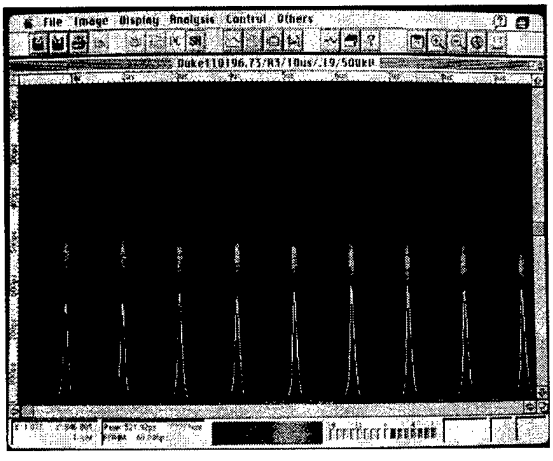


Figure 3: Dual-sweep streak camera image of SER from the OK-4 at $\lambda = 450$ nm, a beam energy of 500 MeV, $V_{rf} = 500$ kV, and $I_B = 0.19$ mA. The time axes are again 800 ps vertical and 10 μs horizontal. In this case, the bunch length of the selected image is 60 ps (FWHM).

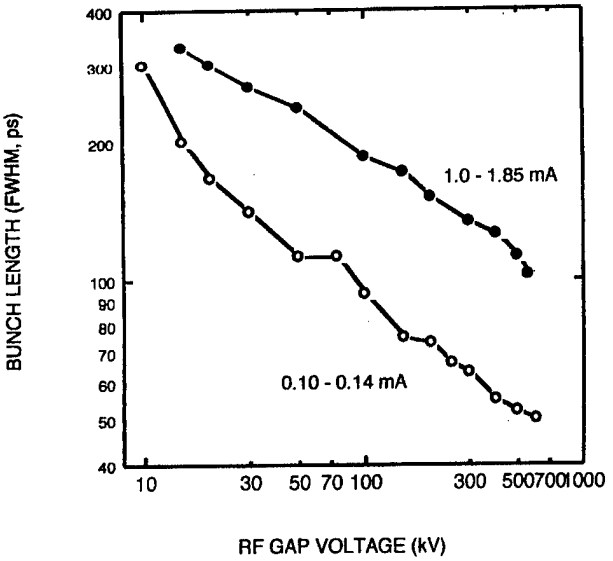


Figure 4: Plot of the variation of beam bunch length with rf gap voltage. The two sets of data are from low current (0.10-0.14 mA) and medium current (1.0-1.85 mA) runs.

3.2 Cavity Length/Orbit Length Synchronism

All measurements in the preceeding section used the retractable pick-off mirror upstream of the resonator cavity mirror. In order to evaluate the feasibility of detecting radiation near 200 nm, we initially used the pick-off mirror for wavelengths down to 220 nm in dual-sweep mode. We then changed to synchroscan sweep only and also changed a relay lens to a 50-mm focal length to provide a smaller focus at the entrance slit of the streak camera. The OK-4 was tuned to about λ = 195 nm, and the 193 nm × 10 nm band pass filter was put in the path to the streak camera. The radiation outcoupled from the cavity was then transported to the streak camera. At that point manual tweaking of the resonator cavity mirrors was done until the observed signal in the monochromator was reduced by 50% between the resonator mirrors' being tuned and detuned. The rf frequency for the storage ring was then varied to change the beam orbit length relative to the fixed resonator cavity length. As the stored beam current decreased, the bunch length shortened to about 40 ps (FWHM). We could then clearly display the relative arrival time of the second pass in the resonator compared to the first pass of the next e-beam bunch. Figure 5 shows an example where the second pass or lower image is 99.5 ps displaced from synchronism. By tracking the second pass's positions, the cavity and e-beam orbit length were synchronized. This preferred length was then used in subsequent lasing experiments within the next few weeks [2].

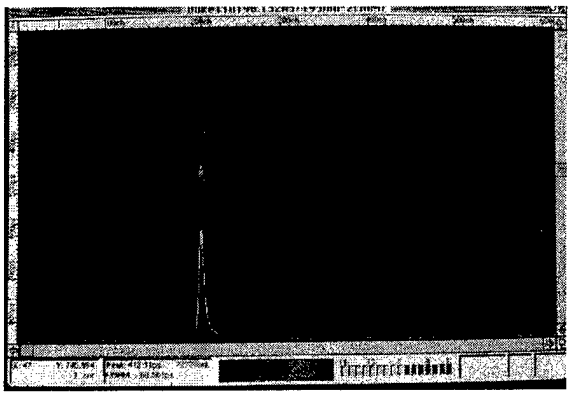


Figure 5: Synchroscan streak image of the SER outcoupled from the resonator cavity at $\lambda \sim 195$ nm. The very low current of 0.04 mA resulted in a bunch length of 44 ps (FWHM). The cavity length is different from the orbit length by 99.5 ps as shown by the vertical displacement of the two images.

4 SUMMARY

In summary, both the dual-sweep and synchroscan options of the streak camera were used to provide key information for the operation of this SR FEL. The source strength of the OK-4 SER was exploited to measure the electron beam bunch lengths at very low currents (<10 μA) and to detect radiation in the deep UV at λ = 195 nm. These results extend the range over which the techniques have been demonstrated on a FEL facility.

5 ACKNOWLEDGMENTS

The authors acknowledge John Galayda (ANL/APS/ASD) and John Madey (Duke FEL Laboratory) for their support of this collaboration. APS work was supported by the U.S. Department of Energy, Office of Basic Energy Sciences, under Contract No. W-31-109-ENG-38.

6 REFERENCES

[1] V. Litvinenko et al., *Nucl. Instrum. Methods* A375, p. 46 (1996).
[2] V. Litvinenko et al., "First UV/Visible Lasing with the OK-4/Duke Storage Ring FEL: Design and Initial Performance," Presented at SPIE's LASE '97, FEL Challenges Conference, February 13, 1997, San Jose, CA.
[3] A. H. Lumpkin, *Nucl. Instrum. Methods* A296, p. 134 (1990).
[4] P. Wang, Duke University, October 1996.
[5] W. Cieslik, Hamamatsu Photonics Corp., C5680 Camera Data Sheets, June 1996.

THE ADVANCED PHOTON SOURCE LOW-ENERGY UNDULATOR TEST LINE

S.V. Milton, J. N. Galayda, and E. Gluskin
Advanced Photon Source, Argonne National Laboratory, Argonne, IL 60439, U.S.A.

Abstract

There are a number of fully commissioned 3rd-generation synchrotron light sources in the world today. So far they have met the demanding requirements of the user community; however, there is always a desire to go beyond what is presently available or even desirable. The Advanced Photon Source (APS) Low-Energy Undulator Test Line (LEUTL) was conceived to address the advancement of synchrotron light sources. The LEUTL uses the existing APS linac and a low-emittance electron gun, and by means of measurements of the beam and generated light, will test new and innovative undulators and push the technology and physics of single-pass, coherent light sources. The design and status of the LEUTL will be described along with its immediate capabilities and those planned for the future.

1 INTRODUCTION

The APS linac is capable of accelerating electrons to more than 700 MeV. Coupled with a high-brightness, low-emittance electron source, it can also be used to explore areas beyond those for which it was originally intended, areas important to the future of synchrotron radiation sources and facilities.

The LEUTL was conceived and designed to examine just such topics. It consists of a high-brightness, thermionic rf gun, the APS linac, and additional beamlines directing the accelerated electron beam into a special-purpose enclosure with attached optical end station building. The LEUTL's purpose is twofold: the first is to fully characterize innovative, future generation undulators, some which may prove difficult or impossible to measure by traditional techniques such as very long small-gap undulators, superconducting undulators, and helical undulators; and the second is to act as a test line to investigate generation of coherent radiation at wavelengths down to a few tens of nanometers.

2 DESCRIPTION

Four modifications to the APS facility are required to make the LEUTL fully operational:

- Installation of a high-brightness thermionic rf gun.
- Addition of beamlines required to bypass both the positron accumulator ring (PAR) and the booster synchrotron (booster).
- Extension of the booster vault into the new LEUTL beamline enclosure and end station building.
- Construction of the undulator test line.

2.1 RF Gun

At the head of the APS linac a high-brightness thermionic rf gun with alpha magnet bunch compression [1] has been installed and is presently being commissioned (Figure 1). Table 1 lists the expected gun and transport system performance. This gun produces an electron beam of sufficient quality for most of the initial planned testing and experiments; however, additional high-brightness beam concepts are being pursued both in collaboration [2] and through an in-house effort using a laboratory-directed research and development award.

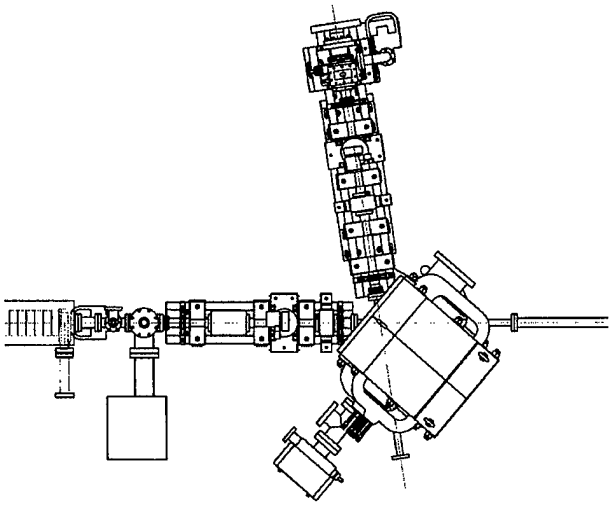


Figure 1: RF gun and transport system.

Table 1: Expected Gun Performance

Energy	3 MeV
Peak current	150 A
Normalized emittance	5π • mm-mrad
Energy spread	1%

2.2 Linac Diagnostics and Transfer Lines

The APS linac is reasonably well instrumented; however, additional beam diagnostics have been added to provide enhanced characterization of the high-brightness electron beam. In particular, optical transition radiation (OTR) screens have been installed at strategic locations. The light generated from these screens will be transported either to radiation-resistant hutches or outside the linac enclosure. Sensitive high-resolution cameras have been procured for detection of the beam profile signals and a 0.6-ps-resolution fast streak camera will be used for bunch length measurement.

0-7803-4376-X/98 /$10.00 © 1998 IEEE

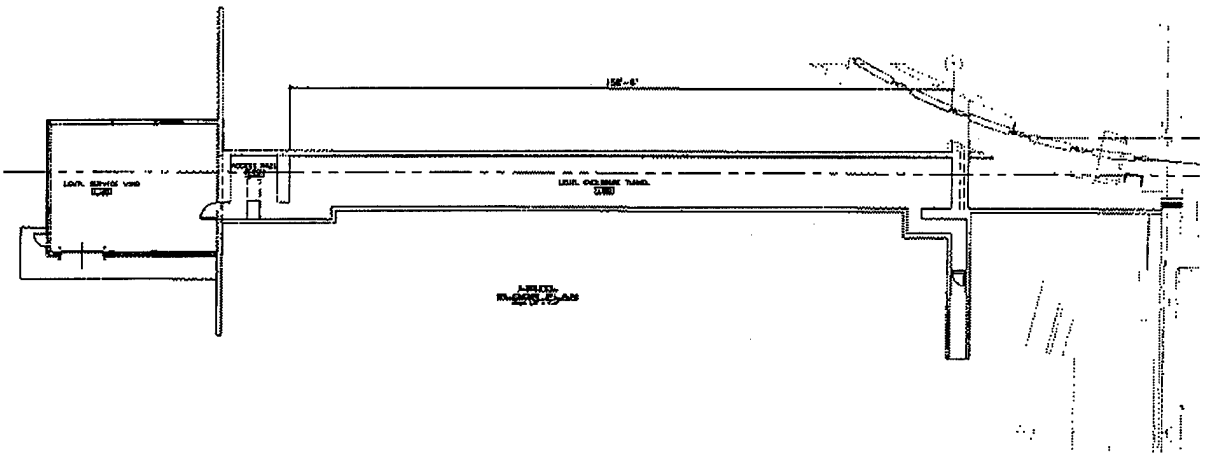


Figure 2: The LEUTL enclosure and end station building.

Following acceleration, two additional sections of beamline are required to guide the beam past both the PAR and booster and into the LEUTL main enclosure. The PAR bypass line is equipped with OTR screens in a 10-m region clear of magnetic elements. This will permit a very accurate characterization of the beam quality after passage through the linac. This OTR screen system will be capable of determining a normalized emittance of $\varepsilon_n = 10\pi$ • mm-mrad to ≈ 6% and $\varepsilon_n = 1\pi$ • mm-mrad to ≈ 20%.

The booster bypass line is approximately 55 m in length. Over 40 m of this length a gentle elevation change of 1 m will be made primarily to avoid interferences with the booster. Theory [3][4] shows that the resultant growth in emittance caused by this bending is negligible.

2.3 Building

Figure 2 shows a layout of the LEUTL building. It consists of two parts: an earth berm covered concrete enclosure for the electron beamline, undulator, and beam dump; and an end station building which houses technical components and the diagnostics for characterizing the light produced by the undulators under test. The beamline enclosure has nearly 50 m of available length and is 12 ft wide. Provisions have been made to house two separate beamlines, one straight ahead relative to the APS linac and the second offset by 5 ft horizontally. The end station building has approximately 1200 square feet of available floor space and can be occupied while beam is being delivered to the LEUTL enclosure.

3 UNDULATOR TESTING

3.1 Beam-Based

The LEUTL will offer a unique method for performing magnetic measurement of undulators. Measurements will be made by passing the electron beam through the undulator while very precisely measuring the beam position and angle. Using this information, a very accurate measure of the first and second field integrals will be made. The measurement will be further enhanced by employing a magnetic telescope arrangement proposed by M. Borland. This system can provide a point-to-point magnification of -13.5 and a similar magnification of 8.8 m/rad in parallel-to-point mode. Further enhancement will be achieved by averaging the position signal over many shots. As an example, consider measurement of the first and second field integrals

$$\int_1 = \frac{\delta x (B\rho)}{M_\theta A} \quad \int_2 = \frac{\delta x (B\rho)}{M_x A}, \tag{1}$$

where δx is the single-pass measurement accuracy, M_θ and M_X are the parallel-to-point (in units of m/rad) and point-to-point magnifications, respectively, and A is the improvement due to averaging. Assume

$$B\rho = 2\,T\cdot m; \quad \delta x = 10\,\mu m; \qquad M_\theta A\,[m/rad] = M_x A = 100\ , \tag{2}$$

then

$$\int_1 = 0.2\,G\cdot cm \quad \int_2 = 20\,G\cdot cm^2. \tag{3}$$

For comparison, 2.5-m-long APS type-A undulators are measured using a traditional magnetic measurement system [5] with repeatability to < 1 G-cm and absolute accuracy of 10 G-cm in the first field integral, and with repeatability to < 100 G-cm^2 and absolute accuracy of 1000 G-cm^2 in the second field integral.

3.2 Light Output

An alternative to beam-based measurements in determining the overall magnetic quality is to use the light generated by the beam/undulator system. This is made possible by the high quality (small emittance and energy spread) of the electron beam. A simulation using various different scenarios was performed by R. Dejus to check the capability of this method [6]. Figure 3 shows the output at the 9th harmonic of the emitted radiation for a typical APS type-A undulator and a

beam of 650 MeV. Most relevant is the comparison between curves 2a and 4a which show the degradation in the amplitude of the 9th harmonic in the presence of typical undulator errors.

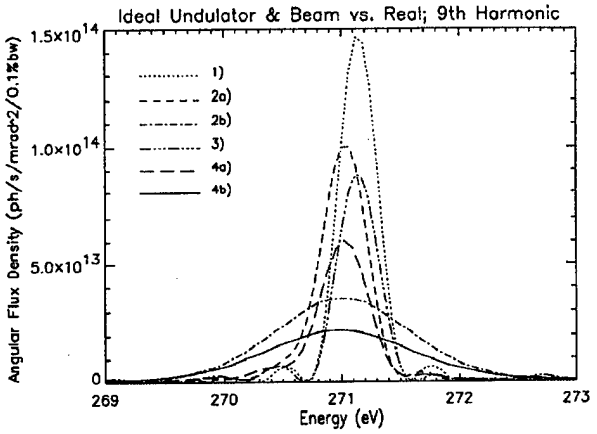


Figure 3: 1) Ideal beam, ideal undulator; 2a) Ideal undulator, beam with emittance (no energy spread); 2b) Ideal undulator, real beam ($\Delta E/E$ = 0.1%); 3) Real undulator, ideal beam; 4a) Real undulator, beam with emittance (no energy spread); 4b) Real undulator, real beam ($\Delta E/E$ = 0.1%).

4 COHERENT LIGHT POSSIBILITIES

The possibility of achieving coherent light generation in a single pass of an undulator at wavelengths less than 100 nm exists with the LEUTL system. Studies have been carried out to determine the requirements of an undulator system used to study the self-amplified spontaneous emission (SASE) process [7]. These studies were based on a conservative estimate of the beam quality from the thermionic rf gun source. The undulator design was optimized with an initial wavelength goal of 120 nm using a 400-MeV electron beam. A simple planar undulator with separated-function external focusing and a fixed gap was chosen. An undulator length sufficient to reach saturation in a single pass would be built up of 2.5-m-long cells with 2 m of undulator and 0.5 m available for external focusing plus diagnostics. The results of calculations and simulations indicate a gain length of 1.5 m with saturation predicted to occur after passage through 15 undulator cells. The principle parameters for this mode of operation are shown in Table 2.

Table 2: Optimized FEL Undulator Design

Wavelength	120 nm
Electron energy	400 MeV
Normalized emittance	5 π mm-mrad
Energy spread	0.1%
Peak current	150 A
Undulator period	27 mm
Magnetic field	1.2 T
Undulator gap	5 mm (fixed)
Focusing	separated quadrupoles
Gain length	1.5 m
Undulator length	15 × 2.5 m

The LEUTL beam energy can be raised to 700 MeV with a commensurate reduction in the output wavelength of the undulator. This and the use of a photocathode rf gun electron source were both considered during the optimization process of the undulator. At the higher energy the system should be capable of achieving saturation down to a wavelength of 40 nm.

5 PRESENT STATUS AND SCHEDULE

The present status of the LEUTL project is as follows. The thermionic rf gun and alpha magnet system is installed with beam produced and delivered straight ahead into a Faraday cup. Further commissioning of the gun awaits completion of a "beam gate" kicker magnet and rework of the rf waveguide, both of which should be ready by July 1997. All primary in-vacuum additional diagnostics hardware has been installed in the linac with some optical transport still remaining to be complete. The PAR bypass will be installed and ready for use by August 1997, and the booster bypass and beamline into the LEUTL enclosure will be completed by early winter of 1997. The LEUTL building will be ready for beneficial occupancy by early summer of 1997. Already designed is a prototypical undulator section for testing single pass SASE-mode operation. This should be available for installation in the fall of 1997. First measurements of undulator properties should begin early in 1998. Upgrade to a high-brightness gun is planned for sometime late in 1998.

4 ACKNOWLEDGMENTS

Work supported by U.S. Department of Energy, Office of Basic Energy Sciences, under Contract No. W-31-109-ENG-38.

REFERENCES

[1] M. Borland, "Cavity Design and Beam Simulation for the APS RF Gun," *APS Light Source Note* **LS-186**, Dec. 1991.

[2] J. Schmerge et al. "SLAC RF Photocathode Gun Test Facility," *SPIE Lase '97 - Free-Electron Laser Challenges Conf.*, San Jose, Feb. 1997, in press.

[3] Y.S. Derbenv, J. Rossbach, E.L. Saldin, V.D. Shiltsev, "Microbunch Radiative Tail-Head Interaction," (DESY) TESLA-FEL **95-05**, 1995.

[4] T. Raubenheimer, "Summary of Linac Working Group," *Micro Bunches Workshop, Upton, NY, AIP Conf. Proc.* **367**, pp.94-106, 1995.

[5] L. Burkel et al., "The Insertion Device Magnetic Measurement Facility: Prototype and Operational Procedures," *Argonne Tech. Bulletin*, **ANL/APS/TB-12**, 1993.

[6] R. Dejus and A. Luccio, "Program UR: General Purpose Code for Synchrotron Radiation Calculations," NIM **A347**, pp. 61-66, 1994.

[7] N. Vinokurov et al., "Design Considerations for the Magnetic System of a Prototype X-ray FEL," *SPIE Lase '97 - Free-Electron Laser Challenges Conf.*, San Jose, Feb. 1997, in press.

GAMMA-RAY PRODUCTION USING MULTI-PHOTON COMPTON SCATTERING

H.Takahashi, Y.An*, M.Nomura
Brookhaven National Laboratory, Upton, New York 11973

Abstract

The nonlinear Compton scattering cross-section for laser light is formulated by treating the electron in the laser field as a dressed electron, in which the laser field is expressed as classical field. In comparison, multi-photon Compton scattering can be represented by the Feynman diagram where the electron is treated as an undressed one; hence, this formula can be applied only to a low intensity laser. To study the effect of the coherency of the photon on Compton scattering, these two formulas were compared for the case of two-photon scattering. The difference might be due to the fact that the Feynman formula cannot take into account the coherency of the photon. To account for the coherency of a laser field in quantum mechanics, therefore, the formula based on coherent-state formalism is required.

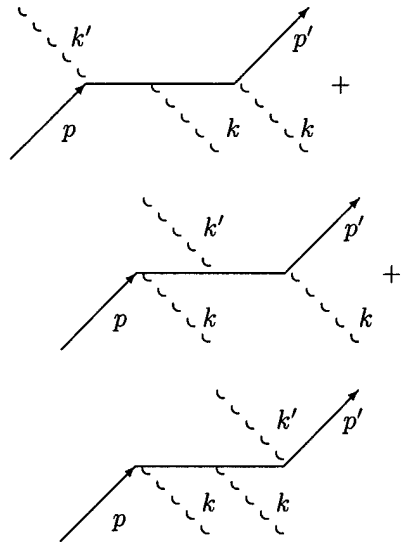
1 INTRODUCTION

There have been many investigations of multiphoton processes in strong electromagnetic fields since the invention of the laser in the early 1960s. Nikishov and Ritus derived formulae for the multiphoton absorption of an electron in a plane electromagnetic field [1]; this effect was observed recently [2]. Other theoretical studies made by the classical approach [3] - [7] and also by the semiclassical scattering theory, as reviewed by Ehlotzky [8], all of which describe multiphoton absorption processes, have contributed to great advances in our understanding. Both the classical approach and the semiclassical theory use the classical way to describe the field of laser beam; therefore, they yield the same results for multiphoton processes [3].

In using quantum theory to describe multiphoton processes in the intense electromagnetic fields of laser beam, one encounters difficulties. The laser beam is a kind of electromagnetic wave which has high density of photons that may be in coherent states; therefore, the usual perturbation theory of Quantum electrodynamics(QED) may be not appropriate for such a case. In the present paper, we calculate the cross-section of Compton scattering of the absorption of two photons by an electron from Feynman diagrams, and compare our results with the semiclassical QED theory [1].

2 FORMULAE OF CROSS-SECTION

We can illustrate the Feynman diagrams for the absorption of two photons by an electron as:



where p and p' are four-vector momentums of the initial and final states of electron, and k and k' are photons. We follow the formulae in ref. [9] to derive the differential cross-section of an unpolarized electron scattering with two unpolarized photons, as shown in the Feynman diagrams, above. The formulae will much simplified if we use the invariant $u = \frac{(kk')}{(kp')}$ and $u_1 = \frac{2(kp)}{m^2}$, then:

$$d\sigma_a = \pi {r_0}^2 \frac{\pi e^2}{2u_1 m^2 \omega} \frac{2\pi}{(1+u)^2} X_a du \qquad (1)$$

where r_0 is the classical radius of electron, and,

$$X_a = -\frac{32}{{u_1}^4}u^4 + \frac{112-16u_1}{{u_1}^3}u^3 + \frac{-116+36u_1}{{u_1}^2}u^2 + \frac{-16+36u_1}{{u_1}^2}u + \frac{16+36u_1}{{u_1}^2} - \frac{16+36u_1}{(1+u){u_1}^2} \qquad (2)$$

To compare our findings with the results in ref. [1], we substitute ω in equation (1) to $\frac{4\pi e^2}{m^2\xi^2}$, as was done in section 101 of ref. [10], where ξ is a parameter of the laser beam's intensity. Then equation (1) becomes:

$$d\sigma_a = \frac{\pi {r_0}^2}{8u_1}\xi^2 \frac{2\pi}{(1+u)^2} X_a du \qquad (3)$$

and the total cross-section can be obtained by integral it over u,

$$\sigma_a = \frac{\pi {r_0}^2}{8u_1}\xi^2 \int_0^{2u_1} \frac{2\pi}{(1+u)^2} X_a du \qquad (4)$$

* Permanant address: Tsinghua University, Beijing 100084, china

0-7803-4376-X/98/$10.00 © 1998 IEEE

The formulae in ref. [1] are probabilities dw rather than cross-sections $d\sigma$, and the initial photon is linearly polarized. Therefore, by integrating the initial polarization angle ϕ, and dividing the incident flux density, then we obtain:

$$d\sigma_b = \frac{16\pi {r_0}^2}{u_1\xi^2}\frac{du}{(1+u)^2}\int_0^{2\pi} d\phi X_b \tag{5}$$

where,

$$X_b = -{A_0}^2 + \xi^2(2+\frac{u^2}{1+u})({A_1}^2 - A_0A_2) \tag{6}$$

where the functions A_0, A_1, and A_2 are those found in APPENDIX of ref. [1]; here, we consider only the case of the absorption of two photon, in this case, we have,

$$A_0(\alpha,\beta) = \sum_{l=-\infty}^{\infty} J_{2+2l}(\alpha)J_l(\beta) \tag{7}$$

where $J_l()$ is Bessel function, A_1 and A_2 can be calculated by formulae in ref. [1]. The total cross-section of the absorption of two photon can be obtained by integral over u and azimuthal angle ϕ,

$$\sigma_b = \frac{16\pi {r_0}^2}{u_1\xi^2}\int_0^{2\pi} d\phi \int_0^{2u_1} \frac{du}{(1+u)^2} X_b \tag{8}$$

The X_b in equation (5) can be expanded by powers of ξ, and the term of ξ^4 order corresponds to two-photon absorption [11]. Because the formula is for linearly polarized plane waves, therefore we should integrate over azimuthal angle ϕ, then we get the term of the ξ^4 order of equation (6):

$$X_c = -3\frac{u^4}{{u_1}^4} + 10\frac{u^3}{{u_1}^3} - \frac{21u^2}{2{u_1}^2} + 5\frac{u}{u_1} + \frac{u^2(u+4)}{2u_1(1+u)} - \frac{u^4}{{u_1}^2(1+u)} \tag{9}$$

and the differential cross-section is:

$$d\sigma_c = \frac{2\pi {r_0}^2}{u_1}\xi^2\frac{2\pi du}{(1+u)^2}X_c \tag{10}$$

the total cross-section can obtained by integral (10):

$$\sigma_c = \frac{2\pi {r_0}^2}{u_1}\xi^2\int_0^{2u_1}\frac{2\pi du}{(1+u)^2}X_c \tag{11}$$

The cross-sections given in above formulae are easy to calculate by computer.

3 NUMERICAL RESULTS

With the formulae discussed in previous section, we can make numerical calculations. For the sake of simplicity, in the following discussion and figures we use "exact" to denote the results with the semiclassical QED (equation 5). Similarly, we use "expansion" to denote the results from the expansion of "exact" formulae and the term "Feynman diagram" to express the results of solving equation (3). The calculated cross sections are all relative to $\pi {r_0}^2$.

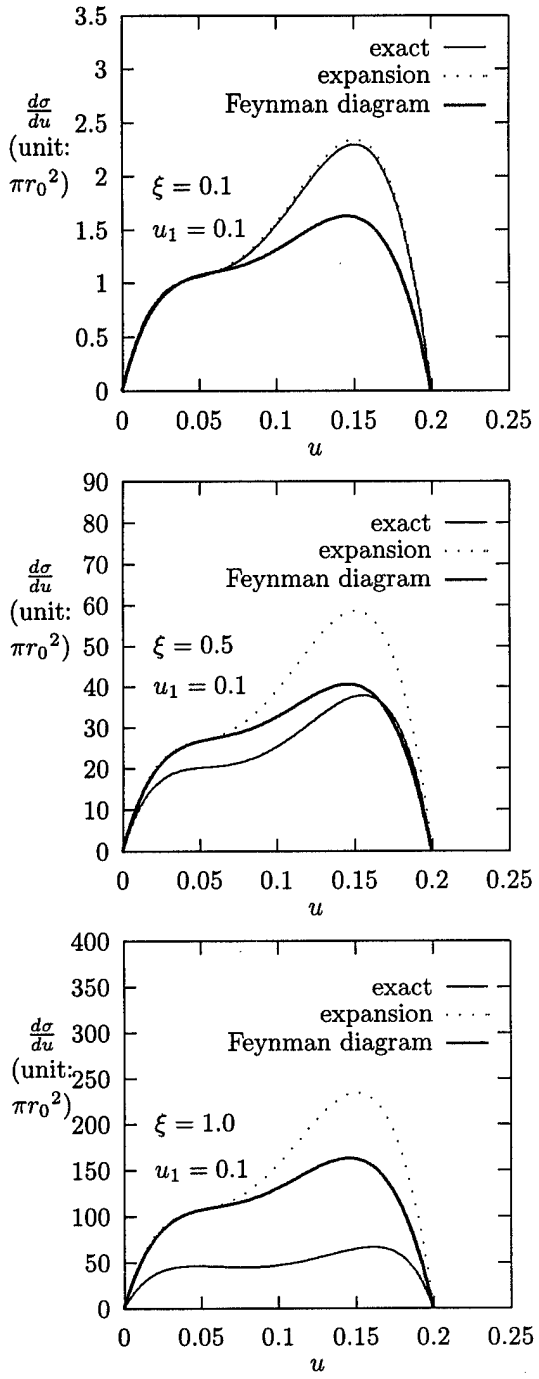


Figure 1: The differnetial cross-sections of an electron scattered by two photons via u.

The three graphs in Figure 1 correspond to differential cross-section of $\xi = 0.1$, $\xi = 0.5$, and $\xi = 1.0$ (top to bottom). When $\xi = 0.1$, the "exact" curve and "expansion" curve are very close, but as ξ increases to $\xi = 1.0$ for instant, the discrepancy between them becomes large. The results from "Feynman diagram" also differ from the "exact"; as ξ increases, at first when $\xi < 0.4$ they become close, after then gradually the difference between them also

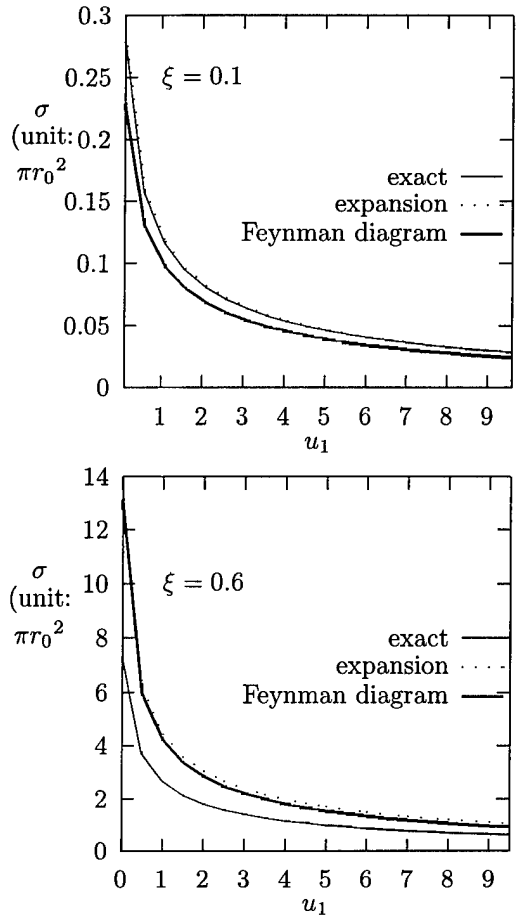


Figure 2: The total cross-sections of an electron scattered by two photons via u_1.

becomes greater. There are no such changes between "expansion" and "Feynman diagram" as ξ increases. These discrepancies supposedly arise from the approximation of the electron state's state to a free state, rather than to a "dressed" state, which means that we have neglected the coherent effects of laser beam. The large ξ signifies the strong intensity of the laser beam which may be related to its strong coherence. However, although there are so many difference between these results calculated by the three methods, they are of the same order of magnitude. Fig. 2 shows the results via another parameter u_1, which is the relative value of the incident particle's energy and the electron's mass. From the figures, we see that the differences between these different theory are not changed by that parameter.

Fig. 3 demonstrates the total cross-section calculated by different theories; their different increases as the intensity of laser beam ξ increases. In the strongest laser beam $\xi \approx 0.6$, either the "expansion" line or the "Feynman diagram" line differ from "exact" line by about 100%. Therefor, if one uses the perturbation theory to consider the intensity field, coherency should be taken into account.

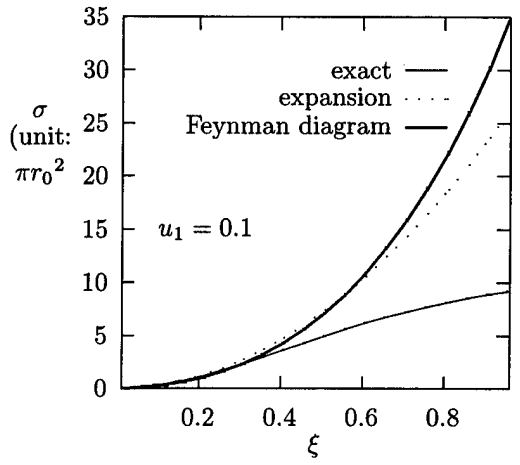


Figure 3: The total cross-sections of an electron scattered by two photons via ξ.

4 CONCLUSION

Our numerical calculations show that the ξ^4 term of the expansion in powers of ξ differs from the results of the perturbation theory of Feynman diagram, but they are in the same order of magnitude. Both the "expansion" and "Feynman diagram" are different from the "exact" results, and the difference becomes larger as ξ increases, which means that the intense laser beam has strong coherent effects.

5 ACKNOWLEDGMENTS

The authors acknowledge to Avril Woodhead for her editoral work on this paper. This work was performed under the auspices of the U.S. Department of Energy under Contract No. DE-AC02-76CH00016, and was partly supported by Power Reactor and Nuclear Fuel Development Corperation.

6 REFERENCES

[1] A.I.Nikishov and V.I.Ritus, Sov. Phys. JETP **19**, 529(1964).

[2] C.Bula, K.T.McDonald, and E.J.Prebys *et al.*, Phys. Rev. Lett. **76**, 3116(1996).

[3] Vachaspati, Phys. Rev. **128**, 664(1962).

[4] E.Esarey, S.K.Ride, M.Baine, A.Ting, P.Sprangle, Nucl. Instr. and Meth. **A 375**, 545(1996).

[5] A.K.Puntajer and C.Leubner, J. Appl. Phys. **67**, 1606(1990).

[6] Lowell S. Brown and T.W.B.Kibble, Phys. Rev. **133**, A705(1964).

[7] A.K.Puntajer and C.Leubner, Opt. Commun. **73**, 153(1989).

[8] F.Ehlotzky, Can. J. Phys. **63**, 907(1985).

[9] F.Mandl and T.H.R.Skyrme, Proc. Roy. Soc. A **215**, 497(1952).

[10] V.B.Berestetskii, E.M.Lifshitz, and L.P.Pitaevskii, *Quantum Electrodynamics*, 2nd ed. (Pergamon Press, New York, 1982).

[11] A.I.Nikishov and V.I.Ritus, Sov. Phys. JETP **20**, 757(1965).

UNIQUE FEATURES OF THE OK-4/DUKE STORAGE RING XUV FEL AND MONOCHROMATIC γ-RAY SOURCE.

V.N.Litvinenko, Y.Wu, B.Burnham, S.H.Park, M.Emamian, J.Faircloth, S.Goetz, N.Hower, J.M.J.Madey, J. Meyer, P.Morcombe, O.Oakeley, J.Patterson, R.Sachtschale, G.Swift, P.Wang
FEL Laboratory, Physics Department, Duke University, Durham, NC 27708, USA
I.V.Pinayev, M.G.Fedotov, N.G.Gavrilov, V.M.Popik, V.N.Repkov, L.G.Isaeva, G.N.Kulipanov, G.Ya.Kurkin, S.F.Mikhailov, A.N.Skrinsky, N.A.Vinokurov, P.D.Vobly, E.I.Zinin
Budker Institute of Nuclear Physics, Novosibirsk 630090, Russia
A.Lumpkin, B.Yang
APS, Argonne National Laboratory, Argonne, IL 60439, USA

Abstract

The OK-4 is the first storage ring FEL operating in the United States. It was commissioned in November, 1996 and demonstrated lasing in the near UV and visible ranges (345-413 nm) with extracted power of 0.15 W [1]. In addition to lasing, the OK-4/Duke FEL generated a nearly monochromatic (1% FWHM) γ-ray beam [2]. In this paper we describe the initial performance of the OK-4 /Duke storage ring FEL and γ-ray source.

1. INTRODUCTION

The OK-4 /Duke storage ring FEL project is a collaboration of the Duke University Free Electron Laser Laboratory and the Budker Institute of Nuclear Physics begun in 1992 [3]. The OK-4 FEL was built and operated in the 240-690 nm range using the VEPP-3 storage ring at Novosibirsk [4]. After commissioning the 1.1 GeV Duke storage ring in November, 1994 [5], the OK-4 FEL made a trip around the globe to Duke in May, 1995. The OK-4/Duke FEL was ready for the first demonstration experiment in November, 1996. The first run on November 13, 1996 with the OK-4/Duke FEL was successful. The OK-4/Duke storage ring FEL demonstrated operation in the near UV/visible range and generated nearly monochromatic 3-15 MeV γ-rays via intracavity Compton backscattering.

2. THE OK-4/DUKE XUV STORAGE FEL

The Duke 1.1 GeV storage ring [5,9] has a 34 meter long straight section dedicated for FEL operation. The present lattice has transverse β-functions of 4 meters in both directions at the center of the OK-4 to optimize the gain. The storage ring RF system [7] operates at 178.5 MHz (64th harmonic of the revolution frequency). Typical OK-4 FEL operation mode applies an RF voltage of 500 kV. The existing 270 MeV injection system limits the maximum stored current to 8 mA/bunch. We plan to improve the efficiency of injection and increase single bunch current to 20-40 mA. Some parameters of the Duke storage ring are summarized in Table I. The main parameters and expected performance of the OK-4 FEL are described in previous publications [4,10]. Table II gives an up-to-date summary of the parameters. The magnetic system of the OK-4 FEL was slightly modified to accommodate a new vacuum chamber and to provide a field-free collision point for the Compton γ-ray source. Two Trans-Rex power supplies (5 kA, 500 V, donated by Fermi Lab) have been repaired, equipped with large external LC filters and are presently used to drive the OK-4 wigglers and buncher. Overall performance of the OK-4 power supplies is close to specifications (50 ppm DC and ripples) and will be improved in the near future using a second stage of regulation and feedback. The controls of the OK-4 FEL are part of the Duke storage ring computer control system [11]. This system provides flexible operation of the OK-4 and the possibility to ramp the energy of the storage ring without changing the OK-4 wavelength.

Table I. Duke Storage Ring Electron Beam Parameters

Operational Energy [GeV]	0.25-1.1
Circumference [m]	107.46
Impedance of ring, Z/n, [Ω]	2.75±0.25
Stored current [mA][a] multibunch	155
single bunch	20[b] /8[c]
Bunch length, σ_s[ps][d] natural	15
with 5 mA in single bunch 60	
Relative Energy spread, σE/E[d] natural	$2.9.10^{-4}$
at 5 mA in single bunch	$1.1.10^{-3}$
Peak Current [A][d] with 5 mA/bunch 12	
with 20 mA/bunch [e]	31
Horizontal Emittance [nm*rad]	
5 mA/ bunch @ 700 MeV	< 10[f]
3 mA/ bunch @ 500 MeV	< 8[f]

[a] Maximum current at 1 GeV is limited to 2-3 mA before crotch-chambers with absorbers are installed;
[b] Per bunch using standard mode of multibunch injection;
[c] In single injection mode with 1 nsec photocathode gun [8];
[d] At 500 MeV, V_{RF}=500 kV;
[e] Expected from broad band impedance model with Z/n = 2.75Ω; *[f] Extracted from the OK-4 spontaneous radiation spectra.*

Table II. OK-4 FEL Parameters Optical Cavity

Optical cavity length [m]	53.73
Radius of the mirrors [m]	27.27[a]
Rayleigh Range in OK-4 center [m]	3.3
Angular control accuracy [rad]	better than 10^{-7}
OK-4 wiggler [4,10]	
Period [cm]	10
Number of periods	2 x 33.5
Gap [cm]	2.25[b]
Kw/I [1/kA]	1.804
Kw	0-5.4

[a] Measured; [b] Increased to accommodate new vacuum chamber.

We have installed temporary crotch chambers (*without absorbers and smooth transitions*) providing passage of

0-7803-4376-X/98/$10.00 © 1998 IEEE

the OK-4 optical beam to facilitate its commissioning. This makes the impedance of the vacuum chambers rather large. According to the bunch length and the OK-4 FEL gain measurements, the impedance of the vacuum chamber is ~2.75 Ohm.

3. COMMISSIONING OF OK-4 FEL AND γ-RAY SOURCE

Three main storage ring operational modes were established (injection energy of 0.265 GeV, at 0.5 GeV and 0.7 GeV the OK-4) along with a number of supplementary modes (between 0.35 and 0.75 GeV) for proper FEL operation. We have created computer tools to vary the OK-4 wiggler current while keeping the betatron tunes stable. It took less than two hours to obtain first lasing. Knowledge of the optical cavity length proved to be very useful [6]. Lasing was demonstrated at a variety of electron energies from 0.265 to 0.55 GeV. A standard operation energy was 500 MeV.

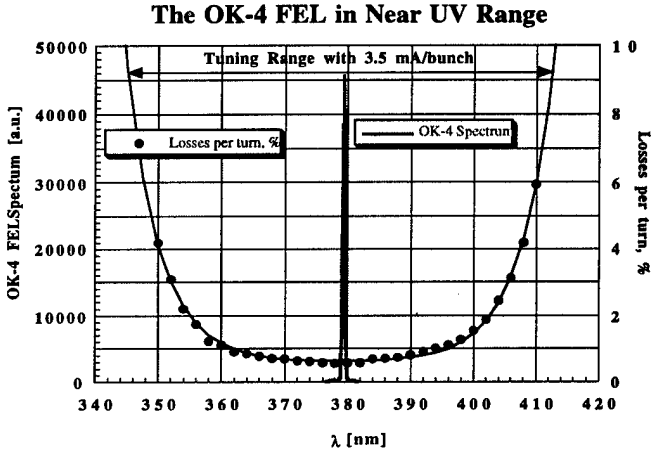


Fig. 1 The tuning range of the OK-4 FEL (with 3.5 mA/bunch at 500 MeV with 500 kV RF voltage) using 380 nm mirrors. The line in the center is a measured time lasing line. This line was tuned ±18% from 345 to 413 nm by changing the current in the OK-4 wigglers. The dots are measured round trip cavity losses and the smooth curve is a fit. Round-trip losses at the edges of the tuning range give the value of the FEL gain at a given current: gain >9% at 345 nm with 3.5 mA/bunch, 500 MeV electron beam and 500 kV RF voltage .

A typical tuning range (obtained by variation of the wigglers' current) and one measured lasing spectrum are shown in Fig.1. Lasing was reasonably easy because the OK-4 gain was at least 10 times higher than its losses at 380 nm. The start-up current for lasing was 0.3 mA, and with 3 mA/bunch we were able to lase in both optical klystron and conventional FEL mode (buncher off). In all cases the optical klystron mode had higher gain and power. Figs. 2 and 3 show a comparison of the measured and predicted gain and extracted power from the OK-4 FEL in the near UV. We have used our self-consistent storage ring FEL code [13] and broadband impedance model to predict the OK-4 performance. The agreement of the measured and predicted values is very reasonable and we can rely on our predictions of the OK-4 FEL gain at 193 nm.

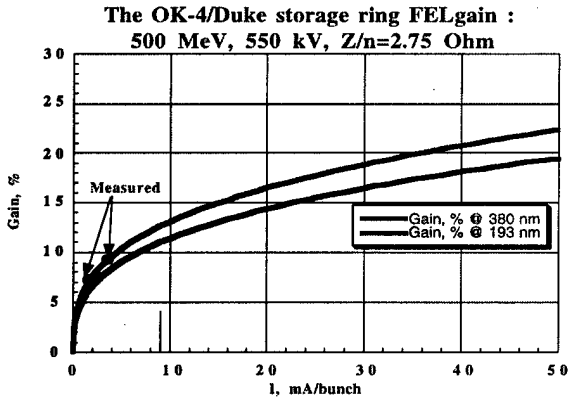


Fig. 2 The measured (dots, 345 nm) and predicted gain (solid lines) for 380 nm and 193 nm of the OK-4.

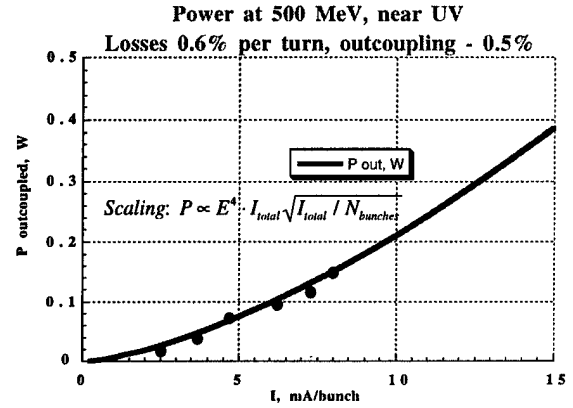


Fig. 3 Measured and predicted extracted lasing power from the OK-4 FEL. More than 80% of the power was extracted.

Table III. Measured Parameters of the OK-4 FEL

Tuning Range (3.5 mA/bunch)]	345-413 nm
Gain per pass (3.5mA/bunch, 345 nm)	>9%
Extracted Power (8 mA, 380 nm)	0.15 W
Induced e-bunch length, σs[ps]	
low current	~35
with 3.5 mA in single bunch	~200
Induced energy spread (3.5mA/bunch), σE/E	0.45%
FEL pulse length [ps]	
low current	~2.5
with 3.5 mA in single bunch	~20
Linewidth σ_λ/λ	$4 \cdot 10^{-4}$ [b]
Lasing life-time	2-4 hours

[a] *Measured; 75 mW per mirror. Accuracy ~ 25%;*
[b] *Time averaged value presumably caused by ripples in power supply, instantaneous value should be ~1·10⁻⁴.*

With expected cavity losses less than 3% [1], the OK-4 should lase at 193 nm with a beam current of a few mA/bunch. With 10 mA per bunch and existing set of mirrors, we expect to lase within the 188-197 nm range. We have observed an increase of the energy spread and bunch length by a factor of 2-3 during lasing. Typical RMS values of the FEL pulse were 5-10 times shorter than the electron bunch length. Operating at very low

current and using very precise tuning of the revolution frequency, we have registered FEL micropulses as short as 2.5 psec RMS with the APS streak-camera. The duration of these pulses is consistent with Super-modes predicted in [14]. Table III gives a summary of the measured OK-4/Duke storage ring parameters.

Monochromatic γ-rays (with 1% FWHM resolution) were produced by operating the OK-4/Duke storage ring FEL with two equally separated electron bunches. This mode provides for head-on collisions of the optical and electron beams at the center of the optical cavity, and the generation of γ-rays via Compton backscattering [12]. Small emittance of the electron beam ensures a high level of correlation between the observation angle θ and the energy of the generated γ-rays:

$$E_\gamma = \frac{4\gamma^2 E_{ph}}{1+(\gamma\theta)^2 + 4\gamma E_{ph}/mc^2};\ E_{ph} = \hbar\omega; \gamma = \frac{E_e}{mc^2}$$

A simple collimator can be used to select the most energetic γ-rays near θ=0. Using a lead collimator with 3 mm diameter (located 30 m downstream from the collision point) and a Ge detector we measured the 1% FWHM energy resolution of the γ-rays. We demonstrated the tunability of γ-ray energy within the 3-15 MeV range tuning both the laser wavelength (±18%) and the energy of the electron beam (265-550 MeV). Most of our shifts were dedicated to these studies and the results will be published elsewhere [2].

After one month of operation, which was mostly dedicated to γ-ray generation and spectrum measurements, the injector for the storage ring was shut down in December, 1997 to condition one of the klystrons. We expect to resume operation of the OK-4 FEL when conditioning is finished.

4. CONCLUSIONS AND PLANS

Commissioning the OK-4/Duke storage ring FEL demonstrated high performance and reasonably high gain. Initial evaluation of the OK-4 FEL parameters is in good agreement with our predictions. We do not expect serious problems when we attempt to lase below 200 nm in the near future. The gain modulator, the permanent crotch-chambers with absorbers, and nitrogen purged beamlines are in progress. The gain modulator will provide for high intracavity power and generation of coherent VUV harmonics. Later this year we plan to begin use of the OK-4 coherent and spontaneous radiation as well as monochromatic γ-rays for user experiments. The user program includes nuclear γ-ray spectroscopy, UV cornea surgery, studies of PMM, photo-absorption and spectroscopy.

Absence of absorbers and permanent crotch chambers prevent us from operating at 1 GeV with full current and limits us to 10 mA at 750 MeV. With these beams we could not go far above a few watts of average laser power. The permanent crotch chambers and absorbers [15] are needed for full power (~100 W) operation of the OK-4/Duke storage ring FEL and full flux operation of the γ-ray source (10^9-10^{11} γs/sec). We plan to install them in 1998. Long term plans for the OK-4 include extension to the VUV range.

5. ACKNOWLEDGMENTS

This work is supported by US Office of Naval Research Contract #N00014-94-0818, AFOSR Contract No.F49620-93-1-0590, DURIP-95 Grant F49620-95-1-0476 and Russian Academy of Sciences. The authors are grateful to P. Cable, G. Detweiler, H. Goehring, J. Gustavsson, M. Johnson, L. Kennard, C.Kornegay, H.Mercado, and J. Widgren (Duke University FEL Lab), V.V. Anashin, A. Bulygin, E.I.Gorniker, A.D.Oreshkov, V.M.Petrov, T.V.Shaftan, I.K.Sedlyarov, E. Szarmes. V.G.Vesherevitch (BINP, Novosibirsk) for their important contributions to the design, construction and commissioning of the OK-4 FEL. The authors would like to thank P.G.O'Shea, J.L.Lancaster (Duke University) and R.Jones (NCSU) for providing single-bunch injection capability. In addition we would like to acknowledge P.G.O'Shea for supervising operation of the linac injector and, J. Gustavsson and J. Widgren for keeping it operating day and night during the OK-4 FEL commissioning. The authors would like to thank R.S.Canon, C.R.Howell, N.R.Roberson, E.C.Schreiber, M.Spraker, W.Tornow and H.R.Weller (TUNL) for γ-ray measurements and characterization. In addition we would like to thank K.D.Straub for the development of the OK-4 FEL user program.

REFERENCES

[1] V.N.Litvinenko et al., SPIE v.2988 (1997) p.188.
[2] V.N.Litvinenko et al., "Gamma-ray Production in a Storage Ring Free Electron Laser", to be published in Physics Review Letters.
[3] V.Litvinenko et al.,, Proc. of PAC'93 ,1993, p.1442.
[4] I.B.Drobyazko et al., NIM A282 (1989) 424.
[5] V.N.Litvinenko et al., Proc. of PAC, 1995, p. 213.
[6] A.Lumpkin et al., "Initial applications of a Dual-Sweep streak camera for the Duke SR OK-4 source", These Proceedings.
[7] P.Wang et al., Proc. of PAC'95, 1995, p. 1841.
[8] P.G.O'Shea et al., "Single bunch injection for SR FEL.", These Proceedings.
[9] Y.Wu et al., NIM A375 (1996) p. 74.
[10] V.N.Litvinenko et al., NIM A375 (1996) p. 46.
[11] Y.Wu et al., Proc. of PAC'95, 1995, p.2214.
[12] V.N.Litvinenko, J.M.J.Madey, NIM A359 (1996) 580; V.N.Litvinenko et al., SPIE v.2521 (1995) 55.
[13] V.N.Litvinenko, NIM A359 (1995) 50; V.N.Litvinenko et al., NIM A358 (1995) pp.334, 369.
[14] G.Datoli et al., Phys. Rev. A (April, 1988).
[15] V.N.Litvinenko et al., SPIE v.2522 (1995) p. 473.

A LASER PULSE TRAPPER FOR COMPTON BACKSCATTERING APPLICATIONS*

D. YU and B. STUART
DULY Research Inc., Rancho Palos Verdes, CA 90275

Abstract

The repetition rate for high peak power, short pulse lasers used in Compton backscattering for production of x-rays, positrons and other reaction products is typically much lower than that for the electron bunches. The production rate can be increased by trapping a laser pulse [1] in a delayed line for repeated collision with a plurality of electron pulses. The temporal and spatial characteristics of a trapped laser pulse are calculated including effects of dispersion, self phase modulation and self focusing through the delay line optics. For ultra short laser pulse, the DULY Box includes a pulse stretcher and a pulse compressor in order to minimize non-linear effects. Experiments are planned to verify and optimize the box design.

INTRODUCTION

The DULY Box [1] is a device which traps a laser pulse in an optical delay line and allows multiple collisions of the laser pulse with electron multibunches. It can be used to enhance the yield of Compton backscattering products such as x-rays, positrons and gamma rays. Enhanced production of positrons or gamma rays can increase the luminosities of future linear colliders. The DULY Box is also potentially applicable to other reactions whose yields depend on the collision frequency with a high intensity laser pulse, e.g. laser isotope separation. The optical delay line can be implemented either in a linear configuration or a ring configuration [2].

The goal of the DULY Box is to preserve the properties of a single laser pulse (temporal and frequency profiles, energy, spot size, focal point, etc.) for as many times of interaction with the target as possible. To achieve this, the design of the DULY Box must avoid linear (group velocity dispersion) and non-linear optical effects (self phase modulation, self focusing) which could otherwise destroy the beam. This is accomplished either by operating in a limited laser parameter space (low energy, long pulse) or by stretching and subsequently recompressing a high-energy, short laser pulse within the delay line. A properly designed amplifier to replenish the energy loss in each round trip is an integral part of the device.

ANALYSIS OF A LONG PULSE VERSION

An analysis of the DULY linear and ring cavities was performed to determine the parameters under which a high peak power laser pulse may be trapped without destroying itself during the propagation in the cavity.

Gaussian vs. Flat-Top Spatial Distribution

Figure 1 compares the near- and far-field profiles of equal-energy Gaussian and flat-top (10^{th} order super-Gaussian) near-field modes. The size of each near-field beam is set to minimize diffraction effects when passing through a 5-cm diameter aperture. As can be seen, the flat-top intensity is 4.5 times less than the Gaussian, leading to greatly reduced nonlinear effects upon propagation through material. The far-field (focal) distributions show the diffraction-limited beam size after focusing with a 10-cm focal length lens. Although a significant fraction (16%) of the energy ends up in the secondary lobes, the flat-top still produces a focal intensity 1.4 times that of the Gaussian. This, coupled with the lower near-field intensity and uniform profile for amplification, make the flat-top the spatial mode of choice for this application even though it must be relay-imaged.

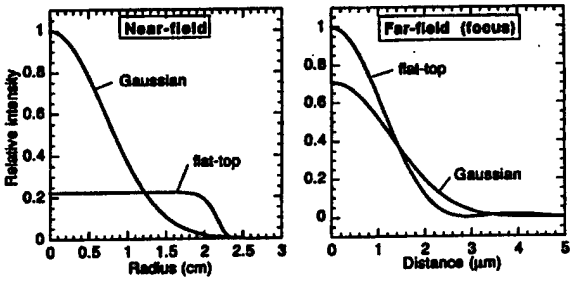


Figure 1 Near- and far-field spatial profile of equal-energy beams which pass through a 5-cm diameter aperture with minimal diffraction and the focused profile of each beam.

Group Velocity Dispersion (GVD) and Self-Phase Modulation (SPM)

A pulse envelope with central frequency ω_0 will propagate through material with group velocity $v_g = \partial\omega/\partial\beta(\omega)$, where $\beta(\omega) = n(\omega)\omega/c$ is the propagation constant. If the pulse is composed of many frequency components (as is a short pulse), the different frequencies will propagate with different velocities. An initially transform-limited pulse will be stretched in time by GVD.

The index of refraction of a material depends on the laser intensity,

$$n(I) = n_0 + n_2|E|^2 = n_0 + \gamma I ,$$

where n_0 is the ordinary index of refraction, n_2 the nonlinear index of refraction, E the pulse electric field, γ the nonlinear index coefficient, and I the laser intensity.

* Work supported by DOE SBIR grant DE-FG-03-94-ER81740.

0-7803-4376-X/98 /$10.00 © 1998 IEEE

This intensity-dependent index change produces a variation of phase in time across a pulse as it propagates through material. SPM leads to spectral broadening of optical pulses through the generation of additional frequency components. Since only the phase of the pulse varies in time, the pulse intensity as a function of time remains the same. However, these additional frequency components may cause temporal broadening through group-velocity dispersion. A measure of the nonlinear phase accumulation of a pulse as it propagates through a length L of material is given by the B-integral,

$$B(I) = \frac{2\pi}{\lambda} \int_0^L \gamma I dz ,$$

where λ is the wavelength of light and z is the propagation direction. Noticeable spectral distortion begins at $B \approx 1.5 - 2.0$.

Pulse Propagation

The nonlinear Schrödinger equation for the complex pulse amplitude A describes propagation through material [3],

$$i\frac{\partial A}{\partial z} = -\frac{i}{2}\alpha A + \frac{1}{2}\beta_2 \frac{\partial^2 A}{\partial T^2} - \gamma |A|^2 A .$$

Loss and gain are included in the term with α. The second term on the right hand side gives the group-velocity dispersion (higher order terms in β can also be added) and the last term includes nonlinear effects with nonlinear coefficient γ. We solve the above equation with the split-step Fourier method [4], where the dispersion and absorption terms are separated from the nonlinear terms. The equation is valid for pulse durations $\geq$ 50 fs. For shorter pulses, higher order terms must be included.

Analysis of Ring Cavity

We will first calculate the effect of GVD in a relay-imaged ring cavity assuming a transform-limited 1.06-μm input pulse of a given duration, no SPM, and material pathlength of 16 cm (KD*P Pockels cell: 3 cm, fused silica lenses/windows: 3 cm, amplifier: 10 cm). Figure 2 shows the increase in pulse duration, including also the higher-order dispersion terms, as the pulse circulates in the ring cavity.

If the initial pulse is not transform-limited it will lengthen at an increased rate corresponding to its excess bandwidth. To maintain a constant intensity at the interaction point the pulse duration must be greater than approximately 5 ps. In this regime the number of interactions will be limited by the nonlinear phase accumulation or B-integral.

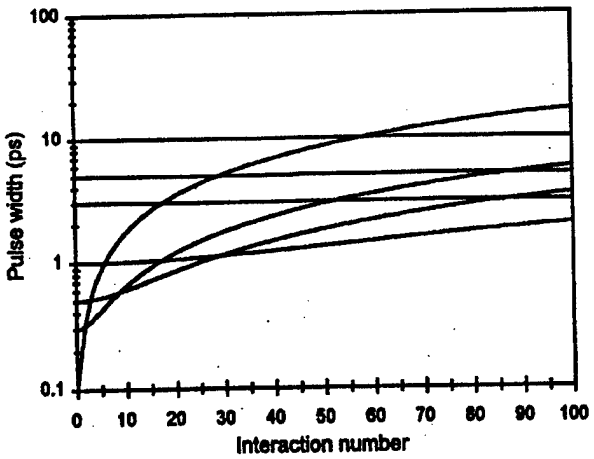
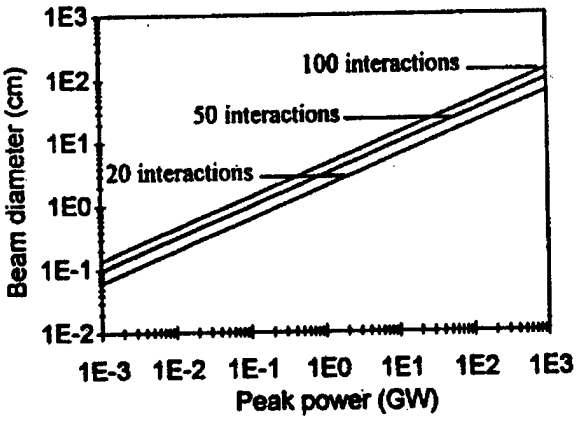


Figure 2 Plot of pulse duration vs. number of interactions for various starting values of pulse lengths.

An approximate expression for the number of interactions (N) possible in the above ring cavity as a function of pulse duration (τ_p, in picoseconds), energy (U, in Joules), diameter (D, in cm), wavelength (λ, in μm), and desired maximum B-integral (in radians) is given by

$$N = 0.036 \frac{B\lambda D^2 \tau_p}{U(13 + 0.5D)} .$$

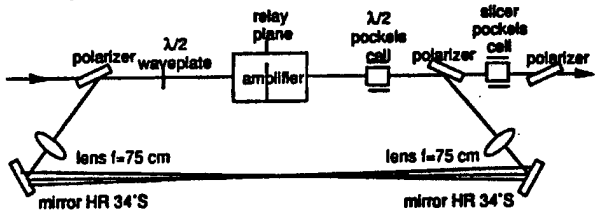
Using the above equation with a target B=2 to limit SPM and self-focusing, we can plot the beam diameter required to achieve a given number of interactions as a function of desired peak power. To trap 1-J, 20-ps pulses (50 GW) for 100 interactions, the beam diameter is 30 cm. The above equation is only a rough guide; as the beam becomes larger the optics need to be thicker.



EXPERIMENTAL DESIGN

A small-scale experiment has been designed to trap 10-20 ps pulses for many (40+) passes without destroying the pulses either temporally or spatially. A flat-top spatial profile with a beam diameter of 6.5 mm was chosen in order to use standard size 9-10 mm diameter optical components (amplifier rod, Pockels cells). This allows trapping of pulses with energy on the order of 1.0 mJ, depending on the number of passes desired.

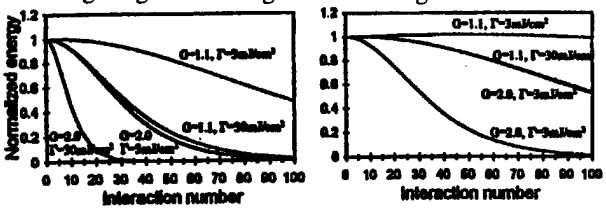
A relay-imaged ring cavity with a round-trip time of approximately 10 ns is shown below. To trap the pulse, the Pockels cell is turned on to its half-wave voltage with rise time < 5 ns. The voltage can be varied while the pulse is trapped to maintain constant intensity at the interaction point. The pulse is switched out for measurement after the desired number of round trips by turning off the Pockels cell. Since a small fraction of light will leak out on each round trip, a slicer Pockels cell is necessary to separate the desired pulse from the sum of the leakage pulses before the diagnostics. The focused spot in the cavity is approximately 300 μm giving an intensity of 10^{11} W/cm^2.



In order not to extract the stored energy from the amplifier too quickly, an amplifier medium with a high saturation fluence ($\Gamma_s=h\nu/\sigma_s$) or low stimulated emission or gain cross section (σ_s) is desired. The circulating fluence should then be maintained at a level well below the saturation fluence. In this analysis we assume the amplifier is pumped once before the circulating pulse arrives. It is also possible to laser-pump the amplifier each round trip. The parameters for some common amplifier materials are listed below.

Gain medium	Wavelength (nm)	Gain cross section (cm^2)	Saturation fluence (J/cm^2)
Nd:YAG	1064	2.8×10^{-19}	0.7
Nd:YLF	1053	1.2×10^{-19}	1.6
Nd:glass	1053/1064	1.4×10^{-20}	4.7-19
Ti:sapphire	1053	2.8×10^{-20}	6.7
Ti:sapphire	800	3×10^{-19}	0.8
Yb:glass	1000-1070	$0.8\text{-}4.0\times10^{-21}$	50-230

The initial gain is determined by the cavity losses, typically 10% per round trip, giving a gain G=1.1. Gains per pass higher than G=2 may be necessary if a pulse stretcher and compressor is included in the ring (see below). In the figures below, we show the calculated pulse energy (normalized) as a function of number of interactions for amplification in Nd:YLF and a low-gain Nd:glass using initial gains of 1.1 and 2.0 and input fluences of 3 mJ/cm^2 (1 mJ, 6.5 mm diameter) and 30 mJ/cm^2. As can be seen, even at very low circulating fluence the energy extraction in Nd:YLF is too rapid to maintain constant energy. The smaller gain cross section of Nd:glass allows better energy balance in trapping the pulse, and a still smaller cross section (Yb:glass) would allow higher gains and higher circulating fluence.



Nd:YLF
$\sigma_s=1.2\times10^{-19}$cm^2

Nd:glass
$\sigma_s=1.0\times10^{-20}$cm^2

DULY BOX FOR ULTRA SHORT PULSE

To trap a recirculating, ultra short (< 1 ps), high power laser pulse in a delay line for repeated interaction with a high rep-rate electron beam, the DULY Box may be installed *in place of* a pulse compressor in a chirped pulse amplification (CPA) high power laser system [2]. A stretched, long pulse, high power, linearly polarized laser beam enters the box via a polarizer. The pulse is then focused and compressed spatially and temporally to interact with an electron pulse. After interacting with the electron pulse, the laser pulse is again stretched and its energy replenished by an amplifier before starting the next round trip. The stretched laser pulse avoids the nonlinear problems as it goes through a dispersive medium and maintains its energy by the loss-compensation amplifier during each round trip. The system implementation of this box uses similar pulse compression and pulse stretching methods as in the standard CPA, except the diffraction gratings should have a very high efficiency and very low loss. Work is in progress on the design and analysis of such a system for an enhanced positron and gamma source for possible linear collider applications.

CONCLUSION

We have analyzed the effects of group velocity dispersion and nonlinear index of refraction upon a laser pulse trapped in a recirculating delay line, and have provided a simple relation between the laser beam size required to stay below a given *B*-integral limit as a function of input pulse parameters and amount of material it passes through.

REFERENCES

[1] P. Chen, D. Bullock, D. Yu, Proc. of γγ Collider Workshop, LBNL (1994); Nucl. Inst. Meth. A355, pp. 130-132 (1995).

[2] D.Yu and D. Bullock, patent pending; D. Yu, patent pending.

[3] G.P. Agrawal, Nonlinear Fiber Optics, Academic Press (1989).

[4] R.A. Fisher and W.K. Bischel, Appl. Phys. Lett. 23, 661 (1973); J. Appl. Phys. 46, 4921 (1975).

HIGH CURRENT FEL OSCILLATOR ON BASE OF MSU ELECTRON ACCELERATORS

V.K.Grishin, B.S.Ishkhanov, T.A.Novicova, Institute of Nuclear Physics of Moscow State University, Moscow 119899

Abstract

Peculiarity of high current FEL with a collective regime of electromagnetic wave excitation is considered. The start value of electron current in a FEL-Oscillator is estimated. Possibilities of such device creation on base MSU electron linear accelerator are discussed.

1 INTRODUCTION

In previous paper [1] it has been shown that a high current FEL (HCFEL) has a high coefficient of signal amplification, and this permits to extend the possibilities to create the coherent short-wave radiation sources. High signal amplification is a result of a collective interaction of an electron beam with an electromagnetic wave which is arisen due to the bunching of particles. The latter can be realised if the density of electron is sufficiency high. An intense beam acquires the properties of optical waveguide, and the electromagnetic radiation is concentrated in the beam volume. Therefore a high current regime can be realised in FEL having a moderate current but low emmitances of particles that is peculiar for an electron accelerators of new generation.

Present paper has two goals. It is of interest how are the properties of HCFEL revealed in a scheme of FEL oscillator? And can we have here any application of this scheme of the MSU electron accelerators?

2 START CONDITION IN HIGH CURRENT FEL OSCILLATOR

Consider a traditional scheme of a charged beam generator. A system constructed along the axis **z** consists of undulator with a period λ_0 and length L_{und} which is located between two mirrors. The mirrors separated by distance $\mathbf{L_m}$ ($\mathbf{L_m > L_{und}}$) are forming an open resonator. Along the axis **z** in a point **z'** placed before the undulator a continuous beam of monoenergetic electrons is being injected into the system (by means of supplementary magnet system). The electron energy is $E = mc^2\gamma_L$ where γ_L is Lorenz's factor , the initial electron velocity is $v_0 = \beta_0 c$. Passing trough the undulator the electrons acquire a transversal velocity $v_\perp = \beta_\perp c$ that permits them to interact with an optical (i.e. transversal) wave. After passage the undulator the electron beam is being deflected from the system (by means of second supplementary magnets).

Analyse start condition of HCFEL oscillator. Let an initial signal of frequency ω be brought in the system. The signal passing through the undulator can be amplified by an electron beam and then being partly irradiated and reflected from the mirrors returns to the initial point. Usually a start condition of FEL oscillator is estimated from one if the amplification of circling signal begins surpass its total absorption. But the HCFEL has its important peculiarities.

An electron beam in the undulator is an electromagnetic medium in which some transversal waves of different modes can propagate in both directions. An initial signal is distributed among the co-travelling with beam waves some of which can interact with the electrons. Its interaction becomes resonant if the double conditions are carried out:

$$\omega = kc;\ k = k_0\beta_{0Z}/(1-\beta_{0Z}) \qquad (1)$$

where k is a wave vector, $k_0 = 2\pi/\lambda_0$,

$$\beta_{0Z} = (\beta_0^2 - \beta_\perp^2)^{1/2}.$$

Practically one can consider only the mostly amplified wave among the co-travelling ones after passing the undulator and only one back travelling wave because an electron beam do not disturb the electromagnetic oscillations in last case.

Hence the final balance of amplification and absorption in system gives the nest condition of reliable generation start (see [2] too):

$$R_1R_2\exp\left(i\int_0^{L_m}(k^+ - k^-)dz\right) = 1 \qquad (2)$$

where $R_{1,2}$ are the coefficients of wave amplitudes reflection from the first and second mirrors respectively (value of R_2 includes the loss of signal due to its irradiation), k^+ and k^- are the wave vectors of forward and back directions for given frequency and mode. Here we take into account that the waves coming in and out from an electron beam are almost not reflected. Outside electron beam

$$k^+ = k = \frac{\omega}{c},\ k^- = -\frac{\omega}{c} \qquad (3)$$

and inside one

$$k^+ = k + \delta k^+;\ \ |\delta k| << k \qquad (4)$$

Hence the equation (2) is reduced to

$$2kL_m + \delta k^+ L_{und} = 2\pi M + i\ln|R_1R_2| \qquad (5)$$

where $M = S - \arg(R_1R_2)/2\pi$, S is an integer.

0-7803-4376-X/98 /$10.00 © 1998IEEE

Separating the real and imaginary parts of (4) one can write

$$2kL_m + \mathrm{Re}(\delta k^+)L_{und} = 2\pi M \qquad (6)$$
$$\mathrm{Im}(\delta k^+)L_{und} = -\ln|R_1 R_2|$$

This equation is written for a given value of frequency. And the first equation in (6) determines conditions when the wave excitation of given mode is possible in beam system. But already after the first wave circulation, the excitation of electromagnetic oscillations in mirror resonator go to play the important role. Therefore it is necessary to add the condition of wave excitation in FEL resonator with the same value of frequency. Such condition produces a relation [3]

$$2kL_m = 2\pi(N + (n+q+1)/2 + \Delta) \qquad (7)$$

where N, n, q are the integers, Δ is a mode shift determined by resonator parameters.

The second equation in (6) determines the start condition for the electron beam current I_b. Really according with a solution of beam linear system the increment of wave excitation $\mathrm{Im}(\delta k^+) = -A I_b^{\alpha}$ (see below). Due to this the second condition in (6) drives to the direct dependence of start value of I_b on $R_{1,2}$, A, α ones:

$$I_{b_{st}} = \left(\frac{\ln|R_1 R_2|^{-1}}{A L_{und}} \right)^{1/\alpha} \qquad (8)$$

The magnitude of $\alpha \approx 1/3 - 2/5$ for a wide and compressed beam respectively [1]. For the latter case

$$A = k_0 \left(\frac{4}{k a_b I_A} \right)^{\alpha} \qquad (9)$$

where I_A= 17 kA, and $k = k_o \gamma_0^2$.

The value of $R_2 = (1 - \varepsilon)^{1/2}$ where factor $\varepsilon << 1$ including the fraction of electromagnetic flow irradiated through the second mirror.

To determine the value of R_1 it is necessary to take into analysis the fact of strong channelling of electromagnetic radiation in the beam volume. As a result the cross-section of electromagnetic flow becomes comparable with of beam one. The electromagnetic flow reflected from the second mirror returns to the first one and then to the undulator expanding due to a diffraction. As a result the fraction of electromagnetic flow returned in the beam volume is reduced to [4]

$$F = \left(\frac{a_b a_E k}{2L_d} \right)^2 \qquad (10)$$

where $a_{b,E}$ are the radius of beam and electromagnetic flow canalized in it, $L_d = 2L_m - L_{und}$. Finally

$$R_1 = F^{1/2} / N^+ \qquad (11)$$

where N^+ is the number of forward travelling waves (usually N^+ = 2-3 [1,2]).

On the whole the collective regime indicates in FEL a relatively weak dependence of start current value on the resonator parameters.

3 FEL OSCILLATOR ON BASE OF MSU ELECTRON ACCELERATORS

In present time in Institute of Nuclear Physics of MSU there are two continuous wave electron accelerators with the particle energy of 1.2-2.3 and 6.6 MeV respectively. The first device is designed for different nuclear and applied studies and has the average current magnitude up to 10-30 mA. The electron beam has small emittances.

The values of γ_0 = 3.4 - 5.6 permit to use this accelerator for producing the electromagnetic radiation in a millimetre and submillimetre range what opens a very important applications in biology and so on. Estimate the start current value.

Let the system and beam parameters be the next: γ_0= 2 cm, $L_m = 2L_{und}$, a_b = 0.1 cm, a_E = 2-3 a_b In this case the value of $I_{b\,st} \approx$ 30 mA is been reached only with $L_{und} \approx$200 cm and $\geq$ 250 cm for the electron energies 1.2 and 2.3 MeV respectively. Thus this accelerator can be used as FEL oscillator though for its reliable operation it is necessary to rise the current amplitude at several times.

The current in the second accelerator do not surpass 100 mkA. And in spite of excellent quality of electron beam this accelerator can be used only as FEL amplifier (in a special regime considered in [1]).

REFERENCES

[1] V.K.Grishin, B.S.Ishkhanov. T.A.Novicova, V.I.Shvedunov, FREE ELECTRON LASER - FEL -STUDY IN INSTITUTE OF NUCLEAR PHYSICS OF MSU, Proceeding of the Particle Accelerator Conference, Dallas, v.1, p.225.

[2] N.C.Erokhin, M.V.Kusilev, S.S.Moiseev e al., Neravnovesnye processy in plasmennoi radiophysike, Nauka Press, Moskva, 1982.

[3] O.Zvelto, Principles of Lasers, Plenum Press, New York.

[4] L.D.Landau, E.M.Lifshits, Theory of Field, § 61, Nauka Press, Moskva.

POSSIBILITY OF X-RAY FREE ELECTRON LASER WITH SINGLE CRYSTAL OPTICAL RESONATOR FOR BRAGG REFLECTION

Y. Miyahara
SPring-8, Kamigori, Ako-gun, Hyogo 678-12, Japan

Abstract

Noting the X-ray reflection coefficient of a single crystal as high as 90 % at a Bragg angle, a possibility of X-ray free electron laser in a storage ring was investigated. An optical resonator composed of four Si single crystal mirrors with diffraction angle 45 degrees provides a light beam size in the optical resonator about 30 μm rms at a wavelength of 0.217 nm. Assuming an electron beam emittance of 46 pm-rad at a beam energy of 3 GeV, and a peak current of 1200 A, we obtain an FEL gain of 39 % for an undulator with a number of periods of 300, which is slightly higher than the radiation loss in the mirrors. At the same time a conceptual design of a storage ring with such a small emittance beam is presented.

1 INTRODUCTION

Free electron laser using an electron beam has attracted a strong concern to produce an intense coherent radiation in a wide range of wavelength. Many efforts have realized FEL's in the wavelength longer than about 200 nm with the aid of a high reflective optical resonator, but not in a shorter wavelength. This is because the reflectivity of light with mirrors is very low in the shorter wavelength. Thus, efforts have been made to develop high reflective mirrors made of multilayers. One of the ways to avoid this difficulty is a high gain single pass FEL or SASE [1]. A rapid progress of RF photo-cathode gun made it possible to produce a high quality electron beam, and a SASE even in X-rays has become a realistic subject, for which, however, a high quality linac with an energy about 10 GeV equipped with a bunch compression system is needed to produce an electron beam emittance compromising a diffraction limit in the order of 10^{-11} rad-m.

Meanwhile, recent progress in storage rings for synchrotron radiation has realized a beam emittance around several nm-rad at an energy of 6~8 GeV. Discussions have started as for the next generation light source with an emittance of sub nm-rad [2, 3]. Such a light source equipped with a number of insertion devices is expected to become a practical tool in a near future. It is noted that the gap height of insertion devices has already been reduced to 10 mm in X-ray storage rings, so that X-rays can be generated with insertion devices at a beam energy about 3 GeV. In addition, it is noted that X-rays can be reflected by 90 % at a Bragg angle with a single crystal [4], which is much stronger agaist heat load than multilayers. Thus, a possibility of an X-ray FEL using a single crystal resonator was first investigated. Apart from the FEL issues discussed here, a storage ring with an emittance smaller than the diffraction limit is in itself very interesting, because the brilliance of undulator radiation increases quadratically as for the number of undulator periods.

In this paper, a crude discussion is presented as for a possibility of an X-ray FEL equipped with a single crystal resonator for Bragg reflection, including a design of a small emittance ring.

2 OPTICAL RESONATOR

By the improvement of crystal perfectness, a single crystal can have a reflection coefficient of 90% at a Bragg angle for X-rays shorter than a few nano-meters. Suppose an optical resonator composed of four Si single crystals (unit cell length is 0.5431 nm) facing each other at 45 deg and separated by 1 and 29 m as shown in Fig.1. The mirror center on the beam axis is away from the electron beam orbit by about 50 cm in the case of a storage ring discussed later. The wavelength λ=0.217 nm is well reflected by the crystal plane (222). Assuming a confocal type of mirrors, we obtain a radiation size ω_0=32 μm at the center between the mirrors and 46 μm at the mirror surfaces. Horizontally polarized radiation generated by the undulator or by the FEL interaction in the optical resonator is reflected in the vertical direction, so that the electric field vector of the radiation is parallel to the mirror surfaces to give the high reflectibity. The reduction of the light pulse intensity per one circulation in the resonator is 34%, so that the FEL gain should be higher than this value. Practically, a high stability of the mirrors is required since the sizes of the radiation and electron beams are very small. To make a confocal mirrors with single crystals might not be easy. Combination of two pairs of mirrors, toroidal and plane, in two directions relaxes this difficulty. Possibly, two-mirror system is better than the four-mirror system.

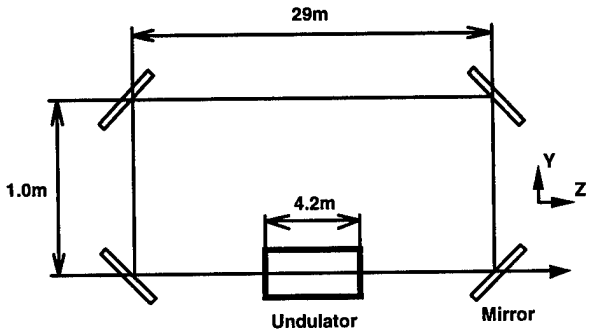


Fig.1 Optical resonator made of single crystals for FEL

0-7803-4376-X/98/$10.00 © 1998 IEEE

3 UNDULATOR

The peak field of the Halbach type undulator is expressed as

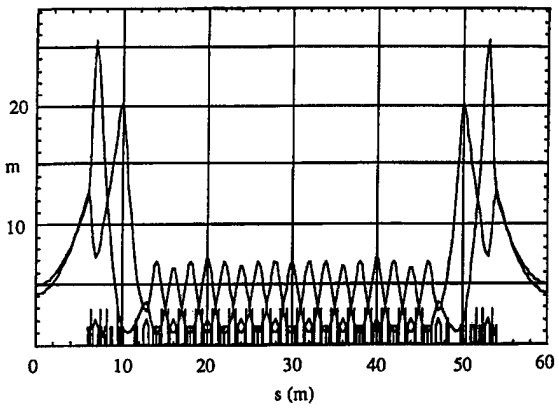
$$B_p=2B_r \frac{\sin(\pi/4)}{\pi/4} \exp\left[-\frac{\pi g}{\lambda_0}\right]\left[1-\exp\left(-\frac{2\pi h}{\lambda_0}\right)\right]$$

We get B_p=0.284 T for the remanent field B_r=1.2 T with the gap height g=8 mm, the undulator period λ_0=1.4 cm and the block height h=λ_0/4, so that $K=0.934B_p\lambda_0$ =0.371. This undulator generates the radiation wavelength λ=0.217 nm at a beam energy of 3.0 GeV. Higher harmonic components of the undulator radiation are weak because of the smaller value of K than 1.

4 FEL GAIN

The FEL gain in the small signal regime is given by

$$G=32(2)^{1/2}\pi^2(\lambda^3\lambda_0)^{1/2}\zeta(K)\frac{I_p}{I_A}\frac{Nu^3}{\Sigma\eta}F(\xi)$$



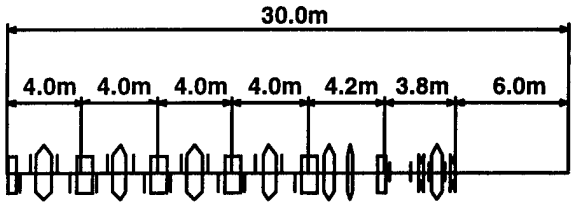


Fig.2 Half unit cell (bottom) and lattice function in a unit cell of the storage ring

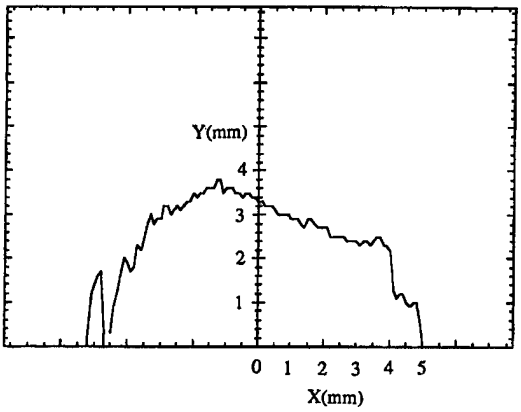


Fig.3 Dynamic aperture of the storage ring

where $\zeta(K)=K^2/2/(1+K^2/2)^{3/2}$, Ip is the peak current, I_A(=17000 A) is the Alfen current, Σ is the cross section of the electron beam, h is the filling factor, and $F(\xi)$ is the gain function. In the storage ring discussed later, we have the natural emittance of electron beam ε_x=46 pm-rad at 3 GeV and the beta function $\beta_x^*\approx\beta_y^*\approx$5 m in the center of the straight section for the undulator. Assuming a full coupling of horizontal and vertical betatron oscillations, we have the beam size $\sigma_x\approx\sigma_y\approx$11 μm, so that $\Sigma=\pi\sigma_x\sigma_y\approx3.6\times10^{-10}$ m^2, and $\eta=(\omega_0/\sigma_{x,y})^2$=8.5.

To get a sufficiently high gain in the gain function, the number of the undulator periods should approximately satisfy the following relation, $N_u < 1/(2\pi\sigma_E/E)$, where σ_E/E is the relative energy spread and given by $\sigma_E/E=6.23\times10^{-4}$. Therefore we assume N_u=300, with the undulator length L_u=4200 mm, for which we have $F(\xi)\approx0.06$. Substituting these values and Ip=1200 A into the gain equation, we obtain G=39%, which is slightly higher than the radiation loss.

5 SMALL EMITTANCE STORAGE RING

To fit to the tunnel of the SPring-8 storage ring with the circumference 1436 m and the periodicity 48, we considered a ring with almost the same circumference and a periodicity of 24. The unit cell of the ring consists of 8 normal cells sandwitched with dispersion suppressors and tune correctors as shown in Fig.2. Two bending magnets of rectangular type with defocusing field and a focusing quadrupole magnet constitute the normal cell, where focusing and defocusing sextupole magnets are installed to suppress the chromaticity. The field gradient in the bending magnets is rather weak as -11.16 T/m, which reduces the bending field as low as 0.327 T. The lattice function is shown in Fig.2. The dispersion function is less than 0.045, which produces the small emittance given above. The dispersion is suppressed to zero with two quadrupole magnets in the suppressor. The straight

Table 1 Storage ring parameters

Beam energy	E	3	GeV
Circumference	C	1440	m
Periodicity	p	24	
Natural emittance	ε_x	46	pm-rad
Compaction factor	α_p	5.68×10^{-5}	
Radiation energy	U_0	235	keV
Energy spread	ε_E/E	6.23×10^{-4}	
Tune	ν_x	84.40	
	ν_y	68.45	
	ν_s	1.39×10^{-3}	
Natural chromaticity	ξ_x	-124.9	
	ξ_y	-106.0	
Damping time	τ_x	65	ms
	τ_y	123	ms
	τ_ε	111	ms
Revolution frequency	f_0	208.2	kHz
Harmonic number	h	2442	
RF frequency	f_{RF}	508.42	MHz
RF voltage	V_{RF}	351	kV
Bucket height	$\Delta E_{max}/E$	1.0	%
Bunch length	σ_τ	20	ps
Average current	I_0	10	mA/bunch
Number of bunches	N_b	24	
Peak current	I_p	1200	A
Bending magnets			
Bending field	B	0.3272	T
n-value	n	1041.96	
Bending radius	ρ	30.558	m
Magnet length	l_B	0.8, 0.4	m
Quadrupole magnets			
Field gradient	B_y'	≤ 16	T/m
Magnet length	l_Q	0.8, 0.6, 0.3	m

section for insertion devices is as long as 12 m for a higher brilliance, which needs rather large peak values of the beta functions. The chromaticity is reduced to zero with focusing and defocusing sextupole magnets installed in the normal cells. The dynamic aperture is as narrow as several mm, as shown in Fig.3.

6 CONCLUSION

In the present paper, we have crudely discussed a possibility of an X-ray FEL in a small emittance ring equipped with a single crystal optical resonator for Bragg reflection. The estimated gain is slightly higher than the radiation loss. There are, however, several subjects such as bunch lengthening, intra-beam scattering and others not considered here yet, which might decrease the gain. Nevertheless, the results obtained here are encouraging to make a further optimization of the FEL system and storage ring, and it is also necessary to consider the beam dynamical issues.

Another important result of the present investigation is the design of the storage ring with an emittance as small as 46 pm-rad at a beam energy of 3 GeV, which is close to the diffraction limit of X-rays. Although the dynamic aperture is very small, it is not beyond practical operation. There are many things to be discussed further, which will be presented elsewhere.

The author is grateful for the use of the computer code BETA.

REFERENCES

[1] C. Pellegrini: 'A 4 to 0.1 nm FEL Based on SLAC Linac', Proceedings of Workshop on Fourth Generation Light Sources, Stanford, February 1992, 364~372.

[2] Y. Cho: 'A Very Low Emittance Lattice', Proceedings of 10th ICFA Beam Dynamics Panel Workshop on 4th Generation Light Sources, Grenoble, January 1996, wg3-43~52.

[3] D. Einfeld and J. Schaper: 'Design of a Diffraction Limited Light Source (DIFL), ibid, wg3-53~66.

[4] M. Yoshimatsu, T.Matsushita and S.Kikuta: 'X-ray Diffraction' edited by K. Kohra, (Kyodo press, 1988 in Japanese), Chap.5.

ON THE ANALYTIC REPRESENTATION OF PERIODIC MAGNETOSTATIC FIELDS

A.V. Smirnov
Russian Research Centre `Kurchatov Institute`, Moscow 123182, Russia

Abstract

A generalized form is considered in a source-free region for the magnetic scalar potential in focusing planar undulators and insertion devices. A number of particular cases is outlined: periodic quadrupole and sextupole focusing, combined-function nonlinear wigglers, twisted undulator, alternating longitudinal field focusing system, an adjustable phase insertion device. A special attention is paid to quadrupole type intrinsic fields including strong periodic focusing. The generalised formalism can be used in particle tracing codes or 3D codes for free electron lasers simulation.

1 INTRODUCTION

Free electron lasers (FELs), synchrotron radiation sources, microwave sources use a great variety of periodic magnetic systems. The development of the shortest wavelength high power FELs [1] requires a long undulator with strong focusing to achieve high gain. Therefore the fields providing intrinsic focusing should be considered in more details. Besides, some novel structure of insertion devices (ID) such as twisted undulator [2] need in specific description of undulator fields in paraxial region.

2 FIELDS IN CARTESIAN FRAME FOR PERIODIC SYSTEMS

There is a well known formula for the magnetic scalar potential in the planar wiggler [3] with a periodic intrinsic focusing of sextupole type. However this formula does not include the real case of intrinsic focusing with a periodic transverse field gradient in planar wigglers (undulators).

Let us consider a magnetostatic system with space period $\lambda_w = 2\pi / k_w$ and adiabatic tapering along the longitudinal axis OZ. The magnetic field $\boldsymbol{B}$ ($\boldsymbol{B} = -\nabla\psi$) can be expanded as a Fourier series in a free-space (interaction) region:

$$\psi = \sum \psi_n(x,y) e^{ink_w z}.$$

For rectangular gap configuration the analytic solutions of Helmholtz equation $\Delta_\perp \psi_n - n^2 k_w^2 \psi_n = 0$ can be derived in the following form:

$$\psi = \mathrm{Re} \sum_n e^{i(n\int_0^z k_w dz + \varphi_n)} \begin{pmatrix} A_n^{(1)} \cosh \mu_{nx}^{(1)} x \dfrac{\sinh \mu_{ny}^{(1)} y}{\mu_{ny}^{(1)}} + \\ A_n^{(2)} \dfrac{\sinh \mu_{nx}^{(2)} x}{\mu_{nx}^{(2)}} \cosh \mu_{ny}^{(2)} y + \\ A_n^{(3)} \cosh \mu_{nx}^{(3)} x \cosh \mu_{ny}^{(3)} y + \\ A_n^{(4)} \dfrac{\sinh \mu_{nx}^{(4)} x}{\mu_{nx}^{(4)}} \cdot \dfrac{\sinh \mu_{ny}^{(4)} y}{\mu_{ny}^{(4)}} \end{pmatrix},$$

$$\mu_{nx}^{(m)2} + \mu_{ny}^{(m)2} = n^2 k_w^2, \; m = 1,2,3,4, \qquad (1)$$

where n is the field harmonic number; φ_n is the initial space shift for the n-th harmonic, $A_n^{(m)}$, $\mu_{nx}^{(m)}$, $\mu_{ny}^{(m)}$, k_w are slowly varying functions of the longitudinal coordinate z: $\frac{d}{dz} \ln\left\{A_n^{(m)}, \mu_{nx,y}^{(m)}, k_w\right\} << k_w$; $A_n^{(m)}$ coefficients (m≠4) define on-axis field Fourier-amplitudes or field gradient Fourier-amplitudes (m=4), and $\mu_{nx}^{(m)}$, $\mu_{ny}^{(m)}$ eigenvalues describe the field shape in transverse plane for each Fourier-harmonic.

2.1 Particular cases

Herewith five particular cases **i**)÷ ∨) are considered.

i) $A_n^{(1)} \neq 0$, $A_n^{(m)} = 0, m \neq 1$

We deal with Scharlemann`s expression (see ref. [3]) for the magnetic scalar potential in the planar undulator with a horizontal wiggle plane. The first term in (1) being expanded in powers of x,y gives the series of periodic fields with an even symmetry with respect to YOZ plane: dipole, sextupole, decapole, etc.
We can consider two subclasses.

a) A conventional wiggler (undulator) with sextupole type (`natural`) focusing (see ref. [3]) at $\mu_{nx}^{(m)2} > 0$, $\mu_{ny}^{(m)2} > 0$.

b) If $\mu_{ny}^{(m)2}$(z) periodically changes its sign along the undulator ($\mu_{ny}^{(m)2} < 0$, $\mu_{nx}^{(m)2} > 0$ and vice versa) we can derive an alternating sextupole strong focusing that was investigated in matrix formalism in [4]. K-V equations [5] describe beam envelope behaviour as Mathieu-Hill equations and allow to treat such focusing in

0-7803-4376-X/98/$10.00 © 1998 IEEE

a source-free region for undulators also. Particle tracing codes can solve the beam transport problem in such undulators taking into account nonlinear effects and the measured magnetic field data (see [6,7] for example).

ii) $A_n^{(2)} \neq 0,\ A_n^{(m)} = 0, m \neq 2.$

The second term in (1) describes the undulator fields with the sextupole type periodic focusing and the vertical (YOZ) wiggle plane. So this case can be obtained from the previous (**i**) case by means of replacement: x ↔ y.

iii) $A_n^{(3)} = 0 = A_n^{(4)}, \mu_{nx}^{(2)} \Rightarrow 0, \mu_{ny}^{(1)} \Rightarrow 0$

at $A_n^{(1)} = -iA_n^{(2)} = const \neq 0.$

This case approximates the fields of a well known helical undulator in Cartesian frame. This form is more suitable for a permanent magnet undulator having only two dipoles over $\lambda_w / 2$ length and angular shift $\pi/2$ between them in the transverse plane.

iv) $A_n^{(3)} \neq 0.$

a) $A_n^{(m)} = 0, m \neq 3.$

We see that the longitudinal magnetic field is not zero on the OZ axis. The transverse magnetic field components are equal to zero on the OZ axis. The transverse field components vanish at $n = 0$ and $\vec{B}_\perp \sim \vec{r}_\perp$ near the axis. This case describes alternating longitudinal field (solenoidal) focusing system. Such systems are very compact and effective for electron beam focusing in travelling wave tubes (TWT) and backward wave oscillator (BWO) tubes.

b) $A_n^{(1)} = 2B_r G_n \cos\left(\frac{nk_w z_o}{2}\right),\ A_n^{(2)} = 0, A_n^{(4)} = 0,$

$$A_n^{(3)} = -i2B_r G_n \sin\left(\frac{nk_w z_o}{2}\right).$$

This case appropriates to the adjustable phase insertion device (APID, see ref. [8]). Here z_o denotes the space shift along the OZ axis between two parallel magnet rows with a constant gap and other notations B_r, G_n are the same as in the ref. [8]. It can be shown that the focusing properties of APID are independent on the undulator strength (i.e. z_o value for APID) in contrary to the adjustable gap insertion devices (AGID) for ultra relativistic electron beams.

2.1.1 Field component having odd symmetry in transverse plane

v) $A_n^{(4)} \neq 0,\ A_n^{(3)} = 0.$

Here $A_n^{(4)} = Q_n(z)$ is Fourier-amplitude of the field gradient for the n-th field harmonic.

The last term in (1) describes the intrinsic periodic focusing fields with odd symmetry with respect to the longitudinal OZ axis. Unlike the previous cases (**i, ii**) corresponding fields can be regarded as quadrupole, octupole, dodecapole, etc. series of fields. Besides, an interchange of signs of $\mu_{nx}^{(4)2}$ and $\mu_{ny}^{(4)2}$ corresponds no longer to a conventional strong focusing. The alternating gradient focusing is caused by $A_n^{(4)} = Q_n(z)$ variation along the undulator. It can be provided by means of both external quadrupoles and special undulator schemes with intrinsic quadrupole focusing.

The combination of the first and the last term in (1) can describe the so-called quadrupole-sextupole wiggler (see ref. [6]) in which, as the name suggests, there are superposed quadrupole and sextupole fields. Such multipole combination produces nonlinear damping effect with negligible energy loss for fluctuating synchrotron radiation in storage rings. Another combined-function nonlinear wigglers (for example, dipole-octupole magnets) produce a large additional energy loss [6].

Let us consider the contribution of ψ_q to a total scalar potential ψ from the last term in (1):

$$\psi_q = \mathrm{Re} \sum_n e^{i(n\int_0^z k_w dz + \varphi_n)} A_n^{(4)} \frac{\sinh \mu_{nx}^{(4)} x}{\mu_{nx}^{(4)}} \cdot \frac{\sinh \mu_{ny}^{(4)} y}{\mu_{ny}^{(4)}}. \quad (2)$$

We can outline three following subclasses.

a) $A_n^{(4)} \neq 0,\ A_n^{(4)} = 0$ for $n \neq 0, \varphi_o = 0: \psi_q = Q_o xy.$

This is a conventional quadrupole focusing with constant gradient. For intrinsic quadrupole focusing Q_0 is the gradient averaged over undulator period.

b) $A_0^{(4)} \neq 0,\ A_n^{(4)} = 0$ for $n \neq 1.$

This is the case of an alternating gradient with quadrupole lenses placed between the poles ($\varphi_1 = 0$, see also ref. [4]) or with canted poles having the same tilt ($\varphi_1 = \pi / 2$).

c) $A_0^{(4)} \neq 0,\ A_0^{(4)} \neq 0,\ A_n^{(4)} = 0$ for $n \neq 0$ and $n \neq 2.$

This case takes place when the local gradient $Q(z) = -\partial B_y / \partial x$ is a periodic function with period $\lambda_w / 2$. As it follows from direct measurements [9-12] the undulators with canted poles [11,12], side magnets [9] and C-shape poles [10] have a such property. It can be assumed that for some other planar undulator schemes (for example, with trapezoidal blocks or offset pole pieces) we have $Q_2 \neq 0$ as well.

Expression (2) describes intrinsic quadrupole focusing and contains Q_o, Q_2, μ_{2x}, φ_2 parameters in addition to the conventional undulator parameters (period, amplitude, etc.). These additional parameters can be defined by means of direct measurements or 3D magnetostatic fields

calculation. To take into account Q_2-effect on beam size, phase synchronism detuning (see [9,10]) we can not apply K-V equations and should use non-averaging and non-linearized particle tracing calculations (e.g. [7]). We expect this effect can appear as a coupling between the vertical and horizontal motions due to the nonlinear cross terms in the undulator focusing strengths expanded as a Taylor series. It would be similar to the effect noticed for the equal focusing undulators with the sextupole type focusing [9,13].

3 TWISTER UNDULATOR FIELDS

The geometry [2,14] looks like helical transformation with period λ_t applied to an original linear undulator structure having period λ_w and provides a combination of fast and slow oscillations of the electron beam. In a source-free region the fields can be represented in terms of $\psi(r,\varphi,\ z)=Re\Sigma R(r)\Phi(\varphi)Z(z)$. Since the longitudinal structure combines two periods λ_t and λ_w, we use nh_t+mh_w as a separation constant. It gives the followng solution:

$$\psi(r,\varphi,z)=\mathrm{Re}\sum_{l,m,n}\begin{pmatrix}A_l C_{n,m} I_l(r(nk_t+mh_w))\times\\ \exp(i(l\varphi-(nk_t+mh_w)z))\end{pmatrix}$$

To define the constants A_l, $C_{m,n}$ the following transverse fields we imply at $r=0$:

$B_r=(B_w cosk_w z+B_t)sin(\varphi+k_t z)$

$B_\varphi=(B_w cosk_w z+B_t)cos(\varphi+k_t z)$,

where B_w and B_t are the amplitudes of the untwisted and helical undulator fields respectively. This form follows from the expression for on-axis undulator field derived from that for planar undulator under twisting transformation [14]:

$B_x=(B_w cosk_w z+B_t)\sin(k_t z)$

$B_y=(B_w \cos k_w z+B_t)cos(k_t z)$.

Under these assumptions one can derive:

$$\psi(r,\varphi,z)=\mathrm{Re}\sum_{m=-1}^{m=+1}\begin{pmatrix}C_m I_1(r(mh_w+k_t))\times\\ \exp(i(\varphi+(mh_w+k_t)z))\end{pmatrix},$$

where $C_0=\dfrac{2iB_t}{k_t}$, $C_{\pm1}=i\dfrac{2B_w}{k_t\pm h_w}$

REFERENCES

[1] R. Tatchyn, J. Arthur, M. Baltay, K. Bane, R. Boyce, M. Cornacchia, T. Cremer, A. Fisher, S.-J. Hahn, M. Hernander, G. Loew, R. Miller, W. R. Nelson, H.-D. Nuhn. D. Palmer, J. Paterson, T. Raubenheimer, J. Weaver, H. Wiedemann, H. Winick, C. Pellegrini, G. Travish, E. T. Scharlemann, S. Caspi, W. Fawley, K. Halbach, K.-J. Kim, R. Schluter, M. Xie, D. Meyerhofer, R. Bonifaco, L. De Salvo. Research and development toward a 4.5-1.5 Å linac coherent light source (LCLS) at SLAC. Nucl. Instr. and Meth. A375 (1996) 274

[2] Yu.P. Bouzouloukov, V.V. Gubankov, A.S. Khlebnikov, N.S. Osmanov, A.V. Smirnov, N.V. Smolyakov and S.V. Tolmachev. Short-period planar undulators development towards twisted structures, Proc. of the 18-th. Int. Free-Electron Laser Conf., Rome, Italy, August 26-31, 1996 (Th P23)

[3] E.T. Scharlemann. Wiggle plane focusing in linear wigglers. J. Appl. Phys. **58** (6), 15 September 1985, 2154-2161.

[4] G. Travish, J. Rosenzweig. Strong Focusing for Planar Undulators. AIP Conf. Proc. No 279. (1992), 277.

[5] I.M. Kapchinskij and V.V. Vladimirskij. Proc. Int. Conf. on High Energy Accelerators (Cern, Geneva, 1959), p. 274

[6] J. M. Jowett. Electron Dynamics with Radiation and Nonlinear Wigglers. CERN Accelerator School, Advanced Accelerator Physics, (Oxford, 16-27 September 1985), published at CERN 87-03 (1987).

[7] A.V. Smirnov. 3D-code UNDYNA for electron beam transport simulations in planar undulators. Preprint IAE-5655/14, Moscow, Russia (1993)

[8] R. Carr. Adjustable phase insertion devices as X-ray sources. Nucl. Instr. and Meth. A306(1991) 391-396.

[9] A.A. Varfolomeev, A.V. Smirnov. Beam Transport Through Undulators Designed for High Power FEMs. Nucl. Instr. and Meth. A 358 (1995) 197

[10] A. Khlebnikov, C. Pellegrini, A. Smirnov, A. Varfolomeev. Beam Transport in KIAE- UCLA Undulator. University of California, Los Angeles, USA. Internal report (1992).

[11] D.C. Quimby, S.C. Gottschalk, F.E. James, K.E. Robinson, J.M. Slater, and A.S. Valla. Development of a 10-meter Wedged-Pole Undulator. Nucl. Instr. and Meth. A285 (1989) 281
J. Pfluger and Yu. M. Nikitina, Undulator schemes with the focusing properties for the VUV-FEL at the TESLA Test Facility. Nucl. Instr. and Meth. A375 (1996) 325

[12] K.E. Robinson, D.C. Quimby, J.M. Slater, T. L. Churchill and A.S. Valla. Field Certification of a High Strength Tapered Hybrid Undulator. Nucl. Instr. and Meth. A259 (1987), 62.

[13] J.J. Barnard. Anharmonic betatron motion in free electron lasers. Nucl. Instr. and Meth. A296(1990) 508-515.

[14] A. Khlebnikov and A. Smirnov, A novel structure of short-period twisted undulator. Spontaneous emission properties; these Proceedings (9P29).

A HIGH-POWER COMPACT REGENERATIVE AMPLIFIER FEL

D. C. Nguyen, R. L. Sheffield, C. M. Fortgang, J. M. Kinross-Wright, N. A. Ebrahim, and J. C. Goldstein
MS H851, Los Alamos National Laboratory, Los Alamos, NM 87545

Abstract

The Regenerative Amplifier FEL (RAFEL) is a new FEL approach aimed at achieving the highest optical power from a compact rf-linac FEL. The key idea is to feed back a small fraction (<10%) of the optical power into a high-gain (~10^5 in single pass) wiggler to enable the FEL to reach saturation in a few passes. This paper summarizes the design of a high-power compact regenerative amplifier FEL and describes the first experimental demonstration of the RAFEL concept.

1 INTRODUCTION

Self-amplified spontaneous emission (SASE) has been demonstrated experimentally in the mm-wave, far-ir and mid-ir regions.[1] Recent interest in SASE has shifted toward shorter wavelengths as this provides the basis of the fourth generation light sources emitting coherent tunable radiation in the deep uv and x-rays. Existing designs of x-ray SASE FELs, however, call for very long wigglers (tens of meters).[2]

One way of reducing the wiggler length is to use optical feedback to synchronously inject the optical power from one pass back to the front of the wiggler to seed the optical buildup of subsequent passes. We called this idea the regenerative amplifier FEL (RAFEL). With a large single-pass gain, the amount of optical feedback can be quite small, e.g. <10%. Since mirrors can easily provide that kind of reflectivity, even in the deep uv and x-ray regions, a small amount of optical feedback translates into substantial saving in the number of gain lengths needed for saturation. Furthermore, this approach allows us to control the output frequency and amplitude and to use a strongly tapered wiggler for improved extraction efficiency. Compared to traditional FEL oscillators, the RAFEL outcouples >90% of the intracavity power, thereby reducing the risk of optical damage while maximizing system efficiency. The RAFEL output efficiency is essentially equal to the FEL extraction efficiency.

2 EXPERIMENTAL SETUP

The RAFEL concept was implemented on the compact Advanced FEL test stand at Los Alamos with the philosophy of a simple system design and minimum number of components. The key components of the RAFEL experiment include a high-current, high-brightness electron linac, a high-gain, high-efficiency wiggler and an optical feedback loop. Figure 1 schematically depicts the RAFEL experimental setup. As details of the RAFEL experimental implementation have been reported elsewhere,[3] only the pertinent parameters of the RAFEL experiment are summarized in this paper (see Table I).

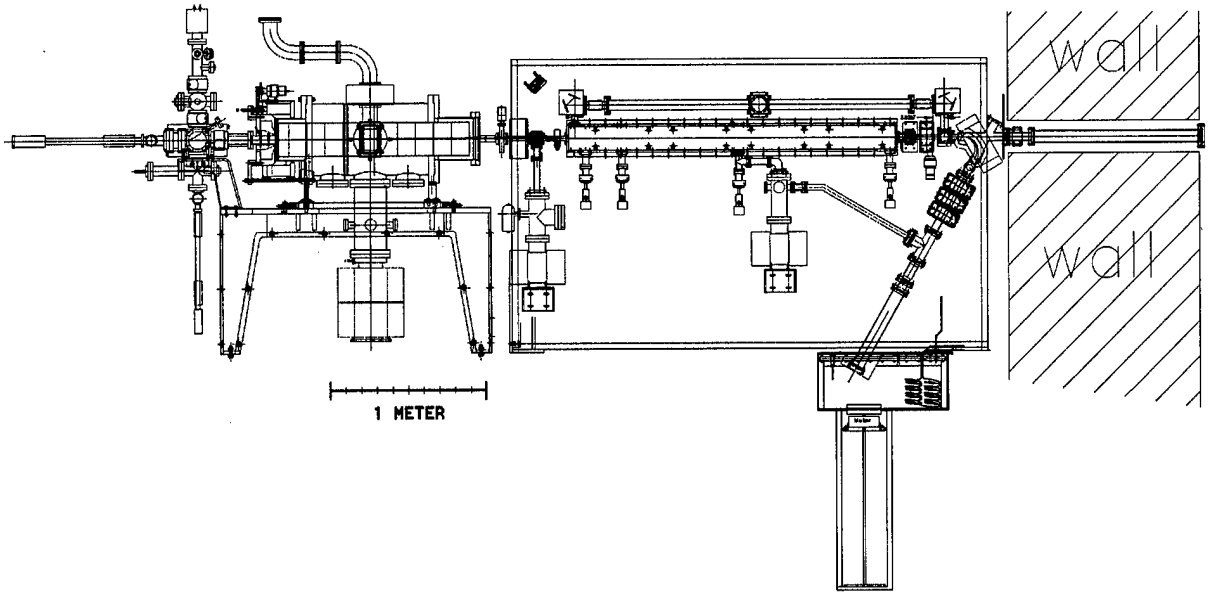


Figure 1. Experimental setup of the regenerative amplifier FEL.

0-7803-4376-X/98/$10.00 © 1998 IEEE

Table I: Summary of experimental parameters

Beam Energy	E	16.5 MeV
Peak current	I_{peak}	3–300 A
Charge/bunch	Q	0.01–5 nC
Bunch length	τ	3.5–16 ps
Bunch separation	T	9.23 ns
Normalized emittance*	ε_n	<7 mm-mrad
Energy spread	$\Delta\gamma/\gamma$	<0.5%
rms radius inside wiggler	r_b	0.2 mm
Wiggler period	λ_w	2 cm (fixed)
On-axis field	B_0	0.7 Tesla
Wiggler length	L_w	1 m uniform 1 m tapered
Taper rate		30% in B
Wiggler gap		5.9–9.5 mm
Betatron period	λ_β	1 m
Wavelength	λ	16.2 μm
FEL parameter*	ρ	0.02
Gain length (3-D)*	λ_G	7.8 cm
Slippage length	L_S	1.7 mm

* At 300 A peak current

The requisite electron beam has been characterized and reported in Ref. [3]. The permanent magnet wiggler has nearly equal two-plane focusing via the sextupole components of the magnetic field.[4] Beam size measurements using OTR screens confirmed the near circular profile and the constant beam radii in the wiggler. The feedback loop consists of two annular mirrors and two 90° paraboloids, forming a simple ring resonator.[5] The present output mirror has a 12 mm diameter hole instead of the designed 14 mm hole.

The forward-directed spontaneous, SASE and RAFEL lights were detected with a sensitive HgCdTe detector. The 16 μm micropulses were detected with a fast Cu:Ge detector. Optical energy measurements were made with calibrated Molectron J50 pyroelectric detectors.

3 RESULTS AND DISCUSSION

The RAFEL without the feedback optics is a SASE experiment with a 1 m uniform wiggler. The observed intensities of the SASE micropulses are completely random with amplitudes varying by more than a factor of ten (Fig. 2). Since the electron beam parameters cannot change significantly on the nanosecond time scale, the SASE amplitude variation are most likely caused by differences in the start-up conditions.

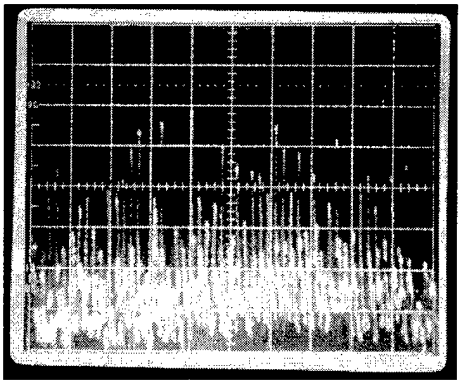


Figure 2. Oscilloscope trace of SASE at 16 μm as detected with a helium cooled Cu:Ge detector.

To determine the SASE single-pass gain, we varied the micropulse charge from 0.01 to 5 nC and measured the infrared light generated in a single pass. The results are plotted on a log-log scale in Fig. 3. The sudden break from linear dependence (slope=1) to quadratic dependence (slope=2) at 0.2 nC is attributed to transition from spontaneous to SASE. From the ratio of the measured SASE power at 5 nC to the spontaneous power at the end of the first gain length, an average SASE gain of X500 is inferred. As the SASE power fluctuates by a factor of ~10 from micropulse to micropulse, we expect the peak gain to be 3 times higher.

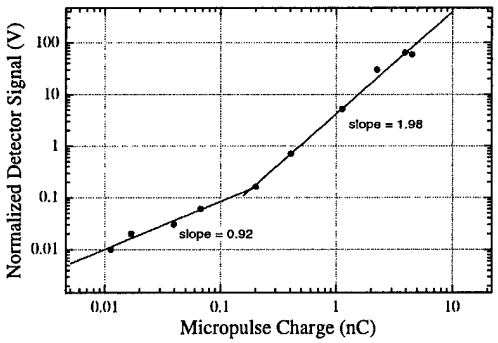


Figure 3. Plot of attenuation-corrected HgCdTe signal vs. micropulse charge on log-log scale.

Shortly after installing the feedback loop, we observed an optical power more than six orders of magnitude above SASE. The measured energy integrated over an 8 μs macropulse (~900 micropulses) was 0.35 J. If the Fresnel loss of the ZnSe vacuum window is accounted for, we have generated 0.5 J of 16 μm light over 8 μs, corresponding to a 60 kW average power over the macropulse. Since these results were obtained with 3 nC electron bunches, we deduced 1% of the beam power was converted to FEL light.

Unlike an FEL oscillator, the RAFEL has a large feedback cavity detuning curve with a fwhm ≥ 1 mm (Fig. 4). The optical buildup near saturation exhibits a large gain (~X6 assuming 66% cavity loss), although this is much less

than the small-signal gain which we could only infer from the SASE measurements. As there are two pulses in the feedback cavity, two sets of micropulses build up from different initial conditions and achieve saturation at different times (Fig. 5). Because of the large outcoupling, the cavity ringdown is fast: the FEL power drops by a factor of 3 in successive passes (Fig. 6). From the ringdown measurements, we estimated that the present outcoupling is less than 66%. This outcoupling differs from the expected 90% partly because of the smaller hole in the output mirror.

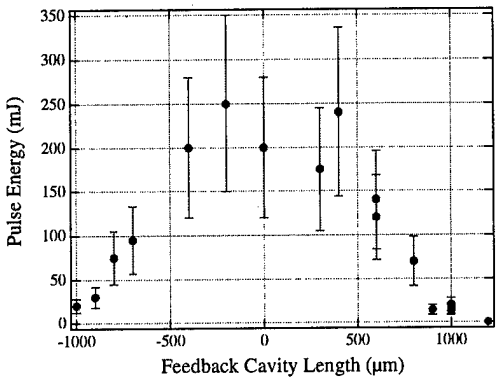
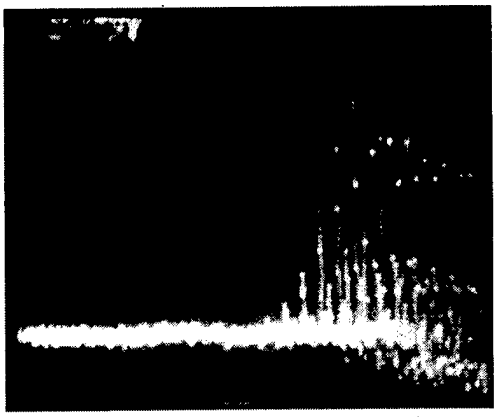
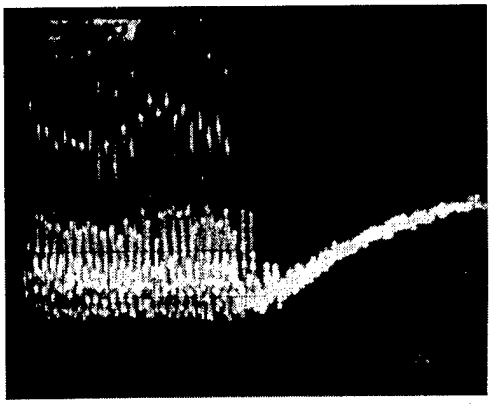


Figure 4. RAFEL feedback cavity detuning curve


Figure 5. Fast buildup of RAFEL to saturation.


Figure 6. RAFEL ringdown shows optical power decaying by a factor of 3 in successive passes.

4 CONCLUSION

We have demonstrated for the first time the regenerative amplifier FEL concept. A single-pass gain greater than 500 was inferred from the plot of SASE intensity versus charge. The RAFEL produced 0.5 J per macropulse at 16 μm, corresponding to 60 kW average power, over an 8 μs macropulse, and a 1% output efficiency. Experiments are in progress to characterize this new regime of FEL operation.

5 ACKNOWLEDGMENTS

The authors thank Roger Warren, Claudio Pellegrini, David Goldstein, Kara Hayes, Michael Weber, Scott Volz, John Plato, Richard Lovato, Claude Conner, and Robert Wheat for their support. This work was conducted under the auspices of the US Department of Energy, supported (in part) by funds provided by the University of California for the conduct of discretionary research by LANL.

REFERENCES

[1] T. J. Orzechowski et al., *Nucl. Inst. Meth.* A **250**, 414 (1986); D. Bocek et al., *Nucl. Inst. Meth.*, A **375**, 13 (1996); R. Prazeres et al., *Phys. Rev. Lett.*, **78**, 2124 (1997).

[2] H. Winnick et al., *Nucl. Inst. Meth.*, A **347**, 199 (1994); J. Rossbach, *Nucl. Inst. Meth.*, A **375**, 269 (1996).

[3] R. L. Sheffield et al., to be published in *Proc. SPIE*, San Jose, 1997.

[4] C. M. Fortgang, to be published in *Nucl. Inst. Meth*, Proc. FEL'96, Rome 1997.

[5] D. C. Nguyen et al., to be published in *Nucl. Inst. Meth*, Proc. FEL'96, Rome 1997.

W-BAND FREE ELECTRON LASERS FOR HIGH GRADIENT STRUCTURE RESEARCH

S. M. Lidia, Lawrence Berkeley National Laboratory,
D. H. Whittum, Stanford Linear Accelerator Center, and
J. T. Donohue, Centre d'Etudes Nucleaires de Bordeaux-Gradignan

Abstract

We analyze two designs for W-Band free electron lasers for application as laboratory instruments in the study of millimeter wave accelerators at high gradient. The first design is based on the linear induction accelerator LELIA (CEA/CESTA, France), employs a 1-kA, 80-ns electron pulse, and corresponds to a helical TE_{11} 200MW W-Band amplifier design. We analyze also a W-Band planar ubitron design making use of a SLAC-modulator, operating with a 480 kV, 300 A, sheet beam gun and producing a 5 MW, 1μs pulse.

1 INTRODUCTION

To reach high gradients in conducting structures a short rf wavelength is required, due to the constraints of *trapping*, *breakdown*, and *pulsed heating* [1]. For copper accelerators, optimized for *[R/Q]*, the scaling for wall quality factor,

$$Q = 2.7\times10^{4} f(\mathrm{GHz})^{-1/2},$$

implies a field decrement time,

$$T \approx 8.6\mu s\, f(\mathrm{GHz})^{-3/2},$$

and a natural fill time in the range of 10ns at W-Band (75-110 GHz). Extrapolation of breakdown scalings at S and X Band indicate that this time-scale is sufficiently short that breakdown may well be inhibited up to gradients beyond 1 GeV/m. Trapping of an initially stationary population of field-emitted electrons is diminished at mm-wavelengths, where even at 1 GeV/m, the gradient wavelength product can be held to values routinely employed on certain high-gradient sections at the SLC [2]. The most critical concern at high-gradient is heating due to Ohmic loss in a *single pulse*, for it is conventional wisdom that the pulsed temperature rise ΔT, should be held to 40° K or lower, due to the cyclic stress limit for copper. To appreciate the significance of this constraint, we note the relation between gradient and pulsed temperature rise for a conventional travelling wave structure with attenuation parameter $\tau \sim 1$, and optimized shunt impedance,

$$G\left(\frac{\mathrm{GeV}}{\mathrm{m}}\right) = 0.25\left(\frac{\Delta T}{40^{\circ}\mathrm{K}}\right)^{1/2}\left(\frac{f}{91.4\mathrm{GHz}}\right)^{1/4}.$$

This constraint is, for some ΔT, unassailable, and motivates the design of structures, and powering schemes that escape the bandwidth constraint for conventionally powered, passive structures [1]. Detailed experimental studies are in progress at SLAC to assess in practice the limit on ΔT [3]. Other concerns have been raised, over the years, concerning the use of short-wavelength structures, particularly: fabrication, and wakefields. Fabrication of such structures is now an accomplished fact [4]. Wakefields, it has been demonstrated [5], can be dealt with in a constructive fashion, making use of the structure itself as a beam-position monitor, and permitting, in principle, precision structure alignment.

The immediate implication of this line of research is however, that one needs a W-Band high-power amplifier, as a laboratory instrument at first, and eventually as an accelerator power source. Commercial amplifiers at W-Band provide at most 3-5 kW [6]. Gyroklystron tube research has resulted in 55 kW power levels [7]. A planar ubitron has been operated at 250 kW [8]. Induction linac driven FELs have output 100 MW at 35 GHz[9], and 2 GW at 140 GHz [11]. To produce a 1 GeV/m gradient in a W-Band structure, and regardless of whether it is an active or passive structure, one needs power levels in the range of 200 MW, for pulse lengths of order 10 ns. There are two conceivable ways to accomplish this with externally generated RF. The first is to generate a low power level, in the range of 5 MW, over a longer, 1 μsec pulse, and perform active pulse compression. The second is to generate the 200 MW directly, in a short pulse. We consider each of these in turn. We will analyze two examples, set down the design parameters required, and confirm them with the help of 1D and 3D simulations. We will consider an rf frequency of 91.39 GHz, the 32nd harmonic of SLAC S-Band, 2.856 GHz.

2 PLANAR UBITRON

The mm-wave planar ubitron would be powered by a SLAC modulator, with space-requirements typical of a klystron test-stand in the SLAC Klystron Test Lab. The wiggler parameters we have in mind are close to those of the sheet beam free-electron laser operated at 250 kW, at the University of Maryland [8]. The focusing scheme is different in that a quadrupole will be considered to provide focusing in the horizontal, at the expense of vertical focusing provided by the wiggler. The geometry is similar to that employed for the 30 MW X-Band FEL at KEK [10].

With beam voltage set at 480 kV, consistent with the available modulator, and beam current set at 300 A consistent with the 5 MW requirement (absent tapering), the wiggler wavelength should be in the range of 1.16 cm for optimal gain at 91.39 GHz. With these parameters, the peak wiggler field on-axis, at optimal gain is 5.1 kG, well within the Halbach limit for NdFeB with Vanadium Permendur, provided the pole gap is held to 4 mm (7 kG). Focusing in the vertical is provided by the wiggler itself. One long quadrupole can be employed to

0-7803-4376-X/98/$10.00 © 1998 IEEE

focus in the horizontal, at the expense of vertical focusing.

Table 1 Parameters for the planar ubitron.

Wiggler Parameters	
wiggler period λ_w	1.16cm
peak wiggler field B_w	5.5kG
# of wiggler periods N_w	60
desirable tuning range	3kG-7kG
Beam Parameters	
voltage V_b	480kV
current I_b	300A
beam full width *2X, 2Y*	2cm, 0.2cm
Waveguide & RF	
inner dimension height, width	0.4cm, 4cm
input power, P_{in}	1kW
gain	37dB
required match to output	VSWR<1.002

Parameters are indicated in Table 1, arrived at taking into account the envelope equation, and, for gain calculation, solution of an analytic dispersion relation that incorporates space-charge, emittance, energy-spread, low energy corrections to the relativistic approximation, and waveguide corrections.

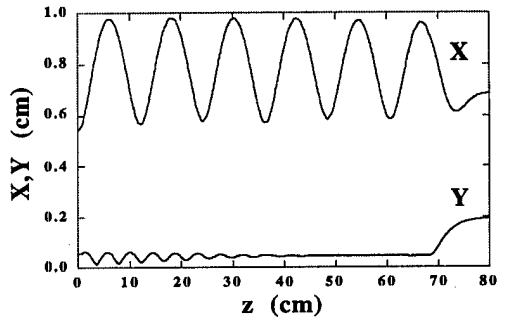


Figure 1 Envelope evolution in the Planar Ubitron.

The 1D scalings provide a gain curve to guide the design. These scalings are being studied numerically with a non-wiggler averaged, particle-in-cell code, incorporating the physical optics as modified by the beam, space-charge, and a realistic wiggler model computed as a sum over coils. This code also provides a feature for tuning of the quad field to maximize transmission, and adjusting of the first two half-period coil currents to minimize betatron launch down the wiggler. Illustrative results for beam transport are indicated in Figure 1.

Beam collection in the first implementation of this design would simply amount to dispersal on the vertical walls of the guide, as the beam exits the wiggler, as seen in Figure 1. Due to the wide sheet character of the beam, and the 5 cm beam spreading length, the heat load is below 50 W/cm^2 at a pulse repetition frequency under 5 Hz.

The gun design for this tube is the most challenging technology feature of the device. The required current density at the entrance plane is 750 A/cm^2. If we ask for a very ambitious cathode loading of 100 A/cm, the required convergence is *x* 7.5 for waist formation near the anode. Taking, as an example, a gun consisting of a section of a cylindrical diode, we find that the unique solution for convergence of 8.1 into a full height of 2 mm corresponds to a cathode radius of 1.247 cm, an anode radius of 0.154 cm, and a half-angle of 40.5°. This solution however corresponds to a field in the gun in excess of 250 kV/cm, too high to be held for 1 μs without arcing. This suggests, at the least, that a simple 2D gun is not likely to be adequate, and opens the problem up to that of 3D gun design, with convergence in both planes, a challenging problem.

3 LIA FEL

Linear induction accelerators have been used successfully in the past to drive free electron lasers operating in the W-band frequency range [9, 10, 11]. Electron beams produced with these accelerators typically have energies ranging from several MeV to tens of MeV, and pulse lengths from tens of nanoseconds to several microseconds. The LELIA accelerator, operated at the Centre d'Etudes Scientifiques et Techniques d'Aquitaine (CESTA) facility, generates a 1 kA, 2.2 MeV beam with an 80 nsec (FWHM) pulse length. Current FEL experiments operate in the amplifier mode, and have shown strong bunching and power production at 35 GHz [12]. This configuration is being studied as a possible bunching device for the drive beam in a two-beam accelerator. Involvement of both the CERN CLIC and the LLNL/LBNL RK-TBA groups is ongoing.

Table 2 Parameters for the LIA FEL

Wiggler Parameters	
wiggler period λ_w	5cm
peak wiggler field B_w	2.7kG
# of wiggler periods N_w	68
Beam Parameters	
voltage V_b	2.2MV
current I_b	900A
beam radius	0.4cm
Waveguide & RF	
inner radius	3.05cm
input power, P_{in}	0.5kW
gain	56dB

We have designed a new helical wiggler for use on the LELIA beamline to drive the FEL resonance at 91 GHz. The parameters are shown in Table 2.

The FEL interaction is simulated with the code WTDI [13]. This code tracks 3D particle motion, and the amplitude and phase of a single frequency vacuum waveguide mode. Space charge effects are included from an approximate analytic model. This allows us to use a

relatively small number of particles (4096) in the simulation.

We have modelled the power and phase fluctuations induced by energy jitter in the drive beam. We assume a maximum fluctuation of ±0.1% of the beam energy over the entire pulse. This fluctuation is primarily due to nonlinearities in the pulse forming network that drives the induction cells, and results in variations of both the peak power and the phase of the output radiation from the FEL. The difference in phase development is shown in Figure 2.

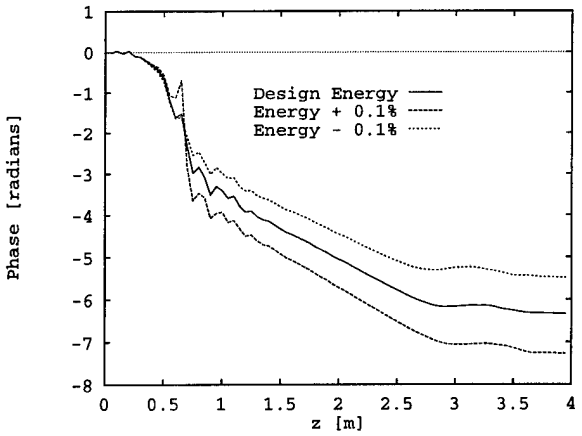


Figure 2 Phase development in the FEL

Clearly, this amount of phase difference over the full pulse length is unacceptable for most applications. Indeed, this has proven to be a fundamental limitation in using FEL's as drivers in two-beam accelerators. However, simple control and feedback systems have been proposed [14] that can reduce this level of jitter to ±0.5% or less, by employing an active compensation circuit to the drive PFN and the input RF signal. In this way, fluctuations in phase may be controlled to with ±2° over a bandwidth of several hundred MHz.

4 CONCLUSIONS

We have seen that, from the point of view of the FEL interaction, the power levels required for high-gradient studies of W-Band structure are achievable with existing facilities in at least two ways. For the Planar Ubitron, the challenge is the gun, and this is a considerable, but not insurmountable challenge. For the induction driven device, the required performance has already been achieved at the ELF facility some 10 years ago.

5 ACKNOWLEDGEMENTS

Helpful conversations and fruitful collaborations with the SLAC Klystron Department are gratefully acknowledged. This work was performed under the auspices of the U.S. Department of Energy by LBNL under contract AC03-76SF00098, and by SLAC under contract DE-AC03-76SF00515.

REFERENCES

[1] D. H. Whittum and H. Henke, *High-Gradient Cavity Beat-Wave Accelerator at W-Band* (these proceedings)

[2] T. Seeman, Ann. Rev. Nucl. Part. Sci. **41** (1991) pp.389-428

[3] Pritzkau, *et al.*, *Experimental Study of Pulsed Heating of Electromagnetic Cavities* (these proceedings)

[4] Chou, *et al.*, *Design and Fabrication of a Traveling-Wave Muffin-Tin Accelerating Structure at 91 GHz* (these proceedings).

[5] Seidel, *et al.*, Proceedings of the XVIII International Linac Conference (CERN, Geneva, to be published).

[6] *MMW Power Klystrons for Remote Sensing and Communications*, Communications and Power Industries (CPI), 45 River Dr., Georgetown, Ontario, Canada L7G2J4.

[7] Blank, *et. al., Experimental Investigation of a W-Band Gyroklystron Amplifier* (these proceedings).

[8] Cheng, *et al.*, IEEE Trans. Plasma Sci. **24** (1996) pp. 750-757.

[9] L. Thoop, *et al.*, Nuc. Instr. & Methods in Phys. Res. **A272**, 15 (1988).

[10] H. Whittum, K. Ebihara, S. Hiramatsu, J. Kishiro, T. Monaka, T. Ozaki, and K. Takayama, IEEE Trans. Plasma Sci. **21**, 136 (1993).

[11] L. Allen, *et al.*, Proceedings of the 1993 Particle Accelerator Conference (Washington, D.C., 1993), 1551.

[12] Gardelle, *et al.*, Phys. Rev. Lett. **76**, 4532 (1996).

[13] Zhang, G. Shvets and J.S. Wurtele Nuc. Instrum. Meth. A **331** (1993) pp. 472-476, and Ge Zhang, Investigation of the Performance of Free-Electron Lasers and Mode Competition in Cyclotron-Resonance Masers (Ph.D. Thesis, MIT).

[14] Hopkins, *et al.*, Proceedings of the 1991 Particle Accelerator Conference (San Francisco, 1991), 1335.

LINAC DESIGN FOR THE LCLS PROJECT AT SLAC*

V.K. Bharadwaj, K. Bane, J. Clendenin, P. Emma, J.C. Sheppard, M.D. Woodley
Stanford Linear Accelerator Center, Stanford, California 94309

Abstract

The Linac Coherent Light Source (LCLS) at SLAC is being designed to produce intense, coherent 0.15-nm x-rays. These x-rays will be produced by a single pass of a 15 GeV bunched electron beam through a long undulator. Nominally, the bunches have a charge of 1 nC, normalized transverse emittances of less than 1.5π mm-mr and an rms bunch length of 20 μm. The electron beam will be produced using the last third of the SLAC 3-km linac in a manner compatible with simultaneous operation of the remainder of the linac for PEP-II. The linac design necessary to produce an electron beam with the required brightness for LCLS is discussed, and the specific linac modifications are described.

1. INTRODUCTION

The proposed LCLS [1,2] project has undergone a significant design revision in the last year. The LCLS, a 0.15-nm x-ray source, requires an extremely high quality electron beam. This beam must simultaneously have peak beam current in excess of 3.5 kA, transverse beam emittances of order 1π mm-mr, energies up to 15 GeV and bunch lengths of 20 μm. Fortunately 15 GeV of linac accelerator will become available at SLAC when the PEP-II Asymmetric B-Factory [3], which uses only the first two-thirds of the existing linac, becomes fully operational in the next few years. This 15 GeV linac, with its existing infrastructure, combined with some modest modifications makes LCLS a feasible and cost effective project.

Figure 1 shows a schematic of the LCLS linac. A new RF Gun and associated Linac-0 (L0) generates a 1-nC, 1π mm-mr beam [4]. This beam is injected onto the existing SLAC linac axis using a dogleg inflector, DL1. The beam

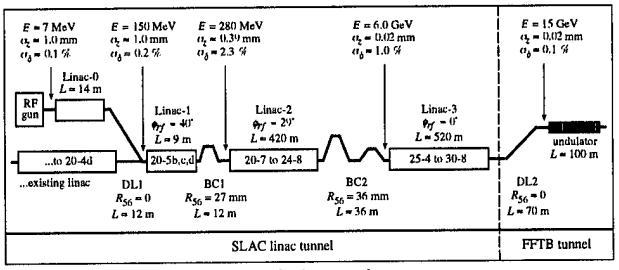


Figure 1. LCLS Linac Schematic

is further accelerated using Linac-1, Linac-2 and Linac-3 (L1, L2, L3) and compressed in two magnetic chicanes, BC1 and BC2. The beam is then transported (beamline DL2) to the LCLS undulator. The L2 and L3 linac hardware is essentially unchanged in the LCLS design. The RF Gun, L0, DL1, BC1, BC2 and DL2 are new installations, although existing components are used where possible. Table I lists the major accelerator parameters for the various sections of the LCLS linac.

Table I. LCLS Linac Parameters

Parameter	*L0*	*L1*	*L2*	*L3*
Initial energy (GeV)	0.007	0.150	0.280	6.0
Final energy (GeV)	0.150	0.280	6.0	5-17
Linac length (m)	12	9	420	523
Initial sector #	20-3	20-5b	20-7	25-4
RF phase (deg)	variable	40	29	0
$\beta_{x,y}$ min/max (m)	—	2/10	10/45	35/65
Phase advance/cell (deg)	—	75	70	30
Initial $\Delta E/E$ (%,rms)	0.1	0.2	2.3	1.1
Final $\Delta E/E$ (%,rms)	0.2	2.3	1.1	<0.1
Bunch length (μm,rms)	~1000	1000	390	20

2. LATTICE DESIGN

The four main considerations in the optics design of the LCLS linac are to 1) minimize the transverse emittance dilution due to misalignments, 2) effect the final bunch compression, 3) allow for the precise measurement of beam parameters, and 4) transport the beam to the LCLS undulator. TRANSPORT and LIAR [5] are the two main simulation tools used in the optics design.

L0 is a new 150 MeV accelerator which consists of four 3-meter s-band accelerating sections displaced 1 meter horizontally from the existing SLAC linac. Its beam dynamics, and hence its design, are dominated by space charge. It is followed by a matching section, diagnostic region and dogleg, DL1, which injects the beam into L1.

L1 is a 130 MeV linac consisting of three existing 3-meter sections. By accelerating the beam off-crest, an input energy-z correlation for BC1 is generated. Given the long bunch length and large energy spread in L1, both dispersion and transverse wakefields are sources of potential emittance growth. The LIAR code is used to study the effects of misaligned components (BPMs, quadrupoles and accelerating structures). By adding a quadrupole/BPM/steering package between each accelerating section, a lattice design with a phase advance of 75°/cell was found to keep the transverse emittance growth to less than 10%, even for very pessimistic misalignment tolerances of 300 μm. Figure 2 shows the lattice functions of L1, BC1 and their associated emittance and energy diagnostic section.

* Work supported by Department of Energy contract DE-AC03-76SF00515

0-7803-4376-X/98/$10.00 © 1998 IEEE

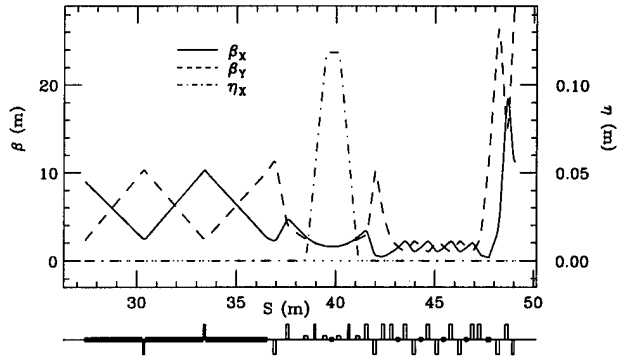


Figure 2. L1 and BC1 Lattice. The small circles on the magnet schematic at the bottom of the plot are wire scanners, four for emittance diagnostics and one for energy measurement.

L2 accelerates the beam to 6 GeV and generates an input energy-z correlation for BC2. In L2 the bunches have 1-2% energy spread, and the 400 μm RMS bunch length is still relatively long. This makes L2 very sensitive to component misalignments. In fact even with an optimized lattice, LIAR simulations still give an unacceptable factor of two transverse emittance growth due to realistic component misalignments. However, SLC experience has shown that this emittance growth can be empirically controlled using "emittance-bumps"[6]. Figure 3 shows LIAR simulation results of such bumps for a 70°/cell phase advance lattice. For 300-μm structure misalignments and 150-μm BPM and quadrupole misalignments, the transverse emittance growth is reduced from 80% to less that 10% (average of 100 seeds).

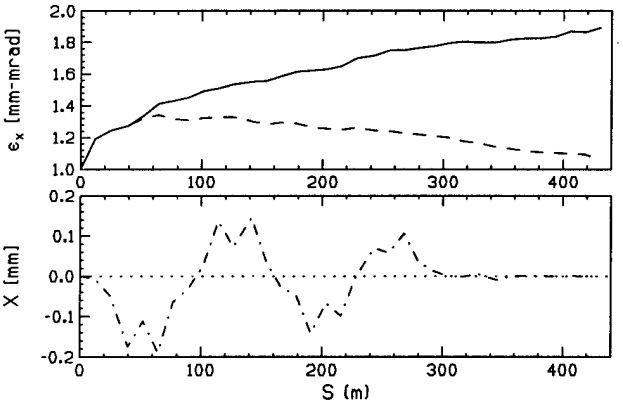


Figure 3. Emittance Bumps in L2. The upper plot the shows emittance dilution without (solid) and with (dashed) emittance bumps. The lower plot shows a typical horizontal orbit distortion due to the bump.

L3 accelerates the beam to a maximum energy of 15 GeV. The bunch is too short to use rf phasing to minimize the energy spread, but fortunately the very strong longitudinal wakefield generated by the 20-μm bunch reduces the 1.1% energy spread exiting BC2 to <0.1% (<0.02% incoherent energy spread) at the undulator. The short bunch effectively eliminates transverse wake effects and the dominant emittance dilution mechanism is due to momentum dispersion generated by quadrupole and BPM misalignments. Simulations show that a weak lattice, with a phase advance of 30°/cell and the nominal SLC quadrupole spacing, reduces the expected emittance growth to less than 10% for component misalignments as large as 300 μm. The LCLS specifications require 5-15 GeV range of electron energies. This is generated in L3 by varying the number of s-band accelerating sections used and by backphasing sections to reduce the final energy.

DL2 transports beam to the undulator, located in the existing FFTB tunnel. Figure 4 shows lattice functions for this beamline. An emittance diagnostic section is also built into the beamline. A four dipole dogleg inflector displaces the beamline 0.9 m horizontally which allows for energy analysis and a stabilizing feedback system.

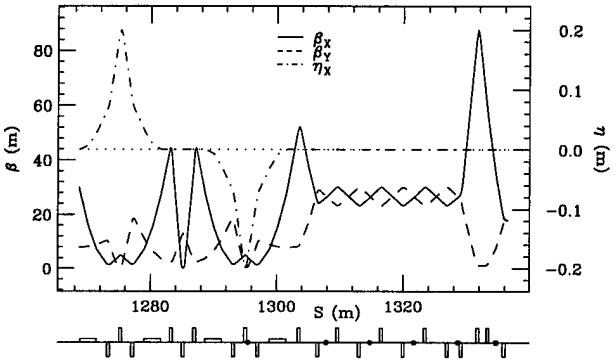


Figure 4. DL2 Beam Transport Line. Note the wire scanners for beam emittance and energy measurement in the magnet schematic.

3. BUNCH COMPRESSION

The LCLS requires peak beam currents in excess of 3.5 kA. Present electron gun technology cannot produce this current, so a series of magnetic chicane bunch compressors is used to reduce the bunch length thereby increasing the beam current. For 1 nC of accelerated charge a bunch length of 20 μm RMS is required. This corresponds to a large compression ratio of 50 for the 1-mm bunch generated by the RF photoinjector.

In designing the LCLS bunch compression scheme, care is taken to minimize non-linear effects arising from longitudinal wakefields, rf curvature and second order momentum compaction, and the sensitivity to phase and charge variations at the gun. Synchrotron radiation effects, both incoherent (ISR) and coherent (CSR), define the minimum chicane length.

Because of the large compression ratio, the LCLS accelerator has two bunch compressors, BC1 and BC2. In addition to making the magnetic chicane design easier, the two-compressor scheme allows for partial cancellation of jitter arising from gun phase and intensity variations. This cancellation seems to work best for gaussian bunch distributions out of the gun. In addition the beam is

partially compressed at a low energy in BC1, and this mitigates emittance dilution due to component misalignment at low energies.

BC1 is a simple four magnet chicane which compresses the bunch from 1 mm to 390 μm at 280 MeV. This compression ratio optimizes the cancellation of the L2 wakefield and the RF curvature and T_{566} non-linearities of L1/BC1. BC2 has a more complicated design driven mainly by the need to minimize CSR effects due the extremely small bunch length and strong bends. Because the energy spread generated by CSR is coherent, two consecutive chicanes of unequal strengths with a **–I** horizontal transfer matrix between chicane centers can be tuned to cancel [7] the longitudinal to transverse coupling as shown in Figure 5.

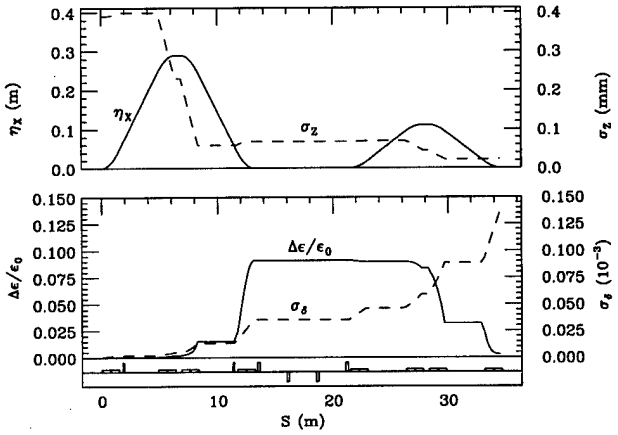


Figure 5. BC2 Double Chicane. The upper plot shows the horizontal dispersion (solid) and the bunch length (dashed) along BC2. The lower plot shows the CSR emittance growth (solid) and energy spread (dashed).

The output bunch length of BC2 is adjustable and can be tuned, along with the rf phase of L2 to compensate for the uncertainty in the magnitude of the L3 wake that sets the final energy spread. Simulations show that a 50% uncertainity can be compensated. Table II lists important BC1 and BC2 parameters. Figure 6 shows the longitudinal phase space at the input to the LCLS undulator.

4. DIAGNOSTICS AND TUNING

The design LCLS beam specifications are especially demanding. The LCLS accelerator naturally breaks down into four logical sections (RF-Gun-L0-DL1, L1-BC1, L2-BC2, L3-DL2). The diagnostic design criterion ensures that there are sufficient measurement devices so that the beam properties out of each accelerator section can be measured well and each section can be tuned to design.

The LCLS accelerator has the standard complement of BPMs, beam toroids, screens and beam scrapers, etc. Beam dumps are installed such that each accelerator section can be individually tuned before beam is sent to the next section and finally onto the LCLS undulator. Emittance measurement is done using a four wire scanner station. A lattice with wires spaced by 45° of phase advance with equal beam sizes at each wire is optimum for emittance diagnostics. One such emittance measurement station is placed after each LCLS section. Additional wire scanners are placed in high dispersion points in DL1, BC1, BC2 and DL2 for energy and energy spread diagnostics.

The short LCLS bunches present a measurement challenge. Detectors using transition radiation and CSR are being designed and zero-phasing L3 can also be used to measure the absolute bunch length.

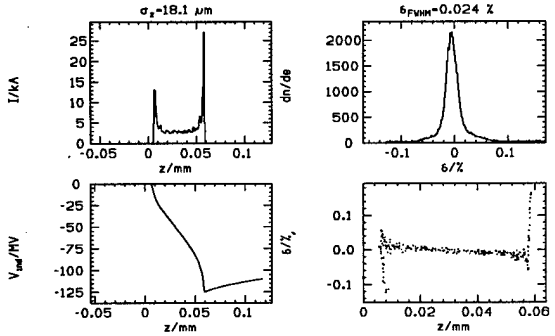


Figure 6. Longitudinal Bunch Distributions to Undulator at 15 GeV. The plot shows z-distribution (top left), energy distribution (top right), longitudinal wakefield (bottom left) and energy-z correlation (bottom right).

Table II. Bunch Compressor Parameters

Parameter	*BC1*	*BC2*
Beam energy (GeV)	0.28	6.0
Initial bunch Length (μm)	1000	390
Final bunch Length (μm)	390	20
Energy spread (%)	2.3	1.1
Momentum compaction (mm)	27.0	35.5
2nd. order mom. comp. (mm)	–40.5	–53.5
Total length (m)	2.8	34.5
Bend angle/magnet (deg)	7.1	3.4/1.3
Bend field (kG)	5.8	7.9/3.0
Max dispersion (m)	0.117	0.29/0.11
ISR emittance dilution (%)	0	1.4
CSR emittance dilution (%)	1.9	0.3

REFERENCES

[1] M. Cornacchia, "Performance and Design Concepts of Free Electron Lasers in the X-ray Region", SLAC-PUB-7433 (1997).

[2] K. Bane et al., "Electron Transport of a Linac Coherent Light Source (LCLS) Using the SLAC Linac", SLAC-PUB-6200 (1993).

[3] PEP-II Asymmetric B-Factory Conceptual Design Report , SLAC-418 (1993).

[4] A. D. Yeremian et al. , "A Proposed Injector for the LCLS Linac", these proceedings.

[5] R. Assmann et al., "LIAR-A Computer Program for Modeling and Simulation of High Performance Linacs", SLAC/AP-103 (1996).

[6] J. Seeman et al., "The Introduction of Trajectory Oscillations to Reduce Emittance Growth in the SLC Linac", SLAC-PUB-5705 (1992)

[7] P. Emma et al., "Emittance Dilution Through Coherent Energy Spread Generation in Bending Systems", these proceedings.

FIRST LASING OF THE ISRAELI TANDEM ELECTROSTATIC ACCELERATOR FREE ELECTRON LASER

J.S. Sokolowski, A. Abramovich, A. Arensburg, D. Chairman, M. Draznin,
A.L. Eichenbaum, A. Gover, H. Kleinman, Y. Pinhasi, Y.M. Yakover,
Department of Physical Electronics, Tel - Aviv University, Israel

A. Rosenberg, J. Shiloh, Rafael, Haifa, Israel

M. Cohen, L.A. Levin, O. Shahal, NRCN, Beer-Sheva, Israel

Abstract

First lasing at 3mm wavelength was achieved on December 4, 1996 in our FEL employing a modified EN-Tandem electrostatic accelerator as the source of energetic free electrons. A Pierce-type electron gun capable of providing a 2A beam was installed at the entrance to the accelerator and operated at 1.4A level, while the wiggler (λ_w=4.4cm, N_w=26) was located in the center of the accelerator, inside the positive HV terminal. The electron gun voltage was V_{gun}=-43kV and the terminal operating voltage V_{term}=1.4MV. The resonator, consisting of two parallel curved plates waveguide terminated by wave splitters at its both ends, was mounted inside the wiggler. Radiation pulses at 100.5 GHz of 2μsec duration and 1200W of power were obtained at intervals of 15 sec.

1 INTRODUCTION

Free electron lasers, with electrostatic accelerators operating as their high voltage sources, have the potential advantage of producing single mode radiation in quasi-cw operation. It is our long term objective to develop such an FEL; a number of modifications to the FEL reported on here will be required in order to achieve this goal. The version completed recently provides short pulses 100GHz radiation. We have also the option to convert it into an FEL of a different wavelength by changing the wiggler period λ_w (a new wiggler) and by changing the beam energy of the accelerator.

2 ELECTRON INJECTION SYSTEM

The parallel flow Pierce-type electron gun[1] designed using the Herrmannsfeldt code[2] was installed at the entrance to the accelerator. The gun employs a 2A Spectra - Mat tungsten dispenser cathode and it is followed by 4 focusing coils and a beam steerer. Helmholz coils surrounding the gun area cancel the earth's magnetic field, which in this low energy area (-43kV) is deflecting the beam quite significantly. The gun platform is isolated at -43kV potential while the gun anode is at ground level. A pulse forming network provides the gate (grid) of the gun with pulses of 6μsec duration and +12 kV in amplitude with respect to the cathode. The steady state voltage of the gate before the pulse arrival is -6kV with respect to the cathode. The vacuum system pressure in the gun area is of the order of 10^{-8} Torr, achieved by a differential pumping system. A retractable beam viewer is located between the second and the third focusing coils and its screen is observed with the aid of a CCTV camera. Occasional measurements of the beam current at this position are possible with minor adaptations.

3 BEAM ACCELERATION AND FOCUSING

In order to enable focusing of the electron beam after acceleration (at the entrance to the wiggler) and before deceleration (at the exit from the wiggler) we have removed one of the accelerating tubes on both sides of the wiggler and replaced them by 3inch diameter stainless steel tubes on which 4 quadrupoles and a steerer were installed[3]. Thus, at the expense of reducing the high voltage terminal potential from 6MV to 3MV maximum we have gained the possibility of beam focusing at the high voltage level. The reduction of the maximum voltage of the machine does not pose any problems to us, since we are presently operating it at 1.4 MV only.

4 BEAM DIAGNOSTICS

The main diagnostic devices used in our setup are retractable fluoresecent viewers and Rogowski coils. A rather flexible retractable viewer is located immediately after the gun, it can be used as a poor-man's Faraday cup, or a pepper-pot for emittance measurements.

The three beam viewers installed inside the accelerator tank are located as follows: the first one at the exit from the accelerator tube, the second at the entrance to the wiggler and the third one at the exit from the wiggler. The beam viewer cameras are installed inside the vacuum area and the signals from the cameras are sent to the control room via fiber optics. We have installed Rogowski coils in only three positions, we measure the current of the gun cathode, the beam current at the exit from the wiggler and the collector current. We have decided to include soon additional Rogowski coils in two other positions; at the entrance to the focusing tube and at the entrance to the wiggler.

0-7803-4376-X/98/$10.00 © 1998 IEEE

5 CONTROL

The basic accelerator control is the same old fashioned one as was used to run the ion accelerator. A new control system was added for pulsing of the electron beam current and for operating the beam focusing, diagnostics and steering, inside the accelerator at the high voltage terminal potential. This control system consists of a personal computer, a digital oscilloscope in the control room, an RS-232-to-fiber optics converter at the input to the accelerator tank, fiber optics along the beam tube inside the tank, a digital control box and analog control current drivers inside the high voltage terminal. Ac power to these units is supplied by a 400Hz, 108V, 1.5 kW generator driven by the belt shaft inside the high voltage terminal. Separate communication systems (using their own fiber optics) transmit the information from the beam viewer screens to the CCTV monitor and the amplitude of the beam current pulses to the oscilloscope.

We have a total of 8 quadrupoles and 4 steerer coils. Since we would like to use additional steerers, we are presently increasing the number of current drivers from 12 to 18 and modifying the digital control system.

6 THE WIGGLER AND THE RESONATOR

The wiggler (Halbach type[4] planar configuration) has 26 periods of 4.4cm each. Inside the wiggler and symmetrical about its axis is located a 100GHz resonator, built of two curved parallel plates forming the waveguiding structure, terminated at each end by a quasioptical Talbot effect wave splitter (see Fig.1). The beam splitters acting as resonator reflectors for the laser radiation allow electron beam to pass through an opening, without disturbing the reflectivity properties. This kind of resonator has low ohmic and low radiation losses, its Q-factor is of the order of $3x10^4$[5,6]. Focusing of the electron beam in the wiggling plane is achieved by the use of two long permanent magnets along the axis of the whole wiggler[7]. The basic parameters of the wiggler and resonator are shown in Table 1.

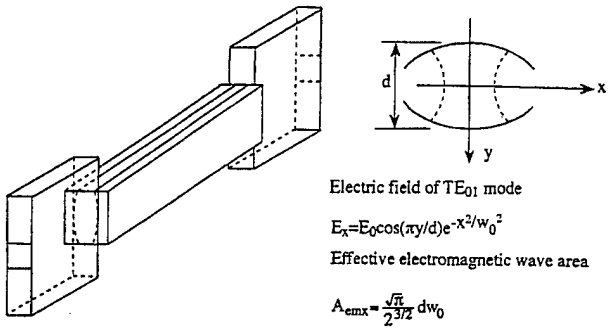


Fig. 1. The resonator.

7 BEAM TRANSPORT AND RECOVERY

The beam, received from the Pierce gun is focused and steered by three focusing coils and a pair of steering coils, enters the accelerating tube. After acceleration the beam continues through the 3inch diameter, 2m long tube on which four quadrupoles lenses and a couple of steering coils are installed. The beam is further focused by these lenses and the viewing screens located before and after the wiggler are used as diagnostics for optimizing the shape, position and diameter of the beam.

We have so far concentrated our efforts mainly on getting an appreciable part of the beam current into the wiggler, so that the basic boundary condition for lasing radiation production would be satisfied. We were able to get about 200mA through the wiggler to the collector, but we know - based on our previous experiments and simulations - that we should be able to transmit nearly all the beam to the collector. Once this is achieved, we shall collect the electron current at a voltage close to ground level (due to the energy loss for the lasing). A floating, 50kV power supply, compensating for this energy loss, will be connected in series between the collector and the gun high voltage platform, and thus we shall be able to recirculate the current. The depressed collector operation will allow the operation of the FEL at much longer pulses and at higher repetition rates thus giving a substantial average power as required in many applications.

Table 1. Basic parameters of the tandem FEL

Accelerator:	
Electron beam energy	E_t = 13-15 MeV
Cathode e-beam current	I_0 = 1.4 A
Wiggler:	
Magnetic induction	B_0 = 2 kGs
Period length	λ_w = 4.44 cm
Number of periods	N = 26
Waveguide resonator:	
Type	Curved parallel plate waveguide
Mode	TE_{01}
Interaction length	L_w = 88.9 cm
Resonator length	L_c = 131 cm
Designed-Q factor	> 20,000
Power round trip losses	1-R < 10%

8 LASING RADIATION AND MEASUREMENT

On the 4th of December 1996 the first lasing pulse was detected (Fig. 2). This radiation pulse width was approximately 0.5μsec while the electron beam pulse was 5 msec wide. During following experimentation we have reached radiation pulses of 3 μsec duration (Fig. 3). This width was limited due to the voltage droop of the high voltage terminal. The stability of the high voltage terminal potential is one of the critical parameters for

laser radiation to occur and be maintained, thus if this condition is not preserved, lasing is discontinued. One can note in Fig. 3 the slow buildup of the radiation pulse (its risetime) and its sudden interruption (the falltime). The radiation decay, after the voltage falls below the lasing value, corresponds to $Q_L = 2\pi\tau_c f = 30{,}000$.

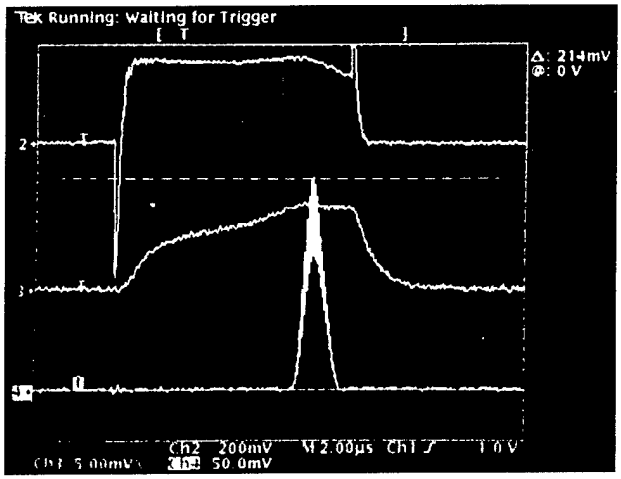


Fig. 2 The first lasing radiation pulse.

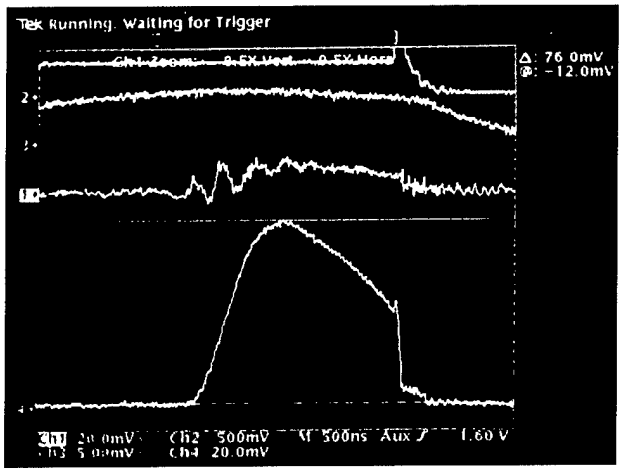


Fig. 3. The widest radiation pulse so far

The measured attenuation of the radiation path through decelerating section of the beam tube to the collector was 42dB. The power translated to the exit from the resonator was 1200W. The frequency of the radiation was checked using a heterodyne system i.e. by mixing the detected wave with a known local oscillator frequency and measuring the beat frequency between them. The measurement resolution was of the order of a few MHz and the FEL frequency was 100.55GHz - rather close to the predicted 100GHz.

9 FUTURE PLANS

Having shown that the FEL operation is close to the theoretical predictions, we will pursue further goals:

a. Gradual increase of the pulse width from the present 3µsec to 1 millisec.

b. Increase of the repetition rate from 1 in 15 seconds to 10/sec.

c. Increase of the lasing power at the exit from the resonator from 1200W to approximately 10kW.

d. Design an installation of an efficient optical transport of the lasing radiation to couple it out of the tank.

e. Adapt the FEL to operation as users' facility for industrial, medical and scientific applications.

10 CONCLUSIONS

The theoretical calculations, assumptions and simulations used in order to design the FEL were proven to be correct - the machine operates at 100.55GHz (predicted 100GHz). The low loss resonator is promising for the objective of achieving high lasing power, once we transport the beam without major losses through the wiggler. The planned improvements to the FEL and its operation in quasi-cw mode (1msec wide pulse at a rate of 10/sec) will allow it to become a users' facility for industrial, medical and scientific applications.

11 ACKNOWLEDGMENTS

We would like to thank the Ministry of Energy, Ministry of Defense and Ministry of Science, The Israel Academy of Sciences, The U.S.-Israel Binational Science Foundation as well as the Reuben Meyer Trust for their encouragement and financial support. The Weizmann Institute of Science, by putting at our disposal the EN-Tandem accelerator enabled the initiation of the project and allowed us to bring it to this successful stage. The Accelerator Laboratory management and staff were extremely helpful. The people who are not with the project any more, but have largely contributed to its success are: I. Ben - Zvi, one of the project's co-initiators and its moving spirit at the early stages, J. Wachtel, E. Skurnik our accelerator expert, A. Goldring project management. The list of people who largely contributed to the success include Jacques Catarivas, the accelerator technician - the living spirit of the machine, D. Tamari and A. Bar-On with their staff at the mechanical workshop and Y. Wolovelsky with his staff at the Instrument Design group.

REFERENCES

[1] A. Gover et al, Proceedings of the 11th International Free Electron Laser Conference, Nucl, Inst. and Meth A 296, (1990) 720.
[2] Herrmannsfeldt, SLAC, Stanford (1979 and 1988).
[3] Cohen et al, Proceedings of the 15th International Free Electron Laser Conference, Nucl. Inst. and Meth. A 341, (1994) ABS 57.
[4] Halbach, Nucl.Inst. and Meth 169, (1980) 1.
[5] Urbanus et al, Nucl. Inst. and Meth A 331, (1993) 235.
[6] Yakover et al, Nucl. Inst. and Meth A 358, (1995) 323.
[7] Cohen et al, Phys. Rev. E 54, (1996) 4178.

RECIRCULATING ACCELERATOR DRIVER FOR A HIGH-POWER FREE-ELECTRON LASER: A DESIGN OVERVIEW

Courtlandt L. Bohn, on behalf of the Jefferson Lab FEL Team, Thomas Jefferson National Accelerator Facility, Accelerator Division, 12000 Jefferson Avenue, Newport News, VA 23606

Abstract

Jefferson Lab is building a free-electron laser (FEL) to produce continuous-wave (cw), kW-level light at 3-6 μm wavelength. A superconducting linac will drive the laser, generating a 5 mA average current, 42 MeV energy electron beam. A transport lattice will recirculate the beam back to the linac for deceleration and conversion of about 75% of its power into rf power. Bunch charge will range up to 135 pC, and bunch lengths will range down to 1 ps in parts of the transport lattice. Accordingly, space charge in the injector and coherent synchrotron radiation in magnetic bends come into play. The machine will thus enable studying these phenomena as a precursor to designing compact accelerators of high-brightness beams. The FEL is scheduled to be installed in its own facility by 1 October 1997. Given the short schedule, the machine design is conservative, based on modifications of the CEBAF cryomodule and MIT-Bates transport lattice. This paper surveys the machine design.

1 INTRODUCTION

Thomas Jefferson National Accelerator Facility (Jefferson Lab) is building a cw, kW-level, 3-6 μm free-electron laser (IRFEL, hereafter called the IR Demo). Its purpose is two-fold: to assess the applicability of the technology for scaling to higher-power devices for potential industrial and defense applications, and to provide a source of intense picosecond infrared light pulses for studies of laser-solid interactions.

An FEL extracts power from a preaccelerated electron beam. Since electron-beam power scales in proportion to its energy and current, compact high-power FELs profit from high-gradient acceleration of high average current. Because superconducting rf (srf) cavities accelerate beam at cw gradients significantly larger than normal-conducting cavities afford, and because their low surface resistances and large beam apertures are ideal for acceleration of high average current, the IR Demo's design is based on srf technology. Moreover, wherever possible, the IR Demo incorporates technologies known to be scalable to high average power.

This paper summarizes the accelerator design and trades which lead to the chosen operating point, and it assesses key technical risks. It also provides a guide to other Conference papers that give details concerning the design.

2 IR DEMO DESIGN

The IR Demo, pictured in Figure 1, comprises a 10 MeV injector and a 32 MeV linac to produce a 42 MeV, 5 mA electron beam for use in lasing. Beam requirements are listed in Table 1. After lasing, a high-acceptance lattice transports the electron beam back to the linac for deceleration down to 10 MeV, then to a dump. Thus, 75% of its energy is put back into rf power for use in accelerating other electrons, thereby reducing rf power requirements, waste heat, and radiation.

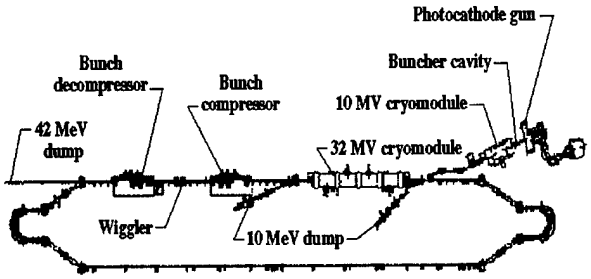


Figure 1. Schematic of IR Demo.

Table 1: Beam Requirements at Wiggler for 1 kW Lasing

Energy	42 MeV
Average current	5 mA
Bunch charge	135 pC
Bunch length (rms)	1 ps at 135 pC
Peak current	50 A
Transverse emittance (normalized rms)	13 mm-mrad*
Energy spread (rms)	210 keV
Longitudinal emittance (rms)	50 keV-deg
Pulse repetition frequency	37.425 MHz
Energy stability (rms)	4×10^{-4}
Timing jitter (rms)	$10^{-8}/f_m$**
Current jitter (peak-to-peak)	< 2%
Beam-position jitter (rms)	100 μm
Beam-angle jitter (rms)	250 μrad
Dispersion	< 2 cm
Horizontal betatron function (at entrance)	47 cm
Vertical betatron function (at center)	50 cm

*allows 3rd-harmonic lasing; 20 mm-mrad suitable for 3 μm.
**f_m is the modulation frequency of the jitter.

To reduce cost and schedule, the IR Demo incorporates where possible components that are commercially available and/or are standard in Jefferson Lab's nuclear-physics accelerator (CEBAF) [1]. The injector [2] comprises a 350 kV cw photocathode gun driven by a commercial Nd:YLF laser [3], followed by a copper buncher cavity and a CEBAF-type 1497 MHz srf cryounit [4] to generate an average accelerating gradient of 10 MV/m, boosting the beam to 10

0-7803-4376-X/98/$10.00 © 1998 IEEE

MeV. The accelerator uses a full CEBAF-type 1497 MHz srf cryomodule [5] to generate an average accelerating gradient of 8 MV/m, boosting the beam to 42 MeV energy. Two commercial 50 kW klystrons power the injector's cryounit. A commercial wiggler [6] and modifications of CEBAF's rf system, control system, and safety system are also included.

By using CEBAF-derived components, modified for high-current operation, we take advantage of Jefferson Lab's experience with building, installing, and operating the 42 cryomodules comprising its 4 GeV accelerator [1]. Beam impingement must also be kept low (<5 μA at >25 MeV) to mitigate radiation damage, shielding requirements, and electronic noise. Low beam loss, aided by intrinsically large apertures of srf cavities and by designing large apertures into the electron-transport system, also supports safe hands-on maintenance. The recirculation lattice is likewise based on a mature design, that used in the MIT-Bates accelerator [7].

Some simplified scaling arguments will illuminate the choice of accelerator parameters in Table 1. FEL power is just the average power in the electron beam multiplied by the average extraction efficiency and the optical cavity output coupling efficiency. Obviously each should be as high as possible to maximize the laser power.

Electron-beam power is the product of energy and current. Considerations like rf-window power handling, beam loading, cathode lifetime, and commercial availability of high-voltage power supplies led us to choose 5 mA for the injector's design current. A cryounit and cryomodule operating at plausible average gradients of 10 MeV/m and 8 MeV/m, respectively, yield 42 MeV energy. The average electron-beam power is therefore 210 kW. Increasing the beam energy would deliver shorter laser wavelength but at additional cost for the accelerating structures.

The extraction efficiency is $\sim(4N)^{-1}$, where N is the number of wiggler periods [8]. Decreasing N increases the extraction efficiency but also increases the energy spread of the exhaust beam and decreases the gain. The lattice can accept nominal 5% energy spread with low-loss transport [9]. The exhaust energy spread in most existing FELs is ~8 times the extraction efficiency, implying N>40 is desirable. We chose N=40 because this also provides reasonable gain.

High optical cavity output coupling efficiency is easy to achieve in the mid-IR since low-loss optical substrates and coatings are available. Low gain requires low output coupling for efficient lasing, leading to high mirror loading and low output coupling efficiency. Our goals are >30% small-signal gain and >90% output coupling efficiency.

Some electrons will be in tails of the phase-space distribution and not contribute to lasing. Experience has shown that the fraction of beam which contributes to the laser is from 80% to 90%. Assuming 80% is useful, an extraction efficiency of 0.625% and an output-coupling efficiency of 90% will provide ~1 kW laser power.

The electron-beam quality required for 3 μm operation follows from standard design formulas [8]. A 40-period wiggler has energy acceptance $(5N)^{-1}$=0.5%. The normalized emittance must satisfy $\epsilon_n \leq \gamma\lambda_r/4\pi$ to ensure the electrons are inside the optical mode. For 42 MeV beam (γ=83) and λ_r = 3 μm, the maximum emittance is 20 mm-mrad. For third-harmonic lasing at 1.6 μm the emittance should be below 10 mm-mrad, and also the energy spread should be below $(15N)^{-1}$=0.17%.. These may be difficult to achieve, but third-harmonic lasing at the 100 W level is feasible with an emittance of 13 mm-mrad and an energy spread of 0.25%. PARMELA simulations affirm this emittance is achievable; machine impedance and beam-breakup thresholds are also well within budget [9]. With 13 mm-mrad emittance, a 50 A peak current provides sufficient gain for stable laser operation.

We are adapting a commercial 74.85 MHz drive laser to 37.425 MHz using an electro-optic modulator as a compromise between required cathode quantum efficiency, peak current, and beam quality. A lower repetition rate would produce more gain but with poorer beam quality and less margin for quantum efficiency. A higher repetition rate would provide insufficient peak current.

Beam-stability requirements were chosen to satisfy FEL stability requirements. Current and timing jitter cause laser-power fluctuations, while beam-pointing jitter can lead to laser-pointing jitter and mode-quality degradation. Energy jitter causes spectral broadening and wavelength jitter. The electron beam is matched to the intrinsic wiggler beta function in the horizontal direction and is matched to the optical-mode profile in the vertical direction.

A spreadsheet incorporating semianalytic formulas for gain and extraction efficiency and benchmarked against simulations was used to estimate performance sensitivities to critical parameters [10]. Sample results are shown in Table 2. As expected, reduced electron-beam power leads to reduced laser power. The power is much less sensitive to the emittance and non-output-coupling losses in the optical cavity. The gain is relatively insensitive to most design parameters with the exception of peak current.

Table 2: Sensitivities to Critical Parameters (at λ_r = 3 μm)

Parameter	Degradation*	Power	Gain
e-beam energy**	-10%	-10%	small rise
average current	-25%	-25%	0%
emittance	+25%	-2%	-14%
output cavity loss	+50%	-4%	0%

* Represents plausible deviations.

** 10% energy degradation yields 20% longer wavelength.

Given the design for energy recovery with low beam loss, instabilities arising from fluctuations of the cavity fields are a concern. Energy changes can cause beam loss

on apertures or phase oscillations during beam transport with concomitant changes in the beam-induced voltage in the cavities that can lead to unstable variations in the accelerating field. An analytic model of the instabilities, including amplitude and phase feedback, and numerical simulations both suggest that, given microphonic noise of amplitude typically found in CEBAF, the rf control system appears to be adequate for stable and robust operation [11].

3 TECHNICAL RISKS AND PLANS

Principal technical risks are operation of the high-brightness injector and achievement of energy recovery from the high-power electron beam while lasing. Space charge is important along the injector beamline, and the cryounit will be heavily beam-loaded. If necessary, the injector can be operated at twice the planned pulse-repetition rate and half the charge per bunch to mitigate space-charge effects [12]. If cathode lifetime becomes a concern, an alternative cathode or cathode-preparation procedure can be used. Though energy recovery has been demonstrated experimentally [13], the approach has never been implemented with high-power beam. A scraper is located in the first leg of the first recirculation bend as a precaution against beam loss. Specifications were established that permit the scraper to serve as an excellent energy-distribution and halo diagnostic, in addition to being a safeguard for machine protection.

Coherent synchrotron radiation (CSR) will be present in the magnetic bends and potentially cause growth in the transverse emittance [14]. Estimates indicate growths of about 10% in each optical chicane surrounding the wiggler, and about 50% in each recirculation bend [15]. Concerns about CSR-induced beam degradation motivated placement of the wiggler at the exit of the linac rather than following the first recirculation bend, resulting in a correspondingly larger machine footprint. However, the calculations carry considerable uncertainty, and the machine is an ideal platform for CSR experiments. Parametric studies of emittance growth in the bunch decompressor following the wiggler and in the first recirculation arc are planned. Stringent beam requirements and plans to study CSR and space charge necessitate extensive diagnostics for commissioning and operating the IR Demo [16].

The wiggler location also permits early first light, i.e., 5 μm light at ~100 W cw power without energy recovery using a 1.1 mA beam . The IR Demo will incorporate an upgraded power supply for the klystrons driving the cryomodule, thus enabling them to run at 8 kW rather than their 5 kW CEBAF specification. Moreover, the wiggler placement establishes symmetry in the recirculation arcs and back leg, simplifying energy recovery [7].

Construction is scheduled to be complete by 30 Sep 97, with commissioning to start on 1 Oct 97. Target dates are: early 1998 for initial data on CSR, spring 1998 for first light, and summer 1998 for high-power operation. While turning on the machine, we will no doubt learn much about producing and transporting high-brightness electron beams.

This work was supported by the U. S. Department of Energy under contract DE-AC05-84-ER40150, the Office of Naval Research, the Commonwealth of Virginia, and the Laser Processing Consortium.

4 REFERENCES

[1] H. Grunder, Proc. 1995 Part. Accel. Conf., IEEE Cat. No. 95CH35843, 1-3 (1996); A. Hutton, "Operation of CEBAF with Heavy Beam Loading", these Proceedings.

[2] H. Liu, J. Benesch, S. Benson, J. Bisognano, D. Douglas, G. Neil, D. Neuffer, C. Sinclair, B. Yunn, *Nucl. Instrum. and Meth. in Phys. Rsch. A*, **358**, 475-478 (1995).

[3] D. Engwall, C. Bohn, L. Cardman, B. Dunham, D. Kehne, R. Legg, H. Liu, G. Neil, M. Shinn, C. Sinclair, "A High-DC-Voltage GaAs Photoemission Gun: Transverse Emittance and Momentum Spread Measurements", these Proceedings.

[4] M. Wiseman, J. Preble, D. Machie, J. Fisher, J. Benesch, L. Phillips, J. Mammosser, "Jefferson Lab IRFEL Injector Cryounit Modifications and Test Results", these Proceedings.

[5] CEBAF Design Handbook (Revised), 14 January 1991.

[6] D. C. Quimby, S. C. Gottschalk, F. E. James, K. E. Robinson, *Nucl. Instrum. and Meth. in Phys. Rsch. A*, **259**, 304-311 (1987).

[7] D. Douglas, "Lattice Design for a High-Power Infrared FEL", and J. Karn, G. Biallas, A. Guerra, L. Harwood, "Magnetic Measurements of the Prototype Dipole for the IRFEL at the Thomas Jefferson National Accelerator Facility", these Proceedings.

[8] C. A. Brau, *Free-Electron Lasers* (Academic Press, Inc., San Diego, 1990).

[9] B. Yunn, private communication.

[10] S. Benson, private communication.

[11] L. Merminga, J. Bisognano, J. Delayen, "Energy Stability in Recirculating, Energy-Recovering Linacs in the Presence of an FEL," Proceedings 1996 EPAC.

[12] K. Jordan, R. Evans, O. Garza, R. Hill, M. Shinn, J. Song, D. Venhaus, "Pulse Selection Control for the IRFEL Photocathode Drive Laser", these Proceedings.

[13] N. Sereno, Ph. D. Dissertation, University of Illinois, 1994; T. Smith, *Nucl. Instrum. and Meth. in Phys. Rsch. A*, **259**, 1 (1987).

[14] R. Li, C. L. Bohn, J. J. Bisognano, "Shielding Effect on the Transient Self-Interaction of a Bunch Entering a Bend", these Proceedings.

[15] C. L. Bohn, R. Li, J. J. Bisognano, "Emittance Growth from Transient Coherent Synchrotron Radiation", Proc. 1996 FEL Conf., Rome, Italy, 21-25 August 1996 (in press).

[16] G. Krafft, K. Jordan, D. Kehne, J.-C. Denard, P. Piot, S. Benson, E. Feldl, J. Song, R. Ursic, "Electron-Beam Diagnostics for Jefferson Lab's High-Power Free-Electron Laser", and P. Piot, J. Song, R. Li, G. Krafft, D. Kehne, K. Jordan, E. Feldl, J.-C. Denard, "A Multislit Transverse-Emittance Diagnostic for Space-Charge-Dominated Beams", these Proceedings.

ELECTRON-BEAM DIAGNOSTICS FOR JEFFERSON LAB'S HIGH POWER FREE ELECTRON LASER

G. A. Krafft, K. Jordan, D. Kehne, S. Benson, J. Denard, E. Feldl,
P. Piot, J. Song, and R. Ursic, TJNAF, 12000 Jefferson Ave., Newport News, VA 23606

Abstract

In this paper the current plans for the diagnostic complement for Jefferson Lab's IRFEL are presented. Diagnostic devices include optical transition radiation beam viewers, both stripline and button beam position monitors, multislit beam emittance measuring devices, coherent synchrotron and transition radiation bunch length monitoring devices, and synchrotron light cameras for measuring the beam profile at high average power. Most devices have update rates of order 1 sec or shorter, and all are controlled through an EPICS control system.

1 DIAGNOSTIC REQUIREMENTS

Accurate beam instrumentation is essential for smooth commissioning of any accelerator. The diagnostics for Jefferson Lab's FEL accelerator [1] have two main purposes: to allow set up of the accelerator and to monitor changes in beam conditions during production runs. Setup of the accelerator will proceed in a low-beam-power mode with significantly reduced average micropulse repetition rates to limit the beam loss and activation of accelerator components. The production runs will occur in a high-average-power CW mode. The diagnostic requirements for the FEL are similar in many respects to that of other electron accelerators. There are, however, a few parameters that require additional emphasis. One would like to obtain short bunch lengths (0.5 psec rms), low average beam loss, and precise steering and beam envelope matching in the wiggler.

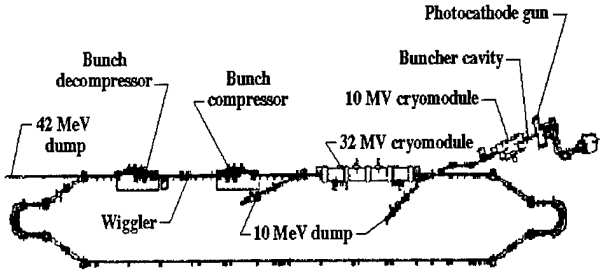


Figure 1: IR Demo Layout

A diagram of the overall facility appears in Fig. 1. Beam, originating in a 350 kV high-average-current injector, is accelerated to 10 MeV, merged onto the main linac beam line, and accelerated to 42 MeV. After passing through the wiggler, the used beam is recirculated to the beginning of the accelerator and its energy recovered, thereby reducing the overall demand on the linac RF systems. In Ref. [1], the main beam parameters are summarized. In Table 1, the performance of the various diagnostic techniques and measurements is summarized.

All of the beam diagnostics devices are to be controlled by EPICS, employing UNIX workstations for executing high-level applications.

2 DIAGNOSTIC SYSTEMS

2.1 Beam Position Monitors

There are thirty Beam Position Monitors (BPMs): one in the injector, nine in the linac straight section including the wiggler, thirteen in the recirculation straight, two each in the recirculation bends, and three in the dump lines. The most stringent requirements are given by the BPM systems in the wiggler region. The required relative resolution through the wiggler is 45 μm rms with a bandwidth of about 10 Hz. During startup the general accuracy should be 500 μm based on aperture restrictions; we are demanding 100 μm resolution on startup. A typical BPM system consists of a beam electrode mounted to the beamline and time domain electronics to resolve the signal.

Two types of beam electrodes are used in the IRFEL: stripline detectors and button detectors. The stripline detector design is modeled after work done at the SSC. It is about 15 cm long, and its principal advantage is the smooth RF transition from the vacuum feed-through to the stripline. The button detectors are identical to those purchased for the B-factory at SLAC. Such detectors are used in regions where, for beam-dynamics reasons, the vacuum chamber is wider than normal. Examples are the recirculation bend regions and the chicanes.

There are two types of BPM electronics, based on those of Jefferson Lab's nuclear physics accelerator. The older first type, called four-channel electronics, detect the output from each stripline in a separate channel [2]. They are principally located on the straight sections of the machine, and are always attached to stripline BPMs. The second type, based on VXI standards, are the so-called switched-electrode electronics (SEE) [3]. In these electronics alternate electrode outputs are switched onto the same detector channel, eliminating one potential source of error compared to a four-channel device. These electronics have relatively high dynamic range in current compared to the four channel systems. They are attached to all the button-type monitors and to the two stripline monitors near the wiggler, to help insure greater reproducibility of the orbit through the wiggler. It is already known that these systems will meet the requirements, given that the

0-7803-4376-X/98 /$10.00 © 1998 IEEE

beam current is so much higher in the FEL than in the nuclear physics accelerator.

2.2 *Bunch Length Monitor*

The bunch length will be determined at several locations in the accelerator. The main measurements will be done at 42 MeV near the wiggler, although, for beam verification purposes, several devices at 10 MeV are planned. Two types of devices are planned: ones based on a destructive coherent transition radiation interferometer used for calibrating and optimizing the bunch length, and devices based on "narrowband" coherent synchrotron radiation detectors which noninvasively monitor bunch length changes.

In the first device, a Michelson interferometer and Golay cell detector are used to measure the power spectrum of transition radiation by autocorrelation. An estimate of the bunch profile can be derived from this spectrum. The University of Georgia is building the interferometers and Golay cells, which are similar to one installed and tested at Vanderbilt. The range of the device is approximately 0.2-5 psec, and it is desired to have a result good to 0.1 psec. Two interferometers will be installed. The first is at the injection point into the main linac and the second is just downstream of the wiggler, i. e., at the location where one would like the bunch length to be minimized.

The second device uses coherent synchrotron emission to monitor the bunch for any changes in the longitudinal distribution while running at full beam power [4]. The device is a replica of previous work at Jefferson Lab, modified for the longer bunch length of the IRFEL bunches as compared to the nuclear physics machine. Three devices are planned for installation. One is in the injector region, one is in the wiggler region, and one is in the recirculation beamline, to check that the bunch length does not grow on recirculation.

2.3 *Beam Viewers*

Optical transition radiation (OTR) viewers will be used to measure beam profile and position throughout the machine. Resolution of the viewers is 50 μm. Charge Injection Device (CID) cameras will be used to image the screen. The only area where there might be a problem is at 10 MeV where the emitted light level is low. If necessary, these can be replaced with fluorescent viewers and harps.

2.4 *Synchrotron Light Monitors*

The critical wavelength for synchrotron emission from a typical 42 MeV bend is about 7.5 μm. We have chosen to use image-intensified CCD cameras to monitor the synchrotron emission. The camera sensitivity is high enough that low-power, pulsed, tune-up beam is observable. Attenuators will be used to prevent camera saturation during high-power running. The cameras are located near each bend of the recirculation dipoles, at the 90° point of the 180° bends, and in the chicane regions. These latter cameras will allow us to monitor the energy spread generated by the laser as the laser turns on.

2.5 *Emittance*

The size of the beam emittance will be determined at three different locations using three distinct methods. In a set of gun characterization experiments [5], a variant of the "two slit" method is used. After the beam is accelerated to 10 MeV, the large space charge in the beam makes envelope measurements questionable. Therefore, we have developed a multislit device for such measurements [6]. Finally, we measure the emittance by envelope fitting for energies of 42 MeV, i. e., after acceleration to full energy.

The nominal value for normalized rms emittance at the 10 MeV injection point is 4 mm mrad. The requirement for first light lasing is about 8 mm mrad. It is desired to measure emittance to within ± 1 mm mrad, covering the range 4-20 mm mrad. Because space charge dominates the beam optics at 10 MeV, it is necessary to reduce the beam intensity to perform a significant measurement. A multislit device was chosen based on the results obtained at UCLA on a similar design. The multislit provides information on α and β for tuning purposes. The device was recently tested with beam. It performs measurements of the required accuracy in real time.

Downstream of the main accelerator, the emittance will be measured by fitting to beam envelopes. Two prominent examples of such measurements are the wiggler emittance measurement, which can involve either three or five OTR viewers in the straight section containing the wiggler, and the back-leg emittance measurement, which involves varying a quadrupole magnet and observing the beam profile on a downstream OTR foil. Profiles may be obtained at six locations in the recirculation straight. The measurements will be analysed using high-level software previously developed for the nuclear physics machine at Jefferson Lab. Eventually, we will use the OTR radiation to obtain the emittance directly as this process is more rapidly completed operationally.

2.6 *Beam Current*

The requirements impose a limit of 2% peak-to-peak fluctuation for current stability. The beam current will be measured by collecting the beam in the dumps. Such measurements give the average current over time scales greater than 1 μsec. The average current is sampled and reported to the control room on a time scale of order 1 sec. Fast measurements are possible by directly monitoring collected current signals. There are six possible dump locations; only three of the dumps are able to handle full beam power.

Also, the stripline BPMs may serve as fast current monitors. Should the need arise, amplitude detecting the 1497 MHz signal on the BPM wires provides a precise measure of the average current at a high speed ($\approx$100 kHz

Parameter	Nominal Value	Span	Technique	Resolution	Bandwidth/ Time scale	Number
Position	Centerline	±5 mm	BPM	100 μm	60 Hz	30
Profile	5 mm	0.1-20 mm	OTR Foil	50 μm	>10 Hz	24+13
Divergence	30 μrad	10-1000 μrad	OTR	1 μrad	1 Hz	
Emittance	9mm mrad	3-25mm mrad	Quad Profile/OTR	3mm mrad	0.1 Hz	2
Charge	135 pC/bunch	10-270 pC	Faraday Cup	5 pC	2 kHz	6
Energy	42 MeV	20-45 MeV	High η OTR	0.01%	1 Hz	3
Energy Spread	280 keV		High η BPM	0.05%	0.01 Hz	3
Bunch Length	0.4 psec	0.2-5 psec	CSR or CTR	0.1 psec	0.01 Hz	3+2
M_{56}	0 cm	±100 cm	RF Phase	1 cm	0.1 Hz	3

Table 1: Requirements for the Accelerator Diagnostics

bandwidth).

2.7 *Path Length/M_{55}/M_{56}*

Measurements of path length are required to set the proper RF phase of the second pass through the linac and to measure M_{56} in the arcs. Path length measurements will be done using the method that is currently employed at CEBAF [7]. In this method, a precision phase detector is used to measure the phase difference between a RF reference signal and a tuned pickup cavity located at the end of the linac. Adjusting the path length will be done by antisymmetrically exciting two correctors before and after the 180° bends in the recirculation arcs. The M_{56} value will be determined by measuring path length differences through the arc at two slightly different beam energies. Path length at CEBAF has been measured to within 50 μm, while M_{56} has been measured to within 1.8 cm.

2.8 *Beam Loss*

The electron beam in the driver accelerator for the FEL has enough power rapidly to burn through the vacuum chamber if it is not adequately protected. The protection system in use for the nuclear physics machine at Jefferson Lab will be adapted for use in the FEL. It is based on fast photomultiplier tubes which rapidly shut the beam down when beam loss is detected. Experience on the nuclear physics machine indicates that losses as low as 100 nA (20 ppm) are detectable by these methods. It is not clear at present whether the continuous beam loss of the full-power beam will exceed this level. If so, an installed beam scraper will be used to localize the loss, allowing loss monitors not in this region to be active without being blinded. The response time of the electronics systems attached to the tubes is of order 1 μsec. Shutdowns within 10 μsec of beam loss detection are anticipated.

3 STATUS AND RESULTS

Presently, the beam diagnostic complement is on schedule to be installed by 30 September, 1997. All hardware choices and most hardware procurements are out. To the extent we are able, early checks of the diagnostics have been undertaken. As summarized in Ref. [6], the multi-slit emittance device has successfully passed its first tests, measuring emittances down to 0.5×10^{-6} m rad with 250 kV beam. More standard emittance measurements using envelope fitting have been used at Jefferson Lab over a number of years, and they present no problems for application to the 42 MeV FEL beam. Our first interferometer is complete, and plans to test the device at Vanderbilt or at Jefferson Lab are proceeding. The path-length system is complete, except for the longitudinal pickup cavity which will be complete in two months. This work supported by U. S. DOE Contract No. DE-AC05-84ER40150, the Office of Naval Research, the Commonwealth of Virginia, and the Laser Processing Consortium.

4 REFERENCES

[1] Bohn, C. L., Recirculating Accelerator Driver for a High-Power Free Electron Laser, these Proceedings.

[2] Hofler, A. S., *et. al.*, Proc. of the 1993 Part. Accel. Conf., pg. 2298 (1993)

[3] Powers, T., *et. al.*, Proc. of the Seventh Beam Instrumentation Workshop, pg. 257 (1996)

[4] Wang, D. X., G. A. Krafft, *et. al.*, Proc. of the Micro bunches Workshop, AIP Conf. Proc. 367, 502 (1995).

[5] Engwall, D., *et. al.*, A High DC Voltage GaAs Photoemission Gun: Transverse Emittance and Momentum Spread Measurements, these Proceedings.

[6] Piot, P., J. Song, *et. al.* A Multislit Transverse Emittance Diagnostic for Space-Charge Dominated Electron Beams, these Proceedings.

[7] Krafft, G. A., *et. al.*, Proc. of the 1995 Part. Accel. Conf., pg. 2429 (1995), and Hardy, D. *et. al.*, Automated Measurement of Path Length and M_{56}, these Proceedings.

NEW HIGH POWER LINACS AND BEAM PHYSICS*

T.P.Wangler, E.R.Gray, and S.Nath, Los Alamos National Laboratory, Los Alamos, NM, 87545, K.R.Crandall, Amparo Corporation, Santa Fe, NM 87504, and K. Hasegawa, Japan Atomic Energy Research Institute, Tokai-mura, Ibaraki-ken 319-11, Japan.

Abstract

New high-power proton linacs must be designed to control beam loss, which can lead to radioactivation of the accelerator. The threat of beam loss is increased significantly by the formation of beam halo. Numerical simulation studies have identified the space-charge interactions, especially those that occur in rms mismatched beams, as a major concern for halo growth. The maximum-amplitude predictions of the simulation codes must be subjected to independent tests to confirm the validity of the results. Consequently, we compare predictions from the particle-core halo models with computer simulations to test our understanding of the halo mechanisms that are incorporated in the computer codes. We present and discuss scaling laws that provide guidance for high-power linac design.

1 OVERVIEW

High-intensity, high-energy proton linacs are being designed for new projects around the world [1]. Typical requirements for these linacs include high peak current (beam current averaged over an rf period) near 100 mA, corresponding to about 10^9 particles per bunch at bunch frequencies of several hundred MHz, and final energies near 1 GeV. An important design objective is to restrict beam losses to levels that will allow hands-on maintenance throughout the linac. If one adopts a hands-on-maintenance criterion that limits the activation level to 20 mRem/hr at a distance of 1 m from a copper accelerating structure an hour after shutdown of the accelerator, the maximum tolerable beam-loss rate can be estimated from calculations reported in Ref. [2]. If the beam-loss rate is expressed in terms of the lost beam power, the loss rate above 100 MeV must be limited to several tenths of a beam-Watt per meter. The LANSCE proton linac, which operates with hands-on maintenance at the 17-mA peak and 1-mA average current levels, achieves typical beam-loss rates above 100 MeV of less than a few tenths of a Watt per meter. The challenge for the new generation of linacs is to provide larger average currents without increasing the beam loss.

Numerical simulation codes with a space-charge calculation based on solving Poisson's equation, provide a practical method of self-consistent calculations for so-called collisionless beams that satisfy Liouville's theorem. Liouville's theorem would be violated in beams that are affected significantly by particle collisions. However, the beam spends only a short time in the linac, typically several microseconds, and one finds that intrabeam scattering [3], resulting from multiple Coulomb collisions, and the Touschek effect [4], resulting from single Coulomb collisions, are small effects compared with the space-charge forces.

Numerical-simulation studies predict that a major threat of beam loss in the new generation of high power linacs is associated with halo induced by beam mismatch [5]. Because there is not a consensus about its definition, halo remains an imprecise term. In any given computer simulation one can unambiguously define an rms beam size, and a maximum particle displacement. Provided that the statistical precision is sufficiently adequate that the results are not sensitive to the motion of a few lone outer particles, the ratio of the maximum displacement to the rms size of the matched beam, which we call the maximum to rms ratio, is a useful figure of merit. Qualitatively, one can describe the evolution of the outer regions of the particle distribution for the case of an initial compact particle distribution (excluding the singular K-V distribution). A compact particle distribution might be arbitrarily defined as having initial position and velocity coordinates that are contained within about 3σ. If this beam evolves in an rms-matched state, an equilibrium distribution develops in which the density at the beam edge falls off within about a Debye length. The Debye tail, whose size is a function of both the rms emittance and beam current, is a consequence of the propensity of the charges in a beam to provide shielding within the beam core. Rms emittance growth and associated growth of the Debye tail can occur, especially through longitudinal-transverse coupling of the space-charge force [6]. For a beam with a given current and emittance, the size of this tail relative to the rms size can be changed by changing the focusing strength. Although there is no consensus about whether to call the Debye tail a halo, values of the maximum to rms ratio larger than about 5 are generally not observed in simulations, and the beam retains a very compact distribution [7].

* Work supported by US Department of Energy

0-7803-4376-X/98/$10.00 © 1998 IEEE

The outer region for a beam, with the same initial compact particle distribution in an rms mismatched state, evolves differently. Many theoretical and numerical studies of halo formation in mismatched beams have been reported, showing larger amplitudes extending well beyond the Debye-tail of a matched beam. For practical estimates of expected mismatch in linacs, values for the maximum to rms ratio as large as 10 to 12 have been observed in simulations, and it is generally agreed that this is called halo. Particle-core models for both a cylindrical beam [8] and a spherical bunch [9] provide quantitative predictions for the amplitudes. In these models the space-charge field from a beam core, oscillating radially in the symmetric breathing mode in a uniform linear-focusing channel, is represented by a hard-edged, spatially-uniform density distribution. The breathing mode appears to produce the largest amplitudes seen in simulations. The amplitude of the breathing-mode oscillation is directly related to the magnitude of the initial rms mismatch of the beam. The behavior of halo particles is studied in the model by representing them with single particles that oscillate through the core and interact with it. The particles slowly gain or lose energy as a result of multiple traversals through the core. A parametric resonance exists [10] when the particle frequency is half the core frequency. The amplitude growth for the resonant particles is self limiting, because outside the core, the net restoring force increases with radius, which produces a dependence of frequency on the particle amplitude; thus the resonant condition is restricted to a range of particle amplitudes. Chaos, which may increase the halo population, is observed at low tune-depression ratios [11].

By numerically integrating the trajectories from the models, the maximum amplitudes have been calculated as a function of an initial mismatch parameter μ, the ratio of the initial rms core size to the matched rms core size. The normalized maximum particle amplitude is described over a useful range of tune-depression ratios by an approximate empirical formula

$$x_{max}/a = A + B|\ln(\mu)|, \qquad (1)$$

where x_{max} is the maximum resonant-particle amplitude, a is the matched rms core size, and A and B are weak functions of the tune-depression ratio, given in Ref. [9]. Approximate values for the cylindrical beam are $A \cong B \cong 4$, and for the spherical bunch, $A \cong B \cong 5$. Equation 1 is not a good approximation for values of μ very near 1, where x_{max}/a rapidly approaches 2 for the continuous beam, and $\sqrt{5}$ for the spherical bunch.

For the spherical bunch geometry, we expect that both the transverse and the longitudinal halo are driven primarily by the breathing mode. In the limit of a prolate spheroid or cigar-shaped bunch with a large aspect ratio, the transverse motion is still dominated by the breathing mode. Then, the longitudinal motion is dominated by the lower-frequency antisymmetric mode [12] in which the radial and longitudinal displacements are out of phase.

2 SCALING OF EMITTANCE GROWTH AND HALO

Assuming that the bunch can be modeled as a long cylinder with a uniform longitudinal profile, we obtain simple scaling formulas for transverse rms emittance growth and maximum particle amplitude for the mismatched beam. It is known that the space-charge-induced rms-emittance growth is a function of the tune depression ratio k/k_0, where k and k_0 are the transverse phase advances per unit length, with and without space charge. For a long cylindrical bunch where end effects can be ignored, and assuming uniform transverse focusing, the rms emittance-growth ratio is a function of the tune depression ratio. In the smooth approximation, where the focusing is represented by an equivalent uniform focusing channel, we may write $k/k_0 = \sqrt{1+u_t^2} - u_t$, where u_t is a space-charge parameter given by

$$u_t = \left(\frac{qI}{16\pi\varepsilon_0 \ell f \gamma^2}\right)\left(\frac{1}{mc^2\beta}\right)\left(\frac{1}{\varepsilon_n k_0}\right). \qquad (2)$$

The parameters appearing in the Eq.(2) are the charge q, rest energy mc^2, average beam current I, effective bunch length ℓ, bunch frequency f, relativistic mass factor γ, velocity (relative to that of light) β, and normalized rms emittance ε_n. The average current is related to the number of particles per bunch N and the bunch frequency, by I=qNf.

The particle-core model for an rms-mismatched beam predicts that the halo particles created by the resonance have a maximum amplitude for a given core-oscillation amplitude. From Eq.(1), the numerical solution predicts that the maximum amplitude is proportional to the matched rms size a of the core, given by

$$a^2 = \frac{\varepsilon_n}{k_0\beta\gamma}\left[\sqrt{1+u_t^2} + u_t\right]. \qquad (3)$$

In the space-charge dominated limit, when $u_t >> 1$, the rms beam size is

$$a^2 \cong \frac{2\varepsilon_n u_t}{k_0 \beta\gamma} = \left(\frac{qI}{8\pi\varepsilon_0 \ell f \gamma^2}\right)\left(\frac{1}{mc^2\gamma\beta^2}\right)\frac{1}{k_0^2}\,, \qquad (4)$$

which is independent of the emittance. The emittance-dominated limit corresponds to $u_t << 1$, and we find

$$a^2 \cong \frac{\varepsilon_n}{k_0\beta\gamma}\left[1+\left(\frac{qI}{16\pi\varepsilon_0 \ell f \gamma^2}\right)\left(\frac{1}{mc^2\beta}\right)\left(\frac{1}{\varepsilon_n k_0}\right)\right]. \quad (5)$$

In Eq.(5), the second term is much less than unity, and smaller emittance results in smaller a and smaller maximum amplitude.

In spite of these scaling results, which show that the maximum amplitude for an rms mismatched beam decreases with increased focusing strength (larger k_0), a consensus does not exist that the strongest transverse focusing yields the optimum solution. First, there is a concern that if the transverse focusing is too strong, the longitudinal space-charge forces will increase and longitudinal halo may become a problem. Then, related to this concern, some argue [13,14] that even at high energies the focusing strengths should be chosen to maintain equipartitioning between all three planes, to prevent the possibility of any energy exchange. If the linac frequency and accelerating gradient are fixed, one finds that because of the reduction in the longitudinal focusing strength with increasing energy, equipartitioning requires that the transverse focusing must also be weakened. This shifts the beam towards a more transverse-space-charge dominated regime, so that, although there is a shorter Debye tail for a matched or nearly matched beam [15], one finds both a larger transverse rms size and larger maximum amplitude [16]. Until some of these questions are resolved, it is prudent to require sufficient adjustability in the electromagnetic-quadrupole focusing to allow an experimental optimization.

3 HALO SIMULATION TESTS

As a test of the capabilities of the space-charge codes to calculate the maximum particle amplitudes, numerical simulation runs were carried out for four different cases using 10^4 particles per run, as summarized in Table 1. Two space-charge codes were used, one based on Gauss' law, and the other is SCHEFF, which is based on a 2-D (r-z) particle-in-cell method [17]. Several initial distributions were used, including Gaussian in both position and velocity space (truncated at 3σ), semi-Gaussian (uniform in space and Gaussian in velocity space, and Waterbag (uniformly-filled ellipsoid in 4-D or 6-D phase space). For each case there is a set of runs for different values of the initial mismatch parameter μ, which is the same in all planes. After the beam sizes were set for a given mismatch parameter, the velocities were scaled to make the emittance the same as for the matched case.

Table 1. Simulation runs for Comparison with the Particle-Core Models.

Fig.	Space-Charge Code	Particle-Core Model	Focusing Channel
1	Gauss	Cylinder	Uniform
2	Gauss and SCHEFF	Cylinder	Uniform
3	Gauss	Sphere	Uniform
4	SCHEFF	Sphere	FODO

Figs. 1 through 4 show the ratio of the maximum particle amplitude from simulation to the rms size of the matched beam, versus the mismatch parameter μ. For Figs. 1, 3, and 4, two curves are shown from the appropriate particle-core model, showing the ratio of the maximum resonant-particle amplitude to the rms size of the matched core. The lower and upper curves are for tune-depression ratios of 0.5 and 0.9. In Fig. 4, the points correspond to a maximum displacement and rms size that are averaged over the lattice period. The simulations for the uniform channels were run for at least 100 plasma periods, sufficient for the amplitudes to reach an apparent asymptotic value. A typical high-power linac may contain a few hundred plasma periods.

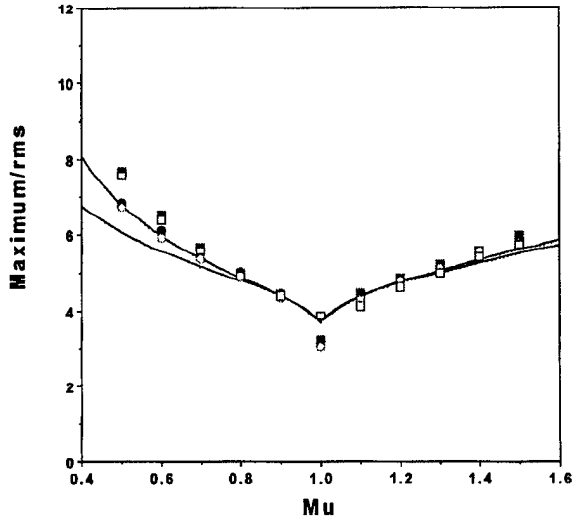


Fig. 1. Cylindrical-beam simulations comparing the particle core-model with the Gauss'-law space-charge code for a uniform-focusing channel. The solid and open symbols are for the initial Gaussian and Semi-Gaussian distributions, and the circles and squares are for tune-depression ratios of 0.5 and 0.9.

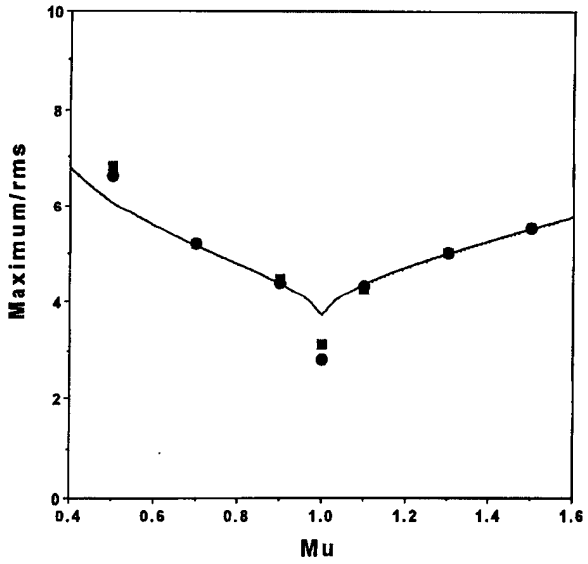


Fig. 2. Cylindrical-beam simulations comparing the cylinder particle core-model with the Gauss (circles) and SCHEFF (squares) space-charge codes for a uniform focusing channel, both for a tune-depression ratio of 0.5. The initial distribution is a 4-D Waterbag.

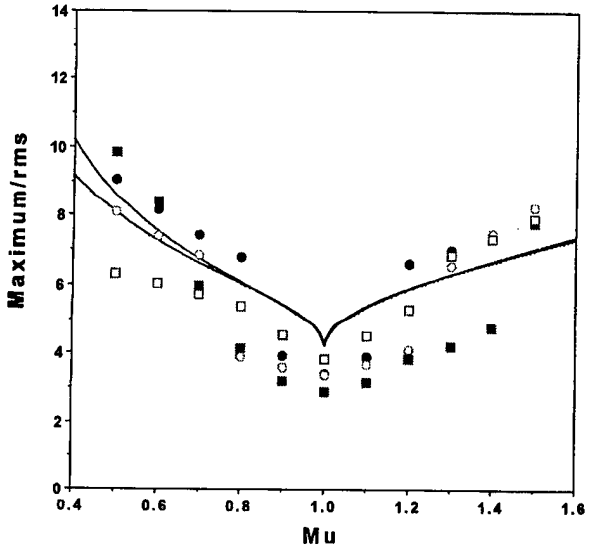


Fig. 3. Spherical-bunch simulations comparing the Gauss' law space-charge code with the sphere particle core-model for a uniform focusing channel. The solid and open symbols are for the initial Waterbag and Semi-Gaussian distributions, and the circles and squares are for tune-depression ratios of 0.5 and 0.9.

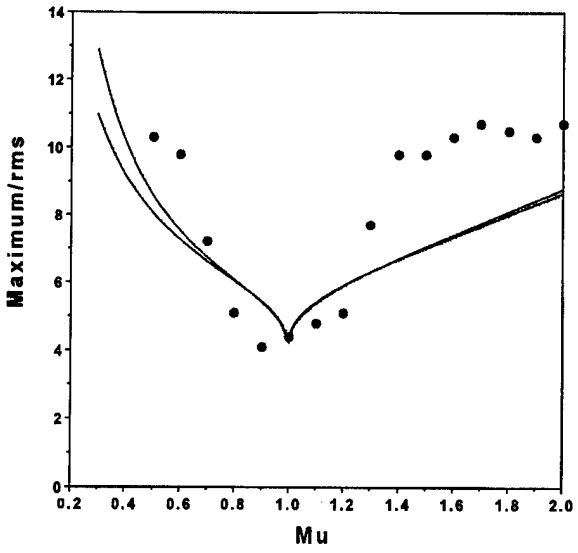


Fig. 4. Simulations comparing the SCHEFF space-charge code with the spherical particle core-model for a 7- to 217-MeV proton linac with 100-mA beam current, and FODO quadrupole-focusing with a variable tune-depression ratio. The initial distribution is a 6-D Waterbag, and the bunches have a variable prolate-spheroid geometry.

The agreement of the maximum amplitudes from the models and the Gauss'-law simulations for the uniform channel in Fig. 1 is remarkably good for both the initial Gaussian and semi-Gaussian distributions. In Fig. 2 the test is extended to the 4-D Waterbag distribution, comparing both the Gauss'-law and the SCHEFF simulation results. Although the details of the maximum amplitude trajectories for the Gauss'-law and the SCHEFF simulations were not exactly the same , the maximum amplitudes agree very well with each other and with the cylinder particle-core model. We consider this result an important initial test of the capability of the SCHEFF code. In Fig. 3, the Gauss'-law simulation for the spherical bunch shows a tendency for some points, especially with μ values near 1, to remain below the curves of the particle-core models. These results suggest that halos may have more difficulty developing from some initial spherical-bunch states. Fig. 4, representing a simulation of a real linac, shows that the SCHEFF results for the larger mismatches (greater deviations from μ=1) are systematically higher than the sphere model by as much as 30%. Deviation of the points from the curves may be caused by inadequacies of either the model, or the SCHEFF space-charge calculations. For the linac simulation, we conclude that the results are consistent with the hypothesis that the breathing mode is the most important, although perhaps not the only driver of the beam halo produced by the simulation codes.

4 CONCLUSIONS

The particle-core models make quantitative predictions about the halo that is formed from the resonant interaction between individual particles and a mismatched-induced core oscillation in the breathing mode. The models predict that the halo will be limited to a maximum amplitude, which depends mostly on the magnitude of the initial mismatch. The simulation results, using two different space-charge codes, confirm the model predictions for the continuous beam in a uniform focusing channel. In other cases, discrepancies are observed, but the largest of these are only about 30%. We interpret the results to be consistent with the hypothesis that the breathing mode is the main source of the halo seen in the simulation codes. We believe that a reasonable estimate for the maximum mismatch-oscillation amplitude corresponds to values μ that may deviate from unity by about 0.3 to 0.4.

We believe that a practical approach to beam-loss control is to inject a high-quality, well-collimated beam into the high-energy linac, and achieve minimal proton-beam loss at high energies by providing strong transverse focusing, carefully controlling the beam centroid, and providing large beam apertures. The optimal choice of transverse focusing strength will depend on the results of subsequent studies of longitudinal halo. Although we are acquiring a better understanding of the causes of beam halo in the simulation codes, and providing a better rationale for the aperture choice, it is prudent to provide a safety margin. Such a margin is necessary to allow for errors and for the possibility of physics effects, which are not treated or are inadequately treated in the present codes. Consequently, to further reduce the risk of high-energy beam loss, we believe that the design of a high-power proton linac can benefit from the use of large-aperture superconducting linacs at high energies, as is now proposed for APT.

5 ACKNOWLEDGMENTS

The authors acknowledge helpful discussions with R. Gluckstern, R. Ryne, J. Bernard, and S. Lund.

REFERENCES

[1] For a list of references to projects see M. Prome, "Major Projects for the Use of High-Power Linacs", Proc. of the XVIII Int. Linear Accel. Conf., 26-30 August, 1996, Geneva, Switzerland, CERN 96-07, 9.

[2] A.P.Fetotov and B. Murin, Proc. of the 1976 Linear Accelerator Conf., Chalk River, Canada, p.377.

[3] M. Reiser, "Theory and Design of Charged Particle Beams," John Wiley & Sons, Inc., New York, 1994. For a nonrelativistic formula that gives an upper limit, see Eq. 6.173 in Section 6.4.2 of the 1st Edition.

[4] H. Bruck, "Circular Particle Accelerators, Institut National des Sciences et Techniques Nucleaires, Saclay, Presses Universitaires de France, 1966, Los Alamos Translation LA-TR-72-10 Rev. See Eq. 30-17, Chapter XXX.

[5] A. Cucchetti, M. Reiser, and T. P. Wangler, Proc. 1991 Part. Accel. Conf., IEEE Cat. No. 91CH3038-7 (1991) 251.

[6] M. Pabst and K. Bongardt, "Halo Simulation in a Realistic proton Linac Design, Proc. of the XVIII Int. Linear Accel. Conf., 26-30 August, 1996, Geneva, Switzerland, CERN 96-07, 9.

[7] R.D.Ryne and T.P.Wangler, "Recent Results in Analysis and Simulation of Beam Halo", Int. Conf. on Accelerator-Driven Transmutation Technology and Applications, Las Vegas, NV, 1994, AIP Conf. Proc. 346, pp. 383-389.

[8] J. S. O'Connell, T. P. Wangler, R. S. Mills, and K. R. Crandall, Proc. 1993 Part. Accel. Conf., Washington, DC(1993) 3657.

[9] T.P. Wangler, R.W. Garnett, E.R.Gray, R.D,Ryne, and T.S.Wang, Dynamics of Beam Halo in Mismatched Beams, Proc. of the XVIII Int. Linear Accel. Conf., 26-30 August, 1996, Geneva, Switzerland, CERN 96-07, 372.

[10] R. L. Gluckstern, Phys. Rev. Lett. 73(1994) 1247.

[11] J. M. Lagniel, Nucl. Inst. Meth. A345(1994) 46; A345(1994) 405.

[12] J. Barnard and S. Lund, these proceedings.

[13] M. Reiser and M. Brown, "RF Linac Designs with Beams in Thermal Equilibrium", Space Charge Dominated Beams and Applications of High Brightness beams, Bloomington, IN, 1995, AIP Conf. Proc. 377, pp. 329-340.

[14] R. A. Jameson, in Advanced Accelerator Concepts, AIP Conf. Proc. 279, (1993), p 969.

[15] L.M. Young, "Equipartitioning in a High Current Proton Linac", these proceedings.

[16] R.W.Garnett, "Linear Accelerator for Tritium Production", ref. 13, pp. 60-73.

[17] K.R.Crandall, unpublished.

THE JAPANESE HADRON FACILITY

Y. Mori, KEK-Tanashi 3-2-1 Midori-cho, Tanashi-shi, Tokyo 188, Japan

Abstract

The present status of the design and R&D works for the accelerators of Japanese Hadron Facility(JHF) are expressed.

1 INTRODUCTION

The Japanese Hadron Facility (JHF) consists of the following three accelerators;[1]

(1) main ring:50 GeV proton synchrotron (50 GeV PS)

(2) booster:3 GeV proton synchrotron (3 GeV BS)

(3) injector:200 MeV proton linear accelerator (200 MeV linac)

The accelerators will be constructed at the north site of KEK. The first stage of beam acceleration is provided by the linac, which accelerates H^- ions up to 200 MeV. The expected peak beam current in the injector linac is at least 30 mA and the pulse duration and the repetition rate of the beam are more than 400 msec and 25 Hz (50 Hz in future), respectively. The H^- beam is injected into the booster by charge-exchange multi-turn injection and accelerated to 3 GeV. The 3 GeV booster will be constructed in the existing tunnel for the present KEK proton synchrotron (PS) main ring. All of the components of the KEK PS main ring, such as dipole magnets, quadrupole magnets, vacuum chambers and others will be removed. The booster is a fast cycling proton synchrotron with a repetition rate of 25Hz. The expected beam intensity in the booster is 5×10^{13} ppp (protons per pulse), therefore, the average beam current becomes 200 mA. The total power of the extracted beam from the booster reaches 0.6MW. The 3 GeV protons are supplied to three experimental facilities; a pulsed spallation neutron source facility (N-arena), a meson facility (M-arena) and an unstable nuclei facility (E-arena), and to the 50 GeV main ring (K-arena).

Protons from the booster are injected into the main ring and accelerated to 50 GeV. The expected beam intensity in the main ring is 2×10^{14} ppp and the repetition rate is about 0.3 Hz. The 50 GeV protons are extracted by slow and fast extraction schemes into two experimental areas; one is for experiments using secondary beams (K, pbar, etc.) and primary beams by slow extraction, and the other is for the neutrino oscillation experiment by fast extraction. When it is operated in a slow extraction mode, the average current and duty factor, which is defined as a fraction of a cycle when beam are available, are 9.4 mA and 0.20, respectively. In addition to acceleration of high intensity protons, heavy ion and polarized proton beams are also requested. Using the 500 MeV booster of the KEK PS as an injector of the 3 GeV booster, it becomes feasible to accelerate these particles.

Typical machine cycle structure is illustrated in Fig.1. Four batches from the booster is injected into the main ring when the main ring stays low field. The 16 buckets out of 17 are filled with beams. Then, the main ring starts acceleration while three other facilities start using 3 GeV beams directly from the booster. Table 1 shows the main parameters of the whole accelerator complex.

2 50GEV MAIN RING

2.1 Lattice Design

The symmetry of the lattice is 4 because of the following requirements. There will be two major physics experimental area downstream. One uses slow extracted beams and the other does fast extracted beams. Slow extraction channel needs a long straight section of more than 50 m to realize a low loss extraction. In addition, abort channel of beams at and slightly above the injection energy needs another long straight section. A long straight section is also needed for RF cavities. The total required RF voltage is estimated as at least 270 kV. With an accelerating field of 10 kV/m, a total length for RF cavities is 27 m. The maximum field strength of bending magnets is 1.8 T and its length is 6.2 m. The field gradient of quadrupole magnets is 20 T/m at maximum and its length is 1.5 m and 2 m depending on a family. The coaxial type RF cavities with high permeability material will be used in the frequency range of a few MHz. The beam transfer line from the booster merges the main ring at one of the missing bend cells in an arc. The beams are injected vertically using some kicker magnets.

Table1: Main parameters of accelerator complex.

200 MeV linac		
	beam emittance	320 πmm-mrad
	accelerated particle	H^-ion
	peak beam current	>30(50)mA (25Hz,400μs)
3 GeV booster		
	beam emittance	54 πmm-mrad
	intensity	5×10^{13}ppp
	repetition rate	25Hz
	beam power	0.6MW
	RF frequency	1.99-3.43MHz
	RF voltage	420kV
	circumference	340m(KEK-PS tunnel)
50 GeV main ring		
	beam emittance	4.1 πmm-mrad
	intensity	2×10^{14}ppp
	repetition rate	0.3Hz
	RF frequency	3.43-3.51MHz
	RF voltage	270kV
	momentum compaction	~10^{-3}
	circumference	1445m (north site of KEK)

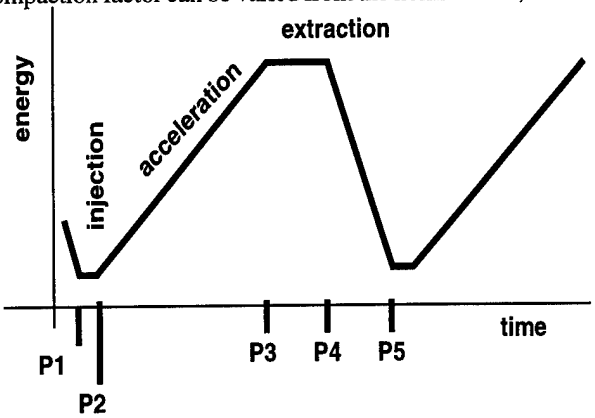
0-7803-4376-X/98/$10.00 © 1998 IEEE

The booster delivers a batch of 4 bunches every 40 ms when it is operated in 25 Hz. Because the circumference of the main ring is 17/4 times that of the booster, 4 booster batches fill 16 buckets of the main ring. One empty bucket is left and it is reserved for necessary time period for excitation of extraction kicker magnets.

In order to achieve high beam intensity and low beam loss in the 50 GeV PS, the following considerations are taken in its design.

(1)Imaginary transition γ lattice

The imaginary transition γ lattice means that the momentum compaction factor is negative and beams never cross transition energy which might cause a large fractions of the beam loss. The betatron oscillation amplitude and dispersion functions are depicted in Fig. 2. We adopted the missing bend scheme which make transition γ imaginary. The basic unit of the lattice is 3 FODO cells. There is no bending magnet in the middle FODO cell, therefore it can be represented as (D/2)BFBDOFODBFB(D/2). We adjust the middle FODO cell length and the strength of 4 quadrupole families, 2 for focusing and 2 for defocusing, to achieve imaginary transition γ. The magnitude of the momentum compaction factor can be varied from the nominal one, which



slow extraction of 50GeV

P1 - P2(injection)	0.12 s
P2 - P3(acceleration)	1.9 s
P3 - P4(extraction)	0.7 s
duty factor	0.20
P4 - P5	0.7 s
total	3.42 s
average current	9.4μA

Fig.1: Typical machine cycle of the main ring.

is determined by horizontal tune, on positive side to slightly less than -0.01 on negative side. When it is too close to zero, higher order effects, such as the momentum compaction factor depending on $(\Delta p/p)^2$ and on space charge tune shift, become relatively large and the lattice is unstable. On the other hand, when its magnitude becomes too large, the betatron oscillation amplitude and dispersion functions tend to diverge, resulting in smaller transverse acceptance. We choose the momentum compaction factor of -0.001 as a nominal value, which gives moderate lattice functions.

(2)Selection of phase advance

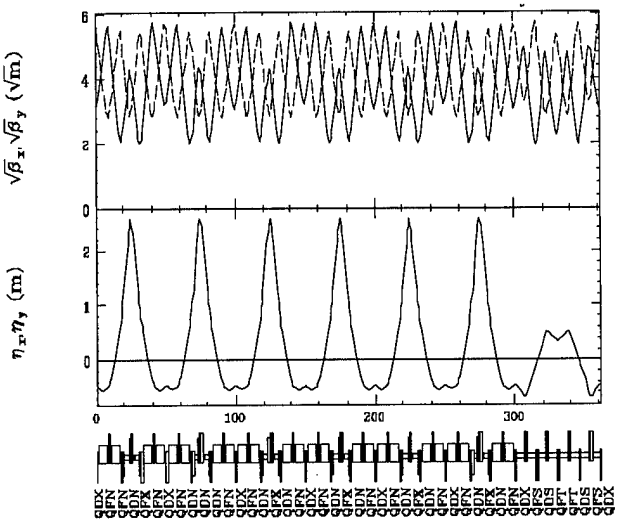


Fig. 2: Betatron oscillation amplitude and dispersion functions in the main ring. The solid line in the top is the horizontal betatron oscillation amplitude and the dashed line is the vertical one. In the bottom picture, the vertical dispersion is zero and the other curve is the horizontal one. One quarter of the ring is depicted.

Self space charge force excites strong resonance coupled with beam envelope modulation if the phase advance is just above 90 degrees[2]. The space charge induced resonances can be cured only by careful tuning of the transverse phase advance. The horizontal phase advance is below 90 degrees and the vertical one is far below 90 degrees making the tune of (21.8, 15.3) in total.

(3)Room for slow extraction hardware

In order to reduce beam loss less than 1 % at the extraction, careful design and simulation are in progress as explained later. At least 50 m long straight section is necessary to put electric and magnetic septa. If that is still not enough, we have an option of putting a pre-septum magnet in the missing bend cell in the preceding arc.

(4)Tunability of the transverse tune

The lattice should have tunability in transverse tunes and stability in lattice functions together. More specifically, the betatron oscillation amplitude and dispersion functions should not change much at least within the tune of +-1 around the nominal tune. In addition, the momentum compaction factor is supposed to be almost constant within the similar tuning range. With the same lattice, by tuning the quadrupole strength such that the phase advance in the arc is equal to integer, the dispersion free long straight can be created.

2.2 Emittance and Acceptance

In order to see whether the main ring has an enough acceptance to accommodate the emittance above, the acceptance is calculated for off momentum particle of 0.5 % with closed orbit distortions (COD) introduced by quadrupole mis-alignments. The distribution of misalignment errors is Gaussian whose rms value is +-0.3 mm. The magnitude of errors more than 2 σ is eliminated. With steering magnets next to each quadrupole magnet, one for each plane, and beam position monitors, one for both planes, the COD

correction is performed. The corrected COD is about ±0.5 mm and the acceptance becomes more than 60 π.mm.mrad. Here we assume a beam pipe of 100 mm diameter. It is less than 40 π.mm.mrad without correction.

From the beam instability point of view, the longitudinal emittance should be more than 3 eVs. On the other hand, that of the booster is 0.6 to 1 eVs, which is obviously not big enough. The larger longitudinal emittance also helps reduce transverse space charge effects because of the higher bunching factor. Therefore, we will blow up the longitudinal emittance either during the acceleration of the booster, or right after the injection of the main ring. With the longitudinal emittance of 3 eVs and the RF voltage of 270 kV, the bunching factor becomes 0.28 and the incoherent and coherent space charge tune shifts are -0.08 and -0.04, respectively. That is not negligible, but small enough.

2.3 Chromaticity Correction and Dynamic Aperture

Since the transition energy is imaginary, operation from the injection to the extraction is always below the transition energy, namely the slippage factor is always negative. The zeroth mode of the head tail instability and negative mass instability are stable with negative chromaticity. The natural chromaticity makes the tune spread due to momentum dispersion too high, the order of +-0.1, so that chromaticity correction is planned, even though it is not necessary to correct it to zero. The chromaticity correction introduces strong nonlinearity by the sextupoles. We have looked at tune shift due to amplitude and the dynamic aperture. The dynamic aperture is defined as the maximum amplitude of particle which survives for 10,000 turns at the flat bottom energy. The sextupoles are excited to make the both chromaticity zero in that test. The tune shift is small and the dynamic aperture is more than 200 π.mm.mrad, that is large enough compared with the physical aperture of 54 π.mm.mrad. The momentum dependence of the dynamic aperture within the range of +-0.5 % is negligible.

2.4 Space Charge Effects

Incoherent space charge tune shift at injection is -0.1 at most even though the total number of particles are 2×10^{14}. At 3 GeV, coherent space charge tune shift becomes not negligible but still less than -0.05. Those value seems not too difficult to deal with, but still careful beam handling is necessary to reduce beam loss. An upgrade plan is already discussed with 2nd harmonic cavities or barrier bucket system. By those additional installations, the space charge tune shift can be even lower than -0.1 and the increase of the beam intensity becomes feasible. More detailed study using multi-particle tracking is in progress.

2.5 Slow Extraction

In an ordinary slow extraction, particles with a large betatron amplitude caused by a resonance are deflected outward by an electric septum. Then, they are extracted from the ring by a chain of magnetic septa. For a high current proton accelerator such as the 50 GeV PS, even a small beam loss in those process will lead to unacceptable levels of radiation. We set a criterion such that tolerable beam loss in the slow extraction process should be less than 1 % for a 10 μA average current. For the present design of the main ring, beam loss process was examined by beam simulations. The third integer resonance was chosen to increase the betatron amplitude of the particles. In this calculation, the septum thickness is chosen to be 50 μm. It is feasible if we consider the deformation of the wires as well as the nominal thickness of the wires. The beam loss less than 1 % is achieved by selecting the septum length less than 1 m and the resonance strength of greater than S=1.5.

There are several new methods to reduce the beam loss. A TRIUMF group has proposed 'an electric pre-septum' [3]. A LANL group has proposed a new magnet with two pairs of magnetic poles with opposite magnetization directions [4]. Recently a new extraction scheme has been proposed in Japan and successfully tested in several facilities [5]. In this method, the separatrix is kept in constant by fixing the betatron tune near the resonance and the horizontal emittance of the circulating beam is increased by a transverse RF field. The angular spread of the beam extracted from the constant separatrix is expected to be very small. We would be able to reduce beam loss at the first septum by using this method. The combination of this method and the electric pre-septum scheme mentioned above is also very effective to reduce the beam loss drastically.

2.6 Magnets and Power Supplies

The main ring consists of 96 bending magnets, 176 quadrupole magnets, and 48 sextupole magnets. Main parameters for magnet design are summarized in Table 1. Based on these requirements, a bending magnet, a quadrupole magnet and a sextupole magnet have been designed.[6]

2.7 *RF system*

The RF voltage cycle is calculated by RAMA. It requires 270 kV, for whole injection and acceleration periods. In order to avoid negative mass and microwave instabilities, the longitudinal emittance is increased during injection. The emittance becomes 3 eVs after increasing the longitudinal emittance. [7] The room placed for the RF cavity in the ring is limited. The requirement for RF voltage per unit length has to be at least more than 10 kV/m. As the practical length of the RF cavity is 3 to 4 m, the required voltage per cavity is about 40 kV. The requirements of RF system performance are summarized in Table 2 Since the beam intensity is very high and harmonics number is 17, beam loading effects and coupled bunch instability are significant problems.

A number of wide band cavities using fine-crystallized soft-magnetic core, "FINEMET", are going to be employed in the main ring. This material is made of a thin layer of soft magnetic tape and has a very high permeability. Although the Q value is relatively small (Q~1), the shunt impedance (=μQf) is fairly large. The characteristics are independent of the RF magnetic field as shown in Fig.3.Since the Curie Temperature of the material is about 600C, a stableoperation at high temperatures is possible.

Development of this new type of the RF cavity has been started and recently, wwe have succeeded in obtaining the RF voltage pwr unit length of about 10kV/m.[8] The

Table 1: Main parameters for design of the main ring magnets

Bending Magnet		
	Magnetic Rigidity	12.76 - 170 Tm
	Field	0.135 T (for 3 GeV)
		1.8 T (for 50 GeV)
	Length	6.2 m
	Number	96
	Active Peak Power	54.0 MW
	Dissipation Power	12.0 MW
	Cooling Water	8.5 ton/min.
Quadrupole Magnet		
	Max. Field Gradient	20 T/m
	Length	1.5 - 2 m
	Total Number (8 families)	176
	Active Peak Power	24.0 MW
	Dissipation Power	7.0 MW
	Cooling Water	5.0 ton/min.
Magnet Aperture		
	B-Magnet 106 mm^h x (106 mm^w for useful)	
	Q-Magnet	132 mm^f

wide band cavity is also suitable to cure the coupled bunch instability as described in the section of beam instabilities.

3 3GEV BOOSTER

3.1 Lattice Design

Since the 3 GeV ring will be constructed in the present KEK PS tunnel, it imposes some geometrical constraints on the lattice. In addition, the high intensity operation requires a few essential cares on the optics. The circumference and superperiodicity should be very similar or the same as the present KEK PS. That is 340 m and 4, respectively. More specifically, the number of the total cells and the local curvature of the arc must be similar to that of the KEK PS, since the width of the tunnel cross section is only 4 m. There should be empty cells to install many rf cavities. The 3 GeV ring repetition is initially 25 Hz and supposed to be upgradable to 50 Hz. The minimum required rf voltage for 25 Hz operation is 420 kV. The straight section of 40 m or more in total is necessary for rf cavities provided that the accelerating field of more than 10 kV/m will be available. For 50 Hz operation, the necessary length of the straight section will be doubled. In order to install injection components including steering magnets for H- painting, one half cell is required. For extraction, 3 half cell is also required for one extraction channel. 6 half cells are then required for N arena and for E, K, and M arenas. In addition, the beam scraper and collector system, those are separated for about

Table 2: RF System requirements.

RF amplitude	40 kV (per cavity)
Harmonic Number	17
Number of Bunches	16
RF Frequency at injection	3.4 MHz
RF Frequency at extraction	3.5 MHz
Intensity per bunch	1.25×10^{13}
Total Gap Impedance	8 kW
Beam Intensity	6.4~6.6 A
Ib	12.8~13.2 A
Acceleration Time	1.9 s
Max. Beam Power	132 kW
Max. fs 30	

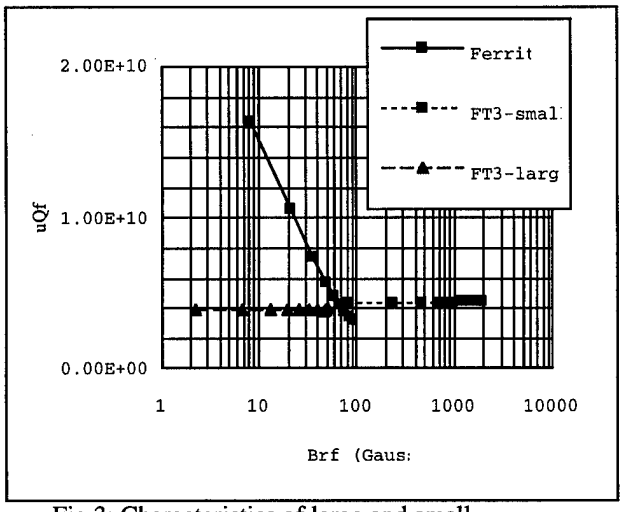


Fig.3: Characteristics of large and small FINEMET(FT3) and typical ferrite cores

180 degree phase advance, needs 4 half cells. The flexibility of adjusting transverse tune with minimum modulation of betatron oscillation amplitude and dispersion functions is desired. The tuning range of a few integer units in both horizontal and vertical planes is expected. Transition energy crossing must be avoided because the beam loss associated with it is inevitable. The higher transition energy, therefore the smaller momentum compaction factor, is also helpful from view point of the longitudinal matching between the 3 GeV and the 50 GeV ring.

In order to satisfy the above-mentioned conditions, a flexible momentum compaction (FMC) lattice has been studied in detail (Fig. 4). The FMC lattice consists of 28 FODO cells as total. The basic unit is 2 FODO cells with 2 bending magnets in the outer half cell. It can be represented as (F/2)BDOFODB(F/2). Three of them together with 1 FODO cell without bending magnets make a superperiod. Consecutive half cell without a bending magnet provides the place for the extraction. The whole ring consists of 4 identical superperiods such that the ring fits in the present KEK PS tunnel. The horizontal phase advance per 2 FODO cells is chosen above 180 degrees, but not too close to 180 degrees, in order to realize FMC. Those adjustments requires 2 focusing quadrupole families and 1 defocusing quadrupole family. The momentum compaction factor can be varied from almost zero to 0.009, which corresponds to 10 or higher in terms of transition gamma. The second order effects on the momentum compaction factor which come from the $(\Delta p/p)^2$ term is also examined and it turns out negligible unless it is too close to zero. We choose 0.006 as the nominal value of the momentum compaction factor. The betatron oscillation amplitude and dispersion functions in the tune range of +-1 around the nominal tune is examined. The tune depen-

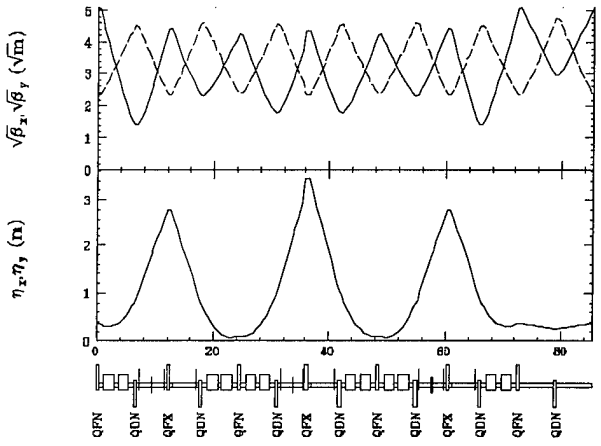


Fig. 4 Flexible momentum compaction (FMC) lattice for the 3GeV booster.

dence of those functions are marginal.

One of the distinguished features of this lattice is that it can provide the additional knob to control the momentum compaction factor. Then it becomes easier to match optically in the longitudinal plane between the 3 GeV and the 50 GeV rings, and to increase synchrotron oscillation frequency to introduce Landau damping. We have also looked into the alternative lattices, namely two options of normal 28 FODO cell lattice, and normal 24 FODO cell lattice. The both normal 28 FODO cell lattices (second and third options) fit most in the KEK PS tunnel simply because the tunnel has originally made for the present 28 cell KEK PS lattice.

3.2 Synchrobetatron Coupling Resonances

Because of the fast cycling nature, the required rf voltage is relatively high, resulting in high synchrotron tune, 0.015 at the injection energy. The synchrobetatron coupling resonance due to dispersion at the rf cavity location becomes one of major concerns to design the 3 GeV ring. Because there is large tune spread due to space charge effects, the transverse tune of some particles in a beam is close on a integer and resonance condition with small number of *m* may be satisfied. We have looked at the rms emittance growth and beam loss due to synchrobetatron coupling resonances by a full 6-D particle tracking. The FMC lattice was taken and multi-particles tracking has been done. When the harmonic number is 4 and synchrotron tune is around 0.015, no rms emittance growth or beam loss has been observed below the horizontal tune of 7.85 even though all the cavities are located at one position so that any cancellation due to symmetry occurs.

4 200MEV LINAC

A 200-MeV proton linear accelerator for the JHF consists of a 3-MeV radio-frequency quadrupole linac (RFQ), a 50-MeV drift tube linac (DTL) and a 200-MeV separated-type drift tube linac (SDTL).[8] An rf frequency of 324 MHz has been chosen for all of the rf structures. An expected peak current of 30 mA for H^- ion beam of 400 μsec pulse duration will be accelerated at a repetition rate of 25 Hz. One of the design features is its high performance for a beam-loss problem during acceleration. It can be achieved by separating the transition point in the transverse motion from that of the longitudinal motion..

The features of the design are as follows:

1. A frequency of 324 MHz has been chosen for all of the rf structures up to 200 MeV.
2. An SDTL has been chosen in an energy range from 50 to 200 MeV.
3. A 3-MeV RFQ has been chosen.
4. A transition energy of 150 or 200 MeV from the SDTL to the ACS has been selected.
5. The klystrons are used for all of the accelerating structures.

Acknowledgment

The author would like to express his sincere appreciation to all of the members of the JHF accelerator design group for preparing the information used in this article.

[REFERENCES]

[1] Y. Mori, et al., Proc. of the 10th Symposium on Accelerator Science and Technology, p. 454, 1995; Y. Ishi, et al., Proc. of the 10th Symposium on Accelerator Science and Technology, p. 326, 1995; S. Machida, et al., Proc. of the 10th Symposium on Accelerator Science and Technology, p. 407, 1995; Y. Mori, et al., Proc. of Fifth European Particle Accelerator Conf., p. 569,1996; Y. Mori (ed.), JHP-30, INS,University of Tokyo, 1996.

[2] S. Machida, Nucl. Instr. and Method A384 (1997)316.;S.Machida et al., Contribution for this Conferece.

[3] U. Wienands, et al., Proc. of the Advanced Hadron Facility Accelerator Design Workshop, 1988.

[4] H. S. Butler, et al., Proc. of the Advanced Hadron Faciity Accelerator Design Workshop, 1988; J. Liu, et. al., Proc. of the Advanced Hadron Facility Accelerator Design Workshop, 1988.

[5] A. Noda, et al., Proc. of Workshop on TARN II, INS-T-493, 63, INS, University of Tokyo, (in Japanese), 1990; K. Hiramoto, et. al., Nucl. Instr. and Method A322(1992) 154; M. Tomizawa, et. al., Nucl. Instr. and Method A326 (1993) 399; K.Noda, et. al., Nucl. Instr. and Method A381 (1996) 194; F. Albrecht, et. al., Proc. of Fifth European Particle Accelerator Conf., 1996, p. 2459.

[6] M. Muto (ed.), JHP-supplement-26, INS, University of Tokyo, 1997.;M.Muto et al.,Contribution for this Conference(1997).

[7] C. Ohmori, et al., Proc. of the 10th Symposium on Accelerator Science and Technology, p. 55,1995; T. Uesugi, et. al., JHP-31, INS, University of Tokyo, 1997.

[8]C. Ohmopri, et al., Contribution for this Conference(1997).

[9] T. Kato, " Design of the JHP 200-MeV Proton Linear Accelerator," KEK report 96-17 (1997).

REVIEW OF RADIOACTIVE ION BEAM ACCELERATORS

Pierre G. Bricault, TRIUMF, 4004 Wesbrook Mall, Vancouver, B.C., Canada, V6T 2A3

Abstract

During the last decade there has been a growing world-wide interest in the possibility of using radioactive ion beams for a variety of fundamental studies in pure and applied science. The possibility of producing intense beams of radioactive nuclei with extreme neutron to proton ratio (N/Z), compared with natural isotopes, has opened a new era in nuclear science. This interest has been generated by the considerable improvements which have occurred over the past 30 year in the field of heavy-ion accelerators, ion source, more particularly, in on-line production and isotope mass separation. The three major techniques used to produce intense radioactive ion beams are the in-flight separation method (IFS), neutron fission product using reactor (NF) and the on-line isotope separation (ISOL). Coupling very intense production sources of unstable nuclei to efficient accelerator structures will lead to the availability of a wide range of nuclei far from stability. This paper reviews the properties of radioactive ion beam accelerators in operation, under construction and proposed around the world.

1 INTRODUCTION

We are at a turning point in the history of nuclear physics. For the first time we can use and expect to use intense radioactive ion beams (RIB) along a very large neutron or proton line for systematic nuclear studies. With the new intense RIB facilities under construction and upgrade of existing facilities it will be possible to have access to new neutron and proton shell closures, and then to test the nuclear shell model. In the past, nuclear reaction studies were restricted to the use of stable nuclear projectile. New dimensions of nuclear physic were introduced because of the development of RIB facilities. Nuclear reactions with RIB of light neutron-rich like ^{11}Li and ^{11}Be led to the discovery of the halo structure of their neutron distribution [1, 2]. A similar structure of the very loosely bounded valence proton was also discovered [3].

This paper covers mainly the new ISOL based RIB facilities and major upgrades of RIB facilities based on in flight separation using the Projectile Fragmentation.

2 PRODUCTION METHOD

2.1 In-flight separation using the Projectile Fragmentation

The projectile fragmentation method is a very powerful method to produce a large variety of intense Radioactive Beams at heavy ion beam energies of ≈ 50 A*MeV to several A*GeV. The production mechanism is characterized by peripheral interaction of the projectile with the target nucleus that leaves the fragment with much of the initial momentum and with a small angular dispersion. This reaction mechanism produces a wide variety of nuclei with a large spread in A, Z and N/Z ratios. Before being useful for any experiments, the RIB has to be purified using several steps: magnetic separator, differential energy loss and velocity filter.

A variation of this method is used at the Michigan state university [4]. Due to the production mechanism this method is limited to RIB close to the stability line.

2.2 The ISOL method

The ISOL method uses a complementary approach to the projectile fragmentation. A high energy beam of light particles (p, d, ^{4}He or n) impinges on a heavy target and produces radioactive nuclides via spallation, induced fission, target fragmentation. The recoils are stopped in the target that is brought to a very high temperature in order to favor the release of radioactive atoms. They diffuse to the surface from which they desorb and then enter an ion source to be ionized.

ISOLDE at CERN [5] is the major example of a facility based on this technique. There are also other facilities using low energy proton beams such as Louvain-la-neuve [6] or heavy ions as the primary beam for RIB production.

2.3 Comparison of the production method

The two major production techniques can be viewed as complementary methods. Each one has advantages and disadvantages. Table 1 gives a summary of advantages and disadvantages for both production methods.

3 ISOL BASED FACILITY

3.1 Louvain-la-neuve

Since the first successful acceleration of ^{13}N in 1989, Louvain-la-neuve has led the way in the field of RIB acceleration, and considerable progress has been made since then [7]. Now the range of post-accelerated ion species spans from ^{6}He to ^{35}Ar. The intensities range from 10^5 pps for $^{35}Ar^{5+}$ and up to $2x10^9$ pps for $^{19}Ne^{2+}$. The energy range now available is between 0.6 to 4.9 A*MeV.

The Louvain-la-neuve facility uses two cyclotrons, and an on-line ECR ion source to produce, ionize and accelerate the radioactive ion beams. The 30 MeV proton beam of the first accelerator, CYCLONE30, is used to produce a large quantity of unstable elements using suitable targets. These elements are injected into an ECR ion source, they are ionized, and after a first magnetic separation, are injected into a second cyclotron, CYCLONE110, which accelerates the beam to the required energy.

The exotic species accelerated so far are mainly noble gases such as ^{6}He, ^{18}Ne, ^{19}Ne, ^{35}Ar, or elements like ^{13}N or ^{11}C which are extracted on-line from the production target, in gaseous form like ^{13}N-N or $^{11}CO_2$ molecules. Due to the quite low energy of the production beam those elements have to be produced using specific targets. The production beam intensity varies between 120 μA and 180 μA, depending on the target material of the charge state required since the target is directly connected to the ECR ion source.

^{18}F is a peculiar case in this list because it is produced by a quite different approach. Due to the high chemical reactivity of this element, the on-line extraction of fluorine from the production target with a high efficiency is difficult. They were successful by using a technique developed by the PET center. After chemical separation the

0-7803-4376-X/98 /$10.00 © 1998 IEEE

$CH_3{}^{18}F$ is transferred in a gaseous form to the ECR ion source.

Table 1. Advantages and disadvantages of the In-flight separation method

Method	Advantages	Disadvantages
in-flight Separation	•Short separation (micro sec.) •Simple target fabrication • High collection efficiency (app. 50%)	• Low primary beam intensity for heavy ions • Target thickness limited by momentum acceptance of the recoil spectrometer • Moderate beam purity, required several stages • Large emittance; transverse and longitudinal •RIB at high energy, difficult to decelerate
ISOL	• Thick Target • Intense Primary Beam are available, highest luminosity • High RIB purity • Low emittance; transverse and longitudinally • Long expertise in the field or target/ion source	• Yield strongly coupled to target/product chemistry, (element dependent) • Delay due to diffusion, desorption and effusion time (element dependent) • Requires a post-accelerator

The acceleration is done using an existing cyclotron, CYCLONE. Unfortunately, the unstable ions are injected together with intense (several orders of magnitude larger) beams of stable elements having almost the same mass over charge ratio (m/q). To achieve a high purity in the final beam, the cyclotron is tuned as a radio-frequency mass spectrometer, so that the intensity of isobaric contaminants is considerably reduced after the acceleration process. In an isochronous field the mass resolving power $R= (q/m)/\Delta(q/m)$ is given by: $R=2\pi\ h\ N\ /\ \sin\phi_0$, where h is the harmonic number, N is the number of turns required to the full energy, and ϕ_0 the initial phase. In order to reach the high mass resolving power the number the number of turns has to be large, which implies a low dee voltage. This has the effect to reduce considerably the acceleration efficiency.

3.1.1 Future upgrade

A new cyclotron is presently under construction, CYCLONE44. It will cover the energy range between 0.2 and 0.8 A*MeV, and it is designed to combine the high acceleration efficiency (one order of magnitude larger than it is in CYCLONE), with a high mass resolving power, in order to provide pure radioactive beams of low intensity in the presence of intense isobaric contaminants. The main challenge in the design of CYCLONE44 lies in the combination of these two requirements. The resolving power is proportional to the number of turns times the harmonic number, thus requiring low dee voltage and high harmonic modes. On the other hand, a large acceleration efficiency can only be obtained if the axially injected low energy beam is perfectly matched to the cyclotron central region acceptance in the six dimensional phase space. This requirement calls for a low harmonic number, high injection voltage and high dee voltage.

3.2 The Holifield Radioactive Ion Beam Facility

The Holifield Radioactive Ion Beam Facility HRIBF has the mission to provide an economic first generation RIB facility [8]. The HRIBF utilizes two existing accelerators, the Oak Ridge Isochronous Cyclotron (ORIC) and the 25 MV tandem. In the past ORIC served as an energy booster for stable heavy ion beams from the tandem. For RIB production this process has been reversed: ORIC will produce the RIB that will be accelerated using the tandem.

The ORIC accelerator is used to bombard a thick target. High intensity light-ion beams such as 50 μA of 100 MeV alphas, 50 MeV deuterons, or 60 MeV protons are transported to the RIB injector to bombard a thick target material. The injector is located in a heavily shielded room which was originally designed to house the experiments utilizing the 1 mA 75 MeV proton beams. The ion source platform houses the target/ion source assembly, the first mass separator stage and a cesium charge exchange cell for conversion of positive ions to negative beam.

The use of the existing 25 MV tandem accelerator was clearly dictated by its availability. Tandem accelerators possess some attributes which make them attractive for this type of application. They have a large phase acceptance, and have the ability to accelerate singly charged particles with low initial velocity. The main disadvantage is the fact that tandem require a negative ion beam. In some cases it is not possible to create negative ions with high efficiency.

3.2.1 Future upgrade of the HRIBF

This first generation RIB accelerator has several limitations; the limited energy provided by the tandem and the limitation in energy of the production accelerator. The low energy of the primary beam limits the intensity of RIB far from the stability. HRIBF has several possibilities for upgrade; 1) they can add a superconducting booster in order to reach the coulomb barrier for heavier masses, 2) replacing ORIC by a modern cyclotron to provide higher primary beam energy and higher intensity.

3.3 The RNB facility at KEK Tanashi (INS Tokyo)

At INS, University of Tokyo, an ISOL based RIB facility in now in operation after 4 years of construction [9]. The INS RIB facility is a prototype for the Exotic Nuclear Beam Arena (E-Arena) of the Japanese Hadron Project (JHP). It was built in order to develop critical techniques such as a highly efficient ion source, a high resolution isotope separator, a versatile RIB accelerator.

The radioactive nuclides are produced in a thick target using a 2 μA proton beam coming from a K=67 SF cyclotron. Three different types of ion sources have been developed to ionize the various elements: surface ionization, Forced Electron Beam Induced Arc Discharge (FEBIAD) and an ECR ion source.

The separated beam with a charge to mass ratio greater than 1/30 is injected at 2 A*keV into a Split Coaxial RFQ (SCRFQ) linac operating at 25.5 MHz. After stripping at 170 A*keV the beam is injected into an Interdigital H type RF structure composed of 4 cavities operating at twice the RFQ frequency (51 MHz) accelerating ions with a mass to charge ratio 1/10. The output energy is variable from 0.170 to 1.05 A*MeV.

3.3.1 *Future RIB, JHP (E-Arena)*

INS and KEK, the National Laboratory for High Energy Physics, have merged as a new organization as of April 1997. The new National Laboratory aims at promoting the JHP. In the E-Arena, it is planned to use a 10 μA proton beam from the 3 GeV rapid synchrotron booster for the production of exotic nuclei.

3.4 SPIRAL project at GANIL

GANIL is a well-known heavy ion facility based at Caen (France) operating since 1983. It is composed of a cascade of three cyclotrons; C01,2, SSC1 and SSC2. The two SSC produce beams up to 95 A*MeV for fully stripped ions. This facility has been producing RIB with the projectile fragmentation method using the recoil spectrometer LISE [10] and SISSI [11]. Some years ago, the beam intensity was upgraded up to $2x10^{13}$ pps for light ions up to Ar. As an extension to the existing RIB facility, GANIL has been funded in December 1993 to develop an ISOL based facility, SPIRAL, using a new K=262 MeV SSC [12].

The primary beam accelerated by the GANIL cyclotrons will bombard a production target located inside a well-shielded cave beneath ground level in the existing machine building. It was shown [13] that using heavy ions as the primary beam can be competitive in some area to the so called classic ISOL where high energy protons are used to bombard a heavy element target. In the case of heavy ions the projectile fragmentation is the process of most importance. In all cases, the reaction products are stopped in the target. The originality of the SPIRAL project lies in the use of an extended range of heavy-ions, up to the maximum available energies of 95 A*MeV for 36 Ar. The chosen target is made from carbon and it is designed in such a way that it can stand very high power density of the Bragg peak.

The new cyclotron under construction (CIME) is a room temperature compact cyclotron of K=265 MeV with an average magnetic field between 0.75 and 1.56 T and an ejection radius of 1.5 m. The energy range is 1.7 to 25 A*MeV. The resonators should be ready in May this year. Then injection is done using a 34 mm radius Mueller type inflector for harmonic 2,3 and 4. For harmonic 5 a new inflector with a radius of 45 mm is under investigation. The extraction is done using two electrostatic and two magnetic channels. One other aspect of the SPIRAL project is the use of a cyclotron like Louvain-la-neuve as a mass spectrometer.

The first proposed beams for SPIRAL will be limited to noble gases elements ^{6,8}He, ^{17,19}Ne, ^{23,27}Ne, ^{32,35}Ar, ^{41,46}Ar and ^{72,77}Kr. The projected intensities range from $5x10^{3}$ for ^{17}Ne to $6x10^{8}$ for ^{6}He.

The first stable beams will be accelerated at the end of 1997, while commissioning of the target and ion source assembly will begin in early 1998.

3.5 REX-ISOLDE RIB facility

A pilot experiment is proposed to study very neutron rich isotopes in the region around the neutron shell closure of N=20 and N=28 after Coulomb excitation and neutron transfer [14]. To do this the plan is to accelerate the ISOLDE beams up to 2 A*MeV by the means of a new linear accelerator. The linear accelerator concept will require the development of a charge state booster capable of producing ions with a charge to mass ratio greater the 1/4.5.

ISOLDE uses the 1 GeV proton beam from the CERN PS booster delivering a 2 μA time averaged proton beam with a pulse at 0.4 to 0.8 Hz rate. This facility is operating since more than 25 years producing a very wide range of isotopes for applied and fundamental sciences research.

REX-ISOLDE is considered like other experimental equipment. The ISOLDE 1+ beam will be injected into a Penning ion trap which will be used as an accumulator and buncher device to convert the DC beam into 50 Hz pulses. These pulses will then be injected into a charge state booster consisting of an Electron Beam Ion Source (EBIS). The pulsed beam will be injected into a 4-rod RFQ that will bring the ions energy from 10 to 500 A*keV, an 11-gap Interdigital H type RF structure then increases the energy to 1.0 A*MeV, and finally three 7-gap resonators accelerate the beam to 2.0 A*MeV. All the linac accelerating structures operate at 108 MHz and the system is pulsed at 50 Hz with a 5% duty cycle.

3.6 EXCYT project, LNS Catania

The Laboratorio Nazionale del Sud is equipped with a 15 MV tandem and now with a K=800 MeV superconducting cyclotron [15]. These accelerators will be reconfigured in order to provide an ISOL type RIB facility.

In order to increase the energy and the intensity from the SC cyclotron, a new 14.5 GHz, 1.4 T, superconducting ECR ion source was constructed for axial injection. The aim is to extract from the SC cyclotron beam currents of the order of 1 μAp. This is a challenge for this type of cyclotron, and the electrostatic deflector will have to stand very high power of the order of 3 kW coming from the extracted beam.

The negative ions will be produced with a new 150 kV injector, similar to the HRIBF concept and injected into the 15 MV tandem accelerator. RIB up to mass 40 will be accelerated above the Coulomb barrier. The EXCYT project has been funded in 1995 and the commissioning of the facility will start in the middle of 1998 and operation in 1999.

3.7 ISAC RIB facility at TRIUMF

In June 1995 the ISAC project was funded to build a RIB facility based on the 500 MeV and 100 μA H- cyclotron [16]. A new beam line is under construction which will guide the beam from the cyclotron vault through the wall into a new tunnel extension. Then beam can be sent to two target stations located into a heavily shielded area. A new building of approximately 5000 m^2 is under construction. This building is divided into two parts, the target handling hall and the accelerator/experimental area hall. The remote handling target concept is based on twenty years of experience in meson production targets. Each target station comprises five modules, primary beam entrance, target/ion source, beam dump and two exit modules containing the front end of the mass separator. All the components are attached at the bottom of a 2 m long steel plug. The target stations are housed in a canyon heavily shielded for a primary proton beam intensity up to 100 μA.

The ion beam from the mass separator can be sent either to the Low Energy Experimental area or to the linear accelerator. The ions with a charge to mass ratio greater than 1/30 are accelerated from 2 A*keV to 150 A*keV by a 4-rod split-ring RFQ operating at 35 MHz in CW mode. After stripping and charge analysis the beam is injected into a Drift-tube linac. The output energy is fully variable from 0.15 to 1.5 A*MeV, using a separated function Drift-Tube-Linac.

A prototype of the split-ring 4-rod RFQ composed of three modules has been tested at full CW power (85 kV inter-electrode voltage) [17].

For the DTL, a new approach was taken in order to deliver a fully variable output energy. Five independently phased IH tanks operating at $\Phi_s = 0°$ provide the main acceleration. Longitudinal focusing is provided by three independently phased 3-gap resonators positioned before the second, third and fourth IH tank. They permit the beam to be kept well bunched over the entire energy range [18].

The first phase (Low Energy Experiments) will be operational by the end of 1998, and the accelerated RIB will become operational a year later.

4 UPGRADE OF PROJECTILE FRAGMENTATION FACILITIES

4.1 Upgrade of the NSCL at Michigan state university

The NSCL has developed a plan to upgrade and couple its existing Superconducting Cyclotron K500 and K1200. Also they propose to replace the present A1200 beam analysis system by an improved A1900 beam analysis system [19]. The upgrade will greatly enhance the performance of the NSCL facility, particularly for studies using radioactive ion beams. The K500 will be disassembled and rotated by 120 degrees from its present orientation. Its central region will be redesigned to allow a more efficient acceleration in the second harmonic mode and to increase the turn separation. A new beam line will be constructed for the coupling between the K500 and K1200 cyclotrons. The beam is then injected radially. After stripping to a higher charge state, the beam will be accelerated to full energy. The improvement in intensity is a result of the lower charge states required from the ECR ion source for the K500⊗K1200 mode. The improvement in energy for mid and high mass nuclei comes from the higher charge state obtained after stripping into the K1200. For example, the maximum energy for 238U will be 110 A*MeV instead of 25 A*MeV in the present configuration. The overall result for RIB production is an increase by a factor 10^3 to $4x10^4$ for ^{11}Li to ^{132}Sn.

4.2 RIKEN upgrade

RIKEN, Accelerator Research Facility (RARF) proposes an upgrade consisting in an intensity upgrade by replacing the high voltage platform by a combination ECR ion source and a 4-rod folded coaxial variable frequency RFQ. In Addition to the existing K540-MeV ring cyclotron (RRC) two new cyclotrons will be built [20]. A K930-MeV room-temperature ring cyclotron (RC4) and a K2500-MeV superconducting ring cyclotron consisting of six sectors (SRC6). The maximum beam energy of the RC4 is 135 A*MeV and 400 A*MeV for SRC6.

The project was formally approved in December 1996 and the design is nearly completed. The commissioning is due for the year 2002. With the combination of new high intensity injector and post-accelerator delivering heavy ion of several hundreds of A*MeV RIKEN will become the most intense source of RIB using the in flight separation technique.

4.3 SIS/GSI (Darmstadt, Germany) upgrade

GSI possesses one of the most powerful projectile fragmentation facilities. SIS can accelerate heavy ions up to 2 A*GeV. Combined with the Fragment Recoil Separator (FRS) a very wide range of radioactive ion beams can be produced. The limiting factor at the moment is the primary beam intensity.

At present SIS uses the original UNILAC as injector, not designed originally to be a dedicated synchrotron injector.

In order to fill the SIS up to its inherent intensity limit the linac has to be modified [21]. The limit is set by the space charge effects at the injection. Improvement on ion source are required.

The choice of $A/q \leq 65$ for the new linac design is in accordance with the "state of the art" for the ion source. For the new pre-stripper linac, a frequency of 36 MHz is chosen, which is one third of the Alvarez frequency.

A novel approach for the RFQ structure is used. The RF mode is the H_{110}- mode which is similar to the one used in Interdigital H type RF structure. The RFQ tank is 1 m in diameter and 9.4 m long. The IH-DTL is composed of two cavities, 9.15 and 10.2 m long. The first tank contains 3 quadrupole triplets and the second only one. Triplets are used for the transverse focusing. Quadrupole magnets are laminated, and the field at the surface of the pole is 1.35 T. With this intensity upgrade SIS will be able to run at the space charge limit in 1998.

5 PROPOSED RIB BASED ON ISOL METHOD

5.1 Argonne National Laboratory

The Argonne concept for a RIB facility is based on the use of the existing superconducting linac as the major part of the post-accelerator. The new components for the RIB facility will be constructed in a new building north of the existing ATLAS facility. The driver accelerator can be a conventional 215 MV linear accelerator or a superconducting linac using a two-gap superconducting niobium resonator.

Acceleration of low q/m RIB will requires a sequence of three new subsystems; a short low frequency RFQ and two sections of superconducting linac optimized for these low charge state ions. After acceleration at energies between 0.5 and 1. A*MeV the secondary beams can be delivered to the new experimental area. For further acceleration the beam will be injected into the actual ATLAS facility.

Prototyping of the 12 MHz split-coaxial RFQ have started, and they plan having a 40 kW RF amplifier running by the end of the summer, and test in the fall, [22].

5.2 PIAFE

The project PIAFE in Grenoble plans to take advantage of the proximity of the high neutron flux (10^{14} n/s/cm^2) from the Institut Laue-Langevin nuclear reactor (ILL). The radioactive ions will be produced via induced fission of ^{235}U by thermal neutrons [23]. After two successive mass-analysis, inside the ILL reactor building, the beam will be sent to a high mass resolution separator, first phase (PIAFE1). In the second phase (PIAFE2), the singly charged ions will be guided to the SARA accelerator complex of the Institut des sciences nucléaires (ISN-Grenoble). Before being injected into the cyclotron the singly charged ions will be converted into higher state using an ECR as charge state breeder. The final energy will be comprised between 2 and 10 A*MeV.

5.3 Beijing Radioactive Nuclear Beam Facility (BRNBF)

The Beijing Radioactive Nuclear Beam Facility proposed and ISOL type RIB facility based on a high intensity proton beam produced by a 70 MeV H$^-$ cyclotron. After mass analysis the RIB will be accelerated using an existing HI-13 tandem accelerator [24].

6 DISCUSSION

The use of intense RIB opens new possibilities and it is a very active field. The demand for high energy RIB beam around the Coulomb barrier is very challenging for accelerator physicists.

The choice of the post accelerator depends on the physics program, which defines the energy and mass range requirements. First generation RIB facilities take advantage of existing accelerators;

- Louvain-la-neuve, cyclotron
- HRIBF, tandem
- EXCYT, tandem

Table 2 shows a list of the advantages and disadvantages of different types of accelerator used or proposed for post-acceleration of RIB.

Together, these RIB facilities will cover a very large energy range, from the low energy required for nuclear astrophysics to the Coulomb barrier, intermediate energies and above the Fermi energy. A new field of experiments will be possible and will give us insight into the nucleosynthesis in stars, novae and supernovae, nuclear structure, and investigation of exotic nuclear matter.

7 ACKNOWLEDGMENT

The author wants to tank all the colleagues from other laboratories who provided important pieces of information for the preparation of this talk, in particular: Dr. M. Lieuvin (SPIRAL/GANIL), Dr. G. Ryckewaert (Louvain-la-neuve), Dr. I. Katayama, Dr. S. Arai, Dr. M. Tomizawa (INS/Tokyo), Dr. J. Garrett (HRIBF), Dr. G. Münzenberg, Dr. F. Nickel, Dr. N. Angert (GSI), Dr. J.L. Belmont (PIAFE/ISN-Grenoble), Prof. D. Habs (REX-ISOLDE/Munich), Dr. J. Nolen, Dr. K. Shepard (ANL), Dr. G. Ciavola (EXCYT/LNS), Dr. G. XiaLing (Beijing RNBF), Dr. Schmor, Dr. G. Dutto and Dr. R. Poirier and Dr. R. Laxdal (ISAC/TRIUMF).

REFERENCES

[1] S. Tanihata, et al. Phys. Lett. B 160:380, (1985)
[2] P. G. Hansen, B. Jonson, Europhysics Lett. 4:409 (1987)
[3] W. Schwab, et al. Z. Phys. A 350:283 (1995)
[4] J. J. Kolata, et al. NIM, B40/41 (1989) 503.
[5] H. L. Ravn and B. W. Allardyce, Treatise on Heavy Ion Science, Ed. D. A Bromley, Vol. III, Nuclei Far From Stability (Plenum Press, New York, 1989)
[6] M. Loiselet, et al. Proc. of the RNBIII, Ed. DJ Morrissey, Edition Frontières, Gif-sur-Yvette (1993) 179.
[7] M. Loiselet, et al. Proc. of the 14th Int. Conf. On Cyclotrons and their Application, Cape Town, South Africa (1995), 629.
[8] A proposal for physics with Exotic Beams at the Holifield Heavy Ion Facility, Feb. 1991, Ed. JD Garrett and DK Olsen.
[9] I. Katayama, et al. INS-Rep.-1163, Sept. 1996.
[10] R. Anne, et al. NIM, A257 (1987)
[11] C. Grunberg, et al. GANIL Int. Rep. R89 09
[12] M. Lieuvin, GANIL Int. Rep. S 95 04
[13] H. L. Ravn, et al. NIM **B88** (1994) 441.
[14] REX-ISOLDE, CERN Report ISC 94-25, Geneva, 1994.
[15] EXCYT project, Status report, LNS 20-5-96
[16] PG Bricault, et al. Proc. Of the XVI Particle Accelerator Conf. Dallas (1995)
[17] RL Poirier, et al. The RFQ prototype for the Radioactive Ion Beam Facility at TRIUMF, Proc. XVIII Inter. Linac Conf., Geneva, Switzerland, Aug. 1996
[18] RE Laxdal and P Bricault, Design of a drift tube linac for the ISAC project at TRIUMF, Proc. XVIII Inter. Linac Conf., Geneva, Switzerland, Aug. 1996
[19] K500⊗K1200, Michigan State University Internal Rep. MSUCL-939
[20] Y. Yano, RIKEN RI-beam Factory Project, this conference.
[21] N. Angert, Status and development of the GSI accelerator facilities, EPAC96 and GIS-95-05 Report, Beam intensity upgrade of the GSI accelerator facility. June 1995.
[22] K. W. Shepard, private communication.
[23] JL Belmont, et al. Proc. Int. Workshop on the physics and techniques of secondary nuclear beams, p. 407, Dourdan, France, 1992. Edited by;. JF Bruandet, B. Fernandez and M. Bex, Ed. Nouvelles Frontières.
[24] Guan XiaLing, this conference

Table 2. Comparison between different post-accelerator

Accelerator	Advantages	•Disadvantages
Tandem	• Can accelerate singly charge ion • Reliable operation, • Energy continuously variable • Good beam quality.	•Require negative ion •Require high voltage injector, not compatible with high radiation field around the target •Require high voltage; V> 25 MV to reach the Coulomb barrier
Cyclotron	• Can obtain high energy at low cost: E ≤ A•20 MeV • Can be use as a mass spectrometer	•Required high charge state; expertise on on-line ion source for singly charged ions only. •Very large contamination of the central region. •Large energy spread
LINAC	• Good transverse and longitudinal emittance • Energy fully variable • Good transmission	•Require low frequency RFQ •CW mode required efficient rf structures

RIKEN RI-BEAM FACTORY PROJECT

Y. Yano and A. Goto, RIKEN Wako, Saitama 351-01, Japan and
T. Katayama, Center for Nuclear Study, School of Science,
University of Tokyo Tanashi, Tokyo 188, Japan

Abstract

The RIKEN Accelerator Research Facility (RARF) has proposed the "RI-Beam Factory" project. In 1997 fiscal year, the construction budget for the first phase of this project has been formally approved. The factory is aimed at providing the world's most intense RI (radioisotope) beams at energies of several hundreds MeV/nucleon over the whole range of atomic masses. RI beams will be generated by the projectile frag-mentation. For the efficient generation a cascade of a K930-MeV ring cyclotron and a K2500-MeV super-conducting ring cyclotron will boost the energy of heavy-ion beams from the existing ring cyclotron up to 400 MeV/nucleon for light ions and more than 100 MeV/nucleon for very heavy ions. Moreover, this factory includes a next generation of the multi-use experimental storage rings (MUSES) consisting of an accumulator-cooler ring, a booster synchrotron ring and double storage rings. The MUSES will enable us to conduct various types of unique colliding experiments.

1 INTRODUCTION

The RARF (RIKEN Accelerator Research Facil-ity) has a heavy-ion accelerator complex consisting of a K540-MeV ring cyclotron (RRC) as a main ac-celerator and two different types of injectors: a fre-quency-variable Wideröe linac (RILAC) and a K70-MeV AVF cyclotron (AVF). The facility provides heavy-ion (HI) beams over the whole atomic mass range and in a wide energy range from 0.6 MeV/ nucleon to 135 MeV/nucleon. One of the remarkable features of this facility is capability of supplying light-atomic-mass RI (radioisotope) beams with the world-highest level of intensity which are produced by means of the projectile-fragment separator, RIPS [1].

In order to further promote experimental programs utilizing RI beams, the RARF undertakes the construction of "RI Beam Factory". The bird's eye view of its layout is illustrated in Fig. 1. The factory is aimed at providing RI beams covering over the whole atomic-mass range with very high intensity in a wide energy range up to several hundreds MeV/nucleon.

2 A CASCADE OF CYCLOTRONS FOR HIGH-INTENSITY RI BEAM PRODUCTION

The factory utilizes the "projectile fragmentation" to generate RI beams of intermediate energies. To enable the efficient generation of such RI beams covering the whole atomic masses, are needed high-intensity primary heavy-ions, up to uranium ions, with the energies exceeding 100 MeV/nucleon. In order to realize those beams, we will construct a cascade of an intermediate-stage ring cyclotron (IRC) with K=930 MeV and a superconducting ring cyclotron (SRC) with K=2500 MeV as an energy booster of the existing RRC. In addition, we will upgrade the RILAC which serves as the initial-stage accelerator by introducing a new pre-injector and a charge-state mulitiplier (CSM). This accelerator complex, which is schematically illustrated in Fig. 2, will possess such perfomance that a 100 MeV/nucleon uranium beam with the intensity over 1 pμA is obtainable.

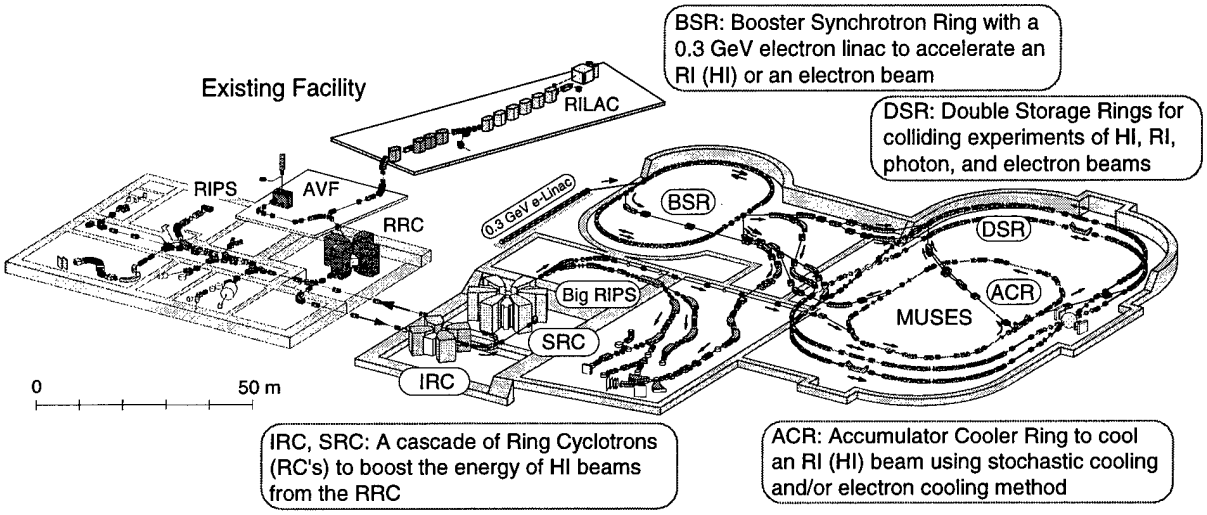


Fig. 1 Bird's eye view of "RI-Beam Factory" layout.

0-7803-4376-X/98/$10.00 © 1998 IEEE

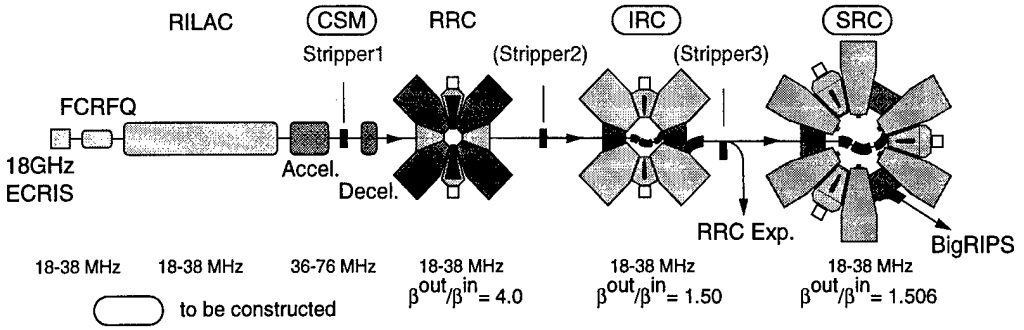


Fig. 2 Conceptual diagram of heavy-ion accelerator complex for RI-beam production.

2.1 Pre-injector for RILAC

The RILAC is stably operational in the acceleration radio-frequency range between 18 MHz and 38 MHz. In order to upgrade the RILAC performance in the beam intensity by one or two orders of magnitude, its new pre-injector system consisting of a frequency-tunable folded-coaxial RFQ linac (FC-RFQ) equipped with an 18-GHz ECR ion source (ECRIS-18) has been developed. In the recent acceleration tests, the FC-RFQ has successfully covered HI beams in the energy-mass region required, and the beam transmission efficiency of about 90 % at the maximum was obtained [2]. In addition, high-intensity highly-charged ion beams have been produced by the ECRIS-18 [3].

2.2 CSM

The CSM consists of an accelerator, a charge stripper and a decelerator. Its functions are to produce higher charge state of ion beams by further increasing the stripping energy and to reduce their magnetic rigidity by decelerating them to the initial energy. With this device the magnetic rigidity of the RILAC beam with a most-probable charge state can be reduced to the acceptable value of the RRC even when the injection velocity into the RRC is increased as shown in Fig. 3. The accelerator and decelerator are of a type of frequency-tunable IH linac whose operational radio-frequencies are twice as that of the RILAC to double an acceleration gradient. Transmission efficiency through the CSM depends only on charge state distribution behind the charge stripper foil.

2.3 IRC-SRC

The maximum beam energy of the SRC is set to be 400 MeV/nucleon for light ions which is achieved at 38 MHz, the maximum radio-frequency in the RILAC. Based on the characteristics of the existing machines, this means that the velocity of the RRC's output beam has to be amplified by a factor of 2.26 by combination of the IRC and the SRC. Harmonic numbers of the IRC and the SRC are chosen to be 7 and 6, respec-tively, while that of the RRC is 9, considering the maximum magnetic field strength and the central space to place the injection elements. The mean injection radius of the IRC is taken to be 7/9 times the mean extraction radius of the RRC, and the velocity gain factor of the IRC to be 1.50 (accordingly that of SRC is to be 1.506). On the above conditions, the mean injection and extraction radii of the IRC are 2.77 m and 4.15 m, respectively, and those of the SRC are 3.56 m and 5.36 m, respectively. The sector angles are taken to be 51° for the IRC and 25° for the SRC, based on the beam dynamics study [4]. The radio-frequency of the IRC and the SRC ranges from 18 MHz to 38 MHz which are the same as that of the RILAC and the RRC. The maximum magnetic field strength in the sector magnets is to be 1.9 T for the IRC and 4.3 T for the SRC. This IRC-SRC system boosts the energy of uranium ions from the RRC up to more than 100 MeV/nucleon.

Geometries and characteristics of the IRC and the SRC thus designed are shown in Fig. 4 along with those of the RRC. The structure and size of the IRC are similar to those of the RRC, and the rf resonators of the IRC and

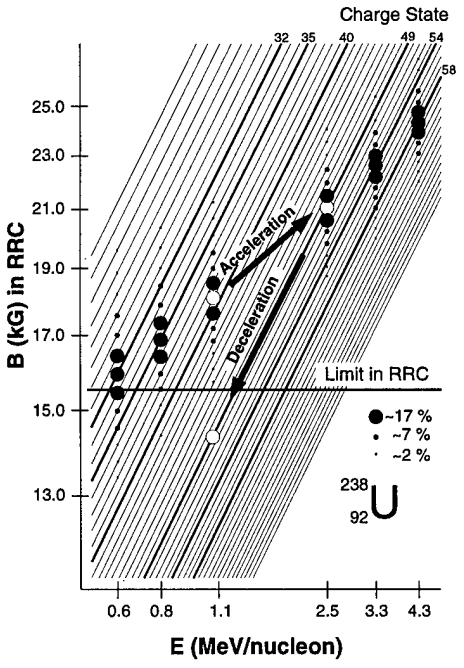
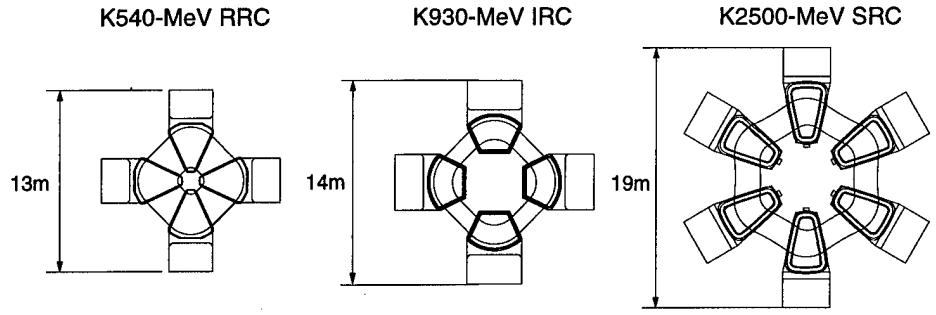


Fig. 3 Principle of the CSM: Size of a dot corresponds to the yields of U ions with re-spective charge states at the stripping (a carbon foil) energy, E. The ordinate represents the necessary bending power in the RRC.



Rinj (m)	0.89	2.77	3.56
Rext (m)	3.56	4.15	5.36
Velocity gain	4.0	1.50	1.51
h	9	7	6
B (T)	1.7	1.9	4.3
Weight (ton)	2,100	2,400	4,000

Fig. 4 Comparison of three ring cyclotrons.

the SRC can also be made to be similar to those of the RRC. Therefore, our effort has been concentrated mainly on the design of the SRC, in particular, on that of its superconducting sector magnets [5] and superconducting injection and extraction systems [6].

As shown in Fig. 5 the IRC's maximum energies are 127 MeV/nucleon for light ions up to around Ar, 102 MeV/nucleon for Kr^{30+}, and 58 MeV/nucleon for U^{58+}. The minimum energy is 25 MeV/nucleon. In the SRC the maximum energies are increased to 400 MeV/nucleon for light ions up to around Ar, to 300 MeV/nucleon for Kr^{30+}, to 150 MeV/nucleon for U^{58+} and to 100 MeV/nucleon for U^{49+}. The minimum energy is 60 MeV/nucleon.

We have undertaken the fabrication of a full-scale model sector magnet of the SRC without a yoke to verify the mechanical and cryogenic design [7]. The superconductors for the main and trim coils have already been complete. This task is scheduled to be finished by the spring of 1998.

In this two-stage cyclotron scheme the simultaneous utilization of the HI beams is possible in both of the existing experimental facility and the new facility, when part of the IRC beam is charge-stripped and is transferred back to the existing facility. As an example, part of a 127 MeV/nucleon $^{16}O^{7+}$ beam from the IRC, the main part of which is injected to the SRC, is charge-stripped to O^{8+} and delivered to the existing facility where the magnetic rigidity of this O^{8+} beam can be accepted.

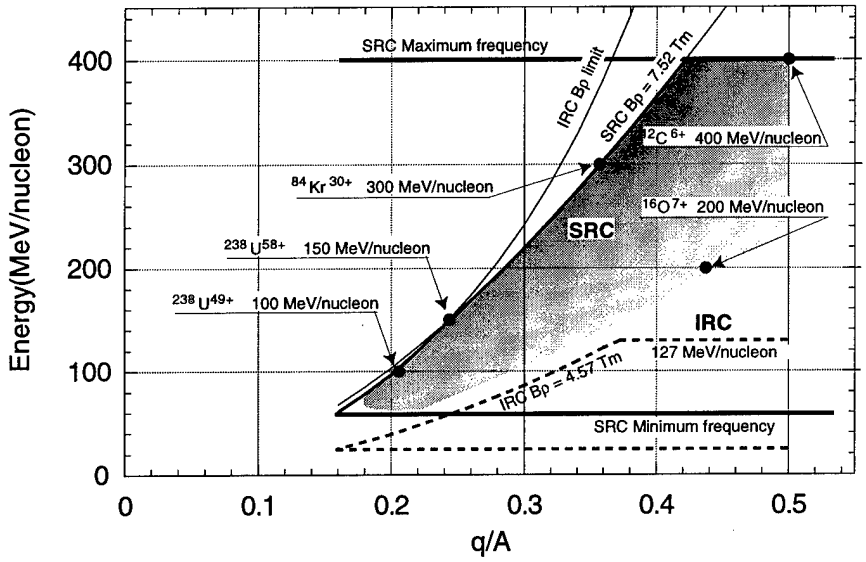


Fig. 5 Maximum HI-beam energy obtainable by the IRC and the SRC for ion species with different charge-to-mass ratos, q/A.

3 MULTI-USE EXPERIMENTAL STORAGE RINGS (MUSES)

The MUSES (Multi-USe Experimental Storage rings) consists of an Accumulator-Cooler Ring (ACR), a Booster Synchrotron Ring (BSR) with an injector electron linac and Double Storage Rings (DSR). It will be installed downstream from the SRC and an RI beam separator, Big-RIPS.

The ACR functions for accumulation and cooling of RI (HI) beams, and is also used for atomic and molecular physics experiments with a cooler electron beam. The BSR works solely for the acceleration of RI (HI) and electron beams. The DSR permits various types of unique colliding experiments: RI (HI) - HI

merging or head-on collisions; collisions between electron and RI (HI) beams; and collisions of RI (HI) beams with a high brilliant X-ray emitted from an undulator which is inserted in one ring of the DSR.

3.1 Production of RI Beams

The SRC's HI beams irradiate a production target and are converted to RI beams through the projectile fragmentation. RI beams generated are the mixture of various RI's; and therefore, they will be purified by means of momentum and charge-state selection at Big-RIPS.

Production rates of RI beams were theo-retically estimated with the computer code INTENSITY2 [8]. In the code, physical nature of projectile fragmentation process is empir-ically treated. Kind of primary beam and thickness of the Be production target were optimized so as to obtain the maximum production rate. Figure 6 shows the result of estimation with the assumption that intensity of the primary HI beam is 1 pμA, and that the acceptance of the Big-RIPS is 10 mrad in angle and 1 % in momentum.

Typical RI-beam quality was also estimated: the momentum spread is ± 0.5 %; the phase width relative to RF frequency is ± 5 degrees; and the transverse emittance is 4.5 π mm·mrad in both horizontal and vertical directions. This beam is transported from the production target point to the injection point of the ACR along the length of 70 m. At the end point of transport line, a

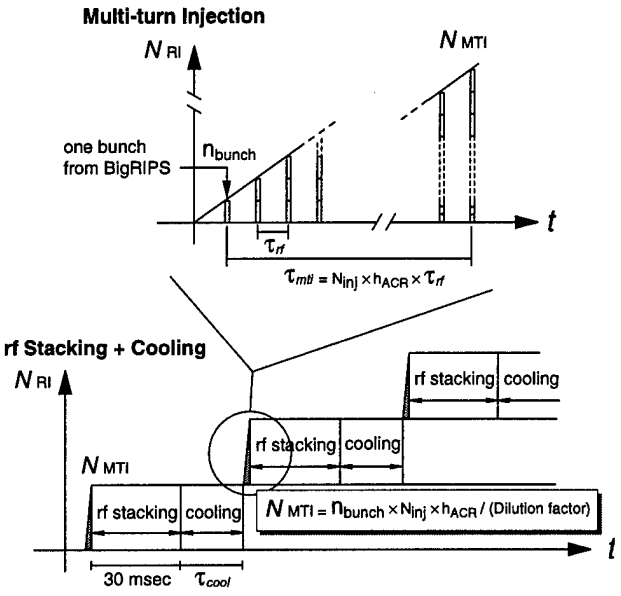


Fig. 7 Time chart of multi-turn injection (top) and rf-stacking plus cooling (bottom) in the ACR. In the figure n_{bunch} denotes the number of RI ions in one bunch coming from the Big-RIPS per τ_{rf} (=1/38MHz–1/18MHz), N_{inj} the number of injected turns (=~40), and h_{ACR} harmonics of the ACR (=30).

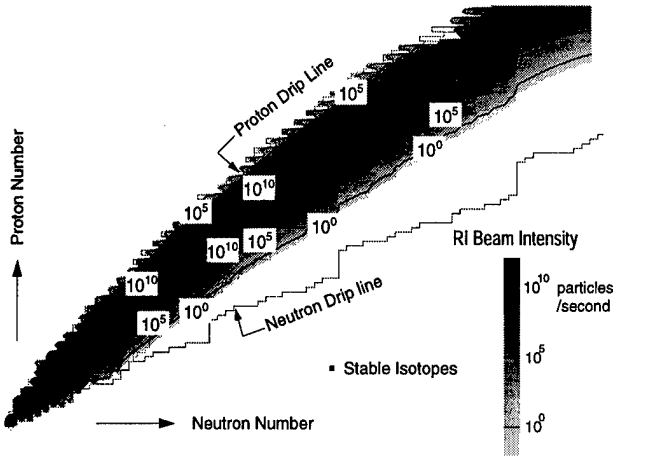


Fig. 6 Production rate of RI-beams per 1 pμA primary beam.

debuncher system with a voltage of 8 MV and harmonics number of 6 will be installed to reduce the momentum spread to ± 0.1 %.

3.2 Accumulation and Cooling of RI beams in ACR

Figures 7 and 8 show the time chart for the accumu-lation process of RI beams in the ACR. RI-beam bunches coming from the Big-RIPS are injected into the ACR by means of the multi-turn injection. Then the rf-stacking associated with the beam cooling is per-formed. Momentum cooling continuously works during the rf-stacking. This process is repeated at intervals of the rf-stacking time of 30 ms plus the cooling time τ_{cool} depending on the RI-beam property.

Simulation study for both of the electron cooling and the stochastic cooling of RI beams was done [9]. As a result, it turned out that the stochastic cooling is much faster than the electron cooling. An electron cooler with length of 3 m and current density of 0.5 A/cm^2 gives, for example, the cooling time of 380 s for ^{6}He and 0.42 s for ^{232}U, whereas a stochastic cooling system composed of a 10 kW feed-back amplifier with a band width of 2 GHz gives 0.20 s and 5.0 ms, respectively. This is due to the property of the RI beam: the intensity is rather weak; and both of the momentum and emittance spreads are large.

The RI beam accumulated in the ACR decays with its own intrinsic life time τ_{life}. The number N_{total} of the RI ions stored in the ACR after the period of τ_{life} is determined by the balance of the supply rate and the decay rate as shown in Fig. 8. The space charge limit was also considered in the estimation of the maximum number of RI ions stored in the ACR. This limit, however, becomes effective only for RI ions neighboring on the stability line with high production rate.

The accumulated RI beams in the ACR will be fast extracted and one-turn injected into the BSR (see Fig. 8.)

3.3 BSR

In the BSR, RI (HI) beams will be accelerated to the energy required for the experiment within 0.3 s, and then will be one-turn injected into the one ring of the DSR (see Fig. 8.) The maximum energies are: e.g., 1 GeV/nucleon for $^{238}U^{92+}$, 1.5 GeV/nucleon for ions of charge-to-mass ratio (q/A) of 1/2 and 3.5 GeV for protons [10]. The slow-extraction channel will also be prepared.

Electrons are accelerated up to 300 MeV by an electron linac and then injected to the BSR. The BSR boosts the electron energy up to 2.5 GeV at the maximum and supply them to the one ring of the DSR. The expected beam current in the DSR is about 500 mA. In order to make a synchronous collision of electrons and RI (HI) ions, the bunch number of electrons are varied from 30 to 45 according to the ion beam energy from 300 MeV/nucleon to 3.5 GeV/ nucleon. The numbers of electrons in a bunch are then 9×10^{10} and 6×10^{10}, respectively.

3.4 DSR

The DSR consists of vertically-stacked two rings of the similar specification. Each lattice structure takes the form of a racetrack to accommodate two long straight sections. These straight sections of one ring vertically intersect those of the other ring at two colliding points: one point is used for the collision between an RI beam and an electron beam at a collision angle of 20 mrad and the other for the merging of RI (HI) beams at a merging angle of 170 mrad. RF cavities and beam injection devices are placed at these long straight sections. Two short straight sections will be used for electron coolers to suppress the beam instabilities and to make a short-bunch ion beams [11].

The ring circumference is 269.6 m, which is 48/6 times the extraction circumference of the SRC, 33.7 m. It means that the harmonic number of the DSR is 48 while that of the SRC is 6. The maximum $B\rho$–value becomes 14.6 Tm when a dipole field strength is 1.5 T at the maximum. Accordingly the maximum energy is 1.0 GeV/nucleon for U^{92+} ions, 1.5 GeV/nucleon for light ions of q/A=1/2, and 3.5 GeV for protons [12].

One of typical experiments conducted at the DSR is the collision of an RI beam with an electron beam to precisely measure charge-density distribution of unstable nuclei [13]. In the experiment, one ring of the DSR will be filled with a high-current electron beam of nearly 500 mA with the energy of up to 2.5 GeV. The lattice of this electron ring is designed so that the emittance of electron beam is 10^{-6} π m·rad from the point of view of the luminosity and beam-beam effect. The parameters of the ion ring are different from those of the electron ring because of the difference between lattices of the colliding section in two rings. Another usage of an electron beam is to generate high brilliant X-ray by an undulator inserted in the electron ring [14]. This X-ray will shine Li-like RI ions circulating in the other ring. By detecting fluorescence emission from the ions, new spectroscopy of unstable nuclei will be possible. For this purpose the electron-beam emittance is required to be as small as 10^{-8} π m·rad. This is achieved by forming the Double Bend Achromat (DBA) system in the arc.

4 CONSTRUCTION SCHEDULE

In the present schedule, the IRC, the SRC, the Big-RIPS and the experimental installation will be completed in 2002. The construction of the MUSES is planned to start in 2003 and to be fully finished in 2009.

REFERENCES

[1] T. Kubo et al., Nucl. Instrum. Meth., **B70** (1992) 309.
[2] O. Kamigaito et al.: in this proceedings.
[3] T. Nakagawa et al.: in this proceedings.
[4] T. Mitsumoto et al.: in this proceedings.
[5] T. Kawaguchi et al.: in this proceedings.
[6] J.-W. Kim et al.: in this proceedings.
[7] S. Fujishima et al.: in this proceedings.
[8] H. Okuno et al.: in this proceedings.
[9] T. Tominaka et al.: in this proceedings.
[10] T. Kubo et al.: in this proceedings.
[11] J. A. Winger et al.: Nucl. Instrum. Meth., **B70** (1992) 380.
[12] Y.J. Yuan et al.: Proc. of EPAC96 (1996) 1338.
[13] T. Ohkawa et al.: in this proceedings.
[14] M. Takanaka et al.: in this proceedings.
[15] N. Inabe et al.: in this proceedings.
[16] T. Katayama et al.: Proc. of 3rd Intl. Conf. on Nuclear Physics at Storage Rings, Bernkastel, Germany (1996), to be published in Nucl. Phys. A.
[17] M. Wakasugi et al.: in this proceedings.

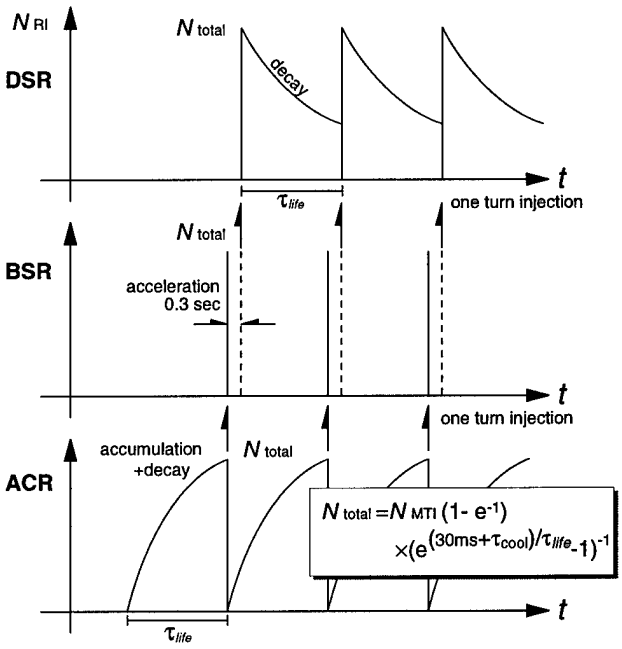


Fig. 8 Time chart of accumulation and acceleration of RI ions in the ACR, BSR and DSR.

STATUS OF THE IUCF COOLER INJECTOR SYNCHROTRON

D.L. Friesel and S.Y. Lee, Indiana University Cyclotron Facility
2401 Milo B. Sampson Lane, Bloomington, IN 47408

Abstract

Construction of a 2.24 T-m, rapid-cycling booster synchrotron is nearing completion at IUCF. Designed to accelerate protons to 220 MeV, it will replace the k200 isochronous cyclotron as an injector of polarized light ion beams (p, d) into the Indiana Cooler. CIS (Cooler Injector Synchrotron) will fill the Cooler to about 10^{11} protons in a few seconds for research. At 30 months into the construction program, all major ring elements are fabricated, assembled, installed and in some cases, commissioned. Ring strip injection and accumulation studies began in March, 1997, ramping studies will start in June, 1997 and Cooler injection studies are planned for late 1997. The status of the construction project and initial beam injection and commissioning results are presented.

1 INTRODUCTION

At the 1995 U.S. PAC, IUCF announced the funding ($2.0M NSF, $1.5M Indiana Univ, 8/94) of and presented major system design and performance goals for a 2.24 T-m booster synchrotron [1, 2, 3, 4, 5] to replace the k200 cyclotron as an injector of polarized ions (p,d) into the Indiana 3.6 T-m electron cooled storage ring [6]. The new injector complex, shown in Fig. 1,

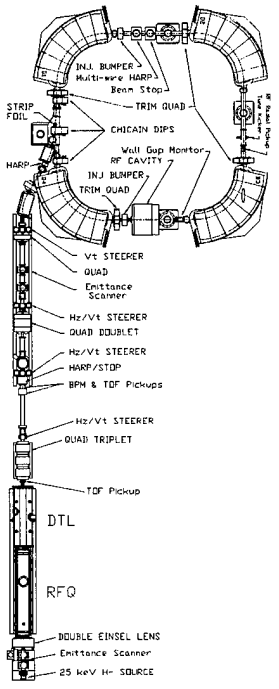


Figure 1: The CIS synchrotron and injection system.

consists of a pulsed, polarized negative ion source (1 mA peak) and 25 keV LEBT, a 7 MeV H^- linac pre-injector, a 9 m long injection beam line, and a rapid cycling (1–5 Hz) 220 MeV proton synchrotron. The lattice chosen for this ring operates below transition, relies on dipole edge angle focusing, and has small dispersion (1.7m) and momentum compaction values (0.62). The small ring circumference (17.37m) presented several accelerator component design challenges. The laminated main dipole magnets (1.27 m radius, 90° bend and 1.7 T maximum field) and the fast extraction kicker and pulse forming network (17 mrad bend, 1m insertion length and 50 nsec risetime) were two such challenges. Several contributions to this conference [7, 8, 9, 10, 11, 12, 13] report on these and other **CIS** accelerator systems completed during the last 24 months. IUCF accelerator operations for research were suspended on November 27, 1996 to install the Linac and assemble the **CIS** ring. Injection and accumulation of 10^{10} protons in the ring was first demonstrated on March 26, 1997. The status of the project, including the initial beam strip injection and accumulation results, is summarized below.

2 RING ASSEMBLY

As the shutdown began, the main dipole and smaller ring magnetic elements were fabricated, field mapping was nearing completion, the Linac pre-injector was undergoing final testing at the factory, and the accelerator vaults and utilities were ready for ring assembly. An unpolarized H^- ion source and 25 keV LEBT was built and the ring injection beam line was assembled and awaiting both the delivery of the Linac and assembly of the ring. The unpolarized source was built from in-house spare parts so that Linac and CIS ring beam development could proceed in parallel with construction of a polarized H^-, d^- source to replace it. For the studies reported here, it routinely delivered 0.4 mA (peak), 25 keV H^- beams, pulsed (50–300 us) at 1–5 Hz with an emittance ($<0.5\pi$ mm-mrad norm.) and convergence (125 mrad Hz & Vt) well matched to the specified RFQ input requirements.

The Linac was delivered in Dec. '96 and evening beam commissioning studies began in Jan. '97 and continued in parallel with daily ring assembly work throughout the 4 month long shutdown. The ring was assembled in its final design configuration except that the extraction kicker and 12° vertical Lambertson magnets were not installed. Their allocated space was used for temporary diagnostic elements (multi-wire HARP, beam stops & emittance scanners) to facilitate the strip injection and accumulation studies. The 4000A ramping main dipole magnet power supply, obtained surplus from FNAL, was completed and initial ramping tests were conducted using the main dipoles. The ferrite tuned rf accelerator cavity was also installed in

0-7803-4376-X/98/$10.00 © 1998 IEEE

the ring. The ring vacuum system, including welded SS dipole vacuum chambers (1mm wall, 5 cm by 10 cm elliptical cross section) incorporating eddy current sextupole correction coils, was completed and evacuated to an average pressure of <0.3 μTorr on March 20, 1997. All ring magnets except the 4 trim quads and the 2 injection bumper magnets were powered and operable via the CIS VISTA control system.

3 RING BEAM DEVELOPMENT RESULTS

Commissioning of the Linac, a commercial 425 MHZ, 3 MeV H^- RFQ coupled directly to a 4 MeV H^- DTL, is reported elsewhere in these proceedings [8]. Briefly, Linac beam transmission (80%), and the 7 MeV H^- beam horizontal emittance ($\epsilon_n < 1.0\pi$) and focussing properties meet the manufacturers guaranteed performance. The injection beam line matches this beam to the optics requirements (*MAD*) at the first ring dipole entrance. Fabricated largely from surplus equipment, it begins with a strong (17 T/m) quad triplet that produces a 6 mm dia. waist at the gap of a 425 MHZ debuncher located 2.5m down stream of the Linac. For these tests, the unfinished debuncher was replaced with a multi-wire HARP [12] to measure Linac transmission and beam profiles. A 6 mm FWHM diameter double waist was achieved here using the calculated (*TR3D*) quad triplet run values, verifying the factory Linac optics predictions. Transmission through the remainder of the 9m beam line to the injection stripper foil is also > 80% using the predicted setup. Of the 400 uA (peak), 25 keV H^- source beam, 320 uA and 250 uA at 7 MeV are transmitted to the HARP following the triplet, and to the stripper foil at injection, respectively. The setup and performance reproducibility of the source, Linac, and beam line is excellent.

Protons are injected into the ring via stripping the 7 MeV H^-beam on a 6.5 mm wide by 25 mm tall 4.5μgm/cm^2 Carbon foil strip fabricated at IUCF. Two bumper magnets located in adjacent straight sections displace the ring equilibrium orbit 20 mm onto the foil during injection. The multi-position foil ladder can be moved transversely to the ring equilibrium orbit to optimize injection. The foil strip improves beam life time and fill rate by increasing the probability that accumulated beam will pass on either side via betatron motion. The calculated foil hit/miss ratio for this configuration is 0.5.

3.1 Ring Strip Injection Performance

Proton beam injection and accumulation were demonstrated at both 3 MeV (RFQ only) and 7 MeV (RFQ + DTL). The action of the missing bumpers was simulated using the ring dipole trims to produce the local orbit bump that displaces the equilibrium orbit onto the carbon foil strip. Injected and accumulated beam is observed on ring dipole entrance and exit BPM's, a Wall Gap Monitor and a multi-wire HARP. The HARP, located between dipoles 1 and 2, is used to view 1st turn injected beam and to close the circulating beam orbit through the first 10 turns or so. A beam stop just behind the HARP measures the strip injection efficiency. Orbit centering and accumulation are optimized using the BPM's and WGM with the HARP and stop removed. 7 MeV proton injection and accumulation profiles, measured with the dipole 2 exit BPM (BPM4), are shown in Fig. 2.

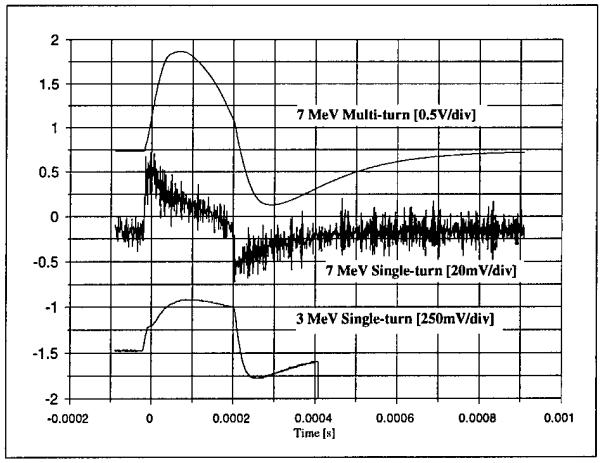


Figure 2: BPM and WGM FET Accumulation Profiles

For these measurements, ring vertical steerer 3 was adjusted from its optimum stored beam value to full output current to prevent multi-turn accumulation to view only the injected beam pulse. The injection pulse length of 220 μsec and the r/c time constant of the BPM amplifier input filter are clearly visible in the single- turn profile. The injected proton beam intensity measured on the stop was 250 μA. The accumulated equilibrium intensity gain of 75 was reached in 100 μsec. A maximum of 18 mA (8×10^{10}protons) were accumulated. Stored beam intensity scales with source intensity, hence the accumulation limit is emittance growth rather than space charge dominated.

A similar injection profile for 3 MeV H^- beam injection is also shown in Fig. 2. The 3 MeV H^- beam is obtained by simply turning off the DTL cavity power. For this beam, an intensity gain of 20 was reached in 75μsec, producing 5 mA of stored protons. The irregular shape of the fill rate after the first 50 usec is likely due to poor centering or injection trajectory.

7 MeV beam accumulation was independently observed by measuring the peak voltage induced across the 3.3 Ω impedance of a wall gap monitor with 200 volts of rf on the accelerator cavity. The WGM voltage is shown in Fig. 3 along with a simultaneous BPM4 accumulation profile. The WGM 57 mV (peak-to-peak) corresponds to 8.5 mA of protons captured in the rf bucket. The rf capture is not adiabatic, only about half the injected beam is captured in the rf bucket, so this measurement is consistent with the simultaneous 17 mA BPM measurement shown. Note that beam capture in the rf bucket at 7 MeV begins only 150 usec after injection start and is completed in about 250 usec. First attempts to capture the 3 MeV beam in an rf bucket were

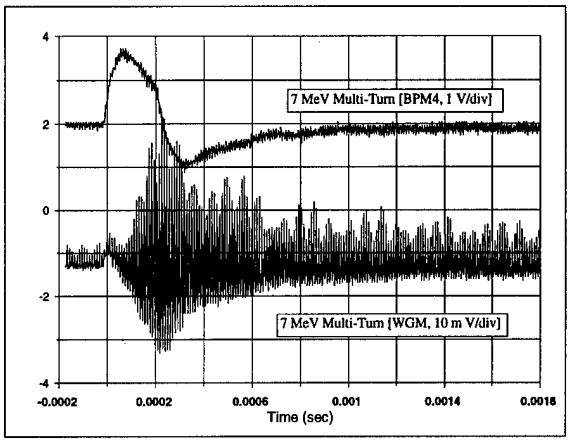


Figure 3: 7 MeV BPM & WGM Accumulation Profiles

not successful, probably because of the short lifetime at this energy. The measured intensity gain and fill rates agree reasonably well with predictions [5]. The 3 to 7 MeV intensity gain ratio (3.5) agrees with calculations, but the measured gains are about a factor of 2.5 smaller than calculated for H^- beams with 1.5% $\Delta T/T$ and $1.0\pi\epsilon_n$ on a 4μg/cm2 Carbon foil. The missing injection bumpers prevent storing the beam long enough to obtain accurate centering information from the ring BPM's and the missing 425 MHz beam line debuncher increases energy spread and reduces life time of the accumulated beam. Measurements at 7 MeV show both short (100 usec) and long (295 msec) 1/e lifetime components, indicating that some beam is displaced off the foil via betatron motion or foil and gas scattering induced energy loss. The shorter life time is that expected for beam on the 4.5 ug/cm^2 foil.

Foil longevity has not been a problem. All development runs were made using the same foil, and without the injection bumpers, the injected and accumulated beam remained on the foil continuously. In routine operation, the injected beam will be on the foil for $\leq 200\mu$sec/sec, a duty factor 5000 times smaller than used for these tests. There is no visible sign of foil deterioration.

3.2 Ring Lattice Parameters

CIS ring Hz and Vt fractional tunes with no trim quad current were measured via the traditional knockout procedure to be 0.49 and 0.77 respectively, which are to be compared with calculated values of 0.491 and 0.783. The stored beam long lifetime component (295 msec) was maximized by adjusting the rf cavity frequency to 2.09683 MHz. For the CIS ring design circumference (17.364 m), this corresponds to a proton beam energy of 6.987 MeV. The rf cavity frequency was varied about this optimum until beam was removed from the ring. The measured frequency width of the stored beam was ± 15 kHz, corresponding to $\pm 1.5\%$ energy acceptance.

4 RING COMPLETION SCHEDULE

Work is continuing to install the injection bumpers and complete the ring ramping controls hardware and software. Main dipole power supply commissioning is proceeding and fabrication of the 20 A, 200 V main dipole trim supplies is underway. Beam ramping development should begin in June with the unpolarized H^- beam, and will continue until the annual December IUCF accelerator shutdown. Fabrication and testing of the extraction kicker should be completed in time for ring installation then. The high energy beam line between CIS and the Cooler ring will also be assembled throughout this period. Unpolarized protons from CIS will initially be injected into the Cooler in January, 1998 following this shutdown. Cooler injection will use the existing the stripping path and ferrite kicker in corner 1. Because of the slow rise and fall times of this kicker, only 2 of the 5 Cooler buckets can be filled in this way. At the CIS design goal of 2.5×10^{10} protons/pulse, this should still give 5×10^{10} stored protons in the Cooler.

5 ACKNOWLEDGMENTS

The successes reported here were the direct result of the skill and dedication of the IUCF technical and professional staff, who installed and debugged a 7 MeV RFQ/DTL Linac and assembled the synchrotron ring, after two years of parts fabrication, during a single 4 month shutdown. The shutdown ended with beam injection and accumulation achieved on the 1st attempt on March 26, 1997, just one week after pumping the completed ring to 0.2 μTorr. There is no substitute for experience and cooperation. Supported by Indiana University and National Science Foundation Grants NSF PHY 93-147-83 & 23-423-10.

6 REFERENCES

[1] D.L. Friesel and S.Y. Lee, IEEE 95CH35843, 336 (1995).

[2] D. Li *et al*, IEEE 95CH35843, 357 (1995).

[3] A. Pei *et al*, IEEE 95CH35843, 1705 (1995).

[4] A. Pei *et al*, IEEE 95CH35843, 1708 (1995).

[5] K. Hedblom, IEEE 95CH35843, 1861 (1995).

[6] R.E Pollock, IEEE 89CH2699-0, 17 (1989).

[7] V. Derenchuk *et al*, "Pulsed Ion Sources for the IUCF Cooler and Injector Synchrotron", this publication.

[8] D.L. Friesel *et al*, "Commissioning of the IUCF 7 MeV H^- Linac Pre-Injector", this publication.

[9] J. Callahan *et al*, "A High Reliability Accelerator Control System", this publication.

[10] A. Pei *et al*, "An RF System for a Compact Synchrotron", this publication.

[11] G.P.A. Berg *et al*, "The CIS Dipole Magnet fabrication & mapping", this publication.

[12] M. Ball *et al*, "Design and Commissioning of BPM's in the Cooler Injector Synchrotron", this publication.

[13] X. Kang *et al*, "Beam Extraction for the Cooler Injector Synchrotron", this publication.

ACCELERATION TEST OF RADIOACTIVE NUCLEAR BEAM AT INS

M. Tomizawa, S. Arai, Y. Arakaki, Y. Hashimoto, A. Imanishi*, S.C. Jeong,
I. Katayama, T. Katayama*, H. Kawakami, S. Kubono*, T. Miyachi*, H. Miyatake,
K. Niki, T. Nomura, M. Okada, M. Oyaizu, Y. Shirakabe, P. Strasser,
Y. Takeda, J. Tanaka, M.H. Tanaka, E. Tojyo, and M. Wada
INS, Institute for Nuclear Study†, Univ. of Tokyo, 3-2-1 Midori-cho, Tanashi, Tokyo 188, Japan

Abstract

First acceleration test of a radioactive nuclear beam was performed in a radioactive beam facility at INS. The ^{19}Ne beam was produced by bombarding a LiF target with 30 MeV protons from an SF cyclotron, and ionized by a ECR ion source. We succeeded to accelerate the $^{19}Ne^{2+}$ ions to 0.72 MeV/u by heavy-ion linacs. The intensity delivered to a secondary target is not yet enough. Further improvements will be done to perform experiments using accelerated radioactive nuclei.

1 INTRODUCTION

The construction of an ISOL-based radioactive nuclear beam facility at INS started in 1992 and completed in 1996. Radioactive nuclei, produced by bombarding a thick target with protons or light ions from an SF cyclotron, are ionized in an ion source, mass-analyzed by an isotope separator on line (ISOL), and transported to a heavy ion linac complex through a 60 m long beam line. The linac complex comprises a 25.5 MHz split coaxial RFQ (SCRFQ) and a 51 MHz interdigital-H (IH) linac, and accelerates heavy ions up to 1 MeV/u. Three beam lines including a recoil mass separator (RMS) were prepared for experiments. This facility is a prototype for the exotic nuclei arena (E-arena) of the Japanese Hadron Facility (JHF), in which 3 GeV,10 μA protons is used as a primary beam, and a radioactive nuclei beam is accelerated up 6.5 MeV/u by an extension of the IH linac[1]. The main purpose of the prototype facility is to study various technical problems for the E-arena in the JHF and to perform pioneering works with respect to nuclear astrophysics. In this paper, a result of first acceleration test of a radioactive nuclear beam is reported together with a summary of the outline and the present status of this facility.

2 OUTLINE AND PRESENT STATUS OF RADIOACTIVE BEAM FACILITY

2.1 *Target and Ion Source*

Production target and ion source technology are crucial part of the ISOL based radioactive technology. High production efficiency of ions, short releasing time and stable operation are required. Three different types of ion sources have been prepared to ionize various elements.

The main part of a surface ionization type is a Ta tube. The inside of this tube is covered with a metal foil with high work function like Re or Ir. This type is effective for atoms with low ionization potentials like alkaline elements. In a plasma type, neutral atoms are ionized by thermal electrons accelerated between a cathode and an anode. Since the forced electron bombardment is the main ionization process, atoms with high ionization potential can be also ionized by this ion source. A 6.4-GHz ECR type with mirror coils is used for the ionization of gaseous elements.

A beam bunching technique is used in the ion sources, when the heavy ion linacs are operated at a pulse mode. The bunching is made by installing an auxiliary electrode just at the exit of the ion source, and applying alternative positive and negative voltages[2, 3]. This bunching method also enables a direct measurement of the ionization efficiency of the ion source[4].

2.2 *Mass Separator*

The beam ionized by the ion source is selected by a mass separator (ISOL)[5]. The ion optical configuration of this separator is divided into two stage, QQDQQ(F1) and QMDMQ(F2), where Q, D and M stand for the quadrupole, dipole and multipole magnets and F the focal point. The multipole magnets and surface coils in the dipole magnets can be used to eliminate higher order aberrations. The first magnetic quadrupole doublet is movable in the axial direction so as to fit for different types of the ion sources. Designed mass resolving powers ($m/\Delta m$) are 9000 and 800 for the beam emittances of 4 and 40 πmm·mrad, respectively. The whole system is insulated from a ground potential so that a negative potential up to 100 kV can be applied. A full extraction voltage can be used in order to obtain a higher mass resolution. A mass resolving power of 5100 was achieved in the test using a stable beam.

2.3 *Low Energy Transport Line*

The ISOL and the heavy ion linacs are connected with a 60 m long transport line[5]. The transport line consists of seven electrostatic deflectors and about 134 electrostatic quadrupole singlets. The electrodes of the quadrupoles have a bore diameter of 36 mm. The acceptance of 170 πmm·mrad is obtained when the phase advance per a focusing period is selected to be 77 degree. The beam line level changes from 1.2 m to 2.3 m to across the TARN II ring,

* Present Address : CNS, Center for Nuclear Science, Univ. of Tokyo, 3-2-1 Midori-cho, Tanashi, Tokyo 188, Japan
† Present Name of Institute : High Energy Accelerator Research Organization, Tanashi Branch

0-7803-4376-X/98/$10.00 © 1998 IEEE

and again to 1.2 m of the linacs level. The achieved vacuum pressure is in the order of 10^{-7} torr, which is needed to suppress the beam loss due to the collision with the residual gases.

2.4 *RFQ*

A split coaxial RFQ (SCRFQ) has been developed to accelerate heavy ions with a small q/A at INS[6]. Design parameters of the SCRFQ are summarized in Table 1. The SCRFQ accelerates ions with a charge-mass ratio greater than 1/30 from 2 to 172 keV/u. The resonant frequency is chosen to be 25.5 MHz to accelerate the ions with $q/A \geq$ 1/60 considering future extension. The duty factor can be operated at 30% to accelerate ions with q/A=1/30 and 100% with $q/A \geq 1/16$. The cavity with 0.9 m in diameter and 8.6 m in length comprises four unit cavities, and each of which is composed by three modules. The intervane voltage was obtained by measuring the endpoint energy of X-rays generated from the cavity. As a result, the resonance resistance (=$V^2/2P$) was 24.55 $\pm$ 0.44 kΩ. Beam tests were conducted using beams from a 2.45-GHz ECR ion source placed at the entrance of the RFQ. The beam transmission efficiency for nitrogen molecules (q/A=1/28) was 90% at a duty factor of 20%, which agrees with the design value.

Table 1: Design parameters of the SCRFQ

Frequency	25.5 MHz
Charge-to-mass ratio	$\geq$ 1/30
Energy	2 $\rightarrow$ 172 KeV/u
Input emittance	291 π mm·mrad
Normalized emittance	0.6 π mm·mrad
Vane length	8.585 m
Number of cells (radial matcher)	172(20)
Max. Intervane voltage	108.6 kV
Max. surface field	178.2 kV/cm
	(2.49 Kilpatrick)
Mean aperture radius (r_0)	0.9846 cm
Minimum aperture radius (a_{min})	0.5388 cm
Max. modulation index (m_{max})	2.53
Margin of bore radius (a_{min}/a_{beam})	1.2
Final synchronous phase	-30°
Focusing strength (B)	5.5
Max. defocusing strength (Δ_b)	-0.17
Transmission (0 mA input)	91.4 %
Transmission (5 mA input)	86.0 %

2.5 *Transport Line between RFQ and Drift Tube Linac*

A transport system between the RFQ and the drift tube linac comprises a charge stripper (C-foil), a rebuncher and two pairs of quadrupole doublets[7]. The charge stripper is used to increase the charge state of the ions with a small q/A. Beam test with the stripper will be soon performed. The rebuncher is a 25.5 MHz double coaxial quarter wave resonator with six gaps. The power consumption in the cavity is less than 1.5 kW also in a maximum operation.

2.6 *Drift Tube Linac*

The ions with $q/A \geq$ 1/10 are accelerated from 172 keV/u to 1 MeV/u by a 51 MHz interdigital-H (IH) linac[8]. To obtain a high acceleration efficiency, π-π drift tubes without transverse focusing element were adopted. The linac has four separated tanks. The output energy can be continuously varied in the whole energy range from 172 keV/u to 1 MeV/u by adjusting rf power levels and rf phases. Three sets of quadrupole triplets are placed between tanks. The design parameters of the IH linac are listed in Table 2 together with the results of low power measurements. The power consumptions were obtained from the effective shunt impedance measured by a bead-pull method.

In the tests with beams ($^{14}N^{2+}$ and $^{20}Ne^{2+}$) from the 2.45-GHz ECR ion source, the transmission efficiencies achieved to 90$\sim$100%. The measured spreads of the output energies roughly agree with designed ones. A variability of the output energy was confirmed in a beam test.

Table 2: Main parameters of the IH linac

	tank1	tank2	tank3	tank4
f(MHz)	51	51	51	51
max. q/A	1/10	1/10	1/10	1/10
T_{out}(MeV/u)	0.294	0.475	0.725	1.053
L_{tank}(m)	0.68	0.90	1.16	1.53
D_{tank}(m)	1.49	1.49	1.49	1.34
D_{bore}(cm)	2.0	2.4	2.8	3.2
D_{tube}(cm)	3.8	4.4	4.6	5.2
L_{gap}(cm)	2.9	3.7	4.5	5.3
Cell No.	9	10	11	12
V_{gap}(kV)	200	250	313	370
unloaded-Q	10681	15387	16230	18490
Z_{eff}(MΩ/m)	264	289	268	218
P(kW)	10.5	15	25	39

2.7 *High Energy Transport and Recoil Mass Separator*

The optical arrangement of the high energy transport downstream of the IH linac comprises QQDQDQQ to make an achromatic condition at a secondary target position. The magnetic rigidity of the system is the same as that of ions with q/A=1/10 and 0.77 MeV/u. Three beam lines were prepared for experiments. One line has a recoil mass separator (RMS) together with a low-background gamma ray detector system[9]. The RMS is designed for low-energy capture reaction study for nuclear astrophysics. It has a mass resolving power of about 60, and the energy spread acceptance of $\pm$5%. The RMS comprises QQEDQQ optical elements, where E is an electrostatic deflector. In recent test, a stable Ne beam (0.72 MeV/u) stripped by a Au thin foil placed at the secondary target position was delivered to a focal plane of the RMS.

3 FIRST ACCELERATION TEST OF RADIOACTIVE NUCLEI

First acceleration test of $^{19}Ne^{2+}$ ($T_{1/2}$=17.3 s) was conducted in the spring of 1997. The ^{19}Ne beam was produced using $^{19}F(p,n)$ reaction with 30 MeV-protons from the SF cyclotron. The used target materials were LiF+C in a powder form with a size of about 1 μm and heated up to 400°C The production rate in the target is estimated to be 2×10^9 with 1 μA, 30 MeV protons. The ECR ion source was in a pulse operation, 2.0 ms in width and 100 Hz in repetition rate, which were determined by the operation of the linac complex. The IH tank-1 through tank-3 were operated to accelerate ^{19}Ne up to 0.72 MeV/u. The rf amplitudes and phases of linacs were set to parameters determined by acceleration tests with stable beams. The ^{19}Ne-transmission efficiency of the linac complex is estimated to over 80% from the contaminated beam current measured by Faraday cups.

In order to measure the beam intensity, the ^{19}Ne beam was stopped at plates or Faraday-cups placed on transport lines. The 511 keV γ-rays by β^+-decay were measured by Ge or CsI detectors. The full-energy detection efficiency of these detectors were calibrated by a standard source of ^{22}Na in advance. The efficiencies of the Ge and CsI detectors are $0.5\sim3\times10^{-3}$ and $0.3\sim1.4\times10^{-4}$, respectively. Figure 1 shows an example of the time spectrum of $^{19}Ne^{2+}$ intensity measured by a Ge detector at the secondary target position. The intensity of ^{19}Ne delivered here was not yet enough. The following improvements will be done after this test;

- The production efficiency of ^{19}Ne ions in the ECR ion source decreases at the primary beam intensity over several hundreds of nA. This seem to be due to undesirable out-gas generated from the target. The target temperature during irradiation of the high power beam must be also controlled at optimum one.
- To produce the ^{19}Ne beam, a LiF was used as a target material. A large amount of ^{19}F ions (a mass difference from ^{19}Ne is about 1/5500) was also produced. It is difficult to separate this contaminant completely by the ISOL. Different target materials may be chosen to avoid it.
- The transmission efficiency of the 60 m long transport line exceeded 70% in the test using a stable beam. But it was worse in this test. We need to search for the optical parameters to optimize the intensity of the ions of interest. Moreover, the beam from this line can not be well matched for the RFQ. More optical elements may be needed to match it.
- The IH tanks have not been operated with a duty factor higher than 20% under maximum powers. In final stage of the commissioning, a challenge of the higher duty operation will be conducted.

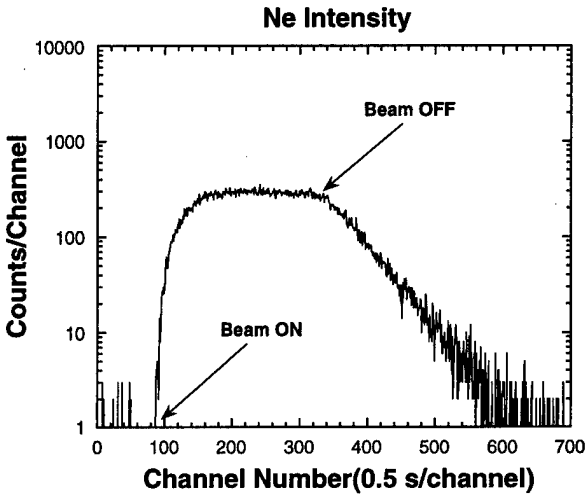


Figure 1: Time spectrum of $^{19}Ne^{2+}$ intensity measured by a Ge detector at the secondary target position. The intensity of primary protons was 100 nA.

4 REFERENCES

[1] T. Nomura: 'Exotic Nuclei Arena in Japanese Hadron Project', INS-Report-780(1989).

[2] Y. Shirakabe *et al.*: 'Bunching of Radioactive Ion Beam in the Millisecond Region -a Pulsed Gating-Potential Method in an Ion Source for On-Line Isotope Separation', Nucl. Instr. and Meth., **A337**(1993)11.

[3] S.C. Jeong *et al.*: 'Beam-Bunching in an ECR Ion Source by the Pulsed Gating-Potential Method', Nucl. Instr. and Meth., **B114**(1996)154.

[4] T. Nomura *et al.*: 'Simple On-Line Method of Measuring the Absolute Ionization Efficiency of an Ion Source', Nucl. Instr. and Meth., **B93**(1994)492.

[5] M. Wada *et al.*: 'High-Resolution Mass Separator and 60 m Beam Transport Line for the Radioactive Nuclear Facility at INS', Nucl. Instr. and Meth. B, to be published.

[6] S. Arai *et al.*: 'Construction and Beam Tests of a 25.5-MHz Split Coaxial RFQ for Radioactive Nuclei', Nucl. Instr. and Meth. A, in press.

[7] K. Niki *et al.*: 'Beam Transport Design for the Linac System in the INS Radioactive Beam Facility', Proc. of 1994 Int. Linac Conf., 1994, p.725.

[8] M. Tomizawa *et al.*: 'Progress Report of the Interdigital-H Linac for Radioactive Nuclei at INS', Proc. of the 5th European Particle Accelerator Conf., 1996, p.780.

[9] S. Kubono *et al.*: 'New ISOL-Based Radioactive Nuclear Beam Facility at INS', Nuclear Physics, **A616**(1997)11c.

ACCELERATION TEST OF THE FOLDED-COAXIAL RFQ LINAC FOR THE RILAC

O. Kamigaito, A. Goto, Y. Miyazawa, T. Chiba, M. Hemmi,
M. Kase, S. Kohara, T. Nakagawa, Y. Batygin and Y. Yano,
The Institute of Physical and Chemical Research (RIKEN),
Wako-shi, Saitama 351-01, Japan

Abstract

A new injector system for the RIKEN heavy-ion linac (RILAC) has been constructed, which consists of a variable-frequency RFQ and an 18-GHz ECR ion source. The RFQ, based on a folded-coaxial resonator with a movable shorting plate, accelerates ions with mass-to-charge ratios of 6 to 26 at up to 450 keV per charge in the cw mode by varying the resonant frequency from 17.7 to 39.2 MHz. Beam tests of the RILAC and the ring cyclotron (RRC) were successfully performed with the new injector system. The beam intensity from the RRC as well as the transmission efficiency through the RILAC has been greatly improved. This paper describes the performance of the RFQ and the results of the acceleration tests.

1 INTRODUCTION

The RIKEN heavy-ion linac (RILAC) is rf frequency-tunable between 17 and 40 MHz, which accelerates various kinds of ions with mass-to-charge (m/q) ratios up to 28 in a wide energy range[1]. A 450 kV Cockcroft-Walton accelerator with an 8-GHz electron-cyclotron resonance ion source (ECRIS) has been used as the injector of the RILAC.

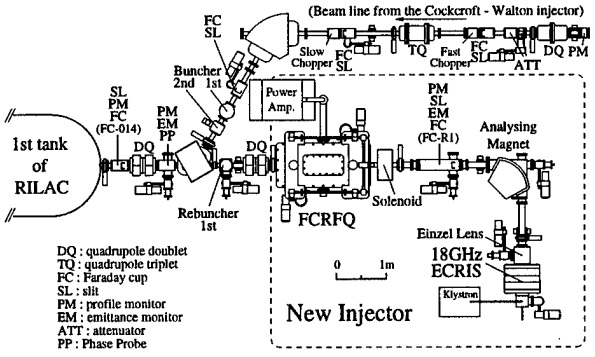


Figure: 1 Schematic drawing of the new injector for the RILAC

In order to increase beam intensities in the RILAC, a new injector has been constructed recently[2], which consists of an 18-GHz ECRIS[3] and a variable-frequency RFQ linac. This injector was installed in the RILAC beam line in August, 1996, as shown in Fig. 1, while keeping the beam line from the Cockcroft-Walton injector alive. In this paper we describe the results obtained from the acceleration tests which started at the end of October, 1996 as well as the outline of the RFQ linac.

2 FCRFQ LINAC

The RFQ resonator is based on a folded-coaxial structure[4]. The distinct features of this folded-coaxial RFQ (FCRFQ) are that it can be operated in a low frequency region and the frequency range is quite large. The design parameters are listed in Table 1.

Table: 1 Design Parameters of the FCRFQ

Frequency	17.7 - 39.2 MHz
Mass-to-charge ratio (m/q)	6 - 26
Input energy	10 keV/q
Output energy	450 keV/q
Input emittance	145 π mm•mrad
Vane length	1420 mm
Intervane voltage	33.6 kV
Mean aperture radius (r_0)	7.70 mm
Minimum aperture radius (a_{min})	4.17 mm
Maximum modulation (m)	2.70
Focusing strength (B)	6.8
Max. defocusing strength	-0.30
Final synchronous phase	-25°

Figure 2 shows a schematic layout of the FCRFQ resonator whose details are given in the reference[4]. The resonator is separable into upper and lower parts, as shown in the figure. All the vanes are rigidly fixed in the lower part. The upper part containing the stem and the movable shorting plate can be removed as a unit. This separable structure permits accurate alignment of the vanes and easy maintenance. The lower part of the tank wall is made of steel (SS400) whose inside is plated with copper to a thickness of 100 mm, while the other parts such as the vanes and the stem are made of oxygen-free copper (C1020). The vanes are three-dimensionally machined within the accuracy of ±50 μm. They are aligned within the same accuracy by taking the estimation of the misalignment effect on the beam transmission efficiency into account[6].

The channels for water cooling are arranged based on a heat analysis. Water for the horizontal vanes is supplied through the front and rear supports of the vanes. That for the vertical vanes and the rectangular tube is provided

0-7803-4376-X/98 /$10.00 © 1998 IEEE

through the inside of the upper stem. The total water flow is 155 *l*/min at the pressure of 7 atm. The resonator is evacuated by two turbo-molecular pumps (1500 *l*/s) on its both sides. The vacuum stays in a range of 5 - 8 × 10^{-8} Torr at a pump head during the operation.

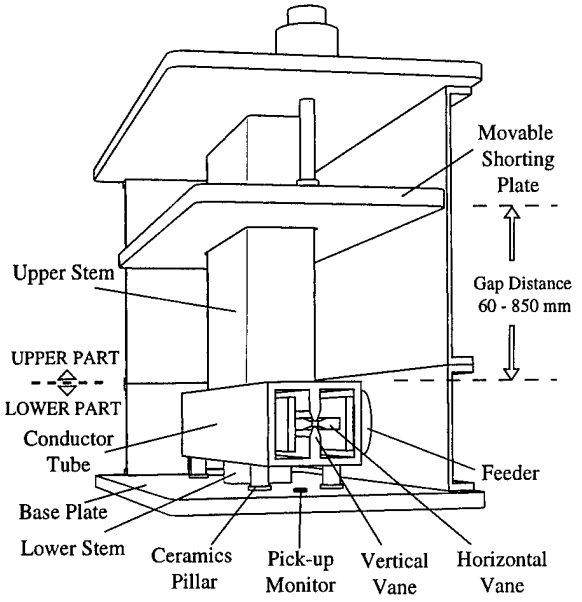


Figure: 2 Schematic drawing of the RFQ resonator. The inner volume of the resonator is about 1700 mm (length) × 700 mm (width) × 1150 mm (height).

The rf power is supplied through a capacitive feeder with an rf power source based on an Eimac 4CW50000E, which has a cw power of 40 kW at maximum between 16.9 and 40 MHz. A capacitive tuner for the fine tuning is placed on the other side of the feeder.

The resonant frequency varies from 17.7 to 36.2 MHz by changing the position of the shorting plate by a stroke of 790 mm, when the lower stem is out of the resonator. When the lower stem is used, the frequency varies from 30.2 to 39.2 MHz. This result is in good agreement with the MAFIA calculation. On the other hand, the measured Q-values and the shunt impedances are about half of the MAFIA calculations. The power losses estimated from the measured shunt impedances are 6 kW at 17.7 MHz and 26 kW at 39.2 MHz for the maximum intervane voltage of 33.6 kV in the cw operation.

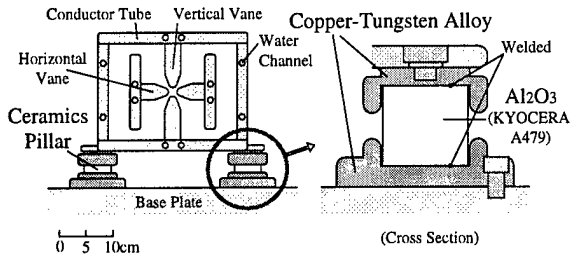


Figure: 3 Schematic drawing of the ceramics pillar.

The key to the stable operations of this RFQ is the ceramics pillar, which stands the high rf voltage. Figure 3 shows the structure of the pillar installed in the resonator. It consists of Al_2O_3, whose nominal loss tangent is 2 × 10^{-4}, welded with copper-tungsten alloy on its both sides. This welding is possible because both materials have similar values of the coefficient of the linear thermal expansion. Since there is no electric field concentration in the ceramic material, it is quite stable even in the operation of the maximum voltage. The power loss in one pillar is estimated to be 20 W at maximum.

3 ACCELERATION TEST

3.1 Preliminary Test

Prior to the installation in the RILAC beam line, we tested the new injector system alone by using Oxygen, Neon, Argon, Krypton, and Tantalum beams[6]. They are indicated by the closed circles in Fig. 4. The maximum transmission efficiency was 88 % with an Ar^{8+} beam of 120 eμA.

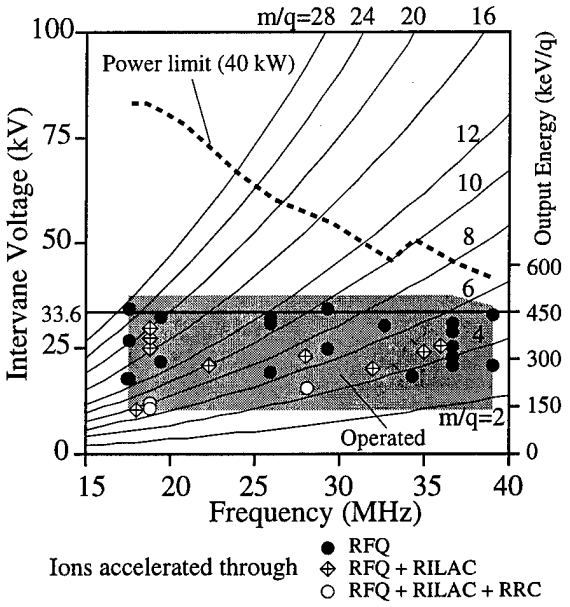


Figure: 4 Performance of the RFQ linac. The abscissa and the ordinate represent the resonant frequency and the intervane voltage, respectively. The output energy, which is proportional to the intervane voltage, is also indicated. The hatched area shows the region where the RFQ has ever been operated in the cw mode. The ions accelerated so far are indicated by the closed circles, the diamonds, and the open circles. The solid curves represent the acceleration condition of ions, each of which is indicated by the m/q-value. The dashed curve shows the maximum attainable voltage with the present power source (40 kW).

The input beam emittance from the ion source was measured to be 150 - 300 π mm•mrad, which decreased as the extraction voltage and/or the charge states of the ions

increased. The output beam emittance was almost independent of the acceleration condition and was in agreement with the PARMTEQ simulation.

The energy distribution of the output beam was measured with the electrostatic deflector placed downstream of the RFQ along with the scanning wire probe. The beam energy was deduced from the beam position measured with the probe, and the voltage applied to the deflector. The measured distributions were found to be well reproduced by the PARMTEQ simulation. The energy spread of the output beam was also measured with the same device. The result was 2-3% at FWHM and was consistent with the simulation.

3.2 Test of the RILAC

The beam matching section between the RFQ and the RILAC consists of two quadrupole doublets and one rebuncher operated in the fundamental harmonics, as shown in Fig. 1[7]. The rebuncher resonator is a quarter-wavelength type with four rf gaps, which is driven by a 1-kW wide-band amplifier. A capacitive phase probe, placed in the chamber before the RILAC, was shown to be important in adjusting the rf phase of the rebuncher.

The ions accelerated so far through the RILAC with the new injector are $N^{2,3+}$, $^{36}Ar^{5+}$, $Ar^{2,4,5+}$, Fe^{7+}, $Kr^{11,18+}$, and Xe^{7+} at the frequencies of 18.0, 18.8, 22.3, 28.0, 28.1, 35.0, 36.0 MHz. They are indicated by the diamonds in Fig. 4.

The transmission efficiency of the RILAC has increased to 70 %, while the original value for the beams from the Cockcroft-Walton injector was 30 %. In the beam tests, however, the transmission efficiency of the injector section did not reach the value obtained in the preliminary tests. This deterioration might come from the small aperture radius of the rebuncher. Therefore, about one half of the ions extracted from the 18-GHz ECRIS are accelerated by the RILAC at present. Nevertheless, this overall efficiency is three times larger than the original value of 15 %. The maximum beam intensity ever achieved by the RILAC with the new injector is 13 pμA for a N^{3+} beam of 2.5 MeV/nucleon.

3.3 Test of the ring cyclotron (RRC)

In December, 1996, we started the acceleration tests of the ring cyclotron (RRC) with the upgraded RILAC. The ions accelerated so far are $^{36}Ar^{5+}$, Fe^{7+}, and Kr^{18+} at the frequencies of 18.8 and 28.1 MHz. They are indicated by the open circles in Fig. 4.

In the first test using an $^{36}Ar^{5+}$ beam, we achieved the beam current of 1 pμA out of the RRC for the first time, where 20 % of the beam extracted from the ion source was accelerated to the final energy of 7.5 MeV/nucleon.

Since highly charged ions are available with the 18-GHz ECRIS, charge strippers are unnecessary for the low-energy beams of medium-heavy ions. This is an advantage from the viewpoint of the beam intensity and the stability. However, the extraction voltage of the ECRIS becomes quite low for the highly charged ions, because the maximum voltage is 10 kV at present. For example, the extraction voltage was only 3 kV in the first test described above. This low voltage causes bad effects both on the intensity and the emittance of the extracted beams.

We are planning, therefore, to raise the maximum extraction voltage of the 18-GHz ECRIS from 10 kV to 20 kV in this summer. New vanes are under fabrication so that the RFQ can accept the upgraded beams.

4 SUMMARY AND OUTLOOK

We have installed the new injector for the RILAC, which consists of the 18-GHz ECRIS and the FCRFQ. The transmission efficiency of the RILAC has increased to 70 %. Moreover, we achieved the beam current of 1 pμA out of the RRC for the first time.

Since the extraction voltage is too low for the highly charged ions, we are planning to raise the maximum extraction voltage of the ECRIS from 10 kV to 20 kV in this summer for further upgrade of the beam intensity. It is expected that this new injector will play an important role in the RI-beam factory project[8].

5 ACKNOWLEDGMENTS

The authors are grateful to Dr. N. Tokuda at KEK and Dr. S. Arai at INS for the usage of the program for vane-cutting as well as for the fruitful information about the vane design. The resonator was fabricated by Sumitomo Heavy Industries, Niihama Work, the rf power source by Denki Kogyo, and the ceramics pillars by KYOCERA Corporation.

REFERENCES

[1] M. Odera *et al.*, Nucl. Instrum. and Methods, **227**, 187 (1984).
[2] A. Goto *et al.*, Proc. 14th Int. Conf. on Cycrotrons and Their Applications, 1995, Cape Town, p. 237 (1995).
[3] T. Nakagawa *et al.*, in this proceedings.
[4] O. Kamigaito et al., Jpn. J. Appl. Phys. **33**, L537 (1994), and Jpn. J. Appl. Phys. **34**, 5799 (1995).
[5] Y. Batygin *et al.*, RIKEN Accel. Progr. Rep. **28**, p.172 (1994).
[6] O. Kamigaito *et al.*, Proc. 18th Int. Linear Accelerator Conference, 1996, Geneva, p. 863 (1996)
[7] O. Kamigaito *et al.*, RIKEN Accel. Progr. Rep. **30**, p.191 (1996).
[8] Y. Yano, in this proceedings.

RECENT LEAD ION STORAGE TESTS ON LEAR

J. Bosser, J. Broere, C. Carli, M. Chanel, C. Hill, R. Ley, A. Lombardi, R. Maccaferri,
S. Maury, D. Möhl, G. Molinari, H. Mulder, E. Tanke, G. Tranquille, M. Vretenar.
PS Division, CERN, CH 1211 Geneva 23, Switzerland.

1. INTRODUCTION

With the completion of the antiproton physics program, the Low Energy Antiproton Ring is now available to be used as an accumulator ring for heavy ions in the LHC injector chain. The proposed scheme for the injection of lead ions [1] is shown in Fig. 1, where an intensity gain of 125 is obtained by accumulating lead ions with electron cooling in the LEAR ring. With a linac cycling at 10 Hz and cooling times faster than 100 ms, 20 pulses can be accumulated in 2 s before transfer to the PS, the next machine in the chain. A number of machine experiments [2] have been performed, and will continue this year, in order to establish the techniques required.

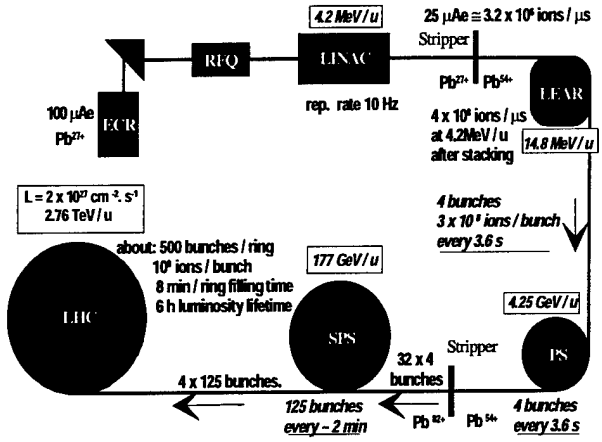


Figure 1. The lead-ion injection scheme for LHC.

2. INJECTION LINE TESTS

The lead ions follow a transfer line which includes a U-turn linking the linac to the transfer tunnel to LEAR. Despite problems matching the beam, we always succeeded in injecting around 10^8 charges per single turn injection.

For the multi-turn scheme, which combines injection into horizontal and longitudinal phase space [3], a number of tests have been made to determine whether the acceptance of the transfer channel is large enough to transmit a momentum width of 8×10^{-3} and to make preliminary measurements on the energy ramping of the linac. In effect, with this type of injection the mean energy of the beam coming from the linac varies during the injection of the pulse. An energy change of 70 keV (corresponding to a momentum shift $\delta p/p = 8\times10^{-3}$) in a time $\Delta t = 60$ μs will increase the number of 'useful' turns that can be injected and make full use of the faster longitudinal cooling.

To test the momentum acceptance of the line, Pb^{53+} and Pb^{54+} ions were simultaneously transmitted by adjusting the magnetic filter line after the stripper to a large momentum width. The two beams passed the whole line, and the beam spots on a scintillator screen in front of the septum were superimposed proving that the momentum acceptance of the line was greater than 18×10^{-3} and also that the residual dispersion of the line at the septum was small, as required by this type of injection.

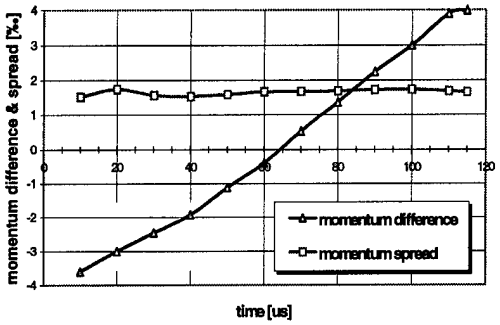


Figure 2. Linac momentum and momentum spread (4σ) versus time for an energy ramped injected beam.

Energy ramping was first tried out by ramping the ITF (Ion Transport Filter) debuncher phase. The maximum momentum change achieved was ±0.2% in 55 μs. This was the fastest ramp which gave stable debuncher operation. By ramping the linac tank 3 RF amplitude synchronously with the debuncher, a momentum swing of ±0.4% in 100 μs was obtained, but a small blow-up of the momentum dispersion along with a low energy tail were observed (Fig. 2). These results were obtained by using the LEAR machine as a spectrometer through measurement of the longitudinal distribution by means of Schottky noise.

machine:	1	4	7
β_x ss1/3 [m]	1.9	9.5	4.8
β_z ss1/3 [m]	6.4	10.5	5
D ss1/3 [m]	3.5	0	5
β_x ss2/4 [m]	1.9	3.6	1.1
β_z ss2/4 [m]	6.4	7.2	6.2
D ss2/4 [m]	1.9	9.9	2
Q_x	2.31	1.62	2.55
Q_z	2.62	2.42	2.7

Table 1. Lattice functions for the LEAR machines 1,4, and 7 that were used in the experiments.

0-7803-4376-X/98 /$10.00 © 1998 IEEE

3. MACHINE EXPERIMENTS

Experiments to test the influence of various parameters such as the machine lattice functions (Table 1) or the electron beam intensity, on the beam lifetime and cooling down times have been performed with lead ions of charge states 52+ to 55+. These different charge states can be selected with sufficient intensity after stripping the beam from the linac at an energy of 4.2 MeV/u.

Ion beam lifetime and vacuum measurements

The beam lifetime τ was measured by recording the ion intensity versus time. The intensity is deduced from the longitudinal Schottky signal where the total power in a frequency band around a harmonic of the revolution frequency was measured. The decay rate, $1/\tau = 1/\tau_{vac} + 1/\tau_{rec}$ has contributions from the charge exchange from the residual gas, $1/\tau_{vac}$,and from the presence of the electron cooling beam, $1/\tau_{rec}$. The former is constant while the latter varies with the electron intensity I_e. By plotting $1/\tau$ versus I_e, (Fig. 3) we can deduce the two contributions to the beam lifetime.

The gas composition can be measured in each straight section of the machine by residual gas analysis and the expected vacuum lifetime can be computed. The vacuum lifetime varied between 10 and 20 s. The proportion of He and CH_4 varied quite strongly between runs even though the average machine pressures did not. Local pressure bumps also play an important role in the lifetime of Pb ions, decreasing it by a factor 2 for example when beam is lost at injection, causing outgassing from the vacuum chamber. Our estimations of the vacuum lifetime agreed well with the theoretical value based on the formula found in [4], and no difference could be detected between the different charge states.

In contrast a very strong dependence on the charge state was found for the lifetime due to the recombination processes with the cooling electrons. The rate coefficients $\alpha_r = 1/\tau_{rec}/n_{eff}$ [in 10^{-8} cm^3 s^{-1}], normalised to the effective electron density seen per turn n_{eff}, were computed for each charge state from the slope of the curves in Fig. 3. Values of 60 were measured in all runs independent of machine settings for Pb^{53+} ions. For the other charge states values between 5 and 12 were observed with an apparent dependence on the machine lattice for Pb^{54+}. These values have to be compared to coefficients of about 2.5 that are obtained from existing theory for radiative electron capture for all the charge states of interest. Attempts to explain these high rates have been made through resonant dielectronic capture [5] and could apply to Pb^{52+}, Pb^{54+} and Pb^{55+}. However the rate for Pb^{53+} indicates that an unusually strong capture resonance or other mechanisms are involved.

To observe capture phenomena, a moveable scintillator screen has been installed in the first bending magnetic downstream from the cooling section. Here we can intercept the $Pb^{(q-1)+}$ ions that are created due to electron capture by the circulating Pb^{q+} ions. When placed in its expected position (25mm horizontally outward from the circulating beam) a strong counting rate was measured which was enhanced when Pb^{53+} ions were in the machine. More refined experiments also using an X-ray detector are under preparation.

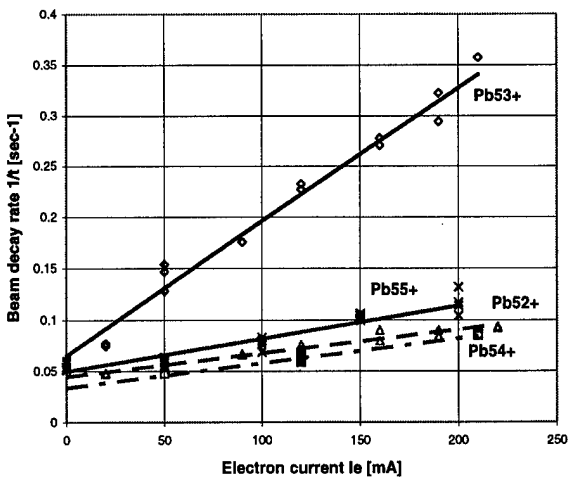


Figure 3. Plot of the inverse lifetime as a function of electron current for all the charge states investigated.

Cooling time measurements

For the accumulation of lead ions using multi-turn injection, the phase space occupied by the in-coming beam has to be quickly reduced to leave space for a new pulse. To accumulate 20 linac pulses in 2 s, cooling down times in all three planes of less than 100 ms are required. The cooling time depends on various parameters, amongst them : the electron beam intensity, the cooling length and the relative angle between the circulating ions and the electron beam. Up to now our tests have focused on obtaining of stable high intensity electron beams and on the influence of the machine parameters on the cooling process. The lengthening of the cooling section is one of our modifications for this year's experiments.

To measure such fast cooling times we have developed a system that measures simultaneously in all three planes the signal from the Schottky pick-ups and then reconstructs the Schottky power distribution profiles as a function of time. The down-mixed Schottky signals are acquired by a PC [6] which performs a FFT on time slices of the data buffer and then displays a mountain range graph of the evolution of the profile. In this manner we are able to monitor the beam size evolution tightly in the three planes, with a time resolution of about 4 ms. A second method to observe the transverse emittance is based on the ionisation profile monitor (BIPM). This uses position sensitive channel plates to detect the ionisation of the residual gas and hence the beam dimensions in the transverse planes.

Two different techniques were used to measure the cooling down times. The first method consists in

recording the beam size evolution for an injected beam, whilst the second analyses the decay of the betatron oscillation of a well-cooled beam deflected by a fast ejection kicker. Typical 2 rms emittance values for an injected beam are : $\Delta p/p=1x10^{-3}$, $\varepsilon_v=7\ \pi$ mm mrad and $\varepsilon_h=50\ \pi$ mm mrad , and the equilibrium values with an electron beam current of 350 mA were $\Delta p/p=0.15x10^{-3}$, $\varepsilon_v=\varepsilon_h=4\ \pi$ mm mrad. For the injected beam, cooling proceeds simultaneously in all three planes whereas with the kick method only the horizontal betatron oscillations can be tested for a beam that is already cooled in the longitudinal and vertical degrees of freedom.

Cooling down times were measured as a function of various parameters including the electron beam current, the lattice parameters at the cooler and the degree of neutralisation of the electron beam [7]. Fig. 4 shows some measurements made on electron beam neutralisation, and in Fig. 5 are displayed the cooling down times as a function of the machine settings.

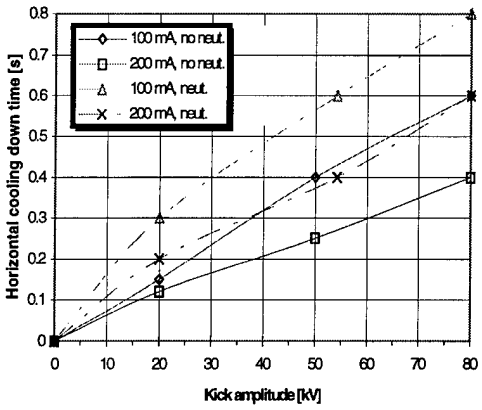


Figure 4. Horizontal cooling down time (40 π mm mrad to 4 π mm mrad) vs. kick amplitude for neutralised and non neutralised electron cooling beams (machine 4 optics).

From the results we have found that there is no advantage in using a neutralised electron beam but that it is important to monitor the degree of neutralisation as, if unstable, it can be detrimental to the cooling process. Cooling times under 100 ms in all planes were measured for $4x10^6$ ions of Pb^{54+}, but an unusual dependence on the lattice parameters has been observed which might indicate large transverse velocities at the edge of the electron beam.

4. CONCLUSIONS AND FUTURE EXPERIMENTS

The required fast cooling times have been obtained, but only at low ion intensity. A factor of more than 100 in intensity has to be gained by multi-turn injection and stacking, and at this high intensity, collective effects can become important.

Charge exchange with the residual gas and recombination with cooling electrons severely limit the lifetime. The choice of Pb^{54+} which has a lifetime of 6 s with a nominal electron current of 400 mA is acceptable.

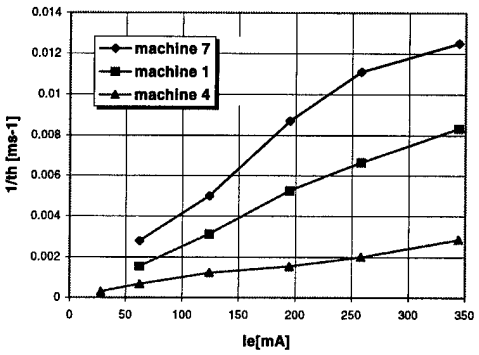


Figure 5. Cooling rate (inverse of the time to go from 40 π to 4 π mm mrad horizontally) as a function of the electron current for 10^7 Pb^{54+} ions for different optical settings.

This year LEAR will run from May to September in a dedicated machine experiment session. Fast bumpers have been installed to test fully the combined multi-turn injection scheme, and the instrumentation in the transfer line and in the machine has also been upgraded. To improve the vacuum quality, pumps have been added at various points around the machine where beam loss is most likely and additional non evaporable getter (NEG) pumps have been installed in the electron cooling section. To further enhance the cooling process, the cooling length has been doubled and the vacuum chamber has been made uniform to avoid problems with electron beam neutralisation.

5. REFERENCES

[1] P. Lefèvre and D. Möhl,'A Low Energy Accumulator Ring of Ions for LHC', Proc. Workshop on Beam Cooling, Montreux 1993, CERN 94-03, p. 411.

[2] J. Bosser, J. Broere, C. Carli, M. Chanel, C. Hill, R. Ley, A. Lombardi, R. Maccaferri, S. Maury, D. Möhl, G. Molinari, H. Mulder, E. Tanke, G. Tranquille, M. Vretenar, 'LEAR Machine Studies to Test Ion Accumulation for the LHC. Summary, March-April 1996', internal report PS/AR/Note 96-09 (MD), 1996.

[3] C. Carli, S. Maury and D. Möhl, 'Combined Longitudinal and Transverse Multiturn Injection in a Heavy Ion Accumulator', This conference.

[4] B. Franzke, 'Vacuum Requirements for Heavy Ion Synchrotrons', Proc. Part. Acc. Conf. IEEE Trans. Nucl. Sci. NS-28 (1981) 2116.

[5] A. Muller, Physica Scripta T37 (1991) 163

[6] G. Tranquille, 'A General Purpose PC Based Data Acquisition System', Proc. 1st International Workshop on PCs and Particle Accelerator Controls, PCaPAC, Hamburg, Oct. 1996.

[7] F. Varenne, 'Neutralisation de la charge d'Espace du Faisceau d'Electrons', Doctoral Thesis, Universite Blaise Pascal, Clermont-Ferrand, Nov. 1995.

THE REX-ISOLDE PROJECT

R. von Hahn, M. Grieser, H. Podlech, R. Repnow, D. Schwalm
Max-Planck-Institut für Kernphysik, Heidelberg, Germany
D. Habs, O. Kester, T. Sieber
LMU Munich, Garching, Germany
A. Schempp
University of Frankfurt, Frankfurt, Germany
G. Bollen, F. Ames
CERN, Geneva, Switzerland
U. Ratzinger
GSI Darmstadt, Darmstadt, Germany
L. Liljeby, K.G. Rensfelt
Manne Siegbahn Institute of Physics, Stockholm, Sweden
P. van Duppen
Instituut voor Kern- en Stralingsfysica, Leuven, Belgium
and the REX-ISOLDE collaboration

Abstract

REX-ISOLDE is an experiment at ISOLDE/CERN with a twofold aim: i) to demonstrate a novel efficient scheme for the acceleration of radioactive ions from the online mass separator ISOLDE. ii) to perform first nuclear physics experiments by studying the structure of neutron rich Na,Mg and K,Ca nuclei in the vicinity of the closed neutron shells N=20 and N=28 by Coulomb excitation and neutron transfer reactions. The radioactive ions are first accumulated in a Penning trap, then charge breeded to a charge to mass ratio of $\geq$1/4.5 in an Electron Beam Ion Source (EBIS) and finally accelerated up to 2.2 MeV/u. The Linac consists of a Radio Frequency Quadrupole (RFQ) accelerator, an interdigital H-type-Structure (IH) and three seven-gap resonators, which allow to vary the energy between 0.8 and 2.2 MeV/u. This paper gives an overview of the different components of the accelerator.

1 INTRODUCTION

REX-ISOLDE (Radioactive Beam EXperiment at ISOLDE) is a pilot experiment with energetic radioactive ions at the new ISOLDE (CERN) [1]. It makes full use of the low energetic 1^+-beams delivered from the on-line mass separator ISOLDE. These ions will be accelerated on the basis of a radically new concept (see fig. 1) . By continuous injection into a Penning trap (REX-TRAP), the 1^+ions are accumulated for 20 ms and cooled by collisions with a buffer gas. Bunches of 10 μs length with improved emittance are then transferred to the EBIS. The dense electron beam of the EBIS, focussed by a strong magnetic field of a solenoid strips the ions up to the stripping limit determined by the electron energy. After a breeding time of 20 ms a 100 μs long bunch is finally extracted.

As the intensity of the radioactive ions is about orders of magnitudes smaller than the intensity of ions from the residual gas, a mass separator between the EBIS and the front end of the LINAC is required. The mass separator consists of an electrostatic 90^0 cylinder deflector and a 90^0 magnetic bender build up in a vertical S-shape. This system has been calculated to third order, providing a q/A-resolution of 1400. The seperator is described more precisely in ref. [2, 3]. The following Linac allows to vary the ion- energy between 0.8 and 2.2 MeV/u. The ions are finally bend onto the target, which might be surrounded by an efficient Ge-detector array (MINIBALL).

2 THE LINEAR ACCELERATOR

2.1 The 4-rod-RFQ

The first acceleration stage of the REX-ISOLDE LINAC is a 4-rod-RFQ which is designed to accelerate radioactive ions with a charge-to-mass ratio larger than 1/4.5 from 5 keV/u to 300 keV/u. The rf quadrupole field provides transverse focusing for the low energy ions while a modulation of the four rods performs a smooth bunching and acceleration of the injected 100 μs bunch. The 4-rod-RFQ is a well tested structure [4], which is already used in the GSI HLI-LINAC [5] and the Heidelberg high-current injector [6]. As the lay-out of the REX-ISOLDE-RFQ is very conservative the maximum voltage which can be obtained should even provide acceleration of ions with charge-to-mass ratios as small as 1/6.5. With a shunt impedance of 100 kΩm the expected power consumption will be about 60 kW.

Design calculations with PARMTEQ have been performed to minimize the divergence of the beam at the exit of the RFQ. It turned out that one can avoid a rapid increase of the radial beam size in the drift tube between the end of the rods and the first triplet of the matching section. Connecting the RFQ to the IH-structure the matching section consists in total of two triplets and a rebuncher.

0-7803-4376-X/98/$10.00 © 1998 IEEE

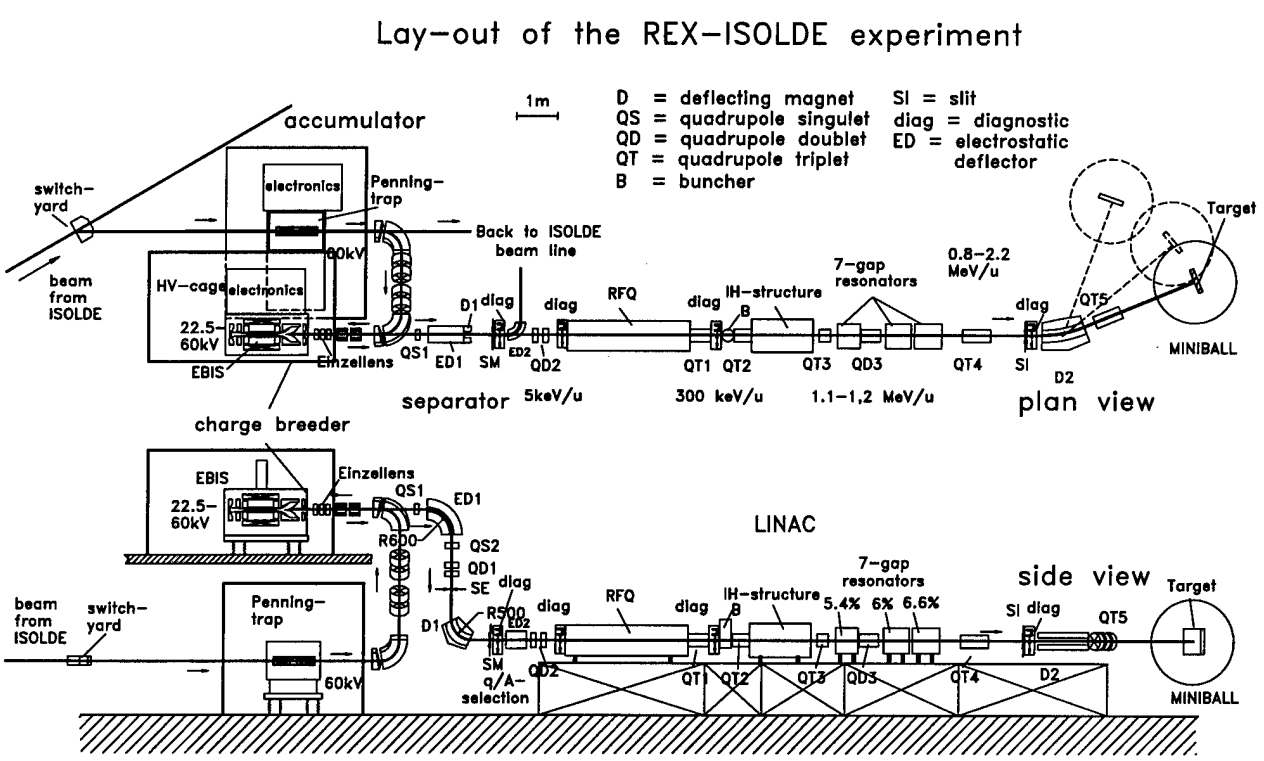


Figure 1: Schematic view of REX-ISOLDE.

2.2 *The IH-structure*

The IH-struture for REX-ISOLDE is a drift-tube structure which has been scaled from similar structures like the GSI HLI-IH-structure or 'tank 1' of the IH-structure of the lead LINAC at CERN [8, 9]. The beam dynamics concept of the 'Combined Zero Degree Structure' [9] was developed and applied for both IH-DTL's mentioned above and resulted in a very reliable beam operation.

The IH-structure accelerates the ions from 0.3 MeV/u to an extraction energy between 1.1 and 1.2 MeV/u. Switching between the two values of the exit energy of the IH-structure can be achieved by adjusting the gap voltage distribution via capacitive plungers.

The electric field distributions of the drift tube structure have been studied by MAFIA calculations. The required undercut length of the magnetic flux inductors for a flat gap voltage distribution, has been investigated as well. The design distribution and the calculated one fits very well for the different final energies. The lower final energy of the IH-structure is important for deceleration of the ions down to 0.8 MeV/u: a deceleration from 1.2 MeV/u down to 0.8 MeV/u by the 7-gap resonators would lead to a non-acceptable phase spread of the ions at the target. The accepted phase/energy spread of the IH-structure are $\pm 10^0/\pm 2.8\%$ respectively. Assuming a shunt impedance of 300 MΩ/m, the total peak power consumption will be 36 kW.

2.3 *The seven-gap resonators*

The last section of the accelerator consists of three 7–gap resonators similar to those built for the new high current injector at Heidelberg [10], but operating at a slightly different eigenfrequency. Each resonator has a single resonance structure (see fig. 2), which consists of a copper half shell and three arms attached to both sides. Each arm consists of two hollow profiles, surrounding the drift tubes and carrying the cooling water. Driven in push pull mode, consecutive drift tubes have opposite potential.

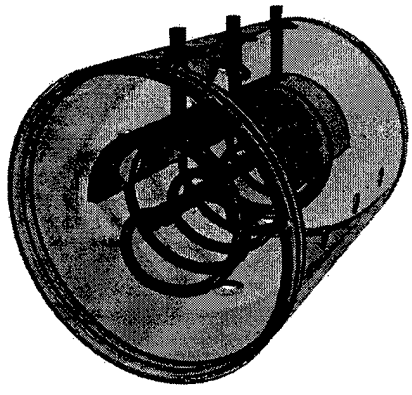


Figure 2: Transparent drawing of a 7-gap resonator.

The development and construction of the three 7–gap–resonators which will allow to vary the energies of the REX-ISOLDE beams between 0.8 and 2.2 MeV/u has been started. Assuming a realistic resonator voltage for each

resonator of approximately 1.75 MV at 90 kW incoupled power [11], the design velocities were fixed to 5.4%, 6.0% and 6.6% of the velocity of light. Three downscaled models (1:2.5) were built in order to optimize the shuntimpedance and the field-distribution at the operation frequency of the amplifiers of 101.28 MHz required by CERN standards. The optimization of the 6.0% low power resonator is already finished.

For the down scaled mmodel we have measured a shuntimpedance of 95 MΩ/m and a Q–value of 3350. Therefore a resonator voltage of about 1.8 MV for the power type resonator can be expected. Table 1 compiles the parameters of the 6.0% power type resonator as expected from the down scaled model.

Parameter	6.0% power type resonator
f [MHz]	101.28
Q–value	5300
Z [MΩ/m]	58
N [KW]	90
U_0 [MV]	1.78

Table 1: Parameters for the 6.0%-power-resonator, extrapolated from the down scaled model. f=frequency, Z=shunt impedance, N=power consumption, U_0=resonator voltage.

The development of the resonators was accompanied by extensive MAFIA calculations. The six arms with drift tubes correspond to six coupled oscillators and produce closely spaced modes. To investigate these modes referring to eigenfrequency and voltage distribution in the gaps MAFIA is a very powerful simulation code. It could be demonstrated that spiral-resonators like 7–gap resonators can be simulated to better than 1% in comparison with experimental results (compare fig. 3).

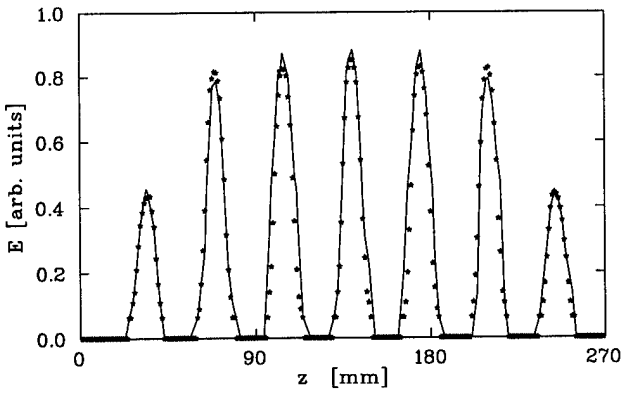


Figure 3: Comparison between the optimized distribution of the electric field in the down scaled 7-gap resonator for $\beta = 6\%$ calculated with MAFIA (solid line) and measured (asterisk).

Extensive beam dynamic calculations were made to optimize the transmission of the beam up to the target. It turns out that for final energies between 0.85 and 2.2 MeV/u nearly 100% transmission can be realized. The acceptance in the x-plane is 1.2 πmm mrad (norm.) and in the y-plane 3.0 πmm mrad (norm.). The bunchlength of the fully accelerated beam (2.2 MeV/u) is 2.4 ns at the target, it can be further improved if necessary by a rebuncher before the target.

3 STATUS

The extension of the ISOLDE experimental hall, starting in January 1996 is finished. The superconducting solenoid for the REX-Trap is delivered and installed at the high voltage platform. The first retardation system is under construction, all mechanical parts including the magnet chamber are in fabrication. The solenoid for the EBIS, a 2 Tesla system, has been ordered and new injection simulations of the injection scheme were performed.

RFQ- and IH-tanks are ordered, for the IH-structure a scaled down model for the parameter optimization is under construction in the mechanical workshop. All three scaled down models of the 7 gap resonators are built and presently optimized by bead perturbation measurements. The full scale tanks are under construction.

The development and construction of all components are expected to keep the time schedule, which foresees the first accelerated beams available in 1999.

This work is funded in part by the German Federal Ministery for Education, Science, Research and Technology (BMBF) under contract No. 06HD802I and No. 06LM868I(2).

4 REFERENCES

[1] Radioactive beam Experiment at ISOLDE: Coulomb Exitation and Neutron Transfer Reactions of Exotic Nuclei, Proposal to the ISOLDE commitee, CERN-ISC94-25

[2] D. Habs, *et al., Proc. of the EMIS-13*, Bad Dürkheim, Germany, 1996, *to be published in NIMB*

[3] O. Kester, *et al., Proc. of the CAARI'96*, Denton Texas, USA, 1996

[4] A. Schempp, *et al., Nucl. Inst. and Meth.* **B10/11**, 831 (1985)

[5] J. Friedrich, *et al., Proc. of the IEEE-PAC91*, San Francisco (California), 3044 (1991)

[6] Kleffner, C.-M., *et al.*, in *Proc. of the EPAC92*, 1340 (1992)

[7] A. Schempp and H. Klein, *et al., Nucl. Inst. and Meth.* **135**, 409 (1976)

[8] U. Ratzinger, *Proc. of the LINAC88*, Williamsburg, CEBAF-89-001, 185-187 (1988)

[9] U. Ratzinger, *Proc. of the IEEE-PAC91*, San Francisco, 567-571 (1991)

[10] von Hahn, R. *et al., Nucl. Instr. and Methods*, A328, 270-274, (1993)

[11] Kleffner, C.M., *Proc. of the IEEE-PAC95*, Dallas, USA

DEVELOPMENT OF HILBILAC FOR INITIAL PART OF ADTT ACCELERATOR

G.Batskikh, V.Pirozhenko, Moscow Radiotechnical Institute
A.Favale, T.Myers, Northrop Grumman Corporation

Abstract

High-Intensity Low-Beta Ion Linear Accelerator (HILBILAC) is developed for application in initial part of CW proton accelerator for the transmutation. The accelerator uses high-efficiency compact accelerating resonator located inside a superconducting focusing solenoid. The results of calculations of the accelerator section with 3 MeV energy and 250 mA beam current are presented along with some results of experimental study. The accelerator offers good capture of injected beam to the acceleration, very low radio-frequency power loss (10 times lesser than known RFQ accelerator), and low peak electrical field in the resonator (2-3 times lesser than RFQ). HILBILAC Pulse Prototype with 1.9 MeV energy and 250 mA pulse current has been designed, the systems of the accelerator are mounted and adjusted.

1. INTRODUCTION

The accelerator under development is intended for application in an initial part of CW proton accelerator for the transmutation [1,2]. It can be used also for material study and materials treatment [5] as well as for Boron Neutron Capture Therapy [4].

According to the concepts for ADTT accelerator architecture, basic parameters of the initial part are the following: beam current - from 100 to 250 mA, operating frequency - 350 MHz or higher, particles energy - 20 MeV, it may be obtained by a few sections. Major problems are focused on the first 3-MeV section, rest sections may be similar[6].

HILBILAC meets theese requirements well. Its scheme contains compact accelerating resonator located inside a bore of superconducting focusing solenoid [3].

2. PARAMETERS OF HILBILAC SECTIONS

At present, experience in HILBILAC designing is based on the mathematic simulation of beam dynamics and resonator electrodynamics [6], the experimental investigation of proof-of-principle accelerator providing 400 mA proton beam current [7], and physical modeling with electron beam providing 5.6 A beam current (scaling to proton beam at 200 MHz) [7].

HILBILAC is capable to accelerate a 250 mA ion beam at frequences of 350 and 700 MHz starting from 100-150 keV injection energy. Separation of accelerating and focusing functions offers a possibility to optimize beam dynamics for obtaining of near to 100% capture efficiency, small diameter and emittance of the beam. Besides, radio-frequency (RF) accelerating structures with high efficiency can be used in the HILBILAC.

In Table 1, calculated parameters of two versions of CW accelerator having 350 and 700 MHz are presented. The 700-MHz version provides filling all RF buckets in the high-energy linac, thus minimizing the charge per bunch and beam losses.

Table 1. HILBILAC sections parameters

Section	CW vers. 1	CW vers. 2	HPP
Frequency (MHz)	350	700	350
Beam current (mA)	250	250	250
Output energy (MeV)	3	3	1.9
Injection energy (MeV)	0.1	0.15	0.1
Accelerator length (m)	3	2.8	1.7
Magnetic field (T)	7	7	7
Beam diameter (mm)	3	3	3
RF power supply (kW)	770	750	475

Since designing of high-intensity CW accelerator poses a few problems, the HILBILAC Pulse Prototype (HPP) has been designed and now is mounted at MRTI. Its parameters also are presented in Table 1.

3. BEAM DYNAMICS

Beam matching between ion injector and accelerating resonator is a problem because injector-resonator distance is large in order to reduse edge magnetic field of superconducting solenoid in the ion source. In the HPP, beam transport channel with two lenses is used. Distribution of the magnetic field is shown on fig. 1 along with variation of beam radius. In the resonator, the beam has 0.15 cm radius and 0.014 cm rms deviation of radius.

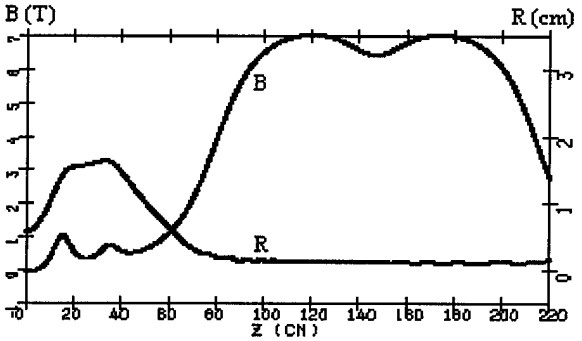


Fig. 1. Magnetic field B and beam radius R in HPP

*Work supported by Northrop Grumman Corporation

To achieve good beam matching and high capture efficiency, adiabatic RF bunching of the beam in rising field is used. Within initial part, the equilibrium phase decreases gradually while accelerating field increases (fig. 2). Major acceleration is made within last part of the accelerator, with acceleration rate of 2.6 MeV/m.

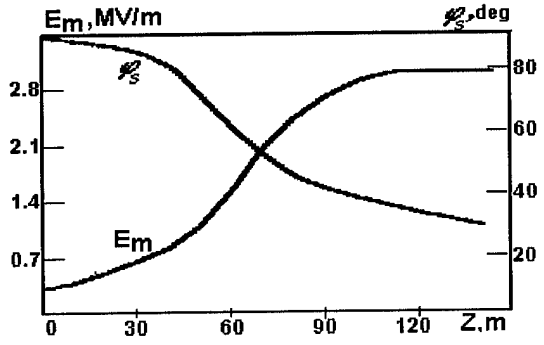


Fig. 2. Accelerating field and equilibrium phase in HPP

On fig. 3 is shown energy spectrum of accelerated beam. Almost all particles lie within 1.8-2 MeV energy range except about 2% that are unaccelerated.

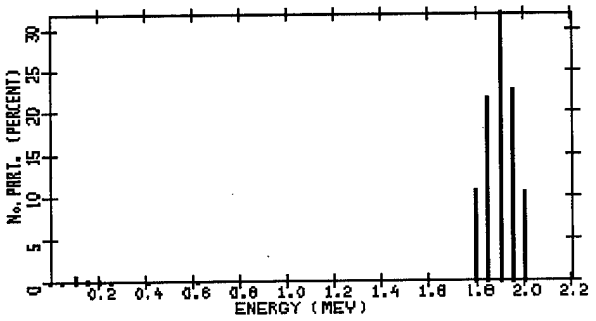


Fig. 3. Energy spectrum of accelerated beam in HPP

4. HILBILAC PULSE PROTOTYPE DESIGN

The ion injector (fig.4, ref.1) uses ion source duoplasmatron type. The transport channel (ref.2) includes two magnetic lenses. Owing to use of magnetic screens and compensating coil, edge magnetic field of the focusing solenoid in the source is under 0.001 T.

The cryostat (ref. 3) includes vacuum envelope, helium vessel for superconducting solenoid and two thermal shields. The superconducting solenoid (ref. 5) has 4.2 K temperature and uses NbTi cables. Magnetic field of 7.9 T was obtained on the tests of the solenoid.

The accelerating resonator (ref. 4) is placed in "warm" cryostat bore. Two coaxial feeders (ref. 6) are used to supply RF power from two output RF amplifiers based on GI-51A vacuum tubes each providing 300 kW pulse RF power.

The beam diagnostic system includes beam profile meter, foil transducer for energy spectrum measurement (ref. 7) and beam emittance meter (ref. 8).

At present, all systems of the HPP have been designed, the systems are manufactured and mounted.

5. ACCELERATING RESONATOR

The resonator has longitudinal RF magnetic field (H-resonator). It consists of cavity, two vanes, a number of drift tubes alternatively connected to the vanes thus forming accelerating gaps (fig. 5). The cavity has hexagonal cross-section with width gradually rising along the resonator. The ends of the vanes are braced to obtain required field distribution. Every drift tube is a thin ring. The stems are of conic shape providing good removal of heat from the drift tubes to the vanes.

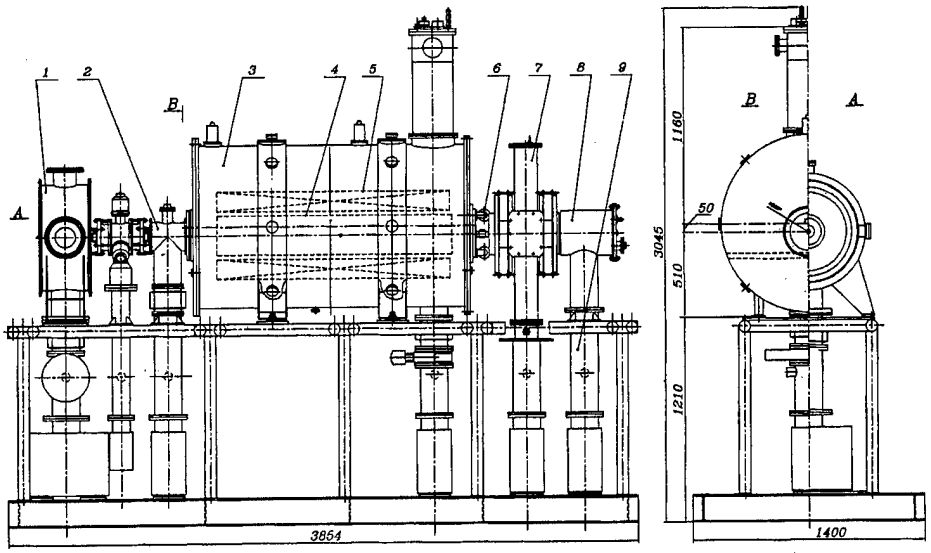


Fig. 4. HILBILAC Pulse Prototype design

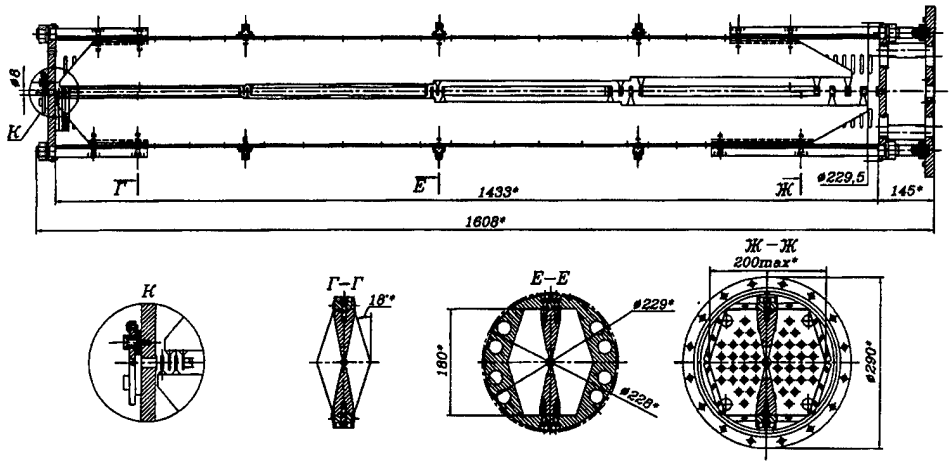


Fig. 5. HILBILAC Pulse Prototype resonator design

The resonator parameters were calculated using 2D REAL and GNOM codes based on the mesh technique. The parameters were checked with RF modeling. In particular, full-scale RF model of HPP resonator was manufactured and tested, field distribution shown on fig. 2 was obtained.

Effective shunt impedance of the resonator vs relative velocity of particles is given on fig. 6. The dots indicate values measured with RF models at 200-300 MHz and scaled to 350 MHz. Measured values are 65-75% of calculated values. The shunt impedance of the structure is very high.

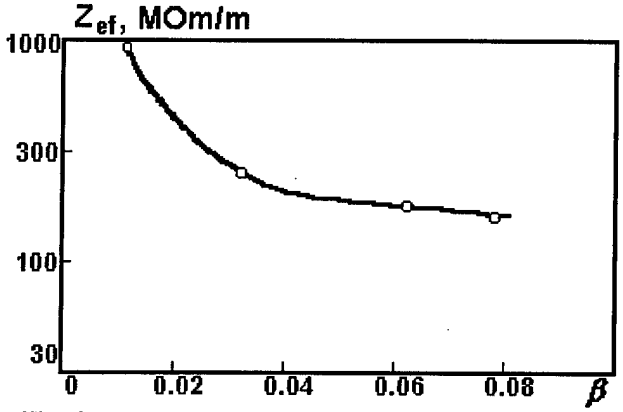


Fig. 6. Measured shunt impedance of the resonator

Table 2. Parameters of the accelerating resonators

Section	CW	HPP
Frequency (MHz)	350	350
Length (m)	2.83	1.43
Number of gaps	215	141
Cavity width (mm)	100-210	92-200
Accelerating field (MV/m)	0.26-2.4	0.26-3
Pick surface field (MV/m)	11	14.7
RF power loss (kW)	42	23
Efficiency	95%	95%

Design of the resonator is well suitable for the technique developed in GRUMMAN and used for BEAR and CWDD [8]. For CW accelerator, the cavity and vanes may be manufactured from TeCu alloy combining high conductivity with good mechanical properties, and electroformed with pure Cu. The design offers good thermal characteristics: local power dissipation does not exceed 10 W/cm^2 and overheating of elements does not exceed 10 °.

6. CONCLUSION

A comparison of HILBILAC and well-known RFQ accelerator in indicated range of parameters shows the following. HILBILAC offers much more limit current of ion beam providing acceleration of 250-mA beam at any frequency without beam funneling. RF power loss in HILBILAC is about 10 times lesser, that gives an economy in RF power and makes more simple the solution of heat removal problem. Peak surface field in HILBILAC is 2-3 times lesser, that ensures more reliable operation. Pay for theese merits is necessity to use the superconducting solenoid.

REFERENCES

[1] G.Lawrence, Proc. of 1995 Particle Accelerator Conf., p. 35-39.
[2] G.Batskikh et al., Proc. of 1994 International Conf. on ADTT, Las-Vegas, p. 83-92.
[3] V.Pirozhenko, O.Plink, ibid, p. 404-410.
[4] V.Pirozhenko, Proc. of 1-st International Workshop on Accelerator-Based Neutron Sources for BNCT, Jackson, 1994, p. 149-159.
[5] S.Schriber, Proc. of 1994 European Particle Accelerator Conf., p. 213-217.
[6] V.Pirozhenko, O.Plink, T.Myers, ibid, p. 261-263.
[7] B.Murin, V.Pirozhenko, O.Plink, Proc. of 1990 Linear Accelerator Conf., p. 707-709.
[8] J.Rathke, L.Young, Proc. of 1994 Linear Accelerator Conf.

A 1- TO 5-MW, RCS-BASED, SHORT-PULSE SPALLATION NEUTRON SOURCE

Y. Cho, Y.-C. Chae, E. Crosbie, K. Harkay, D. Horan, R. Kustom, E. Lessner, W. McDowell, D. McGhee, H. Moe, R. Nielsen, G. Norek, K. Peterson, K. Thompson, J. Wang, and M. White
Argonne National Laboratory, 9700 South Cass Avenue, Argonne, Illinois 60439-4800 USA

Abstract

Two accelerator configurations, the linac/compressor ring scheme and the linac/RCS scheme, are commonly used to provide the proton beam power for a short-pulse spallation neutron source. In one configuration, a full-power linac provides the beam power and a compressor ring shortens the pulse length from 1-ms down to 1 μs. In the other, rapid cycling synchrotrons (RCSs) provide the beam power and also shorten the pulse length. A feasibility study of a staged approach to a 5-MW proton source utilizing RCS technology, allowing intermediate operation at 1 MW, was performed at ANL and is presented in this paper. This study is complementary to a study in progress at ORNL based on a linac and an accumulator ring. Our 1-MW facility consists of a 400-MeV injector linac that delivers 0.5-mA time-averaged current, a synchrotron that accelerates the beam to 2 GeV at a 30-Hz rate, and two neutron-generating target stations. In the second phase, the 2-GeV beam is accelerated to 10 GeV by a larger RCS, increasing the facility beam power to 5 MW.

1 INTRODUCTION

Three of the four pulsed sources now in existence use the RCS scheme; the other uses the linac/compressor scheme. Our concept uses RCS technology to attain, in two stages, a beam power of 5 MW. It complements the linac/compressor ring work mentioned below [1,2].

Two ongoing studies, the European Spallation Source (ESS) [3] being designed in Europe, and the National Spallation Neutron Source (NSNS) being designed at ORNL [4] by a collaboration including BNL, LBNL, and LANL, are using the linac/compressor ring scheme.

Distinct differences exist between the two methods. The linac/compressor ring tends to have a beam energy around 1 GeV, while the RCS energy is generally higher than 1 GeV. A high-energy linac is costly to build and to operate, making a linac with energy much higher than 1 GeV economically unattractive, and the beam current of an RCS is usually space-charge limited, thus the final beam power is obtained by increasing the energy. We chose a 2-GeV RCS for the 1-MW source and a 10-GeV RCS for the 5-MW source, leading to a beam current requirement of 0.5-mA for both machines.

1.1 Repetition Rate

The 30-Hz repetition rate was chosen after extensive consultation with IPNS users at ANL. The peak flux of a 30-Hz machine is twice that of a 60-Hz machine operating at the same average beam power, with a longer time separation between pulses. About half of the proposed NSNS instruments cannot operate at 60 Hz due to overlaps between consecutive pulses. The repetition rate has implications on the accelerator configuration since it is very difficult to operate a multi-MW linac/accumulator ring system at low repetition rates.

1.2 Upgrade Path or Phased Approach to 5 MW

The 2-GeV and 10-GeV cascading RCS system allows the 2-GeV RCS (RCS-I) to be used as a booster for the 10-GeV RCS (RCS-II). The booster/main ring arrangement enables us to reach 5-MW operation in two-stages. A 1-MW, 2-GeV facility is built in the first stage, and RCS-II with its associated building and support structures is added later to increase the facility power to 5 MW. First, the 2-GeV beam is extracted to the target stations via transfer lines; the 10-GeV target-station extraction line is completed along with RCS-II.

1.3 Beam Loss Considerations

A 5-MW facility based on a 1-GeV linac requires a 5-mA average current, while a 10-GeV RCS system requires 0.5 mA. A factor of 10 fewer protons must be handled by the RCS, giving it a strong advantage with respect to potential beam losses. Beam losses usually occur during injection and capture, not during acceleration or extraction. It is therefore preferable to have the minimum possible injection energy so that if there are losses, they occur at low energy and result in less activation. Beam transfer from RCS-I to RCS-II uses highly efficient bunch-to-bucket transfer.

2 FACILITIES DESCRIPTION

2.1 Facility Layout

Figure 1 shows the overall layout of a site-independent, self-contained 5-MW facility, consisting of: a 400-MeV H^- linac, 2- and 10-GeV RCSs, 10- and 30-Hz target stations, and beam transfer lines from both synchrotrons to both target stations. Also shown in Figure 1 are a central laboratory and office building to house the facility staff and two laboratory and office modules for users. The total building area is about 82,000 m^2. The installed electric power is ~ 80 MVA, with an expected average power usage of 45 MVA at 5 MW. Table 1 summarizes parameters of RCS-I and RCS-II.

0-7803-4376-X/98/$10.00 © 1998 IEEE

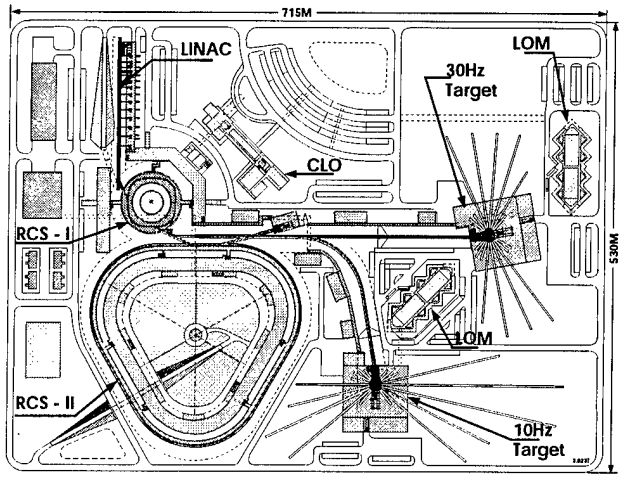


Figure 1: Site-independent 5-MW facility layout.

Table 1: Parameters of RCS-I and RCS-II

Parameters	RCS-I	RCS-II	
Circumference	190.4	761.6	m
Super-periodicity	4	3	-
Total number of cells	28	75	-
Nominal straight-section length	2.90	4.28	m
Bending radius	6.62	26.39	m
Horizontal tune, ν_x	6.82	19.19	-
Vertical tune, ν_y	5.73	19.13	-
Transition Energy, γ_t	5.40	14.47	-
Nat. chromaticity, $\xi_x=(\Delta\nu)_x/(\Delta p/p)$	-7.23	-24.78	-
Nat. chromaticity, $\xi_y=(\Delta\nu)_y/(\Delta p/p)$	-6.88	-26.24	-
Maximum β	12.0	20.3	m
Maximum η function	2.2	1.1	m

2.2 Target Stations for 1-MW and 5-MW Operation

Our plan is to reuse the 1-MW target stations, with some modifications, for the 5-MW source. The biological shield is the most costly item in a target station. The shield, which can cost some tens of million dollars, is usually made of iron and steel. The shielding of a 5-MW target is $\approx\sqrt{2}$ thicker than that of a 1-MW target. The actual neutron-generating target and moderator assembly cost around a million dollars but have a volume of only about one cubic meter. The target station's mechanical structure should therefore be designed to accommodate the shielding thickness of a 5-MW target-moderator assembly, including potential geometry changes.

3 THE 2-GEV ACCELERATOR SYSTEM

A detailed description of the 1-MW accelerator system appears elsewhere [1,2], thus only a brief summary is presented here. The previous work mainly addressed a site-specific design utilizing existing buildings and infrastructure of the former Zero Gradient Synchrotron (ZGS) facility. The ZGS enclosure accommodates a 200-m-circumference ring, and a 2-GeV energy permits use of that enclosure. The ring energy could easily be increased if a site-independent optimization were made. The choice of a 2-GeV beam energy fixed the average beam current at 0.5 mA, which in turn set the required number of protons/pulse at 1.04×10^{14} for a 30-Hz repetition rate.

3.1 Lattice, Aperture, and Stacked Beam Emittance

The lattice is described in detail in [1]. Desired features include: 1) a transition energy » 2 GeV so there is a large slip factor, $\eta = |\gamma^{-2} - \gamma_t^{-2}|$, to facilitate radio-frequency (rf) beam manipulation, 2) dispersion-free straight sections equipped with rf systems and the H^- injection stripper foil, and 3) at least 20 m total length of straight-section space for rf cavities. The large rf space requirement is because, in the 1- to 2-MHz frequency range, typical cavity energy gains are 10 kV/m, and the required peak rf voltage is estimated at 200 kV. To achieve the desired features, a 90° phase advance FODO cell was chosen as the normal cell. A dispersion-suppressor cell is constructed by removing one dipole from a normal cell. Empty cells are obtained by removing both dipoles from a normal cell. The straight-section length is obtained by adding as many empty cells as required. A periodicity of four was chosen to best use the existing ZGS enclosure.

An assessment of the ring magnet apertures was made, taking into consideration the lattice functions and the machine apertures. A ring acceptance of 750 π mm mr makes the physical dimension of the aperture close to that of ISIS. Injected beam will be stacked within an emittance of 375 π mm mr to provide some space for beam scraping and catching of the scraped beam. This leaves a space equivalent to 40% of the beam size between the chamber wall and the beam.

3.2 Injection, Rf Capture, and Acceleration

Using the required 10^{14} protons/pulse, a planned allowable incoherent space charge tune shift of 0.15, and a stacked beam emittance of 375 π mm mr, we can calculate the $\beta^2\gamma^3$ term of the Laslett equation. The relativistic parameters, β and γ, come from the injection energy, so an injection energy of 400 MeV satisfies the 10^{14} protons/pulse requirement. As noted above, a lower injection energy is a desirable feature. The linac operates at a 30-Hz repetition rate with a pulse length of 0.5 ms, giving a duty factor of 1.5%. The peak current of the macropulse is 44 mA, with 75% of the beam chopped to facilitate no-loss injection. The chopper is located between the ion source and the radio-frequency quadrupole. Either Penning- or volume-type negative hydrogen sources could be used as they are capable of delivering ~50mA peak current with a 1.5% duty factor. The injection of H^- ions enables us to paint both transverse phase-space planes in a preset manner. The linac energy spread is adjusted for longitudinal phase-space painting to fill the total bucket area of 9 eV s.

The number of injected turns will be about 500. The desired proton distribution is achieved by injecting H^-

ions through a 250-μg/cm^2-thick carbon stripper foil using programmable injection positions and angles in the transverse phase planes. The horizontal closed orbit is moved away from the foil as injection progresses, using four bumper magnets. The vertical injection angle is programmed. Programming of the horizontal injection position and the vertical injection angle results in the expected K-V particle distribution.

The rf acceleration voltage is related to the dB/dt of the ring dipole, thus it is desirable that dB/dt be fairly low. This is achieved at a 30-Hz repetition rate by energizing the ring at a 20-Hz rate and de-energizing it at a 60-Hz rate. The required peak rf voltage is lowered by 1/3.

Since beam loss prevention is one of the most important concerns in multi-MW proton sources, an extensive simulation study to eliminate beam losses was performed [1]. Variable parameters in the Monte Carlo tracking calculation included the rf voltage programming during injection and capture, the ring magnet dB/dt, incoming beam energy spread, gap length after chopping the linac macro-pulse, and desired Δp/p of the beam throughout the acceleration cycle in order to satisfy the Keil-Schnell longitudinal stability criteria. We tracked 5×10^4 macro-particles representing 10^{14} particles with 75% chopped (25% discarded) beam and an incoming-beam energy spread of ± 0.4%. We can inject and accelerate to 2 GeV with no losses. In addition, the study resulted in a determination of the optimum rf voltage programming for no-loss acceleration, and the algorithm to control Δp/p of the beam to satisfy the Keil-Schnell criteria. Details are presented in [1].

The coupling impedance between the circulating beam and its surroundings in the RCS is dominated by space-charge effects that vary with the beam energy. Both longitudinal and transverse stability have been studied extensively and are described in references [5,6].

4 THE 10-GEV ACCELERATOR SYSTEM

Figure 1 shows the 5-MW facility layout, obtained by adding an RCS of energy ≥ 10 GeV adjacent to the 1-MW facility. RCS-I is a booster for the 10-GeV machine. The 1-MW target stations are upgraded as described earlier. A preliminary description of RCS-II is given in [7].

4.1 Lattice, Beam Transfer, and Injection

The RCS-II lattice has the same requirements as the RCS-I lattice. We use the 90° phase advance FODO structure as the normal cell, a missing dipole FODO cell for the dispersion suppresser cell, and FODO cells without dipoles as the straight section cells. A total straight section length of 200 m is required to accommodate the rf cavities that produce ≈ 2000 kV of rf voltage. RCS-II's circumference must be an integer multiple of that of RCS-I so the rf systems are harmonically related. The harmonic relationship between the two rings is essential in making the bunch-to-bucket transfer from the smaller ring to the larger ring. This feature of transferring bunches from RCS-I to waiting buckets of RCS-II permits no-loss injection into the large ring. The lattice and its performance on single particle dynamics are described in [7].

The RCS-I rf system has a harmonic number 2 and a frequency range from 2.2 to 2.9 MHz. To improve the efficiency of RCS-II's rf system, a harmonic jump occurs in the 10-GeV ring. This is achieved by giving RCS-II a frequency range of 4.4 to 5.8 MHz. Bunch-to-bucket matching between the two rings is achieved by adjusting the rf voltage of RCS-I at extraction and the rf voltage of RCS-II at injection. Figure 2 shows the phase-space distribution at injection into RCS-II.

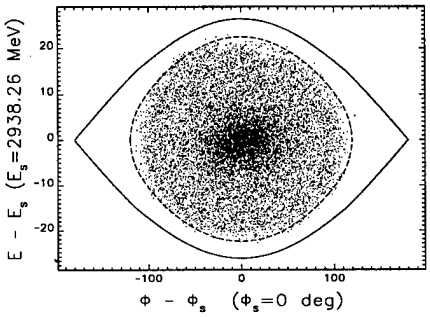


Figure 2: Rf bucket and bunch phase-space distribution from RCS-I at injection into RCS-II. The dotted line indicates the contour enclosing an area of 3.7 eV s.

4.3 Impedance and Collective Instability

RCS-II operates below transition energy. The coupling impedance is dominated by space charge effects, and an analysis similar to that for RCS-I was also performed.

5 ACKNOWLEDGMENTS

Work is supported by the U.S. Department of Energy, Office of Basic Energy Sciences, under Contract No. W-31-109-ENG-38. We acknowledge D. Haid for graphics help and C. Eyberger for editorial assistance.

6 REFERENCES

[1] "IPNS Upgrade - A Feasibility Study," ANL Report ANL-95/13 (April, 1995).

[2] Y. Cho et al., "A 2-GeV, 1-MW Pulsed Proton Source for a Spallation Source," EPAC-96, Sitges, Spain, 10-14 June 1996, pp. 524-526 (1996).

[3] G. Bauer et al., eds., "ESS - A Next Generation Neutron Source for Europe," ESS-96-53-M, Nov 1996.

[4] B. R. Appleton, these proceedings.

[5] K. Harkay and Y. Cho, "Transverse Instability Analysis for the IPNS Upgrade," Proc. of the 1995 Particle Access. Conf., Dallas, TX, May 1995, pp. 3004-3006 (1996).

[6] K. Harkay, Y. Cho, and E. Lessner, "Longitudinal Instability Analysis for the IPNS Upgrade," Proc. of the 1995 Particle Accel. Conf., Dallas, TX, May 1995, pp. 3001-3003 (1996).

[7] Y. Cho et al., "A 10-GeV, 5-MW Pulsed Proton Source for a Spallation Source and a Muon Collider," EPAC-96, Sitges, Spain, 10-14 June 1996, pp. 521-523 (1996).

STATUS OF THE TRIUMF-ISAC FACILITY FOR ACCELERATING RADIOACTIVE BEAMS

P.W. Schmor, R. Baartman, P. Bricault, M. Dombsky, G. Dutto, S. Koscielniak,
R.E. Laxdal, F. Mammarella, G.H. Mackenzie, R. Poirier, L. Root,
G. Stanford, G. Stinson, I. Thorson, J. Welz
TRIUMF 4004 Wesbrook Mall, Vancouver, B.C., Canada V6T 2A3

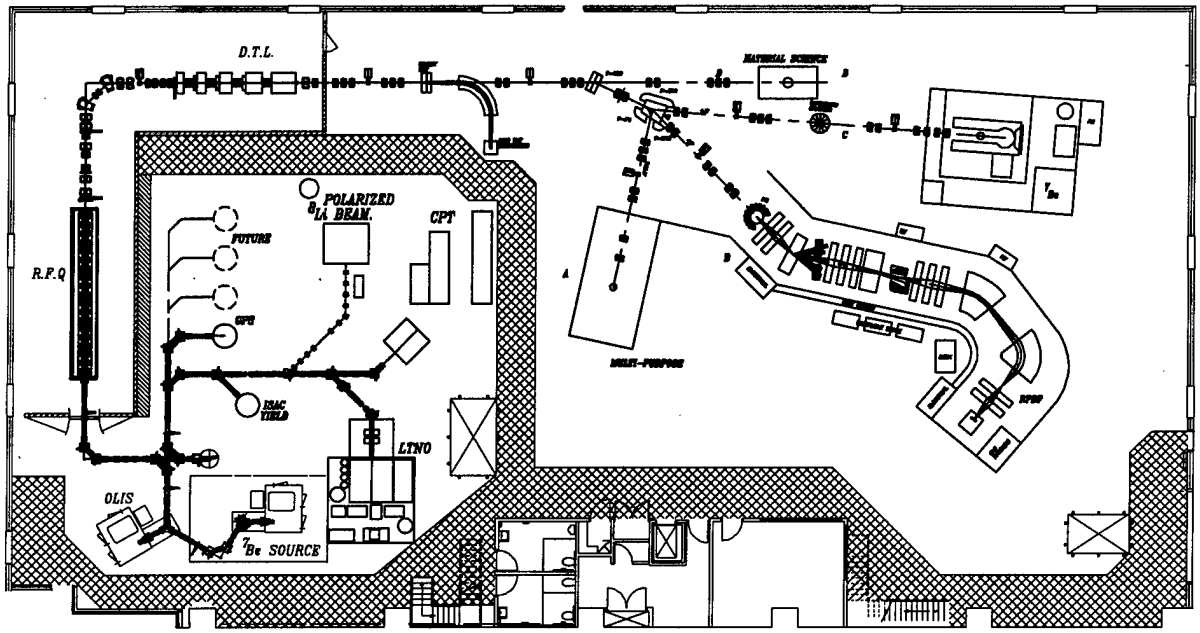
Abstract

ISAC, a new facility for accelerating intense beams of unstable ions, is under construction at TRIUMF. The radioactive nuclei will be produced by up to 100 A of 500 MeV protons impinging on one of two target/ion source stations located in an underground vault. The ionized beam will be transported by electrostatic ion optics to a high acceptance, high resolution mass analyser. Following mass selection the beam is transported vertically to grade level and then horizontally to either a low energy experimental area or to a system of accelerators. First, a 35 MHz cw RFQ accelerates isotopes with q/A >1/30 from 2 keV/u to 150 keV/u. Following the RFQ the beam is passed through a stripper and magnetic bend to select a charge state with q/A 1/6 prior to rebunching and injection into a cw drift tube linac (DTL) operating at 105 MHz. The output beam, with energy continuously variable from 0.15 to 1.5 MeV/u, is transported to one of a number of experimental stations. This paper briefly outlines the plans, schedule and status of the project.

1 INTRODUCTION

A five-year plan, designed to provide TRIUMF with an intense radioactive ion beam facility by the year 2000, was approved in June 1995. The plan includes (i) The extraction of a high intensity (100 A) proton beam from the 500 MeV H- cyclotron into a dedicated beam line (2A) transporting the beam to a new 5000 m^2 facility; (ii) A remotely handleable 50 kW target/ion-source beam - dump system for the production of low energy radioactive beams up to 60 keV for singly charged ions; (iii) A high resolution (1/10000) mass selection system; (iv) A low energy transport system (LEBT) and experimental area; (v) a linear accelerator system, consisting of an RFQ and an interdigital H- DTL, accelerating ions with A 30 to energies between 150 keV/u and 1.5 MeV/u; and (vi) a transport system for the accelerated beams (HEBT) and corresponding experimental area (see fig. 1).

The facility will allow strengthening of the radioactive beam research initiated ten years ago (using a 1 A 500 MeV proton beam) on the TISOL facility [1]. It will also allow new astrophysics, material science, life science and other fundamental research to take place at energies up to 1.5 MeV/u for light (A 30) ions. The limit in mass and energy was dictated by budget limitations and experimental priorities. However, the new building was



0-7803-4376-X/98/$10.00 © 1998 IEEE

designed to be compatible with acceleration to 6.5 MeV/u. A new plan to expand the mass range and energy range beyond present limits is being developed for the period after the year 2000. For energies less than 60 keV, all isotopes produced by the target/ion source system can be delivered to the low energy experimental area.

2 FACILITY

When fully commissioned, beam line 2A will direct a 100 A proton beam to the ISAC targets and will be one of four primary beam lines into which beam may be extracted simultaneously from the H- cyclotron. Low intensity beam has already been extracted into the front end portion of 2A over an energy range from 472 to 510 MeV. Simultaneous low-intensity extraction into lines 1A and 2A has also been demonstrated to be feasible, despite intrinsic vertical oscillations of the internal cyclotron beam in the extraction region.

The new ISAC building, is divided into a shielded building and an experimental building. The sealed, heavily shielded section, houses the highly radioactive and potentially contaminated target/ion source assemblies, extraction systems, the pre-separator magnet, and ancillary systems (cooling, vacuum, decontamination and storage facilities). A remotely controlled 20-ton crane and two hot cells are integral parts of this building. Construction is well advanced with concrete pouring nearly complete. The structural steel erection is well under way. The installation of services is in progress. The buildings will be available starting this summer.

3 TARGET/ION SOURCE SYSTEM

All highly activated and potentially contaminated components such as production targets, beam dump, ion sources and initial focusing devices will be located at the target station within the target hall along with the primary radiation shield and services required to operate the target station components. Hot cells, assembly area and a decontamination and storage facility will be included within the target hall. The target facility is located in a canyon surrounded by steel and concrete shielding, and consists of a large vacuum tank with five separate modules: entrance, target, beam dump and two exit modules housing beam-optics components. The target module is made up of a 2m long shielding plug on the bottom of which are the ion source and the extraction system. The target/ion source assembly will be biased to give extraction voltages up to 60kV. The target station modules are all designed to be handled remotely. The shielding is designed to allow access by personnel into the target hall with beam on target.

4 MASS SEPARATOR

The mass separator front end includes an electrostatic triplet followed by an electrostatic doublet. Preliminary mass selection will be done using a 60 magnet having a resolving power around 300. The focal plane of this magnet accepts a large portion of the beam within a ±10% mass range. The slit-selected beam is then transported to the main mass separator which is designed to provide mass separation with energy spread focusing at the focal plane. This is based on two magnetic sectors, placed at different electrostatic potentials. The design will allow good mass separation even with an ion source having several tens of eV energy dispersion.

Table 1-Separator Specifications

Separator Specifications	
Mass range	< 238 amu
Ion beam energy	≤ 60 keV
Mass dispersion	5m or 5 cm/%
Resolving power	≤ 10000

5 LEBT

The ion beam from the mass separator is transported vertically to grade level and is to be switchable between the low energy experimental area (LE) and the accelerator. A switchyard allows an off line source to supply beam to either the RFQ or the LE experimental area while simultaneously, the mass separator can supply beam to the LE or the RFQ, respectively. All the optics in the LEBT are electrostatic: quadrupoles are typically 50 mm long by 25mm bore radius, bends are each 45, with spherical electrodes, 250mm in radius. The RFQ, having no bunching section, accepts bunches ±30 in length. A sawtooth rebuncher (four harmonics) located 5m upstream of the RFQ operates at 11.67 MHz, yielding bunch separation of 86ns and 80% of the beam within the RFQ longitudinal acceptance for acceleration. More details can be found elsewhere in these proceedings [3].

6 ISAC ACCELERATOR

A description of the various components of the ISAC accelerator system has already been reported elsewhere [3]. Recent progress, design definitions or improvements will be summarized below. Basic specifications are given in Table 2 and the layout in Figure 1.

6.1 RFQ

The reference design for the RFQ [4] is a four-rod split ring structure operating cw at 35 MHz. Full power tests on a single ring were completed last summer [5] and on a three ring module assembly last fall [6]. The 8 metre long vacuum tank and the RFQ components have been released for manufacturing, allowing the low energy seven-ring portion of the final RFQ to be assembled and tested with beam in its final location by spring 1998. The final RFQ is 760 cm long with 19 rings in 40 cm long modules. The cross section of the vacuum tank is rectangular to facilitate alignment of the modules and

copper plating of the vacuum tank. The alignment philosophy is to construct a solid base, maintain tight manufacturing tolerances, construct the modules using precise jigs and fixtures and edm-machine the critical mounting surfaces for the electrodes after assembly [6].

Table 2-Accelerated Beam Specifications for ISAC

Input Beam	
Injected energy	2 keV/nucleon
Ion mass	A 30
Ion charge	1 (initially)
Beam emittance (100%)	50 mm mrad at injection
Output energy range	0.15 E 1.5 MeV/u
Resolution E/E	0.1%
Duty factor	100%

6.2 MEBT

The MEBT is made up of three sections. In the first section, the beam from the RFQ is focused in three dimensions on to the stripping foil to minimize emittance growth due to multiple scattering and energy straggling. Five quadrupoles provide the transverse focus and a two-gap, 105MHz spiral resonator between the second and third quadrupoles will focus the beam in time. There is also provision to incorporate a chopper to eliminate beam from the adjacent two sparsely populated 35 MHz buckets. The quadrupoles act optically like a typical 4Q system but the third quadrupole is replaced by two quadrupoles separated by a drift space to allow the chopper to be placed where the beam is parallel in x. The chopper slits would be placed just upstream of the foil. The second section consists of a 90 achromatic bend (QQDQQDQQ) with charge selection slits at the symmetry plane. The section is very compact to reduce beam debunching. The last section includes a 35 MHz folded /4 rebuncher, at the image point of the charge selection section, and four quadrupoles to provide a three dimensional match at the DTL entrance. This buncher is now being developed in collaboration with LBNL.

6.3 *Drift-tube Linac*

The separated function ISAC DTL [7] will accelerate ions of 1/3 q/A 1/6 to a final energy fully variable from 0.15 to 1.5 MeV/u. Five independent 105 MHz interdigital H-mode cavities provide the acceleration, while quadrupole triplets and three gap split-ring resonator bunchers between IH tanks provide transverse and longitudinal focusing. To reduce final energy the high energy IH tanks are turned off sequentially and the voltage and phase in the last operating tank is varied. Beam simulations show that the DTL can accelerate beams with little or no emittance growth over the complete energy range. Design of the first IH tank is well under way with fabrication to be completed by the end of the year. We are collaborating with INR Moscow on the design and fabrication of a working prototype for the split-ring resonator bunchers [8]. The complete DTL is scheduled to be fully commissioned by the end of 1999.

7 HEBT

The HEBT comprises three sections. In the first section the beam is captured from the DTL and matched to the HEBT with five quadrupoles. The 5Q system allows the insertion of a chopper if required. A 90 analysing magnet can be positioned in the periodic section to check the beam energy and energy spread off line during commissioning and accelerator tuning. The beam is directed to the various experimental areas with an asymmetric QQDQQDQQ achromatic system where the last bend is a large switching magnet. At present four areas are envisaged but there will be capability for more areas as the science program evolves. To maintain the bunched structure of the lowest velocity beams (=1.8%) 35 MHz rebunchers are positioned every 8-10m.

REFERENCES

[1] K. Oxorn, et al, "The Installation of a Prototype On-line Isotope Separator at TRIUMF (TISOL), Nucl. Inst. & Methods, B26 (1987) 143.

[2] PG. Bracelet et al, Proc. Of the XVIII Int. Lin. Acol. Conf, CERN 36-07, Vol 1, p399.

[3] R. Baartman and J. Welz, "60 keV Beam Transport Line and Switchyard for ISAC", these proceedings.

[4] P.G. Bricault and H.R. Schneider, "Simulation of the TRIUMF Split Ring 4-rod RFQ with MAFIA", Proc. 1995 Particle Accelerator Conf., p1125 (1995).

[5] R.L. Poirier et al, "The RFQ Prototype for the Radioactive Ion Beams Facility at TRIUMF", Proc. XVIII LINAC Conference, CERN, p405 (1996).

[6] R.L. Poirier et al, "Construction Criteria and Prototyping for the ISAC RFQ Accelerator at TRIUMF", these proceedings.

[7] R. Laxdal et al, "A Separated Function Drift Tube Linac for the ISAC Project at TRIUMF, these proceedings.

[8] Y. Bylinsky, et al, "A Triple Gap Resonator Design for the Separated Function DTL at TRIUMF, these proceedings.

ANOMALOUS, INTENSITY DEPENDENT LOSSES IN Au(32+) BEAMS

M. Blaskiewicz*, L. Ahrens, H. Calvani,
AGS Dept. BNL, Upton NY 11973-5000 USA

Abstract

Anomalous, intensity dependent losses in Au(32+) beams have been observed in the AGS Booster. No collective signal is expected, or observed, but increasing the number of injected ions decreases the beam lifetime. The loss rates for Au(32+) are compared with those for Au(15+) .

1 INTRODUCTION

The AGS Booster is a rapid cycling proton and heavy ion synchrotron. The beam pipe has an average radius of 7 cm and the Booster's circumference is $C = 202$ m with betatron tunes ≈ 4.8. When accelerating gold the pressure of the backround gas is $P \approx 2 \times 10^{-11}$ Torr. The injection momentum of the ions is 9 GeV/c and the extraction momentum of 70 GeV/c was reached in 0.55 s for Au(15+) and 0.10 s for Au(32+) . A strongly intensity dependent loss in the Au(15+) beam has been reported previously[1]. In this note we report a qualitatively similar behavior for the Au(32+) .

Machine studies with Au(15+) were conducted in September 1994 and with Au(32+) in January 1997. In both cases the Booster magnet cycle was modified to include porches of constant field, so that data could be collected at a fixed beam energy. The data consisted of digitized current transformer traces taken under various conditions. During the magnetic porch the number of ions in the ring as a function of time $N(t)$ was fitted by an exponential $N(t) \approx N_0 \exp(-\alpha t)$ where α is the inverse life time or loss rate. For some of the data there was clear evidence that the losses were not a simple exponential, but without a theory we had no reasonable parameterization.

2 REVIEW OF Au(15+) DATA AND Au(32+) DATA

Figure 1 shows the equilibrium loss rate as a function of the number of injected Au(15+) ions.

The low intensity loss rates $\approx 0.1 s^{-1}$ are roughly consistent with scattering off residual gas at a pressure of 2×10^{-11} Torr. The lack of a coherent signal, and the insensitivity of the loss rate to the presence of rf suggests that the intensity dependent loss rates are due to the beam creating targets with which it subsequently scatters. This hypotheses is also consistent with the observation that the instantaneous loss rate depends on the intensity earlier in the cycle and on previous cycles.

The dependence of the loss rate on machine history was observed in two ways. In equilibrium, where the same number of Au(15+) ions were injected every cycle, the average loss rates are as shown in Figure 1. What is not obvious from the figure is that the number of ions at the end of the Booster cycle was not monotonic with the number of injected ions. For example, with a momentum of $p = 30$ GeV/c with 2×10^9 ions injected there were 1×10^7 ions remaining after 1.5s, while for 1×10^9 ions injected there were 2×10^8 ions remaining after 1.5s.

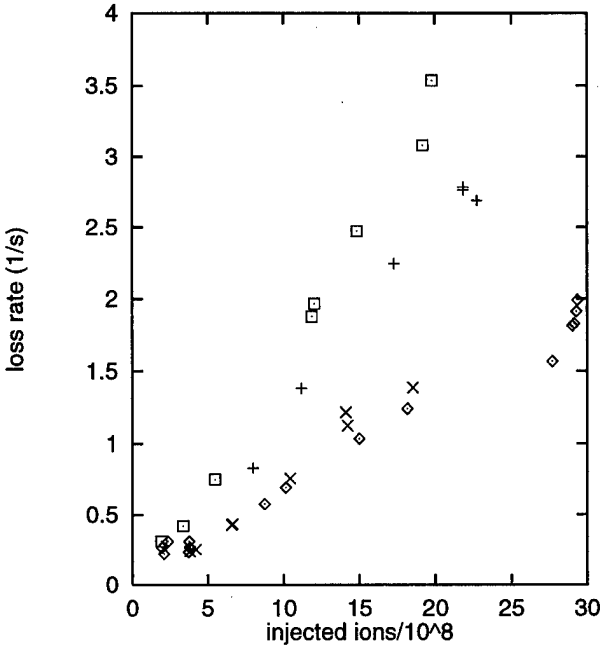


Figure 1: Au(15+) loss rate versus number of injected ions for momenta of: 9 GeV/c (diamonds), 15 Gev/c (crosses), 30GeV/c (squares), and 60 GeV/c (Xs)

The history dependence of the loss rates was observed when the beam was turned off for several cycles and the machine was allowed to "cool". The loss rate for the first cycle after cooling was $\approx 50\%$ smaller than the equilibrium value, and loss rates on subsequent cycles monotonically approached the equilibrium value.

Taken together these observations provide compelling evidence that the Au(15+) beam influences the background gas. We also note that the background gas is affected before a significant fraction of the beam is lost, since enhanced loss rates are apparent very early in the cycle.

Figure 2 shows the equilibrium loss rate as a function of the number of injected Au(32+) ions. A clear trend in the Au(32+) loss rate with intensity is apparent. The Au(32+) data were not as good as the Au(15+) data because of intensity limitations and generally smaller loss rates. At-

* Work supported by United States Department of Energy

0-7803-4376-X/98/$10.00 © 1998 IEEE

tempts to measure memory affects and variations in the loss rate during a given Booster cycle were inconclusive. On the other hand, we see no reason to believe a qualitatively different loss mechanism for the two cases.

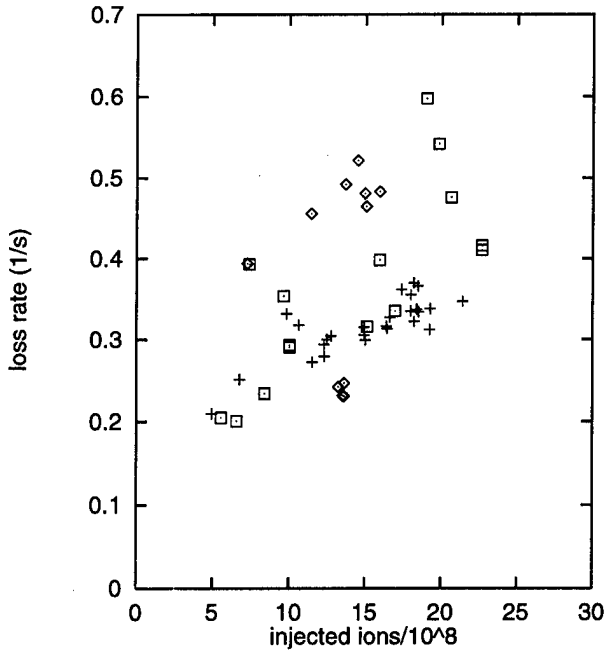


Figure 2: Au(32+) loss rate versus number of injected ions for momenta of: 20 GeV/c (diamonds), 27 Gev/c (crosses), 40 GeV/c (squares)

3 DISCUSSION

Straight lines were fit to the loss rates in Figures 1 and 2, yielding the change in loss rate with the number of injected ions as a function of momentum. These derivatives are shown in Figure 3. For scattering off residual gas the loss rate is given by

$$\alpha = \sum_j v n_j \sigma_j(v)$$

where v is the beam velocity and n_j and $\sigma_j(v)$ are the density and total charge changing cross section for scatterers of the jth type. Only n_j would vary with beam intensity. Assume that any scatterers are uniformly distributed within the vacuum chamber and that only one species is responsible for the change in loss rate with intensity. Then the change in the number of scatterers N_s with the number of injected ions N_b is given by

$$\frac{dN_s}{dN_b} = \frac{V_r}{\sigma v}\frac{d\alpha}{dN_b}$$

where $V_r = 3.1m^3$ is the total vacuum volume in the ring. Set $\sigma = \sigma_{16}10^{-16}cm^2$, $p = p_9$GeV/c, and $d\alpha/dN_b = \alpha' 10^{-8}\mathrm{s}^{-1}$. The beams are non-relativistic so $dN_s/dN_b = 1.9 \times 10^6 \alpha'/(p_9\sigma_{16})$, and for Au(15+) at $p = 30$ GeV/c, $dN_s/dN_b = 1 \times 10^4/\sigma_{16}$. For Au(32+) at $p = 20$ GeV/c, $dN_s/dN_b = 7 \times 10^3/\sigma_{16}$. For $\sigma_{16} = 10$ there are several hundred scatterers generated by each Au(15+) ion.

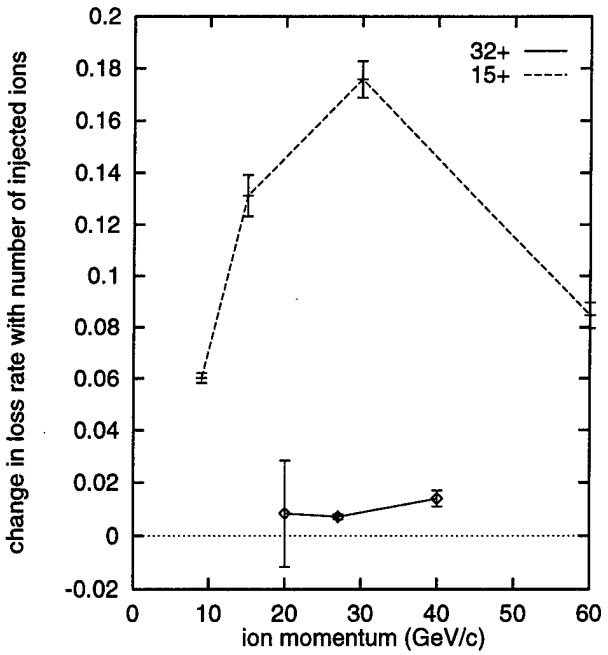


Figure 3: change in loss rate with the number of injected ions, $d\alpha/dN_b$ ($\mathrm{s}^{-1}10^{-8}$) versus ion momentum, p (GeV/c). The error bars are one standard deviation.

For a beam velocity $v = 0.15c$, a gas pressure of $P = 2\times10^{-11}$Torr, and a low intensity loss rate of $\alpha = 0.25\mathrm{s}^{-1}$ the data predict a loss cross section of $\sigma_\ell = 0.87\text{Å}^2$. This is a rather large cross section and to model the intensity dependent losses even larger cross sections appear necessary.

To model the losses, assume that hydrogen (H_2) is the main vacuum component at low beam intensity. After the beam is injected it interacts with the hydrogen via a total cross section σ_t^H which can result in charge exchange σ_ℓ^H or just momentum transfer. When the hydrogen molecule hits the wall, with an energy large compared to kT, it desorbs M molecules of type A. Molecules of type A remain in the beam pipe for a time τ_A before sticking on the wall. Since no significant rise in pressure is noted, assume that the amount of hydrogen is essentially constant. Then,

$$\frac{dN_b}{dt} = -\frac{vN_b}{V_r}\left(\sigma_\ell^A N_A + \sigma_\ell^H N_H\right), \quad (1)$$

$$\frac{dN_A}{dt} = +\frac{MN_b v}{V_r}\left(N_H\sigma_t^H + N_A\sigma_t^A\right) - \frac{N_A}{\tau_A}. \quad (2)$$

In equation (1) N_b is the number of gold ions in the beam, N_A is the number of molecules of type A, N_H is the number of molecules of H_2 and σ_ℓ^H and σ_ℓ^A are the charge exchange cross sections for H_2 and molecules of type A, respectively. It is assumed that molecules of both types are distributed uniformly throughout the entire volume of the vacuum chamber V_r. In equation (2) there are M molecules of type A liberated by each molecule that is

scattered by the beam, and σ_t^A is the cross section for momentum transfer between the beam ions and molecules of type A. These equations were numerically integrated using a 4s repetition period with beam present for 2s each cycle, as was done during the Au(15+) study. The calculation was continued until a nearly periodic solution was obtained and average loss rates were calculated.

If we assume that the molecule in question is CO and that the stripping cross sections vary as the square of the target atomic numbers[3] then $\sigma_\ell^A \approx 50\text{Å}^2$. Assume that two CO molecules are liberated per energetic molecular impact and that the CO lifetime is $\tau_A = 20$ s. Additionally, assume that the total cross sections for momentum transfer are ten times the cross sections for charge transfer; $\sigma_t^H = 10\text{Å}^2$ and $\sigma_t^A = 500\text{Å}^2$. With these assumptions the modeled Au(15+) loss rates as a function of the injected number of ions are shown in Figure 4. The loss rate is monotonic in the cross sections and significantly smaller cross sections did not accurately model the Au(15+) data.

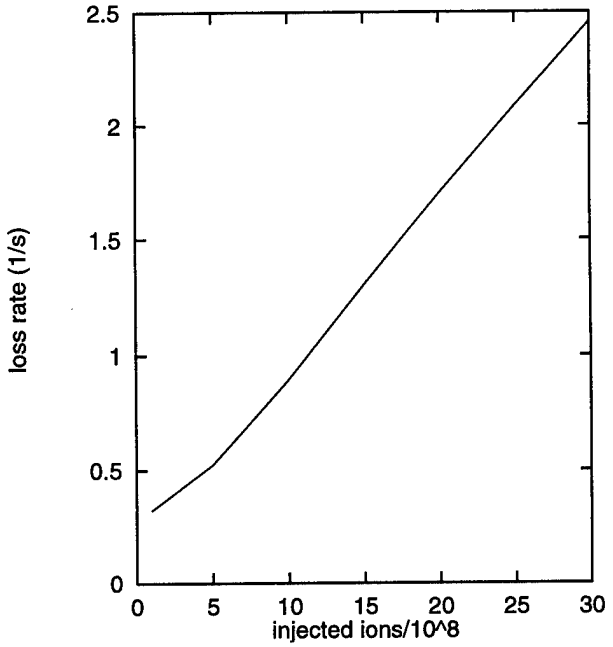


Figure 4: Modeled Au(15+) loss rate s^{-1} versus number of injected ions.

The change in gas composition with beam intensity should be measurable using mass spectroscopy. Such a measurement will provide additional constraints on any model. Since the Au(32+) Coulomb field is significantly greater than the field of Au(15+) we expect any change in backround gas composition to be present when accelerating significant amounts of Au(32+) . Hence, this model can be tested without returning to Au(15+) running.

For the Au(32+) data significantly smaller values of σ_ℓ^A are indicated. On the other hand, if the far field Coulomb force is responsible for the momentum transfer cross section σ_t^A, then σ_t^A should be larger for Au(32+) than for Au(15+) . If this is the case the charge exchange cross sections for Au(15+) are much greater than simple scaling laws would indicate.

4 ACKNOWLEDGEMENTS

We thank H.C. Hseuh for providing valuable information with regard to vacuum conditions in the AGS Booster.

5 REFERENCES

[1] M. Blaskiewicz, L.A. Ahrens, H.C. Hseuh, T. Roser, Y. Shoji, K. Zeno PAC95.

[2] H.C. Hseuh, BNL Booster Tech Note # 116, (1988).

[3] H.D. Betz, Rev. Mod. Phys., Vol 44, pg 465 (1972)

ACCUMULATOR RING LATTICE FOR THE NATIONAL SPALLATION NEUTRON SOURCE

C.J. Gardner*, Y.Y. Lee and A.U. Luccio
Brookhaven National Laboratory, Upton, NY 11973.

Abstract

The Accumulator Ring for the proposed National Spallation Neutron Source (NSNS) [1] is to accept a 1.03 millisecond beam pulse from a 1 GeV Proton Linac at a repetition rate of 60 Hz. For each beam pulse, 10^{14} protons are to be accumulated via charge-exchange injection. A 295 nanosecond gap in the beam, maintained by an rf system, will allow for extraction to an external target for the production of neutrons by spallation. This paper describes the four-fold symmetric lattice that has been chosen for the ring. The lattice contains four long dispersion-free straight sections to accomodate injection, extraction, rf cavities, and beam scraping respectively. The four-fold symmetry allows for easy adjustment of the tunes and flexibility in the placement of correction elements, and ensures that potentially dangerous betatron structure resonances are avoided.

1 THE LATTICE

The lattice for the accumulator ring will consist of four superperiods, each containing a 90° arc and a long straight section [2]. The layout of the accumulator is shown in Figure 1. Each arc will consist of four identical FODO cells and will have a total betatron phase advance of 2π which will ensure zero dispersion in the long straight sections. The arc half-cells will be 4 meters long and consist of a half-quadrupole, a 1.55 m space, a 1.5 m long dipole, a 0.45 m space, and a half-quadrupole. Two identical FODO cells without a dipole will form each long straight section. Here the half-cells will be 5.793 meters long and the phase advances will be adjusted so that the horizontal and vertical tunes of the ring are 5.82 and 5.8 respectively. The lattice functions for one superperiod are shown in Figure 2 where the plot runs from the center of one long straight section to the next. The relevant ring parameters are given in Table 1.

Table 1: NSNS Accumulator ring parameters

Kinetic Energy	1.0 GeV
Magnetic Rigidity	5.6575 T-m
Circumference	220.688 m
Periodicity	4
Structure	24 FODO
Beam Emittance	120 πmm-mrad
Ring Admittance	312 πmm-mrad
β_{max}(x/y)	19.2/19.2
X_p(max/min)	4.1/0.0 m
$\nu_{x/y}$	5.82/5.80
Natural $\xi_{x/y}$	-6.6/-7.3
γ_t	4.93

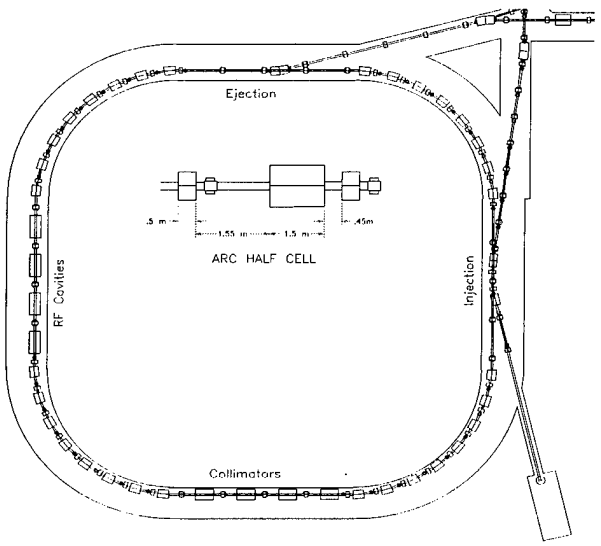


Figure 1: Accumulator ring layout.

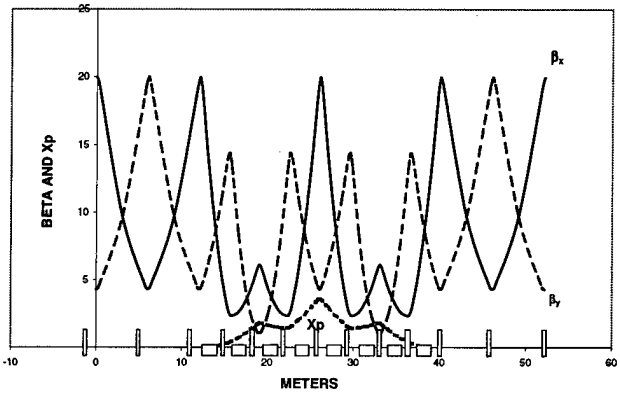


Figure 2: Accumulator lattice functions.

The four superperiods of the ring are labeled A, B, C, and D, and run sequentially along the beam direction from the beginning of one arc to the next. The order of magnets in each superperiod X is DHX1, QVX1, DHX2, QHX2, ..., DHX8, QHX8, QVX9, QHX10, QVX11, and QHX12, where D and Q denote dipoles and quadrupoles and H and V refer to the horizontal and vertical planes. The long

* Work sponsored by the Division of Material Sciences, U.S. Department of Energy, under contract DE-AC05-96OR22464 with Lockheed Martin Energy Research Corp, for Oak Ridge National Laboratory.

0-7803-4376-X/98 /$10.00 © 1998 IEEE

Table 2: Tunability and Chromaticity Behavior.

$\Delta p/p$ %	$\Delta\nu_x$	$\Delta\nu_y$	$\beta_{x,max}$ $\beta_{y,max}$ [m]	$X_{p,max}$ $X_{p,min}$ [m]	ΔFQ ΔDQ %
0.0	0.0	0.0	19.2	4.1	0.0
			19.2	0.0	0.0
0.0	-0.5	0.0	21.9	4.1	-18.1
			17.8	0.0	-4.3
0.0	0.0	-0.5	17.8	4.1	-4.3
			21.9	0.0	-18.1
0.0	-0.5	-0.5	20.1	4.1	-24.8
			20.1	0.0	-24.8
0.5	-0.03	-0.04	19.9	4.16	
			19.3	-0.1	
1.0	-0.06	-0.07	20.5	4.23	
			19.5	-0.2	

straight section in A runs from QVA9 through QHA12 and will be used for injection. Similarly, the long straight sections in B, C, D will be used for beam scraping collimators, rf cavities, and extraction respectively. In the arcs, the 1.55 m space between a quadrupole and the downstream dipole will contain a beam position monitor (pickup electrode) followed by a correction package and a vacuum pumping port. The correction package will consist of a dipole corrector and either a skew quadrupole or higher-order multipole corrector. Position monitors and correction packages will also be located downstream of each quadrupole in the long straight sections. Other available space in the lattice will be used to accommodate tune meter kickers, a transverse damping system, and clearing electrodes, to name a few.

The beam will have a full emittance, both horizontal and vertical, of 120π mm-mrad and the ring will have a full acceptance of 312π mm-mrad, which is twice the full beam emittance plus an allowance of 1 cm for the maximum possible orbit errors. The ring must also accept a maximum beam momentum spread of $\pm 1\%$ and the quadrupoles QHX4 at the centers of the arcs will be 50% larger than the others to meet this requirement. The quadrupoles QHX10 in the centers of the long straights will also have larger apertures to allow for the injection orbit bumps and for the extraction kicker and septum displacements.

2 TUNABILITY AND CHROMATIC BEHAVIOR

It will be desirable for the accumulator ring to run with different sets of betatron tunes. Small tune changes are expected in normal ring operations, however tune changes of up to half a unit may be implemented in special operations for accelerator studies. Table 2 shows the behavior of the beta function for a tune change of 0.5 units. As can be seen in the Table, a change in tune of half a unit results in a change of less than 15% in the beta function, with no change in the dispersion function. Because the chromatic behavior is nonlinear, the betatron functions for an off-momentum particle might show significant changes, but for this lattice, even at 1% off-momentum, the maximum ever expected, the betatron functions and the dispersion behave very well.

In practice the desired tunability will be achieved by dividing the main windings of the quadrupoles into three families, with the magnets of each family connected in series to a separate power supply. The first family will consist of all 28 arc quadrupoles (QVX1, QHX2, ..., QVX7); the second will consist of all 12 focusing quadrupoles (QHX8, QHX10 and QHX12) in the long straight sections; and the third will consist of all 8 defocusing quadrupoles (QVX9 and QVX11) in the long straights. The current in the first family will be adjusted so that the phase advance of each arc is 2π, thereby ensuring zero dispersion in the long straight sections. The currents in the second and third families will then be used to adjust the tunes. The quadrupoles will also have trim windings which will be divided into four families. These will be used for fine tuning the lattice. In particular they will allow for independent adjustment of the currents in the quadrupoles at the center (QHX10) and the ends (QHX8 and QHX12) of the long straight sections. This is important in the A superperiod, for example, where the injection setup depends on the setting of the QHA10 quadrupole.

3 CORRECTION ELEMENTS

To compensate for unavoidable field imperfections and magnet alignment errors, the accumulator ring will have a set of correction elements consisting of horizontal and vertical dipoles, skew quadrupoles, sextupoles, skew sextupoles, and octupoles. Trim windings on the lattice quadrupoles will allow for any necessary quadrupole corrections. The correction elements will be contained in packages located downstream of the position monitor at each lattice quadrupole. Each package, except those downstream of the quadrupoles QHX10 (at the centers of the long straight sections), will contain a horizontal or vertical dipole and either a skew quadrupole or higher-order multipole. The packages downstream of quadrupoles QHX10 will contain only horizontal dipoles. Thus, there will be a total of 24 horizontal and 24 vertical dipoles. Each superperiod will have four skew quadrupoles (QSX1, QSX3, QSX5, QSX7) located in the correction packages downstream of quadrupoles QVX1, QVX3, QVX5, and QVX7; two sextupoles (SHX8, SVX9) located downstream of QHX8 and QVX9; two skew sextupoles (SSVX11, SSHX12) located downstream of QVX11 and QHX12; and three octupoles (OHX2, OHX4, OHX6) located downstream of QHX2, QHX4, and QHX6.

Closed orbit correction is discussed in Ref. [3].

4 RESONANCE CORRECTION

Because the ring will operate at very high intensities for which stringent limits on losses will be imposed, the possibility of beam loss due to resonance excitation must be

considered. The second, third and fourth-order resonances between tunes of 5 and 6 are shown in Figure 3. Although the space-charge tune spread of the beam is expected to be small (~ 0.1), there are a number of resonance lines sufficiently close to the working point to be of concern. Moreover, even though lines such as those excited by normal and skew quadrupoles are far from the working point, they can cause unfavorable distortions of the betatron functions. The four-fold symmetric lattice allows placement of correction elements so that either even or odd harmonics (in azimuth θ) can be produced for the correction of the following resonances. Detailed calculations are underway to determine the required magnet strengths.

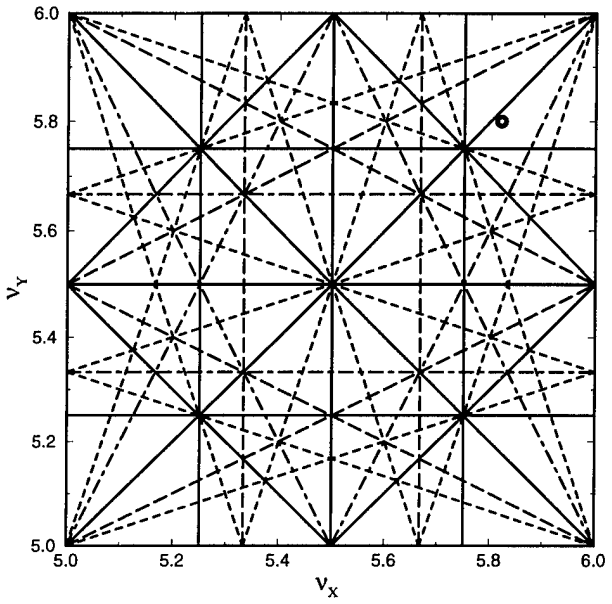


Figure 3: Accumulator Tune Chart. The circle shows the working point. Solid and short-dashed lines indicate second and fourth-order resonances; long-dashed and dot-dashed lines indicate third-order.

4.1 Second-Order Resonances

The $2\nu_x = 11$ and $2\nu_y = 11$ resonances can be corrected by exciting the trim windings on the quadrupoles with harmonic 11 in azimuth θ. (To produce an odd harmonic, magnets separated by $\theta = 180°$ are excited with equal but opposite currents.) Similarly, the sum resonance $\nu_x + \nu_y = 11$ can be corrected by exciting the skew quadrupole correctors with harmonic 11; the difference resonance $\nu_x - \nu_y = 0$ can be corrected (or enhanced if coupling between the two planes is desired) by exciting these correctors with harmonic 0.

4.2 Third-Order Resonances

The $3\nu_x = 17$ and $\nu_x + 2\nu_y = 17$ resonances can be corrected by exciting sextupoles with harmonic 17. The eight sextupole correctors allow for independent correction of the two lines. Similarly, the $3\nu_y = 17$ and $\nu_y + 2\nu_x = 17$ resonances can be corrected with the eight skew sextupole correctors.

4.3 Fourth-Order Resonances

The fourth-order resonance lines are driven by octupoles (both normal and skew) and those closest to the working point pass through the point $\nu_x = \nu_y = 5.75$ in Figure 3. The effects of these lines can be reduced by exciting the octupole correctors with harmonic 0. Schemes for correcting specific lines are under investigation. The octupole correctors also allow for Landau damping of transverse instabilities.

5 STRUCTURE RESONANCES

One consideration in our choice of a lattice was the avoidance of structure resonances. The 4-fold symmetric lattice has fourth-order structure resonances at betatron tunes of 5 and 6; third-order at tunes of 5.333 and 6.666; and second-order at a tune of 6. However, none of these are near the proposed working point. A 3-fold symmetric lattice that has been considered in previous design studies, on the other hand, has fourth-order structure resonances at a betatron tune of 3.75 which is right on top of the proposed working point for this lattice. Although these resonances may not hurt the ring performance, they are best avoided.

6 REFERENCES

[1] W.T. Weng, et. al., "Accumulator Ring Design for the NSNS Project", these proceedings.

[2] Y.Y. Lee, "The 4 Fold Symmetric Lattice for the NSNS Accumulator Ring", BNL/NSNS Tech.Note No. 026, February 14, 1997.

[3] C.J. Gardner, "Closed Orbit Distortion and Correction in the Four-Fold Symmetric NSNS Ring", BNL/NSNS Tech.Note No. 031, April 14, 1997.

MINI-BUNCHING THE AGS SLOW EXTERNAL BEAM*

JW Glenn, L Ahrens, T Hayes BNL, R Lee UC-Irvine

Abstract

Test and modeling toward providing a continuos string of proton bursts of a few nano-seconds every 3 to 10 micro-seconds for the two second BNL AGS spill are presented.

1 INTRODUCTION

Two new proposed experiments at the AGS require well bunched beam. The specification for a muon to electron conversion experiment is a burst of a few nano-seconds every few micro-seconds with only a part in 10^8 leakage between bursts. Another experiment to measure the muon lifetime needs 10 micro-seconds between bursts. The AGS started extracting mini-bunches in 1974 for Fainberg and Kalogerapoulos to measure anti-neutrons. Bunches were <~4 ns spaced every 220 ns. This technique kept the beam bunched in the main RF buckets and moved only the edge of the bunch into the extraction transverse resonance by slowly shifting the RF frequency[1,2]. There has been no further interest in this technique until a new crop of proposals developed from the AGS 2000 Workshop [3].

1.a Mini Bunches every 3 Micro-seconds.

The plan for this rate of delivery is to only fill one of the eight RF buckets in the AGS. This bunch is then accelerated to full energy and, as the RF is left on, kept bunched. After the extraction resonance is established, the radius is slowly moved out, using a signal from the servo that controls the spill rate to modify the rate of radial change, until all the beam has kissed the resonance and been extracted. The actual beam bursts in the slow beam are much shorter than the bunches in the AGS as only the edge of the rotating bunch touches the resonance.

Mini Bunches Every 10 Micro-seconds.

The approach to achieve 10 micro-seconds between bursts is to use an RF dipole as is used to spin flip on intrinsic resonances during polarized proton acceleration[4]. This dipole will kick horizontally and be "tuned" to one third the rotation frequency of those particles being extracted or ~124 kilo Hertz. The phase of the kick will be such as to enhance only one of the three separatrixes of those particles being extracted within the one populated bucket in the accelerator. This will prevent particles from passing the fixed unstable points on two corners of the stable area and enhance escape on to the separatrix at the remaining one.

2 LONGITUDINAL MODELING

The equation modeled is:

$$\ddot{\phi} = W_o^2 * (\sin\phi - \sin\phi_s)$$

$$[W_o^2 = \frac{eV\eta f_{RF}^2 2\pi}{\beta^2 Eh}]$$

where ϕ and equivalent W_o^2 were calculated using equations in Ref 5. Normal conditions used were: RF voltage = 20 KV & $\dot{B}/B$ = 0.001 /Sec., producing buckets with the following: stable phase = 0.17^o, half height = 68 MeV.

An ensemble of particles were started for all phases within a bunch that fills 10% of the bucket and the "resonance", ϕ where the particle makes a "first crossing", is moved down. Each time a particle exceeds a new ϕ, a point is plotted on to the screen at the current phase and ϕ. The resultant plot shows the phase extent of beam as it is extracted. As the bunch only fills the bucket to 10% on flattop, particle population is contained within less than ~40% of peak amplitude. The full width of bunches here is less than 20 nano-seconds.

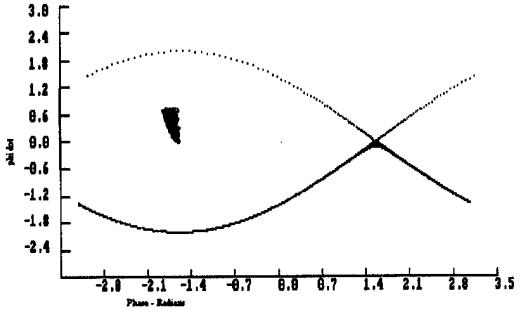


Figure 1 Phase of Extraction for Various Amplitudes of Synchrotron Oscillations.

3 TRANSVERSE MODELING

Behavior was tracked using equations from Ref 6. They are for tracking position in an "*XY*" space every three revolutions and were modified to be Symplectic by M Blaskowitz. They are:

$$X_{n+1} = (X_n + \varepsilon * Y_n)/(1 - 6 * E * Y_n)$$

$$Y_{n+1} = Y_n - \varepsilon * X_{n+1} + 3 * E * [(X_{n+1})^2 - (Y_n)^2]$$

[Where eta space variables X is related to displacement by $\sqrt{\beta}$ and Y to angle, both rotated to match the phase of the sextuples; ε is the tune difference from the resonance

*This work is supported by US department of Energy.

0-7803-4376-X/98/$10.00 © 1998 IEEE

and E to drive sextuple strength. which is normalized to make X_o, the size of the stable region, unity.]

An ensemble of 2000 particles with an initial gaussian distribution in this space were tracked. Particles motion was starting with a large $\mathcal{E}$. Tune difference was slowly shifted to zero, $\mathcal{E}$ shrank to zero, and the location of the particle plotted every 36 turns (12 passes through the above equations). [Without tune shift, the particle path did not change during 1.9 seconds of simulated coasting (sixty thousand passes); on a 586, this took less than two minutes (only 5 times the time of travel of particles in the AGS)]. Figure 2 shows trajectories for normal 1/3 integer extraction, Figure 3 shows the trajectories for particles with the RF dipole on with 1.5 gauss-meters of field. The dipole is simulated by a .003 increment in Y every three turns.

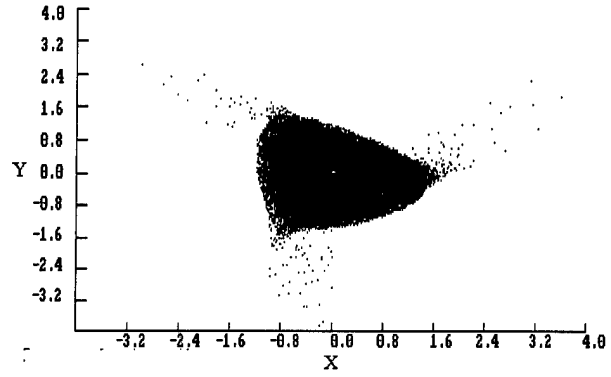


Figure 2 Extraction Separatrixes, RF Dipole Off

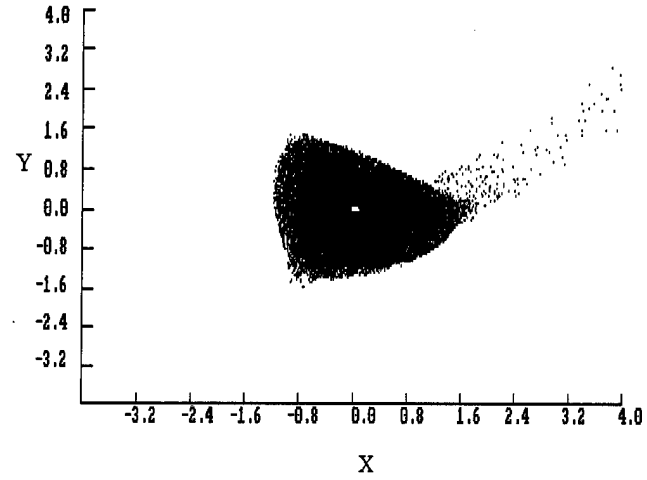


Figure 3 Extraction Separatrixes, RF Dipole On

4 BEAM TESTS

Bunched Slow Extraction from the AGS was tested quickly with one of the two buckets filled in the Booster. The kickers for transferring beam between the Booster and the AGS were miss-timed to only both be on when the one bunch was transferred. With only one RF bucket filled beam was accelerated, left bunched on flat top, extracted and targeted. The arrival time of secondaries from the target was compared to the time of a rotation clock signal from the RF system that divides the RF by eight (buckets) starting with the first injected bunch. Secondaries show an RMS bunch widths of ~6 nano-seconds occurring every 3 micro-seconds. There was a few parts in 10^5 "leakage" between buckets as seen in Fig 4.

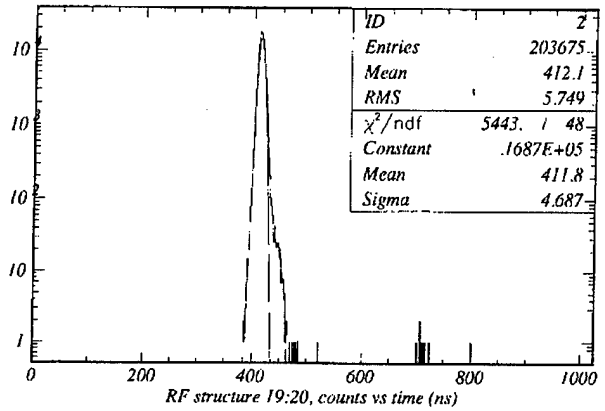


Figure 4 Single Mini-Bunch - Data

This small amount of beam trickled into the adjacent bucket during the zero $\dot{B}$ time on the AGS magnet reserved for injection. This leakage may be stemmed by better RF control and shortening the time beam is stored here, also if there remains beam in the adjacent bucket after this effort, this bucket will be emptied by extracting it with the Fast Beam kicker during acceleration.

Beam tests for 10 micro-second structure may be done this summer using the tune meter kicker

REFERENCES

[1] Barton "Some Comments on AGS Bunch Areas" BNL AGS DIV 74-3, 1974

[2] Fainberg & Kalogeropoulos "The AGS Beam Structure" EP&S 74-2 or BNL 18938, 1974

[3] AGS 2000 Workshop Proceedings, BNL 52512, 1996

[4] M Bai, et. al. "Overcoming Intrinsic Spin Resonance by Using an AC Dipole", these proceedings.

[5] CERN's ".SELECTION OF FORMULAE" .."CERN/MPS-SI/Int DL/70/4, pp30-31

[6] M Month, "Effects of Sextupoles ....", BNL AGSCD-17, 1967

MICRO-BUNCHING THE AGS SLOW EXTERNAL BEAM*

JW Glenn, M Brennan, L Littenberg, J Rose, C Woody, A Zoltsman BNL
P Bergbusch, TRIUMF and Dick Mjka, YALE

Abstract

Measurements and modeling are presented on BNL's AGS operation of the slow External Beam with sub-nanosecond beam bunching for the full two second spill.

1 INTRODUCTION

The Brookhaven AGS can now operate with a few hundred pico-second beam bursts in its Slow External Beam. "Micro-bunching" was developed to meet the requirements of a new generation of users:[1] 1) About 100 pico-sec RMS bursts every 50 nano-second for time of flight momentum determination of incoming GeV/c level Ko's to measure the $K_L \rightarrow \pi^o . \nu . \bar{\nu}$ branching ratio. 2) A bunched beam with 30 pico-sec bursts to "prebunch" Kons for a 12 GeV/c RF separated beam to eliminate the first bunching cavity section, increasing the K flux per proton and shortening the secondary beam. And 3), Sub-nanosecond bursts would be appropriate in test beams for collider detectors.

In 1980 Ch Steinbach and R Cappi used the 200 MHz SPS prebunching cavity in the PS to reduce the low frequency (<1 KHz) ripple on the PS spill. RF structure as an undesirable side effect was expected, not found to cause the users problems, and thus not investigated [2]. Bunching is achieved by forcing a debunched beam between empty barrier buckets at the extraction radius. We presently use the 93 MHz longitudinal dilution cavity. With 20 KV per turn on this cavity, modeling predicts 130 pico-second bunches with ~11 nsec spacing; at present, bunches of 330 ps have been seen with high intensity protons and 250 ps with ions.

2 LONGITUDINAL MODELING

The first test with Heavy Ions showed <2.5 nsec bunches and spill ripple reduction over a surprising four kilo-Hertz variation in VHF frequency. Another early run with protons showed less than 0.6 nsec bunches, over about a hundred Hertz range. To better understand these observations we required a computer simulation of longitudinal motion of beam in the AGS with this setup.

The equations modeled are given in Ref 3. Normal conditions used were: VHF (93 MHz) voltage = 20 KV & $\dot{B}/B =$ 0.002 /Sec., producing buckets with the following: stable phase = 0.35^o , half height = 10 KV, & length = 344^o (a 16^o or 0.48 nsec gap between buckets). Particles were started well out of the bucket with a large $\dot{\phi}$. Location of a particle was plotted every 20 micro-sec equivalent (.01 radians of synchrotron oscillation) as a small dot. To better demonstrate this motion, Fig 1 is plotted with 15 times normal $\dot{B}/B$ (or one fifteenth RF voltage) to separate trajectories. The approximate location of part of the separatrix around the empty bucket and beyond is sketched in as solid lines]. As the AGS field falls, the particle spirals out since it is not in a bucket. Being above transition energy, $.\dot{\phi}$ decreases with increasing radius. At a particular radius the transverse tune reaches 8 2/3, and the particle is extracted. The $\dot{\phi}$ where extraction occurs is the difference between the frequency associated with extraction and the RF frequency. This $\dot{\phi}$ can be adjusted, thus as the beam could be set up to extract at any $\dot{\phi}$. The particle phase is recorded for many different $\dot{\phi}$'s for the first pass through that particular value (the emphasized points on Fig 1 show these "first crossings" of the extraction radii). Note: $\dot{\phi}$ in these figures is "normalized" to the synchrotron frequency of 235 Hz and the phase is offset by pi/2 to better see the gap between buckets.

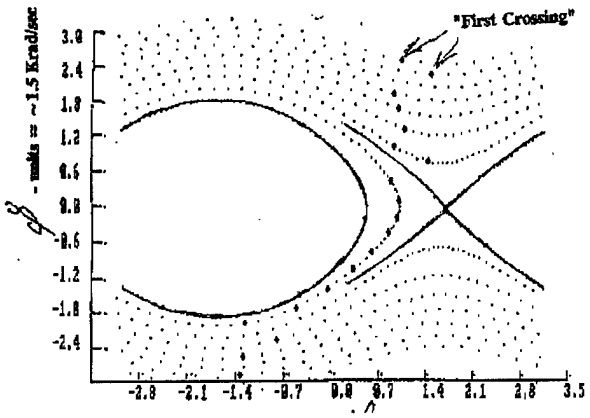


Figure 1 Particle Trajectory Between the Buckets,

Fig 2 shows the "first crossing" (large dots Fig 1) results for 300 particles evenly spaced phases at an initial The first crossing of each of a series of momenta, shown as a

This work partially supported by US Department of Energy.

0-7803-4376-X/98 /$10.00 © 1998 IEEE

series of short lines of many dots of slightly different phases at different phi dots.

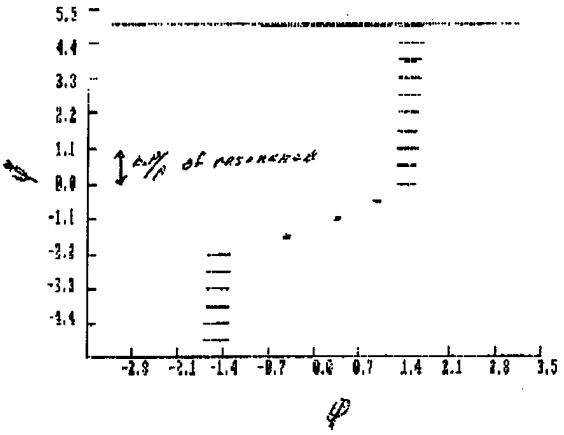


Figure 2 First crossings for 300 Particles

The assumption is that when the beam crossed the transverse resonance, the beam will be extracted almost immediately. Thus the distribution in phase at many possible extraction resonance radii were plotted. Fig 3 shows a histogram of particle population versus time.

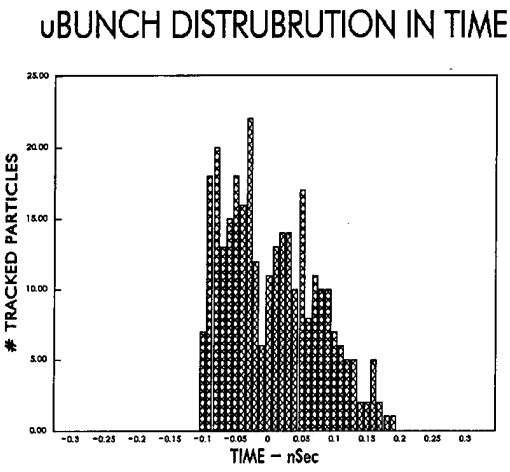


Figure 3 Histogram of Particles at Extraction vs Time

One result was that the beam will be bunched at the 120 psec level over a broad range of frequencies implies spill structure reduction over this range as it is inversely related to bunch length [Ref 1]. Another was that bunch widths of 30 pico-seconds RMS can be seen if the bucket is centered above the extraction radius. These results do require that all particles are quickly extracted together. This assumption is not completely valid. There are two corrections required.

2.1 Momentum width

The actual transverse tune of a particle is dependent its transverse oscillation amplitude. This amplitude distribution implies a momenta range of 2 parts in 10^4 (this extent in $\dot{\phi}$ is shown on Fig 2). The phase of the extracted beam is a mixture of $\dot{\phi}$'s and their various phases thus making the bunches wider. This correction is large is just below synchronous frequency, unfortunately where the bunches appear narrowest.

2.b Transverse Modeling Delay in extraction -

There is some difference in the time to extract particles of the same momentum, broadening the bunches as a function of phi dot. The details of the transverse modeling and initial conditions are discussed in another paper [3].

For each particle, the time to extraction (blow-up), was recorded if it wasn't retrapped. The average and RMS spread in delay time was calculated. These trackings were done for various rates tune change. A plot of variation in delay versus $\dot{Q}$ (Fig 4) shows that the product

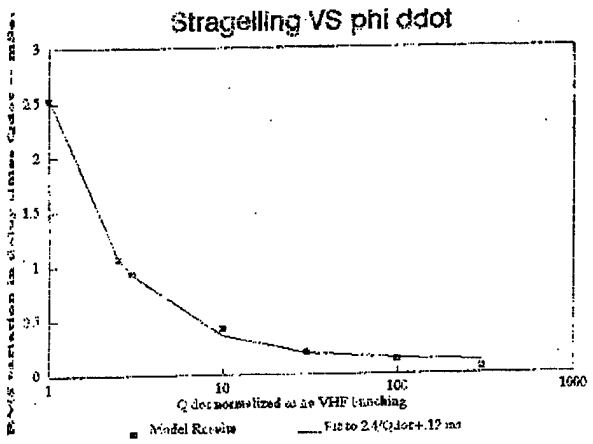


Figure 4 Spread in Time to Extraction

is invariant over the range of interest. The spread in delay to extraction multiplied by $\dot{\phi}$ for the resonance causes an added spread in phase, and thus bunch width.

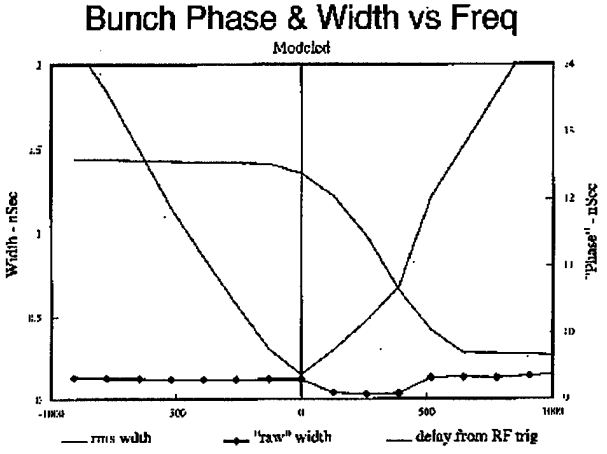


Figure 5 Phase and Width

This effects bunch width if the bucket is not synchronized, thus widths of 130 psec are still expected over about +/- 50 Hz. At larger phi dot's the effect will be large and bunching should disappear. This result is added to width expected from longitudinal modeling is plotted in Fig 5 with the "raw" widths from longitudinal modeling. During the tune-up of VHF cavity frequency, narrow bunches were not seen at frequency differences that still resulted in reduced spill structure.

The above modeling was also done for an 80 KV VHF RF system, four times the present voltage. The minimum predicted width here is 80 psec RMS or 62% of the width at 20 KV, consistent with the 50% expected from simple calculations.

3 EXPERIMENTAL RESULTS

Bunch widths were measured using fast (<100 ps) counters in an electron beam looking at the Slow Beam. The timing trigger was a discriminator fed by a RF signal from the cavity. The delay relative to the trigger for each electron was recorded. Scatter plots of electron delay vs time into the spill showed a variation in width during the spill. The middle 15% of the spill was separately analyzed. Runs was taken for a selection of frequencies in the VHF cavity. Average time delay, "phase" and variation in delay "width" are plotted verses the frequency over the results of modeling; the zero frequency was chosen to match minima in width and the delays were matched at mid frequency. The is good agreement in the variation in phase and the shape of the width curve. The widths are almost twice expected.

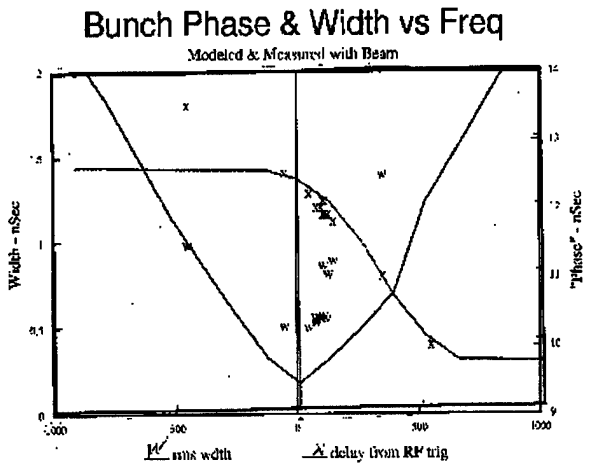


Figure 6 Model and Data [X W]

Also installed for this test was an old 200 MHz acceleration cavity, modified to resonate at 186 MHz, to be used as a bunching detector. It generated over a volt of signal with the 5 microAmps in the SEB. The hope is to use the phase of this signal to servo the extraction frequency

The last run was made with Gold ions into a few micron thick quartz cherenkov counters, good to 50 pico-sec. Also installed: a phase locked loop on the RF to reduce noise and a step recovery diode before the discriminator to sharpen timing. Widths for this run were as low as 250 pico-seconds. Note that the time distribution is more symmetric than the model prediction.

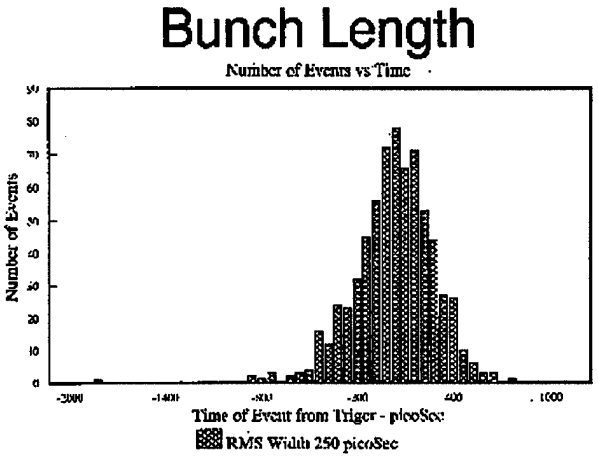


Figure 7 Time Histogram of Events

Again there was a drifting of the width over the spill and at rates up to few tens of hertz.

To achieve ~100 ps widths with 50 ns spacing between bunches, a low frequency RF system cavity will be provided for bunch spacing and the 93 MHz cavity, with possibly a 200 MHz one, to sharpen up the bunches. Foe 30 ps bunches the 200 MHz cavity will be run at ~100 KV.

REFERENCES

[1] AGS 2000 Workshop Proceedings, BNL 52512, 1996

[2] Cappi & Steinbach "Improvement of the Low Frequency ..." CERN/PS/OP 80-10 & IEEE NS-28, No 3, June 1981, pp 2806

[3] JW Glenn, et. al., "Mini-Bunching the AGS Slow External Beam", these proceedings.

ACCUMULATOR RING DESIGN FOR THE NSNS PROJECT *

W.T. Weng, J. Alessi, J. Beebe-Wang, M. Blaskiewicz, L. Blumberg, M. Brennan, C. Gardner, Y.Y. Lee, A.U. Luccio, H. Ludewig, D. Maletic, D. Raparia, A. Ruggiero, S.Y. Zhang
AGS Department, Brookhaven National Laboratory, Upton, NY 11973.

Abstract

The goal of the proposed National Spallation Neutron Source (NSNS) is to provide a short pulse proton beam of about 0.5μs with average beam power of 1MW. To achieve such purpose, a proton storage ring operated at 60Hz with 1×10^{14} protons per pulse at 1GeV is required. The Accumulator Ring (AR) receives 1msec long H^- beam bunches of 28mA from a 1GeV linac. Scope and design performance goals of the AR are presented, other possible technological choices and design options considered, but not adopted, are also briefly reviewed.

1 INTRODUCTION

The Oak Ridge National Laboratory is leading a conceptual design for a next generation pulsed spallation neutron source, the National Spallation Neutron Source (NSNS) [1]. There are three major accelerator systems included in Brookhaven's area of responsibility. First is the High Energy Beam Transport (HEBT) system [2]. Secondly, the Accumulator Ring (AR) system and thirdly, the Ring to Target Beam Transport (RTBT) system [3]. This paper describes the design of the AR itself whose magnet and tunnel layout is shown in Fig. 1.

The proton Accumulator Ring is one of the major systems in the design of the NSNS. The primary function of the AR is to take the 1GeV H^- beam of about 1msec length from the linac and convert it into a 0.5μs beam through a stripping foil in about one thousand turns. The final beam should have 1.0×10^{14} protons per pulse, resulting in 1MW design average beam power at 60Hz repetition rate. Provisions have been reserved for a future upgrade to 2MW beam power by doubling the stored current to 2.0×10^{14} proton per pulse without changes in both the magnet and vacuum system.

One of the major performance requirements is to keep the average uncontrolled particle loss during the accumulation time to less than 2.0×10^{-4} per pulse. The reason of this stringent requirement is to keep the residual radiation to such a level that the hands-on maintenance is possible except for a few localized areas, such as: injection, extraction and collimation. To achieve this goal, special care have been exercised in the H^- stripping, the RF stacking, and the collimator design.

This paper describes the final product of the intensive R&D efforts in the past two years. During that period, we have studied many possible technologies and design choices. Some of the considerations and rationals of choices are given here for comparison.

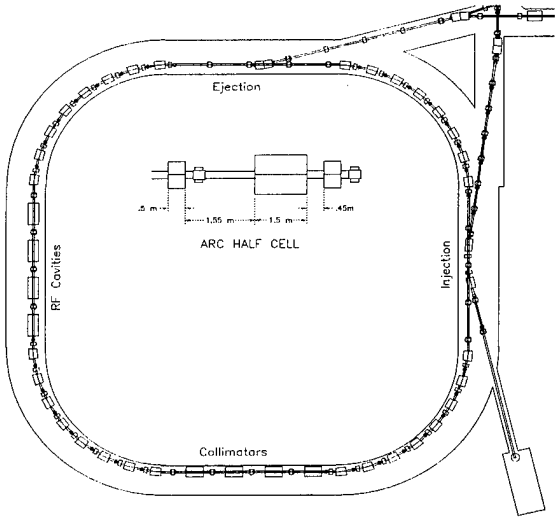


Figure 1: Layout of the accumulator ring.

a. *Accumulator Ring vs Rapid Cycling Synchrotron.* The AR option is chosen for better injection efficiency, no eddy current effects and shorter beam-in-ring time to avoid coherent instabilities.

b. *One vs Two Ring Tunnels.* Separate tunnels for future upgrade is chosen for its simplicity in mechanical design, reliability in future operation, accessibility for maintenance, and low initial capital investment. Both the performance goal and specific design of the second ring can be decided at the time of upgrade.

c. *FODO vs Triplet Lattice.* A FODO lattice is chosen for its smoothness in betatron function variation around the ring. Such a property will minimize the possible envelope oscillation for beam with large space charge tune shift.

d. *Normal vs Isochronous Lattice.* Our choice is for a normal lattice, even if, at a first look, isochronous lattice may offer the advantage of constant longitudinal extend of the injected beam. However, it hurts in many other ways. For example, the higher order chromatic effects in lattice, reduction in dynamic aperture, and the reduction in Landau damping for transverse instabilities.

e. *Single, Dual, Barrier Cavity RF Systems.* The dual harmonic RF system is chosen for its advantage in

* Research on the NSNS is sponsored by the Division of Material Sciences, U.S. Department of Energy, under contract number DE-AC05-96OR22464 with Lockheed Martin Energy Research Corporation for Oak Ridge National Laboratory.

0-7803-4376-X/98 /$10.00 © 1998 IEEE

higher bunching factor and established performances. The barrier cavity system holds promises of keeping the beam within the confine of the RF bucket and leaving the gap clean. However, it requires more RF stations and the beam dynamics related to beam loading and coherent instabilities is not well-understood.

2 LATTICE, H^- INJECTION AND RF STACKING

The accumulator ring of the National Spallation Neutron Source (NSNS) will have a four-fold symmetric lattice. The lattice will accommodate the long straight sections required for the injection system, the extraction system, the RF cavities, and the beam scraping system. The straight sections will be dispersion free, which is desirable, especially for the RF cavities and the injection system. The lattice will provide ease of betatron tuning and flexibility of operation. Unlike lattices of lower symmetry, a lattice of four-fold symmetry will assure that there are no dangerous betatron structure resonances other than for the integer tune. Details of lattice design is given in ref. [4]. Lattice functions and other salient performance and design parameters of the accumulator ring are summarized in Table 1.

Table 1: NSNS Accumulator ring parameters

Beam Average Power	1.0 MW
Kinetic Energy	1.0 GeV
Average Current	1.0 mA
Repetition Rate	60 Hz
Ion Source Peak Current	35 mA
Linac Peak Current	27.7 mA
Beam Duty Cycle	6.18 %
Linac Pulse Length	1.03 msec
Beam Loss (Controlled/Uncontrolled)	< 2 / 0.02 %
Number of Turns Injected	1225
Revolution Period	0.8413 μsec
Revolution Frequency	1.1886 MHz
Circumference	220.688 m
Space-Charge Tune-Shift	< 0.1
Bunching Factor (Dual RF Systems)	0.405
Number of Protons/Ring	1.04×10^{14}
Beam Emittance (Transverse, norm.)	217 πmm-mr
Tunes ν_x/ν_y	5.82 / 5.80
β_{max}(x/y)	19.2 / 19.2 m
Dispersion X_p(max/min)	4.1/0.0 m
Transition Energy γ_t	4.93
RF Voltage (1^{st} Harmonic)	40 kV
RF Voltage (2^{nd} Harmonic)	20 kV
RF bucket	17 eV-sec
Beam Emittance (Longitudinal)	10 eV-sec
Beam Gap (injection)	295 nsec
Injected Pulse Length	546 nsec
Vacuum	10^{-9} Torr

The most demanding system in the design of the 1MW short pulse spallation neutron source is the H^- multi-turn injection into the storage ring. For the NSNS accumulator ring, a carbon foil of 400μg/cm^2 is assumed. The stripping efficiency for 1GeV incident H^- beam is about 99.8%. The temperature rise for the 1MW design is estimated to be about 3200°C. In addition, it has been found that [5]

a. Stripping losses in passage of the H^- beam through the B=3kG field in a DC bump dipole magnet upstream of the stripper foil are negligible.

b. A fraction $f(H^o)$ =8.19×10^{-3} of the incident H^- beam will emerge as H^o from a 400μg/cm^2 carbon stripper foil and must be disposed of in an external dump.

c. Field ionization of the H^ocomponent in the B=2.41kG field of a quadrupole downstream of the foil will lead to negligible uncontrolled losses.

d. Fractional losses from nuclear non-elastic interactions in the foil as low as 1.26×10^{-5} can be realized with rapidly (exponentially) collapsing injection bumps and "smoke-ring" injection scheme which result in very small multiple foil traversals of $< N_t >$=2.43 traversals/injected proton.

e. Multipole Coulomb and nuclear elastic scattering fractional losses out of a ring acceptance of $A_{x,y}$=330πmm-mrad for the above injection conditions are 1.35×10^{-5}, well below our loss criterion of $<10^{-4}$. With the small area stripper foil (8mm H × 4mm V) used for the above estimates, 2.2% of the incident H^- beam misses the foil and will be deflected by a magnet to an external dump.

To accumulate all the particles needed and keep them in proper azimuthal distribution, a dual harmonic RF system is employed. The fundamental RF system will provide 40kV and the second harmonic RF system will provide 20kV to form a flattened RF bucket for particle trapping with resulting bunching factor of about 0.4. Such a RF system will reduce the incoherent tune shift by 25%. The 4-dimensional multi-particle tracking program *Accsim* is needed to follow the 1200 turns of particles in the ring. The resultant beam distributions in real space and in RF phase space are shown in Fig. 2 and Fig. 3 respectively [6]. Much more work has to be done in this exercise to determine the optimal combination of RF waveform and injection strategy.

3 BEAM LOSSES AND THEIR CONTROLS

There are many possible beam loss mechanisms in addition to the foil stripping mentioned above. The important ones include:

a. Resonance crossing due to space charge tune shifts and magnetic imperfections. This will be minimized by controlling the tune shift to be less than 0.1 unit and provide all necessary multipole corrections up to order 3.

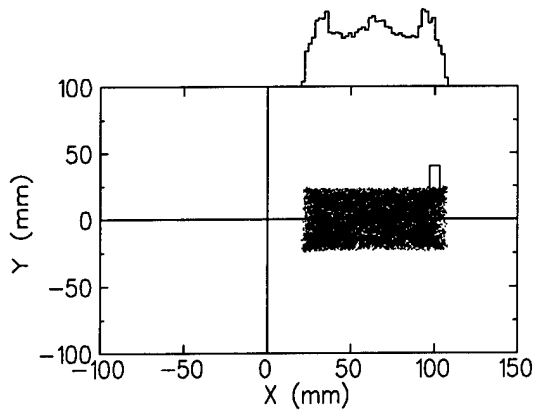


Figure 2: The resultant beam distributions in real space. *Accsim* snapshot at 1200 turns. Pseudo barrier RF.

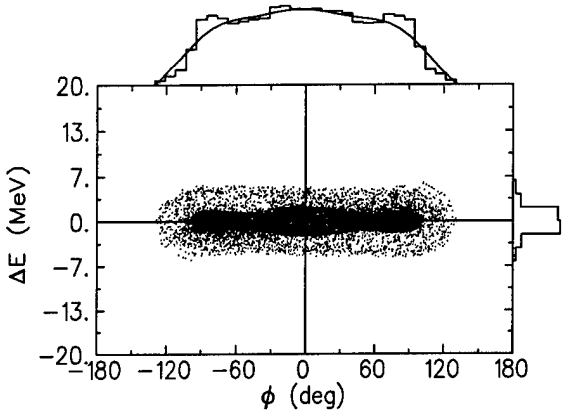


Figure 3: The resultant beam distributions in RF phase space. *Accsim* snapshot at 1200 turns. Pseudo barrier RF.

b. Coherent instabilities induced by impedance of the vacuum components. Careful studies have shown that all known instabilities will not occur with our design choices, except possible transverse instability. Further reduction of impedance will be attempted and a transverse damper will be provided to damp possible transverse instability [7].

c. $e-p$ instability can limit the achievable intensity if excessive e^- generation is allowed to occur. For the NSNS design, a vacuum pressure of less than 10^{-9}Torr and clear beam gap of 295 nsec should keep the neutralization coefficient below 10^{-3} which will keep the beam stable. TiN coating of the vacuum chamber has been considered to further reduce the secondary emission of the electrons [8].

d. Halo formation has been proposed as one of the possible beam loss mechanisms due to the particle-core resonance effect. Detailed studies will be carried out to better understand this phenomenon and its impact on the ring design and ultimate performance.

To contain those particles inadvertently migrating toward the wall, after all careful considerations and provisions, a collimator system is designed to catch the bulk of them before hitting the wall. Four collimators, 3.2m each, enclosing a 4π solid angle around the source point and stuffed with segmented material to capture all secondary particles generated by the incident protons will be provided to reduce the radiation effects by a factor of 100. This way, most of uncontrolled losses will occur at the collimator, leaving ring components relatively intact for reliable operation [9].

4 UPGRADE TO HIGHER POWER

The design presented in this paper is for initial performance of 1MW average proton beam power. All accelerator issues, such as: space charge, tune shift, coherent instabilities, $e-p$ instabilities, ...etc. have been considered and designed for 2MW capability. For phase I upgrade to 2MW performance, the peak current for the linac will be increased for 28mA to 56mA. No major changes in the ring will occur except modification in the kicker pulser and increase of shielding around high loss areas.

The most straightforward way to achieve 4MW is to build second identical ring and combine the beam power into single target station. In that case, the injection time into one ring will be reduced from 1msec to 0.5msec. If the community of the users require more peak power, a bigger accumulator ring or synchrotron to higher beam energies can also be contemplated.

5 ACKNOWLEDGMENTS

The authors would like to thank the assistances and contributions to this work from many staff members from BNL and the NSNS collaboration Laboratories.

6 REFERENCES

[1] B.R. Appleton *et al.*: 'The NSNS Collaboration', Proc. of EPAC'96, p.575, Sitges, Spain, 1996.

[2] D. Raparia *et al.*: 'The NSNS high energy beam transport line', in these proceedings.

[3] D. Raparia *et al.*: 'The NSNS ring to target beam transport line', BNL/NSNS Tech. Note #6, October, 1996.

[4] Y.Y. Lee, C.J. Gardner and A.U. Luccio: 'Accelerator ring lattice for the National Spallation Neutron Source", in these proceedings.

[5] L.N. Blumberg and Y.Y. Lee: 'H^- charge exchange injection into the 1GeV NSNS accumulator', BNL/NSNS Tech. Note #3, November, 1996.

[6] A.U. Luccio, J. Beebe-Wang and D. Maletic: 'Proton Injection and RF Capture in the National Spallation Neutron Source', in these proceedings.

[7] A.G. Ruggiero: 'Space charge and coherent effects in the NSNS storage ring", BNL/NSNS Tech. Note #7, June, 1996.

[8] A.G. Ruggiero: '$e-p$ instability in the NSNS accumulator ring', in these proceedings.

[9] H. Ludewig, S. Mughabghab and M. Todosow: 'NSNS ring system design study, collimation and shielding', BNL/NSNS Tech. Note #5, November, 1996.

CONVERSION OF THE PS COMPLEX AS LHC PROTON PRE-INJECTOR

F. Blas, R. Cappi, V. Chohan, D. Cornuet, G. Daems, D. Dekkers, R. Garoby, D. Grier, J. Gruber, E. Jensen, H. Koziol, A. Krusche, K.D. Metzmacher, F. Pedersen, J. Pedersen, U. Raich, J.P. Riunaud, J.P. Royer, M. Sassowsky, K. Schindl, H. Schönauer, M. Thivent, H. Ullrich, F.Völker, CERN, 1211 Geneva 23, Switzerland

Abstract

CERN's Large Hadron Collider (LHC) [1][2] will be supplied with protons from the injector chain Linac2-PS Booster (PSB)-PS-SPS (Fig. 1). The required transverse beam brilliance (intensity/emittance) is almost twice that of current PS beams and the LHC bunch spacing of 25 ns must be impressed on the beam before its transfer to the SPS. The scheme involves new RF harmonics in the PSB and the PS, an increase of the PSB energy, and two-batch filling of the PS. After a successful test of the main ingredients, a project for converting the PS complex was launched in 1994. Major additions are (i) h=1 RF systems in the PSB, (ii) upgrading of the PSB main magnet supply from 1 to 1.4 GeV operation, (iii) new magnets, septa, power supplies, kicker pulsers for the PSB-PS beam transfer, (iv) 40 and 80 MHz systems in the PS, (v) beam profile measurement devices with improved resolution. A significant part of the effort is being provided by TRIUMF under the Canada-CERN co-operation agreement on the LHC.

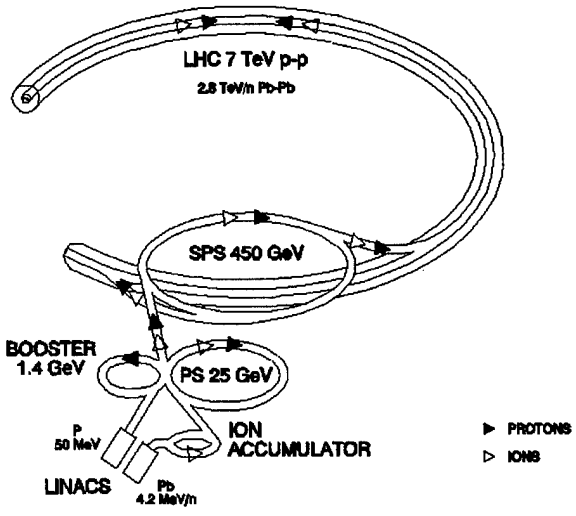


Fig. 1: The LHC injector complex.

1 LHC REQUIREMENTS

Supplying the LHC with protons from the existing chain of injectors may appear straightforward at first sight. However, the beam has to fit into the tiny LHC dynamic aperture, and must also have the brilliance required for LHC's desired luminosity. While the intensity is well within the capabilities of the PS complex (Linac2, PSB, PS), the beam brilliance requested (here defined as intensity per bunch/normalised rms emittance) needs to be up to twice that of current beams. LHC proton beam parameters at collision (7 TeV per beam) at various stages of operation are summarised in Table 1.

	Commis-sioning	Nomi-nal	beam-beam limit
Luminos. [$cm^{-2}s^{-1}$]	10^{33}	10^{34}	$2.5\ 10^{34}$
bunch spacing [ns]	25		
bunches/beam	2835		
protons/bunch	$1.7\ 10^{10}$	10^{11}	$1.7\ 10^{11}$
$\varepsilon^* (=\beta\gamma\sigma^2/\beta_{x,y})$ [μm]	1.0	3.75	3.75

Table 1: LHC proton beam parameters at collision. Note that $\varepsilon^* = \varepsilon_x^* = \varepsilon_y^*$.

The injector chain has to produce beams corresponding to the nominal performance; wherever possible, a higher performance level is aimed at, to potentially fill the LHC up to the beam-beam limit and to provide an operational margin.

2 A SCHEME TO REDUCE SPACE CHARGE

With a beam brilliance corresponding to the LHC beam-beam limit, the space-charge tune shifts (ΔQ) are almost twice the present figures at the PSB (50 MeV) and PS (1 GeV) injection energies, leading to unacceptable beam blow-up and loss.

2.1 Double-batch filling of the PS to reduce space charge in the PSB

Usually the four PSB rings (each 1/4 of PS circumference) are transferred sequentially (3-4-2-1), to fill the PS in one pulse. The LHC beam would generate, at PSB injection, a $\Delta Q = 0.9$, far beyond the "hard" limit of 0.55. With two PSB pulses to fill the PS, the intensity per PSB pulse is halved and ΔQ reduced to 0.45.

2.2 RF harmonic 1 in PSB for two-batch filling of the PS

With the RF equal to the PSB revolution frequency, there is just one bunch per ring (5 at present) and two-batch filling of the PS becomes feasible. Appropriate phasing of the bunch in each ring before extraction enables the four

0-7803-4376-X/98/$10.00 © 1998 IEEE

bunches to be lodged in ½ of the PS (Fig. 2), which can then accommodate a second batch.

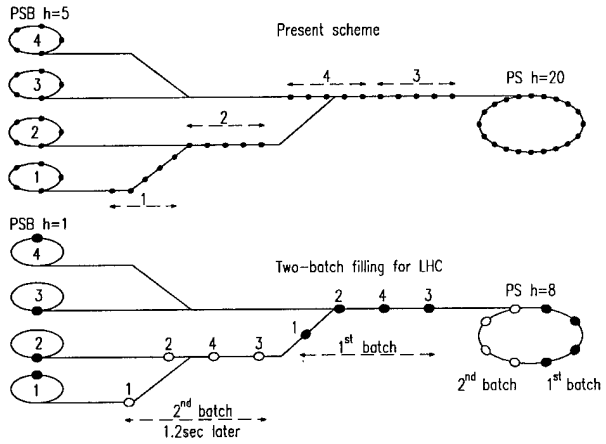


Fig. 2: PSB-PS four-ring transfer schemes.

2.3 PSB energy to 1.4 GeV to reduce tune spread in PS

The first batch from the PSB dwells for 1.2 sec on the PS injection plateau until the second batch arrives and is particularly vulnerable to a large ΔQ. The increase of the PSB energy will reduce the tune shift from 0.3 to a more comfortable 0.2.

For convenience, the main machine parameters of the LHC injector chain (including the SPS [3]) are compiled in Table 2. Note that the RF harmonic number 84 in the PS corresponds to the LHC bunch spacing of 25 ns which is impressed on the beam in the PS on the 25 GeV extraction flat top.

	PSB	PS	SPS
kinetic energy [GeV]	1.4	25	450
repetition time [s]	1.2	3.6	16.8
number of pulses to fill downstream machine	2	3	2x12
number of bunches	1/ring	8(16)/84	243
p/pulse nominal [10^{11}]	43	84	240
beam-beam	72	140	405
p/bunch nominal [10^{11}]	11	10.5/1.0	1.0
beam-beam	18	17.5/1.7	1.7
emittance ε* [μm]	2.5	3.0	3.5

Table 2: The LHC proton injector chain.

3 MAJOR HARDWARE UPGRADES

The 50 MeV proton linac is now equipped with a 750 keV RFQ and produces a beam of unprecedented brightness: 150 mA in ε* = 1.2 μm during 120 μs. Ways to increase this intensity to 180 mA (albeit during only 20 μs) are under study.

3.1 New RF systems in PSB

New h=1 ferrite-filled RF cavities with a frequency swing of 0.6 to 1.7 MHz, 8 kV, will accelerate one bunch in each ring. Moreover, the present h=5 cavities will be modified for a tuning range of 1.2 to 3.9 MHz (h=2) to flatten the bunches and thus reduce the space charge Q-shift in the low-energy part of the cycle.

3.2 Upgrading the PSB to 1.4 GeV

Raising the PSB output energy from 1 to 1.4 GeV implies an increase of the main dipole field by 26% to 0.87 T and of the quadrupole gradient to ~5 T/m. Beam measurements at these field levels have shown no sign of saturation. However, the main power supply needs upgrading: putting into service a fourth rectifier-inverter group, renewal of 18 kV transformers, including the reactive power compensation system, and implementing new controls circuitry.

3.3. PSB-PS beam transport to 1.4 GeV

The bending power of most of the magnetic elements of this line cannot be increased by 26%. Eight dc septum magnets are to be replaced by pulsed ones, three vertical bending magnets, six quadrupoles, and a series of correction dipoles are to be rebuilt with laminated yokes [4] and equipped with new power converters. This will permit the change of beam energy from pulse to pulse. The eight kicker magnets are being refurbished with more powerful pulsers [5].

3.4. Acceleration on new RF harmonics in the PS

The PS RF cavities are tuned to h=8 so as to accommodate the 8 PSB bunches (Fig. 2). These are then accelerated to 3.5 GeV/c where they are split to 16 bunches, followed by acceleration on h=16. New low-level electronics to cope with these harmonics is being built.

3.5. 40 and 80 MHz RF systems in the PS [6]

The LHC bunch spacing of 25 ns as well as bunch length matching (<4 ns) to the SPS are obtained with fixed-frequency RF systems. A 40 MHz cavity (300 kV) bunches the beam on h=84, whereas two 80 MHz systems (600 kV) are added to shorten the bunches, to fit into the SPS 200 MHz buckets. The design features a sophisticated mechanical short-circuit, as well as a powerful feedback to prevent high-intensity beams from suffering beam loading effects.

3.6. Beam diagnostics

Several systems are to be improved owing to the small size of the LHC beam, the new RF harmonics, and the intricacies of two-batch filling. Of particular relevance is the resolution of beam profile measurement devices (SEM grids, fast wire scanners) which must be increased by more than a factor 2.

4 BEAM TESTS - PAST AND FUTURE

4.1. Major results obtained so far

A partial test to check the proposed LHC proton filling scheme in the PS complex was carried out in late 1993 [7]. Only PSB ring 3 was used; its hardware was adapted by means of prototypes and pushing some elements beyond their safe limits. It has demonstrated that a proton beam can be produced at 25 GeV that meets the LHC specifications in terms of intensity and ε^* and confirmed the main ingredients of the scheme. More recently, the newly installed 40 MHz cavity was successfully used to bunch the beam with 25 ns spacing; the fast feedback system lowers the cavity impedance sufficiently to prevent high-intensity beams from becoming unstable.

4.2 Main beam dynamics issues [8][9]

The last line in Table 2 highlights the tight emittance budget available in the injector chain; every effort has to be made to avoid transverse blow-up. While space-charge detuning sweeps the beam over stop-bands and leads to an unavoidable emittance increase in the synchrotrons, emittance can be conserved in beam transport systems: mis-steering is to be minimized by automatic procedures, and corrected with fast dampers; mismatch is to be tackled by on-line quadrupole correction [10].

The new RF systems and harmonics will need intensive study [11]: (i) keeping the PSB h=2 RF in step with the h=1 RF even at highest intensity; (ii) bunch splitting from 8 to 16 in the PS; (iii) techniques to de-populate the bunch centre (for lowering space charge); (iv) RF gymnastics in the debunching/recapture process (from h=16 to h=84) at 25 GeV.

Another issue is to make sure that the proposed modifications do not jeopardize the beams for other users.

ITEM	STATUS	TRIUMF PART
PSB h=1 RF systems (4)	prototype in one ring	ferrites power supplies
PSB h=2 RF systems (4)	one cavity com-mutable h=5/h=2	
PSB main supply	control circuitry being tested	transformers (10) var compensator
PSB-PS kicker pulsers (7)	prototype tests	study on pulse-flattening [5]
PSB-PS septa (8) and supplies	two are operational	
PSB-PS line magnets (14) and power supplies	magnets: ½ are ready; supplies: prototype tested	all magnets [4], all power supplies
PS 40 MHz cavities (2)	one cavity operational	model studies, tuners, HOM dampers, HV supplies
PS 80 MHz cavities (3)	in fabrication	
wire scanners (8) 4 rings, H+V	prototype tests in PSB	design + fabrication
fast blade profile monitor in PSB	prototype being designed	design and fabrication

Table 3: Status of major hardware systems, TRIUMF contributions.

5 STATUS OF THE "PS FOR LHC" PROJECT

The project of converting the PS complex for the LHC was launched in 1994 and will be finished by 2000. Right from the start, a fruitful collaboration with TRIUMF has been established, formalised in 1996 by a CERN-TRIUMF cooperation agreement on the LHC. About one quarter of the funds and manpower required are being furnished by TRIUMF (Table 3).

In summary, the aim of the project is to deliver routinely to the SPS a beam of nominal characteristics (81 bunches, each 10^{11} p, $\varepsilon^* < 3.0$ μm, $\varepsilon_L \sim 0.35$ eVs), and possibly more intensity, by 1999. Presently everything indicates that this goal will be met. This will enable the SPS to assess, in time, its upgrading scheme.

6 ACKNOWLEDGEMENTS

The excellent collaboration with the colleagues at TRIUMF and the timely provision of resources are instrumental in the good progress of the "PS Conversion for LHC" project. The authors are particularly indebted to the TRIUMF coordinator, E. Blackmore, as well as to M.J. Barnes, G. Clark, M. Craddock, D. Dale, F. Jones, R. Keitel, S. Koscielniak, F. Mammarella, A.K. Mitra, A. Otter, R.L. Poirier, P. Reeve, K. Reiniger, G.D. Wait.

REFERENCES

[1] The LHC Study Group, The Large Hadron Collider, Conceptual Design, CERN/AC/95-05 (LHC).
[2] L. Evans, LHC status and plans, this conference.
[3] P. Collier (editor), The SPS as injector for LHC, conceptual design, CERN-SL-97-07, March 1997.
[4] G. Clark, A. Otter, P. Reeve, Magnets for the CERN PS Booster transfer line, this conference.
[5] G.D. Wait, M.J. Barnes (TRIUMF), K.D. Metzmacher, L. Sermeus (CERN), The application of saturating inductors for improving the performance of the CERN PS kicker systems, this conference.
[6] R. Garoby, D. Grier, E. Jensen (CERN), A.K. Mitra, R.L. Poirier (TRIUMF), The PS 40 MHz bunching cavity, this conference.
[7] The PS staff, reported by K. Schindl, Partial test of the PS complex as LHC proton injector, Proc. 4th EPAC, London 1994, p. 500.
[8] K. Schindl, The PS Booster as pre-injector for LHC, Proc. 3rd Int. Workshop on High Brightness Beams for Large Hadron Colliders ("LHC96"), Montreux, Switzerland, Oct. 1996, to be published in Part. Acc.
[9] R. Cappi, The PS in the LHC injector chain, LHC96, Montreux, Switzerland, Oct. 1996, to be published in Particle Accelerators.
[10] B. Autin, L. Giulicchi, A. Jansson, M. Lindroos, A. Lombardi, M. Martini, K. Schindl, Automated emittance preservation in the PS complex, this conference.
[11] R. Garoby, Longitudinal limitations in the PS complex for the generation of the LHC proton beam, LHC96, Montreux, Switzerland, Oct. 1996, to be published in Particle Accelerators.

COMBINED LONGITUDINAL AND TRANSVERSE MULTITURN INJECTION IN A HEAVY ION ACCUMULATOR

Ch. Carli, S. Maury, D. Möhl, CERN/PS, CH 1211 Geneva 23, Switzerland

Abstract

After the completion of the antiproton programme, the Low-Energy Antiproton Ring (LEAR) will be able to serve as an accumulator ring for heavy ions in the injector chain of the Large Hadron Collider (LHC). For injection and accumulation, a scheme is proposed, which exploits both the longitudinal and the transverse acceptances of LEAR. Compared to a classical multiturn injection, a factor 3 to 5 in intensity is gained for the set of parameters pertaining to this case; furthermore emittances, which are more favorable for electron cooling, result. The principle is outlined and computer simulations are presented.

1 INTRODUCTION

To prepare intense bunches of ions for injection into the LHC, it has been proposed [1] to cool and accumulate heavy ions in LEAR or a similar ring constructed for this purpose. Particles coming from the linac are injected by multiturn injection and cooled and stacked by electron cooling; the process is repeated until the required intensity is reached. In order to increase the number of injected particles and to obtain a particle distribution more favorable for electron cooling, an injection scheme has been proposed [2], which exploits both the longitudinal and the transverse acceptances.

Computer simulations to investigate this new technique of combined longitudinal and transverse injection for LEAR have been performed. Some results will be presented here. A more detailed description of the simulations can be found in [3]. A summary of recent experiments in view of ion accumulation is given in [4].

2 PRINCIPLE

The principle of combined longitudinal and transverse multiturn injection is best explained with the help of Fig. 1. As for convential multiturn injection, a local deformation of the closed-orbit (the"bump") is created and decreases during the injection of the linac pulse. The linac energy is ramped in such a manner, that at the injection septum the closed-orbit corresponding to the instantaneous linac energy remains fixed, or changes only by a small amount.

For conventional transverse multiturn injection, the linac energy is constant and the closed-orbit moves away from the septum as the bump decreases. Thus a large emittance of the circulating beam results whereas the momentum spread is ideally the same as that of the incoming beam. With the combined injection (which has some similarities with the "painting" used in H^- injection [5]) both longitudinal and transverse phase space are exploited and transverse emittance can be traded for momentum spread.

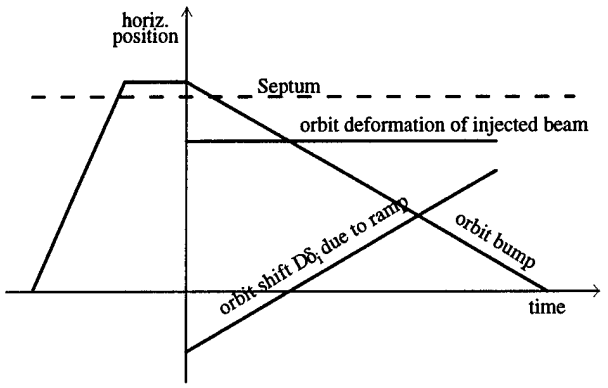


Figure 1: Horizontal positions for an example of combined longitudinal and transverse multiturn injection. The closed-orbit bump decreases during the injection of the pulse as for conventional multiturn injection. The momentum of the incoming beam is ramped $p = p_0(1 + \delta_i(t))$, which leads to an additional time dependent orbit shift $D\delta_i(t)$ (where D is the dispersion) for the incoming beam. The bump decrease and the energy ramp are adjusted, such that the instantaneous closed-orbit of the injected particles remains fixed.

3 LEAR LATTICES

With the fixed geometry of LEAR different "machines" can be obtained varying the currents in the quadrupole families. For the injection a small horizontal β function and a large dispersion are necessary; whereas for the electron cooling we expect vanishingly small dispersion and intermediate β in both transverse phase spaces to be advantageous. In Fig. 2, the Twiss functions are shown for two of the machines used for the simulations; (a) shows standard LEAR and (b) the machine best for combined injection, but with β functions a little too large for electron cooling.

A third lattice used for the simulations has smaller β-functions at the cooler, but leads to a situation less suitable for the injection.

4 SIMULATIONS

The injection process is simulated with a Monte-Carlo method. Each particle is described by its coordinates in the two transverse phase spaces, the relative momentum deviation and the time. First a Gaussian beam with particle coor-

0-7803-4376-X/98/$10.00 © 1998 IEEE

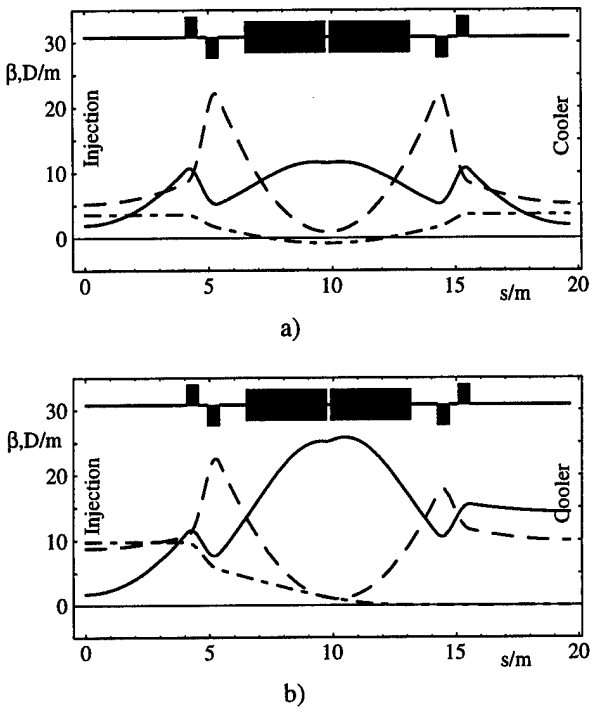


Figure 2: Lattice functions (the solid and dashed lines represent the horizontal and vertical β-function respectively, the dot-dashed line is for the dispersion) for one fourth of the machine extending from the center of the injection to the center of the electron cooling straight section for (a) standard LEAR and (b) a lattice improved for combined multiturn injection. The lattice functions in the rest of the accelerator are obtained by mirroring and repetition.

dinates corresponding to given Twiss parameters is generated at the injection septum with a random number generator. The injected particles are tracked through the accelerator consisting of the lattice magnets (dipoles, quadrupoles), closed-orbit bumpers, aperture limitations and the injection septum. Particles hitting an aperture limitation or the septum or falling outside an acceptance of 50 μm at the end of the injection are counted as lost. In simulations of a purely transverse process, the transverse acceptance had to be increased to 150μm to permit injection of a sufficient number of turns.

For the beam coming from the linac the following characteristics (corresponding to one standard deviation) were taken from [6] :

emittance	:	$2.1\ \mu m$
relative momentum spread	:	$0.2\ 10^{-3}$

In addition to the (instantaneous) spread, the mean momentum of the linac beam changes with time; this ramp has been limited to $\delta < 6\ 10^{-3}$. Further it is required that the distance from the center of the stack to the vacuum chamber must be at least 2.5 times the standard deviation of the stack. This leads to the following phase space volumes (2.5 rms) reserved for the stack (volumes expected for 1 rms taken from [1]) :

horizontal emittance	:	$(2.5)^2 \cdot 10\ \mu m = 62.5\ \mu m$
vertical emittance	:	$(2.5)^2 \cdot 5\ \mu m = 31.2\ \mu m$
rel. momentum spread	:	$2.5 \cdot 0.5\ 10^{-3} = 1.25\ 10^{-3}$

where the contributions due to momentum spread and due to horizontal betatron oscillations have to be added quadratically.

For the model of the accelerator, the real apertures available were followed as close as possible, after removing 10 mm in order to account for closed-orbit distortions up to ± 5 mm.

To optimize the injection efficiency all parameters of the incoming beam (position, angle, Twiss parameters, momentum) and the position of the injection septum are varied. The mean momentum of the stack is such that it is near the inner wall of the vacuum chamber, whereas the injection is from outside.

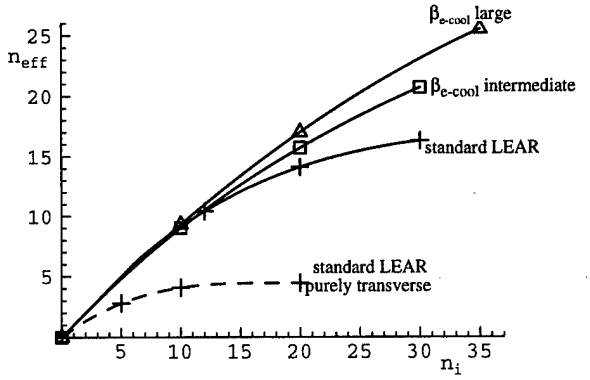


Figure 3: Number of 'efficient' turns n_{eff} accepted per injection as a function of the number of injected turns n_i for optimizations of combined multiturn injection. The crosses are for standard LEAR; triangles and squares are for injection into improved lattices with large and intermediate betatron functions at the electron cooler. For comparision, efficiencies for a purely transverse process and standard LEAR machine are given as a dashed line. In the latter case the full acceptance (150 μm) of LEAR is used whereas in all other cases the emittance was limited to 50 μm to permit faster cooling.

In Fig. 3 the number of turns accepted as a function of injected turns is plotted for various conditions. Phase-space plots for injection of 20 turns into the standard LEAR machine and into the machine best suited for combined injection (but expected to be less appropriate for electron cooling) are given in Figs. 4 and 5. For the incoming beam three phase space ellipses with small momentum deviations were overlapped; they separate after injection due to the dispersion. One notes that this separation is more important for the improved lattice because the normalized Dispersion $d/\sqrt{\beta}$ at the injection septum is increased; this is a consequence of improving the lattice for combined injection with a limited linac energy ramp.

For comparision, a plot of the horizontal phase space for the purely transverse process and the standard LEAR

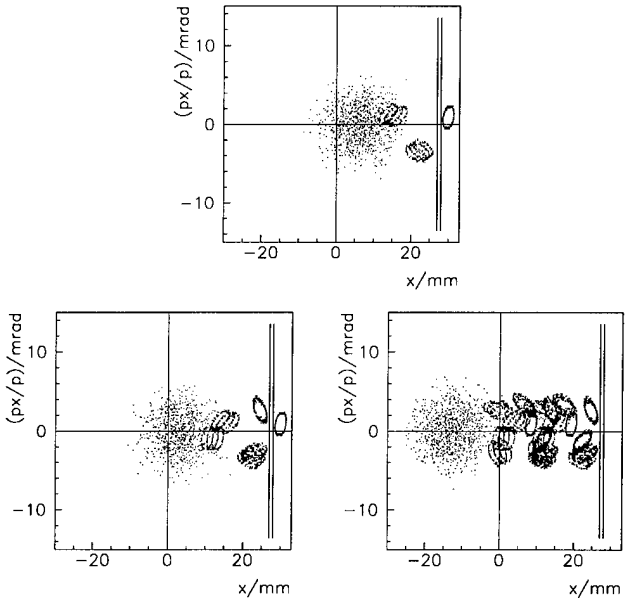


Figure 4: Plots of the horizontal phase space for the combined longitudinal transverse multiturn injection into the standard LEAR machine. 20 turns are injected; the three plots show the particles after 2, 5 and 20 turns.

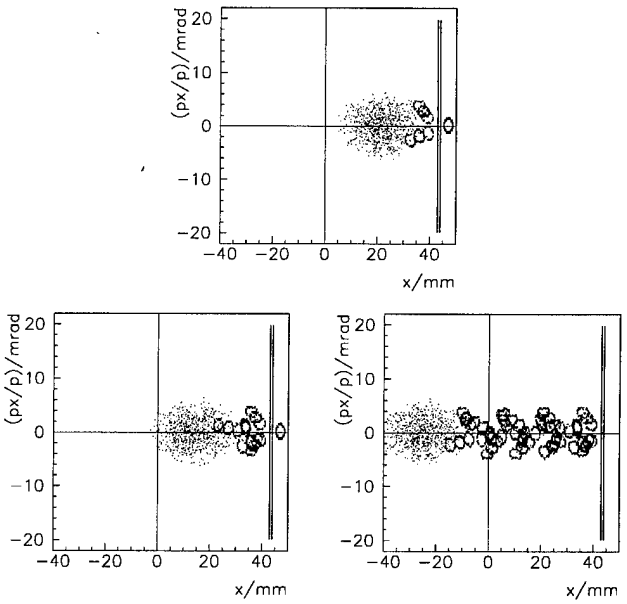


Figure 5: Plots of the horizontal phase space for the combined longitudinal transverse multiturn injection into the improved lattice with large β at the cooler. 20 turns are injected; the three plots show the particles after 2, 5 and 20 turns.

machine is given in Fig. 6. One notes, that particles are injected only in a ring-shaped region of the phase space around the stack.

5 CONCLUSIONS

Comparing the number of turns that can be injected with a given efficiency, one notes that a factor of 3 to 5 is gained with combined injection as compared to the purely transverse process (in the standard LEAR machine); another factor of 2 can be gained if the lattice is modified. In addition a smaller emittance of the injected beam, more favorable for electron cooling, is possible with the combined injection.

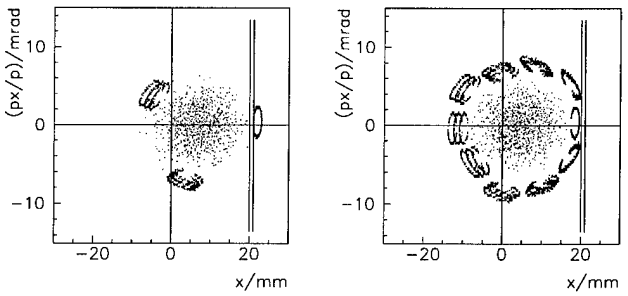


Figure 6: Plots of the horizontal phase space for purely transverse multiturn injection into the standard LEAR machine. 10 turns are injected; the two plots show the particles after 2 and 10 turns.

6 REFERENCES

[1] P. Lefèvre and D. Möhl, *A low Energy Accumulation Ring of Ions for LHC*, CERN/PS 93-62 and LHC Note 259.

[2] S. Maury and D. Möhl, *Combined Longitudinal and Transverse Multiturn Injection into a Heavy Ion Accumulator Ring*, internal note (CERN) PS/AR/Note 94-12.

[3] Ch. Carli, *Simulation of Multiturn Injection into LEAR in View of Ion Accumulation*, internal note (CERN) PS/DI/Note 96-24.

[4] J. Bosser, J. Broere, C. Carli, M. Chanel, C. Hill, R. Ley, A. Lombardi, R. Maccaferri, S. Maury, D. Möhl, G. Molinari, H. Mulder, E. Tanke, G. Tranquille, M. Vretenar, *Recent Lead Ion Storage Tests on LEAR*, this conference.

[5] D. Raparia, C.W. Planner, G.H. Mackenzie and J.R. Richardson, *Efficient Capture in an Accumulator, of 20000 Turns of Beam Injected from TRUMF*, Proc. of PAC 1985 (Vancouver), IEEE Trans. Nucl. Sci. NS-32, p 2456.

[6] N. Angert, M.P. Bourgarel, E. Brouzet, R. Cappi, D. Dekkers, J. Evans, G. Gelato, H. Haseroth, C.E. Hill, G. Hutter, J. Knott, H. Kugler, A. Lombardi, H. Lustig, E. Malwitz, F. Nitsch, G. Parisi, A. Pisent, U. Raich, U. Ratzinger, L. Riccati, A. Schempp, K. Schindl, H. Schönauer, P. Têtu, H.H Umstätter, M. van Rooij, D. Warner and M. Weiss, *CERN Heavy-Ion Facility Design Report*, CERN 93-01.
and
N. Angerth, W. Bleuel, Y. Bylinsky, H. Gaiser, H. Haseroth, G. Hutter, H. Kugler, E. Malwitz, R. Popescu, M. Rau, U. Ratzinger, R. Scrivens, E. Tanke, D. Warner, *The IH Linac of the CERN Lead Injector*, proceedings of the 1994 international linac conference, Tsukuba, Japan

THE ANTIPROTON DECELERATOR: AD

S. Baird, D. Berlin, J. Boillot, J. Bosser, M. Brouet, J. Buttkus, F. Caspers, V. Chohan, D. Dekkers, T. Eriksson, R. Garoby, R. Giannini, O. Grobner, J. Gruber, J.Y. Hémery, H. Koziol, R. Maccaferri, S. Maury, C. Metzger, K. Metzmacher, D. Möhl, H. Mulder, M. Paoluzzi, F. Pedersen, J.P. Riunaud, C. Serre, D.J. Simon, G. Tranquille, J. Tuyn, and A. Van der Schueren
CERN, CH–1211 Geneva 23, Switzerland

Abstract

A simplified scheme for the provision of antiprotons at 100 MeV/c based on fast extraction is described. The scheme uses the existing $\bar{p}$ production target area and the modified Antiproton Collector Ring in their current location. The physics programme is largely based on capturing and storing antiprotons in Penning traps for the production and spectroscopy of antihydrogen. The machine modifications necessary to deliver batches of 1×10^7 $\bar{p}$/min at 100 MeV/c are described. Details of the machine layout and the experimental area in the existing AAC Hall are given.

1 INTRODUCTION

The scenario used up to the end of 1996 involved 4 machines downstream the antiproton production target: the Antiproton Collector (AC), the Antiproton Accumulator (AA), the Proton Synchrotron (PS) and the Low Energy Antiproton Ring (LEAR). They were used to collect, cool and decelerate antiprotons in the following sequence:

1) Antiprotons, produced by 26 GeV/c protons on the production target, are collected and precooled at 3.57 GeV/c in the AC.
2) They were transferred to the AA where they are accumulated and further cooled.
3) A bunch of a few 10^9 $\bar{p}$ was taken from the AA and sent to the PS every 30 minutes to several hours.
4) This bunch was decelerated in the PS from 3.57 to 0.6 GeV/c.
5) It was then transferred to LEAR, where cooling (at 3 or 4 intermediate momenta) and deceleration brought the full intensity to low energy.

This scheme was designed as an 'annex' to the antiproton source for the Sp$\bar{p}$S (the SPS used as a $\bar{p}$-p collider at 300 GeV per beam). A simplified solution [1], using the modified AC and renamed AD (Antiproton Decelerator), is now being implemented. The antiproton physics programme will continue at the AD start in 1999, and LEAR will be converted into an ion accumulator for LHC [2].

2 AD OVERVIEW

The existing target area and the AC ring [3] in its present location (Fig.1) are used whereas the AA is dismantled. The basic AD cycle with the different intermediate levels is sketched in Fig. 2. After injection into the AD, bunch rotation is applied as in the AC to reduce the momentum dispersion of the antiproton batch. Then the beam is stochastically cooled at 3.5 GeV/c and 2 GeV/c and further decelerated in several steps. The next cooling level is at 300 MeV/c where the transverse emittances have grown to 33π mm·mrad and a $\Delta p/p$ of 0.2%. Electron cooling is applied and, finally, after deceleration down to 100 MeV/c, the beam is again electron-cooled. Beam characteristics and the cooling times are shown in Table 1.

The experimental area will be inside the AC ring. The shielding will be reinforced so that the users are allowed to access the area during $\bar{p}$ production and deceleration.

Table 1 - Transverse emittances and momentum spread before (i) and after (f) cooling, and cooling times. Only adiabatic increase due to deceleration is considered

p	ε_i	ε_f	$\Delta p/p_i$	$\Delta p/p_f$	t	Cooling process
[GeV/c]	[π mm.mrad]		[%]		[s]	
3.57	200	5	1.5	0.1	20	Stochastic
2.0	9	5	0.18	0.03	15	
0.3	33	2	0.2	0.1	6	Electron
0.1	6	1	0.3	0.01	1	

0-7803-4376-X/98/$10.00 © 1998 IEEE

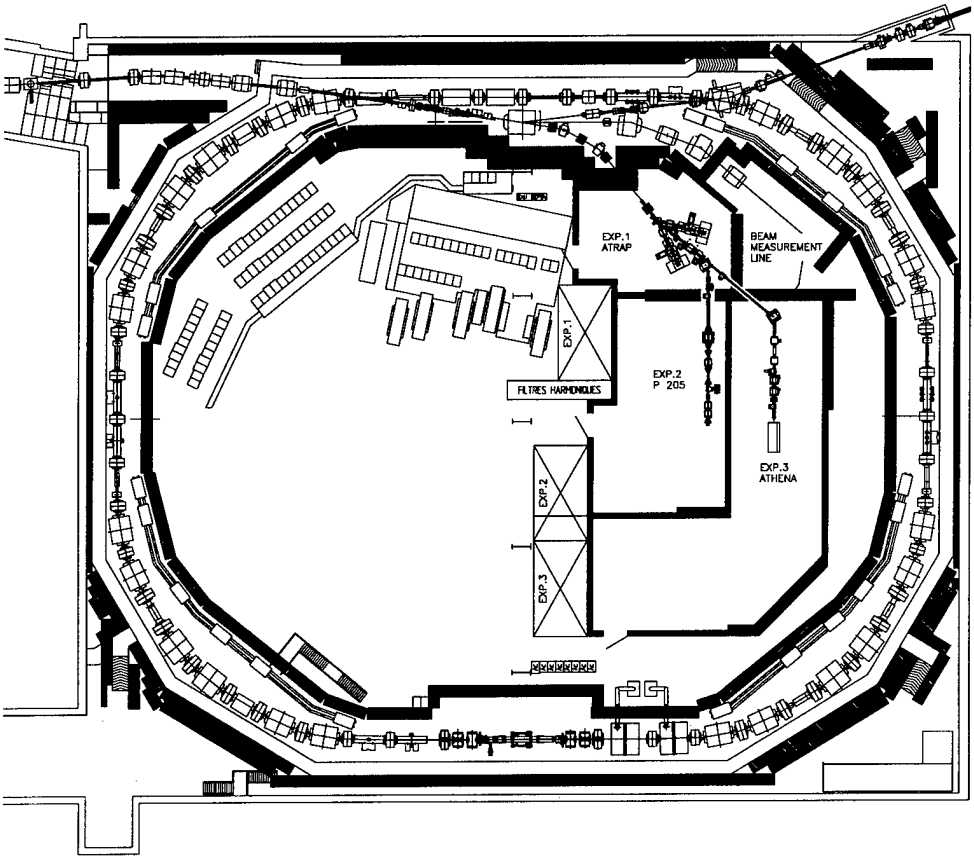


Fig. 1: AD layout.

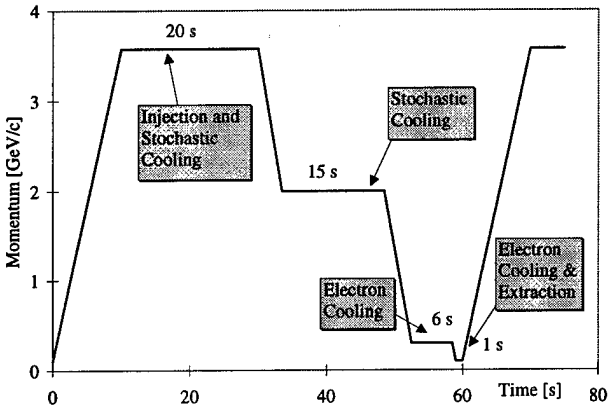


Fig. 2: Basic AD deceleration cycle.

Estimated characteristics of the ejected bunch are: 10^7 $\bar{p}$'s in one pulse of 0.2-0.5 μs length, with a repetition cycle of about 1 minute.

3 AD LATTICE

Detailed study [4] has led to the conclusion that suitable location for the electron cooling device is in a long straight section opposite to the injection section. The central quadrupole has to be removed. To reduce the strength of quadrupoles required for matching, it is proposed to add an additional quadrupole at the upstream and downstream end of the cooling insertion.

Phase advances between the pick-ups and kickers of the stochastic cooling have been adjusted by modifying the strength of other AD quadrupoles outside the cooling insertion. Further study to compensate the tune shift given by the solenoid of the electron cooler, calculations of the dynamical aperture are under way. The AD lattice functions is shown in Fig. 3. During study sessions made in the AC during 1996, it was found that orbit correction is necessary [4] to reach low momenta.

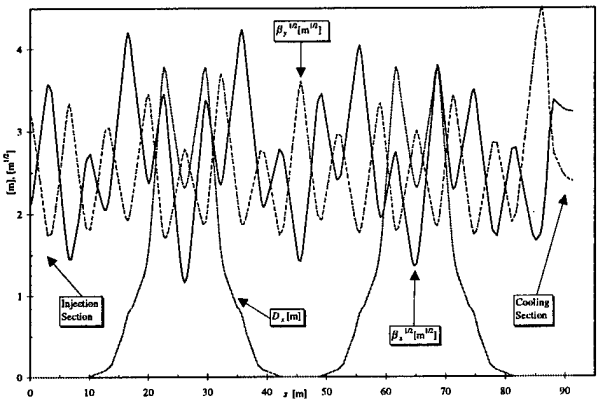


Fig. 3: The lattice functions of the AD where $\beta_H^{1/2}, \beta_V^{1/2}$ and D are shown on half a ring starting in the middle of the injection section.

4 SYSTEMS INVOLVED

4.1 Antiproton Production

The primary beam of 10^{13} protons at 26 GeV/c hitting the antiproton production target will be similar to the present one. It will, however, benefit from developments carried out in view of the use of the PS as part of the LHC injector chain [5].

Antiprotons emerging at 3.5 GeV/c from the target will be focused and matched to the transport line acceptance of 200π mm·mrad by a magnetic horn pulsed at 400 kA.

4.2 Radiofrequency Systems

The 5×10^7 $\bar{p}$'s injected in the AD will be trapped by the existing 9.5 MHz (h=6) rf system, as in the present scheme, and a bunch rotation will be applied in order to reduce the energy spread. The beam will then be decelerated with the present 1.6 MHz (h=1) rf system whose frequency range will be extended down to 0.5 MHz and changes of harmonic numbers at intermediate energy levels will be performed.

This rf system will also be used to shorten the bunch at 100 MeV/c prior to extraction

4.3 Beam Cooling Systems

Stochastic cooling is needed at 3.57 GeV/c and 2 GeV/c (Fig. 1), for which band I (0.9 to 1.6 GHz) and band II (1.6 to 2.4 GHz) of the present systems will be employed. The pick-ups and kickers of band I remain in their present location. The band II system will be located in the present band III location. At 2 GeV/c band I is used to compensate the adiabatic beam blow-up due to the deceleration. The pick-up sensitivity is reduced by a factor of 2 compared to 3.57 GeV/c. Band III (2.4 to 3.2 GHz) is not used as the gain in the cycle time would not be significant and space is needed for the electron cooling system.

Electron cooling will be applied at low momenta, especially at 300 and 100 MeV/c (Fig. 2). With only minor modifications, the existing LEAR cooler can be used in the AD.

4.4 Vacuum

Amongst the different effects of the residual gas which have an influence on the quality of the antiproton beam, both the single scattering loss and the multiple scattering blow-up become very important at low momenta.

In the presence of cooling, with a time constant of 1 s for the large beam, an equilibrium emittance of ~20π mm·mrad would be reached with the vacuum conditions of AC. For efficient capture of antiprotons in a Penning trap, equilibrium emittances <1π mm·mrad at 100 MeV/c are important. Therefore, an improvement of the present vacuum conditions by about a factor 20 is required.

4.5 Power Converters

In order to guarantee a current stability at low energy, active filters must be added on the main power converters. The trimming power supplies used in the AC will have to run below the present minimum controllable current. It is proposed to build new power converters which will be stable down to a very small current.

5 OPERATION

During setting-up with protons, the radiation level induced by a beam of 3×10^{10} protons will be too high to allow access to the hall. Therefore, the hall and the AD ring will be considered as primary zone. During normal $\bar{p}$ operation, the new shielding configuration will reduce the dose rate in the hall; in this case it will be considered as a secondary zone.

6 CONCLUSION

The modified AC as an antiproton decelerator will deliver a dense beam of 10^7 $\bar{p}$ every minute at 100 MeV/c with bunch lengths between 200 and 500 ns. This simplified scheme opens the possibility for an antiproton physics programme based on fast extracted beams. CERN will provide the framework for the AD but cost and manpower for the project will be provided by the user laboratories, who also will help with the operation.

7 REFERENCES

[1] AD Study Group, S. Maury (editor) : 'Design Study of the Antiproton Decelerator: AD', CERN/PS 95-43 (AR), 1995.

[2] The LHC Study Group: 'The Large Hadron Collider: Conceptual Design', CERN/AC 95-05 (LHC), 1995.

[3] ACOL Study Group, E. Wilson (editor): 'Design Study of an Antiproton Collector for the Antiproton Accumulator (ACOL)', CERN 83-10, 1983.
Koziol and S. Maury: 'Parameter List for the Antiproton Accumulator Complex (AAC)', Edition 1994, CERN/PS 95-15, 1995.

[4] P. Belotschskii, C. Carli, T. Eriksson, R. Giannini, S. Maury, D. Möhl, and F. Pedersen: 'Beam Optics Issues for the Antiproton Decelerator (AD)', this conference.

[5] R. Cappi, R. Garoby, S. Hancock, M. Martini, J.P. Riunaud, K. Schindl, H. Schonauer, 'Beams in the PS Complex During the LHC Era', CERN/PS 93-08 (DI) Rev., 1993.

OVERVIEW OF THE RECENT OPERATION OF THE AAC AND LEAR FOR THE LOW-ENERGY ANTIPROTON PHYSICS PROGRAMME

S. Baird, J. Boillot, F. Caspers, M. Chanel, V. Chohan, T. Eriksson, R. Ley,
S. Maury, C. Metzger, D. Möhl, H. Mulder, F. Pedersen, and G. Tranquille
CERN, CH–1211 Geneva 23, Switzerland

Abstract

This paper reviews the recent performance of the AAC and LEAR. Activities on the AAC include the successful exploitation of a magnetic horn as an antiproton collector lens and an energy-saving mode of operation, which has been possible since 1992, when LEAR became the only client of the AAC. LEAR worked in its full momentum range between 100 MeV/c and 2 GeV/c, with performance (intensities, ejection modes and spill length) exceeding the design specifications. Improvements are described, which contributed to the quality of the beam delivered to experiments. The reliability and availability of the antiproton machines are also discussed.

1 INTRODUCTION

The operation for the period following the SPS Collider run in 1991 to the close-down of AAC and LEAR in December 1996 are reviewed. During this five-year period, the AAC was operated only for the low-energy antiproton physics [1]. Typically, the AAC ran for around 5 800 h/year and, as LEAR took a small fraction of the possible daily production, the antiproton complex has operated a third of the time in the "energy-saving mode".

2 AAC OPERATION

2.1 Antiproton Production

In December 1991 the 20 mm lithium lens was reinstalled after a breakdown of the 400 kA magnetic horn. The cause of the failure was investigated and the mechanical reinforcement (stronger fixing flanges) was improved. One of the new horns was successfully tested over 1.3×10^6 pulses in the laboratory and, to complete the consolidation progamme [2], two cradles, specially studied to improve air cooling and the positioning of the collector after the target, were equipped with the improved horns.

The 20 mm lithium lens, which had been so reliable over three years, broke down in April 1995. A short-circuit developed in its primary transformer winding, and it had to be replaced by a magnetic horn. Such a horn collects about 15% less antiprotons, and the loss of $\bar{p}$ collection was compensated by running the production for a longer time.

The yield (Table 1) defined as the number of antiprotons measured on the injection orbit of the collector ring per incident 26 GeV/c proton, slowly decreases as the production beam intensity increases.

Table 1: Operational yields, measured for 1.5×10^{13} primary protons.

20 mm lithium lens (1992-1994)	53×10^{-7} $\bar{p}/p$
400 kA magnetic horn (1995-1996)	45.2×10^{-7} $\bar{p}/p$

2.2 AC and AA Rings

The different systems of the AC and AA rings have had fairly stable operation during the last five years. No major modifications or improvements have been carried out; however, a re-alignment of both rings had to be made because the gradual compacting of the ground had strongly restricted the vertical acceptances.

Machine development sessions on the AAC were mainly carried out simultaneously with normal running and aimed at maintaining the performance level of the machines. Deceleration of proton beams in the AC was studied in view of a simplified low-energy antiproton source [3].

2.3 Energy Saving Mode

With LEAR being the only consumer of the antiprotons produced in the AAC, there was a need to reduce the energy consumption. It was very efficient to accumulate $\bar{p}$ at maximum stacking rate and maximum number of PS-cycles during short periods. Once the AA was full, the AC ring, injection line elements as well as other elements used only for $\bar{p}$ production could be switched off or operated with reduced power, saving about 4 MW of electrical power. The PS production cycles were converted to other use or put in standby mode, further increasing the power savings. Antiproton transfers to LEAR from the coasting AA beam could continue as before. The AA to LEAR transfer efficiency actually increased due to a reduction in the transverse emittances of the AA stack.

3 LEAR OPERATION

A single bunch of antiprotons was transferred from the AA to the PS at 3.5 GeV, decelerated in the PS to 609 MeV/c and subsequently transferred to LEAR where through acceleration or deceleration and beam cooling, the beam was made available to physics experiments in the range of 105 MeV/c to 2 GeV/c.

0-7803-4376-X/98/$10.00 © 1998 IEEE

At the extraction flat top(s), the beam was either fast extracted in single bunches or ultra slowly using third-order stochastic extraction [4]. LEAR could supply several physics experiments at a time either switching single bunch extraction, or through beam splitting in the transfer line during ultra-slow extraction. In this way, typically 5 physics experiments could take data in parallel.

3.1 Stochastic and Electron Cooling

Stochastic cooling is available in the entire energy range of LEAR. It is normally applied at the 609 MeV/c and above and optionally during ultra-slow extraction at the extraction momentum. Electron cooling is applied at momenta below 350 MeV/c.

There are two stochastic cooling systems comprising high-gain pick-ups connected to correction kickers through variable delays. The first system is reserved for operation above 200 MeV/c and the second only at 105 MeV/c and below. All 50 Ω matching resistors and the pick-up electronics of this last system are cryogenically cooled in order to increase the signal to noise ratio. In the last years, the low-energy stochastic cooling systems have been used as wide-band dampers, providing the extra power and bandwidth needed to stabilise the dense beams that are obtained by electron cooling. Stochastic cooling is also used during ultra-slow extraction to counteract the blow-up of the circulating beam due to scattering on the residual gas.

The electron cooling, inherited from the ICE experiment, has undergone a number of major overhauls before its fully operational configuration. LEAR is the only machine to use electron cooling [5]. The modifications include the development of a variable intensity electron gun which has made it possible to increase the electron current on the cooling flat tops, a major upgrade of the vacuum systems in the cooling section, a feedback system on the high-voltage power supply to compensate for any change in the electron beam space-charge potential and the improvement of the controls for more reliable operation. These changes provided the physics community with high-quality antiproton beams at low energy and with a much improved duty cycle (electron cooling is applied typically for 15 s on the flat top as opposed to 5 min with stochastic cooling).

3.2 Stochastic Extraction

Consolidation of the noise generation hardware of the stochastic extraction system [6] improved the ultra-slow extraction of large stacks, of $\approx 10^{10}$ particles, at low momenta (<300 MeV/c). An extracted flux feedback system was put in operation to replace the parameter driven feed-forward system. This reduced the setting up time of the process and introduced the possibility to change the particle flux instantaneously at user request. It also allowed for very long low-intensity particle spills from large stacks. A typical spill is shown in Fig. 1. The longest constant flux spill lasted 14 hours.

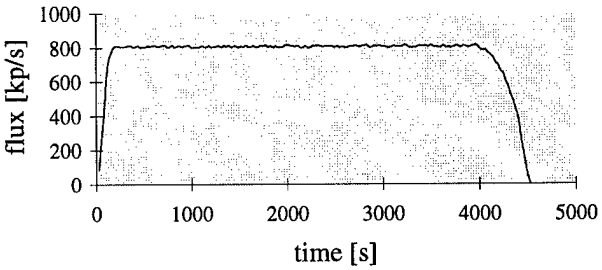


Figure 1: Antiproton spill with flux feedback.

Because of the improved spill control, the antiproton flux to the physics experiments could be kept close to the required value and as a result a net increase in the integrated flux was observed. This is one of the major factors in the improved performance of LEAR over the last 2 years.

4 OVERALL OPERATION PERFORMANCE

The total number of antiprotons injected into LEAR per year is shown in Fig. 2. The steady increase in the number of spills/year continued throughout the life of the machine. The small decrease seen in 1991 and 1992 was due to the push for increased spill length rather than any reduction in running time. The sharp dip in 1987 is due to the shutdown for the installation of the AC.

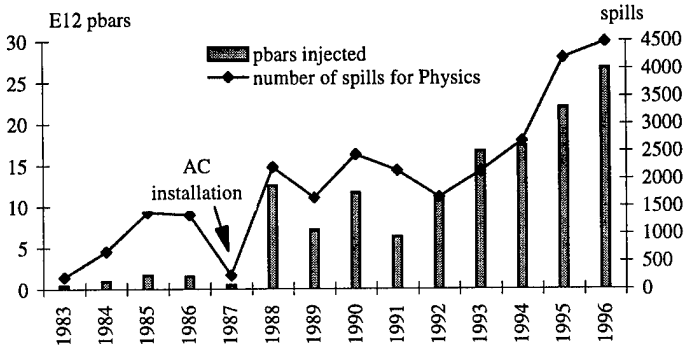


Figure 2: 1983-1996 LEAR running statistics.

After this installation, LEAR clearly profited from the increased antiproton flux available and the average intensity/spill continued to increase from 1988 right up to the end of the antiproton programme in 1996. A major effort was made to improve the overall efficiency of the AAC/PS/LEAR operation, leading to a very significant reduction in the time taken to refill LEAR. The use of the electron cooling helped to reduce the deceleration time by around 5 min/spill. These and other measures significantly reduced the waiting time between LEAR spills. As a result the number of spills was more than doubled for an increase of only 20% in time. In addition, the quality of each spill (peak intensity/average intensity) was also improved by careful adjustments of the extraction parameters, spill form and duty factors. All these factors provided a large increase in the total integrated antiproton flux to the LEAR users. The number of antiprotons injected into LEAR was almost tripled between 1992 and 1996, (Fig. 3). As antiprotons are expensive to produce, particular attention was paid to the overall efficiency of the transfer and deceleration process. One of the most critical areas was the injection of the antiproton bunch into the PS at 3.5 GeV/c. Any transverse emittance blow-up here, translates directly into beam losses during deceleration to 609 MeV/c. Therefore, the transverse injection oscillations were automatically measured and stored and any necessary corrections were automatically calculated and applied. A feedback system took care of small pulse-to-pulse variations in the PS injection process. It was also very important to monitor the beam trajectories from the AAC to the PS and from PS to LEAR, as any drift resulted in unwanted beam losses. At the end of the LEAR operation, the global transfer efficiency from the AAC to LEAR, i.e. the total number of antiprotons injected into LEAR divided by the total number ejected from the AAC in a year, was around 75%.

The actual time scheduled for the LEAR antiproton physics operation each year is shown in Fig. 3.

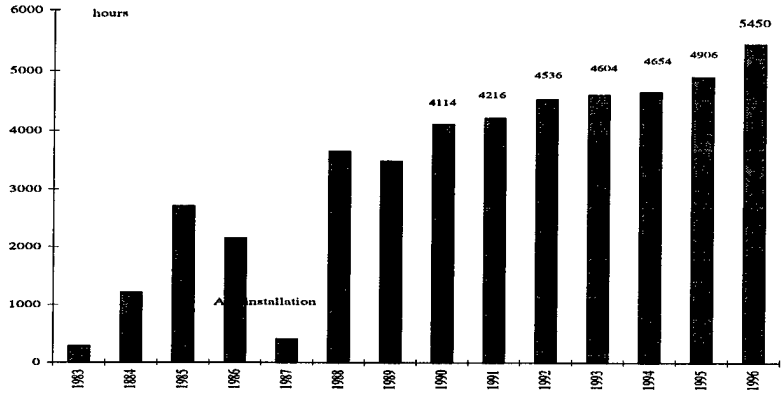


Figure 3: LEAR hours scheduled for antiproton physics (1983-1996).

5 CONCLUSION

This unique low-energy antiproton facility worked with good efficiency and reliability. The antiproton programme was completed in December 1996.

The machines involved will be reborn with a new lease of life. LEAR will be used as a lead ion accumulator ring (LEIR) for LHC and the AC ring converted into an 'Antiproton Decelerator' (AD). A new simplified antiproton source opens the possibility for a new antiproton programme at CERN.

6 REFERENCES

[1] G. Carron, F. Caspers, V. Chohan, S. Maury, C. Metzger, F. Pedersen, T.R. Sherwood, L. Thorndahl: Proc. XVth Int. Conf. On High Energy Accelerators, Hamburg 1992, CERN/PS/92-41 (AR), 1992.

[2] D. Boimond, M. Frauchiger, T. Kurtyka, M. Lubrano di Scampamorte, R. Maccaferri, S. Maury, L. Nikita, and J.C. Schnuriger: 'Consolidation of the 400 kA Magnetic Horn for AAC Antiproton Production', CERN/PS 94-02 (AR), 1994.

[3] S. Baird, D. Berlin, J. Boillot, J. Bosser, M. Brouet, J. Buttkus, F. Caspers, V. Chohan, D. Dekkers, T. Eriksson, R. Garoby, R. Giannini, O. Grobner, J. Gruber, J.Y. Hémery, H. Koziol, R. Maccaferri, S. Maury, C. Metzger, K. Metzmacher, D. Möhl, H. Mulder, M. Paoluzzi, F. Pedersen, J.P. Riunaud, C. Serre, D.J. Simon, G. Tranquille, J. Tuyn, B. Williams: 'Design Study of the Antiproton Decelerator: AD', CERN/PS/96-43 (AR), 1996.

[4] S. van der Meer: 'Stochastic Extraction - A Low Ripple Version of Resonant Extraction', CERN/PS/AA/78-6, 1978.
R. Cappi, R. Giannini, W. Hardt: 'Ultra-Slow Extraction', Proc. Physics at LEAR with Low-Energy Cooled Antiprotons, Erice, Italy, 1982, p. 49.

[5] J. Bosser, M. Chanel, R. Ley, D. Möhl, J.C. Perrier, G. Tranquille, D.J. Williams: 'Operational Aspects of Electron Cooling at the Low Energy Antiproton Ring', PAC91, San Francisco, USA, 1991, p. 2832.

[6] S. Jacobsen, G. Molinari, H. Mulder: 'A Feedback System to Control the Flux during Ultra Slow Extraction at LEAR', EPAC96, Sitges (Barcelona), Spain, 1996, p. 1845.

THE PROTON SYNCHROTRON DESY III

W.Ebeling, J.R.Maidment,
Deutsches Elektronen Synchrotron DESY,
Notkestrasse 85, 22607 Hamburg,
Germany

Abstract

Desy III is one link in the chain of injectors for HERA, the electron/positron - proton colliding beam storage ring. Because of the relatively low injection (kinetic) energy of 50 MeV space charge plays a significant role in determining the achievable accelerated current. The luminosity in HERA is critically dependent on the transverse beam brightness hence the need to examine, and where possible minimise, emittance blow-up. Measurements of the beam emittance as a function of intensity in Desy III and the derived incoherent space charge tune shift are presented and discussed. Finally some preliminary investigations with regard to upgrading the injection energy via a pre-booster are described.

1 INTRODUCTION

The Desy III synchrotron accelerates protons from a momentum of 0.31 MeV/c to 7.5 GeV/c in approximately 2s. Injection is from a 50 MeV H^- Alvarez linac using charge exchange in a thin ($34\mu g.cm^{-2}$) carbon foil. The linac output current is around 14 mA with a variable pulse length set in normal operation to $33\mu s$ corresponding to ten turns. The RF system consists of a single, ferrite tuned, cavity operating between 3.2 and 10.3 MHz providing harmonic number 11. Transition is not crossed during the acceleration ramp. The original design requirement was for an output intensity of $1 \cdot 10^{11}$ particles per bunch equivalent to some 165 mA circulating in 11 bunches. In routine operation some 10% more current is achieved while the maximum observed current corresponds to 25-30% above the design value. Although the longitudinal bunch area specified in the original proposal[1] is achieved, the assumptions regarding transverse emittance have yet to be met. This is the main topic reported on here.

It should be noted that injection and subsequent acceleration is accompanied by particle loss. The injection efficiency, measured as the ratio of the charge circulating immediately after the n-turn injection compared to that contained within the linac pulse, is 85% to 90%. Thereafter about 55% of this beam survives until full energy with the losses confined to the first 250 ms of the acceleration cycle ie ceasing after a momentum of circa 1 GeV/c. This transmission behaviour does not depend upon the number of injected turns below that required for the maximum achievable intensity.

The occurrence of longitudinal bunch oscillations has been reported elsewhere[2]. A feedback system[3] is installed which damps the dipole modes but is only activated during the magnet flat-top when the revolution frequency is constant. The threshold for the onset of the oscillations is around an intensity equivalent to 60 ma in flat-top Thus during acceleration the observed beam horizontal profile at higher intensities is somewhat influenced by radial synchrotron oscillations and to a much lesser extent by bunch shape oscillations. Although the shape oscillations are not damped by the feedback there is a negligible contribution to longitudinal mismatch at extraction and injection into Petra, the next accelerator in the injector chain.

2 EMITTANCE MEASUREMENTS

Desy III is equipped with residual gas monitors to measure the beam profile in each plane and a single wire scanner to measure the horizontal profile.[4] Both systems produce a beam profile resulting from a time integration. The residual gas monitor is based on the readout of a video camera whilst the wire scanner traverses at $\sim 1\ ms^{-1}$. Comparison of the profiles yielded by each system at peak energy show excellent agreement.[5]

The residual gas monitors, which measure the average profile on 4 consecutive cycles, have been used to acquire profile data over a wide range of beam intensity and momentum. The first conclusion is that there is a blow-up of the emittances in both planes between injection (flat bottom) and full energy (flat top). This is shown in Figures 1 and 2. where the horizontal and vertical emittances are plotted as a function of accelerated current. Due to the transmission losses already mentioned even if no blow-up occurred there would be a factor of ~ 2 reduction in the phase plane density.

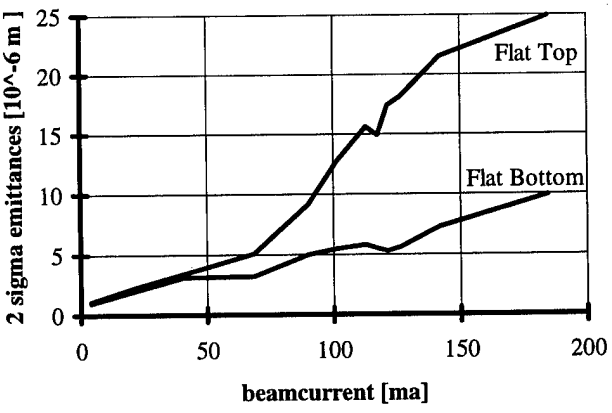


Figure 1: Horizontal emittance vs accelerated current.

Measurements of the emittances at the exit of the linac, using charge deposition on wire harps, yield ε_h =

0-7803-4376-X/98 /$10.00 © 1998 IEEE

$3.2 \cdot 10^{-6}$m and $\varepsilon_v = 2.5 \cdot 10^{-6}$m for the horizontal and vertical *normalised, 2σ* emittances respectively. To within the measurement errors, which may be of the order of 25%, the same values are recorded in flat bottom for at most 2-turn injection. No increase in emittance could be detected for 2-turns with up to an additional 20 passages of the proton beam through the stripping foil. At this low intensity there is no evidence of emittance blow-up between injection and top energy.

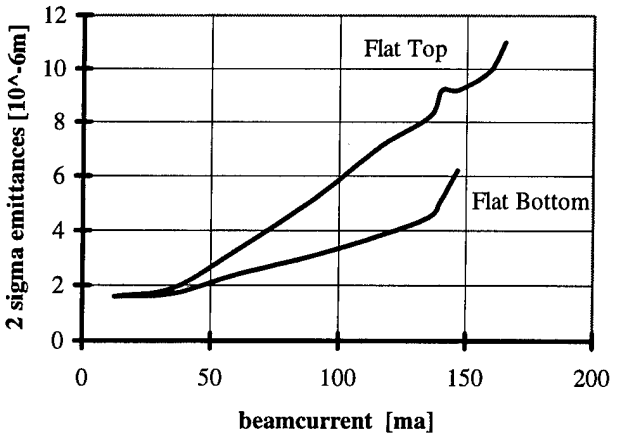


Figure 2: Vertical emittance vs accelerated current.

The injection of further linac turns leads to a recorded emittance at injection which increases approximately linearly with current. There is an additional blow-up during acceleration which also shows an approximately linear increase with intensity, rising to a factor of ~2 under standard operational intensities.

3 TRANSVERSE SPACE CHARGE

Space charge is considered to be the most significant effect limiting the maximum achievable beam brightness. We may write the expression for the vertical detuning as:

$$\Delta Q_v = \frac{N r_p F G}{\pi \varepsilon_v \left(1 + \sqrt{\frac{\varepsilon_h}{\varepsilon_v}}\right) B_f \beta \gamma^2} \qquad (1)$$

Where N is the total number of circulating protons, r_p = classical proton radius, F ($\sim$ 1) takes account of the image forces, G ($\geq$ 1) is a transverse distribution factor, B_f is the bunching factor (average/peak current) and ε is the transverse *normalised, 2σ* emittance. The subscripts h and v refer to the two transverse planes.

Measurements of the (vertical) emittance as a function of time/momentum during the cycle together with the the bunch length allow the derivation of the tune shift. The bunch length is measured using a resistive wall monitor with bandwidth of order 1GHz. To evaluate ΔQ_v we have used F=G=1 in equation1 and for the bunching factor have assumed a parabolic line density which is in good agreement with measurements.

Figure 3 shows typical results for the vertical emittance versus time during acceleration for two different end intensities while figure 4 is a plot of the derived variation of the vertical tune shift for an end intensity of 180 ma. Although ΔQ_v has a maximum value of ~0.6 at the start of acceleration it is not clear that incoherent space charge effects are responsible for the blow-up observed during the whole cycle for high intensity beams. The initial phase space density of low current beams yields similar large tune shifts.

We have not observed coherent betatron oscillations during the acceleration cycle. We may speculate that the radial synchrotron oscillations, whose amplitude increases with increasing intensity and which are not damped until flattop, impose additional good field requirements to maintain transverse emittance. Desy III is equipped with the minimum number of multipole magnets required to independently influence/compensate all 3^{rd} and 4^{th} order betatron sum resonances spanned by a space charge tune spread of 0.4. Skew quadrupoles are incorporated to correct the coupling. To date studies with these systems have been confined to achieving increased accelerated intensity. They are not activated in standard operation. Further studies of their influence on emittance are planned.

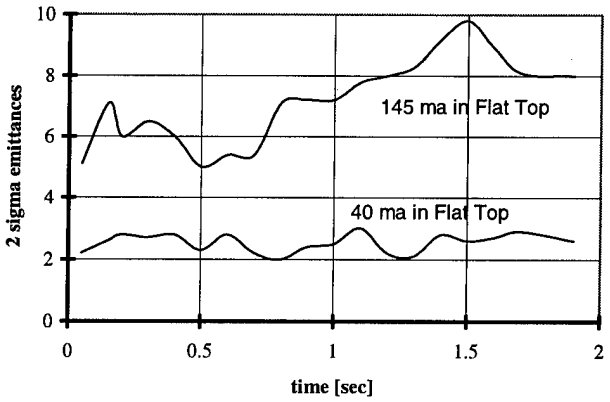


Figure 3: Vertical emittance vs time during acceleration.

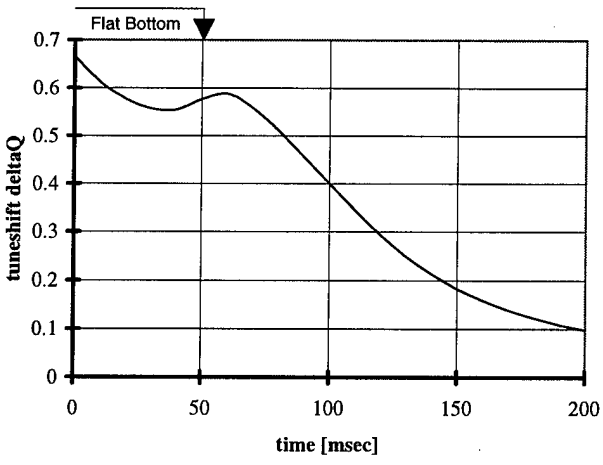


Figure 4: Derived (vertical) tune shift vs time.

4 UPGRADE OPTIONS

Short term improvements concentrate on reducing the observed losses. At present orbit correction is via dc-powered elements. It may be advantageous to incorporate time dependent correctors. We observe a systematic increase of the orbit radius shortly after the start of acceleration indicative of a dipole field tracking error. Improved read-out electronics for the position monitors are essential and system tests are underway.[6]

A study has been made of increasing the injection energy using additional linear accelerator structures in the space between the present Alvarez linac and the synchrotron tunnel.[7] An increase of injection energy to 170 MeV is considered feasible. This would theoretically reduce the space charge tune shift, at constant phase space density, by a factor of 2.

Somewhat more promising is a study in progress based on the use of an intermediate booster.[8]. Sited in the existing building alongside the present linac this would accelerate 2 bunches to 800 MeV kinetic energy using a 1 Hz magnet cycle which is the maximum repetition rate of the linac. The space charge tune shift in the booster would be moderate and that in Desy III reduced by a factor of 3 to 5 depending on the chosen bunch intensity.

Use of such a booster requires bunch to bucket transfer to Desy III using fast (ca. 70 ns risetime) kickers. The ten bunches would be boxcar accumulated using 5 booster transfers. Measurements have been made on an 800 MeV flat-top in Desy III which gave a beam lifetime of 270 s and no observable emittance increase over 2.7 s. The additional accumulation time produces a negligible increase in the overall Hera filling time.

5 ACKNOWLEDGEMENTS

We would like to thank K.Wittenburg and J Schwarz for their assistance in obtaining the profile measurements.

6 REFERENCES

[1] E.Bakewicz et al, "Desy III: Design Report", Internal report DESY HERA 1986-11, 1986.

[2] W.Ebeling et al, "Improvements in performance of Desy III",Proc. XVth Int. Conf. on High Energy Accelerators, p112, Hamburg, 1992.

[3] R.D.Kohaupt, "Feedback Systems at Desy", Proc. 5th Europ. Part. Accel. Conf., p180, Sitges, 1996.

[4] W.Hain et al "Beam Profile Monitors for the Hera Proton Accelerators", Proc. 2nd Europ. Part. Accel. Conf. p759, Nice, 1990.

[5] K.Wittenburg, "Emittance measurement in the proton accelerators at Desy", Proc. Int. wkshp. on Particle Dynamics in Accelerators, Tsukuba, 1994.

[6] M.Wendt. Private Communication

[7] S.K.Esin et al "Desy Linac III Upgrade Study", Proc. XVIIIth Int. Linear Accel. Conf., p190, Geneva, 1996.

[8] V.Balbekov et al. "Desy III Booster Design Study", To be published

STATUS OF THE EUROPEAN SPALLATION SOURCE DESIGN STUDY

I S K Gardner[1], H Lengeler[2], K Bongardt[2], H Klein[3], G H Rees[1] and C M Warsop[1]
on behalf of the ESS Study Group. [1] Rutherford Appleton Laboratory (RAL), UK;
[2]Forschungszentrum Julich (FZJ), Germany; [3]J W Goethe Universitat (JWGU), Germany.

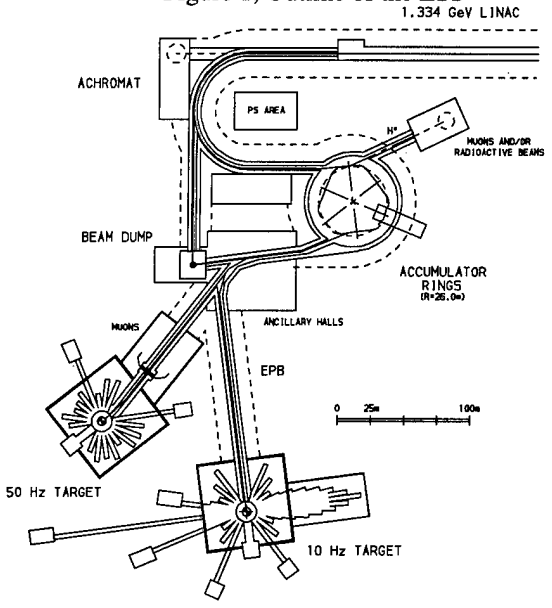
Abstract

The status of a study for a European Spallation Source (ESS) is reported along with a description of the reference design. The design of the 5 MW, 1.334 GeV machine is dominated by the need to keep beam loss at a low enough level to allow hands on maintenance for most areas. All accelerator sections are designed to be far away from space charge limits. The design allows scraping of the H^- Linac beam in all three phase planes (horizontal, vertical and momentum) prior to injection into the two accumulators. Key elements of the R & D programme that will validate the design are identified.

1 ESS DESIGN STUDY STATUS

The first phase of the ESS Project was completed at the end of 1996, with the conclusion of the Feasibility Study and publication of the Reference Design [1]. This work identified areas of research required to validate the design, and is the basis for planning the next 'R&D' Phase of the study which is outlined in Section 6.

Figure 1, Outline of the ESS



2 ESS REFERENCE DESIGN

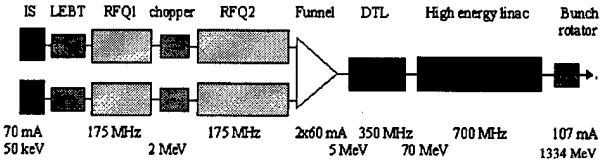
The Reference Design consists of a 1.334 GeV H^- Linac, which develops the full 5 MW beam power at 50 Hz, followed by two Accumulator Rings which operate in parallel to compress the proton pulse to 1 μs. Two spallation targets are included, one for 50 Hz operation and the other for 10 Hz, see Figure 1.

The Linac provides a peak current of 107 mA (at 6% duty cycle) over two successive 0.6 ms injection pulses into each ring. To minimise injection losses, the 1.2 ms injection pulse is chopped at the ring revolution frequency of 1.67 MHz, and linac halo is removed in a long collimation section in the injection line. Charge exchange injection is over 1000 turns, accumulating 2.34×10^{14} protons per ring. Fast extraction from each ring, on successive turns, yields the 1 μs pulse required.

3 THE ESS LINAC

Two 70 mA H^- ion sources feed RFQs whose beams are funnelled together at 5 MeV into a 350 MHz, 70 MeV DTL. Next, a 700 MHz coupled cavity linac accelerates the beam up to the final energy of 1.334 GeV. See Figure 2. The momentum of the beam is ramped and the spread is reduced by a bunch rotator. Hands on maintenance is a more important criterion than either capital or operating cost minimisation.

Figure 2, Proposed Linac Scheme



3.1 Low Energy Section

The H^- ion source requirements of 70 mA at 6% duty cycle have not yet been achieved. The most promising candidates are developments of the ISIS Penning source, which has already delivered 55 mA, or an RF driven volume source [1]. As neutralisation effects in the transport system between the ion source and RFQ have not been demonstrated for H^- at high intensities, an integrated ion source-RFQ ESS test stand is to be built at RAL. Various parts will be delivered by the ESS collaborators. Details of the 2 MeV chopping line and the 5 MeV funnelling line are given in [1].

3.2 DTL and CCL Linacs

After acceleration to 70 MeV in a conventional 350 MHz DTL, the particles are injected into a 700 MHz CCL. The injection energy is below the neutron production threshold of ~120 MeV. The CCL at high

0-7803-4376-X/98 /$10.00 © 1998 IEEE

energy is the most sensitive for beam loss. It is also the most expensive, for both capital and operating cost.

Optimisation of capital and 10 years operating costs leads to a field gradient of 2.8 MV/m and length 663 m. By decreasing the full current transverse tune with energy, even for the 214 mA bunch current at 700 MHz, the transverse and longitudinal tune ratios are ~0.8 all along the ESS linac. This non space charge dominated design leads to rms emittance growth of < 10%. Most important for beam loss is the reduced halo outside the dense core. Monte Carlo simulations with $\leq 10^6$ particles have been run for the DTL and the CCL in sequence [2]. There is strong transverse-longitudinal coupling associated with the non-uniform space charge density of a bunched beam. The linac is expected to achieve the low loss design goal after an initial start-up period.

3.3 RF Power for CCL

Each klystron feeds only two cavities and is designed to deliver 2 MW peak RF power, which is 30% more than the sum of beam and cavity dissipation power. No modulating anode is foreseen for this single beam klystron. A bouncer has been designed for a modulator delivering 6 MW DC power for 1.2 msec pulses at 50 Hz. The AC to DC efficiency is about 85% and the pulse flatness is better than ±0.5% [1]. This modulator may be used to power a pair of 2 MW peak RF power klystrons. The replacement of Gate Turn Off (GTO) thyristor switches by Insulated Gate Bipolar Transistors (IGBT) is promising for reducing costs and control problems. A test stand is planned for studying the series connection of IGTBs up to a blocking voltage of 5 kV for each. Costs are reduced as all modulators are designed for the same DC power; a central housing of modulators for many klystrons using common energy storage and control systems is possible. More detailed studies are planned to evaluate this arrangement.

Attention has to be given to the RF control system. Uncorrelated amplitude and phase errors, of ±1% and ±1° respectivley, will cause an oscillation of the beam centre of about 0.6 MeV at the linac end. This is near the limit for low loss ring injection.

3.4 Superconducting Option

Superconducting cells are an interesting option for the high β linac. Detailed studies are to be performed for accelerating the ESS beam from 70 MeV to 1.334 GeV by using 5-cell 700 MHz superconducting Nb cavities at 2K. A constant gradient of 10 MV/m is chosen. Two cavities are connected to one klystron. The total linac length is 300 m. About 30% saving of capital and operating cost is expected for this sc linac compared to the nc reference design, if amplitude and phase can be stabilised to better than ±1%, ±1° respectively. RF errors due to the Lorentz force detuning may be compensated by stiffening the cavities and applying digital feedback from feedforward tables. The cavity to cavity and pulse to pulse frequency shift of ±30 Hz, as measured for a stiffened 1.3 GHz sc TESLA cavity due to microphonics, causes an intolerable phase shift of ±3° at low β and ±1.2° at high β. Unlike electron linacs, phase errors in different cavities connected to one klystron do not add up to give a common energy fluctuation. To achieve the very stringent limits required, methods such as connecting only one cavity to a klystron, or increasing the cavity bandwidth by lowering the loaded Q-value, are being considered in cooperation with the TESLA RF control group at DESY, Hamburg.

4 THE INJECTION TRANSFER LINE

The injection line is involved with collimation, momentum ramping and bunch rotation. For low loss in the rings, linac halo is removed. In the transverse planes unnormalised emittances are collimated at 2.54 π mm mr. To allow phase space painting in the ring, the momentum is ramped linearly through injection. The instantaneous δp/p is adjusted with bunch rotator cavities, which compensate for space charge induced phase width growth. The total momentum range, spread plus ramp, is collimated at $0.0\% > \delta p/p > 0.4\%$.

There are three sections; the initial drift and matching section, an achromatic bending region, and a final vertical separation and optical matching section. All collimation systems in the line utilise stripping foils and magnet fields to separate and remove unwanted beam efficiently. Magnets have C shaped cores, open on the outer radius for easy removal of stripped beam.

The first section includes the momentum ramping cavity and debuncher at the upstream end, four horizontal betatron collimators at successive phases of 45° and, at the down stream end the bunch rotator. The 180° achromatic bending region has a mean radius of 42.5 m to keep fields low and prevent H^- stripping. This provides a peak normalised dispersion of 5.5 $m^{1/2}$ for momentum collimation; two momentum pre-collimators allow reduction of magnet apertures required. The achromat has four superperiods, each containing low field combined function magnets in a triplet configuration. Beam dynamics are similar to a circular machine above transition, with minimal debunching. Four vertical betatron collimators are also included in the achromat, placed at relative phases of 45°. After the achromat the line splits into two ring matching sections, 2 m vertically apart. A vertical splitting magnet, with a rise time of 100 μs, deflects the beam appropriately.

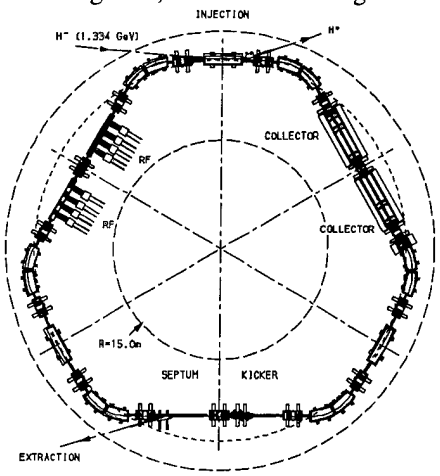
5 ESS ACCUMULATOR RINGS

5.1 Accumulator Lattice and Injection

The 1.334 GeV accumulators have a mean radius of 26 m, and a three superperiod lattice utilising quadrupole

triplets to provide alternate achromatic bending regions and long dispersionless straights. This fullfills requirements for extracted pulse length, low loss injection, RF, extraction and collimation. Beam emittances are large (collimated at 260 π mm mr) to keep betatron tune depressions below 0.1 at the design intensity of 2.34×10^{14} per ring. For full design see [1].

Figure 3, Accumulator Rings



During injection the beam is painted in all three planes to minimise space charge effects. The beam momentum is ramped linearly through injection and the large dispersion at the foil (5.66 m) correlates this longitudinal painting to that in the horizontal plane. Vertically a programmed symmetrical bump at the foil anti-correlates vertical amplitudes. One topic for research is the effect of space charge on the painted transverse emittance and related loss.

The injection system requires careful design, main requirements are: specified dispersion for injection painting; efficient removal and collection of H^0, H^-; low field to prevent pre-stripping and efficient collection of stripped electrons to prevent foil heating. Manufacture and verification of graphite foil performance is part of the R&D program. Interactions of recirculating protons with the foil cause losses, and measures to minimise the number of foil traversals are: collapsing vertical orbit bump, optical mismatch at injection, RF steering after injection, two unsupported edges on the foil and the large machine acceptance.

5.2 *RF System and Extraction*

The chopped linac beam is injected unmatched into the bucket of the dual harmonic RF system (h=1,2). RF voltage and frequency laws have been determined by stability and injection criteria, and optimised with space charge codes [3]. There are four RF cavities per ring, providing a peak total voltage of 27 kV/turn. A small frequency sweep is used for final RF steering, and a 200 ns beam gap allows for the rise time of the single turn extraction system. Extraction uses four push-pull lumped kickers, which deflect the beam by 15.8 mr to a septum magnet half a straight downstream.

Precautions against instabilities include profiled aluminium vacuum chambers, shielded bellows, low impedance extraction kickers and further R&D work.

5.3 *Loss Collection in Accumulator Rings*

Total loss in each ring is estimated at <0.02% and is mainly due to foil interactions. Most loss will be localised in a well shielded, dispersionless collection region. Collimation and aperture limits are 260 and 480 π mm mr respectively. Most operational loss will be stopped on a betatron collimation system and a special momentum tail system. The latter intercepts particles losing energy at the high dispersion point of the foil, by intercepting their enhanced betatron motion at 180° phase shift downstream. The system of collimators is being optimised for most efficient collection of particles, including effects of growth rate, outscattering, misalignment and fault conditions.

6 RESEARCH & DEVELOPMENT PROGRAM

An application for CEC support under the TMR scheme has been submitted. Research topics and participants are summarised in Table 1 for the 3 year TMR R&D program. An ESS test stand with ion source, chopper and RFQ is to be built at RAL, and beam loss studies will continue.

Table 1, Summary of Topics and Participants

Subject	Participants
Ion Sources	RAL, JWGU
2 MeV RFQ	RAL, JWGU, TUE, FZJ, HMI
Chopper Design	TSL, JWGU, TUE, FZJ, HMI
Space Charge Codes	FZJ, RAL JWGU, INFN
Foil & Injection Studies	RAL, HMI
Diagnostics	U Aarhus, TSL, FZJ, HMI, JWGU
Linac Cavity and RF	TUE, FZJ
Impedance Modelling	INFN, RAL

Participants are: RAL, JWGU, FZJ, Univ. of Aarhus (U. Aarhus), The Svedberg Laboratory (TSL), Istituto Nazionale di Fisica Nuclear (INFN), Eindhoven Univ. of Technology (TUE), Hahn Meitner Institut (HMI). Other institutes may join as studies progress.

The anticipated ESS programme is: completion of R&D by 2000, two years engineering design, six years construction, two years commissioning ending by 2010.

REFERENCES

[1] ESS A Next Generation Neutron Source for Europe, Volume 3, The ESS Feasibility Study, March 1997.

[2] M Pabst et al, Proc. of this conference.

[3] C Prior, ESS Report, ESS 94-7-R, November 1994.

INTENSITY LIMITATIONS IN FERMILAB MAIN INJECTOR

W. Chou, Fermilab,* P.O. Box 500, Batavia, IL 60510, USA

Abstract

The design beam intensity of the FNAL Main Injector (MI) is 3×10^{13} ppp. This paper investigates possible limitations in the intensity upgrade. These include the space charge, transition crossing, microwave instability, coupled bunch instability, resistive wall, beam loading (static and transient), rf power, aperture (physical and dynamic), coalescing, particle losses and radiation shielding, *etc.* It seems that to increase the intensity by a factor of two from the design value is straightforward. Even a factor of five is possible provided that the following measures are to be taken: an rf power upgrade, a γ_t-jump system, longitudinal and transverse feedback systems, rf feedback and feedforward, stopband corrections and local shieldings.

1 INTRODUCTION

High intensity beams are often in demand when proton synchrotrons are operated in fixed target mode or in antiproton or neutrino production mode. In the past half century, scores of proton synchrotrons have been built and tremendous amount of knowledge has been accumulated in their design and operations for understanding where the bottlenecks are and how to conquer them. One of the best examples is Ref. [1], which shows how various measures were taken on the PS Booster at CERN for increasing the beam intensity by an order of magnitude in 15 years. At this moment, the AGS at BNL holds the world record of the highest beam intensity (6.3×10^{13} ppp) in a proton synchrotron.

The design goal of the beam intensity in the Main Injector at Fermilab is modest: 3×10^{13} protons per pulse. But it is by no means the intensity limit. This paper investigates a number of sources that could possibly become bottlenecks. The "Top 10" list is:

- Space charge.
- Microwave instability.
- Coupled bunch instability and resistive wall.
- Beam loading.
- Robinson instability.
- RF power.
- Transition crossing.
- Dynamic and physical aperture.
- Coalescing.
- Particle losses and radiation shielding.

These are in random orders and will be discussed in sequence. They will be re-ordered in the end of the paper to establish a priority list.

Other sources, such as intrabeam scattering and residual gas scattering are considered not to be important. Lattice mismatch, beta-beat and beam steering could be important but it may be more appropriate to study them when machine operation begins.

2 SOURCES OF INTENSITY LIMITATIONS

2.1 *Space charge*

The space charge may cause emittance growth (especially in the transverse phase space) and particle losses (from resonances). When the space charge limit is reached, the transverse emittance would grow as bunch intensity increases, while keeping their ratio a constant. The characteristic parameter is the Laslett tune shift, which comes from both the space charge and image charge. In the Main Injector, it is -0.08 at 6×10^{10} protons per bunch at injection. It would become -0.4 if the beam intensity is increased by a factor of five, assuming the same transverse emittance. Such a big tune shift would cross a number of resonance lines. A standard way to cure it is to employ stopband corrections, which have been successful in many machines, including the AGS.

2.2 *Microwave instability*

Table 1 is the impedance budget of the Main Injector. The total longitudinal $Z_{\|}/n$ is 1.6 Ω, the total transverse $Z_{\perp}$ is 2.2 MΩ/m. The threshold of microwave instability and transverse mode coupling instability is also listed in the table. It is seen there is a safety margin of 4-5. When the intensity is increased by a factor of 5, one might see transverse mode coupling, which, however, has never been observed in any proton machine. A possible solution to push the intensity even higher is by intentional blow up of the longitudinal emittance, which has been used at CERN for years.

2.3 *Coupled bunch instability and resistive wall*

The 18 rf cavities in the Main Ring (MR) will be re-used in the Main Injector. The longitudinal coupled bunch instability driven by the higher order modes (HOM) in these cavities have been observed in the MR. At present there are two narrow-band passive dampers for the modes 128 and 225 MHz. It is not clear which modes would be dangerous when these cavities move to the MI. The calculation shows the growth time at nominal intensity is about 10 ms in the MI, which can be damped by active feedback. As beam intensity increases by a factor of 5, the growth time would de-

* Operated by Universities Research Association Inc. under Contract No. DE-AC02-76CH03000 with the U.S. Department of Energy.

0-7803-4376-X/98/$10.00 © 1998 IEEE

Table 1. Main Injector Impedance Budget

Component	Number	Impedance	
		$Z_\parallel/n$ (Ω)	$Z_\perp$ (MΩ/m)
RF cavities (HOM)		0.09	0.023
Main cavities (53 MHz)	18		
Coalescing (2.5 MHz)	5		
Coalescing (5 MHz)	1		
2nd harmonic (106 MHz)	1		
Transitions (tapered)		0.012	0.01
RF section	10		
Inj section	2		
Bellows (shielded)	552	0.37	0.67
Flange gaps (shielded)	552	-	-
Weldments	2208	0.001	0.005
Gate valves (shielded)	34	0.04	0.05
Pump ports (screened)	577	0.1	0.07
Beam position monitors	208	0.18	0.3
Kickers		0.3	0.6
p inj (1.1 m)	3		
$\bar{p}$ inj/p extr (2.24 m)	2		
$\bar{p}$ extr (2.2 m)	2		
Abort (2.2 m)	2		
Lambertson laminations		0.1	0.3
Lambertson joints		0.3	0.1
Lambertson-quad	12		
Lambertson-Lambertson	6		
Lambertson-dipole tube	10		
Resistive wall		0.11	0.092
Total		1.6	2.2
Instability threshold:			
At 8.9 GeV/c		39	7.9
At 120 GeV/c		8.0	16

crease by a similar portion, which makes the feedback more demanding. Hence, it is desirable to install a wide-band passive damper in the cavity to damp all the HOM above certain frequency, say, 200 MHz. A new version of the simulation code MAFIA, v.4, allows its frequency domain solver to deal with lossy materials such as ferrite. This can be a useful tool in the investigation of such a damper.

The resistive wall instability has a much faster growth time, about 1.2 ms at 3×10^{13}, which is about 100 turns. The specification of the transverse feedback has a damping time of 20 turns. Therefore, it should be able to handle higher beam intensity.

2.4 *Beam loading*

The transient beam loading gives a phase modulation due to the gap in the bunch train. The worst case is when there is only one batch in the machine. In this case the phase modulation is about 20°. Another beam loading effect is the instability driven by the fundamental mode of the cavity due to detuning. Although calculation shows it would not happen in the MI because of its high revolution frequency (90 kHz), the observation of such kind of instability in the MR even in the Booster causes concern. Presently mode dampers are used. There is also a plan to build fast rf feedback to suppress it. But the power amplifier needs to work in the linear region (class A or AB) for this purpose. The current Fermilab amplifier is class C. Modification is thus needed.

2.5 *Robinson instability*

The first type Robinson instability is rarely seen in proton machines thanks to their low synchrotron frequency. The second type, however, could occur at high intensities when the relative beam loading factor exceeds 2. The value of this parameter in the MI is 1.4 at nominal intensity. It would cross the threshold even with a moderate intensity upgrade. Therefore, fast rf feedback (or feedforward) is also necessary in this respect.

2.6 *RF power*

The ramp rate in the MI is 260 GeV/s. The total rf power is 3.6 MW. Therefore, the maximum number of protons

that can be accelerated at this ramp rate is about 8×10^{13}. This is a hard bottleneck. If one wants to accelerate more protons, then either one needs to purchase more rf power or the ramp rate needs to be reduced.

2.7 Transition crossing

During transition crossing, there could be longitudinal emittance dilution as well as particle losses. Both are observed in the MR. This process is complicated and involves several mechanisms: nonlinear effect, bunch length mismatch due to space charge, scraping due to limited momentum acceptance, microwave and negative mass instabilities, *etc.* This problem will not be as severe in the MI as in the MR, because the MI has higher ramp rate, lower $Z_{\|}/n$, smaller emittance and larger momentum acceptance. However, during intensity upgrade, transition crossing could become a critical point. Therefore, a conceptual design of a γ_t-jump system is being worked out.[2] The plan is to implement it at high intensity operations.

2.8 Dynamic and physical aperture

The sagitta and good field quality of the MI magnets result in large dynamic aperture. The required dynamic aperture is 40π mm-mrad. The tracking shows it is as big as $120\ \pi$. Therefore, there should be no problem in dynamic aperture.

However, there are certain areas in the ring where the physical aperture is noticeably small, in particular, in the MI52 region. It is the injection point of 8 GeV antiprotons and extraction point of 120 and 150 GeV protons. It is conceivable that this area would be a radiation hot spot due to large amount of particle losses. Possible solutions include the use of large aperture quadrupoles, local shielding and careful beam steering.

2.9 Coalescing

The main concern is the microwave instability that could develop during adiabatic debunching, when the bunch length σ_b becomes longer while the energy spread σ_p becomes smaller. According to the Keil-Schnell criterion, the instability threshold goes linearly with σ_b but quadratically with σ_p. Therefore, the threshold would be lower. As a matter of fact, if the minimum full bunch height is 12 MeV during debunching, the impedance threshold would be as low as 1 Ω even at nominal intensity (6×10^{10} per bunch). More study needs to be done on this subject. More rf voltage will certainly help, because it allows larger longitudinal emittance.

2.10 Particle losses and radiation shielding

The DOE regulation gives a upper limit of annual operational losses, which is 1.0×10^{19} at 8 GeV and 0.41×10^{19} at 120 GeV. At the nominal intensity of 3×10^{13} ppp, 10% loss rate would mean 5×10^{15} particle losses per hour. Thus, the annual operation time would be limited to 2000 hours. If the beam intensity goes up by a factor of 5 but the loss rate is still 10%, then the allowed machine operation time will be reduced to 400 hours. Therefore, one must keep the loss under control during the intensity upgrade.

3 CONCLUSIONS

When the beam intensity goes beyond the design value of the beam intensity in the MI, the potential bottlenecks would likely appear in the following order. The possible solutions are given in the parenthesis.

1. RF power. (Needs money to purchase more power.)
2. Transition crossing. (γ_t-jump)
3. Instabilities and coalescing. (Low machine impedance, passive and active dampers)
4. Beam loading and Robinson instability. (Fast rf feedback and feedforward)
5. Space charge. (Stopband correction)
6. Physical aperture limit at MI52 and the associated particle loss and radiation shielding problem. (Large aperture quads, local shielding, careful beam steering)

As a conclusion, it seems to increase the MI beam intensity from 3×10^{13} by a factor of 2 is straightforward, provided that the Booster is capable to deliver twice as many protons to the MI (which may require multi-turn injection from the Booster by use of slip stacking or other techniques). A upgrade by a factor of 5 is also possible, provided all the measures discussed above would be taken. This would bring the intensity to 1.5×10^{14}. Further increase, say, by another factor of 2, would be difficult.

4 ACKNOWLEDGEMENTS

A number of people have contributed to the contents of this paper through discussions with the author. They are: P. Martin, D. Wildman, K-Y. Ng, D. McGinnis, J. Marriner, J. MacLachlan, D. Johnson, C. Bhat, S. Mishra and S. Holmes. The author is indebted to them.

5 REFERENCES

[1] G. Gelato *et al.*, Proc. Particle Accelerator Conference, p. 1298 (1987).

[2] W. Chou *et al.*, 'The Design of a γ_t-Jump System for Fermilab Main Injector,' this conference.

DESIGN OF A γ_t-JUMP SYSTEM FOR FERMILAB MAIN INJECTOR

W. Chou, B.C. Brown, S. Fang, J. Leibfritz, K.-Y. Ng, H. Pfeffer and I. Terechkine
Fermilab,* P.O. Box 500, Batavia, IL 60510, USA

Abstract

In order to control the beam emittance and reduce the particle losses during the transition crossing at high intensity, a conceptual design of a γ_t-jump system for the FNAL Main Injector is presented. It is a first-order system employing local dispersion inserts at existing dispersion free straight sections. The goal is to provide a jump of $\Delta\gamma_t$ from +1 to –1 within 0.5 ms. The system consists of 8 sets of pulsed quadrupole triplets. These quads have pole tips of the hyperbolic shape and thin laminations. The power supply uses a GTO as the fast switch and a resonant circuit with a 1 kHz resonant frequency. The elliptical beamtube is made of Inconel 718, which has high electrical resistivity and high strength. Details of the lattice layout and subsystems design are presented.

1 INTRODUCTION

The Main Injector (MI), which is under construction at Fermilab, is a proton synchrotron with an injection energy of 8 GeV and maximum energy of 150 GeV. The transition energy is about 20 GeV. There is a transition crossing during acceleration, similar to the present Main Ring (MR), which is to be replaced by the MI. During transition crossing, both longitudinal emittance dilution and particle losses are observed in the MR. However, the MI has a number of important improvement in its design, including higher ramp rate, lower machine impedance, smaller beam emittance, larger momentum acceptance and bigger aperture. Furthermore, the design beam intensity of the MI is moderate (3×10^{13} ppp). Therefore, it is believed that there should be no problem when particles cross the transition at nominal beam intensity in the MI. However, from the experience of other machines, *e.g.*, the AGS at BNL, transition crossing could become a severe bottleneck in intensity upgrade. It is thus decided to carry out a conceptual design of a γ_t-jump system for the MI and to make sure there is enough room in the lattice should such a system doom to be implemented.

Two other schemes for dealing with the transition crossing problem have also been considered. One is the imaginary γ_t lattice. It was excluded because of the constraint of the tunnel footprint. Another is the focus free scheme using higher harmonic rf cavities. It is good for tackling nonlinear effects. But its effectiveness is unknown for high intensity beams when the collective effects (bunch length mismatch due to space charge, microwave and negative mass instabilities) are dominant. The γ_t-jump, on the other hand, is a matured technique and has been successfully employed in a number of proton machines such as the PS at CERN and PS at KEK, the AGS at BNL and the Booster at Fermilab. Therefore, it is decided to focus on the γ_t-jump design. Meanwhile, the existence of dispersion free straight sections in the MI lattice provides an opportunity to employ a first order jump system, which has not been possible for the other machines mentioned above due to the lack of such type of regions in their lattice.

* Operated by Universities Research Association Inc. under Contract No. DE-AC02-76CH03000 with the U.S. Department of Energy.

2 DESIGN GOAL

The nominal ramp rate of the MI is about 260 GeV/s. In order to have an effective γ_t-jump, the jump rate should be at least one order of magnitude higher. The two characteristic time scales during the transition, namely, the non-adiabatic time and non-linear time, are about 2 ms in the MI. This implies the jump amplitude, $\Delta\gamma_t$, should be 1.5 or more. Based on these parameters, the following choice is made — The γ_t of the lattice should have a jump from +1 to –1 within 0.5 ms. This gives a jump rate of $\Delta\gamma_t/\Delta t = 4000$ s^{-1}, about 15 times faster than the ramp rate.

3 LATTICE LAYOUT

The design uses a first-order system, making use of the dispersion free straight sections in the MI lattice[1]. The jump is provided by 8 sets of pulsed quadrupole triplets. Each triplet has two quads in the arc and one of twice integrated strength in the straight section, with a phase advance of π between each quad. The main advantage of such a design is the perturbation to the original lattice is localized. In particular, the dispersion increase during the jump is small. Figures 1-3 show the changes of β-function, dispersion function and tune when $\Delta\gamma_t$ varies between –1 and +1.

4 SUBSYSTEMS DESIGN

4.1 The pulsed quadrupoles

Each quad in the arc has an integrated field of 0.85 T-m/m and a length of 20 inches. Each one in the straight section has double strength (1.7 T-m/m) and double length (40 inches). Thus, a triplet actually consists of four identical quads. In two straight sections (MI30 and MI60), the β-function and phase are mismatched. Therefore, the strength and length of the quads in these two sections need some adjustment.

The pulsed quad has pole tips of the hyperbolic shape. There are two reasons to choose this pole tip: (*a*) It has higher inductance than that with circular coils. This means it uses lower driving current, which is advantageous to the power supply design. (*b*) The MI beam pipe is of elliptic shape, which fits better in hyperbolic pole tips than in circular coils.

0-7803-4376-X/98/$10.00 © 1998 IEEE

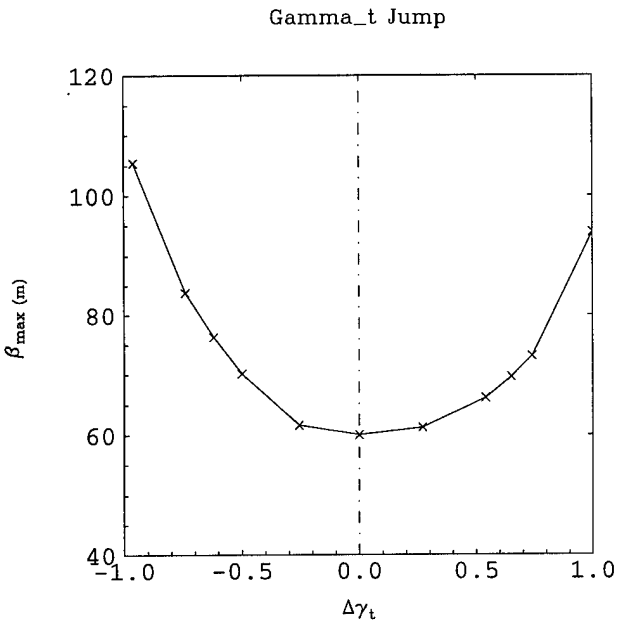


Figure 1: Maximum β-function *vs.* $\Delta\gamma_t$.

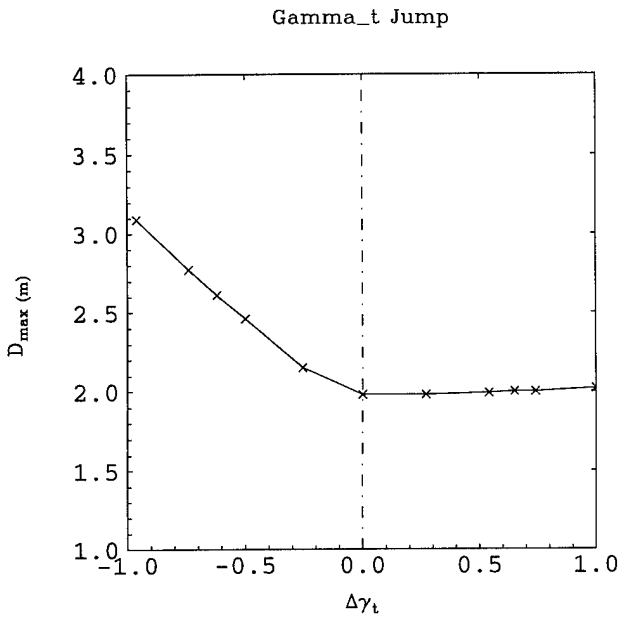


Figure 2: Maximum dispersion function *vs.* $\Delta\gamma_t$.

The laminations use thin (0.025") silicon steel in order to minimize the eddy current losses.

4.2 The power supply

4.2.1 The system

The system consists of 8 power supplies. Each power supply drives a four-magnet quadrupole (*i.e.*, a triplet) string. The turn numbers per pole in the magnet design is chosen such that the magnet current is minimized yet the magnet voltage is limited to below 1.5 kV. This limit is compatible with both magnet insulation values and power supply component ratings. Each magnet has an inductance of 288 μH and a peak current of about 200 A. Its resistance is less than

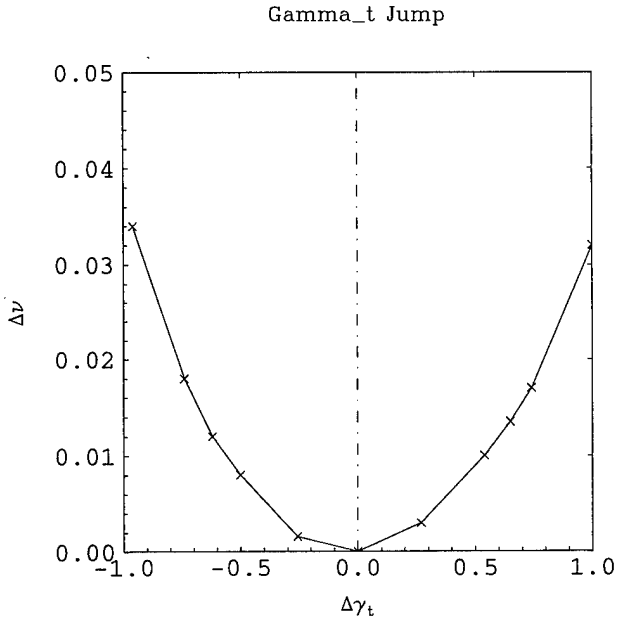


Figure 3: Tune change *vs.* $\Delta\gamma_t$.

20 mΩ. The power supply design is shown in Figure 4.

4.2.2 Circuit operation

The pulse begins when the GTO (gate turn-off thyristor) is turned ON. This applies 125 volts on the load, and charges the load current to 195 A within 3 ms. At this time the GTO is turned OFF, and the magnet load rings with the capacitor (27.5 μF) as a resonant circuit with a 1 kHz resonant frequency. The circuit rings through one half cycle, at which point the magnet current has reversed and the capacitor voltage has come back to zero. The ringing is terminated by the SCR switch in the end-of-pulse clipper, which is turned ON to prevent the capacitor from charging positively. The magnet current subsequently decays with a 3 ms time constant.

4.2.3 Eddy current losses

The ringing described above indicates what would happen in a high Q system with small losses. However, the ac losses at 1 kHz are substantial in both the magnet and the beam pipe. From measurements on various magnets at the laboratory,[2] and from calculations of expected eddy current and core losses, one expects the losses to be equivalent to those in a 4 Ω resistor placed in parallel with each magnet. The 16 Ω resistor in Fig. 4 represents the total magnet loss elements. With this resistance, the Q of the circuit is less than 0.5, and the magnet will not ring close to its peak current.

4.2.4 The current pump

In order to ring to the full negative current of 195 A, a section called the current pump is added. It consists of a 1.6 mH choke and a diode. During the time the GTO is turned ON, the choke charges up to 200 A parallel with the magnet

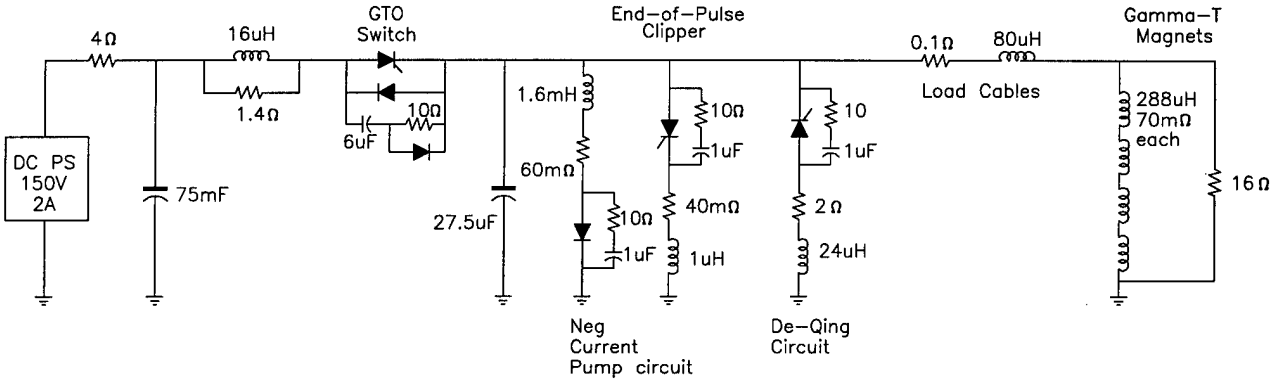


Figure 4: The power supply circuit design.

load. When the GTO is turned OFF, the current stored in the choke draws charge out of the capacitor and allows it to generate as large enough pulse to reverse the magnet current fully. The advantage of introducing a current pump is to enable us to fully reverse the load current without switching in a negatively charged capacitor. The disadvantage is the GTO must conduct twice the current as it would in the lossless case. Moreover, the choke is a substantial component; it stores more energy than the entire magnet load.

4.2.5 De-Qing

The magnitude of $\Delta\gamma_t$ on the negative side can be controlled by the de-Qing circuit, which is triggered if it is desired to terminate the pulse early and create an asymmetric current waveform. This feature is useful for the bunch length match before and after the jump.

4.3 The beam pipe

The beam pipe in the γ_t-jump section is elliptical, matching the regular MI beam pipe size, and is made of Inconel 718. Inconel has higher yield strength than the stainless steel. The wall thickness t is 0.025", thinner than the MI stainless steel pipe which is 0.060". It also has low electrical conductivity σ. The product σt of Inconel 718 pipe is four times smaller than that of the stainless steel pipe. This means the eddy current losses and magnetic field distortion will be smaller by the same ratio. This is the main reason for choosing this material. Compared with ceramic pipes, the manufacturing of Inconel pipes is easier, and the transition from Inconel to stainless steel is simpler. Several prototype pipes have been made. Vacuum tests show they are mechanically stable and vacuum tight. The stress and deflection analysis using theoretical model and 3-D ANSYS simulations is in agreement with the measurement. For more details the reader is referred to Ref. [3].

5 SPACE INVENTORY IN THE LATTICE

The present MI lattice is already crowded. In order to find space to install the eight triplets, the following measures would have to be taken:

1. To remove four (out of a total of 54) horizontal sextupoles.
2. To remove four (out of a total of 62) octupoles and the adjacent ion pumps.
3. To move the antiproton extraction kickers and proton abort kickers downstream by one meter, respectively.
4. To adjust the position of some diagnostics (Schottky, multiwire and low level rf pickup).
5. To shorten the BPM ends by 1" and bellows by 2" at four locations. (At these locations, the maximum available space is only about 16", which means the magnet current would have to be increased by 20% in order to reach the same integrated field strength as a 20" magnet.)

6 CONCLUSIONS

This paper presents a feasible design of a γ_t-jump system for the Main Injector. It is by no means optimized. The purpose is to demonstrate there is a solution if such a system needs to be installed, even though it may not be the best one. At this moment, the magnet design is being revised, in particular, the end part, which could have appreciable contribution to the ac losses due to the longitudinal field component[4]. A complete conceptual design report, including the cost estimate, is being prepared.

7 ACKNOWLEDGEMENTS

The authors wish to thank P. Martin, L. Sauer, S. Holmes and C. Bhat for useful discussions during this study.

8 REFERENCES

[1] V. Visnjic, Phys. Rev. Lett., v. 73, p. 2860 (1994).

[2] S. Fang and W. Chou, 'Analysis and Measurements of Eddy Current Effects of a Beam Pipe in a Pulsed Magnet,' this conference.

[3] J. Leibfritz, 'FNAL Main Injector γ_t-Jump Beam Pipe Design,' this conference.

[4] F. Mills, private communication.

DESIGN AND SIMULATION OF THE ANTIPROTON RECYCLER LATTICE

D.E. Johnson, C.S. Mishra, S.D. Holmes, N. Gelfand, J.A. Holt, L. Michelotti
Fermi National Accelerator Laboratory *

Abstract

The Recycler is a new antiproton storage ring designed to improve antiproton production and allow recovery of antiprotons at the end of stores in the Fermilab Tevatron. The ring will be situated in the Main Injector enclosure, with a circumference of 3319 meters, and will operate at 8 GeV. The design of the Recycler utilizes permanent magnets. Lattice design considerations and performance modeling will be described.

1 LATTICE DESCRIPTION

The Recycler ring [1] is composed of fifty four arc FODO cells (17.288 meter cell length) with eight zero dispersion straight sections distributed around the ring following the symmetry of the new Fermilab Main Injector(MI). [2] There are three lengths of straight sections; four 3 half-cell, two 4 half-cell, one 8 half-cell, and one high beta, for future addition of electron cooling. Each straight section is bounded on either side by a dispersion suppressor insert made up of four 12.966 meter half-cells. The phase advance of the arc and straight section cells is μ_x=85.4 and μ_y=79.2 degrees giving rise to a base tune of Q_x=24.425 and Q_y=24.415. Each focusing/defocusing location contains either two gradient magnets (F or D) or two quadrupoles. The lattice functions for the complete ring are shown in Figure 1.

The Recycler ring will be installed at an elevation of 56 inches above the centerline of the MI. The geometry of the Recycler closely resembles that of the new MI with the exception that the cell lengths of the dispersion suppressor cells on either side of the RR60 straight section were increased by two meters in order to move the closed orbit about .5 meter to the outside thus bypassing the Main Injector RF cavity power amplifiers. In order to keep the path length between the machines matched the cell lengths of this straight section were shortened. This straight section (RR60) additionally contains a phase trombone [3] that will be used for tune adjustments of up to $\pm$0.5 units.

The Recycler ring is composed of two types of permanent magnet combined function magnets, 216 long "arc" magnets which have dipole, quadrupole, and sextupole components, and 128 short "dispersion suppressor" magnets which only have dipole and quadrupole components, and 74 permanent magnet quadrupoles. The Recycler ring is designed to match the momentum of the new permanent magnet 8 Gev injection line.

* Operated by the Universities Research Association under contract with the U. S. Department of Energy

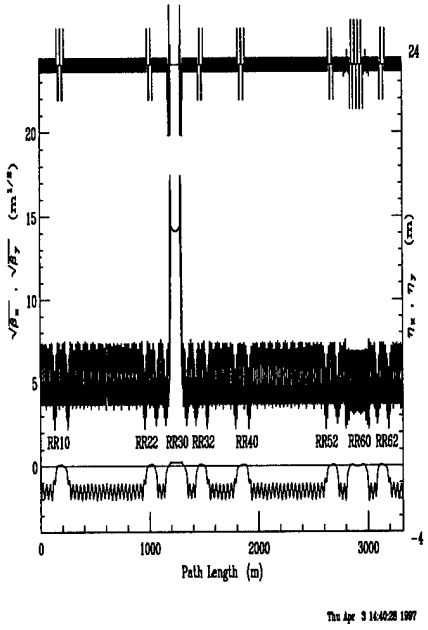


Figure 1: Lattice Functions of the full ring.

2 PERFORMANCE PROJECTIONS

The Recycler ring is unique in that it is the first storage ring to be built using permanent magnet technology for all bending and focussing elements. The exclusive use of permanent magnets dramatically reduces the cost of the magnets by avoiding the expense of coil winding and removes the necessity of power supplies and magnet cooling systems. It does however, require careful attention to the lattice and magnet design. Lattice issues related to the base operating tune, tune adjustment, closed orbit distortions[4, 5], optical function distortions [6], momentum aperture, and resonance widths[7], as well as magnet issues related to strength variations, transverse field uniformity, longitudinal field uniformity, and temperature stability[8] have been addressed through semi-analytical analysis and tracking studies to validate the base design [1]and to specify the exact properties of the magnets. We present here the results of the tracking studies used in determining the required magnet field specifications.

2.1 Tracking Calculations

Tracking studies were performed using the thin element tracking code TEAPOT [9] Although beam is expected to be stored for hours, with cooling times of tens of minutes, tracking studies were done for 10^5 and 10^6 turns representing 1 to 10 seconds beam time. We require the survivability

0-7803-4376-X/98/$10.00 © 1998 IEEE

of particles with oscillation amplitudes corresponding to at least 70π mm-mr (normalized) over the full $\pm 0.3\%$ momentum aperture of the Recycler. This oscillation amplitude corresponds to the vertical physical aperture and provides a 75% margin relative to the specified 40π mm-mr dynamic aperture.

Performance in the presence of a mixture of alignment and magnetic field errors is tested by launching an array of particles at different amplitudes. Particles are tracked with betatron oscillation amplitudes relative to a corrected orbit. Following the introduction of the errors the tune is adjusted to the nominal tune for zero momentum offset using the phase trombone. The particles are launched with equal horizontal and vertical emittance, which corresponds to a horizontal displacement 'A' and a vertical displacement $\sqrt{\beta_y/\beta_x}$A. Particles are tracked with a constant momentum offset. Net chromaticities in both planes are set to -2. Simulations are performed for five different seeds with a maximum of 100,000 turns tracked.

A survival plot of the five seeds displaying how many turns a particle survived as a function of the initial launch amplitude is shown in Figure 2. The dynamic aperture of the machine is defined as the smallest amplitude particle that *did not* survive the full 100,000 turns. From figure 2 we see that the dynamic aperture of the Recycler is predicted to be 21.7 ± 1.5 mm corresponding to a normalized emittance of $68.4 \pm 9.7\ \pi$ mm-mr.

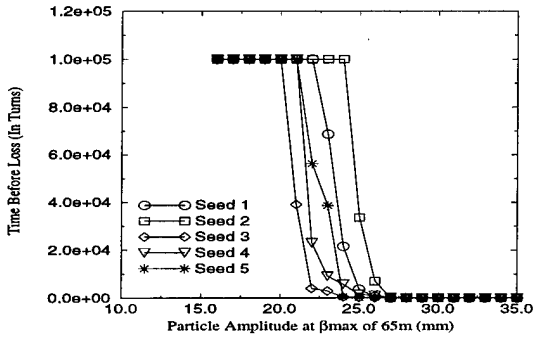


Figure 2: Dynamic Aperture of the Recycler. The number of turns survived is shown as a function of launch amplitude for five different collections of systematic and random alignment and magnetic field errors and a momentum offset of 0.3%.

The dynamic aperture as a function of momentum offset for the the largest amplitude particles that survived 100,000 turns is shown in Figure 3. This plot indicates an aperture in excess of 50 π mm-mr is maintained over the full momentum spread expected in the antiproton stack.

The detuning effect of the higher order multipoles is seen by looking at the change in fractional tune as a function of particle oscillation amplitude. Figure 4 shows amplitude dependent tune shift in the presence of only the sextupole in the long combined function magnets and in the presence

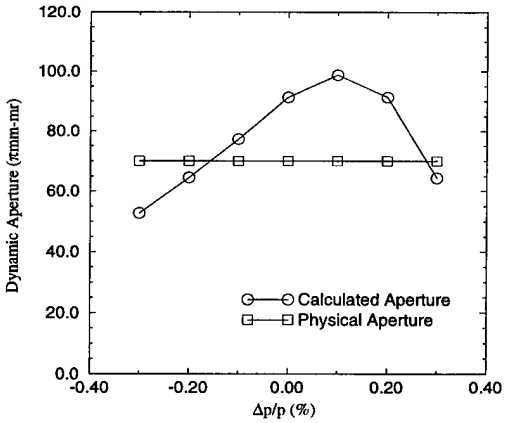


Figure 3: Dynamic Aperture as a function of momentum offset over the full range of the antiproton stack.

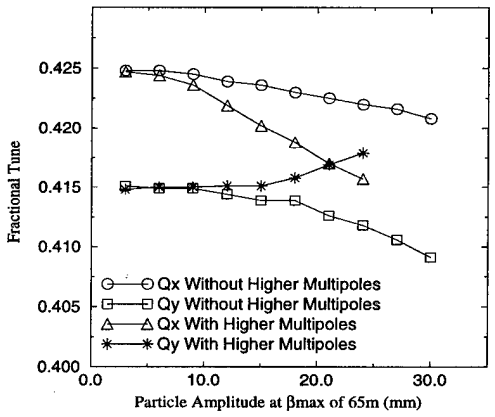


Figure 4: Fractional Tune as a function of particle amplitude for a lattice with and without higher multipoles.

of all multipole errors listed in Table 2.

2.2 *Correction Schemes*

Since the Recycler will not have active orbit correctors other than those required around the injection and extraction areas, the correction strategy will be based upon measuring the orbit and adjusting the transverse positions of the 15 most effective gradient magnets. Random alignment errors with a sigma of 0.25 mm in each plane and a roll with a sigma of 0.50 mr were assigned to all gradient magnets, quadrupoles, and beam position monitors. In addition, a field error,σ_{BL}/BL, of 5E-4 for all gradient magnets was included. With these errors the uncorrected orbit is expected to show peaks of up to 15 mm. A model in which 15 gradient magnets were chosen to be moved was analyzed and shown to produce a corrected orbit with a rms of less than 1 mm and peak distortion under 3 mm. Th maximum transverse motion of any gradient magnet was on the

order of 2 mm, well within the tolerable mechanical motion allowed.

Global tune adjustment is accomplished by adjusting the local phase advance through the phase trombone located at RR60. The phase trombone utilizes five families, each with two adjustable quadrupoles, to adjust the local phase over a range of ± 0.5 with no perturbation to the optical functions outside the trombone region.

The natural chromaticity of the ring is compensated to -2 in both planes by the addition of a sextupole component in the long "arc" gradient magnets. Additional control of the chromaticity, with ± 5 units of adjustment, will be provided by two families of sextupoles.

Compensation of coupling due to systematic and random skew quadrupole errors and alignment errors (roll) will be controlled via two skew quadrupole circuits. Although, the location of the circuits provides acceptable global decoupling, all tracking simulations performed to date have have utilized a coupled lattice.

2.3 Magnetic Field Quality Specifications

The specification on the tolerances for the strength of the dipole, quadrupole, and sextupole components of the combined function magnets are derived from studies related to: the sensitivity of the lattice to systematic and random strength variations of both the long and short gradient magnets and their effect on the closed orbit,[4] the sensitivity of the lattice on the systematic and random strength variations of the gradient in the gradient magnets and their effect on the optical function distortion, [6]and the required sextupole strength for the compensation of the natural chromaticity. These strength tolerances are summarized in Table 1.

Table 1: Magnet strength tolerances for Recycler combined function (CF) magnets.

Performance Measure	Tolerance (Sys.)	Tolerance (Random)
Abs. bending strength of long CF magnet	5E-4	5E-4
Ratio of short/long bend strength in CF magnets	5E-4	5E-4
Ratio of quad. to nominal dipole in CF magnets	2E-4/in.	1E-4/in.
Ratio of sext. to nominal dipole in CF magnets	1E-4/in.^{2}	1E-4/in.^{2}
Field flatness over ± 25 mm	$\pm$1.5E-4	$\pm$1.5E-4

Based upon the tracking studies and dynamic aperture analysis, the magnet field quality specifications are given for both the systematic and random strength variations in the dipole, quadrupole, and sextupole components and well as the harmonic content and field uniformity of the combined function magnets and quadrupoles. These are summarized in Table 2.

Table 2: Modeled Multipole Components in the Combined Function Magnets, in Fermilab units.

Multipole Component	Normal (Sys.)	Normal (Ran.)	Skew (Sys.)	Skew (Ran.)
Quadrupole	1	1	.5	1
Sextupole	0.5	1	–	0.5
Octupole	0.5	0.5	–	0.5
10-pole	0.2	0.5	–	0.5
12 to 18-pole	0.1	0.5	–	0.5

3 SUMMARY

The design of the Recycler ring has been established. Semi-analytical and tracking studies were used to specify the required field uniformity necessary for beam storage. Four prototype gradient magnets with dipole, quadrupole, and sextupole have been built and measured which meet the specifications for field strength and field uniformity.[10] The detailed design and specification of harmonic correction systems, and specialty magnets to be used for injection/extraction systems continues.

4 REFERENCES

[1] "The Fermilab Recycler Ring Technical Design Report", Fermilab TM-1991, November 1996.

[2] The Fermilab Main Injector Technical Design Handbook, August 1994.

[3] Al Garren and Dave Robin, "A Phase Trombone for the Recycler", internal MI note MI-0181, July, 1995.

[4] S.D. Holmes and C.S. Mishra, "Recycler Closed Orbit Distortion from a Systematic Mismatch Between Long and Short Combined Function Magnet Strengths", internal MI note MI-0157, February, 1996.

[5] S.D. Holmes,"Recycler Closed Orbit Distortion Expected from Random Magnetic Element Strength and Alignment Errors", internal MI note MI-0158, March, 1996.

[6] S.D. Holmes and C.S. Mishra, "Recycler Beta Function Distortions from Systematic and Random Gradient Errors in Combined Function And Quadrupole Magnets", internal MI note MI-0160, April, 1996.

[7] S.D. Holmes, "Evaluation of Resonance Widths from Recycler Magnetic Field Multipoles, internal MI note MI-0165, April, 1996.

[8] J.-F. Ostiguy, "Permanent Magnet Stability:Addendum", internal MI note MI-0177, July, 1996.

[9] l. Schachinger and R. Talman, Particle Accelerators 22, 1987.

[10] W. G. Foster, "The Fermilab Permanent Magnet Antiproton Recycler Ring", session 3C.01, these proceedings.

An IMAGINARY-γ_t LATTICE WITH DISPERSION-FREE STRAIGHTS FOR THE 50 GeV HIGH-INTENSITY PROTON SYNCHROTRON

K.Y. Ng
Fermi National Accelerator Laboratory,* P.O. Box 500, Batavia, IL 60510

Abstract

The 50 GeV proton synchrotron, proposed by the Institute of Nuclear Study of Japan (INS), requires zero-dispersion straight sections for polarized-beam operation. A new preliminary lattice that contains two straight sections with nonzero dispersion and two with zero dispersion is presented. The γ_t of the whole ring remains imaginary. Some analysis of the lattice is discussed.

1 INTRODUCTION

In order to reduce beam loss, the 50-GeV proton synchrotron of the Japan Hadron Project (JHP), designed by the INS, will operate with an imaginary-γ_t [1]. The lattice is 4-fold symmetric. Each quadrant consists of 6 flexible momentum-compaction (FMC) modules [2] and a long straight section of about 60 m in length. Each FMC module is 3 FODO-cell long. The dispersion in the long straight sections vary between -0.71 and 0.58 m. Although the dispersion is small, it is always more appealing to have zero-dispersion straights. This is especially true when the synchrotron is accelerating a polarized beam. To obtain zero dispersion in one straight section and in another straight section on the other side of the ring, a special excitation of the quadrupoles needs to be turned on so as to allow a dispersion wave and a betatron wave to flow through half of the ring. Aside from the inconvenience of having a special power supply, this excitation also brings about unwanted high betatron functions and high dispersion functions, which will eventually limit the performance of the accelerator at high intensities. In this paper, we suggest the introduction of dispersion suppressors. A preliminary lattice that contains two straight sections with nonzero dispersion and two with zero dispersion is presented. The details are given in Ref. 3.

2 DISPERSION SUPPRESSOR

The standard FMC module of the JHP ring is shown in Fig. 1 with its lattice elements, betatron functions and dispersion. To study its dispersion property, the module is plotted in the normalized dispersion space in Fig. 2(a), with $\sqrt{\beta_x}D' + \alpha_x D/\sqrt{\beta_x}$ versus $D/\sqrt{\beta_x}$ [2]. Here, D and D' are, respectively, the dispersion function and its derivative with respect to the longitudinal coordinate s, β_x and $\beta'_x = -2\alpha_x$ are, respectively, the horizontal betatron amplitude function and its derivative.

A thin dipole of bending angle θ will be represented by a horizontal advance of $\sqrt{\beta_x}\theta$. Outside the dipoles, the plot

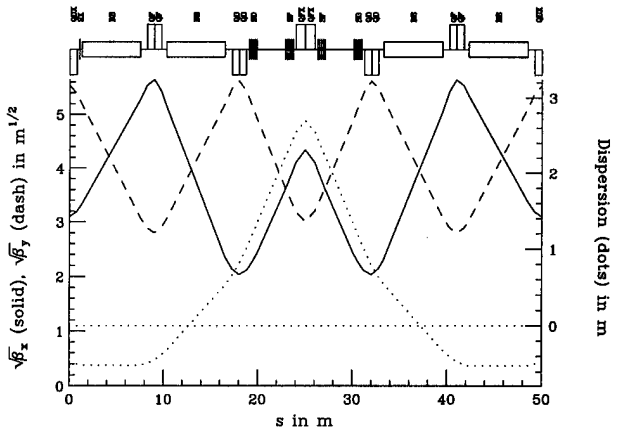


Figure 1: The standard FMC module of the JHP ring.

becomes an arc of a circle centered at the origin with phase advance equal to the horizontal Floque phase advance. We see that the module starts off from the quadrupole QDX with zero β'_x and D', but with dispersion -0.5213 m. The first two dipoles BB are represented by two long straight lines pointing mostly to the right. Note that these line are not exactly horizontal, because the dipole is far from a thin element and there is a phase advance across it. If we chop up the dipoles into smaller elements, this straight line will be curved. However, it will still be quite different from the arc of a circle with center at the origin of the plot. The deviation just represents the angle-bending nature of the dipole. After the dipoles, follows an arc of a circle centered at the origin leading to the center quadrupoles QFX, which have the largest $D/\sqrt{\beta_x}$. The other half of the module is just the mirror image of the first half, coming back to the starting point.

In order to be a dispersion suppressor, we must alter the lattice so that the end of the module stops precisely at the origin of the dispersion space. To accomplish this, we must first make the radius of the arc smaller in the upper half of the dispersion plane, and second we must use an exact amount of dipole to bring the module to $D = 0$ and $D' = 0$ at the point when this arc reaches roughly 180°. The suppressor constructed in this way is shown in Fig. 3 and its dispersion plot in Fig. 2(b). The construction starts from pulling out the second dipole, so that the module continues with a smaller arc until the quadrupole QFFX. To facilitate lattice matching, although unnecessary, we treat this temporarily as a point of symmetry, that is with $\beta'_x = \beta'_y = D' = 0$. After that we continue as in the case of the standard FMC module with the exception that the last dipole, called B4, is shortened so that the module lands exactly at $D = 0$, $D' = 0$. In order not to deal with a fractional dipole, the amount B4 has been shortened,

* Operated by the Universities Research Association under contracts with the U.S. Department of Energy.

0-7803-4376-X/98 /$10.00 © 1998 IEEE

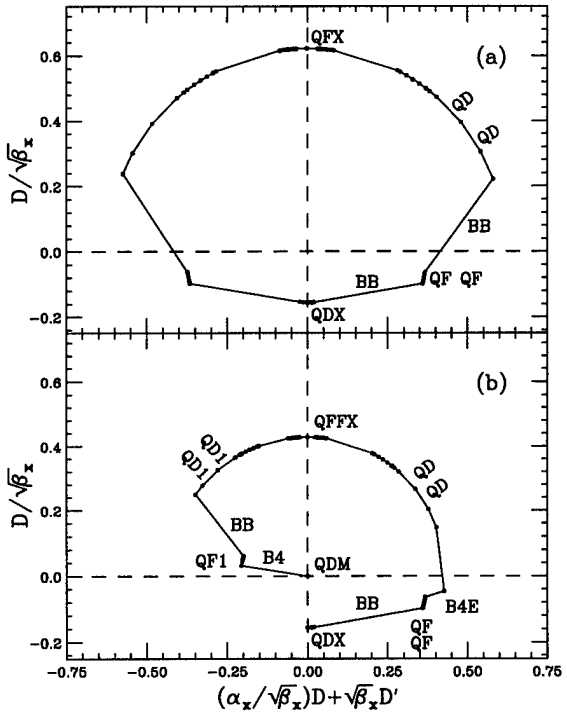


Figure 2: The standard FMC module and dispersion suppressor in the normalized dispersion plane.

called B4E, is placed in the space where the second dipole has been pulled out. In other words, one normal dipole has been pulled out, and another normal dipole has been chopped up into two parts B4 and B4E, 83% and 17% of the normal dipole. The chopping up of a normal dipole for the dispersion suppressor seems to be inevitable. This is very similar to the situation of the dispersion suppressor in a FODO-cell lattice, where one can avoid chopping up dipole only when the phase advance of each cell is exactly $\pi/3$.

As shown in Fig. 3, the dispersion suppressor is not very much different from the standard FMC module. It has a length of 48.7269 m, maximum/minimum dispersion of $1.8632/-0.5148$ m, maximum/minimum horizontal betatron function 31.84/4.22 m and maximum/minimum vertical betatron function 32.32/7.17 m. The vertical and horizontal tune advances are 0.721/0.545, which are very close to the 0.740/0.531 for the standard FMC module. Best of all, this suppressor has also an imaginary transition gamma of $\gamma_t = 69.05i$, so that the whole ring can still retain its imaginary-γ_t property.

3 LONG STRAIGHT SECTIONS

There will be two long straight sections that are dispersion-free and two that are not. The straight with dispersion, which joins two standard FMC modules together, consists of 4 FODO cells with a total length of 61.2524 m. The zero-dispersion straight is inserted between two dispersion-suppressors. It also contains 4 FODO cells with a total length of 62.2938 m.

Now the whole ring can be assembled. We start from

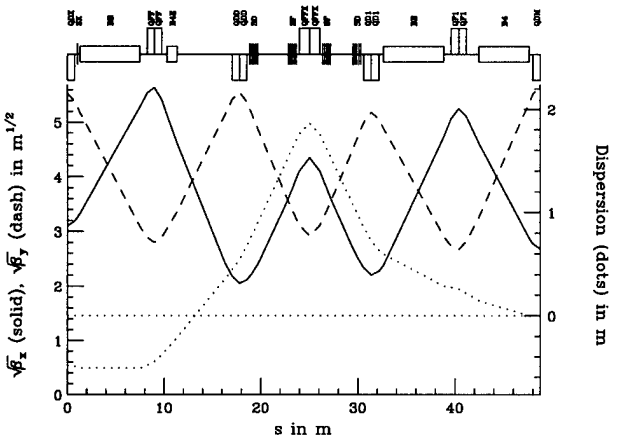


Figure 3: The lattice structure of the dispersion suppressor.

the center of the non-dispersion-free straight section, then 5 standard FMC modules, the dispersion suppressor, and then the dispersion-free long straight section. We make a mirror reflection about the center of the dispersion-free straight to arrive back at the center of the other non-dispersion-free straight. This complete one half of the ring. The whole ring has now only 92 dipoles each of length 6.2 m. Since the beam particles are to be accelerated to the maximum total energy of 50 GeV, the maximum bending field of the dipole becomes 1.837 T, which is high but is still possible. There is enough space to increase the length of the dipoles from 6.2 m to 6.3 m, thus reducing the bending field to 1.808 T.

4 SEXTUPOLE CORRECTION

In general, quadrupoles of the FMC modules are stronger than those in the usual FODO lattice. As a result, larger natural chromaticities will be generated and sextupoles of larger strengths will be required for their corrections. The corrections are mainly made by the two families of sextupoles SF and SD as shown in Figs. 1 and 3. There each SF or SD is represented by 5 thin sextupoles in the lattice code. Just after the entrance defocusing quadrupole of each FMC module, there is a third family SX, which is used for fine adjustment. For example, the chromaticity corrections have been made by setting the strength of each SX to be 0.105 m^{-2} and each of the thin SF and SD 0.0572 m^{-2} and -0.0933 m^{-2}, respectively. The amplitude-dependent betatron tunes are $\nu_x = 21.0954 + 130\epsilon_x - 116\epsilon_y$ and $\nu_y = 15.4433 - 116\epsilon_x + 134\epsilon_y$, where the emittances ϵ_x and ϵ_y are measured in πm. We see that with $\epsilon_x = \epsilon_y = 50\times10^{-6}$ πm, the largest tune spread is only 0.0067, which is quite acceptable for a non-storage ring.

Another measure of nonlinearity introduced by the correction sextupoles is the single-particle smears, which are defined as the fractional rms distortion of the Poincaré torus at any phase advances in the horizontal and vertical phase spaces. The smears can be expressed analytically in terms of the distortion functions [4]. We see from Fig. 4 that the rms vertical smear reaches only about 0.1%, which is very small, and the horizontal smear is still smaller. The full smears will be roughly $\sqrt{2}$ times the rms values, which are

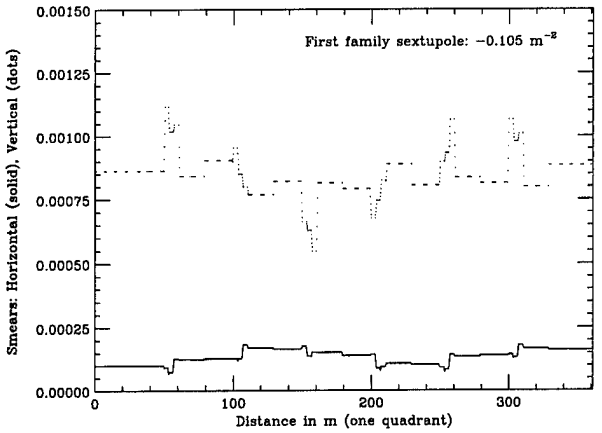


Figure 4: The horizontal and vertical single-particle smears for one quarter of the accelerator ring.

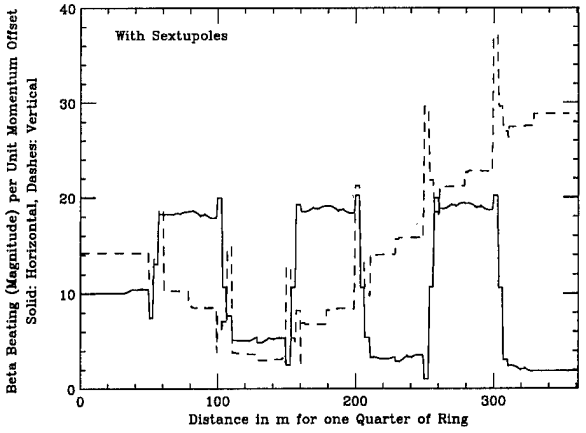


Figure 5: The magnitudes of the horizontal and vertical beating vectors for one quarter of the accelerator ring.

much less than the 7% nonlinear criterion of the former Superconducting Super Collider. We also see that the smears are step-like, constant over a region and exhibit a jump only when a sextupole is encountered.

5 BETATRON BEATINGS

In this FMC-type lattice, it is impossible to place a sextupole beside every quadrupole to correct for local chromaticities. As a result, particles with a momentum offset will see a different set of betatron functions. The fractional change in the betatron function per unit momentum deviation $\Delta\beta/\beta|_\psi$, horizontal or vertical, at phase advance ψ, is called "beat factor" [5]. Each beat factor can be made complex by introducing the imaginary part $-\frac{d}{d\psi}\frac{\Delta\beta}{2\beta}|_\psi$. As a vector, the complex number just rotates at a tune of 2ν, except when crossing a field gradient k of infinitesimal length ℓ where the real part jumps by $\frac{1}{2}\beta k\ell$. Note that the field gradient can come from quadrupoles, sextupoles, the centripetal force of the dipoles as well as the edges of the dipoles. The magnitudes of the beat vectors are plotted in Fig. 5, the largest being around 30. Considering that the momentum spread of the beam is only 0.5% at injection, the relative change in betatron function is at the most 15% which is not excessive at all.

The harmonic analysis of the beat factors is also important, because it gives us some clues to reduce the beat factors. Choosing the mid-point of a non-dispersion-free straight as the point having zero phase advances, the lattice is almost left-right symmetric (aside from the sextupoles SX). The Courant-Synder J_p's then become almost real:

$$J_p = \int_{-\pi\nu}^{\pi\nu} k(\psi')\beta^2(\psi')\cos\frac{p\psi'}{\nu}d\psi' \ .$$

Each beat factor can be expanded as

$$\left.\frac{\Delta\beta}{\beta}\right|_\psi = -\frac{J_0}{\pi\nu} - \frac{2\nu}{\pi}\sum_{p>0}\frac{J_p\cos\frac{p\psi'}{\nu}}{4\nu^2-p^2} \ .$$

We find that the sextupoles do produce beat waves in the harmonic space. This is because they have not been placed at the proper phase advances for confinement or cancellation. The tunes of the lattice are $\nu_x = 21.0954$ and $\nu_y = 15.4433$, so that the important Fourier components are $p = 42$ for the horizontal and $p = 31$ for the vertical. Because of the two-fold symmetry of the lattice, $p = 31$ does not occur. As for $p = 42$, the horizontal beat factor is not large because $2\nu_x$ is still far from 42. However, we do see the beat waves exhibit large magnitudes at $p = 28$. This comes about because each of the two straight sections has a vertical tune advance of ~ 0.60 which is not too far from the vertical phase advance of 0.53 for each FMC module. On the other hand, their horizontal tune advances are 1.00 and 0.70, respectively, for the straights with dispersion and the one without. They average out to roughly the horizontal tune advance of a FMC module. Thus, the contributions of the sextupoles add up. As a result, there appears to be roughly a 7-fold symmetry in a superperiod. Hopefully, $p = 28$ is quite far away from a multiple of the tunes and the contribution of this harmonic has not been too large. To reduce this contribution, the vertical phase advance of the straight section must be increased.

6 SUM RESONANCES

Sum and difference resonances should also be studied. We note that $2\nu_y + \nu_x = 51.982$ is too close to the third integer sum resonance. This happens because this preliminary lattice is just a simple modification of the original INS lattice [1], which also sits at this third integer sum resonance. However, we believe that this resonance can be avoided by a more careful design of the lattice.

7 REFERENCES

[1] This analysis is based on a recent lattice design released by the INS.

[2] S.Y. Lee, K.Y. Ng, and D. Trbojevic, Phys. Rev. **E48**, 3040 (1993).

[3] K.Y. Ng, *An Imaginary-γ_t Lattice with Dispersion-Free Straights for the 50 GeV High-Intensity Proton, Synchrotron*, Fermilab Internal Report TM-1997, 1997.

[4] N. Merminga and K. Ng, *Analytic Expressions for the Smear due to Non-linear Multipoles*, Fermilab Report FN-505, 1989.

[5] E.D. Courant and H.S. Snyder, Ann. Physics **3**, 1 (1958).

MULTIPLE INJECTIONS WITH BARRIER BUCKETS

K.Y. Ng
Fermi National Accelerator Laboratory,* P.O. Box 500, Batavia, IL 60510

Abstract
Multiple injections into the 50 GeV proton synchrotron, proposed by the Institute of Nuclear Study of Japan, from a 3 GeV booster using barrier buckets are simulated. For four successive injections of 4 bunches each time, having a half momentum spread of 0.5%, the final coasting beam in the synchrotron has a momentum spread of roughly $\pm 1.0\%$ in the core, with a tail extending up to $\pm 2.5\%$. The choice of debunching time, barrier velocity, barrier voltage, and barrier width is analyzed. Some beam kinematics relating to the barrier buckets are discussed.

1 INTRODUCTION

The Main Ring of the Japan Hadron Project (JHP) is a high-intensity fast-cycling synchrotron. The 16 bunches with a total of 2×10^{14} protons are injected from the booster in 4 batches cycling at the rate of 25 Hz. In order to minimize the high space charge, it has been suggested the use of rf barrier waves during the injection [1]. Such a simulation is described below. The detail and some beam kinematics relating to the barrier buckets are given in Ref. 2.

2 CHOICE OF DEBUNCHING TIME

The ring has an imaginary transition gamma of $\gamma_t = 27i$ giving a slip factor at injection $\eta = -0.05813$. For a bunch to debunch until the part with maximum momentum spread $\delta = +0.005$ meets the part with $\delta = -0.005$ longitudinally, $t_{\rm debunch} = T_0/(2|\eta\delta|) = 8.28$ ms is required, where $T_0 = 4.9526$ μs is the revolution time with the ring circumference taken as $C_0 = 1442$ m. We will use $t_{\rm debunch} = 10$ ms in the simulation.

3 CHOICE OF SQUEEZING TIME

In this simulation, we inject into the ring, as shown in Fig. 1, 4 bunches, each containing 1000 macro-particles distributed randomly in its elliptical envelope with maximum momentum spread $\delta = \pm 0.005$ and width $\Delta\tau = \frac{1}{17\times 8}T_0$; i.e, the full width is a quarter of the rf wavelength at revolution harmonic $h = 17$. After debunching for 10 ms, two square rf barrier waves are introduced at $\tau = 0$ on the phase axis. One barrier is fixed while the other moves slowly at the rate of $\dot{T}_2 = -3.884 \times 10^{-5}$ to the right until a space corresponding to four $h = 17$ rf wavelengths or 1.165 μs is opened. The time taken will be 30 ms, so that 40 ms has just elapsed and the next injection of 4 more bunches from the booster is just in time, as is illustrated in Fig. 2. The procedure then repeats. After debunching for another 10 ms and introducing rf barrier waves with squeezing for 30 ms, the third injection is ready as shown in Fig. 3. Another 10 ms of debunching and 30 ms of squeezing by barrier waves lead to the fourth injection in Fig. 4. Finally, we allow for another 10 ms of debunching before recapturing by the $h = 17$ rf system for acceleration. In the above, T_2 is the width of the rectangular part of the bucket. Since the moving barrier pulse squeezes the bucket, $\dot{T}_2 < 0$. In order that the longitudinal emittance of the bunch inside the barrier bucket is conserved, we must have [3] $|\dot{T}_2| \ll \frac{1}{2}|\eta\delta| = 1.45 \times 10^{-4}$. Therefore, the rate of barrier movement chosen in the simulation should be slow enough.

4 CHOICE OF BARRIER VOLTAGE AND WIDTH

The amount of momentum spread δ_b the pair of square barrier pulses can trap is given by [3]

$$\delta_b = \sqrt{\left(\frac{2}{\beta^2|\eta|}\right)\left(\frac{eV_0T_1}{E_0T_0}\right)}\,, \qquad (1)$$

where E_0 is the total energy of the particle and β is velocity relative to the velocity of light. Note that the barrier voltage V_0 and barrier width T_1 in Eq. (1) become $V_0T_1 \to \int_{\rm barrier} V(\tau)d\tau$, when the barrier wave is of arbitrary shape than square. To confine $\delta_b = 0.018$ say, we need $V_0T_1 = 173.26$ kV-μs . It is not good to use too small a barrier voltage, because this will make the width of the barrier too wide. Remember that the stable bucket consists of a rectangular part where particles do not see the barrier pulses and two curved parts where the particles are exposed to the barrier voltage. A large barrier width increases the curved parts of the bucket and more particles will be left outside the bucket when the barrier waves are switched on. Too narrow a barrier width is also not desired. This will boost the barrier voltage to too high a value, making it more difficult to generate. Also, whenever a particle drifts towards the barrier, it will gain or lose energy by an amount equal to V_0 per turn, independent of whether the barriers are moving or not. If this change in energy is too large, some particles may be thrown outside the maximum momentum offset $\delta_{\rm max}$ of the bunch even when the barriers are not moving. In order to preserve the conservation of the bunch area, the barrier voltage must be limited to $eV_0/(\beta^2E_0) \ll \delta_{\rm max}$. This constraint gives $V_0 \ll 18600$ kV using $\delta_{\rm max} = 0.005$. We actually choose $V_0 = 625$ kV and $T_1 = 0.30$ μs in our simulation. Then, a particle with $\delta = 0.005$ will lose its extra energy in approximately $E_0\delta/(eV_0) = 31.4$ turns and penetrate the barrier by an amount approximately equal to $\tau_{\rm penetrate} = |\eta|\beta^2E_0T_0\delta^2/(2eV_0) = 0.0314$ μs. These barrier waves can produce a bucket height of $\delta_b = 0.0187$ when $\tau_{\rm penetrate} = T_1$, the barrier width.

5 MOMENTUM-OFFSET DISTRIBUTION

To get an estimate of the momentum spread of most of the particles after each squeezing by the barrier pulse, we ne-

* Operated by the Universities Research Association under contracts with the U.S. Department of Energy.

0-7803-4376-X/98/$10.00 © 1998 IEEE

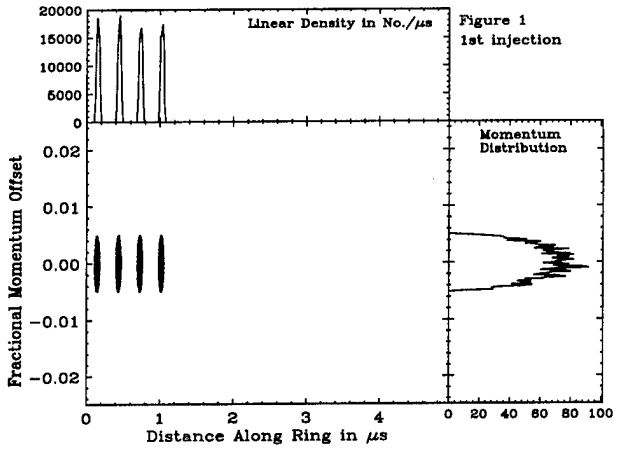


Figure 1
1st injection

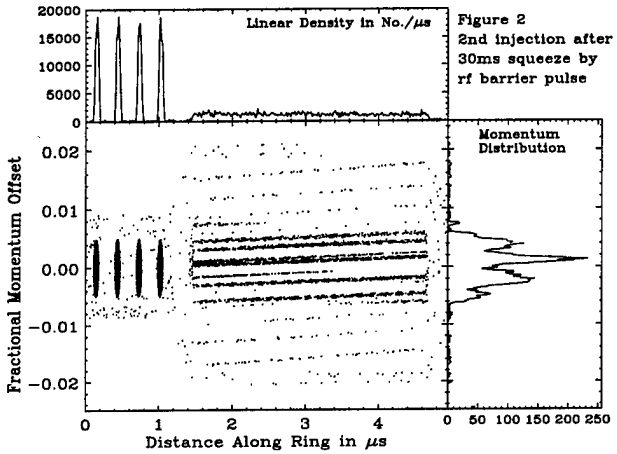


Figure 2
2nd injection after 30ms squeeze by rf barrier pulse

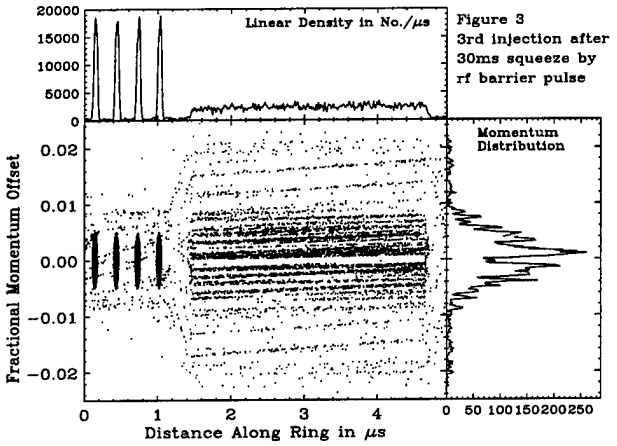


Figure 3
3rd injection after 30ms squeeze by rf barrier pulse

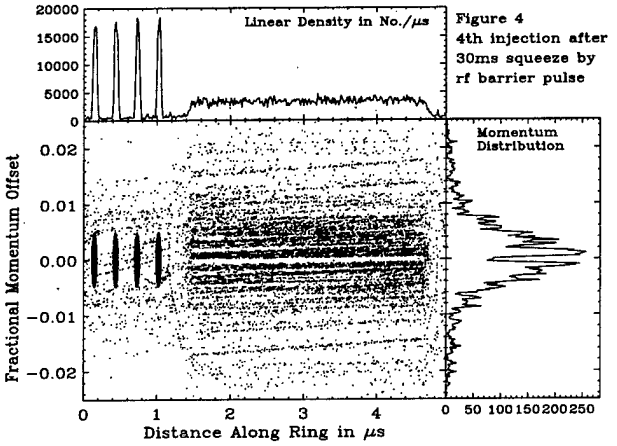


Figure 4
4th injection after 30ms squeeze by rf barrier pulse

glect the curved part of the barrier bucket. The rectangular part of the bucket has a width of $T_{2\,\mathrm{init}} = T_0 - 2T_1$ at the time when the barrier waves are introduced, and becomes $T_{2\,\mathrm{final}} = \frac{13}{17}T_0 - 2T_1$ at the end of the squeeze. The momentum spread will be increased by the factor $F = (T_0 - 2T_1)/(\frac{13}{17}T_0 - 2T_1) = 1.356$. Ideally, in the fourth injection after the third squeezing by the rf barrier, the momentum spread should increase only by the factor $F^3 = 2.547$ to $\delta = \pm 0.0127$. We see in Fig. 4a that for most part of the beam, the momentum spread actually increases by such a ratio after 3 barrier squeezes. However, there is a small part of the beam having momentum spread as large as $\delta = \pm 0.025$ or even ± 0.030. This is because the above consideration is correct only for a bunch that is initially at equilibrium inside the barrier bucket. Here, the beam particles are *captured* into the barrier bucket when the barrier pulses are turned on. Since we have a debunching before capturing into the barrier bucket, particles can be anywhere along the phase axis at the time of capture. For those particles that are captured into the curved parts of the bucket and are very close to the boundaries of the bucket, they can acquire large amount of energy through the barrier pulses and leave the barrier pulse with much larger momentum offset than the estimate given above. It can be seen in Fig. 1 that there are particles with momentum offsets much larger than $1.356 \times 0.005 = 0.0068$ after the first squeeze by the moving barrier pulse. There are also particles that have not been captured into the barrier bucket at all. For a particle with initial momentum offset $\delta_{i0} > 0$ outside the stable barrier bucket, it will first drift across the moving barrier pulse as in Fig. 5, and result in a momentum offset of δ_{f1} given by

$$\left(\delta_{f1} + \frac{\dot{T}_2}{|\eta|}\right)^2 = \left(\delta_{i0} + \frac{\dot{T}_2}{|\eta|}\right)^2 + \delta_b^2 , \qquad (2)$$

where $\dot{T}_2$ is negative. The particle then drifts across the stationary barrier pulse to the space opened up by the moving barrier, after making synchrotron drifting once around the ring. The momentum offset will be reduced to δ_{i1} with $\delta_{f1}^2 = \delta_{i1}^2 + \delta_b^2$. Since the initial momentum offset is at most $\delta_{i0} = 0.005$, during the first synchrotron *rotation* (not oscillation or libration) outside the barrier bucket, we have therefore $\delta_{f1} = 0.0194$ and $\delta_{i1} = 0.0067$. On the average, this particle will encounter the moving barrier pulse 4 times during the 30 ms squeeze time. At the end of the first squeeze, we have $\delta_{f4} = 0.0206$. After that there is another 10 ms of debunching and some of these large-momentum-offset particles can land outside the barrier bucket again when the next barrier pulses are turned on. Thus, for the second squeezing, there may be particles having $\delta_{i0} = 0.0206$ to start with. At the end of the second squeeze after another 4 encounters with the moving barrier pulse, we obtain $\delta_{f4} = 0.0282$ by solving again Eq. (2). Continuing on in this way until the end of the third squeeze, we will have some particles with the largest momentum offset of $\delta_{f4} = 0.0340$. When we analyze the momentum distribution in Fig. 4 more carefully, we do find

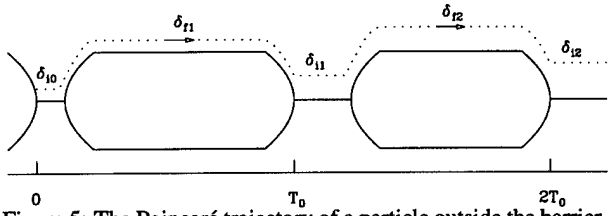


Figure 5: The Poincaré trajectory of a particle outside the barrier bucket with the left barrier pulse moving to the right.

18 macro-particles out of 16,000 in the momentum-offset range of 0.025 to 0.030, and 1 particle in the range of 0.030 to 0.035.

The above analysis depends on the time-integrated barrier voltage only. However, if we use a higher barrier voltage while keeping V_0T_1 constant, more particles will be captured into the larger stable barrier bucket, although the bucket height remains the same. Thus, the probability for particles to attain large momentum offsets outside the bucket becomes smaller. Moreover, because the larger barrier voltage increases only the rectangular area of the bucket but not the bucket height, the bunch area that has momentum offset within $\delta = \pm 0.005$ (for the first injection) will be relatively larger. Thus not so many beam particles will attain higher momentum offsets via synchrotron oscillations. When one of the barrier pulse moves, more particles will follow the momentum-offset increase. A simulation by doubling the barrier voltage to $V_0 = 1250$ kV while halving the barrier width to $T_1 = 0.15$ μs actually shows less particles landing at larger momentum-offsets. However, as was pointed out in the previous section, too high a barrier voltage is not desired.

6 DISCUSSIONS

6.1 Bunch width at injection

The simulation results depend very strongly on the momentum spread of the bunches at injection, but are very insensitive to the initial bunch length, since there is always a debunching period before every squeeze. In practice, however, the initial bunch length cannot be too long, because some gaps must be provided for the kicker rise and fall times. In the above simulations, the total bunch length is $\frac{1}{4}$ of a $h = 17$ rf wavelength. Thus the space between the end of the squeezed barrier bunch and the first bunch in the next injection is $\frac{3}{8}$ of a $h = 17$ rf wavelength, or 109 ns. There will be a gap of similar length between the fourth bunch and the front of the squeezed barrier bunch. These gaps will be long enough for the injection.

6.2 Double barrier pulses

Instead of using one negative pulse and one positive pulse to set up the barrier bucket and perform the bunch squeezing, we may utilize instead a pair of identical double pulses. Each double pulse consists of a positive voltage V_0 of duration T_1 followed by a negative voltage $-V_0$ of duration T_1 similar to one sinusoidal period of an rf wave. At switch-on, the two pulses overlap each other. As one pulse moves to the right while the other one remains stationary, the space opened up by the moving pulse also forms a stable barrier bucket between the negative half of the moving pulse and the positive half of the stationary pulse. Thus some particles will be trapped there and they will have their momentum offsets decreased gradually, because this bucket is becoming wider. However, there are disadvantages also. The particles that are trapped in the space opened by the moving barrier can be lost when the kicker is fired for the next injection. Also, stable barrier bucket only starts to form after the moving barrier moves a distance of T_1. Before that, the two barrier pulses overlap at least partially. At switch-on, the two barrier pulses overlap completely; i.e., an equivalent pulse height of $2V_0$ width T_1 followed by pulse height of $-2V_0$ width T_1. The barrier bucket forms at this moment will have a bucket height $\sqrt{2}\delta_b = 0.0257$ instead, where δ_b is the bucket height when single barrier pulses are used. Thus particles will bound off from the barriers having much larger momentum offsets. A simulation with the double barrier pulses using $V_0 = 625$ kV and $T_1 = 0.30$ μs shows that the momentum distribution spreads out wider.

6.3 Pros and cons of the method

There are pros and cons for using the barrier pulses in multiple injections. The advantage is obviously the much shorter exposure of bunches of very high linear intensity to the vacuum chamber, and we hope that no collective instabilities would develop during this shorter duration. For example, the linear linear density in Figs. 1 to 4 has been reduced by a factor of $\sim$ 6, and the reduction will be more significant if the bunch width at injection becomes narrower. The disadvantage is that microwave instability can develop during debunching when the local momentum spreads of the debunched bunches become small enough. Also, because of the introduction of the barrier pulses and the movement of one of them sends quite a number of beam particles to large momentum offsets, the momentum spread of the final beam will become much larger. Finally, there must be another recapturing of the beam particles into the $h = 17$ rf buckets for acceleration. Beam loss will become inevitable during the recapturing. Thus, there will be beam loss as well as emittance blowup during the whole procedure, which may or may not be tolerable.

Another method is to lengthen the bunches in the booster by bunch rotation and perform simple bucket-to-bucket injection into the main ring. For example, the local linear density will be reduced by a factor of 3.2 already, if each bunch is lengthened to occupy 80% of the $h = 17$ bucket. The gap between two consecutive bunches becomes 58 ns and is still long enough to accommodate the kicker rise or fall time. Since no recapturing will be necessary, the beam loss during injection can be kept to a minimum.

7 REFERENCES

[1] Some preliminary simulations have been performed at the Institute of Nuclear Study of Japan.

[2] K.Y. Ng, *Injection of JHP Main Ring Using Barrier Buckets*, Fermilab Report FN-654, 1997.

[3] S.Y. Lee and K.Y. Ng, *Particle dynamics in storage rings with barrier rf systems,* 1996, to appear in Phys. Rev. **E**.

THE FERMILAB ACCUMULATOR RING LATTICE UPGRADE

S. O'Day and M. Church, Fermilab*, P.O. Box 500 Batavia, IL 60510

Abstract

The Fermilab Antiproton Source Accumulator ring lattice will be changed to accommodate the planned upgrade of the Accumulator stacktail momentum cooling system. The bandwidth of the stacktail system will increase from 1-2 GHz to 2-4 GHz. This bandwidth change will provide the system with the additional cooling force necessary to stack a factor of two more flux than the present system. The lattice must be modified to halve the slip factor η of the machine as a result. Reducing η from -.023 to -.012 will avoid the Schottky band overlap which causes excessive beam heating and will permit the use of conventional notch filters for gain shaping. The new η will be achieved by replacing six high dispersion region quadrupoles and installing thirty-six quadrupole current shunts. Machine aperture, pickup to kicker phase advance and injection/extraction efficiency have not been compromised in the new lattice.

1 INTRODUCTION

During Collider Run II which is scheduled to begin in 1999, the antiproton flux is expected to increase from 2×10^7 to 8.1×10^7 particles per second. Doubling the bandwidth and halving η is expected to double the flux that one can stack in the Accumulator storage ring. A flux of 12 mA/hr was attained during an experiment where proton secondaries from the target were stacked with the machine polarity reversed. This is a lower limit for the maximum attainable stacking flux in the present machine. A macroparticle simulation of the proposed system shows that it can stack at least 24×10^{10} particles/hr[1].

2 LATTICE MODIFICATIONS

2.1 Theoretical Background

The slip factor η is expressed in terms of γ=E/m and γ_t (which is γ at the transition energy) by the expression:

$$\eta=1/\gamma^2-1/\gamma_t^2$$

The momentum compaction factor α is equal to $1/\gamma_t^2$ is related to the dispersion D_x and radius of curvature ρ by:

$$\alpha=\langle D_x / \rho \rangle$$

From these expressions, it is clear that in order for the Accumulator's slip factor (η=-.023) to become less negative(smaller in absolute value), γ_t must increase and the average D_x must decrease. The most straightforward way to accomplish this is with a dispersion bump[2] in each sector.

2.2 Principal Design Considerations

The Fermilab accumulator ring has a circumference of 474m. It is divided into six sectors and has three-fold symmetry. Each of the six sectors is a reflection of its neighbor and contains 5 dipole and fourteen quadrupole magnets[3]. The gross features of the Accumulator are shown in figure 1.

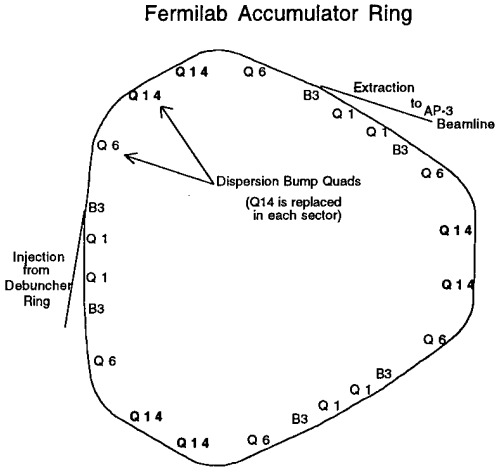


Figure 1. The Fermilab Accumulator. Quadrupoles Q6 and Q14 are the most important elements for the lattice upgrade. New Q14's are being built for Collider Run II.

The second figure shows the horizontal dispersion in one sector(1/6) of the ring. A dispersion bump using quadrupoles at the locations shown will reduce the average D_x enough to make the slip factor change required for the stacktail momentum system upgrade. The Methodical Accelerator Design(MAD) program[4] was used to design the new Accumulator lattice.

2.3 Lattice Optimization

Design constraints have been imposed on the new lattice beyond the principle goal of reducing η by a factor of two[5,6]. The machine parameters which are required for stochastic cooling operation follow:

* Operated by the Universities Research Association under contract with the U.S. Department of Energy

0-7803-4376-X/98/$10.00 © 1998 IEEE

•the betatron phase advance from stochastic cooling pickups to kickers is an odd multiple of $\pi/2$.
•the β functions at the pickups and kickers are maintained so that the sensitivity of existing hardware is unaffected.

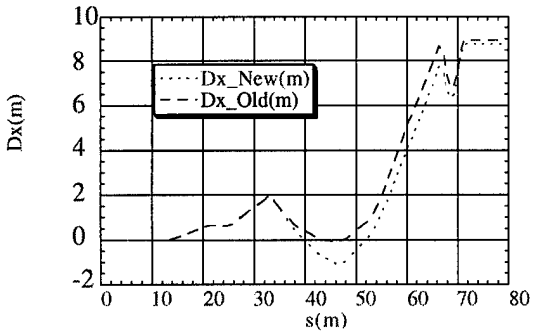


Figure 2. Model predictions for the horizontal dispersion function. The present lattice is compared with the proposed lattice.

The machine parameters which are required for storage ring operation follow:
•the fractional part of the horizontal and vertical tunes must be kept roughly the same in the new design to insure a comfortable margin away from resonances across the momentum aperture.
•the betatron phase between injection/extraction pulsed septa and kickers must be an odd-multiple of $\pi/2$.
•the transverse apertures are close to an un-normalized 15π mm-mrad(see figures 3,4,5,6 and Table 1).

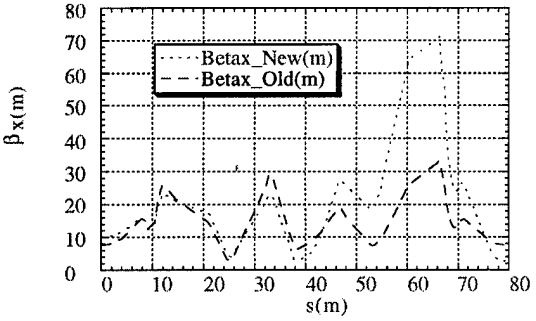


Figure 3. Model predictions for the horizontal β function. The present lattice is compared with the proposed lattice for 1/6 of the ring. The new β_x(max) is larger in the high dispersion section where it minimally impacts A_x.

Table 1. Lattice parameters which change with upgrade.

Machine Parameter	Present	Upgrade
η	-.023	-.012
Dx(min)	0.m	--1.1m
Dx(max)	8.95m	8.75m
βx(max)	34m	71m

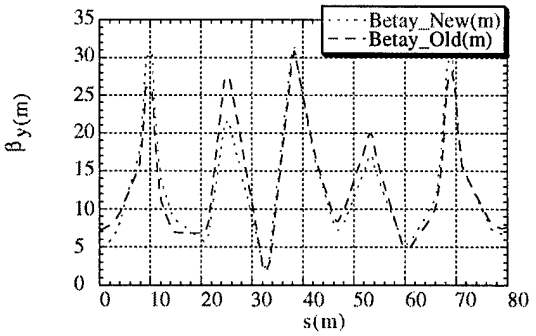


Figure 4. Model predictions for the vertical β function. The present lattice is compared with the proposed lattice.

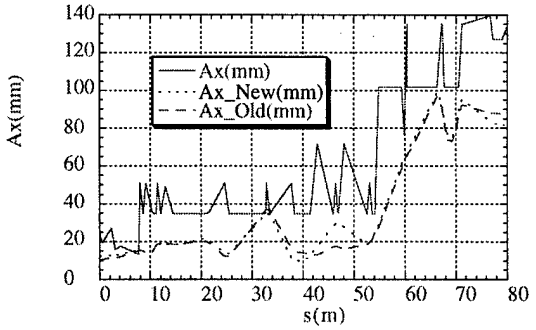


Figure 5. Model predictions for the horizontal machine aperture. The present lattice is compared with the proposed lattice using D_x and β_x assuming a 15π mm-mrad un-normalized emittance beam. Known aperture limitations are shown as the solid curve.

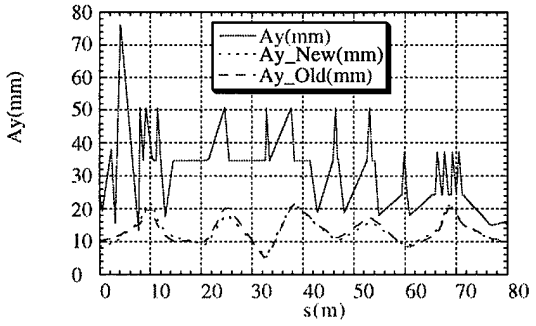


Figure 6. Model predictions for the vertical machine aperture. The present lattice is compared with the proposed lattice using β_y with a 15π un-normalized emittance beam. Known aperture limitations are shown as the solid curve.

2.4 Hardware Implementation

To satisfy all the conditions mentioned in previous sections, it will be necessary to replace one Q14(see figure 1) high dispersion section quadrupole and to add six quadrupole shunts in each sector at locations Q3,6,8,10,11 and 14. The new quadrupole will be a TeV1 style LQC magnet[3] 30.4" long with a 6.625" pole tip diameter. The magnet will have 76 turns. Table 2 shows the fractional quadrupole gradient changes relative to the

present design. Previous magnetic field measurements and saturation effects have been taken into account[7].

Table 2. Changes to the Accumulator quadrupole gradients.

Magnet	Gradient(T/m)	Proposed/Present
Q1	10.3809	.9885
Q2	-10.3809	.9885
Q3	10.3809	.8995
Q4	9.6633	.9853
Q5	9.7413	.9918
Q6	9.6633	1.1030
Q7	9.7413	.9918
Q8	9.6633	.9804
Q9	9.7413	.9818
Q10	4.0877	.9913
Q11	8.9399	.9913
Q12	-8.9399	1.0140
Q13	-8.9399	1.0140
Q14	8.9399	1.0850

3 MEASUREMENTS

Physics measurements were made to improve upon the model of the existing Accumulator. This is useful since the new design is based on the old.

Tune versus revolution frequency measurements are shown in figures 7 and 8. Deviations from the model reflect non-linearities in the machine which are not in the model. The horizontal dispersion measurements made in 1995 and 1996 are shown in figure 9. These measurements show reasonable agreement with the model everywhere except in the A20 high dispersion section. It is believed that uncertainty in beam position monitor gain accounts for the observed differences. Horizontal and vertical β function measurements have been made by varying quadrupole shunts where they exist in the machine. Although the data are not shown, variations from the model are approximately ten percent.

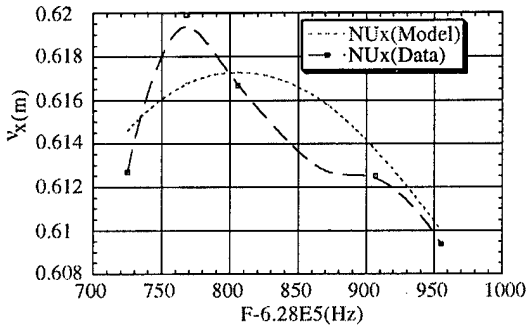


Figure 7. Horizontal tune data vs. model predictions for the existing Accumulator ring.

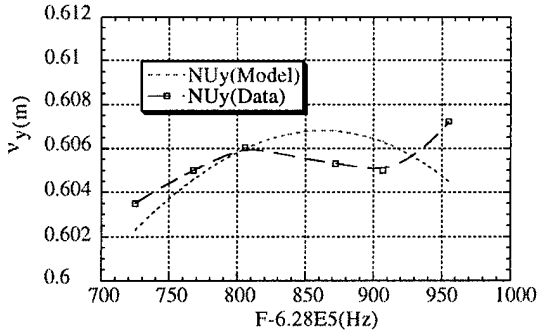


Figure 8. Vertical tune data vs. model predictions for the existing Accumulator ring.

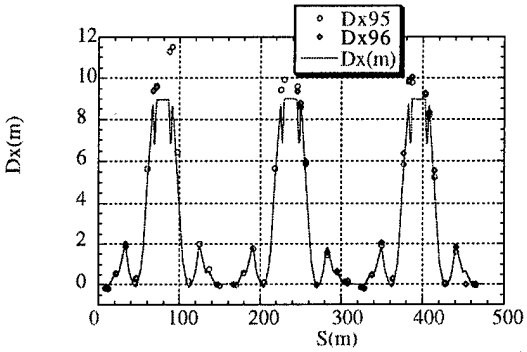


Figure 9. Horizontal dispersion data vs. model predictions for the existing Accumulator ring.

4 SUMMARY

A new lattice design is being implemented as an Accelerator Improvement Project to support the upgrade of the Accumulator stacktail momentum stacking system. This design is based on a model of the existing machine whose predictions compare well with measurements.

REFERENCES

[1] F.Bieniosek, M.Church, G. Jackson, S.O'Day, R.Pasquinelli,"Antiproton Production and Cooling at the Tevatron", Proc. of the Fifth European Particle Accelerator Conference,p.8-12(1996).

[2] R. Servranckx, K. Brown,"Circular Machine Design Techniques and Tools",NIM A258:525(1987).

[3] Fermilab, "Design Report for the Tevatron I Project", Batavia, IL(1984).

[4] H. Grote, F. Iselin,"The Methodical Accelerator Design Program",CERN/SL/90-13(AP).

[5] V. Visnjic,"Antiproton Accumulator in the Main Injector Era (2)", FERMILAB TM-1812(1992).

[6] G. Dugan, Fermilab Pbar Internal Note 530.

[7] B.C. Brown et al.,"Data Acquistion System Design for Production Measurements of Magnets for the Fermilab Antiproton Source", IEEE Trans. Nucl. Sci.,NS-32,p.2050(1985).

INTENSITY UPGRADE STUDIES AT THE KEK-PS

Hikaru Sato and Crew of the Intensity Upgrade Study
Accelerator Laboratory, High Energy Accelerator Research Organization (KEK)
Tsukuba-shi, Ibaraki-ken, 305 Japan

Abstract

Intensity upgrade studies have been performed at the KEK-PS for recent years in order to meet the need of new physics researches, especially the long base line neutrino oscillation experiment. Studies are concentrated on the reduction of the beam losses during injection, at the acceleration start and at the passing the transition energy. Obtained results up to date are 6.8 x 10^{12} particles at the acceleration start and 6.1 x 10^{12} particles after acceleration, however an average beam intensity of 3-5 x 10^{12} ppp are currently supplied for the experiments due to the beam loss during the slow extraction. We report the present results of these studies.

1 CURRENT STATUS OF THE KEK-PS OPERATION

The KEK-PS consists of four accelerator complex, two 750KeV Cockcroft Walton pre-injectors, 40MeV injector linac, 500MeV booster synchrotron and 12GeV main ring. One pre-injector is utilized for ordinary H^- operation and another one was used for D^- and/or alpha ion operation. Figure 1 shows a layout of the KEK-PS complex. After the counter experiment started on 1976 using the secondary beam from an internal target and the fast extraction for bubble chamber experiment, the KEK-PS has been operated successfully to serve an intense proton beam for the past two decades.[1] Proton, deuteron and alpha beam have been serving by the half integer slow extraction to East and North counter halls. In those days, beam intensity at the booster extraction and in the main ring were $6x10^{11}$ppp and $2x10^{12}$ppp, respectively. Beam bunches accelerated in the booster except to the main ring are utilized as NML (Neutron and Meson Laboratory).

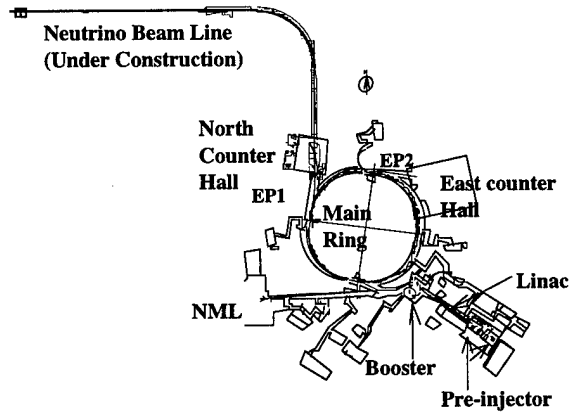


Figure 1. Layout of the KEK-PS Complex.

As the results of much effort, the beam intensity was increased to $5.4x10^{12}$ppp in the main ring on 1989 and $2.4x10^{12}$ppp for NML on 1990. Although the highest beam intensity in the main ring was upgraded to $5.95x10^{12}$ ppp on 1994, an average intensity for utilities is still 3-5 x 10^{12} ppp due to protection of radio activation. In order to increase the beam intensity for the need of new physics researches, especially the long base line neutrino oscillation experiment, studies are concentrated on the reduction of the beam losses during injection, at the acceleration start and at the passing the transition energy.

2 MACHINE STUDY FOR THE INTENSITY UPGRADE

Every effort to realize the upgrade of KEK-PS have been devoted. Booster synchrotron accelerates more than 2 x 10^{12} ppp for NML. If the main ring can accept and accelerates the beam of this intensity with no beam loss, 10^{13} ppp beams could be expected for main ring utility. However, the circulating beam intensity is limited to about 6 x 10^{12} ppp for some reasons. The machine study has continued to make clear the cause and curing of the difficulty in order to realize the beam intensity upgrade. First of all, several tools for the machine study were developed, such as an upgraded injection error monitor, a fast beam loss monitor which can observe it turn by turn using computer workstations and so forth.

Table 1. Aperture of the Main Ring. (πmm mrad.)

	Mechanical	Measured
Horizontal	135.0	81.0
Vertical	31.0	15.0

Transverse Aperture Survey

The aim of the first study was to concentrate the main ring beam injection problem on 1995. The local aperture measurements of the main ring were performed to make clear the real orbit center in the vacuum chamber. The twenty eight steering dipoles were excited independently to make a local bump orbit at each section in the main ring. The vertical aperture seems to be determined by the diameter of the vacuum chamber in the bending magnet. The orbit was set to the center of the vacuum chamber as decided above, then the beam survival were measured to make clear and maximize the acceptance with dependence on the injection error. As the result of this study, the closed orbit, especially vertical, seems essential for the beam loss at the injection. Table 1 shows the main ring aperture of the calculated value from

0-7803-4376-X/98 /$10.00 © 1998 IEEE

real mechanical dimension and the measured value, respectively. It is still unknown that the reason of difference between the mechanical and measured aperture.

Higher Order Resonance Correction

The usual operating point of PS main ring was at ν_x=7.12 and ν_y=7.25. In order to avoid beam loss due to the space charge detuning for a high intensity beam, it should be select rather higher operating point. However, a third order resonance, $\nu_x + 2\nu_y = 22$, and fourth order resonances, particularly $4\nu_y=29$ and $2\nu_x + 2\nu_y = 29$ seem to be obstacles. The correction of these resonances were established by the sextupole magnets and the octupole magnets using rather low intensity beam, about 4 x 10^{11}ppp. After fixed the correction parameter, the high intensity beam, 1.3 x 10^{12}ppp, were injected from booster and measured the tune mapping of beam survival as shown in Figures 2a and 2b. A fast beam loss is brought near integer operating point, on the other hand a slowly beam loss is brought at around larger than .25.

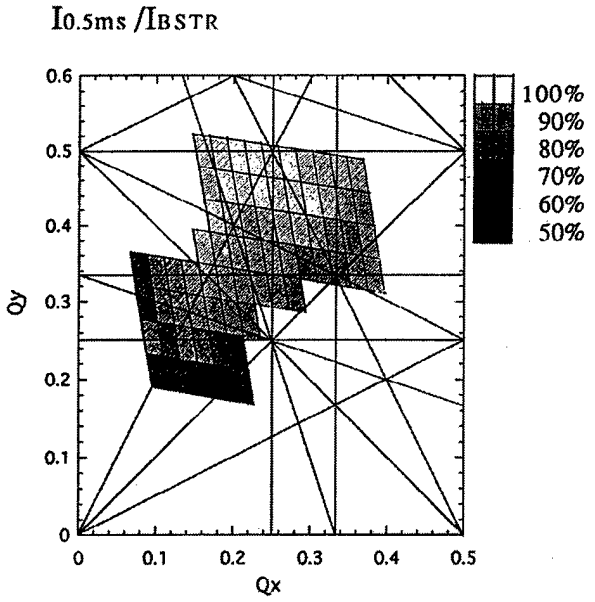


Figure 2a. Beam survival tune mapping of high intensity beam after resonance correction. Ratio between the intensity of booster extraction and 0.5ms after injection.

These show that there are no region where more than 70% of the beam survives. It seems that these forth order resonances are caused by the space charge induced quadrupole imperfection.[2] In order to reduce the quadrupole imperfection, several correction quadrupoles are necessary, however there are no installation space in the ring. Then, the panofsky type hybrid quadrupole magnet, which will be use for both of quadrupols for the imperfection correction and dipoles for the COD correction, are considering. At this present, the vertical tune was changed to 5.25 to curing the effect of the forth order resonance. However, the intensity is still same as the old operating point.

From the view point described above, the re-alignment of the main ring magnet in the vertical plane was done on the summer shut down, 1996. The injection efficiency has increased up to 95-97%, although it was less than 93% before re-alignment.

Another studies on the longitudinal acceptance measurement and the broad band reactive impedance measurement so forth were performed on 1995.[3]

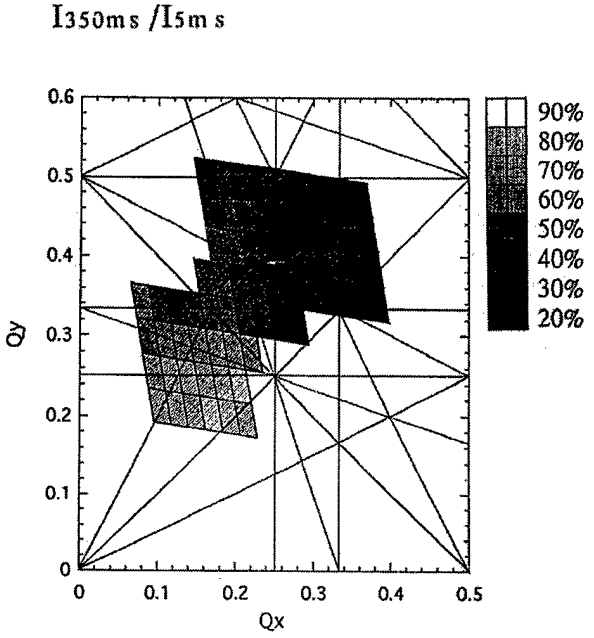


Figure 2b. Beam survival tune mapping of high intensity beam after resonance correction. Ratio between the intensity of 5ms and 350ms after injection, respectively.

Beam Loss During Acceleration

Major beam loss during acceleration is at the acceleration start and at the transition crossing. As the recent studies, following facts come to our knowledge. Some head-tail instability occurs several tens milliseconds after acceleration start [4] and the microwave instability occurs after crossing the transition energy.[5]

First one of these phenomena depends on of course the chromaticity, and this occurred after changing the vertical operating point. The total chromaticity, caused by the eddy current in the vacuum duct inside the bending magnet and the remnant of the sextupole magnet etc., becomes positive 80ms after acceleration. Mode one phenomena disappears by the correction of chromaticity. Various mode of the head tail instabilities occur depend on the chromaticity so the study is under going to clear more detail.

Depend on the knowledge of a proton-klystron model [6] for the microwave instability, a part of the vacuum ducts between the bending magnet and the quadrupole magnet and the beam position monitor (BPM) except high radioactive position were replaced on the summer shut down, 1996. The emmitance brow-up after this replacement clearly decreased.[5]

Figure 3 shows an acceleration efficiencies, intensity ratio between acceleration start and end, and it's

improvement effect. Closed circles are the data during rather high intensity operation several years ago. Open circles are the data after last summer shut down.

5.5-6.1 x 10^{12} ppp at the acceleration end for about 20 minutes have been achieved at the high intensity trial operation on October, 1996. The acceleration efficiency of this trial are also shown in Figure 3.

Reduced the harmonic number seems advantage method in order to beam trapping at the acceleration start. Harmonic six operation has been considering instead of usual nine harmonics, but this is not better since one bunch should be taken out due to the rise time of kicker described later.

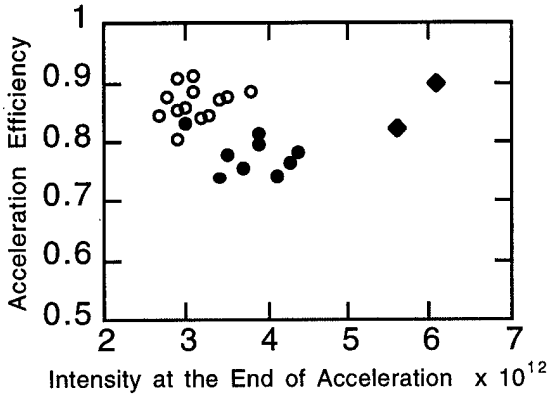


Figure 3. Acceleration efficiency, intensity ratio between acceleration start and end, at the former high intensity operation in 1989 and after improvement of duct impedance. Closed circles are the 1989 data. Open circles are the data after BPM and B-Q duct replacement. Closed diamond are the typical results at the high intensity trial after that.

3 DESIGN OF THE FAST EXTRACTION SYSTEM

Fast extraction of full circulating beam should be requested for the neutrino oscillation experiment.[7] At this present, KEK-PS equipped two slow extraction lines and one internal target beam line. A switching the fast extraction and the slow extraction is considering for multi user requests.

According to the careful orbit analysis for the feasibility using existing slow extraction devices, such as bump and septum magnets system, the changeable system of the extraction kicker and electro-static septum in the same vacuum chamber has decided in stead of former design, which is the small kicker distribution system.[8] A large orbit excursion is the problem since the extracted beam passes through non linear magnetic field region of both bending and quadrupole magnets. Table 1 shows a typical calculation results.

In order to extract the beam during one turn, the kicker magnetic field should have a rise time less than 30ns and more than 1.1μs flat top since the harmonic number is nine and bunch length is about 125ns. The time space between the beam bunches of 30ns is so short for the rise time of fast kicker magnet that one bunch is taken out to obtain the time space for rise time. This means 155ns available for the kicker rise time. The field strength is requested higher than 0.11T and this should be realized within the space of 3m in one long straight section. In order to double of the kicker magnetic field and save the transmission time, the distributed small kickers with the Blumelein system was decided to construct. Prototype one has just constructed and is under exciting test.[9] However, eight bunches acceleration means the beam intensity is reduced to eight ninth. If we adopt the harmonic number six operation, the space between bunches increase to 60ns, but one bunch should be still taken out, then this is not advantage method. First rise kicker magnets are strongly desired.

4 SUMMARY

Acceleration of about 6x10^{12} ppp intense beam has achieved, however, an average intensity during normal operation has been still 3-5 x10^{12} ppp. Since much studies have been concentrated to make clear the beam loss problem the reason of the beam loss is getting to understand little by little.

Twenty years has passed since the KEK-PS constructed, then several equipments and parts become decrepit. The failure time has increased for recent a few years. It was about 3% before 1992, but more than 5% recently. Taking into consideration for this problem is also important subject for the reliability of machine operation.

ACKNOWLEDGMENTS

The author would like to express their sincere thanks to Professors I. Yamane, the director of PS division, and K.Nishikawa, Institute of Particle and Nuclear Studies (IPNS), KEK, for there encouragements. He is much indebted to many colleagues of PS group for their discussions and collaborations.

REFERENCES

[1] K. Nakai and T. Ohshima Summary of Experimental Programs at the KEK-PS in KEK-PS 1980's, 1990 and KEK-PS 1990-1994, 1994
[2] Y. Shoji et.al., Presented in this conference, 8V.37.
[3] Report on the 1995 Spring Machine Study at KEK 12 GeV Proton Synchrotron, KEK Internal 95-12 (in Japanese)
[4] T. Toyama et.al., Presented in this conference, 2V.10.
[5] K. Takayama et.al., Presented in this conference, 3B.06.
[6] K. Takayama et al., Phys. Rev. Lett. 78 (1997) 871
[7] K. Nishikawa et al., KEK Preprint 93-55/INS Report 297-93-9
[8] H. Sato et al., Proc. of the 1995 Part. Accel. Conf., 1995, p.1909
[9] T. Kawakubo et al., Proceedings of the 5th European Particle Accelerator Conference. p.2441. KEK Preprint 97-1 A

OVERVIEW AND STATUS OF THE LOS ALAMOS PSR INJECTION UPGRADE PROJECT*

D. H. Fitzgerald, H. Ahn, B. Blind, M. J. Borden, R. J. Macek, F. Neri,
M. A. Plum, C. R. Rose, H. A. Thiessen, C. A. Wilkinson, and M. V. Zumbro
Los Alamos National Laboratory, Los Alamos, NM 87545

Abstract

An upgrade is in progress to the Los Alamos Proton Storage Ring (PSR) to allow direct injection of the H^- beam into the ring and provide a beam bump system to move the circulating beam off the stripper foil. The primary benefits of this upgrade are matching the transverse phase space of the injected beam to the PSR acceptance and reduction of foil hits by the circulating beam by a factor of ten. Foil thickness is optimized to minimize the combination of circulating-beam losses plus losses due to excited H^0 states produced at injection. An overall factor of five reduction in losses is expected. The project comprises extensive modifications of the injection line, the injection section of the ring, and the waste-beam transport line. We will discuss the goals of the project, present an overview of the technical design, and describe the status of the implementation plan.

1 INTRODUCTION

In the injection upgrade project, the overall performance objectives for PSR and the beam delivery system for the LANSCE neutron spallation source are:

- 100 μA @20 Hz routine operation
- Beam availability > 85%
- Less than 5% downtime from intervals > 8 hours

Beam losses at PSR and the resulting radioactivation of ring components are the dominant factors limiting average beam current, a significant cause of equipment failure, and a major element in repair times. Reducing the beam loss rate is key to achieving the performance improvements.

Losses of the circulating beam in PSR are primarily caused by nuclear and large-angle Coulomb scattering in the injection stripping foil. [1,2] These losses can be reduced by keeping the stored beam off the foil. The present, two-step injection process converts H^- to H^0 in a stripper magnet, then H^0 to H^+ in the stripper foil. This produces significant emittance growth in the bend plane of the stripper magnet and a substantial mismatch of the injected beam. Both factors severely limit the use of injection painting to keep the circulating beam off the foil. To eliminate these problems and implement effective injection painting we are replacing the two-step process by one-step (H^- to H^+) injection of the beam. Direct H^- injection provides the capability to tailor the injected beam parameters for optimal painting.

2 DESIGN

As shown in Fig. 1, we will implement direct H^- injection by using a dipole (which is part of the PSR lattice) to merge the incoming H^- beam with the circulating proton beam. A thin carbon foil after this dipole strips the H^- primarily to protons that are captured in the ring.

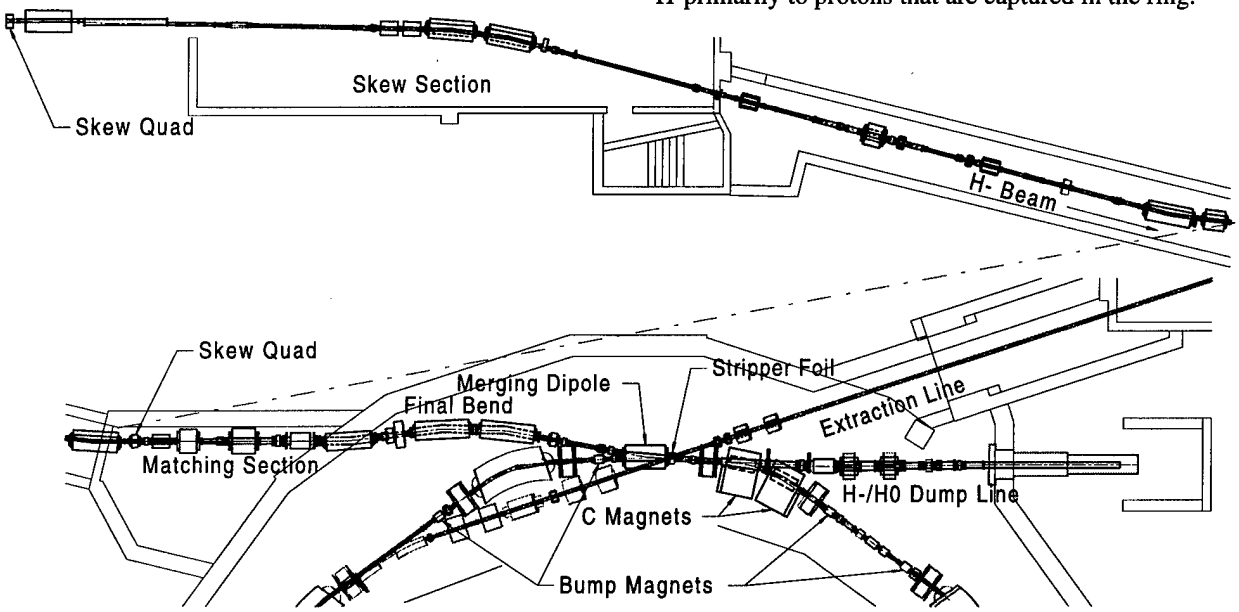


Figure 1. Layout for PSR Injection Upgrade

0-7803-4376-X/98 /$10.00 © 1998 IEEE

The project comprises extensive modifications of the injection line, PSR injection section, and H^-/H^0 dump line.

2.1 Beam Injection

The beam from the linear accelerator has a non-Gaussian transverse distribution, but it is bounded by an ellipse with rms emittance 0.8 π mm mrad. This emittance was used in the design calculations, together with a total momentum spread of ±0.5% (a generous postulate).

The beam injection design is described in detail in Ref. 3. Three sections compose the injection line shown in Fig. 1. A skew section transports the beam from the H^- transfer line to PSR level. The skew section is rolled by approximately 27° to accomplish an elevation change of 3.35 m. A four-quadrupole matching section is used to tailor the beam at the stripper foil to optimize phase space painting. A final bend diverts the beam around a PSR dipole and injects the beam into the merging dipole.

The skew section is achromatic to prevent dispersion-related emittance growth and beam centroid motion caused by beam energy shifts. A general drawback of skew lines is that skewed beam-line elements couple the transverse planes, leading to projected emittance growth. In this design, skew quadrupoles upstream and downstream of the skew section are set, together with a quadrupole at the dispersion crossover point, to uncouple the beam transfer matrix and so avoid emittance growth for all input beams.

The matching section is in a dispersionless region in order to decouple tuning of transverse and longitudinal beam parameters. The nominal injected beam has upright transverse phase space ellipses with rms parameters: x = 1.0 mm, x' = 0.80 mrad and y = 1.6 mm, y' = 0.50 mrad. The injected beam is offset by: x_0 = 7.21 mm, x_0' = -1.96 mrad, y_0 = 22.5 mm, y_0' = 3.10 mrad. Zero-dispersion injection is used to reduce the injected beam size and, thus, the number of foil hits by the circulating beam. The matching section has sufficient tuning flexibility to accommodate the normal range of input beams and to produce an adequate range of beam parameters at injection in PSR.

Hands-on maintenance of the injection line components requires minimal beam losses. In general, losses occur because the beam is too large for the aperture, or is mis-steered, or because H^- is stripped in the magnetic fields. The nominal aperture in the injection line is at least 6.6 times the rms beam size including momentum spread. Thus, scraping losses should be negligible, even with reasonable steering errors. Dipole fields have been kept below 3.8 kGauss and quadrupole fields have been kept correspondingly low to avoid excessive losses. [3]

Alignment or field errors can cause emittance growth or steering errors, leading to incorrect injection match and increased beam losses in PSR. The effects of injection-line errors were studied using particle-tracking codes in the injection line and PSR. Alignment and field errors twice the design tolerances (see below) were used in the simulations. Circulating beam losses from foil hits and scraping did not increase, while the fraction of injected beam missing the foil increased insignificantly (<1%).

2.2 PSR Reconfiguration and Beam-Loss Reduction

Changes to PSR include the 6.8° injection dipole, bump magnets to produce the closed orbit bump and the replacement of the first dipole downstream of injection by two C magnets. To accommodate the merging dipole, the bend angles of the dipoles on either end of the straight section must be reduced. The net result is an increase in the PSR circumference of 2.8 cm, requiring an increase of 2 MeV in the beam central energy, i.e., to 799 MeV.

The design for offset injection and closed-orbit bump was optimized by simultaneously minimizing foil hits by the circulating beam while keeping the injected beam ellipse completely inside the ring acceptance ellipse. Injection is offset in both planes, and the vertical closed-orbit bump in the injection section is collapsed linearly to zero by the end of injection, as shown in Fig. 2.

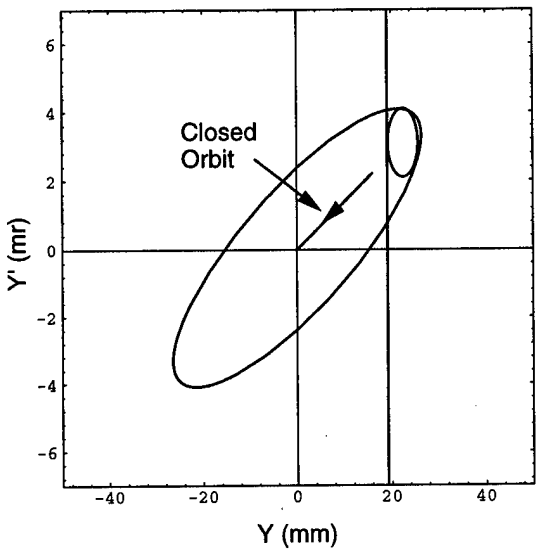


Figure 2. Closed orbit bump is collapsed linearly to zero during the injection period.

ACCSIM simulations show that offset injection and painting reduce the average number of foil hits by the circulating beam to 35 for 2300 turns injected, a ten-fold reduction over H^0 injection. A second source of PSR losses is excited H^0 states produced at injection and stripped in the first ring dipole. These losses are minimized by increasing the thickness of the foil. Fig. 3 shows the results of an optimization study of losses *vs.* foil thickness. With an optimized foil thickness of 400 $\mu g/cm^2$, losses are reduced by a factor of 5 from that for present PSR operation with a 200 $\mu g/cm^2$ foil.

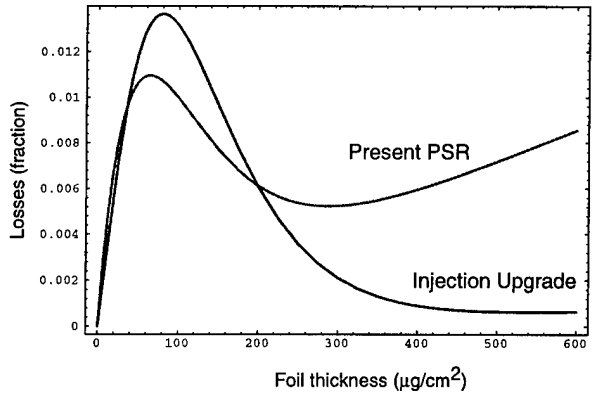


Figure 3. Total losses *vs.* foil thickness.

2.3 H/H^0 Beam Dump Line

The offset injected beam at the stripper foil requires increasing the aperture in the downstream bending magnet to accept H^0 produced in the foil and the unstripped H^-. Therefore, we are replacing the present dipole by two existing C magnets, the first having a 50% larger vertical aperture than the present dipole. In the dump line, the diverging H^- and H^0 beams must be combined and transported with minimum losses. To design this line, a particle tracking code was developed that takes into account the initial beam distributions and stripping distributions for H^- to H^0 in the first C magnet. The final design incorporates a dual-plane bending magnet to aim the beams at the beam dump and a quadrupole doublet to combine and focus the beams at the beam stop.

3 IMPLEMENTATION

To implement the upgrade requires: 11 dipoles (including two C magnets), one dual-axis bending magnet, 15 quadrupoles, and 11 steering magnets. To reduce costs we used existing magnets where possible, so only eight new magnets (five designs) are needed. The C magnets have the most stringent central-field quality requirements: 10^{-4}. All magnet power supply needs can be met from the existing pool, although 14 must be upgraded to improve regulation or better match the load. To satisfy design specifications, the C magnets will require power supply regulation of 10^{-5}, while the dipoles in the final bend require 2×10^{-5}. The required regulation for the quadrupoles is 10^{-3} except for the last quadrupole in the matching section, which requires 10^{-4}. The closed-orbit bump will be produced using four programmable, pulsed magnets [4] located as shown in Fig. 1.

In the particle-tracking studies the following critical alignment tolerances were found to be acceptable:

- Dipoles: 1 mm longitudinal, 1.7 mrad roll
- Quadrupoles: 0.25 mm transverse, 1.7 mrad roll

These required tolerances can be obtained by standard alignment techniques at LANSCE, which are capable of attaining 0.1 mm in position and <1 mrad in angle.

Procurement and fabrication are about half completed, and the project is on track for installation beginning in August 1997; commissioning is scheduled for May 1998.

4 TECHNICAL SPECIFICATIONS

Table I contains the PSR injection upgrade specifications

Table I. PSR Parameters After Injection Upgrade

Parameter	Value
Current, repetition rate	100 μA @ 20 Hz
Protons per pulse	3.1×10^{13} ppp
Beam energy	799 MeV
PSR accumulation time	825 μs
Injected beam time spread	250 ns
Input beam phase space Transverse Longitudinal	 0.8 π mm-mrad rms 0.063% dp/p rms
Injection line acceptance Transverse Longitudinal	 35 π mm-mrad ±0.5% δp/p
Injected beam offset (x_0,x_0') = (y_0,y_0') =	 7.21 mm, -1.96 mrad 22.5 mm, 3.10 mrad
Closed orbit bump (linear) from (y_0, y_0') = to (y_0, y_0') =	 16.0 mm, 2.2 mrad 0.0 mm, 0.0 mrad
Foil thickness	400 μg/cm²
RF volts per turn, lin. ramp	6-10.5 kV
Harmonic no., freq. (time)	1, 2.795 MHz, (358 ns)
Tune	$\nu_x = 3.172$, $\nu_y = 2.142$
Max. tune depression	$\Delta\nu_x = -0.071$, $\Delta\nu_y = -0.106$
Stored beam 95% emittance ε_x = ε_y = dp/p =	 35 π mm-mrad 49 π mm-mrad ±0.34%
Frac. of beam missing foil	2.6%
H^- stripped to H^0	0.6%
Foil hits per proton	30.5
Stored beam loss (incl. 0.022% nucl. scatt.)	(0.046 ± 0.005%) total
Extraction losses	0.008%
Excited H^0 losses	0.048%

REFERENCES

[1] R. Macek, *et al.*, Proceedings of the European Particle Accelerator Conference (1988) 1252.
[2] R. J. Macek, *et al.*, Proceedings of the 1993 Particle Accelerator Conference (1993) 3739.
[3] Barbara Blind and Andrew J. Jason, 'PSR Injection Line Upgrade', these proceedings.
[4] C. R. Rose, *et al.*, 'Overview of the Bump Magnet System at the Los Alamos Proton Storage Ring', these proceedings.

* Work supported by the US DOE and DoD.

COMPARISON OF BEAM TRANSPORT SIMULATIONS TO MEASUREMENTS AT THE LOS ALAMOS PROTON STORAGE RING

C. Wilkinson, F. Neri, D. H. Fitzgerald, B. Blind, R. Macek, M. Plum, O. Sander, H.A. Thiessen,
Los Alamos National Laboratory, Los Alamos, NM 87544

Abstract

The ability to model and simulate beam behavior in the Proton Storage Ring (PSR) of the Los Alamos Neutron Science Center (LANSCE) is an important diagnostic and predictive tool. This paper gives the results of an effort to model the ring apertures and lattice and use beam simulation programs to track the beam. The results are then compared to measured activation levels from beam loss in the ring. The success of the method determines its usefulness in evaluating the effects of planned upgrades to the Proton Storage Ring.

1 SIMULATION

For the model, the dimensions and positions of the PSR beam line elements were obtained from drawings and documentation and were verified by measurements wherever possible. Aperture dimensions included as-built variations, if known. The resulting DIMAD lattice geometry was checked against a 2-d computer layout of the ring. One unverified point remained after this effort: a limiting aperture in the vacuum pipe of the insertion magnet and ring bender, SRBM01. Loss patterns do not indicate that such a restriction exists.

The PSR clear apertures on either side of the beam pipe center are plotted in Figure 1 and the minimum of the apertures on either side is plotted in Figure 2. The smallest apertures in the horizontal direction are found in the extraction kickers (2.58 and 2.90 cm), the extraction septum magnet (4.52 cm), and the unverified vacuum chamber aperture in bender SRBM01 (2.52 cm). For the rest of the ring, the minimum horizontal apertures (4.78 cm) are in the Beam Position Monitors (BPM's) in the quadrupoles and are close to the value for the ring dipole magnets. The horizontal apertures are widest in the beam elements that must handle both circulating and incoming or exiting beams. In the vertical direction, the smallest apertures are in the special vacuum chambers in the ring dipole magnets which must also accommodate the injected (SRBM01, 4.63 cm), unstripped (SRBM11, 4.26 cm), and extraction beams (kickers, 4.34 cm). The remaining ring dipoles and the QU BPM's have the next smallest apertures (4.73 cm).

The beam envelopes were generated by tracking particles in ACCSIM and then using the emittances containing a chosen beam fraction in a DIMAD simulation. The ACCSIM simulation included injection halo, wide-angle Coulomb scattering, momentum spread, and apertures. Beam parameters and characteristics are included in Table 1. For the present PSR, emittances containing 99.95% of the beam tracked by ACCSIM were used in the DIMAD simulation. The momentum spread, $\Delta p/p$, was found to be 0.32%. This includes RF effects of the buncher and is consistent with what is actually seen in operation.

The simulated PSR beam envelopes are plotted inside the clear apertures in Figure 1. The ratio of the minimum clear aperture to beam size is plotted in Figure 2. With the

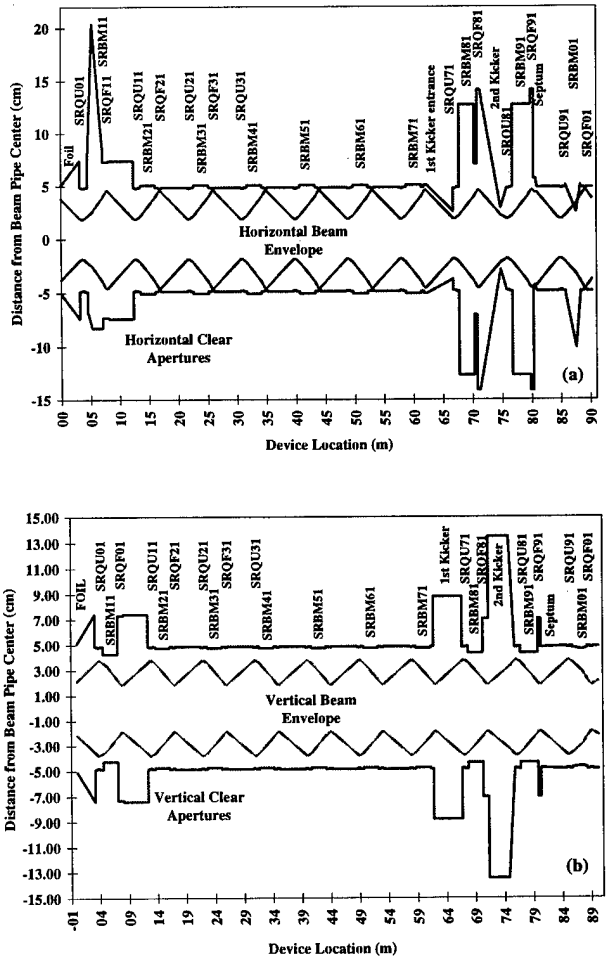


Figure 1(a) and (b). The horizontal and vertical beam envelopes plotted inside the physical clear aperture for the present Proton Storage Ring.

0-7803-4376-X/98/$10.00 © 1998 IEEE

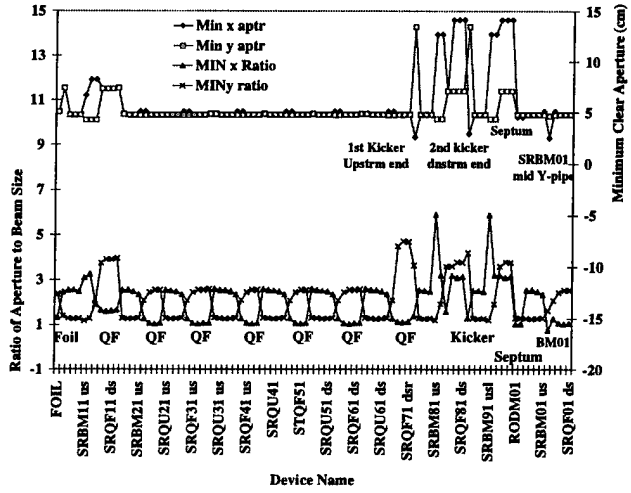


Figure 2. Minimum physical clear apertures and minimum aperture to beam ratios for the present Proton Storage Ring.

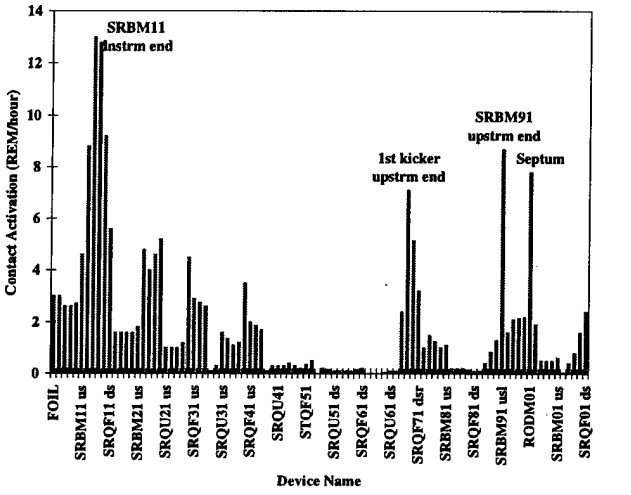


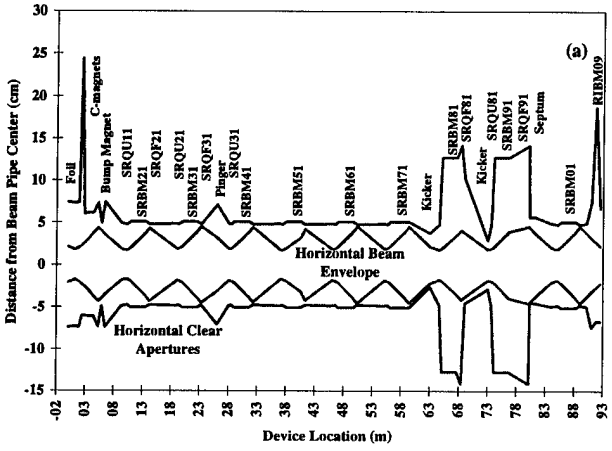
Figure 3. Average measured activation on contact for the present PSR.

exception of the questionable aperture in SRBM01, the limiting aperture for the PSR is in the extraction septum magnet, as given by the aperture ratio of 1.039 in the horizontal direction. The focusing quadrupoles horizontal aperture ratios are only slightly larger, at 1.043, followed by the extraction kickers, at 1.11 and 1.31 respectively. The limiting apertures are distributed around the ring, with no aperture significantly more limiting than any other. Particles reaching a large radius will be lost at the first limiting aperture they encounter and are therefore likely to be lost close to their point of generation.

2 COMPARISON TO MEASUREMENT

A comparison of loss patterns in the PSR corroborates the model of distributed limiting apertures. The averages of several contact measurements of component activation taken over the last five years are plotted in Figure 3. The losses in the injection region are known to come from nuclear scattering, wide-angle coulomb scattering, injection beam halo, and excited H^0 states that strip in the first bender field. Particles from these effects are generated at or near the stripper foil. The activation pattern shows that the major injection losses occur in the first four sections of the ring, with peaks at the limiting aperture quadrupole magnets. The large peak in the first bender, SRBM11, is caused primarily by excited H^0's that strip in SRBM11. The upstream apertures shadow the later limiting apertures, so fewer losses are seen in sections five and six.

Activation in the extraction region follows a similar pattern. Although some of the losses are not completely understood, the majority come from beam halo, extracted beam tails, beam in the gap, and unextracted beam. The activation peaks occur at the limiting apertures: the front end of the first kicker, the exit of the second kicker and the entrance of the following ring bender, and the septum magnet. Activation after the unverified constriction in the



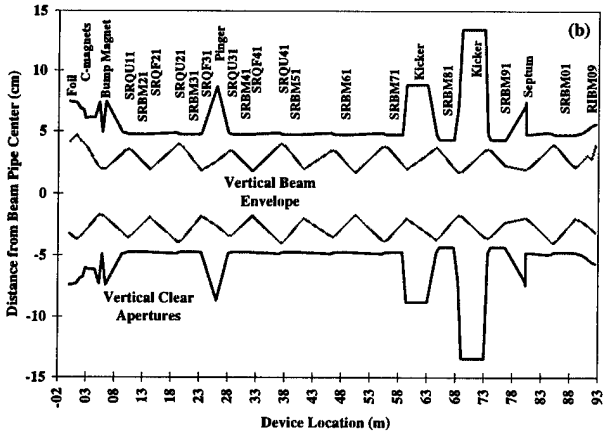


Figure 4 (a) and (b). The horizontal and vertical beam envelopes plotted inside the physical clear aperture for the planned LRIP improvements.

bender, SRBM01, is not consistent with the assumed narrowness of the beam pipe, which in any case will be changed for the LRIP improvement.

3 APPLICATION TO IMPROVEMENTS

The same type of modeling and analysis was applied to the planned upgrade of the ring injection, which is part of the LANSCE Reliability Upgrade Improvement Project (LRIP) scheduled for installation in late 1997. The improvements include direct H^- injection, better matching of the injected beam to the ring acceptance, fewer foil traversals achieved by vertical bumping of the circulating beam and increased vertical beam size, thicker foil, and a change to C-magnets just downstream of the foil. The majority of these changes are intended to reduce ring losses by reducing the number of foil traversals per proton. The present and post-LRIP beam parameters are listed in Table 1. The emittance used for the post-LRIP beam included a slightly larger beam fraction, 99.99%, than that used for the present PSR beam. The results of the analysis are plotted in Figures 4 and 5.

The same pattern of distributed limiting apertures is seen for the LRIP analysis as for the present PSR. The septum aperture ratio is the same and the ratios at the limiting focusing quadrupoles are slightly improved to an average of 1.08. A vertical bump magnet in section 1 becomes the first limiting aperture after the stripper foil, but its aperture equals that of the other limiting apertures. Thus, the LRIP improvements do not introduce new limiting apertures or decrease the aperture ratios, even when more beam is included in the LRIP beam envelope than for the PSR.

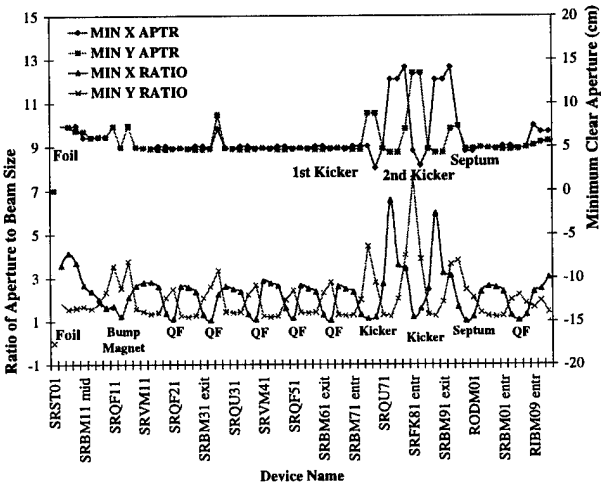


Figure 5. Minimum physical clear apertures and aperture to beam ratios for the LRIP Proton Storage Ring.

4 SUMMARY

The modeling of the present Los Alamos Proton Storage Ring gives aperture to beam size ratios that are consistent with the losses as indicated by contact activation measurements. The success in matching present limiting apertures to losses implies that the method is useful in analyzing planned improvements to the PSR. An analysis of the LANSCE Reliability Improvement Project predicts that there are no major changes in the distribution and size of the limiting apertures, indicating that the improvements have not made the loss situation worse due to the introduction of new limiting apertures.

Table 1. Parameters for the present PSR and the planned LRIP improvements.

	PSR **75 μA @ 20 Hz, 250 ns**	**LRIP** **100 μA @ 20 Hz; 250 ns**
Injection Point Lattice	$\alpha_x = 1.891$, $\beta_x = 9.151$ m $\alpha_y = -0.705$, $\beta_y = 4.560$ m	$\alpha_x = 0.629$, $\beta_x = 2.776$ m $\alpha_y = -1.423$, $\beta_y = 10.931$ m
Injected Beam Emittance	$\varepsilon_x = 7.2$, $\varepsilon_y = 4.20$ (4 σ) mm-mrad	$\varepsilon_x = 3.2$, $\varepsilon_y = 3.2$ (4 σ) mm-mrad
Injected Beam dp/p	36% 0.037 Δp/p & 64% 0.063% Δp/p	36% 0.037 Δp/p & 64% 0.063% Δp/p
Bumping	none	$y^1 = 16.0$ mm, $y^{1'} = 2.2$ mrad to 0,0 in 825 μs
Horiz. Accept. Def. Apert.	47.8 mm at Quads; 44.9 mm at sept.	47.8 mm at Quads; 44.9 mm at septum
Vert. Accept. Def. Apert.	47.8 mm at center of Quads	47.8 mm at center of Quads
RF Buncher Voltage	8 kV at 2.8 MHz, ramped from 4 kV	10.5 kV at 2.8 MHz, ramped from 6 kV
Frac. of Beam missing Foil	1.25% plus 7.4% through foil	2.56% plus 0.58% through foil
Tunes	$\nu_x = 3.172$, $\nu_y = 2.142$	$\nu_x = 3.172$, $\nu_y = 2.142$
Max. Tune Depressions	$\Delta\nu_x = -0.158$; $\Delta\nu_y = -0.125$; 2.20×10^{13} p	$\Delta\nu_x = -0.071$; $\Delta\nu_y = -0.106$; 3.12×10^{13} p
Stored Beam 95% Emitt.,	$\varepsilon_x = 27.0$, $\varepsilon_y = 39.0$ mm-mrad	$\varepsilon_x = 35.0$, $\varepsilon_y = 49.0$ mm-mrad
Stored Beam 95% Δp/p	±0.32%	±0.34%
Foil Hits/Proton	307.4 (650 μsec Injection)	35.0 (825 μsec Injection)
Stored beam losses (scatt.)	0.152% multiple; 0.105% nuclear	0.0244 ±0.005% mult.; 0.0217 % nucl.
Excited H^0; Extract. Losses	0.259%; 0.05% respectively	0.048%; 0.0078% respectively

ACCUMULATOR RING H⁻ INJECTION OPTIMIZATION STUDIES

J. D. Galambos, J. A. Holmes, and D. K. Olsen
Oak Ridge National Laboratory, Oak Ridge TN, 37831-8218

Abstract

H^- ion injection into an accumulator ring is a limiting process for future high-intensity pulsed spallation neutron sources. To facilitate the injection design process, a method has been developed to access a tracking code, ACCSIM [1], from within an optimization package [2]. The optimization tool is a C++ interactive driver with steepest decent and genetic algorithm optimization methods and parallel computing capabilities. Some injection parameters varied in the optimization process are the H^- beam size and position, the foil configuration and thickness, and the horizontal and vertical bump time profiles. Constraints and figures-of-merit include maximum allowed foil temperature, maximum allowed space charge tune shifts, maximum allowed foil traversals, and maximum allowed beam losses. Application of this method to accumulator ring injection in the proposed National Spallation Neutron Source (NSNS) is presented.

1 BACKGROUND

In NSNS an intense H^+ beam is built up in an accumulator ring by stripping an incident 1 GeV H^- beam at injection. The H^- ions and stripping foil are necessary to overcome Liouville's Theorem in merging the injected beam into the circulating H^+ beam. Building up the circulating beam is an intricate process requiring a time-dependent bump of the reference orbit over ~1200 turns to obtain the required emittances and distributions. In addition, other considerations impact the process. Because of the high beam intensity, uncontrolled beam line losses must be kept to a minimum ($<10^{-4}$). The temperature of the carbon stripping foil must not exceed 2750° C. The tune shift induced by the space charge in the circulating beam must be small (<0.15) to avoid resonances. To minimize beam losses and satisfy these constraints, a number of parameters can be varied: the H^- beam size and position, the foil configuration, the horizontal and vertical bump time profiles, the foil thickness, and the longitudinal parameters. The problem of injection into the NSNS accumulator ring is thus one of optimization. With this in mind, a method has been developed to call a tracking code, ACCSIM[1], from within an optimization package[2]. We apply this method to minimize beam losses during accumulator ring injection into the proposed NSNS.

2 MODEL DESCRIPTION

2.1 Overall Configuration

The optimization of NSNS ring injection is accomplished by calling the particle-tracking code, ACCSIM, from the SUPERCODE driver Shell. SUPERCODE is an interactive C++ shell that incudes optimization tools. In this case we utilize a Genetic Alogrithm (GA) option to perform the optimization. The information flow between codes is shown schematiccaly in Fig. 1. The optimizer creates a population, each member consisting of a set of selected values for the indpendent variables, and passes each member to a distinct copy of ACCSIM (which is used by SUPERCODE as a "function evaluator"). These copies can reside on separate workstations, or on separate nodes of a parallel computer. Each copy of ACCSIM then performs a calculation using its input and returns the constraint and Figure-of-Merit (FOM) values. These are then used by the GA routine to create a new generation, and the procedure is iterated to convergence. The message passing is done using PVM [3] with which we have used up to 20 workstations in parallel.

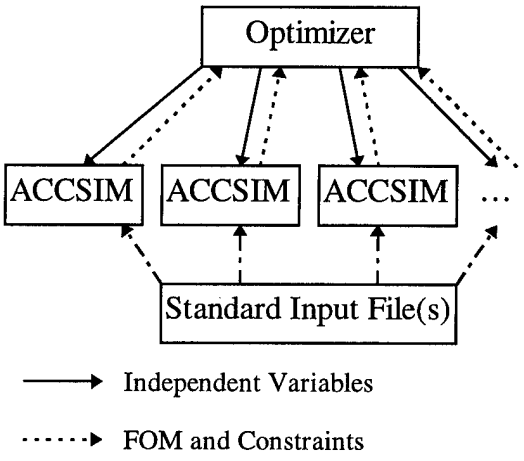


Fig. 1 Overview of information flow in the optimization setup.

0-7803-4376-X/98 /$10.00 © 1998 IEEE

2.2 *ACCSIM Modifications*

To facilitate the present studies, a number of additions were made to ACCSIM: (1) exponential decay (x,y) bump profiles, (2) foil temperature calculation, (3) in-foil nuclear elastic scattering (NES) loss fraction calculation, (4) foil-induced fractional 4&5 excited state H^0 production calculation, (5) injected beam coordinates and final bump location to obtain specified final painted emittances, and (6) message passing to/from the optimizer as discussed.

2.3 *Problem Formulation*

The constraints are listed in Table 1 and the variable parameters in Table 2. The Figure-of-Merit is minimum beam loss (NES + H^0 4&5 state losses). The tune shift depends on the longitudinal parameters through the bunching factor. This dependence will be explored in future work. Present calculations were performed with the following longitudinal parameters: first harmonic RF at 30 keV and the ring transit frequency and 65% longitudinal bunch length.

Table 1. Constraints on Calculated Quantities.

Constraint
Peak Foil Temperature $\leq$ 2750 °C
Peak x tune shift < 0.15
Peak y tune shift < 0.15

To find optimal solutions, the parameters listed in Table 2 are allowed to vary within the indicated bounds.

Table 2. Variable Input Parameters.

Bound:	Lower	Upper
Linac Beam x/y Beta (m)	1	50
Initial Bump x/y offset (mm)	0	15
Normalized bump x/y e-fold time scale	1	10
foil thickness (mg/cm^2)	50	1000

3 RESULTS

Table 3 shows the results of injection optimization studies performed to date. Due to the "fuzziness" of the GA optimizer there are occasional borderline violations of constraints. The total loss rate is the sum of the nuclear elastic scattering (NES) and the H^0 4&5 state excitation rates in the stripping foil. Small angle Coulomb scattering is ignored here, but will be considered in future studies. The bump rates are exponential decay rates in the bumped beam position. The initial bumped beam is centered at the x and y offsets relative to the injected beam center. The circulating beam center after injection is positioned to yield the desired transverse emittances. Large bump rates lead to hollow profiles in the corresponding phase space. Small bump rates lead to peaked beam profiles. Except when beam center fixed in y, all the parameters in Table 3 are varied by the optimizer to minimize total losses and to satisfy the constraints.

3.1 *Presentation of Results*

Most of the following studies have constant offsets in y. The resulting y-y' phase space beam profile is a hollow ring. The x bump rates are slow, leading to peaked beam profiles in x-x' phase space.

The first three cases in Table 3 examine the effect of the foil edge configuration on the loss rate. The most striking feature is the large loss rate for a single-edged foil. This results from a higher particle-foil impact rate than for the other cases. The results for the two- and three-edged cases are very similar, showing no advantage with a three-edged foil. However, a three-edged foil can be used to collimate the beam.

The second study shown in Table 3 consists of four cases differing in the fraction of the injected beam allowed to miss the foil. This portion of the beam remains H^- and goes to the beam dump. When 2% or more of the beam is allowed to miss the foil, the foil-induced beam losses decrease measurably. This is caused by fewer foil impacts per particle, which results from the placement of the injected beam closer to the foil edge when more beam is allowed to miss the foil.

In some estimates as much as two-thirds of the beam energy loss promptly leaves the foil, which implies reduced foil heating. In the third study, the energy deposition formulation for the beam in the foil was arbitrarily halved. With this reduced heating the optimizer selected a thicker foil to eliminate the excited state H^0 losses while still satisfying the foil temperature constraint.

In the next study, the nuclear elastic scattering cross section was arbitrarily tripled. The main effect on the solution was an enhancement of the NES losses. The other quantities show little effect. For foil thicknesses around 600 mg/cm^2, the H^0 loss rate is strongly decreasing, while NES losses increase linearly. Hence, the tendancy toward thinner foils from tripling the NES cross section is countered by the tendancy toward thicker foils driven by the H^0 loss rate.

The remaining studies include orbit bumps (hence phase space painting) in both x and y. Reductions occur in all losses, in foil impacts per particle, and in x space charge induced tune shifts, together with an increase in foil thickness made possible by the reduced particle hit rate. The optimal bump rates are slow in y and fast in x, so the resulting phase space distributions are peaked in y-y' and hollow in x-x'. Hence, the additional degrees

of freedom provided by a variable y bump allow improved solutions compared to x bump alone.

The final study involves the selection of a different figure-of-merit, namely minimum number of foil traversals. The optimizer achieves this by selecting a very narrow injected beam that can subsequently clear the foil in the circulating beam. To satisfy the foil temperature constraint, given the intense injected beam spot, the optimizer is forced to make the foil very thin. The resulting excited H^0 losses are huge, so that the solution is technically unacceptable, but the value of 1.8 foil hits per particle is indeed small.

3.2 Summary

The coupling of optimization with accelerator physics techniques provides a systematic automated approach to the solution of complicated design problems. Applications of such an approach to injection into the NSNS ring yield sensible solutions that could otherwise be obtained only via trial and error.

4 FURTHER STUDIES

A number of enhancements to the present study will be pursued. These involve (1) the inclusion of Coulomb scattering effects of beam particles impacting the foil, (2) an enhancement of the current simple treatment of space charge effects to include orbit effects and resonances, and (3) enhanced modeling of the longitudinal beam dynamics to facilitate longitudinal phase space painting into rings with generalized RF systems including several harmonics.

5 ACKNOWLEDGEMENTS

This research is sponsored by the Division of Materials Sciences, DOE, under contract DE-AC05-96OR22464 with Lockeed Martin Energy Research.

6 REFERENCES

[1] F. W. Jones, "User's Guide to ACCSIM", TRIUMF Design Note TRI-DN-90-17, (1990).

[2] S. W. Haney, et al., Fusion Technology, **21**, (1992), 1749.

[3] http://www.netlib.org/pvm3/book/pvm-book.html

Table 3. Summary of Optimization Runs

Case Studies	FOM - Fractional Loss ($x10^{-4}$)			Foil Hits / Part.	Constraint Values			Variable Parameter Values				
	Total Loss	NES Loss	H^0 Loss		Max Dn_x	Max Dn_y	Foil Tmp (°C)	Bump Rates r_x, r_y	x,y Offset (mm)	b_x Inj. (m)	b_y Inj. (m)	Foil Thick mg/cm^2
Foil Edge												
1 Edge, 1% Miss	3.90	3.21	0.68	29.8	0.16	0.15	2724	1.3, ∞	5.7, 15.1	29.2	21.9	581
2 Edge, 1% Miss	1.81	1.41	0.40	12.4	0.16	0.15	2667	1.3, ∞	6.6, 15.1	38.5	21.9	612
3 Edge, 1% Miss	1.95	1.46	0.49	13.1	0.17	0.15	2742	1.3, ∞	5.0, 15.8	42.7	15.3	600
% Miss Foil (2 Edge)												
0.5% Miss	1.64	1.45	0.20	11.9	0.17	0.15	2755	1.3, ∞	4.5, 15.1	34.6	21.6	653
1.0% Miss	1.81	1.41	0.40	12.4	0.16	0.15	2667	1.3, ∞	6.6, 15.1	38.5	21.9	612
2.0% Miss	1.38	1.26	0.12	10.0	0.16	0.15	2769	1.3, ∞	5.0, 15.1	34.6	21.6	679
4.0% Miss	1.39	0.90	0.49	8.1	0.16	0.15	2712	1.5, ∞	5.4, 15.0	30.0	22.1	600
Foil E-Dep (2-Edge)												
100% Dep., 1% Miss	1.81	1.41	0.40	12.4	0.16	0.15	2667	1.3, ∞	6.6, 15.1	38.5	21.9	612
50% Dep., 1% Miss	1.70	1.62	0.08	12.4	0.15	0.13	2662	1.6, ∞	3.4, 17.1	46.4	6.9	703
s_{NES} x 3												
2 Edge, 1% Miss	5.18	4.77	0.41	14.0	0.16	0.15	2747	1.2, ∞	4.5, 16.0	46.9	14.1	610
3 Edge, 1% Miss	3.98	3.30	0.68	10.2	0.16	0.16	2707	1.5, ∞	8.9, 15.0	30.	22.6	582
Y-Bump												
2 Edge, 1% Miss	1.41	1.21	0.21	10.0	0.12	0.15	2733	6.9,1.2	5.7, 6.0	35.7	22.1	650
2 Edge, 4% Miss	1.07	0.96	0.11	7.6	0.10	0.15	2742	6.2,1.3	6.3, 4.8	37.6	21.1	686
3 Edge, 1% Miss	1.43	1.27	0.16	10.3	0.11	0.15	2741	5.7,1.2	3.7, 5.9	37.8	21.1	663
3 Edge, 4% Miss	1.18	0.97	0.21	8.1	0.12	0.15	2745	4.1,1.3	6.3, 5.5	33.5	21.4	649
Min. Traversals												
3 Edge, 4% Miss	469	0.02	469	1.8	0.12	0.13	2748	3.8,1.	6.0 , 0.2	6.2	1.3	71

A POSSIBLE UPGRADE FOR ISIS

M R Harold, R G Bendall, T A Broome, I S K Gardner, M G Glover, C R Prior,
C W Planner and G H Rees. CLRC RAL

Abstract

The Rutherford Appleton Laboratory's neutron spallation source ISIS is running at its design intensity of 200 μA and demand for experimental time is 2.4 times that available. Studies have shown that it is possible to increase the accelerated current to nearly 300 μA by installing four 2nd harmonic RF cavities in the synchrotron. This scheme, together with the other necessary changes to the ISIS Facility, are described. Compared with the capital value of the Facility, the expense of providing the extra 100 μA is shown to be very modest.

1 INTRODUCTION

ISIS consists of an 800 MeV proton synchrotron feeding a heavy metal target at 50 Hz. Neutrons are generated and moderated to feed 16 instruments which are used for the study of condensed matter. In addition to the large number of neutron users, there are installations for the study of neutrinos and muons. All of these experiments would benefit from an increase in the proton intensity. An additional target station to operate at 10 Hz would suit many of the neutron experiments and there is also great interest in radioactive beams. A study is in progress to see how such facilities can best be fitted into the ISIS complex. This paper describes how it is possible to increase by 50 % the synchrotron beam intensity, which is presently limited by space charge to about $2.5\ 10^{13}$ protons per pulse (ppp). The increase in current must be achieved without losing any more beam than is lost at present.

2 THE DUAL HARMONIC SYSTEM

The power necessary to accelerate 200 μA is provided by 6 RF stations disposed round the synchrotron (see Fig 1). These produce a peak of 140 kV per turn during the 10 ms acceleration period. Typical beam losses are 1% during injection, when the RF volts are extremely low, and 10% during trapping, which lasts for about 1.5 ms. Most of the lost protons are collected on beam scrapers, and with the loss concentrated in less than 1/5th of the circumference hands-on maintenance is the norm. Any increase in intensity should not result in further losses.

When a second harmonic component (h=4) of the correct phase and amplitude is added to the accelerating RF (h=2), the longitudinal phase acceptance is increased so that more particles can be accelerated without necessarily leading to increased loss. Such a scheme was successfully applied to NIMROD, the 7GeV predecessor of ISIS, and has been used on other accelerators, but never (we believe) on a fast-cycling machine.

A detailed analysis of a system for ISIS [1] showed that simply adding an h=4 component, variable in phase and amplitude, does not allow stable acceleration throughout the cycle; it is also necessary to increase the fundamental amplitude. As it would be difficult to find space in the ring for a 7th fundamental station, it is

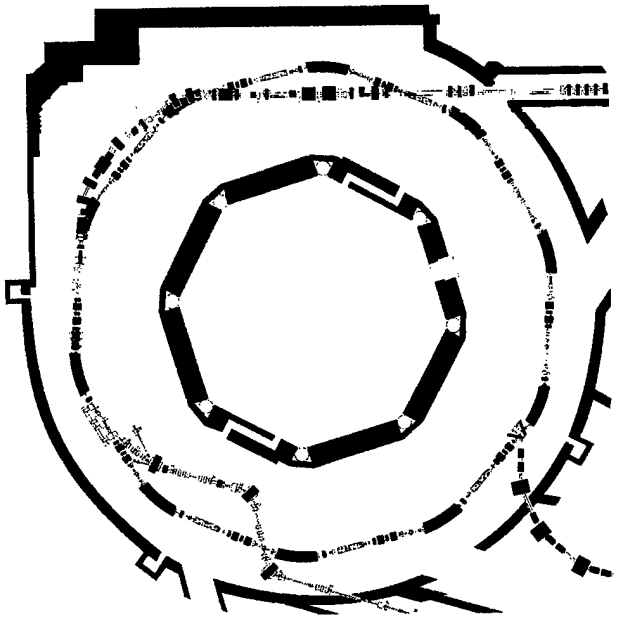


Figure 1 The ISIS 800 MeV synchrotron

fortunate that the present cavities have a little voltage in hand and should be adequate for the task. A simulation using less than 20,000 particles showed that, with the various restrictions pertaining with ISIS, the phase and amplitude of the h=4 component have to be programmed within tight limits if extraneous loss is to be avoided. This is particularly so for the last 2.5 ms of acceleration. Figure 2 clearly shows the distortion and enlargement of the RF bucket due to the higher harmonic.

There will be a small increase in momentum spread, which should not be significant, but there is a possibility of a small amount of loss later in the cycle - up to 6 ms. This could be troublesome due to the higher

0-7803-4376-X/98/$10.00 © 1998 IEEE

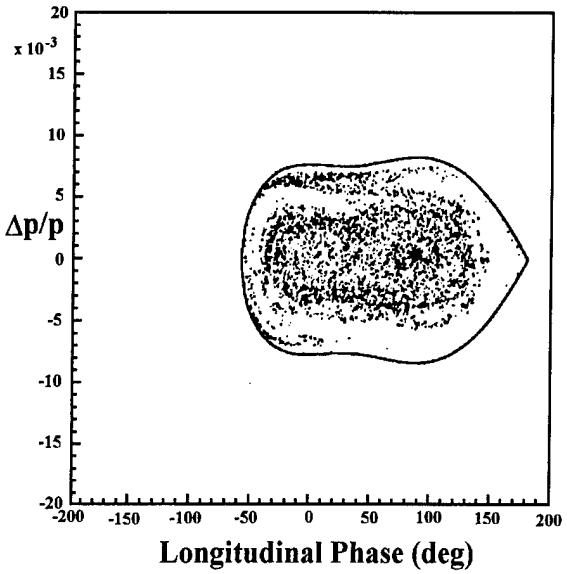


Figure 2 Longitudinal phase space 2.5 ms after injection

momentum of the lost particles, but small changes to the phase and amplitude functions should bring the loss earlier. Table 1 gives the expected inventory of injected, accelerated and lost particles per pulse for the 200 μA and 300 μA cases.

TABLE 1

Accel'd current	Injected protons	Accel'd protons	Lost protons
200 μA	$2.9\ 10^{13}$	$2.5\ 10^{13}$	$4\ 10^{12}$
300 μA	$4.1\ 10^{13}$	$3.7\ 10^{13}$	$4\ 10^{12}$

3 HARDWARE

The 2nd harmonic cavities will be shortened versions of the fundamental cavities (Fig 3). About half the original length, they will be installed in four short straight sections which can be made available in the ten superperiod ring (see Fig 1). Two steering magnets will have to be re-located elsewhere, and two position monitors will be lost, but these changes will have little effect on the running of the machine. The cavities will be assembled at RAL, as were the fundamental units. The original drawings, jigs and fixtures are all available.

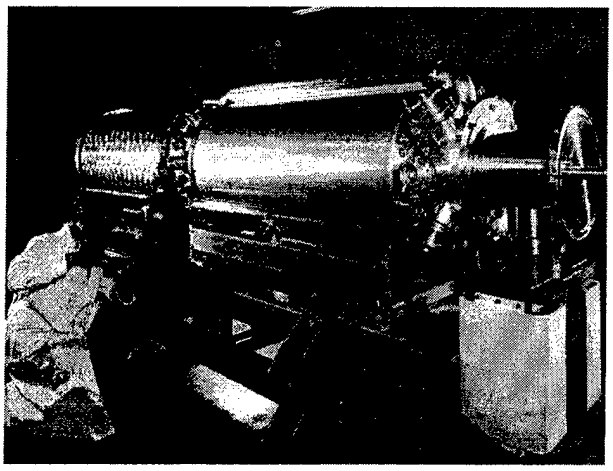


Figure 3 A fundamental RF cavity

The frequency range to be covered by the new cavities is 2.6 - 6.2 MHz, so the low level RF technology will be essentially unchanged. Regarding the high power RF, however, it is hoped to collaborate with Argonne National Laboratory and KEK National Laboratory in Japan in testing a cathode follower driver. Two of the four cavities would be powered in this way to simplify the phasing. Workers at KEK (and at PSR, LANL) have used a triode cathode follower to drive an RF cavity, and shown it to behave in a stable manner at a fixed frequency [2]. The low impedance of the cathode follower circuit should result in low induced volts and obviate the need for feed-forward compensation.

The objective would be to demonstrate that cathode followers behave in a stable way under frequency modulation conditions, and that the beam-induced voltages are as calculated. The design will be such that it will be relatively easy to revert to the present fundamental circuit should it be necessary. The total cost of the cavities, power supplies and distribution (including manpower) is estimated to be £4.6M.

4 INJECTOR REQUIREMENTS

In order to provide the $4.1\ 10^{13}$ ppp necessary for 300 μA operation, the output of the 70 MeV injector must increase from 22 to 30 mA of H^- ions. The ion source has been developed so as to give 50 mA with a 250 μsec pulse length, but the 665 kV Cockroft-Walton pre-injector is now very elderly and is to be replaced by an RFQ in 1998.

The linac tank RF modulator systems may not be robust enough to withstand the increased beam loading. Steps necessary to overcome this include uprating the modulators' capacitor banks and charging systems, and replacing the modulating switch tubes and the RF drivers to the penultimate 4616 tetrode amplifiers. A test rig is also required to study and eliminate parasitic oscillations in the TH116 output tube which will become more critical at the higher output level.

5 EFFECTS ON THE NEUTRON TARGET

Because a second target station would cost far more than the 300 μA upgrade, we have to assume that initially, at least, the present target will have to be able to cope with the extra beam power. The performance of the two tantalum targets used so far suggests that at least a one year life time can be expected at the higher intensity. It is probable that the plates will have to be reduced slightly in thickness, but this is straightforward and of low cost.

Development work on the tantalum target is proceeding at present and the requirements for 300 μA can be anticipated to ensure that any changes for higher power can be made easily. The use of uranium as a target material at this intensity can probably be ruled out.

The moderator cooling is adequate for the higher intensity but the reflector cooling on the top section is already marginal at 200 μA, and the design does not allow the water flow to be increased. A new top section will be required for running at 300 μA. The existing top section will be retained as a spare, so there will be no immediate disposal cost.

Regarding the shielding, all the dose rates will increase by 50%. This should not be a problem in the generally accessible areas but the rates in the neutron beam line enclosures with the shutters closed must be reviewed and it would be prudent to allow for shielding upgrades.

6 COSTS

The RF proposal has been costed in detail [3] and a summary is given in Table 2. Manpower costs are included.

TABLE 2

Item	Cost (£k)
4 LPRF systems	410
4 RF cavities	1270
4 HPRF amplifiers	420
4 HPRF power supplies	1830
Distribution	190
Civil engineering	480
Linac changes	700
Target reflector	700
Extra shielding	50
TOTAL (ex VAT)	**6050**

6.1 Additional running costs

The annual electricity costs of running ISIS are about £2M. The cost of running the four extra systems, assuming 5500 hours operation per year, will be £0.36M. The full marginal annual running cost is shown in Table 3, which allows for the fact that the linac will be fitted with tubes that are more expensive to replace.

TABLE 3

Item	£k
Linac Power tubes	25
2nd Harmonic Systems:	
Power tubes	70
Spares	20
Maintenance	20
Electricity	360
TOTAL (ex VAT)	**470**

7 SUMMARY

The ISIS Facility has a replacement cost of about £150M and cannot meet the demand for its neutrons, muons and neutrinos. The primary proton current can be increased by 50% at a capital cost of £6M and extra running costs of £0.5M per annum.

REFERENCES

[1] Studies of Dual Harmonic Acceleration in ISIS. C R Prior, A-11, ICANS-XII, RAL Report 94-025

[2] Very Low Output Impedance RF System for High Intensity Accelerators. Y Irie, A-131, ibid.

[3] ISIS Synchrotron 2nd Harmonic Costing. M G Glover and R G Bendall. ISIS/SYN/3/96

DESIGN OF BOOSTER SYNCHROTRON FOR MUSES

T.Ohkawa, RIKEN, Wako, Saitama 351-01, Japan
T.Katayama, Center for Nuclear Study, School of Science, University of Tokyo
Tanashi, Tokyo 188, Japan

Abstract

The Booster Synchrotron Ring (BSR) is a part of Multi-USe Experimental Storage rings (MUSES). BSR functions exclusively for the acceleration of ion and electron beams. The maximum accelerating energy is, for example, to be 3 GeV for proton; 1.45 GeV /nucleon for light ions of q/A=1/2; 800 MeV/nucleon for heavy ions of q/A=1/3. Electron beam is accelerated to 2.5 GeV from the injection energy 300 MeV. The accelerated ion and electron beams will be fast extracted and injected into the Double Storage Rings (DSR) by one turn injection. As another operation mode, ion beams will be slowly extracted for the experiments. In this paper, results of lattice study and injection and extraction procedures of the BSR are presented.

1 LATTICE REQUIREMENTS AND CONSTRAINS

The lattice structure is to be as compact as possible. Basically FODO structure is used, and we adopt a racetrack type to accommodate two long straight sections. They are used for the devices for fast and slow extraction of ion and electron beams and RF cavities.

The circumference of BSR is 179.716m which is 32/6 times the SRC extraction radius, and the maximum magnetic rigidity is 14.6Tm. Those values are determined by a requirement that heavy ions with q/A=1/3 are accelerated up to the energy of 800 MeV/nucleon. Transition γ was set to be as high as 4.22, being satisfactory value for beam stability.

2 BSR LATTICE DESCRIPTION

As shown in Fig.1, the BSR consists of two arc sections and two long straight sections. Each arc section is mirror symmetrical system, and there are two bending cells. Each bending cell is a dispersion suppresser arc, and consists of four FODO cells because this number of cells is specified to raise γ_t sufficiently large. The dispersion in the straight sections outside the arc section is zero. The length of a dipole magnet of 1.911 m is determined by the circumference specification. The maximum magnetic field of a dipole (1.5 T) is determined by required maximum rigidity of 14.6 Tm. The lattice is specified for eight families of quadrupoles; QF1 and QD1, QF4 and QD4 in the arcs, QF2 and QD2, QF3 and QD3 in the long straight sections. The structure of one FODO cell and short straight section in the arc are given as follows.

$$\text{cel}=\text{QF1}\,\underline{d_1}\,\text{B}\,\underline{d_2}\,\text{QD1}\,\underline{d_1}\,\text{B}\,\underline{d_2}$$

$$\text{str2}=\text{QF4}\,\underline{d_3}\,\text{QD4}\,\underline{d_s}\,\text{QD4}\,\underline{d_3}\,\text{QF4}$$

Then, the lattice of each arc section (60.365 m) is

arc=(cel,cel.cel,cel,str2,-cel,-cel,-cel,-cel)

In this structure, d1 (d2) is 0.925 m (0.475 m) drift space which are used for sextupole magnets for chromaticity correction and kicker magnets for COD correction.

The two long straight sections are mirror symmetry structure. The lattice of each section (23.876 m) is

$$\text{str1}=\underline{d_s}\,\text{QF2}\,\underline{d_3}\,\text{QD2}\,\underline{d_s}\,\text{QD3}\,\underline{d_3}\,\text{QF3}\,\underline{d_3}\,\text{QD3}\,\underline{d_s}\,\text{QD2}\,\underline{d_3}\,\text{QF2}\,\underline{d_s}$$

where, d_S is a free space with a length of 4.276 m which is used for RF cavities, injection kickers or other device.

Then, the whole lattice of BSR is described as follows.

BSR=(arc,str1,arc,str1)

Tune values are chosen from the tune diagram shown in Fig.2. The parameters of the lattice are summarized in Table 1. The β and dispersion functions are shown in Fig.3. Transition γ is 4.643 and the peak dispersion is 3.730 m. The peak β function are 14.028 m in horizontal direction and 15.089 m in vertical direction. The calculation is performed using the MAD program.

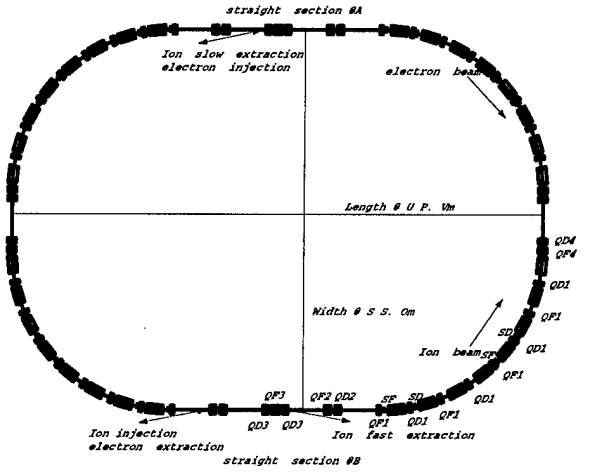


Fig.1 A Layout of BSR

0-7803-4376-X/98/$10.00 © 1998 IEEE

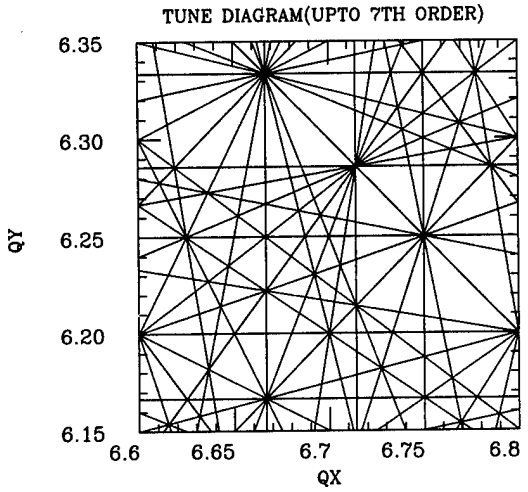


Fig.2 Tune diagram

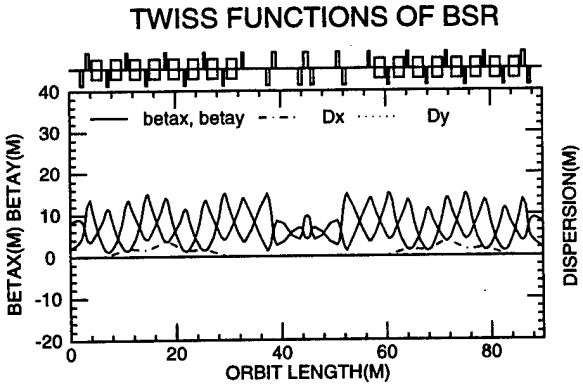


Fig.3 β and dispersion functions along the lattice

Table 1. Lattice Parameter of BSR

Circumference	C=179.7159 m
Average Radius	R=28.603 m
Max. Magnetic Rigidity	Bρ=14.6 Tm
Momentum Compaction	α=0.0437
Transition gamma	γ_t=4.643
Betatron Tune Values	Qx/Qy=6.700/6.220
Natural Chromaticity	Q'x/Q'y=-8.896/-8.321
Max.β Amplitude	βx/βy=14.028m/15.089m
Max.Dispersion	Dx/Dy=3.730m/0.0

3 DYNAMIC APERTURE

The dynamic aperture might be seriously reduced when chromaticity is corrected. The reason for this is due to the low average value of dispersion in a ring, corresponding to high γt. In this lattice, natural chromaticity values are -8.896 (horizontal) and -8.321 (vertical), and are corrected by two families of sextupoles SF and SD, (focusing and defocusing), associated with their respective qurdrupoles as indicated in Fig.1. Same family's sextupoles in one bending cell, are located π apart in phase in order not to excite the resonance with particular amplitude and phase. The normalized field strengths of sextupoles required to correct chromaticity are relatively large: 9.036 m^{-3} for the SF and -15.000 m^{-3} for the SD. The tracking results of the beam with $\varepsilon_x=125\pi$ mm.mrad, $\varepsilon_y=5\pi$ mm.mrad and fully corrected chromaticity, are shown in Fig.4. The largest initial betatron amplitude for which particles are still on a stable orbit is defined as a dynamic aperture. The above tracking results show that the dynamic aperture of BSR is larger than $\varepsilon_x=125\pi$ mm.mrad and $\varepsilon_y=5\pi$ mm.mrad. Next, we calculate the tracking for the beam with $\varepsilon_x=750\pi$ mm.mrad, $\varepsilon_y=30\pi$ mm.mrad, $dp/p=10^{-3}$ and fully corrected chromaticity when all magnet elements have been misaligned (misalignments are ±100μm and rotations are ±0.1mrad) and field errors (sextupole components of dipole magnets are ±0.1 m^{-3}) introduced randomly. These tracking results shows that the dynamic aperture of BSR is as large as $\varepsilon_x=750\pi$ mm.mrad and $\varepsilon_y=30\pi$ mm.mrad.

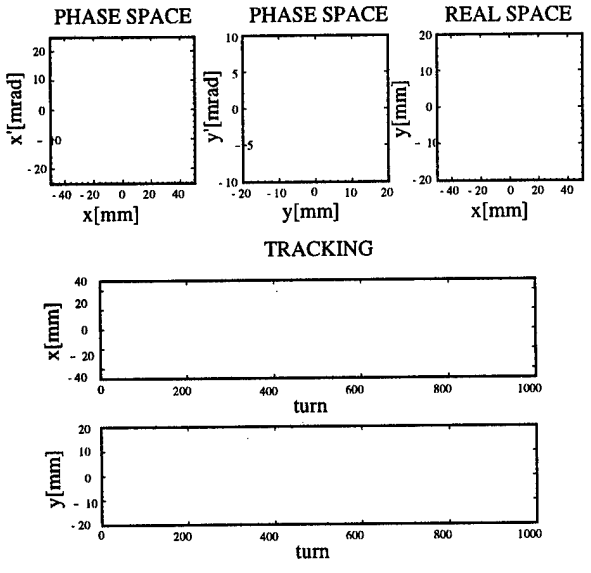


Fig.4 Result of single-particle tracking

Further tracking has to be performed to obtain information about the main sources of dynamic aperture reduction and to estimate the level of multipolar content tolerable in the dipoles.

4 INJECTION AND EXTRACTION

An arrangements of the injection and extraction magnets are shown in Figs 5 and 6. The BSR lattice is designed to be able to operate with two different extraction mode for ion beams; fast extraction and slow extraction.

As seen in Fig.5, an electrostatic septum(ES), four septum magnets(SM1, SM2, SM3, SM4) and three bump magnets(BM1) are used for the electron beam multi-turn injection. These magnets except bump magnets, are used for ion beam slow extraction which is carried out by using third order resonance (ν_{res}=20/3).

As seen in Fig.6, three septum magnets(SM2, SM3, SM5), four bump magnets(BM2) and ten kicker magnets(K1) are used for the ion beam one turn injection. These magnets are also used for electron beam fast extraction. The ion beam from the ACR is injected into the septum magnet SM5 at an angle of with respect to the straight section of the BSR.The ion beam is finally kicked and placed in the reference orbit by the kicker magnets.This kicker magnets are used for ion beam fast extraction. So, kicker magnets must be risen and fallen less than 50 ns.

5 SUMMARY

We have designed the lattice of BSR which satisfies fundamental requirements. This lattice is required to be further investigated in detail for the installation of all the necessary hardwares. Optimization of the lattice of the BSR is under progress.

REFERENCES

[1] N.Golubeva,etc.,"A Racetrack lattice with missing magnets for the BOOSTER",TRIUMF,1991.

[2] T. Katayama et al., Proc. 5th European Particle Accelerator Conf., p.563 (1996).

[3] T. Ohkawa et al., Proc. 5th European Particle Accelerator Conf., p.929 (1996).

[4] S. Watanabe et al., Proc. 5th European Particle Accelerator Conf., p.2340 (1996).

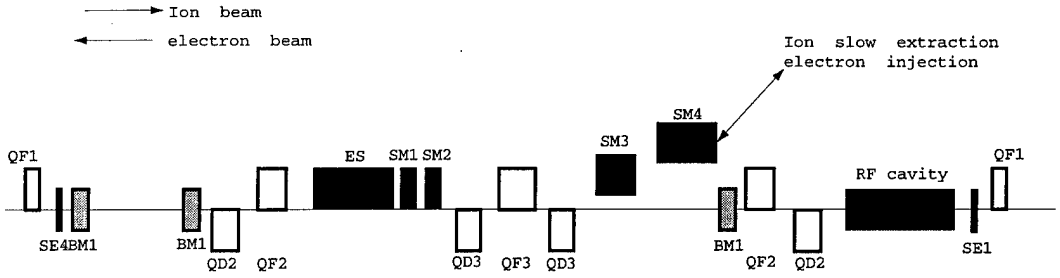


Fig. 5 An arrangement of straight section A

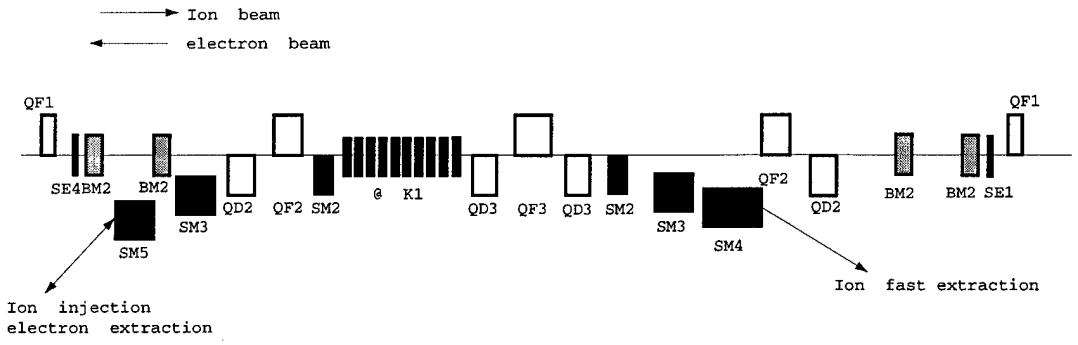


Fig. 6 An arrangement of straight section B

ELISA - AN ELECTROSTATIC STORAGE RING FOR ATOMIC PHYSICS

Søren Pape Møller, Institute for Storage Ring Facilities, University of Aarhus
DK-8000 Aarhus C, Denmark

Abstract

The design of a new type of storage ring (synchrotron) for heavy ions using electrostatic deflection and focusing devices is described. Such a storage ring will be attractive for many atomic-physics experiments, and also for basic research in neighboring fields such as chemistry and biology.

1 INTRODUCTION

Storage rings were initially developed for storage of high-energy particles in particle-physics laboratories. In the last decade, storage rings have also been introduced in atomic-physics and intermediate-energy physics laboratories with great success, see [1]. These low- and medium-energy storage rings were modelled after the storage rings in the high-energy laboratories, in particular LEAR [2], using magnetic bending and focusing devices (e.g. magnets and quadrupoles) and only using electrostatic devices in special cases, e.g. electrostatic septa. These low-energy storage rings have stored particles of very low momentum and velocity. As extreme examples, ASTRID [3] has stored $^4He^-$ ions at an energy of 5 keV, corresponding to a momentum of 4 MeV/c and a beam of $^{12}C_{70}^-$ at 25 keV with a velocity of 0.00025 c.

The new development [4] summarized in the present paper is a design of a storage ring for low, but yet finite, energy particles using electrostatic devices, in particular electrostatic deflectors and quadrupoles. The device is called ELISA for ELectrostatic Ion Storage ring, Aarhus. Although the energy is limited to rather low values, this is not an issue for several experiments.

The advantages of such a ring as compared to a magnetic storage ring are both technical and fundamental. Examples of more technical advantages are no remanent fields, no hysteresis and no cooling water. A more fundamental advantage is the absence of magnetic fields, which may e.g. induce transitions between the hyperfine levels of the circulating ions. Such an electrostatic ring can also be made much smaller than a magnetic one, which in itself can be advantageous, but it also means that heating and cooling of the vacuum chambers surrounding the beam is easy. In this way lower pressures can be envisaged by cooling.

ELISA-type rings are thought to be storage devices, but electrostatic rings could just as well be operated in synchrotron mode. Actually, much faster acceleration than in magnetic rings is possible due to the absence of eddy currents.

The other storage device used to confine charged particles for extended periods in a small volume is the electromagnetic trap. Comparing with an electromagnetic trap, the electrostatic storage ring allows easy access to the ion beam. Furthermore, electrons and atomic/molecular fragments created either spontaneously or by the interaction with an electron- or laser-beam can easily be detected. In particular neutral fragments will be easily detected at the end of straight sections. This issue, although seemingly trivial, is actually a very important feature of storage rings used for atomic-physics experiments [4].

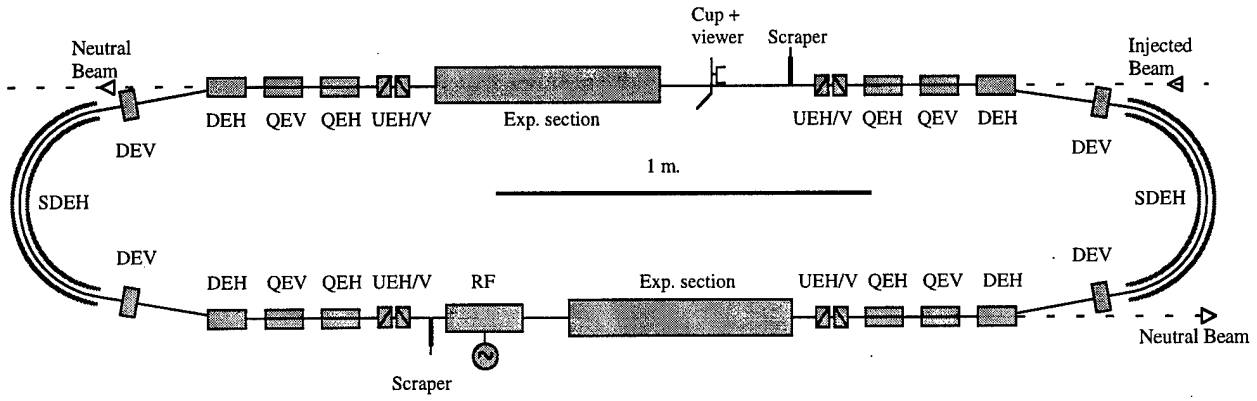


Figure 1 Layout of the ELISA storage ring.

0-7803-4376-X/98/$10.00 © 1998 IEEE

There is one fundamental difference between a ring based on electrostatic and magnetic elements: The longitudinal energy is conserved in the magnetic case, but this is not the case for an electrostatic device. Clearly, an ion traversing an electrostatic deflector off-axis will meet a longitudinal component of the deflecting field and will be accelerated or decelerated at the entrance and exit of the device. This means that there will be an inherent coupling between the longitudinal and transverse directions. It also means that the focusing in a deflector will be different for the electrostatic and the magnetic case.

Initially, we believed that ELISA would be the first electrostatic storage ring. An electrostatic storage ring/synchrotron was, however, built and tested successfully in the mid 50'es, before starting the construction of the AGS at Brookhaven [5]. This ring was built to test the principles of alternating-gradient focusing and transition crossing, and was as such very succesful. The ring was designed for 1-10 MeV electrons and had a circumference of 43 m. This so-called "electron analog" is to the authors knowledge the only electrostatic synchrotron/storage ring ever built, and one might speculate why this is so. One reason is undoubtedly that the low-energy rings are descendants of the high-energy rings where magnetic devices are beneficial.

2 TECHNICAL DESCRIPTION

The electrostatic storage ring presently being built has a race-track shape as shown in fig. 1. This is the most simple lattice with straight sections, but clearly different lattice configurations are possible as for magnetic storage rings. In the following, we shall briefly outline some details. Comparisons with a magnetic storage ring will be made, and here ASTRID [3], familiar to the author, has been chosen.

2.1 Optics - the lattice

The lattice is defined by two 160° spherical electrostatic deflectors (SDEH), four 10° parallel plate deflectors (DEH) and four pairs of electrostatic quadrupoles (QEV, QEH) in the two straight sections.

The resulting lattice functions are shown in fig. 2 corresponding to tunes of Q_H = 1.21 and Q_V = 1.44. The strong focusing from the 160° deflectors is seen to result in a very narrow waist in the middle of the deflectors. Furthermore, an almost round beam is obtained in the straight sections. The lattice is quite flexible, and straight section lengths between 0.6 m (as indicated in fig. 1) and 1.2 m can easily be accomodated. The horizontal and vertical tunes can be adjusted between 1 and 2. For closed-orbit correction, four vertical ± 1° steerers (DEV) are arranged as shown in the fig. 1. Horizontally, the two 160 ° and the four 10° deflectors will be used for closed-orbit corrections.

The injection system consists of a chopper in the injection beamline and one of the 10° deflectors used as a pulsed inflector giving a single-turn injection. Injection will initially be made from an isotope separator.

All electrodes close to the beam will be gold-plated in order to avoid oxide layers and the potentials across such insulating layers. The required voltages, apertures and other relevant numbers are given in the table.

2.2 3D tracking simulation

The optics has first been designed using linear transfer matrices for hard-edged elements in ordinary lattice programs. In this way, fig. 2 was produced.

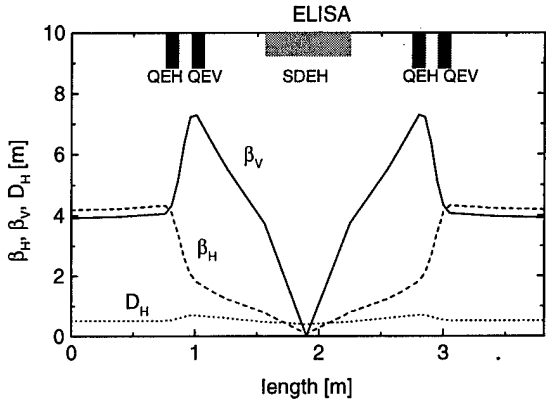


Figure 2 Lattice functions for half the circumference.

Secondly, the program SIMION [6] has been used for inclusion of fringe fields etc. SIMION is an ion optics simulation program that models ion optics with 3D electrostatic potential arrays determined by solving the Laplace equation outside electrodes. Ions has been traced (flown) through the machine for many turns, and stability has been verified for hundreds of turns for not too large starting amplitudes.

2.3 Radio Frequency System and Diagnostics

Although no acceleration is envisaged in ELISA, bunching of the beam will be useful for bunched-beam observations. Hence a driven drift tube rf-system of 20 cm length will be installed. 30 V on the drift tube will give 1 V peak rf corresponding to $\Delta p/p = 0.7$ % for harmonic number 1. This can be achieved with a rf-signal generator and a small amplifier. The required frequency range is 10 kHz - 500 kHz.

The diagnostics for ELISA will consist of a viewer, a Faraday cup, four sets of horizontal and vertical pick-ups for bunched beam observation, Schottky noise detection, two sets of horizontal and vertical scrapers, and a current transformer.

Finally, observations of the neutral beam emerging from the two straight sections will be very useful.

GENERAL PARAMETERS	
Injection energy	25 keV
Circumference	7.62 m
Revolution time	3.5μs (p), 93μs (C_{60})
Betatron tunes (Q_H, Q_V)	1.21, 1.44
Chromaticities (ξ_H,ξ_V)	-1.7, -1.3
Momentum compaction (α_p)	0.42
160° spherical deflectors	
Electrode radii	235 and 265 mm
Nominal voltages	± 4.0 kV
10° deflectors	
Plate distance	50 mm
Plate length	100 mm
Nominal voltages	± 2.2 kV
Electrostatic quadrupoles	
Inscribed radius	26.2 mm
Electrode length	50 mm
Nominal voltages	± 0.43 kV
Chopper and inflector	
rise/fall time	< 200 nsec.

2.4 Intensities and lifetimes

The maximum current that can be stored is usually limited at low energy by the space-charge tune shift. Hence, we should be able to store currents comparable to that in ASTRID, up to around 10 μA corresponding to some 10^8 particles.

The lifetime of a beam of singly-charged ions at low energy is determined by interactions with the residual gas, either electron-capture or electron-loss. Cross sections for these processes are approximately velocity-independent at small velocities, and hence a longer life-time is expected at low velocities, since the traversed target thickness becomes smaller. Furthermore, it is easier to obtain a low pressure in a small ring than in a large one. We design for a pressure around 10^{-11} mbar, which should give lifetimes in the 10-1000 sec. region. The short lifetimes apply to loosely bound negative ions.

Intra-beam scattering is the scattering between beam particles, which can lead to emittance growth. As an example, we have calculated the intra-beam scattering times (1/e folding times) for a 25 keV beam of singly-charged ions with mass M = 24, a current of 10 μA, momentum spread $\Delta p/p = 3\ 10^{-3}$, horizontal emittance of ε_H = 30 π mm mrad, vertical emittance ε_V = 15 π mm mrad using the program ZAP [7]. We get a longitudinal scattering time of τ_L = 36 sec., a horizontal scattering time of τ_H = 162 sec. and a vertical scattering time τ_V = 65 sec. The emittances and momentum spread have been chosen to get roughly equal scattering times in all three planes. These scattering times are comparable to the lifetimes of positive particles. We note here, that intra-beam scattering times scale as $\tau \propto T^{3/2} A^2/(N q^2)$, where T is the kinetic energy, A and q the ion mass (in amu) and charge, and N the number of circulating ions. Hence heavier ions will have significantly larger scattering times.

3 POTENTIAL PHYSICS EXPERIMENTS

The applications of ELISA-type storage rings exploits the specific properties such as simplicity, use of electric fields and absence of magnetic fields, low residual gas pressure and easy access to beam particles and decay products. In particular, storage of ions with any mass is possible at the design energy of 25 keV [8], including fullerenes, proteins and macro-molecules. We refer to [4] for further speculations about possible experiments.

The limitation for the actual ELISA ring is the rather low storage energy, which however is not a principal constraint for this type of storage ring, and one can envisage electrostatic storage rings with energies up to tens of MeV's with circumferences below 100 m.

4 CONCLUSIONS AND OUTLOOK

A new general type of storage device for charged particles has been described.

At the time of the present conference the ELISA storage ring is being assembled at our institute, and the commissioning will start this summer.

5 ACKNOWLEDGEMENTS

Several persons have contributed to the design and concept of ELISA. In particular, V. Toft has converted the ideas to engineering constructions and L.H. Andersen has brought the physics ideas and potential experiments into the design.

REFERENCES

[1] S.P. Møller, Proc. of the fourth European Particle Accelerator Conference, eds. V. Suller and Ch. Petit-Jean-Genaz, London 1994, p. 173, World Scientific.

[2] P. Lefevre, D. Möhl and G. Plass, Proc. 11th Int. Conf. On High Energy Accelerators, Geneva, 1980, EXS 40 (1980) 53.

[3] S.P. Møller, Proc. of the 1993 Particle Accelerator Conference, editor S.T. Corneliussen, Washington D.C., 1993, p. 1741.

[4] S.P. Møller, accepted for publication in Nucl. Instrum. Methods in Phys. Res. A.

[5] G.K. Green and E.E. Courant in Handbuch der Physik, Band XLIV, Springer-Verlag, Berlin 1959, p. 319.

[6] David A. Dahl, SIMION 3D, Version 6.0, User's Manual, distributed by Ion Source Software, P.O. Box 2726, Idaho Falls, ID 83403, USA.

[7] ZAP USER'S MANUAL, M.S. Zisman, S. Chattopadhyay, and J.J. Bisognano, dec. 1986, Lawrence Berkeley Laboratory, University of California, LBL-21270 UC-28.

[8] Actually for very heavy ions, the beam will sag in the straight sections owing to gravity, eventually limiting the mass to a finite value. This effect was realized by J.S. Nielsen.

A PROTON DRIVER FOR THE MUON COLLIDER SOURCE WITH A TUNABLE MOMENTUM COMPACTION LATTICE*

D. Trbojevic, J.M. Brennan, E.D. Courant, T. Roser, and S. Peggs
Brookhaven National Laboratory, Upton, NY, 11973, USA,
K.Y. Ng, C. Johnstone, and M. Popovic at FNAL, and J. Norem at ANL

Abstract

The future Muon Collider will have a luminosity of the order of 10^{35} cm^{-2-1} during 1000 turns when the muons decay. This requires 10^{12} muons per bunch. The muon source is a 30 GeV proton driver with 2.5 10^{13} protons per pulse. The proton bunch length should be of the order of 1 ns. Short bunches could be created by a tunable momentum compaction lattice which would bring the momentum compaction to zero in a short time. This isochronous condition would allow bunches to shear and become very short in time. We present a lattice where the momentum compaction is a tunable parameter at fixed horizontal and vertical betatron tunes. The values of the maxima of the dispersion function are kept small. We examine two kinds of lattices, with combined function as well as normal dipole and quadrupole magnets.

1 INTRODUCTION

The muon collider progress report and its components are described in other reports at these proceedings[2],[3],[4],[5] etc. Muons will be created through pion decay. The proton driver, a high intensity ~30 GeV synchrotron, delivers compressed and focused bunches to a heavy metal target, generating pions which are captured and transfered to a linac. The proton bunches need to be very short (of the order of 1 ns) to minimize the final muon longitudinal phase space and reduce the cost of the muon phase rotation section. It is very desirable to have a proton synchrotron without transition crossing and with *tunable* momentum compaction α. RF manipulations could be performed very easily if the momentum compaction is adjustable, but this requires unchanged betatron tunes. A finite synchrotron frequency is preferable for stability. There have been many previous reports on *harmonic modulation* of the lattice[6][7], a *missing dipole* approach by U. Wienands[8] and the a recent report by B. Autin[9]. We reported earlier a *flexible momentum compaction* (FMC) approach[10] which represents a possible solution for the design of such a lattice. Because the Proton Driver would require fast acceleration and a lot of cavities, the *missing dipole* solution for momentum compaction control looks very preferable. The drawback is dispersion in the cavities. We report a lattice design method which uses the FMC modules with *missing dipoles*in a standard FODO cell lattice, to make the momentum compaction tunable. With small adjustments of the quadrupoles on both sides of the missing dipoles in the FMC module the transition energy γ_t may be changed to any desired value without changing the betatron tunes.

2 THE *MISSING DIPOLE* CELL

Three standard FODO cells are used to produce an imaginary γ_t lattice by having two dipoles missing within the central cell, as previously reported[8].

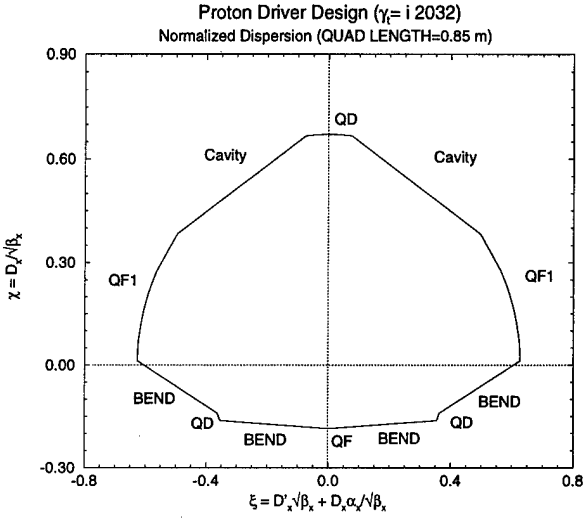


Figure 1: Imaginary γ_t lattice with *missing dipole* FODO cells lattice.

The length of the cell is selected by setting the limit on a dipole magnetic field strength to B~1 T[11]. The betatron functions have maxima of β_x=27.1 m and β_y=27.8 m, with an imaginary transition energy of γ_t=i 2032. The "FMC-method" of lattice design, described earlier[12], uses the normalized dispersion function. The *Missing Dipole* FODO lattice, tuned to be an imaginary γ_t lattice, is presented in normalized dispersion space in Fig. 1. The middle FODO cell without dipoles is shown in the upper part of the ξ and χ diagram where the dispersion is positive. The oscillations of the dispersion function are within a range from D_{max}=1.42 m to D_{min}=-1.00 m. The dispersion values in the regular 90° FODO cell, made of the same elements, oscillates between from D_{max}=1.39 m to D_{min}=0.68 m. The betatron functions of the *missing dipole* FODO cells are presented in Fig. 2.

There are many synchrotrons still in operation today (AGS at Brookhaven National Laboratory, Fermilab Booster, PS at CERN, etc.) which were built with com-

* Work performed under the auspices of the U.S. Department of Energy

0-7803-4376-X/98/$10.00 © 1998 IEEE

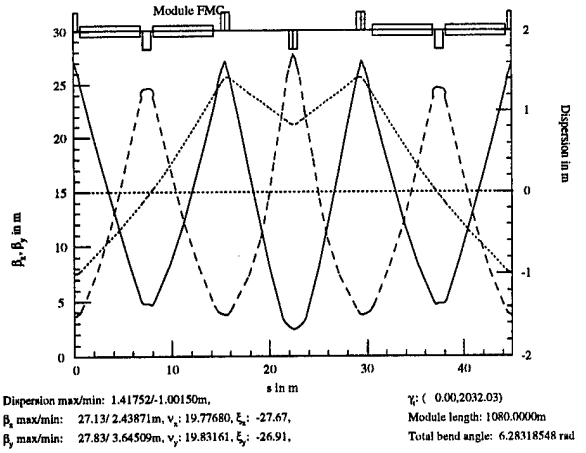


Figure 2: Imaginary γ_t lattice with *missing dipole* FODO cells.

bined function magnets. The same method of lattice design is applied with combined function dipole FODO cells in Fig. 3. The betatron functions have little different maxima β_x=22.2 m and β_y=41.9 m and the dispersion function oscillates from D_{max}=1.49 m to D_{min}=-0.85 m.

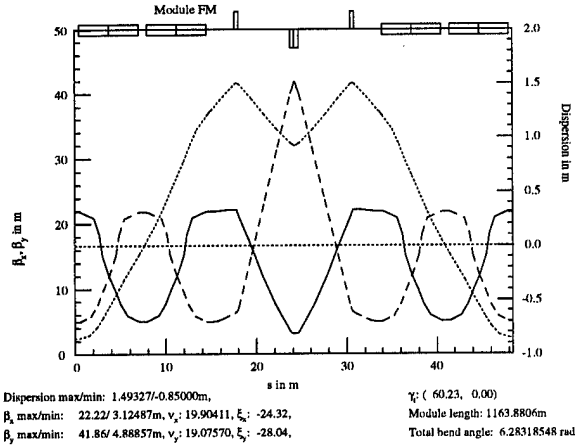


Figure 3: The *missing dipole* FODO cell lattice with combined function dipoles.

3 TUNABLE MOMENTUM COMPACTION WITH *MISSING DIPOLE* FODO CELLS LATTICE

The horizontal and vertical betatron tunes have to remain unchanged if the momentum compaction of the accelerator is required to change during the operation. This was an additional constraint to the design. We have demonstrated[10] that the momentum compaction of a *Flexible Momentum Compaction* module can be adjusted to almost any value by choosing the value of the minimum dispersion function at the beginning of the module and adjusting the gradients of the quadrupoles. The length of the FMC module was kept constant. The momentum compaction dependence on the value of the minimum dispersion function in a different FMC module is presented in Fig. 4. A very similar quad and the minimum of the dispersion function adjustments in these *missing dipole* FODO cells are performed (see Table 1). First, positions of the focusing quadrupoles QF1 in the central FODO cell were allowed to be a variable parameter, keeping a constant length of the FODO cell as well as the horizontal and vertical betatron tunes. The quadrupoles length was selected[11] to be L=0.85 m. A distance of the focusing quad with respect to the end of the dipole is labeled D1, while the other side towards the RF cavity is D2.

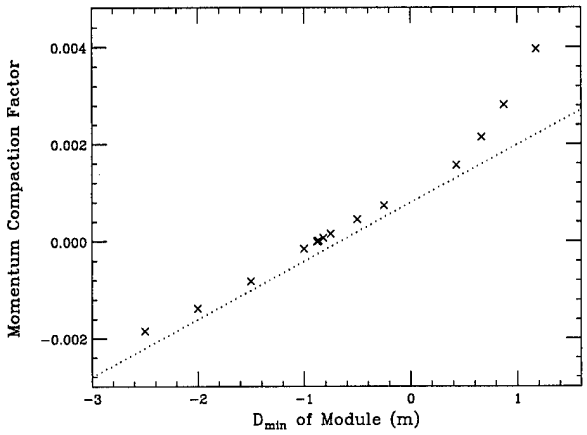


Figure 4: The momentum compaction α dependence on the initial negative value of the dispersion function in a different FMC module.

Table 1

D1(m)	D2(m)	α	D_{min}	D_{max}
0.567	1.041	0.0004110	-0.88	1.442
0.654	0.955	0.0001770	-0.81	1.428
0.679	0.929	0.0001100	-0.97	1.425
0.692	0.916	0.0007659	-0.98	1.423
0.706	0.902	0.0000408	-0.99	1.420
0.721	0.888	0.0000048	-1.00	1.418
0.723	0.886	0.0000000	-1.00	1.417
0.734	0.874	-0.0000297	-1.01	1.416
0.761	0.848	-0.0000978	-1.03	1.411
0.808	0.800	-0.0002106	-1.06	1.402
0.839	0.769	-0.0002884	-1.08	1.397

A positions of the focusing quadrupole QF1 is selected at the isochronous condition (or when α=0). A solution, for the tunable momentum compaction for the *missing dipoles* FODO cells, was found by splitting the focusing QF1 quadrupoles into two new QFS and QF2 quadrupoles, at the beginning and the end of the central FODO cell with missing dipoles. The betatron functions within the momentum compaction tunable lattice are presented in Fig. 5.

The momentum compaction was tunable by adjusting gradient values in the two new quadrupoles as presented in Table 2. The dispersion values presented in Table 1 are in meters. It is important to note, The betatron tunes values at all quadrupole settings for the corresponding γ_t values were kept within an error of $\leq 10^{-4}$.

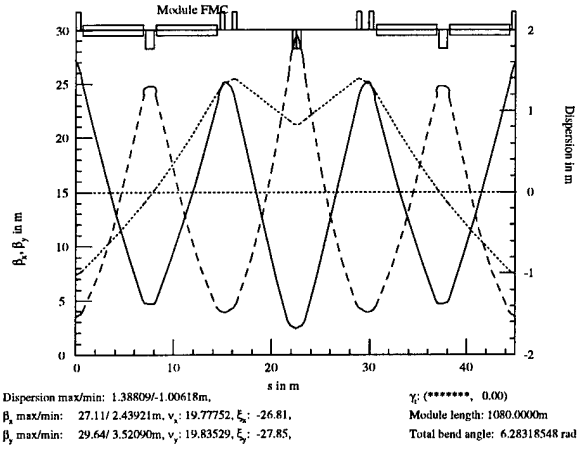


Figure 5: The *missing dipole* FODO cell lattice with tunable momentum compaction.

Table 2

GFS(T/m)	GF2(T/m)	α	D_{min}	D_{max}
12.89	38.60	0.000424	-0.88	1.43
17.23	35.36	0.000191	-0.81	1.41
19.52	33.56	0.000021	-0.86	1.41
20.49	32.77	0.000001	-0.88	1.40
27.23	27.08	0.000000	-1.01	1.39
27.28	27.04	0.000003	-1.01	1.39
27.50	26.85	0.000015	-1.01	1.39
32.93	21.93	0.000335	-1.10	1.37

Table 2 shows the dependence of the transition energy γ_t on the gradients in the two quads. More details of this is shown in Fig. 6.

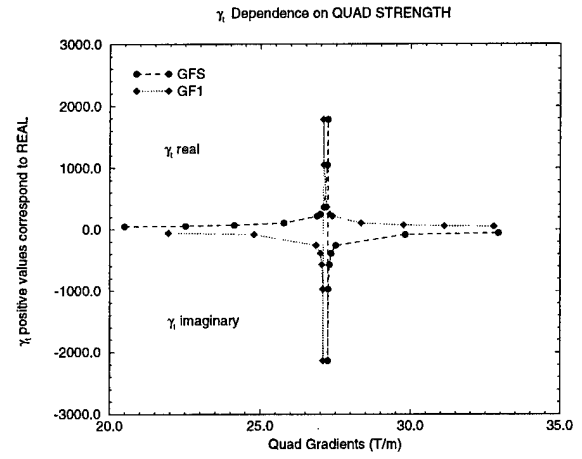


Figure 6: Transition energy, γ_t, dependence on the quad gradients.

4 CONCLUSIONS

The proton driver for the muon collider requires very short bunches of the order of 1 ns. The proton driver is a fast cycling machine which requires a lot of RF cavities distributed around the ring. This is why the *missing dipole* FODO lattice design was combined with the *Flexible Momentum Compaction* method. The drawback of this design is not having zero dispersion at the cavities. An abrupt change of the momentum compaction at the end of the accelerating cycle, would shear the bunches and make them very narrow in time but wide in momentum. A lattice with a tunable momentum compaction, fulfilling this condition, keeps the dispersion function within small values in the range of D$\approx \pm$1m to allow a large momentum aperture. This lattice might be also suitable for RF manipulations, where instead of the RF frequency change one can use the tunable momentum compaction. An experiment at the AGS to examine the creation of short bunches by a sudden change in momentum compaction has been proposed and accepted. This experiment will be performed at the transition energy by using the γ_t quadrupoles to produce a required difference in the momentum compaction.

5 REFERENCES

[1] R.B. Palmer, "Progress on $\mu^+\mu^-$ Colliders", these proceedings.

[2] J. Norem, C. Ankenbrandt, J. Griffin, C. Johnstone, F. Mills, A. Moretti, R. Noble, M. Popovic, Z. Qian, M. Brennan, T. Roser D. Trbojevic, and J. Wei, "The Proton Driver for the $\mu^+\mu^-$ Collider", these proceedings.

[3] D. Neuffer and A. Van Ginneken, "μ-Ionization Cooling Simulation Results", these proceedings.

[4] R.C. Fernow, J.C. Gallardo, and R.B. Palmer, "Ionization Cooling using a FOFO lattice", these proceedings.

[5] D. Summers, D. Neuffer, Q.S. Shu, and E. Willen, "Acceleration for the $\mu^-\mu^+$- Collider", these proceedings.

[6] A.I. Iliev, *Analytic Approach to Design of High Transition Energy Lattice with Modulated β Function*, Proc. of 1991 IEEE Part. Accel. Conf. (1991) San Francisco, California, pp. 1907-1909.

[7] G. Guignard, *A Lattice with no Transition and Largest Aperture*, Proc. of 1989 IEEE Part. Accel. Conf. (March 20-23, 1989) Chicago, IL, pp. 915-917.

[8] E.D. Courant, A.A. Garren, and U. Wienands, "Low Momentum Compaction Lattice Study for the SSC Low Energy Booster", Proc. of 1991 IEEE Part. Accel. Conf. (1991) San Francisco, California, pp. 2829-2831.

[9] B. Autin, R. Cappi, R. Garoby, J. Gruber, J.P. Riunaud, and K.H. Schindl, "PS-XXI, a new 32 GeV proton synchrotron in the LHC injector chain", private comunication.

[10] S.Y. Lee, K.Y. Ng, and D. Trbojevic, Minimizing dispersion in flexible-momentum compaction lattices, Physical Review E, Vol. 48, Number 4 (October 1993) pp. 3040-3048.

[11] T. Roser, private communications.

[12] D. Trbojevic, D. Finley, R. Gerig, and S. Holmes, *Design Method for High Energy Accelerator without Transition Energy*, Proc. of Second European Particle Accelerator Conference, Nice, France (June 1990) pp. 1536-1538.

CORRECTION OF DEPOLARIZING RESONANCES IN ELSA

C. Steier, D. Husmann
Universität Bonn, Physikalisches Institut, Nußallee 12, 53115 Bonn, Germany

Abstract

At the 3.5 GeV electron accelerator ELSA (Bonn University) an upgrade for polarized electrons is under way. A source of polarized electrons (GaAs crystal, electrons produced by photoeffect using circular polarized laserlight) is operational. Recently, studies have been started to minimize the losses in polarization level due to crossing of depolarizing resonances, which necessarily exist in circular accelerators (storage rings). Calculations concerning different correction schemes for the depolarizing resonances in ELSA are presented, and first results of measurements, done by means of a Møller polarimeter in one of the external beamlines, are mentioned.

1 INTRODUCTION

The electron stretcher ring ELSA[1] is operational since 1987, both as a continuous beam facility for external fixed target experiments and part of the time as a dedicated synchrotron light source. The accelerator complex consists of two LINACs, each equipped with sources of polarized and unpolarized electrons, a fast cycling booster (50 Hz) and the storage ring ELSA (Fig. 1). External beams can be provided beween 0.5 and 3.5 GeV with currents between some pA and 100 nA[1]. A slow resonance extraction on a third integer resonance excited by sextupoles is used. The extraction time can be varied between 20 ms and some minutes.

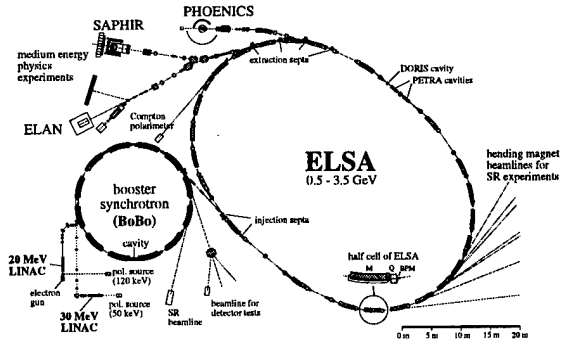


Figure 1: Site plan of the ELSA facility at Bonn University.

Starting 1997/1998 experiments with longitudinal polarized electrons or circular polarized photons (produced by bremsstrahlung) will be carried out. Because of the intensity requirements of an external target, the polarized electron beam cannot be produced by self polarization due to the Sokolov-Ternov effect. Instead, a low energy polarized electron source has to be used. With strained GaAs or superlattice crystals it is possible to achieve a polarization level of more than 70% at the source.

In order to preserve the polarization level to the experimental target, several depolarizing resonances (both in the booster and in the storage ring) have to be crossed and corrected. This has been successfully done in several proton accelerators but not yet in an electron storage ring. Some calculations will be presented to show the differences. The applied correction techniques also differ from the scheme which is applied in high energy electron storage rings to obtain a high equilibrium polarization.

In a flat ring only the vertical component of the polarization is preserved. Every spin vector precesses around this direction and the precession frequency depends only on the energy of the corresponding particle: $Q_{sp} = \gamma a$, where Q_{sp} is the spin tune (i.e., the number of precessions in the restframe of the particle in one turn), γ the relativistic Lorentz factor and a the gyromagnetic anomaly ($1.16 \cdot 10^{-3}$ for electrons). Depolarizing resonances arise from resonant coupling of the spin precession to periodic horizontal magnetic fields. They can be divided into two main categories:

1. intrinsic resonances due to the vertical betatron oscillations in quadrupoles and the resulting horizontal magnetic fields: Resonance condition is $\gamma a = kP \pm Q_z$, where k is an integer, P the supersymmetry of the ring ($P = 2$ for ELSA) and Q_z the vertical betatron tune;

2. imperfection resonances due to magnet errors and the resulting vertical closed orbit distortions: Resonance condition is $\gamma a = k$.

The change in polarization level after the linear crossing of an isolated resonance (with equal strength for all particles) is given by the Froissart-Stora equation[2]

$$\frac{P_f}{P_i} = 2 \cdot \exp\left(-\frac{\pi \mid \epsilon_r \mid^2}{2\alpha}\right) - 1, \qquad (1)$$

where ϵ_r is the resonance strength and α the crossing speed ($\alpha = \frac{\dot{\gamma a}}{\omega_{rev}}$ for imperfection and $\frac{\dot{\gamma a}}{\omega_{rev}} \pm \frac{\dot{Q}_z}{\omega_{rev}}$ for intrinsic resonances).

2 INTRINSIC RESONANCES

The strength of an intrinsic resonance is different for each individual particle and depends on its vertical betatron amplitude. To calculate the depolarization one has to integrate Eq. (1) over the vertical phase space. But since the resulting formula has the same qualitative behaviour, the following qualitative discussion can be carried out using Eq. (1).

[1] Electron Stretcher Accelerator

0-7803-4376-X/98 /$10.00 © 1998 IEEE

There are two possibilities to avoid depolarization: For small resonance strength or high crossing speed the polarization vector stays unchanged. For high strength or low crossing speed a spinflip (with conservation of the absolute value) is possible. For an electron accelerator like ELSA, the second possibility is not applicable for intrinsic resonances. At imperfection resonances the situation is somewhat different which will be discussed later.

To reduce the strength of intrinsic resonances, tests to decrease the emittance coupling have been done. A coupling ratio of less than 5% could be achieved during the whole ramping phase (below 1% during flat top). But even then, three of the intrinsic resonances are sufficiently strong to cause a significant depolarization. So additionally the crossing speed has to be increased. For this purpose a pulsed system of Panofsky type quadrupoles with ferrite yokes has been designed that shifts the vertical tune rapidly during resonance crossing[3].

The design was optimized with respect to the inductance of the magnet and the multipole composition of the field. For earlier designs of similar magnets (IUCF, KEK or ELSA) only two-dimensional simulations have been used. They underestimated the inductance of the magnet by more than a factor of two. We suspected the field of the conductor loops at the end of the magnet and the stray fields to be the source of the discrepancy. In a three-dimensional simulation both effects are included naturally. The result of a 3D simulation using MAFIA[4] for the inductance of our magnet was 14.4 μH in comparison to 6.4 μH from a 2D simulation. As a check for the validity of this result, we also did 3D simulations of several already existing ironless or ferrite quadrupoles and we could reproduce their measured inductances to about 10%.

The main problem causing higher multipole components is the skin effect (the rise time of the magnet is 10 μsec and the peak gradient 1.2 T/m). This has been simulated and a coil arrangement was chosen to minimize the unwanted multipoles.

2.1 Ion Problems

Ions produced by scattering on the residual gas molecules can be captured in the electric potential of the beam. They introduce an additional space charge that results in a shift of the betatron tune. This problem does not exist for proton accelerators, where depolarizing resonances have been successfully crossed in the past.

Furthermore there can be a coherent instability between the captured ions and the electron beam if a certain threshold number of captured ions is reached. The instability strongly increases the emittance of the electron beam and causes a sudden change in the vertical tune (Fig. 2). This increases the strength of intrinsic resonances and requires the tune jump to be enlarged. For a homogeneous filling of ELSA, the instability threshold is reached for relatively low currents at injection energy. Therefore cures against the instability have to be applied[5].

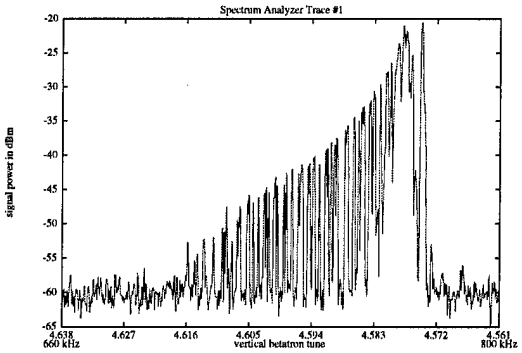


Figure 2: Spectrum of the coherent vertical oscillation of the beam (averaged over 10 sec) around the $5-Q_z$ betatron tune sideband ($Q_z^{nom} = 4.575$). No external excitation of the beam is applied.

At ELSA, first a gap in the filling structure (filling only 1/3 of the ring) was applied during synchrotron radiation runs. Later this has also been used for external experiments, but the gap has to be smaller in order to keep a high duty factor. A second possible cure is the application of beam-shaking (resonant vertical excitation of the beam close to a sideband of the vertical tune). This is now integrated into the routine operation with high currents below 1.6 GeV. Also clearing electrodes can be used. Their installation is under way and first tests have been carried out. Overall the coherent instability is suppressed for beam parameters relevant for polarized electron operation. Also the tuneshift could be kept at an acceptable level.

3 IMPERFECTION RESONANCES

The strength of imperfection resonances is roughly proportional to the average vertical closed orbit distortions. Unfortunately, the achievable overall orbit quality during ramping is not sufficient to avoid a significant depolarization. Therefore one concentrates on the closed orbit harmonic(s) that is (are) driving a specific resonance. Because the crossing speed of imperfection resonances is determined by the ramping speed only (which is more or less fixed), the only parameter to vary is the resonance strength.

3.1 Adiabatic Spinflip

The spin motion in an electron storage ring is strongly affected by the synchrotron motion and the stochastic emission of synchrotron radiation[6]. Therefore the dependence of the final polarization on the resonance strength is more complicated than in Eq. (1). To calculate this, one starts with the formula describing the spin precession close to a resonance in a spinor representation. Then one has to include the synchrotron oscillation, the emission of photons and the ramping into the terms containing γ. Afterwards it can be solved by pertubation methods and numerical integration.

These calculations show that it is possible to achieve a

nearly perfect spinflip up to the 4th imperfection resonance at ELSA (Fig. 3). The required resonance strength is about $2 \cdot 10^{-3}$. This can easily be achieved by the help of two existing correctors and the required closed orbit distortion will be safely inside the machine aperture. The advantage of a spinflip over a harmonic correction is the smaller sensitivity to corrector and measurement errors. Thus it is fast to optimize and should be very reproducible once established. At higher energies a spinflip is still possible, but is combined with significant depolarization. Therefore a harmonic correction scheme is planned for these resonances.

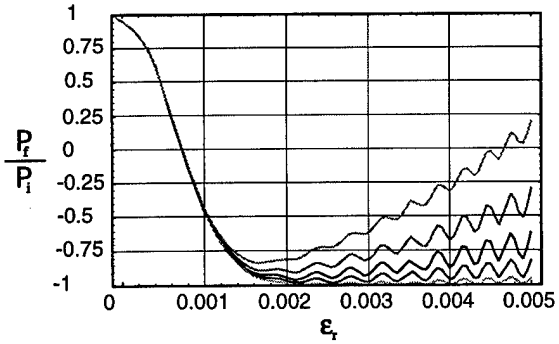


Figure 3: Simulation of depolarization due to crossing of the 3rd (lowest curve), 4th, 5th, 6th or 7th (top curve) imperfection resonance plotted against the resonance strength. The graphs have been calculated with ELSA standard beam parameters and a ramping speed of 6 GeV/s.

3.2 Harmonic Correction

The aim of the harmonic correction is the reduction of the degrees of freedom of the optimization problem by correcting only the closed orbit harmonics relevant for the actual resonance. Therefore it is possible to optimize the initial corrector settings calculated from closed orbit data by measurements of the actual depolarization. For simulations concerning different correction methods a program to calculate resonance strengths based on the Courant-Ruth formalism[7] (used in combination with MAD[8]) has been written. As a result, specifications for an upgrade of the corrector system have been formulated.

4 EXPERIMENTAL STATUS

A source of polarized electrons is operational and first tests with a superlattice crystal were carried out. A low energy Mott polarimeter downstream from the source and a high energy Møller polarimeter in an external beamline can be used for measurements. During several machine development runs longitudinal[2] polarization behind the storage ring has been measured[3] at 1.27 GeV with the Møller polarimeter. Currently several investigations are going on to optimize the polarization level at that energy.

[2]In the external beamline the spin orientation is rotated from vertical to longitudinal.

[3]using a bulk GaAs crystal at the source

Within this year an internal Compton polarimeter will come into operation at the storage ring. It will be calibrated by observation of the polarization build-up due to the Sokolov-Ternov effect. To choose suitable optics, tracking studies with SITROS[9] have been carried out. Afterwards each of the resonances will be studied in detail. The two tune jump quadrupoles will be installed in the end of 1997. An upgrade to improve the speed of the corrector dipoles will be carried out this year and also the beam position monitors are currently equipped with new electronics.

Beam based alignment measurements have been started (the k-values of all quadrupoles can be varied separately) in order to improve the precision of the closed orbit correction and to calibrate the optics model of ELSA[10]. First results indicate that the lattice errors are sufficiently weak, such that gradient error and other higher order depolarizing resonances cause no problems.

5 SUMMARY

The program to correct depolarizing resonances at ELSA has been started. To produce polarized electrons a GaAs-type source is used. A low and a high energy polarimeter are operational and first measurements of the polarization level behind the main ring have been done. Such studies of resonance crossing during ramping have not been performed at other electron storage rings yet. The design of a system of pulsed quadrupoles for the crossing of intrinsic resonances is finished. Cures for ion problems, which are specific of electron accelerators, are implemented. Simulations show that a spinflip can be achieved up to the 4th imperfection resonance to minimize depolarization. For higher energies synchrotron oscillations and synchrotron radiation become too strong. Therefore harmonic correction schemes have been simulated and upgrades of the corrector system with respect to the results are under way.

6 REFERENCES

[1] K.H. Althoff *et al.*, ELSA – One year experience, Part. Acc. 27 (1990) pp. 101-106.

[2] M. Froissart and R. Stora, Nucl. Instr. Meth. 7 (1960) p. 297

[3] T. Toyama, C. Steier *et al.*, Crossing of Intrinsic Depolarizing Resonances in ELSA, Bonn-ME-97-01.

[4] T. Weiland, MAFIA, the ECAD System, Darmstadt (1994).

[5] C. Steier, Vielteilcheneffekte bei der Elektronen-Stretcher-Anlage ELSA, Bonn-IB-95-40 (1995).

[6] K. Yokoya, Effects of Radiative Diffusion on the Spin-Flip in Electron Storage Rings, Part. Acc. 14 (1983) pp. 39-61.

[7] E.D. Courant and R.D. Ruth, Acceleration of Polarized Protons, Report BNL-51270 (1980).

[8] H. Grote and F.C. Iselin, The MAD Program, User's Reference Manual, SL Note 90-13 (AP) (Rev. 4) CERN (1995).

[9] M. Böge, Analysis of Spin Depolarizing Effects in Electron Storage Rings, DESY 94-087 (1994).

[10] J. Keil, D. Husmann, Beam-based Calibration of the Linear Optics Model of ELSA, these proceedings.

CONTINUOUS ELECTRON–ENERGY VARIATION OF THE EINDHOVEN RACETRACK MICROTRON

W.H.C. Theuws, J.I.M. Botman, H.L. Hagedoorn
Eindhoven University of Technology, Cyclotron Laboratory,
P.O. Box 513, 5600MB Eindhoven, The Netherlands.

Abstract

For the Eindhoven racetrack microtron, which has been designed as a fixed–energy accelerator at 75 MeV, continuous electron–energy variation between 45 and 90 MeV can be obtained by taking the microtron's orbit pattern as constant and varying certain parameters. The microtron injector is a linac producing electrons between 6 and 12 MeV. The microtron cavity potential and the magnetic guide fields must be adapted to the injection energy in order to fulfil the synchronism condition. The racetrack microtron's transversal and longitudinal acceptance are effected by electron–velocity deviations from the speed of light, which are different for each extraction energy. An account of these effects is presented together with the energy–setting measurements by using one of the microtron magnets as a spectrometer.

1 ISOCHRONISM

The Eindhoven racetrack microtron, see Fig. 1, has a 10 MeV, 2998 MHz travelling–wave linac (type M.E.L. SL75/10) as injector. In the microtron a 5 MeV standing–wave cavity accelerates the electrons 13 times, such that the extraction energy is 75 MeV[1]. Although the microtron has been designed as a fixed–energy machine[2], the extraction energy can be varied continuously without changes in hardware.

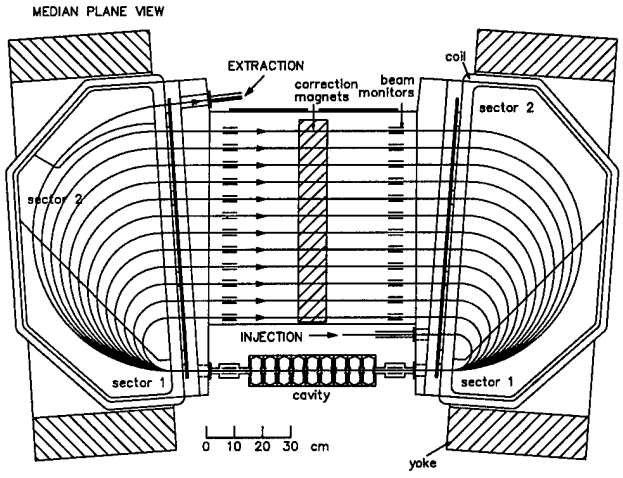


Figure 1: The 10–75 MeV Eindhoven racetrack microtron.

For isochronous acceleration the revolution time of each orbit in the accelerator must be an integer multiple of the RF–period, $1/f_0$. The isochronism condition for the first orbit is given by:

$$t_1 = \frac{2L}{\beta_1 c} + \frac{2\pi}{B_r e c^2}(E_0 + E_{inj} + E_{cav}) = \frac{\mu}{f_0}, \quad (1)$$

with L is the microtron drift length, B_r the resonant magnetic field of the 180 degrees bending magnets, E_0 the electron's rest energy, E_{inj} the kinetic energy at injection, E_{cav} the cavity potential, β_1 the relative velocity in the first orbit with respect to the speed of light, and μ the initial harmonic number. For isochronism the time–difference between two successive orbits, n and $n-1$, must be an integer multiple of the RF–period as well:

$$\Delta t = \frac{2L(\beta_{n-1} - \beta_n)}{\beta_{n-1}\beta_n c} + \frac{2\pi}{B_r e c^2} E_{cav} = \frac{\nu}{f_0}, \quad (2)$$

where ν is the incremental harmonic number. This condition can only be fulfilled for all orbits if the electrons are highly relativistic, i.e., $\beta_{n-1} = \beta_n = 1$. With this assumption two basic relations for a racetrack microtron can be derived, viz.

$$E_{cav} = \left(\frac{\nu}{\mu - \nu - 2Lf_0/c}\right)(E_0 + E_{inj}), \quad (3)$$

and

$$B_r = \frac{2\pi f_0}{e c^2}\frac{E_{cav}}{\nu}. \quad (4)$$

The frequency, f_0, and the injection energy, E_{inj}, are dictated by the linac–parameters, and have to be 2998 MHz and 10 MeV, respectively. The incremental harmonic number, ν, is chosen 2 in order to get well–separated orbits in the microtron (about 60 mm[2]). The cavity potential, E_{cav}, is chosen 5 MeV. The drift length, L, and consequently the initial harmonic number, μ, have to be sufficiently large to create enough space for the cavity. For $\mu = 26$ the drift length, L, is given by Eq. (3), which yields 0.99 m. The resonant magnetic field, B_r, is given by Eq. (4), and yields 0.524 T.

The isochronism condition is slightly violated as the particle velocity is not exactly equal to the speed of light. This implies that it takes a particle a little longer to complete an orbit. For the first orbit the extra time needed is 4.7 ps, which corresponds to 5.1 degrees of the RF–period. For the next orbits this phase–difference becomes less as the particle velocity increases, viz. 3.1, 2.2, 1.6 degrees, etcetera. Isochronism is not effected seriously by these phase–differences, as the stable phase–interval, given by[3]:

$$\Delta\phi = \arctan\left(\frac{2}{\pi\nu}\right), \quad (5)$$

0-7803-4376-X/98/$10.00 © 1998 IEEE

equals 18 degrees for the Eindhoven microtron.

The use of two–sector bending magnets, see Fig. 2, instead of homogeneous bending magnets does not violate the isochronism conditions at all. For homogeneous bend-

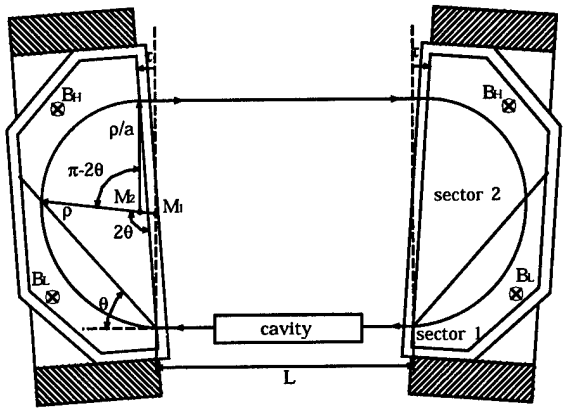


Figure 2: Two–sector bending magnets. The high magnetic field, B_H, is equal to a times the low magnetic field, B_L, which is linear with B_r[2].

ing magnets the orbit length of the n^{th} orbit is: $s_n = 2L + 2\pi\frac{p_n}{B_r e}$ (p_n is the momentum of the n^{th} orbit). For the two–sector magnet the orbit length is:

$$s_n = 2L + 2\frac{2\Theta a + \pi - 2\Theta + (a-1)\sin 2\Theta}{1 + \frac{1}{\pi}(a-1)(2\Theta + \sin 2\Theta)}\frac{p_n}{B_r e}, \quad (6)$$

which is linear with momentum just as for homogeneous bending magnets. This implies that the two–sector magnets do not influence isochronism; there is only a different relation between the resonant magnetic field and momentum.

2 ENERGY VARIATION

Different combinations of E_{inj}, E_{cav} and B_r can fulfil the basic microtron Eq. (3) and (4) as well. These three parameters can be changed without changes in hardware. The injection energy is provided by the linac, which can be varied continuously between 6 and 12 MeV. The cavity potential and resonant magnetic field can be adapted to the injection energy. The other parameters apparent in equations (3) and (4) can be kept constant.

The microtron's extraction energy is given by

$$E_{extract} = E_{inj} + 13E_{cav}, \quad (7)$$

in which $E_{cav} \approx \frac{1}{2}E_{inj}$ according to Eq. (3). Thus the extraction energy can be varied continuously between about 45 and 90 MeV. But, for lower extraction energies isochronism is violated more severely. An account of this effect is presented in the next sections.

3 TRANSVERSAL ACCEPTANCE

Energy variation as described in the previous section uses a constant orbit pattern. This means that all 'obstacles' that limit the transversal acceptance are at the same positions relative to the beam. Consequently the transversal acceptance is not influenced by energy variation.

However, this is not exactly true as the orbit pattern does not remain exactly constant. The bending radius, ρ, is linear with $\gamma\beta$. So for high energies ρ is linear with γ, which is linear with energy. But, for lower energies β plays a role as β is not linear with energy.

Consider the worst–case situation: $E_{inj} = 6$ MeV, and consequently $E_{cav} \approx 3$ MeV. This means that the energy in the first orbit is 9 MeV, which means $\beta = 0.999$. The relative influence for the bending radius ρ is $1 - \beta$, which is 0.1%. As $\rho \approx 0.1$ m for the first orbit, this means that $\delta\rho \approx 0.1$ mm. This is negligible with respect to the 10 mm space, which is available for the beam.

Thus the transversal acceptance is not influenced by energy variation.

4 LONGITUDINAL ACCEPTANCE

The longitudinal acceptance is calculated using Dôme's equations describing the dynamics of the synchrotron motion[4].

The phase ϕ_n and the energy E_n are defined just after the n^{th} cavity passage. The deviation of the phase and the energy from the synchronous value are given by $\Delta\phi_n = \phi_n - \phi_s$ and $\Delta E_n = E_n - E_{s,n}$ ($n = 1, 2, 3, ...$), respectively. The dynamics of the synchrotron motion is described by the finite difference equations:

$$\Delta\phi_{n+1} = \Delta\phi_n + \frac{2\pi\nu\Delta\epsilon_n}{\beta_n}, \quad (8)$$

and

$$\left(\frac{\Delta\epsilon}{\omega_s}\right)_{n+1} = \left(\frac{\Delta\epsilon}{\omega_s}\right)_n + \left(\frac{1}{\omega_s}\right)_n \left(\frac{\cos(\phi_s + \Delta\phi_{n+1}) - \cos\phi_s}{\cos\phi_s}\right), \quad (9)$$

with $\Delta\epsilon_n = \Delta E_n / E_{cav}$.

However, perfect isochronism is assumed in these equations. The violation of isochronism as a result of the fact that the electrons do not exactly have the speed of light (see Section 1) can be incorporated by adding a term $\Delta\phi_{\beta,n}$, which accounts for this effect, to the right–hand side of Eq. (8).

The longitudinal acceptance is calculated from Dôme's equations. For a regular grid of combinations of initial deviations $\Delta\phi_1$ and $\Delta\epsilon_1$ Dôme's equations are applied 13 times. If $\Delta\epsilon_n$ remains small during these calculations the position in longitudinal phase–space is considered as accepted. The longitudinal acceptance is linear with the extraction energy from 1.0 deg MeV for $E_{extract} = 45$ MeV

to 2.1 deg MeV for $E_{extract} = 90$ MeV. However, the acceptance plot is not perfectly centred around the origin. It is more off–centre for lower energies. This implies that an initial phase off–set and injection–energy off–set have to be applied. For extremely high energies the longitudinal acceptance stabilizes at about 11 deg MeV, but this is for extraction energies of about 1 GeV or higher, which is practically impossible to achieve with the Eindhoven racetrack microtron.

5 SPECTROMETER

When the extraction energy is chosen the injection energy and cavity potential can be calculated from Eqs. (3) and (7). The initial phase off–set and injection–energy off–set of the electron bunches can be determined from longitudinal–acceptance calculations (see Section 4). Then the injection energy, the cavity potential and the initial phase off–set are to be adjusted. The injection energy is determined by the injection line; the cavity potential by an RF–attenuator; and the phase by an RF phase–shifter.

The left–hand microtron magnet will be used to measure these three energy parameters[5]. This magnet is excited such that the beam is extracted immediately after the first cavity passage without recirculating in the microtron, see Fig. 3. The excitation current of the magnet in combination

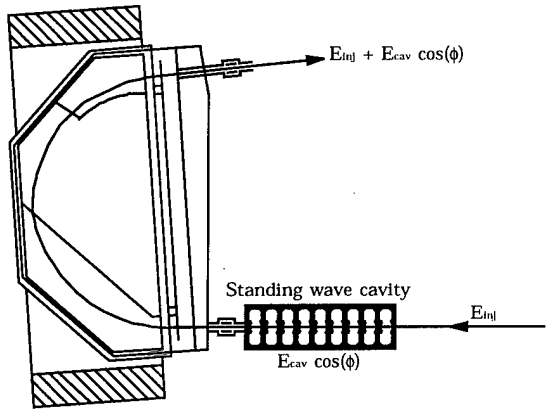


Figure 3: Left–hand RTM–magnet used as spectrometer.

with the beam–position monitors just before and behind the magnet give the mean energy of the beam. This energy is measured for different settings of the phase shifter, which results in a sine–like form of the energy as a function of phase,

$$E = E_{inj} + E_{cav} \cos \phi. \qquad (10)$$

The injection energy, E_{inj}, is the mean of the function. The cavity potential, E_{cav}, is the amplitude of the harmonic part. Moreover, the phase–difference, ϕ, is calibrated.

The absolute measurement accuracy of the 'spectrometer' is estimated to be 2%. The relative measurement accuracy is only about 0.2%, as the alignment errors of the beam–position monitors just before and behind the magnet and the absolute value of the magnetic field do not influence the relative accuracy.

6 CONCLUSIONS

Continuous electron–energy variation is very well possible with the Eindhoven linac–racetrack microtron combination without changes in hardware. The extraction energy can be varied between about 45 and 90 MeV. For lower extraction energies the longitudinal acceptance of the racetrack microtron decreases as the isochronism conditions are slightly violated by particle–velocity deviations from the speed of light. Moreover, the extraction energy cannot be varied dynamically as the microtron parameters that have to be varied are not controlled by dynamic control loops.

The injection energy and cavity potential can be measured within about 2% by using one of the microtron magnets as spectrometer. These measurements are not accurate enough for proper acceleration in the microtron[2], however the exact values are not important as long as $\frac{E_{cav}}{E_{inj}}$ is in agreement with Eq. (3). The relative measurement accuracy of the spectrometer is estimated to about 0.2%, which is accurate enough. The resonant magnetic field can be adapted to the exact values according to Eq. (4).

7 REFERENCES

[1] Theuws, W.H.C., Botman, J.I.M., Hagedoorn, H.L., Leeuw, R.W. de, Timmermans, C.J., *The 75 MeV racetrack microtron Eindhoven*, Proc. Lin. Acc. Conf., Geneva (1996) pp. 92–94.

[2] Webers, G.A., *Design of an electron optical-system for a 75 MeV racetrack microtron*, Ph.D Thesis, Eindhoven University of Technology (1994).

[3] Kapitza, S.P., Melekhin, V.N., *The microtron*, translated from Russian by I.N. Sviatoslavsky, Harwoord Academic Publishers, London (1978).

[4] Dôme, G., *Theory of RF acceleration*, Proc. Cern Accelerator School, advanced accelerator physics (1980) pp. 110–143.

[5] Theuws, W.H.C., Leeuw, R.W. de, Gossens, L.W.A.M., Spoek, P.M., Botman, J.I.M., Timmermans, C.J., Hagedoorn, H.L., *Diagnostic system of the Eindhoven linac–racetrack microtron combination*, Proc. Eur. Part. Acc. Conf., Barcelona (1996) pp. 1615–1617.

THE ANKA INJECTOR

D. Einfeld[1], F. Perez[2], R. Rossmanith[1] and R. Walther[1]

[1] ANKA, Forschungszentrum Karlsruhe, D-76021 Karlsruhe, Germany
[2] Lab. Sincrotro Barcelona-IFAE, Campus UAB, E-08193 Bellaterra, Spain

Abstract

ANKA [1] is a 2.5 GeV synchrotron radiation storage ring under construction at the Forschungszentrum Karlsruhe in Germany. The beam is accelerated up to 0.5 GeV in a booster synchrotron and afterwards injected into ANKA. In ANKA the beam is accumulated to 200 mA (second stage: 400 mA) and afterwards accelerated to 2.5 GeV. The injector system will consist of a pre-injector with an end energy of 20 or 50 MeV, a booster synchrotron and transport channels. The booster synchrotron should be as simple and inexpensive as possible. In the following three different concepts for designing the booster synchrotron are compared.

1 THE SELECTION OF THE OPTICAL CODE

For a compact and low energy accelerator the length of a bending magnet is comparable with the bending radius. In this region the basic beam optical parameters such as emittance and damping times are significantly influenced by edge effects. The beam parameters are calculated via the 5 synchrotron integrals I_1 to I_5 [2]. I_4, which describes the emittance and the damping times, consists of two parts: the contribution from the bending magnets and the contribution from the edge effects [2]

$$\Delta I_4 = - \sum_{polefaces} \frac{\eta_{poleface.} \tan\Phi}{\rho^2}$$

wherein η is the dispersion, Φ is the pole face angle in the usual definition and ρ is the bending radius. The sum has to be taken over all pole faces of the machine. For high energy synchrotrons and storage rings the contribution from the edges is negligible; hence, many programs like MAD [3] and BETA [4] do not take these effects into account. The codes DIMAD [5] and RACETRACK [6] take the edge effects fully into account. Both the horizontal emittance ε

$$\varepsilon = C_q \gamma^2 \frac{I_5}{I_2 - I_4}$$

and the horizontal damping partition numbers

$$J_x = 1 - \frac{I_4}{I_2}, \quad J_\varepsilon = 2 + \frac{I_4}{I_2}$$

depend on I_4. In the following parameters depending on I_4 were calculated with the program DIMAD. Beta-functions and the momentum compaction factors were calculated either with the program MAD or DIMAD.

In the following three layouts of boosters are compared. Only booster synchrotrons which are radiation damped in all 3 directions are considered: they can be operated with power supplies of any repetition rate, for instance 1 Hz, 3 Hz or 10 Hz.

2 OPTICAL COMPARISON OF THREE DIFFERENT DESIGNS

a. The booster synchrotron introduced in the ANKA proposal

The optics of the booster synchrotron introduced in the ANKA proposal [7] is shown in fig. 1. The lattice consists of 8 45° bending magnets and 2 quadrupole families.

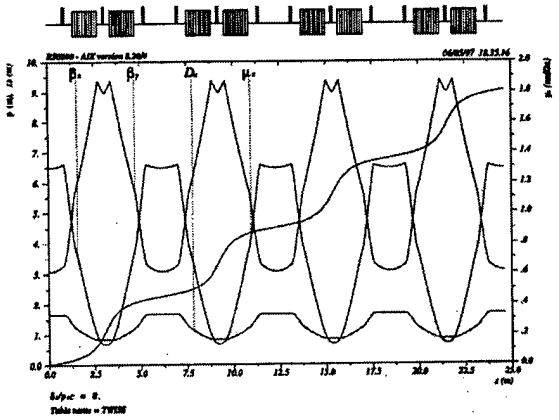


Fig. 1 β_x, β_y, η and horizontal phase advance of the booster synchrotron from the ANKA proposal (MAD calculations). The optical parameters are listed in Table 1.

b. Weak focusing booster synchrotron

An example of a simple weak focusing booster synchrotron is shown in fig. 2. It consists only of four 90 degree sector bending magnets with a gradient. The parameters for a zero pole face angle are listed in table 1. Using a pole face angle ≠0 can improve emiitance and α significantly.

0-7803-4376-X/98/$10.00 © 1998 IEEE

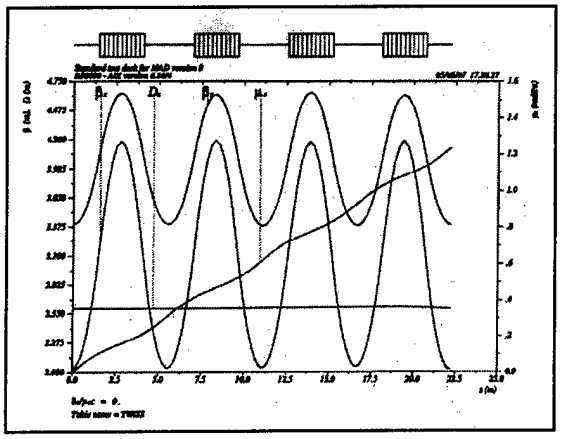


Fig.2 A simple weak focusing synchrotron consisting of only 4 bending magnets with a gradient (MAD calculations)

c. Strong focusing booster synchrotron with a gradient in the bending magnets

An example of a strong focusing booster synchrotron with 90^0 bends with gradients and 1 quadrupole family is shown in fig. 3.

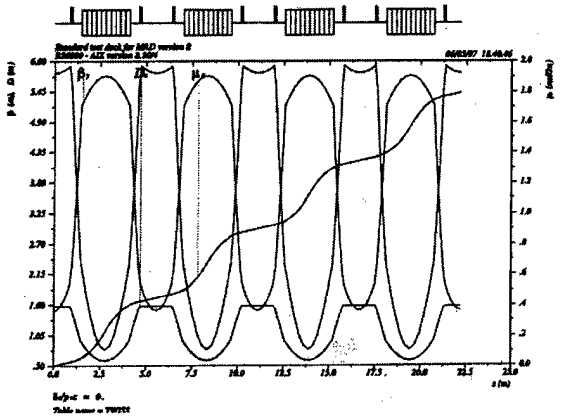


Fig. 3 A strong focusing booster synchrotron with a gradient (MAD calculation)

d. Table of the optical parameters

The optical parameters of the three machines are compared in Table 1. The most significant differences between the three machines are in the emittances and the momentum compaction factors.

e. The evolution of the emittance

With the parameters listed in table 1 the evolution of the emittances during acceleration is shown in fig. 4. In the given example the acceleration time is 0.1 sec. The emittance of 7. 10^{-7} at the beginning is given by the injection process.

Parameter	proposal	weak focusing	strong focusing
bending radius [m]	1.66	1.66	1.66
number of bending magnets	8	4	4
field index	0	0.36	0.25
circumference [m]	24.6	22.2	22.2
pole face angle [degree]	22.5	0	45
momentum compaction	0.26	0.73	0.2
Q_x/Q_y	1.81/0.8	1.23/0.89	1.79/1.2
emittance [mm.mrad]	0.14	0.87	0.058
τ_x [sec]	0.023	0.04	0.015
τ_ε [sec]	0.025	0.009	0.015
σ_ε	$3.3\ 10^{-4}$	$3.\ 10^{-4}$	4.10^{-4}

Table 1 Comparison of the optical parameters of the three boosters

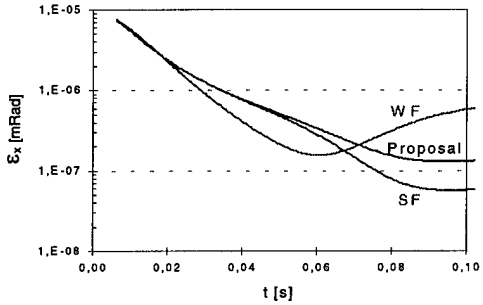


Figure 4: Evolution of the transverse emittance during acceleration. It is assumed that the acceleration time is 0.1 sec. WF: weak focusing. SF strong focusing booster with gradient from fig. 3.

3 LONGITUDINAL ACCEPTANCE

The longitudinal acceptance of the booster at injection and during ramping is mainly determined by the energy of the beam, the RF voltage and α.

a. RF system

The synchrotron radiation loss at maximum energy will be around 4 keV/turn, 40 W for a 10 mA beam. Assuming a pillbox type cavity with a shunt impedance of 3 MΩ and an overvoltage factor of around 7 the power dissipated on the wall of the cavity will not exceed 120 W.

The simplest solution for the ANKA-booster RF system is a 200 W solid state amplifier (as in SRS booster [8]). With this amplifier the peak RF voltage is 25 kV. The voltage is constant during acceleration. Only a low level control loop for the phase for synchronizing the booster with the pre-injector and the storage ring exists.

b. Longitudinal acceptance

Figure 5 shows the separatrix for the three boosters at 20 MeV. The maximum gives the longitudinal energy acceptance: 0.85% for the proposal, 0.5 % for the weak focusing (WF) and 1.0 % for the strong focusing (SF). The differences come mainly from the different momentum compactions of the boosters.

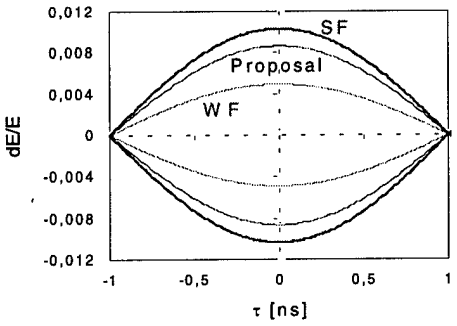


Figure 5: Separatrix for the three boosters at 20 MeV with an RF peak voltage of 25 kV.

The capture efficiency also depends on the time structure of the beam. With a bunch distance of 0.33 ns only about 4 out of 6 bunches will be accepted by the RF bucket in the booster. With a 500 Mhz pre-buncher at the exit of the gun each bunch finds a corresponding bucket.

Figure 6 shows the typical evolution of the beam envelope during ramping. Once the electrons are captured there will be no losses during the acceleration due to longitudinal oscillations since the emittance is faster reduced than the acceptance.

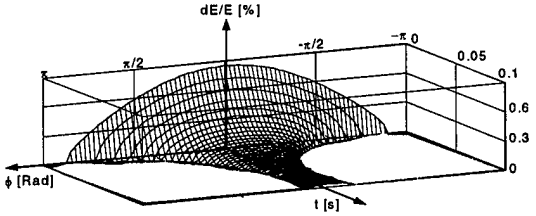


Figure 6: Evolution of the longitudinal beam envelope during ramping for the proposal booster.

The quantum lifetime depends on the momentum compaction factor: the larger α, the shorter the quantum lifetime. Assuming again a 200 W amplifier the quantum lifetime for the proposal booster and the SF is around 5 min, for the WF it is only 300 ms. With an acceleration time of 0.1 sec the WF booster will have an additional beam loss of 35% due to the quantum excitations.

4 PRE-ACCELERATOR

The pre-injector can be either a linac or a microtron. Both can be equipped with a 500 MHz prebuncher. Table 2 compares the different possibilities under the assumption that the current is 10 mA at 500 MeV. In these calculations a loss of 75% is assumed due to transversal oscillations during injection and acceleration.

	500 MHz Prebuncher	Proposal [mA]	WF [mA]	SF [mA]
Linac	Yes	70	198	54
	No	116	327	88
Microtron	Yes	14	21	14
	No	17	29	16

Table 2. Beam intensity at pre-injector exit

5 INJECTION AND EJECTION

The two types of boosters require different injection and ejection schemes. Fig. 7 shows the closed orbit distortion in the case that only one kicker for the WF and the SF booster is used for injection. The weak focusing booster needs a large aperture.

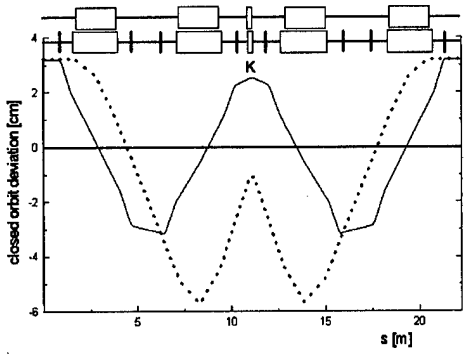


Fig. 7 Kicker bump with one kicker in a WF (dotted line) and a SF (solid line) booster. In the case of the WF booster two kickers are needed.

7 LITERATURE

[1] D. Einfeld et al., ANKA-Status, these Proceedings
[2] R. H. Helm et al., IEEE, NS-20, 973
[3] H. Grote and F. Iselin, CERN/SL/90-13(AP)
[4] L. Farque et al., ESRF-SR/LAT 88-08
[5] R. V. Servranckx et al., SLAC-285, UC-28(A), 1985
[6] A. Wrulich, DESY, 84/026
[7] H. O. Moser et al., ANKA Proposal, FZ Karlsruhe 1995, unpublished
[8] S. Hill, SRS, private communication

THE IASA RACETRACK MICROTRON FACILITY, A PROGRESS REPORT

E. Stiliaris, H. Avramopoulos, D. Baltadoros, M. Barbarosou, S. Cohen, D. Economou, T.A. Filippas, E.N. Gazis, A. Karabarbounis, M. Malagari, D. Maroulis, N.H. Papadakis, C.N. Papanicolas, N. Patavalis, P. Phinou, H. Rahmani, N. Sparveris, N. Uzunoglou, N. Vodinas
Institute of Accelerating Systems and Applications, P.O.Box 17214, GR–10024 Athens, Greece
and H. Herminghaus*, *Inst. f. Kernphysik, Univ. Mainz, Germany*

Abstract

The Institute of Accelerating Systems and Applications (IASA) is pursuing research and facilitates postgraduate studies in traditional and cross-disciplinary areas where accelerators play an important role. The first major facility of IASA, now under construction, is a 242 MeV two-stage CW cascade microtron. During the ongoing period of civil construction a staging area has been set up for the installation of the injector and the testing of several key subsystems. A progress report on this project is presented here.

1 INTRODUCTION

The first large scale facility of IASA is a 242 MeV microtron[1]. It is being constructed largely out of the components of the NBS/LANL CW RaceTrack Microtron (RTM) [2] supplemented by those of the University of Illinois R&D RTM project[3]. The available equipment from the above two projects combined with the additional equipment produced by IASA in the last two years, allows a design based on a cascade (two stage) RTM. The accelerator comprises of a 6.5 MeV injector and two cascaded RTMs (RTM1 and RTM2) with output energies 41 MeV and 242 MeV respectively (Fig. 1).

Two interfacing sections match the output of the injector to the acceptance of RTM1 and the output of the latter to the acceptance of RTM2. They also serve to transport the beam to experimental areas. Both RTMs are designed for variable energy extraction[4][5]. The main characteristics of the machine are summarized in Table 1.

	INJ	RTM1	RTM2
Injection Energy [MeV]		6.5	41
Gain per Turn [MeV]		1.32	8.04
Number of Recirculations		26	25
Max Output Energy [MeV]	6.5	41	242
Max Current [μA]	600	100	100
Frequency [MHz]	2380	2380	2380
Incremental Number ν		1	1
Magnets Field [T]		0.2196	1.338
RF Power Consum. [KW]	118.7	29.0	169.3
Spacing [m]	8.8	3.25	8.7

Table 1: The main characteristics of the IASA Cascade RaceTrack Microtron

* Supported by the EU, TMR-Programme ERBFMBICT961234

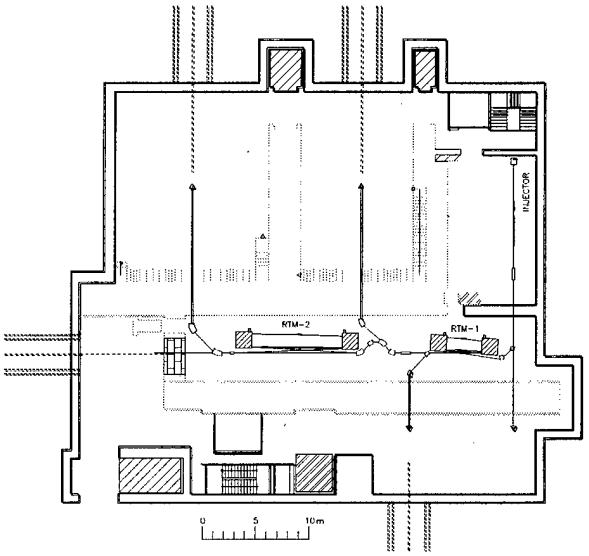


Figure 1: Layout of the planned IASA CW cascade (two-stage) microtron. The accelerator vaults and experimental areas are shown.

2 DESIGN AND OPTICS CALCULATIONS

The design philosophy is such as to result in stable operation, simple tuning and optimal use of the available linac sections, RF equipment and End-Magnets.

The injector consists of a 100 keV electron gun, a chopping and bunching system, a capture section, a preaccelerator and a booster. This design increases the initial NIST injector energy of 5 MeV to 6.5 MeV. Its optics has extensively been studied with the code PARMELA[6]. Most favorably, it turned out that the injector can be tuned such as to match RTM1 longitudinally without any further measures. This is demonstrated in Fig. 2[7].

Both microtron stages use quadrupole doublets on either side of the linac for transverse focusing, and both use the MAMI schemes[8] for injection and extraction, respectively. For RTM1, it was possible to apply a variant of this extraction scheme which provides achromatic extraction directly[9].

The first microtron (RTM1) is designed to operate with an asymptotic synchronous phase of 18 deg. The choice of that particular phase is made on the basis of keeping the longitudinal acceptance of RTM1 sufficiently high while relaxing the need of an extremely demanding control of the RF stability and injector output energy. The accelerating

0-7803-4376-X/98/$10.00 © 1998 IEEE

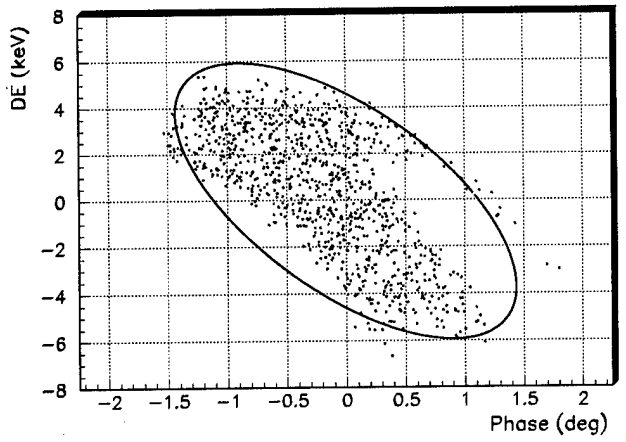


Figure 2: PARMELA simulation of the 6.5 MeV injector: Longitudinal emittance (dots) with the input eigenellipse of RTM1 with 6.5π keV deg. Chopper range is $\pm 30°$.

section consists of a 15 cell (0.95 m) RF structure, to be constructed by reconfiguring the two 4 m main linac sections of the original NIST RTM. The second (RTM2) is to be operated at a synchronous phase of 16 deg as a best compromise between RF stability demands and energy width. The accelerating section consists of a 93 cell (5.9 m) RF structure, assembled by reconfiguring the NIST structure.

Microtrons and interfacing systems have been designed using the interactive codes OMEN for first order beam dynamics and LONGIDYN for nonlinear longitudinal dynamics[10]. Main design goals were ease of manufacture and operation, while finding a best match between layout of machine and civil construction (see Fig. 1)[9]. The design thus obtained was finally checked independently by the higher order code PTRACE[11] which also allowed to study the effects on cross coupling and quadrupole imperfections. For the latter, a sextupole moment of 2% at the pole tips (aperture radius = 10 mm) of all quadrupoles has been assumed. These calculations reproduced the design within close limits.

The results for RTM1 as the most critical subsystem are briefly communicated:

The acceptance ("bucket") of a microtron, as well known, has a rather irregular shape as roughly indicated by the dotted line in Fig. 3. For practical purposes, it is wise to consider some inner polygon of the bucket as useful area which might be called "practical emittance". It is drawn in Fig. 3 in bold line covering an area of 219π keV deg. The design emittance of 6.5π keV deg is shown for comparison (ellipse).

Using the practical emittance for the longitudinal phase space and a value as high as thirty times the design transverse emittance at injection (which is very conservatively assumed as 0.17π mm mrad at 6.5 MeV) it was verified by PTRACE that the RTM1 operation is stable even under those quite unfavorable conditions.

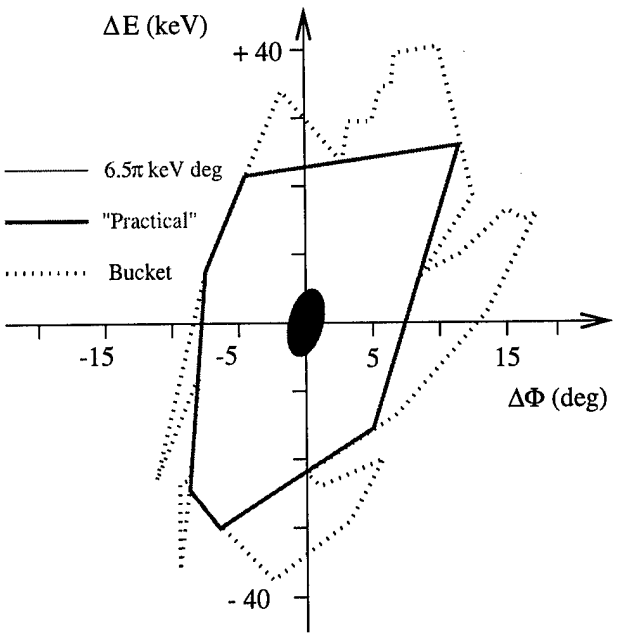


Figure 3: Calculated acceptance for RTM1 shown together with the design emittance (ellipse) and the practical emittance.

3 INJECTOR STATUS

The electron gun and the 100 keV chopping and bunching system have been installed. Several changes from the original NIST installation have been made at the electron gun to incorporate a new High Voltage Power Supply, an Isolation Transformer, and new control electronics (VME based) for the High Voltage terminal of the gun. So far, the system has been successfully operated in D.C. mode. The RF supply of chopper and buncher is being prepared. A beam line for measuring the transverse emittance of the beam is under construction[12], while a second line for measuring the longitudinal emittance of the beam is being designed[13].

4 RF SYSTEM AND MAGNET LAB

The currently adopted RF architecture for the cascade RTM calls for two power sources, both based on the Varian VKS 8270 klystrons. The first source will drive the 100 keV beam line, the capture, preaccelerator and boost/matching section, while the second the RTM1 and RTM2. The RF power needed for the implementation of both stages is shown in Table 2.

	INJ	RTM1	RTM2
Acc. Length [m]	4.7	1	6
Acc. Grad [MV/m]	1.3-1.5	1.5	1.5
Gain Amplitude [MeV]	6.65	1.388	8.36
Diss. RF Power [KW]	114.9	25.5	149.2
Beam RF Power [KW]	3.8	3.5	20.1
Total RF Power [KW]	118.7	29.0	169.3

Table 2: RF-related parameters for the IASA Microtron

The Magnet Lab deals with the powering, controlling and testing of all magnetic elements. Its major task is the field mapping of the small components, as well as of the End-Magnets.

5 CONTROL SYSTEM

The Control System for the IASA Microtron is totally revised, since the architecture of the NIST and UIUC machines is considered to be outdated[14]. The new system is being developed on the EPICS environment using Sun Sparc Stations and VME electronics.

The system architecture for the 100 keV injector has been finalized and in the major part realized. This includes the full control of the basic magnetic elements (solenoids, steerers), the high voltage power supply for the e-gun and monitoring of various readout parameters (currents at apertures, vacuum, etc.). An EPICS control screen created with the display manager (medm) for the IASA RTM injector is shown in Fig. 4.

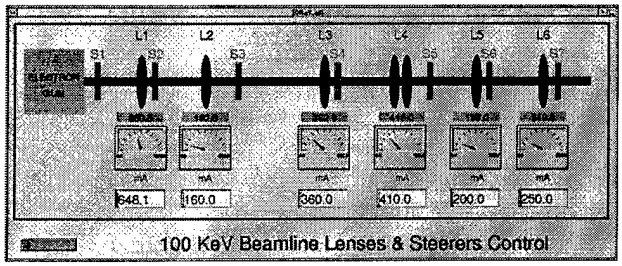


Figure 4: EPICS display screen (medm) for the control of the solenoids and steerers of the 100 keV injector

Further development of the system includes the integration of the programmable filament and bias supplies for the electron gun via fiber-optics for dc and pulsed beam operation, interlocks and other safety controls.

6 CONCLUSION

The two-stage cascade scheme for the Athens CW Microtron described here has been chosen because of its simplicity, stable operation and optimal use of the available equipment. The design of the accelerator is for all practical purposes completed. The 100 keV injector line has been installed and the first electron dc beams have been extracted. Basic elements of the electron gun and the injector line are controlled by a new system based on the EPICS environment.

7 REFERENCES

[1] A. Karabarbounis *et al.*, *The IASA RaceTrack Microtron Facility*, 5th European Particle Accelerator Conference, EPAC96, Sitges, Spain (1996) TUP047G, pp. 560–562.

[2] S. Penner *et al.*, *Progress Report on the NBS/Los Alamos RTM*, IEEE Transactions on Nuclear Science, Vol. NS–32 (1985) pp. 2269–2271.

[3] L.S. Cardman, *The Illinois Cascade Microtron: A proposal for a High Duty Factor, Intermediate Energy Electron Accelerator*, IEEE Transactions on Nuclear Science, Vol. NS–30 (1983) pp. 3267–3273.

[4] A.V. Filippas *et al.*, *Optics for the IASA CW RTM*, 5th European Particle Accelerator Conference, EPAC96, Sitges, Spain (1996) TUP046G, pp. 557–559.

[5] H. Herminghaus, *Conceptual Design of a Two Stage Microtron Cascade in "Beam Highway" Configuration*, IASA Internal Report (Dec. 1996).

[6] Lloyd M. Young, *PARMELA, A Particle Dynamics Code for Electron Linacs*, Accelerator Operations and Technology Division, Group AOT-1, Los Alamos (1995).

[7] N.H. Papadakis *et al.*, *Optimization of the 6.5 MeV Injector at the IASA Microtron*, IASA Internal Report (1997).

[8] H. Herminghaus *et al.*, *The Design of a Casceded 800 MeV Normal Conducting C.W. RaceTrack Microtron*, NIM **138** (1976) pp. 1–12.

[9] H. Herminghaus, *Revised First Order Design of the IASA Microtron Cascade*, IASA Internal Report (1997).

[10] H. Herminghaus, *OMEN - Optik Menu, An Interactive Program for Beam Optics*, Private Communication (1995).

[11] K.H. Kaiser, Private Communication.

[12] H. Herminghaus, *Transverse Beam Diagnostics for Maquette*, IASA Internal Report (Feb. 1997).

[13] M. Malagari, *A Device for the Measurement of the Longitudinal Phase-Space for the IASA*, Diploma Thesis, National Technical University of Athens (1997) unpublished.

[14] E. Stiliaris *et al.*, *Control System Implementation for the IASA Microtron*, 5th European Particle Accelerator Conference, EPAC96, Sitges, Spain (1996) TUP043L, pp. 1784–1786.

EXTRACTED BEAMS FROM IBA'S C235

D. Vandeplassche, W. Beeckman, S. Zaremba, Y. Jongen
IBA, Chemin du Cyclotron 3, B – 1348 Louvain-la-Neuve, Belgium, and
T. Tachikawa, Sumitomo Heavy Industries, Niihama, Japan

Abstract

IBA's proton therapy cyclotron (C235) has produced extracted 235 MeV proton beams and has fulfilled its factory tests. Model calculations have played an important role all along the course of this project: 2D and 3D magnetic fields, closed orbit analyses, particle trackings, beam transport layouts ... These calculations and the corresponding tools are evaluated by a comparison to experiment.

1 INTRODUCTION

The purpose of this contribution is to describe the present status of IBA's C235 cyclotron as seen from an *a posteriori* viewpoint by the calculation team. Hence we will compare calculations and measurements of several subsystems of the cyclotron, and evaluate them.

2 MAGNETISM

Modelling of the magnetic circuit using Vector Fields Opera2d and Opera3d codes has been described in Ref. [1]. It must be stressed that, though a 3D approach is compulsory, the high mesh density offered by 2D models makes them much better suited for the description of mechanical details or of small variations. The *pseudo-2D* behaviour of C235 allowed us to fully exploit the complementarity of the 2 approaches: due to the full saturation of the magnet different radial slices are almost independent, and hence each slice may be adequately described by an appropriate 2D-like axisymmetrical model.

Using his technique allowed us to reach the final profile of the radial pole edge in just one iteration[1].

The gradient corrector (*GC*) was also designed that way. A series of models corresponding to several radial cuts and covering the azimuthal span of the *GC* have been built. They provided us with calculated shapes of the *GC* plates and quantified the strong influence the *GC* had on the inner adjacent pole field (closest approach ~4 mm).

The calculated field map obtained in this way has been extensively used for the design of the extraction channel *before* the field was measured. The comparison with the experimental field map showed a very good agreement[2].

The permanent magnet quadrupoles (*PMQ*) were also designed from purely 2D models. The distance between these elements and the poles is large enough to avoid magnetic interaction, and the geometry of the quadrupoles fulfills the requirement for linear symmetry. Hence they have been described by a single 2D model with a simulated external field, and using a BH-curve provided by the manufacturer of the Sm_2Co_{17} material.

The real quadrupoles were mapped. The fitted field gradient is 19.1 T/m against a model value of 19.2 T/m and an almost identical deviation from linearity. The effective limit is found to be 3 mm outside the magnet.

3D models were also used to help shimming the pole edges in the process of isochronisation, in order to know the field redistribution caused by geometrical modifications (which is a fundamentally 3D process). This response function has thus been obtained via a series of 3D models, each one featuring a "unit cut" at a given radius. Here again the success of the method is undeniable.

3 BEAM OPTICS

The (Q_H, Q_V) diagram (Fig. 1) obtained from the closed orbit analysis of the circulating beam shows that a couple of potential resonance zones are crossed during acceleration.

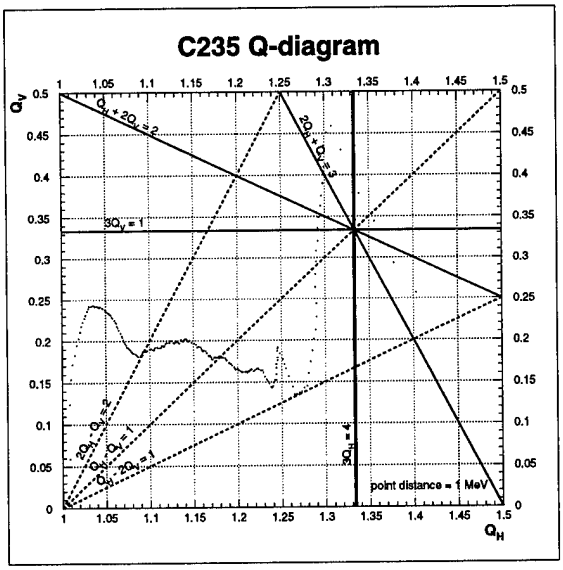


Figure 1: Working diagram throughout the acceleration in C235, as obtained from closed orbits in the final field map.

Coarse experimental betatron tunes are obtained from radial probe diagrams and are in good agreement with the computed values.

The $Q_H - Q_V = 1$ resonance did actually show up during the initial beam tests. The calculations predicted this resonance not to occur since the skew quadrupole field components that drive it are neither present in the model nor in the measured median plane field map. The origin of the upper/lower asymmetry causing these skew components is still unknown. The experimental solution of slightly dif-

0-7803-4376-X/98 /$10.00 © 1998 IEEE

fering currents in the upper and the lower coil to cope with this problem has not yet received a calculated confirmation.

We also added a Q-corrector on the pole edge so as to cross the resonance as fast as possible by changing the shape of the working line. A realistic corrector is too small for a 3D simulation, but an upscaled version was calculated and has shown the correct properties (size and radial distribution of the Q-correction).

4 EXTRACTION CHANNEL

Besides magnetic models, extensive particle tracking in the horizontal plane and beam optics computations have been carried out through the extraction channel, i.e., electrostatic deflector, *GC* and *PMQ* doublet (Fig. 2).

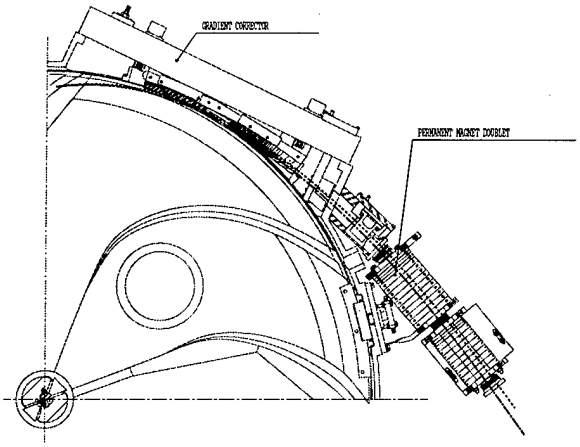


Figure 2: Comparison of the experimental (dash-dotted line) and the simulated (broken line) extraction paths.

Though the design of the channel was revised several times as new computational or experimental data were available, it must be stressed that the final design was good enough and the mechanical solution flexible enough for all the elements to be used as-built, giving a good practical measure of the quality and reliability of the calculations.

Particle tracking in the horizontal plane not only provides the extracted central path and the phase space diagram of the beam along its trajectory but also information about the non-linearities in the channel as well as hints to minimize them. It further allows to simulate radial current density plots and to compare them with experimental values obtained with the radial probe. Finally it permits a check of the accelerated beam optics through the effects of

- couplings between radial motion and acceleration
- hidden effects of the *large* first harmonic content
- energy spread

As initial conditions we always chose the central position and the Twiss parameters obtained from a closed orbit analysis, adding a known amount of off-centering if required. The assumed emittance comes from an early estimate. However, since the extraction from C235 is a multiturn process, the emittance of the extracted beam is in no direct relationship with that of the circulating beam.

The initial extracted beam tests have provided us with the geometrical path of the beam center and with beam profiles. It is found that the extracted beam is systematically at lower radial positions than in the simulations (Fig. 2), which in turn influences the optical properties. The circulating beam is intercepted at a slightly smaller radius because this position gives a better overall efficiency. The effect is partly corrected by shortening the *GC*. It is probable that the real beam suffers from optical imperfections which occur very close to the radial pole edge and which do not show up in the simulations. A Q-corrector has been added on a purely experimental basis, but a retrofit into the model has not been possible.

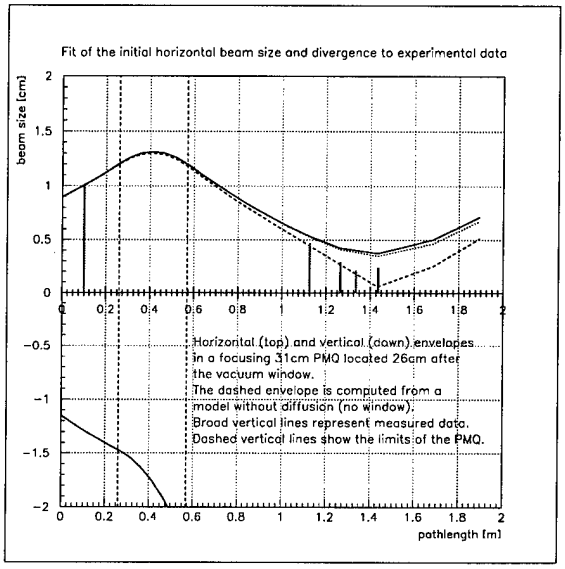


Figure 3: Beam envelopes with a focussing permanent magnet quadrupole, starting at the Al exit window.

During the design phase the extraction line optics were obtained according to the following recipe:

1. track particles (typ. 500) through the electrostatic deflector and the *GC* up to the entry of the first *PMQ*.
2. make the phase space plot at this position and fit the Twiss parameters and the emittance.
3. run *MAD* with the initial conditions of point 2 on the beam line made up by the quadrupole doublet, with end condition $\alpha_H = \alpha_V = 0$, and with the 2 quadrupole lengths as parameters.

Experimentally the following scenario was used:

1. visualize the beam spot on a quartz at several positions along the path with a *focussing PMQ* installed.
2. visualize the beam spots with a *defocussing* quad.

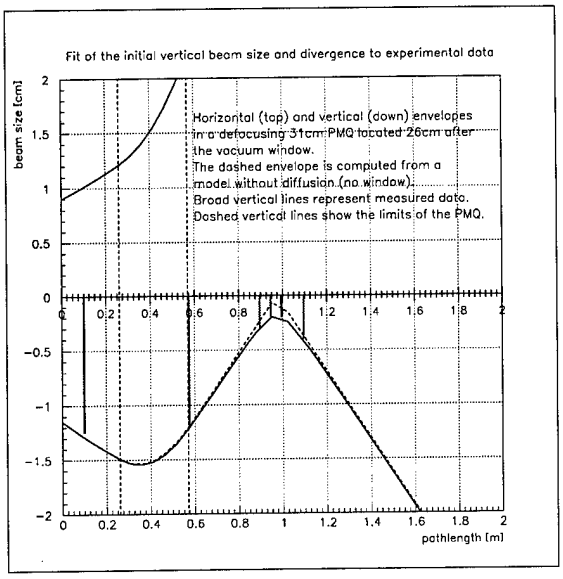


Figure 4: Beam envelopes with a defocussing permanent magnet quadrupole, starting at the Al exit window.

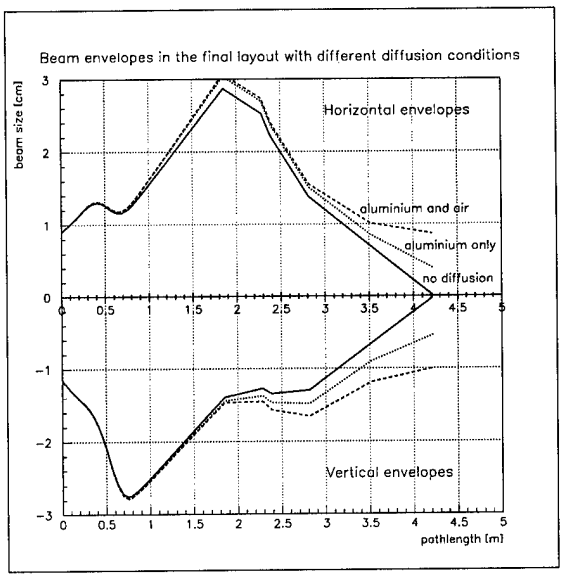


Figure 5: Beam envelopes in the extraction line for various multiple scattering conditions.

3. build realistic optical models of the 2 preceding setups, including measured *PMQ* (see Section 2), residual horizontally defocussing field gradient present between the main coils and multiple scattering caused by the Al exit window (1 mm) and the subsequent air layer (experimental conditions during the test).

4. using *TRANSPORT*, match the initial beam parameters to the observed beam spots.

The results of both fits are given in Figs. 3 and 4.

Starting from the initial values a new model of the line up to the Energy Selection System (incl. the 2 active quads at the exit of the cyclotron) has been made. Since 100% transmission cannot be obtained within the $\emptyset$ 56 mm vacuum pipes, the figure of merit for these calculations is the transport efficiency of the line, using as a constraint a double waist and a horizontal/vertical equivalence at the ESS. The resulting beam envelopes are shown in Fig. 5.

5 CONCLUSION

From its official start to the first extracted beams, the C235 project has taken three years. This performance is largely due to the successful calculations which have been performed beforehand and all along the course of the construction.

Knowing the reality now, we may state that magnetic field calculations generally give an excellent agreement, and the combination of 3D and 2D modelling may be a powerful tool for the description of even very small details. However, a full description of an isochronous field and of the tiny Q-correctors requires a finer meshing in the 3D models. Furthermore it is necessary to reduce the symmetry of the model from 8 down to 2 or even 1 if a realistic description of the machine is wanted. This makes us expect a 3D code capable of handling $\sim 10^6$ nodes. There are discrepancies between the beam simulations and the real beam, and some experimental observations can not be reproduced. Some of these discrepancies can be explained, but some are inherent to our model. Particle tracking must include the vertical motion and the coupling between the 2 planes — however, we do not have a magnetic model giving rise to skew quadrupole components ... This being said, it remains that the tracking results have been extremely useful for the design of the extraction components.

6 REFERENCES

[1] W. Beeckman, A. Laisné, Y. Jongen, D. Vandeplassche, S. Zaremba, J.C. Amélia, G. Lannoye, T. Satoh, T. Tachikawa, M. Sano, Proc. 14th Int. Conf. on Cyclotrons and their Applications, Cape Town (1995) 218–221.

[2] W. Beeckman, M. Schuwer, D. Vandeplassche, S. Zaremba, J.C. Amélia, G. Lannoye, H. Miyazaki, ibid 222–225.

THE COOLER SYNCHROTRON COSY FACILITY

H. Stockhorst, U. Bechstedt, J. Dietrich, R. Maier, S. Martin, D. Prasuhn, A. Schnase, H. Schneider, R. Tölle, Forschungszentrum Juelich GmbH, P.O.B. 1913, D-52425 Juelich, Germany

Abstract

The cooler synchrotron COSY Jülich is now running continuously with its experimental programs. The machine covers the whole momentum range from 600 MeV/c up to 3.3 GeV/c and delivers up to $3 \cdot 10^{10}$ protons. Electron cooling is applied up to 645 MeV/c. Stochastic cooling will enhance the beam quality in the range from 1.5 to 3.3 GeV/c. Substantial progress in developing the machine was made to increase the intensity and quality of the beam for internal as well as external experiments. In addition, a polarized proton beam could be successfully accelerated up to 2 GeV/c.

1 THE COSY FACILITY

The COSY accelerator complex [1] comprises several ion sources, the refurbished isochronous cyclotron, a 100 m long injection beam line, the COSY-ring and extraction beam lines to the external experiments. The ion sources are a H_2^+, H^-, D^- and a H^- polarized ion source. The injector cyclotron (JULIC) is now running continuously with H^- beams with a momentum of 296 MeV/c. Currents of approximately 10 μA are fed into the accelerator ring via stripping injection. This injection technique has proven to be very reliable when the H_2^+ ion source was used. The well-tried injection scheme is also applied for polarized H^- beams.

The ring has a circumference of 183.47 m and stands out for its great flexibility in tuning the lattice optics to the needs of the internal as well as external experiments. Sixteen quadrupoles in each 40 m long straight section of COSY grouped as four triplets allow the ion optics to be tuned such that the sections act as telescopes with a 1:1 imaging giving either a π or a 2π phase advance. At the same time optimized beam conditions for the two internal experimental stations located in the target telescope can be adjusted. The other one (cooler telescope) contains the accelerating rf-cavity, the electron cooler, scrapers, Schottky pick-ups, and current monitors.

The arc sections have a length of 52 meters each. They are composed of three identical elements that have in themselves a mirror symmetry. A half-cell has a QF-bend-QD-bend structure with the option to interchange focusing-defocusing for added flexibility in adjusting the tune. This structure leads to a six fold symmetry for the total magnetic lattice of the ring. Stripping target and bumper magnets for injection and electrostatic and magnetic septum for extraction are located in one arc-section. Besides the diagnostic kickers and the elements for the ultra slow extraction the other arc-section contains the internal target station where the COSY-11 experiment has been installed. At the connecting points where the arc sections meet the target telescope the stochastic cooling pick-ups are built in. The corresponding kickers are located in the cooler telescope section.

In total 18 sextupoles are installed. They can be grouped into 11 families. Three of them are placed in the arcs and eight are in the telescopes.

At present three internal experiments are in operation, the COSY-11, COSY-13 and the EDDA-experiment. The latter two are located in the target telescope.

Extraction beam lines guide the beam to three external experiments. One site being the large magnetic spectrometer BIG KARL, the other the Time of Flight facility (TOF), and the third (NEM) is foreseen for experiments with low proton momenta (800 MeV/c). A fourth beam line is under discussion for experiments requiring longitudinal polarization.

A typical machine cycle lasts between 5 seconds and one hour. At injection the ring is filled up with $2 \cdot 10^{11}$ protons corresponding to the space charge limit. At maximum momentum, 3.5 GeV/c, up to $3 \cdot 10^{10}$ protons have been measured.

2 INTERNAL EXPERIMENTS

There is a very intimate relation between internal experiments and the accelerator as they affect each other in a direct way. EDDA [2] is an internal experiment at TP2 that has been set up to measure excitation functions with high precision. The basic design is a thin horizontally oriented fiber target that intercepts the beam combined with a cylindrical detector system surrounding the thin walled beam pipe. Due to its construction the EDDA experiment is not only a tool for medium energy physics but also an excellent probe for investigating and verifying beam properties of COSY with high precision [3]. This experiment has special requirements on the beam to achieve optimal measurement conditions. This concerns the lateral stability and the orientation of the phase space ellipses. It is the latter point where the flexibility of the target telescopes proved invaluable [3]. Moreover, it was proven that the lattice allows to shift transition energy upwards during acceleration so that no transition jump is needed [3]. This property allows to take excitation data even when ramping up the machine to flat top energy.

Different conditions have to be satisfied for the COSY-11 and COSY-13 experiments. Both take data in flat top of the machine [2].

To enhance the machine flexibility the control system has been updated to allow to run COSY with supercycles. At present each supercycle consists of three different machine settings which can be combined independently as shown in figure 1. The set up has been made for the COSY-13 experiment and allows a quick comparison of measurements close to the threshold of the reaction.

0-7803-4376-X/98 /$10.00 © 1998 IEEE

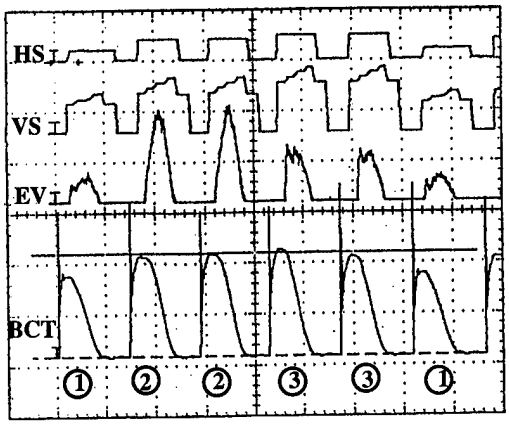


Figure 1: Beam current transformer signals (BCT) for a supercycle in COSY. Each cycle, labelled by one, two and three corresponds to momenta 1.7, 2.25 and 2.68 GeV/c, respectively. The event rate (EV) has its maximum value within cycle two. The upper two traces are the currents of the horizontal (HS) and vertical (VS) steerer magnets which optimize the event rate.

The machine starts with cycle one delivering protons with momentum 1.7 GeV/c at flat top. In the next two cycles, labelled with two, a momentum of 2.25 GeV/c is available. They are followed by two cycles, labelled by three, at 2.68 GeV/c flat top momentum finishing the supercycle. Besides the beam current transformer signal (BCT) the figure shows the event rate (EV) as well as the currents of the horizontal (HS) and vertical steerer magnets (VS) to optimize the event rate.

Since the installation of electron cooling in 1993 [4] it has been shown the an electron cooled beam could be successfully accelerated to flat top energy. Recently several experiments with the electron cooler have been carried out to increase the injection efficiency by stacking. Figure 2 shows the beam current as a function of time during stacking.

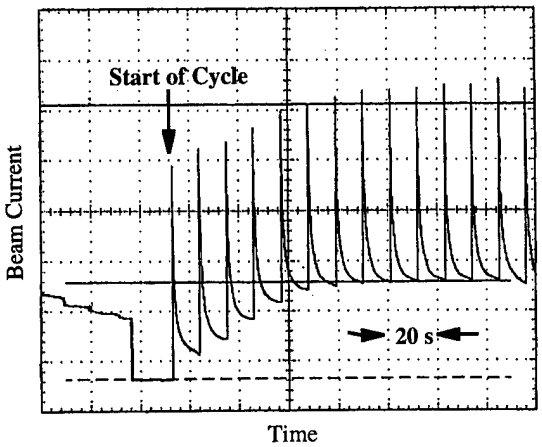


Figure 2: Increasing beam current during stacking

Each spike corresponds to a new injection into COSY. During injection the beam is electron cooled decreasing the transverse as well as the longitudinal emittance. By properly adjustment of the dipole field the beam is slightly slowed down to move on an inner orbit. This prevents that the already circulating beam hits the stripping target when the next injection process begins. As proposed by [5] it can be seen that the number of stacked protons increases until an equilibrium limit of the cooled beam is reached after nearly 50 s. Each injection is accompanied by a sudden beam loss which results from the fast cooling of the injected beam to the space charge limit. This limit increases during stacking so that the number of stored particles increases. Since the space charge limit is proportional to the emittance [4] the number of stored particles can be enlarged if the cooling force is properly counterbalanced by transverse heating. Further experiments will be carried out to study the stacking mechanism in detail.

During 1996 polarized protons were injected and successfully accelerated to 2 GeV/c [1]. The polarization was measured continuously during acceleration with the internal experiment EDDA. Further progress is expected if the already installed tune jump system to overcome depolarizing resonances [1] will be used.

3 EXTERNAL EXPERIMENTS

Resonant extraction and stochastic extraction [6] are applied to serve external experiments. Beams with momenta up to 2.75 GeV/c have been delivered to three experimental collaborations.

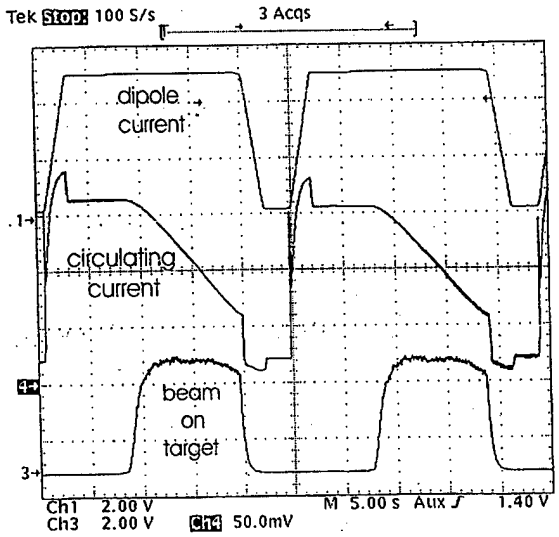


Figure 3: Two cycles show the extracted beam (beam on target) together with dipole current and the circulating beam. The spill length is approximately 14 s.

Conventional extraction at COSY is made by creating a third order resonant condition by sextupole excitation and sweeping the horizontal tune through the resonance by quadrupole ramping. At present typical spill lengths of the order of 10 s are requested with $2 \cdot 10^{10}$ protons per spill. The extraction efficiency of nearly 85% was reached. Further progress was made in stochastic extraction (figure 3). First experiments were carried out at 2.75 GeV/c. Instead of moving the horizontal tune by quadrupoles the

optic was kept fixed and a rectangular shaped noise was swept over the beam distribution. Because of the finite horizontal chromaticity the protons will then diffuse towards the resonance where they are extracted. A precalculated sweep frequency program was applied to prepare a rather flat spill without prior beam shaping [6].

4 STOCHASTIC COOLING

The COSY stochastic cooling system [1] operates in the frequency range from 1 GHz to 3 GHz divided into two bands (1 - 1.8) GHz and (1.8 - 3) GHz. At present the horizontal pickup (4 m length) is installed in the ring consisting of two tanks each 2 m long. Also, one of the two vertical pickup tanks is now placed in the ring. The other one completing the system will be installed in May, 1997. The pickups are cryogenically cooled down to nearly 60 K. Uncooled preamplifiers with a noise temperature below 50 K are mounted outside the vacuum tanks. The rest gas pressure can be kept on 10^{-10} hPa. The position of the electrode bars are independently adjustable and thus allow for closed orbit suppression. Programmable delays permit an energy adjustment from 1.5 GeV/c up to the maximum momentum 3.3 GeV/c. Two kicker tanks of length 2 m are installed for the horizontal and vertical plane, respectively. Similar to the pickups the electrode bars are independently movable. Measurements of transverse and longitudinal Schottky spectra of an unbunched beam with $3 \cdot 10^{10}$ protons have been carried out with good signal-to-noise ratio [1].

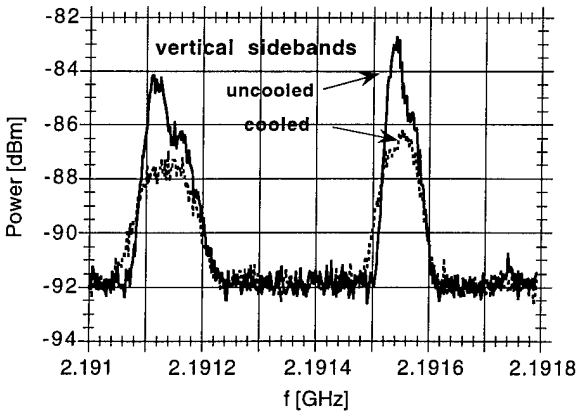


Figure 4: First stochastic cooling of the vertical beam emittance. The emittance is cooled by a factor of two.

Hardware transfer function measurements (HTF), i.e. sending an excitation around 0 dBm to the kicker and measuring the response from the pickup without beam, have proved that the mounted ferrite material is sufficient to damp propagating modes in the vacuum chamber [7]. In recent experiments vertical beam transfer function measurements (BTF) have been carried out to gain experience in adjusting gain and phase of the vertical cooling system in band I. In addition open/closed loop measurements were done to optimize the system gain. A first result is shown in figure 4 indicating vertical stochastic cooling of a debunched beam with $1.5 \cdot 10^{10}$ protons at pc = 3.39 GeV. The figure shows a lower and upper sideband in the frequency range of band II near the 1392th revolution harmonic of the beam. The vertical emittance before cooling (thick curve) is reduced by approximately a factor of two within 5 minutes (dotted curve). The long cooling time reflects the large number of stored protons but is also partly due to a yet not optimized lattice resulting in a large mixing factor in this case. Future measurements will include the EDDA experiment which is an excellent tool to probe beam profiles.

5 SUMMARY AND OUTLOOK

In 1996 in total 6520 hours were scheduled. From this the machine was in operation for 6174 hours. In total 4248 hours were available for the user of COSY. Proton numbers up to $3 \cdot 10^{10}$ are accelerated to the design momentum of 3.3 GeV/c. A polarized proton beam could be successfully accelerated. To ensure polarization during acceleration a tune jump system has been installed at the beginning of 1997. Measurements of the fast quadrupoles and the corresponding power supply have shown that their design specifications are very well fulfilled. Machine runs with polarized protons using the jump system will be carried out. In addition, improvements of the stochastic extraction as well as increasing the beam intensity are given high priority to further exploit the machine's potential for medium energy physics. In first investigations of the stochastic cooling system a reduction of the vertical emittance was observed. The work on transverse and longitudinal (filter method) stochastic cooling is still continuing.

Considerable work is done for a new device for experiments at internal targets, the 0^0 facility ANKE [2], to study nuclear medium effects. The realization of the facility, for which three additional large dipole magnets will be installed in the COSY ring, made progress in the completion of the concept studies and in construction. The 0^0 facility will be located between two triplets of the cooler telescope.

REFERENCES

[1] R. Maier et al., `Cooler Synchrotron COSY`, Storage Rings 1996

[2] O.W.B. Schult et al., `The Physics Research Program at COSY-Juelich`, Proc. 14th RCNP, Osaka, Int. Symp. on Nuclear Reaction Dynamics of Nucleon-Hadron Many Body Systems, eds. H. Ejiri et al., world scientific 1996, p. 460

[3] R. Tölle et al., `Conditioning the Cooler Synchrotron COSY for Internal Experiments`, EPAC96, Barcelona 1996

[4] R. Maier et al., `Electron Cooling in COSY Juelich`, EPAC90, Nice 1990

[5] H. Poth and D. Möhl, `Elektronenkühlung in COSY Juelich`, COSY-Arbeitstreffen Bad Honnef 16./17. Dec. 1985, Germany, Juel-Spez-345 (1986)

[6] H. Stockhorst et al., `Beam Extraction at the Cooler Synchrotron COSY`, EPAC96, Barcelona 1996

[7] F. Caspers, `Experience with Stochastic Cooling of Particle Beams`, Int. Symp. on Multi-GeV High Performance Accelerators and Related Techniques`, OSAKA, Japan, 12-14 March 1997, to be published

BEAMS FOR GAMMASPHERE AT THE LBNL 88-INCH CYCLOTRON

D.J. Clark, D. Collins, R. Dwinell, A. Guy, S. Lundgren, C.M. Lyneis, M.A.McMahan, D. Syversrud and Z. Q. Xie, Lawrence Berkeley National Laboratory

Abstract

The new transport system from the 88-Inch Cyclotron to the Gammasphere facility is described. Included are discussions of the ECR sources, operation, beam diagnostics, mechanical construction, vacuum system and beam optics.

1 INTRODUCTION

The 88-Inch Cyclotron at Lawrence Berkeley National Laboratory is the present home of Gammasphere, a powerful gamma ray array for studying the structure of nuclei. Gammasphere has been operating as a national facility since April of 1993, running 104 major experiments and over 12,000 hours since then. The majority of Gammasphere experiments run to date have used compound nucleus reactions at energies just above the Coulomb barrier (≈5 MeV/u) to make specific nuclei of interest for nuclear structure studies, especially nuclei that have been found or predicted to exhibit very large deformations at high spins, called superdeformed (with an axis ratio of 2:1) or hyperdeformed (with an axis ratio of 3:1). In order to make these nuclei, beams of medium mass are generally used, and often rare isotopes are required. Modest intensities are needed, on the order of ≤ 5 pnA at the target. Other Gammasphere experiments have used transfer reactions to make nuclei far from stability and study their structure. Here much heavier beams are needed at higher energies. To date, the heaviest beam run for these experiments has been ^{162}Dy. Gammasphere running has occupied 52% of the scheduled Cyclotron time.

In order to meet the needs of these experiments, a new beamline was constructed with improved vacuum, beam diagnostics, and optics systems, shown in Fig. 1.

2 OPERATION

The ECR [1] and AECR-U [2] sources supply heavy ion beams to the Cyclotron. The ECR source started regular operation in 1985. It is a 2-stage source with the main stage operating at 6.4 GHz. It can use either of two types of ovens, with temperatures up to 700 deg. C and 2000 deg. C to provide solid material feed radially into the plasma. The AECR-U source has a single stage operated originally at 14 GHz. It has been upgraded by increasing the magnetic field, using multiple frequencies of 14 and 10 GHz and using an aluminum vacuum chamber. With the AECR-U the Cyclotron can now supply beams to Gammasphere up to mass 200 at 5 MeV/u. Both high and low temperature ovens are available for the source, with 2 radial insertion positions. The source-cyclotron system is efficient enough to run rare isotopes such as ^{54}Cr and ^{76}Ge from natural feed material. ^{36}S is enriched to 2.5% and ^{48}Ca to 39%. The overall beam delivery system to Gammasphere has had a 98% uptime.

During beam development using a sample 200 MeV Ar^{9+} beam, the optics were refined, and a Microsoft Excel GENTUNE predictive spreadsheet for

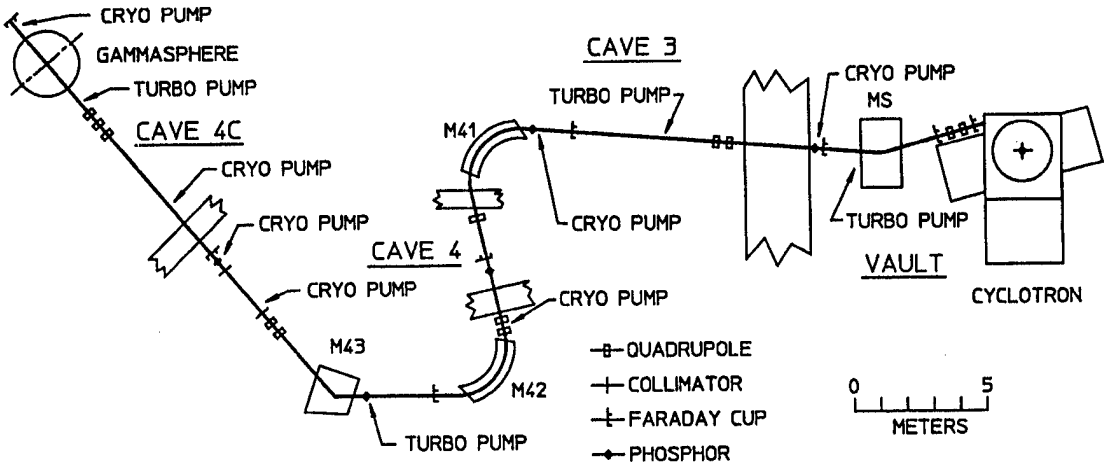


Figure: 1 Mechanical layout of beamline.

0-7803-4376-X/98/$10.00 © 1998 IEEE

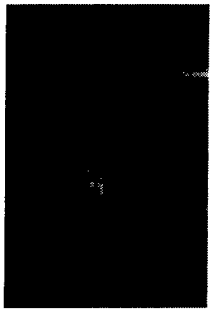


Figure: 2 Beam spot on phosphor at focus in Cave 4.

quadrupoles and bending magnets was created for all reasonable combinations of ion species and energy. This supplanted the older QuickBasic MASTER program.

Five ZnS phosphors provide first level optic diagnostics, with beam levels typically around 100 epA. Six magnet-suppressed Faraday cups are available for checking transmission, and 11 combinations of adjustable slits or plungeable collimators can be used to define beam spot size and to reduce halo on target.

Once the Cyclotron tune is completed and the GENTUNE values are loaded, the remaining optics tuning is very quick, typically around five minutes from Cyclotron exit until the beam is in Gammasphere. Focusing is not usually done on the phosphors; beam spot shape and position are compared on a go/nogo basis against benchmarks. Optimizing the tune on target is done typically by reducing the beam on a collimator at the target, relative to the beam on a Faraday cup at the end of the line. Fulfilling even the most complex requirements typically take less than 20 minutes. The transport from the cyclotron along the 50 m beamline to the target reaches 50% transmission with careful tuning. The predicted beam size on the target is 3 mm diameter. This has been verified experimentally. The beam size can be increased by defocusing the beam with the triplet just before Gammasphere. The beam spot on a phosphor at the last focus before Gammasphere in Cave 4 is shown in Fig. 2. The rectangular box is 4 cm x 4 cm. The phosphor is mounted at 45 deg. to the beam direction. Normally, a .75 cm collimator is plunged here to define the spot size, transmitting most of the beam while removing most of the halo.

The beam pulse width can be reduced to 1-2 ns FWHM by using cyclotron internal beam collimators and a Fast Faraday Cup described in the next section.

3 BEAM DIAGNOSTICS

Phosphors, Faraday cups, fixed diameter beam collimators and guillotines (beam stops) can be mounted to standardized plunging drives. They are in-house designed units which are controlled from the control room. Color coding of the external support bracket helps to identify which type of internal device is in use. Adjustable slits are electric motor driven with linear potentiometer position sensing and are controlled from the control room.

A fast response Faraday cup is normally placed in the downstream end of Cave 4. It was designed and constructed by cyclotron staff. It uses a 50 ohm line at the beam stop, tapering down to a 50 ohm cable at the back of the cup, which carries the signal through a vacuum seal. The signal then goes through a fast amplifier (HP 8447F), to a low loss Heliax cable to bring the signal to a sampling oscilloscope (Tektronix TDS 820) in the Control Room. In the control room the various cyclotron parameters can be tuned for narrow phase width when desired, while watching the beam pulse on the scope. Two retractable slits inside the cyclotron at a beam radius of 5-15 inches are useful to define the beam phase width. Each slit has two blades with separate drives for gap width and radius position. Using these slits the phase could be reduced to 1-2 nanoseconds FWHM for Gammasphere type beams of 5-6 MeV/u, where cyclotron frequencies are 15-16 MHz.

In order to provide a test of the beam pulse width independent of the fast Faraday cup, and to be able to measure lower-intensity beams , a small, plungeable scintillator/photo-tube assembly was installed just prior to the fast Faraday cup in the Cave 4C beam line. This scintillator measured the timing of the beam relative to the RF. Since it detects individual beam particles it normally needs a beam attenuator upstream. The width of the beam pulse was comparable to that measured by the fast Faraday cup.

A BaF gamma ray detector has also been used outside the beam pipe at the same location to measure beam pulse shape by detecting gammas from a beam stop. It gave similar results to the above methods.

4 MECHANICAL SYSTEMS

1.1 Earthquake Safety

Quadrupole magnets which were added to the beam line were first aligned, then bolted to the floor for an earthquake safe installation. Existing quadrupole installations remain counter weighted to prevent tipping during an earthquake. Extensive reinforcement of the Gammasphere cave shielding was done for earthquake protection.

1.2 Vacuum System

The vacuum system uses stainless steel beam pipe, aluminum beam boxes and turbo and cryopumps. The stainless steel beam pipe sections making up the 50 m long beamline were electropolished and UHV cleaned for improved vacuum. The aluminum vacuum pumping stations and diagnostic boxes were UHV cleaned for high vacuum service. Fluorocarbon rubber is used for both static and dynamic seals to reduce outgassing. Beam line isolation valves are interlocked on upstream and down stream pressures. They have position indication and control both locally and in the Control Room.

Roughing the beam line is accomplished by a system of locally controlled vacuum pumping stations utilizing turbomolecular pumps, with pumping speeds of 300-500 l/s for nitrogen, backed with rotary vane pumps.

For the final vacuum the turbopumps continue to pump the beamline and a system of cryopumps is added, each with a pumping speed of 1500 l/s for nitrogen. Each pump is locally controlled and is connected to the beamline through an interlocked gate valve for isolation during servicing. The cryopumps are regenerated by a dry pump or LN_2 trapped rotary vane pump. Pumpdown time from atmosphere to operating pressure is 15 minutes. Bayard-Alpert ionization gauges positioned midway between pumping stations give indication of the beamline pressures of 1 x 10^{-6} to 1 x 10^{-7} torr after a day of pumping.

Beamlines are vented to atmospheric pressure using dry nitrogen which is piped from the main LN_2 tank vaporizer/economizer system, providing 7.9 l/s (1000 cu. ft./hr.) of dry nitrogen at 3.1x 10^5 pascals (45 psi) throughout the experimental areas. Venting to dry nitrogen has improved the pumpdown speed and the final pressure.

5 BEAM OPTICS

The new optics was designed to meet the following requirements of beam on target:

1. Beam emittance on target is minimum: no energy spread contribution.
2. Beam spot size on target is as small as 3 mm diameter for some experiments.
3. Maximum beam divergence is adjustable.
4. Transmission from ion source to target should be maximum, to make possible runs with low source intensity (rare isotopes or high mass).
5. Beam collimators producing background radiation should be kept away from the target, preferably in an upstream cave.

The resulting solution is shown in Fig. 3. The half beam envelopes are shown for the "x" or horizontal direction in the top half of the plot, and for the "y" or vertical direction in the bottom half of the plot. The top and bottom boundaries of the plot space at 5 cm represent the beam pipe radius for the standard 4 inch diameter pipe and the quadrupoles. Eta(x) is the dispersion, or $\Delta p/p$ ray.

To meet the condition of minimum emittance at the target, the Δp ray should cross the axis at the target and be travelling along the axis. The solution uses an additional quad singlet, and a doublet, between M41 and M42. These quads keep the Δp ray to small amplitude and give the desired trajectory along the axis after the last dispersive element, M43. A central ray with a momentum displacement $\Delta p/p$ of .075% is shown diverging from the axis, slightly in MS and more in M41 and M42. This Δp ray represents the beam energy spread, which adds to the horizontal size of the beam. A quad triplet is used in Cave 4C to give good control over the beam spot shape on target. The triplet is placed close to the target to get the demagnification for a small spot size. For Gammasphere optics, this brought the total number of elements to 12 quadrupoles, four large bending magnets, and ten small steering magnets.

The requirement of keeping the last collimators away from the target is met by having them behind the Cave 4C wall in the upstream cave, Cave 4. They are plungeable from the Control Room. They consist of 3 plates with different hole sizes for forming an object for the quad triplet in Cave 4C. Selection of the hole size gives control over the beam spot size on target. Another set of collimators is further upstream, near the previous quad . These are 4 independent jaws, controllable from the Control Room, which control divergence of the beam on target by controlling beam size at the position in the previous cave where the beam is large.

The design of the beam line has satisfied all the requirements, and this solution is now the one routinely used for Gammasphere. This beam optics was designed using the LATTICE code, a user friendly version of TRANSPORT written by J. Staples of LBNL.

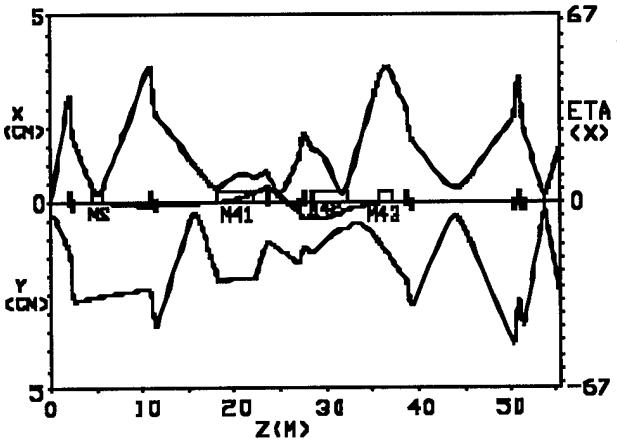


Figure: 3 Beam optics layout.

6 ACKNOWLEDGEMENTS

The authors wish to thank the Cyclotron engineering groups, shops, and crew for the successful completion of this project. G. Wozniak and M. Maier made important contributions to the beam pulse width measurement. This work was supported by the Director, Office of Energy Research, Division of Nuclear Physics of the Office of High Energy and Nuclear Physics of the U.S. Department of Energy under Contract DE- ACO3-76SF00098.

REFERENCES

[1] C.M. Lyneis, Proceedings of the International Conf. on ECR Ion Sources and their Applications, East Lansing, NSCL Report #MSUCP-47, 1987, p. 42.

[2] Z. Q. Xie and C. M. Lyneis, Proceedings of the 13th International Workshop on ECR Ion Sources, College Station, Texas, Feb 1997, to be published.

A COMPACT SUPERCONDUCTING CYCLOTRON FOR THE PRODUCTION OF HIGH INTENSITY PROTONS*

H. Blosser, D. Johnson, D. Lawton, F. Marti, R. Ronningen, J. Vincent, National Superconducting Cyclotron Laboratory, Michigan State University, East Lansing, MI 48824-1321 USA

Abstract

This paper reviews a study of a compact superconducting cyclotron to accelerate 200 microamps of protons to 250 MeV. The basic cyclotron structure is the same as that developed in a previous study of a 250 MeV cancer therapy cyclotron, the chief difference in the study reported here being much higher beam current (x10,000) than in the therapy cyclotron to meet desired specifications for the 'Driver' accelerator of an ISOL type radioactive beam facility. The increase in current is far below (x1/50) the axial space charge limit of the proposed cyclotron, but longitudinal space charge requires changing the extraction system from a single turn to a multi-turn system thereby increasing beam losses. Leading design uncertainties, namely the overall efficiency of the multi-turn extraction system and the distribution of radioactivity generated by lost beam are addressed herein; results indicate reasonable residual activity in the cyclotron from the perspective of customary 'hands-on' maintenance operations.

1 INTRODUCTION

Oak Ridge National Laboratory is reviewing accelerator systems appropriate for use as an upgraded primary production (or 'Driver') accelerator in their Holifield Radioactive Ion Beam Facility. Tentative beam specifications for this new Driver accelerator are 100 to 200 microamps of protons at 250 MeV.

Many accelerator systems are intrinsically capable of providing the desired beams i.e. linac, separated sector cyclotron, compact cyclotron, negative ion cyclotron, etc. and with either superconducting or room temperature as a design option for most of the above. The study discussed in this paper selects one of the above options, namely the compact superconducting cyclotron for more detailed review, this option offering advantages in size and cost relative to other systems, but with added innovation in that beam power considerably exceeds levels which have thus far been achieved in cyclotrons of this type. (A second paper describes features of a room temperature separated sector cyclotron to achieve the same goals.)

2 K250 CYCLOTRON STRUCTURE

Basic features of the K250 cyclotron are shown schematically in Figure 1 and have been described in a previous NSCL report [1]. The basic structure is a four sector dee-in-valley design with spiral hills to provide adequate axial focusing. The superconducting coil is mounted in an annular cryostat as is typical in compact superconducting cyclotrons.

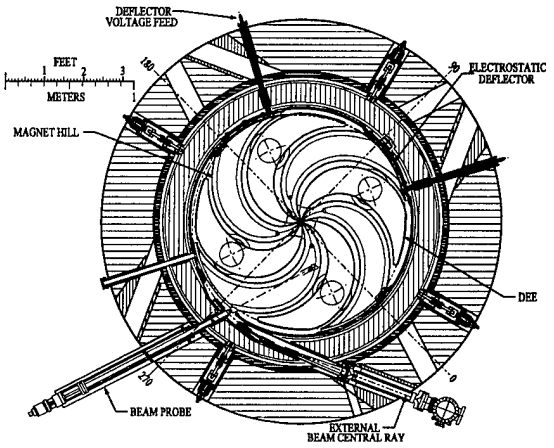


Figure 1: Median plane section of the K250 proton cyclotron: Note azimuthal coordinate labels at 0, 90, 180, 270 deg: Extraction system entry /exit at 60/340.

The 4 dee radio-frequency system operates on the 2nd harmonic of the orbital frequency so that the total in-out energy gain from each of the 45 degree dees is approximately 1.4 times the peak voltage to ground of the dee. Two opposite dees in the four dee system are galvanically coupled by the central region electrode system; the intervening dees at +/- 90 degrees are driven capacitively from the primary pair by the central region coupling and tuned individually to the push-pull mode relative to the primary pair by servo adjustment of 'fine' tuning elements.

Beam extraction uses two 45 degree electrostatic deflectors followed by a line of five inert magnetic quadrupole elements which guide the beam through the edge field of the magnet and compensate the strong radial defocusing of the edge field so as to maintain a nearly uniform beam profile through the complete extraction trajectory.

The ion source will follow the design used in the Harper Hospital neutron therapy cyclotron; this simple cold cathode system routinely produces 200 microamp beams from a 1.4 mm dia. exit hole in a 6.4 mm dia. molybdenum chimney. The vacuum system design separates beam chamber and coil cryostat vacuums into two separate systems so that the beam chamber can be

0-7803-4376-X/98 /$10.00 © 1998 IEEE

opened as desired without disturbing the superconducting coil. Other cyclotron subsystems are routine in character and well described in the previous report [1] and are therefore not reviewed here.

3 SPACE CHARGE EFFECTS

The beam in the proposed cyclotron is accurately described by the 'uniform charge' approximation and, using 500 keV for the expected energy gain-per-turn from the 8 gap accelerating system, 5 mm for the full beam height, +/- 10 rf degrees for the beam phase width, 36 Mhz for the orbital frequency, and 0.2 for the minimum NuZ, the usual formula [2] gives 11 milliamps for the limiting current. The x50 factor between the axial limit and the desired beam current then implies no significant space charge effects in the axial behaviour of the beam.

The other primary space charge consideration in an isochronous cyclotron is the longitudinal effect [3] which acts to enhance the energy gain of the leading particles in the beam phase wedge and decrease the energy on the trailing edge of the wedge. If 'single-turn' (i.e. no-loss) extraction is the goal, this effect sets a lower limit on the energy-gain-per-turn and on the beam phase width and these limits are incompatible with a compact cyclotron structure such as envisaged here. This cyclotron must therefore operate in a broad phase, multi-turn extraction mode with the extraction trajectories separated from the internal circulating beam by the thin septum of the first electrostatic deflector. The main goal of the studies summarized herein is then to realistically assess the efficiency which can be achieved in such an extraction system, and secondarily to estimate the distribution and intensity of the radioactivity induced in the cyclotron due to particles lost in the extraction process.

4 ORBIT COMPUTATIONS

Our study of deflector efficiency uses an extensively tested set of cyclotron computer programs which track orbits from ion source to extraction in a highly realistic fashion. In the central region the codes include detailed maps of the electric field derived from 3D relaxation calculations of the central region electrode structure. Away from the central region, orbits are transferred to a faster 'Z4' code which includes non-linear terms in the axial motion through fourth order; for added speed the Z4 code represents acceleration gaps by delta functions (in the correct spiral location and with the radial impulse of the spiral gaps included). Finally a special 'Septum Penetration' code is used to track orbits which hit the (Copper) septum, with energy loss introduced via a table derived from detailed Monte Carlo calculations (the effect of multiple scattering in the septum is not yet included in the calculation).

A massive initial condition ensemble is used to represent the extensive phase space volume of the multi-turn beam. Specifically this volume 1) uses 41 rf times (220, 220.5, ..., 240 degrees) to span the 'phase width' of the 10 eV beam leaving the source, 2) at each of these rf times 16 radially displaced rays are added at the entry point of the Z4 code (distribution: 1+8+8 on eigenellipses with average radial amplitudes of 0, 0.44, & 0.88 mm respectively), and 3) finally, for each radial ray at each rf time an eight point axial eigenellipse of 1.6 mm average amplitude is added. The total ensemble of tracked orbits is then 41x17x5 = 3485 (the last factor being 5 rather than 9 due to the median plane symmetry of the fields). Figure 2 gives a histogram plot (at the azimuth of the deflector entrance) of number of orbits vs. radius with the 'toward-the-cyclotron-center' corner of the deflector septum indicated by the light vertical line.

At the deflector entry the 3485 rays from the acceleration family transfer to the Septum Penetration program which tracks the rays until they they arrive at a beam stop at the exit of the deflector or, in the case of rays penetrating the septum, until they hit the vacuum tank wall at some azimuth (no rays actually stop in the septum due to the range of the 250 MeV beam). With the deflector entrance radius positioned as shown in Figure 2 and with a 0.25 mm septum thickness, 3309 of the 3485 rays (95.0%) pass cleanly through the deflector -- if the septum thickness is reduced to 0.13 mm the transmitted group increases to 3401 (97.6%).

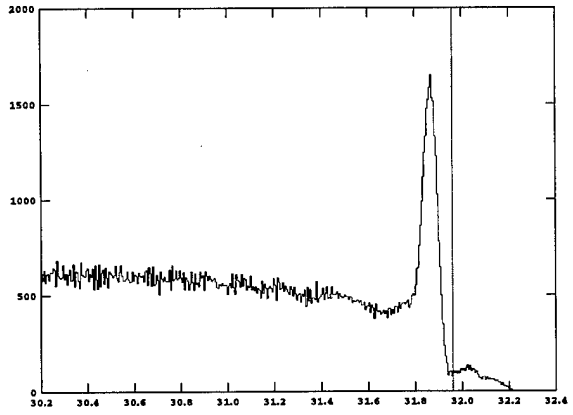


Figure 2: Radius histogram of 3485 ray family at azimuth 60 deg (radius in inches): Tracking ends where the azimuth 60 radius first exceeds 31.96 inches.

Fig. 3 shows a sample of trajectories of rays which hit the septum; the outer circle in this Figure is the 33 inch radius inner wall of the beam chamber vacuum tank with the inset double line in the 45 degree upper arc showing the aperature of the first electrostic deflector. Almost all of the rays which penetrate the septum hit the vacuum tank wall in the azimuthal region at the right (around 60 degrees upstream from the deflector entrance) with a few rays being as much as 120 degrees upstream. The most upstream cluster of rays (those which experience the largest energy loss in the septum) show substantial axial defocusing coming from alignment of the trajectories with a defocusing edge of one of the magnet sectors; higher

energy rays hit the wall further upstream and show reasonable axial focusing.

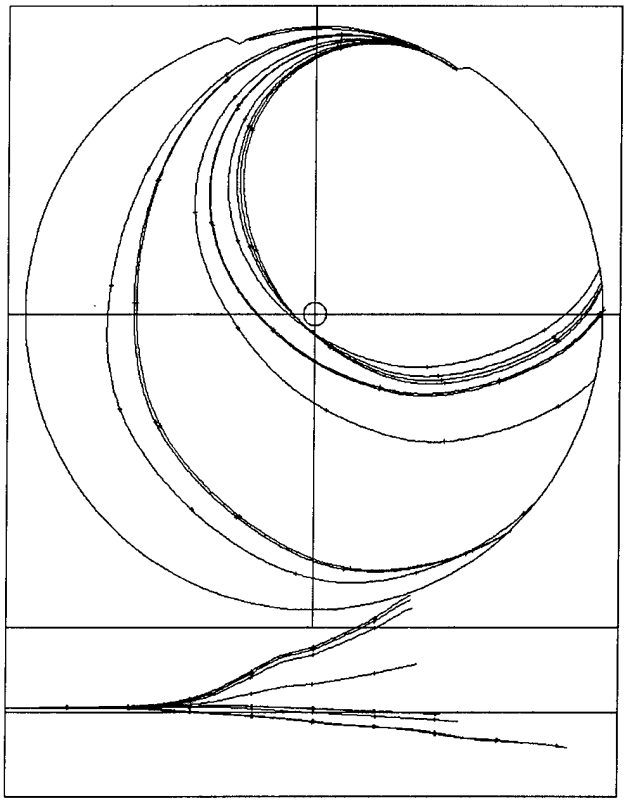


Figure 3: Top - Polar plot of selected orbits (rf times 200, 205, ..., 220 deg) which penetrate deflector septum: Bottom - Z vs path length for these orbits.

5 INDUCED RADIOACTIVITY ESTIMATES

Estimates of radioactivity induced in the cyclotron by the lost beam depend on many factors and are accordingly difficult to make in an accurate way. A previous lower energy cyclotron, the 72 MeV 'Phillips Injector' at the Paul Scherrer Institute operated for a number of years with a 200 microamp external beam and with with 93% extraction efficiency in the multi-turn mode [4]; this group moreover maintained careful records of integrated beam current and of radiation dose received by maintenance personnel (the latter being of course the final most important factor in judging the viability of a high-current accelerator based on multi-turn extraction).

The orbit computations from the previous section indicate that careful attention to fabrication details and tolerances, in conjuction with a septum of 0.13 mm (or smaller) thickness, can reduce extraction losses to the 2.5% range, i.e. lower than the PSI Phillips Injector by a factor of 3. The thick-target neutron yield at 250 MeV on Copper (the stopping material for most protons in the Phillips Injector) is higher by a factor of 12.5 than at 72 MeV [5], but, if Carbon is used for the septum and for the lost beam collectors on the vacuum tank wall, the 250 MeV yield is reduced by a factor of 3.3 relative to Cu, so that total neutron production in the K250 will be nearly the same (i.e. 12.5/3/3.3=1.3) as in the Phillips Injector.

Neutron yield is moreover far from being the only important factor in estimating residual radiation hazards. The increased range at 250 MeV (63 vs 7.4 mm in Cu) relative to 72 MeV tends to bury, disperse, and self shield induced activity. Cossairt [6] plots the 'Danger Parameter' representing radiation level in 4pi cavities in various materials uniformly irradiated by protons of various energies. For Cu the danger parameter (24 hours after a 365 day irradiation) increases by x3.7 in going from 50 to 500 MeV (the nearest energies at which results are quoted) whereas in C the parameter decreases by 1/2.1 for the same energy change. Interpolating, 250 MeV stopping in C is inferred to be only about 1/8 as dangerous as 72 MeV stopping in Cu [7].

Finally we note that actual radiation records [4] for the Phillips Injector group at PSI for the three years 1982-84 (years where the integrated extracted beam exceeded 500 milliamp-hours/year) averaged 103 mSv/year total for the group. If this work is shared by four people the annual dose is at 1/2 of allowable tolerance, and as noted in the previous paragraph there is good reason to expect radiation levels in a graphite stopping environment to be lower by x1/24 compared to the PSI Phillips injector. Relatively simple remote handling systems could easily lower this dose level by additional significant factors.

6 CONCLUSIONS

With a graphite septum, and graphite outer wall liners at beam loss points, maintenance radiation levels should be reduced by more than an order of magnitude relative to the level of the PSI facility, and since maintenance exposures at that facility were well below present tolerance levels, it is reasonable to project a comfortable margin for 'hands-on' maintenance of a 250 MeV, 200 microamp cyclotron of the type suggested herein.

REFERENCES

[1] H. Blosser, D. Johnson, F. Marti: 'Design Study for a 250 MeV High Current Cyclotron: Compact Superconducting Option', MSUCL-1070(1997).

[2] H. Blosser, M. Gordon: 'Performance Estimates for Injector Cyclotrons', Nuc. Instr. Meth. 13(1961)101.

[3] M. Gordon: '...Longitudinal Space Charge Effect...', Proc. Fifth Intl. Cyc. Conf: (Oxford 1969) 305.

[4] T. Stammbach (private communication: May 1997).

[5] T. Kato, T. Nakamura: 'Estimation of Neutron Yields .....': Nuc. Instr. Meth. A311(1992)548.

[6] J. Cossairt: 'Topics in Radiation at Accelerators', US Particle Accel. School (Jan 1993) TM-1834.

[7] Beam tests at NSCL show Pyrolytic graphite to be an excellant septum material.

*Supported by US National Science Foundation (PHY-9528844) and by Lockheed Martin Energy Systems (22X-SW033V).

A SEPARATED SECTOR CYCLOTRON FOR THE PRODUCTION OF HIGH INTENSITY PROTONS*

F. Marti, H. Blosser, D. Johnson, D. Lawton and J. Vincent
National Superconducting Cyclotron Laboratory,
Michigan State University, East Lansing, MI 48824, USA

Abstract

We describe in this paper the design of a separated sector cyclotron (SSC) for the production of an intense beam of 230 MeV protons. The goal was an accelerator that could be used as the driver of an ISOL type Radioactive Ion Beam Facility.

1 INTRODUCTION

The purpose of this study is the conceptual design of an accelerator for the Holifield Radioactive Ion Beam Facility (HRIBF) at Oak Ridge National Laboratory (ORNL) to produce 200 μA of protons at energies of approximately 200-250 MeV, that would fit in room C110 at ORNL. The choice in this option of a separated sector cyclotron (SSC) is driven by the desire of minimizing the losses in the accelerator. Most of the losses in an isochronous cyclotron usually occur at the deflector septum during extraction. The radius gain between turns should be increased as much as possible to decrease these losses. The radius gain per turn due to the energy gain, in abscence of any other off-centering mechanism is given approximately by:

$$\Delta R = R \frac{\Delta E}{E} \frac{\gamma}{\gamma + 1} \frac{1}{\nu_r^2}$$

Where R is the extraction radius, E is the final energy, ΔE is the energy gain per turn, γ is the relativistic factor and ν_r is the radial focusing frequency. Increasing the voltage of the RF system is the obvious way of increasing the energy gain, but it is limited by sparking and power limitations. Increasing the radius of the cyclotron is the other parameter that we have used in this design to increase the turn separation. One of the boundary conditions in this study was the desire to obtain a cyclotron design that would fit in room C110 at ORNL. Under this condition we estimated that 3.7 m is the maximum extraction radius compatible with fitting the cyclotron in that room. These decisions of increasing the cyclotron size and RF voltage come at a price, the accelerator cost increases. This SSC option then emphasizes reliability and lower technical risk over cost. Our design has benefitted from past experience developed mainly at two laboratories: the National Accelerator Center (NAC) at Faure, South Africa [1], and the Paul Scherrer Institut (PSI) at Villigen in Switzerland [2]. Both laboratories operate large separated sector cyclotrons that accelerate protons in similar ranges of energies and intensities. The NAC cyclotron is a multi-ion, variable energy machine that accelerates protons up to 220 MeV, with currents of up to 200 μA at 66 MeV. The PSI accelerators are single ion, fixed energy. They accelerate protons to 72 MeV in their Injector II and to 590 MeV in their ring cyclotron with intensities above 1.5 mA. The PSI cyclotrons can be described as state of the art in high intensity operation. The extraction efficiency is 100 % even at 1.5 mA.

A companion paper describes a different option: a compact superconducting cyclotron [3].

2 SECTOR MAGNETS

One of the first decisions to be made in the design process is the number of sectors in the magnet and the angular width of each sector necessary to achieve the final energy of approximately 250 MeV. To avoid the effects of resonances like the $\nu_z = 1$ and the $\nu_r = N/2$ we have selected four sectors and a magnet sector angle of 34 degrees (f= 34/90=0.378).

The magnetic field of the sector magnets was studied with the finite element code TOSCA. We have adopted a minimum magnet gap of 3.8 cm with the assumption that the magnet surface close to the median plane will be part of the vacuum chamber. We expect to obtain an isochronous field by shaping the pole tip surface and thus eliminate the need for trim coils. We would like to have the magnetic field approximately constant inside the sector magnet along each orbit for a given energy, and change according to the isochronism requirements for different energies. With this purpose the TOSCA grid was designed with construction circles that followed the theoretical (hard edge approximation) closed orbits. The points along these circles have assigned to them a constant gap value. After obtaining a polar grid from the TOSCA

* Work supported by ORNL contract 22X-SW033V and NSF Grant PHY-95 28844

0-7803-4376-X/98/$10.00 © 1998 IEEE

model we isochronized the field and found the difference between the calculated field and the field required to maintain isochronism during acceleration. This difference was used to change the gap as a function of energy and a new model was calculated. After several iterations a reasonable approximation to the isochronous field was obtained with errors of less than 100 gauss and less than 50 over most of the radius. A top view of the whole SSC in Room C110 at ORNL is shown in Figure 1. A view of the sector magnets is shown in Figure 2.

3 BEAM DYNAMICS

The equilibrium orbit (closed orbit) properties were calculated in the polar grid obtained from TOSCA. These results confirmed the choice of sector angle maintaining the operating point away from deleterious resonances.

A conceptual design of the injection system is similar to the injection system used at NAC [4]. The beam is injected at an energy of 8 along one of the two valleys not used for the main RF cavities. Two deflecting elements with fields of 12.0 kG and 1.15 kG are used to bend the beam into the accelerated orbit. As the turn separation between central rays at injection is large, 4.0 cm for an energy gain of 1 MeV, there is no problem in accommodating a septum between turns. The actual dee voltage profile may reduce this energy gain significantly.

A plan view of the extraction system is shown in Figure 3. The maximum radius of the 231 MeV internal beam ellipse is plotted as well as the central ray of the extracted beam.

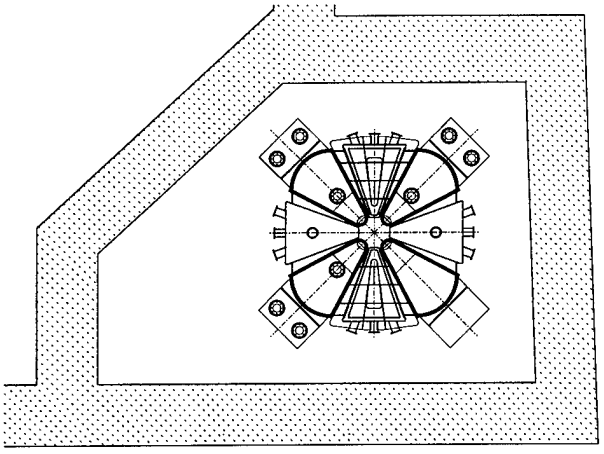


Figure 1 Plan view of the SSC installed in Room C110 at ORNL.

This system closely resembles the extraction system of the NAC SSC [4]. The beam extraction is started by increasing the separation between the final orbit and the internal beam with an electrostatic deflector (ED) with a relatively low field of 25 kV/cm extending from θ=-44 to θ=-32 degrees (l ≈0.64 m).

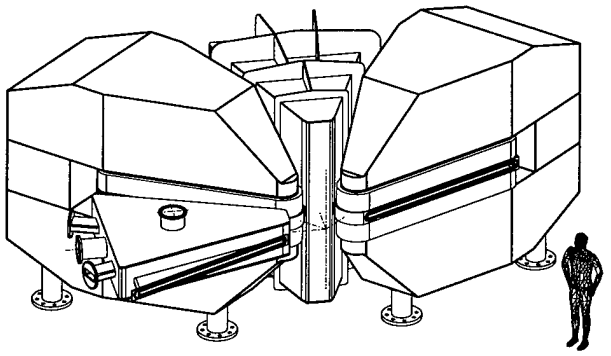


Figure 2 Partial view of the SSC showing two of the sector magnets and two of the valley vacuum chambers.

Approximately 90 degrees later, from θ=44 to θ=50 degrees (l ≈ 0.30 m) the turn separation is sufficient (1.5 cm) to insert a septum magnet (SM1) of low field (0.1 T), (see Figure 4). This septum magnet is located inside the dee. The next deflection is produced by a second septum magnet (SM2) located from θ=116 to θ=128 degrees (l ≈ 0.65 m). The separation here is 12 cm allowing a higher field (0.4 T) magnet. Finally a bending magnet (BM) with a field of 1.0 T is used to clear the next sector magnet.

The phase spread of the beam will produce an energy spread and a radial spread that will reduce the turn separation from the theoretical monoenergetic beam separation. To reduce this deleterious effect it is desirable to accelerate a narrow phase width, but space charge forces increase the energy gain of the ions in the leading edge of the bunch and decrease the energy gained by the ions in the tail of the bunch. This effect tilts the bunch effectively increasing the turn width and decreasing the separation between consecutive turns.

Analytic treatments of space charge effects in cyclotrons are not very detailed due to the complexity of the problem, and mostly give a qualitative idea of how the different parameters enter in the analysis. Numerical calculation of space charge effects in cyclotrons are still very primitive and no hard limits can be obtained from them. Instead we use approximate formulas to compare our design with cyclotrons running in the high intensity regime (PSI Injector II and Ring cyclotron). According to W. Joho [5] the voltage spread induced by the longitudinal space charge forces can be estimated from the formula:

$$\Delta U_{SC} = 2800\Omega \frac{< I > n^2}{\frac{\Delta\Phi}{2\pi}\beta_f}$$

A figure of merit is the ratio of the space charge induced voltage spread to the voltage gain per turn. This ratio for our design falls in between the corresponding values for the PSI cyclotrons. Both of these accelerators achieve 100 % extraction.

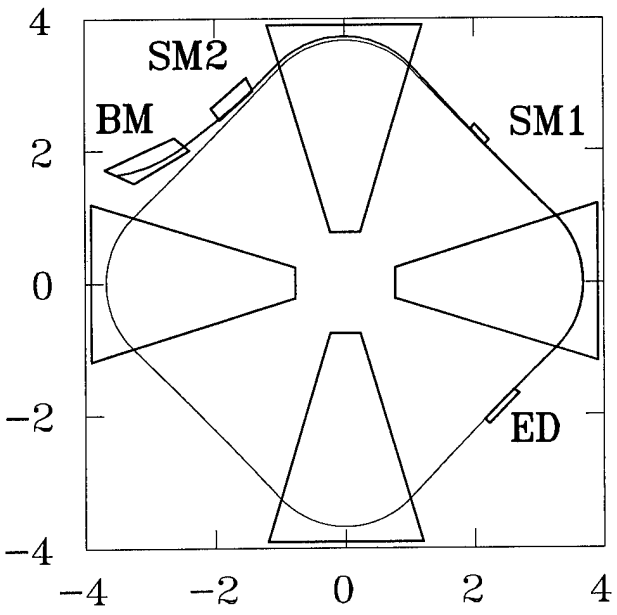


Figure 3 Top view of the extraction system.

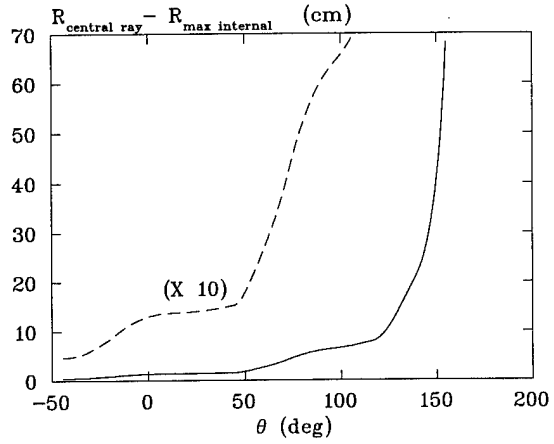


Figure 4 Difference in radius between the central ray of the extracted orbit and the maximum radius of the internal beam.

A solution to the turn broadening produced by a large beam phase width is obtained by using a flat-topping RF system. Additional electrodes are utilized that are excited with the third and ninth harmonic of the fundamental RF frequency. The result of particle tracking in the actual magnetic field with fundamental and higher harmonics showed that the addition of a third harmonic energy gain of 23.5 % of the fundamental is optimum. This additional voltage increased the phase interval corresponding to an energy spread less than 10 % of the energy gain per turn from just a few degrees to 25 degrees. If a ninth harmonic component is included the acceptable phase width is 43 degrees. The ninth harmonic cavity would certainly be a challenging project, running at 300 MHz. Serious design work should be done to determine its feasibility.

4 RF AND VACUUM

The main accelerating system consists of two dees placed in opposite valleys. The ion orbital frequency is 8.3 MHz giving RF in fourth harmonic of 33.2 MHz.. The cavity has been calculated using the program WAC [6]. For a peak voltage of 250 kV on the dees the estimated total power is 150 kW.

The beam chamber consists of the valley sections and sector magnet sections. The steel surfaces in the sector magnets constitute the beam chamber itself. Plating of the steel is necessary to avoid corrosion problems. The valley sections are of two kinds depending if the RF resonators fill the valley or if it is a valley used for injection, extraction or diagnostics. The design adopted for the vacuum seals has been copied from the PSI Injector II seals. It consists of metallic inflatable seals of toroidal shape that are deflated to disassemble the beam chamber and inflated when assembled. This mechanism allows radial motion of the four valley sections with respect to the sector magnets for fast assembly-disassembly.

CONCLUSIONS

The present study showed that it is posible to design a SSC that would fit in Room C110 at ORNL to produce 200 μA of 230 MeV protons. Preliminary injection and extraction systems have been designed. Flattopping cavities are needed to decrease the energy spread and reduce the losses on the extraction septum.

ACKNOWLEDGEMENTS

We would like to thank A. H. Botha from NAC and P. Sigg from PSI for sharing with us extensive information about their facilities.

REFERENCES

[1] A. H. Botha et al., Proc. of the 11th Intl. Conf. On Cyclotrons and Their Applications, Tokyo 1987, p. 9.
[2] U. Schryber et al, Proc. of the 14th Intl. Conf. On Cyclotrons and Their Appl., World Scientific, 1995, p. 32.
[3] H. Blosser et al., this conference.
[4] S. Schneider and P. F. Rohwer, Proc. of the 11th Intl. Conf. On Cyclotrons and Their Applications, Tokyo 1987, p. 476.
[5] W. Joho, Proc. Ninth Intl. Conf. On Cyclotrons and Their Appl.,Caen 1981, p. 337.
[6] See www.3pco.com.

CONCEPTUAL DESIGN OF A HIGH FIELD ULTRA-COMPACT CYCLOTRON FOR NUCLEAR PHYSICS RESEARCH

J. Schubert and H. Blosser, National Superconducting Cyclotron Laboratory, Michigan State University, East Lansing, MI 48824

Abstract

We have studied the feasibility of using an existing wide-bore 8 T magnet as a component of an ultra-high-field cyclotron. Such a machine would use the highest magnetic field of any cyclotron to date, viz. 7.6 T averaged azimuthally with 8.5 T in the hills. The K95 `Eight Tesla Cyclotron' would have roughly the same magnetic rigidity (Bρ) as the Oak Ridge Isochronous Cyclotron in a package of only one fourth the radius, with a corresponding reduction in cost. Such a cyclotron could accelerate particles with a charge state Q/A = 1/4 to a final energy of 5 to 6 MeV/nucleon, the energy range currently being used to study superdeformed, high angular momentum nuclei that result from glancing collisions. Studies have stressed achieving sufficient vertical focusing (ν_z) despite the high magnetic field level, and finding a central region geometry that fits comfortably in the limited space available while providing centering and early-turn focusing properties that are similar to those of less compact machines.

1 INTRODUCTION

The Eight Tesla Cyclotron is conceived as a two stage project. The first stage of the project will be to build an internal beam cyclotron to accelerate He^+ from a PIG ion source to an internal beam stop. The design parameters for this stage are listed in Table 1. In this configuration the miniature cyclotron would demonstrate the ability of a high field magnet to provide adequate focusing to deliver a beam from the center of the machine to the extraction radius, and the current available for extraction could be measured. At a later time the accelerator could be converted from a test stand to a nuclear physics tool by replacing the internal ion source with an axial injection system and installing an extraction system. The cyclotron would then accelerate heavy ion beams of any species capable of producing a charge state near Q/A = 1/4.

2 THE MAGNETIC FIELD

The Eight Tesla Magnet has been in operation with flat poletips since 1994[1]. The magnet excitation reported in Table 1 was chosen because this is the highest current at which the magnet has operated reliably to date. Further development work on the magnet should make it possible to raise the average field with sectored pole tips to 7.8 T. This would place the RF frequency comfortably inside the FM band, allowing us to use a commercially available transmitter intended for FM radio stations, rather than a more expensive custom built transmitter.

Table 1. Internal beam cyclotron parameters

ORBIT PARAMETERS	
Charge state	0.250
Final energy	5.93 MeV
Final radius	18.9 cm
Turn number	178
MAGNET	
Magnet bending limit	95 MeV
Rigidity	1.42 Tm
Ampere-turns	3.1×10^6
Central magnetic field	7.58 T
Maximum hill field	8.47 T
Minimum valley field	6.75 T
Iron weight	8 tons
Pole radius	19.9 cm
Hill gap	2.54 cm
Valley gap	29.8 cm
Sector number	3
Sector spiral	7.46^o/cm
Sector width at max radius	62.1^o
RF SYSTEM	
Harmonic number	3
RF frequency	87.1 MHz
Peak dee voltage	28.5 kV

The poletips are small enough that we plan to machine sectors out of a single piece of iron for each pole. The equilibrium orbit properties for the calculated magnetic field are shown in Fig. 1. The iron in the pole tips is saturated, so raising the overall field level <B> has little effect on the third harmonic component, B_3. Our B_3 peaks at 8 kG which is almost identical to the case for the 4.6 T Harper medical cyclotron. Flutter focusing depends on the ratio of B_3/<B>, so the higher the field, the smaller the contribution of flutter focusing to the total ν_z. Although ν_z is sufficient at middle energies, it rises slowly near the center so that the central focusing cone and electrostatic focusing are more important to the early turns in the high field machine than in its low field predecessors.

In this design it was necessary to incorporate iron into the ion source in order to shape the central field

0-7803-4376-X/98/$10.00 © 1998 IEEE

cone. Otherwise the poletip design is very similar to the three previous superconducting cyclotrons built at the NSCL. Because this is a fixed energy single charge state machine we may accomplish all needed field shaping with hill and valley shims so no trim coils are needed.

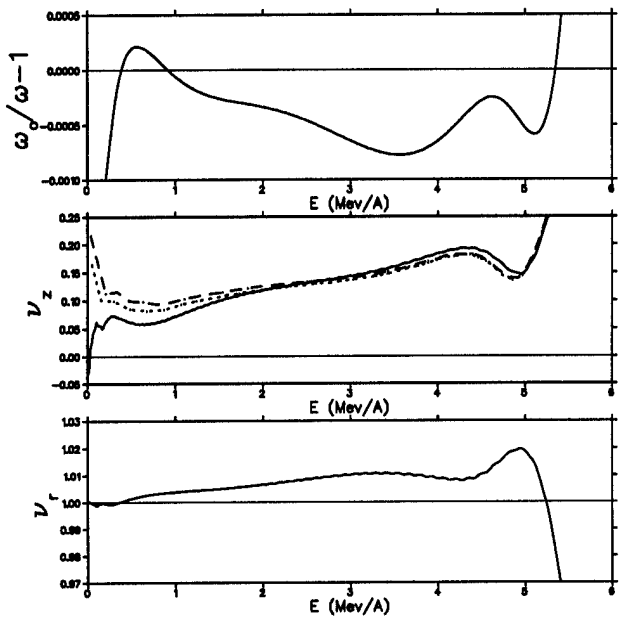


Fig. 1: Equilibrium orbit properties as a function of energy. Top: orbital frequency relative to isochronous frequency. Middle and Bottom: axial and radial focusing frequencies calculated by the E.O. code. Also plotted are the total axial focusing frequencies for accelerated orbits leaving the ion source at RF times τ_0 = 207°(dashed line) and 201°(dotted line.) Peak dee voltage occurs at τ= 270°.

3 THE CENTRAL REGION

The central region was initially scaled from that of the Harper medical cyclotron[2] using the Reiser formula[3], which describes the geometrical enlargement or reduction of ion orbits for changes of the magnetic field, charge-to-mass ratio, and dee voltage. The Harper geometry is reduced by a factor of 0.80.

Electric fields in the central region are computed by RELAX3D[4] and then orbits are tracked by the NSCL code, CYCLONE[5]. Initial conditions for orbit simulations were chosen by running a variety of orbits in the scaled central region. Particles that left the chimney at an RF time τ_0 = 204° were found to be the best centered (relative to other starting times) and were presumed to best characterize the beam in the actual Harper cyclotron.

The scaled geometry was then modified to further optimize beam centering in preparation for extraction studies. The design was also improved in several ways to compensate for the magnetic focusing that is lost due to the higher field. The optimized central region layout can be seen in Fig. 2. The first accelerating gap (from the chimney to the field free region at the center of the puller) has been shifted 4° clockwise by the orbit code to simulate lengthening the puller gap in order to shift all phases in the positive direction. Fig. 3 shows the average phase per turn calculated from the time that a particle arrives at the electrical center of each gap.

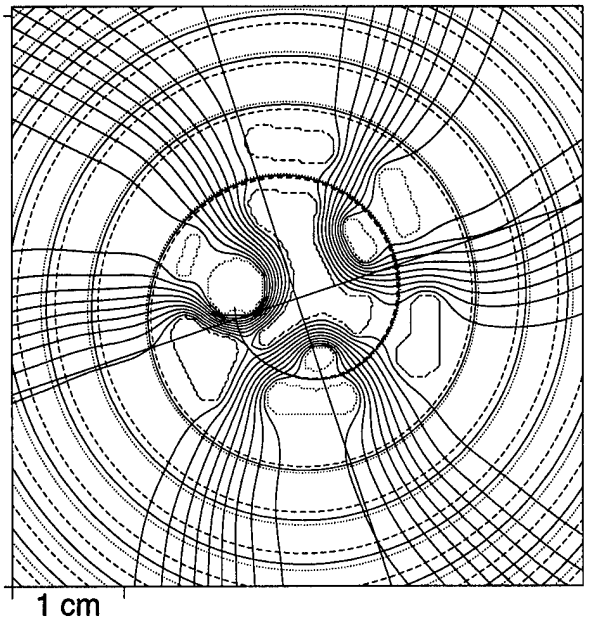


Fig. 2: Central region equipotential field map, and the first few orbits for beam leaving the ion source at RF times τ_0 = 201°, (dotted line) 204°, (solid line) and 207° (dashed line).

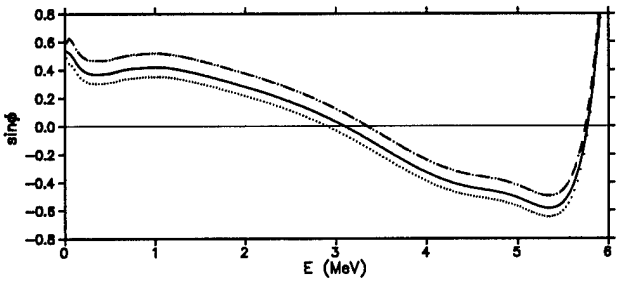


Fig. 3: Turn average phase for the three orbits of Fig. 2.

The first gap position and cone field size have been chosen to keep the average phase near +30° for the first 1 MeV of acceleration (about 30 turns) in order to maximize electrostatic axial focusing in the region where the magnetic contribution to ν_z is below 0.1. The total focusing plotted in Fig. 1 is measured from half cycles of vertical oscillations of a ray that is displaced 2 mm vertically at the puller and then accelerated to full energy.

Axial confinement was investigated for starting times from τ_0 = 201°-207°. The maximum displacements in axial position and momentum (at the puller) which remain within the beam aperture approximate an ellipse corresponding to a total (normalized) acceptance of 1.0π mm-mrad for the range of starting times studied.

Similar studies of orbits that are displaced radially at the puller indicate a normalized radial acceptance of at least 0.15π mm-mrad for the same range of starting times.

4 FEASIBILITY OF AXIAL INJECTION

In order to produce heavy ion beams the cyclotron would need an external ion source and an axial injection system. A spiral inflector geometry can be scaled from the design used in the K500 and K1200 cyclotrons[6] by holding the tilt parameter k′ constant[7]. The height and width of the inflector are inversely proportional to the magnetic field, so the scaled inflector is 0.81 cm tall and 1.25 cm in diameter. If a new central region were scaled from the K1200[8] the resulting first turn diameter would be 2.5 cm. The scaled inflector is too large to perfectly match the scaled central region, but the discrepancy is only 15% so the needed adjustments should be minor.

The electric field in the inflector gap increases in proportion to the magnetic field. The scaled inflector would have a 2 mm gap with a 24 kV/cm electric field, which is comfortably within the operating range of such devices.

The primary difficulty appears to be machining and properly positioning the miniature inflector electrodes. More detailed studies may be necessary to investigate increasing the gap height and the corresponding electrode voltage.

5 FEASIBILITY OF EXTRACTION

We plan a resonant extraction system where the first harmonic field perturbation is produced by a set of iron rods (1" in diameter) similar to the Chalk River trim rods[9]. The rods eliminate all space and cooling issues associated with trim coils and they can be centered at the radius where ν_r = 1, so that only a small displacement is needed to produce a sufficient first harmonic.

The turn separation produced by a 5 gauss field perturbation can be seen in Fig. 4. Here the τ_0 = 204° central ray from the internal ion source central region has been tracked from the ion source to the likely position of an electrostatic extraction channel. The septum would be located near a radius of 18.5 cm. A phase space is defined by eight rays displaced from the central ray at the puller to form a 1 mm diameter circle. Each of the eight rays' starting phase has been adjusted so that its energy gain is similar to that of the central ray. The first harmonic perturbation causes little distortion of the phase space while providing a turn-center to turn-center separation of 2 mm.

The low first harmonic used for the initial off centering helps to minimize the axial expansion of the beam which occurs at the $\nu_r = 2\nu_z$ resonance roughly ten turns after the ν_r = 1 resonance. A beam which fills the 7.5 mm puller aperture has a height of roughly 5 mm at the entrance to the electrostatic deflector.

From this point a pair of 56° long electrostatic deflectors in successive hills, followed by a 64° electrostatic deflector located behind a dee, can extract the beam with an electric field of 130 kV/cm in a gap 2.5-3.5 mm wide, which is within the range of electric fields used successfully at the NSCL[10].

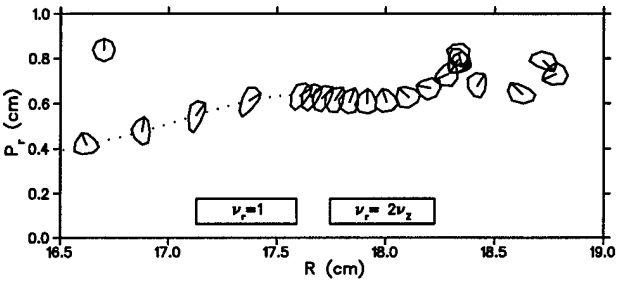


Fig. 4: Radial phase space behavior of a family of accelerated rays plotted at the azimuth of the electrostatic deflector entrance. The shape of the initial phase space (at the puller) relative to the central ray is indicated at the upper left. Radial momentum p_r is divided by $\omega_0 m$ to yield units in cm.

6 CONCLUSION

The miniaturization of cyclotron components for an 8 T magnetic field poses no critical problems for the energy and charge-to-mass ratio studied. Such a machine would be a natural extension of the development work already performed for super-conducting cyclotrons.

REFERENCES

[1] J.W. Kim, Ph.D. thesis, MSU-NSCL (1994).
[2] H. Blosser *et. al.*, *IEEE Trans. Magn.*, 25,no 2, 1746 (1989).
[3] M. Reiser, NIM 18-19, 370, (1962).
[4] C. J. Kost and F.W. Jones, `RELAX3D User's Guide and Reference Manual', TRIUMF, Canada (1992).
[5] MSU NSCL Accelerator Group, `Z3CYCLONE Instruction Manual', (1992).
[6] F. Marti and A. Gavalya, Proc. of the 11th Int. Conf. on Cyclotrons, Tokyo, 1986.
[7] J.L. Belmont and J.L. Pabot, *IEEE Trans. Nucl. Sc.*, NS-13:191-193, (1966).
[8] D. Johnson and F. Marti, NSCL Annual Report, 125, (1989)
[9] C.B. Bigham, NIM 131, 223, (1975).
[10] T. Antaya *et. al.*, NSCL Annual Report, 198, (1980-1981).

POLARIZED ELECTRONS IN THE AMPS STORAGE RING

G. Luijckx, P.W. van Amersfoort, H. Boer-Rookhuizen, J. F.J. van den Brand, F.B. Kroes, C.W. de Jager*, L.H. Kuijer, J. B. van der Laan, R. Maas, J. G. Noomen, I. Passchier, M.J.J. van den Putte, all at NIKHEF, Amsterdam, NL
I. Koop, B. Militsyn, BINP, Novosibirsk, Russia; A.S. Terekhov, ISP, Novosibirsk, Russia

Abstract

AmPS is a 300-900 MeV electron ring. The machine was designed as a pulse stretcher to provide continuous external beams. After years of successful operation in this mode the nuclear physics program now concentrates on experiments with stored beams interacting with internal gas targets. These experiments require currents between 50 and 200 mA through 60 cm long 15 mm wide cylindrical target cells. Gas pressures in the open-ended cells correspond to target thickness of 10^{14} to 10^{16} atoms/cm^2. Strong stray fields from a spectrometer and from target holding fields disturb the closed orbit. Under operational conditions the linac provides a maximum energy of 700 MeV, so ramping is required to achieve 900 MeV. To further increase the luminosity at the target a reduced emittance lattice based on the existing magnet configuration has been designed. Late 1996 a polarized electron injector as well as a "Siberian Snake" to control the spin on the internal target became operational. The polarized injector delivers a few mA to the linac so stacked injection in the ring is required. With strained InGaAsP cathodes a polarization of 80 % was obtained. Test results, performance and prospects are presented.

1 INTRODUCTION

NIKHEF is a nuclear physics and high-energy physics research institute. The storage ring AmPS provides high duty factor (d.f.) beams for the in-house electron scattering experiments. The experiments use several detectors measuring in coincidence. The real to accidental coincidence ratio is directly dependent of the d.f. of the beam on target. In pulse stretcher mode the ring provides routinely external beams up to 10 μA @ 300 to 700 MeV. For experiments with internal targets up to 150 mA @ 300 to 700 MeV is available. An energy of 950 MeV was achieved in Spring 1997 during accelerator physics experiments. Details on the design and the performance of the ring were reported earlier, an extensive list of references is available [1]. A collaboration between NIKHEF, the Budker Institute of Nuclear Physics (BINP) and the Institute of Semi-conductor Physics (ISP) allowed to add a polarized electron source and a siberian snake to the AmPS accelerator facility. A first internal target (IT) experiment with polarized electrons was performed in Fall 1996 with on average a stored current of ~ 5 mA @ 650 MeV. Meanwhile systematic commissioning of key systems improved the cathodes lifetimes, the stored current and the polarisation degree.

2 AmPS with POLARIZED ELECTRONS

2.1 Self polarization

Due to the emission of synchrotron radiation the electron spins will be aligned with the direction of the magnetic field (i.e. transverse polarization). The time constant of this 'Sokolov-Ternov effect' in practical units [2] is

$$\tau_0[hr] = 2.75\times10^{-2}\,\frac{\rho^2 R[m^3]}{E^5[GeV]}$$

The maximum polarization degree is about 92 %. Since the desired spin-orientation at the target location is longitudinal, an additional insertion device is needed to re-orient the spin. For AmPS at E = 800 MeV the self-polarization time $\tau_0 \approx 30$ hr, not very useful with gas IT's.

2.2 Injection of polarized electrons

Because of the long self-polarization time it was decided to inject polarized electrons directly into AmPS. In order to obtain the desired longitudinal polarization at the IT location, some spin manipulation is necessary.
The spin tune ν_0 is given by $\nu_0 = \gamma.a$, γ is the Lorentz factor and $a = (g-2)/2$. In practical units this relation is expressed as $\nu_0 = E[MeV]/440.65$. Only at energies being integer multiples of this 'magic energy' of 440.65 MeV will the spin tune be integer. At these energies a longitudinal polarization at the IT location will be maintained without additional insertions (assuming injection with the proper polarization direction!). At all other energies the spin tune is not integer and a special device, e.g. a Siberian Snake, is needed to make the spin tune integer. A Snake rotates the spin by p along the longitudinal beam axis, which introduces in the x–plane an additional spin rotation of $2(p - \nu_0/2)$; in one revolution the spin rotates by ν_0, so the net rotation per revolution is just 2p, independent of energy, see Fig. 1. To produce longitudinal polarization at the IT location, an energy–dependent polarization of the injected electrons is required, since ν_0 *does* depend on energy. To rotate the spin over π, a solenoid with a field integral of

$$\int \frac{B_s\,dl}{B\rho} = \pi \qquad (1)$$

is required. The total length of the AmPS solenoids is 1.624 m, so from (1) the field requirement follows:

$$B_S\,[T] = 6.45\,E[GeV].$$

Superconducting solenoids are needed to reach this field magnitude.

* now at TJNAF, Newport News, VA, USA

0-7803-4376-X/98/$10.00 © 1998 IEEE

2.3 Beam optical effects

A solenoid will introduce strong coupling between the two transverse planes. In order to remove this coupling the solenoid has been split into two parts, and the total Snake includes two 45°–rotated end quadrupole doublets and a strong central quad. This structure possesses the following transfer matrix:

$$M = \begin{pmatrix} -1 & 4.7 & & \\ 0 & -1 & & \\ & & 1 & 4.7 \\ & & 0 & 1 \end{pmatrix}$$

In the horizontal plane the Snake behaves as a 4.7–m drift space, with a tune advance of $\Delta\nu_x = 0.5$ (as $\cos\mu_x = -1$). Vertically the Snake is just a 4.7–m drift length. To first-order, the x–y coupling has been removed. When the Snake is operated, AmPS is run with a slightly modified lattice configuration, in order to compensate the additional horizontal tune shift.

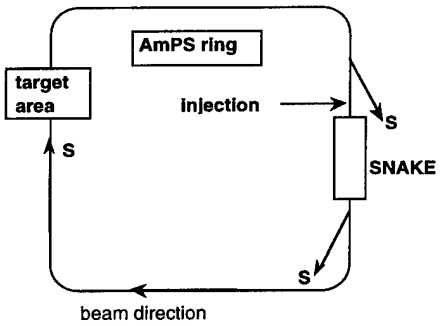


Fig. 1 Spin orientation in AmPS with Snake on.

3 THE POLARIZED ELECTRON SOURCE (PES)

PES mainly consists of a loading chamber, a preparation chamber, a 100 keV photo-cathode gun, a Ti:Sapphire laser with an optical circuit, a Z-shape spin manipulator, a Mott polarimeter and a 300 keV r.f. post-accelerator.
Cathodes are inserted into and extracted from the source UHV system through the loading chamber. With a magnetic manipulator cathodes can be exchanged between the loading and the preparation (prep) chamber. The prep chamber can store up to 4 cathodes. One cathode can be prepared to a Negative Electron Affinity (NEA) surface state at a time. Also the quantum efficiency and the lifetime (at He-Ne laser wavelength) can be measured in the prep. chamber. Cathodes are exchanged between the prep. chamber and the photocathode gun by means of 2nd magnetic manipulator, within a typical time of 15 min.
The photocathode gun is designed with double vacuum chambers and a double high voltage insulator [3]. The latter allows for the permanent connection of the preparation and loading chamber. The cathode operates at **-100 kV**. Pulsing this power supply with the injection frequency (typ. 1 Hz, max. 10 Hz) and with a pulse length of 600 μs increased the cathode lifetime from 4 to 180 h with respect to the former d.c. mode of operation. The photocathode is illuminated by Ti:Sapphire laser. Its wavelength range is from 700 to 850 nm at intensities up to 1kW per pulse. By means of an electro-optic pulse slicer, with a variable delay and width, the laser pulse length can be set in the range 0.4 - 4 μs. The laser produces linearly polarized light. A λ/4 plate converts the polarization to circular. The intensity of the pulses is adjustable by a rotatable Glanprism. The laser spot on the cathode can be adjusted by a variable diaphragm which is projected onto the cathode surface. The laser pulses are synchronized with the h.v. power supply pulses.
From the gun the 100 keV electrons are guided through two 45° bending magnets towards the Z-shape spin manipulator. Here the electron spin orientation can be adjusted by an arbitrary angle. The principle of the spin rotator is based on the Illinois-CEBAF design [4] . It precesses the spin such that the maximum longitudinal polarization can be achieved at the internal target location of the storage ring AmPS. To match the injection requirements of MEA the polarized electrons are accelerated to 400 keV by a post-accelerator. This accelerator consists of two 2856 MHz cavities, one for prebunching and one for acceleration. The beam is inflected in MEA by an α magnet. Fig. 2 shows a lay-out.

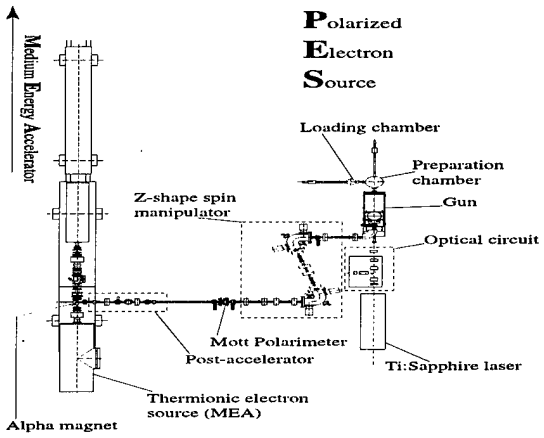


Fig. 2. Overview of the polarized electron source

Diagnostics: the polarization degree of the electrons is measured with a Mott polarimeter based on an existing design [5]. The polarimeter is positioned downstream of the Z-shape spin manipulator because the measurement is sensitive to the transverse polarization of the beam.
To determine the polarization degree the electrons are scattered on a 100 nm thick gold foil. Other foils with different thickness are used to calibrate the polarimeter. Four silicon surface barrier detectors detect the scattered electrons. Two detectors are mounted at +120° and -120° to measure the scattering asymmetry. The other two detectors are mounted at +50°, and -50° and monitor the instrumental asymmetries. The current transmission along the beampath of the source can be measured with 2 current transformers and also with a Faraday cup when the alpha magnet is not powered.

Six screens provide information on the beam shape and position along the beam path of the polarized electrons. Selection of the cathodes is a tedious job, especially since a high quantum efficiency is not necessarily related to a high current output. The best cathodes so far provided 30 mA at 50 % polarization and 10 mA at 70 % polarization. The transmission in to MEA is ~ 25 to 30 %.

4 SIBERIAN SNAKE

The snake consists of 2 mirror symmetric sections. Each section is composed of 2 "skew" (90°) quadrupoles, one superconducting (SC) solenoid and one "normal" quadrupole. The SC solenoids are warm bore types. Each solenoid consists of 5 coils that are connected in series. The inductance of a coil is ~ 450 mH and a 0.2 Ω resistor is externally connected across each coil giving an L/R of ~ 2 s. The maximum current is ~ 300 A yielding a field of 6.5 T , good for 1 GeV. NbTi (NT-50) wire with a ø of 0.85 mm is used for the coils as well as for the leads from the coils to the outside world. There is one cryostat that feeds both solenoids with liquid He. The "heat" shields are now cooled by the return He gasflow reducing the consumption of He from the original 150 to 70 liter/24 h.

5 POLARIMETER

To measure the polarization of the stored electrons in the AmPS ring, a polarimeter based on spin-dependent Compton scattering has been designed and constructed. The cross section for elastic photon-electron scattering depends on the product of longitudinal electron polarization (P_z) and circular photon polarization (S_3) by:

$$d\sigma/dE = \sigma_0(1 + P_z S_3 \alpha_{3z})$$

where σ_0 is the unpolarized cross section and α_{3z} the analyzing power (which is of the order of 2% at 1 GeV). The polarimeter consists of a Argon-ion laser, an optical path for the laser beam, and a gamma-detector to measure the energy of the backscattered photons. The Argon-ion laser produces a CW beam of 10 W in TEM_{00} mode at 515 nm. The optical path contains remotely controllable mirrors to transport the laser light to the interaction region and lenses to maximize the density of the laser light. A Pockels cell and a quarter-wave plate are used to create left and right circularly polarized light. Photons which are Compton scattered, have energies up to 30 MeV and are detected with a pure CsI crystal of 10x10x24 cm^3. A lead shield surrounds the crystal, while a plastic scintillator is placed in front of the detector to veto charged particles. Initial tests with the polarimeter have shown that we can optimize the overlap of the electron and laser beam by means of the remote controlled mirrors. 88% of all detected photons originated from Compton scattering with a rate normalized to the beam current of 3.5 kHz/mA.

6 RESULTS

A current of 150 mA is routinely stored in AmPS by 3 turn injection and stacking of 2 mA polarized e^- pulses from the linac MEA. This was achieved by precise matching of the pulses of the 2 injection kickers.

The polarization life time of the electrons stored in AmPS was measured see fig. 3. These measurements indicate that the polarization life time is long enough to enable IT experiments using the polarized electron beam, because then the ring is refilled typically every 10 minutes. The measurements also show that there is no significant loss of polarization during injection, even with multi-turn injection and stacking.

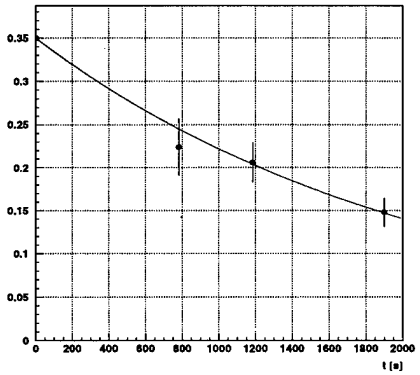


Fig. 3. Polarization (vertical axis) versus time [s]. Stored current at t = 0: 120 mA.

Due to a destructive quench of several of the SC leads to the solenoid coils the commissioning had to stop end of January 1997. One of the solenoids is still operational and it will be tried to maintain polarization in the ring with this solenoid. This only works well close to the magic energy of 440 MeV.

7 PROSPECTS

Internal target experiments with polarized electrons will be resumed early 1998, after the repair of the snake.

High-luminosity: a first lattice design [6] for a threefold reduction of the stored beam emittance proved extremely sensitive to some quadrupole settings. The design could be adapted allowing for "offsets" up to 3 % without deteriorating the reduced emittance nor the betafunction amplitude at the internal target. The emittance will be measured indirectly by measuring the size of the beam profile with a system based on compton scattering [7].

Ramping: starting from 650 MeV the energy could be successfully ramped to 950 MeV in 15 min. (without IT cell and with electrons from the thermionic gun). The current loss (includig lifetime effects) during ramping was typically 50 % with starting currents of 75 mA.

REFERENCES

[1] G. Luijckx et al.," The AmPS ring: Actual Performance and Future Plans", Proc. of the 1995 Particle Accelerator Conference and International Conference on High-Energy Accelerators, p. 330.
[2] A.W. Chao, IEEE Trans. Nucl. Sc., Vol. NS-30, No 4, Aug. 1983)
[3] N.H. Papadakis et al., Proc. International Workshop on Polarized Beams and Polarized Gas Targets, Cologne 1995, World Scientific.
[4] D.A. Engwall et al., Nucl. Instr. and Meth. A324 (1993) 409.
[5] T.J. Gay, F.B. Dunning, et al., Rev. Sci. Instr. 63, 114 (1992)
[6] R. Maas and G. Luijckx, Reduced emittance lattice for AmPS, proc. EPAC 96, p. 457
[7] R. Tamoschat et al., Emittance Measurement at AmPS and Delta using Laser Compton Scattering, proc. EPAC 96, p 1707

NUMERICAL ANALYSES OF THE INJECTION AND EXTRACTION TRAJECTORIES FOR THE RIKEN SUPERCONDUCTING RING CYCLOTRON

S.Fujishima, H.Okuno, T.Tominaka, T.Mitsumoto, T.Kubo, T.Kawaguchi, J.-W.Kim,
K.Ikegami, N.Sakamoto,S.Yokouchi, T.Morikawa, Y.Tanaka, A.Goto, and Y.Yano
The Institute of Physical and Chemical Research (RIKEN), Wako, Saitama, 351-01, Japan

Abstract

Current status of numerical analyses of the injection and extraction trajectories for the RIKEN superconducting ring cyclotron is described. With numerical analyses, the difference of trajectories in the elements and required fields of the elements are minimized. As a result, layouts and specifications of the elements are optimized.

1 INTRODUCTION

For the RIKEN RI Beam Factory project[1], a six-sector superconducting ring cyclotron (SRC) is designed[2][3]. The SRC has strong stray fields from the sector magnets, and these fields strongly depend on the condition of acceleration. Thus, the trajectories of various beams differ very much from each other. And besides, the injection and extraction elements must be placed in small space limited with the sector magnets, the RF-cavities, and the beam chambers. These difficulties make the design of the injection and extracion systems challenging. The injection system consists of four bending magnets (BM1, BM2, BM3, and BM4), three magnetic inflection channels (MIC1, MIC2, and MIC3), and an electrostatic inflection channel (EIC). The extracion system consists of a bending magnet (EBM), three magnetic deflection channels (MDC1, MDC2, and MDC3), and an electrostatic deflection channel (EDC)[4].

To analyze the injection and extraction trajectories of the SRC, we modified a computer program originally developed to analyze injection beam trajectories of the existing four-sector normal-conducting RIKEN Ring Cyclotron (RRC). In this computer program, a Lorentz equation concerning the time is solved with Runge-Kutta-Gill method. Magnetic fields of sector magnets used in these analyses were calculated with a 3D-code 'TOSCA'. Magnetic field of each element was approximated to be constant in the element, and was added on the field of sector magnets. Voltage of double-gap cavity was assumed to be 230 kV at injection and 276 kV at extraction.

Table 1 shows energies and magnetic rigidities of typical beams.

In the case of 200 MeV/u(ext.) $^{16}O^{7+}$ and 150 MeV/u(ext.) $^{238}U^{58+}$, the difference of Bρ between the two beams becomes maximum, so that the difference of trajectories between the beams also becomes maximum. To minimize the bore of the elements, the difference of trajectories must be suppressed as small as possible.

Table 1: Energies and magnetic rigidities of typical beams.

	Energy Inj. [MeV/u]	Energy Ext. [MeV/u]	Bρ Inj. [Tm]	Bρ Ext. [Tm]
$^{16}O^{7+}$	74.2	200	2.89	4.90
$^{16}O^{7+}$	126.7	400	3.83	7.25
$^{238}U^{58+}$	58.0	150	4.57	7.52

2 INJECTION

Figure 1 shows schematic layout of the injection elements and the injection trajectories of typical beams.

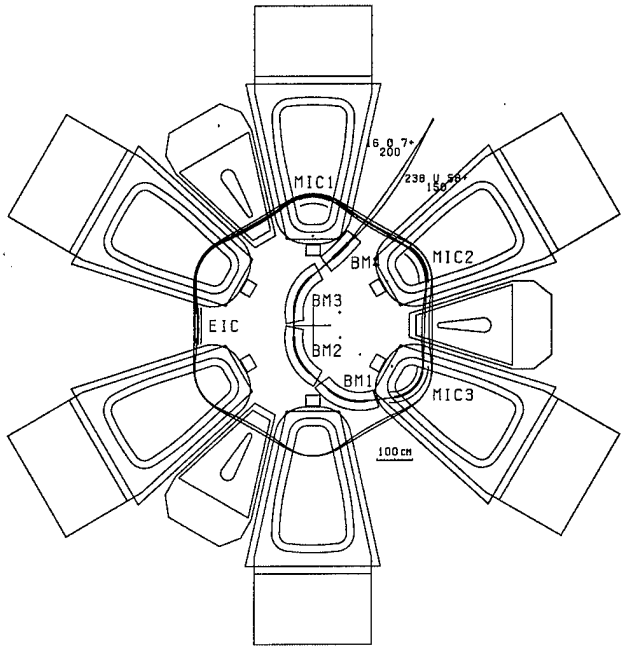


Figure 1: Schematic layout of the injection elements and the injection trajectories of typical beams.

Table 2 shows characteristics of the injection elements. For the acceleration of 400 MeV/u(ext.) $^{16}O^{7+}$, the EIC and MIC1 should generate the maximum fields. For the injection of 150 MeV/u(ext.) $^{238}U^{58+}$, the MIC2, MIC3, BM1, BM2, and BM3 should generate the maximum fields. The length of each element was determined in consideration of balance between the difference of trajectories in the element and required field of the element. Table 3 shows the differences of trajectories in the injection elements.

0-7803-4376-X/98/$10.00 © 1998 IEEE

Table 2: Characteristics of the injection elements.

	Radius [cm]	Angle [deg]	Length [cm]	B or E maximum
EIC	variable	variable	100	95 kV/cm
MIC1	111	46.5	90	0.18 T
MIC2	110	52.5	101	0.27 T
MIC3	87	73.9	112	1.5 T
BM1	132	52.0	120	4.02 T
BM2	130	52.0	118	3.92 T
BM3	128	52.0	116	3.96 T
BM4	492.5	7.0	60	-0.8,+0.7 T

Table 3: Differences of trajectories in the injection elements.

	Difference [cm]
EIC (movable)	10
MIC1	1.0
MIC2	1.2
MIC3	1.2
BM1	0.9
BM2	0.7
BM3	0.5
BM4	2.3

2.1 EIC

Figure 2 shows the difference of trajectories in the EIC. The maximum change in the radius of the orbit is about 10 cm. Accordingly, the EIC must be movable in the radial direction by 10 cm, and the radius of curvature of the EIC should be adjustable in the range from about 10 m to almost infinity.

Performance of the EIC determines the turn separation between the first equilibrium orbits and the injection trajectories at the MIC1. The turn separation at the MIC1 is required about 5 cm to place the MIC1. To give this turn separation, the EIC is required to generate the maximum electric field of 95 kV/cm and to have the length of 1 m.

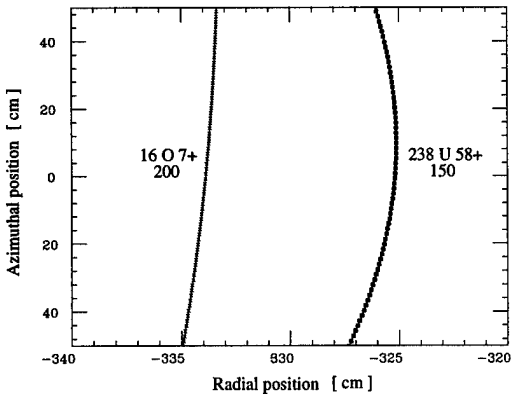


Figure 2: Difference of trajectories in the EIC.

2.2 MIC1

The MIC1 is required to generate the magnetic field of 0.18 T at the maximum with normal-conducting coils. Figure 3 shows the turn separation at the MIC1.

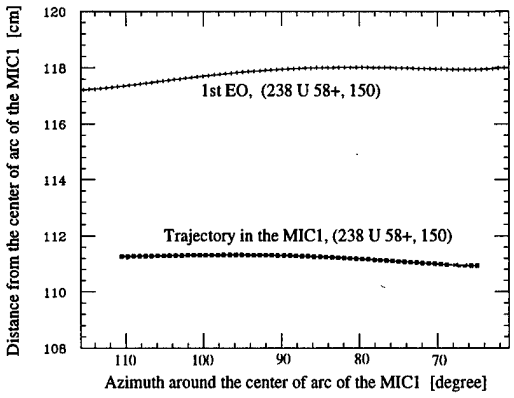


Figure 3: Turn separation at the MIC1.

2.3 MIC2

The MIC2 is required to give appropriate turn separation about 25 cm for the MIC3. To give this turn separation, the MIC2 generates the magnetic field of 0.27 T at the maximum with normal-conducting coils. The turn separation at the MIC2 is about 10 cm, so that the MIC2 has more space for coils than the case of the MIC1. Thus, the MIC2 can accomplish the maximum magnetic field of 0.27 T with almost the same current density as that of the MIC1.

2.4 MIC3

The MIC3 is required to generate the magnetic field of 1.5 T at the maximum with superconducting coils. The position of the MIC3 was determined in consideration of effective use of background magnetic field by the sector magnet.

2.5 BM1

The BM1 is required to generate the magnetic field of 4 T at the maximum with superconducting coils. The edge size and width of the BM1 are required as small as possible. Because the space to place the BM1 is extremely restricted by a yoke-link and a cryostat of the sector magnet. Because of high field and small space, design of the BM1 is most challenging[5].

2.6 BM2 and BM3

The BM2 and BM3 are required to generate magnetic field of 4 T at the maximum with superconducting coils.

2.7 BM4

The BM4 must accept various beams coming from a pre-accelerator. The beams come through a long valley with

stray fields from sector magnets, so that the increment of the difference of trajectories in the BM4 is inevitable. To minimize the difference of trajectories, the BM4 generates magnetic field not only positive but also negative. The range of the field is from -0.8 T to +0.7 T, and the field is generated with superconducting coils. Therefore, the difference of trajectories in the BM4 can be less than 2.3 cm.

Figure 4 shows the difference of trajectories in the BM4.

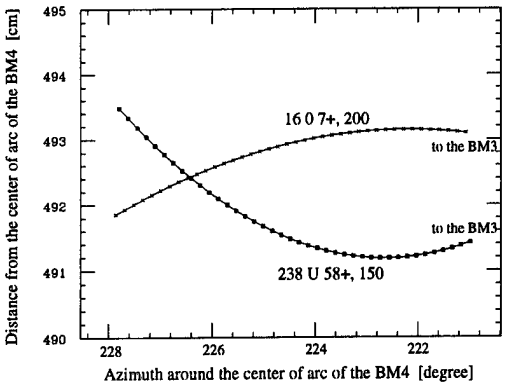


Figure 4: Difference of trajectories in the BM4.

3 EXTRACTION

The extracion system is similar to the injection system, so that the extraction trajectories were analyzed in almost the same way as for the injection trajectories. Analysis of the extraction trajectories has just been started.

Figure 5 shows schematic layout of the extraction elements and the extraction trajectories of typical beams.

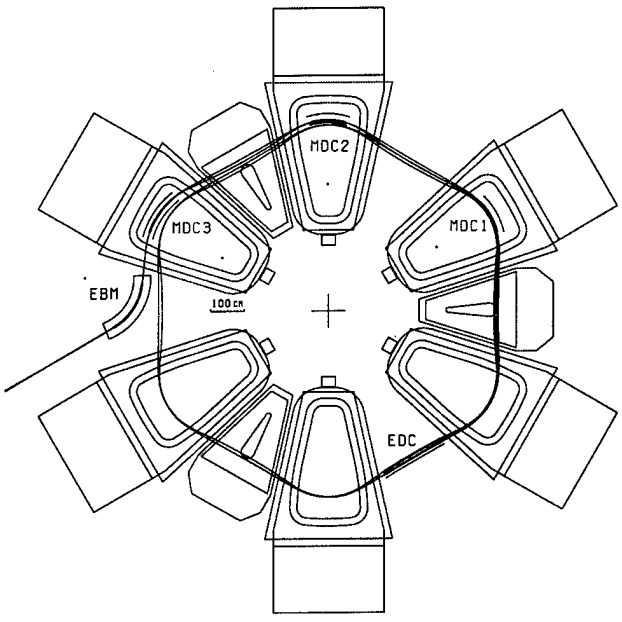


Figure 5: Schematic layout of the extraction elements and the extraction trajectories of typical beams.

Table 4 shows characteristics of the extraction elements. For the extraction of 400 MeV/u(ext.) ^{16} O $^{7+}$, the EDC, MDC1, and MDC2 should generate the maximum fields. For the extraction of 150 MeV/u(ext.) ^{238} U $^{58+}$, the MDC3 and EBM should generate the maximum fields.

Table 4: Characteristics of the extraction elements.

	Radius [cm]	Angle [deg]	Length [cm]	B or E maximum
EDC	variable	variable	200	100 kV/cm
MDC1	185	32.0	103	0.2 T
MDC2	190	32.0	106	0.3 T
MDC3	230	30.0	120	1.12 T
EBM	170	54.0	160	3.9 T

4 CONCLUSION

Layout and characteristics of the injection elements of the SRC have almost been determined. Preliminary layout and characteristics of the extraction elements have also been determined. Further optimization will be continued.

5 REFERENCES

[1] Y.Yano *et al.*, 'RIKEN RI-Beam Factory Project', in this proceedings.

[2] T.Mitsumoto *et al.*, 'Orbit Analysis for the RIKEN Superconducting Ring Cyclotron', in this proceedings.

[3] T.Kawaguchi *et al.*, 'Design of the Sector Magnets for the RIKEN Superconducting Ring Cyclotron', in this proceedings.

[4] H.Okuno *et al.*, 'Design Study of the Injection and Extraction Systems for the RIKEN Superconducting Ring Cyclotron', in this proceedings.

[5] T.Tominaka *et al.*, 'Design Study of the Injection and Extraction Elements for the RIKEN Superconducting Ring Cyclotron', in this proceedings.

ORBIT ANALYSIS FOR THE RIKEN SUPERCONDUCTING RING CYCLOTRON

T. Mitsumoto, A. Goto, T. Kawaguchi, J.-W. Kim, Y. Tanaka, T. kubo, H. Okuno, T. Tominaka, S. Fujishima, K. Ikegami, N. Sakamoto, T. Morikawa, S. Yokouchi and Y. Yano
The Institute of Physical and Chemical Research (RIKEN), Wako, Saitama, 351-01, JAPAN

Abstract

An "RI beam factory" has started to be constracted as the next project of the RIKEN Accelerator Research Facility (RARF)[1]. The "RI beam factory" aims at production and acceleration of radioactive isotope beams covering the whole mass region. It requires the energy of ion beam to be higher than 100 MeV/nucleon. To accomplish this requirement, the following two ring cyclotrons have been adopted as post-accelerators of the existing RIKEN Ring Cyclotron (RRC): a 4-sector ring cyclotron for the first stage (IRC) and a 6-sector superconducting ring cyclotron for the second stage (SRC). The sector magnet of the SRC has to be flexible enough to generate isochronous fields in a wide range of energies and for various q/A values. In this report we describe the isochronous field generation and orbit analysis of the SRC.

1 INTRODUCTION

The maximum acceleration energy of the SRC was determined by experimental requirements. The SRC is expected to boost the energy of ion beam up to 400 MeV/nucleon for light heavy ions like carbon and 150 MeV/nucleon for very heavy ions like uranium. Beam current is expected to be more than 100 pμA for light heavy ions and about 0.2 pμA for 150 MeV/nucleon uranium ions. Figure 1 shows the region of expected ions from the SRC (grey area) and typical ions (white circle).

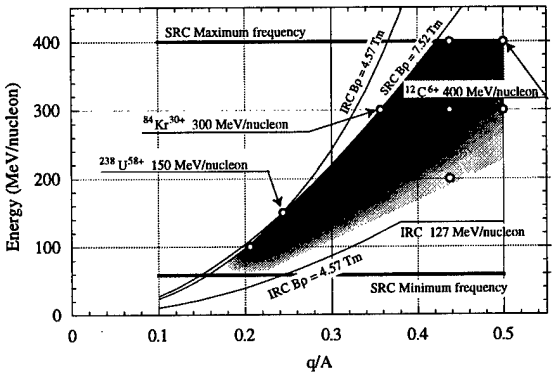


Figure 1: Performance expected for the SRC.

Main parameters of the SRC are listed in Table 1. Figure 2 shows a layout of the SRC. Six sector magnets, three RF cavities and injection and extraction devices together with injection and extraction orbits are displayed.

Table 1: Main parameters of the SRC.

Number of sectors		6
Harmonics		6
Mean radius	injection	3.56 m
	extraction	5.36 m
RF frequency		18 - 38 MHz

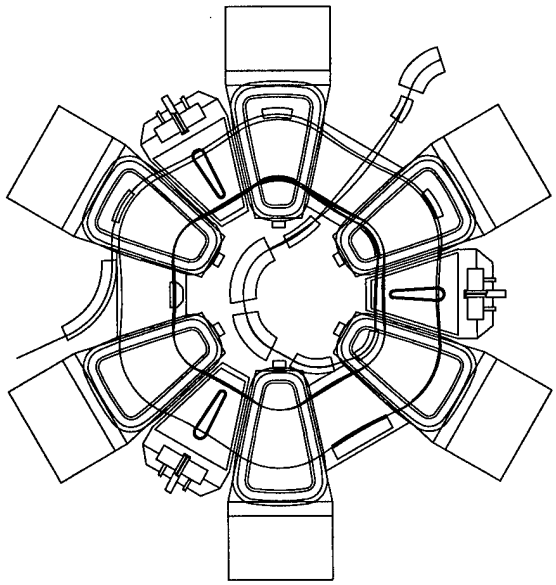


Figure 2: Layout of the SRC.

2 ISOCHRONOUS FIELD GENERATION

The maximum magnetic field is required for the acceleration of 150 MeV/nucleon $^{238}U^{58+}$. The magnetic field of the sector magnet is 4.0 T at the injection and 4.3 T at the extraction. In the case of 400 MeV/nucleon $^{16}O^{7+}$[1], the magnetic field is 3.3 T at the injection, and 4.1 T at extraction side. Field distribution for typical ions are shown in Fig. 3.

The sector magnet of the SRC has a set of superconducting main coils for base field generation, five sets of superconducting trim coils for coarse fitting to the isochronous field and about 20 sets of normal conducting trim coils for fine adjustment.

Magnetic field distribution is calculated by three dimentional code TOSCA[2]. Working path of the radial and axial betatron frequencies for typical ions are shown in Fig. 4.

0-7803-4376-X/98 /$10.00 © 1998 IEEE

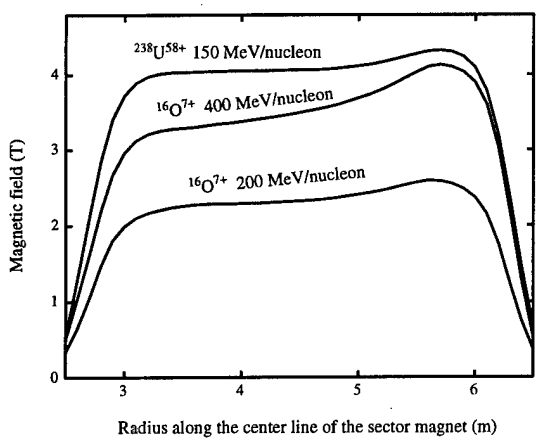


Figure 3: Magnetic field strengths along the center line of the sector magnet for typical ions.

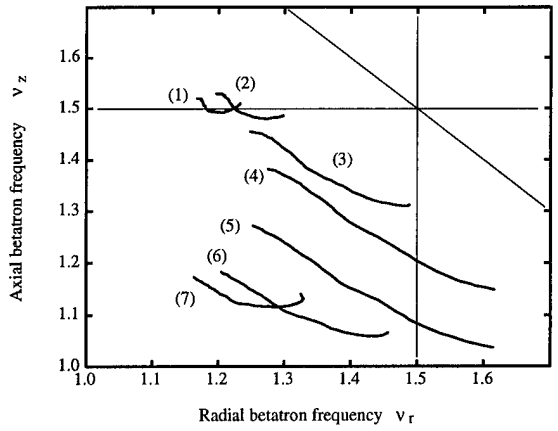


Figure 4: Working paths of the radial and axial betatron frequency of typical ions for the SRC are shown: (1) 100 MeV/nucleon $^{238}U^{49+}$, (2) 150 MeV/nucleon $^{238}U^{58+}$, (3) 300 MeV/nucleon $^{84}Kr^{30+}$, (4) 400 MeV/nucleon $^{16}O^{7+}$, (5) 400 MeV/nucleon $^{12}C^{6+}$, (6) 300 MeV/nucleon $^{12}C^{6+}$ and (7) 200 MeV/nucleon $^{16}O^{7+}$.

2.1 *Pole and superconducting main coil*

Size of the superconducting main coil is 284 mm (width) x 310 mm (height). The maximum excitation current is 6 MA for one sector magnet (two coils). The superconducting main coil is installed inside a He vessel made of stainless steel which is tightly fixed to the cold pole. Pole gap is 380 mm. For details, see Refs. [3] and [4].

Smaller sector angle causes larger vertical focusing force. From the viewpoint of minimizing the maximum field and magnetic forces, however, a large sector angle is preferable. Therefore, edge of the pole has a straight line from the injection side to the middle of the sector with the wide angle of 25 deg. Then the pole shape has a curvature in order to increase the axial betatron frequency ν_z at the extraction side.

Figure 5 shows the radial and axial betatron frequencies of three different pole shapes for 400 MeV/nucleon $^{12}C^{6+}$. The radius of curvature of 8.0 m increases ν_z value by 0.12 at the extraction radius compared with the straight pole. Required excitation current of the main coil dose not increase but the currents of superconducting trim coils at the extraction side increase.

2.2 *Superconducting trim coil*

Five sets of superconducting trim coils are placed on the inner surface of the cold pole. Two sets at the extraction side have current returns at the extraction side, which are not wound along beam orbits but just straight in the beam region in order to avoid concave curveture of conductors. The other three sets have current returns at the injection side. The first coil on the injection orbit is wound along beam orbit, then it gradually becomes straight towards the extraction side.

Figure 6 shows the configuration of the superconducting trim coils.

Using the five sets of superconducting trim coils, it is possible to adjust various distributions of isochronous fields within ±0.1%. Further fine adjustment will be done with the trim coils of room temperature.

3 ORBIT ANALYSIS: RESONANCE

Working paths of radial and axial betatron frequencis for the SRC are spread in a wide region of the ν_r-ν_z diagram because various conditions of ions have to be accelerated. Some of the working paths lie near the resonance lines. We studied influences of the resonance, under the condition that the manufacture error or mis-alignment from the design values was 1 mm.

The reason for this assumption is the following:

- The pole and the superconducting coils in cryogenic vessels are supported by the thin rod from room temperature. They are affected by large force from room temperature yoke.
- Direct measurement of the pole position at low temperature is difficult, and moreover measurement of the main coil in He vessels is impossible.
- The pole gap (380 mm) is four or five times larger than normal conducting cyclotron. So larger error than a normal separate sector cyclotron should be tolerable.

3.1 *Integer resonance: ν_z = 1.0*

In the case of high energy acceleration, the axial betatron frequency ν_z goes down toward 1.0 as the energy increases. Influence of resonance line ν_z=1 was studied by the a computer simulation. Figure 7 shows an example of the calculation for 400 MeV/nucleon $^{12}C^{6+}$ in the case that the working path of the betatron frequency crosses ν_z=1 resonance.

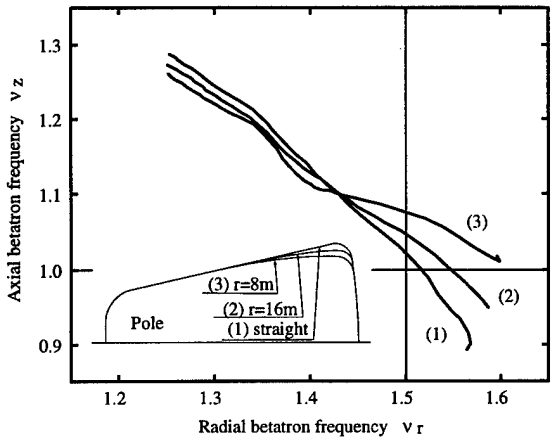


Figure 5: Effect of the curveture of the pole at the extraction side. The betatron frequencies in the case of (1) straight, (2) curveture of 16-meter radius and (3) curvature of 8-meter radius are shown.

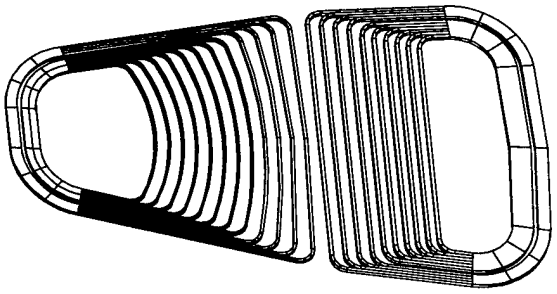


Figure 6: Configuration of the superconducting trim coils. Two of five sets have current returns at the extraction side and the others have current returns at the injection side.

In this calculation, magnetic field was perturbed to have the first-order harmonics simulated that one sector magnet and another sector magnet of opposite side were vertically displaced 1 mm and -1 mm, respectively. Amplitude of vertical oscillation increases fatally when the beam crosses the resonance. It is impossible to accelerate ions across the resonance line of ν_z=1. Minimum ν_z was found to be set 1.04 in order to avoid the influence of the resonance.

3.2 Half integer resonance ν_z=1.5 and ν_r=1.5

In the case that the extraction energy is higher than 300 MeV/nucleon, the working path crosses the ν_r=1.5 line. For ions of energy less than 150 MeV/nucleon with small q/A, the working path crosses the resonance line ν_z=1.5.

By a preliminary estimation, influence of half integer resonance ν_z=1.5 and ν_r=1.5 was found to be small.

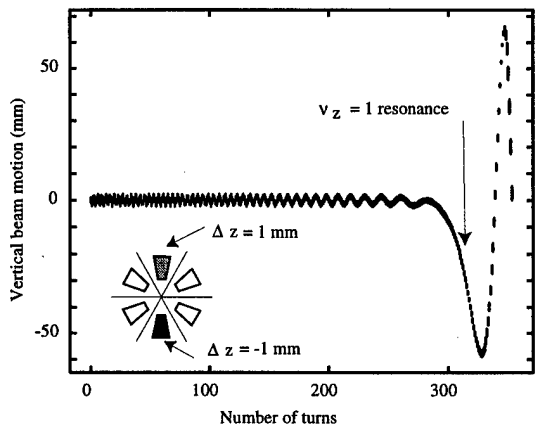


Figure 7: Effect of ν_z=1 resonance.

4 SUMMARY

Design study of the sector magnet for the SRC for the RIKEN RI beam factory has been carried out. Combination of the superconducting main coil, superconducting trim coils and normal conducting trim coils can generate isochronous field for various ions. The minimum axial betatron frequency is set to be 1.04 in order to avoid the ν_z=1 resonance.

5 REFERENCES

[1] Y. Yano *et al.*, 'RIKEN RI-Beam Factory project', this conference.

[2] Vector Field Limited, Oxford, England.

[3] T. Kawaguchi *et al.*, 'Design of the Sector Magnets for the RIKEN Superconducting Ring Cyclotron', this conference.

[4] T. Kubo *et al.*, 'Design of a Model Sector Magnet for the RIKEN Superconducting Ring Cyclotron', this conference.

DESIGN STUDY OF ACCUMULATOR COOLER RING FOR MUSES

K. Ohtomo, Institute of Physical and Chemical Research (RIKEN), Wako, Saitama 351-01, Japan,
T. Katayama, Center for Nuclear Study, School of Science, Univ. of Tokyo, Tanashi 188, Japan

Abstract

An RI beam factory project is proposed by the Institute of Physical and Chemical Research (RIKEN) as a next new facility for nuclear physics. The accelerator system for this project, consists of main 2 parts, one is Super-conducting Ring Cyclotron (SRC) and the other is a storage ring system named MUSES. An Accumulator Cooler Ring (ACR) is a part of Multi-USe Experimatal Storage rings (MUSES). It is used for the accumulation and cooling of the radioactive isotope (RI) beams which are produced by the beam from SRC and pass through a fragment separator. The large momentum spreads of these RI beams will be significantly reduced by the electron cooling and stochastic cooling devices in the ACR. Devices for multi-turn injection and RF stacking are also prepared in order to increase the beam current. The simulations and designs of these devices are presented in this report.

1 LATTICE

1.1 Requirements for Lattice

Lattice of the ACR shall be designed by taking the following requirements into account:

1) Electron cooler requires a long straight free space (nearly 8 m) free from dispersion.
2) Stochastic cooling devices require a pair of dispersion-free space for a pickup and a kicker, and the phase advance of the betatron oscillation should be nearly $k\pi/4$ between them.
3) Multi-turn injection requires the sections where the phase advance of the betatron oscillation is nearly π, to arrange kickers and septum magnets.
4) RF stacking requires a dispersion in the multi-turn injection section and a space for tunable RF cavity.
5) Accumulation of high current beams requires a large acceptance in the horizontal plane ($=125\pi$.mm.mrad) and a large momentum spread ($\Delta p/p = \pm 2\%$).

1.2 Design of Lattice

Optimized design is shown in Table 1 and Figs. 1 and 2. The ACR lattice consists of two arc sections and two long straight sections, as shown in Fig.1 and is given as follows.

ACR = CELL--STRC--2CELL--STRC--CELL ,

where STRC denotes the long straight section and CELL the half of the arc section. A CELL is symmetric and decomposed into two half elements, HCELL.

Table 1 Lattice Parameters of ACR

Circumference	C=168.4836 m
Average Radius	R= 26.815 m
Max. Magnetic Rigidity	$B\rho$ = 8.0 T.m
Max. Beam Energy	E = 400 MeV/u (Z/A=1/2)
Momentum Compaction	α = 0.0402042
Transition Gamma	γ = 4.987
Betatron Tune Values	Qx/Qy = 4.555/3.540
Natural Chromaticity	Q'x/Q'y = -5.058/-6.571
Max. β-Amplitude	$\beta x/\beta y$= 18.33m/24.53m
Max. Dispersion	Dx/Dy= 4.518m/0.0m

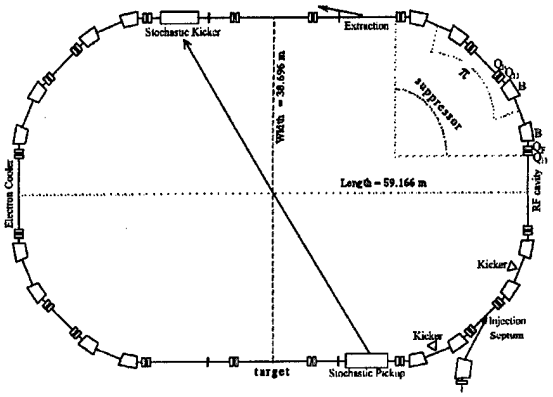


Figure: 1 The Layout of ACR.

CELL = (HCELL, -HCELL)

A HCELL is:

HCELL = -(Lr)--QD-QF--B--(Lk)--B--QD-QF--(Li)- ,

where QF and QD are the focusing and defocusing quadrupoles, B bending magnets, and L long drift space. Each CELL functions as a dispersion suppresser and makes the free dispersion space at Lr, where RF cavities or electron coolers are located. Horizontal and vertical beta functions are designed at nearly equal value because RI beam shape should match with cylindrical electron flow at an electron cooler. An injection kicker and septums occupy at Lk in one CELL, where the lattice has the maximum value of the horizontal dispersion. A couple of stochatic cooling devices are positioned at two Lr, set on opposite side in ring. The residual Lr sections are used for beam extraction devices.

The two long straight sections are given as follows:

STRC = ---QC---QD-QF--(Le)--QF-QD---QC--- ,

where Qc is a quadrupole for chromaticity correction. Le is a long drift space of 8 m for an internal target or for another experiment equipments.

0-7803-4376-X/98 /$10.00 © 1998 IEEE

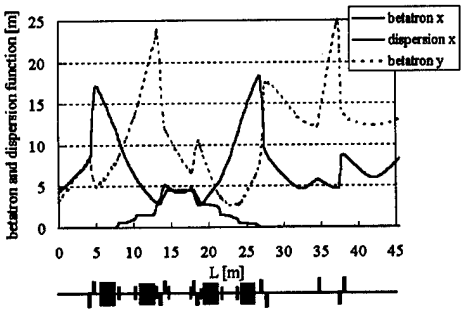


Figure: 2 β and dispersion functions in quarter of ACR

2 INJECTION

The multi-turn injection combined with RF stacking method is used in ACR. The local closed orbit is deformed by two bump magnets. The beam is injected onto an injection orbit, which has the momentum difference of +1% from the central orbit. After the multi-turn injection, the RF frequency changed gradually and the beam is stacked at the bottom orbit, which has the momentum difference –2% from the center. In a normal operation, the stacking period is 30msec and after 30 times of stackings the beam is extracted from ACR. The total repetition cycle is 1Hz, which is as same as an acceleration cycle of Booster Synchrotron Ring.

2.1 Pre-Debunching Devices

The momentum spreads of RI beam from the fragment separator is relatively large. The required RF voltage to capture them in RF buckets is proportional to the square of Δp/p. The value reaches 600kV on the assumption that Δp/p equals ±0.5% and the stacking efficiency is assured to be 80%.[1] This high voltage seems difficult to realize with ferrite loaded RF cavity. Then we are planning to install the debuncher cavities in the injection line just previous to the injection kicker.

Simulations in 6-dimentional phase spaces were performed and the typical result are shown in Fig. 3. Here the debuncher cavity are positioned at 100m downstream from the fragmet separator. The RF frequency of debunchers is 144-228MHz, 6-times higher than that of stacking cavity in ACR, and the total RF voltage of debunchers is set to be 3MV in the case of the beam energy of 400MeV/u. This voltage fulfills that the initial momentum spreads of ±0.5% is compressed to ±0.15%, which corresponds to the required RF voltage at stacking cavity of 70kV. It is achivable value with ferrite loaded cavity.

A type of debuncher cavities is a re-entrant λ/2 push pull and semi-tunable by changing the gap distance for various energy of RI beam. The structure is designed by superfish and the shape is cylindrical and the inner dimensions of cavity are 900mm in diameter and 600mm length with sliding nose for frequency tunability. The RF voltage is 800kV per a cavity and the number of cavity is 4.

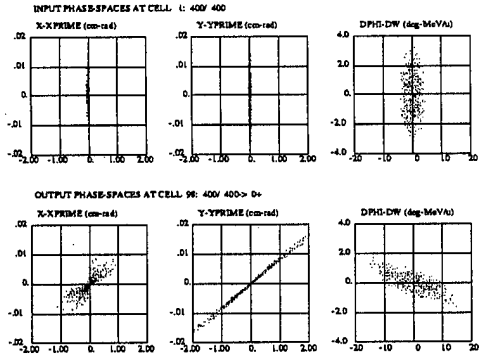


Figure: 3 De-bunching effects on phase space. The total RF voltage is set to be 3MV. Upper three figures are particles at the fragment separator and lower three are that after the debuncher.

2.2 Deflection Devices

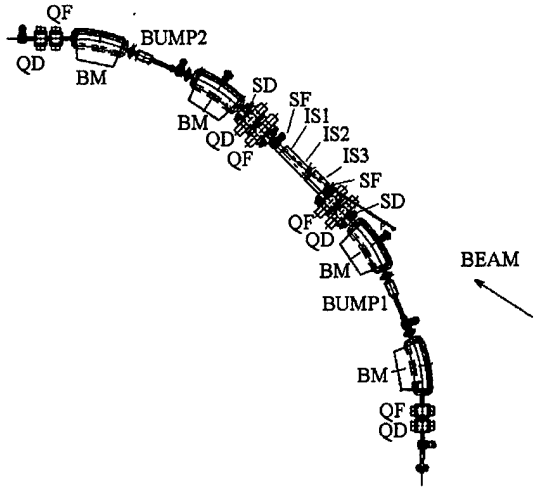
The devices for beam injection are located at half of arc section shown in detail in Fig. 4.

A couple of bump magnets are positioned apart from each other π in betatron phase. The magnetic field of these magnets are excited like a half-sine wave, of which a top magnetic field is 0.16 T corresponds to the beam of the maximum magnetic rigidity 8 Tm. The half period of half-sine is 300 μsec and a repetition cycle is 30 Hz.

The maximum displacement between the bump and central orbit is 104 mm at the first injection septum magnet. The deflection magnetic field of septum magnet is 1 T and the length is 500mm. Upstream of this, the second and third injection septum are set. The deflection magnetic fields are 1 T and 1.2 T and the lengths are 500mm and 625mm, respectively.

Some modification at the return yoke of the nearest Q magnet are required to make a clearance of the injected beam path from the debunchers.

Figure: 4 The layout of the injection devices.



2.3 Devices for RF stacking

The parameters of RF stacking cavity are listed in Table

2.

Table 2 Parameters of RF stacking cavity

Peak RF voltage	100kV
Initial Frequency Range	18-38MHz
Max. Frequency modulation width for RF Stacking	2.6%
Modulation Period	30msec
Max. Cavity free space	8m
Min. Q value	585
Max. Dissipation Power at Tuner Cavity	8kW
Max. Dissipation Power at Main Cavity	13kW
Max. Total Dissipation Power	21kW

A proposed cavity consists of two parts. The main cavity is a coaxial $\lambda/4$ and semi-tunable by changing the gap distance according to the energy of RI beam. The additional cavity is loaded with ferrites to change frequency rapidly for stacking . The frequency modulation method is based on the cavity of a proton booster synchrotron at Fermi Lab.[2] and the model cavity considered at TRIUMF.[3] A schematic drawing of the cavity are shown in Fig. 5.

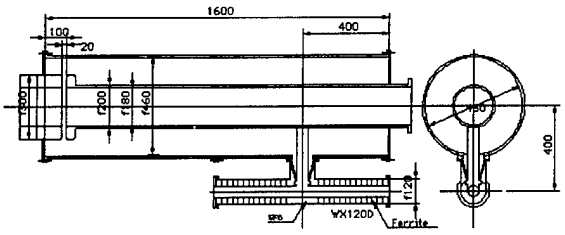


Figure: 5 The ferrite loaded cavity for RF stacking.

The length of the main cavity is 1600mm and the tuner cavity is connected directly with the inner duct of the main cavity at the position 1200mm apart from the gap. The length of the tuner cavity is 1400mm. The maximum frequency modulation width are attained with changing RF permeability ratio from 3 to 4. The dissipation power at the tuner cavity including ferrite is evaluated by superfish with complex module. The maximum power is 8kW and Q value is 585. The dissipation power at main cavity due to surface loss is also calculated as 13kW. The total dissipation power amounts to about 21kW.

Presently R&D works on the measurement of characteristics of real size ferrites are in progress.

3 CONCLUSION

The lattice design of ACR has been completed and the technical designing for basic devices such as magnets are now in progress. The model test for ferrite tuned stacking cavity is scheduled in this year.

REFERENCES

[1] Y.J. Yuan, et al.: 'Simulation of RF Stacking Combined with Cooling Effects', EPAC, 1996, p1338-1340.

[2] J.E. Griffen and Q.A. Kerns: 'NAL Main-Ring Cavity Test Results', IEEE Trans. On Nucl. Sci., NS-18, 241, 1971

[3] R.L. Poirier and T. Enegren: 'Status of RF Development work on a Ferrite Tuned Amplifier Cavity for the TRIUMF Kaon Factory', IEEE PAC, Washington D.C., 1987, p1499. (1987)

DESGIN STUDY OF THE INJECTION AND EXTRACTION SYSTEMS FOR THE RIKEN SUPERCONDUCTING RING CYCLOTRON

H. Okuno, T. Tominaka, S. Fujishima, T. Mitsumoto, T Kubo, T. Kawaguchi, J.-W. Kim,
K. Ikegami, N. Sakamoto, S. Yokouchi, T. Morikawa, Y. Tanaka, A. Goto, and Y. Yano,
The Institute of Physical and Chemical Research (RIKEN), Wako, Saitama, 351-01, Japan

Abstract

In the RI beam factory project,[1] an intermediate-stage ring cyclotron and a six-sector superconducting ring cyclotron (IRC and SRC)[2, 3] are designed to boost the energy of the ion beams available from the existing RIKEN Ring Cyclotron (RRC). The output energies designed to the SRC are 400 MeV/u for light ions such as carbon and are 150 MeV/u for heavy ions such as uranium. In the present report, we describe the recent status of design study of the injection and extraction systems for the SRC.

1 INJECTION SYSTEM

The injection energies (E_{inj}), required to obtain the designed output energies (E_{ext}), for three kinds of ion beams, are shown in Table 1. Figure 1 shows an example of the trajectories of injected beams in the SRC. The beams are injected through one of the magnetic valleys into the central region of the SRC, which are then radially guided to their first equilibrium orbits. The transport system consists of four bending magnets (BM1, BM2, BM3 and BM4), three magnetic inflection channels (MIC1, MIC2 and MIC3), and an electrostatic inflection channel (EIC). The MICs are inserted in the gap between the pair of poles of the sector magnets to increase the bending power of the sector field locally. The EIC is placed in the position where the trajectories of injected beams match finally with the first equilibrium orbits. The radial-injection method as shown in Fig. 1 is the most straightforward one adopted in many ring cyclotrons. However, to apply the same method on the SRC is more difficult than on the normal conducting ring cyclotron, because a strong negative fringe field exists in the valley region for the SRC and so the beam trajectory strongly depends on the acceleration condition.

	Charge	E_{inj} (MeV/u)	E_{ext} (MeV/u)
^{16}O	8+	127	400
^{84}Kr	30+	103	300
^{238}U	59+	58	150

Table 1: Energies of the injected and extracted beams at the full- power operation of the SRC.

In order to accept the changes in the beam trajectory, the elements should be movable or have a large bore. We adopted the latter method for the elements, except for the EIC, which is required to move as large as 10 cm at the maximum in the radial direction. It is important to make

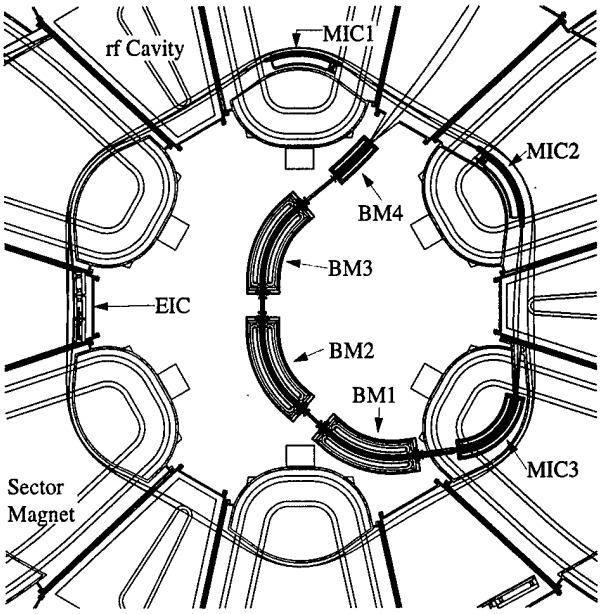


Figure 1: A schematic layout of injection elements for the SRC, and possible trajectories for the injected beam.

the change of the beam trajectories inside the elements as small as possible. In the numerical analysis of the injection orbits[4], we concentrated our effort on minimizing them (Δx). Obtained results from such an analysis are shown in Table 2, together with their parameters.

1.1 BMs

The BM1, BM2, BM3 and BM4 are required to be superconducting magnets in order to produce the required magnetic fields. The strong stray fields from the sector magnets make these bending magnets difficult to be constructed, because we can not use an iron yoke for magnetic shielding. The total flux of the stray field in the center region of the SRC is large enough to saturate the iron. Thus, we adopted active-shield-type magnets for the BMs although more magnetic motive force is needed than the case of an iron-shield-type magnet.

The specifications of BM1 are listed in Table 3. The space available for the BM1 is verly limited: the BM1 has a space of as small as about 20 cm in the radial direction. In the coil-end region coil supports and cryostat walls need to be accommodated within the space of about 10 cm. In the design of the BM1 magnet, mainly the following two

0-7803-4376-X/98 /$10.00 © 1998 IEEE

	Radius (cm)	Angle (deg.)	B or E (max.) (T) or (kV/cm)	Δx (cm)
EIC	–	–	95	10
MIC1	111	46.5	0.18	1.0
MIC2	110	52.5	0.27	1.2
MIC3	87	73.9	1.5	1.2
BM1	132	52.0	4.02	0.9
BM2	130	52.0	3.92	0.7
BM3	128	52.0	3.96	0.5
BM4	492.5	7.0	-0.8,+0.7	2.3

Table 2: Parameters of the injection elements and changes (Δx) in the trajectories obtained from the numerical analysis of injection orbits.

points were taken care: One is that coil structures should be simple because non-straight coils are difficult to wind and the other is that effective length of the field should be as long as possible compared with the real coil length. The proposed coil structures are shown in Fig. 2. This structure has no bend-up in the coil end and the effective length of the field is only 6 cm shorter than the real coil length. Magnetic field analysis[5] show that the superconducting coils can produce the required field with the current less than 50% of the critical current, and that the BM1 can be installed in the limited radial space. Figure 3 shows a schematic drawing of the BM1 on the due position of the SRC. In the near future, the model of the BM1 will be made to test this design.

Item	Value
Type	Iron free Active shield
Maximum field	4.02T
Homogenity	1×10^{-3} /cm^2
Beam Bore	40 (Horizontal) × 20 (Vertical) mm^2
Radius	1320mm
Angle	40deg.
Fringe Field	± 20 cm
Space limit in the radial direction	about ± 20cm
Space for the coil end region	about 10cm

Table 3: Main specifications of the BM1.

1.2 MICs

The MIC1 and MIC2 are normal conducting magnetic channels. Several types of devices can be used as the MIC, for instance, an iron shim, septum coils or a combination of the shim and septum coils. The use of the septum coils is essential for our machine since the magnetic field inside the

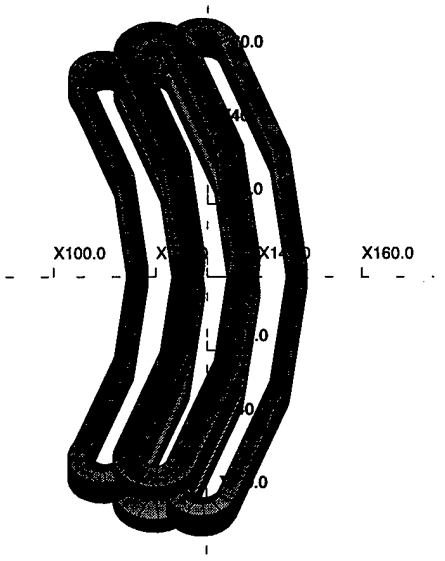


Figure 2: Coil structure of the BM1

MIC must be adjusted in a wide range from low to a considerably high value in accordance with the wide variety of the accelerated particles and energies. Iron shim is not used since uniformity of the field can not be obtained with it in the region of more than 2 T. Figure 4 shows a schematic drawing of the MIC1. Magnetic analysis for these two elements showed that about 20 turns of coils can produce the requied fields of the MIC1 and MIC2.

The MIC3 is the superconducting magnetic channel. The coil structure is under study. This superconducting channel is the most difficult among the superconducting injection elements of the SRC since the curvature is small and the maximum field in the coil is high. A model of the channel will be made to test feasibility of the channel.

1.3 EIC

The EIC needs to move by about 10 cm in the radial direction and vary its curvature. The channel having three divided structres shown in Fig. 5 has been proposed. Its gap is 10 mm and its field is 95 kV/cm. The maximum EV value is confined to be 9500 kV^2 /cm well below the critical value of 15000 kV^2/cm for the sparkover. Conventional stepping moters can not be used to move the EIC because the magnetic field at the EIC is more than 0.1 T. Tests of the oil cylinder for this purpose are under study.

2 EXTRACTION SYSTEM

Examples of the extraction orbits is shown in the Fig. 5 of[4]. The optimization of the extraction trajectories is in progress. The elements similar to the injection system will be used for the extraction system.

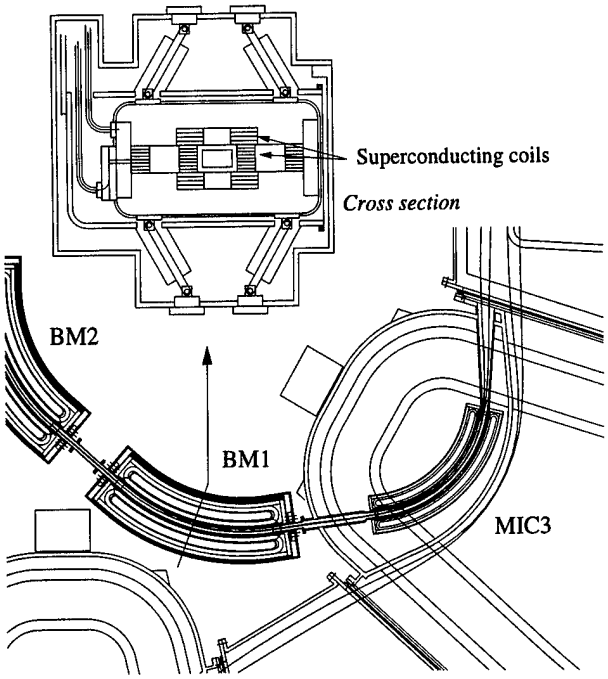


Figure 3: Location of the BM1 in the SRC together with its cross section. Injection and the first equilibrium orbits for $^{16}O^{8+}$ (200 MeV/u) and $^{238}U^{58+}$ (150 MeV/u) are also shown.

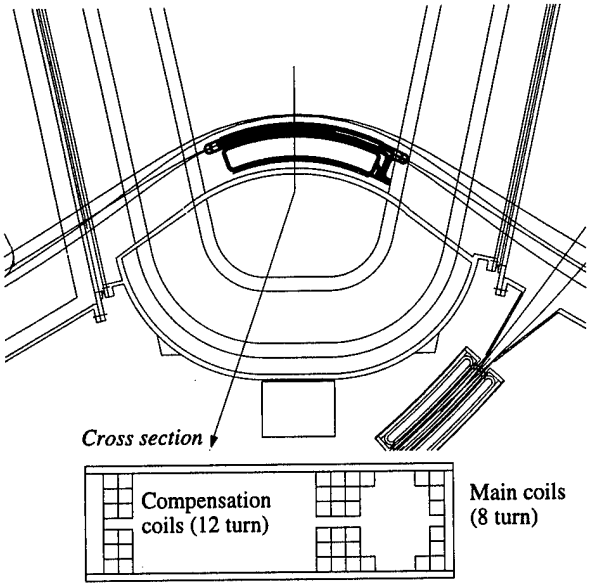


Figure 4: Location of the MIC1 together with its cross section. Injection and the first equilibrium orbits for $^{16}O^{8+}$ (200 MeV/u) and $^{238}U^{58+}$ (150 MeV/u) are also shown.

3 REFERENCES

[1] Y. Yano *et al.*, 'RIKEN RI-Beam Factory project', in this proceedings.

[2] T. Mitsumoto *et al.*, 'Orbit Analysis for the RIKEN Superconducting Ring Cyclotron', in this proceedings.

[3] T. Kawaguchi *et al.*, 'Design of the Sector Magnets for the RIKEN Superconducting Ring Cyclotron', in this proceedings.

[4] S. Fujishima *et al.*, 'Numerical Analyses of the Injection and Extraction Trajectories for the RIKEN Superconducting Ring Cyclotron', in this proceedings.

[5] T. Tominaka *et al.*, 'Design Study of the Injection and Extraction Systems for the RIKEN Superconducting Ring Cyclotron', in this proceedings.

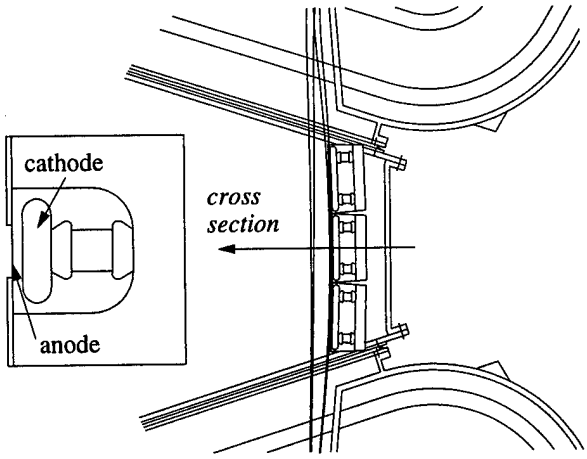


Figure 5: Location of the EIC together with its cross section. The first and the second equilibrium orbits for $^{16}O^{8+}$ (200 MeV/u) and $^{238}U^{58+}$ (150 MeV/u) are also shown.

STATUS OF THE HMI-RFQ-INJECTOR

O. Engels, A. Schempp
Institut für Angewandte Physik, Johann Wolfgang Goethe-Universität, 60054 Frankfurt, Germany
W. Pelzer, H. Homeyer
Hahn-Meitner-Institut, 14109 Berlin, Germany

Abstract

The new injector of the ISL (Ionen-Strahl-Labor, Berlin) consists of an RFQ-section and an ECR-source. The RFQ-section consists of two closely coupled VE- (Variable Energy) RFQs. They are designed for direct injection into the cyclotron, with a small energy spread and a duty factor of 100 %. The status of the project will be discussed.

1 INTRODUCTION

The scientific program at the ISL, the former VICKSI- (Van de Graff Isochron Cyclotron Kombination für Schwere Ionen) facility has changed from nuclear physics to solid state physics [1]. The VICKSI-facility consists of two external injection beamlines, a Van-de-Graff and a Tandem injector with a separated sector cyclotron as postaccelerator. To meet the demands of the solid state physics users the Tandem injector will be replaced by a combination of an ECR-source mounted on a 200 kV platform and a two stage VE-RFQ. The ECR-RFQ-combination will accelerate the ions to energies between 0.09 and 0.36 MeV/n to cover the range of final energies out of the cyclotron between 1.5 and 6 MeV/n.

2 RFQ-PARAMETERS

To stretch the energy range of the injector the RFQ is split into two RFQ stages, mounted in one vacuum-tank. Each stage with a length of 1.5 m consists of a ten stem 4-Rod-RFQ-structure. With a power consumption of 20 kW per stage an electrode voltage of 45 kV at 85 MHz for q/a=0.125 and 35 kV at 120 MHz for a q/a=0.15 will be possible.

The RFQs will be driven in two different modes of operation. In the high energy mode both RFQs accelerate, the output energy of the cyclotron is between E_{out}=3 MeV/n and E_{out}=6 MeV/n with a harmonic number of 5 for the cyclotron. In the low energy mode the second RFQ has a detuned phase and works as a quadrupole transport channel. The energy range of the cyclotron in this mode is between E_{out}=1.5 MeV/n and E_{out}=3 MeV/n. The cyclotron works on the harmonic number 7. In both modes the frequency of the RFQ is tuned to the eighth harmonic of the cyclotron frequency.

A schematic view of the structure with the movable tuning plate to vary the frequency is given in figure 1, the main parameters of the RFQ and the cyclotron are given in table 1.

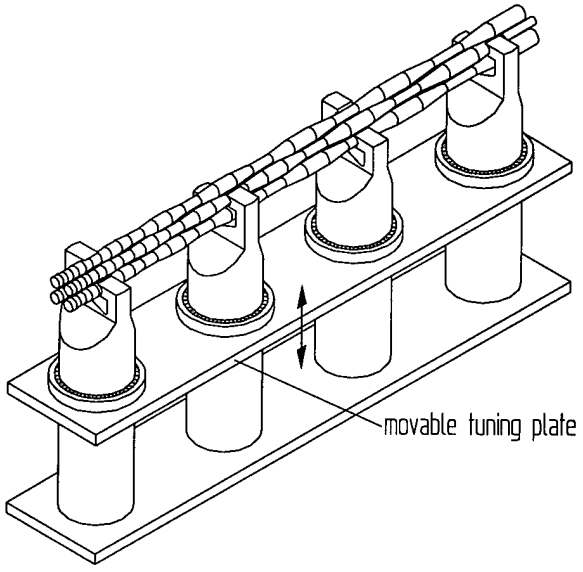


Figure 1: Scheme of the VE-RFQ.

RFQ:	low energy mode	high energy mode
Ein [keV/n]	15 / 30	
E_{out} RFQ1 [keV/n]	90 / 180	
E_{out} RFQ2 [keV/n]	90 / 180	180 / 360
energy gain factor RFQ1	6	
energy gain factor RFQ2	1	2
charge-to-mass-ratio	1/5 - 1/8	
frequency [MHz]	85 - 120	
electrode voltage [kV]	45	
length / diameter [m]	3 / 0.5	

Cyclotron:	
injection radius [m]	0.43
extraction radius [m]	1.8
frequency [MHz]	10 - 20
max. dee-voltage [kV]	140 (peak)
energy gain factor	16.8 - 18.6

Table 1: Main parameters of the RFQ and the cyclotron

0-7803-4376-X/98 /$10.00 © 1998 IEEE

The RFQ output emittance depends largely on the input conditions. For matched input beams with an energy spread $\Delta E/E < 1.5$ %, a normalized emittance $\varepsilon_n < 0.5\ \pi$ mm mrad and a bunch length $\Delta t < 1$ ns a transmission of 100 % is expected. To reach this beam quality it is necessary to have a buncher-chopper system between the ECR and the RFQs.

The ECR-source is mounted on the 200 kV platform formerly used for the Tandem. The vertical beam is bent 90°, passes through the buncher-chopper system and will be injected into the RFQs. The final matching into RFQ1 will be done by a triplet lens. The beam from RFQ2 is transported through the injection beamline of the cyclotron, to which a rebuncher has been added to obtain a proper time focus for the entrance of the cyclotron.

3 RF-PROPERTIES

The important rf-properties like Q-value, shuntimpedance, flatness and the relation between the movable tuning plate and the frequency as seen in figure 1 were calculated with the code MAFIA Ver. 3.2 [2] at the beginning of the project [3]. They are compared with the first low level measurements made in February 1997.

The main point of interest is the relation between the tuning plate position and the frequency as well as the dependence of the shuntimpedance and the Q-value on the frequency, as shown in figures 2, 3 and 4. The dots represent the measured values.

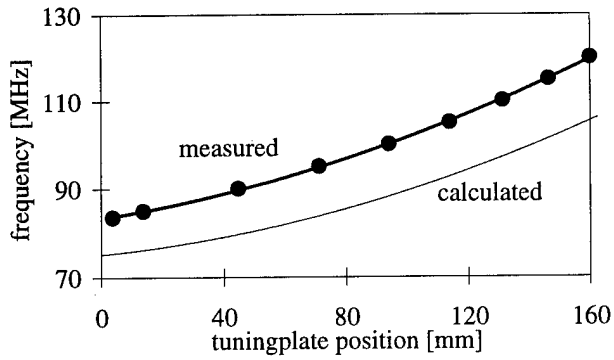


Figure 2: Relation between the position of the tuning plate and the frequency.

There is a good agreement of measurement and calculation in the way how the frequency varies by moving the tuning plate. As seen in several calculations before made with MAFIA the measured frequency is generally above the calculated one. The modulation of the RFQ-electrodes for the electrodynamical calculation is approximated by 4 unmodulated rods, which have the same capacity as a two-dimensional cut of four modulated rods with the average aperture. This approximation might be a reason for the offset.

Figure 3 shows the relation between the frequency and the Q-value, figure 4 shows the relation between the frequency and the shuntimpedance.

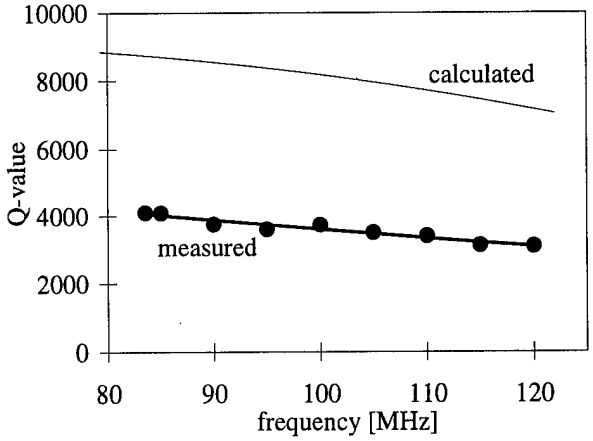


Figure 3: Relation between the frequency and the Q-value.

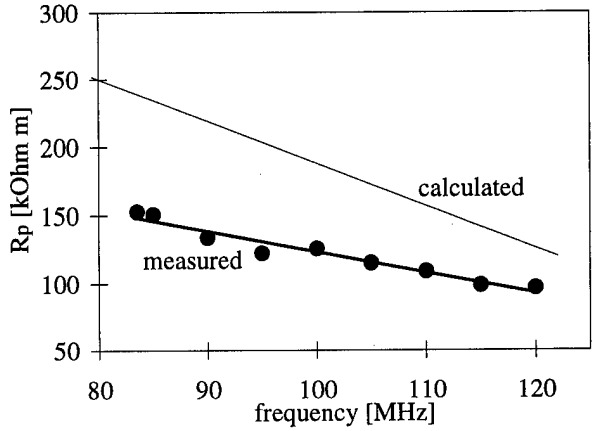


Figure 4: Relation between the frequency and the shuntimpedance.

There is a factor of 2 between the calculations and the measurements for the Q-value. This is a known effect of MAFIA and has been observed with other RFQ-resonators as well [4]. There are different reasons for the more optimistic results for complex structures. On the one hand a simplification for the electrodes is made, as explained above. On the other hand the transition resistance between the RFQ parts are totally neglected.

These effects are not intrinsic for MAFIA; due to the immanent computer limits, a limited matrix size of the resonator geometry has to be used. With a finer grid the results should fit better. Anyway, the code MAFIA is very helpful for structure optimization [5].

Another point of interest is the electrode voltage along the RFQ (flatness). Calculations have shown that the flatness is a function of the frequency. The value of 3 % at the highest frequency is noncritical and improves at lower frequencies, as shown in figure 5.

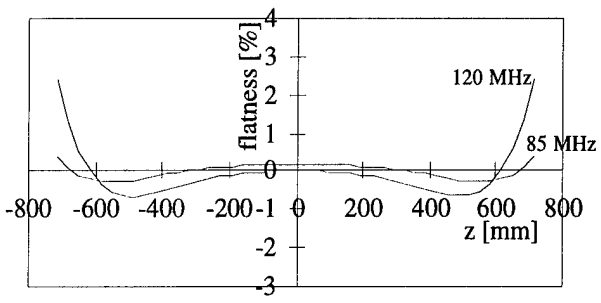


Figure 5: Calculated flatness .

4 STATUS AND SCHEDULE

The alignment of the electrodes of the two RFQ-stages is finished. The maximum misalignment in relation to the theoretical beamline is 70μm. The alignment was measured with an optomechanical system, having the electrodes readily assembled for operation, and not on a bench before mounting. Figure 6 shows a picture of the electrodes mounted in the chamber.



Figure 6: Electrodes mounted in the chamber.

First high power rf-tests started in March 1997, with 24 hours of operation with an preamplifier (rf-power 200 W). With full cooling operation and an adjusted transmitter controlling device the applied rf-power could instantaneously be increased to 20 kW in cw-mode in thermal equilibrium. No further frequency tuning of the resonator structure with the slow tuner was necessary. No ponderomotive effects were detected.

These tests confirmed the ability of the RFQ to work under the design conditions. The only cooling problems were caused by the slow tuner and the coupling loop. An improved tuner and a slightly modified cooling have been set-up in the meantime.

Testing of the second rf-transmitter with the 50 Ohm dummy load, the final tuning of the transmitter controlling device as well as the completion of the main computer control are the next steps to be undertaken at NTG in Gelnhausen.

REFERENCES

[1] H. Homeyer, K. Ziegler, NIM B64 (1992) 937-942
[2] T. Weiland, Computer Modelling of two- and three-dimensional cavities, IEEE NS-32 (1985) 2738
[3] O. Engels, NIM B113 (1996) 16-20
[4] O. Kamigaito, EPAC96 (1996) 786
[5] K. Kaspar, EPAC96 (1996) 1973

A TWO-BEAM RFQ FOR ION BEAM FUNNELING*

A. Firjahn-Andersch, J. Madlung, A. Schempp, H. Zimmermann,
Institut für Angewandte Physik, Johann Wolfgang Goethe-Universität, 60054 Frankfurt am Main, Germany

Abstract

The front end of a spallation source linac, e.g. for the european spallation source (ESS) and also a heavy ion inertial fusion (HIIF) driver injector has to provide a high current and small emittance ion beam which cannot be provided by one single ion source. The space charge forces at the low energy part of the linac are the strongest current limitations. For these reasons the required beam will be reached by several funneling stages, where two identically bunched ion beams are combined into a single beam with twice the frequency, current and brightness. For the most critical first funneling stage a two-beam RFQ, where two beams are bunched and accelerated in a single r.f. cavity and a novel scheme for an r.f. funneling deflector operating at low voltages has been developed. With the use of convergent incoming beams, the funneling structure will be placed around the beam crossing position. The experimental setup of a combination of a two-beam RFQ with such a deflector for funneling of two He^+-beams at low energies will be presented.

1 INTRODUCTION

The proposed ESS RFQ injector system consists of two parallel 54 mA RFQ-linacs, operating at 175 MHz. The beams will be combined in a new funnel system to a 107 mA beam at 350 MHz [1].

Each RFQ-line is split into two sections, one from 50 keV to 2 MeV and the second from 2 MeV to 5 MeV with the chopping line between the two RFQs to enable chopping with an unneutralised beam at a moderate energy to reduce the required chopping voltages but at an energy high enough so that the beam can be transported through the line with a minimum emittance growth. For the funnel section a new design is used, where now a two-beam RFQ will bring the beams close together. Thereby the beams can be combined in a single resonator driven rf-deflector. Figure 1 shows a schematic drawing of the ESS RFQ injector system.

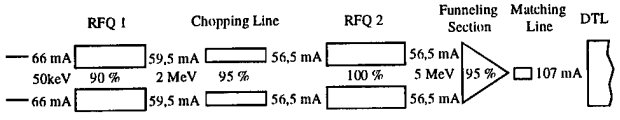


Figure 1: Schematic drawing of the ESS RFQ injector system.

A heavy ion inertial fusion (HIIF) driver could start with a set of low frequency RFQs which employs electrical r.f. focusing and provides bunched ion beams with high transmission [2,3]. The layout of a HIIF injector is shown in Figure 2.

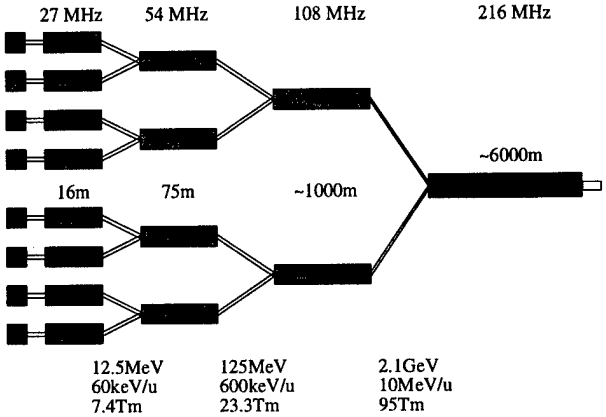


Figure 2: Layout of a 27...216 MHz HIIF injector system for 200 mA of Bi^+.

Initial funneling experiments have been done with systems of discrete elements such as quadrupole doublets and triplets, debunchers, deflectors and bending magnets [4,5,6].

2 THE TWO-BEAM RFQ

A new system with a two-beam RFQ and a resonator driven deflector has been investigated. A first two-beam funneling experiment includes a two-beam RFQ where the beams are bunched and accelerated with a phase shift of 180° between each bunch. In the two-beam RFQ the beam separation at the RFQ exit can be kept small. Therefore the r.f. funneling deflector system can operate at low voltages. To study the properties of the new two-beam RFQ resonator, different types of prototype resonators were built and tested. Also calculations with the electrodynamics CAD program MAFIA [7] have been done for comparison with the low-level measurements.

For the ESS case, a combination of a two-beam RFQ, which joins the two separated RFQ 2-resonators, and a single- or multi-gap deflector has been proposed. Figure 3 shows a scheme of the ESS funneling section. In table 1, the main parameters of the two-beam RFQ and the rf-deflector are shown.

* Work supported by the BMBF

0-7803-4376-X/98/$10.00 © 1998 IEEE

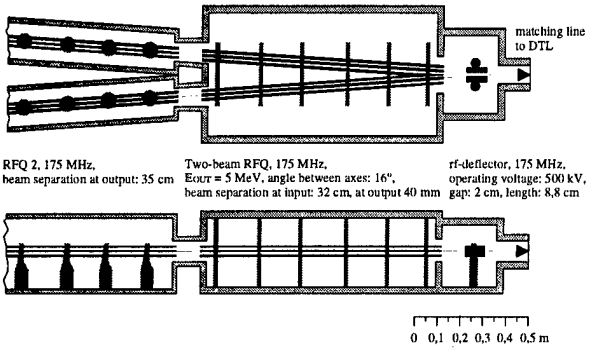


Figure 3: Scheme of the ESS funneling section.

Two-beam RFQ	
f_0 [MHz]	175
E_{in} [MeV]	5
E_{out} [MeV]	5
Length [m]	1
N_{cav} [kw]	250
Angle between beam axes [mrad]	284
R.f. deflector	
f_0 [MHz]	175
Voltage [kV]	500
Length [cm]	8.8
N_{cav} [kw]	65
Beam separation at input [mm]	12.6

Table 1: Main parameters of the two-beam RFQ and the r.f. deflector for the ESS funneling section.

3 THE MULTIGAP DEFLECTOR STRUCTURE

The electrode geometry of the multigap deflector consists of some deflector plates divided by spaces or sections with larger aperture with equal length. In this geometry, the particles will see the deflecting field in one direction several times but the deflection in the opposite direction is always less. The length of the capacitors have to be proportional to the particle velocity and to the inverse of the frequency of the deflector system.

For beam funneling, the frequency of the deflector has to be the same as the accelerator frequency, so that the bunches from different beam axes will see opposite field directions because of the phase shift of 180° between each bunch. If the two incoming beams are parallel, the cell length of the deflector has to be $\beta\lambda$ (β = v/c with c = speed of light and λ = wavelength of the deflector frequency) to get a displacement only. If the two beams are not parallel, the cell length has to be $\beta\lambda/2$ to reach a maximum change of the beam angle [8]. The r.f. resonator for the multigap deflector will be a structure as it is used for 4-Rod-RFQs with two stems. Each stem is electrically contacted with one of the deflector electrodes and will sustain the other electrode by a ceramic support. For longer electrodes it is possible to use an r.f. structure with more stems to preserve mechanical stability.

4 THE TWO-BEAM FUNNELING EXPERIMENT

The funneling experiments in Frankfurt will be carried out with He^+ ions to facilitate ion source operation and beam diagnostics. Two small multicusp ion sources and electrostatic lenses, built by LBNL [9,10], will be used.

The ion sources and injection lenses will be attached directly on the front of the RFQ with an angle of 76 mrad, the angle of the beam axes of the two-beam RFQ. Figure 4 shows a photograph of the ion source attached to the very compact electrostatic injection system.

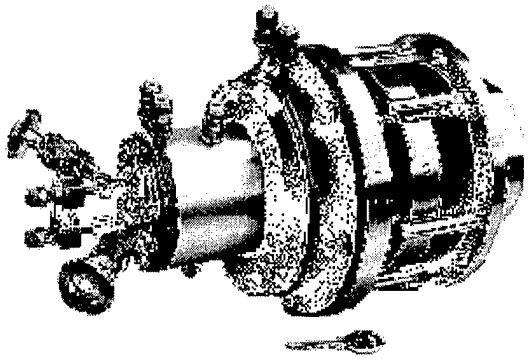


Figure 4: Photograph of the multicusp ion source attached to the injection system.

Figure 5 shows an emittance plot of the ion beam behind the extraction system. The divergent part is originated by the neutral beam and is therefore negligible.

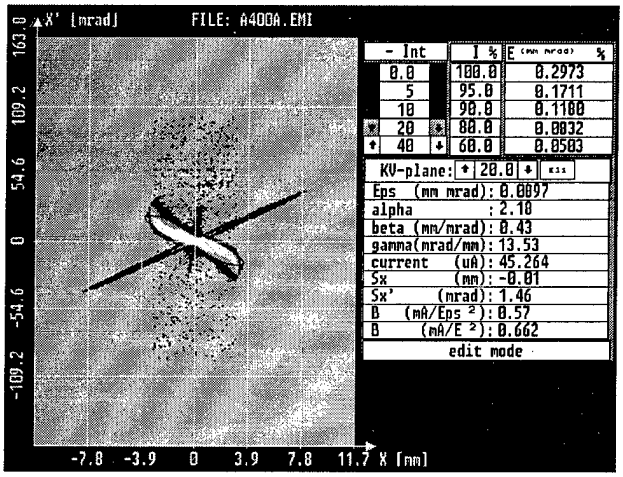


Figure 5: Emittance plot of the ion source.

With this angle of 76 mrad the distance between the two beams at the RFQ input will be more than 160 mm and about 40 mm at the output. The electrodes are supported by eight flat stems. To achieve a proper voltage distribution along the electrodes, the distance between the supports has to be reduced along the resonator.

Behind the RFQ the funneling deflector will be placed before the beam crossing. Figure 6 shows the experimental set-up of the funneling experiment. Beam

diagnostics in front of and behind the RFQ and behind the funneling deflector are in preparation. The funneling resonator is under construction and a prototype for r.f. measurements has been finished.

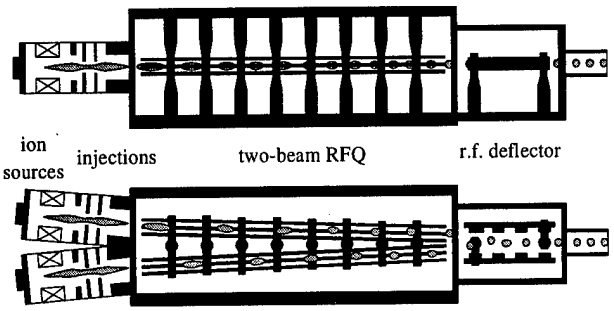


Figure 6: Experimental set-up of the two-beam funneling experiment.

Two-beam RFQ	He^+	Bi^+
f_0 [MHz]	54	27
Voltage [kV]	10.5	180
R_p-value [kOhm·m]	150	250
Quality factor	2000	3000
T_{in} [keV]	4	230
T_{out} [MeV]	0.16	12.54
Length [m]	2	16
Angle between beam axes [mrad]	76	76
Multigap funneling deflector		
f_0 [MHz]	54	27
Voltage [kV]	6	273
Length [cm]	54	233
Beam separation at input [mm]	40	44

Table 2: Main parameters of the experiment with He^+ and the design parameters of a first HIIF funneling stage for Bi^+.

5 CONCLUSION

Figure 7 shows a photograph of the low energy end of the two-beam RFQ. For first r.f. measurements unmodulated electrodes have been mounted. With these electrodes, a resonance frequency of about 57 MHz and a quality factor of 2500 was measured. Due to the lower capacity of the unmodulated electrodes compared to the modulated ones, the design frequency of 54 MHz should finally be reached. The RFQ electrode design is finished. The RFQ electrodes are divided in two parts with different functions. The first part (Figure 8) bunches and accelerates the ion beam the output energy, the second part consists of a drift length and the matching to the funneling deflector.



Figure 7: Photograph of the low energy end of the two-beam RFQ with prototype electrodes mounted.

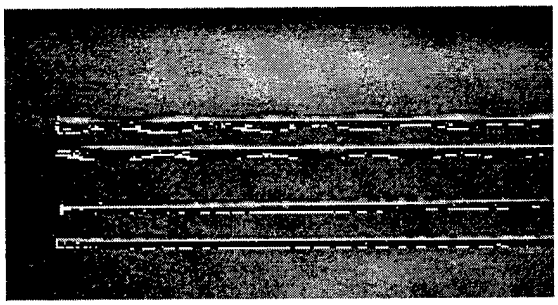


Figure 8: Photograph of the low- and the high-energy end of the two-beam RFQ ectrodes.

REFERENCES

[1] A. Schempp, J. Madlung, A. Firjahn-Andersch, H. Deitinghoff, G. Parisi, RFQ-, Chopping- and Funneling-studies for the ESS-Injector Linac, Proc. XVII Int. Linac Conf., CERN 96-07 (1996) p. 47.

[2] A. Schempp, A HIIF Funnel Injector System, GSI-Report, GSI-95-06 (1995) p. 26.

[3] W. Barth, A. Schempp, Funneling Study with a Low Energy Proton Beam, Proc. PAC91, San Francisco, IEEE 91CH30387 (1991) p. 3076.

[4] K. Bongardt and D. Sanitz, Funneling of Heavy Ion Beams, Primary Report, Kernforschungszentrum Karlsruhe, 11 04 02P14C (September 1982).

[5] J.F. Stovall, F.W. Guy, R.H. Stokes and T.P. Wangler, Beam Funneling Studies at Los Alamos, Nucl. Instr, and Meth. A278 (1989) p. 143.

[6] K.F. Johnson, O.R. Sander, G.O. Bolmer, J.D. Gilpatrick, F.W. Guy, J.H. Marquardt, K. Saadatmand, D. Dandoval and V. Yuan, A Beam Funnel Demonstration: Experiment and Simulation, Part. Acc., Vols. 37-38 (1992) p. 261.

[7] T. Weiland, Computer Modelling of two- and three-dimensional cavities, IEEE NS-32 (1995) p. 2738.

[8] J. Madlung, A. Schempp, A.Firjahn-Andersch, A Novel Design for Heavy Ion Beam Funneling, Fusion Engineering and Design 32-33, Elsevier Science S.A., (1996) p. 229

[9] K.N. Leung, Multicusp Ion Sources, Proc. 5th Int. Conf. on Ion Sources, Beijing, China, 1993, Rev. Sci. Instrum. 65(4), April 1994, p. 1165.

[10] R. Keller in: The Physics and Technology of Ion Sources, Edited by I. G. Brown, Wiley-Interscience Publication, New York

DESIGN OF A HIGH CURRENT H$^-$-RFQ INJECTOR *

A. Schempp, H. Vormann,
Institut für Angewandte Physik, Johann Wolfgang Goethe-Universität,
Frankfurt am Main, Germany

Abstract

High current H$^-$-RFQs are injectors for the planned new spallation sources like ESS and NSNS. Critical points are the high current, the low emittance and the high duty factor of the injector. The strongest existing spallation source ISIS at RAL presently is still operating with a Cockroft-Walton injector. RAL now will upgrade that column by a new RFQ injector, where some of the features of the new proposed ESS injectors can be tested. A Four-Rod RFQ at 202 MHz with a duty factor up to 10% and H$^-$ currents of 50 mA are input values for the rf-structure design and beam dynamics. Results of this design work will be presented.

1 GENERAL

The most critical point of the RFQ operation is a high duty cycle. Table 1 shows RFQ structures in operation or designs. One can see that the duty cycle of these types is bigger than the average duty factor values of other structures.

RFQ	Beam Current	Duty cycle
HLI	U^{28+} 5 µA	25 %
HSI	U^{4+} 25 mA	1 %
DESY	H^- 20 mA	< 0.1 %
CERN	H^- 150 mA	< 0.1 %
Design:		
APT	H^+ 100 mA	100 %
ESS	H^- 107 mA	6.5 %
RAL	H^- 50 mA	10 %

Table 1: Different RFQ Structures.

1.1 High Duty Cycle RFQs

The first c.w. RFQ applications were the normal conducting IFMIF [1] and the cryogenic CWDD [2], the APT (Accelerator Production of Tritium) [3, 4] and Ground Test Accelerator RFQs.

* This work is supported by the BMBF.

In both cases cooling was a critical part of the design and required most engineering efforts. For the Four-Rod structure c.w. operation was done at early work for convenience at rather low average power [5].
We have started again investigation of high duty factor RFQs: The GSI-HLI has a duty factor of 25 % and a thermal power of 15 kW/m, the cyclotron injector for the HMI Berlin will operate at continuous wave and 15 kW/m, too.
A special resonator for c.w. operation has been built and tested [6]. This prototype is a four-stem model with unmodulated electrodes for testing RF properties. It had 16 small viton seals (water - vacuum). Although this concept worked reliably at 20 kW thermal power (20 kW c.w.), it will not be used in a real working RFQ, as the use of water-vacuum seals is not the choice for operational reliable Four-Rod RFQs at high power operation. For an operating RFQ the 10 % duty factor envisaged for RAL is one step in the direction of continuous wave.

1.2 Intense Spallation Ion Source

The ISIS at Rutherford has a long term operation experience with Penning sources [7, 8]. Recently, more than 55 mA of H$^-$ ions have been extracted stably with 2.5 % duty cycle. The 6.5 % d. c., as required for ESS, can be possible with more cooling operation.

1.3 ESS Specifications and Requirements

The design concept for the european spallation source project ESS [9] requires beam currents of 107 mA at the beginning of the DTL. Two RFQ injector linacs with 54 mA each are funnelled into that first DTL stage at an energy of 5 MeV. The beam has to be bunched, so that it can be accelerated in a High Energy Linac to an energy of 1.334 GeV, and then be injected into two compressor rings. Therefore two beams with 54 mA each have to be funneled in a two beam RFQ and a Funnel Section, with a bunch repetition rate of 350 MHz. For a proper operation of the compressor rings the Linac beam has to be chopped with a 60 % duty factor at the ring revolution frequency of 1.67 MHz (360 ns pulse and 240 ns gaps, within a macro pulse of 1.2 ms).

0-7803-4376-X/98/$10.00 © 1998 IEEE

2 SPALLATION SOURCE APPLICATION

The RAL Injector

The ISIS-Facility at the Rutherford Appleton Laboratories is still the most powerful pulsed neutron source in operation. The Linac consists of a 665 keV Cockroft-Walton injector and an Alvarez DTL (202 MHz), accelerating up to 70 MeV for charge exchange injection into the 800 MeV ISIS-Synchrotron. The average beam current is 0.2 mA, the beam power at the target as high as 160 kW.

The existing H^- Penning ion source works at an extraction voltage of 35 kV. The Cockroft-Walton generator will be replaced by a Four-Rod RFQ, which must be able to accelerate H^- ions with a beam current of 50 mA. It is designed in a way that for future upgrade the current can be increased up to 100 mA with 85 % transmission.

The Four-Rod RFQ Resonator

The principle of a Four-Rod RFQ structure is shown in figure 1. The electrodes are carried by stems, which are about 10 mm thick, in case of typical small values for the power loss. If higher power losses have to be considered, special cooling pipes (see figure 4) have to be inserted and therefore the stems have to be thicker. MAFIA Calculations have been made concerning the resonance frequency as function of the thickness of the stems. Figure 5 shows the resonance frequencies for different stem thicknesses. Other MAFIA calculations gave the distribution of the power loss on the RFQ structure, as shown in the following table.

Power Loss Distribution	
Electrodes	34 %
Stems	44%
Ground Plate	22 %

For the new RFQ injector rf power supplies up to 300 kW are available at RAL, but only about 200 kW will be necessary, plus 35 kW beam loading. With the duty cycle of max. 10 % (four times more than the duty factor at present) the thermal power is about 20 kW, for that reason a special cooling concept for the RFQ resonator will be used, which follows the design successfully tested at GSI. A backing cooling tube at the electrodes will be used for that resonator (figures 1, 3 and 4).

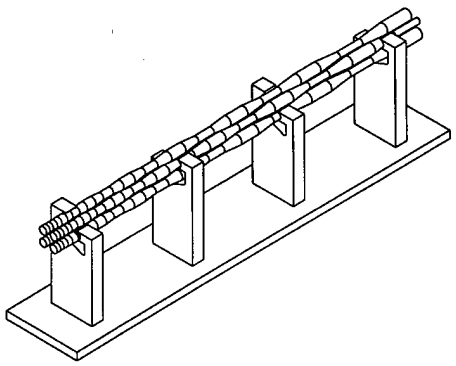


Fig. 1 : Principle of a Four-Rod RFQ Structure.

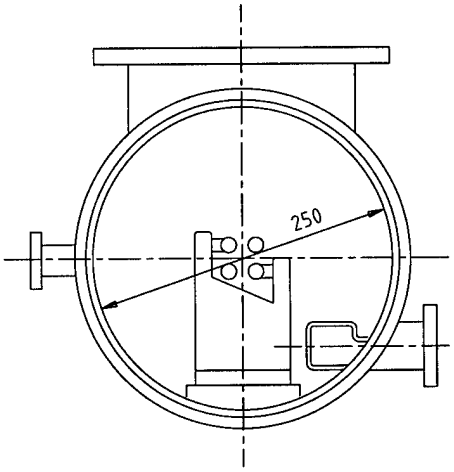


Fig. 2: Typical cross section of a Four-Rod RFQ resonator.

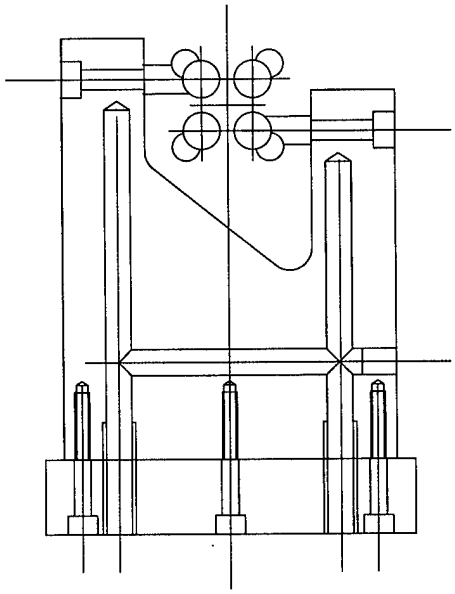


Fig. 3: Cross-section of the stems.

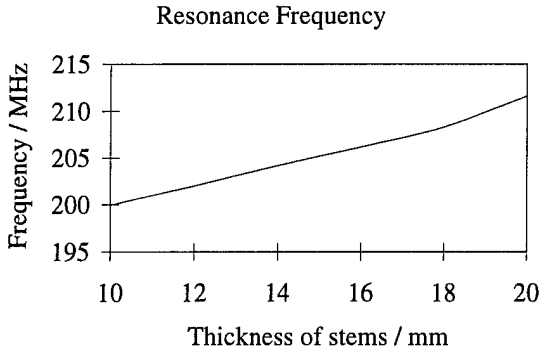


Fig. 4: Resonance frequency for different stems.

3 PARTICLE DYNAMICS

Particle dynamics calculations have been done with the code PARMTEQ [10]. The results are shown in figure 5, the output emittances for 50 mA in the following table.

Beam dynamics parameters	
$\varepsilon^{in}_{rms\ norm}$	1.00 πmmmrad
$\varepsilon^{out}_{rms\ norm}$ (50 mA)	1.05 πmmmrad
$\varepsilon^{out}_{rms\ norm}$ (100 mA)	1.15 πmmmrad
$\varepsilon_{l,\ rms}$	0.07 °MeV

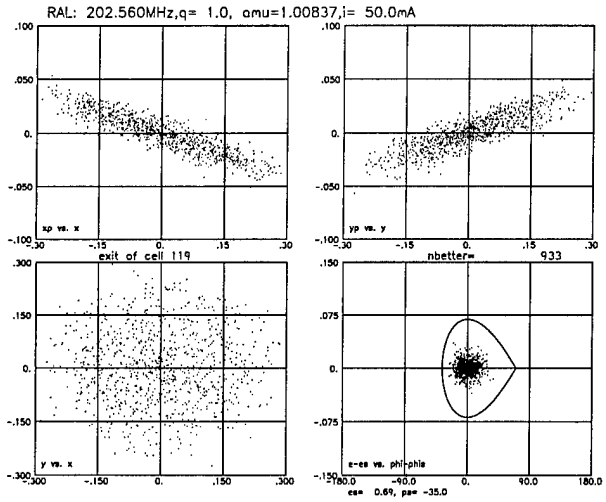


Fig. 5: Particle Output Distribution of the RAL-RFQ.

4 STATUS OF THE WORK

The electrode design calculations for the RAL-Injector are finished. Decisions concerning the resonator design have been made, taking into account the high duty cycle requirements. The construction of the resonance structure is now in progress. RAL has already prepared a complete test stand, where the properties of the new structure will be tested before it can finally replace the Cockroft-Walton generator at the ISIS Linac.

ACKNOWLEDGEMENTS

We would like to thank Charles Planner for the support and for the long lasting efforts to bring the RFQ project to a start. We would also like to thank our group members for support and help, especially A. Firjahn-Andersch, J. Madlung, O. Engels and U. Bessler.

REFERENCES

[1] D.D. Armstrong, ´Recent Performance of the FMIT RFQ´, Proc. Linac 84, GSI 84-11(1984), p. 53,

[2] G. McMichael, J. Carwardine, I. Clarkson, P. Den Hartog, R. Paopsco, G. Pile, L. Sagalovsky, T. Yule, ´CWDD Accelerator at Argonne - Status an Future Opportunities´, Proc. EPAC 94, p. 131,

[3] G. Lawrence, D. Barlow, J. Billen, B. Bing, K. C. D. Chan, R. Garnett, R. Gentzlinger, E. Gray, D. Gurd, F. Krawcyzk, M. Lynch, S. Nath, A. Regan, D. Rees, A. Rohlev, B. Rusnack, R. Ryne, J. D. Schneider, D. Schrage, R. Shafer, J. Sherman, J. Stovall, H. Takeda, P. Tallerico, T. Wangler, R. Wood, L. Young, ´Conventional and Superconducting RF Linac Design for the APT Project´, Proc. Linac 1996, p. 710,

[4] D. Schrage, P. Roybal, L. Young, W. Clark, R. Depaula, F. Martinez, A New RFQ Linac Fabrication Technique, Proc. Linac 94, KEK, Tsukuba (1994) p.152,

[5] A. Schempp, H. Klein, H. Deitinghoff, P. Junior, M. Ferch, A. Gerhard, K. Langbein, N. Zoubek, ´Zero-Mode-RFQ Development in Frankfurt´, Proc. Linac 84, p. 150,

[6] U. Beisel, ´Aufbau und Untersuchung eines RFQ-Beschleuniger-Moduls für hohe mittlere Leistungen´, Diploma Thesis, Institut fuer Angewandte Physik, Frankfurt (1996),

[7] R. Sidlow, P.J.S. Barratt, A. P. Letchford, M. Perkins, C. W. Planner,´Operational Experience of Penning H^- Ion Sources at ISIS´, Proc. EPAC 1996, p. 1525,

[8] N. D. West, ´The Rutherford Laboratory 70 MeV Linear Accelerator´, Proc. Linac 79, p. 88,

[9] A. Schempp, J. Madlung, A. Firjahn-Andersch, H. Deitinghoff, G. Parisi, ´RFQ-, Chopping-, and Funneling-Studies for the ESS-Injector´, Proc. XVII International Linear Accelerator Conf., CERN 96-07 (1996) p. 47,

[10] J. Billen, L. Young, ATO, LANL Code Group.

PROTOYPE OF A SUPERCONDUCTING RFQ FOR A HEAVY ION INJECTOR LINAC

G. Bisoffi[ζ], V. Andreev[⊗], E. Bissiato[ζ], F. Chiurlotto[ζ], M. Comunian[ζ], E. Corradini[⊥], H. Dewa[℘], A. Lombardi[ζ], A. Pisent[ζ], A.M. Porcellato[ζ], T. Shirai[℘], E. Tovo[⊥], R. Tovo[⊥]

[ζ]INFN - Laboratori Nazionali di Legnaro, Padova, Italy

[⊗]Institute for Theoretical and Experimental Physics - Moscow, Russia

[⊥]Dipartimento di Ingegneria Meccanica - Università di Padova, Padova, Italy

[℘]Nuclear Science Research Facility - ICR - Kyoto University, Kyoto, Japan

Abstract

Two superconducting radiofrequency quadrupoles, SRFQ1 and SRFQ2, resonating at 80 MHz, will provide acceleration from $\beta=v/c=0.009$ to 0.035 in PIAVE, the new injector for the superconducting linac ALPI at INFN – Laboratori Nazionali di Legnaro [1]. The construction of the full niobium structures was preceded by the development of a full size stainless steel prototype of SRFQ2 (fig.1), through which most of the construction techniques also applying to the niobium cavities, electromagnetic characterization of the resonator and its mechanical vibration spectrum can be investigated. This paper presents the most relevant design issues of the superconducting RFQ resonators and the construction techniques adopted.

1 INTRODUCTION

Preliminary analysis of a heavy ion accelerator for very low energies consisting of six short superconducting RFQs was proposed in 1988 [2] and in 1991 [3]. To study the feasibility of a superconducting RFQ the third of these six resonators was prototyped at Stony Brook using the technology of electroplating lead onto a copper base [4]. The construction of a full niobium prototype of a high current superconducting RFQ is being carried out at Argonne [5], where a proof of principle of a small unmododulated RFQ, obtained on a modified split ring resonator, yielded a CW peak electric field of 128 MV/m [6]. At INFN-LNL the following scheme is proposed [7]: two SRFQs accelerate a highly charged heavy ion beam from an ECR ion source, located on a 350 kV platform, and prebunched through a three harmonic buncher [1]. Eight quarter wave resonators (QWRs) follow, to match the optimum velocity ($\beta=0.055$) at the beginning of ALPI. Table 1 summarizes the characteristics of SRFQ1 and SRFQ2, whereas the geometry of SRFQ2, which was prototyped in a full scale stainless steel model, is shown in fig.1.

When designing a superconducting RFQ, besides obeying the constraints dictated by the beam dynamics for the vanes [7], other specifications typical of superconducting resonators must be considered. First of all the SRFQ diameter is limited to 800 mm to keep the size of the cryostat reasonable: a four-rod-RFQ is chosen, since the four-vane-RFQ would be 50% larger in size. The choice of the superconductor was essentially between lead and niobium. Lead, electrochemically plated onto copper, gives peak surface fields which are not larger than $\approx$ 16 MV/m, too low for our application.

	SRFQ1		SRFQ2	
	in	out	in	out
Length (mm)		1304.		752.
m	1.2	3.0	3.0	3.0
a (mm)	7.	5.	8.	8.
E_p (MV/m)		25.5		25.5
U (J)		1.5		4
$\varnothing_{tank}$ (mm)		460.		620.
H_p (Gauss)		280.		295.
Q - expected		$7x10^8$		$9x10^8$
$P_{diss,4K}$ (W)		7		7
f (MHz)		80.		80.

Table 1: SRFQs parameters

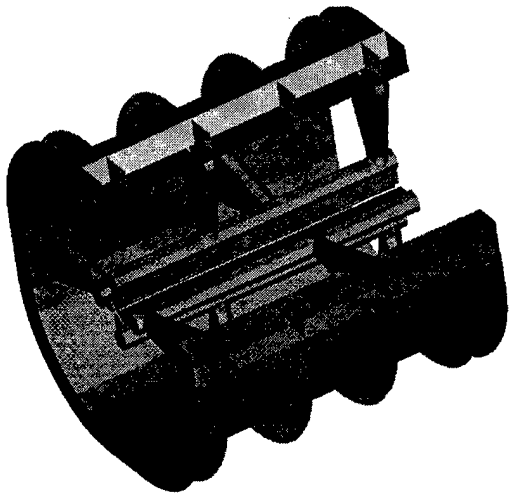


Fig.1 Geometry of SRFQ2

R&D of niobium sputtering onto copper would have taken too long for the short-term scale of an approved project. We opted for full 3 mm thick niobium (RRR ≈300) for

0-7803-4376-X/98 /$10.00 © 1998 IEEE

the whole resonator except the thicker vanes. Though quite expensive and not trivial to assemble by electron beam welding (EBW), it yields high fields with a fairly established technology. The quite low thermal conductivity forces to bring the liquid helium bath close to the whole surface exposed to the fields: stems are then hollow, vanes are carved and equipped with a hollow cylinder on the back, filled with liquid helium so as to bring the cooling liquid close to the dissipating surfaces. The peak surface electric field E_p = 26 MV/m is quite conservative e.g. with respect to the values reached at INFN-LNL for full niobium QWRs [8]. The peak magnetic field, H_p < 300 Gauss, is well below the critical field of Nb at 4 K.

A scheme of alternate stems for oppositely charged electrode couples has the merit of halving the magnetic field on the surface of the modulated vanes and it allows to exploit the end-gaps of the SRFQ as accelerating gaps [7].

2. ELECTROMECHANICAL STABILITY

Superconducting cavities are characterized by an intrinsicly high Q and by a consequently narrow bandwidth around the resonant frequency. The necessary phase locking of an on-line superconducting cavity to a master clock is therefore extremely sensitive to resonant frequency variations caused both by the liquid helium pressure changes and by environmetal mechanical noise and microphonics. The solution is usually a combination of electronic control and development of a stable mechanical design. A comprehensive description of phase and amplitude control of a superconducting resonator is given in ref. 10. It is shown [11] that the ideal amount of resonator overcoupling that minimizes the total RF-amplifier power is found when $\Delta f_L = \delta f_{max}$, Δf_L being the loaded bandwidth and δf_{max} the maximum frequency deviation to be controlled, provided that $\delta f_0 << \delta f_{max}$, where δf_0 is the intrinsic bandwidth. The RF power amplifier must be capable of a maximum output power P_{max} = 1 kW to reach $\Delta f_L = \pm$ 10 Hz. Resonant frequency variations due to pressure fluctuation on the liquid helium are usually slow enough to be controlled inserting the mechanical fine tuner into a separate phase feedback circuit. Resonant frequency jitters due to environmental noise and microphonics can be counteracted, in a design phase, through a robust mechanical design of the resonator. The mechanical design of SRFQ2 [12] aimed at pushing the lowest mechanical vibration mode of the resonator up to the highest possible frequency. By developping particularly rigid stems and with the fundamental support of a stiffening jacket welded outside the resonator tank (fig. 1), this frequency was pushed to 143±15 Hz. Fig. 2 shows the vibration pattern of the lowest frequency mode, as evaluated with the 3D-FEM code I-DEAS [13]. In our case the stored energy is far higher in SRFQ2 (4 J) than in SRFQ1 (1.5 J) and this was the main reason to choose the former for a full size stainless steel prototype. The prototype is being assembled at present: beside enabling to test EBW and assembly techniques, it will allow to experimentally evaluate the vibration spectrum of the resonator, both on the shelf and inside the warm and cooled cryostat.

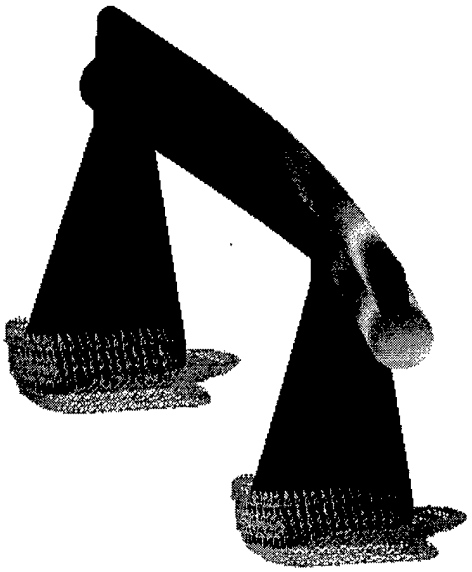


Fig. 2 Pattern of the lowest mechanical vibration mode of a single SRFQ2 electrode.

3. ASSEMBLY, ELECTRON BEAM WELDING AND FREQUENCY TUNING

As mentioned above the resonator parts are made of 3 mm thick niobium sheet. The assembly procedure is not trivial and a large effort has been put on its optimization. For the Nb SRFQ2 it is foreseen to follow the same assembly and welding steps which are being adopted for the stainless steel model. SRFQ2 is built up in quarters: for the sequence of assembly, EBW and rough frequency tuning

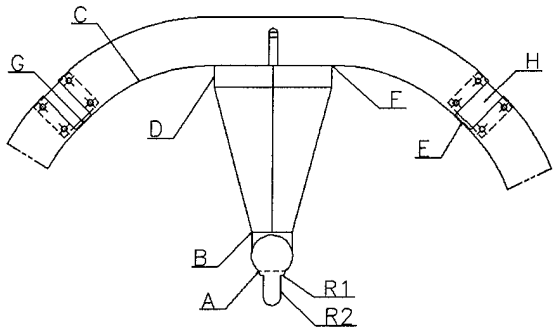


Fig. 3 Procedure of SRFQ2 assembly and EBW

we refer to fig.3.

After the stems are assembled, the still unmodulated vanes are welded to the rear cylinders ((A) in fig.3): these are extruded at the longitudinal position of the stems with extrusions which are only ≈ 2% smaller in diameter

than the cylinder themselves: the joints are properly machined and EBW between extruded parts and stems is done (B). At this stage both transverse reference planes (R1 and R2 in fig.3) and modulation are obtained by means of a computer controlled milling machine. The 10 mm wide 60 mm high stiffening ribs are, in parallel, EB-welded outside the resonator tank (C). It should be noted that, in the full niobium SRFQ2, the stiffening ribs will be mostly made out of Ti instead of Nb, so as to increase the rigidity of the stiffening structure. However, in order to avoid the risk of titanium diffusion into the 3 mm thick niobium wall during the high temperature electron beam welding of the ribs to the tank, a 6 mm high standard quality niobium insertion is foreseen between the two: the welding time should be short enough to avoid this phenomenon [13] but no experimental tests were performed yet.

The length of the lower straight part of the stems (D), and consistently the length of the straight edges of the quarters of the resonator tank (E), are kept conservatively large and are then stepwise reduced (rough frequency tuning) so as to bring the resonator frequency to the desired value (estimated to be around 79.9 MHz, thus taking thermal shrinking of niobium between 300 and 4 K into account): the frequency range of such a procedure is $\Delta f \approx 1.6$ MHz and the sensitivity $\Delta f/l_s \approx 100$ KHz/mm, l_s being the stem length [12]. After rough tuning the stems are welded to the resonator tank (F). This is done from the inside of the RFQ, so as to keep the highest weld quality possible, and in two passes for the sake of symmetry of the deformation introduced by EBW. Finally the four SRFQ quarters are EB-welded together from the outside (G). The latter two welding steps follow the last rough frequency estimation and require particular care since the SRFQ frequency must fall within the range of the fine tuning, which is $\Delta f = \pm 100$ kHz [10]. Fine tuning is obtained by pushing and pulling both end plates of the resonator by ±2.5 mm with respect to 20-mm-thick 750-mm-long ERGAL bars, bolted to the end flanges of the resonator.

The continuity of the stiffening ribs on the resonator tank is eventually obtained by filling in the gaps with properly shaped insertions (H).

The stainless steel model is being rough tuned at present and fig.4 shows a photo of it during the first assembly [15].

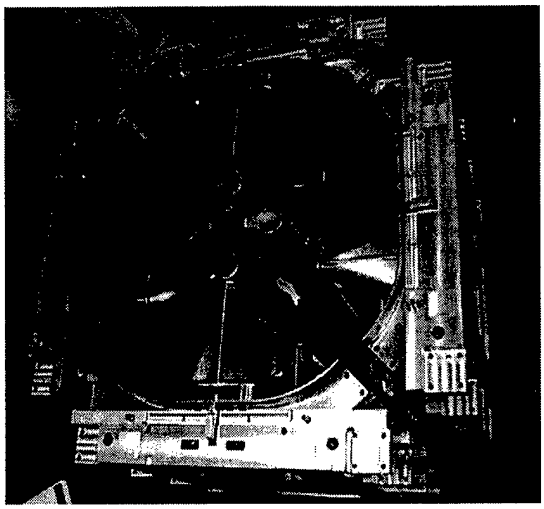


Fig. 4 Photo of the stainless steel model of SRFQ2 during the procedure of assembly and rough tuning in an external jig.

REFERENCES

[1] A. Lombardi et al., these proceedings.

[2] I. Ben-Zvi, Nuclear Instruments & Methods A287(1990) 306-308

[3] I. Ben-Zvi, A. Lombardi, P. Paul, Particle Accelerators, 1991, Vol. 35, 177-192

[4] I. Ben-Zvi, A. Jain, J.W. Noé, P. Paul, H. Wang and A. Lombardi, Nuclear Instruments & Methods B79 (1993) 711-713

[5] K.W. Shepard, W.L. Kennedy and K.R. Crandall, Proc. of the 1993 IEEE Particle Accelerator Conference, Washington, 1042-1044

[6] J.R. Delayen, K.W. Shepard, Appl. Phys. Lett. 57 (5), 30 July 1990, 514-516

[7] A. Pisent and M. Comunian, these proceedings.

[8] A. Facco and J.S. Sokolowski, Nuclear Instruments & Methods A328 (1993) 275-278

[9] I. Ben-Zvi, M. Birk, C. Broude, G. Gitliz, M. Sidi, J.S. Sokolowsi, J.M. Brennan, Nuclear Instruments & Methods A245 (1986) 1-12

[10] J.R. Delayen, G.J. Dick and J.E. Mercereau, IEEE Trans. on Nuclear Science, Vol. NS-24, N.3,June 1977, 1759-1761

[11] G. Bisoffi, G. Algise and A. Lombardi, Proc. of the 7th Workshop on RF-Superconductivity, Gif-sur-Yvette 1995, 677-681

[12] I-DEAS Finite Element Modeling, Structural Dynamics Research Corporation, 2000 Eastman Drive, Milford, OHIO 45150, USA

[13] C. Antoine, DAPHNIA-CEA, private communication

[14] M. Bartsch et al., Computer Physics Communications 72 (1992) 22-39

DEVELOPMENT OF THE ITEP 27 MHZ HEAVY ION RFQ*

V.A. Andreev, A.A. Kolomiets, V.I. Pershin, V.N. Sidorenko, R.M. Vengrov, S.G. Yaramyshev
Inst. of Theoretical & Experimental Physics (ITEP), B. Cheremushkinskaja 25, RU-117259 Moscow
O.V. Ershov
Institut for High Energy Physics (IHEP), Protvino, RU-142284 Moscow Region
G. Parisi
Inst. für Angewandte Physik (IAP), Frankfurt University, Robert-Mayer-Str 2-4, D-60054 Frankfurt

Abstract

A 27 MHz RFQ is presently under development and construction at ITEP, Moscow. It is based on a 90°-apart-stem geometry ("ring-connected RFQ") and its parameters have been chosen to accelerate ions with charge to mass ratio of 1/60 to energies of 110 keV/u. It can also be considered as a prototype for a new 10 MHz RFQ, to be used as the initial part of a heavy ion accelerator for inertial fusion.

In this paper the 27 MHz RFQ status is presented and some simulations of RF efficiency and field distribution, carried out with MAFIA codes, are given for the 10 MHz resonant structure.

1 INTRODUCTION

Much work has been carried out at ITEP during several years for the development of a structure to accelerate intense heavy ion beams. Presently, RFQ structures are considered as the only choice for the initial part of high-power heavy ion accelerators. Because of the low charge to mass ratio (1/60), a low operation frequency is needed, around 10÷30 MHz.

Several different resonant structures have been proposed and investigated for this low-frequency RFQ: 4-rod, Split-ring, Split-coaxial, 4-rod Spiral, etc. However, all of them have some intrinsic drawbacks for low frequencies high duty cycle RFQs.

The 4-rod structure, used in a number of heavy ion linacs, is mechanically simple and has relative small size, but it has an intrinsic presence of dipole components in the operating field and a ripple of the inter-electrode voltage along the structure (due to an extremely high capacitance between a stem supporting a pair of electrodes and the not connected pair). The dipole component is present also in the other considered RFQs which, furthermore, have low mechanical rigidity. It can be reduced to some extent by proper choice of RFQ parameters, but a high intensity RFQ must allow to preserve the injected beam brightness, therefore the field distribution should be dipole free. Moreover, the structure must be easily tuneable, and a reliable stabilisation of the operational mode should be provided.

That is why the development of a new resonant structure for low frequencies, which has perfect quadrupolar symmetry of focusing field, uniform field distribution along axis, which is mechanically stable and suitable for high duty cycle operation, is still actual.

As result of this work, a new structure (henceforth called "ring-connected RFQ") was proposed, investigated and tested by numerical simulations and cold model measurements. It is the advanced version of the so-called "4-ladder RFQ", based on a 90°-apart-stem geometry [1][2], with rings connecting the stems and rods connecting the rings. This allows to lower both the resonant frequency and the size, while achieving a sufficiently high shunt impedance and consequently RF efficiency. A combination of quadrupole and coaxial modes is excited in the structure, which provides a reliable separation between operating mode and dipole ones. Tests showed that it is the most suitable solution for the initial part of a high intensity heavy ion linac.

This 27 MHz RFQ was designed to accelerate 15 mA of U^{4+} ions from 1.5 to 110 keV/u, for upgrading the ITEP injector [3]. It will also allow to continue the research program on heavy ion beam interactions with dense plasma started at GSI-Darmstadt on the "Maxilac" accelerator, which has now been shut-down.

Moreover, it can be considered as the prototype of a 10 MHz RFQ to be used as a heavy ion driver for inertial fusion. The development of high current heavy ion linacs is required for inertial fusion installation: therefore designing and testing prototypes of accelerating structures for the low energy part of the linac are essential.

2 STATUS OF THE 27 MHZ RFQ

The construction of the new RFQ started two years ago in ITEP; for the mechanical design and manufacturing of some RFQ parts, IHEP-Protvino is involved, but it will be assembled, tuned and commissioned in ITEP, which is also in charge of the experimental study of its parameters and of beam dynamics. Numerical simulations with MAFIA codes were done in IAP-Frankfurt.

Parameters of the RFQ, resulting both from simulations and RF measurements on a scaled (1:2) cold model, were chosen to fit the existing equipment in

* Work in Moscow and Protvino is supported by GSI. Work in Frankfurt is supported by BMBF.

0-7803-4376-X/98 /$10.00 © 1998 IEEE

ITEP, such as vacuum tank, ion source, high voltage platform and technological systems, beam outlet systems and diagnostics. They are the following:

Length of the vacuum tank	12.0 m
Inner tank diameter	1.2 m
Outer diameter of the rings	0.81 m
Aperture radius	0.64 cm
Peak E-field on the electrode surface	2.2 Kilpatric
Transmission at 15 mA	96 %
Specific shunt-impedance (R_{sh})	1.49 MΩ·m
Emittance	0.3 mm·mrad

Most parts of the RFQ structure have already been built in the IHEP workshop and delivered to ITEP: the oxygen-free-copper electrodes are ready; the inductor rings and the connecting rods, manufactured from an aluminium alloy, have been copper-plated. Other parts, as tuning elements, are near to be completed.

While the existing vacuum tank is being prepared for structure accommodation, a portion of the RFQ (see Fig. 1) has been assembled in room for testing the alignment and tuning procedures.

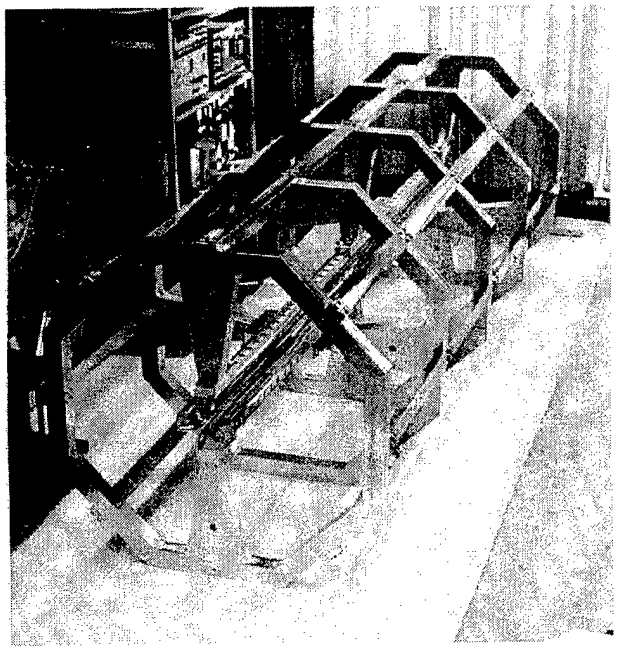


Figure 1: The 4-cell portion of RFQ assembled in ITEP.

The schedule of main expected results in 1997-98 is the following:

- alignment, tuning, measurement of field distribution of the assembled RFQ portion (under operation);
- upgrade of the RF power system and feeding elements; preparation of the U^{4+} ion source to work as pre-injector of the RFQ; development of the diagnostic equipment; manufacture of new tuning and control systems; upgrade of vacuum system; simulation of beam dynamics with parameters measured at the ion source test bench;
- commissioning and achievement of the required beam parameters;
- experiments on intense heavy ion beam dynamics, especially about processes which lead to beam emittance growth and particle losses.

3 STUDY OF THE 10 MHZ RFQ

After assembly, alignment and tuning, the 27 MHz RFQ parameters will be measured (field distribution, shunt impedance, Q-value, power dissipation, etc.). After commissioning, the intense heavy ion beam dynamics will be investigated. The obtained experimental data will be used to develop a prototype of the initial part of a high current linac driver for heavy ion inertial fusion.

The 10 MHz RFQ will have the same structure type but larger dimensions. Numerical simulations by MAFIA codes have been performed in IAP-Frankfurt to design it; the proposed geometrical dimensions are the following:

Length of a cell	1.84 m
Inner tank diameter	2.10 m
Outer diameter of the rings	1.60 m
Inner diameter of the rings	1.44 m
Width of the rings	80 mm
Ring-connecting rods cross-section	40 × 80 mm
Electrode supports width	80 mm
Aperture radius	12 mm
Curvature radius of electrode tips	12 mm

A drawing of a single cell of the structure is shown in Fig. 2. The resulting parameters are the following:

Resonant frequency (f_q)	10.0 MHz
Dipole frequencies (f_d)	14.5 / 15.2 MHz
Separation (f_d–f_q)	4.5 / 5.2 MHz
Q-factor	22.3×10^3
Specific shunt-impedance (R_{sh})	5.1 MΩ·m
Voltage uniformity (dV/V)	1.4 %

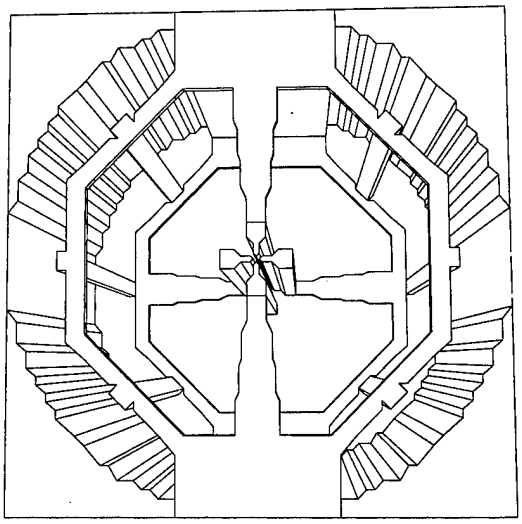


Figure 2: MAFIA plot of the 10 MHz RFQ (1 cell).

A few plots of the electric and magnetic field inside the structure are shown in Figs. 3, 4, 5, 6 and 7.

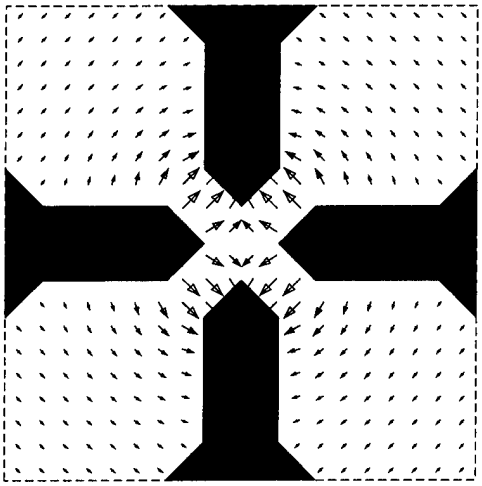


Figure 3: MAFIA plot of the electric field in a transverse section trough the electrodes (detail).

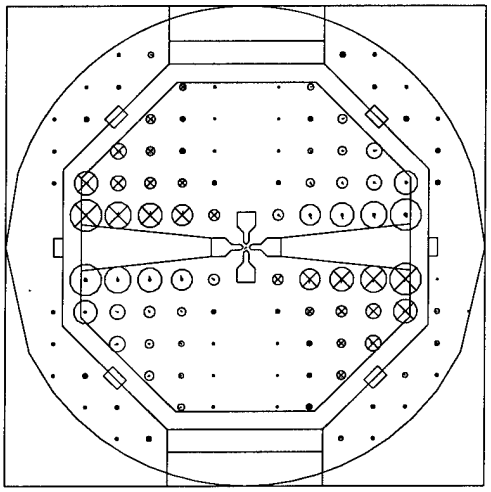


Figure 4: MAFIA plot of the magnetic field in a transverse section in the middle of a ring.

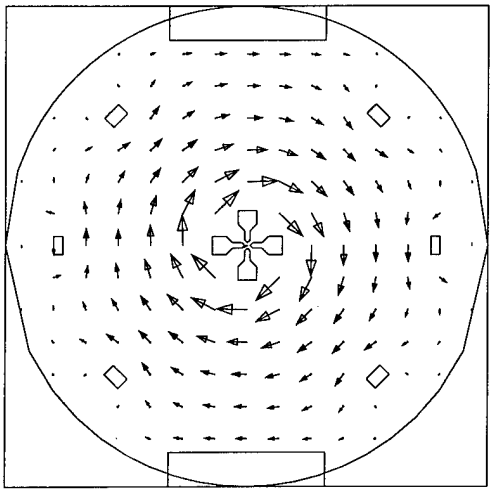


Figure 5: MAFIA plot of the magnetic field in a transverse section in the middle of the cell.

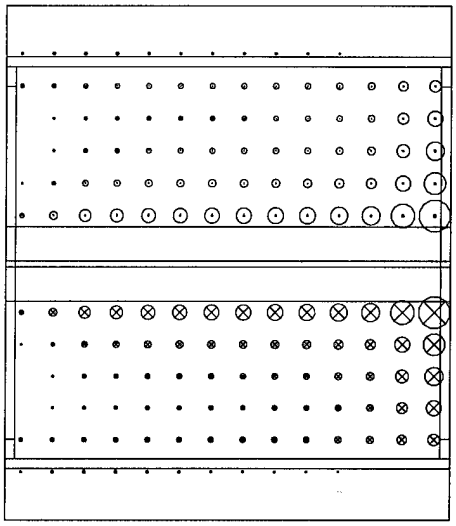


Figure 6: MAFIA plot of the magnetic field in a longitudinal section in the middle of the vertical plane.

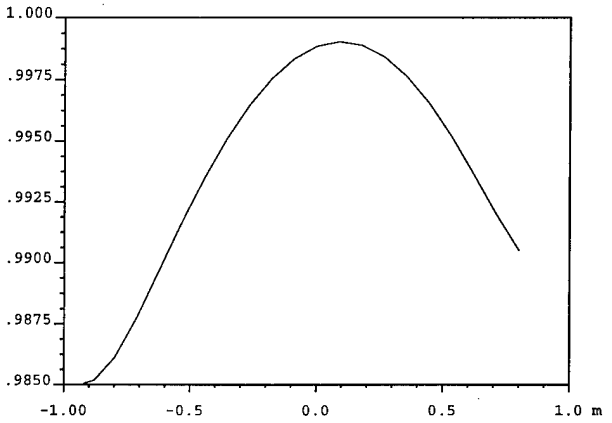


Figure 7: MAFIA plot of the normalized inter-electrode voltage.

4 CONCLUSIONS

A new RFQ structure for accelerating heavy ions was investigated, developed and tested by numerical simulations and measurements on a scaled cold model. Its manufacture is now almost completed in ITEP.

It will accelerate 15 mA of U^{4+} ions to 110 keV/u, allowing to carry out experiments on the interaction of a high intensity heavy ion beam with dense plasma.

This structure can be considered as the prototype of a 10 MHz RFQ to be used as heavy ion driver for inertial fusion. Some preliminary design is simulated by MAFIA codes, which can be base for real structure development.

5 REFERENCES

[1] V.A. Andreev, G. Parisi, "90°-apart-stem RFQ Structure for Wide Range of Frequencies", Proc. PAC'93, Washington, D.C., May 1993, p. 3124.

[2] V.A. Andreev, G. Parisi, "A 90°-apart-stem Low Frequency RFQ", Proc. EPAC'96, Sitges, Spain, June 1996, p. 789.

[3] V.A. Andreev, A. Kolomiets, S. Yaramishev, J. Klabunde, "Low frequency High Duty Cycle Heavy Ion RFQ", Proc. Linac'94, Tsukuba, Japan, August 1994.

A 6.7-MEV CW RFQ LINAC*

D. SCHRAGE, L. YOUNG, W. CLARK, T. DAVIS,
F. MARTINEZ, A. NARANJO, & P. ROYBAL
Los Alamos National Laboratory

Abstract

A 6.7-MeV 350 MHz, cw Radio Frequency Quadrupole proton linac has been designed and is being fabricated for the Accelerator Production of Tritium Project at Los Alamos. This eight-meter long structure consists of four resonantly-coupled segments and is being fabricated using hydrogen furnace brazing as a joining technology. Details of the design and status of fabrication are reported.

1 INTRODUCTION

The linear accelerator for the Accelerator Production of Tritium Project (APT) [1] will include a 6.7-MeV Radio Frequency Quadrupole (RFQ) linac. The first phase of the project, the Low Energy Demonstration Accelerator (LEDA) [2], is to demonstrate performance of the RFQ plus a CCDTL [3] to 20 MeV. The technical specifications for the APT/LEDA RFQ are given on Table 1.

TABLE 1: APT/LEDA RFQ SPECIFICATIONS

PARAMETER	VALUE
Frequency	350.00 MHz
Particle	H^+
Input Energy	75 keV
Input Current	105 mA
Input Emittance, trans./norm.	0.020 π-cm-mrad rms
Output Energy	6.7-MeV
Output Current	100 mA
Output Emittance, trans./norm.	0.022 π-cm-mrad rms
longitudinal	0.174 deg-MeV
Transmission	95%
Duty Factor	100 %
Peak Surface Field	1.8 Kilpatrick
Average Structure Power	1.2 MW
Average Beam Power	0.7 MW
Average Total Power	1.9 MW
RF Feeds	12 Waveguide Irises
Average Heat Flux	11 Watt/cm^2
Maximum Local Heat Flux	65 Watt/cm^2
Resonant Segments	4 @ 2.0 meters each
Brazed Sections	8 @ 1.0 meters each
Slug Tuners	128 total
Length	8.0 meters
Weight	5000 lb.
Inlet Coolant Temperature	50°F
Operating Temperature	85°F

The design and construction of an RFQ to deliver an average proton current of 100 mA at 6.7-MeV is a significant challenge for the beam dynamics and thermal management. The original concept of the APT/LEDA RFQ was developed in 1993 [4]. Since then a number of the physics parameters have changed to reflect revised requirements for matching to the LEBT and CCDTL as well as to take advantage of improvements in the transport codes [5]. Along with this, the fabrication concept has changed from the electroformed-joint design developed for the BEAR Project [6] to a furnace-brazed design [7].

Subsequent sections of this paper describe the cavity design, the engineering design, and the present status of the fabrication.

2 PHYSICS DESIGN

The physics design is discussed in detail elsewhere in these proceedings [5]. The parameters are plotted in Figure 1.

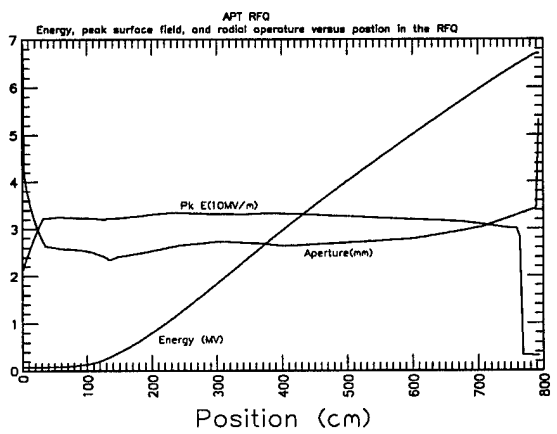


Figure 1: Calculated Physics Parameters
(Peak Surface Fields are Divided by 10)

3 CAVITY DESIGN

The cavity cross-section is the "conventional" triangular shape with a significant longitudinal variation in the width of the vane skirt. The skirt profile is shown on Figure 2. This profile minimizes the power deposited on the cavity walls.

The 8-meter-long structure is designed as four resonantly coupled 2-meter-long segments [8] to assure longitudinal stabilization. Stabilizer rods [9] on the inter-

* Work supported by the US Department of Energy

0-7803-4376-X/98/$10.00 © 1998 IEEE

segment coupling plates and end walls provide azimuthal stabilization without the scalloping of the on-axis fields associated with vane-coupling rings [10] or pi-mode stabilizers [11].

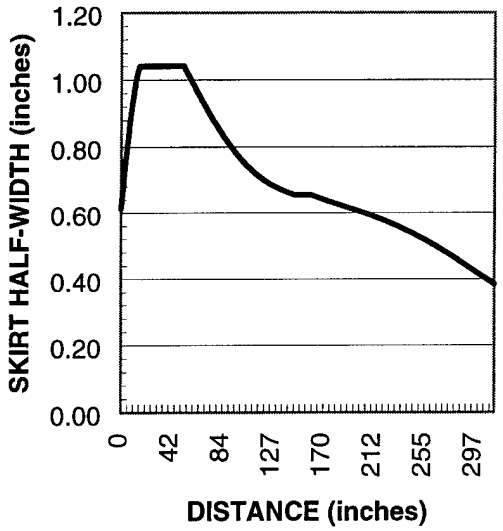


Figure 2: Vane Skirt Width Variation

4 ENGINEERING DESIGN

The cavity is fabricated as eight one-meter-long sections each consisting of two major and two minor vanes. There are 24 longitudinal coolant passages in each of the sections to remove the 1.2 MW of average structure power. These are machined into the OFE-copper substrate and then plugs are brazed on. In order to provide coolant passages as near as possible to the vane tips, the vane tips are fabricated separately and brazed onto the vane bases. These are the only water-to-vacuum braze joints and they are a double joint of nearly one-inch width. This is shown on Figure 3.

For resonance control, the tip coolant passages ("A" & "B") are operated with 50°F coolant while the temperature of the coolant in the outer ("C,", "D," "E," & "F") passages is modulated to maintain the cavity on resonance. The rf power in each of the four resonant segments is significantly different (A = 188, B = 318, C = 361, & D = 398 KW respectively) and the inlet temperature of the coolant is varied accordingly. The error signal for the resonance control system is derived from the reflected power. A compromise between longitudinal temperature variation in the sections and flow-erosion considerations led to a decision for a maximum bulk velocity of 15 ft/sec. The total flow through the cavity is 1,190 GPM. The peak surface heat flux on the cavity walls is 13 W/cm^2 at the high-energy end. The peak temperature on the cavity wall surfaces is predicted to be 100°F.

The peak surface heat flux in the undercut region at the high-energy end is predicted to be 65 W/cm^2 with the peak temperature in this region predicted to be 130°F.

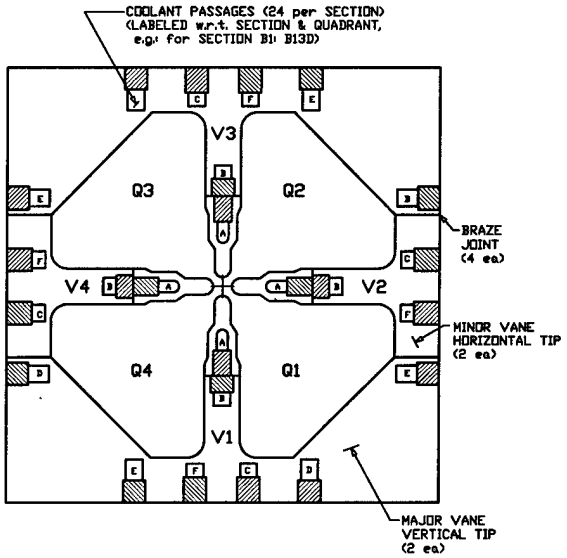


Figure 3: RFQ Cross-Section

The 50°F inlet coolant temperature requires a refrigeration system instead of the cooling tower more commonly used for linacs. The cooling tower would provide an inlet coolant temperature of about 105°F with correspondingly higher peak surface temperatures on the cavity walls and end undercut regions. The higher temperatures on these surfaces would have higher thermal loads due to increased surface electrical resistance. Additional rf power would also have been required with the higher coolant inlet temperature.

The beam loss will be approximately 5 mA of H^+ and will occur in the first section. The vacuum system will have eight 8-inch cryopumps which includes installed redundancy to allow regeneration while the linac operates. This was necessary to meet the APT availability requirement.

Power is supplied to the cavity through 12 waveguide irises (Figure 4). There are three 1-MW klystrons which will normally operate at 2/3 rated capacity. This will extend both rf window and klystron lifetimes. In the event of a klystron failure, the RFQ can operate with the remaining two klystrons.

5 FABRICATION STATUS

Detail design of the APT/LEDA RFQ began in October of 1995. The RFQ cavity is being fabricated and brazed in the LANL shops. At the present time, three of the eight sections have been completed and machining of components of the remaining five sections is underway. A photo of Section A2 is shown in Figure 5.

6 ACKNOWLEDGMENT

Other institutions participating in the RFQ project include LLNL (vacuum system), AlliedSignal (resonance control

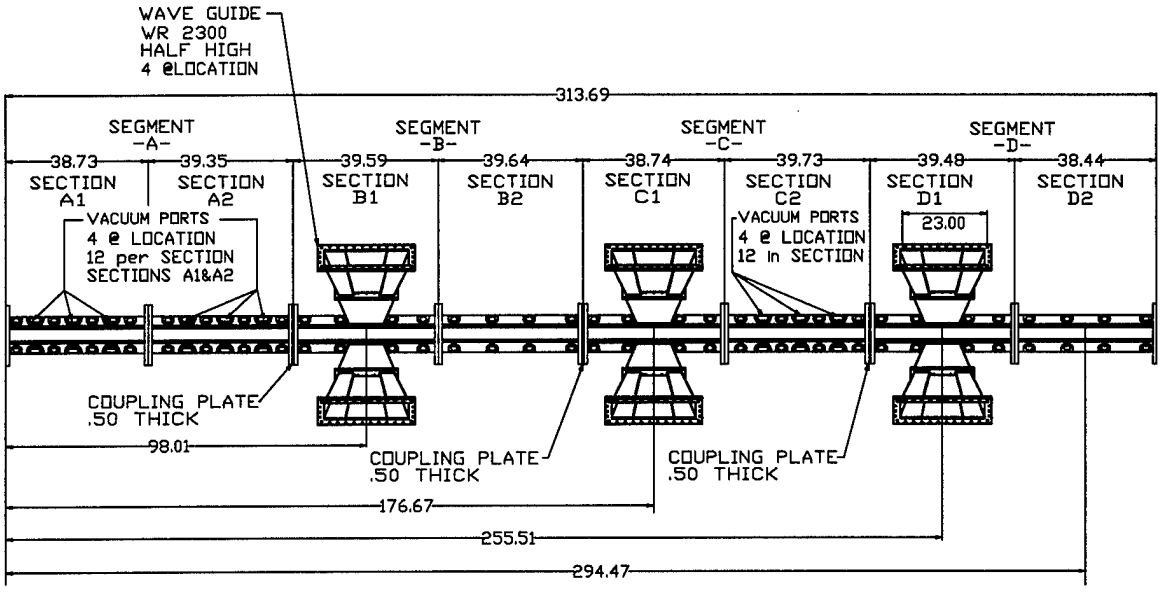


Figure 4: APT/LEDA RFQ Schematic

cooling system), and Northrop-Grumman (engineering support).

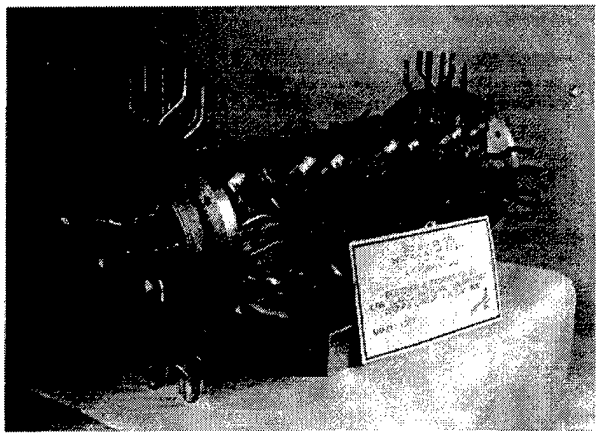


Figure 5: APT/LEDA RFQ Section A2 After Furnace Brazing

7 REFERENCES

[1] G. Lawrence & T. Wangler, "Integrated Normal-conducting/Superconducting High Power Proton Linac for APT," these proceedings.

[2] J. H. Billen, et al, "A New RF Structure for Intermediate-Velocity Particles," Proc. of the 1994 Linear Accel. Conf., Tsukuba, Japan

[3] J. D. Schneider & K.C. Chan, "Progress Update on the Low-Energy Demonstration Accelerator (LEDA)," these proceedings.

[4] D. Schrage et al, "Conceptual Design of a 7-MeV RFQ Linac for the Accelerator Production of Tritium," LANL Report LA-UR-93-1790, 1993

[5] L. M. Young, "Simulations of the LEDA RFQ 6.7-MeV Accelerator," these proceedings.

[6] D. Schrage, et al, "A Flight-Qualified RFQ for the BEAR Project," Proc of the 1988 Linear Accel. Conf., Williamsburg

[7] D. Schrage, et al, "A New RFQ Fabrication Technique," Proc. of 1994 Linear Accel. Conf., Tsukuba, Japan

[8] L. Young, "Segmented Resonantly-Coupled Radio-Frequency Quadrupole (RFQ)," Proc. of the 1993 Particle Accel. Conf, Washington, D.C.

[9] M. Vretenar, "RFQ Field Stabilization Use Dipole Suppressers,' Proc. of the 1st Workshop on INFN Eliosatron Project, Rice, Sicily, (1986)

[10] H. Schneider & H. Lancaster, "Improved Field Stability in RFQ Structures with Vane Coupling Rings," IEEE Trans. Nucl. Sci. NS-30, No. 4., (1983)

[11] A. Ueno, et al, "The π-Mode Stabilizing Loop for Four-Vane Type RFQ's," Proc of the 1990 Linear Accel. Conf., Albuquerque, NM

NSNS RFQ MECHANICAL DESIGN†

Matthew D. Hoff, Craig Fong, Martin Fong, John W. Staples
Ernest Orlando Lawrence Berkeley National Laboratory, Berkeley, California, 94720

Abstract

A 402.5 MHz, 6% duty factor RFQ is being designed for the National Spallation Neutron Source (NSNS). The 6% duty factor and RFQ length will present formidable design challenges. To this end, an RFQ materials test program is underway. A cold model test facility is being designed. Results of cooling calculations have begun. Plans for cavity construction, rf and vacuum seals, alignment, structural support and hot models are discussed.

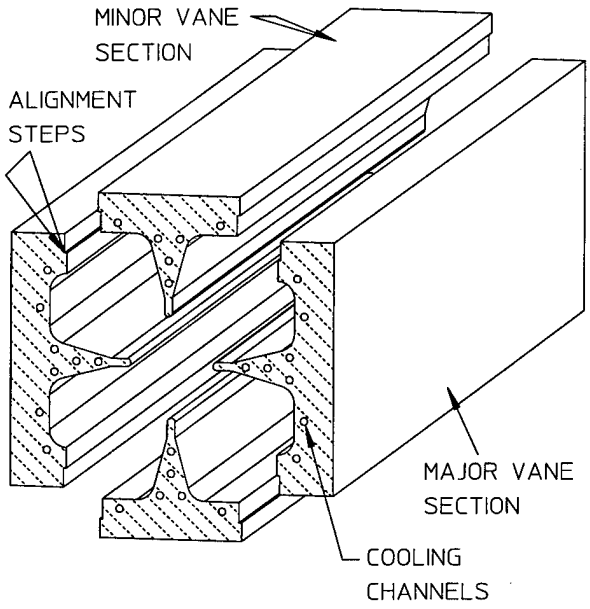


Figure 1. Vacuum-furnace Braze Assembly
Exploded view
Flanges and ports not shown for clarity.

CONSTRUCTION

We have designed the basic size of the RFQ at 3.7 meters long by 215 mm square cross-section, not including the flange, which is 292 mm square. The RFQ will be divided into four modules of varying length. The longest module is 950 mm in length while the shortest module is 900 mm. We are studying a vacuum-furnace brazed, self-aligning technique for fabrication, (See Figure 1) We plan to braze together four vane sections to create modules that in turn bolt together to form the full length RFQ as shown in Figure 2.

The RFQ is divided into four modules all under one meter in length to simplify fabrication, oven brazing and handling. A development program will be integrated with the hot model testing to verify this construction technique.

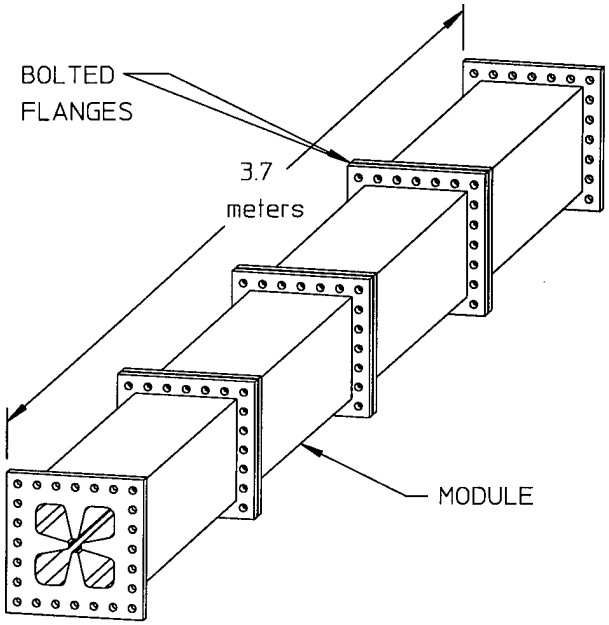


Figure 2. Four Module RFQ Assembly

MATERIALS

We have currently selected Glidcop AL-15 [1] (an alumina dispersion-strengthened copper) because of the vacuum-furnace braze technique and the close tolerance requirements for the cavity. Glidcop will not anneal in the brazing oven and will not creep from residual stress, making it ideal for our close tolerance application. Module connecting flanges can be fabricated of either Glidcop or stainless steel. Raw Glidcop billets can be sized to include the flanges, saving an oven brazing cycle, but requiring more material and machining. Stainless steel flanges would have greater strength than Glidcop, but would require a braze cycle. We will investigate both options. Anticipating accelerated erosion due to ion sputtering by the 6% duty factor, we plan on investigating the hardening of vanetips by ion implantation of a refractory metal such as tantalum. The Plasma Applications Group at LBNL has developed advanced techniques of surface modification using ion guns to harden copper surfaces.

† This research is sponsored by the Lockheed Martin Energy Research Corporation under the U.S. Department of Energy, Contract No. DE-AC05-96OR22464, through the Lawrence Berkeley National Laboratory under Contract No. DE-AC03-76SF00098.

0-7803-4376-X/98/$10.00 © 1998 IEEE

RF TUNING

The coarse frequency will be determined by computation with 3-D electro-dynamic codes and refined by physical modeling. The actual RFQ modules will be fabricated with a frequency slightly higher than required and a groove machined in the length of the cavity wall to bring the frequency into the desired tolerances. The groove will be cut using a wire EDM machine with a throat opening greater than the length of the modules. The RFQ design incorporates forty-eight tuners, (See Figure 3). We plan to adapt the design of the PEP-II tuners [2] which have been developed for a similar wall power density and 476 MHz frequency, but a 100% duty factor. The PEP-II tuner has a piston area of 7500 sq. mm, while the NSNS tuner will be 200 sq. mm with a motion of $\pm$ 2 mm. The tuners use silver-plated Glidcop rf contacts sliding on rhodium-plated copper piston. Hence, we need only to scale down the size of the design. Because of the anticipated rf losses, the tuners are water cooled. The physics design of the RFQ is further discussed in a companion paper at this conference[3].

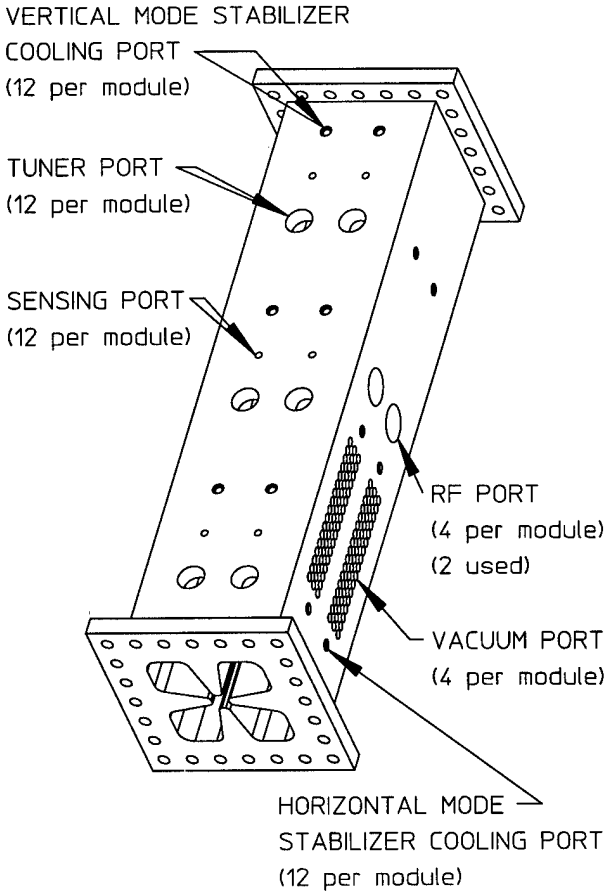


Figure 3. Module Port Configuration
Port configuration is identical on the opposing hidden surface.

DRIVE LOOPS

We plan to distribute 800 kW of rf power into the RFQ at eight locations. At 100 kW per input, eight water cooled drive loops will be used. Drive loops will be located, in pairs, in the center of each module. Drive loop pairs will be located in opposing quadrants. To promote even power distribution, drive loops will alternate between adjacent quadrants in adjacent modules. To maintain symmetry in the cavity design, all modules will have four drive ports in the center, but only two will be used, with the other two capped off.

VACUUM SYSTEM

An array of holes with diameters small enough to attenuate rf leakage will be machined into each major vane component resulting in four pump-out ports per module. Conceptual design indicates that four turbomolecular and two cryo pumps should be used for pumping the entire RFQ. Each vacuum pump manifold covers two adjacent ports on a module side. Unused vacuum ports will be covered. Vacuum calculations indicate this arrangement can pump down to a pressure of 10^{-7} torr, which will meet operational requirements.

SEALS

Current plans are to join RFQ modules with a bolted flange utilizing a Helicoflex[4] seal, backed up with an O-ring. The Helicoflex seal fulfills both the rf and vacuum requirements. We expect the rf current across the bolted joint to be low, well within the capabilities of the metal clad, high contact pressure Helicoflex seal. We view the back-up O-ring seal as cheap insurance for a major vacuum joint. Local rf current will be sustained at the vanetips by capturing a canted spring ring between them. Large flanges, such as the vacuum ports will be sealed with O-rings. Smaller seals, such as the tuners, may use copper knife-edge type seals.

π MODE STABILIZER BARS

LBNL has chosen to use π Mode Stabilizer bars that were pioneered at KEK [5]. These stabilizers are mechanically simple, inexpensive to fabricate and easy to cool. Preliminary design calls for six pairs per module, twenty-four pairs total.

ANSYS CALCULATIONS

Initial ANSYS [6] analysis of the nominal RFQ cross-section showed the following results. Thermal distribution calculations show a 5° C rise for the cross-section. Thermal stress, along with vacuum loading, is calculated at less then 650 psi. Net thermal deflection at the vanetip and cavity wall is less then .001 mm resulting in a calculated frequency shift of .001%. Further analysis of the RFQ vane end region and other potential hot spots will be carried out as the design matures. The cooling water flowing through the vane is calculated to rise less than 3° C.

COOLING CIRCUITS

Multiple cooling circuits will be gun bored and their locations are based on ANSYS analysis. The gun boring method allows us to place cooling closer to the vane tips. In locations where a port must cross a cooling passage, a port sleeve with a cooling channel on the outside bore will be inserted (during a furnace braze cycle) to allow the coolant to flow around the port, (See Figure 4). The cooling passages will be brazed shut at the ends and connecting water passages radially bored in from the outside.

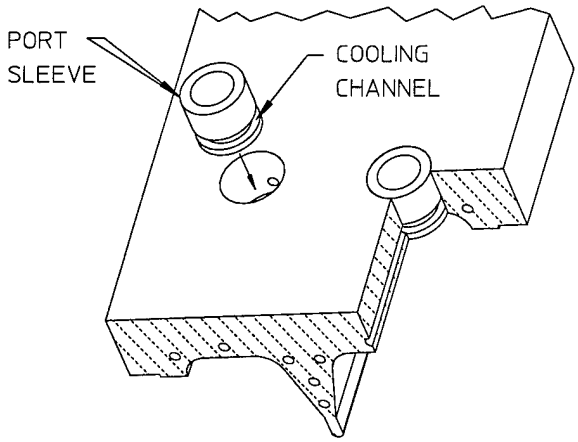


Figure 4. Port Sleeve Cooling

ALIGNMENT

We plan to address the alignment of vanetips in the individual modules by machining alignment steps into the major and minor vane sections and braze using a "zero gap" technique, (See Figure 1). The "zero gap" technique entails fixturing the components with metal to metal contact and placing the wire braze material in machined grooves that open to the contact surface. The groove location and size is designed to deposit the correct amount of braze material through out the joint. The metal to metal contact assures precise alignment and tolerance control. The four modules will then be mounted on a strongback structure (raft) that will align the modules to each other, support vacuum pumps and facilitate transportation.

STRUCTURAL SUPPORT

The smaller strongback structures (rafts) holding the modules will be mounted on a larger, overall support structure (girder) holding the entire NSNS Front End. This girder will facilitate easy instrumentation access and modification, yet provide stiff, rugged support. This structure may also double as a shipping fixture.

COLD MODELING

A modular cold model structure has been designed for low power rf testing without vacuum. Starting with short, standard sections, we will work our way up to a final full length model. Preliminary test are planned for the mode stabilizer rod spacing and location. Vanetip end geometry, tuners, rf drive ports and absolute frequency will also be tested.

HOT MODELING

Design is progressing on a test stand for testing small RFQ structures under vacuum and full rf power, hence the term "hot". We plan on testing rf joints, multipactoring reduction techniques, rf feed loops and cooling on this test stand. Initial test will be on a short two vane structure to simplify fabrication, eventually working our way up to a full scale cross-section.

INSTRUMENTATION

Instrumentation design is in the discussion stage only at this time. Forty-eight wall-field sensing loops are planned, as are four spark detectors and cavity temperature monitors. Full monitoring of the water cooling system is anticipated to include flow rate, temperature and water quality. All rf tuners will be monitored for temperature and position during operation.

CONCLUSION

We have presented a four-vane, oven-brazed, Glidcop RFQ, assembled in four modular sections. Initial ANSYS calculations indicate an excellent thermal design showing thermal stress below 650 psi and thermal frequency shift under .001%. We are confident that our development program will verify our fabrication technique and successfully overcome the challenge of a 6% duty factor, 3.7 meter long RFQ.

REFERENCES

[1] Glidcop Products Information Bulletin, SCM Metal products Inc., 1988

[2] H.D. Schwarz et. al., *Development of a Movable Plunger Tuner for the High-Power RF Cavity for the PEP-II B Factory.* this conference.

[3] J. W. Staples et al, *The NSNS Front End Accelerator System*, this conference.

[4] Helicoflex is a registered trademark. Helicoflex Company, Columbia, SC., USA

[5] A. Ueno et al., *Beam Test of the Pre-Injector and the 3-MeV H- RFQ with a New Field Stabilizer PISL,* Linac 96

[6] ANSYS finite element code, Rev 5.3, ANSYS, Inc. Canonsburg, Pa. USA

STATUS OF THE RFD LINAC PROTOTYPE*

D.A. Swenson, F.W. Guy, J.W. Lenz, Linac Systems, Waxahachie, TX 75165
K.R. Crandall, Consult Crandall, and J.M.. Potter, JP Accelerator Works, Inc.

Abstract

A 2.5-MeV prototype of a "Compact 12-MeV Proton Linac for PET Isotope Production" is under construction at Linac Systems. This unit will serve as the "proof of principle" for the revolutionary new Rf Focused Drift tube (RFD) linac structure. Both the prototype and the production unit will operate at 600 MHz. The prototype comprises a 25-keV proton ion source, an einzel-lens-based LEBT, a 0.65-m-long RFQ linac to 0.8 MeV, and a 0.35-m-long RFD linac to 2.5 MeV. The two linac structures will be resonantly coupled together and powered by a collection of planar triodes. The entire assembly will be evacuated by 2 turbomolecular pumps and 1 ion pump. The alignment philosophy is based on precision machining and "hard socket" for installation of the drift tubes. Fabrication methods for achieving the required precision will be described. Installation of a Laboratory Building to house the prototype is nearing completion. The prototype is scheduled for completion in the fall of 1997. The status of this project after 7 months of funded activity will be reported.

1 INTRODUCTION

The RFD linac structure[1-5] resembles a drift tube linac (DTL) with radio frequency quadrupole (RFQ) focusing incorporated into each "drift tube". As in conventional DTLs, these drift tubes are supported on single stems along the axis of cylindrical cavities excited in the TM_{010} rf cavity mode. The RFD drift tubes comprise two separate electrodes, operating at different electrical potentials as determined by the rf fields in the cavity, each supporting two fingers pointing inwards towards the opposite end of the drift tube forming a four-finger geometry that produces an rf quadrupole field distribution along the axis. The fundamental periodicity of this structure is equal to the "particle wavelength", $\beta\lambda$. The particles traveling along the axis traverse two distinct regions, namely gaps between drift tubes where the acceleration takes place, and regions inside the drift tubes where the rf quadrupole focusing takes place.

2 RFD DRIFT TUBE GEOMETRIES

The drift tube body and stem geometries, which are so fundamental to the RFD linac structure, continue to evolve. The transverse quadrupole fields, which produce the quadrupole focusing, are now pretty much isolated from the longitudinal gap fields by the drift tube bodies. That is, the four fingers, which produce the rf quadrupole fields, are now compleely enclosed within the bodies of the drift tubes, instead of being exposed to the gap fields as they were in previous designs. The stems that support the two halves of the drift tube must do so without shorting out the rf excitation of these electrodes. Now, instead of using the inductance of the stems to isolate the two halves of the drift tube, we plan to use the coupling of the stem geometry to the magnetic fields of the linac to provide an rf excitation equal to that derived from the coupling of the drift tube bodies to the electric fields of the linac.

We are designing for a drift tube diameter of 36 mm, a gap length (G) to cell length (L) ratio of 0.25, a quad length (Q) to cell length ratio of 0.5, and a bore hole radius of 1.5 mm. The energy range for the POP prototype is 0.8 to 2.5 MeV. The cell lengths, at 600 MHz, range from 21 mm to 36 mm. The cross section of the drift tubes for cell lengths of 22, 26, 30 and 34 mm are shown in Fig. 1. The upper half of the cross section shows the horizontal plane of a horizontally focusing quadrupole and the lower half of the cross section shows the vertical plane of the same quadrupole.

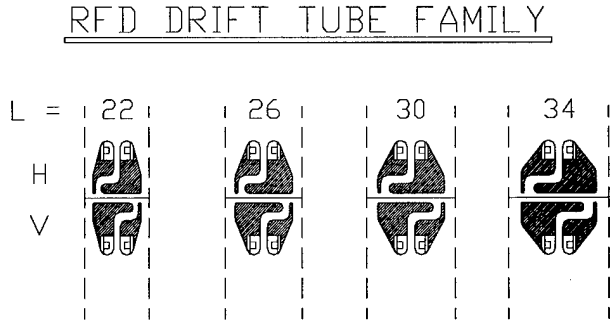


Figure 1: Cross Sections of RFD Drift Tubes.

The goal is for the RFD lens excitation derived from the capacitive coupling of the drift tube bodies to the electric fields of the linac mode to be equal to that derived from the inductive coupling of the drift tube stems to the magnetic fields of the linac mode. The latter is evaluated from SUPERFISH field information with the aid of the CHARGE-2D program. The former is evaluated with the aid of the CHARGE-3D program.

The desired lens excitation is determined by the beam dynamics. A constant voltage across the lens, independent of cell length, results in a constant phase advance per unit cell, which results in a constant beam diameter throughout the linac. A constant lens voltage

* Supported by the National Institute of Mental Health (NIMH).

0-7803-4376-X/98 /$10.00 © 1998 IEEE

implies a declining ratio of lens voltage to cell voltage as the cell length (and voltage) increases. We are designing for a lens voltage of 40.5 kV, which corresponds to a V_L/V_C ratio that ranges from 0.23 to 0.15 over the length of the POP prototype.

3 RFD BEAM DYNAMICS

We have decided to terminate RFD linac tanks at a mid-gap location. That is, the end cells are what we would call "half cells". This obviates the need to design special RFD lenses that would function properly on the end walls. We have recently modified the RFD linac beam dynamics program, PARMIR, to accommodate that decision.

The acceleration and focal properties of these end cells can be determined from the electric field distribution along the axis of the cell and adjacent beam pipe. SUPERFISH calculations reveal that these fields reach their maximum intensity near the center of the "half gap" and that the tails of the distribution lack the symmetry of normal linac cells. This lack of symmetry poses the question of where best to apply the transverse and longitudinal "kicks" to simulate the action of these fields on the beam. We have decided to adopt the point about which the S integral vanishes as the effective center of the cell, leaving us with the normal linac energy gain expression, where the T, TP, and SP integrals are evaluated about this same point.

SUPERFISH runs are made for half-cell/bore-tube geometries corresponding to energies where tank ends are expected to occur. The locations of the effective centers of these cells are determined and the T, TP, S and SP factors are evaluated about these effective centers. The value of E_0 is independent of the choice of origin over which it is integrated and will be the same as that of its neighboring full cell. As the effective gap of the half cell is smaller than that of a normal "full cell", the transit time factor (T), will be higher than that of the neighboring full cell. These data are extracted from a series of SUPERFISH runs and the result are presented to the beam dynamics code, PARMIR, in tabular form as a function of the particle velocity, β. When PARMIR encounters the need to generate an end cell of a tank, it interpolates the data in this table to the β of the end cell to get the data needed for generating the half cell.

4 RF CAVITY FIELD CALCULATIONS

For a complete analysis of the RFD linac structure, some 3D rf calculations are needed. Outside the drift tubes of the RFD linac structure, the geometry and fields are axisymmetric; inside the drift tubes, the geometry and fields are highly three-dimensional. Although the three-dimensional portion of the problem occupies less than 1% of the total cavity volume, the fields in this region represent a majority of the fields that the particles see. The effect of this region on the resonant frequency of the structure is important. The rf efficiency of the structure depends, to some extent, on the power dissipation in this region of the structure. The design of the drift tube cooling circuit requires some knowledge of the distribution of the power losses in this region. The allowable excitation will be limited by the electric field intensities on the surfaces of this region.

The common 3D rf codes are MAFIA, ARGUS, HFSS, and SOPRANO. To date, calculations of the field distributions and power losses in the RFD linac structure have been made with MAFIA, HFSS, and SOPRANO. All calculations confirm that the structure performs as expected. SOPRANO[REF] has an enormous advantage over MAFIA in that it can have a fine mesh in one portion of the problem volume, surrounded by a coarse mesh for the rest of the problem volume. Vector Fields has produced a sample calculation of this geometry for us.

5 RFD DRIFT TUBE BODY AND STEM DESIGN

The RFD drift tube body and stem design comprises two half-body electrodes, with a total of four fingers to create the rf quadrupole field along the axis, supported on two water-cooled support blades that emanate from a single stem that mounts in a single hole through the linac tank wall.

The stem/blade assembly will be a 4-layer stainless steel sandwich requiring two hydrogen-furnace braze cycles for completion. In the first braze cycle, two halves of the blades will be joined together to form a support blade complete with a machined cooling channel. In the second braze cycle, two blade assemblies will be brazed together to form a complete stem/blade assembly with connections to the parallel blade cooling channels. The stem portion of this assembly will be machined to a circular cross section and precision ground to a cylindrical surface for installation into a reamed hole in the tank wall. The stem and hole will be keyed to control the angular orientation of the drift tube. At this point, portions of the stem/blade assembly will be copper plated.

To achieve the required precision in the location of the body halves relative to the stem base, the stem/blade base will be held in a precision jig, coolant will be circulated through the stem/blade assembly, and the inner surface of the circular annuli at the end of the blades will be cut by the wire EDM process to form a precision seat for the body halves, accurately located relative to the precision ground cylindrical surface of the stem base.

The body electrodes are made from oxygen-free copper. The body electrodes for each drift tube will be different to accommodate the changing velocity of the accelerated particles, whereas the two halves of each drift tube will be identical. The drift tube half-bodies will be joined to the stem/blade assembly by a third hydrogen-furnace braze cycle. A trial run at the fabrication of several drift tubes is underway.

6 RFD LINAC TANK DESIGN

The RFD linac structure will be relatively short (0.35 m) as it need only go to 2.5 MeV. The linac tank, consisting of a thick-walled (22-mm) aluminum tube with a rectangular bar of aluminum welded to one side, represents the principal structural element of the linac. The linac tank for this prototype is 0.38 meters in diameter and weighs 42 kg. The tank is copper plated on the inside and anodized on the outside.

The tank will be oriented with the welded bar at the bottom. The purpose of the welded bar is to provide a thicker wall on which to mount the drift tubes. After all the tank welds are finished and it has been heat treated, the mounting holes for the drift tubes will be precision bored through the thickened tank wall. These holes represent "hard sockets" for the drift-tube stems. No provision is made for further alignment of the drift tubes.

The finished drift tube assemblies are inserted into their hard sockets from the inside of the tank. This requires that the completed drift tube assembly be somewhat shorter than the inner tank diameter. We insist on being able to remove and reinstall any drift tube without disturbing its neighbors. The principal drift-tube-stem vacuum seal is a proprietary copper seal. A secondary elastomer seal on each stem provides for vacuum-checking convenience and a backup vacuum capability.

7 ION SOURCE

The ion source will be a scaled-down version of an early LAMPF duoplasmatron. Some attempts to scale this source to smaller sizes have suffered from magnetic field saturation problems and duty factor limitations. Improvements in the magnetic and cooling circuits promise to rectify these problems.

The ion source will operate at a potential of 25 kV and produce a proton beam of at least 15 mA at a duty factor up to 2%. The filament power will be about 175 W (35 A at 5 V). The magnet power will be about 60 W (2.5 A at 25 V). The hydrogen gas flow is estimated at about 2 SCCM. It will have a length of 152 mm and a diameter of 210 mm. The ion source is currently under design at JP Accelerator Works, Inc. It is scheduled for delivery in the fall of 1997.

8 RF POWER SYSTEM

The rf power system, based on a multiplicity of high power planar triodes, will produce a peak power of 240 kW at a pulse duty factor of 0.5%. It will consist of a chain of two intermediate power amplifiers (IPA1 and IPA2) and one final power amplifier (FPA). The IPAs will be rack mounted while the FPA will be mounted in close proximity to the accelerator. IPA1 will use one YU-141 planar triode and IPA2 will use two YU-141s. The FPA will utilize an all new single cavity configuration of 12 planar triodes in parallel.

This system is currently under development at JP Accelerator Works, Inc., features easy tube replacement (individual cathode assemblies), a broadband cathode circuit (no tuning required), a light weight cavity assembly, built-in phase and amplitude control, and a PC-based control system with fiber-optically isolated control modules and professional controls software. The system is scheduled for delivery in June, 1997

9 VACUUM, COOLING, AND CONTROLS

The vacuum system for the proof-of-principle prototype will consist of one turbo pump on the ion source/LEBT, one turbo pump on the RFQ linac structure, one ion pump on the RFD linac structure, and two rotary vane roughing pumps. These pumps have been procured.

We will strive for metal seals where they are convenient or where they involve critical components that are hard to replace (drift tubes, for example). We will accept elastomer seals on some of the large joints between tank sections and end plates.

The cooling system for the proof-of-principle test will be a recirculating system, based on a single commercial unit with a temperature control capability of ±1°C and a capacity of 3 kW. Some deionized cooling capacity will be needed for the high voltage parts of the rf power system. An additional 5 kW of cooling, without sophisticated temperature control, will suffice for the rest of the system.

The control requirements for RFD linac systems are understood to be very modest. The control system for a production system will involve a PC-based computer with commercially available control modules and commercially available control-oriented software. The plan for the prototype is to implement a skeleton of such a system to establish its potential. Its principle function will be to support important personnel safety and equipment protection functions, some beam diagnostic measurements, and some data-logging functions to assist in accident reconstruction. The control of most accelerator equipment on the prototype will be accomplished manually in the course of developing the required controls procedures.

A new 1200 square foot laboratory has just been completed to support the development of the RFD linac structure. Newly acquired equipment includes a network analyzer, a vector voltmeter, an rf power meter, and a bead perturbation setup. The support structure for the POP prototype have been installed in the new laboratory.

10 REFERENCES

1. D.A. Swenson, 1994 Linac Conf., pp 804.
2. D.A. Swenson, et.al., 1995 PAC Conf., pp 342.
3. D.A. Swenson, et.al., 1996 EPAC Conf.
4. D.A. Swenson, et.al., 1996 Linac Conf., pp 411.
5. D.A. Swenson, 1996 Denton Conference.

BEAM DYNAMICS STUDIES ON THE ISAC RFQ AT TRIUMF

S. Koscielniak, R.E. Laxdal, R. Lee, L. Root
TRIUMF, 4004 Wesbrook Mall, Vancouver, B.C., Canada

Abstract

An 8 m long split-ring RFQ linac is being constructed at TRIUMF as part of the ISAC radioactive beam project. The RFQ is designed to accelerate unstable nuclei with $q/A \geq 1/30$ from 2 keV/u to 150 keV/u. Several unusual beam dynamics studies have been pursued during the latter stages of the design. To furnish engineering alignment tolerances, particle tracking in the 10-term potential was performed to estimate the RFQ performance with respect to vane displacement errors; the results are compared with a simple analytical model. In order to explore fringe field effects, particle tracking studies through computed three-dimensional fields at the RFQ entrance and exit were made to optimize the radial matching section (RMS) to the LEBT optics, and to appraise the value of a transition cell[9]. In this paper we describe the methods and results of the beam dynamics simulations and summarize final specifications for the RFQ.

1 INTRODUCTION

The ISAC project conceptual design[1] consists of an ISOL and two c.w. linear accelerators: a 35 MHz RFQ and a 105 MHz drift tube linac (DTL). The Radio Frequency Quadrupole (RFQ) beam dynamics design[2] has stabilized with the following values: focusing parameter $B = 3.5$, characteristic radius to pole tip (r_0) and vane transverse radius of curvature $\rho = r_0 = 0.741$ cm, modulation index $1.1 \leq m \leq 2.6$, local bore radius $0.37 \leq a(\text{cm}) \leq 0.71$ and inter-vane voltage $V = 74$ kV. An unusual feature of the design is the constant synchronous phase of $\phi_s = -25°$ as a consequence of an external multi-harmonic buncher[5] operating at 11.66 MHz fundamental frequency. The buncher introduces an 86 ns pulse spacing into the beam that is useful in some physics experiments. The tapering down of the focusing parameter, B, toward the RFQ exit, in an earlier design, has been eliminated in favour of exit 'transition cells'. The RMS has been customized to minimize beam size and convergence at the RFQ entrance. The RMS is immediately followed by accelerating cells with $m = 1.1$, and a transition cell has been introduced to avoid the discontinuity.

2 RADIAL MATCHING SECTION

The longitudinal profile of the vane tips is obtained from an analytic expression[4] for the RMS potential. Since the vane cross-sections are semi-circles of radius ρ with straight vane extensions and differ from those assumed in the analytic study the RMS region of the RFQ has been modelled using RELAX3D[13, 6].

The transverse emittance orientation required at the RFQ entrance is determined using TRACK[11] to trace the matched ellipses at the exit of the RMS backwards through the RELAX3D potentials and then back to the last matching quadrupole located 9 cm in front of the tank entrance. The emittance growth due to aberrations in the 4Q matching section at the RFQ entrance is found to decrease as the distance from quadrupole to RMS decreased and as the number of cells in the RMS increased. A quadrupole to RMS spacing of 17.8 cm and a 10 cell RMS section, producing 0.7 % emittance growth for a $50\pi\mu$m emittance beam, is used in the final design.

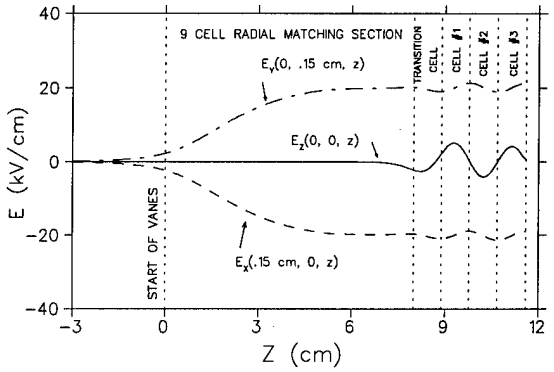


Figure 1: The fields in the RMS calculated using RELAX3D.

A transition cell with a sinusoidal half-period longitudinal vane shape is used to join the unmodulated RMS vanes to the first modulated cell. To make room for this, the RMS is shortened to nine cells, and the tenth cell is the transition cell. This section of the RFQ along with the first three accelerating cells is modelled using RELAX3D, and the calculated electric fields are shown in Fig. 1. Particles are tracked through the calculated RMS potential grids and are then fed into PARMTEQ and accelerated through the RFQ. For comparison, particles are also simulated using PARMTEQ only. The results show that the transition cell has no significant effect on the RFQ's acceptances or output emittances and so acts as a successful bridge through this non-adiabatic region.

3 CPACK CALCULATIONS

Eight term potentials calculated by CPACK[10] are used in PARMTEQ to study beam dynamics of the accelerating section of the RFQ. In order to maintain synchronism and optimum transverse focussing, the analytic two-term potential values for the local aperture a and the modulation m are adjusted using a procedure similar to that described in references[3, 2], so that with the revised cell parameters, the two lowest order, CPACK calculated, coefficients are

0-7803-4376-X/98 /$10.00 © 1998 IEEE

equal to their two term potential values. After the adjustments to a and m, PARMTEQ calculations using the 8-term CPACK potentials give results nearly identical to those produced using the ideal two term potential.

4 EXIT TRANSITION CELL

Crandall[9] suggested terminating the high energy end of an RFQ with a transition cell which would connect the exit of the last modulated cell to a section of unmodulated vane having a constant radius to pole tip r_0, hence zero on-axis potential. This makes the final energy easier to calculate analytically and by adjusting the length of the unmodulated section, the orientation of the output transverse emittances may be changed. In our case we calculate with RELAX3D the potentials at the exit and so can accurately predict the final energy, however we have found that the transition cell allows us to exert more control on the output energy and RFQ length. The ISAC RFQ, as designed, uses a simplified version of Crandall's transition cell.

The ISAC RFQ must have an output energy of 150 keV/u, and, from rf design considerations, a length of $\approx$ 760 cm while GENRFQ/PARMTEQ originally produced a design of 759.38 cm and 150.5 keV/u. To lengthen the design and to decrease the energy, the last cell was converted into a transition cell with a sinusoidal half period to bring the vanes to quadrupole symmetry. A 0.62 cm long unmodulated vane section follows the transition cell to bring the RFQ vanes to the correct length. A RELAX3D model of the exit region is shown in Fig. 2. Ray tracing through the RELAX3D calculated potentials indicates that this combination will produce a beam with an energy of 150.08 keV/u and with emittances which the 4Q optics section downstream of the RFQ can easily handle.

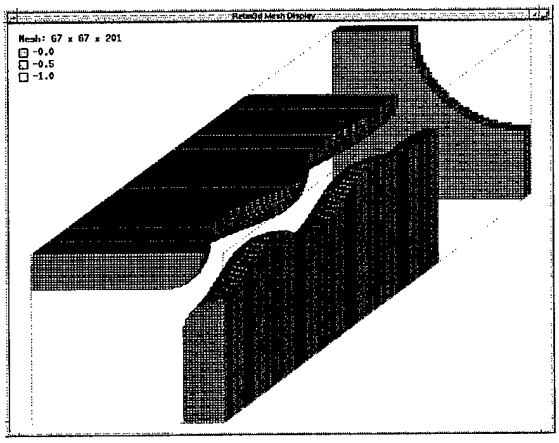


Figure 2: A RELAX3D model of the exit region showing three regular cells, a transition cell and a short unmodulated end section.

Additional RELAX3D simulations using differing lengths L_u of the unmodulated section are summarized in Figure 3, and show how changing L_u can alter the transverse Twiss parameters. Given some freedom on the final length of the vanes, the transition cell and parallel vane drift can be effectively used to tailor the transverse characteristics of the output beam.

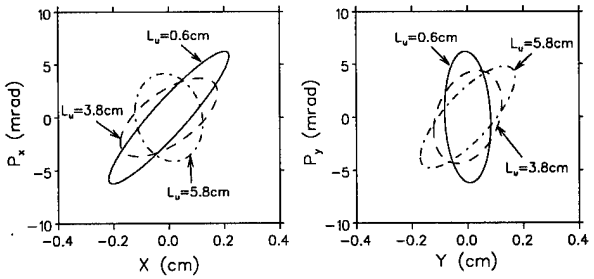


Figure 3: Output emittances for end cells composed of a transition cell and an unmodulated vane of length L_u.

5 CALCULATED RFQ PERFORMANCE

The final RFQ performance simulations are done using an initial particle ensemble with matched transverse emittances of $\epsilon = 50\pi\mu$m and the 11.66 MHz pre-bunched longitudinal distribution shown in Figure 4(a). Particles are tracked through the RMS RELAX3D entrance grid, through the RFQ's acceleration section using PARMTEQ and the the 8-term CPACK potentials, and finally through the transition cell RELAX3D exit grid. 81 % of the beam is captured into the central RFQ bucket, 3.5 % of the beam is captured into satellite buckets located between the central buckets, and 15 % of the beam is transported to the RFQ exit but not accelerated. Transversely the emittance growth is $\sim$3 %. An ellipse in longitudinal phase space of area 0.22π keV/u·nsec encloses 98 % of the particles at the RFQ exit as shown in Figure 4. The beam quality is adequate for injection into the DTL[12] which will follow the RFQ.

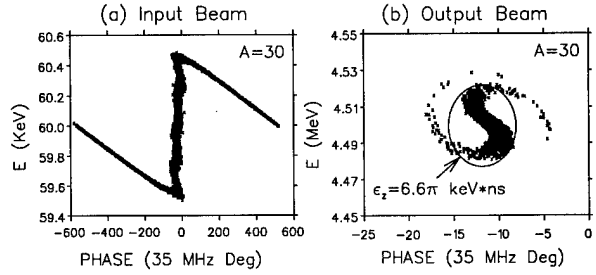


Figure 4: Input and output longitudinal emittance.

6 SENSITIVITY ANALYSIS

An essential part of a design study is to perform a sensitivity analysis of the performance (transmission and emittance) with respect to injection errors of the beam and mechanical errors of the accelerating/focusing structure. Further details and numerical values appear in Reference [2].

6.1 Beam injection errors

The PARMTEQ program was modified so that the description of a field-corrected RFQ could be read from file. Based upon tracking an ensemble of 4400 particles (with the 8-term potential) with various initial injection errors it appears there is a quadratic dependence of the transverse

emittance growth on transverse injection errors, e.g. Figure 5.

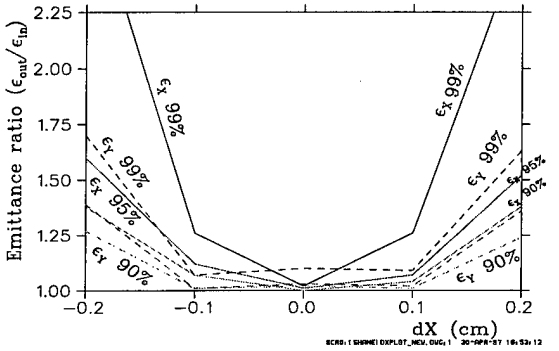


Figure 5: Emittance growth vs horizontal displacement.

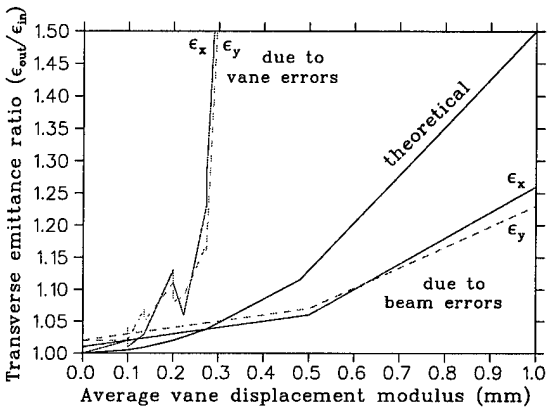


Figure 6: Comparison of simulation with a simple model.

6.2 *Vane position errors*

The vane displacement study was performed with the TRIUMF versions of RFQCOEF[10] and PARMTEQ. The RFQ m, a, l description is fed into COEF so that vane displacements can be added and new potential function coefficients calculated.[1] When vanes are moved, the 8-term potential is supplemented with dipole and sextupole components to give a 10-term potential. The dipole coefficients were calibrated against analytic[7] estimates. Let us number the vanes counter-clockwise, and suppose that the pair of vanes 2&4 both move upward an amount δ, while vanes 1&3 remain fixed. The potential function is:

$$\begin{aligned}\Phi &= (V/2)\left\{A_{01}(r^2\cos 2\theta + 2\delta\times r\sin\theta)\right. \qquad (1)\\ &+ \left. A_{10}\cos kz[I_0(kr) + k\delta\times I_1(kr)\sin\theta]\right\}\ .\end{aligned}$$

Based upon the mechanical support and connections two types of vane displacement are important: (i) where vanes 1&3 and/or 2&4 move as pairs with radial errors (likely vibrational modes); and (ii) where all vanes twist (likely thermal deformation). As a means to 'roll together' the variety of cases it was decided to plot emittance growth and transmission versus the average modulus of the vane displacement. The transverse emittance growth dependence on vane error appears to be quartic, Figure 6. The longitudinal inverse 'brilliance' [where $B_z^{-1} = \epsilon_z/(\text{survival fraction})$] has a quadratic dependence on vane error.

6.3 *Emittance growth*

Non-linear terms in the equation of motion give rise to an amplitude dependence of the betatron tune and to amplitude increase; so that emittance grows. Let dX and dX' be alignment and angle errors of the beam centroid. Let $\hat{x}$ the beam half-width and $\hat{x}'$ the maximum divergence (i.e on the envelope). If filamentation (due to tune spread) is complete but there is no change in action, the emittance growth ratio can be estimated[8][7] (assuming $\alpha \approx 0$) as follows:

$$\epsilon_{\rm new}/\epsilon_{\rm old} = 1 + 2\left[dX^2/\hat{x}^2 + (dX')^2/(\hat{x}')^2\right]\ . \qquad (2)$$

For the particular case of a constant displacement δ of a pair of vanes, we substitute $dX = \delta$, $dX' = 0$ to obtain the theoretical curve of Fig. 6. For the ISAC, the emittance is $\epsilon_{\rm old} = 0.1\pi$ mm.mrad (normalized), $\hat{x} = 2$ mm and $\hat{x}' = 0.05$ mradian.

[1] Even for zero displacements, there were small changes in the A_{01} and A_{10} coefficients, but this inaccuracy has since been corrected.

6.4 *Conclusion*

The emittance growth due to vane errors grew faster than the theoretical quadratic dependence, which implies the 'action' must be increasing. The emittance growth due to beam errors grew slower than the theoretical dependence, which implies that filamentation is not complete. Clearly, vane errors are more damaging than injection errors.

7 REFERENCES

[1] P. Schmor *et al*: *Status of the TRIUMF-ISAC Facility for Accelerating Radioactive Beams*, these proceedings.

[2] S. Koscielniak *et al*: *Beam Dynamics of the TRIUMF ISAC RFQ*, ibid.

[3] S. Koscielniak: *Correction of Field Errors in ISAC RFQ*, Proc. EPAC '96, Sitges Spain.

[4] S. Koscielniak: *Vane profiles in the radial matching section of the ISAC RFQ*, TRI-DN-96-7.

[5] L. Root: *Beam dynamics feasibility study for a pre-RFQ subharmonic buncher*, TRI-DN-96-9.

[6] R. Lee: *ISAC RFQ Radial Matching Section Beam Tracking*; TRI-DN-ISAC-13.

[7] S. Koscielniak: *Analytic formulae for the dipole coefficients of an RFQ cell with displaced vanes*, TRI-DN-ISAC-14.

[8] P.J. Bryant: *Introduction to Transfer Lines and Circular Machines*, pp.31-33, CERN 84-04.

[9] K. Crandall: Proc. Linac '94, pp.227-229.

[10] N.J. Diserens: *RFQCOEF, a package for extracting the harmonic coefficients*, Proc. Linac '84, Darmstadt, Germany.

[11] J. Staples: personal communication.

[12] R. Laxdal, *et al*: *A Separated Function Drift-Tube Linac for the ISAC Project at TRIUMF*, these proceedings.

[13] F. Jones: *A Graphical User Interface for RELAX3D*, these proceedings.

CONSTRUCTION CRITERIA AND PROTOTYPING FOR THE ISAC RFQ ACCELERATOR AT TRIUMF

R.L. Poirier, P. Bricault, G. Dutto, K. Fong, K. Jensen, R. Laxdal, A.K. Mitra, G. Stanford

TRIUMF, Vancouver B. C. Canada

Abstract

The ISAC RFQ consists of an 8 metre long 4-rod split ring structure resonating at 35 MHz. The rods are vane-shaped and are supported by 19 rings. The challenge of the mechanical design is the stringent, +/- 0.08 mm, positioning tolerance on the four rod electrodes for 150 kW cw operation. A 1.2 metre long prototype with three full-scale modules, each comprising one ring and 40 cm of electrode, has already been built and successfully tested to full power. This enables us to complete the basic electrical and mechanical design for the final unit. The initial 7-ring portion of the final RFQ will be assembled first, together with an off-line source and a portion of the LEBT, so that RF parameters and beam dynamics behavior in the injection region can be tested as soon as possible. For the final RFQ the cross-section of the vacuum tank will be square, rather than circular. This will facilitate alignment of the modules and copper plating of the vacuum tank. The scope of the paper is to report the latest results from the full power tests on the prototype and to describe mechanical and RF design features including RF coupling, alignment philosophy and the copper plating technique.

1 INTRODUCTION

The accelerating system of the ISAC radioactive ion beams facility consists of an RFQ and a post - stripper DTL [1]. Singly charged ion beams with A $\leq$ 30, delivered from the on line mass separator with an energy of 2 keV/u, will be accelerated to 150 keV/u through the RFQ and then to a maximum energy of 1.5 MeV/u through the DTL structure [2]. The low charge-to-mass ratios of the ions dictates a low operating frequency to achieve adequate transverse focusing, and cw operation is required to preserve beam intensity. The reference design [3] for the RFQ is a four rod split ring structure operating cw at 35 MHz. Full power tests on a single module [4] were completed last summer and on a three module assembly last fall. The RFQ accelerator section is 8 meters long and is designed in 40 cm long modules with 74 kV potential between the electrodes. The alignment philosophy is to construct a solid base, maintain tight manufacturing tolerances, assemble with jigs and fixtures and EDM machine the critical mounting surfaces for the electrodes after assembly.

2 PROTOTYPE MEASUREMENTS

Figure 1 is a photograph of the three modules ready to be installed in the tank. As in the one module test the electrodes were aligned only to +/- 0.250 mm but the average alignment was within the +/- 0.08 mm tolerance.

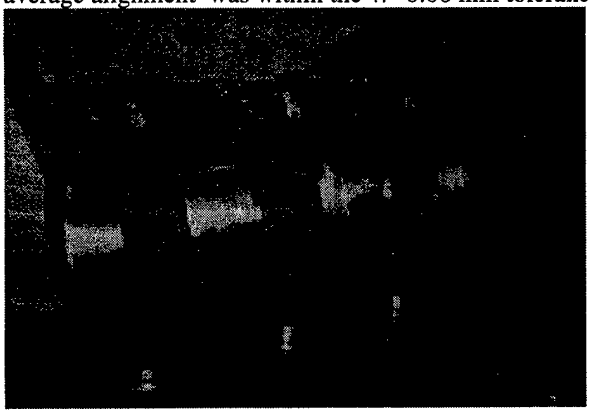


Figure 1. Photograph of the three modules ready to be installed in the tank.

Many longitudinal bead pull measurements were made between adjacent electrodes. The measurement shown in figure 2 is an average value of the field variation for the four electrodes.

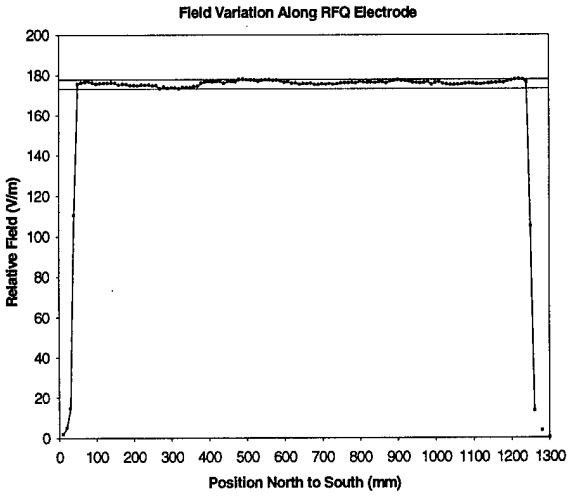


Figure 2. Field variation along the 120 cm length of the RFQ

A +/- 1.35% field variation along the 120 cm of RFQ was achieved. Considering the rough alignment, this is in close agreement with the beam dynamics specification of +/- 1.0% field variation along the 8.0 meters of the ISAC RFQ [5]. Table 1 summarizes the measured and MAFIA

0-7803-4376-X/98/$10.00 © 1998 IEEE

calculation parameters on the three modules and compares them to the single module test. In both cases, a movement of less than +/- 0.050 mm was observed when the voltage was slowly increased to 85 kV and a dynamic movement of less than +/- 0.025 mm was observed due to cooling water and vacuum pumps. At the same time the frequency of the RFQ decreased by 24 kHz from signal level to full power compared to 36 kHz for the single module test. When the voltage was instantaneously applied a movement of 0.150 mm was observed on the electrode in the direction away from the beam center and returned to its aligned position within 6 minutes compared to 0.200 mm and 3 minutes respectively for the single module tests. The close agreement of the measured frequency of 34.38 MHz compared to the Mafia value of 34.16 MHz for the 3 module tests gives us confidence for the design of the 19 module assembly for the ISAC RFQ. Because the one ring module is in a three ring tank, the difference in frequency between measured and MAFIA values is greater.

Table 1. RF Measurements on the RFQ Prototype

Parameters	One Module		Three Modules	
	Measured	MAFIA	Measured	MAFIA
Q	7200	14000	7150	14500
R/Q	62.7	69.5	26.1	24.5
kW/module	8.0	3.7	6.45	3.4
Freq. (MHz)	35.18	34.40	34.38	34.16

The operating pressure at full power for the single module tests was 9.5 x 10-7 torr. However with the increased power for the three modules the pressure increased by almost an order of magnitude to 8.5 x 10-6 torr. This proved to be too much for the coupling loop RF window which failed after 15 hours of continuous operation. The vacuum was improved by a long mild bake out and by replacing the end cover vacuum seals with Viton "O" rings. This enabled us to reach a base pressure of 5.5 x 10-8 torr and a pressure of 1.1 x 10-6 torr with RF on. As expected, a measurement with the mass spectrometer indicated the highest component to be water vapor. This factor of 20 from RF off to RF on, can be explained by the outgassing due to high operating temperature in a section of the vacuum tank that did not get properly copper plated [2]. A new copper plating technique has been designed and tested for the final RFQ tank and we expect that this will eliminate the outgassing problem. Subsequently we were able to run 100 hours continuously at 20 kW, 40 hours continuously at 30 kW and subsequent runs for 17 and 14 hours at 30 kW without failure of the coupling loop RF window. This gives confidence in designing the 150 kW RF window required for the ISAC RFQ (see figure 3).

3 RF CONTROLS

For the RFQ prototype, a simplified control system is used. The control turns on, turns off or pulses the RF. The cavity voltage can be feedback regulated in the pulsed or cw mode. Adaptive feedback control can be turned on in pulsing mode to reduce the turning on transient. All these are achieved using a stand alone digital signal processor. For the 8 meter long RFQ, the control system will be housed in a VXI mainframe. The VXI slot-0 controller will provide supervisory and communication tasks for the controller.

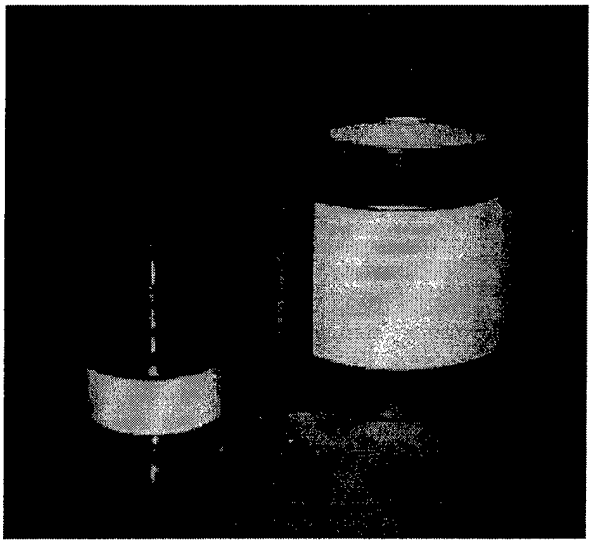


Figure 3. Photograph of the RF windows for the prototype and ISAC RFQ

4 RFQ VACUUM TANK

Unlike the prototype, the vacuum tank for the ISAC RFQ, shown in figure 4, is square in cross-section. Note that the tank is split diagonally by an "O" ring flange into two triangular parts, tank base and tank lid. The copper plating is easier to do in two parts. Also we maintain full unobstructed side access to the RFQ modules for ease of installation and alignment. The tank weighs approximately 12 tons and is constructed of plate steel which will be chemically treated (descaled) and surface ground before fabrication. The tank base forms a stable internal horizontal platform on which to mount the RFQ components. It is a 1.58 cm (5/8") thick steel plate mounted on two heavy "I" beams running the full length of the tank with attached footpads. The vertical back plate is 3.8 cm (1.5") thick and will have most of the penetrations for vacuum pumps, vacuum gauges, RF coupling loop and RF diagnostics. The triangular shaped lid is 1.25 cm (1/2 ") thick reinforced by tubular section ribs and weighs approximately 5 tons. The copper plating is a cyanide bath process which uses a different chemical solution than that used to copper plate the prototype tank.

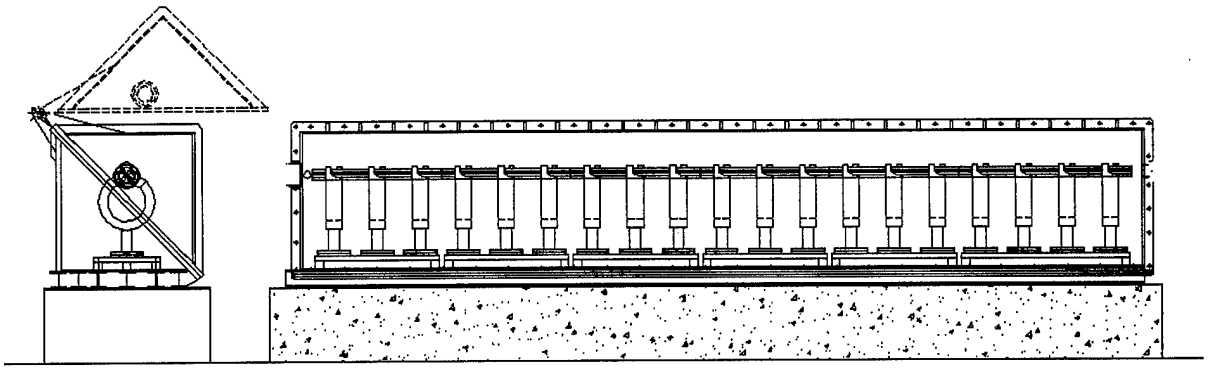


Figure 4. RFQ vacuum tank installed on its concrete pad with lid removed and RFQ modules installed

Each piece is plated separately to avoid the possibility of a section of the tank not being uniformly copper plated due to air trapped in the solution. Several sample coupons have been successfully copper plated, giving a much better copper plating finish than the prototype tank.

5 RFQ ALIGNMENT

Maintaining the tight alignment tolerance of +/- 0.08mm over the 8 meter length of the four electrode, 2 arm structure requires special manufacturing and assembly techniques and procedures.

The pedestal type structure with cantilevered electrode mounting has inherent stability considerations including static deflections, thermal distortions, mechanical vibrations and manufacturing tolerances. Static deflections are primarily a factor in the electrode itself. We expect to see the electrode displaced in the order of 10 to 15 microns between supports. Thermal effects are minimized by extensive cooling within the assembly and separating the heat affected areas from the structural supports. The vibration effects are largely indeterminate, however displacement amplitude has been minimized by increasing structural stiffness. Empirical data from the prototypes indicate vibration effects are not a significant factor.

Manufacturing and assembly tolerances could easily consume all of the alignment error budget. Tight controls must be maintained to meet our target. As the critical item is the position of the electrodes, accuracy starts there. Manufacturing technology limits us to 25 microns on the electrode straightness. This, combined with simple deflection constitutes up to half of our alignment error budget. Thus we must achieve a near perfect electrode mounting surface on each of the 38 electrode mounts. They must all be nearly identical and in the ideal position within a few microns. To achieve a near ideal individual ring assembly we must eliminate the accumulation of tolerances which can produce a substantial assembly error. This is accomplished by assembling the ring structure in a precision fixture from a series of moderate accuracy components. The fixture serves to position the components within an envelope of acceptability to ensure that the assembly falls within the range of the finishing operation. Once everything is assembled, a final high precision operation machines the electrode mounting faces relative to the ring base plate within an accuracy envelope of 5 microns. The individual ring assemblies are then positioned on a platen surface of equal accuracy, thus establishing a uniform beam centerline. The orientation and positioning of the ring bases are established through precision machining of reference datum on the base and platen. During installation in the tank a laser will define the centre line. Digital targets mounted on the rings will provide positional feedback capable of a couple of micron accuracy. This feedback will allow the platen assembly of three or four rings to be oriented precisely to the beam.

6 ACKNOWLEDGMENT

The authors wish to thank R. Roper, B. Waraich, P Harmer, J. Tanguay and Q. Walker for the mechanical design, fabrication and assembly work, B. Uzat and J. Lu for the amplifier work, and P. Bourquin and W. Pirkl from CERN for helpful discussions on the fabrication, assembly and alignment of the RFQ.

REFERENCES

[1] P. Schmor et al, "Status of the TRIUMF ISAC-Facility for Accelerating Radioactive Beams", These proceedings

[2] R. Laxdal et al, "A Separated Function Drift Tube Linac for the ISAC Project at TRIUMF", These proceedings

[3] P.G. Bricault and H. R. Schneider, "Simulation of the TRIUMF Split Ring 4-Rod RFQ with MAFIA", Proc. 1995 Particle Accelerator Conf. and Int. Conf. on High-Energy Accelerators, p1125 (1995)

[4] R.L. Poirier, P.J. Bricault, K. Jensen and A.K. Mitra, "The RFQ Prototype for the Radioactive Ion Beams Facility at TRIUMF", Proc. XVIII LINAC Conference, CERN, p405 (1996)

[5] S. Koscielniak, TRIUMF, Private communication.

A HIGH-POWER RADIOFREQUENCY FOCUSING CONTINUOUS WAVE ELECTRON LINAC

N.P. Sobenin[a], D.V. Kostin[a], V.I. Shvedunov[b], and W.P. Trower
World Physics Technologies, Blacksburg VA 24060 USA

Abstract

To simplify construction and reduce beam current losses, we introduce **R**adio **F**requency focusing in a high-power **C**ontinuous **W**ave **E**lectron **LIN**ear **AC**celerator by employing **R**ectangular **C**avity **B**iperiodical **S**tructures that have quadrupole-like focusing properties.

1 INTRODUCTION

The next generation compact high-power industrial electron accelerators will be high efficiency CWELs whose multi-megawatt average power beams will have energies up to 10 *MeV*. These CWEL accelerating structures must possess contradictory properties of high inter-cell coupling required for high beam and heat loading and also high shunt impedance. Strong RF focusing is also desirable since it would simplify the accelerator design and increase the accelerated current.

We use a horizontally focusing RCBS in our compact 70 *MeV* pulsed **R**ace-**T**rack **M**icrotron [1] to simplify the design. RCBSs have been realized with circular beam holes [2] as well as with rectangular beam slots [3]. By changing the aperture geometry, elongating it horizontally or vertically, and varying the cavity dimensions, we can change the focusing sign and strength from 0 to ~1,000/m^2.

It is known experimentally that increasing a biperiodic structure inter-cell coupling decreases its shunt impedance since the surface current distribution in both the coupling and accelerating cells are changed. Using extensive three-dimensional computer simulations coupling slot and cell geometries have been optimized to achieve large coupling with little decrease in the shunt impedance [4]. Our optimized RTM RCBS with no coupling slots [5] has a ~5% coupling which we achieved with only ~6% shunt impedance decrease. Here we present a RF focusing RCBS with optimized focusing, coupling, and shunt impedance for a high power CWEL.

2 RF FOCUSING OPTIMIZATION

In Fig. 1 we show the normalized horizontal (x) and vertical (y) focusing gradients, G_x and G_y, respectively, and effective shunt impedance for a RCBS with rectangular beam slots but with no coupling slots.

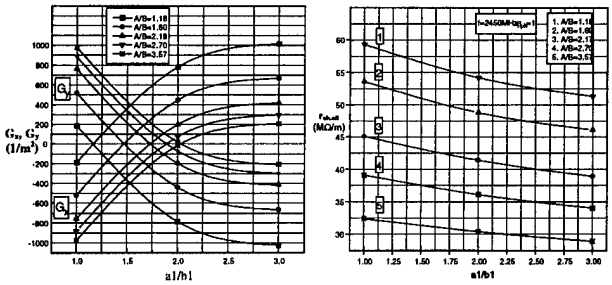


Fig. 1. Focusing gradient and shunt impedance with a_1/b_1.

The **E**lectro**D**ynamics **C**haracteristics depend on the ratios a_1/b_1 and A/B defined in Fig. 2. For a $\pi/2$ mode phase velocity equal to the speed of light ($\beta = 1$) at 2,450 *MHz*, we obtained $-G_x$ and $+G_y$ up to ~1,000/*m*^{2} with a large A/B and a square or circular ($a_1/b_1 = 1$) beam hole by vertically elongating the structure. With a A/B $\approx$ 1 and large a_1/b_1 the focusing gradients were the same but with opposite sign.

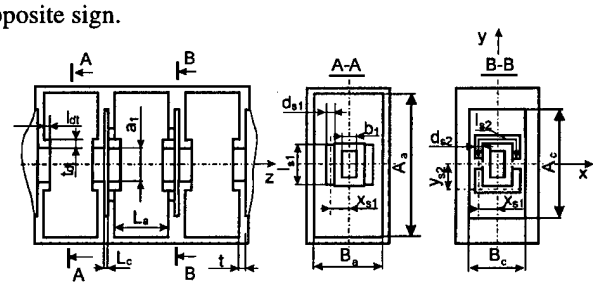


Fig. 2. RCBS with rectangular beam and coupling slots.

3 COUPLING AND SHUNT IMPEDANCE OPTIMIZATION

In biperiodic structures the coupling aperture dimensions and location modify differently accelerating and coupling cell eigenfrequencies [6]. Since the cell frequency detuning is inversely proportional to the cell volume and the accelerating cell is much larger than the coupling cell, a tuned structure with a high coupling requires a very small (A_c,B_c) coupling cell surface as seen in Fig. 2.

Fig. 3 shows the strong magnetic field in the coupling cells of the tuned structure that provides the inter-cell coupling. For small coupling cells and coupling slots close to axis, the surface current integral induced by this field in the coupling cells is small. Thus RF losses and shunt impedance change little from a structure without coupling slots.

Permanent addresses: [a]Electrical Engineering Department, Moscow Engineering Physics Institute, Moscow, Russia and [b]Institute of Nuclear Physics, Moscow State University, Moscow, Russia.

0-7803-4376-X/98/$10.00 © 1998 IEEE

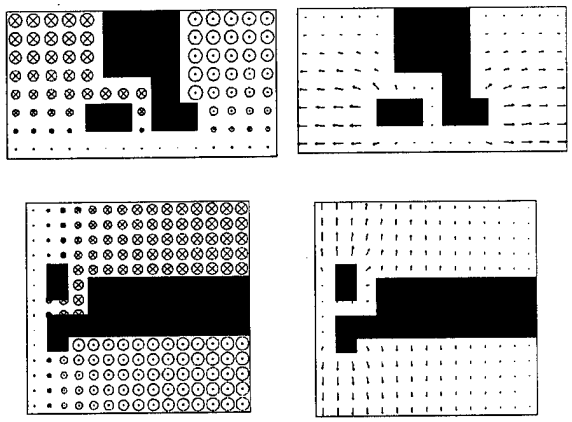
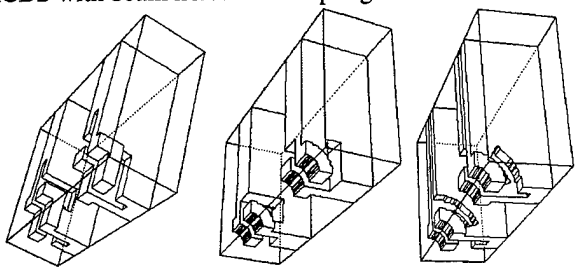


Fig. 3. Magnetic and electrical fields at xOz-yOz for a RCBS with beam holes and coupling slots.



(a) (b) (c)

Fig. 4. Three RCBS structures.

Table I. Structure dimensions in mm.

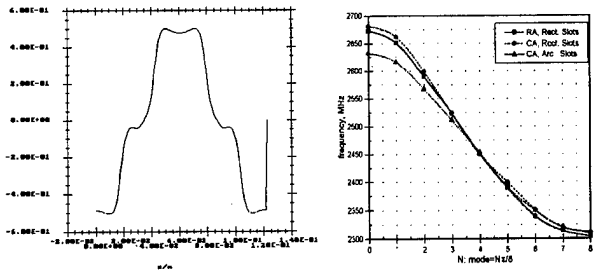
	(a)	(b)	(c)
A_a	130.00	130.00	130.00
A_c	68.00	36.00	130.00
B_a	63.84	65.40	64.96
B_c	44.00	36.00	50.70
$2r_1$	---	12.00	12.00
a_1	24.00	---	---
b_1	12.00	---	---
$D=\lambda_w/2$	61.20	61.20	61.20
L_a	44.00	44.00	44.00
L_c	4.60	4.60	4.60
T	6.30	6.30	6.30
l_{dr}	4.00	4.00	4.00
t_{dr}	6.00	6.00	6.00
x_{s1}	15.00	15.00	16.00
l_{s1}	36.00	35.00	32.00
d_{s1}	6.00	6.00	8.00
y_{s2}	21.00	15.00	16.00
l_{s2}	48.00	49.00	40.00
d_{s2}	6.00	6.00	8.00

We investigated three highly coupled RCBS variants. The first, which is appropriate for our RTM and is seen in Fig. 4(a), has rectangular beam and coupling slots. The second, seen in Fig 4(b), has circular beam holes and is coupled by rectangular slots. In the third, shown in Fig. 4(c), there are circular beam holes and the coupling is by circular holes. RCBSs with circular beam holes hold an advantage for CWELs because they have larger shunt impedance for the same focusing gradient as $a_1/b_1 = 1$ rectangular slotted structure. RCBS (b) has smaller coupling cells than (c) and has larger coupling with approximately the same EDC. Table I list the dimensions and Table II gives the EDC for these three structures.

Table II. Structure electrodynamics characteristics.

	(a)	(b)	(c)
k_c (%)	15.1	15.2	13.2
$r_{sh,eff}$ (MΩ/m)	40.4	48.9	48.8
G_x (m^{-2})	+275	−680	−650
G_y (m^{-2})	−275	+680	+650
Q	12,400	13,400	13,000

The axial longitudinal electrical field for structure (b) is seen in Fig. 5(a) and was obtained for a tuned structure consisting of two coupling cells, an accelerating cell, and two half accelerating cells and terminated with electric walls. Fig. 5(b) shows the structure dispersion.



(a) (b)

Fig. 5. (a) On-axsis E_z and (b) dispersion characteristics.

4 HIGH-POWER CWEL BEAM DYNAMICS

For pulsed electron LINACs beam focusing is most important after the injector, before the electrons become relativistic. However, focusing is critical in a high-power CWEL which in some respects is intermediate between a proton and a pulsed electron LINAC. Heat dissipation and efficiency limit the CWEL energy gain to only 1-4 *MeV/m*, so to achieve 10 *MeV*, several *MW* 'industrial strength' electron beams requires focusing to overwhelm the strong repulsive space charge forces. Thus, RCBSs that both accelerate and focus beams are desirable.

We explore these RCBS possibilities for a CWEL with a 2 *MeV/m* energy gain producing 10 *MeV*, several hundred *mA* beams. The initial relativistic 2 *MeV* beam is accelerated in a short β_{ph}= 1 section with a ~10° electron bunch prepared by a chopper, pre-buncher, and capture section. At 2 *MeV/m*, depending on the shunt impedance, between ~80 and 150 *kW/m* of RF power must be dissipated and 1 *MW/m* of RF power is required to accelerate a ~500 *mA* beam. For a several hundred kW CW S-band RF source, this accelerating structure will consist of short sections of several accelerating cells each whose number we vary to achieve the desired focusing.

The i^{th} accelerating cell focal length, f_i, is related to the

normalized focusing gradients by

$$1/f_i = -\frac{\lambda^2 \sin\varphi_0}{8\pi p_i} G_{x,y}(0,0)_n E_{z1}(0,0), \quad (1)$$

where λ is the RF wavelength, φ_0 is the accelerating phase, $E_{z1}(0,0)$ is the first harmonic amplitude, and p_i is the longitudinal momentum. Since the distance between accelerating cells is much less than the individual cell focal length, an N cell structure focal length is

$$\frac{1}{F_\Sigma} \approx \sum_{i=1}^{Ncell} \frac{1}{f_i} = \frac{p_1}{f_1} \sum_{i=1}^{Ncell} \frac{1}{p_i} = \frac{p_1 N_{cell}}{f_1 \bar{p}}, \quad (2)$$
$$\frac{1}{\bar{p}} = \frac{1}{N_{cell}} \sum_{i=1}^{Ncell} \frac{1}{p_i}$$

For horizontal/vertical cell dimensions, A/B, of ~2, a RCBS with circular beam holes, has a ~680/m^2 focusing gradient, a 2 *MeV/m* energy gain, a ~4 *MeV/m* first harmonic amplitude, and, from eqn.(1), a ~1.5 *m* single cell focal length at 2 *MeV*. From eqn.(2), a six cell section focal length is ~0.3 *m*.

In our RCBS zero phase particles get the maximum energy gain and, in contrast to our RTM, negative phases give stable longitudinal dynamics. For a ~–30° accelerating phase, the focal length for a 2 *MeV* beam is doubled to ~0.6 *m* and increases with beam momentum until at 10 *MeV* it is ~2.5 *m*. This focal length increase can be partially compensated for, if necessary, by shifting the accelerating field phase. On the other hand transverse space charge forces decrease as the square of the energy, so a focal length increase is not very important.

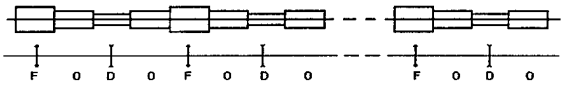


Fig. 6. High-power CWEL with RF focusing.

To focus the beam in both transverse planes, we rotate each RF quadrupole-like singlet section sequentially through 90° and separated them by axially symmetric accelerating structure drift spaces seen in Fig. 6.

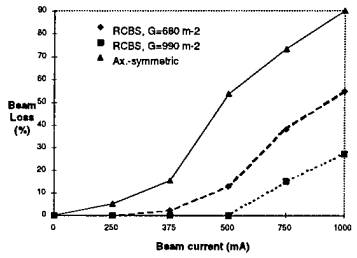


Fig. 7. CWEL beam loss with and without RF focusing.

Fig. 7 shows the beam current losses with the injected beam current calculated for an axially-symmetric LINAC and our RCBS LINAC with focusing gradients of 680 and 990/m^2 using A/B ~4. These calculations take into account space charge forces [7].

5 CONCLUSIONS

We have shown that a high focusing RCBS LINAC can accelerate a 500 *mA* beam from 2 to 10 *MeV* with no beam losses while a traditional axially symmetric LINAC begins to loose beam at ~100 *mA*. Although much remains to be done before achieving a final high power RF focusing CWEL design, we are encouraged.

6 ACKNOWLEDGEMENTS

This work is supported in part by NSF DMI-9560721. We have benefited greatly from our many vigorous discussions with Ed Knapp.

REFERENCES

[1] V.N. Melekhin, A.I. Karev, V.I. Shvedunov, N.P. Sobenin, and W.P. Trower, in *Proc. 5th European Particle Accelerator Conf.*, Ch. Petit-Jean-Genaz ed. (World Scientific, Singapore, 1996) vol.2, p.1380; V.I. Shvedunov, A.I. Karev, V.N. Melekhin, N.P. Sobenin, and W.P. Trower, in *Proc. 1995 Particle Accelerator Conf.*, L. Gennari, ed. (IEEE, Piscataway, 1995) vol.2, p.807; and W.P. Trower, A.I. Karev, V.N. Melekhin, V.I. Shvedunov, and N.P. Sobenin, *Nucl. Instrum. Meth.* B99 (1995) 736.

[2] N.P. Sobenin, V.N. Kandrunin, A.I. Karev, V.N. Melekhin, V.I. Shvedunov, and W.P. Trower, in *Proc. 1995 Particle Accelerator Conf.*, L. Gennari ed. (IEEE, Piscataway, 1996) v.1, p.1827.

[3] D.V. Kostin, V.N. Melekhin, V.I. Shvedunov, N.P. Sobenin, and W.P. Trower, in *Applications of Accelerators in Research and Industry, J.* Duggan, ed. (Am. Inst. Phys., Washington D.C., 1997) v. CP392, p. 1135.

[4] L.V. Kravchuk and V.V. Paramonov, in *Proc. 18th Intl. Linac Conf. (LINAC-96)* 1996, v.1, p.490.

[5] R. Klatt, F. Krawczyk, W.R. Novender, C. Palm, and T. Weiland. in *Proc. 1986 Linear Accelerator Conf.*, SLAC-303 p.276 (1986). A version the MAFIA code was obtained by V.S. from T.W in 1989.

[6] N.P. Sobenin and B.V. Zverev, *Electrodynamic Characteristics of Accelerating Cavities* (Energoatomizdat, Moscow, 1993) 220 pp. (in Russian).

[7] V.G. Gevorkyan, A.B. Savitsky, M.A. Sotnikov, and V.I. Shvedunov, *Computer Codes for Simulation of Beam Dynamics in Recirculating Accelerators*, VINITI deposit number 183-b89 (1989) in Russian -- RTMTRACE code.

THE BEAM LOADING EFFECT IN THE MULTICAVITY LINEAR ACCELERATOR AND THE REQUIREMENTS FOR THE RF CONTROL SYSTEM

Yu. Senichev*, Aarhus University, Aarhus, Denmark

Abstract

This work has been done in the frame of ESS collaboration. The high intensity proton beam with 60 mA average current is supposed to be accelerated in the ESS linac up to 1.3 GeV. The ratio between the beam power and the losses power is changed along the accelerator from 0.6 to 0.7. With such a strong beam loading effect, the amplitude and phase RF field instabilities cause the growth of the effective longitudinal emittance at the exit of the multicavity linear accelerator. It gives rise to the difficulties with the injection of the beam in the ring. We define the requirements to the RF control system, taking this effect into account.

1 INTRODUCTION

At present the neutron source projects are developed in Europe, USA and Japan. Its are based on $1.0 \div 1.5$ GeV linac and the compressor ring or the high cycling synchrotron with the full maximum beam power of 5 MW[1]. The dominating design principle for the accelerators is the minimisation of beam losses. The maintenance and repair require that high energy beam losses are kept below 1 nA/m. In addition, the linac has to be optimised for low loss injection into the ring. Due to these problems the longitudinal and transverse emittance growth has to be comprehensively explored. The author of this work studies such a phenomena as the effective longitudinal emittance blow up. Owing to the random-regular character of the time-space deviation of the accelerating field, each single bunch undergoes the different exposure. With increasing of an energy the length and the relative momentum spread of the single bunch is adiabatically damped, but in the same time the effective sizes grow up with a number of the cavity. The distortion of the electromagnetic field has a lot of sources. We are interested the RF power or the beam switch off and on and the instability of the power supply or the beam current. Taking into account the feedback system, the reaction of the cavity on any random perturbation is described by the regular function, which has the time scale of change determined by the cavity inertia and the feedback delay. In other words two neighbour bunches have to have very similar parameters and the energy-phase deviation along the bunch train depends on the feedback and the cavity parameters. The fundamental mode change is recognised by the beam as the time distortion of the average field and it can be stabilised by the feedback system. The excitation of the modes with the variation along the cavity results in the space distortion. It is not under the control of feedback system and can be minimised by the relevant choice of the cavity parameters. The author has paid attention to this effect in the high intensity linear accelerator, working under ESS project[3].

* on leave from Institute for Nuclear Research, Moscow.

2 ERRORS COMPENSATED BY FEEDBACK

To stabilise the average field in the cavity the feedback system is used. The standard feedback system includes the object with the transition function $W_c = \frac{K_c e^{-p\tau_c}}{pT_c+1}$ and the feedback system itself with the transition function $W_f = \frac{K_f e^{-p\tau_f}}{pT_c+1}$, where K_c, K_f are the gain coefficients, τ_c, τ_f are the time delays and T_c, T_f are the inertia in the direct and feedback circuit respectively. The transition function of the cavity applied by the feedback is $W(p) = \frac{W_c(p)}{1+W_f(p)W_c(p)}$ and the original function of the closed loop is:

$$X(t) = \frac{X_0}{1+K_t}\left[1 - \frac{\omega_1}{\omega_0}e^{-\delta t}\sin(\omega_0 t + \theta)\right], \qquad (1)$$

where

$$\delta = \frac{T_f + T_c - K_t\tau}{2T_cT_f + K_t\tau^2}, \omega_1^2 = \frac{K_t+1}{T_fT_c + 0.5K_t\tau^2},$$
$$\omega_0^2 = \omega_1^2 - \delta^2, K_t = K_fK_c, \tau = \tau_f + \tau_c, \tan\theta = \frac{\omega_0}{\delta},$$

where X_0 is the initial stepwise perturbation. The parameter δ determines the stability of the system. The maximum coefficient for the stable regime is $K_t \leq \frac{T_f+T_c}{\tau}$. Actually it has to be less, since the control time in response to the perturbation grows with K_t. In the same time the residual error equals to $\frac{X_0}{1+K_t}$. To realise the required gain coefficient the generator has to have the power reserve . The extra power depends on the ratio between the perturbation and the required residual error. For ESS this value equals to 30% of the nominal power to stabilise the amplitude and phase of $\pm 1\%$ and $\pm 1^0$ respectively. Thus the efficiency of the control system is determined in the first approximation by the ratio of the cavity feeling time and the time delay in the closed loop of the feedback system. There are lot of methods how to compensate the delay τ_f in the feedback system itself. One of them is the time leader unit applying the generator, which has to have the transition function similar to the direct circuit transition function. However no method compensates the natural delay of the signal in the cavity and the ultimate coefficient is restricted by the value $K_t \approx \frac{T_c}{\tau_c}$. The natural delay is equal to the one run time of the power along the cavity.

0-7803-4376-X/98 /$10.00 © 1998 IEEE

3 ERRORS UNCOMPENSATED BY FEEDBACK SYSTEM

The nature of these uncompensated errors lies in the difference between the irradiation of the generator and the beam. This is based on the different nature of the sources. In the first case the source is at rest:

$$j^g(z,t) = j_m\delta(z-z_0)e^{-i\omega t} \tag{2}$$

in the second one the source moves with the velocity v:

$$j^b(z,t) = j_m\delta(z-vt)e^{-i\omega t} \tag{3}$$

The electromagnetic field (electrical component) is represented as the sum of incident E_s and reflected E_{-s} waves:

$$E = \sum(C_sE_s + C_{-s}E{-s}) + \frac{4\pi}{i\omega\epsilon}j_z^b, \tag{4}$$

where

$$C_s(z,k) = \frac{1}{N_s(k)}\int_{z_1,z} j_kE_{-s}dv,$$

$$C_{-s}(z,k) = \frac{1}{N_{-s}(k)}\int_{z_2,z} j_kE_sdv$$

Substituting the expression for current in these integrals, we can find out:

- The generator current excites **all modes** of the cavity.
- The beam current excites that modes only, which have the phase velocity less than the beam velocity, what accords to **Cherenkov irradiation**.
- The generator irradiates in **both directions** from the power extraction point and the front of wave goes with the group velocity.
- The beam irradiates **back only**, but it fills the cavity with the phase velocity, that is practically instantaneously. So we should consider the beam as the distributed source along cavity.

In the waveguide approximation after "n" reflections we can write the expression for the total field irradiated by the generator located at one of the end of cavity. It is the stepwise function:

$$E = E_me^{i\phi}e^{-\alpha z}$$
$$\left[1 + ... + (1 + e^{-2\alpha z}\dot{G}_1\dot{G}_2)e^{-2\alpha z}\dot{G}_1\dot{G}_2\right], \tag{5}$$

or for the steady value:

$$E = E_me^{i\phi}e^{-\alpha z}\frac{1-e^{-2\alpha Ln}}{1-e^{-2\alpha L}} \tag{6}$$

where $E_me^{i\phi}$ is the travelling wave field, α is the attenuation constant determined by $\alpha L = \frac{\tau_{gr}}{\tau}$. The one run time of the power along the cavity is $\tau_{gr} = \frac{L}{v_{gr}}$, where v_{gr} is the group velocity. The group velocity depends on the phase velocity v_{ph} and the coupling coefficient K_{coupl} of the accelerating structure and equals $v_{gr} = \frac{\pi}{4}K_{coupl}v_{ph}$. The filling time is determined by the quality factor Q and the resonant frequency ω. From (6) the ratio between the steady value of E and the travelling wave amplitude E_m is $\tau/2\tau_{gr}$, or using $E = (P_{generator}R_{sh})^{1/2}$,we have

$$E_m = \frac{2\tau_{gr}}{\tau}(P_{generator}R_{sh})^{1/2}. \tag{7}$$

Without beam all power is spent for the losses compensation $P_{generator} = P_{losses}$. To compensate the beam loading (fundamental mode) we have to extract the additional power from the generator $P_{generator} = P_{beam}/\cos\varphi_s$. Thus, the initial step amplitude for the stepwise function (5) is:

$$\frac{E_m}{E} = \frac{2\tau_{gr}}{\tau}\left[(\frac{P_{beam}}{P_{losses}\cos\varphi_s} + 1)^{1/2} - 1\right]. \tag{8}$$

In particular for ESS, where $P_{beam}/P_{losses} \approx 70\%$ the value $E_m/E \approx 7\%$. To minimise this perturbation the beam has to be injected with the finite front of the pulse current. However even in the steady regime any perturbation of few percents causes the extra power injection with the sharp front due to the high gain coefficient of the feedback system. In that case to estimate the perturbation we should use the extra power P_{extra} instead P_{beam} in the formula (8) and we get $E_m/E \approx 3\%$. Thus during the pulse current acceleration such a perturbation will "walk" along the cavity. The beam sees its as the accelerating field modulation. The characteristic time of this perturbation is determined by the frequency beat between the fundamental and the nearest modes. For ESS it is about $1 \div 2$MHz. To decrease these distortions we have to do one of the following:

- to use shorter cavity
- to use the accelerating structure with the higher coupling coefficient
- to use the structure with the higher quality factor

From this point of view it would be interesting to compare the normal cavity with the high coupling coefficient and the super conductive cavity. However, we should understand how these distortions influence the beam parameters.

4 THE EFFECTIVE PARAMETERS OF THE BEAM

We are interested in the motion in the perturbed electromagnetic field:

$$E = E_0 + \delta E(z,t) = E_0(1 + \frac{\delta E_m}{E_0}\sum_k e_k\cos k\nu t), \tag{9}$$

where $\nu = \frac{2\pi}{T_c}$ is the minimum frequency of perturbation with the period of the length cavity T_c. This kind of perturbation gives arise the parametric or external resonance in

the longitudinal plane. To avoid these resonances the parameters of the cavity have to be in compliance with the condition[2]:

$$T_c \leq \frac{4\pi k}{\Omega_0 \cos^{1/2}\varphi_s}, \delta E e_k \leq \frac{2\Omega_0 \sin\varphi_s}{\cos^{1/2}\varphi_s}, \qquad (10)$$

where Ω_0 is the synchronous frequency when the synchronous phase $\varphi_s = -90^0$. Obviously this condition restricts us in the cavity length or the accelerating field amplitude. Let us suppose we have designed the accelerator, which avoids the resonance condition. In this case any perturbation can be considered as a high frequency kick. It causes the phase deviation of the bunch from the separatrix centre after passing through n cavities:

$$\langle\Delta\psi\rangle_{centre} = \left(\langle\delta\varphi\rangle^2 + \langle\cot\varphi_s \frac{\delta E}{E}\rangle^2\right)^{1/2} n^{1/2}\mathcal{K}(k) \qquad (11)$$

and the energy deviation

$$\langle\Delta W\rangle_{centre} = \gamma^2 p_s v_s \frac{\Omega}{\omega}\langle\Delta\psi\rangle_{centre}, \qquad (12)$$

where $\mathcal{K}(k)$ is the harmonic number function. In the first approximation $\mathcal{K}(k) = \frac{\pi k/\mu}{(\pi k/\mu)^2 - 1}$, where μ is the advanced phase per the cavity. Thus, the energy spread of the bunch centres grows, as

$$\langle\Delta W\rangle_{centre} \propto n^{1/2}\gamma^{3/2}\beta^{3/2}\mathcal{K}(k), \qquad (13)$$

and the energy spread of single bunch:

$$\langle\Delta W\rangle_{bunch} \propto \gamma^{3/4}\beta^{3/4}, \qquad (14)$$

These expressions show the effective momentum spread is significantly determined by the spread of the centres. This effect has been calculated numerically for ESS side coupled linac in the work[4].

5 THE REGULAR COOLING OF BEAM

So, the effective longitudinal emittance is determined by the time-space distortions in the cavity. The lowest characteristic frequency of this process is most sensitive for the beam and inversely proportional to the inertia of units included in the closed loop. In particular for ESS this frequency is 150 kHz. Let us consider such a control system, when the phase perturbation of the accelerating field is compensated by the amplitude or contrary. Ideally it would be, when $\delta\varphi = \cot\varphi_s \delta E/E$. The energy deviation δW in that case equals zero. But the question is how to realise such a simple idea? The answer is the time of flight procedure. This procedure supposes the measurement of the flight phase and the correction of it either by the RF phase or by the RF amplitude until the coincidence with the designed value with accuracy Φ :

$$\left|\omega\int_0^{L_{cavity}}\frac{dz}{c\beta} - \omega\int_0^{L_{cavity}}\frac{dz}{c\beta_s}\right| \leq \Phi \qquad (15)$$

In that case the bunch energy deviation after passing through the cavity will be:

$$\Delta W \leq \left|\gamma_2 p_s v_s \frac{\Omega\Phi}{\omega\sin\mu} + \Delta\psi\tan\frac{\mu}{2}\right|. \qquad (16)$$

Schematically this procedure is shown for the relative velocity on figure 1. Thus, we do not have the factor $n^{1/2}$ and the velocity (energy) deviation is determined by the current cavity.

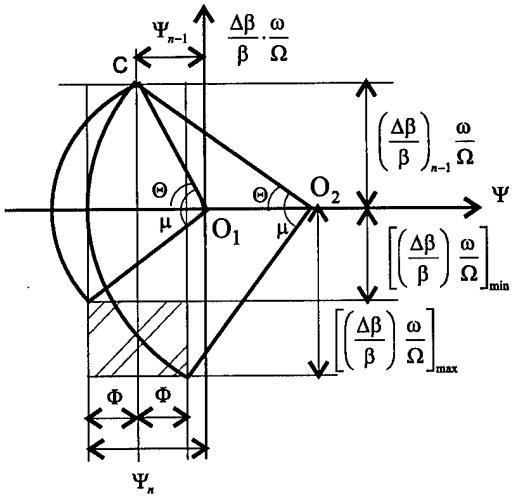


Figure 1: The phase diagram for the flight time procedure.

6 CONCLUSION

This material allows us to compare the normal and the super conductive accelerators and how each option influences the beam quality. On the one hand due to small ratio τ_{gr}/τ the superconductive cavity has no spatial distortion of the electromagnetic field and we do not have the errors uncompensated by feedback system. On other hand the higher accelerating field amplitude, the stronger influence of the residual errors to the spread of the bunch centres. From this point of view the most appropriate variant is the normal structure with the high coefficient of the coupling $\sim 50\%$.

7 ACKNOWLEDGEMENTS

The author is very grateful to Professors H. Lenger, H. Klein and Drs. K. Bongardt, M. Pabst for great interest in this work and for helpful discussions at ESS meetings.

8 REFERENCES

[1] H. Lengeler, "Proposals for Spallation Sources in Europe", Fourth European Particle Accelerator Conference, London, 1994.

[2] Yu. Senichev, "Transient effect in a high-intensity proton linear accelerator", Particle Accelerator, 1995, v.50, pp.237-259

[3] Yu. Senichev, "Beam loading affect in ESS linac", Third General ESS Meeting, ESS 95-24-M report May 1995

[4] K. Bongardt, M. Pabst, "Beam dynamics in the 1.3 GeV high intensity ESS coupled cavity linac", Proc. EPAC, Sitges, Spain, 1996

A SUPERCONDUCTING LINAC FOR THE ENERGY AMPLIFIER

Alessandro G. Ruggiero
AGS Department. Brookhaven National Laboratory. Upton, NY 11973.

*Abstract**

Because of the safer and more reliable mode of operation, a Superconducting Linac has been proposed as the proton beam accelerator which drives a nuclear plant based on the concept of the Energy Amplifier. An example based on the net generation of 400 MW (electric) is described. This requires a proton beam energy of 1 GeV with a continuous beam current of 10 mA, corresponding to a beam power of 10 MW. Two frequencies cases, 360 and 805 MHz, have been considered for the Linac design. Performance and cost comparison for the two cases are given.

1 THE CONCEPT OF THE ENERGY AMPLIFIER

It was proposed by Bowman [1] and Rubbia [2] that it is possible to sustain a nuclear fission chain reaction under subcritical conditions by providing the required balance of neutrons with a steady flow of neutrons from the spallation of an intense beam of protons on a solid target. This is a granular mixture of inertial material, like Tungsten or Lead, and fissionable material, for instance Th^{232}. This method has the advantage of a safer operation since the chain reaction, if needed, can be easily controlled by acting on the proton accelerator.

An example of Energy Amplifier based on these concepts was also given [3]. The power plant assumed as the driver a continuous proton beam of 1 GeV with an average intensity of 10 mA, that is an average power of 10 MW. With realistic assumptions, it was demonstrated that the device could be capable to deliver 400 MW on an external load, with an extra 25 MW for the operation of the proton accelerator and another 5 MW for the facility surrounding the complex.

The original concept of the Energy Amplifier assumed one or two cyclotrons as the proton accelerator [4]. But there are several serious technical concerns with the operation of cyclotrons at very large beam power, which deal with space charge effects at injection, components activation due to slow beam losses caused by the narrow gap of the accelerator magnet, and the complexity of the beam extraction. Thus, as an alternative it was proposed [3] to use a Superconducting Linac (SCL) as the proton accelerator. The Linac would remove several of the technical concerns of the cyclotrons. For instance, at the intensity level of 10 mA, space charge effects are small, understood and easily controlled. The ratio of the physical aperture to the beam size is also very large, which essentially eliminates the problem of activating the Linac itself by the slow beam losses. The RF architecture and the operation is simple. Lastly, very important, a large electric to beam energy conversion efficiency is expected, close indeed to the 40% level used in the cited example.

*Work performed under the auspices of the U.S. Department of Energy.

2 THE SUPERCONDUCTING LINAC

The Linac is made of three sections: the Front-End, the Normal Conducting Linac, and the Superconducting Linac proper. The Front-End is made of a 12-mA positive-ion source followed by an RFQ. The Normal Conducting Linac accelerates the 10-mA proton beam to 100 MeV. It is actually made of two parts. The first part accelerates the beam to 20 MeV and is a typical Drift Tube Linac with permanent magnets inserted in the drift tube themselves. The second part is made of a Cavity-Coupled Drift Tube Linac which optimizes acceleration of protons in the velocity range $\beta = 0.1$ to 0.4.

The last section is the Superconducting Linac proper which accelerates the beam from 100 MeV to 1.0 GeV. The analysis and the design concepts of a Superconducting Linac are discussed in [5]. A Superconducting Linac is made of an alternating sequence of Warm Insertions and Cryo-Modules. The Warm Insertions are needed to accommodate beam steering and focussing magnets, beam position monitors and vacuum pumps. The Cryo-Modules house the RF Cavities. A Cryo-Module is made of a number of Cavities, and each Cavity is made of a number of Cells.

The Linac design is based on a constant energy gain per Cryo-Module. The optimum Transit Time Factor (TTF) is obtained by adjusting the Cell length d so that, denoting with λ the RF wavelength, $d = \beta\lambda / 2$. As the beam is accelerated, β varies, and the Cell length d has to be adjusted accordingly. This would not be practical since all Cryo-Modules would look different in shape and size. A more practical solution is obtained by dividing the Superconducting Linac in two sections. Each section is made of Cavities with Cells of the same length, shape and size, corresponding to a geometrical $\beta = \beta_0$ in proximity of the middle of the accelerating range. There is a penalty of lowering the TTF which can be compensated with an increase of the axial electric field. This way all the Cryo-Modules in the same section are identical in shape and size.

We shall assume in the following that each Cavity is individually driven by a single RF Coupler. To resolve phase adjustment to a sufficiently high degree, one should not allow more than two cavities under the same Klystron. The preferred mode of operation is to provide the same amount of power to all the RF Couplers in the same Linac section. Because the Cavity-Cell-Coupler configuration is

0-7803-4376-X/98 /$10.00 © 1998 IEEE

the same for all Cryo-Modules in one section, the energy gain per Cryo-Module is also the same.

The original proposal of the Superconducting Linac [3] made use of an RF system operating at 805 MHz in line with similar assumptions made at Los Alamos National Laboratory. Later other studies and designs of the Superconducting Linac [6] considered the frequency of 360 MHz. The purpose of our work, which is summarized here is to compare the performance and the cost for these two frequency choices.

3 DESIGN OF THE 10-MW SUPERCONDUCTING LINAC

A list of the general parameters of the 1.0 GeV Superconducting Linac is given in Table 1. To reduce the wall-dissipated losses we have taken a temperature of 2° Kelvin for the cavities. There are 4 Cells per Cavity and 4 Cavities per Cryo-Module. The synchronous RF phase angle for acceleration is -30°. Transverse focussing is provided by arranging quadrupoles in the Warm Insertions in a typical FODO arrangement with a betatron phase advance of 90° per FODO cell in both planes. Bunch area and beam emittances are also shown in Table 1.

Table 1. The 1.0-GeV Superconducting Linac

Total Beam Power (CW)	10 MW
Beam Current	10 mA
Ion Source Current	12 mA
Initial Kinetic Energy	100 MeV
Final Kinetic Energy	1.0 GeV
Temperature	2.0 °K
Cells / Cavity	4
Cavities / CryoModule	4
Cavities / Klystron	2
No. of RF Couplers / Cavity	1
RF Phase Angle	-30°
Method for Transverse Focussing	FODO
Betatron Phase Advance / FODO cell	90°
Normalized rms Emittance	0.30 π mm mrad
rms Bunch Area	1.725 π μeV-s

A more detailed list of parameters for the two sections of the Superconducting Linac is given in Table 2, where the two frequency cases are also compared to each other. For both cases the first section accelerates protons from 100 to 300 MeV, the second section from 0.3 to 1.0 GeV. We define as a period the combination of a Warm Section and the following Cryo-Module. As noted and expected, because of the relatively low number of particles per bunch, the losses to the Higher-Order Modes (HOM) of the Cavities are negligible. The required cryogenic power is estimated assuming a conservative static loss in the cryostats of 5 W/m. The AC-to-RF efficiency for Klystrons is taken to be 58.5%. The cryogenic efficiency is 0.4%.

Table 2. Comparison of SCL at two different Frequencies

Frequ. (MHz)	360		805	
	L-E	H-E	L-E	H-E
Velocity, β: in out	0.428 0.653	0.653 0.875	0.428 0.653	0.653 0.875
Cell Refer. β_0	0.48	0.69	0.48	0.69
Cell Length, cm	19.99	28.73	8.94	12.85
No. of Periods	16	22	36	51
Total Length, m	141.6	225.5	143.6	235.4
Period Length, m	8.85	10.25	3.99	4.62
Cryo. Length, m	6.650	8.049	2.990	3.616
Warm Insert., m	2.2	2.2	1.0	1.0
Quad. Length cm	67	67	30	30
Bore Radius, cm	11	11	5	5
Transitions, cm	67	67	30	30
Pwr/Coupl., kW	32.5	80.0	14.0	35.0
Gain/Per., MeV	13.0	32.0	5.6	14.0
Surf. Imped., nΩ	20.80	20.80	24.00	24.00
Q_0, in 10^9	5.70	8.20	4.94	7.10
ZT^2, ohm/m	490	1,013	223	461
Diss. Power, kW	3.73	2.98	9.05	7.63
HOM - Power, W	16	22	79	113
Cryog. Pwr, kW	4.28	3.89	9.67	8.67
RF Power, MW	2.70	9.45	2.71	9.46
AC Power, MW	5.69	17.13	7.05	18.34
Efficiency, %	35.14	40.86	28.37	38.18

We have assumed CW mode of operation. Moreover, we have allowed an extra 35% of RF power as contingency to allow phase and amplitude tuning of the Cavities.

As one can see the overall efficiency is indeed close to 40% as originally projected. In particular, the amount of power in the RF Coupler, which has been chosen so that the surface field never exceeds the limit of 17 MV/m, is within the technical demonstrated capabilities.

4 COST

The capital cost of the Superconducting Linac is estimated assuming 100 k$ / m for the Warm Insertions and 300 k$ / m for the Cryo-Modules. The tunnel cost is taken to be 70 k$ / m. All the required parameters are shown in Table 3. The cost of Klystrons, including waveguides, windows, etc..., depends on their number, RF architecture, and total RF power required. An extra 35% of RF power has also been added for the tune-up operation of the Linac. The cost of the refrigeration plant is estimated assuming 2 k$ per Watt at 2 °Kelvin. The distribution of the AC power has also a cost, taken at 0.14 $ per Watt. The summary given in Table 4 shows a total of 160 - 185 M$ for the Superconducting Linac, to which one should add the cost of the front-end and of the normal-conducting section, which could be another 30-35 M$. The accelerator cost is expected to be only a small fraction of the total cost of the facility, which includes the target station, the energy recovery and electrical transformation systems, the processing plant, etc... etc... Once in full operation, it is of course expected that the cost of the operation of the facility will not include the AC electric power, since this will be provided by the plant itself. Nevertheless, during the early commissioning stages, the AC electric power may be provided only externally and at full cost. A total of 20 - 25 MW of AC power is then required, that somewhere in USA may contribute to an operational cost of 7-8 M$ a year, assuming that the Linac is to be available at least 75% of the yearly time.

5 COMPARISON AND CONCLUSIONS

The comparison of the performance of the two frequency cases is given in Table 2, and that of the cost in Table 4. No major differences are noticed between the two cases. The number of Modules (and of periods) is lower, by about half, in the 360 MHz case than in the 805 MHz case, but the periods are about twice as long and the cryostats are larger.

Table 3. Cost and Other Parameters

AC-to-RF Efficiency	0.585 for CW mode
Cryogenic Efficiency	0.004 @t 2.0 °K
Electricity Cost	0.05 $/kWh (in USA)
Availability	75% of yearly time
Normal Conducting Structure Cost	100 k$/m
Superconducting Structure Cost	300 k$/m
Tunnel Cost	70 k$/m
Cost of Klystron (*)	1.68 $/W of RF Power
Cost of Refrigeration Plant	2k$/W @ 2.0 °K
Cost of Electrical Distribution	0.14 $/W of AC Power

(*) Assuming a single step of RF power splitting

The overall length is about the same, 270 m in both cases. Because the focusing period is longer, the quadrupole gradient is weaker in the low frequency case, and the beam size is larger. Yet, the ratio of cavity aperture to beam size is larger at 360 MHz. The most important difference is the wall-dissipated power: a total of 6.7 kW at 360 MHz, and 16.7 kW at 805 MHz. This gives a negligible impact to the total RF requirement, which is essentially given by the beam power, but a substantial contribution to the required Cryogenic power which from 8 kW at 360 MHz increases to 18 kW at 805 MHz, with a corresponding increase of the AC power for the Cryogenic plant from 2 to 4.5 MW respectively. As a result, the overall efficiency is somewhat lower at the high frequency case. There is about a 20 M$ difference in the capital cost, with the low frequency case being less expensive. This difference is the consequence of the larger dissipated power in the 805 MHz frequency case. Though the difference in absolute values are not large, the 360 MHz frequency would actually represent a better choice. For instance, the lower number of modules required, could lead to an easier construction and maintenance of the facility.

Table 4. Cost Comparison

Frequ. (MHz)	360		805	
	L-E	H-E	L-E	H-E
Operat. Cost, M$/y	1.87	5.628	2.316	6.023
Capit. Cost: (M$)				
RF Klystrons	4.54	15.88	4.55	15.89
Electr. Distrib.	0.797	2.398	0.987	2.567
Refrig. Plant	8.55	7.78	19.34	17.34
Warm Struct.	3.52	4.84	3.60	5.10
Cold Struct.	31.92	53.12	32.29	55.32
Tunnel	9.91	15.78	10.06	16.48
Total Cost (M$)	59.24	99.81	70.83	112.7

6 REFERENCES

[1] Bowman C. et al. Nucl. Instr. Meth., A320, 336 (1992).

[2] Carminati F. et al., CERN/AT/93-47 (1993).

[3] A.G. Ruggiero, BNL 63527, AGS/AD/97-1, Brookhaven National Laboratory. October 1996.

[4]Rubbia C. et al, Proceed. of EPAC94, Vol. 1, page 270, London, June 27 - July 1, 1994.

[5]A. G. Ruggiero, "Design Considerations on a Proton Superconducting Linac", BNL 62312, August 1995.

[8] Meeting on EA - Accelerator, Legnaro, October 1996.

LOW-BETA STRUCTURES FOR CW OPERATION

H. Leboutet, S.Joly
Commissariat à l'Energie Atomique - B.P. 12 - Bruyères-le-Châtel, France
C.Perraudin
Thomson-CSF AIRSYS - 91195 Saint-Aubin Cedex, France

Abstract

Arcing problems and mechanical instabilities may limit the output energy of cw RFQ's even below 2 MeV. Between 2 and 10 MeV, Alvarez type DTL's are not convenient. The proposed structures are derived from slot-coupled, iris loaded, π-mode, 5-cell resonators. But the noses are shaped so that they provide a large enough space at atmospheric pressure to accommodate a magnetic quadrupole, to insure a FODO-type focusing. The beam sees a 3π or a 5π delay-line. Those structures are well suited for 350 MHz, or above, operating frequency, where there is enough space for water pipes to insure a sufficient cooling for cw operation. The focusing quadrupoles are entirely in the air and easily accessible. Fabrication is substantially the same as slot-coupled CCL's and beam dynamics is intermediate between 2π and 4π Alvarez structures.

1 INTRODUCTION

CW operation at room temperature concerns, at least, the low-energy part of any linear proton accelerator, even when superconductivity is used above about one hundred MeV.

The injector part of a long and powerful accelerator used for production purposes must be essentially reliable, stable, immediately available, and especially free from abrupt changes in current due to arcing. The design has to be exaggeratedly safe :

- cw operation at room temperature implies drastic cooling problems on the accelerator RFQ as well as the following Alvarez structures in order to maintain good mechanical stability,
- cw reliable RF power sources are actually klystrons, whose lower frequency is 350 MHz,
- a conventional Alvarez linac requires a minimum of space for the drift tubes, at least 10 cm of geometric period, for a reliable construction. At 350 MHz, $\beta\lambda$ = 10 cm corresponds to 6.5 MeV.

Consequently, in the conventional state of the art, one is faced with the unevitable situation of a rather long RFQ with rather high voltages on the vanes, followed by an Alvarez-type tank with focusing quadrupoles fitted into the drift tubes. The technology of these two structures has yet to be validated for a cw operation. The next limitation is arcing when the Kilpatrick coefficient Kp reaches values around 1.8. Published experimental results [1,2] seem to recommend to stay below 1.3-1.4 Kp for cw safe operation.

After these considerations may come the cost optimization: low-voltage DC kilowatts for the quadrupole magnets vs RF-klystron-produced kilowatts for the RFQ. One way out is to go to much lower frequencies, and try to fabricate powerful enough RF sources.

The situation becomes different and the technology easier when, as in the TRISPAL project [3], the required current is around 40 mA; then, good, reliable, easy to cool accelerating structures can be built down to $\beta\lambda$=4 or 5 cm, which would correspond to 1.5- 1.6 MeV at 350 MHz. The RFQ output energy could stay below 2 MeV, eventually down to 1.6 MeV. At these reduced currents, a Kilpatrick coefficient of 1.4-1.45 will drastically reduce the risk of arcing.

2 LOW-BETA STRUCTURES

A possible structure is represented in Figures 1 to 3. Compared to the conventional DTL, the "posts" are made big enough to contain the quadrupoles and are vacuum-tight so that the quadrupoles are in the air , easy to fabricate and cool, with relaxed limitations in volume and easy access for maintenance of all individual quadrupoles.

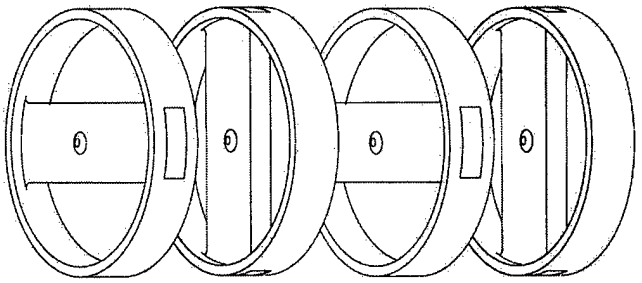


Figure 1 : Cells assembly with 90 degrees rotation between cells.

0-7803-4376-X/98/$10.00 © 1998 IEEE

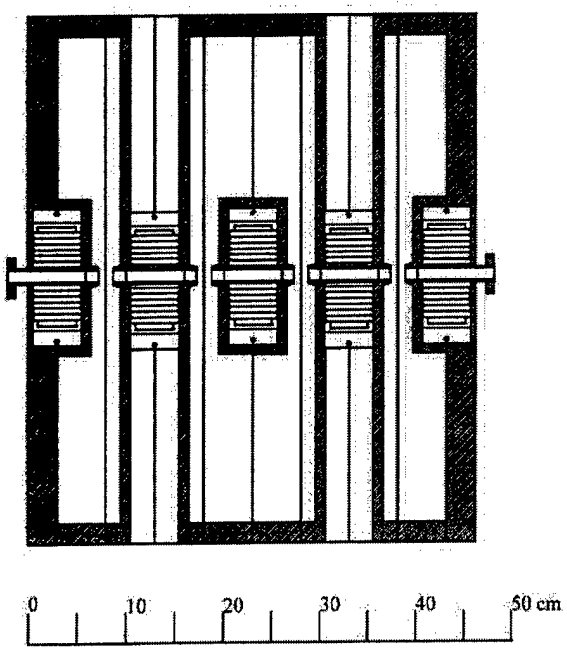


Figure 2 : 4-cells assembly in 2 βλ zero mode at 1.6 MeV with FODO focusing.

Compared to the iris-loaded waveguide, there is no fondamental difference except that the irises are partially thicker. RF-wise, when used as a resonant structure made of a certain number of cells coupled together, only the zero and the π-modes are of interest. As seen by the beam, the interaction can occur on any of the π , 2π , 3π , 4π , 5π , ... modes . As seen by the engineer, the mechanical period must have a minimum length of 10 cm to allow for the quadrupole, the flanges and the accelerating gap. The region of interest of this kind of sructure is given in Figure.4.

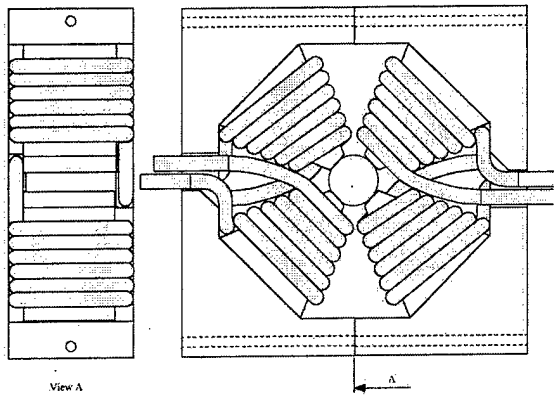


Figure 3 : Quadrupole assembly.

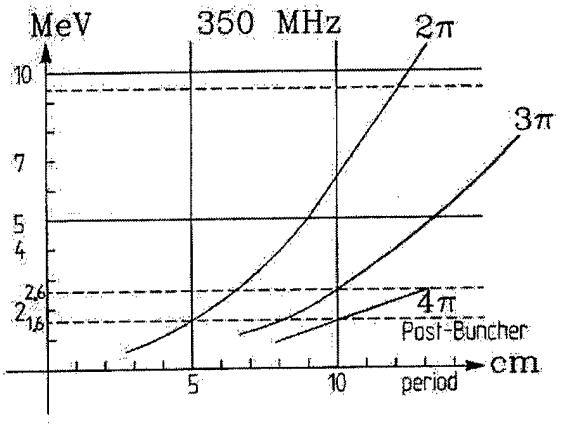


Figure 4 : Validity region of the structure.

3 HIGH-POWER INJECTOR

Figure 5 shows the general layout of the proposed injector for a cw high-power accelerator. The resonant tanks are separated in units of 125 kW-RF inputs as has been safely decided in the TRISPAL project. The RFQ output energy is limited to 1.6-1.8 MeV to reduce mechanical and cooling difficulties and save RF power. As it seems convenient for RF distribution purposes and mechanical stability concerns, to safely limit the RFQ output energy below 2 MeV, then a short 4π structure, about 100 cm long, must be inserted as a "post-buncher" to cover the gap up to 2.6 MeV. The matching transition between the RFQ and the following line is considered as a critical place, more critical at lower energy. After that,a 3π-line is adequate up to 10 MeV. A chicane can then be installed for a "clean up" of the bunches to drastically reduce their contribution to a "halo" forming downstream.

The beam out of the RFQ is divergent radially and the space charge causes an increase in the axial dimension of the bunches. Mechanical requirements imply flanges and alignment infinitely short. The solution taken here is conventional :

- control of the phase oscillation at the output of the RFQ so that the beam is not divergent, and if possible slightly convergent,
- modify the last cell of the RFQ to reduce and equalize the divergence in x and y directions,
- use a very short but powerful triplet of qudrupoles transforming the divergent into a convergent beam and re-arrange the gradients of the three first quadrupoles of the FODO structure to transform a convergent or parallel beam into what fits the FODO line taking into account

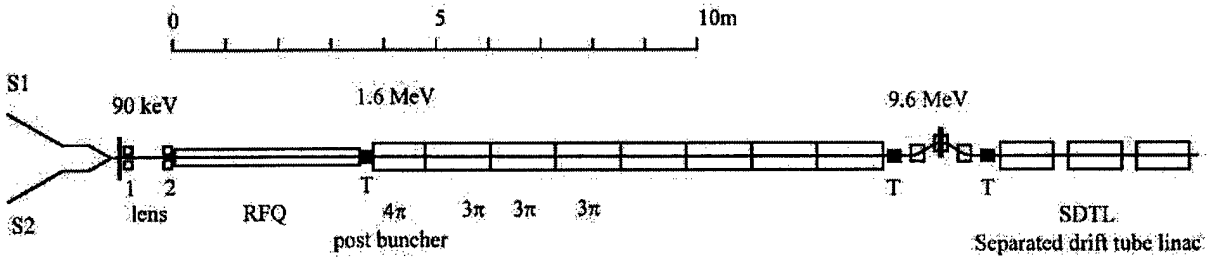


Figure 5 : General layout of the cw injector.

both the RF defocusing lens and space charge effects. The control is made by using a "macro-particle" code.

The next most difficult transition region which cannot be avoided when using this scheme, is the FODO to doublet focusing transition which is planned here in the 10 MeV-region. By taking advantage of this necessary difficulty, this transition can include a "clean up" system cutting "tails" and "feathers" of the bunches, to prevent any contribution to halo formation downstream.

Above 10 MeV, the "short-DTL" structure, as described in Reference [4], can be used.

REFERENCES

[1] S.O. Schriber : 'Factors limiting the operation of structures under high gradient', Proc. LINAC-86 Conference, Stanford, June 2-6, 1986, SLAC-Report-303 (sept.86) p.591.

[2] A. Gerhard, M.Kurz, J. Brutscher, A. Schempp, H. Klein : 'RF sparking experiments at 108.5 and 216 MHz' ; Proc. XIIIth International Symposium on Discharges and Electrical Insulation in Vacuum, Paris, June 27-30, 1988, Editions de Physique, p. 492.

[3] M. Promé : 'Major projects for the use of high-power linacs', Proc. LINAC-96 Conference, Geneva, August 26-30, 1996, CERN-SIR, p.9.

[4] C. Bourat : 'A DTL with short tanks and external focusing for high-power cw linacs', this Conference.

IPHI, THE SACLAY HIGH-INTENSITY PROTON INJECTOR PROJECT

J-M. LAGNIEL
Commissariat à l'Energie Atomique - DSM - GECA
CEA-Saclay - LNS, 91191 Gif-sur-Yvette Cedex, France

S. JOLY, J-L. LEMAIRE
Commissariat à l'Energie Atomique - DAM - DRIF - DPTA - SP2A
B.P. 12 - 91680 Bruyères-le-Châtel, France

A. C. MUELLER
Centre National de la Recherche Scientifique - IN2P3 - IPN/Orsay
91406 Orsay Cedex, France

Abstract

High-power accelerators are being studied for several projects based on high-flux neutron sources driven by proton or deuteron beams. Since the front end is the most critical part of such accelerators, it has been decided to build a High-Intensity Proton Injector (IPHI) designed to accelerate a cw 100 mA beam up to 11 MeV. The aim is to validate design codes, test technical choices, demonstrate operational reliability and measure the beam parameters in order to optimize the high-energy part of the accelerator. The design chosen for IPHI (ECR source, RFQ, DTL and diagnostic line) and the construction schedule are presented.

1 INTRODUCTION

Accelerators for high beam power (> 1 MW) are studied for several applications such as fundamental research, accelerator-driven transmutation technologies (transmutation of radioactive wastes, tritium production), material science, energy production (hybrid reactors and fusion)... [1] [2]. For most of these applications, high-power proton or deuteron beams are used to produce high neutron fluxes with characteristics which cannot be obtained from nuclear reactors. One of the main advantages of an accelerator-driven neutron source is its flexibility : the neutron flux can be continuous or pulsed with time characteristics defined by users and the energy of the neutrons can be adjusted (14 MeV neutrons for the fusion material tests). In addition, problems associated with reactors such as potential impact on the environment, supply of highly-enriched uranium, cost associated with spent fuel processing and decommissioning can be avoided or greatly minimized. However, this new generation of accelerators has to produce multi-MW beams. This is one to two orders of magnitude higher than the most powerful machines in operation today.

Careful attention must be paid to optimize the design of such high-power accelerators. On one hand, one needs to provide desired beam with high reliability for the operational life cycle. On the other hand, the capital and operational costs need minimization. The two main issues in this regard are the requirements of extremely low beam loss [3] and high availability. The final design results from a compromise between the technical risk and the total cost of the project. A good compromise is difficult to achieve without a serious R&D program focused on the important issues mentioned above. Since rf linacs have emerged as the accelerators of choice for pulsed or cw beams above 5 MW, we have undertaken a comprehensive demonstration program for the low-energy part of such machines.

2 IPHI R&D PROGRAM AIMS

IPHI is a R&D project proposed by the CEA with collaborations from CNRS. The project is also supported by Thomson-CSF-AIRSYS, a company with experience in the construction of accelerators for medicine, industrial and military applications. The project aim is to build a 11 MeV "Injector for Protons with High Intensity" (> 100 mA) capable of operation with duty cycle up to 100% (see section III). The goal of the R&D program is to gain knowledge necessary to optimize both design and cost of several projects of interest to the IPHI partners :

- TRISPAL, the French project for tritium production [2],
- IFMIF, the International Fusion Materials Irradiation Facility [4],
- ESS, the European Spallation neutron Source [5],
- nuclear waste transmutation and next generation of exotic beam facilities.

After an analysis of the best R&D program to undertake which would serve all these projects, a proposal to build the IPHI prototype has been made. The same has been done in Canada (the Chalk River Injector Test Stand is presently undergoing tests at Los Alamos [6]), in Japan (JAERI Basic Test Accelerator [7]) and in USA at Los Alamos (Low-Energy Demonstration Accelerator [8]). Each of these high-power accelerator front ends (under test or in progress) has different designs and would therefore provide complementary knowledge bases for optimization of both design parameters and costs of this new class of high-power accelerators. They specifically will allow :

- validation of the beam dynamics codes by testing them in the low-energy sections where space-charge effects are dominant,

0-7803-4376-X/98/$10.00 © 1998 IEEE

- knowledge of the beam distribution at an energy where halo considerations become crucial (~10 MeV),
- demonstration of a specific set of technological choices and adequacy of design codes (RF cavities, RF systems, temperature control systems, diagnostics for high-power beams,...),
- accumulation of data on reliability, availability and maintainability, cost of the accelerator components and ability of the manufacturers to build them.

It is clear that all that information gained at low energy is essential to optimize a high-energy machine.

3 LAYOUT

The High-Intensity Light-Ion Source **SILHI** is the first stage of the IPHI prototype. It has been designed to produce high-intensity proton or deuteron beams (> 100 mA) at 95 kV with up to 100% duty cycle. Design started in mid-1994 with funding from CEA, and teams from CEA-DSM (Saclay and Grenoble) and 'Laboratoire National Saturne' (CEA-DSM and CNRS-IN2P3). A 2.45 GHz ECR source was chosen in light of the excellent performances achieved at Chalk River and Los Alamos. This type of source has also several advantages compared to the other source types :

- no filament or RF antenna,
- low microwave power (< 1 kW),
- very high gas efficiency,
- good beam stability,
- high proton or deuteron fraction (> 90%).

Within two weeks of the end of the construction (July 1996), a 46 mA cw total beam current was extracted at 70 kV using a $\phi = 10$ mm aperture plasma electrode (plasma density : J = 58 mA / cm^2). Six months later, a 107 mA cw beam current was obtained at the nominal extraction voltage (95 kV) with a $\phi = 8$ mm aperture plasma electrode (J = 213 mA / cm^2). Continuous beam above 90 mA are now accelerated routinely. Measured beam characteristics are reported in Ref. 9.

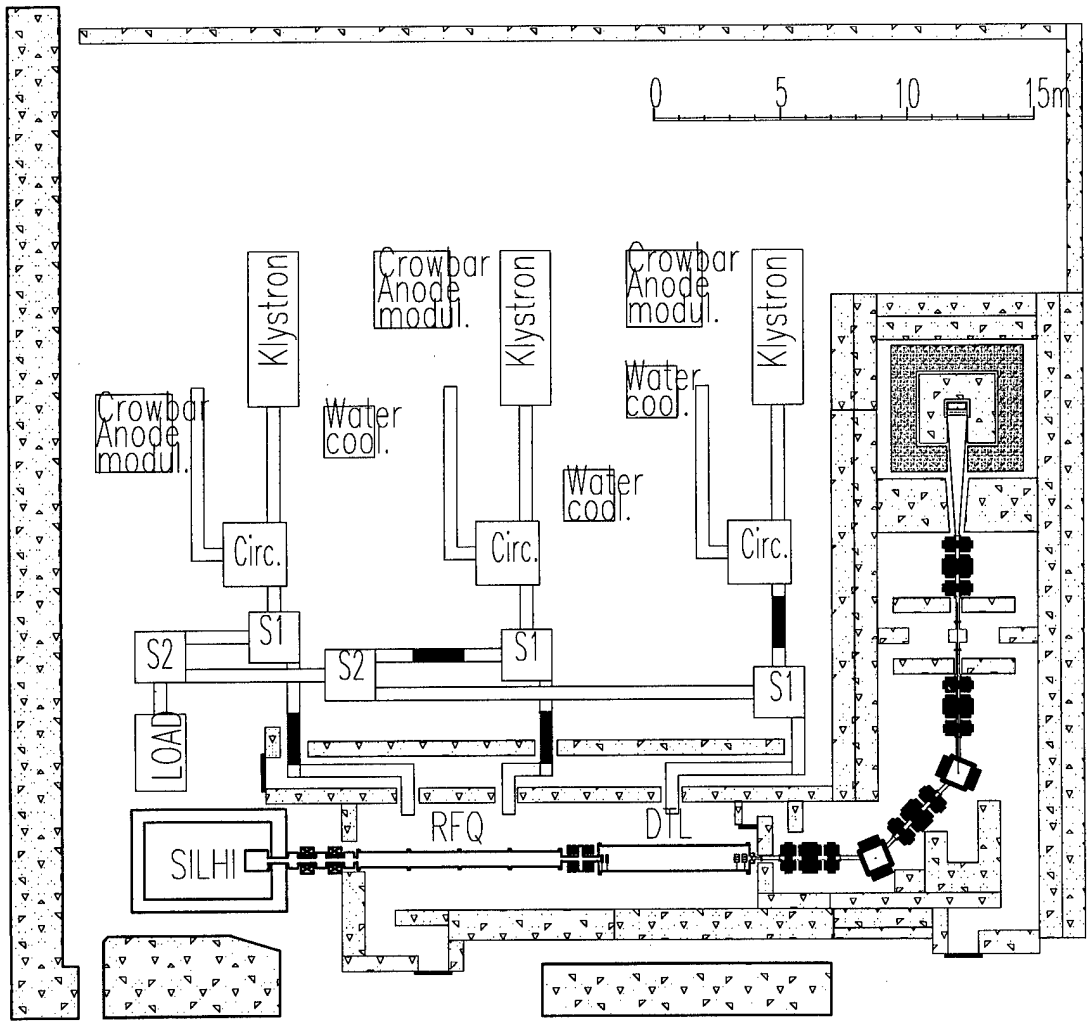


Figure 1 : Layout of the IPHI prototype

The next steps of the IPHI project concern the construction of a RFQ followed by a DTL tank in order to reach 11 MeV (fig.1). The IPHI partners are ready to support both construction and manpower costs for this new stage since 1997.

The **IPHI RFQ** will be a ~7 m long four-vane structure following the developments at the Los Alamos National Laboratory. As in the APT RFQ, the cavity will be brazed and will be made from several separately tunable segments assembled with RF couplings [8]. The IPHI RFQ is designed to work with two 352 MHz high-power RF generators of the CERN (LEP) and ESRF type. For the present design, beam dynamics calculation shows a beam transmission of 97% for 100 mA with both multipoles and image-charge effects taken into account. Investigations are presently being done to improve this design (same transmission with a maximum electric field lower than 1.8 Kilpatrick criterion...). The final energy is 5 MeV, the lowest energy which allows to build the first drift tube of the 352 MHz DTL using electromagnetic quadrupoles.

It is planned to build a **Beam Matching Section** between the IPHI RFQ an DTL in order to keep some freedom for the tunings and to leave enough room to install diagnostics.

The **IPHI DTL** will be a 6 m long Alvarez structure designed to accelerate beam to 11 MeV. The choice of a conventional DTL structure for IPHI is mainly done to avoid emittance growth and halo formation which can be induced when the energy gain per focusing period is high. A 2π mode DTL structure with a FODO focusing period leads to the shortest focusing period ($2\beta\lambda$) with the best ratio for the linear radial focusing strength (quadrupoles) over the nonlinear RF defocusing effect. Also, many DTL Alvarez structures have successfully demonstrated their capabilities to accelerate very high pulsed beam currents (200 mA and above) worldwide. The main issue for a high duty-cycle DTL is to cool the low-energy drift tubes which house high-gradient quadrupoles. Studies undertaken for the IPHI project indicate that the drift tubes can be adequately cooled for the 352 MHz cw structure above 5 MeV. The first task on the IPHI DTL will be to build a hot prototype with a small number of drift tubes (2 or 3) for feasibility demonstration.

The **IPHI Diagnostic Line** being studied will provide both transverse and longitudinal emittance measurements for the RFQ beam (up to 500 kW) and subsequently for the full DTL beam (up to 1 MW). It is planned to vary the focusing and energy dispersion properties of this line to perform these measurements using non-destructive profile monitors. The beam halo will be measured on collimators located all along the line.

4 CONCLUSION

The final decision for the IPHI project is expected by June 1997. A favorable decision will allow to start this R&D program for the future generation of high-power linear accelerators. This will be mainly funded by CEA with a total investment budget of 90 MFF (~M$ 18). The total manpower need is estimated to be 240 man-years for the entire duration (1997-2002) of the project with 50 man-years per year during the construction period (1998-2000).

The IPHI prototype will be installed in the CEA-Saclay Center. The key dates are :

- 06/2000 : first RFQ beam
- 06/2001 : end of the RFQ tests (500 kW beam)
- 09/2001 : first DTL beam
- 12/2002 : end of the program (1 MW beam)

5 ACKNOWLEDGEMENT

The authors gratefully acknowledge the SILHI and IPHI Team members for the large amount of excellent work already done. The contributions of C. Perraudin and C. Bourat have been also highly appreciated. They sincerely thank all the authorities who support the project : M. Olivier, J. Faure, S. Harar and C. Césarsky for CEA-DSM; J. Daussy, A. Joubert and J. Bouchard for CEA-DAM; S. Galès, F. Dupont and C. Détraz for CNRS-IN2P3; J. Courau for Thomson-CSF-AIRSYS. Many thanks also to our colleagues and friends from LANL, JAERI and IFMIF Team for fruitful discussions with special thanks to S. Nath.

REFERENCE

[1] S.O. Schriber, "Survey of proposed high intensity accelerators and their applications", EPAC94 Proc., June 1994, Vol.1 p.213.

[2] M. Promé, "Major projects for the use of high power linacs", LINAC96 Proc., August 1996, Vol.1 p.9.

[3] J-M. Lagniel, "Halos and chaos in space-charge dominated beams", EPAC96 Proc., June 1996, Vol.1 p.163.

[4] IFMIF CDA Team, "International Fusion Materials Irradiation Facility Conceptual Design Activity, Final Report", Edited by M. Martone, ENEA-Frascati, Italy, December 1996, RT/ERG/FUS/96/11.

[5] "Outline design of the European Spallation Source", Edited by I.S.K Gardner, H. Lengeler and G.H. Rees, September 1995, ESS report 95-30-M.

[6] J.D. Schneider et al., "Installation of a cw radiofrequency quadrupole accelerator at Los Alamos National Laboratory", LINAC94 Proc., August 1994, Vol.1 p.149.

[7] K. Hasegawa et al., "The R&D status on the front end of the high intensity proton accelerator in JAERI", LINAC96 Proc., August 1996, Vol.2 p.665.

[8] J.D. Schneider, "APT accelerator technology", LINAC96 Proc., August 1996, Vol.1 p.22.

[9] P-Y. Beauvais al., "First beams of the CEA-Saclay cw high-intensity microwave source", PAC97, 6W #5347.

STATUS ON LINACS DEVELOPED AT INSTITUTE OF ATOMIC PHYSICS-BUCHAREST, ROMANIA

D.Martin, C.Oproiu, A.Radu, S.Marghitu, I.Indreias,
Institute of Atomic Physics, Accelerator Laboratory
R.Cramariuc, A.Margaritescu, ICPE-Electrostatica, Bucharest, Romania
G.Cojocaru, TRIUMF, Vancouver, B.C., Canada

Abstract

The features and physical characteristics of two linacs, ALIN- 10 and ALID-7, built in Romania, as well as their applications in the field of radiation research and technology are presented. Both linacs are of traveling-wave type driven by 2MW peak power S-Band magnetrons and operate with two independent switchable modulators to perform a single pulse, or pulse trains of accelerated electrons.

1 INTRODUCTION

Potential industrial applications indicate the need for electron accelerators in the energy range 0.5 MeV to 10 MeV and with currents of 1-20 mA[1]. However, according to the last conclusions [2, 3, 4] which resulted from our radiation research with regard to the polymeric flocculants (PA and PV types) production obtained by electron beam irradiation, the use of low power-high energy linacs begins to become economically attractive for this type of application. Indeed, the estimate of processing rates for a linac of 1kW output power and 5-10 MeV energy is up to 2000 kg/h for the PA type polymeric flocculants and up to 500 kg/h for the PV type. Also, our recent investigations concerning the use of simultaneous electron beam and microwave irradiation, demonstrate that some material processing, such as polymerisation and sterilization, need a lower electron absorbed dose in the case of the simultaneous use of electron beam and microwave irradiation in comparison with electron beam irradiation only.

2 THE CONSTRUCTIVE CHARACTERISTICS OF THE LINACS BUILT AT IAP

The first linac, AL-3 of 3 MeV and 200 W, was built in 1996 at the Accelerator Laboratory from Institute of Atomic Physics (IAP) to satisfy the needs of scientists engaged in radiation research. To implement the irradiation processes which provide distinct advantages over conventional processes, years of research combined with engineering activities have culminated in the development of two evolved electron linear accelerators: ALIN-10 of 6 MeV and 100 W and ALID-7 of 5.5 MeV and 700 W.

The ALIN-10 linac is designed as a laboratory installation. It is located in a horizontal configuration, its use including both, electron and X-ray beam production for fundamental research. As fixed equipment, it is adapted to specific needs of more efficient use of the electron beam treatment by using a post-acceleration beam focusing and bending to project electron beam at right angle to the accelerating structure.

The ALID-7 is an industrial equipment having a turning accelerating structure. It is now installed in a vertical position to provide more beam processing flexibility and to meet the wide needs of future applications.

Both ALIN-10 and ALID-7, are of traveling-wave type, driven by 2 MW (peak power) magnetrons (English Electric Valve) operating in S-band. The electrons are injected from diode type guns in the accelerating structure operating in the $\pi/2$ mode. The first portion of the accelerating structures (iris-loaded circular guides) is a variable phase velocity buncher and the remainder has a uniform section, for a phase velocity equal to speed of light. Except some special components, such as magnetrons and ferrite isolators, all microwave devices such as accelerating structures, mode transducers, waveguide windows, high power loads, bends and tee junctions are built in Romania. The high power loads [5] used for ALIN-10 and ALID-7 are multimode right circular cavities (200 mm diameter and 60 mm length) filled with a high loss dielectric (water cooled silicon carbide disk of 200 mm diameter and 25 mm length). These loads have a very simple construction, are compact, light, easily to match over a broad band (200 MHz) and, therefore, suitable for service at the end of an accelerating structure.

Waveguide windows are made by suitable modification of the output glass-metal cylindrical structure retrieved from the depreciated power magnetrons. The broad band matching (100 MHz) of this structure was obtained by using short cylindrical-rectangular transitions with inductive elements (small diameter metallic cylinders) symmetrically placed in its rectangular portion. Fig.1 shows the ALID-7 microwave system photograph. During and after acceleration, the electrons are subjected to a succession of electromagnetic devices for beam focusing, beam projecting through 90° (only for ALIN-10) and beam sweeping in a horn-shaped vacuum chamber. The scanning frequency, amplitude and waveform of sweep electromagnet current, beam size, maximum permissible distance between impact of two

0-7803-4376-X/98/$10.00 © 1998 IEEE

pulses, pulse rate and conveyor speed were carefully adjusted for a uniform treatment to be attained. The scanner geometrical parameters are the same for both, ALIN-10 and ALID-7: 32.2° semi-angle, 39.7cm height, 4 cm window width and 50 cm window length. The dose uniformity on the swept surface is ensured by specially designed waveforms for the scanner electromagnet current. ALIN-10 has a linear conveyor (10 m length and 50 cm width) and ALID-6 a circular conveyor (325 cm average diameter, 50 cm width).

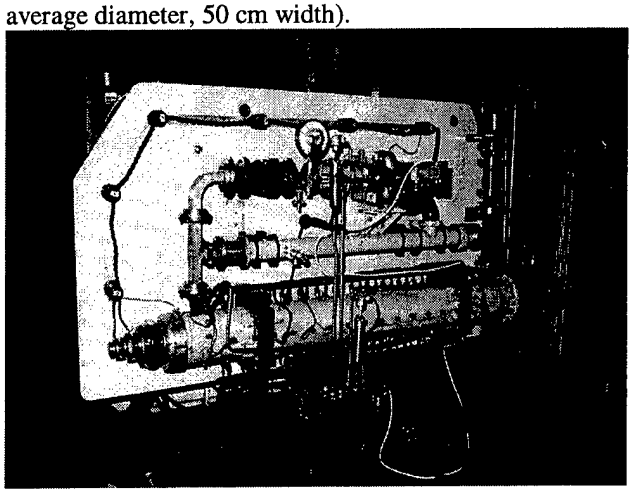


Fig.1 The microwave system of the ALID-7 linac

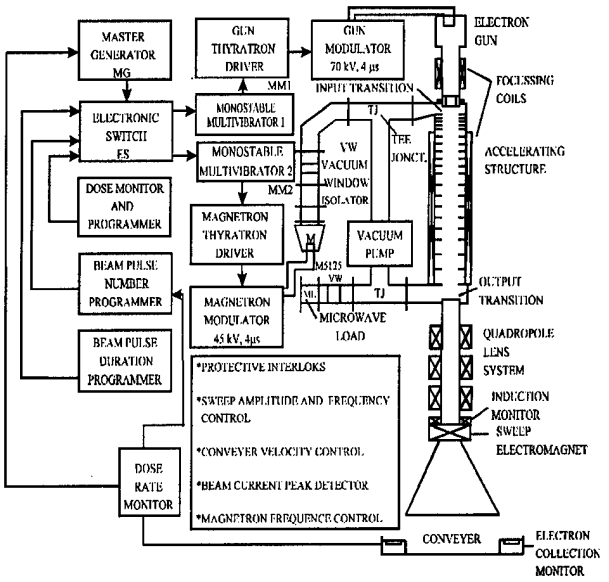


Fig.2 The system configuration of the ALID-7 linac

3 THE FEATURES AND PHYSICAL CHARACTERISTICS OF THE LINACS ALIN-10 AND ALID-7.

3.1.The features.

An important feature of our linacs with diode type guns is an original control technique [7] for obtaining programmed single electron beam shots and pulse trains, with desired pulse number, pulse repetition frequency and pulse duration by discrete pulse temporal position modulation of the gun electron pulses and magnetron microwave pulses. For this flexibility, two separate modulators are provided: a gun modulator and a magnetron modulator. This method combines the unsophisticated construction of the diode gun and better temporal flexibility of the beam, generally available when using triode type guns. A block diagram of this kind of modulation applied to ALID-7 is shown in Fig.2. The accelerator triggering system has two branches: the gun branch and the magnetron branch. The master generator MG, which synchronizes all the system units, delivers pulses at a programmed repetition rate (up to 250 pulses/s) at the monostable multivibrators MM1 and MM2. The pulses of the gun thyratron driver and magnetron thyratron driver are formed from the trailing edges of the MM1 pulses and MM2 pulses, respectively. The electronic switch ES may discretely change the duration of the MM1 pulses in the gun branch. When the electronic switch is not activated, the MM1 delivers long pulses and there is no overlapping of the electron gun and magnetron pulses an thus there is no accelerated electron beam at the accelerator output. The instabilities in the transitory regimes of the gun and magnetron are avoided by operating the accelerator a certain time without accelerated beam and then, by pushing "beam start button" the overlapping of electron gun and magnetron pulses are obtained, the variation in absorbed dose to pulse to pulse being reduced. Programmed absorbed dose, programmed irradiation time, programmed beam pulse number or other external events may interrupt the coincidence between the gun pulses and magnetron pulses and then the irradiation regime. The beam pulse duration may be continuously adjusted from 0.25 μs to T_M-T_F, where T_M is length of magnetron pulse and T_F is fill-time of the accelerator guide. The duration of the short beam pulses is limited only by the values of the gun pulse leading edge and of the magnetron pulse trailing edge. Slow variation of the absorbed dose rate is composed by means of an automatic control system of the pulse repetition frequency in the master generator. Another facility, which was specially designed to be used together with our linacs, is a reaction chamber built to permit simultaneous accelerated electron beam and microwave irradiation. As an initial step, an experimental model of reaction chamber (EMRC-1), excited by a single slotted waveguide system, has been developed in order to study the chemical, physical and biological effect caused by a microwave power up to 850 W and 6 MeV accelerated electron beam in their simultaneous passage through a wide variety of material samples: monomers mixture in aqueous solution, medical products, gases mixture containing nitrogen oxides and sulfur dioxide, ammonia and water vapor and other. Fig. 3 shows ALID-7 scanner and EMRC-1 set up in series. EMRC-1 is a rectangular chamber of 50X25X25 cm^3 using an injection system

consisting of a microwave power-controlled generator for a 2.45 GHz CW magnetron of 850 W maximum output power, a launcher to fit to waveguide WR430, a dual directional coupler for direct and reflected power monitoring, a tree stub tuner for impedance matching and an applicator based on five inclined series slots cut in the broad wall of a WR430 waveguide. Scanned electron beam is perpendicularly introduced to the upper- end plate of EMRC-1, passing through a 100 μm thick aluminium window and the microwave power is coupled to the chamber sidewall via the slotted waveguide system.

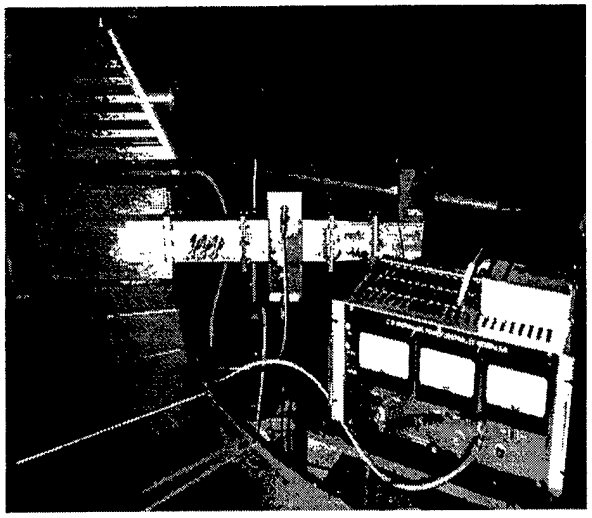


Fig.3 The ALID-7 scanner and EMRC-1 in series

3.2.The physical characteristics.

The physical characteristics of the beam which are of great interest for material processing, are: electron beam power, which represents the basic processing capability of a given source for a "required dose", and energy beam, which determines the depth to which the electron beam will penetrate the product. Along with this, the dependence of electron beam average power (P_B) on the input accelerator characteristics as well as beam loading characteristic have been investigated for the determination of the optimum values of peak beam current (I_B) and average beam energy (E_B) to produce maximum beam average power at the end of the accelerating process.

The peak beam current was measured by means of a ferrite ring pulse transformer and the average beam power by applying calorimetric method [8]. The average beam energy was determined from beam power characteristics. The calorimetric method was very suitable for electron beam power maximization as a function of the gun voltage (V_G), magnetron voltage (U_M), magnetron frequency (F_M) and peak beam current. The optimum values to produce maximum output beam power are recorded in Table 1.

Table 1

Linac	E_B (MeV)	I_B (mA)	U_M (kV)	U_G (kV)	F_M (MHz)
ALIN-10	6.23	75	43.5	68.4	2997.5
ALID-7	5.5	130	43.5	65	2998.6

4 THE ALIN-10 and ALID-7 LINACS DESTINATION

Our major research object is focused on the application of the electron accelerators to environmental engineering. As an initial step, the preparation of polymeric flocculants for waste water treatment was developed. Thanks to remarkable properties of the electron beam technologies developed over recent years in our institute for the polymeric flocculants preparation [2,3,4], it was proved that high energy linacs with modest output beam power, from a few hundred watt to one kilowatt, became economically attractive for their commercial production. The required dose for our types of flocculants , based on polymerization of the aqueous solution containing proper monomer mixture, such as acrylamide, acrylic acid and acetate vinyl, is smaller by a factor of 10 to 100 as compared to the dose requirement for other polymeric material production. Also, using the simultaneous electron beam and microwave treatment the required absorbed dose is again much decreased and some properties, as linearity and molecular weight are improved.

Our recent investigation on the sterilization of a wide variety of materials including foods and medical waste by simultaneous electron beam and microwave treatment demonstrates once more that the required beam dose level is much decreased.

5 CONCLUSIONS

The electron accelerators developed at Institute of Atomic Physics, Accelerator Laboratory, are to be used for various industrial applications at pilot-scale level thanks to the innovative electron beam technologies applied in the polymeric flocculants field. In addition to this, by using simultaneous electron beam and microwave treatment the industrial application of small-output power-high energy linacs will be more extended and the electron beam costs will decrease. Also, new and promising results are expected in material research by applying the method of the simultaneous electron beam and microwave treatment.

REFERENCES

1.Trageser A.D., Nucl.Instr. and Meth. 11(1961)p.248.
2.Martin D. et al., Radiat.Phys.Chem., Vol45,No.4 (1995),p. 615;
3.Martin D. et al., Nucl.Instr.and Meth.in Phys.Res.B113(1996), p.106;
4.Martin D. et al, Progr.Colloid Polym.Sci 102 (1996),p.147;
5.Martin D. et. al., Rev.Roum.Sci.Tech.-Electrotechn. et Energ.,17 (1972)p.723
6.C.Oproiu et al., Rev.Roum.Phys.,Tome 23, No.6, (1978) p.635.
7.Martin D. and Nemes M., Nucl.Instr. and Meth. 105 (1972)p.605;
8.Martin D., Radu.A.,Baciu G., Rev.Roum.Phys.23 (1978)p.1007.

A HIGH CURRENT SUPERCONDUCTING PROTON LINAC FOR AN ACCELERATOR DRIVEN TRANSMUTATION SYSTEM

C. Pagani, G. Bellomo, P. Pierini, G. Travish, D. Barni, A. Bosotti, R. Parodi*
INFN Sezione di Milano, LASA, Via Fratelli Cervi 201, 20090 Segrate (MI), Italy
*INFN Sezione di Genova, Via Dodecaneso 33, 16146 Genova, Italy

Abstract

High current CW proton linac accelerators have been recently proposed for a number of applications based on the use of a large flux of spallation neutrons. In this context, an R&D program on an accelerator driven system for nuclear waste transmutation has been recently approved in Italy. Our specific task is to develop, together with the national industry, a design of the high energy part of the proton accelerator, along with prototype development for the most critical components. In this paper we present a revised version of the design proposed at Linac'96, using five cell cavities, rather than the original four cells. This modification, together with a new criterion for using the transit time factor curve for non resonant proton velocities, results in a more modular and efficient design. A 1.6 GeV linac, operated at 25 mA, allows to reach 40 MW beam power. The beam power upgrade is achievable using additional couplers per cavity.

1 PROJECT OVERVIEW

An R&D program has started in Italy on an accelerator driven system for nuclear waste transmutation. In the recently approved two year program, starting in January 1998, two Italian research agencies (INFN and ENEA) will be supported to study, together with other institutions and the national industry, critical components of the accelerator driven system. In the following we present a revised version of the reference design, originally proposed at Linac'96 [1], and the rationale behind the parameter choices.

More generally, a number of applications have been recently proposed for high current proton linacs, including nuclear waste transmutation, energy production by sub-critical reactors, spallation neutron sources and trit-ium production [2]. These applications share in common a number of requirements on the accelerator. A high average current, high energy proton beam is needed. Additional requirements include high wall plug efficiency and low particle losses to guarantee the hands-on maintenance of the system. While these systems differ in the detailed parameters desired, they generally operate in the space charge dominated regime.

A number of accelerator configurations for the system in question have been considered in the literature. While this paper focuses on the superconducting linac option, it is worth mentioning alternatives.

Cyclotrons are presently limited to beams up to 1 MW, and can conceivably be extended up to a few MW. Still, cyclotrons possess the advantage of being compact and so they could be candidates for a demonstration plant.

Room temperature linacs offer a mature technology, but suffer from a much lower RF efficiency and high heat loads in CW operation.

One approach, which relies on well tested technology and provides efficient use of wall plug power, combines a low energy section based on a room temperature linac, and a high energy section based on β-graded superconducting structures.

The low energy section of such a system poses a number of challenges; however, a number of existing technologies address the regime of interest. For instance, proton sources in excess of 100 mA have been demonstrated, RFQs operating with more than 100 mA are operating and DTL structures at high current, up to 200 MeV exist, albeit at low duty cycle.

Here we consider systems with energy greater than 1 GeV and average beam power in excess of 30 MW. Moreover, we address only the high energy section (above 100 MeV) of the system. In the design presented in Section 4 we choose a final beam energy of 1.6 GeV, very close to the Los Alamos APT design [3]. The final choice of beam energy and current is heavily influenced by the specific application and is outside of the scope of the present paper.

The following sections of this paper illustrate the approach followed to design the high energy section from 100 MeV to the target energy of 1.6 GeV.

2 THE 350 MHZ SC LINAC OPTION

The motivation for turning to superconducting technology is twofold: high RF efficiency is readily achieved, which is important for CW operations, and large apertures are possible, which are relevant to minimizing particle loss.

The choice of operating frequency is set by a few general considerations. CERN has operated the LEP2 cavities at 350 MHz, and has added extensive experience at this frequency to the accelerator community. A number of cavity production tools and test stands are available in European companies as a result of the LEP2 development. Additionally, the 350 MHz choice matches existing RFQ and DTL designs.

Frequencies higher than the LEP frequency imply smaller physical dimensions for the cavities and associated components, but require a more complex 2 K cryogenics.

The injection energy of 100 MeV is mainly determin-

0-7803-4376-X/98/$10.00 © 1998 IEEE

ed by elliptical superconducting cavity constraints. Elliptical cavities for low energies (matched $\beta<0.5$) have a short active length and a low accelerating gradient, resulting in a poor "real estate" gradient from an expensive structure. Alternative schemes for the low energy section may allow the extension of the initial section to higher energy (>100 MeV). Nevertheless, elliptical cavities can capture efficiently the 100 MeV beam and higher injection energies have little impact on performance.

Due to the wide proton velocity variation from 100 MeV to over 1 GeV, and to the limited velocity acceptance of any resonant accelerating structure, the linac has to be sectioned. Analysis indicates three sections are sufficient to cover the energy range from 100 MeV to 1.6 GeV.

3 OPTIMIZATION CONSIDERATIONS

There are a number of constraints and practical arguments which limit the usable parameter space. A central need is to make the machine cost effective in terms of both capital and operational costs. In general, the capital cost is reduced by decreasing the length of the accelerator, while the operational cost is reduced by having "efficient" acceleration — good RF to beam coupling. Additionally, the RF is a major component of the system cost, and care must be taken to optimally use the klystron's power rating, while saving a proper margin for controls and mismatching.

On the basis of the existing 1.3 MW CW LEP klystron, a nominal power of 1 MW is used for beam acceleration in most of the linac structures. This power feeds four cavities in the high energy section (one cryomodule) and six (two cryomodules) in the intermediate one. For general machine reliability, the first section uses smaller klystrons (500 kW) feeding four cavities (two cryomodules). This scheme is compatible with further current upgrading, based on multiple RF coupler operation.

Efficient use of the cryostats is also demanded because of the capital cost, however beam dynamics considerations affect the arrangement of the accelerating cavities.

A major consideration is the need to keep the beam size well under control, and this implies a limit on the focusing lattice period length. In turn, the focusing period, in combination with the need for warm diagnostic boxes in each cell, sets limits on the cryomodule length. The cost and the added length of the cold/warm transitions require a compact focusing scheme, thus a singlet scheme seems less desirable than a doublet focusing structure.

It is standard practice to use multicell cavities in order to increase the ratio between the active and physical cavity length. The velocity acceptance of the cavities decreases with the number of cells in the structure, and that, in turn, can affect the number of sections needed in the linac for efficient acceleration. Increasing the active cavity length also increases the RF power needed for the beam acceleration, which must be within the limits of the available coupler technology [4].

Five cell cavities represent the best compromise to preserve a three section linac design, while the maximum number of cavities per cryomodule has been limited respectively to two, three and four, on the basis of the focusing scheme outlined above. The considerations presented in this section, combined with basic beam dynamics, and details of the specific system being considered, yield the present reference design.

4 A DESIGN FRAMEWORK

For our design, we assume the parameters and limits given in Table 1. The assumed values for the peak electric field and RF power transmitted through the couplers have been previously achieved CERN test bench values [4]. The nominal current of 25 mA is reachable with a single coupler per RF cavity. To provide a possible beam current upgrade, the cavities will be designed from the beginning with multiple coupler ports, despite the fact that the present design parameters are based on a one coupler solution.

The minimum cavity matched ("effective", not geometric) β has been set to 0.5 based on preliminary electromagnetic and mechanical studies. The reference design of such a cavity, which features an appropriate stiffening structure and an iris radius of 10 cm, has a peak surface to accelerating field ratio of 3.2. For the assumed peak surface field of 15 MV/m and considering the poor packing factor of the active cavity length to the lattice period the average "real estate" accelerating gradient of the low β section is 1 MeV/m.

Table 1: Parameters and limits used for the design of the superconducting linac.

Parameter	Value
Initial Energy	100 MeV
Final Energy	1600 MeV
Beam Current	25 mA
Beam Power	40 MW
Peak Surface Field	$\leq$ 15 MV/m
Minimum Cavity β	0.5
RF Coupler Max. Power	250 kW
Available Power/Klystron	1 MW

The procedure for determining the β values and the transition energies of the sections depends strongly on the operating range allowed by the cavities. Initial studies utilized an operating range which was symmetric in the velocity acceptance curve [1], while present work relies on an asymmetric approach.

The present method sacrifices some RF efficiency in the first part of each linac section for improved average (real estate) acceleration gradient. Since the particle velocity changes most rapidly at low energies, the initial few cavities in each section are used for velocity matching by operating them at lower RF power than the subsequent cavities. Such an approach allows the totality of a section's cavities to operate closer to the maximum acceler-

ating gradient (see Fig. 1), while the best klystron efficiency is set for the majority of a section's cavities which, in the last part of each section, operate at a constant energy gain, independently of the proton velocity.

Moreover, the smooth ramping of the effective energy gain at the entrance of each linac section is expected to help the beam matching between the different lattice periods. In the high energy section the energy gain per cavity of 10 MeV and a better packing factor allows a real estate gradient of 2.5 MeV/m.

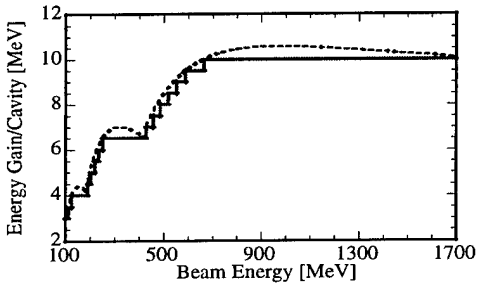


Figure 1: Maximum (upper line) and actual (lower line) energy gain along the accelerator as a function of the beam energy, assuming a peak surface field of 15 MV/m and synchronous phase φ_s= -30°.

In Table 2 we list parameters for the three sections. Note that a shorter lattice period is used at the lower energy ranges, as is required to compensate the effect of transverse RF defocusing.

Table 2: Machine and lattice parameters.

Parameter	**Value**		
Total length	~ 720 m		
Number of cells/cavity	5		
Number of couplers/cavity	1		
Section	**1**	**2**	**3**
Section total length [m]	96	146	475
Injection energy [MeV]	100	190	428
Section period [m]	8	11.2	15.3
# of cavities/section	24	39	124
# of cavities/cryomodule	2	3	4
# of cavities/klystron	4	6	4
Klystron rating (kW)	500	1300	1300
Cavity matched β	0.5	0.65	0.85
Accel. Gradients [MV/m]	4.3	5.4	6.4
Power/coupler [kW] / 25 mA	100	160	250

The linear beam dynamics with space charge has been studied; and a procedure for matching the beam between the linac sections has been devised. The matching of the short period FODO structure of the DTL to the long period doublet structure in the SC linac is still under investigation.

A lattice, consistent with the above machine parameters is shown in Fig. 2. The maximum needed quadrupole integrated strength is approximately 1.6 T, which is achievable within the 60 cm reserved for each quadrupole in the 3 m intermodule section. A normalized emittance of 1 π mm-mrad (transverse) and 1 π deg-MeV (longitudinal) has been assumed [3], and a constant synchronous phase of -30° has been used along the linac.

5 R&D PROGRAM

On the basis of the present reference design, the objective of the two year program, for the high energy part of the linac, is to develop the technology of the most crucial components, while finalizing the design of the machine.

We plan to develop, together with the industry, Nb single cell cavities at the lowest beta, to be measured at CERN, and a complete five cell copper structure for mechanical and RF warm tests. A complete copper, Nb sputtered, cavity at the highest beta is also planned; the R&D on single cells being in progress at CERN [5].

ACKNOWLEDGEMENTS

We are grateful to Simone Visonà for the cavity studies and Massimo Bonezzi for the technical drawings.

REFERENCES

[1] C. Pagani, G. Bellomo, P. Pierini, Proc. of the XVIII Int. Linear Acc. Conf., eds. C. Hill, M. Vretenar, CERN 96-07, (1996) p.107.
[2] M. Prome, Proc. of the XVIII Int. Linear Acc. Conf., eds. C. Hill, M. Vretenar, CERN 96-07, (1996), p. 9.
[3] J. Schneider, Proc. of the XVIII Int. Linear Acc. Conf., eds. C. Hill, M. Vretenar, CERN 96-07, (1996) p. 22; and APT Conceptual Design Report, LANL.
[4] G. Geschonke, Proc. of the XVIII Int. Linear Acc. Conf., eds. C. Hill, M. Vretenar, CERN 96-07, (1996), p. 910.
[5] E. Chiaveri, Private communication.

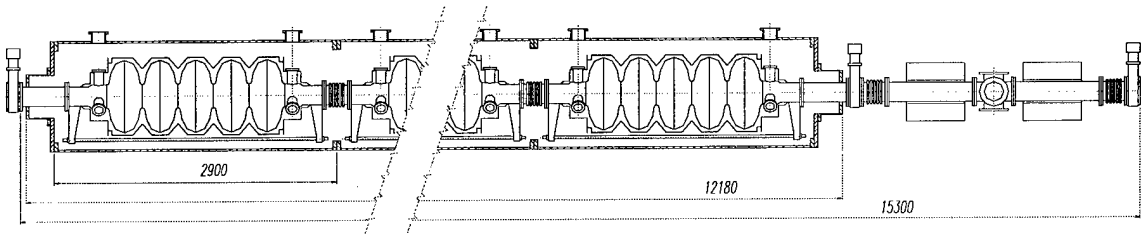


Figure 2: Layout of the basic cell in the high energy section (the low and intermediate energy sections differ only in the cryomodule length). The 3 m intermodule distance accomodates the quadrupole doublet, steering magnets (not shown), and a diagnostic and pumping box. The beam pipe aperture is maintained at 20 cm or greater throughout the linac.

THE NEW POSITIVE ION INJECTOR PIAVE AT LNL

A. Lombardi, G. Bassato, A. Battistella, M. Bellato, G. Bezzon, L. Bertazzo, G. Bisoffi, E. Bissiato, S. Canella, M. Cavenago, F. Cervellera, F. Chiurlotto, M. Comunian, A. Facco, P. Favaron, G. Fortuna, S. Gambalonga, M. Lollo, M.F. Moisio, V. Palmieri, R. Pengo, A. Pisent, M. Poggi, A.M. Porcellato, F. Scarpa, L. Ziomi
INFN-LNL, via Romea 4, I35020 Legnaro (PD), ITALY
I. Kulik, ILTPE Kharkuv, Russia; A. Kolomiets, S. Yaramishev, ITEP, Moscow, RUSSIA
H. Dewa, Institute for Chemical Research, University of Kyoto, JAPAN

Abstract

The construction of a positive ion injector for the linac ALPI, named PIAVE, at Laboratori Nazionali di Legnaro was funded in 1996. The beam parameters of the injector, consisting of two Superconducting Radio Frequency Quadrupoles (SRFQ) and eight superconducting Quarter Wave Resonators (QWR) for an equivalent voltage of about 8 MV (U^{28+} beam), are fixed. The building is ready, infrastructures and beam transport lines are being ordered. The superconducting RFQ's are in the prototyping phase. The general status of the project is reported in this paper, including cryostat and cryogenics, bunching systems, diagnostic devices and electronic control systems.

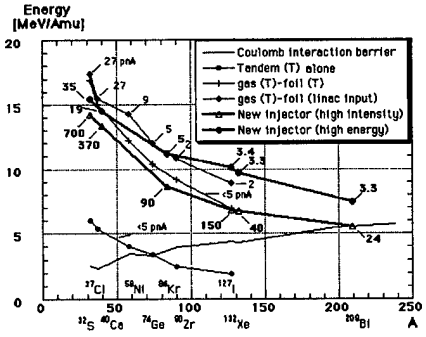


Figure: 1 Performances of the Legnaro accelerator complex including the foreseen upgrading given by PIAVE.

1 SCOPE OF PIAVE

Presently the Legnaro accelerator complex consists in a XTU tandem followed by the superconducting linear booster ALPI. It delivers ion beams to the experimental rooms with beam intensities on the target of few particle-nA, masses ranging from protons to masses of the order of 100 amu (^{81}Br) and energies well above the Coulomb barrier as it is shown in figure 1 [1]. The main constraint for the existing facility is the presence of the stripping section inside the tandem that limits the performance of the accelerator complex towards the heavier masses, up to 200 amu, and the beam intensities. On the other hand the nuclear physicists are interested to the very heavy ion beams with energies around the interaction barrier.

As a consequence of this request a new injector for the ALPI booster has been proposed at the beginning of 1996. The injector PIAVE (Positive Ion Accelerator for Very-low Energy) is meant for increasing the mass range of the facility up to lead ion. PIAVE will use the beams generated by the ECR Ion Source Alice placed on a high voltage platform operated at 350 kV [2].

Figure 1 describes the performance of the tandem-ALPI complex and compares it with the foreseen capability of PIAVE in terms of specific energy of the beam versus the mass number. The values indicated near the curves are the beam currents on the target, in particle-nA, including a realistic transmission coefficient in ALPI of 50%. It clearly shows the possibility of reaching the heaviest masses keeping the energy of the beam above the Coulomb barrier and with beam currents on target more than adequate for nuclear physics experiments.

The project has a three years time schedule and a cost of about 8 Billion Italian Liras.

2 THE ACCELERATOR

PIAVE is a superconducting linac operating at a rf frequency of 80 MHz and containing two SRFQ resonators followed by eight QWR's. It accelerates beams from β=0.0089 to β=0.045, in the case of a $^{+28}U^{238}$ beam, for an efficient injection into ALPI. The cavities are located inside three cryostats: one containing the two SRFQ and two, similar to the ALPI ones, containing four QWR's each.

The accelerator is connected to the ECR source, placed on the high voltage platform, on one side and to ALPI on the other side by matching lines containing the bunching systems to perform the longitudinal matching of the beam. The beam dynamics analysis of the whole system is completed [3] and the various component of the matching lines are in different phases of construction.

Figure 2 shows the layout of the machine, including the ECR high voltage platform.

The high voltage platform housing the ECR source is placed on a concrete base and its output beam line and accelerating column is displaced, both vertically and horizontally, with respect of PIAVE. The resulting transport line deflects the beam of 180^0 guiding it on a line some 5 meters below and some 2 meters to the left

0-7803-4376-X/98/$10.00 © 1998 IEEE

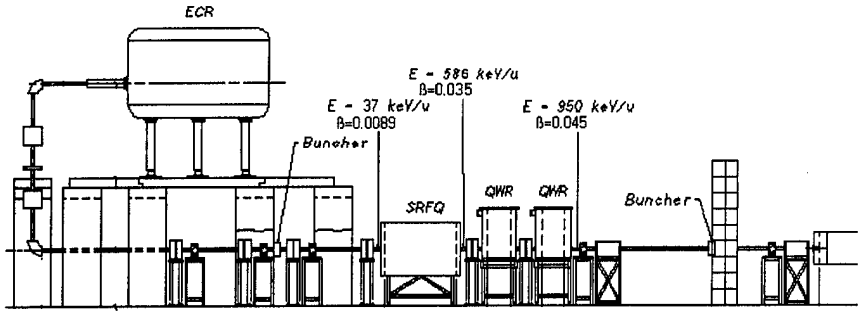


Figure: 2 The Layout of PIAVE

of the ECR output one, following the beam direction. All the magnetic elements of the line were ordered.

The beam analysis is performed by a magnetic spectrometer on the high voltage platform. Therefore the magnetic elements of the line are meant only for the transverse matching of the beam into the SRFQ's and to create the required beam waist at the buncher location.

The beam dynamics studies [3] determined the need for a very efficient bunching system with a low transverse emittance increase. The result of that is a quite innovative design of a triple harmonic buncher [4] realized with two independent cavities as it is shown in figure 3. The two cavities operate at 40-120 MHz and 80 MHz respectively.

The buncher, combining the absence of grids and the use of three harmonics, has a bunching efficiency of ≈68% and it requires a rf power of less than 100 W which allows the use of a room temperature system without severe cooling problems. The cavities are powered by three independent solid state amplifiers controlled by standard ALPI rf controllers. The operation of the first cavity at 40 and 120 MHz is possible due to the different field distribution of the two modes with a careful displacement of the tuners, the couplers and the pick-ups.

In the beam velocity range $0.009 \leq \beta \leq 0.035$ the acceleration is performed by two SRFQ resonators operating at 80 MHz and made of niobium sheets electron-beam welded [5]. The accelerating structure of ~2.5 meters long is split into two different resonators housed in the same cryostat. This choice is dictated by the limitation in the maximum storable energy inside a cavity compatible with the rf phase locking [6].

The novelty of the project, with respect of similar facility already operating in other laboratories, is the presence of the superconducting RFQ [7]. The beam dynamics specifications, the bunching of the beam, which is made before the RFQ with a triple frequency buncher described above, and the particular care put in the design of the cavity both for rf and vibration control reasons are the main peculiarities of the SRFQ design. The complete design of the SRFQ resonators is almost finished and the first stainless steel prototype is in its final construction stage [8].

The accelerating structure is changed, passing from the SRFQ to the QWR, following the indications of the beam dynamics studies at an energy of 578 keV/u, that means $\beta=0.035$ for the nominal uranium beam mentioned above. This beam velocity is too low for the injection into ALPI low β resonators. Therefore a section containing eight QWR's with an optimum β of 0.047 is foreseen for PIAVE. These cavities are similar to the ALPI ones and the first example is now under construction following the production procedures fixed for the ALPI resonators [9].

The matching line between PIAVE and ALPI contains two quadrupole triplets, an achromatic 90^0, made of two bending magnets with a quadrupole singlet using the standard ALPI 'L-Bends', as well as two room temperature bunchers [3].

3 DIAGNOSTICS

To operate the machine eight diagnostic boxes are foreseen in the two beam transport lines. The boxes are equipped with the Beam Profile Monitors and longitudinal phase space diagnostics. Current monitors for the transmission control are located in several boxes.The main issue for this BPM's is the beam intensities expected from the ECR. We would like to use as much as possible our experience with ALPI where the BPM's are harps made of wires 20 μm thick [10]. These BPM's have severe problems with the beam intensities and beam power foreseen for PIAVE, as it has been already experienced with the tandem beams before the charge analysis. The possible solution is to use strips instead of wires for the harps. Alternative solutions, such as residual gas detectors and rotating wires, will be considered.

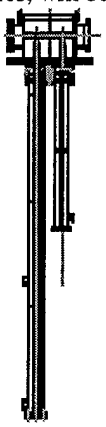


Figure: 3 Schematic of the PIAVE triple harmonic buncher

A transverse emittance measuring box is under construction for the commissioning of the low energy beam transport line and, afterwards, of the SRFQ and QWR's accelerator sections. The apparatus is able to measure beam spots of 60 mm and maximum divergence of 240 mrad with an angular resolution of 3 mrad. The emittance measurements box when it is placed at the output of the SRFQ section and moreover after the QWR section requires a dissipation of thermal power of the order of hundreds Watts.

4 RF AND CONTROL

The resonator controller is an evolution of the ALPI QWR's controller. It operates in self-excited loop mode and locks the cavity phase by adding to the signal driving the amplifier with a reactive component in response to a phase error detection [11,12]. Improvements have been brought to the electronic board to reduce the phase-amplitude cross-talk and to make more accurate the search of the resonance peak. In order to broaden the SRFQ bandwidth to a range of ±10 Hz, a solid state power amplifier delivering 1 kW CW in class AB will be used.

The new injector control system is an extension of the ALPI system and it is based on VME crates connected via Ethernet to UNIX workstation (DEC Alpha) for the operator interface. Some changes have been made to increase the performance; in particular the old CPU boards (68030) have been substituted by new ones equipped with the PowerPC processor running at 200 MHz clock. These boards provide a full support for the Fast Ethernet (100 Mbit/s) and this can be an option for a further system upgrade. The VME CPU boards operate under the real time OS Tornado (by Wind River Inc.).

5 STATUS OF THE PROJECT

The project, which started officially in July 1996, is now in its construction stage for many components.

The ECR source is placed in its final position onto the high voltage platform and has been tested successfully with noble gas beams in May 1996. The resolution of the ion analysis proved to be satisfactory enabling to distinguish ^{132}Xe from ^{134}Xe and to detect a 10 V ripple in the ion source voltage. The high voltage power supply is ready to be installed and tested to the nominal voltage of 350 kV. The electrical power needed by the ECR equipment is provided onto the platform via an insulating transformer with a total power of 135 kVA at 380 V which has been already ordered. For general use with metals, a rf induction oven was built and an oven was tested up to 1950±100 ^{0}C. The beam after the accelerating column is foreseen for the beginning of 1998.

The magnetic elements of the transport lines have been already ordered and are expected to be delivered by the end of 1997. By that time all the ancillary systems, such as vacuum and diagnostics, will be ready for mounting.

The SRFQ2 stainless steel prototype is in its assembly stage and is expected to be finished by the middle of 1997. The niobium pieces for the resonator has been acquired.

The triple harmonic buncher has been designed and it will be ready for testing by the end of may 1997.

The test cryostat for the SRFQ resonators, with the internal screens and reservoirs made in titanium, is under construction.The cryogenic plant for PIAVE has to deliver 130 W at 4.5 K and 600 W at 80 K. The cooling power at 80 K will be provided by liquid nitrogen. A new refrigerating system for the liquid helium has been considered to avoid the overloading of the ALPI system.

In the framework of the PIAVE project a scaled model of a SRFQ working at 160 MHz in dummy cavity has been made for the first attempt of magneto-sputtering deposition of thin films. The preliminary results are encouraging both concerning the uniformity of deposition and the stability of the plasma.

REFERENCES

[1] 'Status of ALPI and Related Developments of Superconducting Structures', by G. Fortuna et al, Proceedings of the XVIII International Linear Acc. Conf., Geneva 1996

[2] 'Commissioning of the ECR source Alice', by M. Cavenago and G. Bisoffi, NIM A328(193) p.262-265, and 'Selection of charge from the ECR Alice without forming a Waist', by M. Cavenago, NIM, A328(1993),266-269

[3] 'Complete simulation of the heavy ion linac PIAVE', by A. Pisent and M. Comunian, these proceedings

[4] 'The triple harmonic buncher for the PIAVE project', by A. Facco and F. Scarpa, to be published in the LNL Annual Report 1996.

[5] 'Superconducting RFQ cavities of the new heavy ion injector at Legnaro', by G. Bisoffi et al., Proceedings of the "Seventh Workshop on RF Superconductivity", Paris, October 1995.

[6] 'Status of the Superconducting RFQ project for the Legnaro New Positive Ion Injector', by A. Pisent et al., Proceedings of EPAC 1996, Sitges (Barcelona).

[7] 'Design of a Superconducting RFQ resonator', by I. Ben-Zvi et al, Particle accelerators 35 (1991) 177

[8] 'Prototype of a Superconducting RFQ for Heavy Ion Injector Linac', by G. Bisoffi et al., these Proceedings.

[9] 'Experience with the bulk niobium low β resonators at LNL', by A. Facco et al., Proceedings of the 7th International Conference on Heavy Ion Acceleration Technology, Canberra, Nucl. Instr. and Meth. in Phys. Res. A 382 (1996) 107-111

[10] 'The beam diagnostic system of ALPI Post-Accelerator', by M. Bellato et al., Proc. of the 3rd EPAC 1992 Berlin.

[11] 'The control and electronics of a superconducting booster module', by I. Ben-Zvi et al., Nucl. Instr. and Meth. A245 (1986)1.

[12] 'Status of the ALPI control System', by G. Bassato et al., Proc. IEEE 7th Conf. on Real Time 91 (1991) 285; 'The Control System of the L.N.L. LINAC', by G. Bassato et al, Proc. of the 3rd EPAC, Berlin 1992.

COMPLETE SIMULATION OF THE HEAVY ION LINAC PIAVE

A. Pisent, M. Comunian,
INFN- Laboratori Nazionali di Legnaro, Padova, Italy.

Abstract

PIAVE is the new injector under construction at LNL for the super conducting linac ALPI. The beam, generated by an ECR source, will be bunched by a three harmonic buncher and accelerated by a couple of super conducting RFQs, followed by eight QWR, for an equivalent voltage of 8 MV (U^{+28} beam). We present here the complete simulation of the injector, where the same ensemble of particles is transported from the buncher up to ALPI. The code used are PARMTEQM, PARMILA and specific software has been written to transport the particles in the field distribution (calculated by MAFIA) of the transition between the two RFQs and in the QWRs accelerating gaps. The performances of this design, especially for what longitudinal emittance is concerned, are discussed in this paper.

PARAMETERS OF THE LINAC

At LNL a new positive ion injector for the super conducting linac ALPI is under construction. The new linac, named PIAVE, will have an equivalent voltage of about 8 MV and will allow the acceleration of ions up to U above the nucleus-nucleus barrier. More details about the project status are given in the general paper [1].

In this paper, after a general overview of the beam parameters of PIAVE (Tab. I), we shall concentrate on the points that have been defined in this last period, namely the Low Energy Beam Transport Line (LEBT), the external bunching, the transition between the two super conducting RFQs. Moreover we show the simulations of the complete injector, where the same ensemble of particles is followed form the buncher up to ALPI.

Table 1
Injector parameters

Source and LEBT			
Ion source	ECR	14 GHz	
Mass to charge ratio	8.5÷1		
Platform voltage*	315	kV	
RMS Emittance	0.1	mm mrad	norm.
Bunching system	3H	40;80;120	MHz
$\Delta\varphi$	±6	deg	80 MHz
ΔW	±0.55	keV/u	
RFQ Accelerator			
Radio Frequency	80	MHz	
Input Energy	37.1	keV/u	β=.0089
Output Energy	586	keV/u	β=.0355
Max. Surface field*	25	MV/m	
Max. stored energy*	≤4	J	RFQ
Acceptance#	≥0.9	mm mrad	(norm.)
Output Emit. RMS	0.1	mm mrad	(norm.)
	≤0.14	ns keV/u	
	SRFQ1	SRFQ2	
Vanes length	137.8	74.61	cm
Output energy	341.7	586	keV/u
Voltage *	148	280	kV
Number of cells	42.6	12.4	
Average aperture R_0	0.8	1.53	cm
Modulation factor m	1.2-3	3	
Synchronous Phase	-40÷-18	-12	deg
QWR Section			
Number of resonators	8		
Output energy*	948	keV/u	β=.045
Radio Frequency	80	MHz	
Optimum β	0.05		
Accelerating Field	3	MV/m	
Shunt impedance	3.2	kΩ/m	
Synchronous Phase	-20	deg	
Matching Line to ALPI			
Number of bunchers	2	(room temperature)	
Buncher eff. Voltage	VT	≤100	kV

THE LEBT

The LEBT is now completely defined, magnets have been ordered to the industry and the construction of the bunchers has been launched.

The line, following the accelerating column, is composed by an achromatic bend, a couple of doublets that make a small waist at the buncher, followed by the second couple of doublets needed for the matching at the RFQ input.

After the analysis of different options we have selected a three harmonics buncher, with 40 MHz as fundamental frequency, at a distance of 3.51 m from the RFQ input. Indeed, since for each harmonic we use a two gaps configuration, the first and the third harmonics are applied in a first buncher, the second harmonic in a second buncher at a distance of 120 mm; all voltages are below 4 kV [2] [3].

The design efficiency of the bunching is such that 70% of the particles are captured by the RFQ with a final RMS longitudinal emittance of 0.13 ns keV/u with nominal focusing. Simpler configurations, like double drift double frequency bunchers, have not the same

* The values are referred to mass over charge ratio $8.5(^{+28}U^{238})$.

We conventionally relate total and RMS values as $\varepsilon=5*\varepsilon_{rms}$

0-7803-4376-X/98/$10.00 © 1998 IEEE

performances, due to the fixed distance between the two bunchers and the consequent difficulty of getting small beam waists in all gaps.

THE RFQS

The major constraints for the RFQ design, dictated by the superconducting nature of the cavities, are the maximum electric surface field E_s (25 MV/m) and the maximum stored energy per resonator U (4 J). This last value is imposed by the RF power needed to keep the resonator locked within the required frequency window of ±10 Hz.

Due to the high costs of a super conducting structure and associated cryostat in the design of the RFQ modulation big emphasis was given to the maximization of the average acceleration; this was pursued with the external bunching, and keeping the modulation factor m, kR_0 (average aperture over modulation wavelength) and intervane voltage V relatively large [4][5]. Moreover the specification for U imposed the use of two electromagnetically decoupled RFQs.

The drift space of 200 mm between the two RFQs electrode terminations determines a certain beam mismatch in SRFQ2 and a consequent problem in keeping the specified acceptance. Cutting the electrodes where the beam envelopes have a waist can minimize the problem [6][7]. This corresponds to a length of

$$\frac{\beta\lambda}{2}\left(\frac{1}{2}-\frac{\phi_s}{\pi}\right)$$

for the last cell of SRFQ1 and correspondingly for the first cell of SRFQ2 (almost *half-cell*).

This *half-cell* has been simulated using MAFIA Electrostatic solver, so to have an accurate description of both the focusing and the accelerating field components. In doing this it is important to take into consideration the (local) electrode voltage relative to ground, determined by the resonator supports geometry. In our resonator the modulation is such that, in first approximation, this special cell has the focussing effect of half-cell (minimum mismatch) and the acceleration of a full cell (maximum acceleration) [8].

SIMULATIONS

Multi-particle simulations have been done using the LANL programs PARMTEQM, in the RFQs, and PARMILA, for the transfer lines and the QWRs section. The same ensemble of 10000 particles is transported from the bunchers up to the end of the accelerator. The space charge can be completely neglected up to 5 μA, while we do not aspect more than 1 μA from the source. In the transition between the two RFQs particle trajectories are calculated with a dedicated code using the MAFIA fields.

In fig. 1 we summarized the result of simulations as function of the initial transverse emittance; namely the RFQ transmission, the total PIAVE transmission (including bunching efficiency), and the longitudinal emittance after the RFQs and after the QWRs are plotted. In the QWR section there is an emittance growth due to the change of longitudinal and transverse focusing structure. Nevertheless correspondingly to the ECR nominal RMS emittance (0.1 mmmrad) 70% of the particles are transmitted with a final longitudinal emittance within the specifications.

In fig. 2 we show the transverse and longitudinal phase space in critical locations for the nominal beam. In particular it is possible to appreciate the longitudinal phase space evolution all over PIAVE and the residual mismatch at the transition between the two RFQs.

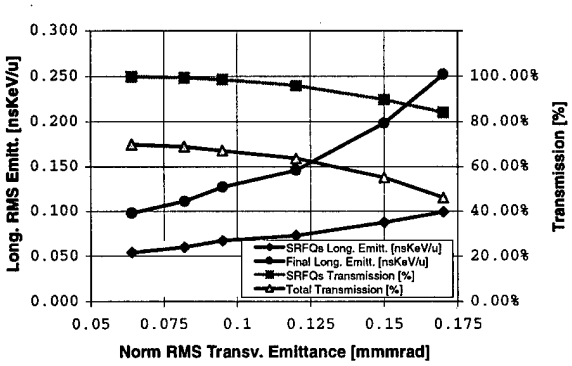


Fig. 1 Long. Emittance and Transmission as function of Transverse Initial Emittance.

ACKNOWLEDGEMENTS

We thank J. Billen and Lloyd Young (LANL) that have provided us the simulation codes, and Augusto Lombardi, Giovanni Bisoffi and Alessandra Lombardi (CERN) for many useful discussions.

REFERENCES

[1] Lombardi et al., "The new positive ion injector PIAVE at LNL" This Conference Proceedings.
[2] M. Comunian, A. Pisent, "LEBT and Three Harmonics Buncher Design for PIAVE" LNL Annual Report, 1996.
[3] Facco, F. Scarpa, "The new triple harmonic buncher for the PIAVE project" ibid.
[4] BenZvi, A. Lombardi and P. Paul, Particle Accelerators 35 (1991) 177
[5] Pisent, "Beam Dynamics of the new LNL Injector" LNL-INFN (REP) 107/96.
[6] Y. Iwashita, H. Fujisawa, Linac Conference Ottawa, 1992, pg. 698-700.
[7] Kolomiets, LNL Internal note.
[8] Pisent, M. Comunian, in preparation.

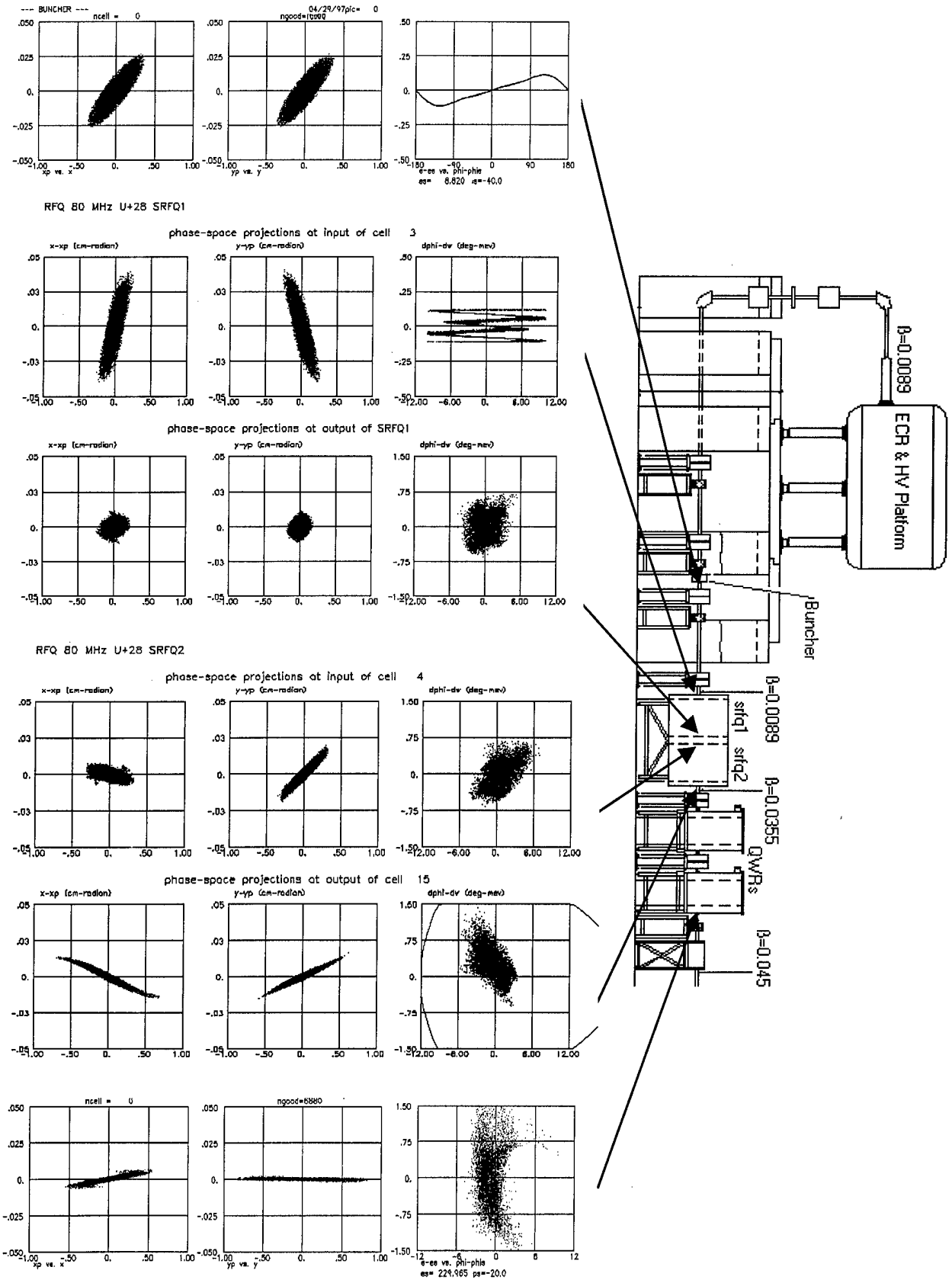


Fig. 2 PIAVE layout and transverse and longitudinal phase space in various locations.

A TRIPLE GAP RESONATOR DESIGN FOR THE SEPARATED FUNCTION DTL AT TRIUMF

Y. Bylinsky, V. Kukhtiev, P.N. Ostroumov, V. Paramonov, INR RAS, Moscow and
R.E. Laxdal, TRIUMF, 4004 Wesbrook Mall, Vancouver, B.C., Canada V6T 2A3

Abstract

A separated function, variable energy, drift tube linac (DTL) operating in cw mode is being built for the ISAC radioactive beam facility at TRIUMF. Longitudinal focussing is achieved by positioning 105 MHz rebunching cavities immediately upstream of the second, third and fourth IH accelerating tanks. The three devices must operate at a relatively low β (2.3%, 2.7%, 3.3%)and deliver peak effective voltages in cw mode of 0.19, 0.26 and 0.32 MV respectively. In addition the geometry must allow a large voltage dynamic range for the variable energy operation. A three gap cavity has been chosen as a trade-off between velocity acceptance and peak effective voltage. Several cavity geometries have been considered in order to identify the optimal geometry for this application. We present here a summary of the available buncher designs.

1 INTRODUCTION

A radioactive ion beam facility with on-line source and linear post-accelerator is under construction at TRIUMF [1]. A separated function drift tube linac (DTL) operating in cw mode is required to accelerate ions of $1/3 \geq q/A \geq 1/6$ to a final energy fully variable between 150 keV/u to 1.5 MeV/u[2]. Five independent interdigital H-type structures operating at 105 MHz and 0^0 synchronous phase, provide the acceleration while quadrupole triplets between IH tanks provide the transverse focussing. Longitudinal focussing is achieved by positioning independently phased, 105 MHz rebunching cavities immediately upstream of the second, third and fourth IH tanks.

The rebunchers have two prime functions. In acceleration mode they are used to match the longitudinal beam characteristics to the next IH accelerating tank. In reduced energy operation the re-bunchers maintain longitudinal transport through the non-accelerating sections of the DTL. The two modes require quite different specifications. The maximum effective voltage is required during the acceleration mode while the bunching mode requires a large variation in the voltage. In addition the re-bunchers must be physically compatible with the upstream quadrupoles and a downstream diagnostic box consistent with the aim to keep the inter-tank lengths short to reduce longitudinal emittance growth due to debunching.

2 RE-BUNCHER SPECIFICATIONS

Both two and three gap structures have been studied. The triple gap cavities are more efficient to deliver effective voltage at the design velocity of the structure but the double gap cavity has more velocity acceptance. The efficiency of the two structures to accelerate at velocities other than the design velocity, β_0, can be calculated from the following:

- for the double gap cavity

$$TT_2 = \frac{2}{\pi}\frac{\beta}{\beta_0}\left[\cos\frac{\pi}{4}\frac{\beta_0}{\beta} - \cos\frac{3\pi}{4}\frac{\beta_0}{\beta}\right]$$

- for the triple gap cavity

$$TT_3 = \frac{1}{\pi}\frac{\beta}{\beta_0}\left[2\sin\frac{\pi}{4}\frac{\beta_0}{\beta} + \sin\frac{3\pi}{4}\frac{\beta_0}{\beta} - \sin\frac{5\pi}{4}\frac{\beta_0}{\beta}\right]$$

Here we have assumed a square field approximation with a cell length given by $\beta_0\lambda/2$. The results are displayed in Fig. 1.

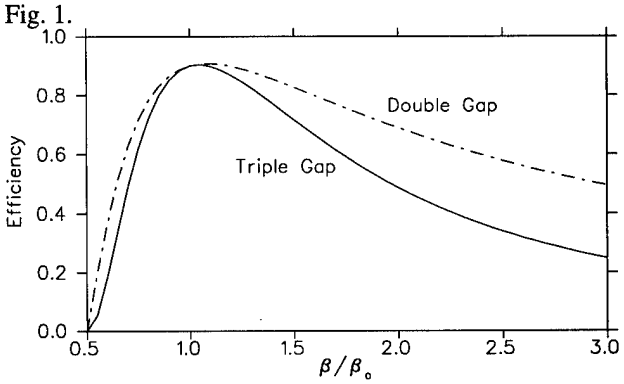


Figure 1: The acceleration efficiency, as a function of beam velocity, of both a two gap and a three gap buncher.

A summary of the buncher specifications for both the two gap and the three gap solutions are given in Table 1 for the design particle of q/A = 1/6. The effective voltage V_{eff} is quoted for the design velocity. V_T is the peak tube voltage. The drift tube aperture is a=14 mm and the frequency is 105 MHz for all cases.

In variable energy mode simulations[3] it was found that, for the design particle of A/q = 6, a minimum buncher setting of 30% of the values quoted in Table 1 was required. This corresponds to an absolute minimum of 15% of the quoted value for A/q = 3. This led to the specification for the re-bunchers of multipactor free operation from 10% to 100% of maximum.

0-7803-4376-X/98/$10.00 © 1998 IEEE

Buncher	β (%)	β_0 (%)	L (cm)	V_{eff} (MV)	V_T (kV)
Double gap					
B1	1.8-2.3	2.3	6.6	.19	118
B2	1.8-3.1	2.3	6.6	.28	175
B3	1.8-4.1	2.3	6.6	.37	230
Triple gap					
B1	1.8-2.3	2.3	9.8	0.19	60
B2	1.8-3.1	2.7	11.6	0.26	78
B3	1.8-4.1	3.3	14.1	0.32	94

Table 1: Summary of parameter specifications for both double gap and triple gap bunchers (B1-B3) for the design particle of q/A = 1/6. The effective voltage V_{eff} is quoted for the design velocity β_0. V_T is the peak tube voltage.

3 SHUNT IMPEDANCE

The specification restricts somewhat the choice of structure. Coaxial λ/4 resonators, spiral resonators (fig. 2), split-ring resonators (fig. 3) and arc-type resonators (fig. 4) have all been considered as candidates for the buncher. All these structures have been generated with MAFIA in order to compare their shunt impedances. Similar drift tube structures are chosen for all resonators in the initial comparison. Shunt impedances and rf losses for the most challenging case, B3, are shown in table 2.



Figure 2: MAFIA plot of half of the internal part of the 2-gap spiral buncher.

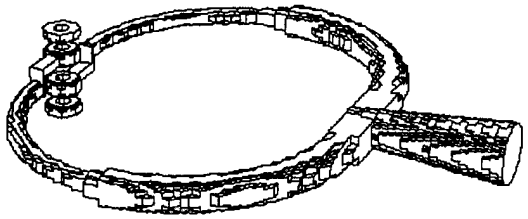


Figure 3: MAFIA plot of internal part of the 3-gap split ring buncher.

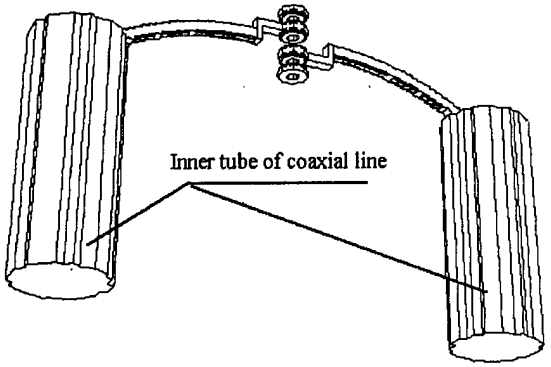


Figure 4: MAFIA plot of internal part of the 3-gap arc-type buncher.

Structure type	Double gap		Triple gap	
	coaxial	spiral	split ring	arc-type
R_p, MOhm	6.6	7.4	14	21.2
P_0, kW	32	29	11	7.5

Table 2: MAFIA results for several buncher structures (B3 specifications). Here P_0 - rf losses; R_p - shunt impedance:

$$R_p = \frac{(V_{eff}/T)^2}{P_0}.$$

From the table it is clear, that the 2-gap structure, either coaxial or spiral, will meet very serious problems with cooling. Also the most efficient arc-type structure was abandoned due to its large size and the absence of performance experience. On the other hand the split-ring structure is known to be quite stable against multipactor discharge and has shown good performance at very high power levels[4]. So, detailed study has been performed only for the split ring structure in order to clarify specifications for all 3 bunchers (see Table 3).

4 MAXIMUM ELECTRIC FIELD GRADIENT

Due to the high drift tube voltage and short gaps high surface electric fields were expected to be a problem. Maximum electric field on the drift tube surface has been estimated by solving an electrostatic problem (Poisson equations) with SUPERFISH. The gap lengths as well as the drift tube curvature have been optimized in order to reduce maximal field gradients. The central gap has been assigned to be two times longer than the two outermost ones ($Lg_c=2Lg_o$), keeping the designed inter-gap distance $\beta_0\lambda/2$ (see fig.5). It allows a slight increase in efficiency as

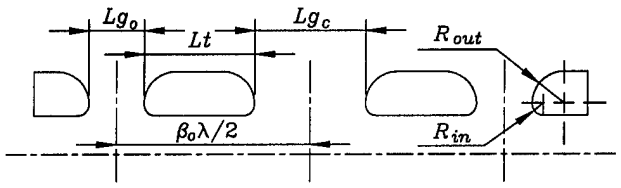


Figure 5: Drift tubes geometry for the 3-gap buncher.

well as a reduction in field gradients by 15%. The central gap length Lg_c is equal to the tube length as a trade-off between acceptable surface fields and sufficient buncher efficiency. Fig. 6 shows the maximum surface field and efficiency dependencies upon the ratio Lg_c/Lt for equal gap lengths (curve 1) and for optimized gaps: $Lg_c=2Lg_o$ (curve 2). The optimal ratio of the drift tube tip radii is about $R_{out}/R_{in}=3$ (see fig. 5). Finally, numbers in Table 3 represent nominal buncher parameters. In addition to the shunt impedance, MAFIA gives the following RF loss distribution among the structure units:

- cavity walls - 30%;

- drift tubes - 10%;
- supporting ring - 60%.

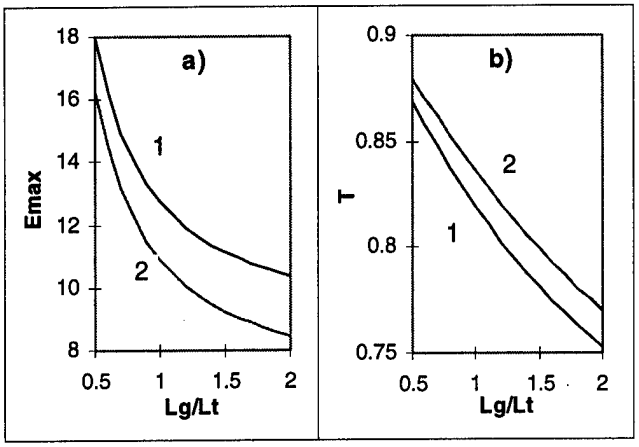


Figure 6: a) maximum surface field and b) acceleration efficiency with the ratio of gap to tube length. Curve 1: $Lg_c=Lg_0$; curve2: $Lg_c=2Lg_0$.

Buncher		B1	B2	B3
V_{eff}	[MV]	0.19	0.26	0.32
Es_{max}	[MV/m]	9.8	11.1	10.9
R_p	[MOhm]	12.0	13.0	14.0
P_0	[kW]	6.4	10.5	14.0

Table 3: Nominal buncher parameters. The quoted shunt impedance values are from MAFIA. The power calculations assume a shunt impedance 75% of the value quoted.

5 MECHANICAL DESIGN

A general view of the equipment in front of DTL tank #2 is shown in the fig. 7. The buncher will be brazed to the downstream diagnostic box due to the tight inter-tank space. Drift tubes, supporting ring as well as cavity are going to be made of copper. Principal dimensions of the structure are collected in Table 4.

Tank diameter	[mm]	550
Tank length	[mm]	98 (116, 141)
Ring diameter	[mm]	350
Ring tube diameter	[mm]	30
Aperture	[mm]	14
Drift tube diameter	[mm]	30

Table 4: Principal dimensions of the split-ring bunchers

The rf amplifier feedback system requires a frequency tuner, which will be made as a movable plate with capacitive coupling to the drift tubes. Cooling channels will go through the tank walls, including the endplates. The most heated ring will require a separated cooling circuit for each half ring with water flow of about 150 cm^3/s. The ring water will also cool the drift tubes.

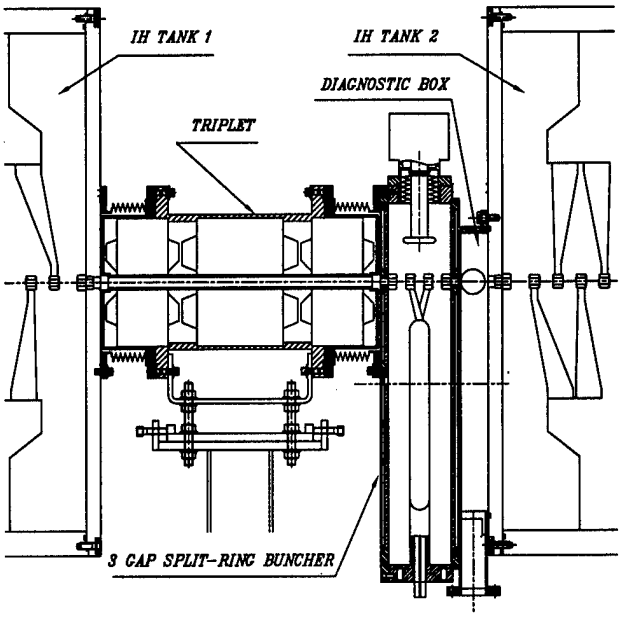


Figure 7: General view of the equipment in the inter-tank space.

6 CONCLUSION

As usual in the design of rf cavities the choices were made as a compromise between contradictory requirements:

- maximum effective voltage;
- minimum surface electric fields;
- minimum rf power consumption;
- minimum size along the beam axis.

The studies show that the 2-gap buncher cannot be used due to extremely high surface field and power consumption. The 3-gap buncher with split-ring structure has been chosen for all DTL bunchers. The arc-type configuration was abandoned due to its large size and absence of performance experience.

In the most challenging case maximum surface fields are moderate (≤11 MV/m) with a rather high heat load (≤14 kW). So the cooling solution together with good mechanical stability should be carefully tested.

A working prototype of Buncher 1 is scheduled to be completed by the spring of 1998.

7 REFERENCES

[1] P. Schmor, et al., Status of the TRIUMF ISAC Facility for Accelerating Radioactive Beams, these proceedings.

[2] R. Laxdal, et al., A Separated Function Drift-Tube Linac for the ISAC Project at TRIUMF, these proceedings.

[3] R. Laxdal, The Separated Function Drift Tube Linac for ISAC, TRI-DN-97-4, TRIUMF Design Note, April 1997.

[4] E. Muller and H. Klein, The Split-Ring Loaded RF Cavity, Nuclear Inst. and Meth. 224 (1984), p.17.

BBU GAIN MEASUREMENTS ON THE ITS 6-MeV, 4-kA LINAC

Paul Allison and David C Moir
Los Alamos National Laboratory

Abstract

The amplification of transverse beam motion by the ITS eight-cell linear induction accelerator (LIA) was measured with a 4-kA beam at frequencies between 710- and 950-MHz. The 3.75-MeV injector beam was deflected with amplitudes of ~ 1 mrad by an RF-driven tunable cavity 84 cm before the linac. The centroid-position waveforms from calibrated B-dot loops were recorded with 5-GS/s digitizers at the linac entrance, exit, and after a further free drift of 108 cm. The FFT amplitudes of the waveforms were used to compute the gains. The code LAMDA, an envelope and BBU model for the linac, was used to interpret the gain curves, using the transverse impedances of the cells as adjustable parameters. The results compare favorably with cell impedances previously measured with a two-wire TSD method.

PURPOSE

Beam-breakup (BBU) was first observed and described at SLAC, where the beam current disappeared (broke up) after going partway down the linac[1] because of the excessive amplitude of transverse motion. This amplitude grows approximately[2] as $\exp(ni_b\omega Z/c^2B)$ for a beam of current i_b in a linac of n cells with peak transverse impedance $\omega Z/c$ and solenoidal magnetic field B. We require for DARHT[3] that the transverse motion at the X-ray target be a small fraction of the inherent spot size of ~ 1 mm. DARHT cells were designed for low transverse impedance, which we measured[4] using the two-wire through-short-delay (TSD) method. The purpose of our BBU experiment is to measure amplification with a 4-kA beam, deducing the frequency dependence of $\omega Z/c$ using our beam dynamics code LAMDA[5], to compare with the TSD measurements.

EXPERIMENT

Beam was deflected in the Y-plane before the ITS linac (Fig.1) entrance with a tunable "tickler" box[6]. Centroid deflections in the X- and Y-planes were measured with beam-position monitors (bpms) at the linac entrance (bpm3), exit (bpm5), and after a field-free drift of 108 cm (bpm6). In effect, the angles at bpm5 are determined by the positions at bpm6 and bpm5, therefore a complete measurement of the centroid motion at bpm5 is made. The tickler box had a single mode below pipe cutoff frequency of ~ 1.2 GHz, with the pipe offset so that RF-deflection of the beam would occur. The bpms were precision B-dot loop types[7], individually calibrated. Each bpm was connected, without integrators, to Tektronix TDS-684 5-GS/s digitizers through 30-db attenuators with cables time aligned through the digitizers to ~ 20 ps. The waveforms were clean but damped by beam loading as it is deflected in the 8-cm length of the box. Since the

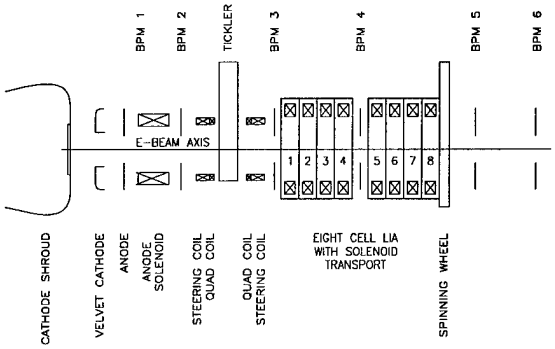


Fig.1 Layout of ITS for BBU experiment

frequency was not an exact multiple of the bin spacing of 20 MHz, the power spectral density (PSD) of the waveforms over 50 ns was summed over ± 3 bins around the peak, adequate to include ~ 99% of the signal. A waveform for bpm6x is shown in Fig.2, along with the FFT analysis, converted approximately to μ. Gains are defined as gx5 = [PSD(bpm5x)/PSD(bpm3y)]$^{1/2}$, and similarly for gy5, gx6, and gy6.

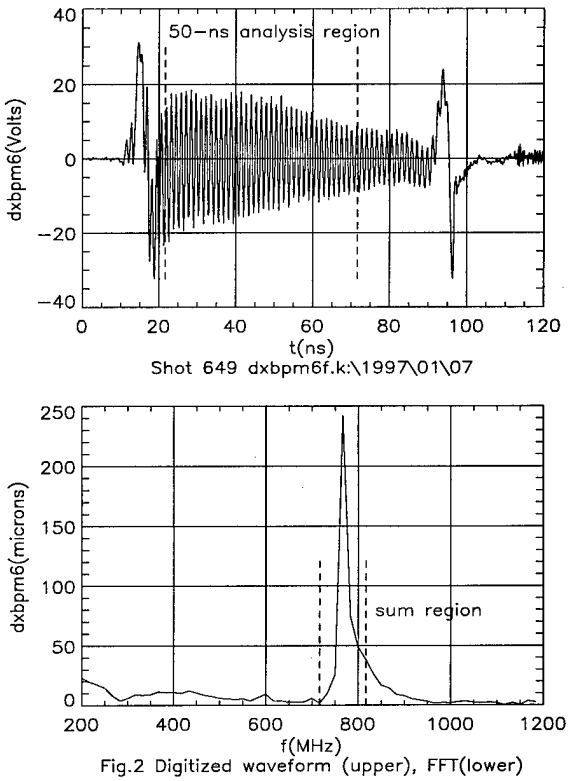


Fig.2 Digitized waveform (upper), FFT(lower)

The injector was operated at 3.75-MeV, 3.8-kA, the linac at 224-kV/cell. The eight linac magnets had a total phase advance of 2.48π with B ~ 700 to 900 G. There

0-7803-4376-X/98/$10.00 © 1998 IEEE

was no observable current loss to bpm6, 734 cm from the cathode, to within our 2% accuracy. Field maps were made of all linac magnets in situ, so that the effects of ferrites and mu-metal shielding on the fields were included, and accurate models of these fields were then used in the codes. We drove the tickler with a 25-W RF amplifier to stabilize the deflection amplitude to ~ 20%.

We did steering experiments[8] at low (~0.3 kA) and at high (3-kA) currents to verify overall accuracy of calibrations of magnets and bpms, data capture and analysis, and code physics. Besides verifying basic calibrations, this led to the discovery that for steady-state steering, the centroid steers as if the beam-potential depression bpd = $(i_b Z_0/2\pi\beta)\ln(R_w/r_b)$ from the wall, R_w = 7.41 cm, to the beam edge r_b were zero. We also discovered that the quadrupole image-field of the beam in the tickler box, $\int \nabla_\perp B dz \approx 5$ G/kA, made the beam highly elliptical (up to ~ 3x at bpm3). Analysis shows that the fractional bpm response error = $3(r_y^2-r_x^2)/4R_w^2$ ~ 20% in some cases (beam radii r_x, r_y). To eliminate this error, we added quadrupole corrector coils (Fig.1) around the tickler box and measured ellipticity near bpm3 as a function of the frequency of the tickler and the corrector settings, then used this data to set the corrector currents for the BBU experiment. Over its full range of ± 20 A, we found that apparent gains at bpm5 and bpm6, near the BBU gain maximum at ~ 760 MHz, varied up to 30% but were not very sensitive to uncertainties around the proper setting of about 6.5 A. To eliminate the quadrupole effect entirely, we measured gains with a circular cavity with TM_{110} modes at 764 MHz. The results closely matched those with the rectangular tickler.

The TSD-measured impedances showed that the TM_{120}-like modes near 800 MHz would dominate over those near 300 MHz. We made our measurements with excitation in the Y-plane only, from 710 MHz up to 950 MHz in 20-MHz steps, then back down at intermediate frequencies. During the downward steps, there was an injector energy shift of about 100 keV, which shifted the up/down gain curves by 5-20%. We took a smooth average of the data, about 250 shots at 23 different frequencies. Out of ten shots at each frequency, typically two were discarded because of low amplitude, the remainder then having gains with a standard deviation of only ≈ 4%.

ANALYSIS

Simulations[9] with the PIC code ISIS show that at 800-MHz, as for steady-state steering[8], the bpd is essentially zero for the centroid dynamics, therefore LAMDA was modified accordingly. The LAMDA model for the centroid has the image-displacement steering of the pipe and of the gaps. We neglected the effect of impedance of three bellows, ~ 1 Ω/cm each. The TSD-measured impedance values for all cell modes were used initially in LAMDA, then the eight values of Q, f, and reZ and imZ at resonance f were varied for the two ~ 800-MHz modes. During the TSD measurements we had observed that with ferrite bias current of 500 A, the impedances declined by ~ 10% and the frequency changed by a few percent, so it is expected that cell parameters under beam conditions may differ slightly from the TSD values.

We define fom = $[\Sigma(gm-gc)^2/\Sigma gc^2]^{1/2}$, summed over all frequencies, as a convenient figure of merit for comparing the measured and calculated gains gm and gc. The fom was calculated for each of the four gains gx5, gy5, gx6, and gy6 and for the magnitudes g5 (= $[gx5^2 + gy5^2]^{1/2}$) and g6. Generally, g5 and g6 are less affected by the imaginary impedances or the energy (phase advance) than the other four gains. We tried to minimize all six fom's simultaneously. Positive fom means that the weighted gm > gc and vice-versa.

The best match of LAMDA to the BBU measurements is shown in Fig.3, having adjusted the injected beam energy to 3.62 MeV, 130 keV or 3.5% below the nominal value. This could mean that the bpd cancellation is not complete under all conditions of our measurements. The magnetic fields are probably accurate to better than 1%, otherwise a possible source of the discrepancy. There is a clear determination from LAMDA of the energy to ~ 1%, however, from the ratio of X- and Y- gain amplitudes at bpm5 and at bpm6. The best values of LAMDA model parameters are shown in the table for the X- and Y-planes, along with the

	TSD	LAMDA
f_x(MHz)	760	790
Q_x	4.5	4.6
reZ_x(Ω/cm)	6.35	6.03
imZ_x(Ω/cm)	-1.8	-1.
f_y(MHz)	785	780
Q_y	5.3	5.5
reZ_y(Ω/cm)	8.8	6.45
imZ_y(Ω/cm)	1	-5.5

TSD-measured values. The LAMDA values are lower by 5% and 27% in X and Y. The average $reZ_{x,y}$(Ω/cm) are 7.6 (TSD) and 6.2 (LAMDA). If the code energy is increased to the nominal 3.75 MeV, then only g5 and g6 can be matched well, in which case the optimum average is 6.8 Ω/cm. We believe that the TSD measurements determined reZ to ±20%, imZ to ±2 Ω/cm. LAMDA fits reZ to ~5%, imZ to ±1 Ω/cm. We might expect the imZ to be near their zero-frequency values[8] of ~ -3.5 and -4.5. Neglect of bellows impedances and other modeling omissions or errors may influence the fit values of any of the parameters, of course, but the BBU experiment determines that reZ is 10-20% lower than the TSD values.

CONCLUSIONS

Measurements of the BBU gains and their theoretical interpretation give results that are close those expected from the TSD measurements but more favorable for DARHT operation. The cancellation of the bpd for centroid motion observed for steering[8] appears to be ~ 1/3 incomplete for our RF frequencies. Beam performance predictions at the DARHT X-ray target used the higher TSD impedances, therefore BBU motion at the target should contribute negligible spot blur.

REFERENCES

[1] W. K. H. Panofsky and M. Bander, RSI Vol.39, No.2, 1968, p.206, "Asymptotic Theory of Beam Break-Up in Linear Accelerators"

[2] George J. Caporaso & Arthur G. Cole, "High-Current Electron Transport", UCRL-JC-108050, Particle Accelerator School September 1991

[3] M. Burns, P. Allison, R. Carlson, J. Downing, D. Moir, and R. Shurter, "Status of DARHT", XVIII International Linac Conference, Geneva, August, 1996.

[4] L. Walling, Paul Allison, M. Burns, D. J. Liska, D. E. McMurry, "Transverse impedance measurements of prototype cavities DARHT", 1991 PAC, San Francisco

[5] T. P. Hughes, T. C. Genoni, R. M. Clark, "Lamda User's Manual", May, 1996, MRC/ABQ-R-1798

[6] Designed by George Caporaso, LLNL, who describes an earlier BBU experiment in G. J. Caporaso, A. G. Cole, K W. Struve, "Beam-Breakup (BBU) Instability Experiments on the Experimental Test Accelerator (ETA) and Predictions for the Advanced Test Accelerator", IEEE Trans. on Nucl. Sci. Vol. NS-30, No.4 August, 1983, p.2507

[7] R. L. Carlson, R. N. Ridlon, and L. E. Stout, RSI 57(10), Oct. 1986, p.2471, "Multigigahertz beam current and position monitor for relativistic electron beams"

[8] Paul Allison, David C. Moir, Gary Sullivan, "Observation of Self-Steering Effects on the ITS 6-MeV Linac", PAC97 conference

[9] T. P. Hughes, "Steering Effects in ITS Experiments", MRC/ABQ-N-576, July, 1996, and recent calculations on the RF steering

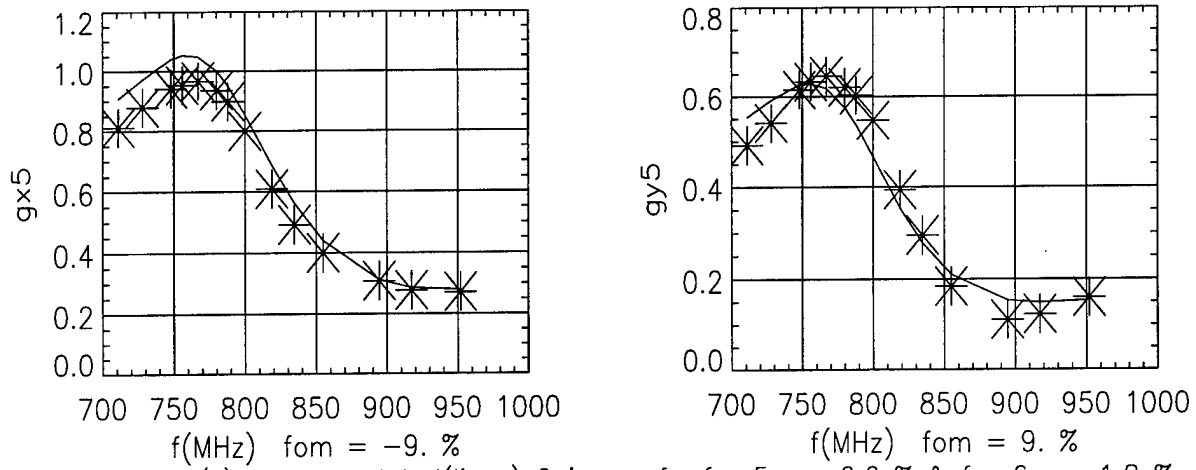
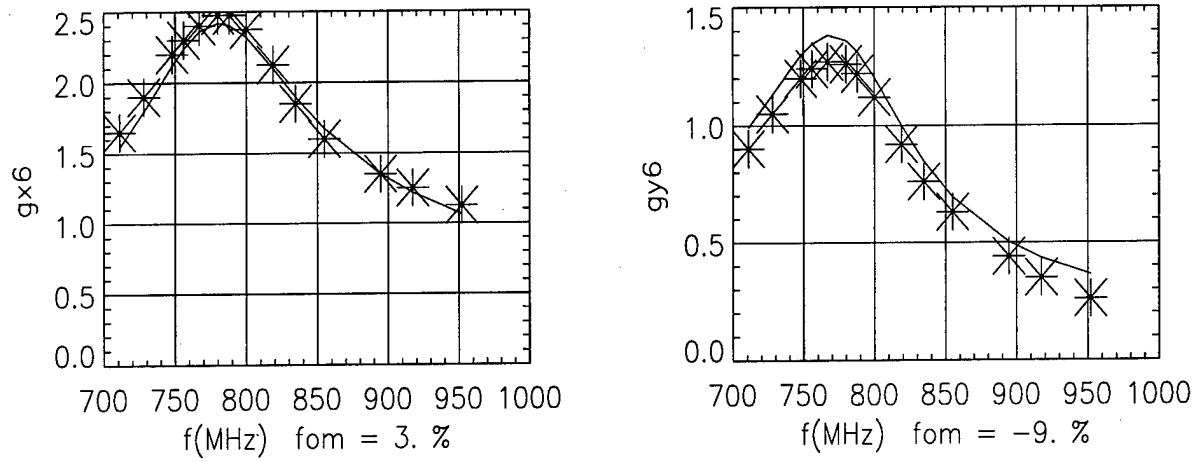


Fig.3 Measured(*) and Calculated(lines) Gains vs f, fom5 = −6.6 % & fom6 = −1.8 %



QUADRUPOLE IMAGE-CURRENT EFFECTS IN THE ITS 6-MeV, 4-kA LINAC

Paul Allison and David C. Moir
Los Alamos National Laboratory

Abstract

The eight accelerating cells for the ITS linear induction accelerator (LIA) are driven with two 50-Ω lines at 250 kV for 60 ns. The wall return currents for the 4-kA beam then pass through these lines, generating a weak steady-state quadrupole field of ~ 3 G integrated strength on axis, which causes a small asymmetry in the nominally round beam at the linac exit. Beam-dynamics simulations with the particle-tracing code SCHAR show that if uncorrected, this would increase the beam emittance at the end of the DARHT 20-MeV linac, therefore quadrupole-corrector coils (QC) were added to each cell, in addition to the existing dipole steering coils. Measurements of the asymmetry of the ITS beam as a function of excitation current of these corrector coils are in good agreement with simulations, giving confidence that there will be negligible emittance degradation from this effect for DARHT.

INTRODUCTION

The DARHT accelerator[1] is designed to produce a 20-MeV, 4-kA beam of 60-ns duration, focused to about 1-mm diam on a tungsten target for flash X-ray measurements of explosive shots. Focusing (by solenoids) and acceleration are axisymmetric, therefore the beam should always be round. However, in initial

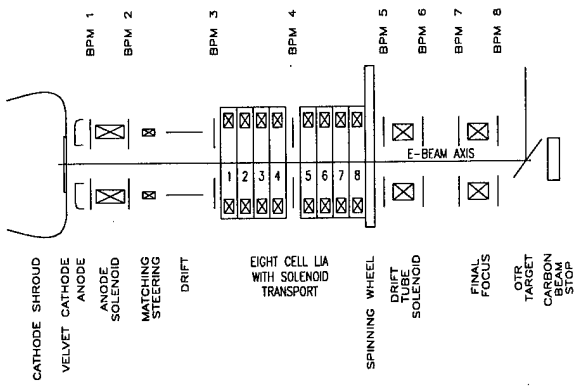


Fig.1 Layout of ITS for quadrupole experiment

measurements on the ITS prototype (layout shown in Fig.1) we found significant asymmetries after acceleration through the first block of eight induction cells, particularly with weak focusing transport. The source of asymmetry is presumably a weak quadrupole image field (QIF) produced by wall return currents into the drive rods of the accelerating cells (Fig.2). Calculations with the code SCHAR[2] showed that the QIF would have a negligible effect under the conditions of the design tune but might lead to significant emittance growth and beam asymmetry under other conditions.

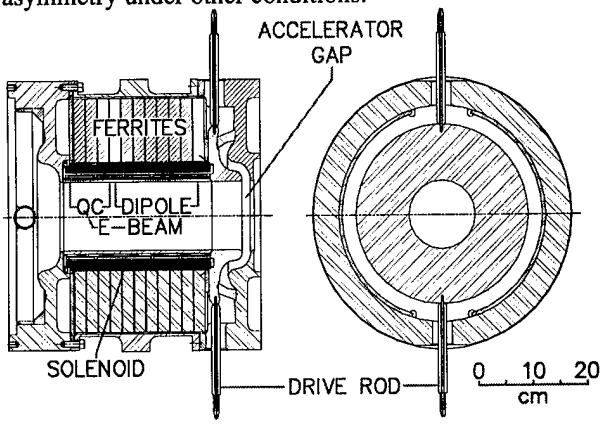


Fig.2 ITS accelerating cell geometry

Our cell uses two drive rods to supply cell voltage. This symmetry eliminates dipole fields produced by the drive rods, which each carry $(i_b + i_f)/2$, where $i_b = 4$ kA and ferrite current $i_f = 500$ A, both approximately constant during the 60-ns pulse. We designed[3] the cell for minimum transverse impedance and discovered during RF measurements[4] of prototypes that the normally degenerate TM_{110}-like modes were split by ~ 100 MHz by the rods coupling into the drive lines, reducing the frequency-averaged impedance by about half. Four drive rods would eliminate the QIF but at the cost of higher transverse impedance.

The integrated strength $b \equiv \int g dz$, with $g \equiv \nabla_\perp B$, of the QIF can be estimated[5] by assuming that the wall current i_b crosses the gap $w = 1.9$ cm, half at 0° and half at 180°, at distance $D = 23.3$ cm from the axis, leading to $b \sim i_b Z_0 w/2\pi c D^2 = 0.70$ G/kA. Calculations[5] with the 3-D code BTEC, using ferrite permeability 250, give $b = 1.0$ G/kA, or 0.77 G/kA without the ferrites. Each cell already had a Lambertson-type dipole steering pair for beam alignment, so we added a quadrupole corrector (QC) circuit to the printed-circuit foil. Since the quadrupole strength depends only on beam current, which is constant through the linac, a single power supply of ~ 3 A can be used to null the QIF.

The single-particle dynamics for continuous solenoidal field B and quadrupole gradient g for a beam without acceleration give $x'' = ky' + Gx$ and $y'' = -(kx' + gy)$, where $k = B/B\rho$ and $G = g/B\rho$. Combining these leads to $y'''' + k^2 y'' - G^2 y = 0$ and

0-7803-4376-X/98/$10.00 © 1998 IEEE

similarly in x, the solution to which is $\exp(i\Omega z)$, where $\Omega^2 = k^2 \pm (k^2+4G^2)^{1/2}$. Thus, there is exponential growth unless $G \equiv 0$. With $g \sim 3$ G/43cm and $B \sim 2$ kG, $\Omega \sim \pm 1/20$ cm, $\pm i/286$ m. The accelerator length L for DARHT is 32.2 m, making the exponential growth factor only ~ 1.1. Emittance calculated with SCHAR grows very rapidly with quadrupole strength but is low at the nominal strength, in qualitative agreement with this simple model. The QIF changes the beam angle r' by $\delta r' \sim br/B\rho$ per cell, which should be made small compared with the thermal spread $\theta \sim \varepsilon_n/\beta\gamma r$, leading to beam radius $r << (mc\varepsilon_n/eb)^{1/2} = 7$ cm for 4rms normalized emittance $\varepsilon_n = 0.14\pi$-cm-rad. For DARHT, r varies from about 1 cm at injection to 0.5 cm at the exit, well under 7 cm.

EXPERIMENT

For this experiment, the QC were added to cells #5-8 only. The QC location (Fig.2) is close to the accelerating gap but displaced by one cell, hence in operation the first QC in DARHT will probably not be used. A field map of the QC in the cell showed that its strength was increased ~ 60% over the air value to 1.1 G/A. We operated all eight linac solenoids at 140 A, about 500 G peak and less than half the design value, to make the beam radius larger to enhance the QIF effect. All four QC's were operated in series over the their maximum range, ± 20 A. The injector was operated at 3.55 MeV, 3 kA, and the accelerating cells were operated at 214 kV each, giving 5.26 MeV final energy.

A line schematic of the experimental set-up for optical measurement of ellipticity is shown in Fig.3. The electron beam is focussed on a 6-μm-thick aluminized Kapton (Al/K) detector that is located 64.2 cm from the center of the final focus magnet. The beam interacts with the foil to produce optical transition radiation (OTR). This visible light is imaged on the photocathode of a gated microchannel plate (MCP). The MCP is gated for 20 ns and timed to be in the center of the 60-ns flat-top of the beam pulse. A cooled ccd camera interfaced to the MCP is used to collect the image data. The rms beam diameter was typically 15 mm. The targets were not damaged for

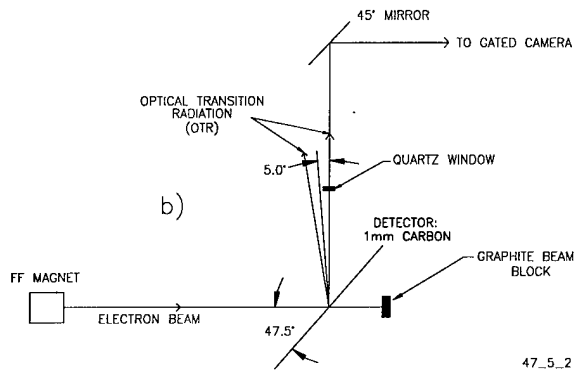
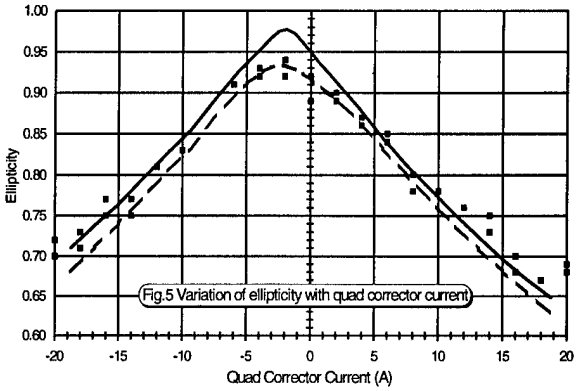


Fig.3 Schematic of OTR measurement

these beam parameters. All of the data were taken with the same micro-channel plate gain and on the same Al/K surface. As a result this data is internally consistent.

Contour plots of the electron beam distribution inferred from OTR measurements as a function of quadrupole magnet current are shown in Fig.4. The inner, intermediate and outer contours correspond to 10%, 40% and 80% of the peak intensity. Beam distribution data at each of the quadrupole currents is analyzed to obtained the rms radius and then the image is rotated 15° and reanalyzed to obtain the rms radius. This process is continued through 165°. The result is the rms radius vs angle for a single beam-pulse distribution. The ratio of minimum to maximum of this rms radius vs angle is the experimental ellipticity, obtained for each QC setting, plotted in Fig.5.



The SCHAR ellipticity at the target (solid curve, Fig.5) is slightly higher than the minimum (dashed curve) a few cm before the target. In SCHAR we used a calibration for QC of 89% of the measured and for QIF of 0.77 G/kA, 75% of the BTEC-calculated value with ferrites. Possibly the properties of the ferrites change in the presence of the solenoidal focusing field, or on the 60-ns time scale the values are different from those assumed. In spite of these differences, the measurements seem well explained by SCHAR.

CONCLUSIONS

We have shown that SCHAR predictions adequately match the measured ellipticity of the beam in ITS as a function of quadrupole corrector current. For the 4-kA matched tune for DARHT, SCHAR predicts ellipticity at the target of ~ 0.97 without using the QC and 0.99 with. Emittance growth is < 4% in either case. For beams mismatched by 50% at the linac entrance, ellipticity decreases to ~ 0.90 without and 0.96 with the QC. Calculated emittance growth is then about 6-12%, independent of either the QIF or QC. The dominant predicted quadrupole effect is therefore a barely observable ellipticity.

ACKNOWLEDGMENTS

We thank Bill Taylor, Dale Dalmas, Chris Gossein and Steve Eversole for ITS operations for these experiments and Joe Baiardo for making drawings.

REFERENCES

[1] M. Burns, P. Allison, R. Carlson, J. Downing, D. Moir, and R. Shurter, "Status of DARHT", XVIII International Linac Conference, Geneva, August, 1996

[2] R. J. Hayden and M. J Jakobson, "The Space Charge Computer Program SCHAR", IEEE Trans. Nucl. Sci., Vol. NS-30, No. 4, August, 1983, p. 2540-2542. SCHAR traces distributions of line currents through an accelerator in steady state to all orders, using 3-D field maps of the accelerator and the self-fields of typically 1000 particles. Emittance growth can occur because of charge redistribution, field aberrations, energy spread across the beam, or the mixing of quadrupoles and solenoids in a transport.

[3] M. Burns, P. Allison, L. Earley, D. Liska, C. Mockler, J. Ruhe, H. Tucker, L. Walling, "Cell design for the DARHT linear induction accelerators", 1991 PAC, San Francisco

[4] L. Walling, Paul Allison, M. Burns, D. J. Liska, D. E. McMurry, "Transverse impedance measurements of prototype cavities for a dual-axis radiographic hydrotest facility", 1991 PAC, San Francisco

[5] Thomas P. Hughes, Robert E. Clark, Paul W. Allison, David C. Moir, "Multipole Field Calculations for DARHT", Beams 94 Conference

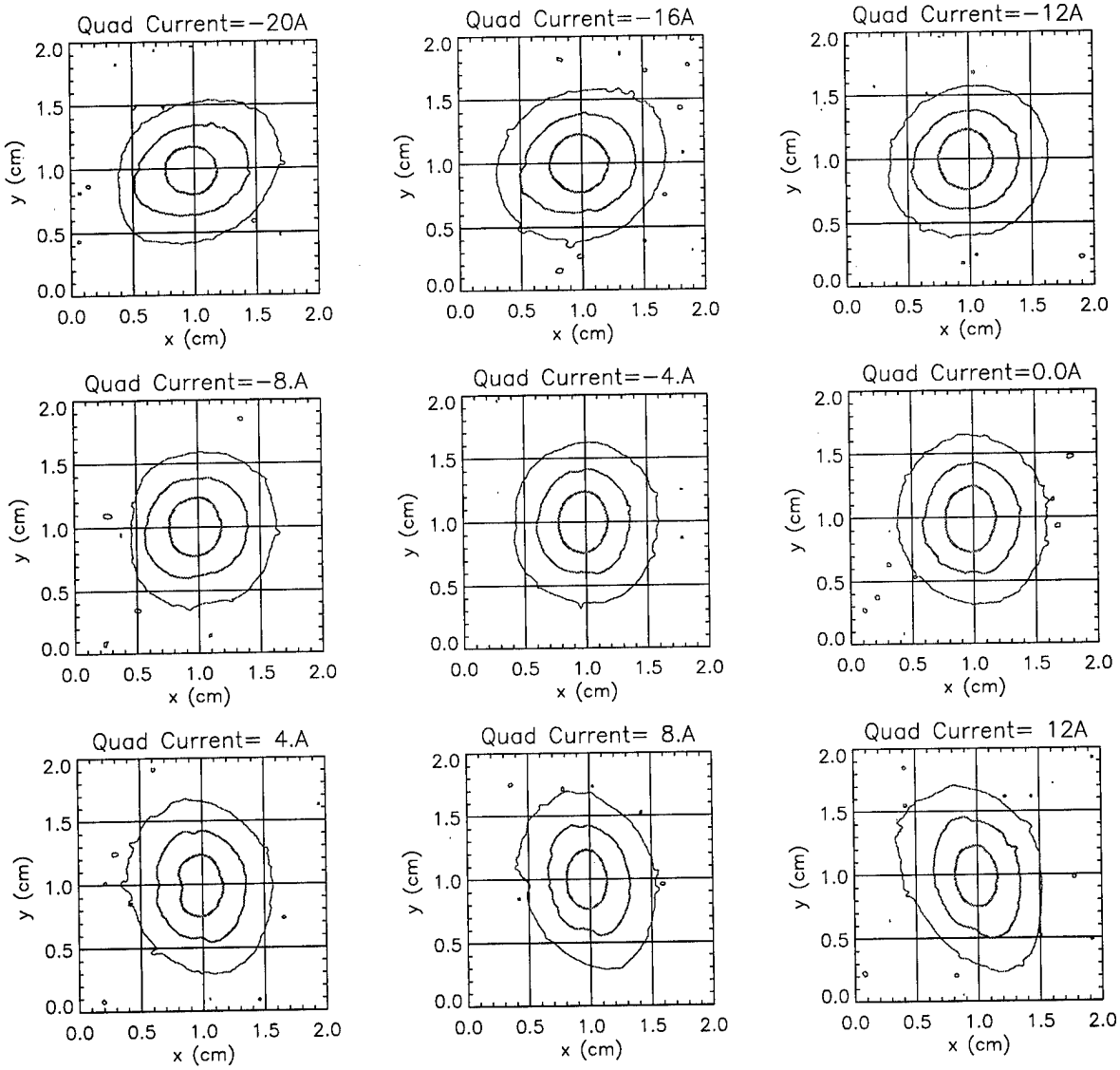


Fig.4 X- and Y-plane beam contours at OTR target vs QC current

OBSERVATION OF SELF-STEERING EFFECTS ON THE ITS 6-MeV LINAC

Paul Allison, David C. Moir, Gary Sullivan
Los Alamos National Laboratory
Thomas P. Hughes
Mission Research Corporation, Albuquerque

Abstract

Beam centroid oscillations were induced in the ITS eight-cell linear induction accelerator (LIA) by steering the beam near the entrance, and position measurements were then made at four locations through the linac. Measurements were in good agreement with code predictions, using the nominal accelerator values, for a collimated beam of ~ 0.3 kA, but to get reasonable agreement for the full 3-kA beam, it was necessary to increase the code value of injection voltage from its known value of ~ 3.7 MeV by ~ 300 kV, approximately the edge beam-potential depression (bpd). Subsequent simulations with the 3D PIC code LSP showed that centroid steering is described more accurately by the total rather than the kinetic energy of the beam. Modification of the beam dynamics code to eliminate the bpd resulted in good agreement with measurement for both 0.3- and 3-kA beams.

PURPOSE

The Integrated Test Stand (ITS) is the first part of the DARHT linac[1] and consists of a 3.75-MeV injector and eight 250-kV induction-linac cells. We are making various beam measurements to compare with design predictions to validate codes and to gain confidence in our ability to predict performance for the full linac. Accurate prediction of centroid motion is important for interpretation of BBU gains[2]. Agreement between position measurements, made at downstream beam position monitors (bpms), and code predictions requires accurate

1. bpm calibrations
2. bpm waveform digitizers
3. bpm analysis programs
4. steering and focusing magnet fieldmaps, polarities, locations, calibrations, readouts
5. beam voltage and current, cell voltage.

Good machine reproducibility and beam roundness[2] are also essential. Code physics must include proper modeling of centroid deflection in the cells caused by image-current effects, a.k.a. imaginary transverse impedances and hereafter called $Z_\perp$. Since these deflections are proportional to $i_b Z_\perp$, then $Z_\perp$ can be inferred by comparing steering experiments (runs) for high- and low-current beams, i_b ~ 3- and ~ 0.3-kA, with otherwise identical linac and injector settings. The goals of the steering experiment were to

1. demonstrate ability to model beam steering
2. deduce $Z_\perp$.

We did six different runs (#1-#6, summarized in the table below) at three injection energies and several currents. The same magnet settings and gap voltages (233 kV) were used for all runs, except for #4 and #6, for which solenoid magnet #7 (Fig.1) was off.

EXPERIMENT

The layout of the experiment (Fig.1) shows the location of the bpms and the steering magnet pair (smx and smy, before the linac), which were used for steering in either the X- or Y- planes. Deflections dx and dy were measured at bpms 3,4,5,6. A 2-cm diam. collimator was placed upstream of the steering magnet for the low-current measurements. The drift-tube solenoid was turned off for all runs.

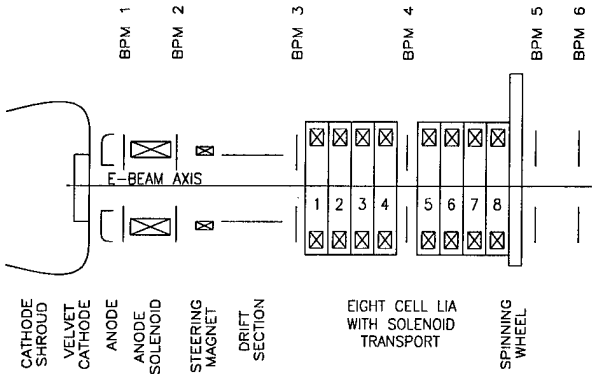
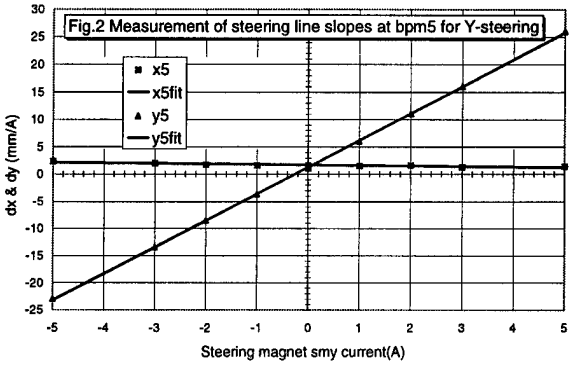


Fig.1 Layout of the ITS steering experiment

For a typical run, smy was varied in steps of 1 A from -5 to +5 A, and the bpm data were analyzed over the central 50 ns of the 60-ns pulse flattop with correction for bpm non-linearities for deflections of up to 30 mm. The steering waveforms were digitized at 700 MS/s with accuracies of a few percent. The deflections dx and dy (Fig.2 shows a sample) were generally quite linear with steering currents and reproducible. The sixteen slopes of the steering lines dx and dy in mm/A for the four bpms



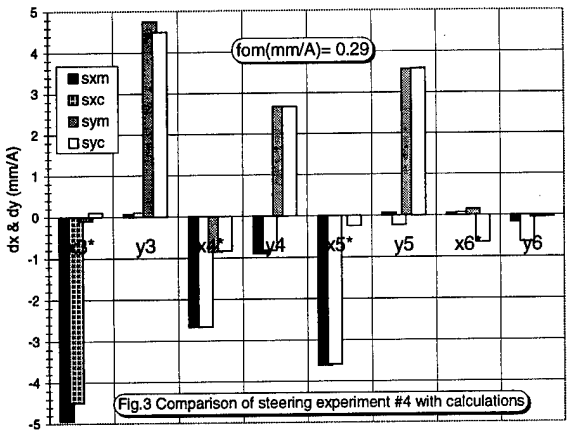
0-7803-4376-X/98/$10.00 © 1998 IEEE

with steering in the two X- and Y- planes constitute a dataset of 16 values that the code must predict for a single run, with the figure of merit fom(mm/A) being defined as the rms difference between the predicted and the measured values. The injector beam energy and the cell $Z_{\perp x,y}$ in both planes were varied to find the minimum fom. The injector energy was known to ~ 2% from other measurements, consistent with the values determined here. A common pair of $Z_{\perp x,y}$ values was used for all six runs.

For the ~ 0.3-kA runs, we initially found good agreement with code using the nominal values of the energy and current (Fig.3 shows run #4). The labels sxm and sxc refer to the eight measured and calculated dx and dy deflections (mm/A) for steering in the X-plane and similarly for sym and syc. Typically the fom for the sixteen measurements for one run was ~ 0.25 mm/A (table), equivalent to ~ 10% accuracy.

#	phi(MeV)	Magnet#7	ib(kA)	fom(mm/A)
1	3	on	.55	0.34
2	3.5	on	.26	0.35
3	3.7	on	.22	0.24
4	3.7	OFF	.22	0.29
5	3.7	on	3.2	0.18
6	3.7	OFF	3.2	0.19

The injector was operated at nominally 3, 3.5 and 3.7 MeV for the low-current runs, which were of course not very sensitive to the gap impedances.



The injector was operated only at 3.7 MeV when the collimator was removed and the 3-kA beam was steered. The agreement with code was poor until we increased the injector energy in the code by ~ 300 kV, approximately the value of the edge bpd = $(i_b Z_0/2\pi\beta)\ln(R_w/r_b)$, where R_w is the wall radius (74 mm) and r_b is the beam radius. We then simulated[3] steering in a solenoid using the 3D electromagnetic PIC code LSP and discovered that steering indeed scaled closely with the total (nominal) beam energy rather than with the depressed (kinetic) energy. Evidently, the forces on the beam on a curved trajectory from ahead and behind act to nearly cancel the effect of the bpd, hence the beam is self-steered.

An estimate of this effect[3] is obtained by considering a section of beam with a stationary trajectory which has local radius of curvature R. We compute the transverse force at a given position due to nearby beam charge and current. The electric and magnetic forces reinforce to give a total self-force of

$$F_\perp^s \approx (ei_bZ_0/2\pi R)\ln(R_w/r_b) \quad (1)$$

where logarithmic divergences have been cut off at R_w (shielding effect of wall) and r_b (finite beam radius). The curved beam orbit due to a transverse magnetic field $B_\perp$ satisfies

$$-m\gamma v^2/R = evB_\perp + F_\perp^s \quad (2)$$

If $\gamma_0 mc^2$ is the undepressed energy, then γ at the edge of the beam is $\gamma_0 - 2(i_b/\beta I_0)\ln(R_w/r_b)$, where I_0 = 17.045 kA, so that Eq. (2) can be rewritten for $\beta \sim 1$ as

$$-\gamma_0/R + (2i_b/I_0R)\ln(R_w/r_b) = eB_\perp/mv + (2i_b/I_0R)\ln(R_w/r_b) \quad (3)$$

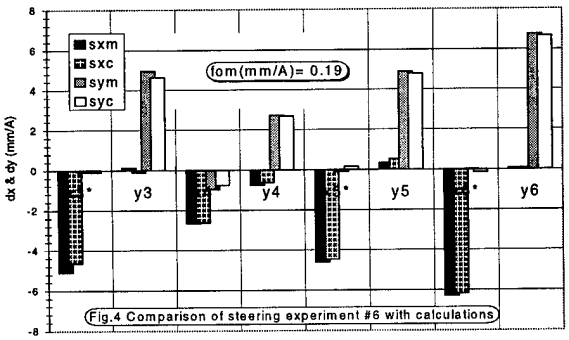
There is an approximate cancellation between the space-charge depression of γ and the beam self-force. Experiment and simulation confirm this cancellation within an uncertainty of ~ 20%. The beam is deflected by $B_\perp$ as though its energy were approximately the total energy $\gamma_0 mc^2$. Similar effects have been calculated[4] for beams in circular accelerators.

The physics in our beam dynamics code xtr for steering had included

1. beam potential depression
2. higher-order space-charge corrections[5] to account for non-uniformity of β across the beam and the diamagnetic B_z enhancement at the beam edge
3. image steering in the gaps, in the constant-radius beam pipe, in bellows, and in bpms

Without having a complete theoretical formulation of the steering, the code has now been modified so that all steering fields act on the centroid as if bpd = 0.

For the 3-kA beam, only the 3.7-MeV energy was used, since it would have been necessary to retune the linac magnets to transport a lower-energy beam. The measurements for run #6 (Fig.4) agree well with code and are quite different from those shown in Fig.3, even though all ITS settings are nominally identical. The only



difference was removal of the collimator and readjustment of the pulsed-power drive to produce the same gap voltages with the different beam loading. The centroid trajectories through ITS for Y-steering for #5 are shown in Fig.5 (solid curves dy, dashed dx), with the measurements overplotted. The trajectories are quite different (Fig.6) if

the edge energy is depressed by the bpd. The relative magnetic fields (1150 G max) are also overplotted.

The image-steering effects on the centroid x_c are proportional to $i_b Z_\perp$, that is

$$\Delta x'_c/x_c = -ei_b Z_\perp/\beta\gamma mc^2$$

so that the fom depends mainly on this product for the gaps, bpms, and bellows. For the bpms and bellows, $Z_\perp$ = -.2 and -1 Ω/cm were used. A value of $Z_\perp \approx$ -3 Ω/cm for the gaps was

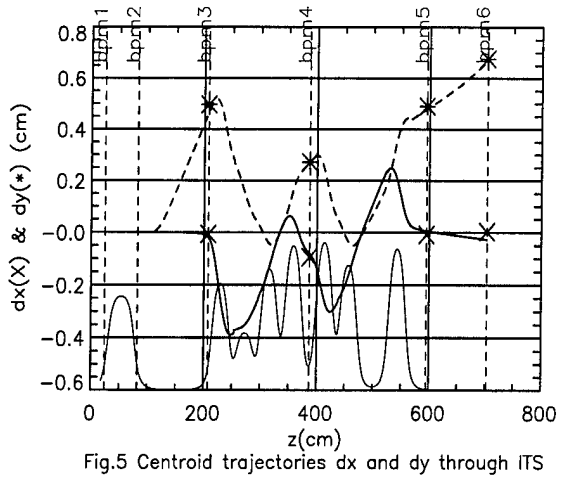


Fig.5 Centroid trajectories dx and dy through ITS

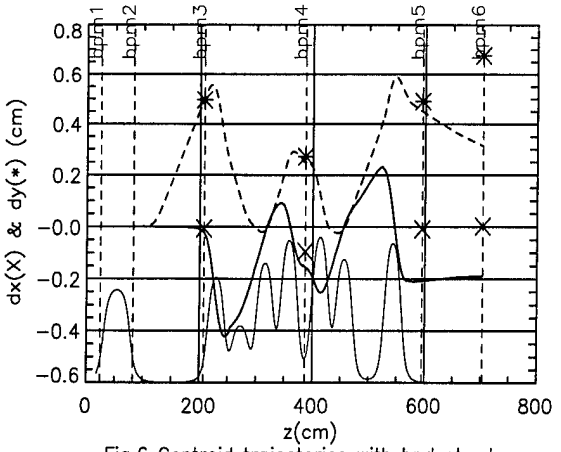


Fig.6 Centroid trajectories with bpd at edge

calculated with the Briggs model[6], compared with a more realistic calculation of -3.6 Ω/cm by Hughes[7]. This value should be modified to $Z_\perp$ = -3.3, -3.9 Ω/cm for the X- and Y- planes by the quadrupole effect[8] for the cells, $\int \nabla_\perp Bdz \approx$ 3G for a 3-kA beam, since it is not taken into account elsewhere in xtr. Except for this quadrupole effect, steering should be symmetric in X and Y. The best xtr fit for all runs gives

$$Z_{\perp\, x,y} = -3.5\pm0.5, -4.9\pm0.7\ \Omega/\text{cm},$$

as determined by the sensitivity of the fom. The strongest image effect is found to be in the gaps.

CONCLUSIONS

Steering measurements and code xtr predictions are in reasonable agreement, using the total, rather than the kinetic, energy at the beam edge for the centroid dynamics. We are unaware of other measurements demonstrating this effect. Six different runs with very different beam conditions were matched to ~ 10% with nominal linac settings and injector parameters. The greatest source of experimental uncertainty may be individual bpm calibration, perhaps ± 5%. Defining sensitivity S as that parameter change which increases the minimum fom by 20%, this set of experiments determines S = 0.7% (phi), 8% (i_b), 12% ($Z_\perp$), and 4% (V gap).

REFERENCES

[1] M. Burns, P. Allison, R. Carlson, J. Downing, D. Moir, and R. Shurter, "Status of DARHT", XVIII International Linac Conference, Geneva, August, 1996

[2] Paul Allison and David C. Moir, "BBU Gain Measurements on the ITS 6-MeV, 4-kA Linac", *Proc. PAC97 Conference.*

[3] T. P. Hughes, "Self-Steering Effects in ITS Experiments", MRC/ABQ-N-576, Mission Research Corp., Albuquerque, July, 1996.

[4] C. A. Kapetanakos, S. J. Marsh, and P. Sprangle, "Dynamics of a high-current electron ring in a conventional betatron accelerator", Particle Accelerators Vol. 14 (1984) p.261, and Edward P. Lee, "Cancellation of the centrifugal space-charge force", Particle Accelerators Vol.25 (1990), p.241.

[5] M. Reiser, "Laminar-flow equilibria and limiting currents in magnetically focused relativistic beams", Phys. Fluids 20, 477 (1977), and T. P. Hughes, T. C. Genoni, et al., Computational Support for ITS and REX, MRC/ABQ-R-1735, April, 1995.

[6] R. J. Briggs, D. L. Birx, G. J. Caporaso, V. K. Neil, T. C. Genoni, "Theoretical and Experimental Investigation of the Interaction Impedances and Q Values of the Accelerating Cells in the Advanced Test Accelerator", Part. Acc. Vol. 18 (1985), pp.41-62.

[7] T. P. Hughes, R. E. Clark, D. R. Welch, and R. L. Carlson, "Computational Support for REX and ITS", MRC/ABQ-R-1797, Mission Research Corp., Albuquerque, June 1996.

[8] Paul Allison and David C. Moir, "Quadrupole Image-Current Effects in the ITS 6-MeV, 4-kA Linac", *Proc. PAC97 Conference.*

AN OVERVIEW OF THE LOW ENERGY DEMONSTRATION ACCELERATOR (LEDA) PROJECT RF SYSTEMS*

J. Bradley III, K. Cummings, M. Lynch, D. Rees, W. Roybal, P. Tallerico,
Los Alamos National Laboratory, New Mexico, USA
and
L. Toole, Savannah River Site, South Carolina, USA

Abstract

Successful operation of the Accelerator Production of Tritium (APT) plant will require that accelerator downtime be kept to an absolute minimum. Over 230 separate 1 MW RF systems are expected to be used in the APT plant, making the efficiency and reliability of these systems two of the most critical factors in plant operation. The Low Energy Demonstration Accelerator (LEDA) being constructed at Los Alamos National Laboratory will serve as the prototype for APT. The design of the RF systems used in LEDA has been driven by the need for high efficiency and extremely high system reliability. We present details of the high voltage power supply and transmitter systems as well as detailed descriptions of the waveguide layout between the klystrons and the accelerating cavities. The first stage of LEDA operations will use four 1.2 MW klystrons to test the RFQ and supply power to one test stand. The RFQ will serve as a power combiner for multiple RF systems. We present some of the unique challenges expected in the use of this concept.

1 INTRODUCTION

The purpose of the LEDA accelerator is twofold. The LEDA accelerator shall validate and demonstrate the front end design of the APT accelerator and shall also serve as a test bed for different accelerator component designs that are competing for use in the APT plant. Each major high-power RF sub-system is described, proceeding from the unit substation which supplies power to the accelerator up to the accelerating cavities.

2 HIGH VOLTAGE POWER SUPPLIES

The high voltage power supply sub-systems convert the AC line voltage from the unit-substation to DC voltages of up to 95 kV which are supplied to the klystrons through the transmitter sub-system. Each power supply must be capable of delivering 2 MW (21 A at 95 kV) to a 350 MHz klystron to produce 1.2 MW of RF power. Power supplies using two different topologies are currently being built for use in LEDA. The design of the power supplies purchased for LEDA has been dictated by the operational requirements of the final APT plant. The plant driven requirements on reliability, cost of operation and cost and time to repair are quite stringent given that over 230 power supplies will be used in the APT plant.

* Work supported by US Department of Energy.

2.1 SCR Controlled Center Tapped Power Supply

SCR controlled power supplies are being built by Maxwell Laboratories for use in the LEDA accelerator. These supplies utilize an SCR bridge which regulates the current through the center tapped transformer primaries to control the secondary output voltage as shown in Fig. 1. Center point control allows the output voltage filter inductance to be placed across the SCR bridge on the low voltage side of the transformer. This placement offers several advantages. The reduction in the filter inductor operating voltage gives increased reliability and reduces cost. The lower voltage also allows an SCR to be placed across the inductor to short out and dissipate the energy stored in the filter inductor in the event of a klystron arc.

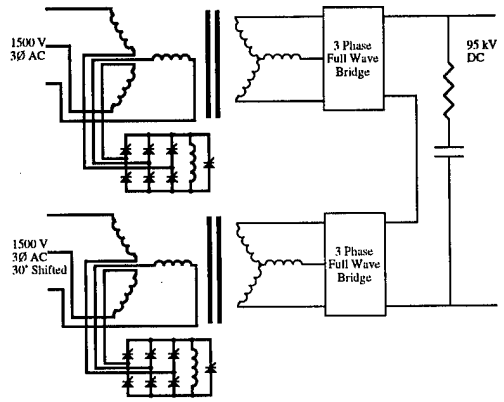


Figure: 1 Secondary voltage is controlled by SCR bridges located in the centers of the transformer primaries.

Two sources of 1500 V, 3-phase power are supplied by the unit-substation. Figure 1 illustrates how one set of 3 phase power is offset by 30° with respect to the other set to produce 12-pulse rectification from two 6-pulse rectifiers whose outputs are wired in series.

The SCR controller and transformer/rectifier sub-units shown in Fig. 1 are located outside the main accelerator building adjacent to the unit-substation. The third sub-unit of the power supply contains the ripple voltage filter capacitor and crowbar circuits. This sub-unit is located inside the accelerator building and adjacent to the klystron. In the event of a klystron arc, the crowbar circuit protects the klystron from stored energy in the filter capacitor and in the power supply cables and from any power supply follow-though energy which enters the tube before the SCRs shut off the current.

0-7803-4376-X/98 /$10.00 © 1998 IEEE

2.2 *IGBT Controlled SSM Style Power Supply*

The second power supply type being built for LEDA is the Insulated Gate Bipolar Transistor (IGBT) controlled Solid State Modulator (SSM) style power supply made by Continental Electronics. The power supply design is based on the Solid State Modulators that are currently produced for AM radio service. Figure 2 shows how these supplies utilize 96 separate rectifying modules wired in series to produce high voltage. The relative phase differences between the sets of 3-phase secondaries on each of the four transformers are arranged to achieve 24-pulse rectification at the output.

A schematic of a single module is illustrated in Fig. 3. Each module contains a full wave, 3 phase rectifying bridge which produces 1.1 kV DC across a small filter capacitor. An IGBT is used to switch the filter capacitor across the output terminals of the module. A diode allows current produced by other modules to pass when the IGBT is turned off.

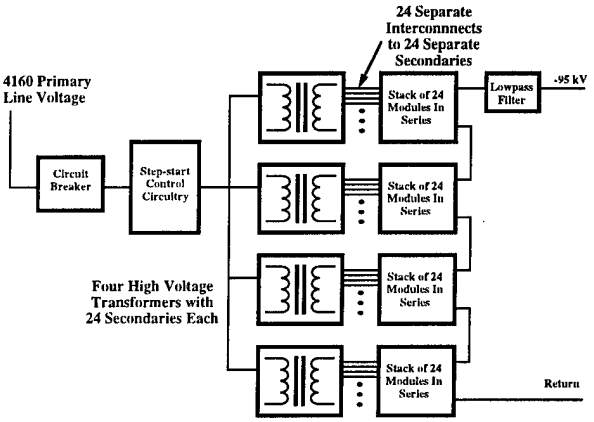


Figure: 2 The secondaries of the HV transformers are arranged to produce 24 pulse rectification.

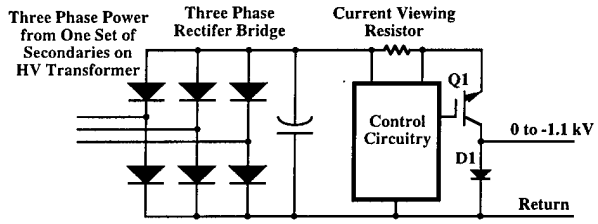


Figure: 3 Each module contains a 3-phase, full wave rectifying bridge.

The IGBT controlled SSM Power Supply has several strengths, the most important being that the fast response of the IGBTs allows the supply to turn off quickly enough to limit the energy in a klystron arc without the use of a crowbar circuit. The elimination of the crowbar circuit reduces power supply cost and increases reliability. A sophisticated diagnostic system allows graceful degradation of the power supply output capability by disabling a failed module or modules and compensating with the remaining modules. The supply also offers an extremely high efficiency (>97%) and power factor (>0.98). These will be critical factors in the operating costs of the APT plant.

3 TRANSMITTERS

The transmitter provides support functions for the klystron. These functions include: klystron magnet power, a solid-state RF drive amplifier and klystron interlocks. The transmitter also includes a cathode referenced voltage source that provides variable high voltage to the modulating anode of the klystron. The modulating anode voltage is derived from and referenced to the cathode voltage as shown in Fig. 4 in order to reduce the tendency for cathode voltage ripple to cause ripple on the RF output of the klystron. Ripple on the klystron RF output power can complicate accelerator phase control issues [1].

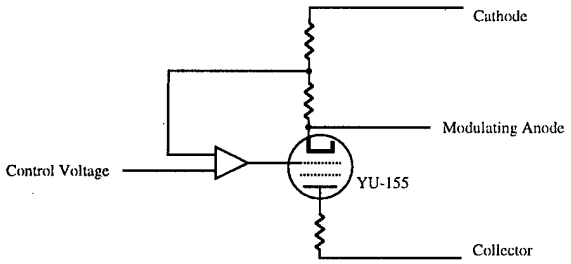


Figure: 4 The modulating anode voltage is derived from the cathode voltage to eliminate the affect of power supply voltage ripple on the klystron current.

4 KLYSTRON AMPLIFIERS

The RFQ is driven by 350 MHz klystrons made by EEV Ltd. Figure 5 shows how these klystrons employ a coaxial RF window to transition from the tube to WR2300 waveguide. The klystron RF windows are similar to the RF windows used at the accelerator [2]. The klystron collector is rated to absorb the full 2 MW of klystron beam power. A full power collector was chosen to allow the RF output power to be shut off quickly (by removing the RF drive) without causing a massive disruption in the amount of electrical power used by the accelerator. The use of a full power collector was motivated by the fact that discontinuities in the power drawn by the accelerator will be a major challenge in the successful operation of the APT plant with the rest of the regional power grid.



Figure: 5 Each 350 MHz klystron is capable of producing 1.2 MW of RF power.

5 CIRCULATORS

350 MHz Y-junction circulators shown in Fig. 6 have been built by AFT for the LEDA project. These circulators are rated to operate into a full-reflection standing wave with the worst-case phase for the circulator while 1.3 MW of RF power is being transmitted by the klystron.

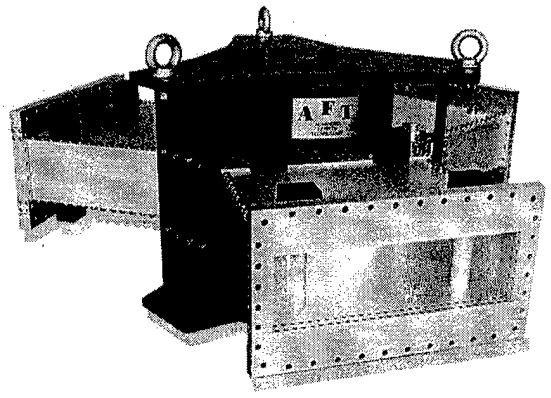


Figure: 6 350 MHz circulators protect each klystron from reflected RF power.

6 WAVEGUIDE RUNS

Three separate WR2300 waveguide runs are used to transport the RF power produced by three 350 MHz klystrons on the mezzanine to the twelve RF windows on the RFQ located in the adjacent tunnel [2].

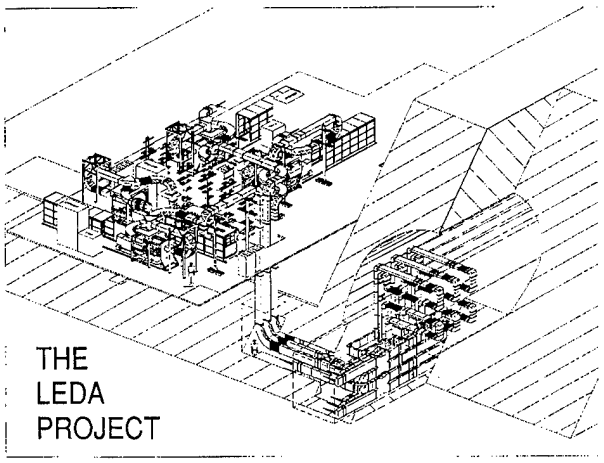


Figure: 7 Three separate WR2300 waveguide runs deliver RF power to the RFQ located in the beam tunnel.

Each waveguide run consists of 64.6 m of WR2300 waveguide as shown in Fig. 7. The three waveguide run lengths have been equalized as much as possible in order to reduce the demands on the three-probe phase shifters and Low Level RF control systems as the waveguide expands and contracts with temperature [1].

7 HIGH-POWER RF WINDOWS

The RF power produced by the klystrons is divided into four equal parts to minimize the stress on the vacuum RF windows at the RFQ [2]. The RFQ portion of the accelerator requires 1.96 MW of RF power, but 3 MW of RF power must be available to implement the supermodule concept as described in Section 9. Half-height WR2300 waveguide is used for the last 22 m of the waveguide run to minimize the space occupied by waveguide. The RFQ portion of the accelerator achieves an RF power per accelerator length of 245 kW / meter.

8 ACCELERATING CAVITIES

An RFQ and various CCDTL configurations will be used throughout the LEDA program. The CCDTL sections will be driven by 700 MHz RF systems which are very similar to the 350 MHz RF systems and will be fully described in a later paper. The first LEDA configuration is shown in Fig. 8. It will test the injector and RFQ and accelerates 100 mA to 6.7 MeV.

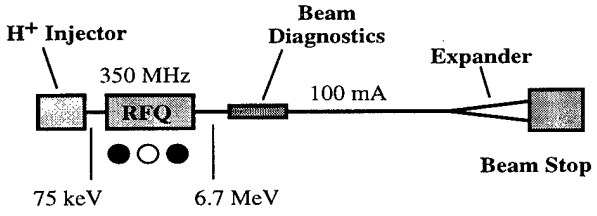


Figure: 8 The initial configuration of the LEDA accelerator will consist of the injector and the RFQ.

9 SUPERMODULE OPERATION

The RFQ portion of the accelerator achieves high reliability through the use of the supermodule concept [3]. In this concept, the RFQ is used as a power combiner for 3 RF systems. Each of these systems is capable of producing 1.2 MW of RF power. If one RF system fails, the accelerator is shut down briefly. The other two RF systems are brought to full power and the accelerator resumes operation. This capability is indicated in Fig. 8 where the three circles below the RFQ represent the three RF systems and filled circles represent the minimum number of RF systems that are required to operate.

REFERENCES

[1] A. Regan, *et. al.*: "APT LLRF Control System Model Results", to be presented at this conference.

[2] K. Cummings, *et. al.*: "Experimental Evaluation Of 350 MHz RF Accelerator Windows For The Low Energy Demonstration Accelerator",to be presented at this conference.

[3] D. Rees, *et. al.*: "Design of 250-MW CW RF System for APT", to be presented at this conference.

COMMISSIONING PLAN FOR A HIGH-CURRENT PROTON LINAC*

K. C. D. Chan, R. L. Barber, R. W. Garnett, J. D. Gilpatrick, K. F. Johnson, G. P. Lawrence, S. Nath, A. Regan, L. Rybarcyk, R. E. Shafer, H. V. Smith, T. P. Wangler, and L. M. Young, Los Alamos National Laboratory, Los Alamos, NM 87545, L. W. Funk, Westinghouse Savannah River Company, Aiken, SC 29808 and K. Crandall, Amparo Corporation, Santa Fe, NM 87504.

Abstract

High-power proton linacs (E>500 MeV) are potentially useful for transmutation applications, such as the production of tritium. In production applications, high availability is essential. Achieving high availability requires an accelerator design that simplifies maintenance and accommodates commissioning procedures designed to minimize tune-up time. These are worthwhile goals for any accelerator, but the high beam powers (170 MW) and heavy beam loading of the Accelerator Production of Tritium (APT) [1] linac introduce significant new challenges. This paper will describe the commissioning plan, as developed to date.

1 INTRODUCTION

The APT accelerator is an integrated normal conducting - superconducting (NC/SC) linac [2]. It has a final beam energy of 1700 MeV and a CW beam current of 100 mA. It starts with a 75-kV injector. Acceleration up to 217 MeV is provided by a RFQ accelerator and a coupled-cavity NC linac. From 217 to 1700 MeV, acceleration is provided by two sections of SC linac: the medium-b and high-b linac sections.

The APT accelerator must demonstrate high reliability and availability. To achieve this, designers must know how the accelerator will be commissioned and operated. The design, commissioning plan and operating plan must be developed in concert to ensure that the required beam instrumentation, controls, and access will be available.

The goal of commissioning is to safely, quickly and reproducibly bring the beam to full current and energy with minimum beam loss, to verify that all systems are working correctly, and to develop a physics model of the beam dynamics that will permit computer-aided automatic beam tuning.

A good physics model and automatic beam tuning are important for achieving high availability. The most difficult source of "emittance noise" to control is the degree of the neutralization [3] in the LEBT, upstream of the RFQ [4]. RFQs have been observed to be effective "emittance filters". Because RF accelerating systems downstream of the RFQ are well understood and known to be capable of consistent performance with good commissioning protocols, automatic beam tuning is believed to be achievable.

2 IMPORTANT ELEMENTS OF COMMISSIONING PLAN

The commissioning plan has been developed using recent commissioning experience from the FNAL linac upgrade and CEBAF. It is also based on the operating experience at the Los Alamos Neutron Scattering Center (LANSCE).

The 170-MW APT linac can quickly activate or destroy components. Therefore, it is therefore essential to approach full power with a low averaged power pulsed beam. Table 1 shows the different beam formats that will be used. A pilot beam is the lowest power beam used for equipment checkout when commissioning begins. Its minimum power is limited by the response of the diagnostics and the pulse rate of the ion source. A calibration beam is used for calibrating the amplitude and phase of the accelerating structures. Its power level is defined by the minimum beam power required by each calibration method. A tuneup beam brings the peak current to 100 mA without exceeding the design power of the full-energy beamstop at the end of the linac (Figure 1) of 3.4 MW. The average power levels of the pilot and calibration beams are comparable to that used for LANSCE tuneup. The LANSCE tuneup beam is a 480-W pulsed beam of 4 Hz, 1-mA peak, and 150-μm long.

Table 1: List of Pulsed-Beam Formats

Beam Types	Repetition Rate (Hz)	Max. Peak Current (mA)	Pulse Length (ms)	Maximum average Power
Pilot	1	1	0.1	170 W
Calibration	1	10	1	17 kW
Tuneup	10	100	1	1.7 MW
APT	(CW)	100	(CW)	170 MW

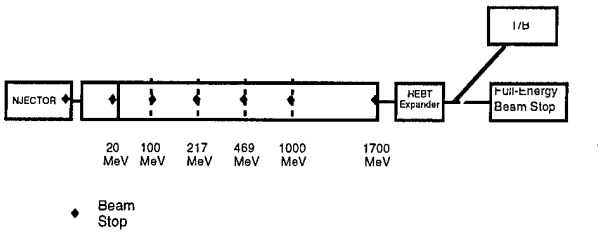


Figure 1. Schematics of APT Linac for Commissioning

* Work supported by the US Department of Energy

0-7803-4376-X/98/$10.00 © 1998 IEEE

Different beamstops (Table 2 and Figure 1) will be required at each commissioning step. A full power beamstop will be installed at the Injector for beam setup and beam abort. A full-power beamstop is required at the 20-MeV point because the beam dynamic up to this energy is highly space-charge dominated. Good beam quality at this point is critical to the beam quality for the rest of the linac. The short APT schedule calls for linac installation by sections. Commissioning of a section will take place while later sections are being installed. To accomplish this, a low-average power beamstop that can be moved to the end of a section is needed. The radiation safety aspect of such a beamstop is currently under study. There is a full-energy, 2% full averaged power, beamstop at the end of the linac. The target/blanket will be used as a beamstop for CW beam tuning at power level from 2 to 100% of the full beam power.

Table 2: List of APT Beamstops

Location	CW or Pulsed	Average Power	Peak Current (mA)	Energy (MeV)
Injector	CW and Pulsed	10 kW	130	0.075
20-MeV	CW and Pulsed	2 MW	100	20
End of Sections	Pulsed	17 kW	10	1700
End of Linac	Pulsed	1.7 MW	100	1700

Measurements using beam diagnostic instrumentation will be used to develop the physics model for automatic tuning. A list of measurements and measurement methods is given in Table 3. A description of the APT beam diagnostics can be found in Reference [5].

3 COMMISSIONING STEPS

The APT-linac commissioning plan has the following steps (Figure 1):

Table 3: Diagnostics for Beam Measurements

Measurements	Method
Current	
CW	Multi-core toroidal
Pulsed	Single-core toroidal
Peak current	Summed BPM signals
Beam loss	Ion chamber
Fast Protect	Ion chamber
Beam centroids	
Position	BPM
Angle	Δ between BPMs
Phase	Capacity probe
Energy	Time of flight
Beam width	
Transverse	Gas Fluorescence or Flying wire
Energy	Dispersive Magnet
Phase	Image Current Probe
Halo	Scraper

1. Installation of linac sections. Sections of linac are defined temporarily at beam energies: 75 kV, 20, 100, 217, 469, 1000, and 1700 MeV. A section will be installed. Equipment will be checked without beam and with the pilot beam. Accelerating structures will be calibrated using the calibration beam.
2. The first 20 MeV will be commissioned to full current using procedures developed in the Low-Energy Demonstration Accelerator.
3. After completing steps 1 and 2, the pulsed tuneup beam will be tuned to design peak current at the full energy beamstop.
4. A CW beam will be tuned to the Target/Blanket System. The current will increase from 2% to 100% in steps.
5. Linac physics-model study and beam-loss minimization will take place.

Methods used in these steps are described in the following subsections.

3.1 Steering

A pilot beam will be used. The principal diagnostics that will be used to establish alignment are the beam position monitors (BPM), of which about 210 will be permanently installed.

Several steering strategies have been investigated [6], of which two are particularly promising: dipole pair and least squares steering. Both are equally effective in keeping the beam centered in the beam channel, but the latter, although it requires somewhat more power supplies, reduces the demands on the steering magnets.

This stage will be carried out with the accelerating cavities detuned to minimize their interaction with the beam. It will be done by linac sections

3.2 Cavity Field Amplitude and Phase for NC Structures

In the normal conducting systems, over the physical region between two beam monitors, a series of phase scans and delta-t measurements [7] will establish the field phase and amplitude required to achieve design longitudinal beam dynamics. The minimum length for this process is one RF "supermodule" [8]. A plot of the beam energy and output phases as a function of the RF amplitude and phase will be compared with simulation to determine the amplitude and phase of the RF cavity field.

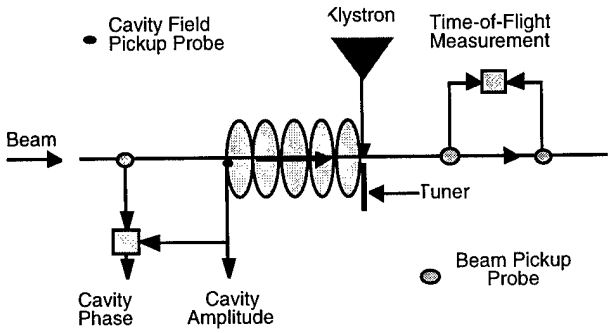


Figure 2. A schematic of the setup for calibrating phase and amplitude of SC cavities

3.3 Cavity Field Amplitude and Phase for SC Cavities

The APT SC linac can operate with some cavities idle. This flexibility requires phase calibration of cavity independent of the number of cavities operating upstream to the cavity being calibrated. Figure 2 shows a schematic of the setup used for calibrating the amplitude and phase of an SC cavity. Capacity pickups will be used immediately upstream of the cryomodule to provide the beam arrival phase. The phase of the cavity field will reference to this arrival phase. By directly referencing to the beam arrival phase, the dependence on the number of operating cavities of cavity phase calibration is minimized. The first step of the calibration procedure is to establish a RF field in the cavity using the klystron while the cavity is resonant in frequency. A calibration beam will then be injected. The calibration of the phase calibration is achieved by adjusting the phase of the RF field until minimum beam induced phase changes of the cavity field are reached. At that time, the RF field is orthogonal to the beam in phase.

Calibrating field amplitude is conceptually more straightforward. The RF field amplitude is measured by field probes that are weakly coupled to the RF field. The field probe is calibrated to ±10% by measuring RF powers before installations of the cavity. Final calibration of the probe will be achieved by measuring the change in beam energy using the time-of-flight method with beam pickups along the accelerator.

3.4 Tuneup of Full Peak and Average Current

After the accelerating structures have been calibrated in RF phases and amplitudes, beam tuneup of the linac will start. The peak current will be increased to 100 mA. The repetition rate will be increased while keeping the average beam power below the design power of the beamstop at the end of the linac. Once acceptable performance has been achieved at this power level, further increases in beam power will take place with the switchyard configured to send the beam to the Target/Blanket.

At the beginning of the tuneup to the Target/Blanket, the peak current will be reduced to less than 2 mA. The reduction of beam current will not affect the component settings along the linac because the linac has been designed for current independent matches [9].

Throughout the process, accelerator performance will be compared to simulations. Beam transmission, transverse beam position, beam energy, transverse and longitudinal beam sizes, transverse match, and beam halo will be measured. Finally, a physics model will be confirmed using the data obtained. Algorithms for minimizing beam loss will be tested.

4 SUMMARY

Work is underway to develop a commissioning plan for the integrated normal/superconducting linac of the APT. If this is developed in concert with the linac design and operation plan, it will lead to high availability. To date, commissioning steps have been determined. Pulsed-beam formats, beamstops, and diagnostics required have been specified. Calibration methods of phase and amplitude of accelerating structures are being investigated.

REFERENCES

[1] Paul J. Lisowski, 'The Accelerator Production of Tritium (APT) Project', these proceedings.

[2] G. Lawrence and T. Wangler, 'Integrated Normal-conducting/Superconducting High Power Proton Linac for APT', these proceedings.

[3] R. Ferdinand, J. Sherman, R. R. Stevens, Jr., and T. Zaugg, 'Space-Charge Neutralization Measurement of a 75 keV, 130 mA Hydrogen Ion Beam', these proceedings.

[4] D. Schrage, L. M. Young, W. Clark, T. Davis, F. Martinez, A. Naranjo and P. Roybal, 'A 6.7 MeV CW RFQ Linac', these proceedings.

[5] J. D. Gilpatrick, J. F. Power, C. R. Rose, R. E. Shafer and R. B. Shurter, 'LEDA and APT Beam Diagnostics Instrumentation', these proceedings.

[6] J. E. Stovall, E. R. Gray, S. Nath, H. Takeda, R. L. Wood, L. M. Young, K. R. Crandall, 'Alignment and Steering Scenarios for the APT Linac', Proceedings of the XVIII International Linac Conference,, Geneva, Switzerland, August 26-30, 1996 p. 686.

[7] T. L. Owens, et.al., 'Phase Scan Signature Matching for Linac Tuning', Linac94 Proceedings, August 1994, Tsukuba, Japan, p893.

[8] J. T. Bradley, III, et. al., 'An Overview of the Low Energy Demonstration Accelerator (LEDA) Project RF Systems', these proceedings.

[9] S. Nath, E. R. Gray, T. P. Wangler and L. M. Young, 'Beam Dynamics Design for the APT Integrated Linac', these proceedings.

SIMULATED PERFORMANCE OF THE SUPERCONDUCTING SECTION OF THE APT LINAC UNDER VARIOUS FAULT AND ERROR CONDITIONS*

E. R. Gray, S. Nath and T. P. Wangler
Los Alamos National Laboratory, Los Alamos, NM 87545

Abstract

The current design for the production of tritium uses both normal-conducting (NC) and super-conducting (SC) structures. To evaluate the performance of the super-conducting part of the linac which constitutes more than 80% of the accelerator, studies have been made to include the effects of various error and fault conditions. Here, we present the simulation results of studies such as effects of rf phase and amplitude errors, cavity/klystron failure, quadrupole misalignment errors, quadrupole gradient error, and beam-input mismatches.

INTRODUCTION

The current Los Alamos design for APT uses an integrated NC/SC structure [1,2]. The SC structure starting at 217 MeV accelerates the 100 mA, cw proton beam to a nominal energy of 1.7 GeV. The beam is delivered onto a production target. through a high energy beam transport (HEBT) section [3].

One of the main advantages [1,4] of having a SC structure at high energies is that it allows a larger bore size reducing the risk of beam loss. In view of the importance of the beam-loss issue, we did study the effect of various types of error conditions and component failures on the beam. Of specific interest are the transverse beam-profile along the length of the linac and quality of the output beam which has direct impact on the transport of the beam through the HEBT.

The high-energy SC linac is comprised of two, medium and high β sections with β=0.64 and 0.82 respectively. The bore radius in the sections are 6.5 cm and 8.0 cm respectively. Two design scenarios for the SC linac section are under consideration [1]. One uses SC quadrupole magnets in a FODO lattice; the other uses doublet room-temperature quadrupoles placed outside the cryostats. The results reported here correspond to the "singlet" SC design. Unless otherwise noted, simulations were done with a beam from the output of the NC structure at 217 MeV which originated at the plasma surface of the ion source [5]. For the error studies, the beam was matched across the NC/SC transition by ramping the quadrupole-strengths down starting at 100 MeV without deliberate consideration of a current-independent match described in Ref.1.

MISMATCHES

Setting errors for the quadrupole gradients, accelerating gradients, or cavity phases can produce beam mismatches. To study the effect of mismatch at the 217 MeV input point, we use an initial waterbag distribution (uniform filling of a 6-D phase-space ellipsoid) at 217 MeV. The waterbag distribution has characteristics that are similar to those seen in real beams; the distribution in any 2-D projection is peaked in the center and falls off gradually at the edges. The mismatched input distributions are derived from the matched ellipses in all three phase-space planes; the ellipse parameters for the matched beam in each plane are scaled to adjust the beam size while leaving the rms-phase-space areas (emittances) constant. Equal mismatches were simultaneously applied in each plane, corresponding to μ=0.7 and 1.3, where μ is defined as the ratio of the initial rms beam size to the matched rms beam size.

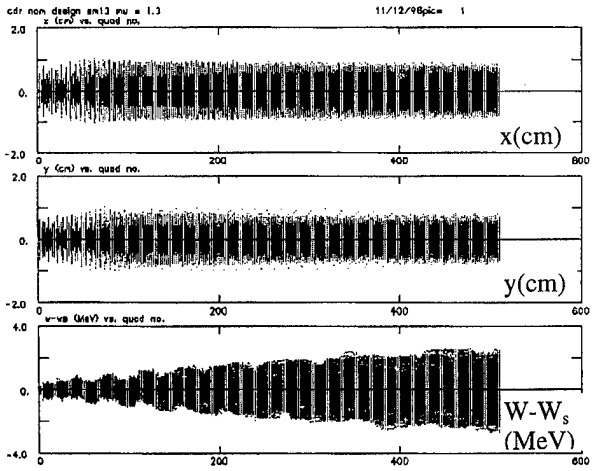


Figure 1. Transverse and longitudinal beam profiles vs. quadrupole number in the SC linac for a mismatched beam of μ=1.3 at 217 MeV with an initial waterbag distribution.

Figure 1 shows both the transverse and longitudinal profiles for μ=1.3. The transverse beam size of the mismatched beam starts to grow immediately after the input, but after several periods settles down to a larger value. At the output end (1.7 GeV) the x rms beam size grows to about 0.82 cm compared to about 0.46 cm for the matched case. The effect of mismatch in the longitudinal space is less pronounced. The output beam energy spread is only slightly larger when compared to the matched case.

The normal error-free output beam looks like a parabolic distribution in x or y. The output distribution for a single point mismatch shows a shoulder on it that depends on the size of the mismatch. For this case, the extent of the distribution seems to be limited as demonstrated by adding the simulations of many 100,000 particle runs to reach several million total particles and as expected from the particle-core halo model [6]. The effect of mismatches for more than one point are still being studied.

* Work supported by the US Department of Energy

0-7803-4376-X/98/$10.00 © 1998 IEEE

ERRORS

Rf Cavity Phase and Amplitude Errors

The rf Power system has feedback loops to maintain the phase and amplitude of the fields in the cavities. Because the klystron power is split to drive multiple cavities, the feedback loop adjusts the klystron phase and amplitude to control the average phase and amplitude error from the driven cavities. The result is that even though the average phase and amplitude of the cavities within an RF module can be controlled by the feedback loop to an average of 1.0° in rms phase and 1% in rms amplitude, each individual cavity can have a larger variation. As a representative case, we have done simulations assuming 10° and 10% rms variations in each cavity with the average rms phase and amplitude for a klystron-driven set of cavities at 1.0° and 1%, respectively. The APT linac structures may experience about half of this level of RF amplitude and phase variations during normal operation.

We performed a set of 20 simulation runs, each with cavity phase and amplitude errors set randomly, assuming a uniform distribution within the above specified limits. The initial particle distribution was obtained from the preceding normal-conducting LE linac section. The results show that the output beam-energy centroid varies by about ±4 MeV, which is acceptable for the HEBT. Transverse rms emittance varies by about ±4%. However, the longitudinal emittance growth, as expected, is higher than the error-free case by about 30%.

Quadrupole Magnet Misalignments

Misalignments are simulated with a program, PARTREX that follows a central particle and a beam ellipse envelope through a sequence of elements using a sequence of matrix transformations in a linear-field approximation. Because the code transports beam ellipses rather than individual particles, it uses considerably less running time, enabling the user to make a statistical analysis of the beam behavior under random misalignments of the large number of quadrupoles in the linac. Each simulation corresponds to a complete set of random errors for each quadrupole in the linac.

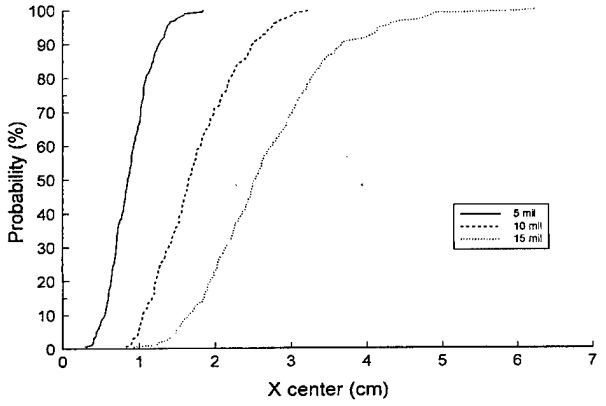


Figure 2. Beam centroid probability plots for rms quadrupole misalignment errors of 5,10 and 15 mil (127, 254, and 381 μm).

Two hundred simulations were made with random rms quadrupole alignment errors. Figure 2 shows the ordered-results for quadrupole misalignment errors of 0.127, 0. 254 and 0.381 mm. For a 0.254 mm rms random misalignment error, there is 95% probability that the beam-center shift will be less than 2.8 cm. The corresponding numbers for 0.127- and 0.381-mm misalignment errors are 1.4 cm and 4.2 cm, respectively.

A 0.254-mm rms uncertainty is a value that has been achieved for SC magnets in other accelerator facilities. A corresponding shift of 2.8 cm or larger with 5% probability suggests that provision should be made for steering in or after the linac. It should be noted, however, that the beam easily cleared the bore of the linac without steering for all the runs.

Practical Set of Machine Errors

We considered a set of realistic errors that include magnet misalignment in displacement, tilt, and roll, quadrupole gradient error, and RF phase and amplitude variations. The numbers used are uniform distribution of errors that have the following RMS widths:

- quadrupole magnet gradient error, ± 1%
- quadrupole magnet tilt error, ± 0.3 degree
- quadrupole magnet roll error, ± 0.3 degree
- average RF phase error, ± 1 degree
- average RF gradient error, ± 1%
- local RF phase error, ± 10 degree
- local RF gradient error, ± 10 %

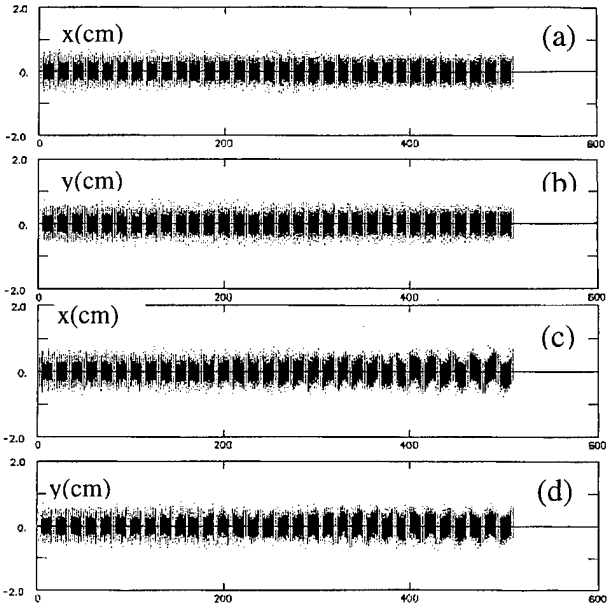


Figure 3. Transverse (x and y) vs. quadrupole number with (a-b) no errors and (c-d) realistic set of errors noted in the text.

Figures 3 (a) and (b) show the x and y profile plots of a normal beam. Corresponding profile plots with the above set of errors are shown in Figures 3 (c) and (d). A small centroid oscillation is observed while the longitudinal profile (not shown) does not show any significant effect.

FAULTS

RF Cavity/Klystron Failure

If a single cavity or a klystron that powers several cavities fails, the beam-entry phase beyond the failure point will be shifted and, unless corrected, would generally result in poor acceleration efficiency and poor longitudinal focusing in the cavities downstream of the failure. Such an uncorrected situation could also lead to radial loss of beam. However, rephasing the linac beyond the point of failure is practicable because the cavities in the SC structure are electrically independent.

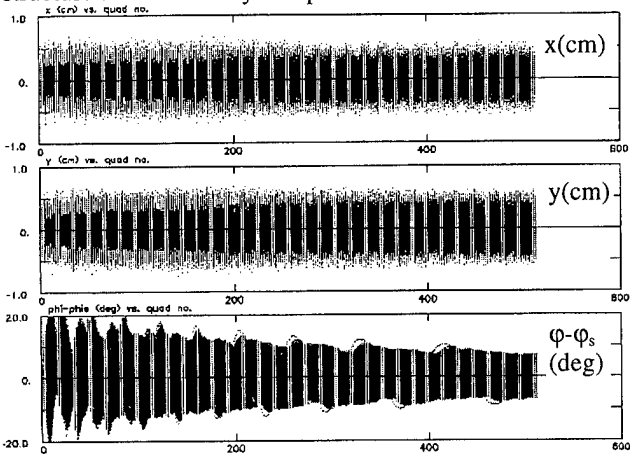


Figure 4. Beam profiles vs. Quadrupole number in the SC linac with the first klystron in the β=0.64 section turned off.

If the rf amplitudes beyond the failure point are not reset, the output centroid energy will be reduced. As expected, the increase in longitudinal emittance is significantly larger than the corresponding increase of the transverse emittance. Also, a larger increase in longitudinal emittance is associated with cavity or klystron failures at the lower-energy end of the linac. This is due to the fact that in the lower-energy part of the SC linac, the longitudinal focusing loss as a result of a single cavity failure is more important, especially for compensation of the space-charge forces.

Figure 4 shows the beam profiles along the length of the SC linac when the first klystron in the β=0.64 section is turned off. There is a large increase in the longitudinal emittance. However, since the longitudinal emittance is of little concern to the HEBT/ Expander system, operation of the linac with a klystron off is not a problem in terms of beam at the target. Though not a major effect on the transverse emittances, this does, however, represent a mismatch with some attendant increase in the tails of the particle distribution.

Quadrupole Magnet Failures

Failure of one or more quadrupole magnets causes an immediate transverse mismatch resulting in subsequent emittance and halo growth. Since the focusing lattice is a FODO sequence, it is not surprising that a failure of an odd number of adjacent magnets causes a larger disruption. A failed pair of magnets early in the machine did not result in beam loss in the linac but did result in emittance growth of nearly a factor of 13. Readjusting the four quadrupoles downstream of the failed ones, a rematch can be achieved that reduces the emittance growth to near a factor of two. The output phase-space distributions with and without errors are shown in Figure 5. There are more particles on the edges of the distribution compared with the error-free case even with quadrupole readjustment.

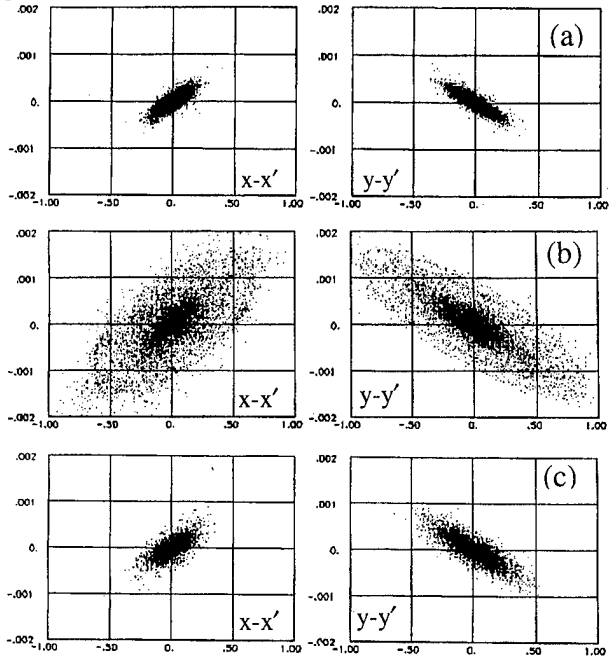


Figure 5. Output phase-space distributions with a pair of quadrupoles at the start of β=0.64 section turned off; (a) no failure, (b) with failure but no adjustment and (c) with downstream quadrupoles readjusted.

CONCLUSION

On the basis of the error studies completed, it can be concluded that none of the error conditions put the beam-edge close to the aperture. Steering magnets in or after the linac should be installed for transporting the beam through the HEBT/Expander system. In case of quadrupole failure, retuning downstream of failed quadrupoles will be necessary for the beam to be transported by the HEBT/Expander system or the cryomodule can be replaced. HEBT can continue to operate with cavity/klystron failure.

REFERENCES

[1] S. Nath et al., "Beam Dynamics for the APT Integrated Linac," this conference.

[2] G. P. Lawrence and T. P. Wangler, "Integrated Normal-conducting/Super-conducting High power Proton Linac for APT," this conference.

[3] R. A. Shafer et al., "Overview of the APT High-Energy Beam Transport and Beam Expanders," this conference.

[4] Los Alamos National Laboratory APT Conceptual Design Report, LA-UR-97-1329, April 1997.

[5] L. M. Young, "Simulations of the LEDA LEBT with H^+, H_2^+, and e^- particles," this conference.

[6] T. P. Wangler et al., "New High Power Linacs and Beam Physics," this conference.

INTEGRATED NORMALCONDUCTING/SUPERCONDUCTING HIGH-POWER PROTON LINAC FOR THE APT PROJECT*

G. P. LAWRENCE and T. P. WANGLER
Los Alamos National Laboratory, Los Alamos NM 87545, USA

Abstract

The baseline accelerator design for the APT (Accelerator Production of Tritium) Project [1] is a normalconducting-superconducting proton linac that produces a CW beam power of 170 MW at 1700 MeV. Compared with the previous all-NC linac design, the NC/SC linac provides significant power savings and lower operating and capital costs. It allows a much larger aperture at high energies, and permits greater operational flexibility. The design has been approved by high-level technical panels and is published in a Conceptual Design Report [2]. The high-energy portion is a superconducting (SC) rf linac employing elliptical-type niobium cavities, while the low-energy portion is a normal-conducting (NC) linac constructed from copper cavities. This provides an integrated accelerator design that makes optimum use of the two technologies in their appropriate regions of application. The NC linac, which consists of an injector, RFQ, CCDTL, and CCL, accelerates a 100-mA beam to 217 MeV. The SC linac is built in two sections optimized for different beam velocity spans, with each section made up of cryomodules containing 5-cell cavities and SC singlet quads in a FODO focusing lattice. Alternate SC linac designs are being studied that employ a doublet focusing lattice using conventional quadrupoles located between cryomodules.

BASELINE NC/SC LINAC DESIGN

The APT linac design is driven strongly by the large amount of rf power required to accelerate the 100-mA CW beam. Efficient conversion is needed at each stage in the power train to minimize capital and operating costs. Parameter selection and cost/performance modeling to achieve this objective have been discussed previously [3]. The current baseline design has evolved from an earlier all-NC linac design [4]. System architecture is displayed in Fig.1, with additional parameters listed in Table 1. The low-energy linac, which is basically the same as in the all-NC design, accelerates a 100-mA proton beam to 217 MeV in copper water-cooled structures. A 75-keV injector housing a microwave-driven ion source generates a continuous 110-mA proton beam. From this input, a 350-MHz, 8-m-long RFQ produces a CW 100-mA beam at 6.7 MeV. The RFQ is built in four resonantly-coupled segments, and rf drive is provided by three 1.2-MW CW klystrons through 12 windows.

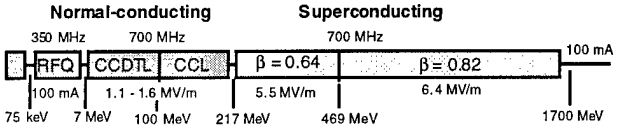


Fig. 1. Architecture of APT integrated NC/SC linac.

The RFQ output is matched into a 700-MHz CCDTL that accelerates it to 100 MeV. The CCDTL is a coupled sequence of 2-gap and 3-gap short DTLs, embedded in an 8-$\beta\lambda$ FODO focusing lattice [5]; the quads are external to the structure. Acceleration continues to 217 MeV in a 700-MHz side-coupled CCL that has the same focusing period. In the CCDTL and CCL, the average accelerating gradient is ramped up to 1.3 MV/m, and accelerating and focusing parameters change smoothly with beta. The result is a linac that has strong focusing at low beam energy and is free from phase-space transitions after the RFQ. Beam dynamics analyses and simulations have shown these factors to be critical in terms of minimizing core emittance growth and the generation of halo [6]. As seen in Table 1, transverse emittance growth is negligible after 20 MeV and longitudinal emittance grows only slightly.

Table 1. NC Low-Energy Linac Parameters

Parameter	RFQ	CCDTL	CCL
Structure gradient (MV/m)	1.38	1.1-1.6	1.6-1.5
Average gradient (MV/m)	1.38	0.4-1.2	1.2-1.3
Length (m)	8.0	102.3	104.3
Synchronous phase (deg)	- (90-33)	- (60-30)	-30
Shunt impedance (MΩ/m)	–	18-52-33	33-37
Phase-adv./period (deg)	–	80	80-35
Quadrupole lattice period		8βλ	8βλ
No. of quadrupoles	–	234	125
Quadrupole G•L prod. (T)		2.6-2.2	2.2-2.0
Trans emitt. (π mm-mrad)*	0.160	0.163	0.163
Long emitt. (π mm-mrad)*	0.405	0.44	0.45
Aperture radius (mm)	2.3-3.4	10-17.5	17.5-25
Aperture : beamsize ratio	–	6.5-14	14-17
Copper rf losses (MW)	1.26	5.0	6.8
Number of klystrons	3	21	27

* Normalized rms values.

The SC high-energy linac consists of a string of cryomodules each containing three or four 5-cell 700-MHz niobium accelerating cavities, alternating with SC quads in a FODO focusing lattice. There are two kinds of cryomodules, each type designed for efficient acceleration in a different velocity range. Cavity shapes [7] in the medium-beta section (217 MeV to 469 MeV) are optimized at β = 0.64, and in the high-beta section at β = 0.82. The shapes are similar to the well-established elliptical designs for electron machines, but are compressed longitudinally in proportion to beta. Because the cavities are short and are driven independently, each section of the SC linac has a broad velocity bandwidth, which allows the gradient profile and output energy to be adjusted over a wide range. Because of the high beam current, the major design push

* Work supported by US Department of Energy

0-7803-4376-X/98/$10.00 © 1998 IEEE

is not for high cavity gradient but high power rf coupler capability. As coupler performance with beam has been demonstrated at about 150 kW and the technology is advancing rapidly, a performance rating of 210 kW has been chosen for the high-β section and 140 kW for the medium-β section. Each cavity is supplied by two antenna-type coaxial couplers mounted on opposite sides of the downstream beam tube. Dual warm coaxial windows are planned, located in the input lines so that they do not see the beam directly.

Fig. 2 sketches the structure of a β=0.82 cryomodule and its rf drive. Each cavity pair is powered by one 1-MW 700-MHz klystron. The quads [8] have SC coils and iron poles, and are similar to the RHIC trim quads. The β=0.64 cryomodules contain three 5-cell cavities, which are powered by one 1-MW klystron, and four SC quads.

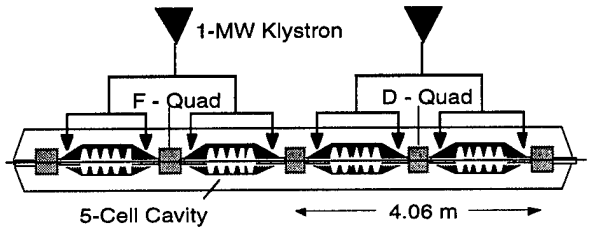


Fig. 2. High-beta cryomodule architecture (β = 0.82)

Table 2. lists key parameters of the two sections of the SC linac. The selection of cavity gradients and numbers of cells per cavity are restricted in both sections by the need to maintain conservative peak surface fields, and power coupler specifications that are close to demonstrated levels. The rf distribution is governed by the need to fully utilize the 840-kW power available from each 1-MW klystron, since the rf system dominates the accelerator cost. A 2K operating temperature for the niobium cavities was chosen to minimize LHe refrigerator and cryodistribution costs. To bound the 2K cryogenic load, the average cavity Q_0 is taken as $5x10^9$, and the static heat leak is estimated at 5 W per meter of cryomodule.

Table 2. Baseline SC High-Energy Linac Parameters

Parameter	β=0.64	β=0.82
Structure gradient (MV/m)	4.8 - 5.5	5.4 - 6.4
Avg. gradient (MV/m)	1.43-1.51	1.89
Peak surface field (MV/m)	14.9 - 17.1	14.0 - 16.6
Section length (m)	204	792
No. of (5-cell) SC cavities	90	312
No. of klystrons (1-MW)	30	156
Synchronous phase (deg)	-30 to -35	-29
Coupler power (kW)	140	210
Power per klystron (kW)	840	840
Trans. phase adv./period (deg)	83 - 67	81 - 32
Quadrupole length (cm)	30.5	45.9
No. of quadrupoles	120	390
Quadrupole gradient (T/m)	6.4-8.1	5.4
Trans. emittance (π mm-mrad)*	0.16 - 0.17	0.17 - 0.20
Long. emittance (π deg-MeV)*	0.36 - 0.46	0.46 - 1.10
Aperture radius (mm)	65	80
Aperture-radius/rms-beam-size	37 - 56	58 - 85
Thermal load @ 2K (kW)	2.3	11.5

* Normalized rms values.

The key beam dynamics [9] goal for the accelerator is to achieve very low beam losses (0.1 nA/m at 1700 MeV) in order to assure unrestricted hands on maintenance. The NC/SC linac design provides apertures that are much larger than the rms beam size, with the largest apertures at high energies where the activation threat per lost proton is greatest. In the NC linac, the aperture increases in steps to 50 mm, while in the SC linac it jumps to 130 mm at 217 MeV, and then to 160 mm at 469 MeV. Strong transverse focusing keeps the beam size small, and in concert with careful matching, minimizes halo generation. Figure 3 summarizes the result, comparing the linac aperture dimension with both rms beam size and the radius of the outermost trajectories in a 100,000 particle simulation. At full energy, the aperture ratio (ratio of aperture to rms-beam-size) is over 80, at the end of the NC linac it is 17, and at 100 MeV it is 14.

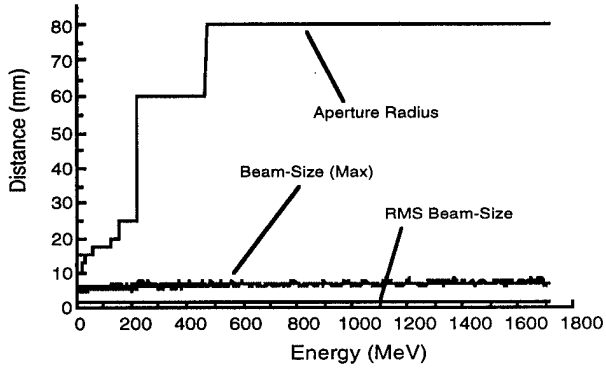


Fig. 3. Aperture radius, rms beam size, & radius of outermost particle for NC/SC baseline linac design.

In order to meet the high availability goal for the accelerator (>85%), redundancy schemes are used to provide excess rf drive in both the NC and SC linacs, but are implemented differently in each. The NC linac is divided into "supermodules" consisting of 100-150 coupled accelerating cells, with each unit supplied by n+1 klystrons (typically 5 to 7), where only n units are needed for operation. When an rf station fails, it is isolated by a waveguide switch, power from the remaining klystrons is increased to compensate, and the supermodule continues to provide the full energy gain needed in that section. In the SC linac, redundancy is provided by including 5% more rf stations and cryomodules than are needed to deliver the nominal 170 MW output power. These are distributed along the high-β linac to compensate for failed units.

Beam simulations show that the SC linac is insensitive to a broad range of construction or operating errors and also can continue to function in a variety of off-normal conditions, including having single klystrons, cavity pairs, and quadrupole pairs out of service. Operational flexibility is enhanced by the retunability of the high-beta section of the SC linac and the adjustability of the cavity gradients.

DOUBLET-LATTICE SC LINAC

The singlet-lattice FODO design for the SC linac meets the performance objectives for APT and provides a very high aperture ratio because of the strong focusing per

unit length. However, because the quadrupoles are inside the cryomodules, construction of these units is complex and relatively expensive. The overall linac architecture is also less than optimum in terms of accessibility of the quads for alignment and space for beam diagnostics. Looking for a better SC linac architecture, we have recently been studying designs based on conventional quadrupole doublets located in the warm regions between cryomodules. This approach simplifies cryomodule construction, shortens the linac by 100 m, reduces the number of quadrupoles, and lowers costs.

Fig. 4 shows the high-β architecture for the alternate SC linac design, and Table 3 summarizes the parameters. Each cryomodule contains 4 cavities, with one klystron driving each cavity pair, using a maximum coupler power of 210 kW. The doublet focusing period is 8.54 m. In the medium-β section, the cryomodules contain two 5-cell cavities, supplied by two power couplers at 124 kW each. A single klystron drives three cavities, so the power of two klystrons is distributed between 3 cryomodules. The doublet period is 4.88 m, providing the relatively strong focusing that the simulations show is needed in this section for good beam control. Beam dynamics for the doublet-based SC linac are discussed in Ref. 9.

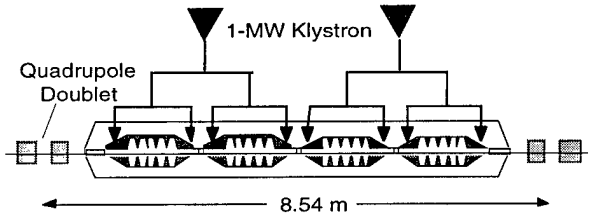


Fig. 4. High-β architecture for doublet-lattice SC linac.

Table 3. Doublet-Lattice SC Linac Parameters

Parameter	β=0.64	β=0.82
Structure gradient (MV/m)	4.24 - 4.85	5.4 - 6.4
Avg. gradient (MV/m)	1.26	2.25
Peak surface field (MV/m)	13.1 - 15.0	14.0 - 16.6
Section length (m)	249	649
No. of (5-cell) SC cavities	102	304
No. of klystrons (1-MW)	34	152
Synchronous phase (deg)	-30 to -35	-29
Coupler power (kW)	123.5	210
Power per klystron (kW)	741.2	840
Trans. phase adv./period (deg)	83 - 67	81 - 32
No. of quadrupoles	102	152
Trans. emittance (π mm-mrad)	0.17 - 0.18	0.18
Long. emittance (π deg-MeV)	0.34 - 0.33	0.33 - 0.39
Aperture-radius/rms-beam-size	37	65

* Normalized rms values.

A high-β section architecture with only two cavities per cryomodule is also being investigated. The latter has stronger focusing than the 4-cavity unit, because of the shorter period, so the beam size is smaller. However, it makes the linac significantly longer than the FODO baseline and more expensive, because of the larger number of components. Beam simulations without errors show that the rms performance is essentially the same for the 2-cavity and 4-cavity cases. However, error and halo studies must be carried through to provide a more conclusive comparison of the two options, especially with respect to how much beam halo is projected into the high-energy beam transport (HEBT).

OTHER DESIGN ASPECTS AND ED&D

There are several other important aspects of the APT accelerator design (not already referenced) that are covered elsewhere in these Proceedings. These include a description of the rf power system [10], the HEBT and expander system [11], and the accelerator commissioning plan [12].

Engineering development and demonstration programs to confirm design and operation of the major components of the NC/SC linac are well underway. The LEDA program [13], which is prototyping the low-energy linac at full power, has the injector performing at APT specifications, and the RFQ [14] is under construction. For the SC linac, complete cryomodule prototypes will be built and tested prior to industrial production. This step will follow construction and testing of "cryounits" that will integrate 5-cell cavities, power couplers, tuners, and cryostat. Preliminary rf field tests on a single-cell β = 0.64 cavity show no problem in meeting the desired Q_0 vs E specifications. Also, recent proton irradiation measurements on niobium test cavities at Los Alamos and Saclay have put to rest the question of performance reduction at high proton dose levels [15].

REFERENCES

[1] P.W. Lisowski, "The Accelerator Production of Tritium (APT) Project," Proc. 1997 Particle Accelerator Conf., Vancouver (May 1997).

[2] APT Conceptual Design Report, Los Alamos Report LA-UR-97-1329, April 15, 1997.

[3] G.P. Lawrence, et al., " Conventional and Superconducting RF Linac Designs for the APT Project," Proc. 1996 Int. Linac Conf., Geneva, 710 (August 1996).

[4] J.H. Billen et al., "A Versatile High-Power Linac for Accelerator-Driven Transmutation Technologies, Proc. 1995 Particle Accelerator Conf., Dallas, IEEE No. 95CH35843, 1137 (1995).

[5] S. Nath et al., "Physics Design of APT Linac with Normal Conducting rf Cavities," Proc. 1996 Int. Linac Conf., Geneva, Aug 1996.

[6] T.P. Wangler, "New High Power Linacs and Beam Physics Issues," Proc. 1997 Particle Accelerator Conf., Vancouver (May 1997).

[7] F.L. Krawczyk et al., "Superconducting Cavities for the APT Accelerator," ibid.

[8] S. Kahn and P. Wanderer, "Magnetic Design of Superconducting Quadrupoles for a SC Linac for APT," ibid.

[9] S. Nath, et al., "Beam Dynamics Design for the APT Integrated Linac," ibid.

[10] D. Rees, "Design of 250-MW CW RF System for APT," ibid.

[11] R.E. Shafer et al., "Overview of the APT High Energy Beam Transport and Beam Expanders," ibid.

[12] K.C.D. Chan et al., "Commissioning Plan for a High-Current Proton Linac," ibid.

[13] D. Schneider and K.C.D. Chan, "Progress Update on the Low-Energy Demonstration Accelerator," ibid.

[14] D. Schrage et al., "A 6.7-MeV CW RFQ Linac,"

[15] B. Rusnak, et al., "In-situ Proton Irradiation and Measurement of Superconducting RF Cavities under Cryogenic Conditions," ibid

OVERVIEW OF PROGRESS ON THE IMPROVEMENT PROJECTS FOR THE LANSCE ACCELERATOR AND TARGET FACILITIES

R. J. Macek, J. C. Browne, T. Brun, J. B. Donahue, D. H. Fitzgerald, R. Pynn, S. O. Schriber, and D. Weinacht, Los Alamos National Laboratory, Los Alamos, NM 87545

Abstract

Three projects have been initiated since 1994 to improve the performance of the accelerator and target facilities for the Los Alamos Neutron Science Center (LANSCE). The LANSCE Reliability Improvement Project (LRIP) was separated into two phases. Phase I, completed in 1995, targeted near-term improvements to beam reliability and availability that could be completed in one-year's time. Phase II, now underway and scheduled for completion in May 1998, consists of two projects: a) implementation of direct H^- injection for the Proton Storage Ring (PSR) and b) an upgrade of the target/moderator system for the short pulse spallation neutron (SPSS) source. The latter will reduce the target change-out time from about 10 months to about three weeks. The third project, the SPSS Enhancement Project, is aimed at increasing the PSR output beam current to 200 μA at 30 Hz and providing up to seven new neutron scattering instruments.

1 INTRODUCTION

During the years 1993-1995 the focus of the program based on the 1 mA, 800 MeV proton linac at Los Alamos shifted from basic research in intermediate energy nuclear and particle physics to neutron science. The accelerator and target facility improvement projects are being undertaken to facilitate this transition from the Los Alamos Meson Physics Facility (LAMPF) to LANSCE. The centerpiece for LANSCE and its neutron science program is the short-pulse spallation neutron source comprising the PSR, the neutron production target facility, and the suite of instruments incorporated in the Manuel Lujan Jr Neutron Scattering Center (MLNSC). When the improvements are completed, LANSCE will provide the US neutron science community with access to a world-class, short-pulse spallation neutron source. The main goals for beam delivery improvements are:

- Operation with > 85% neutron beam availability for up to 8 months per year with <5% down time from intervals > 8 hours.
- 100 μA @ 20 Hz from PSR with acceptable losses in the ring at the end of the LANSCE Reliability Improvement Project.
- 200 μA @ 30 Hz from PSR with acceptable losses in the ring at the end of the SPSS Enhancement Project.

2 THE RELIABILITY IMPROVEMENT PROJECT

High neutron beam reliability (as measured by neutron beam availability with respect to established schedules) has been of paramount concern to the users of LANSCE. Neutron beam availability prior to and including 1993 operations was in the range of 50-75%. This level of availability along with access restrictions to experimental rooms (ER-1) surrounding the neutron production target were major impediments to a successful user program in neutron scattering. The reliability improvement project was undertaken in 1994 to address these issues.

2.1 Phase I – Near-term Reliability Improvements

A large list of potential improvements were identified and prioritized by their expected contribution to improved beam availability. However, average down time is not a complete measure of the impact on users. For the typical neutron scattering experiment of 2 or 3 days duration, the distribution of the length of down time intervals is also highly significant. The impact of short down times is often equivalent to a reduction in average current while longer down times can seriously disrupt the experimental plan. Therefore, in the final selection, greater priority was given to treating the sources of long down time intervals, especially those greater than 8 hours.

The main improvements of Phase I are listed below:

- Several H^- source and injector reliability improvements
- Upgrade of the "soft-vacuum" for tank 1 of the linac
- Several linac rf reliability/availability improvements
- DC beam switching (H^-) to replace the pulsed kicker switching
- PSR reliability/maintainability improvements
  - Reconfigured extraction region of PSR for improved maintainability
  - Refurbished H^0 line and vacuum system
  - PSR Pulsed-Power Improvements (upgrade of ring injection line kicker modulator and improvements to the extraction kicker modulators)
- Upgrade of the extraction line beam position monitoring (BPM) system
- Some PSR controls converted to EPICS

0-7803-4376-X/98/$10.00 © 1998 IEEE

- Measures to improve operability and serviceability of MLNSC target/moderator cooling systems
- Improved MLNSC target cell shielding
- Improvements to the Radiation Security System (RSS) which in conjunction with improved shielding allows access to ER-1 by trained experimenters under limited access conditions

Phase I was 95% completed by the start of beam operations in July of 1995. One measure of success, but not solely attributable to the Phase I hardware improvements, is the improved neutron beam availability of 83% and 84% (and greatly reduced fraction of down time from intervals greater than 8 hours) which was experienced in 1995 and 1996, respectively. Further characterization of improvements in reliability and availability is shown in the graph of Figure 1 where the unavailability for major subsystems during the period 1988 – 1992 is compared to the year 1995, the first year after the completion of Phase I. Similar results were obtained for 1996 operations.

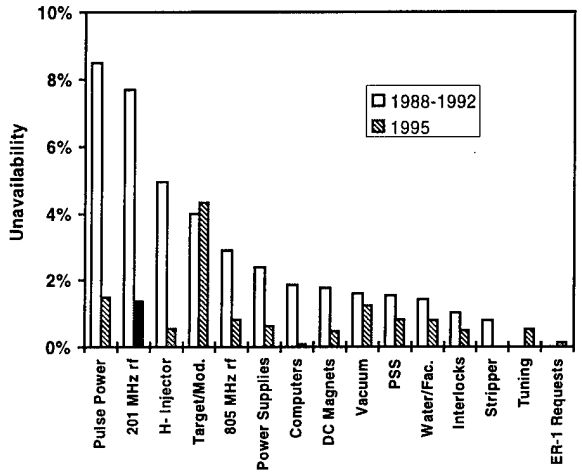


Figure 1. Main contributors to down time.

2.2 Phase II – Longer-term Reliability Improvements

Two projects requiring extensive preparations and a lengthy installation period constitute Phase II of the reliability improvement project. The first project, conversion of the beam injection into PSR from the present two-step process (H^- to H^0 to H^+) to direct injection of H^- beam in one step (H^- to H^+), addresses the root cause of beam losses in the ring. [1] The second, an upgrade of the spallation neutron production target system, will lead to a target that can withstand 200 μA average current and can be replaced in three weeks instead of the 10 months needed for the existing target/moderator system. [2]

2.2.1 PSR Injection System Upgrade

Beam losses at PSR and the resulting radio-activation of ring components are the dominant factors limiting average beam current, a significant cause of equipment failure, and a major element in repair times. Present radiation levels in the injection and extraction regions of the ring are at the limit for practical hands-on maintenance. Reducing the beam loss rate is key to improving maintainability, raising beam current and limiting radiation exposure to personnel who must work on ring components.

Beam losses at PSR are now well understood. First turn losses are now known to arise from the production of excited states of H^0 produced in the stripper foil [3,4]. Stored beam losses are the most prevalent and arise from nuclear and large angle Coulomb scattering as stored beam traverses the stripper foil [5,6]. Reduction of stored beam losses would result from measures that reduce foil traversals but the present H^0 injection scheme severely constrains injection painting. The direct H^- injection upgrade for PSR, first proposed in 1987, avoids these constraints and allows optimum injection painting. [7,8]

The PSR injection upgrade starts with a reconfiguration of the injection line to bring H^- beam to a low-field DC merging magnet placed in the injection section of the ring which functions to merge the H^- and the stored H^+ orbits. The H^- beam is converted to H^+ in a stripper foil located after the merging magnet. A programmed, closed-orbit vertical bump at the foil moves the injected beam off the foil for nearly optimal injection painting. Painting in the horizontal plane is achieved by offsetting the injection point. Important details of the injection upgrade are covered in other papers in these proceedings. [1,8,9]

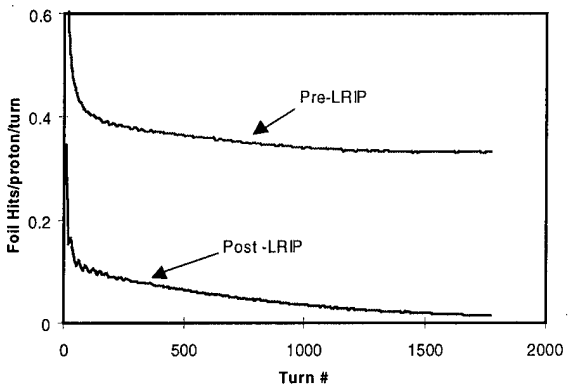


Figure 2. Simulation of foil hits in PSR injection systems.

The main benefit of the new injection system, a large reduction in the foil hits, is computed in ACCSIM simulations to be a factor of 10. This can be seen in more detail in Figure 2 which compares calculated curves of the foil hits per turn per proton for the present and the new injection systems. After optimizing foil thickness to reduce total losses, the overall reduction in beam losses is estimated in the simulations to be a factor 4.5.

2.2.2 Target and Moderator System Upgrade

Replacement of components of the existing target, moderator or reflector system is an intensive, lengthy (~10 months), hands-on operation that results in very significant radiation dose to workers. Failure rates of target system components are rather uncertain but the risk of a long down time is considerable. To date there have been no failures of the tungsten target. However, there have been two failures of the liquid hydrogen moderators in the past 5 years that had a very serious impact on the programs dependent on cold neutrons. For these reasons, upgrade of the target system for faster replacement is of high priority.

The concept of the target upgrade is a single-piece assembly that can be removed remotely in one operation. The assembly will contain a water-cooled target, moderators, reflectors, beam diagnostics and some shielding that fits into a vacuum chamber in the bulk shielding. An overhead crane and access port through the target cell roof will be added so that the target module can be lifted remotely into a shielded cask. For more details see reference [2] in these proceedings.

3 SPSS ENHANCEMENT PROJECT

The US neutron scattering community strongly supports higher beam intensity (both peak and average) from the short pulse spallation neutron source. After LRIP is successfully completed the opportunity exists to reach 200 μA @ 30 Hz with further modest upgrades of the SPSS at LANSCE.

3.1 H- Ion Source and Injector Upgrade

The present H^- ion source limits the H^- current from the linac to ~ 6.5 mA averaged over the PSR chopping pattern. To reach the goal of 200 μA @ 30 Hz requires about 50 % more peak current from the H^- ion source and injector. More current, up to the 17 mA capacity of the linac, is desirable to reduce storage time (hence beam losses in the ring) and to reduce the bunch length in PSR.

A source with twice the intensity and half the emittance of the present surface conversion source is desired. A project to develop the needed source and injector modifications is underway in collaboration with experts at LBNL. Progress is reported in reference [10] of these proceedings.

3.2 RF Buncher Upgrade for PSR

To reach the peak intensity of 4.2 x 10^{13} protons per pulse required for 200 μA @ 30 Hz one must deal with the limits imposed by the PSR instability. The preponderance of evidence to date supports the e-p hypothesis for this instability i.e., coupled oscillations of low-energy electrons trapped in the potential well of the circulating proton beam. [11,12] The threshold intensity for the instability is most strongly influenced by rf buncher parameters, especially the buncher voltage, as is shown in Figure 3. This behavior is consistent with the e-p hypothesis and is the basis for the buncher upgrade to control the PSR instability.

A project is underway to upgrade the existing rf buncher in PSR to produce a wave form with up to 18 kV peak voltage at the fundamental of the revolution frequency. When this is completed a second buncher that produces 15 kV at the second harmonic will be added to produce a better bunching factor.

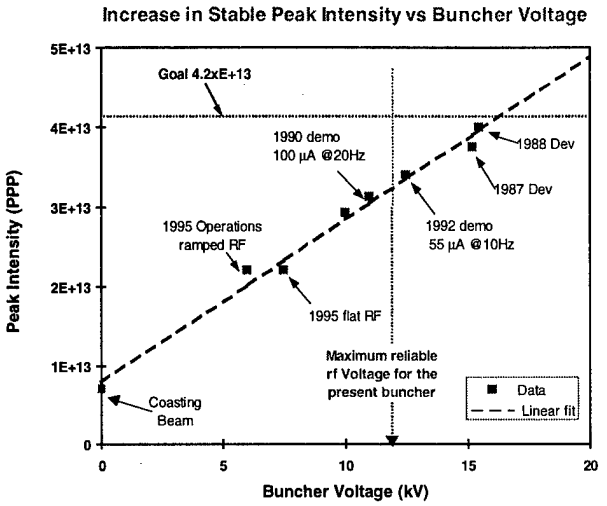


Figure 3. Threshold intensity vs Buncher Voltage.

REFERENCES

[1] D. H. Fitzgerald, *et al.*, 'Overview and Status of the Los Alamos PSR Injection Upgrade Project', these proceedings.

[2] J. B. Donahue, *et al.*, 'LANSCE Short-Pulse Spallation Source Target Upgrade', these proceedings.

[3] R. Hutson and R. Macek, Proceedings of the 1993 Particle Accelerator Conference (1993) 363.

[4] R. J. Macek, *et al.*, Proceedings of ICANS XII, (1993) Volume 2, A-25.

[5] R. Macek, *et al.*, Proceedings of the European Particle Accelerator Conference (1988) 1252.

[6] R. J. Macek, *et al.*, Proceedings of the 1993 Particle Accelerator Conference (1993) 3739.

[7] R. J. Macek, Proceedings of ICANS X, (1988) 91.

[8] Barbara Blind and Andrew Jason, 'PSR Injection Line Upgrade', these proceedings.

[9] C. R. Rose, *et al.*, 'Overview of the Bump Magnet System at the Los Alamos Proton Storage Ring', these proceedings.

[10] A. B. Wengrow, *et al.*, 'Development of a High Duty Factor, Surface Conversion H^- Ion Source for the LANSCE Facility', these proceedings.

[11] D. Neuffer *et al.*, NIM, A321 (1992) 1-12.

[12] M. Plum, *et al.*, 'Recent Experimental Evidence for the Los Alamos Proton Storage Ring Instability', these proceedings

BEAM DYNAMICS ASPECTS FOR THE APT INTEGRATED LINAC*

S. Nath, K. R. Crandall+, E. R. Gray, T. P. Wangler and L. M. Young
Los Alamos National Laboratory, Los Alamos, NM 87545

Abstract

The accelerator-based production of tritium calls for a high-power cw proton linac. The current Los Alamos design uses an integrated approach in terms of accelerating structure. The front part of the accelerator uses normal-conducting (NC) structures while most (>80%) of the linac structure is superconducting (SC). Here, we report the beam-dynamics rationale used in the integrated design and present particle simulation results.

INTRODUCTION

The linac for the production of tritium calls for 100 mA of cw proton beam to be delivered onto a production target. Previous design [1] consisted entirely of normal-conducting structures. In that design, we minimized the number of transitions between accelerating structures. In addition, the phase advances per unit length in both the transverse and longitudinal motion were tailored to be continuous at the only transition point i.e. RFQ and the CCDTL at 6.7 MeV. The structure beyond 100 MeV was also a NC coupled-cavity structure.

At higher energies, however, there are some advantages of using SC rf-cavity structures discussed in detail elsewhere [2,3]. In brief, it allows comparatively larger bore size minimizing the risk of beam loss - an issue of utmost importance for such a high power linac. Considerably more operational flexibility is another advantage of using SC structures at higher energies. A substantially higher power efficiency is obviously the major attraction in terms of life-time operational cost. To arrive at an optimum integrated design, we studied several design-schemes in terms of lattice, focusing strength and number of accelerating cavities per cryomodule in the SC section. The design features of the linacs are described in an accompanying paper [3]. In the following sections, we describe the beam dynamics and simulated performances of a few of the design-options studied so far.

DESIGN OVERVIEW

At present, 217 MeV, which corresponds to the end of a supermodule in the NC section is chosen as the transition energy between the NC low-energy (LE) linac to the SC high-energy (HE) linac. It is a good compromise in terms of the desire to switch at the lowest possible energy to maximize the benefits of the SC linac, and confidence in the SC-cavity performance for the shortened elliptical cavity which increases with the design velocity.

Beyond 217 MeV, the SC structures accelerate the beam to a nominal energy of 1.7 GeV. The HE SC linac is comprised of two sections, a medium-β section with identical cavities optimized for a velocity β=0.64, and a high-beta section with identical cavities optimized for a velocity β=0.82. Each section consists of a sequence of identical cryostats. The rationale for the two-velocity section/5-cell-cavity architecture is based on the velocity-acceptance characteristics of the cavities as a function of the number of cells per cavity. Detailed analysis is contained in Ref. 2.

Two design scenarios for the SC linac section are considered. One uses SC quadrupole magnets laid out in a FODO lattice. The magnets are contained within the cryostats alternating with the cavities. In another option, the quadrupole magnets are laid out in a doublet (FDO) lattice outside the cryomodules. Heretofore, we refer them to as singlet and doublet design respectively.

SINGLET DESIGN

In the singlet design, there are three Nb cavities in the β=0.64 section, while the β=0.82 section contains four cavities per cryomodule. The medium-β section accelerates the beam through a nominal energy range from 217 MeV to 469 MeV with an average or real-estate accelerating gradient ranging from 1.43 to 1.51 MV/m. The high-β section ranges from 469 MeV to 1700 MeV with an average accelerating gradient of 1.89 MV/m. The beam dynamics parameters are listed in Table 1. The length of the focusing period in the transition from the normal to the SC section approximately doubles from 2.0 m to about 3.4 m.

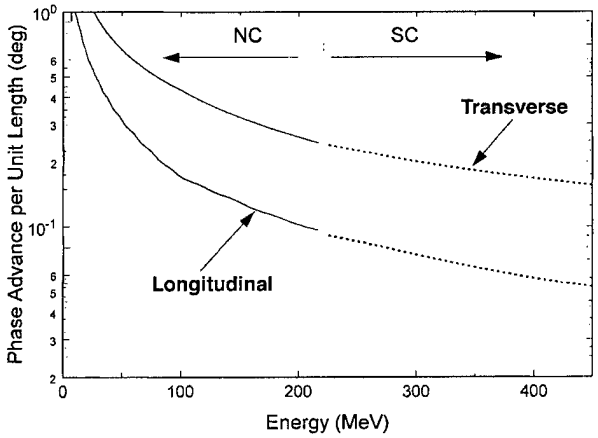


Figure 1. Zero-current transverse and longitudinal phase advance per unit length (degree/cm) across the transition between the NC and SC linac at 217 MeV.

No separate matching section is used to match the beam across the NC/SC transition. Instead, matching is achieved by smoothly ramping the quadrupole strengths, beginning at 24 MeV, so that the focusing strength across the transition is smooth. From 24 MeV to 100 MeV, the gradient is scaled down as $1/\beta^{0.25}$. The strength is scaled

* Work supported by the US Department of Energy
+ Amparo Corporation, Santa Fe, NM 87540

0-7803-4376-X/98/$10.00 © 1998 IEEE

as $1/\beta^{0.40}$ from 100 to 155 MeV, and as $1/\beta^{0.48}$ from 155 to 217 MeV. This prescription results in a continuous zero-current phase advance per unit length as shown in Figure 1. The average (i.e. real-estate) accelerating gradients across the transition are almost equal as are the average design phases. This makes the zero-current longitudinal phase advance per unit length also continuous across the NC/SC transition point.

Table 1. Beam Dynamics Parameters for the Singlet SC linac without equipartitioning

Parameter	Medium-β Section	High-β Section
Quadrupole lattice type	FODO	FODO
Lattice half period	1.70	2.03
Synchronous phase (deg)	-25 to -35	-30
σ_{t0} = Trans. phase adv. per period (zero current)	80 to 52	57 to 25
σ_t = Trans. phase adv. per period (space charge)	42 to 25.4	28.3 to 14.4
σ_{l0} =Long. phase adv. per period (zero current)	26 to 14.5	25 to 7.5
σ_l = Long. phase adv. per period (space charge)	9.1 to 5.8	4.5 to 0.7
σ_t / σ_{t0}	0.5	0.5 to 0.6
σ_l / σ_{l0}	0.3 to 0.2	0.2 to 0.1
Trans. Emit. (π-cm-mrad)	0.0163 to 0.0166	0.0166 to 0.0164
Long. Emit. (π-cm-mrad)	0.045 to 0.046	0.046 to 0.050
Ratio of aperture radius to matched rms beam radius	39 to 43	54 to 70

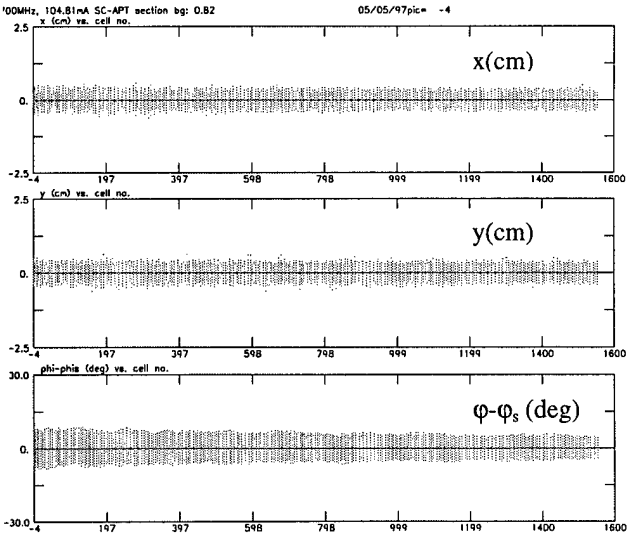


Figure 2.. Transverse and longitudinal profile plots in the "singlet" SC linac from 469 MeV to 1.7 GeV for non-equipartitioned mode of operation.

In the context of the optimization process for the singlet-lattice design, the quadrupole gradient profiles along the linac must be chosen. As one possibility, merits of equipartitioning [4, 5] were investigated. Detailed results are described in an accompanying paper [6]. Figure 1 and Table 1 correspond to a non-equipartitioned case. For the equipartitioned case, we have a similar, smooth transition as is shown in Ref. 6. The ratio σ_{0l}/σ_{0t} decreases from 0.55 at 25 MeV to 0.30 at 1.7 GeV. In the equipartitioned linac, on the other hand, the ratio is nearly constant throughout the linac. It should be noted that equipartitioning requires operating the linac with reduced transverse focusing strength above 25 MeV. The quadrupole strength at the end of the equipartitioned linac is about 55% of the strength in the non-equipartitioned linac.

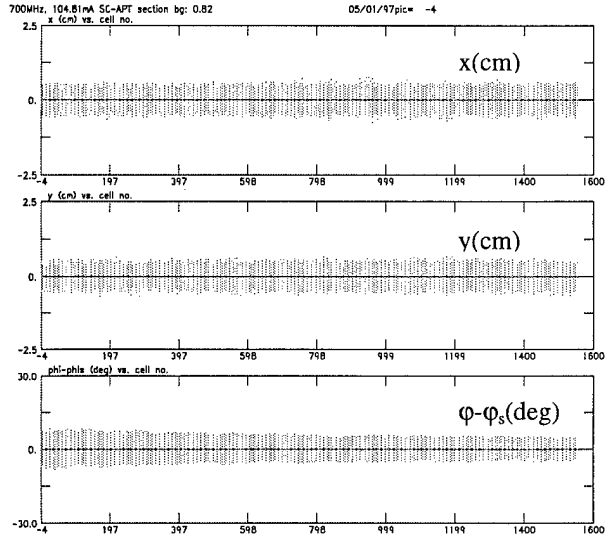


Figure 3. Transverse and longitudinal profile plots in the "singlet"super-conducting linac from 469 MeV to 1.7 GeV for equipartitioned mode of operation.

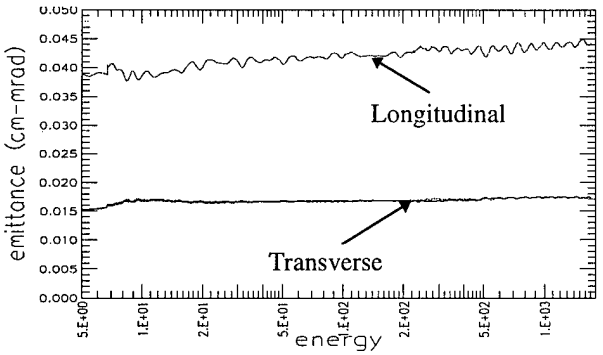


Figure 4. Longitudinal and transverse rms normalized emittance vs. energy for full current in the "singlet" SC linac for equipartitioned mode of operation.

Simulation results without any errors for both the equipartitioned and un-equipartitioned mode are shown in Figures 2 through 4. Initial beam distribution of 100,000 particles originating at the plasma surface of the ion source are followed [7] through the entire linac. Beam-profile plots for full current from 469 MeV to 1.7 GeV in the un-equipartitioned and equipartitioned cases are shown in Figures 2 and 3 respectively. Relative to the rms size, the beam is smaller in the equipartitioned case but in

absolute terms, the beam-size is roughly 55% larger. No oscillations in the profiles indicate a good match in the transition region. Longitudinal and transverse emittance as a function of energy for the equipartitioned case are plotted in Fig. 4. The optimum choice for the quadrupole gradient profile in the final design will also depend on the results of the linac performance, when errors are included.

DOUBLET DESIGN

In the doublet design for the SC section, the cryomodules contain only the Nb cavities; the room-temperature quadrupoles are placed outside. For the β=0.64 section, there are two cavities per period. In the β=0.82 section, two configurations were studied; one with two cavities per period and the other with four cavities per period.

In order to achieve a current independent matching between the normal-conducting and SC structure, the quad strengths in the NC section need to be ramped down more than was done in the singlet design. The period-length at 217 MeV for the NC and the SC structures are about 2.0 m and 4.9 m respectively. In order to achieve the same phase advance per unit length at the transition, we start tapering down the field gradient of the quadrupoles in the NC section starting at 100 MeV where σ_{0t}=77.2°. Quadrupole gradients are ramped down to make σ_{0t}=32.7° at 217 MeV reducing the phase advance by equal amounts per period. In the longitudinal plane, σ_{0l} per unit length are the same at the transition for φ_s= -30°.

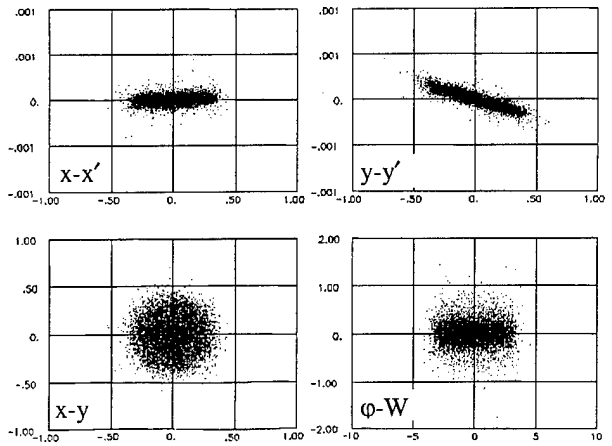


Figure 5. Output phase-space distributions at 1.7 GeV for the doublet design with four cavities per period in the β=0.82 section.

The matching between the β=0.64 and β=0.82 SC-sections starts with finding suitable design phases for the last period of the β=0.64 section and the first period of the β=0.82 section. The phases in the β=0.64 section are then ramped appropriately to achieve a smooth longitudinal transition. For the design with two cavities per period in the β=0.82 section, the quads in the β=0.64 section need to be ramped up from 5.75 to a final value of 7.75 T/m to match the σ_{0t}=80° value in the first period of the β=0.82 section. For the design with four cavities per period, period-lengths are longer. Here, in addition to ramping the quadrupole gradients in the β=0.64 section, the gradients in the interface need to be adjusted slightly.

Good matching is achieved for all currents between zero and 100 mA in both the designs described above. It should be emphasized that no special difficulties were encountered in achieving a current independent singlet to doublet match at 217 MeV. The output phase space distributions at 1.7 GeV for the design with four cavities per period in the β=0.82 section are shown in Figure 5. The output phase space distributions for the design with two cavities per period look very similar except that it has slightly smaller transverse rms dimension. In both the designs, there is very small growth in the transverse emittance. Figure 6 shows the relationship between maximum rms -beam-size, aperture-size, and maximum transverse coordinate of a particle as a function of energy.

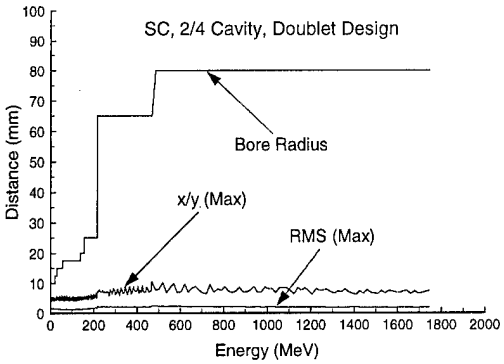


Figure 6. Maximum rms beam-size, aperture size and maximum transverse coordinate of the outermost particle vs. energy.

CONCLUSION

Beam-dynamics simulations show that both singlet and doublet designs are viable options for the SC linac section. An integrated NC/SC design using either of the options provides the beam quality required for the APT.

REFERENCES

[1] S. Nath et al., "Physics Design of APT Linac with Normal Conducting RF Cavities," Proceedings of the 1996 Linear Accelerator Conference, Geneva, Switzerland, August 26-30, 1996.

[2] Los Alamos National Laboratory APT Conceptual Design Report, LA-UR-97-1329, April 1997.

[3] G. P. Lawrence and T. P. Wangler, "Integrated Normal-conducting/Superconducting High Power Proton Linac for APT," this conference.

[4] R. A. Jameson, "On Scaling and Optimization of High Intensity Low-Beam-Loss RF Linacs for Neutron Source Drivers," AIP Conference Proceeding 279, ISBN 1-56396-191-1.

[5] M. Reiser, "Theory and Design of Charged Particle Beams," John Wiley & Sons, Inc., p573 (1994).

[6] L. M. Young, "Equipartitioning in a High Current Proton Linac," this conference.

[7] L. M. Young, "Simulations of the LEDA LEBT with H^+, H_2^+, and e^- particles," this conference.

AVAILABILITY RESULTS FOR THE LANSCE ACCELERATOR COMPLEX

N. T. Callaway, R. W. Garnett, K. W. Jones, M. A. Oothoudt, and B. D. Ray,
LANSCE Division, Los Alamos National Laboratory, Los Alamos, NM 87545, USA

Abstract

The results of an analysis of operations data from the 1996 run-cycle of the LANSCE accelerator complex will be presented. Frequency and history of operational events including system and component failures which affect beam availability have been tracked. Some of the significant downtime incidents will be described and analyzed in detail. These results will be used to improve future operations and beam availability.

1 INTRODUCTION

The Los Alamos Neutron Science Center (LANSCE) accelerator complex (formerly known as LAMPF) consists of an 800-MeV linear accelerator, a proton storage ring (PSR), and a variety of production targets and experimental areas. Two beams are presently accelerated simultaneously on alternating cycles of the rf.

The linear accelerator consists of two 0.75-MeV Cockroft-Walton injectors, one supplying H^+ ions while the other supplies H^- ions, a separate low-energy beam transport (LEBT) line for each beam species, a 0.75 to 100-MeV drift-tube linac (DTL) operating at 201.25 MHz, a 100-MeV transition region (TR), and a 100 to 800-MeV side-coupled linac (SCL) operating at 805 MHz. Peak beam currents typically range from 12 to 18 mA for varying duty factors to give a maximum average beam current of 1 mA. The number of particles per bunch is of the order of 10^8 in the linac.

Beams from the linac are directed to various experimental areas and into the PSR via a beam switchyard. The 800-MeV H^+ beam is presently sent to an experimental area (Area A) where it interacts with a series of different target materials for the Accelerator Production of Tritium (APT) program. Up to 3 μA of the 800-MeV H^- beam is sent to the Weapons Neutron Research Facility (WNR) where it strikes a target producing an intense white-neutron source. Since variable proton pulse widths are available, time-of-flight experiments for neutron energies ranging from a few MeV to 800 MeV are possible.

The PSR functions as a high-current accumulator or pulse compressor to provide intense pulses of 800-MeV protons to the Manual Lujan Jr. Neutron Scattering Center (Lujan) spallation neutron-production target. The 800-MeV H^- ions from the linac are transported to a high-field stripper magnet where they are converted to H^0 ions. The H^0 beam then enters the magnet focusing lattice of the ring through a dipole where the final stripping to H^+ occurs. The PSR operates at a repetition rate of 20 Hz. An entire linac macropulse is accumulated per turn with up to 2800 turns accumulated prior to single-turn extraction.

In addition to the accelerator, as with any complex facility, there are major support systems which must be functioning properly and which affect beam delivery and availability. These systems include cooling water, ventilation, rf power, magnet power supplies, vacuum, and safety systems. Tracking of the effects of these systems on beam availability is important for reliable operation.

2 AVAILABILITY TRACKING

During scheduled operation of the LANSCE accelerator complex, an availability logging (AVL) system [1] utilizing automatically archived accelerator data and electronic control room log entries, is used to track the frequency and causes of accelerator and facility downtime. Beam availability is defined as the fraction of scheduled beam time delivered.

Historically, such data was manually collected by the accelerator operators. The AVL system is intended to automatically gather and report most of the data. The main shortcoming of the AVL system is its inability to automatically assign causes of downtime. Therefore, manual input of information by the accelerator operators is still necessary and the availability tracking is done using a combination of the automated software programs, written specifically for this purpose, and a spreadsheet for final data analysis and plotting. The AVL system consists of two major subsystems: Data Acquisition and Data Analysis software. These are discussed in the sections below.

2.1 Data Acquisition Components

The data acquisition subsystem consists of three programs which interact to gather data while the facility is in operation. These programs are started when the control system is booted and run either as background or interactive processes.

The program AVL_LOGGER runs as a background process and writes output to files. Data is acquired once per minute. The top-level equipment readiness status of each section of the facility (i.e., major areas like the linac, a beam transport line, etc.) is interrogated. If any top-level status is found to be "bad," a script is executed for that section, all "bad" statuses are logged, and output is written

0-7803-4376-X/98/$10.00 © 1998 IEEE

to a file. The AVL_LOGGER program does not do any data analysis; it only logs the data to a file on disk.

The program CMLOGGER also runs in background once per minute. This program reads a number of current monitors, logic states, and the beam duty factors. This information is also written to a file. CMLOGGER compares the operation production current thresholds, which are maintained in a data system, in real-time with the current monitor values. The program sends a message to the CCRLOG program, which maintains an electronic log of control room activities, when beam currents drop below or rise above the specified production current thresholds.

The CCRLOG program displays messages in the log corresponding to the change in the production states of the beams. If beam currents are out of production tolerances for more than 2 minutes, the program prompts the operator for information about the causes of downtime since the system can not do this automatically.

2.2 Data Analysis Components

The data analysis subsystem consists of a set of sorts and filters on the raw data to collect and tabulate information both by cause of downtime and fraction of total downtime. The analysis is performed by a set of command files, most often run automatically as a batch job. The final stage of analysis is to use a spreadsheet to produce graphs which are displayed to track availability, for maintenance, and for historical archiving.

3 DATA ANALYSIS FOR 1996

Data from the AVL system has been compiled and analyzed [2] for the 1996 calendar year. Each calendar year of operation of the LANSCE accelerator complex is subdivided into several "run-cycles." Each run-cycle is generally followed by a period of equipment maintenance. The calculated availability for each run cycle for each area where beam was delivered and the cumulative 1996 results are shown in Table 1. The availability is calculated by taking the ratio of the amount of time the beam current was above the specified production threshold and the total scheduled beam time. Beam time to each area is generally scheduled months in advance of production. Our operations goal for 1996 was to provide greater than 80% availability for all beams delivered. These goals were met with the exception of beam delivery to Area A which will be discussed in detail in the next section.

The AVL system allows tracking and categorization of downtime by system. This data is useful in determining which systems are the most frequent causes of facility downtime. Figures 1-3 are plots of percentage of scheduled operation lost (downtime) as a function of subsystems of the LANSCE accelerator complex. Downtime caused by subsystems of the accelerator affect delivery of beam to all areas. These sources of downtime are common to all three plots. For example, failures of rf system components (labeled RF-201 and RF-805 in the figures) in the accelerator will affect beam availability to all three experimental areas.

Table 1 - Summary of LANSCE beam availability for 1996. Availability is calculated for each experimental area where beam is delivered using the time the beam current was above the specified production threshold.

	Area A (%)	WNR (%)	Lujan (%)
Cycle 71	-	73.2	69.0
Cycle 72	87.2	87.4	88.7
Cycle 73	31.8	89.3	88.9
1996 Ave	63.5	82.2	81.4

As can be seen in Figure 1, a significant source of beam downtime for Area A (>30% of scheduled production) was due to problems related to target operations. For both the WNR area (data shown in Figure 2) and the Lujan area (data shown in Figure 3), beam availability was generally high with 4-4.5% downtime attributed to DC magnet power supply failures.

During every operating period of the LANSCE accelerator there are also many short beam interruptions lasting 1-2 minutes in duration. This is not apparent from the figures above. For example, during one run cycle there were 330 total periods of downtime. Of these, 199 were of short duration and contributed to only 0.46% of the total downtime. These short-duration downtime periods are primarily caused by a machine "Fast Protect" where beam is automatically gated off due to an out-of-tolerance condition. Most of these events are transient in nature and usually require no operator intervention to be corrected.

4 SIGNIFICANT DOWNTIME INCIDENTS

Two significant downtime incidents are discussed in detail below. Each of these incidents caused extended periods of downtime which significantly affected beam availability of the LANSCE accelerator complex during 1996 operations.

4.1 Area A - H^+ Beam Delivery

A series of highly successful experiments were run in Area A in 1996. The experiments consisted of placing a group of stacked inserts, each made of a different target material, into the H^+ beam. Metallurgical and corrosion studies were carried out on the various inserts.

The success of these experiments relied on control of the environment surrounding each insert. Five periods of downtime were caused by water leaks of unknown origin (perhaps from localized heating by the beam) developing in the first insert (tungsten). Although the accelerator maintained the capability to deliver beam as scheduled, the target requirements for these experiments precluded beam delivery. The accumulated downtime from these five periods was approximately 24.2 days, which is 28.9% of the total run-cycle time.

This failure falls into the category of unanticipated equipment failures. Since these target inserts are often of a unique mechanical design, easily replaceable spares often do not exist. Failures of this kind demonstrate the importance of proper water system design and maintenance.

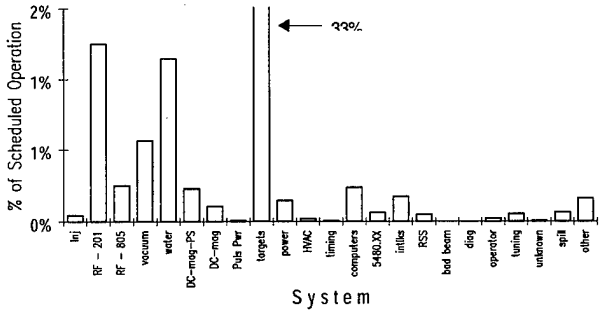


Figure 1: Causes of downtime for H^+ beam delivery to Area A histogrammed by system.

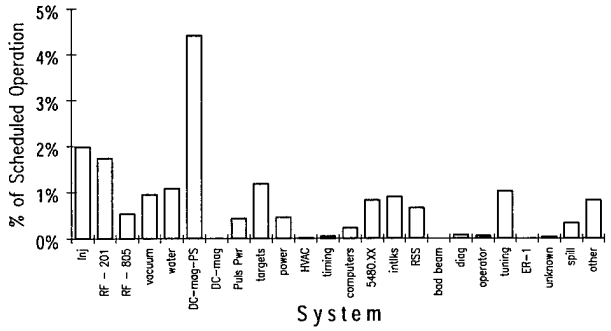


Figure 2: Causes of downtime for H^- beam delivery to the WNR area histogrammed by system.

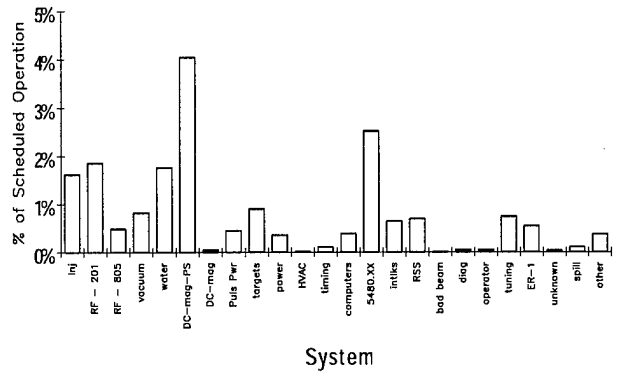


Figure 3: Causes of downtime for H^- beam delivery to the Lujan area histogrammed by system.

4.2 Lujan - H^- Beam Delivery

Although the average availability of beam during 1996, as seen in Table 1 above, to the Lujan area was high, the significantly lower availability during Cycle 71 was caused by a catastrophic failure of a magnet power supply for the main benders of the PSR. This caused approximately 6.3 days of downtime.

The current regulation capability of the power supply was lost due to component failure of the controller and subsequently it tripped off-line. In an attempt to diagnose the problem, repair technicians re-energized the power supply. Because of the loss of current regulation, 40% of the output capacitors, a 75-volt power supply and fuses for some of the magnet shunts were destroyed.

Replacement of the capacitors and fuses was carried out using parts on hand. The power supply was ordered from the vendor, was readily available, and was shipped overnight. The power supply controller was determined to be a custom designed part for LANSCE and was not immediately available from the vendor. A replacement IC was not immediately available. About four days were required to design and fabricate a robust substitute circuit at LANSCE for use in the interim.

This failure emphasizes the importance of refresher training for problems which are not common and to review knowledge which is not often used [3]. Also, having spare parts on hand is required for timely failure recovery and high availability. It may also be of value to periodically review availability of replacement parts for aging systems and upgrading or replacing them with more readily available parts.

5 SUMMARY

The AVL system described in this paper has been used to track beam availability and to identify the most frequent system failures affecting availability at the LANSCE accelerator complex during the 1996 operating period. It is our goal to further develop the AVL system capabilities so that predictions, such as mean-time-between-failures, may be made in the future. We also hope to use our availability data and past lessons-learned to help implement a more structured system of preventative and corrective maintenance, and to identify systems or components in need of upgrade or replacement.

REFERENCES

[1] M. A. Oothoudt, "AVL User Information Manual," Los Alamos National Laboratory Report, AOT-6-94-135, August 1994.

[2] M. A. Oothoudt and K. W. Jones, "Los Alamos Neutron Science Center Availability for 1996," Los Alamos National Laboratory Report, AOT-6-97-49-TR, February 1997.

[3] J. C. Sturrock, Los Alamos National Laboratory Report, AOT-6-96-41-IR, August 1996.

PROGRESS UPDATE ON THE LOW-ENERGY DEMONSTRATION ACCELERATOR (LEDA)*

J. D. Schneider and K. C. D. Chan, APT Project Office, Los Alamos National Laboratory, Los Alamos, New Mexico, 87545

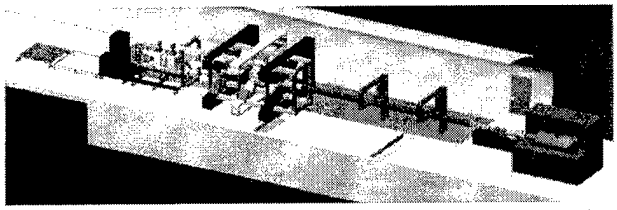
Abstract

As part of the linac design for the accelerator production of tritium (APT) project, we are assembling the first approximately 20 MeV portion of this cw proton accelerator. Primary objective of this low-energy demonstration accelerator (LEDA) is to verify the design codes, gain fabrication knowledge, understand LEDA's beam operation, and be able to better predict costs and operational availability for the full 1700 MeV APT accelerator. This paper provides an updated report on this past year's progress that includes beam tests of the 75 keV injector, fabrication of the 6.7 MeV radio-frequency quadrupole (RFQ), preparation of the facility, procurement and assembly of the rf system, and detailed design and documentation of many pieces of support equipment. First tests with the 6.7 MeV, 100 mA, cw beam from the RFQ are scheduled for late 1998. References are given to many detailed papers on LEDA at this conference.

1 INTRODUCTION

This overview paper will present only an executive summary of the many activities completed and underway on LEDA, the low-energy demonstration accelerator. In the process, we will reference the many recent publications and the several papers at this conference that provide much detail on LEDA activities.

LEDA is designed as a prototype [1] of the first approximately 20 MeV portion of the accelerator production of tritium (APT) accelerator [2] that will be built at Savannah River. Prototyping the first 20 MeV should significantly increase our confidence in this critical space-charge dominated structure [3,4,5]. LEDA's beamline components will include a 75 keV proton injector, a 6.7 MeV RFQ, and approximately 20 MeV of CCDTL coupled-cavity drift-tube linac), a hybrid between a standard DTL and a CCL structure.



Conceptual layout of the LEDA accelerator, showing injector, RFQ (behind waveguides), a section of the CCDTL, and the shielded beam stop.

Although being built at Los Alamos, and being led by Los Alamos personnel, LEDA represents a collaboration between several organizations. Major participants include: Westinghouse Savannah River Corporation, Lawrence Livermore National Laboratory, Allied Signal, Brookhaven National Laboratory, and heavy involvement by the APT Prime contractor, Burns and Roe Enterprises teamed with General Atomics. LEDA is intended to become the confirmatory prototype for the plant accelerator.

Even though output energy is low (20 MeV), the average beam power (2.0 MW) of LEDA will rank it as the highest power proton accelerator in the world. Clearly, radiation shielding and power handling are important design issues.

Most equipment ordering and detailed design on LEDA began in November, 1995, although some conceptual design was begun earlier. In the following paragraphs, we summarize the LEDA status as of early May, 1997.

2 SUBSYSTEM DESCRIPTION

Injector:

The LEDA injector is, at this time, the only fully operational part of the beamline hardware. This injector must supply a dc beam of at least 110 mA of protons at 75 keV into the radio-frequency quadrupole (RFQ) accelerator. The operational injector uses a 2.45 GHz microwave ion source, a single-gap extractor, and dual magnetic solenoids to provide this beam. The ion source requires only 500-800 Watts of power to create a suitable plasma from which a 90% proton beam with >30% gas efficiency may be extracted [6].

The single-gap, spherically convergent extractor provides a beam with emittance of less than 0.2 π mm-mrad (normalized).

The low-energy beam transport (LEBT) uses two solenoids and two steering coils to ensure a proper match into the RFQ. A well-cooled variable-iris device will be used to control injected current, and a microwave power modulator will be used to provide beam pulsing. Multiple extended beam runs with this injector have shown it capable of required current, emittance, stability; and measured erosion rates show a predicted maintenance-free lifetime exceeding 400 hours. LEBT physics design

* Work supported by the US Dept of Energy, Defense Programs.

0-7803-4376-X/98/$10.00 © 1998 IEEE

[7,8] is in good agreement with mechanical design [9] and detailed measurements [10].

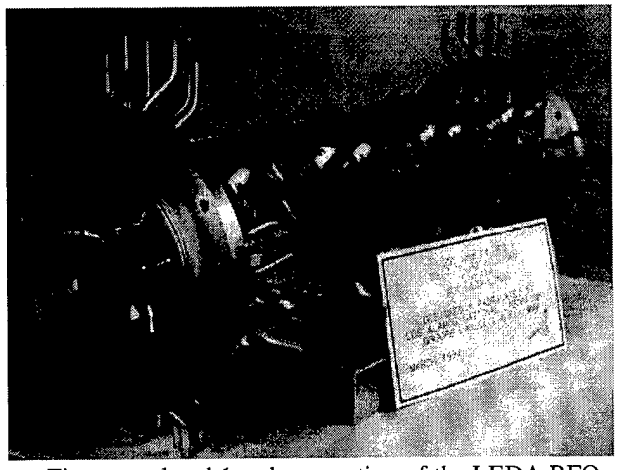
During the summer of 1997, the LEDA injector will be used to inject a 50 keV proton beam into the CRITS (Chalk River Injector Test Stand) RFQ. Beam operation with this 1.25 MeV cw RFQ will provide an additional confirmation of injector beam quality and will help to verify RFQ design codes.

RFQ:

LEDA's RFQ [11] is unique in terms of its long physical length (8 meters), high output energy (6.7 MeV), large beam power (663 kW), and cooling requirements (1.27 MW). It is constructed as an all-brazed, 100% copper (OFE) structure, assembled from eight separate 1-m long sections [12]. When in operation, its only active resonance control is by modulation of input water temperature.

Of the eight separate sections, three are used for 350 MHz rf power feed via four 250 kW coupling irises, three are used to provide vacuum pumping. Each section includes ports for 16 static slug tuners, used only for tailoring initial field distribution. Design and fabrication of the main structure is being done by and at Los Alamos. Livermore National Laboratory (LLNL) is responsible for the vacuum system [13], and Allied Signal's Kansas City Plant is doing the resonance-control cooling system. Specialists from Northrup/Grumman Corporation assisted with structural and thermal analysis, design reviews, and tuning.

At this point, the first two sections of the RFQ have seen the final fabrication steps; all others are in advanced stages of machining and brazing. These first three completed sections are leak-tight, dimensionally correct and appropriately tuned for rf fields. The eight sections of the complete RFQ will be assembled into four tuned segments, with inter-coupling plates to distribute RF power. Assembly of the entire structure should be complete in January, 1998, and first beam should be seen 6--11 months thereafter.



First completed 1-m long section of the LEDA RFQ.

CCDTL:

This new 700 MHz structure [14] promises to capture the best features of a DTL and a CCL, using either one or two simple drift tubes inside each π-mode cavity. All quadrupole focus magnets are outside the drift tubes and cavities, so alignment is not critical. Extensive measurements with a 'cold-model' calibrated our 3-D design codes and helped to tailor the coupling slots between all cavities. Within the next few months, a 'hot model' will be used to test structure cooling and response.

RF power systems:

LEDA will require a number of approximately 1-MW cw rf power systems [15] to power the RFQ and CCDTL cavities. Three 1.2 MW 350 MHz systems will feed into the RFQ. Three 700-MHz 1.0 MW systems will be needed for the CCDTL. In addition, LEDA facilities will be used to qualify and test all rf system components.

The first two 350 MHz klystrons have been shipped to Los Alamos, two 1-MW circulators have arrived, and the first transmitter (klystron electronics) is on hand. The first high-voltage power supply should ship soon. Meanwhile, crews at Los Alamos are assembling and checking all available components and support systems. Two 350 MHz rf vacuum windows were tested [16] with power levels of 950 kW. During operation, these windows will be run at 250 kW. During the last several months of 1997, we will be testing all rf components and preparing the setup of the three 350 MHz stations [17] needed for supplying power to the RFQ.

Low-level rf systems:

The sophisticated controls and electronics of the LLRF system will set and maintain proper phase and amplitudes of all accelerating cavities [18,19], distribute reference signals along the beam line and provide many feedback signals from the cavity and beam pickup devices.

Controls:

LEDA will use a distributed control system. EPICS was originated for GTA and has since been highly developed by use at the APS (Advanced Photon Source) and Jefferson Lab, in addition to nearly 50 world-wide locations, plus embraced and enhanced by at least three commercial ventures. Many systems will have localized control with dedicated PLCs, but all operational status and control commands can be accesses through the EPICS operator interfaces. Input/output controllers or IOCs will provide this local interface (through VXI and VME hardware) and provide links into the centralized database-driven communication. An EPICS station and all peripherals have been controlling the LEDA injector for more than the past two years. Automated control routines provide a prompt and complete hands-off, full-beam recovery from any interruption such as a high-voltage sparkdown.

Beam transport and beam stop:

The purpose of LEDA's beamline components after the accelerator are to safely carry the beam to a high-power dump, and to do confimatory measures of beam parameters. Initial testing will be done with a very simple transport line [20], merely to confirm RFQ performance. Later, a magnetic lattice similar to that used with the CCDTL can help to predict the critical matching between the different structures.

For tests at both 6.7 MeV and 11 MeV, the beam will impinge either on graphite tiles or a nickel-plated copper plate. This beam stop plate will be mounted inside a large vacuum vessel and surrounded by one-meter thick magnetite concrete to shield against both prompt and residual neutrons and gammas. A linearized 2-D beam rastering system [21] will be used to uniformly distribute the beam power over the beam stop surface.

Beam Diagnostics:

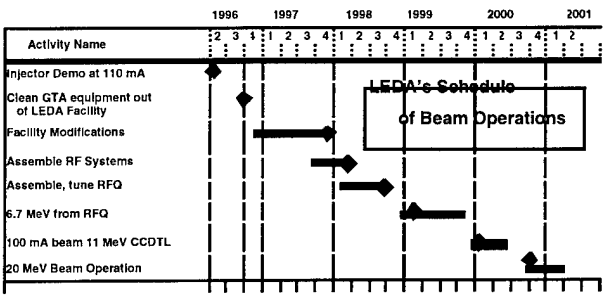
An important and essential feature of LEDA is the use of extensive (mostly non-interceptive) diagnostics [22] to measure and characterize the beam position [23,24], phase and energy [25]. This information will be used to confirm and refine accelerator designs.

Facility Modifications:

LEDA is being assembled and will be operated in the former GTA (Ground Test Accelerator) facility. This experimental structure, with a 140 m long buried beam tunnel, was built to house a 100 MeV, 100 mA, 5% DF accelerator. It is thus generally appropriate for LEDA, but requires upgrades to greater than 10 MW of ac power and cooling water.

Safety Systems:

Operational run-permit will be incorporated into the EPICS control system, with scores of interlocks to ensure that components and systems are operated only when the risk of equipment damage is very low. A hard-wired fast-protect system will ensure the near-immediate (10--20 μs) turnoff of the beam in event of beam spill as detected by fast ionization chambers. Totally separate from both these equipment safety systems, a personnel access control system (PACS) will be used to ensure that all personnel are excluded from the beam tunnel whenever beam or high rf power might be present. This PACS is very similar to the recently upgraded system in use at LANSCE.



An environmental assessment (EA) was completed and approved for LEDA more than one year ago. Other than the increased use of ac power and water for cooling, environmental impacts from LEDA are extremely minor. Meanwhile, a draft safety analysis document (SAD) has been prepared and reviewed. This SAD is complete except for some refinements on the beamstop radiation calculations.

3 SUMMARY

The LEDA project is on schedule to progressively assemble and test major components of a high-power, cw accelerator, first at 6.7 MeV, then 11.2 MeV, and finally at approximately 20 MeV. This collaboration of several national laboratories and international industries should advance significantly the technology of high-current, high-power accelerators.

4 REFERENCES

[1] J. D. Schneider, "APT Accelerator Technology," Proc. XVIII Int. Linac Conf. (Geneva, 26-30 Aug. 1996), pp. 22--26

[2] G. Lawrence, et al, "Integrated Normal-conducting/Super-conducting High Power Proton Linac for APT," this conf.

[3] L.M. Young, "Simulations of the LEDA RFQ 6.7-MeV Accelerator," this conf.

[4] L. M. Young, "Equipartitioning in APT Linac," this conf.

[5] S. Nath, et al, "Beam Dynamics Design for the APT Integrated Linac," this conf.

[6] J. D. Sherman *et al.*, "Development of a 110-mA, 75-keV Proton Injector for High-Current, CW Linacs," Proc. XVIII Int. Linac Conf. (Geneva, 26-30 Aug. 1996), pp. 701-3.

[7] H.V. Smith , et al, "Simulations of the LEDA LEBT H+ Beam," this conf

[8] L. M. Young, "Simulations of the LEDA LEBT with H+, H2+, and e- particles," this conf.

[9] L. Hansborough *et al.*, "Mechanical Engineering for the LEDA Injector," this conf.

[10] R. Ferdinand, *et al.*, "Space-Charge Neutralization Measurement of a 75-keV, 130-mA Hydrogen-Ion Beam," this conf.

[11] L.M. Young, "An 8-m Long Coupled-Cavity RFQ Linac," Proc. 1994 Int. LINAC Conf. (Aug., 1994, Tsukuba, Japan), 178.

[12] D. Schrage, et al, "A 6.7 MeV CW RFQ Linac," this conf.

[13] S. S. Shen, et al, "APT/LEDA RFQ Vacuum Pumping System," this conf.

[14] R. L. Wood, et al, "Thermal/Structural Design and Fabrication Development of High-Power CCDTL and CCL Structures," Proc. XVIII Int. Linac Conf. (Geneva, 26--30 Aug. 1996 pp. 752--4.

[15] D. Rees, "Design of 250-MW CW RF System for APT," this conf.

[16] K. Cummings, "Experimental Evaluation of 350 MHz RF Accelerator Windows for the Low-Energy Demonstration Accelerator," this conf.

[17] J. Bradley, "An Overview of the Low Energy Demonstration Accelerator (LEDA) Project RF Systems," this conf.

[18] Y. M. Wang, et al, "Algorithm and Implementation of APT Resonant Control System," this conf.

[19] A. Regan, et al, "APT LLRF Control System Model Results, " this conf.

[20] R. E. Shafer et al, "Overview of the APT High-Energy Beam Transport and Beam Expander"., this conf.

[21] C. R. Rose, et al, "A 200-A, 500-Hz, Triangle Current Wave Modulator and Magnet Used for Particle-Beam Rastering," this conf.

[22] J. D. Gilpatrick, et al, "LEDA and APT Beam Diagnostics instrumentation, " this conf.

[23] C. R. Rose, et al, "The LEDA Beam Position Measurement System," this conf.

[24] C. R. Rose, et al, "Description and operation of the LEDA Beam Position Measurement Module," this conf.

[25] J. F. Power, et al, "Design of a VXI Module for Beam Phase and Energy Measurements for LEDA," this conf.

PHYSICS DESIGN OF THE NATIONAL SPALLATION NEUTRON SOURCE LINAC*

H. Takeda, J. H. Billen, and S. Nath
Los Alamos National Laboratory, Los Alamos NM 87545, USA

Abstract

The National Spallation Neutron Source (NSNS) requires a linac that accelerates a H^- beam to 1.0 GeV. The NSNS linac starts with a radio-frequency quadrupole (RFQ) accelerator, which is followed by a drift-tube linac (DTL), a coupled-cavity drift-tube linac (CCDTL), and a conventional coupled-cavity linac (CCL). In this paper, we focus on the DTL, CCDTL, and CCL parts of the accelerator. We discuss the linac design parameters and beam dynamics issues. The design rationale of no separate matching sections between different accelerating sections maintains the current independence of beam behavior.

LINAC DESIGN AND BEAM DYNAMICS

The NSNS linac starts with a 2.5-MeV RFQ followed by a beam transport and matching section that includes a fast chopper. We report studies of a matched beam from the exit of the beam transport section injected into the 2.5-to-20-MeV DTL, which is followed by a CCDTL[1] and a conventional CCL. Figure 1 shows schematically the layout of the CCDTL and CCL sections of the linac. We use the term segment to refer to a contiguous section of accelerating structure plus the space between cavities for electromagnetic quadrupole lenses. After the DTL, we maintain a constant 11-$\beta\lambda$-long transverse focusing period through the rest of the linac, where $\beta\lambda$ is the distance traveled by a particle of velocity βc in one rf period.

A future upgrade of NSNS from 1 to 4 MW total beam power will require duplication of the components below 20 MeV and installation of a beam funnel. The rest of the linac remains the same, except for a reconfiguration of the rf modules to handle the added beam power. The original installation of the CCDTL and CCL will include a sufficient number of power irises for the upgrade.

Drift-Tube Linac: 2.5 to 20 MeV

The 402.5-MHz DTL accelerates the 2.5-MeV beam to 20.27 MeV. Permanent-magnet quadrupole lenses inside the drift tubes, arranged in a FOFODODO lattice, provide the transverse focusing. The lattice period has length 4 $\beta\lambda$ at 402.5 MHz. At the front end, each lens has Gl = 24 kG, which corresponds to a zero-current transverse phase advance σ_{0t} = 74 deg/period. The transverse focusing gradually weakens to Gl = 17.08 kG, σ_{0t} = 59 deg/period at the exit. The longitudinal phase advance σ_{0l} starts at 61 deg/period and ends at 40 deg/period. The accelerating gradient is kept constant at E_0 = 3.0 MV/m.

*This work sponsored by the Division of Materials Sciences, US Department of Energy, under contract number DE-AC05-96OR22464 with Lockheed Martin Energy Research Corporation for Oak Ridge National Laboratory.

In the CCDTL, the rf structure frequency doubles. Also, the periodicity of the transverse focusing lattice changes to 11 $\beta\lambda$ at 805 MHz, which is a 37.5% increase in length compared to 4 $\beta\lambda$ at 402.5 MHz. We use this frequency and focusing period through the CCL.

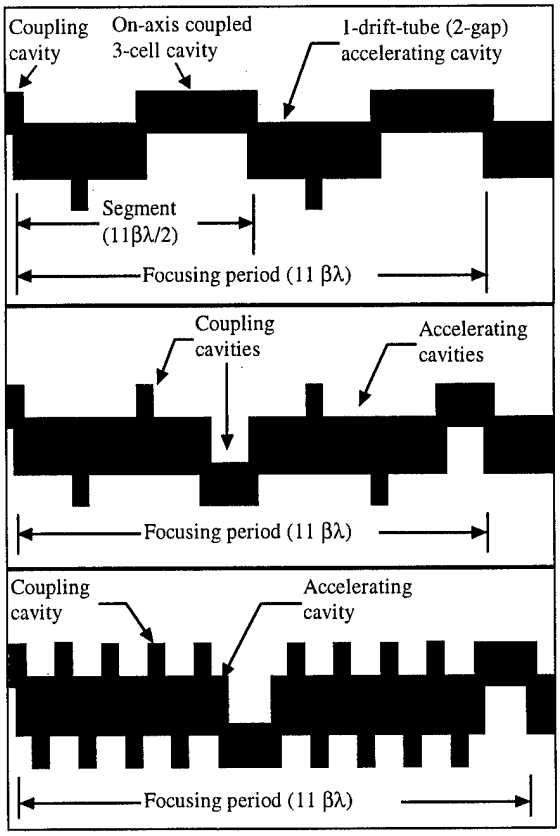


Figure 1. Layout of CCDTL and CCL sections. From 20 to 67 MeV (top), segments contain two cavities plus a 5$\beta\lambda$/2 space for a magnet. From 67 to 95 MeV (middle), segments contain three cavities plus a 1$\beta\lambda$ space. Above 95 MeV (bottom), the CCL has nine cavities and a 1$\beta\lambda$ space.

Coupled-Cavity Drift-Tube Linac: 20 to 95 MeV

The top part of Figure 1 shows two 2-gap cavities in a CCDTL segment for the energy range from 20 to 67.7 MeV. Each cavity contains one internal drift tube mounted on stems. Electromagnetic quadrupole magnets mounted external to the rf structure provide the transverse focusing. The bore radius in this section is 1.059 cm. At 67.7 MeV, we switch to three 2-gap cavities per segment, as shown in the middle part of Figure 1. At this point, the bore radius increases to 1.505 cm. In a symmetric design all the cavities of a segment are identical: their length

0-7803-4376-X/98/$10.00 © 1998 IEEE

corresponds to the average velocity of the particles in the segment. Successive segments lengthen as β increases.

The choices for frequency and focusing lattice impose conditions on matching between structures. We require that σ_{0t} and σ_{0l} be continuous across the transition between the DTL and CCDTL. For both x and y transverse planes, σ_{0t} = 59.0 deg/period and σ_{0l} = 39.6 deg/period for a period of 4 $\beta\lambda$ in the 402.5-MHz DTL. In the CCDTL, we need σ_{0t} = 80.0 deg/period and σ_{0l} = 55.0 deg/period for a period of 11 $\beta\lambda$ at 805 MHz. At 20 MeV, the required strength of the quadrupole magnets in the CCDTL FODO lattice is Gl = 22.77 kG, and the required accelerating gradient is E_0 = 2.40 MV/m. We match the DTL output beam into the CCDTL by adjusting the first four quadrupole gradients and the first two CCDTL cavity gradients. The phases of these cavities are set to –90 degrees to act as bunchers. When the funnel is eventually installed, it will provide a beam that matches the beam characteristics at the output of the DTL.

The design rf phase through the CCDTL ramps smoothly from –40 degrees at 20 MeV to –30 degrees at 95 MeV. The accelerating gradient is discontinuous across changes in the rf structure so that the average of E_0T over a focusing period is continuous, where T is the transit-time factor. Figure 2 shows E_0 as a function of beam energy along the accelerator.

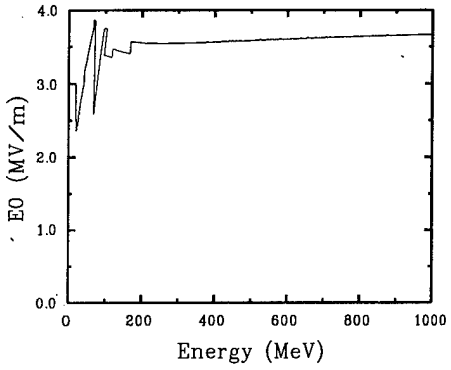


Figure 2. Accelerating gradient versus energy. The discontinuities between structures make accelerating field per unit length vary smoothly.

Coupled-Cavity Linac: 95 MeV to 1 GeV

A CCL segment consists of 9 identical cavities as shown in the bottom of Figure 1. Drift spaces for quadrupole magnets have length $\beta\lambda$. For a nearly constant accelerating gradient E_0 ~ 3.36 to 3.67 MV/m, the longitudinal focusing drops substantially through the CCL: σ_{0l} = 75.0 deg/period at entry and σ_{0l} = 17.0 deg/period at 1 GeV. To reduce the energy transfer from the transverse to the longitudinal phase plane, we reduce the quadrupole strength Gl from 22.65 to 10.5 kG.

The computer code PARMILA[2] designs the cavity for each segment and simulates the beam-dynamics performance through all sections of the linac. We inject a beam of 10,000 macroparticles into the DTL with 27.5 mA peak current. Figure 3 shows the x position, phase, and energy profiles through the CCL to the final energy of 1 GeV. Figure 4 shows the beam phase space distributions x-x′, y-y′, and Δϕ-ΔW at the center of the last quadrupole magnet. The figure also includes a plot of the x-y spatial distribution.

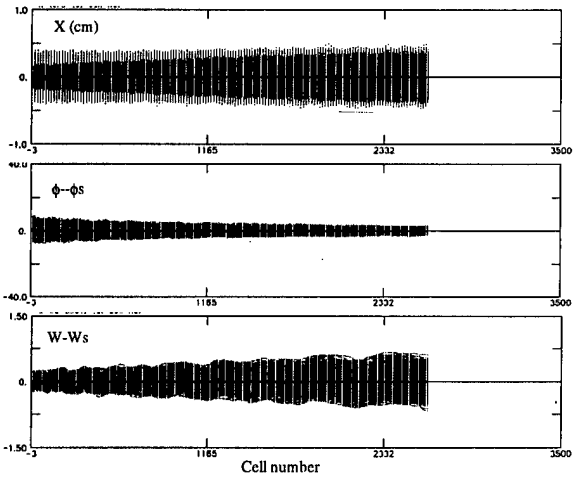


Figure 3. Beam profiles along the CCL versus cell number. The top panel shows the x position, the middle shows phase, and the bottom shows energy.

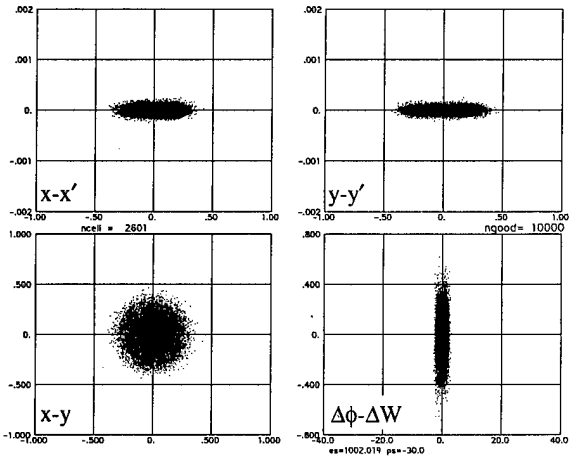


Figure 4. The beam phase space distributions at the center of last quadrupole lens in the CCL.

DESIGN PARAMETERS

In designing the rf cavities, the bore radius in the CCDTL and CCL strongly affects the cavity efficiency as measured by the shunt impedance. Figure 5 shows the effective shunt impedance per unit length ZT^2 calculated by the SUPERFISH [3] program for several series of cavities optimized for good shunt impedance. The data presented here include the effects of power losses on stems in the CCDTL as well as an estimate of the additional power losses near coupling slots in both the CCDTL and CCL. We chose cavities with ZT^2 larger than about 35 MΩ/m. The CCDTL has three different bore radii starting at 1.059 cm and the CCL has four bore radii increasing up to 2.216 cm.

Table 1 lists a few of the design parameters for the three sections of the NSNS linac. Most parameters have been defined elsewhere in this paper. The synchronous

phase of the design particles is ϕ_s, the initial and final energies of a section are W_i and W_f, and L is the length.

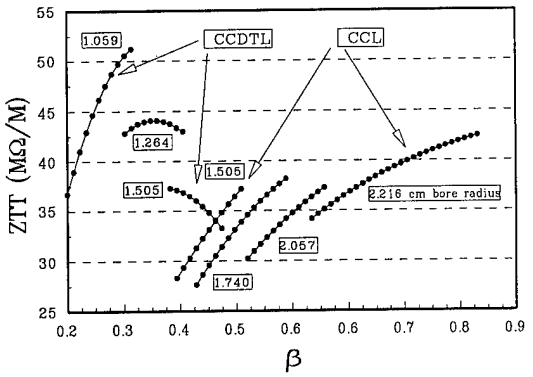


Figure 5. Shunt impedance computed by SUPERFISH depends on the beam velocity β and the cavity bore radius.

Table 1. Linac Parameters.

Structure	DTL	CCDTL	CCL
Lattice	FOFODODO	FODO	FODO
f (MHz)	402.5	805.0	805.0
E_0 (MV/m)	3.0	2.36 to 3.70	3.38 to 3.67
G*l* (kG)	24.0 to 17.1	22.8	22.7 to 10.5
ϕ_s (degrees)	−30	−40 to −30	−30
W_i (MeV)	2.5	20.27	95.39
W_f (MeV)	20.27	95.39	1000.0
L (m)	8.71	59.34	424.4

BEAM CHARACTERISTICS

The beam emittances were calculated by the simulation code PARMILA starting from the DTL entrance at 2.5 MeV to the CCL exit at 1 GeV. We started with an emittance of 0.0175 π cm-mrad for both transverse phase planes and 0.08865 π MeV-deg for the longitudinal phase space. The G*l* product of the quadrupole magnets changes through the CCL to gradually reduce the beam partitioning ratio [4,5] from 1.8 at 100 MeV to 1.4 at 1 GeV. A partitioning ratio of 1.0 corresponds to an equipartitioned beam. A value larger than unity indicates an excess of transverse focusing. Figure 6 shows the transverse (x and y) normalized rms emittance and the longitudinal normalized emittance along the linac. An unavoidable mismatch between the DTL and CCDTL causes some emittance growth and an increase in beam size early in the CCDTL, but the emittance and size remains nearly constant through the rest of the linac.

The rms beam radius and the maximum size in the x coordinate are plotted in Figure 7. The figure also shows the drift-tube inner radii along the linac. The maximum beam radius of 5 mm compared to a large beam tube reduces the beam loss in the linac. The consequences of beam loss are more serious at high energy than at low energy. The smaller bore radii below 200 MeV improve the shunt impedance.

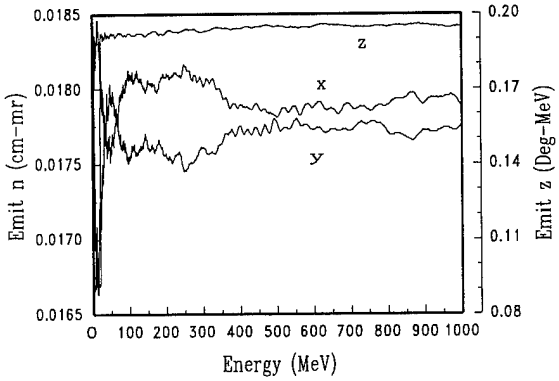


Figure 6. Transverse (x and y) and longitudinal (z) normalized emittances versus beam energy.

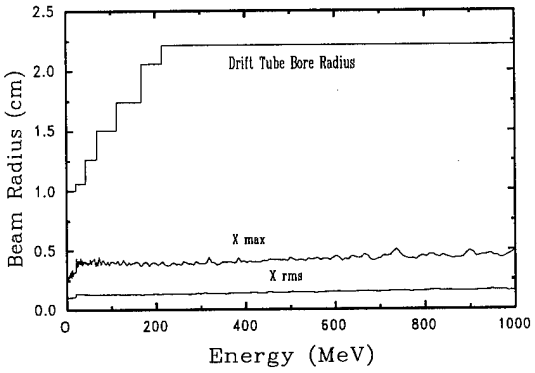


Figure 7. The beam's maximum radius and the rms radius along the linac compared to the beam aperture.

CONCLUSION

The current design of the NSNS linac shows that we can accelerate beam from the DTL through the CCL to 1 GeV without appreciable emittance growth or beam-size growth. The beam is well contained within the aperture. The match between the DTL and the CCDTL might be further refined to reduce the emittance growth at that junction. Also, the funnel section that combines two DTL beams into the CCDTL requires further work.

REFERENCES

[1] J. H. Billen, F. L. Krawczyk, R. L. Wood, and L. M. Young, "A New RF Structure for Intermediate-Velocity Particles," Proceedings of the 1994 International Linac Conference, Vol. 1, p. 341 (August 21-26, 1994).

[2] H. Takeda and J. E. Stovall, "Modified PARMILA Code for New Accelerating Structures," Proceedings of the 1995 Particle Accelerator Conference, p. 2364 (May 1-5, 1995, Dallas, Texas).

[3] J. H. Billen and L. M. Young, "POISSON SUPERFISH," Los Alamos National Laboratory report LA-UR-96-1834 (revision April 22, 1997).

[4] L. M. Young, "Equipartitioning In A High Current Proton Linac," this conference.

[5] Martin Reiser, "Theory and Design of Charged Particle Beams," John Wiley & Sons, Inc., p. 573 (1994).

THE NSNS FRONT END ACCELERATOR SYSTEM*

John W. Staples
Lawrence Berkeley Laboratory, Berkeley, California 94720

ABSTRACT

The National Spallation Neutron Source (NSNS) front-end accelerator comprises a 65 keV LEBT, a 2.5 MeV RFQ and a matching accelerating a 55 mA H^- beam with a 6% duty factor. Critical design issues are the 6% beam duty factor, the 5 free space-wavelength long 402.5 MHz RFQ, and nanosecond chopping of the beam before it enters the first DTL. The conceptual design of the front-end systems will be presented, with experimental validation of some of the proposed subsystems.

NSNS CONFIGURATION SUMMARY

The NSNS front end provides a 2.5 MeV, 28 mA H^- beam at 6% duty factor to the rest of the 1 GeV linac, supplied by LANL, which in turn injects a 1 GeV storage ring. Approximately 1200 turns of H^- beam is accumulated into the storage ring by stripping injection, then extracted in a single turn, supplying 1 MW of average beam power to a neutron production target at a 60 Hz pulse rate. Future options increase the front-end beam current to 55 mA for 2 MW power at the target, and then further double the beam power to 4 MW by funneling two injectors together at the 20 MeV point.

The Front End comprises the ion source, (described elsewhere in these proceedings [1],) the electrostatic LEBT, the RFQ and the MEBT including a fast beam chopper.

LEBT (LOW ENERGY BEAM TRANSPORT)

The LEBT will transport up to 70 mA of beam from an rf-excited volume ion H^- source to the RFQ operating at 6% duty factor. The LEBT comprises an electrostatic extraction gap, followed by two einzel lenses with a final output energy of 65 keV within a length of 10 cm.

To permit chopping in the ion source and the LEBT and to eliminate neutralization turn-on time, the beam will be fully unneutralized. The entire LEBT is electrostatic, with a high-voltage extraction gap followed by two sets of einzel lenses with a minimum aperture-to-beam diameter ratio of approximately two.

*This research is sponsored by the Lockheed Martin Energy Research Corporation under the U.S. Department of Energy, Contract No. DE-AC05-96OR22464, through the Lawrence Berkeley National Laboratory under Contract No. DE-AC03-6SF00098.

Figure 1 shows the trajectory of a 28 mA H- beam from the ion source plasma boundary (left) to the start of the RFQ vane. A transverse field at the split einzels deflects the beam up to 25 mrad with an emittance increase of less than 10% [2]. Beam chopping is included by applying a ±3 kV square wave across opposing quadrants of either einzel lens. Transverse steering is accomplished by moving the entire ion source-LEBT assembly on a sliding joint at the LEBT-RFQ interface while the LEBT is under vacuum.

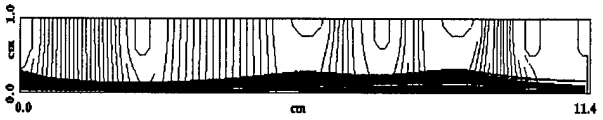


Figure 1. 28 mA Beam Envelope in LEBT

A five-segment Faraday cup, doubling as a beam stop, and a vacuum gate valve will be included in the 1 cm space between the last einzel electrode and the RFQ entrance flange. The Faraday cup will comprise a center button and an outer ring, divided into four quadrants. Half the beam will target the center button, and the rest of the beam will be divided on the other four quadrants. The last einzel lens will be brought to ground potential when the Faraday cup is swung in from the side, which will not significantly alter the beam size at the Faraday cup position. The vacuum valve will isolate the RFQ from atmospheric pressure during ion source maintenance.

RFQ

The RFQ accelerates the 35-70 mA H^- beam from 65 keV to 2.5 MeV. A 59 mA input beam with rms normalized emittance of 0.2 π mm-mrad results in 55 mA accelerated, a transmission efficiency of 93%. The long buncher section produces an rms longitudinal output emittance of 89 keV-degree at 55 mA output without increasing at the 28 mA level due to bunch overcompression.

The vanetip geometry uses a constant-transverse radius design with $\rho_T = r_0 = 0.336$ cm. This results in very low multipole error fields for this particular design, as the emittance blowup in the RFQ is less than 10% at 55 mA. The constant transverse radius vanetip is a great convenience, as it permits cutting the vanetip shape with a form cutter, reducing the risks of variable radius vane cutting. The minimum longitudinal radius is 1.49 cm, a very easy radius to accommodate with a form cutter.

0-7803-4376-X/98/$10.00 © 1998 IEEE

The two most challenging aspects of the RFQ are the 6.1% beam duty factor, and the 3.7 meter length, corresponding to 5 free-space wavelengths.

Previous LBNL-built RFQs have strapped opposing vanes together with vane coupling rings (VCRs), which move the dipole frequencies away from the TE_{120} quadrupole mode, significantly relaxing the assembly tolerances. For this RFQ, the high duty factor prompted us to select pi-mode stabilizers, used successfully on the high duty-factor Japanese Hadron Collider RFQ injector, instead of VCRs.

The pi-mode stabilizer, pioneered at KEK, consist of pairs of rods placed through the RFQ, alternately in the horizontally and vertical planes [3]. Operating experience with the KEK RFQ using pi-mode stabilizers show that the maximum contamination of the desired quadrupole field configuration by both dipole modes and unwanted longitudinal tilt from high-mode longitudinal modes is less than 1%. That RFQ is four free-space wavelengths long, this one is five.

A power of 590 kW excites the cavity to 76 kV peak voltage between the vanetips, including an additional 50% margin for actual cavity losses compared to theoretical losses in the Glidcop© AL-15 cavity material. With 55 mA accelerated beam to 2.5 MeV, an additional 135 kW is required, for a total of 725 kW, with 19% beam loading.

A 1-MW 402.5 MHz klystron will provide power to a 21-inch waveguide, which will be split into eight 3-1/8 inch semi-flexible coaxial feeds, each driving the RFQ at 8 drive ports with loop couplers, located in pairs along opposing sides the RFQ.

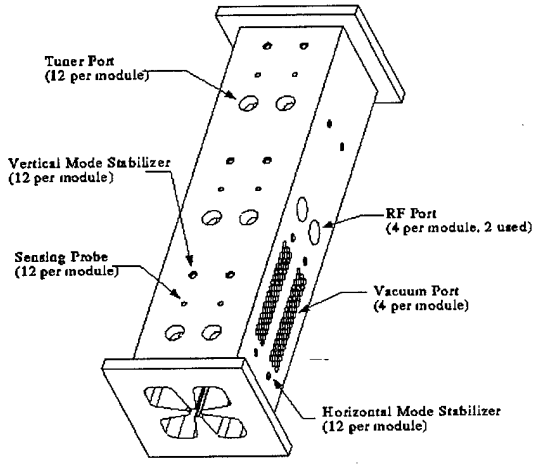


Figure 2. One 1-meter-long RFQ module

The high r.f. duty factor results in an average power dissipation of 1.9 watts/cm^2 in the outer wall of the cavity with hot spots at the ends of the vanes of up to 6 watts/cm^2.

Each module will have water cooling passages gun-drilled in the 93 cm long section from both ends, and then brazed shut at the ends. Connecting water passages will be bored radially from the outside. The steady-state temperature variation in the RFQ body is less than 3° C and the material stress is below 600 psi.

Four vane-cavity segments are brazed together to form a 93-cm long module Each vane-cavity segment is machined from a solid block of Glidcop, insuring that the vane tip and the joint to adjoining sections are in close dimensional tolerance with each other, a technique proven in a previous 400 MHz RFQ built at LBNL [4].

The mechanical design eliminates demountable r.f. joints in regions of high r.f. wall currents by brazing four Glidcop pieces together forming each RFQ module. The entire RFQ will be assembled of 4 of these brazed modules with demountable vacuum and r.f. joints. The four RFQ modules will be joined with a circumferential Helicoflex vacuum and r.f. seal, and the vanes themselves by sections of canted spring ring. The Helicoflex seal will be surrounded by a back-up O-ring vacuum seal. Figure 2 shows the intermodular joint.

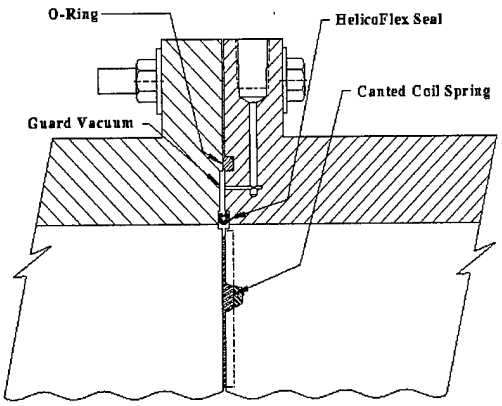


Figure 3. RFQ intermodule rf and vacuum joint

Vacuum ports are arrays of holes and will be machined symmetrically in all 4 quadrants to guarantee r.f. symmetry. Local tuners will be used to compensate the depressed cutoff frequency of the RFQ waveguide to level out variations in the vane tip voltage distribution. The RFQ vacuum will be in the 10^{-7} Torr region.

The RFQ will incorporate 48 tuners, 3 per quadrant in each of the four modules each with an active piston area of 2 cm^2 and a motion range of ±2 mm. The r.f. sliding contact will be similar to that of the PEP-II tuners, which operate at about 476 MHz with a 100% duty factor in cavities with similar wall power density as ours. Those tuners use silver-plated Glidcop r.f. contacts sliding on rhodium-plated surfaces of the copper tuner body.

A full-scale prototype RFQ will be built and operated at LBNL with beam for an prolonged test period to uncover any problems with the design. A production RFQ will then be made and incorporated into the actual NSNS injector system. The mechanical design is further discussed in a companion paper at this conference [5].

MEBT (MEDIUM ENERGY BEAM TRANSPORT)

The MEBT transports the 2.5 MeV, 402.5 MHz r.f. bunched and 1.2 MHz chopped beam from the RFQ to the DTL. A major MEBT function includes the 2.5-5 nsec, 1.2 MHz beam chopper. (Two slower risetime choppers are located upstream in the ion source and the LEBT.) The tandem operation of the choppers provides an on/off intensity ratio of $1{:}10^{-5}$.

The first traveling-wave chopper deflects the beam off the axis; the second chopper deflects the beam back parallel to the axis. This chopper-antichopper combination insures that deviation from perfect waveform in the chopper (ringing) will not cause axis shift of the beam itself as it enters the DTL. The traveling-wave choppers and their 2.5 nsec rise/fall, 900-volt power supplies will be designed and constructed by LANL.

The most stringent MEBT design requirement is preservation of transverse emittance from the RFQ to the DTL. The average linear external focusing force provided by the quadrupoles is strong in comparison to the nonlinear space-charge forces, making the MEBT relatively space-charge independent. The quadrupole filling factor in the beam line is high, requiring all the other MEBT equipment fit in narrow inter-quad gaps.

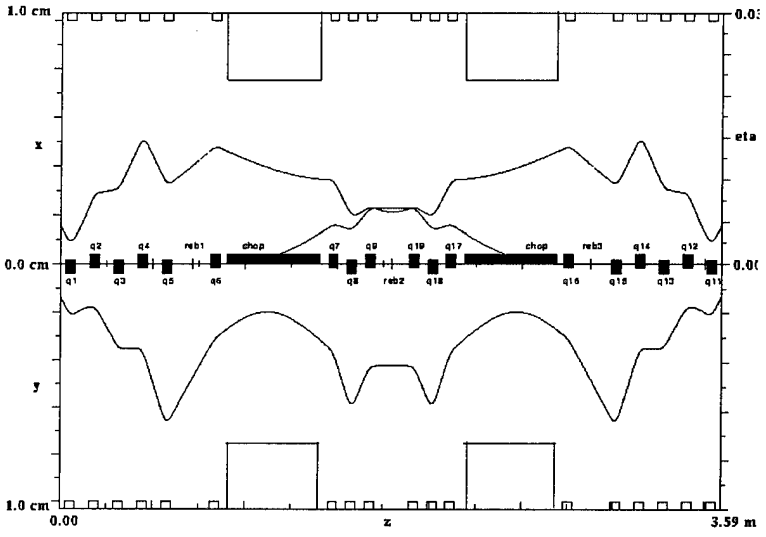


Figure 4. Beam Envelope in MEBT

The six quadrupole system at the beginning of the MEBT slowly relaxes the very rapid phase advance the beam experiences in the RFQ. The focusing system matches the beam size in the chopper by placing a waist in the transverse plane in the middle of the chopper, and minimizes the beam size at the exit of the chopper in the deflecting plane, producing a minimum beam size to maximum beam displacement at the chopping aperture ("chopper stopper").

The quadrupoles have a 1 cm pole tip radius and an effective length of 5 cm. The quadrupoles will be of two types, and will allow at least a ±30% field variability. The quads with less than 3 kG poletip field will be simple iron-core, water-cooled EM design featuring end-clamps. The highest-strength quads will use permanent magnets with variable energization from additional PM material connected to a rotatable outer soft iron ring. Both designs must operate in vacuum, and six of the quadrupoles will provide beam steering by adjustable transverse offset.

Figure 4 shows the beam envelope in the MEBT. The two long objects are the chopper and the antichopper. Three 402.5 MHz rebuncher cavities are in the other large gaps. The peak gap voltage on the first and third cavities if 55 kV, with the central cavity operating at 35 kV. The peak r.f. power requirement is 15 kV at 35 kV gap voltage.

The beam line alternates quads and short beam boxes. Rather than combining all the quads together in a single package inside a common vacuum chamber ("coffin"), the quads are mounted around sections of vacuum pipe between short diagnostic beam boxes with some quads inside the short beam boxes. This technique isolates sensitive diagnostic equipment from the strong electromagnetic interference generated by the bunched beam in the environment of large beam boxes.

Diagnostic equipment will occupy the short beam boxes between the quadrupoles. These diagnostic devices will include slit-type emittance measurement equipment, Faraday cups, flying wires, beam toroids, residual-gas profile monitors and a beam stop.

ACKNOWLEDGMENTS

This work was aided by efforts of Rick Gough, Matt Hoff, Alex Ratti, Craig Fong, Ka-Ngo Leung, Daniela Wutte and Matthaeus Leitner with additional assistance from Steve Lewis, Martin Fong, Ross Schlueter, Mike Green, Dave Humphries, Sam Mukherjee, Greg Stover and Jim Hinkson.

REFERENCES

[1] Ka-Ngo Leung et al, this conference.

[2] J.W.Staples, M.D.Hoff and C.F.Chan, *All-Electrostatic Split LEBT Test Results*, Linac 96.

[3] A. Ueno et al, *Beam Test of the Pre-Injector and the 3-MeV H- RFQ with a New Field Stabilizer PISL*, Linac 96

[4] S. Abbott et al., *Design of an Integrally Formed RFQ*, 1989 PAC.

[5] M. Hoff et al, *NSNS RFQ Mechanical Design*, this conference.

A PROPOSED SUPERCONDUCTING BOOSTER LINAC FOR THE HRIBF

J. D. Bailey, ORNL*/JIHIR†, and D. K. Olsen, ORNL

Abstract

A 42 MV Superconducting (SC) Booster Linac is proposed for the Holifield Radioactive Ion Beam Facility (HRIBF). The linac, consisting of 56 superconducting, quarter wave, 120 MHz, independently phased, 2 gap resonators, will be used to boost Radioactive Ion Beams (RIBs) accelerated by the 25 MV NEC tandem, to Coulomb barrier energies for use in nuclear physics research near the proton and neutron drip lines. The design potential of 42 MV is sufficient to boost the beams of mass 180 above the Coulomb barrier using the most probable charge state, 15+, from single foil stripping in the tandem terminal. Linac parameters and layout are presented with accompanying beam dynamic calculations. In addition, an upgrade of the existing pre- tandem beam bunching system is proposed to further preserve the RIB intensity through better longitudinal phase space matching into the linac.

1 INTRODUCTION

HRIBF is providing RIB's for nuclear physics and astrophysics experiments using the ISOL technique. Radioactive atoms are created from nuclear reactions with light-ion beams from ORIC, a compact flexible K100 cyclotron. After diffusing from the target and desorbing from surfaces, these radioactive atoms are ionized, magnetically separated, charge exchanged, and then transported through a second high-resolution separator into the 25 MV tandem, where they are accelerated to energies of interest for nuclear and astrophysics. The tandem is capable of accelerating mass 80 above the Coulomb barrier with single foil stripping in the terminal, and mass 130 above the Coulomb barrier with a second foil stripping 1/3 of the way down the high energy acceleration tube. RIB's are very difficult to produce and have very low intensity, so maximizing the total transmission from the RIB source target to the experimental target is essential.

The Nuclear Science Advisory Committee has identified the National Isotope Separator On Line (ISOL) RIB Facility as the next major construction by the DOE Nuclear Physics program[1]. A possible very cost effective reconfiguration of the existing HRIBF into the National ISOL Facility would be to: (1) use as much of the existing building-6000 heavily shielded area and experimental apparatus as possible, (2) replace ORIC with an approxinmately 200 MeV proton linac or cyclotron, (3) extend the existing RIB injector with a new platform for the production of intense neutron-rich fission fragment RIBs produced by proton bombardment of a high-temperature thick actinide target, and (4) construction of a SC linac booster for the tandem to allow acceleration of fission fragment RIBs above the coulomb barrier with single foil stripping in the tandem[2]. These changes, shown in Fig. 1, will allow physicists to explore nuclei far from stability, learning more about solar processes, and the neutron and proton drip lines.

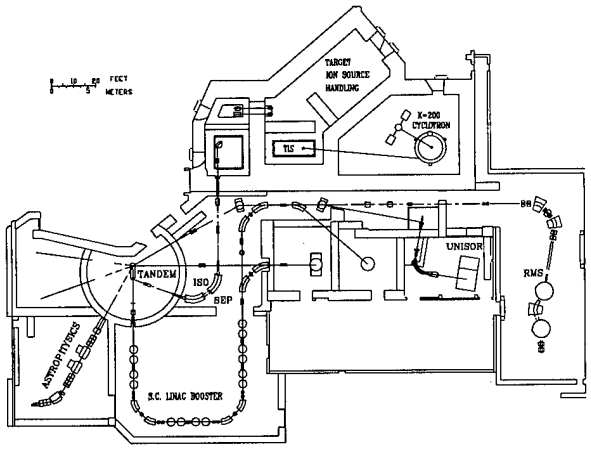


Figure 1 Floor plan depicting the conversion of the HRIBF into the National ISOL Facility. The main changes are a new driver accelerator, a modified target ion source platform, and the addition of a superconducting linac to boost the tandem beam.

These changes can be constructed together or in a phased approach. This paper describes a SC linac for this approach. As a booster, this linac could be used to accelerate fission fragment RIBS produced using ORIC with the existing RIB injector, or from a 200 MeV proton accelerator with a new high-power RIB injector. It can also be built without shutting down the present facility, with only minimal interruptions to the schedule.

2 LINAC LAYOUT

The most important requirement for the booster is to accelerate fission fragments above the Coulomb barrier with single stripping which corresponds to the accelera-

* Research sponsored by the Oak Ridge National Laboratory, managed by Lockheed Martin Energy Research Corporation for the U.S. DOE under contract number DE-AC05-96OR22464.

† The Joint Institute for Heavy Ion Research is the University of Tennessee, Vanderbilt University, and the ORNL; it is supported by the members and by the U.S. DOE under contract number DE-FG05-87ER40361 with the University of Tennessee.

0-7803-4376-X/98/$10.00 © 1998 IEEE

tion of 15+ A=180 to 5.5 MeV/A. This maximum mass is 180 for two reasons: (1) the maximum fission fragment mass is ~180, and (2) the elements with A>180 tend to be refractory and will not readily release from targets. To provide RIBs of A<180 using the most probable charge state with single stripping with the tandem operating at 22 MV terminal, requires the addition of an effective 42 MV booster linac.

The linac will be similar to the linac at ALPI[3], which provides accelerating fields of 5 MV/m, and is one of the latest in a long line of improvements on heavy ion superconducting booster linacs. Simple niobium quarter-wave resonators with 18 cm inside diameters will be cooled, by pot boiling of liquid He, in sets of four, inside ~1.1 m diameter cylindrical stainless steel cryostats. Quarter-wave resonators were chosen because of their wide use, mechanical stability, simple construction, and high accelerating fields.

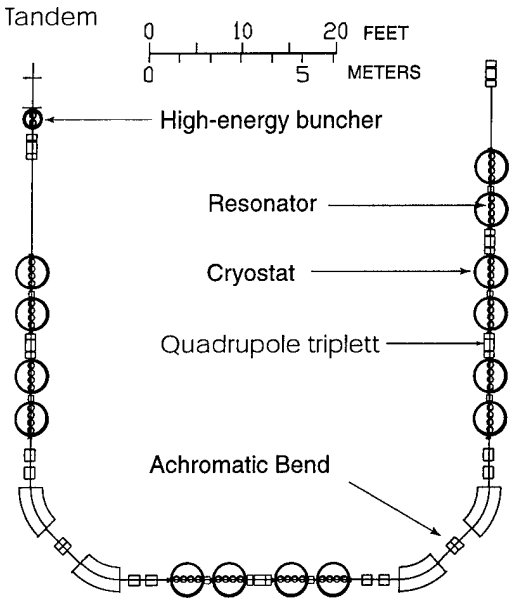


Figure 2 The linac has 14 cryostats, each cooling 4 niobium superconducting 1/4λ resonators. The configuration depicted uses quadrupole triplets for transverse focusing. Achromatic bends are used to wrap the linac back upon itself.

About 56 resonators operating at 5 MV/m are needed for an average transit time factor of 95%, using a synchronous phase of 20 degrees, and allowing for a downtime fraction of 5%. Various velocity and frequency configurations of these resonators were investigated in detail to obtain the highest possible energies for A=6-180 with single stripping and A=40-238 with a second stripping at the linac entrance. Many configurations are more than adequate; however, the simple and flexible configuration of 56 β=0.086 120 MHz resonators seems about optimum. Longitudinal phase space matching between the Tandem and the linac, will be achieved with the addition of a high energy buncher before the linac, and a possible modification of the tandem low energy buncher. A high energy chopper may also be added in the tandem exit line. A two frequency linac design was discarded because of a loss of longitudinal phase space.

A possible layout for the booster is shown in Fig. 2. As shown, the linac consists of three sections separated by 90 degree achromatic bends. Quadrupoles, in FODO cells and in doublets and triplets, each separated by one or two cryostats, were investigated to confine the beam radially. Figure 2 shows a round-beam triplet configuration. Other configurations are also acceptable. RIBs could be accelerated by the tandem and transported to the nuclear physics areas with or without the booster. A new ~5000 sq. ft building will be needed to house the booster.

3 OPTICS

The tandem beam has a 1 π mm mrad transverse emmittance, with a waist at the exit slits of the tandem[4]. Small energy variations in the tandem translate through the mass and energy analyzing magnets into a small walk in the beam centroid. In high intensity operation, the vertical part of this walk is used to control the tandem potential, and beam energy to 10^{-5}[5]. For low intensity, the energy can be regulated to 10^{-4} using terminal potential stabilizers. Figure 3 shows a typical energy spread produced by stripping in the tandem terminal calculated with TRIM92[6]. This energy spread is lower than the tandem energy regulation of 35 keV, but, because of the long drift path in the tandem terminal, it can dominate the time spreading of the beam. The RIB source energy spread is dominated by the charge exchange canal, measured at 50 eV for an As beam.

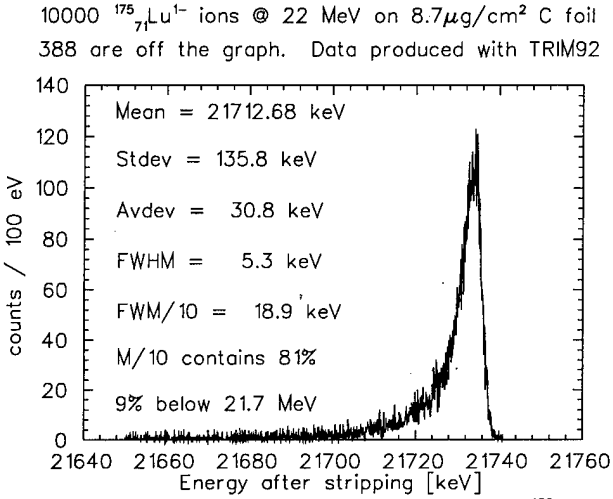


Figure 3 Beam energy spread from stripping ^{175}Lu to 15+ in an equilibrium thickness ^{12}C foil, in the tandem terminal. This translates into time spreading, and is a major component of the time spreading in the tandem beam ~1 ns.

The low energy buncher will be operated at 10 MHz. The present double drift buncher routinely bunches 50% of the beam into 6° RF, or 1.7 ns. A replacement 4f buncher based on that of Lynch[7], will bunch 66% into 4° RF, or 1.3 ns. A small debunching will occur due to path length differences and beam energy spread and variations. This debunching is ≅1 ns. The beam pulse width seen by the high energy buncher will then be ~2 ns.

The high energy buncher, operating at the linac frequency with a 1f and a 2f SC resonator, sees a pulse ~90° RF wide with an energy spread of 40 keV. As a buncher, it can add about ±1.3 qMeV to the beam energy spread. Table 1 shows the longitudinal acceptance of the SC linac when operated at a synchronous phase of 15°, for a range of heavy ions, and their most probable charge state after stripping in the tandem terminal operating at 22 MV. The longitudinal acceptance is at maximum energy spread, and does not correspond to maximum phase spread. The corresponding distances to bunch a 2 ns bunch are also given. An 8 m drift will be sufficient to longitudinally match the bunched tandem beam to the SC linac acceptance. Figure 2 shows a 5 m drift length. The extra 3 m of drift will require moving a cooling tower, and a 14 in. water pipe.

Table 1 SC Linac longitudinal acceptance at maximum energy spread, and drift length necessary to bunch a 2ns wide bunch, for various beams exiting a 22 MV tandem using the most probable charge state.

A	6	40	80	100	120	140	175	238
Q_{mn}	3	11	13	14	15	15	15	16/43
ΔE MeV	3.8	6.6	5.4	5.2	5.8	4	4.2	10
Δφ deg	17	15	13	9	9	8	5	9
L_{bun} m	5.0	5.7	6.2	6.4	5.8	7.8	6.6	2.6

The 90° achromatic bends present a rather long drift space for the beam to unbunch. This causes a reduction in phase space acceptance, but as shown above, the beam can still be bunched into the reduced phase space, and transmitted through the tandem. If the decision is made to extend the new building addition, it would be advantageous to accelerate only on the first and third legs, using a rebuncher in the middle of the second leg to improve the linac transmission and optics.

The transverse optics are designed by subdividing the linac into cells consisting of two cryostats separated a quadrupole triplet. Each cell is designed with a 90° phase advance. The achromats are designed with point to point focusing.

Figure 4 shows the results of a survey of linac performance over the range of useable fission fragments. Useable is defined as a combination of long half lives, and intense productions[8]. The SC linac will provide Coulomb barrier energies over the entire range.

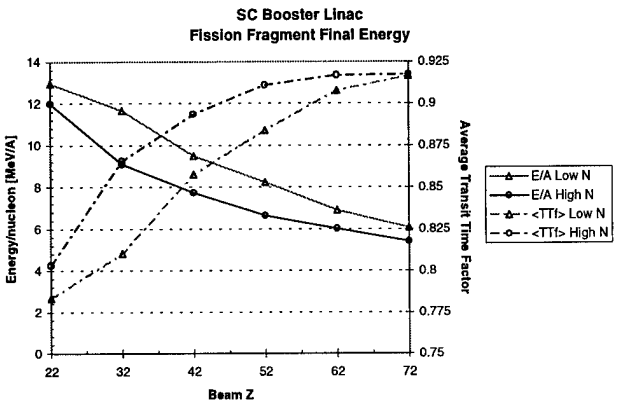


Figure 4 Final beam energy of useable fission fragments as a function of Z. Results for both the high and low mass useable fission fragments are shown. Also shown are the corresponding average transit time factors. Optimized for high masses, the SC linac is still efficient over the fission fragment mass range.

REFERENCES

[1] 'Nuclear Science: A long Range Plan', Nuclear Science Advisory Committee, (DOE/NSF, USA) (1996).

[2] D.K. Olsen, *et al.*'The National RIB Facility Project.' ORNL Physics Division Progress Report (1996).

[3] A. Facco, *et al.*'Bulk Niobium Low-, Medium- and High -β Superconducting Quarter Wave Resonators for the ALPI Postaccelerator'. 1993 Particle Accelerator Conference. (IEEE, Piscataway) (1993) pp 849-851.

[4] W.T. Milner, *et al.* 'Transport of DC and Bunched Beams through a 25 MV Folded Tandem'. IEEE Transactions on Nuclear Science, Vol. **NS-22**, No. 3 (1975), pp. 1697-1701.

[5] D.K. Olsen, *et al.* 'Calibration of the HHIRF Tandem Accelerator Energy Analyzing Magnet.' NIM **A254** (1987) pp 1-6.

[6] J.F. Ziegler, *et al.* 'The Stopping and Range of Ions in Solids.' (Pergamon Press, New York) (1985).

[7] F.J. Lynch, *et al.* 'Beam Buncher for Heavy Ions.' NIM **A159** (1979) pp 245-263.

[8] Private communication, J.D. Garrett, ORNL (1997).

A 100 MEV MULTITANK DRIFT TUBE LINAC FOR PROTON ACCELERATION

G. D'Auria, C. Rossi, Sincrotrone Trieste, Italy.

Abstract

Following the demand for a proton beam accelerator capable of accepting protons from a RFQ at about 6 MeV and of accelerating them up to 100 MeV, a new MultiTank Drift Tube Linac (MTDTL) structure has been developed and a detailed theoretical study is being carried out to design such a linear accelerator which already shows some important advantages: technological simplicity, compactness, high efficiency, relative low costs.

1 INTRODUCTION

After the request for a warm pre-injector for the Energy Amplifier [1] was made, a review of the existing possibilities was performed and a modular structure proposed which represented a good compromise between the need to keep the overall efficiency as high as possible and the necessity of a very reliable accelerator, easily aligned and serviced.

A first tentative proposal was presented in Legnaro in the end of October [2] and more detailed calculations were performed for the Preliminar Design Study [3].

The starting point for the proposed MTDTL was that if one looks at the behaviour of the shunt impedance per unit length in a drift tube structure, it is easy to see that its value doesn't change after some meters of RF structure. Having chosen a resonating frequency of 352 MHz, we saw that, with a length per tank between 1 and 2 meters, the shunt impedance per meter already stays over 80% of its maximum value. The possibility of reducing the quadrupole number and of keeping them outside of the tanks allows, on the other hand, an increase in the effective shunt impedance, which contributes to increase the efficiency.

The segmentation as it has been designed follows the decision of limiting the maximum RF power per tank at 200 kW, to allow the adoption of coaxial feedthroughs [4]. The aim of simplifying the RF power distribution system, by means of coaxial components as far as possible, we expect will be justified by a reduction in the whole plant complexity.

A prototype tank has been built to have a comparison between the parameter values calculated by Superfish [5] and the actual ones, to check some technological solutions and to study the gap field stabilization. At present the first measurements performed already seem to support the assumptions made for the calculations.

2 THE ACCELERATING STRUCTURE

The injection energy has been chosen equal to 6 MeV, but it can be lowered to 4.5 or 5 MeV in order to adjust the compromise between good efficiency of the RFQ injector and a reasonable DTL injection energy.

As it is known, the defocusing effect of an RF gap is more effective in the low energy end of the accelerating structure, it is then convenient to increase the beam energy as fast as possible; on the other hand the aim of keeping the focusing quadrupoles outside the accelerating tanks led to a compromise regarding the tank length and the number of RF gaps per tank. Another factor which has been taken into account is the limitation of the longitudinal emittance growth, whilst keeping a smooth variation of the longitudinal phase advance. This has been obtained by modulating in a convenient way the energy gain per gap in the first tanks by acting on the transit time factor according to the $\beta\gamma$ variation of the beam. Since the beam losses have to be kept at the lowest possible value, the influence of so called parametric resonances must be minimized, limiting the large value increase of the beam transverse amplitudes; this has been pursued by matching the 30 mA beam keeping the transverse tune depressions in the range of $0.85 \div 0.9$.

The triplets of quadrupoles have been placed in the intertank space which varies along the Linac from 3 to 2 $\beta\lambda$; in the future optimization of the MTDTL a considerable reduction of this space is foreseen, to gain in compactness.

In the following figure the energy gain per meter is reported as a function of the accelerator length.

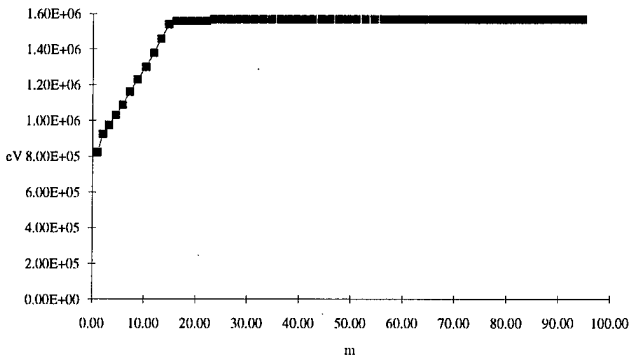


Figure 1: Energy gain per meter vs. MTDTL length.

The whole accelerator is divided into 58 tanks, with a variable number of RF gaps, the tank radius ranges from 0.25 to 0.31 m and it is planned to have not more than three different families of tanks of different diameter, in order to standardize the tank production. Table 1 summarizes the structure parameters, which have been divided in two regions: up to 30 MeV beam energy and from 30 to 100 MeV.

0-7803-4376-X/98/$10.00 © 1998 IEEE

Energy sections (MeV)	6 to 30	30 to 100
Number of tanks	18	40
Tank length (m)	0.7 ÷ 1.2	1.0 ÷ 1.3
Number of gaps / tank	5 ÷ 8	3 ÷ 5
Tank radius (m)	0.31	0.25
Bore radius (mm)	10 ÷ 15	10
Total length (m)	24.9	62.1
Resonating frequency (MHz)	352	352
ZT^2 (MΩ/m)	24 ÷ 32	32 ÷ 33.5

Table 1: RF structure parameters of the MTDTL

Some linear beam dynamics simulations have been performed up to the energy of 30 MeV by means of the code TRACE-3D[5] and in the following table the values of the parameters have been reported, together with the values at 100 MeV, which have been extrapolated.

Energy sections (MeV)	6 to 30	30 to100
Energy in (MeV)	6.0	30.76
Energy out (MeV)	30.76	101.
Synchronous phase (deg)	- 60 ÷ -30	- 30
Field gradient (MV/m)	1.2 ÷ 2.0	2.0
Transit time factor	0.8 ÷ 0.91	0.91
Beam current (mA)	30	30
Input ε_{xy} (π mm mrad) n. RMS	0.35	0.355
Output ε_{xy} (π mm mrad) n. RMS	0.355	0.357
Input ε_z (π deg MeV) n. RMS	0.25	0.4
Output ε_z (π deg MeV) n. RMS	0.4	0.46

Table 2: Beam parameters in the two energy sections.

The estimation of non linear effects is under way by means of the code PARMILA [5]; the beam dynamics through some tanks has already been calculated, confirming the results from TRACE-3D, some more time is needed to complete the simulations.

Some efforts have still to be performed to improve the longitudinal matching between different tanks, especially in the low energy end of the MTDTL; as regards the beam transport, good transverse beam control has been found keeping the quadrupole gradient inside the 30 to 60 T/m range.

3 THE PROTOTYPE TANK

A prototype tank has been built to check the Superfish simulations which have been performed on the first tank of the MTDTL; the TM_{010} field lines are drawn in the following figure, the real tank dimensions are 0.686 m length and 0.312 m radius.

This is a quite simplified tank, lacking the actual RF feedthrough, stems and tuner, but it is consistent with the geometry used in the Superfish calculations, so that the scaling factor can be considered a realistic one.

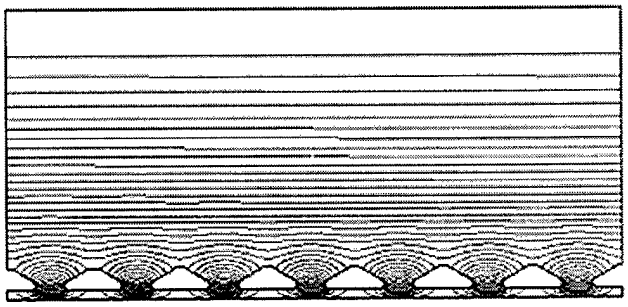


Figure 2: TM_{010} Electric field lines in tank #1

In the following table the calculated parameters are compared with the measured ones, it must be stressed that the 20% of difference in the measurement of the unloaded Q is the expected one with this kind of program.

TANK #1 PARAMETERS	Superfish	measured
Resonating frequency (MHz)	352.04	351.97
Unloaded Q	54263	43883
r (MΩ)	22	17.8
ZT^2 (MΩ/m)	32	25.9

Table 3: Comparison between Superfish and the measured parameters on Tank #1

The value of r, in table 3, is given by the product of ZT^2 times the tank length.

As is pointed out in another contribution in this conference [4], the calculation of the power requirements has been done in a conservative hypotesis and has led to consider for this first tank the value of 16.5 MΩ as the effective shunt impedance.

4 CONCLUSION

The proposal of a Multi Tank Drift Tube Linac which has been presented must be considered a very preliminary one and still a lot of work has to be done. We have verified the simplicity of the alignment procedure, which can be done on bench quickly and with very high accuracy. The modular solution seems to be extremely good as regards technological simplicity and efficiency and we have verified that a reasonable beam dynamics is possible. The crucial point will lie on the RF plant costs which seems to be the conclusive topic in the final choice.

REFERENCES

[1] C Rubbia and J.A. Rubio, A Tentative Programme Towards a Full Scale Energy Amplifier - CERN/LHC/96-11.

[2] Meeting on EA Accelerator-Legnaro, October 1996.

[3] D. Bulfone et al., Preliminary Design Study for the Linear Accelerator of the Energy Amplifier - ST/M - 96/7.

[4] G. D'Auria and C. Rossi, The RF Low Level and Power Distribution of the 100 MeV Proton MultiTank Drift Tube Linac - this conference.

[5] J. Billen et al., LANL Accelerator Design Codes Documentation, PARMILA, SUPERFISH and TRACE-3D - Los Alamos, 1990.

THE RF LOW LEVEL AND POWER DISTRIBUTION OF THE 100 MeV PROTON MULTITANK DRIFT TUBE LINEAR ACCELERATOR

G.D'Auria, C. Rossi, Sincrotrone Trieste, Italy

Abstract

The Sincrotrone Trieste proposal for a 100 MeV proton accelerator, driving a 1÷2.5 GeV booster Linac for the Energy Amplifier Project, is based on a Multi-Tank Drift Tube Linac (MTDTL) structure, since it seems to be the most simple and efficient solution for a high power, CW proton beam. The optimization of the RF system, in terms of efficiency and cost, is a crucial point in the design of the MTDTL. A possible solutions for the low level distribution and the RF power distribution are presented and analisys of the efficiencies are given.

1 INTRODUCTION

The Energy Amplifier Project, as proposed by C. Rubbia in [1,2], has been conceived for energy production as well as the incineration of the actinide waste from nuclear reactors. One of the main tasks to fullfil the stringent requirements imposed by the project is the generation of a CW proton beam with tens of MW nominal power, i.e. 30 mA @ 1GeV. No existing machine can deliver at the moment a proton beam with these characteristics and, following a suggestion by C. Rubbia, the accelerator scheme to drive the E.A. is based on a multi stage Linac [3]. The low energy injector must provide a proton current at a sufficient energy level for an efficient injection and acceleration in the main Linac. For our purposes the injection energy has been set to 100 MeV and a maximum beam current of 30 mA was assumed; this could be eventually reduced to 10÷12 mA in the near future if the energy of the main Linac could be raised to 2.5 GeV (i.e. redeployment of the existing CERN LEP superconducting RF cavities at the end of their operation expected in 2000). Since the feasibility and the reliability of the whole machine are of paramount importance, it is mandatory to keep an adequate safety margin for the machine design parameters. The scheme proposed for the pre-injector is based on the use of a commercial 3/6 MeV RFQ followed by a conventional DTL up to 100 MeV. The sequence RFQ-DTL, already successfully used in many other laboratories, is a conservative choice for a proton machine in this energy range. Nevertheless, to avoid the use of long DTL, which are difficult to tune and suffer from many difficulties coming from the necessity to house the focusing elements inside the drift tubes, as well for the high power involved, we adoped a MultiTank DTL (MTDTL) accelerating scheme, splitting the whole injector (6÷100 MeV) in a sequence of a short DTL tanks fed at a convenient power, whilst long DTL tanks would require more complicated solutions for the RF power feeding. Such a scheme would have the following advantages:

i) the focusing elements are placed outside the accelerating tanks, leaving the drift tubes free from quadrupoles, leading to a simplified heat removal from stems and drift tubes and an improvement in the temperature stability;

ii) the required RF power per tank can be kept below 200 kW, with the consequent advantage in employing standard coaxial components, already developed and available on the market, i.e couplers, feed-throughs, etc. for the RF distribution system.

The resulting disadvantages, like the slight increase in power loss and the need for a greater number of RF sources, are in our opinion acceptable. The efficiency loss of the accelerating tanks could be compensated by a higher shunt impedance due to a proper shaping of the drift tube profiles.

The length of each tank has been fixed by taking into account the previuos conditions togheter with beam dynamic requirements. The table below summarizes the main machine parameters.

Input Energy	6	MeV
Output Energy	100	MeV
Beam Current	30	mA
RF-frequency	352.21	MHz
Structure gradient	1.47÷2.44	MV/m
Average gradient	1.0÷1.8	MV/m
Number of tanks	58	
Number of gap/tank	3÷8	
Total length	87	m

Table 1. Main machine parameters.

2 RF POWER REQUIREMENTS

The suggested pre-injector design (6÷100 MeV) [4] will include 58 tanks in total with lengths ranging from 0.7 to 1.3 meters and with 3÷8 gaps per tank; Fig.1 gives a sketch of two 5-gap tanks with focusing and diagnostic elements.

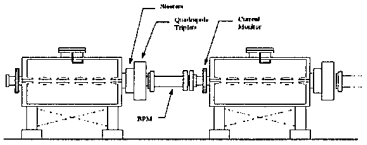


Figure 1. Two 5-gap tanks.

In Fig.2, a preliminary layout of the proposed RF distribution scheme is shown.

The whole machine will be supplied by 16 RF plants; in table 2 the power needs per plant, for 30 mA proton beam, are summarized. The reported data have been evaluated assuming an effective shunt impedance per tank ranging from 20÷25 MW; to be consevative, the values taken are roughly 10% below the corresponding ones measured of a seven gap prototype tank already assembled and tested in our laboratory. Numerical

0-7803-4376-X/98 /$10.00 © 1998 IEEE

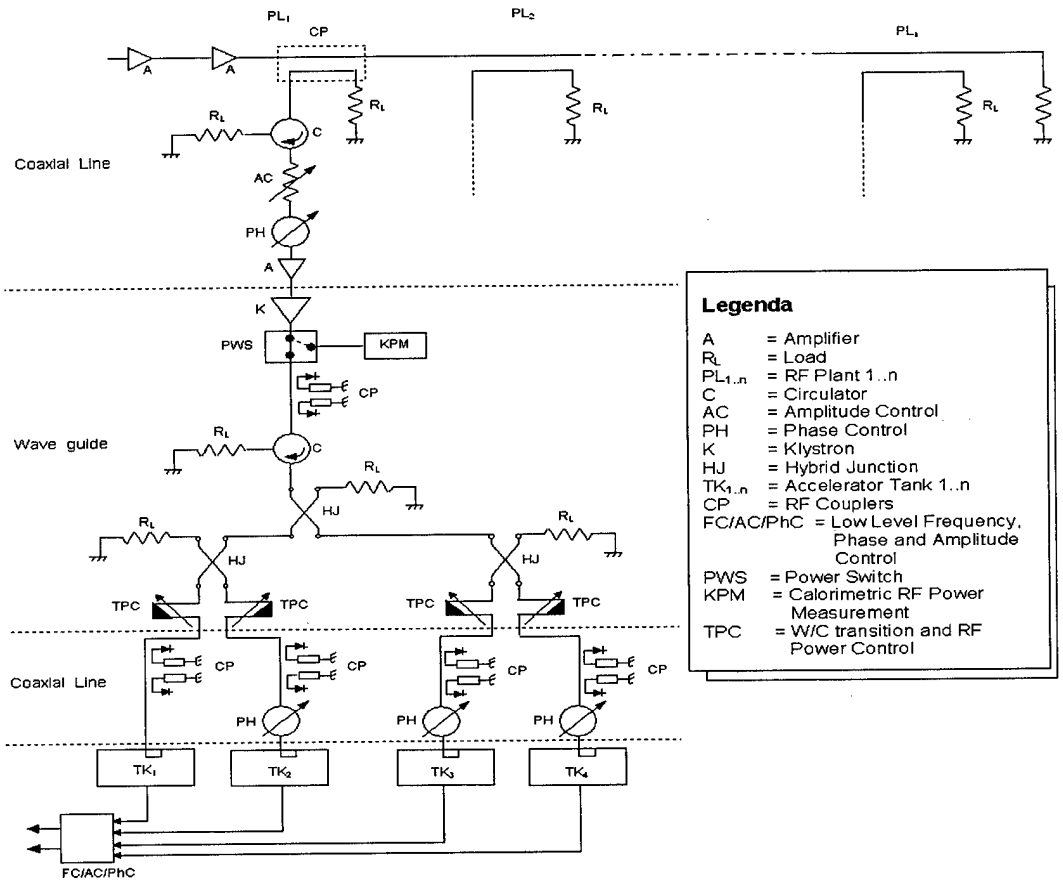


Figure 2. RF distribution layout

simulations made with Superfish on the same tank give an effective shunt impedance roughly 30% greater.

The first three plants could be fed with three CW 220÷250 KW klystrons, using a slightly modified version of the Thomson TH 2145, while for each remaining plant, a 1.1 MW tube, already in use at CERN, could be used. We have sorted the tanks to minimize the unbalanced power losses per plant since hybrid junctions are used to divide the power. For reliability reasons, the operating power level for each plant has been kept well below the maximum allowable for the tubes. We also alalysed the concept where the same 250 KW tube is used for all tanks, employing in total 55 klystrons, but a cost comparison made on the basis of informations supplied by two klystron manufacturers, EEV and TTE, was not in favour to such a solution. The main parameters of the two klystrons are listed in table 3.

Plant No.	No. of tanks for plant	No. of gap/tank	Total power (KW)	Unbalanced power (KW)
1	2	7	92	6
2	2	8	141	11
3	2	8	191	15
4	4	7/8	573	41
5	4	6/7	667	11
6	4	5/6	616	7
7	4	5	664	10
8	4	5	718	9
9	4	4	632	6
10	4	4	664	6
11	4	4	696	6
12	4	4	728	6
13	4	4	760	6
14	4	3	614	3
15	4	3	630	3
16	4	3	646	3
		Total power	9032	149

Table 2. RF power requirements for plant

	CERN Tube	TH 2145 or equiv.
Operating Frequency (MHz)	352.21	368 (to be tuned)
Typically Output Power (KW)	1100	200÷250
Efficiency (%)	65	>62
RF gain (DB)	>40	>40
Operating Voltage (KV)	100	40
Operating Current (A)	20	9.8
Total No. of Tubes to be employed	13	3

Table 3. Klystron main parameters

For the first three plants, the whole power distribution is carried out using standard 6 $^{1/8"}$ and a 9 $^{3/16"}$ coaxial lines, while for the remaining plants a WR 2300 waveguide distribution is foreseen. In this case a waveguide to coaxial transition adapter on each tank has to be provided. The RF power tuning on each tank is achieved by means of a special designed waveguide to coax transition with a remote controlled end plate short, or with a capacitive plug tuner. Further analysis will be done in the future to confirm the validity of these solutions.

On each tank we plan to control the frequency togheter with the phase and the amplitude of the resulting electic field. The frequency will be tuned and compensated by means of a proper stub, driven by a phase discriminator that compares a reference signal with the signals coming from two loops, opposite in phase and coupled with the tank. The voltage amplitude at the tank gaps could be kept constant by means of a voltage comparator while the phase control could be realized using a scheme based on a mixer which allows a rather constant sensitivity against large power variations at the input.

3 ELECTRIC EFFICIENCY

From the electric power consumption point of view, the overall efficiency of the machine has to be as large as possible. The efficiency of the whole system can be written as [5]:

$$\eta_{tot} = \eta_{ac/dc}\,\eta_k\,\eta_{tr}\,\eta_{rf/beam}$$

with:

η_{tot} wall-plug to beam efficiency;

$\eta_{ac/dc}$ conversion AC/DC efficiency;

η_k klystron efficiency;

η_{tr} trasmission line efficiency;

$\eta_{rf/beam}$ accelerating cavity efficiency.

The accelerating cavity efficiency can be expressed as:

$$\eta_{rf/beam} = \left(\frac{E_0}{R_{sh} \cdot I_{beam} \cdot \cos\phi} + 1 \right)^{-1}$$

A preliminary estimation of the overall machine efficiency is summarized in the table below:

Conversion AC/DC	$\eta_{ac/dc}$	0.9
Klystron	η_k	0.6
RF Trasmission Line	η_{tr}	0.9
Accelerating Cavity	$\eta_{rf/beam}$	0.3
Wall-plug to Beam	η_{tot}	0.14

Note that η_{tr} has been evaluated averaging the efficiency on the different tanks with a mean structure gradient of 1.3 MV/m and that η_{tot} doesn't include the power requirements for the focusing elements.

4 CONCLUSIONS

A first proposal for the RF distribution system of the 6÷100 MeV CW proton Linac, based on a MTDTL, has been reported. As already said, the main reasons for adopting a modular solution, are coming from feasibility and reliability considerations, even if the cost of the RF plants could strongly affect the final choise. However, the estimated 14% efficiency seems to be consistent with the expected values reachable by means of longer DTL structures as well.

REFERENCES

[1] C.Rubbia et al., "A realistic Plutonium Elimination Scheme with fast Energy Amplifiers and Thorium-Plutonium Fuel", CERN/AT/95-53 (ET), Geneva (1995).

[2] C.Rubbia and J.A. Rubio, "A Tentative Programme towards a Full Scale Energy Amplifier", CERC/LHC/96-11 (EET), Geneva (1996).

[3] D. Bulfone et al., "Preliminary Design Study for the Linear Accelerator of the Energy Amplifier", ST/M-96/7.

[4] G. D'Auria and C. Rossi, "A 100 MeV Multi Tank Drift Tube Linac for Proton Acceleration, this conference.

[5] G.P. Lawrence, "Critical design issues of high intensity proton Linacs", Proc. 1994 EPAC, London June, 1994.

LINEAR BEAM DYNAMICS IN THE SUPERCONDUCTING LINEAR ACCELERATOR OF THE ENERGY AMPLIFIER

F. Iazzourene, C. Pasotti, A. Wrulich
Sincrotrone Trieste, SS 14, Km 163.5 in Area Science Park, 34012 Basovizza, Trieste - Italy

Abstract

For the design of the linear optics of the superconducting linear accelerator for a Full Scale Energy Amplifier, a computer code is under development for the 3-dimensional linear motion with space charge and transverse cavity effects included. A sequential matching routine allows an easy optimization of the optics for the long structure of the linear accelerator. The program is described and first results of the optics optimization for the linear accelerating structure are discussed.

1 INTRODUCTION

A possible scenario of accelerators to drive a full scale Energy Amplifier was proposed in [1] by C. Rubbia. Based on this proposal a preliminary study was performed in [2] for the overall concept and some of the accelerator systems.

The accelerating system proposed consists of a warm part for the low energy range with a final energy of 100 MeV, followed by a superconducting linear accelerator which is built up by three different types of low beta accelerating cavities and LEP type cavities in the final stage. Each of the different structures has to cover a wide range of particle velocity variation with a corresponding loss in efficiency. The optimization of the overall structure and the derivation of the cavity lengths, (i.e. β_0, since $L_{cell}=\beta_0\lambda/2$) is described in [3]. All cavities are built up by four cells. Several cavities are housed in the same cryostat, varying from 7 for the low energy structure, to 4 for the high energy end. Each cryostat is preceded by a normal conducting quadrupole doublet for transverse focusing.

2 COMPUTER CODE DESCRIPTION

2.1 Basic Concepts

In order to take the loss in efficiency in consideration for particle velocities βc which are largely deviating from the cavity β_0, the computer code LINAD was developed for linear optics calculation and tracking. Major parts of the code closely follow the concepts developed for TRANSPORT and TRACE3D [4,5]. LINAD calculates the envelopes of a bunched beam, represented by a 6*6 σ matrix, and tracks single particles along the linac structures. The drifts and the magnets are represented by a 6*6 matrix as in the program Transport [5], while the accelerating elements are treated in the thin element approximation. Each cavity can be subdivided in an arbitrary number of segments in order to handle the acceleration and the transverse cavity effects in a more accurate way. As in [4], the space charge effects are derived from an approximation of the electric field given by an uniformly charged ellipsoid as described by Lapostolle in [6].

The electromagnetic field in a 4-cell cavity (assuming radial deviations from the center which are small as compared to the cavity dimensions) can be analytically expressed by:

$$E_z = E_o \sin\left(\frac{2\pi z}{\beta_o\lambda}\right)\sin\left(\frac{2\pi z}{\beta\lambda}+\phi\right)$$

$$E_r = -\frac{E_o \pi r}{\beta_o\lambda}\cos\left(\frac{2\pi z}{\beta_o\lambda}\right)\sin\left(\frac{2\pi z}{\beta\lambda}+\phi\right)$$

$$B_\theta = \frac{E_o \pi r}{\lambda}\sin\left(\frac{2\pi z}{\beta_o\lambda}\right)\cos\left(\frac{2\pi z}{\beta\lambda}+\phi\right)$$

with E_0 the amplitude of the axial field, r the distance from the symmetry axis, $\beta_0 c$ the geometrical velocity of the cavity, βc the beam velocity and ϕ the synchronous phase (defined as the phase difference between the particle passing the center of the symmetric structure and the zero crossing of the accelerating wave).

2.2 Acceleration

To take care of the beam velocity change along the cavity, each cell of the cavity can be cut in an arbitrary number of segments. Corresponding to the energy gain in the cavity segment, the beam velocity is then updated before entering the subsequent one.

The voltage seen by the particle passing one cavity segment defined by the coordinates z_1 and z_2 is then given by [3]:

$$V = \int_{z_1}^{z_2} E(z)\,dz = \frac{E_o}{k_o^2 - k^2}\Big[-k_o \cos(k_o z)\sin(kz+\phi) + k\sin(k_o z)\cos(kz+\phi)\Big]_{z_1}^{z_2}$$

where $k_0 = \frac{2\pi}{\beta_0\lambda}$, $k = \frac{2\pi}{\beta\lambda}$.

For a four cell structure with the length $2\beta_0\lambda$ we find for the total accelerating voltage:

$$V = \frac{E_o\lambda}{\pi}\cdot\frac{\beta^2\beta_o}{\beta_o^2-\beta^2}\sin\left(2\pi\frac{\beta_o}{\beta}\right)\cos\phi$$

Figure 1 shows the energy gain per segment (with 100 segments per half cavity) as a function of the longitudinal position in the cavity, for two different operation modes.

0-7803-4376-X/98/$10.00 © 1998 IEEE

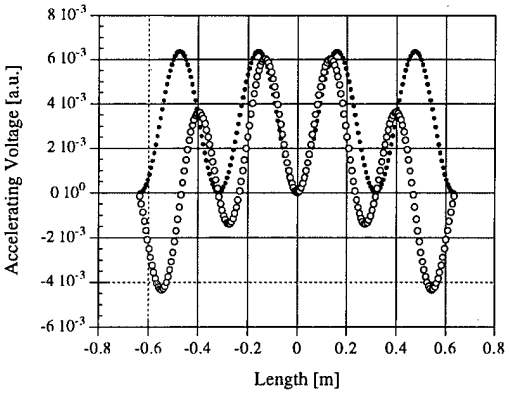


Figure : 1 Energy gain per segment (for zero synchronous phase) in a 4-cell cavity with β_0=0.75, as a function of longitudinal position. Two different particle velocities are shown, corresponding to β=0.75 (black dots) and β=0.55.

The possibility for a numerical integration of data points (representing the accelerating field) from a file, was also implemented. This allows an improvement of the sinusoidal approximation for the accelerating field and to include more realistic models, as for instance proposed in [3] or fields derived by numerical computations.

2.3 Transverse Cavity Effects

Transverse cavity effects can greatly alter the focusing in the linear structure. From the electromagnetic fields we can derive the transverse force for the general case of particles which are largely deviating in velocity from the one the cavity is optimized for (x stands for the horizontal and vertical plane):

$$F_x = q\left(E_r - \beta c\ \beta\right) = -\frac{E_o q \pi}{\beta_o \lambda}\{$$
$$\cos\left(k_o z\right)\sin\left(kz+\phi\right)+\beta_o\beta\sin\left(k_o z\right)\cos\left(kz+\phi\right)\}\cdot x$$

The transverse kick generated by a cavity segment is then obtain by integration over the segment length:

$$p_x = \frac{E_o q}{4c}\left\{\frac{1+\beta\beta_o}{\beta_o+\beta}\cos\left[\left(k+k_o\right)z+\phi\right]\right.$$
$$\left.+\frac{1-\beta\beta_o}{\beta_o-\beta}\cos\left[\left(k-k_o\right)z+\phi\right]\right\}_{z_1}^{z_2}\cdot x$$

For a 4-cell structure with the length $2\beta_o\lambda$ we find for the total transverse momentum generated by the cavity (only valid if the change in velocity over the cavity length can be neglected):

$$p_x = -\frac{qE_o}{\gamma^2 c}\cdot x\cdot\frac{\beta_o}{\beta_o^2-\beta^2}\sin\left(2\pi\frac{\beta_o}{\beta}\right)\sin\phi$$

Figure 2 shows the transverse momentum generated per segment as a function of the longitudinal position in the cavity. Two different operation modes are considered.

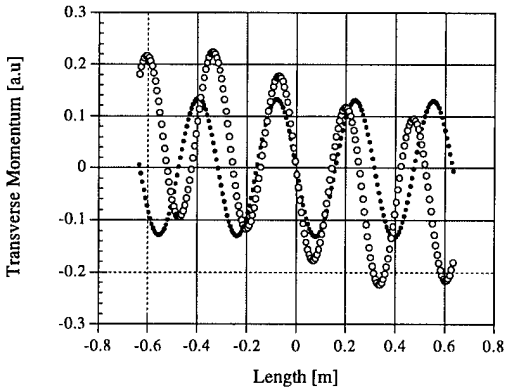


Figure : 2 Transverse momentum per segment (for zero synchronous phase) in a 4-cell cavity with β_0=0.75, as a function of longitudinal position. Two different particles velocities are shown, corresponding to β=0.75 (black dots) and β=0.55.

2.4 Matching Routines

Different types of matching routines are foreseen which allow a sequential matching of the transverse and longitudinal optics along the structure, together with the adjustment of beam energy. For the moment the following matching options are available:

- Energy at the exit of an element or energy gain at a specific acceleration element.
- Longitudinal and/or transverse phase advances between two elements.
- Structure end values of β_x, α_x or/and β_y, α_y or/and β_ϕ, α_ϕ.

At the moment the operation of the code is limited to the treatment of quadrupole magnets for transverse focusing and multicell cavities for acceleration. The matching of the longitudinal phase advance is at present functional for the multicell cavities. The code determines the synchronous phase ϕ for the multicell cavity if chosen as a tuning parameter and sets the desired phase advance for the selected range. In case of transverse phase matching, the program determines the gradient in the quadrupoles indicated by the user.

3 FIRST RESULTS FOR THE LINAC STRUCTURE OPTICS

Some initial optics calculations were performed for various parts of the superconducting linac structure. The following procedure was adopted for these calculations:

- Find the RF phase ϕ at the entrance of each cavity in order to get a good compromise between the energy gain the longitudinal phase advance and the longitudinal betatron function,
- Perform the transverse matching to get a correct transverse phase advance and a smooth variation of the transverse betatron functions,
- See the behaviour of the phase advances and the betatron functions in the presence of the space charge effects. If the tune depressions are too low or/and the betatron functions oscillate too much, rematch the phase advances.

Figure 3 shows the transverse and longitudinal β functions along 5 periods of a β-graded LEP structure. The 4-cell cavity is optimized for β_0=0.8 while the initial β of the particles is β=0.69. Zero current is assumed, which means that the optics is not affected by space charge forces (but just by transverse cavity effects).

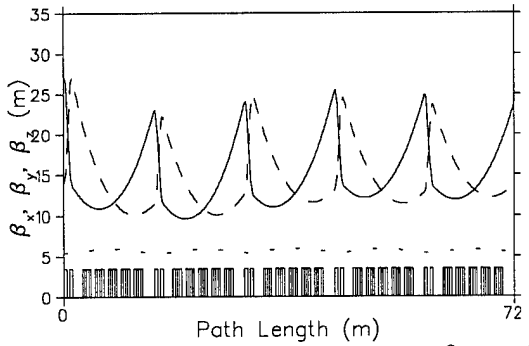


Figure : 3 Transverse and longitudinal β functions along 5 periods of the low beta structure with β_0=0.8; for zero beam current.

The same section is shown in figure 4 for a beam current of 20 mA, after re-matching of the structure. The corresponding phase advances and the tune depressions are shown in figures 5 and 6, respectively.

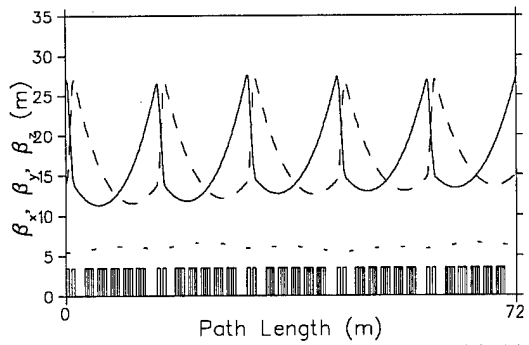


Figure : 4 The same parameters as figure 3 with 20 mA beam current (after rematching).

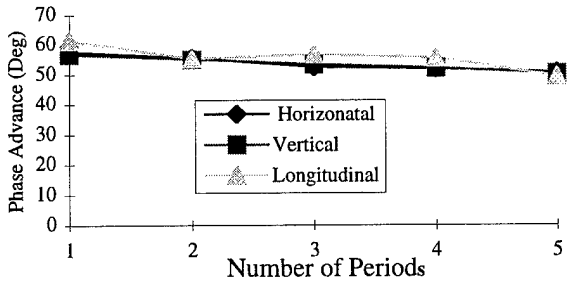


Figure : 5 Phase advances for a 20 mA beam current.

Figure 7 shows the energy gain over the structure length. The increase in effciency, i.e. energy gain with higher β can be clearly observed.

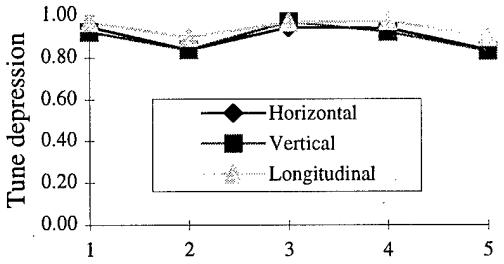


Figure : 6 Tune depression for a 20 mA beam current along 5 periods of the EA3 structure, β_0=0.8.

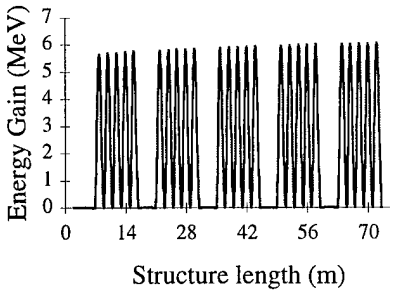


Figure7 : Energy gain over 5 periods of the low beta structure with β_0=0.8.

4 CONCLUSIONS

A new computer code has been developed which accurately treats the acceleration in multicell cavities for particles with velocities which deviate largely from the velocity for which the cavity is optimized. Each cavity can be subdivided in an arbitrary number of segments in order to take care of the energy increase in the structure. Acceleration. as well as transverse cavity effects can therefore be treated in an improved manner.

In addition sequential matching routines have been implemented which allow an easy matching of long linac structures with many periods.

First results of calculations for the superconducting linac proposed in [1,2] as a driver for a full scale Energy Amplifier were presented.

REFERENCES

[1] C. Rubbia and J.A. Rubio : 'A Tentative Programme towards a Full Scale Energy Amplifier', CERN/LHC/96-11 (EET) - Geneva , 15 July, 1996.

[2] D. Bulfone et al., 'Preliminary Design Study for the Linear Accelerator of the Energy Amplifier', ST/M-96/7, Sincrotrone Trieste, December 1996.

[3] A.Wrulich, 'Optimization of the Accelerating Structure for the Superconducting Linear Accelerator of the Energy Amplifier', this conference.

[4] 'TRANSPORT' by K.L. Brown, D.C. Carey, Ch. Iselin and F. Rothacker. CERN 80-04, Geneva, 18 March 1980.

[5] 'TRACE3D', by K.R. Crandal and D.P. Rustoi. Los Alamos, December 1990.

[6] P.M. Lapostolle, CERN report AR/int. SG/65-15, Geneva, July 1965.

OPTIMIZATION OF THE ACCELERATING STRUCTURE FOR THE SUPERCONDUCTING LINEAR ACCELERATOR OF THE ENERGY AMPLIFIER

A. Wrulich, Sincrotrone Trieste, Italy

Abstract

The superconducting linear proton accelerator of the original proposal by C. Rubbia for a Full Scale Energy Amplifier is composed of three different low beta cavity sections for the low energy part and makes use of the LEP accelerating structures at the high energy end [1]. An optimization of the structure distribution is performed, based on an improved model for the accelerating field.

1 EFFECTIVE ACCELERATION FOR AN IDEAL FIELD

In order to judge the importance for an improved model of the accelerating field for the optimization of the accelerating structure we start with an ideal field which is approximated by a sine wave.

1.1 Accelerating Voltage for Arbitrary Particle Velocities

The space and time dependence of an idealized accelerating electric field in a cavity is given by:

$$E(z,t) = E_o \sin 2\pi\left(\frac{z}{\beta_o\lambda}\right)\sin\omega(t-t_o) \qquad (1)$$

with E_0 the longitudinal electric field amplitude, z the longitudinal coordinate, λ the RF wave length, β_0 the beta for which the cavity is optimized and ω the angular rf frequency.

For the temporal coordinate of a particle which is moving with speed βc, we have:

$$t = \frac{z}{\beta c} \qquad (2)$$

The voltage seen by the particle passing the cavity is then given by integration of (1) along the cavity, i.e.

$$V = E_o \int \sin 2\pi\left(\frac{z}{\beta_o\lambda}\right)\sin\frac{2\pi c}{\lambda}\left(\frac{z}{\beta c}-t_o\right)dz \qquad (3)$$

For a structure with 2n cells in total we then find for the accelerating voltage:

$$V = \frac{E_o\lambda}{\pi}\cdot\frac{\beta^2\beta_o}{\beta_o^2-\beta^2}\cos(n\pi)\,\sin\left(n\pi\frac{\beta_o}{\beta}\right)\cos\phi \qquad (4)$$

with $\phi = (2\pi c/\lambda)t_0$ the synchronous phase, which can be set to zero for the subsequent considerations without loss of generality.

In the special case of $\beta=\beta_0$ we find for the accelerating voltage:

$$V(\beta=\beta_o) = E_o\, n\left(\frac{\beta\lambda_o}{2}\right) \qquad (5)$$

As can be easily verified, the limits of the particle beta for which acceleration can be performed, i.e. whenever expression (4) is positive are given by:

$$\left[\frac{n}{(n+1)}\right]\beta_0 < \beta < \left[\frac{n}{(n-1)}\right]\beta_0$$

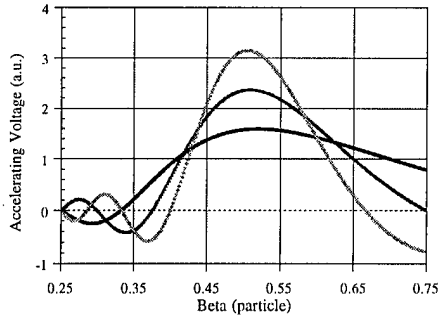


Figure : 1 Accelerating voltage (without the factor $E_0\lambda/\pi$ in equation 4) for 3 different structure lengths (4, 6 and 8 cells), for a structure optimized for β_0=0.5.

Figure 1 shows the accelerating voltage for different cell numbers for a structure optimized for β_0=0.5. For larger cell numbers the voltage decays more rapidly and the total acceleration range is narrowed down. There is also a slight shift of the maximum accelerating voltage to higher betas, which becomes more pronounced for smaller cell numbers. It is caused by an increase in average voltage of a single cell for particles with betas higher than the nominal one (it is assumed here that the particle is passing at zero phase the center of a cell structure with an even number of cells). The reduction of this shift with higher cell numbers is then due to the loss of synchronism.

1.2 Optimization of the Three Different Low Beta Structures

In a first step the accelerating voltage is kept constant for the low beta structures with different cavity betas. By using expression (4) we can optimize the three different structures to get the maximum overall acceleration efficiency.

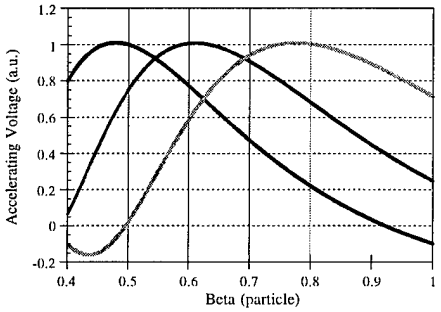


Figure : 2 Accelerating voltages for the three different low beta structures (optimized for β_0=0.46, 0.59, 0.75 from left to right) as a function of particle beta.

0-7803-4376-X/98/$10.00 © 1998 IEEE

Figure 2 shows the accelerating voltages for the three optimized low beta structures as a function of the particle beta, covering the energy range from 100 MeV to 1 GeV. The minimum efficiency at the intersection points between two different structures is 92.4%.

1.3 Optimization of Low Beta Structures with Variable Peak Fields

So far the optimization was performed by assuming that the maximum accelerating field achieved for LEP [2] can also be applied for the low beta structures. Numerical cavity calculations performed in [3] have revealed that by reducing the length of the cavity, the surface electric and magnetic peak fields are increase. In order to maintain the peak fields as for the LEP cavities, the accelerating field must be reduced with the length of the structure. For the initial cavity design an increase of the peak field for constant accelerating field, proportional to the inverse of the length was found. This in turn implies that the electric field in equation (4) has to be replaced by $E=\beta_0 E_0$. In a further optimization step [3] a considerable reduction of the peak field could be achieved, leading to the modified condition for the accelerating field, $E = (0.33+0.66\ \beta_0)E_0$.

For the optimization of the overall efficiency we have to derive the maximum integrated voltage over the beta range β_1 to β_2, defined as:

$$V_t = \frac{E(\beta_0)\lambda}{\pi} \int_{\beta_1}^{\beta_2} \frac{\beta^2 \beta_0}{\beta_0^2 - \beta^2} \sin\left(2\pi \frac{\beta_0}{\beta}\right) d\beta$$

Figure 3 presents the results of the optimization procedure in a form showing the accelerating voltage/cavity as a function of the kinetic energy. E_0 was chosen to be 12 MV/m which corresponds to the maximum gradient reached with the LEP cavities for $\beta=1$ (note: $V(\beta=\beta_0)L_{cav}=E_0\beta\lambda_0$).

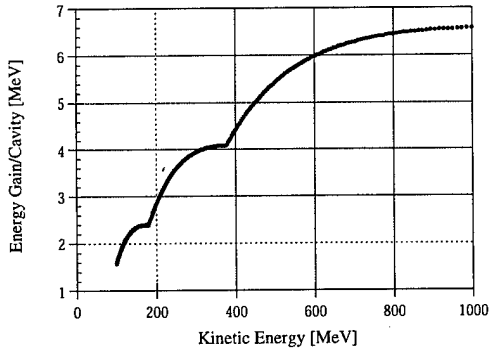


Figure : 3 Accelerating voltage/cavity as a function of kinetic energy (cavity betas β_0: 0.46, 0.59, 0.75, number of 4-cell cavities: 35, 54, 111)

It becomes evident from the graph, that the scaling of the accelerating voltage has created a shift of the structure beta towards higher energies. Only the lower branch of the quasi symmetric distribution is taken for the acceleration, since the accelerating voltage at the lower branch for larger β_0, is larger than in the upper branch for a symmetric arrangement.

2 EFFECTIVE ACCELERATION FOR A REALISTIC FIELD

In the following we introduce an analytical model for the accelerating field, based on results of different numerical calculations for cavities with different lengths.

2.1 Approximation of the Numerically Evaluated Field

The real cavity field has been divided in 3 distinct regions with separate analytical approximations:

I $\underline{0 < z < 3/4\ \beta_0\lambda}$: It is assumed that the field is undisturbed in this region.

II $\underline{3/4\ \beta_0\lambda < z < \beta_0\lambda}$: Is approximated by a cos-function with an increased period length

III $\underline{3/4\ \beta_0\lambda < z < \infty}$

Figure 4, shows a comparison between the approximation and the numerically evaluated field, and also indicates the three areas with different analytical approximations.

After matching the field values and the slopes at the connection points, we find the following expressions:

$$E_I = -E_0 \sin\left[\frac{2\pi}{\beta_0\lambda} \cdot z\right]$$

$$E_{II} = E_0 \cos\left[\frac{2\pi}{\beta_0\lambda} \cdot q\left(z - \frac{3}{4}\beta_0\lambda\right)\right] \qquad (6)$$

$$E_{III} = E_0 \cos\left(\frac{\pi}{2}q\right) \exp\left[-\left(\frac{2\pi}{\beta_0\lambda}\right) q \tan\left(\frac{\pi}{2}q\right)(z-\beta_0\lambda)\right]$$

with q as a matching parameter, which is given by the ratio of a/b, as indicated in the drawing.

Based on the numerical data of the different numerical calculations for cavities with different lengths, a scaling for the matching parameter q has been derived, which for the various cavity types can be approximated by the linear relation: $q = 0.33 + 0.688\ \beta_0$.

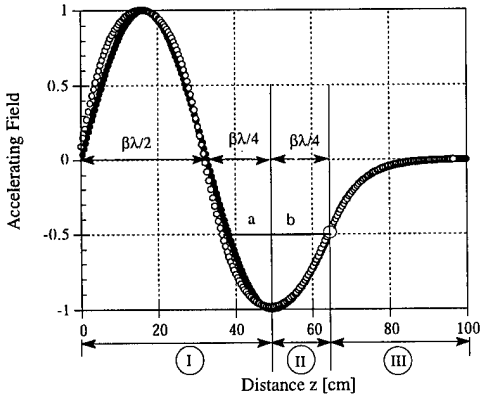


Figure : 4 Comparison of the numerically evaluated field with the analytical model (black dots), for q=0.625 and β_0=0.48.

In order to get the contributions of the 3 distinct field approximations to the accelerating voltage we have to perform the integration over the corresponding region:

$$V_i = \int E_i(z) \sin\left(\frac{2\pi}{\beta\lambda} \cdot z\right) dz \qquad (7)$$

which leads to:

$$V_I = \frac{E_0 \lambda}{\pi} \cdot \frac{\beta_0^2 \beta}{\beta^2 - \beta_0^2} \cos\left(\frac{3}{2}\pi \frac{\beta_0}{\beta}\right)$$

$$V_{II} = \frac{E_0 \lambda}{\pi} \cdot \frac{\beta_0 \beta}{(q\beta)^2 - \beta_0^2} \left\{ \beta_0 \left[\cos\left(2\pi \frac{\beta_0}{\beta}\right) \cos\left(\frac{\pi}{2} q\right) - \cos\left(\frac{3}{2}\pi \frac{\beta_0}{\beta}\right) \right] + q\beta \left[\sin\left(2\pi \frac{\beta_0}{\beta}\right) \sin\left(\frac{\pi}{2} q\right) \right] \right\}$$

$$V_{III} = \frac{E_0 \lambda}{\pi} \cdot \frac{\beta \cos\left(\frac{\pi}{2} q\right)}{1 + p^2} \left[\cos\left(2\pi \frac{\beta_0}{\beta}\right) + p \sin\left(2\pi \frac{\beta_0}{\beta}\right) \right]$$

with $p = \frac{\beta}{\beta_0} q \tan\left(\frac{\pi}{2} q\right)$

The contributions of the terms V_I, V_{II} and V_{III} are separately drawn in figures 5 for the 'Real Field' and the Ideal Field .

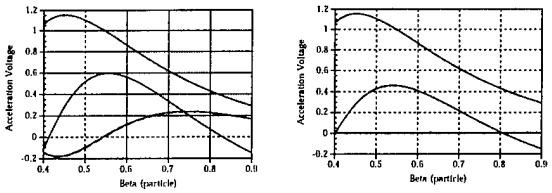


Figure : 5 Contributing terms to the accelerating voltage (without the factor $E_0\lambda/\pi$ in equations 7). Real Field (left) and Ideal Field (right), where V_I gives the largest and V_{III} the least contribution.

By comparing the two graphs we find an enhanced second term for the Real Field. On the other hand we get a negative contribution from the third term for betas lower than a certain threshold, since the particle is exposed to a decelerating field when it enters this region. This can easily be seen by looking at figure 4 for the Real Field. If the motion is synchronized to the structure beta, the particle finds an increased field in section II but sees then an out of phase field when it enters section III. For higher velocities also the third term contributes and we therefore get a shift of the maximum towards higher betas.

2.2 Optimization of the Three Low Beta Structures for a Realistic Field

Due to the fast decay of the accelerating voltage for the real field towards lower betas, the optimum structure betais here shifted back towards smaller betas [4,5]. The results of the optimization are presented in figure 6.

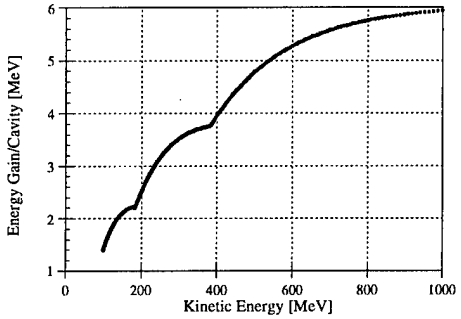


Figure : 6 Accelerating voltage/cavity as a function of kinetic energy (cavity betas β_0: 0.49, 0.64, 0.80, number of 4-cell cavities: 36, 63, 131)

The importance of an appropriate field model is visualized in figure 7, where the accelerating gradient/cavity is drawn as a function of kinetic energy, assuming the Real Field, for a structure optimized for the Ideal Field. A considerable mismatch at the transition between two structures occurs.

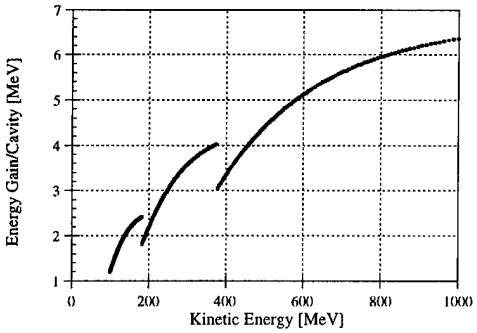


Figure : 7 Accelerating gradient/cavity vs. kinetic energy, computed with the realistic field for a structure optimized for the ideal field.

3 CONCLUSIONS

It was suggested in [1], that a sequence of 3 low beta structures be used for the Energy Amplifier to cover the energy range from 100 MeV to 1 GeV. The effective acceleration voltages have been optimized for the 3 different structures, using the ideal sinusoidal field and an improved analytical approximation of the Real Field derived by numerical calculations in [2] and [3].

An optimization of the overall accelerating structures was performed for two different cases. In a first step it was assumed that the achievable gradient is identical in all structures [4]. In a second step the limits given by the surface fields have been included in the optimization [5].

REFERENCES

[1] C.Rubbia and J.A.Rubio: 'A Tentative Program Towards a Full Scale Energy Amplifier', CERN/LHC/96-11 (EET).

[2] D.Boussard et al.: 'Preliminary Parameters of a Proton Linac Using the LEP2 RF System when Decommissioned', SL-RF Technical Note No. 96-4.

[3] C.Pasotti, P.Pittana, M.Svandrlik: 'SC EA1 Multicell Structure for b=0.48, First Results', Sincrotrone Trieste Internal Note, August 1996.

[4] A. Wrulich: 'Acceleration Efficiency of Low Beta Structures for the Energy Amplifier (using the Real Field for the Accelerating Structures), ST/M-96/5, August 1996.

[5] A. Wrulich: 'Optimization of the Accelerating Structure for the Superconducting Linac of the Energy Amplifier', ST/M-97/1, January 1997.

A DTL WITH SHORT TANKS AND EXTERNAL FOCUSING FOR HIGH POWER CW LINACS

C. Bourat, C. Perraudin
Thomson-CSF Airsys, Bagneux,-France-

Abstract

Recently, major projects, for the transmutation of nuclear waste, the production of tritium or more generally for the production of neutrons by spallation, have been proposed using high power linacs and a CW operation. See for example [1] or [2]. In this context, the manufacturing of the low or medium energy part of the linac with a standard DTL, appears to be a tricky job, particularly the insertion of high gradient quadrupoles into the drift tubes, with a specific cooling system needed for CW operation, and many brazing or welding processes. Moreover the reliability and the maintenance of the DTL could be affected sooner or later. It is proposed in this paper to use a DTL with short tanks (let say 2 to 5 cells) with a focusing system outside the tanks. The mechanical design is in that way very simplified, the drift tube geometry can be optimised for a better shunt impedance, the cooling system is easy and efficient and the alignment problem is greatly reduced. This concept is applied to a 5 MeV to 100 MeV CW proton linac operating at 352 MHz, with a 40 mA beam current, and shows moreover that the linac global efficiency is increased compared with a classical approach. Preliminary beam dynamics studies are included.

1. INTRODUCTION

A classical DTL could generally be divided in long Alvarez-type tanks, with a FODO focusing system integrated inside the drift tubes. As part of the design of new high power proton linacs operating in a CW mode, the cavities cooling system is thus an important task to take into account. It must be designed to ensure the removal of heat due to high RF wall losses on drift tubes and quadrupole heating at once. This is especially difficult at low energy where the drift tubes are short and the quadrupole gradient could be high. In that case the bore diameter should be moreover minimised, adding a restriction to the beam dimensions. The manufacturing of such drift tubes, including a compact quadrupole, its power feeding with cooled wires, the cooling circuit for the drift tube itself, and associated with the stem, implies in particular many multi-stages brazing and welding processes which are significative in terms of risks and costs. To date, two solutions among others have been proposed to move the focusing system outside the tanks:

- the Coupled-Cavity DTL (CCDTL) developed at Los Alamos [3], designed to work at 700 MHz for the APT linac.
- the Separated-type DTL (SDTL) from KEK [4], [2] at 432 MHz, for medium proton energies between 150 MeV and 300 MeV

2. A SDTL FOR LOW ENERGY PROTON BEAM

It is proposed here to apply the SDTL concept at 352 MHz [1], with a CW operating mode, for low proton energies from say 5 MeV to 100 MeV, just behind an RFQ for example, in place of a conventional DTL.

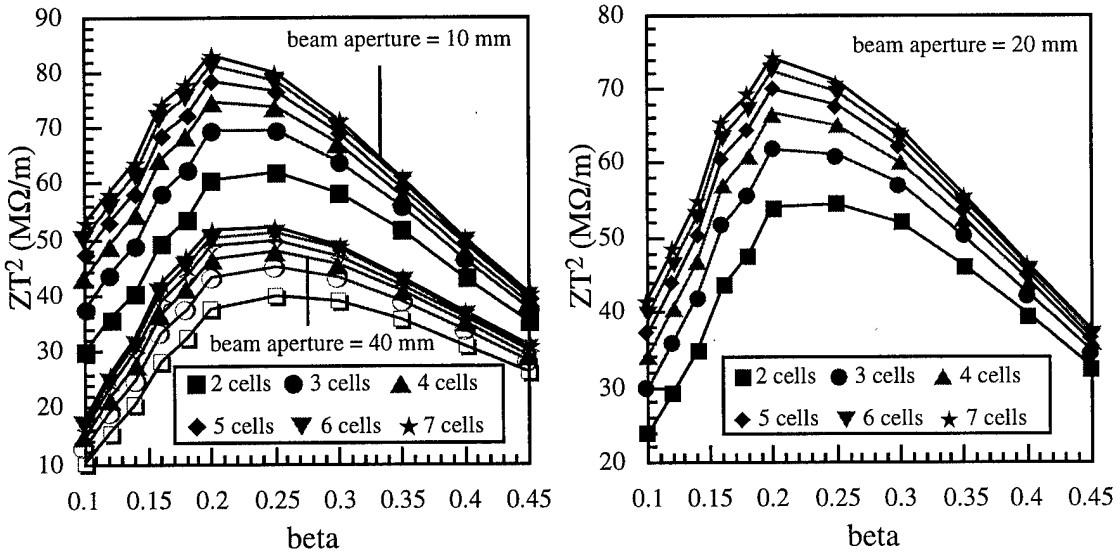


Fig.1 Shunt impedance (100 %) for multi-cells tanks (352 MHz). Bore radius = ϕ10 mm, ϕ20 mm, ϕ40 mm

0-7803-4376-X/98/$10.00 © 1998 IEEE

The tanks are necessarily short, with few cells to not lengthen too much the transverse focusing period. They are not RF coupled together, but are fed independently with a power splitting scheme, according to the power that couplers can handle. Several potential advantages, previously mentioned elsewhere, could be pointed out:

- a mechanical simplification and efficient cooling of the drift tubes, including its inner part exposed potentially to the beam
- a better shunt impedance with an optimised geometry, or alternatively a greater beam aperture if desired.
- post-couplers in short tanks no longer needed
- lower manufacturing costs

The overall SDTL has the following properties:

- easier to align with a magnetic axis separated from the RF one.
- diagnostics could be set up between tanks.
- a manufacturing simplicity implies in principle a better reliability and maintenance.

2.1 The SDTL Shunt Impedance

No quadrupoles inside the drift tubes allows to optimise its geometry to find the best shunt impedance. The outer drift tube radius is minimised, leading to a light and compact tube, including exclusively a cooling circuit. See for example fig. 2. The gap of the cell is optimised for a maximum ZT^2. Two key points must be kept in mind:

- the limited number of cells implies that the power losses in end walls have to be taken into account for the global shunt impedance of the tank.
- the reduced size of the drift tube, associated with a short gap, could lead to a high peak field on copper.

This maximum field is here arbitrarily limited to about 1 Kilpatrick (i.e. 18.4 MV/m at 352 MHz) which is enough conservative to avoid sparking. This restriction applies to tanks below 16 MeV, which are thus non-optimised for maximum shunt impedance, with a gap larger than expected.

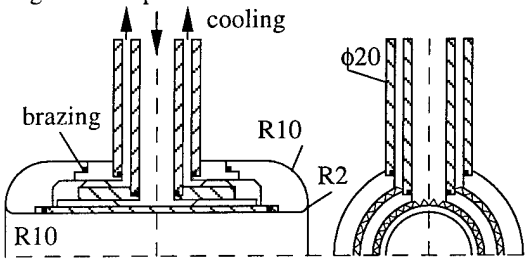


Fig.2 A SDTL Drift Tube with cooling system

Superfish [5] computations are made with various beam apertures from ϕ10 mm to ϕ40 mm, versus the particle velocity from β=0.1 (4.7 MeV) to β=0.45 (112.4 MeV) and the global ZT^2 is thus estimated for multi-cells tanks from 2 to 7 cells. (Fig. 1). The maximum shunt impedance is obtained around 20-30 MeV, which justifies the use of a SDTL at low energy. Compared with a conventional DTL with a same bore radius, a 40% to 70% increase in ZT^2 could be gained particularly above 15 MeV.

2.2 A 5MeV to 100 MeV SDTL Linac

The design of the linac includes at the beginning some beam dynamics constraints. To limit the longitudinal phase advance without current σ_{0l} below 90 deg, on account of beam stability, short tanks with 2 cells are used at low energy, with an RF power level restricted to 62.5 kW max, which is also compatible with the maximum field on copper. The number of cells is gradually increased up to 5 cells at 23 MeV. The transitions in number of cells are smoothed by choosing specific laws of synchronous phase, while keeping a regular and constant RF power splitting scheme (1/16 and 1/8 of 1 MW klystrons). The design is an iterative process between the beam dynamics, the parameters of the tanks and the choice of transitions.

The solution proposed here includes a drop of 17.5% on the theoretical shunt impedance , as a safety margin. The beam current is 40 mA CW. The beam aperture is kept constant at 20 mm. The parameters are the following:

- 8 klystrons (1 MW, 352 MHz) of which the two first are divided by 16 (62.5 kW per tank), and others divided by 8 (125 kW per tank)
- 80 tanks, 336 βλ cells, divided as follows:
  - 2 cells (tanks 1 to 12, 5 MeV to 8.8 MeV, ϕ_s=48 deg to 52 deg)
  - 3 cells (tanks 13 to 20, 8.8 MeV to 13.5 MeV, ϕ_s=40 deg)
  - 4 cells (tanks 21 to 32, 13.5 MeV to 23 MeV, ϕ_s=35 deg to 45 deg)
  - 5 cells (tanks 33 to 80, 23 MeV to 103.2 MeV, ϕ_s=25 deg to 30 deg, up to tank 40, and ϕ_s=30 deg beyond)
- active length = 83.36 m
- average field E_0T = 1.44 MV/m
- average shunt impedance ZT^2 = 42.6 MΩ/m
- copper power losses = 4.07 MW
- beam power = 3.93 MW
- efficiency = 49.1 %

The high energy part of the SDTL beyond 20 MeV, because of its high shunt impedance, compensate largely the low energy part which is not designed at its potential maximum capability, due to the transitions and large synchronous phase (which however increases the phase acceptance). This SDTL example shows in fact a gain of at least 10% in efficiency compared with a standard DTL which could be designed even with a smaller beam aperture. The SDTL saves 1 or 2 klystron power units.

The overall linac uses here a doublet focusing scheme which is well suited to the set up of free space between the quadrupoles for various beam diagnostics. Here, a regular βλ drift is used. In that case the total length of the linac is 124 m (about 1.5 times the active length) which

is also 20% or 30% longer than a standard DTL. A triplet focusing could also be used, leading to a longer linac, but with the advantage of a round beam in the cavities. Fig 3 shows the main parameters of the beam dynamics for an initial 40 mA matched beam, with an ellipsoidal uniform space charge model and 5 times the RMS beam emittance at the output of an RFQ before the SDTL. (i.e. ε_{tn} = 1.2 π mm.mrad normalised, and ε_l = 0.6 MeV.deg)

3. CONCLUDING REMARKS

The SDTL scheme presented here seems to be an attractive solution for a low energy high power linac operating in the CW mode, especially for its manufacturing simplicity and its potential low cost. It uses moreover an independently-phased cavities scheme, well known in superconducting linacs [6], which must be favourable for larger velocity acceptance. Nevertheless, a great care must be taken for the beam dynamics at low energy, because of the transitions and the matching to the RFQ [7]. Other lay-out schemes are now under investigation for a smoother beam behaviour.

REFERENCES

[1] M. Promé, "Major Projects for the use of High Power Linacs", LINAC-96, CERN 96-07, p. 9

[2] Y. Yamazaki, "Design Issues for High-Intensity, High-Energy Proton Accelerators", LINAC-96, CERN 96-07, p. 592

[3] J.H. Billen and al. "A New RF Structure for Intermediate-Velocity Particles", LINAC-94, Tsukuba,p. 341

[4] T. Kato, "Proposal of a Separated-type Proton Drift Tube Linac for a medium-energy Structure", KEK internal report 92-10

[5] K. Halbach, R.F. Holsinger, Particle Accelerators 1976 Vol. 7, pp 213-222

[6] K.C.D. Chan, "Conceptual Design of a Superconducting High-Intensity Proton Linac", LINAC-96, CERN 96-07, p. 580

[7] J.H. Billen, H. Takeda, L.M. Young, "Smooth Transverse and Longitudinal Focusing in High-Intensity Ion Linacs", LINAC-96, CERN 96-07, p. 587

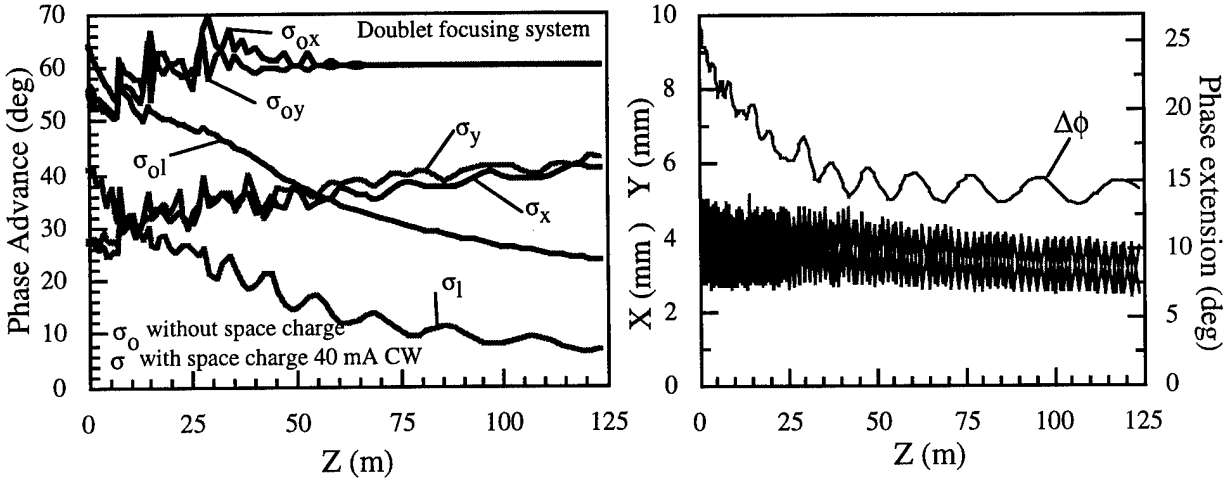


Fig. 3 Phase advance laws along the SDTL, Transverse beam envelopes and Phase extension

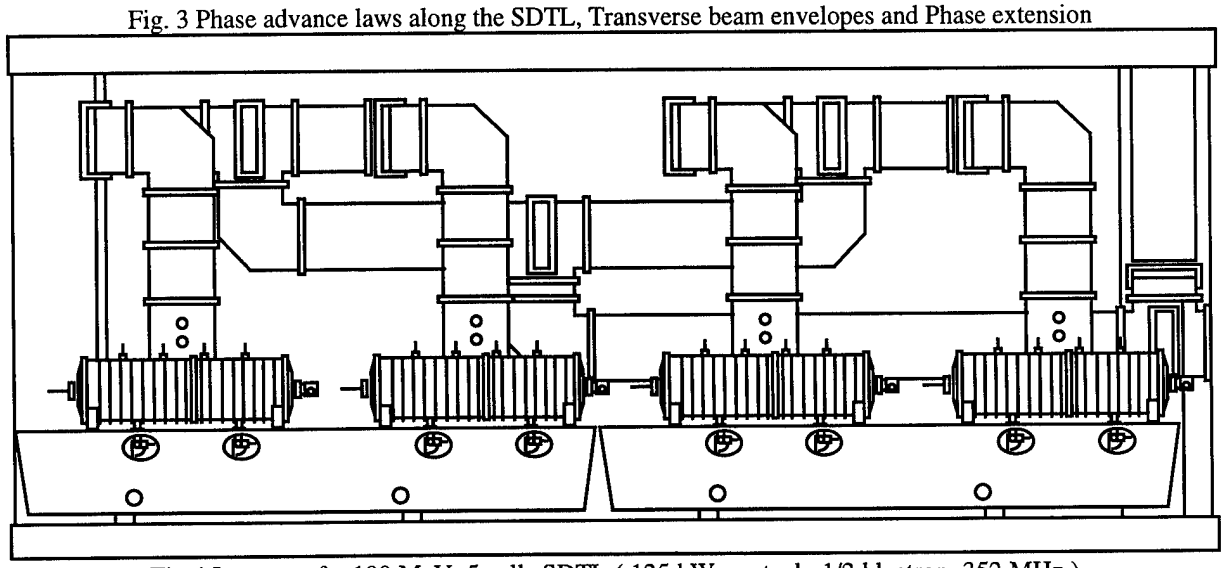


Fig.4 Lay-out of a 100 MeV, 5 cells SDTL (125 kW per tank, 1/2 klystron, 352 MHz)

A SEPARATED FUNCTION DRIFT-TUBE LINAC FOR THE ISAC PROJECT AT TRIUMF

R.E. Laxdal, P.G. Bricault, T. Reis
TRIUMF, 4004 Wesbrook Mall, Vancouver, B.C., Canada V6T 2A3
D.V.Gorelov, INR RAS, 60th October Anniversary Prospect 7A, Moscow 117312, Russia

Abstract

A variable energy drift tube linac (DTL) is required as part of the post-accelerator for the ISAC project at TRIUMF. A novel *separated function* DTL concept has been developed. Five independent interdigital H-type structures, each operating at 105 MHz and 0° synchronous phase, provide the acceleration, while quadrupole triplets and triple-gap split-ring resonators placed between IH tanks provide periodic transverse and longitudinal focussing respectively. Beam simulations show that the DTL can accelerate beams with little or no emittance growth over the complete energy range. MAFIA has been used to optimize the rf structures. Design and fabrication of the first IH tank is underway. Results of the beam dynamics and MAFIA studies, as well as the final linac specifications are presented. The status of the DTL engineering is summarized.

1 INTRODUCTION

A radioactive ion beam facility with on-line source and linear post-accelerator is being built at TRIUMF. [1] The accelerator chain comprises a 35 MHz RFQ [2] to accelerate beams of $q/A \geq 1/30$ from 2 keV/u to 150 keV/u and a post stripper, 105 MHz variable energy drift tube linac (DTL) to accelerate ions of $1/3 \geq q/A \geq 1/6$ to a final energy between 0.15 MeV/u to 1.5 MeV/u. Both linacs are required to operate *cw* to preserve beam intensity.

A *separated function* DTL concept has been developed.[3, 4] Five independently phased IH tanks operating at $\phi_s = 0°$ provide the main acceleration. Longitudinal focussing is provided by triple gap, split-ring resonator structures[5] positioned before the second, third and fourth IH tanks. Quadrupole triplets placed after each IH tank maintain transverse focussing. To achieve a reduced final energy, the higher energy IH tanks are turned off sequentially and the voltage and phase in the last operating tank is varied. A schematic drawing of the DTL is shown in Fig. 1. Diagnostic boxes are placed between the bunchers and the IH tanks.

2 BEAM DYNAMICS AND SPECIFICATIONS

2.1 Full Energy Mode

The code LANA [7] has been used to study the beam dynamics and to set the general specifications for the tanks. MAFIA has been used to model the rf characteristics. At full voltage the beam dynamics are typical for a 0° accelerating structure[6] with the benefits that the acceleration efficiency is optimum and rf defocussing is reduced. The calculated beam envelopes for the full energy case are shown

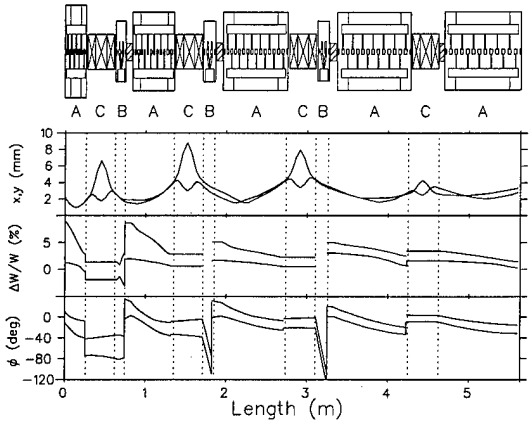


Figure 1: Schematic drawing of the ISAC variable energy 105 MHz DTL (upper figure) consisting of five IH tanks (A), three split-ring resonators (B) and quadrupole triplets (C). Beam envelopes (lower figure) define the x and y maximum half sizes and the energy and phase spread in the beam as a function of linac length. The calculations are for a beam with normalized emittances of 0.25π μm and 1.6π keV/u·ns longitudinally.

in Fig.1 for matched, normalized emittances of 0.25π μm and 1.6π keV/u·ns. The strong periodic focussing yields small beam sizes and increased acceptance. The longitudinal and transverse acceptance are 4.8π keV/u·ns and 0.6π μm respectively. A summary of before and after emittances for the full energy mode using particles simulated through the RFQ and MEBT for two different MEBT conditions are given in Table 2.1.

The gross specifications of the five IH tanks and the three split-ring resonators for the design particle of $q/A = 1/6$ are given in Table 2. The chief design considerations are the variable energy requirement and the *cw* operation. The quantity of cells in each tank is chosen to satisfy both transverse beam size requirements and debunching constraints in variable energy mode. Tank apertures are chosen to give sufficient transverse acceptance while maintaining a gap-to-aperture ratio of at least 1.2 for efficient acceleration.

Case		ϵ_x (π μm)	ϵ_y (π μm)	ϵ_z (π keV/u·ns)
A	in	0.221	0.192	1.95
	out	0.236	0.210	2.06
B	in	0.199	0.194	0.737
	out	0.209	0.194	0.737

Table 1: Beam quality before and after DTL for two MEBT setups. Quoted emittances are normalized and contain 98% of particles.

0-7803-4376-X/98/$10.00 © 1998 IEEE

Each triplet unit has an effective length of 32 cm, with a bore aperture of 28 mm and a maximum gradient of 67 T/m. They will occupy a 40 cm space between tanks.

Maximum accelerating gradients are determined by restricting the total power per unit length to less than 20 kW/m based on shunt impedance calculations with MAFIA. The drift tube aperture is significantly larger (see table) in Tank 2-5 than in Tank 1. The increased capacity of the larger tubes requires a lower tank radius than that of Tank 1 to obtain the desired resonant frequency. Ridge parameters, in particular the ridge base width and ridge length, were varied in MAFIA to alter the inductance for frequency correction. In all cases the drift tube wall thickness of the IH tanks is 5 mm. This results in a reasonably conservative peak surface field in the last tanks of 14 MV/m. The peak surface field in the bunchers is reduced by careful shaping of the drift tubes[5].

2.2 *Variable Energy Operation*

A plot of the tank voltage and phase required for a given final energy is shown in Fig. 2. Each point represents a tune that has been simulated. In all the cases for input beams of 1.6πkeV/u·ns the final emittance was $\epsilon_z \leq 1.7\pi$keV/u·ns. For a reduced voltage the particle bunch is phased negatively with respect to the synchronous phase so that as the particles lose step with the synchronous particle and drift to more positive phases they gain the required energy. Below some minimum voltage (set by multi-pactoring criterion) the phase alone is used to fine tune the output energy. For the lower energies the upstream buncher is used to match the beam to the de-tuned tank. The buncher following this tank is then used to capture the diverging beam. The three gap split-ring structure [8] is chosen for its large velocity acceptance and large multipactor-free voltage range. The three bunchers must operate over β regimes given by 1.8%→2.2%, 1.8%→3.1%, 1.8%→4.1% respectively and over voltage ranges from 15% to the tabulated value. Three resonators with gap structures synchronized to beam velocities of $\beta = 2.3\%, 2.7\%$ and 3.3% have been specified.[5]

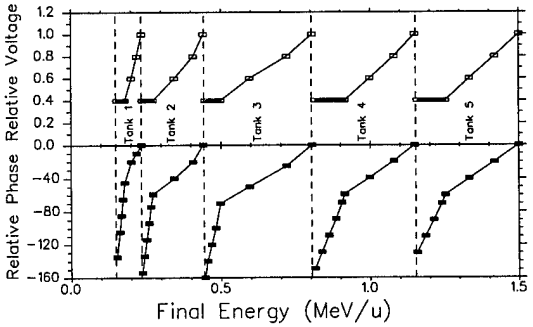


Figure 2: Tank voltage and phase required for a certain final energy. Upstream tanks are turned off. The full energy case corresponds to tank voltages of 1.0 and phases of 0°.

In Fig. 3 we show the initial and final position of a grid of particles in longitudinal phase space after acceleration in Tank 1 for two different tank voltages, $V = 0.4$ and 0.8. Distortion of phase space occurs for phases greater than that of the maximum energy gain. Below this the energy gain falls off nearly linearly. The diagram is useful in choosing the proper matching conditions entering the detuned cavity to reduce emittance growth during acceleration and to minimize phase spread in the next debunching cavity.

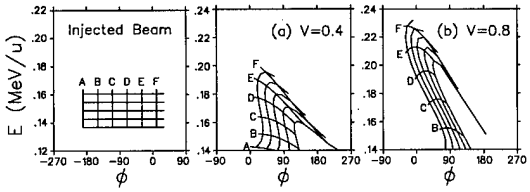


Figure 3: Final positions in $E-\phi$ space of initial grid of particles after acceleration through Tank 1 for voltages of 40% and 80% of the full energy setting.

3 TANK 1

The first IH tank (Tank 1) will be fabricated on an accelerated schedule as a working prototype for the other IH tanks. The engineering design is presently under review in preparation for detailed design. Detailed dynamics studies were completed prior to the engineering design and are reported below.

3.1 MAFIA *Optimization*

In an IH structure the capacitance is concentrated in the drift tubes. Hence as the cell length increases with β along the tank, with corresponding decrease in capacitance, the field profile will be asymmetric, higher at the first half of the cavity and falling off towards the end-plates. This leads to an uneven power distribution in the stems and a non-uniformity in the peak surface field on the tubes. In the case of Tank 1 the small length results in extra capacitance between the end plates and the ridge support. Shifting the ridge support to an asymmetric position improves the asymmetry at the expense of the shunt impedance. By varying the gap to cell length ratio, g/ℓ (Fig. 4(a)) the field profile on axis can be flattened (Fig. 4(b)). Note that although the g/ℓ variation changes the distribution of the field in a cell there is no substantial change in the distribution of the average field along the tank. However the peak surface field in each cell is made more uniform as is the power loss per stem. In flattening the maximum accelerating field the peak surface field variation in Tank 1 is reduced from 18% to 5%.

3.2 *Beam Dynamics through Realistic Fields*

The specifications and initial beam simulations of the DTL were calculated using a square field approximation in LANA. For Tank 1, these calculations were repeated with three-dimensional fields output from MAFIA to check the analytic gap-focussing calculation in the square wave model and to calculate accurately the effect of the E_y field

Tank -	No. Cells	L (cm)	a (mm)	R (cm)	$\beta_{out}(\%)$ $\beta_{in} = 1.5$	$\overline{E_o \cdot T}$ (MV/m)	E_s (MV/m)	V_{eff} (MV)	Z (MΩ/m)	P_ℓ (kW/m)	P (kW)	E_{out} (MeV/u)
1	9	26	10	46	2.2	2.1	10	0.5	480	12	3.3	0.23
2	13	50	14	38	3.1	2.4	12	1.2	495	16	7.8	0.44
3	15	77	16	38	4.1	2.5	14	2.0	464	18	14	0.78
4	14	90	16	38	5.0	2.4	14	2.2	400	19	17	1.14
5	13	98	16	38	5.6	2.3	14	2.2	365	19	19	1.50
B1	3	10	14	28	2.2	1.9	9.8	0.19	77		6.4	0.23
B2	3	12	14	28	3.1	2.3	11	0.26	75		11	0.44
B3	3	14	14	28	4.1	2.3	11	0.32	72		14	0.78

Table 2: Parameter specifications for each IH tank and buncher (B1-B3) for the design particle of $q/A = 1/6$ in full energy mode. All cavities operate at 105 MHz. Here L is the length, a is the tube aperture, R is the tank radius, $\overline{E_o \cdot T}$ is the effective field gradient, E_s is the peak surface field, Z is the effective shunt impedance and P_ℓ is the power per unit length. The quoted shunt impedance values are from MAFIA. The power/unit length and power calculations assume a shunt impedance 75% of the value quoted.

on axis (dipole component) caused by the IH stem structure. A comparison of the transverse and longitudinal calculations using both the square wave model and the realistic field simulations compared very closely.

The dipole component plus the effective integrated voltage from the field is plotted in Fig. 4(c). This field produces a maximum deflection of 0.6 mrad with a maximum shift in beam centroid of 12 μm. The cumulative deflection is negligible due to the alternating nature of the kick. Nevertheless some steering will be incorporated into the quadrupoles to allow for fine tuning of the beam position.

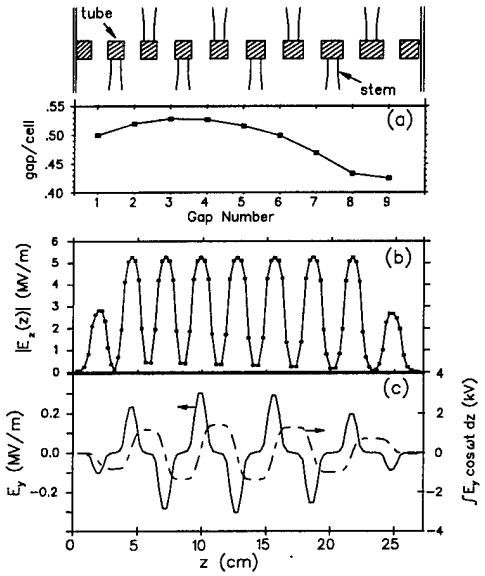


Figure 4: Tank 1 longitudinal (b) and vertical (c) field profiles from MAFIA for the gap to cell length ratio shown in (a).

3.3 *Engineering*

The tank and ridge are fabricated from mild steel. Cooling channels will be drilled in the ridge and hollow copper cooling inserts will be fit on the end plate in the vicinity of the beam entrance and ridge end. Stems are fabricated from copper and cooled through two holes drilled from stem base to near the drift tube. In order to minimize the ridge length for a given stem base, the stems are all longitudinally asymmetric, with tube positions not centered on the base. Water is supplied through a separate cooling circuit drilled into the ridge. The interior of the tank is to be copper plated with a bright acid finish to a thickness of 0.25 mm. Tuning is done through a capacitive plate with a servo-drive controlled via an rf pick-up loop.

4 CONCLUSIONS

The *separated function* DTL concept provides a low power solution to achieve variable energy heavy ion acceleration in the low β regime without significant increase in the longitudinal emittance. Signal level tests on Tank 1 are expected in early 1998. A working prototype of a split-ring resonator is scheduled to be completed by the spring of 1998. Other IH tanks are scheduled for testing in early 1999 with the DTL to be fully commissioned by the end of 1999.

5 REFERENCES

[1] P. Schmor, *et al.*, *Status of the TRIUMF ISAC Facility for Accelerating Radioactive Beams*, these proceedings.

[2] R. Poirier, *et al.*, *The RFQ Prototype for the Radioactive Ion Beams Facility at TRIUMF*, these proceedings.

[3] R. Laxdal and P. Bricault, *A Drift Tube Linac for the ISAC Project at TRIUMF*, Proc. 1996 Linear Accelerator Conf., Geneva, (1996).

[4] R. Laxdal, *The Separated Function Drift Tube Linac for ISAC*, TRIUMF Design Note, TRI-DN-97-4, April, 1997.

[5] Y. Bylinsky, *et al. A Triple Gap Resonator Design for the Separated Function DTL at TRIUMF*, these proceedings.

[6] U. Ratzinger, *Interdigital IH Structures*, Proc. 1990 Linear Accelerator Conf., Los Alamos, p. 525, (1990).

[7] D.V. Gorelov, *et al.*, *Use of the LANA Code for the Design of a Heavy Ion Linac*, these proceedings.

[8] E. Müller and H. Klein, *The Split Ring Loaded RF Cavity* Nuclear Inst. and Meth. 224 (1984), p. 17.

DESIGN OF THE SOURCE DEVELOPMENT LAB BUNCH COMPRESSOR

W.S. Graves, I. Ben-Zvi, E.D. Johnson, S. Krinsky, J. Skaritka, M.H. Woodle,
L.-H. Yu, National Synchrotron Light Source, Brookhaven National Lab, Upton, NY 11973
T.O Raubenheimer Stanford Linear Accelerator Center, Stanford, CA

Abstract

The accelerator at the Source Development Lab at BNL consists of a 1.6 cell RF photocathode electron gun followed by a 230 MeV SLAC-type linac that includes a magnetic chicane bunch compressor. The nominal specifications call for a 10 ps FWHM bunch of 2nC charge to be compressed in time by a factor of 25 at an energy of 85 MeV. The design of the compressor magnets and the beam dynamics from the gun through the magnetic chicane are described.

1 INTRODUCTION

Next generation light sources and linear colliders will operate with electron beams that occupy very small 6D phase space volumes. The Source Development Lab (SDL) is designed to take advantage of the latest methods for producing these high brightness beams, including the use of short-pulse lasers to tailor electron beam pulse shapes produced by RF photocathode guns, the latest generation BNL-type photocathode, and magnetic pulse compression to squeeze the beam longitudinally to a very short bunch length and high peak current. At the NSLS the primary use for this beam will be the production of short wavelength light through the FEL interaction and by Thomson scattering of an infrared laser. Our FEL uses the NISUS wiggler [1] as part of a high-gain amplifier which can be operated in several configurations which provide tunable radiation at wavelengths from 1μm to below 100 nm. In combination with the gun laser, Thomson scattering from the linac beam can provide tunable x-rays from 100 to 300 keV.

This paper briefly reviews the accelerator, then focuses on the design of the magnetic bunch compressor and the beam dynamics through the compressor.

2 ACCELERATOR COMPONENTS

The electron source [2] is a radio-frequency photocathode developed by a collaboration from BNL, SLAC, and UCLA. It consists of a 1.6 cell RF structure driven at 2856 MHz. The maximum gradient is 140 MV/m, yielding an exit energy of approximately 8 MeV.

To produce electrons in the RF gun, the photocathode is illuminated with 266 nm light generated by frequency tripling the fundamental from a Ti:Sapphire laser. Up to 0.4 mJ of UV light is available with a tunable pulse length ranging from 60 fs to 20 ps which should be more than sufficient to produce several nancoulombs of charge from a copper cathode. A square transverse intensity profile with a 65 degree wavefront tilt is used to match the beam onto the RF photocathode. The square intensity profile is optimal for emittance correction. The wide bandwidth of the Ti:Sapp laser allows for longitudinal pulse shaping so that nonlinear emittance correction may be investigated.

The linac currently consists of four SLAC-type constant-gradient linac tanks operating at 2856 MHz, with provision for installation of a fifth section. The first two linac tanks are used to accelerate the beam to approximately 84 MeV, where it enters the magnetic chicane. The final two linac tanks following the chicane accelerate the beam to a maximum energy of 230 MeV.

3 CHICANE DESIGN

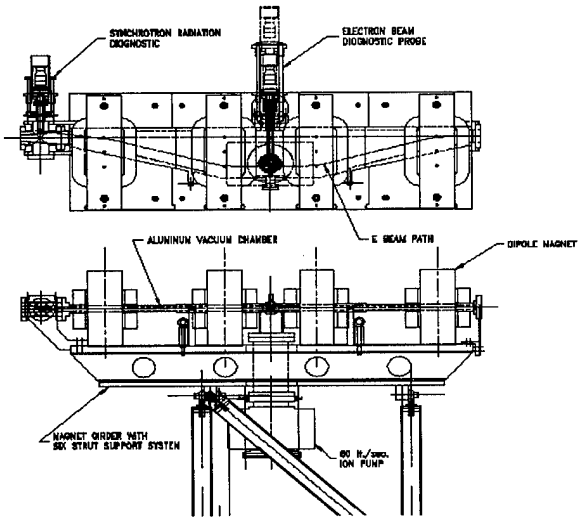


Figure 1: Magnetic chicane.

The SDL bunch compressor is made up of three major components: the dipole mangets, the vacuum vessel system with the beam diagnostics, and the mechanical support system. The 4 dipoles are fabricated from solid blocks of 1008 low carbon steel. Steel dowel pins at the magnet midplane accurately locate the yoke blocks. Each magnet uses eight air-cooled pancake coils of 16 turns. Current density is held to less than $1.5\mathrm{A/mm}^2$ to avoid thermal distortion. The coils also extend away from the iron to allow natural convection cooling. The field strength is 4.5 kG, magnetic length is 19 cm, and the gap is 3 cm. The magnetic design was optimized with the three dimensional code TOSCA.

The aluminum vacuum chamber is machined in halves and seam-welded at its periphery. Two CCD cameras are used as electron beam and synchrotron radiation diagnos-

0-7803-4376-X/98 /$10.00 © 1998 IEEE

tics. The electron beam probe is injected through the center of the vacuum chamber. It has a YAG crystal[3] and mirror to observe beam shape. It also has 3 slots 0.3, 0.6, and 1.0 mm wide, respectively, so that slice emittance may be studied. The slots may also be used to select a fixed energy bandwidth for transmission to the wiggler. The local emittance and local energy spread are key determinants of single-pass FEL performance. The probe may be moved to any tranverse position in the chamber by a stepper motor. The maximum displacement of the beam is 14 cm at 84 MeV. The compressor may be operated at any value from zero field to full strength. The synchrotron radiation monitor is used to observe emission as the beam passes through the final bend magnets. A variable position mirror is needed to accommodate potential magnet repositioning. The CCD mount is also moveable to accomodate variations in the direction of radiation emission.

A six strut system was selected to support the magnet girder. The struts simplify survey and alignment and take the place of a separate stand. The struts are bolted to a steel ground plate which is bolted and grouted to the floor.

Drift distances are 38 cm between outer magnets and 25 cm between the central magnets. For a given compressor length it is desirable to maximize these outer drifts (from magnets 1 to 2, and 3 to 4) in order to minimize the emission of coherent synchrotron radiation (CSR). The separated magnet configuration also reduces coupling between adjacent magnets. The outer magnets may be placed in either of two positions; the normal operating position is shown in Figure 1, the other position has them placed adjacent to the inner magnets. The latter position generates a greater portion of the path-length difference in the bends, and will be used to investigate the effects of coherent synchrotron emission on beam emittance and energy distribution.

4 BUNCH COMPRESSION DYNAMICS

There are several methods of producing short electron bunches, but they are not all applicable to the high charge ($\geq$ 1 nC) regime. The electron bunch length immediately adjacent to the cathode surface is approximately equal to the input laser pulse length. It is possible to produce short bunches in the RF gun through two mechanisms. The Ti:Sapp laser can produce 100 fs pulses directly, or a longer laser pulse may be timed at an advanced RF phase so that velocity bunching [4] occurs in the first 1/2 cell of the gun. Both of these methods are applicable to small beam charges ($\ll$ 1 nC) only. At higher charges the low energy and high charge density in the gun cause both bunch-lengthening and emittance growth due to space charge forces. This paper describes bunch compression via magnetic rotation at higher energies, where space charge forces are small.

The bunch compression, ΔL, due to energy spread is

$$\Delta L = R_{56}\,\frac{\Delta E}{E} + T_{566}\left(\frac{\Delta E}{E}\right)^2 \qquad (1)$$

where $R_{56} = \int ds\,\eta/\rho$, η is the dispersion, ρ is the bending radius inside the compressor magnets, $\Delta E/E$ is the correlated spread in beam energy produced by running the bunch off-crest in the linac, and T_{566} is the appropriate second order matrix element. For the chicane configuration with four equal-length magnets, the dominant R_{56} term can be written [5]

$$R_{56} = 2\theta^2(L_{dft} + \frac{2}{3}L_{mag}) \qquad (2)$$

where θ is the bend angle in each magnet, L_{dft} is the drift distance between magnets, and L_{mag} is the length of each magnet. The drift distance from magnet two to three does not affect the compression, and may be made larger or smaller to accomodate diagnostics or beamline length constraints. Equation 2 shows that the drifts contribute more to ΔL than do the bends. For a fixed chicane length, CSR will be reduced by maximizing the drifts.

Nonlinear components of the longitudinal bunch distribution are produced by curvature of the RF waveform and longitudinal wakefields generated in the linac. These nonlinearites may be partially corrected [6] by the T_{566} element of the magnetic field. For our design $T_{566} = -7.4$ cm and $\Delta E/E = 1\%$ yielding a second order path length difference of just 7.4μm, too little to correct aberrations in the distribution. Investigations are underway to study longitudinal pulse shaping to balance the curvature due to wakefields and RF.

Conservation of the longitudinal emittance requires that the uncorrelated energy spread of the bunch grow in inverse proportion to the bunch length reduction. The maximum energy spread that the FEL will tolerate sets a limit on the amount of compression that may be achieved. The input beam to the compressor is expected to have an uncorrelated RMS energy spread of .04% and a FWHM bunch length of 10 ps. The FEL and scattering experiments will tolerate approximately 1% energy spread at the compressor (0.4% at the wiggler), hence we may compress the beam by a factor of 25 for a compressed FWHM of a few hundred femtoseconds. Figures 2 and 3 show the results of a PARMELA simulation of 2 nC of charge represented by 1000 macro particles. The peak current after compression is 10 kA in a bunch length of 200 fs FWHM. The actual performance will depend on the details of the bunch distribution and wakefields generated.

Short, high current bunches generate significant coherent synchrotron radiation (CSR) at wavelengths near the bunch length and longer. The CSR power generated by N particles bending through an angle θ is [7]

$$P[\text{watts}] = 2.42\times10^{-20}\frac{N^2}{\rho^{2/3}[\text{m}]\;\sigma^{4/3}[\text{m}]}\frac{\theta}{2\pi} \qquad (3)$$

where ρ is the the bending radius and σ is the RMS bunch length. The SDL chicane parameters are $\rho = 1.25$ m, $\theta = 0.25$, and $\sigma = 50\mu$m. This yields an output power of 65 kW. The CSR is emitted predominantly in the final bend of the chicane. The total emitted CSR energy is 0.4 mJ near 60μm wavelength. We plan to detect the CSR spectrum for

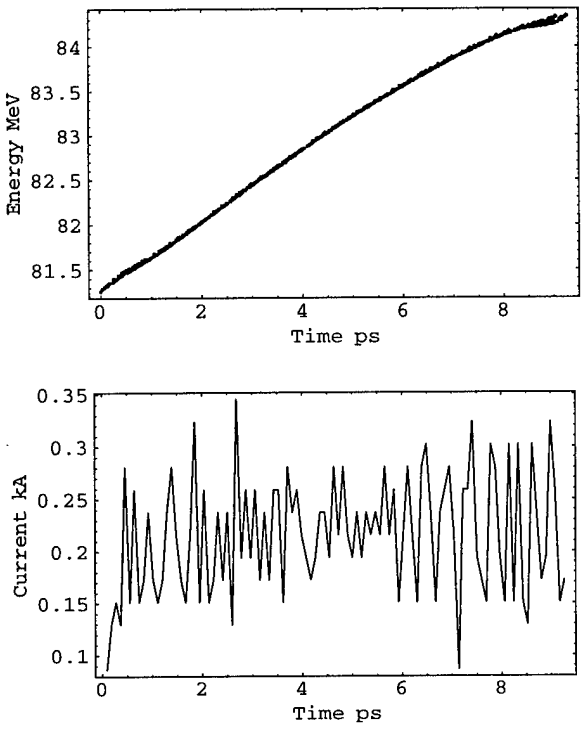


Figure 2: PARMELA simulation of energy-chirped beam entering chicane.

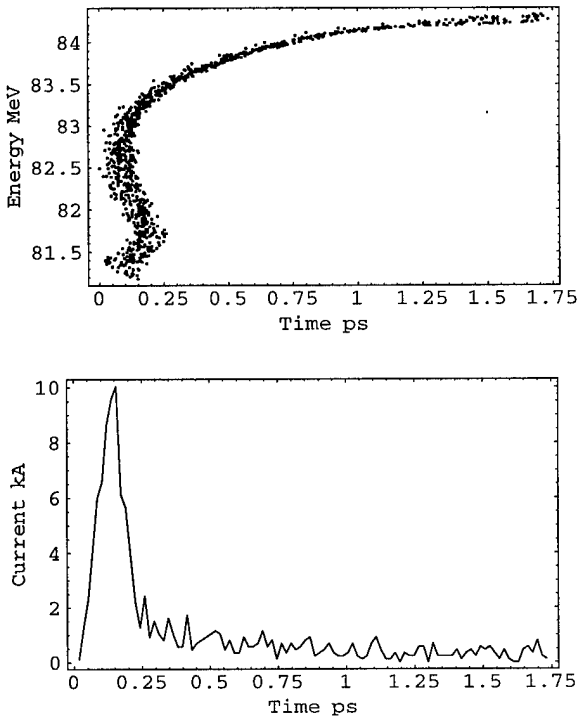


Figure 3: PARMELA simulation of compressed bunch exiting chicane.

use as a bunch length diagnostic. The total beam power is $P_{beam} = IV = 8.4 \times 10^{10}$W. Thus the energy loss due to CSR is $4 \times 10^{-4}/0.17 = 0.2\%$, a modest increase over the 1% induced energy spread.

Emittance dilution is of course anticipated to accompany the compression process, and calculation of its magnitude represents an active area of research[8]. The SDL accelerator with its compressor should provide an experimental platform for measuring these effects. Emittance growth is minimized by bringing the beam to a tight focus (increasing its divergence angle) in the final chicane bend. There is a quadrupole triplet installed just upstream of the chicane for this purpose.

5 SUMMARY

The design of the SDL electron bunch compressor has been described including its structure, magnetic properties and the electron beam dynamics. It is currently under construction. This compressor is expected to compress a 10 ps FWHM, 2 nC into 200 fs FWHM bunch length. This yields a peak current of 10 kA.

6 ACKNOWLEDGEMENTS

We thank Bruce Carlsten and Lloyd Young of LANL for much help with the PARMELA code. This work performed under the auspices of the U.S. Department of Energy Contract DE-AC02-76CH00016.

7 REFERENCES

[1] D.C. Quimby et al. Development of a 10-meter wedged–pole undulator. *Nucl. Inst. and Meth.*, A285:281–289, 1989.

[2] D.T. Palmer et al. Microwave measurements of the BNL/SLAC/UCLA 1.6 cell photocathode RF gun. In *1995 Particle Accelerator Conf.*, pages 982–984, 1995.

[3] W.S. Graves, E.D. Johnson, P.G. O'Shea. A high resolution profile monitor. In *IEEE Particle Accelerator Conference*, 1997.

[4] X.J. Wang et al. Experimental observation of high-brightness microbunching in a photocathode rf electron gun. *Physical Review E*, 54:3121–3124, 1996.

[5] T.O. Raubenheimer, P. Emma, S. Kheifets. Chicane and wiggler based bunch compressors for future linear colliders. In *1993 Particle Accelerator Conf.*, pages 635–637, 1993.

[6] B.E. Carlsten. Nonlinear subpicosecond electron-bunch compressor. Technical report, Los Alamos Nat. Lab, 1995. LA-UR-95-3933.

[7] J.B. Murphy et al. Longitudinal wakefield for an electron moving on a circular orbit. Technical report, National Synchrotron Light Source, 1996. BNL 63090.

[8] B.E. Carlsten, T.O. Raubenheimer. Emittance growth of bunched beams in bends. *Phys. Rev. E*, 51:1453–1470, 1995.

ELECTRON BEAM DYNAMICS FOR A LOW-ENERGY ELECTRON LINAC

A.F.J. Hammen, J.I.M. Botman, R.W. de Leeuw, H.L. Hagedoorn, W.H.C. Theuws.
Eindhoven University of Technology, Cyclotron Laboratory,
P.O. Box 513, 5600MB Eindhoven, The Netherlands.

Abstract

Linac characteristics have been calculated from linac structure dimensions, and have been inserted in the power diffusion equation. Assuming a constant beam current along the linac, the EM wave power has been retreived. Numerical computer simulations, using the EM wave power as input, have been used to calculate the beam current along the linac, which has been inserted in the power diffusion equation again. In particular these procedures have been applied to the Eindhoven 10 MeV linac, for which extensive measurements have been carried out. The calculation process converges after a few iterations and yields the load line, and the radial and longitudinal emittances, which are in agreement with the measurements.

1 INTRODUCTION

At the Eindhoven University of Technology, the Racetrack Microtron Eindhoven (RTME) [1] will be coupled to the Eindhoven 10 MeV, 2998 MHz travelling-wave linac (type M.E.L. SL75/10). Therefore, linac beam characteristics, in particular the load line, radial and longitudinal emittance have been simulated and measured. In the simulations, space charge effects have been neglected, because of the rather low beam current. Simulations have been compared to calculations based on Hamiltonian theory [2] as well, with an excellent agreement between these methods [3]. Simulations have been carried out with the code Parmela [4].

2 EM WAVE POWER ALONG THE LINAC

For Parmela simulations, the amplitude of the longitudinal component of the electric field, E_z, as a function of the longitudinal co-ordinate, z, must be inserted in the input file.

This amplitude is obtained from the power of the EM wave, P, in the linac as a function of z, which is calculated using the power diffusion equation [5]:

$$\frac{dP(z)}{dz} = -\frac{\omega_{\phi_0}}{v_g Q_{010}} P(z) - I_b(z)\cos(\phi_a)\sqrt{\frac{\omega_{\phi_0}}{v_g Q_{010}} r_{sh} P(z)}. \quad (1)$$

The parameters ω_{ϕ_0}, v_g, Q_{010} and r_{sh}, which stand for the EM wave frequency of the linac operating in the ϕ_0-mode, the group velocity of the EM wave, the unloaded quality factor of a TM_{010} wave in a pillbox corresponding to a linac cell and the shunt impedance per unit lenth, are calculated from the linac structure dimensions [6].

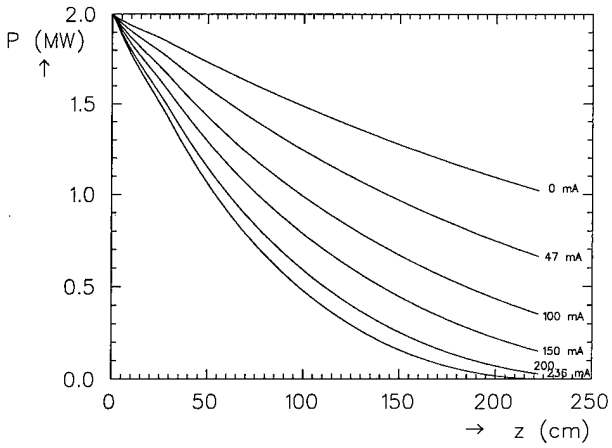


Figure 1: The EM wave power in the Eindhoven 10 MeV linac as a function of longitudinal co-ordinate for various values of final beam current (indicated in the figure). The power at $z = 0$ is 2 MW, corresponding to the magnetron power.

Assuming a constant beam current $I_b(z)$ along the linac and a mean accelerating phase $\phi_a = 30°$ in equation (1), $E_z(z)$ is calculated, using [5]:

$$E_z(z) = \sqrt{\frac{\omega_{\phi_0}}{v_g Q_{010}} r_{sh} P(z)}. \quad (2)$$

$E_z(z)$ is inserted in the Parmela input file yielding a first approximation for $I_b(z)$, which is inserted in equation (1), yielding a better approximation for $E_z(z)$. This $E_z(z)$ is inserted in Parmela again. In this way, $P(z)$ is calculated in an iterative process, which is convergent within 1% in three steps.

An approximation of the mean energy increase of the electrons, ΔE, is given by:

$$\Delta E = \int_{z=0}^{L} E_z(z)\cos(\phi_a)dz, \quad (3)$$

in which L is the total length of the linac. It appears that $I_b(z)$ does not depend much on ϕ_a, for a fixed final beam current. So ϕ_a is calculated by matching the mean final energy from Parmela and from equation (3), using $I_b(z)$ determined iteratively.

With this value of ϕ_a, which extends from 30° at $I_b(z) = 0$ to 35° at the maximum final beam current of 236 mA, one more iteration is applied. The results of the $P(z)$ cal-

0-7803-4376-X/98/$10.00 © 1998 IEEE

culations for several final beam currents are presented in figure 1.

3 LOAD LINE

The simulated load line is constructed by determining the energy value of the peak in the energy spectrum of Parmela simulations at different final beam currents. The measurement of the load line is performed in a standard spectrometer measurement using a dipole magnet with a slit behind it to select the energy and a Faraday cup, to measure the current. At different beam currents, the energy of the peak has been measured. Results are presented in figure 2.

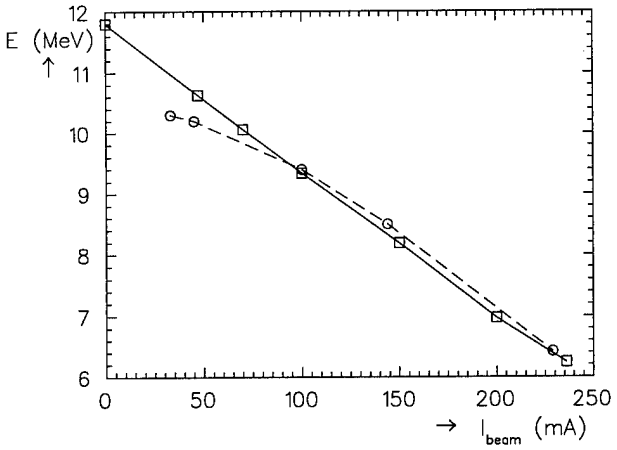


Figure 2: Simulated (□) and measured (○) load lines of the Eindhoven 10 MeV linac.

Above 75 mA, simulations and measurements agree well. Differences at lower beam currents may be due to measurement inaccuracies and to uncertainties in shunt impedance calculations.

4 RADIAL EMITTANCE

Using Parmela, the 90% radial emittance, ϵ_{90}, has been simulated at a 70 mA (corresponding to 10 MeV electrons) setting and is presented in figure 3. The emittance yields ϵ_{90} = 18.5 mm·mrad. Measurements have been performed, using a set-up consisting of two movable slits in the horizontal and vertical plane at a distance of 58 cm from each other, with a Faraday cup behind the second slit, to measure the current. The measurements have been corrected for the finite slit thickness and results have been fitted to an ellipse [3]. Results in the transversal x- and y-directions are: $\epsilon_{90,x}$ = 11 mm·mrad and $\epsilon_{90,y}$ = 17 mm·mrad.

Differences between simulation and measurements are due to measurement inaccuracy, to the absense of space charge calculations and to the fact that Parmela uses a Floquet series expansion of the electric field, which is not completely valid in the a-periodic initial part of the linac. Differences between x and y measurements are attributed to measuring inaccuracies, to structure imperfections and to

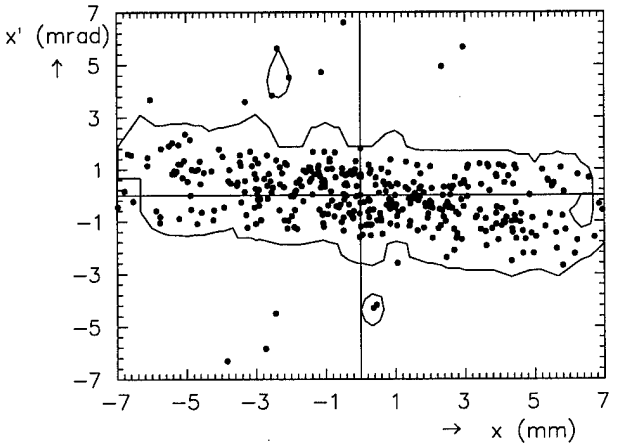


Figure 3: The simulated radial emittance of the Eindhoven 10 MeV linac, the contour determines the 90% emittance, the dots represent the simulated test particles.

non-rotational symmetric influences, like the electron gun and the coupling in of the RF power.

5 LONGITUDINAL EMITTANCE

Using Parmela, the longitudinal emittance has been simulated at a 70 mA (10 MeV) setting and is presented in figure 4.

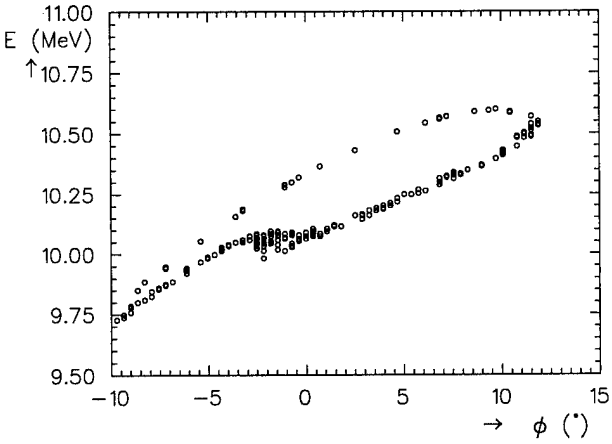


Figure 4: The simulated longitudinal emittance, presented as phase-energy relation, of the Eindhoven 10 MeV linac.

From the longitudinal emittance the energy spectrum can be constructed. This spectrum has also been measured, using the same set-up as in the load line measurement. However, due to the magnitude of the radial emittance, the energy spectrum can not be measured sufficiently accdurately, using this set-up. Therefore, it has been calculated what signal would be measured, assuming the simulated spectrum as input for the measurement set-up [3]. The simulated and the measured energy spectrum as well as the

calculated measurement spectrum, assuming the simulated spectrum as input, are presented in figure 5.

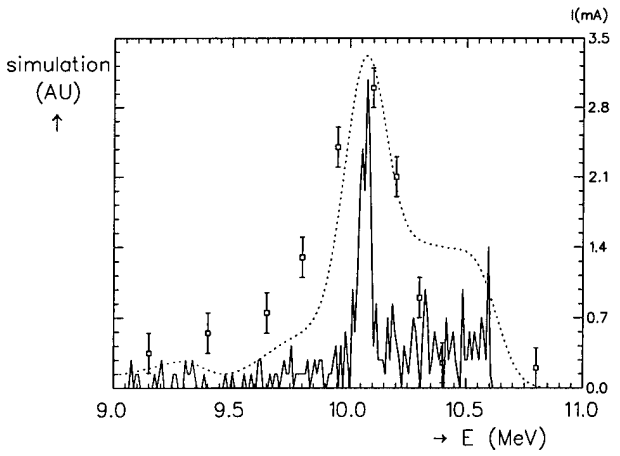


Figure 5: The simulated energy spectrum (solid line), the simulated energy spectrum as would be measured in the used set-up (dotted line) and the measured spectrum (□) (units on right axis) of the Eindhoven 10 MeV linac.

The agreement between measured spectrum and calculated measurement spectrum is rather good, from which it is concluded that the real energy spectrum is about equal to the simulated spectrum. Furthermore, it follows that the calculation of the longitudinal is quite realistic.

6 INJECTION PHASE DEPENDENCY

In the initial part of the linac, particles are homogeneously distributed over the RF wave, because of the fact that the RF period is much shorter than the duration of macro pulse fed to the electron gun. Each injection phase interval leads to a specific contribution in the final energy spectrum and the final total emittance. By selecting an optimal 50° part of the total injection phase distribution, a final beam is obtained with a 3.7° final phase spread and a 1.3% final energy spread, the 90% radial emittance of this beam is 8.1 mm·mrad. Thus a much higher beam quality is obtained, compared to figures (3) and (4). Injection of this higher quality beam in the RTME is prefered, because of better matching and a higher quality beam at the end of the RTME.

7 CONCLUSIONS

Linac beam characteristics have been determined, with measurements and simulations. There is a good agreement between these methods, which means that the method used to calculate the EM wave power along the linac is correct and that the simulated linac characteristics are quite reliable.

Comparing the beam characteristics to the acceptance of the RTME [7], the current that will be accepted in RTME is more than adequate [3] and [8].

8 REFERENCES

[1] Theuws W.H.C., Botman J.I.M., Hagedoorn H.L., Leeuw R.W. de, Timmermans C.J., *The 75 MeV racetrack microtron Eindhoven*, LINAC 96. Proc. of the XVIII International Linear Accelerator Conference, Geneva (1996), 92-94.

[2] Hagedoorn H.L., Botman J.I.M., Leeuw R.W. de, Stas R.J.W., *Orbit dynamics in a low energy electron linear accelerator*, EPAC 96. Proc. of the fifth European Particle Accelerator Conference, Barcelona (1996), 944-946.

[3] Hammen A.F.J., *Particle dynamics in the 10 MeV TUE electron linac*, Internal Report, M.Sc. Thesis, Eindhoven University of Technology (1997).

[4] Parmela, *Reference manual*, Los Alamos Accelerator Code Group, Los Alamos National Laboratory, Los Alamos, USA (1987).

[5] Leiss J.E., *Beam loading and transient behavior in travelling wave electron linear accelerators* in *Linear accelerators*, Lapostolle P.M., Septier A.L. eds., North Holland Publ. Comp., Amsterdam (1970) 147-172.

[6] Gao J., *Analytical formulae for the resonant frequency changes due to opening apertures on cavity walls*, EPAC 92. Proc. of the third European Particle Accelerator Conference, Berlin (1992) 865-867.

[7] Webers G.A., *Design of an electron-optical system for a 75 MeV racetrack microtron*, Ph.D. Thesis Eindhoven University of Technology (1994).

[8] Theuws W.H.C., Kemper A.H., Ridderhof E.J., Timmermans C.J., *Electronic detection circuit for a stripline beam position monitor*, EPAC 96. Proc. of the fifth European Particle Accelerator Conference, Barcelona (1996), 1618-1620.

FABRICATION OF BIPERIODIC DAW CAVITY

Y. Iwashita, H. Ao, A. Noda, H. Okamoto, T. Shirai, M. Inoue, Accelerator Laboratory, NSRF, ICR, Kyoto University, T. Kawakita, Core Engineering Department, Nuclear Energy Systems Engineering Center, Mitsubishi Heavy Industries, Ltd., M. Matsuoka, Electronic Systems & Space Systems Engineering Department, Kobe Shipyard & Machinery Works, Mitsubishi Heavy Industries, Ltd. and K. Koyama, Research and Development Department, Nuclear Development Corporation

Abstract

Fabrication techniques for the biperiodic DAW cavity have been investigated for these years. The basic dimensions are optimized by computer simulations and cold model tests. According to results of material tests, all of the parts facing to the inside are made of OFC. In order to improve the properties of a bridge coupler, which is installed between two 1.2-m long accelerating tube, choke structure is implemented.

1 INTRODUCTION

The biperiodic DAW cavity for electron acceleration is under fabrication and test. The operating frequency is designed at 2857MHz so that it can replace one of the existing disc-loaded waveguide accelerating tubes. The injection energy for the acceleration test is intended to be about 60MeV. It consists of two of 1.2-m long accelerating tube and a coaxial bridge coupler that connects the two tubes. The bridge coupler has an RF coupler, a vacuum port, and three frequency tuners.[1] Recent progresses in fabricating a power model for a real acceleration of electrons are described in this paper.

2 MATERIAL TEST

At first, chromium copper (Cr-Cu) was considered as the material for mechanically severe portions, because of the mechanical complexity of the DAW.[2] Cr-Cu, however, was found to have some undesired properties for the DAW cavities as following:

1) the outgas from the Cr-Cu surface is three to four times larger than that from the OFC surface,
2) the composition of Cr-Cu changes after the parts are furnace brazed (900°C), which decreases the strength and
3) the oxidization of the surface on Cr-Cu is caused.

2.1 Outgas

The outgas characteristic was measured for Cr-Cu. The shape and the size of the specimen are shown in Fig. 1.

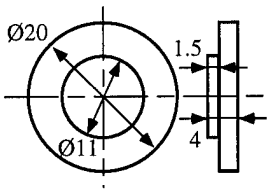


Figure 1: The dimensions of the specimen for outgas test.

	H	O
Cr-Cu	1.3 ppm	2 ppm
OFC (Class 1)	0.6 ppm	1 ppm

Table 1: Impurities in the material for outgas test.

Hydrogen and oxygen impurities are listed in Table 1. The pressure of H_2 gas was measured at 500°C for more than 30 minutes. The pressure reached its maximum value at 14 minutes after the heating started. The result showed that the outgas rate of Cr-Cu is three to four times that of OFC. The value was 2.7×10^{-6} Torr•l/cm^2/s at 30 minutes after heating, which was 47% of the maximum value. The time dependencies for both the Cr-Cu and OFC specimen were similar except for the absolute value.

2.2 Heat test

Test pieces made of Cr-Cu (Cu-0.94%Cr) and OFC were provided for a heat test. The shapes of the specimens are half cylinders as shown in Fig.2. Hydrogen and oxygen impurities are listed in Table 2. Figure 3 shows the temperature change that simulates the furnace brazing procedure.

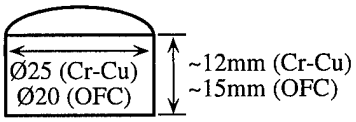


Figure 2: The dimensions of the specimen for heat test.

	H	O
Cr-Cu	1.3 ppm	2 ppm
OFC (Class 1)	0.5 ppm	1 ppm

Table 2: Impurities in the material for heat test.

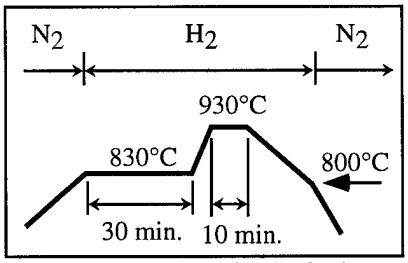


Figure 3: Temperature change for heat test.

0-7803-4376-X/98/$10.00 © 1998 IEEE

Although the OFC specimen did not show any change in its surface color, the surface of the Cr-Cu specimen changed its color dark. A microscopic inspection showed the existence of two layers on the surface of the Cr-Cu specimen. The medium layer had a thickness of 10 μm and seemed to be pure copper. The very surface layer was so thin that it could be barely recognized. The composition of the inner portion of Cr-Cu specimen changed after the parts were heated up, which may cause decrease of the mechanical strength of the material.

In order to identify the chemical composition of these layers, we carried out a measurement with an X-ray diffraction method for chemical elements of Cu, Cr, O, H, N and C. Then only Cu and Cr_2O_3 were found for above elements. The result showed that the very surface thin layer and the 10 μm layer were made of Cr_2O_3 and pure copper, respectively. The origin of the oxygen was not clear: whether it comes from the atmosphere or the inside of the material. Because both the possible oxygen sources cannot be controlled in the current facility, the oxidization of the surface is difficult to be avoided.

Thus, OFC is considered as a material for the whole structure of DAW except for the outer water jacket.

3 BRIDGE COUPLER

Two 1.2m-long accelerating tubes are coupled by a coaxial bridge coupler, which has an RF coupling slot, an evacuation port and frequency tuners (Fig. 4). The RF power is fed through the coupling slot on the coaxial bridge coupler. The spool in the bridge coupler is supported by four straight pipes connected to the body of the bridge coupler, so that the cooling water can go through the spool. The electric field distributions in the bridge coupler for the accelerating mode and the coupling mode are shown in Fig. 5.

The spool in the bridge coupler is upheld by four supports that are located at the center of the bridge coupler so that disturbance of the electric field for the accelerating mode becomes small. On the other hand, they disturb the electric field distribution of the coupling mode, which raises the coupling mode frequency about 200 MHz. This frequency shift is too large to be compensated by modifying only the spool shape and dimensions, even with an inter-rim at the center of the spool. In order to cure this situation, we adopted the choke structure in the spool supports (see Fig. 6). Because

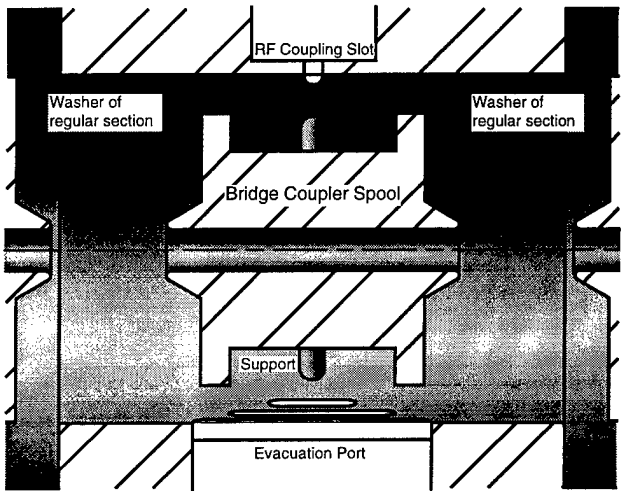


Figure 4: Coaxial bridge coupler.

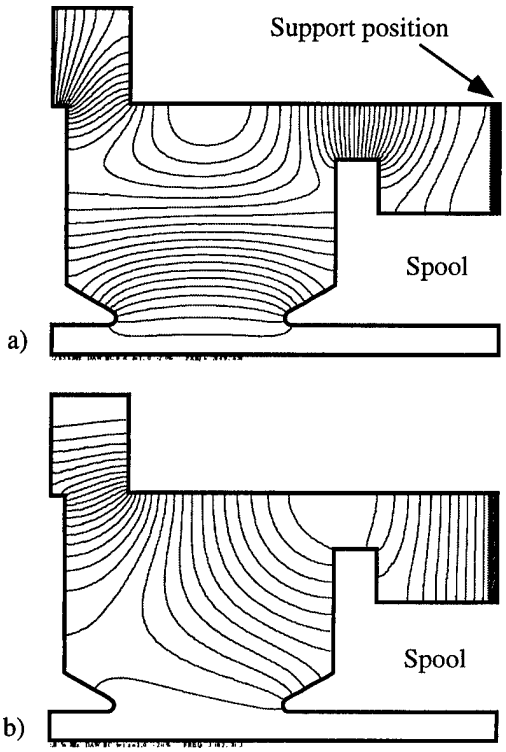


Figure 5: The field distribution in the coaxial bridge coupler; a) the accelerating mode, b) the coupling mode.

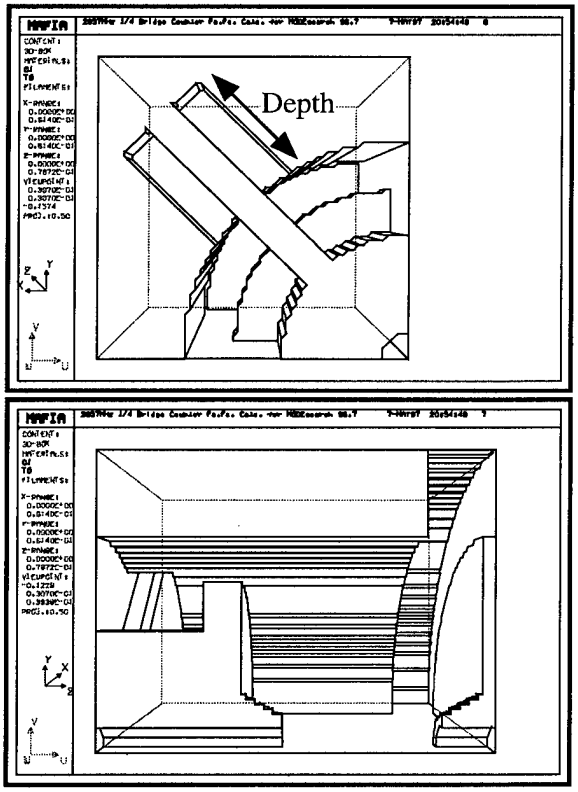


Figure 6: Choke structure implemented for the supports.

a support is connected to a $\lambda/4$ coaxial line, it is practically insulated from the outer wall. The coupling mode frequency can be adjusted by the depth of the choke. On the other hand, the accelerating mode frequency is not affected by the choke.

3.1 MAFIA calculation

MAFIA calculations were performed to show the choke effect. Because no inter-rim is implemented on the spool for simplicity, the coupling mode frequency (fc) does not match with the accelerating mode frequency (fa). The outer cylinder is approximated by a square for ease in meshing. The calculated frequencies are listed in table 3. Because the original fc (without support) is 200 MHz higher than fa, the choke is used in over-compensation way.

	fa [MHz]	fc [MHz]
without support	2847	3078
with support	2856	3243
with choke depth=23.5	-	2917
with choke depth=24.8	2852	2855
with choke depth=25.5	-	2824

Table 3: Effect of the choke depth.

3.2 Coupling Mode Frequency of Cold Model

Cold model tests were carried out to determine the choke depth. The geometry difference from the MAFIA model was the approximated outer cylinder of the choke. The accelerating mode frequency decreased only 3 MHz with the implementation of the choke structure. Figure 7 shows the depth dependence of the coupling mode frequency in conjunction with the MAFIA results. Taking account of the practical mesh, the difference between the calculations and the measurements are reasonable. The rough parameters were obtained from these results. The precise tuning can be done with minor adjustment of the spool dimensions. The tilt sensitivity[3] with 9 gap-regular section on each side was up to 10 %/MHz in the cold model (see Fig. 8). On the other hand, that without the choke was as much as 50 %/MHz. The difference is much more drastic if only the values around the bridge coupler are compared.

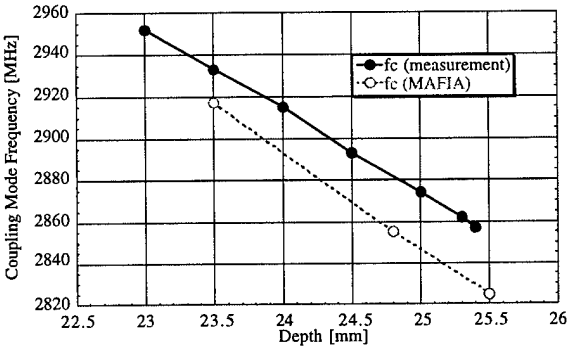


Figure 7: Coupling mode frequencies as functions of the choke depth.

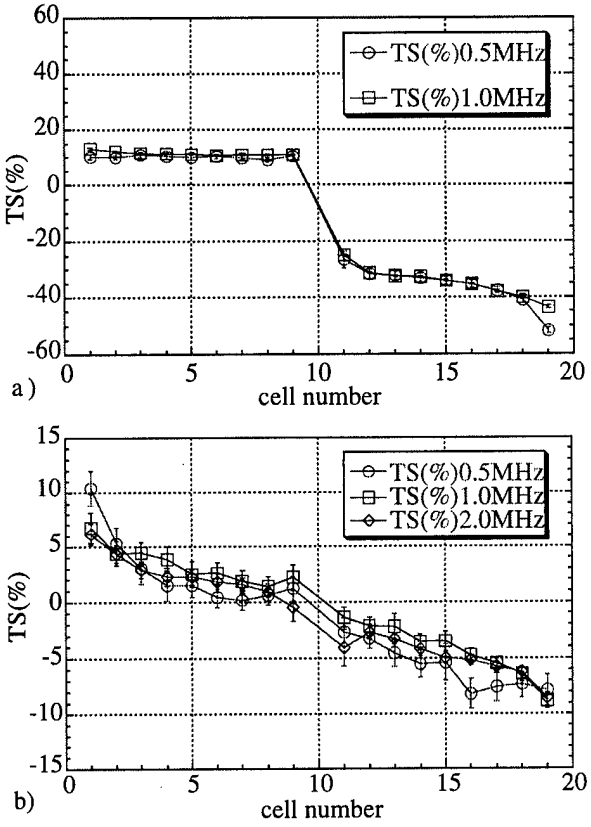


Figure 8: Tilt sensitivity a) without choke , b) with choke

4 CONCLUSION

According to the results from the material tests, OFC was chosen as the material for fabrication and the accelerating tube was designed. The choke structure was implemented on the supports for the spool in the bridge coupler. Because the washers should be water-cooled, they have cooling grooves in them. The fluid and thermal calculations were also performed for the groove design. We are preparing for a power test and a beam acceleration test including the measurement of the power model tank.

5 ACKNOWLEDGEMENTS

The authors are grateful to Mr. Tonguu for his technical support to accomplish the measurement. The present work is supported by a Grant-in Aid for Scientific Research from Ministry of Education, Science, Sports and Culture. Computation time was provided by the Supercomputer Laboratory, Institute for Chemical Research, Kyoto University.

6 REFERENCES

[1] Y.Iwashita, et al.,: `Cold Model Test of Biperiodic L-Support Disk-and-Washer Linac Structure', Proc. of the 1995 Particle Accelerator Conference, Dallas, p.1093 (1995)

[2] Y. Iwashita, et al.,: `Power Model of Biperiodic DAW Cavity', Proc. of the 1996 International Linear Accelerator Conference, Geneva Switzerland, p.857 (1996)

[3] J.H. Billen, `Field Stability in Two-Stem Drift-Tube Linacs', 1988 Linac Conf., CEBAF, CEBAF-Report 89-001, p.125 (1989)

PRESENT STATUS OF THE ELECTRON LINAC AS THE INJECTOR FOR KSR

T. Sugimura,T. Shirai, H. Tonguu, Y. Iwashita, A. Noda and M. Inoue,
NSRF, Institute for Chemical Research, Kyoto University,
Gokasho, Uji-city, Kyoto, 611, Japan

Abstract

At Kyoto University, a 300 MeV electron storage ring, KSR, has been constructed for the research of the synchrotron radiation light. As an injector of the ring, an S-band electron linac with the energy of 100 MeV was constructed in October, 1995, and have been operated since then. We measured the transverse emittance of the 100 MeV electron beam using a profile monitor made of a fluorescent screen and quadrupole lenses. The horizontal and vertical ones are 0.44 π·mm·mrad and 1.3 π·mm·mrad, respectively. The beam from the linac is being used for the experiment of the parametric X-ray radiation from the silicon crystal at rather low duty factor.

1 KSR AND LINAC SYSTEM

1.1 KSR

An electron storage ring, KSR, is under construction at the Nuclear Science Research Facility, Institute for Chemical Research, Kyoto University. This ring will be used for the research with the synchrotron radiation light from bending magnets and an insertion device. It is also planned to be used as a pulse stretcher of the electron beam from the linac. Figure 1 shows the layout of KSR and a Linac. The circumference of the ring is 25 m and the maximum energy is 300 MeV.

1.2 Linac

As the injector for KSR, the electron linac has been ready for injection. The main parameter is shown in the Table 1.

Table 1 Main parameters of the injector.

Output beam Energy	100 MeV (100 mA)
Typical current	100 mA
Pulse width	1 nsec ~ 1 μsec
Maximum repetition	20Hz
Acceleration structure	2π/3 mode, constant gradient type
Length of accelerating structure	3 m*3
Operation frequency	2857 MHz
Acceleration electric field	15 MV/m (without beam loading)

The electron gun has a thermionic cathode with a maximum extraction voltage of -100 kV. The cathode and grid assembly is Y796 (Eimac). The beam pulse width can be changed from 1 ns to 1 μs. A standing wave reentrant cavity is used as a prebuncher and the resonant frequency is 2857 MHz, which is the same as that of the

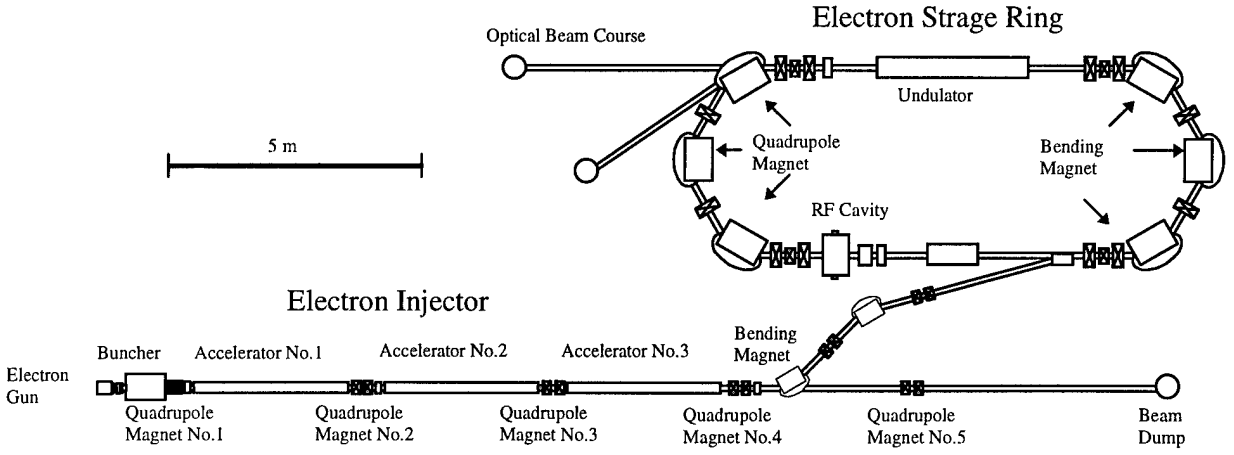


Fig. 1 The layout of the KSR and the injector.

0-7803-4376-X/98 /$10.00 © 1998 IEEE

main accelerating structures. A buncher subsequent to the prebuncher is a traveling waveguide with 21 cells. 4 sets of solenoid-focus coils surround the buncher.

The accelerating structure has constant gradient with $2\pi/3$ mode. For the beam focusing, quadrupole lenses are installed in the high energy section. Four ITT-8568 klystrons are used as RF sources for the accelerating structures. The maximum output peak power of these klystrons is 21 MW. Their maximum repetition rate is 21 Hz.

2 EMITTANCE MEASUREMENT

We measured the emittance of the output electron beam from the linac in order to prepare for the beam injection to KSR.

2.1 Basis of the emittance measurement

The transfer matrix M from a point ***i*** to another point ***o***, in which there are quadrupole magnet lenses, is given as

$$\begin{pmatrix} x_o \\ x_o' \end{pmatrix} = M \begin{pmatrix} x_i \\ x_i' \end{pmatrix} = \begin{pmatrix} m_{11} & m_{12} \\ m_{21} & m_{22} \end{pmatrix} \begin{pmatrix} x_i \\ x_i' \end{pmatrix} , \quad (1)$$

where x is the beam position, and x' means dx/dz.

Using m_{ij}, the twiss parameters is transformed in a following way,

$$\begin{pmatrix} \beta_o \\ \alpha_o \\ \gamma_o \end{pmatrix} = \begin{pmatrix} (m_{11})^2 & -2m_{11}m_{12} & (m_{12})^2 \\ -m_{21}m_{11} & 1-m_{12}m_{21} & -m_{12}m_{22} \\ (m_{21})^2 & -2m_{22}m_{21} & (m_{22})^2 \end{pmatrix} \begin{pmatrix} \beta_i \\ \alpha_i \\ \gamma_i \end{pmatrix} \quad .(2)$$

If the beam size is measured N times with the various focusing power of the quadrupole magnet, σ and m_{ij} change their values. Let's denote

$$\begin{aligned} (m_{11})^2 &= a_n , \\ -2m_{11}m_{22} &= b_n , \\ (m_{12})^2 &= c_n . \end{aligned} \quad (3)$$

σ_n are expressed in the following way,

$$\begin{pmatrix} \sigma_1^2 \\ \sigma_2^2 \\ \vdots \\ \sigma_N^2 \end{pmatrix} = \begin{pmatrix} \varepsilon\beta_1 \\ \varepsilon\beta_2 \\ \vdots \\ \varepsilon\beta_N \end{pmatrix} = \begin{pmatrix} a_1 & b_1 & c_1 \\ a_2 & b_2 & c_2 \\ \vdots & \vdots & \vdots \\ a_N & b_N & c_N \end{pmatrix} \begin{pmatrix} \varepsilon\beta_i \\ \varepsilon\alpha_i \\ \varepsilon\gamma_i \end{pmatrix} . \quad (4)$$

The following formula (6) defines Q.

$$Q = \sum_{k=1}^{N} \left\{ \varepsilon\beta_k - \left(a_k\varepsilon\beta_i + b_k\varepsilon\alpha_i + c_k\varepsilon\gamma_i \right) \right\}^2 . \quad (5)$$

The $\varepsilon\beta_i$, $\varepsilon\alpha_i$ and $\varepsilon\gamma_i$ are decided by the least square method with minimizing the Q.

From the relation of,

$$\beta \cdot \gamma - \alpha^2 = 1 , \quad (6)$$

ε_k is derived as following,

$$\varepsilon = \sqrt{\varepsilon\beta_i \cdot \varepsilon\gamma_i - (\varepsilon\alpha_i)^2} . \quad (7)$$

2.2 Measurement and result

The fluorescent screen made of aluminum oxide(Al_2O_3) doped with chromium oxide was installed on the beam line at the downstream of the quadrupole magnets. The magnets QD4, QF4 is located at the downstream of the accelerator No.3. Figure 2 shows the layout of the experimental setup. The fluorescence from this screen is observed with a CCD camera through a surface mirror. The image data was taken into the computer through the video image freezer.

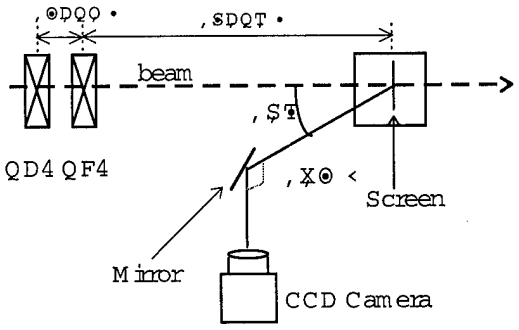


Fig. 2 Experimental setup layout

The image data were projected on the horizontal and the vertical planes. Because it can be assumed that a beam has a gaussian distribution, the least square method was applied. The function form used is given as follows.

$$f(x) = a \cdot \exp\left(\frac{-(x-b)^2}{2\sigma^2} \right) + c , \quad (8)$$

where a, b, c and σ are fitting parameters. The standard deviation of gauss distribution is used as the beam size.

Figure 3 (a) and (b) show the square of beam size as a function of the field gradient of the quadropole magnet lens. The solid lines show the fitting curves calculated by least square method using eq. (5).

The emittances at the exit of the linac are measured as 0.44 π·mm·mrad in the horizontal direction, and 1.3 π·mm·mrad in the vertical direction. The Twiss parameters are listed in the Table 2.

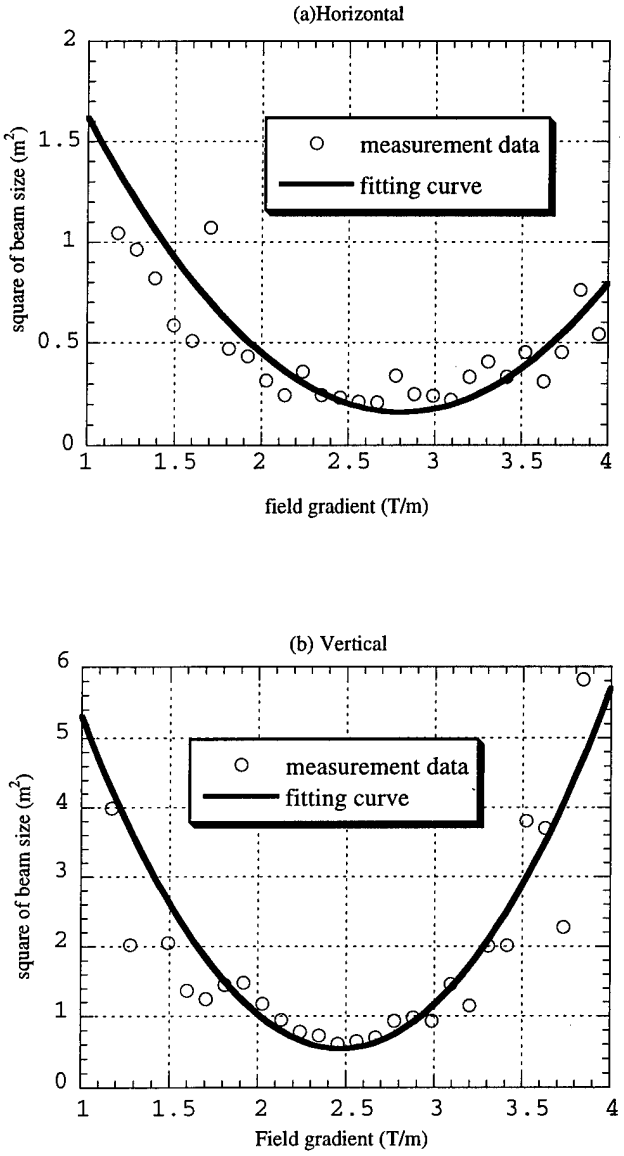


Fig. 3 Square of beam size in horizontal direction (a) and vertical direction (b). Markers show the measured data and a line shows a fitting curve.

Table 2. The measured twiss parameters.

	β (m)	α	γ(1/m)
Horizontal	3.3	-0.79	0.49
Vertical	5.5	-0.72	0.27

2.3 Discussion

In KSR the maximum of vertical Beta function and the mechanical aperture are 27 m and 36 mm, respectively. So the beam from the linac can be accepted by the KSR in vertical direction to say nothing of the horizontal.

Asymmetry in the horizontal and vertical emittance at the exit of linac suggests existence of alignment error of quadrupole magnet lenses.

3 IMPROVEMENT OF CHARACTERISTICS OF THE BEAM FROM LINAC

The Parametric X-ray is being observed using the beam from the linac [7]. In this experiment, the request for the beam emittance is quite severe on the target. But observation of the beam profile on the target is difficult due to the low current and low duty factor, though it is quite necessary for the beam tuning. In order to increase the duty factor the utilization of KSR as a stretcher is proposed [6][8].

The momentum spread of the beam has an influence on the beam size and the efficiency of the injection to the KSR. The measured momentum spread of 100 MeV beam is approximately 2 % even for the pulse width of 100 ns. It is slightly worse than the value obtained by the calculation. To make matters worse, beam pulse width becomes 260ns for 3-turn injection to the KSR whose harmonics number and the revolution frequency are 10 and 116.7 MHz, respectively. This increases the momentum spread. In order to improve the efficiency of the injection in terms of momentum spread, the best operating parameters are being searched using profile monitors, especially in the low energy section of the linac

REFERENCES

[1] "Construction of 100 Mev electron linac at I.C.R. and it's beam measurement.",(in Japanese), T. Sugimura, master thesis, Kyoto Univ., 1996.

[2] "Beam Profile Monitor Using Alumina Screen And CCD Camera", Y. Hashimoto.et al., The 8th symp. On Accelerator Science and Technology.

[3] "Emittance Calculations for the Stanford Linear Collider Injector", J.C.Sheppard, et al., IEEE Trans. Nucl. Sci. NS30 (1983) 2161

[4] "System of the 100 MeV Electron Injector for KSR", T.Shirai, et al., Bull. Inst. Chem. Res., Kyoto Univ., Vol73, No.1,1995

[5] "100 Mev Electron Linac in Kyoto university", T.Shirai, et al., Proc.20th Linear Accelerator Meeting in Japan.

[6] "Stretcher Mode of the Electron Storage Ring, KSR", A.Node,et al, Beam Sience and Technology, NSRF, ICR,Kyoto Univ., Vol2,1997

[7] "Observation of Parametric X-Ray Radiation from 80 MeV Electron Beams", Y.Hayakawa,et al, Beam Sience and Technology, NSRF, ICR,Kyoto Univ., Vol2,1997

[8] "Electron Storage and Stretcher Ring, KSR", A.Node,et al, Beam Sience and Technology, NSRF, ICR,Kyoto Univ., Vol1,1996

UPGRADING OF THE LNLS INJECTION SYSTEM

D. Wisnivesky°, F. S. Rafael, O. R. Bagnato, R. A. Picoli, A. C. Lira, A. R. Silva and C. Pardine.
Laboratório Nacional de Luz Síncrotron - LNLS/CNPq
Cx Postal 6192, 13083-970 Campinas SP Brazil
°also IFGW/ UNICAMP

Abstract

The energy of the injection linac and transport line into the LNLS synchrotron storage ring will be increased to 170 MeV by doubling the microwave power of the linac.

The new system will operate with 4 klystrons, delivering 25 MW pulses into each one of 4 accelerating SLAC-type structures. This paper describes the design and construction and tests of 2 new klystron modulators, microwave drive system, waveguides, as well as the upgrading of the power supplies for the linac and transport line magnets.

1 INTRODUCTION

At present, the injection system into the LNLS storage ring is made up of a 120 MeV linac followed by a short transport line [1]. Accumulation of current is done at low injection energy followed by ramping up to 1.37 GeV. This corresponds to almost a twelve-fold dynamic range. The combination of relatively low energy accumulation and large energy ramping limits the high energy current to around 50 mA. To increase the accumulated current at low energy as well as the ramping efficiency, a higher energy linac would be required. Consequently, it was decided to upgrade the injection energy by increasing the microwave power in the linac. By doubling the number of klystrons it would be possible to attain 170 MeV at the output of the linac, which according to the available ramping data, will suffice to overcome the most critical range of energies.

2 THE LINAC

The present linac, which has been in operation since the beginning of 1996, comprises 4 SLAC-type accelerating structures. Each structure is fed with 12 MW, 3 μs-long microwave pulses produced from two split-output 25 MW klystrons. The waveguide system has a short section with pressurized SF6, as required by the klystron manufacturer, separated by ceramic windows from the vacuum waveguide stretches. An extra ceramic window is located at the input coupler of each accelerating structure to avoid leakage of SF6 into the accelerators in case of a breakdown in the first window. Figure 1 shows a top and side view of the linac klystron number 1. The waveguide that goes into the first structure has a 26 dB coupler to derive power for the prebuncher. The second waveguide is provided with a high power phase shifter used to adjust the electron's energy gain. The second klystron and waveguide arrangements are similar to the first one except for the absence of the coupler.

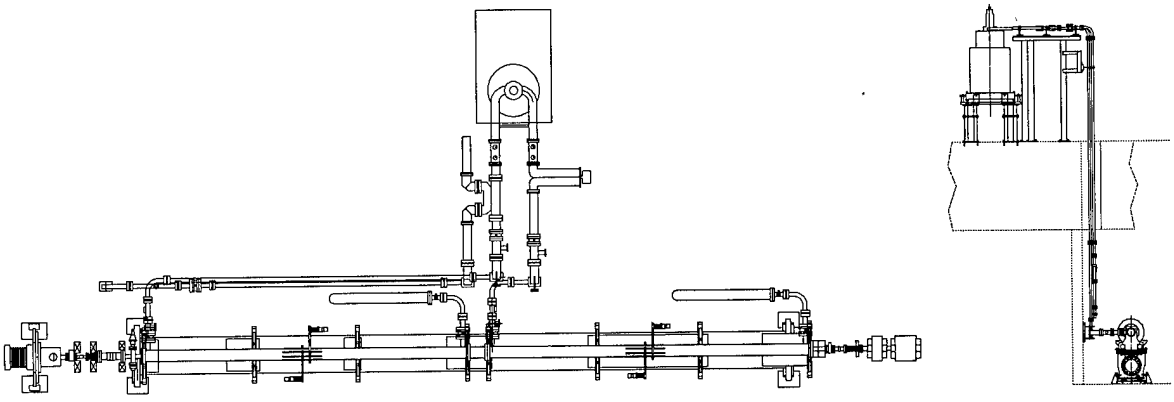


Figure 1: top and side view of the present linac waveguide system for the first and second accelerating structures.

0-7803-4376-X/98/$10.00 © 1998 IEEE

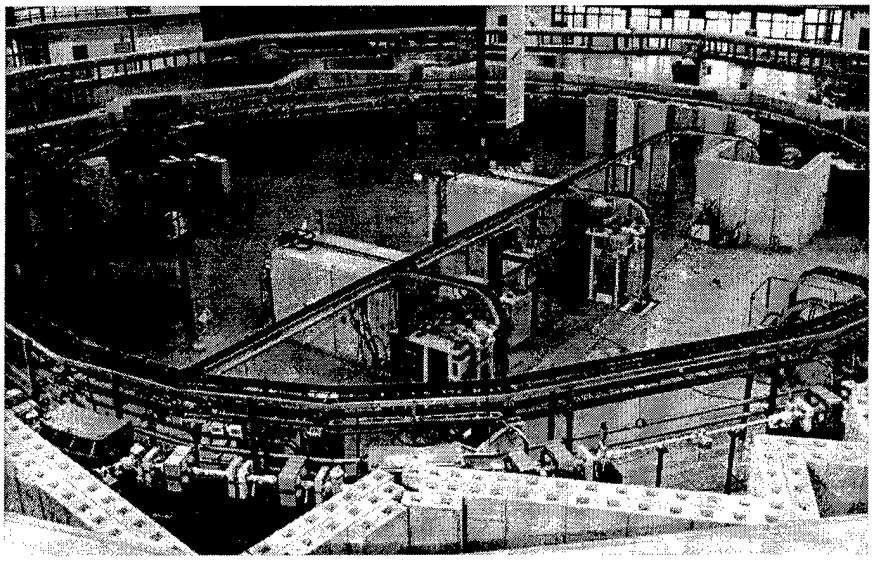


Figure 2: linac modulators and klystrons shown on the central part of the storage ring hall.

Figure 2 shows the distribution of linac equipment on the inside area of the storage ring. The linac is mounted in an underground tunnel below the inner part of the storage ring. At the storage ring floor level, occupying 1/3 of the available space, are the 2 high-power klystron modulators and the medium-power klystron and modulator. The new klystrons and modulators will be placed on the free space to the right.

3 THE UPGRADING

One way to increase the linac energy would be to enlarge the microwave power delivered to the accelerating structures. This could be done by adding 2 more 22 MW Klystrons, the corresponding high and medium power drivers and a new waveguide system. Since the linac does not have a buncher, the efficiency of the first structure is low and its energy gain is about 17 MeV, much smaller than the corresponding gain in the other three structures, which is about 34 MeV each. Thus, with 22 MW pulses, the expected energy increase will be more than 40% with the electron's energy reaching 170 MeV at the linac output. Measurements performed during ramping of the stored current show that 170 MeV is a safe starting point to increase accumulation and ramping efficiency to the desired values [2].

Figure 3 shows the new arrangement of the microwave system that distributes the power into the first and second accelerating structures. As can be seen, the output of the existing Thomson TV 2015B6 klystrons is combined in a 3 dB hybrid and delivered into the first structure, while a new ITT 8568 klystron, is used for the second structure. Similar arrangements are used for the third and fourth accelerating structures. The high power phase shifters, which are used at present to adjust the microwave phase between the 1-2 and 3-4 structures, will be used now to maximize the output power in the hybrid ports. The combining hybrids have been machined and brazed in house and are constructed and tested to operate in high vacuum. A ceramic window separates the SF6 region from the vacuum waveguide. The hybrid forth port is terminated with a full-power water load which requires SF6 and again is separated with a ceramic window.

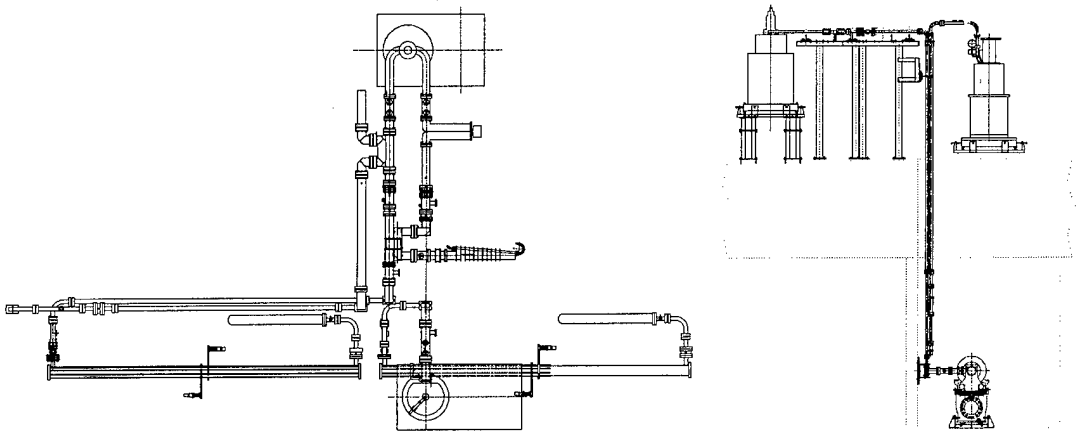


Figure 3: top and side view of the new arrangement of klystrons for the first and second accelerating structures.

Two new modulators will be added to the existing ones. Each one includes a pulse-forming network (PFN) comprising 24 HV capacitors which produces 3 μs-long pulses. The two existing HV power supplies, used with the present modulators, will be adequate to charge the 2 additional PFN, since the pulsing rate is very small. The pulsing rate is determined by the damping time of synchrotron oscillations (~ 6 s) and is typically about 0.6 Hz at 120 MeV injection energy, although it may go up to 7 Hz for waveguide conditioning. The PFN charging voltage stability has proven to be a critical parameter to keep the linac energy variations below 0.2 %, as required for low energy accumulation. Initially, the PFN voltage will be regulated using a standard d'Quing circuit. Later on, a regulated current source will be used to charge the PFN to full voltage. This should improve the stability of the klystron output power as well as avoid several other disadvantages of the resonant charging method such as: discharge of the PFN before triggering of the thyratron and mains current surges during the charging of the HV capacitor filter.

Special consideration has been given to the medium power microwave system. In order to drive the high-power klystrons, 250 W are needed for the Thomson klystrons, and 150 W for the ITT ones. A system of medium-power drivers is used to drive the high-power klystrons. These drivers use a series of 2 high-frequency EIMAC triodes model 8847, which can easily deliver 500 W of regulated peak power at the output.

4 CONCLUSIONS

A program to increase the linac injector energy has been initiated. This includes doubling the microwave power by including two more high-power klystrons. Two new pulse-forming networks and auxiliary equipment, providing 3 μs-long pulses, have been built and tested. The waveguide system, adequate for the new power system, is ready. This involved machining, brazing and testing 28 pieces including straight sections, curves, 3 dB hybrids, power monitors, arc detectors and vacuum flanges. The new medium-power microwave system, based on pulsed high frequency triodes is in the construction stage. The installation of the upgraded linac is planned to start in the second semester of 1997, during the next scheduled shutdown of the LNLS machine.

REFERENCES

[1] A. R. Rodrigues et al. "LNLS Commissioning and Operation". In these proceedings.

[2] A. R. Rodrigues et al. "Ramping Efficiency Studies in the LNLS Synchrotron Light Source". In these proceedings.

OPERATION AND STATUS OF THE ELETTRA INJECTOR LINAC

G. D'Auria, D. Daclon, P. Del Giusto, M. Milloch, A. Milocco, A. Pozzer, V. Rizzi, C. Rossi, A. Tomicich, Sincrotrone Trieste, Italy

Abstract

The injector Linac of the ELETTRA Storage Ring has been operating since 1993 providing a 1.0 GeV electron beam. Since that time many technical problems have been solved to increase the machine reliability by progressively upgrading all the machine sub-assemblies. Here the machine operation and the status of the upgrading program are described.

1 INTRODUCTION

Starting from 1993 the ELETTRA Linac is routinely running as injector for the Synchrotron Light facility ELETTRA, providing a 1.0 GeV electron beam. The machine is made up of two different parts: a 100 MeV preinjector and a booster Linac up to 1.0 GeV; a complete description of the whole machine can be found in [1,2]. Even if the Linac is mainly used as the storage ring injector, in the last few years additional scientific activities, have been considered, i.e. an IR/FIR FEL experiment set-up [3], as well as the installation of a movable OTR (Optical Transition Radiation) measurement station [4,5].

In the past year the machine was operated for roughly 3500 hours/year most of which, 90%, for injection and maintenance, while the remaining 10% has been used for the upgrading program and new activities.

In the same period, to improve the overall efficiency of the machine, the following upgradings have been undertaken[6]:

a) improving the poor reliability of some critical machine sub-assemblies via a re-design of the timing system, the control and interlock system ecc;
b) because the booster Linac is SLED equipped, the RF power and the pulse length from the klystron tubes have been set to avoid to exceed a gradient of 24÷26 MV/m on the accelerating waveguides which up to now seems to be a reliable value for convenient operation;
c) constant monitoring procedure for the klystron operating parameters and some other critical components has been implemented to prevent sudden replacements with consequent long machine downtime.

2 OPERATION

The ELETTRA Storage Ring is generally run on a three/four week basis followed respectively by one/two week shutdowns with roughly 82% of the total beam time for Users and the remaining for machine studies. Except for the machine study shifts, where the Linac is continuously kept in operation 24 hours/day, Storage Ring injection requires the Linac once per day in the morning with typically 1÷2 mA/sec injection rate. After injection the Linac is kept in operation for plant monitoring, machine optimization and service; FEL and OTR operations are generally implemented after the daily injection. The Linac can also be operated in single bunch mode, with 2 ns current pulses at 10 Hz, but for the present the storage ring is operated in multibunch mode. The main parameters for the injection and for the FEL operations are listed in the table below:

Measured parameters:	Injection	FEL
Operating Energy	1.0 GeV	30 MeV
Maximum Energy	1.1 GeV	75 MeV
Macropulse width	2 or 10÷150 ns	6 μsec
Macropulse repet. rate	10 Hz	10 Hz
Current	up to 30mA @ 70ns	> 100 mA @ 6 μsec
Energy spread	± 0.5 %	± 0.5%
Micropulse pattern	Single/Multi bunch	2 ns @ 25 MHz p.r.r.
Emittance	not measured	3.38 p mm mrad

Table 1: Injection and FEL operating parameters.

Table 2 reports some operating parameters for the RF plants together with the obtained energy gain per accelerating section. The energy gain of the pre-injector has been kept lower than the maximum achievable to increase the plant safety margin with a consequent improvement in reliability. The maximum reachable energy from the injector, without compromising the efficiency, is 1.08÷1.10 GeV, we have also operated at energies up to 1.2 GeV but in this case the higher electric field inside the accelerating structures causes many RF field breakdowns with an unacceptable increase in the machine downtime.

RF Plant	Klys. Filam. hours	RF Power (MW)	RF Pulse lenght (μs)	Energy gain (MeV)
MDK0	15247	38	2.0	85
MDK1	15893	41	2.7	134
MDK2	15386	43	3.0	152
MDK3	15656	42	2.7	145
MDK4	14975	42	2.4	141
MDK5	15115	43	3.0	150
MDK6	14407	42	3.2	156
MDK7	14305	42	2.5	139

Table 2: RF plant operation.

As is reported in the table 2, up to now we have operated each RF plant for roughly 15000 hours and at the the beginning of '97 we have also started the klystron replacement program. The first Thomson TH 2132A tube

0-7803-4376-X/98/$10.00 © 1998 IEEE

has been replaced in February '97 on the pre-injector RF plant MDK0; the tube has been kept operating for 14645 hours in approximately 6 years at 40 MW/3μsec power level. It is necessary to point out that the klystron failure was identified in the electric field breakdown inside the tube probably due to slow accumulation of cathode fragments on the anode surface during operation and that no considerable decrease in the microperveance was observed during the long operating period. During '95 to '96 we have also substituted five EEV CX 1536X thyratron tubes with more than a mean 10000 hours of operation.

The histograms in Fig.1 and Fig.2 give respectively the percentage per run of the Linac downtime during '96 as % of the total running hours, and the Linac sub-systems downtime statistics as percentage of the total Linac downtime.

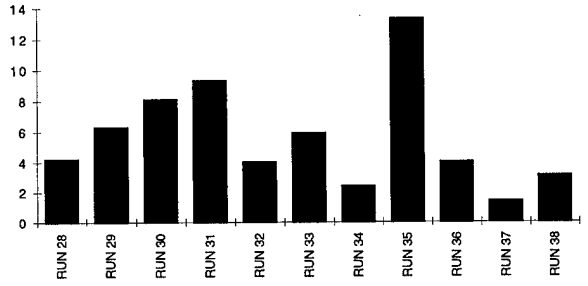


Figure 1: Linac overall downtime statistics during 1996.

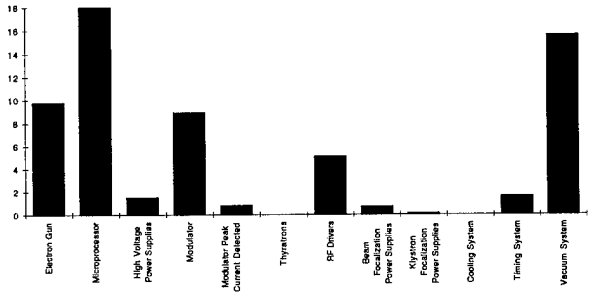


Figure 2: Linac subsystems downtime statistics (run 28÷38) in percentage of the total machine downtime.

It is necessary to point out that the anomalous 13.3% value of the run 35 results from a vacuum leak suffered by the last accelerating section (11.0% downtime) and that during run 30 we had serious problems on the electron gun (7.8% downtime, for the replacement of the cathode). Anyway, it seems reasonable to assume a mean value of 6 to 7 %, for the downtime of the machine during the whole '96. Looking at Fig.2 and taking into account the random contribution due to the section seven vacuum leak, and to the cathode replacement, it is necessary to point out that the main fault source still remains the machine control system. If we include the general service faults (electricity, water ecc.), the overall Linac contribution to the ELETTRA beam downtime in '96 goes up to roughly 9%.

3 MACHINE UPGRADING PROGRAM STATUS

As already said, in order to improve the low reliability of the machine, a re-design of some sub-systems has been undertaken.

The New Linac Timing System: to avoid suffering from problems deriving from trigger instabilities, a prototype of the new Linac timing system has been realized and tested on the field [7]. It is based on a local reference clock from a 50 MHz signal, synchronous to the ELETTRA master oscillator. The five kinds of trigger given to each of the eight RF plants are supplied by delay boards developed at Sincrotrone Trieste and housed in a VXI crate for noise immunity; they have fully programmable trigger outputs which can be delayed from 10ns up to 1.2ms, 10ns/step and each one can be independently interlocked to an external trigger. An in-phase synchronization with the start injection signal will allow a real bucket by bucket storage ring filling. At the end of '96 the first trigger board has been successfully tested on the machine and we plan to implement the whole system during '97.

The New Control and Interlock System: at present the control system operates with a centralized architecture and no special care had been given by the supplier to the signal distribution system as well as grounding and noise problems. The new control system [8] will be built with a spread architecture: all the machine will be divided into 9 blocks, which we will call plants and each plant will have an intelligent local processing unit where the low level software manages the local processes and talks with the high level software running on the workstations of the control desk, see Fig.3. The goal is to have a modular system keeping all the signals as close as possible to the related plant to prevent noise propagation and grounding interference between different plants. Up to now several prototype boards have been developed and are under testing, i.e. a fast sample/hold board for pulsed signals, a conversion board V/F, RF detecting boards, a programmable trigger board for the acquisition of pulsed signals out of the noise region, etc.; Fig.4 gives a block diagram of the analog signal acquisition layout. We plan to assembly a prototype of a complete VME acquisition crate on a plant before the end of this year. The interlock system, made up of a local relay chassis per plant, is now being assembled and we hope will be ready to start the tests on the first chassis before August.

RF plant upgrading: for the RF modulators we have completely developed a new heating chassis, completely integrated with the new control and interlock systems, for both klystrons and thyratrons; it allows to keep the filament heating currents at 80% of the nominal values during the machine stand-by to get both an extended tube life time and a very fast machine restart if necessary.

Moreover, a new pulsed 300W 3GHz RF solid state preamplifier for the klystrons has been developed in collaboration with Milmega LTD, UK and the first prototype is at present successfully running on an RF plant.

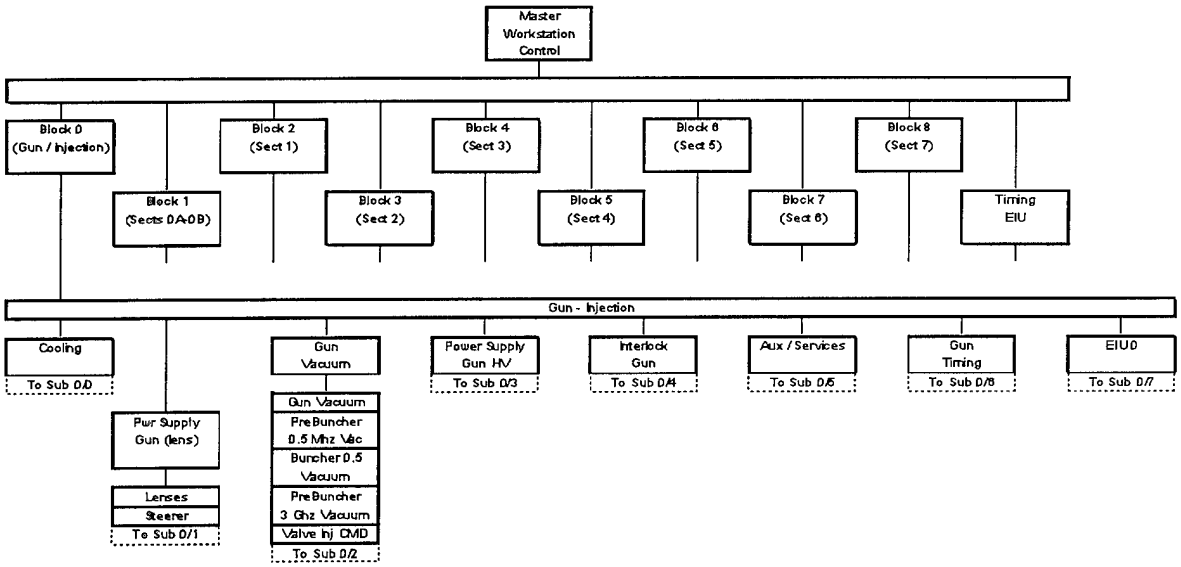


Figure: 3 Block diagram of the new machine control system with an exploded view of the block Ø.

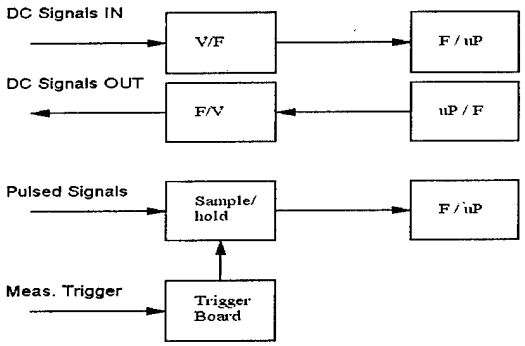


Figure 4: Layout of the analog signals acquisition scheme with voltage/frequency converters.

4 CONCLUSIONS

In the last two years, an intense activity program has been carried out on the ELETTRA Injector Linac to assure a reliable routine operation of the machine. The operating statistics for '96 show that the overall machine downtime has been kept inside an acceptable value (less than 10%) even before the full upgrading of the machine. By the first part of '98 we expect to implement the new control and interlock systems and thereafter we plan to set to work on the machine diagnostics for fast beam optimization. Moreover in the future we also intend to stimulate a growth of other scientific activities which can be carried out in a time sharing basis with ring injection.

REFERENCES

[1] C. Bourat et al., "The 100 MeV Preinjector for the Trieste Synchrotron" (IEEE Particle Accelerator Conference Proceedings, Chicago, USA, March 1989).

[2] D. Tronc et al., "The Elettra 1.5 GeV Electron Injector", (IEEE Particle Accelerator Conference Proceedings, San Francisco, USA, May 1991).

[3] R.P. Walker et al., "The FERMI FEL Project at Trieste", Nucl. Instr. & Meth. Vol. A 375, p. 252 (1996).

[4] C. Rossi et al., "A new OTR Based Diagnostic System for the Trieste Linac Injector of ELETTRA", this conference.

[5] D. Giove et al., "Optical Transition Radiation Measurements on the ELETTRA Linac", this conference.

[6] G. D'Auria et al., "The Elettra Injector Linac upgrading program", European Particle Accelerator Conference, Sitges, June 1996.

[7] M. Ferianis et al., "The New Timing System for the ELETTRA Linac" European Particle Accelerator Conference, Sitges, June 1996.

[8] L. Bulfone et al., "Design and Development of a New Control System for the ELETTRA Linac", European Particle Accelerator Conference, Sitges, June 1996.

BACKWARD TRAVELING WAVE ELECTRON LINAC*

Chen Huaibi, Huang Yuanzhong, Lin Yuzheng, Tong Dechun, Ding Xiaodong
Department of Engineering physics, Tsinghua University, Beijing 100084

Abstract

Future electron linacs will require high gradient acceleration. This paper studies the high shunt impedance backward traveling wave electron linac accelerating structure (BTW). Experiments were performed to prove the feasibility of the BTW structure.

INTRODUCTION

Wide use of electron linacs requires improved accelerating units. The direct approach of improving structure shunt impedance has been made these decades for SW structures. But similar progress has not occurred with the forward E-coupled TW structure. New proposals were recently made using the H-coupled backward TW geometry in the $3\pi/4$ mode and in the $7\pi/8$ mode [1]. The idea is to dissociate the RF coupling region from the beam-field interaction region as is the case in SW, to allow optimization. All modes between $2\pi/3$ and π can be chosen but a compromise must be found between high Q values and sufficient coupling for moderate slot apertures [2]. In addition, it is difficult to adjust the frequency of each cell. Therefore, the lower $3\pi/4$ mode was chosen to be.

Backward traveling wave properties

The BTW accelerator structure combines the advantages of traveling waves and standing waves. The forward TW electrically coupled on-axis structure (the classical "disk-loaded waveguide") is remarkable for its good adaptation and short filling time. The SW magnetically coupled off-axis is remarkable for its high shunt impedance. The BTW advantages are: (i) with reference to the forward TW, the presence of noses insures good shunt impedance, (ii) with reference to SW, BTW has no complicated coupling cells. However, since the RF input is near the beam exit and the buncher is near the RF exit, the field level depends on the line attenuation and for long pulses on the beam loading [3].

The Tsinghua university accelerate laboratory has developed a set of BTW accelerating tube. Initial experiments have demonstrated that the BTW accelerating structure is a promising accelerating structure.

$3\pi/4$ BACKWARD TW STRUCTURE DESIGN

General design

Figure 1 shows the structure which consists of 32 cells plus input and output couplers. These couplers are magnetically coupled to the structure and to the external RF wave guides. The working frequency is 2856 Mhz. The total length is 1.16 meter. The input coupler should be located at the beam exit for the backward TW structure.

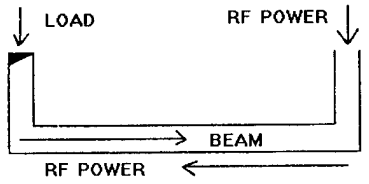


Fig.1 BTW structure

Cell design

Figure 2 shows the cell geometry with a beam aperture diameter of 7 mm and coupling slots corresponding to vg/c=1% for a bandwidth of 27 Mhz. The cells are all identical and are rotated by 90 degrees relative to each other to avoid having coupling slots face to face. The distance between noses, optimized using the SUPERFISH code for a half-cell geometry, is 21.4 mm for the optimum effective shunt impedance.

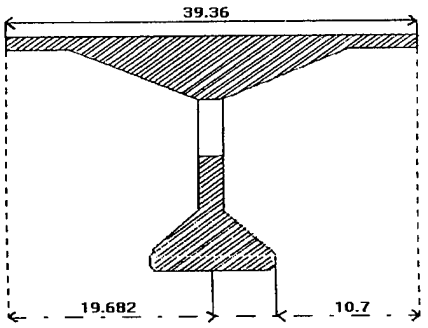


Fig.2 BTW cell geometry

Physical design

Figure 3 gives the phase oscillations curves, The radial beam envelope is shown in figure 4.

* Supported by the National Natural Science Foundation of China

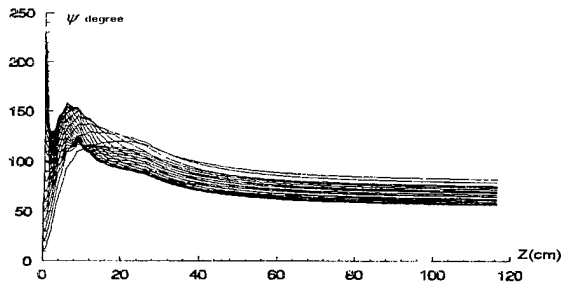


Fig.3 BTW acc. tube phase oscillation

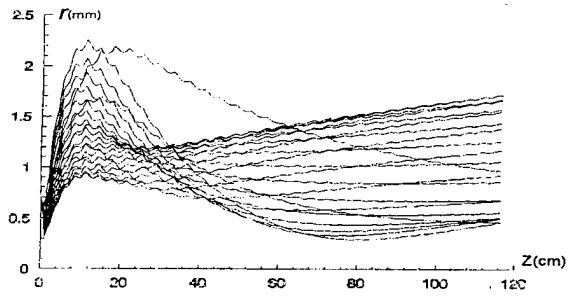


Fig.4 BTW acc. tube radial beam envelope

MATCHING AND TUNING

The tuning process is intended to adjust the phase shift in every cavity to the design value. The uniform cavity chain was tuned by tuning each cavity in the $\pi/2$ mode at a frequency of 2866 Mhz. The cavities will then operate at a frequency of 2856 Mhz in the $3\pi/4$ mode.

Matching is done by adjusting the dimensions of the coupler cavities so as to insure a low standing-wave ratio at the input and output of the structure. The accelerating traveling wave structure is obtained by adjusting the coupler so that the RF power arriving through a rectangular waveguide is coupled to the structure without reflection from the input aperture of the first cavity, the coupler cavity. The problem is how to carefully determine the dimensions of the coupling aperture. The basic ideas are based on Kyhl's method presented in a SLAC note [4], and Chanudet's method which was used at LAL [5].

COLD MEASUREMENTS OF THE STRUCTURE

$\rho \sim f$ curve

It is well known that $\rho \sim f$ curve in a TW accelerating tube is much flatter than that in a SW accelerating tube, especially in the near region of f_0, where ρ is nearly constant. The frequency range of VSWR below 1.2 should be 1~4 Mhz, with a minimum VSWR approximately equal to 1.0. For our BTW accelerating tube, the measured minimum VSWR is 1.02, and the frequency range of VSWR below 1.1 is 2 Mhz. (Figure 5)

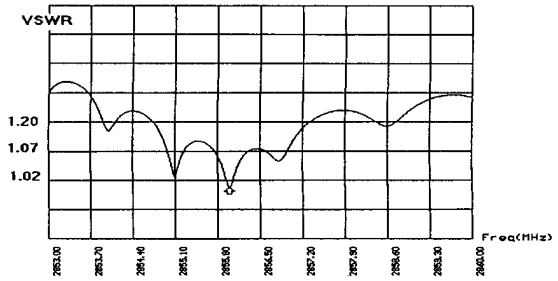


Fig.5 $\rho \sim f$ curve of the BTW acc. tube

TW field Distribution

Figure 6 shows the measured result of the electrical field distribution on-axis. Including the input and output couplers, the measured attenuation coefficient is A=0.24 Np.

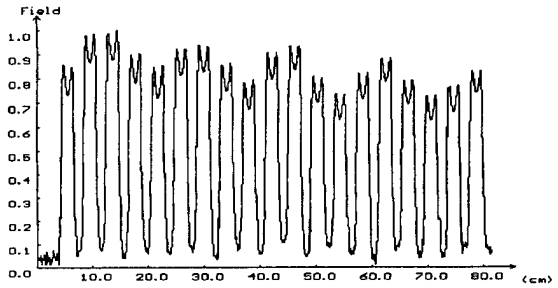


Fig.6 BTW structure electrical field distribution

Other microwave parameters

RF parameters of H-coupled cells must be measured to know their shunt impedance. The Q and R/Q factors of the cavity chain were measured with a coupling slots angle of 30 degrees in the $3\pi/4$ mode for the SW. The dispersion curve is shown in figure 7.

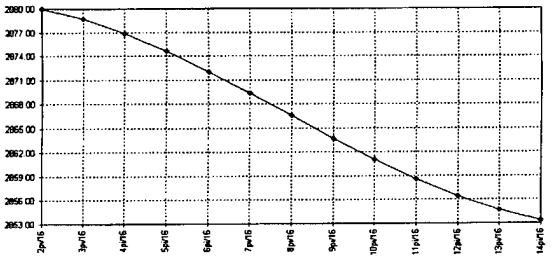


Fig.7 BTW structure dispersion curve

The effective TW shunt impedance can be obtained from these measurements using the classical relation: Zeff(TW)=2Zeff(SW). and the following cell RF parameters, Q=13000, R/Q=7056 ohm/m, and Zeff=85.7 Mohm/m. Table 1 gives a comparison of the measurement data with the design values.

Table1 Comparison of measured data with design values.

	calculated values	experimental results
shunt impedance	103.2 $M\Omega/m$	85.7 $M\Omega/m$
group velocity	0.82% c	0.81% c
Q value	13000	13000
coupling coefficient	1%	1.01%
attenuation coefficient	0.286 $/m$	0.329 $/m$

COMPARISON OF THE BTW STRUCTURE WITH THE DISK-LOADED ACCELERATING TUBE

Table 2 gives a comparison of the design parameter for a 9 MeV $3\pi/4$ H-coupled (BTW) accelerating tube and the $2\pi/3$ E-coupled (disk-loaded waveguide, i.e. FTW) used as a radiation source for inspecting large containers at customs.

A 40 kev electron beam with a converging will be to be injected into the BTW accelerating tube. The design values of the electron beam focal spot size are less than 3 mm diameter and a pulsed beam current of 170 mA with 3.5 MW input RF power.

CONCLUSION

The design presented in this paper adopts a backward traveling wave structure to bunch and accelerate electrons proving the feasibility of developing the BTW accelerating tube. The BTW structure has several advantages. The BTW structure shunt impedance is higher than that of a disk loaded waveguide. In addition, the BTW is a backward wave structure, which is beneficial for efficiently using the microwave power, especially in the bunching section which has varying phase velocity.

The cold measurements data are now available for the design and the RF adjusting of a $3\pi/4$ H-coupled backward TW structure. Results of this research suggests that the backward traveling wave accelerating structure is preferable, because BTW has a higher effective shunt impedance, a shorter filling time and is more stable to operate.

Table 2 : Comparison between $2\pi/3$ FTW and $3\pi/4$ BTW

	BTW accelerating tube	FTW accelerating tube
coupling pattern	magnetic coupling	electric coupling
operating mode	traveling wave	traveling wave
operating frequency	2856 Mhz	2856 Mhz
operating mode	$3\pi/4$	$2\pi/3$
shunt impedance	85.7 $M\Omega/m$	62 $M\Omega/m$
coupling coefficient	1%	2%
Q factor	13000	14200
group velocity	0.82% c	1.6% c
attenuation factor	0.3 $/m$	3 db
total length	1.16 m	2.21 m
buncher length	20.8 cm	42.6 cm
buncher number	9	17
capture factor	60%	80%
peak field	15.7 MV/m	6.7 MV/m
average field	10 MV/m	5 MV/m
external focusing (coil)	without	4

A 9 MeV BTW accelerating tube operating in the $3\pi/4$ mode has been designed with a 1.16 m single section and a buncher as radiation source for inspecting large containers at customs.

REFERENCES

[1] R.H.Miller, SLAC-303, 1986, P200.

[2] P.Girault, " 4pi/5 backward TW structure tested for electron linacs optimization ", EPAC88, 1988, P1114.

[3] D.Tronc, " A new electron linac injector design up to 200 MeV ", IEEE PAC1991, 1991, P3008.

[4] E.westbrook, " Microwave impedance matching of feed waveguide to the disk-loaded accelerator structure operating in the 2pi/3 mode ", SLAC-TN-63-103, December 1963.

[5] M.Chanudet, " Matching of the coupler cavity to traveling wave structures at any operating mode ", LAL/RT 93-06, June 1993.

14MeV SINGLE-SECTION SW GUIDE FOR MEDICAL ACCELERATORS[1]

Jin Qingxiu, Lin Yuzheng, Tong Dechun, Li Quanfeng, Yang Yue, Sun Jingqing, Hu Shaoguang
Chen Bingyi*, Li Yuezeng*, Sun Baoyu*, Zou Yang*, Hu Wensheng*
Department of Engineering Physics, Tsinghua University, Beijing 100084
*Beijing Institute of Electronics & Vacuum Technology, Beijing 100016

Abstract

A 14MeV, on-axis coupled, S-band waveguide for medical accelerators was built and tested between 1993 and 1995. The accelerator design, the results of cold and hot tests and the beam performance are given in this paper.

INTRODUCTION

Recently electron linacs are widely used in China and low energy medical electron linacs with energies of from 4 to 10 MeV can be manufactured by several organizations in China. However, new medium and high energy electron linacs must be developed to meet the demand in radiotherapy. There is also evidence that certain tumors can be more effectively treated with a combination of low- and high- energy photons or of photons and electrons. As a result, a single machine that can produce both low and high energy x-rays together with a wide range of electron energies would be very useful. Such multi-energy accelerators are currently offered by foreign companies. Based on our past works, we began development of multi-energy electron linac structures for the domestic market in 1991. A single-section 14 MeV standing-wave accelerating structure providing two X-ray modes and several electron modes was the first one developed for medical use in China.

GENERAL DESCRIPTION

The guide was designed for X-ray energies of 6 or 15MV and electron beam energies of from 6 to 14MeV. The guide has a single 1.45m long section, operated in the $\pi/2$ mode at 2998MHz. Its microwave of power source is a S-band magnetron, MG5260, whose output power can be adjusted to a maximum peak power of 2.6MW. The beam energy is varied by changing the input RF power, injection voltage and injected current.

The cavity configuration must be carefully optimized to obtain 14MeV beam energy within a 1.45m long accelerating guide. The optimized shunt impedance is as high as 105 MΩ/M but our experience shows that the practical impedance is at most 85% of the theoretical value.

The guide contains 30 accelerating cells with 29 coupling cells, divided into three homogeneous regions with distinctive phase velocities and field configurations. These regions respectively contain 1, 3 and 26 accelerating cells.

The electron gun has a triode structure with a 8mm diameter cathode. The gun emits up to 1A of beam current over a voltage range of 7 to 15KV. A 270° deflection system was adopted for achromaticity and small beam spot size.

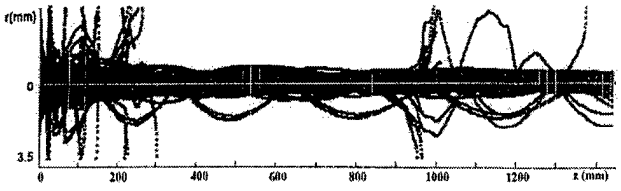


Fig.1 Radial multiparticle track for 15MV X-ray mode without any focusing solenoid

PHYSICAL DESIGN

The design of the buncher and the selection of the operating parameters are compromises between the two X-ray energy modes and are meant to optimize the spectrum sharpness at 12MeV. As a result, the capture efficiency for the 6MV mode is relatively low. For the 6MV mode, the input power was reduced and the beam loading was increased while maintaining the rf phase focusing.

The longitudinal and transverse beam dynamics were calculated using the LONGN and TRSVN [1] codes. The result was checked using a multiparticle trace code. Fig.1 shows the radial multiparticle track for the 15MV X-ray mode without any focusing solenoid.

Tables 1 and 2 summarize the design characteristics and parameters for each operating mode.

Table 1. Design characteristics

length	1.45 m
frequency	2998 MHz
power	2.6 MW
coupling	1.7 fixed
shunt impedance	89 MΩ / m
injection voltage	7~15 kV
coupling coefficient k	3.3%

[1] Supported by the Major Research Project of the Eighth-Five Plan (1991~1995) of China

0-7803-4376-X/98/$10.00 © 1998 IEEE

Table 2. Design parameters for each operating mode

parameter	x-ray mode		electron mode				
Beam energy(MeV)	6	13.5	6	8	10	12	14
Injection voltage(kV)	15	7	10	10	10	10	7
Injected current(mA)	900	130	45	36	26	17	17
Peak power(MW)	1.80	2.20	0.9	1.0	1.1	1.5	2.2
Beam current(mA)	120	35	5	5	5	5	5

TUNING AND COLD TEST

The mode spacing of the coupled cavity chain for the $\pi/2$ mode can be expressed as $k\pi/2N$, where k is the cell-to-cell coupling factor and N is the total number of cells in the chain. For a long cavity chain with 59 cells, the coupling factor k should be large enough so as to ensure stability of operation. However, increasing k can cause a decrease in the figure of merit, Q_0, for the entire tube, thus causing the shunt impedance, ZT^2, to decrease. The coupling factor was experimentally determined to be slightly more than 3%, which would not cause a decrease in ZT^2. Also, the dispersion diagram shows that the group velocity for the guide is as high as 0.04, which is enough for phase stability and to meet the tolerance requirement.

The location of the coupler affects the passband performance. The PPDW code was used to analyze and calculate the passband characteristic of the input coupler when placed in different cells. The PPDW code which is based on equivalent circuit theory, was developed to analyze microwave characteristics of arbitrarily composed, coupled cavity chains. Figs. 2 and 3 show the modules of complex reflection as a function of frequency for the coupler located in the 1st and the 21st cavities respectively. Locating the coupler in the 21st cavity suppresses the modes immediately adjacent to the $\pi/2$ mode. The coupler was adjusted for overcoupling of 1.78 at zero beam loading as a compromise between the two x-ray modes.

The guide design has the field configuration of the guide separated into three steps. Therefor the coupling factors , k , of the coupling cell to both accelerating cells to the coupling should vary at the location of the field configuration variation. The coupling factors were varied by modifying the coupling apertures on both webs of the second and eighth on-axis coupling cells.

The shunt impedance and the field flatness of the entire guide were measured using the bead-pull technique. An automated phase-lock frequency tracking system and a precise and accurate computerized data acquisition system were developed for the measurement. The field distribution of a 1.45m long accelerating structure was measured in 3 minutes with a precision of 0.1 KHz and a step size of 0.5mm. Fig.4 shows the measurement system schematic drawing. Fig. 5 shows the measured and the theoretical results for the electric field distribution along the beam axis of the guide.

The tuning results for the guide are: the stop band is less than 20KHz; the frequency uniformity of various cavities is better than 200KHZ; the shunt impedance of the entire guide is 89 MΩ/M; and the field flatness in the accelerating section is better than 3%.

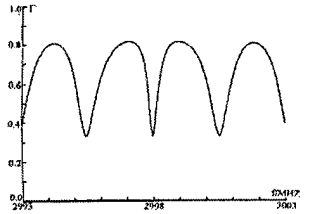


Fig.2 Rf power fed into the A_0 cavity

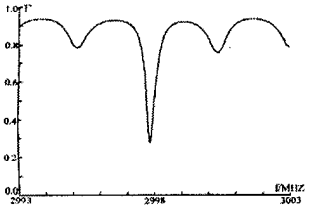


Fig.3 Rf power fed into the A_{22} cavity.

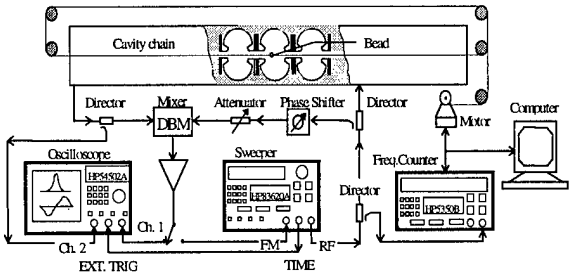
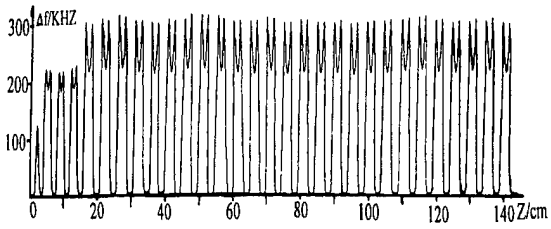
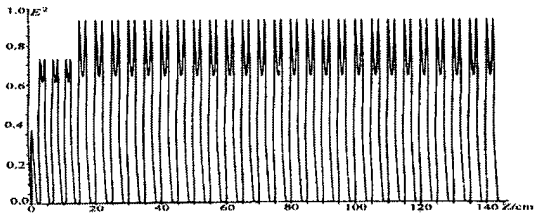


Fig.4 Bead-pull measurement system



(a) Measured



(b) Calculated

Fig.5 Electric field distribution along the beam axis of the guide

MECHANICAL DESCRIPTION

Since our brazing technology can control frequency errors to within $\pm$ 0.3MHz, the guide did not need further tuning after brazing. Fig.6 shows the entire guide after brazing.

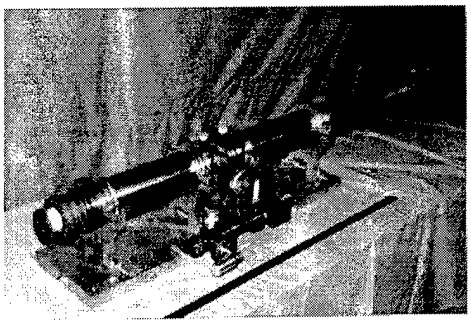


Fig.6 The brazing guide

The rf horn assembly is a short section of standard OFHC S-Band waveguide brazed into the coupler. The rf assembly has a vacuum port cut into the side and a ceramic rf window braze assembly welded to it.

The final assembly of the guide includes an electron gun, a rf window, a 2 l/s vacuum pump, a vacuum envelope for beam transport through the 270° bending magnet, support tubing, and an anti-dark current solenoid near the buncher end.

The structure was designed to be baked-out and sealed-off; however, several bakeable flanges were also used at the gun, the 270° deflection system, and the pinch-off. The guide was baked-out and pinched-off initially. Any component that fails can be easily replaced. After baking out a cold vacuum of 1x 10^{-6} Pa is typically achieved.

HIGH POWER TEST

Table 3 compares the calculated result and the measured beam characteristics.

Table 3

beam	beam energy/MeV		beam current/mA	
	calculated	measured	calculated	measured
X-ray	6	6.2	120	160
Electron-beam	14	15	5.0	28

The beam energy was measured using the aluminum absorption method. The beam current was measured using a Faraday cup and a beam transformer. The guide was shown to provide a 15MeV electron beam, thus satisfying the design requirement.

The measured beam spot size was less than 1.2x1.8cm after the beam passed through a 1.45m long accelerator guide and a 270° deflection system without any focusing solenoid. The focus is the result of rf phase focusing, an asymmetrical first bunching cavity and converging beam injection.

Commissioning tests of two 14MeV SW guides have been completed in two domestic medical linacs. One of them is being installed at a hospital in Beijing by the Beijing Medical Equipment Institute.

REFERENCES

[1] Yue Yang, Research on low-energy standing-wave electron linear accelerating structure, Th. M, (1994)

[2] Victor A. Vaguine, Electron linear accelerator structures and design for radiation therapy machines, IEEE Transactions on Nuclear Science, Vol. NS-28, No.2, p1884-1888, (April, 1981)

[3] Kenneth Whitham, 20 MeV S-band standing waveguide, IEEE Transactions on Nuclear Science, Vol. NS-22, No.3, p1328-1333, (June, 1975)

[4] Eiji Tanabe, Gard Meddaugh, Variable energy standing wave linear accelerator structure, p191-193

[5] Kenneth Whitham, 12 MeV S-band standing waveguide, IEEE Trans. on Nuc. Sci., Vol. NS-18, No.3, p542-544

A PORTABLE X-BAND ON-AXIS STANDING WAVE LINAC STRUCTURE

Sun Xiang, Tong Dechun, Jin Qingxiu, Lin Yuzheng, Sun Jingqing, Hu Shaoguang, Du Taibin, Duan Xiuming
Department of Engineering Physics, Tsinghua University, Beijing 100084, PRChina
Chen Bingyi, Li Yuezeng, Zou Yang, Hu Wensheng
Beijing Institute of Electronics & Vacuum Technology (BIEVT), Beijing 100016, PRChina

Abstract

A portable X-band on-axis standing wave electron linear accelerating structure has been developed that is suitable for portable radiation therapy and radiography. The phase-focusing technique is used. The design parameters of a 2 MeV, X-band, on-axis coupled, SW accelerating guide operated in the $\pi/2$ mode is described. A prototype 150 mm long structure has been machined, brazed and sealed, and the experimental data of the cold tests and beam tests are presented.

INTRODUCTION

The many advantages of using higher RF frequencies for electron linear accelerators include higher shunt impedance, higher breakdown threshold level, smaller size and short fill time. In addition, increasing the RF frequency increases the accelerated beam energy for a fixed input RF power [1][2]. An extremely small accelerator structure with high shunt impedance is needed for medical and industrial applications. The Accelerator Laboratory at Tsinghua University, which has extensive experience with S-band electron linacs, having studied X-band SW electron linacs since 1991, is currently developing a prototype 2 MeV, X-band SW accelerating guide. One objective is to study the fabrication and tuning techniques of X-band accelerating structures. Work is also proceeding on the development of a portable 6 MeV X-band SW accelerating structure for medical electron linacs.

STRUCTURE OPTIMIZATION

Three types of X-band accelerator structures have been developed, the disc-loaded structure[1], the side-coupled structure[1], and the coaxially coupled structure[2][3]. However, the Accelerator Laboratory prefers the on-axis structure for X-band SW linac based on our experience of fabricating S-band structures. This structure has advantages similar to the coaxially coupled structure which offers a significantly smaller diameter than the side-coupled structure. In addition to small size and less weight, the cylindrical symmetry structure is simpler to machine and braze.

The two important limits that influence the effective shunt impedance are the beam aperture radius and the thickness of the copper web between the accelerating cavities. Decreasing the beam aperture radius and the thickness of the copper web increases the effective shunt impedance. However, the size of the beam hole is limited by the beam transverse transmission. Our dynamic simulation calculations showed that the beam aperture diameter should be 4.0 mm. The web thickness is related to the coupling cavity which must be inserted between the two accelerating cavities in the on-axis coupled structure and to thermal conductivity requirements. The web thickness was chosen to be 2.8 mm and the coupling cell length was chosen to be 1.0 mm.

As shown in Table 1, the on-axis structure offers about the same shunt impedance and outer diameter as the coaxial structure. Although the theoretical effective shunt impedance of the on-axis structure is less than for the side-coupled structure, our experience shows that the actual shunt impedance of both structures are similar with S-band linacs.

Table 1. Parameters for X-band (9300 MHz) Accelerator Structures

Structure	Disc-loaded	Side-coupled	Coaxial	On-axis
Type of Operation	TW	SW	SW	SW
Mode of Operation	$2\pi/3$	$\pi/2$	$\pi/2$	$\pi/2$
Effective Diameter (cm)	3.2	5.3	3.2	3.2
Effective Shunt Impedance(MΩ/m)	80	145	130	133
Beam Aperture Diameter (mm)	8.0	4.0	4.0	4.0

PHYSICAL DESIGN

A 2 MeV X-band on-axis SW accelerator was designed with a guide that is approximately 150 mm long and with 11 accelerating cells and 10 on-axis coupling cells. It uses 5 accelerating cavities as a buncher. The structure is operated in the $\pi/2$ mode with an average effective shunt impedance of 121.4 MΩ/m. The RF power is supplied by a tunable coaxial magnetron of 1.0 MW peak power at X-band (9305 to 9325 MHz). The pulse coaxial magnetron was developed by BIEVT.

To minimize the size and weight of the structure and to improve the beam spot as well as the transmission, the phase-focusing technique was used without a bulky, external magnetic focusing device[1][2][4]. It is well known in alternating phase focusing, that the electrons alternate between ahead of the accelerating crest where they are

0-7803-4376-X/98/$10.00 © 1998 IEEE

longitudinally focused and behind the crest where they are radially focused. By choosing the right phase velocity taper and by tapering the magnitude of the buncher field levels from cavity to cavity, the RF field in the buncher region provides transverse focusing as well as longitudinal bunching and acceleration. An injection voltage of 16 kV is used with a converging injection beam. The electron beam focal spot size is less than 1.0 mm and the pulsed beam current is 75 mA with 0.6 MW input RF power. The capture efficiency is about 30% . Some performance data for the guide is shown in Fig. 1 to Fig. 4.

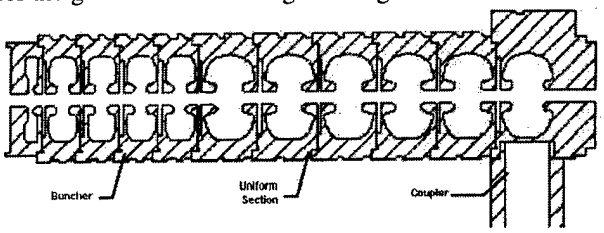


Fig. 1. Schematic Illustration for On-axis Structure

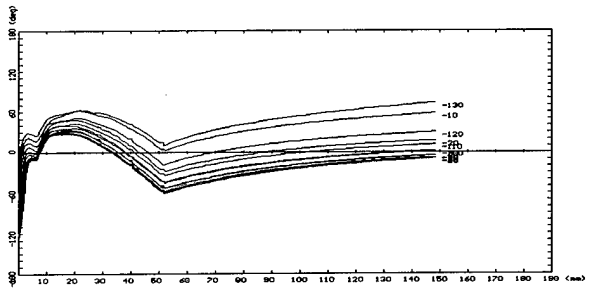


Fig. 2. Longitudinal Orbits for Various Input Phases

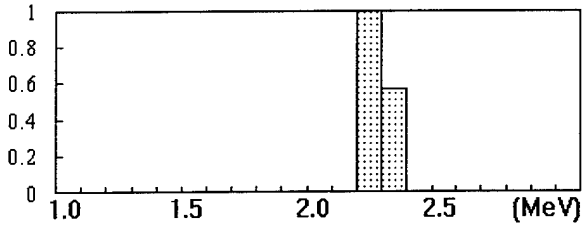


Fig. 3. Energy Spectra

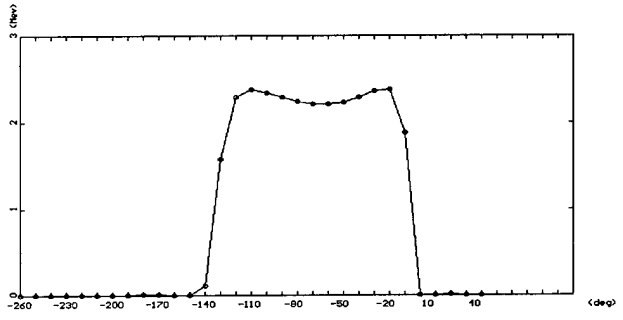


Fig. 4. Energy Spectra as a Function of Input Phase

TUNING AND LOW POWER TESTS

After careful machining, the cavities were assembled and tuned. The fabrication and tuning of the prototype X-band structure were strongly interrelated and must progress carefully due to the high operating frequency. The frequencies were measured using a HP8757D network analyzer. Both accelerating and coupling cavities were isolated and measured by inserting two probes into the cavity drift tubes one by one. The two probes serve to short out adjacent cavities as well as the RF transmission. The tuning was iteratively repeated since the states of adjacent cavities has some effect on these measurements. The position and size of the probes greatly influences the measurements; therefore, the probe optimization is very important.

The guide tuning results are: The frequency uniformity is $\pm$ 1.5 MHz for the accelerating cavities and $\pm$ 2.0 MHz for the coupling cavities. The stop band is less than 2.0 MHz. The nearest neighbor coupling, k_1 for accelerating section, is 3.7%. The nearest neighbor coupling factors for the buncher section were adjusted to meet the field configuration. The bead pull data is shown in Fig. 5. The passband characteristic of the guide is shown in Fig. 6. Before brazing, the measured Q of the guide was 6050. The coupling factor of the waveguide coupler, β, is 2.12 at zero beam loading.

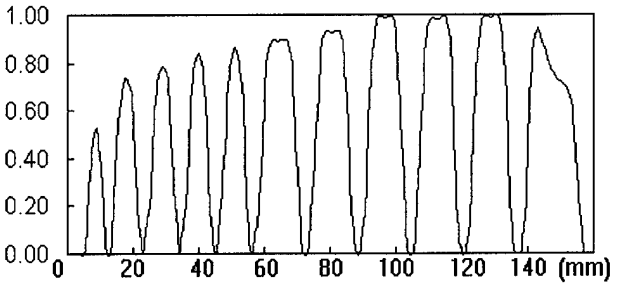


Fig. 5 On axis Bead Drop Data

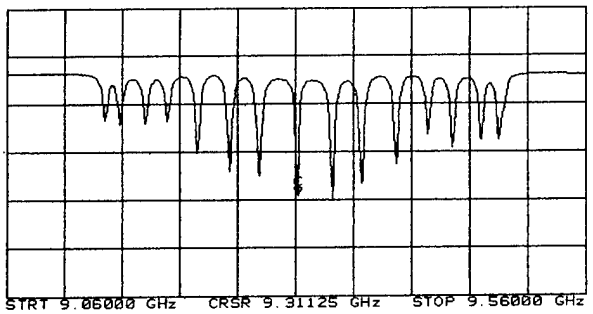


Fig. 6 Modules of Complex Reflection vs. Frequency

The brazing was done in collaboration with BIEVT. The electron gun, RF waveguide, RF window, glass window and ion pump were designed and fabricated at BIEVT. The overall structure was then brazed, evacuated and sealed. No post-braze tuning of the guide was done. The dispersion curves for the guide are shown in Fig. 7.

The final measured Q for the guide is 7100 with a β of 2.24. The average shunt impedance for the whole guide is about 105.0 MΩ/m. Fig. 8 is a photograph of the 2 MeV On-axis SW Guide.

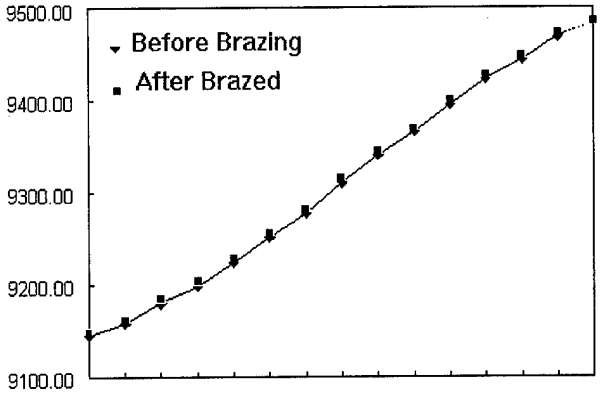


Fig. 7 Dispersion Curve for On-axis Coupled SW Accelerator Structure

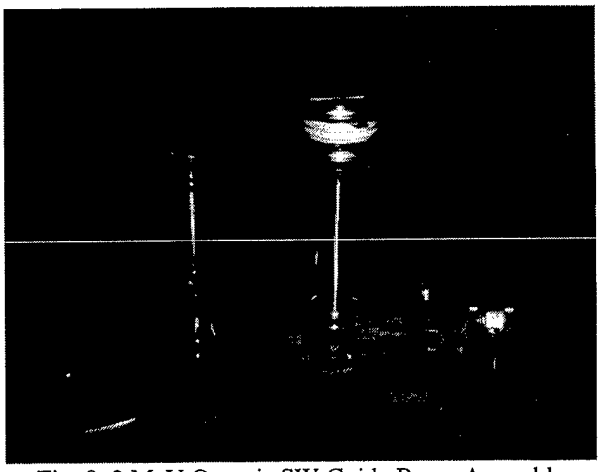


Fig. 8. 2 MeV On-axis SW Guide Braze Assembly

BEAM TESTS

The structure beam tests have been completed in Tsinghua University Accelerator Laboratory in collaboration with BIEVT and the China Institute of Atomic Energy. The design parameters and the experimental data of the beam tests are shown in Table 2.

Table 2. System specifications

	Theory	Experiment
Electron Energy (MeV)	2.3	2.4
Electrical Length (mm)	148.5	148.5
RF Frequency (MHz)	9300.0	9316.5
RF Peak Input Power (MW)	0.60	0.68
Injection Voltage (kV)	16	17
Capture Efficiency	30%	30%
Peak Beam Current (mA)	75	>90
Target Spot Size (mm diameter)	<1.0	<0.7

REFERENCES

[1] R.G. Schonberg, et al., "Portable, X-Band Linear Accelerator System", IEEE Trans. NS-32, No. 5, pp. 3234-3236, Oct., 1985

[2] E. Tanabe, et al., "An X-Band Coaxial Standing Wave Linear Accelerator Structure", 1986 Linear Accelerator Conference Proceedings, Stanford, CA, USA, pp. 455-457 1986.

[3] E. Tanabe, et al., "A Small Diameter Standing Wave Linear Accelerator Structure", IEEE Trans. NS-32, No. 5, pp. 2975-2977, Oct., 1985.

[4] R.H. Miller, et al., "RF Phase Focusing In Portable X-Band, Linear Accelerator", IEEE Trans. NS-32, No. 5, pp. 3231-3233, Oct., 1985.

BEIJING RADIOACTIVE NUCLEAR BEAM FACILITY(BRNBF)

The BRNBF project group (written by Guan Xialing)
China Institute of Atomic Energy
(P.O.Box 275 Beijing, 102413)

1. INTRODUCTION

It is well recognized that the radioactive nuclear beam (RNB) promises a bright future in significant areas of nuclear physics and related sciences[1] . Proposals for RNB facilities have been put forward in many countries, that are in various stages of completion.

In order to promote the fundamental and applied research of nuclear physics in the foremost frontier, China Institute of Atomic Energy (CIAE) has proposed the Beijing Radioactive Nuclear Beam Facility (BRNBF), which is an extension of the existing HI-13 tandem accelerator. The proposed BRNBF is an ISOL type radioactive nuclear beam facility.

The plan view of the Beijing Radioactive Nuclear Beam Facility is shown in Fig.1.

A new intensity proton cyclotron accelerator will be built to provide proton beam with 70 MeV 200μA. A thicktarget/ion--source system will produce the interesting exotic radioactive nuclear beam which will then be isotopically separated by an on-line mass separator. The beam then pass through a charge exchange canal to inject its charge state to negative ion and to inject into the HI-3 tandem.

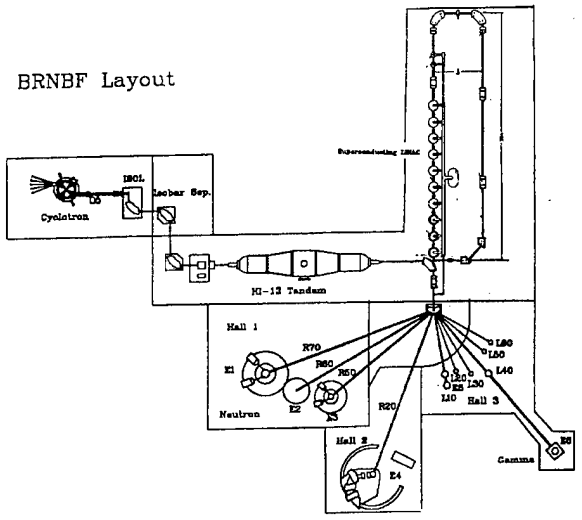


Fig.1. plan view of the BRNBF

A super conducting heavy ion linac accelerator will be built as a post accelerator, which can give the energy gain of 17MeV/q. By this facility an intensity of more than 10^9 pps, 5MeV/u radioactive exotic ion beam for mass up to A=140 will be expected. Investigation has shown that the BRNBF is technologically feasible in China. The BRNBF will be an advanced and competitive facility on the world in the first decade of next century[2]. It will be a major tool for searching for new nuclides and studying the nuclear structure physics, nuclear astro-physics, nuclear reaction mechanism, atomic physics, material science, life science as well as other application of nuclear physics.

The three accelerators of BRNBF can be operated in five different modes.

a) Single cyclotron operation.
b) Single tandem operation.
c) Combination of tandem and linear .
d) Combination of cyclotron and tandem.
e) Combination of three accelerators.

II. PRE-ACCELERATOR CYCIAE 70

As the pre-accelerator, a new proton cyclotron will be built on the west to pre-existing HI-13 tandem accelerator, and will provide 70MeV, 200μA proton beam, which will be used to bombard thick targets for producing radioactive nuclei.

The new cyclotron machine which called CYCIAE 70 combines the advantages of solid-pole and separator sector cyclotrons of three system: external negative hydrogen ion source and injection system; magnet and RF system; stripping foil and beam transportation system.

Since 1995, some R & D programs for CYCIAE 70 have been carrying out. For example, the beam dynamics, the magnet computation and test of Dee and RF cavity model have been carried out. In addition, 3.5 mA negative hydrogen ion source has been developed in CIAE.

III ISOL SYSTEM

The mass separator is composed of the target/ion source system, match lenses, 90° magnet with ρ=1.3m and charge exchange canal. Whole equipment of the spectrometer are located on a high-voltage platform with potential up to 300kV. The platform connect the primary proton beam line and the isobar separator system beam line by two accelerator tubes. The layout of the ISOL system is shown in Fig. 2.

Production rates for various exotic elements such as C, O, F, Na, Si, P, Cl, K, Cu. As, Nb, Tc, Rh, up to In using (p,xn), (d,xn) reactions by proton, or deuteron beam at 50-70 MeV are the region of 10^8--10^{11} atoms/pμA/s. In general, the production efficiency of primary beam to exotic nuclei is about 0.1%. The conversion efficiency of exotic atoms to charged ion inside the ion source can be estimated as 30%. The efficiency of beam transportation from ion source, through on-line isotope separator, to the entrance of tandem accelerator is about 50%. In addition, most elements which have lower electron affinities are difficult to be ionized into negative ions directly. They have to pass through the charge exchange canal to convert

0-7803-4376-X/98/$10.00 © 1998 IEEE

the charge state from positive to negative. The conversion efficiency is about 30%.

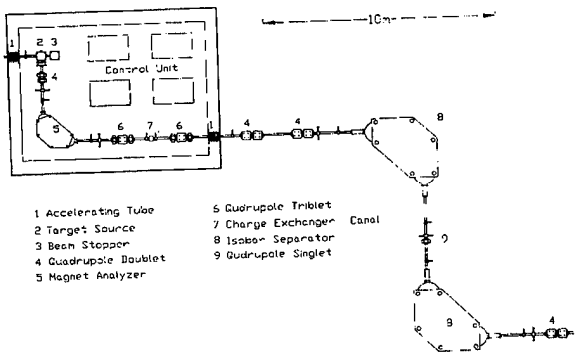


Fig.2.: The layout of the ISOL system

A modified version of the ISOLDE type electron beam plasma source will be chosen as the main source at BRNBF, which has been selected and redesigned for OR-RIBF facility at Oak Ridge National Laboratory [3],[4] .Desirable properties of the target materials are fast diffusion and effusion release of RIB species, such as, high production cross section; high melting point; low vapor pressures at high temperatures and large diffusion coefficients. In order to achieve a high performance isobar separator, the second high resolving mass separator at ground potential has been designed with two 90° ρ=2.5m opposite bending magnets. The mass resolving power is about 20,000 at the image slit of the second magnet.

Due to the interactions of the intense primary proton beam in the target activate the target itself and the second neutrons activate the source structural materials, the platform room should be shielded by a heavy concrete and a remote handling system for the routine maintenance of the target-ion source has to be needed.

IV. SUPER CONDUCTING LINAC.

In order to extend the region of stable and the radioactive ion species with energy higher than relative Coulomb barrier, a superconducting linac as a booster following the tandem accelerator has to be planned to build. The sketch of the booster linac is shown in Fig. 3 A new post stripper accepts the high energy beam coming from the tandem. Two 45° magnets form a L-bending transport line with one single quadrupole lens being inserted in between, to preserve isochronism and achromatism of the symmetric beam line. Two quadrupole triplets focus the beam to the object slit of the second isochronism and achromatism system to be composed of two 90° magnets and a single quadrupole lens in between. The mode of the resonator for linac sections is the cylindrical coaxial quarter wave resonator (QWR) which was very successful developed at Weizimann Institute[5] , University of Washington [6] , Stony Brock[7], Legnaro Laboratory[8] and JAERI[9]. Their experience shows that the excellent frequency stability, the simple structure for manufacture and balance electrically, the broad curve of the transit time factor, the low peak surface field values and wide energy per nucleon range together with the low cost constitute are the important advances in technology of superconducting resonators for heavy ion linac.

In the proposal facility, the QWR resonators should cover the β_i values from 0.05 to 0.10 and β_0 values from 0.10 to 0.16. We choose 20 cavities of the optimum low β section with β_l=0.07 for frequency of 108 MHz and 20 cavities of the optimum high β section with β_h=0.10 for frequency of 144 MHz.

The concept design of the RF system, the control system, the vacuum system and the beam optics for the superconducting Linac accelerator have finished. The R & D of the mechanical and electrochemical preparation of the substrate of the cavity, the technology of the Niobium-sputtered copper QWR resonators have been testing in Peking University.

V. CONCLUSION

The proposal for radioactive nuclear beam is anextension project of the present tandem accelerator. The pre-accelerator provides the primary beam and the radioactive beam. The post-accelerator increase the energy, not only for the radioactive ion but also for the stable ion. The existing tandem accelerator, switch magnet, experimental area and the date acquisition system are used to perform the radioactive nuclear experiments.

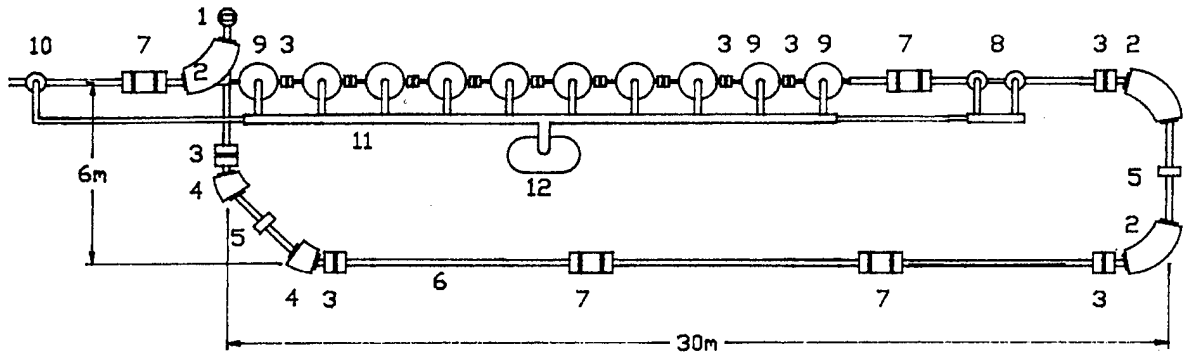
In order to reach the internationally advanced level in the area of radioactive nuclear beams in a period as short as possible, the existing technology, both home and abroad, will be adopted in the proposal.

a) A 30 MeV, 350μA high intensity proton cyclotron constructed by CIAE delivered beams in October, 1994. The proposed 70 MeV, 200μA cyclotron will used the similar technology.

b) The existing tandem has been in good operating condition since it put into operation in 1987. The main fragile spare parts are home made. The expertise of the technical staff is compatible to the BRNBF operation and maintenance.

c) The proposed superconducting LINAC is the same type as being built in the United States, Japan, Italy, and Israel. The Know-how would help our project. Peking University has accumulated rich experience in the R & D of superconducting cavity. Collaboration of CIAE and Peking University is important in constructing the LINAC.

d) On-line isotope separators have been build in both CIAE and Institute of Modern Physics (IMP) in China. The target/ion source technology can be learnt from CERN and ORNL.



1	Stripper	5	Quadrupole Singlet	9	Cryostat
2	90Deg Magnet	6	Beam Line	10	Debuncher
3	Quadrupole Doublet	7	Quadrupole Triplet	11	Transport Line
4	45Deg Magnet	8	Buncher	12	Refrigerator

Fig. 3 sketch of the booster linac

REFERENCES

[1] Nuclei, Nucleons, Quarks, Nuclear Science in 1990's -- A Long Range Plan for Nuclear Science, NSAC (1989).

[2] D.K.Olsen, Nucl, Instr, and Meth A328(1993)303

[3] G.D.Alton et al., Nucl. Instr and Meth A328 (1993) 325

[4] G.D.Alton et al., Nucl. Instr and Meth (1996) 207,225

[5] I Ben-Zxi et al., Nucl. Instr and Meth 12(1983)73

[6] D.W.Stom et al., Nucl. Instr, and Meth A287 (1990) 247

[7] J.W. Noe, Rev. Sci. Instr.57(1986) 757

[8] G.Fortuna et al., Nucl. Instr. and Meth A328 (1993) 236

[9] S.Takeuchi Proc. of Japan-China Joint Symposium (1990)p-79

DEVELOPMENT OF THE HOLIFIELD RADIOACTIVE ION BEAM FACILITY

B.A. Tatum for the HRIBF Operations Staff
Oak Ridge National Laboratory*

Abstract

The Holifield Radioactive Ion Beam Facility (HRIBF) construction project has been completed and the first radioactive ion beam has been successfully accelerated. The project, which began in 1992, has involved numerous facility modifications. The Oak Ridge Isochronous Cyclotron has been converted from an energy booster for heavy ion beams to a light ion accelerator with internal ion source. A target-ion source and mass analysis system have been commissioned as key components of the facility's radioactive ion beam injector to the 25MV tandem electrostatic accelerator. Beam transport lines have been completed, and new diagnostics for very low intensity beams have been developed. Work continues on a unified control system. Development of research quality radioactive beams for the nuclear structure and nuclear astrophysics communities continues. This paper details facility development to date.

1 INTRODUCTION

The Holifield Radioactive Ion Beam Facility (HRIBF) [1] of Oak Ridge National Laboratory was formally dedicated on December 12, 1996, and approved for high intensity operation as a National User Facility, the first of its kind in North America. The HRIBF will be the first radioactive ion beam (RIB) facility in the United States devoted to low-energy nuclear structure and astrophysics research. Light ion beams from the Oak Ridge Isochronous Cyclotron (ORIC) are utilized to bombard targets in the target/ion source (TIS) assembly on the -300kV RIB injector platform. Radioactive ions diffuse from the target and are ionized, then mass separated. Subsequently, the RIB is transported to, and accelerated by, the 25 MV tandem electrostatic accelerator (Tandem) prior to transport to any of several experimental devices.

2 ORIC DEVELOPMENT

ORIC development centers around the production of proton, deuteron, and alpha beams which are required for initial RIB production. The operational objectives are to increase beam energy and intensity while minimizing machine activation, and also to increase machine reliability. Goals and present status of beam development are shown in Table 1. Beam intensities have been intentionally limited by source aperture size during the development phase to minimize machine activation. The ORIC has provided up to about 5 microamps of 42 MeV protons to the target/ion source to produce ^{69}As and ^{70}As beams. The beam current is being increased in stages to study radiation and beam-heating effects on the target materials and to minimize residual radioactivity. Thus far, no adverse effects have been observed. Proton beam current will be increased to 50 μA as development progresses to produce RIBs of sufficient intensity for the experimental research program.

Table 1: ORIC Beam Development

Beam	Goal	Status
proton	60 MeV, 50 μA	42 MeV, 5.0 μA
deuteron	50 MeV, 50 μA	49 MeV, 0.4 μA
alpha	75 MeV, 200μA	75 MeV, 1.6 μA

ORIC is in the middle of a four year Accelerator Improvement Project (AIP) to accomplish the stated objectives. Central region development for separated turns and high extraction efficiency is a focal activity. Presently, extraction efficiencies are less than 50%, but modifications currently underway are designed to increase efficiencies to 75%. The result will be improved beam production with less activation of key components such as the electrostatic deflector and extraction channels. New ion source heads and an improved gas handling system have resulted in cathode lifetimes in excess of 200 hours. The design simplifies source maintenance for minimal personnel radiation exposure. Improved beam diagnostics have been installed including a multi-segmented radial probe and beam scanning system which provides both radial and axial beam profiles.

Machine reliability has been greatly increased in several areas. The deionized water system has been simplified and flow switches rebuilt for reliable component protection. Several aging power supplies have been or will be replaced, eliminating chronic down-time. A majority of ORIC controls have been moved to the Vista control system from the obsolete Modcomp and older hardwired systems. Complete controls wiring and interface module replacement has resulted in a more robust and easily maintainable system. RF system modifications are also a part of the AIP Project, including the replacement of the 20kV, 30A power supply required by the anode of the RCA 4648A power amplifier tube.

3 RIB INJECTOR DEVELOPMENT

The RIB injector [2] consists of all equipment on the -300kV platform (target ion/source, first stage magnetic mass separator, electrostatic quadrupoles, and cesium vapor charge exchange cell) and the transfer beam line (electrostatic quadrupoles and second stage magnetic mass separator) to the 25 MV Tandem. Great progress has been made in understanding and optimizing the performance of the elements of the RIB injector.

Routinely, the beam exiting the ion source via the extract electrode is steered onto the optical axis of the RIB injector by using the first two of the four electrostatic quadrupoles

* Research sponsored the U.S. Department of Energy under contract number DE-AC05-96OR22464 with Lockheed Martin Energy Research Corporation.

0-7803-4376-X/98 /$10.00 © 1998 IEEE

immediately after the ion source as steerers. The first steerer bends the beam so that it crosses the optical axis at the position of the second steerer. The second steerer bends the beam parallel to the optical axis.

Total transmission through the RIB injector from the ion source to the Tandem is 28% for ^{70}Ge ions. Essentially all loss is in the charge exchange cell; transmission of positive ions through the cell with no cesium vapor is 70%, and the measured negative ion fraction is 40%. All other elements, including the second stage mass separator, transmit the beam without measurable loss. The transmission of the entire system from the ion source through the Tandem is about 6%, corresponding to a transmission through the Tandem itself of 20%. These measurements were made with a 50 keV ^{70}Ge beam on the high voltage platform, accelerated to 200 keV, and injected into the Tandem.

The design mass resolution of the second stage mass separator is 1 part in 20,000 and is limited by the size of the beam at the object of the separator in the dimension corresponding to the bending plane of the separator. Transmission of 100% has been achieved with a size corresponding to a resolution of 1 part in 7500 (FWHM). With this tune, a resolution of 1 part in 10,000 with 60% transmission or 1 part in 20,000 with 20% transmission is achievable. Based on analysis of an experimental study of the energy loss straggling in the charge exchange cell, the intrinsic resolution of the second stage mass separator is conservatively estimated to be better than 1 part in 10,000. Operation of the second stage mass separator with full transmission at the design mass resolution will be the major development project on the RIB injector during the coming year.

After bombardment with an intense light ion beam, the TIS vacuum enclosure may contain up to 100 Ci of residual activation, prohibiting prompt manual removal of the TIS from the -300kV platform for examination, repair, or interchange. Thus, to minimize delays in the experimental program, a Remote Handling System (RHS) is used to remove the TIS from the platform.

The RHS consists of three major components: (1) a six-degree of freedom robotic arm, designed to withstand 10^8 RAD total dose, mounted on the high voltage platform next to the TIS; (2) a conveyor that extends from the high voltage platform room through the cyclotron vault and into a shielded storage room; and, (3) a robotic gantry crane in the shielded storage room.

The RHS only operates with ORIC beam off, and platform and TIS high voltage off. The TIS is remotely disengaged from the RIB injector vacuum system and moved to a retracted fiducial position on the TIS table. The robotic arm picks up the TIS, places it in a stainless steel Contamination Control Box (CCB) which sits on the remotely-extended end of the conveyer, and places a dust-tight cover on the CCB. The end of the conveyer with the CCB retracts into the wall and the conveyor moves the CCB to the shielded storage room where it is picked up by the robotic gantry crane and placed inside a lead cask. The crane is capable of placing a lead lid on top of the cask. The RHS also reverses this sequence to install a new TIS on the RIB injector. RHS reliability was confirmed by the successful performance of 50 consecutive repetitions of the removal and installation processes using a 250 pound source mock-up, which is twice the weight of a normal TIS. The time required to remove and install a source was 41 minutes, and no human intervention was required during the 34 hour period. The RHS is fully programmable and communicates with the RIB injector VISTA-based control system, and also has manual controls.

Several engineering modifications have been made to the RIB Injector. All air and water valves associated with the TIS have been moved to the instrumentation platform. The extract electrode drive mechanism has been moved to the top of the Faraday cage to minimize radiation damage to the drive motor and associated limit switches. Flexible spring mountings have been installed on the extract electrode to allow easier movement. The self sealing features of the water connections to the TIS have been removed to improve reliability of cooling water flow. The positioning pin arrangement for the TIS base plate and table has been modified to accommodate the RHS. All elastomer O-rings in the extraction region have been replaced with metal O-rings. The acrylic supports for the deceleration tube and for the extraction area ceramic insulators have both been replaced with radiation resistant G10 supports.

4 TANDEM ACCELERATOR DEVELOPMENT

The Tandem is fully devoted to RIB development, routinely providing stable ion beams in support of TIS studies and experimental apparatus commissioning during periods between RIB acceleration.

The combination of the Tandem and the on-line isotope separator (UNISOR) provides a valuable tool for testing new target materials and ion source concepts. The high reliability and low operating cost of the Tandem has permitted completion of 15 experimental runs over the past year for target/ion source development. Thus far, the Tandem has provided both proton and deuteron beams for this program and addition of a helium negative ion source is being considered. The proton beam is administratively limited to an energy of 40 MeV and current of 10 nA due to shielding limitations around the UNISOR target region and the desire to limit activation of the Tandem components. The high sensitivity of the isotope separator allows measurements to be carried out at these low beam intensities while minimizing residual radioactivity and personnel exposure to radiation. The emphasis during the past year has been on development of liquid germanium targets for production of ^{69}As and ^{70}As beams, and alumina targets for production of ^{17}F and ^{18}F beams. The first program is essentially completed and an ^{69}As beam has been provided to the experiment end station. The fluorine beam development program has had good success using thin aluminum oxide fiber targets and a negative ion source is being developed to provide these beams to the research program in the near future.

Tandem equipment has been upgraded for improved safety, environmental compliance and better operation for the RIB experimental program. For improved safety, the Tandem radiation safety system was upgraded for three reasons: *(1)* to comply with DOE order 5480.25 and related ORNL Facility Safety Procedure, *(2)* to improve system

electrometers by replacing old electrometer circuitry which was based on obsolete electronics and *(3)* to extend the system to the new Recoil Mass Separator (RMS) experimental area to provide the convenience of a permissive entry system to RMS experimenters.

To comply with freon-reduction guidelines, the Tandem stable-ion injector's Freon 113 cooling system was replaced with a recirculating water-cooled system with a liquid-to-air heat exchanger. All components of the system are installed in the limited space on the ion source platform. A mixed-bed resin deionizer keeps water conductivity at 14 megaohm-cm.

Tandem energy-analyzing magnet coils were replaced with new coils of a modified design in August 1995 after instabilities became apparent during a period of routine accelerator operation in February of 1994. The cause of instabilities was an internal short in one of the magnet coils. The magnet was operated with fewer turns for several months at a 50% reduction in bending power. Energy-analysis versus magnet field was calibrated using a time-of-flight method resulting in an analyzed beam energy accurate to at least 0.1%.

5 LOW INTENSITY BEAM DIAGNOSTICS

Beam diagnostic requirements at the HRIBF vary from the measurement of high intensity ORIC beams used in production to typically low-intensity radioactive beams. Below is a list of methods and devices used for monitoring radioactive beams.

5.1 Non-Invasive Sampling

- An ionization sampler of the residual gas by the beam particles which is 3-D sensitive (10^0-10^7 p/s)

5.2 Invasive Readout

- (Alumina) with sensitive CCD video camera (104-109 p/s)
- Phosphor X-Y position sensitive avalanche type gas detector (100-106 p/s)
- Sensor based on detecting ions or electrons emitted by the beam hitting a metal plate (10^0-10^7 p/s)

The sensor, based on detecting emissions from a metal plate [3], shown in Fig. 1, is being used at several dead sections of the accelerating tubes. It is mounted with mechanical actuators that place it in the beam path.

6 ACCELERATOR CONTROL SYSTEM

The accelerator control system is built around Vsystem, a commercial toolkit from Vista Control Systems. Vsystem provides a foundation for a distributed, data driven system in which a real-time database is used to dynamically configure system behavior and provide a common mechanism for interprocess communication. In addition, Vsystem includes Vdraw which is an X Window based GUI builder. All human interface screens have been created with the assistance of Vdraw.

A portion of the software runs in an environment in which a VAX 4000 model 90 running VMS supports the X Terminals on which the Vdraw screens are displayed, and three rtVAX300 processors running VAXELN perform the

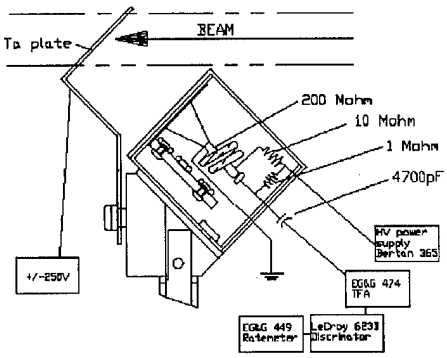


Figure 1. Invasive Readout.

I/O processing and house the real-time databases. I/O devices include numerous RS232 and RS485 serial interface modules in addition to Allen-Bradley remote I/O scanners and programmable logic controllers (PLCs). The ORIC, RIB injector, and a number of beamlines are controlled by these components.

The control system upgrade for the tandem accelerator and related beamlines was started some time after work on ORIC and the injector began. At the same time, a new multiplatform version of Vsystem became available. Consequently, an Alpha workstation running Digital UNIX was chosen to support the human interface displays and a Heurikon 68060 CPU running VxWorks was selected to control the I/O devices and house the real-time databases. I/O hardware for the tandem consists of devices connected to a CAMAC serial highway and is not included in the upgrade.

Currently, the RIB injector subsystem is fully implemented, the ORIC is largely implemented, and integration testing is proceeding for the Tandem and associated beamlines. Future plans include the replacement of the VAX/VMS workstation with an Alpha workstation running Digital UNIX. In addition, Allen-Bradley ControlNet processors, with perhaps one Heurikon 68060 CPU, will replace the VAXELN CPUs.

7 CONCLUSIONS

Considerable progress has been made at the HRIBF in both radioactive ion beam and machine development. Future directions will focus on expansion of the array of RIB beams available for research and higher intensity RIB production with the intent of maintaining a world-class research complex.

REFERENCES

[1] D. K. Olsen et al., Proc. Second Int Conf on Radioactive Nuclear Beams, Louvain-la-Neuve, Belgium, August 1991, ed. By TH. Delbar (Adam Hilger, Bristol, 1992), p. 131; A proposal for Physics with Exotic Beams at the Holifield Heavy Ion Research Facility, edited by J. D. Garrett and D. K. Olsen, February 1991.

[2] D. T. Dowling, et al., Status of the Radioactive Ion Beam Injector at the Holifield Radioactive Ion Beam Facility, Proceedings of the 1995 Particle Accelerator Conference and International Conference on High Energy Accelerators, Dallas, TX, May 1-5, 1995.

[3] M. Meigs, D.Haynes, C.Jones, C.Lecroy, "A New Beam Intensity Monitoring System with Wide Dynamic Range for the Holifield Radioactive Ion Beam Facility," Proceedings of the 1995 Particle Accelerator Conference and International Conference on High Energy Accelerators, Dallas, TX, May 1-5, 1995.

EXPERIMENTS IN HEAVY ION FUSION BEAM PHYSICS AT LBNL, LLNL, AND THE UNIVERSITY OF MARYLAND

J.W. Kwan, Lawrence Berkeley National Laboratory, Berkeley, CA

Abstract

A heavy ion fusion driver must be capable of accelerating an intense ion beam to GeV beam energies. The final beam pulse current can be as high as a few kA using beam compression in an induction linac. Combining beamlets at low energy may prove to be economical as long as there is no significant emittance growth. Focusing of the final beam pulse from the reactor chamber wall to the target can be enhanced by using a plasma channel to guide the ion beam. Experiments at LBNL on ion sources, injector, the combiner and plasma channel focusing are discussed. One possible way to reduce the cost of a driver is to use an induction recirculator. Experiments at LLNL are exploring this concept by studying the transport and bending of space-charge-dominated ion beams. At the Univ. of Maryland the behavior of space-charge dominated beams is being simulated with low-energy electrons. They studied emittance growth, halo formation and beam pulse compression.

1 INTRODUCTION

The goal of a heavy ion fusion driver is to deliver particle beam power for igniting a fusion target about 5 mm in diameter. To do so, the required beam energy is ≈ 5 MJ and the pulse length should be ≈ 10 ns in order to achieve a peak power ≈ 10^{15} W/cm^2. Furthermore, the energy must be deposited within a short penetration range, e.g. 0.02 to 0.2 g/cm^2 of the target material. For heavy ions with atomic masses ≈200, the allowable kinetic energy is ≤ 10 GeV [1,2].

Figure 1 is the block diagram of a typical heavy ion fusion driver using induction linacs [3]. Starting with a 2 MeV injector, which may contain up to 100 beams at 1 A per beam, the ions will be accelerated to 100 MeV kinetic energy using electrostatic quadrupole (ESQ) focusing. Above this kinetic energy, the ion velocity is high enough such that magnetic quadrupole focusing becomes more effective. Since an optimal design of the ESQ channel has a smaller bore size and less transportable current than that of the magnetic quadrupole, combining beams at the transition point will minimize the overall cost of a driver. Of course, this is only true if the beam combining process does not significantly degrade the beam quality for the final focusing of beams onto the target.

Assuming an average acceleration rate of 1 MV/m, a 10 GV machine will be 10 km long. One way to reduce the accelerator length is to use lighter ions or high charge state heavy ions which require less beam voltage but more beam current (in the form of more beam channels). For ions of the same q/m ratio, and for a fixed range, the heavier ions are more advantageous because of the higher kinetic energy per nucleon. Another way is to use a

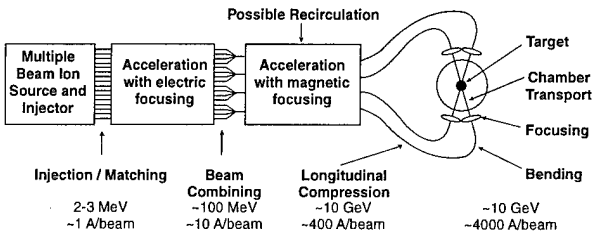


Figure: 1 Block diagram of an HIF induction linac driver.

circular machine so the beams go around many times. Ultimately, the final choice will depend on the physics, the technical difficulties and most importantly the cost.

The increase in ion velocity amplifies the beam current if the beam bunch length remains constant. Furthermore, the acceleration pulse can be arranged to compress the bunch length by giving more kinetic energy to the particles at the rear, therefore producing additional current amplification. In fact, beam compression continues into the drift region beyond the accelerator until the longitudinal space-charge repulsion force eliminates the velocity gradient. While the beam bunch is still in the accelerator, the space-charge repulsion must be balanced by the transverse focusing forces from the quadrupoles and by longitudinal forces due to specially shaped acceleration voltage pulses.

At the final stage of beam focusing, the beam current can be as high as 4 kA/beam. The ability to focus such high current beam onto a 3-mm radius spot size depends greatly on the beam emittance. Some novel ways to relieve the stringent emittance requirement include schemes such as plasma lens and plasma channel beam transport.

Experiments that were designed to address many of these beam physics issues are ongoing at Lawrence Berkeley National Lab (LBNL), Lawrence Livermore National Lab (LLNL) and the University of Maryland (UM). This paper briefly describes some of the more recent experiments and plans.

2 EXPERIMENTS AT LBNL

2.1 Ion Sources and Injectors

Based on beam transport considerations, a 2-MeV injector should provide a beam with a line charge density of approximately 0.25×10^{-6} C/m. The actual beam current will depend on the ion velocity (or equivalently the square root of the charge/mass ratio). For a potassium ion beam, the corresponding beam current is 0.8 A per ion source. For HIF driver applications, the required pulse length at the ion source is about 20×10^{-6} s with a rise time preferably not more than 1×10^{-6} s and a repetition rate of 10 Hz.

0-7803-4376-X/98/$10.00 © 1998 IEEE

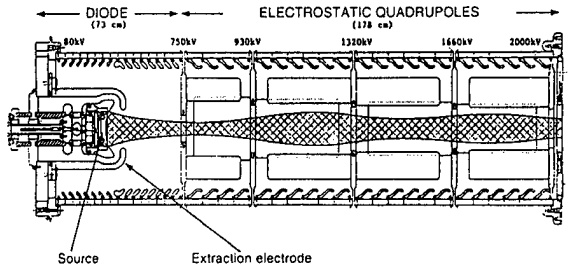


Figure: 2 Schematic Diagram of the 2-MeV ILSE injector.

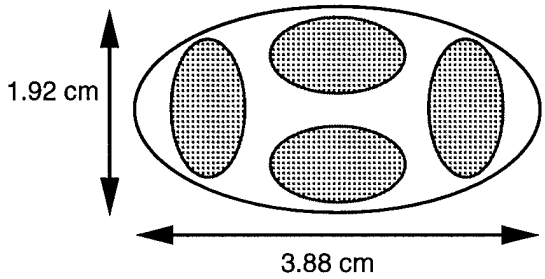


Figure: 3 Four beams emerging from the combiner.

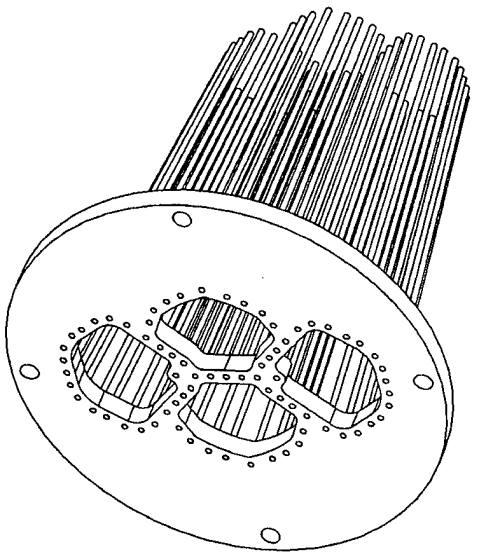


Figure: 4 The wire cage used for combining beams.

So far, the surface ionization sources have been selected in most HIF driver designs. The surface ionization type of ion sources can efficiently produce singly charged alkali ions such as Cs^+ and K^+. The major advantages of this type of ion source are the absence of gas flow, excellent beam current control and low emittance (due to low ion temperature and a solid emitter boundary). The main concerns here are the source lifetime, the alkaline vapor delivery system, and the deposition of alkaline vapor onto beam line components. Other types of ion sources should be considered according to their unique properties, for example, a gas source is suitable for generating Hg, Xe, Ar and Ne ions, whereas a metal vapor vacuum arc (MEVVA) source or a laser source would be more appropriate for high charge state ions such as those of Gd and Bi.

Previously, an alumino-silicate ion source has been developed for a 2 MeV injector built for the ILSE/Elise project [4]. A schematic diagram of the ion source and injector is shown in Fig. 2. The injector performance was satisfactory in delivering up to 0.8 A of K^+ ion beam with a normalized edge emittance < 1 π-mm-mrad and it continues to serve as a useful facility for studying HIF beam dynamics including beam profile control and matching the acceptances.

Although this ion source has met the original specifications, the latest conceptual designs for the next HIF research facility calls for an injector with an ion source that has a current density ≥15 mA/cm^2 of K^+ (a factor of 4 increase compares to the previous case). A recent experiment has shown that such current density is within the capability of the alumino-silicate ion sources and vapor-fed contact ionizers [5]. The major reason for choosing a high current density, compact size injector is to reduce the overall cost of a fusion driver.

2.2 Beam Combining

The previous MBE-4 experiment on multiple beam transport in induction linacs was successfully completed to show that under optimum conditions the current amplification could be achieved without significant emittance growth [6]. The same facility is now being used for a beam combining experiment.

Fig. 3 shows a layout of 4 beams, each having an elliptical cross-section, arranged in such a way as to be enclosed by a minimum size ellipse. As these beams propagate downstream, they will start to merge into each other forming a single inseparable beam. The merge is not perfect because the empty space within the ellipse boundary is irreversibly blended into the final beam area and the beam emittance.

To minimize the emittance growth, the beams must be brought together independently (i.e. avoid space-charge interaction) until they are closely packed. This is done by using 4 channels of ESQ with a 6° converging angle (w.r.t. center-line) commonly aimed at a merging point where a combined function element called the "wire cage" is located. The device is shown in Fig. 4. It is made of many 1-mm diameter tungsten rods biased at various potential so that the correct Dirichlet boundary condition is established to give both quadrupole field for focusing and dipole field for steering the beams into the proper positions.

The technical difficulties in this experiment are due to the requirements of precise beam alignments and high electric field at the wire cage. Preliminary experimental results [7] are in general agreement with the computer beam simulations.

2.3 Plasma Lens and Channel Transport for Final Focus

The final stage of focusing a very high current heavy ion beam onto the target can be a limiting factor in determining the port size on the chamber wall as well as the number of ports required. Many schemes have been proposed and the major differences among them are the level of space charge and beam current neutralization. While the non-neutralizing lens is only applicable to low current, low charge state ions coupled with a high

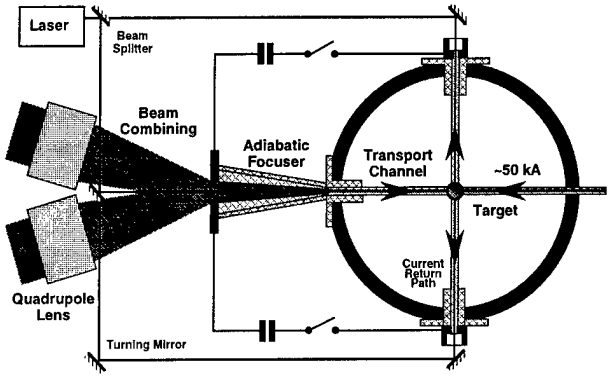


Figure: 5 A proposed scheme for final focus using adiabatic lenses and a discharge channel transport.

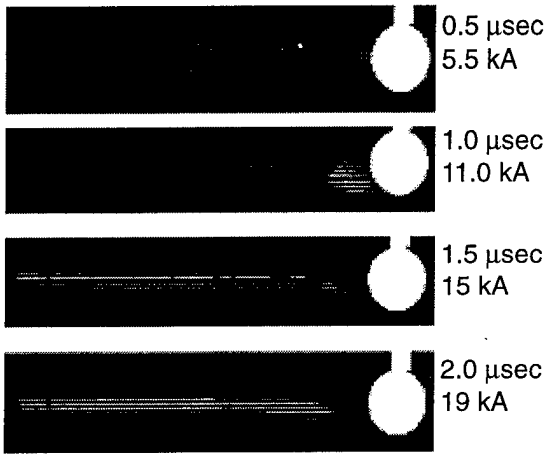


Figure: 6 Photographs of the plasma channel at various times after the laser trigger.

vacuum in the reactor chamber, neutralizing plasma lens can handle large current (>100 kA), highly stripped ions and are compatible with a moderate chamber pressure. Furthermore, focusing by the plasma lens is achromatic and is insensitive to the beam emittance [8].

Since the beam radius can easily decrease by a factor of more than 3 in passing through the lens, one way to match the focusing properties to this change is by using a tapered discharge tube to adiabatically increase the focusing power along the z-axis. Typically, the entrance radius can be 4-5 times larger than the exit radius. Figure 5 illustrates a final focusing scheme using conventional quadrupole lenses in conjunction with adiabatic lenses and followed by a high current plasma channel to transport the tightly focused ion beam across the chamber radius (≈5 m).

An adiabatic lens experiment was set-up at the 2-MeV injector facility. By passing a small beam through a tapered discharge tube, it was found that the beam current density at the exit changed by a factor of more than 50 between the cases with and without the plasma lens focusing [9].

In a separate experiment, inside a chamber filled with a mixture of nitrogen and benzene, an excimer laser was used to preionize a beam path and then followed by a high voltage discharge [9,10]. The plasma channel produced has a radius of 35 mm, 40 cm long, and up to 19 kA of discharge current. Breakdowns due to surrounding grounded structures was more problematic than hydrodynamic instabilities. In order to simulate the current paths in a reactor chamber (see Fig. 5), a metal ball with the supporting rod as the return current path is inserted at the middle of the experimental chamber to intercept the plasma channel. A series of pictures of the plasma channel at various times after the laser trigger is shown in Fig. 6. The kink at the tip where the electrical current turns a 90° corner is due to the lack of symmetry (purposely arranged in this experiment) from the self-magnetic force. The phenomenon disappeared when the return current was allowed to flow symmetrical on the far side.

3 EXPERIMENTS AT LLNL

A recirculating induction accelerator can reduce the driver cost because it "recycles" the same set of components (≈ 100 laps) for beam acceleration. Similar to an induction linac, the acceleration voltage is provided by induction cores but at a more modest gradient. Nevertheless, the acceleration is rapid enough to avoid the resonant losses of typical circular rf-driven accelerator. Since the ion beams are non-relativistic, the high voltage pulses applied to the induction cores must be continuously adjusted as the beams gain energy. In practice, the dynamic range is about 10-20 times energy gain for each ring, so it will take at least 3 rings to build a 10 GeV driver [11,12].

There are 4 main critical issues in developing the recirculator: (1) power handling, including energy recovery of the dipole magnets, at high repetition rate; (2) beam loss due to inadequate vacuum ($<10^{-10}$ Torr is required); (3) beam dynamics; and (4) feed-back controls.

A small prototype recirculator is being developed at LLNL for experimental studies [13]. Figure 7 shows a schematic diagram of the machine and its designed parameters are tabulated in Table 1. Recently, in a series of experiments, a 65-kV, 1.6-mA K^+ beam was sent through an electrostatic quadrupole matching section,

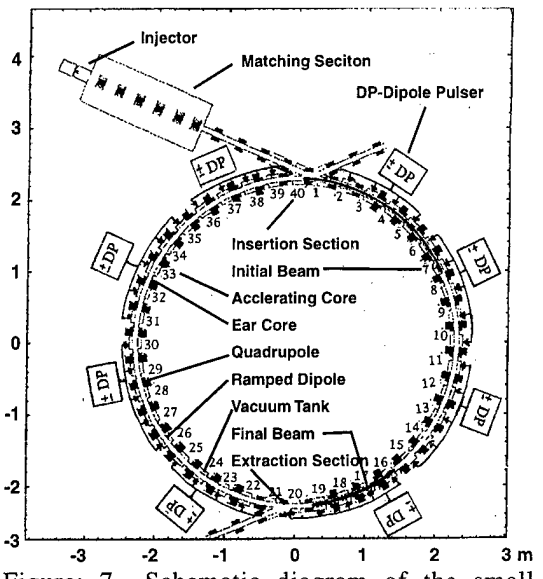


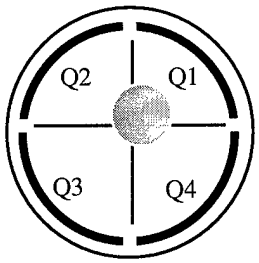
Figure: 7 Schematic diagram of the small recirculator.

Ion species	K^+ (mass 39)
Beam energy	80 - 320 keV
Beam current	2 - 8 mA
Pulse duration	4 - 1 μs
Nominal number of laps	15
Circumference	14.4 m
Number of half-lattice period	40
Pipe radius	3.5 cm
Maximum beam radius	1.5 cm
Permanent magnet (at pipe wall)	0.29 T
Undepressed phase advance	78° - 45°
Depressed phase advance	16° - 12°

Table: 1 Design parameters of the small recirculator.

which is followed by a straight transport line of 8 permanent-magnet quadrupole lenses, and then by a 45 degree bend of 5 half-lattice periods. The bending is effected by carefully shaped electric deflector plates.

A special capacitive probe was developed to monitor the beam centroid position [14]. Such non-interceptive beam diagnostics are essential for beam steering corrections in the recirculator. The probe consists of 4 sensing electrodes symmetrically located around the axis, see Fig. 8. The beam centroid x and y positions can be expressed as simple algebraic expressions of the different charges accumulated on the 4 sensors. Excellent agreement was obtained in comparing the measured beam positions against the calculated values.



$$x \approx \frac{\pi R(Q1+Q4-Q2-Q3)}{4(Q1+Q2+Q3+Q4)}$$

$$y \approx \frac{\pi R(Q1+Q2-Q3-Q4)}{4(Q1+Q2+Q3+Q4)}$$

$$I \approx \frac{v(Q1+Q2+Q3+Q4)}{L}$$

Figure: 8 The capacitive probe as non-interceptive beam diagnostic (R is radius, I is beam current, v is beam velocity, and L is probe length).

4 EXPERIMENTS AT THE UNIVERSITY OF MARYLAND

4.1 Merging Multiple Beams

A low energy electron beam is being used to conduct experiments simulating heavy ion (space-charge dominated) beam transport physics. The facility is a 5 m long periodic solenoid focusing channel system; typical beam parameters are: beam energy 2.5 - 5.0 kV, current 30 - 200 mA, and pulse duration from a few nanoseconds up to a few microseconds. By using a mask with 5 small apertures, arranged in a cross pattern, to produce 5 beamlets, the charge homogenization and emittance growth effects were observed [15]. The experimental set-up is shown in Fig. 9. It was found that the beamlets eventually merged into an almost uniform density single beam. The measured merging distance and the emittance

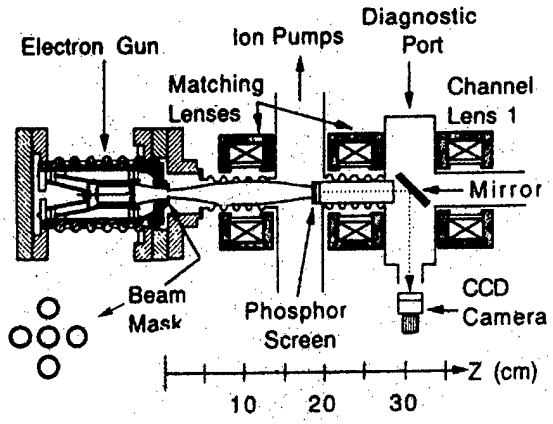


Figure: 9 Schematic of the multi-beam experiment

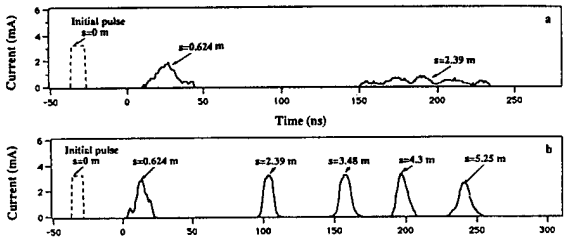


Figure: 10 Comparison between drift expansion and rectangular pulse restoration: (a) free expansion of a 300 eV, 3.3 mA, 7 ns bunch; (b) beam profiles with restoration.

growth are in good agreement with theoretical prediction as well as computer simulations. The merging distance was near 1/4 beam plasma period and the emittance growth is minimized (a factor ≈3) for rms matched beams. For rms-mismatched beams the halo formation has been observed for the first time in a controlled experiment.

4.2 Space-charge Wave Experiments

The geometry factor g is important in longitudinal beam dynamics because it relates the E_Z associated with a perturbation in a beam with the line-charge density variation. By measuring the velocities of the fast and slow (forward and backward in the beam frame) space-charge waves, Wang *et al* deduced the g factor and confirmed the theoretical model [16] that $g=2\ln(b/a)$ where b and a are the pipe radius and the beam radius respectively.

It was also found that a space-charge wave will be partially transmitted and partially reflected at a bunch end [17]. If the beam edge length is much smaller than the perturbation wavelength, there is full reflection and conversely if the ratio is large, then there is no reflection. In addition, by passing the beam through a 1 m long glass tube coated with a layer of indium-tin-oxide on the inside wall (a resistive pipe), the experiment demonstrated the growth of localized slow waves and the decay of fast waves in the long wavelength range [18].

4.3 Longitudinal bunch expansion and Compression

The ends of an initially rectangular line-charge beam bunch usually experience erosion during beam transport.

One way to counter this effect is to apply an "ear" pulse to longitudinally confine the beam particles. An experiment was done by imposing a linear velocity gradient at the beam edge of an eroded beam profile to restore the rectangular shape [19]. Figure 10 shows the beam profiles with and without the restoration.

4.4 Future Development

Figure 11 shows the schematic of a 1.7 m radius electron ring proposed by the Univ. of Maryland. The machine has 36 lattice periods, a 4.9 cm bore radius, a 8.1 G/cm gradient. The quadrupole length is 4.4 cm and has a diameter of 5.3 cm. Injection beam energy is 10 keV and the current is 100 mA. The average beam radius is 1.04 cm with an initial emittance of 10 mm-mrad. Further information on the electron ring development can be found in other papers presented in this meeting [20].

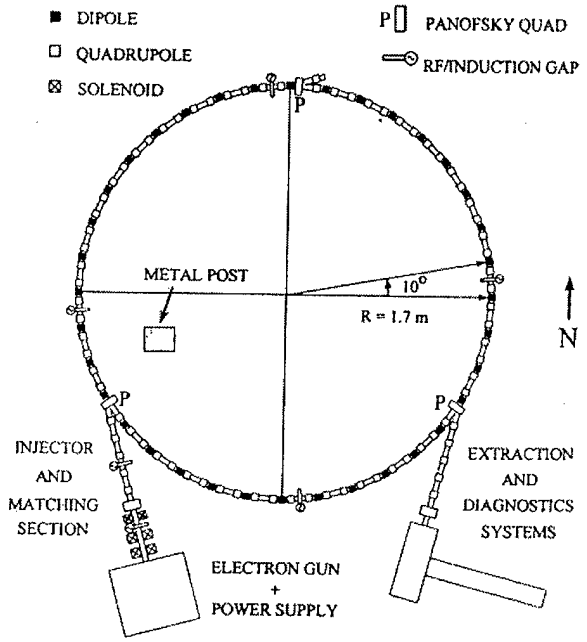


Figure: 11 Layout out of proposed electron ring at the University of Maryland.

5 SUMMARY

The experimental program at LBNL is investigating various means to optimize the accelerator architecture in order to reduce the cost of an induction linac HIF driver. Experiments include high current density ion source and injector, beam combining, and unconventional final focusing. The LLNL approach is to develop the concept of recirculator. In the University of Maryland, electron beams are being used to study many interesting phenomena related to the transport and acceleration of a space-charge-dominated beam bunch. So far, almost all the experiments are scaled down to a much reduced beam energy and current level. In order to make progress towards the construction of a fusion driver, there is an urgent need of a full scale experimental facility for heavy ion fusion research.

6 ACKNOWLEDGEMENTS

The author wish to thank R. Bangerter, A. Faltens, P. Seidl, S. Yu, T. Fessenden, and M. Vella at LBNL, A. Friedman and J. Barnard at LLNL, and M. Reiser and J. Wang at the Univ. of Maryland for their support. This work is supported by the Office of Fusion Energy, US DOE under contract No. DE-AC03-76SF00098.

REFERENCES

[1] J.D. Lindl, R.L. McCrory and E.M. Campbell, Phys. Today 45, No 9, 32, (1992).

[1] W.J. Hogan, R.O. Bangerter and G.L. Kulcinski, Phys. Today 45, No 9, 42, (1992).

[3] R.O. Bangerter, Proc. of Inter. Symp. on Heavy Ion Inertial Fusion, Frascati, Italy, May 25-28, 1993, Nuovo Cimento 1445 (1993).

[4] S.S. Yu, *et al*, Proc. of Inter. Symp. on Heavy Ion Inertial Fusion, Princeton, New Jersey, Sept. 6-9, 1995, Fusion Engineering and Design 32-33, 309, (1996).

[5] J.W. Kwan, W.W. Chupp, and S. Eylon, 6W.25, paper in this conf. proceeding.

[6] W.M. Fawley, et al, Phys. Plasmas 4 (3), 880, (1997)

[7] P.A. Seidl, *et al*, 8V.46, paper in this conf. proceeding.

[8] E. Boggasch, Appl. Phys. Lett. 60, 2475, (1992).

[9] A. Tauschwitz, *et al*, Proc. of Inter. Symp. on Heavy Ion Inertial Fusion, Princeton, New Jersey, Sept. 6-9, 1995, Fusion Engineering and Design 32-33, 493, (1996).

[10] T.J. Fessenden, and M.C. Vella, HIFAR Note #474, Lawrence Berkeley National Lab, (1997)

[11] J.J. Barnard, *et al*, Phys. Fluids B: Plasma Phys., 5, 2698, (1993)

[12] A. Friedman, *et al*, Proc. of Inter. Symp. on Heavy Ion Inertial Fusion, Princeton, New Jersey, Sept. 6-9, 1995, Fusion Engineering and Design 32-33, 235, (1996).

[13] J.J. Barnard, *et al*, Proc. of Inter. Symp. on Heavy Ion Inertial Fusion, Princeton, New Jersey, Sept. 6-9, 1995, Fusion Engineering and Design 32-33, 235, (1996).

[14] F.J. Deadrick, J.J. Barnard, T.J. Fessenden, J.W. Meridith and J. Rintamaki, Proc. Particle Accel. Conf. Dallas, TX, May 1995, p2557.

[15] M. Reiser, C.R. Chang, D. Kehne, K. Low, and T. Shea, Phys. Rev. Lett. 61, 2993, (1988).

[16] J.G. Wang, H. Suk, D.X. Wang, and M. Reiser, Phys. Rev. Lett. 72, 2029, (1994).

[17] J.G. Wang, D.X. Wang, H. Suk, and M. Reiser, Phys. Rev. Lett. 74, 3153, (1995).

[18] H. Suk, J.G. Wang, Y. Zou, S. Bernal, and M. Reiser, 2V. 28, paper in this conf. proceeding.

[19] D.X. Wang, J.G. Wang, and M. Reiser, Phys. Rev. Lett. 73, 66, (1994).

[20] M. Reiser, et al, 6C.6, 9P.93, 9V.35, 9V. 37, 9V. 38, papers in this conf proceeding.

PBFA Z: A 55 TW/4.5 MJ ELECTRICAL GENERATOR*

R. B. Spielman, W. A. Stygar, K. W. Struve, J. F. Seamen
Sandia National Laboratories, Albuquerque, NM 87185-1194

Abstract

PBFA Z is a new 55 TW/4.5 MJ short pulse electrical driver located at Sandia National Laboratories. We use PBFA Z to magnetically-implode plasma shells. These configurations are historically known as z pinches. The pulsed power design of PBFA Z[1] is based on conventional single-pulse Marx generator, water-line pulse-forming technology used on the earlier Saturn[2] and PBFA II[3] accelerators. PBFA Z stores 11.4 MJ in its 36 Marx generators, couples 4.5 MJ in a 55-TW/105-ns pulse to the output water transmission lines, and delivers up to 3.0 MJ and 40 TW of electrical energy to the z-pinch load. Depending on the initial load inductance and the implosion time, we attain peak currents of 16-20 MA with a rise time of 105 ns. Current is fed to the z-pinch load through self magnetically-insulated transmission lines (MITLs). Peak electric fields in the MITLs exceed 2 MV/cm. The current from the four independent conical disk MITLs is combined together in a double post-hole vacuum convolute with an efficiency greater than 95%. The measured system performance of the water transmission lines, the vacuum insulator stack, the MITLs, and the double post-hole vacuum convolute differed from preshot predictions by ~ 5%. Using a 2-cm radius and a 2-cm length tungsten wire array with 240, 7.5-μm diameter wires (4.1-mg mass) as the z-pinch load, we achieved x-ray powers of 200 TW and x-ray energies of 1.85 MJ as measured by x-ray diodes and resistive bolometry.

1 INTRODUCTION

The PBFA-II accelerator[3] at Sandia National Laboratories was originally used by the light-ion-beam ICF Program. We have made major modifications to the accelerator in order to optimize coupling to magnetically-imploded loads, typically z pinches. The facility, in operation since September 1996, has been renamed PBFA Z. Much of its electrical design and design philosophy was descibed in detail in Ref. 1.

This paper describes the electrical performance of PBFA Z and summarizes the overall pulsed power design and modeling that lead to the successful operation of the largest z-pinch driver in the world. To date PBFA Z has conducted more than 65 shots. We have demonstrated the generation of greater than 50 TW of electrical power in the constant impedance water tranmission lines in a 2.5-MV, 100-ns FWHM voltage pulse. The measured forward-going electrical energy is nearly 5 MJ.

The electrical energy is transmitted through a water-vacuum insulator interface and conducted via self magntically-insulated vacuum transmission lines (MITLs) to the z-pinch load. PBFA Z delivered a peak current of 18 MA to a low inductance z-pinch load. The load, a tungsten wire array, generated a peak x-ray power of 200 TW and an x-ray yield of 1.85 MJ.

The overall electrical design of PBFA Z pushed the limits of pulsed power engineering. The physics of MITLs and vacuum convolutes is still not well understood. Issues such as radiation-driven vacuum gap closure and limits on current density near the load need to be studied in detail in the future. PBFA Z is studying some of these fundamental pulsed power concerns while addressing the z-pinch physics necessary for the next generation of drivers.

2 PULSED POWER DESIGN

As described in detail in Ref. 1, PBFA Z's pulsed power design is based on Marx generator/water pulse-forming technology. PBFA Z contains 36 nearly identical modules. In each module a Marx generator, with 60, 1.3-μF capacitors charged to a voltage of 90 kV, delivers its energy to a water-dielectric coaxial capacitor in 1 μs. The capacitor reaches a peak voltage of 5 MV. A low-jitter laser-triggered gas switch is used to couple the energy into a second, lower inductance coaxial water capacitor in 200 ns. Self-breaking water switches are used to transfer the energy into a 0.12-Ω constant impedance water transmission line. The electrical pulse at this point has a voltage of 2.5 MV and a pulse width of 105-ns FWHM. The total power generated in the accelerator at this point is 50 TW. The electrical energy is delivered to an insulator where is passes into the vacuum portion of the accelerator. The electrical energy is then fed through four vacuum MITLs, through a vacuum convolute, to the z-pinch load. A schematic of PBFA Z is shown in Figure 1.

2.1 Water transmission Lines

The water transmission lines used on PBFA Z are a bi-plate, constant-impedance, constant-anode/cathode-gap design. This was done to optimize the energy efficiency of the transmission lines and to maximize the coupling of the energy in the transmission lines to an inductive load. The impedance of each of the 36 lines was 4.32 Ω. Each water line has a voltage and current monitor. (See Section 3.) We can accurately measure the voltage and current and, hence, the power and energy in each water transmission line. These measurements allow us to verify the operation of the water lines. These measurements are complicated

0-7803-4376-X/98 /$10.00 © 1998 IEEE

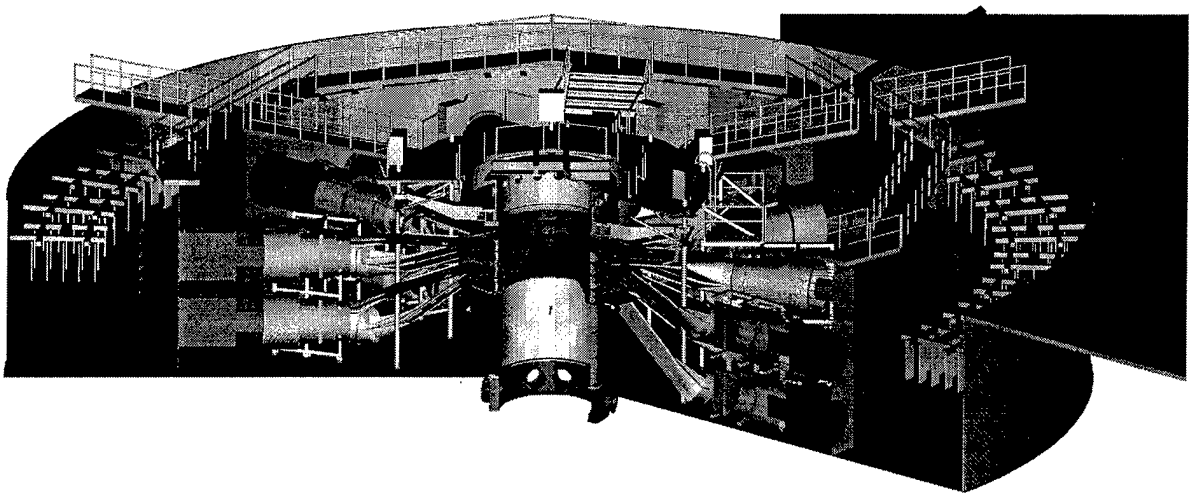


Figure 1 A schematic of PBFA Z showing the Marx generators, the water pulse forming section, the insulator stack, and the diagnostic line-of-sight.

by the spatially- and temporally-varying behavior of the electrical pulse and its reflection from the load. The transmission line gap is fixed at 14 cm. The peak voltage in the water lines varies with the proximity to the load due to the superposition of the reflected pulse on the main pulse. The water transmission lines were modeled with electrostatic codes to examine the issues of enhanced and fringing electric fields.

2.2 Insulator Stack

The insulator stack (See Figure 2.) is the boundry between the water dielectric and the vacuum that is necessary to drive the z-pinch load. The insulators, nearly 4 m in diameter, are made from Rexolite™, a high-density cross-linked polystyrene. Experience has shown that Rexolite™ has superior mechanical and electrical properties when compared with PMMA or polycarbonate. The electric field was carefully "graded" across each insulator to equalize the stress on each insulator component. The insulator stack was designed with a 2-D electrostatic code and then the final design validated with a 2-D electromagnetic code. We expect that future, more advanced designs, will use electromagnetic design codes exclusively. The voltages and currents were measured at each of the insulator stacks. (See Section 3.) These data gave a very accurate measure of the power and energy through the insulator stack boundary.

2.3 MITLs

One of the great achievements of PBFA Z is the design of the magnetically-insulated vacuum transmission lines (MITLs). The MITLs consist of four separate, conical disk feeds coupled together at the vacuum convolute. (See Section 2.4.) These MITLS operate successfully at a peak electric field of 2MV/cm with vacuum gaps as small as 1 cm. Issues such as vacuum electron flow and plasma formation were addressed with 2-D electromagnetic particle-in-cell (PIC) computer codes [1]. These MITLs must operate at fields 10X greater than the explosive emission threshold on the cathode and must hold off the full accelerator voltage for 100-150 ns. We place current monitors at two radial locations and 3-6 azimuthal postions in each of the four MITLs to better study losses.

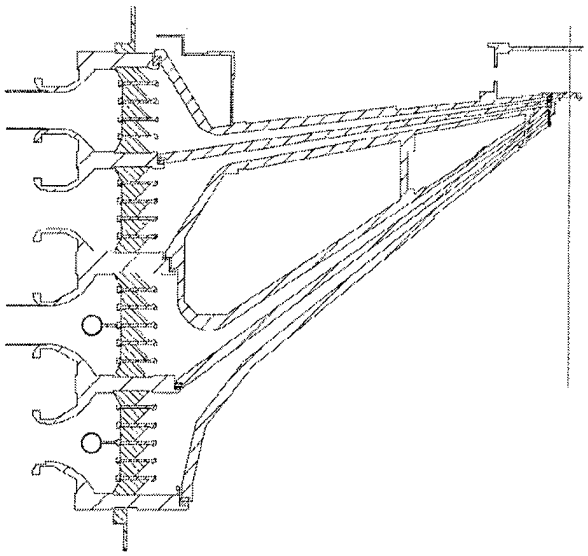


Figure 2 A schematic of the PBFA-Z insulator stack and MITLs is shown. Note, only half of a cylindrically-symmetric section is displayed. The diameter of the insulator stack is nearly 4 m.

2.4 Vacuum Convolute

The most critical part of the vacuum power flow is the double post hole convolute that couples the four, conical disk MITLs together. This is done in order to combine the current from each level and deliver the summed currents to a single z-pinch load. A vacuum convolute is necessarily a three dimensional object and will necessarily have a

number of magnetic field nulls. It is the electron losses through these nulls that drive the convolute design. We based the PBFA Z design on the successful Saturn design. In addition, the convolute was partially modeled using QUICKSILVER [1], a 3-D E&M PIC code. A drawing of the convolute is given in Figure 3.

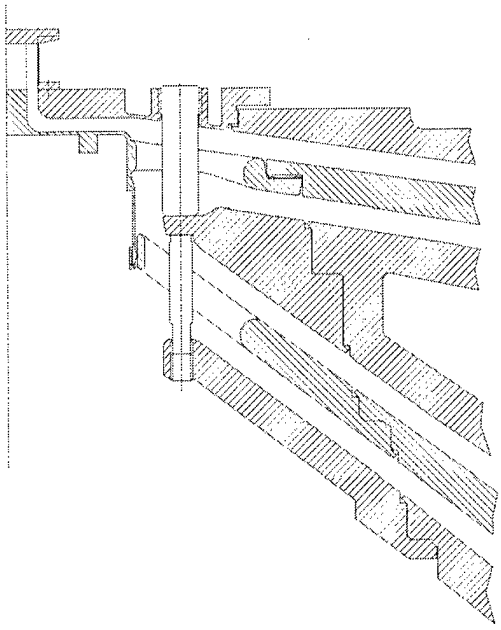


Figure 3 A line drawing of the posthole convolute for PBFA Z. The drawing shows the anode and cathode connections presently in use.

3 ELECTRICAL DIAGNOSTICS

One of the most important parts of any successful accelertor is the attention paid to electrical diagnostics. This is particularly true of single shot, pulsed accelerators. We field a full complement of diagnostics on every shot. With thirty six modules, this translates into hundreds of waveforms per shot.

3.1 Diagnostic Description

The operation of the Marx generators is monitored with 36, current viewing resistors (CVRs) located at the ground connection. The voltages on the water-dielectric intermediate store (IS) capacitors are measured with capacitively-couple voltage monitors, commonly referred to as dV/dt or V-dot monitors. Again, there are 36 of these V-dot monitors. The operation of the laser triggered gas switches is checked with these IS V-dot monitors. The electrical output of the IS capacitors charges the second intermediate store capacitor (the Line 1 or L1 capacitor). Again there are V-dot voltage monitors at this location. AS many as 36 monitors are used to measure the voltage and switching of the L1 capacitors. The output of the L1 capacitors is monitors with 36, V-dot voltage monitors and 36, magnetic loop current probes (B-dot monitors). These final 72 monitors give us a complete measure of the timing, voltage, current, power, and energy in each of the 36 accelerator modules. The voltage and the current at the insulator stack is again measured with 6, V-dot probes and 3, B-dot probes on each of the four levels. Current in the MITLs is measured with up to six B-dot probes at two separate radial positions in each of the four MITLs. The total load current is monitored with up to four B-dot probes located about 5 cm from the z-pinch load.

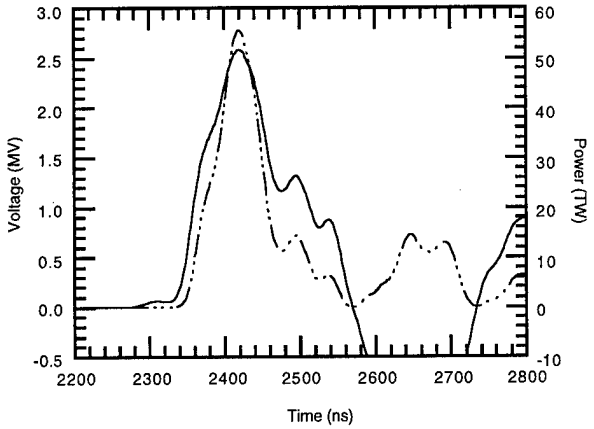


Figure 4 The average voltage (solid line) and total power waveforms in the water transmission lines measured on Shot 51.

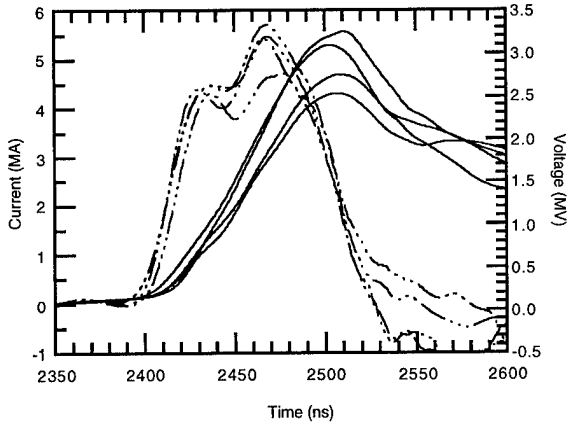


Figure 5 The currents (solid lines) and voltages for each level of the insulator stack measured on Shot 51.

3.2 Calibration

Calibration of all of the diagnostics is critical. Some of the calibrations are done in-situ with pulsers and reference monitors placed near the diagnostics under calibration while other calibrations were done externally. In all cases the pulsers are designed to provide electrical test pulses with nearly the same rise time as the actual accelerator pulse. The reference monitors are carefully calibrated against NIST-traceable standards. All calibration waveforms are stored and are available for examination or further checking at any time in the future. Typical

electrical diagnostic calibrations were accurate to ~ 2-4%. We believe that the total error, including data acquisition and systematic errors, for most of the electrical diagnostics is better than 5%.

4 ELECTRICAL PERFORMANCE

This section of the paper describes the actual performance of PBFA Z element by element in the accelerator.

4.1 Water Transmission Lines

Measurements of voltage and current in the constant impedance water transmission lines comprise the backbone of the electrical performance of the accelerator. These data give the module spread, voltage, power, and energy for the entire accelerator. Figure 4 shows the voltage waveform from a single module of PBFA Z. The peak voltage is 2.5 MV with a 105-ns FWHM pulse. The power shown is the 36 times the power of a single line. These data give a total forward-going energy for the accelerator of ~ 4.5 MJ.

The peak stress measured in the water lines was 180 kV/cm. The water lines on PBFA Z can successfully operate at this stress level. Data show that breakdowns in the water transmission lines is dominated by edge effects, joints, and gaps. We see no evidence of electrical breakdown or losses in the uniform field portion of the water transmission lines.

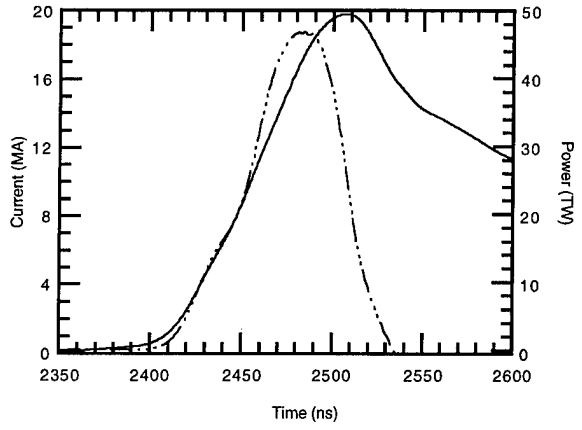


Figure 6 The total current (solid line) and power at the insulator stack measured on Shot 51.

4.2 Insulator Stack

Data show that the insulator stack is exposed to peak voltages exceeding 3 MV. Our data show that at peak electric fields of ~ 100 kV/cm the insulator stacks never flash. This voltage hold off value is at the extreme limit of classical insulator breakdown described in Refs. 1&4. In fact, even upon voltage reversal (after peak current) when the voltage reaches as low as -1 MV the insulator holds off the voltage for as long as 200 ns. Figure 5 shows the voltage and current waveforms measured on each of the four insulator stacks for PBFA-Z Shot 51. Figure 6 shows the total current through the insulator stack together with the electrical power (I*V) passing through the insulator stack. The peak electrical power measured on Shot 51 was 46.8 TW. The measured electrical energy at the insulator stack for Shot 51 was 2.9 MJ.

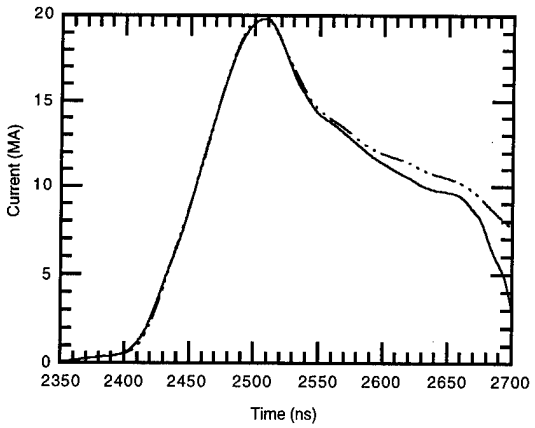


Figure 7 The total stack current (solid line) is plotted with the total MITL current for Shot 51. The stack flashes at ~ 2675 ns.

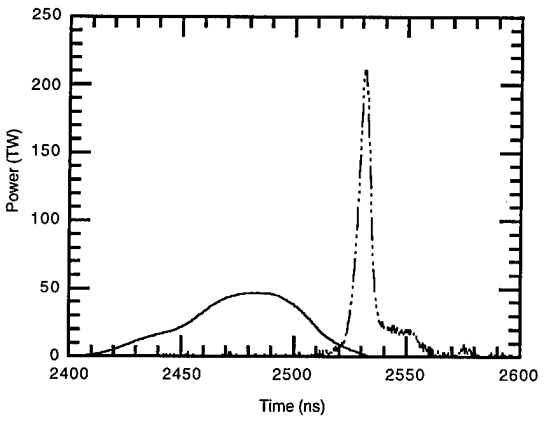


Figure 8 The total stack power (solid line) is plotted together with the x-ray power for Shot 51.

4.3 MITLs

Data from MITL current monitors for Shot 51 show that there is 100% current transfer from the insulator stack to a location just radially inside the MITL current monitors (a location just over 1 m from the load). The total current in the MITLs is compared with the total insulator stack current in Fig. 7. Note that the current has exactly the same shape as the insulator stack current at all times except when the insulator stack flashes late in time. At that time all of the magnetic flux is trapped in the MITLs and will only slowly LR decay away. MITL current data from other shots with MITL current monitors just outside

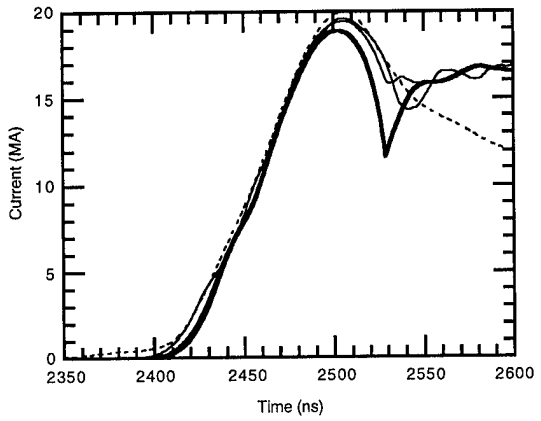


Figure 9 The total stack and MITL currents (dashed lines) for Shot 51 plotted together with the Screamer calculated values (solid lines). The Screamer load current is the bold line.

the vacuum convolute (30 cm from the load) show no MITL current losses to that radial location.

4.4 Comparison of Data with Modeling

The final piece of data required to compare with circuit calculations is from the z-pinch load. We measure the implosion time and have accurate knowledge of the initial load mass and radial position. The load data, the measured inductances, together with water transmission line, stack, and MITL current and voltage data allows a detailed model of the entire pulsed power system. We use the Sandia Screamer code[5] with only one adjustable parameter, the effective loss impedance at the vacuum convolute, to model PBFA-Z power flow.

Figure 8 shows the power and relative timing of the x radiation to the total insulator stack power. The timing accuracy of the two signals is measured to be ~ 2 ns. Note that the z pinch provided a 4X power gain over the electrical power delivered to the insulator stack. Using this time information and knowing that the load dynamics places a severe constrain on the actual current driving the load we calculate all relevant voltages and currents in the system. Figure 9 plots the stack and MITL currents against Screamer calculated values. In addition, the Screamer prediction for the actual load current (not measured) is included. The agreements are excellent. Using the same modeling methodology with a large number of shots has given us confidence in this technique for extracting the actual load current for a wide range of load parameters.

5 CONCLUSIONS

PBFA Z, representing the culmination of marx-driven water-pulse-line technology, is the world's most powerful electrical accelerator. We are successfully operating at the 50-TW design point. We routinely couple MJ's of electrical energy into imploding z-pinch loads thereby generating x-ray powers of 200 TW and x-ray energies of 1.85 MJ.

PBFA Z will be available for the next decade for a variety of scientific uses. Experimenters can access unique regions of plasma density and temperature parameter space for basic science and defense applications.

ACKNOWLEDGEMENTS

The author would like to thank the invaluable assistance of a large number contributors, throughout government and industry, without whose pulse power expertise this work would have been impossible. In particular, the authors acknowledge the significant contributions made by P. Corcoran, I. Smith at Pulse Sciences, Inc, San Leandro, CA.

*This work was supported by the United States Department of Energy under Contract DE-AC04-94AL85000.

REFERENCES

[1] R. B. Spielman, et al., *Proc. Of the Tenth IEEE Pulsed Power Conf.*, Albuquerque, NM 1995, pp. 396.

[2] D. D. Bloomquist, et al., *Proc. of the Sixth IEEE Pulsed Power Conf.*, Arlington, VA edited by P. J. Turchi and B. H. Bernstein (IEEE, New York, 1987), p. 310.

[3] B. N. Turman, et al., *Proc. Of the Fifth IEEE Pulsed Power Conf.*, Arlington, VA 1985, pp. 155.`[B. N. Turman, et al., *Proc. Of the Fifth IEEE Pulsed Power Conf.*, Arlington, VA 1985, pp. 155.

[4] J. C. Martin, Fast Pulse Vacuum Flashover, SSWA/JCM/713/157 and AFWL High Voltage Notes, Note 2, 16 March 1971.

[5] M. L. Kiefer, K. L. Fugelso, K. W. Struve, M. M. Widner, SCREAMER, A Pulsed Power Design Tool, 25 August 1995 (Sandia Internal Document).

3D PARTICLE SIMULATIONS OF SPACE-CHARGE-DOMINATED BEAMS IN HIF ACCELERATOR EXPERIMENTS

D. P. Grote, A. Friedman, and S. M. Lund, LLNL, L-440 P. O. Box 808, Livermore, CA 94550
I. Haber, NRL, Code 6790, Washington DC 20375

Abstract

The development of a high current, heavy-ion beam driver for inertial confinement fusion requires a detailed understanding of the behavior of the beam, including effects of the large self-fields. This necessity makes particle-in-cell (PIC) simulation the appropriate tool, and for this reason, the three-dimensional PIC/accelerator code WARP3d is being developed. WARP3d has been used extensively to study the creation and propagation of ion beams both to support experiments and for the understanding of basic beam physics. An overview of the structure of the code is presented along with a discussion of features that make the code an effective tool in the understanding of space-charge dominated beam behavior. A number of applications where WARP3d has played an important role is discussed, emphasizing the need of three-dimensional, first principles simulations. Results and comparisons with experiment are presented.

1 INTRODUCTION

The mainline approach of the U.S. for a driver for energy production by inertial confinement fusion is a heavy-ion induction accelerator. The beams used for heavy-ion fusion (HIF) have a large enough current that the space-charge effects dominate the behavior of the beam, in comparison to thermal effects. The necessity of including the significant space-charge makes theoretical analysis of the beam difficult, but makes the use of particle simulation techniques (used in plasma physics) ideal.

One- and two-dimensional particle-in-cell (PIC) codes have played a significant role in the understanding of space-charge dominated beam dynamics. Often though, full three-dimensional models are required to capture all of the relevant physics; there is much interaction of the longitudinal and transverse dynamics of the beams. Examples of cases where full-three dimensional simulation is necessary are the study of beam ends and longitudinal compression in a quadrupole lattice and the examination of various element misalignments and non-axisymmetric field errors. For these reasons, the three-dimensional PIC/accelerator code WARP3d is being developed.

WARP3d[1] is a three-dimensional PIC code developed expressly for the purpose of simulating the behavior of high-current, space-charge dominated beams. The applications of interest are ongoing and future accelerator experiments in the HIF program and ultimately a full scale driver for inertial fusion energy power production. We are well on our way toward a source-to-target modeling capability needed for modeling a full scale driver.

2 OVERVIEW OF WARP3d

The WARP3d code combines the PIC technique with a description of the "lattice" of accelerator elements. In the PIC model, the calculation of the self-fields of the beam is done by solving Poisson's equation (i.e. electrostatic only) on a 3-D mesh which can move with the beam. Only electrostatic beam fields are important throughout most of an HIF accelerator since, with the large ion mass, the velocity is well below the speed of light, only reaching ~0.3 c at the end. The particles are advanced using the full Lorentz equation, including the self electric field as well as the applied electric and magnetic fields. The beams can be created in their entirety at the start of the simulation or by injection. The injection can be off of a plane or a curved surface and can be at a set current or space-charge limited. Both steady-state and time-dependent simulations can be made. The steady-state algorithm is based on the algorithm used in EGUN[2].

The lattice is a general set of finite-length accelerator elements including quadrupoles for focusing, dipoles for bending, and induction gaps for acceleration, as well as more general elements with arbitrary fields. Another set of elements in the 3-D model specifies the locations and curvatures of bends. These are not physical elements but are the appropriate coordinate transformations needed to follow the beam around the bends. The calculation of the self-fields is also altered to include the curvature of this "warped" space.

The fields of the lattice elements can be specified at any of several levels of detail. At the lowest level, the lattice elements can be hard-edged with an axially uniform field over the extent of the element. Here, the "residence correction" method is used in the particle mover, scaling the applied field by the fraction of the velocity step spent inside the element, to ensure that the particles receive (to a good approximation) the correct impulse from each element independent of the timestep size and thus allowing larger timesteps to be used. The fields of elements may also be specified in more detail and more generally either via axially dependent multipolar field composition or via field description on a 3-D mesh. The electrostatic elements can alternately be implemented from "first principles" by self-consistently including the conductors in the field solution, using a subgrid-scale boundary resolution algorithm to afford a realistic description of the geometry.

WARP3d makes use of a number of modern programming practices such as use of an interpretive scripting language, coarse grained objects, and parallel processing.

0-7803-4376-X/98/$10.00 © 1998 IEEE

3 BEND EXPERIMENT

A recirculating induction accelerator has the potential of significantly reduced cost as a driver for heavy-ion fusion. There are a number of physics and engineering issues that still need to be examined. For that reason, the heavy-ion fusion group at LLNL has begun experiments leading up to a small scale recirculator which will have dimensionless parameters similar to those of a driver scale recirculator[3]. The bend experiment is the first step of the sequence and may be the first detailed examination of the behavior of a space-charge dominated beam in a bent lattice with quadrupole focusing.

In the current state of the experiment a matching section of seven electric quadrupoles is followed by eight permanent magnetic quadrupoles in a straight lattice, and then by five more magnetic quadrupoles which are in a bent lattice with electric dipoles between the quadrupoles to bend the beam. The total bend angle is 45°. The beam of singly-charged potassium ions is injected with an energy of 80 keV, a current of 2 mA, and a radius of 5.5 mm. The space charge of the beam depresses the phase advance per lattice period from 70° to 20°. The transport line is in total about five meters long.

The goals of the simulations are, in combination with experimental results, to understand the behavior of the beam in the bend and to fully characterize the beam to allow thorough understanding of what will be inserted into the completed ring.

Previous analytical work[4] and simulation[1] has shown that as a beam enters a bend, it experiences a growth in emittance which is related to the axial thermal spread of the beam. As a beam with a thermal spread enters a bend, the particles with different axial velocities will separate due to dispersion. This separation leads directly to an increase in RMS emittance, and as the nonlinear space-charge density due to the separation thermally mixes, the separation leads to an increase in the true emittance which is related to the beam temperature. In the length of the current 45° bend experiment, only the increase in RMS emittance will be observed.

This growth in emittance can be used as an indirect measurement of the axial thermal spread in the experimental beam. The thermal spread is estimated from the temperature of the emitter to be < 0.1% of the axial velocity, too small to be measured directly. By comparing the emittance growth seen in the experiment with that of simulations, a better estimate can be obtained.

In most of the simulations, the beam is formed by injection from the aperture at the end of the diode. The field of the electric quadrupoles is obtained from a multipolar decomposition of the fields calculated from "first principles" in a separate WARP3d calculation including the geometry of the electric quadrupole conductors. The field from the magnetic quadrupoles is obtained analytically; knowing the arrangement of the permanent magnets which make up the quadrupoles, the field can be calculated and

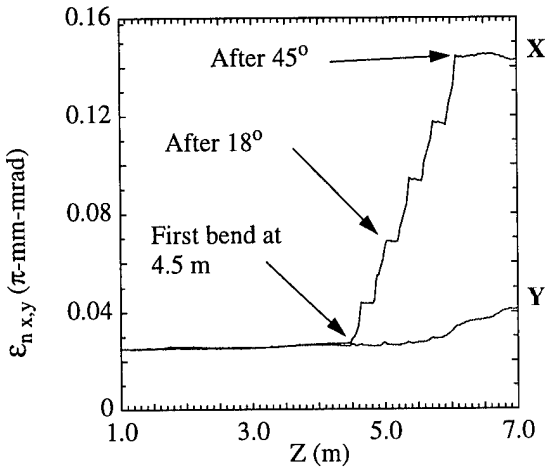


Figure 1: Normalized emittance at mid-pulse as the beam moves along the accelerator. The rise in the x emittance is due to the axial thermal spread of the beam in the bend. The y emittance begins to rise to match x. The thermal spread is 0.22% of the beam velocity.

then decomposed into multipolar components. The field from the dipoles is obtained by another first-principles solution of Laplace's equation including the carefully-shaped electric dipole plates. The field in a 3-D region around the plates is saved and applied directly to the particles.

Typically, 100,000 simulation particles and a $64 \times 32 \times 256$ field grid are used. About 800 timesteps are taken for the beam to travel completely though the lattice, taking 20 minutes on 32 processors of a Cray T3D.

With a thermal spread of 0.22% of the axial beam velocity, roughly the same as the transverse thermal spread, a significant emittance growth is seen as shown in figure 1. Figure 2 compares the transverse phase space in the plane of the bend before and after the bending. The spreading is very evident. In the plots, the particle shading is determined by the axial velocity, showing the separation of the different velocity classes. The particles with smaller x' are those with higher axial velocity; the beam is bending towards positive x so the particles with higher axial velocity are bending less and thus have more negative x and x'.

A series of simulations was carried out with varying axial thermal spread. Figure 3 shows the final emittance after a 45° bend versus the axial thermal spread. The increases in emittance for the velocity spreads shown are all well within acceptable limits for a beam to be injected into the ring. Note that for these runs, the fields of the matching electric quadrupoles were applied using the hard-edged approximation, to reduce the time of the simulation. Comparison with runs using the decomposed first-principles fields show little difference in the emittance growth.

Extensive simulations of the full small scale recirculator experiment have also been carried out. The simulation

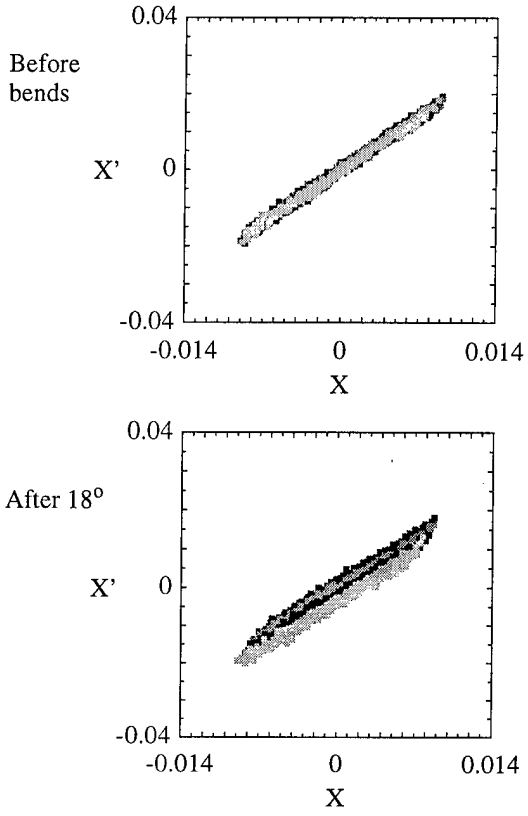


Figure 2: Phase space in the plane of the bend before and after an 18° bend. The shading of the particles based on axial velocity shows the spreading from the bend. The particles with larger velocity have smaller x'.

results show emittance growth from multi-lap operation that is well within acceptable limits. That work is discussed more fully in reference [1].

4 MARYLAND BEND EXPERIMENT

The University of Maryland has an experimental electron beam program that is examining the dynamics of high-current, low energy beams. Currently there exists a one meter long, 4 kV, 20 mA, injector test assembly[6]. In the planning stages is a ring[7]. The WARP3d code is beginning to be used in the examination of the experiments and in validation of the designs.

The focus to date has been on simulating the existing injector transport line. The focusing in the accelerator is obtained from printed circuit quadrupoles which were designed with a 3-D magnetics program. The fields from these quadrupoles are calculated in the 3-D magnetics program and are empirically fit to an analytic formula which is used in the simulation. Similarly, the fields from a solenoid, which is used to initially focus the beam as it comes off of the source, can be calculated and applied in the simulation. The calculated 3-D field structure can be applied directly in the simulation, but this has not been done yet. The simulated beam is created by continuous injection at a constant current at the end of the diode and is allowed to fill the system axially until a steady-state is reached.

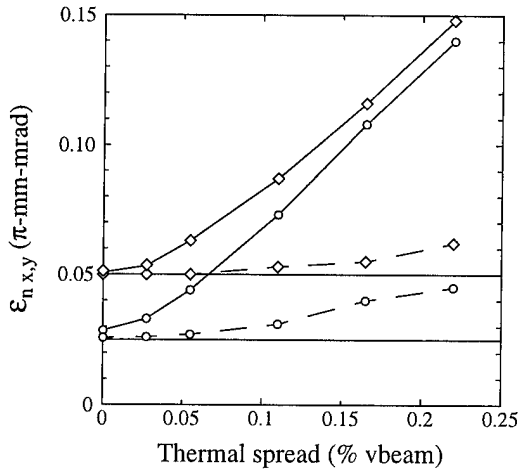


Figure 3: Final normalized emittance of the beam midpulse with changing axial thermal spread for two different initial emittances, 0.025 and 0.05 π-mm-mrad. Solid line is in the plane of the bend, dashed is out of plane. The horizontal lines show the initial emittance. Comparison with the emittance from the experiment will give an indirect measurement of the axial thermal spread.

As there is no experimental data yet, comparisons were made with another code, namely the envelope code SPOT[8]. Good agreement was found between the codes. There were minor differences, though, due in part to the fact that WARP3d allows a more complete description of the solenoid fields including the radially varying transverse fields. Use of the more complete description changes the effective focusing of the solenoid. The future plans are to use WARP3d to examine the design of the full electron ring. That work will rely heavily on the capability of WARP3d to model the transport of high-current beams around bends.

5 ELECTROSTATIC QUADRUPOLE INJECTOR

An injector for a driver-scale accelerator will be required to produce multiple beams with a high current. In order to examine the relevant physics and engineering issues, a driver scale injector experiment is being carried out at LBNL[5]. The injector design consists of a diode to extract a beam from a source, followed by a series of electric quadrupole focusing elements which have their voltages arranged to produce a net accelerating gradient down the axis.

The injector produces a 1 A beam of singly-charged potassium ions at 2 MeV. A major goal was production of a beam of low emittance. Since there are a number of issues in the design of the injector which can lead to emit-

tance growth, an effort was started to study the injector with simulation. The major issue is the large size of the potentials of the electric focusing quadrupoles relative to the energy of the beam. That potential can cause a significant transverse variation of the axial velocity which distorts the beam, leading to emittance growth; this is referred to as the "energy effect".

The experiment has been simulated extensively using WARP3d. Initial simulations were of a smaller scale, proof of principle experiment and help demonstrate the feasibility of the injector design and improve upon it. The major improvement was knowledge of how much to increase the diode voltage. With that increase, the focusing potentials are a smaller fraction of the beam energy and the distortion due to the energy effect is less. Also, the beam is more easily focused and can be made smaller, further reducing the size of the distortion. The diode voltage is limited, though, on the upper end by breakdown considerations. Increasing the diode voltage from 500 kV to 750 kV was shown by the simulations to significantly reduce the emittance growth while staying below the voltage breakdown threshold.

Self-consistent simulations of the full-scale experiment have been carried out[1]. The beam is created by space-charge limited injection off the emitting surface. The full geometry of the diode region and of the electric quadrupole structure is included self-consistently, creating the applied fields and the image fields. Comparisons between simulation and experiment have shown excellent agreement in the beam size and divergence as well as in the shape of the beams transverse phase space.

The experimental results, though, have shown an unanticipated beam hollowing and non-linear transverse charge density distribution. Simulations of the experiment have eliminated such causes as the energy effect, and suggest that the hollowing could results from a nonuniform distribution generated in the diode. Studies of this phenomenon continue.

6 BEAM COMBINER

An optimal design of a driver may require the combining of multiple beams in order to take advantage of cost efficiencies of an architecture with many beams at low energy and few beams at high energy. The HIF group at LBNL is carrying out an experiment to examine beam combining[9]. The major issue is the increase in the emittance resulting from the filling of phase space between the beams when they are combined.

WARP3d is being used to simulate the beam transport. To date, the code has only been used for simulations of the matching section leading up to the combiner section. Fairly good agreement with the experimental results have been obtained. There is a small difference in the phase rotation which is likely due to uncertainties in the initial conditions which are used in the simulation. The simulations are shedding light on the cause of an unanticipated essing in phase space. These simulations are described in more detail in reference [10]. Our future plans include simulation of all of the experiment from the source through the combiner.

7 AVLIS

Though not within the HIF program, simulations for the atomic vapor laser isotope separation (AVLIS) program provide a means to further the use and utility of the WARP3d code. The AVLIS program is using an electron beam to melt and vaporize the material to be separated. The electron gun has shown anomalous asymmetric beam behavior that cannot be studied with axisymmetric codes. We have begun to use WARP3d to examine the gun with space-charge limited injection of the electrons off the emitter surface and use of magnetic fields calculated by TOSCA and specified on a 3-D grid. The full conductor geometry is simulated using subgrid-scale conductor resolution.

An additional focus of the simulations is placing tolerances on the construction of the gun diode. A series of simulations has been carried out offsetting various pieces of the diode to examine the degradation of beam quality. These simulations are made possible by the three-dimensional code.

8 CONCLUSIONS

The necessity of self-consistency in the self-field calculation and of full dimensionality in the study of the transport of high-current beams relevant for HIF has lead to the development of WARP3d, a three-dimensional particle-in-cell/accelerator code. Though this code is still under development, it has been successfully used in a wide range of applications, some of which have been described above. The major uses have been examination of beam dynamics in ongoing accelerator experiments being carried out by the U.S. HIF program. The code has been used to study, among other issues, injection, transport though lattices with non-linear fields, transport through bent lattices, and misalignments. WARP3d has played and continues to play an important role in the development of our understanding of high-current beam dynamics and in the analysis of high-current beam experiments.

9 REFERENCES

[1] D. P. Grote, *et. al.*, "Three-Dimensional Simulations of High Current Beams in Induction Accelerators with WARP3d", *Fus. Eng. & Des.*, 32-33 (1996) 193-200.

[2] W. B. Herrmannsfeldt, "EGUN-An Electron Optics and Gun Design Program", technical report 331, SLAC, 1988.

[3] C. Sangster, "Status of the LLNL Experiments in Bending and Recirculating", this conference, 8V47.

[4] J. J. Barnard, H. D. Shay, S. S. Yu, A. Friedman, and D. P. Grote, "Emittance growth in Heavy Ion Recirculators", 1992 Linear Accelerator Conference Proceedings, Ottawa, Canada, vol. 1, p 229, AECL Research, (1992).

[5] S. Yu, *et. al.*, "Heavy Ion Fusion 2 MV Injector", in *Proceedings of the 1995 Particle Accelerator Conference*, Dallas, TX, pp 1178-82, IEEE, 1995.

[6] S. Bernal, *et. al.*, "Transport of Space-Charge Dominated Electron Beams in a Printed-Circuit Quadrupole Channel", this conference, 9V36.

[7] J. G. Wang, *et. al.*, "Design and Development of an Electron Recirculator for Study of High Current Beam Dynamics", this conference, 6'C6.

[8] C. K. Allen, *et. al.*, IEEE Cat. 95CH35843, 2324 (1996).

[9] P. A. Seidl, *et. al.*, "A Scaled Beam-Combining Experiment for Heavy Ion Inertial Fusion", this conference, 8V46.

[10] W. M. Fawley, *et. al.*, "Numerical Simulation Studies of the LBNL Heavy-Ion Beam Combiner Experiment", this conference, 8V45.

EXPERIMENTS INVESTIGATING THE GENERATION AND TRANSPORT OF 10-12 MeV, 30-kA, mm-SIZE ELECTRON BEAMS WITH LINEAR INDUCTIVE VOLTAGE ADDERS

M. G. Mazarakis, J. W. Poukey, J. E. Maenchen, D. C. Rovang, P. R. Menge, J. S. Lash, D. L. Smith, J. A. Halbleib, S. R. Cordova, K. Mikkelson, J. Gustwiller, and W. A. Stygar
Sandia National Laboratories, P.O. Box 5800, Albuquerque, NM 87185-1193
D. R. Welch, Mission Research Corporation, Albuquerque, NM 87106
I. Smith and P. Corcoran, Pulse Sciences Incorporated, San Leandro, CA 94577

Abstract

We present the design, analysis, and results of the high-brightness electron beam experiments currently under investigation at Sandia National Laboratories. The anticipated beam parameters are the following: energy 8-12 MeV, current 35-50 kA, rms radius 0.5 mm, and pulse duration 30-60 ns FWHM. The accelerators utilized are SABRE and HERMES III. Both are linear inductive voltage adders (IVA) modified to higher impedance and fitted with magnetically immersed foilless electron diodes. In the strong 20-50 Tesla solenoidal magnetic field of the diode, mm-size electron beams are generated and propagated to a beam stop. The electron beam is field emitted from mm-diameter needle-shaped cathode electrode and is contained in a similar size envelope by the strong magnetic field. These extremely space charge dominated beams provide the opportunity to study beam dynamics and possible instabilities in a unique parameter space. The SABRE experiments are already completed and have produced 30-kA, 1.5-2.5 FWHM electron beams, while the HERMES-III experiments are currently under way.

INTRODUCTION

The experiments reported here were motivated by the success of converting RADLAC II (an induction linac) into an equal impedance (~ 120 ohm) inductive voltage adder coupled to a magnetically immersed foilless diode (RADLAC II/SMILE) [1]. The inductive voltage adder (IVA) technology is relatively simple and couples a self-magnetically insulated transmission line (MITL) [2] with an induction linac to generate a new family of induction accelerators. In these accelerators, the particle beam which drifts through the multiple cavities of conventional induction linacs is replaced by a metal conductor which extends along the entire length of the device. The voltage addition of the accelerating cavities is therefore accumulated in the TEM Poynting vector rather than in a sequentially accelerated electron beam.

In the next sections, we present results and analysis of the SABRE [3] experiments and a progress report on HERMES-III [4] experiments.

SABRE EXPERIMENTS

SABRE IVA has 10 inductively insulated cavities, each rated at 1.0 MV, designed to operate at 40 ohms in negative polarity and 20 ohms in positive polarity. For these experiments, SABRE was modified to increase the output voltage and proportionally reduce the current, delivering the same energy. It was, therefore, operated at 9-12 MV and 100-120 kA. The major accelerator modifications were to reduce the total number of pulse forming lines by half and to design and construct a new cathode electrode. Thus, each cavity was fed by a single pulse forming line, doubling the accelerator impedance which was further increased to 120 ohms by the new smaller diameter cathode electrode [5,6,7].

The design of the MITL voltage adder and the foilless diode (Fig. 1) were validated with a large number of particle-in-cell simulations. Because of the large range in space and time scales, the entire design was divided into three parts: the voltage adder; the transition region, where the coupling from the MITL into the immersed diode was studied, and finally, the immersed diode where the beam generation and beam parameters were analyzed in fine detail (Fig. 2). The diode simulations represent an ideal situation assuming no ion emission from the target, perfect cylindrical symmetry and no instabilities between counterstreaming electrons and ions.

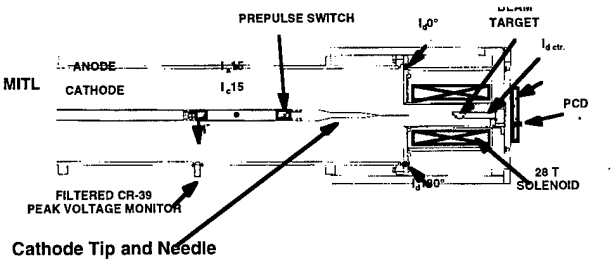


Figure 1. Schematic diagram of diode design and transition region, showing details and B-dot monitors.

0-7803-4376-X/98/$10.00 © 1998 IEEE

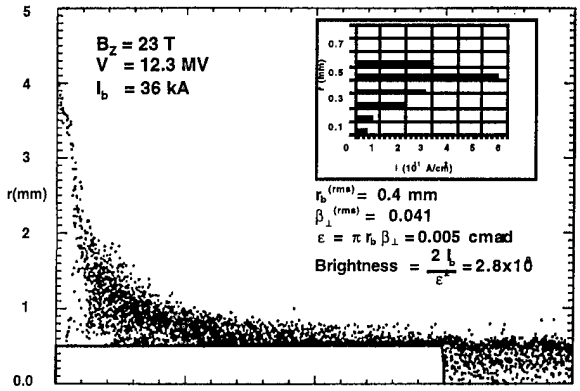


Figure 2. High-resolution diode simulation calculating the beam parameters.

The intense electron beam produced by the SABRE foilless diode quickly produces an ion-emitting anode plasma. The ions, mostly protons, are accelerated toward the cathode with a current reduced roughly by the ratio of the ion-to-electron beam velocity (3 kA ions versus 30 kA electrons for typical SABRE parameters). The electrostatic attraction between the two beams is considerable and various forms of the two-stream instability can be excited, including sausage, hollowing, hose, and filamentation. These instabilities can cause large deflections and heating of the beam which would increase the beam spot size in the absence of a strong axial magnetic field (B_Z). According to theory and IVORY simulations, a 30-T or higher field controls these instabilities in the linear regime and allows 0.5 to 0.75 mm radius beams. The experimental results are in very good agreement with IVORY simulations [8] (Table I). Figure 3 presents two time-integrated pinhole x-ray images of the beam on the anode target for two magnetic field strengths: 6 T (Fig. 3a) and 28.5 T (Fig. 3b).

Table 1

	Beam Spot FWHM (mm)	
B_Z (T)	Experiment	IVORY Simulation
6	3.1	2.83
29	1.5	1.25

SABRE experiments demonstrated that a magnetically immersed foilless diode driven by an inductive voltage adder can produce 1.5 mm (FWHM) electron beams. A ~ 30 T solenoidal magnetic field controlled the ion hose instability and kept it in the linear regime. The experimentally measured voltage, current, x-ray dose, $\beta_\perp$, and spot size are in excellent agreement with analytical theory and numerical simulations.

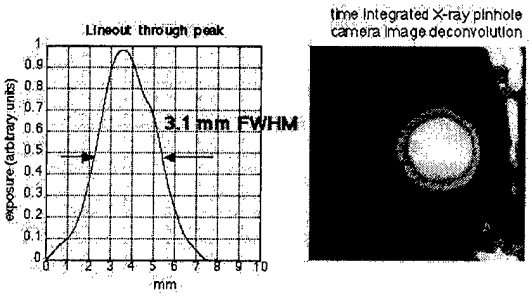


Figure 3a. Time-integrated x-ray images of the beam for B_Z = 6 T.

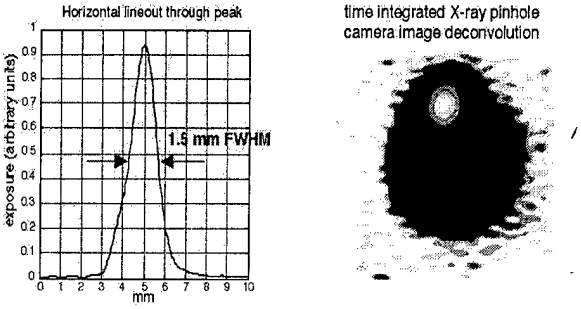


Figure 3b. Time-integrated x-ray images of the beam for B_Z = 29 T.

HERMES-III EXPERIMENTS

We currently utilize the HERMES-III accelerator to extend SABRE results to higher voltage (12 MV), longer pulse length (~ 70 ns FWHM), and higher diode magnetic field (50 T). The higher magnetic field should produce even smaller beam spot sizes of the order of 0.75 mm FWHM. The increased voltage and pulse length are required to achieve 1 kRad x-ray dose at 1 m from the Ta target.

HERMES III is larger than SABRE, having 20 inductively insulated cavities, each rated to a 1-MV maximum voltage. It routinely produces 18-20 MV, 700-kA electron beam in normal operation, but in the present experiments, we operate it at lower voltage (12 MV), reduced current (150 kA), and longer pulse (~ 70 ns FWHM). A number of modifications from the original configuration were necessary to achieve this performance: the pulse forming line length was doubled, a new cathode electrode increased the final impedance to 110 ohms, and the Marx generators were charged to lower voltage (60 kV). The cantilevered cathode electrode is now of much smaller radius and longer (18 m). To increase its strength continuous tapered sections were utilized instead of the stairstep design approach of previous voltage adders [5,6]. The outer cylinder of the extension MITL also has conical sections to reduce the radius down to SABRE size. Thus, the same magnetically immersed diode (Fig. 1) assemblies are utilized with HERMES III. In addition, a smaller, 50-Tesla, cryogenic diode was designed and constructed.

HERMES III is a very reliable accelerator and performed as expected. We produced with great reproducibility 12 MV, 150 kA, 70 ns FWHM pulses with 50 ns flat top at the output end of the long extension MITL.

During SABRE experimentation we observed a severe decrease in the diode impedance near the peak of the voltage pulse. It was attributed to a 100-kV prepulse arriving 200 ns before the main pulse. A flashover prepulse suppression switch solved the problem. For the diode impedance to remain constant, besides the prepulse switch, the diode chamber pressure had to be better than 2×10^{-6} torr. In HERMES III, we measured a similar amplitude prepulse. Two prepulse flashover switches were installed in series on the cathode electrode 30 cm upstream from the AK gap. Unfortunately, because of unexpected air and oil leaks inside the accelerator column, we are as yet unable to take advantage of the available long pulse and make the diode operate at constant impedance for the entire 70 ns. Fig. 4 shows voltage, diode current and diode impedance for SABRE normal operation (Fig. 4a) with prepulse flashover switch in place and good vacuum. Fig. 4b presents similar HERMES III diode parameters with the present poor vacuum (7×10^{6}) and oil contaminated system. At the beginning of the pulse, the impedance appears reasonable, and the first few frames of the x-ray framing camera [6] show beam spot sizes similar to SABRE and in good agreement with the simulations. However, very soon the diode impedance collapses and the beam disappears. Opening the AK gap to 20 cm seems to help the diode operation and substantially delay the impedance decay.

Currently, we are in the process of identifying and fixing the accelerator air leaks. To solve the oil leak problem, a number of accelerating cavities will be replaced, diffusion pumps will be installed in the accelerator, and sections of the extension MITL will be provided with cryowalls.

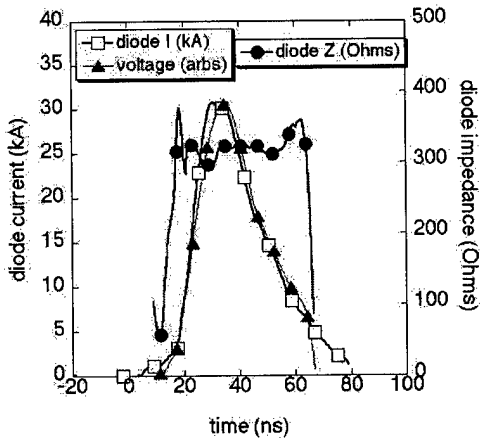


Figure 4a. A constant impedance diode shot with SABRE.

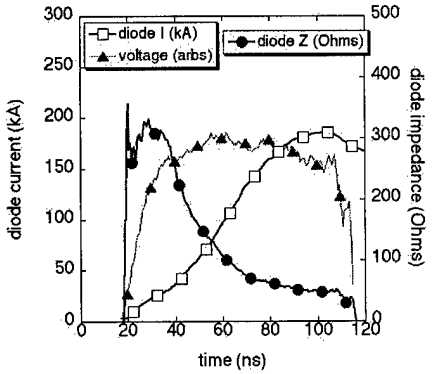


Figure 4b. The impedance of the HERMES-III diode decays with time, probably due to poor accelerator vacuum and oil contamination.

CONCLUSIONS

We have designed, constructed, and experimentally tested immersed diodes and high-impedance voltage adders for SABRE and HERMES III, which should generate very intense high-brightness electron beams of millimeter size. In our first experimental validation of the design with SABRE, ion-hose instabilities have imposed a lower spot size limit of 1.5-mm FWHM to the beam. The 50-T HERMES-III experiments should further minimize the ion-hose effect and reduce the beam spot size to ~ 0.7 mm FWHM. Unfortunately, in our first experimental campaign, poor accelerator vacuum and oil leaks prevented us from reaching our goals which we hope to achieve in the very near future.

ACKNOWLEDGMENTS

Sandia is a multiprogram laboratory operated by Sandia Corporation, a Lockheed Martin Company, for the U.S. DOE under Contract DE-ACO4-94AL85000.

REFERENCES

[1] M. G. Mazarakis, J. W. Poukey, S. L. Shope, C. A. Frost, B. N. Turman, J. J. Ramirez, and K. R. Prestwich, *Proc. 8th Int. IEEE Pulsed Power Conf.*, (San Diego, CA, 1991), p. 86.

[2] J. M. Creedon, *J. Appl. Phys.* **48** (3), 1070 (1977).

[3] J. Corley, J. A. Alexander, P. J. Pankuch, C. E. Heath, D. L. Johnson, J. J. Ramirez, and G. J. Denison, *Proc. 8th Int. IEEE Pulsed Power Conf.*, (San Diego, CA, 1991), p. 920.

[4] J. J. Ramirez, K. R. Prestiwch, E. L. Burgess, J. P. Furaus, R. A. Hamil, D. L. Johnson, T. W. L. Sanford, L. E. Seamons, L. X. Schneider, and G. A. Zawadzkas, *Proc. 6th Int. IEEE Pulsed Power Conf.*, (Arlington, VA, 1987), p. 294.

[5] M. G. Mazarakis, J. W. Poukey, D. Rovang, S. Cordova, P. Pankuch, R. Wavrik, D. L. Smith, J. E. Maenchen, L. Bennett, K. Shimp, and K. Law, in *Space Charge Dominated Beams and Applications of High Brightness Beams*, edited by S. Y. Lee, (AIP, New York, 1996), p. 479.

[6] M. G. Mazarakis, J. W. Poukey, D. C. Rovang, J. E. Maenchen, S. R. Cordova, P. R. Menge, R. Pepping, K. Mikkelson, D. L. Smith, J. Halbleib, and W. A. Stygar, *Appl. Phys. Lett.* **70** (7), 832 (1997).

[7] M. G. Mazarakis, J. W. Poukey, C. A. Frost, D. L. Johnson, S. L. Shope, J. A. Halbleib, K. R. Prestwich, B. N. Turman, and I. Smith, *Proc. IEEE Int. Conf. on Plasma Science*, (Tampa, FL, 1992), p. 104.

[8] D. R. Welch, M. A. Mostrom, and R. E. Clark, Mission Research Corporation internal report MRC/ABQ-R-1766 (1995); MRC/ABQ-R-1792 (1996).

LINEAR INDUCTION ACCELERATOR APPROACH FOR ADVANCED RADIOGRAPHY

George J. Caporaso, Lawrence Livermore National Laboratory, Livermore, California 94550, USA

Abstract

Recent advances in induction accelerator technology make it possible to envision a single accelerator that can serve as an intense, precision multiple pulse x-ray source for advanced radiography. Through the use of solid-state modulator technology repetition rates on the order of 1 MHz can be achieved with beam pulse lengths ranging from 200 ns to 2 μsecs. By using fast kickers, these pulses may be sectioned into pieces which are directed to different beamlines so as to interrogate the object under study from multiple lines of sight. The ultimate aim is to do a time dependent tomographic reconstruction of a dynamic object. The technology to accomplish these objectives along with a brief discussion of the experimental plans to verify it will be presented.

1 INTRODUCTION

Induction linacs, because of their kiloampere current capability are used as intense flash x-ray sources. A novel approach, illustrated in Fig. 1 is to generate a train of several pulses in one accelerator which can be sectioned into pieces by kickers and directed down different beamlines. These pieces will go through kickers and several large angle bends in order to arrive at the x-ray targets simultaneously.

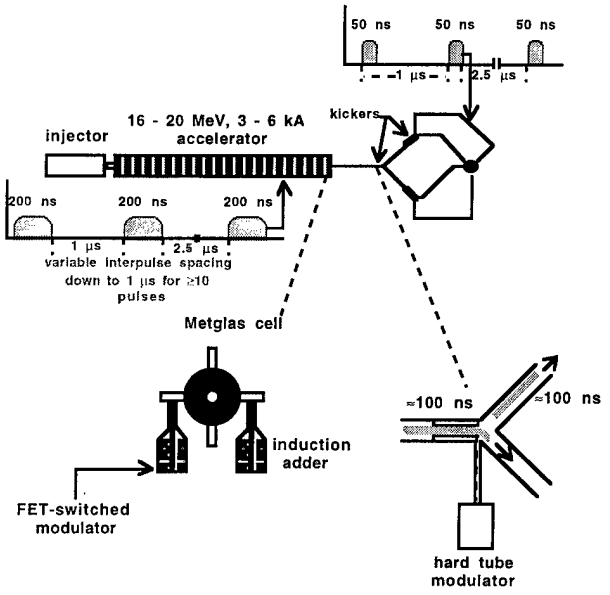


Fig. 1 Schematic of induction linac advanced radiography concept

The electron beam is focused to a small spot, typically of order 1 mm, onto a Bremsstrahlung target. The x-ray brightness depends on the electron beam's final spot size and divergence angle, and hence on its emittance. The performance of a radiographic machine using a single accelerator as a driver depends on whether beam quality can be preserved throughout these beam manipulations. The effects of space charge forces on the emittance growth in these bends has been calculated and appears to be small [1].

2 ARM SOLID-STATE MODULATOR

The ARM (Advanced Radiography Machine) solid-state modulator concept is shown in Fig. 2. The voltage to be applied to the load (ultimately an accelerator cell) is that of the precharged capacitor. A suitable switch alternately connects and disconnects the capacitor from the load. Another branch of the circuit acts independently to reset the magnetic core material of the induction cell to prepare it for another voltage pulse.

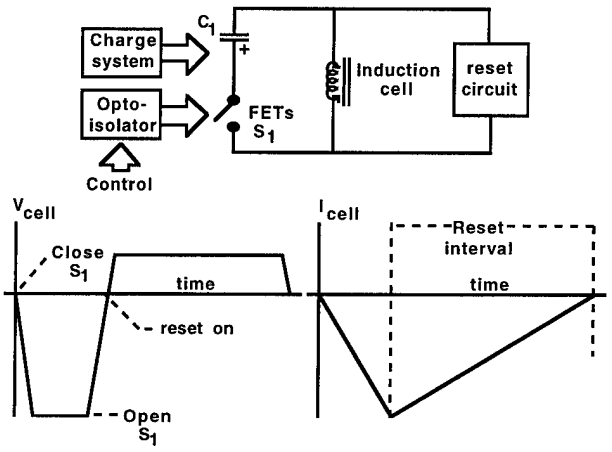


Fig. 2 Schematic of solid-state modulator concept

In this case the switch is a series-parallel array of FET's (Field Effect Transistors). These devices are inherently fast but have limited voltage and current capacity. Thus, they must be arranged in parallel to handle large currents and in series to handle high voltages. Fig. 3 shows a switch circuit board with 12 FET's capable of handling 1.2 kA at approximately 1 kV. Many of these circuit boards along with reset boards and the primary energy storage capacitors are arranged around a Metglas core to form the

0-7803-4376-X/98 /$10.00 © 1998 IEEE

ARM-II modulator shown in Fig. 4. This modulator has successfully operated at its design parameters of 15 kV (open circuit voltage) and up to 6.7 kA (where it is internally current limited) for pulses between 200ns up to 2μsecs in duration.

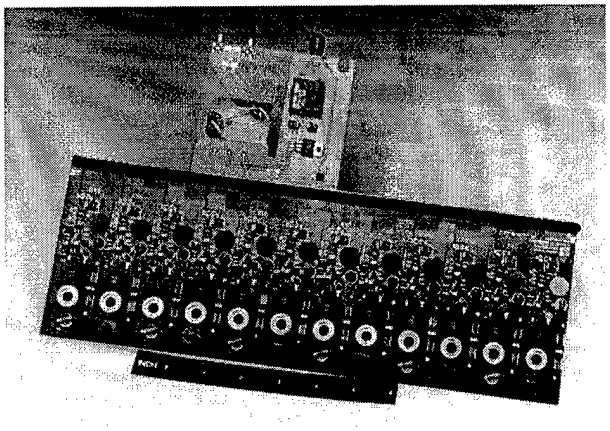


Fig. 3 ARM-II switchboard containing 12 FET's

The modulator has been fired at full power into a short circuit and operated without damage. Without reset the modulator can produce a string of 200 ns pulses at a repetition rate of 2 MHz.

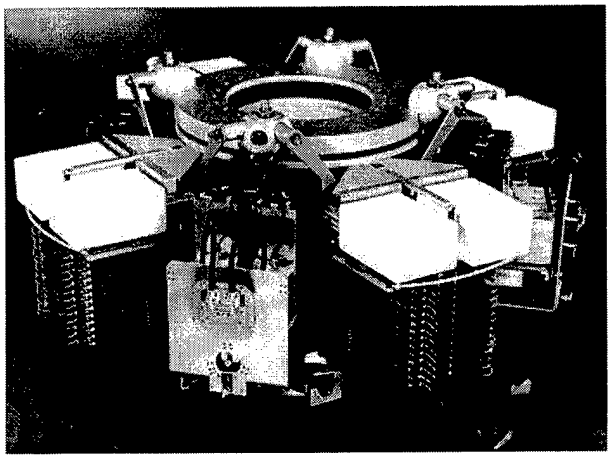


Fig. 4 Assembled ARM-II modulator

Fig. 5 shows a pulse sequence that might be used for advanced radiography. It consists of 1 1μsec pulse followed by a string of 3, 200 ns pulses followed by a 2 MHz burst of 5, 200 ns pulses.

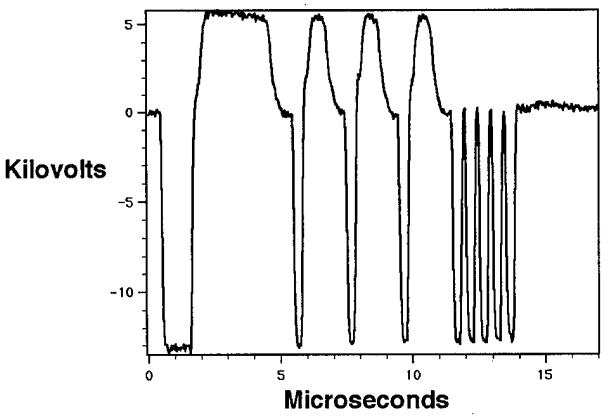


Fig. 5 A candidate accelerating pulse format for advanced radiography

3 FAST KICKER SYSTEM

The kicker system concept is illustrated in Fig. 6. It consists of stripline electrodes and is very similar to a stripline BPM. By driving the downstream end of two of the electrodes with a fast pulser the beam can be deflected in one plane. A D.C. bias dipole wound over the kicker is used to steer the beam to one of the two desired output positions in the absence of a pulse. When the pulser is activated, the voltage and current on the strips overcome the bias field and switch the beam to the other output position. The kicker is followed by a drift space in which the effects of the kicker are amplified. A separation of several centimeters in the two output positions is readily achieved but a large angular separation between the two beams is not. The beams are then passed through a D.C. septum magnet which changes the angles of the two output beams fairly abruptly so that there will be room to insert additional focusing lenses.

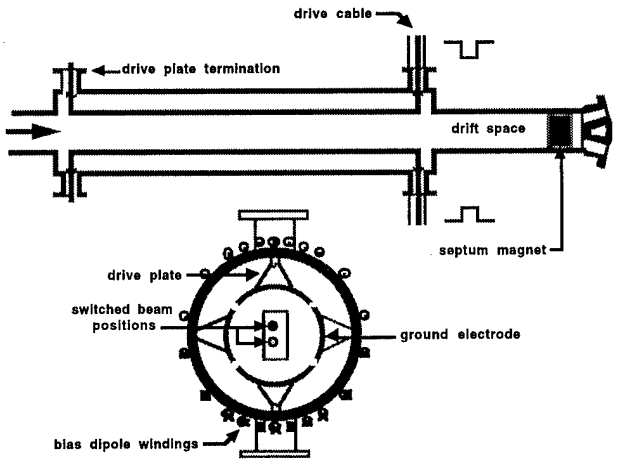


Fig. 6 Fast kicker system

The passage of a high current beam through the kicker will induce currents and voltages in the structure which will act to amplify the effects of the externally applied

deflecting signals [2, 3]. These effects can be made small in a properly designed system and can be compensated by using a pulser with an adjustable output waveform. A very fast pulse risetime is desired in order to minimize the amount of beam that is lost on the septum pipe. The pulses are provided by a hard tube modulator with a bandwidth on the order of 40 MHz. This system is essentially an amplifier which can provide a pulse that is custom tailored to accommodate the effects of any beam induced voltage in the system. Because kiloampere level beam currents will pass through the kicker relatively large voltages will be generated which will run up the drive cables to the pulser where they will reflect and come back down to the kicker perturbing subsequent sections of the beam. One way to eliminate these reflections is to use a transit time isolated cable system. Unfortunately for the time windows under consideration (10's of μsecs) the skin effect in conventional conductors makes this impossible without unacceptable high frequency attenuation. The attenuation and dispersion can be greatly reduced by using a superconducting delay line [4].

4 ETA-II EXPERIMENTS

In order to test various aspects of kicker performance and to verify the preservation of beam quality through large angle achromatic bends a series of experiments will be performed on the ETA-II induction accelerator [5]. ETA-II produces high quality electron beam pulses of 6.3 MeV at 2.2 kA with an energy flat top of ±1% over 40 ns. A series of extensive kicker/septum measurements are planned for the 1997 fiscal year. Beam induced voltages, and their effect on steering, emittance growth and pulser response will all be measured as a function of beam current from roughly 100 A up to the full current of the machine (2.2 kA). Eventually, the ARM three-stage inductive adder will be used to power a long pulse accelerator cell installed on the ETA-II beamline to provide a complete system test of the solid-state modulator technology with an actual beam load.

5 CONCLUSIONS

We have presented a concept for an advanced radiographic system that should be capable of providing multiple lines of sight to an object with a temporal sequence of pulses at a very high repetition rate sufficient to image a dynamic object.

6 ACKNOWLEDGMENTS

The author gratefully acknowledges helpful discussions with Hugh Kirbie. The work was performed under the auspices of the U.S. Department of Energy by LLNL under contract W-7405-ENG-48.

REFERENCES

[1] Yu-Jiuan Chen, "Space-Charge Forces Of A Dc Beam In A Continuous Bend", this conference.

[2] B. Poole, G. Caporaso and W. Ng, "Wake Properties of Stripline Beam Kicker", this conference.

[3] G. Caporaso, Yu Ju Chen and B. Poole, "Transmission Line Analysis of Beam Deflection in a BPM Stripline Kicker", this conference.

[4] Yu Ju Chen and G. Caporaso, "A Novel Design for a High Power Superconducting Delay Line", this conference.

[5] J. Weir, et. al., "ETA-II Experiments for Determining Advanced Radiographic Capabilities of Induction Linacs", this conference.

PERFORMANCE OF THE SPIRAL LINE INDUCTION ACCELERATOR

J.R. Smith, V.L. Bailey, H. Lackner, and S.D. Putnam

Pulse Sciences, Inc
San Leandro, CA 94577

Abstract

A proof-of-concept experiment (POCE) to demonstrate the performance of a novel recirculating induction accelerator has been completed. The Spiral Line Induction Accelerator employs a unique combination of features (spiral beamline, shielded off-axis gaps, and stellarator focussing fields) which permits efficient, high-current operation with a compact device.[1] Initial experiments demonstrated acceleration of 2 and 10 kA beams to 5.5 MeV and acceleration of a 12.5 kA beam to 4.5 MeV by transport around a full turn with two passes through a single accelerating unit. Recent tests with the completed POCE hardware achieved the program goal with acceleration of a 2.4 kA beam to 9.5 MeV.

1 INTRODUCTION

The Spiral Line Induction Accelerator (SLIA) is a compact high-current accelerator with two accelerating units placed on each side of a racetrack geometry (Fig. 1). An electron beam is recirculated through the accelerating units using a spiral beamline for simple injection and extraction. A solenoidal magnetic field confines the beam in the accelerating units; and toroidal, vertical, and stellarator fields are used for transport through the bends. The $l = 2$ stellarator or helical quadrupole fields [2] permit transport of a high current beam with large energy spread (design goal: transport of injected beam with $\leq$ 20% energy spread), and a shielded gap design permits off-axis accelerating gaps which are necessary for the spiral line geometry. This report describes a SLIA POCE experiment which consists of circulation around three 180° bends with two passes through each of the two accelerating units.

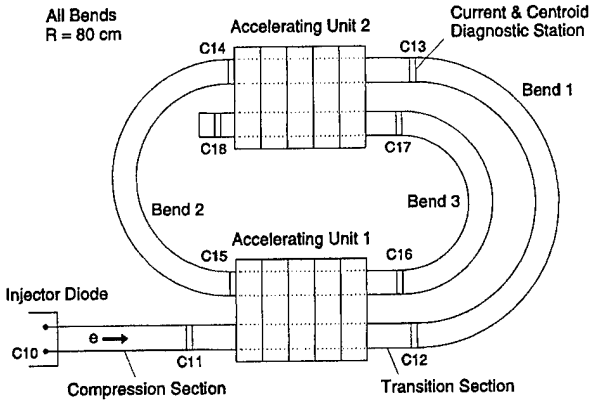


Figure 1. SLIA layout and diagnostic stations.

Major issues pertinent to SLIA operation are: (1) transport efficiency, (2) energy bandwidth of small aperture bends, (3) excitation of transverse beam deflection modes in the cells, i.e. the beam break-up instability (BBU), and (4) beam envelope matching on and off the stellarator bends.

The field-free injector diode uses a velvet cathode in a Pierce field geometry. The energy variation during the current risetime is ~ 65%, and ~ 100% during the falltime. The compression region consists of six solenoids tuned to provide a field profile which minimizes envelope oscillations for peak and near-peak injected energies. Beam diameter at the compression exit for these experiments is 12 mm. Each accelerating unit has five induction acceleration cavities, and each cavity has two off-axis accelerating gaps. Each gap produces a 300 kV, 83 ns FWHM accelerating pulse. The toroidal field in the accelerating units was ~ 2 kG. Transition sections 56.7 cm long are inserted between the accelerating units and bends 1 and 3. These allow diagnostic access and capability for addition of matching coils if needed.

The three 180° bends all have an 80 cm major radius and a 3 cm beampipe radius. Each bend has three layers of windings as outlined in the table below.

Table 1. Typical field values in the bends.

Toroidal (kG)	Vertical (G)	Stellarator (G/cm)
3.5 - 3.8	221 - 342	87 - 105

The stellarator pitch is 62.8 cm in bend 1, 83.8 cm in bend 2, and 125.7 cm in bend 3. These values allow operation of the bends as first order achromats. No steering or matching coils were used in the experiments reported here although experiments to validate two matching techniques [3] were conducted during the program.

There are nine B-dot stations labeled C10 through C18. Each station has 4 B-dots oriented at 90° intervals. Beam current is determined from addition of the 4 B-dot signals and beam centroid displacement is derived using a ratio equation involving the signals from opposing B-dots. A time integrated camera which images a Cherenkov converter is used to infer beam size. The target for this diagnostic consists of (1) a carbon disk and (2) two quartz plates separated by conducting mesh for

0-7803-4376-X/98/$10.00 © 1998 IEEE

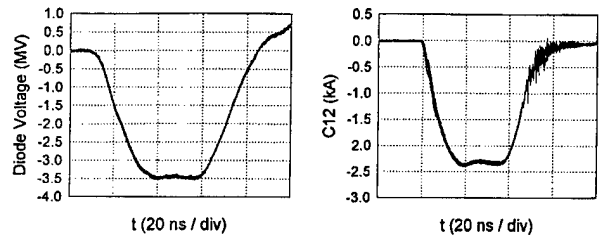


Figure 2. Seven shot overlay of diode voltage and C12 current

charge bleed-off.

2 BEAM MEASUREMENTS

Figure 2 shows reproducibility of diode voltage and C12 current for a seven shot overlay. Low energy electrons are not matched to the fields in the compression region and execute large radial oscillations in the compression region and accelerating unit. This produces current occlusions responsible for the oscillations observed during the falltime of the C12 current. In later work insertion of apertures in the compression section eliminated these oscillations. Beam centroid motion during ~ 25 ns of the current pulse at the end of the linear section of the accelerator (C12) was +/- 0.3 mm, the limit of resolution of the B-dot array.

Beam current and displacement at C16, C17, and C18 are given in Fig. 3. Beam displacement is shown for current ≥ 80% of the maximum current. The beam current profile is maintained throughout the transport with minor perturbations. During the mid-pulse at C16 and C17 (entrance and exit of bend 3) both x and y displacements are ≤ 1 mm and vary ≤ +/- 0.5 mm. During the midpulse at C18 x-displacement is 3 mm and varies ≤ +/- 0.5 mm, and y-displacement is ≤ 2 mm with oscillations ~ +/- 1 mm amplitude. The significantly larger displacements during the pulse rise and fall time are due to large energy mismatch in the bends which results in off-axis, larger angle trajectories at the bend exits.

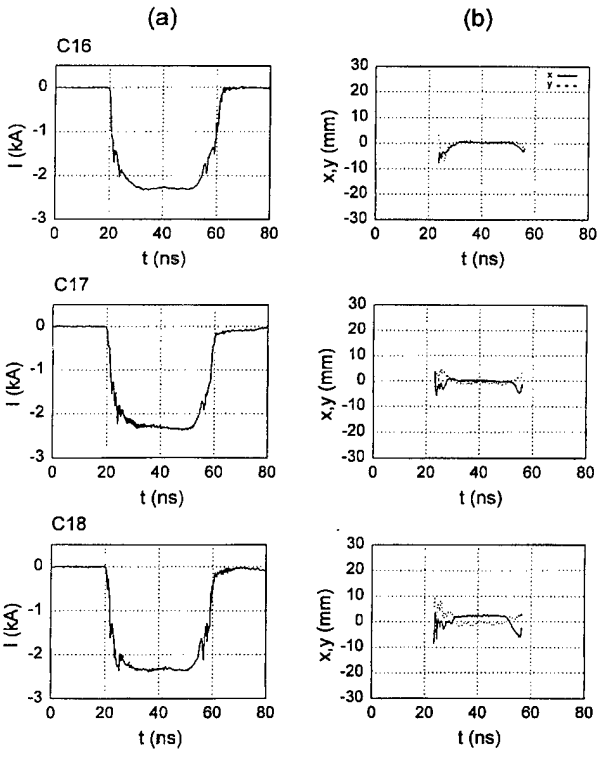


Figure 3. (a) Beam current. (b) Beam displacement. Shot # 4496.

Figure 4 gives maximum beam current, beam energy, and total beam charge as a function of axial position in the spiral line. The plot begins at the entrance to accelerating unit 1. The data points on the current and charge plots correspond to B-dot stations C12 - C18. The energy curve shows acceleration from the injector energy (3.5 MeV) to the final design energy (9.5 MeV). The loss of charge between C12 and C13 is due to loss of lower energy electrons in the risetime and falltime which are below the energy acceptance of bend 1. There is no additional loss of charge from C13 to C18. The small fluctuations are within the +/- 3•C accuracy of the measurement. The maximum current level is maintained throughout the spiral line.

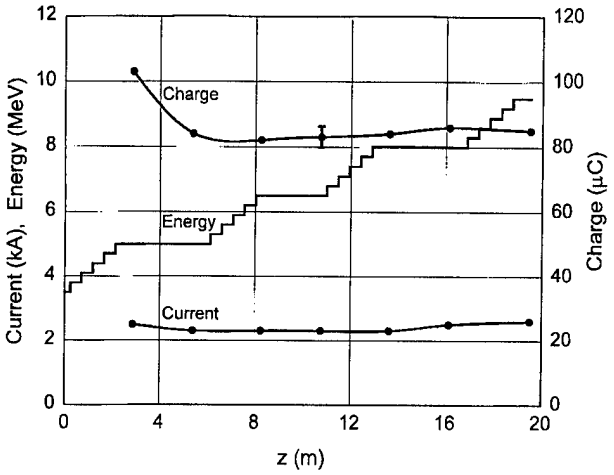


Figure 4. Beam current, energy (kinetic plus potential), and charge vs. beamline location.

The total system energy bandwidth is determined by comparison of the transported current and the diode voltage (Fig. 5.) The transported current pulse measured at C18 is identical to the injected current (C10) except the leading and falling edges are truncated as shown by the vertical lines in Fig. 5. Electrons which are ≥ 80% of the peak injected energy are transported through the entire spiral line; therefore the system energy bandwidth is 20%.

A time-integrated measurement of beam profile recorded immediately downstream of C18 is given in Fig. 6. The black outer boundary is the 60 mm beampipe

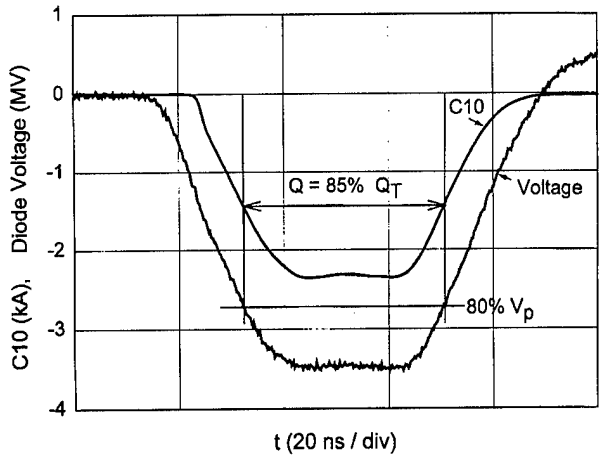


Figure 5. Determination of system energy bandwidth.

diameter. The full-width half maximum (FWHM) of the Cherenkov light is 18.6 mm. Calibration of light output with current density is required to rigorously determine beam width from this measurement. Previous work at lower beam voltage has demonstrated good agreement between light output and beam size.[4]

The two main modes of BBU growth are 1.0 and 1.8 Ghz from RF cold tests of a prototype cell/cavity.[5] Excitation frequencies below 900 MHZ do not couple through the coaxial section of the shielded gaps. No evidence of BBU growth was observed in any of the SLIA experiments even though no Q-reduction ferrite pieces were incorporated in the cells. Asymptotic formulas suggest BBU gains as high as ~230 for the 1.0 Ghz mode with some experimental parameters.

Stellarator fields are used to increase energy bandwidth in the bends. If stellarator fields are turned off energy bandwidth is reduced. Current rise and fall times

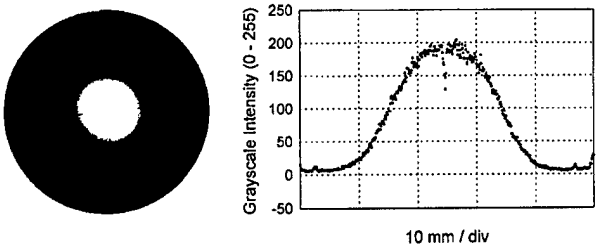


Figure 6. Cherenkov image of electron beam at the accelerator exit, and a line scan across a diameter. Cherenkov diameter = 18.6 mm, x-displacement = 0.6 mm, y-displacement = 0.6 mm. Shot # 4306.

which consist of lower energy electrons are significantly affected by the reduced bandwidth. This is demonstrated by comparison of risetime and falltime features at C18 for two cases: (1) all bends had stellarator fields - Fig. 3, and (2) only bend 3 had a stellarator field - Fig. 7.

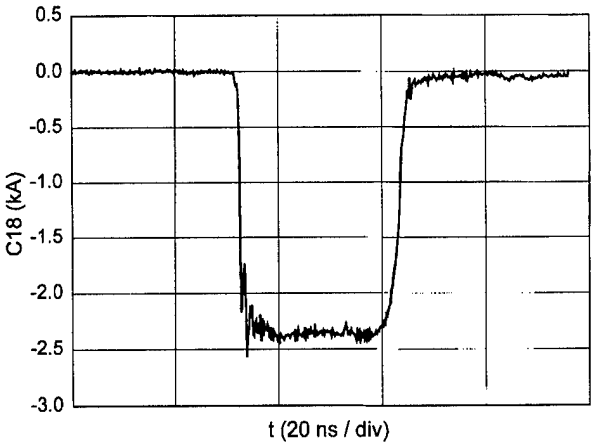


Figure 7. Current at C18 for shot without bend 1 and bend 2 stellarator fields. Risetime = 0.6 ns, FWHM = 31 ns. Shot # 4502.

3 SUMMARY

The SLIA proof-of-concept experiment has demonstrated acceleration of the 2.4 kA beam with an initial energy spread of 20% to full design energy. There was no measurable loss of charge after the first bend which eliminated electrons with energy outside the design energy bandwidth. At the accelerator exit the indicated beam diameter was 18.6 mm, and transverse centroid oscillations during the midpulse were less than ~ +/- 1 mm. Shot-to-shot reproducibility of current profiles and spot size were excellent. No oscillations due to BBU were observed, and no matching or additional steering were required for efficient transport.

4 ACKNOWLEDGMENTS

The excellent technical work by John Lisherness of Pulse Sciences, Inc. and the support of William Freeman of the Naval Surface Warfare Center and Dr. Bertram Hui of the Defense Advaned Research Projects Agency are very much appreciated. Theoretical support by the Naval Research Laboratory and Science Applications International (McLean, VA) during the early phase of the program and by Mission Research Corporation (Albuquerque, NM) throughout the program is gratefully acknowledged. This work was sponsored by DARPA and monitored by NSWC.

REFERENCES

[1] S. D. Putnam, 1987 IEEE Particle Accelerator Conference, Conf. Record 87CH2387-9, p. 887. V. Bailey et al., ibid.

[2] C. Roberson et al., *Particle Accel.* **17**, p. 79 (1985).

[3] M. Tiefenback et al., 1991 IEEE Particle Accelerator Conference, Conf. Record 91CH3038-7, p. 3195; J. Krall et al., *J. Appl. Phys.* **77**, p. 463 (1995).

[4] J. P. Lidestri et al., 1991 Particle Accelerator Conference, Conf. Record 91CH3038-7, p. 3120.

[5] J. Edighoffer, 1991 IEEE Particle Accelerator Conference, Conf. Record 91CH3038-7, p. 3117.

AIRIX PROTOTYPE TECHNOLOGICAL RESULTS AT CESTA

P.Anthouard, J.Bardy, C.Bonnafond, P.Delsart, A.Devin, P.Eyharts, P.Eyl, D.Guilhem, J.Labrouche, J.Launspach, J. de Mascureau, A.Roques, M.Thevenot, D.Villate, L. Voisin, Commissariat à l'Energie Atomique,Centre d'Etudes Scientifiques et Techniques d'Aquitaine, BP N°2 - 33114 Le Barp , France
and E.Merle, J.C.Picon, Commissariat à l'Energie Atomique, Centre d'Etudes de Vaujours - Moronvilliers, 51490 Pontfaverger-Moronvilliers, France.

Abstract

AIRIX Flash X-ray Radiographic facility is based on a 4 MeV - 3,5 kA pulsed electron injector and a 16 MeV induction accelerator. The accelerator will consist of 64 induction cells powered by 32 H.V. generators operated at 250 kV. The final 20 MeV electron beam will be focused on a target designed for X -ray conversion. At CESTA, PIVAIR is a testbed designed as a validation step of AIRIX up to 8 MeV. The injector has been connected with 16 accelerating cells, increasing electron beam energy to 7.2 MeV. Two kinds of induction cells have been developed and tested .A focusing experiment is planned for electron beam spot diameter measurements. After this step, beam focusing on a target will be experimented for X-ray source characterization.

1 INTRODUCTION

AIRIX induction accelerator has been designed to produce a 16-20 MeV, 3.5 kA, 60 ns high brightness electron beam for flash X-ray radiography application. Obtaining the final 2 mm focal spot size requires a low energy spread ($\Delta E/E \leq 1\%$) and a small emittance electron beam. These objectives have governed each component design: pulse power sources (injector and H.V. generators), induction cells (magnetic alignment and H.F. response) in order to minimize emittance growth ($\Delta\varepsilon \leq 10$ %) along the accelerator.

The first studies began at CESTA in 1992 with the development of two prototypes: a 250 kV pulsed generator and a versatile induction accelerating cell.

PIVAIR facility (Fig 1) is a validation step of AIRIX up to 8 MeV and consists of a 4 MeV pulsed electron injector, sixteen induction cells powered by eight H.V. generators, and a beam focusing section.

In the following sections, we shall describe the experimental set up and results which lead to the technological choices for AIRIX accelerator.

2 INJECTOR

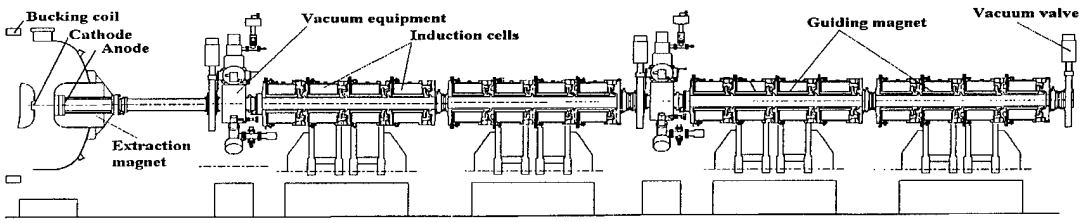
The injector consists of a 4 MV good flatness pulsed generator developed by PSI [1] and a vacuum diode designed by LANL for the DARHT project. Acceptance tests at CESTA in early 1994 have demonstrated a 4 MeV-3.5 kA beam with a low energy spread (± 1% over 60 ns). The beam normalized emittance was measured at 1600 ± 300 π.mm.mrad with the pepper pot method. The injector has exhibited an excellent reproducibility and a low command fire jitter (0.5 ns at 1σ) over more than 8000 shots performed in the 3 to 4 MeV range.

3 HIGH VOLTAGE GENERATORS

A high voltage pulsed generator has been designed to drive two induction cells with 250 kV, 75 ns pulses with less than ± 1% flat top deviation. Eight generators are currently operating on PIVAIR induction LINAC with the rated specifications according to the beam energy spectrum measured.

4 INDUCTION CELLS

Each induction cell comprises 11 ferrite cores (250 mm I.D., 500 mm O.D., 25 mm thick) housed in a non magnetic stainless steel body, a 4 layers bifilar wound solenoïd magnet and two printed circuit dipole trim coils. The 19 mm width accelerating gap has been shaped in order to obtain good voltage holdoff and minimize the beam coupling with the gap cavity to reduce BBU instability.



Figur 1 : PIVAIR set-up

0-7803-4376-X/98 /$10.00 © 1998 IEEE

4.1 Cell design and H.V.testing

The first induction prototype cell was operated with the prototype H.V. pulse generator and pure resistive loads in the 200 to 300 kV range [2] in order to test different set-up (gap geometry and insulators, fe rrite types,...). Two types of cell were finally selected to be tested with a 3.5 kA beam on PIVAIR test bed (Fig 2):

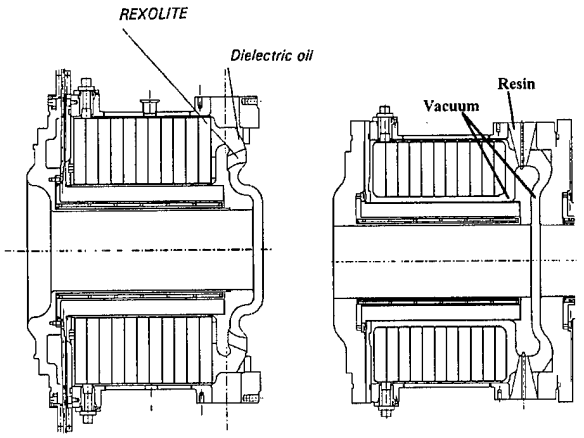


Figure 2: PIVAIR induction cells

4.1.1 Rexolite cell

In this technology, the ferrite cores are insulated with oil and the gap insulator is made of reticulated polystyrene (Rexolite) ; viton O-rings provide vacuum tightness (10^{-6} Torr).

4.1.2 Ferrite under vacuum cell

In such a cell, gap insulator is suppressed and dielectric oil is replaced by vacuum. The vacuum interface and high voltage insulation are transferred on cable heads.

4.2 Ferrite improvement

The first tests performed with TDK PE 11 B ferrite pointed out the need for increasing available flux swing in order to maintain a 75 ns flat top at 250 kV. TDK PE 16 ferrite were tested but the specific ferrite developed by CEA-LR exhibited a 15% flux swing gain. They were successfully tested on PIVAIR and choosen to furnish AIRIX induction cells cores.

5 DIAGNOSTICS

Specific, accurate and time resolved diagnostics have been developed in order to monitor (BPM) and to characterize (spectometer, emittancemeter, beam imaging using OTR or Cerenkov) the electron beam; they are more detailed in a companion paper [3]

6 PIVAIR RESULTS

6.1 Alignment

The 50 meters lenght AIRIX accelerator will consist of sixteen cell blocks (each block is a four induction cell assembly) completed by a drift pipe and a focusing magnet.The cell magnetic misalignement must be minimized in order to reduce chromatic effects.The objective is to enclose all the cell magnetic axes into a 250 µm diameter cylinder with an angle spread lower than 500 µrad around the reference beam axis. Moreover we want to be able to control the accelerator alignement between two shots without using the beam axis (i.e without breaking vacuum), so a new external reference must be defined .

A first procedure, using a prism technique and four lasers [4] has been abandonned for accuracy problems.

In the new procedure, the beam axis reference is defined with respect to a vertical plane and an horizontal plane (Fig 3). Two WPS (Wire Positioning System) and three HLS (Hydrostatic Levelling System) detectors are necessary to ajust these two planes [5]. Both detectors use capacitive probes and were studied by ESRF.

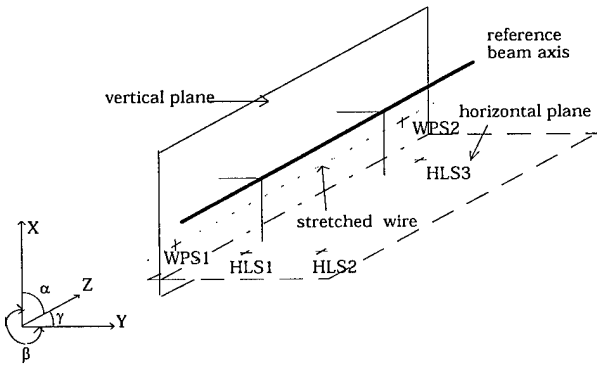


Figure 3: external reference

The alignment procedure consists of 3 steps:

- the reference beam axis is defined into the accelerator building and two standard references are set up to materialize this axis.
- each block ,which consits of 4 cells mechanically aligned and assembled on a Standard Mounting Bench (SMB), is aligned with respect to the SMB standard references (fig 4) by means of the WPS and HLS detectors. The third HLS is replaced by a bank indicator.

The detector values are recorded in a block data file

- the cell block previously aligned on the SMB reference axis is then transported on the accelerator line in order to be aligned on the beam reference axis. The final alignment is obtained when the HLS and WPS detectors reproduce the block data specifications previously recorded on the SMB.

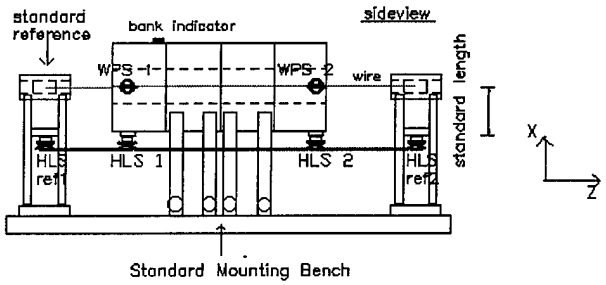


Figure 4: cell block alignment on the bench

The SMB, very sensitive to thermal or vibration perturbations, has been entirely automatised for each cell alignment and could be operated by night to avoid human work perturbations.

The first HLS network is going to be tested in the PIVAIR accelerator set up and environment by the end of this year. As the WPS wire can't be installed before the end of AIRIX accelerator assembly, the full scale alignment system will not be set up and tested before the end of next year.

6.2 Induction cell characterization

6.2.1 Rexolite cells

The first 4 cells, using TDK PE 11 ferrites, demonstrated a 210 kV per cell "routine" accelerating level with a 4 MeV-3.5 kA injected electron beam. For higher accelerating voltages, ferrite saturation occured and a reverse peak voltage appeared accross cell gap, leading to a flashover. Thanks to the magnetic flux gain obtained with CEA-LR ferrites, the next 4 cells exhibited a 250 kV working voltage (1 MeV energy gain per block measured with the time resolved spectrometer) over a few hundreds shots, but a growing number of flashovers occured during reverse and direct voltage. Even after carefull cleaning and refurbishing, a durable and reliable working hasn't been reached. We suspect a bad vacuum thightness on some of the Rexolite insulator vacuum O rings but didn't manage to fix it.

6.2.2 Ferrite under vacuum cells

Two blocks of four cells have been constructed in order to test on PIVAIR facility two different gap shapes , designed to minimize transverse impedance .
The first H.V tests exhibited current leakage between ferrite cores and the internal diameter of the metallic housing. This led to increase the ferrite core internal diameter to 270 mm in order to improve HV insulation . Consequently the ferrite section and available magnetic flux were lowered. This was partly balanced by adding a 12^{th} core (only 12 mm thick). These cells were successfully tested at 300 kV on the HV testbed before being assembled on PIVAIR accelerator line. To obtain the right vacuum level in the beam pipe (10^{-7} Torr),this technology recquired 2 days heating at 70 °C in order to dehydrate ferrites .The tests with a 3.5 kA beam demonstrated a 250 kV working voltage for the two kinds of cell. This value was confirmed by energy spectrum measurements but the available voltage flat top accros the accelerating gap was 7% shorter (compared to Rexolite cell) which necessitated to carefully synchronize injector and pulse generators. Reliability testing (1000 shots at 250 kV) revealed no flashovers for the "flat gap" cells during the main voltage pulse and a few flashovers during the main pulse and reverse polarity postpulses for the "curved gap" cells. This led to choose the ferrite under vacuum technology with flat gap for the AIRIX accelerator.

After disassembling the "curved gap"cell block, we carefully inspected gap and ferrite surface and we found that some plastic shims (used to maintain insulation distance beetween the first ferrite toroïd and the gap electrode) were certainly involved into the flashovers occurence. Removing these shims resulted in a noticeable reliability improvement demonstrated over 400 shots.
In order to delay the ferrite saturation and decrease overvoltages stresses we decided to add a 13^{th} ferrite core: each AIRIX cell will consist of thirteen 24 mm thick ferrite cores. This, partially balanced by some mechanical changes, will imply a 1.2 meter lenght increase for the final AIRIX accelerator.

7 PIVAIR AND AIRIX SCHEDULE

PIVAIR focusing section is now under construction. A focusing experiment at 7 MeV and electron beam spot characterization are planned before summer. Then it will be necessary to extend PIVAIR building before begining the first radiography experiment and X-ray spot characterization.

At Moronvillier site, AIRIX building is quite finished. AIRIX injector has been assembled by the end of february and is now under acceptance test.

8 REFERENCES

[1] Pulse Sciences Inc., 600 Mc Cormick street, San Leandro, CA 94577, USA
[2] Status of the AIRIX induction accelerator
P.Eyharts et al, CEA CESTA, Le Barp, France
Proceedings of PAC 95, Dallas,May 1995.
[3] Beam transport and characterization on AIRIX prototype at CESTA
P.Eyharts et al, CEA CESTA, Le Barp, France
This conference
[4] AIRIX alignment and high current beam diagnostics
D.Villate et al, CEA CESTA, Le Barp, France
Proceedings of PAC 95, Dallas,May 1995.
[5] Status of AIRIX alignment and high current electron beam diagnostics
C.Bonnafond et al, CEA-CESTA, Le Barp France
Proceedings of EPAC 96, Barcelona, June 1996.

BEAM TRANSPORT AND CHARACTERIZATION ON AIRIX PROTOTYPE AT CESTA

P.Eyharts, P.Anthouard, J.Bardy, C.Bonnafond, P.Delsart, A.Devin, P.Eyl, D.Guilhem, J.Labrouche, J.Launspach, J.de Mascureau, A.Roques, D.Villate, L.Voisin
Commissariat à l'Energie Atomique,CESTA, BP N°2 - 33114 LE BARP - FRANCE
and E.Merle, J.C.Picon, *CEA,CEV-M, 51490 PONTFAVERGER - MORONVILLIERS, FRANCE.*

Abstract

Designed to produce an X-ray dose of 500rads @ 1m, AIRIX flash X-Ray Radiographic facility will consist of 4 MeV/3.5 kA pulsed electron injector and 16 MeV induction accelerator powered by 32 H.V. generators. Construction of PIVAIR accelerator (8 MeV AIRIX prototype) is now ended at CESTA.The injector has been connected with 16 accelerating cells in order to study beam transport and centering procedures. Accurate,time resolved diagnostics have been used to measure beam characteristics and a tickler experiment has been planned to estimate BBU instabilities. In this paper all experimental data recently obtained will be discussed and first conclusions for AIRIX will be given.

1 INTRODUCTION

After four years of experiments on PIVAIR prototype at CESTA,AIRIX flash X-ray radiographic machine is now under construction and will be commissionned by CEA at Moronvilliers in 1999.This installation will generate an intense bremsstrahlung X-ray pulse of 500 rads @ 1m using an electron beam of 3.5 kA/4 MeV produced by a pulsed diode injector and accelerated up to 20 MeV by 64 induction cells driven by 32 H.V. generators.

Final design of AIRIX has been decided this year on the base of performances obtained with PIVAIR accelerator after a series of experiments involving electron beam. At first, high voltage tests performed on this facility have permitted to choose generators and induction cell technologies: the results of this work are presented in a companion paper elsewhere in this conference[1].

Then, electron beam delivered by PIVAIR has been extensively characterized by using time resolved diagnostic equipments in order to measure beam position, energy and emittance. During these experiments, a beam transport and centering procedure has been defined and tested with success along the accelerator.

Finally, a tickler experiment has been carried out with 8 induction cells in order to estimate the BBU predictive capability of numerical models.

All experimental measurements made to date on PIVAIR will be summarized and discussed in the following sections of this paper. Section 2 will describe the facility and sections 3 to 7 will discuss the beam experiment results.

2 PIVAIR FACILITY DESCRIPTION

The construction of PIVAIR installation started at CESTA in 1994 with the injector assembly and testing. Using a velvet cathode as electron source this generator is able to produce in routine 4 MeV/3.5 kA beam with an energy spread less than ± 1 % over 60 ns pulse duration. By the end of 1995 eight induction cells were connected to the diode and last year another module of eight cells was added. All PIVAIR cells are designed to deliver the same acceleration to the beam (250 keV) but they differ by the insulation technology used in the high voltage region: eight cells use an oil-insulated ferrite core and a reticulated polystyrene as accelerating gap insulator, the other cells use vacuum to insulate ferrite and consequently no gap insulator[1][2].

Influence of these configurations on beam characteristics will be discussed below.

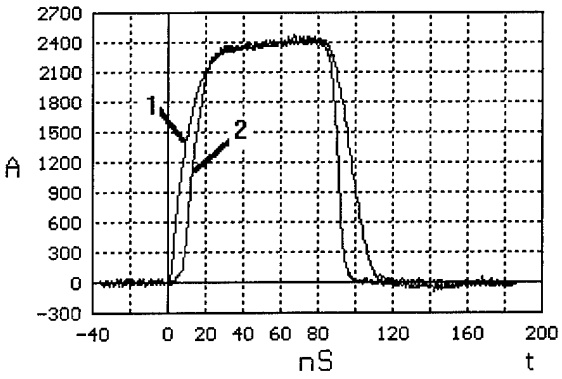
3 BEAM MONITORING

Beam transport along the accelerator is controlled by seven Beam Position Monitors (BPM). Three BPM are placed at the injector output on the drift tube and one BPM after each block of four cells. Specially developed for this application,they use four electrical loops to determine centroid position by measuring B_Θ field associated with the beam .

Tests performed on PIVAIR have demonstrated a resolution of ±200 μm and a sensitivity of 20 μm .The bandwidth was limited to 400 MHz by the integrator technology but was considered sufficient for AIRIX. However, we have observed a decrease of electron pulse rise time as beam progresses through the accelerator. As shown on figure 1 rise time was 25 ns at the injector exit and 10 ns after 16 accelerating cells. We think that this effect is due to the loss of low energy electrons during transport. If this phenomena grows with the number of cells on AIRIX accelerator, BPM bandwidth will have to be improved in order to maintain the same resolution.

An optical diagnostic is also used on PIVAIR to monitor beam position and help beam centering. It is based on measurement of Cerenkov light generated

0-7803-4376-X/98/$10.00 © 1998 IEEE



Fi gure 1: Beam profile at injector output (1) and accelerator output (2).

by interaction of electrons with an aluminized PET plastic foil. In this diagnostic the light is imaged with a streak camera to get a time resolved measurement.

We have compared results given for beam position by Cerenkov diagnostic and BPM. Currently a ± 1.5 mm discrepancy was observed between the two methods; but due to calibration difficulties, it was impossible to evaluate independently the Cerenkov method accuracy.

As this diagnostic is not suitable at energy higher than 10 MeV,we have developed for AIRIX another optical diagnostic using Optical Transition Radiation (OTR),phenomena which occurs when a charged particle crosses the interface between two medium having different dielectric indices.Tests performed on PIVAIR with the same PET foil were very satisfying.

Unfortunatly,optical diagnostics are interruptive and their absolute accuracies are not known so they are only utilized for rough beam centering. However, they allow measurement of beam profile which is of a great interest for emittance evaluation.

4 BEAM TRANSPORT AND CENTERING

PIVAIR beam transport and centering is carried out with an iterative method that involves both experimental measurements and calculations made with an envelope code knows as ENV.

The procedure begins with optical measurements of beam radius at the injector output for different sets of anode magnet currents.The results permit to deduce numerically initial beam characteristics (diameter,envelope slope,emittance) which are used as data entry for ENV calculations of cell guiding magnet currents.These values are choosen in order to transport the beam at constant diameter. Typical beam diameters on PIVAIR are 72 mm at the cathode and 40 mm in the accelerator.

Beam centering is realized every block of 4 cells using ENV calculations and BPM measurements.Electron beam is first centered at entrance of block n°1 with the help of dipole trim coils placed on the drift tube.Then beam position is measured at the output of the same block for different sets of cell trim magnet currents.From these measurements ENV code determines current values that allow centering at the block exit.The same procedure is applied to the next block.

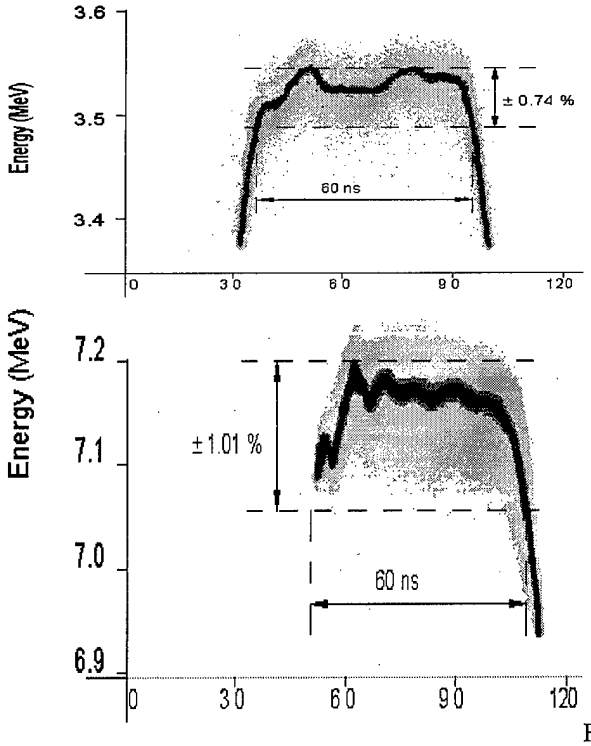
This step by step tuning method has been tested with success on PIVAIR giving a centering accuracy of ± 200 µm. It will serve as a basic procedure for AIRIX beam transport.

5 BEAM ENERGY MEASUREMENTS

Beam energy has been measured with a time resolved spectrometer placed at different locations along the accelerator.This apparatus described in a previous paper [3] is able to measure energy spectrum with a very high resolution (0.2 %) by means of an electromagnet coupled with an array of optic fibers and a streak camera.

Maximum energy measured at the output of the sixteen PIVAIR induction cells was 7.2 MeV; this value is less than the design value of 8 MeV because accelerating pulses on Rexolite cells were limited to 200 kV to avoid high voltage flashovers.

The spectrum profile has been compared with spectrum obtained at the injector exit (figure 2). Both exhibit an energy spread around ± 1% peak to peak over 60 ns beam duration. Nevertheless, we observe on the accelerator spectrum a slight broadening of the trace which is not yet explained.



Fi gure 2: Beam energy spectrums at injector output (3.55 MeV) and 16 cells accelerator output (7.2 MeV).

Another series of experiments have been performed at 5.5 MeV in order to compare spectrums

measured after acceleration with Rexolite cells and vacuum cells.No significant difference was noted between the two technologies(figure3).

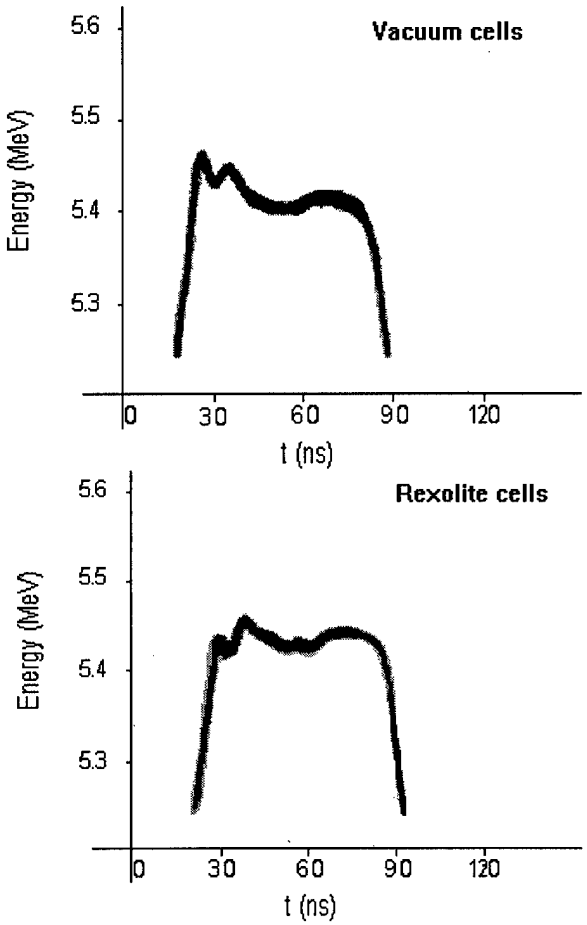


Figure 3: Energy spectrums obtained after acceleration with Rexolite or vacuum cells.

6 EMITTANCE MEASUREMENTS

Emittance has been determined using the three gradient method by measuring the beam radius at the injector output for different sets of extraction magnet current.The data have been fitted with ENV envelope code to obtain normalized rms emittance.

Experimental results show that emittance value depends on the optical diagnostic (Cerenkov or OTR) used to measure the beam radius. For a 3 kA/3.6 MeV electron beam we have extracted the following emittances:

$\varepsilon_{n,rms}$(Cerenkov)= 780 π.mm.mrad

$\varepsilon_{n,rms}$(OTR)= 700 π.mm.mrad

The same experiment was conducted at the accelerator exit but varying the guiding magnet current on the sixteenth induction cell.In this case beam energy was 6.2 MeV and measurements have given the results mentioned above:

$\varepsilon_{n,rms}$(Cerenkov)= 1300 π.mm.mrad

$\varepsilon_{n,rms}$(OTR)= 700 π.mm.mrad

Although the difference between emittances measured by the two diagnostics are not yet explained we note that in both cases the emittance is low.This result agrees well with calculations made for PIVAIR cells.

7 BBU EXPERIMENTS

Design of PIVAIR cells have been made in order to limit development of BBU instabilities by minimizing the transverse impedance of the accelerating gap.

First series of experiments using the two wires method have confirmed the transverse impedance predicted by PALAS code for both technologies used on PIVAIR.

The goal of this new experiment was to validate the BBU calculation code SITAIR by measuring, at the exit of eight Rexolite cells, the amplification of beam transverse oscillation initiated by a tunable tickler cavity.

Typically we have measured initial oscillations of 0.06-0.1 mm for frequencies ranging from 700 to 900 MHz.The cavity was excited by a 3 kA /3.6 MeV beam and driven by an external 23 W rf source.The magnetic guiding field was set around 300 Gauss.In these conditions we have observed a maximum BBU gain of 8 at 780 MHz. To date the best agreement (±15%) with SITAIR code was obtained for a transverse impedance real part of 800 Ω/m.

To complete this work we must now calculate the imaginary part of transverse impedance that will optimize the fitting of experimental data with code calculations.

CONCLUSIONS

Thousands of tests realized on PIVAIR since 1994 have demonstred that technologies of accelerator sub-systems are adequate for AIRIX. Electron beam characteristics predicted by the numerical codes have been obtained; but we must verify that they are sufficient to achieve a small radiographic source size after focussing on tantalum target.This work is in progress at CESTA and will be ended this summer.

REFERENCES

[1] AIRIX Prototype Technological Results at CESTA
P.Anthouard et al.,CEA-CESTA,Le Barp,France
Proceedings of this conference

[2] Status of the AIRIX Induction Accelerator
P.Eyharts et al.,CEA-CESTA,Le Barp,France
Proceedings of PAC 95,Dallas,May 1995

[3] AIRIX Alignment and High Current Beam Diagnostics
D.Villate et al.,CEA-CESTA,Le Barp,France
Proceedings of PAC 95,Dallas,May 1995

ETA II EXPERIMENTS FOR DETERMINING ADVANCED RADIOGRAPHIC CAPABILITIES OF INDUCTION LINACS

J. T. Weir, G. J. Caporaso, J. C. Clark, H. C. Kirbie, Y.-J. Chen, S. M. Lund, G. A. Westenskow and A. C. Paul
Lawrence Livermore National Laboratory

Abstract

LLNL has proposed a multi- pulsed, multi-line of sight radiographic machine based on induction linac technology to be the core of the advanced hydrotest facility (AHF) being considered by the Department of Energy. In order to test the new technologies being developed for AHF we have recommissioned the Experimental Test Accelerator (ETA II). We will conduct our initial experiments using kickers and large angle bending optics at the ETA II facility. Our current status and our proposed experimental schedule will be presented.

1 INTRODUCTION

LLNL has proposed using induction linac technology as the driver for the AHF system being considered by the Department of Energy. The concept includes building a long pulse accelerator (200 ns.) and using a stripline beam kicker and septum magnet system to chop the long pulse into shorter pulses (50 ns.) The pulsed kicker will induce a small angular difference between the front and the back of the beam before it runs through the septum magnet. The septum magnet is a dc magnetic field designed with the left half of the field oriented up and the right half oriented down. This septum greatly magnifies the angular differences between the two pulses which will be routed to separate beam lines. (Figure 1) By repeating the process the two beams can become four beams which will converge on the target area and give four lines of sight in the radiographic chamber. High beam quality (low emittance) must be maintained during the chopping and transporting of the pulses. To validate the kicker and transport technology, experiments are needed, measuring the effects on beam quality of a kicker and a large angle transport beam line. We have chosen to resurrect the Experimental Test Accelerator (ETA II) as the test bed for these validation experiments.

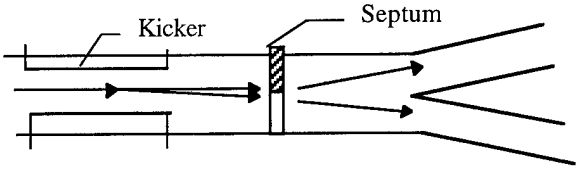


Figure 1

2 THE ACCELERATOR

ETA II is a linear induction accelerator that was designed to accelerate electrons for use as the driver in a free electron laser experiment. The facility was shut down in 1992 with various components being scavenged for other projects. In the Spring of 1996, we began looking at ETA II as a possible test bed for the AHF experiments. On the negative side was the fact the system had not been run for more than four years, many of the components were missing and many of the remaining subsystems were in disrepair. The advantage of resurrecting ETA II was in having a dedicated system that would permit precision measurements of kickers and transport lines. The ETA II parameters were well known and would scale easily to an AHF system. (Table 1) By the summer of 1996 it was decided to resurrect ETA II and the work began.

ETA II Accelerator Parameters

Energy	6.3 MeV..
Current	2 kA.
Pulse Width	60 ns.
Energy Regulation	+/- 1%
Repetition Rate	1 Hz.

Table 1

The injector and each of the sixty accelerating cells were disassembled and fitted with new O-rings and vacuum seals. The high voltage insulators were cleaned or replaced and vacuum and fluid system were overhauled. Missing vacuum pumps and valves were recalled from other programs and missing equipment was replaced.

Each of the four pulse power units (MAGS) was completely disassembled and rebuilt and the power supplies for the solenoid magnets and steering magnets were brought back on line.

In the control room, we brought up the computers for the safety system, the mechanical system, the pulse power and magnetic control systems and the data acquisition and analysis system. In many cases we had to restore the programs from archived backup tapes as the original could not be located or would not execute.

By December of 1996 we had the injector running and by April of 1997 we had the full accelerator running at 2 kA. and 6.2 MeV.

In order to compare the refurbished accelerator with its past performance an emittance measurement was made at

0-7803-4376-X/98 /$10.00 © 1998 IEEE

the 2.5 MeV. point (after the first 20 cells) using a pepper pot emittance diagnostic. The pepper pot mask was drilled with a pattern of 0.0568 cm. diameter holes and was 86.85 cm. from the phosphor coated viewing plate. An emittance of 17 cm.-mrad. (uncorrected for space charge) was measured with a beam current of 1700 amps. This corresponds to a whole beam brightness of 3 x 10^8 A(m-rad)^2 which is the same value measured after 20 cells in 1990.

After we achieved full power operation of the accelerator and measured the emittance, we began the installation of the first experimental beam line.

3 THE EXPERIMENTAL BEAM LINE

We are currently building the first of our experimental beam lines. The purpose of these first experiments will be to measure the quality of the beam before and after our preliminary kicker design. The beam line will be laid out as one continuous straight section with no splitting of the beam line after the septum. After the end of the accelerator, the beam is transported by discrete solenoids through an energy analyzer, a solenoidal emittance selector, a final focusing magnet, the kicker, the septum, and finally to the pepper pot emittance diagnostic.(Figure 2) In this initial experiment we will use a static dipole magnetic field over the kicker and by choosing the polarity of the dipole field and the applied voltage to the kicker we can select either section of the chopped beam to be directed into the diagnostic beam line.

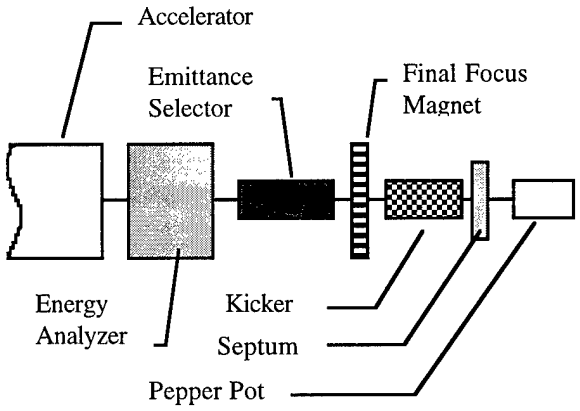


Figure 2

4 THE INITAIL EXPERIMENTS

Our initial experiments should begin in June of 1997. We will begin by measuring the quality of the beam delivered to the experimental section. Energy measurements will be taken and the timing of the accelerator cells will be adjusted until we have less than 1% energy variation across the central 40 ns. of the beam. Maintaining a minimum energy sweep prevents the build up of the corkscrew motion of the beam through the accelerator which can lead to degraded emittance. Energy variations of less than 1% were recorded on ETA II before it was shut down in 1992.

After the energy tests, we will run the beam through the solenoidal emittance selector. In addition measuring the whole beam brightness, the emittance selector will be used as a knob on the current entering the kicker section. Changing the current in the accelerator requires retuning the accelerator and this can be a time consuming task. We will run the accelerator at a standard current (2 kA.) and then use the emittance selector to adjust the current to the experimental section.

Next, we will transport the beam to the pepper pot diagnostic for a detailed emittance measurement. For these measurements the kicker and the septum magnet will be replaced with blank section of beam pipe. This will give us the baseline performance of the beam.

At this point we will install the kicker system without the septum magnet. We will run a series of tests on the kicker in an un-powered mode. We need to measure the effects of beam induced voltages on the kicker rods as a function of beam current and beam centroid offset. The primary diagnostic for this set of experiments will be the beam current and position monitors down stream of the kicker. We will also repeat the emittance measurement to ensure we have not degraded the beam quality.

Next we will begin running the high voltage pulser (9 kV.) to the kicker deflection rods. Issues we need to investigate include reflections of the power pulses back to the pulser and possible emittance growth in the kicked beam.

Our final set of experiments in this configuration will involve installing the septum magnet and measuring the effect of the septum's field on the beam emittance.

Once we have successfullly tested the preliminary kicker/septum design we will use the data we collect to modify the design as necessary and begin the construction of our next beam line.

5 FUTURE EXPERIMENTS

Another key technology we will study using the ETA II test bed will be the issue of beam transport. In order for the long pulse technology to work we must be able to route the pulses through long transport lines involving bends as large as 90 degrees. This transport must be done without degrading the beam quality if the radiographic spot size is to be kept small. We will begin our transport studies by removing the kicker/septum section of our beam line and replacing it with a 30 degree bend on classical magnetic transport. We will then measure the quality of our beam after this bend. These experiments should begin by December of 1997. If the magnetic transport is shown to be successful we will replace the magnets with the kicker/septum system and repeat the

transport experiments. These experiments should begin in the spring of 1998 and will use a modified kicker/septum system that has been designed with the data from our earlier experiments.

Our final transport experiment would be to construct a beam line with a pair of kickers and a 90 degree bend. This beam line would address most of the key issues associated with the LLNL long pulse proposal for AHF. Proving our ability to use multiple kickers and transport the beam through large angle bends without degrading the beam quality would be a large step towards implementing the long pulse AHF technology.

In addition to the kicker and transport issues we will study, LLNL is working on the pulsed power and advanced cell design that will be necessary to create a long pulse induction linac. When the pulsed power modules and test cell have completed their laboratory testing they will be brought to ETA and installed in our beam line. Operating the test cell with the advanced pulsed power system in the actual accelerator environment will be a final demonstration for these key elements.

6 CONCLUSIONS

We have brought the ETA II accelerator out of mothballs and tested it at full current and voltage. The beam quality has been measured and it is identical with the high quality beam that was being produced before the accelerator was shut down. ETA II is ready to be the test bed for the kicker and transport experiments necessary to validate the LLNL long pulse proposal for the AHF accelerator. We are installing our first beam line now and should begin our experiments in June of 1997.

7 ACKNOWLEDGMENTS

The work was performed under the auspices of the U. S. Department of Energy by the Lawrence Livermore National Laboratory under contract W-7405-ENG-48.

800-keV ELECTRON INDUCTION INJECTOR WITH HIGH AVERAGE POWER

G. Mamaev, A.Ctcherbakov, A. Glazov, V. Krasnopolsky, T. Latypov,
S. Mamaev, S. Poutchkov, I. Tenyakov,
Y.Teryoshkin, S. Vlasenko,
Moscow Radiotechnical Institute of Russian Academy of Sciences

Abstract

For many applications of intense electron beams, including flash radiography and free-electron lasers, multikiloampere currents and low emittance are required. The report deals with the development of an injector ensuring these demands.

Design parameters of the injector are 800 keV beam energy, 2...5 kA current, 80 ns pulse flat top and 100 Hz repetition rate. The average power of the series of pulses is 40 kW.

The injector contains seven induction modules in series to generate 0.8 MV diode potential. The voltage contributions of seven modules, at 120 kV each, are summed along the cathode stem as it threads through the seven units. The modules use amorphous alloy and permalloy cores. The injector has been designed to provide two modes of operation: with a low and high current electron beam respectively. A velvet cathode and a mesh-less anode are used to produce an electron beam with the current of 2 kA and the brightness of 2.4 10^3A/(cm rad)^2 in the first mode. A 800 keV, 5 kA electron beam is derived by a mesh anode in the second mode. The modules of the induction injector and its parameters are described in this report.

1 INJECTOR DESIGN

1.1 General configuration

The injector consists of a high voltage generator, seven induction modules, a ceramic cone insulator and a vacuum tank with an accelerating gap. The electron source mounted on the stem consists of a velvet cathode placed on a field forming electrode. The tapered insulator assembly separates the oil-filled induction modules from the vacuum diode. The generator [1] is a two-stage magnetic power compressor with a thyratrons switch. The voltage pulse is produced by a water-filled pulse forming line (PFL) with the impedance of 3.3 Ohm. PFL is connected to the induction cells by using two parallel rigid 20 Ohm oil transmission strip lines. Each of the induction cells has six identical connnections. Two of them are used for line connections, and four for compensating water resistors that load the pulse power source in parallel with the cell. The injector design is shown in Fig.1.

1.2 Induction cells

The magnetic material in the 1.5 m tank is packaged into seven independent 120 kV induction cells. Oil is used as dielectric and cooling fluid surrounding the magnetic material. The cathode stalk of 105 mm O.D. runs in the center of the injector and the full diode voltage appears across the A-K gap at the load end. The actual average effective length of each cell is 180 mm, giving an accelerator gradient of 0.7 MV/m.

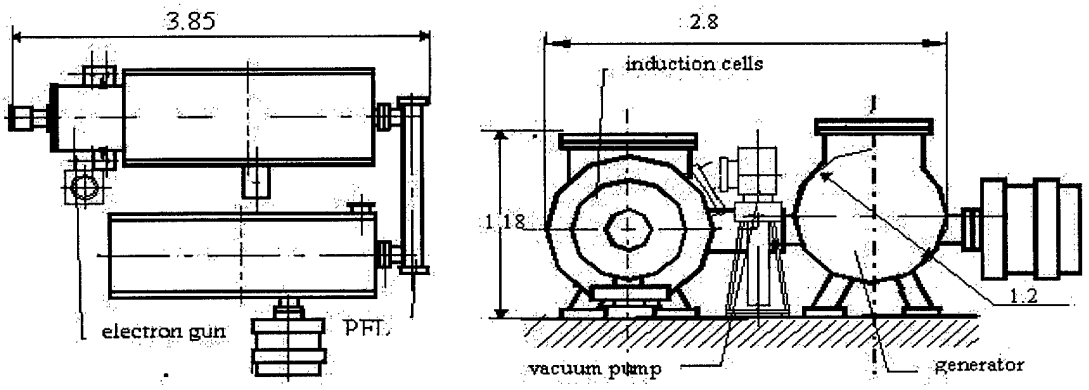


Figure: 1 The injector design.

0-7803-4376-X/98/$10.00 © 1998 IEEE

The four of the seven induction cells consist of five 24 kV permalloy cores with 200 mm I.D., 380 mm O.D. and 25 mm thickness. The other three cells consist of seven 17 kV amorphous alloy cores with 300 mm I.D., 430 mm O.D. and 20 mm thickness.

Particular attention has been given to the design and construction of the induction cell to minimize the voltage between amorphous alloy layers in the cores. In order to solve this problem a high voltage gap is situated in the mid-plane of the induction cell. After calculation of the voltage distribution inside the induction cell we reached the following conclusion. Under the operating conditions wave effects are insignificant as a result of attenuation in amorphous alloy.

The voltage across each core is a vector sum of a curl field and an electrostatic field. It is important that the curl field is the same on each core, and the electrostatic field is different and depends on the capacitive division of the voltage and the core position inside the induction cell. In our design, the radial voltage on the face surface of the cores is no more than one half the voltage over the gap. As a result, the voltage between amorphous alloy layers in the cores is no more than (13...15) V, assuming that the operating conditions of insulation between layers are acceptable. To make the cores, a new technology was used [2]. The insulation coating with high dielectric characteristics is applied during the winding. The computer assistance used during the process of termomagnetic treatment allows to impove magnetic characteristics and reduce the core weight. For example, the experimental results of amorphous alloy 9KCP cores testing show that the puncture voltage is no less than 12 V/wrap, ΔB is 2.2 T and the magnetisation field is no more than 2 kA/m.

The value of magnetization current of the injector amorphous alloy cores was measured without the beam. It is about 2.0 kA under the following conditions: the voltage is 13 kV, the time is 80 ns. The voltage and curent waveforms are presented in Fig.2.

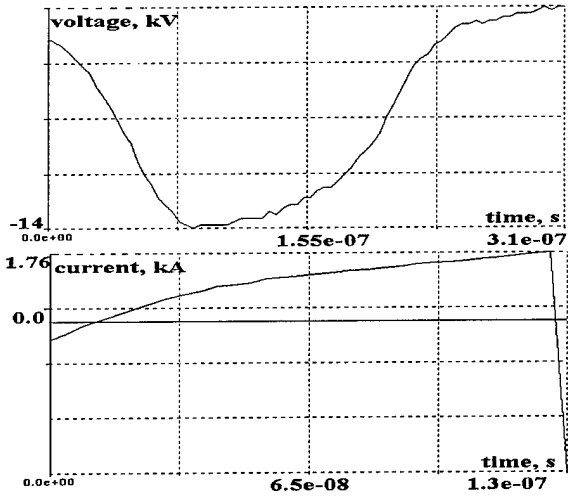


Figure: 2 The voltage and curent waveforms.

The design induction cell parameters provide the core current no more than (2.5-3) kA. Consequently, the core efficiency is (40-44)% in the first mode and (62-70)% in the second mode which that is not bad. These data allow to investigate pull of design parameters of the injector on the waveform of the beam current. The induction cells with the transmission strip lines and PFL were modeled using MC3 simple circuit code. Previously, equivalent parameters of the circuit have been calculated analytically. The waveforms of the current for two modes of the injector operation are shown in Fig. 3. As shown, the droop of the pulse current is nothing more than 10%. This is ensured by a matching water capacitor.

1.3 Electron gun

The cathode assembly is mounted at the small diameter end of the ceramic cone insulator. It consists of a focus electrode, a velvet cathode and a bucking coil. In the first mode, the electron source is a 80 mm diam velvet cathode. The purpose of the focus electrode use is to aid in focusing the beam and to minimize the electric field enhancement at the edge of the emitter. The focus electrode made from the stainless steel has the field stress no more than 150 kV/cm. The A-K gap is about 50 mm and the anode aperture is 90 mm diam.

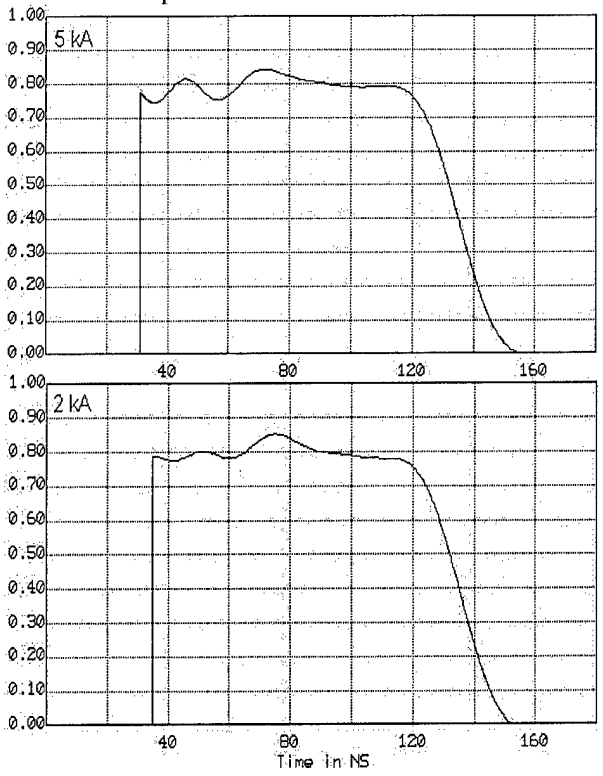


Figure: 3 The wave forms of a current for two modes of injector operation.

The cathode is designed to be operated with nearly zero magnetic field component normal to its surface in order to minimize the canonical angular momentum of the

extracted electron beam. This is accomplished with two coils placed over the A-K region. The magnetic field is generated by a 180 mm-I.D. backing coil in the vacuum diode and a 130 mm-I.D. air-core extraction magnet which center is located 100 mm from the cathode. The axial magnetic field strength in the centre of the extraction magnet is about 0.8 kG. To arrive at the final diode design, the computer 2D codes EGUN [3] and SAM were used. The simulation geometry (SAM) is shown in Fig.4. The numerical calculation gave the following results: the rms beam radius is 2 cm, the rms emittance is 80 cm mrad and the current density on the cathode surface is about 30 A/cm^2. The simple variant of the cathode assembly without a focus electrode was also calculated by EGUN code. The simulation geometry is shown in Fig.5. This is a basic variant of the cathode assembly with the parameters similar to the previous variant.

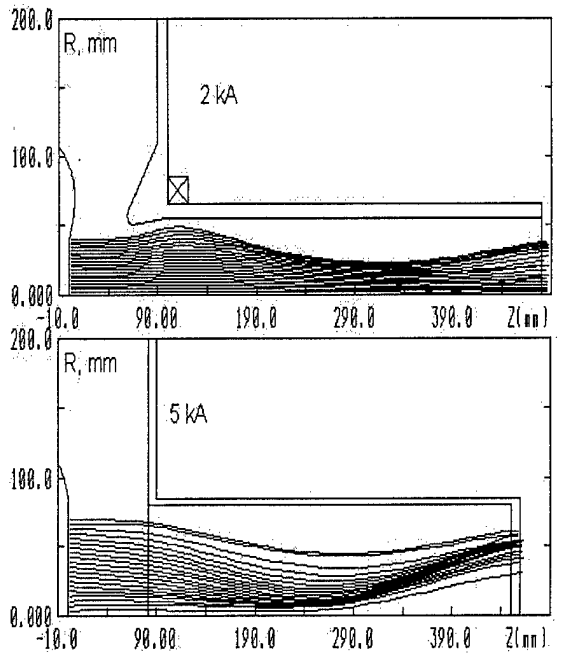


Figure: 4 The simulation geometry.

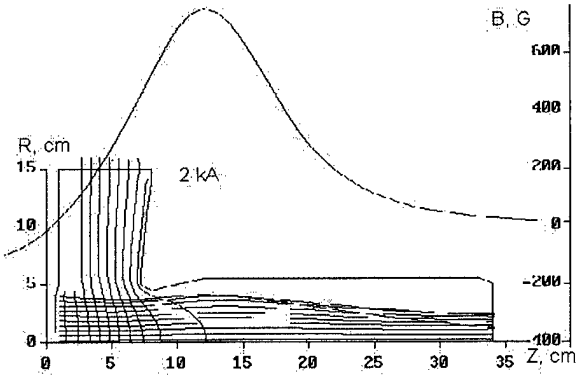


Figure: 5 A basic variant of the cathode assembly.

In the second mode the 140 mm diam replacement velvet cathode without a focus electrode is used. In this case the anode is planar and consists of a grid. The anode grid is fabricated by stretching 0.08 mm thick tungsten wire on a pattern of slots cut into the supporting rings. The width of the openings between the wires is less than 5mm. The diode configuration showing the electron trajectories is indicated in Fig.4.

1.4 Ancillary arrangements

To measure the parameters of the electron beam and induction cells in the exploitation mode the following monitors are used: a capacitive (E - dot) monitor located inside the vacuum tank versus the cathode assembly, Rogowski coil on the cathode stalk, a resistive probe and an electron collector, where electrons are stopped, and Rogowski coils in the induction cells.

The vacuum in the vacuum tank of the electron gun is ensured by 500 l/s turbomolecular pump.

2 CONCLUSION

We suppose to have the injector in operation within the current year. The generator is expected to be built and installed in coming months. Now we have all the induction cells made.

REFERENCES

[1] G. Mamaev et al: '150 kV Magnetic Pulse Compressor', this conference.

[2] G. Mamaev et al: 'Technology for Production of Amorphous Alloy Large Scale Cores', this conference.

[3] W. Herrmannsfeldt: 'EGUN, An Electron Optics and Gun Design Program', SLAC Report 331, SLAC,1988.

OUTPUT BEAM CHARACTERISTICS OF 150 MEV MICROTRON

T. Hori, H. Tsutsui, D. Amano, M. Washio
Lab. for Quantum Equip. Tech., Sumitomo Heavy Ind., Ltd., 2-1-1 Yato, Tanashi, Tokyo 188 Japan
J. Yang
Dept. of Physics, Tokyo Metropolitan Univ., 1-1 minamioosawa, hachioji, Tokyo 192-03 Japan
K. Tani
Kansai Research Establishment, JAERI, 608-9 Higashishionokoji, Shimogyo-ku, Kyoto 600 Japan

Abstract
Sub-picosecond electron pulses are desirable for generating femtosecond X-ray pulses. By numerical simulation, it has become clear that racetrack microtron (RTM) has unique features to produce very short electron bunches by itself. In addition, it has proved experimentally that RTM has beneficial characteristics to accelerate only an excellent quality beam in both emittance and energy spread. The measured and calculated results of such distinctives are shown in this paper.

1 INTRODUCTION

High quality X-ray beam of the pico- to femtosecond pulse width is an indispensable tool for the investigation of various phenomena in the same time scale. Thomson Scattering between electrons and laser beams is considered to be the most promising to generate such the excellent X-ray pulses[1]. For such the purpose, it is inevitable to obtain a high quality electron beam of very short and low emittance pulses.

RTM has been proved to be the best candidate to realize the above interaction because of its compactness which is essential in those experiment. When we adopt new technology of RF gun with photo cathode[2] in the injection system of conventinal RTM, sub-picosecond electron pulses will be extracted as an output beam with no other sophisticated technology such as the bunch compressing magnets system.

In order to acquire the basic knowledge of such the conventional RTM[3,4], which is popular as the injectors of many compact SR rings, we have carried out the measurements of 150 MeV beam. We also performed various simulations numerically and compared the results with measured ones. Those simulations have shown us the new concept, which was bunch shortening effect of RTM. It becomes very advantageous when we intend to product femtosecond electron bunches in the future.

2 EMITTANCE MEASUREMENTS

Figure 1 shows the top view of 150 MeV RTM. It has two 180 deg. bending magnets (BM) with reverse field ones in front of them, one accelerating cavity of 0.5 m long placed on the first orbit near the injection point, and the 80 keV low energy injection system using a thermionic gun. While circulatng RTM, vertical focusing is mainly given by the effect of field gradient of BM and horizontal focusing by the only single quadrupole (QSF) on the same axis as the cavity (see Figure 2). Main parameters of 150 MeV RTM are listed in Tabel 1. We have manufactured four RTMs since 1988, the principle values of them are the same up to now, suitable for a injector of SR rings and not for making as short pulses as possible. We once measured the emittance of low energy 80 keV beam from the thermionic gun keeping the record about 50~100π mm.mrad since then.

Emittances (εx, εy) of the 150 MeV beam were evaluated from the measurement of various beam profiles (σx, σy) observed on the screen monitor #2 of the beam transport line (BT) in Figure 2. Profiles were controlled by changing the focusing force of two quadrupoles, Q1 and Q2. The measured (σx, σy)'s are fitted to the following equations by the rms method;

$$\sigma_x = \left(\varepsilon_x \cdot \beta_x + \eta^2 (\Delta p/p)^2\right)^{1/2}$$

$$\sigma_y = \left(\varepsilon_y \cdot \beta_y\right)^{1/2},$$

where the dispersion η = 0.854 m at the exit of 150 MeV RTM. An example of the fitted results is shown in Figure 3 as a function of Q1 strength.

Thus, Twiss parameters and emittances were obtained at the entrance of the extraction magnet. We compared various calculated values and concluded the followings as the most probable value;

(εx, εy) rms = (0.11π, 0.07π) mm.mrad
ΔE/E = ±0.06 %

There exists a possibility, however, that those values may vary about a factor of 2 or so for the horizontal parameters, εx and ΔE/E, because of their coupled effects. On the contrary, there is little room to vary for the vertical parameter, εy, because it behaves independently.

Figure 4 shows the simulation results assuming the initial emittance of the 80 keV beam as 100π mm.mrad, where ellipses in the figure represent the calculated rms emittance at the extraction magnet. In the figure, εx looks much larger than •y because of the momentum dispersion. The simulated results are;

(εx, εy) rms = (0.035π, 0.015π) mm.mrad
ΔE/E = ±0.05 %

Compared both the emittances, the measured values are slightly larger than the calculated ones by a factor 3~5 except the energy spread. When taking into account the difference of both situations, that is, simulations have been carried out under the ideal condition, it should be

0-7803-4376-X/98 /$10.00 © 1998 IEEE

reasonable to find such the level of mismatch in the characteristics of accelerated beam.

3 BUNCHING EFFECT

We have done much simulations of RTM so far. The most innovative discovery among them is the bunch shortening effect of the normal RTM. This fact suggests us the possibility to have much the shorter pulses than the length normally expected from the width of its orthodox longitudinal acceptance, which lies at around 32 degree. It is equivalent to 32 picosecond when the common S-band 2856 MHz is adopted as the frequency of accelerating cavity. From Figure 5, we can see the evidence of this effect, that is, even the 100π mm.mrad initial emittance, the main part of the accelerated electrons are gathered together rather in a short range of the phase. We investigated the relationship between initial and final phases of the beam, limitting the initial emittance of 80 keV beam to 10π mm.mrad. Figure 6~7 are obtained from such the condition. If looking precisely into the distribution of final phase in Figure 6 excepting the tails dropping out to both the sides, we can extract the substance of the bunching effect in Figure 7. Here the bunch shortening effect is much more obvious, 1σ of this peak is estimated to 0.36 degree, which corresponds to 0.7 picosecond FWHM. As seen in Figure 7, when limitted the initial phase within 4 degree which is to be a width of the beam from an RF gun, initially the broad beam in phase becomes the very sharply bunched beam finally.

4 CONCLUSION

The low emittance beam of RTM was proved by the measurements of the 150 MeV accelerated beam, which agreed slightly well to the values prospected by numerical simulations. The results predict that we can easily have sub-picosecond electron pulses in hand when the conventional thermionic gun is replaced by an RF gun with photocathode.

*This work was done under the collaboration of Sumitomo Heavy Ind. and Japan Atomic Energy Reserch Institute in 1996 fiscal year.

REFERENCES

[1] M. Washio, et al., "Femtosecond X-ray Pulse Generation Using a Low Emittance Electron Beam and a High Power Laser", 7th China-Japan Bilateral Symp. on Radiation Chem., Oct. 28, '96, Chengdu, China.

[2] D. T. Palmer, et al., "Microwave Measurements of the BNL/SLAC/UCLA 1.6 Cell Photocathode RF Gun", PAC95, May 1-5, 1995, Vol.2, pp.982-984.

[3] T. Hori et al., "Improvement of 150 MeV Racetrack Microtron", PAC91, May 6-9, 1991, Vol.5, pp.2877-2879

[4] T. Hori et al., "Racetrack Microtron : Injector for Compact SR Light Source AURORA"(in Japanese), Sumitomo Heavy Ind.'s Tech. Review, vol.39, No.116, Aug. 1991, pp.46-62.

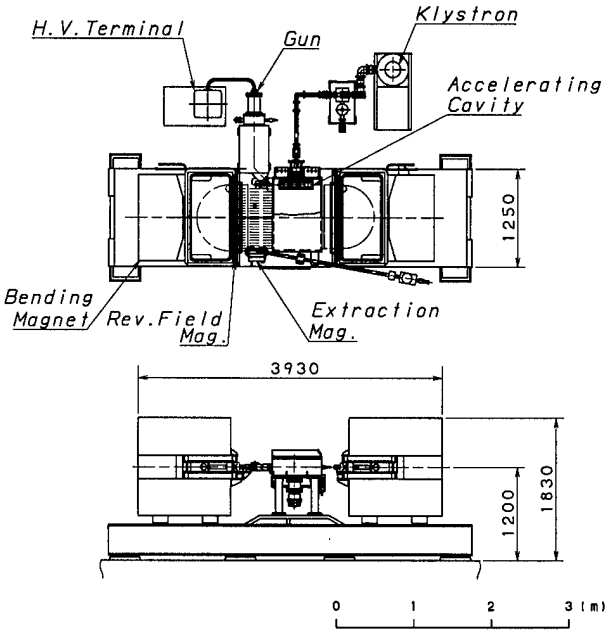


Figure: 1 Top view of 150-MeV microron with conventional injection system.

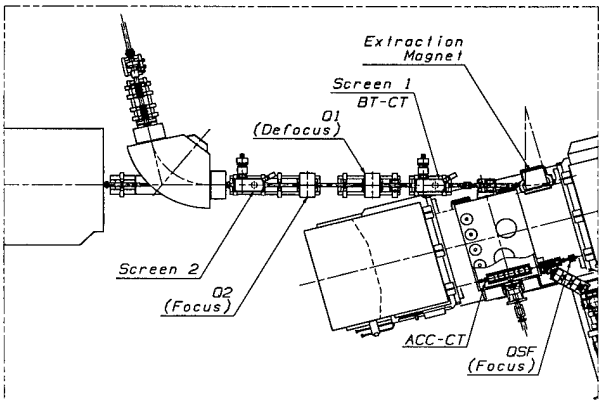


Figure: 2 Device layout used in emittance measurements.

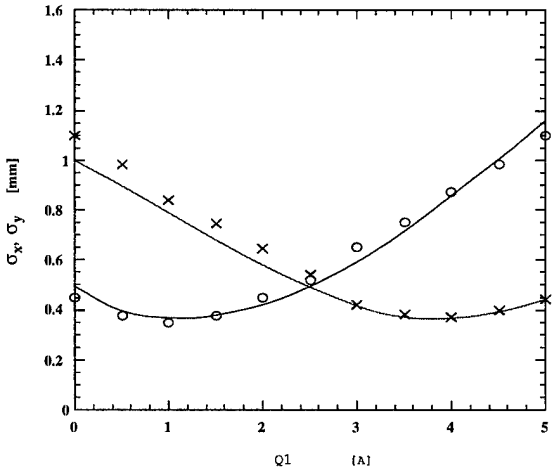


Figure: 3 One of many fitted results derived from measured beam profile.

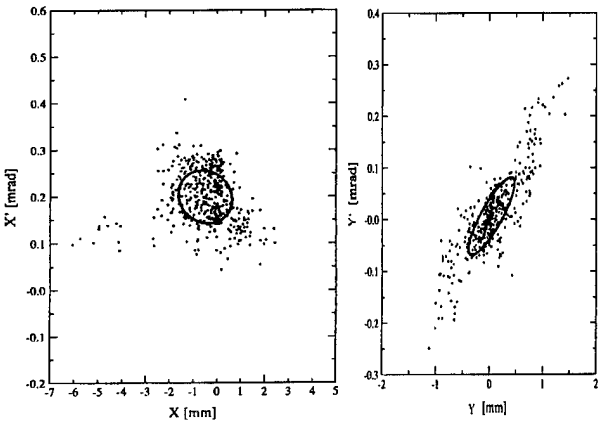
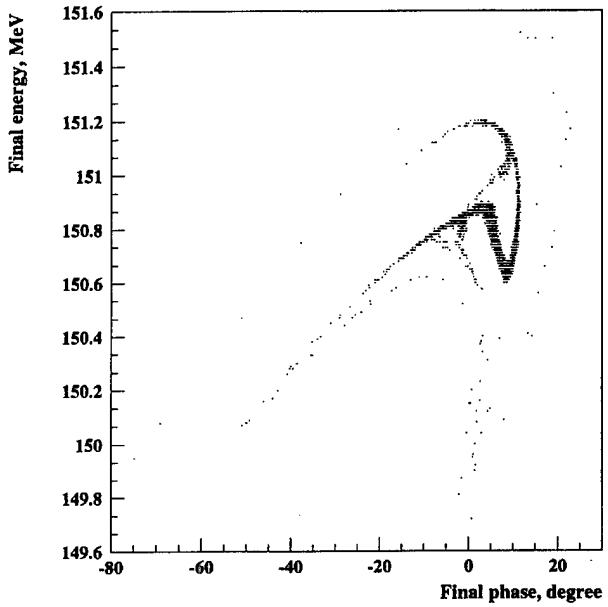


Figure: 4 Caluculated εx and εy (rms) of 150 MeV beam.



Figur: 5 Energy vs. phase of 150 MeV beam.

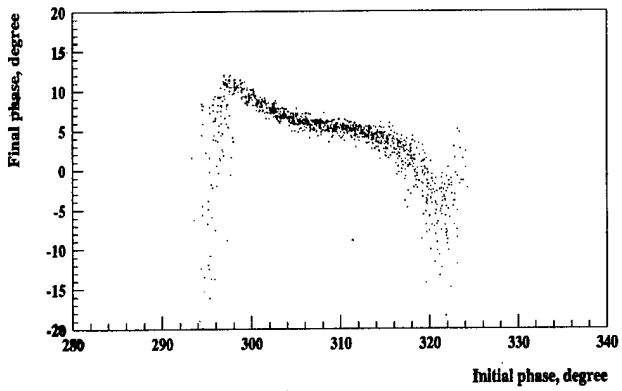


Figure: 6 Correlation between initial and final phase.

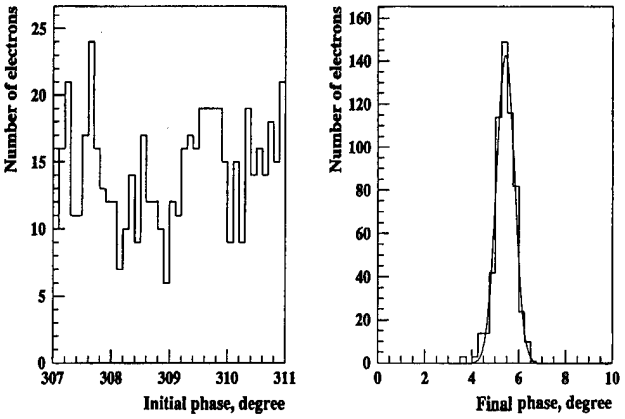


Figure: 7 Effective bunching of RTM from broad initial phase to narrow final phase.

Injection Energy	80	keV
Final Energy	150	MeV
Peak Current	10	mA
Pulse Width	0.1~4.0	μsec
Repitition Rate	1~100	Hz
Emittance	<1π	μm.rad
Energy spread	±0.1	%
Circulating No.	25	laps
Energy gain	6.0	MeV/lap
Bending Field	1.23	Tesla
Field Gradient	0.14	Tesla/m
Reverse Field	0.3	Tesla
RF Frequency	2856	MHz
RF Pulse Width	6.0	μsec
Acc. Tube Type	S.C.C.	
Accelerating Gradient	15	MV/m
Bohr Diameter	1.0	cm
RF Power Source	6.0	MW

Table: 1 Principal parameters of 150 MeV microtron

CONSTANT-CURRENT CHARGING SUPPLIES FOR THE ADVANCED PHOTON SOURCE (APS) LINEAR ACCELERATOR MODULATORS

R. Fuja, A. E. Grelick, D. Meyer, G. Pile, and M. White
Advanced Photon Source, Argonne National Laboratory,
9700 South Cass Avenue, Argonne, Illinois 60439-4800 USA

Abstract

The APS [1,2] linac beam energy must be stable to within ±1% to match the energy acceptance of the positron accumulator ring. The klystron pulse modulators [3,4] must therefore provide a pulse-to-pulse repeatability of 0.1% in order for the beam to have the required energy stability. The modulators have had difficulty achieving the necessary repeatability since the pulse forming network (PFN) charging scheme does not include a deQing circuit. Several of the major charging circuit components are also less reliable than desired. In order to increase operating reliability and to improve pulse-to-pulse stability, it is planned to replace the high voltage power supplies in all modulators with constant-current power supplies. A new modulator charging supply that contains two EMI [5] series 303 constant-current power supplies was constructed. Each of these EMI supplies delivers 1.5 A at up to 40 kV. One supply is sufficient for linac operation at up to 45 Hz, and two supplies in parallel enable linac operation at the nominal rf repetition rate of 60 Hz. This paper discusses test results from the new modulator, and also describes the existing modulators and their performance limitations.

1 INTRODUCTION

In the five existing APS linac modulators, a 12-pulse unregulated power supply and a 22-Henry inductor are used to resonantly charge a 0.704-μF PFN capacitance to the desired voltage through a tetrode switch tube. When the switch opens, energy in the charging inductor increases the PFN voltage to a higher value. This new PFN voltage level can vary from pulse to pulse depending on the voltage level of the charging supply. The charging supply's output voltage is affected by the rather frequent AC line voltage fluctuations. The 60-Hz, 20-kV charging supply, the tetrode switch tube, the 22-Henry charging inductor, and other ancillary equipment require control and protection circuitry and also a fair amount of space.

The heat generated by the 100-A tetrode filament current must also be dealt with. Use of a series tetrode as the charge-controlling element is not ideal, because screen grid current can become excessive as the plate voltage drops to a value near the screen grid voltage.

The PFN is normally charged to 33 kV, and for ± 0.1% regulation, a ± 33-V variation can be tolerated. Use of a 22-Henry charging inductor means that the current in the inductor is required to remain to within ± 5 mA at the time the tetrode opens. This is impossible in this non-deQed configuration because of the large stored energy in the inductor.

AC line variations of 3% can easily be seen during normal running, and power line variations of 5% can happen at certain times of the day.

In order to overcome the limitations of the present configuration, a sixth modulator and klystron system, eventually intended as an on-line spare, was fitted with two EMI series 303 constant-current charging supplies. These supplies are rated at 40 kV and 1.5 A, and are capable of an average power output of 30kW. In the next section, we compare regulation of the new modulator with constant-current supplies to regulation of our standard modulators with resonant-charging systems.

2 TEST RESULTS

Power supply regulation data were obtained for both types of charging systems while the 1000-A, 2-Hz pulsed, booster synchrotron power supplies were off and also while they were on. The modulator PFN set point voltage, the actual measured modulator PFN voltage, and the incoming AC line voltage were logged and analyzed using software from the SDDS toolkit [6]. Power supply regulation data for the two types of charging systems were captured using the built-in envelope detector on an HP 54542 A oscilloscope.

With the booster synchrotron pulsed supplies ramping at full power, there are PFN voltage variations of ± 0.55% when the resonantly-charged PFNs are charged to 33.9 kV, as can be seen in Figure 1. With the booster supplies off, the PFN voltage regulation provided by the resonant-charging system was ± 0.3% of 32.5 kV.

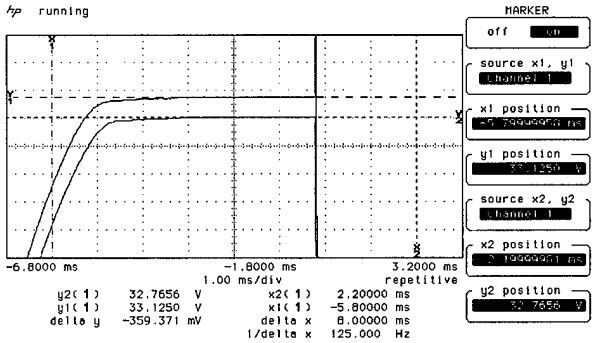


Figure 1: The resonant-charging system regulates to ± 0.55% with the 2-Hz synchrotron pulsed supplies on.

0-7803-4376-X/98/$10.00 © 1998 IEEE

The constant-current charging system held the PFN voltage to ±0.125% with the booster pulsed supplies ramping at full power and with the PFN charged to 31.6 kV, as can be seen in Figure 2. The constant-current supplies regulated the PFN voltage to ± 0.125% of 31.3 kV with the booster pulsed magnets off. The constant-current charging supplies were operated in pulsed mode, with charging initiated for 12 ms at a 30-Hz rate.

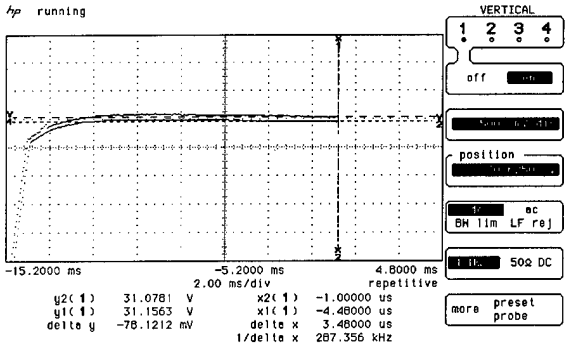


Figure 2: The constant-current charging system regulates to ± 0.125% with 2-Hz synchrotron pulsed supplies on.

Figure 3 shows variations in the PFN voltage and in the line voltage over a six-hour period on a typical day. The PFN set-point was constant during this period. Figure 3(a) shows the actual PFN voltage during that time, and Figure 3(b) shows variations in line voltage over the same time period. The measured PFN voltage follows the AC line voltage quite closely.

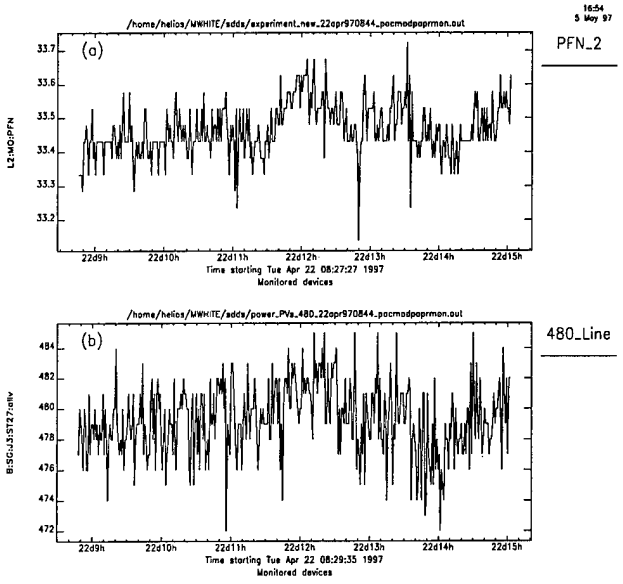


Figure 3: (a) PFN voltage and (b) AC line voltage variations over a six-hour period.

3 DISCUSSION

The resonant-charging system, as presently configured, is inadequate to provide a regulation of better than ± 0.55% under changing line voltage conditions, as can be seen very clearly in Figure 4. Figure 4 is a single-shot plot of a resonantly charged PFN taken while the booster synchrotron supplies were pulsing at full power and at a 2-Hz rate.

The effect of the 2-Hz pulsed synchrotron supplies on the regulation of the PFN charged by constant-current supplies is not evident, as shown in Figure 5.

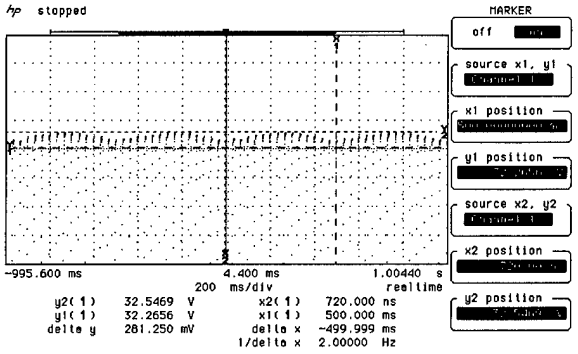


Figure 4: The 2-Hz pulsing of the synchrotron supplies appears as an inter-pulse ripple on the voltage of the resonantly-charged PFN.

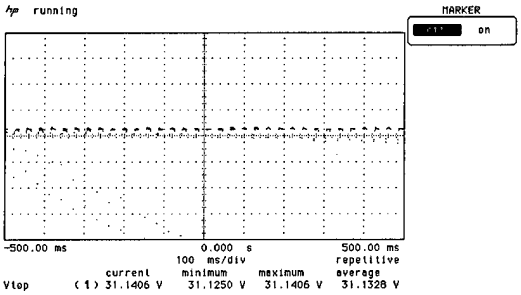


Figure 5: Regulation of constant-current supplies with pulsed supplies running at full power and at a 2-Hz rate.

4 CONCLUSION

Under constant AC line voltage conditions, the regulation produced by the two different charging systems is quite similar. The difference becomes evident as the AC line varies, and poor regulation sometimes even leads to operational difficulties. Although data are not presented here, the PFN voltage for some of the resonantly charged systems has been observed to vary as much as 1 kV out of 33 kV. The constant-current supplies are able to charge the PFN to within ± 39 V, independent of the actual PFN voltage level.

Both charging systems have experienced reliability difficulties. One of the tetrode circuits had a chronic problem with oscillations that proved extremely difficult to control and has led to a number of tube failures. One constant-current supply experienced several infant-mortality failures, including one that caused oscillations. In the long term however, it is expected that use of the semiconductor-based power supplies will result in a modulator availability that is superior to that of the resonant-charging circuit with a tube.

The new modulator supplies are very compact, freeing up a lot of real estate as shown in Figure 6. We are able to

eliminate a motorized 3-phase variable transformer, a high voltage step-up transformer, a high voltage rectifier assembly, a switching element, and a charging inductor, along with related control and safety circuitry. The standard double-width rack that contains most, but not all, of the resonant-charging system components is shown in Figure 7. An additional outboard cabinet, not shown, is also required.

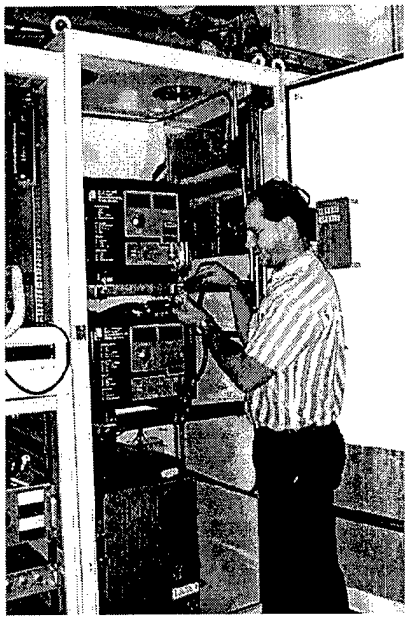


Figure 6: One single-width cabinet contains two constant-current power supplies.

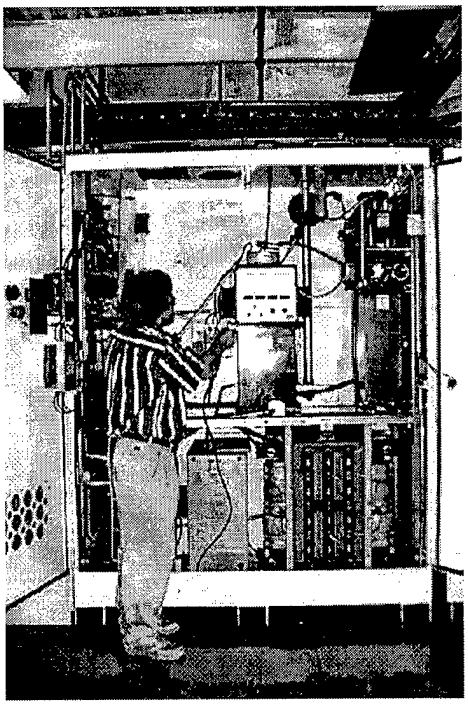


Figure 7: A double-width high voltage power supply cabinet contains most of the resonant-charging system.

A new control system is being developed that will incorporate the built-in diagnostic functions of the constant-current supplies and will eliminate unneeded functions in the existing control system. Considerable attention will be devoted to signal and power filtering, cable and connector shielding, electronic chassis screening, and chassis and rack grounding. The system will be modular, utilizing commercially available PLC technology, but will be re-engineered into an environment that will make it much less susceptible to interference or failure.

Large power system transients have been experienced during klystron conditioning. High voltage transient breakdowns or "arcs" have previously caused component failures in the existing power and control systems. These types of problems cause radio frequency interference (RFI). The effects are mostly seen as pickup on signal cables, and they result in spurious operation of interlocks as well as erratic behavior of electronic circuits. RFI/electromagnetic-compatibility testing, utilizing bulk-current injection and conducted-emission techniques, will be used on the new control system. These tests will help to make the new control system reliable without compromising the high bandwidth required of its control and monitoring circuits.

5 ACKNOWLEDGMENTS

Work is supported by the U.S. Department of Energy, Office of Basic Energy Sciences, under Contract No. W-31-109-ENG-38. Many thanks to G. Trento and T. Jonasson for assembling the sixth modulator and for adapting the new charging system to the existing control system.

6 REFERENCES

[1] "7-GeV Advanced Photon Source Conceptual Design Report," ANL-87-15, April 1987.

[2] M. White et al., "Construction, Commissioning, and Operation of the Advanced Photon Source (APS) Linear Accelerator," Proc. of the XVIII International Linac Conference, Geneva Switzerland, 26-30 August 1996, pp. 315-319.

[3] T. Russell and A. Cours, "Klystron Modulator Operation and Upgrades for the APS Linac," Proceedings of the 1995 Particle Accelerator Conference, 1-5 May 1995, Dallas, Texas, pp. 1559-1561 (1996).

[4] "APS Linac Klystron and Accelerating Structure Gain Measurements and Klystron PFN Voltage Regulation Requirements," N. S. Sereno, LS Note 257, April 1997.

[5] Electronic Measurements Inc. 405 Essex Rd. Neptune, NJ. 07753.

[6] M. Borland and L. Emery, "The Self-Describing Data Sets File Protocol and Toolkit," Proceedings of the 1995 ICALEPCS Conference, pp. 653-662 (1997).

NEW RESULTS ON ELECTRON EMISSION FROM PZT FERROELECTRIC CATHODES*

D. Flechtner, Cz. Golkowski, J. D. Ivers, G. S. Kerslick, J. A. Nation, and L. Schächter
Laboratory of Plasma Studies & School of Electrical Engineering,
Cornell University, Ithaca, NY 14853, USA

Abstract

Ferroelectric cathodes may offer a source of high current density electron beams for applications where the use of conventional cathodes is limited by the required current density, cathode poisoning, or lifetime. In a ferroelectric cathode, electrons are emitted when the spontaneous polarization is rapidly changed by a pulsed electric field applied across the ferroelectric. When no additional voltage is applied to a planar diode gap, emission current densities are on the order of $\sim 1\ A/cm^2$. When an additional field is applied to the gap, we have measured current densities of up to 100 A/cm^2. In this paper we report on two topics:(1) beam extraction into a drift tube at low (10-20kV) voltage and, (2) electron emission, transverse to an applied magnetic field, from a cylindrical ferroelectric cathode. In the former case we report on emission of a 20A beam current in a 300ns pulse repetitively pulsed at rates up to a power supply limited $\sim 50Hz$. The cathode is located in the fringing region of a 3kG solenoid magnetic field. In the second case we find, at low applied gap voltages, that the magnetic field required to suppress the radial current flow is considerably in excess of that predicted for the applied electric field.

1 INTRODUCTION

The study of electron emission from ferroelectrics has advanced through the last several years to the point that we can now consider them for use in electron guns. Among the possible advantages of such emitters is their insensitivity to poisoning, and the possibility of obtaining much larger emission current densities than can normally be obtained from a thermionic cathode. In order to proceed beyond this point requires, (i) a measurement of the emission characteristics at the high applied voltages normally used in electron guns and, (ii) a demonstration of their viability at high repetition rates and, (iii) measurements on the life of ferroelectric cathodes. We have carried out and report in this, and a companion paper [1], an investigation of the first two of the above features. The repetition rate measurements were made at 15kV in an arrangement in which the electrons emitted from an appropriately pulsed 1.8cm diameter ferroelectric disk are injected into a 5cm diameter drift tube located 2.8cm from the surface of the cathode. The flow is focussed by a converging magnetic field into a 1 cm diameter channel. The anode cathode voltage was provided by a 300ns pulse transformer operated at repetition rates of up to 50Hz. The emitted current was found to be stable and equal to 20A.

In the high voltage gun experiment peak currents of 200A have been obtained with the cathode-drift tube gap about 6.5cm and the cathode voltage in the 400-500kV range.

In addition to the above measurements we have recently initiated a new experiment designed to help elucidate the electron emission mechanism(s) further, and also to provide a possible new means of generating an annular electron beam. In this experiment a 2.5cm long, 2.5cm diameter PZT sample is mounted in a coaxial diode assembly with an anode cathode separation of 1cm. An axial applied magnetic field is used to determine the cut-off condition for radial current flow. As the radial current decreases with increasing applied magnetic field an axial current flow develops with the flow in an annular channel of radius approximately equal to that of the ferroelectric cylinder.

The detailed experimental results and their implications are discussed in the following sections.

2 EXPERIMENTAL DATA

The essential features of the gun system are shown schematically in figure 1, where the ferroelectric cathode is located in the fringing field of a solenoid field coil system. Note that this arrangement does not produce a constant radius beam as it propagates through the system. The flow is indeed sharply focussed at certain axial locations; it is however a confined flow which does not intercept the tube walls.

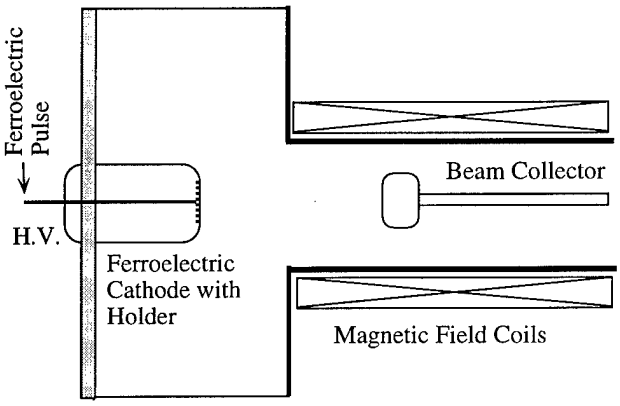


Figure 1: Schematic of 15kV ferroelectric gun experiment.

We show in figure 2 experimental data for the beam current in the 15kV gun experiment. The beam current is an overlay of 46 consecutive events at a power supply limited 47Hz.

* Work supported by USAFOSR through the MURI Program and by the US Dept. of Energy.

0-7803-4376-X/98/$10.00 © 1998 IEEE

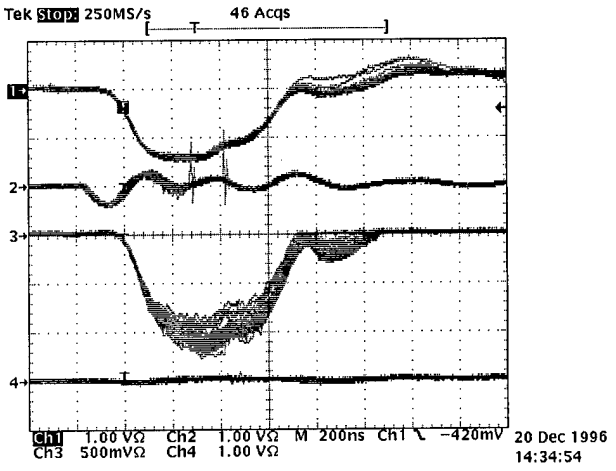


Figure 2: Ferroelectric cathode emission at ~50Hz. Ch1: V_{gap}, 12kV/div; Ch2: I_{ferro}, 70A/div; Ch3: I_{anode}, 10A/div.

In figure 3 we show a schematic of the radial diode assembly with data obtained at applied voltages of 1.75 and 40kV in figure 4. In figure 4 the radial and axial current flows are shown as a function of the strength of the axial magnetic field. The critical field, required to suppress single particle radial current flow, is indicated on the figures. The 40kV data were obtained using a pulse line feeding a 3:1 step up transformer The pulse line has an output impedance of 300Ω and generates a 300ns duration pulse which is triggered separately, and subsequently to the ferroelectric. A 500Ω resistor is placed in parallel with the vacuum diode. This limits the voltage excursion if the ferroelectric fails to emit. Typically delays between the two pulses are $\sim 600 \pm 300$ns.

We show in figure 5 typical data from the radial and axial current monitors at 40kV for low ~0.07T and high ~ 0.2T axial magnetic fields. As the magnetic field is increased the radial current drops to a value close to zero while, as expected, the axial current increases. Peak axial currents of about 250A have been monitored.

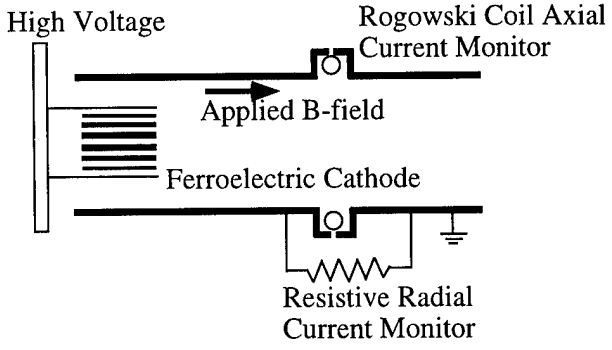
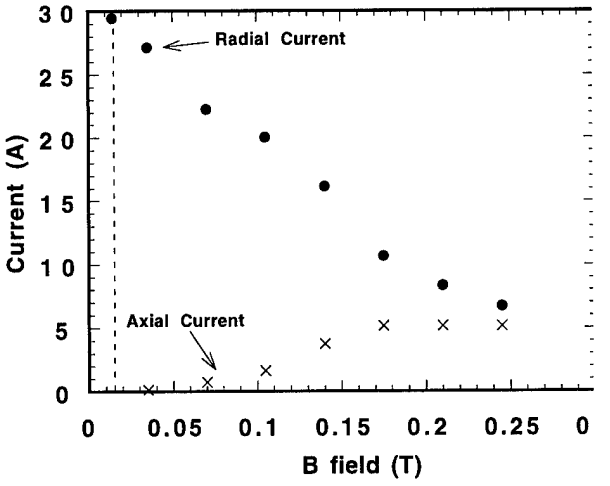


Figure 3: Schematic of cylindrical ferroelectric cathode experiment.



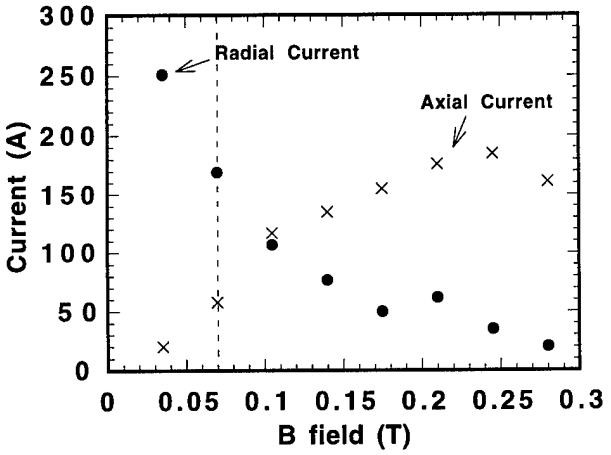


Figure 4: Axial and radial current as a function of applied B field for two applied voltages: 1.75kV (upper frame) and 40kV (lower frame). The critical B field in each case is indicated by the vertical dashed line.

3 DISCUSSION OF RESULTS

50Hz Repetition Rate Data: The data presented gives an encouraging view of the potential of ferroelectric cathodes for use in high repetition rate experiments. It is worth noting that the current is limited in these experiments by the potential depression in the drift space. A further feature is the effect of conditioning on the beam current. These experiments were carried out in relatively poor vacuum 10^{-5} Torr and the emission repeatibility improved dramatically with time. Arcing at the anode surface could be inferred from current flow from the anode to the cathode. This process was rapidly reduced to a very low probability with operation at even modest repetition rates. The data presented were obtained after a few thousand shots had been obtained with the assembly.

Electron current in radial diode geometries: The experiment to measure the emission transverse to an applied axial magnetic field was designed to show the potential of the ferroelectric as a source for production of an annular

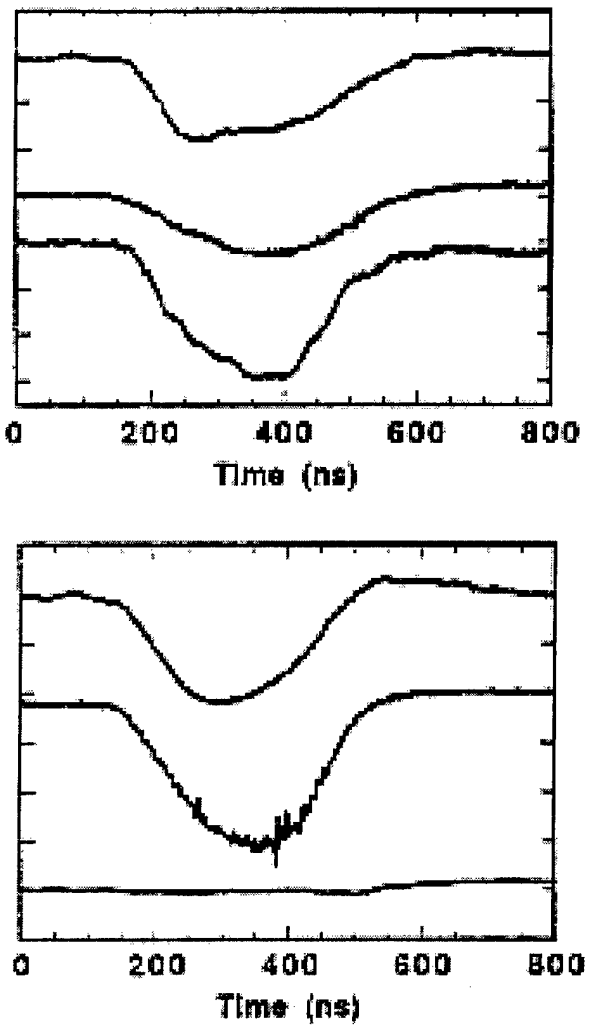


Figure 5: Radial and axial currents emitted from cylindrical ferroelectric for B=0.07T (upper frame) and B=0.2T (lower frame). Top waveform: V_{diode}, 25kV/div; Middle waveform: I_{axial}, 100A/div; Bottom waveform: I_{radial}, 80A/div.

electron beam and further to help clarify the emission process from the ferroelectric diode. Three mechanisms have been proposed to account for the observed emission current densities [3]. The first entails the emission of electrons with an initial velocity, the second the formation of a deep potential well resulting from the field enhanced ejection of the electrons, and the third plasma formation and subsequent anode-cathode gap closure. As regards these mechanisms we have never detected electrons with initial energies exceeding $\sim$ 600V. This initial energy is insufficient to account for the observed current flow in our experiments. Based on the radial current flow at magnetic fields strengths well in excess of the critical field for magnetic insulation, the low voltage ($\sim 2kV$) data shown in figure 4 would imply a potential well depth of order 80kV. The more rapid fall off of the radial current close to the critical field at high applied potentials is consistent with this observation. The third mechanism is based on the concept of an ambi-polar like motion across the anode cathode gap. Based on the measured injection electron energies a limited number of protons could achieve velocities of about 10 cm/μs (higher atomic number ions would give lower velocities). Gap closure, albeit with low plasma density, could then occur in the 1 cm radial gap in times of order 100ns. At the high voltages ($\sim$ 30 – 60kV) used in these experiments the sense and magnitude of the applied electric field would tend to result in the ion motion being suppressed close to the anode and negate this process. The observation of reverse diode current flow at late times ($\geq$ 0.6μs indicates that the diode eventually fills with plasma. Based on these observations we conclude that the deep potential well is probably the dominant mechanism at early time and that plasma controlled flow dominates at later times. We note, from events in which the ferroelectric is switched during the main anode cathode voltage pulse, that axial current flow dominates at high magnetic fields and follows the applied voltage pulse with zero delay, following the start of the ferroelectric switching current. The radial current flow is much smaller than the axial flow in these conditions and does not start typically until there has been a sufficiently large change from the remnant polarization of the medium. This is consistent with the time taken to form a deep potential well.

4 CONCLUSIONS

The observations reported in this paper show that electron beams can be produced from ferroelectric cathodes, at interesting current levels for high power microwave generation. The production of 200-300A beams in both radial and axial emission configurations at current densities of order 75A/cm^2 has been achieved. The data obtained in the radial flow configuration experiment sheds additional light on the emission mechanisms from ferroelectrics. This work is continuing.

5 REFERENCES

[1] *A Ferroelectric Cathode, Electron Gun for High Power Microwave Research*, J. D. Ivers, D. Flechtner, Cz. Golkowski, G.S. Kerslick, and J.A. Nation, Proc. PAC'97 Conference, Vancouver May 1997.

[2] *Ferroelectric Cathodes as Electron Beam Sources*, D. Flechtner, G.S. Kerslick, J.D. Ivers, J.A. Nation, and L. Schachter Proc. PAC 95 Conference, Vol II, 1036, 1995.

[3] *Ferroelectric Sources and their Application to Pulse Power: A Review*, C.B. Fledderman and J.A. Nation. To be published in IEEE Trans on Plasma Physics, 1997.

A FERROELECTRIC CATHODE, ELECTRON GUN FOR HIGH POWER MICROWAVE RESEARCH *

J. D. Ivers, D. Flechtner, Cz. Golkowski, G. S. Kerslick, and J. A. Nation
Laboratory of Plasma Studies & School of Electrical Engineering,
Cornell University, Ithaca, NY 14853, USA

Abstract

A pulse modulator, previously described at the 1995 PAC meeting, has been reconfigured to improve the pulse shape at a slightly lower beam energy, but with a higher current (500kV,1kA). The device has been run at rated voltage and current into a resistive load for pulse durations in excess of 250ns and at $\sim 0.1Hz$ repetition rate. The modulator, which is designed for use in our high power microwave research program, has been coupled to an electron gun which uses a ferroelectric cathode and has been operated in this mode producing a 500kV, 200A electron beam. We report in this paper on the revised design and performance of the modulator and present preliminary data on the electron gun design and characteristics. The recessed ferroelectric cathode is located in the fringing field of a 3kG solenoidal magnetic field so that the emitted current will be compressed to about a $\leq$ 0.6cm diameter pencil beam, suitable for use in high power microwave amplifier experiments. The cathode emission is initiated by a 100ns, 2kV pulse inductively decoupled from the ground by a coaxial cable wound around the transformer core. The pulse transformer, which is driven by three pairs of plus/minus charged 5Ω pulselines, feeds a step-up transformer giving a matched output impedance of $\sim$ 500Ω. It is switched independently of the ferroelectric trigger to provide maximum operating flexibility. Results will be reported on all aspects of the system design and operation.

1 INTRODUCTION

As part of our high power microwave generation research program we are developing a low repetition rate modulator/electron gun. The modulator uses a ferrite core transformer the design of which is an evolution of a device previously reported in the PAC95 Conference [1]. We require a pulse with a flat top of order of or greater than 250ns at a voltage of 500kV and with a beam current of 200-500A, depending on the application. We have also been involved in the study of ferroelectric cathodes and plan to investigate their suitability for use as a high current density electron beam source. In the following sections we summarize the modifications made, since our last report, to the modulator and describe the implementation of the ferroelectric cathode. Our present gun experiments concentrate on extending the current-voltage characteristics of the ferroelectric to $\sim$ 500kV with a lesser effort made to generate a useful electron beam. Designs are in hand for the actual gun based on EGUN simulations. Up until the present we have generated a $\sim$ 420kV, 200A electron beam in a pulse with a relatively flat top of $\sim$250ns. The ferroelectric cathode, which is command triggered $\leq 2\mu s$ before the diode voltage pulse, produces the 200A beam at an average current density of 75 A/cm^2.

* Work supported by USAFOSR through the MURI Program and by the US Dept. of Energy.

2 MODULATOR DESIGN MODIFICATIONS.

The modulator design, which was originally reported at the PAC95 meeting, has been run as either two 6:1 step up transformers operated in series or as a 12:1 step up transformer run with a single set of cores. The lower gain, compared to that reported at PAC95, was needed to reduce the rise time of the output pulse. In both configurations the system is now driven by three pairs of plus/minus 40kV charged 5Ω pulse lines and hence has an output impedance of $\sim$500 Ω. At the rated voltage the energy stored in the pulse lines is $\sim$ 300J. The modulator is switched by a command triggered pressurized gas switch. A shunt resistor (R$\geq$ 900Ω) is used to limit the voltage excursion if the diode current is not properly initiated. The shunt resistor is also used, together with a 10 kΩ gun voltage resistive monitor located along the insulator stack of the gun. A schematic of the transformer is given in figure 1. We show the two core arrangement of 6:1 step up transformers in the figure. An additional change made since the last report is that the volt-second product of the driver pulse transformer has been increased by approximately 16 %. As previously reported the system is immersed in transformer oil, but is now connected to an electron gun. Base pressures are at present limited to about 10^{-5} Torr but plans are in hand to operate the system at lower pressures. The system is now set-up to include an automatic reset of the ferrite cores and to operate in a command trigger mode. Previous results were limited to self break switch operation. More detail on the experimental set up of the modulator is provided in [1].

The electron beam is generated from a 1.8cm diameter, 1mm thick disk of PZT coated with a front surface 200μm silver grid. Emission from ferroelectrics has been described elsewhere [2], where extensive references to the current literature are presented. Emission from the ferroelectric is initiated by the application of a fast rising pulse generated by krytron switched PFNs coupled to the rear surface of the ferroelectric. The pulser is connected to the ferroelectric by a length of RG178 wound around the transformer core adjacent to the secondary windings. The winding inductively decouples the transmission line from the experimental ground. The impedance is reduced to $\sim$12.5Ω,

0-7803-4376-X/98 /$10.00 © 1998 IEEE

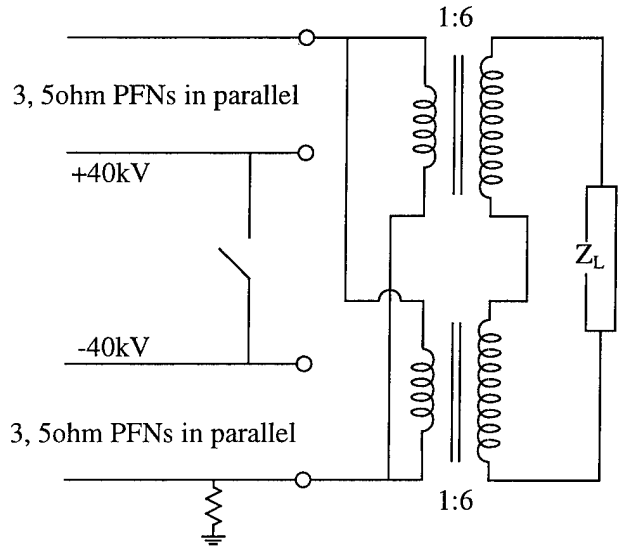


Figure 1: Schematic of pulse transformer.

to provide a fast rise time on the ferroelectric pulse, at the cathode by a 2:1 transformer. In the experiments reported in this paper the tests focussed on determining the emission characteristics of the ferroelectric and not on beam production. This was necessary since no tests of ferroelectric emission have been reported in diodes or electron guns with anode cathode voltages in excess of 50 kV, and the scaling characteristics are required to design the electron gun. The ferroelectric cathode was flush mounted at the center of a 10cm diameter cathode shank. The gridded ferroelectric surface was recessed about 0.3 cm from the front surface of the cathode shank. A confined, but not laminar, electron beam was generated in a converging magnetic field reaching a peak value of up to 3kG about 4cm into a 5cm diameter drift tube. The drift tube was located approximately 6.5cm from the front of the cathode. The beam was collected on a 2.5cm diameter collector about 10cm into the drift tube. EGUN simulations show that the beam will all enter the drift tube and be collected on the center conductor. The beam current is monitored by a Rogowski coil attached to the collector.

3 EXPERIMENTAL DATA

The level of electron emission from the ferroelectric cathode was determined by measuring the current collected on the center conductor in the drift tube. In the absence of a trigger pulse to the rear of the ferroelectric no current was monitored. If the ferroelectric pulse was applied more than 2 μs prior to the diode voltage the beam current remained zero, whereas pulsing the ferroelectric at times $\leq$ 2.0μs prior to the gun pulse consistently generated an electron current pulse. This result is consistent with previously reported data [3]. Figure 2a shows representative data obtained for the beam current when the delay between the two pulses was about 1.8μs. The current rises to its maximum value in about 200ns and shows a relatively flat top duration of about 250ns. The voltage pulse shown in figure 2b was obtained at 500kV using the two core series winding arrangement feeding a 900Ω resistive load. Note that the 16% increase in the core volume was not in place at the time these records were obtained.

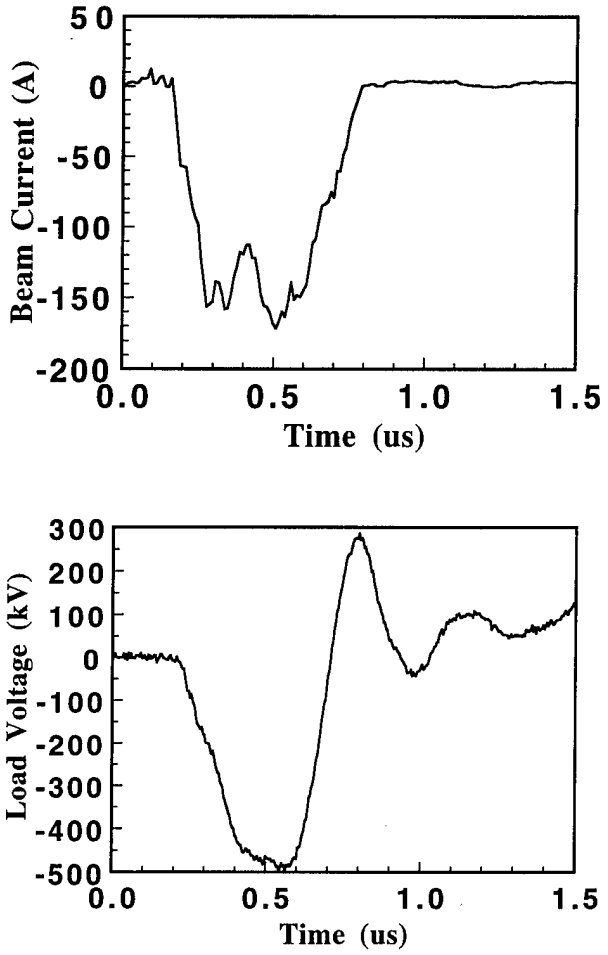


Figure 2: Beam current (100A/div) and the secondary voltage for the 3.3Ω line driven transformer.

In figure 3 we show a plot of the beam current versus the gun voltage to the three halves power. The linear plot indicates a gun perveance of 0.8μperv. Previous lower voltage data show, in vacuum diodes, a current level enhanced by a factor of $\sim$ 100 over that predicted by the Child Langmuir law. At present it is not clear whether the differences are due to the gun voltage or to the long delay (2μs) between the triggering of the ferroelectric and the application of the gun voltage. Our earlier observations at $\leq$ 50 kV also showed that the diode current dropped to zero with delays in excess of 2μs. In order to achieve the microwave powers desired in the TWT amplifier research program we require at least 200 A beams. This level of emission has been achieved in the present experiments from an exposed 2.8 cm^2 ferroelectric cathode at an average beam current of nearly 75 A/cm^2. Unpublished data, also presented in a companion paper at this meeting, report 20A, emission at

15 kV at a repetition rate of 50 Hz [3]. Although measurements have been made of the emittance of electron beams generated from ferroelectric cathodes no data has been reported under the high voltage, high current conditions achieved in these experiments.

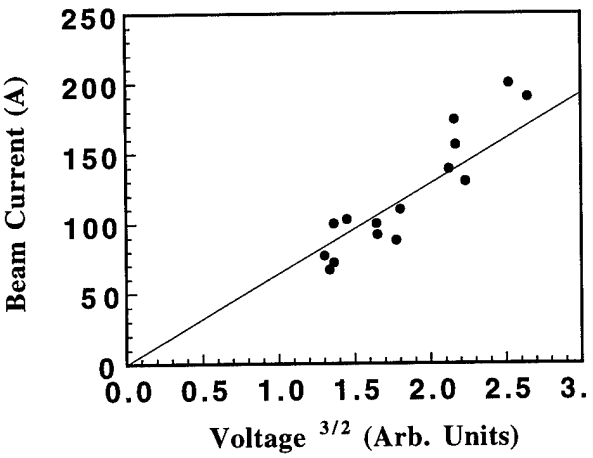


Figure 3: Beam current vs Diode Voltage raised to the three halves power.

4 DISCUSSION OF RESULTS

In the present set of experiments we have reported modifications made to the pulse transformer used to drive the ferroelectric cathode-electron gun. Two configurations have been investigated for the modulator, of these the two 6:1 step up transformers have proved to be the most satisfactory as regards the pulse rise time. The data, on the electron gun emission, were obtained with a single core 12:1 step up transformer.

These electron emission data reported here are the first results on electron beam generation at gun voltages in excess of 50 kV. With the existing delays between the ferroelectric and gun voltage pulses it is not surprising that the beam current was in close accord with that expected on the basis of space charge limited emission, as determined by the EGUN program. The observed currents are consistent with those obtained from EGUN using a 1.8 cm diameter cathode with a gap of about 5-6 cm. The emission is consistent with plasma formation on the front surface of the cathode allowing the high current densities. The current densities obtained are predicted by EGUN with gaps of about 5 cm and are consistent with gap closure velocities of order 2 cm/μs, typical of the figure found in pulse power driven field emission diodes. Previous work has indicated that the emission from a ferroelectric cathode is controlled by the ferroelectric for times of up to about 1 μs after pulsing of the ferroelectric and that plasma effects may dominate at later times. Work is presently in progress studying the emission under conditions where the delay time between the ferroelectric pulse and the diode voltage is reduced below $\sim 1\mu$s.

5 CONCLUSIONS

We have demonstrated operation of a 500kV, 1000Ω electron beam generator capable of delivering a 250ns pulse duration at a low repetition rate. The system will be used to generate 200-500A beams for use in our new 35 GHz source research program. The extension to 500A beam currents may require a larger active emission area. EGUN simulations have been made indicating a suitable gun configuration, which has not yet been tested.

Work is in progress testing the ferroelectric emission process with shorter time delays than the 1.8 μs used in these experiments. The work reported here and in the companion paper (ref 3) at this conference are believed to be the first demonstrations of:

a. ferroelectric cathode emission in MW power level electron guns,

b. ferroelectric cathode operation at 50 Hz repetition rates with current levels of order 20A.

6 REFERENCES

[1] *Design and Operation of a 700kV, 500A Modulator*, J. D. Ivers, G. S. Kerslick, J. A. Nation and L. Schächter, *Proceedings of the 1995 Particle Accelerator Conference*, Dallas, Texas, May 1-5, 1995, vol.2 p1219.

[2] *Ferroelectric Cathodes as Electron Beam Sources*, D. Flechtner, G.S. Kerslick, J.D. Ivers, J.A. Nation, and L. Schachter Proc. PAC 95 Conference, Vol II, 1036, 1995.

[3] *Ferroelectric Sources and their Application to Pulse Power: A Review*, C.B. Fledderman and J.A. Nation. To be published in IEEE Trans on Plasma Physics, 1997.

THIRTY MEGA-WATT KLYSTRON MODULATOR DEVELOPMENT AT THE DUKE UNIVERSITY FREE-ELECTRON LASER LABORATORY*

Richard J. Sachtschale, P.G. O'Shea, G. Swift
Duke University, Box 90319, Durham, NC, USA 27708-0319

Abstract

The Duke FEL Lab requires no less than ten additional 30 mega-watt S-Band RF modulators to satisfy requirements for the storage ring and future linac projects. Ideas focusing on economy of cost and space utilization will be presented along with their current status. These ideas range from rebuilding old *SLAC* klystrons with commercially available dispenser cathodes, using inexpensive industrial PLC technology for modulator instrumentation and control, to a proposed modulator driving twin klystrons. This last item is especially applicable to reducing cost and space requirements.

1 KLYSTRON REFURBISHMENT

Roughly half the cost of an RF modulator system is the output klystron. A number of old *SLAC* klystrons with oxide cathodes are at Duke. The cathodes in these tubes suffer from reduced electron emission due to their more than thirty years of age. By using the services of our in-house vacuum shop and technicians, along with a dispenser cathode package designed by HeatWave Technologies, we will attempt to give our old *SLAC* klystron tubes a second useful life.

1.1 Cathode Replacement

Removal of the old cathode necessitates opening the klystron at the weldment above the ceramic high-voltage bushing. This allows the bottom of the tube containing the cathode and heater filament to be removed from the upper vacuum shell containing the anode and collector body. Following careful inspection and photographic documentation of the disassembled components, the cathode, focus electrode, heater filament and ceramic bushing were reassembled and sent to HeatWave for evaluation.

HeatWave will design, produce and mount a cathode package with the following attributes:

- Dispenser style cathode with integral heater filament
- Molybdenum heat shield and mounting canister
- Attachment of focus electrode to the perifery of the cathode
- Provision for mounting the package in the ceramic bushing that allows for easy swap and replacement

* Work supported by ONR contract N00014-94-1-0818.

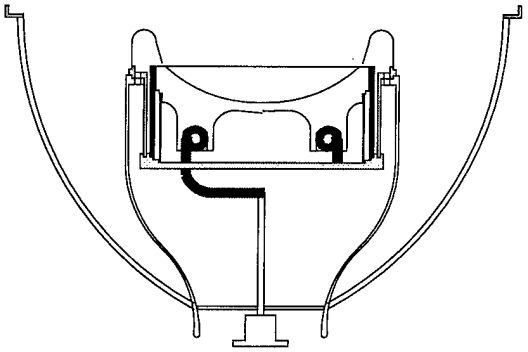


Figure 1: Cut-away section of dispenser cathode assembly in high voltage ceramic bushing

1.2 Cathode Filament Power

Dispenser cathodes require a higher operating temperature than oxide cathodes, see Reference[1]. This translates to an increase in the electrical power delivered to the heater filament. AC filament power is delivered to the cathode via the bifilar secondary windings of the high-voltage pulse transformer. The filament is connected to a coaxial terminal at the base of the high-voltage bushing. The cathode is also connected to the outer conductor of the coaxial terminal. To keep the filament current manageable through the windings of the pulse transformer, an auto-transformer is used to step-up the current after passing through the pulse transformer windings. The auto-transformer floats electrically with the klystron cathode voltage which is pulsed to 260kV.

The pulse transformer, filament auto-transformer and other associated hardware for driving the klystrons were designed for the old dispenser cathode requirements. The power required for the dispenser cathodes is approximately 300W. The filament auto-transformer was tested into a dummy load and was found to be limited to 360W. This is the lower limit of power required for the dispenser cathode being provided by HeatWave. Prior to commissioning the refurbished klystron, the cathode surface has to be *formed* by heating the dispenser matrix to above typical operating temperature. This causes the barium emitter material to melt and migrate up through the sintered tungsten matrix of the cathode bed, providing a uniform emitter surface. Due to the power limitation of our filament transformer, we will attempt to form the cathode at the end of the vacuum bakeout.

0-7803-4376-X/98/$10.00 © 1998 IEEE

1.3 *Klystron Vacuum Bakeout*

Once the klystron has been reassembled with its new cathode, it will have to go through a vacuum bakeout. We have done this previously using heater tapes and bakeout blankets, see Reference[2]. For future bakeouts a dedicated oven has been built. It was fabricated in-house and is about the size of a telephone booth. This will allow a quicker, easier and more uniform bakeout of the klystron.

Toward the end of the vacuum bakeout, when the oven temperature has come down to ambient, the cathode will be formed using a suitable power source.

2 MODULATOR CONTROLS

The modulators that provides the high-voltage pulse to drive the klystrons are relatively simple devices compared to other technologies in common use today. They consist of a high-voltage dc power supply, storage capacitors configured with inductors as a Pulse Forming Network, a high current switch(hydrogen thyratron or SCR stacks) to switched the stored charge from the pfn to the klystron pulse transformer, instrumentation, controls, interlocks and support electronics.

2.1 *PLCs*

Programmable Logic Controls are a mature technology that provide the following features to an automation application:

- Easily configurable Input/Output points
- State-Machine style management of event responses
- Consolidated operator interface
- Remote communications port
- Logging of event responses
- Proven reliability in harsh industrial environments
- Highly cost effective

These features have greatly simplified the task of automating and monitoring modulator operation. The consolidation of local front panel indicators and controls into a single interface module costing no more than a single analog panel meter, has resulted in significant cost reduction. This also translates to simpler wiring and panel layout.

2.2 *Surge and Fault Protection*

Power transformers and thyratron filaments require protection from in-rush currents at turn-on. Typically this has been done with current-limiting resistors that are shunted at some predetermined time following turn-on by a time-delay relay. In the case of thyratron filaments, variacs are typically used to ramp the power to the filament by an operator. In both of these cases Negative Temperature Coeffiecient Thermistors can be used.

NTC thermistors have a relatively high resistance at room temperature. As they heat up their resistance drops. This provides automatic surge protection during turn-on of reactive devices (e.g. power transformers) or cold filaments. They have been used reliably for years in motor start circuits. They are available in a wide range of sizes and ampacities.

During a klystron arc the modulator must be protected from the voltage reversal due to the sudden load mismatch caused by the arc. A common method for doing this is by using an end-of-line clipper wired across the end of the pfn. The clipper consists of a diode stack, a matched load and a voltage triggered switch (e.g. a calibrated spark gap). During normal operation the diodes are reverse biased. When a voltage reversal occurs across the pfn, that exceeds the breakover voltage of the spark gap, the diodes become forward biased and the energy reflected back from the load during a fault is dumped in the matched load in series with the diodes and spark gap. Such spark gaps cost several hundred dollars depending on their size. A cost effective alternative to the calibrated spark gap switch is a Metal Oxide Varistor. Below it's transition voltage, the MOV behaves like a large resistor (hundreds of mega-ohms). As it's transition voltage is reached, it's resistance drops acting like a lossy switch. MOVs come in a wide range of sizes and packaging styles. For modulator pfns insulated with transformer oil, an unpackaged MOV of the style used in electrical utility transformers for lightning fault protection are ideal and inexpensive (more than an order of magnitude less expensive than calibrated spark gaps).

3 DUAL KLYSTRON MODULATOR

Developed lab and service spaces never seem to be large enough. This may become obvious soon after occupancy if planning was casual and hasty or it may not occur until later in the evolution of a successful lab that has been blessed with careful and studied planning. Most labs likely fall in between these extremes. Service buildings that house power, controls and support equipment always seem to be the first to become filled to over flowing. It will be attempted to prevent this situation from occurring by optimizing the space requirements for the modulators in our service buildings.

One way to do this that seems straight-forward and realizable is to use one modulator to drive two klystrons. Due to the low repetition rate (5 pulses/sec) and short pulse width (2 microseconds), the only significant item that requires changing are the pfn capacitors and inductors. The F-243 hydrogen thyratrons switches are being operated more than an order of magnitude below their maximum specifications. The modulator cabinet has the additional room needed for the larger pfn. This is because the cabinets were originally built to house a resonant charging high-voltage supply. Such supplies require substantial reactive components. The space required for these components is no longer required with the use of modern, switch-

ing, capacitor charging supplies from Maxwell Labs and other vendors.

4 ACKNOWLEDGEMENTS

We would like to recognize the patient expertise of Kim Gunther at HeatWave for his patient cooperation in trying to address the many constraints involved with finalizing a dispenser cathode specification.

5 REFERENCES

[1] 'Microwave Tubes', by A. S. Gilmour, Jr., published by Artech House, 1986.

[2] 'In-House Repair of a 30 Megawatt, S Band Klystron', R. Sachtschale, P.G. O'Shea, M. Ponds, G. Swift, proceedings of the 1995 Particle Accelerator Conference, published by the American Physical Society, 1996.

A THYRATRON TRIGGER WITH LOW JITTER

C. Jensen, D. Qunell, FNAL, P.O. Box 500, Batavia IL 60510 USA

Abstract

A very low jitter trigger is required for the Main Injector Proton Injection kicker. The trigger is also designed to be reliable against thyratron arc down to the trigger grid. The trigger uses a wide band coaxial cable transformer that operates at 1500 V with a 500 ns pulse width and a 10% – 90% rise time of 20 ns. An FET is used as the switch and a very low inductance capacitor is used to store the trigger energy. Typical total jitter between TTL trigger pulse and the 50% load current value has been measured at < 2 ns over a period of 8 hours and 10^5 pulses. About half this jitter is attributed to the trigger system, and the other half to the thyratron. The trigger has been subjected to several thyratron sparks without problem. The paper will present the trigger schematic, waveforms, components and the thyratron connections.

1. TRIGGER CIRCUIT

The trigger circuit uses several minor variations on a standard pulse generator. Most of the design effort was in component selection, circuit board layout and transient immunity. The schematic is shown in Fig. 1. This is not a capacitor full discharge circuit. Capacitors C29 and C30 discharge only about 6% during a pulse.

The 750 V power supply that charges C29 and C30 is not shown in Fig. 1 and neither are the thyratron trigger negative bias voltage and the thyratron DC priming current. These thyratron support supplies are derived from the thyratron filament supply. Detailed discussions of all the major components follow.

1.1 FET Switch

One novel component is the FET switch. This switch, from DEI Inc., has a ceramic low inductance package so that it may be used for high power amplifiers up to 15 MHz. The package has coplanar line connections. There are two source leads on either side of the gate and two source leads on either side of the drain. The DE375-X2 102N20 has a voltage breakdown rating of 1000 V, an average current rating of 20 A, drain–source voltage fall and rise times of approximately 7 ns and a price of approximately $200. This device has a measured voltage fall time (90%–10%) in our circuit of ~ 10 ns.

It was experimentally determined that the peak FET drain current should be limited to two or three times the average current rating to achieve the fast rise and fall times. In initial prototyping, the DE375-102N10, a smaller FET with an average current rating of 10 A, was used. In the prototype circuit the peak drain current was ~ 60 A and the drain–source voltage was 850 V. The measured drain–source voltage fall time with this FET was 50 ns. Using the same gate circuit with the higher average current DE375–X2 FET, the drain–source voltage fall time was reduced to 10 ns. Subsequent modifications to the circuit have reduced the peak drain current to 30 A.

The operating voltage of the FET is 750 V in the final design. This level is relatively close to the FET breakdown voltage, however the inverse diode across the transformer primary and the very low inductance of the primary capacitor limit the normal transient voltages to 900 V. The inverse diode and primary load resistor also reset the pulse transformer. Thyratron arc down transients are somewhat clamped by the MOV and current limited by the 49 Ω resistor. The body diode of the FET protects it from overvoltage and R8-R11 limit the body diode current.

The drive circuit for the high voltage FET was also a substantial design effort. A very fast FET driver from Unitrode, the UC1711JE, was chosen as the first power stage. The two drivers in this package are paralleled to drive peak currents of ~ 3 A into the next stage, a voltage follower. This discrete complimentary FET driver has an $R_{DS(ON)}$ resistance of 150/300 mΩ for the N/P channel devices. These devices have a silicon gate to increase switching speed and all the driver components are surface mount parts to reduce lead inductance. The zener diode voltage drop of 5.1V is slightly less than twice the gate source threshold voltage of the drive FETs. This biases both FETs slightly on to reduce delay times. Finally, the power supply bypass capacitors consist of three 0.1μF surface mount capacitors each for the +15 V and -5 V supplies. In addition, a 33 μF Aluminum electrolytic capacitor and 1 μF leaded ceramic capacitor were used on each supply. The layout of all the drive components was done to minimize inductance. Because of the electrical and mechanical design of the DE375-X2, the drain current flows primarily through the source leads next to the drain and the gate current flows primarily through the source leads next to the gate. This further decreases the fall time since the gate circuit does not have to overcome the drain source leads L dI/dt drop.

1.2 Pulse Transformers

There are two high voltage pulse transformers used in this circuit and each had it own unique problems. X1 is used to allow the FET to be source grounded. This avoids further complications on an already difficult gate drive circuit. X2 is used to isolate the thyratron high voltage, nominally 30 kV during the pulse, from the trigger circuit. The use of two transformers also allows some effective clamping components to be used. The first transformer is a coaxial cable transformer. In the prototype, this transformer provided a 1:2 step up ratio in addition to isolation. The advantage of that construction was a reduction in the leakage inductance of the second pulse transformer. Unfortunately, the required core size for the second transformer was already substantial because of the required volt seconds and use of only a single turn on the primary.

0-7803-4376-X/98/$10.00 © 1998 IEEE

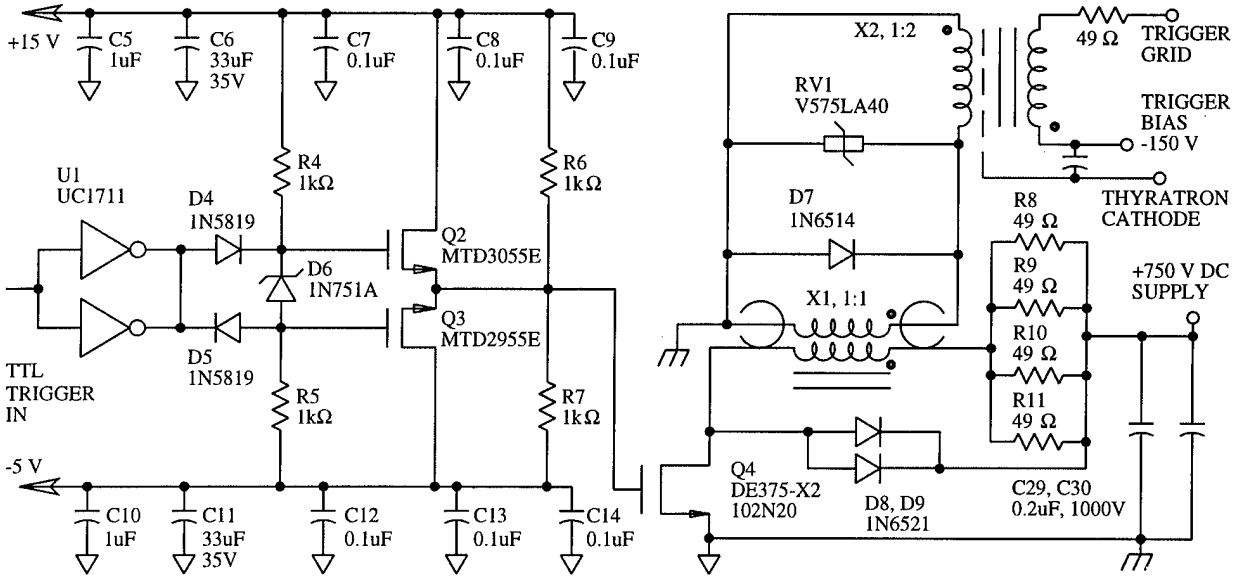


Figure 1, Thyratron Trigger Schematic

X1 is constructed of two parallel 1.5 m lengths of 0.047 inch outer diameter 25 Ω coaxial cable, Precision Tube # 25DA047. The core used is 4 pieces of a Ceramic Magnetics 3000–4 two hole balun core made from CMD5005 ferrite. There are 4 turns through each hole and the total cross sectional area is approximately 9 cm^2. In order to shield the 750 V DC voltage on the cable, for personnel safety, the center conductor is the primary and the outer conductor is the secondary. The total leakage inductance of the transformer is less than 100 nH. The transformer has adequate core area for a volt second rating of approximately 0.5 mV•s without any bias. The corona extinction voltage of the coaxial cable is approximately 850 V_{rms} at 60 Hz which is sufficient for very long lifetime.

The polarity of the transformer is particularly important in this application to achieve fast rise times. Since the cable is charged between pulses, a traveling wave is launched down the coaxial cable of the pulse transformer when the FET is closed. The current in the secondary is in the correct direction to provide full voltage into a matched load when the wave exits the other end of the transformer. In this respect, the rise time of the output pulse is limited mainly by the FET switching time when driving into a matched load. This is strictly true only if the 12.5 Ω resistor in series with the energy storage capacitor is not present. In practice this resistor increases the rise time by less than 30%.

X2 has a single turn primary and a two turn secondary. To achieve high isolation voltage, the center conductor and polyethylene of a piece of RG220/U is used as the primary. An electric field screen with a gap in the middle is place over this piece of cable and then the secondary is wound with 10 parallel pieces of AWG #22 wire. The cores used for this transformer have a total cross sectional area of 14.5 cm^2 and are made of Ceramic Magnetics CMD5005 material. Even with this substantial core and because of the single turn primary, a bias drive of 15 A/m is required to achieve a 0.2 mV•s rating. The bias current (2 A turns) is provided by a third winding and blocking inductor on the high voltage side (not shown in the diagram). The X2 transformer bias supply is derived from the thyratron filament supply on the high voltage side.

1.3 Other Components

One component that was specially ordered for the circuit was a very low inductance 0.2μF, 1000V capacitor from Electronic Concepts. This capacitor, #5PT-11635K, was designed to have a 10 year life at 1000 VDC and has an internal inductance of approximately 10 nH. The construction is an extended foil / polypropylene capacitor with 2" wide leads for each connection. The capacitor is packaged in an IC style dual inline pin package with 40 pins per side.

The trigger circuit also provides a closed relay contact back to the control system when all the DC voltages on the trigger board are within ±5% of the nominal values.

2 THYRATRON CIRCUIT

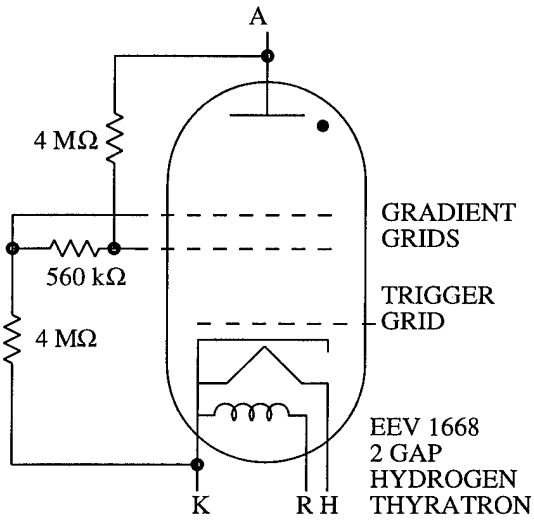


Figure 2, Thyratron Cross Connection Scheme for Proton Injection Kicker

The thyratron connection is also different from standard practice. EEV Inc. suggested using a "cross connection" at the gradient grids, Fig 2. This applies a reverse bias, in reference to the anode – cathode voltage, across the drift space between each pair of gradient grids. The voltage must be substantial enough to start a glow discharge in the drift space. The main benefit of this connection is a dramatic reduction in the delay time between successive gap breakdown in the thyratron.

The filament and reservoir supplies are 20 kHz switching supplies. They are not rectified on the high voltage side. The high voltage isolation required for these transformers is the same as the trigger and the same design is used. These isolation transformers have the same single turn primary, but the secondary has 15 to 20 turns. As previously mentioned, the filament transformer has further auxiliary windings to provide power for thyratron trigger and priming biasing.

3 SYSTEM RESULTS

The measured rise time (10% - 90%) on the thyratron trigger grid is approximately 20 ns as shown in Fig. 3 The data was captured with a HP54540 scope and Tektronix P5100 probe. Fig. 4 shows the measured jitter on the actual proton injection kicker system, measured from the TTL trigger signal to the measured current in the magnet load resistor. This is the envelope of the measured current. The peak to peak difference at the 50% current level after 4 hours and 50,000 pulses is 1 ns. The oscilloscope contributes approximately 200ps of jitter.

REFERENCES AND ACKNOWLEDGMENTS

This work is supported by the U.S. Department of Energy under contract No. DE-AC02-76CHO3000.

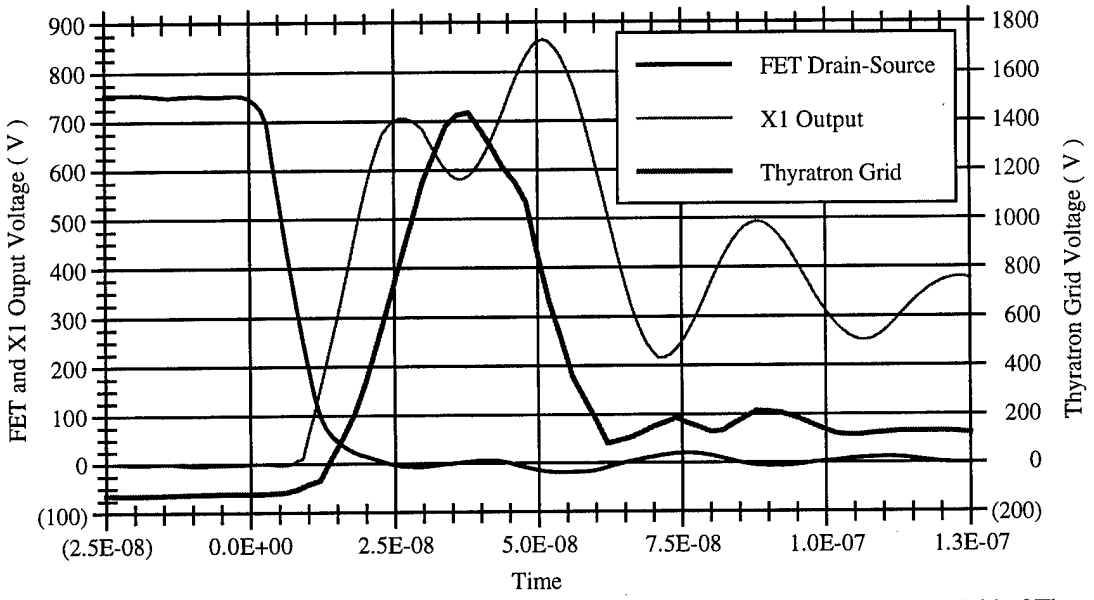


Figure 3: Measured Trigger Circuit Waveforms at Main Switch FET, Output of X1 and Trigger Grid of Thyratron

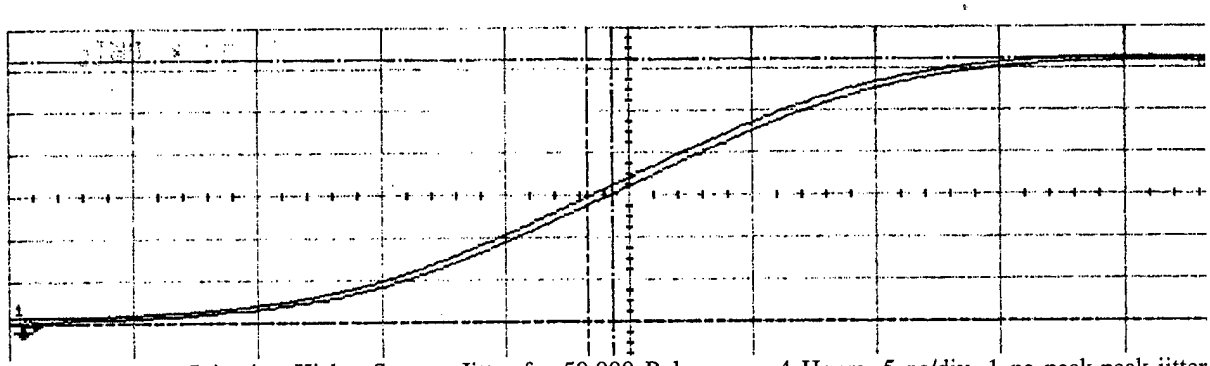


Figure 4: Proton Injection Kicker System Jitter for 50,000 Pulses over 4 Hours, 5 ns/div, 1 ns peak-peak jitter From TTL Trigger to 50% Current Level

A 40 KV, 3.1 Ω PFN FOR THE MAIN INJECTOR ABORT KICKER

C. C. Jensen, FNAL, P.O. Box 500, Batavia IL 60510 USA

Abstract

The Main Injector abort kicker system has been run at full voltage. The system was required to operate with a PFN to meet specifications. The system was designed to operate in air to allow for easier maintenance. The topology chosen has the thyratron cathode grounded, a grounded PFN and a floating pulse transformer. The system is also required to have low EMI because of the proximity of low level controls. Several problems related to the pulse transformer and to operation in air are addressed and some solutions are presented.

1 CIRCUIT DESIGN

Siting constraints have forced the abort kicker modulator to be located ~100 m from the kicker magnet itself, much further than the existing distance of ~12 m in the Main Ring and ~40 m in the Tevatron. At the same time, the rise time of the field has been decreased from 1.8 μs in the Main Ring to 1.0 μs in the Main Injector. To meet specifications, a pulse forming network is required in place of the circuit used in the Main Ring [1] and Tevatron. The Main Injector Abort Kicker specifications are shown in Table 1. A more detailed explanation on the requirement for using a pulse forming network is given in [2].

The circuit function is straight forward with the possible exceptions of the transformer secondary snubber circuit and the 0.05 μF capacitor added to the high voltage bus connection. This capacitor is added where the high voltage bus connects to the pulse transformer. It is used to compensate for the added inductance of the bus.

The transformer secondary snubber circuit is required because the load time constant is longer than the rise time of the PFN. It provides a mechanism to control the initial voltage applied to the magnet, and then damp the reflections that come back from the magnet to the modulator. There is an optimum value of capacitance that makes the current at the magnet rise rapidly but not overshoot by more than 5%. The value depends on the cable length between the magnet and the modulator, on the transformer leakage inductance, and on the load time constant.

Table 1, Main Injector Abort Kicker Specifications

Field rise time (10% – 70 %) (10% – 90 %)	700 ns 1 μs
Field flat top duration	>9.8 μs
Flatness (ΔB/B) during pulse	± 10%
Field fall time	NA
∫B dl (Total kick/2 Magnets)	0.37 kG m (8 GeV) to 2.51 kG m (150 GeV)
Repetition Rate	0.7 Hz
Magnet Inductance	5.05 μH
Magnet Current	2700 A

2 IMPLEMENTATION

The original design for the abort modulator had all components assembled in a single 24" x 30" x 75" high relay rack. Due to partial discharge problems with several components, a more spacious layout was implemented. Six commercial EMI/RFI shielding enclosures, Schroff® Eurorack HF 1, were purchased for the two modulators. Three enclosures were then joined together to form a final cabinet that is 79" long x 34" wide by 61" high. Each section contains a major pulse power component and is arranged for easy and rapid maintenance.

2.1 PFN Cabinet

The first cabinet contains the PFN, shorting safety relay and end of line termination. The PFN consists of 13 capacitors and 12 inductors. These inductors may be tuned approximately ±5% by changing the length of the coil. This can be done with the system energized. The capacitors are double ended Maxwell capacitors rated for 10^8 pulses at 40 kV charge voltage. The inductor coils are placed parallel to each other and alternately wound right handed and left handed. This positioning of the coils adds coupling between sections to achieve a flatter pulse response.

There is only one connection to frame ground in the

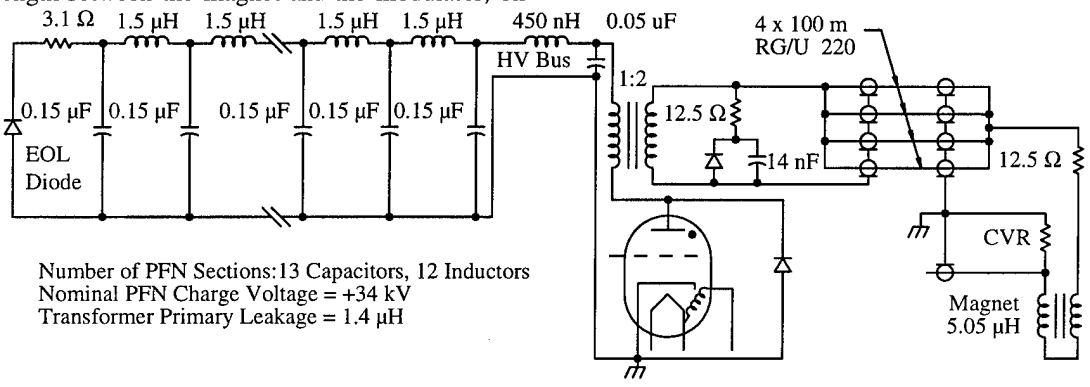


Figure 1, Schematic of Main Injector Abort Kicker System

0-7803-4376-X/98/$10.00 © 1998 IEEE

modulator and this is done at the thyratron. This location was chosen because of the multiple number of connections required between ground and the thyratron. The return bus at the PFN then rings up to about 1 kV during the pulse. The PFN is constructed in a polycarbonate housing which is isolated from the enclosure by standoffs rated for 1 kV_{rms}.

The safety shorting relay and end of line clipper diode and resistor are also in the PFN cabinet. The shorting relay is mounted for gravity return. A modified wire wound resistor from Ohmite, rated at 1 kW average power, is used as the load dump. The modification was to replace a metal frame that runs the length of the resistor with a G–10 frame. This allows the part to be rated for 20 kV pulse voltage and two are used in series. The end of line clipper resistor is made from a stack of 15 ceramic composition resistors, HVR Inc. #W0825A0R2J, rated at 5 kV each. The end of line diode is an assembly from CKE Inc., C03–1689, rated at 60 kV and 11 kA for 10 μs.

2.2 Thyratron Cabinet

The next cabinet contains the thyratron, the thyratron support electronics, and the modulator interlocks. The thyratron trigger circuit, support electronics and interlocks are contained inside a shielded enclosure inside the thyratron cabinet. Initially, a Litton L–4988 thyratron was purchased for the switch. Subsequently, six excess ITT, now Triton, F-241 thyratrons became available. The F-241 has shown acceptable service life under similar conditions in the modulators for the SLAC linac. The Fermilab operating conditions have a much lower repetition rate, but a slightly higher A•s rating per pulse. Two parallel stacks of inverse diodes, 9 pieces Micro–Semi UDD–7.5 per stack, were connected across the thyratron to further ease the operating conditions. These provide a low loss path for reverse currents through the thyratron.

Triggering requirements for this thyratron could be met with the trigger system already designed for the Main Injector Proton Injection Kicker [3]. A 1:3 transformer was used at the output of the trigger circuit to get an open circuit voltage of 2100 V.

In the bottom of this cabinet is mounted a 1.48 m long high voltage bus that connects the PFN, the pulse transformer and the thyratron. Fermilab has successfully used a low inductance stripline bus in air at 12 kV DC for another modulator project [4] so extending the operating voltage to 40 kV DC was reasonable. Several 2D electric field models were made with Opera-2D software from Vector Fields. This was the basis for the bus design. Two tall narrow insulators are used to provide sufficient spacing between the high voltage conductor and two ground conductors. This reduces the electric field stress enough to prevent partial discharge in the air. A thin wide insulator is used between the tall insulator and the ground conductor to get sufficient tracking distance. The insulating material used is polycarbonate because of its excellent electrical and good mechanical properties. Initial testing of the entire bus structure has resulted in a 19 kV_{rms} 60 Hz corona extinction level. The source of the partial discharge appears to come from high voltage connections at the ends. For long life, an extinction level of 25 kV_{rms} is desired and will require further improvements.

2.3 Pulse Transformer Cabinet

The last cabinet contains the pulse transformer, the secondary snubber circuit and the output cable connectors. Free space is required in this section to maneuver the pulse transformer in and out of the cabinet.

The prototype pulse transformer had severe corona problems. The insulation was a cast epoxy that gave sufficient voltage holdoff, however the lifetime of the transformer was in question because of a low corona extinction voltage. The subsequent transformer for the system was specified to use oil as insulation. A solid barrier between primary and secondary windings was also required because the transformer primary will be at 40 kV for 2 seconds during accelerator flattop. Also, 60 kV DC bushings, Isolation Design Model 404, were specified to reduce corona from the connections.

The manufacturer of the first production transformer ordered under the new specification experienced several additional problems. First, the primary windings required additional bracing to protect against shifting during shipment. Second, the leakage and magnetizing inductance were both out of specification. After winding repairs were made, the leakage inductance met specifications but the magnetizing inductance was still small by a factor of two. However, during testing the transformer passed 5000 pulses at 200% nominal operating voltage. It was decided to accept the transformer in order in continue to make progress with modulator development.

The 60 Hz corona extinction level was measured at Fermilab to be approximately 6 kV rms. This level seems inconsistent with long lifetime, however the corona extinction level for the transformer was not specified. It is not obvious that the 60 Hz corona levels are indicative of life for this pulse application. The slow 0.5 second charging time and the fast discharge are definitely not AC operating conditions. Fermilab has many high voltage cables that last 10^8 pulses with a slow charge to 60 kV and pulse discharge, but they also have had measured corona extinction voltages of less than 25 kV_{rms}.

3 TEST RESULTS

Preliminary tests at low voltage indicated that all magnet current specifications had been met. However, after running at full voltage, the magnet current rise time (10 % – 90 %) has increased from 1.0 μs to 1.3 μs. Upon returning to low voltage, the increased rise time is still present. The cause is unknown for certain, but a change in leakage inductance of the transformer is suspected given the problems the vendor had with bracing. Another more experienced vendor has been contracted for the next transformer and that unit has just been tested successfully and shipped.

The measured PFN voltage and current are shown in Fig. 2. The voltage is measured on the primary high side of the transformer with a Northstar VD-60 probe and the current is measured at the thyratron anode with a Pearson 3025 CT. The magnet current is measured with a 2.5 mΩ CVR and shown in Fig. 3. The flat top specification for ripple and length have been met. The ripple is under ±5% and the 90% – 90% pulse length is now 9.7 μs. The pulse length can be further extended by approximately 700 ns because the design allowed for the addition of one more PFN section. However, this should not be necessary when the rise time specification is met.

4 CONCLUSIONS

The modulator has run at rated voltage. The problem of pulse transformer leakage inductance has been solved with the new manufacturer.

The cost of each finished modulator is approximately 130k$ for parts and materials, 800 hours for shop labor and 3000 hours for assembly and testing labor. While the parts cost is substantially more than the old Main Ring abort kicker system, an increased cost was anticipated because the specifications ruled out the technique used for that kicker system.

REFERENCES AND ACKNOWLEDGMENTS

This work is supported by the U.S. Department of Energy under contract No. DE-AC02-76CHO3000.

[1] Abort Kicker Power Supply Systems at Fermilab, G. Krafczyk, G. Dugan, M. Harrison, K. Koepke, E. Tilles, IEEE Trans. Nuc. Sci., Vol. NS-32, No. 5, October 1985, pp. 3581-3583

[2] Fermilab Main Injector Abort Kicker System, C. C. Jensen, J. A. Dinkel, Proceedings 1995 PAC, Dallas TX, pp. 1239-1241

[3] Kicker System for 8 GeV Proton Injection, D. Qunell, C. Jensen, D. Tinsley, Proceedings 1997 PAC, Vancouver BC

[4] A 2nd Long Pulse Modulator for TESLA Using IGBTs, H. Pfeffer et. al., Proceedings of 1996 EPAC, Sitges Spain, pp. 2585-2587

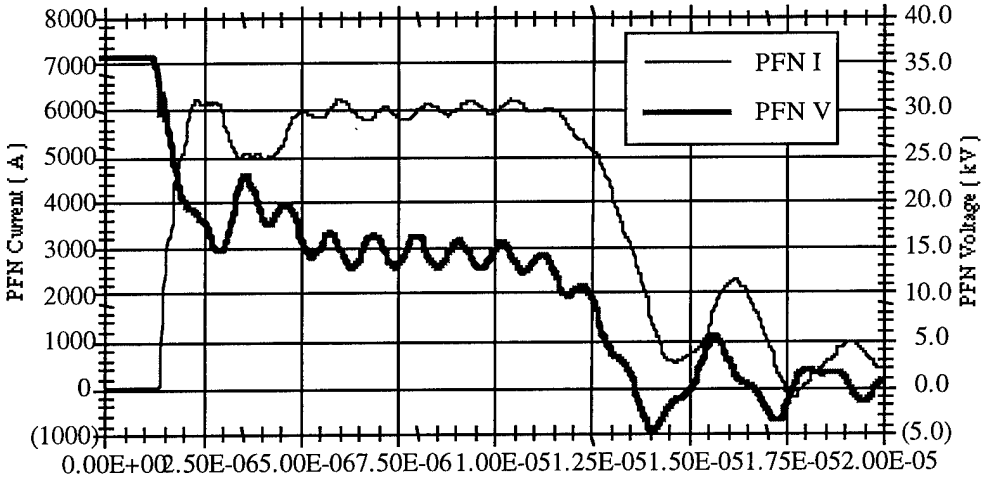


Figure 2, Measured PFN Voltage and Current Waveforms at Nominal Operating Level

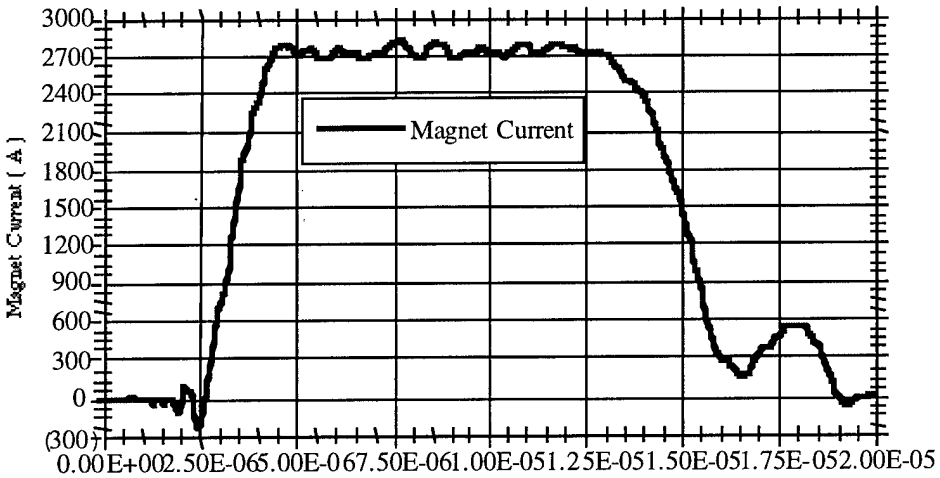


Figure 3, Measured Magnet Current Waveform at Nominal Operating Level

KICKER SYSTEM FOR 8 GEV PROTON INJECTION

D. Qunell, C. Jensen, D. Tinsley
Fermi National Laboratory, P.O. Box 500, Batavia, IL 60510

Abstract

This kicker functions to inject 6 batches of 8 GeV beam vertically into the Fermilab Main Injector from the Booster. The trajectory of this beam must be bent 1.05 mr to place it onto equilibrium orbit. This kicker system produces a nominal integrated field kick of 0.309 kG-m. Specifications require a 1.6 microsecond pulse with a 50 ns risetime (1%-99%) and a 150 ns falltime (99%-5%). The system is comprised of three magnets and power supplies. Each is composed of a resonant charger, a 25Ω PFL, a thyratron-based pulsed power supply, a ferrite "C" magnet, and a Fluorinert™-cooled resistive load. Design details and measurements are presented.

1 INTRODUCTION

This system is being developed to replace the existing kicker that injects protons from the Booster to the Main Ring. The existing system does not provide a fast enough risetime. First, the current risetime of the thyratron is slow because the dc charging system requires a low reservoir level to avoid prefires. Second, the parasitic inductance of the thyratron housing limits the risetime of the circuit. Also, the control system is being upgraded to use components common throughout Main Injector and newer TeV kickers. Power supplies of this type will be also used in the Fermilab Recycler and future Booster upgrades. In addition to meeting design specifications, this kicker was also developed to meet reliability, serviceability and cost objectives.

Prefires and fail-to-fires must be kept less than one per every million shots. Lifetime is also important; over 10^8 shots are necessary to achieve 5 years of service. While this is most applicable to the thyratron, the magnet and resonant charging unit must also last a similar amount of time without any high voltage breakdown or other failure modes.

Serviceability was another major concern. Unlike previous power supplies which were large forced air or oil cooled tanks, this design is a compact Fluorinert™ cooled system. Replacement of a complete power supply takes less than an hour, while even the replacement of a thyratron is a fairly simple task requiring less than four hours. In general, an effort was made during the design to improve the ease of servicing all system components.

Of course, cost was another design consideration. The systems had to adhere to project budgets and schedules throughout the design and development phase.

Initial system specifications [1] are tabulated in Table 1. Some preliminary measurements are also included. These specifications are subject to revision.

∫ Bdl	0.309 kG-m
Kick Angle	1.05 mr vertical
Horizontal Aperture	101.6 mm
Vertical Aperture	50.8 mm
Magnets Required	3
Field Rise Time (1%-99%)	<50 nsec
Flattop	1600 nsec
Field Fall Time (99%-5%)	<150 nsec
Flattop Stability	±1%
Post Flattop Stability	±1% of full field
Magnetic Length	0.83 m
Gap Height	111.1 mm
Gap Width	63.5 mm
Nominal Field	0.136 kG
Characteristic Impedance	25 Ω
Number of Cells	26
Measured Magnet Fill Time	26 nsec
Measured Inductance per Cell	~29 nH
Measured Capacitance per Cell	~45 pF

Table 1: Specifications and Measurements

2 DESIGN

2.1 Power Supply

The power supply consists of a PFL, a thyratron pulser and a resonant charging system, as shown in Figure 1. This system must produce a 1.6 microsecond pulse with fast rise and fall times. It must operate at a 15 Hz repetition rate, producing 6 pulse "bursts" every few seconds. Minimization of prefires and fail-to-fires is a major design consideration. A lifetime of over 10^8 shots is required.

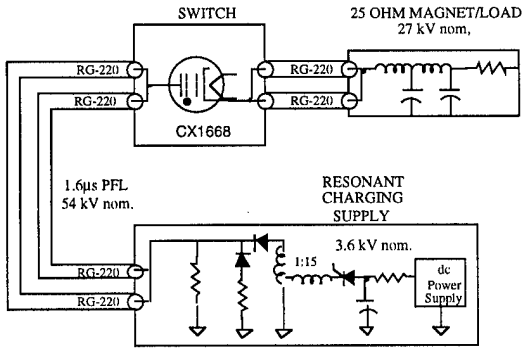


Figure 1: Diagram of Kicker System

0-7803-4376-X/98/$10.00 © 1998 IEEE

Each PFL consists of two lengths of RG-220 type cable. The cable itself is AA-5966, manufactured by Times Microwave Systems under a custom Fermilab specification. It is similar to standard RG-220 cable except that it has the addition of a foil shield bonded to the polyethylene. The two 50 Ω cables are installed in parallel to make a 25 Ω system. These cables are cut to nominal 160m lengths to determine the 1.6 μs pulse width. Cables delivered to Fermilab from Times passed a 500,000 pulse acceptance test at 66 kV. The falltime of the system is dominated by the skin-effect of the cable.

The pulsed power supply shown in Figure 2 consists of a thyratron switch, a trigger system, and associated filament/reservoir power supplies. These components are mounted in a Tin-plated Aluminum housing. This housing is compact to minimize parasitics that adversely affect the system risetime. The thyratron is cooled by 3M Fluorinert™ FC-40 liquid. This also provides the necessary high-voltage insulation. Connections to the PFL and load cables are made with custom connectors designed by Isolation Designs, Inc [2].

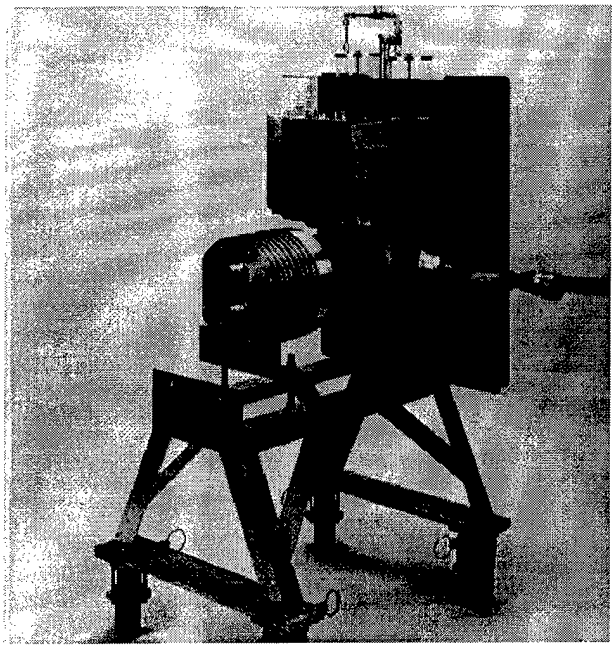


Figure 2: 25 Ω Pulsed Power Supply

Fermilab tested various 2-gap and 3-gap thyratrons. The best results were obtained with a hollow anode EEV CX1668 using a "cross-connection" bias scheme [3]. This decreases the overall system delay, and effectively reduces the risetime by minimizing the time between the breakdown of the two gaps. Biasing is accomplished with 4 MΩ resistors on the gradient grids; no capacitors were used in the bias network. An adjustable DC power supply and a 20 kHz DC-AC converter are used to power the filament and reservoir. This minimized the size of the transformer which provides isolation between high and low voltage components. Also in the thyratron housing is a fast thyratron trigger system [4].

A resonant charging supply is used in this system, primarily to allow the thyratron to operate at a higher reservoir power level than would be possible with a direct charging DC system. The higher reservoir power level improves the current risetime in the magnet significantly. In addition, the resonant charging system operates in about 300 μs, allowing fast repetition rates.

The resonant charging system is comprised of a 5 kV DC power supply which charges a capacitor. The capacitor size can be varied depending on the length of the PFL being resonantly charged. On command, an SCR switch discharges the capacitor into a step up transformer. The transformer assembly, made by Stangenes Industries, has a nominal 1:15 step up ratio. In addition, it incorporates the charging diodes, a 25 Ω resistor/diode back-termination network, and a 500 kΩ discharge resistor in its oil-filled housing. The discharge resistor will discharge the PFLs between pulses at the 15 Hz rep rate to prevent accidental overcharges, should a fail-to-fire occur. The PFLs connect directly to the transformer assembly via Isolation Designs connectors.

2.2 Magnet

Like the power supply, a new 25 Ω magnet has been developed to replace the existing Main Ring injection magnet. A "C" magnet design is used, incorporating 26 cells with inductance and capacitance tuned to provide a matched 25 Ω system. Vector Fields OPERA-2d software was used in analyzing and optimizing the field linearity in the beam tube gap.

Each cell is comprised of a high frequency Nickel-Zinc ferrite block. The ferrite is CMD 5005, made by Ceramic Magnetics [5]. The ferrites are 2.54 cm thick, and have a 0.635 cm spacing. Adjacent ferrites are cross-coupled with a single turn of copper strap and a series 10 Ω ceramic composition resistor [6]. Finally, each cell has a small parallel plate capacitor that forms a matched 25 Ω system with the magnet inductance. Standard high-voltage ceramic capacitors were determined to have too much stray inductance for this application. This capacitor is simply a small metallic plate connected to the busbar that forms a small capacitance with the top of the magnet case. The top of the case can be machined such that the distance between the capacitor electrodes can be varied to allow for precise matching of the impedance. OPERA-2d software was used to design the capacitor. An impedance analyzer will be used to ensure the production magnets are properly trimmed.

The magnet is potted in Grace Stycast 5952 Silicon Rubber. This is a high dielectric constant material which is used to achieve the proper capacitance between the parallel-plate capacitors. Most kicker magnets at Fermilab have used a transparent RTV material. While this allows for simple inspection of failures, it did not

provide the high dielectric constant necessary in this design. The Stycast material does have the disadvantage that is it opaque, and will make locating repairs difficult. The potting material also provides high voltage insulation in the magnet. Since repairs are likely to be difficult, peak field stresses in the magnet were universally kept below half of the dielectric strength of the material.

Like the power supply and resonant charging unit, Isolation Designs connectors are incorporated into the magnet to facilitate connection to the RG-220 type cable that runs between the magnet and power supply. Capacitive pickup probes at the input and output are used to monitor the magnet voltage. In addition, the magnet may incorporate a saturable reactor and a speed up network to improve performance [7]. Preliminary tests have shown that a small saturable reactor at the input of the magnet does improve the risetime. Acceptable results were obtained using 3.23 cm^2 of CMD 5005 ferrite with no air gap. This ferrite had an ID of 1.27 cm and an OD of 3.81 cm. The ferrite was mounted directly over a 1.27 cm conductor inside the magnet. Larger amounts of ferrite improve the 10%-90% risetime significantly, but also cause unacceptable reflections later in the pulse. Further tests will determine if a small "speedup" capacitor on the output of the magnet can improve the risetime.

2.3 Resistive Load

Attached directly to the magnet is a 25 Ω load, comprised of ten disc resistors manufactured by HVR. These resistors are mounted in a low inductance, tapered housing. They are individually selected to be matched to the proper resistance at nominal operating temperatures and voltages. The resistors are cooled by a passive, evaporative cooling system using Fluorinert™ FC-72 liquid. Heat is transferred by copper plates between resistors to the Fluorinert™ in the center hole. Dow Corning Sylgard® 184 RTV provides high voltage insulation. A current viewing resistor is included for monitoring the current waveform.

3 MEASUREMENTS

Initially, we compared measurements from a printed circuit field coil and the difference of the two capacitive pickup probes. More recently, we have started some preliminary measurements on the prototype magnet with a novel ferrite probe [8]. All these measurements show reasonable agreement. A measurement of the rising edge of the magnet field using the new ferrite probe is shown in Figure 3. As the load was not at nominal operating temperature, there is a slight impedance mismatch in the system for these measurements. This mismatch is a partial cause of the small oscillation on the flattop. The parasitic inductance and capacitance of the thyratron housing are other factors. These measurements were taken at 20% over nominal field ratings. This is about 66 kV, and is the upper limit due to reliability of the PFLs and the thyratron. Typical observed jitter at these levels is about 1.5 ns. No saturable reactor or "speed-up" capacitor is installed for these measurements.

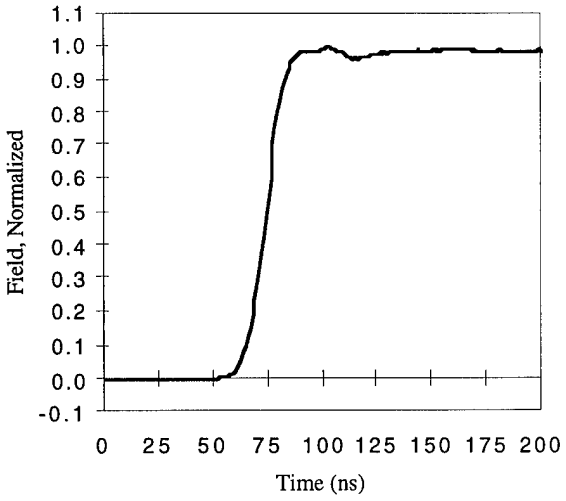


Figure 3: Magnet Field vs. Time

4 CONCLUSION

Preliminary field measurements on the prototype kicker system show that the system meets specifications except for flattop stability, which is better than ±2%. Final system components are being procured and assembled for installation in 1998. We intend to measure the first production magnet later this year using an 8 GEV proton beam. Based on those measurements, we may include a saturating ferrite and capacitive speed up network to improve performance over measurements presented here.

5 ACKNOWLEDGMENTS

The authors acknowledge John Dinkel and Ken Kellogg of Fermilab for their contributions to this project. We would also like to thank M. Barnes and G. Wait at TRIUMF for various technical exchanges over e-mail.

REFERENCES

[1] The Fermilab Main Injector Technical Design Handbook, November, 1995.
[2] A. Donaldson , et al., "High Voltage Pulse Cable and Connector Experience in the Kicker Systems at SLAC," IEEE Particle Accelerator Conference , Vol. 5, pp3159-3161 , May 1991.
[3] Ron Sheldrake, EEV Corportation, Private communication
[4] C. Jensen, D. Qunell, "A Thyratron Trigger with Low Jitter," These Proceedings.
[5] C. Jensen, J. Dinkel, "Comparison of Ferrite Materials for Pulse Applications," IEEE Transactions On Magnetics, Vol. 31, No. 1, January 1995.
[6] B. Hanna, J. Dinkel, C. Jensen, D. Qunell, R. Reilly, D. Tinsley, J. Walton, "A New Fast Rise Time Kicker System For Antiproton Injection Into The Tevatron," IEEE Particle Accelerator Conference Proceedings, Vol. 3, pp 1900-1902, May 1995.
[7] M.J. Barnes, G.D. Wait, "Effect of Saturating Ferrite on the Field in a Prototype Kicker Magnet", EPAC94, London, pp2544-2546.
[8] W. Pellico, P. Colestock, "Pulsed Magnetic Field Measurement System," These Proceedings.

HIGH POWER MODULATOR FOR LINEAR INDUCTION ACCELERATOR SILUND-21

G.V. Dolbilov, A.A. Fateev
Joint Institute for Nuclear Research, 141980 Dubna, Moscow Region, Russia

Linear induction accelerator SILUND-21 is under construction at the Joint Institute for Nuclear Research (Dubna). SILUND-21 will provide electron beam with the energy up to 10 MeV, peak current $\sim$ 1 kA and pulse duration 50 – 70 ns. This report presents description of nanosecond accelerating voltage scheme for the SILUND-21 accelerator. The main feature of our approach consists in the use of powerful, low-voltage generator ($V \simeq 42$ kV) and low-resistance load ($R \simeq 0.5\ \Omega$). A high power in nanosecond pulses ($W \sim 1$ GW) is achieved in nonlinear compression schemes with distributed parameters which compress electromagnetic energy in time.

1 INTRODUCTION

The SILUND-21 linear induction accelerator (10 MeV, 1 kA, 50 – 70 ns) will serve as a base of experimental facility to study microwave electronics, FEL physics and two beam acceleration [1]. SILUND-21 accelerator is constructed using the equipment of LUEK-20 accelerator developed for experimental investigations of the collective method of acceleration [2, 3]. Nevertheless, there are two principal distinctions between LUEK-20 and SILUND-21 accelerators. First, LUEK-20 accelerator has been used to accelerate compact, 4 – 6 mm long electron-ion rings, so there was no need in essentially rectangular form of the accelerating voltage. In the case of SILUND-21 we need good quality rectangular pulse of about 50 ns duration. Second, the equivalent beam current load was less then 100 A in LUEK-20 accelerator, so there were no severe requirements to the value of stray inductance of junctions. The beam load will be larger by the order of magnitude in SILUND-21, so, the main problems of upgrading the LUEK-20 equipment consist in partial reconstruction of induction sections and in design of a new modulator.

2 ACCELERATING MODULE

The accelerator consists of seven identical accelerating modules. Each module provides approximately 1.5 MeV accelerating voltage at 1 kA beam load. The general layout of the accelerating module is presented in Fig. 1. Induction section (1) consists of 36 permalloy cores combined in pairs. The core exciting windings of each pair are commutated in parallel. The input impedance of the section is equal to about 0.5 Ω at nominal beam load.

Vacuum pumping of the accelerator volume is provided by sputter-ion pumps (3) via channels placed in the gap (4). Electron beam diagnostic devices are also placed there.

The accelerating ceramic tube consist of 6 sections separated by cone earthing diaphragms. Cone diaphragms play also the role of screens reducing the intensity of interaction between the electron beam and dielectric waveguide and form accelerating gaps. The amplitude of accelerating voltage at each of six accelerating gaps of the accelerating section is equal to 250 kV.

Focusing of the electron beam is provided by solenoid. The solenoid winding is sectional and the number of the sections is equal to the number of permalloy cores. Design parameters of the solenoid power supply allow one to provide the guiding magnetic field with the amplitude up to 1.4 T and pulse duration about of 0.8 ms.

Pulses of accelerating voltage with the amplitude of 42 kV, duration of 50 – 70 ns and rise time of about 5 ns are formed by modulator (2) with 0.5 Ω internal resistance. TGI1-2500/50 hydrogen thyratron (2500 A, 50 kV), which is used as a commutator, does not provide commutation of the required level of the peak power, so power compression schemes are used to increase the peak power.

3 MODULATOR SCHEME

The modulator scheme (see Fig. 2) is based on the application of the nonlinear power compression technique and is similar to that of the SILUND-20 accelerator [4]. More than ten years of successful operation of the SILUND-20 accelerator have proved the validity of technical solutions for the modulator.

The process of pulse power compressing in microsecond range is relatively simple and could be realized without significant efforts. The main problems arise when designing power compression scheme is operating in nanosecond range with pulses of rectangular form.

Modulator scheme consists of two main parts. The first one is traditional compression scheme with lumped-elements, which includes initial pulse forming circuit (thyratron, C1, L1) and one compression cell (C2, L2).

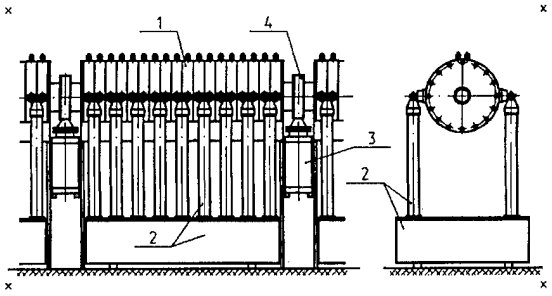


Figure 1: Accelerating module

0-7803-4376-X/98/$10.00 © 1998 IEEE

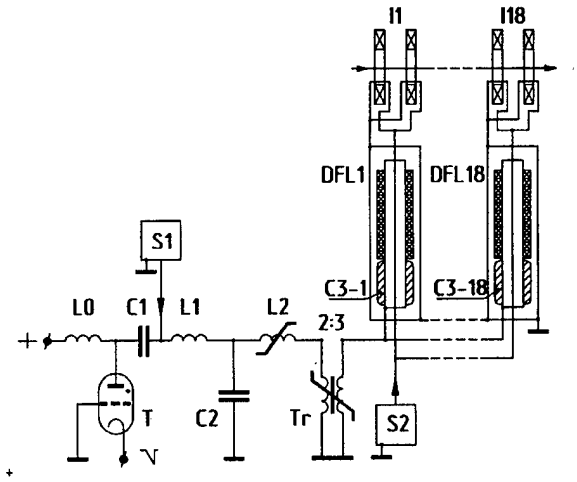


Figure 2: Modulator scheme

The second part is an output forming stage which includes forming lines and nonlinear transformer Tr.

The severe requirements to the modulator of SILUND-21 accelerator (low output impedance and short rise time of the output pulses) completely exclude the possibility of using lumped-element chains in the output stage. As a result, the lines with distributed parameters (both linear and nonlinear lines with ferrits) should be used in the output stage. In this case the processes of power compression and forming of rectangular shape of the pulse take place simultaneously in the output stage.

Hydrogen thyratron T operates in a pulsed mode with 3 μs pulse duration and provides commutation of 10 kA current at 30 kV voltage. Permalloy reactor L2 and saturable transformer Tr play the roles of ferromagnetic switches. The initial pulse is compressed in the traditional stage and then it charges the forming stage consisting of nonlinear double forming lines (DFL1 – DFL18) with the additional correcting capacities (C3-1 – C3-18). DFLs are charged within 1 μs time period. During this process the transformer Tr is not saturated. Each DFL consists of two coaxial lines. The external line is partially filled with ferrite rings. The rest volume of DFL is filled with rectified water. With respect to the charge current the ferrite is saturated and the efficiency of the energy transfer is about 0.9.

When the voltage amplitude in the DFL reaches its maximum, the transformer Tr is saturated and becomes to serve as a commutator forming a voltage swing with the relatively long front which then becomes shorter and forms $\sim$ 5 ns rise time of the driving pulse. Such a way to form output pulses allows one to reach a high ratio of compression and to obtain rectangular pulses of 60 ns duration from sinusoidal pulse of 1 μs duration.

The initial magnetization of the ferromagnetic materials in the nonlinear elements is adjusted by two ambipolar current sources (S1 and S2). This technique provides a high precision of the initial magnetization value.

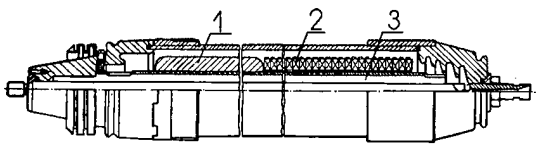


Figure 3: Nonlinear double forming line. 1-correcting capacity, 2-ferrit cores with screens, 3-internal linear line.

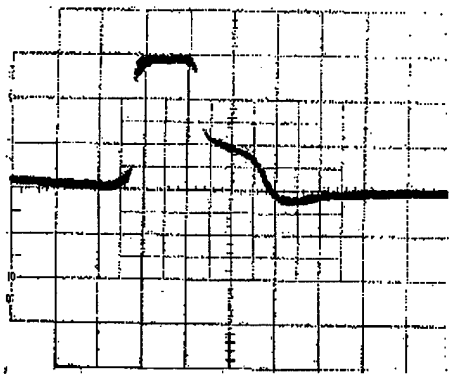


Figure 4: Oscillogram of the output pulse. Amplitude scale is 15 kV/div. Time scale is 50 ns/div.

4 DOUBLE FORMING LINE

Preliminary construction of the double forming line is shown in Fig. 3. All metallic parts are manufactured of stainless steel. Insulating parts are made of plastic. Ferrit cores are placed into metallic screens which increase linear capacitance and protect ferrit against electrical fields.

5 TEST MEASUREMENTS

The specimens of the double forming lins and water rectification systems are being manufactured and assembled in an experimental hall. This setup allows one to test the double forming lines under conditions close to operating regime.

Operating experience has been showing that the water rectification system maintains the required value of the water resistivity in the line larger than 2 MΩ cm. This value corresponds to the discharge time of 14 μs. DFL are tested with charging voltage up to 50 kV with the rise time of about 0.8 μs. The commutation time is about 200 ns. The rectangular pulses of $\sim$ 60 ns duration are formed at the equivalent load consisting of two permalloy cores and resistor. The oscillogram of the output pulse is presented in Fig. 4.

6 ACKNOWLEDGEMENT

The authors wish to acknowledge Dr. I. Ivanov for his constant encouragement. We also would like to express our thanks for the support from all technical groups.

7 REFERENCES

[1] G.V. Dolbilov et al., Nuclear Instrum. and Methods **A 375**(1996)100.

[2] G.V. Dolbilov et al., Proc. EPAC94 (London, 1994). World Scientific, 1994, Vol.1, p.748.

[3] G.V. Dolbilov et al., Proc. of the 1994 International Linac Conference (Tsukuba, Japan), Tsukuba, KEK, 1994, Vol.1, p.357.

[4] G.V. Dolbilov, A.A. Fateev, V.A. Petrov, A.I. Sidorov, Proc. of the 1994 International Linac Conference (Tsukuba, Japan), Tsukuba, KEK, 1994, Vol.1, p.360.

A 200-A, 500-Hz, TRIANGLE CURRENT-WAVE MODULATOR AND MAGNET USED FOR PARTICLE BEAM RASTERING*

C. R. Rose and R. E. Shafer
Los Alamos National Laboratory, Los Alamos, NM 87545

Abstract

This paper describes a simple 2D beam-rastering system to uniformly spread a 100-mA 6.7-MeV cw proton beam over a 50-cm by 50-cm beam stop. The basic circuit uses a 20-mF capacitor bank, a IGBT (insulated gate bipolar transistor) full-wave inverter, and a 1-mH ferrite dipole magnet to produce a ± 500-Gauss peak triangular-waveform deflection field at 500 Hz. A dc input voltage of 200 volts at 2.6 amps (520 watts) produces a 160-ampere peak-to-peak triangular current waveform in the ferrite magnet at 500 Hz. For dual-axis rastering, two ferrite dipoles are used, one at 500 Hz, and the other at 575 Hz, to produce a uniform 2D beam distribution at the beam stop.

The paper will discuss the IGBT modulator and ferrite deflector in detail, including current and voltage waveforms, and the ferrite magnet B-dot (dB/dt) signal.

1 INTRODUCTION

High energy particle beams, if narrowly focused, can exceed the power density limitations of the beam stop. Currently, there are several approaches available to diffuse the energy of the beam across the beam stop. One technique involves defocusing the beam. Another is to raster the beam across the beam stop to reduce the peak power at any one location. This paper describes a design for a beam-rastering system comprised of a ferrite-dipole magnet and triangle current-wave modulator. In the complete system, both the x- and y-axes will be rastered. To date, one system has been designed, built, and tested at full current at the required frequencies of 500 Hz and 575 Hz. These frequencies were determined empirically to provide uniform power distribution over the beam stop.

2 MAGNET

The magnet is approximately 20 cm (W) by 23 cm (H) by 30 cm (L) with an 8-cm by 8-cm aperture. With a 40-turn coil, the inductance is about 1.1 mH. At 80 A, the field inside the bore is 500 G. Fig. 1 is a picture of the first magnet developed to prove the concept.

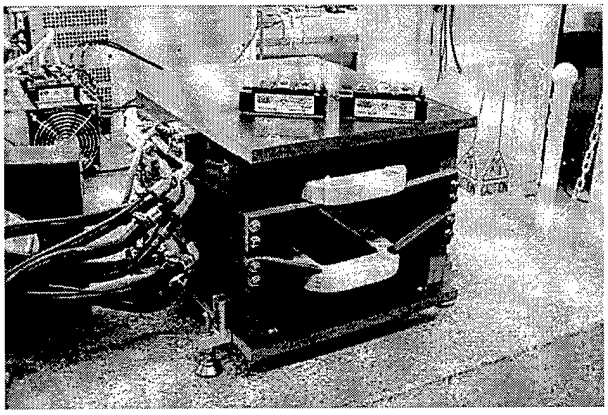


Fig. 1 Picture of the magnet with the IGBTs on top.

3 MODULATOR

The modulator uses two International Rectifier half-bridge IGBT modules configured into an H-bridge as shown in Fig. 2. A TTL level pulse generator provides the Q and Q-bar timing signals to the IGBT drivers. The IGBTs are switched in pairs; Q1 and Q4 switch together, then Q2 and Q3 switch on during the last half cycle. The bypass diodes in the IGBTs switch on when their respective IGBT turns off allowing the inductive energy

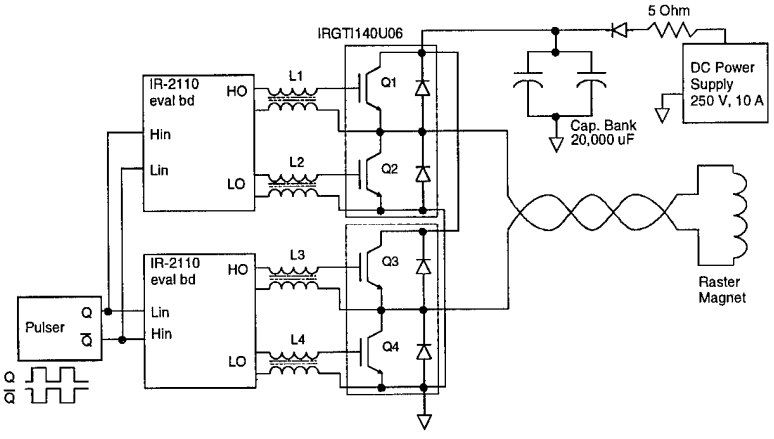


Fig. 2 Electrical schematic of the beam-rastering modulator.

* Work supported by the US Department of Energy.

in the magnet to return to the capacitor bank. The common-mode chokes eliminate large dV/dt transients at the output of the driver cards and help to protect the IR-2110 driver ICs. The two IGBT modules, the charging diode, and the series resistor are mounted on a heatsink for cooling. The IR-2110 IGBT driver boards are mounted on the side of the heatsink. A picture of the modulator is shown in Fig. 3. The IGBTs are rated at

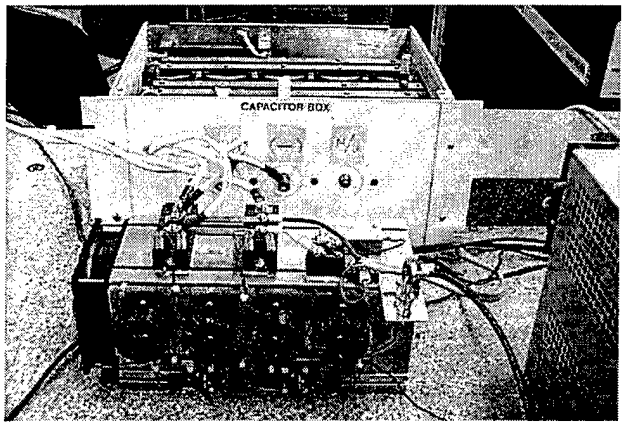


Fig. 3 View of the modulator showing the heatsink, the drivers, and the IGBTs.

140 A, 600 V, and have a switching risetime of under 90 ns. The capacitor bank consists of ten 2000-μF high rms-current-rated capacitors.

4 SYSTEM OPERATION

The modulator has been tested and operated successfully at both 500 and 575 Hz. The data shown and included in this paper are at 500 Hz. Several tests were run on the system including measuring the total power dissipation as a

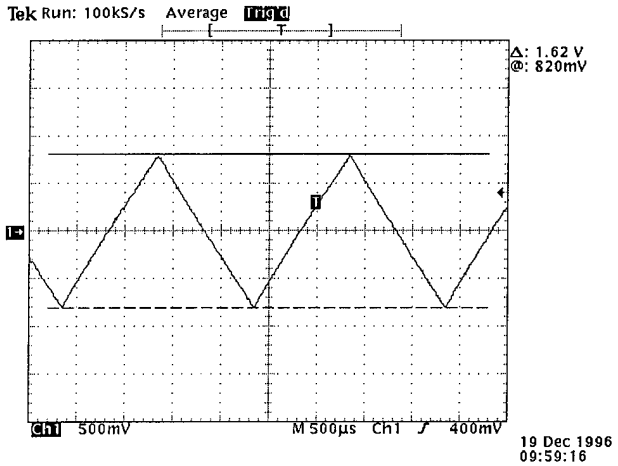


Fig. 4 Data of the triangle magnet current.

function of frequency, the output current levels, and the magnetic field levels inside the magnet. A typical magnet current waveform is shown in Fig. 4.

In this figure, the modulator was operating at 200-V dc, 2.6-A dc, and yielded a magnet current of 162 $A_{p\text{-}p}$. The measurement equipment consisted of a Pearson #101 current transformer (100 A/V) and a Tektronix TDS-340A oscilloscope. Current measurements were also done using a Pearson #3025 with 40 A/V sensitivity.

To measure the quality of the magnetic field inside the magnet, a B-dot (dB/dt) loop was used. The B-dot voltage signal is shown in Fig. 5 along with a superimposed current waveform for timing and reference purposes. The risetime of the B-dot signal is about 2 μs.

The B-dot loop consisted of a one-turn wire loop in the magnet aperture with a cross-sectional area of about

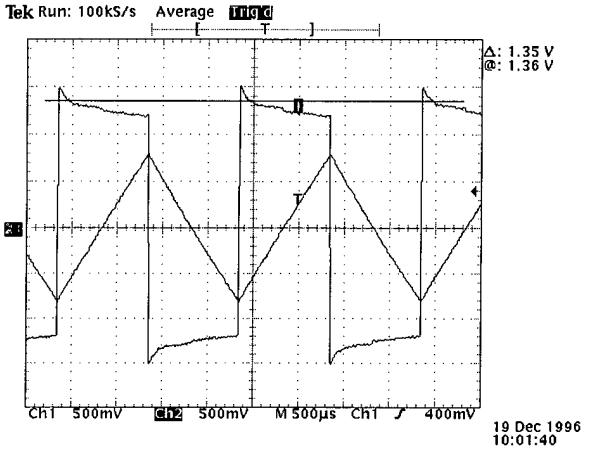


Fig. 5 Magnet current and B-dot loop waveforms.

124 cm^2. Overshoot in the B-dot is due to eddy currents in the copper magnet coil. The L/R droop is also observable. Both effects have been simulated and confirmed with SPICE simulations.

The circuit shown in Fig. 2 was operated and power dissipation data were taken. This data is shown Fig. 6.

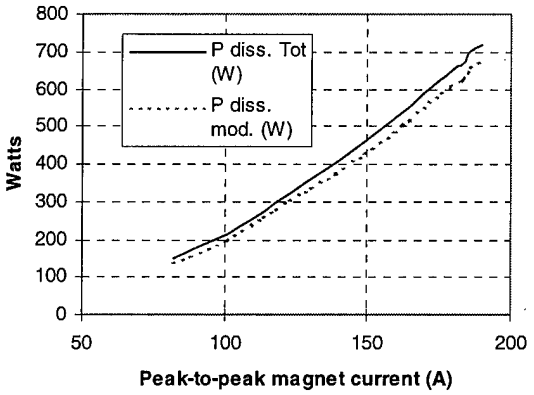


Fig. 6 Plot of modulator dissipation with and without the 5-Ohm series resistor.

The top curve is total power dissipation including the 5-Ω series resistor. The lower curve excludes the resistor. The 5-Ω resistor and charging diode help to isolate the dc power supply from the large current transients in the IGBTs and inductor.

The expected rastering pattern for two rastering magnets operating at 500 and 575 Hz, and 1000 gauss p-p is shown in Fig. 7. The beam-spot rms width should

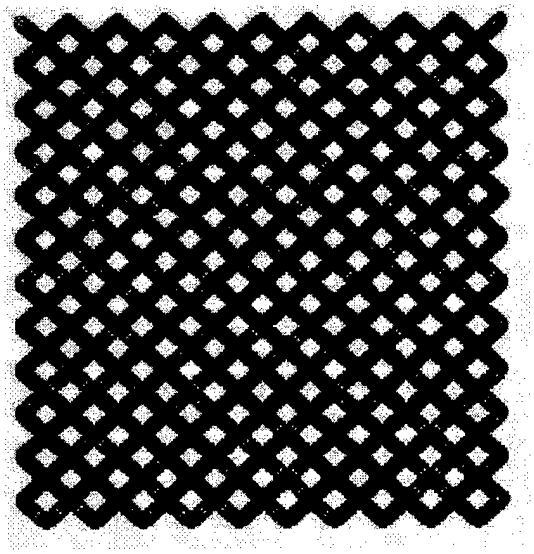


Fig. 7 Plot of the rastering pattern from two rastering magnets operating at 500 and 575 Hz.

be at least half the spacing between the traces to achieve ± 5% uniformity in beam power density. Because of eddy-current limitations, a ceramic beam tube is required. The inner surface should have a one skin-depth metalization to carry the beam image currents.

5 CONCLUSIONS

The basic concept of using IGBT switches to create a triangular current waveform in a raster magnet works well. Two rastering magnets operating at non-harmonic frequencies will provide a uniform 2D rastering pattern. The 40-turn magnet coil will be redesigned to reduce the eddy-current losses and the L/R droop.

ACKNOWLEDGEMENTS

The authors would like to thank and acknowledge the help and contributions of D. Redd and B. Shurter who helped with the assembly and testing of the modulator.

ARBITRARY WAVEFORM GENERATOR FOR ELECTROSTATIC DIPOLES IN A HEAVY ION RECIRCULATOR

D.P. Berners, L.L. Reginato, *Lawrence Berkeley National Laboratory*

Abstract

The Lawrence Berkeley National Laboratory is working in close collaboration with the Lawrence Livermore National Laboratory in the investigation of using a recirculating induction accelerator as a driver for Heavy Ion Fusion. The deflection dipoles in the recirculator require precise high voltage electrical waveforms. These waveforms are of a parabolic shape and rise to a peak voltage level of 28 kV in 240 μs. A voltage reference is generated internally which is completely adjustable through the computer. The voltage reference is compared to the output voltage and the error signal drives a pulse width modulator carrier frequency of 100 kHz. The high frequency carrier is stepped up with five stages of ferrite transformers, rectifiers and filters to generate a completely adjustable waveform of up to 28 kV which follows the computer generated voltage reference.

1. INTRODUCTION

The small Heavy Ion Fusion Recirculator Ring under construction at the Lawrence Livermore National Laboratory (LLNL) will require precisely tailored waveforms to bend the beam around the circumference (Fig. 1). The bending field will be electrostatic (rather than magnetic) and its strength must increase during acceleration in precise synchronism with the increase in particle energy. This requirement leads to the need for a precisely programmable power supply which can be adjusted through a computer from 7 kV to 28 kV (Fig. 2). As shown in Fig. 1, forty bipolar bending dipoles are spaced around the recirculator. Each dipole is a capacitive load and, with the additional cable capacitance, a total reactive load of 300 pF must be driven by the programmable power supply. Considering the rate of rise in voltage, an average current of 50 mA is required during the 240 μs pulse for each positive and negative power supply. Commercially available programmable power supplies did not meet our requirements and the cost of custom made units would have been prohibitive. It was decided that an in-house effort would be appropriate since the power supplies could be made to satisfy all of the physics requirements with no additional features at a very reasonable cost. Also, for economic reasons, as many dipoles as possible will be driven in parallel from a single power supply. The number of dipoles that can be driven is determined by the output impedance of the high voltage stages. The high voltage stages consist of ferrite transformers wound in such a way as to minimize the leakage inductance.

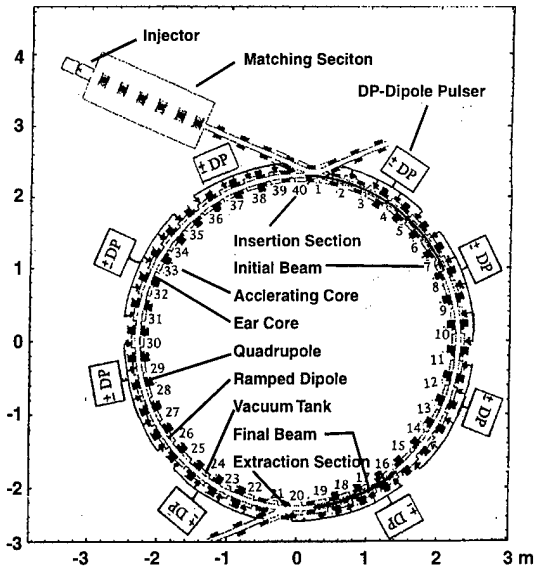


Figure: 1 The Small Heavy Ion Fusion Recirculator Ring.

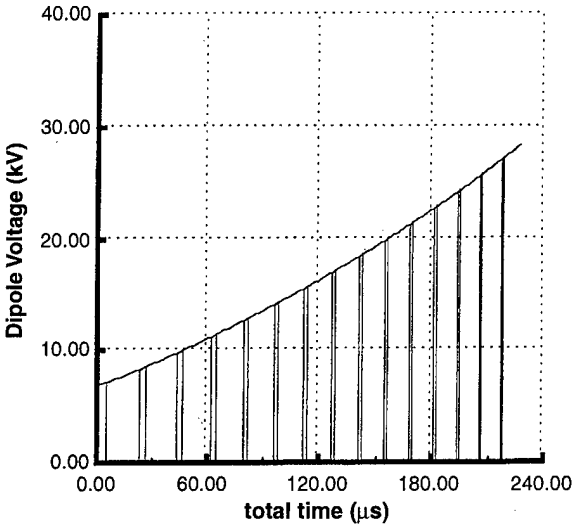


Figure: 2 Required electrostatic bending dipole field.

2. SYSTEM ARCHITECTURE

The basic requirement boiled down to building a DC to pulse converter with the appropriate bandwidth to precisely reproduce the required reference waveform. Several options were investigated but the one which appeared most efficient was one which used pulse width modulation in the feedback loop. The block diagram for the arbitrary waveform generator is shown on Fig. 3. The reference waveform required to bend the beam in the

0-7803-4376-X/98/$10.00 © 1998 IEEE

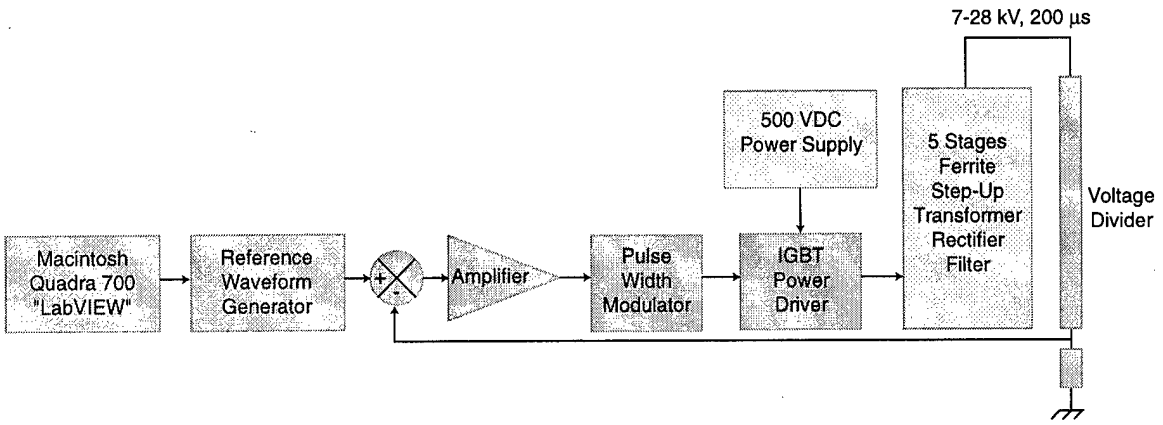


Figure: 3 Block diagram of the arbitrary waveform generator.

recirculator is shown on Fig. 2. This waveform can easily be adjusted by the accelerator tuner through the Macintosh computer using the software LabVIEW. The reference is compared to the output voltage and the error signal adjusts the pulse width modulator to insure that the high voltage output is a precise reproduction of the reference. The feedback loop gain and response are adjusted at the amplifier stage. The insulated gate bipolar transistors (IGBT) provide the switching power that drives the input ferrite 12:1 step-up transformer which is coupled to the other four stages of one-to-one transformers. The secondaries of all five transformers are connected in series to provide a 60:1 step up ratio (Fig. 6). The carrier frequency of 100 kHz was chosen since it provided sufficient slewing rate to accurately generate the high voltage waveform in a full wave rectifier system. A low pass filter consisting of an inductor in series with the distributed dipole and cable capacitance provided the smoothing function. Five stages of ferrite transformers were chosen rather than a single high voltage step-up transformer because it resulted in lower overall leakage inductance, a better distribution of the high voltage, and a higher safety factor.

It is estimated that the capacitance of the dipole and ten feet of 100 ohm high voltage cable will have a capacitance of 300 pF. The high voltage system was developed and tested by loading it with 2500 pF, hence, up to eight dipoles can be driven by one waveform generator.

3. REFERENCE GENERATOR AND INTERFACE

The reference generator must be capable of accurately duplicating the waveform dictated by the heavy ion beam transport dynamics (Fig. 2) and be capable of easily being adjusted during the beam tuning process. The commercially available waveform generators had many features which were not necessary and as such cost considerably more than the budget allowed. It was decided that a simple waveform generator which met all of the performance and cost requirements could be developed in-house and that LabVIEW, which was already in use on other experiments, could provide a simple user interface. Fig. 4 is a simplified block diagram of the reference generator and interface. The software LabVIEW on a Macintosh Quadra 700 programs the reference board through a GPIB parallel port. The data for the pulse can be stored on a spreadsheet, can be derived from an equation, or can be derived graphically from within the LabVIEW driver.

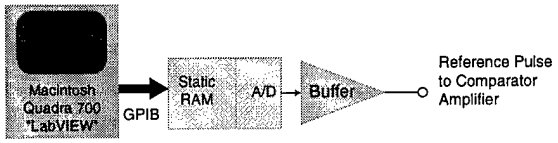
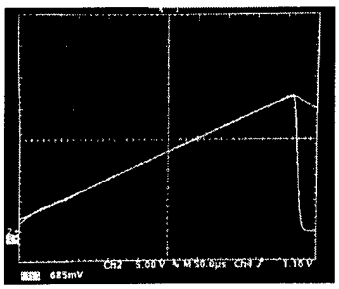
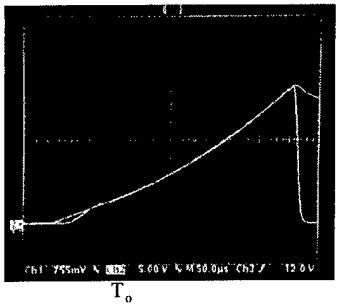


Figure: 4 Simplified block diagram of the reference generator and interface.

The pulse is produced digitally at a sample rate of 1 MHz with 12 bit precision for the data. Static RAM is used to hold the data which is sent to an analog to digital converter (A/D) in sequence. The pulse shape is defined by 512 integers between zero and 4095 which corresponds to an output voltage of zero to 5 volts with a maximum duration of 512 µs. This reference pulse is exactly proportional to the high voltage required on the electrostatic dipoles. The reference voltage is compared to the output voltage and the pulse width modulator (PWM) automatically sets the pulse duration to generate the desired voltage. Due to switch inpedances the time constant for charging the cable and dipole capacitance is considerably shorter than the discharge time constant. Components in the power stage were chosen such that the rise time would be sufficient to track the (monotonically increasing) desired pulse. To achieve the highest possible bandwidth, a small phase margin was chosen in the control loop. Because of this, a step function at the input results in an overshoot by the system. The slow discharge time constant results in unacceptable recovery time from an overshoot. To eliminate the problem a

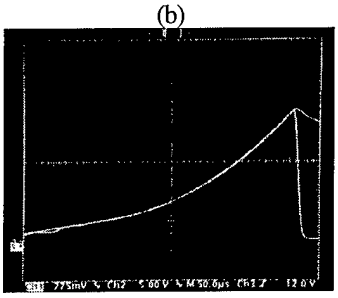


(a)



T_o

(b)



(c)

Figure: 5 Superimposed waveforms of the reference and the high voltage outputs.

smooth ramp is introduced before the pulse to prevent a discontinuity at the beginning of the useable pulse.

4. TEST RESULTS

The waveforms of the reference and the high voltage output shown on Fig. 5, were taken driving the equivalent capacitance of eight dipoles. Although there is a slight discrepancy between the two waveforms at the beginning of the pulse, the active region, which consists of the 240 μs at the end of the pulse, tracks the reference to better than 1%. The waveforms include a linear ramp and two parabolas of different curvature. Each waveform can be adjusted to a precision of 0.1% in amplitude and timing. The most representative of the required shape (Fig. 2) is the waveform 5(b). The bending field provided by this waveform would be synchronized to the acceleration cycle so that the heavy ions enter the ring at point T_0 or where the voltage is about 7 kV and would recirculate and gain energy over the next 240 μs where the voltage has ramped to 28 kV.

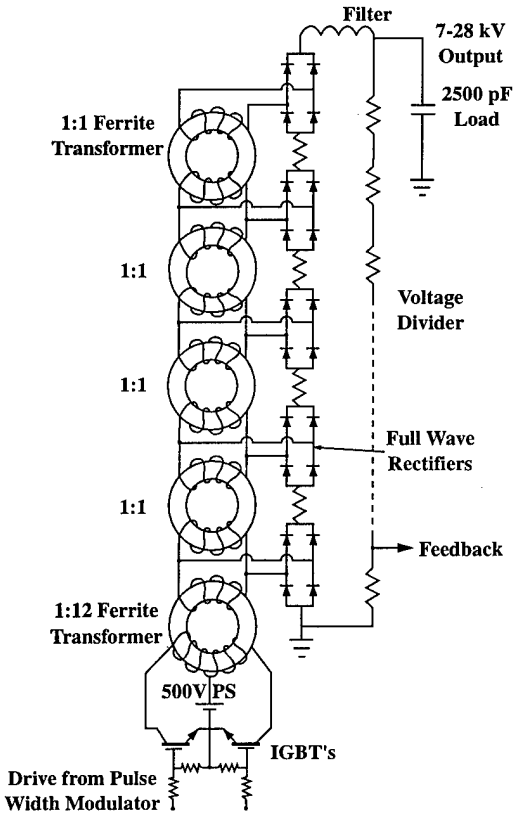


Figure: 6 High Voltage Drive

.5. CONCLUSION

Limited funding directed our efforts in the development of a fully programmable high voltage waveform generator for steering a heavy ion beam around a recirculator. The design was based on inexpensive components and was optimized to fully satisfy the physics requirements. Projecting the cost of this prototype toward the complete system for the recirculator, it appears that it should be well within the allowed budget .

6. ACKNOWLEDGMENTS

We are grateful to Tom Fessenden for directing our efforts to insure that the physics requirements were satisfied and we are grateful to Bill Strelo and his technical staff for the coordination and fabrication efforts.

Work supported by the U.S. Department of Energy under Contract DE-AC03-76SF00098.

REFERENCES

[1] J.J. Barnard, et al., "Study of Recirculating Induction Accelerators as Drivers for Heavy Ion Fusion," UCRL-LR-108095, 1991.

[2] T.J. Fessenden, "Accelerator Waveform Synthesis and Longitudinal Beam Dynamics in a Small Induction Accelerator," PAC 1995 Proceedings, p.825.

[3] A. Friedman, et al., "Progress Toward a Prototype Recirculating Induction Accelrator for Heavy Ion Fusion," PAC 1995 Proceedings, p. 828.

DYNAMICS OF MAGNETIC INSULATION VIOLATION IN SMOOTH-BORE MAGNETRONS

A.V. Agafonov,
P.N. Lebedev Physical Institute of RAS, Leninsky Prosp. 53, Moscow 117924, Russia,
V.M. Fedorov, V.P. Tarakanov
High Energy Density Research Center, IVTAN, 13/19, Izhorskaja, Moscow, 127412, Russia

Abstract

The efficiency of large and high-power magnetrons of GW power levels is less than 30% and inherent pulse-length and repetition rate limitations seem to exist because of use of explosive field emission. Another approach is the development of low voltage, high-efficiency magnetrons utilizing a secondary emission magnetron array with high repetition rate. The numerical model of nonstationary, nonuniform secondary electron emission from a cathode surface has been developed. The results of first steps in computer simulations of electron cloud formation inside a smooth-bore magnetron under the condition of back-bombardment instability (BKB) are presented. Calculations have been performed for a coaxial smooth-bore magnetron and for magnetrons with different types of azimuthal inhomogeneities which could promote the growth of BKB. The results of computer simulation are in agreement with experimental data. The main calculations of the beam dynamics were carried out with PIC-code KARAT.

1 INTRODUCTION

Problems of magnetic insulation violation inside a vacuum coaxial diode (magnetron diode — MD) with dense electron flow in crossed $\vec{E}\times\vec{B}$ fields are considered. It is known that the magnetic field suppresses the mobility of charged particles in the direction perpendicular to the magnetic field at distances exceeding the Larmor radius r_{eL} ($d_{AK} > r_{eL} = v_e/\omega_{ec}$, v_e — maximum velocity, $\omega_{ec} = eB_0/mc\gamma_e$ — cyclotron frequency). This effect, so-called magnetic insulation, is almost perfect in axisymmetrical systems with low density electron flow ($en_e d_{AK} \ll V_{AK}/d_{AK} = E_0$). Experimental investigations of MD with high density electron flow ($en_e d_{AK} \sim E_0$) show an appreciable value of electron current to the anode (leakage current) $\bar{J}_{er} \neq 0$. This is due to the occurrance of azimuthal variations of charge density distribution. Attempts to construct a model of MD allowing to estimate the leakage current I_{eA} or the power of back-bombardment flow of electrons with surplus energy to cathode surface have not been successful earlier [1], [2] nor later [3].

Computer simulations have been performed using 2.5-D electromagnetic PIC code KARAT [4] for the MD with parameters close to experimental [1], and with an external voltage source $V_0(t)$ connected to MD via an RL-circuit. Note that calculations without the external circuit could lead to meaningless physical results.

The yield of secondary electrons from the cathode are described by a modified expression [5] to take into account the dependence of the yield on the energy of electrons and the angle between the direction of electron velocity and the perpendicular to the cathode surface, and also the threshold of secondary emission:

$$k_{sec} = (1 - \cos\alpha) + \frac{\pi}{2}\sigma_{sec}x^{0.55}\exp(-0.45x), x > 0,$$

$$k_{sec} = 0, x \leq 0,$$

where x = (w - w_{sec1})/w_{sec2}, $\sigma_{sec} = 2$ is the maximum coefficient of secondary emission, α the angle of incidence (see above), w the kinetic energy of primary electrons, w_{sec1} = 100 eV is the threshold value of the energy incident on the surface, w_{sec2} = 600 eV is the energy corresponding to the maximum yield of secondary electrons.

2 MAIN RESULTS

Let us consider first the process of electron cloud formation inside an axisymmetrical MD under the condition of homogeneous initial emission of a low current beam from the cathode. The main parameters of MD are radius of the anode r_A = 0.53 cm, radius of the cathode r_K = 0.33 cm; external longitudinal magnetic field B_0 = 2.5 kGs ($B_0/B_{cr} \simeq$ 1.15, $\omega_{ec}/2\pi$ = 7 GHz, period of cyclotron rotation 0.14 ns); the voltage rise time to maximum value of V_{0m} = 12 kV is 2 ns; maximum emission current of the primary beam I_{em} = 2 A.

For given voltage and geometry of MD the Child-Langmuir current through the MD without a magnetic field equals approximately $I_{CL} \simeq$ 200 A (here and below currents and charge densities correspond to linear values per cm of length in the longitudinal direction). Electrotechnical parameters are $\tau_{L/R}$ = 0.25 ns, τ_{RC} = 0.24 ns, where C is the capacitance of MD. Drift velocity of electrons in crossed fields is $\bar{v}_{e\theta} = cE_0/B_0 = 2.4\times10^9$ cm/s, if the electric field is estimated as V_{0m}/d_{AK}.

Dependences of voltage V_{AK} on MD and current in anode circuit I_{AK} on time, and dependences of the numbers of primary N_{e0} and secondary N_{es} electrons inside MD and secondary emission current I_{es} on time are shown in Fig. 1. In Fig. 2 configurations of electron flows at different times are shown.

Inevitable presence of electric field fluctuations due to noise, discreteness of flow and random conditions of emission of electrons lead to redistribution of the energy of electrons. Under conditions of conservation of full energy and

0-7803-4376-X/98/$10.00 © 1998 IEEE

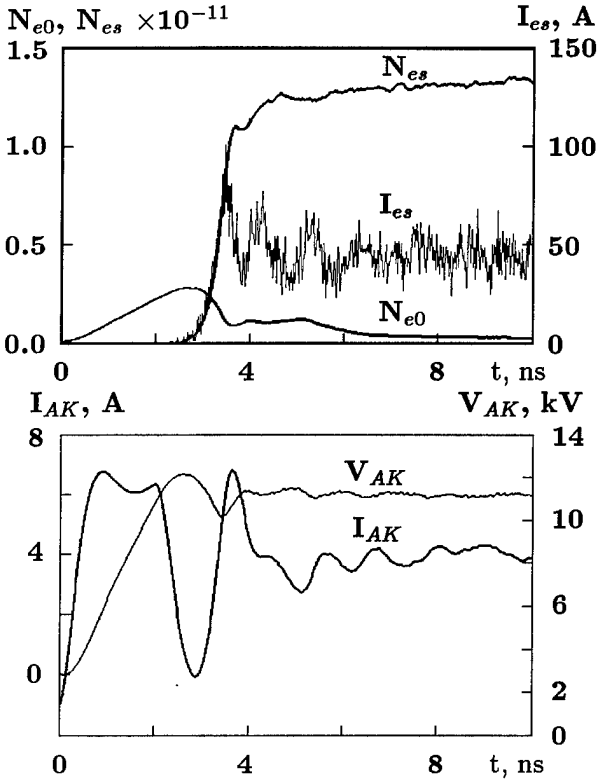


Figure 1: Dynamics of store of primary N_{e0} and secondary N_{es} electrons and the dependence of secondary emission current I_{es} on time (above); the dependences of the voltage V_{AK} on MD and the current in anode circuit I_{AK} on time (below).

momentum a part of the electrons lose energy under the action of the field and drifts to larger radii towards the anode. Another part of the electrons increases its energy and returns to the cathode with an energy exceeding the threshold value for secondary emission.

In view of indicated reasons, the emission of secondary electrons is nonuniform. This effect leads to an intensification of the cathode back-bombardment process and to fast and effective growth of secondary electrons inside MD. The growth of secondary emission current is accompanied by a drop in voltage (see Fig. 1). The secondary-emission current exceeds the primary-beam current by more then order of magnitude and subsequently exerts a determining action on the operation of the MD. The MD passes over to a condition of self-sustaining emission and the primary beam can simply be disconnected. After the transient process, a stable formation consisting of three main bunches is formed. This electron flow rotates as a whole with approximately constant angular velocity.

In Fig. 3 the distributions of electrons reaching the anode (f_{eA}) and returning back to the cathode (f_{eK}) are presented for energy and for angle. The average energy of electrons reaching the anode equals $\bar{w}_{eA}$ = 7.4 keV and at the cathode the average energy $\bar{w}_{eK}$ = 0.44 keV. Thus, for the given conditions $\eta_{BKB} = (eV_{AK} - \bar{w}_{eA})/eV_{AK} = 34\%$

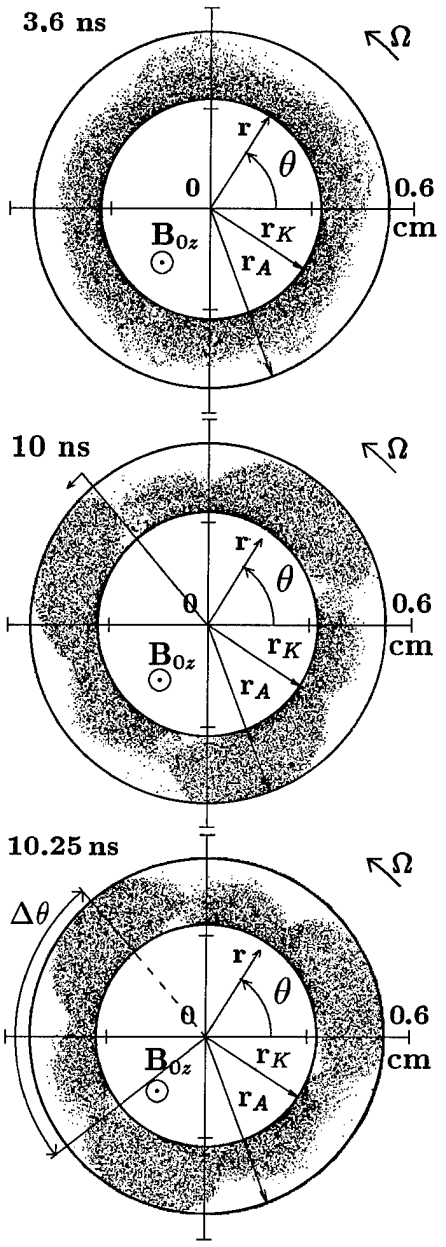


Figure 2: Formation of electron cloud inside MD under the condition of homogeneous emission of low-current primary beam. The rotation of electron cloud as a whole with angular frequency $\Omega \simeq 2\pi \times 10^9$ s^{-1} at 10 ns and 10.25 ns is shown in the last two figures.

for power of back-bombardment flow $P_{eK} \simeq 15$ kW and power of beam reaching the anode $P_{eA} \simeq 30$ kW.

Fig. 4 shows flow configurations for various variants of emission of primary and secondary electrons. The nonuniformity of various types leads to the following main effects: broadening of the functions of distribution of electrons at the anode for energy and angle of incidence; formation of flows with non-regular azimuthal structure; change of the spectrum of field frequencies. However, integral characteristics of flow (total charge in the gap, leakage current of

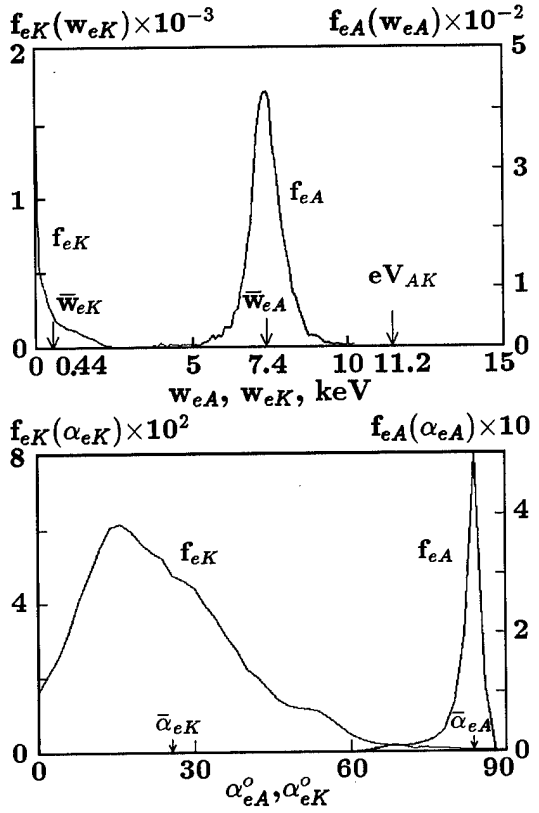


Figure 3: Distribution functions of electrons for energy (above) and angle of incidence (below) at the anode and the cathode.

electrons at the anode) practically do not change, i.e., the system is stable relative to the initial conditions.

3 CONCLUSION

The selfconsistent picture of an electron flow formation inside secondary emission MD has been described. The existence of quasistationary, rotating state of an electron flow has been shown under conditions of conservation of full power and full momentum of the system. This state is characterized by the transformation of supplied power to a power of back-bombardment flow with the efficiency exceeding 30% and to a power of a leakage beam to the anode (magnetic insulation violation). The results are close to the data [1].

Work supported by RFFI under grant 96-02-19215a.

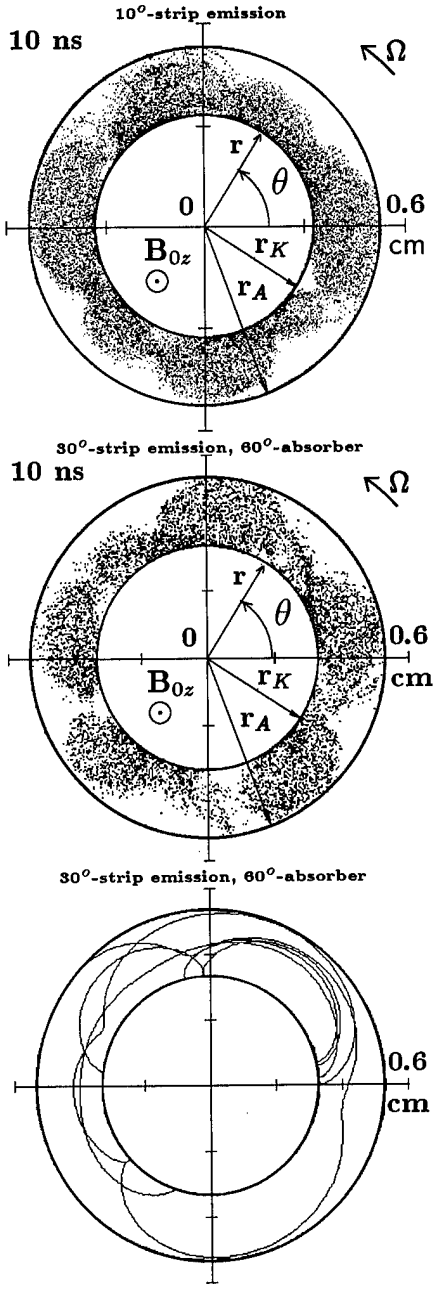


Figure 4: Configurations of electron flows inside MD at t = 10 ns: a uniform emission of primary beam of 2 A from a cathode having a 20° strip with no emission of secondary electrons; emission of primary beam of 2 A from a 30° strip at the cathode having a 60° strip with no emission of secondary electrons; trajectories of electrons which are emitted at t = 5 ns and observed for 2 ns.

4 REFERENCES

[1] R.L. Jepsen and M.W. Muller. Enhanced emission from magnetron cathodes. J. Appl. Phys. 1951, v. 22, 1196 - 1207.

[2] Okress E. (ed.). Crossed-field microwave devices. Academic Press. N.Y., 1961.

[3] V.M. Fedorov, W. Schmidt, Th. Westermann. Ion beam generation with inhomogenious anode and cathode plasmas. Proc. 9th Intern. Conf. on High-Power Particle Beams. Washington, USA, 1992, v. 2, 747–755.

[4] P.V. Kotetashwily, P.V. Rybak, V.P. Tarakanov. KARAT — Tools for a Computer Experiment in Electrodynamics, Institute of General Physics, Moscow, Russia, Preprint no. 44, 1991.

[5] V.B. Baiburin, V.P. Eremin. Analytical models of cylindrical M-type amplifiers of forward and backward waves. Radiotechnics and Electronics, 1992, v. 37, 503–512.

BRILLOUIN FLOW IN A MAGNETRON DIODE AS THE KINETIC MODEL LIMIT

A.V. Agafonov and V.S. Voronin
P.N. Lebedev Physical Institute, Leninsky Prosp. 53, Moscow 117924, Russia

Abstract

Two classes of approaches that have received the most attention to describe the important space charge dynamics in a magnetron are Brillouin flow and the double-stream kinetic model. It is supposed that in the first case electrons move parallel to the electrode surfaces and in the second case they move in cycloidal orbits performing a single turn. Precise analysis of electron dynamics in fully selfconsistent kinetic equilibria in a smooth-bore magnetron shows that for a given external magnetic field and a voltage there exists a multiplicity of natural equilibrium states, differing as to structure of electron trajectories and emission current density. The value of emission current density differs from one to another type of equilibrium and can aspire to zero under the same condition of space charge limited flow due to a large number of revolutions of electrons around the cathode. The greater the number of revolutions the closer the main parameters of the kinetic flow to the Brillouin one. The comparison of analytical calculations and the results of computer simulation of transient processes of Brillouin flow formation from initially kinetic flow are presented.

1 INTRODUCTION

Despite the great number of works about magnetron operation, a detailed description of electron dynamics under strong space charge influence is complicated by the nonlinear nature of a field-particles system. In particular, there is no satisfactory solution even to the problem of electron flow formation in a magnetron with a smooth anode (a coaxial magnetron diode). In the work presented here it is shown that within the framework of accepted kinetic descriptions of a coaxial magnetron diode, multiple steady states of electron flow are possible for a given diode geometry and the same set of external parameters (applied voltage and external magnetic field). These states are distinguished by the number of electron revolutions around the cathode and the current emitted from the cathode. Direct transition from kinetic flows to Brillouin flow as a limit is shown. Numerical simulation helps to investigate the dependence of steady state properties of electron flow on its history of formation. Comparison of analytical data and results of numerical simulation is made with the purpose to analyse the conditions of applicability for existing analytical models.

2 THEORETICAL MODELS

Usually it is supposed for a magnetron that in an initial stage magnetically insulated axially symmetric rotating electronic flow is formed. As a rule, the description of electron flow is based on two models: a hydrodynamic parapotential model, or Brillouin flow[1, 2], in which electrons rotate along circular trajectories around the cathode, and a kinetic two-flow model[3, 4], in which electrons move along cycloid trajectories, beginning and coming to an end on the cathode surface. It is necessary to emphasize that in the latter case it was always supposed that an electron makes a single revolution along a cycloid independent of the geometry of the diode (plane or cylindrical).

It is easy to show for a plane diode that at the top of a cycloidal trajectory radial velocity and electromagnetic force both equal zero. Thus it is possible to "connect" another descending (that usually is done), or ascending trajectory, then continuing them symmetrically up to the cathode, i.e. the top of trajectories in the plane diode is a point of solution branching.

But for a coaxial cylindrical diode it was shown[5] that artificial connecting of trajectories is impossible: the cylindrical metrics removes degeneration. And the structure of a kinetic flow differs in that the angular movement of electrons around an axis can significantly exceed 2π. The more the number of electron revolutions, the greater the time the electron stays in the diode gap, and there should be less emission current from the cathode surface. Thus, the steady state of an electron flow depends on the value of emission current chosen (and an electric field on the cathode surface equal to zero corresponding to a space charge limited current; but the value of emitted current is much less than limiting current and, basically, can approach zero).

3 PARAPOTENTIAL (BRILLOUIN) MODEL[1]

A system of units in which $c = e = m_e = 1$ is hereafter used. The electronic flow consists of circular trajectories with radii r filling completely or partially the gap between the cathode with radius r_k and anode with radius r_a: $r_k < r < r_e, r_e \leq r_a$.

Outer (boundary) parameters — anode voltage (γ_a-1) and (kept in a short pulse regime) average value of magnetic induction in the diode gap B_0 — are connected to parameters of an electronic flow by the relations

$$ln\left(\frac{r_e}{r_k}\right) = \int_0^{A_e} \frac{dx}{\sqrt{(C^2+x^2)(1+x^2)}},$$

$$\gamma_a = \gamma_e + r_e E_e ln\left(\frac{r_a}{r_e}\right),$$

$$r_a A_a = \frac{r_a^2 - r_k^2}{2} B_0 = r_e A_e + \frac{r_a^2 - r_e^2}{2} B_e$$

0-7803-4376-X/98/$10.00 © 1998 IEEE

from which in that specific case $r_e = r_a$ (electronic flow occupies the whole anode-cathode space) is essentially only the last relation between an average magnetic induction and diode voltage:

$$(r_a^2 - r_k^2)B_0 = 2r_a\sqrt{\gamma_a^2 - 1}.$$

4 KINETIC (EMISSIONING) MODEL[4].

This analytical model, supposing presence of an emission current from the cathode coming back on the cathode, is described by a system of equations for $\gamma(r)$, $A(r)$

$$\frac{1}{r}\frac{d}{dr}\left(r\frac{d\gamma}{dr}\right) = \frac{f_0}{r}\frac{\gamma}{\sqrt{\gamma^2 - 1 - A^2}},$$

$$\frac{d}{dr}\left(\frac{1}{r}\frac{d}{dr}(rA)\right) = \frac{f_0}{r}\frac{A}{\sqrt{\gamma^2 - 1 - A^2}},$$

$$\frac{d\gamma}{dr} = E, \quad \frac{1}{r}\frac{d}{dr}(rA) = B,$$

where the constant f_0 is proportional to density of cathode emission current. On the cathode $\gamma(r_k) = 1$, $A(r_k) = 0$, $E(r_k) = 0$, $B(r_k) = B_k$, and the outer boundary of electron flow is at radius r_e, at which electrons turn back to the cathode and the radial pulse of electrons $p_r = \sqrt{\gamma^2 - 1 - A^2}$ is equal to zero. In this model anode voltage and average value of magnetic induction are connected to parameters of an electronic flow by the relations:

$$\gamma_a = \gamma_e + r_e E_e ln\left(\frac{r_a}{r_e}\right),$$

$$r_a A_a = \frac{r_a^2 - r_k^2}{2}B_0 = r_e A_e + \frac{r_a^2 - r_e^2}{2}B_e$$

The results of calculations on these models are shown in Fig. 1 for the same external conditions (voltage and external magnetic flux) and with zero electric field on the cathode. The Brillouin smooth solution and three kinetic ones from a set of possible number of layers (n = 1, 2, 4) are shown. With increasing number of layers, emission current from the cathode tends to zero, electrons make more and more revolutions before coming back to the cathode, and a kinetic solution gradually approaches the Brillouin one. In the situation when magnetic field is much stronger than electric field, the Brillouin solution appears to be the only possible one. Thus the kinetic solution occurs only if the electric field on the cathode is not equal to zero. We note that in the inverted magnetron diode (with the anode on inner surface) only a single-layer kinetic solution exists, which points to the essential influence of cylindricity on electron flow within the diode. In "plane" approximation for the kinetic model the criterion for restriction of number of layers by any value is not present, and the usual choice of n = 1 is in essence arbitrary.

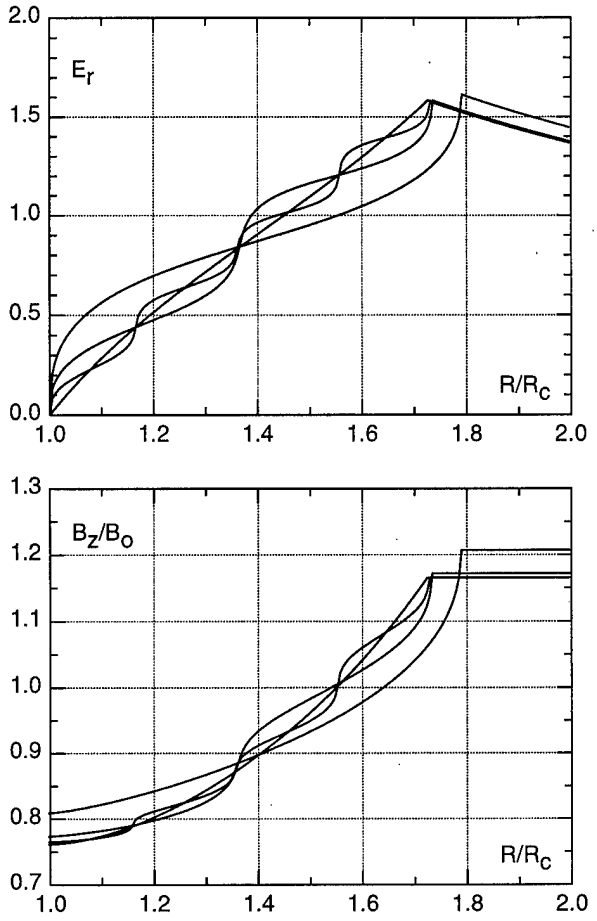


Figure 1: Kinetic (n=1,2,4) and Brillouin models of a rotating beam (E(r) upper, B(r) lower) for the same external conditions (voltage and magnetic flux).

5 TEMPORAL EFFECTS AND THEORETICAL MODELS

Discussion of effects observed in a magnetron diode had as its basic purpose to show that theoretical models describing, one should think, one and the same situation actually correspond to various physical conditions. We shall illustrate this by an example, comparing analytical results and numeric simulation realized with a PIC-code KARAT[6].

Modeling of particle emission in KARAT code can be realized in two ways: (1) by setting the law for temporal change of emitted current, the value of which can be less than, or more than limiting current, the applied voltage being fixed (this situation corresponds to emission from photocathodes or external injection of a beam through the surface of the emitter); and (2) by setting the law for temporal rising of diode voltage to some constant value, emission current being fixed at a value greatly exceeding the value limited by space charge (this situation corresponds to thermionic cathode). In Fig. 2 typical distribution functions of particles in these two cases are shown. In the first case a single electron revolution in a cycloid is realized (symmetric two-peak distribution of electrons on a pulse p_r)

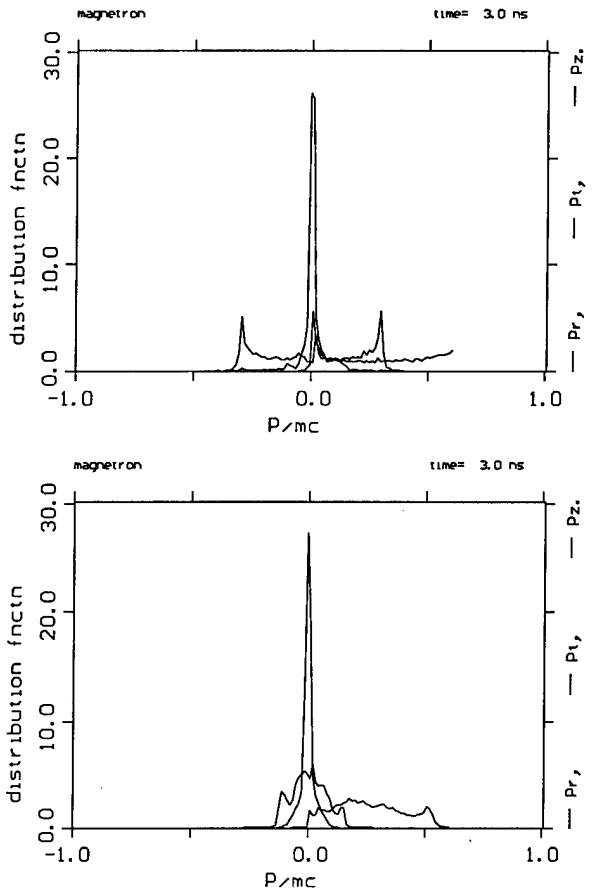


Figure 2: Example of distribution functions.

without accumulation of charge in an accelerating gap; in the second case — symmetric distribution of particles on a pulse p_r with capture of electrons during voltage increase, growth of number of particles in diode gap and multiturn dynamics of electrons.

6 DISCUSSION

Both theoretical models give about the same physical results. Recall that the equations describing Brillouin flow can be deduced on the basis of the same approach used for the kinetic model [7]. Under conditions of conservation of full energy of particles and canonical angular momentum

$$P_\theta = r(p_\theta + A) = const,$$

the next general set of equations can be derived:

$$(r\gamma^2 v_z')' + \gamma\left(\frac{v_\theta P_\theta'}{v_z}\right)' = 0,$$

$$(r\gamma^2 v_\theta')' - \frac{\gamma^2 v_\theta}{r} - r\gamma\left(\frac{P_\theta'}{r}\right)' = 0,$$

where the prime denotes d/dr.

For the case of a magnetron diode with a cathode surface coinciding with a magnetic flux surface we have $P_\theta =$ const and

$$r\gamma^2 v_z' = const.$$

The constant equals zero (i.e., $v_z =$ const) in this case and we have the same equations as in Section III [8].

Therefore, it is not surprising that a direct transition exists from kinetic flow to a Brillouin one as a limit.

Work supported by RFFI under grant 96-02-19215a.

7 REFERENCES

[1] A.V. Agafonov, V.S. Voronin, A.N. Lebedev, K.N. Pazin. JTP, 1974, v. 44, p. 1909.

[2] J.M. Creedon. J. Appl. Phys., 1977, v. 48, p.1070.

[3] R.V. Lovelace, E. Ott. Phys. Fluids, 1974, v. 17, p. 1263.

[4] V.S. Voronin, A.N. Lebedev. JTP, 1973, v. 43, p. 2591.

[5] A.V. Agafonov, D.B. Orlov. Proc. of the 1989 IEEE Particle Accelerator Conference, Chicago, USA, v. 2, p. 1397.

[6] P.V. Kotetashwily, P.V. Rybak, V.P. Tarakanov, Inst. of Gen. Phys., Moscow, Russia, prepr. no. 44, 1991.

[7] M. Raiser. Phys. Fluids 1974, v. 20, p. 477.

[8] A.V. Agafonov, Proc. of the 1995 IEEE Particle Accelerator Conference, Dallas, USA, v. 5, p. 3272.

A NOVEL DESIGN FOR A HIGH POWER SUPERCONDUCTING DELAY LINE

Yu Ju (Judy) Chen and George J. Caporaso
Lawrence Livermore National Laboratory

Abstract

Potential designs for a high power superconducting delay line of approximately 10ms duration are described. The transmitted signal should have low dispersion and little attenuation to recapture the original signal. Such demands cannot be met using conventional metal conductors. This paper outlines a proposal for a new transmission line design using low temperature superconducting material which meets system specifications. The 25W line is designed to carry pulsed signals with an approximate rise time of 8nsec and a maximum voltage magnitude of 25kV. Predicted electrical design and performance of the line will be presented.

1 APPLICATION OF THE LINE

The line will be used to provide transit time isolation of the reflections expected to be generated in the kicker of an AHF accelerator [1]. The kicker will operate with beam currents of 3 to 6 kA and will launch beam-induced voltages up the transmissions lines connecting it to its pulsers. The most straightforward way to eliminate the effects of these reflections is to transit time isolate the kicker from the pulser. Thus the 10 μsec line will actually allow a 20 μsec operational interval.

2 WHY USE SUPERCONDUCTORS?

2.1 Attenuation

The general expression for attenuation is

$$\alpha = \frac{1}{2}\frac{R_s}{Z_0}\sqrt{\frac{\omega}{2}}$$

where R_s is the skin-effect impedance dependent on the geometry and resistivity of the structure [2].

For a coax where a and b are the inner and outer diameter, R_s is derived to be

$$R_s = \frac{\sqrt{j\omega\mu}\Gamma_r^2}{2\pi}\left[\frac{1}{a^2}-\frac{1}{b^2}+\frac{1}{2\Gamma_r a}\frac{I_0(a/\Gamma_r)+I_2(a/\Gamma_r)}{I_1(a/\Gamma_r)} + \frac{1}{2\Gamma_r b}\frac{K_0(b/\Gamma_r)+K_2(b/\Gamma_r)}{K_1(b/\Gamma_r)}\right]$$

where I_n and K_n are the modified Bessel functions of the first and second kind. Γ_r is associated with the skin depth and is

$$\Gamma_r = \begin{cases} 1/\sqrt{j\omega\mu\sigma} & \text{normal conductor} \\ 1/\sqrt{j\omega\mu\sigma + 1/\lambda^2} & \text{Type I superconductor} \end{cases}$$

where λ is the penetration depth of the superconductor. At high frequencies the expression simplifies to a more familiar expression [2][3].

$$R_s = \frac{\sqrt{j\omega\mu}}{2\pi}\Gamma_r\left(\frac{1}{a}+\frac{1}{b}\right).$$

Suppose the line was made of copper (σ = 5.92e7$(\Omega\text{-m})^{-1}$) and the inner and outer diameters were 2cm and 3cm respectively. With an 8nsec. rise time, we used 125MHz to be the highest critical frequency, which is about 3 times that of the roll-off frequency. For 125MHz, α = 7.658e-4/m. For a 3km line, this corresponds to a power attenuation of $(1\text{-}e^{-2\alpha\cdot 3000m})$=98.9%. The signal has virtually disappeared!

On the other hand, for the same set of dimensions, a niobium (λ=39nm[1] ,σ=8.03e6$(\Omega\text{-m})^{-1}$) line yields an α of approximately 5.1025e-6$(1+j)$/m. The imaginary term contributes to the inductance of the line. The power attenuation is now 3% at 125MHz which is an upper limit. This is the most compelling reason to use a superconducting line.

3 DESIGN OF A SUPERCONDUCTING LINE

The size of the transmission line is fundamentally limited by the critical field of the superconducting material. Of the type I conductors, niobium (Nb) is the most generous material since it has the highest critical B-field of .206T [2] at T=0K.

Assuming the distribution for the critical field to be $B_c(T) = B_c(0)[1-(T/T_c)^2]$, the critical field at 4.2K (the usual operating point of liquid helium) is .1635T. The B-field of a structure can be written as $B=gI$ where g is a geometry factor. The condition on g is therefore $g \le B_c/I$.

[1] see back cover of [3].

0-7803-4376-X/98/$10.00 © 1998 IEEE

3.1 Coaxial line

For a concentric coax, $g=\mu/2\pi r$ where r is either the inner or outer radius of the line. This yields the condition that $r>\mu I/2\pi B_c$. If one wants to operate at 20% of maximum capacity, then $a=.2\mu I/2\pi B_c$ where a is the inner radius. The current on the line can be as high as 1kA. This requires that a=6.12mm.

Since the layer of niobium only needs to be much greater than the penetration depth λ, a thin coat of approximately .5um will be deposited on a copper substrate as shown in Fig. 1. The need for a metal substrate will be discussed in section 4. The area between the two conductors will be filled with a material that may or may not have dielectric properties. The inner conductor should be hollow to allow helium to flow through the tube.

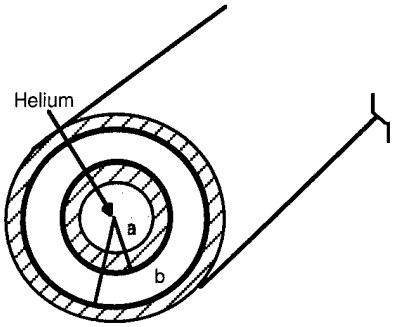


Fig. 1. Coaxial line with Nb layers deposited on copper tubes

Design 1: The outer conductor radius, for an impedance of 25Ω, is 9.28mm. Design 2: If one puts in a dielectric material of ε_r=10, the outer radius goes up to 22.85mm. The advantage of the dielectric is that the length of the line is reduced by a factor of $1/\sqrt{10}$ which yields a length of 948m.

3.2 Stripline

For manufacturing considerations, it may be easier to fabricate striplines instead of coaxial lines. The solution for the stripline problem, both open and closed, has been derived by Primozich [4]. As it turns out, a stripline with a dielectric filler is too dispersive (see section 5). Therefore, the design cannot have a dielectric material. Design 3: The stripline dimensions are shown in Fig. 2.

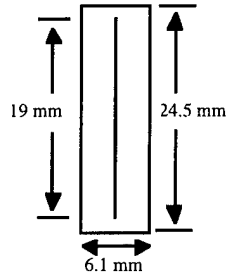


Fig. 2. Dimensions of stripline design

3.3 Sheath helix

Sheath helix lines are like coaxial lines, only the inner conductor is wrapped at an angle. These are slow wave structures and ideal for a delay line. However, they are more dispersive than regular coax. Fig. 3 shows two sets of two overlayed 10kV pulses. The solid line is the actual signal at the output of the line and the dotted is the output had there been no dispersion. These plots are derivations based on Lund [5] and are for uncurved lines only.

Design 4: Fig. 3(a) corresponds to a line with ε_r=1, b/a=1.15, p(pitch)/a=2.1, and v/c=.336. The line length is reduced to about 1/3 of the original length. Part (b) corresponds to ε_r=3, b/a=1.4, p/a=2.75, and v/c=.264. The second line yields a slightly slower wave but at the cost of increased dispersion as evident by the wiggles at the rising part of the pulse.

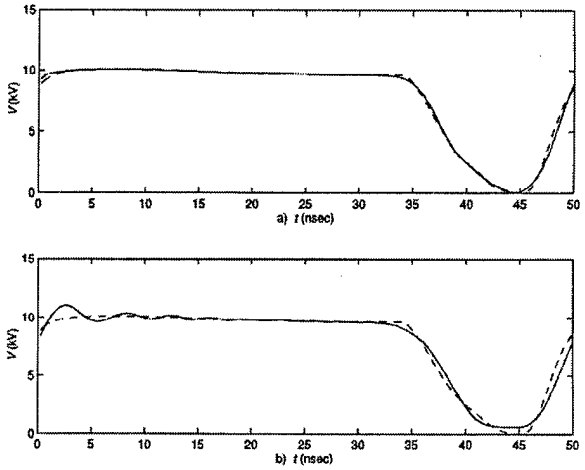


Fig. 3. a) — 10 kV pulse at output of line for sheath helix without dielectric, – – same pulse if line were non-dispersive
b) same as a) except line has dielectric. Wiggles indicate more dispersion

The sheath helix line is presented here as a backup design in case the stripline is not easy to manufacture because of it's length or the dielectric used for the coaxial line proves to be lossy or difficult to work with.

4 THE NEED FOR A SUBSTRATE

Niobium can be deposited on copper as illustrated in Fig. 1 where the fields and currents flow. The copper acts as a stabilizer in case the superconducting portion exceeds critical current and quenches. Quenches can distort the original signal by introducing transient high resistance to the line.

Copper is also a much less expensive conductor than niobium so the minimal use of niobium is advantageous from a bulk material cost point of view. In addition, if the helix line is chosen as the final design, a

substrate for the inner conductor will need to be implemented.

5 DISPERSION

The previous section has already shown that dispersion from skin depth is negligible for a superconducting line. The dispersion on the superconducting transmission line, instead, is caused by wrapping the long line onto either a drum or into a pancake shape. The electromagnetic problem for a curved coax has been solved in [7].

The propagation constant for a curved coax is as follows

$$\gamma^2 = \gamma_0^2\left[1+\frac{A_2}{R^2}+O(\frac{1}{R^4})\right]$$

where $\gamma_0=\omega\sqrt{\mu\varepsilon}$, $A_2=A\omega^2+B$, and $R=R(s)$. The constants A and B can be found in [7]. For a pancake design, the outer cable radius is, as a function of s, the total length, and R_0, the inner radius,

$$R(s)=\sqrt{R_o^2+\frac{2bs}{\pi}}$$

If one wants to find the total dispersion at the end of the line, the propagation constant would need to be integrated over the length of the line since it varies with s. In other words,

$$e^{-j\gamma s} \rightarrow e^{-j\int_0^s \gamma ds'}$$

Therefore, the phase shift of the signal at the end of the line is

$$\Delta\phi = -\frac{A_2(\omega)}{2}\gamma_0\int_0^s \frac{ds'}{R^2(s')} = -\gamma_0\frac{\pi A_2}{4b}\ln\left(1+\frac{2bs}{\pi R_0^2}\right)$$

The phase velocity and $\Delta\phi$ for design 2 is plotted in Fig. 4. As one can see in Fig. 4b, the phase distortion is less than 1° at the end of the line. The striplines were treated as equivalent coax lines to estimate the dispersion due to bending.

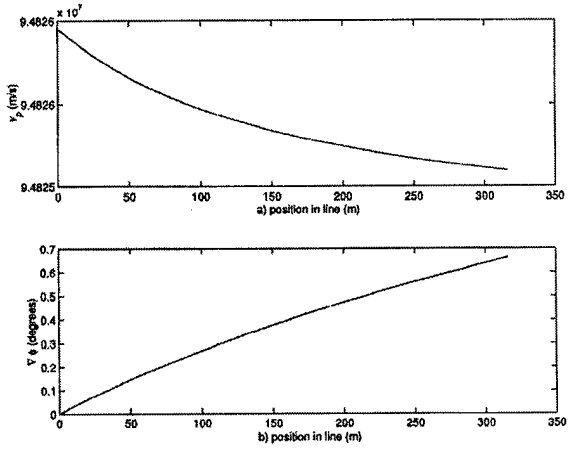


Fig. 4. a) phase velocity as function of position in a pancake-wound coax line
b) it's corresponding phase shift at 125 MHz

The parameters for designs 1-3 were run through a kicker dynamic code to examine the acceptability of the output signal. All 3 designs produced clean output signals. An output plot of design 2 is shown in Fig. 5 where R_0=1m.

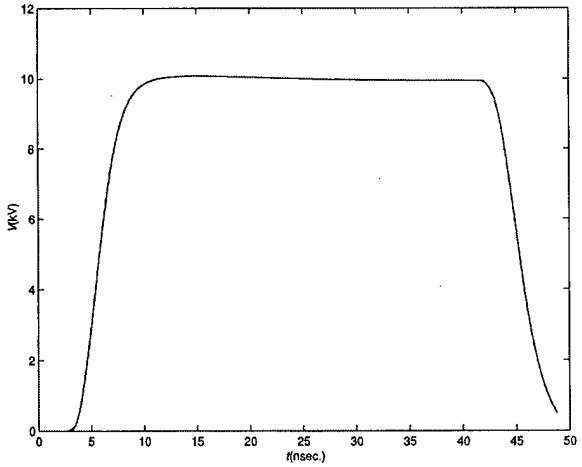


Fig. 5. Design 2 placed in kicker dynamics program produced almost exact replication of original pulse (figure actually has 2 overlapping curves)

6 CONCLUSION

Attenuation in long transmission lines made use of superconductors a necessity. The attenuation in the superconducting line is very small, with joints connecting sections of the line contributing to most of it. Dispersion, on the other hand, can arise simply from the geometry of the line. Curved lines and helix lines are subject to dispersion. Two coaxial lines, one stripline, and a sheath helix design were presented. The challenge of fabricating the line will determine which design is ultimately adopted.

7 ACKNOWLEDGEMENTS

The authors would like to acknowledge the technical support of Michael Krogh of AlliedSignals and Steve Sampayan. This work was performed under the auspices of the U.S. Department of Energy by the Lawrence Livermore National Laboratory under Contract No. W-7405-Eng-48.

REFERENCES

[1] G. J. Caporaso, "Linear Induction Accelerator Approach for Advanced Radiography," these proceedings.

[2] R. E. Matick, "Transmission Lines for Digital and Communication Networks," reissued by IEEE PRESS, 1995

[3] T. Van Duzer, C. W. Turner, "Principles of Superconductive Devices and Circuits," published by Edward Arnold, Ltd., 1981.

[4] F. G. Primozich, **AIEE**, May 1955.

[5] C. O. Lund, **RCA Review**, March 1950.

[6] M. N. Wilson, "Superconducting Magnets," published by Oxford University Press, 1983.

[7] J. J. Krempasky, IEEE Transactions-MTT, v38, n6, June 1990.

HIGH-PERFORMANCE INSULATOR STRUCTURES FOR ACCELERATOR APPLICATIONS*

S. E. Sampayan, G. J. Caporaso, D. M. Sanders, R. D. Stoddard, D. O. Trimble, Lawrence Livermore National Laboratory, Livermore, CA 94551, and J. Elizondo, M. L. Krogh, and T. F.Wieskamp, Allied Signal Corporation, FM&T, Kansas City, MO 64141

Absract

A new, high gradient insulator technology has been developed for accelerator systems. The concept involves the use of alternating layers of conductors and insulators with periods of order 1 mm or less. These structures perform many times better (about 1.5 to 4 times higher breakdown electric field) than conventional insulators in long pulse, short pulse, and alternating polarity applications. We describe our ongoing studies investigating the degradation of the breakdown electric field resulting from alternate fabrication techniques, the effect of gas presssure, the effect of the insulator-to-electrode interface gap spacing, and the performance of the insulator structure under bi-polar stress.

I. INTRODUCTION

It is experimentally observed that insulators composed of finely spaced alternating layers of dielectric (<1mm) and thin metal sheets have substantially greater vacuum surface flashover capability than insulators made from a single uniform substrate [1]. In the previous work we showed these structures to sustain electric fields 1.5 to 4 times that of a similar conventional single substrate insulator [2]. We also previously reported on the capability of these structures under various pulse conditions and in the presence of a cathode and electron beam. Further, we have explored the properties of these structures in the context of switching applications, investigating their behavior under high-fluence photon bombardment [3] and the effect on RF modes [4,5]. Here we describe our on-going studies on the degradation of the breakdown electric field resulting from alternate fabrication techniques, the effect of gas pressure, the effect of the insulator-to-electrode interface gap spacing and on initial testing that subjects the insulator to bi-polar pulses.

A high-gradient insulator consists of a series of very thin (<1mm) stacked laminations interleaved with conductive planes. This insulator technology was originally conceived and disclosed by Eoin Gray in the early 1980's [6] and resulted from experimental observations that the threshold electric field for surface flashover increases with deceased insulator length [7,8].

Some understanding of the increased breakdown threshold of these structures may be realized from the basic model of surface flashover. A simplified vacuum surface breakdown model suggests that electrons originating from the cathode-insulator junction are responsible for initiating the failure [9]. When these electrons are intercepted by the insulator, additional electrons, based on the secondary emission coefficient of the surface, are liberated. This effect leaves a net positive charge on the insulator surface, attracting more electrons and leading to escalation of the effect or SEEA breakdown.

It has been shown that full evolution of the discharge occurs within 0.5mm [10]. Thus, placing slightly protruding metallic structures at an equivalent interval is believed to interrupt the SEEA process and allow the insulator to achieve higher gradients before failure. Alternate modifications to this explanation include the effects of insulator shielding and equilibration of the induced surface charge. As a result, electron impact on the surface is modified. Or, alternately, by separation of the insulator into N-1 additional decoupled sub-structures, a local breakdown on the insulator cannot propagate to the remainder of the structure.

In this paper we describe our on-going work in which we have performed additional studies on the effect of various fabrication techniques, the effect of gas pressure, the effect of the insulator-to-electrode interface spacing, and on initial testing which subjects the insulator to bi-polar stress.

II. APARATUS

Small sample testing (approximately 2.5cm diameter by 0.5cm thick) was performed in a turbo-molecular pumped, stainless-steel chamber at approximately 10^{-6}T. High voltage was developed with a 10J "mini-Marx". The Marx developed a pulsed voltage of approximately 1 to 10μs (base-to-base) and up to 250kV amplitude across the sample. Diagnostics consisted of an electric field sensor and a current viewing resistor. Failure of the insulator was determined by a prompt increase in Marx current and a prompt collapse in the voltage across the sample.

Several small sample insulators were fabricated by interleaving layers of 0.25mm fused silica, formed by depositing gold on each planar insulator surface by a sputtering technique and then bonding. Bond strength between the gold layer and substrate using this technique was measured to exceed 10kpsi. Alternate samples were also fabricated from lexan and other polymer materials. To perform the breakdown experiments, the structure was slightly compressed between highly polished bare

0-7803-4376-X/98 /$10.00 © 1998 IEEE

aluminum electrodes that establish the electric field for the tests.

After a short conditioning phase, we applied up to 150 to 200 shots to a given structure and attempted to determine if any damage to the structure occurred that significantly altered the breakdown characteristics. At these applied energies, we generally did not observe any degradation. These data were then reduced to reliability plots by determining the total number of successful shots over the total number of applied shots. In these data we define the electric field as the applied voltage divided by the total insulator length. We define reliability at a given electric field as the total number of successful shots over the total number of shots.

III. RESULTS

We observed flashover of the small samples at approximately 175kV/cm for the fused silica substrates (fig. 1). The effect of pulse width from 1 to 10μs on this breakdown threshold was well within the statistical nature of our data. The trend in conventional insulator technology (fig. 2) for 0°-insulators indicates a threshold of approximately 50kV/cm. Thus, a net increase in the performance over conventional technology was a factor of approximately 3.5.

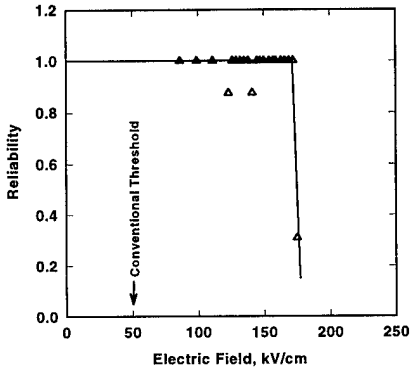


Figure 1. Pulsed surface breakdown reliability of a ground-fused silica high-gradient insulator.

A finish grinding operation was generally performed on the outside diameter. Since this process is time-consuming, an alternate fabrication means was pursued. To simplify fabrication, we attempted an ultrasonic machining process. Although it was possible to fabricate the part in a single operation, the surface was left slightly rougher. Comparison with these samples showed significantly more scatter and a slightly decreased breakdown threshold of 25% (fig. 3).

The structures were also subjected to increased pressures to determine susceptibility to breakdown (fig. 4). In these data a fixed reliability was established at the various pressures. All data was then normalized to a mean breakdown electric field. Susceptibility to breakdown stays relatively constant up to about the 10^{-3}T range, at which point, the field at which breakdown occurs decreases rapidly. Also shown are data from previous work by Smith [11]. It appears that the new structures show a lower breakdown electric field threshold than that of the previous data at these elevated pressures.

Any insulator not in full contact with the electrode surface will show a higher susceptibility to breakdown and lower reliability at a given electric field. This effect results from the enhanced electric field that occurs between the insulator/electrode interface gap. To investigate this effect with these new structures, shims were placed between the cathode electrode and insulator, and the reliability at a given electric field were determined. This data, normalized to the configuration where the insulator was flush with the electrode, is shown figure 5. In these tests, we observed the reduction in the capability of the insulator to be strongly reduced from about 90% of full capability for a 12-μm interface gap to less than 60% for a 125-μm interface gap.

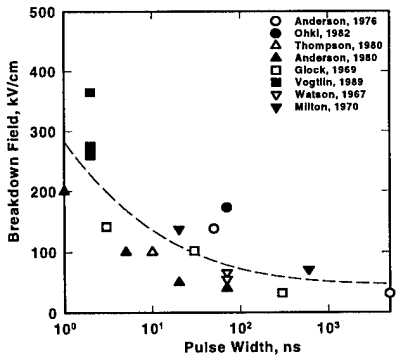


Figure 2. Pulsed surface breakdown electric field as a function of pulse width for single substrate, straight wall insulators.

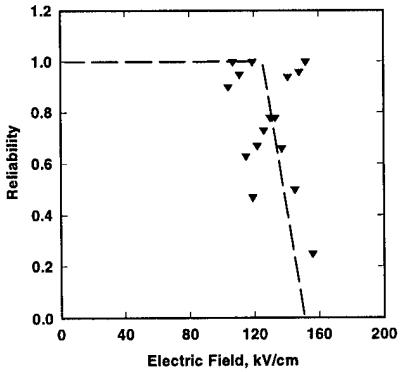


Figure 3. Pulsed surface breakdown reliability of a fused silica high-gradient insulator fabricated using an ultrasonic fabrication technique.

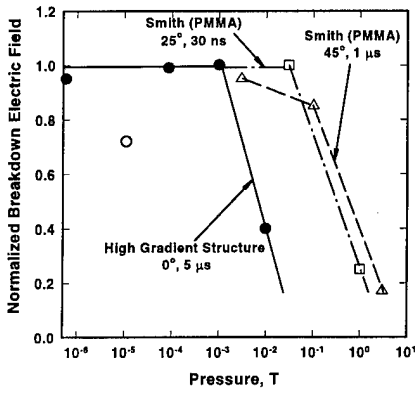


Figure 4. Effect of gas pressure on the performance of high-gradient insulators.

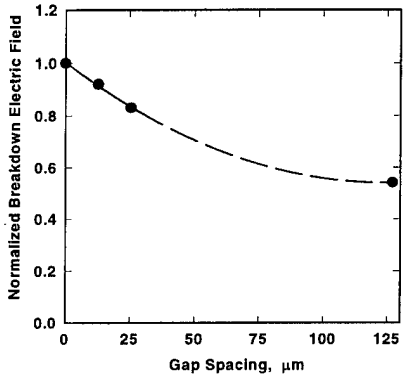


Figure 5. Effect of an increased electrode/insulator interface gap.

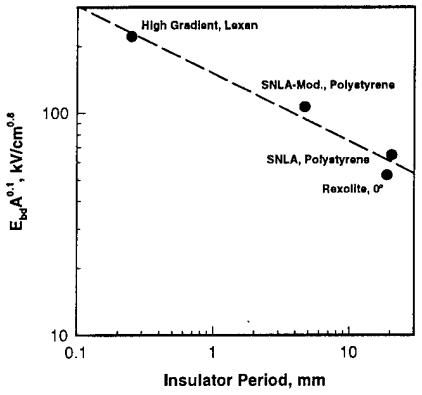


Figure 6. Result of bipolar testing of the high gradient insulator. Comparison with conventional data [12].

We have also begun testing these structures under bi-polar stress. The applied pulses were generated by placing an inductor between the insulator and allowing the Marx generator to undergo un-damped oscillation (τ_p=500ns). This technique would subject the insulator structures to approximately 10 fully reversing pulses. Results are shown in figure 6. Comparison with previous data, scaled to area, shows a strong dependence on the insulator period. Increased performance over conventional technology (Rexolite, 0°) was exceeded by a factor of 4.

IV. SUMMARY

We are developing a high gradient insulator technology for accelerator systems which consists of alternating layers of conductors and insulators with periods of order 1 mm or less. These structures perform many times better (about 1.5 to 4 times higher breakdown electric field) than conventional insulators in long pulse, short pulse, and alternating polarity applications.

V. REFERENCES

*Performed under the auspices of the US Dept. of Energy by LLNL under contract W-7405-ENG-48.

[1] J. Elizondo and A. Rodriguez, Proceedings of the 1992 15th International Symposium on Discharges and Electrical Insulation in Vacuum, Vde-Verlag Gmbh, Berlin, Germany, pp. 198-202.

[2] S. Sampayan, et. al., Proceedings of the 1995 Particle Accelerator Conference, (IEEE), New York, N.Y., pp.1269-1271.

[3] S. Sampayan, et. al., Proceedings of the 1995 Particle Accelerator Conference, (IEEE), New York, N.Y., pp. 2123-2125.

[4] T. L. Houck, et. al., these proceedings.

[5] C. C. Shang, et. al., these proceedings.

[6] E. Gray, private communication.

[7] O. Milton, IEEE Trans. Electr. Insul., Vol. EI-7, pp. 9-15.

[8] A. S. Pillai and R. Hackam, J. Appl. Phys., Vol. 53(4), pp. 2983-2987.

[9] H. C. Miller, G. E. Aerospace Report, (GEPP-TIS-1064-UC-13).

[10] W. Glock and S. Linke, Cornell University Report, Laboratory of Plasma Studies, Ithaca, N.Y., (No. LPS 24, 1969).

[11] I. D. Smith, "Pulsed Breakdown of Insulator Surfaces in Poor Vacuum," unpublished AWRE report, Aldermaston, United Kingdom.

[12] R. A. Anderson and W. K. Tucker, J. Appl Phys., Vol. 58(8), pp. 3346-3349

150 kV MAGNETIC PULSE COMPRESSOR

G.Mamaev, T.Latypov, S.Mamaev, S.Poutchkov, A.Ctcherbakov, I.Tenyakov
Moscow Radiotechnical Institute of Russian Academy of Sciences

Abstract

The generator is based on a magnetic pulse compression circuit, its repetition rate is one pulse per some minutes. The generator consists of a thyratron switch, a resonant transformer (1:7 step up), a storage capacitor, a water-filled pulse-forming line and two saturable magnetic switches from amorphous alloy with a high induction of saturation, a high ratio B_r/B_s and a high resistance of the insulation. A special attention has been paid to the reliability of the installation.

1 GENERATOR DESIGN

The high voltage, high power (6.0×10^9 W) generator with 150 ns duration of the pulse was designed. This generator can be used with low impedance devices. Many applications such as start circuits of high-voltage discharge and high current electron injectors, etc. require a generator with these parameters. The general parameters of the generator are:

Output voltage	150 kV
Output impedance	4 Ohm
Output pulse duration	150 ns
Build-up time	20...30 ns
Pulsed-oscillator starting time (jitter)	5...10 ns
Repetition rate	1 pulse/s

The generator is created under the traditional scheme with a magnetic compression [1]. It consists of a water-filled pulse forming line (PFL), a two stage pulse compressor, capacitor stores, a switch and a step-up transformer. The two stage compressor is placed in two oil-filled tanks. The generator is shown in Fig. 1 and its design is shown in Fig. 2.

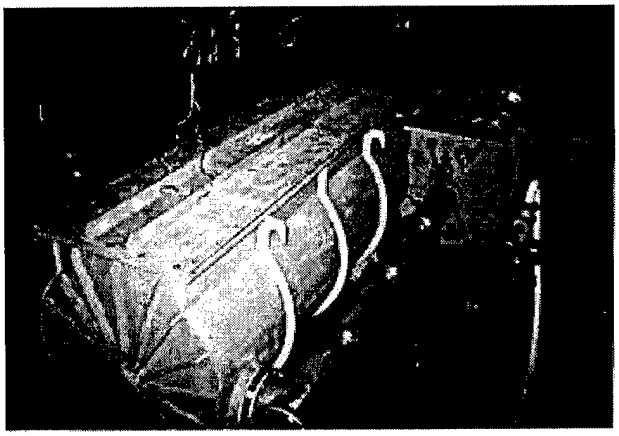
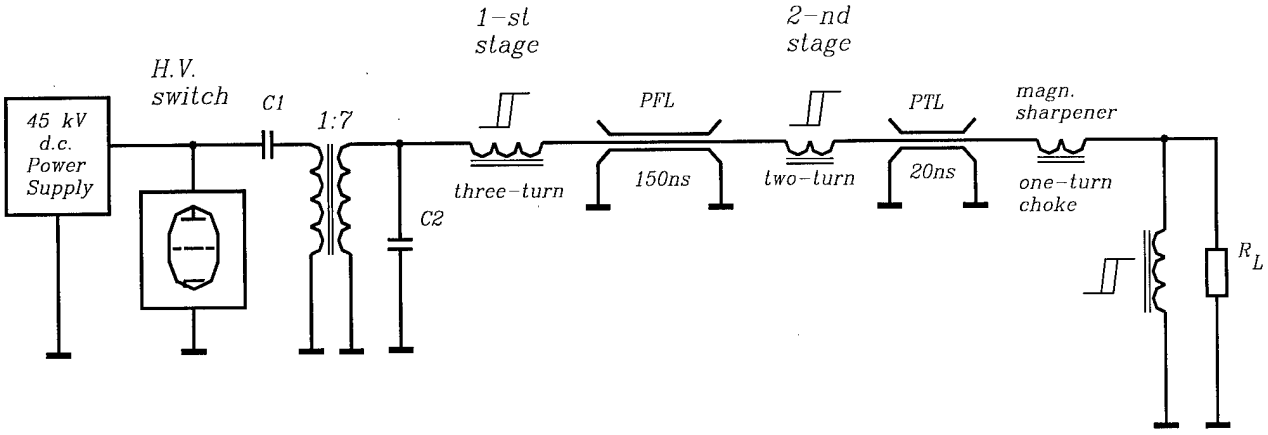


Figure: 1 The generator.



Fgure: 2 The generator design.

The generator is based on a two-cycle scheme of demagnetization of switching magnet ferromagnetic cores and a step-up transformer [2]. This scheme of demagnetization allows to reduce corporeal consumption. The current of demagnetization is formed by a passive LC network and two pulses of different polarity are obtained. The first current pulse serves to demagnetize the cores switching magnets of pulse compressors, the second pulse

0-7803-4376-X/98/$10.00 © 1998 IEEE

serves to demagnetize the core of the step-up transformer. The low-voltage connection of the secondary winding is used for the demagnetization current supply. The switching on of the generator occurs at a certain time, when the process of demagnetization of the step-up transformer core comes to the end. The demagnetization device is placed in a special box.

The generator is operated in the following way. The controlled up to 45 kV DC voltage source charges the primary store C_1 (1.2mkF, 50 kV). The primary switch is a hydrogen thyratron. The critical pulse current for the thyratron switch, the primary store and the step-up transformer is more than 20 kA. The hydrogen thyratron operates in the regime with a grounding control grid [2]. In this regime the thyratron cathode is used for running the primary switch rather than for current producing. As a result the critical pulse current of the thyratron increases considerably. JINR's investigation of TGI-2500/50 thyratron operating regime exposed its high reliability in the regime with a grounding control grid. It seems to be provided by the effective water-cooling of the anode and grid and pumping of the emitted gas after each pulse of the generator.

The secondary store C2 (0.02 mkF) is a low-inductance high current capacitor of a special design. It is charged up to (300-320) kV in 1.6 mks by the step-up transformer. The design cross section of the three-turn switching magnet core in the first stage pulse compressor is 290 cm^2 and its weight is 200 kg. The permissible discharge current of the secondary store C2 determined by the connector design is 30 kA. The store C2 is discharged through the magnetic switch of the primary stage pulse compressor.

The C2 store being discharged in 0.45 mks through the saturated switch of the first compression stage, charges a forming water-filled line up to (300-320) kV. The water line charging time has been chosen to match the triple duration of forming pulse. The deionized water resistance can be no more than 200...300 kOhm×cm, it simplifies the demands for water supply system. The water line discharging current (of about 37 kA) flows through the short transmission line (20 ns) into a sharper after the second magnetic switch flipping and then into the load. The sharper is not used now. The load consists of several low-inductance bulk TVO-60 resistors. A one-turn magnetic switch can be used in the second compression stage but a two-turn switch is much lighter and cheaper. With a two-turn switch, the built-up time and the pulse droop slightly rise. The designed cross-section is 118 cm^2 and its weight is 87 kg. We expect to have the built-up time of 20-30 ns by the use of the sharper. In adjusting the generator load was shunted by a saturatable one-turn switch with the projected flipping time of above 150 ns. Including the switch cuts the output pulse built-up time.

Permalloy and amorphous alloy cores manufactured using special technology are used in generator switches. This technology was developed especially for amorphous alloy ribbon and it allows to achieve the squareness ratio coefficient more than 0.9, the saturation induction of above 1.45 T and the pack factor coefficient above 0.7 [3]. We could not complete generator adjusting without construction redesigning because of the break-down of the capacitor battery C1 bushing. Then, there was a high concentration of water in the oil. The vacuum desicciation was uneffective due to the low temperature at the production area. We are going to carry out additional desicciation procedures and oil warming.

To provide adjusting and reparing of the generator some capacitor voltage dividers were installed:

at the primary winding of the step-up transformer;
at the secondary winding of the step-up transformer;
at forming line unput and output;
at the generator output.

Two transformers for current measuring were also installed at forming line input and output.

REFERENCES

[1] D.Brix, E.Cook and others:' The Application of Magnetic Switches as Pulse Sources for Induction Linacs', IEEE Trans. On Nuclear Science, Vol. 1, NS-30, No 4, August,1983.

[2] О. Архипов и др.: 'Линейный индукционный ускоритель трубчатого пучка.' Труды VIII международной конференции по мощным пучкам заряженных частиц. Новосибирск, 1990, том 2, стр. 809.

[3] G. Mamaev, I. Bolotin, S. Mamaev, S. Poutchkov, Ctcherbakov, I. Tenyakov: 'Technology for Production of the Amorphous Alloy Large Scale Cores', This conference.

TECHNOLOGY FOR PRODUCTION OF AMORPHOUS ALLOYS LARGE SCALE CORES

G. Mamaev, I. Bolotin, A. Ctcherbakov, S. Mamaev,
S. Poutchkov, I. Tenyakov
Moscow radiotechnical institute of Russian Academy of Sciences

Abstract

High average power pulsed accelerators are enabling the potential use of high peak power technology in a number of different industrial application areas such as material processing, food processing, stack gas cleanup and the destruction of organic contaminants etc.

The development and commercial availability of amorphous alloys allowed the development of new class of short pulse duration, high peak current, high average power accelerator that is capable of efficient repetitive operation up to 10^4 pps (pulses per second) using semiconductors, thyratrons and saturable core magnetic switches. The saturable switches are now employed in high current, high average power systems, such as CLIA, TBA and COBRA accelerators and others. It is known, that optimum magnetic properties of amorphous alloys for use with high dB/dt applications are achieved only with core annealing. With increasing magnetization rates there are increase interlaminar voltage and core loss (cause by interlaminar eddy currents). Ribbon for such cores have to be coated with interlaminar insulation coating. As a rule, manufacturers of large scale cores use amorphous alloys (2605SC, 2605CO or 2705 METGLAS™) without annealing, but with interlaminar insulation (mylar or special paper). With such technology core has high interlaminar break voltage, but nonoptimal magnetic properties: - induction Bm, squareness ratio B_r/B_s (SR), pack factor (PF) and increased losses.

The paper addresses the spesialists associated with development and manufacturing efficient (low loss), most compact, inexpensive and reliable cores with inorganic insulation coating, for magnetic pulse compression circuit (MPC), magnetic switches (MS), inductors for linear accelerators (ILA), high voltage pulse transformers (HVPT), pulse power transformer (PPT) etc.

1 INTRODUCTION

With creation of pulse high-power accelerators the rather important role is connected with technological aspects of cores manufacturing. The magnetic cores of powerful accelerators can have the rather large sizes and weight. High induction B_s, squareness ratio B_r/B_s, high pack factor, insulation coating with the high electrical characteristics, low losses - there are the main requirements for cores manufacturing technology. The important influence have also other reasons: cost efficiency, availability of simple in maintenance equipment for cores manufacturing with high output, possibility of automation, low power consumption, ecological safety etc.

At present, [1,2,3,4] toroidal configuration cores with size range from 130×50 mm to 1500×800 mm (OD×ID), wounded with an insulating layer of mylar or special paper and are exclusively used **without annealing or thermomagnetic treatment** (TMT). There are also data in [2] about annealing ribbon (obviously below 300°C) before wounding. For the technology of core manufacturing with TMT and insulation coating there are severe restrictions for materials, which can be used as insulation - a high heat distortion of arround 450°C, high heat conductivity, possibility to change coating thickness, high electrical characteristics of insulation coating, strong adhesion, thermal expansion (TE) of coating must be the same or closed to TE of amorphous alloys under winding. These restrictions badly complicate the design of such technology, especially for large-sized cores. By the literature [1... 7] in high average power systems are mainly used the magnetic cores with the characteristics, appropriate to magnetic properties a ribbon of amorphous alloys "as cast", i.e. B_{max}=1.2-1.3 T (with H=80A/m), squareness ratio SR= 0.5-0.7. Obviously, that squareness ratio and losses of ready cores are far from those values, which can be obtained with TMT (for a longitudinal magnetic field).

2 SHORT TECHNOLOGY DESCRIPTION

Technological prosesses of winding large scale cores from amorphous alloys with applying insulation coating and computer aided TMT have been developed in Moscow radiotechnical institute (MRTI) of Russian Academy of Sciences. The equipment for manufacturing cores from amorphous Fe-base alloys (with high Curie temperature) with a minimum ID from 25 mm, maximum OD up to 600 mm and width of a ribbon up to 50 mm was made. The main features of the developed technology are following: - additional ribbon cleaning, applying insulation coating in special bath with insulation solution (modified Na liquid glass), preliminary drying in special vertical tunnel, check quality of coating and finally - winding. The winding is carried out with tension beforehand given and supported with high accuracy by the special servosystem. All this processes are carried out on special mashine, developed in ÌRTI and shown on Figure 1. The mashine for core winding works, as a rule, act in a semi-automatic mode, the interference of an operator is necessary only in case of ribbon breakaway or abnormal disconnecting (bad quality of insulation etc.). After winding and preliminary

0-7803-4376-X/98/$10.00 © 1998 IEEE

control of insulation quality the cores are located in special furnace for annealing (TMT).

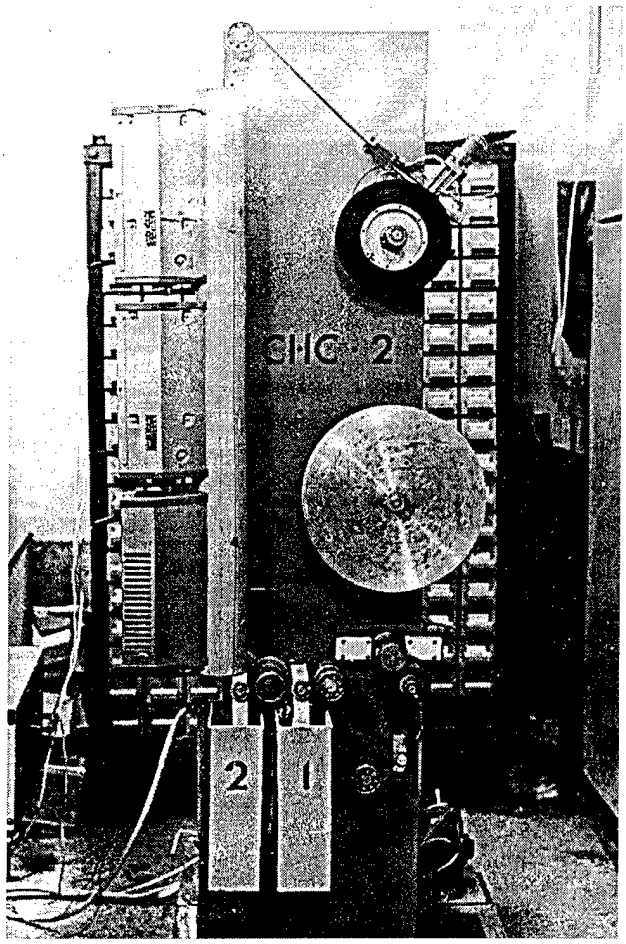


Figure: 1 The mashine for core winding works.

The main features of furnace, that is shown on Figure 2, are following: amount of cores for contemporary annealing up to 4, automatic loading and unloading mode, computer control modes of TMT, possibility of



Figure: 2 The furnace for cores with OD up to 700mm.

annealing (and cooling) with longitudinal field (up to 2500 A/m for cores with OD up to 500 mm).

With PC aid operator, through the special interface chooses a mode of TMT and a program of the measurements of current values, the main magnetic and other core characteristics. Some factors are taken into account for speed of heating and finite temperature: brand of alloy, presence or absence of insulation coating, amount of contemporary anneling cores, size or weight of core(s). Intermediate temperature platform with temporary hold-up are availability. Uninterrupted, during the TMT process mesurement core's magnetic characteristics and the speed and sign of their changes, allow (using specially developed algorithm) to reach optimal magnetic core properties for power pulse applications.

3 THE REACHED RESULTS

Computer aided TMT and insulation coating make possibility to provide minimum of H_c, maximum of B_m, high SR B_r/B_s (0.9-0.95) and rather high μ_{eff} (for dB/dt up to 30T/mksec), low loss. The technology allows also to use inexpensive amorphous Fe base alloys with small Co contents (about 9 %) and to reach parameters compared to parameters of cores, made from more expensive alloys.

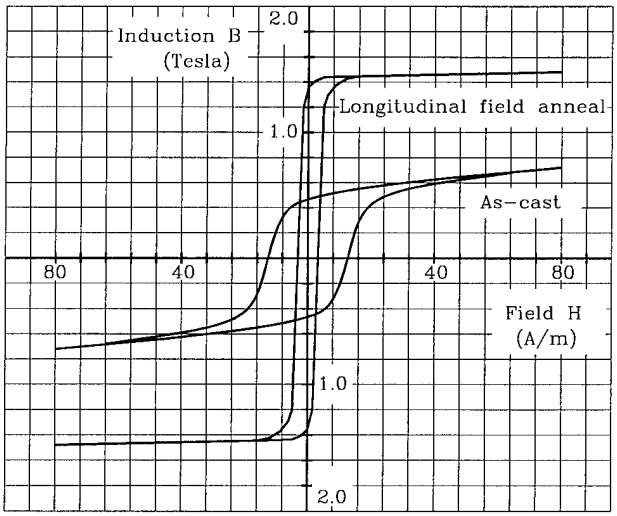


Figure: 3 Typical quasistatic (50 Hz) hysteresis loops for alloy 9KCP.

The method of applying of insulation coating provides thickness of coating layer from approximately 0.2mkm up to 3mkm and its value depends on smoothing of ribbon surface and magnetization rate dB/dt (pulse duration). Electrical characteristics of insulation after core annealing (up to 450°C): $\rho=10^7$-10^{15}Ohm×m, break-down voltage =15-30V/mkm. Correlation coefficients between B_r, winding tension, PF and between break-down voltage, coating thickness, PF has been founded. It allows to achieve high output suitable cores with given properties and dispersion not exceeding 10%. Such technology is espesially suitable for researche and optimization of TMT

modes for cores with different sizes and weights, with or without insulation coating.

With the purpose of saving high values of the core magnetic characteristics and also for elimination or weakening of influence on the annealed core mechanical stresses and/or climatic conditions, at once after TMT and preliminary test measurements the core covers over special silicon compound with temporary and thermal shrinkage closed to zero. This process can be carry out under vacuum. After full hardening (within 72 hours) the check cycle of measurements of ready core are carried out (50Hz and pulse). The results of this measurements are write to computer's memory in form of label, with the indication of core number, dimensions, weight, brand of alloy, conditions of measurements and all main characteristics (including view of a hysteresys loop with different values of a field). The characteristics of cores from different alloys are formed in Table 1.

	30KCP after TMT	9KCP after TMT	2605SC as cast	2605CO as cast
B, T 80A/m	>1.5	>1.45	<0.7	<1.2
SR 80A/m	>0.95	>0.92	<0.6	<0.9
B, T 800A/m	>1.56	>1.56	<1.3	<1.3
SR 800A/m	>0.92	>0.9	<0.5	<0.7-0.8
PF	>0.7	>0.7	<0.7	<0.7

Table 1: The static core characteristics from differrent alloys.

The data of alloys 2605SC, 2605CO are taken from [1,2,5,6].

The measurement of the pulse characteristics of cores was carried out in 1-cosine voltage saturation mode on the specially developed device with the following parameters: U_{max} = 40 kV, f = 800 kHz, r = 2 Ohm.

4 CONCLUSION

About 1500 kg cores with different weights (ID×OD from 25×50 up to 460×220 mm) was manufactured during 1994-1996. The export order on cores for the accelerator similar to the CLIA was executed. Also cores for the pulse modulator (report is represented on this conference) was manufactured. The assemblage of the accelerator for delivery on export comes to an end, the cores was produced after described technology. In the whole technology has shown the reliability, stability and rather high output of suitable products (cores). The economic index of technology also are rather high. Unfortunately a thickness of a ribbon and its quality (stability of properties, geometry and especially quality of a surface) do not allow to realize all advantages of considered technology.

In the further it is planned:

- to carry out experiments on additional processing of a ribbon (polishing and purge off a thin surface defect layer) and use thin ribbon (13-18 mkm), that will allow to use cores from such ribbon with pulse duration up to 50 nsec;
- to use for core manufacture nanocrystalline alloys with low saturation magnetostriction and low μ_{sat}.

REFERENCES

[1] L. Reginato et al.: 'Engineering conceptual design of the relativistic klystron two-beam accelerator (TBA) based power sourse for 1-TeV next linear collider'.

[2] T.F. Godlove et al.: 'Pulse modulators for ion recir culator Cells'.

[3] Eugene L. Neau: 'High average power, high current pulsed accelerator technology'.

[4] S. Ashby et al.: 'CLIA-A compact linear induction acceerator system'.

[5] David L. Smith et al.: 'COBRA accelerator for San dia ICF diode research at Cornell University'.

[6] S. Yu et al.: 'RF power source for a 1 TeV next linear collider' .

[7] B.G. Kim et al.: 'Magnetic properties of very high permeability, low coercivity and high electrical resis tivity in Fe87Zr7B5Ag1 amorphous alloy', J.Appl.Phys.77(10),15 May 1995.pp.5298-5302.

[8] I. Bolotin, A. Ctcherbakov, G. Mamaev, S. Mamaev, S. Poutchkov: 'Main features of technology for manufacturing of amorphous cores with interlaminar insulation coating', 'Amorphous presision alloys: technology, properties and applications'VI Interna tional conference, 19-20 September, 1996, Borovichi, Russia.

THE PEP-II ABORT KICKER SYSTEM*

J. de Lamare, A. Donaldson, A. Kulikov, J. Lipari
Stanford Linear Accelerator Center

Abstract

The PEP-II project has two storage rings. The HER (High Energy Ring) has up to 1.48 A of electron beam at 9 GeV, and the LER (Low Energy Ring) has up to 2.14 A of positron beam at 3.1 GeV. To protect the HER and LER beam lines in the event of a ring component failure, each ring has an abort kicker system which directs the beam into a dump when a failure is detected. Due to the high current of the beams, the beam kick is tapered from 100% to 80% in 7.33μS (the beam transit time around the ring). This taper distributes the energy evenly across the window which separates the ring from the beam dump such that the window is not damaged. The abort kicker trigger is synchronized with the ion clearing gap of the beam allowing for the kicker field to rise from 0-80% in 370nS. This report discusses the design of the system controls, interlocks, power supplies, and modulator.

1 SYSTEM SPECTIFICATIONS

The PEP-II beam abort kicker system is designed to divert the stored beam of the HER and LER rings into a beam dump in the event of beam based trigger or a equipment failure trigger [1]. The HER and LER abort systems operate independantly, and their operating parameters are listed in Table 1. The rings will be operated 274 days per calendar year with scheduled maintenance 2 days per month. It is anticipated that the rings will need full refilling 3 times per day due to a failure in one of the ring's subsystems [2]; meaning, the abort system typically could be triggered 3 times per day.

	HER (at 9 GeV)	LER (at 3.1 GeV)
Max. Bend Angle	1.7 m-rad	2.1 m-rad
Magnetic Field	600 G	394.5 G
Kick Direction	Down	Down
Magnet Current Amplitude (without overshoot)	4800 A	3156 A
Magnet Current Risetime	370ns Max.	370ns Max.
Magnet Current Droop (in 7.33μs)	100%-80%	100%-80%
Max. Pulse Rep. Frequency	0.5 Hz	0.5 Hz
Typical Pulse Rep. Time	8 hr.	8 hr.

Table: 1 Abort Kicker Operating Parameters

The beam abort system must be reliable to insure that the beam won't drill a hole through a vacuum vessel in the event of a ring failure. Therefore, there is redundancy in key system components--particularly triggers. Also, the system is self triggering in the event of a power loss, disconnected input trigger cable, or detected non-critical internal fault. Though only one abort system is needed to extract the beam, a second system is planned in each ring which is triggered in the event of a detected fault of the first system, some 7.33μs delayed or one revolution of the beam from the first kicker [3].

2 SYSTEM COMPONENTS

The abort kicker subsystems are: Controls and Interlocks, Modulator Ancillary Circuitry, Modulator, and Magnet.

2.1 Controls and Interlocks

The system control hardware consists of Camac modules which are controlled by micro-controllers which in turn are controlled by a mainframe computer. The various Camac modules include: an Isolated Digital Output Module (IDOM) for command functions, an Isolated Digital Input Module (IDIM) to provide status information, a Smart Analog Module (SAM) for recording analog readbacks, a Simple Timing Buffer (STB) for command triggering, and a Beam Abort Trigger System (BATS) for emergency triggering. There is also an Abort Kicker Modulator Controller which is a 19" rack mounted chassis that acts as the interface between the Camac controls and the Modulator with its ancillary cicuitry. The controller is discussed in more detail below.

2.2 Modulator Ancillary Circuitry

The Modulator Ancillary Circuitry provides the power and the triggering necessary for modulator operation. There are two grid drivers, modified BIRA SCR Thyratron Driver 730-788, which are redundant in function. They provide the thyratron grid 2 pulse which initiates current in the magnet. Redundant drivers are necessary to insure that the system is still functional in the event of a malfunction of one driver. A Thyratron Keep Alive/Bias Power Supply chassis generates -130 VDC for the grid 2 bias, and the 100mA of keep alive current for grid 1 of all thyratrons within the modulator. The Thyratron Heater/Reservoir Power Supply is powered by a ferro-resonant transformer which stabilizes the AC voltage. This chassis provides adjustable AC power for the modulator thyratrons, a time-out interlock to allow thyratron heating on startup, and sends voltage and current readbacks to the control system. A Low Voltage Power Supply (LVPS), Glassman Series ER 0-3kVDC, charges one of the modulator's pulse capacitors. It is named the

* Work supported by the Department of Energy under contract No. DE-AC03-76SF00515

0-7803-4376-X/98/$10.00 © 1998 IEEE

LVPS only because the High Voltage Power Supply (HVPS), Glassman Series LT 0-30kVDC, generates a considerably higher voltage. The HVPS also charges a pulse capacitor in the modulator.

2.3 Modulator

The modulator generates the high current pulse to the magnet. The circuit design is discussed in more detail later. The modulator cicuitry is housed in a 53cm x 54.5cm x 56cm box which is located directly under the abort kicker magnet (Fig. 1). The magnet connections are made with 5 cm wide aluminum bus, approximately 20cm long, and spaced 3.8cm apart. The modulator is air cooled and uses an air filter to limit the dust intake. The ambient air temperature of the ring tunnel is expected to be 40° C, thus the modulator components are rated appropriately.

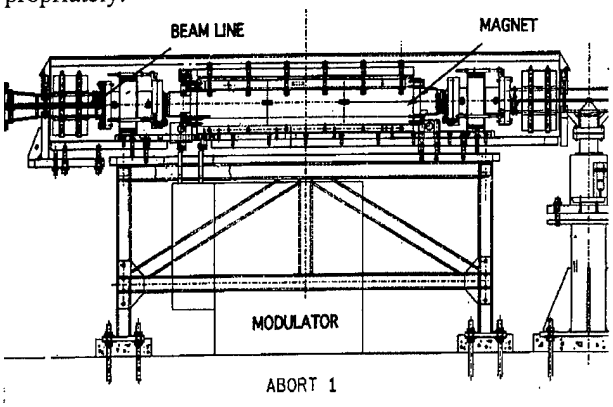


Figure: 1 Abort kicker magnet and modulator assembly

2.4 Magnet

The magnet is a single turn, H-type magnet made from blocks of Ceramic Magnetics CMD5005 ferrite. The HER magnet ferrite is 0.85m and the LER magnet ferrite is 0.55m in length. For a detailed description of the magnet design see Reference 4.

3 ABORT KICKER CONTROLLER

3.1 Controls

The abort kicker system was intentionally given a minimum number of controls such that it will not inadvertantly be manipulated. The system may be remotely turned on, turned off, reset, and switched between command trigger mode with emergency trigger to emergency trigger only mode. What the system lacks in control, it more than makes up for in diagnostics. There are a number of status bits reporting system functionality. Particularly important are the trigger statuses. The trigger sequence from the redundant BATS and Grid Driver triggers to the magnet voltage are all monitored. These diagnostics are useful to determine whether a trigger module needs repair or when self triggering occurs.

The analog readback data is stored in history buffers. These include: thyratron heater and reservior current, thyratron keep alive current, thyratron bias voltage, pulse capacitor voltages, and magnet current. Because the modulator is seldom triggered, the anaolg magnet current pulse is read by a sample and hold circuit, converted to digital, and then back to analog for monitoring by a SAM. This method eliminates the droop of a sample and hold circuit. A running history of all analog readbacks is recorded in the control system main frame computer.

3.2 Interlocks

The system is designed such that it is self protecting for most failures. In the event of a power loss or a failure of the modulator or its ancillary circuitry, the modulator is triggered by the BATS. The controller sends two statuses to the BATS--System O.K. and System Failing. If the modulator is O.K., then it is triggerable by a command trigger. If the status is not O.K., then the system is not ready and cannot be triggered. When the system is failing, then the system is triggered by the BATS. A list of the interlocks and the system status is given in Table 2. All of the interlocks are inhibited when the thyratron heater interlock is timing out and when a trigger command is detected.

Description	System Status
HV Fail High (V > 102%)	Not Ready
HV OK	Trigger Ready
HV Falling (0 > Slope • -1%/ms)	Failing
HV Fail Low (V < 98%)	Not Ready
LV Fail High (V > 102%)	Not Ready
LV OK	Trigger Ready
LV Falling (0 > Slope • -1%/ms)	Failing
LV Fail Low (V < 98%)	Not Ready
HV Keep Alive Current High	Failing
HV Keep Alive Current OK	Trigger Ready
HV Keep Alive Current Low	Failing
LV1 Keep Alive Current High	Failing
LV1 Keep Alive Current OK	Trigger Ready
LV1 Keep Alive Current Low	Failing
LV2 Keep Alive Current High	Failing
LV2 Keep Alive Current OK	Trigger Ready
LV2 Keep Alive Current Low	Failing
HV Bias Voltage Low	Failing
HV Bias Voltage OK	Trigger Ready
LV Bias Voltage Low	Failing
LV Bias Voltage OK	Trigger Ready
HV Htr./Res. Current High	Failing
HV Htr./Res. Current OK	Trigger Ready
HV Htr./Res. Current Low	Failing
LV Htr./Res. Current High	Failing
LV Htr./Res. Current OK	Trigger Ready
LV Htr./Res. Current Low	Failing
Heater Current Time-Out	Not Ready
Heater Current Time-Out OK	Trigger Ready
AC Fail	Failing
AC OK	Trigger Ready
Rack Over-Temperature	Failing
Rack Temperature OK	Trigger Ready
Grid Driver Failure	Not Ready
Grid Drivers OK	Trigger Ready

Table: 2 Abort Kicker Interlocks and their system status.

4 ABORT KICKER MODULATOR

The modulator is made up of three CX1622 thyratrons, two pulse capacitors, a damping resistor, and many other supporting components. Figure 2 shows the simplified modulator circuit. Because of the shape of the pulse, the circuit design is such that it has two parts: a high voltage part and a low voltage part. The high voltage part is made up of one CX1622 thyratron and a 0.15μf, 50kV low inductance pulse capacitor. The capacitor charges through the magnet, and likewise discharges through the magnet when the thyratron is triggered. The resulting pulse generates a voltage on the magnet of -25kV.

The low voltage part of the circuit consists of two parallel CX1622R thyratrons, a 100μf, 4kV low inductance pulse capacitor, and a 0.2∘ damping resistor made from 50 parallel 2W carbon composition resistors. Each thyratron is supported in a slotted cylindrical housing which acts as the current return path for low inductance. All of the thyratron cathodes are grounded at a common point. Because stray inductance in the low voltage circuit contribute to the current overshoot, the inductance of all circuit connections is minimized.

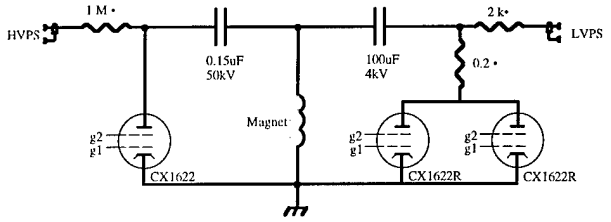


Figure: 2 Simplified Modulator Schematic

As the high voltage thyratron is triggered by the redundant grid drivers, the voltage at the magnet and the low voltage circuit goes to -25kV, and a half sine current pulse is initiated in the magnet, with the high voltage circuit capacitance and inductance determining the current risetime. The low voltage thyratrons are triggered in parallel with a pulse formed by a current transformer positioned on the connection from the modulator to the magnet. Therefore, the low voltage thyratrons will always be triggered when the high voltage thyratron conducts whether from a command trigger or a self trigger.

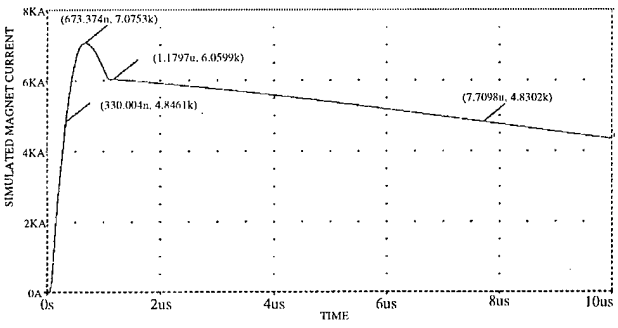


Figure: 3 Simulated Magnet Current Waveform

As the magnet voltage swings through zero, the low voltage thyratrons become positively biased, and conduction begins. Initially, the magnet supplies current through the low voltage circuit up to a point where the R-C network of the circuit gives the waveshape an exponentially decaying tail.

The circuit was modeled with a circuit simulation program. The model included the stray inductances of the capacitors and thyratrons, the inductance of the magnet connection, and a model of the magnet as given in Reference 4. Using the model, the first 10μs of magnet pulse is shown in Figure 3. The overshoot results from the stray inductance in the low voltage circuit which limits the circuit's current risetime and allows for the high voltage circuit current to swing past its peak.

5 CONCLUSIONS

The modulator has been completed and tested into the magnet. Figure 4 shows the test results. The model is in good agreement with the test results. The controller isn't yet completed, so the total system has not yet been tested. Within the year the total system will be field tested with beam.

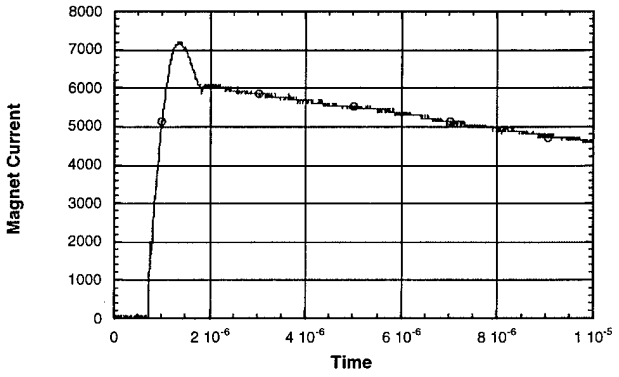


Figure: 4 Abort kicker current test results.

6 ACKNOWLEDGEMENTS

We want to thank Piotr Blum for his efforts in the assembly of the modulator, the design and fabrication of many of its parts, and for the assembly of many of the subsystems. We also want to thank Joe Olszewski for his dedication and support on this project.

REFERENCES

[1] W. Barry, et. al.: 'Criteria for Beam Abort in PEP-II', SLAC-PEP-II-AP-NOTE-9-94, June 1994. 2pp.

[2] J. Dorfan, M. Zisman: 'PEP-II Operational Efficiency: Assumptions and Guidelines--Part I', SLAC-PEP-II-TECHNICAL-NOTE-18, Mar 1993. 2pp.

[3] A. Kulikov, et. al.: 'PEP-II Abort Systm Specifications', SLAC-PEP-II-TECHNICAL-NOTE-61, Oct 1994. 13pp.

[4] G. C. Pappas, et. al.: 'The PEP-II Injection Kicker System', PAC97

NLC KLYSTRON PULSE MODULATOR R&D AT SLAC*

R. Koontz *SLAC*, M. Akemoto *KEK*, S. Gold *SLAC*, A. Krasnykh *JINR*, Z. Wilson *SLAC*

Abstract

The basic elements of a klystron pulse modulator are: a charging supply, a PFN with energy storage capacitors, a thyratron switch tube, and a pulse transformer. The design group mentioned above is working on the system requirments of an NLC modulator, is carrying out tests on components, and building a prototype NLC modulator of conventional, but optimized design. A PFN using Russian K15-10 type high energy density glass capacitors has been constructed and tested into a conventional pulse transformer and klystron load. Rise time is less than 400 nsec. Developmental work with thyratron manufacturers is being started. Similarly, R&D pulse transformers developed in cooperation with industry are being tested.

1 KLYSTRON PULSE MODULATOR REQUIREMENTS OF NLC

An X-band 75 MW PPM klystron has been developed and operated successfully at SLAC. The present technical specifications for a two klystron pulse modulator assembly are listed below. These specifications change as the klystron design is optimized, so the NLC modulator design must be adaptable to these changes.

Parameters	Operating value
Beam voltage	500 kV
Beam current (2 kly)	530 amps
Pulse width (flat top)	1.5 μsec
Pulse rep rate (PRF)	120 PRF
Rise time (10 - 90%)	less than 400 nsec
Pulse Top Ripple	2%
Droop	2%
Primary charge voltage	up to 80 kV
Pulse transformer ratio	14/1

On the civil side of NLC planning, space is at a premium partly due to construction cost, so the pulse modulator and support electronics must be designed to fit in a modest size area, be compatible with the RF delivery waveguide layouts, be energy efficient, and allow for effective servicing during operation. We categorize these requirements in three general classifications:

- Ergonomic design
- Reliability & Maintainability
- Power Efficiency

1.1 Ergonomic design

In the NLC system design, the klystron modulator is recognized as just one component of the general RF delivery system which must mate smoothly with other parts of the complex. Fig. 1 shows an initial configuration of a two klystron-modulator assembly in which all pulsed high voltage components are housed in a cylindrical oil tank which also mounts the two klystrons. Except for the thyratron and its carrier which can be changed in place, all other servicing including klystron and modulator component replacement is done at a depot after the whole two tube assembly is removed from the housing location. The term "ergonomic design" refers to the need in the design phase to consider what components will fail, how accessible are these components for replacement, and what diagnostics will be put in place to detect and identify fault conditions preferably before they do collateral damage.

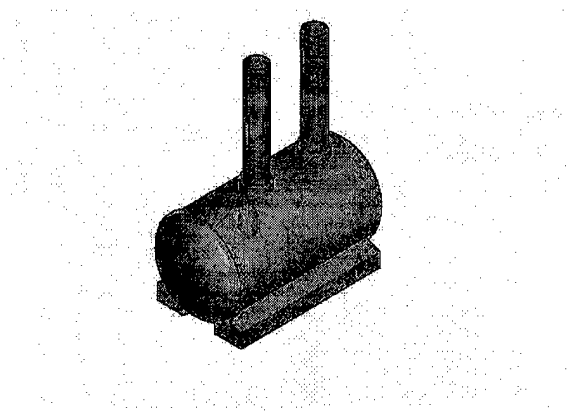


Fig 1. Klystron & Modulator Assembly

1.2 Reliability & Maintainability

The NLC design contains over 2,000 pulse modulators. While some M of K redundancy will be used in the system design of the RF power sources, individual RF power sources including the modulators will have to have very high MTBF ratings, well over 12,000 hours. Similarly, failed units must be capable of being changed out and the station put back on line quickly, ideally in less than 4 hours (MTTR - Mean Time to Repair). Quick changing of whole klystron-tank assemblies and depot repair help to keep MTTR low. Even in the depot, though, the hours to diagnose, disassemble, repair, and retest the klystron-modulator assembly must be kept low to minimize the size of the sustaining maintenance organization.

1.3 Power Efficiency

Electricity is a major operating cost of the NLC. The overall power efficiency from 480 volt input to usable klystron electron beam must be maximized to minimize operating cost. Keeping the charging power supply and modulator systems simple can produce high efficiency designs. Some areas, cathodes, have inherent inefficiencies. A klystron load is not a true resistance, but a perveance (non-linear) which cannot be matched during rise and fall times of the drive pulse. Beam current during rise time is not usable for producing RF, and thus represents an energy loss which can be minimized with faster rise time. The whole pulsed high voltage system

0-7803-4376-X/98/$10.00 © 1998 IEEE

has stray capacity which must be charged and discharged each pulse. All these are energy loss mechanisms which must be taken into account in the modulator design.

2 TEST BED CIRCUIT AND COMPONENT DEVELOPMENTS AND RESULTS

A high voltage modulator tank and test position in the Test Lab at SLAC has been modified into a Test Bed for NLC components. Figure 2 is a picture of the oil tank showing the thyratron, PFN and pulse transformer being tested. Figure 3 is a simplified schematic of the test circuit.

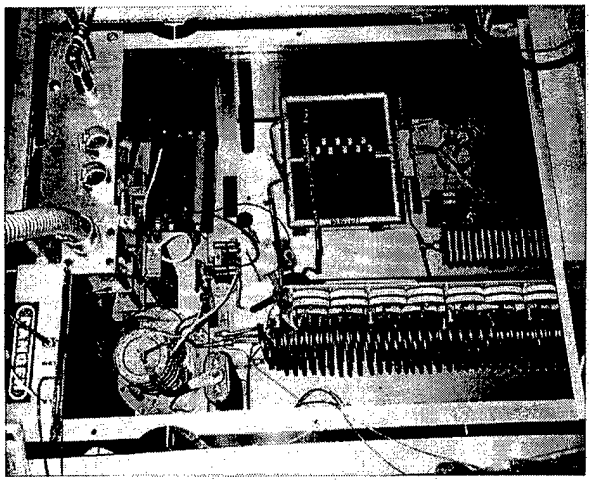


Fig 2. Test Bed for NLCModulator

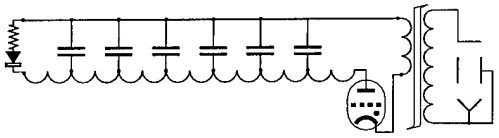


Fig 3. Test Circuit Schematic

The components to be studied for development and optimization for an NLC modulator are the PFN with its associated capacitors, the pulse transformer and the high voltage switch, which is still envisioned as a thyratron. The initial purpose of this development is to physically realize a simple, reliable modulator design which will meet the basic requirements of the NLC. The NLC modulator requirements are still evolving as an interdependent part of Klystron development, pulse compression and the high power RF ransmission system and the overall Linac tunnel construction.

2.1 High Energy Density Pulse Capacitors

The PFN under test is comprised of high energy density glass capacitors which are manufactured in St. Petersburg, Russia. These capacitors are made from a crystaline glass with a dielectric constant of 1000 and have a standard value of 10nF @ 40kV. A single capacitor, approximately 4î in diameter and æî thick including end connections, is shown in Figure 4. Two capacitors are placed in series to get to 80kV. The PFN has to store approximately 500 joules to deliver a pulse for two 75MW klystrons. The PFN will be made up of 40



Fig 4. Russian K15-10 Glass Capacitor

capacitor sections of 5nF each. The first testing of this configuration will be four parallel lines. Each line will have ten sections and an impedance of approximately 19.3 ohms, for a total PFN impedance of 4.8 ohms. The PFN coils are designed with mutual inductance to help flatten the pulse top. See Fig 5.

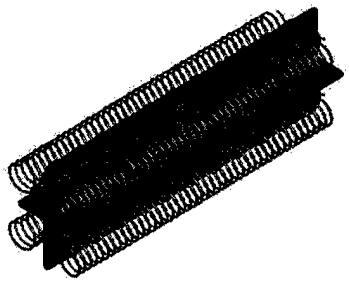
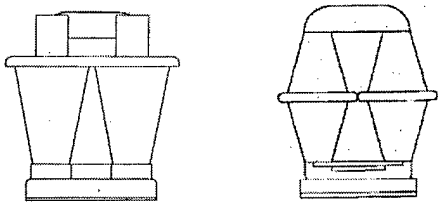


Fig 5. Four Parallel PFN Configuration

It is anticipated that a tuning method at low voltage will be studied to eliminate the need for high voltage hot tuning of the modulator. This also means that klystron variations will be minimized and klystrons will be installed in matched pairs.

2.2 Pulse Transformer Designs

The pulse transformer is one of the more critical elements of the modulator. The transformer leakage inductance and distributed capacitance are often the limiting factor in pulse rise time. Much of these characteristics are controlled by the physical geometry of the transformer. The geometry is dictated by voltage standoff and cross sectional core area required. Stangenes industries designed a 14:1 pulse transformer of standard configuration. This transformer is designed with higher voltage gradients and is therefore smaller than previous models. The outline of this transformer is shown in Fig 6a. Northstar Research has designed a double basket transformer depicted in Fig 6b.



a) Conventional b) Double Basket

Fig 6. Pulse Transformer Outlines

Preliminary tests using the Stangenes Industries conventional pulse transformer and a standard 5045, 15:1 ratio, pulse transformer are compared in Fig 7. As seen both the rise time and fall time of the output pulse are greatly improved and approach the base NLC requirement.

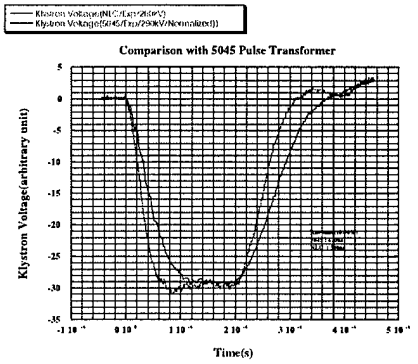


Fig 7 Transformer Beam Pulse Comparison

We are planning test and analyze the Northstar Research double basket transformer configuration in the same circuit and make a direct comparison of the two design approaches. Prior to these tests, the test bed layout will be reconfigured to minimize loop inductances and control noise. Future pulse transformer development plans include investigating other core materials and stripline transmission line transformers.

2.3 Thyratron Developments

The thyratron remains as the most stable choice for the high voltage switch at this time. Thyratrons already exist which meet the voltage and current handling characteristics required, namely 80kV and 10kA. There are three major thyratron manufacturers in the western world and all three are aware our basic requirement. Long history with the SLC at Stanford Linear Accelerator Center has shown the thyratron be one of the more frequent failures for the modulator assembly. The reliability of the NLC is an integral part of the design and therefore even in the first cut early stages components and assemblies are being assigned values for MTBF. The required thyratron MTBF is 50,000 hours. This is a factor of five+ over the existing SLC thyratron. We plan to continue to work with the manufacturers in their development of a low cost, more reliable thyratron. Another factor in operating the large number of modulators and thyratrons is to eliminate the need for thyratron ranging (adjusting of the reservoir voltage during thyratron lifetime). EEV proposes a scheme, which they have used successfully, to pre-pulse grid 1 instead of using DC to initiate a plasma at the cathode. We plan to set up this pre-pulsing arrangement in the Test Lab with thyratrons from different manufacturers to test and optimize the effects. Future advances in stacked solid state switches with regard to power handling, di/dt and reliability may in time make them the choice to replace the thyratron.

2.4 High Efficiency, Capacitor Charging Supplies

Physical size of the high voltage charging supply will also have a large impact on the NLC design. The power supply system needs to charge the PFN to approximately 80kV at a repetition rate of 120 Hz. The PFN capacitance is 200 nF. It is desirable that the entire charging system fit into a 19" rack cabinet and be as small as practical. There are existing capacitor charging power supplies commercially available at lower voltage and power levels. This technology needs to be expanded to the NLC requirement. There are also multiple schemes for pulse charging of the PFN which require further investigation. The power supply community is being encouraged to develop supplies that will meet our requirements

3. DEVELOPMENT PROGRAM PROJECTIONS

We are currently projecting NLC modulator development work for the next eighteen months. We have two operational test areas, one in the Klystron Test Lab, and a second in the fourth modulator position of the NLCTA (End Station B - SLAC).

3.1 NLCTA Prototype Operation

The prototype klystron & modulator assembly shown in Fig. 1 will be completed in design and assembled in the Klystron Test Lab. After the usual testing, characterization, and shakedown, it will be installed in NLCTA and begin operational running to collect lifetime data for both the modulator, power supply, and klystrons.

3.2 Component Development with Industry

In the Klystron Test Lab, the more open test bed as shown in Fig. 2 will continue to be used to test various capacitor and PFN configurations, optimized pulse transformer designs, and when they become available from manufacturers, prototype long life thyratrons. The secondary systems associated with modulator and klystron operation will be developed and optimized for low cost production Participation of industry will be most important as in all of these areas, the quality, longevity, and cost of the components and sub-systems available will determine the configuration of the final modulator design. Even though we have adopted a very simple, conventional design for the prototype NLC modulator, there is still time to consider other ideas that could lead to a lower cost, higher efficiency, and more reliable design. We will work with interested parties on any promising developments.

*Work supported by Department of Energy contract DE-AC03-76SF00515.

R. Koontz rfkap@slac.stanford.edu
M. Akemoto akemoto@slac.stanford.edu
S. Gold slg@slac.stanford.edu
A. Krasnykh krasnykh@slac.stanford.edu
Z. Wilson wilson@slac.stanford.edu

DEVELOPMENT OF THE PULSE TRANSFORMER FOR NLC KLYSTRON PULSE MODULATOR*

M. Akemoto†, S. Gold, A. Krasnykh and R. Koontz
Stanford Linear Accelerator Center, Stanford University, Stanford, CA 94309, USA

Abstract

We have studied a conventional pulse transformer for the NLC klystron pulse modulator. The transformer has been analyzed using a simplified lumped circuit model. It is found that a fast rise time requires low leakage inductance and low distributed capacitance and can be realized by reducing the number of secondary turns, but it produces larger pulse droop and core size. After making a tradeoff among these parameters carefully, a conventional pulse transformer with a rise time of 250ns and a pulse droop of 3.6% has been designed and built. The transmission characteristics and pulse time-response were measured. The data were compared with the model. The agreement with the model was good when the measured values were used in the model simulation. The results of the high voltage tests are also presented.

1 INTRODUCTION

The klystron pulse modulator for the Next Linear Collider(NLC) requires to produce a 500kV, 530A, 1.5μs flat top pulse to drive a pair of PPM-focused 75MW klystron[1]. The R&D of basic elements, a charging supply , a PFN, a thyratron switch tube and a pulse transformer for a prototype NLC modulator are being performed at SLAC[2].

The power efficiency of the modulator is extremely important. The effective output power of the modulator is the power of the flat-top portion of the high voltage output pulse. Since a pulse transformer is a major contributor to the waveform, the pulse transformer requires a fast rise time. In order to achieve a rise time that is less than 400ns, we have improved the design of a 14:1 pulse transformer by tradeoffs among the droop, the core size and the rise time. The test transformer has been built, and low and high voltage tests have been performed.

2 ANALYSIS OF THE PULSE TRANSFORMER

In order to simplify the analysis, we consider the simple geometrical arrangement with rectangular core. A single-layer secondary is wound over a one-layer primary and the distance between layers is constant[3].

2.1 Equivalent circuit

Figure 1 shows an equivalent circuit for the pulse transformer. The L_P is primary inductance, the L_S is secondary inductance, the L_L is leakage inductance, the C_D is distributed capacitance, the L_D is distributed leakage inductance. These circuit elements can be calculated from the geometrical constants of the transformer, dielectric constant of the insulation, and the permeability of the core material.

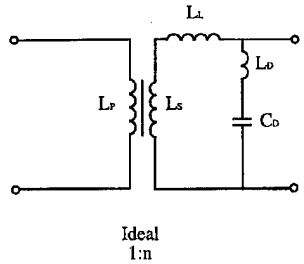


Figure 1. Equivalent circuit for the pulse transformer.

2.2 Droop and core size

The droop D_r is given by

$$D_r = \frac{R_{kly} \cdot \tau}{2L_s} ,$$

where R_{kly} is klystron impedance, τ the pulse width and L_S the secondary inductance.

The cross-section area of the core A is given by

$$A = \frac{V_s \tau}{\Delta B} \frac{1}{N_s} ,$$

where V_S is the voltage of secondary, N_S the number of secondary turns and ΔB the total magnetic flux density swing of the core. Thus, the cross-sectional area of the core is inversely to proportional to the number of secondary turns.

Since the secondary inductance L_S is calculated by

$$L_s = \frac{\mu_0 \mu_e A \cdot N_s^2}{l} ,$$

where μ_0 is the permeability of free space, μ_e the effective magnetic permeability, l the length of the magnetic path. Thus, the droop D_r is given by

$$D_r = \frac{\Delta B \cdot R_{kly}}{2\mu_0 \mu_e V_s} \frac{l}{N_s} .$$

The droop is propoportinal to the length of the magnetic path and inversely to proportional to the number of secondary turns.

2.3 Rise time

The rise time t_r is determined by

$$t_r \propto \sqrt{L_L \cdot C_D} .$$

The leakage inductance L_L is calculated by

*Work supported by the Department of Energy contract DE-AC03-76SF00515
† Visiting from KEK, permanent address: 1-1 Oho, Tsukuba-shi, Ibaraki-ken 305 Japan

0-7803-4376-X/98/$10.00 © 1998 IEEE

$$L_L \propto \frac{\mu_0 \Delta \cdot u \cdot N_s^2}{L},$$

where Δ is the distance between layers, u the average circumference of the layers and L the winding length.
The distributed capacitance C_D is calculated by

$$C_D \propto \frac{\varepsilon_0 \varepsilon_r u \cdot L}{\Delta}\left(\frac{n-1}{n}\right)^2,$$

where ε_0 is permittivity constant of free space, ε_r the dielectric constant of the insulation and n turn ratio. Therefore, from using $u \approx 4\sqrt{A}+\pi\Delta$, the rise time is given by

$$t_r \propto \sqrt{\varepsilon_r}\sqrt{\frac{V_s \cdot \tau}{\Delta B}}\sqrt{N_s}\frac{n-1}{n}.$$

It is found that the rise time strongly depends on the number of the secondary turns rather than turn ratio.

2.4 Tradeoffs

From the above analysis, it is found that a fast rise time requires low leakage inductance and low distributed capacitance and can be realized by reducing the number of secondary turns, but it produces larger pulse droop and core size. Thus, fast rise time and low droop are contrary to each other. Since a droop of several percentage can be compensated by making adjustments to the PFN, we can improve the rise time by tradeoffs among these parameters.

3 FABRICATION OF TEST PULSE TRANSFORMER

The conventional pulse transformer has been carefully optimized and designed by the model calculations. The transformer is an isolation transformer type with two parallel primary basket windings, and with two parallel tapered secondary basket windings as shown in Figure 2. It has been fabricated by Stangenes Industries, Inc.

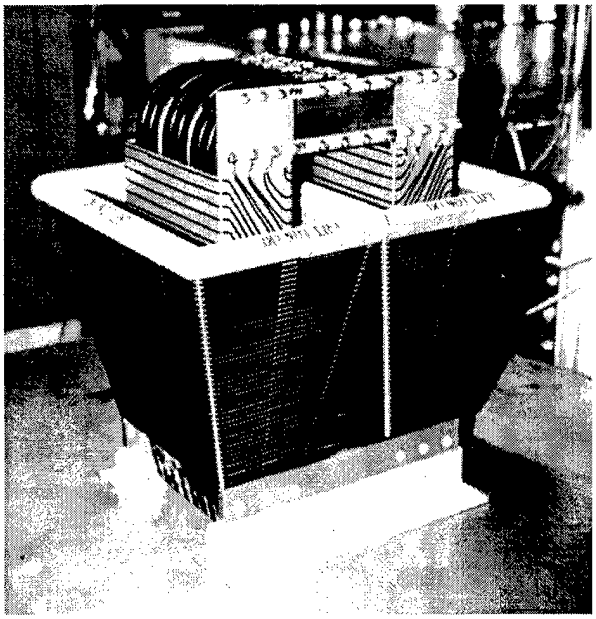


Figure 2. Side view of the pulse transformer.

Parallel primaries and secondaries are wound on each leg providing bifilar characteristics. The core is made up of 3 smaller subcores strapped together. Each subcore is wound from 0.002-inches thick, silectron grain-oriented silicon steel ribbon. Table 1 and 2 shows specifications and parameters of the pulse transformer, respectively.

Table 1. Specification of the pulse transformer

Primary voltage	33.2 kV
Primary current	5320 A
Secondary voltage	465 kV
Secondary current	380 A
Output impedance	1224 Ω
Flat top pulse width	1.5 μs
Pulse droop	3.6 %
Rise time	250 ns
Turn ratio	1:14
Pulse repetition rate	180 pps

Table 2. Parameters of the pulse transformer

Parameters	unit	
Total magnetic flux density swing	T	2.0
Effective magnetic permeability		1,500
Core packing factor	%	89
Area of the core	m^2	0.0102
Distance between layers in the high-voltage side	mm	52
Distance between layers in the low-voltage side	mm	6
Mean magnetic-path length	m	1.04
Effective winding length	mm	260
Circumference of the primary layer in the low-voltage side	mm	538
Number of primary turns	turns	3
Number of secondary turns	turns	42

4 LOW VOLTAGE TEST[4]

4.1 Electrical parameters

The primary inductance, secondary inductance, leakage inductance and the distributed capacitance between the primary and the secondary windings were measured in air with a LCR meter (BK Precision 875A). In the model calculation, the shape of the tapered basket and distribution of voltage along the windings were considered. The measured and calculated values are summarized in Table 3. It should be note that the calculated value does not include the inductance of the shorting strap across the primary. If the shorting is 100nH, 19.6μH should be subtracted from measured value. We are investigating the discrepancy between the calculations and the measurements.

Table 3. Electrical parameters for the pulse transformer

Item	unit	Model calculated value	Measured value
Primary Inductance	μH	130	55.2
Secondary Inductance	mH	25.48	10.81
Distributed capacitance	pF	25	33
Leakage inductance	μH	80.36	122.2

4.2 Transmission characteristics

The transmission characteristics of the pulse transformer were measured in air with the network analyzer(HP 3577A). The test circuit is shown in Figure 3.

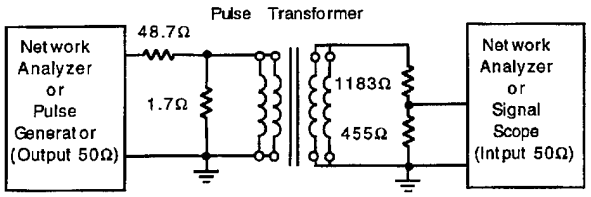


Figure 3. Test circuit.

Figure 4 shows the data of the amplitude and phase for the transformer as a function of frequency. A remarkable feature of the measurement data is a prominent sharp dip at 7.198MHz. This frequency corresponds to $1/2\pi\sqrt{L_D C_D}$. Therefore, the distributed inductance L_D is determined to be 14.8μH by using measured distributed capacitance. The broken curve in this figure shows result simulated by a computer code Micro-Cap IV using electrical parameters of the measured values. The simulation gives a good fit to the data.

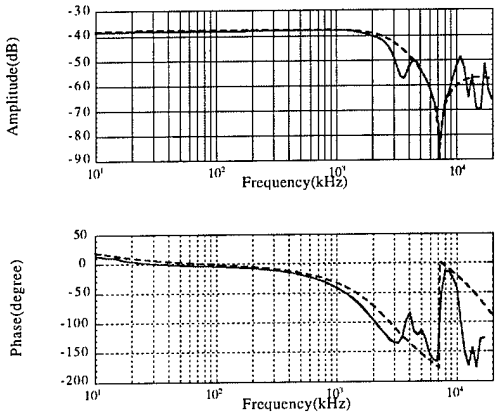


Figure 4. Amplitude and phase for the pulse transformer as a function of frequency.

4.3 Pulse response

A square low-voltage pulse signal with a width of 2μs was fed to the primary side, and the output pulse waveform was measured in air with the oscilloscope as shown in Figure 3. The result is shown in Figure 5. The rise time(10-90%) was 190ns. The broken curve in this figure shows simulated result. The simulation gives a good fit to the data.

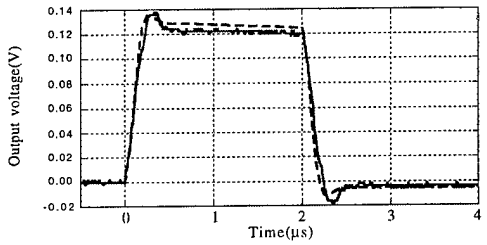


Figure 5. Pulse response of the pulse transformer.

5 HIGH VOLTAGE TEST IN OIL

The high voltage test of the pulse transformer connected to a 5045 klystron has performed. The transformer was installed in the Test Stand 3 modulator oil tank. Figure 6 shows an example of the klystron voltage waveform. The PFN was not adjusted to make a flat-top. A high voltage pulse with a rise time of 380ns(10-90%) was successfully generated. The broken curve in this figure shows simulated result. In this case, a total of distributed capacitance included klystron and tank was estimated to be 250pF.

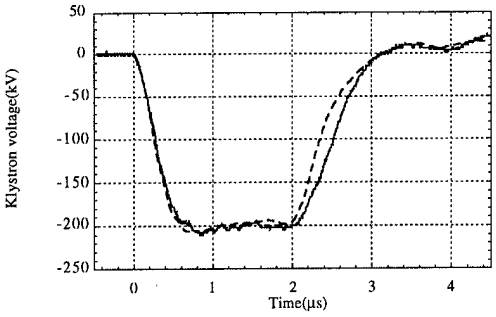


Figure 6. Output pulse waveform at the klystron.

6 SUMMARY

For the NLC klystron pulse modulator, we have improved pulse transformer design of 14 to 1 ratio by tradeoffs among the droop, the core size and the rise time. In the high voltage test of the transformer using a klystron load, a rise time of 380ns was successfully generated. The data calculated by the lumped circuit model are in agreement with the measured data. The model can also be used to optimize the design further.

7 ACKNOWLEDGEMENTS

The authors wish to thank George Caryotakis and Ronald Ruth for their support of this project.

8 REFERENCES

[1] The NLC Design Group: 'Zeroth-Order Design Report for the Next Linear Collider', SLAC-474, 1996.

[2] R. Koontz, M. Akemoto, S. Gold, A. Krasnykh and Z. Wilson: 'NLC Klystron Pulse Modulator R&D at SLAC', this cnference.

[3] N. G Glasoe and J.V. Lebacqz: 'Pulse Generators', Massachusetts Institude of Technology Radiation Laboratory Series, vol. 5, McGraw-Hill Book Company, New York, 1948.

[4] M. Akemoto and S. Gold: 'Analysis of the pulse transformer by a lumped circuit model', to be published.

A FAST 60 kV RESONANT CHARGING POWER SUPPLY FOR THE LHC INFLECTORS

M.J. Barnes, G.D. Wait, TRIUMF
E. Carlier, L. Ducimetière, U. Jansson, G.H. Schröder, E.B. Vossenberg, CERN.

Abstract

The injection kicker systems for the two LHC beams will each consist of four magnets and four pulse forming networks (PFNs), discharged by thyratron switches. Fast resonant charging systems (RCS) are used to charge the PFNs within 1 ms to 60 kV: fast charging minimises the number of unwanted erratically thyratron discharges. The stability and pulse to pulse reproducibility of the PFN voltage must be maintained to a precision of $\leq \pm 0.1\%$. Each RCS consists of a 2.4 mF primary capacitor bank, connected via a Gate Turn-Off thyristor (GTO) and a 1:23 step-up transformer to two PFNs, each with an effective capacitance of 0.96 μF. The PFNs are discharged 400 μs after the end of the charging period into the kicker magnets. The RCS include novel features such as a GTO used in Gate Assisted Turn-off (GAT) mode and a low-leakage inductance, high voltage, step-up pulse transformer. This paper presents a basic design for the RCS, and the optimisation of the electrical circuit using PSpice. The RCS are designed, constructed and tested at TRIUMF in collaboration with CERN as part of the Canadian contribution to the LHC project.

1 INTRODUCTION

The European Laboratory for Particle Physics (CERN) is designing a Large Hadron Collider (LHC) to be installed in an existing 27 km circumference tunnel. The LHC requires Injection Kicker Systems, devices for fast deflecting the incoming particle beams onto the accelerator's circular trajectory. Two pulsed systems, of 4 magnets and 4 PFNs each, are required for injection[1,2]. The injection sequence, during normal operation, consists of 12 pulses with a period of 16.8s. However the RCS will be tested at 0.2 Hz, continuous. Fig. 1 shows a schematic of the RCS and the notation utilised for component names.

The RCS will simultaneously charge two 5 Ω PFNs, which are connected in parallel (Fig. 1), to 60kV before the thyratrons are triggered. The stability and pulse to pulse reproducibility of the PFN voltage must each be maintained to a precision of better than $\pm 0.1\%$[3]. Each RCS will have a 2.4 mF storage capacitor bank ($C_{storage}$) charged up to 2.5 kV. The storage capacitor bank is connected to the primary of a 1:23, low leakage inductance, step-up transformer, via a GTO and series diode. Each of two 5 Ω PFNs is connected to the secondary of the transformer via a cable, a charging resistor (R_{charge}) and a diode stack (D_{charge}). Each 5 Ω PFN can be considered to be a 0.96 μF capacitor during the charge cycle. The PFNs are discharged through a kicker magnet using thyratrons.

When the GTO is gated-on, a resonance is excited between the storage capacitor bank, the PFN capacitance and the leakage inductance of the pulse transformer. Energy is transferred from the storage capacitors to the PFNs. When the PFN voltage has reached its maximum value the high voltage diode stack, connected in series with each PFN, stops the resonance and electrically disconnects the charged PFN from the transformer. The GTO switch turns-off, and the storage capacitor bank is recharged, at constant current, in a few seconds.

Fig. 2 shows typical GTO current, PFN voltage, and the secondary voltage associated with the pulse transformer. The period of time when the positive voltage across the transformer secondary is increasing in magnitude is referred to as the *charge time*; the period when the positive secondary voltage is reducing in magnitude is referred to as the *backswing time*. The *effective charge time* (ECT) is the sum of the *charge time* and *backswing time*.

RCS's are used to charge the PFNs in order to reduce as much as possible the number of erratic thyratron turn-ons.

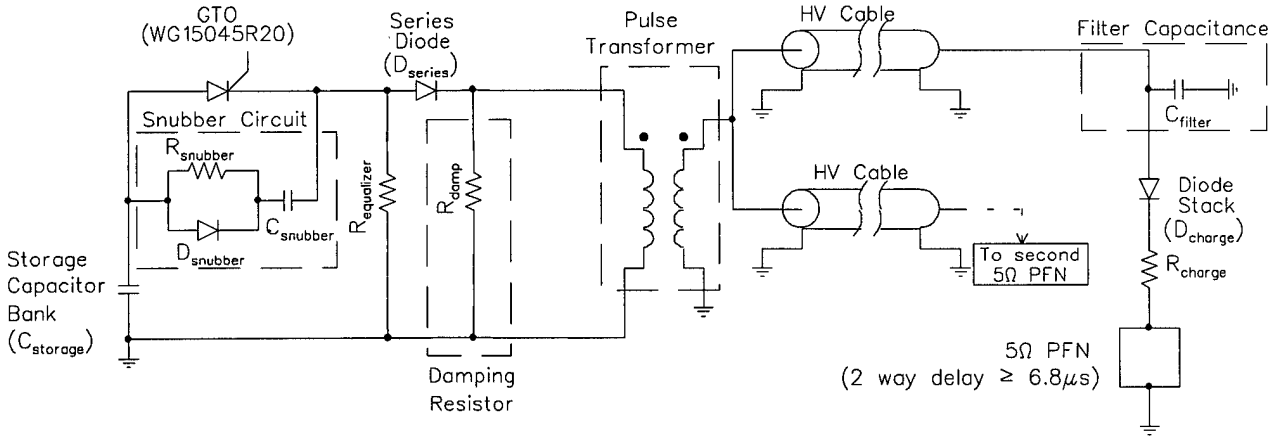


Figure 1. Schematic of Resonant Charging Supply

0-7803-4376-X/98/$10.00 © 1998 IEEE

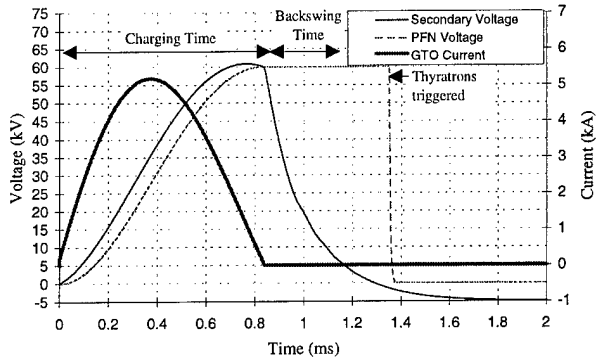


Figure 2. Typical secondary voltage, PFN voltage and GTO current waveforms

This number is dependent upon the time period that there is high voltage across the thyratrons, hence it is advantageous to minimise the ECT of the RCS.

2 POWER SEMICONDUCTOR SWITCH

If a thyratron turns-on erratically, during the recovery period of the power semiconductor switch, the semiconductor can be subjected to a forward dV/dt of 90 V/μs[4]. An SCR with suitable ratings for use in the RCS has a turn-off time (t_q) of typically several hundred microseconds. During the recovery period, forward voltage cannot be applied across the semiconductor switch without it turning on, and an SCR has a limited capability to withstand positive dV/dt when forward voltage is reapplied. A GTO used in GAT mode, with suitable ratings for use in the RCS, would have a t_q time of typically 10 μs. In GAT mode negative voltage is applied to the GTO gate just before the main current falls to zero. A suitable GTO is the WG15045R20[5].

3 SNUBBER COMPONENTS

The purpose of the snubber circuit is to limit the dV/dt across the GTO to an acceptable value. During normal operation, the ECT is increased at a rate of 32 μs/μF of the snubber capacitor value, and thus it is desirable to minimise the value of the snubber capacitor. A detailed consideration of several abnormal operating conditions resulted in the choice of a snubber capacitor with a nominal value of 2 μF. The 2 μF limits the maximum predicted dV/dt across the GTO, when a thyratron turns-on erratically during the recovery time, to 90 V/μs[4] which is believed to be a safe value for the WG15045R20.

The snubber resistor limits the magnitude of discharge current, from the snubber capacitor, into the GTO. The value of the snubber resistor is a compromise between a large value to limit this discharge current, and a small value for a relatively short time-constant for discharging the snubber capacitor. If the time-constant is too long, the snubber capacitor may still have a significant voltage across itself following the normal loop of conduction current through the GTO. A nominal snubber resistor value of 50 Ω represents a reasonable compromise.

4 DAMPING RESISTOR

The purpose of the damping resistor is to reduce the ECT and therefore the size of the transformer too. Without a damping resistor the ECT is 2100 μs, and the transformer volt-time integral (VTI) approaches 79 V.s., referred to the terminals of the secondary winding.

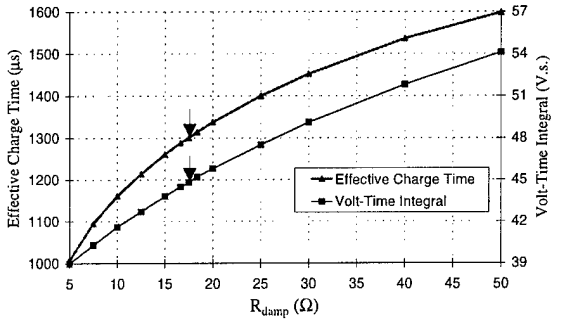


Figure 3. ECT and VTI as a function of the value of the damping resistor

Fig. 3 shows plots of ECT and the transformer VTI as a function of the damping resistor value (R_{damp}). Reducing the resistance increases both transformer reset time and the initial current into the GTO at turn-on: the reset time is the elapsed time at which the transformer core is reset to its initial value. In addition, dissipation in the damping resistor increases significantly with low resistance values (Fig. 4). The peak negative secondary voltage, following backswing, reduces as the resistance value is decreased. A low amplitude of negative voltage reduces the electrical stress on the secondary components.

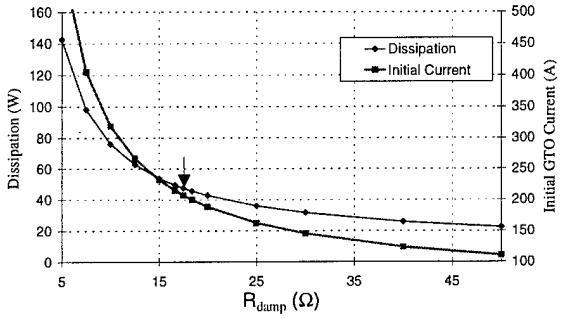


Figure 4. Damping resistor dissipation and initial GTO current as a function of the resistor value

A damping resistor value of 17.5 Ω±5% gives a reasonable compromise: 17.5 Ω results in a conservative value of initial current through the GTO immediately following turn-on (230 A), a transformer VTI of 45 V.s., an acceptable ECT (1300 μs), a minimum secondary voltage of –6 kV, a damping resistor dissipation of 48 W, and a reset time of 60 ms.

5 TRANSFORMER TURNS RATIO

The charge time is determined approximately by the leakage inductance of the transformer and the effective capacitance. The effective capacitance during the charge time is approximately equal to the series sum of the PFN

capacitance, referred to the primary, and the value of the storage capacitor bank. The capacitance of the PFN is determined by the impedance of the PFN and its delay. Choosing a maximum storage capacitor voltage minimises the capacitance of the storage capacitor bank, and the charge time. A single WG15045R20 GTO is used for the RCS; Westcode recommend that the GTO be used with a DC blocking voltage of not more than 2.8 kV in the RCS. The transformer turns-ratio influences the ECT for the PFN. To evaluate the optimum, PSpice[6] simulations have been carried out[7,8]. For the optimisation it has been assumed that the value of the leakage inductance referred to the primary of the transformer reduces in inverse proportion to the square of the turns ratio, which can be true over a limited range[9]. However the value of the PFN capacitance referred to the primary of the transformer increases in proportion to the square of the turns ratio. The backswing time is dependent upon the sum of the parasitic capacitance of the secondary winding, and the capacitance of each of the HV cables and filters. This capacitance referred to the primary winding increases in proportion to the turns ratio squared: hence the backswing time increases with increasing turns ratio. Hence the optimum value for the turns ratio is dependent upon the effective capacitance during the backswing time. Fig. 5 shows a plot of both storage capacitance value and ECT as a function of turns-ratio. To limit the nominal value of the storage capacitor bank to 2.4 mF, a turns ratio of 1:23 is chosen.

6 CHARGING RESISTOR

The purpose of the charging resistor is to both limit fault current if the thyratrons erratically turn-on during the charging cycle and, together with the filter capacitors,

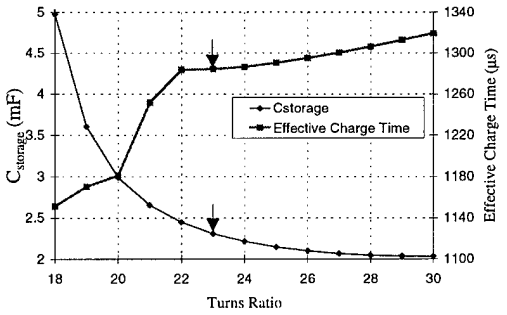


Figure 5. Storage capacitor value and ECT as a function of transformer turns-ratio

limit maximum dV/dt across the transformer secondary if the Dump Switch (DS) thyratrons turn-on erratically.

Without filter capacitors, the secondary dV/dt would be almost four times greater than that recommended for the transformer[7,8]. A time-constant of approximately 360 ns, for the charging resistor and filter capacitor, limits the maximum dV/dt across the transformer secondary, when both DS thyratrons turn-on simultaneously from maximum PFN voltage, to below 120 kV/µs[7,8]: this dV/dt is safe[9]. The optimum value of charging resistor has been determined using PSpice. The storage capacitor bank pre-charge voltage was selected to give the required PFN voltage. The time-constant of the charging resistor and filter capacitor was kept as 360 ns. The pre-charge on the storage capacitor bank is below 2.7 kV for charging resistor values of less than 100 Ω.

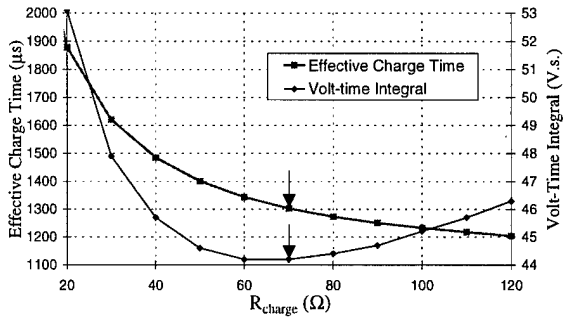


Figure 6. ECT and VTI versus the value of the charging resistor (C_{filter} x R_{charge} = 360 ns)

Fig. 6 shows a plot of ECT and VTI versus the value of charging resistor. A minimum VTI is required for a value in the range of 60 Ω to 70 Ω, and the VTI curve climbs less steeply for values greater than 70 Ω. In addition the ECT decreases for increasing values of charging resistor. Thus a nominal value of 70 Ω has been selected.

7 CONCLUSION

This paper has described the process employed for optimising component values for a 60 kV RCS for the CERN LHC inflector system. The often conflicting requirements have been considered in selecting component values.

REFERENCES

[1] L. Ducimetière, U. Jansson, G.H. Schröder, E.B. Vossenberg, M.J. Barnes, G.D. Wait. "Design of the Injection Kicker Magnet System for CERN's 14 TeV Proton Collider", Tenth IEEE International Pulsed Power Conference, Albuquerque, 1995, pp1406-1411

[2] M.J. Barnes, G.D. Wait, L. Ducimetière, U. Jansson, G.H. Schröder, E.B. Vossenberg, "Kick Stability Analysis of the LHC Inflectors", EPAC96, June 1996, Barcelona. pp2591-2593.

[3] Technical Specification SL/Tech.Spec.96-6(BT), "Resonant Charging Power Supply For LHC Injection Kicker Prototype", Prévessin, 11 May 1996

[4] M.J. Barnes, G.D. Wait, L. Ducimetière, E. Carlier, U. Jansson, G.H. Schröder, E.B. Vossenberg, "Operation Modes of the Fast 60 kV Resonant Charging Power Supply for the LHC Inflectors", Proc. of 11th IEEE Pulse Power Conference, Baltimore, June 1997.

[5] Westcode Semiconductors, "Gate Turn-Off Thyristor (Symetrical blocking type.) Types WG15026Rxx to WG15045Rxx", August 1996, Rat.Rep.96G9, Issue-3.

[6] MicroSim Corporation, 20 Fairbanks, Irvine, California. CA 92718. Tel (714) 770 3022.

[7] M.J. Barnes, G.D. Wait, "Design and Optimization of the 66 kV Resonant Charging Power Supply for the LHC Injection Kickers", Design note TRI-DN-96-22, December 1996.

[8] M.J. Barnes, G.D. Wait, "Design and Optimization of a 60 kV Resonant Charging Power Supply", Design note TRI-DN-96-16, August 1996.

[9] Private communication with Magne Stangenes, Stangenes Industries Inc., 1052 East Meadow Circle, Palo Alto, California 94303

THE APPLICATION OF SATURATING INDUCTORS FOR IMPROVING THE PERFORMANCE OF THE CERN PS KICKER SYSTEMS

G.D. Wait, M.J. Barnes, TRIUMF, Vancouver, Canada,
K.D. Metzmacher, L. Sermeus, CERN, Geneva, Switzerland

Abstract

Kicker magnets are used for injection and extraction in the CERN PS. The addition of the LHC facility to the complex of accelerators at CERN requires an improved performance of the existing kicker magnet systems in the CERN PS. The injection kicker field must rise and fall from approximately 1% to 99% of full strength during the 96ns time interval between bunches, whereas the extraction kicker field must rise from approximately 0.5% to 99.5% of full strength during a gap of 121ns created in the beam. The kicker magnet systems require pulse forming network (PFN) voltages of up to 80kV. Displacement current arising from the turn-on of a multi-gap thyratron can significantly increase the effective rise-time of the kick. Saturating inductors can be used to reduce both the effect of the displacement current and the rise-time of the main current pulse. This paper describes the results of measurements on a system which includes saturating inductors. Some of the measurements are compared with theoretical predictions.

1 INTRODUCTION

Three gap deuterium filled thyratrons[1] are used as switches for the PS kicker magnet systems. The individual gaps in a three gap thyratron break down in sequence. Initially the gap closest to the cathode conducts and the full PFN voltage is shared between the centre and anode gaps. Approximately 40ns to 50ns later the centre gap starts to conduct and the full PFN voltage builds up across the anode gap. The collapse of voltage across one gap causes a displacement current to flow in the parasitic capacitance of off-state gaps. The displacement current flows in the external circuit and hence through the kicker magnet, and thus can increase the effective rise-time of the kick. One promising method of decreasing the effect of the displacement current involves the use of a "displacement current saturating inductor" (DISI) connected on (or near) the input of a kicker magnet. A "switching loss saturating inductor" (SLSI) may be connected adjacent to the thyratron anode to reduce the switching losses[2], so that thyratron life can be extended. This also improves the pulse voltage rise-time[3] and permits the adjustment of the thyratron reservoir voltage without any change in rise-time[4].

2 MEASUREMENTS

2.1 Circuit

Recent measurements have been carried out at TRIUMF in collaboration with CERN as part of the Canadian contribution to the LHC project. The test circuit consists of an 80kV pulse generator which can deliver 40kV pulses into a kicker magnet. The pulse generator is a 30Ω system, on loan to TRIUMF from CERN PS Division, and has been modified to permit testing with saturating inductors (SLSI) connected on the thyratron anodes (fig.1). The kicker magnet is a 10 cell, 31.5Ω prototype transmission line kicker magnet which was built at TRIUMF[5] as part of the KAON factory project definition study. This kicker magnet is based on the design of those of the CERN PS division[6]. The kicker magnet is housed in a vacuum tank and operated with PFN voltages of 60kV and 80kV for the tests described here. Measurements were performed with and without saturating inductors and with the kicker terminated in either a short-circuit or 30Ω. The circuit configuration is shown in figure 1. The one-way delay of τ_x and τ_m is 220ns and 26ns respectively. τ_s is 36ns for a resistive terminator and is 6ns when a short-circuit is placed at the output to the kicker magnet, at the Lemo connector that is at the base of the vacuum tank.

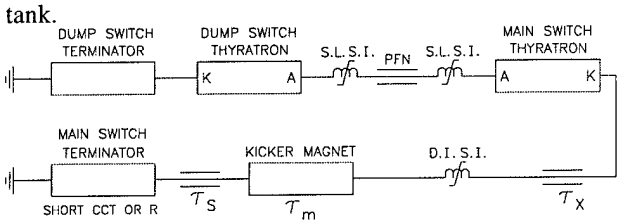


Figure 1. Block diagram of pulse generator and kicker magnet test system.

The inductance characteristics of the saturating inductor is related to the cross-sectional area (CSA) of the ferrite. Ferrite toroids, manufactured from CMD5005[7], were connected on the input to the kicker magnet. The DISI ferrite is quite thin (2.5mm), with an inner diameter of 40mm and a total CSA of 12cm^2. Previous measurements[8] have shown that the pre-pulse field is improved when 12cm^2 of thin ferrite is used, rather than 12cm^2 of thick (10mm) ferrite. The SLSI consists of 60cm^2 CMD5005 ferrite with an inner diameter of 1cm and an outer diameter of 7cm. The stray capacitance from the SLSI to ground enhances a 3rd pre-pulse displacement current peak in the voltage pulse[4].

2.2 Measurement System

Capacitive pickups were installed on the high voltage capacitance plates at the input and output of the magnet to measure the input (V_{in}) and output (V_{out}) voltages. The field in the kicker magnet is determined from $\int(V_{in}-V_{out})dt$. An analogue integrator was connected on a channel of a

0-7803-4376-X/98/$10.00 © 1998 IEEE

Tektronix TDS724A digital oscilloscope. The integrator time constant is approximately 2.6μs. This time constant is a compromise between too small a value, which results in considerable droop of a flat-top voltage, and too large a value which results in parasitic inductance of the integrator affecting the measured signal[8].

Signal averaging methods were employed in the TDS724A oscilloscope so that each waveform measured was the result of averaging 200 pulses. This improves the signal to noise ratio and permits accurate measurements of the pre-pulse displacement current. Measured data was transferred to a PC for processing. Software, which was developed at TRIUMF, reads in the data, and provides data manipulation functions which include: correction for droop of the analogue integrator; normalisation and phase advance/delay. The files are then read into Probe[9] for further processing.

The voltage droop associated with the analogue integrator is compensated for by analysis methods presented in a previous paper[8]. There is also a small portion of the signal (2%) which is due to inductive coupling in the signal cables situated inside the vacuum tank. The inductive coupling component was derived from measurements with the magnet terminated with a short circuit. This small correction was applied to the voltage waveforms from the capacitive pickups before calculating the field.

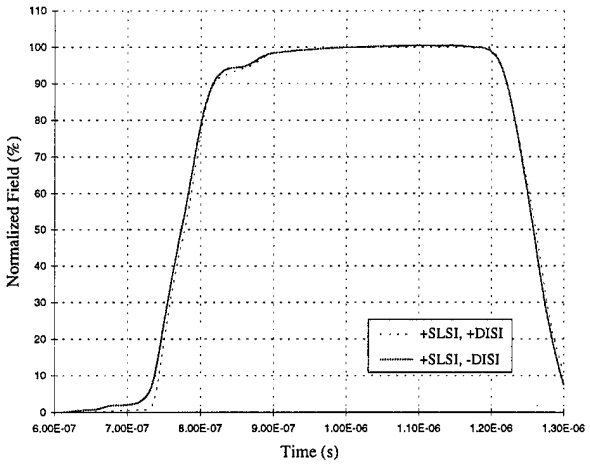


Figure 2. Magnet field at 80kV PFN with MS and DS SLSI, in a 31.5Ω kicker terminated with a short circuit, with and without a 12cm^2 DISI.

2.3 Measurement Results

Figure 2 shows the results of measurements with a PFN voltage of 80kV, a short-circuit terminator, a MS SLSI and a DS SLSI. The dashed line shows the kicker magnet field with 12cm^2 DISI. The solid line shows the field without a DISI. Note that there is a notch (undershoot) at the beginning of the flat-top of the field. This is due to a mismatch at the input to the magnet caused by the inductance of the housing for the DISI ferrite. The short-circuit is applied external to the vacuum tank and thus there is an inductance to ground at the output which also contributes a small amount to the notch in the pulse. PSpice calculations showed that this notch can be corrected by installing speed-up networks at the input and the output to the magnet each consisting of 200pF in series with 30Ω to ground.

PFN (kV)	MS SLSI	DISI	Term	0.5% rise-time (ns)	1.0% rise-time (ns)
60	no	no	R	152	144
60	yes	no	R	166	158
60	no	yes	R	105	76
60	**yes**	**yes**	**R**	**117**	**71**
60	no	no	SC	170	142
60	yes	no	SC	180	153
60	no	yes	SC	125	88
60	**yes**	**yes**	**SC**	**120**	**91**
80	no	no	R	156	148
80	yes	no	R	165	157
80	no	yes	R	111	81
80	**yes**	**yes**	**R**	**111**	**65**
80	no	no	SC	176	150
80	yes	no	SC	183	155
80	no	yes	SC	130	93
80	**yes**	**yes**	**SC**	**128**	**89**

Table 1. Measured field rise-times to 90% in the TRIUMF prototype kicker magnet under various conditions.

Rise-time measurements were performed without any speed-up networks. Since there is a notch in the flat-top of the pulses we present the data with rise-time definitions of 0.5% to 90% and 1% to 90%. This permits a consistent comparison of the effect that the ferrites have on the pre-pulse displacement current. Table 1 shows field rise-times for both 60kV and 80kV on the PFN, with and without ferrites, with a resistive terminator (R) and with a short-circuit (SC) terminator. In all cases there is a DS SLSI but this will not influence the front edge of the pulse. The DS SLSI reduces ripple at the trailing edge of the flat-top of the pulse which is caused by the DS anode displacement current.

In table 1 the rows in bold face are those in which there is both a DISI and a MS SLSI. The rise-times for 60kV and 80kV are the same. The short-circuit rise-times are longer than the resistively terminated rise-times as is expected since the fill-time is 64ns (52ns+12ns for the output stripline) for the short-circuit case compared with 26ns for the resistively terminated case. There is a marked improvement in the rise-times if a DISI is used. The MS SLSI with no DISI causes an increase in the rise-time, due to a large 3rd displacement current peak; this shows up in the voltage waveforms but is not apparent in the integral, since the integration tends to blend the 3rd peak into the rising edge. The rise-time from 0% to 0.5% is 90ns when a DISI is installed for the short circuit case (fig. 3), so that a very small error in pre-pulse amplitude can introduce a large error in rise-time, depending on the rise-time

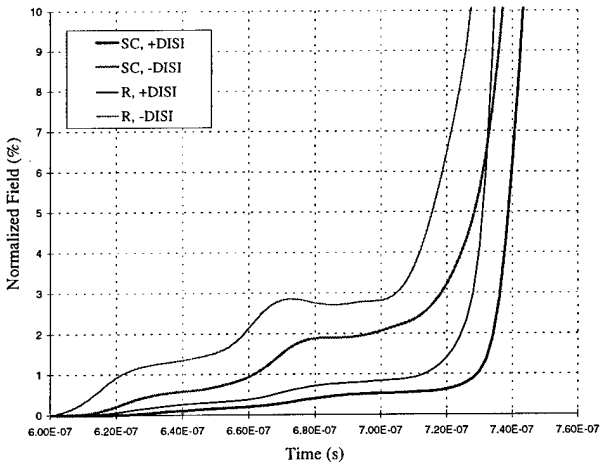


Figure 3. Pre-pulse kicker field with 80kV PFN, DS and MS DISI, with and without a 12cm^2 DISI, with a short-circuit terminator or a resistive terminator.

definition. This probably explains why for some of the cases, a slight improvement of rise-time occurs when there is a DISI with a MS SLSI, and in other cases it appears to improve without a MS SLSI.

Figure 3 shows the pre-pulse field for an 80kV PFN voltage with a MS SLSI installed. The magnitude of the pre-pulse field with no DISI is 2.8% (2%) of the full field with a resistive (short-circuit) terminator. The magnitude with a 12cm^2 DISI is 0.9% (0.6%) of the full field with a resistive (short-circuit) terminator. The measured pre-pulse field with a resistive terminator and without any ferrites is 3.2% of the full field (fig. 4)

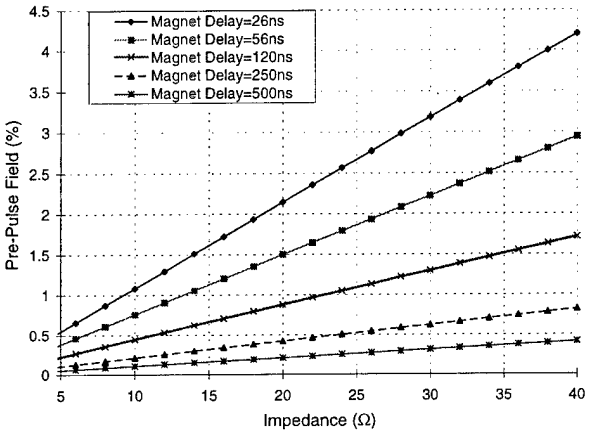


Figure 4 Calculated pre-pulse field amplitude as a function of magnet impedance and delay time without ferrites.

3 CALCULATIONS

The magnitude of the pre-pulse field, due to displacement current is dependent on the impedance of the kicker system. Fig 4 shows a plot obtained from PSpice calculations of the pre-pulse field versus magnet impedance for various magnet fill-times for the case without a SLSI or DISI in the circuit. The flat-top current in a kicker magnet, for a fixed PFN voltage increases as the magnet impedance reduces but the displacement current is almost constant. Therefore the amount of ferrite required to reduce the pre-pulse ripple is reduced for low impedance systems.

Theoretical calculations were performed to optimize the PS injection kicker (FAK) configuration, which is a 15Ω system operating at 80kV PFN voltage, using a PSpice model[9] of a thyratron[10]. The fill-time of the FAK with a resistive terminator is 56ns, which is to be compared with 64ns for the short-circuit TRIUMF magnet. The goal is to achieve a 0.5% to 99.5% field rise-time of 121ns. The simulation carried out includes a DISI where the CSA has been optimised to 3cm^2. However experience with the KAON prototype 30Ω kicker magnet at TRIUMF[8], operating at a PFN voltage of 50kV, showed that the DISI is slightly less effective at suppressing the effects of displacement current than predicted; thus 4cm^2 may be required for the FAK. Including a CSA of 3cm^2 reduces the theoretical field rise-time from 184ns to 134ns. In addition the values of four speed-up component networks have been optimized (with lossy transmission lines modelled). The resulting predicted field rise-time (0.5% to 99.5%) is 127ns.

4 CONCLUSION

The measurements show that there is considerable reduction in the field rise-time with the inclusion of a DISI in the circuit ahead of the kicker magnet. The use of a SLSI has only a slight benefit for the rise-time. However a MS SLSI will cause a reduction in thyratron switching losses and permits the reservoir voltage to be adjusted without affecting the rise-time. The measurements confirm calculations and thus show that the calculations for the PS kicker are quite realistic.

REFERENCES

[1] EEV, Chelmsford, Essex, U.K

[2] L. Ducimetière, D.C. Fiander "Commutation Losses of a Multi-gap High Voltage Thyratron". IEEE Conf. Record of the 1990 19th Power Modulator Symposium. pp248-253

[3] M.J. Barnes and G.D. Wait, "Improving the Performance of Kicker Magnet Systems" Proc. of XVth International Conference on High Energy Accelerators, Hamburg, July 1992, pp191-193.

[4] G.D. Wait and M.J. Barnes, "Thyratron Lifetimes, a Brief Review" presented at the Modulator-Klystron Workshop at SLAC for future Linear Colliders, SLAC Report 481, Oct, 1995.

[5] M.J. Barnes and G.D. Wait. "Comparison of Measured and Predicted Inductance per Cell for a Traveling Wave Kicker Magnet" Pres. at EPAC, Barcelona, June 1996, pp2588-2590.

[6] D.C. Fiander, K.D. Metzmacher, P. Pearce, "Proc. of the KAON PDS Magnet Design Workshop", Vancouver, Oct. 1988, pp71-79.

[7] Ceramic Magnetics Inc., New Jersey, USA

[8] M.J. Barnes and G.D. Wait, "Effect of Saturating Ferrites on the Field in a Prototype Kicker Magnet", Proc. of EPAC, London, June 1994, pp2544-2546.

[9] MicroSim Corporation, 20 Fairbanks, Irvine, California 92718. U.S.A.

[10] M.J. Barnes and G.D. Wait, "A Mathematical Model of a Three-Gap Thyratron Simulating Turn-On", Proc. of the 9th Int. Pulsed Power Conf., Albuquerque, June 1993, pp293-296.

AUTHOR INDEX

A

Abramenko, N.I. 2773
Abramovich, A. 906
Abs, M. 3816, 3857
Adachi, T. 3470
Adolphsen, C. 439, 554, 608, 1673, 1676, 2119, 2186, 2256, 2580, 2852, 3027, 3042, 3192
Agafonov, A.V. 1299, 1302, 3141
Ahn, H. (JAERI) 648, 760
Ahn, H. (LANL) 1012
Ahrens, L. 69, 89, 98, 101, 959, 965, 1460, 1478
Aiello, G. Roberto 2113, 2122
Aizatsky, M.I. 3810
Akai, K. 2902, 2974, 2977, 2986, 3069, 3087, 3090
Akasaka, N. 455, 530, 533, 536, 1831, 2902, 2974, 2977, 2986, 3069
Akemoto, M. 587, 1319, 1322
Akre, J. 2067
Akre, R. 506, 1569, 3021, 3024, 3027
Alessi, J. 89, 162, 970, 1460, 2023, 2711
Alexahin, Y. 312
Alexeev, N.N. 261
Alford, O. 3562
Alforque, Rudy 3693
Allen, C.K. 1526
Allen, C.W. 596
Allen, M. 3004
Allen, T. 3796
Alley, R. 1981, 2849
Allison, Paul 1138, 1141, 1144
Allison, S. 439, 2359, 2470, 3027
ALS Stability Task Force 784
Alzofon, D. 2253
Amano, D. 1266
Amano, S. 757
Amatuni, A.Ts. 690, 693, 695
Ambrosia, M. 3872
Amelia, J.-C. 3816
Ames, F. 947
Amman, M. 3807
An, Y. 402, 880
Anamkath, H. 3796
Anders, A. 2678
Anderson, D.E. 590, 3734
Anderson, E.B. 369
Anderson, K. 3837
Anderson, S. (SLAC) 596
Anderson, S. (UCLA) 736, 1965
Anderson, S. (IUCF) 2968
Andersson, Å. 345
Ando, A. 757, 1385
Andreev, V.A. 1087, 1090
Andreev, V. (Dubna) 2452
Andrews, D.E. 3413
Andrianov, S. 2419
Anerella, M. 3338, 3356
Anferov, V.A. 78
Ang, Z. 3377
Ankenbrandt, C. 144, 396, 399
Anthouard, P. 1254, 1257
Ao, H. 1203
Appleton, Bill R. 20
Arai, S. 938
Arakaki, Y. 938, 1557
Arakawa, D. 1548, 1599, 1908
Araki, N. 201
Araki, S. 587
Archuleta, T.A. 2829
Arduini, G. 168, 171, 1858
Arensburg, A. 906
Areti, H. 3681
Ärje, J. 2672
Arnett, D. 2253
Arnold, J. 1813
Arroyo, F.C. 3476
Artoos, K. 3586
Arutunian, S.G. 695
Asaka, T. 2511, 2814
Asano, K. 2908, 3087, 3090
Asaoka, Seiji 2458, 3616
Aspenleiter, J. 2947, 3497
Assadi, S. 127, 1771, 2323
Assmann, R. 449, 497, 500, 503, 506, 608, 687, 1331, 1523, 2119, 2580
Atkinson, R. 439, 3042
Aune, B. 425
Ausset, P. 2720
Autin, B. 1362, 2314
Averill, R. 348, 2274, 3407, 3743
Avrakhov, P.V. 3126
Avramopoulos, H. 1042
Avsec, S. 2481
Ayzatsky, N.I. 651
Azorsky, N.I. 3126

B

Baartman, R. 956, 1415, 2675, 2778
Baba, H. 530, 593
Babcock, R. Chris 2562
Babzien, M. 621, 675, 2687
Bacher, R. 2446
Bagnato, O.R. 1209
Bai, M. 1346, 1460, 1478
Bailey, J.D. 1177
Bailey, R. 66
Bailey, V.L. 1251
Baine, M. 611
Baiod, R. 3272, 3278, 3288
Baird, S. 979, 982
Bajikar, S. 461
Baker, G.D. 190
Bakhtiari, Shervin 3842, 3845
Balakin, V.E. 3126
Balakirev, V.A. 651
Ball, M. 1481, 2081
Ball, M.J. (Penny) 3404
Balling, P. 1984
Baltadoros, D. 1042
Bane, K. 506, 509, 515, 554, 608, 903, 1673, 1738, 1789, 1873, 1876, 2189, 2580
Barale, P. 3312
Barbarosou, M. 1042
Barber, R.L. 1150
Bardy, J. 1254, 1257
Barillas, G. 3024
Barlow, D. 83, 193, 3309
Barnard, John J. 1929, 1932
Barnes, B. 2326
Barnes, John N. 86
Barnes, M.J. 1325, 1328
Barnes, P. 3075
Barni, D. 1126
Barov, N. 627, 1996
Barraza, Juan 2210
Barry, W. 772, 2344
Bartelson, L. 3461
Barth, W. 1897
Bartolini, R. 1469, 2568
Barton, D. 101
Bassato, G. 1129
Batskikh, G.I. 950
Battistella, A. 1129
Batygin, Y. 941, 1786, 1941
Bauer, G.S. 3785
Baumgartner, W. 439, 3042
Baynham, E. 3386
Bazzani, A. 2568
Beauvais, P-Y. 2720
Bechstedt, U. 1048
Bedermann, K. 3123
Beebe, E. 2711
Beebe-Wang, J. 970, 1882
Beeckman, W. 1045, 3816
Behne, D. 3622
Belkacem, A. 150
Bellato, M. 1129
Bellomo, G. 1126
Bellomo, P. 315

Belochitskii, P. 312, 1382
Belomestnykh, S. 1718, 3075
Belorgey, J. 3365
Belser, C. 3619
Ben-Zvi, I. 645, 675, 1197, 1971, 2687, 2790, 2793, 2843, 2846
Benapfl, M. 3568
Bendall, R.G. 1021
Benedikt, M. 1376, 1379
Benesch, J. 3108, 3758
Benjegerdes, R. 3212
Benson, S. 912
Benveniste, V.M. 2767
Berezin, A.K. 651
Bereznitsky, S.L. 261
Berg, G.P.A. 264, 2737, 3303
Berg, J.S. 107, 1712
Berg, W.J. 871
Bergbusch, P. 967
Berger, J.C. 2696
Bergl, J. 2493
Berkvens, P. 3571
Berlin, D. 979
Bernal, S. 1650, 1855, 1959, 2143
Bernard, M. 2823
Berners, D.P. 1296
Bertazzo, L. 1129
Bertenelli, F. 3586
Bertolini, L. 3562, 3619, 3622
Bertsche, K.J. 3263, 3283
Berz, Martin 2416
Besler, C. 315
Bestea, V. 3854
Bezzon, G. 1129
Bharadwaj, V. 315, 903, 2855
Bhat, C.M. 243, 1590, 3242, 3245, 3672
Biallas, G. 3333, 3752
Bickley, M. 2128
Biedron, S.G. 324
Bieniosek, F.M. 234, 1403, 3837
Bigelow, N.P. 2867
Biino, C. 80, 165
Billan, J. 3365, 3377
Billen, J.H. 1171, 3138
Biller, Ye.Z. 3810
Billing, Michael 2317
Billquist, P.J. 2702
Bilodeau, D. 2081
Bini, C. 572
Biryukov, V. 177, 179, 249
Bish, P. 3212
Bishofberger, K. 736
Bisoffi, G. 1087, 1129
Bisognano, J. 1641, 1644, 2128
Bissiato, E. 1087, 1129
Bizek, Hana M. 1493, 1496
Bjork, M. 2253
Bjorklund, E.A. 2464
Blackmore, E.W. 3831
Blank, M. 3150, 3180
Blas, F. 973
Blaskiewicz, M. 89, 959, 970, 1554, 1578, 1581
Blell, Udo 1727
Bleser, E. 89
Blind, B. 83, 193, 270, 1012, 1015, 3728
Bliss, N. 3598
Blokhin, A.I. 258
Blokland, W. 2032
Blondel, A. 366
Blosser, H. 1054, 1057, 1060
Blum, E.B. 3494
Blumberg, L. 159, 970
Bobyleva, L.V. 488
Bocchetta, C.J. 826, 829, 2353, 2356
Boer-Rookhuizen, H. 1063
Bogacz, S.A. 1697
Bogard, D. 2720
Bogdanovich, B. 276, 2773, 3869
Böge, M. 366, 1356, 1436, 1439
Boggia, A. 2729
Bohl, T. 1813, 1849
Bohn, C. 909, 1641, 1644, 2693
Boillot, J. 979, 982
Bollen, G. 947
Bolotin, I. 1313
Bolshakov, A.E. 261
Bong, E.L. 2253
Bong, P. 439
Bongardt, K. 988, 1846
Bonnafond, C. 1254, 1257
Borasi, F. 2696
Borchard, P. 3180
Borden, M.J. 187, 1012
Bordry, F. 66
Boriskin, V.N. 3810
Borland, M. 742, 2052, 2410, 2487, 3224
Bosch, R.A. 862
Boscolo, A. 2011
Bosland, P. 817
Bosotti, A. 1126, 3657
Bosser, J. 944, 979
Bossert, R. 3389
Botman, J.I.M. 1036, 1200
Bottura, L. 66, 3377
Bourat, C. 1191
Bourdon, J.C. 2823
Boussard, D. 2879
Bovet, C. 1987
Bowden, G. 464, 672, 3330
Bowling, Bruce 2526
Bowman, J. 3622
Boyce, R. 838
Bradley, S. 348, 2099
Bradley III, J. 1147
Brandt, D. 312
Braun, H.H. 479
Braun, J. 3123
Brautti, G. 2729
Bravin, E. 366
Breizman, B.N. 1635
Brennan, J.M. 69, 89, 396, 399, 967, 970, 1030
Brennan, S. 838
Bretin, J.-L. 225
Bricault, P. 925, 956, 1105, 1194, 2675
Brinkmann, R. 336, 1572, 1679
BRNBF Project Group 1224
Broadbent, A.J. 3413, 3494
Brodowski, J. 3233
Broere, J. 944, 3123
Bromberek, D. 2929
Broome, T.A. 1021
Broome, W. 2305
Brouet, M. 979
Brown, B.C. 994, 3242, 3245, 3254, 3257, 3260, 3263, 3269, 3286, 3288
Brown, I. 2678, 3752
Brown, K. (BNL) 69, 89, 98
Brown, K.(TJNAF) 2271
Brown, K.A. 1460, 2149, 2213, 2302
Brown, Nathan A. 1894, 2562
Brown, R.J. 2737
Brown, R.L. (SLAC) 2186
Brown, R.L. (BNL) 3230
Brown, Thomas A. 2559
Brown, V. 439
Brown, W. 2690
Browne, J.C. 1159
Browne, M. 439
Brugnoletti, B. 2253
Brumwell, F.R. 156
Brun, T. 190, 1159
Brunelle, P. 817, 1406
Brunet, J.-C. 3368, 3586
Brüning, O. 107, 1715, 1816, 1858
Bruno, D. 3449, 3452
Bruns, W. 2651
Bucalossi, J. 2717
Buhler, S. 2823
Buldakovsky, V.N. 184
Bulfone, D. 826, 2353, 2356, 2467, 3527
Buller, T.L. 2950
Bultman, N.K. 190
Bunce, G. 1460
Burke, D. 608

Burkhardt, H. 1532, 1813, 1819
Burla, P. 66
Burnham, B. 883
Burns, A. 1987, 2026
Burris, H.R. 611
Bushuev, A. 2838
Buttkus, J. 979
Buxton, W. 2155
Bylinsky, Y. 1135
Byrd, J. 769, 772, 775, 778, 1514, 1563

C

Cai, Y. 1454, 2583, 2586, 2636
Calame, J. 3144, 3159
Calder, R. 3586
Call, M. 2473
Callahan, J. 2449
Callaway, N.T. 1165, 2464
Callin, R.S. 3045
Calvani, H. 959
Camariuc, R. 3854
Cameron, P. 1460, 2152, 2215
Cammarata, Jim 3693
Campedel, C. 3586
Canella, S. 1129
Cao, Z. 3318
Capek, K. 2198
Capista, D. 144, 1721, 2061
Caporaso, G.J. 1248, 1260, 1305, 1308, 1861, 2627, 2630, 2633
Cappi, R. 973
Cardman, L. 2693
Carli, C. 944, 976, 1379, 1382
Carlier, E. 225, 1325
Carlson, Randolph L. 1867, 2826
Carlsten, B. 1914, 2832, 3129, 3132, 3135
Carr, G.P. 2464
Carson, J.A. 3291
Carter, A. 2099
Carwardine, J. 2281, 2290
Cary, John R. 2592, 2654
Caryotakis, G. 439, 2894
Casas-Cubillos, J. 3206
Caspers, F. 75, 107, 979, 982, 1587
Caspi, S. 3212, 3398
Cassel, R. 439, 3482
Castellano, M. 2137
Castillo, V. 2155
Castle, M. 3168
Catani, L. 2137
Cavallari, G. 1858
Cavenago, M. 1129
Ceci, N. 2169, 2729
Celata, C.M. 1926, 2761, 3807
Cerniglia, P. 2502
Cervellera, F. 1129
CESR Operations Group 372
Chae, Y.-C. 953, 1700
Chai, J.S. 3825
Chairman, D. 906
Chan, A. 2413, 2517
Chan, K.C.D. 1150, 1168, 3096
Chanel, M. 944, 982, 1587
Chang, C.H. 3536, 3539
Chang, H.P. 841
Chang, L.H. 1487, 1638, 1691, 2377, 3048, 3051, 3054
Chang, Peace 853, 1409, 1487, 3533
Chang, S.S. 1638, 2858, 3048, 3054
Chang, Y.I. 1638
Chao, A.W. 1523, 1563, 1738, 1834, 1873
Chao, Yu-Chiu 2125, 2262, 2526
Chaput, R. 817
Charlton, Lowell A. 86
Chase, B.E. 2326
Chattopadhyay, S. 687, 1984
Chautard, F. 479
Chavanne, J. 3506, 3509
Chehab, R. 2823
Chel, S. 817, 1709, 2311, 2823
Chen, Bingyi 1218, 1221
Chen, C.S. 2371, 2374, 2523, 3488, 3539, 3749
Chen, C.T. 3749
Chen, Chiping 1938
Chen, Huaibi 1215
Chen, J. (DULY) 2802, 3120
Chen, J. (SRRC) 3749
Chen, J.R. 847, 3642
Chen, J.S. 2374, 2479, 3488, 3539, 3749
Chen, Jenny 853, 2371, 2374, 2523, 3488, 3539
Chen, P. 687, 1789
Chen, S.-Y. 2657
Chen, Tong 2164
Chen, W. 3297
Chen, X. 402
Chen, Y.J. 1260, 1305, 1861, 1864, 2633
Cheng, D. 3619
Cheng, G.-T. 2183
Cheng, J. 3168
Cheng, W.-H. 422, 1514, 1614
Chepegin, V.N. 249
Cherepakhin, A. 234
Chernikov, V.I. 184
Chesnokov, Yu. 249
Chester, N. 3248, 3291
Chiang, I.H. 2149, 2213
Chiang, John 850
Chiba, T. 941, 2672
Chiba, Y. 3828
Chida, K. 1557
Chin, A.H. 1984
Chin, M. 2235, 2253
Chin, P. 1855
Chin, Y. 1545, 1566, 1596, 1656
Chiurlotto, F. 1087, 1129
Cho, M.H. 593, 823
Cho, Y. 953
Chohan, V. 973, 979, 982
Choi, E.H. 1870
Choi, J. 823
Choi, J.J. 3159
Chojnacki, E. 363, 3075, 3177
Chou, P.J. 464, 542, 672
Chou, W. 110, 113, 130, 991, 994, 1724, 3251
Chow, K. 3212
Chowdhary, M. 2383
Chu, C.M. 1346, 1481
Chubar, O. 3509
Chung, S.M. 3633
Chupp, W.W. 1926, 2755
Church, M. 1006, 2055
Cinnamon, J. 3678
Cisneros, G. 439
Clark, D.J. 1051
Clark, George S. 3336
Clark, J.C. 1260
Clark, S. 439, 2473, 3027
Clark, W. 1093
Clarke, J.A. 3386, 3503
Claus, R. 2284, 2359, 2365, 2470
Clausen, M. 2403, 2446
Clauser, T. 2169
Clayton, C. 678, 681, 687, 2870
Claytor, N. 150
Clément, M. 80, 165
Clendenin, J. 903, 2849
Clerc, G. 2899
Clifford, T. 101
Cline, D.B. 621, 675
Clout, Peter N. 2532
Coates, M.C. 3494
Coffman, F. 2473
Cohen, M. 906
Cohen, S. 1042
Cojocaru, G. 1123, 3854
Colby, E. 2873
Cole, M. 3177
Colestock, P. 16, 127, 2873, 3716
Collier, P. 66, 3206
Collins, B. 2253
Collins, D. 1051
Collins, I. 3586

Collins, J. 2449
Colomb, D. 3619
Colomp, P. 3571
Comunian, M. 1087, 1129, 1132
Conde, M. (ANL) 627, 633, 639, 1996
Conde, M. (UCLA) 2873
Conkling Jr., C.R. 2496
Connolly, R. 69, 98, 101, 2152, 2215, 2947
Constant, T. 439
Cooke, S.J. 2431
Coombs, R. 3386
Coosemans, W. 560, 3645
Copeland, M.R. 464, 672
Corbett, J. 342, 832, 838, 1457, 1490, 2586
Corcoran, P. 1245
Cordova, S.R. 1245
Corlett, J. 2116, 2344, 3639
Corlier, M. 817
Cornacchia, M. 838, 1457, 1490
Cornali, R. 1813
Cornelis, K. 171, 1813
Cornelius, Wayne D. 3636
Cornuet, D. 973
Corradini, E. 1087
Corredoura, P. 2359
Corsini, R. 563
Cortopassi, C. 3221
Corvin, C. 439, 3746
Courant, E. 405, 1030, 1371, 3359
Cours, A. 2941
Cozzolino, J. 3338
Craddock, M.K. 153
Craievich, A. 811
Cramariuc, R. 1123
Crandall, K. 915, 1099, 1150, 1162, 2574
Crane, G. 2413
Crane, M. 2473, 2476
Crawford, C. 243
Crisp, J. 2072, 2166
Crofford, M. 2265
Crosbie, E. 953
Cruikshank, P. 3206, 3368, 3586
Ctcherbakov, A. 1263, 1313
Cullen, J.R. 3583
Cummings, K. 1147, 3183, 3725
Cuttone, G. 2038
CYCIAE 30 Engineering Group 3834

D

D'Alsace, R. 2305
d'Amico, T. 566, 1362
D'Auria, G. 826, 1180, 1182, 1212, 2002
D'yachkov, M. 107, 1587, 2648
da Cruz, M.T.F. 2998
Daclon, D. 1212
Daclon, F. 826
Daems, G. 973
Dahl, L. 1897
Dahlerup-Petersen, K. 3206
Dainelli, A. 2169
Dalin, J.-M. 3586
Dallin, L.O. 716
Daly, E. 2014, 2253, 3619
Danby, G. 3233
Danilov, V.V. 1499, 1759, 1777
Danly, B. 2690, 3144, 3150, 3159, 3180
Danowski, G. 2308
Davies-White, W. 838
Davis, T. 1093
Dawson, C.L. 2956, 3598
de Jager, C.W. 1063
de Lamare, J. 1316
de Leeuw, R.W. 1200
de Lima, J.A. 2998
de Loos, M.J. 2577
De Martinis, C. 2002, 2038
de Mascureau, J. 1254, 1257
De Vito, Bill 3693
de Vries, J. 808, 1987, 3221
Dean, T. 439, 3027
Decker, F.-J. 449, 497, 500, 503, 506, 509, 608, 687, 1569, 1876, 3021
Decker, G. 698, 745, 2281
Decking, W. 778, 799
Degen, C. 2502
Degtyarev, I.I. 252, 255, 258
Dehler, M. 518
Dehning, B. 366, 3648
Deitinghoff, Horst 1900
Dejus, R. 3224
DeKamp, J. 278
Dekkers, D. 973, 979
Del Giusto, P. 1212
Delahaye, J.P. 482, 563
Delferrière, O. 2720
Dell'Orco, D. 3212
Dell, F. 69, 98, 219
Delsart, P. 1254, 1257
DELTA Group 724
Delvigne, T. 3857
Denard, J. 912, 2198, 2204
Deng, J.J. 1855, 1956, 1959
Den Hartog, P.K. 3224, 3556
Deregel, J. 3365
Derenchuk, V.P. 2737
Desavouret, E. 3395, 3713
Desforges, B. 3206
Desgranges, C. 2717
Desmon, M. 2823
Devin, A. 1254, 1257
Devlin, D.J. 2829
DeVolder, Barbara G. 2174
Devred, A. 3365
Dewa, H. (JAERI) 648, 760
Dewa, H. (Kyoto) 1087, 1129
Dey, J. 2032, 3018
Diaczenko, N. 3443
Dieperink, J.H. 225
Dietderich, D. 3212
Dietrich, J. 1048
Dikansky, N.S. 1795
Dikiy, N.P. 3840
DiMarco, J. 3269, 3272, 3389, 3395
Dimonte, N. 3690
Ding, X. 1968, 2802
Ding, Xiaodong 1215
Dinkel, John 234
Dinneen, T. 150
DiStefano, James 86
Diviacco, B. 1520, 3524, 3527
Doble, N. 80, 165
Dodd, E. 2657
Dodson, G. 348
Doets, M. 3630
Dohlus, M. 2008, 2550, 2553, 2612
Dolbilov, G.V. 1290, 3126
Dölling, R. 174, 246
Dombsky, M. 956, 2675
Donahue, J.B. 190, 1159
Donahue, R. 3807
Donald, M. 1454, 2583
Donaldson, A. 390, 1316
Dong, Lan 3300
Donohue, J.T. 900
Dooling, J.C. 156
Doolittle, L. 3758
Doose, C. 745, 2293, 3227, 3577
Doub, J.M. 3473
Douglas, D.R. 1351
Dovbnya, A.N. 651, 2820, 3810, 3840
Dovgenko, B.A. 3455
Dow, K. 348, 3407
Dowell, D.H. (CEA) 2684
Dowell, David H. (Boeing) 1888, 1891, 2950
Drago, A. 2284
Dragusin, M. 3854
Draznin, M. 906
Drewsen, M. 1560
Drivotin, O. 1944
Drozdovsky, A.A. 3848
Drozhdin, A.I. 116, 133

Drury, M. 3105, 3108
Du, Taibin 1221
Duan, Xiuming 1221
Ducas, V. 1362
Ducimetière, L. 225, 1325
Dudnikov, V.G. 2714
Duffy, P. 3562
Dugan, G. 318, 3215, 3380, 3383
Duke, Jonathan 204
Duke FEL Lab 24
Dunham, B. 1947, 2201, 2484, 2693, 3755
Durieu, L. 228
Dutto, G. 956, 1105, 2675, 2781
Duval, P. 2446
Duzenli, C. 3831
Dvoeglazov, A. 2419
Dwinell, R. 1051
Dykes, D.M. 2956, 3078
Dzengeleski, J. 3407

E

Earley, L.M. 3135
East, G. 1481
Ebeling, W. 985
Ebrahim, N.A. 897
Ecklund, S. 3330
Eckoldt, Hans-Joerg 3458
Economou, D. 1042
Edwards, H. 2873
Ego, H. 2971
Ehrlich, R. 3075
Ehst, D. 393
Eichenbaum, A. 906
Eichner, J. 439, 3042
Eickhoff, H. 3801
Einfeld, D. 336, 763, 1039, 3613
El-Shazly, M.N. 3607, 3610
Elizondo, J. 1308
Elleaume, P. 2210, 3506, 3509
Elliott, T. 3443
Elsener, K. 80, 165, 168, 171
Elzhov, A.V. 488
Emamian, M. 883
Emery, L. 742
Emma, P. 452, 608, 903, 1679, 2580, 2855
Endo, K. 3470
Endo, M. 820
Engelmann, G. 1813
Engels, O. 1078
Engwall, D. 2201, 2693
Erdt, W. 3368
Erickson, R. 596
Eriksson, M. 345, 3527
Eriksson, T. 979, 982, 1382
Ershov, O.V. 1090
Esarey, E. 611, 630
ESS Study Group 988
Etkin, A. 3230
Euteneuer, H. 1902
Evans, B. 3831
Evans, J. 3123
Evans, L.R. 61
Evans, R. 2529
Evans Jr., K. 2281, 2290
Evtushenko, Yu.A. 3455
Eyharts, P. 1254, 1257
Eyl, P. 1254, 1257
Eylon, S. 590, 2755, 2832, 3719, 3722
Eysselein, F.G. 3410
Ezura, E. 2902, 2974, 2977, 2986, 2992, 2995, 3069, 3087

F

Fabris, A. 826, 829, 1735
Fabris, R. 826
Facco, A. 1129, 3084
Fahmie, M. 808, 2344
Fainberg, Ya.B. 651
Faircloth, J. 883
Faltens, A. 195, 1926
Fan, Mingwu 3834
Fan, T.C. 3536, 3539
Fang, J.M. 621
Fang, S. 2049, 3057
Fang, Si J. 994, 3242, 3251
Fant, K. 3004, 3039
Farias, R.H.A. 811, 2096, 2238, 3324, 3740
Farkas, David 599
Farkhondeh, M. 348
Farrell, Ken 86
Fartoukh, S. 470
Fateev, A.A. 1290
Faucett, J.A. 2464
Faure, J. 2720
Faus-Golfe, A. 1356, 1442
Favale, A.J. 950
Favaron, P. 1129
Fawley, W.M. 1923, 1926
Fazio, M.V. 3135
Fedorov, V.M. 1299
Fedorova, A. 1502, 1505, 1508
Fedotov, Alexei V. 1744, 1747, 1750
Fedotov, M.G. 883
Fedotov, Yu.S. 255
Feher, S. 3389, 3395
Feinberg, B. 150
Feinerman, A.D. 461
Felch, K. 3180
Feldl, E. 912, 2198, 2204
Feng, P.K. 3452
Feng, S.K. 2437
Feral, B. 3586
Ferdinand, R. 2720, 2723
Ferguson, P.D. 190
Ferguson, Patrick 3129
Ferianis, M. 826, 2002, 2011
Ferioli, G. 171
Fernow, R. 408
Ferrando, O. 228
Ferraz, R.O. 3628
Ferreira, M.J. 811, 3324, 3628
Feschenko, A.V. 2078
Fidecaro, G. 168, 171
Filhol, J-M. 751
Filippas, T.A. 1042
Finocchiaro, Paolo 2038
Fiorito, R.B. 675
Firjahn-Andersch, A. 1081
Fischer, R. 611
Fischer, W. 69, 98, 101, 210, 222, 3341, 3359
Fischer, W.E. 3785
Fisher, A. 315, 2014, 2253, 2840, 2849
Fisher, J. 3108
Fitch, M.J. 2867
Fitzgerald, D.H. 1012, 1015, 1159, 1611, 2743
Fitzgerald, J. 2072
Flechtner, D. 1272, 1275
Fliflet, Arne W. 3153
Flood, Roger 2131
Flynn, G. 817, 1517, 1709
Fockler, J. 2633
Foley, K.J. 3230
Fong, Craig 1096
Fong, K. 1105, 2049, 3057
Fong, Martin 1096
Fontana, J.R. 675
Forrestal, J. 3669
Fortgang, C.M. 897, 3135
Fortuna, G. 1129
Foster, G.W. 363, 3257, 3260, 3263, 3280, 3286, 3392
Fowkes, R. 439, 2911, 3045, 3189, 3195
Fowler, W.B. 3254, 3257, 3260, 3263
Fox, J. 2284, 2362, 2368
Fox, W. 2737, 3303
France, A. 2720
Franco, G.S. 811
Franks, R.M. 3007
Franzini, P. 3413
Freedman, S.J. 2770
Freund, A. 80

Friedl, J. 724
Friedman, A. 1240, 1923
Friedrichs, C. 3473
Friesel, D. 264, 935, 2737, 2811, 3303
Frigola, P. 736
Frischholz, H. 2911
Fry, A.R. 2867
Fuja, R. 1269
Fujieda, M. 2992, 2995
Fujishima, S. 1066, 1069, 1075, 3419, 3422, 3428, 3440
Fujita, H. 339
Fujita, Y. 3819
Fukuma, H. 306, 1566, 1596
Fuller, R. 439, 2186, 3027, 3042
Fumelli, M. 2717
Funahashi, Y. 587
Funakoshi, Y. 301, 306
Funk, W. 1150
Furman, M.A. 1617
Furuya, T. 2908, 3087, 3090
Fusellier, J. 2823
Futami, Y. 3822

G

Gabriel, Tony A. 86
Gaedke, R. 3443
Gagliano, J. 3552, 3580
Gahl, J.M. 3725
Gai, W. 627, 633, 636, 639, 1996
Galambos, J.D. 1018, 3851
Galayda, J.N. 877
Galbraith, P. 3648
Galdi, V. 1753
Galimberti, A. 826, 2353, 2356
Gallardo, J. 405, 408, 616, 621, 675
Gallet, B. 3365
Gambalonga, S. 1129
Gamp, A. 3162
Ganetis, G. 3353, 3356, 3651
Ganguly, A.K. 3156, 3171
Gao, J. 1602, 1605, 1608
Gardner, C. 89, 962, 970
Gardner, I.S.K. 988, 1021
Gareyte, J. 1356
Garnett, R.W. 1150, 1165, 2743
Garoby, R. 973, 979, 2953
Garren, A. 411, 838, 868
Gärtner, W. 3410
Garvey, J.D. 3291, 3395
Garvey, T. 2823
Garza, O. 2529, 3681
Gassner, D. 2149
Gatignon, L. 80, 165
Gavidia, A. 2067
Gavrilov, N.G. 883
Gaydosh, M.. 3666
Gayet, P. 1858
Gazis, E.N. 1042
Gelbart, William Z. 3842, 3845
Gelbke, C.K. 34
Gelfand, N. 997
Geller, J. 2149
Genet, M. 3368
Genevey, P. 3365
Gentner, M. 330
Gentzlinger, R.B. 3096
Gentzlinger, Robert C. 2914
Gerken, E. 3725
Geschonke, G. 1858
Ghiroso, W. 1926
Ghosh, A. 3353, 3356, 3398
Giachino, R. 1813
Giannini, R. 979, 1382
Gikal, B.N. 3610
Gill, P.F. 3583
Gillespie, George H. 1894, 2559, 2562
Gilpatrick, J.D. 83, 1150, 2041, 2090, 2093, 2232
Gioumousis, A. 2253
Giovannozzi, M. 1445, 1451, 1469, 2568, 2571
Giove, D. 2002, 2038, 3657
Giulicchi, L. 2314
Giuressi, D. 2353, 2356
Glass, H.D. 3242, 3257, 3260, 3263, 3269, 3286
Glatz, J. 1897
Glazov, A. 1263
Glenn, J.W. 89, 965, 967, 1478, 2149, 2155
Glock, H.-W. 521, 527
Glover, M.G. 1021
Glover, T.E. 1984
Gluckstern, Robert L. 1744, 1747, 1750, 1950
Gluskin, E. 877, 3224
Gobin, R. 2720
Goddard, B. 309
Godlove, T. 1855, 1956, 1959
Goeppner, G.A. 2207
Goetz, S. 883
Gold, S. 439, 1319, 1322, 3027, 3042
Gold, Steven H. 3153
Goldberg, D.A. 3001
Goldstein, J.C. 897, 2174
Golkowski, Cz. 1272, 1275
Gonçalves da Silva, C.E.T. 811
Goodzeit, Carl L. 3404
Gorchenko, V. 2452
Gordon, D. 681
Gorelov, D.V. 1194, 2621
Goto, A. 930, 941, 1066, 1069, 1075, 2672, 3419, 3422, 3428, 3440
Gottschalk, S.C. 675
Gou, Z.Y. 1729
Gouffon, P. 3239
Gough, R. 2675, 2758, 2770, 3737
Gougnaud, F. 2823
Gould, H. 150
Gourlay, S.A. 3209, 3398
Gournay, J.F. 2823
Gover, A. 906
Govil, R. 654
Gower, F. 3796
Gracia, J. 315
Graf, M.A. 2767
Grafström, P. 80, 165
Granatstein, V.L. 3168
Grandinetti, R. 3651
Graves, W.S. 1197, 1993, 2437, 3497
Gray, E.R. 83, 915, 1153, 1162
Gray, R. 315
Green, M.A. 868, 3401
Greene, J. 2696
Greenslade, M. 3413
Greenwald, S. 2547, 3699, 3702, 3705
Greenwald, Z. 2547, 3705
Greenwood, J.B. 2705
Greer, J. 2344
Gregory, S. 2633
Grelick, A. 1269, 2941, 3174
Grier, D. 973
Grier, E. 2953
Grieser, M. 947
Griffin, J. 396, 399, 1724
Grimm, T.L. 663
Grimmer, J. 3556
Grippe, J. 439
Grishanov, B.I. 237
Grishin, V.K. 889, 3866
Gröbner, O. 979, 3542, 3586, 3589
Groeppner, G.A. 3552
Gros, P. 2720
Gross, R. 3743
Groß, P. 174
Grote, D.P. 1240, 1923
Grote, H. 1356, 1442
Gruber, J. 973, 979
Grudiev, A.V. 2609
Guerra, A. 3333
Guharay, S.K. 2681
Guigli, J. 2067
Guignard, G. 458, 473, 482, 566
Guilhem, D. 1254, 1257
Gulbekian, G.G. 3607, 3610
Guo, Z.Y. 1566, 1828

Gupta, R. 3344, 3347, 3356, 3362, 3398
Gustafson, R. 3260
Gustwiller, J. 1245
Guy, A. 1051
Guy, F.W. 1099
Gyr, M. 168, 171

H

Ha, K.M. 3479
Haber, I. 1240, 1923
Haberer, Th. 3801
Habs, D. 947
Haddock, P.C. 3135
Haebel, E. 1858
Hafizi, B. 666, 3153
Hagedoorn, H.L. 1036, 1200
Hagel, J. 458
Hagestedt, A. 763
Haggard, J.E. 3257, 3263, 3266
Hahn, A.A. 2166, 2226
Hahn, H. 210, 213, 216, 1706
Hahn, K. 1926
Hahn, U. 2134
Haid, D. 3669
Haimson, J. 2808
Haines, John 86
Halbach, Klaus 3728
Halbleib, J.A. 1245
Halvarsson, B. 2026
Hamilton, B. 1481, 2081
Hamm, R.W. 2811
Hammen, A.F.J. 1200
Han, Y. 3297
Han, Y.J. 3633
Hangst, J.S. 1560
Hanna, S. 439, 539, 3042
Hannaford, C. 3212
Hansborough, L.D. 2740
Hansen, B.C. 3872
Hansen, Robert J. 3153
Hansen, U. 3123
Hanson, A. 3096
Hanson, D.L. 1935
Hanus, X. 817, 1709
Hao, Y. 3297
Haouat, G. 1841
Haque, T. 3452
Hara, K. 3087, 3090
Hara, M. 2971
Harding, D.J. 3242, 3245, 3257, 3263, 3269, 3272, 3275, 3278, 3286, 3288, 3291
Hardy, D. 2265
Hardy, L. 751
Harkay, K. 953, 1575, 1700, 2052, 2944, 3577
Harkewicz, R. 2702
Harnden, W. 3212
Harold, M.R. 1021
Harris, G. 3580
Harrison, M. 69, 101, 219
Harrison, S.M. 3413
Harss, B. 2696
Hartemann, F.V. 2858
Harteneck, H. 3568
Hartill, D. 1718, 2164, 3236
Hartmann, H. 2499
Hartmann, W. 3123
Hartung, W. 3075
Haruyama, Y. 1557
Harwood, L. 3333
Hasegawa, K. 915
Hashimoto, S. 757
Hashimoto, Y. 584, 938
Hatanaka, K. 3359, 3416, 3434
Hatch, K. 3743
Hathaway, D. 3622
Hayano, H. 494, 584, 587, 2980
Hayes, T. 965
Haynes, W.B. 2914, 3096, 3135
Hays, T. 3075, 3177
He, P. 675
Heiberger, M. 3816
Heifets, S. 1563, 1620, 1682
Helm, R. 608
Hemery, J.-Y. 228, 979
Hemker, R.G. 2870
Hemmi, M. 941, 2672
Henderson, S. 291, 1472, 1542, 1765, 2029, 2164
Hendrickson, L. 452, 497, 608, 2122
Henestroza, E. 590, 1926, 2832, 3719, 3722
Henke, H. 351, 464, 542, 672, 2134
Henrichsen, K. 66, 3648
Herbeaux, C. 817
Herer, A. 3857
Herminghaus, H. 1042
Hernandez, M. 733, 2017, 2840
Herr, W. 168, 171, 309, 312
Herrup, D. 2058
Hershcovitch, A. 1792, 2678, 2711
Hertzbach, S. 608
Hess, C. 3395
Hettel, R. 838
Heydari, H. 2603, 2784
Hezel, T. 3512
Higashi, A. 3822
Higgins, S. 3755
Higley, H. 3212
Higo, T. 494
Hilbert, B. 3206
Hill, A. 3004
Hill, Barrey W. 1894, 2562
Hill, C. 944
Hill, J.O. 2461
Hill, R. 2529
Hillman, A. 2281
Himel, T. 2425, 2473, 2476
Hindi, H. 2284, 2362
Hinkson, J. 775, 2110, 2235, 2253
Hinode, F. 354, 578, 587, 2980, 2983
Hiramatsu, S. 1566
Hiramoto, K. 1653, 3294, 3813
Hirata, K. 384, 1780, 1783
Hirota, J.I. 3294
Hirshfield, J.L. 666, 3153, 3156, 3171, 3863
Ho, C.H. 2858, 3048
Ho, Wendy 3842, 3845
Hoag, H. 439, 539
Hock, J. 2149
Hodapp, T.R. 2232
Hodgkins, D.J. 2740
Hoff, Lawrence T. 2395
Hoff, Matthew D. 1096
Hofler, A. 2201
Hofmann, A. 838, 1813, 1858
Hofmann, Ingo 1852
Hogan, B. 3168
Hogan, M. 736
Hogge, J.P. 2690
Hogrefe, R. 3669
Holben, S. 3165
Holik, P. 439
Holmes, J.A. 1018
Holmes, Michael 796
Holmes, R. 3562
Holmes, S. 439, 3027, 3042, 3192
Holmes, S.D. 47, 997
Holt, J. 72, 997
Holtkamp, N. 581, 2008, 2078, 2104, 2726
Holtzapple, R.L. 509
Homeyer, H. 1078
Honda, T. 2084, 2146
Honma, T. (Chiba) 1557
Honma, T. (Hokkaido U.) 2565
Horan, D. 953, 2926, 2935, 2941, 3111, 3687, 3690
Hori, T. (Sumitomo) 1266, 2642
Hori, T. (SPring-8) 2511, 2814
Hornekær, L.H. 1560
Horsky, T.N. 2767
Horton-Smith, S. 1981
Hosino, M. 1557
Hosono, K. 1557
Hosoyama, K. 3087, 3090

Hou, R. 3297, 3318
Houck, T. 590, 2627, 2633, 3719, 3722
Hovater, Curt 2861
Howells, M. 778
Hower, N. 883
Hoyer, E. 3221
Hoyt, M. 3004
HRIBF Operations Staff 1227
Hsieh, H. 3619
Hsiung, G.Y. 3642
Hsu, Ian C. 850, 2047, 2183
Hsu, K.T. 841, 847, 853, 1487, 2259, 2371, 2374, 2377, 2523, 3488, 3539, 3749
Hsu, Y.J. 850, 3642
Hsue, C.S. 1409, 1487, 3533
Hsue, K.T. 1409
Hu, K.H. 3539
Hu, Shaoguang 1218, 1221
Hu, Wensheng 1218, 1221
Hua, D. 3807
Huang, Bingsong 3300
Huang, Fuhe 3300
Huang, H. (BNL) 89, 1460, 1478, 2155, 2538
Huang, H. (IHEP) 1566
Huang, J.Y. 823, 2107, 2350, 3015, 3479
Huang, N. 1388, 1448, 1780
Huang, Yuanzhong 1215, 3764
Hubbard, E. 3816
Hubbard, R.F. 611, 630
Hughes, Thomas P. 1144, 1867, 2826
Hülsmann, P. 521, 524, 527
Humphrey, R. 439
Humphries, D. 3315
Humphries Jr., S. 2428
Hunt, D. 3619
Hunt, W. 2449, 2737
Hurh, P.G. 2166, 3283
Hurn, T. 3816
Hus, J.L. 684
Husmann, D. 330, 1033, 1373
Huttel, E. 763, 3613
Hutter, G. 3123
Hutton, A. 281, 2383
Hwang, C.S. 3536, 3539
Hwang, J.Y. 2858
Hwu, K.H. 3749

I

Iazzourene, F. 826, 829, 1185
Ichac, J.-P. 2899
Igarashi, I. 1599
Ikegami, K. 1066, 1069, 1075, 3419, 3422, 3428, 3440
Ikegami, Masanori 1911
Ilhoff, E. 2241
Imai, Y. 3425
Imanishi, A. 938
Inabe, N. 1400, 2672
Indreias, I. 1123, 3854
Ingalls, W.B. 2743, 2764
Ingold, G. 3527
Ingrassia, P. 1460
Inoue, M. 339, 1203, 1206, 3294, 3819
Intensity Upgrade Study Crew 1009
Irwin, J. 360, 482, 512, 608, 1341, 2583, 2636
Isaeva, L.G. 883
Ishi, Y. (INS) 1962
Ishi, Y. (Mitsubishi) 2908, 3087
Ishikawa, Y. 3822
Ishimaru, H. 110
Ishkhanov, B.S. 889, 3866
Issinsky, I. 181, 184
Itano, A. 201, 2347
Ito, Y. 2511, 2814
Itoh, M. 859
Ivanenko, A.I. 3604, 3607
Ivanov, I.N. 491, 1391, 3126
Ivers, J.D. 1272, 1275
Iverson, R. 315, 687
Iwashita, Y. 339, 1203, 1206, 1798, 3294, 3819
Izawa, M. 1566, 2171, 2989, 3066

J

Jablonka, M. 2823
Jackson, A. 703, 778
Jackson, G.P. 3257, 3260, 3263, 3280, 3286
Jackson, J. 3233
Jacob, J. 1551
Jacobs, G. 2726
Jacobs, K. 348, 2099
Jaeschke, E. 713
Jagger, J. 363, 2699
Jahnel, L.C. 811, 2096, 2238, 3740
Jain, A. 3309, 3338, 3347, 3353, 3356, 3362, 3651
Jaisle, A. 3443
Jakob, A. 174, 246
Jakob, H. 2026
Janenko, V. 276
Jankowiak, A. 2140
Janssen, D. 2796, 2838
Jansson, A. 2314
Jansson, U. 1325
Jark, W. 3527
Jarvis, H. 608
Jason, Andrew 270, 3138, 3728, 3731
Jayamanna, K. 2675
Jeanneret, J.B. 153
Jenkins, D.M. 3413
Jenner, D. 2968
Jensen, C. 1281, 1284, 1287
Jensen, D. 3330
Jensen, E. 973, 2953, 3060
Jensen, K. 1105
Jeon, D. 1346, 1481
Jeong, S.C. 938
Jeram, B. 2481
Jiang, C.L. 2696
Jiang, X. 2932, 2938
Jimenez, M. 1858
Jin, L.H. 1388
Jin, Qingxiu 1218, 1221, 3764
Jobe, K. 1981
Jobe, R.K. 3021, 3027
Johnson, B.M. 2678
Johnson, C. 563
Johnson, D. (NSCL) 1054, 1057
Johnson, D. (LANL) 1611
Johnson, D.E. 997, 3272
Johnson, E.D. 1197, 1993
Johnson, J. 808
Johnson, Jeffrey O. 86
Johnson, K.F. 1150, 2232
Johnson, L. 439
Johnson, P.E. 2950
Johnson, R. 2110, 2122, 2253
Johnstone, C. 119, 396, 399, 411, 414, 1030
Johnstone, John A. 240
Joly, J.M. 2823
Joly, S. 1117, 1120, 2684
Jones, C.R. 2799
Jones, F.W. 1882, 2597, 2600
Jones, G. 3619
Jones, J. 2699, 2929
Jones, K.W. 1165
Jones, R. 439, 518, 545, 548, 551, 554
Jones, W.P. 2737
Jongen, Y. 1045, 3770, 3816, 3857
Jongewaard, E. 439, 3189
Jonker, M. 1813
Jordan, K. 912, 2204, 2529
Joshi, C. 11, 678, 681, 687
Jöstingmeier, A. 2553, 2612
Jowett, J.M. 312
Judd, D. 195
Judkins, J. 3004, 3039
Juillard, M. 817, 2823
Jung, D.H. 2107
Junquera, T. 2823

K

Kaan, A.P. 3630
Kabe, A. 3087, 3090
Kabel, A. 2550
Kagaya, S. 587
Kageyama, T. (RIKEN) 2672
Kageyama, T. (KEK) 2902, 2974, 2977, 2986, 3069
Kahn, S. 3309, 3350, 3356
Kaiser, K.-H. 1902
Kakiuchi, S. 3294
Kaljuzhny, V.E. 2008, 2104
Kaltchev, D. 153
Kamada, S. 1831
Kamigaito, O. 941, 2672
Kaminsky, V.I. 3869
Kamitsubo, H. 6
Kamiya, Y. 856, 2146, 2989, 3066
Kamps, T. 2134
Kanai, T. 3822
Kanaya, Noriichi 2458, 3616
Kanazawa, M. 201, 2347, 3819, 3822
Kando, M. 648, 760
Kane, Steve 3693
Kang, X. 264, 1346, 1481, 2968
Kang, Y. 461, 1575, 2296, 2699, 2929, 2932, 2935, 2938, 2941, 2944, 3687
Kao, C.C. 727
Kaplan, R. 1718, 3075
Karabarbounis, A. 1042
Karantzoulis, E. 826, 829
Karas', V.I. 651
Karasyov, S.P. 2229
Karl, F. 3651, 3693
Karliner, M. 2796, 2838
Karn, J. 2383, 3333
Kase, M. 941, 2672, 3327
Kashiwagi, S. 494, 587
Kasimer, K.U. 2461
Kassab, L.R.P. 3239
Kasuga, T. 1566, 1664
Katayama, I. 938, 1557
Katayama, T. 92, 930, 938, 1024, 1072, 1400, 1786, 1807, 3359, 3416, 3431, 3434, 3437, 3521
Kato, S. 1596
Kato, T. 3822
Katoh, M. 2084
Katsouleas, T. 681, 684, 687, 2870
Kawachi, K. 820, 3822
Kawaguchi, H. 2565
Kawaguchi, T. 1066, 1069, 1075, 3359, 3419, 3422, 3425, 3428, 3431, 3440
Kawakami, H. 938
Kawakita, T. 1203
Kawashima, Y. 2971
Kazacha, V.I. 488
Kazakov, S.Yu. 3126
Kazimi, R. 1947, 2484, 3755
Keane, J. 2069
Keesee, M. 2201
Kehne, D. 912, 2204, 2484, 2693, 3755
Keil, E. 104, 309, 363
Keil, J. 1373
Keller, R. 775, 778, 781, 784, 787
Kelly, Darren R.C. 3547
Kelly, E. 3362
Kennedy, K. 3568, 3619
Keppler, P. 165
Kerby, J. 3398
Kerns, J. 3619
Kersevan, R. 3559, 3592
Kerslick, G.S. 1272, 1275, 3117
Kester, O. 947
Kewisch, J. 69, 98, 222
Khabarov, M.V. 3607
Khan, S. 1703, 1810
Khlebnikov, A.S. 3518
Kiang, L. 1481
Kidman, R. 3096
Kihara, T. 1798
Kijima, Y. 2908, 3087
Kikutani, E. 306, 1566, 1596, 2332, 2335
Kim, C. 778, 790, 808
Kim, C.K. 3633
Kim, Eun-San 384
Kim, J.-S. 3719, 3722
Kim, J.-W. 1066, 1069, 1075, 3419, 3422, 3425, 3428, 3440, 3825
Kim, J.K. 2657
Kim, K-J. 1984
Kim, K.H. 2107
Kim, S. 3577
Kim, S.H. 745, 2293, 3227
Kim, T.Y. 1593
Kimura, W.D. 675
King, F. 3568
King, N.S.P. 3096
Kinkead, Allen K. 3153
Kinosita, H. 757
Kinross-Wright, J.M. 897
Kirbie, H.C. 1260
Kirby, G.A. 3209
Kirby, R. 3568
Kircher, F. 3365
Kirchgessner, J. 3075, 3177
Kirichenko, A. 2452
Kirk, H. 408
Kirsebom, K. 80
Kiselev, A.V. 2805
Kiselev, V. 1463, 1466
Kiselev, V.A. 651
Kishek, R.A. 3198
Kishiro, J. 1548, 1599, 1908
Kishiyama, K. 2110, 3622, 3625
Kitagawa, A. 3822
Kitamura, Hideo 3515
Klabunde, J. 1897
Klaffky, R.W. 2305
Klaus, F. 3123
Kleeven, W. 3816
Kleffner, C. 2078, 2726
Klein, H. 174, 246, 521, 524, 527, 988
Klein, W. 2422, 2535
Kleinman, H. 906
Klem, J. 168, 171
Klimine, P. 3407
KLOE Collaboration 3413
Knauf, A.B. 3710
Knott, M. 3669
Ko, I.S. 823, 2107, 2350, 3015, 3479, 3633, 3663
Ko, J.J. 1870
Ko, K. 387, 439, 2589, 3033
Koba, K. (KEK) 1548, 1599
Koba, K. (Miyazaki U.) 1908
Kobayashi, T. (JAERI-RIKEN) 2814
Kobayashi, T. (Tsukuba) 2902, 2974, 2977, 2986, 3069
Kobayashi, Y. 856, 1566, 2084, 2171
Koepke, K. 2873
Kohara, S. 941
Kohno, T. 201
Koiso, H. 1394
Kojima, Y. 3087, 3090
Koldenhoven, R. 3669
Kolomiets, A. 1090, 1129, 1905, 2735, 2965, 3848
Kondoh, S. 648, 760
Kondratiev, B.K. 2735
Konecny, R. 633, 636, 639, 1996
Konstantinov, S. 2838
Koontz, R. 439, 1319, 1322, 3021, 3027, 3042
Koop, I. 1063, 1433
Korhonen, T. 587
Korovin, O.P. 1511
Korsbjerg, T. 2920, 2923
Kos, N. 3586
Koscielniak, S. 956, 1102, 1647, 2389
Koseki, T. 856, 1756, 2146, 2989, 3066
Kostin, D.V. 1108, 2008, 2104
Kotaki, H. 648, 760
Kotov, V.I. 249

Kotseroglou, T. 687, 1981, 2849
Kouda, S. 3822
Kourbanis, I. 144, 1721, 2061, 2323
Koutchouk, J.-P. 66, 1356, 1442
Kovalenko, A. 184, 2452
Kowalkowski, J.B. 2461
Kowalski, S. 348, 2274
Koyama, K. 1203
Koyama, T. 375
Koziol, H. 973, 979
Kozlov, O. 181
Kozodaev, A.M. 2965, 3848
Kozyrev, E.V. 3114
Kponou, A. 1460, 2023, 2711
Krafczyk, G. 3291, 3461
Krafft, G.A. 739, 912, 2020, 2128, 2204, 2265, 2268
Kraft, G. 3801
Kraimer, Martin R. 2403
Krainz, G. 3206
Kramer, S.L. 748, 2305
Krasnopolsky, V.. 1263
Krasnykh, A. 1319, 1322
Krastelev, E.G. 3141
Krause, U. 3801
Krawczyk, Frank L. 2914, 3093, 3731
Krebs, Gary F. 793, 796
Kreischer, K.E. 2690
Krejcik, P. 608, 1623, 1626, 3030
Krevet, B. 3512
Kriens, Wilhelm 231
Krietenstein, B. 2645
Krinsky, S. 727, 1197, 2161, 2287
Kroc, T.K. 3269
Kroes, F.B. 1063
Krogh, M.L. 1308, 2627
Kroll, N. 429, 439, 518, 548, 551, 554
Kroupa, M. 2535
Kruchkov, J. 2838
Krueger, K. 1460
Krusche, A. 973
Krushelnick, K. 611
Krüssel, A. 763
Kuba, A. 2511, 2814
Kubo, K. 354, 494, 587, 1484, 2980, 2983
Kubo, T. 1066, 1069, 1075, 3419, 3422, 3425, 3428, 3440
Kubo, Tadashi 3467
Kubono, S. 938
Kudinov, V. 276
Kudo, Hirofumi 2146
Kuijer, L.H. 1063
Kukarnikov, S.I. 491
Kukhtiev, V. 1135
Kulik, I. 1129
Kulikov, A. 315, 1316, 2253, 3639
Kulikov, I. 2452
Kulipanov, G.N. 883
Kumada, M. 820, 2347, 3327, 3822
Kuner, B. 2493
Kuo, C.C. 841, 847, 850, 853, 1409, 1487, 1638, 2377, 3048, 3051, 3054, 3533
Kuo, C.H. 2259, 2371, 2374, 3749
Kuo, T. 2675
Kupper, R.R. 2737
Kurakin, V.V. 3848
Kurennoy, Sergey S. 1732, 1950, 3731
Kurita, N. 2014, 2110, 2253, 3639
Kurkin, G.Ya. 883
Kurnaev, O. 234
Kurokawa, S. 381, 1566, 1596
Kurz, M. 521, 527
Kusche, K.P. 621, 675
Kushnir, V.A. 651, 3810
Kustom, R. 461, 953, 1575, 2296, 2929, 2941, 2944, 3174
Kutner, V.B. 3604
Kuybeda, R.P. 3848
Kuzay, Tuncer 2210
Kuzmiak, M. 1391
Kwan, J.W. 1230, 2755
Kwan, Thomas J.T. 2174
Kwiatkowski, S. 2947
Kwon, M. 823, 2350, 3015
Kyser, R.H. 3159

L

Labrador, A. 1560
Labrouche, J. 1254, 1257
Lackner, H. 1251
Laclare, J.-L. 817, 1406, 1517
Ladeuze, M. 3816
Lagniel, J-M. 1120, 2720
Lahey, T. 2473
Lai, B. 461
Lai, C.Y. 1638
Lai, P.-C. 2047
Laird, R. 2490, 2926
Lalayan, M.W. 2104
Lamanna, G. 2169
Lambaise, R.F. 3452
Lambertson, G. 1617, 2344
Lambiase, B. 3449
Lamm, M.J. 3389, 3395, 3398
Lamont, M. 309
Lampel, M.C. 2562, 2615
Lancaster, J.A. 2799
Lange, R. 2493
Langenbeck, B. 2594
Langenbrunner, J. 1611
Langton, J. 2014, 2253
Lannoye, G. 3816
Larsen, R. 2284
Larson, D. 1403, 3248, 3837
Lash, J.S. 1245
Latham, P.E. 3150
Latypov, D. 3443, 3446
Latypov, T. 1263, 1311
Lau, W.K. 847, 1487, 1638, 1691, 2377, 2858, 3048, 3051, 3054
Lau, Y.Y. 3198
Lauckner, R. 66
Launspach, J. 1254, 1257
Laverty, M. 3057
Lavine, T. 439, 1676, 3027, 3042, 3192, 3675
Lawrence, G.P. 83, 1150, 1156
Lawson, W. 3168
Lawton, D. 1054, 1057
Laxdal, R. 956, 1102, 1105, 1135, 1194, 2621
Laycock, S. 3816
Lazarev, N.V. 2965, 3848
Lebedev, V. 1560, 2128, 2383
LeBlanc, G. 342, 345, 832
Leboutet, H. 1117
Lee, C.-H. 2183
Lee, D.H. 850
Lee, E. 195
Lee, J.C. 844
Lee, M. 2586
Lee, P.B. 657
Lee, R. (UC Irvine) 965
Lee, R. (TRIUMF) 1102
Lee, S. 687
Lee, S.C. 3663
Lee, S.Y. 264, 396, 399, 935, 1346, 1460, 1478, 1481, 2968
Lee, T. (Pohang) 823
Lee, T. (DULY Research) 2802, 3036, 3120
Lee, Y. 2667, 2675, 2770, 3737
Lee, Y.Y. 159, 162, 962, 970
Leemans, W. 630, 654, 657, 687, 1984
Legg, R. 2201, 2265, 2383, 2693, 3755
Leibfritz, J. 994, 3601
Leinbach, R. 3221
Leitner, M.A. 2758, 2764, 2770
Lemaire, J-L. 1120
Lenci, S. 3183
Lengeler, H. 988
Lenkszus, F. 2281, 2490, 2926
Lenz, J.W. 1099
Leonhardt, W.J. 3230, 3583
Leroy, P-A. 2720

Le Sage, G.P. 2858
Lessner, E. 327, 953
Letchford, A.P. 1846
Letta, P. 2383, 2484
Leung, K-N. 2675, 2758, 2761, 2764, 2767, 2770, 3737, 3807
Level, M.-P. 817, 1406, 1517
Levichev, E. 1463, 1466
Levin, L.A. 906
Levush, B. 2431, 3144, 3150, 3159, 3180
Levy, C.D.P. 2781
Ley, R. 944, 982
Leyman, D. 3816
LHC Magnet Team 3371
Li, L. 3297
Li, N. 3312, 3318
Li, Quanfeng 1218
Li, R. 1641, 1644, 2204
Li, S.P. 1566
Li, X. 633, 1996
Li, Y. (Maryland) 1855, 1959
Li, Y. (IHEP) 3297
Li, Yuezeng 1218, 1221
Li, Yulin 3559, 3592, 3595
Li, Zenghai 599
Liakin, D.A. 2965
Lidia, S. 590, 900, 2624
Liehr, M. 2708
Lietzke, A. 3212
Liiou, A.V. 2078
Likhachev, S.P. 3866
Liljeby, L. 947
Limberg, T. 491, 2550
Limborg, C. 838
Limon, P.J. 3389, 3395, 3398
Lin, Glory 850
Lin, K.K. 2259, 2371, 2374, 2523, 3749
Lin, Liu 811, 2096, 2238, 3740
Lin, M.C. 1638, 3048, 3051, 3054
Lin, S.J. 1638, 2377, 3048
Lin, X. 387, 3033
Lin, Y.K. 853
Lin, Yuzheng 1215, 1218, 1221
Lindgren, L-J. 345
Lindroos, M. 2314
Linebarger, W. 596
Ling, Guan Xia 1224
Linnecar, T. 1813, 1816, 1849
Linnik, A.F. 651
Linscott, I. 2284
Lipari, J. 1316
Lira, A.C. 811, 1209, 3476
Lisowski, P.W. 708, 3780
Littauer, R. 1472, 1542
Littenberg, L. 967
Litvinenko, V. 874, 883
Liu, C.Y. 3488
Liu, D.K. 1566
Liu, F. 2678, 3752
Liu, H. 1947, 2693
Liu, K.B. 3488
Liu, W.B. 1388
Liu, Y. 621, 675
Liu, Y.C. 847, 853, 2259, 2858
Lockey, R. 2711
Loew, G.A. 439
Loewen, R. 439, 539, 3042, 3189, 3192, 3195
Lokhovitskii, A.E. 252, 255, 258
Lollo, M. 1129
Lombardi, A. (CERN) 944, 2314
Lombardi, A. (INFN) 1087, 1129
Lonza, M. 826, 2353, 2356
Lorenz, R. 2134, 2137, 2392
Losito, R. 3063
Lou, W. 3236
Louie, W. 3338
Loulergue, A. 817, 2684
Lozowski, W.R. 2737
Lu, Fuhai 3162
Lucas, William 3595
Luccio, A. 92, 207, 962, 970, 1460, 1882, 2538, 3359
Luchini, K. 808
Ludewig, H. 970
Ludewigt, B.A. 3791
Luger, G. 2422, 2535
Luhmann Jr., N.C. 2858
Luijckx, G. 1063
Lujan, R.E. 3096
Luke, P.N. 3807
Lumpkin, A. 775, 871, 874, 883, 1700, 1999, 2052, 2207
Lund, S.M. 1240, 1260, 1929, 1932
Lundgren, S. 1051
Luo, G.H. 847, 850, 853, 1638, 3048
Lupton, William 2403
Lussignol, Y. 2823
Lyles, J. 3473
Lynch, D.R. 3494
Lynch, M. 1147, 3138
Lyneis, C.M. 1051, 2770
Lysenko, A.P. 1433
Lysenko, W. 1917, 2574
Lyudmirskiy, E.A. 249

M

Ma, L. 1566, 2075
Ma, R. 3831
Maas, R. 1063
Maccaferri, R. 944, 979
MacDonald, A.R. 2508
Macedo, D. 2096
Macek, R. 190, 1012, 1015, 1159, 1611
MacGregor, I. 2413
Machida, S. 1656, 1670, 1908, 1962, 2995
Machie, D. 3108
MacKay, W. 69, 98, 101, 210, 222, 2541
Mackenzie, G. 956, 2675
Mackenzie, R. 2476
MacLachlan, J. 1590, 2556
MacLaren, S. 1926
Madey, J.M.J. 24, 883, 2799
Madlung, J. 1081
Madsen, N. 1560
Maenchen, J.E. 1245
Maeng, A.H. 3663
Maezawa, Hideki 2458, 3616
Mahler, G. 2155
Mahoney, K. 3565, 3678, 3681, 3684
Maidment, J.R. 985
Maier, R. 1048
Mailian, M.R. 695
Mainaud, H. 560
Maines, J. 3224
Mais, H. 1825
Maisheev, V.A. 249
Majka, Dick 967
Major, J. 165
Makarov, A. 3248, 3291
Makarov, I.G. 3114
Makdisi, Y.I. 1460
Makino, K. 1336
Makoveev, V.K. 1391
Maksimchuk, A. 2657
Malafronte, A.A. 2998
Malagari, M. 1042
Malamud, E. 363
Maletic, D. 970, 1882
Malitsky, N. 375, 2434
Maloney, M. 3096
Mamaev, G. 1263, 1311, 1313
Mamaev, S. 1263, 1311, 1313
Mammarella, F. 956
Mammosser, J. 3102, 3108
Mancini, D. 461
Mane, V. 69, 98, 2158
Mangra, D. 745, 2938
Manka, C. 611
Mansur, Louis K. 86
Manvell, Benjamin 3595
Margaritescu, A. 1123, 3854
Marghitu, S. 1123, 3854
Marhauser, F. 521, 527
Mariam, F. 1460, 3359

Marin, A. 3645
Marks, N. 3386
Marks, S. 802, 3221
Marlats, J.-L. 817
Marneris, I. 2308
Marone, A. 3353
Maroulis, D. 1042
Marriner, J. 72, 144
Marsh, K. 678, 687
Marshall, T. 642, 666
Martens, M.A. 72, 136
Marti, F. 278, 1054, 1057
Martin, D. (Bucharest) 1123, 3854
Martin, D. (SLAC) 1457, 1490
Martin, P.S. 139, 243, 3242, 3245, 3269, 3272, 3275, 3278, 3288
Martin, S. 1048
Martinez, D.G. 2232
Martinez, F. 1093
Martinez, R. 2232, 3309
Martini, M. 1362, 2314
Martins, M.N. 2998
Martlew, B.G. 2443
Martono, Hendy 2562
Marutsuka, K. 267, 1908
Marx, M. 491
Maryokhin, S.V. 2229
Mashaw, A. 3737
Mashiko, K. 339
Maslov, M.A. 258
Massmann, P. 2717
Massoletti, D. 778, 808
Masunov, E.S. 2835
Mathewson, A. 3586
Matsuda, Kooji 3813
Matsumoto, H. 455, 530, 533, 581, 587, 593
Matsumoto, S. 306, 1596
Matsuoka, M. 1203
Matufuji, N. 3822
Matuk, C.A. 2767
Maury, S. 944, 976, 979, 982, 1382
Mavric, G. 2481
May, M.P. 3257, 3263, 3280, 3286
Mazarakis, M.G. 1245
Mazur, P. 3389, 3392
McAllister, B. 348, 2099
McCammon, D. 2968
McCormick, D. 1981, 2189, 2253
McCullough, R.W. 2705
McCurdy, A.H. 3159
McDaniel, B. 1472, 1542
McDonald, M. 2675
McDowell, W. 953, 3669
McGee, M.W. 3283
McGhee, D. 953
McGill, R. 2253
McGinnis, D. 144, 1721, 2323
McIntosh, E. 2571
McIntosh, P.A. 2223, 2956, 3078
McInturff, A.D. 3212, 3389
McIntyre, Gary 3693
McIntyre, P. 3443, 3446
McJunkins, P. 3443
McMahan, M.A. 1051
McManamy, Thomas J. 86
McMichael, G.E. 156
Mead, J. 2502
Mecklenburg, B. 2808
Meddahi, M. 309, 312, 1813
Medvedko, A.S. 3455
Medvedko, E.A. 2113, 3455
Medvedyeva, Ye.P. 3840
Meincke, O. 1858
Meisner, K. 2326
Meitzler, C.R. 3872
Melissinos, A.C. 2867
Meller, Robert E. 2505
Mencik, M. 2823
Mendonsa, R. 3796
Menegat, A. 464, 672, 3036, 3045
Meneghetti, J. 3619
Meng, W. 3233
Menge, P.R. 1245
Menshov, A.A. 2078
Méot, F. 121, 1987
Merinov, I. 2244
Merl, R. 745, 2281
Merle, E. 1254, 1257
Merminga, L. 1694, 2320
Merrill, F. 1611, 2743
Metzger, C. 979, 982
Metzmacher, K. 973, 979, 1328
Meyer, D. 1269
Meyer, E.A. 2740
Meyer, J. 883
Meyer, S. 2413, 2517
Meyerhofer, D. 2840
Michelini, P. 3527
Michelotti, L. 997
Michnoff, R. 2218
Mikhailichenko, A. 318
Mikhailov, S.F. 883
Mikhailov, V. 181, 184
Mikkelsen, U. 80, 165, 168
Mikkelson, K. 1245
Miles, J. 1356
Militsyn, B. 1063
Miller, E. 2473
Miller, R. 439, 518, 539, 548, 551, 554, 599, 2687, 2790, 2840, 2843, 2846, 2849, 2852, 2855, 3042
Miller, T. 3619
Millich, A. 563
Milloch, M. 1212
Millos, G. 3568
Mills, J.A. 3230
Mills, Mark R. 2122
Milocco, A. 1212
Milovanov, O.S. 2104
Milton, B.F. 3775
Milton, S. 324, 877, 1700, 2699, 3577
Milward, S.R. 3209, 3494
Minaev, S.A. 2645
Minamihara, Y. 3221
Minato, T. 3425
Minister, J. 439
Minty, M.G. 354, 357, 449, 506, 509, 608, 1563, 1569, 1741, 1873
Minuzzi, F.A. 3628
Mirzojan, A.N. 2078
Mishra, C.S. 139, 997, 1771, 3269
Mistry, N.B. 3559, 3592, 3595
Mitchell, D. 3389
Mitchell, M. 3021, 3024
Mitra, A. 1105, 2953, 3060, 3063
Mitrochenko, V.V. 651, 2817, 2820, 3810
Mitsuhashi, T. 766, 859, 2084
Mitsumoto, T. 1066, 1069, 1075, 3419, 3422, 3428, 3440
Mitsunobu, S. 2908, 3087, 3090
Miura, A. 530
Miura, T. 2983, 3066
Miyachi, T. 938
Miyahara, Y. 891
Miyamoto, S. 757
Miyatake, H. 938
Miyazawa, Y. 941, 2672
Mizuno, A. 2511, 2814
Mizuno, H. 2902, 2974, 2977, 2986, 3069, 3767
Mochihashi, Akira 1664
Mochizuki, T. 757
Moe, H. 953
Mohammadzadeh, Ahmad 2380
Möhl, D. 944, 976, 979, 982, 1382
Moir, D.C. 1138, 1141, 1144, 2829
Moisio, M.F. 1129
Mokhov, N. 116, 124, 133, 393, 414, 3672
Molau, N.E. 2627, 2633
Molinari, G. 944
Møller, S.P. 80, 165, 1027, 2920, 2923
Molodozhentsev, A.Y. 491, 1391
Momal, F. 3206
Monchinsky, V. 184, 2452
Montag, C. 485
Montoya, Debbie I. 2914
Moog, E. 2207, 3224

Moor, E.J.F. 3494
Moore, C.D. 141
Moore, C.I. 611
Moore, John M. 2562
Moraru, R. 3854
Morcombe, P. 883
Moretti, A. 3018
Morgan, G. 3356, 3362
Morgillo, A. 3353
Mori, W. 681, 684, 687, 2870
Mori, Y. 920, 1656, 1670, 1908, 1962, 2992, 2995, 3306
Morii, Y. 2347, 3828
Morikawa, T. 1066, 1069, 1075, 3419, 3422, 3428, 3440
Morita, Y. 3087, 3090
Morpurgo, G. 1858
Morris, J. 3209
Morrison, L. (ANL) 2929
Morrison, L. (LBNL) 3212
Morrison, M. 3212
Morrissey, D.J. 198
Mortazavi, P. 3494
Morton, P. 1611
Morvillo, M. 75, 107
Moser, H.O. 763, 3512
Mosnier, A. (Saclay) 467, 817, 1661, 1709, 2311, 2823
Mottershead, C. Thomas 1397
Mouat, M. 3831
Mueller, A.C. 1120
Mugge, M. 3622
Mulder, H. 944, 979, 982
Mulhollan, G.A. 2849
Muller, Tom 3693
Müller, I. 2493
Müller, R. 2493
Müller, W.F.O. 524
Mullins, L. 3562
Muñoz, M. 814
Murai, T. 3087
Murakami, T. 3822
Muratore, J. 3347, 3353, 3356, 3362
Muratore, P. 3338
Murokh, A. 736
Muto, M. 584, 3306
Myakishev, D.G. 2609
Myers, S. 1
Myers, T.J. 950

N

Naba, T. 2983
Nadji, A. 817, 1406, 1517
Nagatsuka, Toshiya 856
Nagl, M. 2078, 2726
Naidenov, V.O. 1511
Naito, F. 2902, 2974, 2977, 2986, 3069
Naito, T. 584, 587
Nakagawa, T. (RIKEN) 941, 2672
Nakagawa, T. (Mitsubishi) 2102
Nakai, H. 3087
Nakajima, K. 648, 760
Nakamura, N. 856, 1756, 2146
Nakanishi, H. 648, 760, 2902, 2974, 2977, 2986, 3069, 3087
Nakayama, H. 1394, 2992, 2995
Nakayama, K. 3828
Nam, S.H. 823, 2107, 3479
Nam Soon-Kwon 1593
Namkung, W. 593, 823
Nantista, C. 439, 1676, 2186, 2256, 2852, 3027, 3042, 3192
Naqvi, S. 3117
Naranjo, A. 1093
Nassiri, A. 461, 1575, 2052, 2296, 2941, 2944, 3111, 3120, 3174, 3491
Nath, S. 915, 1150, 1153, 1162, 1171
Nation, J.A. 1272, 1275, 3117
Naumann, O. 1551
Nawrocky, R.J. 2069
Naylor, Graham 2210
Neel, J. 817
Nelson, E.M. 1837
Nelson, R. 3165
Nelson, S.D. 2633
Neri, F. 193, 273, 1012, 1015, 3788
Nesterenko, I.N. 1433, 1762
Nesterov, V. 439
Nesterovich, A. 276, 2773, 3869
Neubauer, M. 3004, 3039
Neuenschwander, R.T. 811
Neuffer, D. 417, 624, 1537, 2905
Ney, S. 3096
Nezhevenko, O.A. 3013, 3114, 3153, 3156, 3186
Nezrick, F. 2867, 2873
Ng, C. 387, 1738, 2116, 2189, 3033, 3562
Ng, K.-Y. 396, 399, 405, 994, 1000, 1003, 1030, 1481
Ng, Wang C. 2630
Nghiem, P. 330, 817, 1406, 1517
Nguyen, D.C. 897, 1990
Nguyen, K. 3144, 3180
Nguyen, M.N. 3482
Nguyen, V. 3102
Nguyen-Tuong, V. 3105
Ni, G. 3297
Ni, Yi 3764
Nicol, T.H. 3257, 3263, 3710
Nielsen, J.S. 1560
Nielsen, R. 953
Niibe, M. 757
Niki, K. 938, 3306
Nikiforov, A.A. 3114
Nikitina, I. 3586
Nikitina, L. 3586
Nishi, M. 3813, 3819
Nishimura, H. 778, 784, 799, 805
Nissley, L. 3816
Nitsch, F. 3123
Njegomir, M.M. 190
Nobes, S. 3209
Noble, R.J. 393
Nobrega, F. 3389, 3398
Noda, A. 339, 1203, 1206, 3294, 3819
Noda, K. 201, 820, 1557, 2347, 3819, 3822
Nogiec, J.M. 3395, 3464, 3713
Nolen, J. 2696
Nomura, M. 402, 880, 2787
Nomura, T. 201, 938
Noomen, J.G. 1063
Noonan, J. 3552, 3580
Nordberg, E. 3075, 3383
Nordby, M. 3330, 3639
Norek, G. 953
Norem, J. 363, 396, 399, 1030
Noriega, R. 2253
Normann, L. 1813
Nosochkov, Y. 838
Novicova, T.A. 889
Novikov, A.V. 2732
Novikov, S.A. 184
Novitski, I. 3398
Novokhatski, A. 467, 1661, 1709
Nuhn, H.-D. 838

O

O'Day, S. 1006
O'Shea, P.G. 1278, 1891, 1993, 2799
O'Sullivan, M. 3681
Oakeley, O. 883
Obina, Takashi 1664
Odagiri, T. 1557
Ogata, A. 648, 760
Ogawa, H. 3327, 3822
Ogitsu, T. 3365
Oh, J.S. 581, 593
Ohashi, Y. 2971
Ohkawa, T. 1024
Ohkubo, Y. 533
Ohmi, K. 1566, 1596, 1667, 1831
Ohmori, C. 1656, 1670, 1908, 1962, 2992, 2995
Ohshima, T. 2971
Ohtomo, K. 1072

Ohtomo, Kiyotaka 3816
Oide, K. 494, 587, 1394, 1484, 1798, 3660
Okada, M. 938
Okamoto, H. 339, 1203, 1798, 1911
Okamura, M. 1460, 3341, 3359, 3431, 3437
Okugi, T. 584, 587, 1484
Okuma, S. 730
Okuno, H. 1066, 1069, 1075, 3327, 3419, 3422, 3440
Oliveira, L.H. 3476
Olsen, B. 101
Olsen, D.K. 1018, 1177, 2775, 3851
Olsen, Jeff J. 2122
Olsen, R. 3485
Olson, C.L. 1935
Olsson, E. 2422, 2535
Omar, A.S. 2553, 2612
Omeich, M. 2823
Onishchenko, I.N. 651
Ono, S. 1557
Oothoudt, M.A. 1165, 2064, 2464
Oproiu, C. 1123, 3854
Oren, T. 3755
Ormond, Kern W. 1822
Orris, D. 3389, 3395, 3713
Osborn, J. 3312, 3318, 3321
Oshita, E. 730
Osmanov, N. 736
Ostiguy, J.-F. 1403, 2556, 3257, 3260, 3263, 3272, 3278, 3286
Ostojic, R. 3209, 3696
Ostreiko, G.N. 3114
Ostrem, D.J. 2464
Ostroumov, P. 1135, 2078, 2621, 2732
Otter, Alan J. 3336
Ottinger, M.B. 1653
Ovsyannikov, D. 1944
Owen, H. 333, 2443
Oyaizu, M. 938
Ozelis, J.P. 3389

P

Pabst, M. 1846
Pachnik, J. 3395, 3713
Padamsee, H. 2884, 3075, 3177
Padmore, H. 3221
Pagani, C. 1126, 3657
Pakter, Renato 1938
Palanque, S. 817
Palmer, D.T. 1968, 2687, 2790, 2840, 2843, 2846, 2849, 2855
Palmer, R. 286, 405, 408, 3401
Palmieri, V. 1129
Pamela, J. 2717
Pan, K.T. 3539
Pantell, R.H. 675
Paoluzzi, M. 979
Papadakis, N.H. 1042
Papanicolas, C.N. 1042
Papis, J.P. 2049
Pappas, G.C. 390
Paramonov, V. 1135, 2726, 2959, 2962
Pardine, C. 811, 1209, 3010
Pardo, R.C. 2696, 2702
Parisi, G. 1090, 1900
Park, D. 3633
Park, H.J. 3015
Park, M.K. 2350
Park, S. 874, 883
Park, Sanghyun 835, 2840
Parker, J.M. 3625
Parker, R. 66
Parker, R.K. 3159
Parkhomchuk, V.V. 1795
Parma, V. 3368, 3374
Parodi, R. 1126
Parsa, Z. 642, 1502, 1505, 1508, 1917
Parzen, G. 1421, 1424, 1427, 1430
Pascholati, P.R. 2998
Pasotti, C. 826, 1185, 1735, 3099
Pasquinelli, R.J. 1403, 3804, 3837
Passchier, I. 1063
Patavalis, N. 1042
Paton, K. 3831
Patteri, P. 572, 2137
Patterson, J. 883
Patterson, J.M. 439
Paul, A.C. 1260
Paul, M. 2696
Pawel, Steve J. 86
Payet, J. 330, 817, 1406, 1517
Pearson, C. 439, 2911, 3192
Pearson, P.S. 2437
Peaupardin, P. 817
Pedersen, F. 973, 979, 982, 1382
Pedersen, J. 973
Peggs, S. 56, 69, 95, 98, 101, 219, 222, 405, 1030, 2158, 3359
Pei, A. 1481, 2968
Pekeler, M. 2917
Pekker, M.S. 1635
Pelaia, T. 1472, 1542
Pellegrini, C. 678, 736, 1457, 1490, 1968, 2687, 2802
Pellico, W. 3716
Pelzer, W. 1078
Pendzick, A. 2213
Peng, Q. 378, 3297
Pengo, R. 1129
Pénicaud, J.-P. 817
Peoples Jr., J. 29
Peperkorn, I. 2078, 2726
Perelstein, E.A. 488
Perevedentsev, E.A. 1759
Perez, F. 763, 1039
Perin, R. 3371
Perini, D. 3410
Perkins, L.T. 2761, 3807
Perraudin, C. 1117, 1191
Pershin, V.I. 1090, 3848
Pershing, D. 3144
Persov, B.Z. 3114
Peschardt, E. 309
Peters, C. 1926
Peters, J. 2726
Peterson, K. 953
Peterson, T. 3392, 3395
Petillo, J. 3144
Petracca, S. 1753, 1783
Petri, H.R. 2737
Petrov, S.P. 3455
Petrov, V. 1795, 2796, 2838
Petrov, V.A. 491
Pett, J. 66
Pewitt, E.G. 3269, 3275
Peyrot, M. 3374
Pfeffer, H. 994, 3461
Pfeiffer, G. 2493
Phillips, L. 3102, 3108, 3752
Phillips, R. 439
Phinney, N. 497, 506, 608
Phinou, P. 1042
Phung Ngoc, B. 2311, 2823
Picard, D.S. 2761
Pickles, T. 3831
Picoli, R.A. 1209
Picon, J.C. 1254, 1257
Piech, R. 2929
Pierini, P. 1126
Pietryka, M. 315, 439, 3666
Pietryla, A. 2281
Pike, C. 2344
Pikin, A. 2711
Pilat, F. 69, 95, 98, 101, 222, 2544, 3359
Pile, G. 1269
Pillai, C. 2064, 2743
Piller, Chip 2131
Pinayev, I.V. 883
Pinchasi, Y. 906
Pinto, I. 1753
Piot, P. 912, 2198, 2204
Pipersky, P. 3221
Pirozhenko, V.M. 950
Pisent, A. 1087, 1129, 1132
Pittana, P. 3099

Pivarč, J. 3604
Pivarč jun., J. 3604
Placidi, M. 366, 1987, 3648
Planner, C.W. 1021
Plate, D. 3221
Plesko, M. 336, 763, 2481
Plotnikov, V.K. 2965, 3848
Plum, M. 187, 190, 1012, 1015, 1611
Podgorny, F.V. 237
Podlech, H. 947
Podobedov, B.V. 1629
Poelker, B.M. 2861, 2864
Poggi, M. 1129, 2169
Pogorelsky, I. 621, 645, 675
Poirier, R. 956, 1105, 2953, 3060, 3063
Polk, I. 3230
Pomasan, Yu. 276
Pomatsalyuk, R.I. 2229
Poncet, A. 3368, 3586
Poole, Brian 1861, 2630
Pope, R. 439, 3042, 3192
Popenko, V.A. 3810
Popik, V.M. 883
Popov, E.O. 1511
Popovic, M. 396, 399, 1030, 1403, 3837
Poppensieker, K. 3801
Porcellato, A.M. 1087, 1129
Poreye, V. 3816
Portante, L. 2998
Porter, T. 439
Postma, O. 3630
Potepan, F. 2467
Potier, J.P. 476
Potter, J.M. 1099
Potukuchi, P. 3072
Pouchkov, S. 1263
Poukey, J.W. 1245
Power, J. 633, 639, 1996
Power, J.F. 193, 2041, 2232, 3731
Pozimski, J. 174, 246
Pozzer, A. 1212
Prabhakar, S. 2284, 2362
Prasuhn, D. 1048
Preble, J. 3108
Prelec, K. 2711
Price, J.S. 2864
Prichard, B. 1611
Prieels, D. 3816
Prior, C.R. 1021
Pritzkau, D. 672, 1626, 3036
Proch, D. 3081
Prokesh, K. 1391
Prokopenko, S.Yu. 2229
Pros, M. 2011
Proudlock, P. 66
Pruss, S.M. 3286
Ptitsin, V. 3359, 3500
Puchkov, S. 1311, 1313
Pugachov, G.D. 3840
Pugh, M.J. 2443, 2508
Putnam, S.D. 1251
Pynn, R. 1159

Q

Qin, Q. 1448, 1566
Qing, Q. 1356
Qiu, Joe X. 1971
Qualls, A. 2449
Quigley, P. 3075
Quimby, D.C. 675
Qunell, D. 1281, 1287

R

Rabedeau, T. 838
Radoiu, M. 3854
Radu, A. 1123
Rafael, F. 811, 1209, 2096, 3324
Rahmani, H. 1042
Rahn, J. 2493
Raia, Guido 2038
Raich, U. 973
Raimondi, P. 449, 452, 503, 509, 608, 687, 1981, 2189
Raino, A. 2729
Rajagopalan, S. 2802
Rakowsky, G. 727, 3497
Ramamoorthy, S. 2287
Ramsell, C.T. 663
Rao, M.G. 3105
Raparia, D. 162, 970, 2023
Raridon, R.J. 2775
Raskopin, A.M. 2965
Ratner, L. 1460, 1478
Ratti, A. 216, 1706
Ratzinger, U. 947, 1897, 2645
Raubenheimer, T. 473, 482, 503, 599, 605, 687, 1197, 1563, 1626, 2580
Rawlinson, B.R. 2443
Rawnsley, W.R. 2049
Ray, B.D. 1165
Redd, D.B. 273
Redden, D.P. 3872
Reece, C. 3105
Reece, K. 89, 1460
Rees, D. 1147, 2428, 2889, 3183, 3725
Rees, G.H. 988, 1021
Reeve, Paul 3336
Regan, A. 1150, 2338, 2341
Reginato, L. 590, 1296
Rehm, K.E. 2696
Reichanadter, M. 243
Reiche, S. 736, 1365
Reichel, I. 1819
Reidelbach, K. 246
Reigle, D. 3669, 3690
Reilly, J. 3075
Reis, D. 2840
Reiser, M. 1526, 1650, 1855, 1953, 1956, 1959, 2143, 2681, 3168
Ren, F. 3297
Rennich, Mark J. 86
Rensfelt, K.G. 947
Repkov, V.N. 883
Repnow, R. 947
Reppond, A. 3872
Reshetnyak, N.G. 2820
Reuter, E. 315
Reymermier, C. 3586
Reyzl, I. 2392
Riabko, A. 1346, 1481
Rice, D. 3236, 3383, 3705
Richards, L. 3443
Riche, A. 563
Richter, M. 3801
Rickard, M.L. 2758
Ridlon, Rae N. 2826
Rieckmann, C. 2553, 2612
Ries, T. 1194
Rifflet, J.M. 3365, 3374
Rifkin, J. 439, 2186, 3042, 3192
Rijllart, A. 3206
Rimmer, R.A. 3001, 3004, 3007, 3039
Rinckel, T. 3303
Ringwall, A. 3330
Risbud, S. 3183
Risselada, T. 1356, 1442
Ritson, D. 113
Riunaud, J.-P. 228, 973, 979
Rizawa, T. 3828
Rizzi, V. 1212
Robert, C. 2899
Roberts, J.E. 190
Robertson, H.P. 3684
Robin, D. 778, 799
Robinson, K.E. 675, 3201
Rodger, E.S. 3230
Rodier, J. 2823
Rodionov, D.A. 3866
Rodrigues, A.R.D. 811, 2096, 3324, 3740
Rodriguez-Mateos, F. 3206
Rogers, J. 318, 369, 1822, 2276, 3215
Rohmig, P. 3368, 3374
Rohrer, U. 3785
Röjsel, P. 345

Rokni, S. 687
Romanov, S. 2452
Romas'ko, V.P. 2820
Romeu da Silva, A. 811
Ronnigen, R. 1054
Root, L. 956, 1102
Ropert, A. 754
Roques, A. 1254, 1257
Rosa, A. 811
Rose, C.R. 193, 1012, 1293, 2044, 2093, 2232
Rose, J. 967
Rosenberg, A. 906
Rosenberg, R.A. 3552
Rosenzweig, J. 627, 678, 736, 1365, 1965, 1968, 2802, 2873, 2876
Roser, T. 89, 207, 396, 399, 1030, 1460, 1478, 2538, 3359
Roshal, A.S. 2835
Ross, J.S.H. 3413
Ross, M. 608, 1626, 1981
Ross, W. 2284, 2359, 2365
Rossa, E. 1987
Rossbach, J. 719
Rossi, C. 826, 1180, 1182, 1212, 2002
Rossmanith, R. 763, 1039, 3512
Roster, W. 439
Rotela, E. 2207, 2929
Rovang, D.C. 1245
Rovelli, Alberto 2038
Roy, A. 3072
Roy, G. 312, 1819, 1858
Roybal, P. 1093
Roybal, W. 1147, 3183, 3725
Royer, J.P. 973
Rubin, D. 318, 372, 3075, 3236, 3654
Rüdiger, H. 2493
Ruggiero, A. 970, 1114, 1578, 1581
Ruggiero, F. 75, 107, 1712, 1753, 1816, 2648
Rukoyatkin, P. 181
Rule, D.W. 675
Rümmler, J. 237
Rusnak, B. 2914, 3096
Russell, A.D. 3275, 3278, 3288
Russell, G.J. 190
Russell, Steven J. 2005, 2177
Rust, K.R. 273
Rusthoi, D.P. 2574
Ruth, R. 439, 482, 539, 548, 554, 605, 1676, 3042, 3192
Ryan, W. 2152, 2215
Rybaltchenko, K. 3645
Rybarcyk, L. 1150, 2514, 2743
Ryne, R.D. 2624

S

Saadatmand, K. 2767
Sabah, S. 2392
Saban, R. 3206
Sabbi, G. 1682, 3398
Sachtschale, R. 883, 1278, 2799
Sachwitz, M. 2137
Safa, H. 3096
Safranek, J. 748, 799, 838, 841
Sagan, David 1765, 1768
Sah, R.C. 847, 850, 853, 2371
Saito, K. 2995
Saito, M. 1557
Sajaev, V. 1463, 1466
Sakai, F. 648, 760
Sakai, H. 2902, 2974, 2986, 3069
Sakaki, H. 2511, 2814
Sakamoto, N. 1066, 1069, 1075, 3419, 3422, 3428, 3440
Sakamoto, T. 587
Sakanaka, S. 354, 2980, 2983, 2989, 3616
Saldin, E.L. 575, 1658
Salzborn, E. 2705, 2708
Sampayan, S.E. 1308, 2627
Sampson, W. 3353, 3356
Sandberg, J. 2308
Sander, O. 1015, 1611, 2743
Sanders, D.M. 1308
Sandweiss, J. 675
Sano, Masami 3816
Sapozhnikov, L. 2359, 2365
Saraph, G.P. 3168
Sarkar, S. 2241, 2274
Sasaki, Shigemi 802
Sass, R. 2473, 2476
Sassowsky, M. 973
Sato, H. 267, 1009, 1460, 1908
Sato, K. 3327
Sato, S. 201
Sato, Y. 1566, 3822
Satogata, T. 69, 98, 101, 210, 2544
Satoh, K. 2983, 3066, 3828
Satoh, Kotaro 306, 2087
Satoh, Takemi 3816
Savino, Ray 3693
Sawada, S. 2992, 2995
Scafuri, C. 826, 2353, 2356, 2467
Scandale, W. 1445, 1469, 1816
Scanlan, R. 3212, 3398
Scarpa, F. 1129
Schächter, L. 1272
Schaefers, F. 3527
Schaffer, H. 3796
Schaffner, S. 2128
Schaller, S.C. 2464
Schaper, J. 336, 763
Scheblein, J.A. 3230
Scheer, M. 1418, 1520, 2606, 3527
Scheitrum, G.P. 3045
Schempp, A. 947, 1078, 1081, 1084, 1897, 2726
Schiffer, J.P. 1560, 2696
Schilcher, T. 2320
Schillinger, B. 2594
Schindl, K. 973, 2314
Schlabach, P. 3248, 3257, 3263, 3392
Schlapp, M. 2702, 2705, 2708
Schlarb, H. 1572
Schlueter, R. 802, 3221, 3230, 3315
Schmalzle, J. 3356
Schmerge, J. 2840
Schmickler, H. 66, 1858, 2026
Schmidt, C.W. 1403, 3837
Schmidt, F. 1356, 1436, 1439
Schmidt, R. 66, 3206, 3209, 3648
Schmitz, S. 569
Schmor, P. 956, 2675, 2781
Schnase, A. 1048
Schneider, G. 3586
Schneider, H. 1048
Schneider, J.D. 1168, 2740
Schneidmiller, E.A. 575, 1658
Schoenlein, R.W. 1984
Schoessow, P. 633, 639, 1996
Schönauer, H. 973, 1587
Schrage, D. 1093, 3625
Schreiber, H.J. 2137
Schriber, S.O. 1159
Schröder, G.H. 225, 1325
Schroeder, C.B. 684
Schryber, U. 3785
Schubert, J. 1060
Schulte, H. 2603
Schultheiss, C. 3452
Schultheiss, T. 3177
Schütt, P. 3162
Schwalm, D. 947
Schwartz, C. 2296, 3111
Schwarz, H. 2359, 3004, 3007, 3039
Scorzato, C. 811
Seamen, J.F. 1235
Sears, J. 3075
Sebek, James J. 835
Sedlak, J. 1391
Sedlyarov, I. 2796, 2838
Seeman, J.T. 315, 1563, 1876
Segel, R.E. 2696
Seidel, M. 434, 439, 500, 554, 2119, 2189
Seidl, P. 1923, 1926
Seitz, Gerald J. 2826
Sekutowicz, J. 3081

Sellier, J.C. 3365
Senichev, Yu. 1111, 2923
Sennyu, K. 2908, 3087
Senyukov, V.A. 3869
Seo, K. 3425
Seo, K.W. 3663
Serafini, L. 1365, 1965, 1968, 2876
Serdobintsev, G.V. 3114
Sereno, N.S. 1700
Sergo, R. 2353, 2356
Serio, L. 3206
Serio, M. 2284
Sermeus, L. 1328
Serre, C. 979
Servranckx, R.V. 153
Sery, Andrey 557
Sessler, Andrew M. 422, 1614
Settakorn, Chitrlada 733, 2017
Sexton, I. 3586
Sgobba, S. 3586
Shafer, R. 83, 1150, 1293, 2232, 3309
Shahal, O. 906
Shamovsky, V.G. 1795
Shang, C. 2627, 2633, 3183
Shank, C.V. 1984
Shapiro, A.H. 2914, 3096
Shapiro, M. 2690
Shapiro, V.E. 1368
Shaposhnikova, E. 1813, 1816, 1849
Sharma, S. 363, 2207, 2929, 3574
Sharonov, S. 3395, 3464, 3713
Shasharina, Svetlana G. 2592, 2654
Shatilov, D.N. 1762
Shatunov, Y. 1433, 3359, 3407, 3500
Shaw, J. 2241, 2274
Shchelkunoff, S.V. 3114
Shcherbakov, A. 1311
Shea, T.J. 2152, 2215, 2502
Sheehan, J. 2687
Sheffield, R.L. 897
Shelley Jr., F.E. 2514
Shen, S. 3625
Shen, W. 3443, 3446
Sheng, I. 2207, 2929, 3574
Shepard, K.W. 3072
Sheppard, J.C. 903
Sherman, J.D. 2723, 2740, 2746
Sherrill, B.M. 198
Sheu, J.T. 3488
Shevtsov, V.Ph. 491
Shi, P. 1560
Shi, Ping 2075
Shibuya, S. 1962
Shiloh, J. 906
Shiltsev, V.D. 237, 420, 1475, 1774, 1777, 2805
Shin, H.M. 1870
Shinn, M. 2529, 2693
Shinoe, Kenji 2146, 3066
Shintake, T. 455, 530, 533, 536, 593, 1981
Shirai, T. 339, 1087, 1203, 1206, 3294, 3819
Shirakabe, Y. 938
Shirakata, M. 267, 1908
Shlakhov, I.N. 2229
Shoaee, H. 1454, 2383, 2425, 2586
Shoji, Y. (KEK) 267, 1908
Shoji, Y. (Himeji) 757, 1385
Shu, Deming 2210
Shu, Q.-S. 624, 2905
Shukla, S. 144
Shulze, M. 1611
Shurter, R.B. 2232
Shurter, R.P. 2829
Shvedov, O.V. 3848
Shvedunov, V.I. 1108, 1902, 3866
Shvets, G. 657, 669
Shvetsov, V.S. 3126
Sibley, C. 2099, 2241, 2274, 3407, 3743
Sidorenko, V.N. 1090
Sidorov, G.I. 1391
Sieber, T. 947
Siemann, R.H. 464, 497, 500, 602, 672, 687, 1629, 2164, 2580, 3036
Siemko, A. 3377
Sievers, P. 3377
Siggins, T. 3752
Sikora, John 1765
Sikora, R. 2152
Silbar, Richard R. 1529
Silke, C. 3816
Silva, A.R. 1209, 3476
Silva, M.B. 3628
Sim, J. 3242, 3395, 3713
Siman-Tov, Moshe 86
Simon, D.J. 979
Simon, R. 763
Simonin, A. 2717
Simonov, E.A. 1762
Simpson, J. 633, 636, 639
Simrock, S. 2320, 2905
Sinclair, C.K. 2693, 2864, 3761
Singh, O. 727, 2161, 2287, 3455, 3494
Skachkov, V.S. 2965, 3848
Skaritka, J. 621, 675, 1197, 2687, 2843
Skoczen, B. 3368
Skopik, D.M. 716
Skrinsky, A.N. 883
Sloan, T. 264, 1481
Smaluk, V. 1463, 1466
Smedley, J. 2790
Smirnov, A. 1795, 3407
Smirnov, A.V. 894, 3518
Smirnov, V. 2244
Smith, D.L. 1245
Smith, G.A.(BNL) 2149, 2215, 2302
Smith, G.A.(FNAL) 3257, 3263
Smith, H. 439
Smith, H.V. 1150, 2746
Smith, I. 1245
Smith, J.D. 2437
Smith, J.R. 1251
Smith, K.D. 3209, 3413, 3494
Smith, R. Scott 2164
Smith, S. 439, 2110, 2113, 2116, 2122, 2253
Smith, S.L. 2443
Smith, T.L. 2299, 2938, 2941
Smith, V. 2253
Smithwick, J. 3212
Snell, Charles M. 2174
Snydstup, L. 2711
Sobczynski, S. 2274
Sobenin, N.P. 1108, 2008, 2104
Søby, L. 1587
Soika, A. 3443
Sokolowski, J.S. 906
Solita, L. 3669, 3690
Solomon, L. 727, 3497
Sommer, M. 817, 1406
Sommer, W.F. 190
Sondericker, Jack 3693
Song, J. 912, 2204, 2529
Song, J.J. 461, 1575, 2941, 2944
Soong, S.B. 2241
Soukas, A. 2308, 3449
Soutome, K. 1385
Sparveris, N. 1042
Spence, W.L. 506, 1673
Spencer, J. 439, 608
Spencer, N. 439
Spentzouris, L. 16
Spielman, R.B. 1235
Spinka, H.M. 1460
Sprangle, P. 611, 630
Sprehn, D. 439
Springer, R.W. 2829
SRC Staff 865
Srinivasan-Rao, T. 2790
Stagno, V. 2169
Stanek, M. 596
Stanford, G. 956, 1105
Staples, John W. 1096, 1174
Stefan, J. 2481
Stefan, P.M. 727, 3497, 3515
Steffen, L. 2446
Stege, R. 2253

Steier, C. 1033
Steimel, J. 144, 1721, 2323
Stein, P. 2711
Steiner, R. 3801
Steininger, R. 763
Stellfeld, D. 1816
Stepin, V.D. 651
Stern, C. 2422, 2535
Stettler, M. 2041, 2044, 2093, 2232
Stevens, A.J. 219
Stevens, R.R. 2723, 2740, 2743, 2746, 2764
Stevens, T. 3619
Stevenson, Nigel R. 3842, 3845
Stiliaris, E. 1042
Still, D. 1721, 2061
Stinson, G. 956
Stirling, W.L. 2714
Stitts, E. 3681
Stockhorst, H. 1048
Stoddard, R.D. 1308
Stoltz, P. 669
Stover, G. 2284, 3734
Stowell, G. 2808
Strait, J.B. 124, 3209, 3389, 3395, 3398
Strasser, P. 938
Street, A.J. 3209, 3413
Strong, Edward 2131
Strozinsky, R. 3021
Strubin, P. 2440
Struve, K.W. 1235
Stuart, B. 886
Stupakov, G. 449, 1563, 1632, 1635, 1685, 1688, 1834, 2180
Stygar, W.A. 1235, 1245
Suda, M. 3822
Suetake, M. 306
Suetsugu, Y. 1566, 1596
Sugai, I. 187
Sugimura, T. 339, 1206, 3819
Suh, J.H. 3479
Suk, H. 1650, 1855, 2143
Sukenobu, S. 3828
Sullivan, Gary 1144
Sullivan, M. 296, 3330, 3562
Summers, D. 624
Sun, Baogen 1664
Sun, Baoyu 1218
Sun, D. 1403, 3018
Sun, J. 3297
Sun, Jingqing 1218, 1221
Sun, Xiang 1221
Sun, Y. 3300, 3312, 3318
Suwada, T. 2253
Suzuki, C. 536
Suzuki, S. 2511, 2814
Svandrlik, M. 826, 829, 1735, 3099
Sveshnikov, B. 2452
Svirtun, V. 3580
Swan, T. 3622
Swenson, D.A. 1099, 3872
Swift, G. 883, 1278
Sylvester, C. 3392, 3395
Syphers, M. 95, 207, 1478, 2155, 3359
Syversrud, D. 1051
Szczech, J. 2702

T

Tabor, M. 3816
Tachikawa, T. 1045, 3816
Tadano, M. 2084
Tadokoro, M. 3294, 3819
Tajima, T. (Texas) 1653
Tajima, T. (KEK) 2908, 3087, 3090
Takada, E. 201, 2347, 3822
Takagi, A. 2992, 2995
Takagi, H. 1908
Takahashi, H. 402, 880, 2787
Takahashi, J. 2998
Takahashi, T. 2908, 2989, 3087, 3090
Takaki, Hiroyuki 856, 2146
Takanaka, M. 1807
Takano, M. 587
Takao, M. 1385
Takashima, T. 2971
Takata, K. 494
Takayama, K. 1548, 1599, 1908
Takayama, T. 2642, 3816
Takeda, H. 1171
Takeda, S. 494, 587
Takeda, Shigeru 581, 3660
Takeda, Y. 938
Takeuchi, N. 859
Takeuchi, Y. 581, 2902, 2974, 2977, 2986, 3069
Takii, T. 730
Taleyarkhan, Rusi 86
Tallerico, P. 1147, 3138
Tallerico, T. 2213
Talman, R. 375, 1472, 1542, 2434
Tamura, F. 3767
Tamura, Kazuhiro 1664
Tan, Cheng-Yang 2221
Tanabe, J. 3312, 3318, 3321
Tanabe, T. 1557, 2992, 2995
Tanabe, Toshiya 3515
Tanabe, Y. (KEK) 2992, 2995
Tanabe, Y. (Toshiba) 3828
Tanaka, H. 1385
Tanaka, J. 938
Tanaka, M. 69
Tanaka, M.H. 938
Tanaka, Y. 1066, 1069, 1075, 3419, 3428, 3440
Tang, C. 1729, 3081
Tang, H. 599, 608, 2849
Tang, J. 2265
Tang, Y. 2287
Tani, K. 1266
Taniuchi, T. 2511, 2814
Tanke, E. 944
Tantawi, S. 439, 3042, 3189, 3192, 3195
Tarakanov, V.P. 1299
Taratin, A. 165
Tarnetsky, V.V. 3114
Tartaglia, M. 147, 3395
Tatchyn, R. 2192, 2195, 2639, 3530
Tatum, B.A. 1227
Taurigna-Quere, M. 2823
Tavares, P.F. 811, 2096, 2238, 3740
Tawada, M. 1394
Taylor, B.D. 2867
Taylor, C. 3212
Taylor, T. 315
Taylor, T.M. 3209, 3696
Tazzioli, F. 2137
Tecker, F. 366, 3645, 3648
Tejima, Masaki 2087
Temkin, R.J. 2690
Temnykh, A. 1718, 1768, 3218, 3654, 3708
Tenenbaum, P. 439, 479, 608
Teng, L. 1359, 2699
Tenishev, S. 2229
Tenyakov, I. 1263, 1311, 1313
Tepikian, S. 69, 98, 101, 222, 405, 2544, 3359, 3651
Terasawa, M. 757
Terebilo, A. 1457, 1490
Terechkine, I. 994, 3248, 3291
Terekhov, A.S. 1063
Terunuma, N. 494, 584, 587
Teryaev, V.E. 3126
Teryoshkin, Y. 1263
TESLA collaboration 425
Tessier, J.M. 2311
Teytelman, D. 2284, 2362, 2368
Theuws, W.H.C. 1036, 1200
Thevenot, M. 1254
Thiessen, H.A. 273, 1012, 1015, 1611, 3788
Thivent, M. 973
Thomas, M.G. 2305
Thomas, R. 3362
Thomlinson, W. 3494
Thompson, K. (SLAC) 608, 2580
Thompson, K. (ANL) 953, 2699

Thompson, P. 69, 98, 101, 3353
Thomson, J. 1563
Thorson, I. 956
Thur, W. 2067
Tian, Bo 3764
Tiede, R. 2645
Tiefenback, M. 2128, 2265, 2271, 3758
Tieger, D. 348
Tighe, R. 2359, 2520
Tikhomirov, A.V. 3610
Tille, T. 2784
Tillghman, A. 439
Timlin, C. 3413
Timm, M. 515
Timossi, C. 805
Ting, A. 611, 630
Tinsley, D. 1287
Tkatchenko, A. 330, 817, 1406
Tkatchenko, M. 817
Tobiyama, M. 306, 1566, 1596, 1664, 2332, 2335
Toda, M. 2992, 2995
Todesco, E. 1445, 1469, 2568
Toelle, R. 1048
Tojyo, E. 938
Tokumoto, S. 2983, 2989, 3066
Toldo, F. 3449
Tolstoluzhsky, A.P. 651
Tomicich, A. 1212
Tomimasu, T. 730
Tominaka, T. 1066, 1069, 1075, 3359, 3416, 3419, 3422, 3428, 3431, 3434, 3437, 3440
Tomitani, T. 3822
Tomizawa, M. 938, 1962
Tomlin, R. 144
Tommasini, D. 763
Tompkins, J.C. 3389, 3395, 3713
Tomura, H. 3822
Tong, Dechun 1215, 1218, 1221, 3764
Tongu, E. 730
Tonguu, H. 339, 1206
Tonisch, F. 2137
Toole, L. 1147
Tordeux, M.-A. 817
Torikoshi, M. 820, 3819, 3822
Tortschanoff, T. 3374
Tosi, L. 826, 829, 1520, 2353, 2356, 3527
Tosin, G. 3324
Tovo, E. 1087
Tovo, T. 1087
Townsend, M. 3209
Toyama, T. 1548, 1599, 1908
Trahern, C. 69, 101, 2544
Trakhtenberg, E. 3224, 3556
Tran, H.J. 1647
Tranquille, G. 944, 979, 982
Trassl, R. 2705, 2708
Travish, G. 736, 1126
Trbojevic, D. 69, 98, 101, 219, 396, 399, 405, 1030, 1371, 3651
Treadgold, J. 3209
Tremaine, A. 736
Tribendis, A. 2796, 2838
Trimble, D.O. 1308
Trofimov, N. 2440
Trombly-Freytag, K. 3713
Tron, A. 2244, 2247
Trotz, S. 2690
Trower, W.P. 1108
Troyanov, E.F. 249
True, R. 3153, 3180, 3186
Trzeciak, Walter 865
Tsarenkov, A. 2452
Tschalaer, C. 348
Tsentalovich, E. 348, 2241
Tsoupas, N. 69, 98, 207, 210, 213, 222, 1460, 2152, 3359
Tsubota, K. 2565
Tsubuku, H. 3822
Tsutsui, H. 1266, 2642
Tsygankov, E. 276
Tumanov, K.D. 3604
Tuozzolo, J. 213, 2149, 3233
Tur, Yu.D. 2820, 3810, 3840
Turchin, V.I. 2735
Turchinetz, W. 348, 2274
Turlington, Larry 2131
Turner, J. 315, 1569
Turner, L.R. 3491
Turner, William C. 422
Tuyn, J. 979
Tzeng, K-C. 2870
Tzeng, R.H. 3051

U

Ueda, A. 2084
Ueda, T. 648, 760
Ueng, T.S. 847
Uesaka, M. 648, 760
Uesugi, T. 1656, 2992, 2995
Uggerhøj, E. 80, 165
Uhm, Han S. 1870, 3147
Ullmann, J. 3096
Ullrich, H. 973
Umezawa, M. 3294, 3813
Umstadter, Donald 2657
Underwood, D. 207, 1460
Underwood, K.K. 497
Urakabe, E. 3819
Urakawa, J. 354, 444, 494, 578, 584, 587, 1484, 2980
Ursic, R. 912, 2131
Uskov, V.V. 651
Uvarov, V.L. 2229, 3810, 3840
Uythoven, J. 1858
Uzat, W. 3057
Uzunoglou, N. 1042

V

Valbuena, R. 3586
Valentino, V. 2169, 2729
Valishev, A.A. 1433
Valter, H. 3123
van Amersfoort, P.W. 1063
van Asselt, W. 89, 1460, 1478, 2155
van den Brand, J.F.J. 1063, 3630
van den Putte, M.J.J. 1063
van der Geer, S.B. 2577
van der Laan, J.B. 1063
Van der Schueren, A. 979
Van Duppen, P. 947
Van Ginneken, A. 393, 417
van Leeuwen, E. 3630
van Oers, W.T.H. 2781
van Oort, J. 3212
van Rienen, U. 524
van Steenbergen, A. 616, 621, 675
Van Vaerenbergh, P. 3506
Van Weelderen, R. 3368
van Zeijts, J. 2128, 2383, 2386, 2526
Vandeplassche, D. 1045, 3816
Vanecek, D. 590, 3722
Varfolomeev, A. 736
Variale, V. 2169, 2729
Variola, A. 2002, 2823
Varisco, G. 3657
Vasiliev, V.V. 3848
Vasilishin, B. 181, 2452
Vasserman, I. 3224
Vazquez, L. 1825
Védrine, P. 3365, 3374
Veness, R. 3586
Vengrov, R.M. 1090, 3848
Venhaus, D. 2529
Venturini, M. 1855, 1953
Verdier, A. 312, 1442
Veremeenko, V.F. 3455
Vetter, A.M. 2950
Vetterlein, R. 3761
Vierlbeck, D. 3123
Vilaithong, R. 2761
Villate, D. 1254, 1257
Vincent, D. 3374
Vincent, J. 1054, 1057
Vinokurov, N.A. 883

Vinzenz, W. 3123
Vishnevskiy, N.K. 249
Visintini, R. 826, 2353, 2356, 3527
Vlasenko, S.I. 1263
Vlieks, A. 439, 3042, 3189, 3192, 3195
Vlogaert, J. 3368, 3410
Vobly, P.D. 883, 1795
Vodinas, N. 1042
Voevodin, M. 184, 2452
Vogel, G. 2032
Vogel, V.F. 3126
Voigt, S. 763
Voisin, L. 1254, 1257
Volfbeyn, P. 657, 1984
Volk, J.T. 3254, 3257, 3260, 3263, 3280, 3286
Völker, F. 973
Volkov, V.I. 184, 2452
Volkov, V.N. 1795, 2796, 2838
vom Stein, P. 2796, 2838
von Hahn, R. 947
Vondrasek, R.C. 2702
Vormann, H. 1084
Vorobiev, P. 3407
Voronin, V.S. 1302
Vossenberg, E. 225, 1325
Vretenar, M. 944
Vylet, V. 439, 3675

W

Wada, M. 938
Wagner, A. 1813, 1858
Wagner, R. 2657
Wagner, U. 3368
Wait, G.D. 1325, 1328
Wakasugi, M. 3521
Wakisaka, K. 730
Wakita, K. 730
Walbridge, D. 3242, 3248, 3269, 3272
Walckiers, L. 66, 3377
Walker, R.P. 826, 829, 1520, 3524, 3527
Walstrom, P. 193, 3309, 3788
Walters, D. 2699, 3552, 3580
Walther, R. 1039
Walz, D. 608, 687
Wan, W. 1801
Wanderer, P. 3309, 3338, 3347, 3350, 3353, 3356
Wang, C.-T. 2047
Wang, C.J. 2374, 3488, 3539
Wang, Ch. 1638, 1691, 3048, 3051, 3054, 3536
Wang, Changbiao 3171, 3863
Wang, Chaoen 3533, 3539
Wang, Chun-xi 360
Wang, D. 1388
Wang, D.X. 1976, 2020, 2320
Wang, F. 348, 2099
Wang, G. 687
Wang, G.W. 1729
Wang, J. (ANL) 953, 2699
Wang, J. (SLAC) 1676, 2852
Wang, J.G. 1650, 1855, 1956, 1959, 2143
Wang, J.M. 2305
Wang, J.Q. 1566
Wang, J.W. 439, 539, 548, 554, 3042
Wang, L.F. 1566, 1828
Wang, M. 3297
Wang, M.H. 1409, 1487, 2377, 3533
Wang, P. 874, 883
Wang, Q. 3117
Wang, S.H. 1566, 1729, 1828
Wang, T.F. 1670, 2696
Wang, T.S. 1611
Wang, W.C. 2633
Wang, X.J. 621, 1971, 2687, 2790, 2793, 2843, 2846
Wang, Xiaoping 3300
Wang, Yi-Ming 2341
Wangler, T.P. 915, 1150, 1153, 1156, 1162, 3138
Warsop, C.M. 988
Washio, M. 1266
Watanabe, I. 1557
Watanabe, K. 593
Watanabe, S. 2347
Watanabe, T. (Tokyo) 648, 760, 1557
Watanabe, T. (Himeji) 757
Watson, W.A. (Chip) 2128, 2383, 2386, 2398, 2403, 2526
Weaver, J. 2840
Weber, R. 3837
Wei, F. 826
Wei, J. 69, 98, 222, 396, 399, 2158, 2544, 3651
Wei, Z.T. 1388, 1448
Weiland, T. 515, 524, 2594, 2645, 3162
Weinacht, D. 1159
Weir, J.T. 1260
Weisse, E. 168, 171
Weisz, S. 1356, 1442, 3696
Welch, D.R. 1245, 1867, 1935
Welch, J. 3236, 3380, 3383, 3654, 3708
Wells, S. 2241
Welz, J. 956, 2778
Wendt, D. 3443
Wendt, M. 2134
Weng, W.T. 42, 162, 970, 1885
Wengrow, A.B. 2758, 2764
Wenninger, J. 366, 3645
Werin, S. 345, 1520, 3527
Westenskow, G.A. 590, 1260, 3719, 3722
Westervelt, R. 2532, 2535
Whealton, J.H. 2714, 2775
Wheeler, S.J. 654
White, G. 1454, 2425, 2586
White, M. 327, 953, 1269, 3174
White, V. 461
Whitham, K. 3796
Whitney, R. 3761
Whittum, D. 351, 500, 542, 602, 687, 900, 2119, 2189, 2586, 3045
Wiatrzyk, J.M. 3209, 3413
Wiedemann, H. 733, 838, 2017, 2840
Wiemerslage, G. 3556
Wienands, U. 315
Wieskamp, T.F. 1308
Wight, G.W. 2781
Wilcox, D. 3183
Wilde, S.B. 2767
Wildner, E. 1362
Wilkinson, C. 1012, 1015, 1611
Wille, K. 2140
Willeke, F. 51
Willen, E. 624, 3347, 3356, 3359, 3362
Williams, B. 228
Williams, D. (SLAC) 390
Williams, D. (LBNL) 2675, 2758, 2761, 2764, 2767, 2770
Williams, L.R. 3368
Williams, N.W. 1460
Wilson, I. 482, 518
Wilson, N.G. 3625
Wilson, P.B. 439, 482, 545, 605, 3042
Wilson, Z. 439, 1319, 3027, 3042
Winick, H. 37, 2687, 2840
Winn, D. 363
Wiseman, M. 3108, 3761
Wisnivesky, D. 811, 1209, 3010, 3476
Witherspoon, S. 2386, 2526
Witkover, R. 101, 2149, 2155, 2215, 2218
Wokas, T. 3248
Wolf, R. 66, 3377
Wolf, Z. 3330
Wolff, D. 3461
Wong, V. 2302
Wood, F. 3159
Woodle, M. 1197, 2687, 2790, 3494
Woodley, M. 497, 903, 1673, 2855
Woody, C. 967
Worm, T. 80

Wright, E. 439
Wright, E.L. 2808
Wrulich, A. 826, 829, 1185, 1188
Wu, G. 3245
Wu, H. 92, 3359
Wu, X. 195, 198
Wu, Y. 874, 883
Wu, Y.Z. 321, 378
Wuensch, W. 518
Wurtele, J.S. 422, 657, 684, 1614
Wüstefeld, G. 1418, 1520, 2606, 3527
Wutte, D. 2758, 2764, 2770, 3737
Wyss, C. 3347

X

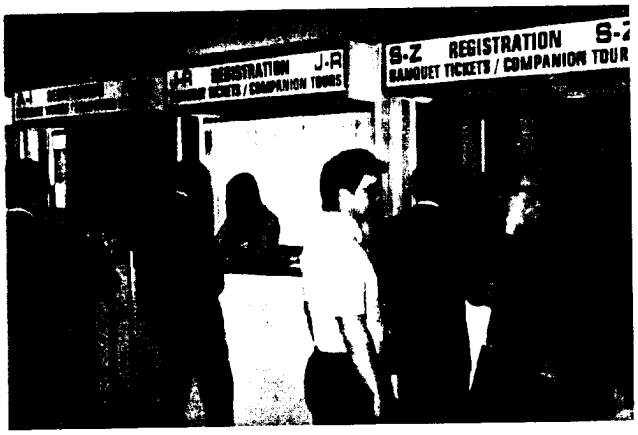
Xiao, A.M. 1448
Xiao, Liling 3764
Xie, Ming 660
Xie, Z. 1051, 2662, 2702, 2770
Xu, S. 3556
Xu, X. (SLAC) 3045
Xu, X. (IHEP) 3312

Y

Yakimenko, V. 675, 2687
Yakover, I.M. 906
Yakovlev, V.P. 2609, 3114, 3153, 3156, 3186
Yamada, S. 201, 820, 3819, 3822
Yamaguchi, A. 3828
Yamamoto, M. 2995
Yamamoto, Noboru 2455, 3660
Yamazaki, Y. 2902, 2974, 2977, 2986, 3069
Yan, Y. 2583, 2586, 2636
Yanagida, K. 2511, 2814
Yang, B. 871, 874, 883, 1700, 1999, 2052, 2207, 3574
Yang, J. 1266
Yang, Ming-Jen 2035
Yang, T.T. 1638, 2377, 2858, 3048, 3051, 3054
Yang, Yue 1218
Yano, Y. 930, 941, 1066, 1069, 1075, 2672, 3419, 3422, 3428, 3440
Yaramishev, S. 1090, 1129, 1905
Yarba, V. 3248, 3291
Yarigin, S.N. 2008, 2104
Yatagai, T. 859
Yazynin, I.A. 252, 255, 258
Yee, C. 2359
Yee, D. 3318, 3321
Yeh, M.S. 2377, 3048
Yeremian, A.D. 439, 599, 608, 1676, 2840, 2849, 2852, 2855, 3042
Yin, B. 3297
Yocky, G. 2189
Yokomizo, H. 2511, 2814
Yokosawa, A. 1460, 1478
Yokouchi, S. 1066, 1069, 1075, 3419, 3422, 3428, 3440
Yokoya, K. 1566, 1596
Yonezawa, H. 533
Yoon, M. 823, 2107, 2350
Yoribayashi, Y. 578
York, R.C. 195, 198, 663, 1855
Yoshida, Masato 3467
Yoshii, M. 1548, 1908, 2992, 2995
Yoshikawa, H. 2511, 2814
Yoshimoto, S. 3087
Yoshioka, M. 581
Yoshizawa, J. 3822
Yosiyuki, T. 1557
Young, A. (SLAC) 2284, 2368, 3027
Young, A. (LBNL) 3221
Young, E. 1472, 1542
Young, L. 1093, 1150, 1162, 1920, 2746, 2749, 2752, 3138
Young, P. 1403, 3018, 3837
Younger, F. 3321
Yourd, R. 3312, 3318
Yu, C.H. 1388
Yu, D. 886, 1968, 2802, 3036, 3120
Yu, I.H. 3015
Yu, L.-H. 1197, 2287
Yu, S. 590, 2832, 3719, 3722
Yuan, D. 2675
Yunn, B. 1694, 2128
Yurkov, M.V. 575, 1658

Z

Zagel, J.R. 2166
Zakutin, V.V. 2820
Zaltsman, A. 967
Zangrando, D. 826, 3524
Zante, A. 3796
Zapalac, G. 2618
Zaplatine, E. 2920, 2923
Zapryagaev, I.A. 3114
Zarecky, M. 3761
Zaremba, S. 1045, 3816, 3857
Zarucheiskiy, V.G. 249
Zaugg, T.J. 2723, 2740
Zavadtsev, A.A. 2008, 2250, 3860
Zawislanski, Peter T. 3807
Zeitlin, M. 1502, 1505, 1508
Zelenski, A. 2781
Zelinski, J. 439
Zeller, A.F. 198
Zeno, K. 89
Zhabitsky, V.M. 2329
Zhan, Xiaowei 2589
Zhang, C. 1566, 1780, 1828
Zhang, Dunan 3300
Zhang, F.Q. 3470
Zhang, J. 3297
Zhang, S.Y. 89, 970, 1584, 1885, 2155
Zhang, T.B. 666
Zhang, Tainjue 3834
Zhang, W. 210
Zhang, X.L. 1566, 1596
Zhao, G. 3297
Zhao, S. 2908, 3087
Zhao, X. 1346
Zhao, Y. 408
Zheng, L. 3297
Zholents, A. 315, 808, 1801, 1804
Zhou, F. 1566, 1729
Ziemann, V. 1412, 1879
Zimmermann, F. 452, 608, 1514, 1563, 1626, 1741, 1789, 1876, 1981, 2189, 2580
Zimmermann, H. 1081
Zinin, E.I. 883
Ziomek, C. 439, 2338, 2359, 3027
Ziomi, L. 1129
Zisman, M. 315, 3312, 3318
Zitvogel, E. 2149, 2215, 2218
Zlobin, A.V. 3389, 3395, 3398
Zlunitsyn, E.S. 3810
Zolfaghari, A. 348
Zolotorev, M. 1801, 1804, 1984, 2180
Zorzano, M.P. 1825
Zotter, B. 1813, 1858
Zou, Y. 1650, 1855, 1959
Zou, Yang 1218, 1221
Zumbro, John D. 1397
Zumbro, M.V. 1012, 2064
Zviagintsev, V. 3084
Zwart, T. 348, 2241
Zykov, A.I. 3810
Zyngier, H. 778

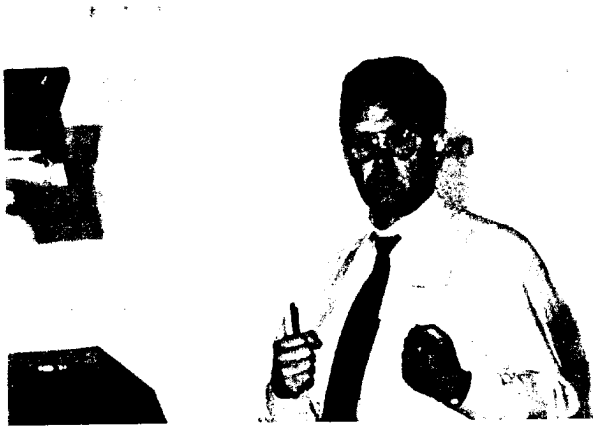

J-R REGISTRATION
S-Z REGISTRATION
BANQUET TICKETS / COMPANION TOUR













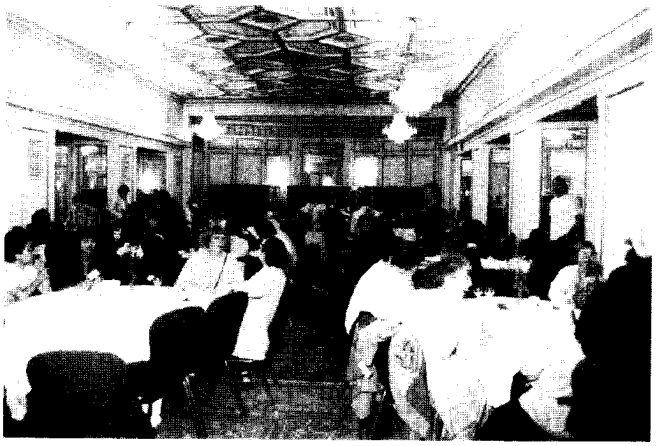




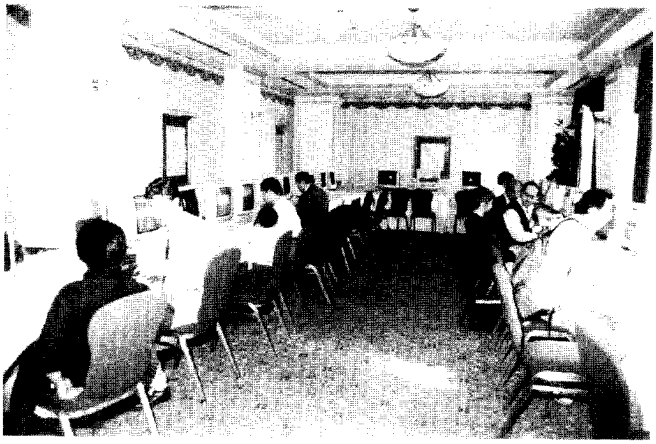



DIVISION
OF PHYSICS
US
PARTICLE
ACCELERATOR
SCHOOL










GMW MAGNET




TITAN
Béta




Linac
Systems


EBCO TECHNOLOGIES INC.


METACERAM


OXFORD




PHILIPS


SIGMAPHI



